Jingwen Mao

Frank P. Bierlein

Mineral Deposit Research:

Meeting the Global Challenge

The 8th Biennial SGA Meeting is held in Beijing, August 18–21, 2005

Sponsored by

China University of Geosciences (Beijing)

Institute of Mineral Resources, Chinese Academy of Geological Sciences

National Natural Science Foundation of China

China Society of Geology

Society for Resource Geology

Society of Economic Geologists

International Association on the Genesis of Ore Deposits

Institute of Geology and Geophysics, CAS

Institute of Geochemistry, CAS

State Key Lab for Mineral Deposit Research (Nanjing University)

Jingwen Mao
Frank P. Bierlein
(Eds.)

Mineral Deposit Research: Meeting the Global Challenge

Proceedings of the Eighth Biennial SGA Meeting Beijing, China, 18–21 August 2005

Volume 1

With 472 Figures (Volume 1)

Springer

Editors

Professor Dr. Jingwen Mao

Chinese Academy of Geological Sciences
Institute of Mineral Resources
26 Baiwanzhuang Road
Beijing 100037
China

Dr. Frank P. Bierlein

University of Western Australia
School of Earth and Geographical Sciences
Tectonics Special Research Centre
35 Stirling Highway
Crawley WA 6009
Australia

Library of Congress Control Number: 2005929130

ISBN-10 3-540-27945-8 **Springer Berlin Heidelberg New York**
ISBN-13 978-3-540-27945-7 **Springer Berlin Heidelberg New York**

Springer is a part of Springer Science+Business Media
springeronline.com

Printed in Germany

Cover design: Erich Kirchner, Heidelberg
Data conversion: Büro Stasch · Bayreuth (stasch@stasch.com)
Typesetting: Dr. Frank P. Bierlein, Australia
Production: Almas Schimmel
Printing: Stürtz AG, Würzburg
Binding: Stürtz AG, Würzburg

Printed on acid-free paper 32/3141/as – 5 4 3 2 1 0

Preface

In June 1965, a small group of European economic geologists gathered in Heidelberg, Germany, at the invitation of Professor G. C. Amstutz and decided to establish the Society for Geology Applied to Mineral Deposits (SGA) and to start a journal to be called *Mineralium Deposita*. The first issue of the journal came out in May 1966, and has now matured to a leading journal in economic geology The first Biennial SGA Meeting was held successfully in Nancy, France, in 1991, with subsequent meetings in Grenada (Spain; 1993), Prague (Czech Republic; 1995), Turku (Finland; 1997), London (United Kingdom; 1999), Krakov (Poland; 2001) and Athens (Greece; 2003). In 2002, the SGA Council decided that its 8th Biennial Meeting in 2005 should be held in Beijing, China, making this the first Biennial Meeting to be convened outside Europe. Significantly, 2005 also marks the 40th anniversary of the SGA. The decision to host this year's premier meeting in Beijing reflects the Society's successful transition from its traditional European focus to a truly global organization, with 24% of SGA members situated in North America, 13% in Australia and Oceania, and 5% in Asia.

Over the last 27 years China has made dramatic progress towards political and economic reform, and opening the nation to the outside world. China's rapid economic development demands increasing amounts of minerals, fuels and materials, and this is currently a major driver for the global economic markets. Specifically, new policies that encourage prospecting and exploration for mineral resources in western China, are attracting both domestic and international mining corporations. This 8th SGA Biennial Meeting in Beijing provides outstanding opportunities for representatives from academia, government organizations and the industry from around the world to come together and exchange ideas, foster collaboration, and establish long-term linkages between China and the global geosciences community.

Three major tectonic metallogenic belts extend, converge and are superimposed in China, namely the Paleozoic Ancient Asia (or Altaides), the Mesozoic to Recent circum-Pacific belt, and the Mesozoic/Cenozoic Tethys. Because of this protracted tectonic evolution, the geological phenomena are complex and diverse. Some Precambrian mineral deposits occur in China, but the most significant deposits in the country, with the highest concentration of metallic elements occur within the Mesozoic extensional regime of East China, within the Cenozoic post-collision regime in Tibet and adjourning areas, and within the Paleozoic subduction – collision – post-collision regime in Xinjiang and Inner Mongolia.

The long mining history in China is reflected by the cover of this volume which shows a picture of mining potash salt in ca. 1,200 year old incorporated in a book of "Tian-Gong-Kai-Wu" published in Ming Dynasty (368 years old), and the old Chinese character of "ore", and the old Chinese character of "ore". Mining has historically played a significant role in the development of both China and many of its neighboring countries. With this in mind, we have arranged 14 sessions focusing on a diversity of relevant topics that include 1) tectonics, lithospheric, and mantle controls on global metallogenic provinces and giant ore deposits; 2) basin evolution: base and precious metal mineralization in sediments; 3) uranium deposits: metallogeny and exploration; 4) magmas and base-metal ore deposits; 5) epigenetic gold systems;

6) submarine ore systems and ancient analogues: global comparisons of VMS (sponsored by IGCP-502); 7) understanding ore systems through precise geochemistry, isotope tracing and microgeochemistry; 8) general economic geology; 9) Mesozoic to recent geodynamic and metallogeny of eastern Asia; 10) metallogeny of the Tethys-Himalayan orogen; 11) geodynamics and metallogeny of the Altaid orogen (sponsored by both IAGOD and IGCP-473); 12) metallogeny of the Au-Ag-Se-Te mineralized systems (sponsored by both IAGOD and IGCP-486); 13) conceptual targeting of mineral deposits; and 14) exploration, discovery, and mine developments in China (sponsored by SEG). Four short courses and workshops will be held prior to the meeting, i.e. 1) "geochemical mapping – regional national and global"; 2) "metallogeny: current theory and exploration models"; 3) "gold deposits: new development and exploration" (sponsored by SEG), and 4) "metallogeny of intrusion-related gold deposits in China and adjacent countries". Another short course on magmatic sulfide deposits ("geology, geochemistry and exploration" will be offered following the meeting. Moreover, a total of 15 pre- and post-meeting field excursions have been organized. These field trips will provide the participants with unique opportunities to visit metallogenic provinces and important deposits in China, Mongolia, Japan, New Zealand, and Iran.

The response to our invitation to meet in Beijing has been exceptional, with over 450 extended abstracts submitted by authors from 39 countries. Following review and editing of all submissions by ourselves and a panel of dedicated reviewers (cf. complete list of reviewers), 400 revised submissions were accepted and are included in this volume. These papers present a diverse and comprehensive snapshot of global mineral resources research and exploration at the beginning of the 21st century.

On behalf of the Organizing Committee, we wish to express our sincere gratitude for the joint sponsorship of the following organizations: China University of Geosciences (Beijing); Institute of Mineral Resources, Chinese Academy of Geological Sciences; National Natural Science Foundation of China; China Society of Geology; Society of Economic Geologists (SEG); International Association on the Genesis of Ore Deposits (IAGOD); Institute of Geology and Geophysics, Chinese Academy of Sciences; Institute of Geochemistry, Chinese Academy of Sciences; and State Key Lab for Mineral Deposit Research, Nanjing University. More than sixty students from around the world and ten professionals from developing countries have received financial grants to assist their participation in the meeting. This was made possible by generous financial donations from 17 mining and exploration companies (Anglo American; Anglogold Ashanti China; BHP Billiton Word Exploration; De Beers; Goldfields Australia; Ivanhoe Mines; Newmont Mining; Oxiana Resources; Placer Dome Exploration; Rio Tinto London; Sino-Oz; Sino Gold; Silvercorp Metals Inc; SRK Consulting; Teck Cominco; Garrison International) and the Specialist Group in Economic Geology of the Geological Society of Australia.

We are extremely grateful to all co-convenors involved in organizing the scientific sessions and for their editing of numerous papers with patience, tolerance and dedication. We also wish to thank the Organizing Committee for their enthusiasm and hard work that made this meeting possible and ensured its international recognition. We are confident this conference will be a milestone in the 40th anniversary year of our SGA and extend a warm welcome to all participants of the 8th Biennial SGA Meeting.

Beijing, August 2005
Jingwen Mao, Frank Bierlein

Contents

8th Biennial SGA Meeting

Organizing Committee

Honorary Chairmen: Meng Xianlai, Shou Jiahua, Tu Guangchi
Chairman: Chen Yuchuan
Vice Chairmen: Wu Ganguo, Zhang Hongtao, Chai Yucheng, Mao Jingwen
Members: Nigel Cook, Richard Goldfarb, David Groves, Craig J.R. Hart, Peter Herzig, Brian Hoal, Deng Jun, Hou Zengqian, Hu Ruizhong, Hua Renmin, David Leach, Li Zhijian, Li Ziying, Liu Dunyi, Nie Fengjun, Jan Pašava, Pei Rongfu, Peng Qiming, Reimar Seltmann, Masaaki Shimizu, Wang Jingbin, Wang Mili, Yao Yupeng, Zhai Mingguo, Zhai Yusheng, Zheng Mianping, Zhou Meifu
Secretary General: Mao Jingwen
Secretary Group: Zhao Caisheng, Zhao Kelin, Meng Dahu
Treasurer: Wang Lijie
SGA Technical Liaison: Bernd Lehmann
Program Committee: David Groves, Craig J.R. Hart, Mao Jingwen, Zhou Meifu
Field Trip Chairmen: Richard Goldfarb, Wang Yitian, Masaaki Shimizu
Short Courses: Nie Fengjun, Timothy Baker
Exhibition Manager: Xu Haiming
SGA Promotion Manager: Gregor Borg
Student Representatives: Jorge Relvas, Zhao Caisheng and Anna Vymazalova
Corporate Representative: Doug Kirwin

Society for Geology Applied to Mineral Deposits (SGA)

Publications: Jingwen Mao, Frank P. Bierlein
Spouse and Guest Activities: Susan Leach, Li Hongyan, An Yulan

Executive Committee:
President: D. Leach (USA)
Vice-President: H. Frimmel (South Africa)
Executive Secretary: J. Pašava (Czech Republic)
Treasurer: P. Herzig (Germany)
Promotion Manager: G. Borg (Germany)
Chief Editors:
B. Lehmann (Germany) – MD European Office;
L. Meinert (USA) – MD North American Office;
M. Chiaradia (Switzerland) – SGA News
Student Representative: A. Vymazalová (Czech Republic)
Past President: P. Fenoll-Hach Alí (Spain)

Regional Vice-Presidents
Africa: I. Nyambe (Zambia)
North America: G. Beaudoin (Canada)
South America: J. Cabello (Chile)
Asia: Mei-Fu Zhou (China)
Australia/Oceania: F.P. Bierlein (Australia)
Middle East: M. Yazdi (Iran)
Europe: R. Herrington (U.K.)

Councillors through December 31, 2005
N. Arndt (France), F. Barriga (Portugal), A. Boyce (U.K.), Ch. Heinrich (Switzerland), J. Mao (China), P. Weihed (Sweden)

Councillors through December 31, 2007
D. Eliopoulos (Greece), A.Gemmel (Australia), V. Shatov (Russia), P. Spry (USA), H. Stein (USA), F. Tornos (Spain)

Ex officio Members, SEG:
President: M. Hitzman (USA)
Executive Director: B. Hoal (USA)

Ex officio Members, IAGOD:
Secretary General: N. Cook (Norway)
Publications Manager: R.Seltmann (U.K)

Scientific Reviewers

Beaudoin, Georges
Laval University, Quebec, Canada

Beaudoin, Yannick
University of Toronto, Toronto, Canada

Bierlein, Frank
University of Western Australia, Perth, Australia

Cabral, Alexandre R.
University Laval, Québec, Canada

Chen, Yanshao
Barrick Exploration, Beijing

Ciobanu, L. Cristiana
University of Adelaide, S.A., Australia

Cook, Nigel J.
University of Oslo, Oslo, Norway

Cooke, David
CODES, University of Tasmania, Hobart, Tasmania, Australia

Coveney, Raymond M.
University of Missouri, Kansas, USA

Emsbo, Poul
U.S. Geological Survey, Denver Federal Center, Denver, Colorado, USA

Fan, Hongrui
Institute of Geology and Geophysics, CAS, Beijing, China

Franklin, Jim
Franklin Geosciences, Ottawa, Canada

Gardner, Parham
Colorado State University, Fort Collins, Colorado, USA

Groves, David
University of Western Australia, Perth, Australia

Gu, Lianxing
Nanjing University, Nanjing, China

Gu, Xuexiang
China University of Geosciences, Beijing, China

Hall, Greg
Placer Dome Asia Pacific, Perth, Australia

Hart, Craig
Yukon Geological Survey, Whitehorse, Canada

Herrington, Richard
Department of Mineralogy, Natural History Museum, London, UK

Hofstra, Albert
U.S. Geological Survey, Denver Federal Center, Denver, Colorado, USA

Hou, Zengqian
Institute of Mineral Resources, CAGS, Beijing, China

Hrischeva, Elitsa
University of Toronto, Toronto, Canada

Hua, Renmin
Nanjing University, Nanjing, China

Ishihara, Shunso
Geological Survey of Japan, Tokyo, Japan

Jiang, Shaoyong
Nanjing University, Nanjing, China

Kirkham, Rodney V.
Horseshoe Gold Mining Inc.Delta, British Columbia, Canada

Kribek, Bohdah
Czech Geological Survey, Prague, Czech Republic

Lambert, Ian
Minerals Division, Geoscience Australia, Canberra, Australia

Li, Jianghai
Beijing University, Beijing, China

Li, Zhiying
Beijing Research Institute of Uranium Geology, Beijing, China

Liu, Jiajun
China University of Geosciences, Beijing, China

Mo, Xuanxue
China University of Geosciences, Beijing, China

Morris, Paul
Geological Survey of Western Australia, Perth, Australia

Mudrovska, Inna
Ukrainian State Geological Prospecting Institute, Kyiv, Ukraine

Mungall, Jim
University of Toronto, Toronto, Canada
Nie, Fengjun
Institute of Mineral Resources, CAGS, Beijing, China
Nokleberg, Warren
U.S. Geological Survey, Menlo Park, Californian, USA
Pagel, Maurice
Universite Paris-X1, Paris, France
Pašava, Jan
Czech Geological Survey, Prague, Czech Republic
Peter, Jan
Geological Survey of Canada, Ottawa, Canada
Pirajno, Franco
Geological Survey of Western Australia, Perth, Australia
Roberts, Paul
CSIRO Exploration and Mining, Kensington, Australia
Romer, Rolf L.
GeoForschungsZentrum Potsdam, Potsdam, Germany
Scott, Steve
Toronto University, Toronto, Canada
Seltmann, Reimar
Natural History Museum, London, UK
Shimazaki, Hidehiko
University of Tokyo, Tokyo, Japan
Smith, Roric
AngloGold Ashanti Beijing Representative Office, China
Stein, Holly
Colorado State University, Fort Collins, Colorado, USA
Sun, Xiaoming
Zhongshan University, Guangzhou, China
Thompson, John
Teck Cominco Corporation, Vancouver, Canada
Tornos, Fernando
Institute of Geology and Mineralogy, Salamanca, Spain
Walshe, John
Division of Exploration and Mining, CSIRO, Perth, Australia
Watanabe, Yasushi
Geological Survey of Japan, Tokyo, Japan
William-Jones, Anthony
McGill University, Montreal, Canada
Zhao, Zhenhua
Institute of Geochemistry, CAS, Gunagzhou, China
Zhou, Meifu
Hongkong University, Hongkong, China
Zhou, Taofa
Hefei University of Sciences and Technology, Hefei, China
Zimmerman, Aaron
Colorado State University, Fort Collins, Colorado, USA

This page intentionally blank

Session 1

Tectonics, lithospheric, and deep mantle controls on global metallogenic provinces and giant ore deposits

Global tectonic settings and deep mantle control on Hg and Au-Hg deposits

A.S. Borisenko, A.A. Obolenskiy, E.A. Naumov
Institute of Geology, Siberian Branch of Russian Academy of Sciences, 630090 pr. Koptyuga 3, Novosibirsk, Russia

Abstract. Three main geodynamic environments are favorable for the developmemnt of ore-forming systems of Hg and Au-Hg deposits: Intracontinental rifts and aulacogens at the ancient cratons, intraplate rifting in the orogenic belts of different ages, and active continental margins of the continents. The isotope-geochemical characteristics of ore-forming systems of Hg and Au-Hg deposits, changes in $^{3}He/^{4}Hg$ ratio, and paragenetic relationship between subcrustal basite and alkaline basite magmatism suggest that mantle plumes played a significant role in their formation.

Keywords. Mercury, gold-mercury deposits, geodynamic settings, mantle plumes, helium isotopes, Ar/Ar dating

1 Introduction

Analysis of the siting of Hg and Au-Hg deposits indicates their joint deposition sites in the well- known metallogenic belts: Pacific-Ocean, Mediterranean, and Central Asia (Obolenskiy and Naumov 2003). The most ancient Precambrian Au-Hg deposits only of Canada, South America and Australia, which are localized in the separate ore districts and controlled by rifting structures of the ancient cratons, occur beyond the limits of the belts. Different geodynamic environments are typical for the Hg and Au-Hg deposits localized within the limits of recognized global metallogenic belts.

2 Global metallogenic belts

The well-known Almaden ore district in the rift structures of the ancient Iberian plate, and the Donetsk basin ore province in the Dnepr-Donetsk aulacogen in the flank of the ancient Ukraine shield, occupy separate positions in the Mediterranean belt, where Mesozoic and Cenozoic Hg and Au-Hg deposits are related to the post Jurassic subduction zones and overlying continental volcanic belts (Bailey et al. 1973; Tanelli et al. 1991). Mercury deposits of the Almaden district are the Silurian-Devonian in age, while mercury deposits of the Donetsk basin are of Permian-Triassic age.

Mercury and Au-Hg deposits of the Central Asian belt, localized in Early Paleozoic and Hercinian orogenic belts, are related to various metallogenic epochs (Table 1). The four main periods of Hg and Au-Hg deposits are distinguished in the Altai-Sayan orogenic region using Ar-Ar dating: Early Paleozoic, Middle Paleozoic, Early Mesozoic and Late Mesozoic. Industrial Hg and Au-Hg deposits of the Altai-Sayan and Tien-Shan ore provinces are related to the most productive Early Mesozoic period. Geodynamic environment of formation of these belts is caused by the intraplate riftogenesis, confined to the large scale displacements along strike-slip faults of

Table 1: Ages of Hg and Au-Hg mineralization

Geological time	Deposit type	Hg minerals in the ore	Method	Age
Late Mesozoic (J_3-K_1)	**Hg, Au-Hg, Hg-Sb-W:** Transbaikalia, West Mongolia, South-Gobi belt	Cinnabar, Hg-sphalerite, metacinnabarite, Hg-gold	Geol. age K-Ar	J_3-K_1 116-131
Early Mesozoic (T)	**Hg (Hg-Sb):** Chazadr (Tuva), Tyutyo (Altai), Kok-Uzek (Altai), Kelyanskoye (Transbaikalie) Karasug (Tien-Shan) **Au-Hg:** Hurimt-Huduk (Mongolia)	Cinnabar, Hg-tetrahedrite, Hg-sphalerite Cinnabar Hg-gold, Hg-fahlore, coloradoite	Ar-Ar - " - - " - K-Ar Ar-Ar K-Ar	227±16.3 231.5±1 234.4±1.3 240-245 235.4 238.6±2.4 246
Middle-Paleozoic (D-C_1)	**Au-Hg:** Murzinskoye (Altai), Kundat (Kuznetsk Alatau)	Hg-gold, Hg-fahlore, saukovit Cinnabar, Hg-sphalerite, Hg-gold	Ar-Ar - " -	358.3±3.8 337.8±2.9
Early Paleozoic (Є-O)	**Au-sulfide-Q:** Lysogorskoye (East Sayan), Kharalskiy district (Tuva)	Hg-gold, schwatzit, cinnabar Hg-gold, Hg-sphalerite	**Ar-Ar** - " -	512±2 486.7±8.2

Late Paleozic – Early Mesozoic age. There are no known mercury deposits of Paleozoic age, and Hg enters into the sulfides and native gold of lode gold and Au-Cu-skarn deposits, and forms complex Au-Hg occurrences related to the granitoids ($D\text{-}C_1$) (Table 1).

A large quantity of Hg and especially Au-Hg deposits are localized mainly in the back-arc rift structures of the Basin and Ranges province, occur in the global Pacific-Ocean metallogenic belt and particularly in its North American branch. The main Au-Hg deposits of the world class occur there, and since their discovery in the 1860s they became one of the major industrial types of Au deposits (Radtke 1985; Muntean et al. 2004).

Mercury deposits are localized within the limits of active continental margins of Andean and Californian types of South and North America in frontal accretion complexes of subduction zones and overlying continental volcanic belts. Mercury deposits of North-East and Far East Russia are situated in similar geodynamic environments. Au-Hg deposits in these structures are minor.

Small Hg and Au-Hg deposits occur in island-arc systems of ensialic type predominantly in the West Pacific-Ocean segment of the belt (Japan, Oceania, New Zealand). The important Au-Hg province of South-East China is situated in this part of the Pacific Ocean belt including large Sb-Hg (Vanshan) and Au-Hg deposits of Carlin type related to the structures of Mesozoic active rifting of South-China craton (Hu Rui-Zhong et al. 2002). Thus, analysis of Hg and Au-Hg deposits localization in global metallogenic belts allows us to establish the main regularities of their position.

3 Geodynamic settings

Proterozoic and Paleozoic deposits occur in rift structures or aulacogens are confined to continental rifts and related genetically to the mantle plumes. Mercury and Au-Hg deposits are located separately as a rule, although Hg mineralization coincides with Au-Hg mineralization in the South-East China province.

Mercury and Au-Hg deposits, whose formation is caused by the intraplate rifting development of anorogenic magmatism and plutonogenic ore-forming systems with complex Cu-Au-Hg ore, occur in the reactivated orogenic belts of different age in Central Asia. The intraplate riftogenesis is completed by basite and alkaline-basite magmatism as dike swarms and epithermal Au-Hg and Hg mineralization at the Permian-Triassic boundary. Mesozoic and Cenozoic Hg and Au-Hg deposits are located at active continental margins. They are known in ensialic island-arcs, accretion complexes of subduction zones, overlying continental volcanic belts, and in the back-arc rifting structures. There is a close relation between Hg and Au-Hg deposits in this geodynamic environment, with common ore-forming epithermal and volcanogenous-hydrothermal systems.

Thus, three main geodynamic environments are favorable for the development of ore-forming systems of Hg and Au-Hg deposits: intracontinental riftogenesis at the cratons, intraplate rifting related to strike-slip faults in the orogenic belts, and active continental margins of the continents. Magmatism of mantle (plume) nature, according to the isotope-geochemical characteristics, arises as volcanogenic-plutonogenic or dike complexes and magmatogenic-hydrothermal ore-forming systems in each of these geodynamic environments. Mercury and Au-Hg deposits are related to the late periods of their development. Ore-forming systems of the Hg deposits may occur separately as well.

4 Mantle plumes and ore forming processes

A mantle origin of ore-forming systems of Hg and Au-Hg deposits is proved by isotopic composition of helium from fluid inclusions in quartz at these deposits (Table 2) (Torgersen et al. 1981, 1982, Cline et al. 2003). Isotope com-

Table 2: $^3He/^4He$ values of ore-forming fluids of Hg and Au-Hg deposits

Deposits	$^3He/^4He * 10^{-6}$
Hg deposits	
Nikitovka (Ukraine)	0,12
Khaidarkan (Kyrgyzstan)	0,06
Vanshan (China)	0,38
Aktash (Altai, Russia)	0,28
Djilkidal (Altai, Russia)	1,6
Sulfur-Bank[1] (USA)	19,4 - 19,9
Uzon[2] (Kamchatka, Russia)	6 - 11,3
Au-Hg deposits	
Travyanskoe (Urals, Russia)	0,8
Novolushnikovskoe (Salair, Russia)	0,6
Lysogorskoe (Sajan, Russia)	0,37
Tereksai (Kyrgyzstan)	<0,41
Kyuchus (Yakutia, Russia)	0,32
Murzinskoe (Altai, Russia)	1,15
Kundat (Kuznetsk Alatau, Russia)	0,2
Getchell[3] (USA)	0,2 - 2
New Zealand[4]	3,1 - 7,4
Steamboat-Springs[1] (USA)	1,48 - 8,36

Data by: 1 – Torgersen & Jenkins (1981); 2 - Rozhkov (1979); 3 – Cline et al. (2003); 4 - Torgersen et al. (1982).

position of He was measured in the laboratory of geochronology and geochemistry of isotopes at the Kola Geological InstituteRAS. The lowest 3He/4He ratios (from 0.12*10-6 to 0.38*10-6) are typical for mercury deposits (Vanshan, Nikitovka). The copper-mercury (Djilkidal) and gold-mercury (Murzinskoe) deposits with the isotopes of helium varying from 1.06*10-6 to 1.6*10-6 belong to the intermediate type. Relatively high-temperature Ni-Co-As and Ag-Sb deposits (Bu-Azzer and Akdjilga) are characterized by a higher proportion of light helium isotope, average 3He/4He ratio varies from 4*10-6 to 18*10-6, respectively (Naumov et al. 2004).

We observed some inverse correlation between 3He/4He values of ore-forming fluids and resources of epithermal Au and Hg deposits from different parts of the world (Table 3).

These data suggest that in a series of deposits: mercury ? copper-mercury ? gold -mercury ? nickel-cobalt arsenide ? silver-antimony, the proportion of mantle helium increases significantly in the composition of ore-forming fluids.

In this series a marked isotope shift in the ä18OH2O of hydrothermal solutions suggests a higher concentration of magmatogenic fluids in their composition (Fig. 1).

Ore-forming systems in different geodynamic environments differ in ore productivity. The unique mercury deposits were formed by ore-forming systems of intracontinental rifts (Nikitovka, Almaden, Vanshan).

Ore-forming systems of overlying subaerial volcanic belts in the Tuscan province in Italy, Idria in Slovenia, and Huancavelica in Peru formed the world- class Hg deposits. Ore-forming systems in subduction zones (deposits of Coastal Ridge in California, USA, Tamvatney, Chukotka, SE Russia) are of the same grade. Ore-forming systems in zones of regional thrusting of the orogens are not so productive (Tien-Shan and Altai-Sayan – Aktash and Chagan-Uzun deposits).

The geodynamic environment of back-arc riftogenesis occupies a special place in formation of highly productive ore-forming systems, an example of which is the Basin and Ranges province. The Nevadan belt occurs in this province, where most of the Hg and Au-Hg deposits are concentrated.

Independent of an approach to explain the origin of tectonic structures of the Nevadan belt, evolution of Cenozoic (40 Ma) magmatism is established on the boundary of 20-15 Ma, when typical bimodal calc-alkaline magmatism gives place to the alkaline-basite, and over 5 Ma to the basite one. That is the most satisfactory explained by the influence of Yellowstone mantle plume and common reconstruction of volcanic arc geodynamic environment on the riftogenesis. The most important ore-magmatic systems of porphyry-Cu-Mo and Au-Hg epithermal deposits were formed at the boundary of 45-35 Ma, and also at 26-22 and 9-5 Ma. The intensity and duration of ore-forming processes in the Nevadan belt may be explained by the consecutive influence of mantle plumes on tectonic structure formation, magmatism, and associated ore-forming process (Pirajno 2000; Muntean et al. 2004).

Thus, mantle alkaline-basite magmatism immediately precedes the Hg and Au-Hg deposits forming in a number of ore provinces, for example Iberian (Higueras and Munha, 1993; Hernandez 1999), Donetsk, South-China (Hu Rui-Zhong et al. 2002), Tuscan (Tanelli, 1991), and Nevadan provinces (Pirajno, 2000).

Age displacements of ore-forming processes relative to the time of the main phase of plume magmatism are

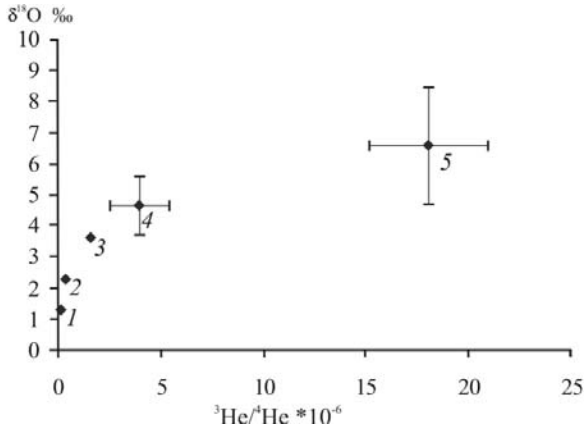

Figure 1: Isotope composition of oxygen and helium of hydrothermal solutions from epithermal deposits, according to isotope data of the O and He in fluid inclusions of minerals from the deposits: 1 – Nikitovka, 2- Vanshan, 3 – Djilkidal, 4 – Bu-Azzer, 5 – Akdjilga

Table 3: Inverse correlation between $^{3}He/^{4}He$ values of ore-forming fluids and resources of deposits

Deposit	Resources (t.roughly)	$^{3}He/^{4}He *10^{-6}$
Au-Hg deposits		
Steamboat springs	1	1.2
Rotorua	2.5	1.2
Murzinskoe	12	1.2
Getchell	100	0.1-1.1
Hg deposits		
Uzon	10	6.0-11.3
Sulfur-Bank	15	19.4-19.9
Djilkidal	100	1.5-1.6
Vanshan	10000	0.38
Nikitovka	40000	0.12

established for the South Siberian and Tien-Shan provinces (Siberian superplume 250-244 Ma, Hg mineralization 230-235 Ma, Tien-Shan alkaline-basite magmatism 255-240 Ma, Hg deposits 236-228 Ma). This is possibly caused by specific development of the structures of intraplate riftogenesis in the orogenic belts, as well as the location of arising under-crust magmatic centers occurred generally as basite and the late alkaline basite dike swarms.

5 Conclusions

Geohistorical analysis, geodynamic environments, and spatial and temporal paragenetic relationship of ore-forming systems of Hg and Au-Hg deposits with mantle magmatism allow consideration of their formation as one of the events related to mantle plumes in the Earth's crustal structures (Pirajno, 2000). The intracontinental rifts (aulacogens) arising in the Early and Middle Paleozoic period, structures of intraplate riftogenesis in the reactivated Paleozoic orogenic belts, and subduction zones and active continental margins in Mesozoic and Cenozoic periods are the most favorable for the localization of ore-forming systems of not only Au-Hg but most of Hg deposits.

Acknowledgements

We are grateful to I. Kamenskiy (KGI RAS) for carrying out He isotope analyses. This work was financially supported by the Russian Foundation for Basic Research (grants 04-05-64485, 04-05-64399) and "Leading scientific schools" (grant 1573.2003.5.).

References

Bailey EH, Clark AL, Smith RM (1973) Mercury. US Geological Survey Professional Paper, No 820. 873

Cline JS, Stuart FM, Hofstra AH, Premo W, Riciputi L, Tosdal RM, Tretbar R (2003) Multiple sources of ore-fluid components at the Getchell Carlin-type gold deposit, Nevada,USA. In: Eliopoulos et al. (eds) Mineral exploration and sustainable development. Millpress, 965-968

Hernandez A, Jebrak M, Higueras P (1999) The Almaden mercury mining district, Spain . Mineralium Deposita. 34, No 5-6, 539-548

Higueras P, Munha J (1993) Geochemical constrains on the petrogenesis of mafic magmas in the Almaden mining district. Terra Abstract, 12-13

Hu Rui-Zhong, Su-Wen-Chao, Bi Xian-Wu, Tu Guang-Zhi, Hofstra AH (2002) Geology and geochemistry of Carlin-type gold deposits in China: Mineralium Deposita 37, No 3-4, 378-392

Muntean JL, Cline J, Johnston MK, Ressel MW, Seedorf E, Barton MD (2004) Controversies on the origin of world-class gold deposits, Part I: Carlin-type gold deposits in Nevada: SEG Newsletter, 59:11-18

Naumov EA, Airiyants AA, Borisenko AS, Borovikov AA, Kamenskiy IL, Reutskiy VN (2004) Helium, carbon and oxygen isotope composition study of the epithermal deposits. In: Khanchuk AI (ed). Metallogeny of the Pacific Northwest: Tectonics, Magmatism and Metallogeny of Active Continental Margins. Vladivostok. Dalnauka, 300-303

Obolenskiy AA, Naumov EA (2003) Global mercury belts and geodynamic position of ore-forming systems of mercury deposits In: Eliopoulos et al. (eds) Mineral exploration and sustainable development. Millpress, 511-515

Pirajno F (2000) Ore Deposits and Mantle Plumes. Kluwer Academic Publishers, Dorbrecht, Netherlands.

Radtke AS (1985) Geology of Carlin gold deposit, Nevada. US Geological Survey Professional Paper, 1, No 1267, 124

Rozhkov AM (1979) Gas composition, Rn radioactivity, $^{3}He/^{4}He$ isotope ratios as indicator of ore-forming conditions and ore deposition from thermal water in Uzon caldera (Kamchatka, Russia): Vulcanologia I Seismologia, 6: 30- 40

Upper mantle composition: Tools for smarter diamond exploration

William L. Griffin
GEMOC Key Centre, Dept. Earth & Planetary Sciences, Macquarie University, NSW 2109, Australia and CSIRO Exploration and Mining, North Ryde, NSW 2113, Australia

Suzanne Y. O'Reilly
GEMOC Key Centre, Dept. Earth & Planetary Sciences, Macquarie University, NSW 2109, Australia

Abstract. The traditional use of major-element data on diamond indicator minerals such as garnet and chromite is based on empirical correlations that have proven unreliable in some exploration situations. The use of trace-element data on these minerals, combined with mantle-mapping techniques, provides clear explanations of both the successes and the failures of the traditional approaches. These techniques make it possible to determine, at an early stage of exploration, both the overall prospectivity of a region and the most appropriate application of indicator mineral chemistry.

Keywords. Diamond exploration, mantle petrology, trace elements, lithosphere mapping

1 Introduction

The formation of known economic deposits of gem diamonds has involved sampling of the subcontinental lithospheric mantle (SCLM) by ascending kimberlitic or lamproitic magmas, and much of our knowledge of cratonic SCLM has been a byproduct of diamond exploration and production. The factors that control the distribution of diamond in the SCLM are still incompletely known, although numerous empirical studies have provided constraints. Early studies of diamond inclusions identified an important suite of harzburgitic minerals, especially low-Ca, high-Cr ("G10") pyrope garnets and high-Cr chromites. The use of these as "indicator minerals" has led to some significant exploration successes (especially in S. Africa and Siberia) but has proven misleading in several other regions, leading to significant waste of exploration resources.

However, developments in the use of mantle-derived xenocryst minerals to map vertical and lateral variations in SCLM composition (Griffin and Ryan 1995; O'Reilly and Griffin 1996) provide tools that can explain both the successes and the failures, and shed light on diamond formation processes that can be used to improve exploration models.

2 Mapping SCLM composition

The application of single-grain thermometers based on Ni in garnet and clinopyroxene, and Zn in chromite (Ryan et al. 1996) allows the depth of origin of each grain to be estimated, by referral of T to a known or assumed geotherm. Such geotherms can also be derived directly from data on garnet and chromite compositions. This approach allows the mapping of mineral chemistry on to depth sections, which contain information on mantle composition, structure and processes (Fig. 1).

3 Examples

As an example, SCLM sections from kimberlites in S. Africa and Siberia (Fig. 1) show that harzburgites (olivine-orthopyroxene rocks), identified as important diamond-bearing rock types in these areas, occur mainly at depths that are in the diamond stability field.

However, in the Lac de Gras area of the Slave Province (northern Canada), "G10" garnets and high-Cr chromites have proven counter-indicative for diamond prospectivity; pipes with the highest proportions of these indicators have low diamond content. One reason for this is apparent in Figure 1. The Lac de Gras SCLM consists of two layers, separated by a sharp discontinuity at 145±5 km. The upper layer is ultradepleted, consisting largely of harzburgite residual after extraction of most basaltic components. The deeper layer (145-190 km) is more fertile (richer in Ca, Fe and Al) and contains little harzburgite; it is interpreted as a subcreted plume head (Griffin et al. 1999, 2004a). Nearly all "G10" garnets and high-Cr chromites come from the upper layer, but only the lowest part of this layer is in the diamond stability field. An analysis of the depth of sampling of Lac de Gras kimberlites shows that those which sampled mainly the upper layer have few diamonds; those that sampled mainly the lower layer are the most diamondiferous.

Studies of inclusions in diamonds from the Lac de Gras area (Davies et al. 1999, 2004) show that the lower layer has a high proportion of diamonds of the superdeep (lower mantle) paragenesis, but about 50% of the diamonds are derived from eclogites, and particularly kyanite eclogites with high-Ca garnets (which thus are a more important indicator mineral). A map of the distribution of eclogites (Fig. 2), constructed from T estimates on xenoliths (Pearson et al. 1999; Aulbach et al. 2004) shows that eclogites are concentrated both near the 145-km discon-

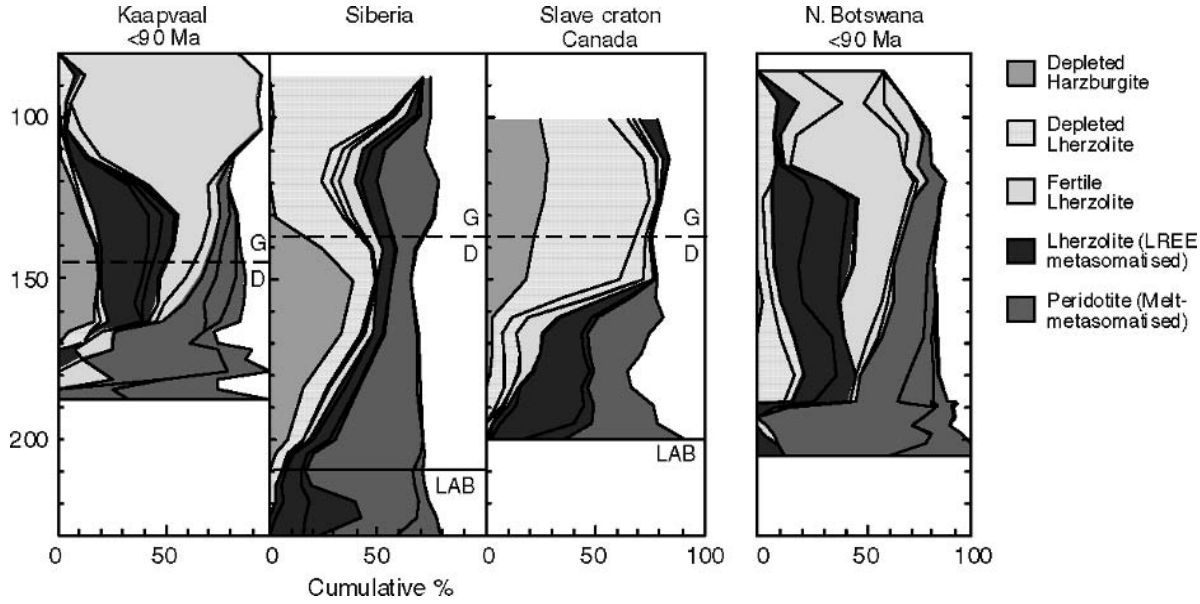

Figure 1: SCLM sections for three representative Archean areas, and the Proterozoic terrain of Northern Botswana. Relative proportions of different rock types have been mapped using major- and trace-element data on concentrate garnets, projected to an empirical geotherm derived for each area. G/D, graphite-diamond transition; LAB, lithosphere-asthenosphere boundary (the base of the depleted lithosphere)

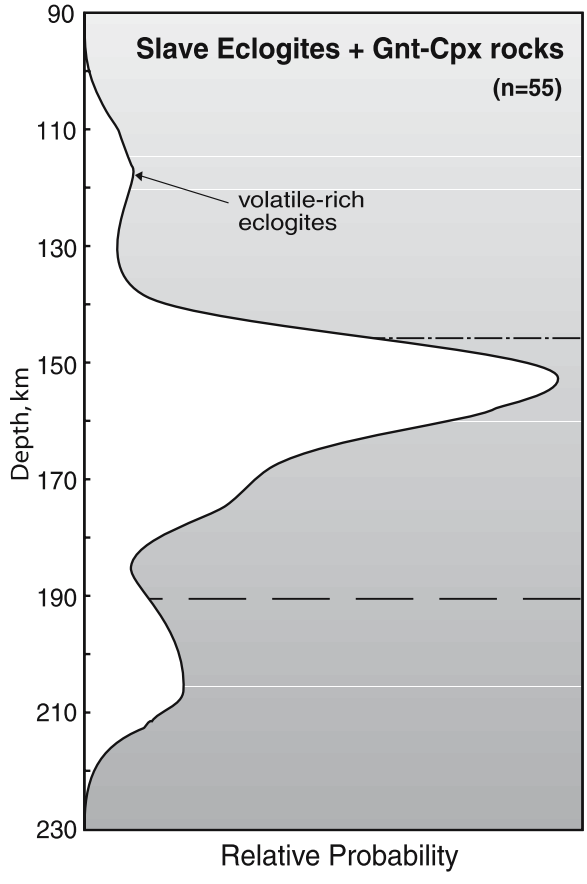

Figure 2: Depth distribution of eclogites in the Lac de Gras area, central Slave Craton

tinuity, and at 180-200 km; the varieties with Ca-rich garnets are preferentially concentrated at the base of the SCLM.

The diamondiferous kimberlites of Botswana (Orapa and Jwaneng fields) contain very few "G10" garnets, but abundant diamonds. An SCLM section (Fig. 1) shows essentially no harzburgites, although Re-Os data show that this SCLM is originally Archean. The abundance of depleted/ metasomatised and fertile lherzolites suggests that the section was refertilised by the introduction of melts during Proterozoic extension and orogeny. In this process, pre-existing harzburgites were converted to lherzolites and their diamonds apparently have been largely destroyed. Diamond inclusion studies show that most of the diamonds in these pipes are derived from eclogitic rocks.

The diamondiferous Group I eclogites are strongly concentrated at the base of the SCLM (Ca 180 km; Fig. 3), and are accompanied by strong melt-related metasomatism (Fig. 1); the non-diamondiferous Group II eclogites are concentrated higher in the SCLM, mostly out of the diamond stability field, which begins at about 150 km depth in this section. This pattern, and eclogite chemistry, suggest that some asthenospheric melts ponded at the discontinuity represented by the base of the SCLM (Group 1) while some penetrated higher into the SCLM (Group II).

In the Arkhangelsk area of western Russia, "G10" garnets are abundant in both diamondiferous and barren kimberlites (Fig. 4). SCLM sections show that the SCLM beneath the barren pipes has been heavily metasomatised

and has a significantly higher geotherm than that beneath the fertile pipes; much of this SCLM has been oxidised and heated by the introduction of magmas (represented by abundant megacryst phases crystallised at high pressure), leading to the destruction of diamonds.

The Proterozoic Brockman kimberlite in the Pilbara Craton of Western Australia contains very high proportions of G10 garnets and high-Cr chromites (Fig. 5), but few diamonds. The SCLM section (Fig. 6) is dominated by extremely depleted harzburgite, much of it within the diamond stability field. However, the trace-element signatures of the garnets show very little evidence of metasomatism. Diamond formation involves the introduction of carbon, which must be fluid-borne, and therefore related to metasomatism. We suggest that the Pilbara SCLM simply never experienced the metasomatism required to introduce carbon; this type of extreme depletion in mantle rock types thus is a negative indicator of diamond potential. While some metasomatic styles appear to destroy diamonds, it is still unclear which of the different metasomatic signatures that can be recognised in these SCLM sections was responsible for diamond formation. Answers may come from ongoing trace-element studies of the diamonds themselves (Griffin et al. 2004b).

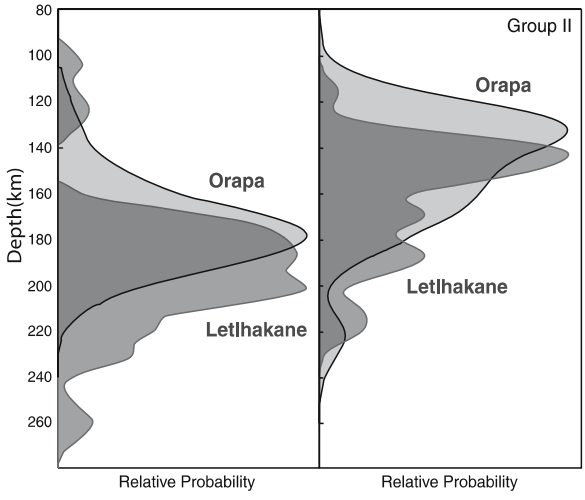

Figure 3: Depth distribution of eclogites beneath the Orapa and Letlhakane kimberlites, N. Botswana. Group I eclogites are diamondiferous; Group II rarely are

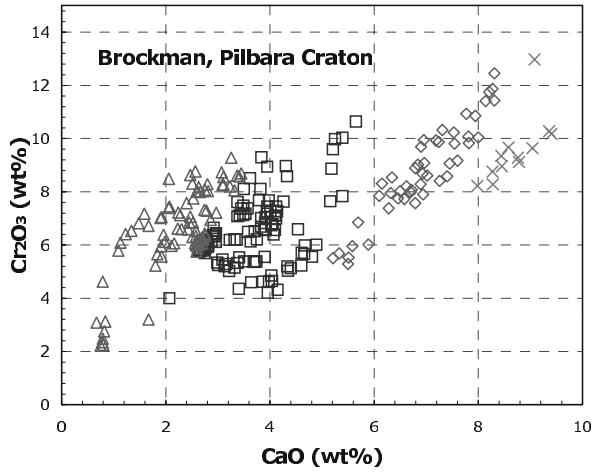

Figure 5: Ca-Cr relationships of garnets from the Brockman kimberlite, Pilbara Craton, W. Australia

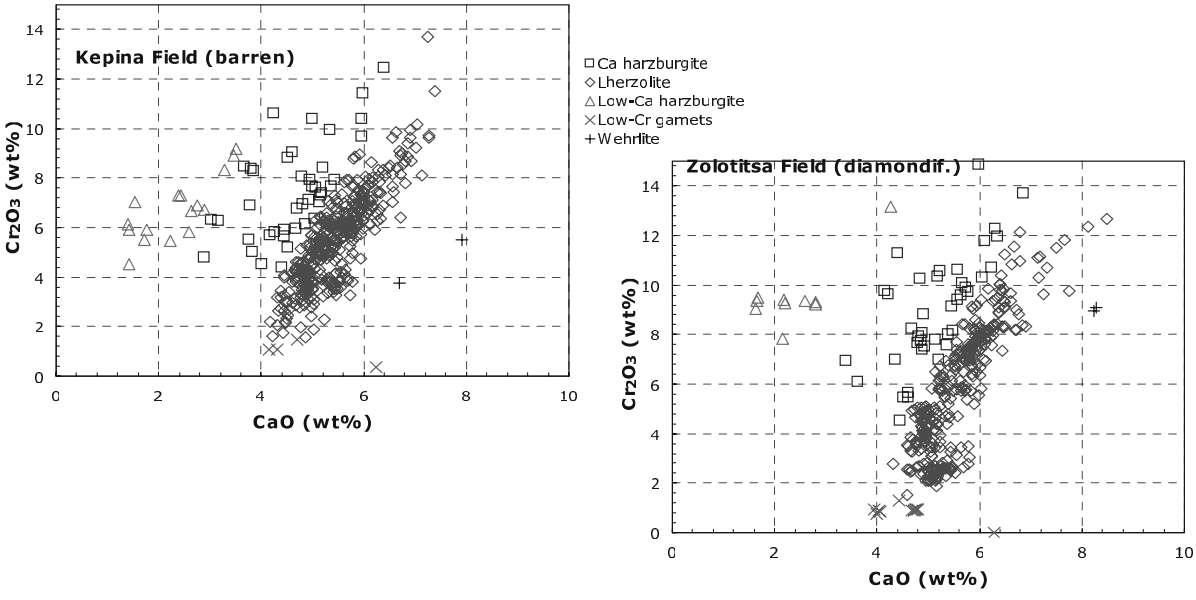

Figure 4: Ca-Cr relationships in garnets from barren kimberlites of the Kepina field, and diamondiferous kimberlites of the nearby Zolotitsa field, Arkhangelsk Province, Western Russia

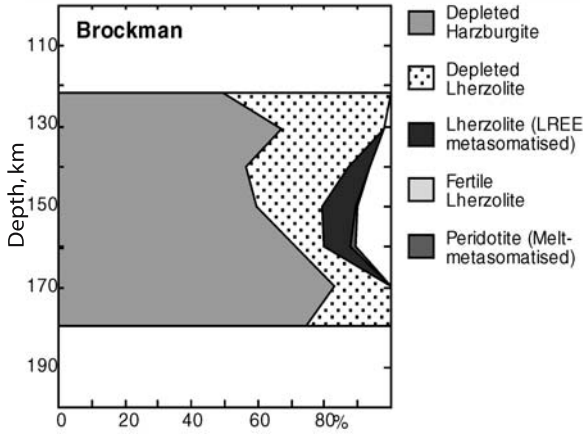

Figure 6: SCLM section from the Brockman kimberlite, Pilbara Craton, Western Australia

4 Exploration applications

SCLM composition can be analysed at early stages of exploration, using garnets and chromites from drainage/loam/till samples to evaluate the diamond potential of specific regions. Such an analysis should be part of the area selection process. It can be used to identify more favourable and less favourable areas, at an early stage of exploration. It can also be used to prioritise individual indicator trails – that is, "Do I really want to find this pipe?" Both approaches can lead to large savings in exploration resources.

Acknowledgements

We are grateful to many colleagues, including those in diamond exploration, for input and stimulating discussions over 20 years. Financial support has been provided by industry partners, ARC, CSIRO and Macquarie University.

References

Aulbach S, Griffin WL, Pearson NJ, O'Reilly SY, Kivi K, Doyle BJ (2004) Mantle formation and evolution, Slave Craton: constraints from HSE abundances and Re-Os systematics of sulfide inclusions in mantle xenocrysts. Chemical Geology 208: 61-88

Davies RM, Griffin WL, Pearson NJ, Andrew A, Doyle BJ, O'Reilly SY (1999) Diamonds from the Deep: Pipe DO-27, Slave Craton, Canada. Proc. 7th Int. Kimberlite Conf., Red Roof Design, Cape Town: 148-155

Davies RM, Griffin WL, O'Reilly SY, Doyle BJ (2004) Mineral inclusions and geochemical characteristics of microdiamonds from the DO27, A154, A21, A418, DO18, DO27 and Ranch Lake kimberlites, Lac de Gras, Slave Craton, Canada. Lithos 77: 39-55

Griffin WL, Ryan CG (1995) Trace elements in indicator minerals: Area selection and target evaluation in diamond exploration. Jour. Geochem. Explor. 53: 311-337

Griffin WL, Doyle BJ, Ryan CG, Pearson NJ, O'Reilly SY, Davies RM, Kivi K, van Achterbergh E, Natapov L M (1999) Layered Mantle Lithosphere in the Lac de Gras Area, Slave Craton: Composition, Structure and Origin. Jour. Petrol. 40: 705-727

Griffin WL, O'Reilly SY, Doyle BJ, Pearson NJ, Coopersmith H, Kivi K, Malkovets V. and Pokhilenko NV (2004a) Lithosphere mapping beneath the North American Plate. Lithos 77: 873-902

Griffin WL, Rege S, Davies RM, Jackson S, O'Reilly SY (2004b) Trace Element Analysis of Diamond by LAM ICPMS: Standardisation, results and directions. Ext. Abst., DeBeers Diamond Conference, Warwick, England

O'Reilly SY, Griffin WL (1996) 4-D lithospheric mapping: a review of the methodology with examples. Tectonophysics 262: 3-18

Pearson NJ, Griffin WL, Doyle BJ, O'Reilly SY, van Achterbergh E, Kivi K (1999) Xenoliths from kimberlite pipes of the Lac de Gras area, Slave Craton, Canada. Proc. 7th Int. Kimberlite Conf., Red Roof Design, Cape Town, 644-658

Ryan CG, Griffin WL, Pearson NJ (1996) Garnet Geotherms: a technique for derivation of P-T data from Cr-pyrope garnets. Jour. Geophys. Res. 101: 5611-5625

Tectonic and lithospheric controls on the heterogeneous temporal distribution of mineral deposits

D.I. Groves, R.M. Vielreicher
Centre for Global Metallogeny, SEGS, The University of Western Australia, Crawley, WA 6009, Australia

R.J. Goldfarb
USGS, Box 25046, MS 964, Denver Federal Center, Denver, Colorado 80225-0046, USA

J.M.A. Hronsky
WMC Resources Ltd, 191 Great Eastern Highway, Belmont, WA 6104, Australia

K.C. Condie
Department of Earth and Environmental Science, New Mexico Institute of Mining and Technology, Soccorro, New Mexico 87801, USA

Abstract. Mineral deposits exhibit extremely heterogeneous distributions, with each major deposit type showing a distinctive, commonly unique, temporal pattern. Individual temporal patterns reflect a complex interplay between formational and preservational forces that, in turn, largely reflect changes in tectonic processes and environmental conditions in an evolving Earth. The first-order drivers were the supercontinent cycle and evolution from plume-dominated to modern-style plate tectonics in a cooling Earth. Consequent decrease in the growth rate of continental crust, and change from thick, buoyant sub-continental lithospheric mantle (SCLM) in the Precambrian to thinner, negatively buoyant SCLM in the Phanerozoic, led to progressive decoupling of formational and preservational processes through time. This affected the temporal patterns of deposit types including orogenic gold, porphyry and epithermal deposits, VHMS, palaeoplacer Au, iron-oxide Cu-Au, PGE, diamond and probably SEDEX deposits.

Keywords. Mineral deposits, temporal distribution, tectonics, lithosphere

1 Introduction

Economic geologists have long been fascinated by the heterogeneous distribution of mineral deposits. Modern studies of mineral deposits have led to refinement of their classification into relatively specific types, such that their distribution in space and time can be defined. Enormous improvements in the robustness, accuracy and precision of mineral chronometers have allowed temporal peaks in the distribution of mineral deposits to become progressively better defined. Temporal patterns of deposit distribution have been broadly defined in the past (e.g. Meyer 1988; Barley and Groves 1992), but it is only in the last decade that details of these temporal patterns have been deciphered. Some periodic changes in the temporal distribution of specific mineral-deposit types may be due to long-term periodic supercontinent formation and breakup, whereas other changes relate to intracratonic extension. However, the distribution of most mineral-deposit types is more complicated than this, with some restricted to very specific periods in Earth history, whereas others occur periodically throughout the rock record.

The heterogenous temporal distribution of mineral deposits broadly can be ascribed to temporal changes in the processes that produce the deposits, or to the depositional environments in which they form, and the preservational potential of the deposit-hosting environments. In turn, temporal changes in ore-deposit forming processes can be ascribed to: 1) secular decrease in global heat flow in a cooling Earth; 2) long-term changes in tectonic processes; and 3) the evolution of the atmosphere - hydrosphere - biosphere system. Tectonic changes may be a consequence of a cooling Earth and may induce short-term fluctuations on long-term evolution of the atmosphere-hydrosphere system. Changes in tectonic regime may affect the preservational potential of terranes in which the mineral deposits formed. There are thus feedback loops in dynamic evolving global systems.

In this paper, several figures are constructed to facilitate the discussion of the temporal distributions of various deposit types. There are a number of critical problems in generating these: 1) it is possible only to include the major deposits within each deposit type; 2) in some places (e.g., central Asian countries, Russia, and China) production and resource data are incomplete or conflicting, 3) even for well-described deposits, total tonnages of metal may vary by a factor of two, 4) for some deposit types, databases are confidential; and 5) the absolute age of many deposits is unknown or debated, and thus time ranges have to be given. Therefore, the figures reflect the temporal distribution of mineral deposits but are indicative rather than definitive in terms of resources (cf. Groves et al. in press a).

2 Brief review of tectonic and lithosphere evolution

Under the influence of a cooling Earth, tectonic processes evolved from mantle-plume dominated, "buoyant" style

of plate tectonics to modern-style plate tectonics (e.g. Abbott and Isley 2002; Condie in press). Coincident with this was a trend from rapid and voluminous formation of juvenile continental crust (major peaks at *c.* 2.7 and 1.9 Ga associated with catastrophic mantle plumes) and the development of equidimensional Archaean-Palaeoproterozoic cratons, to less voluminous crustal growth and the evolution of highly elongate orogens. Progressive decrease in mantle plume intensity and frequency led to progressive evolution of thinner, less-buoyant SCLM (e.g. Poudijom Djomani et al. 2001). Juvenile continental crust and its SCLM root were linked through their subsequent history (e.g. Griffin et al. 2003), strongly influencing their metallogenic and preservational potential. Formational and preservational processes would have been linked in the early Earth but progressively decoupled in the Proterozoic and Phanerozoic (Groves et al. in press b). Temporal patterns are presented for several, relatively redox-insensitive, mineral deposits whose secular variation is linked to a cooling Earth and changes in tectonic processes

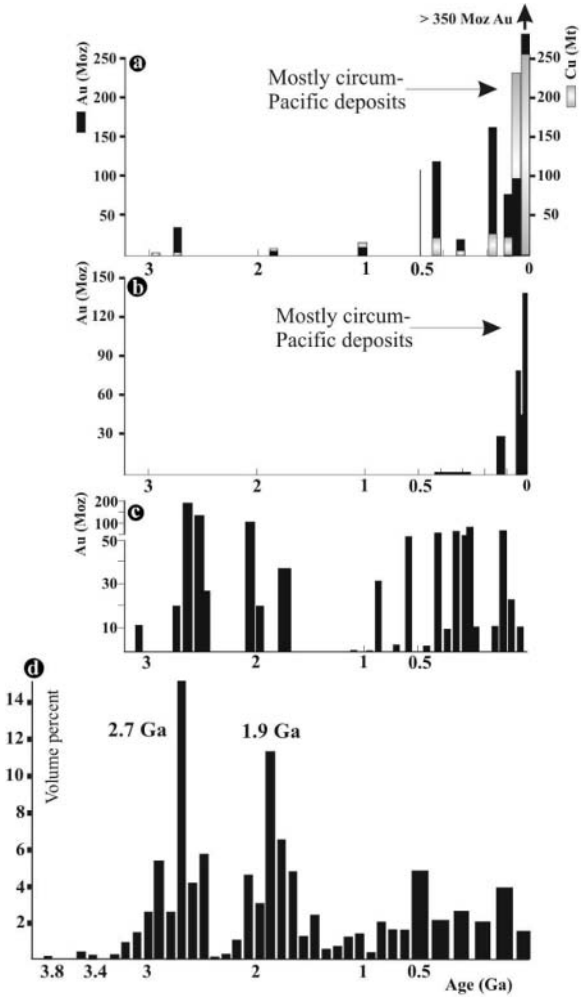

Figure 1: Temporal distribution of epigenetic Au±Cu±Ag deposits compared with the temporal evolution of juvenile continental crust: a. Porphyry Cu-Au deposits: b. Epithermal Au-Ag deposits: c. Orogenic gold deposits:: d. Temporal evolution of continental crust growth: from Condie (2000)

3 Synthesis of temporal patterns and their causes

Mineral deposits show heterogeneous distributions, with each specific group having a distinctive temporal pattern that relates to the conjunction of formational and preservational processes in an evolving Earth. Only Ni-Cu deposits show a direct relationship to a cooling Earth, with komatiite-hosted ores restricted to the Archaean and Palaeo-proterozoic.

Some deposit types, for example epithermal deposits and, to a lesser extent, porphyry deposits, show almost purely preservational patterns with virtual restriction to the late Phanerozoic (Fig. 1a,b), because they form at high crustal levels in arc settings in convergent margins with high uplift rates and rapid erosion (e.g. Sillitoe 1997). Other deposits, such as orogenic gold and VHMS deposits that formed throughout Earth history during major crust-forming events (Fig. 1d), show mixed formational and preservational patterns (Figs. 1c, 2a,b). These relate to secular changes in tectonic processes from strongly plume-influenced buoyant-style plate tectonics in the latest Archaean and early Palaeoproterozoic to modern-style plate tectonics from the Neoproterozoic onwards. The cones-quences included evolution from thick, buoyant SCLM beneath broadly equidimensional Archaean-Palaeoproterozoic cratons, which preserved the orogenic gold and VHMS deposits, to thinner, negatively buoyant SCLM beneath elongate Phan-

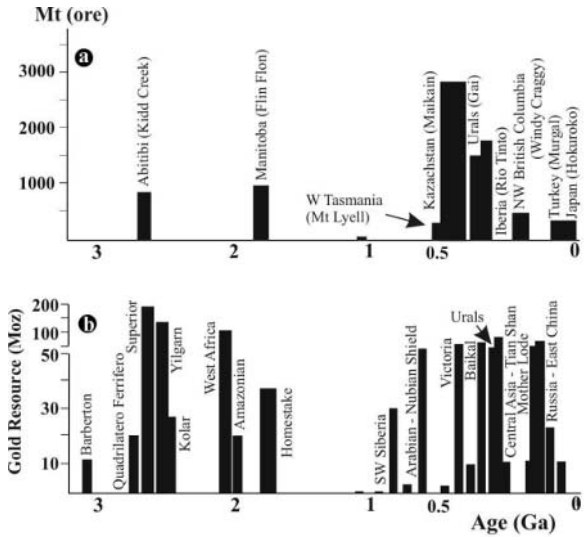

Figure 2: Temporal distribution of VHMS deposits compared with that of orogenic gold deposits. a. VHMS deposits: b. Orogenic gold deposits

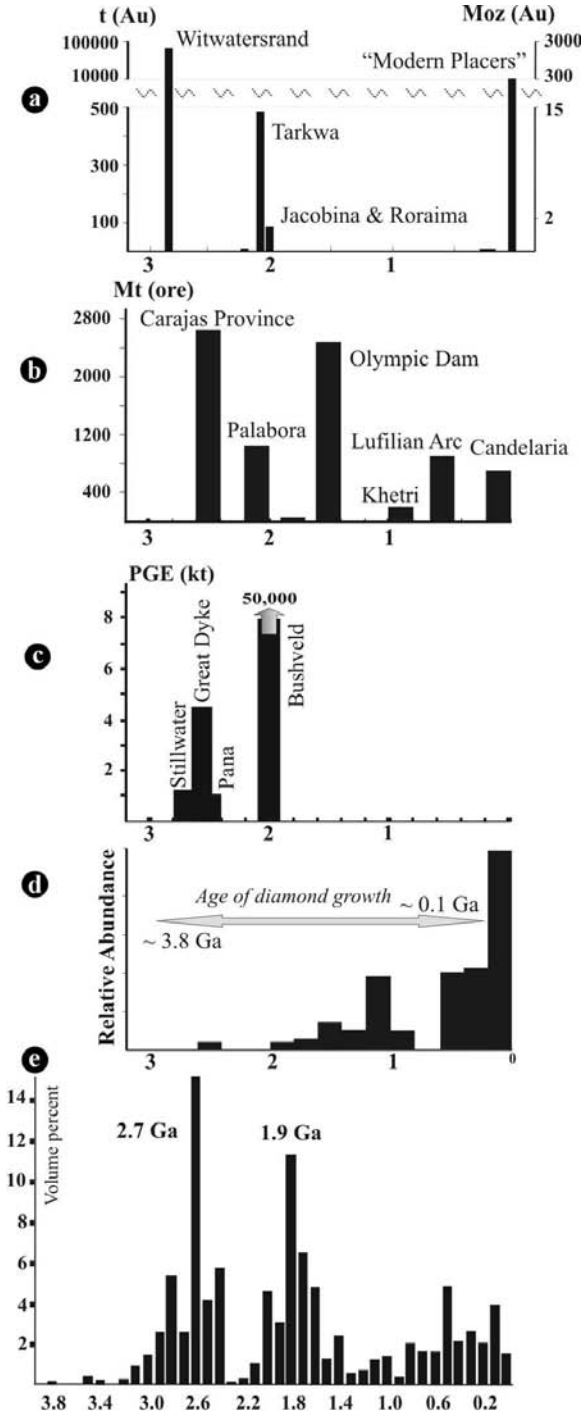

Figure 3: Temporal distribution of palaeoplacer and placer gold deposits, iron-oxide copper-gold deposits, PGE deposits in layered intrusions and primary diamond deposits, compared with secular evolution of juvenile continental crust. a. Palaeoplacer and placer gold deposits: b. Iron-oxide copper-gold deposits with significant Cu-Fe sulphides and gold: c. PGE deposits in large layered intrusions: d. Primary diamond deposits: e. Juvenile continental crust growth

erozoic orogenic belts that were more susceptible to uplift and erosion, leading to non-preservation of these deposits in Meso- and Neo-proterozoic belts (e.g. Goldfarb et al. 2001).

Thus, crustal and metallogenic formational and preservational processes were linked in the early Earth but became decoupled in the Mesoproterozoic to Recent. Giant gold palaeoplacers were also by thick early Precambrian SCLM (e.g. Frimmel et selectively preserved in foreland basins underlain al. in press), with a major hiatus and then the re-appearance of large gold placers in the Tertiary to Recent from erosion of orogenic gold deposits in the hinterland to foreland basins (Fig. 3a). Other types of mineral deposits appear to require the prior existence of thick, stable, early Precambrian SCLM, with low geothermal gradients and incompatible element-rich metasomatism of marginal SCLM, for formation. Hence, these make their first appearance in the Late-Archaean or Palaeoproterozoic. These include IOCG deposits (Fig. 3b), PGE deposits in layered intrusions (Fig. 3c) and primary diamond deposits (Fig. 3d). They, however, show drastically different temporal patterns, with giant PGE deposits and IOCG deposits mainly restricted to the Precambrian (Fig. 3b,c) due to their relatively deep crustal level of emplacement, or protection by cover rocks. In contrast, economic diamond deposits became progressively more abundant towards the late Phanerozoic (Fig. 3d) because of their high crustal level of emplacement and susceptibility to weathering of their hosts.

A schematic diagram, Figure 4, shows the preservational environments of mineral deposits whose temporal patterns are related to tectonic processes. First-order controls on sedimentary rock-hosted lead-zinc deposits are more problematic. The SEDEX deposits first formed in the early Mesoproterozoic, following the assembly of the first giant supercontinent and related generation of large rift basins with appropriate structural and sedimentary architecture (e.g. Betts et al. 2002), and again during the assembly of Pangea (e.g. Lydon 1996): precise processes are equivocal.

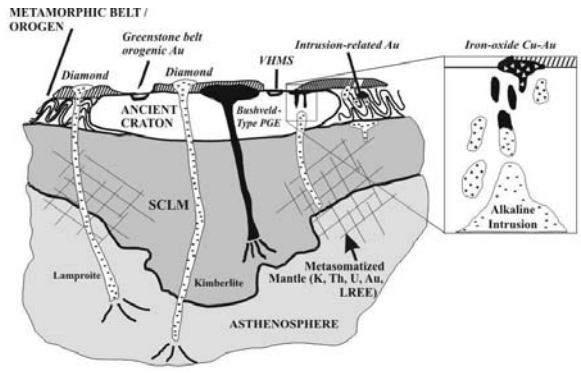

Figure 4: The preservational environments of mineral deposit types with a strong tectonic control as related to Archaean SCLM. From Groves et al. (1987) and Kerrich et al. (2000)

The MVT deposits formed in carbonate platforms with a direct connection to distal orogenic belts. The more important examples show a more restricted temporal distribution, probably due to the requirement of permeable, reactive limestone reef sequences, combined with suitable low-latitude climatic conditions and topographic drivers for long-distance fluid flow, best met during assembly of Pangea (e.g. Leach et al. 2001).

Acknowledgements

We are grateful to colleagues at the Centre for Global Metallogeny at UWA, particularly N. Vielreicher, and D. Leach at the USGS, and to Rob Kerrich, for their discussions on this topic.

References

Abbott DH, Isley AE (2002) The intensity, occurrence and duration of superplume events and eras over geological time. Journal of Geodynamics 34: 265-307

Barley ME, Groves DI (1992) Supercontinent cycles and the distribution of metal deposits through time. Geology 20: 291-294

Betts PG,Giles D,Lister GS, Frick LR (2002) Evolution of the Australian lithosphere. Australian Journal of Earth Sciences 49: 661-695

Condie KC (2000) Episodic continental growth models: afterthoughts and extensions. Tectonophysics 322: 153-162

Condie KC (in press) Supercontinents and superplume events: distinguishing signals in the geologic record. Physics of the Earth and Planets International

Frimmel HE, Groves DI, Kirk J, Ruiz J, Chesley J, Minter WEL (in press) The formation and preservation of the Witwatersrand goldfields, the largest gold province in the world. Economic Geology

Goldfarb RJ, Groves DI, Gardoll S (2001) Orogenic gold and geologic time: A global synthesis. Ore Geology Reviews 18: 1-75

Griffin WL, O'Reilly SY, Abe N, Aulbach S, Davies RM, Pearson NJ, Doyle BJ,Kivi K (2003) The origin and evolution of Archean lithospheric mantle. Precambrian Research 127: 19-41

Groves DI, Ho SE, Rock, NMS, Barley ME, Muggeridge MY(1987) Archean cratons, diamond and platinum; evidence for coupled long-lived crust-mantle systems. Geology 15: 801-805

Groves DI, Vielreicher RM, Goldfarb RJ, Condie KC (in press a) Controls on the heterogeneous distribution of mineral deposits through time. Journal of the Geological Society

Groves DI, Condie KC, Goldfarb RJ, Hronsky JMA., Vielreicher RM (in press b) Secular changes in global tectonic processes and their influence on the temporal distribution of gold-bearing mineral deposits. Economic Geology

Tectonic controls on the endowment of Archean cratons in VHMS deposits: Evidence from Pb and Nd isotopes

David L. Huston, David C. Champion, Kevin F. Cassidy
Geoscience Australia, GPO Box 378, Canberra, ACT 2601, Australia

Abstract. Comparison of Pb and Nd isotopes of the well-endowed Abitibi-Wawa Subprovince with the poorly endowed Eastern Goldfields Province implies that volcanic-hosted massive sulfide (VHMS) endowment in Archean terrains is controlled by crustal character. The Abitibi-Wawa Subprovince contains mostly primitive crust formed in a wide extensional environment. The high heat flow, promoted by thin crust and high level intrusions, and the extensional structures that characterize such an environment encouraged the formation of extensive VHMS deposits. In contrast, extensional environments are limited to a relatively narrow zone in the Eastern Goldfields Province. Although this zone contains VHMS deposits, they are not abundant enough to create high endowment. Provinciality of Pb isotopes in lode Au deposits from near Leonora in the Eastern Goldfields Province supports the concept of a rift-like zone.

Keywords. Archean metallogeny, VHMS deposits, Pb isotopes, Nd isotopes, Eastern Goldfields Province, Abitibi-Wawa Subprovince

1 Introduction

The late Archean Eastern Goldfields Province of Australia and the Abitibi-Wawa Subprovince of Canada are two of the most richly mineralized regions in the world, producing significant portions of global Au, Zn, Cu and Ni. Although these regions have many geological similarities, including age (~2.7 Ga), lithological assemblages and styles of mineralization, the metallogenic endowment of these terrains differs. Although both provinces are well endowed with Au, they differ substantially in known endowment of VHMS deposits. The Abitibi-Wawa Subprovince is well endowed with Zn-Cu-bearing VHMS deposits, but the Eastern Goldfields Province contains few significant VHMS deposits.

Several reasons have been proposed for these differences in endowment, including impediments to exploration (e.g. weathering) and differing tectonic environments (Groves and Batt, 1984). We use published Pb isotope analyses of galena from VHMS deposits and new whole-rock Nd isotope analyses to determine tectonic factors that may account for differences in metallogenic endowment.

2 Lead and neodymium isotope systematics

Lead and Nd isotopes provide direct and indirect constraints on the age and tectonic environment of orebodies and their host rocks. In the Archean, Pb isotopes behave in a more systematic manner than later in Earth's history as processes that fractionate the parent elements to Pb, U and Th were not as widespread at that time. Consequently, models have been developed for Archean Pb isotope evolution that accurately date Pb-bearing mineral deposits. The Western Superior model (Thorpe et al. 1992) applies in the North Pilbara Terrain of Western Australia and Archean terrains in southern Africa as well as the western Superior Province in Canada. The Abitibi-Wawa model (Thorpe 1999) applies mostly in the Abitibi-Wawa Province. These models can predict the age of many deposits to within 10 million years of ages provided by independent methods. These models also produce μ values ($^{238}U/^{204}Pb$ ratios integrated to the present), which indicate the character of the Pb source.

Neodymium isotopes also reflect crustal character. One measurement of this is the two stage Nd depleted-mantle model age (T_{2DM}), an indication of the time when the source of a magmatic rock differentiated from depleted mantle. The closer T_{2DM} is to the magmatic age, the younger the source and the more recent the inferred crustal growth.

3 Lead isotopes in Archean VHMS deposits

Figure 1 plots published least-radiogenic analyses (Browning et al. 1987; McNaughton et al. 1992; Thorpe et al. 1992;

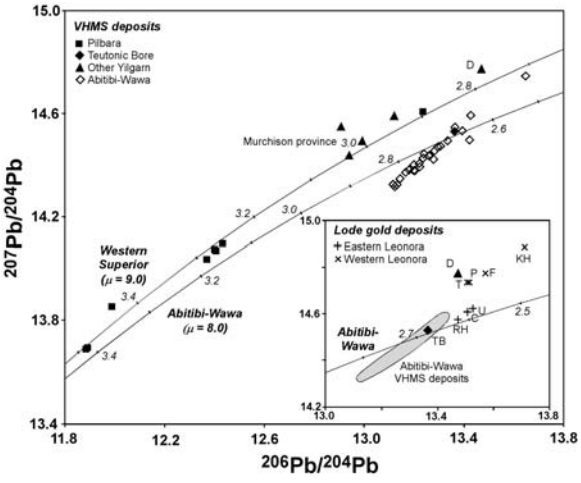

Figure 1: Variations in last radiogenic Pb isotope compositions of galena from Archean VHMS deposits. The inset shows variations of VHMS and lode Au deposits in the Leonora area. Deposit abbreviations as in Figure 2

Thorpe, 1999; Huston et al. 2002) of galena from 3.47-2.69 Ga VHMS deposits in the Abitibi-Wawa Subprovince, the Eastern Goldfields Province, the Murchison Province (in Australia) and the North Pilbara Terrain. The upper of the two data arrays on Figure 1 is defined by deposits from the Pilbara and Murchison, and is interpreted to reflect variations in the ages of the deposits. The ages of the Pilbara deposits are well modelled by the Western Superior evolution curve (shown), although deposits from the Murchison Province are not. The lower array, which is defined almost exclusively by deposits from the Abitibi-Wawa Subprovince, mostly reflects changes in μ as the age range of these deposits is narrow (2.73 to 2.70 Ma). Because the upper array plots above and to the left of the lower, its sources are more evolved than deposits in the Abitibi-Wawa Subprovince.

Importantly, the Teutonic Bore deposit, which is the most important VHMS deposit in the Eastern Goldfields Province, plots on the array defined by the Abitibi-Wawa Province, with its model age well predicted by the Abitibi-Wawa model. According to Thorpe (1999), this deposit is the only VHMS deposit outside the Abitibi-Wawa Subprovince described by the Abitibi-Wawa model.

4 Neodymium and lead isotope variations in the Leonora Area: Evidence for younger crustal growth

Figure 2 illustrates variations in T_{2DM} for 2.67-2.63 Ga granites that have intruded the Eastern Goldfields Province in the Leonora area (unpublished data of D. Champion and K. Cassidy). These results define a 100 km wide, NNW-SSE trending zone with T_{2DM} only slightly older than the age (~2.7 Ga) of the rocks the granites intrude. Outside of this zone, T_{2DM} values are much older than the ages of their hosts, suggesting the presence of a ~100 km wide zone of younger crustal growth. The origin of this rift-like zone is uncertain, its interpretation dependent on whether crustal growth was autochthonous or allochthonous. The only significant VHMS deposits in the Eastern Goldfields Province, the Teutonic Bore and Jaguar deposits, and several other prospects are located within or along the margins of this rift-like zone. Deposits in the Golden Grove district in the Murchison Province also are also located within a rift-like zone with distinctive Nd isotope values. Lead from the Teutonic Bore deposit is more primitive than Pb in the Duketon prospect to the east of the rift-like zone. These limited data are consistent with Pb isotope data from lode Au deposits in the Leonora area (inset to Figure 1). Lode Au deposits from within the rift-like zone have more primitive Pb isotopes than deposits to the west. Moreover, galena from the three deposits within the rift-like zone give Abitibi-Wawa model ages of 2.635-2.630 Ga, consistent with the ~2.630 Ga age for most Au deposits in the Eastern Goldfields Province (Yeats et al. 1999). In summary, VHMS and lode Au deposits in the Eastern Goldfields rift- like zone have more primitive Pb than deposits outside this zone.

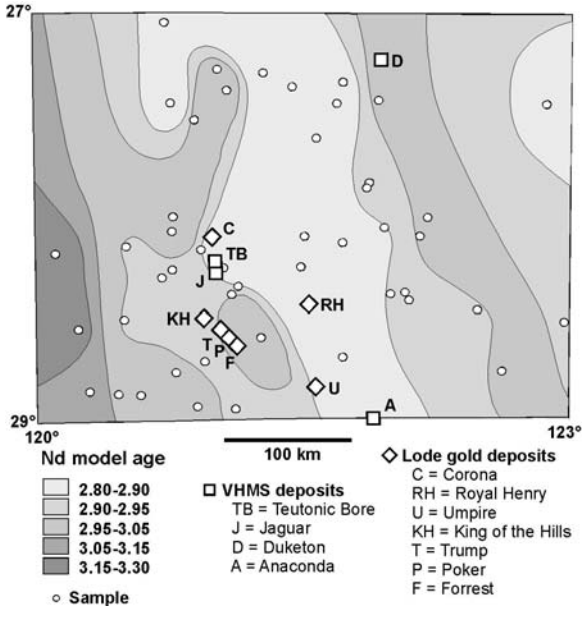

Figure 2: Variations in Nd model ages (T_{2DM}) and the location of selected mineral deposits in the Leonora area

5 Variations in μ from VHMS deposits: An indication of extension in the Abitibi-Wawa Subprovince

Figure 3 illustrates variations in μ values for least-radiogenic galena analyses from VHMS deposits in the Abitibi-Wawa Subprovince. As noted by Thorpe (1999), VHMS districts in the Abitibi-Wawa Subprovince individually have very uniform Pb isotope compositions. However, Figure 3 suggests that this provinciality extends beyond the district scale: μ values show pronounced spatial variations at the regional scale. Although the exact details of the contouring in Figure 3 could be argued, the data require that VHMS districts in the east-central part of the subprovince (e.g. Noranda, Bousquet and Val D'Or districts) have significantly higher μ than deposits to the north and west (e.g. Matagami and Manitouwadge districts). Moreover, Figure 4 suggests that variations in μ are also time-dependent, with older deposits having lower μ.

Ayer et al. (2002) and Bleeker et al. (1999) argued that the Abitibi-Wawa Subprovince formed autochthonously, with younger volcanic sequences built upon a substrate of older sequences. Variations in μ (Figures 3 and 4) support this interpretation. The increase in μ with age suggests that VHMS deposits and their host volcanic sequences became progressively more evolved, with a greater crustal component, with time. This is consistent with Ayer et al. (2002), who found that younger volcanic sequences

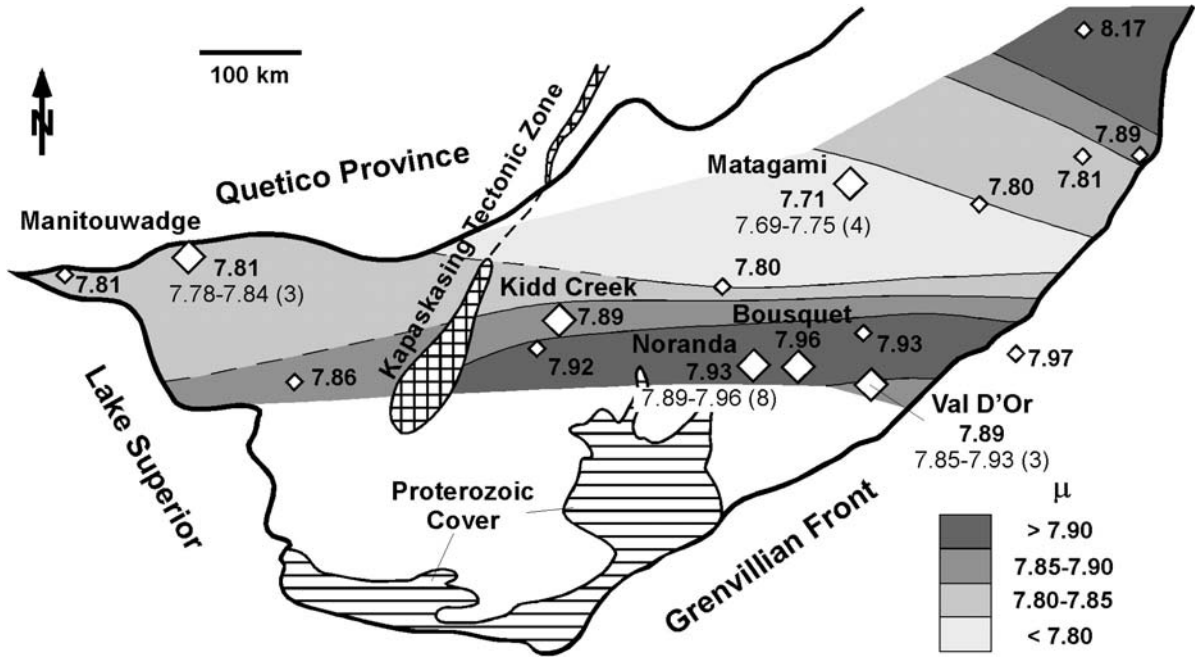

Figure 3: Variations in μ for VHMS deposits in the Abitibi-Wawa Subprovince (values calculated from least radiogenic Pb isotope galena analyses from Thorpe [1999] using the Abitibi-Wawa model, with number of deposits in districts in parentheses)

commonly contained inherited zircons from the older sequences. The east-central zone of high μ values corresponds broadly to younger greenstone belt assemblages of Ayer et al. (2002).

However, Pb from nearly all VHMS deposits in the Abititi-Wawa Subprovince is more primitive than Pb in both VHMS and lode deposits from the Eastern Goldfield Province, including the rift-like zone. The Abitibi-Wawa Subprovince appears to be unique among Archean terrains for its primitive character, as indicated by Pb isotopes and by Nd T_{2DM} of volcanic rocks (calculated from data of Ayer et al. 2002) that are within 100 million years of emplacement ages.

One mechanism to produce the highly primitive crust that characterises the Abitibi-Wawa Subprovince is progressive extension. The distribution of μ in Figure 3 suggests possible extension about an east-west trending axis, with a width of up to 500 km. This contrasts with the narrow (~100 km) rift-like zone identified in the Eastern Goldfields Province.

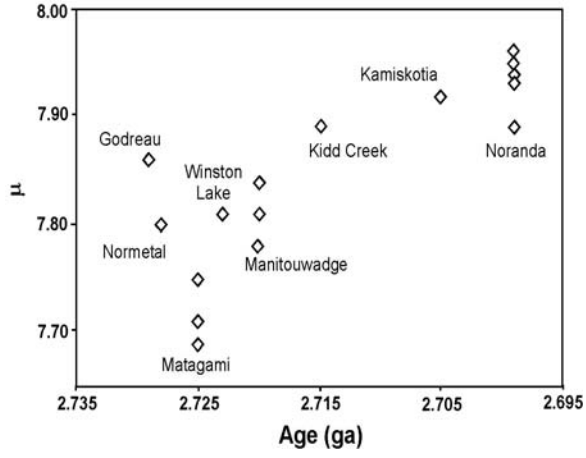

Figure 4: Relationship between age and μ for VHMS deposits in the Abitibi-Wawa Subprovince (values calculated from least radiogenic Pb isotope galena analyses using the Abitibi-Wawa model). Each symbol represents one deposit; districts with multiple deposits plot as vertical arrays

6 What controls the endowment of VHMS deposits in Archean terrains?

Lead and Nd isotope data suggest fundamental differences in the tectonic character of the Eastern Goldfields Province and the Abitibi-Wawa Subprovince. The Eastern Goldfields Province is characterized by evolved crust with relatively narrow rift-like zones that contain the only known significant VHMS deposits. In contrast, the Abitibi- Wawa Subprovince is characterized by more primitive crust, possibly formed in a wide (500 km?) extensional zone that was active over a period of 50 million years. Hence, we infer that the high endowment of VHMS deposits in the Abitibi-Wawa Subprovince is a consequence of its unique tectonic character, which would have resulted in both a high heat flow and extensional structures to channel fluid flow. As this primitive, extensional environment was not extensive in the Eastern

Goldfields (and Murchison) Province, it does not have comparable VHMS endowment. However, rift-like zones identified using Nd isotopes have high potential for significant VHMS deposits in Western Australia. It is interesting to note that many of the larger VHMS districts (e.g. Kidd Creek and Noranda) are associated with the zone of high μ in the east-central part of the Abitibi-Wawa Subprovince.

Cassidy et al. (2005) suggest the metallogeny of komatiite-associated Ni sulfide (KANS) deposits is also controlled by crustal character in the Yilgarn Craton. As KANS deposits favor evolved crust with old Nd T_{2DM} ages, the apparent low endowment of the Abitibi-Wawa Subprovince for KANS deposits may be related to the primitive character of the crust, although other factors, such as exploration effectiveness, may also be important.

7 Exploration implications

In the Eastern Goldfield (and Murchison) Province, rift-like zones, as defined by Nd isotopes, are most prospective for VHMS deposits. Similar rift-like zones may also exist in the North Pilbara (e.g. Whundo belt) and other "more evolved" Archean terrains. The most prospective part of the Abitibi-Wawa Subprovince may the east-west, higher μ belt between Kidd Creek and Val D'Or.

Acknowledgements

This contribution benefited from comments by W Bleeker, A Galley, P Thurston, L Black and R Skirrow. It is published with permission of the CEO of Geoscience Australia and dedicated to the memory of Dr Shen-Su Sun who guided the authors through many of the intricacies of understanding isotope geochemistry.

References

Ayer J, Amelin Y, Corfu F, Kamo S, Ketchum J, Kwok K, Trowell N (2002) Evolution of the southern Abitibi greenstone belt based on U-Pb geochronology: autochthonous volcanic construction followed by plutonism, regional deformation and sedimentation. Precamb Res 115: 63-95

Bleeker W, Parrish RR, Sager-Kinsman, A (1999) High-precision U-Pb geochronology of the Late Archean Kidd Creek deposit and Kidd volcanic complex. Econ Geol Mon 10: 43-70

Browning P, Groves DI, Blockley JG, Rosman KJR (1987) Lead isotope constraints on the age and source of gold mineralization in the Archean Yilgarn block. Econ Geol 82: 971-986

Groves DI, Batt WD (1984) Spatial and temporal variations of Archaean metallogenic associations in terms of evolution of granitoid-greenstone terrains with particular emphasis on the Western Australian Shield. In: Archaean Geochemistry: the Origin and Evolution of the Archaean Continental Crust. Springer-Verlag, pp 73-98

Cassidy KF, Champion DC, Huston DL (2005) Crustal evolution constraints on the metallogeny of the Archean Yilgarn Craton. This volume.

Huston DL, Sun S-S, Blewett R, Hickman AH, Van Kranendonk M, Phillips D, Baker D, Brauhart C (2002) The timing of mineralization in the Archean North Pilbara Terrain, Western Australia. Econ Geol 97: 733-755.

McNaughton NJ, Cassidy KF, Dahl N, Groves DI, Perring CS, Sang JH (1992) Lead isotope studies. In: Ho SE, Groves, DI, Bennett (eds) Gold deposits of the Archaean Yilgarn Block, Western Australia: nature, genesis and exploration guidelines. University of Western Australia Publication 20: 395-407

Thorpe RI (1999) The Pb isotope linear array for volcanogenic massive sulfide deposits of the Abitibi and Wawa Subprovinces, Canadian Shield. Econ Geol Mon 10: 555-576.

Thorpe RI, Hickman AH, David DW, Mortensen JK, Trendall AF (1992) Constraints to models for Archaean lead evolution from precise U-Pb geochronology for the Marble Bar region, Pilbara craton, Western Australia. In: Ho SE, Groves, DI, Bennett (eds) Gold deposits of the Archaean Yilgarn Block, Western Australia: nature, genesis and exploration guidelines. University of Western Australia Publication 22: 395-407

Neoproterozoic and Early Palaeozoic metallogenies in the Dinarides, South Tisia, Pelagonides and Serbo-Macedonian Mass

Ivan Jurkovic
Faculty of Mining-Geol.-Petroleum Engineering, Pierottijeva 6, Zagreb, Croatia

Abstract. The documented Neoproterozoic rocks and ore deposits are known in the Pelagonides (Central Macedonia) and presumed on the basis of superposition in the Serbo-Macedonian Mass (Lower Complex). Paleontologically documented Cambrian-Ordovician (the Early Palaeozoic) complexes are in the Medvednica Mt., the Drina-Ivanjica area (the Golija complex), in the West Macedonia and in the Vlasina Complex (SE Serbia). Presumed Early Palaeozoic complex is situated in the South Tisia, in the Una-Sana area and in the Mid-Bosnian Schist Mts.

Keywords. Neoproterozoic, Early-Palaeozoic, metallogeny, Serbo-Macedonian Belt

1 Neoproterozoic metallogeny of the Pelagonides (Central Macedonia)

The Neoproterozoic block of the Pelagonides is situated between the Early Palaeozoic Complex of the West-Macedonia on the west and the Vardar zone on the east (Fig. 1). It is composed of three rock series: a) the oldest gneiss-mica-schist series 1-1.5 km thick (gneisses, mica-schists, amphibolites and amphibole schists; b) the mixed series (albitized gneisses, schists, cipolins); c) marble series (2-3 km thick), the youngest one, with the dominant dolomitic marbles and subordinate calcitic marbles. Porphyroid, syncollisional granitoids and post-collysional quartz-diorite, quartz monzonite, schistose granodiorids intruded before 10^9 Ma in the Neoproterozoic complex. The biggest magmatic mass is "the Prilep granite" of 120 km^2.

The Neoproterozoic complex is metamorphosed in amphibolite facies with transition in epidote amphibole facies. This complex is separated from the West-Macedonian Early-Palaeozoic complex by reverse fault.

Ore deposits genetically bounded to the Prilep granite are: a) aplite veins, b) pegmatites mainly in gneisses, less in granodiorites and in mica-schists. Their length is averagely 100 m (maximum is 500 m). The thickness varies from 1 to 3 m (some to 5-10 m, very rarely to 25 m). The parageneses consist of microcline as the main mineral; albite-and albite-oligoclase are rare constituents. The biggest number of pegmatite occurrences is concentrated in the Vitolište and Kokra areas c) quartz veins, small in size (50 m long, 2 m thick) occur in the areas of Paralovo, Makovo and Skočivir villages. Bigger (200 m long and 10 – 20 m thick) quartz veins occur in the upper parts of the Babuna river. d) Small occurrences of uranium minerals have been found in pegmatites of the Selečka Mt. and in the iron ores genetically bounded to amphibolite schists (Dunje, Kokra). e) Polymetal Pb-Zn ore deposits are situated near villages Berikovo and Nezilovo in the source area of the river Babuna. These deposits are of metamorphosed contact – pneumatolitic and hydrothermal origin (Pb, Zn, Cu, Ba, Fe, U, Mn, Li, Rb, Cs, Ti minerals) with the world known parageneses. f) East of the town Prilep (the Kozjak Mt.) 2-3 km thick series of dolomite-marble occur (the famous quarry Sivec). At the locality Pletvar are some mines of calcite marble. Marble quarries are situated on the Kave Mt., near the village Nežilovo, and on the Bel Kamen Mt. g) Between the Kajmakčalan Mt. and at the village Živojino micaschists occur with significant quantities of garnet and staurolite and east of Prilep with disthene. From the weathered garnet-staurolite and garnet disthene metamorphic rocks originated rich residual deposits (the village Staro Lagovo).

2 Neoproterozoic and Early Palaeozoic metallogenies of the Serbo-Macedonian Mass

The Serbo-Macedonian Mass (SMM) is situated along the western margin of the Carpatho-Balkanides. Its western boundary is represented by the Vardar zone. The SMM consists of two principal complexes of metamorphic rocks:

1. The lower complex consists of rocks metamorphosed to the amphibolite facies – mica gneiss, micaceous schists, quartzites, some marble and migmatite. The complex is about 11 km deep. It is provisionally separated as the Proterozoic.
2. The upper or Vlasina complex lies unconformably and transgressively over the lower one. This complex predominantly consists of rocks metamorphosed to the green-schists, sporadically to the amphibolite facies. It is about 5 km deep, and its age is the Riphean /Lower Cambrian.

The SMM includes volcano-sedimentary complexes of mafic composition and Lower Palaeozoic and Hercynian granitoids. Crystal-line areas of the SMM are thrust over adjacent tectonic units.

2.1 Ore deposits of the Serbo-Macedonian Mass - the Lower Complex

In the Lower complex, the Precambrian mineralization involves sedimentary and volcano-sedimentary types, dominated by iron and titanium-iron mineral associations.

a Volcano-sedimentary and sedimentary iron deposits are numerous, but small in size. They occur as stratiform beds in amphibolites (Pasjaca, Car Sedlar) and/or in sandstone metamorphosed into gneiss (e.g. Zitni Potok deposit). The ore is mostly composed of magnetite, locally hematite as well, accompanied by minor sulphides. Disseminated sulphide mineralization hosted by gabbro and/or amphibolite occurs sporadically. Titanium mineralization of volcano-sedimentary origin is related to meta-gabbro and/or amphibolite. Sphene and ilmenite are the main minerals (Jastrebac Mt.). Metamorphogenic graphitic mineralization at Pasjaca Mts. occurs as thin subparallel veinlets along foliation of micaschists. Kyanite metamorphic deposits are small in size. Glasovik at Pasjaca Mt. deposits contain 30 % of kyanite.

b Ore deposits associated with granites of the Lower complex includes: Numerous pegmatite deposits are found in the Lower complex. Some of them are large in size and economically very significant. Feldspars, mostly microcline, and quartz are the principal mineral constituents of pegmatite, accompanied by albite-oligoclase, pertite, musco-vite, rare biotite, locally by berile, sphene, zircon, garnet, tourmaline, apatite and uraninite. Feldspars, both potassium and sodium, as well as potassium-sodium composition are exploited in numerous quarries. Some beryl and muscovite are recovered as by-product in the area of Prokuplje. The major pegmatite deposits are known south of Prokuplje (Vidojevicki Krs, Dobrotic, Beli Kamen Pasjaca ets.), then pegmatites related to the Bujanovac granite, near the Kukavica granitoid and at Ograzden Mt. Uranium mineralization occurs sporadically in the granites, only the Slatina river deposit has been explored.

2.2 The Upper or Vlasina Complex

The Vlasina complex is characterized by the dominance of mineralization related to volcano-sedimentary association; complex mineralization related to the Palaeozoic granitoids is almost unknown.

1. Volcano-sedimentary deposits: Massive sulphide mineralization is related to specific litho-stratigraphic units of the volcano-sedimentary complex. Pyrite and chalcopyrite are the dominant minerals. a) Massive pyrite bodies at Monastirica with traces of zinc, silver and gold are of small economic importance due to its low grade. Similar copper mineralization is found southwards at Bukovik and Razanj. b) Lead Zinc mineralization probably related to spilite keratophyre suites and copper-nickel mineralization associated with amphibolite are small in size. c) Small stratiform magnetite deposits within the greenschists (Crna Trava and north of the Vlasina Lake) and stratiform titanium magnetite beds in the amphibolite of Mitrasinci, Republic of Macedonia. d) Stratiform quartzite deposits sporadically containing huge reserves are rather frequent in the Vlasina complex.
2. Sedimentary deposits: Lisina phosphate deposit is related to the Ordovician metamorphites-metapelites composed of upper series (sericitic-chloritic schists interbedded by marble and calcschists), and lower series represented by metasandstones and biotite schists. Phosphorite bed (16-32 m thick, containing 2-19% P_2O_5) is deposited between the upper and lower series. The phosphorite of Lisina originated from the apatite-bearing sandstone.

3 Remnants of the Early Palaeozoic units of the South Tisia included in the Variscan complex

Variscan formations of South Tisia crop out in the Slavonian Papuk, Psunj and Krndija Mountains and in the Moslavacka Mt. Palaeozoic complexes are composed of two groups. Predominant are low-and medium grade metamorphic rocks with migmatite and granitoids. In the Slavonian Mts. these are Barrovian type metamorphic sequences characte-rized by zoned distribution of index minerals: chlorite – biotite – garnet – staurolite - sillimanite (or kyanite) Lower-grade parts of the sequences consist of varieties of greenschist, pyhyllite and chloritoid schist. In Moslavačka gora Mt. only medium-grade metamorphic sequences of the Abakuma-type with cordierite and andalusite crop out. Metaclastic rocks from the lowermost part of the Slavonian Barrovian-type metamorphic sequence contain palynomorphic sequence of Silurian (?) to Early Carboniferous age.

The K-Ar values obtained from the amphibole in ultramafic tectonites varies from 527 to 506 Ma. K-Ar measurements on hornblende concentrates from metamorphic rocks gave 568 to 421 Ma suggesting that the Barrovian sequence includes remnants of pre-Variscan units which so far cannot be mapped.

4 Early Palaeozoic metallogenies

The Una-Sana area - most of Palaeozoic formations belong to the Lower-Middle Carboniferous underlain by subordinate Devonian limestones. In upper part of the Early Carboniferous flysch sequence has been found remnants of Early Palaeozoic trilobites and palinological material which are believed to be Early Palaeozoic in age.

The Medvednica Mountains - The central part of the Medvednica Mt. is composed of metamorphic rocks (greenschists) Paleozoic in age. The bigger part is composed of paraschists while the subordinate part (orthogreenschists) is represented by metadiabases, and subordinate by epidote + sericite schists, and amphibole schists. Along 7 km long contact zone (ortho/paraschists) or near to this contact in the orthomagmatic rocks formed numerous discontinuous small iron ore deposits (1-3 m thick, 15-30 % Fe). The contact zone is characterized by ferrugineous and siliceous rocks, muscovite-chloritoid schists, quartz-stilpnomelane-magnetite schists and magnetite-hematite-quartz ore deposits genetically bounded with the Ordovician/Silurian volcanogeno-sedimentary formation, basic in character.

The Drina-Ivanjica Palaeozoic (Golija) complex - is composed largely of the Drina formation, about 1600 m thick, which form the multiple folded Drina anticlinorium and the Ivanjica block. The Cambrian-Ordovician Drina Formation is composed of metaclastics, subordinate limestones, metadiabases and metatuffs. The lowermost parts of the Drina Formation are underlain by Neoproterozoic basement. The oldest fossiliferous rocks in the Drina-Ivanjica complex are Early Palaeozoic in age. In the Drina-Ivanjica Cambrian-Ordovician various iron-ore and manganese-ore formations of non-economic interest are included. Different ore parageneses occur in the following upwardly sequential zones: a) Fe-chlorite (thuringite) with up to 15 % magnetite; b) Fe-chlorite with hematite; c) magnetite and Fe-chlorite-bearing quartzites, and d) magnetite-bearing zone. The thickness vary from 0.3 to 1 m, Fe content from 11 to 35 %.

Mid-Bosnian Schist Mountains (MBSMts.) - In the area between the towns Busovaca-Fojnica, in the north-eastern part of the MBSMts. occur rock units of presumed Cambrian-Ordovician age. They are incorporated in the Variscan formations and are represented by gneisses and amphibolite schists associated with predominant metaclastics and metarhyolites. Their geological age is not as yet supported by fossils and K-Ar whole rock and mineral ages. The oldest K-Ar age of 343 Ma was obtained on whole rock phyllite from the area of Fojnica. This age suggests a Visean thermometamorphic event, a metamorphic overprint on inferred pre-Variscan complex. This complex is tectonically overlain by Silurian magmatic-metamorphic formations sug-gesting their Early Palaeozoic age. In the area of Busovaca a few ferrugineous quartzites, 0.3-0.5 thick, are interlayered in

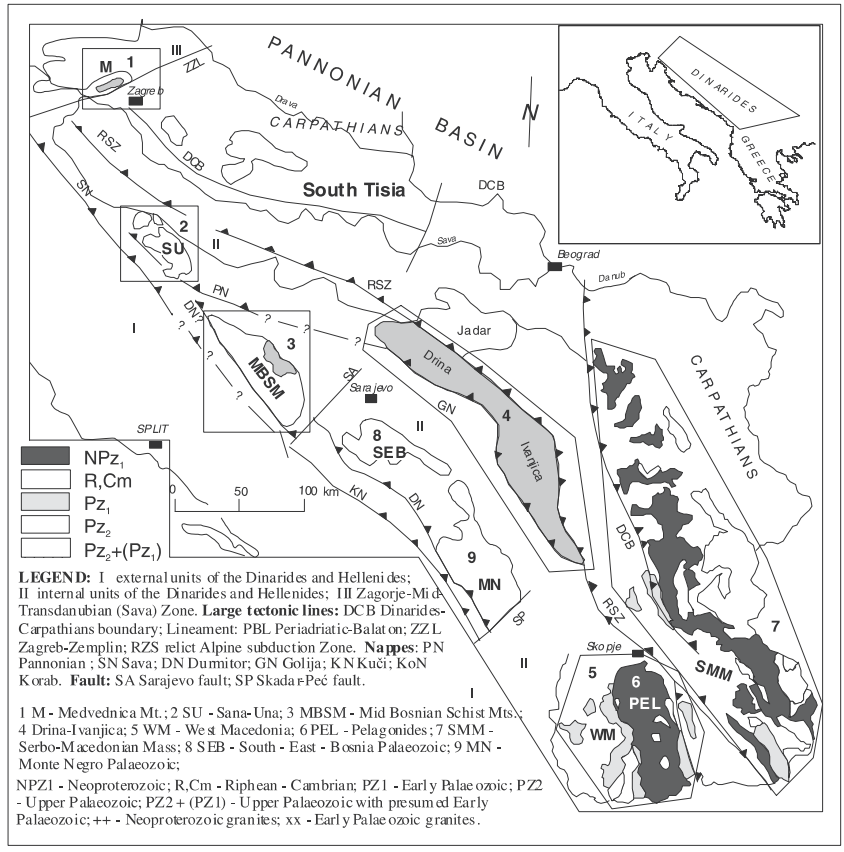

Figure 1: Neoproterozoic and Early-Paleozoic complexes in the Dinarides, South Tisia and Serbo-Macedonian Mass

Lower Palaeozoic metasediments. In the paragenesis quartz predominates over magnetite, Fe-chlorite, hematite and chalcopyrite. In the same area, actinolite-epidote-chlorite ortho-greenschists, interlayered in metasediments are rhythmically interlayered by beds, 15-30 cm thick. Composed of chrome-spinel (4.52 % ZnO and 1.15 % MnO, accompanied by siderite, quartz, albite, Cr-magnetite, hyalophane, phengite, Cr-chlorite and chalcopyrite. In the Krecevo-Kiseljak-Fojnica- Busovaca area occur numerous predominantly small and subordinate middle sized quartz veins. The veins contain 99-97.5% SiO_2, accessories are chlorite, sericite and pyrite. The quartz veins are predominantly synkinematic, some are post-kinematic.

The Early Palaeozoic ore deposits in the West Macedonia - Fossiliferous Cambrian and Ordovician, 4 – 5 km thick have been found on the Stogovo, Karaorman, Pelister, Kruševo, Pesjak and Dobra Voda Mts. It is volcano-sedimentary complex, in the deepest part predominant basic and acid volcanites; metaclastic rocks are subordinate. The higher parts are composed of metaterrigene sediments, subordinate are orthogreen-schists. From metallogenic point ofview the Early Palaeozoic complex of West Macedonia is characterized by the dominance of mineralization related to volcanic-sedimentary association. Mineralization related to the Ordovician (456 Ma) granitoids is of small economic importance.

On the western part of the Stogovo Mt., in the Ordovician schists is situated relatively big manganese deposit Kara Deva and some smaller ones Uzinica, Babin Srt, Denariza. The main primary mineral is rodochrosite, subordinate are siderite and pyrite. The ore contains 20-24 % Mn. Subordinate secondary minerals are psilomelane and pyrolusite. Numerous relatively small iron ore deposits (20–38 % Fe) have been found in the Cambrian-Ordovician schists of Stogovo, Karaorman Slavej and Babuna Mts. The mean ore minerals are chamosite and magnetite. In the contact-metamorphic zone of the Ordovician granitoids, rocks rich on sillimanite and cordierite occur. Very small Cu, Zn, Pb ore occurrences, long quartz veins and rare pegmatites are related to this granitoid.

References

Jankovic S, Serafimovski T, Jelenkovic R, Cifliganec V (1997) Proceed Symp Plate-tectonic aspects of Alpine metallogeny in the Carpatho-Balkan region, Stip, 29-68

Jurkovic I, Pamic J (2001) Nafta 52(9):267-284, Zagreb

Pamic J, Jurkovic I (2002) Int J Earth Sci 91:538-554

Pamic J, Balogh K, Hrvatovic H, Balen D, Jurkovic I, Palinkas L (2004) Mineralogy and Petrology 82:65-79, Vienna.

Mantle control for a giant Neoproterozoic epithermal silver deposit: Imiter (Morocco)

Gilles Levresse
UNAM, Centro de Geociencias, Campus Juriquilla, 76230 Santiago de Queretaro, Mexico

Alain Cheilletz
CRPG-CNRS UPR A2300 and ENSG-INPL, BP 20, 54501 Vandoeuvre-lès-Nancy Cédex, France

Dominique Gasquet
Université de Savoie, CISM-EDYTEM, CNRS – UMR 5204, Campus Scientifique, 73376 Le Bourget du Lac Cédex, France

Moulay Rachid Azizi-Samir
Reminex - Groupe ONA, 26 Av. Allal El Fassi, Tissir 36-40, Marrakech, Morocco

Abstract. The giant epithermal Ag-Hg deposit of Imiter (Morocco) is investigated to test a possible transfer of chalcophile elements from the mantle to superficial crustal levels during Pan-African times. The accretion of the Anti-Atlas belt at the West African continent is characterized by a four stage succession of events, that is, extension, subduction, moderate collision and extension. The strongest metallogenic activity which is dominated by base- and precious metal deposit formation, occurs during the late extensional stage at the Precambrian-Cambrian transition. In the Imiter Ag-Hg deposit, the origin of metals and ligands, deduced from S, fluid inclusions, He, and Re/Os data obtained on sulphide phases and gangue minerals, had a dominantly mantle source.

Keywords. Epithermal deposit, mantle source, Neoproterozoic, Anti-Atlas, Morocco

1 The Imiter Ag-Hg deposit (Morocco)

The Imiter deposit is located on the northern side of the Saghro massif, which constitutes, with the other Proterozoic inliers (Ifni, Kerdous, Akka, Bou Azzer, Sirwa and Ougnat) the Anti-Atlas orogenic belt of Morocco (Fig. 1) bordering over more than 700 km from the Atlantic ocean to Algeria the northern side of the western African Craton WAC (Ennih and Liegeois 2001; Fekkak et al. 2001). Magmatic activity extends from the Palæoproterozoic to the Neoproterozoic and corresponds to two successive periods of crustal accretion during the Eburnean (Birimian) and Pan-African orogenies. The widespread early Palaeozoic cover makes the geology of Anti-Atlas a reference for the Precambrian/Cambrian boundary. The Imiter Ag-Hg deposit is precisely dated at 550 Ma (zircon ion-probe U-Pb dating from associated rhyolites; Levresse 2004) coeval with regional extensional tectonic activity characterizing the P/K transition. Imiter is a world-class silver deposit with currently identified resources of 10 000 metric tones (t) metal. It was formerly interpreted through a black-shale remobilization model (Leistel et Qadrouci 1991) but is now considered as a case of Neoproterozoic epithermal mineralization (Levresse 2001 ; Cheilletz et al. 2002). The Imiter Ag-Hg deposit is hosted by black shales and volcanics of Middle and Late Neoproterozoic age, respectively, and unconformably overlain by a Palaeozoic sedimentary succession. The silver mineralization is genetically related to felsic volcanic rocks (domes and dykes) dated at 550±3Ma (Levresse, 2001). This epithermal event postdates a discrete base metal episode associated with granodiorite intrusions dated at

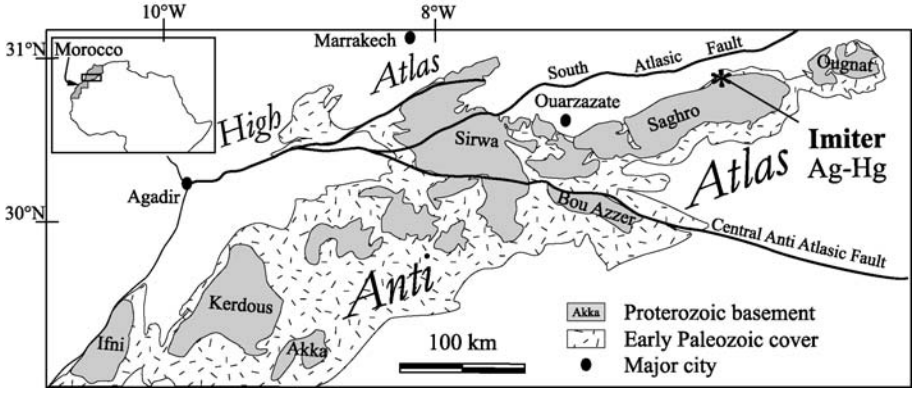

Figure 1: Major geological units of the Anti-Atlas belt in southern Morocco and position of the Imiter deposit

572±5Ma (ion-probe U–Pb dating on zircon; Levresse 2001). Wall-rock alteration associated with the epithermal silver event was minimized by the neutrality of the hydrothermal fluids. The silver mineralization is structurally controlled by the Imiter fault zone which experienced two successive tectonic regimes (Levresse 2001).

The earlier and predominant regime led to the development of normal faults trending N80°E; the second sinistral strike-slip regime led to reactivation of the normal faults, inducing an anastomosed geometry. The epithermal silver event is divided into two successive stages characterized by two different gangue minerals, quartz and dolomite, in extensional veins, hydraulic breccias and quartz-dolomite laminations. Impressive decakilogram Ag-Hg° plates occur in the extensive fault zones and brecciated areas. Mercury content in Ag-amalgam increases from the quartz- to dolomite stage and ranges from 10 to 30% and from 20 to 40% respectively. Mineralogical textures in both stages are complex (association, replacement). Sulphides are the earliest phases. These are, in decreasing abundance, pyrite–arsenopyrite, sphalerite, galena and chalcopyrite. Sulphides occur mostly as aggregates or as xenomorphic. They are strongly corroded by native silver, sulphides and sulphosalts. Silver sulphosalts everywhere precipitated in association with or as replacement of sulphides. Imiterite is most common as needles in dolomitic geodes, associated with cinnabar and argentite. Oxydation is scarce and locally limited to the upper levels of the deposit.

2 A mantle source for metals and ligands

The origin of the metals and ligands (sulphides) was deduced from S, fluid inclusions, He, and Re/Os data obtained on sulphide phases and gangue minerals. Sulphur isotope analyses show the existence of two distinct isotopic reservoirs, one in pyrite from the surrounding black shale country rocks ($\delta^{34}S_{CDT}$=-38‰) and the other in pyrites associated with a synchronous rhyolitic dome ($\delta^{34}S_{CDT}$=-7 to -2‰). The $\delta^{34}S_{CDT}$ values of the silver mineralization event range from -28 to -2‰ and are interpreted as resulting from preferential degassing of SO2 in ascending fluids, as well as mixing between the magmatic isotopic reservoir and a country rock reservoir. Helium isotope analyses of sulphides and gangue minerals yield similar results, with 3He/4He ratios ranging from 0.76 to 2.64Ra. These data and the absence of 20Ne in the analyzed fluid inclusions suggest a mantle origin for the fluids associated with the epithermal silver event. Osmium isotopic ratios have been measured for the first time in Ag° and Ag–sulphosalts. These data and those obtained on other sulphide phases directly associated with the Ag mineralization show measured 187Os/188Os ratios of 0.142-0.197 indicating a dominantly mantle source for the associated Os. Combined with helium isotopes, these data clearly indicate that the main source of the elements (ligands and metals) is from the mantle. The source of the fluids in the Imiter Ag deposit model, unlike in classic epithermal models (Sillitoe 1993; Hedenquist et al. 2000), is hypogene. The low salinity of the fluids (Tmi = 5.9 to 0.0°C) pleads in favor of silver transport as a bisulphur complex (AgHS). The low salinity of the fluids, as well as their gas content (CO_2=50-100%, H_2S=23-36%, N_2=24-48%, of the gas phase), is characteristic of precious metal deposits of the epithermal type (Hedenquist et al. 2000).

3 Geodynamic evolution of the Anti-Atlas during Pan-African times

Regional and local isotopic analysis in conjunction with detailed tectonic and magmatic studies, permit development of a coherent genetic model to Imiter Ag deposit in the Anti Atlas geodynamic evolution. Seven major magmatic episodes are now clearly identified in the Anti-Atlas (Saquaque et al. 1992; Ennih and Liégeois 2001; Hefferan et al. 2002; Thomas et al. 2002) corresponding to major changes in geochemical characteristics and tectonic environments. These magmatic events can be grouped into four major geodynamic-stages (Fig. 2):

1. Ocean opening restricted to Bou Azzer (Fekkak et al. 2001) and probably to the Sirwa massif (Thomas et al. 2002). The age of this phase is not well constrained. However it seems to be, at Bou Azzer, coeval or older than 788±8 Ma which corresponds to the age of thermal metamorphism linked to the emplacement of a gabbroic dyke assumed to belong to the ophiolitic pile (Leblanc and Lancelot 1980). In the Sirwa inlier it appears to be coeval or older than 743±14 Ma, the age recently obtained by Thomas et al. (2002) for a tonalite protolith of an orthogneiss of the ophiolitic sequence from the Bleida Group (Thomas et al. 2002). It is more certainly contemporaneous with plagiogranite emplacement dated at 762±Ma (Samson et al. 2003).
2. Subduction contemporaneous with calc-alkaline magmatism not precisely dated (Saquaque et al. 1992), the dip direction of the subduction, toward North or South, is still matter of debate.
3. a. Obduction (Bou Azzer) related to the so-called B1 tectonic event, low-grade metamorphism, partially molten gneisses and to calc-alkaline intrusives. In fact, the age of B1, recognized in the whole AA, is only constrained in the Central AA at 690-660 Ma. These ages were indirectly obtained either on the associated calc-alkaline metaluminous magmatism supposed to be synchronous with B1, dated at 661±23 Ma (U-Pb, Mifdal and Peucat, 1985), or on metamorphic rocks at the contact of the intrusions at 685±15 Ma and far from intrusions at 663±13 Ma (U-Pb, Thomas et al. 2002). No date was obtained

for B1 in the western and eastern AA and it is uncertain if B1 has the same age in the whole AA.

b. A minor and sporadic collision phase characterized by the emplacement of granodiorites, at 615±12 Ma (Ducrot and Lancelot, 1977), coeval with the "B2" tectonic event. This phase corresponds to the definitive ocean closure.

c. An extensive (595-570 Ma) magmatic episode characterized by intermediate to felsic (mainly high-K calc-alkaline) intrusions; this episode is related to base-metal ore deposits (Cu-Pb-Zn; Levresse, 2004) and constitutes a transition towards the main late Neoproterozoic distensive tectonic event.

4. a. A high-K calc-alkaline to alkaline magmatism ends the late (570-545Ma) Neoproterozoic time. It is linked to precious metal (Au-Ag) deposits. Preliminary Sr-Nd isotopic data for the 595-570 Ma plutonic event and 570-545 Ma volcanic episode from Saghro-Imiter indicate the same low $^{87}Sr/^{86}Sr$ (0.702 to 0.706) and $^{143}Nd/^{144}Nd$ (0.5116 to 0.5119) initial ratios, attesting to mixing between mantle and lower crust sources. This relatively primitive Sr signature is also attested by a low $^{187}Os/^{188}Os$ ratio obtained on pyrites from the rhyolitic domes, dykes and silver mineralization. The calculated Nd model ages on 595-570Ma old granites and 570-545 Ma old felsic volcanics rocks fall in a rather restricted range from 1561 to 1161 Ma suggesting an unique source of middle Proterozoic age for these two episodes of felsic magmatism. A similar middle Proterozoic source is also invoked for the felsic volcanism of the Sirwa window (Thomas et al. 2002).

b. Alkaline volcanism at 531±5Ma, which post-dates the late Neoproterozoic magmatism and heralds the starts of the Palæozoic times.

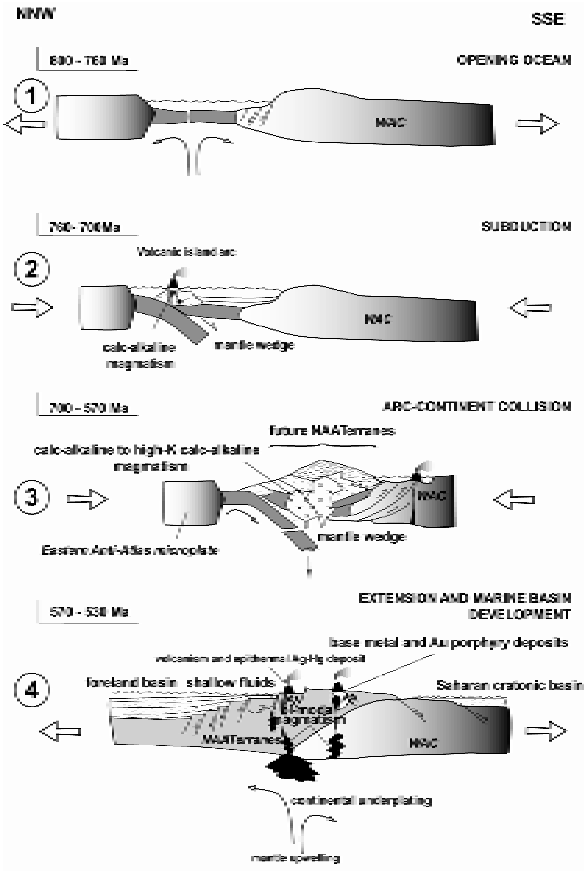

Figure 2: Geodynamical restoration of the Pan-African Anti-Atlas belt at the northern limit of the WAC

4 Conclusion: Imiter as a Precambrian analogue to modern epithermal deposits

An active margin is developed during the stage 3 of the evolution described above. The 570-530 Ma stage 4 characterizes the transition to a passive continental margin coupled with extensional tectonics and the development of marine basins to the north and the Saharan cratonic basin to the south. During this period, magmatism and metallogenic activity have a long common history (e.g. felsic volcanism and the Ag-Hg giant deposit of Imiter: Cheilletz, 2002; Levresse et al. 2004). They have mantellike and *pro parte* infracrustal signatures. Thus, large volumes of juvenile materials, precious metals and chalcophile elements are added to the continental crust. The post-collisional features, related extensive high-K calc-alkaline magmatism, and marine basin development, together indicate high heat flow contribution due to continental underplating and/or mantle upwelling. This geodynamic control is particularly fruitful for the development of superficial hydrothermal mineralization as epithermal or base metal porphyry deposits (Cheilletz et al. 2002). Moreover, huge metal transfers suggest the existence of verticals drains able to mobilize the deepest parts of the lithosphere. This model which involves a large part of the lower crust and the mantle, is in opposition with the re-mobilization model previously elaborated to explain the origin of giant precious metal deposits, such as Imiter, from local superficial convective cells (Leistel and Qadrouci, 1991).

Acknowledgments

This study was supported by several scientific cooperation grants to A.C. and D.G. from the Reminex-SMI-Managem Group (Morocco) and the Ministry of Industry (France), # 98 2 24 00 30 and 00 224 0002. O. Ennaciri, is thanked for assistance during field work. Technical assistance from E. Deloule, M. Champenois, D. Mangin and C. Rollion-Bard (sulphur isotope ion probe analyses), B. Marty, L. Zimmermann (Ne/He), and L. Reisberg, C. Zimmermann (Re/Os, Sr/Nd) is gratefully acknowledged.

References

Cheilletz A, Levresse G, Gasquet D, Azizi Samir MR, Zyadi R., Archibald DA (2002) The Imiter epithermal deposit (Morocco): new petrographic, microtectonic and geochronological data. Importance of the Precambrian-Cambrian transition for major precious metals deposits in the Anti-Atlas. Mineralium Deposita 37: 772-781

Ducrot J, Lancelot JR (1977) Problème de la limite Précambrien-Cambrien: étude radiochronologique par méthode U-Pb sur zircon du Jbel Bobo (Anti-Atlas marocain). Can. J. Earth Science, 14: 2771-2777

Hefferan KP, Admou H, Hilal R, Karson JA, Saquaque A, Juteau T, Bohn M, Samson SD, Kornprobst J (2002) Proterozoic blueschist-bearing mélange in the Anti-Atlas mountains, Morocco. Precambrian Res, 118: 179-194

Ennih N, Liégeois JP (2001) The Moroccan Anti-Atlas: the West African craton passive margin with limited Pan-African activity. implications for the northern limit of the craton. Precambrian Res, 112: 289-302

Fekkak A, Pouclet A., Ouguir H, Ouazzani H, Badra L, Gasquet D (2001) Géochimie signification géo-tectonique des volcanites du Cryogénien inférieur du Saghro (Anti-Atlas oriental, Maroc). Geodinamica Acta 14/6: 373-385

Hedenquist JW, Arribas RA, Gonzalez-Urien E (2000) Exploration for epithermal gold deposits. Rev. Economic Geology, 13: 245-277

Leistel JM, Qadrouci A (1991) Le gisement argentifère d'Imiter (protérozoïque supérieur de l'Anti-Atlas, Maroc). Contrôles des minéralisations, hypothèse génétique et perspectives pour l'exploration. - Chron. Rech. Min, 502: 5-22

Levresse G (2001) Contribution à l'établissement d'un modèle génétique des gisements d'Imiter (Ag-Hg) Bou Madine (Pb-Zn-Cu-Au) et Bou Azzer (Co-Ni-As-Au-Ag) dans l'Anti-Atlas marocain. - Unpublished thesis, Univ. INPL-Nancy, 191

Levresse L, Cheilletz A, Gasquet D, Reisberg L, Deloule E, Marty B, Kyser K (2004) Osmium, sulphur, and helium isotopic results from the giant Neoproterozoic epithermal Imiter silver deposit, Morocco: evidence for a mantle source. - Chemical Geology, 207: 59-79

Mifdal A, Peucat JJ (1985) Datations U/Pb et Rb/Sr du volcanisme acide de l'Anti-Atlas marocain et du socle sous-jacent dans la région de Ouarzazate. Apport au problème de la limite Précambrien-Cambrien. Sci. Géol. Bull, 38: 185-200

Samson SD, Inglis JD, D'Lemos RS, Admou H, Blichert-Toft J, Hefferan K (2003) U-Pb age, geochemistry, and Nd-Hf isotopic composition of Neoproterozoic plagiogranites within the Tasriwine Ophiolite, Siroua inlier, Anti-Atlas orogen, Morocco. Abstract, First meeting of IGCP

Saquaque A, Benharref M, Abia H, Mrini Z, Reuber I, Karson J (1992) Evidence for a Pan-African volcanic arc and wrench fault tectonics in the Jbel Saghro, Anti-Atlas, Morocco. Geologische Rundschau 81: 1-13

Thomas RJ, Chevallier LP, Gresse PG, Harmer RE, Eglington BM, Armstrong RA, de Beer CH, Martini JEJ, de Kock GS, Macey PH, Ingram BA (2002) Precambrian evolution of the Sirwa Window, Anti-Atlas Orogen, Morocco. Precambrian Res. 118: 1-57

Formation of giant Ni-Cu sulfide deposits in dynamic magma conduits

C. Li, E.M. Ripley
Department of Geological Sciences, Indiana University, Bloomington, IN 47401, USA

Abstract. Key factors for the formation of world-class magmatic Ni-Cu deposits include sulfide saturation in magma, large magma/sulfide ratio and accumulation of sufficient quantity of immiscible sulfide liquid in limited localities. Results from two well-known Ni-Cu deposits in the world, the Talnakh deposits in Siberia, Russia and the Voisey's Bay Deposit in Labrador, Canada, indicate that a dynamic magma conduit in the upper crust is an ideal environment in which these factors can prevail.

Keywords. Ni-Cu deposits, magma conduit, Talnakh, Voisey's Bay

1 Introduction

Except for the Sudbury Ni-Cu deposits that are related to an unique meteorite impact event, many other giant Ni-Cu deposits related to continental magmatism occur in dynamic magma conduit systems at upper crustal levels. This is not surprising because a dynamic conduit in the upper crust is an ideal environment for assimilation of S-rich country rocks, accumulation of immiscible sulfide liquids in hydralic traps and upgrading of metals in the sulfide liquids by new pulses of fertile magma (i.e. large resultant magma/sulfide ratio). The best examples of world-class Ni-Cu deposits that occur in dynamic magma conduits are the Talnakh Ni-Cu deposits in Siberia, Russia (Li et al. 2003) and the Voisey's Bay Ni-Cu deposit in Labrador, Canada (Li et al. 2001).

2 Results from Talnakh

At Talnakh, the host intrusions consists of multiple rock units. Major sulfide mineralization is closely associated with the basal gabbro unit. Different rock units in the intrusion are not related to each other by in situ differentiation, but rather by different pulses of magma sucessively flowing through the conduit. Evidence for this interpretation includes the discontinuity of Ni concentration in olivine inclusions (1000 versus 2000 ppm Ni with similar Fo), in plagioclase and pyroxene, and the contrasting S isotopic compositions of different rock units ($\delta^{34}S$ values of 1.5 versus up to 14 per mil). The ^{34}S–enriched sulfur in the intrusions is thought to have been introduced via circulating fluids that transported sulfur from evaporites in the underlying sedimentary sequence to the magma in the conduit. The immiscible sulfide liquids that segregated during sulfur contamination settled down in the wider parts of the conduit as the magma continued to ascend. Successive pulses of new magma entered the conduit, reacted with the early sulfide and displaced much of the early magma in the conduit.

3 Results from Voisey's Bay

At Voisey's Bay (Figs. 1, 2 and 3), important sulfide accumulations are associated with a breccia unit that contains abundant paragneiss xenoliths in the base of an upper chamber, as well as the feeder dyke connecting the upper chamber to a lower chamber.The feeder dyke of the Voisey's Bay intrusion consists of multiple rock units that cannot be related to each other by in situ differentiation of a single magma but are most consistent with emplacement of multiple pulses of magma from the lower chamber. Variations of S isotopic composition and metal concentrations in the sulfide ores suggest that sulfide saturation was initiated by contamination with S-rich paragneiss

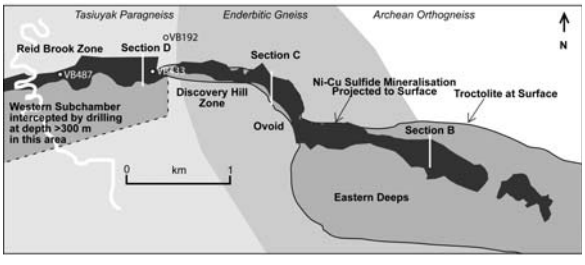

Figure 1: Plan view of the Voisey's Bay intrusion

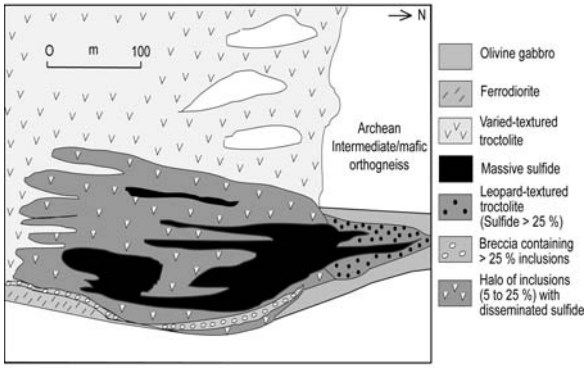

Figure 2: Simplified section through the lower part of the Eastern Deeps

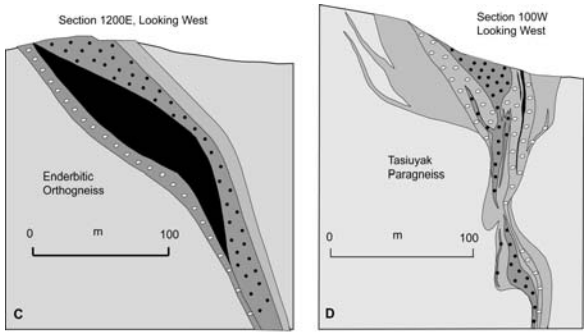

Figure 3: Cross-sections of the feeder dyke of the Voisey's Bay intrusion

in the lower chamber. The immiscible sulfide droplets were brought up by the fractionated magma from the lower chamber along the conduit leading to the overlying chamber. The sulfide droplets became concentrated to form massive accumulations in the swellings of the conduit and at the entrance of the conduit to the upper chamber. Successive surges of more primitive magma through the conduit reacted with some early sulfides and thus increased the metal tenors in the sulfides.

References

Li C, Ripley EM, Naldrett AJ (2003) Compositional variations of olivine and sulfur isotopes in the Noril'sk and Talnakh intrusions, Siberia: implications for ore-forming processes in dynamic magma conduits. Economic Geology 98: 69-86

Li C, Ripley, EM, Naldrett AJ (2001) Critical factors for the formation of a nickel-copper deposit in an evolved magma system: lessons from a comparison of the Pants Lake and Voisey's Bay sulfide occurrences in Labrador, Canada. Mineral Deposit 36: 85-92

Synchronous vertical and horizontal tectonism during the late stage of Archean cratonization: An important process in gold mineralization?

Shoufa Lin, Andrew Parmenter, Jen Parks
Department of Earth Sciences, University of Waterloo, Waterloo, Ontario, N2L 3G1, Canada

Abstract. Both vertical and horizontal tectonism played an important role in Archean tectonic evolution. These two processes have independent driving forces and should not be mutually exclusive. In the Superior Province in Canada, there is convincing evidence for synchronous vertical and horizontal tectonism at the late stages of Archean cratonization, and horizontal shearing (a result of horizontal tectonism) is concentrated in synclinal keels (a result of vertical tectonism). The Timiskaming-type sedimentary rocks were deposited in the keels during this process. The synclinal keel-shear zone association provided a link between the upper crust and the lower crust or mantle, and might have served as a conduit for mineralizing fluids and magma that were generated in the crust and/or mantle during the process. Such a process in the late stage of Archean cratonization can readily explain the common association of gold deposits with greenstone belts in synclinal keels, shear zones, late felsic to intermediate intrusions and Timiskaming-type sedimentary rocks.

Keywords. Vertical tectonics, horizontal tectonics, gold mineralization, Archean, cratonization, Superior Province

1 Introduction

Two contrasting processes have been proposed for Archean tectonics: "vertical tectonism" driven by density inversion and "horizontal tectonism" driven by regional horizontal tectonic stress. Many Archean geologists now accept that processes similar to present-day plate tectonics (a form of horizontal tectonism) existed in some form in the Archean, particularly in the Neoarchean (van Kranendonk 2004 and references therein). On the other hand, detailed field-based studies have continued to document convincing evidence for vertical tectonism (van Kranendonk et al. 2004 and references therein). Considering that the driving forces for vertical and horizontal tectonism are independent, the two processes should not be mutually exclusive. It is therefore conceivable that at some point in time and space, the two processes might operate synchronously (and potentially interactively), although direct (as opposed to circumstantial) evidence has rarely been reported. In this paper, we summarize evidence for synchronous vertical and horizontal tectonism in the Superior Province in Canada and suggest that such a process in the late stage of cratonization played a very important role in gold mineralization.

2 Synchronous vertical and horizontal tectonism in the northwestern Superior Province

As part of a multidisciplinary program to better understand the tectonic evolution of the Superior Province, detailed studies have been conducted in major greenstone belts in the northwestern Superior Province, including the Gods Lake, Knee Lake, Carrot River, Cross Lake and Island Lake belts (Fig. 1a). The results show that both horizontal tectonism (in a form similar to present-day plate tectonics) and vertical tectonism have played a significant role in the tectonic evolution of this part of the Superior Province, and there is convincing evidence for synchronous vertical and horizontal tectonism at the late stages of cratonization. The geological evolution of the Cross Lake greenstone belt is typical of the greenstone belts in the area and is described here as an example (based on Parmenter 2002).

Supracrustal rocks of the Cross Lake greenstone belt consist of two main groups: the >2760 Ma Pipestone Lake Group and the unconformably overlying <2704 Ma Cross Lake Group. The former consists of mafic volcanic and minor sedimentary rocks, and the latter is a fining-upward fluvial to marine sedimentary sequence consisting of polymictic conglomerates, sandstones, argillite-rich horizons and turbidites.

Detailed structural analysis revealed four major generations (G1-G4) of structures in the Pipestone Lake Group and three generations (G2-G4) in the Cross Lake Group. Clasts in the latter contains a pre-depositional foliation (interpreted as S1). The main features of the four generations of structures and their tectonic interpretations are schematically shown in Figure 2. The nature of G1 is enigmatic due to poor preservation. It might represent the major phase of collisional deformation, thrusting, and greenstone belt amalgamation proposed based on data from other greenstone belts in the area. G2 is characterized by the development of a belt-scale synclinorium cored by supracrustal rocks and flanked by granitoid domes (Fig. 2b-c). During G3, large-scale shear zones were developed along supracrustal-pluton contacts, under amphibolite-facies conditions. Movement along these shear zones was oblique with dominant pluton-side-up dip-slip component and minor dextral strike-slip component (Fig. 2d). During G4 deformation, these shear zones were reactivated under greenschist

facies conditions and exhibited similar kinematics as G3 (Fig. 2e). Although the pluton-side-up dip-slip movement component continued, dextral strike-slip movement component was much more significant.

The G2 structures and the dip-slip components of G3-G4 are best explained by gravity-driven vertical tectonism, with subsidence of the dense volcanic sequence (sagduction) and concurrent diapirism of underlying sialic material (Fig. 2b-e). On the other hand, the dextral strike-slip components during G3-G4 are consistent throughout the Superior Province and are best explained by horizontal tectonism related to regional dextral transpression. During most part of the G2-G4 deformation history,vertical and horizontal tectonism was synchronous. During G2 and at least the early stage of G3, vertical tectonism was dominant, whereas during G4 horizontal tectonism prevailed. These relationships indicate that G2-G4 may represent a transition from dominantly vertical tectonism, in the form of diapirism and sagduction, to dominantly horizontal tectonism, in the form of regional transcurrent shearing.

The overall map pattern of the northwestern Superior Province (Fig. 1a-b) is consistent with the presence of both vertical and horizontal tectonism. In areas where vertical tectonism is dominant, the granitoid domes tend to be rounded with greenstone belts occurring in-between in synclinal keels, for example, in the interior of the Sachigo subprovince (lower right corner of Fig. 1a-b). In areas where horizontal tectonism is more significant, both the domes and the greenstone belts are elongated and the general geometry is more "linear" (Fig. 1a-b). Deformation related to horizontal tectonism tends to be localized in shear zones coincident with elongated synclinal keels (Fig. 1a).

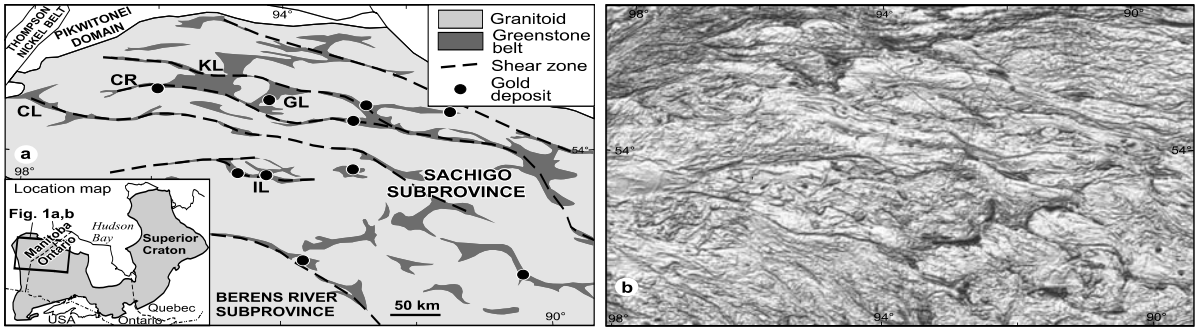

Figure 1: (a) Map showing the distribution of greenstone belts, granitoids and gold deposits and the general geometry of the northwestern Superior Province. (b) A shaded relief image of the total magnetic field of the same area. CR: Carrot River; CL: Cross Lake; GL: Gods Lake; IL: Island Lake; KL: Knee Lake. Magnetic map from the Geological Survey of Canada

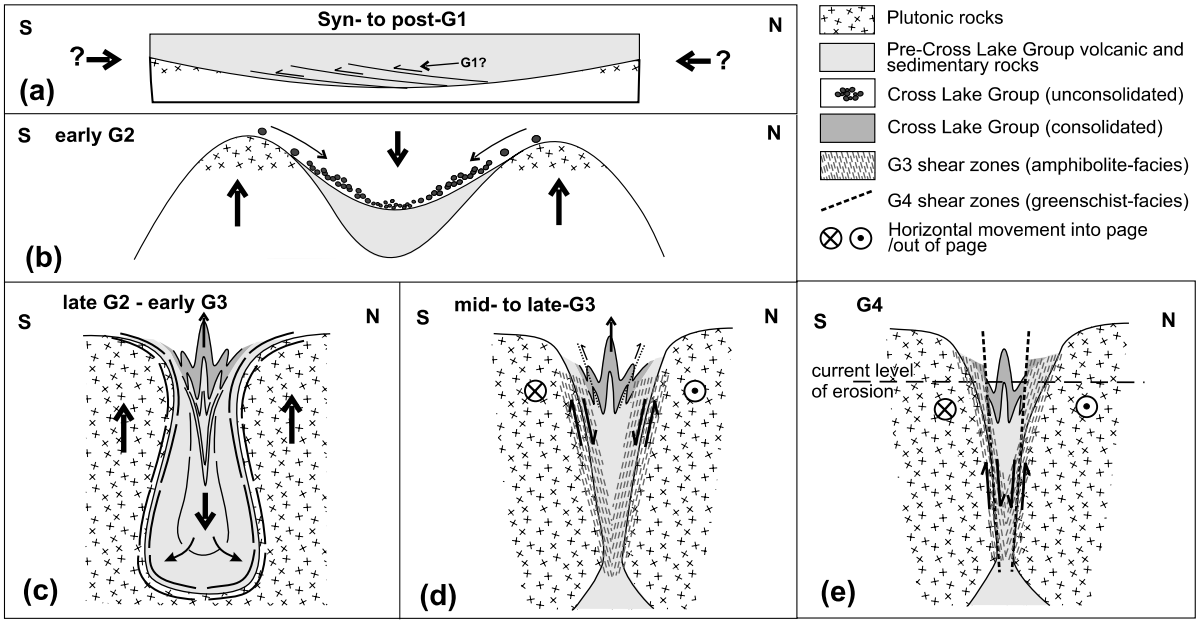

Figure 2: Schematic diagrams showing the structural evolution of the Cross Lake greenstone belt (modified from Parmenter 2002). See text for explanation. Note that movement along G3 and G4 shear zones in (d) and (e), respectively, have both dip-slip and strike-slip components, with the dip-slip component being dominant during G3 and the strike-slip component more important during G4. (c) is modified from Dixon and Summers (1983).

2.1 Deposition of Timiskaming-type sedimentary rocks during vertical tectonism

In many greenstone belts in the Superior Province (and other Archean cratons), a sequence of sedimentary rocks similar to the Cross Lake Group lie unconformably on older greenstone sequences. These "Timiskaming-type" sedimentary rocks show sedimentary features for a structurally controlled basin (Thurston and Chivers 1990). They are commonly spatially associated with, and have traditionally been interpreted as deposits in pull-apart basins genetically related to, late strike-slip shear zones (equivalents of G4 shear zones here). However, data from various greenstone belts in the northwestern Superior Province indicate that basin development and sedimentation were most likely penecontemporaneous with G2 and the onset of vertical tectonism (Fig. 2b; Parmenter 2002). Greenstone-belt subsidence (sagduction), concurrent with diapirism and uplift, provides an ample mechanism for the development of tectonic basins in the synclinal keels between the flanking granitoid domes. A similar interpretation has been proposed for similar sedimentary sequences in the east Pilbara in Australia (e.g. van Kranendonk et al. 2004) and in the Slave Province in Canada (Bleeker 2002). Parks (unpublished data) dated ~400 detrital zircon grains from samples collected at various stratigraphic positions of such a sedimentary sequence in the Island Lake greenstone belt (Fig. 1a) by the LA-MC-ICP-MS method. The results indicate an unroofing pattern in the flanking domes that is consistent with such an interpretation.

3 Implications for Archean gold mineralization

Archean gold deposits dominantly occur in greenstone belts and are spatially associated with major deformation zones that are believed to have served as conduits for mineralizing fluids (e.g. Fig. 1a). There is also a close spatial relationship of gold deposits with post-volcanic, syn- to late-tectonic, felsic to intermediate intrusive rocks and Timiskaming-type sedimentary rocks (Colvine et al. 1988 and references therein). In addition to displaying a spatial association with gold deposits, these syn- to late-tectonic intrusions and sedimentary rocks seem to occur more frequently or dominantly in the deformation zones that host gold mineralization. The latter indicates that their emplacement/deposition might also have been controlled by the deformation zones (Colvine et al. 1988 and references therein). In some deposits, it can be demonstrated that there is a genetic link between these intrusions and gold mineralization. In others, such a direct link cannot be demonstrated and may not exist.

Synchronous vertical and horizontal tectonism at the late stages of cratonization can readily explain the above spatial associations and potential genetic links, and is potentially a very important process in Archean gold mineralization. At the beginning of the process, the greenstone sequence overlaid and insulated the sialic crust, while the crust was likely being "underplated" or intruded by mantle-derived magmas (see Colvine et al. 1988 and references therein; Beakhouse 2003). As a result, the crust below the greenstone sequence was significantly heated and its viscosity significantly lowered creating a gravitational instability and initiating vertical tectonism. This resulted in subsidence of the dense volcanic sequence in the synclinal keels concurrent with diapirism of underlying sialic material in the flanking domes. The Timiskaming-type sedimentary rocks were deposited in the synclinal keels, unconformably overlying the volcanic sequence. The synclinal keels, with steep contacts, are favourable locations for localized horizontal shearing associated with regional transpression, resulting in elongated synclinal keels in which the supracrustal rocks are strongly deformed and foliated. These rocks are thus much more permeable than the granitoids in the flanking domes. Meanwhile, mineralizing fluids and felsic to intermediate magma were generated in the crust and/or upper mantle. They followed these deformation zones up to the upper crust, forming gold deposits and intrusions in the supracrustal rocks, including in the Timiskaming-type sedimentary rocks and in the intrusions emplaced during the process. An important feature of this model is that the mineralizing fluids and the fluid conduits are genetically related, both being generated as a result of Archean cratonization.

3.1 Potential examples

The features summarized above are shared by many gold deposits in both the northwestern and southern Superior Province, implying a common tectonic process for gold mineralization. The spatial association of Timiskaming-type sedimentary basins with major auriferous shear zones such as the Destor-Porcupine fault and the Cadillac-Larder Lake fault is well documented.

The Dome Mine is a potential example of gold deposits formed during synchronous vertical and horizontal tectonism. The deposit is spatially associated with the Dome Fault (a branch of the Destor-Porcupine fault), quartz porphyry intrusions and the Timiskaming Group (conglomerate and slate; Fig. 3). The last unconformably overlies older metavolcanic and metasedimentary rocks, including metabasalt (greenstones). The supracrustal rocks are folded and sheared, and the geometry of the conglomerate layer defines an overall syncline, with a second-order central anticline flanked by two synclines (Fig. 3). The overall kinematics and geometry are very similar to that of Figure 2c-e. Gold mineralization mainly occurs near the crest of the anticline, in stockworks in the conglomerate and in zones parallel to the foliation and lithological contacts in the greenstones. It occurred during folding and shearing, and its location is apparently con-

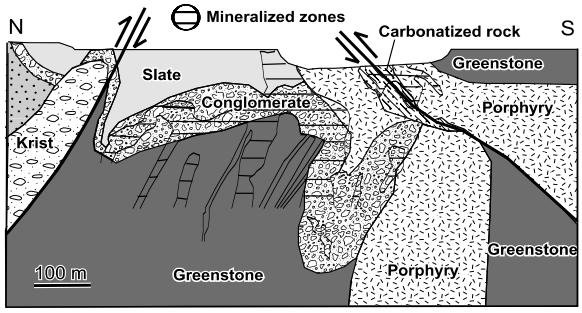

Figure 3: A section of the Dome mine, Timmins, Ontario (modified from a field trip handout supplied by, and published with permission of, the Dome Mine). See text for discussion.

trolled by the (permeable) conglomerate and the geometry of the anticline. The steep foliation and lithological contacts might have served as fluid conduits, the conglomerate as a fluid trap and the slate (shale) as an impermeable cap.

The Hemlo gold deposit is another potential example. Here, gold mineralization, Timiskaming-type sedimentation, shear zone deformation and late-tectonic magmatism are spatially associated and were synchronous (Lin 2001). They occurred at ca. 2677 Ma, probably synchronous with diapirism in a major granitoid dome to the south.

References

Beakhouse GP (2003) A magmatic hydrothermal model for Arcean lode gold deposits: A working hypothsis (poster). http://www.mndm.gov.on.ca/mndm/mines/ogs/posters/OEGS_2003/BeakhousePoster5.pdf

Bleeker W (2002) Archean tectonics: a review, with illustration from the Slave craton. In: Fowler CMR et al. (eds), The Early Earth: Physical, Chemical and Biological Development, Geological Society [London] Special Publication 199, : 151-181

Colvine AC, Fyon JA, Heather KB, Marmont S, Smith PM, Toop DG (1988) Archean Lode Gold Deposits in Ontario. Ontario Geological Survey Miscellaneous Paper 139

Characteristics of isotope geochemistry of deep mantle constraints on metallization in alkali-enriched porphyry systems

Liu Xianfan, Lu Qiuxia, Long Xunrong, Tao Zhuan, Song Xiangfeng
Chengdu University of Technology, Chengdu, Sichuan, China

Abstract. Numerous well-developed alkali-rich porphyry polymetallic deposits occur in the eastern Jinshajiang-Ailaoshan fracture, western Yunnan. These alkali-rich porphyries of this region are known to contain mantle xenoliths. Pb-Si-Sr-Nd isotope geochemistry suggests that silica-rich mineralizing fluids tend to replace and alter the country rocks and rockbodies, and to be contaminated with crustal rocks, thus forming ore deposits during the generation of alkalic magma. The mineralizing process of silica-rich fluids is essentially a continuation of mantle fluid metasomatism during mineralizing processes in the crust. The action of the mantle fluids is not only an internal constraint to widespread Cenozoic mineralization but also an important geochemical constraint for the formation of large and superlarge deposits in western Yunnan, China.

Keywords. Mantle fluid process, alkalic porphyry, xenolith, isotope geochemistry, mineralization

1 Introduction

Western Yunnan, close to the eastern margin of the Qinghai-Tibetan plateau, is a Cenozoic intracontinental deformed region with well-developed polymetallic mineralization associated intimately with tectonics, juvenile magmas and fluids. Some of the most important deposits of this region are alkali-enriched porphyry deposits located in the eastern Jinshajiang-Ailaoshan fracture belt. These include the Machangqing Cu-Mo-Au deposit and Jingchangqing Au deposit in Xiangyun, and the Bei'ya Pb-Au and Yao'an Pb-Ag-Au deposits in Heqing. We have studied the Pb-Si-Sr-Nd isotopic compositions of the above four deposits as well as the ultramafic mantle xenoliths from aegirinite syenite porphyries occurring in Liuhe Village, Heqing County, Yunnan Province. Sodium-rich microlite-glass is located in the ultramafic xenoliths (Liu et al. 2000). Our study shows that the glass originated from mantle fluid metasomatism. In addition, the mineralogical features of the xenoliths show that these xenoliths are characterized by upper mantle rocks which have been modified to a certain extent by enriched mantle fluid metasomatism in the mantle environment, at low-degrees of partial melting (Liu et al. 2003).

Generally, the different type ore deposits, which are all structurally controlled, and are related to alkali-enriched magma and mantle fluid processes, have the following geological features: ore bodies occur as veins or disseminated veinlets in porphyries, contact zones between porphyries and country rocks, and country rocks. As the ore formation temperature changes from high?medium high ?medium low?low, the ore type varies from Mo? Cu-Mo? Pb-Zn-Fe? Au-Ag. Thus, there is a sequential metallogenic effect from intrusive through contact zones to country rocks, with high-temperature metallization changing to low- temperature (Liu et al. 2002). This suggests that the country rocks can partly provide ore materials, in a fluid process, but they are not the main source. Alkali-rich magma and associated upper-mantle fluids, which moved along large-scale deep faults, are the main sources of ore materials for the alkali-rich porphyry deposits.

2 Lead isotope geochemistry

As can be seen in Figure 1 and Figure 2, the plots are highly scattered, suggesting that the alkali-rich porphyries and the xenoliths they carried have a very similar compositions of lead isotopes, and that the alkalic magma and silica-rich ore-fluid had an initial and principal com-

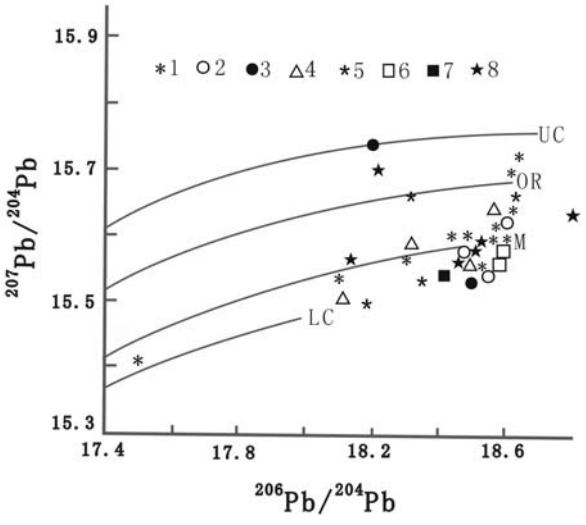

Figure 1: Lead isotope in alkali-rich porphyries, deep xenoliths and characteristic minerals 1.porphyry; 2.feldspar phenocrysts; 3.silicified quartz; 4. pyrite; 5. galena; 6. specularite; 7. altered porphyry; 8. deep xenoliths; UC:upper crust; OR:orogenic belt; M:mantle; LC:lower crust. (based on Zartman, et al. 1981)

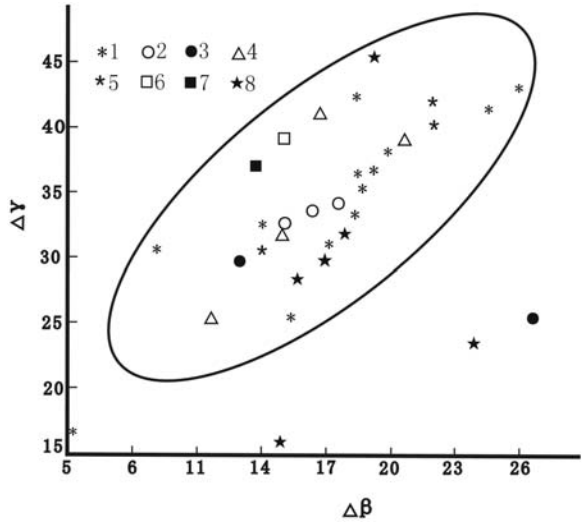

Figure 2: Δγ–Δβ of lead isotope in alkali-rich porphyries, deep xenoliths and characteristic minerals. 1. legends 1~8 is identical to one fig.1; 2. Δβ=(β–βM)/βM×1000; 3. Δγ=(γ–γM)/ γM×1000; 4. β=207Pb/204Pb of samples; 5. γ=208Pb/204Pb of samples; 6. βM=208Pb/204Pb of mantle=15.33; 7. γM=208Pb/204Pb of mantle=37.47 8.limits trap: mixed lead of homogenization between crust and mantle (from Zhu Bingquan, et al.1989)

mon source of lead, which originated from the mantle. But crustal or strata lead may have been incorporated into the alkalic magma and the mineralizing fluid as they ascended along fault systems. Thus lead of different origins were well mixed during orogeny resulting in the shifting of the data points toward OR or even UC.

3 Silicon isotope geochemistry

The silicon isotope composition of characteristic rocks and minerals related to mineralization for the typical deposits in this area, as shown by Table 1 and Figure 3, indicate following features: The silicon istope compositions vary greatly for diffirent type and occurrence of samples. Based on the dynamic fractionation principle of silicon isotopes, our study shows that silicified quartz and hemimorphite and pure quartz enclosures could represent silica-rich mineralizing fluids; lamprophyre, alkali-rich porphyries and the xenoliths they carried, feldspar and quartz phenocryst could represent alkali-rich magma. Both $\delta^{30}Si$ values are quite different, and they do not vary in different layers or bodies. The former is –0.1‰~–2.4‰, with the latter 0.0‰~0.4‰. In addition, Ca-Cr-pyralspite related to mineralization and mineralized rocks (containing porphyry and sandstone) could represent the products of interaction between silica-rich mineralizing fluid and crustal rocks. Their $\delta^{30}Si$ value are 0.3‰~0.7‰. However, silicon isotope compositions vary greatly in different layers and lithologies (0.2‰~0.7‰).

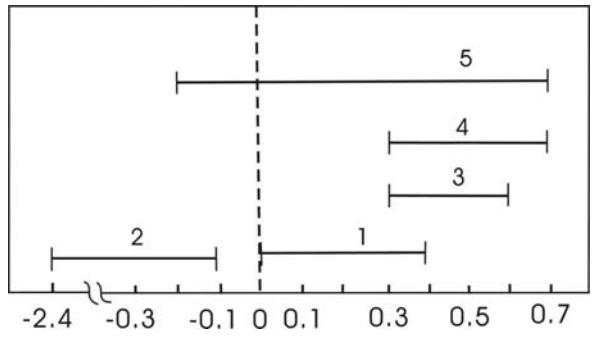

Figure 3: Diagram showing the distribution of silicon isotope compositions of the alkali-rich porphyry, hypo xenoliths, strata country rocks and characteristic minerals from the typical deposits in the study area. 1.alkali-rich porphyry and lamprophyre and deep xenoliths; 2.silicified quartz, hemimorphite and pure quartz enclosure; 3.mineralization porphyry and sandstone; 4.Ca-Cr-pyralspite related to mineralization; 5.strata country rocks (O_1,T_1, K_2)

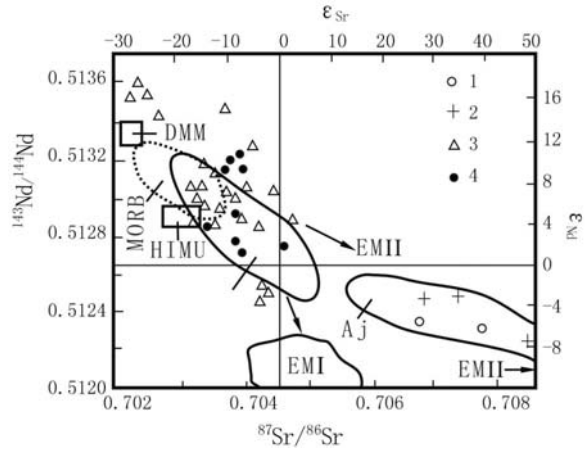

Figure 4: Diagram of Sr-Nd isotope of the alkali-rich porphyries and deep xenoliths they carried. 1. syenite porphyry (the host), Liuhe; 2. deep senoliths in the syenite porphyry, Lihue (from Deng Wanming, et al. 1998); 3. data from Tatsumoto, et al. 1992 and Song, et al. 1988; 4. data from Liu Congqiang, et al., 1996; The Aj field: Alkalic porphyries and alkaline volcanic rocks in western Yunnan (from Deng Wanming, et al. 1998 and Zhang Yuquan, et al., 1997); The Ad field: Cenozoic basalts in eastern China (from Liu Congqiang, et al. 1996;); the four end members of mantle are based on Hart, 1984; MORB show mid-ocean ridge basalts

The above distribution of silicon isotope compositions may suggest that the silica-rich mineralizing fluids, which are characterized by low negative silicon isotope values with almost no dynamic fractionation, have the nature of primary mantle, and that alkali-rich magma, which is characterized by positive silicon isotope values after quite dynamic fractionation, was derived from a source in enriched namtle formed by mantle metasomatism. The $\delta^{30}Si$ values (0.3‰~0.7‰) of Ca-Cr-pyalspite and mineralized rocks are higher than those (0.0‰~0.4‰) of representation alkali-rich magma. This suggests that the

Table 1: Composition of silicon isotope of the alkali-rich porphyry, deep xenoliths, strata country rocks and characteristic minerals from the representative deposits in the study area

Ser. No	Sample No	Rock or mineral	δ^{30}Si‰	Sample occurrence
1	MM-9-2	quartz phenocryst	0.1	biotite quartz monzo-porphyry
2	MM-32-1	silicified quartz	−0.1	Cu-Mo-bearing quartz vein
3	MM-30	lamprophyre dike	0.4	in monzo-porphyry
4	MM-15	mineralization sandstone	0.4	Au-bearing strata country rock (O_1)
5	MM-16	sandstone	−0.2	strata country rock(O_1)
6	HL-81	aegirinite syenite-porphyry	0.0	deep xenoliths-bearing host rock
7	HL-71-4	Ca-Cr-phyralspite	0.7	in garnet-diopsidite of deep xenoliths, as polycrystal aggregates
8	HL-72	amphibolized phlogopite-garnet-diopsidite	0.1	deep xenolith in aegirinite syenite-porphyry
9	HL-76	amphibolized biolite-granulite	0.0	xenolith in aegirinite syenite-porphyry
10	HL-79	pure quartz enclosure	−0.3	xenolith in aegirinite syenite-porphyry
11	A-328-2	feldspar phenocryst	0.4	in syenite-porphyry
12	HB-55-3	Hemimophite	−2.4	in Pb-Zn-bearing altered rock
13	HB-56-7	Ca-Cr-pyralspite	0.3	in skarnization porphyry
14	HB-56-3	Siltstone	0.7	strata country rock (T_1)
15	YAJ-8	syenite-porphyry	0.0	host rock-body from Yao'an
16	YAJ-13	mineralization porphyry	0.3	Au-bearing altered porphyry
17	YAJ-27	mineralization sandstone	0.5	Au-bearing altered sandstone(K_2)
18	YAJ-29	sandstone	−0.2	strata country rock (K_2)
19	XJ-37-2	Quartz phenocryst	0.0	in quartz syenite-porphyry
20	XJ-39-1	Silicified quartz	−0.2	Au-bearing quartz vein

Note: Samples 1~5 from the Machangqing deposit; Samples 6~10 from the Liuhe intrusion in Heqing Country; Samples 11~14 from the Beiya deposit; Samples 15~18 from the Yaoan deposit; Samples 19~20 from the Jinchangqing deposit; Analyzed by Wan Defang of the Institute of Mineral Deposit, Chinese Academy of Geological Sciences (analytic precision>0.1‰).

former have more intense silicon isotopic dynamic fractionation than the latter, and the nature of the silica is changed from silica-rich mineralizing fluid to porphyry and to country rocks. Such a process of silica-rich mineralizing fluid is essentially the continuance of the metasomatism of mantle fluids during crustal mineralization.

4 Sr-Nd isotope geochemistry

The distribution of Sr-Nd isotope compositions of the alkali-rich porphyries and the deep xenoliths they carried basically coincide (Fig. 4), and they fall into the field of EM, showing a much stronger tendency toward the enriched mantle than xenoliths in basalts from eastern China. Tatsumoto, et al. (1992) and Liu et al. (1996) considered that EMI and EMII end members of enriched mantle existed in continuental lithospheric mantle in eastern China based on the Sr-Nd isotopes study of Hannuoba basalts and deep xenoliths they carried. This may suggest that mantle metasomatism in continental lithosphere was developed to a greater extent in western China than in eastern China. It is may be of fundamental importance to the understanding of why Cenozoic than in mineralization in western China is generally better developed than in the eastern part of the country.

5 Conclusion

As is clear from the above discussions and the study of mineralogy (Liu Xianfan et al. 2003) and trace element geochemistry (Liu et al. 2002) of deep xenoliths in the area, the deep xenoliths are very similar to their host rocks in a lot of aspects. In the present state of knowledge, this phenomenon may be explained by: (1) The xenoliths have been highly reworked by the alkalic magma into which they were trapped; (2) the xenoliths have been replaced by a fluid derived from the asthenosphere prior to being trapped by the alkalic magma; and (3) the xenoliths of garnet-diopsidite, which are of mantle derivation and show character of fluid metasomatism, are representative of an alkalic magmatic event. Compehensive studies have shown that the second and third explanations tell important features of deep mantle control in metallization for alkalic magma. It is reasonable especially as evidenced by the

mantle microcline glass from deep xenoliths[1]. Such asthenosphere-derived fluid, as regarded by Van der Laan (1994), may serve as an ideal agent for the transport of minor and ore-forming elements, and result in mantle metasomatism. It is the mantle fluid metasomatism that leads to significant enrichment of incompatible elements such as Si, Al, Na, K and ore forming elements. It also results in the transition of the Sr-Nd isotopic characters from a type of depleted mantle to that the enriched mantle, and cause the effect of series mineralization from rockbody?country rock corresponding high?low temperature. It is the action of fluids that is the internal constraint on the widespread cenozoic mineralization and an important geochemical background for the formation of large and super-large deposits. The complicated mineralization phenomena of Cenozoic era in Sanjiang region of western Yunnan may be better understood and interpreted by the study in mantle fluid metasomatism.

Acknowledgements

The study was supported by the project of National Natural Science Foundation of China (Grant No: 40473027).

References

Deng WM, Huang X, Zhong DL (1998) Alkali-rich porphyry and its relation with intraplate deformation of northern part of Jinsha River belt in western Yunnan, China, Science in China (Series D), 41(3): 297

Ding TP, Jiang SY, Wan DF, Li YH (1994) Silicon isotope geochemistry. Beijing: Geological Publishing House, 50~63 (in Chinese)

Hart, SR (1984) A Large-scale isotope anomaly in the southern hemisphere mantle, Nature, 309:753~757

Liu CQ, Xie GH, Zheng TZ (1996) Geochemistry of REE ans Sr, Nd isotopes of mantle xenoliths in Hannuoba basalt. Acta Petrologica Sinica, 12(3):382~389

Liu XF, Liu JD, Zhang CJ (2002). Effect of Series Mineralization of Mantle Fluid Metasomatism. Mineral Deposits,21: 1002~1004 (in Chinese)

Liu XF, Liu JD, Zhang CJ (2003) Study of elements geochemistry characteristics for ultramafic deep xenoliths in alkali-rich porphyry. Journal of Mineralogy and petrology, 23(3): 39~43 (in Chinese)

Liu XF, Yang ZX, Liu JD (2003) Mineralogical features of ultramafic deep xenoliths in alkali-rich porphyry. Geotectonica et Metallogenia 27(1~2): 81~90

Liu XF, Zhan XZ, Gao ZM (1999) Deep xenoliths in alkalic porhyry, Liuhe, Yunnan, and implications to petrogenesis of alkalic porphyry and associated mineralizations. Science in China (Series D), 42(6): 627~635 (in English)

Liu XF, Zhan XZ, Gao ZM (2000) Na-rich microlitegrass in deep xenoliths, Liuhe, Yunnan: discovery and implications. Journal of Geodynamics 29: 141~147

Song Y, Frey FA (1988). Geochemistry of peridotite xenoliths in basalt from Hannuoba, Eastern China: Implications for subcontinental mantle heterogeneity. Geochim. Cosmochim. Acta, 53: 97~113

Sun SS, Mcdonough W (1989) Chemical and isotopic systematics of oceanic basalts: implication for mantle composition and processes. Geol. Soc. Spec. Publ, 42: 313~345

Tatsumoto M, Basu AR, Huang WK (1992) Sr, Nd and Pb isotopes of ultramafic xenoliths in volcanic rocks of Eastern China: enriched components EMI and EMII in subcontinental lithosphere. Earth Planet Sci. Lett., 113: 107~128

Vander LSR (1994) MARID and mantle metasomatism. Mineralogical Magazine, 58A: 505~516

Zartman RE, Doe BR (1981) Plumbotectonics: The model. Tectono. Physics, 75: 135~162

Zhang YQ, Xie YW (1997) Geochronology of Ailaoshan-Jinshajiang alkali-rich intrusive rocks and their Sr and Nd isotopic characteristics. Science in China (Series D), 40(5): 524

Zhu BQ, Liu BL, Li XH (1989) Nd-Sr-Pb isotopic characteristics and the model of three compositions mixing-four systems recycle in continent and oceanic mantle. Science in China (Series B), 19(10): 1092~1102

The formation of a mantle-branch structure in western Shandong and its constraints on gold mineralization

Shuyin Niu, Aiqun Sun, Huabin Hu, Baode Wang, Chuanshi Xu
College of Resources, The Shijiazhuang University of Economics, 302 Huainan Road, Shijiazhuang 050031, China

Jingwen Mao
China University of Geosciences, 29 Xueyuan Road, Beijing 100083, China

Abstract. On the basis of regional strata, magmatic activity, ring and radial faults, gently dipping detachments, geophysical information and isotopic age, this paper discusses the characteristics of mantle-branch structure in western Shandong. According to the characteristics of ore-control structures, gold deposits in the Luxi mantle-branch structure are divided into ductile shear zone type and detachment-slip layer type deposits. The detachment-slip layers type deposit, including the Guilaizhuang gold deposit and Mofanggou gold deposit are significant economic types. The $\delta^{34}S$ values of pyrite associated with gold mineralization exhibit a narrow range of -0.71 to 2.99‰, implying that the sulfur was probably derived from the mantle or magma, whereas the $\delta^{18}O_{fluid}$ and δD values suggest that the ore-forming fluids of the gold deposits mixed with meteoric water in the shallow level.

Keywords. Western Shandong, mantle-branch structure, gold deposits, zircon SHRIMP U-Pb dating, stable isotope

1 Introduction

The western Shandong (Luxi) region, located in the southeastern edge of the North China Craton and separated by the Tanlu fault from the Jiaodong gold province (the largest gold producing area in China) has drawn attention for its unique geological characteristics and abundant mineral resources in the last ten years (Yu, 2001; Niu et al. 2004). Although the geology has been well studied, the evolution of geology and the structural controls mineralization are still open to debate. On the basis of the setting of ore-formation and the characteristics of geochemistry, this paper discusses the formation of a mantle-branch structure in western Shandong and its constraints to the gold mineralization.

2 Characteristics of the mantle- structure in western Shandong

2.1 Occurrence of regional strata

Similar to other areas in the interior of the North China Craton, the strata of the Luxi region consist of Archean and Paleoproterozoic basement, and Meso- Neoproterozoic and Paleozoic cover strata. Regionally, they are characterized by a circulas distribution with Taian-Pingyi as a center. The center comprises a well-developed magmatic and metamorphic complex, which is surrounded by Paleozoic cover strata. This suggests an extensional tectonic setting, with the basement uplifted and the cover strata detached outwards in the Luxi region (Fig. 1).

2.2 Extensive magmatic activity

The Luxi terrane contains well developed Mesozoic mantle-derived magmatic rocks, including intrusives, potash-rich volcanics and lamprophyres. The intrusive rocks, with extensive distribution but relatively small size, are variable in lithology. According to lithological assemblages, they can be subdivided into: (1) monzodiorite porphyry– monzonite porphyry, syenite porphyry assemblage, (2) pyroxenite– monzodiorite– syenite assemblage, (3) olivine gabbro– pyroxene diorite(amphibole diorite)-quartz monzonite assemblage, (4) diorite (porphyry)-quartz monzodiorite(porphyry)- granite (porphyry) assemblage, (5) carbonatite.

Strontium and Nd isotopic compositions of Mesozoic potash-rich volcanic rocks, lamprophyres and carbonatite in Luxi and its adjacent area share similar characteristics, such as $^{87}Sr/^{86}Sr$ values of potash-rich volcanic rocks in Mengyin Basin from 0.708715 to 0.711418–ε_{Nd} from -11.47 to -17.54, ε_{Nd} of lamprophyres from -11.57 to -19.64 (Qiu et al. 2001). $^{87}Sr/^{86}Sr$ ratios of Luxi carbonatite vary from 0.70998 to 0.71048–ε_{Nd} from -14.1 to -16.7 (Chu et al., 1997;Yin et al. 2001). All higher $^{87}Sr/^{86}Sr$ ratios and lower ε_{Nd} values reflect that these rocks have the characteristics of crustal material, but potash-rich volcanic rocks and lamprophyres in the Mengyin Basin exist mantle xenoliths as chrome-diopside and chrome- phlogopite, which shows mantle genesis of these rocks.

2.3 Radial and ringed fault systems

Faults in western Shandong are generally distributed in concentric ring and radial shapes outward from the Xinzhai- Sishui- Pingyi- Mengyin area in the central part of the area. The concentric ring faults may be divided into three basically complete ring structures from the inner part outward: (1) the Feicheng-Yiyuan-Linyi-Qufu ring fault, (2) the Juye-Liangshan-Jinan-Zibo ring tectonic belt, and (3) the Matouji- Fanxian- Liaocheng-Huantai ring fault.

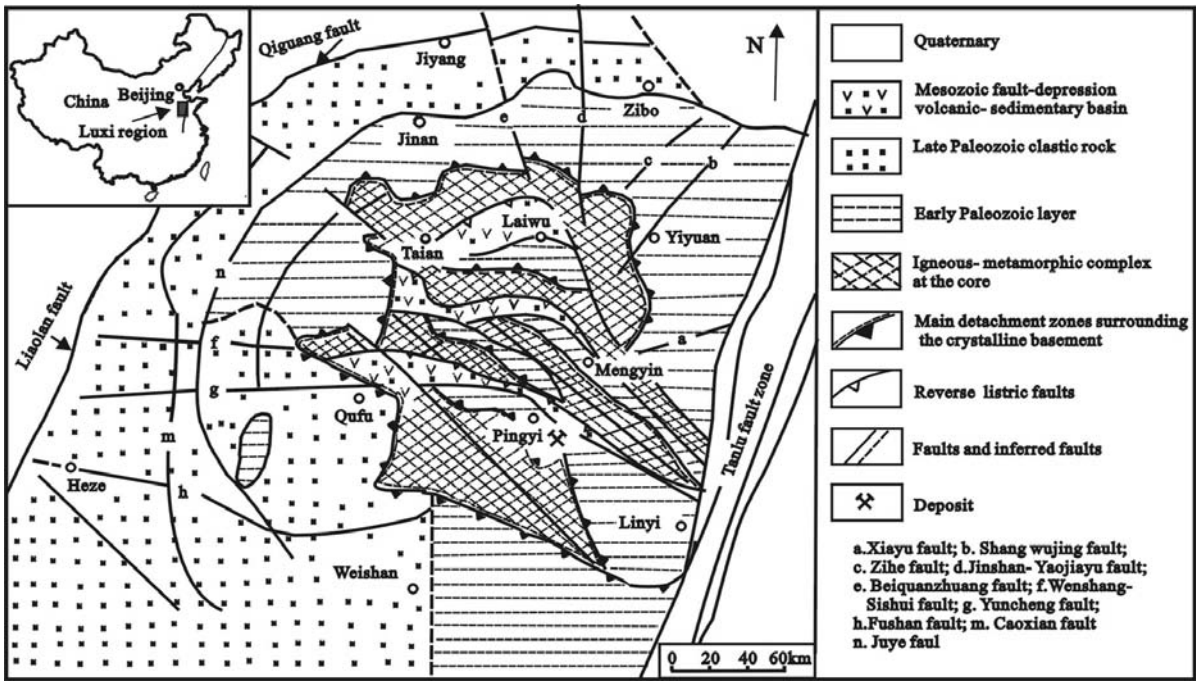

Figure 1: Tectonic sketch map of western Shandong

The radial faults comprise mainly the Nishan, Yuncheng, Wenshang- Sishui, Feicheng, Wenzu, Jinshan-Yaojiayu and Shangwujing faults. The faults generally dip steeply and show the tensile character. The intersection of the radial and concentric ring faults indicates that they are the product of the same stress field and the same tectonic phase. Generally, these radial and ringed faults occur in the early uplift of mantle-branch structure, and reflect a relatively small vertical relief of uplift.

2.4 Geophysical evidences for the Mesozoic mantle-branch structure

Three-dimensional velocity images from seismic tomography demonstrate that high-velocity blocks (Vp is more than 8.3Km/s) exist in the upper part of the mantle whose Vp is 7.8 ~ 8.0Km/s (Lu et al. 2000). A structural profile of crust-mantle from Beijing to Okinawa shows two mantle upwelling areas whose Vs is lesser than 4.2 ~ 4.3 km/s (Feng et al. 1996). They correspond to two sub-mantle plumes, one situated in the Okinawa ocean trough, and the other the North China sub- mantle plume with the Bozhong region as a center (Niu et al, 2002). The Luxi mantle-branch structure is a second-order unit of the Bozhong sub- mantle plume. Synthetic outcomes from man-made seismic exploration and geodesic electrical sounding further show that upper mantle obviously uplifts around Linyi in the Luxi mantle-branch structure.

2.5 Units of the Luxi mantle-branch structure

The mantle-branch structure — a third-order unit of a mantle plume, is a complex structure developed in shallow lithosphere during multiple evolution of mantle plume (Maruyama, 1994). The mantle-branch structure is generally composed of three units: magmatic and metamorphic complex, surrounding detachment-slip layers, and overlap fault volcanic basin, which are related each other.

2.6 Evolution of the Mesozoic mantle- branch structure

According to the ages of Mesozoic magmatic rocks, magmatic activity can be divided into two stages, one is in early Jurassic epoch, when the Tongshi alkali complex rock body formed, dated at 175.7±3.8Ma by the $^{206}Pb/^{238}U$ weighted mean age; the other is in early Cretaceous epoch, ranging from 110Ma to 130Ma, when Jinan, Guodian, Tongjin, and Laiwu rock masses formed. Statistics (n=95) from the ages of these rocks by K-Ar or $^{40}Ar/^{39}Ar$ dating show that most data cluster between 132Ma and 110Ma (Lin et al., 1996; Qiu et al., 2001). Thus, it is inferred that the activities of Mesozoic mantle-branch structure in western Shandong have two peak periods: early Jurassic epoch and early Cretaceous epoch, with the latter more extensive. This is consistent with the viewpoint that the early Cretaceous epoch represents the climax of a global mantle plume (Larson, 1991). In the light of extensive Neocene volcanism in the Bohai region (Gu et al. 2000),

This page intentionally blank

the Luxi mantle-branch structure has undergone three active periods and three inactive periods since Mesozoic-Cenozoic era. This suggests that the lithosphere of eastern China has undergone a process of uplift-fallback since the Mesozoic-Cenozoic era.

3 Genesis of gold deposits in the mantle-branch structure

3.1 Types of gold deposits

There are numerous gold deposits or occurrences in the Luxi mantle-branch structure. Although the characteristics of gold deposits are different, all of them occur in two tectonic units of the Luxi mantle-branch structure (the magmatic- metamorphic complex core and detachment-slip layers). According to the characteristics of the ore-controlling structure, gold deposits in the Luxi mantle-branch structure are divided into two types, that is, ductile shear zone type and detachment-slip layer type. The former, which comprised Huamawan, Yuejiazhuang and Buwa gold deposits (or occurrences), occur along NW-trending ductile shear zone, and are temporally and spatially related to Mesozoic intrusive rocks, and the latter, including Guilaizhuang gold deposit and Mofanggou gold deposit with total gold reserves of 45 tons, constitute the main gold deposits in western Shandong.

3.2 Geochemistry of detachment-slip layer type gold deposits

$\delta^{34}S$ values of pyrite from silicified and carbonatized monzodiorite porphyry, igneous breccia and mineralized dolostone of the Guilaizhuang and Mofanggou gold deposits range from -0.71 to 2.99‰ (Lin et al. 1997), close to those of the mantle sulfur, suggesting a mantle or magma source of sulfur in the ores. The δD values of detachment-slip layer type gold deposits in western Shandong range from –48 to –70‰, and the $\delta^{18}O_{fluid}$ values of ore fluids of the Guilaizhuang gold deposit vary from –1.13‰ to +5.07‰, being notably deviated from the $\delta^{18}O_{fluid}$ range (5.5 to 9.5‰) of magmatic water, which suggest that the ore-forming fluids of the gold deposits mixed with meteoric water.

3.3 A proposed gold mineralization model

A proposed gold mineralization model is as follows. The NW-trending steeply dipping ductile shear belt cuts deep-seated pyrolite of the mantle sub- plume beneath North China, resulting in decompression to form anatectic magma. The magmatic complex was emplaced at the main detachment between Cambrian carbonate rocks and Neoarchean granodiorite or Paleoproterozoic monzogranite. The magmatic hydrothermal fluids and Au-rich ore-forming fluids migrated upward along the detachment zone and deposited gold on the ductile shear belt and detachment-slip layers.

Acknowledgements

This project is supported by the National Natural Science Foundation of China (No. 40272088).

References

Chu T, Shen W (1997) Isotopic geochemistry of apatite from carbonatite in central Shandong. Acta Mineralogica Sinica, 17, No 1: 82-85

Feng F, Song L (1996) Mantle diapir tectonics: thermo-dynamic analysis of circum-western Pacific Basins. Earth Science, 21, No 4: 383-394

Gu L, Dai T, Fan W (2000) Mesozoic-Cenozoic volcanism and the significance of deep processes in the Bohai region. Geotectonica et Metallogenia, 24, No1: 9-17

Larson R L (1991) Latest pulse of earth, evidence for a mid-Cretaceous superplume. Geology, 19: 547-550

Lin J, Tan D, Jin Y (1996) $^{40}Ar/^{39}Ar$ ages of Mesozoic igneous activities in western Shandong. Acta Petrologica et Mineralogical, 15, No 3: 213-220

Lin J, Tan D, Yu X, Li B, Li Y, Xu W (1997) Genesis of Guilaizhuang gold deposit of western Shandong. Shandong Science and Technology press, Jinan: 1-160

Lu F, Zheng J, Li W, Chen M., Cheng Z (2000) The main evolution pattern of Phanerozoic mantle in the eastern China:the "Mushroom cloud" model. Earth Science Frontiers, 7, No. 1: 97-107

Maruyama, S (1994) Plume tectonics. Geol. Soc. Japan, 100, No.1: 24-49

Niu S, Hu H, Mao J, Sun A, Xu C, Hou Q (2004). Structure in wester Shandong and its genetic mechanism. Geology in China, 31, No.1: 34-39

Qiu J, Xu X, Luo Q (2001). Potash-rich volcanic rocks and lamprophyres in western Shandong province: ^{40}Ar-^{39}Ar dating and source tracing. Chinese Science Bulletin, 46, No.18: 1500-1508

Yin J, Zhou X (2001) Characterization of trace elements and Sr, Nd isotopes of carbonatites in the western Shandong province. Bulletin of Mineralogy, Petrology and Geochemistry, 20, No. 4: 09-314

Yu X (2001) Ore-froming series and model of Tongshi Gold field in Pingyi, Shandong province. Geology of Shandong, 17, No.3-4: 5 9-64

The evolution of lithospheric domains: A new framework to enhance mineral exploration targeting

Suzanne Y. O'Reilly
GEMOC National Key Centre, Department of Earth and Planetary Sciences, Macquarie University, NSW, 2109, Australia

Jon Hronsky
WMC Resources Ltd., PO Box 91, Belmont, WA, 6894, Australia

William L. Griffin
GEMOC National Key Centre, Department of Earth and Planetary Sciences, Macquarie University, NSW, 2109, Australia and CSIRO Exploration and Mining, North Ryde, NSW 2113

Graham Begg
WMC Resources Ltd., PO Box 91, Belmont, WA, 6894, Australia

Abstract. A new approach to global exploration targeting is essential for the discovery of new world-class ore deposits. Understanding the lithosphere-scale context of resource formation and location may provide the next step-change in enhancing exploration success. Knowledge of the nature of trans-lithospheric structure and discontinuities and the delineation of deep lithosphere domains with fundamentally different composition, architecture and evolution is providing a new framework for exploration. This enhances understanding and prediction of the location of ore-deposits derived from a variety of deep lithospheric processes including mantle-derived magmatic and fluid flow (and associated thermal transfer) and deep crustal reworking and partial melting. Relevant resource deposits include Ni-PGE, Cu, Au and diamonds, while these methods also reveal important parameters about basin formation that are potentially important for oil and gas occurrence.

Keywords. Lithospheric mantle; exploration targeting; diamonds; magmatic nickel deposits

1 The lithospheric context

The last twenty years have seen a systematic decline in the performance of the global minerals exploration industry; in the 1990s approximately three times as much was spent to make a major discovery as in the 1970s. This decline is now widely recognised by the industry, leading to an increased emphasis in some of the exploration sector on focussed research, targeted at improving exploration performance. Economic analysis indicates that the Expected Monetary Value of an exploration project is most sensitive to the quality of the initial area selection decision. When searching for new giant ore deposits, the most important targeting is done at the broad regional scale, resulting in ground acquisition of the order of a few thousand square kilometres. Therefore, improving the quality of regional targeting decisions becomes a primary driver of enhancing exploration success.

The primary focus of modern mineral exploration must be on giant metal ore-deposits and high-grade diamond-producing deposits, in order to achieve profitability. The essential challenge in targeting lies in discriminating between areas prospective for such significant deposits and those likely to host only minor deposits. Historically, the discipline of Economic Geology has not focussed much on this problem, but has concentrated on developing an understanding of the processes of ore formation. The few published studies to consider the factors that produce giant ore deposits have compared and contrasted deposit-scale parameters. In all cases, the conclusions have been that there are no unique features at the deposit scale that characterise giant deposits.

However, giant ore deposits must be thought of as mass-concentrative systems that are constrained, for fundamental reasons of mass-balance, to operate over very large scales. In this perspective, the ore deposit itself becomes merely the final focus of a much larger-scale system. Therefore, the concepts and observations of the greatest significance to predictive targeting for giant ore systems are those related not to the deposit environment itself, but to the much larger entity — the ore system. In this context, critical questions become: how large is the ore system; what are its fundamental controls; and how can such systems be recognised in the datasets available to mineral exploration?

Our approach, based on detailed studies of the nature of the lithosphere, is based on the concept that giant ore systems are the product of lithosphere-scale processes. Although the details of such processes will vary between deposit styles, a critical common factor is the large-scale structure of the lithosphere; with large ore deposits more likely to be associated with lithosphere-scale domain boundaries.

2 4-D lithosphere mapping

4-D Lithosphere Mapping (eg O'Reilly and Griffin, 1996; O'Reilly et al. 2001a) is a unique approach to understanding lithospheric architecture and evolution based on in-

tegration of petrologic, geochemical, tectonic and geophysical datasets. The mantle is the ultimate source of Earth's atmosphere, oceans, crust and fluids that deposit a wide range of ores, so the nature of the bulk of the Earth lying beneath the crust is of fundamental importance to understanding the formation and localisation of many resources.

Several lines of evidence indicate that the subcontinental lithospheric mantle (SCLM) is heterogeneous, with domains hundreds to thousands of kilometres across that are underlain by different types of upper mantle with different histories and styles of crust-mantle interaction. Fragments of the upper mantle (xenoliths) brought to the surface in volcanic rocks show that mantle volumes of different age differ significantly in composition, thermal state and density (Griffin et al. 1998a; O'Reilly et al. 2001). These data also show abrupt changes in mantle composition and structure across major terrane boundaries, even within single cratons, indicating that these boundaries extend to depths of at least 200 km (Griffin et al. 2003a) and represent significant discontinuities in the SCLM. Such domain boundaries reflect the large-scale geodynamic processes by which continents have been constructed, broken up and reassembled throughout Earth history. The mapping of such boundaries, and the definition of their timing and origin, therefore provides fundamental new insights into Earth processes, providing the basis for a new conceptual approach to global mineral exploration.

3 Change in nature of the subcontinental lithosphere through time

The secular evolution of SCLM composition has been documented by the detailed mapping of mantle sections in terms of composition, "stratigraphy" and thermal state, using xenocrystic and xenolithic material brought to the surface in volcanic rocks (e.g. kimberlites, lamproites and basalts). This work has shown a clear correlation of SCLM composition with the age of the last major tectonothermal event in the overlying crust. The Archean/Proterozoic boundary represents a major change in the nature of lithosphere-forming processes. Archean SCLM is highly depleted (very low in basaltic components such as Ca, Al and Fe), commonly strongly stratified, and contains rock types not found beneath terranes affected by younger tectonothermal events (Fig. 1). It is relatively thick (180 – 220 km) and has a present-day low goethermal gradient. Phanerozoic lithospheric mantle is thinner (80-100km), has a high geothermal gradient and is compositionally more fertile (higher contents of Fe, Ca and Al). Proterozoic mantle has intermediate characteristics.

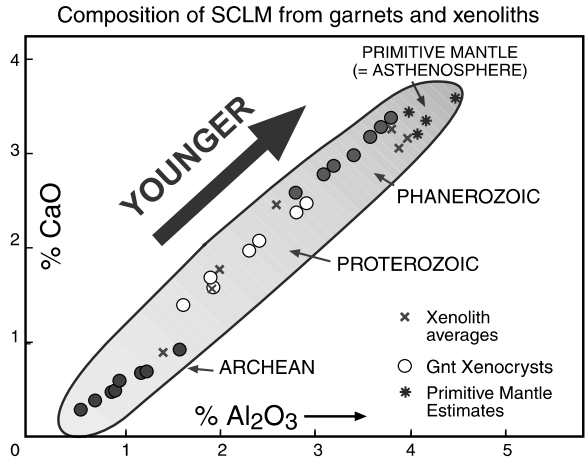

Figure 1: Change in average composition of newly-formed lithospheric mantle through time

These compositional variations in different SCLM volumes result in differences in the density and elastic properties of lithospheric mantle of different age (Fig. 2; Poudjom Djomani et al., 2001a). Archean and Proterozoic mantle roots are highly buoyant; they cannot be delaminated but require mechanical disaggregation (lithospheric thinning and/or rifting) and infiltration of upwelling fertile material to be destroyed or transformed. This buoyancy, when combined with the refractory nature of Archean SCLM, offers a simple explanation for the thickness and longevity of Archean lithospheric keels. By contrast, *Phanerozoic* SCLM is relatively dense (compared with asthenosphere) for observed thicknesses (~100km) and tends to be in a precarious state of neutral

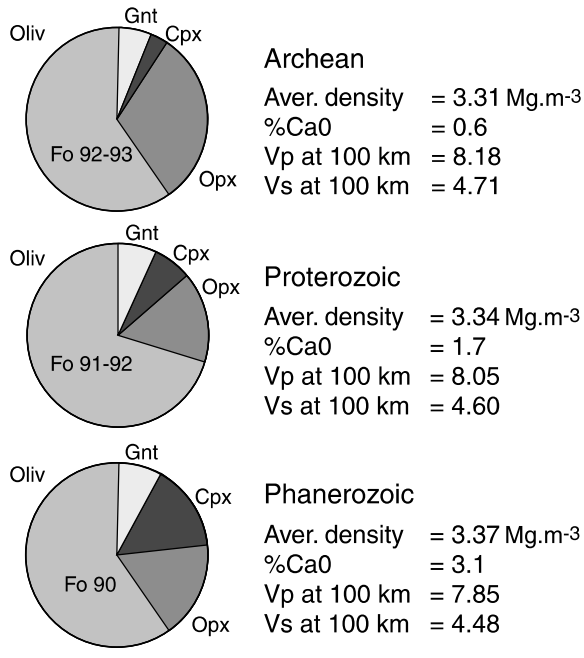

Figure 2: Properties of lithospheric mantle of different ages. Densities calculated at standard T and P, shear wave velocity (*Vs*) and compressional wave velocity (*Vp*) at 100 km (O'Reilly et al. 2001)

buoyancy. Thus it is easily delaminated especially if there is a kinetic trigger such as collision.

The contrasting properties of different mantle domains require lateral contrasts in composition, density, depth and seismic response for present-day lithospheric domains. Such lateral contrasts create lithospheric discontinuities and may affect thermal convection geometries; these boundaries may be foci for fluid flow though the lithosphere.

4 Tracking linked crust and mantle events

The broad relationship between crustal age and SCLM composition suggests a strong link between crustal formation and the generation of continental roots, and a persistent coupling between the crust and the underlying SCLM.

GEMOC has developed the unique TerraneChron^{TM} approach to studying the processes of crustal generation on the terrane scale, using integrated U-Pb dating, and Hf-isotope and trace-element analysis of single zircon grains from stream sediments (eg Belousova et al., 2004; O'Reilly et al, 2004). We have also developed unique techniques for dating mantle depletion events, using *in situ* Re-Os analysis of sulfides in mantle-derived xenoliths, providing geochronology about mantle events such as stabilisation age of the particular mantle volume and the timing (and nature) of subsequent fluid-related mantle events for the first time (eg Spetsius et al. 2002; Griffin et al. 2004). The combination of these novel approaches now allows a detailed analysis of the temporal and geochemical relationships between tectonic events in the crust and mantle. Such knowledge helps to provide information on the nature and timing of large-scale fluid movement and/or thermal transfer from the mantle to the crust with relevance to ore-forming processes related to magmatic episodes with or without significant crust reworking (eg fluid infiltration into and melting of deep crust regions).

5 Focussing the pathways for mantle fluids to reach the crust

The integration of geophysical data with geochemical data has proven powerful in revealing the nature of the deep crust and lithospheric mantle. Coupled with the mantle domains with vertically resolved spatial rock type distribution, we are able to define discrete lithospheric mantle regions and discontinuities (vertical and horizontal).

We have integrated the petrological and geochemical information with long-wavelength geophysical (gravity, magnetic and heat flow) data as well as detailed seismic tomography to extend our lithosphere mapping from the vertical "virtual drill-holes" of the mantle sampling sites to regional scales. A productive approach has been the use of detailed analysis of the Effective Elastic Thickness (Te) of the lithosphere to test the relationships of these domains to lithospheric strength and lithosphere composition. Te assessment involves inversion of gravity and topographic data and results in the delineation of regions of different lithospheric strength that are interpreted as reflecting relative rheological domains. Combining the Te with detailed stratigraphic and tectonic analyses of crustal history has led to an understanding of the evolution of lithosphere domains. Detailed T*e* analysis across the Slave Craton (Canada) and Siberia, areas of importance in diamond exploration, has shown that kimberlites occur at features identified as gradients in lithosphere strength and that the kimberlites avoid strong cratonic core regions. In the Slave Craton, the observed Te gradient coincides with the expression of a major crustal suture zone that dips to the east near the surface. The combination of geochemical information from the mantle-derived samples and the Te results indicate that this suture dips sharply at depth to be near vertical in the lithospheric mantle. This provides an empirical link between this major lithosphere structure, clearly imaged in the Te, and the zone of kimberlite emplacement. An analogous relationship between Te gradient and kimberlite emplacement is seen in the Siberian lithosphere (Poudjom Djomani et al, 2001b). We consider that Te gradients can identify fundamental zones of weakness or lithospheric discontinuities that have important consequences as pathways to focus the transfer of mantle fluids (including magmas) to the overlying crust and therefore have considerable significance in large-scale exploration targeting for economic deposits related to mantle fluids such as kimberlites and Ni deposits related to magmatic processes.

6 The North China Craton – a case history of lithosphere change

The North China Craton provides a cogent example of significant lithosphere change crucial to exploration for diamond-bearing kimberlites in that region. In the eastern Sino-Korean craton, eruptions of Ordovician kimberlites provide mantle samples (xenoliths and disaggregated minerals) that show the mantle at that time was thick, cool, diamondiferous and typically Archean in composition (Fig. 3); it probably had survived for at least 2 Ga (Griffin et al. 1998b). Tertiary lamprophyres and basalts that erupted through the same terranes about 400 m.y. later, sampled only a thin (<120 km), hot and fertile lithosphere. Within those 400 m.y., rifting with associated asthenospheric upwelling has disaggregated and thinned the Archean lithospheric root as revealed in detailed tomography as well as by the mantle xenolith sampling. One important consequence of understanding the nature and timing of lithospheric change is the

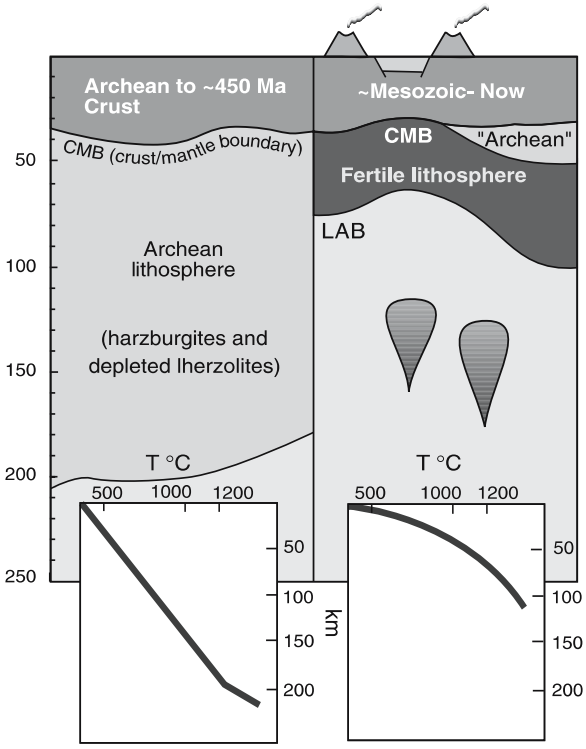

Figure 3: Lithosphere evolution in eastern part of Sino-Korean craton (Griffin et al. 1998b)

common exploration concept that diamond-prospective regions require a deep, ancient lithospheric root. This does not exist today in north China although kimberlites erupted before the lithosphere thinning may be diamondiferous.

Acknowledgments

We wish to acknowledge many colleagues who have contributed to these concepts and participated in related research with us, and all the visionary industry colleagues who have helped us shape our related research over many years. This work has been strongly supported by many ARC grants, Macquarie University and many industry partners.

References

Griffin WL, O'Reilly SY, Ryan CG, Gaul O, Ionov D (1998a) Secular variation in the composition of subcontinental lithospheric mantle. In Braun J, Dooley JC, Goleby BR, van der Hilst RD, Klootwijk CT (eds), Structure & Evolution of the Australian Continent, Geodynamics Volume 26, AGU, Washington D.C. pp 1-26

Griffin WL, Zhang A, O'Reilly SY, Ryan CG (1998b) Phanerozoic evolution of the lithosphere beneath the Sino-Korean Craton. In: Flower M, Chung SL, Lo CH, Lee TY (eds), Mantle Dynamics and Plate Interactions in East Asia Mantle Dynamics and Plate Interactions in East Asia, AGU Geodynamics vol. 27: 107-126

Griffin WL, O'Reilly S.Y, Natapov LM, Ryan CG (2003) The evolution of lithospheric mantle beneath the Kalahari Craton and its margins. Lithos 71: 215-241

Griffin WL, Belousova EA, Shee SR. Pearson NJ, O'Reilly SY (2004) Archean crustal evolution in the northern Yilgarn Craton: U-Pb and Hf-isotope evidence from detrital zircons. Precambrian Research 131: 231-282

O'Reilly SY, Griffin WL (1996) 4-D lithospheric mapping: a review of the methodology with examples. Tectonophysics 262: 3-18

O'Reilly SY, Griffin WL, Poudjom Djomani Y, Morgan P (2001) Are lithospheres forever? Tracking changes in subcontinental lithospheric mantle through time. GSA Today 11: 4-9

O'Reilly SY, Griffin WL, Belousova EA (2004) TerraneChron™: Delivering a competitive edge in exploration. Abstract, 27 Sep – 1 Oct 2004 SEG Conference, Predictive Mineral Discovery Under Cover, Perth, Western Australia

Geodynamic considerations of Uralian metallogeny

Victor N. Puchkov
Institute of Geology Ufimian Scientific Centre, K Marx st. 16/2 450 000 Ufa Russia

Abstract. The analysis of relationships between metallogeny and geodynamics in the Urals made by preceding researchers in recent times has proven that they are related. However, in the present study more attention is paid to metallogeny of the platform (Middle Jurassic-Paleogene) and neotectonic (Late Cenozoic) stages. It is also updated by new information concerning the Wilson cycles preceding the platform stage. It includes a revised understanding of geodynamic development of the Timanides (ocean formation in the Late Riphean and collision in the Late Vendian) and of the Uralides (a new interpretation of relationships between Tagil and Magnitogorsk arcs, arc-continent collision in the Late Devonian, subduction jump in the Early Carboniferous, and thrust stacking in the Late Carboniferous-Permian). More attention is paid to the problem of plumes and their role in metallogeny of the fold belt. It is shown that many well-defined types of ore deposits have become additional geodynamic indicators themselves. At the same time, it is taken into account that many deposits are polygenetic and different stages of their formation belong to different geodynamic stages.

Keywords. Metallogeny, geodynamics, Timanides, Uralides, plumes

1 Introduction

The Urals, one of the oldest mining provinces of the world, produces significant amounts of raw materials. The Uralian deposits make up about a quarter of the total value of all Russian mineral resources. Many deposits are exhausted, but the region still has large resources. However most of the readily discovered deposits have been found. That is why it is so important to study geodynamics as a framework for all considerations concerning the ore origin, keeping in mind that they are closely related.

2 Structural division of the Urals

The structural zoning of the Uralides (Puchkov, 1997)is as follows (Fig. 1): a) Preuralian foredeep, filled with Permian molasse; b) West Uralian zone, with a predominant development of intensely folded and westward-thrusted shelf and bathyal Paleozoic sediments; c) Central Uralian zone, with Precambrian complexes exposed; d) Tagil-Magnitogorsk zone, limited from the west by the Main Uralian Fault (MUF) and represented mostly by Paleozoic complexes of the oceanic floor and island arcs; e) East Uralian zone characterized by the presence of Precambrian terranes, and along with them, Paleozoic oceanic and island arc complexes; f) Transuralian zone, the westernmost, composed of pre-Carboniferous complexes of different geodynamic character, probably accretionary in nature, covered unconformably by the Lower Carboniferous calc-alkaline volcanic rocks.

The history of the Urals reveals several stages, which allows the following vertical division of the Urals: a) The Archean-Paleoproterozoic (Pre-Timanides), an immediate extension of the crystalline basement of the East-European platform under the Urals. b) The Meso-and Neoproterozoic Timanides, which reveals a series of successive rift events prior to final Late Pre-Cambrian collision and orogeny (Puchkov, 2003). c) The Cambrian-Early Jurassic Uralides, primarily connected with the Paleouralian Ocean. The ocean opened as a result of Late Cambrian-Ordovician epicontinental rifting and subse-

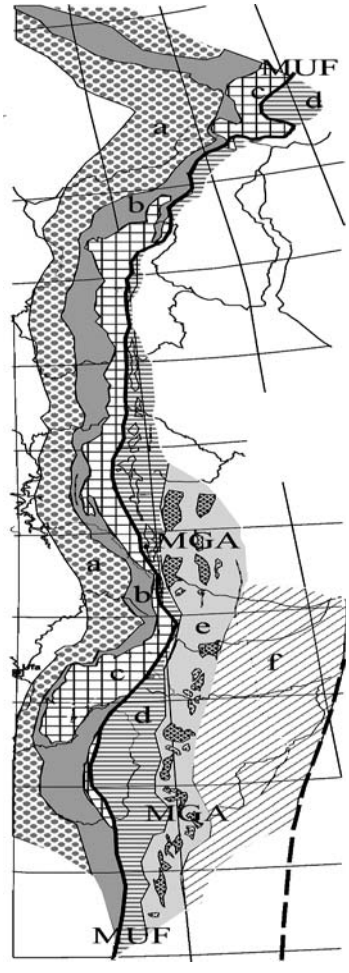

Figure 1: Structural zones of the Uralides; a - f – zones (see text), MUF – Main Uralian Fault, MGA – Main Granite Axis

quent oceanic spreading and closed through subductions in the Late Ordovician to Early Carboniferous, and collisions in the Late Paleozoic and Early Jurassic. d) Jurassic-Paleogene platform complex, formed when the orogen was finally eroded to a peneplain (Sigov, 1969), giving way to deep weathering. e) Late Cenozoic neo-orogenic complex, formed when new mountains rose along some tectonic lines of the Uralides. Each complex has its zoning and each zone its own metallogeny.

3 The Archean-Early Proterozoic complex

The metamorphic complexes of this stage, preserving relics of granulite metamorphism, is exposed in the Urals in the rather small Taratash massif and probably in some other small blocks. Sedimentary-metasomatic quartz-magnetite deposits of minor importance belong to them. A feature of this crystalline complex is its deep burial, both sedimentary and tectonic.

4 Timanides

Much more widespread at the surface are Meso- and Neoproterozoic complexes. Owing to a structural unconformity between the Timanides and Uralides, the nature of the Mezo-Neoproterozoic formations in the Polar Urals strongly differ from that of the Southern-Northern Urals. In the Central Uralian zone of the Polar Urals were Neoproterozoic oceanic and subduction zones. For that reason, the Polar Urals hosts copper-pyritic, pyritic-polymetallic, copper-skarn, and Mo-Cu-porphyry deposits (Dushin, 1997). Conversely, the Meso-Neoproterozoic formations of the Southern-Northern Urals belong to a deep aulacogen-type ensialic sedimentary basin and host stratiform siderite and magnesite deposits, hydrothermal fluorite, SEDEX barite-polymetallic, Sukhoy Log-type Au-Pt mineralization, ilmenite and chromite deposits in stratified intrusions (Ovchinnikov, 1998).

5 Uralides

The development of the Uralides corresponds to a classic Wilson cycle and comprises epicontinental rifting in the Uppermost Cambrian-Lower-Middle Ordovician, formation of an ocean with continental passive margins (only one of them is preserved in the Urals), development of an eastward subduction in the Late Ordovician to Late Devonian, arc-continent collision in the Late Devonian, formation of an Andean-type subduction zone in the Early Carboniferous, and continental collisions in the Late Moscovian to Permian and in the Early Jurassic).

The metallogeny of the Ordovician epicontinental rifting is represented by copper sandstones and barite-polymetallic stratiform deposits, associated with Ordovician rift volcanic rocks. Subalkaline magmatism and carbonatitic metasomatism of the Late Ordovician-Early Silurian in the Middle Urals have led to formation of rare metal deposits. We suggest that it is a trace of a plume at the continental margin tied up to the process of new ocean development. Further transformations of this mineralization could be connected with collision.

The metallogeny of the oceanic stage is much more variable. In the sedimentary successions of a passive continental margin, rift formations are followed by purely sedimentary formations demonstrating a facies transition from shelf to continental slope zone (Puchkov, 1997). Shelf sediments contain (or produced) hydrocarbons, coal and bauxite. In the bathyal successions, the most important are stratiform Ba and Mn (low-temperature seep?) deposits.

The ophiolites (oceanic formations) host Cr, PGE, VMS (Cyprian type) and gold. But formation of all these deposits did not stop at the oceanic stage. The largest concentrations of chromite are associated with restites: they are by-products of mantle depletion which went on not only in the MORs, but at the island-arc stage as well. It must be remembered that the island-arc volcanism results mainly from a partial melting of a supra-subductional mantle wedge (e.g. Stern, 2002). Therefore subduction participated in reworking of dunite-peridotite complex of ophiolites and in ore formation.

Most of the Uralian VMS deposits are associated with island arcs, representing products of ancient black smokers (e.g., Herrington et al. 2002). Manganese mineralization, associated with cherts of mostly Middle Devonian age in the Magnitogorsk zone was probably due to processes of on-bottom deposition by colder, remote hydrotherms.

Along with VMS deposits, several other sulfide types are connected with island arcs. Among them are Mo-Cu-porphyry deposits of the South Uralian Magnitogorsk arc, gold deposits in the hangingwall of MUF (Sazonov et al. 2001), serpentinite-hosted sulfide copper-nickel-cobalt deposits of MUF zone. There is a discussion if the latter deposits belonged to MOR or to a Magnitogorsk forearc.

The massifs of the platinum-bearing belt hosted by the Tagil arc in the Middle and Northern Urals are composed of dunite, pyroxenite, gabbro, gabbro-amphibolite forming big concentric-zonal massifs. They are believed to belong to the island-arc stage (Ivanov and Shmelev, 1996). The belt got its name from native platinum that originally was produced from placers. Platinum had been supplied to these placers from chromite bodies of the nearby dunite massifs. A special role as an active factor of ore mineralization in the belt was played by magmatic stratification and thermochemical activity of comparatively young gabbro-norite intrusions, forming transitions from magmatic segregations of vanadium-rich titanomagnetite to skarn-magnetite and skarn-hydrothermal deposits (Ovchinnikov 1998).

In the Early Devonian, the active stage of development of Tagil zone as a whole came to an end. After that, in the

Emsian-Middle Devonian, the arc was divided into two zones. In the west, volcanic activity gave place to formation of carbonate shelf with sub-equatorial lateritic weathering and bauxite deposition. In the eastern part of Tagil arc, subductional magmatism was still going on, giving birth to skarn-magnetite and copper-skarn mineralization (Ovchinnikov, 1998). We explain it by a suggestion that the extinct Tagil arc was included into the younger Magnitogorsk arc as a microcontinent.

In the Late Devonian, a collision took place between continental passive margin and Magnitogorsk island arc in the Southern Urals. The stage was accompanied by some economic mineralization (e.g. rutile, quartz, metamorphic pyritic deposits, jadeite, gold in and around MUF). Collision and accretion of the continent were followed by a jump of the subduction zone and a formation of an Andean-type margin in the east of the Urals. Skarn-magnetite and copper-magnetite-skarn mineralization, as well as Cu-porphyry deposits accompanied this event.

The continent-continent collision stage started in Moscovian time, when all the oceanic crust was subducted. It led to formation of the Uralian orogen and Preuralian foredeep. Intense thrust stacking and formation of a crustal root have resulted in anatexis and emplacement of Permian granites. Together with transpressional style of deformations, it created elevated heat and fluid production, partial melting in the lower crust and abundant fluid conduits in the upper crust, which was favourable for an intense metasomatism, hydrothermal activity and formation of specific deposits.

The Preuralian foredeep hosts deposits of hydrocarbons, coal, salt, copper sandstones, manganese. The distribution of many deposits along the foredeep was ruled by climate (salt and copper sandstones in arid climate and coal – in colder and wet conditions).

In the Central Uralian zone, Alpine-type veins with different kinds of quartz formed. In the MUF and some other suture zones, processes of metasomatism and formation of quartz lode component of gold deposits were active, controlled structurally by strong transpressional deformations and geochemically by generation of heated fluids (Koroteev et al. 2001; Sazonov et al. 2001). In the East Uralian zone, formation of the Main Granitic axis (MGA) of the Urals had been almost completed in the Permian. To the massifs of the Upper Devonian - Lower Carboniferous subduction granodiorite-tonalite formation, Permian collision and anatexis added intrusions of granite (Bea et al. 2002). The igneous activity was accompanied by formation of quartz, gold (with the final stage of golden quartz lode formation) and deposits of rare metals and precious stones, often combined. It is believed that metamorphic-metasomatic alteration of peridotites of that time resulted in rich antophyllite-asbestos deposits.

The Triassic epoch, apart of coal deposition, was characterized by an intense trapp volcanism probably connected with the widest Permian/Triassic Uralo-Siberian superplume. Lamproite dikes post-dating trapps and prospective for diamonds are developed along the whole western boundary of the magmatic province.

6 The Middle Jurassic-Paleogene platform complex

This stage is characterized in the Urals by processes of very mild and restricted erosion, weathering, karst formation over limestones and sulphates, combined with accumulation of raw materials. Karst depressions hosted small deposits of coal, bauxite, iron, placers. Another type of"niches" for burial of exogenic deposits were shallow valleys developed in the eastern slope of the Urals, obliquely to the structural grain of the Uralides. They control clusters of small bauxite deposits, different placers and also uranium. In the western slope of the Middle Urals, paleo-valleys control diamond placers (Sigov, 1969). The recent discoveries of endogenic, tuffisite type of diamond deposits in the Uralian placer field also must be mentioned, though their endogenic nature is still under serious doubt. Very large wide-areal sedimentary iron deposits were controlled by swampy lowlands and shore lines of the West Siberian sea. Deep weathering was also the cause of the origin of gossans, developed over some VMS deposits and produced tons of free gold. Linear and areal silicate Ni ores are connected with weathering of serpentinites along their contacts with carbonates. Naturally alloyed iron ores are widely developed. Poor carbonate iron and manganese ores are transformed into small, but economic oxidized ores.

7 The Late Cenozoic neotectonic complex

The moment when the Ural mountains began to grow again came in the Late Oligocene or even later. It is most important as the time of final emplacement of placers. Once created in previous epochs, placers could not simply disappear, dissipate or shift horizontally, but just moved downwards into new, transversal valleys. In the Miocene a South Uralian coal basin was formed in sulfate karst depressions of the Preuralian foredeep.

8 Conclusions

Using the example of the Uralian foldbelt we conclude that the metallogeny of the province is controlled in the first instance by the following factors: 1) Presence, proportion or absence of oceanic, marginal, rifting, subduction, or other specific geodynamic-indicative complexes. 2) Position of these complexes within the structure and in relation to the Earth's surface. Both orogenic and epirogenic movements led to their burial or exhumation to a depth which determine feasibility of exploration and

exploitation of their deposits. 3) Intensity of orogenic reworking of primary complexes through deformation, metamorphism and anatexis, resulting in the origin or upgrading of deposits. 4) Climatic and tectonic conditions, controlling development of hypergenic deposits. Presence of rocks able to form karst cavities; development and burial of river valleys; that is, factors, controlling weathering and burial of its products. 5) Secondary orogeny (without a Wilson cycle), influencing the processes of exhumation, burial, transportation, erosional elimination or redistribution of deposits. 6) Connection of some mineralization processes with plume tectonics.

The above research reveals also the importance of deposits of many types as additional geodynamic indicators.

Acknowledgements

The study was supported by Programs No5 and No7 of the Presidium RAS and Department of the Earth Sciences RAS

References

Stern RJ (2002) Reviews of Geophysics, 40(4): 3- 1-39

Bea F, Fershtater G, Montero P (2002) Granitoids of the Uralides: Implications for the Evolution of the Orogen. In: Brown D, Juhlin C, Puchkov V (eds) Mountain Building in the Uralides: Pangea to the Present. AGU Geophysical Monograph Series 132: 211-232

Dushin VA (1997) Magmatism and geodynamics of paleocontinental sector of the North of the Urals. "Nedra", Moscow, 213 (in Russian)

Herrington RJ, Armstrong RN, Zaykov VV, Maslennikov VV, Tessalina SG, Orgeval JJ, Taylor RNA (2002) Massive Sulfide deposits in the South Urals: Geological setting within the framework of the Uralide orogen. In: Brown D, Juhlin C, Puchkov V (eds) Mountain Building in the Uralides: Pangea to the Present. AGU Geophysical Monograph Series 132: 155-182

Ivanov KS, Shmelev VR (1996) The Platinum-bearing belt of the Urals – magmatic trace of the Early Paleozoic subduction zone. Doklady of Academy of Sciences, geology 347: 649- 652 (in Russian)

Koroteev VA, Sazonov VN, Ogorodnikov VN (2001) Ore genesis and geodynamics of the Paleozoic history of the Urals. Lithosphera 1: 52-63 (in Russian)

Magmatic Cu-Ni-PGE mineralization at a convergent plate boundary: Preliminary mineralogic and isotopic studies of the Duke Island Complex, Alaska

E.M. Ripley, C. Li, J. Thakurta
Department of Geological Sciences, Indiana University, 1001 E. 10th Street, Bloomington IN 47405 U.S.A.

Abstract. The Duke Island complex is one of more than thirty ultramafic bodies of Cretaceous age located in a belt of ~40 km width that stretches along the 560 km length of the Alaskan panhandle. Recent drilling operations have detected the presence of large volumes of low-grade massive and disseminated sulfide mineralization hosted within an olivine clinopyroxenite body that appears to cross-cut other ultramafic rock types. Assays show a maximum of 2.08% Cu, 0.25% Ni, and 1 gram/ton combined Pt + Pd. Prior to the recent discoveries Alaskan-type ultramafic complexes were thought to be poor prospects for world-class magmatic Cu-Ni-platinum group element (PGE) sulfide deposition. One reason for this assessment relates to the fact that although PGE placers are often found in association with the ultramafic complexes, base metal sulfides have only rarely been found in the host rocks. PGE mineralization appears to be primarily associated with chromite-rich occurrences in dunitic portions of the complexes, and most of the PGEs are housed in alloys, tellurides, or antimonides. For these reasons the complexes are thought to have formed in very low fS_2 environments. A second reason for not suspecting the presence of magmatic sulfides is that the linearly arranged Alaskan-type complexes are thought to have formed in compressive regimes related to subduction processes. Very few large magmatic Cu-Ni-(PGE) sulfide deposits are associated with subduction zones, although some researchers believe that komatiites (host to many Ni-sulfide deposits) may have formed in Archean to Proterozoic subduction zones. Two pre-requisites for the formation of large Cu-Ni-(PGE) deposits are: 1) a supply of readily available S from country rocks and 2) localization of immiscible sulfide liquids in magma conduit systems where they have the opportunity to exchange metals with large volumes of metal-bearing magma. An analysis of the tectonic and petrologic environments of the Duke Island complex suggests that immediate country rocks are indeed sulfide-bearing (some may include Triassic volcanogenic massive sulfide deposits), and that the complexes probably served as feeder systems for arc-related volcanic activity. Sulfur isotopic values of the mineralization at Duke Island range from -15 to 4.6‰, and are strongly suggestive of the involvement of country rock sulfur. Nickel contents of olivine (Fo_{77-85}) are variable; grains associated with a high proportion of sulfide are Ni-depleted (to values <100 ppm), whereas grains in sulfide-deficient zones contain up to 1000 ppm Ni. Our preliminary data suggests that the complex may represent an excellent target for the localization of Cu-Ni-(PGE) mineralization in a tectonic environment that in the past may have been overlooked in terms of sulfide potential.

Keywords. Ni-Cu-PGE deposits, subduction zones, Duke Island Complex

1 Introduction

The largest mafic-rock-related Cu-Ni deposits (with varying amounts of PGE) are located in a variety of tectonic settings. Deposits that currently contain the highest tonnages of Ni reserves and resources are shown in Figure 1, and include Sudbury, Noril'sk, Jinchuan, Voisey's Bay, Uitkomst, the Duluth Complex, and several komatiite-related deposits. In brief, key elements for the generation of such large deposits appear to be related to the availability of metals and sulfur (whether of external or magmatic origin), as well as to concentrating and potentially upgrading immiscible sulfide liquids.

Deposits in intrusive rocks associated with the Permo-Triassic Siberian flood mechanisms of basalt province at Noril'sk and the Midcontinent Rift-related flood basalts (the Duluth Complex and several other troctolitic to gabbroic intrusions) illustrate the importance of externally derived sulfur in large volume rift systems (e.g. Godlevsky and Grinenko 1963; Gorbachev and Grinenko 1973; Ripley 1981; Ripley and Al-Jassar, 1987; Arcuri et al. 1998; Li et al. 2003).

Voisey's Bay, Noril'sk, and Jinchuan have been shown to be magma conduit systems where large volumes of magma may have been transported and reacted with trapped sulfide liquid (e.g. Lightfoot and Naldrett 1999; Naldrett and Lightfoot 1999; Li et al. (2004). Exchange reactions involving Fe and more chalcophile metals such as Cu or Ni are thought to have led to an increase in metal tenor of the accumulated sulfide liquid. External S may have played a significant role in the genesis of mineral-

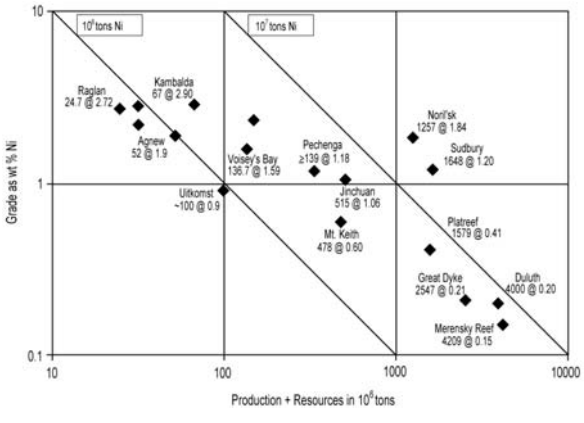

Figure 1: Production plus reserves and resources of Ni in major magmatic sulfide deposits of the world (after Naldrett, 1999)

ization at Voisey's Bay and Jinchuan as well (e.g. Ripley et al. 1999, 2002, in press). Sudbury is a rather unique example of a bolide impact-generated melt sheet (e.g. Therriault et al., 2002; Lightfoot et al. 2001). Even here the interaction between melts and crustal sedimentary material may have been critical for ore formation. Komatiite-related deposits, such as those at Kambalda, Thompson, and Raglan are thought to be related to the interaction between high-temperature lavas and sulfidic sediments in lava channels (Lesher and Keays, 2002). Nickel from the ultramafic lavas is thought to react with externally derived sulfur, and the immiscible sulfide liquid may be concentrated in a number of structural or topographic traps.

There are many other, generally smaller, Cu-Ni occurrences associated with mafic intrusive rocks around the world. Some of these are under active exploration and may someday supplant those discussed above as "world-class, high tonnage" deposits. We have conducted sulfur isotopic studies of a number of prospects from around the world, and although the absolute values of the analyses remain proprietary, we can unequivocally state that the importance of externally derived S in magmatic ore genesis continues to be a key evaluative factor.

The tectonic settings of both the well-known and lesser-known deposits are in some cases very clear and in some cases very speculative. Flood basalt provinces are prime exploration targets because of deposits such as those at Noril'sk and those associated with the Midcontinent Rift. The deposits at Voisey's Bay are thought to be associated with plume-related extension following continental collision (Ryan 2000). The troctolitic host rocks of the Voisey's Bay deposit are part of the Nain Plutonic Suite that straddles the suture zone between the Churchill (largely Proterozoic) and Archean Nain provinces. For many years komatiites were thought to be produced in dry, plume-related extensional environments (e.g. Arndt 1998). This theory has recently been challenged by workers who believe that hydrous, basaltic komatiites, in particular, may be equivalent to boninites and were produced in subduction zone environments (e.g. Parman et al. 2001; Stone et al. 2003). If true, this broadens the types of tectonic environments that may host large magmatic Cu-Ni deposits.

2 Alaskan-type ultramafic complexes

Alaskan, Ural-Alaskan, or "zoned ultramafic" intrusions (Taylor, 1967; Johan, 2002) are well known for associated PGE placer deposits and magnetite prospects. The intrusives are commonly concentrically zoned, with dunite cores surrounded by clinopyroxenite and hornblendite. Orthopyroxene and plagioclase are missing or occur in very low abundance. Magnetite is a common mineral in the pyroxenites, hornblende pyroxenites, and hornblendites, with concentrations locally up to 20 wt.%. Chromite is present only in the dunites, and occurs as stratiform segregations and irregular veins. The tectonic environment of the intrusions is not always agreed upon; they may occur within linear belts suggestive of a subduction zone-arc setting (central Urals and southeast Alaska), or as less regularly arranged bodies near the margins of stable cratons (e.g. Aldan-type along the Siberian Craton).

The presence of PGE alloys and the lack of base-metal sulfides in the dunites and chromite-bearing rocks has led researchers to conclude that the Alaskan-type complexes represent low-S systems (e.g. Johan, 2002). Only a few (Salt Chuck, Giant Mascot, GabbroAkarem-an Aldan-type complex) are known to contain significant quantities of magmatic sulfide mineralization. It has been suggested that because the belts which contain the ultramafic intrusions probably represent subduction zones, large volumes of S-rich mafic magmas should not be expected. However, ophiolites of supra-subduction zone origin (e.g. Prichard et al. 1996; Walker et al. 2002) are thought to represent high degree partial melts of fluid-fluxed mantle wedge material. Certainly the interaction of these magmas with sulfur derived from country rocks could initiate a favorable ore-forming environment. The belt of Alaskan-type complexes in southeastern Alaska has been linked to nearby volcanic rocks of the Gravina sequence (see below) along a major accretionary suture. Taylor (1967) and Irvine (1974) proposed that the complexes were feeders for large volumes of volcanic rocks. Murray (1972) proposed that linearly arranged Alaskan type complexes were genetically associated with andesitic lavas in subduction zone environments. The potential volume of magma with which the Alaskan complexes may have been associated could, therefore, have been very large, and not a deterrent to the formation of magmatic Cu-Ni-PGE sulfide deposits. Magma throughput in conduit systems is thought to be an important process for the upgrading of sulfide masses in strongly mineralized systems (Naldrett 1999; Ripley and Li, 2003). Although the volume of magma may have been less than in many flood basalt systems, there is no reason to suspect that the process could not have occurred in chambers and conduits associated with the Alaskan complexes.

3 Results from Duke Island

The Duke Island complex is a well-known Alaskan-type complex that consists of two spatially distinct, well exposed ultramafic bodies that are interpreted to be parts of the same intrusive system at depth. The intrusions are composed of dunite and wehrlite cores surrounded by concentric zones of olivine clinopyroxenite, hornblende-magnetite clinopyroxenite and gabbro. The complex is intruded by late hornblendite and hornblende plagioclase pegmatite. Recent investigations have identified significant sulfide mineralization associated with the complex.

This page intentionally blank

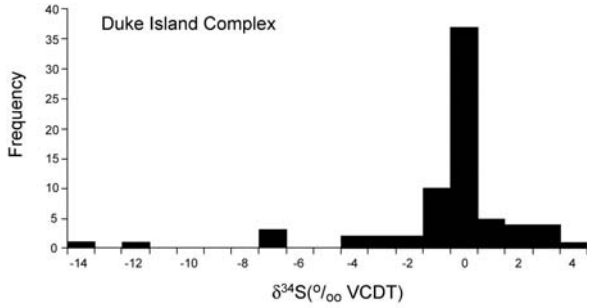

Figure 2: Sulfur isotopic values from Duke Island

Assays range up to 2.8% Cu, 0.25% Ni, and 1 gram/ton combined Pt + Pd. In areas of high sulfide concentration Cu/Ni ratios vary between 2 and 4, whereas in low sulfide zones the ratio drops to ~0.8. Pyrrhotite is the most common sulfide mineral present, with local concentrations of chalcopyrite and pentlandite.

Olivine in the ultramafic rocks varies from Fo_{77} to Fo_{85}; Ni in olivine ranges from less than 100 ppm to ~1000 ppm. Olivine in sulfide-poor rock types shows a negative correlation between Ni and Fe, characteristic of fractional crystallization. Olivine in sulfide-rich rocks contains less than 400 ppm Ni and shows no correlation between Ni and Fo content. Although Ni-exchange between sulfide and olivine is clear, the high-Ni olivine population indicates that under appropriate conditions, a Ni-rich sulfide liquid could be generated.

Sulfur isotopic values range from -15 to 4.6‰, with over 70% of the values between -2 and 2‰. Although most of the sulfur isotopic ratios are consistent with a mantle origin for S, the wide range in $\partial^{34}S$ values indicates that country rock sulfur has also been involved in sulfide genesis (Fig. 2).

Our preliminary data suggest that mineralization at Duke Island is characterized by geochemical signatures that at the very least are intriguing in terms of the prerequisites for world-class Cu-Ni-PGE ore formation. Additional geochemical and petrological studies at Duke Island are in progress. Current results suggest that the potential for mafic rock-related Cu-Ni-PGE deposits in convergent plate settings should not be overlooked.

References

Arcuri T (1998) Sulfur and oxygen isotopic studies of the interaction between pelitic xenoliths and mafic magma at the Babbitt and Serpenting Cu-Ni deposits, Duluth Complex, Minnesota. Econ Geol 93: 1063-1075

Godlevsky MN, Grinenko LN (1963) Some data on the isotopic composition of sulfur in the sulfides of the Noril'sk deposit. Geochem 1: 335-341

Gorbachev NS, Geinenko LN (1973) The sulfur isotope ratios of the sulfides and sulfates of the Oktyabv'sk sulfide deposit, Noril'sk region, and the problem of its origin. Geokhimiya 8: 1127-1136

Irvine TN (1974) Petrology of the Duke Island ultramafic complex, southeastern Alaska. GSA Memoir 138, 240

Johan Z (2002) Alaskan-type complexes and their platinum-group element mineralization. In: Cabri LJ (ed) The Geology, Geochemistry, Mineralogy, and Mineral Beneficiation of Platinum-Group Elements. CIM Special Volume 54: 669-720

Lesher CM, Keays RR (2002) Komatiite-associated Ni-Cu-(PGE) deposits. In: Cabri LJ (ed) The Geology, Geochemistry, Mineralogy, and Mineral Beneficiation of Platinum-Group Elements. CIM Special Volume 54: 579-618

Li C (2003) Compositional variations of olivine and sulfur isotopes in the Noril'sk and Talnakh intrusions, Siberia: Implications for ore-forming processes in dynamic magma conduits. Econ Geol 98: 69-86

Li C (2004) Compositional variations of olivine from the Jinchuan Ni-Cu sulfide deposit, Western China: Implications for petrogenesis and ore genesis. Mineral Dep 39: 159-172

Lightfoot P, Naldrett AJ (1999) Geological and Geochemical relationships in the Voisey's Bay intrusion, Nain Plutonic Suite, Labrador, Canada. Geol Assoc Can Short Course Notes 13: 1-30

Lightfoot PC (2001) Chemical evolution and origin of nickel-sulfide mineralization in the Sudbury Igneous Complex, Ontario, Canada. Econ Geol 96: 1855-1876

Murray CG (1972) Zoned ultramafic complexes of the Alaskan type: Feeder pipes of andesitic volcanoes. In Shagam RE et al (eds), Studies in Earth and Space Sciences (Hess Volume). GSA Memoir 132: 313-335

Naldrett AJ (1999) World-class Ni-Cu-PGE deposits: Key factors in their genesis. Mineral Dep 34: 227-240

Naldrett AJ, Lightfoot PC (1999) Ni-Cu-PGE deposits of the Noril'sk region, Siberia: their formation in conduits for flood basalt volcanism Geol Assoc CanShort Course Notes 13: 195-249

Parman SW (2001) The production of Barberton komatiites in an Archean subduction zone. Geophys Res Lett 28: 2513-2516

Prichard HM (1996) A model to explain the occurrence of platinum- and palladium-rich ophiolite complexes. Jour Geol Soc London 153: 323-328

Ripley EM (1981) Sulfur isotopic studies of the Dunka Road Cu-Ni deposit, Duluth Complex, Minnesota. Econ Geol 76: 610-620

Ripley EM (1999) Sulfur and oxygen isotopic evidence of country rock contamination in the Voisey's Bay Ni-Cu-Co deposit, Labrador, Canada. Lithos 47: 53-68

Ripley EM (2002) Paragneiss assimilation in the genesis of magmatic Ni-Cu-Co sulfide mineralization at Voisey's Bay, Labrador: ä^{34}S, ä^{13}C, and Se/S evidence. Econ Geol 97: 1307-1318.

Ripley EM, Li C (2003) Sulfur isotopic exchange and metal enrichment in the formation of magmatic Cu-Ni-(PGE) deposits. Econ Geol 98: 635-641

Ripley EM et al. (in press) Mineralogic and stable isotopic studies of hydrothermal alteration at the Jinchuan Ni-Cu deposit. Econ Geol

Ryan B (2000) The Nain-Churchill boundary and the Nain Plutonic Suite: A regional perspective on the geologic setting of the Voisey's Bay Ni-Cu-Co deposit. Econ Geol 95: 703-724

Stone WE (2003) Hydromagmatic amphibole in komatiitic, tholeiitic, and ferropicritic units, Abitibi greenstone belt, Ontario and Quebec: evidence for Archean wet basic and ultrabasic melts. Mineral Petrol 77: 39-65

Taylor HP Jr (1967) The zoned ultramafic complexes of southeastern Alaska. In Wyllie PJ (ed) Ultramafic and Related Rocks. John Wiley and Sons, Inc, New York, 96-118

Therriault AM (2002) The Sudbury Igneous Complex: A differentiated impact melt sheet. Econ Geol 97: 1521-1540

Walker RJ (2002) The osmium isotopic composition of convecting upper mantle deduced from ophiolite chromites. Geochem Cosmochim Acta 66: 329-345

The tectonics and metallogeny of the Precambrian of the Aldan-Stanovoy Shield

A.P. Smelov, V.F. Timofeev
Diamond and Precious Metal Institute, Siberian Branch, Russian Academy of Sciences, 39, Lenin av., 677891, Yakutsk, Russia

Abstract. The Aldan-Stanovoy Shield, located in the southeastern North Asian craton, resulted from the collision of Archean protocratons and Paleoproterozoic microcontinents in the period of 2.0-1.9 Ga. The tectonic structure of the Aldan-Stanovoy Shield is defined by a combination of terranes differing in age and degree of metamorphism. These are the West Aldan granite-greenstone terrane, the Central Aldan superterrane (Nimnyr granulite-orthogneiss and Sutam granulite-paragneiss terranes), the East Aldan superterrane (Uchur granulite-paragneiss and Batomga granite-greenstone terranes), as well as the Tynda tonalite-trondhjemite-gneiss and the Chogar granulite-orthogneiss terranes. The boundaries between the terranes are faults and collision suture zones. The overlap assemblages include diversified sedimentary and volcanogenic–sedimentary rocks of Paleoproterozoic age. We have recognized within the Aldan-Stanovoy shield: (1) pre-collisional metallogenic zones; (2) the collision-related Kalar-Uchur metallogenic belt of Paleoproterozoic age; and (3) the Chara-Uchur post-collisional belt related to intracontinental rifting in the late Pale-oproterozoic.

Keywords. Tectonics, metallogeny, Precambrian, Aldan-Stanovoy Shield

1 Introduction

The tectonic structure of the Aldan-Stanovoy Shield was studied and mapped using the methods of terrane analysis. There are several large terranes which are bounded by faults and collisional suture zones (Fig. 1).

The West Aldan composite terrane of granite-greenstone type consists of several terranes which are made of greenstone and tonalite-trondjhemite complexes. The metamorphic grade of these rocks changes from greenschist to amphibolite facies. The granite-greenstone complexes were formed and metamorphosed during two episodes (> 3.0 and 3.0-2.6 Ga). The age of amalgamation of these terranes into a single composite terrane is 2.6 Ga.

The Central Aldan superterrane of granulite-orthogneiss type consists of Nimnyr and Sutam terranes, which consist of Archean and Paleoproterozoic rocks. The age of the peak metamorphism is 2.1-1.9 Ga. The earlier metamorphic events are possible in the orthogneiss complexes of these terrane.

The East Aldan Paleoproterozoic superterrane consists of the Batomga terrane of granite-greenstone type and Uchur terrane of granulite-paragneiss type. The age of granulite facies metamorphism is 2.1-1.9 Ga in the Uchur terrane.

The Tynda composite terrane of tonalite-trondjhemite type contains small tectonic slabs and blocks which consist of paragneiss complexes. The metamorphic grade of the paragneisses is amphibolite and granulite facies. The high-grade metamorphism is older than 2.5 Ga.

The collisional suture zones separate different terranes and were formed at 1.9 Ga. The zones consist of tectonic slabs and blocks with different rock assemblages of neighbouring terranes. This mixture experienced the combined structural and metamorphic reworking (from greenschist to granulite facies). They are commonly characterized by a higher content of basic and intermediate rocks.

The tectonic position and age of terranes is defined by collision of the Archean and Paleoproterozoic terranes into a single structure, the Aldan-Stanovoy Shield, and the processes of collapse of the orogenic belts at 1.9-1.7 Ga.

With regard to collisional structures, we have recognized within the Aldan-Stanovoy Shield (fig. 1): (1) pre-collisional metallogenic zones; (2) the collision-related Kalar-Uchur metallogenic belt of Paleoproterozoic age; and (3) the Chara-Uchur post-collisional belt related to intracontinental rifting in the late Paleoproterozoic (Parfenov et al. 1999; Nokleberg et al. 2003).

2 Pre-collisional metallogenic zones

Two pre-collisional metallogenic zones of Archean age, West Aldan and Sutam, are established in the Aldan-Stanovoy Shield.

2.1 West Aldan metallogenic zone

The West Aldan metallogenic zone lies within the West Aldan granite-greenstone composite terrane composed of linear greenstone belts made up of metavolcanogenic-sedimentary rocks dated at 2.8-3.2 Ga, which are surrounded by areas of tonalite-trondhjemite gneiss, granite. The West Aldan zone contains large Fe deposits and Au and Pt occurrences in greenstone belts.

The Temulyakit-Tungurcha Au ore district extends sublongitudinally for 200 km and is 50 km wide. It is made up of Late Archean metavolcanogenic-sedimentary and metasedi-mentary deposits of greenstone belts as well as tonalite-trondhjemite gneisses and different-type granites. The Lemochi Au occurrence is in the central part of

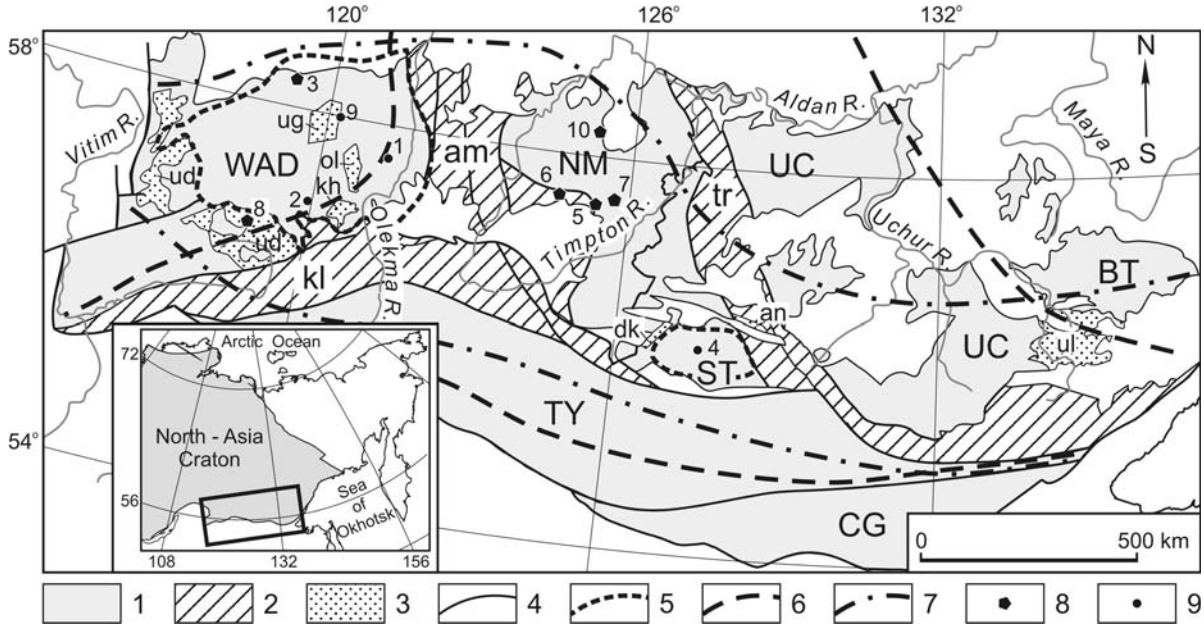

Figure 1: Metallogenic Map of the Aldan-Stanovoy Shield. 1 - Terranes: Granite-greenstone (WAD = West Aldan, BT = Batomga), Tonalite-trondhjemite gneiss (TY = Tynda), Granulite-orthogneiss (NM = Nimnyr, CG = Chogar), Granulite-paragneiss (ST = Sutam, UC = Uchur); 2 - Collision suture zones (kl = Kalar, am = Amga, tr = Tyrkanda; 3 - Paleoproterozoic overlap assemblages (ud = Udokan, ug = Uguy, ol = Oldongso, kh = Lover Khani, an = Atugey-Nuyam, dk = Davangra-Khugdin, ul = Ulkan basins); 4 - Faults; 5 - Pre-collisional metallogenic Zones (West Aldan and Sutam); 6 - Kalar-Uchur Collision-related metallogenic belt; 7 - Chara-Uchur Post-collision rift-related metallogenic belt; 8 - Deposits; 9 - Occurrences. The Batomga and Uchur terranes make up the East Aldan superterrane, and the Nimnyr and Sutam terranes form the Central Aldan superterrane. *Deposits and occurrences:* 1 - Lemochi, 2 - Olondo, 3 - Tarynnakh, 4 - Olimpiyskoe, 5 - Tayozhnoe, 6 - Dyosovskoe, 7 - Foydorovskoe, 8 - Udokan, 9 - Usuu, 10 - Seligdar. Inset shows location of the region

the Tasmiele greenstone belt. Gold ore is associated with pyrrhotite-bearing metabasalt, quartz veins and veinlets, quartz-tourmaline and quartz metasomatites, diaphthorites, and metagabbro. Maximum Au concentration (14.1 g/t) is found in metabasalt.

The Tokko-Khani Au ore district is 10-30 km wide and extends sublongitudinally for 200 km within the limits of the Olondo greenstone belt formed from metamorphosed volcanites and volcanogenic-sedimentary and intrusive rocks. At the Olondo Au occurrence, the amount of Au in metabasites and metahyperbasites varies from 1 to several tens of mg/t. Sampling of one of the metasomatite zones shows that Au is evenly distributed over the orebodies in amounts of 3-5 g/t.

The Imalyk Fe ore district is 300 km long and 20-30 km wide and occurs in the Tarynnakh greenstone belt of Late Archean age. The Tarynnakh Fe deposit extends sublongitudinally for 25 km and is 3-4 km wide. The deposit consists of three orebodies separated by granite, gneiss and schist of varying composition. The orebodies are traced for 22.5 km and are 330 m thick. The ores are dominated by fine-grained hornblende magnetite ferruginous quartzite. Cummingtonite-magnetite, chlorite-magnetite, and magnetite varieties are also present. Iron quartzite is interlayered with quartz schists and quartzite up to 1.4-3.3 km thick, as well as with amphibole-plagioclase schist and amphibolite 0.5-7 m in thickness and granitoids as thick as 0.2-8 m. Iron ore reserves of the Tarynnakh deposit are estimated at about 2 billion tonnes averaging 28.1% Fe_{total} and 21.0% $Fe_{magnetite}$.

2.2 Sutam metallogenic zone

The Sutam zone lies in the south of the Central Aldan superterrane, within the limits of the Sutam terrane consisting of gneiss dated at 2.5-3.0 Ga and subjected to the granulite facies metamorphism at high pressure. The Olimpiyskoe iron deposit is 11 km long and 3-4 km wide. Two rock groups are identified here. The first is magnetite-hypersthene and magnetite-two mica gneiss interbeded with amphibole-two mica and magnetite-two mica-plagioclase schists. The rocks form the core of an antiform. The iron ore horizon, consisting of magnetite and hypersthene-magnetite quartzite, is restricted to the outer part of the antiform. The second rock group, making up the core of a synform, consists of feldspar quartzite interlayered with garnet- and sillimanite-bearing varieties. Eleven lenticular orebodies 0.5-4 km thick and 20-200 m long are identified here. They consist of medium- and coarse-grained banded hypersthene-magnetite quartzite. $Fe_{magnetite}$ varies from 25.3 to 36.98%, S- from 0.08 to 0.13%.

3 Kalar-Uchur collision-related metallogenic belt

The Kalar-Uchur metallogenic belt covers a large part of the Aldan-Stanovoy shield and certainly continues northward beneath the platform cover. Its formation was related to collision of the Early Precambrian terranes into a large continental block. The collision was accompanied by the formation of collision suture zones separating terranes, metamorphism of the granulite and amphibolite facies within the terranes, and by calc-alkaline and subalkaline granitoid magmatism.

The belt includes several metallogenic zones (Kalar-Stanovoy, Amga-Stanovoy, and Tyrkanda-Stanovoy) coinciding with the collision zones, which bear Au, Ag, and Pt mineralizations. Several metallogenic zones lie within the terranes. The Dyos-Leglier metallogenic zone contains large Fe skarn deposits. There are the Timpton and Uchur metallogenic zones with large, long-known phlogopite skarn deposits.

3.1 Dyos-Leglier metallogenic zone

The Dyos-Leglier matallogenic zone includes the South Aldan and Emeldzhak ore districts.

The South Aldan Fe ore district contains the Leglier, Dyos, and Sivagli groups of deposits. The largest are the Tayozhnoe and Dyosovskoe deposits. The Tayozhnoe Fe skarn deposit consists of silicate-magnetite ores (magnetite skarns), magnesian skarns, calciphyre, and biotite gneiss. Host rocks include amphibole gneiss and schist and high-alumina gneiss and quartzite-gneiss. They are intruded by meta-ultrabasite and metagabbro-diorite units. In plan, the deposit is shaped like a horse-shoe curved to the north-west and in section it is a recumbent synform steeply dipping to the south-west. Concordant and en-echelon orebodies are 2 km long and 10-100 m thick. Pyrite, pyrrhotite, and chalcopyrite are constantly present. Some beds contain ludwigite and ascharite. Mineralization and the amphibolite facies metamorphism are dated at 2.1-1.9 Ga. The iron content is 20-60% (average 39.8%), S amounts to 2.12%, and P is practically absent (P_2O_5=0.1%).

3.2 Timpton metallogenic zone

The Timpton metallogenic zone occupies the south-eastern part of the Nimnyr granulite-orthogneiss terrane. It extends for 250 km and is 250 km wide in the south and 50 km in the north. The phlogopite deposits and occurrences tend to occur in diopside and phlogopite-diopside schists, marbles, and calciphyres of Paleoproterozoic age (2.3-2.1 Ga) metasomatized into coarse-grained phlogopite-diopside skarns dated at 1.9-1.8 Ga. The Foydorovskoe deposit occurs on the northern limb of a latitudinal synform under the same name. It extends for 5 km and is 100-150 m wide. The mica-bearing zones are 20-200 m long and 3-12 m thick and include some phlogopite-bearing bodies of different orientation consisting of phlogopite, diopside, hornblende, scapolite, apatite, and actinolite. Phlogopite forms nest-like accumulations varying in size from 0.5x1 m to 1.5x6 m The phlogopite content ranges from 15 to 86.9 kg/m^3.

4 Chara-Uchur post-collision rift-related metallogenic belt

The Chara-Uchur metallogenic belt extends latitudinally across the northern area of the Aldan-Stanovoy shield (Fig. 1). It was formed in the late Early Proterozoic between 1.9 and 1. 7 Ga. The belt was related to rifting, resulting in the formation of grabens, bimodal volcanism, and the emplacemet of alkali granitoids, alkali-ultrabasic and basic rocks and carbonatites. The belt includes the Uguy-Udokan metallogenic zone of Cu sandstone, the Nimnyr metallogenic zone with a large apatite and REE deposit in carbonatites, the Upper Aldan metallogenic zone with piezoquartz deposits, and the Davangra-Nalurak metallogenic zone of Fe oolitic ores and REE mineralization.

4.1 Uguy-Udokan metallogenic zone

The large Udokan Cu sandstone deposit is to the southwest of the study area, within the Udokan basin trough filled in with thick (up to 10 000 m) clastic and minor carbonate rocks dated at 2.2-1.8 Ga. On the territory of Yakutia, the rocks corresponding to the Udokan group fill in relatively small graben-like Uguy, Oldongso, and Lower Khani basins, unconformably overlying various crystalline rocks of the West Aldan terrane. The best-studied are Cu deposits of the Uguy basin. The Usuu Cu occurrence is in the Charodokan formation which is traced for 25 km along the eastern flank of the Uguy basin and includes lagoonal-bar facies. Three thick horizons of Cu mineralization are recognized here. The lower horizon corresponds to carbonate-sandy rocks. Cupper mineralization occurs as rare Cu-sulfide disseminations. The middle horizon is associated with quartzitic sandstones bearing more abundant Cu-sulfide disseminated mineralization. Thickness of the horizon attains locally 60 m with Cu content up to 1%. The upper horizon is characterized by disseminated Cu-sulfide mineralization in sandy dolomites of brecciform structure and cross-bedded sandstones with a carbonate matrix. It is 84 m thick, with Cu to 0.11-1%.

4.2 Nimnyr metallogenic zone

The Nimnyr metallogenic zone of apatite ores in carbonatites extends longitudinally for 400 km in the northern Aldan-Stanovoy shield and is 40 km wide in its central part. The zone includes eleven ore deposits and

occurrences. The Seligdar deposit of apatites in carbonatites represents an asymmetric stock 2 by 1.0 km in area, narrowing down to a few hundreds of square meters at a depth of 1.6 km. The stock includes carbonatites and apatite-carbonate-quartz ores.

4.3 Davangra-Nalurak metallogenic zone

The zone lies within the Atugey-Nuyam and Davangra-Khugdin grabens located in the Centeral-Aldan superterrane. The grabens consist of thick quartz and arkose sandstone units with gravelstone horizons. REE occurrences are restricted to the gravelstone and conglomerate horizons which are 15-30 long and have a thickness varying from a few meters to 150 m. Principal minerals in the heavy fraction of the rocks are monazite and zircon (up to 95%). The conglomerate-gravelstone horizons of the Davangra-Khugdin graben contain 0.1-1% Ce, 0.01-0.3% La, 0.01-0.3% Y, and 0.01-0.03% Hf, whereas those from the Atugey-Nuyam graben contain 0.1-0.8% Ce, 0.01-0.1% Y, 0.03-0.05% La, 0.01-1% Ta, and up to 0.005% Nb.

Acknowledgements

The work has been completed within the framework of the International Project on "Mineral Resources, Metallogenesis, and Tectonics of Northeast Asia". We are grateful to the Siberian Branch, RAS for financial support of Projects NN 69, 161 and 6.7.6.

References

Nokleberg, WJ, Miller RJ, Naumova, VV, Khanchuk, AI, Parfenov, LM, Kuzmin, MI, Bounaeva, TM, Obolenskiy, AA, Rodionov, SM, Seminskiy, ZhV, Diggles, MF (Eds), (2003) Preliminary publication Book 2 from Project on Mineral Resources, Metallogenesis, and Tectonics of Northeast Asia. Open-File Report 03-203, Version 1.0, US Geological Survey, US Department of the Interior, USA, CD-Version.

Parfenov, LM, Vetluzhskikh, VG, Gamyanin, GN, Davydov, YuV, Deikunenko, AV, Kostin, AV, Nikitin VM, Prokopiev, AV, Smelov, AP, Supletsov, VM, Timofeyev, VF, Fridovskiy, VYu, Kholmogorov AI, Yakovlev YuV (1999) Main Metallogenic Units of the Sakha Republic (Yakutia), Russia. J. Internetional Geology Review 41: 425-456

New classification of magmatic sulphide deposits in China and metallogenesis related to small intrusions

Tang Zhongli, Yan Haiqing, Jiao Jiangang
College of Earth Science and Land Resource, Chang'an University, No.126, Yanta Route, Xi'an, China

Li Xiaohu
Lanzhou University, Lanzhou 730000, China

Abstract. Many important metals, such as Ni (Cu, Co) and PGE, are taken from magmatic sulfide deposits. The magmatic sulphide deposits in China can be divided into four types according to their tectonic setting, size of intrusion, ore deposit mode, deposit scale, rock types and metallogenic elements. The four types are: (1) Deposits hosted in intra-continental small intrusions; (2) Deposits associated with continental flood basalts; (3) Deposits associated with small intrusions in orogenic belts; and (4) Deposits related to ophiolites. Among them the first type is the most important in China. According to the experience of prospecting, we propose that there are big potentialities for prospecting ore deposits in small intrusions. Mineralization not only occurs in small mafic-ultramafic intrusions, but also in small intermediate-felsic intrusions with important economic value.

Keywords. Magmatic sulfide deposits, new classification, small rockbodies, metallogenesis

1 Classification of magmatic sulphide deposits

Previous classifications of magmatic sulphide deposits are mainly focused on the controlling factors of geological settings and rock types (Tang, 1996; Liu, 1998). These classifications were helpful for prospecting and research. However, as the development of geological studies advances, small intrusions have been recognized as being important in mineralization. It thus is necessary to put forward a new classification as detailed in Table 1.

2 Characteristics of different types of magmatic sulphide deposits

2.1 Deposits hosted in intra-continental small intrusions

This type of deposits usually occurs in rifts at the margins of Palaeo-continents. In China, these deposits are of Proterozoic age. Mafic and ultramafic magmas originated from mantle emplaced in deep-seated magma chambers. Due to melt-separation and crystallization differentiation, four melt layers formed and include sulfide melt, sulfide-rich silicate magma, sulfide-bearing magma and silicate magma from the base upward.s The four-layer magmas penetrated into different spaces once or several times, and formed several to tens rock groups (or zones). Intrusions are, however, not usually mineralized. We propose classification criteria for small intrusions (i.e. less than an area of 10 square kilometres). Mineralization related to small intrusion is the main metallogenic pattern in China, such as the deposits in Jinchuan, Chibaisong, Tongdongzi and Xiaonanshan.

2.2 Deposits associated with continental flood basalts

This type of deposits formed in igneous intrusions related to the extrusion of large-scale continental flood basalts in the geological history. One characteristic of this type of ore deposits is that the hosting intrusions show a close spatial relationship with the flood basalts. According to the main metallogenic element association, the deposits can be divided into two subtypes: Ni-Cu-Co-Pt and Pt-Pd-Ni-Cu ones. The former is mainly composed of Ni and Cu, such as the Baimazhai and Dapoling deposits; and the latter is mainly composed of Pt and Pd, such as the Jingbaoshan and Yangliuping deposits.

2.3 Deposits associated with small intrusions in orogenic belts

This type of deposit formed during post-orogenic extension mainly in Carboniferous-Permian in China. The metallogenic mechanism is similar to ore deposits in intra-continental small intrusions.

2.4 Deposits related to ophiolites

From the base to top, ophiolites generally consist of four parts: ultra-mafic complex, gabbro cumulative complex, mafic sheet dyke complex and mafic volcanic complex, each of which has different mineralization (Zhang, 2000). The mineralization usually occurs during the stage of growth and movement of oceanic crust. However, the oceanic crust is a dismembered slice in orogenic belts due to tectonic emplacement. Different parts of the opliolites show diverse mineralization. Some ore deposits belong to this type in China, such as those of Jianchaling in Proterozoic Era, and Shijuli, and De'erni.

Table 1: Types of magmatic sulfide deposits in China

Tectonic setting	Intruding way	Ores-hosted main rocks	Deposit mode	Deposit scale	Main metallogenic elements
Palaeo-continent	Small intrusion	Lherzolite	Jinchuan	Supper large	Ni, Cu, Co, Pt
		Diabase,Gabbro	Chibaisong	Middle	
		Gabbro-Diabase	Tongdongzi	Small	
		Gabbro	Xiaonanshan	Small	
	Intrusion associated with the continental flood basalt	Diorite-Gabbro-Diabase- Pyroxenite	Dapoling	Small	Ni, Cu, Co, Pt
		Diorite-Gabbro-Peridotite	Limahe	Middle	
		Gabbro-Pyroxenite-Peridotite	Baimazhai	Middle	
		Diabase-Gabbro-Peridotite	Jinbaoshan	Large	Pt, Pd, Ni, Cu
		Gabbro-Peridotite	Yangliuping		
Orogenic belt	Small Intrusion	Enstatatite	Hongqiling	Large	Ni, Cu, Co, Pt
		Gabbro-Peridotite-Lherzolite	Huangshan	Large	
		Norite-Olivine Norite	Kalatongke	Large	
	Ophiolites	Basalt-Clastic rock-Jade	Shijuli	Middle	Cu, Zn
		Talc- Magnesite Orthopyroxene-Pyroxenite Olivine	Jianchaling	Large	Ni
		Pyroxenite-Peridotite-Orthopyroxene-Pyroxenite Olivine	De'erni	Large	Cu, Zn, Co, S

3 Metallogenesis of small rock-bodies

3.1 The main type of magmatic sulfide deposits in China

The first three types of magmatic deposits are spatially and temporally associated with small intrusions (Table 1). Super large deposits (such as Jinchuan) and large scale ones such as Hongqiling, Kalatongke, Huangshan, Jinbaoshan are also hosted in small intrusions. Ni-Co-PGE metal resources in China mainly come from this type of ore deposits. Although some magmatic sulfide deposits, such as De'erni and Jianchaling, are related to ophiolites. They are less important in terms of their economic values.

3.2 Concept on magmatic deposits in small intrusions

Tang (2002) suggested a model for magmatic deposits in small intrusions. This can be summarized as following: Large-scale, rich ore bodies form in small magmatic intrusions or nearby; the size of small intrusions is typically less than 10 square kilometers, and some are less than one square kilometer; the mineralized proportion (the volume of orebody /the volume of intrusion x 100%) of small intrusions is high. The mineralized proportion is more than 43% in Jinchuan, Kalatongke ore deposit is more than 50%, and No. 7 ore body of the Hongqiling ore deposit is more than 90%.

3.3 Small intrusions in three geological settings

Some small intrusions occur in rifts at the margin of the Palaeo-continent, and their metallogenic epochs are mainly at Palaeo-Proterozoic and meso-Proterozoic (such as the Chibaisong and Jinchuan deposits), and Paleozoic (such as the Xiaonanshan deposits). Some small intrusions are at the margin of the Palaeo-continents, and associated with the continental flood basalts. Their metallogenic epochs are mainly late-Proterozoic (such as the Dapoling deposits), and Paleozoic (such as the Limahe, Baimazhai, Jinbaoshan and Yangliuping deposits). Some small intrusions in orogenic belts are related to post-orogenic extension. Their metallogenic epochs are mainly Paleozoic (such as the Kalatongke, Hongqiling, and Huangshan deposits).

3.4 Key factors for formation of magmatic deposits in small intrusions

The magmatic ore deposits in small intrusions occur along deep faults. For instance, the suture between the North China block and Qilian mountains on the southern side of the Jinchuan ore deposit; the Kangguertage – Huangshan deep fault on the southern side of the Huangshan ore deposit; the Huifahe deep fault on the southern side of the Hongqiling ore deposit and the Eerqisi

This page intentionally blank

north-west deep fault on the northern side of the Kalatongke ore deposits all provided channels for mantle magmas to ascend and mineralize. Olivine-rich magmas and orthopyroxene-rich magmas are helpful for metallogenesis. Olivine-rich magma is characterized by high temperature and high nickel content, and is easy for contaminating SiO_2-rich country rock. The ore deposits of Jinchuan, Huangshan, Baimazhai, Noril'sk, Voisey's Bay are associated with olivine-rich magmas. Orthopyroxene-rich magmas may have the same significance as olivine-rich magmas. No.7 ore body of the Hongqiling ore deposit and Kalatongke ore deposit formed from orthopyroxene-rich magmas. There are wo types of sulfur source. Firstly, there is a small change in the values of $\delta^{34}S$, which are close to zero and distributed with normal distribution, indicative of characteristics of magmatic sulfur The Jinchuan, Hongqiling, Kalatongke, Huangshan, Chibaisong and Sudbury are the examples of this. Secondly, there are large scale variations in $\delta^{34}S$, which appear to be related to contamination with crustal sulfur. The Limahe, Noril'sk and Voisey's Bay are samples for this type. From the above discussion, we can state that mantle sulphur is the main characteristic of magmatic deposits in small intrusions in China. As the host intrusion is small in size, the ore bodies are relatively big and cannot derive solely from the small intrusion itself. Thus, during or prior to the emplacement of the intrusion, partial crystallization and liquation of magma must have occurred in the deep seated magma chambers, where the magma formed several parts: ore magma, sulfide-rich magma, sulfide-bearing magma and ore-free silicate magma from the base upwards. Then the differentiated magma penetrated into different spaces within the crust once or several times. In general, after the crystallization and differentiation and liquation of magma, the volume of ore-free silicate magma is much larger than the total volume of ore magma, sulfide-rich magma and sulfide-bearing magma. During the magma ascending, ore-free silicate magma penetrated into different spaces to form intrusive complex or erupt to the surface to form lavas. The remeining magma comprising ore magma, sulfide-rich magma and sulfide-bearing magma can penetrate into the same space, such as occurred in the Jinchuan, Kalatongke, Baimazhai and Limahe deposits, or penetrate into different spaces, such as the No.1 and No.7 ore bodies of the Hongqiling deposits. By comparison with local liquation, the ore/rock proportion of the small intrusions is much higher than average. This mechanism can explain why a small intrusion is accompanied by a large or supper large deposits.

4 Further study on magmatic deposits in small intrusions

Prospecting for this type of magmatic sulfide deposits started in 1980s in China. The Noril'sk-Talnanhk deposits are the other examples, with major reserves of copper and nickel within an area of 3 square kilometers. The Voisey's Bay deposits cover an area of less than 1 square kilometers. Some researchers have put forward "why are there no major Ni-Cu sulfide deposits in large layered mafic-ultramafic intrusions?" (e.g. Maier 2001).

From the present study on magmatic sulfide deposits, the deposits in small intrusions are Cu-Ni-PGE deposits with higher tenor of Cu and Ni than PGE, but the deposits in large layered intrusions are Pt-Pd deposits with low tenor of Cu and Ni. As there are no large layered intrusions in China, we should pay more attention to prospecting for Cu-Ni-PGE deposits in small intrusions.

On the other hand, metallogenesis in intrusions is not only important to mafic-ultramafic rocks, but also have important economic value and academic significance in intermediate-acidic rocks.

References

Naldrett AJ (1999) World-class Ni-Cu-PGE deposits: key factors in their genesis. Mineralium Deposita 34: 227-240

Liu YX, Tang HS, Wu HZ (1998) Types and ore–control factors of Cu-Ni sulfide deposits in China. Mineral Resources and Geology 12: 86-90. (in Chinese)

Tang ZL (196) Main types of magmatic sulfide deposit in China. Acta Geology Gansu 5: 45-64. (in Chinese)

Tang ZL (2002) Magmatic ore deposits in small intrusions in China. Engeering Science 4 : 9-12.(in Chinese)

Maier WD, Chusi L, De Waal S (2001) Why are there no major Ni-Cu sulfide deposits in large layered mafic-ultramafic intrusions? Canadian Mineralogist 39: 547-556

Zhang Q, Qian Q, Wang Y (2000) Rock Assemblages of Ophiolites and Magmatism beneath Oceanic Ridges. Acta Petrologica et Mineralogica 19: 1-7 (in Chinese)

Geodynamic controls on giant metallogenic provinces: Insights from gold provinces in southeast Australia

I.M.A. Vos
*ACRC / pmd*CRC, School of Geosciences, Monash University, PO Box 28e,VIC 3800, Australia*

F.P. Bierlein
*TSRC / pmd*CRC, School of Earth and Geographical Sciences, University of Western Australia, 35 Stirling Hwy, Crawley, WA 6009, Australia*

P.S. Heithersay
*PIRSA / pmd*CRC, GPO Box 1671, Adelaide, SA 5001, Australia*

G.S. Lister
RSES, Australian National University, Mills Rd, Canberra, ACT 0200, Australia

Abstract. The geodynamic processes that control large-scale accumulations of ore are poorly understood. It has commonly been suggested that massive ore deposits are generated through a combination of factors in the Earth's system. In the Lachlan Fold Belt of southeastern Australia, world-class orogenic gold and porphyry gold-copper deposits formed simultaneously at ~440 Ma in distinct tectonic settings. The driving mechanism that controlled the extraordinary temporal coincidence of these deposits remains largely unexplained. We propose that the interplay of a mega-subduction system and mantle processes could explain the generation of the giant ~440 Ma gold deposits and related metallogenic, tectonic, magmatic and sedimentary events elsewhere in Australia.

Keywords. Metallogeny, giant ore deposits, 440 Ma, Gondwana, mega-subduction, mantle upwelling

1 Introduction

The Lachlan Fold Belt in southeastern Australia is host to a variety of mineral deposit types, and is internationally recognized as being an area of extraordinary gold endowment (e.g. Bierlein et al. 2002). A disproportionally large number of mineralisation ages for gold deposits in the Lachlan Fold Belt concentrate around 440 Ma (e.g. Perkins et al. 1995; Foster et al. 1998). These include the world-class lode-gold deposits at Bendigo, Stawell and Ballarat, and the porphyry copper-gold deposits at Cadia and Northparkes. Although these deposits reflect distinct mineralisation styles that formed in different tectonic settings (e.g. Gray et al. 2002), their similar formation ages record an extraordinary coincidence for which the driving mechanism remains enigmatic. Similarly, the first-order controls on large ore accumulations formed throughout Earth history remain a matter of debate. To gain insight in what processes control the coincident deposition of world-class ore deposits in distinct tectonic settings, we focus on the ~440 Ma event in Australia.

Throughout most of the Palaeozoic, Australia was situated on the margin of Gondwana inboard of a giant subduction system that essentially surrounded the supercontinent (Fig. 1). We propose that changes of subduction zone dynamics, for instance slab break-off, along continental margins are controlling factors for the generation of large ore deposits. In a supercontinent - mega-subduction zone setting, break-off of a portion of the subducting slab could account for the formation of extraordinary large ore deposits.

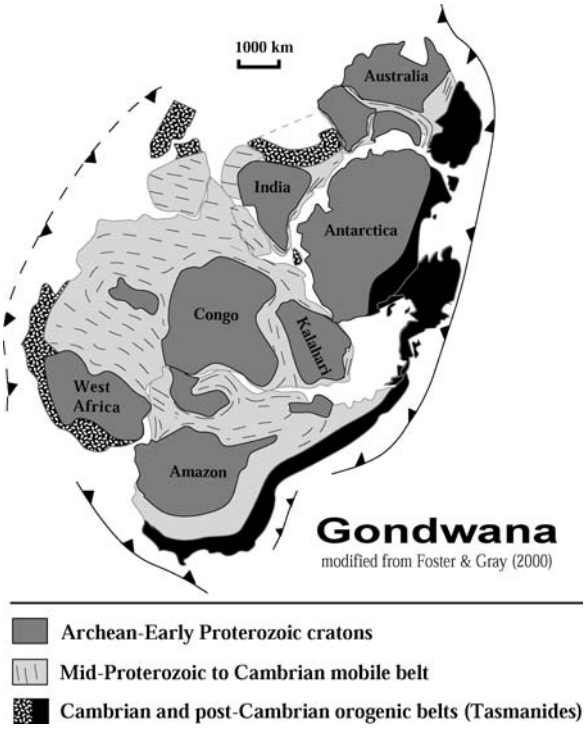

Figure 1: Gondwana surrounded by a mega-subduction zone around the Ordovician – Silurian boundary. Active subduction occurred on the margin of the Australian craton (top-right), where the Tasman Fold Belt System (or Tasmanides) was formed

Table 1: Summary of ~440 Ma gold deposits in the Lachlan Fold Belt based on $^{40}Ar/^{39}Ar$ geochronology

Deposit	Style	Tonnage	Age (Ma)	Reference
Ballarat East	or	67.9	455 ± 2	Foster et al. (1998)
			~440 Ma	Bierlein et al. (2001)
Bendigo	or	693.2	439 ± 2	Foster et al. (1998)
			442 ± 4	Bierlein et al. (2001)
Browns Creek	sk	28.5	425 ± 4.5	Ewers et al. (2002)
Cadia	por	259.6	440 ± 3	Perkins et al. (1995)
Copper Hill	por	16.8	447 ± 5	Ewers et al. (2002)
Fosterville	or	>4	381 ± 2	Bierlein et al. (2001)
Gidginbung	por		461.5 ± 4.7	Perkins et al. (1995)
Glendale	por		439.3 ± 2	Perkins et al. (1995)
Goonumbla	por		440 ± 1.1	Perkins et al. (1995)
Lake Cowal	por	99.6	439.6 ± 1.0	Perkins et al. (1995)
North Parkes	por	1.4	439 ± 1.1	Perkins et al. (1995)
Sheahan-Grants	sk		440	Ewers et al. (2002)
Stawell	or	123.9	439 ± 2	Foster et al. (1998)
Tarnagulla	or	>20	419 ± 2	Bierlein et al. (2001)
Wattle Gully	or		441 ± 3	Foster et al. (1998)

Abbreviations: or = orogenic gold; sk = skarn; por = porphyry Au-Cu.

2 The ~440 Ma event in Australia

The occurrence of a significant large-scale event is suggested based on the abundance of ~440 Ma aged events in Central and Eastern Australia. Their distribution is illustrated in Figure 2 and includes the following events:

1. Simultaneous orogenic lode gold and porphyry gold-copper mineralisation in the Lachlan Fold Belt (e.g. Bierlein et al. 2002; Table 1).
2. Large-scale geodynamic changes in the Lachlan Fold Belt (e.g. Vandenberg et al. 2000; Vos et al. 2003).
3. A magmatic-hydrothermal event in the Mt. Painter Inlier, southern Australia (Elburg et al. 2003).
4. Extensive lead-zinc mineralization in the Flinders Ranges, southern Australia (Groves et al. 2003).
5. Large-scale geodynamic changes in the Arunta Inlier, central Australia (e.g. Mawby et al. 1999; Scrimgeour and Raith, 2001; Hand et al. 2002).

3 Slab break-off – a possible driving force?

We suggest that the simultaneous occurrence of events in Australia that include the genesis of world-class gold deposits is caused by a single broadly synchronous phenomenon around 440 Ma. We hypothesise that an episode of mantle upwelling has been triggered by slab break-off along a portion of the mega-subduction zone outboard of south-eastern Australia at ~440 Ma. The introduction

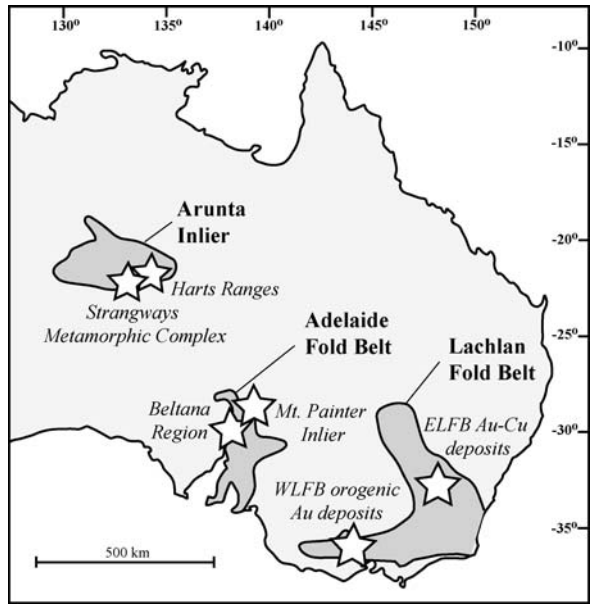

Figure 2: Distribution of ca. 440 Ma ages and events in Australia. Stars indicate ~440 Ma localities; see text for details. WLFB / ELFB = Western / Eastern Lachlan Fold Belt

of heat and fluids in response to mantle upwelling caused the generation of the massive gold provinces in south-eastern Australia. The magnitude of this event was such that it is considered to have caused a ripple effect that intiated changes in lithospheric conditions elsewhere in Austrilia.

Throughout Earth history, a connection between heat anomalies and gold mineralisation has been recognised (e.g. Barley et al. 1998; De Boorder et al. 1998; Goldfarb et al. 2001). In addition, most Mesozoic to recent orogenic gold mineralisation in the Pacific Rim has been associated with accretion of arcs or oceanic plateaus and rapid migration of subduction zones (Goldfarb et al. 1998). During these processes, peripheral orogens undergo major crustal contraction and crustal thickening (Collins 2003).

Previous studies in southeastern Australia suggest that subduction lock-up in response to subduction of a buoyant seamount or arc collision occurred along the south-east Australian margin at ca. 455 Ma and controlled crustal contraction inboard of the subduction system (e.g. Glen et al. 1998; Squire and Miller 2003). While such a process might explain regional geodynamic changes in the Lachlan Fold Belt, it fails to account for the wider occurrence of events at 440 Ma elsewhere in Eastern and Central Australia. As part of the mega-subduction zone system surrounding Gondwana, we envisage that the arrival of a buoyant seamount or arc in the subduction system would have created a regional heterogeneity. At ~440 Ma, a portion of detached following subduction resistance outboard of southeastern Australia.

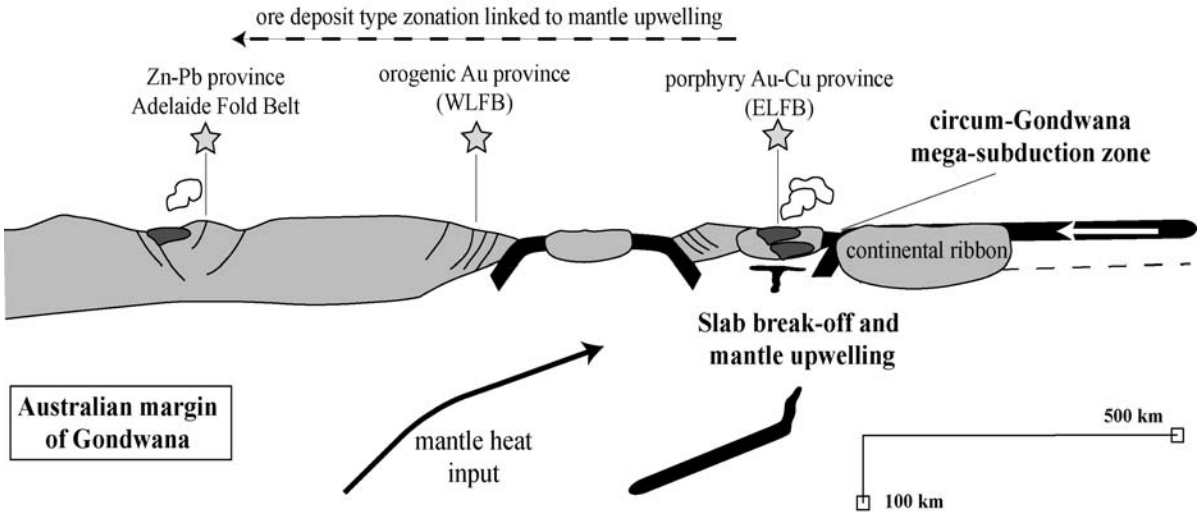

Figure 3: Schematic cross-section of southeastern Australia around 440 Ma illustrating break-off of a portion of the mega-subduction zone on the margin of Gondwana. Slab break-off triggers mantle upwelling, which in turn controls the generation of world-class mineral deposits provinces, including the world-class orogenic and porphyry gold-copper provinces in the western and eastern Lachlan Fold Belt (ELFB and WLFB, respectively). Due to the giant scale of the subduction system, related effects were propagated far inboard of the subduction margin and caused geodynamic changes elsewhere in Australia

The removal of the cooling effect from subduction allowed mantle upwelling and depressurisation and caused significant changes in the geodynamic framework in the southeast Australian portion of Gondwana. The instantaneous introduction of mantle heat has played an important role in ore deposition as well as other magmatic and tectonic events and depositional changes that occurred around 440 Ma elsewhere in Australia. The interplay of these processes is illustrated in Figure 3.

4 A crucial role for slab break-off in the generation of giant ore deposits?

Could generation of giant ore deposits have been controlled by heat anomalies associated with slab break-off and related effects? De Boorder et al. (1998) recognised a spatial correlation between hot regions in the lithosphere as indicated by results from seismic tomography that are interpreted to represent detachment of a cold slab or lithospheric root and mineralised areas in the European Alpine Belt. Metallogenic provinces like the Witwatersrand basin and Palaeoproterozoic basins of West-Africa are also suggested to reflect the interactions of mantle plumes with long-lived convergent margin systems (Barley et al. 1998). Kerrich and Wyman (1990) proposed a model for Archaean lode-gold mineralisation that includes metamorphic dehydration of submarine volcanic and sedimentary rocks following terrane accretion and cessation of active subduction. Clearly, heat anomalies along long-lived convergent margins form a crucial element in models for world-class mineralisation. The long-lived nature of convergent margins allows long-term enrichment of the margin lithosphere in response to repeated episodes of arc and marginal-basin magmatism, and subduction (Barley et al. 1998). However, the mechanism that triggers generation of world-class metallogenic provinces during these episodes is poorly understood.

The coincidence of the genesis of giant ore deposits with anomalous thermal conditions along subduction margins as illustrated in this paper and elsewhere (e.g. Qiu and Groves 1999) suggests that instantaneous changes in subduction dynamics, like slab break-off, play a crucial role in the generation of giant ore deposits.

Acknowledgements

The study reported herein was conducted as part of the first author's PhD project funded by the predictive mineral discovery Cooperative Research Centre (pmd*CRC).

References

Barley ME, Krapez B, Groves DI, Kerrich R (1998) The late Archaean bonanza; metallogenic and environmental consequences of the interaction between mantle plumes, lithospheric tectonics and global cyclicity. In: Percival JA, Ludden JN (eds). Earth's evolution through the Precambrian, Montreal, Canada: 65-90

Basden H (1998) Geology of New South Wales; Synthesis 2, Geological evolution, 666

Bierlein FP, Arne DC, Foster DA, Reynolds P (2001) A geochronological framework for orogenic gold mineralisation in central Victoria, Australia. Mineralium Deposita 36: 741-767

Bierlein FP, Gray DR, Foster DA (2002) Metallogenic relationships to tectonic evolution; the Lachlan Orogen, Australia. Earth Planet Sci Lett 202: 1-13

Collins WJ (2003) Slab pull, mantle convection, and Pangaean assembly and dispersal. Earth Planet Sci Lett 205: 225-237

De Boorder H, Spakman W, White SH, Wortel MJR (1998) Late Cenozoic mineralization, orogenic collapse and slab detachment in the European Alpine Belt. Earth Planet Sci Lett 164: 569-575

Elburg MA, Bons PD, Foden J, Brugger J (2003) A newly defined Late Ordovician magmatic-thermal event in the Mt. Painter Province, northern Flinders Ranges, South Australia: Aust Jour Earth Sci 50: 611-631

Ewers G, Evans N, Hazell M, Kilgour B (2002) OZMIN mineral deposits database, Geoscience Australia (web)

Fergusson CL, Phillips D (2001) 40Ar/39Ar and K-Ar age constraints on the timing of regional deformation, south coast of New South Wales, Lachlan Fold Belt: problems and implications. Aust Jour Earth Science 48: 395-408

Foster DA, Gray DR (2000) Evolution and structure of the Lachlan Fold Belt (Orogen) of Eastern Australia. Ann Rev Earth Planet Sci 28: 47-80

Foster DA, Gray DR, Kwak TAP, Bucher M (1998) Chronology and tectonic framework of turbidite-hosted gold deposits in the Western Lachlan fold Belt, Victoria: 40Ar-39Ar results. Ore Geol Rev 13: 229-250

Glen RA, Walshe JL, Barron LM, Watkins JJ (1998) Ordovician convergent-margin volcanism and tectonism in the Lachlan sector of east Gondwana. Geology 26: 751-754

Mineral systems, hydridic fluids, the Earth's core, mass extinction events and related phenomena

John L. Walshe, Bruce Hobbs, Alison Ord, Klaus Regenauer-Lieb
CSIRO Exploration and Mining, ARRC, 26 Dick Perry Av, Kensington, Western Australia 6151, Australia

Andy Barnicoat
Geoscience Australia, Canberra, ACT, Australia

Abstract. We argue that hydridic fluids from the deep-earth are an important fluid type in mineral systems. The Carboniferous through Triassic interval of Earth history is used to illustrate our hypothesis that flux of hydridic fluid is a causative link between many earth processes such as mass extinction, evolution of ocean chemistry, climate change, anoxia, large-scale volcanism and mineral systems. The Earth's core is considered the dominant reservoir of hydrogen. An enhanced flux of hydridic fluids mobilizes the mantle and sustains tectonism and metallogenesis over 100s of millions of years.

Keywords. Mineral systems, hydridic fluids, Earth's core, mass extinction

1 Why are metal resources rare?

Metal accumulations within the Earth are rare occurrences and the accumulations of high grade, large tonnage metal deposits much more so. Most models of formation of these deposits are based on some combination of processes that operate within the middle to upper crust and the hydro- and bio-sphere: metamorphism, basin dewatering, de-volatilization of magmas, sea floor metamorphism, meteoric fluid circulation, fluvial winnowing and detrital accumulations. But these are relatively common Earth processes. Arguably such common processes ought to give rise to more common occurrences of the giant deposits. So is the "special-ness" of the major metal accumulations a function of rare combinations of common processes or have we yet to understand some key elements of the mineral systems that produced the giant deposits? We argue that anhydrous fluids, composed dominantly of H_2 - CH_4 - H_2S (hydridic fluids in the sense of Larin, 1993) are an important fluid type in the mineral systems that produced the Earth's giant mineral deposits and provinces. The hints from the available stable and radiogenic isotope data and from mineral systems such as the Archean gold provinces, that afford an opportunity to study a crustal section, is that these fluids are sourced from deep within the earth. In this contribution we explore the questions of "where" within the earth, what are the properties of such fluids at P and T and what other earth processes could have been affected, possibly effected, by such fluids?

2 Sources and potential reservoirs of hydridic fluids: The Earth's core?

Given present knowledge of the Earth, two obvious reservoirs of hydridic fluids are within serpentinized mantle wedges of subduction zones and within the Earth's core, or at least the outer parts of the core. Sleep et al. (2004) discuss the formation of H_2 saturated fluids from serpentinization of ultramafic rocks. Magnetite and awaruite ($FeNi_3$) catalyze methane and organic matter formation abiotically within serpentinite. Such extremely reduced fluids will not be stable in the presence of water-bearing silicate melts, thus limiting potential sites of hydridic fluid reservoirs to relatively cold, serpentinized upper mantle. The "flat slab" setting is one possible loci in modern arc settings and interestingly there is a correlation of some giant porphyry and epithermal deposits with zones of low angle subduction in several of the important mineral provinces of the Pacific Rim. Recently Ranero and Sallarès (2004) have provided geophysical evidence (anomalously low seismic velocities and densities of the crust and upper mantle) for serpentinization of the crust and mantle of the Nazca plate during bending at the north Chile trench.

Alternatively the hydridic fluids may be sourced from the core of the Earth. Williams and Hemley (2001) reviewed the development over the last seventy years of the concept of a hydridic core, noting the importance of the experimental work (Antonov et al. 1980) in demonstrating the significant increase in affinity between hydrogen and iron with increasing pressure such that a stoichiometric iron hydride forms at high pressure. Okuchi (1997) concluded that hydrogen may be the primary light element in the core accounting for the major part of the 10% density deficiency of the outer core.

3 Hydridic fluids and metallogenic epochs?

Some first order observations about the temporal distribution of giant deposits through Earth history provide clues as to the dominant source of H_2. Gold deposits are distributed heterogeneously through Earth history with two Precambrian peaks at about 2800 to

2500 and 2200 to 1600 Ma. There is a notable gap in the record from 1600 to 600 Ma with major gold provinces and deposits (including Cu-Au deposits) occurring in the last 600 million years of Earth history. Lead - zinc deposits are also distinctly time bound with the most significant epochs occurring at the Paleoproterozoic - Mesoproterozoic transition and in the late Paleozoic (Devonian through Permian). The formation of most classes of deposits are broadly related to plate-tectonic processes but these "Earth-scale" epochs of metallogenic province formation lasting up to 0.5 billion years with time gaps up to approximately a billion years suggest an additional control beyond plate tectonics. A core-mantle involvement in metallo-genesis, possibly linked to mantle overturn and plumes of hydridic fluids from the D''- layer, provides an attractive explanation for the large-scale temporal pattern of metallogenic epochs.

4 Composition of hydridic fluids

Hydrogen has potential to complex with most elements of the periodic table at high temperature and pressure to form hydrides. As hydrides are unstable in the presence of water their distribution within the Earth will reflect the distribution and state of water. The alkali and most alkali earth elements form ionic hydrides. Group 3 through 7 elements (e.g. Al, Si, N, S, Cl) form covalent hydrides. The formation of hydrides by most transition elements, lanthanides (REEs) and actinides allows the possibly of transport of a wide range of elements of metallogenic interest (e.g. Ti, V, Cr, Co, Mo, W, U, Th, Au, PGEs) within the mantle and under appropriate circumstances within the crust by fluids other than silicate melts.

There is potential for alkali-rich hydridic fluids, including a significant component of alkali halide, to promote alkali metasomatism on mixing with silicate melts, aqueous or carbonic fluids in the crust/upper mantle, generating reduced, alkali-rich, aqueous fluids via for example:

$$NaH + H_2CO_3 \longrightarrow Na^+ + HCO_3^- + H_2$$

with the potential for acid production via

$$H_2CO_3 \longrightarrow H^+ + HCO_3^-$$

Such reactions will be rapid, irreversible and exothermic. The decreasing stability of hydrides with increasing atomic number within any Group of the Periodic Table (Mackay and Mackay, 1968) implies Na ± Li - metasomatism will be favoured over K - metasomatism. At low pressure hydridic fluids are likely to evolve to low density HSCO fluids dominated by H_2 with components of H_2S, CH_4, HCl and CO.

5 Mass extinction events and related phenomena

If hydrogen degassing from the Earth's core was a significant, although probably episodic, process through Earth history, then there ought to be a range of phenomena that reflect the process, in the mantle, the crust, other than giant base and precious metal deposits, as well as in the biosphere and hydrosphere. Mass extinction is one obvious phenomenon to consider. No single cause has been established for the five major mass extinction events of the Phanerozoic that occurred at the end of the Ordovician, Permian, Triassic and Cretaceous, and in the late Devonian, or for the numerous lesser extinction events. The most dramatic loss of species occurred at the Permian–Triassic boundary, ca the time of the Siberian flood volcanism, recently dated at 252.6 ± 0.2 by Mundil et al. (2004). This is also a time of formation of MVT style Pb-Zn deposits (e.g. mid-continent USA; Coveney et al. 2000) and there is evidence of mantle volatiles in these mineral systems (Kendrick et al. 2002).

Newell (1967) originally related marine mass extinctions to eustatic falls of sea level. Hallam and Wignall (1999) affirm that nearly all major biotic crises coincide with rapid global sea-level changes but emphasis a strong link between transgression, spread of anoxic bottom waters and marine extinctions. The extinction at the Cretaceous - Tertiary boundary at 63.4 Ma has been widely attributed to a bolide impact (Alvarez et. al., 1980) but evidence for similar impacts as a causal mechanism for mass extinctions is either weak or non existent (Hallam and Wignall, 1999). Pope (2002) has argued that impact dust was not the cause of the Cretaceous-Tertiary mass extinction. Correlation of large igneous provinces with mass extinction events (Siberian Traps, end-Permian; Central Atlantic Magmatic Province, end-Triassic; Deccan Traps, end Cretaceous) led to suggestions of a causative link (see e.g. Wignall, 2001). More recently, Morgan et al. (2004) have suggested the causative events may be large explosive releases of carbon-rich gas triggered by mantle plume incubation beneath cratonic lithosphere, prior to the onset of continental rifting. Sudden CO_2/CO and SO_2 release into the atmosphere would provide the primary killing mechanism of the extinction event. The shock waves associated with these 'Verneshot' events could generate the reported 'impact signals' at times of great mass extinction thus obviating the need to appeal to bolide impacts.

Extensive geochemical studies reveal deviations in $\delta^{13}C$, $\delta^{18}O$ $\delta^{34}S$, $^{86}Sr/^{87}Sr$ and $^{3}He/^{4}He$ in sediments across extinction intervals (Ryskin, 2003; Berner, 2004; Hotinski et al., 2004 and references therein). Negative excursions in $\delta^{13}C$ in carbonate, up to 8 ‰ at the Permo-Triassic boundary are explained by the breakdown of methane hydrates stored in sediments with methane release to the hydrosphere and atmosphere leading to anoxia greenhouse conditions and mass extinction. The negative deviation in $\delta^{13}C$ at

the Permo-Triassic boundary is preceded by a positive deviation through the Permo - Carboniferous; one of the major "ice-house" periods of Earth history. δ^{34}sulfate shows a negative excursion through the Permo - Carboniferous to values of ca +10 ‰ at the Permo - Triassic boundary and δ^{34}S in sulphide show remarkables shift to ca - 2 ‰ close to the boundary (Kajiwara et al. 1994).

6 Degassing of the Earth's core and mass extinction

We use the Permo - Carboniferous through Permo - Triassic interval of Earth history to illustrate our hypothesis that flux of hydridic fluid may be the link between catastrophic events such as the Permo – Triassic extinction and other less dramatic phenomena and processes. We assume an enhanced but not extreme flux from the Earth's core through the Permo – Carboniferous sufficient to promote methanogen growth in the hydrosphere utilizing CO_2 and H_2 as the energy sources. Reduction of CO_2 to CH_4 led to a progressive transfer of atmospheric CO_2 to methane hydrates in oceanic sediments, a positive deviation in oceanic δ^{13}C and a shift to cooler climates. Mantle sulphur carried in the hydridic fluids (δ^{34}S = zero) caused the δ^{34} seawater - sulfate values to decrease to ca +10 ‰. Relatively high Na concentrations in seawater during the Permian (Lowenstein et al. 2001) may be attributed to the NaH component of hydridic fluids. The Permo-Triassic extinction event marked an extreme flux from the $D^{//}$- layer of the Earth's core, leading to wet-spot development in the mantle via the reaction

$$4H_2 + CO_2 \longrightarrow CH_4 + 2H_2O$$

extensive melting and volcanic activity. The violent release of a toxic gas mix (CO_2, CO, CH_4, H_2S, H_2 and noble gases) to the atmosphere, possibly via 'Verneshots' poisoned life and induced greenhouse warming. The event in the hydrosphere was marked by a switch to negative excursions in δ^{13}C, reflecting the increased abundance of CH_4 in the atmosphere and onset of anoxia. The positive spikes in δ^{34}S of sedimentary pyrite to ca -5 to -2 ‰ marked the transient dominance of mantle sulphur in the hydrosphere. Arguably, the extreme flux of hydridic fluid was a significant factor in the formation of the Late Permian MVT Pb-Zn provinces; a response to enhanced input of reduced sulphur from the mantle as well as enhanced reduction of crustally derived sulfate by thermochemical and/or biotic reduction.

7 Mechanisms of hydrogen release: Wilson Cycle and metallogenesis

We envisage three levels of fluid transfer from the core to the surface (i) plume transport of the hydridic fluids to the base of the lithosphere with enhancement of H-bearing phases in the transition zone below the 410km discontinuity; (ii) upwelling of the 410 km discontinuity as function of slab breakoff after large scale ocean closure and consequent remobilisation of the entire upper mantle with a release of hydridic fluids 100 to 200 million years later and consequent melting and mineralisation, late in the tectonic cycle. This is likely to be the time of maximum flux of hydridic fluids into the lithosphere and maximum potential for metallogenic events; (iii) transfer of H-fluids into the lithosphere by ductile shear zone development and reactive transport (i.e., retrogression and hydrothermal alteration of the lithosphere) with subsequent initiation of subduction (thus a new Wilson cycle).

8 Conclusions

The hypothesis of an episodic hydrogen flux from the Earth's core provides an explanation for many phenomena through Earth history and links both catastrophic and uniformitarian processes to provide a more holistic picture of Earth evolution. Some of the potentially related phenomena include initiation of Wilson cycles, large-volume magma eruptions, global anoxia, green house - ice house cycles, mass extinction events, strength and polarity of Earth's field, metallogenic epochs including formation of oil and gas deposits and diamond growth in the mantle. Epochs of enhanced but episodic flux may last up to 100s of millions of years but extreme flux is short lived; possibly lasting less than a million years.

Acknowledgements

We acknowledge the Predictive Mineral Discovery Cooperative Research Centre, pmd*CRC, CSIRO Exploration and Mining and Geoscience Australia for support and permission to publish.

References

Alvarez LW, Alvarez W, Asaro F, Michel HV (1980) Extraterrestrial cause for the Cretaceous - Tertiary extinction. Science 208:1095-1108

Antonov VE, Belash IT, Degtyareva VF, Ponyatovsky EG Shiryaev VI (1980) Obtaining iron hydride under high hydrogen pressure. Dokl Akad Nauk SSSR 252:1384 -1387

Berner RA (2002) Examination of hypotheses for the Permo-Triassic boundary extinction by carbon cycle modelling. PNAS 99:4172-4177

Coveney, RMJr, Ragan VM, Brannon JC (2000) Temporal benchmarks for modeling Phanerozoic flow of basinal brines and hydrocarbons in the southern Midcontinent based on radiometrically dated calcite. Geology 28:795-798

Hallam A, Wignall PB (1999) Mass extinctions and sea-level changes. Earth Science Reviews 48:217–250

Hotinski RM, Bice KL, Kump LR, Najjar RG, Arthur MA (2004) Ocean stagnation and end-Permian anoxia. Geology 29: 7-10

Kajiwara Y, Yamakita S, Ishida K, Ishiga H, Imai A (1994) Development of a largely anoxic stratified ocean and its temporary massive mixing at the Permian/Triassic boundary supported by the sulphur isotopic record. Palaeogeography Palaeoclimatology Palaeoecology 111: 367-379

Kendrick MA, Burgess R, Leach D, Pattrick RAD (2002) Hydrothermal fluid origins in Mississippi Valley-Type Ore Deposits: Combine Noble Gas (He, Ar, Kr) and Halogen (Cl, Br, I) Analysis of Fluid Inclusions from the Illinois-Kentucky Fluorspar District, Viburnum Trend, and Tri-State Districts, Midcontinent United States. Economic Geology 97:453-469

Larin VM (1993) Hydridic earth: the new geology of our primordially hydrogen-rich planet. Editor on translation C. Warren Hunt, Polar Publishing, Calgary

Lowenstein TK, Timofeeff NM, Brennan ST, Hardie LA, Demicco RV (2001) Oscillations in Phanerozoic seawater chemistry: Evidence from fluid inclusions. Science 294:1086-1088

Mackay KM, Mackay RA (1968) Introduction to Modern Inorganic Geochemistry. International Textbook Company Limited, London

Morgan JP, Reston TJ, Ranero CR (2004) Contemporaneous mass extinctions, continental flood basalts and 'impact signals': are mantle plume-induced lithospheric gas explosions the causal link? Earth and Planetary Science Letters 217:263 -284

Mundil R, Ludwig KR, Metcalfe I, Renne PR (2004) Age and Timing of the Permian Mass Extinctions: U/Pb Dating of Closed-System Zircons. Science 305:1760-1762

Newell ND (1967) Revolutions in the history of life. Geological Society America Special Paper 89:63-91

Okuchi T (1997) Hydrogen partitioning into molten iron at high pressure: implications for Earth's core. Science 278: 1781-1784

Pope KO (2002) Impact dust not the cause of the Cretaceous-Tertiary mass extinction. Geology 30:99-102

Ranero CR, Sallarès V (2004) Geophysical evidence for hydration of the crust and mantle of the Nazca plate during bending at the north Chile trench. Geology 32:549-552

Ryskin G (2003) Methane-driven oceanic eruptions and mass extinctions. Geology 31:741-744

Lead isotopic composition of rutiles from the Chinese continental scientific drill (CCSD) hole and its genetic significance for the superlarge rutile deposit in Maobei, Jiangsu Province

Wang Denghong
Institute of Mineral Resources, Beijing 100037, China

Li Huaqin
Yichang Institute of Geology and Mineral Resources, Hubei 443003, China

Chen Yuchuan
Chinese Academy of Geological Sciences, Beijing 100037, China

Xu Jue, Yu Jinjie, Chen Zhenyu
Institute of Mineral Resources, Beijing 100037, China

Wang Ping'an
Institute of Geomechanics, Beijing 100037, China

Abstract. The central orogenic belt in China, which extends from the Kunlun Mountains in the west to the coast in the east, has experienced a complex tectonic evolution. Based on the Chinese Continental Scientific Drill (CCSD) Hole, this paper reports that the Pb isotopic composition of rutiles selected from surface, from 350m depth and from 500m depth in core are variable, with high content of radiogenic Pb at the middle and later stages of the step-by-step leaching process. This suggests that the rutile-bearing eclogites might have experienced two times of subduction and exhumation.

Key words. Rutile, Pb isotopic composition, tectonic setting, subduction, exhumation, CCSD

1 Introduction

The Maobei rutile deposit is located in the Maobei-Jiangma area, about 15km southwest of Donghai county, Jiangsu Province, and hosted within the gneiss-eclogite assemblage of the Early Proterozoic Donghai Group. There are ten lens- and bed-like orebodies, ranging from 600m to 2640m in length. The complex ores are composed mainly of rutile, ilmenite, garnet and omphacite, and are disseminated, vein-like or have others features. The content of TiO_2 in ores on averaged is 2.13%, with the average contents of garnet and omphacite at 40.5 and 20%, respectively. This rutile deposit was formed by deformation, with residual ores distributed widely on the surface of its weathering crust. Dating the fluid inclusions within the un-deformed quartz from rutile-eclogites in the North Jiangsu terrane gives a Rb-Sr isochron age of 208Ma (Wang et al. 2003), suggesting that the crystal quartz-bearing rutile-eclogite finished deformation at the end of Indosinian (Liu et al. 2004).

The Chinese Continental Scientific Drill (CCSD) Hole cut through the Maobei rutile deposit. Different kinds of mineralization such as rutile ores, ilmenite-magnet-pyromelane mineralization, crystal quartz, serpentine ores and U-Th enrichments have been discovered in the CCSD cores, but the rutile ores are concentrated only within its top 800m (Xu et al. 2004).

Based on the systematic logging of 5100 meter of core from the CCSD, titanium mineralization occurred in three sections from surface to 2000m deep. (1) The first mineralized section is the rutile ore bed located from surface to 607m deep, which is composed of rutile- eclogite, zoisite-kyanite rutile eclogite, rutile-V-Ti-magnetite eclogite, garnet-biotite-hornblende-plagioclase gneiss, garnet-amphibolite, or garnet-biotite-muscovite granitic gneiss, with rutile normally enriched within interbedded eclogites. The rutile contents of all kinds of eclogites generally range from 2% to 3%, in place from 3% to 5%, with highest TiO_2 contents (normally 3~5%, in place 5~10%) occurring in fresh rutile- eclogite, quartz rutile-eclogite and pyrite-rutile- eclogite. (2) The second section of mineralization, from 930m to 1011m deep, is mainly composed of quartz-rutile-eclogite, phengite-rutile eclogite, kyanite-rutile-eclogite and garnet-biotite-plagioclase-gneiss, with rutile contents ranging from 3% to 5% (up to 10% locally). (3) The third section of mineralization, from 1595m to 1993m deep, is composed of phengite-rutile-Ti-magnetite-ilmenite eclogite, uralite-rutile eclogite, kyanite- rutile eclogite, epidote-garnet amphibolite and biotite-muscovite-granitic gneiss. Titanium mineralization is concentrated in the phengite-rutile-ilmenite eclogite, with rutile contents ranging from

2% to 3%, ilmenite averaging at 1%, Ti-ilmenite ranging from 1% to 3%, and pyromelane from 1% to 3%. Generally, the rutile and ilmenite content decrease corresponding to increase of phengite, because rutile normally forms ilmetite during retrograde metamorphism.

2 Samples, analytical methods and results

Because the CCSD intersects the Maobei rutile deposit, the core samples from CCSD are the ideal representative materials for the deposit. Hence, rutiles used in this study were selected from rutile-eclogites at surface, at 350 m and at 500m depth of the CCSD, respectively. The analytical work was done in the isotopic geochemistry open-laboratory of the Chinese Survey of Geology, and the method is the same step-leaching method as that described by Frei and Kamber (1995) and Frei et al. (1997). The process of pure mineral selection can be simply described as follows: picking out single rutiles under binocular microscope, washing with 0.1mol/LHCl purified water, encapsulating rutiles in the teflon high-press smelting vessels, adding 4mol/L HBr, then leaching the samples step by step at the time intervals of 40 minutes, 3 hours, 6 hours and 13 hours. The residual materials, after leaching, are decomposed by HF+ HNO_3 within the same vessel. The step-leaching fluid is transferred into HCl+HBr solution. The purified lead is extracted by anion-exchange column, in preparation for mass spectrometric analysis after drying. The lead isotopic ratio was determined by the MAT-261 adjustable multiple- acceptor thermionization mass spectrograph. Silica gel was used as a transpiration agent, and standard sample SRM981 was used to control mass fractionation. The results are listed in Table 1.

Table. 1: Lead isotopic compositions of rutiles from the Chinese Continental Scientific Drill Hole

Sample No.	$^{206}Pb/^{204}Pb$	$^{207}Pb/^{204}Pb$	$^{208}Pb/^{204}Pb$	Th/U
D1-1(1)	17.536±0.039	15.494±0.039	37.883±0.087	3.95
D1-1(2)	17.192±0.058	15.097±0.052	37.026±0.113	3.67
D1-1(3)	17.115±0.098	15.091±0.093	36.919±0.213	3.66
D1-1(4)	17.172±0.010	15.009±0.013	36.804±0.028	3.56
D1-1(5)	17.417±0.106	15.269±0.091	37.341±0.226	3.72
D1-1(6)	26.301±0.181	16.17±0.114	38.588±0.310	1.57
D1-1(7)	17.412±0.048	15.273±0.046	37.417±0.109	3.76
D1-1(8)	17.467±0.049	15.291±0.042	37.503±0.098	3.78
D1-1(9)	17.524±0.069	15.247±0.059	37.392±0.141	3.68
D1-1(10)	17.481±0.078	15.224±0.068	37.334±0.168	3.68
D1-1(11)	17.82±0.007	15.517±0.007	38.094±0.042	3.89
D1-1(12)	32.391±0.158	16.096±0.063	37.758±0.167	0.55
D5-1	18.157±0.033	15.576±0.027	38.144±0.059	3.74
D5-2	17.864±0.049	15.437±0.042	37.823±0.108	1.50
D5-3	17.429±0.102	15.079±0.083	36.966±0.226	3.51
D5-4	17.372±0.133	15.099±0.107	36.994±0.224	3.56
D5-5	17.71±0.054	15.368±0.047	37.624±0.119	3.71
D5-6	30.584±0.070	16.147±0.048	38.139±0.101	0.62
D5-7	17.912±0.113	15.484±0.101	37.879±0.243	3.74
D5-8	18.168±0.096	15.662±0.083	38.428±0.188	3.87
D5-9	17.714±0.051	15.33±0.046	37.623±0.111	3.70
D5-10	17.558±0.056	15.261±0.052	37.535±0.131	3.73
D5-11	17.85±0.024	15.488±0.026	37.994±0.060	3.82
D5-12	50.181±0.489	17.158±0.173	38.293±0.412	0.33
D8-1	17.943±0.251	15.427±0.293	37.867±0.588	3.70
D8-2	18.208±0.139	15.719±0.056	38.591±0.154	3.93
D8-3	17.841±0.051	15.485±0.029	37.685±0.274	3.69
D8-4	17.979±0.082	15.609±0.063	37.925±0.428	3.74
D8-5	90.209±0.676	17.73±0.299	35.708±0.264	0.12
D8-6	18.827±0.122	16.203±0.085	40.287±1.058	4.37
D8-7	18.481±0.391	15.917±0.332	39.117±0.832	4.03

D1-1 from surface open pit, D5 from rutile eclogites (TiO_2= 4.40~5.36%) at 350m depth, D8 from pyrite-rutile eclogites (TiO_2=2.25%) at 500 m depth.

3 Discussion

The analytical results are listed in Table 1 and Figures 1 to 3. Figure 2 shows the variation of Pb isotopes with the leaching time interval, while Figures 3 is the tectonic diagrams of lead isotopes outlined by Zartman and Doe (1981) and Norman and Leeman (1989), respectively. As shown in Figures 1 and 2, the CCSD rutiles do not plot the same Pb isotope growth curve, with some abrupt changes in Pb isotopic composition. The first four leaching steps for the D5 sample and D1-1 sample, and the first three leaching steps for the D8 sample give concordant and relative stable values of $^{206}Pb/^{204}Pb$ ratio, suggesting that the different rutile samples evolved within the same isotopic system at the late stage of crystallization.

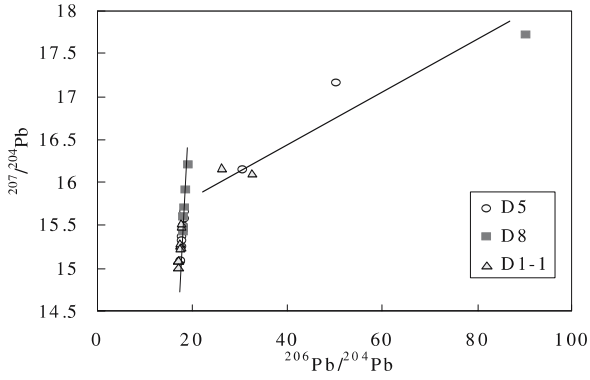

Figure 1: $^{206}Pb/^{204}Pb$ vs. $^{207}Pb/^{204}Pb$ diagram of rutiles from the CCSD

At that time, the tectonic environment for the formation of rutiles was concordant and relatively stable. However, the fifth leaching step for the D5 sample, the fourth leaching step for the D8 sample, and the fifth leaching step for the D1-1 sample give highly variable $^{206}Pb/^{204}Pb$ ratios, with smooth $^{206}Pb/^{204}Pb$ values occurring at the subsequent leaching steps. After the rutile samples were leached thoroughly, the final steps give obviously different $^{206}Pb/^{204}Pb$ ratios and different exchange rates of the $^{206}Pb/^{204}Pb$ ratios for different samples, indicating that the Pb isotopic system of the primary environment for the rutile-formation out of equilibrium. During the whole process of step-leaching, the $^{207}Pb/^{204}Pb$ ratios and $^{208}Pb/^{204}Pb$ ratios are also variable, especially the $^{208}Pb/^{204}Pb$ ratios, but their variety tendency is similar to that of the $^{206}Pb/^{204}Pb$ ratios. That is to say, the Pb isotopic system during the growth of rutiles has been altered, perhaps due to a change in geotectonic setting. In the lead isoto-

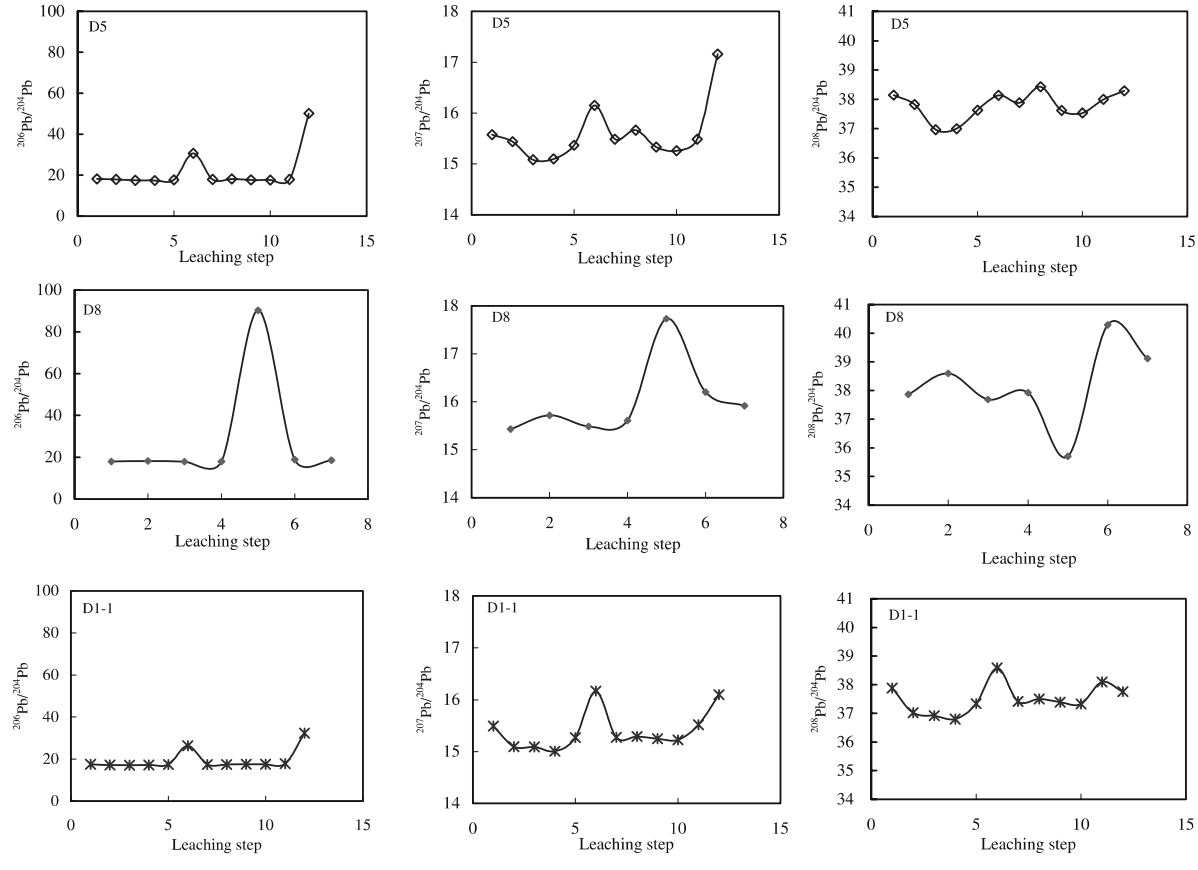

Figure 2: Variation in Pb isotopic compositions of rutiles during the stages of step-leaching

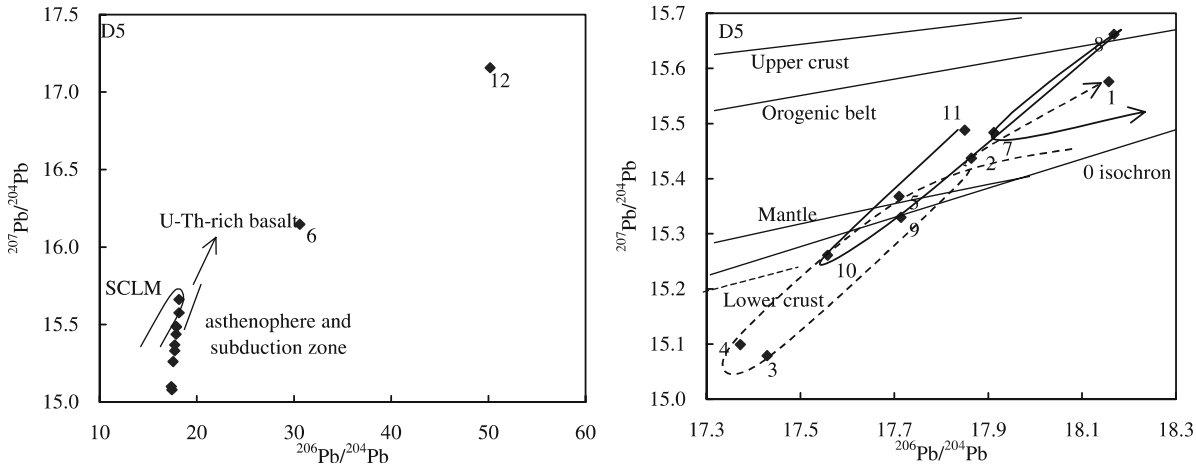

Figure 3: Pb isotopic tectonic model diagram for the D5 rutile sample (after Zartman et al. 1981; Norman and Leeman 1989). The number in the diagram represents the leaching step, i.e No.11 shows the Pb isotopic composition of the core of rutile minerals. The solid and dashed lines represent the first and second times of subduction and exhumation, repectively. The D1-1 and D8 samples provide similar plots

pic tectonic-model plot (Fig. 3), the rutiles mainly plot in the area of lower crust and SCLM, suggesting a SCLM environment for the formation of rutiles. If the step-leaching result represents the whole growth history of the rutiles, then the variation of lead isotopic composition might correspond to a change in tectonic environment. If so, the changing path of Pb isotopic composition of rutiles shown in Figure 3 can give information of the history of tectonic evolution as follows: (1) the source rocks of rutiles might be U-Th rich basalts with radiogenic Pb isotopic composition, (2) the basalts were incorporated into an orogenic belt and subducted into the lower crust or mantle, but rapidly exhumed to a sub-surface environment, (3) the upper crust imprinted a changing record of high content of radioactive elements, and (4) there was a second subduction into lower crust and exhumation on to an orogenic belt. Helium isotopic and PGE geochemistry studies on the same rutiles or rutile-bearing eclogite samples and structure analysis also suggest that the studied samples and the Maobei rutile deposit might have been metamorphosed more than one time (Chen et al. 2003; Wang et al. 2005).

4 Concluding remarks

Although this is the first time for the step- leaching method is applied to study the history of the Maobei rutile deposit, some important clues are as follows:

1. Pb isotopic composition can provide useful information to construct the evolution of tectonic environments.
2. The regular variation of Pb isotopic composition recorded in rutiles from the Maobei deposit, hosted within the east part of the central orogenic ultra-high pressure metamorphic belt, thus provides information on double subduction and exhumation for that UHP metamorphic belt. This is in agreement with the geochronological, tectonic and geochemical studies of Chen Y C et al. (2003), Xu et al. (2003), Yang J S et al.(2003), Xu J et al. (2004), Wang D H et al. (2005) and others, which suggest that the central orogenic belt located in China has suffered at least two regional metamorphic events, the first in the Caledonian and the second in the Indosinian.

Acknowledgements

This study was supported by the CCSD program. Xu Zhiqing, Yang Jingsui and other scientists work for CCSD are acknowledged for their help during the in-situ and laboratory study.

References

Chen YC, Xu J, Yu JJ, Wang DH, Li CJ (2003) Preliminary study on mineralization of the upper 0–2000m part of the CCSD hole. Unpublished report, 1–86 (in Chinese)

Frei R, Kamber BS (1995) Single mineral Pb-Pb dating. Earth and Planetary Science Letters, 129(1-4): 261–268

Frei R, Villa IM, Naegler TF, Kramer JD (1997) Single mineral dating by the Pb-Pb step-leaching method; assessing the mechanisms. Geochimica et Cosmochimica Acta, 61(2): 393–414

Modes of occurrence of H_2 in mantle-derived rocks

M.J. Zhang, P.Q. Hu, P. Zheng
Department of Geology, Lanzhou University, Lanzhou 730000, P. R. China

X.B. Wang, L.W. Li
State Key Lab of Gas-Geochemistry, Institute of Geology and Geophysics, CAS, Lanzhou, P. R. China

Abstract. The Earth's mantle contains trace amounts of H_2 which played an important role in metallogenesis and mantle evolution. The identification of the modes of occurrence of H_2 in mantle-derived rocks is of great value in the study of mantle fluids. In this paper, H_2 contents of olivine, orthopyroxene and clinopyroxene of lherzolite xenoliths and clinopyroxene of pyroxenite xenoliths in Damaping, Hebai province, China have been measured by vacuum stepwise heating mass spectroscopy. The relation between H_2 contents and heating temperatures, total volatiles, crushing sizes of sample, and FTIR absorbance spectra are discussed. Theses suggest that H_2 occurs mainly in gas-liquid inclusions, and secondarily in structural hydroxyl (OH) of mantle-derived rocks, and H_2-rich metasomatic fluid was involved in the evolution of the upper mantle beneath the Northern China craton.

Keywords. Hydrogen, mantle-derived rock, Damaping, China

1 Introduction

Hydrogen is one of the most important volatiles in the solar system. Some of the H_2 preserved in the Earths mantle plays a significant role in mantle partial melting, metasomatism, mantle plume events, prodigious metal inventory, bonanza metallogenic provinces and hydrocarbon generation, and has implications for evolution of Earths mantle (Bell et al. 1995; Wood, 1997; Barley et al. 1998; Jin et al. 2004). For example, the distribution of H_2 shows peak concentration coincident with the PGE and gold reef in the Dovyren mafic-ultramafic layered complex, Russia (Konnikov et al. 2000). Hydrogen concentrations, incorporation and diffusion mechanism in olivine and pyroxene have been extensively studied. Results show that H_2 is present in mantle minerals, and structural OH has been identified in these nominally anhydrous minerals (Skogby et al. 1989; Smyth et al. 1991; Bai et al. 1992; Liu et al. 1993; Ingrin et al. 1995; Zhang et al. 2004). In the present study, variations in H_2 content of olivine, orthopyroxene and clinopyroxene in lherzolite and clinopyroxene from pyroxenite xenoliths and infrared spectra have been determined to reveal the occurrence modes of H_2 in mantle-derived rocks in Damaping, China.

2 Samples and experiments

Very fresh olivine, orthopyroxene and clinopyroxene separates for this study were hand- picked under a binocular microscope from lherzolite and pyroxenite xenoliths of Cenozoic alkali basalt in Damaping, Hebei province, China. Then, mineral separates were divided into five parts and crushed and sieved to size of 0.9, 0.2, 0.1, 0.06 and 0.03mm, respectively. The samples were ultrasonically cleaned in 0.3 mol/l HCl, distilled water and CH_2Cl_2, respectively, to remove secondary carbonate and surficial contamination of organic matter, flushed with distilled water and dried at 110°C. A vacuum stepwise heating MAT-271 mass spectrometer was employed to determine the contents of H_2 in mantle minerals in ten 50-min heating steps from 300 to 1200°C in 100°C increments: volatile extraction apparatus and detailed experiment process are described by Zhang et al. (2004). The systematic standard deviation of H_2 was typically 1mol% at most. Olivine and orthopyroxene for infrared spectra measurements were degassed at 120°C, 600°C, 900°C and 1200°C, respectively, and cooled sequentially at room temperature in a vacuum line. The specimens were prepared by the pressed powder pellet method. Infrared absorption spectra were obtained at room temperature using a Nicolet 10DX Fourier transform infrared spectrometer.

3 Modes of occurrence of H_2 in mantle rocks

The contents of H_2 and total volatiles released from olivine, orthopyroxene and clinopyroxene in lherzolite and pyroxenite are related to the heating temperature and sample crushing size. Hydrogen and total volatiles show synchronous releasing peaks at heating temperatures of 400-500°C and 700-900°C (Fig. 1), Table 1 lists the contents of H_2 at releasing peaks of 400-500°C (LTP) and 700-900°C (HTP). The contents of H_2 are well correlated to the contents of total volatiles (Fig. 2), which indicates that H_2 has a similar origin to total volatiles. Clinopyroxene in pyroxenite has the highest content of H_2 at 700-900°C (Fig. 1), which implies that pyroxenite formed under conditions of high P_{H2} (Skogby et al. 1989). This indicates a H_2-rich metasomatic fluid in the evolution of the upper mantle beneath the Northern China craton.

On the other hand, H_2 contents released from mantle-derived rocks are related to crushing sizes of sample. With decreasing crushing sizes of sample, H_2 contents increase. Orthopyroxene has the highest content of H_2 in crushing sizes of 0.11mm.

Organic contamination and gases adsorbed on the sample surface and in cracks and secondary inclusions were removed completely by means of efficient sample cleaning and pretreatment. Hence, the H_2 released from mantle-derived rocks during stepwise heating could be

derived from three sources: (1) reactions among gaseous components released from minerals, (2) OH^- in mineral structure and H^0 in structural vacancies, and (3) gas-liquid inclusions. Each source is discussed below:

1. The H_2 could have been created by reactions [1-4] at high-temperature:

$$C+H_2O \longrightarrow H_2+CO \quad [1]$$

$$CO_2+CH_4 \longrightarrow 2CO+2H_2 \quad [2]$$

$$CH_4+2H_2O \longrightarrow CO_2+4H_2 \quad [3]$$

$$2Fe_3O_4+H_2O \longrightarrow 3Fe_2O_3+H_2 \quad [4]$$

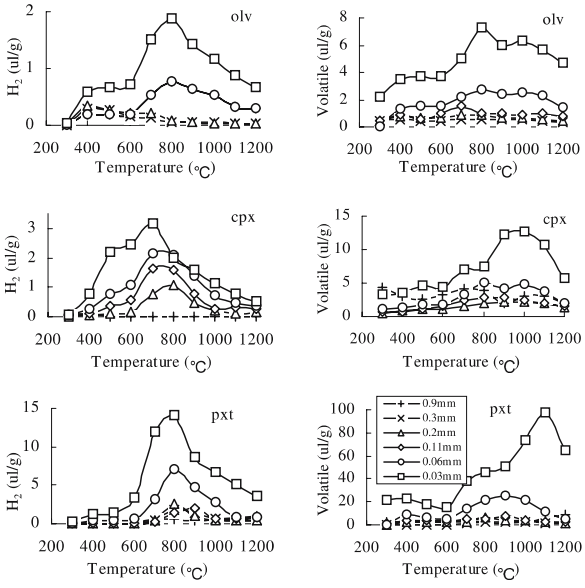

Figure 1: The content variations of H_2 and total volatile with heating temperatures and sample crushing size. olv= olivine in lherzolite; opx=orthopyroxene in lherzolite; cpx= clinopyroxene in lherzolite; pxt= pyroxenite

H_2O, CO_2, CH_4 etc. gaseous components released from mantle-derived rocks could react and form H_2 by the above four reactions in the quartz sample tube or in mineral interiors at high temperature. Because a liquid nitrogen cool trap has been used to cool and isolate the CO_2, H_2O and heavy hydrocarbons etc. released from minerals from the sample quartz tube of high temperature in each heating step, H_2 is only created in mineral interiors by the above reactions. Thus, it is the real composition of H_2 in equilibrium state of mantle conditions at high temperatures (Zhang et al. 2000, 2004).

2. The H_2 could be from OH^- in mineral structure and H^0 in structural vacancies. Extensive infrared spectroscopic studies show that small amounts of OH^- are present in mineral structures of mantle olivine and pyroxene (Skogby et al.,1989; Smyth et al.1991; Bai et al.1992; Ingrin et al.1995), but structural OH^- is difficult to lose, although it could be lost after heating at 1000°C for 24 hrs (Bell et al. 1995; Kohn,1996). H_2 contents from structural OH and structural vacancy H^0 in either olivine or pyroxene could increase with increasing sample surface area in small sample crushing sizes (Skogby et al. 1989).

   Infrared spectra of olivine and orthopyroxene degassed at 120°C, 600°C, 900°C and 1200°C are shown in Figure 3, IR absorbance peak of OH^- at a wavelength of about 3400cm^{-1} show that the contents of OH^- are not reduced in samples degassed at 600°C and 900°C compared with those dried at 120°C, but are reduced in samples degassed at 1200°C; Liquid H_2O decreased in samples degassed at 600°C and 900°C, due to the degassing of burst gas-liquid inclusions. These results imply that H_2 releasing peaks of both 400-500°C and 700-900°C in stepwise heating are not derived from the loss of structural OH^- in mantle-derived minerals, although H_2 released at 1200°C may partly be from structural OH^-.

3. H_2 could be in gas-liquid inclusions. Gas- liquid inclusions in mantle xenoliths were formed during mantle uplift by decompressional exsolution of gaseous components dissolved in pyrolite at high temperature and

Table 1: The contents (ul.STP/g) of H2 at low-T releasing peak (LTP) and high T releasing peak (HTP)

Sample	H_2 Peak	Sample Size (mm)					
		0.9	0.3	0.2	0.11	0.06	0.03
olv	LTP		0.73	0.83	0.44	0.56	1.96
	HTP		0.37	0.42	0.77	3.04	7.49
opx	LTP	0.42	0.83	0.07	0.07	0.15	0.52
	HTP	1.25	0.39	1.47	2.53	1.07	0.75
cpx	LTP	0.16		0.31	1.07	2.12	5.46
	HTP	0.03		2.70	4.77	7.16	9.09
pxt	LTP	0.27	0.01	0.17	0.08	1.24	5.98
	HTP	4.28	4.66	5.11	5.40	18.88	49.92

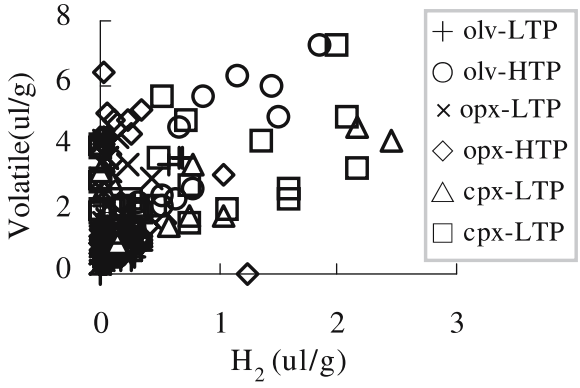

Figure 2: The relationship between H2 content and total volatiles. Abbreviations as in Figure 1 and Table 1

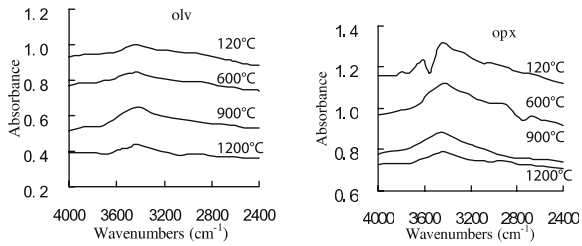

Figure 3: FTIR absorbance spectra of olivine (olx) and orthopyroxene (opx) after H_2 releasing at different temperature. Abbreviations as in Figure 1

pressure, which results in higher internal pressure of gas-liquid inclusions. Mantle xenoliths in Damaping have three kinds of gas-liquid inclusions. One is an early stage of gas-liquid inclusions which have regular shapes, such as ball, egg or negative crystal, with smaller sizes (0.005-0.02mm), These were closed systems in the melting and uplift of upper mantle. Another is a late stage of gas-liquid inclusions which have irregular shapes, such as tree-branch or bead-string, with larger sizes (0.01-0.1mm). Some micro-cracks occur at the sides of the fluid inclusions and demonstrate that this kind of inclusion did not behave as a closed system in the melting and uplift of upper mantle. The third type is reprinted by large quantities of ultra-microscopic gas-liquid inclusions blow ì m in diameters. The formation temperatures of gasliquid inclusions are between 987°C and 1296 °C (Xia, 1984), and homogenization temperatures are from 861°C to 1074°C (Liu et al. 1981).

The decrepitation temperature of gas-liquid inclusions depends on homogenization temperature and the thickness of the wall of the gas-liquid inclusion, which is related to crushing size of sample (Zhang et al. 2000; Anderson et al. 2001). Because of higher interior pressures of gas-liquid inclusions in mantle minerals, their decrepitation temperature is lower than their homogenization temperature (Liu et al. 1993). Hence, it is deduced that the releasing peak of H_2 at 400-500°C is derived mainly from the decrepitation of late-stage gas-liquid inclusions. Lower H_2 contents imply that H_2 was leaked from late-stage gas-liquid inclusions caused by their lack of closed-system behaviors. The releasing peak of H_2 at 700-900°C (close to homogenization temperatures of gas-liquid inclusions), the largest releasing peak, is derived dominantly from the decrepitation of early-stage of gas-liquid inclusions.

The amounts of H_2 released from gas-liquid inclusions are controlled by both preserved amounts and amounts of decrepitation of gas-liquid inclusions. Larger crushing sizes of samples preserved more gas-liquid inclusions, but the thicker wall of early-stage gas-liquid inclusions (small size) prevented gas-liquid inclusion decrepitation, which resulted in smaller amounts of H_2 released at 700-900°C in larger crushing sizes of samples. At smaller crushing sizes of samples, most late-stage gas-liquid inclusions (big size) are broken, which results in the lack of a releasing peak of H_2 at 400-500°C in smaller crushing size of samples. When the crushing size of samples is appropriate for both preserved amounts and decrepitation amounts of gas-liquid inclusions, H_2 show the highest releasing peak. Orthopyroxene in lherzolite shows a H_2 releasing peak at crushing sizes of 0.11m (Table 1), H_2 contents decreased in smaller sized samples, which demonstrates decrepitation of gas-liquid inclusions.

The amounts of H_2 released in olivine increased rapidly with lower crushing sizes, resulting from numerous ultramicroscopic gas-liquid inclusions, not from structural OH^- or structural vacancy H^0. This is because larger crushing size of samples (0.3, 0.2mm) have very low H_2 contents released at 700- 900°C, which could be caused by the difficulty of the decrepitation of gas-liquid inclusions, not problems with the loss of structural OH or structural vacancy H^0.

It is concluded that the two peaks of H_2 release in stepwise heating of mantle-derived rocks are from late-stage gas-liquid inclusions, early-stage gas-liquid inclusions and ultramicroscopic gas- liquid inclusions.

4 Conclusions

Hydrogen is mainly preserved in gas-liquid inclusions in mantle minerals, especially early stage gas-liquid inclusions, and only secondly in structural OH and structural vacancy H^0. The H_2 release characteristics of pyroxenite shows that there was H_2-rich metasomatic fluid involved in the evolution of the upper mantle beneath the Northern China craton. These H_2-rich mantle-derived fluids were injected into crust (Dongying Depression) and have important effects on hydrocarbon generation from kerogen degradation (Jin et al. 2004).

Acknowledgments

This work was financially supported by Natural Science Foundation of China (Grant: 40273009) and Lanzhou Institute of Geology, CAS. We are very grateful to Prof. David Groves and Geoffrey Clarke for their critical reviews.

References

Anderson T, Neumann E (2001) Fluid inclusions in mantle xenoliths. Lithos 55: 310-320

Bai Q, Kohlstedt DL (1992) Substantial hydrogen solubility in olivine and implications for water storage in the mantle. Nature 357: 672-674

Barley ME, Krapez B, Groves DI, Kerrich R (1998) The Late Archaean bonanza: metallogenic and environmental consequences of the interaction between mantle plumes, lithospheric tectonics and global cyclicity. Precambrian Research: 91, 65-90

Bell DR, Ihinger PD, Rossman GR (1995) Quantitative analysis of trace OH in garnet and pyroxenes. Amer. Mineral 80: 465-474

Ingrin J, Hercule S, Charton T (1995) Diffusion of hydrogen in diopside: dehydration experiment. J. Geophy. Res,100: 15489- 15499

Jin ZJ, Zhang LP, Yang L, Hu WX (2004) A preliminary study of mantle-derived fluids and their effects on oil-gas generation in sedimentary basins. J. Petroleum Sci. Eng41: 45-55

Kohn SC (1996) Solubility of H_2O in nominally anhydrous mantle minerals using ^1H MAS NMR. Amer. Mineral 81: 1523-1526

Konnikov EG, Meurer WP, Neruchev, SS, Prasolov, EM, Kisov EV, Orsoev DA (2000) Fluid regime of platinum group elements (PGE) and gold-bearing reef formation in the Dovyren mafic-ultramafic layered complex, eastern Siberia, Russia. Mineral. Deposita 35: 526-532

Liu CS, Shen WZ, Chen PR (1993) Hydroxyl silicate melting-fluid-inclusions. Chinese Science Bulletin 38: 2067-2068 (in Chinese)

Liu RX, Yang ME, Xu, HJ (1981) Preliminary study on ultra-mafic xenoliths of alkali basalts in Northeastern China. Seism. Geol. Sinica 3: 1-16 (in Chinese)

Skogby H, Rossman GR (1989) OH^- in pyroxene: an experimental study of incorporation mechanisms and stability. Amer. Mineral 74: 1059-1069

Smyth JR, Bell DR, Rossman GR (1991) Incorporation of hydroxyl in upper mantle clinopyroxene. Nature 351: 723-735

Wood BJ (1997) Hydrogen: an important constituent of the Core? Science 278: 1727

Xia LQ (1984) Highly dense CO_2 fluid inclusions in peridotitic inclusions in some alkali-basalts from east China. Acta Mineralogical Sinica 4: 133-142 (in Chinese with English abstract)

Zhang MJ, Wang XB, Li LW (2000) An appraisal of different experimental method in the determination of fluid composition in mantle-derived rock. Geological Review 46: 160-166 (in Chinese with English abstract)

Zhang MJ, Wang XB , Liu G, Zhang TW, Bo WR (2004) The compositions of upper mantle fluids beneath Eastern China: Implications for mantle evolution. Acta Geologica Sinica 78: 125-130

Controls of magmatism and hydrothermal activities on mineralization in the Emeishan flood basalt Province, SW China

Zhu Bing-Quan, Zhang Zheng-wei, Hu Yao-Guo
Guangzhou Istitute of Geochemistry, Chinese Academy of Sciences, Wushan, Guangzhou 510640, China

Abstract. Correlations of metallogenic elements and geochronological data from the Emeishan flood basalts indicate that Cu-Ni-PGE, Fe-Ti-V, native Cu-Ag and Pb-Zn-Ag-Ge deposits were related to fractionation processes of different magmas in deep and shallow magma chambers at initial and final stages of eruption. Synvolcanic hydrothermal activities also played an important role in the formation of these deposits.

Keywords. Emeishan flood basalts, Cu-Ni-PGE, Fe-Ti-V, native Cu-Ag and Pb-Zn-Ag-Ge mineralization

1 Introduction

Deposits of Cu-Ni-PGE sulfides, Fe-Ti-V oxides, native Cu-Ag and Zn-Pb-Ag-Ge sulfides related to flood basalts have been progressively found in large igneous provinces (LIPs), such as the Siberia, Midcontinent, Emeishan and Newark LIPs. Figure 1 shows the distribution of metal deposits related to the Emeishan LIP (ELIP) along eruption channels, indicating that the ELIP is one of the few LIPs with a complete metallogenic system. A huge volume of magma usually erupted in a short time interval (1-3 m.y.) in many LIPs and gave no opportunities for magma fractionation and mineralization. However, strong magma fractionation and crystallization, and synvolcanic hydrothermal activities occurred during the initial and final stages of magma etuption in some LIPs, and provided mechanism of these metallogeneses.

2 Magma fractionation in deep magma

2.1 Chambers at an initial stage

High Ti-P flood basalts (HTB) (TiO_2>2.5%, P_2O_5>0.3%, Ti/Y>500 and Nb>20ppm) from the eastern part of the ELIP have high backgrounds of Cu (mean 207 ppm), Zn (mean 143 ppm), V (mean 381 ppm) and Pt+Pd (mean 30 ppb). There are positive correlations between Ti and Cu and Ti and Zn (Fig. 2). HTB and high-Mg basalts, with Mg# varying from 32-65, show a positive correlation between Ti and P with TiO_2/P_2O_5 ≅10 (Fig. 3) and $\varepsilon_{Nd}(t)$ ≅0~+2, near those of primitive mantle. Geochemical evidence indicates that enrich-ments of metallogenic elements in HTB are related to crystal fractionation of magmas derived from fractional partial melting of primitive mantle under sulfur-depleted conditions.

Komatitic picrites in the ELIP have Ni (mean 970 ppm) and Cr (mean 2280 ppm) and have features similar to primitive magma ($\varepsilon_{Nd}(t)$≅0, Nb<3 ppm, Zr<60ppm, and flat REE pattern and spider diagram of HFSE), and similar to Noril'sk and Duluth (Fig. 4). Sulfur addition to primitive magmas with a komatitic composition would induce

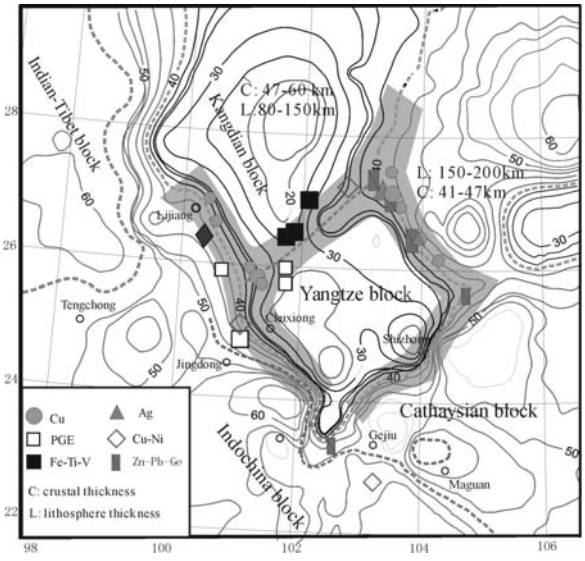

Figure 1: A map showing geochemical and geophysical fields in ELIP area, as well as distribution of related metal deposits. Shadow area represents eruption channels. Contour lines are Pb isotopic vectors (Zhu 2003)

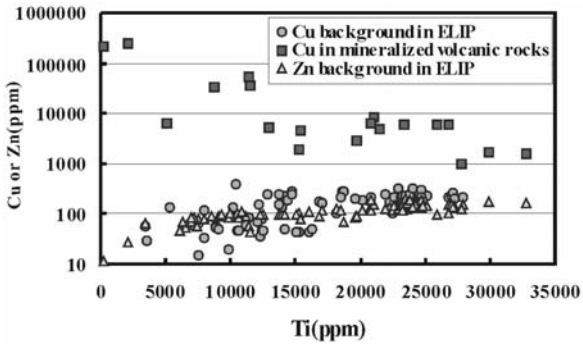

Figure 2: Cu-Ti and Zn-Ti correlations in the ELIP basalts and mineralized volcanic rocks

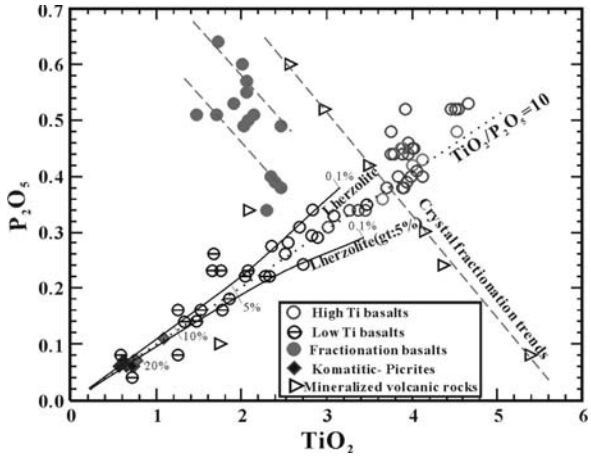

Figure 3: TiO_2-P_2O_5 correlations for ELIP; % numbers are partial melting degrees of mantle lherzolites (the data for low Ti basalts from Xu et al. 2001)

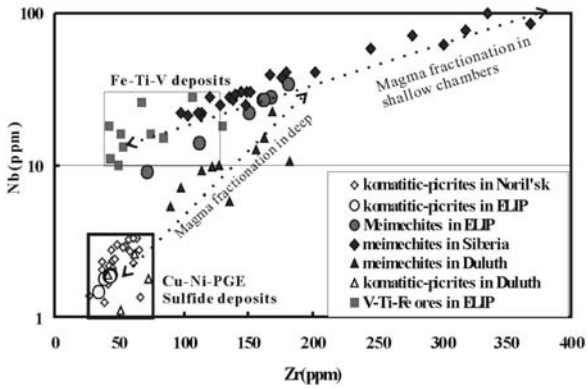

Figure 4: A Nb-Zr correlation diagram for ultramafic lavas and intrusive bodies from the Emeishan, Siberian and Supeior LIPs. Boxes show data areas for rocks with Cu-Ni-PGE and Fe-Ti-V mineralization (data from Sobolev et al. 1992; Shirey et al. 1994; Hawkesworth et al. 1995; Chung and Jahn 1995)

Ni-Cu-PGE sulfide mineralization. Meimechites with high Nb contents (>10 ppm) are products of magma fractionation in shallow chambers and related to Fe-V-Ti metallogenesis, are instead of Ni-Cu-PGE mineralization. Therefore HTB and komatitic picrites are the key metallogenic magmas in the ELIP.

3 Crystal fractionation in shallow magma chambers at the final stage

Titanomagnetite crystal fractionation in shallow magma chambers beneath eruption channels during the final stage played an important role for native copper and Fe-Ti-V mineralization, which caused strong negative correlations between Ti and P and Cu and Ti in contrast to those of cumulative magmas fractionation as mentioned above (Figs 2-3). These magma fractionations also appear in the Fenner trend in close environments with low oxygen fugacity and the Bowen trend in open environments with high oxygen fugacity, which formed a volcanic suite from ultramafic to andesitic rocks, including volcanic breccias, vesicular lavas, agglomerates, welded tuffs and small intrusive dikes, which distribute along the eruption channels with a NW strike. There are clear negative correlations between SiO_2 and TiO_2 and SiO_2 and FeOt (total) and positive correlation between Ti and V in these rocks (Fig. 5). Zr and Nb also shows good positive correlation for Cu ores, as induced by magma crystal fractionation and hydrothermal activities (Fig. 6). Cu solubility in magma increases with increasing in oxygen fugacity (Ripley and Brophy, 1995). Thus, native copper mineralization is commonly associated with low Ti tholeiitic-andesitic rocks derived from HTB magma fractionation. Based on this regularity, native copper deposits have been widely found in the border areas between the Yunnan and Guizhou provinces (Zhu et al. 2003). Fe-V-Ti deposits are related to the ultramafic – mafic rocks in the central and eastern parts of the ELIP (Fig.1). However, these magma fractionations did not induce Zn and Cu-Ni sulfide mineralizations.

4 Late stage hydrothermal activities

A Zn-Pb-Ag-Ge mineralization zone parallel to that of the native copper in the eastern part of the ELIP was controlled by the deep tectonic structures with NW strike, which are also related to eruption channels of the EFB (Fig. 1). A sharp gradient of the thickness of the lithosphere, and a Pb isotopic steep zone can delineate the concealed tectonic structures (Zhu et al. 2000). Hydrothermal alteration, including silification, actinolite, zeolite, bitumen and carbonate alteration, is associated with native copper mineralization along the eruption channel zones over a wide area. T-P conditions of alteration minerals, vitrinite reflectance R_0 of bitumen, and temperature determination of liquid inclusions indicate a temperature range from 400°C to 100°C (Zhu et al. 2003). Although isotopic dating for ELIP gave an eruption age range of 251-265 Ma (Zou et al. 1997; Zhou et al. 2002; Lo et al. 2002), $^{40}Ar/^{39}Ar$ dating of alteration minerals (laumontites) from three native copper deposits in Ludian, Yongshan and Huize of Yunan and Guizhou provinces yields consistent plateau ages (228-226 Ma) (Zhu et al. 2005), which are in agreement with results of Sm-Nd and Rb-Sr isochron dating for sphalerites from the Qilingchang Zn-Pb-Ge deposit in Huize (228-225 Ma) (Huang et al. 2004). The hydrothermal activitities mobilized some elements including Zn, Ge, Cu, Zr, Nb, Th and U (Fig. 6). Therefore, genesis of the large and super-large Zn-Pb-Ag-Ge deposits in the northeastern Yunnan was also associated with the hydrothermal activitities following the HTB eruption. The traditional opinion for the genesis of these deposits, regarded as SEDEX

This page intentionally blank

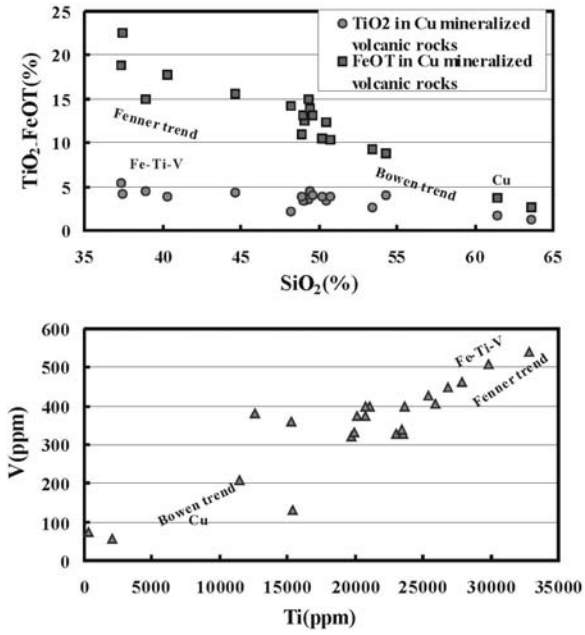

Figure 5: SiO2-FeO and SiO2-TiO2 inverse correlation (upper) and Ti-V positive correlation (lower) in magma crystal fractionation of shallow magma chambers

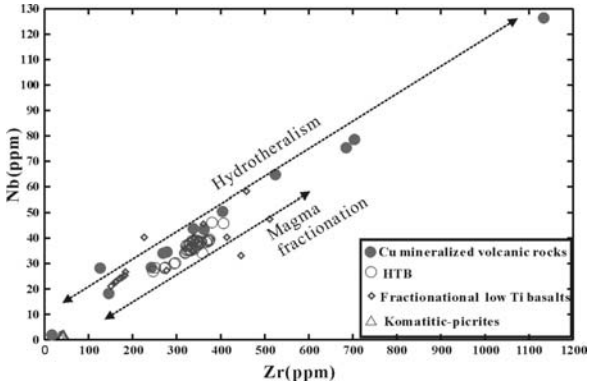

Figure 6: Zr-Nb correlation for mineralized volcanic rocks and host rocks

deposits hosted in Carboniferous -Devonian strata, is thus incorrect. The hydrothermal activitities following lava eruption lasted for about 30 m.y., which is comparable to that in the Keweenawan Peninsular (Bornhorst et al. 1988). The native copper ore bodies with high grades were closely associated with zeolitization and bituminization. Thus, the hydrothermal activitities formed native copper and Zn-Pb-Ag-Ge sulfide deposits within the ELIP.

Acknowledgements

We are grateful to Chinese Academy of Sciences for support through KZCX2-SW-125 Project

References

Bornhorst TJ, Paces JB, Grant NK, Obradovich JD, Huber NK (1988) Age of native copper mineralization, Keweenaw Peninsula, Michigan. Econ Geol 83: 619-625

Chung S-L, Jahn BM (1995) Plume-lithosphere interaction in generation of the Emeishan flood basalts at the Permian-Triassic boundary. Geol 23: 889-892

Hawkesworth CJ, Lightfood PC, Fedorenko VA, Blake S, Naldrett AJ, Doherty W, Gorbachev N (1995) Magma differentiation and mineralization in the the Siberian flood basalts. Lithos 34: 61-88

Huang ZL, Chen J, Han RS (2004) Geochemistry and genesis of the Huize super-large Pb-Zn deposit in Yunnan, and its implications for relationship between the Emeishan basalts and Pb-Zn mineralization. Geological Press, Beijing

Lo CH, Chung SL, Lee TY, Wu G (2002) Age of the Emeishan flood magmatism and relations to Permian–Triassic boundary events. Earth Planet Sci Lett 198:.449-458

Ripley, EM, Brophy JG (1995) Solubility of copper in silicate melts as a function of oxygen and sulfur fugacities, temperature, and silicate composition. Geochim Cosmochim Acta 59: 5027-5030

Sobolev AV, Kamenetsky V, Kononkova NN (1992) New data on Siberian meymechite petrology. Geochem Int 29: 10-20

Shirey SB, Klewin KW, Berg JH, Carlson RW (1994) Temporal changes in the sources of flood basalts: isotopic and trace element evidence from the 1100 Ma old Keweenawan Mamainse Point formation, Ontario, Canada. Geochim Cosmochim Acta 58: 4475-4490

Xu Y, Chung SL, Jahn B-M, Wu G (2001) Petrologic and geochemical constraints on the petrogenesis of Permian –Triassic Emeishan flood basalts in southwestern China. Lithos 58: 145-168

Zhou M-F, Malpas J, Song XY, Robinson PT, Sun M, Kennedy AK, Lesher CM, Keays RR (2002) A temporal link between the Emeishan large igneous province (SW China) and the end-Guadalupian mass extinction. Earth Planet Sci Lett 196: 113-122

Zhu B-Q, Dong Y-P, Chang X-Y, Zhang Z-W (2000) Relation of isotopic geochemical steep zones with geophysical fields and tectonics in the junction area of the Cathaysian, Yangtze and Indochina plates, Acta Geol Sin 74: 236-240

Zhu B-Q, Hu Y-G, Zhang Z-W, Chang X-Y (2003) Discovery of the copper deposits with features of the Keweenawan type in the border area of Yunnan-Guizhou Provinces. Science in China (D) 46(supp) :60-72

Zhu B-Q, Dai T-M, Hu Y-G, Zhang Z-W, Chen G-H, Peng J-H, Tu X-L, Liu D-H, Chang X-Y (2005) 40Ar/39Ar and U-Th-Pb dating for native copper mineralizations of two stages from the Emeishan flood basalts in the northeastern Yunnan Province, China(in Chinese with English abstract). Geochimca 34: 235-247

Zou R, Zhu BQ, Sun DZ, Chang XY (1997) Geochronological study on crust – mantle evolution and mineralization in the Red River belt (in Chinese with English abstract). Geochimca 26: 46-56

This page intentionally blank

Session 2

Basin evolution: base and precious metal mineralization in sediments

Iron transport in redbeds during the genesis of sediment-hosted stratiform copper deposits

A.C. Brown
Department of Civil, Geological and Mining Engineering, École Polytechnique de Montréal
P.O. Box 6079, Station Centre-Ville, Montreal, QC, H3C 3A7, Canada

Abstract. While oxidized, chloride-rich, intersti-tial brines produce redbeds from rapidly deposited coarse-grained rift-basin fills, the redbeds may be leached of their trace copper contents, thereby providing a source of copper for the formation of sediment-hosted stratiform copper deposits in nearby greybeds. The reddening process should lower the Eh of the brine such that the brine becomes suitable for iron solubility. In a simple conceptual analysis, iron could be transported toward the greybeds ahead of the infiltration by cupriferous brines.

Keywords. Sediment-hosted stratiform copper, rift basin, redbed, progressive diagenetic reddening, copper, iron, metal solubility, metal transport, Eh-pH, brine evolution, genetic model

1 Introduction

Genetic models for sediment-hosted stratiform copper deposits (SCDs) commonly call upon the leaching of footwall redbeds by oxidized chloride-rich interstitial brines to provide the copper and associated metals now found in adjacent greybeds (Boyle 1989; Brown 1992, 1997; see Fig. 1). A closer examination of the Eh-pH conditions favorable for copper mobilization in brines reveals that conditions suitable for significant iron solubility are only moderately more reducing than those favorable for copper solubility. Furthermore, significant solubilities for iron and copper can be related to the progressive diagenetic reddening process that creates redbeds from immature coarse rift-filling sediments. A conceptual analysis of probable Eh-pH conditions in the interstitial brine during the reddening process suggests that, in the general genetic model for SCDs, partial iron mobilization could preceed copper infiltration toward the base of the greybeds.

2 Diagenetic formation of redbeds and metal leaching

Rift-filling redbeds, a product of slow diagenesis, consist initially of immature clastic debris accumu-lated in rift basins during rapid erosion of adjacent highlands. The reddening of such debris, involving the oxidation of common iron-bearing minerals by oxidized pore fluids to produce iron hydroxides and oxides, is progressive and may take place over millions of years (Walker 1967, 1989; Zielinski et al. 1983). If the pore fluid is a brine (formed, for example, by the drainage of coeval evaporite pans on surface or by the leaching of evaporite beds within the rift basin fill), metals such as copper may be released to the pore fluids during the progressive diagenetic alteration and may then be transported to greybed sites for deposition as SCDs. The dependence of a favorable copper solubility on the formation of reddened sediments imposes an important time constraint on the formation of SCDs: they cannot precede the reddening process.

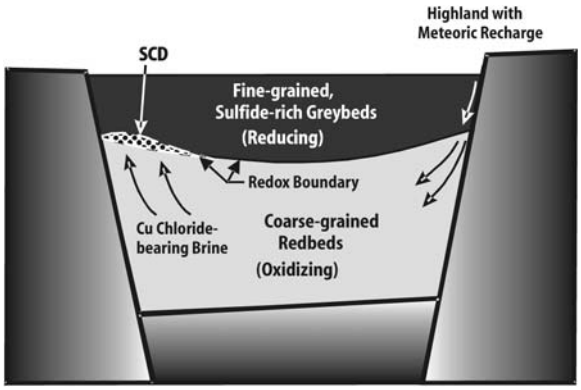

Figure 1: A general genetic model for SCDs, based on a highland recharge of meteoric waters which evolve to redden the rift sediments and to become saline and capable of transporting copper into the base of overlying reduced sulfide-rich sediments (adapted from Brown in print)

During reddening, iron is also leached from the immature sediment and is commonly thought to be redeposited immediately at the microscopic scale as goethitic and hematitic pigments in and around the original iron-bearing minerals (Walker 1989). The production of these pigments is a very slow process, which would depend largely on the rate of introduction of oxidants by the pore fluid. The ultimate stability of the pigments is assured by an abundance of oxidants, as would exist above the Fe^{2+}/$Fe(OH)_3$ transition of an Eh-pH diagram for the Fe-O-H system (Fig. 2).

3 Iron solubility during reddening

At low temperatures, iron is soluble as Fe^{2+} in reduced, acidic aqueous solutions (Fig. 2) and would probably be

still more soluble with the formation of iron-chloride complexes in a sulfur-poor, chloride-rich brine. However, Eh-pH conditions leading to the formation of redbeds deep within an intracontinental rift basin are unlikely to have been truly reducing or significantly acid at the site of reddening. Conditions during active reddening are more likely to have been close to the $Fe^{2+}/Fe(OH)_3$ or Fe^{2+}/hematite transitions due to the pH-buffering effect of the reddening process itself: oxidants would be consumed by the produc-tion of iron hydroxides (e.g. goethite) and hematite, and any significant acidity would be neutralized by reactions such as plagioclase and biotite alterations to form smectite. Those conditions are neither acid nor reducing in our common usage of those terms, but neither are they oxidizing as we would say of conditions within the broad iron-hydroxide or hematite stability fields where the reddening process is essentially complete. They are in fact transitional conditions in which the contours of solubility of iron may represent ppm levels of Fe^{2+} in solution (see the lower ellipse of Fig.2), and possibly still higher levels due to the formation of iron chloride complexes in a saline pore fluid.

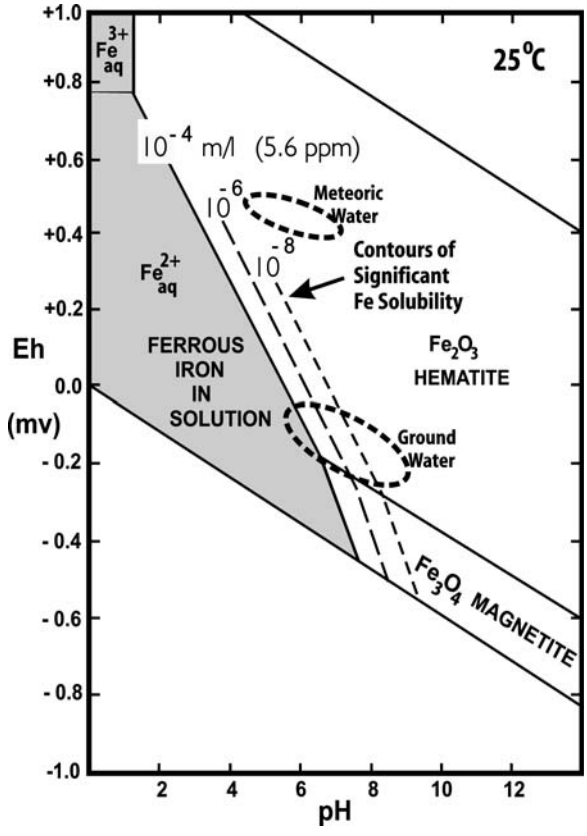

Figure 2: Stabilities of aqueous iron species in equilibrium with iron oxides for a low-temperature Eh-pH diagram. The upper ellipse represents typical Eh-pH conditions for surface and near-surface meteoric water (from Garrels 1960). The lower ellipse represents near-neutral pH, reducing conditions under which Fe^{2+} would be significantly soluble in the pore waters of rift-basin sediments undergoing reddening.

4 Copper solubility during reddening

Contours of copper solubility in a low-temperature chloride brine have been determined by Rose (1976, 1989) (Fig. 3). Compared to the poor solubility of copper in fresh water, the addition of 0.5 M NaCl to induce the formation of soluble copper chloride complexes opens up an area of important copper solubility centered around pH = 7 and Eh = 0.1± 0.1 mv (see the central ellipse of Fig. 3). With the superposition of the ellipses from Figures 2 and 3, it becomes clear that, as expected, copper has its most favorable solubility distinctly above the Eh-pH conditions of the de-oxygenated pore fluid capable of mobilizing iron.

Note also that the Eh conditions favorable for copper transport in a near-neutral pH brine are decidedly lower than the highly oxidizing conditions of 'meteoric water'. In other words, descending meteoric water attains opti-

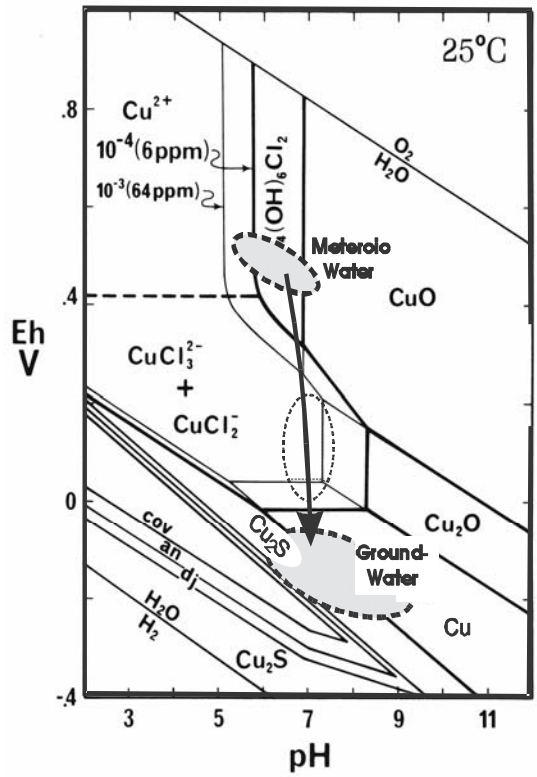

Figure 3: Stabilities of aqueous copper chloride complexes in equilibrium with cupriferous minerals for a low temperature Eh-pH diagram, with Cl- = 0.5M and ∑S = 0.001M. The central ellipse represents near-neutral pH, mildly oxidizing conditions especially favorable for the solubility of cuprous chloride complexes. The upper and lower ellipses have been transferred from Figure 2

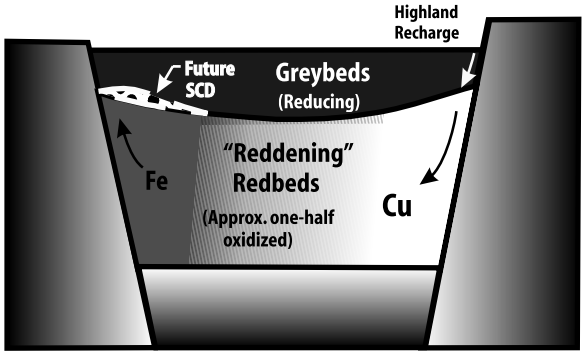

Figure 4: A modified Figure 1 showing the transport of iron and copper during the reddening of rift-basin sediments, with iron largely preceding copper toward an incipient SCD, in a more oxygen-depleted brine than that for copper transport.

mum conditions for copper transport after a significant but not complete depletion of its oxygen. This conclusion suggests that copper mobilization is most efficient within the zone of active reddening where the Eh of the pore brine is evolving progressively from highly oxidizing to reduced conditions. Combined with the earlier conclusion that copper mobilization follows early diagenetic reddening, this additional constraint suggests that copper transport should be optimal in the immediate vicinity of and essentially contempora-neous with the reddening process.

5 Discussion

Figure 4 reproduces the traditional concepts of Figure 1, with modifications to take into account the new perspectives on copper and partial iron solubilities during the reddening of immature rift sediments. Both metals are considered to be significant constituents of a low-temperature brine which evolves from an initial input of meteoric water. Iron is undoubtedly released from the ferruginous silicates during diagenetic reddening, as observed by Walker and associates, and trace amounts of copper are simultaneously released, first to be adsorbed on early goethite, then to be re-released to the pore brine as goethite crystallizes to form the hematitic pigment typical of redbeds. With more advanced oxidation, the pore brine may become highly depleted in oxygen and a portion of the goethite and/or hematite may also be taken into solution and circulate across the basin sediments. The ultimate fate of that mobilized iron remains largely undefined.

The above analysis results from a compilation of several earlier well-known independent observations which, once assembled into a single concept, provide new perspectives on the mobility of two important metals associated with SCD mineralization. The analysis itself is far from exhaustive, for it is only reasonable to ask, for example, what other metals should be examined in a similar manner. If iron is mobilized, should not manganese, with still higher solubilities at the Eh-pHs of the 'ground water' ellipse, be a more obviously mobilized metal? Or should other metals, such as those considered by Rose (1989) (silver, cobalt, lead, zinc and uranium) or those known to be associated with SCDs in greater or lesser amounts (silver, cobalt, lead, zinc, uranium, gold, molybdenum, selenium, mercury, PGEs) be brought into the analysis.

The answer is of course 'yes', although with some serious reservations. As Rose (1989) noted, the behavior of metals during the multistage process of leaching from source minerals and from intermediate-stage goethitic precipitates remains a largely untested and poorly understood aspect of the simple diagenetic leaching model. Rose and Bianchi (1985) investigated the retention capacities of goethite and provide some important insights into the ability of goethite to adsorb metals and to subsequently release metals to a pore-filling brine as goethite crystallizes to hematite. However, they found important variations in retention behavior between metals according to the salinity, temperature, pH and Eh of the solutions, and Rose (pers. comm, 2001) suggests as well that the particular mix of ions (Cl^-, SO_4^{2-}, CO_3^{2-}, Ca^{2+}, Mg^{2+}…) in the pore solution could significantly alter the retention behaviors and ratios of metals released to a brine.

At our current incomplete level of understanding of such aspects, it nevertheless appears that the basic features of redbed reddening are known from the petrographic studies of Walker and associates, and the derivation of a cupriferous solution is essentially unavoidable during reddening if the low-temperature pore solution is sufficiently saline and has an Eh-pH which evolves through the favorable range outlined by the central ellipse of Figure 3.

Iron mobilization may be unavoidable too where the reddening process further depletes the brine in oxygen and Eh-pH conditions approach those of the lower (i.e. 'ground water') ellipse of Figure 3. If so, evidence iron transport and redeposition should exist in the vicinity of SCD mineralization. Three examples deserving examination in this context may be cited: the syn-ore stage hematitic Rote Fäule associated with the Kupferschiefer SCDs; a multitude of iron oxide occurrences known in the Copperbelt-hosting Lufilian Arc of central Africa; and the abundant high-iron chlorites of the basal Nonesuch Formation at the White Pine SCD. Another possibly distantly-related copper-iron mineralization that could be re-examined in this regard would be the low-temperature sediment-affiliated members of the iron oxide-copper-gold family of mineralization.

References

Brown AC (1992) Sediment-hosted stratiform copper deposits. Geoscience Canada, Vol.19, No.3, 125-141 (reprinted in Sheahan PA and Cherry ME, eds, Ore Deposit Models, vol. 2, 99-115, Geological Association of Canada, Reprint Series 6, 1993)

Brown AC (1997) World-class sediment-hosted stratiform copper deposits: characteristics, genetic concepts and metallotects. Australian Journal of Earth Sciences 44: 317-328

Brown AC (in print) Refinements for footwall redbed diagenesis in the sediment-hosted stratiform copper deposits model. Economic Geology

Boyle RW, Brown AC, Jefferson CW, Jowett EC, Kirkham RV, eds (1989) Sediment-Hosted Stratiform Copper Deposits. Geological Association of Canada, Special Paper 36, 710

Garrels RM (1960) Mineral Equilibria. Harper and Brothers, New York, 254

Rose AW (1976) The effect of cuprous chloride complexes in the origin of red-bed copper and related deposits. Economic Geology 71: 1036-1048

Rose AW (1989) Mobility of copper and other heavy metals in sedimentary environments. In: Boyle RW, Brown AC, Jefferson CW, Jowett EC, Kirkham RV, eds, Sediment-Hosted Stratiform Copper Deposits. Geological, Associ-ation of Canada, Special Paper 36, 97-110

Rose AW, Bianchi GC (1985) Adsorption of Cu, Ag, and other metals on Fe-oxides as a control on elemental composition of stratiform and redbed copper deposits. Geological Society of America, Abstracts with Program, 17: 702

Walker TR (1967) Formation of red beds in modern and ancient deserts. Geological Society of America, Bulletin 78: 281-282

Walker TR (1989) Application of diagenetic alterations in redbeds to the origin of copper in stratiform copper deposits. In: Boyle RW, Brown AC, Jefferson CW, Jowett EC, Kirkham RV, eds, Sediment-Hosted Stratiform Copper Deposits. Geological Association of Canada, Special Paper 36, 85-96

Zielinski A, Bloch S, Walker TR (1983) The mobility and distribution of heavy metals during the formation of first cycle red beds. Economic Geology 78: 1574-1589

Application of scanned digital imagery to ore texture interpretation at the Century zinc deposit, NW Queensland

Lucy H. Chapman, Patrick J. Williams, Rod S. Hill
School of Earth Sciences, James Cook University, Townsville 4811, Australia

Kevin L. Blake
Advanced Analytical Centre, James Cook University, Townsville 4811, Australia

Abstract. Digital SEM imagery including X-ray mapping and spectral cathodoluminescence (CL) studies support the previously-proposed diagenetic replacement mode of origin for the large Proterozoic shale/siltstone-hosted Century zinc deposit in northwest Queensland. CL effectively distinguishes different generations of quartz and sphalerite and reveals that the weakly mineralized siltstone beds were replaced by locally pervasive diagenetic silica and microconcretionary siderite prior to ore deposition. This may have destroyed the depositional permeability of these rocks and promoted infiltration of mineralizing fluids into the shale bands in the ore sequence. Micro-replacement textures in which sphalerite has replaced pyrobitumen, pyrite and siderite are incompatible with thermochemical sulphate reduction model for mineralisation and favour a mechanism involving a chemically-reduced, sulphur-bearing ore fluid with metal transport, possibly facilitated by organic complexes. Zn in microconcretionary siderite records the infiltration of sulphur-poor, zinc-bearing fluids prior to main phase sphalerite mineralization. Late stage honey coloured sphalerite has similar Mn and Fe contents but weak CL compared to main phase sphalerite. The time interval represented by the two mineralization phases is unknown.

Keywords. Century zinc deposit, SEM, X-ray mapping, cathodoluminescence

1 Introduction

The Zinifex Century mine, approximately 250 km NNW of Mount Isa in northwestern Queensland Australia, is currently the world's second largest single mine producer of zinc. The Century deposit is one of several large sedimentary-hosted Zn-Pb-Ag deposits associated with carbonaceous intervals in the sequence of the late Palaeoproterozoic "Isa Superbasin" (Southgate et al. 2000) and had a estimated initial resource of 118 Mt with 10.2% Zn, 1.5% Pb and 36 g/t Ag (e.g. Broadbent et al. 1998). Much of the ore is extremely fine-grained and the current study was undertaken to investigate possible applications of SEM-based scanned digital imaging to ore texture interpretation in ore genesis and metallurgical studies.

2 Geological background

The Century deposit is hosted by interbedded carbonaceous shales and siltstones near the top of the Isa Supersequence (Southgate et al. 2000). These are considerably younger (1595 ± 6 Ma) than the host rocks of the large Pb-Zn-Ag deposits near Mount Isa (ca 1653 Ma), and at McArthur River (ca 1640 Ma) (Page and Sweet 1998). The ca 40 m thick mineralized interval is part of 300 m thick siltstone-shale sequence, underlain by massive carbonaceous shales and overlain by sandstones. Siltstones in the vicinity of the orebody are distinguished by high siderite-contents and stylolitic fabrics (Broadbent et al. 1998). The ore-bearing sequence is laterally terminated by faults, and above, by an unconformity with Cambrian limestones. The ore-bearing sequence has been subdivided into 4 main units designated 1 to 4 from the youngest to oldest (Broadbent et al. 1998). Unit 4 forms the lower ore zone in the mine and consists largely of mineralized black shale. Unit 3 forms an inter-ore waste band and is composed of stylolitic sideritic siltstones. Unit 2 is a thick mineralized black shale forming most of the upper ore zone resource. Unit 1 forms marginal ore and is dominated by stylolitic sideritic siltstone with 4 thin sulphidic shale interbeds.

Pyrite and sphalerite are the most abundant sulphides with pyrite being relatively concentrated in rocks immediately above and below the orebody. Galena is comparatively minor and concentrated to the southeast (Broadbent et al. 1998). About 95% of the sphalerite is white to grey and occurs in laminated to aggregated forms that broadly follow the fabric in the host rocks. It is strongly concentrated in shale intervals and about half is specifically hosted in pyrobitumen-rich laminae (Broadbent et al. 1998). About 5 % of the total sphalerite occurs in late stage vein and breccia settings that also host the majority of the galena. It is unclear whether these features formed shortly after main phase sphalerite mineralization or represent a completely separate phase of later fluid migration. Subordinate galena is disseminated in grains up to 1 mm in size that are mostly concentrated in discrete bands up to a few cm thick in shale.

3 Methods of study

Large samples of fresh rock from each subunit of the mineralization sequence stratigraphy as described by Broadbent et al. (1998), were obtained in the Century open cut shortly after the early stages of mining had continu-

ously exposed the southeastern part of the deposit. The samples were slabbed and polished thin sections were prepared from selected areas. These materials were used to achieve a general characterization of textures at hand sample, optical microscope and SEM scale. Combined WDS and EDS multi-element X-ray maps and cathodoluminescence (CL) images (cf. Fig. 1) were generated using a Jeol JXA-8200 electron probe microanalyser fitted with a CSIRO-developed XCLent 256 channel spectrometric CL system.

4 Results

Images of a sample containing early fine-grained grey sphalerite and a veinlet of late-stage honeycoloured sphalerite reveal that the former is characterized by a complex extremely fine-scale CL texture whereas the latter has a very subdued CL response (Fig. 1a). The early sphalerite also has quite variable CL brightness and spectral characteristics. The cause of this is not immediately clear as no obvious chemical distinctions were observed amongst the limited range of minor elements investigated with both types have similar low Mn- and very low Fe-contents (Fig. 1a).

Siderite rich layers in the Unit 1 siltstones have a distinctive microconcretionary texture (Broadbent et al. 1998, Fig. 1b). SEM images show that where unmineralized, these bands can be almost entirely composed of siderite and fine-grained diagenetic silica which can be distinguished from the few preserved primary quartz grains by its CL

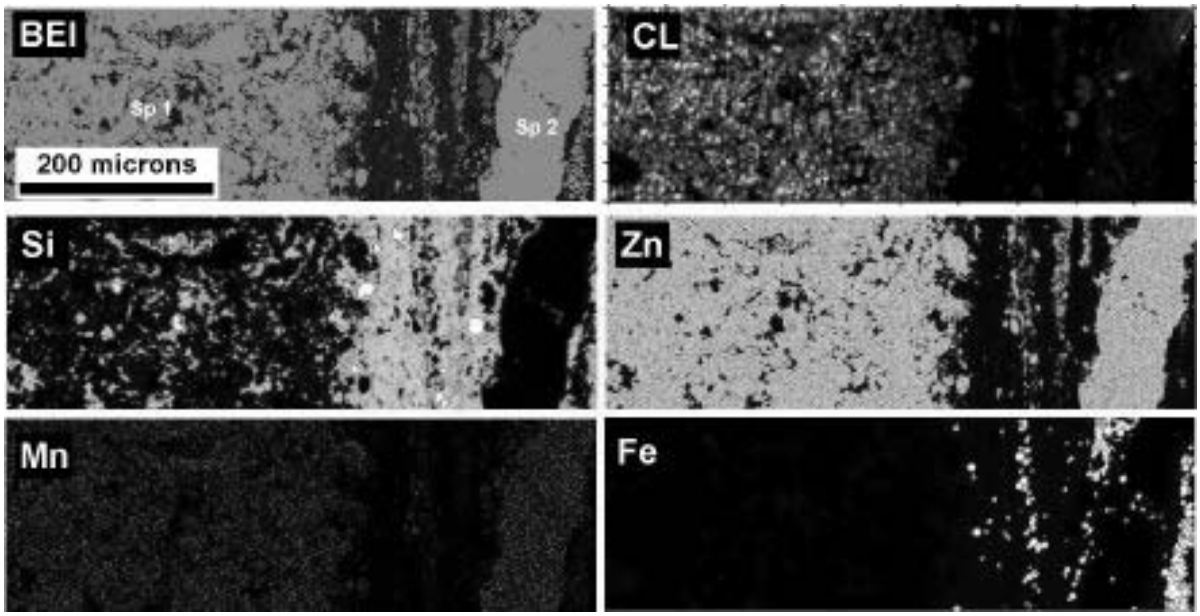

Figure 1a: Images of a sample of Century ore (Unit 4, Lower Ore Zone) illustrating applications of integrated scanned image technology to characterization of sphalerite. Sphalerite distribution is obvious as brighter areas in in the BE image and Zn X-ray map. Early layer-parallel sphalerite (Sp 1) has high CL brightness (and complex polychromatic CL texture though this is not seen in greyscale images) and occurs in fine-scale intergrowth with quartz and other silica-bearing minerals. Late fracture-controlled sphalerite (Sp 2) has a very subdued CL.

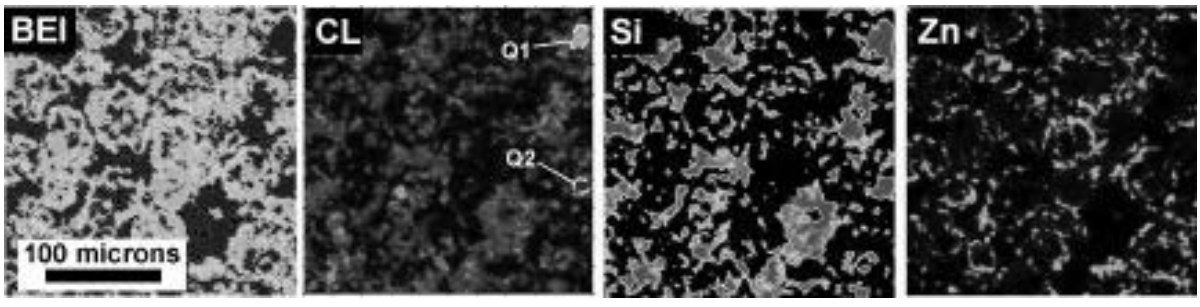

Figure 1b: Images of part of an unmineralized siltstone from Unit 1 which is shown to predominantly comprise diagenetic siderite (bright in BEI) and silica with just a few preserved sedimentary quartz grains (e.g. Q1 and Q2). The siderite is microconcretionary in character and compositionally-zoned with high Zn-contents in the youngest growth zones.

texture (Fig. 1b). Broadbent et al. (1998) undertook spot microprobe analyses of siderite microconcretions and proposed these revealed a time progression from Mn and Zn-bearing cores to relatively Mg-rich rims. However, new X-ray mapping reveals that siderite textures are more complex and include cases where Zn-poor siderite is rimmed by Zn-rich siderite (Fig. 1b). It also revealed that Mn and and Zn are actually decoupled from each other.

SEM imaging revealed a variety of textures involving sulphide minerals that have implications for the interpretation of mineralization processes. Disseminated galena grains are revealed to have a porphyroblastic or nodular character and to have complex internal textures involving microinclusions of sphalerite and apparent epitaxial overgrowths on enclosed detrital quartz grains (Fig. 2a). Pyrobitumen seams in ore bands are commonly replaced by crowded aggregates of fine-grained pyrite with both phases showing evidence of their having been replaced by sphalerite (Fig. 2b). Where sideritic bands are mineralized they display clear evidence that sphalerite post-dates, and in some cases has selectively replaced the siderite (Fig. 2c).

5 Discussion

Broadbent et al. (1998) proposed that the Century deposit originated by the influx of an oxidized metal-bearing fluid into a pre-existing zoned oil and gas reservoir leading to sphalerite deposition by thermochemical sulphate reduction (TSR). An issue with the Broadbent et al. model is the need explain how the Zn-bearing fluids were channelled into the organic-rich shale units that might be expected to be the least permeable in the sequence, particularly given that the ore deposit occurs in a part of the basin sequence distinguished by thinly bedded units and containing relatively massive black shale below, and sandstones above (Broadbent et al. 1998). The current study supports the general concept that main phase sphalerite mineralization occurred in rocks with a prior history of organic maturation and diagenesis. At SEM scale the sideritic siltstones reveal extensive diagenetic replacement of their primary grain textures by finegrained silica as well as siderite which is likely to have had a profound effect on their porosity/permeability characteristics at the time of mineralization. Where they are mineralized, the siltstones display evidence of fracturing that was probably coupled to reaction-enhanced permeability (sphalerite replacement of siderite; Fig. 2c). This echoes another situation described by Uysal et al. (2004) where organic matter-rich shales developed enhanced porosity and permeability characteristics in a process linked to hydrocarbon expulsion whereas organic matter-poor shales, siltstones and sandstones in the same sequence had been sealed by diagenetic quartz and carbonate.

In a TEM investigation of Century ore samples, McKnight (2004) found that organic matter contains

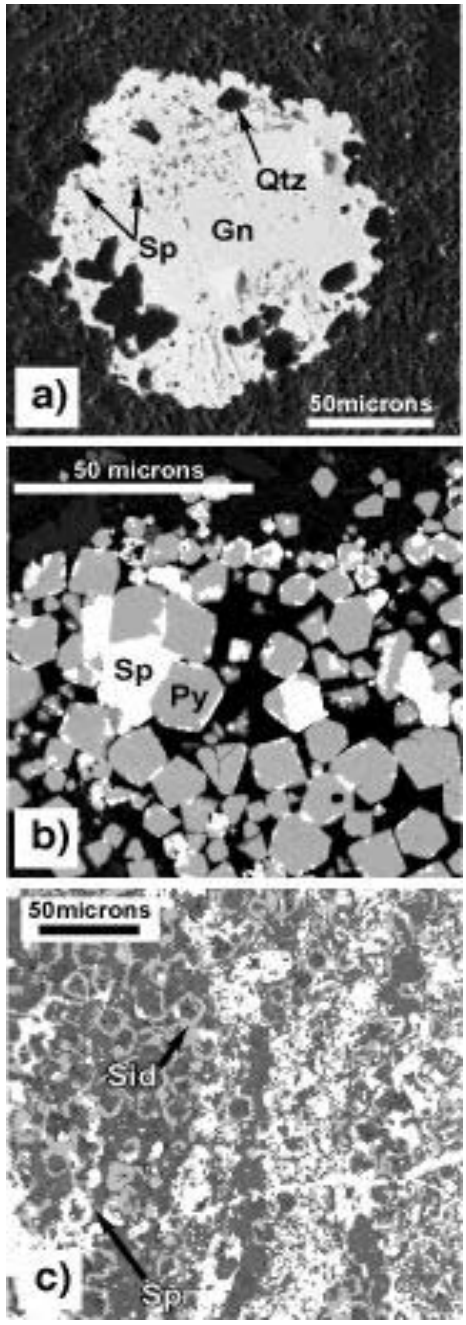

Figure 2: Electron microscope images of replacement textures involving sulphides from the Century upper ore zone sequence. (a) Galena (Gn) "porphyroblast" in Unit 1 siltstone (secondary electron image reveals aspects of the grain texture in the host rock). The galena contains zones of sphalerite (Sp) microinclusions and idiomorphic quartz (Qtz) grains that probably developed by epitaxial overgrowth on detrital grains. Sample from unit 1. (b) Fine grained pyrite (Py) developed in a pyrobitumen (black) seam within Unit 150 shale (a thin marginal ore band in the upper ore sequence). Sphalerite (Sp) has replaced both pyrobitumen and pyrite. Backscattered electron image. (c) Microconcretionary siderite (Sid -darker grey material is predominantly silica, cf.

ultrafine crystallites of sphalerite (> 100 nm) and proposed an alternative model for mineralization involving cotransport of Zn, S and hydrocarbons. Likewise sphalerite replacement of iron minerals (siderite, pyrite; Fig. 2) are inconsistent with the TSR model as no oxidized iron bearing reaction products are present and Fe must have been removed in the (reduced) fluid phase. The temperatures of main phase mineralization at Century are presently unconstrained. Chen et al. (2003) discussed similar concepts with reference the HYC deposit at McArthur River and pointed out that hot (> 250° C) reduced fluids have the capacity to cotransport sulphur and metal and would potentially be rather more aggressive mineralizing agents than other types of fluids envisaged for shale-hosted Pb-Zn-Ag mineralization.

Digital SEM imagery has many potential applications in geometallurgical studies aimed at better understanding the processing behaviour of ores. SEM-based imagery should evidently be the preferred means of characterizing sphalerite textural relations in Century ores and particulate samples (concentrates and tails) as these are commonly too fine-scale to be resolved by other means. CL provides a new means of discriminating different generations of sphalerite in processing products and X-ray maps (cf. Fig. 1b) should be invaluable in estimating the quantities of nonsulphide (unrecoverable) zinc thereby allowing better monitoring of actual concentrator performance.

Acknowledgements

This study was instigated by Ian Kelso (then senior mine geologist) and made possible by financial and logistical assistance from the Century mine.

References

Broadbent GC, Myers RE, Wright JV (1998) Geology and origin of shale-hosted Zn-Pb-Ag mineralization at the Century deposit, northwest Queensland: Economic Geology 93: 1264-1294

Chen J, Walter MR, Logan GA, Hinman MC, Summons RE (2003) The Paleoproterozoic McArthur River (HYC) Pb/Zn/Ag deposit of northern Australia: organic geochemistry and ore genesis. Earth and Planetary Science Letters 210: 467-79

McKnight S (2004) Application of high voltage transmission electron microscopy to the study of ultra-fine grained ores. The AusIMM New Leaders Conference , Ballarat 21-22 April, 2004

Page RW, Sweet IP (1998) Geochronology of basin phases in the western Mt Isa Inlier, and correlation with the McArthur Basin: Australian Journal of Earth Sciences, 45: 219-232

Southgate PN, Bradshaw BE, Domagla J, Jackson MJ, Idnurm M, Krassay AA, Page RW, Sami TT, Scott DL, Lindsay JF, McConachie BA, Tarlowski C (2000) Chronostratigraphic basin framework for Palaeoproterozoic rocks (1730-1575Ma) in northern Australia and implications for base metal mineralisation. Australian Journal of Earth Sciences 47: 461-483

Uysal IT, Glikson M, Golding SD, Southgate PN (2004) Hydrothermal control on organic matter alteration and illite precipitation, Mt Isa Basin, Australia. Geofluids, 4: 131-142

Diagenetic origin of the Luzhou copper deposit, Yunnan Province, China

Wengen Chen, Bin Xia
Guangzhou Institute of Geochemistry, Laboratory of Marginal Sea Geology, Chinese Academy of Sciences, Guangzhou 510640,China

Abstract. The Luzhou sandstone-hosted copper deposit in the Chuxiong Basin is hosted by the Cretaceous Maotoushan Formation. Ore is localized in paleo-river channels on the limbs of gently folded anticlines. Sedimentologic, paragenetic, isotopic and mineral zoning studies suggest that the deposit was formed where oxidized Cu-rich basinal fluids were reduced during early diagenesis.

Keywords. Cretaceous stratiform-copper deposit, Luzhou, Chuxiong basin

1 Introduction

Sandstone-hosted copper deposits in the Chuxiong Basin represent an important metallogenic district in China. The district contains six medium-sized (average 17.2 million tonnes of ore at 1.4 % Cu grade) copper deposits, including Luzhou, Haojiahe, Dacun, Tuanshan, Wadizhu and Geyizha, and more than ten smaller deposits that average tonnages and grades of 2.15 million tones at 1.06 % Cu. The Luzhou contains 30.86 million tonnes of ore at an average grade of 1.32% Cu. The genesis of these deposits has been a source of controversy with proposed models including (1) sedimentation-reworking concentration of Cu (Qin et al. 1993; Zhuang et al. 1996; Ran and Zhuang 1998), or (2) hydrothermal mineralization during diagenesis (Chang 1975).

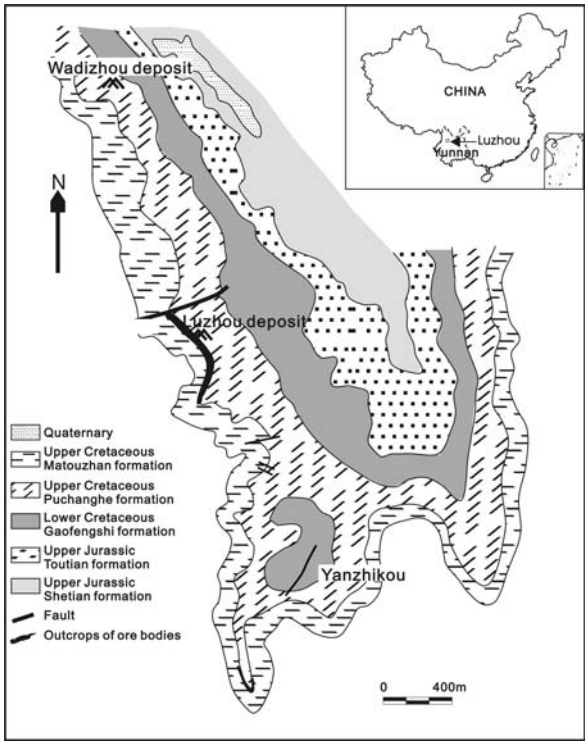

Figure 1: Geologic map of Luzhou Cu deposit.

2 Geologic setting

The Chuxiong Basin formed on the Permian Emeishan basalt on the southwestern margin of the Yangtze Craton. The basin stratigraphic sequence contains Late Triassic coal-bearing formations at the base, overlain by Jurassic-Cretaceous redbed sandstones and caped by a Tertiary evaporite gypsum-salt sequence. North-trending extensional faults controlled second-order depressions in the basin. The largest copper deposits are distributed along the western margin of the Yuanmou Old Land. The Luzhou copper deposit is hosted in the Upper Cretaceous Matoushan Formation (Fig. 1).

3 Geologic characteristics of the Luzhou copper deposit

The base of the Matoushan Formation contains conglomerates and gravels that unconformably cover the Lower Cretaceous Puchanghe Formation. Conglomerates are overlain by an upwards-fining sequence of sandstones, siltstones, mudstones and calcareous mudstones. Ore is hosted in medium- to fine-grained sandstones directly above the conglomerates.

The Luzhou deposit contains several stratiform ore zones with strike lengths ranging between 140 m and 3 km, widths between 80 and 460 meters, and an average thickness of 12 m (ranging from 1 m to 36 m). Ore is localized in paleo-river channels now situated on the limbs of gently folded anticlines.

The dominant ore mineral in the deposit is chalcocite that is disseminated in the sandstones and formed prior to pore-filling diagenetic cements. A second stage of chalcocite occurs in fractures that cut diagenetic minerals. Ore minerals are zoned from hematite below the ore through chalcocite-bornite-chalcopyrite and pyrite at the

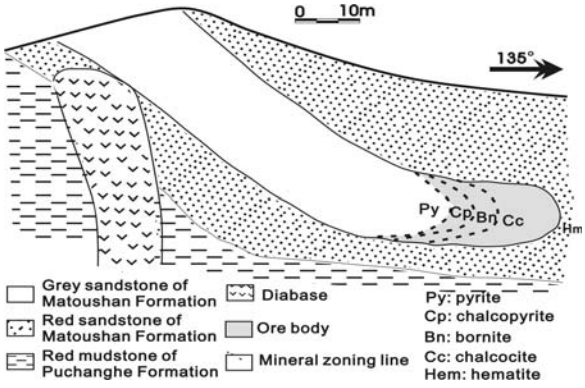

Figure 2: Schematic cross section of the showing mineral zoning of the Luzhou Cu deposit.

top of ore zones. Previous studies have suggested that ore zoning is the result of repeated and superimposed hydrothermal events. Our petrographic studies, however, suggest that copper mineralization took place at a redox interface where oxidized Cu-rich fluids were progressively reduced. The observed zoning of reduced minerals above ore and oxidized below are also inconsistent with supergene concentration of Cu.

4 $\delta^{34}S$ values of ore minerals

The $\delta^{34}S$ values of 44 sulfide minerals separated from the Luzhou Cu deposit range between –31.4‰ and –1.84‰, with most values ranging between -18‰ to -16‰ (Fig. 3). These low values suggest a sulfur source that originated from biogenic reduction of sulfate.

5 Genesis of the copper deposit

Mineralization in the Luzhou deposit is stratiform and localized by a combination of paleo-river channels and gently folded anticlines. Paragenetic relationships suggest mineralization took place during diagenesis and low sulfur isotope values of ore minerals indicate sulfur was sourced from biogenic sulfate reduction (Schmidt and McDoald 1979). The timing of mineralization suggests that that Cu-rich oxidized brines were driven out of the basin during burial and compaction. Localization of ores in permeable beds within the limbs of anticlines com-

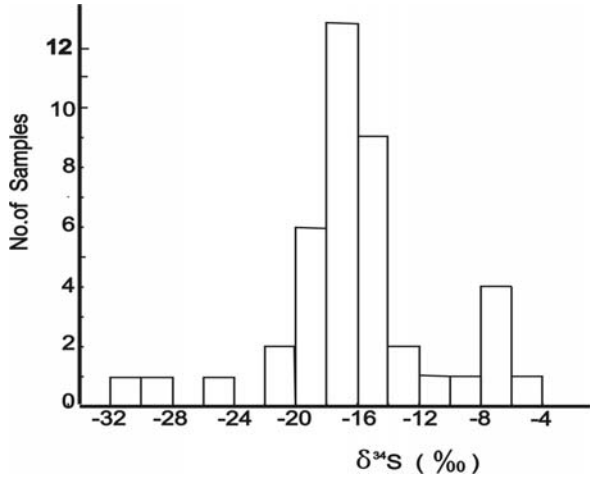

Figure 3: Distribution of sulfide $\delta^{34}S$ values. Analysed minerals include pyrites, chalcopyrites, bornites and chalcocites.

bined with the zoning of redox sensitive minerals suggests ores were formed by progressive reduction of the ore fluid, possibly through fluid mixing, in permeable zones.

Acknowledgements

This work was supported by the CAS Knowledge Innovation Project (grant KZCX2-SW-117). Jan Pasava, Ray Coveney and Poul Emsbo have revised the manuscript.

References

Cheng Y (1975) A preliminary discussion on the genesis of sandstone-hosting copper deposits in a certain area of China and ore-controlling factors. Acta Geologica Sinica 59: 28-44 (in Chinese with English abstract)

Qin D, Meng Q, Yang M (1993) Sedimentation-reworking origin of the Haojiahe copper deposit in Mouding. Mineral Deposits 12: 97-106 (in Chinese)

Ran C, Zhuang H (1998) Geochemistry of the Assemblage of Copper, salt and inorganic deposits in the Chuxiong Basin. Beijing: Science Press, 1998, 19-40 (in Chinese with English abstract)

Schmidt V, McDoald DA (1979) Texture and recognition of econdary porosity in sandstones SEPM, Spec. Pub., No. 26: 175-207

Zhuang H, Ran Ch, He M (1996) Interaction between copper, salt and organic matter and the formation of the sandstone-type copper deposits in the Chuxiong Basin. Acta Geologica Sinica, 70: 162-172 (in Chinese)

An overpressured fluid system associated with the giant sandstone-hosted Jinding Zn-Pb deposit, western Yunnan, China

Guoxiang Chi, Hairuo Qing
Department of Geology, University of Regina, Regina, Saskatchewan, Canada S4S 0A2

Chunji Xue, Rong Zeng
Faculty of Geological Sciences and Resources, Chang'an University, Xi'an 710054, China

Abstract. The Jinding Zn-Pb deposit is hosted in continental clastic rocks in the Meso-Cenozoic Lanping-Simao Basin in western Yunnan. The deposit has been compared to SEDEX, MVT, and sandstone-hosted types (SST), all assuming intra-basinal origins for the ore-forming fluids. The driving forces of fluid flow and the pressure system have not been systematically investigated. This paper presents field and fluid-inclusion evidence to show that the Jinding mineralizing system was strongly overpressured. The common occurrence of CO_2-rich fluid inclusions and the high fluid pressures suggest a mineralizing system markedly different from most other sediment-hosted base metal deposits including SEDEX, MVT and SST. Numerical modeling of basinal fluid flow indicates that sediment compaction alone in the Lanping-Simao Basin cannot produce any significant overpressure. Tectonic thrusting can significantly increase fluid pressure, but is not enough to cause the high fluid overpressure indicated by fluid inclusions. Input of extra-basinal fluids (e.g. deep-sourced CO_2) into the basin may have contributed to the development of the overpressured mineralizing system.

Keywords. Sandstone-hosted, Zn-Pb deposits, Jinding, sedimentary basin, overpressure, fluid inclusions, numerical modeling

1 Introduction

The Jinding Zn-Pb deposit is located in the Meso-Cenozoic Lanping-Simao Basin in western Yunan. With a reserve of approximately 200 Mt ore grading 6.1% Zn and 1.3% Pb (i.e. a metal reserve of about 15 Mt), Jinding is one of the largest Zn-Pb deposits in the world. The nature of the mineralization at Jinding has been the subject of a number of scientific debates, focusing on whether the mineralization is syngenetic or epigenetic (see Xue et al. 2005). Most previous studies assumed the mineralizing fluids were intra-basinal (e.g. Kyle and Li 2002), although some connections with deep-seated (mantle) processes have been suspected (Yin et al. 1990; Xue et al. 2003). No studies have been carried out regarding the pressure regime of the fluid system, regardless of syngenetic or epigenetic origin.

In this paper, we propose that the fluid system associated with the Jinding deposit is strongly overpressured, based on filed observations and fluid inclusion data. Using numerical modeling of basinal fluid flow, we further propose that the observed high fluid pressures were partly caused by thrusting of lithified rocks over soft sediments, and fluids external to the basin (likely deep-sourced) may have contributed to the development of the overpressures.

2 Regional geology

The Lanping-Simao basin is an intracontinental basin developed on the Changdu-Lanping-Simao micro-plate between the Yangtze Plate to the east and the Tibet-Yunnan Plate to the west, separated by the Lancangjiang and Jinshajiang-Ailaoshan faults (Fig. 1). The basin evolved from an inherited marine and marine-continental basin in Triassic period, through a continental depression basin in Jurassic-Cretaceous period, to a continental pull-apart basin in Cenozoic. The strata of the basin consist of, in ascending order, the Upper Triassic Waiguchun (T3w), Sanhedong (T3s), Wailuba (T3wl) and Maicuqing (T3m) formations, followed by a hiatus and then Middle Jurassic Huakaizuo (J2h) and Upper Jurassic Zhuluba (J3z) formations, Lower Cretaceous Jingxing (K1j), Nanxing (K1n) and Hutoushi (K1h) formations, an Upper Cretaceous hiatus, and Eocene Yunlong (E1y), Guolang (E2g), Baoxiangshi (E2b) formations and undivided Upper Eocene sediments (E3). Except T3s that is composed of limestones and Ey that in part contains limestone fragments, all other units are composed of siliciclastic rocks with varying proportions of sandstones and shales. Cenozoic tectonic events include regional westward thrusting, local uplifting, and alkaline igneous activities of 68 to 23 Ma (see Xue et al. 2005).

3 Local geology

The Jinding deposit occurs as tabular ore bodies hosted in sandstones of the Jingxing Formation (K1j) and sandstones and carbonate breccias of the Yunlong Formation (E1y) near a NS-trending, high-angle normal fault, the Pijiang fault (Figs. 1 and 2). K1j rocks were thrusted over E1y along a flat-lying fault (the F_2 fault, Fig. 2). The strata above F_2 (the Jinding nappe or allochthonous system) are overturned, whereas those below F_2 (autochthonous system) remain in normal position (Fig. 2).

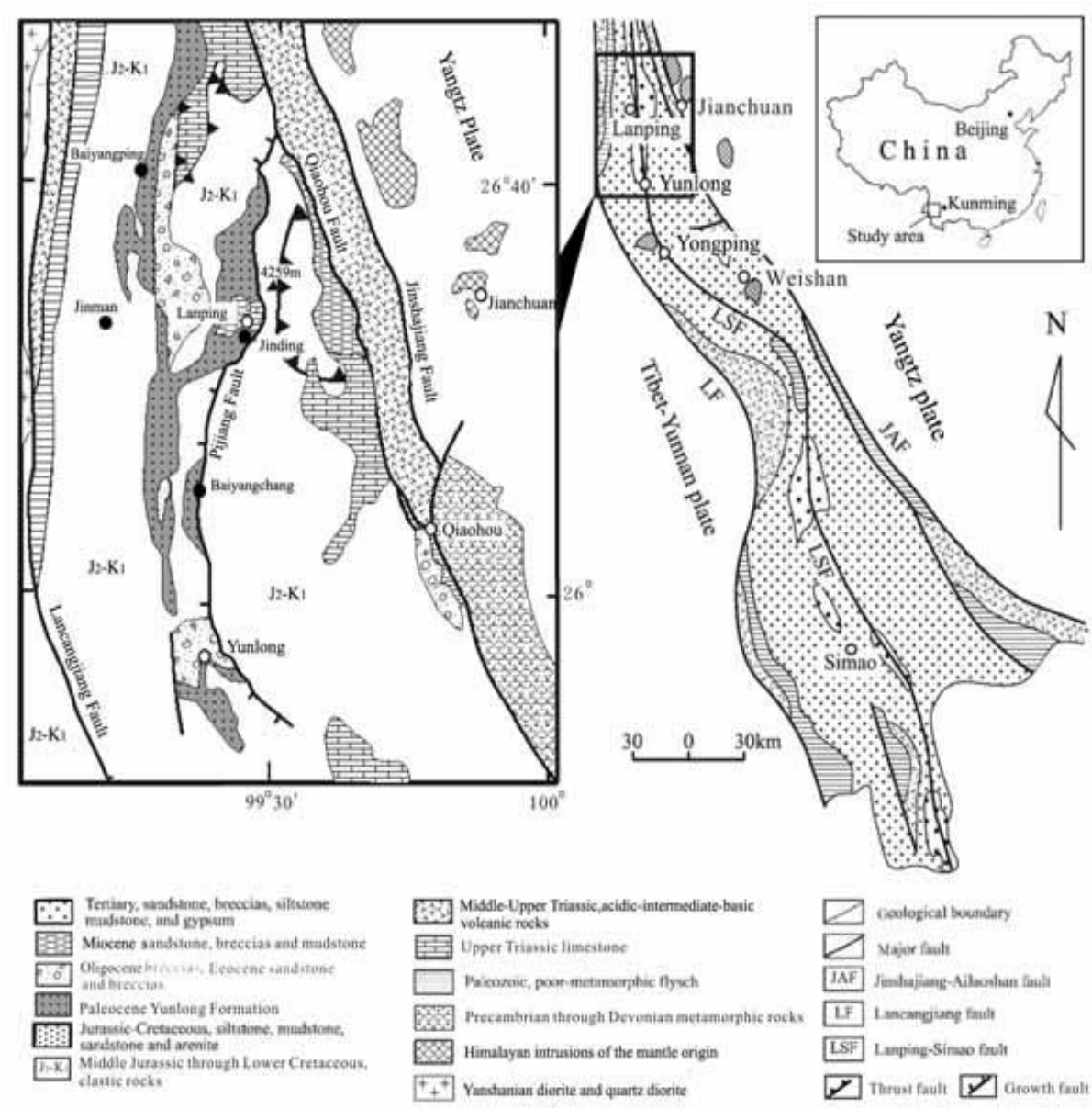

Figure 1: Location and major structural features of the Lanping – Simao Basin in western Yunnan, China, with enlargement of the northern part where the Jinding deposit is located (after Xue et al. 2005).

The deposit consists of a number of ore bodies that are distributed around a doming structure called the Jinding dome. Both the strata above and below F_2, and the thrust fault plane itself, are folded by the dome, indicating the doming process postdated thrusting. The fact that Zn-Pb ores occur both above and below the F_2 fault suggests that mineralization also postdated the nappe emplacement, possibly related to the doming process. Zn-Pb mineralization similar to that around the Jinding dome, controlled by the same thrusting fault, occurs in the vicinity of the Jinding deposit, e.g. the Tuzishan occurrence, a few kilometers northeast of Jinding.

4 Indicators of high fluid pressures

4.1 Hydrofracturing

A significant portion of the Jinding ore deposit is hosted in carbonate breccias in E1y, which have been interpreted as alluvial fan or fan delta complex related to the Pijiang growth fault (Kyle and Li 2002). The matrix of the breccias is generally red-colored sandstone. Locally, limestone fragments are surrounded by an mm-wide halo characterized by a pale color indicating reduced conditions (Fig. 3A). It is possible that some of the carbonate fragments

may have been brought up by overpressured, reduced hydrothermal fluids mixed with sediments.

Angular fragments of sandstones in the matrix of sandstones in the Hutoushi Formation (K1h) (Fig. 3B), seen at the core of the Jinding dome, may be related to hydrofracturing and infilling of soft sediments. Multidirectional fractures and angular breccias of limestone cemented by calcites and sulfides (pyrite and sphalerite) (Fig. 3C) are common in the Sanhetong Formation (T3s). These features are likely related to high fluid pressures and hydrofracturing.

4.2 CO_2-rich fluid inclusions

A number of fluid inclusion studies have been carried out in the Jinding deposit (see Xue et al. 2005), most reporting basinal brines with variable salinities (e.g. Kyle and Li 2002). CO_2-rich fluid inclusions were reported in several studies (e.g. Yin et al. 1990; Xue et al. 2002). The presence of CO_2-rich fluid inclusions is unusual for a sediment-hosted Zn-Pb deposit, and potentially indicates high fluid pressures.

Abundant CO_2-rich fluid inclusions were found in calcite closely associated with sphalerite and galena in the Tuzhishan occurrence. The fluid inclusions range from carbonic-only to aqueous-only, with variable carbonic/aqueous ratios. This is interpreted as a result of immiscibility and heterogeneous trapping. The melting temperatures of CO_2 range from -58.5° to -57.0°C, indicating dominance of CO_2 and presence of other gases such as CH_4. The homogenization temperatures (Th) of carbonic inclusions (to liquid) range from -6.8° to 21.3°C. The Th values of aqueous inclusions coexisting with the carbonic inclusions range from 110° to 133°C. Using the Th values of aqueous inclusions to approximate the trapping temperatures and isochores of carbonic inclusions, the fluid pressures are estimated to be 513 to 1364 bars (Fig. 4). The pressure variation may be related to fluctuation between hydrostatic and lithostatic or supralithostatic regimes.

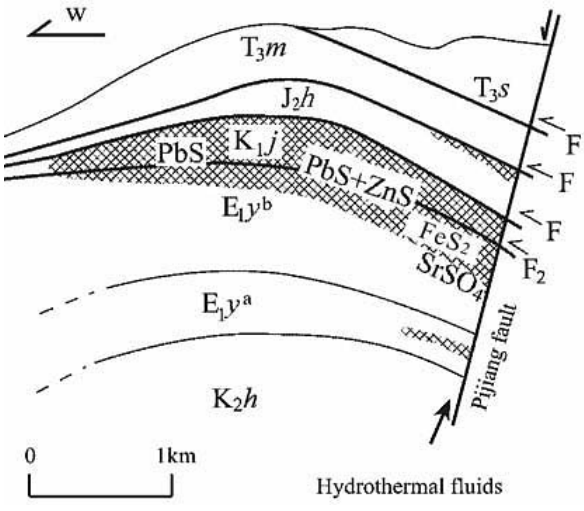

Figure 2: A sketch geological section of the Jinding Zn-Pb deposit (after Xue et al. 2005).

5 Numerical modeling of overpressures

High fluid pressures may have been caused by sediment compaction, loading of the nappe, or input of deep-sourced fluids into the basin. We have examined the effect of sediment compaction and thrusting with numerical modeling using the Basin2 program (Bethke et al. 1993). The inputs of the modeling are lithology, thickness and duration of the strata in the Lanping-Simao Basin from T_{3w} to E_3, based on data from the Third Geological Team (1990). The results indicate that, considering sediment compaction alone, the maximum fluid overpressure dur-

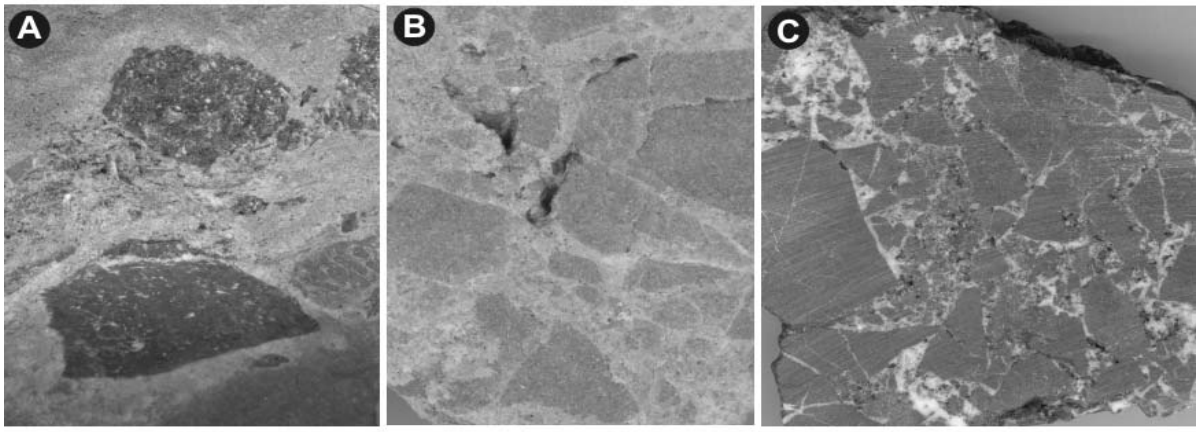

Figure 3: (A) Limestone fragments in matrix of red sandstones, with a halo of pale color, Yunlong Formation (E_{1y}). (B) Angular fragments of sandstone in sandstone matrix, Hutoushi Formation (K_{1h}). (C) Angular fragments of limestone in matrix of calcite with pyrite and sphalerite, Sanhedong Formation (T_{3s}).

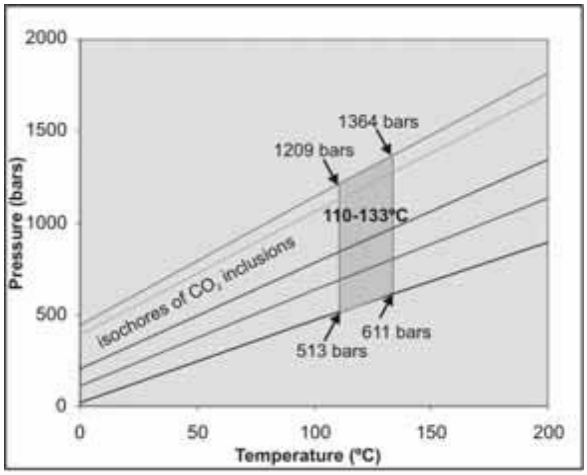

Figure 4: Isochores of carbonic fluid inclusions and inferred pressures for the temperature range of 110°C to 133°C.

ing the evolution history of the basin was less than 10 bars. However, if the loading of the nappe is considered, fluid overpressures increase significantly. The thickness of the Jinding nappe as is preserved is about 600 m, and it is unknown how much has been eroded. In the numerical model, we assume that the nappe was 2 km thick and thrusted over the whole basin from 55.8 Ma (end of Yunlong Formation) to 50 Ma. The results indicate fluid overpressures up to 100 bars were developed throughout the basin underneath the nappe. However, this overpressure is still not enough to explain the high pressures indicated by fluid inclusions.

6 Discussion and conclusions

High fluid pressures are indicated by fluid inclusions and hydrofracturing in the Jinding deposit and nearby occurrence. The pressure regime, the occurrence of CO_2-rich fluid inclusions, together with Pb and noble gas isotopic data (Xue et al. 2005) all point to an origin different from other major types of sediment-hosted Zn-Pb deposits including SEDEX, MVT, and SST. The high fluid pressures can not be explained by sediment compaction, even if the loading of the nappe has been considered. Inputs of fluids from a deep-seated source may be responsible for the strongly overpressured fluid system.

Acknowledgements

This study was supported by NSERC (grants to Chi and Qing) and NSFC (grants to Xue: 40272050, 40427054).

References

Bethke CM, Lee MK, Quinodoz H, Kreiling WN (1993) Basin modeling with Basin2, A guide to using Basin2, B2plot, B2video, and B2view. University of Illinois, Urbana, 225

Kyle JK, Li N (2002) Jinding: A Giant Tertiary sandstone-hosted Zn-Pb deposit, Yunnan, China. SEG Newsletter 50: 8-16

Third Geological Team (1990) Explanatory text of the 1:50,000 Lanping-Madeng geology map. Yunnan Bureau of Geology and Mineral Resources, 131

Xue C, Chen Y, Wang D, Yang J, Yang W (2003) Geology and isotopic composition of helium, neon, xenon and metallogenic age of the Jinding and Baiyangping ore deposits, northwest Yunnan, China. Sciences in China (series D) 46: 789-800

Stratiform Sb and Au mineralizations in the Hercynian Dúrico-Beirã area (North Portugal)

Helena Couto, Frederico Sodré Borges
Departamento de Geologia da Faculdade de Ciências da Universidade do Porto, Centro de Geologia da Universidade do Porto, Porto, Portugal

Abstract. Preceeding the main Hercynian Au-As-Sb metallogenic hydrothermal event, metallic preconcentrations (Au, Sb, Pb) occurred during the sedimentation of the Paleozoic, namely in the Precambrian (?) and/or Cambrian layers bearing volcanic prints, in the volcano-sedimentary lower Ordovician and in the basal Carboniferous breccia. The most evident lithostratigraphic control in the Dúrico-Beirão mining district concerns the Au-As mineralization hosted by the Arenigian alternances along the Eastern limb of the Valongo Anticline, with important syn-diagenetic concentration of gold related to exhalative "black-layer", with pyrite-arsenopyrite. Lithostratigraphic controls are not so evident for the Sb-Au mineralizations that occur west of the Western limb of the Valongo Anticline. Nevertheless, all the studied deposits are hosted by competent sequences, mainly conglomerates, arenites and pelites from the Precambrian (?) and/or Cambrian (Montalto Unit) with acid volcanic rocks intercalated in the base, and in some cases by the Carboniferous basal breccia (paleo-placer type).

Keywords. Stratiform Sb-Au deposit, black layers, organic matter, exhalative, acid volcanic rocks

1 Introduction

As a result of a general paragenetic study (Couto et al. 1990; Couto 1993), gold-antimony mineraliza-tions of the Dúrico-Beirão district were separated into two types: Sb-Au and Au-As. Two gold impoverished types are also present: Pb-Zn-(Ag) and W-Sn. The Sb-Au and Au-As deposits are each located in two distinct areas, and they are related to different lithostratigraphic and structural controls. In this paper we will consider the lithostratigraphic controls of the mineralizations. Ore deposits are mostly of the vein type but some mineralizations are stratiform.

2 Geological setting

The Dúrico-Beirã region is situated near the southwestern boundary of the axial part of the Hercynian folded belt, in the Central-Iberian Zone.

Country rocks consist of a NW striking band of folded metasedimentary rocks, surrounded by pre- to post-orogenic Hercynian granites (Fig. 1). The litho-stratigraphical sequence begins with Precambrian (?) and/or Cambrian, subdivided into two no formal units (Couto 1993). The Terramonte Unit is a thick flyschoïd sequence, showing some turbiditic characters. The Montalto Unit consists of alternating pelite and quartzite layers ending by thick polygenic conglomerates.

Weathered volcanic acid rocks and exhalites are present at the base of the Unit. Ordovician, discordantly overlying the Precambrian (?) and/or Cambrian, begins with platform deposits, followed by interbedded fine grained and coarse grained detritic sediments, indicating subsident and tectonically stable sedimentation conditions. Sedimentary layers bearing prints of volcanic origin are intercalated in the Arenigian alternating sequence (Couto 1993; Couto et al. 2003). The locally reduced thickness of Silurian and the frequent gap of Devonian indicate the evolution to tectonically more and more unstable conditions. In the area these rocks of marine facies form an important geological structure, known as Valongo Anticline. Carboniferous sediments are deposited on this folded and weakly metamorphosed (epizonal) basement, in continental basins.

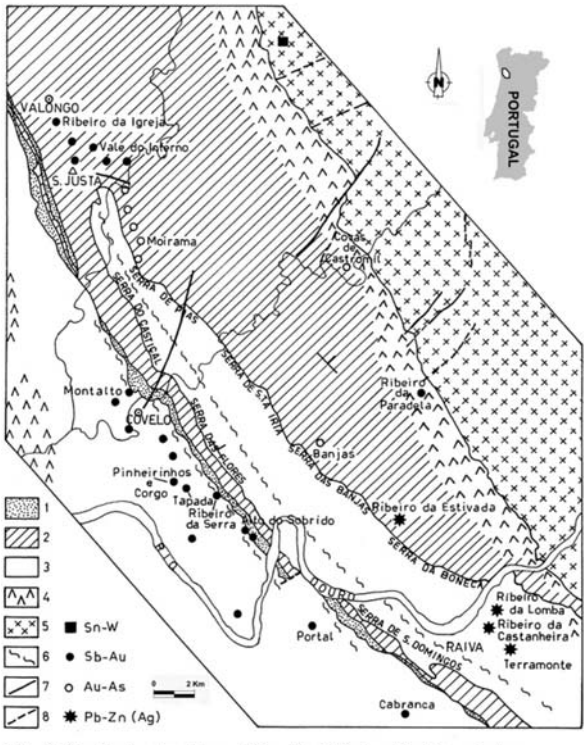

Fig. 1 Geological setting of the the Dúrico-Beirão mining district (modified after Couto et al. 1990). 1 - Carboniferous; 2- Ordovician - Devonian: 3- Precambrian (?) and/or Cambrian; 4 - contact metamorphism; 5 - post-Stephanian granite; 6 - shear-zone; 7 - fault; 8- supposed fault.

3 Litho-stratigraphic controls of the ore deposits

Couto (1993) showed that the different types of mineralization are not submitted to the same litho-stratigraphic controls.

In the Montalto area, volcano-sedimentary layers occur in the base of Montalto Unit (Couto 1993). Quartzic layers alternating with millimetric to centimetric layers composed of Mg-ripidolite, ilmenite, paragonite and scarce pyrophyllite, angular quartz crystals and sericite flakes resulting from feldspar alteration, are interpreted as an exhalite. Layers of green and violet rocks spotted by small yellowish to brownish balls (Fe- and Ti-Fe-oxydes), with a matrix of sericite and subordinate carbonate and irregular layers of angular quartz crystals, resulted from the recrystallization of a partly vitreous acid volcanic primary rock. The upper Arenigian alternating sequence is one of the best regional marker, mainly composed of banded arenitic, siltitic and pelitic beds. They are characterized by the presence of exhalative-sedimentary intercalations (black layers) and of distal volcanogenic prints in the sediments.

Black layers, well exemplified in Banjas mine (Au-As), are mainly composed of chlorite, muscovite, quartz and kaolinite. Accessory minerals are tourmaline and zircon. Opaque minerals, predominantly pyrite and arsenopyrite (gold-bearing), are frequent. This syngenetic arsenopyrite has a low grade of arsenic (mean As+Sb= 27.2 at%) indicating low temperatures of deposition (volcanic origin). Organic matter represented by fusinitizated fragments is present, and migrabetumes and hydrocarbons are not excluded (Couto 1993; Couto et al. 2003). Sporadic occurrence of transported algal and bryozoan remains suggest that these intercalations of carbonaceous fine-grained black sediments are related with episodic development of anoxic conditions (Couto et al. 2004). Subconcor-dant thin quartz "veins" are interbedded in black layers. These flat veins are interpreted as detritic and chemical siliceous rocks (quartzite and chert) crystallized or recrystallized during the circulation of hydrothermal mineralizing fluids (Couto et al. 2003).

Native gold visible to the naked eye was observed most frequently in the black layer, particularly in the sub-concordant quartz veins. Similar black layers with disseminated sulfides and native gold were also observed in the Ribeiro da Igreja and Vale do Inferno mines (Sb-Au). In the area of Ribeiro da Estivada mine (Pb-Zn-Ag with low local gold contents) six layers with the same composition were analysed. All the samples have Au (8-151ppb) and Sb (8-124ppm).

Uncommon lithologies interpreted as volcanogenic prints in the sedimentary environment, were observed in the Arenigian alternating sequence all around the Valongo Anticline. The most frequent are laminæ with angular, wedge- or needle-shaped quartz crystals, and flakes of sericite probably resulting from feldspar crystals alteration.

The Carboniferous basal breccia in Alto do Sobrido mine (Sb-Au) area is, no doubt, the most favourable country rock, with significant anomalies in gold, reaching 2g/t. The amount in As (mean 141,6 ppm), Sb (201-1731 ppm) and Pb (5-1740 ppm) are also anomalous.

4 Discussion

The most evident litho-stratigraphic control in the Dúrico-Beirão mining district is the location of the Au-As deposits in the Arenigian alternating sequences, characterized by the presence of volcanogenic prints and black layers with organic matter. The genetic relationships between the ore deposits and this particular lithologic levels may be explained by three main factors according Couto et al. (2003): (1) Mechanical characters, depending on the competence of the rocks, (2) Topochemical reaction between the mineralizing fluids and the "black-layer" bearing carbonaceous matter and disseminated sulfides, (3) Existence of metallic concentrations in the Arenigian alternating sequence (Au -30 ppb, Sb -16 ppm, Pb -135 ppm). In such an environment, the pyrite-arsenopyrite-gold bearing black layer may be interpreted as an exhalative-sedimentary deposit. These black layers, that occur in metric anticlines related with the first phase of the Hercynian orogeny, were interpreted by Combes et al. (1992) as "saddle-reef" structures, connected with the same mineralizing event that originated the veins. More recent mineralogic and petrographic studies complemented with analytical data, suggest the existence of sin-diagenetic metallic concentrations in the black layers, previous to the main mineralizing hydrotermal episode (Couto 1993; Couto et al. 2003). The black layers show evidences of volcanic activity and of detritic origin (Couto 1993). Part of the gold could be proceeding from the margin of the basin and concentrated by the organic matter, in accordance with the model considered for Kirk et al. (2001) for the auriferous deposit of Witwatersrand (South Africa). The presence of carbonaceous black shales or black slates is frequently reported in the close environment of massive sulfide deposits hosted by volcano-sedimentary series, e.g. at Neves Corvo mine (Leca 1985) in the Iberian Pyrite Belt. Pasava et al. (2003) suggested that Devonian black shales and organic matter played an important role at the the origin of tin-polymetallic deposits in the Dachang mining district. Otherwise, most of the Dúrico-Beirão Sb-Au veins are emplaced in heterogeneous sequences characterized by alternating layers of competent and uncompetent rocks of the Precambrian (?) and/or Cambrian, and rarely in the Carboniferous basal breccia. Nevertheless, the existence of volcano-sedimentary layers has to be reported, notably in the vicinity of Sb-Au deposits as Montalto. Metallic positive anomalies com-

This page intentionally blank

pared to the clark values have been detected in these intercalations (Au = 488-787 ppb; Sb = 145-508 ppm). In the Carboniferous basal breccia (Au = 253 ppb-2 ppm; Sb = 201-1791 ppm; Pb = 5-1740 ppm) the metallic anomalies are related to a pre-concentration of paleo-placer type.

References

Combes A, Cassard D, Couto H, Damião J, Ferraz P, Urien P (1992) Caractérisation structurale des minéralisations aurifères de l'Arénigien dans la région de Valongo (Portugal). Chronique de la Recherche Minière 509: 3-15

Couto H (1993) As Mineralizações de Sb-Au da região Dúrico-Beirã. Ph.D. thesis, Univ. of Porto, Vol. 2, 606

Couto H, Roger G, Moëlo Y, Bril H (1990) Le district à antimoine-or Dúrico-Beirão (Portugal): évolution paragénétique et géochimique; implications métallogén-iques: Mineralium Deposita 25: 69-81

Couto H, Roger G, Moëlo Y, Borges FS (2003) Mina das Banjas: controlo das mineralizações auríferas pelas alternâncias do Arenigiano. Ciências da Terra (UNL), Lisboa, nº esp. V, CD-ROM, F25-F28

Couto H, Borges FS, Roger G, Gutiérrez-Marco JC (2004) The Ordovician of Valongo Anticline (Portugal). Erlanger Geologische Abhanlungen – Sonderband 5. International Symposium on Early Palaeogeography and Palaeoclimate . Abstracts 28

Kirk J, Ruiz J, Chesley J, Titley S, Walshe J (2001) Detrital model for the origin of gold and sulfides in the Witwatersrand basin based on Re–Os isotopes. abs. Geol. Soc. Am. Abstr. Programs 32 (7): A-79

Leca X (1985) La découverte des amas sulfurés cachés de Neves-Corvo (Sud du Portugal). Essai de méthodologie, Chronique de la Recherche Minière 479: 51-62

Pasava J, Kribek B, Dobes P, Vavrin I, Zák K, Delian F, Tao Z, Boiron MC (2003) Tin-polymetallic sulfide deposits in the eastern part of the Dachang tin field (South China) and the role of black shales in their origin. Mineralium Deposita 38: 39-66

Origins of Au-Pt-Pd-bearing Ni-Mo-As-(Zn) deposits hosted by Chinese black shales

Raymond Coveney
Department of Geosciences, University of Missouri, Kansas City, MO 64110-2499, USA

Jan Pasava
Czech Geological Survey, Klarov 131, 118 21 Praha 1, Czech Republic

Abstract. Textural relations and other features suggest PGE that (Platinum group element-bearing) Mo-Ni sulfide beds of South China and similar beds from Canada most likely originated by venting of hydrothermal fluids to the sea floor during sedimentation.

Keywords. Pt, Pd, Mo, Cambrian, black shale, Zunyi, nickel

Unusual PGE-Au-bearing non-placer deposits consisting of Fe, Ni, As, and Mo sulfides (Fan et al. 1973; Chen et al. 1982; Fan 1983) occur in black shales, at or close to the Precambrian-Cambrian unconformity. The deposits occur in a 1600 km belt that extends across south China, with most known ore-grade occurrences located in Guizhou and Hunan. Lott et al. (1999) concluded that the deposits formed by sedex processes as did Steiner et al. (2001) and Pašava et al. (2004). This inference is based primarily on the exceptionally high grades for the ores which contain >2-4% Ni and Mo. The main host for Mo is a new mixed layer C/MoS_2 phase named MoSC by Kao et al. (2001) (Fig. 1). Data for primary fluid inclusions hosted by alteration and gangue minerals associated with the ores are consistent with the presence of high temperature (+200°C) fluids of extremely variable salinity during mineralization (Lott et al. 1997). Polymictic textural relations (Fig. 1) also fit with syngenetic deposition of the ores (Orberger et al. 2003; Pašava et al. 2004).

Figure 1: Collage of reflected light photographs of the polymictic Ni-Mo sulfide ore bed of Tianeshan, near Zunyi, Guizhou. Widths of field approximately 2 mm. Note compositional variation of consisting of varying proportions of a layered C/MoS2 phase (MoSC), iron and nickel sulfides, apatite, and organic matter. The light gray horizontal wavy band that extends through the middle of the photograph in the lower left-hand corner of the figure consists almost entirely of the new mixed layer (MoSC) that was first described by Kao et al. (2001). The presence of about 50 mole % carbon MoSC indicates that MoSC is not jordisite as is commonly supposed. Width of field = 2 mm.

Hulbert et al. (1992) and Orberger et al. (2003) have also proposed hydrothermal origins for Devonian Pt-Pd-Au-bearing mineralization at the Nick and other prospects in the Yukon of Canada (Fig. 2) but Goodfellow (2002) proposes an origin by bolide impact, which had previously been proposed by Fan (1983) for the Chinese ores.

Mao et al. (2001) have concluded that ore constituents for the Chinese shales may have been derived from seawater. Lehman et al. (2004) have shown the feasibility of seawater derivation given certain assumptions that seem to be reasonable. Furthermore Lehman et al. (2004) have suggested that metal associations and precious metal ratios, including Au:Pt:Pd near 1:1:1, are difficult to reconcile with hydrothermal origins. Luo et al. (2004) have suggested that Mo may have been derived from lower Cambrian K-bentonites. Available Re-Os dates from several laboratories (Horan et al. 1994; Mao et al. 2001; Jiang et al. 2004; Liu et al. 2004) are consistent with a lower Cambrian age of ore deposition. It is commonly assumed that the Ni-Mo deposits form a continuous layer but this is not certain, nor is it clear whether the different Ni-Mo occurrences are coeval as opposed to diachronous. Although there is evidence for remobilization of ore constituents (Orberger et al. 2005), most textural features are consistent with syngenetic origins (Fig.1). However, available radiometric ages are not sufficiently precise to distinguish among the three possible modes of origin that have been proposed. The origins of the deposits remain to be resolved definitively, but are important in part because they constitute a largely untested alternative to conventional sources of precious metals, especially platinum group elements. The temporal evidence suggests that the deposition of the Chinese deposits may have coincided with the Cambrian Explosion of Life and the end of Snowball Earth, but a causal relationship to this boundary is uncertain, and in any case would not apply to the Canadian deposits formed long after the start of the Paleozoic Era.

Figure 2: Cambrian-age Ni-Mo sulfide ore from Tianeshan, near Zunyi, Guizhou sitting on a sample of Devonian-age mineralized Ni sulfide from the Nick deposit, Yukon.

References

Chen NC, Yang X, Liu D, Xiao X, Fan DL, Wang L (1982) Lower Cambrian Black argillaceous and arenaceous rock series in south China and its associated stratiform deposits. Mineral Deposits 1: 39-51 (in Chinese)

Coveney RM Jr, Chen NS (1991) Ni-Mo-PGE-Au-rich ores in Chinese black shales and speculations on possible analogues in the United States. Mineral Deposits 26: 83-88

Fan DL (1983) Polyelements in the lower Cambrian black shale series in southern China. In Significance of Trace metals in Solving Petrogenetic Problems and Controversies (ed. SS Augustithis), Theophrastus Publications : 447-474

Fan TL, Yang HC, Wang LF, Chen NC (1973) Petrological and geochemical characteristics of a nickel-molybdenum-multi-element-bearing Lower Cambrian black shale from a certain district in south China (in Chinese). Geochimica 9: 143-164

Goodfellow WD (2002) A meteorite impact origin for late Devonian Ni-PGE sulphide and associated tsunami deposits, northern Yukon, Canada: (abs): 11th Quadrennial IAGOD meeting Windhoek (CD)

In JW M, Bierlein F (eds.), Mineral Deposit Research: Meeting the Global Challenge, Proceedings of the 8th SGA Biennial Meeting (August 18-21, 2005 Beijing)(in press)

Kao L, Peacor DR, Coveney RM Jr, Zhao G, Dungey KE, Curtis MD, Penner-Hahn JE (2001) A C/MoS2 mixed-layer phase (MoSC) occurring in metalliferous black shales from southern China, and new data on jordisite: American Mineralogist 86: 852-861

Lehman B, Mao JW, Ma DS (2004) Extreme enrichment in early Cambrian sulfide-rich black shale in south China: A seawater model: Geological Society of America, Abstracts and Programs 36: 199

Liu SR (2004) Source of Lower Cambrian platinum group elements in black shales in Hunan and Guizhou provinces, China and the Re-Os isotope dating. Science in China (Sect. D) 32: 568-575

Lott DA, Coveney RM Jr, Murowchick JB (1999) Sedimentary exhalative nickel-molybdenum ores in South China. Economic Geology 94: 1051-1066

Luo T, Ning X, Li X, Ling R, Zhu D, Yao L, Gao Z (2003) Discovery and preliminary study of K-bentonite in the lower Cambrian, Zunyi, Guizhou province (in Chinese) Mineral Studies Reports 23: 296-302

Luo T (2005) Alkaline volcanism in the early Cambrian in Zunyi, Guizhou province :(1) primary research of k-bentonite" (in Chinese) Acta Petrologica Sinica" (in review)

Mao JW, Lehmann B, Di AD, Zhang GD, Ma DS, Wang YT, Zeng MG, Kerrich R (2002) Re-Os dating of polymetallic Ni-Mo-PGE-Au mineralization in Lower Cambrian black shales of South China and its geologic significance. Economic Geology 97: 1051-1061 (see also discussions Economic Geology (2003) 98: 661-664

Orberger B, Pašava J, Gallien JP, Daudin L, Pinti D (2003) Biogenic and abiogenic hydrothermal sulfides: controls of rare metal distribution in black shales (Yukon Territories, Canada) Journal of Geochemical Exploration 78-79: 559-563

Orberger B, Wagner C, Vymazalova A, Pašava J, Kříbek B (2005) Rare metal sequestration and mobility in mineralized black shales from the Zunyi region, South China

Pašava J, Kříbek B, Žák K, Vymazalová A, Hailing Deng, Taiyi Luo, Chaoyang Li, Mingguo Zeng (2004) New data on the origin of Lower Cambrian Mo-Ni-PGE black shales in Guizhou Province, south China. Proceedings of the 32nd IGC, August 20-28, 2004 Florence

Steiner M, Wallis E, Erdtmann BD, Zhao YL, Yang RD (2001) Submarine-hydrothermal exhalative ore layers in black shales from South China and associated fossils-insights into a Lower Cambrian facies and bio-evolution. Palaeogeography, Palaeoclimatology, Palaeoecology 169: 165-191

A scale-integrated structural analysis of the Mount Isa Zn-Pb-Ag deposit and implications for genesis

Toby P. Davis
School of Earth Sciences James Cook University, Townsville, Queensland 4811, Australia
Present address: SRK Consulting Pty Ltd. 1064 Hay St, West Perth, WA, 6005, Australia

Abstract. This study analyses the structural geology of the Mount Isa Zn-Pb-Ag orebody from mine to micro scales in order to determine the role of tectonic structure in its evolution. Features of Zn-Pb-Ag deposit are compared to the nearby copper ores as the two ore types are potentially related. A ubiquitous correlation between the metal distribution and tectonic structures exists at all scales. Disharmonic folds are located central to high grade shoots, where as continuous folds are located along the margins of orebodies. Contours of metal grade and ratio of the main metal species are parallel D_4 fold hinges and silica-dolomite alteration fronts throughout the Zn-Pb-Ag deposit. The timing of mineralisation is shown by sulphide-structural overprinting relationships. The scale integrated nature of this study means that features examined are highly representative of the deposit. The Zn-Pb-Ag deposit is made up of bedding parallel sulphide accumulations at a range of scales. However, in all textural variations of these bands the all constituent sulphides can be shown to overprint tectonic structures. Consequently, for the first time the contribution of remobilisation of a pre-deformation deposit at Mount Isa can be confidently discounted. The structural features of the copper and Zn-Pb-Ag and copper ores are the same though exhibited at different scales. Zn-Pb-Ag and copper mineralisation occurred at similar times in the fourth regional deformation.

Keywords. Mount Isa, stratiform sediment hosted Zn-Pb-Ag, copper, remobilisation, syntectonic mineralisation

1 Introduction

The Mount Isa Zn-Pb-Cu-Ag deposit is one of the largest and most enigmatic base metal accumulations on Earth. This study is a scale integrated analysis of the structural geology of the Mount Isa Zn-Pb-Ag orebody ranging from the mine scale metal distribution to micro structures of the complete range of sulphide textures present in the deposit. The aim is to determine the role of structure in the evolution of the Mount Isa Zn-Pb-Ag ores. A comparison with the nearby copper orebodies is included because the two ore types are potentially related. Prior to mining the base metal deposit contained in excess of 405 million tonnes of ore including 150 Mt at 7 % Zn, 6% Pb and 150 g/t Ag and 255 Mt at 3.3 % Cu (Forrestal 1990; McGoldrick and Large 1998; Waring et al. 1998) in spatially separate copper and Zn-Pb-Ag orebodies.

The Mount Isa base metal deposit is located on the western margin of the Leichhardt River Fault Trough in the Western Fold Belt of the Mount Isa Inlier, northwestern Queensland, Australia (Fig. 1). It lies east of, and adjacent to the Mount Isa and Paroo faults and is traversed by folds that formed during the Isan Orogeny (1610-1500 Ma). The orebody is hosted by the Urquhart Shale, a dolomitic sedimentary sequence in the Upper Mount Isa Group.

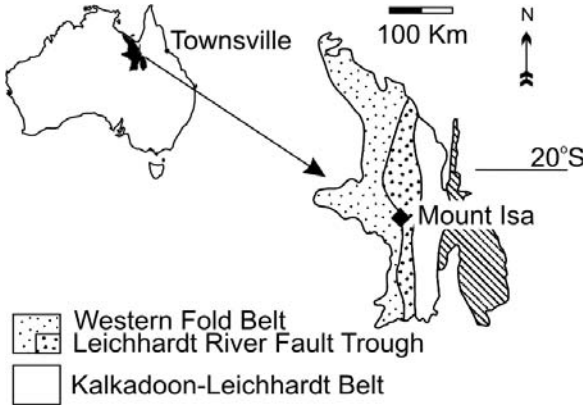

Figure 1: The Mount Isa Inlier and its main tectonic units.

The Zn-Pb-Ag orebody contains a series of conformable lenses that consist of centimetre scale bedding parallel sulphide bands and breccias and belongs to the stratiform sediment hosted Zn-Pb-Ag class of deposits (Large et al. 2002; Fig. 2). Other deposits in this class include Red Dog (Alaska), Sullivan (Canada), HYC (Northern Territory), Century (Queensland), and George Fisher-Hilton (Queensland). In contrast to the Zn-Pb-Ag orebody, the copper orebodies at Mount Isa are discordant at the mine scale and consist of cross-cutting breccias.

2 Previous work

The genesis of the Mount Isa base metal deposit is controversial because of apparently conflicting features between and within the copper and Zn-Pb-Ag orebodies. Early workers (Blanchard and Hall 1937; Grondijs and Schouten 1937) considered the deposits to be epigenetic based on the proximity of ores to folds and high strain zones. This model was replaced by predeformation mineralisation models, including exhalative and diagenetic depositional styles, to explain the conformable nature of sulphide bands within the Zn-Pb-Ag ores (Murray 1961; Neudert 1986; McGoldrick and Large 1998; Large

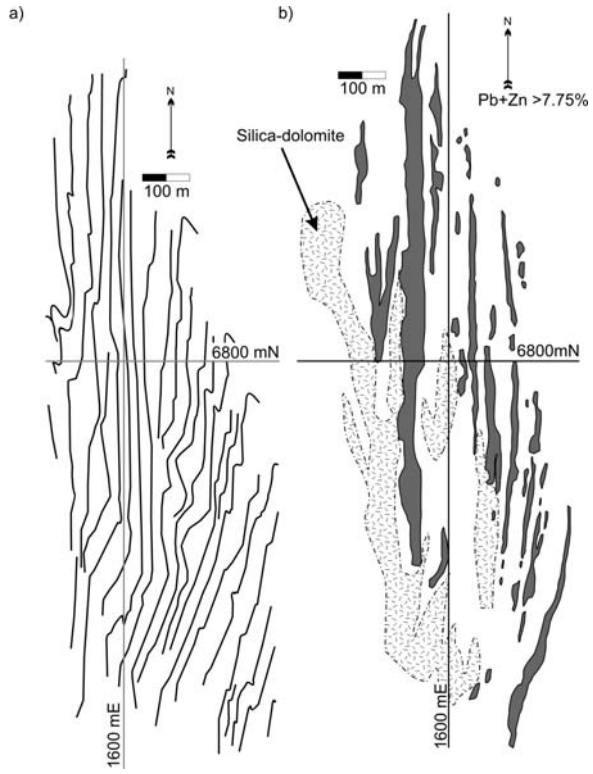

Figure 2: a) Bedding plan in the Lead Mine at Level 9 (3080 mRL). NNW-SSE-striking fold zones are defined by bedding orientations that deviate from the dominant N-S to NNE-SSW-striking fabric. b) Level 12 (2910 mRL) plan of Pb+Zn > 7.75 % and silica-dolomite alteration in the Mount Isa Lead mine.

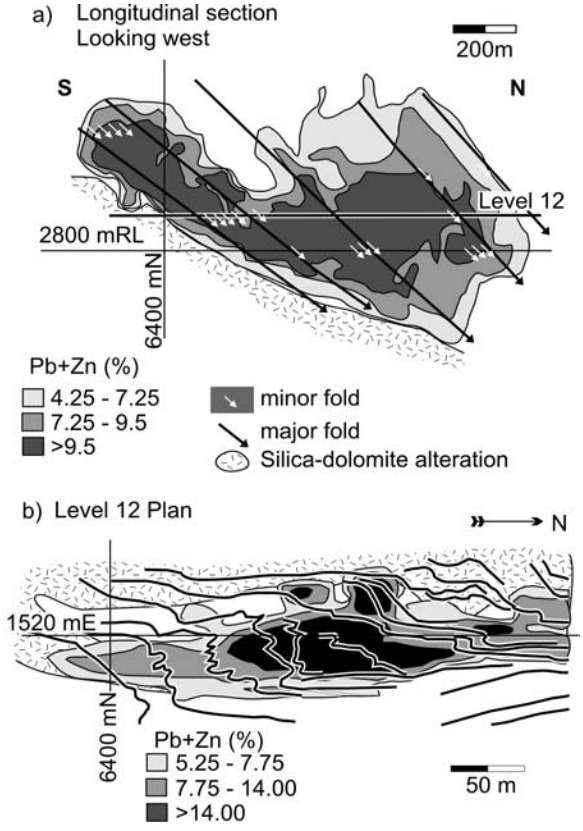

Figure 3: Relationship between the metal distribution and tectonic structures in the Zn-Pb-Ag deposit. a) Longitudinal section looking west orebody C. b) Plan through level 12, demonstrating the metal distribution is centred on disharmonic folds.

et al. 1998). In these models, various discordant features documented by the earliest workers were attributed to remobilisation (McDonald 1970; McClay 1979). Evidence of syntectonic sulphide deposition presented by Perkins (1997) has largely been dismissed as an effect of remobilisation because of the ambiguous representivity of these features (Betts and Lister 2002; Large et al. 2002). However, remobilisation has never been documented at Mount Isa.

3 Structural geology

The mine-scale fabric is dominated by NNE-SSW-striking bedding in the south that progressively rotates to N-S in the north of the mine (Fig. 2). This fabric is traversed by numerous NNW-SSE-striking, asymmetric and ENE-verging folds that formed in D_4. The Zn-Pb-Ag orebody contains ten sheetlike Zn-Pb-Ag ore lenes located around the northern margin of the discordant quartz-dolomite bodies, locally referred to as silica-dolomite, which host the breccia hosted copper ores. The ore lenses are up to 1.2 km long and plunge in the range of 23-60° towards 323-348°, which is parallel to the plunge of F_4 fold hinges. Longitudinal sections show the ore lenses contain NNW-plunging high grade shoots that are parallel to their margins and coincidental with NNW-plunging folds that are disharmonic within the lenses. Similarly orientated folds are located along the margins of the ore lenses but these folds are continuous across them (Fig. 3).

Metal zonation patterns through out the Zn-Pb-Ag orebody show Pb:Zn contours are parallel to F_4 fold hinges and silica dolomite fronts. The remarkably continuous nature of the lead distribution and the simple and parallel shapes of the Pb:Zn contours indicate deposit is undeformed and there has not been any differential remobilisation of sulphide species.

4 Textural analysis

The Mount Isa Zn-Pb-Ag orebody consists of conformable sulphide bands and breccias whose enveloping surfaces are parallel to layering at hand specimen and exposure scales. The range of textural variation in the bands and breccias and their distribution has been determined

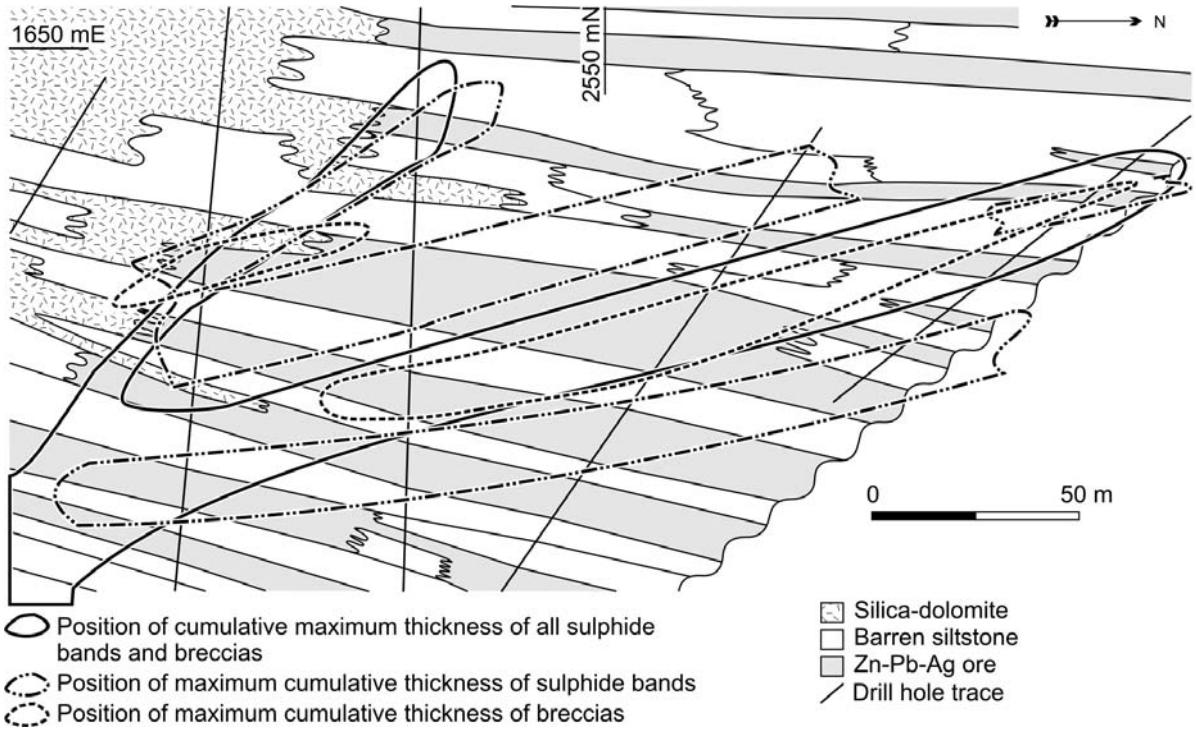

Figure 4: Plan showing the distribution of sulphide textural groupings is the same a the hinges of F4 folds. The combined thickness of all bands and breccias has a NNW-SSE-striking peak plus a NW-SE striking one north of the silica-dolomite alteration front. Sulphide bands (microcrystalline and fine grained styles excluding microbreccias) display two NNW-SSE-striking peaks that straddle the combined styles peak. Breccias have a NNW-SSE-striking cumulative thickness peak coincidental with the combined styled peak and a peak area north of the silica-dolomite alteration front.

by systematically logging drill core throughout the orebody. Sulphide bands were classified by the dominant sulphide species and its grain size into the following categories; microcrystalline pyrite bands, microcrystalline sphalerite bands, fine grained sphalerite bands and microbreccias, galena bands, and nodular layers. All bands contain the same paragenetic sequence, Fe-dol, cte-qz, py, sp, gn, cp with sulphides overprinting tectonic structures. Microcrystalline pyrite is the earliest sulphide phase in the sequence and overprints several generations of crenulation cleavages.

The breccias are classified according to the pattern of brecciation into foliation fill, fold clast and rounded clast breccias. These contain the same paragenetic sequence as the banded ore styles described above, which clearly overprints tectonic structures including foliations and folds.

The deposit is zoned with respect to the ore textures described above (Fig. 4). It contains a core of breccias surrounded by sulphide band textural styles. All ore textural styles have NNW-SSE-trending distribution, which is the same orientation as fold-hosted mine-scale high-grade shoots.

5 Discussion

The Zn-Pb-Ag orebodies at Mount Isa formed in the fourth regional deformation without remobilisation from a pre-existing accumulation in the vicinity. The structural controls on mineralisation are demonstrated by the ubiquitous relationship between the metal distribution and folding at mine scale, sulphide-foliation overprinting relationships in all ore textural styles at micro scales and the distribution of ore textural styles through the deposit.

Synchronous copper and Zn-Pb-Ag mineralisation is indicated by their similar and ore-structural relationships at a range of scales. Their spatial separation is the result of processes acting during mineralisation and could reflect the influence of a change in the size of structures between the orebodies on the chemistry of the mineralising system.

Bedding parallel sulphide textures in the Zn-Pb-Ag orebody are not diagnostic of pre-deformation mineralisation as has been proposed by previous workers because such features can form by structural processes as demonstrated at Mount Isa. The bedding parallel nature of sulphide accumulations reflects the strong influence of

rock type on strain partitioning and ultimately the localisation of structurally controlled fluid flow. Rock type based competency domains occur at a range of scale from individual beds to the formation scale. At Mount Isa shale and shale dominated packages experienced the higher progressive strains and consequently now host ore sulphides.

The scale integrated nature of this study and the widespread spatial distribution of the data mean that the features presented here are highly representative of the deposit. In the past, features demonstrating tectonically controlled sulphide deposition have had a questionable representivity, which has meant they were able to be dismissed as being the products of remobilisation without actual evidence of this process being presented. Remobilisation processes can be confidently discounted as having a significant influence of the formation of the Mount Isa Cu-Zn-Pb-Ag deposit.

References

Blanchard R, Hall G (1937) Mount Isa ore deposition Econ Geol 32: 1042-1057

Betts PG, Lister GS (2002) Geodynamically indicated targeting strategy for shale-hosted massive sulphide Pb-Zn-Ag mineralisation in the Western Fold Belt, Mount Isa Terrane. AJES 49: 985-1010

Davis TP (2004) Mine-scale structural controls on the Mount Isa Zn-Pb-Ag and Cu orebodies. Econ Geol 99: 543-559

Forrestal PJ (1990) Mount Isa and Hilton Silver-Lead-Zinc Deposits. In: Hughes FE (ed) Geology of the Mineral Deposits of Australia and Papua New Guinea. Australasian Institute of Mining and Metallurgy, Melbourne: 927-934

Grondijs HF, Schouten C (1937) A study of the Mount Isa ores. Econ Geol 32: 407-450

Large R, Bull S, Selley D, Yang J, Cooke D, Garven G, McGoldrick P (2002) Controls on the formation of giant stratiform sediment-hosted Zn-Pb-Ag deposits: with particular reference to the north Australian Proterozoic. In: Cooke DR and Pongratz J (eds) CODES Special Publication 4, Giant Ore Deposits: Characteristics, genesis and exploration. University of Tasmania, Hobart, 269

McClay KR (1979) Folding in the silver-lead-zinc orebodies. Mount Isa. Australia, Trans IMM 88: B4-B14

McDonald JA (1970) Some effects of deformation on sulfide-rich layers in lead-zinc orebodies, Mount Isa, Queensland. Econ Geol 65: 273-358

McGoldrick PJ, Large RR (1998) Proterozoic stratiform sediment-hosted Zn-Pb-Ag deposits. AGSO J Geol and Geophys 17: 189-196

Murray WJ (1961) Notes on Mount Isa geology. Proc AusIMM 197: 105-136

Neudert M (1986) A depositional Model for the Upper Mount Isa Group and implication for ore formation. Unpubl PhD. Thesis, Australian National University, Canberra: 324

Perkins WG (1997) Mount Isa lead-zinc orebodies: replacement lodes in a zoned syndeformational copper-lead-zinc system?. Ore Geol Rev 12: 61-110

Waring CL, Heinrich CA, Wall VJ (1998) Proterozoic metamorphic copper deposits. AGSO J Aust Geol Geophys 17: 239-246

Fluid system and ore-forming dynamics of the Yuebei Basin, China

Jun Deng, Liqing Yang, Xueming Chen, Qingfei Wang, Yan Liu
State Key Laboratory of Geological Processes and Mineral Resources, China University of Geosciences, Beijing 100083 and Key Laboratory of Lithosphere Tectonics and Lithoprobing Technology of Ministry of Education and University of Geosciences, Beijing 100083, China

Abstract. The fluid system of the Yuebei Basin was developed by three kinds of ore-bearing fluids during the late Palaeozoic. The first, called the Dabaoshan fluid was related to magmatic hydrothermal processes and formed multi-metal deposits during submarine volcanic hydrothermal sedimentation. The second, the Fankou type fluid is related to circular hydrothermal fluid in deep formation and formed SEDEX type low to middle temperature Pb-Zn-Ag-Hg deposits. The third, the Hongyan type fluid is related to diagenetic compressive water of basin and formed a single low temperature pyrite deposit. Based on the study of ore deposits features in the basin, comprehensive research on temperature field, dynamic field and chemical field of the fluid system shows that fluid system in the Yuebei basin mainly includes multi-origin of ore-forming materials, entirety of ore-forming process and significance of dynamic controlling on ore-forming processes, all of these are controlled by the regional tectonic regimes.

Keywords. Fluids system, ore-forming process, tectonic regime, Yuebei basin

1 Geological setting

The Yuebei basin is located in the northern Guangdong province, 24°~25°20' north latitude, 113°~114° east longitude. The outside margin of the basin consists mainly of pre-Devonian metamorphic rocks, while its cover rocks are late Palaeozoic, Mesozoic and Cenozoic strata. The Devonian strata are widely distributed in the basin, which overlies the Caledonian unconformity. The north boundary of the basin is composed by the Zhuguangshan granite belt. To the south is the Fogang granite belt. Stratabound deposits are well developed in the basin, including the large and middle size Fankou ore deposit, the Dabaoshan ore deposit and the Hongyan ore deposit. Most ore deposits occur in carbonate strata of early Devonian and late Carboniferous age. The basin edge is mostly controlled by EW and NNE linear structures, which corresponds to two mantle gradients, namely, the EW-trending Nanling gravity gradient belt and the NNE-trending Ganxi-Yuexi gravity gradient belt. The two belts cross the entire Guangdong province and extend to Jiangxi province. The NNE faults appear to control the later magmatic intrusion, the change of palaeography and distribution of ore deposits.

2 Geological characteristics of ore deposits

The south-western margin of the Yuebei basin, contains dozens of medium to large pyrite deposits (typified by the Hongyan deposit) which are related to basin compressive fluids and forming a 6 km long pyrite belt in Yingde area. At the eastern margin of the basin occurs the Dabaoshan middle-high temperature multi-metal deposit pertaining to submarine volcanic hydrothermal deposition. And the northern margin is host to the Fankou middle-low temperature SEDEX type Pb-Zn-Ag-Hg deposits.

3 Types of ore-forming fluids in basin and their composition

Three types of ore-forming fluid occurred in the basin. In the Hongyan area, fluid inclusions belong to Na-Ca-Cl type, as their $X(Na^+)>(K^+)$. NaCl-equivalent salinity (11.2%) is rather high for fluid inclusions and are similar to that of oil-field sludge water or ore-forming fluids in Mississippian valley type deposits. Ore-forming fluids in Fankou deposit and Dabaoshan deposit show the feature of $X(K^+)> (Na^+)$. The fluid of the Fankou deposit is of K-Ca-Cl type. The K-Ca-F (Cl) type occurs in the Dabaoshan deposit. Tens of deposits in Hongyan area are located in dolomite, which occurs as a lens and sphenoid in limestone. Except for dolomite, no evaporite minerals such as anhydrite occur in the strata. Rocks are medium to fine grained and display features of "fog centre" and "bright centre". X-ray crystal power diffraction indicates the degree of order of dolomite is up to 0.80 and Ca, Mg content is close to ideal chemical composition of dolomite ($CaCO_3$, $MgCO_3$ = 1:1 molar fraction), and $\delta^{13}C_{PDB}$ is 0.236‰, $\delta^{18}C_{PDB}$, 0.832‰. These imply that dolomite in Hongyan area is not the sediment of high salinity brine solution, but is the result of digenetic fluids replacing limestone in basin.

4 Source of ore-forming material for basinal fluid

150 samples in Fankou deposit were analyzed for S isotopes. The average value for $\delta^{34}S$ concentration is +17.29‰, suggesting that S derived from the reduction

of sulfate from seawater. The $\delta^{34}S$ of the Hongyan ore deposit ranges from -22‰ to -8‰ in the Hongyan deposit, and it can be inferred that S derived from biogenic processes. The ore-forming process probably involved biological agents and the deposit is thought as sedimentation-modification stratabound deposit (Chen 1992) with most of S derived from sulfate in seawater. In Dabaoshan deposit, $\delta^{34}S$ shows highly concentration near 0, that is, -3‰~+3‰, and its mode, +1.5‰, reflecting that S is derived from the mantle (Chen 1994).

12 samples in Hongyan deposit were analyzed for their Pb isotope in galena, pyrite and bulk rock. Except for one 187 Ma age for galena, model ages approximate those of Devonian strata. These show the same source of sedimentation and ore-forming materials. According to a mixed calculation model of Pb source, it is believed that about one third Pb derived from the crust, two thirds from the mantle. The young model age for one galena is thought to be the result of late magmatic intrusion (Caishanding magmatic rocks in Yanshan period).

Pb isotope compositions of Fankou deposit were analyzed in galena, pyrite, bulk limestone, bulk diabase. μ ranges from 9.73 to 9.90, Th/U value in galena is relatively low (3.11). These reflect Pb derived from crust where part of Pb came from the radioactive decay of U.

In the Dabaoshan deposit, Pb isotope compositions of sulphates reflect Pb sources that include crust, island arc and ocean volcanic rocks.

Isotope compositions for mineral inclusions in the Fankou deposit range from -40‰ to -83‰ for δD and 0‰ to -8‰ for $\delta^{18}O$. These reflect derivation from basement formation water and atmospheric water at a late stage of mineralization. Fourteen carbonate rock and calcite samples that coexisted with Pb and Zn minerals in the Fankou deposit were for $\delta^{14}C$ and $\delta^{18}O$ isotopes and compositions that resemble normal seawater carbonate.

Based on the above analysis, it is apparent that fluid system in Yuebei basin has multiple sources, including mantle and crust (magmatic water, basement formation water and sea water). However, each individual deposit shows evidence of mixed fluids. For example, the Hongyan deposit shows evidence for mantle, crustal and magmatic fluids. Data for the Fankou deposit imply a combination of crustal fluid and seawater.

5 Migration track of the fluid system of the Fankou deposit

In the Fankou deposit, a long and narrow band of zoned mineralization parallels a contemporaneous fault. Because of changing physical and chemical conditions, especially dilution of fluid salinity, ore-bearing fluids erupted along contemporaneous fault and then deposited minerals in the following sequence: pyrite-quartz, sphalerite-galena, siderite, and ankerite. And the residual fluids diffused outwards; as a result, dolomite and calcite develop widely and show obviously zoning.

Based on the analysis of Zn and Pb contents and ω(Zn)/ω(Pb) in Sh5 ore-body, near the cross of two groups of contemporaneous fault, both Pb and Zn and ω(Zn)/ω(Pb) in the trend surface map show a close upheaval, where there is not only an area enriched in Pb and Zn, but also a zone of pyrite displaying high decrepitation temperatures. These may indicate the location of an eruption centre of submarine hydrothermal fluid.

The temperature estimates for the Sh5 ore-body show temperature falling with distance from the faults cross (the likely fluid eruption centre), and the highest temperature points, that is, 305°C, 300°C, 298°C, 292°C, occur near the intersection of two groups of faults, with points less than 200°C located at the edge of the ore-body. Temperature field shows regular change on plane that reflects fluids fanned outwards from the centre, which is similar to the distribution trend of Zn, Pb and Zn/Pb.

Near the intersection of two groups of faults, brecciated ores develop in sulphide accumulations, in which sphalerite color is dark, and some sphalerite solid solution separated from chalcopyrite. These indicate high ore-forming temperature. As highly mineralized near the eruption centre, the biology remains slumped from other place is almost replaced by pyrite or sphalerite and forms mould biology replace texture. As the ore-forming temperature fell with distanc from the eruption centre, mineralization became relatively weak. The color of sphalerite is pale-green. The ores become banded or laminated instead of brecciated and biological remnants are less well developed; only relic with disseminated or rimmed texture can be seen occasionally. At the edge of ore-bodies, ores develop lamellar structure, and galena content diminishes, the sphalerite content rises relatively, and decrepitation temperatures are lower.

A study of the ore-body temperature field via systemic testing temperature of mineral inclusions, together with geochemical and geological methods, permit determination of the location of the eruption centre of submarine hot spring and the moving direction of ore-forming fluids.

6 Ore-forming dynamics

The three types of ore deposits in the Yuebei area display a close relation to fault and uplift. Ancient uplift and faults provided necessary conditions to form Fankou, Hongyan and Dabaoshan types of ore deposits. In the three types of deposits, ores show syngenetic or epigenetic rudaceous-brecciated structure, and its breccias include wall rocks and ores. In the Xiniu ore deposit, 2.5~3 cm circinal breccias replaced by pyrite occur widely. These breccias might

This page intentionally blank

be the result of further rounded after structural collapse. In the Fankou ore deposit, a large amount of rudaceous, brecciated ores or limestone breccias developed in ore-body and in its wall rocks. Some micro-crack occurred in ore-body, and sulfides or marine argillaceous sediments deposited on the crack surface, but additional marine sediments were deposited. These reflect ore-forming processes accompanying structural (or tectonic) evolution.

Because of the different scale of ore-controlling fault, fluid circulation and location of the ores, different types of stratabound deposits show different ore-forming process. For example, the Dabaoshan deposit is located near a deep fault and its formation has a close relation to submarine volcanic exhalation and magmatic superimposition. The ores show multi-stage mineralization and coarse-grained crystal textures; mineral compositions are complex; and the mineralization association is W-Mo-Bi-Fe-Cu-Pb—Zn-Au-Ag-S et al. In the Hongyan ore deposit, which is controlled by faults and formed at a relatively shallow depth, mineral compositions are simple, with pyrite ores showing colloform structure; the main mineralization association is Fe-S.

On the northern margin of the Quren basin, galena-sphalerite-pyrite mineral deposits occur from west to east, such as the Yanliutang, Hongzhuchong, Fankou, Tieshiling deposits. But in the Yingde basin, only a single pyrite deposit is present. This may be because of different tectonic scale and depth. At the northern margin of the Quren basin, deposits are controlled by the structure of long time activity, EW striking and parallel to the unconformity plane between Cambrian and Devonian, and absent tidal-flat clastic rock facies (Cen and Yu 2001). Pb isotope compositions are very similar in the Yangliutang, Fankou and Tieshiling deposits. Their projected points focus on the evolution line of orogenic belt and upper crust and the results imply they are from the same source and mineralized early or late along the same EW striking structure.

7 Discussion and conclusions

Our results lead to the following conclusions: First, ore-forming material came from multiple sources, that is, fluids from the mantle, magmatic hydrothermal fluid, metamorphic hydrothermal fluid and basinal compressive fluid. Second, entity of ore-forming process, fluid is important in ore-forming process, because it can assimilate, transit and unload the ore-forming materials. Third the ores were controlled by dynamic processes a compaction fluid system, a gravity fluid system and a thermal dynamic fluid system.

In the Fankou Pb-Zn deposit, my of Pb isotope is 9.39~9.90, omega 37~40, and k about 4.0, these reflect most Pb derived from crust. But in the coordinate of κ-my and omega-κ, the range of project points is large, and in the coordinate of $^{207}Pb/^{204}Pb$-$^{206}Pb/^{204}Pb$, a part of the points locate in the range of oceanic volcanic rock. So part of Pb may come from upper crust in Fankou deposit. It is the result of mixing and homogenization between Pb from mantle and crust. plate tectonism and magmatism have led to migmatization and homogenization of different source of Pb. The oceanic volcanic sediment blended with crust material by plate underthrusting and then melted, the remobilized metal material rose along fault to form deposits. In the Fankou, Yangliutang and Dabaoshan deposit, diabase magma intruded after mineralization. So the rising of deep material and ore-forming process is controlled by regional plate tectonism.

Most of the margins of the Yuebei Basin were controlled by linear structures. These EW and NNE structures controlled the whole evolution process of Yuebei basin. From Caledonian period (early Palaeozoic era) to Hercynian-Indosinian period, then to Himalayan period, the strike direction of plate movement changed from SN to NW-NE, then to NW-NE. The change of direction affected the properties of basin and tectonics, e.g., basin properties changed from interarc trough to back arc basin to fault basin, and tectonic, from miogeosyncline to paraplatform, then to active platform or geodepression. Magmatic rocks, changed from ultrabasic, to intermediate to acid. The extensive volcanic activity weakened (double models). As a result, the large scale of acid magma intruded and erupted outside of the area. So the change affected the type of deposit, that is, from exogenetic deposit, endogenetic deposit to stratabound deposit, part of exogenetic deposit changed into endogenetic deposit or superimposed modification deposit.

Acknowledgements

We would like to thank Academician Zhai Yusheng for his help and instruction. This study is supported jointly by the "Key Project of Science and Technology Research" (No.03178) and the "Trans-century Training Program for Outstanding Talents" of the Ministry of Education and the Chinese National Nature Sciences Foundation (No.40172036).

References

Cen K, Yu C (2001) Coupled system of flow-reaction-transportation of ore-forming fluid and metallogenesis. Earth Science Frontiers, 8(4): 328

Chen X (1992) The tectonic evolution, ore-forming model and forecast of stratabound deposit of Yuebei basin. Beijing: Geological Publishing House. 56-78

Chen Y (1994) Metallogenic mechanism and ore-controlling geological factors of the stratabound lead, zinc and sulphur deposits in northern Guangdong. Mineral Deposits(in Chinese), 13(2): 112-126

Synthesis and structure of single-crystal marcasite

Milan Drábek
Czech Geological Survey, Geologicka 6, 152 00 Prague 5, Czech Republic

Milan Rieder
VSB-Technical University of Ostrava, 17. listopadu 15, 708 33 Ostrava-Poruba, Czech Republic

Abstract. Marcasite single crystals were synthesiz-ed directly by a reaction of aqueous solutions containing Fe^{2+} and Fe^{3+} with H_2S and polysulphides at 200°C. It might be that natural marcasite formed according to some similar recipe, making use of an interaction of H_2S and polysulphides with pore fluids containing Fe^{2+} or Fe^{3+} e.g. iron sulphates or chlorides. The structure of synthetic marcasite was refined from synchrotron diffraction data by the Rietveld method.

Keywords. Marcasite, hydrothermal growth, crystal structure, single crystals

1 Introduction

Iron sulphides, pyrite and its dimorph marcasite, are the most abundant sulphides in the Earth's crust. The growth of pyrite and marcasite has been studied by many authors (e.g. Allen et al. 1912; Rickard 1969; Murowchick and Bernes 1986; Schoonen and Barnes 1992 a, b, c), Marcasite is reported to be difficult to grow experimentally, yet the preparation of marcasite single crystals was reported by Allen et al. as early as 1912.

2 Techniques and methods

A modified experimental technique of Allen et al. (1912) was used. A steel autoclave with a Teflon insert contained 1M sodium thiosulphate solution ($Na_2S_2O_3.5H_2O$) and in it was placed a teflon beaker with Fe^{2+} or Fe^{3+} solutions [$FeCl_2$; $Fe(NH_4.SO_4)_2.12H_2O$ - (ammonium iron (III) sulfate -12 hydrate); $FeSO_4.7H_2O$; $Fe_2(SO_4)_3$] (Fig. 1.). The temperature was 200° C, pressure <15 MPa, run times ranged between 11 and 1650 hrs.

At ≈ 200 °C thiosulphate - $Na_2S_2O_3.5H_2O$ breaks down to produce hydrogen sulphide,

$$Na_2S_2O_3 + H_2O \Leftrightarrow Na_2SO_4 + H_2S$$

Marcasite crystals grow by interaction of slowly generated hydrogen sulphide with the ferric salt solution,

$$FeSO_4 + 4\,H_2S \Leftrightarrow FeS_2\,(mc) + 3S + 4H_2O$$

In systems where sulphur and H_2S is present, polysulphides can form by several reaction paths (Murowchick & Barnes) such as

$$H_2S + S \Leftrightarrow H_2S_{n+1}$$

Marcasite can thus also originate by the reaction:

$$Fe^{2+} + H_2S_n \Leftrightarrow FeS_2\,(mc) + S^0_{n+1} + 2H^+$$

The morphology of run products was examined on a Tesla Scanning Microscope. Run products were routinely examined by X-ray powder diffraction (diffractometer Philips), one sample was selected for synchrotron diffraction at ESRF, Grenoble. Using the Rietveld technique (Schneider 1994) the synchrotron powder data yielded a good quality refinement of the crystal structure of marcasite.

3 Discussion and results

Marcasite was synthesised at 200°C. In addition to marcasite, only native sulphur was detected in run products, but no pyrite or pyrrhotite. There is no evidence that an iron monosulphide grew before or simultaneously with marcasite. Marcasite crystals form coatings on the surface of iron-containing solutions and coat walls of the Teflon beaker. The crystals of marcasite are well developed, up to 0.5 mm in size, and have a prismatic habit (Fig. 1). In some places, marcasite crystals cluster in globular aggregates (Fig. 3). We observed no differences in the shape of marcasite crys-

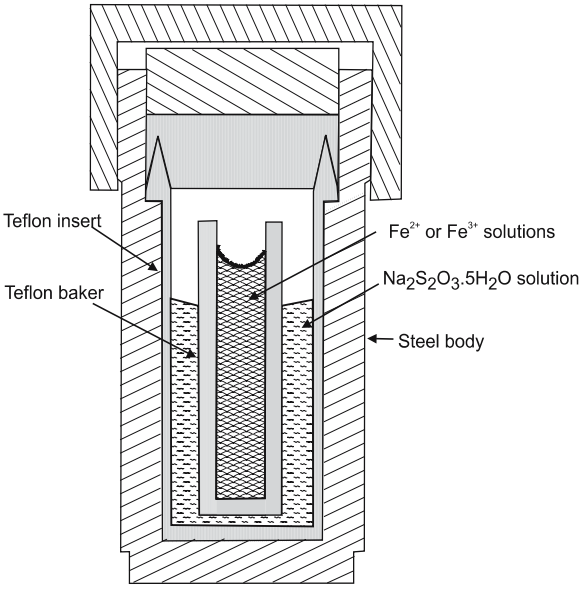

Figure 1: Autoclave used for the synthesis of marcasite crystals.

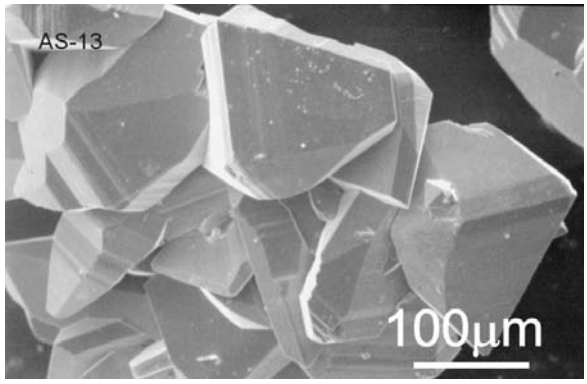

Figure 2: As-13, SEM micrograph of marcasite formed by reaction of H_2S with 1M $FeSO_4$ solution, 200 °C for 165 hours.

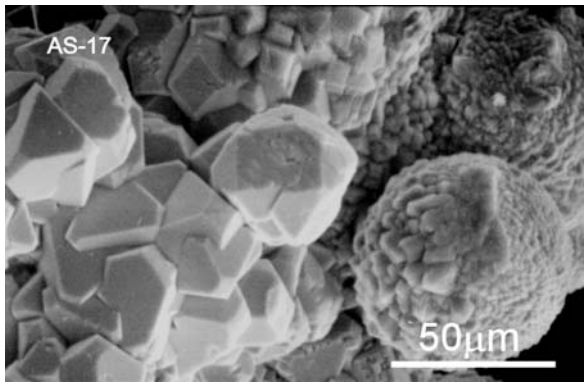

Figure 3: As-17, SEM micrograph of marcasite formed by reaction of H_2S with 1M $FeSO_4$ solution, 200 °C for 80 hours.

tals grown on the surface of different Fe-containing solutions. The yellow colour of Fe-containing solutions at the end of the experiments indicates the presence of mixed polysulphides in solution (Cotton and Wilkinson 1972).

4 Refinement of the marcasite crystal structure

The structure of synthetic marcasite was refined from synchrotron diffraction data by the Rietveld method. The space group *is Pnnm*, and the results of the refinement appear in Table 1.

A complete description of the structure can be reduced to two different Fe-S bond lengths and four different S-S bond lengths, S_2-S_{3a}, S_2-S_3, S_3-S_4, S_2-S_4, and S_2-S_6; the "inter-octahedral" bond is designated S_2-S_{3a}. Also included are data of Buerger (1931).

5 Conclusions

Marcasite single crystals were synthesized directly by a reaction of aqueous solutions containing Fe^{2+} and Fe^{3+} with H_2S and polysulphides at 200 °C. The reaction proceeds fairly rapidly at 200 °C, and marcasite grows in well-developed crystals. It might be that natural marcasite formed according to some similar recipe, making use of an interaction of H_2S and polysulphides with pore fluids containing Fe^{2+} or Fe^{3+} e.g. iron sulphates or chlorides.

Table 1: Results of Rietveld structure refinement of synthetic marcasite compared to single-crystal data Buerger (1931). Diffraction data from ESRF, Grenoble

parameters	synthetic marcasite synchrotron	marcasite, Å from kX Buerger (1931)
unit-cell parameters		
a (Å)	4.4446 (2)	4.436
b (Å)	5.4246 (2)	5.414
c (Å)	3.3864 (1)	3.381
atom coordinates[(3)]		
x (S)	0.2004 (2)	0.200
y (S)	0.3787 (2)	0.378
occupancy factor[(4)]		
n (Fe)	0.253 (1)	0.25
n (S)	0.486 (2)	0.50
temperature factor		
B_{11}(Fe)	1.67 (3)	-
B_{22}(Fe)	1.64 (4)	-
B_{33}(Fe)	1.68 (3)	-
B_{12}(Fe)	0.00 (3)	-
B_{11}(S)	1.43 (4)	-
B_{22}(S)	1.31 (5)	-
B_{33}(S)	1.60 (4)	-
B_{12}(S)	0.00 (3)	-
interatomic distances (Å)		
Fe – S_1	2.239 (1)	2.231
Fe – S_2	2.252 (1)	2.251
S_2 – S_{3a}	2.215 (1)	2.212
S_2 – S_3	2.972 (1)	2.971
S_3 – S_4	3.123 (1)	3.114
S_2 – S_4	3.228 (1)	3.222
S_2 – S_6	3.386 (1)	3.381
agreement factor R_{wp} (%)	7.1	-
wavelength (Å)	0.62061	-
2 Θ range (°)	10-50	-

Acknowledgment

The research was supported by grant No. 205/99/0176 from the Czech Grant Agency. The research at ESRF Grenoble was performed in 1999 on beamline BM01B, as part of experiment CH-681; we wish to thank Hermann Emerich and Wouter van Beek who were instrumental in collecting the data. Mgr. A. Gabasová took the SEM photos.

References

Allen ET, Crenshaw JS, Johnson J (1912) The mineral sulphides of iron. A. Journ. Sci., 33: 169-236

Buerger MJ (1931) The crystal structure of marcasite. Am. Mineral. 16: 361-395

This page intentionally blank

Cotton FA, Wilkinson G (1972) Advanced Inorganic Chemistry, 421-457 Interscience Publisher, New York

Murowchick JB, Barnes HL (1986) Marcasite precipitation from hydrothermal solutions. Geochimica et Cosmochimica Acta 50: 2615-2629

Rickard DT (1969) The chemistry of iron sulfide formation at low temperatures. Stockoholm Contrib. Geol. 20: 67-95

Schneider M (1994) Program for Rietveld analysis of X-Ray and neutron powder diffraction patterns. EDV-Vertrieb

Schoonen MAA, Barnes HL (1991) Reaction forming pyrite and marcasite from solution: I. Nucleation of FeS_2 below 100°C. Geochimica et Cosmochimica Acta 55: 1495-1504

Schoonen MAA, Barnes HL (1991) Reaction forming pyrite and marcasite from solution: II. Via FeS precursors below 100°C. Geochimica et Cosmochimica Acta 55: 1505-1514

Schoonen MAA, Barnes HL (1991) Mechanism of pyrite and marcasite formation from solution: III Hydrothermal processes. Geochimica et Cosmochimica Acta, 55: 3491-3504

Lower cambrian metallogenesis of south China: Interplay between diverse basinal hydrothermal fluids and marine chemistry

Poul Emsbo, Albert H. Hofstra, Craig A. Johnson, Alan Koenig, Richard Grauch
U.S. Geological Survey, MS 973, Box 25046, Denver, Colorado 80225, USA

Xing-chun Zhang, Rui-zhong Hu, Wen-chao Su, Dao-hui Pi
Key Lab of Ore Deposit Geochemistry, Inst. of Geochem., Chin. Acad. Sci., Guiyang 550002, China

Abstract. The lowermost Cambrian metalliferous black shales of southern China represent a unique metallogenic province. The shales host a wide range of world-class synsedimentary metal deposit types. The diverse metal assemblages in these deposits are best explained by venting of multiple hydrothermal fluids including reduced H_2S-rich brines, petroleum, and oxidized brines into the basin. Coincident formation of shales that are extraordinarily rich in organic carbon and metals suggest a rapid increase in bioproductivity and anoxic/dysoxic conditions during ore formation. We propose that basinal fluids were the source of biolimiting nutrients that caused eutrophication and basin-wide anoxia. The dramatic geologic and geochemical changes in this basin demonstrate the possible impacts of hydrothermal systems on the generation and sequestration of organic matter, formation of black metalliferous shales, and chemical changes of seawater.
Keywords. Yangtze, black shales, brine, petroleum, sedex, anoxia, carbon, barite, nickel, molybdenum, gold, platinum, phosphate

1 Introduction

The earliest Cambrian black shales of southern China host a remarkable array of synsedimentary deposits. These diverse deposit types include sedex Ba, Ni-Mo-PGE-Au, U, V, Se, Au, Mn, metalliferous black shales, and PO_4 deposits (Coveney et al. 1994). These distinct deposit types have generally been viewed independently and a variety of conflicting genetic models have been proposed. Models call on different metals sources (i.e. hydrothermal, seawater, riverine, diagenetic) and depositional mechanisms (biogenic accumulation, redox changes, sulfide and carbonate generation and precipitation). Yet, these deposits are all hosted in correlative strata of the same sedimentary basin, are sometimes interbedded, and occur along the same mineralizing trends (Coveney et al. 1994). These spatial and temporal relationships suggest a common genetic link. The goal of this paper is to take a holistic view of the lower Cambrian metallogenesis and explore the possible interrelationships of these diverse sediment-hosted deposits.

2 Lower Cambrian geologic setting and stratigraphy

Neoproterozoic continental rifting formed the large northeasterly-trending Nanhua rift basin that shaped the edge of the Yangtze craton (Wang and Li 2003). This rift basin architecture controlled subsequent upper Neoproterozoic and lower Cambrian sediment depositional patterns (Fig. 1). Platform carbonates covered much of the Yangtze craton during this time. Outboard, a series of silled shale basins formed during the sag phase of the rift (Wang and Li 2003). Deeper parts of these smaller sub-basins were filled with black shales that were flanked by shallow water sediments on their margins (Fig. 1). The orientation of these topographic depressions reflects continued movement along large basement faults that formed during the main phase of rifting. Metalliferous and highly carbonaceous (>10% TOC) shales that formed in these basins represent the base of the lowermost Cambrian Niutitang Formation (and correlative units). This extraordinary black shale province occurs along the entire southern and northern margins of the Yangtze craton and covers approximately $1x10^6$ km^2 (Wang and Li 1991).

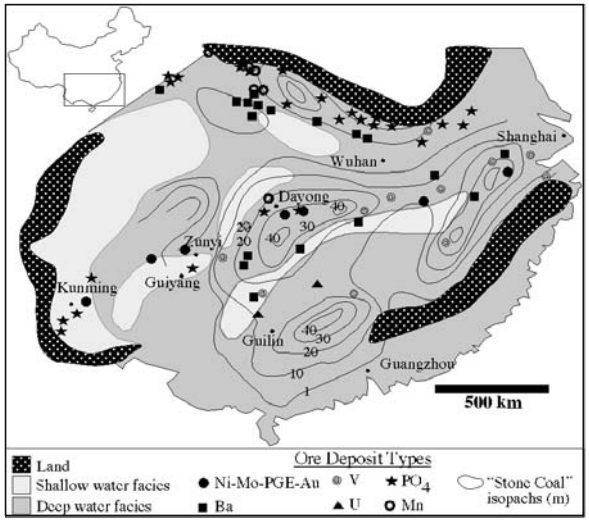

Figure 1: Simplified upper Neoproterizoic/Lower Cambrian paleogeographic map of south China (Li,1986, Coveney et al. 1994), showing locations of synsedimentary deposits including Ni-Mo-PGE-Au, vanadium, and uranium deposits, and stone coal isopachs (Coveney et al. 1994), barite (Wang and Li 1991: Clark et al. 2004), phosphate (Li 1986), and Mn (Hein et al. 1999).

3 Diversity of syn-sedimentary deposit types

The lower Cambrian organic-rich metalliferous black shales host a series of the world's largest barite (± witherite) deposits that account for ca. 50% of the world's barite production (Clark et al. 2004). Barite is interbedded with organic- and vanadium-rich shales, phosphate, and Mn mineralization that are the distal expressions of economic deposits containing these metals (Coveney et al. 1994; Clark et al. 2004; Wang and Li 1991). Bioaccumulation of barite from upwelling of nutrient-rich waters has been proposed for the formation of these deposits (Jewell, 2000). However, the deposits display all the geologic characteristics and radiogenic/stable isotopic compositions of other Paleozoic barite deposits that are hydrothermal synsedimentary-exhalative (sedex) in origin (Emsbo and Johnson 2004; Clark et al. 2004).

The black shales also contain a unique mineralization type that is characterized by a sulfide-rich horizon ranging in thickness from <1 cm to 2 m and can be traced over the entire 1600 km southern paleocoastline of the Yangtze craton (Fig. 1). It is yet uncertain if this horizon is a continuous bed or concentrated around a series of mineralized centers, but the ore horizon occurs in the same stratigraphic position and, where exposed, is continuous for many km's (Mao et al. 2002; Lehmann et al. 2003; Coveney 2003). The horizon shows elemental abundances reaching the following levels: 20% TOC, 18% Mo, 10% P_2O_5, 8% Ni, 2.5% As, 0.5% Cu, 0.2% Se, 0.15% Sb, 0.2 % Ba, 20 ppm Re, 2 ppm Au, 1.2 ppm Pt, 0.7 ppm Pd, 500 ppm U, 100 ppm Hg, and 20 ppm W. The element ratios of ore metals vary little in the horizon. The ore mineralogy is distinctive and includes jordisite (amorphous Mo-S-C), pyrite, vaesite, bravoite, minor arsenopyrite, chalcopyrite, covellite, sphalerite, millerite, polydymite, gersdorffite, sulvanite, pentlandite, tennantite, tiemannite, violarite, and native Au (Murrowchick et al. 1992; Coveney 1994; Lott et al. 1999). The horizon also contains clasts of bitumen that are partially replaced by phosphate and sulfide minerals (Murrowchick et al. 1992; Steiner et al. 2001). These bitumen clasts are interpreted as rounded fragments of algal material (Murrowchick et al. 1992; Lott et al. 1999) or as tar clots formed from migrated petroleum generated by hydrothermal heating of the carbonaceous footwall rocks (Steiner et al. 2001). The remarkable metal enrichments in this horizon have been variously interpreted as being the result of hydrothermal venting of basinal sedex brines (Coveney et al. 1994; Lott et al. 1999; Murowchick et al. 1994; Steiner et al. 2001), extraestrial impact, diagenetic concentration, and synsedimentary enrichments from seawater (Mao et al. 2002). Opponents of sedex hydrothermal models have shown that the metal assemblage is unusual for hydrothermal deposits, has conflicting chemical solubilities in a hydrothermal fluid, and are unzoned within the horizon, which is not typical of sedex deposits.

Another notable feature of this shale sequence is its high organic contents. Centers of the shale basins contain highly carbonaceous combustible shales (<35% TOC) that are up to 40 m thick (Fig. 1). This marine alginite is locally called a "stone coal" because it is mined as an energy source (Coveney 1994). Shales are also metalliferous and contain 0.1 to 0.3% Mo, 0.05 to 0.2% Ni, and 0.5 to 0.9% V (Emsbo 2004; Steiner et al. 2001). The shale also locally hosts a series of V, U, Au and Se deposits/occurrences that are generally coincident with the paleobathymetric lows of the shale basins (Fig 1). In addition, a series of large Mn deposits occur on the margin of the shale basins (Coveney et al. 1994; Hein et al. 1999). Finally, phosphate beds are interbedded with all the above-described mineralization. Where these beds thicken, they form Chinas largest phosphate deposits. Many of the phosphate mines also produce Mn and phosphate is enriched in most of the metals described above. In total, these deposits represent one of the largest phosphate districts in the world.

Conventional and well-established models call on the upwelling of nutrient-rich ocean waters into the basin to form the stone coals, Mn, and phosphate deposits. Introduced nutrients result in an increase in bioproductivity causes basin-wide anoxia and the formation of black shales. Metals in the shales, Mn, and phosphate deposits are thought to be scavenged from seawater through bioaccumulation, sulfide generation, and by the precipitation of metals at redox fronts (Hein et al. 1999; Jewell 2000; Clark et al. 2004).

4 Diversity of hydrothermal fluids

The occurrence of sedex barite deposits establishes that the lower Cambrian was a period of intense hydrothermal venting along the entire margin of the Yangtze craton. Their geologic setting in a large intracratonic rift basin and formation during the sag phase in smaller sub basins is classic for world-class sedex deposits. The large size of these barite deposits in the absence of ore-grade base metals is strong evidence that the ore fluids were reduced H_2S-rich basinal brines (Emsbo 2000; Hofstra and Emsbo 2004). Small base metal occurrences within the shale sequence suggest more oxidized basinal brines may also have vented locally within the basin.

The diversity of metals concentrated in the Ni-Mo-PGE-Au horizon, however, is inconsistent with formation from a single hydrothermal brine (Lehman et al. 2003; Hofstra and Emsbo 2004). Petroleum-exhalative or "petrex" mineralization might explain this unusual metal assemblage (Emsbo 2004). Our chemical analyses of modern petroleum and bitumen from over mature reservoirs (Emsbo 2004, Emsbo and Koenig 2005), chemi-

cal modeling (Hofstra and Emsbo 2004), hydrous pyrolysis experiments (Grauch et al. 2004) and analyses of petroleum in modern hydrothermal vents on the seafloor (Koski et al. 2004) have shown that these metals are all highly soluble and transported in petroleum. Mass balance estimates show that amount of metals transported by large petroleum systems far exceed the amount of metals in conventional ore deposits and that contained in the entire modern ocean (Emsbo 2004). Petroleum discharged into a basin would form a sea-surface slick and distribute the petroleum over large areas. Its contained metals would be liberated and deposited as the oil was volatilized, water-washed, oxidized and biodegraded. This might explain the distribution of the horizon over a large area and the lack of distinct chemical zoning. Remaining insoluble and difficult to biodegraded organic compounds (ca. 1-10% of the petroleum) would coalesce and form clots of bitumen "tar balls" that would tend to sink as their density increased and as they incorporated mineral mater. The bitumen clots that comprise much of the south China ore horizon and are variably replaced by pyrite and phosphate support this hypothesis. Moreover, our recent laser ablation ICP-MS analysis of the bitumen confirms it is highly enriched in ore metals (Emsbo et al. 2004).

Analyses of modern brines and chemical modeling show Mn concentrations are commonly enriched by an order of magnitude above other ore metals in both H_2S-rich reduced and oxidized brines (Hofstra and Emsbo 2004). On the seafloor Mn is highly soluble under anoxic conditions. Thus any Mn vented into an anoxic basin would disperse and only precipitate at redox boundaries in the basin as MnO and Mn carbonates. Although phosphate occurs in all deposit types and large phosphate accumulations are common in sedex deposits (cf. Howards Pass, Broken Hill), PO_4 is relatively insoluble in oxidized and reduced brines and its solubility in petroleum is not well known (Hofstra and Emsbo 2004). It is thus uncertain, perhaps unlikely, that a hydrothermal fluid introduced phosphate.

Modern sedimentary basins invariably contain reduced and oxidized brines and petroleum within different reservoirs. Thus, it is reasonable to expect that all of these fluids would migrate and discharge during a massive fluid migration event. In fact, evidence of multiple fluid compositions during the formation of exhalative deposits are common. The Red Dog deposit in Alaska, for example, contains one of the worlds largest barite deposits that likely formed from reduced brines. Barite is cut by the world's largest Zn deposit that undoubtedly formed from oxidized brines (Emsbo 2000; Johnson et al. 2004). In addition, the S and O isotopic composition of barite shows compelling evidence for hydrocarbons venting during barite formation (Johnson et al. 2004).

5 Link between hydrothermal fluids and marine chemical and biologic processes

Traditionally, the presence of organic-rich metalliferous black shales, phosphate, and Mn deposits (and, in some cases, all the above-described deposits) are explained by coastal upwelling of cold nutrient-rich ocean waters onto the continental shelf. The increased nutrients in shallow marine environments are thought to cause, as observed along modern upwelling coastlines, a surge in bioproductivity and corresponding eutrophication, anoxic/dysoxic conditions, and sequestration organic carbon. In this model, metal and phosphate in the shale are sourced from seawater and accumulated through variety biogenic and chemical mechanisms.

Alternatively, the hydrothermal basinal fluids may have been the source of nutrients. Brines contain very high concentrations of biolimiting nutrient (NH_4, reduced C, trace metals, Ba and Si). Moreover, potentially significant amounts of nutrients in liquid petroleum and gas (e.g. C, CH_4, N, H_2S) may have accompanied brine discharge. Recent estimates have shown the flux of nutrients in large sedex hydrothermal systems can exceed that of the entire modern riverine flux into the ocean (Emsbo 2004). The immense flux of brines and petroleum required to form the hydrothermal deposits imply a nutrient flux of global proportion. Such a nutrient flux into a single sedimentary basin would undoubtedly cause massive increases in primary bioproductivity. Resulting eutrophication would establish anoxic conditions and preserve organic matter. The diversity of hydrothermal fluids explains the extraordinary metal enrichments in the black shales. However, the low solubility of phosphate in hydrothermal fluids suggests that it was not introduced by the brines. A plausible phosphate source, other than seawater, might be remobilization of phosphate adsorbed on detrital ferric oxyhydroxides as the seas become anoxic.

An appealing aspect of this model is that it explains the temporal and spatial coincidence of these phenomena. Overall, the enormous flux of biolimiting nutrients and metals delivered to the ocean by hydrothermal fluids may have been sufficient to form the metal deposits and trigger basin-wide anoxia and the associated biologic, and chemical changes in the sedimentary basin.

References

Clark SB, Poole FG, Wang Z (2004) Comparison of some sediment-hosted, stratiform barite deposits in China, the United States, and India. Ore Geology Rev 24: 85-101

Coveney RM Jr (2003) Re-Os dating of polymetallic Ni-Mo-PGE-Au mineralization in lower Cambrian black shales of south China and its geological significance; discussion. Economic Geology 98: 661-662

Coveney RM, Grauch RI, Murowchick JB (1994) Metals, phosphate and stone coal in the Proterozoic and Cambrian of China; the geologic setting of precious metal-bearing Ni-Mo ore beds. SEG Newsletter 18: 1-11

Emsbo P (2000) Gold in Sedex deposits. Reviews in Economic Geology 13: 427-438

Emsbo P (2004) Genetic links among syngenetic metal accumulations in sedimentary basins: Giant sediment-hosted metal deposits to metalliferous black shales. GSA Abstracts 36: 199

Emsbo P, Johnson CA (2004) Formation of modern and Paleozoic stratiform barite at cold methane seeps on continental margins: Comment: Geology 32: e64

Koski RA, Stakes DS, Lamothe PJ, Crock JG, metal enrichments in hydrothermal petroleum from sediment-covered spreading centers, northeast pacific ocean: GSA Abstracts 36: 200

Grauch RI, Lewan MD, Lamothe PJ, Landis GP, Emsbo P (2004) Element partitioning into generated petroleum and hydrothermal fluids as determined by hydrous pyrolysis of retort shale. GSA Abstracts 36: 200

Hein JH, Fan D, Ye J, Liu T, Yeh H (1999) Composition and origin of Early Cambrian Tiantaishan phosphorite-Mn carbonate ores, Shaanxi Province, China. Ore Geology Reviews 15: 95-135

Hofstra AH, Emsbo P (2004) Solubility of metals and nutrients in brines: implications for ore deposits, bioproductivity, and anoxia in sedimentary basins. GSA Abstracts 36: 200

Jewell PW (2000) Bedded barite in the geologic record. In Glenn CR, Prevot-Lucus LJ (eds), Marine Authigenesis: From Global to Microbial, 66 SEPM Special Publication, 174-161

Johnson CA (2004) sulfur and oxygen isotopes in barite deposits of the western Brooks Range, Alaska, and implications for the origin of the Red Dog massive sulfide deposits. Economic Geology 99: 1435-1448.

Lehmann B, Mao J, Li S, Zhu G and Zhai M (2003) Re-Os dating of polymetallic Ni-Mo-PGE-Au mineralization in lower Cambrian black shales of south China and its geological significance. Economic Geology 98: 663-665

Li YY (1986) Proterozoic phosphorite-regional review: China. In Cook PJ, Shergold JH (eds), Phosphates of the world, Proterozoic and Cambrian phosphorite: 42-62

Lott DA, Coveney RM Jr, Murowchick JB, Grauch RI (1999) Sedimentary exhalative nickel-molybdenum ores in south China; A special issue on organic matter and ore deposits; interactions, applications, and case studies. Economic Geology 94: 1051-1066

Early-diagenetic sulphides in sediment-hosted deposits: A textural and geochemical study from an unmetamorphosed QPC gold placer, Belle-Brook, New Zealand

D.M. Falconer, D. Craw
Department of Geology, University of Otago, Dunedin, New Zealand

K. Faure
Institute of Geological and Nuclear Sciences, Lower Hutt, New Zealand

L. Lawrance
School of Earth and Geographical Sciences, The University of Western Australia, Crawley, Australia

Abstract. In many sediment-hosted ore deposits the timing of mineralisation and the role of diagenetic, syngenetic and epigenetic processes in the ore genesis is a contentious issue. Such uncertainty is inevitable in the absence of well-constrained unmetamorphosed assemblages. This study shows that fine-grained early-diagenetic sulphides formed at low temperature in unmetamorphosed auriferous quartz pebble conglomerates (QPC) at Belle-Brook in southern New Zealand have a variety of diagenetic textures and geochemical signatures similar to those attributed to metamorphic and/or hydrothermal processes in a variety of giant sediment-hosted ore deposits. Both sedimentary and diagenetic processes associated with the QPC at Belle-Brook gold are relatively well-constrained, and hence the mineralising processes are more easily understood than those from older sediment-hosted deposits.

Keywords. Early diagenesis, iron sulphide, marcasite, framboidal pyrite, quartz pebble conglomerate

1 Introduction

Diagenetic fine-grained (<1 mm) Fe-sulphides are common and important components of many sediment-hosted gold and base-metal deposits worldwide: e.g. Witwatersrand, Mt Isa Inlier – McArthur Basin, Broken Hill, Kupferschiefer, Viburnum Trend. A central issue regarding the genesis of many sediment-hosted ore deposits is the timing of ore mineralisation and the role of diagenetic, syngenetic and epigenetic processes with regard to the timing of ore mineralisation (Large et al. 1995; Large et al. 1998; Oszczepalski 1999; Marshall and Spry 2000; Frimmel and Minter 2002; Robb 2005). Sulphide mineralisation is particularly problematic because of the lack of criteria to distinguish between early-diagenetic textures and those resulting from regional metamorphism and/or hydrothermal mineralisation. For example, recrystallised/annealed textures and atoll structures in ore sulphides in metamorphosed terranes are commonly attributed to metamorphism, despite similar textures occurring in sulphides from unmetamorphosed sediments. Fine-grained diagenetic sulphides in unmetamorphosed sediments are well known for their propensity to act as efficient scavengers of trace metals. However, the extent of remobilisation of these trace-metals both within sulphides and through unmetamorphosed sediments is not widely appreciated. Similarly, sulphide diagenesis has a significant effect on remobilisation in unmetamorphosed sediments of gold as indicated by the precipitation of supergene gold and quartz.

This poster documents a variety of early-diagenetic sulphide textures that occur at Belle-Brook in eastern Southland, New Zealand, in an unmetamorphosed Tertiary quartz pebble conglomerate, which may aid the interpretation of similar sulphide textures in older sediment-hosted deposits.

2 Local geology

Belle-Brook is the site of a small-scale alluvial gold mine that contains abundant early-diagenetic sulphide minerals. The local stratigraphy consists of Miocene – Pliocene non-marine fluvial to fluvial-deltaic sediments deposited by a large meandering river system, and preserved in a basinal setting. The local structure is dominated by a series of steeply-dipping north to northeast-striking reverse faults of the Dunsdale Fault System. Belle-Brook is adjacent to the downthrown side of one of these major faults. Cenozoic uplift resulted in local redeposition of variably quartz-rich QPC during the late Miocene and Pliocene. At Belle-Brook QPC horizons (75-90 % quartz) within the broader non-marine fluvial sequence are generally less that one metre thick.

Detrital and diagenetic sulphide minerals occur in the QPC at Belle-Brook, which is supported by sulphur isotope data, which range from -45 to +18 per mil (relative to VCDT). Detrital sulphides are principally euhedral py-

rite and arsenopyrite (1-4 mm in diameter). Similar grains are common in the heavy mineral faction of sediments derived from the Otago Schist. Early-diagenetic sulphides are less common regionally, and predominantly occur in localised saturated QPC, as fine-grained framboidal pyrite and marcasite (< 1 mm in diameter), anhedral lump marcasite (up to 20 cm in length), with rare euhedral marcasite and pyrite.

3 Early-diagenetic sulphides

3.1 Morphology

Marcasite is the predominant sulphide mineral in the heavy mineral faction of the QPC at Belle-Brook. Marcasite occurs as either fine-grained framboids (< 200 μm in diameter) or larger-scale aggregated masses of framboids up to a few centimetres in diameter. Framboidal marcasite is composed of interpenetrating euhedral marcasite microcrysts (10-30 μm in diameter). Smaller aligned octahedral? microcrysts (< 1 μm across) are observed in the larger microcryst faces where disrupted by dissolution, producing a 'wool ball' texture. Large aggregated masses in which individual framboids are indistinct are referred to as 'lump' marcasite. These anhedral marcasite masses are dull grey in colour and up to 20 cm in length. As well as occurring freely, lump marcasite is commonly found as an overgrowth on quartz cobbles in outcrop and on ground surfaces and tailings heaps. In general marcasite is well-preserved with few alteration products occurring on surfaces. Sulphur isotope values ($\delta^{34}S$ -12 to -20) for both framboidal and lump marcasite are consistent with non-marine bacterial sulphate reduction.

In comparison to framboidal marcasite, framboidal pyrite is relatively rare. Individual pyrite framboids are 10-40 μm in diameter and composed of densely packed octahedral microcrysts (1 μm in diameter). Sub-spherical polyframboidal masses of pyrite are up to 300 μm in diameter. Framboidal pyrite is typically well-preserved with few alteration products. Rare euhedral (cubic) pyrite is found occurring on strongly altered lump marcasite. Framboidal pyrite is assumed to be diagenetic.

Although uncommon, small striated rhombohedral crystals (1-5 μm across) of authigenic arsenopyrite are observed along cleavages on parent detrital arsenopyrite crystals. Scorodite, was not observed on either parent or the potentially authigenic arsenopyrite crystals.

3.2 Geochemistry

The anhedral lump marcasite contains elevated concentrations of Ni (180-20,157 ppm), Co (195-7,010 ppm), As (219-6,861 ppm) and Cr (34-1,449 ppm), and to a lesser extent, Zn, Pb, Cu and W. With the possible exception of rare discrete Ni-Co oxide crystals, these trace elements are assumed to occur in solid solution. Microprobe analysis confirms Ni ± Co-rich (1-21 wt.% Ni) colloform-style bands within the marcasite (Falconer 2003; Falconer et al. in press). Rare oscillatory-zoned As-rich and Ni-rich marcasite are observed. Bulk trace element data is not available for framboidal marcasite or euhedral pyrite. However, Ni-rich colloform-style bands are observed in framboidal marcasite, and it is probable that trace elements elevated in lump marcasite, are also elevated in the framboidal marcasite.

3.3 Texture

In polished section, the marcasite framboids comprise finely-divided radial marcasite crystals that have concentric colloform-style bands (< 1 μm wide) about the centre of the framboid. These colloform-style bands are very subtle under reflected light, but distinctive using the electron microprobe, and are commonly conspicuously hexagonal in appearance.

Lump marcasite exhibits a variety of fine- to coarse-grained radial, fibrous, lath, bladed, plumose, polygranular, massive and replacement (i.e. of organic material) textures, along with a variety of Ni ± Co-rich colloform-style bands. The colloform-style bands are either constrained within the original individual framboid, or occur over 100's of microns spanning over many aggregated framboids. On a large scale (100's of microns) fine-grained radial marcasite is colloform banded, in which the 1-2 μm bands are associated with variably altered Ni-rich marcasite. Similar to colloform banded marcasite, is concentric banded marcasite which is crystallographically controlled and associated with massive marcasite. A variety of banded textures are inferred to be secondary rather than primary based on spatial associations, which may imply remobilisation of solid-solution nickel within the sulphide lattice. Lump marcasite exhibits a variety of recrystallisation textures within a single section, ranging from progressively deformed framboids that aggregate, and exhibit a straightening of grain boundaries, development of 120° triple-junctions, and ultimately, develop into a massive groundmass.

Diagenetic pyrite and marcasite are rarely observed together, but where they are pyrite is the earlier of the two, and generally observed as framboidal pyrite either surrounded by radial marcasite, or within a massive marcasite groundmass. In lump marcasite, atoll (ring) structures are observed where marcasite replaces framboidal pyrite within radial marcasite.

Lump marcasite is characterised by ubiquitous fractured, brecciated and disaggregated detrital quartz grains that feature conspicuous embayments along grain margins.

This page intentionally blank

3.4 Pyrite – marcasite association

Where pyrite and marcasite occur together in lump marcasite, paragenetic relations indicate that pyrite is a precursor to marcasite formation. This is consistent with the observation (SEM) of framboidal pyrite with localised overgrowths of marcasite crystals. Another interpretation of this 'overgrowth' relationship is a possible transformation of framboidal pyrite to framboidal marcasite. Two main observations may indicate this transformation. (1) polygonisation and recrystallisation of octahedral microcrysts in framboidal pyrite into pentagonal or hexagonal arrays (5-10 μm wide) (2) the development of marcasite microcrysts in recesses between pyrite framboids that progressively cover, and, ultimately replace pyrite framboids. Both of which correspond with the size of marcasite microcrysts that make up framboidal marcasite.

4 Discussion

Although early-diagenetic sulphide minerals are ubiquitous in sediment-hosted ore deposits, there is little appreciation for their development during early diagenesis. Sulphide textures are often ascribed to metamorphism simply because sediments have been deeply buried and undergone metamorphism. Annealed textures in sulphides are reported to occur in response to greenschist facies metamorphism and upwards (Craig and Vokes 1993). In this study, annealed and recrystallised textures are a characteristic feature of lump marcasite suggesting that fine-grained framboidal sulphides recrystallise at temperatures much lower than presently assumed. Similarly, atoll structures are interpreted to indicate replacement of framboidal pyrite during metamorphism (England and Ostwald 1993). Atoll structures are observed in marcasite at Belle-Brook, indicating that such replacement may also occur at lower temperatures. Solid state conversion of marcasite to pyrite is well known and reportedly occurs at 157°C (Murowchick 1992; Craig and Vokes 1993), but little is documented about conversion from pyrite to marcasite as may be indicated by textures from Belle-Brook (Falconer 2003). The implications of such supergene processes have important economic significance. For example, rounded porous pyrite with typical marcasite ghost textures within the Witwatersrand deposit, variously interpreted as a replacement of carbonates, evaporates and pisolites (England et al. 2003; Phillips and Law 2000) could have formed from early-diagenetic sulphides. In turn, the stability of these sulphides, or lack of stability, is used to help constrain the state of the Archean atmosphere (Phillips et al. 2001, Frimmel in press). The ready formation of early-diagenetic sulphides under oxidising conditions at the surface at Belle-Brook puts into question their use as guides to establishing palaeoenvironmental conditions.

5 Conclusions

Establishing the genesis of sulphide minerals in sediment-hosted deposits is essential for establishing the role of diagenetic, syngenetic or epigenetic processes in relation to the timing of ore mineralisation and formation of ore deposits. Young unmetamorphosed sediment-hosted deposits such as Belle-Brook provide relatively well-constrained examples of the behaviour of early diagenetic iron sulphides and provide valuable insight into the subtleties of sulphide transformation and behaviour that is usually obscured by overprinting associated with metamorphism and/or hydrothermal processes that accompany ore mineralisation in the giant sediment-hosted deposits.

References

Craig JR, Vokes FM (1993) The metamorphism of pyrite and pyritic ores: an overview. Mineral Mag 57: 3-18

England BM, Ostwald J (1993) Framboid derived structures in some Tasman fold belts base-metal deposits, New South Wales, Australia. Ore Geology Reviews 7: 381-412

England GL, Rasmussen B, Krapez B, Groves DI (2002) Palaeoenvironmental significance of rounded pyrite in siliciclastic sequences of the Late Archaean Witwatersrand Basin: oxygen-deficient atmosphere or hydrothermal alteration? Sedimentology 49: 1133-1156

Falconer DM (2003) Sediment-hosted gold and sulphide mineralisation, Belle-Brook, Southland, New Zealand. Unpublished MSc thesis. University of Otago Library

Falconer DM, Craw D, Youngson JH, Faure K (in press) Gold and sulphide minerals in Tertiary quartz pebble conglomerate gold placers, Southland, New Zealand. Ore Geol Rev.

Frimmel HE, Minter WEL (2002) Recent developments concerning the geological history and genesis of the Witwatersrand gold deposits, South Africa. SEG special publication 9: 17-45

Frimmel HE (in press) Archaean atmospheric evolution: evidence from the Witwatersrand gold fields, South Africa. Earth Sci Reviews

Large DJ, MacQuaker J, Vaughan DJ, Sawlowicz Z, Gize AP (1995) Evidence for low-temperature alteration of sulfides in the Kupferschiefer copper deposits of southwestern Poland. Econ Geol 90: 2143-2155

Large RR, Bull SW, Cooke DR, McGoldrick PJ (1998) A genetic model for the HYC deposit, Australia: based on regional sedimentology, geochemistry, and sulphide-sediment relationships. Econ Geol 93: 1345-1368

Marshall B, Spry PG (2000) Discriminating between regional metamorphic remobilization and syntectonic emplacement in the genesis of massive sulphide ores. In Spry PG, Marshall B, Vokes FM (eds) Metamorphosed and metamorphogenic ore deposits. SEG: 37-79

Murowchick JB (1992) Marcasite inversion and the petrographic determination of pyrite ancestry. Econ Geol 87: 1141-1152

Oszczepalski S (1999) Origin of the Kupferschiefer polymetallic mineralization in Poland. Mineralium Deposita 34: 599-613

Phillips GN, Law JDM (2000) Witwatersrand gold fields: geology, genesis and exploration. SEG Review 13: 439-500

Phillips GN, Law JDM, Myers RE (2001) Is the redox state of the Archean atmosphere constrained? SEG newsletter 47: 1-18

Robb LJ (2005) Introduction to ore-forming processes. Blackwell Publishing, United Kingdom

Geochemistry and provenance of clastic metasedimentary host rocks of the Rosh Pinah Zn-Pb-Ag(-Cu-Au) deposit, Southern Namibia

Christoph D.K. Gauert
Petrology and Economic Geology Research Group, Institute for Geological Sciences, Martin-Luther-University Halle-Wittenberg, Von-Seckendorff-Platz 3, 06120 Halle, Germany

Abstract. Whole-rock analyses of clastic to chemi-cal metasedimentary rocks of the Rosh Pinah (RP) and Wallekraal Formations of the Port Nolloth Group, eastern Gariep Belt, provide insights into the provenance and depositional history of the early Rosh Pinah Graben. The findings of this study propose the following provenance of clastic material: Based on immobile trace elements and REE data, source terranes for quartzo-feldspathic material could be fractionate I-type granites such as the Goidab Massif, the Vioolsdrif Granite and granites of the De Hoop Subgroup, all from the palaeoproterozoic Richtersveld Terrain (2.0 Ga). Mafic basement material derived from distal sources such as gabbro and tonalite of the Vioolsdrif Suite are regarded to have contributed to the occurrence of ferromagnesian elements in the argillite. Proximal mafic source rocks are excluded due to low log (Fe_2O_3/K_2O) ratios reflecting strong weathering. RP clastic metasediments have chemical features of passive margin to active continental margin greywakes, mainly from a felsic arc source with increasing old sediment component possibly from a passive continental margin setting. The generally high $(La/Th)_{CN}$ ratios of RP metasediments could be explained by detrital input of rocks from the volcanic Orange River Group, showing calcalkaline geochemistry (Reid 1997), and from alkali granite and syenite bodies of the Richtersveld Suite (Frimmel et al. 2004).

Keywords. Provenance, geochemistry, metasediments, Rosh Pinah Zn-Pb-Ag(-Cu-Au), REE, immobile trace elements, passive to active continental margin source, calcalkaline geochemistry

1 Introduction

Syn-sedimentary stratiform Zn-Pb-Ag(-Cu-Au) sulphide mineralisation, frequently linked to banded iron formation of the same area, is developed within the Neoproterozoic tectono-metamorphic belts of Namibia (e.g. Tsongoari, Rendezvous, Rosh Pinah).

Economic deposits with and without associated bimodal volcanism in Southwestern Gondwana are found both in southern Africa and eastern South America. Neoproterozoic basin evolution commenced with the break-up of a late Mesoproterozoic supercontinent resulting in continental rifting exploited by siliciclastic material (Frimmel and Jonasson 2003). Coarse clastic basal rift deposits are followed by a transgressive carbonate-shale succession representing the transition from early rift to passive continental margin sedimentation. A regressive sequence is followed by basin inversion causing post-glacial carbonate and siliciclastic flysch deposits in foredeep positions (Frimmel and Jonasson 2003). Host rocks to the large stratiform orebodies at RP are highly silicified black shale and dolomitised limestone within a major quartzo-feldspathic package.

In this study, results of a geochemical and provenance investigation are reported aiming at characterising and fingerprinting the variable source of metasedimentary rocks in the Rosh Pinah district of the eastern Gariep Belt. These findings may allow a more accurate assessment of the sedimentary infill potential for zinc, lead, copper and silver in this region thereby contributing to an improved understanding of the processes that control the source of base metal mineralisations.

2 Results of major element, REE and immobile trace element studies

Compositional data for some 325 samples of unmineralised argillite, feldspathic sandstone, and carbonaceous sandstone show well-defined correlations among major, trace and rare earth elements (REE, $n \approx 110$) that reflect mixing lines between original quartz-rich and clay-rich precursor sediments. Abundances of ferromagnesian elements (V, Cr, Sc), high field strength elements (Ti, Th, Nb, Ta) and REE (La to Lu) are highest in fine-grained argillites. Sample groups are distinguished on the basis of total REE contents versus $(La/Yb)_{CN}$ ratios, and on La/Th ratios and $Fe_2O_3{}^C$ content. The groups appear to be independent of sedimentary sorting and are interpreted to reflect different source terranes. The dominant siliciclastic rocks in the Rosh Pinah and northern adjacent area consist of metamorphosed arkoses, subarkoses, wackes, shales, and minor (sub-)litharenites (Fig. 1) as supported by a classification scheme of terrigenous sandstones and shales after Herron (1988). Due to intermediate to low log (SiO_2/Al_2O_3) values, sediments are regarded as relatively mature, and strongly weathered as shown in their predominantly low log (Fe_2O_3/K_2O) ratios reflecting a feldspar dominance over ferromagnesian minerals. Rare earth element patterns of all samples are also similar to the pattern of upper crust with light rare earth enrichment, pronounced negative Eu anomalies and relatively flat heavy rare earth patterns (Fig. 2). The majority of the samples

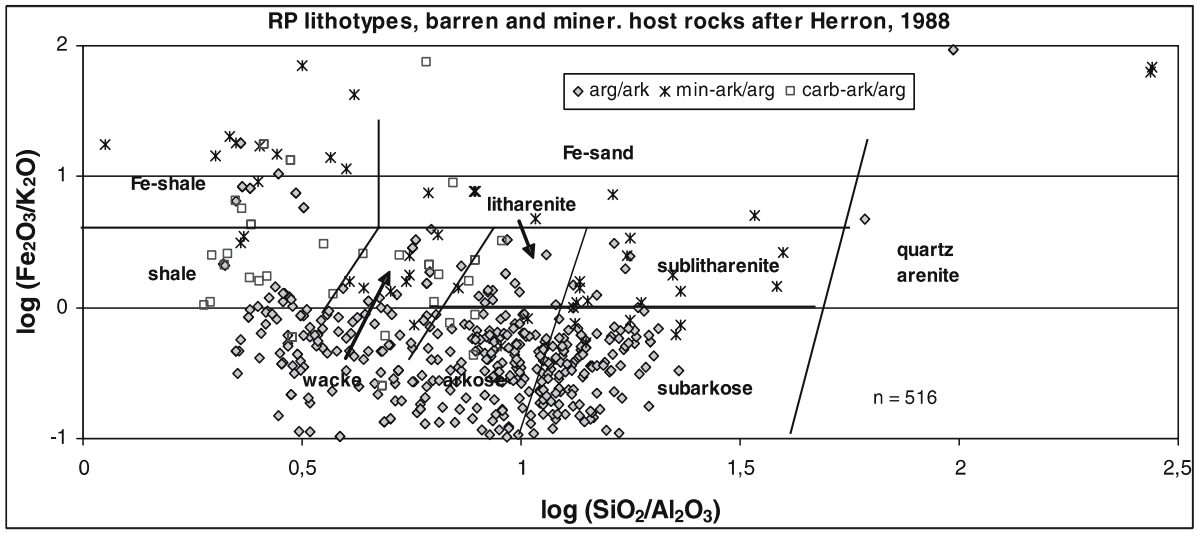

Figure 1: Rosh Pinah metasediment compositions in the classification scheme of terrigenous sandstones and shales using $\log(Fe_2O_3/K_2O)$ vs. $\log(SiO_2/Al_2O_3)$ by Herron (1988) after Pettijohn et al. (1972).

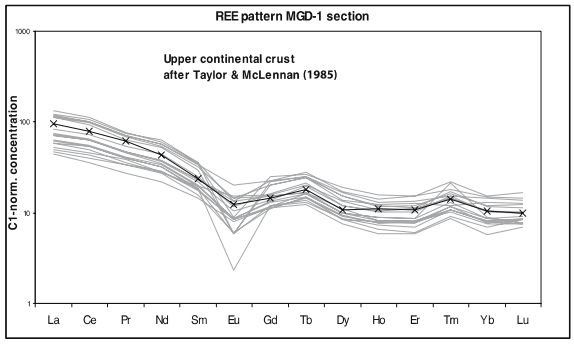

Figure 2: Chondrite-normalised rare earth element pattern of argillaceous to quartzo-feldspathic arenites in the Rosh Pinah District.

are characterised by moderate to steep REE slopes, high La/Ta ratios and weakly elevated Th and U concentrations.

3 Provenance of Rosh Pinah metasediments - insights from REE and trace element data

$(La/Th)_{CN}$ ratios as used by (Slack and Höy 2000) show moderate to very high values (3,04 to 21,8) for Rosh Pinah metasediments suggesting derivation largely from calc-alcalic igneous or metaigneous rocks. Elevated $Fe_2O_3{}^C$ (non-sulphide total iron, > 2.5%) relative to SiO_2 for approximately half of the samples and generally high $(La/Th)_{CN}$ ratios (approx. 7 to 14,09) record erosion of a mixed provenance comprised of evolved metagranitic rocks with a small fraction of iron-rich detritus believed to be derived from magnetite or hematite iron formations. Rosh Pinah metasediments have Th/Sc ratios between 0,56 and 1,59 and trace element characteristics that are consistent with upper crustal derivation. Trace element patterns point to a decreasing to absent juvenile contribution. This trend is indicated by smaller negative Eu anomalies, less marked high field strength depletion, less variation in Th/Sc ratios with values >1. RP metasediments are characterised by acidic arc signatures, with La/Th ratios close to the field of upper continental crust (Fig. 3).

The findings of this study propose the following provenance of clastic material: RP metasediments can be discriminated in their tectonic setting, due to their variability in their TiO_2, Al_2O_3/SiO_2 and Fe_2O_3 + MgO contents (Bathia 1983). Most samples show chemical characteristics of passive continental margin sediments. RP samples can be attributed to a predominantly quartzose sedimentary provenance, distinguished by discriminant functions after Roser and Korsch (1988), which are based on the raw oxides of TiO_2, Fe_2O_3, MgO, Na_2O and K_2O and their ratios to Al_2O_3 respectively.

Most RP metasediments have too high La contents for a contribution from active to passive margin sediments according to Bathia and Crook (1986) but plot in or near the field of continental arcs (Fig. 3). On a log basis, data from these elements suggest for the metasediments both an Archean and a Post-Archean provenance based on their generally high Th and La contents (Taylor and McLennan 1985) (Fig. 4). All samples have low Cr and Sc, but high Co contents, and nearly all have high Th/Sc ratios (>0,6), precluding a significant component eroded from mafic or ultramafic rocks. Most samples plot in the field of continental arc sediments with a minor overlap into fields for active continental and passive margin sediments on a

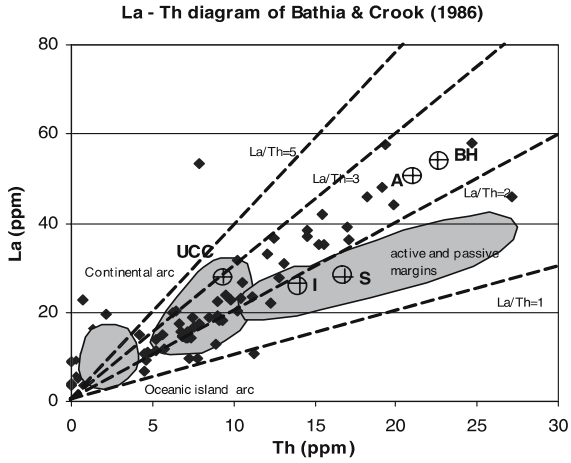

Figure 3: Rosh Pinah metasediments in the La-Th diagram of Bhatia and Crook (1986). UCC = average upper continental crust (Taylor and McLennan 1985); I, S, and A = average I, S, and A-type granites of White and Chappell (1983); BH = average Broken Hill (Australia) clastic metasedimentary rock (Slack and Stevens 1994)

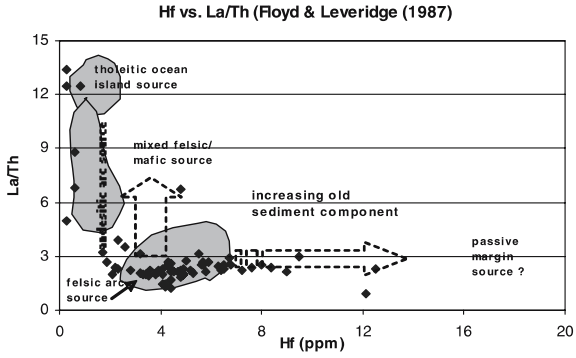

Figure 4: Hf vs. La/Th diagram of Floyd and Leveridge (1987) abbreviations as for Figure 3.

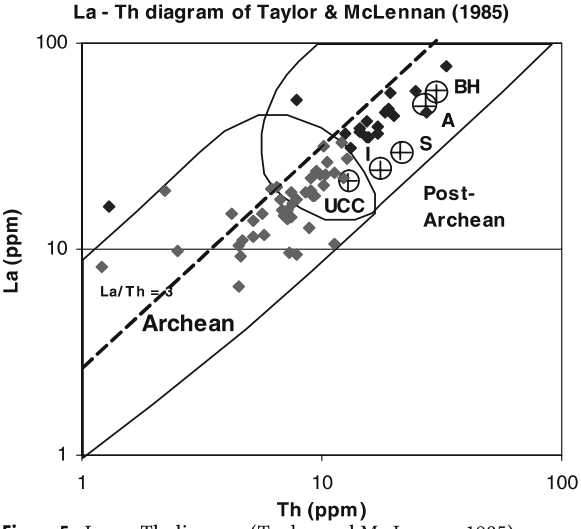

Figure 5: La vs. Th diagram (Taylor and Mc Lennan 1985).

La/Sc vs. Ti/Zr diagram (Bhatia and Crook 1986). Results from Hf and La/Th plot (Floyd and Leveridge 1987) suggest mainly a felsic arc source with increasing old sediment component possibly from a passive margin source and little input from a andesitic to no input from tholeiitic ocean island (Fig. 5). Immobile trace elements and REE used for evaluation of granitic source rocks attribute most RP metasediments to the field of fractionated I-type granitoids, some to A-type granitoids and I-, S- and M-type granitoids. Based on the isotopic composition of ore lead showing elevated $^{207}Pb/^{204}Pb$ ratios, Frimmel et al. (2004) suggest an Eburnean (ca. 2.0 Ga) volcanic arc material to provide the main sediment source for the metasedimentary siliciclastic host by erosion. The former is best preserved in the Richtersveld Terrane, that represents the largest volume of post-Archaean juvenile crust in southern Africa.

4 Palaeotectonic settings of the eastern Gariep Belt

Palaeotectonic settings of Gariep Belt metasediments at RP are evaluated using discriminant diagrams based on data for relatively immobile trace elements and REE (Bhatia and Crook 1986) in the following way:

Diagrams using La-Th-Sc and Th-Sc-Zr/10 show argillaceous, carbonaceous and ferruginous RP clastic sediments with chemical features of passive margin to active continental margin greywakes. Samples of the RP and Wallekraal Formations show considerable scatter on a La-Th plot largely falling outside the fields for continental arcs and active and passive margins. Immobile trace elements and REE data point towards fractionate I-type granites such as Goidab Massif, Vioolsdrif Granite and De Hoop Subgroup to be source terranes for quartz and feldspar-rich basal rift deposits. Mafic basement material could be involved in forming a transgressive shale succession. It could derive from distal sources such as gabbro and tonalite of the Vioolsdrif Suite as evidenced in the occurrence of ferromagnesian elements in the argillite. RP clastic metasediments have chemical features of passive margin to active continental margin greywakes, mainly from a felsic arc source with increasing old sediment component possibly from a passive margin source. The intrusive bodies of the Bushmanland and Kakamas Terranes to the south and north (Frimmel et al. 2004) could represent sources of evolved metagranitic rocks, possibly with a small fraction of iron-rich detritus having derived from magnetite or hematite iron formations such as the older diamictite deposited in the immature continental rift of the Gariep Belt. A subsequent major regressive sequence is followed by set in of basin inversion, post-glacial carbonate and siliciclastic flysch deposits in foredeep positions. Proximal mafic source rocks are excluded due to low log (Fe_2O_3/K_2O) ratios reflecting

strong weathering and therefore small amount of ferromagnesian minerals. RP type mineralisation is confined to a narrow failed-rift graben. Massive sulphide precipitation took place during eustatic sea-level drop, triggering starvation of the Rosh Pinah Graben. The availability of a fertile basement or clastic derivatives from it are regarded as local control for provision of dissolved iron (Frimmel and Jonasson 2003). The generally high $(La/Th)_{CN}$ ratios of RP metasediments could be explained by detrital input of rocks from the volcanic Orange River Group and from alkali granite and syenite bodies of the Richtersveld Suite.

Acknowledgements

The author thanks Gregor Borg, EGRG of MLU geosciences for finances and the access to analytical facilities. Thanks also to Eric Mouton, Lex Geraghty of KumbaResources for logistic support.

References

Bathia MR (1983) Plate tectonics and geochemical com-position of sandstones. Journal of Geology 91: 611-627

Bathia MR, Crook KAW (1986) Trace element cha-racteristics of graywakes and tectonic discrimination of sedimentary basins. Contrib. Mineral. Petrol. 92: 181-193

Floyd PA, Leveridge BE (1987) Tectonic environment of the Devonian Gramscatho basin, south Cornwall: framework mode and geochemical evidence from turbiditic sandstones, J Geol. Soc. 144: 531-542

Frimmel HE, Jonasson I (2003) The controls on Neoproterozoic basemetal sulphide mineralisation: In: Mineral Exploration and Sustainable Development, Eliopoulos et al. (eds), 661-664

Frimmel HE, Jonasson I, Mutiba P (2004) An Eburnian base metal source for sediment-hosted zinc-lead deposits in Neoproterozoic units of Namibia: Lead isotopic and geochemical evidence: Mineralium deposita 39: 328-343

Herron MM (1988) Geochemical classification of terrigenous sands and shales from core or log data: Journal of sedimentary petrology 58: 820-829

Pettijohn FJ, Potter PE, Siever R (1972) Sand and sandstones. Springer-Verlag, New York

Reid DL (1997) Sm-Nd age and REE geochemistry of Proterozoic arc-related igneous rocks in the Richtersveld Subprovince, Namaqua Mobile Belt, Southern Africa. Journal of African Earth Sciences 24: 621-633

Roser BP, Korsch RJ (1988) Provenance signatures of sandstone-mudstone suites determined using discriminant function analysis of major-element data. Chemical Geology 67: 119-139

Taylor SR, McLennan SM (1985) The continental Crust: its composition and evolution; Blackwell Scientific Publications, Oxford, 312

Wernecke breccia, Canada: A large-scale Proterozoic IOCG system related to basin evolution

Julie A. Hunt
Yukon Geological Survey, 2099 Second Ave., Whitehorse, Yukon Territory, Y1A 2C6, Canada and Economic Geology Research Unit, James Cook University, Townsville, QLD 4811, Australia

Timothy Baker, David Gillen
Economic Geology Research Unit, James Cook University, Townsville, QLD 4811, Australia

Derek J. Thorkelson
Simon Fraser University, Burnaby, British Columbia, Canada

Abstract. Iron oxide-copper-gold (IOCG) minera-lization occurs within and peripheral to a large-scale Proterozoic breccia system known as Wernecke Breccia. The breccia and related mineralization appear to have formed, independent of a magmatic cycle, during the expansion of over-pressured, hot, highly saline, basinal fluids into weak and/or permeable regions of the strata during the temporal evolution of the Wernecke Basin. The mineralization contains abundant magnetite and hematite and is similar to typical IOCG deposits. However, the formation of the Wernecke Breccia IOCG system in a thick evaporite-bearing sedimentary package also has similarities to the formation of sediment-hosted copper deposits such as those in the Mount Isa area and the Zambian copper belt.

Keywords. Wernecke Breccia, iron oxide-coppergold, IOCG, Yukon

1 Introduction

Iron oxide-copper-gold (IOCG) mineralization and extensive metasomatic alteration are associated with an Early to mid-Proterozoic breccia system known as Wernecke Breccia that extends over several hundred kilometres in the north central part of the Yukon Territory, Canada (Fig. 1; cf. Bell 1986; Thorkelson 2000). Present genetic models for IOCG systems invoke the involvement of magmatism as a source of fluids and/or as a source of heat to drive fluid circulation (cf. Hitzman et al. 1992; Pollard 2000, 2001; Barton and Johnson 1996, 2000). New data from Wernecke Breccia indicate IOCG mineralization can form in a non-magmatic environment as a result of the evolution of basinal brines.

2 Geological framework of the Wernecke breccia IOCG system

Wernecke Breccia occurs in areas underlain by the Wernecke Supergroup (WSG) an approximately 13 kilometre-thick package of Early Proterozoic, dominantly marine, fine-grained sedimentary rocks and carbonates that were deposited as two clastic to carbonate grand cycles (Delaney 1981; Thorkelson 2000). Small Early Proterozoic (ca. 1710 Ma) igneous bodies known as the Bonnet Plume River Intrusions (BPRI) cross-cut WSG strata and are spatially associated with Wernecke Breccia (cf. Thorkelson et al. 2001 a, b). Rare subaerial volcanic rocks, known as the Slab volcanics, occur in the eastern part of the study area (ibid).

Strata of the WSG were deformed and metamorphosed to greenschist grade during the Racklan Orogeny, a period of pre-1600 Ma contractional deformation (cf. Thorkelson 2000; Thorkelson et al. 2001b; Brideau et al. 2002). The timing of BPRI and Slab volcanics relative to Racklan deformation is uncertain (ibid).

3 Wernecke breccia and IOCG mineralization

3.1 Wernecke breccia

Bodies of Wernecke Breccia occur in weak and/or permeable regions (e.g. fold hinges, shear zones, permeable strata) throughout the WSG but are most abundant in the lower part of the stratigraphy (Delaney 1981; Lane 1990) where there is a transition from evaporite-bearing calcareous metasedimentary rocks to overlying carbonaceous shale (Hunt et al. 2005). The breccia bodies range from a few centimetres to several kilometres across and vary from clast- to matrix-supported. Clasts within the breccia were locally derived from proximal host rocks and range from < 1 centimetre to several hundred metres across (cf. Thorkelson 2000; Hunt et al. 2005). Early phases of breccia are preserved as clasts within later breccia. Matrix to the breccia is made up of rock fragments and hydrothermal precipitates consisting largely of feldspar (albite and/or potassium feldspar), carbonate (calcite, or dolomite/ankerite, locally siderite) and quartz.

3.2 Mineralization and alteration

IOCG mineralization made up dominantly of magnetite, hematite and chalcopyrite occurs as multiple episodes of veining and disseminations within and peripheral to Wernecke Breccia (cf. Bell 1986; Thorkelson 2000; Hunt

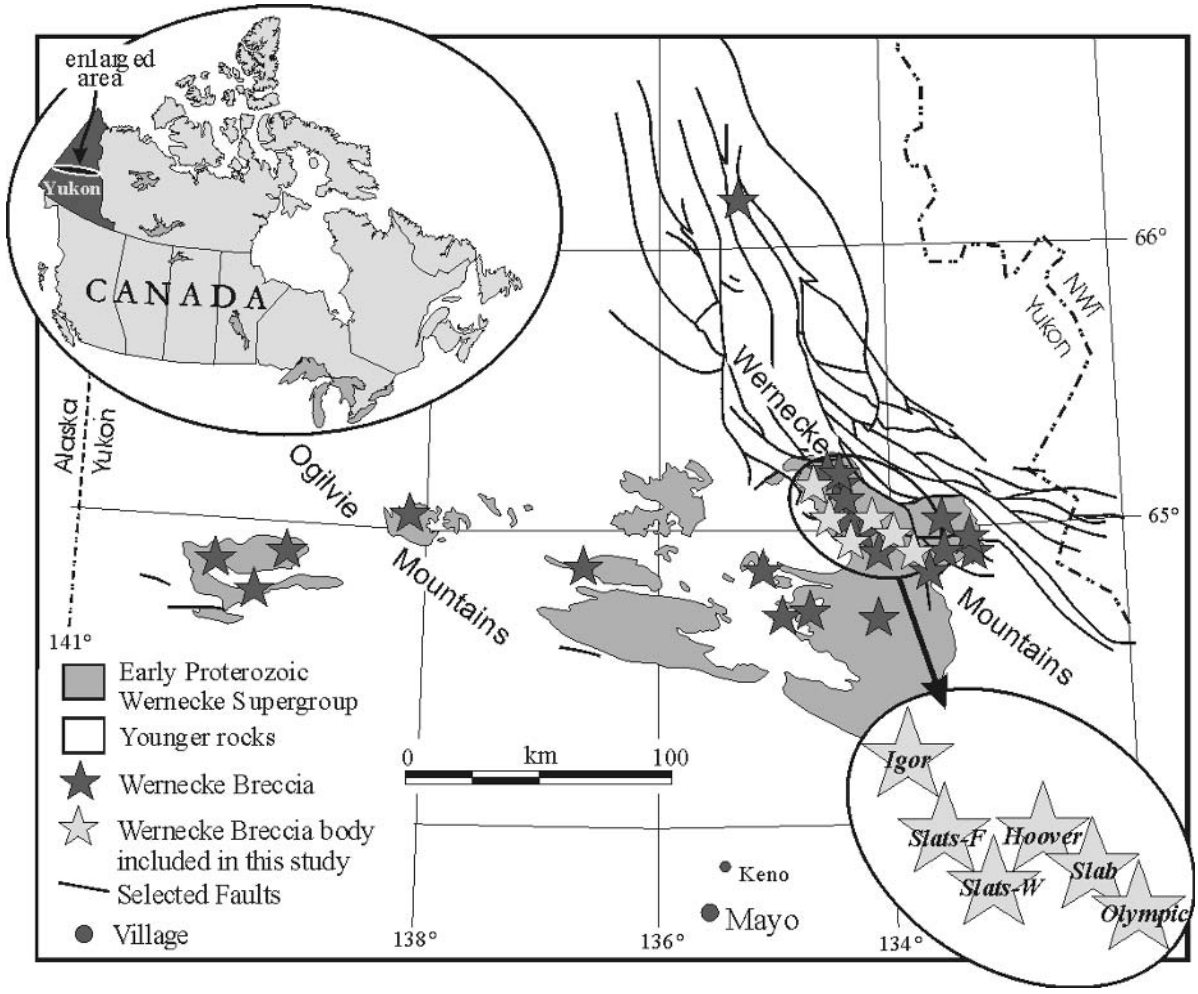

Figure 1: Location of Wernecke Breccia, distribution of Wernecke Supergroup and location of IOCG prospects included in this study (modified from Thorkelson 2000).

et al. 2005). Sodic and/or potassic metasomatic alteration extends tens to hundreds of metres away from the breccia and is overprinted by widespread carbonate alteration.

4 Formation of Wernecke breccia

Wernecke Breccia was produced in WSG sediments that: 1) had undergone diagenesis and compaction; partial dissolution of evaporites during these processes would have caused disruption of intercalated and overlying sediments and led to the formation of solution breccias; 2) had been affected by syn-depositional faulting; 3) had been intruded by BPRI; 4) had reached elevated temperatures due to burial and metamorphism and 5) had been affected by at least one phase of metamorphism (Thorkelson 2000; Hunt et al. 2005).

Fluid inclusion and isotopic data indicate breccia-forming/mineralizing fluids were largely basinal in origin (Hunt 2004; Hunt et al. 2005). The lack of an obvious major intrusive heat sourcec suggests fluid circulation may have been driven by tectonic, gravity and/or density processes. Thus, in contrast to other IOCG systems where magmatism plays a significant role, the formation of the Wernecke Breccia IOCG system appears to be related to the temporal evolution of the Wernecke basin and to be independent of a magmatic cycle.

Wernecke Breccia mineralization contains abundant low TiO_2 iron oxides and is therefore similar to deposits in the IOCG class (cf. Hitzman et al. 1992). However, the formation of the Wernecke Breccia IOCG system by basinal fluids derived from a thick, evaporite-bearing sedimentary sequence, independent of a magmatic cycle, also bears many similarities to sediment-hosted copper deposits such as those in the Zambian Copper Belt and the Mount Isa district (Australia) that were formed during the evolution of the host sedimentary basins.

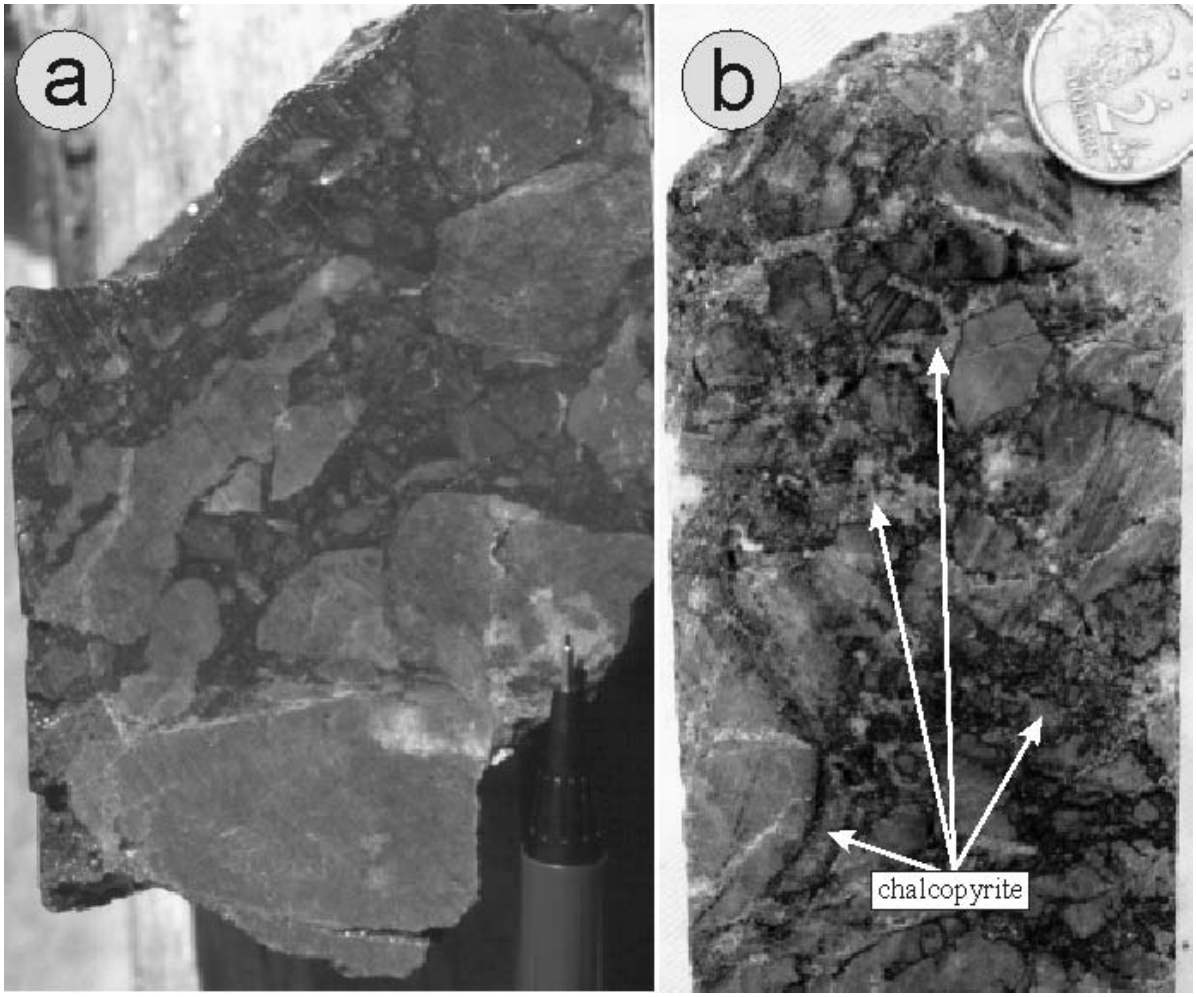

Figure 2: Photographs of Wernecke Breccia: a) typical breccia and b) mineralized breccia with chalcopyrite matrix.

Acknowledgements

Newmont Mines Ltd, Archer, Cathro & Associates Inc., Monster Copper Resources, Blackstone Resources, Equity Engineering and Pamicon Developments are thanked for access to properties and information. Support for this project was provided by Yukon Geological Survey, Australian IPRS, JCU and pmd*CRC scholarships, JCU MRG and an SEG student research grant.

References

Barton MD, Johnson DA (1996) Evaporitic source model for igneous-related Fe oxide-(REE-Cu-Au-U) mineralization. Geology 24: 259-262

Barton MD, Johnson DA (2000) Alternative brine source for Fe-oxide(-Cu-Au) systems: implications for hydrothermal alteration and metals. In: Porter TM (ed), Hydrothermal Iron Oxide Copper-Gold & Related Deposits: A Global Perspective, volume 1: PGC Publishing, Adelaide: 43-60

Bell RT (1986) Megabreccias in northeastern Wernecke Mountains, Yukon Territory: Current Research , Part A, Geological Survey of Canada, Paper 86-1A, 375-384

Brideau MA, Thorkelson DJ, Godin L, Laughton JR (2002) Paleoproterozoic deformation of the Racklan Orogeny, Slats Creek (106D/16) and Fairchild Lake (106C/13) map areas, Wernecke Mountains, Yukon. In: Emond DS, Weston LH, Lewis LL (eds), Yukon Exploration and Geology 2001, Exploration and Geological Services Division, Yukon Region, Indian and Northern Affairs Canada: 65-72

Delaney GD (1981) The mid-Proterozoic Wernecke Supergroup, Wernecke Mountains, Yukon Territory. In: Proterozoic Basins of Canada, Geological Survey of Canada, Paper 81-10, 1-23

Hitzman MW (2000) Iron oxide-Cu-Au deposits: what, where, when and why? In: Porter TM (ed), Hydrothermal Iron Oxide Copper-Gold & Related Deposits: A Global Perspective, volume 1: PGC Publishing, Adelaide: 9-25

Hitzman MW, Oreskes N, Einaudi MT (1992) Geological characteristics and tectonic setting of Proterozoic iron oxide (Cu-U-Au-REE) deposits. Precambrian Research 58: 241-287

Hunt JA (2004) The geology and genesis of iron oxide-copper-gold mineralisation associated with Wernecke Breccia, Yukon, Canada. PhD Thesis, James Cook University, Australia: 120

Hunt JA, Baker T, Thorkelson DJ (2005 – in press) Regional-scale Proterozoic IOCG-mineralized breccia systems: examples from the Wernecke Mountains, Yukon, Canada. Mineralium Deposita

Lane RA (1990) Geologic setting and petrology of the Proterozoic Ogilvie Mountains breccia of the Coal Creek Inlier, southern Ogilvie Mountains, Yukon Territory. MSc Thesis University of British Columbia, Vancouver, Canada: 223

Pollard PJ (2000) Evidence of a magmatic fluid and metal source for Fe oxide Cu-Au mineralisation. ? In: Porter TM (ed), Hydrothermal Iron Oxide Copper-Gold & Related Deposits: A Global Perspective, volume 1: PGC Publishing, Adelaide: 27-41

Pollard PJ (2001) Sodic(-calcic) alteration in Fe oxide-Cu-Au districts: an origin via unmixing of magmatic-derived H_2O-CO_2-NaCl ± $CaCl_2$-KCl fluids. Mineralium Deposita 36: 93-100

Thorkelson DJ (2000) Geology and mineral occurrences of the Slats Creek, Fairchild Lake and "Dolores Creek" areas, Wernecke Mountains, Yukon Territory. Exploration and Geological Services Division, Yukon Region, Indian and Northern Affairs Canada, Bulletin 10, 73

Thorkelson DJ, Mortensen JK, Creaser RA, Davidson GJ, Abbott JG (2001a) Early Proterozoic magmatism in Yukon, Canada: constraints on the evolution of northwestern Laurentia. Canadian Journal of Earth Science 38: 1479-1494

Thorkelson DJ, Mortensen JK, Davidson GJ, Creaser RA, Perez WA, Abbott JG (2001b) Early Mesoproterozoic intrusive breccias in Yukon, Canada: the role of hydrothermal systems in reconstructions of North America and Australia. Precambrian Research 111: 31-55

Use of petrophysical characterisation techniques in receptivity definition for carbonate-hosted MVT deposits

Kip Jeffrey
Department of Geology, University of Leicester, UK

Abstract. Lithostratigraphically controlled replace-ment mineralization in the South Pennine Orefield, UK, has been studied to ascertain the petrophysical characteristics of receptive horizons. These exhibit significantly different pore parameters but mineralization is more directly controlled by the presence of hydrophobic, low solubility and low porosity horizons that create 'intracarbonate ponding surfaces' on which downward fluid movement is retarded and fluids focussed along the upper interface. For deposit formation a strong contrast is required with the overlying units so that the enhanced fluid flow and residence time can initiate and propagate replacement. The mechanical properties of the overlying units are also important. This represents a new conceptual approach to defining receptivity and for the first time allows receptive units to be identified by their essential and measurable petrophysical signatures. These techniques are already being used in an on-going exploration programme.

Keywords. Replacement mineralisation, petrophysics, MVT deposits, receptivity, carbonate hosted, fluorite, South Pennine Orefield, UK

1 Introduction

The fluorite–barite deposits in the South Pennine Orefield, UK are found in a well-explored MVT district within the central and northern Pennine Hills. They are hosted by Carboniferous Limestone, capped by Namurian Shale, with the limestones being sporadically interbedded with tuff and lava horizons (Aitkenhead et. al. 1985). The South Pennine Orefield is an exhumed carbonate platform with and lagoonal to reef facies transitions are observed particularly around the northern and eastern outcrop of the limestone. Mineralisation is concentrated on the eastern edge of the platform.

The area has a long history of working with the galena content of the vein and replacement mineralization being exploited for lead since probably the Roman times. Current working is for fluorite and barite, with minor, galena and aggregates as by-products. Over the last 50 years working has focussed on the major vein systems and these have been extensively mined both on surface and in underground mining operations. As these high-grade deposits have become depleted, and world prices for fluorite declined due to strong international competition, there is greater need to discover large, economic, near-surface deposits amenable to open pit extraction. The replacement mineralisation associated with the vein systems includes bedding replacements, breccia domes and 'pipe complexes' or mantos (Butcher and Hedges 1987; Jeffrey 1997). These have often been discovered fortuitously, and represent some of the largest ore bodies exploited to date (e.g. Masson, Dirtlow Rake etc). Their distribution is irregular and has hitherto been unpredictable. The traditional structurally controlled settings have already largely been examined and deposits worked. There are however a number of large deposits that are found without such structural control where lithostratigraphic factors appear to dominate. This replacement mineralization has been reported as occurring mainly within units dominated by coarse crinoidal limestone and only rarely found in the darker fine-grained facies (Stevenson and Gaunt 1971).

The literature on MVT deposits and other lithostratigraphically controlled carbonate deposits frequently refers to horizons that preferentially host the mineralization as being receptive or replacive. This observation is however usually justified in terms of general comments on its probable higher porosity or permeability as the controlling factor. Joint density has also been suggested in some cases. The nature of what actually controls receptivity is however almost never identified.

The study reported here involved the use of simple petrophysical and microstructural techniques to examine the stratigraphic section through the limestones in an area well known for its replacement deposits. The mineralization in the Castleton study has been studied for over 20 years and the units that preferentially hosted deposits have been identified. The samples from each horizon could therefore be designated replacive or non-replacive and any systematic differences identified.

The original hypothesis was that the organic matter that caused the darker colour in some units might play a role in mediating reactions between the limestone and hydrothermal fluids responsible for the mineralization. Fortunately the limestones have not undergone significant diagenetic, metamorphic or structural modification since the mineralising events and so the limestones examined now are very similar to those encountered by the hydrothermal fluids (Walkden and Williams 1991).

The techniques included wettability, mercury intrusion porosimetry, nitrogen adsorption surface area, dissolution rate, and major oxide chemistry.

2 Sampling

Samples were taken from each lithostratigraphic unit in the large Hope Cement works quarry (Fig. 1) that exposes a 160m vertical section of limestones representing almost the full section of the uppermost Dinantian Limestones that host mineralization. Sampling was undertaken close enough to the mineralization to minimise the potential for significant lateral facies variation but sufficiently distant to avoid test results reflecting alteration associated with the mineralization itself. Each sample was characterised by the suite of tests described above and the preferentially mineralised horizons highlighted. The fluorite-barite replacement mineralization comprised a series of flattened domal structures restricted to a few horizons. The margins of the mineralization showed preferential replacement in some individual beds, replacement fronts with the limestone host rocks and variable silicification. The centre of the mineralised bodies is frequently brecciated and contained abundant clay.

3 Results

The graphs in Figure 2 indicate the responses three of the tests. It is clear that the upper mineralised zone and specifically the most intensely mineralised units are located at a critical interface associated with the least wettable horizon in the succession. This unit is also the least soluble and has a very low surface area. The geometry of the replacement mineralization in this zone clearly indicates that it was initiated on the upper surface of this unit but subsequently developed in the units above it and to a much lesser extent in one unit below.

The unit immediately above the interface is extremely wettable, more soluble and has high surface area. Other units in the mineralised zone share some of these attributes. The mineralised zone is floored by the next hydrophobic and low solubility unit down from the initiation horizon. The lower mineralised zone does not show such interface control but is located mainly within the most soluble carbonate unit within the succession.

Figure 1: Oblique air photo of the Hope Cement Works Quarry looking west, in August 2003. Mineralisation is found at two levels in the main faces.

4 Model

The original floor of the upper mineralised horizon has a characteristic signature with a highly hydrophobic, low surface area, and low dissolution rate. A highly contrasting easily wetted, high surface area, porous and soluble unit, overlies this. The interface between was the loci for the mineralization and focussed the fluids for replacement to be initiated in the overlying unit. The thinly bedded nature of these provided easy upward stoping as the replacement and associate dissolution selected some thin beds and destabilised others leading to breccia formation and in-fill of the mineralised zone. As the mineralization developed the resistant, hydrophobic low solubility, footwall was breached and replacement permeated down until the next hydrophobic, and resistant unit was encountered. This represents a 'secondary floor' and formed the final base of the deposits.

The hydrophobic units therefore forms an 'intra-carbonate ponding surface' but the mineralization appears to require a strong contrast such that the units above are hydrophilic and porous enough to accept the fluids focussed by the unit beneath.

The mineralization also exploits the most highly soluble units in the succession although these are certainly not the most pure and the relationship of chemical purity, microstructure and mineral composition to this dissolution rate is still under investigation. Identification of carbonate units with these 'fingerprints' allows receptive packages of limestone stratigraphy to be identified and targeted. Combining this with information on regional fluid flow pathways and local structural controls allows exploration targets to be defined. Predictive exploration for these previously difficult to locate deposits has become possible and is underway.

5 Conclusions

This represents a new conceptual method for identifying horizons and lithofacies that have enhanced potential for hosting mineralization. It identifies in this setting for the first time the critical combination of petrophysically distinct units needed to locate mineralization in carbonate sequences devoid of the usual gross lithological or structural controls. The concept of intracarbonate ponding surfaces based on wettability, porosity and surface area characteristics is already being used for exploration within the orefield and has led to wider understanding of the localising factors and controls on a number of the other orebodies in the area.

This page intentionally blank

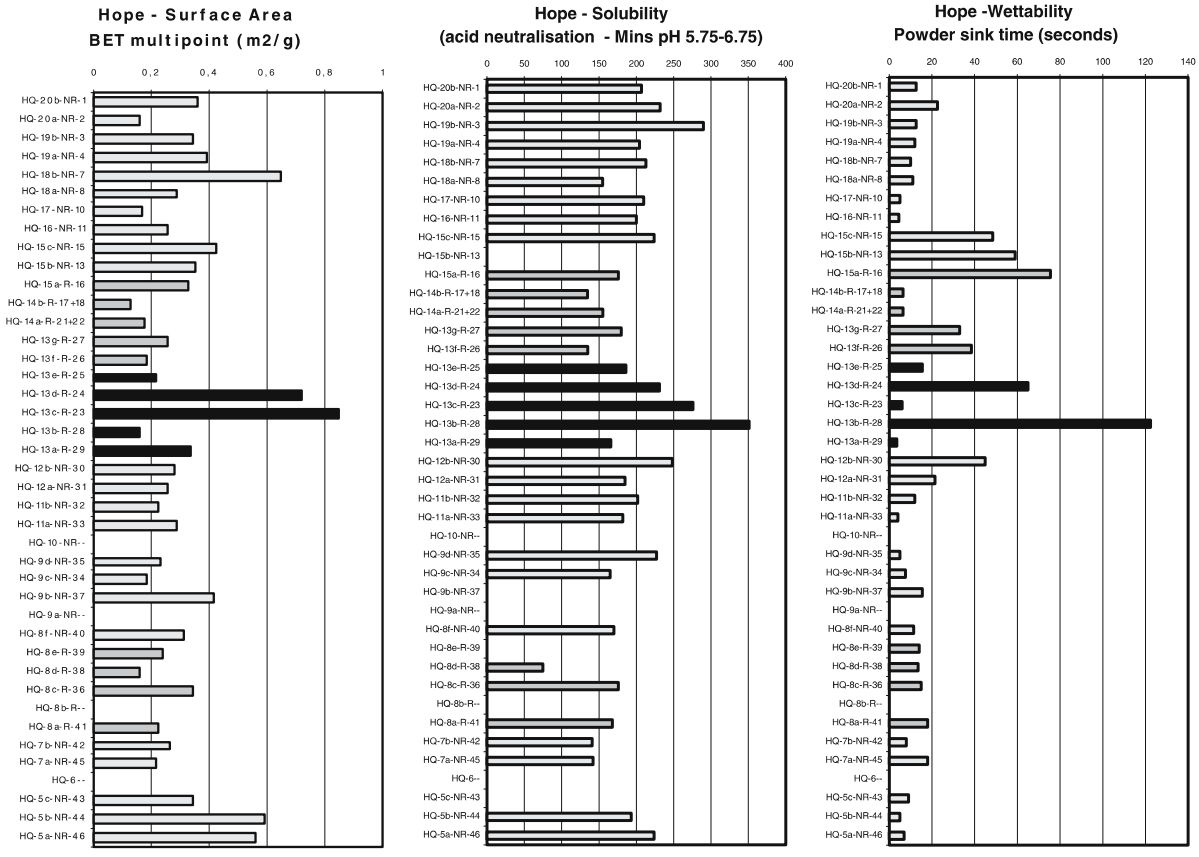

Figure 2: Results of wettability, dissolution rate and nitrogen adsorption surface area analysis for the stratigraphic succession in which the lithostratigraphically controlled fluorite-barite deposits are located. Limestone units –light grey, Upper and lower replacive zones in mid grey, main mineral hosting units in the upper replacive horizon detailed in black.

Acknowledgements

The author would like to thank DTI Technology Foresight LINK funding – FIESTA project for the financial support to undertake this project along with Glebe Mines Ltd, Geomatrix, Geosoft and MIRO for their financial and logistical contributions, and support during the work.

References

Aitkenhead N, Chrisholm JI, Stevenson IP (1985) Geology and Country around Buxton, Leek and Bakewell. Memoirs of the British Geological Survey, Sheet 111. Memoir of the Geological Survey of Great Britain, 168

Butcher NJD, Hedges JD (1987) Exploration and extraction of structurally and lithographically controlled fluorite deposits in Castleton – Bradwell area of the Southern Pennine Orefield, England. Trans. Inst. Min. Metall.(Sect B) B96: 149-155

Jeffrey CA (1997) Replacement mineralization styles and breccia dome formation at Dirtlow Rake fluorite-barite deposit, Castleton, England. Trans. Inst. Min. Metall.(Sect B), 106: 15-23

Stevenson IP, Gaunt GD (1971) Geology of the country around Chapel-en-le-Frith, Sheet 99. Memoir of the Geological Survey of Great Britain, 433

Walkden GM, Williams DO (1991) The diagenesis of the late Dinantian Derbyshire-East Midlands carbonate shelf, central England. Sedimentology 38: 643-670

Geological and economic conditions of the Gar iron ore deposit development (Amur region, Russia)

V.V. Kichanova, V.D. Kichanov
Division of Regional Geology and Hudrogeology Amur Research Center FEB RAS, 2, B.Khmelnitsky St., Blagoveshchensk, Russia

Abstract. The Russian Far Eastern territory con-tains more than 10000 million tones (mt) of unexploited iron ore. The Gar deposit contains reserves of 388 mt at a cutoff grade of 40% (iron oxide) and proven and probable reserves of 600 mt. Ores are amenable to coke-free metallurgy. Technological testing by an electro-metallurgical method produced high quality. Availability of cheap power in the area and its proximity to North East Asia suggests that the Gar deposit may be economically favorable to develop.

Keywords. Amur region, iron ore deposit, prospected reserves, capital expenses

1 Introduction

The Gar iron deposit is located in the Amur Region of Russia. The deposit is located 140 km to the northeast of town Svobodnii and 80 - 90 km from the BAM and Shimanovsk - Chagoian railway. The proximity of the Amur Region to the developing market of North East Asia suggests it may be economically favorable to mine (Kichanova 2003).

2 Geology of the Gar deposit

Ore in the Gar deposits is hosted in a metavolcanic-metasedimentary sequence that is intruded by Proterozoic and early Paleozoic gabbros and granites (Zimin 1985). The deposit occurs over and area of 1.5 by 4 km in the core of syncline that strikes northeast (Gar syncline), and is cut northwest striking faults (Figs. 1 and 2).

A total of 56 stratiform ore zones with the thickness between 2 to 49 m and length between 80 and 500 m have been defined by 500 m-deep drill holes.

3 Chemical composition of the ore

High grade magnetite ore account for 37 % of the ore reserves and averages (in%): Fe – 55.68; FeO – 22.22; SiO_2 – 10.65; TiO_2 – 0.34; K_2O – 0.10; Na_2O – 1.48; Al_2O_3 – 2.77; CaO – 5.63; MgO – 1.70; MnO – 0.31; S – 1.02; P – 0.18; H_2O – 0.12. About 54% of high-grade ores are low phosphate and contain PO_4 - 0,08% and S – 1.68%. Phosphorus correlates with apatite, brimstone with sulfides. Chemical composition of middle-grade ores that account for 63% of the reserves average (in %) : Fe – 32.64; FeO – 13.74; SiO_2 – 24.67; TiO_2 – 0.39; K_2O – 0.36; Na_2O – 1.22; Al_2O_3 –6.66; CaO – 10.98; MgO – 2.73; MnO – 0.35; S –

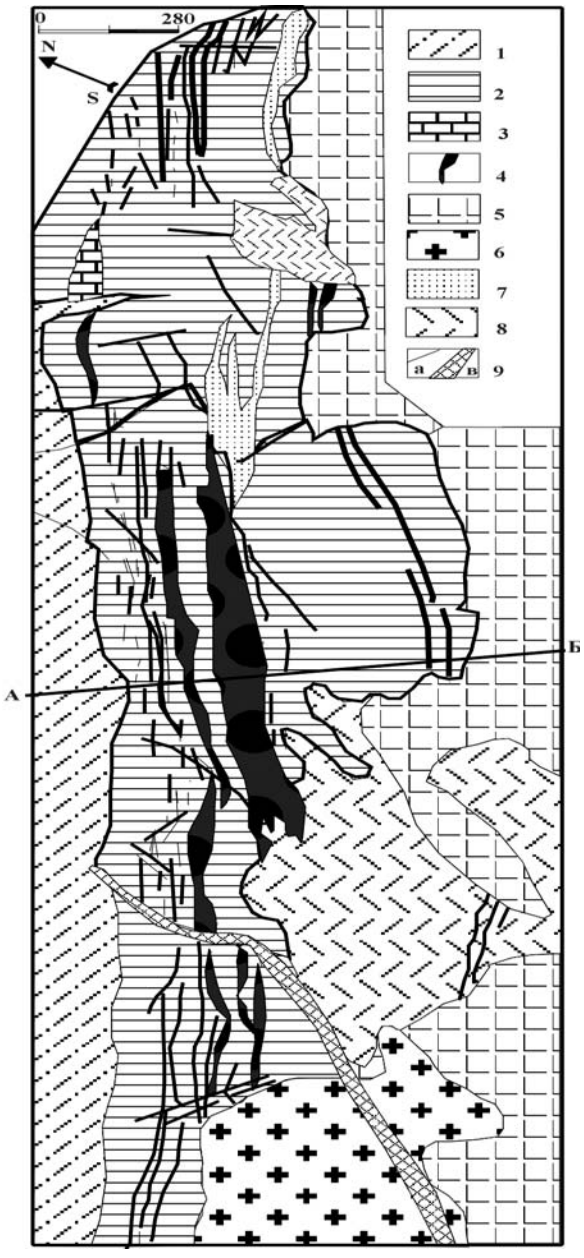

Figure 1: Geological map of the Gar Fe deposit (Vasiliev et al. 2000). 1. Proterozoic chlorite-albite schist. 2. Ore bearing strata: albite, amphibole-albite and amphibole schist. 3. Marbles. 4. Magnetic iron ore. 5. Gabbro intrusion. 6. Granite stock. 7. Garnet-pyroxene and pyroxene skarns 8. Skarn. 9. Fault zone.

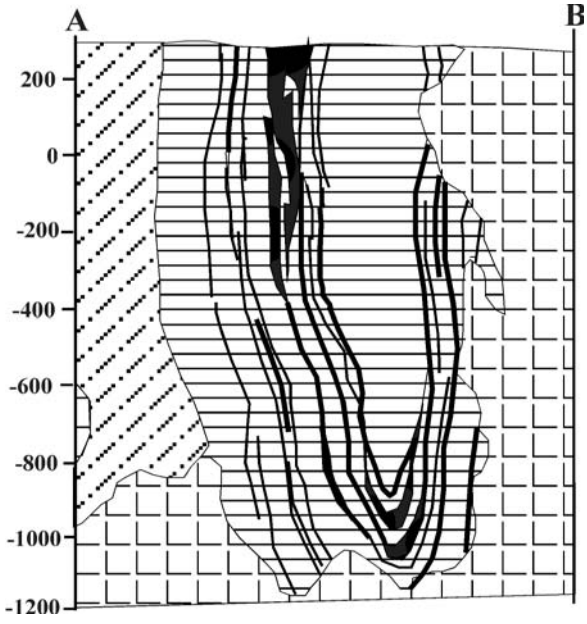

Figure 2: Geological cross section of the Gar Fe deposit. (Vasiliev et al. 2000)

1.99; P – 0.22; H_2O –0.22. Main ore minerals are magnetite, mushketovite, maghematite, ferric oxide. Ores commonly contain pyrite, chalcopyrite, sphalerite, galena, bornite, covelite, chalcocite, pyrrhotite, molybdenite, and malachite. Trace element analyses of 39 samples indicate Au of up to 1.6 g/t; Cu - up to 0.77%, Mo - up to 0.01% (in quartz-spurs up to 0.72%), Co - 0.01%, Ni - 0.02%, Mg - up to 1.16%, chromium pentoxide - up to 0.03%, vanadium pentoxide - 0.01%.

Technological tests made by the plant "Sibelectrostal" indicate that the high quality concentrate contained $Fe_{tot.}$- 69.6%. silica - 1.68%, phosphorus - 0.02%, brimstone - 0.07%. The rich ores with low content of phosphorous with low brimstone does not require enrichments and can be used for melting conversion pig irons or reprocessing by the strait deoxidation method to obtain high quality steels by the electrometallurgical method.

4 Mining

A previous resource estimate indicates that open-cut mining is possible to a depth of 435 meters and reserves of 388.8 mt at Fe - 41.7%, PO_4 - 0.21% and S - 1.13%. The inclusion of possible ore indicates that the Gar deposit could contain up to 600 mt (Zimin and Konoplev 1989). The Selemdginsky iron-ore region, to which the Gar deposit related, contains four other deposits including the Selemdzhinsky, Glybokinsky, Aldikonsky and Shimanovsky. Vasiljev et al. (2000) estimated 2590 mt combined reserves.

A sympathetic federal and regional mining climate, favorable tax situation, cheep labor costs, availability of cheep power, and location near emerging markets in North East Asia suggest the Gar deposit might be favorable to mine.

References

Kichanova VV (2002) To the question about joining the external row material market of a company "Dragless". The materials of the 4th regional scientific-practical conference. Blagoveshensk: 115-117

Kichanova VV (2003) Peculiarities of the row iron ore market of the North East Asian countries and perspectives of the Amure region to enter the market. "Ecological and economical problems of the nature usage in Upper Amure", Blagoveshensk

Vasiliev IA, Kapanin VP, Kovtonyuk GP, Melnikov VD, Luznov VL, Danilov AP, Sorokin AP (2000) Raw-mineral base of the Amure region on the edge of centuries. Blagoveshensk: 32-35

Zimin SS (1985) About genesis of iron ores of Garinskoe deposit in Amure region. Geology, magmatism and mineralization of Priamurie. Vladivostok: 3-6

Zimin SS, Konoplev II (1989) Perspectives of the Selemdzhinskaya iron ore zone. Iron ores of the Far East. Vladivostok: FEB AS USSR: 76-83

Palaeofluid flow in siliciclastic Lower Carboniferous rocks: Evidence from stable isotopes and fluid inclusions, Rhenohercynian Zone, Czech Republic

Jan Kucera, Klára Kucerová-Charvátová
Institute of Geological Sciences, Faculty of Science, Masaryk University, Brno, Czech Republic

Phillipe Muchez
Afdeling Fysico-chemische Geologie, Katholieke Universiteit Leuven, Belgium

Walter Prochaska
Department of Applied Geosciences and Geophysics, University of Leoben, Austria

Abstract. Post-Variscan Zn, Pb, Cu vein minera-lisation occurs within the Lower Carboniferous siliciclastic rocks at the eastern border of the Bohemian Massif. Saddle dolomites are associated with this vein mineralisation and indicate a NW-SE oriented fluid flow through the Palaeozoic rocks. The major control on this fluid flow pattern is exerted by faults. Eutectic temperature and crush-leach analyses indicate H_2O-NaCl-$CaCl_2$ type of basinal brines. Homogenization temperatures regionally decrease from 147° to 80°C and salinities from 26.5 to 17 wt.% eq. NaCl. Temperatures correlate well with an increase of $\delta^{18}O$ values from 15.5 to 22.5‰ SMOW and $\delta^{13}C$ values from -5.6 to -3.1‰ PDB.

Keywords. Bohemian Massif, dolomite, stable isotopes, fluid inclusions, crush-leach analyses

1 Introduction

Post-Variscan vein mineralisation occurs in Devonian and Carboniferous rocks at the eastern border of the Bohemian Massif. In the larger region, post-Variscan hydrothermal activity also includes large Mississippi Valley-type deposits in Poland (Silesia-Cracow Zn-Pb district). This paper discusses small Zn, Pb, Cu occurrences which are hosted by siliciclastic Lower Carboniferous rocks of the Nízký Jeseník Upland (Losert 1957). The aim of this study is determine the origin and possible migration paths of the mineralising fluids.

2 Geological setting

The Nízký Jeseník Upland is situated at the eastern border of the Bohemian Massif. This area represents the eastern part of the European Rhenohercynicum zone. Lower Carboniferous greywackes, siltstones, shales and conglomerates of the Moravice and Hradec-kyjovice formations (Kumpera 1983) are typical host-rocks of the mineralisation. The basement mainly consists of Devonian limestones and the Proterozoic Brunovistulicum unit, containing magmatic and metamorphic rocks (Dudek 1980). This autochtonous sequence has been overthrusted from the east by the West Carpathian units of Alpine age.

3 Stable isotope study

The regional trend of the isotope compositions shows an increase of the $\delta^{18}O$ values from E to W and NW, from 15.5 to 22.5‰ SMOW. The same trend is documented for $\delta^{13}C$ values which range from -5.6 to -3.1‰ PDB (Fig. 2). This trend corresponds with a decrease of the homogenization temperatures. Taking into account the homogenization temperatures (see below), calculated isotopic are between +0.4 and +3.6‰ SMOW.

4 Fluid inclusion study

4.1 Microthermometry

Microthermometric measurements have been performed on 361 inclusions in saddle dolomite from seven localities. In saddle dolomite, small (1-4m) two-phase (L+V) primary fluid inclusions were analysed. Homogenization temperatures (Th) range from 64° to 147°C and final melting temperature from -13.1° to -29.6°C (Tab. 1). Calcu-

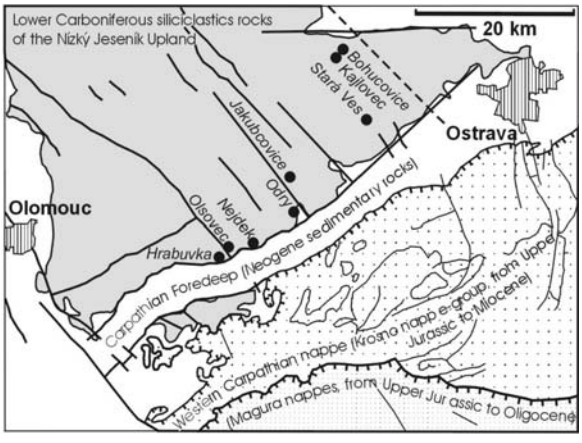

Figure 1: Position of studied localities on the eastern margin of the Bohemian Massif.

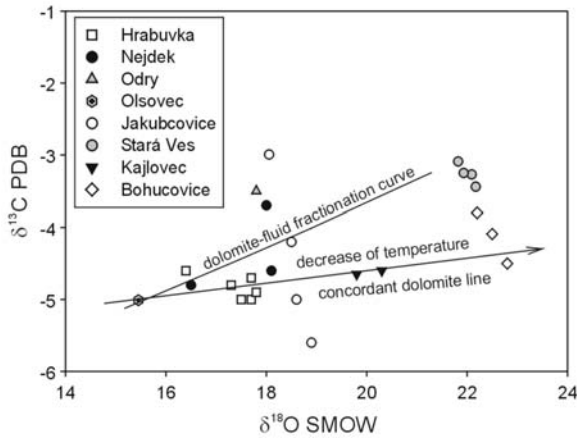

Figure 2: Oxygen and carbon isotopic composition of saddle dolomites. Lower Carboniferous, Nízky Jeseník Upland.

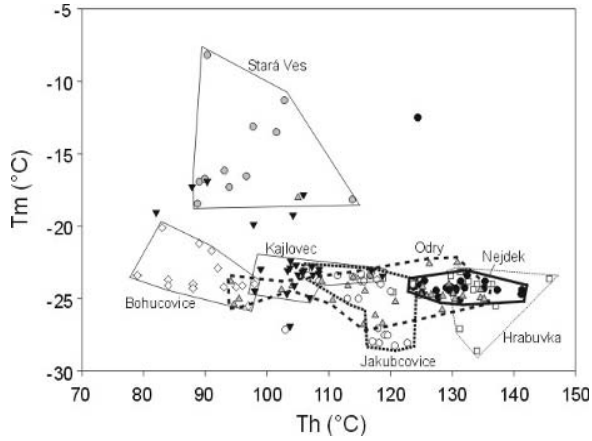

Figure 3: Th – Tm plot from mainly primary fluid inclusions in saddle dolomites. Lower Carboniferous, Nízky Jeseník Upland.

Table 1: Microthermometric data of saddle dolomites

Locality	Th °C (mean value)	Tm °C (mean value)
Hrabuvka	120.5 to 147.5 (133.3)	-23.0 to -27.1 (-24.0)
Nejdek	114.2 to 141.3 (129.5)	-23.2 to -25.1 (-24.3)
Odry	83.3 to 138.0 (120.8)	-18.0 to -26.8 (-24.7)
Jakubcovice	104.4 to 124.4 (116.2)	-19.2 to -29.6 (-23.7)
Kajlovec	75.3 to 120.9 (103.2)	-16.9 to -26.9 (-23.0)
Stará Ves	63.5 to 113.8 (96.2)	-13.1 to -22.8 (-17.2)
Bohucovice	73.0 to 98.0 (88.0)	-20.1 to -25.5 (-24.0)

lated salinities after Oakes et al. (1990) range from 17.0 to 26.5 wt.% eq. NaCl. Eutectic temperatures within the range from -43.7° to -52°C represent the H_2O-NaCl-$CaCl_2$ type of enclosed fluids. It was not possible to measure the final melting temperature of hydrohalite due to the small size of the inclusions. Th regionally decreases from E to W and NW. This trend correlates well with the slow decrease of the salinity of the fluid inclusions in the dolomites (Fig. 3).

4.2 Crush-leach analyses

Eight dolomite samples have been analysed for the Na, Cl, K, Li, Br and F content in their fluid inclusions by crush-leach analyses. Density calculations of fluid inclusions were carried out using the programme BULK of Bakker (2003). Molar ratios of Cl/Na range from 1.5 to 1.8, Cl/Br ratios vary between 210 and 269. Total dissolved solids range from 196 to 268 g/l. These values could represent saline brines. The relative concentrations of potassium (K/Cl molar ratio between 0.0148 and 0.0409) and lithium (Li/Cl molar ratio between 0.0009 and 0.0028) further indicate that the fluids interacted with siliciclastic rocks (mainly illitisation; Fig. 4). Na/Br, Cl/Br and Na/Cl ratios suggest a major contribution of an evaporitic brine as a source for the high salinity. A log Br vs. log Cl plot for these samples shows that the most dolomites plot near the seawater evaporation trajectory (McCaffrey et al. 1987; Fig. 5). However, in detail a linear trend can be observed. This could reflect mixing between a bittern brine and a lower salinity fluid.

5 Discussion and conclusion

Eutectic temperature determinations and crush-leach analyses from fluid inclusions in saddle dolomites indicate the presence of H_2O-NaCl-$CaCl_2$ type of basinal brines. These brines were migrated through siliciclastic rocks of Early Carboniferous age. The main migration pathways for hydrothermal fluids were NW-SE and probably NE-SW faults. The fluid transport towards the NE correlates with a decrease of the homogenization temperature in fluid inclusions and an increase of oxygen isotopic values in dolomites as documented Rye and Williams (1981) from deposit McArthur River in Australia. The subbdued slope of concordant dolomite line (Fig. 2) vs. the theoretical dolomite-fluid fractionation curve (Rye and Williams 1981) is apparently caused by the interaction with the organic matter. Decreasing of temperature correponds with concommitant decreasing fluid salinities (Fig. 3) and larger interaction with surrounding rocks, e.g. illitisation (Fig. 4). Also important is the decrease of the Br and Cl content with salinity (Fig. 5). Dolomite from Stará Ves, which is not situated near a fault shows a mixing with a los salinity water. The trend of mixing with a low salinity waters is absent in the other localities. Microthermometric and crush-leach analyses of fluid inclusions are very similar with those of the Silesia-Cracow MVT district. Low temperature and high saline fluids are probably adherent to same fluid flow along NW-SE and NE-SW faults. Mineralising fluids could have been driven

This page intentionally blank

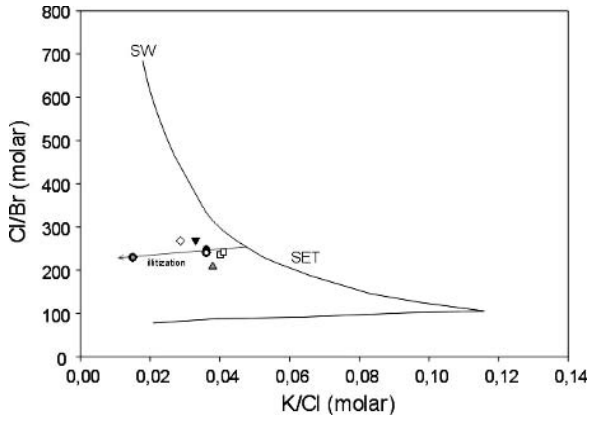

Figure 4: Cl/Br versus K/Cl plot of saddle dolomites. Symbols as in Fig. 2. SET = Seawater Evaporation Trajectory (data after McCaffrey et al. 1987).

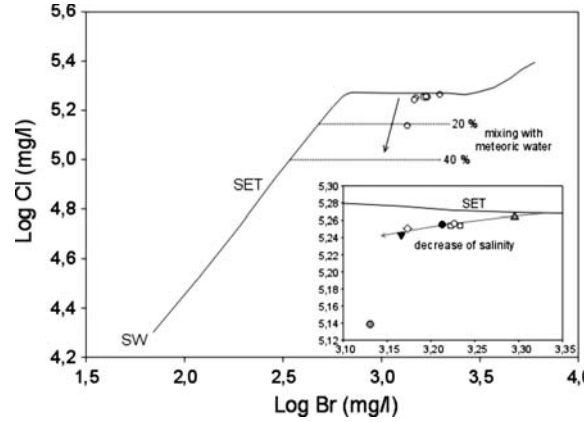

Figure 5: Log Cl versus log Br plot of saddle dolomites. Inset displays a linear trend in the Cl-Br data. Symbols as in Fig. 2. SET = Seawater Evaporation Trajectory (data after McCaffrey et al. 1987).

by a dilatational pump mechanism (Heijlen et al. 2003), or gravity-driven flow model (Leach et al. 1996). The age of this mineralisation is dated to the Early Cretaceous (Heijlen et al. 2003) or Middle Tertiary (Symons et al. 1995; Leach et al. 1996).

Acknowledgements

Investigation was granted by FRVS 584/2003 and GACR 205/00/0356. The doubly polished wafers were carefully prepared by H. Nijs. We also thank the reviewers.

References

Bakker RJ (2003) Package FLUIDS 1. Computer programs for analysis of fluid inclusion data and for modelling bulk fluid properties. Chem Geol 194: 3-23

Dudek A (1980) The crystalline basement block of the Outer Carpathians in Moravia: Bruno-Vistulikum. Rozpr. Čs. Akad. Věd, Ř. mat. přír. Věd, vol. 90, 8, 85 Prague

Heijlen W, Muchez Ph, Banks DA, Schneider J, Kucha H, Keppens E (2003) Carbonate-Hosted Zn-Pb deposits in Upper Silesia, Poland: Origin and evolution of mineralizing fluids and constraints on genetic models. Econ Geol 98: 911-932

Kumpera O (1983) Geology of the Lower Carboniferous horst of Jeseník. Knih. Ústř. Úst. geol., 172 p. Prague (in Czech)

Leach DL, Viets JG, Kozlowski A, Kibitlewski S (1996) Geology, geochemistry, and genesis of the Silesia-Cracow zinc-lead district, southern Poland. Society of Economic Geologists Special Publication 4: 144-170

Losert J (1957) Deposits and occurrences of lead-zinc ores in the north moravian Culm. Rozpr. ČAVU, 67, 4, 1-61. Prague (in Czech)

McCaffrey MA, Lazar B, Holland HD (1987) The evaporation path of seawater and the coprecipitation of Br and K with halite. J Sedim Petrol 57: 928-937

Oakes CS, Bodnar RJ, Simonson JM (1990) The system NaCl-$CaCl_2$-H_2O: The ice-liquidus at 1 atm total pressure. Geochim et Cosmochim Acta 54: 603-610

Ohmoto H, Rye RO (1979) Isotope of sulfur and carbon. in Barnes HL Ed., Geochemistry of Hydrothermal deposits, John Wiley & Sons, 509-567

Rye DM, Williams N (1981) Studies of the Base Metal Sulfide Deposits at McArthur River, Northern Territory, Australia: III. The Stable Isotope Geochemistry of the H.Y.C., Ridge, and Cooley Deposits. Econ Geol 76: 1-26

Symons DTA, Sangster DF, Leach DL (1995) A Tertiary age from paleomagnetism for Mississipi Valley-type zinc-lead mineralisation in Upper Silesia, Poland. Econ Geol 90: 782-794

Zheng YF (1999) Oxygen isotope fractionation in carbonate and sulfate minerals. Geochem J 33: 109-126

Origin and significance of calcite-marcasite-pyrite mineralisation in siliciclastic Lower Carboniferous rocks, eastern margin of the Bohemian Massif, Czech Republic

Klára Kucerová-Charvátová, Jan Kucera
Institute of Geological Sciences, Faculty of Science, Masaryk University, Brno, Czech Republic

Zdenek Dolnícek
Department of Geology, Palacký University, Olomouc, Czech Republic

Abstract. Field and petrographic observations co-mbined with fluid inclusion measurements, geochemical data, and stable and radiogenic isotope results place important constraints on the genesis of calcite-marcasite-pyrite veinlets located in the Lower Carboniferous siliciclastic rocks of the Nízký Jeseník Upland. These data suggest that the veinlets formed from hydrothermal fluids derived from marine water that migrated, along with petroleum, out of the Carpathian Foredeep in Miocene time.

Keywords. Bohemian Massif, calcite-marcasite mineralisation, stable isotopes, fluid inclusions

1 Introduction

Calcite-marcasite-pyrite veinlets (CMPVs) are located in the Lower Carboniferous siliciclastic rocks of the Nízký Jeseník Upland at the eastern border of the Bohemian Massif, and they were studied in the Jakubcovice and Hrabuvka quarries (Dolnícek and Slobodník 2002; Kucera 2002). A combination of field and petrographic observations, the latter using the transmitted and reflected light microscopy, cathodoluminescence and fluorescence, were used to resolve the paragenetic sequence. Major and trace element compositions, isotope ratios of Sr, C, and O with parameters of fluid inclusions were determined in calcites, and the trace element and sulphur isotope compositions were measured for sulphides, both with the aim to resolve the problem of these veinlets, that are rare and different from other veins and mineralisations in this area. It concerned mainly the problems of the timing and particular conditions of their formation.

2 Paragenetic relationships of calcite-marcasite-pyrite veinlets

The CMPVs of thicknesses between 0.1 and 5 cm, from the lower two levels of the Jakubcovice quarry, are stockworks in greywackes, but they are rare in shales. The veins relevant to this type are usually drusy, banded and brecciated, with no features of any younger deformation. These CMPVs cut all structural fabrics in the rock and strike NNE-SSW and WNW-ESE, i.e. the directions which characterize the majority of the post-Variscan hydrothermal veins in the eastern part of Culmian rock massifs, in the outcropping part of the Western Carpathian foreland.

In the CMPVs, two generations of calcite precipitates can be discerned according to overall appearance and analyses. Calcite I consists of alternating bands of light brown and whitish colours, and Calcite II is clear, filling the last open cavities in veins. The first generation of calcites in veinlets contain small amounts of pyrite and marcasite crystals (determined in reflected light) which are arranged as alternating lamellar to patchy intergrowths in framboides, complex coatings or cauliflower-shaped aggregates, the objects that are commonly smaller than 3 mm.

The veinlets texturally similar to those at the Jakubcovice quarry, also thinner than 5 cm, were found also at Hrabuvka. In this second quarry, the Calcite I occurs in bothryoidal or layered mass, which is rich in fine-grained and intergrown pyrite-marcasite with occurrence of framboidal pyrites.

Rare sphalerite dots are usually coupled with accumulations of iron sulphides. The Calcite II granular to drusy incrusting, with growth in relict cavities, is the youngest mineral in unweathered CMPVs.

3 Chemistry of mineralisation

The chemical compositions of calcites from the Jakubcovice quarry were analyzed using atomic absorption spectrophotometry, in combination with microprobe techniques. The Jakubcovice Calcite I yields contents of 0.12 wt.% MnO, 0.24 wt.% FeO and 1.3 wt.% MgO. Calcite II yields contents of 0.04-0.13 wt.% MnO, ~0.0 wt.% FeO, 0.19-0.74 wt.% MgO and 0.0-0.17 wt.% SO_3. The latter calcites have, thus, considerably fluctuating contents of manganese, and they are apparently depleted in magnesium and iron. The concentrations of rare earth's elements show similarly a trend to decrease, even though the Calcite I of Hrabuvka has considerably low contents of these elements (REE around 0.28 $mg.kg^{-1}$). In this context, the pyrite-marcasite aggregates of Hrabuvka are low in Co and Ni (0.18 $mg.kg^{-1}$ Co, and less than 0.06 $mg.kg^{-1}$ Ni). However, arsenic was elevated (up to 0.8 wt.% As). Sphalerite showed 2.5 wt.% Fe, having the concentrations of Cd below detection limits.

4 Fluid inclusion analyses

The primary fluid inclusions in calcite types I and II, in both quarries, are typically single-phased aqueous liquid types, that are spherically or polygonally shaped, and have typically 2-15m diameters. The milky bands in Jakubcovice Calcite I contain brownish coloured inclusions that are most likely identical with embedded crude oil or its degraded compounds. However, the other, i.e., brownish coloured bands contain decreased number of all fluid inclusions. The single-phase liquid inclusions indicate trapping temperatures of under or about 50°C, and ice melting temperatures between 0 and -5.1°C indicate that the fluids can correspond to salinity between 0 and 8 wt.% eq. NaCl (Bodnar 1993). The eutectic temperatures measured for these inclusions are between -14.1 and -19.2° C, giving the characteristics to the system of H_2O-NaCl(±KCl) (Spencer et al. 1990).

The Hrabuvka Calcite I contains two types of fluid inclusions. The first type of single-phase liquid inclusions is indicative of trapping temperatures under or about 50°C, with eutectic temperatures between -26 and -45°C, and indicative of the H_2O-NaCl(±$MgCl_2$±$CaCl_2$) system. The salinity determined in embedded fluids varies from 0.7 to 6.7 wt.% eq. NaCl, it is, according to Tm, between -0.4 and -4.2°C (compare also Bodnar 1993).

Second type of inclusions in calcites contain dark inclusions filled by the hydrocarbons that floress blue in UV light. Gas-chromatographic analyses of enclosed bitumen documented the prevalence of alkanes $nC_{14} - nC_{19}$, whereas aromatic hydrocarbons were found in very small concentrations. Other characteristic feature of these inclusions is the relatively low content of isoprenoid hydrocarbons ($Pr/nC_{17} = 0.53$, $Ph/nC_{18} = 0.62$) and their well-balanced ratio (Pr/Ph = 1.11). It is typical for complex migration fronts that have deep and long circulation, where the source rocks of hydrocarbons deposited, at least in part, in pelagic conditions.

5 O, C, Sr and S isotope values of vein minerals

The Jakubcovice Calcite I has $\delta^{13}C$ values between -27.6 and -48.9‰ and $\delta^{18}O$ values between -4.2 and -6.5‰ PDB. A sample of Calcite II provided similar but little less anomalous $\delta^{13}C$ and $\delta^{18}O$ values of -32.7‰ and -5.0‰ PDB, respectively. The calculated $\delta^{18}O$ composition of water in equilibrium with calcite at 50° C is between 0.35 and 2.5 ‰ SMOW (O'Neil et al. 1969), and the calculated $\delta^{13}C$ values for HCO_3 at 50°C are between -29.3 and -50.2 ‰ PDB (Deines et al. 1974).

The Hrabuvka calcites I and II are almost undifferentiated, and they provided $\delta^{13}C$ values between -15.3 and -38.1‰, with $\delta^{18}O$ values that typically range from -2.5 to -8.2 ‰ PDB. Similarly, the calculated isotope composition yield values of $\delta^{18}O$ ranging between -1.1 and 2.5‰ SMOW, and $\delta^{13}C$ values between -17.1 and -39.8‰ PDB.

The Hrabuvka Calcite I has, for example, an $^{87}Sr/^{86}Sr$ ratio of 0.7095 that is significantly lower than host greywacke ($^{87}Sr/^{86}Sr = 0.7127$). This significant difference suggests that Sr was not significantly sourced from surrounding greywacke, but corresponds to input of hydrothermal fluid from quite distant sources in compressed Carpathian foredeep.

Marcasite from Jakubcovice have $\delta^{34}S$ values about 18.8 ‰ CDT. Such a high value may be caused by bacterial reduction of Tertiary seawater sulphate (Ohmoto and Goldhaber 1997). However, the Hrabuvka marcasites have distinctly different values that range between -54.3 and -15.8 ‰ CDT. This would not disprove the above mentioned process of bacterial reduction of the marine sulphate, especially if the long movement of migration front (many tens of kilometres or more) or mixing with deep and old local aquifers are considered as possible additional parameters of this Miocene low-temperature hydrothermal system (compare the values by Ohmoto and Goldhaber 1997).

6 Discussion and conclusion

The structural, geochemical, isotopic, and fluid-inclusion characteristics of the calcite-marcasite-pyrite veins (CMPVs) suggest that they were formed from one low-temperature hydrothermal system of very young age. About 50° C hot and saline fluids most likely correspond to marine water that was expelled from the Miocene Carpathian Foredeep and migrated farther into the rock massif of the foreland. Low $\delta^{13}C$ values of calcite with hydrocarbons in fluid inclusions are co-indicative of synchronous petroleum migration. The isotopic values of $\delta^{34}S$ and presence of framboids of Fe-sulphides are tentatively interpreted as a possibility of that the significant source of sulphur was in the bacterial reduction of the seawater sulphate. The late phases in banded calcites of the type I are often characterized by presence of "collomorphic" calcite precipitates, intergrown marcasites-pyrites, traces of sphalerites. The anomalous values on C and S isotopes of CMPVs make possible the further investigation of bacterial influences in the time span from the origin of these fluids to precipitation of minerals in these relatively young veinlets.

Acknowledgements

Grants FRVS 2572/2005 and GACR 205/00/0356. Authors gratefully acknowledge the constructive criticism of several anonymous reviewers.

This page intentionally blank

References

Bodnar RJ (1993) Revised equation and table for determining the freezing point depression of H_2O-NaCl solutions. Geochim Cosmochim Acta 57: 683-684

Deines P, Langmuir D, Harmon RS (1974) Stable Carbon isotope ratios and the existence of a gas phase in the evolution of carbonate ground waters. Geochim Cosmochim Acta 38: 1147-1164

Dolníček Z, Slobodník M (2002) Calcite-marcasite mineralisation with hydrocarbon inclusions in Culmian greywackes from Hrabuvka, Nízký Jeseník Upland. Proceedings of abstracts, Herlany (in Czech)

Kučera J (2002) Hydrothermal mineralization on the eastern part of the Culm of the Nízký Jeseník Upland. MS diploma thesis PřF MU. Brno (in Czech)

Kumpera O (1983) Geology of the Lower Carboniferous horst of the Nízký Jeseník Upland. Knih. Ústř. Úst. geol., 172 p. Prague (in Czech)

Ohmoto H, Goldhaber M (1997) Sulfur and carbon isotopes. In: Barnes HL (ed) Geochemistry of Hydrothermal Ore Deposits 3rd Ed., Wiley, New York: 517-611

O'Neil JR, Clayton RN, Mayeda TK (1969) Oxygen isotope fractionation in divalent metal carbonates. J Chem Phys 51: 5547-5558

Spencer RJ, Möller N, Weare JH (1990) The prediction of mineral solubilities in natural waters: A chemical equilibrium model for the Na-K-Ca-Mg-Cl-SO_4-H_2O systems at the temperatures below 25°C. Geochim Cosmochim Acta 54: 575-590

The distribution of SEDEX Pb-Zn deposits through Earth history

D. Leach, E. Marsh
U.S. Geological Survey, MS973, Box 25046, Denver, CO 80225, USA

D. Bradley
U.S. Geological Survey, 4200 University Drive, Anchorage, AK 99508, USA

S. Gardoll
University of Western Australia, Centre for Global Metallogeny, SEGS, Crawley, WA 6009 Australia

D. Huston
Geoscience Australia , GPO Box 378, Canberra 2601, Australia

Abstract. The emergence of SEDEX ores in the rock record at about 1.8 to 2.2 Ga can be related to the hydrosphere and atmosphere progressively becoming oxidized and therefore sulfide-poor and sulfate-rich, evolution of sulfate-reducing bacteria, and fundamental changes in the Earth crust. The reason for the apparent change in tectonic setting of SEDEX deposits from intracratonic rifts in the Proterozoic to passive margins is unclear. Phanerozoic SEDEX deposits formed in paleolatitudes that mirror modern evaporative belts, suggestive of a brine reflux origin for passive margin SEDEX deposits.

Keywords. Sediment hosted lead-zinc deposits, SEDEX

1 Introduction

The reasons for the uneven distributions of certain classes or ore deposits in the geological record are generally attributed to secular variations in geological processes that controlled the formation and destruction of these deposits (e.g. Meyer 1981; Sangster 1990; Hutchinson 1992; Barley and Groves 1992; Titley 1993). We examine the secular distribution of SEDEX lead-zinc deposits (Fig. 1) that is based on the metal resource data (Leach et al. 2005) for 148 SEDEX (sedimentary exhalative deposits) lead-zinc deposits. Despite the inherent "exhalative component" in the term "SEDEX", direct evidence of an exhalite component in the ore or alteration assemblage is not recognized for many SEDEX deposits. The age of mineralization is commonly considered to be synsedimentary, however, some deposits formed in a subseafloor diagenetic environment (i.e. Red Dog, Alaska) and some formed during burial diagenesis (i.e. Century, Australia). Nevertheless, the age of formation is assumed to be the same or very close to the age of the host rocks.

SEDEX ores are mainly restricted to two groups: one in the Proterozoic and another in the Phanerozoic (e.g. Goodfellow 1994 and references therein, Large et al. 2005 and references therein, Leach et al. 2005 and references therein). The Proterozoic group (at about 1.4 to 1.8 Ga) includes the large deposits in the Mt. Isa-McArthur basin of Australia (Large et al. 2005) the Sullivan deposit in Canada and the deposits in the highly metamorphosed rocks of the Aravalli-Delhi belt of northwestern India. The Phanerozoic ores includes the large Red Dog, Alaska deposits and the deposits in the Selwyn basin, Canada. The older age group corresponds to SEDEX deposits in failed continental rifts (rift-sag basins), whereas deposits of the younger age group formed along passive continental margins (e.g. Large et al. 2005 and references therein, Huston et al. in prep.).

We discuss the possible reasons for the emergence of SEDEX deposits and examine the tectonic factors that may have influenced their distribution in the rock record. Recent fluid inclusion studies of the Red Dog deposit together with analysis of the distribution of SEDEX deposits using GIS and plate reconstructions provide insights into why some Phanerozoic basins are fertile for SEDEX and others barren.

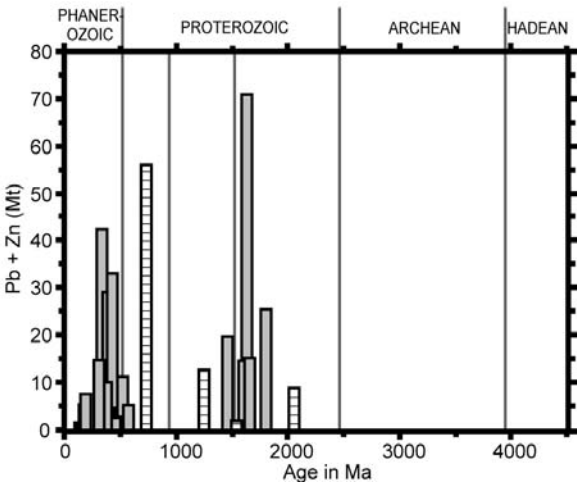

Figure 1: Distribution the combined lead and zinc in SEDEX deposits vs. their presumed age. Data from Leach et al. 2005. The bars represent the mid-points of the ages of the deposits. Bars with horizontal lines include deposits with extreme uncertainty (~ ± 300 my) for the ages of the ores.

2 Emergence of SEDEX deposits evolution of the hydrosphere and atmosphere

SEDEX lead-zinc deposits form mainly from oxidized (reduced-sulfur poor) fluids; therefore, their appearance is likely a consequence of the evolution of the Earth, particularly changes in the composition of the hydrosphere and atmosphere. SEDEX deposits and their closely affiliated ores, MVT deposits, are not known to have formed prior to about 2.2 Ga (Leach et al 2005 and references therein). The oldest significant SEDEX deposits (~1.8 Ga) are those of Aravalli-Delhi belt of India (e.g. Goodfellow 1994 and references therein, Leach et al 2005 and references therein). The early Proterozoic (2.5-1.8 Ga) is a major period of change in Earth's history. Prior to 2.4 Ga, the atmosphere and (for the most part) the hydrosphere, were reduced. Between 2.4 Ga and 1.8 Ga, the atmosphere became oxygenated, with the hydrosphere also progressively becoming oxidized, sulfide-poor and sulfate-rich. Importantly, chemical changes in the hydrosphere probably did not occur uniformly, but instead were more rapid in restricted basins (Fig. 2) than the open ocean (Rye and Holland 1998; Farquhar et al. 2001; Huston and Logan 2004 and references therein). Prior to 2.2 Ga, the reduced oceanic chemistry prevented formation of SEDEX deposits. With the minor exception of a sulfate-rich upper oceanic layer prior to 3.2 Ga, the oceans were generally reduced and virtually sulfate-free during the Archean and earliest Proterozoic (Huston and Logan 2004). Changes in oceanic geochemistry probably led to the flowering of SEDEX deposits, beginning at ~1.8 Ga in India, with continuing between 1655 and 1575 Ma in Australia. Huston and Logan (2004) suggested that the oxygenation of the hydrosphere proceeded unevenly, beginning with small basins and culminating at ~1.8 Ga with final oxygenation of deep oceanic basins. The earliest, small SEDEX deposits may have formed in small basins, with the general oxygenation of the seawater allowing the formation of large deposits beginning at 1.8 Ga. A second aspect that may be important is the evolution of sulfate-reducing bacteria by this period. These bacteria may have been critical in the production of H_2S at the site of deposition, allowing deposition of ore metals.

The specific tectonic factors controlling the emergence of SEDEX deposits are elusive, because the two settings in which they are known—rifts and passive margins—appear to have existed back as far as 3 Ga (e.g. Kusky and Hudleston 1999; Tinker et al. 2002). Nonetheless, there are some potentially important tectonic changes that occurred about 1.8 Ga. The emergence of SEDEX deposits came at a time when global radiogenic heat production was about 1.5 times as great as today (Pollack 1997) and plates, accordingly, may have been smaller. Furthermore, by 1800 Ma, it was likely that the first cycle of supercontinent breakup and reassembly was nearing completion (Meert and Mukherjee 2004) and over 80% of the preserved continental crust had formed (Collerson and Kamber 2000).

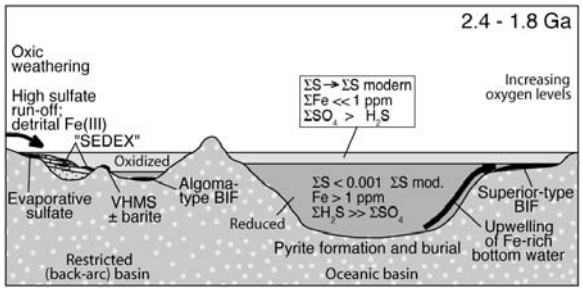

Figure 2: Model for evolution of the hydrosphere between 2400 and 1800 Ma. During this period the hydrosphere became progressively oxygenated, with this process occurring initially in small basins prior to spreading to oceanic basins. In this model, SEDEX deposits would have formed initially in small basins.

3 Passive continental margins and the Mesoproterozoic to Neoproterozoic "gap"

A preliminary survey of passive margins through time (Bradley and Rowley 2004) revealed two main intervals when the earth had passive margins: ~2650 to ~1750 Ma, and ~1050 Ma to present (Fig. 3). Curiously, passive margins of the older age group appear to be barren of SEDEX deposits, whereas those of the younger group host important deposits. Rift basins are common through Earth

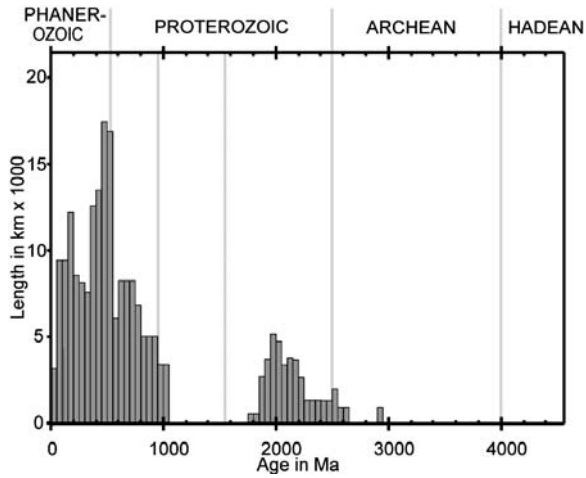

Figure 3: Histogram showing lengths of ancient passive margins plotted against geologic age. Not shown are extant passive margins, which formed between 180 Ma and the present and which today total 180,000 km in length. The deep-water facies belts of these modern margins (where SEDEX deposits might be found) have not yet been uplifted during collision. Also not represented are a few margins in the late Archean (e.g. North China craton) and Mesoproterozoic (e.g. Urals) that are poorly dated.

history (Sengor and Natalin 2001) and yet only during a comparatively short interval in the late Paleoproterozoic did they host significant SEDEX deposits.

The apparent change in tectonic setting of SEDEX deposits remains a mystery, as does the meaning of the Mesoproterozoic to Neoproterozoic "gap" in the number of SEDEX deposits (Fig. 1). Although the Mesoproterozoic to Neoproterozoic does contain significant SEDEX ores (e.g. 542-900 Ma includes Gorevsk deposit in Russia and 900 and 1600 Ma includes Balmat deposit in the USA), this is a relatively quiet time for SEDEX formation and other types of ores (e.g. MVT, VMS, SEDEX barite). This gap could be partly due to deposit preservation and destruction. SEDEX ores that form in passive continental margins may have a higher potential for destruction relative to ores in intracontinental rifts due to the eventual plate convergence and uplift of orogenic fold belts along continental boundaries. However, if this were the main explanation for the Mesoproterozoic to Neoproterozoic gap, we would expect to see a better correlation between SEDEX deposits and passive margins in the rock record.

4 The fertility of Phanerozoic passive continental margins

A "reflux brine" model (Fig. 4) was suggested for the genesis of the giant Red Dog deposit (Leach et al. 2004). In this model, brines are produced in a seawater evaporative environment within shelf carbonates sequences. These brines infiltrate into the underlying basement rocks, extract heat and metals, and discharge into the reduced sediments in a passive margin basin. An important feature of this model is that generation of the brine occurs in high evaporation climatic regions. The principal arid zones for modern Earth are located about 30° N and S of the equator (Warren 1989).

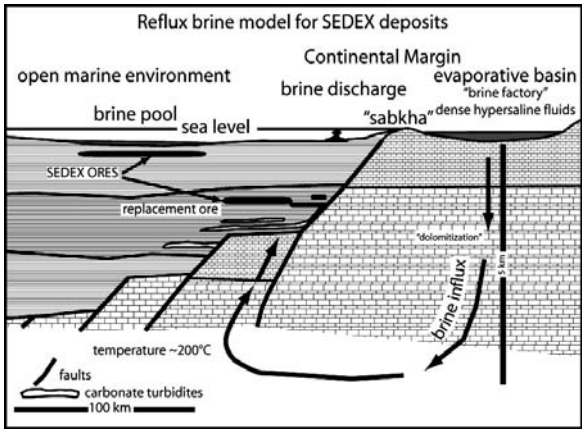

Figure 4: Reflux brine model for the formation of SEDEX ores in continental passive margin basin.

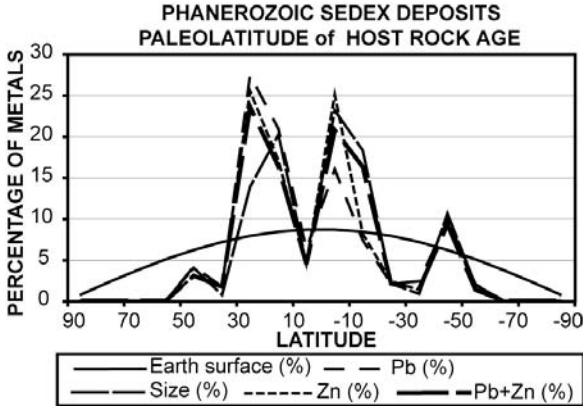

Figure 5: Total metal content of SEDEX deposits (expressed as a percentage of the total of all Phanerozoic deposits) summarized by paleo-latitude at time of deposit formation. Area% defines the surface area of the Earth and the theoretical random distribution of SEDEX deposits.

To test if the brine reflux model can be applied to other Phanerozoic SEDEX deposits, the distribution of the paleolatitudes of the deposits at the time of mineralization can be determined. This is accomplished by an analysis of the distribution of SEDEX deposits in a GIS (Geographical Information System) plate-tectonics database. The approach uses GIS to query results from plate-tectonic reconstructions (Scotese 1999) and quantify both spatial and temporal patterns. Figure 5 summaries the percentage of metal content of all Phanerozoic SEDEX deposits vs. paloelatitudes for ore deposition. The Earth surface area, defined as percentage of the total surface area of the Earth defines the expected distribution of SEDEX deposits (assuming distribution is random).

Considering the uncertainties in plate reconstructions, age of ore deposition and the paleolatitudes of global arid belts, the metal distributions remarkably mirror present day latitudes of high evaporative zones. This observation may provide one aspect of why some passive margins are fertile whereas others are barren of SEDEX. Passive margins basins that do not evolve in high evaporative areas of the Earth have significantly less potential to have been exposed to ore-forming brines.

References

Barley ME, Groves DI (1992) Supercontinent cycles and the distribution of metal deposits through time. Geol 20: 291-294

Bradley, DC, Rowley, DB (2004) Lifespans of passive margins and Atlantic-type ocean crust since 2500 Ma: Penrose Conference on Secular Variation in Tectonics and Allied Fields, Geol Soc of Am, St. George, Utah, Oct. 22-28, 2004 (abst) 7-8

Collerson KD, Kamber BS (2000) Evolution of the continents and the atmosphere inferred from Th-U-Nb systematics of the depleted mantle. Science 283: 1519-1522

Farquhar J, Bao H-M, Thiemens M (2000) Atmospheric influence of the Earth's earliest sulfur cycle. Science 289: 756-758

Goodfellow W (2004) Geology, genesis and exploration of SEDEX deposits, with emphasis on the Selwyn Basin, Canada. In: Deb M, Goodfellow WD (eds) Sediment hosted Lead-Zinc sulphide deposits; Attributes and models of some major deposits in India, Australia and Canada. Narosa Publishing House: 24-99

Huston DL, Logan GA (2004) Barite, BIFs and bugs: Evidence for the evolution of the Earth's early hydrosphere. Earth and Planetary Science Letters 220: 41-55

Huston DL, Stevens B, Southgate P, Muhling P, Wyborn L (in review) Australian Zn-Pb-Ag mineral systems: a review and analysis

Hutchinson RW (1992) Mineral deposits and metallogeny: Indicators of Earth's evolution. In: Schidlowski, M, (ed) Early organic evolution: implications for mineral and energy resources. Springer-Verlag Berlin Heidenberg: 521-544

Kusky TM, Hudleston PJ (1999) Growth and demise of an Archean carbonate platform, Steep Rock Lake, Ontario, Canada. Can Jour of Earth Sci. 36: 565-584

Large RR, Bull SW, McGoldrick PJ, Derrick G, Carr G Walters S (2005) Stratiform and stratabound Zn-Pb-Ag deposits of the Proterozoic sedimentary basins of northern Australia. In: Henquist J, Thompson J, Richards JG (eds) SEG 100th Anniversary Special Publication (in press)

Leach DL, Marsh E, Emsbo P, Rombach C, Kelley K, Anthony M (2004) Nature of the hydrothermal fluids at the shale-hosted Red Dog zinc-lead-silver deposits, Brooks Range, Alaska. Econ Geol 99: 1449-1480

Leach DL, Sangster DF, Kelley KD, Large RR, Garven G, Allen CR, Gutzmer J, Walters S (2005) Sediment-hosted lead-zinc deposits: a global perspective. In: Henquist J, Thompson J, Richards JG (eds) SEG 100th Anniversary Special Publication (in press)

Meert JG, Mukherjee D (2004) Supercontinents through time: status of the issues: Penrose Conference on Secular Variation in Tectonics and Allied Fields. Geol Soc of Amer, St. George, Utah, Oct. 22-28, 2004. 36-37

Pollack HN (1997) Thermal characteristics of the Archean. In: M.J. De Wit and L.D. Ashwal, editors: Greenstone Belts, Clarendon Press, Oxford: 223-232

Rye R, Holland HD (1998) Paleosols and the evolution of atmospheric oxygen; a critical review. Amer Jour Sci. 298: 621-672

Sangster D (1990) Mississippi Valley-type and sedex lead-zinc deposits; a comparative examination: Transactions, Inst Mining Metal Section B, 99: B21-B42

Sengor AMC, Natal'in BA (2001) Rifts of the world: Geol Soc America Special Paper 352, 389-482

Scotese CR (1999) The Global Plate Tectonic Model, unpubl. report

Tinker J, de Wit M, Grotzinger J (2002) Seismic stratigraphic constraints on Neoarchean-Paleoproterozoic evolution of the western margin of the Kaapvaal Craton, South Africa. So African Jour Geol. 105: 107-134

Titley SR (1993) Relationship of stratabound ores with tectonic cycles of the Phanerozoic and Proterozoic: Precam Res. 61: 295-322

Warren JK (1989) Evaporite sedimentology: Importance in hydrocarbon accumulation. Englewood Clifs, Prentice Hall. 285

Epigenetic hydrothermal features of the Emeishan basalt copper mineralization in NE Yunnan, SW China

Houmin Li, Jingwen Mao, Yuchuan Chen, Denghong Wang
Institute of Mineral Resources, Chinese Academy of Geological Sciences, 26 Baiwanzhuang Rd., Beijing 100037, China

Changqing Zhang, Hong Xu
Faculty of Geosciences and Resources, China University of Geosciences (Beijing), 29 Xueyuan Rd., Beijing 100083, China

Abstract. Native copper in basalt copper deposits in NE Yunnan, SW China, formed in fissures of basalt or in carbonaceous sedimentary interbeds of basalt together with organic matter such as bitumen. The mineral fills in fissures of bitumen and replaces plant fragments. Bitumen is of organic origin, with its $\delta^{13}C_{V\text{-}PDB}$ values ranging from –27.3 to –33.1‰. The ^{40}Ar-^{39}Ar ages of the gangue minerals zeolite and actinolite in copper ores are 226 to 238.6 Ma and 134 to 149.1 Ma respectively, indicating the occurrence of two copper mineralization stages. All these suggest that the copper mineralization is of epigenetic hydrothermal origin.

Keywords. Basalt copper deposit, epigenetic hydrothermal mineralization, organic matter, Emeishan basalt, NE Yunnan, SW China

1 Introduction

The Emeishan basalt is widely distributed in SW China. There are many traces of copper mineralization, copper mineralization occurrences and small-scale copper deposits in the basalt. Mining of this type of copper deposit goes back to ancient times and numerous old adits are left. Mining is still conducted by local people now. From 1958 to 2002 some geological and mineral departments have performed prospecting and evaluation for this type of copper in several periods and it was considered that copper mineralization was of volcanic-hydrothermal origin during the late stage of basaltic eruption and had no economic value because of disperse mineralization. No fruitful results were obtained during the mineral prospecting.

In 2002 Zhu et al. (2002a, b, 2003) reported that a copper deposit closely related to bitumen has been found in basalt on the Yunnan-Guizhou border region. This finding again attracted geologists' attention to the Emeishan basalt copper deposits. Study, prospecting and exploration of this type of basalt copper deposit have been carried out once again since then.

In this paper, we will introduce the epigenetic hydrothermal features of this type of basalt copper deposit in NE Yunnan.

2 Geological setting of the basalt copper deposits

The Emeishan basalt is widely distributed in the border region of Yunnan, Guizhou and Sichuan provinces, SW China, covering an area of more than 300,000 km^2. It formed in a rift environment on the western margin of the Yangtze craton in the early Late Permian. The rock belongs to continental flood basalt and may be related to the Emei mantle plume (Chung and Jahn 1995).

The Emeishan basalt stratigraphically belongs to the Upper Permian Basalt Formation and disconformably overlies carbonate rocks of the Lower Permian Qixia and Maokou formations. The Basalt Formation is divided in ascending order into four members: the First Member, mainly volcanic breccia; the Second Member, mainly porphyritic massive basalt; the Third Member, also mainly porphyritic massive basalt; and the Fourth Member, mostly massive basalt with some amygdaloidal basalt and local tuff and carbonaceous sedimentary interbeds (Yunnan Bureau of Geology and Mineral Resources 1989).

The Basalt Formation is disconformably overlain by coal measures of the Upper Permian Xuanwei Formation, which are in turn conformably overlain by Triassic and Jurassic red clastic rocks. Locally Cretaceous sandy conglomerate unconformably overlies old strata of different ages.

Regional faults are well developed in the basalt and mostly strike NE and ENE. The axis of folds is also mainly oriented in a NE direction. These faults and folds occurred in the Late Jurassic.

No significant magmatic activity occurred after eruption of the Emeishan basalt in the area.

3 General characteristics of the basalt copper deposits in NE Yunnan

The basalt copper mineralization in NE Yunnan is stratabound (Fig. 1). The lower part of the Fourth Member of the Basalt Formation is the main mineralization horizon, 50 to 100 m thick and composed of 3 to 5 basalt flows. Each flow consists of massive basalt in the lower part and amygdaloidal basaltic breccia or amygdaloidal basalt in the lower part, often intercalated with carbonaceous conglomeratic mudstone and tuff between the flows.

The carbonaceous conglomeratic mudstone commonly contains plant fragments. There are generally 1 to 3 layers of copper mineralization and sometimes as many as 5 layers. The copper orebodies and mineralization bodies, tens of centimetres to 2 m thick, mainly occur in schistose amygdaloidal basalt, amygdaloidal basaltic breccias

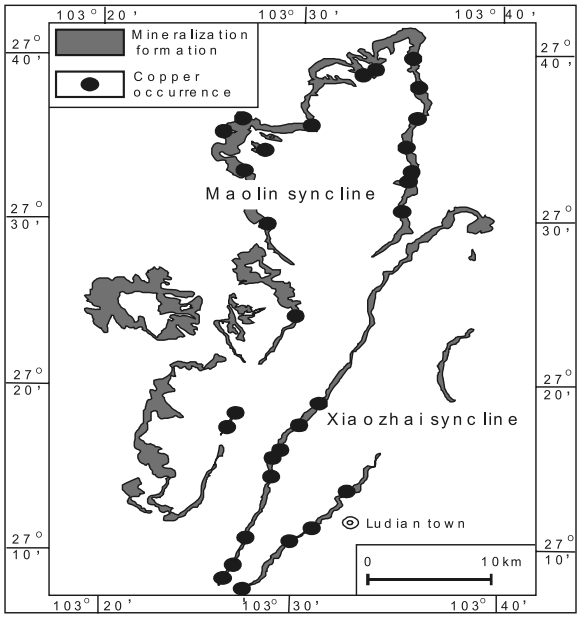

Figure 1: Distributions of the Emeishan flood basalt and basalt copper occurrences in NE Yunnan, SW China.

and carbonaceous sedimentary rocks along the contact zone of different basalt flows. The footwall and hanging wall of the orebodies are generally massive basalt. The dominant metallic minerals in the basalt are native copper and those in carbonaceous sedimentary interbeds are native copper and minor chalcocite. The dominant gangue minerals include bitumen, carbon, laumontite and quartz with subordinate calcite, pumpellyite, epidote, chlorite and prehnite (Li et al. 2004a; Zhu et al. 2002a, 2003).

4 Evidence of epigenetic hydrothermal mineralization of the basalt copper deposits in NE Yunnan

4.1 Geological evidence

Bitumen fills along fissures of basalt (Fig. 2), while native copper fills along fissures in bitumen (Fig. 3). Native copper and chalcocite have replaced the plant fragments in the conglomeratic carbonaceous mudstone (Fig. 4) and some quartz chalcocite veins penetrate the carbonaceous mudstone and gravels therein. All these features suggest that palaeo-petroleum, the precursor of the bitumen, was trapped in the fissures of the basalt after cooling of the basalt, and that native copper mineralization occurred later than the transformation of petroleum into bitumen (Li et al. 2004a).

4.2 Geochemical evidence

Figure 4: Chalcocite (bright) replaces plant fragments and the texture of the plant is preserved. Polished section; plane polarized light; 1.2 × 0.8 mm. Sample taken from the Naoyingyan

Figure 2: Bitumen (black) fills the fissures of basalt (grey). Field photo of the Sujiaqing copper deposit in NE Yunnan.

Figure 3: Native copper (white) fills the fissure of bitumen (grey). Polished section; plane polarized light; 0.6×0.4 mm. Sample taken from the Dadi copper deposit, NE Yunnan.

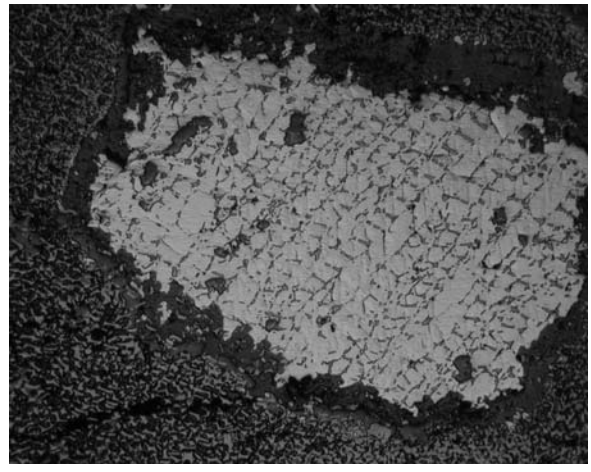

Figure 4: Chalcocite (bright) replaces plant fragments and the texture of the plant is preserved. Polished section; plane polarized light; 1.2×0.8 mm. Sample taken from the Naoyingyan copper deposit, NE Yunnan.

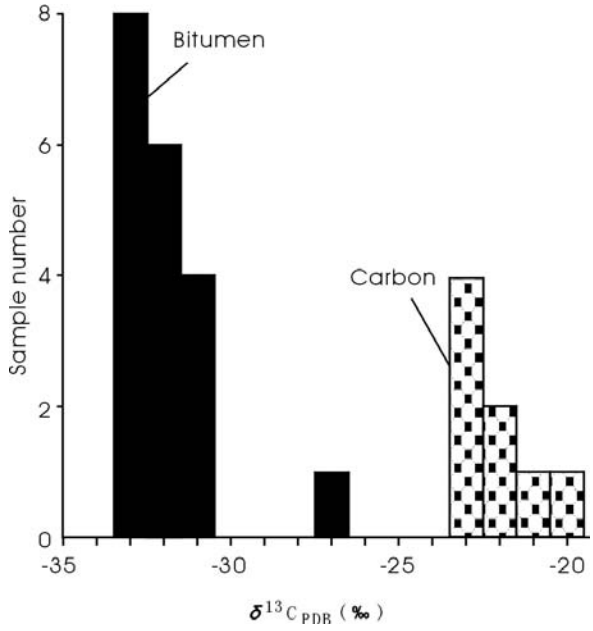

Figure 5: Carbon isotopic compositions of bitumen and carbon in basalt copper ores, NE Yunnan, SW China.

copper deposit, NE Yunnan. The $\delta^{13}C_{V\text{-}PDB}$ values of the bitumen in copper ore hosted in basalt range from –27.3‰ to –33.1‰, showing the organic carbon isotope feature and suggesting that the bitumen, unlike basaltic magma derived from the mantle, is of organic origin rather than inorganic origin. However, there is no relation between bitumen and its nearby carbon material in the carbonaceous mudstones, for the $\delta^{13}C_{V\text{-}PDB}$ values of the carbon material in copper ore hosted in carbonaceous sedimentary rocks range from –20.2 to –23.2‰, which is obviously different from those of the bitumen (Fig. 5). All these suggest that the palaeo-petroleum – the precursor of the bitumen – is allochthonous and epigenetic and that copper mineralization that occurred later than it is naturally also epigenetic (Li et al. 2004b; Mao et al. 2003).

4.3 Isotope chronological evidence

The ^{40}Ar-^{39}Ar ages of laumontite, actinolite and heulandite in the basalt copper ores in NE Yunnan range from 226 to 228 Ma, from 235.7 to 238.6 Ma and from 134 to 149.1 Ma respectively (Zhu et al., 2004). The U-Th-Pb isochron age of the bitumen copper ore is 136 Ma (Zhu et al. 2004). These ages are 30 to 120 Ma younger than the ages of the Emeishan basalt (260 Ma or so), suggesting that the basalt copper mineralization in the area is epigenetic. No age is presently available for the copper mineralization.

5 Discussion and conclusions

The Emeishan basalt, containing up to 200 ppm Cu and covering an area of >300,000 km^2, can provide adequate source materials for the epigenetic hydrothermal copper mineralization. The distinct epigenetic hydrothermal and stratabound features and extensive distribution of the basalt copper mineralization in NE Yunnan imply that large-scale epigenetic hydrothermal activities and copper mineralization occurred in the basalt area. This type of basalt copper mineralization is similar to the Keweenaw basalt copper deposit (Hamilton 1967; Bornhorst et al. 1988; Davis and Paces 1990; Hoa and Mauk 1990, 1996; Mauk et al. 1992; Buruss and Mauk 1996): both occur in continental flood basalt in the continental rift environment of a craton and might be related to the mantle plume; the dominant Cu mineral is native copper; the ore bodies are hosted in the amygdaloidal basaltic breccias and amygdaloidal basalt and their sedimentary interbeds in the upper part of the basalt flows. The dominant gangue minerals are characterized by a low-temperature assemblage of laumontite, epidote, and quartz. The hydrothermal mineralization is epigenetic; and the ages of mineralization are 20 to 30 Ma younger than those of basaltic eruption (Zhu et al. 2003; Li et al. 2004a). Therefore, compared to the Keweenaw native copper deposits, the native copper mineralization in the Emeishan basalt has a great ore potential for prospecting.

Acknowledgements

We are grateful to our colleagues of the Yunnan Bureau of Geology and Mineral Exploration and Development and Guizhou Bureau of Geology and Mineral Exploration and Development for their assistance in the field work and the laboratory of the Institute of Mineral Resources, Chinese Academy of Geological Sciences for the assistance in the indoor work. This study was financially supported by the Major State Basic Research Program of People's Republic of China (No. G1999043211) and China Geological Survey Project (No. 200310200002).

References

Bornhorst TJ, Paces JB, Grant NK, Obradovich JD and Huber NK (1988) Age of native copper mineralization, Keweenaw peninsula, Michigan: Economic Geology 83: 619-625

Buruss RC, Mauk JL (1992) Proterozoic oil in fluid inclusions in the Midcontinent rift: Implications for the origin of oil at White Pine, Michigan: Geol Soc. Am abstr. Prog. 24: A213

Chung SL, Jahn BM (1995) Plume-lithosphere interaction in generation of the Emeishan flood basalts at the Permian-Triassic boundary: Geology 23: 889-892

Davis DW, Paces JB (1990) Time resolution of geologic events on the Keweenaw Peninsula and implications for development of the Midcontinent Rift system: Earth and Planetary Science Letters 97: 54-64

Hamilton SK (1967) Copper mineralization in the upper part of the Copper Harbor conglomerate at White Pine, Michigan: Economic Geology 62: 885-904

Hoa ES, Mauk JL (1996) Relationship between organic matter and copper mineralization in the Proterozoic Nonesuch Formation, northern Michigan: Ore Geology Reviews 11: 71-87

Hoa ES, Meyers PA, Mauk JL (1990) Organic geochemical study of mineralization in the Keweenaw Nonesuch Formation at White Pine, Michigan: Org. Geochem. 16: 229-234

Li HM, Mao JW, Xu ZB, Chen YC, Zhang CQ, Xu H (2004a) Characteristics of copper mineralization distributed in huge Emeishan basalt district of northeast Yunnan province and west Guizhou province: Acta Geoscientia Sinica 25(5): 495-502 (in Chinese with English abstract)

Li HM, Mao JW, Zhang CQ, Xu H, Chen YC, Wang DH (2004b) Isotopic geochemistry of Emeishan basalt copper deposits in northeast Yunnan and west Guizhou: Mineral Deposits 23(2): 232-240 (in Chinese with English abstract)

Mao JW, Wang ZL, Li HM, Wang CY, Chen YC (2003) Carbon and oxygen isotope components in the Permian basalt-hosted copper deposit in Ludian area, Yunnan: Implication for the mineralization process: Geological Review 49 (6): 610-615 (in Chinese with English abstract)

Mauk JL, Kelly WC, Van Der Pluijm BA, Seasor RW (1992) Relations between deformation and sediment hosted copper mineralization: Evidence from the White Pine portion of the mid-continent rift system: Geology 20: 427-430

Yunnan Bureau of Geology and Mineral Resource. (1989) Encyclopedia of the Geology of Yunnan Province. Beijing: Geol. Pub. House (in Chinese)

Zhu BQ, Chang XY, Hu YG, Zhang ZW (2002a) Discovery of Yanhe copper deposit in the Yunnan-Guizhou border area and a new train of thought for copper prospecting in the large igneous province of Emeishan flood basalts: Advance in Earth Sciences 17(6): 912-917 (in Chinese with English abstract)

Zhu BQ, Dai TM, Hu YG, Zhang ZW, Chen GH, Peng XY (2004) The isotopic dating evidences of two periods of hydrothermal mineralization in the large igneous province of Emeishan basalts in northeast Yunnan, China: Bulletin of mineralogy, Petrology and Geochemistry 23 (Supp.): 108 (in Chinese)

Zhu BQ, Hu YG, Zhang ZW, Chang XY (2003) Discovery of the copper deposits with features of the Keweenaw type in the border area of Yunnan and Guizhou provinces: Science in China ser. D 46 (Supp.): 60-72

Zhu BQ, Zhang ZW, Hu YG (2002b) Discovery of economic strata-bounded volcanic tuff breccia-type copper deposits in northeast Yunnan province: Geological Bulletin of China 21 (8-9): 21 (in Chinese)

Geologic characteristics and ore-controls of the Fenghuoshan copper ore deposit, Qinghai province, China

Li Wenming[1,2], Song Zhongbao[2], Liou Zhiyong[3], Li Changan[2], Li Zhucang[1], Li Hongpu[3]
[1]*Chang'an University, Xian 710054,Shaanxi, China*
[2]*Xi'an Institute of Geology and Mineral Resources, Xi'an 710054,Shaanxi, China*
[3]*Qinghai Institute of Geological Survey, Xining 810012, Qinghai, China*

Abstract. The Fenghuoshan copper ore deposit is hosted by the lower to middle part of a continental red rock series of the Upper Cretaceous Fenghuoshan Group in the Hoh Xil Basin in the northern Qinghai-Tibet Plateau. Host rocks consist mainly of dust coloured celadon medium to fine grained lithic quartzose sandstone. Copper-stained layers have lower clay contents and high contents of siliceous or calcareous cement, which formed as a hypabyssal lake deposit or delta-front deposit. The ore deposit is composed of 42 copper ore bodies and five silver ore bodies. Ore bodies are shaped as beds or lenses and wallrock alteration isn't obvious. The ore minerals are composed of chalcocite, digenite and a few of bornite, chalcopyrite, pyrite, galena, sphalerite and argentite. The $\delta^{34}S$ of ore minerals range from –16.77 to 10.92‰ relative to CDT. Sulfur in the ore was probably derived from a mixture of sedimentogenic sulfate and biogenic H_2S in different proportions, but the sulfur of ore remains close to biogenic sulfur in composition. The main controls of the ore deposit include the comparatively steady continental sedimentary basin, the land source denudation area with high copper content and iron-copper ores, periodic changes of climate and sedimentary environment, the reducing conditions resulting from abundant carbon in moderate-sized sandstone bodies. The genetic type of the Fenghuoshan copper ore deposit belongs to the sandstone type copper deposit in Mesozoic fault basin on the stable block.

Keywords. Cupreous sandstone deposit, geologic characteristics, Fenghuoshan, Hoh Xil, Qinghai Province

1 Introduction

The Fenghuoshan copper ore deposit is one and only sandstone type copper deposit so far in Qinghai Province in China, it is located in the middle of Fenghuoshan Basin in the northern Qinghai-Tibet Plateau and the Qinghai-Tebit Highway and the Qinghai-Tebit Railway is being constructed run through the middle part of the ore district. The Fenghuoshan copper ore deposit was discovered when the anomalies of geochemical exploration was checked in 1990, its copper reserves has increased by means of survey, appraising and drilling works in recent years.

2 Geological setting

The Fenghuoshan copper ore deposit is located in the Upper Cretaceous Fenghuoshan continental fault basin on the Jinshajiang stylolitic belt. The basement of basin, with a total thickness up to 23km, is composed of Triassic system, Permian-Triassic Hantaishan Group and Carboniferous-Permian Xijir Ulan Group, the contact relations among which are all angular unconformity (Zhang and Zheng 1994; Qinghai Bureau of Geology 1991). The Cretaceous cover rock of basin is Fenghuoshan Group with a thickness up to 5747m, which is composed of rufous sandstone, mudstone, conglomerate and a few of celadon cupreous sandstone, grey-black bioclastic limestone and grey thin layer gypsum. The emergence of strata in the Fenghuoshan copper ore district consist mainly of the sandstones with limestone interbeds (K_2fn^a) and the sandstones (K_2fn^b) of the lower to middle part of the Fenghuoshan Group (Fig.1). The former contacted directly with the ancient continent is the primary ore-bearing rock series, which consists of interbedded reddish medium to fine grained lithic quartzose sandstone, siltstone, silty mudstone and a few of celadon medium to fine grained lithic quartzose sandstone. The calculated contraction of the Fenghuoshan Group in S-N direction in the Erdaogou is about 40% (Coward et al. 1990).

The deep fault related to the Jinshajiang stylolitic belt and its sub-faults and the Fenghuoshan Syncline along 290° direction are main structures in the ore district.

The Fenghuoshan Syncline consists of sands-tones with limestone interbeds and the cupreous sandstone emerges in its limbs.

The Zangmaxikong monzonite-porphyry stock (0.7km^2) intruded the sandstones with interbedded limestone in the northern ore district. The monzonite-porphyry with porphyritic texture consists mainly of feldspar (70%), aegirine-augite (15%-10%), biotite (5%-10%) and quartz, its chemical compositions shows the following features: Rittmann idexes (sigma) = 5.52~5.76, $Al_2O_3/(CaO+Na_2O+K_2O)$ = 0.6477/0.7055 (molecular ratios), total REE content =329.1, being relatively rich in LREE (LR/HR= 28.38), obvious Eu negative anomaly (δEu=0.479), so the monzonite–porphyry belongs to the sub-aluminous alkaline rock with high K content, and it has undergone a crystallization differentiation in certain degree. K-Ar ages of the monzonite–porphyry in the Zangmaxikong stock are 33Ma~38Ma (Zhang et al. 1994), which is a intrusive body in the Eogene Period. The three fault zones whose attitude are 160°∠60°~70° have obvious mineralization of galena,

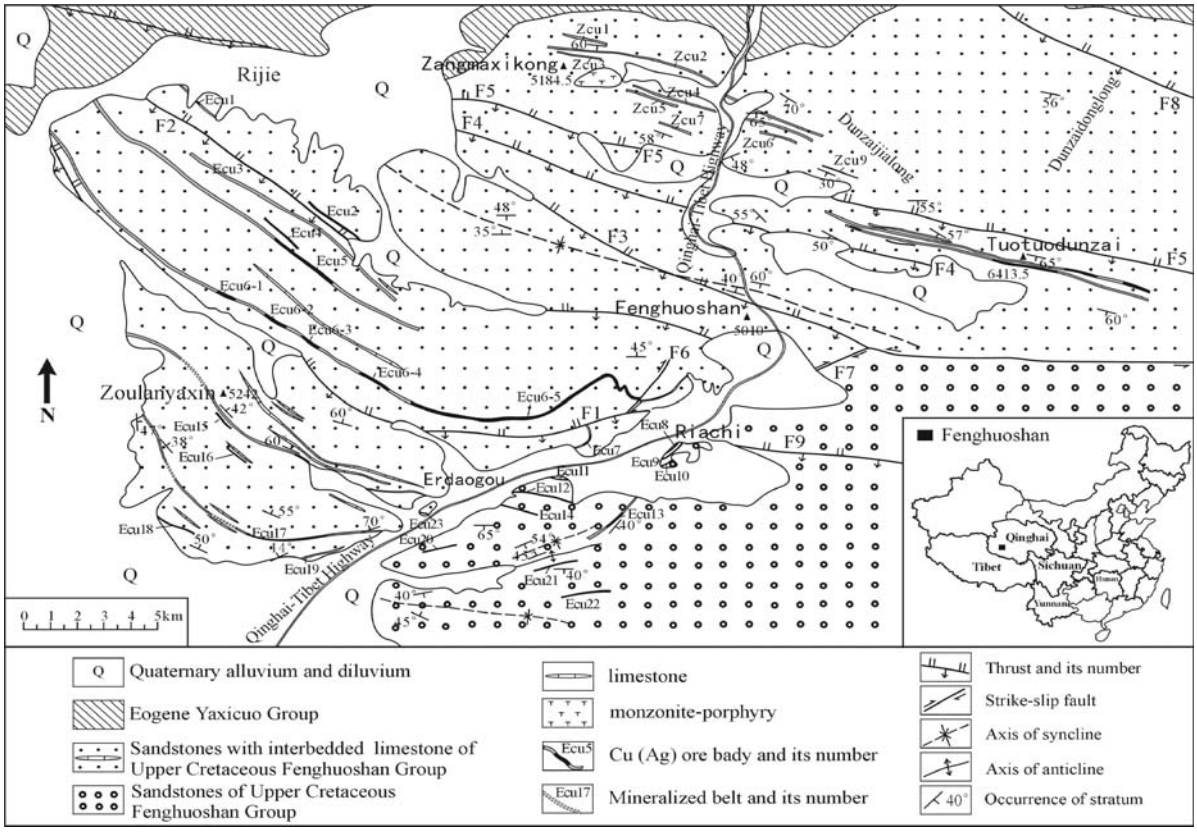

Figure 1: Geological Map of Fenghuoshan Copper Ore Deposit in Qinghai Province, China (Edited on the data of Qinghai Institute of Geological Survey 2003).

argentite, malachite and azurite in the Zangmaxikong stock, the Ag content of the fresh monzonite-porphyry is 73.6 g/T, therefore the silver mineralization in the Zangmaxikong block is closely related to the intrusive activity of the Zangmaxikong stock.

3 Geologic characteristics of the ore deposit

The copper ore bodies are hosted in sandstones with interbedded limestone (K_2fn^a) and sandstones (K_2fn^b) in the lower to middle part of the Upper Cretaceous Fenghuoshan Group. Host rocks consist mainly of dust-coloured ~ celadon medium to fine grained lithic quartzose sandstone and a few of celadon fine-grained arkosic quartzose sandstone, and celadon siltstone. Copper-stained layers have lower clay contents and high contents of siliceous or calcareous cement, which formed as a hypabyssal lake deposit or delta-front deposit. The main copper ore badies are hosted in the sandstone bodies of the underwater distributary channels.

The Fenghuoshan copper ore deposit consists of 42 copper ore bodies and five silver ore bodies, which are located in the Erdaogou, the Tuotuodunzhai and the Zangmaxikong ore blocks. The Erdaogou ore block consists of 23 copper ore bodies, in which the lengths of ore bodies are 200m to 1580m, the thickness of ore bodies are 1.01m to 9.81m, the attitudes of the main ore bodies are 200°- 230°, 40°-70°, Cu tenors of ore are 0.24%-2.10% (wt). The Tuotuodunzhai ore block consists of 14 copper ore bodies, in which the lengths of ore bodies are 600m-1240m, the thickness of ore bodies are 1.05m-5.07m, the attitudes of the ore bodies are 170°-200°, 50°-77°, Cu tenors of ore are 0.41%-3.17% (wt). The Zangmaxikong ore block consists of two copper ore bodies and five copper-sliver ore bodies, in which the lengths of ore bodies are 200m-1190m, the thickness of ore bodies are 1.40m-6.09m, the attitudes of the ore bodies are 155°-180°, 57°-65°, Cu tenors of ore are 0.32%-2.29% (wt), the average Ag tenors of ore is 260.38 g/t.

Ore bodies are shaped as beds or lenses with branching, convergences, local thickening and pinch outs. Wall-rock alteration is not obvious. The outcrops of bodies are oxidized and contain malachite and azurite. Sulfide ore bodies locally appear in the Ri'achi, the Tuotuodunzhai and the Zangmaxikong ore blocks along the dip direction of the ore bodies, in which the ore minerals consist of chalcocite, digenite and a few of bornite, chalcopyrite, pyrite, galena, sphalerite and argentite, the vein minerals

consist of quartz, plagioclase, alkali-feldspar, clay minerals, calcite and sericite.

The structures of ores are mainly disseminated, sparse disseminated structure and a few of dense disseminated and banded structure. The textures of ores are mainly allotriomorphic granular texture, then hypidiomorphic granular, poikilitic, eutectic, rimmed and microstockwork texture. The industrial types of ores are divided into the copper ores and the copper-silver ores, the copper-silver ores mainly distribute in the Zangmaxikong ore block and the copper ores distribute in the other ore bodies.

The Fenghuoshan copper ore deposit has medium-sized copper deposit prospective, its copper resources forecasted is 140,000 tons ~ to 400,000 tons.

4 Genesis of ore deposit

4.1 Source of ore-forming material

The sulfur isotopic compositions of ores may provide the clues of source-sulfur. The $\delta^{34}S$ of ores range from –18‰-13‰, and range mainly from –1‰-4‰, in the stratabound copper ore deposits. The $\delta^{34}S$ of ore minerals in the Fenghuoshan copper ore deposit range from –16.77‰ to 10.92‰ relative to CDT, and the average of $\delta^{34}S$ is –3.07‰. The $\delta^{34}S$ of ores are in obvious variety in the ore deposit, and the anomalous change of $\delta^{34}S$ even appears in the same ore block, these are the isotopic features of the sedimentary sulfur is reduced by bacteria (Zheng et al. 2000). Sulfur in ores underwent a series of geochemical cycles during mineralization, in which the most important course leading sulfur isotopic fractionation is the reduction of bacteria. It may be imagined that the bacteria lived in a micro-surroundings, and only reduce sulfate in the neighbouring region. As the duration of reducing sedimentary environment is brief, the reduction of bacteria is unhomogeneous in the copper-stained layers so that it leads the sulfur isotopic unhomogeneous of ores in the ore district. The explanation is reasonable that sulfur in the ore was probably derived from a mixture of sedimentogenic sulfate and biogenic H_2S in different proportions. Because the average $\delta^{34}S$ (-3.07‰) of ores is negative and the abundant carbonized fragments of plants exist in ores, the sulfur of ore remains close to biogenic sulfur in composition. The sulfur in the Fenghuoshan copper ore deposit is sedimentary sulfur, and bacteria were active during mineralization.

The Fenghuoshan copper ore deposit is hosted in the Upper Cretaceous fault basin on the Carboniferous to Triassic stable block. Several features indicate that the land-source denudation region of the Fenghuoshan basin, specially the strata and the igneous rocks with high copper content and iron-copper ores, not only provide a great deal of detrital sediment into the basin, but also provide the copper of forming ore deposit at the same time.

The silver ore bodies in the ore district occur near the silver-rich Zangmaxikong stock, the three fault zones have lead-silver mineralization in the Zangmaxikong stock, so the silver-source of ores was derived from the magmatic hydrothermal fluid related to the intrusive Zangmaxikong stock.

4.2 Genetic type of ore deposit

The above characteristics of the Fenghuoshan copper ore deposit are basically similar as the sandstone type copper deposit in the central Yunnan, western Sichuan and western Hunan in China, So the genetic type of the Fenghuoshan copper ore deposit mainly belongs to the sandstone type copper deposit in Mesozoic fault basin on the stable block, and the local copper-silver ore bodies were superimposed by the silver-bearing magmatic hydrothermal fluid. The formation of the deposit underwent roughly in four stages: (1) weathering and denudation of cupreous rocks on old land and forming cupreous crust of weathering, (2) fast transport of cupreous weathering products and formation of cupreous sedimentary layers, (3) dissolution, migration and enrichment of cupreous sediment and forming copper ore bodies in diagenetic process, (4) silver superimposed mineralization of magmatic hydrothermal fluid.

5 Ore controls for mineralization

The main controls of the ore deposit are as follows:

1. A comparatively steady continental sedimentary basin.

   The Indosinian movement causes the Hoh Xil region to rise and become a continent, accompanying strong tectonic deformation and magmatic intrusion. The region underwent a long-term interruption of sedimentation from the Jurassic Period to the Early Cretaceous Epoch, the weathering and denudation of the basement rocks formed a giant cupreous crust of weathering. In the Later Cretaceous Epoch, the strong differential elevation and subsidence along the previous and newborn faults in the region formed the Fenghuoshan basin. The basin went through a complicated evolutionary process that the basin was from expansion to reduction and the center of subsidence moved towards the north, the continental red clastic rocks with the thickness up to 5747m deposited in the basin.
2. The land-source denudation region with high copper content and iron-copper ores.

   The clastic compositions of the clastic rocks are complicated in the Fenghuoshan Group. For example, the gravels in conglomerate consist of sandstone, tuff, basic volcanic rock and limestone. The debris in sand-

stone includes basic volcanic rock, siltstone, silty mudstone, carbonaceous argillite, silicalite and other rock types. The clastic compositions of the clastic rocks are the same as the compositions of the underlying Carboniferous to Later Triassic basement rocks; therefore the land source denudation region is the basement uplift region about the Fenghuoshan basin. The copper abundance in the basement rocks are $33x10^{-6}$-$116x10^{-6}$; the copper content is up to $92x10^{-6}$ in the gravels of basic igneous rock; a lot of the Indosinian iron-copper ores develop in the Kaixinling in the south of the ore district, the land-source denudation region with high copper content and previously formed iron-copper ores is the source-copper of the Fenghuoshan ore deposit.

3. Periodic changes of climate and sedimentary environment

   The Fenghuoshan copper ore deposit is hosted in the light-coloured interbeds in the red rock series. The thick red rock layers represent the rapid transportation and accumulation in the oxidative water medium in the hot arid climate. Thin pale layers reflect the region appeared several times brief warm moist climate alternating with the hot arid climate, in which the plant flourished on the uplift region, a lot of plant debris entered the lake with the river, the bacteria decomposed the organic matter and produced H_2S in the bottom of basin, the Cu^{2+}, Fe^{2+} from land-source region combined with H_2S, formed sulfide. The alternative changes of the red rock layers and the light-coloured rock interbeds just represent the periodic changes of climate and sedimentary environment in the Upper Cretaceous Fenghuoshan basin.

4. Reducing conditions resulting from abundant carbon in moderate-sized sandstone bodies

   The sandstone bodies are efficient carriers of sulfide. The moderated-sized sandstone bodies are the precondition of the formation of the Fenghuoshan sandstone copper ore deposit. The copper-stained layers contains abundant carbonized plant shards from thick tree trucks to small leaves, the copper minerals always distribute in the carbonized plant shards, therefore the intensity of copper mineralization is obviously controlled by the content of carbonized plant shards. The copper ore bodies only appear in the celadon sandstone layers in which Fe exists in silicate and sulfide, the celadon sandstone layers with abundant organic matter form in the reducing conditions, so the deposit and enrichment of copper only occurs in the reducing conditions.

6 Conclusions

The Fenghuoshan copper ore deposit is hosted by the light-colour interbeds in the lower to middle part of a continential red rock series of the Upper Cretaceous Fenghuoshan Group in the Hoh Xil Basin, its genetic type mainly belongs to the sandstone type copper deposit in Mesozoic fault basin on the stable block.

The main controls of the ore deposit include the comparatively steady continental sedimentary basin, the land-source denudation area with high copper content and iron-copper ores, periodic changes of climate and sedimentary environment, the reducing conditions resulting from abundant carbon in moderate-sized sandstone bodies.

Geological and geochemical characteristics of the Changba and Dengjiashan Pb-Zn deposits in the Qinling orogenic belt, China

Guoliang Ma
Department of Geology and Geologic Engineering, Laval University, Quebec, G1K 7P4,Canada and Faculty of Resources, Chang'an University, Xian 710054, Shaanxi Province, China

Georges Beaudoin
Department of Geology and Geologic Engineering, Laval University, Quebec, G1K 7P4,Canada

Abstract. The Changba and Dengjiashan deposits are characterized by stratiform and lenticular orebodies with bedded and laminated structures. The major minerals are sphalerite, pyrite, galena, quartz, calcite, ankerite and barite. They are rich in ^{34}S and Eu, depleted in Ce, and show a Pb isotope signature between the Upper Crust and Mantle reservoirs. The world-class Changba deposit is hosted in Mid-Devonian Eifelian clastic rocks and limestone, underlain by a lens of sulfide-cemented breccia. The Dengjiashan deposit, however, is hosted in younger Givetian chert, with more breccia and vein type ores. It is concluded that the deposits formed as exhalative accumulations in Mid-Devonian sedimentary basins. The Changba deposit formed on a continental slope, whereas the Dengjiashan deposit formed in an organic bank environment.

Keywords. Sedex, lead-zinc, China, isotope, stable

1 Introduction

The Middle Devonian Qinling orogenic belt (Fig. 1) contains two types of Zn-Pb deposits: 1) stratiform massive sulfide lenses hosted in fine-grained clastic rocks mainly located in the northern part of the belt, such as the Changba deposit (Ma et al. 2004); 2) stratabound massive sulfide lenses hosted in chert in the southern part of the belt such as the Dengjiashan deposit.

The geological, mineralogical, geochemical and isotopic data presented here are used to understand the origin of the Changba and the Dengjiashan Pb-Zn deposits.

2 Regional geological settings

The Qinling Range comprises two belts divided by the transcrustal Shangnan Suture: the north and south Qinling fold belts (NQFB and SQFB, respectively). The NQFB was the southern active continental margin of the North China Craton, whereas the SQFB was the northern passive margin of the Yangtze Craton (Zhang 1988). The NQFB comprises a Proterozoic metamorphic complex of metagraywackes, marbles and metatholeiites, and an ophiolite suite. A Proterozoic metamorphic complex of paragneiss, marble, tholeiite, and alkaline basalt, Cambrian carbonaceous rocks and Silurian and Devonian sequences form most of the SQFB (Liu 1990).

The Devonian sedimentary rocks that host the Changba and the Dengjiashan deposits, were deposited in subordinate faulted basins identified by beaches, tidal flats, inner shelves, carbonate platforms, outer shelves and semi-deep to deep-water transitional zones of shelves to continental slopes environments (Liu 1990). The outer shelves facies is divided into subbasins where sedimentary facies range from clastic carbonate to fine clastic-argillaceous-carbonate, corresponding to shallow and deep water environments, respectively. Large Pb-Zn deposits occur mainly on both sides of restricted carbonate banks on the outer shelves. In vertical section, the ore-hosting strata commonly change rapidly from clastic-carbonate rocks to turbidite, and then to fine clastic-carbonate rocks.

3 The Changba Pb-Zn deposit

The Changba orebodies are in an overturned, south dipping sequence with stratigraphic polarity towards the north. A post-ore, reverse fault displaced and separated sulfide ore-bodies into the Changba and the Lijiagou segments. The Changba deposit contains 80.4 Mt of ore with average grades of 1.32% Pb and 7.04 % Zn in its Changba segment and 62.1 Mt of ore with average grade of 1.31% Pb and 7.34% Zn in the Lijiagou segment. The Pb+Zn reserve is 11.2 Mt with a (Zn +Pb)/Zn ratio of 1.2.

The Middle Devonian Anjiacha Formation hosts almost all of the Pb-Zn ore-bodies. It is composed of fine-grained clastic rocks intercalated with limestone and dolomite. Although fossils are rare, stratigraphic correlations with strata to the east suggest an Eifelian age (Du 1986). The Changba-II orebody, which accounts for more than 70% of the metal reserves, is lens-shaped and occurs concordantly in biotite quartz schist, trending in a general EW direction, with a 60° to 90° S dip, a length of 380 m and a thickness up to 49 m. The sulfide beds are interlayered with schist and marble. The Changba-II bedded sulfides exhibit a mineral zonation from the bottom upward: bedded sphalerite ore intercalated with quartz albitite, interbedded pyrite and massive sphalerite ore, and bedded sphalerite ore intercalated with bedded barite at the top.

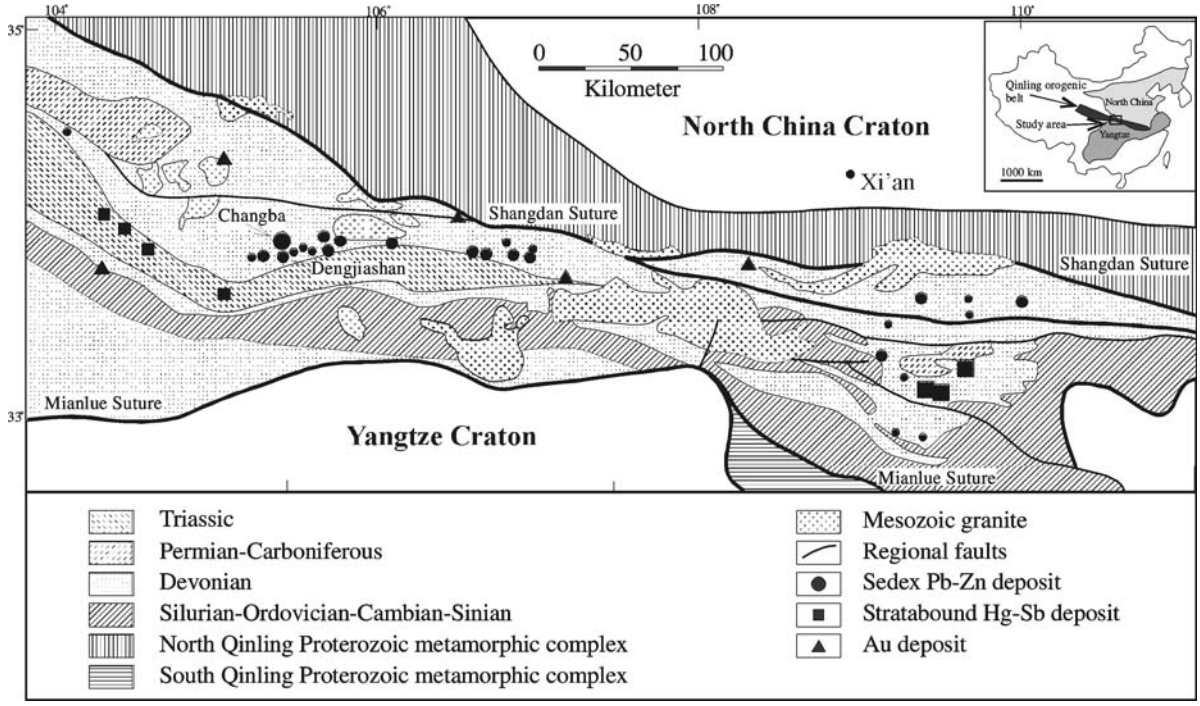

Figure 1: Regional geological map showing mineral deposits in the Qinling orogenic belt, China. The size of the mineral deposit symbols indicates relative size of the deposits (after Qi and Li 1993).

A 30 m thick lens of brecciated and altered rocks occurs to the south, in the stratigraphic footwall of the overturned Changba-II sulfide orebody. The breccia consists of grey-white angular fragments (up to 20 cm by 4 cm in size) of quartz albitite (30 – 90% Ab) cemented by quartz and coarse-grained pyrite, sphalerite, galena and pyrrhotite. Remnants of grey biotite-quartz schists in the core of some albitite fragments indicate that albitite formed by the alteration of the host biotite-quartz schist. This breccia lens bears similarities with the fragmental units in the footwall of the Sullivan deposit (Anderson and Höy 2000).

Sulfur isotope compositions range from +9.9 to +25.4 ‰ for sphalerite (n = 40, average = + 20.7 ‰), from +8.1 to +29.3 ‰ for pyrite (n = 60, average = +21.4 ‰) and from +8.9 to +24.2 ‰ for galena (n =30, average = + 18.2 ‰). The S isotope composition of barite ranges from +20.8 to +31.5 ‰, with an average $\delta^{34}S$ of +24.5 ‰ (n = 6).

Pb isotope ratios from 11 galenas range from 17.847 to 18.459 for $^{206}Pb/^{204}Pb$, 15.420 to 15.874 for $^{207}Pb/^{204}Pb$ and 38.014 to 38.785 for $^{208}Pb/^{204}Pb$. The Pb isotope compositions form an array spreading from values typical of the Mantle reservoir to values more radiogenic than the Upper Crustal reservoir (Doe and Zartman 1979). The enrichment in ^{208}Pb suggests that the lead in has a significant Lower Crustal Pb component.

The REE of the ores and wall rocks show fractionated REE patterns with $(La/Lu)_N > 1$. Most of them exhibit fractionated LREE patterns, and flat HREE patterns. Another important similarity among the samples is the slight depletion (0.72 – 0.98) in Ce. The content of REE from high to low is: biotite quartz schist > massive sulfide ores > marble and dolostone. The REEs contents of breccia lens, quartz albitite, bedded ore are close to the value of biotite quartz schists.

4 The Dengjiashan Pb-Zn deposit

The orebodies in the Dengjiashan deposit are hosted by metamorphosed Devonian sedimentary units that crop out in the cores of the Dengjiashan and Mogou isoclinal anticlines. Drilling indicates mineral resources of more than 25 Mt with an average of 4.77 % Zn, 1.27 % Pb, 14 ppm Ag, 0.1 ppm Au, 160 ppm Cd and 650 ppm Hg.

The host Middle Devonian Xihanshui Formation comprises an upper argillaceous and a lower carbonate member. The lower carbonate member comprises more than 190 m of grey to dark grey bioclastic micrite with thin layers of calcarenite. The upper argillaceous member comprises interbedded phyllites and micritic limestone with abundant brachiopod bioclasts. The sulfide ores are hosted in chert in gradational contact with the footwall lower carbonate member and in sharp contact with the hangingwall upper argillaceous member. The limestone and phyllites of the Xihanshui Formation host sixteen orebodies, of which the two largest are the #1 (Dengjiashan anticline) and #9 (Mogou anticline). Orebody #1 is up to

20 m thick, strikes east-west for approximately 4 km, and continues 300 m downdip to the south., whereas orebody #9 is 2 km long and at least 350 m downdip, with an average thickness of 6.3 m and a thickness up to 21 m.

The ores are composed of intergrowths of sphalerite, galena, and pyrite, with minor chalcopyrite, tetrahedrite, cinnabar and pyrargyrite. The gangue is dominated by quartz, calcite, barite, and ankerite, with minor amount of sericite, chlorite, celsian, cymrite and albite. Primary sedimentary and diagenetic textures and structures such as bedding and lamina are preserved, but the lenticular sulfide orebodies are characterized by recrystallized, vein and breccia structures related to the tectonic and metamorphic events after the emplacement of the ores.

The REE patterns of the sulfide ore, chert and limestone exhibit positive Eu anomaly with Eu* ($2 \times Eu / (Sm + Gd)$) ranging from 1.6 to 16.5. They are similar to those of the East Pacific Rise submarine hydrothermal fluids and of pure hydrothermal precipitates of the Red Sea (Henderson 1984), suggesting that the cherts and sulfide ores were deposited from exhalative hydrothermal fluids. Another characteristic of chert, limestone and sulfide ore samples is a negative Ce anomaly, which is characteristic of oxidized Devonian seawater (Wright et al. 1987).

Ninety sphalerite, pyrite, galena and barite samples from orebodies #1 and #9 yield $\delta^{34}S$ values ranging from +10.5 to +22.3 ‰ for sphalerite, +4.2 to +21.1 ‰ for galena, -7.2 to +23.3 ‰ for pyrite and +14.9 to +31.0 ‰ for barite. It is noteworthy that galena, sphalerite and pyrite have similar maximum $\delta^{34}S$ values at 21-23 ‰. These high $\delta^{34}S$ values in Dengjiashan sulfides are typical of sedimentary exhalative deposits (Large 1983).

Ore galena has $^{206}Pb/^{204}Pb$ ranging from 17.827 to 18.176, $^{207}Pb/^{204}Pb$ ranging from 15.454 to 15.705, and $^{208}Pb/^{204}Pb$ ranging from 37.661 to 38.312. These values plot between the Orogene and Upper Crust reservoir curves of Doe and Zartman (1979) in the $^{207}Pb/^{204}Pb$ - $^{206}Pb/^{204}Pb$ diagram. An enrichment in ^{208}Pb indicates a contribution of thorogenic Pb from a Lower Crust reservoir.

5 Comparison between the Changba and the Dengjiashan deposits

The Changba deposit is hosted by the Middle Devonian Eifelian Anjiacha Formation, which formed in a continental slope environment, whereas the Dengjiashan deposit is in the Middle Devonian Givetian Xihanshui Formation, which formed in a carbonate platform or organic bank environment. The lithofacies imply that the Dengjiashan deposit was closer to the margin of the Xicheng sub basin relative to the Changba deposit. The sedimentary environments range from open platform facies, through organic bank facies, stagnant depression facies to marine facies, affected by an extensional tectonic regime. Ore deposition occurred during the transition from shallow water platform to deeper water basin conditions. No important magmatic activity is known during mineralization, because all plutonic rocks intruded during the Mesozoic and Lower Paleozoic (Ma et al. 2004). The concordant, lenticular orebodies in the Dengjiashan deposit are hosted in chert between marble and phyllite, whereas the concordant stratiform orebodies in the Changba deposit are hosted in schist and limestone. Sulfide lenses in the Changba deposit have more pyrite with a gangue of quartz-calcite-albite-barite, but the Dengjiashan deposit is characterized by quartz-calcite-ferrodolomite-barite. Primary sedimentary bedding and lamination structures are found in both deposits. The breccia lens underlying the Changba-II orebody could represent a sedimentary breccia expulsed along synsedimentary faults that also channelized hydrothermal fluids to the seafloor, as proposed for the Sullivan deposit (Anderson and Höy 2000).

Both deposits have wide ranges of $\delta^{34}S$ values which are interpreted to be a result of mixing between Devonian seawater BSR (min values) in a sulfate restricted subbasin (max barite) with heavy hydrothermal TSR sulfide (max sulfide values) injected into the subbasin to form the sulfide lenses. REE patterns in Dengjiashan, are comparable to modern exhalative fluids, and display negative Ce and positive Eu anomalies that are absent in the Changba deposit. The persistence of a negative Ce anomaly would indicate oxidizing seawater at Dengjiashan compared to Changba, whereas the positive Eu could represent feldspar leaching in the basement or sedimentary cover sequence. The lead isotope composition of the two deposits are quite similar, forming an array between the Upper Crust and the Mantle reservoirs, indicating that lead in both deposits was derived from the mixture of underlying sedimentary rocks and basement of the Qinling orogenic belt.

6 Conclusions

The formation of the lead-zinc deposits in the Middle Devonian was controlled by the tectonic setting and sedimentary environment. During the Eifelian in Changba, the south shore of the Qinling Sea was under extension, which formed faulted basins on the north margin of the Yangtze craton and caused convection of oxidized seawater in pores or fractures of the pre-Devonian sedimentary rocks. This heated seawater leached metals from the rocks along its flow path. At the same time, seawater sulfate was reduced by bacteria under closed conditions to form sulfides. Residual sulfate at the bottom of the faulted basin became enriched in ^{34}S. Hydrothermal fluid carrying TSR sulfur was injected into the sub basin, where a drop in temperature and mixing with the H_2S-riched bottom seawater resulted in the precipitation of the massive sulfide lenses. Where the feeder zone was near the center

of the sub-basin, the breccia zone underlies the bedded orebodies. Later, during Givetian time, subsidence of the carbonate platform and the Dengjiashan deposit formed from a distal hydrothermal fluid discharge site that accumulated into a local depression on the seafloor.

Acknowledgements

Professor Sijing Qi, Ying Li and Zhangren Zen are thanked for their help in the research.

References

Anderson D, Höy T (2000) Fragmental sedimentary rocks of the Aldridge Formation, Purcell Supergroup, British Columbia. The geological environment of the Sullivan deposit, British Columbia, Geological Association of Canada Mineral Deposit Division Sp. Pub. 1: 259-271

Doe BR, Zartman RE (1979) Plumbotectonics, the Phanerozoic. In: Barnes, HL (ed.) Geochemistry of hydrothermal ore deposits, 2nd Edition. John Willy & Sons, NY: 22-70

Du DH (1986) Devonian System in the Qinling-Bashan district, Shaanxi, China: Xi'an Jiaotong University Publishing House, Xi'an: 358

Henderson P (1984) Rare earth element geochemistry. In: Henderson, P (ed.) Development in geochemistry, 2nd, Amsterdam, Elsevier: 510

Large DE (1983) Sediment-hosted massive sulfide lead-zinc deposits: An empirical model. In: Sangster DF (ed.) Sediment-hosted stratiform lead-zinc deposits, Mineralogical Association of Canada Short Course Handbook: 1-30

Liu B (1990) Devonian sedimentary environment and evolution of the sedimentary basin in Zashui-Zhen'an District, East Qinling Mountains, China Acta Sedimentologica Sinica 9: 35-56 (in Chinese, with English abstract)

Ma G, Beaudoin G, Qi S, Li Y (2004) Geology and geochemistry of the Changba SEDEX Pb-Zn depsit, Qinling orogenic belt, China. Mineralium Deposita

Wright H, Schrader H, Holser WT (1987) Paleoredox variations in ancient oceans recorded by rare earth elements in fossil apatite: Geochim Cosmochim Acta 51: 631-644

Zhang GW (1988) Formation and evolution of the Qinling orogenic belt. Northwestern Univ Press, Xi'an: 192 (in Chinese with English abstract)

Pyrite trace element halos to northern Australian sediment-hosted Zn-Pb-Ag deposits

Rodney C. Maier
CODES SRC, University of Tasmania. PO Box 252-79, Hobart, Tasmania 7005, Australia

Peter J. McGoldrick
CODES SRC, University of Tasmania. PO Box 252-79, Hobart, Tasmania 7005, Australia

Abstract. Subtle primary halos form around many sedimenthosted Zn-Pb deposits. Northern Australian deposits may also have pyrite halos, representing the first paragenetic stage of the mineralising fluids. The occurrence of trace elements within this pyrite has potential to provide vectors to the orebody or delineate mineralised from barren systems. Pyrite trace element compositions from rocks surrounding the McArthur River sediment-hosted Zn-Pb deposit, Northern Territory, Australia have been analysed by LA-ICPMS. Analysis was conducted for 25 elements. Over 95% of all pyrite analysed contained >0.10 wt% of trace elements, of which, Co, Ni, Cu, Zn, As, Sb, Ba, Tl, Pb, Mn, Mo, Ag, Bi and Sn are found in abundances significantly greater than detection limits. The host sediments contain no significant levels of Cu, Co, Ni, Pb, Zn. Concentrations of Co, Cu, Ni, Tl and Zn are significantly elevated at the orebody and hangingwall equivalent stratigraphy. As, Ba, Mo, Sb, Sn are slightly elevated at the orebody equivalent stratigraphy. Spatial distribution patterns of the trace elements are erratic, possibly reflecting variations in pH, oxidation state, or temperature across the basin at the time of formation.

Keywords. SEDEX, McArthur river, pyrite, trace elements, LA-ICPMS

1 Introduction

Primary halos to sediment-hosted Zn-Pb deposits are typically broad, but subtle and are identified from whole rock chemical variations. However, northern Australian sediment hosted Zn-Pb deposits also have close associations with highly pyritic sediments. A synsedimentary model of formation for these deposits (e.g. Large et al. 1998) predicts that this pyrite represents the first paragenetic stage produced by the mineralising fluids. Pyrite can contain measurable quantities of trace elements either as inclusions, or within the crystal lattice. This property suggests that a study of pyrite trace element contents has the potential to provide vectoring information in prospective (highly pyritic) areas or to distinguish mineralized hydrothermal systems from those that are barren.

In this study, laser ablation (LA-ICPMS) analysis of pyrite has been undertaken from systematic drill core and underground samples near the giant McArthur River deposit, Northern Territory, Australia.

2 Study area

The McArthur River deposit is the largest known example of a stratiform, sediment hosted deposit and has a geological resource of 237 Mt grading 9.2% Zn, 4.1% Pb and 41g/t Ag (Gustafson and Williams 1981). This Proterozoic age deposit has undergone minimal structural disruption and metamorphism, thus making it an ideal location to conduct such a study. Work currently in progress also involves the study of a large, low-grade sedimentary Zn-Pb system known as the Bluebush prospect, NW Queensland, Australia. This prospect covers an area approximately 10 km x 10km, with average grades of 1.0% Zn. To date, no economic mineralisation has been discovered. The Bluebush prospect will provide a comparison to the mineralised system at McArthur River.

3 Background information

This investigation builds on previous studies that recognized significant elemental and isotopic zonation around the McArthur River deposit e.g. Lambert and Scott (1973),

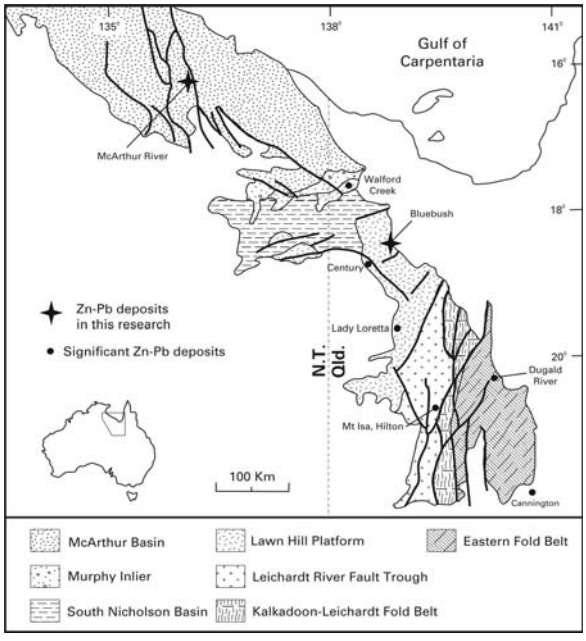

Figure 1: Map showing the location of the two deposits in this study, the location of other significant sediment-hosted Zn-Pb-Ag deposits, and the location of basins and major tectonic elements in the Carpentaria Zinc Belt. Modified from Betts et al. 2003.

Large et al. (2000) and Large et al. (2001). The results of these studies suggest that zonation of specific mineral chemistry may be present.

Many significant reviews have documented the occurrence of trace elements within pyrite (e.g. Craig and Vaughan 1990; Abraitis et al. 1994). Watson et al. 1995 have also shown the effectiveness of bacterially produced gel – a probable precursor to framboids, at absorbing trace elements.

4 Sampling strategy

Samples for this research have been collected at regular downhole intervals from drill cores 0.3, 6, 15 and 23 km away from the orebody, representing the overlying, hangingwall, orebody and underlying equivalent stratigraphy. Additional samples have been collected from underground exposures of "fringe ore". These were selected to cover significant variations in zinc content, from ore grade (~19% Zn) through to sub-economic levels (>5% Zn) along laterally continuous beds.

5 Analytical method

Analytical methods in early pyrite studies (eg Loftus-Hills and Solomon 1967) typically used wet chemical analysis of bulk mineral separates. The data was potentially compromised by inclusions of other sulphide minerals and multiple generations of sulphide deposition.

The principle analytical method used in this research is laser ablation ICPMS. Studies using other microbeam analytical methods (e.g. Cabri et al. 1985; Griffin et al. 1991; Huston et al. 1995) have limitations such as relatively large beam size, high detection limits, prohibitive costs and long analytical times compared to LA-ICPMS. Analyses to date have used an 8 - 10 μm beam, a spatial resolution of a few microns, and median detection limits for most elements less than 5 ppm. This is important considering the northern Australian deposits are characterised by fine grained sulphides.

Pyrite at McArthur River can be <5 μm and host sediment contamination needs to be considered.

The recognition and rejection of analysis compromised by inclusions can reasonably be achieved, initially by interrogation of the LA-ICPMS spectra, and confirmed by statistical analysis of the data. Invariably during LA-ICPMS, small amounts of the host sediments are ablated with the pyrite. To quantify this contribution, micro-analysis of the host sediments, adjacent to the target pyrite grains have also been conducted.

6 Results

Analysis was conducted for 25 elements. The total concentration of trace elements in pyrites was low. Over 95% of all pyrite analysed contained >0.10 wt% of trace elements, of which, Co, Ni, Cu, Zn, As, Sb, Ba, Tl, Pb, Mn, Mo, Ag, Bi and Sn are found in abundances significantly greater than detection limits.

The host rocks are typically composed of dolomite, quartz and muscovite. LA-ICPMS analysis indicates no significant levels of Cu, Co, Ni, Pb, Zn are contained within these minerals. Minor host sediment contamination of Mn, Ba, As, and possibly Sb and Tl to the pyrite analysis cannot be discounted.

Downhole plots of the pyrite trace elements indicate that Co, Cu, Ni, Tl and Zn concentrations are significantly elevated at the orebody position, relative to the hangingwall and overlying formation pyrites. As, Ba, Mo, Sb, Sn are slightly elevated at the orebody equivalent position, relative to the hangingwall and overlying formation pyrites.

Spatial distribution patterns of the trace elements are erratic. This may be reflecting variations in pH, oxidation state, or temperature across the basin at the time of formation, in turn controlling pyrite uptake of the available trace elements. Future work aims to resolve these relationships.

Acknowledgements

This work has been supported by a CODES SRC postgraduate scholarship. Thanks to the project supervisors Dr. Peter McGoldrick and Prof. Ross Large. Additional financial support from Anglo-American and logistical support from McArthur River Mines were provided. Steve Pevely, Damian Nihill, Joe O'Brien, Andrew Allan and Greg Blain are thanked for assistance during field work.

References

Abraitis PK, Pattrick RAD, Vaughan DJ (2004) Variations in the Compositional, Textural and Electrical Properties of Natural Pyrite: A Review. International Journal of Mineral Processing 74: 41-59

Betts PG, Giles D, Lister GS (2003) Tectonic Environment of Shale-Hosted Massive Sulfide Pb-Zn-Ag Deposits of Proterozoic Northeastern Australia. Economic Geology 98: 557-576

Cabri LJ, Campbell JL, Gilles Laflamme JH, Leigh RG, Maxwell JA, Douglass Scott J (1985) Proton-Microprobe Analysis of Trace Elements in Sulfides from Some Massive-Sulfide Deposits. The Canadian Mineralogist 23: 133-148

Craig JR, Vaughan DJ (1990) Compositional and Textural Variations of the Major Iron and Base-Metal Sulphide Minerals. In: P.M.J. Gray, Bowyer GJ, Castle JF, Vaughan, D.J., & Warner, N.A. (Editor), Sulphide Deposits - Their Origin and Processing. The Institution of Mining and Metallurgy, London: 1-16

Griffin WL, Ashley PM, Ryan CG, Sie SH, Suter GF (1991) Pyrite Geochemistry in the North Arm Epithermal Ag-Au Deposit, Queensland, Australia: A Proton-Microprobe Study. The Canadian Mineralogist 29: 185-198

Huston DL, Sie SH, Suter GF, Cooke DR, Both RA (1995) Trace Elements in Sulfide Minerals from Eastern Australian Volcanic-Hosted Massive Sulfide Deposits; Part I, Proton Microprobe Analyses of Pyrite, Chalcopyrite, and Sphalerite, and Part II, Se-

This page intentionally blank

lenium Levels in Pyrite; Comparison with $\delta^{34}S$ Values and Implications for the Source of Sulfur in Volcanogenic Hydrothermal Systems. Economic Geology 90: 1167-1196

Lambert IB, Scott KM (1973) Implications of geochemical investigations of sedimentary rocks within and around the McArthur zinc-lead-silver deposit, Northern Territory. Journal of Geochemical Exploration 2: 307-330

Large RR, Bull SW, Cooke DR, McGoldrick PJ (1998) A genetic model for the H.Y.C. Deposit, Australia; based on regional sedimentology, geochemistry, and sulfide-sediment relationships. Economic Geology 93: 1345-1368

Large RR, Bull SW, McGoldrick PJ (2000) Lithogeochemical halos and geochemical vectors to stratiform sediment hosted Zn-Pb-Ag deposits; Part 2, HYC Deposit, McArthur River, Northern Territory. Journal of Geochemical Exploration 68: 105-126

Large RR, Bull SW, Winefield PR (2001) Carbon and oxygen isotope halo in carbonates related to the McArthur River (HYC) Zn-Pb-Ag deposit, North Australia; implications for sedimentation, ore genesis, and mineral exploration. Economic Geology 96: 1567-1593

Loftus-Hills G, Solomon M (1967) Cobalt, Nickel and Selenium in Sulphides as Indicators of Ore Genesis. Mineralium Deposita 2: 228-242

Watson JHP, Ellwood DC, Deng Q, Mikhalovsky S, Hayter CE, Evans J (1995) Heavy Metal Adsorption on Bacterially Produced FeS. Minerals Engineering 8: 1097-1108

Darhand copper occurrence: An example of Michigan-type native copper deposits in central Iran

Nima Nezafati
Department of Economic Geology and Leibniz Laboratory for Applied Marine Research, Freiberg University of Mining and Technology, Brennhausgasse 14, D-09596 Freiberg, Germany

Morteza Momenzadeh
Zarneh Research Institute, 34 Forth 12m street, Jenah Highway, Tehran, Iran

Ernst Pernicka
Institute of Prehistoric Archaeology, University of Tuebingen, Schloss Hohentuebingen, D-72070 Tuebingen, Germany

Abstract. The Darhand copper occurrence consists of disseminated, veinlet and pocket-shaped native copper mineralization in Late to Mid-Eocene basalt located 200 km south of Tehran, in the middle of the Orumieh-Dokhtar metallogenic belt, in central Iran. The submarine amygdaloidal spilitic basalt, which hosts the mineralization has undergone a propylitic alteration (chloritic, epidotic) as well as a low-grade metamorphism resulting in zeolites and prehnite-pumpellyite-quartz. The pockets, veinlets and amygdales of prehnite, epidote, chlorite and laumontite (zeolite), which fill the open spaces of basalt, host most of the copper mineralization. The Cu mineralization in veinlets, pockets and amygdales is composed of cuprite > native copper > malachite > tenorite > chrysocolla. The round and ellipsoidal grains of native copper and cuprite range up to 2cm in size. With the exception of rare scattered pyrite grains in the host rock, no sulfide minerals were observed in the mineralization. The Cu content of the ore reaches 3.5 % with rather high values of silver (6 ppm). Also the copper concentration in the submarine basalt is anomalously high with 250 ppm. The mineralization is bound to a definite basalt layer underlying the Oligo-Miocene limestone.

The Darhand copper mineralization shares some similarities with the Keweenawan native copper deposits in Michigan, USA. They both appear to be similar in the petrology and in the alteration of their host rocks as well as in their mineral association and ore characteristics. They differ only in the age of the host rocks.

Keywords. Michigan type copper deposits, amygdaloidal basalt, Darhand, Natanz, central Iran

1 Introduction

The Orumieh-Dokhtar metallogenic belt extends from the northwest to the southeast of Iran. Different types of copper deposits, including porphyry ones, are located in this belt. Not many of those deposits are reported to carry native copper. The Darhand copper occurrence was first recognized and investigated by the first author in 1999. The mineralization is hosted by Late to Mid Eocene amygdaloidal basalt and displays a type of metallogeny (high copper, elevated silver) and mineralogy (paucity of sulfide minerals) that is similar to the Michigan Keweenawan native copper deposits (Huber 1975; Wilson and Dyl 1992). This paper introduces the Darhand copper mineralization and compares it with the Keweenawan copper deposits. The stratabound nature of the occurrence may lead to the discovery of further deposits of this type in central Iran.

2 Geologic setting

The Darhand copper occurrence is located 200 km south of Tehran and 4.5 km east of Natanz, in the middle of the Orumieh-Dokhtar metallogenic belt, of central Iran. This belt is indeed part of Thethyan-Eurasian metallogenic belt (Jankovic 1977). The Orumieh-Dokhtar belt hosts most of the Iranian copper deposits, such as Cu-Mo porphyries, VHMS, stratiform deposits, skarn and vein type deposits that are mainly related to Tertiary volcanic activity. Although copper is dominant, other metal resources of lead, zinc, gold and manganese are found in this belt.

The important rock units of the study area are Cretaceous limestone, Late Eocene submarine amygdaloidal basalt, and ignimbritic tuff and breccia. Overlying these Tertiary formations is Oligo-Miocene limestone (Qom formation) with an unconformity (lack of Lower Red Formation). The amygdaloidal basalt trends NE-SW dipping east (N30E) lies below an ignimbritic tuff and breccia unit. The copper mineralization at Darhand is completely confined to this basalt and does not appear at all in adjacent formations.

3 Local geology

The Darhand copper mineralization is stratabound and covers an elongated area of 3 km^2. Cuttings for the construction of a highway through this area imply the continuation of the mineralization to a depth of at least 3m. Inspection of hand specimens indicates that amygdales are 0.1-2 cm in diameter. They are filled with calcite, chlorite, zeolite and prehnite. There are also veins, veinlets and pockets of the same material as long as 2m with N-S, E-W and NE-SW trends. Petrographic investigations car-

ried out in this study show that the amygdaloidal layer is porphyritic basalt with open spaces filled by prehnite, carbonate, zeolite, chlorite, and some quartz. In some samples plagioclase and olivine have been converted to pumpellyite. The skeleton texture in the plagioclase crystals implies a fast cooling rate of the magma. In general, the rock shows the characteristics of spilitic basalts.

The most important alteration of the amygdaloidal basalt is propyllitic (chlorite, epidote), which is pervasive. Argillic and sericitic alterations are much less abundant. In addition to alteration, the rock has experienced a low-grade metamorphism to zeolites and prehnite-pumpellyite-quartz. According to XRD studies the zeolite is laumontite [$(CaAl)_2$ $Si4O_{12}$, $4H_2O$]. The presence of amygdales and pockets of prehnite, zeolite, calcite, chlorite and quartz makes the rock appear similar to Swiss cheese with filled holes.

4 Ore mineralogy and metal association

The mineral association in the Darhand occurrence includes native copper, cuprite, tenorite, malachite and chrysocolla which are disseminated in the pockets, veinlets and amygdales of prehnite, chlorite, zeolite, calcite and quartz in the form of round and ellipsoidal grains up to 2 cm. Malachite impregnation is seen in parts of the host rock where prehnite-carbonate increases in the rock. Cuprite grains are usually coated by tenorite. The aggregation of copper grains comprises 2-60 vol% of the pockets and amygdales. Also the host rock contains small grains of native copper. In the center of some small amygdales, malachite patches are visible.

Ore microscopy reveals the presence of native copper, cuprite, tenorite, malachite, and chrysocolla which have open space filling and dissemination textures. No sulfide mineral has been observed in the pockets. The only sulfide mineral is pyrite, which was rarely observed in the samples taken from host rock. The maximum copper content is 3.5% with about 6 ppm silver analyzed by ICP-MS. The other elements are not anomalous. The concentration of copper in the host rock is 250 ppm, which indicates a rather high anomaly.

5 Conclusions

According to its geologic setting, type of alteration and metamorphism, host rock petrography and ore paragenesis, the Darhand copper occurrence shows strong similarities to the native copper deposit located on the Keweenaw Peninsula, Michigan, USA. The most significant differences are the different ages of the host rocks, namely Precambrian for Michigan and Late-Mid Eocene for Darhand. The latter also lacks the presence of chalcocite.

There are some other similar deposits in Iran like the mineralization in the Tarom zone in northwest Iran, namely Qeshlaq (Bazin and Huebner 1969) and Ghebleh Boulagh (Behzadi 1994), all in Eocene volcanics. According to the characteristics of the Darhand occurrence and published data from Huber 1975, Wilson and Dyl 1992 and Behzadi 1994, the probable mineralization stages of this deposit are as follows:

- intrusion of a gas-rich basaltic magma in the sea floor;
- formation of open spaces and fractures in basalt due to the fast cooling of the magma; tectonic movements simultaneously caused a weak metamorphism in the rock;
- during metamorphism copper was liberated from the silicate minerals by the action of chloride containing hydrothermal fluids, heated by the hot core of the magma, and precipitated in the rock;
- egression of the volcanic body out of the water and oxidation of the mineralization.

If we apply the above-mentioned scenario to the Darhand occurrence, we can consider this mineralization as syn-genetic volcanogenic. Since the amygdaloidal basalt is vast and spread out not only in the area but over all of central Iran and the Orumieh-Dokhtar zone and due to the stratabound nature of the mineralization, it is highly likely that larger and more economical mineralizations of this type may be found. It is of interest to note that some ancient settlements and metallurgical workshops have been discovered in the vicinity of Natanz where native copper was formed by hammering (Hasanalian, personal communication). Although no trace of old mining was found in the area of Darhand yet, it is possible that further fieldwork may encounter them in the future.

References

Bazin D, Hübner H (1969) Copper deposits in Iran. Geological Survey of Iran, Report No. 13

Behzadi M (1994) Economic geological investigations of the Ghebleh Boulagh copper occurrence in Lower -Tarom, Zanjan Province, Iran, MSc thesis (in Persian), Shahid Beheshti University

Huber NK (1975) The geologic story of Isle Royale National Park. U.S. Geological Survey Bulletin 1309

Jankovic S (1977) The copper deposits and geotectonic setting of the Thethyan-Eurasian metallogenic belt. Mineralium Deposita 12: 37-47

Nezafati N (2000) Study on metallic minerals of the Natanz Area, Iran, MSc thesis (in Persian), Research Institute for Earth Sciences. Geological Survey of Iran

Wilson M, Dyl S (1992) Michigan Copper Country. Mineralogical Record, Inc. Tucson, AZ, Vol.23, No.2: 1-76

Zhu B, Hu Y, Zhang Z, Chang X (2003) Discovery of the copper deposits with features of the Keweenawan type in the border area of Yunnan and Guizhou provinces. Science in China Series D, Vol.46 Supplement: 60-72

Rare metal sequestration and mobility in mineralized black shales from the Zunyi region, South China

B. Orberger
Département des Sciences de la Terre, UMR 4846 IDES, Univ. Paris XI, Bât. 504, 91405 ORSAY Cedex, France

C. Wagner
Laboratoire de Pétrologie, Modélisation des Matériaux et Processus , FR32 Univ. Pierre et Marie Curie, Place Jussieu, F- 75251 Paris Cedex, France

A. Vymazalová, J. Pašava, B. Kříbek
Czech Geological Survey, Geologicka 6, 152 00 Prague 5, Czech Republic

J.-P. Gallien
Laboratoire Pierre Süe, CEA-CNRS, UMR 9956, CEA Saclay, F-91191 Gif sur Yvette Cedex, France

Abstract. The micromineralogical and chemical study of two black mineralized shales from the Zunyi region show that they experienced a low diagenetic degree still preserving microbial phosphate and sulfides and poorly crystallized phases composed of metals or Al and Si. The two shales differ in diagenetic vein mineralogy. CH11 is carbonate-rich whereas CH25 is sulfate-rich. As CH11 is twice enriched in the redox sensitive elements Ni, Se, As, Mo, Sb, U, Zn, Pb, Cd, a remobilization by CO_2 (may be derived from organic matter oxidation) rich fluids is suggested. Seawater characteristic REE element patterns, but Se/S-ratio typical for a volcanogenic environment, favor a fluid mixture during early diagenesis.

Keywords. Black shales, Cambrian, rare metal mineralization, molybdenum, selenium, arsenic, nickel, organic carbon, phosphates

1 Introduction

The processes and mechanisms of rare metal concentrations in black shales are explained by syn-sedimentary enrichment from sluggish seawater under anoxic, sulfate reducing conditions which was episodically replenished by upwelling oxidizing seawater (Mao et al. 2002) or by syn-sedimentary infiltration of diffuse dense metal and hydrocarbon-rich hydrothermal fluids (Coveney et al. 1992; Lott and Coveney 1996; Steiner et al. 2001). The Lower Cambrian black shales (> 10 wt. % organic carbon) at the base of the Nuitiang Formation (S-China) host up to 2 m Fe-Ni-Mo sulfide ore layers with a lateral extension of over 1000 m (Mao et al. 2002). The shales are also 10 to 100 times enriched in Mo, Se, As, Sb, Cr, V, U, Zn, Cu, PGE, P, Ba and others compared to average black shales (Mao et al 2002). Iron, Ni, Mo, As, Cu, U, Zn, Ba and P form sulfides, native gold, barite, uraninite, REE-Y and Ca-phosphates (Kao et al. 2001; Steiner et al. 2001). A micro mineralogical SEM-EDX study combined with EMP and PIXE analyses on sulfides, carbonates, phosphates, combined with whole-rock geochemical data of two different samples from the ore layer of the Zunyi region (Huangjiawan mine) were used to locate trace elements and to reconstruct the diagenetic history.

2 Results

2.1 Mineralogy and Mineral chemistry

Both shale samples have a layered brecciated texture showing partly disrupted organic matter (OM) lenses often cut by micrometric veins (Fig. 1a). The OM lenses are partly microbially mineralized, either in concentric, alternating layers of phosphate and Fe-sulfide spherules. Inframicrometric Ca-phosphate spherules agglomerated to larger spherules, and to euhedral apatites (Fig. 1b) occur with Fe-sulfides interstitial to OM. Nanometric sulfide spherules can form polygonal framboidal pyrite (Fig. 1c) in biotites, which is intergrown with diagenetic albite, or rutile. Mica grew also on sulfide rims at the border of organic matter. Diagenetic brannerite occurs around biotite (Fig. 1d). Phosphate, K-Al-Si gel-like textures are frequent. They may contain traces of S, Ni and Fe or host nanometric Fe-sulfides (Figs. 1e,f). Poorly crystallized Fe-Ni-As-Mo-S phases also occur, presenting the precursors for the major sulfides. During advancing diagenesis, sulfurization proceeds and remobilized microbial phosphates precipitated as massive apatite in the crosscutting veins together with Ni-sulfides (Fig. 1g), Ni-Fe-As sulfides, Mo-sulfides (MoS_2), euhedral pyrite, rarely chalcopyrite, and locally chlorite. Mo-sulfides were found interstitially to OM and include typically microbial derived pyrite (Fig. 1h). Shale CH11 differs in mineralogy being characterized by a veinlet network of carbonates and apatites, and a higher abundance of Mo-sulfides and sphalerite, whereas veinlets in shale CH25 are filled with barite, gypsum, apatite and sulfides. Vein carbonates only present in CH11, are high Mg calcite, containing < 8000 ppm Fe, 3000 ppm Mn, < 800 ppm Th, < 600 ppm F and locally 200 ppm U. They contain several hundreds ppm of S (SO_4?) and light rare earth traces. Sr can reach 500 ppm. Biogenic and abiogenic Ca-phosphates are present in both shales. They contain similar traces of F (average 3.5 wt.%) and Th (up to

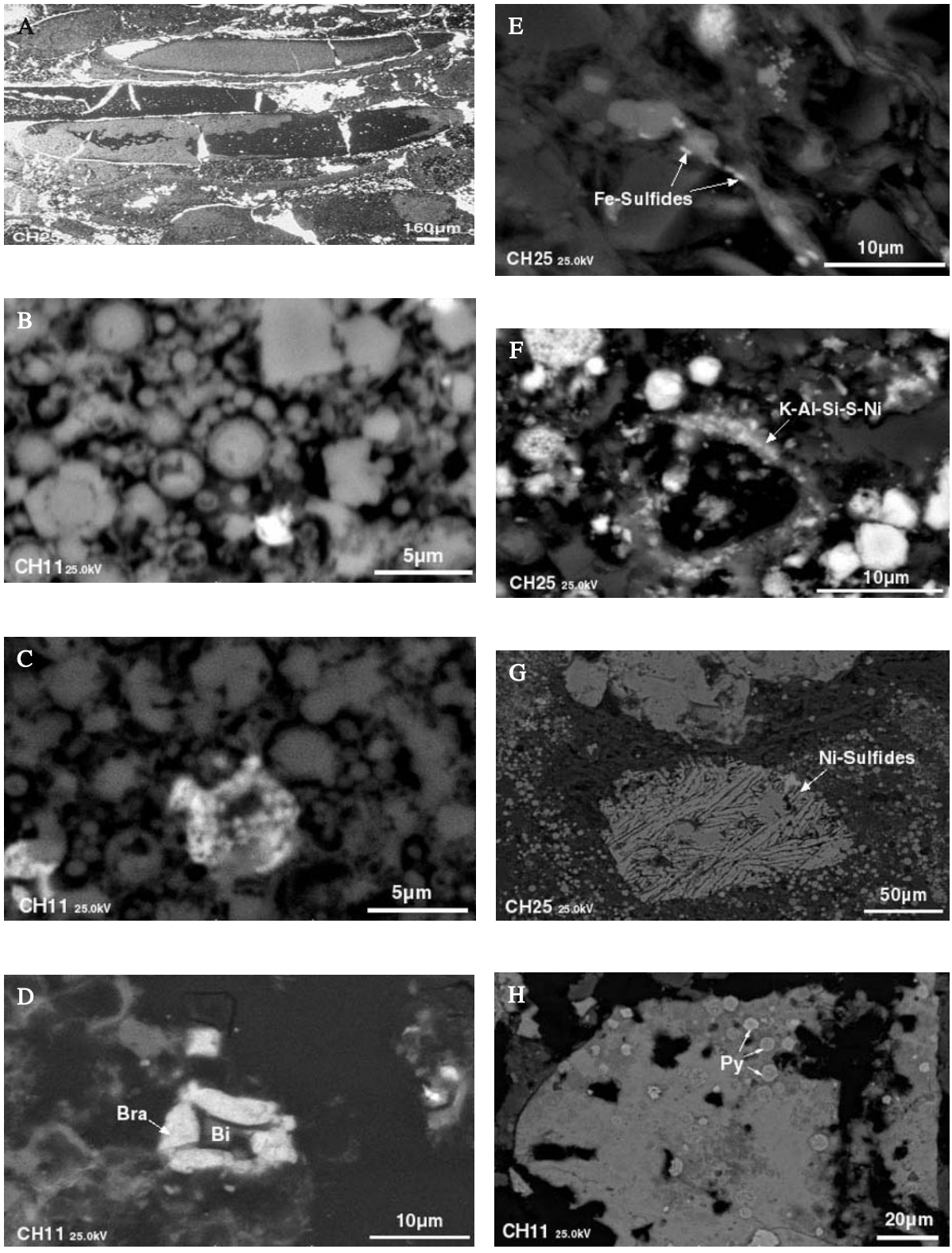

Figure 1: A - sulfurized and phosphatized organic matter (OM) lenses crosscut by veins, B - Ca-phosphate spherules on OM, C - pyrite spherules agglomerating to polygonal pyrite, D - brannerite around biotite, E - gel like phosphate containing sulfide crystals, F - K-Al-Si amorphous material containing sulfides, G - Ni-sulfides, H - MoS_2 including biogenic pyrite

1300 ppm). Mg, U, Cl and Na contents are higher in CH11 (Mg : average 0.13 wt.% , U: < 2000 ppm, Cl : 0.088 wt.%, F/Cl = 39, Na : 0.124 wt.%) than in CH25 (Mg : average 0.09 wt.% , U : < d.l, Cl : 0.012 wt%, F/Cl : 292, Na : 0.05 wt.%). S (SO_4?), is also higher in CH 11 compared to CH25. Only pyrite (py) and MoS_2 were analyzed. Pyrite of CH11 is richer in Ni (2.8-5 at%) compared to that of CH25 (0.01-0.4 at.%). Mo-sufides are three times richer in Ni than py. Pyrites contain in general several hundreds of ppm, rarely thousands of ppm Se, whereas MoS_2 host several thousands of ppm to about 1 at.% of Se.As contents are similar in py and MoS_2 (average 0.63at.%). Cu is in general below 0.08 at.%. Zn is preferentially partitioned into MoS_2, Cd and Pb were found as traces in both sulfides.

2.2 Geochemistry

Both shales contain about 13 wt.% organic C and 17.5 wt.% S. Shale CH25 is four times richer in SiO_2 than CH11, and contains higher Al_2O_3, K_2O and TiO_2, and Fe_{tot}. CH11 contains more than twice amounts of CaO, 10 wt. % of CO_2 and higher Ni, Se, As, Mo, Sb, U, Zn, Pb, Cd. This suggests a co-genetic process and fractionation (?) from Ba, Cu, Cr, Nb, Ta, Th, which are richer in CH25 (Tab. 1). The two samples show also one order of magnitude difference in the Se/S ratio (1.05×10^{-2} : CH11, 6.3×10^{-3} : CH25). It is interesting to note that, in spite of a highly reducing environment most of the iron was analyzed as trivalent iron. This might be due to intermediate oxidation states produced by biological processes.

REE pattern are identical for the two samples. They are characterized by a slight Ce and Eu negative anomaly indicating that seawater was the major fluid involved during precipitation and that no major Ce-bearing minerals are present (Fig. 2).

Table 1: Whole rock geochemical analyses of shales CH11 and CH 25. Note that C and part of the S is included in the LOI

wt.%	CHI-11	CHI-25	ppm	CHI-11	CHI-25
SiO_2	6.91	26.64	Er	9.88	8.7
Al_2O_3	1.46	7.3	Eu	5.49	5.95
Fe_2O_3	14.15	16.42	Ga	6.43	20.16
MnO	0.09	<L.D.	Gd	21.8	23
MgO	3.95	1.26	Ho	3.84	3.52
CaO	13.96	5.56	La	122.1	161.2
Na_2O	0.09	0.11	Lu	0.79	0.72
K_2O	0.29	1.92	Mo	69940	31170
TiO_2	0.06	0.37	Nb	1.039	6.145
P_2O_5	5.21	3.68	Nd	98.73	122.3
LOI	35.49	28.18	Ni	19520	13850
Total	81.66	91.44	Pb	531	299
Corg.	13.07	12.56	Pr	23.4	30.13
CO_2	58.57	48.68	Rb	8.98	62.14
FeO	0.77	0.88	Sb	344	194
S	18.89	16.71	Sm	19.7	22.7
Se (ppm)	2015	1075	Sr	467	303
As	11570	6186	Ta	0.08	0.54
Ba	868	1843	Tb	3.05	3.22
Bi	6.38	10.03	Th	2.05	8.81
Cd	106	57	Tm	1.24	1.03
Ce	182	266	U	425	190
Co	142	154	V	477	353
Cr	30	77	Y	232	173
Cu	895	1101	Yb	6.28	5.63
Dy	18.53	17.78	Zn	5377	879

3 Discussion and conclusions

Mo is preferentially trapped by sulfur-rich OM, and that organically fixed Mo remains immobilized as diagenesis progresses (Tribobillard et al. 2004). Our study shows that although both shales have similar $C_{org.}$ and S contents, and significant OM sulfurization, significant differences in rare metal concentration occur (Tab. 1). It is suggested that CO_2 (+/-P_2O_5) and CaO- in CH11 and SiO_2 in CH25 activities might, at least in part, have controlled the As, Mo, Se, Pb, Zn, +/- Ni and U enrichment in CH11, and the Ba, Ti, Cr, Nb, Ta, Rb enrichment in CH25. Both shales show important vein patterns with different mineralogy (carbonates-apatites in CH11, and sulfates-apatites in CH25), suggesting the same fluid event. These fluids were oxidizing and alkaline stabilizing sulfates, carbonates and phosphates. CO_2 might be generated during OM decay. If seawater is the origin of Mo and other metals (Mao et al. 2002), e. g.marine MoO_4^{2-} might become fixed in Mo-Fe-S cuboidal structures associated with pyrite (Vorlicek et al. 2004). The reaction pathway would involve conversion of MoO_4^{2-} to MoO_3S^{2-}, $MoO_2S_2^{2-}$ and MoS_3^{2-} in the presence of > 10^{-5} M biogenic H_2S. In the absence of S° do-

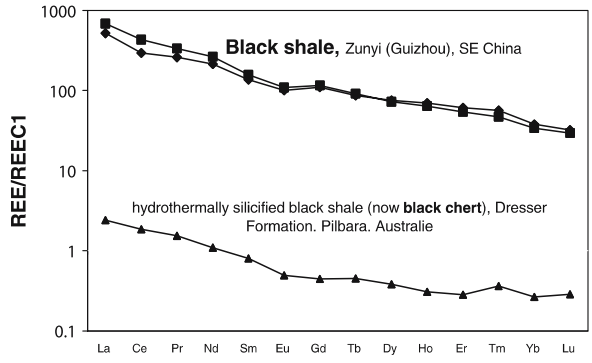

Figure 2: C1 normalized REE pattern of the two shales CH 11 (rhombs) and CH11 (squares)

nors, sulfide may replace the final O ligand to produce MoO_4^{2-} as a slow process. In the presence of S° donors, a faster reaction producing thermodynamically stable MoO_4^{2-} is possible through polysulfidic intermediates (Vorlicek et al. 2004). In the studied samples, Mo-sulfide mineralized OM was not observed. MoS_2 precipitated only interstitial to phosphatized-pyritized OM around biogenic pyrite. It contains about 7 wt% Fe and 3 wt. % Ni. Pure Ni-sulfides occur in veinlets in OM. However, colloidal Ni-Mo-S nodules are described from the Huangjiawan mine (Mao et al. 2002). In order to explain the rare metal concentration in these particular samples, we suggest an in-situ remobilisation process of the metals during early diagenesis related to desorption and biomineralization during OM decay, and precursor colloidal phases (K-Al-Si, Fe-Ni-As-Mo-S), followed by remobilization through fluid circulation shortly later. Hot hydrothermal fluid (99-263°C) influx was proposed based on fluid inclusions in quartz veinlets crosscutting the ore (Lott and Coveney 1996). The diagenetic degree of CH11 and CH25 is very low, and Mo should be immobile (Tribobillard et al. 2004). However, mobilization could have been produced by change in redox conditions during Ba-Si-Fe-Ca rich fluid infiltration, leading to the oxidation of sulfidic sulfur and OM. As these fluids reached a high $P_{CO2,}$ they became enriched in Mo, Se, As etc., migrated and precipitated into shale CH11. Although REE-patterns have strong seawater signature, they are identical with the REE pattern of an Archaean black chert that has a black shale precursor and derived from a hydrothermal dike (Orberger et al. 2004). A pronounced Eu positive anomaly from ore horizon was reported by (Steiner et al. 2001) favoring hydrothermal fluid influx. A volcanogenic environment is also supported by the high Se/S ratio of 10^{-2}-10^{-3} in this study. A mixture of seawater and hydrothermal fluids might be realistic.

Acknowledgments

Financal support: GDR Transmet, PAI Barrande, UMR IDES 4818 and FR 32 (Université Paris VI).

References

Coveney RM Jr, Murowchick JB, Grauch RI, Chen N, Glascock MD (1992) Gold and platinum in shales with evidence against extraterrestrial sources of metals. Chem Geol 99: 101-114

Kao LS, Peacor DR, Coveney RM Jr, Zhao G, Dungey KE, Curtis MD, Penner-Hahn JE (2001) A C/MoS_2 mixed-layer phase (MoSC) occurring in metalliferous black shales from southern China, and new data on jordisite. Am Min 86: 852-861

Lott DA, Coveney JM Jr (1996) Fluid-inclusions evidence for the origins of organic-rich Chinese nickel-molybdenum ores. Abstr. of 30th IGC, Beijing, Vol.2, 8-14 August: 713

Mao J, LehmannB, Du A. Zhang G, Ma D, Wand Y, Zeng M, Kerrich R (2002) Re-Os dating of polymetallic Ni-Mo-PGE-Au mineralization in Lower Cambrian black shales and its geologic significance. Econ Geol 47: 151-1061

Orberger B, Pinti D, Westall F (2004) Black shale origin of an Archean chert from the Dresser Formation, North Pole (Pilbara, Australia). Field Forum on Processes on the early Life (4-9 July), Barberton, South Africa

Steiner M, Wallis E, Erdtmann BD, Yuanlong Z, Yang R (2001) Paleogeography, Paleoclimatology, Paleoecology 169: 165-191

Origin of the Nchanga copper-cobalt deposits of the Zambian Copperbelt

Stephen Roberts, Ross McGowan
School of Ocean & Earth Science, Southampton Oceanography Centre, University of Southampton, Southampton, SO14 3ZH, United Kingdom

Adrian Boyce
SUERC, Scottish Enterprise Technology Park, East Kilbride, Glasgow, G75 0QF, United Kingdom

Abstract. The Cu-Co deposits of the Nchanga Mine in the Zambian Copperbelt are consistently hosted by arenites or arkoses with mineralization progressing for short distances into overlying shales. The ore horizons show a consistent association with flat-lying structures and in the Upper Orebody, are developed within thrust controlled antiformal structures. Hydrothermal alteration includes phlogopite ± sericite followed by dolomite precipitation. and available stable $\delta^{34}S$ of sulfides and $\delta^{13}C$ data for carbonates are consistent with "in situ" thermochemical reduction of a sulphate rich fluid. The new data reported here suggest a strong link between Cu and Co ore formation in the Zambian Copperbelt and the development of structures during basin inversion and the onset of the Lufilian orogeny.

Keywords. Copperbelt, cobalt, copper, sedimentary basins, sulfur isotopes

1 Introduction

The Zambian Copperbelt forms the southeastern part of the 900km-long Neoproterozoic Lufilian Arc; an approximately 550-530Ma old Pan-African fold belt. The Copperbelt preserves a spectacular scale of copper and cobalt mineralization, including the Nchanga deposits (Fig. 1). At Nchanga, two major economic concentrations of copper (and cobalt) are hosted by arenites and shales of the Lower Roan sequence of the Katangan Supergroup (Fig. 2). The Lower Orebody (copper only) and Upper Orebody (copper and cobalt) are hosted within arenitic units and within the base of overlying shales.

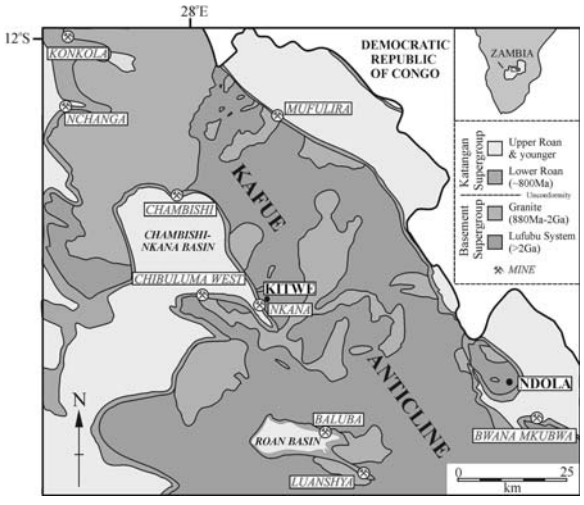

Figure 1: Location map of the Nchanga Mine.

2 Tectonics

Two distinct structural regimes are recognized in the Nchanga area, a weakly deformed zone of footwall

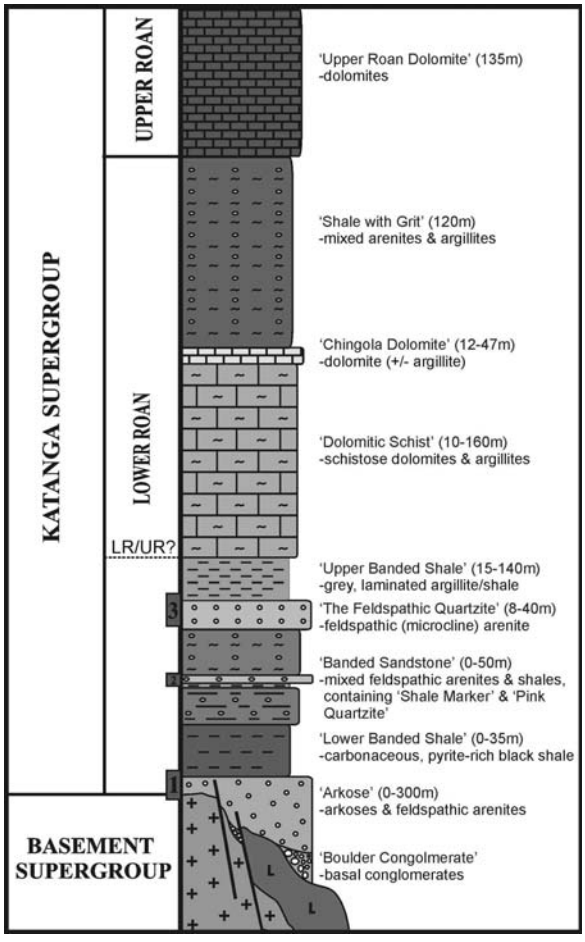

Figure 2: Stratigraphy of the Nchanga deposits showing the major lithologies, mining terms and the stratigraphic location of major orebodies: (1) Lower Orebody, (3) Upper Orebody.

siliciclastics, and a moderately to tightly folded zone of meta-sediments of the Katangan succession, excluding the Lower Arkose (Fig. 3).

The fold geometry of the Lower Roan package, shows vergence towards the NE and is controlled by internal thrust fault-propagation folds that detach at the top of the Lower Arkose or within the base of the overlying stratigraphy (Fig. 3). Faulting and folding are considered to be synchronous, as folding predominantly occurred at the tips of propagating thrust faults, with local thrust breakthrough.

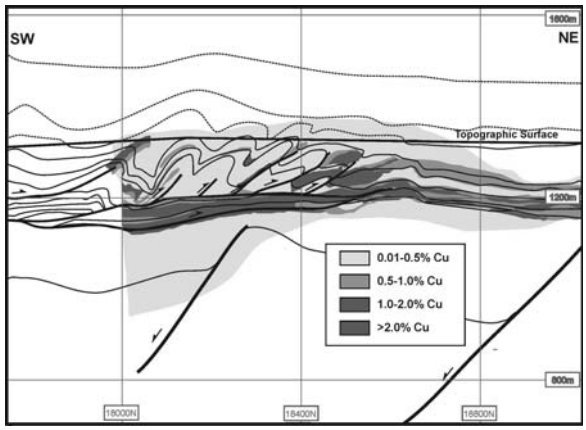

Figure 3: The distribution of mineralization at Chingola B (based on copper grade boundaries) plotted on to the section Mineralization is strongly related to the fault-propagation folds and controlling thrusts.

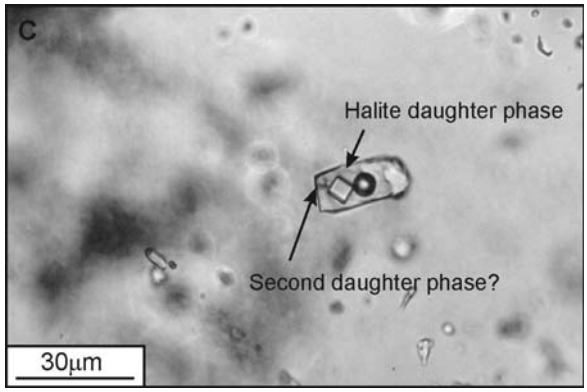

Figure 4: Saline fluid inclusions within quartz-carbonate-sulfide veins in proximity to ore horizons.

3 Ore mineralogy

The sulfide mineralogy includes pyrite, bornite, chalcopyrite and chalcocite, although in the Lower Orebody sulfide phases are partially or completely replaced by malachite and copper oxides. Carrollite is the major cobalt-bearing phase and is restricted to within a feldspathic arenite (Upper Orebody) and in particular within fault-propagation fold zones (Fig. 3). Hydrothermal alteration minerals include dolomite, phlogophite, sericite, rutile, quartz, tourmaline, and chlorite.

4 Fluid inclusion and stable isotope data

Quartz veins from the mine sequence show halite saturated fluid inclusions (Fig. 4) ranging from ~31-38 wt% equivalent NaCl, with homogenisation temperatures (ThTOT) between 140–180°C. Sulphur isotope data of diagenetic pyrites in the lower orebody show distinct, relatively low, sulphur isotope signatures ranging from $\delta^{34}S$ –1‰ to –17‰ whereas arenite- and shale-hosted copper and cobalt sulphides show $\delta^{34}S$ from –1‰ to +12‰ for the Lower Orebody and +5‰ to +18‰ for the Upper Orebody. There is also a clear distinction between the mean of $\delta^{34}S$ +12.1 ± 3.3‰ (n = 65) for the Upper Orebody compared with +5.2 ± 3.6‰ (n = 23) for the Lower Orebody (McGowan et al. 2003).

The $\delta^{13}C$ of dolomites from the units above the Upper Orebody give $\delta^{13}C$ values of +1.4‰ to +2.5‰, typical of marine dolomite.

However, dolomite from within shear-zones and alteration assemblages within the Upper Orebody show more negative $\delta^{13}C$ values: –2.9‰ to –4.0‰ and –5.6‰

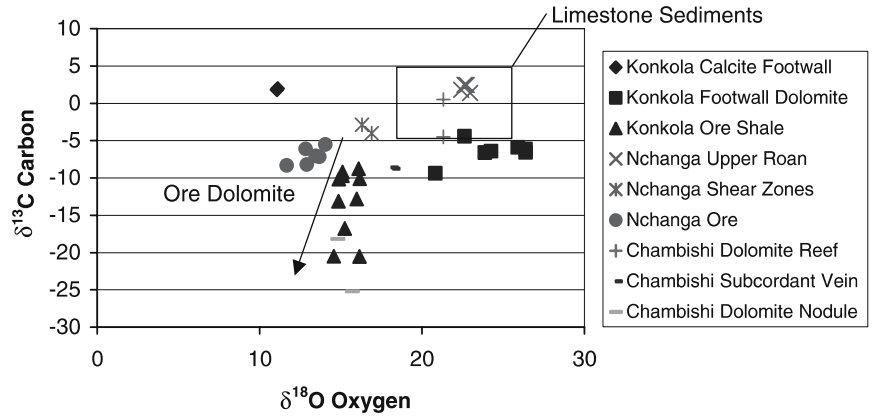

Figure 5: Carbonate data from the Copperbelt Deposits host rocks and Upper Roan lithologies. Konkola and Chambishi data from Sweeney et al. 1986 and Annels 1989.

This page intentionally blank

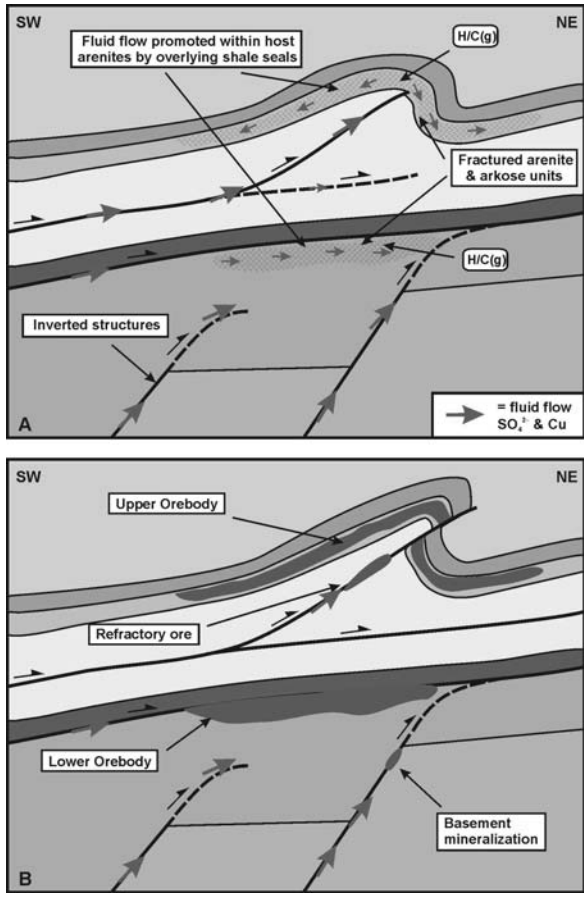

Figure 6: Models of ore formation in the Copper belt.

to –8.3‰, respectively. Similarly, Shear Zone and Upper Orebody dolomites show $\delta^{18}O$ values of +11.7‰ to +16.9‰, compared to Lower Roan dolomites, which show $\delta^{18}O$ of +22.4‰ to +23.0‰ (Fig. 5).

5 Summary

These data suggest a strong link between ore formation and the development of structures during basin inversion and the onset of the Lufilian orogeny. Ore horizons are consistently hosted by arenites with mineralization progressing for short distances into overlying shales, with Co ore horizons consistently associated with small thrust controlled antiformal structures. The hydrothermal alteration around the ores, initially suggests lower pH conditions (phlogopite ± sericite) followed by dolomite precipitation and is consistent with "in situ" thermochemical reduction of a sulfate rich fluid.

References

McGowan R, Roberts S, Foster RP, Boyce AJ, Coller D (2003) Origin of the copper-cobalt deposits of the Zambia Copperbelt: An epigenetic view from Nchanga. Geology 31: 497-500

Sweeney M, Turner P, Vaughan DJ (1986) Stable isotope and geochemical studies of the role of early diagenesis in ore formation, Konkola Basin, Zambia Copperbelt. Economic Geology 81: 1838-1852

Annels AE (1986) Ore genesis in the Zambian Copperbelt, with particular reference to the northern sector of the Chambishi Basin. In Boyle R.W et al. (Eds) Sediment-Hosted Stratiform Copper Deposits. Geological Association of Canada Special Paper 36: 427-452

Alpine type Pb-Zn-deposits (APT) hosted by Triassic carbonates

Erich Schroll
Institute of Mineralogy and Crystallography, University of Vienna, Althanstraße 14, A-1090, Vienna, Austria

Abstract. Pb-Zn deposits hosted by Triassic carbo-nates of the Eastern and Southern Alps are classified as APT deposits. The initial resources and reserves are totally estimated with up to 10.1^6 t Pb+Zn. Geological, mineralogical, geochemical and isotopic data indicate APT deposits as a subclass of low temperature Pb-Zn deposits hosted by carbonates which are usually referred as MVT deposits.

Keywords. Lead, zinc, isotopes, sulfur, Bleiberg, MVT

1 Introduction

Numerous Pb-Zn occurrences are known in Triassic sediments of the Eastern and Southern Alps (Fig. 1). Pb-Zn ores also occur in the Central Alps and in the adjacent European platform of South Germany. The ores are hosted by the Anisian dolomitic Muschel- kalk and by Carnian limestone, dolomite and shale. Economically important deposits occur along the Periadriatic Lineament (Fig. 1): In north Bleiberg (Austria) and Mežica (Slovenia) in the Drau Range and in south Raibl/Cave di Predil and Salafossa in Italy. They are hosted by Carnian sediments. Deposits hosted by Anisian carbonates are generally small. Ores were mined in Topla (Slovenia) and in Auronzo (Italy). In the Northern Tyrolian Alps (western Northern Calcareous Alps), affiliated deposits were hardly economic. All these Pb-Zn deposits were classified as Alpine-type (APT) or Bleiberg-type (Brigo et al. 1977). The origin of these deposits was explained controversially by syn- and diagenetic/epigenetic models (Brigo et al. 1977) and the epigenetic MVT-model (Zeeh and Bechstädt 1994). In the Southern Alps, the Gorno Pb-Zn district in the Bergamasco Alps (Italy) is also hosted by Carnian sediments. The Gorno deposits were in- cluded into APT or classified as MVT (Rodeghiero and Camana 1999) and partly as SCT (Siliceous Crust-Type; Brigo et al. 2001). Moreover, further Pb-Zn occurrences are known in the Triassic of the Alps. Few of them were of economic interest in the past.

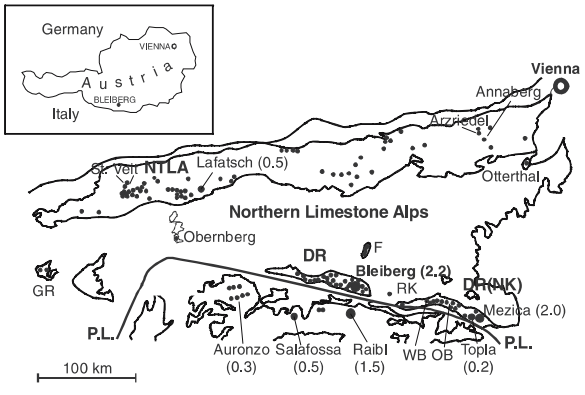

Figure1: Pb-Zn deposits and occurrences hosted by Triassic rocks in Eastern and Southern Alps which are separated by the Periadriatic Lineament (P.L.). Numbers in parenthesis are total production or estimated initial reserves and resources in 10^6 t Pb+Zn. Abbreviations: GR Graubünden, WB Windisch- Bleiberg, OB Obir, RK Rudnik, F Flattnitz; DR Drau Range, NK Northern NTLA Northern Tyrolean Calcareous Alps. Locations from Weber (1977a).

The aim of this contribution is to define the term APT by geological, mineralogical, geochemical and isotopic characteristics in the Alpine realm and to investigate whether the term ATP is qualified for a subclass of low temperature Pb-Zn deposits hosted by carbonates.

2 Geological setting

The ore-bearing Mesozoic carbonates overlie Permian and Lower Triassic sandstones, which cover a metamorphic basement. In the Northern Calcareous Alps, the Mesozoic strata were thrusted and folded by Late-Cretaceous nappe tectonics. The Drau Range was only affected by burial heating (Rantitsch 2001). The Eastern Alps and the Southern Alps are separated by the Periadriatic Lineament (Fig. 1) with a Paleogene/Neogene displacement of ca. 120 km. Triassic rocks show regionally different lithofacies types. The economically important APT deposits are hosted by the Carnian lagunal Wetterstein facies (limestone and dolomite). The local ore bearing Raibl Beds are composed of shale (or marl in Raibl) intercalated by carbonates. Overlying rock sequences are not affected by Pb-Zn mineralisation. In the Alps as well as in Southern Germany, extensive Pb-Zn ore occurrences are hosted by the Germanic lithofacies of the Triassic. In the Alps, small deposits (e.g. Rudnik, Flattnitz) are hosted by Triassic carbonates, which are tectonically intercalated into the pre-Alpine base- ment. Metamorphosed deposits were also described, e.g. Lengenbach/Switzerland (Knill 1996).

3 Mineralogical and geochemical characteristics

The mineral association is composed of galena, sphalerite, subordinately iron sulfides, ± barite and/or fluorite. The Pb/Zn ratio ranges between 1 and 1/20. Ba is corre-

lated with Pb, and F with Zn. Deposits of the Carnian stage contain fine-grained sphalerite and coarse-grained galena. Ores of the Anisian stage tend to fine-grained sulfides. Grain size of minerals is partly controlled by the thermal overprint, which varies between burial heating and medium-grade metametamorphism. Sphalerites are poor on Fe and locally influenced by enrichments of sedimentary iron sulfides.

Ores of the Anisian stage display higher Ag and Cu grades than the ores from the Carnian stage. Lead ores of the Carnian stage of the Drau Range district and Raibl and Salafossa are extremely poor on Ag. Zinc ores display higher contents of Ag than lead ores. Contrary, lead and zinc ores from the Northern Tyrolian Calcareous Alps are rich on Ag (100 to 200 ppm) and Cu (100 to 500 ppm). The APT zinc ores are indicated by Ge-Tl-As association and Ga/Ge ratios <1. The Ge grade amounts up to 1500 ppm in zinc ores from Bleiberg (average 200 ppm Ge) and Raibl (average 500 ppm Ge). Contrary, sphalerite from the Gorno district shows Ge-Cu association and enrichment of Ga. Sphalerites from the eastern Northern Calcareous Alps are relatively poor on trace elements, whereas galena is mostly Ag-bearing (Schroll 1996).

4 Isotopic characteristics

4.1 Lead isotopes

Homogeneous isotopic compositions are reported from Bleiberg and almost all deposits of the Drau Range district, from Raibl and from the Northern Tyrolian district (Köppel and Schroll 1988). The ore leads derived from feldspars (Köppel and Schroll 1988). The two-stage model of lead isotope evolution (Stacey and Kramer 1975, t_1=3.7 Ga) reveals appro- ximately realistic uranogenic model ages for common rock lead. Fig. 2 and 3 display uranogenic and thorogenic model ages (t_2) plotted against the geochemical parameters μ_2 and W_2, i.e. $^{238}Pb/^{204}Pb$ and $^{232}Th/^{204}Pb$ after. The thorogenic model ages are generally lower than the stratigraphic ages. Both diagrams show clearly that model ages of galena from ore districts of Northern Tyrolian Calcareous Alps, the Drau Range and Southern Alps are correlated with μ_2 and W_2 ("APT-trend"). This fact indicates a mixing of orogenic (Hercynian) lead and upper crustal lead. The ore lead of each deposit is isotopically homogeneous with few exceptions. Only Topla does not plot in the field of the APT-trend. The Topla ore lead corresponds to Devonian source rocks. Orogenic lead is typical for primary rock lead and lateral secreted galena ("nodule galena" in Fig. 2 and 3) and for lead of deposits hosted by the Germanic facies (Köppel and Schroll 1988).

With few exceptions the t_2/W_2-diagram (Fig. 3) is comparable to the t_2/μ_2 -diagram (Fig. 2). In the diagram of the uranogenic lead (Fig. 2), lead from Mežica is nearly identical to lead from Bleiberg, while the diagram of thorogenic lead indicates that the source of Mežica ore lead was not identical in all. The APT trend, however, is distinctly recognizable. The occurrences hosted by the Germanic facies are separated in both diagrams. The t_2-μ_2 diagram of uranogenic leads (Fig. 2) demonstrates model ages which are stratigrapically too high (B-type lead) or too young (J-type lead). Radiogenic lead is indicated in lead ores from Oberberg/Brenner or Lengenbach/Binn Valley. Tiny galena crystals from Carnian evaporites showed an uranogenic model age at –2000 Ma (in Weber 1997b). Fig. 2 displays scattered data for the metamorphosed Anisian deposit Lengenbach/ Binn Valley (Switzerland). Ore lead that originates from shale or argilliferous matter tends to realistic model ages (N-type lead).

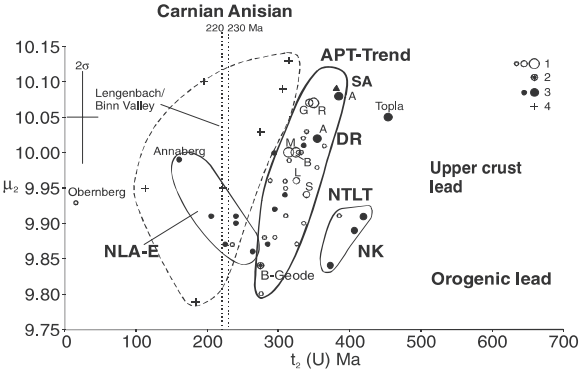

Figure 2: t_1-w_1 of uranogenic leads ($^{206}Pb/^{207}Pb$). Abbreviations; 1 Carnian deposits, 2 nodule galena (B-geode), Bleiberg, 3 Anisian deposits, 4 Lengenbach (Switzerland), A Auronzo, B Bleiberg, G Gorno, L Lafatsch, M Mežica, R Raibl, S Salafossa; SA Southern Alps, DR Drau Range, NK Northern Karavancs, NTLT Northern Tyrolean Calcareous Alps, NLA-E Northern Calcareous Alps –East.

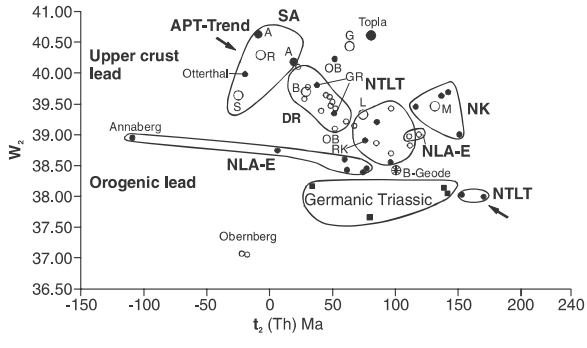

Figure 3: t_2 -w_2 diagram of thorogenic lead (208Pb). Abbreviations: 1 Carnian deposits, 2 nodule galena (B-geode), Bleiberg. 3 Anisian deposits, 4 Lengenbach/ Binn Valley (Switzerland); A Auronzo, B Bleiberg, G Gorno, GR Graubünden, HOB Obir, L Lafatsch, M Mežica, R Raibl, S Salafossa , RK Rudnik. Laed isotope data: Köppel and Schroll (1988), Knill (1996) and in Weber (1997b).

4.2 Sulfur isotopes

Sulfur is derived from the coeval seawater, evaporites and partly epigenetic sulfur. The $\delta^{34}S$ values of the coeval seawater differ in the Anisian stage with about 25‰ and in the Carnian stage with ca. 16‰ (Schroll and Rantitsch 2005). Figure 4 displays the $\delta^{34}S$ range from selected deposits. Four main types of $\delta^{34}S$ pattern are distinguished: (1) Deposits with a wide spread of $\delta^{34}S$ values of sulfide sulfur and a trend to isotopically depleted sulfur > – 20 ‰ and $\Delta\ \delta^{34}S$ values ($\delta^{34}S_{seawater} - \delta^{34}S_{sulfide}$) of up to 40 ‰ (e.g. Topla, stratiform ores at Bleiberg); (2) Deposits with a medium spread of $\delta^{34}S$ values of sulfide sulfur and $\Delta\ \delta^{34}S$ values ($\delta^{34}S_{seawater} - \delta^{34}S_{sulfide}$) > 30‰ (e.g. vein-type ores at Bleiberg and Mežica); (3) Deposits with sulfide sulfur around 0 ‰, a small spread of $\delta^{34}S$ values of sulfide sulfur and $\Delta\ \delta^{34}S$ values ($\delta^{34}S_{seawater} - \delta^{34}S_{sulfide}$) of < 20‰ (e.g. Gorno); (4) Deposits with heavy sulfide sulfur, a small spread of $\delta^{34}S$ values of sulfide sulfur and $\Delta\ \delta^{34}S$ values ($\delta^{34}S_{seawater} - \delta^{34}S_{sulfide}$) < 10 ‰, (e.g. Arzriedel, Lower Austria).

Type 1 is characteristic for activity of sulfide reducing bacteria (SRB) in an open system and bacterial sulfate reduction (BSR). Early diagenetic ores as well as last stage mineralisation were triggered by BSR. Type 2 indicates other conditions for SRB or a mixing with other sulfur sources. Type 3 may be explained by epigenetic hydrothermal sulfur. Type 4 is typical for thermal sulfate reduction (TSR).

4.3 Strontium isotopes

Strontium isotope geochemistry of carbonate and sulfate samples from Bleiberg indicate two main sources: seawater and ore fluid (Schroll 1996).

4.4 Carbon and oxygen isotopes

$\delta^{13}C$ and $\delta^{18}O$ values from carbonates, gangue minerals and cements follow the diagenetic trend. The transition of the fluid regime to meteoric water is linked with uplift tectonics (Schroll 1996, Schroll et al. accepted).

5 Fluid chemistry

Crush-and-Leach data suggest that the metals were leached and transported by Cl-rich fluids. The Cl/Br-Na/Br diagram displays the evaporitic trend. Mixing with meteoric water is not identifiable. Late- diagenetic processes are indicated by Na-depletion of fluids (Schroll and Prochaska 2004).

6 Discussion

The Pb-Zn occurrences of the Eastern Alps are subdivided into the deposits of the APT group and uneconomical occurrences: of the early-diagenetic extensive type mineralization (Laznicka 1985) and genetically different occurrences formed during the Alpine orogeny. The second group is characterized by orogenic or radiogenic lead. Mineralizations during Alpine orogeny are indicated by TSR, e.g. Annaberg, Arzriedel (Fig. 4), and radiogenic lead, e.g. Obernberg/Brenner and some occurrences hosted by Carnian evaporates (Fig. 4).

The APT group is signified by homogeneous lead isotopes (Köppel and Schroll 1988). Thus, prolonged large scale paleohydrologic systems have to be supposed (Heijlen and Muchez 2003). The APT deposits are characterised by stratigraphic control (in Weber 1997b), by sedimentary ore textures (Schulz 1964), by trace and minor element geochemistry (Schroll 1996), by isotopically depleted sulfide sulfur isotopes (Schroll and Rantitsch 2005), by SRB activities in early-genetic ores (Kucha et al. 2005), by saline ore fluids (Schroll and Prochaska 2004) and fluid-rock interactions at low temperatures (Möller 1987). It is important to note that the mineralogical and geochemical characteristics of the Gorno ores are comparable with ores from the classic MVT-deposits.

The classic MVT districts (Leach 1994) – proposed as subclass Viburnum Trend (VTT, Bradley and Leach 2003) – show major differences compared to APT, e.g. large time gap to the stratigraphic age, oilfield or coalfield brines, dominance of TSR, preferably coarse grained ores, sphalerite Ga-Ge-Cu association, radiogenic lead isotopes, heterogeneity of lead isotopes in growth zoning of crystals. Lateral flow of meteoric fluids led to heterogeneous and radiogenic lead (Heijlen and Muchez 2003). Apart from the lead isotopy, deposits, which are generally classified as MVT, correspond widely to features of the classic MVT (Misra 2000).

APT deposits, however, are similar to IRT (Irish type) regarding stratiform ores, sedimentary ore textures and BSR derived sulfide sulfur in early-diagenetic ores. How-

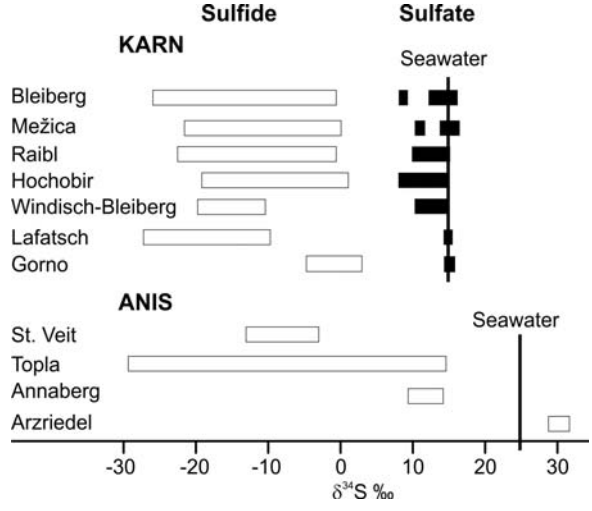

Figure 4: Sulfur isotopes in sulfides and sulfates show the difference between Carnian and Anisian deposits.

ever, a significant difference is the high fluid temperatures at IRT deposits (Anderson et al. 1998).

APT-deposits are a subclass of the generic class "Low-temperature Pb-Zn deposit hosted by carbonates" (LTC). Sheppard and Sharef (1990) proposed the term "shale and carbonate hosted (CSH) deposits" to avoid the problematic MVT term. Each generic term should be free of geographic context, like VMS und SMS. Compared with IRT and MVT deposits, APT-ores display properties from both types.

7 Conclusions

The Pb-Zn occurrences of the Eastern and Southern Alps hosted by Triassic are not genetically uniform. They originate from saline fluids reacting with silicates at all time. The activity of hydrothermal fluids ranges from lateral segregation to large scale paleohydrologic system. The origin of the APT- deposits, however, is related to basinal developments and geological events during the platform stage. The APT deposits are affected by their thermical history during burial and the Alpine orogeny. APT-deposits are distinguishable from other ore occurrences hosted by Triassic carbonates.

The APT-deposits define a subclass of "Low-temperature Pb-Zn deposit hosted by carbonates" whose ores were placed near to the surface on a carbonate platform, not influenced by thermal sulfate reduction.

References

Anderson IK, Ashton JH, Boyce A.J, Fallick AE, Russel MJ (1998) Ore depositional processes in the Navan Zn-Pb deposit, Ireland. Econ.Geol. 93: 535-567

Bradley DC, Leach DL (2003) Tectonic controls of Mississippi-Valley type lead zinc mineralization in orogenic fores-lands. Mineralium Deposita 38: 65-667

Brigo L, Kostelka L, Omenetto P, Schneider H-J, Schroll E, Schulz O, Štrucl I (1977) Comparative reflections on four Alpine Pb-Zn deposits. In: Klemm D, Schneider H-J (eds) Time- and Strata-bound Ore Deposits, Springer, Berlin, Heidelberg, New York: 273-293

Brigo L, Camana D, Rhodeghiero, Potenza R (2001) Carbona- te-hosted siliceous crust type mineraliztion of Carnic Alps (Italy, Austria). Ore Geology Reviews 12: 199-214

Heijlen W, Muchez P (2003) Paleohydrologic and geodynamic framework of carbonate-hosted Zn-Pb mineraliztion in Europe and North America: Insights from fluid composition and Pb isotope systematics. In: Eliopoulis D et al. (eds) Mineral Exploration and Sustainable Development 2: 681-684

Generation of hydrocarbons: Mechanism of reaction, geologic and experimental evidence

N.G. Stenina
Institute of Geology SB RAS, Novosibirsk, 630090, Russia

A.K. Gutakovskii
Institute of Physics of Semiconductors SB RAS, Novosibirsk, 630090, Russia

L.M. Plyasova
Institute of Catalysis SB RAS, Novosibirsk, 630090, Russia

Abstract. A reaction for synthesis of hydrocarbons is considered in terms of a conceptual aqua-complex [$2SiO_3$ – OH_2 – $M^{n+}2M^{m+}O'_4$] (n = 1, 2; m ≥ 3, O' - volatiles). Structural and chemical rearrangements are catalyzed within clay medium. Catalytic reactions are triggered by energy disequilibria in mineral systems caused by strain from the burial and compaction of sediments and by rock deformations during which C substitutes for Si in argillaceous rocks. Organic matter reduces C, which participates in the synthesis of hydrocarbon products. At present, this reaction is taking place in the bottom sediments of the Solenoe Lake (Kulunda steppe) located within one of several tectonic zones that parallel the main orogenic belt of the Altai. Geologic evidence and results of complex study of the bottom sediments support the relevancy of the proposed reaction mechanism, which combines "organic" and "inorganic" viewpoints on the origin of oil and gas.

Keywords. Hydrocarbons, clay, aqua-complex

1 Introduction

Prospecting for and extraction of oil and gas deposits depend strongly on understanding how the formation of hydrocarbon products occurs in nature. At present, there are two contrary extant concepts of origin of oil and gas. One, the "organic" theory, refers to data from stereochemistry, which implies formation from natural hydrocarbon products including those ones typical of bio-organics and notes that many large deposits are hosted by sedimentary rocks rich in organics. The proponents of the "inorganic" view address to numerous cases of hydrocarbon mineralization in rocks of various kinds and to a lack of balance between the petroleum bodies and the buried fossils.

As discussed at recent conferences , applications from the field of geodynamics may help solve this problem. Geodynamics implies an active role of the mineral continuum in the formation of mineral deposits. Specifically, the accepted theory with its notions of "source", "transport" and "deposition" of metals gives way to an understanding of an active role of the whole mineral continuum whose evolution "works" for concentrating useful elements in deposits, and of the energy aspect of these processes. However, after putting the problem this way we face the question of wondering what specific mechanism guides the alteration of the rock matter. And does a universal mechanism for various rocks exist? If the Earth can be viewed as a single entity, the answer is likely to be yes.

2 The Aqua-complex approach

The concept of the aqua-complex [2(Si, T) O_3 – OH_2 – $M^{n+}2M^{m+}O'_4$] (Fig. 1) is based on data obtained from studies of the alteration of minerals in the rocks of gabbro-granite series (Stenina and Distanova 1991). The aqua-complex is composed of three parts: the left part (SiO_2) is acid, the right (MO_2) is basic; the water molecule is presented as a charged tetrahedron built up in the centre, as a redox bridge between both parts. This model is supported by the "quartz" – water structure proposed by Bernal and Fowler (1933). On the basis of our own and published data, the aqua-complex was proposed as a geochemical entity, responsible for: i) the diversity of mineral matter, ii) structural-chemical transformation and redeposition of mineral matter, iii) element associations, iv) formation of granitic melt, v) conversion of energy within the Earth's crust (Stenina 1995).

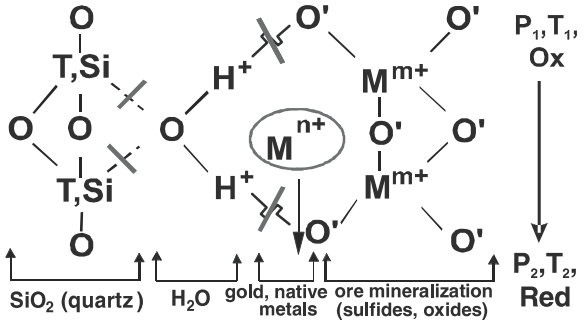

Figure 1: Model for aqua-complex: T – tetravalent ions (C, Sn, Pb, U); M^{n+} - uni and di--valent cations (Na, Au, Cu, Fe^{2+}, etc).; M^{m+} - multivalent ions (Al, Fe^{3+}, As, Mo, etc.); O` - volatiles; --- donor-acceptor, ~ - hydrogen bonds. Combined state as a structural unit of mineral-forming medium and disintegration into quartz–water-ore as a result of redox inversion and/or P, T drops in mineral system.

Table 1: Energies of chemical bonds with oxygen (from Gurvich et al. 1974)

Elements	E (kcal/mol)
C (T)	**256,16 ± 0,08**
Si	190 ± 2
U	180 ± 4
Al (M^{m+})	120 ± 3
Fe	97 ± 3
W	160 ± 10
Y	170 ± 3
Nb	180 ± 3
La (REE)	190 ± 10
Cu (M^{n+})	63 ± 10

In metamorphism, the aqua-complex concept explains the driving forces and mechanisms of mineral replacement. The latter is stimulated by eliminating the excess energy caused by strain in rock deformation and sediment burial-compaction. The aqua-complex possesses a wide range of energies due to varied bond strengths of T and M cations within oxygen polyhedra (Table 1). Energy imbalances in a mineral system are reduced by the extraction from mineral matter of cations with appropriate M (T) — O bond energies and incorporating them into new species. This induces mineral matter to rearrange, and such a process parallels metamorphic replacement. Rock-forming silicates have complex structures with $[SiO_4]$ and $[AlO_4]$ tetrahedra as the major building units. It is unlikely that their transformation goes through complete disintegration and the formation of entirely new phases from separate atoms. The aqua-complex, the smallest unit from which all minerals may be derived, performs structural-chemical rearrangements. In effect, the left part of the aqua-complex corresponds to quartz and other simple oxides; the right side – to complex oxides, sulfides and other salts. Integration of both parts and whole aqua-complexes can yield a great diversity of silicate minerals. Atomic rearrangements in the mineral-forming medium proceed by exchange of chemical bonds, facilitated by water. Generation of hydrocarbons in sedimentary rocks was considered in terms of the aqua-complex concept.

3 Mechanism of reaction of synthesis of hydrocarbon products

In diagenesis, atomic rearrangements in the primary sediments proceed by exchange of chemical bonds facilitated by water. This process stops abruptly when a mineral system suffers drastic fluctuations in pressure, temperature or redox conditions. Under these conditions the weak donor-acceptor and hydrogen bonds, which exist between dipole water molecule and both, left and right radicals are broken, and the aqua-complexes disintegrate to SiO_2, water and MO_2 (Fig. 1). Ca (Sr, Ba) also play a significant role in destroying aqua-complexes. The structure of electron-shells prevents their incorporation into these species. Therefore, when the evolving matter confronts with the Ca-rich rocks, mineralization of the aqua-complex components occur. As a result, argillaceous-limestone-organics sediments are replaced by a quartz-silicate-carbonate association with sulfide, hydrocarbon and graphite mineralization. Figure 2 illustrates such transformations. Kaolinite, the most abundant phase in the early minerals, corresponds stoichiometrically to the (Si, Al) aqua-complex (compare Fig. 1 and the scheme in Fig. 2). Its matrix acts as a nucleus for mineral transformations. Strain in the argillaceous-carbonate-organic matter caused by rock deformation (tectonics) and burial compaction need to be reduced. This could occur by extraction of elements with higher energies of bonding with O than Al has (120 kcal/mol), incorporating them into the aqua-complexes, and the formation through these intermediaries of new mineral phases. Carbonaceous matter however, universally distributed in sediments, prevents such metamorphic reactions. The only possibility of reducing the excess energy is to substitute Si by C in the left part of the aqua-complex. Such a replacement proceeds easily because C ($2p^2$) and Si ($3p^2$) have the same outer electron-shell structure, but the energy of C-bonds in oxygen tetrahedra (256 kcal/mol) greatly exceeds that for Si (190 kcal/mol). As sediments are subjected to deformation, the resultant energy balance in the mineral system is relaxed through the substitution of Si in clay by C. Organic matter provides reducing potential in the aluminosilicate matter, that is, in the network formed by kaolinite aqua-complexes. This stimulates their disintegration and reduction of the constituent radicals. The behavior of C is of particular interest. C^0 generated during reduction can become graphite, and also it can participate in both oxidizing and reducing reactions to yield MCO_3 and C_nH_m products. At the point of redox transformation a metamorphic reaction proceeds (see Fig. 2). C_nH_m end products of this reaction cannot be regarded as completely new products. Primary humic and sapropelic organics are subjected to complex modifications and reworking on the clay matrix during diagenesis. First, together with carbonates, organics yield C to substitute for Si in kaolinite and other silicates. Second, an exchange of H and C occurs between the biogenic and mineral components of sediments. Third, at the expense of clay-carbonaceous material, vigorous synthesis of new hydrocarbon products occurs. Modified biogenic compounds are incorporated into the new phases, and this determines the complex characters of petroleum and other mature hydrocarbon products. Clay plays the role of a major reactive medium in these transformations due to the weak donor-acceptor and hydrogen bonds, which facilitate redistribution of chemical bonds within the aluminosilicate continuum.

4 Geologic and experimental evidence

The proposed processes seem to be taking place in the Solenoe Lake, located in the pre-Altai Kulunda steppe. Solenoe Lake is one of the numerous small lakes containing mineralized water as several kilometers-wide chains (Fig. 2). The chains of lakes parallel the southwestern–northeastern extension of the main ridges of the Altai Mountains. In the Kulunda steppe, they are distinguished by coniferous forests. These features allowed us to suggest that mineralized lakes owe their

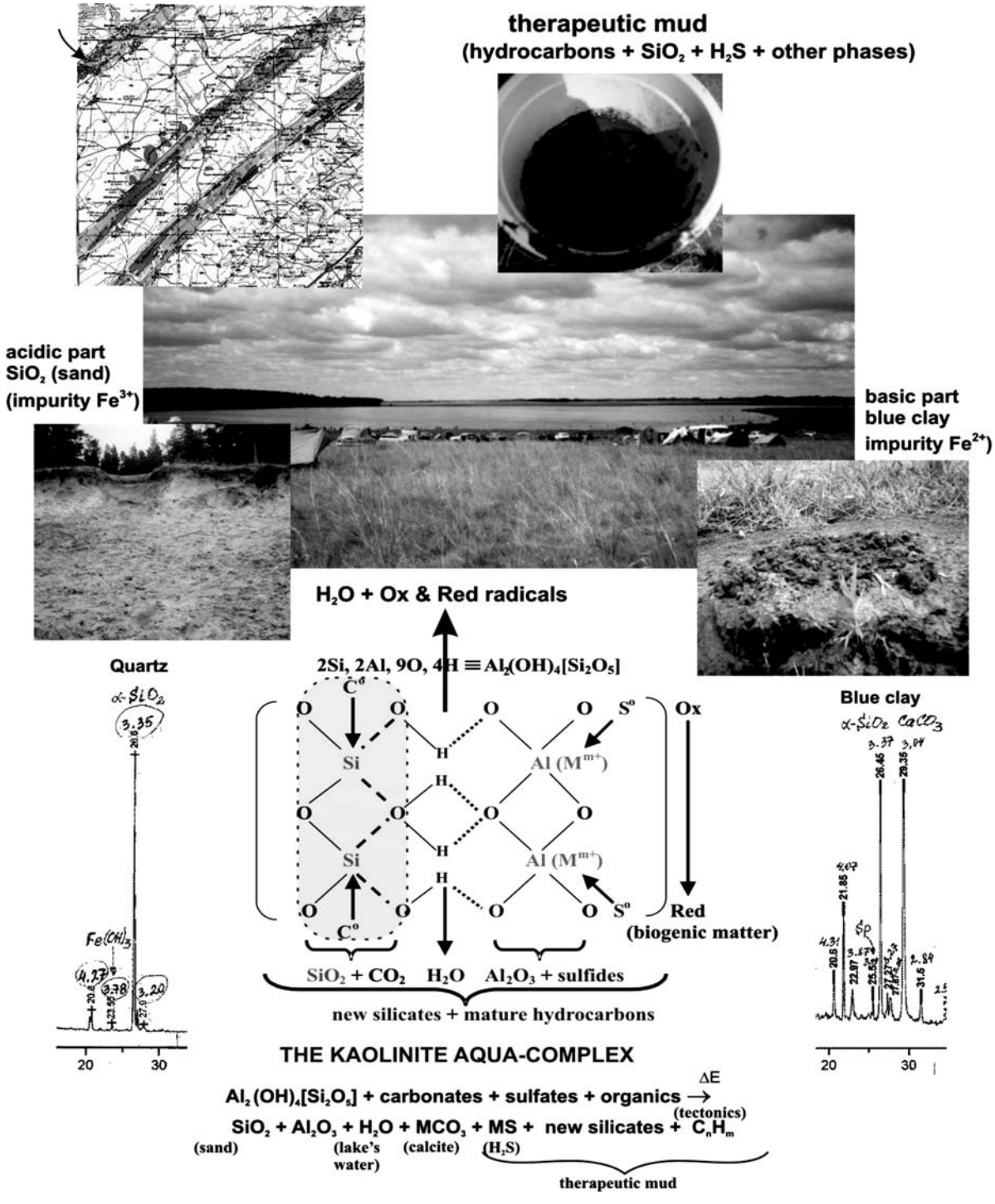

Figure 2: Geologic setting for the formation of hydrocarbons within a kaolinite matrix.

origin to the oscillatory fluctuations of tectonic strains caused by Altai orogeny. Rock deformations generate extra strain energies, which initiate our proposed reaction in sediments. The end products of this reaction are easily recognized in the Solenoe Lake (Fig. 2). Its left shore is composed of quartz sand.

Mineralized water of the lake itself stems from the water liberated from the central part of the aqua-complex. Hydrocarbon products are generated at the bottom sediments Solid products of the reaction like new carbonates, silicates, and others are recorded by X-ray analysis of the clayey matter presenting the soil of the right lake's shore. It resembles true grey-blue clay. However, X-ray powder diffraction detected no peaks of the clay minerals (Fig. 2). On the other hand, careful examination illustrated dark masses that stand out in the light-colored clay. They differ from the light-colored "clay" in having a simpler composition, a lower content of $CaCO_3$ and a higher content of SiO_2. TEM study showed that light-color argillaceous product is composed of well-faceted small crystals and larger amorphous particles. In the dark-colored "clay" no one well-faceted crystalline particle was observed. All products are presented by the fine poorly crystallized phases. The atomic structure of the semi-amorphous particles is apparent from HREM images that readily show the atomic rearrangements occurring within the clay matrix and explain why "blue clay" exhibits no peaks of clay minerals.

5 Conclusions

TEM and HREM data prove the mechanism of synthesis of hydrocarbon products on the clay matrix suggested on the basis of the aqua-complex concept. This mechanism combines previously antagonistic "organic" and "inorganic" viewpoints on the origin of oil and gas.

References

Bernal JD, Fowler RH (1933) A theory of water and ionic solutions, with particular reference to hydrogen and hydrogen ions. J.Chem.Phys 10: 515-548.

Geodynamics of the oil and gas basins (2004) Abstracts of the 2-and International Conference. IM Gubkin State University of Russia of Oil and Gas, Moscow (in Russian)

Gurvich LV, Karachevtsev GV, Kondrat'ev VN, Lebedev YA, Medvedev VA, Potapov VK, Khodeev YS (1974) Energies of breaking of chemical bonds. Potentials of ionization and electron affinity. Nauka, Moscow (in Russian)

Stenina NG (1995) Energy aspect in the formation of granitic magma and ore deposits. Pasava J, Kribek B, Zak K (eds) Mineral deposits: from their origin to their environment impacts, Balkema, Rotterdam: 539-541

Stenina NG, Distanova AN (1991) Structural-chemical transformations of silicate minerals as the indicator of their genesis (on the example of Kaakhem pluton rocks, Tuva). OIGG&M SB RAS, Novosibirsk (in Russian)

N_2-Ar-He tracing systematics of ore-forming fluids: A case study from the Songxi large-scale Ag(Sb) deposit, eastern Guangdong Province, China

Sun Xiaoming, Xu Li, Xue Ting, Chen Binghui, Sun Kai
Department of Earth Sciences, Sun Yatsen University, Guangzhou 510275, P.R.China

David I. Norman
Department of Earth and Environmental Sciences, New Mexico Institute of Mining and Technology (NMT), Socorro, NM87801, USA

Abstract. The Songxi Ag(Sb) deposit is a large-scale new type Ag(Sb) deposit discovered in the early of 1990's. There exist arguments on its genesis between submarine basic volcanic exhalation and shallow-seated medium-low temperature volcanic hydrothermal filling, with the ore-forming fluid either composed mainly of submarine hot brine, or derived mainly from magmatic water, and some amount of meteoric water. Analyses of N_2-Ar-He and He isotopic compositions in fluid inclusions clearly show that the ore-forming fluids of Songxi Ag(Sb) deposit are composed predominantly of formation water or basinal hot brine, the contents of magmatic water in the fluid inclusions are quite low, usually lower than 5%. According to the source of ore-forming fluids, the Songxi Ag(Sb) deposit should be belong to sedimentary basinal brine transformed deposits.

Keywords. Ore-forming fluid, N_2-Ar-He tracing systematics, sedimentary basinal hot brine, Ag(Sb) deposit

1 Introduction

The source of ore-forming fluids is one of the most important issues in studying a hydrothermal deposit. To date, the most common indicator of hydrothermal fluids's source is still δD-$\delta^{18}O$ isotopic composition analysis of fluid inclusions (Taylor 1974, 1997). Due to the following limitations of this method - 1. it needs several grams of pure minerals; 2. oxygen isotopes would have been exchanged between the fluid inclusions and oxygen-bearing host minerals such as quartz; 3. on a $\delta D/\delta^{18}O$ diagram, different fluids overlap to some extent - that it is necessary to explore some new indicators of ore-forming fluids. In recent years, several researchers have studied the source of ore-forming fluids by using of Sr isotopes (Wei et al. 1996) and He-Ar isotopic systematics (Hu et al. 1997), and some advances have been made.

Based on a vast amount of gas analyses from geothermal fluids in New Zealand and elsewhere, Giggenbach (1986) firstly introduced the concept that ratios among trace gases such as N_2, Ar and He could be used to estimate the magmatic, crustal and meteoric gaseous constitutes in geothermal fluids. The reason is that each of the three sources has distinctive plotting field in the NAH ternary diagram (Fig. 1) (Giggenbach 1991, 1992). Since the mid-1980's, Norman et al. (1987) have been analyzing gaseous composition in fluid inclusions in various ore deposits by means of quadrupole mass spectrometer. Based on the large amount of analytical data and the previous work of Giggenbach, Norman et al. (1994, 1996) proposed that the N_2-Ar-He ratios could be used as a new indicator of hydrothermal fluid source.

2 Geological setting of the deposit

The Songxi Ag(Sb) deposit is a large-scale, new type silver deposit. Tectonically, the deposit is located in the southern section of the Yong-Mei depression, which possesses some characteristics of a continental rift, and situated at the northern margin of Caigangshang Mesozoic volcano-sedimentary basin. The major host rocks are carbonaceous shale and sedimentary tuff in upper section of Early Jurassic Songling Formation. The mining district was intruded by andesite basalt dykes. Locally, the thickness of

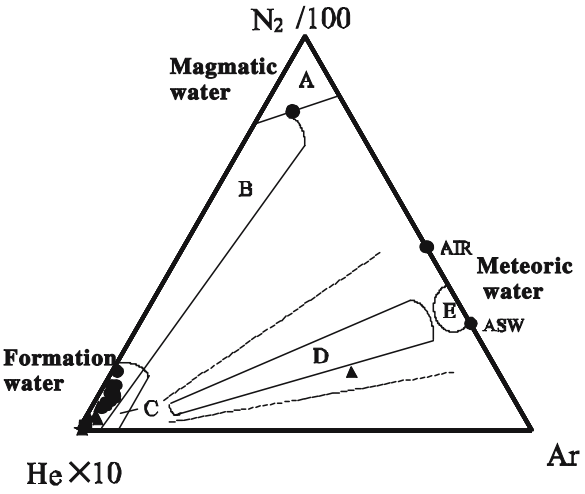

Figure 1: N_2-Ar-He ternary diagram of Songxi Ag(Sb) deposit. A. magmatic water field; B. formation water (sedimentary brine) field; C. rift basalt/rhyolite associated water field; D. deep-circulating meteoric water field; E.shallow-circulating meteoric water, including sea water, field. ASW: air-saturated water. The fields of various waters came from Norman et al. (1994).

the dykes is several tens meters. Most of the ore bodies are lenticular to vein-shaped. The major ore type is sulfide-quartz vein, and the predominant ore minerals are pyrite, stibnite, arsenopyrite and sphalerite. An EW-striking and SE-dipping open anticline has been recognized in the mining area. Compared with the known silver deposits in China and other countries, the deposit has some specific characteristics, such as the specific Ag-Sb mineralizing association and the obvious mineralizing zones of silver and antimony. In terms of genesis of the deposit, two different viewpoints were proposed: submarine basic volcanic exhalation (Zheng 1996) and shallow-seated medium-low temperature volcanic-hydrothermal filling (Yao et al. 1996). The former believed that the ore-forming fluids were composed predominately of submarine hot brine, while the latter thought that it was composed mainly of magmatic water, and a little meteoric water was mixed in the late stage.

3 Analytical method

Trace gases N_2, Ar and He in fluid inclusions were analysed at the New Mexico Institute of Mining and Technology (NMT), USA. Pure mineral samples (about 100mg each, 0.5-1.0mm in diameter) are put into swift crushing tube while being heated at about 100°C and pumping for at least 8*h* , until a pressure lower than $2x10^{-7}$Pa is attained in the gas extraction line. Crush the mineral samples in the vacuum chamber housing the mass spectrometer, and the released volatiles are quickly removed by the vacuum pumping system to a gas mass spectrometer in about one second. The volatile species are measured by a BALZER QMS420 quadrupole gas mass spectrometer. Analytical precision is usually better than 5%. The method is described in more detail in Norman et al. (1996). The He isotopic compositions in fluid inclusions were measured in the Mineral Deposits Institute of Land and Mineral Resources Department in China. Dry the mineral samples over at 105°C, then put the samples into a furnace while being heated at 500°C for about 1h. The released gases are purified and then analyzed by a Ukraine-made MI-1201G inert gas mass spectrometer. The ^{3}He is collected by a electronic multiplier, while the ^{4}He by a Faraday cup. The blank values of the ^{3}He and ^{4}He are $8x10^{-15}Cm^3STP$ and 8×10^{-10} Cm^3STP respectively. The analytical precision is 1-5%. The method is described in detail by Norman et al. (1987).

4 Analytical results and discussion

Trace gases N_2, Ar and He contents and He isotopic compositions of fluid inclusions in Songxi are presented in Tab.1. In the NHA diagram (Fig. 1), most of the analytical data are plotted in the field B and C, in other words, in the fields of crustal water (formation water or sedimentary brine) and rift basalt/rhyolite associated water) (Giggenbach 1991, 1992), excepting one datum. But in Table 1, the ^{3}He/^{4}He ratios of all the samples are lower than that of air ($1.4x10^{-6}$), R/Ra<1, so it is impossible for the ore-forming fluids to have derived mainly from rift basalt/rhyolite associated water, because studies show that the magmatic water associated with rift basalt/rhyolite should have R/Ra >4. Besides, it's reasonable to say that the hydrothermal fluids didn't came mainly from meteoric water or sea water, otherwise, most of tha data would be plotted in field D and E in Figure 1. Thus, the ore-forming fluids of the Songxi deposit can only be composed mainly of formation water or sedimentary hot brines.

From description of the geological background mentioned-above, the Songxi is situated in the Yong-Mei depression, which possesses some characteristics of continental rift. Is it possible for some mantle-derived magmatic water (MDMW) had been added into the orefroming fluid? From Table 1, we find that the R/Ra ratios of hydrothermal fluids vary between 0.0579 and 0.4464, averaging 0.2159. The known R/Ra ratios of MDMW are 6~9R/Ra (Stuart et al. 1995). Assuming 10% MDMW had been mixed with the ore-forming fluid, the mixture of the fluids would have a ^{3}He/^{4}He ratio greater than 0.6Ra, which is higher than those of Songxi. So the content of MDMW in the ore-forming fluid is quite low, usually lower than 5%, and not higher than 10% at most.

The study of N_2-Ar-He tracing systematics has provided new evidences for genesis of the Songxi Ag(Sb) deposit. According to source of the ore-forming fluids, the Songxi deposit should be belong to sedimentary basinal hot brine transformed deposits. The assumed mineralizing processes of the deposit are as follows: in the middle to late stage of Yanshanian Movement, affected by rifting and magma intrusion, the geothermal gradient in the Caigangshang volcano-sedimentary basin, which accumulated thick sediments from the Middle Devonian Period, increased greatly. The sedimentary basinal brine trapped in the sedimentary layers moved laterally to margin of the basin along sedimentary layers because of overburden pressure and increasing geothermal gradient. The expelled fluid would be transported to some favorable structure positions for mineralization such as tension fractures occurred in axial plane of the anticline, within which the ore minerals deposited.

Acknowledgements

This work is jointly supported by the National key Basic Research Development Program in China (No. 2002CB412610), NSFC (No.49773195, No.49502029, 40173025), Natural Sciences Foundation of Guangdong Province (No.970123), Trans-century Training Program Foundation for Talents by the Ministry of education of China. SXM thanks Prof. Andrew Campbell and Ms. Beverly Chomiak for their help during visiting NMT.

Table 1: N_2-Ar-He Contents (mol%) and He Isotopic Compositions of Fluid Inclusions in Songxi Ag(Sb) Deposit.

sample no.	mineral	location	ore type	mineral association**	crushing no.	N_2	Ar	He	$^3He/^4He \times 10^{-6}$	$^4He \times 10^{-6}$ (cm^3STP/g)	R/Ra*
97201Q	quartz	TD8 in -13m	Ag-Sb ore	Sb+Q	1	0.581166	0.000053	0.006866			
		section, Baoshan			2	0.519665	0.000074	0.003480			
					3	0.373786	0.000329	0.007253	0.242	0.48	0.1729
					4	0.608874	0.000152	0.018548			
					5	0.232133	0.000026	0.019687			
97201Sb	stibnite	TD8 in –13m	Ag-Sb ore	Sb+Q	1	0.259227	0.000164	0.038851	0.081	1.79	0.0579
		section, Baoshan			2	0.013119	0.000024	0.000962			
97209	quartz	TD4 in –13m	Ag-Sb ore	Q+Sb	1	0.220098	0.000145	0.013427			
		section, Baoshan			2	0.097213	0.000052	0.009473	0.484	0.32	0.3457
					3	0.305190	0.000096	0.011707			
97210	pyrite	TD4 in –13m	Ag ore	Py	1	0.790980	0.000577	0.007547	0.625	16.6	0.4464
		section, Baoshan			2	2.148841	0.051975	0.001275			
97257	quartz	ZK609, 208.75m	Ag ore	Asp+Sph	1	0.654579	0.000141	0.015407			
				+Sb+Q	2	0.530185	0.000176	0.013898	0.096	1.98	0.0686
					3	0.080460	0.000243	0.006304			
97299	quartz	ZK609, 407.75m	Ag ore	Py+Q	1	0.939319	0.000489	0.007163			
					2	0.517790	0.000285	0.007803	0.285	0.57	0.2036
					3	0.359293	0.000272	0.004058			

*R is $^3He/^4He$ ratios of samples, Ra is $^3He/^4He$ ratio of atmosphere($1.4x10^{-6}$). **Mineral: Q: quartz: Sb: stibnite: Py : pyrite; Asp: asenopyrite; Sph: sphalerite.

References

Giggenbach WF, Glover RB (1992) Tectonic and major processes governing the chemistry of water and gas discharges from the Rotorua Geothermal Field, New Zealand.Geothermics 21: 121-140

Giggenbach WF, Matsuo S (1991) Evaluation of results from Second and Third IAVCEI Field Workshops On Volcanic Gases, Mt.Usu, Japan, and White Island, New Zealand. Appl Geochem 6:125-141

Giggenbach WF (1992) The composition of gasses in geothermal and volcanic systems as a function of tectonic setting. In: Kharata and Maest(eds). Water-Rock Interaction, Balkema: 873-878

Giggenbach WF (1986) The use of gas chemistry in delineating the origin of fluid discharges over the Taupo volcanic: A review. Proc Intel Volcanol Congress, New Zealand 5: 47-50

Hu RZ, Bi XW, Turner G (1997) He-Ar systematics of fluid inclusions in pyrites from Machangqin copper deposit, Science in China 27(6): 503-508

Li YH, Song HB, Li JC (1997) Relation between polymetallic modules and submarine hydrothermalism in the central Pacific Ocean. Chinese Science Bulletin 42: 1980-1983

Norman DI, Moor JN,Yonaka B (1996) Gaseous species in fluid inclusions: a tracer of fluids and indicator of fluid processes. Proceedings of 21st Workshop on Geothermal Reservoir Engineering, Stanford University: 1-8

Norman DI, Musgrave J (1994) N_2-Ar-He compositions in fluid inclusions: indicators of fluid source. Geochim Cosmochim Acta 58: 1119-1131

Norman DI, Sawkins FJ (1987) Analysis of gases in fluid inclusions by mass spectrometer. J Chem Geol 61:1-10

Stuart M, Burnard PG, Taylor RP (1995) Resolving mantle and crustal contributions to ancient hydrothermal fluids: He-Ar isotopes in fluid inclusions from Pal Hwa W-Mo mineralization, South Korea. Geochim Cosmochim Acta 59: 4663-4673

Sun XM, Norman DI, SUN K, Chen BH, Chen JD (1999) N_2-Ar-He Systematics and Source of ore-forming fluids in Changkeng Au-Ag deposits, Central Guangdong, China, Science in China (Series D), 42(5): 474-481

Taylor HP (1997) Oxygen and hydrogen isotope relationships in hydrothermal mineral deposit. In: Barnes H L(ed). Geochemistry of hydrothermal Ore Deposits (Third edition), New York: Wiley: 229-302

Taylor H P (1974) The application of oxygen and hydrogen isotope studies to problems of hydrothermal alteration and ore deposition. Econ Geol 69: 843-883

Wen CS, Tu GC (1996) δD-$\delta^{18}O$-$^{87}Sr/^{86}Sr$ theoritical model for source of ore-forming fluids, Science in China 26(4): 373-377

Yao DX, Li ZL, Ye YF (1996) Geology and genesis of the Baoshan silver (antimony) deposit in eastern Guangdong , Mineral Deposits 15(2): 123-132 (in Chinese with English abstract)

Zheng QN (1996) Geological characteristics of a Ag(Sb) deposit formed by submarine basic volcanic exhalation. Mineral Deposits 15(3): 238-248 (in Chinese with English abstract)

Geochemistry and gold content of the Triassic cabonaceous cherts of the Sikhote-Alin, Russia

Yu.G. Volokhin, A.I. Khanchuk, V.V. Ivanov, V.T. Kazachenko, V.V. Sattarova
Far East Geological Institute of FEB RAS, 159, pr. Stoletiya, Vladivostok, Russia

Abstract. Triassic carbonaceous cherts are widesp-read in the Sikhote-Alin fold belt. They occur in a 4 to 20 m-thick sequence of interbedded cherts, carbonaceous cherts, and argillites that ranges in age from Upper Olenekian to Upper Anisian. The carbonaceous cherts are marine radiolarian rocks that contain 0.3 to 8.5 wt. % C_{org}. The majority of these rocks have undergone textural and mineralogical changes to a middle stage of catagenesis. Their organic matter contains low-grade oxidized humic acids with quinone, $>CH_2$, $-CH_3$ hydrocarbon groups. The $\delta^{13}C$ values are between –27.3 and –32.5 ‰. Carbonaceous cherts are anomalously enriched in V, B, Cu, Ni, Mo, Ag, and locally Au.

Keywords. Carbonaceous chert, geochemistry, precious metals, Triassic, Sikhote-Alin, Russia

1 Introduction

Mikhailov and Volokhin (1980) were the first to describe the carbonaceous cherts of the Sikhote-Alin fold belt. Subsequent fieldwork combined with stratigraphic, sedimentologic, and structural studies have defined the stratigraphy and age of the carbonaceous chert (Volokhin et al. 2003). Previous geochemical study of the carbonaceous chert and associated rocks has included major and trace element (Sn, Pb, Zn, Cu, Ni, Co, Cr, B, Ag, Mo, and Ga) analyses (Mikhailov and Volokhin 1980; Volokhin 1988). Advances in analytical methods have allowed the analysis of a wide range of elements that have previously not been recognized in the carbonaceous cherts of the Sikhote-Alin fold belt.

2 Geological setting of carbonace-ous cherts

The Triassic sediments of the Sikhote-Alin fold belt represent a basinal sequence that is up to 500 m-thick and ranges in age from Upper Olenekian to Rhaetian. Sediments are composed of interbedded siliceous mudstones, cherts and carbonate sediments. The carbonaceous cherts occur at the base of the sequence in siliceous offshore facies, but also in carbonate-siliceous facies (Fig. 1). Carbonaceous cherts comprise a 4-20 m-thick unit that we have informally named the Phtanitic member (Volokhin et al. 2003). This member consists of alternating beds of light-gray chert, argillite, and carbonaceous chert (15 - 30%, rarely up to 50%). The Phtanitic member overlies olive-green clayey cherts or siliceous mudstones and is underlain by dark-gray bedded cherts (Fig. 2). The age of the Phtanitic member is diachronous and varies from the Late Olenekian - Middle Anisian (Dalnegorsk) to the Middle Anisian (other sites) (Volokhin et al. 2003).

3 Methods

The mineralogy of the Phtanitic member was studied using light, TEM, and SEM microscopy, and X-ray diffraction. Major oxides and trace elements were analyzed with wet chemistry, and X-ray fluorescence, ICP-AES, and ICP-MS. Au and Pt were determined with ICP-MS, fire assay and AAS. Ten samples of carbonaceous cherts were dissolved with 0.1N NaOH for 3 days at the room temperature to obtain organic matter extracts. UV spectra of

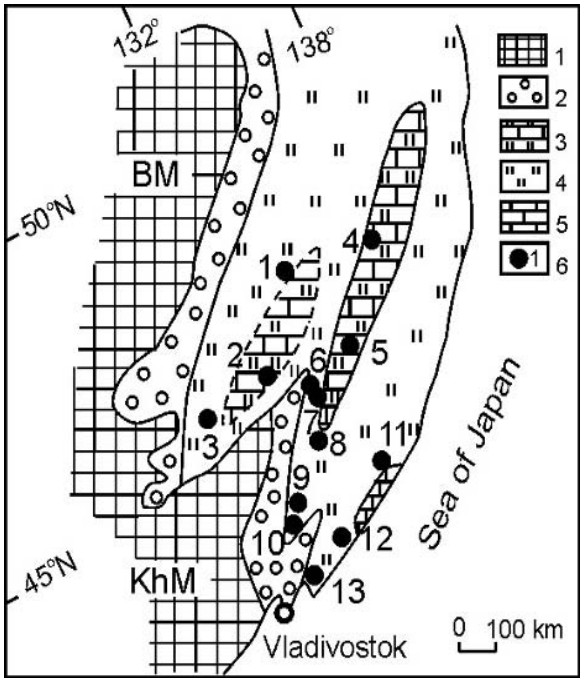

Figure 1: Locations of the Triassic carbonaceous cherts at the Sikhote-Alin folded belt. 1, ancient sialic massifs: BM – Bureya massif, KhM – Khanka massif; 2-5, types of the Triassic: 3, terrigenous shelf sediments; 3, bedded chert facies, 4, facies of bedded chert associated with micritic limestone, 5, reef limestone facies, 6, carbonaceous chert sections: 1, Khabarovsk; 2, Bikin; 3, Shichang; 4, Anuy; 5, Khor; 6, Matai; 7, Katen; 8, Dalnya; 9, Ogorodnaya; 10, Breyevka; 11, Dalnegorsk; 12, Olga; 13, Koreyskaya.

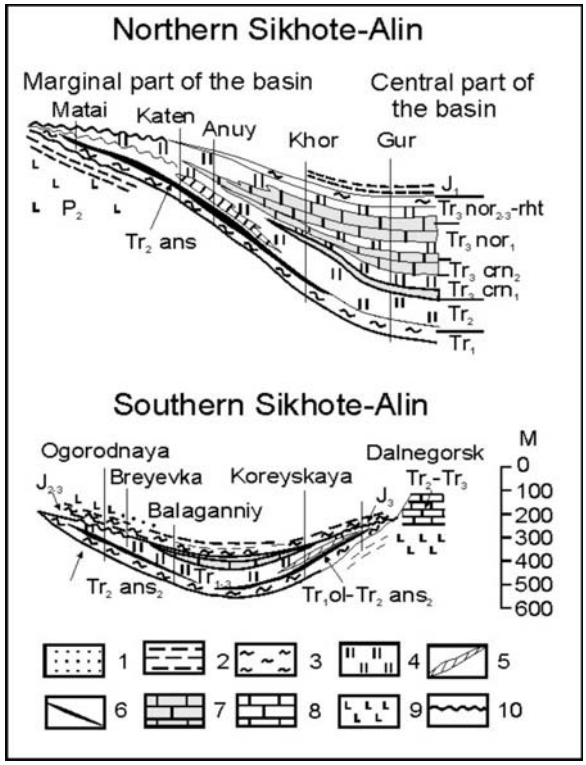

Figure 2: Position of the Phtanitic member in the Triassic siliceous formation (Volokhin et al. 2003).1, sandstone; 2, mudstone and siltstone; 3, siliceous shale and clayey chert; 4, gray and green chert; 5, red chert; 6, carbonaceous chert; 7, pelagic limestone; 8, reef limestone; 9, basalt and tuff; 10, stratigraphic hiatus.

the extracts were measured using a UV-spectrometer (Cecil CE 7200; Cambridge, England). IR-spectra of samples and their water-alkaline extracts in KBr were measured using IR-spectrometer with Fourier-transformation Vector-22 (Bruker, FRG).

4 Components and mineral composition

Carbonaceous cherts are primarily composed of recrystalized radiolarian skeletons, sponge spicules, quartz cements, clay minerals, and dispersed organic matter. They also contain grains of quartz and feldspar, and small clasts of basalt and claystone. The clay fraction of the carbonaceous cherts consists of dioctahedral (b=9.04 Å) $2M_1$ illite and minor amounts of 1M illite (Volokhin et al. 2003). Illite is also the dominant clay mineral in light-gray chert. Some thin dust-sized gold particles were found in residues of dissolved carbonaceous chert. Pyrite with minor chalcopyrite and pyrrhotite also occur in the carbonaceous chert. The maturity of carbonaceous matter in the cherts is variable. Regionally it consists of amorphous kerogen and bitumen, but it has been recrystalized to thin-dispersed graphite around magmatic bodies.

Table 1: UV- and IR-spectra of water-alkaline extracts from carbonaceous siliceous rocks

Sampe No.	IR-bands of humate ν_{max} (cm^{-1})	IR-bands of humate ν_{max} (cm^{-1})	UV-bands of humate ν_{mx} (cm^{-1})
Go-17	1084 Si-O	1670 Ar=O, 2924 CH_3, CH_2	n.d.
H-153	1089 Si-O	1672 Ar=O, 2927 CH_3, CH_2	270 Ar-H
H-155	1089 Si-O	1671 Ar=O, 2928 CH_3, CH_2	n.d.
H-155d	1092 Si-O	1670 Ar=O, 2926 CH_3, CH_2	270 Ar-H
R-102	1093 Si-O	1652 Ar=O	340 Ar=O
R-120	1087 Si-O 2922 CH_3, CH_2	1670 Ar=O, 2927 CH_3, CH_2	n.d.
Dg-2	1088 Si-O 2923 CH_3, CH_2	1670 Ar=O, 2923 CH_3, CH_2	n.d.
C-111	1090 Si-O 2927 CH_3, CH_2	1668 Ar=O, 2925 CH_3, CH_2	n.d.
C-153	1091 Si-O 2924 CH_3, CH_2	1672 Ar=O, 2925 CH_3, CH_2	n.d.
C-159	2090 Si-O 2924 CH_3, CH_2	1670 Ar=O, 2923 CH_3, CH_2	n.d.

Ar – aryl (phenyl, naphtyl etc.), *Alk* – alkyl (methyl, ethyl, etc.), *Ar=O*, quinone; *n.d.* – not determined.

Table 1: UV- and IR-spectra of water-alkaline extracts from carbonaceous siliceous rocks All water-alkaline extracts from carbonaceous rocks contain humate (Table 1). There are weak but characteristic absorption bands on UV-spectra at 270 nm (aromatic compounds) and 340-350 nm (quinone). This agrees with IR-spectroscopy results that show absorption bands at 1652-1672 cm^{-1} (quinone groups), and 2923-2928 cm^{-1} (methyl and methylene groups). The humate from carbonaceous cherts are low-grade oxidized. The preservation of hydrocarbon groups suggests a rather incomplete transformation of organic matter of the Triassic carbonaceous cherts.

5 Geochemistry of carbonaceous rocks

The carbonaceous rocks of the Phtanitic member contain C_{org} from 0.3 to 8.54 wt. %. An average C_{org} in carbonaceous clayey cherts (2.28 wt. %) is twice as high as carbonaceous cherts (1.08 wt. %). $C_{carbonate}$ is commonly less than 0.05 wt. %. $S_{tot.}$ varies from 0.004 to 0.7 wt. % with a mean of 0.14 wt. %. Sulfide sulfur dominates (~83%) over sulfate. The carbonaceous cherts are enriched 2-3 times V and 20-50 times in Mo and Ag above ordinary cherts. The elements content in places reach as much as 1300 ppm of V, 200 ppm of As, 890 ppm of Zn, 490 ppm of Cu, 350 ppm of Ni, 10 ppm of Ag, and 180 ppm of Mo. The most significant regional variation is found for Ba: 127-379

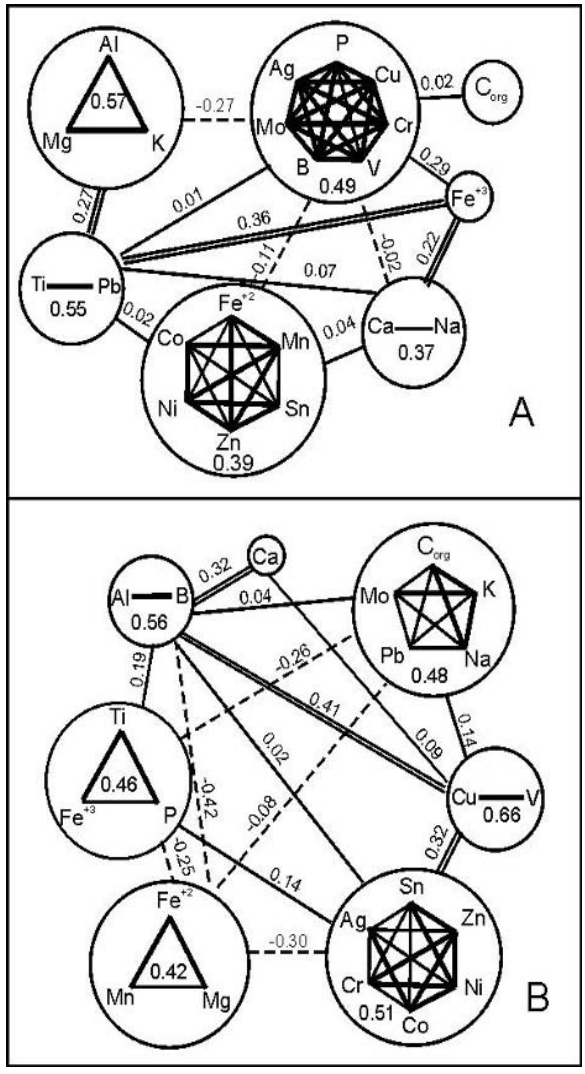

Figure 3: Element associations in carbonaceous siliceous rocks of the Sikhote-Alin. A, carbonaceous clayey chert; B, carbonaceous chert. Bold lines show correlations significant with 95% confident probability. Dashed lines connect antagonistic groups

ppm (Ogorodnaya) to 7000 ppm (Gornaya). Concentrations of other elements (ppm): Pb (5-300), Cu (25-950), Ni (35-350), Co (0,5-180), Cr (10-120), Cd (0,062-0,233), Hg (0,01-0,08), Tl (0,28-1,16), U (0,53-7,25), Th (1,48-5,43), Se (0,3-3), Rb (36-100), In (0,025-0,045), Cs (4-13), La (4-21), Ce (9-38), Bi (0,08-0,37), and Ge (4-8).

Element associations (Fig. 3) based on correlation coefficients (SiO_2 excluded) are shown on the structural schemes of Tkachev and Yudovitch (1975). In carbonaceous clayey cherts the associations of Al-Mg-K, Ca-Na, and Ti-Pb appears to be a terrigenous component. Trace elements associations separate into two distinct groupings. The assemblage of P-Cu-Cr-V-B-Mo-Ag suggests that these elements were dominantly accumulated by organ-

Table 2: Carbon isotope composition of carbonaceous cherts of the Phtanitic member

Sample No.	Section	SiO_2, %	C_{org}, %	$\delta^{13}C_{PDB}$, ‰
U-15	Big Ussurka	90,15	2,96	-30,2
U-16		85,48	6,04	-30,0
U-18		88,12	3,95	-27,6
Go-17	Gornaya	72,94	1,32	-30,1
H-153		78,18	2,21	-27,7
H-155		88,25	1,55	-27,9
H-169		87,45	1,99	-27,7
R-102	Dalnegorsk	87,10	1,42	-27,3
R-120		68,60	5,85	-27,3
C-156	Koreyskaya	74,46	8,54	-29,0
C-159		78,01	5,58	-27,9

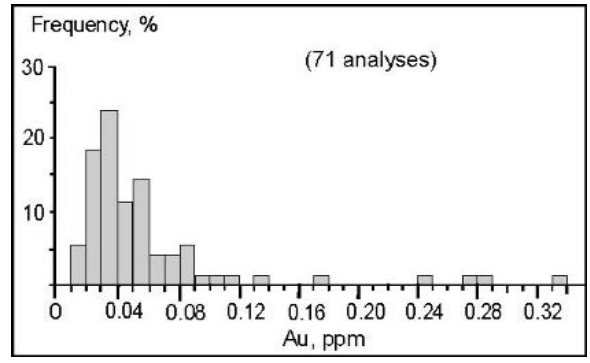

Figure 4: Frequency of Au distribution in carbonaceous cherts of the Ogorodnaya section

ics matter. The grouping of Fe^{+2}-Mn-Sn-Zn-Ni-Co (chalcophile elements) suggests they accumulated in sulfide minerals. Al, B, and Ca belong to of terrigenous silicate group as of Fe^{+3}-Ti-P.

In carbonaceous cherts there is a strong correlation of K and Na with C_{org}. The Sn-Zn-Ni-Co-Cr-Ag and Cu-V groups tend being connected with authigenic sulfides. However with the exception of Mo and Pb, the majority of elements generally accumulating in carbonaceous rocks show a poor correlation with C_{org}. The absence of a direct correlation might result from the oxidation and loss of organic compounds during post-sedimentation processes. The initial organic matter in sediments was likely 2-3-times that measured in the rocks.

The $\delta^{13}C$ of organic of the carbonaceous rocks vary within from –27, 3 to –32, 5‰ PDB (table 2). These values are close to those of Paleozoic bitumen and oil (Galimov 1973).

In recent sediments of the continental slope of Japan the close values of $\delta^{13}C$ (from –23 to -29‰) have lipid of marine organic matter (Shirinsky et al. 1974).

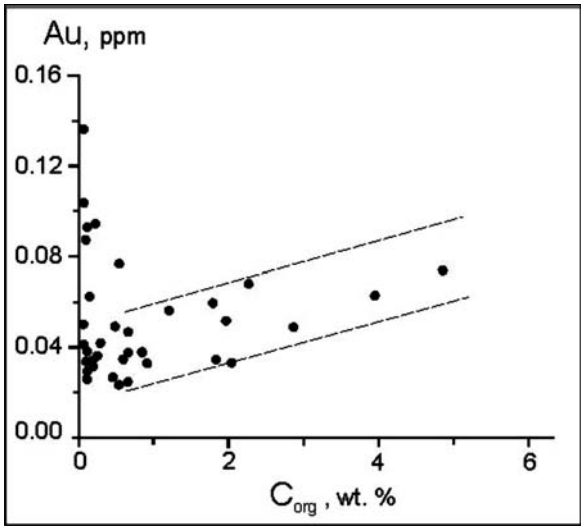

Figure 5: Au vs. C_{org} in rocks of the Phtanitic member.

6 Gold and platinum distribution

A detailed study of the gold distribution in the Phtanitic member reveals a heterogeneous distribution. Au was above detection in 50% of carbonaceous and in 60% of non-carbonaceous samples of the Ogorodnaya section (ICP-MS).

The maximum of Au was found in carbonaceous chert having the high SiO_2 content and relatively low C_{org} (0.3-0.5%). In non-carbonaceous cherts the Au concentration reaches 0.68 ppm (ICP-MS). An average Au content (anomalous samples excluded) is 0.017 ppm (ICP-MS) and 0.052 ppm (AAS). Fire assay with atomic-absorption finish gave Au lognormal distribution with mode 0.035-0.040 ppm (Fig. 4). This is 4 times higher than the clarke concentration in black shales (8-10 ppb, by Yudovitch and Ketris 1994). The positive correlation between Au and C_{org} in rocks containing >0.5% C_{org} (Fig. 5) suggests a genetic link between Au and organic matter.

The 7 samples with <0.5% C_{org} and high Au may indicate the redistribution or addition of Au during post-sedimentation processes. The Pt and Pd concentration was above their 0.001 ppm detection limit in 13 of 56 samples of carbonaceous cherts (fire assay with AAS finish). The maximum of Pt and Pd measured in Ogorodnaya carbonaceous rocks was 0.13 and 0.02 ppm, respectively.

Acknowledgments

We thank Drs. OV Chudaev, SA Shcheka (FEGI), AV Kurika, VP Glazunov (PIBC FEB RAS), for a methodical help and critical comments to manuscript. This work is supported by RFBR (grant 04-05-65269).

References

Galimov EM (1973) The carbon isotopes to the oil-gas geology (in Russian). Nedra, Moskow: 384

Mikhailov MA, Volokhin YG (1980) Geochemical peculiarities of carbonaceous siliceous rocks of the Far East. In Geochemistry and Petrochemistry of sedimentary complexes of the Far East. FESC Ac. Sci. of the USSR, Vladivostok: 3-16

Tkachev YA, Yudovitch JE (1975) Statistical processing of geochemical data: methods and problems (in Russian). Nauka, Leningrad: 233

Yudovitch JE, Ketris MP (1994) Admixture elements in black shale (in Russian). Nauka, Ural publ. firm, Ekaterinburg: 304

Volokhin YG (1988) Geochemical criteria for correlation of chert units and paleogeographic reconstruction (in Russian). Lithology and Mineral Resources 3: 64-81

Volokhin YG, Mikhailik EV, Buryi GI (2003) Triassic siliceous formation of the Sikhote-Alin (in Russian). FEB RAS, Vladivostok: 252

Genesis of PGE-polymetallic deposits in lower Cambrian black rock series, southern China: Evidence from fluid inclusion and inert gas isotopic studies

Wang Min[1,2], Sun Xiaoming[1,2], Ma Mingyang[1]
[1]Department of Earth Sciences, Sun Yat-sen University, Guangzhou 510275, China

[2]Key Laboratory of Marginal Sea Geology, Guangzhou Institute of Geochemistry & South China Sea Institutes of Oceanology, Chinese Academy of Sciences, Guangzhou 510640, China

Abstract. Microthermometric measurements of fluid inclusions in the PGE-polymetallic deposits hosted in the Lower Cambrian black rock series in Southern China were performed, and two types of fluid inclusions were identified. Type I are of NaCl-H_2O system with low to medium salinity, and their homogenization temperatures (Th) and salinities are 106.9 ~ 286.4°C and 0.8 ~ 21.8 wt% NaCl eq. respectively; Type II are of $CaCl_2$-NaCl-H_2O system with medium - high salinity, and their Th and salinities ranging from 120.1 to 269.6°C and 11.4 to 31.4 wt% NaCl eq. Characteristics of fluid inclusions in the PGE-polymetallic ores and carbonate-quartz stockworks in the underlying phosphorites are nearly the same, that they may represent the ore-forming fluid of main metallogenetic stage. The mode value of Th of those fluid inclusions is about 170°C, while their salinities possess a remarkable bimodal distribution pattern with two modal values of 27~31 wt% NaCl eq. and 4~6 wt% NaCl eq.; Inert gas isotopic analyses combined with microthermometric measurements of the fluid inclusions suggest that the ore-forming fluids of main metallogenetic stage were probably formed by mixing of basinal hot brine with $CaCl_2$-NaCl-H_2O system and seawater with NaCl-H_2O system. Finally, a new metallogenic model is proposed.

Keywords. Fluid inclusion, basinal hot brine, inert gas isotopes, PGE-polymetallic deposits in black rock series, Southern China

1 Introduction

Ni, Mo, V, Cu, U, Ba, rare earth elements (REE) and specially platinum group elements (PGE) are extraordinarily enriched in the Lower Cambrian black rock series of Yangtze Platform in Southern China, and locally formed a new type of PGE deposit – Ni-Mo-PGE deposits or ore spots, within which Zhangjiajie and Zunyi are the most representative ones (Coveney and Chen 1991; Coveney et al. 1992; Mao et al. 2001; Wang et al. 2004). There exist three major opinions on the genesis of this kind of deposit: normal seawater sedimentary model (Fan 1983; Mao et al. 2002), submarine exhalative hydrothermal deposition model (Coveney and Chen 1991; Coveney et al. 1992; Li et al. 2000; Lott et al. 1999) and multi-stage metallogenic model (Zhang et al. 2002).

2 General geology of the ore deposits

Precious metals such as PGE are predominantly occurred in the Cambrian Ni-Mo-PGE bearing black shale ore layers. The thickness of the ore layers is usually 20~30cm, locally 50~80 cm. Observations under microscope show that the ores are mainly composed of clay mineral, feldspar, quartz, carbonate mineral, organic matter, jordisite and pyrites. Pyrite, one of the most important ore minerals in diameter of 1~5 mm, mainly occurred as laminated and lentiform, occasionally disseminated structures. Quartzes are of fine-grained and anhedral crystals in diameter as large as 50 μm. Carbonate minerals occur as microgranules or micritic aggregates with greatly-varied diameters.

In the underlying Cambrian phoshorites of the Ni-Mo-PGE bearing black shale ore layers in Daping deposit of Zhangjiajie in Hunan Province, many stockworks with a thickness of several millimeters were recognized, which filled with carbonate minerals and quartzes and vertically cut the strata.

3 Microthermometric measurements

There are quite a limited number of fluid inclusions in quartz and carbonate minerals in PGE-polymetallic ores, the size are usually <5μm and mostly 2~3μm, occasionally 10μm; the vapor/liquid ratio is about 10%~20%, occasionally 30%; For comparison, numerous fluid inclusions are found in carbonate-quartz stockworks in phosphorites underlying the ore layer, the sizes are usually 2~3μm and smaller than those in the ores; The gas/liquid ratio is 10~30%, occasionally 50%.

150 data pairs of Th and salinities of primary and pseudosecondary fluid inclusions were collected in this study. Based on compositions and phases in fluid inclusions, two types of inclusions were recognized in this study: Type I with NaCl-H_2O system and low salinity; Type II with $CaCl_2$-NaCl-H_2O system and medium to high salinities.

Microthermometric measurements demonstrated that the freezing temperatures of the type I inclusions were -57~-45°C, and their Teu (the eutectic point of NaCl-H_2O aqueous system) and Tm were about –21°C°Cand -13.9~-0.5°C respectively. The freezing temperatures of type II inclusions were commonly -83°C~-58°C, and the initial melting started when the inclusions slowly heating to the temperature -55~-52°C, the initial melting of the liquid phase started and vapour bubbles started to

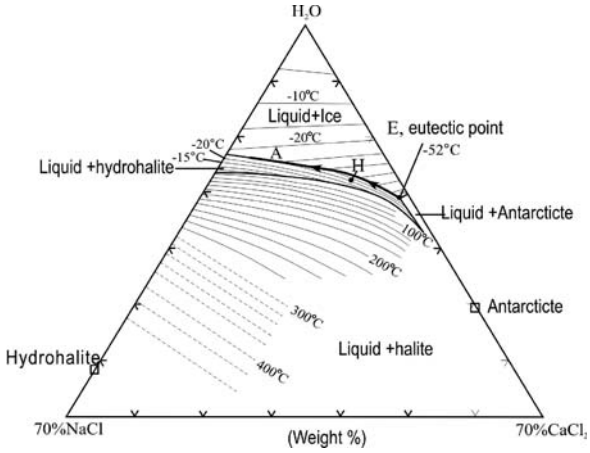

Figure 1: Phase diagram of $CaCl_2$-NaCl-H_2O system in fluid inclusion (after Shen et al 2003).

bounce about gently. Thus, the equilibrium eutectic point of type II inclusions, which is the eutectic melting point of $CaCl_2$-NaCl-H_2O aqueous system shown on the point E in Figure 1, can be estimated to be = -52°C. During the following, heating the liquid phase moved along EA-cotectic line of ice and hydrohalite ($NaCl{\cdot}2H_2O$) on Figure 1. When the rising temperature reached -34.3 ~-24°C, the ice crystals in the inclusions gradually melted. The hydrohalite ($NaCl{\cdot}2H_2O$) in the fluid inclusions melted completely between-27.5°C and -14.1°C during continuously heating. The point of liquid phase left the cotectic line and moved toward the point of the hydrohalite on the NaCl-H_2O boundary, until intersecting the isotherm line of the dissolved hydrohalite. Points of intersection represent the compositions of the liquid phase. For the inclusions whose ice crystal and hydrohalite melted at -34.3°C and -27.5°C separately, its corresponding composition consisting of 8%NaCl, 22%$CaCl_2$ and 70%H_2O (H on Fig. 1) and the apparent salinity is 30 wt% NaCl eq.

4 Analytical results and discussion

Th of fluid inclusions from the PGE poly-metallic ore are 106.9~286.4°C, with a mode value of 160~170°C; those in carbonate-quartz stockworks in phosphorites are 120.1~256.8°C, with a mode value of about 170°C, suggesting that the Th of fluid inclusions in the ores and the stockworks are quite similar, and their Th represent the ore-forming fluid's temperatures of main metallogenic stage.

Salinities of fluid inclusions in the ores are 0.8~33.4 wt% NaCl eq. and possess a remarkable bimodal distribution pattern with mode values of 30~32 wt% NaCl eq. and 4~6 wt% NaCl eq., the densities are 0.730~1.035g/cm^3; The salinities and the densities of fluid inclusions in carbonate-quartz stockworks in phosphorites are 4.2~30.6 wt% NaCl eq. and 0.870~1.068 g/cm^3 respectively, and the former also shows a remarkable bimodal distribution pattern with mode values of 27~28 wt% NaCl eq. and 4~6 wt% NaCl eq. The measured results demonstrate that the salinities and the densities of fluid inclusions in the PGE-polymetallic ores are similar to those of the underlying carbonate-quartz stockworks, that they may be used to represent those of the ore-forming fluid of main metallogenic stage.

Lott et al. (1999) had observed coexistence of fluid inclusions enriched in gaseous phases with those in liquid phases in PGE-polymetallic ores, and thought that boiling might have been occurred during metallogenisis. We found no evidence of coexistence in the samples that we studied, but detailed observation of fluid inclusions let us believed that mixing of different fluids might have been occurred during ore-forming process, the evidence include: The greatly varied gas/liquid ratios varying between 5% to 40%; Coexistence of pure aqueous and nearby gas-liquid phases fluid inclusions in the carbonate-quartz stockwork in phosphorite (Fig. 2A); Concomitance of fluid inclusions with a $CaCl_2$-NaCl-H_2O system (medium-high salinities) and those with a NaCl-H_2O system (low-medium salinities) in the PGE-polymetallic ores (Fig. 2B). These observations imply that mixing between brine with a medium-high salinity and fluid with a low to medium salinity might have been occurred in the formation of the PGE polymetallic ores. The bimodal distribution patterns of salinities mentioned above may reflect fluid mixing.

He-Ar isotopic compositions of fluid inclusions trapped in pyrites in the PGE-polymetallic ores were systematically analyzed by using an inert gas isotopic mass spectrometer, and the results indicate show that the ore-forming fluids possess low $^3He/^4He$ ratios, ranging from 0.43×10^{-8} to 26.39×10^{-8}, with corresponding R/Ra ratios of 0.003~0.189 (R represents the real $^3He/^4He$ value of samples, and Ra represents the $^3He/^4He$ ratios of atmosphere, usually 1.4×10^{-6}); The $^{40}Ar/^{36}Ar$ ratios 258 ~ 287, closing to these of the air-saturated water. He-Ar isotopic studies indicate that the ore-forming fluids were mainly composed of formation water or basinal hot brine and air-saturated water (sea water), the content of mantle-derived fluid or deep-derived magmatic water might be negligible (Sun et al. 2004). The inert isotopic analyses provided evidences for the fluid mixing in the metallogenetic process from another aspect.

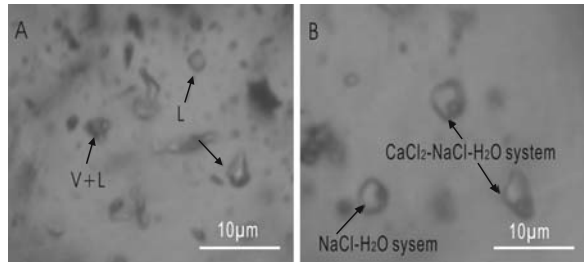

Figure 2: Coexisting fluid inclusions expressed for fluid mixing.

This page intentionally blank

5 New metallogenic model

In the Early Cambrian, the basinal hot brine trapped in the Caledonian basins, which were distributed along southern margin of South China Craton and accumulated giant thick sediments, was expelled and migrated laterally along strata because of the pressure caused by overlying sediments. The basinal hot brine absorbed Ni, Mo, V, PGE from the around rocks and transformed to be ore-bearing hydrothermal fluids with $CaCl_2$-NaCl-H_2O system and medium-high salinity, then ascended along faults and mixed with sea water of NaCl-H_2O system, and finally formed PGE-polymetallic deposits or spots in the black rock series during the Early Cambrian (541.3±16Ma, Mao et al. 2001). The nearly vertical carbonate and quartz filled stockworks underlying the ore layers probably represent remains of ascending channel-way of the basinal hot brines.

Acknowledgements

This work was jointly supported by the Natural Science Foundation of China (NSFC) (No. 40173025, 49928201), National key Basic Research Development Program in China (No. 2002CB412610), the project of Key Laboratory of Marginal Sea Geology, Guangzhou Institute of Geochemistry & South China Sea Institutes of Oceanology, CAS (No. MSGLCAS03-4), the project of State Key Laboratory of Organic Geochemistry, Guangzhou Institute of Geochemistry, Chinese Academy of Sciences (No OGL-200301) and the Trans-century Training Program Foundation for Talents by the Ministry of education.

References

Coveney RM Jr, Chen NS (1991) Ni-Mo-PGE-Au-rich ores in Chinese black shales and speculations on possible analogues in the United States. Mineralium Deposita 26: 83-88

Coveney RM Jr, Murowchick JB, Grauch RI (1992) Field relations, origins and resource implications for platiniferous molybdenum-nickel ores in black shales of South China. Exploration and Mining Geology 1:21-28

Li SR, Gao ZM (2000) Source tracing of noble metal elements in Lower Cambrian black rock series of Guizhou-Hunan Provinces, China. Science in China (Series D) 6: 625-632 (in Chinese with English abstract)

Lott DA, Coveney RM Jr, Murowchick JB (1999) Sedimentary exhalative nickel-molybdenum ores in South China. Economic Geology 94:1051-1066

Mao JW, Zhang GD, Du AD (2001) Geology, Geochemistry, and Re-Os isotopic dating of the Huangjiawan Ni-Mo-PGE deposit, Zunyi, Guangzhou Province-with a discussion of the polymetallic mineralization of basal Cambrian black shales in South China. Acta Geologica Sinica 2: 234-243

Shen K, Zhang ZM, Van Den Kerkhof AM(2003). An unusual high-density and saline aqueous inclusions from the ultra-high pressure metamorphic rocks in the Southern Su-Lu region, eastern China. Chinese Science Bulletin 10: 1076-1081

Sun XM, Wang M, Xue T, Ma MY, Li YH (2004) He-Ar isotopic systematics of fluid inclusions in pyrites from PGE-polymetallic deposits in Lower Cambrian black rock series, South China. Acta Geologica Sinica 2: 471-475

Trace Metals in Solving Petrogenetic Problem and Controversies. Augustithis, S.S. Ed, Athens: 447-474

Wang M, Sun XM, Ma MY (2004) Geochemistry of Ore-forming Fluid and Its Metallogenetic Significances of PGE-polymetallic Deposits in Lower Cambrian Black Rock Series, Southern China. Acta Scientiarum Naturalium Universitatis SunYatseni 5: 98-102 (in Chinese with English abstract)

Zhang GD, Li JL, Qiong QR(2002) Enrichments features and patterns of PGE metals in black shales from Zunyi area, Guizhou Province. Mineral deposit 4: 377-385 (in Chinese with English abstract)

Preliminary study of the source of base metals in MVT deposits of the Canning Basin, Western Australia

Andy R. Wilde, D.C. McPhail[1], J. Brugger[2]
School of Geosciences, Monash University, Melbourne, Australia
[1]now at the Department of Earth & Marine Sciences, Australian National University, Canberra, Australia
[2]now at Museum of South Australia, Adelaide, South Australia

S. McKnight
School of Science & Engineering, University of Ballarat, Victoria, Australia

D. Garnett
Becquerel Laboratories, Lucas Heights, NSW, Australia
now at: Tropical Savannas Management CRC, Charles Darwin University, NT, Australia

Abstract. New bulk chemical and mineralogical data for unmineralized sediments and a review of published lead isotope and permeability/porosity data indicate that Carboniferous and Devonian feldspar-rich sandstones and siltstones are the most likely reservoirs for ore-forming brines and metals in the eastern Canning Basin, Australia. The Anderson Formation and Tandalgoo Sandstone are characterized by extreme depletion in Pb and Zn relative to Cu. Conversely, limestones and dolomites of the Devonian and Carboniferous rift-fill are enriched in Pb and Zn relative to Cu. This enrichment is interpreted to be due to hydrothermal processes, suggesting that carbonate rocks of the Carboniferous-Devonian rift-fill sequence could be targeted for MVT deposits. Furthermore, anomalous Au, As and Sb in limestone of the Pillara Formation suggests that the possibility of Carlin-style gold deposits merits some consideration.

Keywords. MVT Zn-Pb deposits, Canning Basin, Australia, mineralogy, bulk chemical analyses, source potential

1 Introduction

In this paper we examine possible source rocks for the Pb and Zn deposits of the Canning Basin, Western Australia. New bulk chemical and mineralogical data are presented. We focus on the abundance and ratios of the base metals Cu, Pb and Zn and also on the presence and abundance of those minerals that might buffer the pH of transient fluids, because these parameters have a crucial effect on metal solubility and leachability.

2 Geology of the eastern Canning Basin

The Palaeozoic to Mesozoic Canning Basin overlies medium- to high-grade Archaean to Proterozoic metamorphic rocks. Its architecture is controlled by major northwest structures, which bound the Fitzroy Trough, Lennard Shelf and Barbwire Terrace (Fig. 1). Previous studies have suggested that sediments of the Fitzroy Trough are a plausible source for metal and brine that formed the MVT Pb-Zn deposits of Cadjebut, Pillara, Goongewa and Kapok, hosted by Devonian reefal limestone of the Lennard Shelf. Seismic data suggest that the Fitzroy Trough contains over 10 km of sediment (Dorling et al. 1996).

Only six drillholes penetrate more than 1 km of Fitzroy Trough sediments within 100 km of the Pb-Zn deposits; the deepest penetrated only 4 km of the sedimentary fill. Thus knowledge of the deeper parts of the Trough is limited to poor quality seismic data.

The oldest rocks penetrated in the Fitzroy Trough are 68 m of sandstone of the Lower Devonian Tandalgoo Sandstone (in Lake Betty #1, Fig. 1) and 500 m of the Devonian Luluigui Formation (also in Lake Betty #1). The Tandalgoo sandstone is consistently present on the Barbwire terrace, where it reaches thicknesses of up to 320m.

Over 1.05 km of the Upper Devonian to Lower Carboniferous Fairfield Group has been intersected in Fitzroy #1. The Fairfield Group comprises the Laurel Formation (limestone and calcareous clastic rocks), Yellow Drum Sandstone (sandstone and silty dolomite) and the Gumhole Formation (dolomite and dolomitic limestone). The Gumhole Formation yielded modest gas flows and traces of residual hydrocarbons in some holes.

Over 1.4 km of lower Carboniferous Anderson Formation was intersected in St George Range #1. It consists of gray sandstone with minor shale and dolomite. Gas flows and traces of residual hydrocarbon have also been recorded in this unit.

The nature of older rocks must be inferred from outcrop and drilling on the Lennard Shelf and Barbwire Terrace. In these areas several kilometers of Silurian (Carribuddy Formation) and Ordovician rocks were intersected. These are dominantly coarse clastic rocks (sandstone and siltstone) with limestone, dolomite and shale. Salt is an important part of the Carribuddy Formation in the western part of the Canning Basin and anhydrite is present locally.

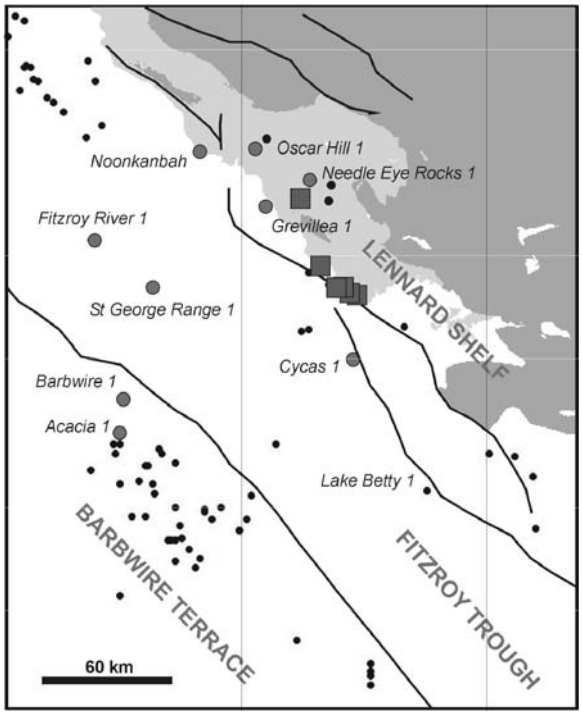

Figure 1: Simplified geology of the eastern Canning Basin. Dark gray – Proterozoic metamorphic rocks, medium gray – Devonian carbonate rocks, white – post-ore rocks. Circles – petroleum wells, large circles – sampled in this study. Squares – Pb-Zn deposits.

3 Carboniferous MVT deposits

Several economic MVT deposits are hosted in shallow-water limestones of the Pillara Formation (Lennard Shelf). Rb-Sr and U-Th dating of ore-stage calcite and sphalerite shows that Pb and Zn were emplaced during the late Devonian to early Carboniferous soon after deposition of the host-rocks (351 ± 15 Ma; Brannon et al. 1995). All of the significant deposits consistently occur in or adjacent to faults located near the transition between platform facies and marginal slope facies, reflecting control on fluid flow by major rift-bounding faults (Muhling 1994; Wilde and Muhling, 2000). The lead-zinc ores generally include sphalerite, galena, and sparry calcite and minor dolomite, marcasite and pyrite. Copper is present in low concentrations. For example, 86 analyses of Western Metals Pb concentrate contained an average of 86 ppm with a maximum of 588 ppm Cu. Few samples contained in excess of 100 ppm Cu. Zn concentrates contain slightly higher Cu with an average of 330 ppm and maximum 654 ppm (154 samples). The weight ratio of Pb+Zn to Cu in the ores is therefore approximately 150.

Fluid inclusion evidence suggests that MVT Pb-Zn deposits of the Lennard Shelf were deposited from hydrocarbon-bearing brines of 5 to 25 wt% NaCl equivalent salinity (Lambert and Etminan 1987; Tompkins et al. 1994) similar in salinity to present-day brines recovered from petroleum exploration drillholes in the western part of the Canning Basin. These brines probably obtained their salinity through halite dissolution. Temperature estimates of mineralisation are in the range 60 to 120°C. The maximum temperature in the Fitzroy Trough, however, may have been as high as 200°C.

4 Bulk chemical data

Approximately 200 bulk chemical analyses were obtained for unmineralized sediments from various petroleum exploration holes up to 100 km from known Pb-Zn occurrences (Fig. 1). These were analyzed for a suite of elements using INAA and AAS. Figure 2 shows the average ratio of Pb, Zn and Cu in different rock types from various stratigraphic units, including basement rocks.

Most rock types, including basement gneiss and diorite, plot close to a straight line. This is interpreted as reflecting the bulk base-metal content of the sedimentary source. Two groups of rocks deviate significantly from this straight line trend. Many Carboniferous and Devonian limestones and dolomites tend to show extreme enrichment in Pb and Zn relative to Cu and often have high average values of these elements. Mudstones of the Silurian Carribuddy Group also show this characteristic. Enrichment of base-metals in rocks of the Fairfield Group has previously been reported by Druce and Radke (1977).

Conversely, the average Tandalgoo Sandstone and Anderson Formation samples plot well below the best-fit line, indicating relative enrichment of Cu with respect to Pb and Zn.

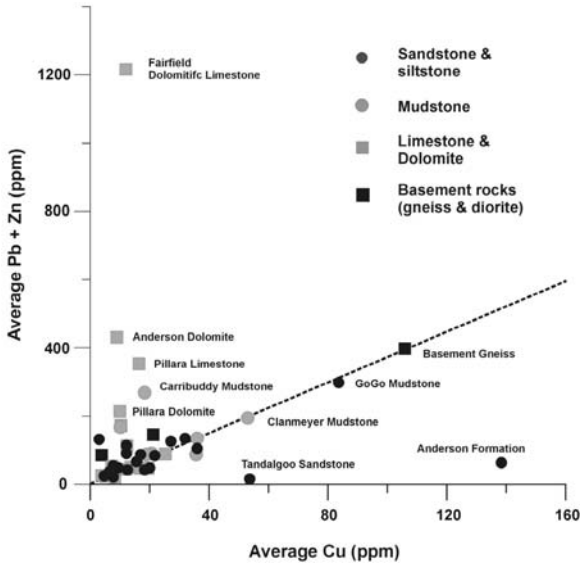

Figure 2: Average base-metal concentration of various stratigraphic units of the Fitzroy trough and Lennard Shelf

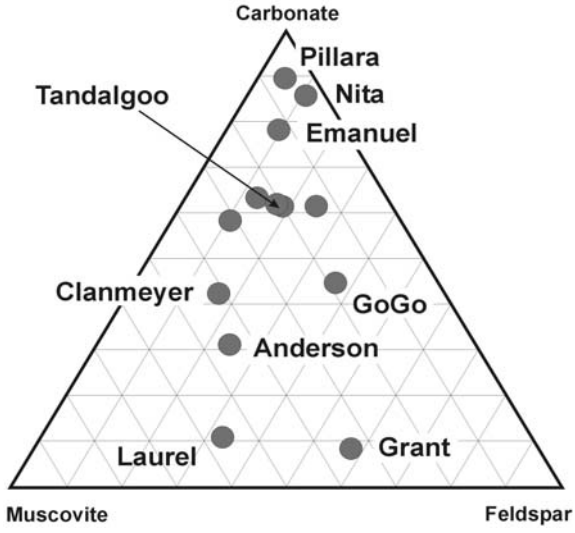

Figure 3: Ternary diagram showing the average modal amounts (vol. %) of carbonate, feldspar and muscovite in various stratigraphic units.

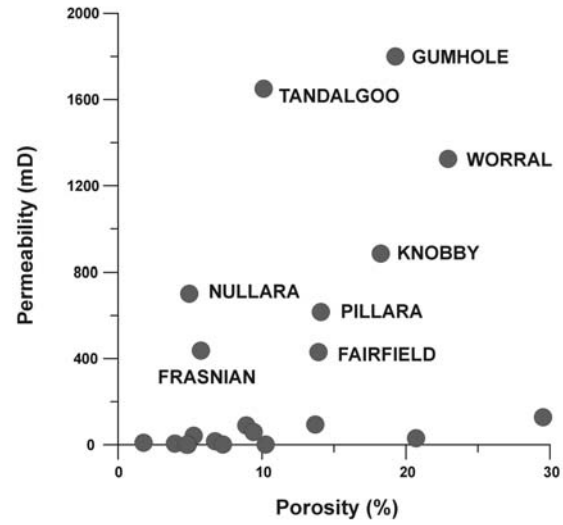

Figure 4: Average porosity and permeability for units intersected in petroleum exploration drillholes. (Data provided by the Western Australian Department of Industry and Resources).

Anomalous gold in association with elevated As and Sb were found in some intervals of limestone of the Pillara Formation (maximum 65 ppb). This and a surprising similarity in pre-Carboniferous geological history raises the possibility of "Carlin-style" gold deposits (see also Wilde and Muhling 2000).

5 Mineralogical data

Splits of the INAA samples were used for XRD analysis at the Universities of Adelaide and Ballarat. Modal mineralogy was quantified using SiroQuant™ ver2.5 software. Figure 3 shows the average carbonate, feldspar and muscovite composition of various stratigraphic units. The preponderance of feldspar and mica in the Anderson, Grant and Laurel Formations is evident.

The abundance of feldspar in these rocks is significant because of its possible role as a repository of Pb (another likely source being clay minerals) and its potential to affect pH (higher values) of transient waters and brines. The Carboniferous and Devonian rocks generally contain more feldspar than the Silurian and older rocks, whereas mudstones and clay-rich sediments form a relatively small part of the stratigraphic packages.

6 Porosity and permeability

The potential for a particular unit to be a viable source for metals depends to some extent on how porous and permeable it was at the time of ore formation as well as the chemical processes operating to transfer Zn and Pb into solution.

Several units retain very high permeability and porosity today (Fig. 4). These are the Tandalgoo Sandstone and also rocks of the Gumhole and Ludlovian Worral Formations. The Pillara and Nullara limestones are also considerably more permeable than most other units.

7 Pb isotope data

Published lead isotope data of MVT ores, basement rocks and clastic sediments within the Fitzroy Trough indicate that much of the lead in the deposits was derived by leaching of feldspathic sands shed from the Kimberley Craton during Devonian extension (Tompkins 1994; Dorling et al. 1996). Figure 4: Average porosity and permeability for units intersected in petroleum exploration drillholes. (Data provided by the Western Australian Department of Industry and Resources).

8 Discussion

The new data presented here suggest that a primary control on the base-metal content of ore-forming brines in the Fitzroy Trough is the inheritance from the sedimentary source, namely Archaean and Proterozoic metamorphic rocks. The abundance of feldspar as determined by XRD is consistent with the hypothesis from Pb isotopic studies that feldspar supplied much of the lead that resides in the deposits. The mineralogical residence of Zn remains uncertain.

Depletion of Pb and Zn together with elevated permeability suggests that the Tandalgoo Sandstone is a prime candidate for a reservoir of ore-forming brines and a source for those metals.

The most probable source of the chlorine in the ore-forming brines is the evaporitic Carribuddy Group, which occurs directly beneath the Tandalgoo Sandstone in several of the sampled wells. There is no direct evidence either from drilling or seismic sections, however, for massive evaporites, although the seismic data are of poor quality.

The Pillara Formation Limestone is host to the bulk of economic Zn and Pb on the Lennard Shelf. Therefore, it is reasonable to speculate that the high Zn and Pb to Cu ratios and absolute concentrations of Pb and Zn in Carboniferous dolomite and limestone reflect post-sedimentation deposition of Pb and Zn, rather than sedimentary inheritance. This needs to be confirmed by petrographic study, but we propose that carbonate-rich rocks of the Carboniferous and Devonian rift-fill could be targeted for economic Pb-Zn deposits.

Acknowledgements

We thank Craig Gwatkin and Dave Hutton of Western Metals for chemical analyses of concentrates and for samples from Kapok. Chemical analyses were performed at Becquerel Laboratories, Lucas Heights, Australia, using funding provided by AINSE (grant 03127), which is gratefully acknowledged.

References

Brannon JC, Cole CC, Podosek, FA (1995) Can All Mississippi Valley-Type Deposits be Radiometrically Dated? *SEG* Intl. Field Conf. Carbonate-Hosted Pb-Zn Deposits. St Louis, MO: 27 – 29

Dorling SL, Dentith MC, Groves DI, Vearncombe JR (1996) Mississippi Valley-type Deposits of the Southeast Lennard Shelf: An Example of the Interplay of Extensional Deformation, Sedimentation and Mineralization. In Sangster D F (ed.), Carbonate-Hosted Lead- Zinc Deposits, Econ. Geol. Spec. Pub: 96-111

Druce EC, Radke BM (1977) Geochemistry of the Fairfield Group, BMR Report, 202, 40

Muhling PC (1994) Lennard Shelf Pb-Zn Mineralization: Abstracts Geol. Soc. Austr. 37: 12th Australian Geological Convention, Perth: 307-308

Lambert IB, Etminan H (1987) Biochemistry and Origin of Sediment-Hosted Base-Metal Deposits. BMR Yearbook: 89-93

Tompkins LA (1994) An Integrated Model or the Genesis of MVT Zn-Pb Mineralization at the Cadjebut Mine, Lennard Shelf, Canning Basin, WA. PhD Thesis, Univ. Western Australia: 178

Wilde AR, Muhling P (2000) Comparison Between the Lennard Shelf MVT Province of Western Australia and the Carlin Trend of Nevada: Implications for Genesis and Exploration. In Cluer JK et al. (eds) Geology and Ore Deposits 2000. The Great Basin and Beyond", Proc. Geol Soc. Nevada, May, 2000: 769-781

Geochemical process model for the Mt Isa Cu-Co-Ag deposits

Andy Wilde, Melissa Gregory, Robert Duncan
*pmd*CRC, School of Geosciences, Monash University, Clayton, Victoria, Australia*

Klaus Gessner, Michael Kühn
CSIRO Exploration & Mining, Kensington, Perth, WA, Australia

Peter Jones
School of Earth Sciences, James Cook University, Townsville, Queensland, Australia

Abstract. We present the results of numerical simulation of chemical processes that formed the Mount Isa copper orebodies. Reduction through wall-rock reaction is the most likely chemical process, although mixing of two fluids of contrasting oxidation state may also have contributed. Most rocks in the Mount Isa region have the ability to reduce oxidized fluids. Porosity (instantaneous fluid to rock ratio) is highlighted as a critical control on ore grade and ratio of Cu to Pb and Zn. Mechanical properties of the host rock may therefore be more important than chemical ones.

Keywords. Mount Isa, copper, geochemical modelling, wallrock reaction, mixing

1 Introduction

Even though a massive volume of data has been accumulated in Mount Isa's 80 year mining history there are many aspects of ore deposition that remain controversial or uncertain. A project of the predictive discovery co-operative research centre was designed to reduce exploration risk by testing chemical and mechanical process models of copper ore formation and creating 3D geometric models of the mine and surrounding areas. This paper focuses on geochemical aspects of the ore-forming processes.

The giant Mount Isa copper deposits are adjacent to but spatially discrete from, similarly large lead-zinc-silver deposits. Both sets of orebodies are hosted by the Proterozoic Urquhart Shale. Copper as chalcopyrite is concentrated in the hanging wall of the Paroo Fault, a high strain zone separating the Urquhart Shale from quartzite, meta-basalt and chlorite schist of the Proterozoic Eastern Creek Volcanics.

Copper grades are highest in thin, silicified and brecciated meta-siltstone layers within the Urquhart Shale, whereas interbedded meta-shale units contain generally sub-economic copper.

2 Fluids and reservoirs

Previous fluid inclusion studies show that the ore-forming solutions at Mount Isa were brines (average 14 wt% NaCl equiv.) at temperatures in excess of 100°C. The true temperatures of formation cannot be accurately determined from fluid inclusion studies, however, because the depth of formation and fluid pressure at entrapment are unknown. Chlorite and illite thermometry suggest that maximum temperatures at the mine site were less than 350°C. There is no evidence of major thermal gradients at the scale of the deposit.

New nuclear microprobe and laser ablation ICP-MS analysis of fluid inclusions in quartz confirm earlier indications that fluid compositions are extremely variable with respect to total salinity, cation ratios and ore metal contents and indicate variability within individual fluid inclusion assemblages trapped at more or less the same time. This is attributed to entrapment of several discrete fluids as well as rapidly varying composition with respect to quartz precipitation.

Evidence for the input of an oxidized ore-forming fluid at Mount Isa includes the presence of a large anhydrite-barite body at the northern end of the copper deposits, the composition of syn-copper chlorite, mica-kaolinite-hematite alteration in faults believed to have been active during ore formation and published sulphur isotope data.

The main reservoirs for oxidised copper-rich brines are believed to be within a basin correlative of the Roper and/or Nathan Groups. Fluid inclusions in the Roper Group are of comparable salinity to late-stage fluid inclusions at Mount Isa (Dutkiewicz et al. 2003). Such basin rocks could have overlain the copper deposits, but no vestiges remain within 100 km of the mine site.

3 Fluid flow paths

Remote-sensed hyperspectral imagery shows high levels of white-mica, kaolinite (and dickite) and hematite along NW-SE faults believed to have been active during ore formation. This is consistent with these faults being aquifers for acidic and oxidized brines. Other possible aquifers include various feldspathic quartzites (including thick examples beneath the mine) which could have been unusually permeable due to a high density of fractures (now infilled with quartz veins). Such rocks tend to contain low masses of reducing minerals making them suitable

for maintaining the flow of oxidized brines. Even so, quartzites in the region often have elevated copper concentrations.

The oxygen isotopic pattern around Mount Isa has previously been suggested as an effective targetting tool for copper (Waring et al. 1998). 3D visualisation and spatial analysis as part of this study, however, revealed that the isotopic patterns are more complex than originally thought and that the $\delta^{18}O$ values correlate better with faults than they do with economic copper. Some of these faults demonstrate post-ore movement and thus the isotopic data may be in part tracking post-ore fluid flow.

4 Driving forces for fluid flow

The absolute age of copper ore formation is poorly constrained. The only direct dating is of several biotite separates using the Ar-Ar technique. Such biotites cannot be related unambiguously to ore formation. New Re-Os isotopic data for various ore and host-rock samples have been obtained as part of this project (Gregory et al. 2004). A preliminary isochron age of 1370 ± 80 Ma is defined by pooling all the available samples (MSWD 49). This is considerably younger than the 1530 Ma age preferred by Perkins et al. (1999).

At least two major fluid flow events have been recognised in the copper orebodies. Textural and paragenetic studies point to an early (pre-copper) fluid flow event with quartz deposited by a cooling (locally upwards flowing) basement-equilibrated fluid. The relative age of this silicification is likely to be contemporaneous with peak deformation (Isan contractional orogeny, D2) or the later D3 deformation event (formerly designated D2.5).
Numerical simulation of deformation-driven fluid-flow at the mine-scale has demonstrated that upward fluid flow patterns would have dominated in contraction (i.e. during the Isan orogeny), while mixed flow patterns (some horizontal component of flow) are much more likely to have occurred in extension or strike-slip (D3 & D4 events; Gessner et al, in press).

Fluid flow could also have been driven by the ambient thermal gradient with predicted flow patterns strongly controlled by the distribution of permeable rock units. We have successfully simulated the formation of the silica-rich alteration by convection within the Paroo fault and adjacent damage zone (Kühn et al. 2004). The Paroo fault need not have been active (slipping) at the time of silicification, as permeability is likely to have been a consequence of the fault being a zone of extreme mechanical inhomogeneity and therefore able to dilate during several periods of applied stress.

Copper ore deposition has been related by several studies to a deformation event currently designated D4, the result of right-lateral transpression. Early silicification is inferred to have played an important role in making the host-rocks at Mount Isa brittle and more susceptible to fracturing and brecciation during the D4 event than rocks that had not undergone this "ground preparation".

Deformed quartz in the copper orebodies was dissolved and replaced by dolomite and eventually chalcopyrite suggesting that the fluid flow field had reversed from upward to downward flow during ore deposition. This is consistent with the need to introduce relatively oxidised and therefore copper-rich fluids into the depositional site from an overlying source.

5 Fluid transport and copper depositional processes

In general, depositional processes include cooling, wall-rock reaction, fluid mixing or unmixing. Unmixing is a process that can be inferred based on fluid inclusion data (entrapment of two-phase fluids) or characteristic vein textures (e.g. lattice-textured quartz after calcite) inter alia. There is no evidence that two-phase fluids were present at Mount Isa, and therefore this process has not been considered further. It is unlikely that the other processes would operate independently. The breccia textures of the Mount Isa copper ore suggest that any mixing and/or cooling would have occurred in the presence of rock. It is important to distinguish the main controls because of the critical implications for exploration. Were cooling to be the main process, ore could occur in a variety of

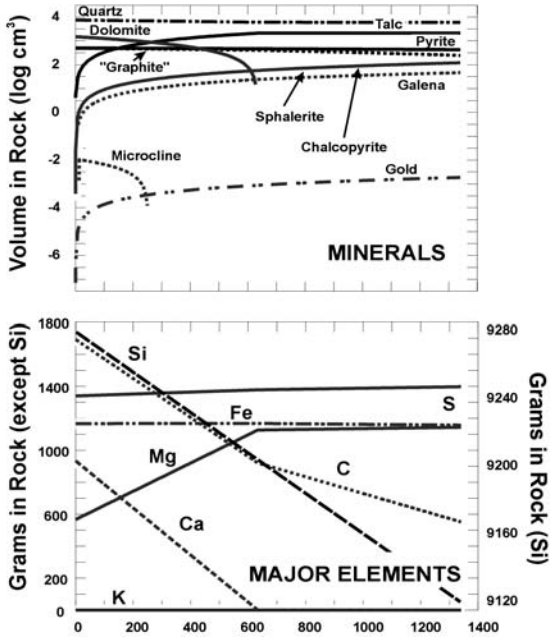

Figure 1: Reaction path model showing interaction of hypothetical ore-forming brine with silicified Urquhart Shale. The mineralogical and bulk chemical changes are similar to those observed in nature.

rocks and the main exploration aim should be to define thermal gradients. Wall-rock reaction requires specific host-rocks. Mixing does not necessarily require a thermal gradient or specific host-rocks.

Previous studies of the Mount Isa copper orebodies have emphasized wall-rock reaction, invoking either redox or pH change as the key depositional mechanism. The presence of pre-copper pyrite has also been suggested as a crucial ingredient via a process of sulphidation of the ore fluids. Textural and isotopic evidence suggests that the latter process did not operate (Perkins 1997). Furthermore, although we have no direct determinations of sulphur in the ore fluids, the presence of barite and anhydrite suggests that high sulphate concentrations are likely.

We have carried out chemical (reaction path) modelling using the software Geochemist's Workbench (GWB) and Hydrochemistry (HCh) in order to assess relative efficiency of depositional mechanisms. Fluid compositions were reconstructed based on fluid inclusion data and ore and gangue mineralogy. The ore fluids were assumed to be somewhat acidic (pH 3.5 at 250°C), since this optimizes the mass of copper that can be transported in oxidised brine. Sensitivity of the calculations to variation in fluid composition was assessed by using several different fluid compositions.

Cooling simulations failed to generate major masses of copper and cooling therefore is likely to have been a contributory factor rather than a key depositional process. Since the oxidized copper-bearing brines are inferred to be flowing downwards into the deposit it is more likely that they are in any case undergoing heating (as is suggested by desilicification).

Wall-rock reaction was assessed by "flushing" over 1,000 kg of hypothetical ore fluids through between 2.5 to 25 kg of rock depending on porosity. This shows that the silicified Urquhart Shale is capable of causing precipitation of chalcopyrite, owing to the presence of carbon as a reductant (Fig. 2) in agreement with some previous interpretations. Consideration of other rock types at Mount Isa, however, shows that many also have the ability to precipitate copper through reduction involving carbonaceous material, magnetite or ferrous silicates.

Porosity (proxied by the instantaneous ratio of fluid to rock at a particular reaction step) is key control on ore grade. This is partly because of its effect on bulk composition and partly because the mass of chalcopyrite precipitated is "diluted" by less rock at higher porosity. At high porosity buffer assemblages are exhausted at lower fluid throughput. One effect of this is illustrated in Fig. 3 which shows two simula-

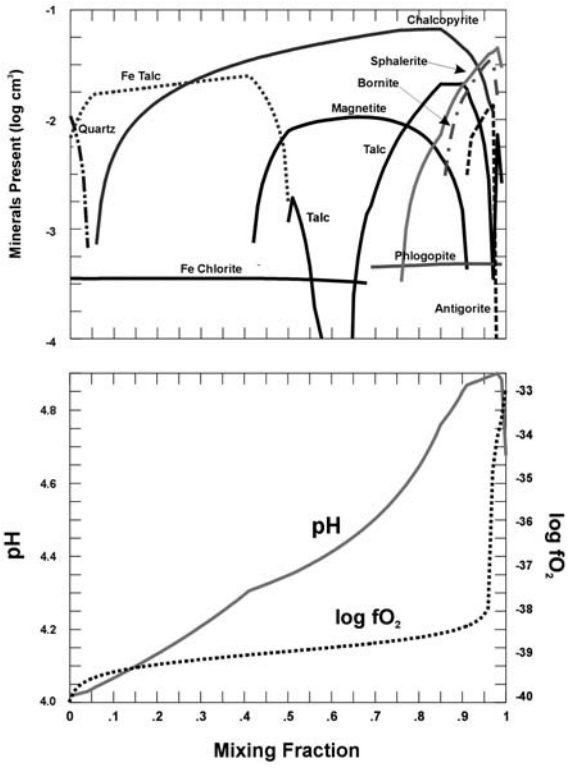

Figure 2: Mass of base-metal precipitated as a result of the flow of hydrothermal fluid through silicified Urquhart Shale at 11% and 54% porosity.

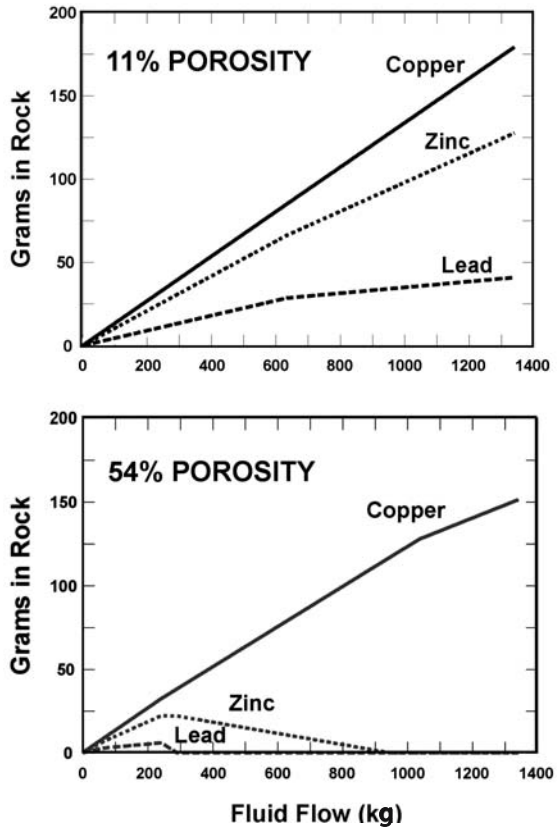

Figure 3: Simulation of mixing of a reduced basement equilibrated brine with oxidized copper-bearing brine.

tions of interaction of hydrothermal fluid with silicified Urquhart Shale that are identical except for porosity. While the mass of chalcopyrite precipitated is similar, the high porosity example shows that lead and zinc are totally dissolved after 250 kg fluid flow. This is due to the complete dissolution of carbon at this point. This may explain the remarkable separation of Cu and Pb-Zn at Mount Isa.

Dissolution of carbonate minerals dyuring fluid flow is calculated to produce losses in rock mass of up to 15%. Such high losses, however, were only observed in calculations that used an extremely high initial porosity suggesting that a mechanical control (such as fracturing) was more important than chemical dissolution in creating the space for copper deposition.

Mixing was simulated using the "flash" option of GWB. A typical example is shown as Fig. 4. The assemblages produced do not reproduce what we see in nature, suggesting that mixing is not the process that formed the copper orebodies or that the presence of rock needs to be taken into account.

Reactive transport calculations using the software SHEMAT are in progress. Preliminary results suggest that mixing of the required mass ratio of end-member fluids could be maintained by convection (Kühn et al. 2004).

6 Chemical process model

An early silicification was produced by dilation at the mechanically inhomogeneous boundary (Paroo fault) between layered pelitic and psammitic rocks of the metamorphosed Urquhart Shale and underlying quartzite and meta-basalt of the ECV. This silicification was crucial in facilitating the development of high porosity and permeability during subsequent deformation.

Ore formation was in response to ingress of oxidized brine from reservoirs in sedimentary rocks above the present level of the deposit, driven by topography or the ambient thermal gradient. Chalcopyrite formation was probably due to wall-rock reaction, although a rigorous examination of wall-rock reaction versus mixing is in progress. Complete spatial separation of Cu and Pb-Zn orebodies may have been a function of the high permeabilities and porosities generated during fracturing of the silicified Urquhart Shale.

Given that many rocks in the region have the ability to reduce an oxidized fluid and precipitate copper, we conclude that the mechanical characteristics of the host-rock and its geometric setting were more important to the formation of the giant Mount Isa deposits than chemical characteristics.

Acknowledgements

The research presented above has benefited from discussions with numerous geologists including Dave A-Izzeddin, James Cleverley, Melanie Coward, Bruce Hobbs, Dan Johnson, Gordon Lister, Mark McGeough, Bill Perkins, Paul Roberts, Justin Tolman and Chris Waring. We would also like to thank Dugi Wilson and Paul Gow of Xstrata Copper for their support.

Mineralization stages and fluid processes in the giant Jinding deposit, western Yunnan, China

C-J. Xue, R. Zeng, S-W. Liu
Faculty of Geological Sciences and Resources, Chang'an University, Xi'an 710054, China

G. Chi, H. Qing
Department of Geology, University of Regina, Regina, Saskatchewan, S4S 0A2, Canada

Abstract. Jinding is the largest Zn-Pb deposit in China, and also the youngest sediment-hosted super-large Zn-Pb deposit in the world. The Jinding mineralization processes are discussed in this paper based on the investigations of the mineral intergrowth. The hydrothermal mineralization experienced three stages: the stage of quartz-sphalerite- galena, the stage of sphalerite-galena-celestite and the stage of galena-calcite-celestite-gypsum. Fluid inclusions in sphalerite and associated gangue minerals show that the homogenization temperatures range from 54° to 309°C and cluster around 110°~150°C, with salinities of 1.6~18.0 wt% NaCl equivalent. The temperature increased and the salinity decreased during the early stage, the temperature was stable and the salinity decreased during the main stage, and both temperature and salinity decreased during the final stage. This temperature-salinity trend probably resulted from mixing of a high- temperature, low-salinity fluid with a low- temperature, high-salinity fluid during mineralization.

Keywords. Jinding deposit, sandstone-hosted, mineralization stages, mineralization fluid processes, fluid inclusions

1 Introduction

The Jinding deposit was discovered in 1960 in the Lanping Basin, SW-China (Fig. 1). Hosted in Cretaceous and Palaeocene terrestrial sandstones, the Jinding deposit is the largest Zn-Pb deposit in China. The Jinding Deposit is related to continental crust movement during the collision of the Indian and Eurasian plates, and is the youngest sediment- hosted super large Zn-Pb deposit in the world (Xue et al. 2003). The genesis of the deposit has been a subject of debate and controversy since the 1980's, and the mineralization fluid process is the key.

In this paper, we investigate the mineral intergrowth, mineralization stage, fluid flow and reveal the mineralization fluid process in the Jinding Deposit. Our results suggest the mixing of mantle- and crust-derived fluid during the Jinding mineralization.

2 Regional geology

The Lanping Meso-Cenozoic Basin is an intracontinental basin developed on the Changdu-Lanping-Simao microplate between the Yangtze Plate to the east and the Tibet-Yunnan Plate to the west, separated by the Lancangjiang and Jinshajiang-Ailaoshan faults (Fig.1). The basin basement is the Palaeo-Tethys marine and terrestrial carbonates, volcanic rocks, and clastic rocks. The Meso-Cenozoic System consist of, in ascending order, the Upper Triassic, Middle-Upper Jurassic, Lower Cretaceous, Upper Cretaceous, Tertiary, and there are several terrestrial gypsum-salt sequences and sedimentary gaps in the basin column. The main fault cuts deeply into the lower crust and upper mantle. In addition, some EW-trending blind structures are also recognizable. Tectonic evolution of the Lanping Basin shows as the Indosinian remained basin, the Yanshanian depression basin and the Himalayan pull-apart basin (Xue et al. 2002).

Himalayan alkali intrusions of mantle-source or mantle-crust mixed sources occur along the margin- and the central-faults of the basin. Some mantle rock xenoliths occur in these alkali intrusions. Several isolated circular structures observed by remote sensing suggest the presence of some thermal anomalies and magma at depth.

The thermal metamorphism developed along the Lanping-Simao fault could result from both deep faulting and heat-driven upwelling along the faults (Luo et al. 1994). High temperature bodies with low seismic velocity and distinct rises of the asthenosphere occur under the Jinding Deposit (Bian 2000).

Deep faulting, magmatism, upwelling of mantle fluid, discordances in the stratigraphic column, and interaction between the crust and the mantle, are the basic geological characteristics of the Lanping Basin and stem from collision of Indian plate and Eurasian plate, This sort of geodynamics is favorable for the material exchange to result in large scale mineralization.

3 Ore geology and mineralization stage

The Jinding ore district has undergone sedimentation, thrusting, heat doming and dome collapse. The mineralization accompanied the local extension and the heat flow upwelling. Ore bodies are usually tabular in shape, distinctly structure-controlled (Fig. 2), and no obvious sedimentary features can be recognised. The cement texture resembles that of typical ores formed when sulfide minerals replace the cement in the highly permeable clastic rocks.

The Jinding hydrothermal mineralization is separated into three stages based on paragenetic studies and min-

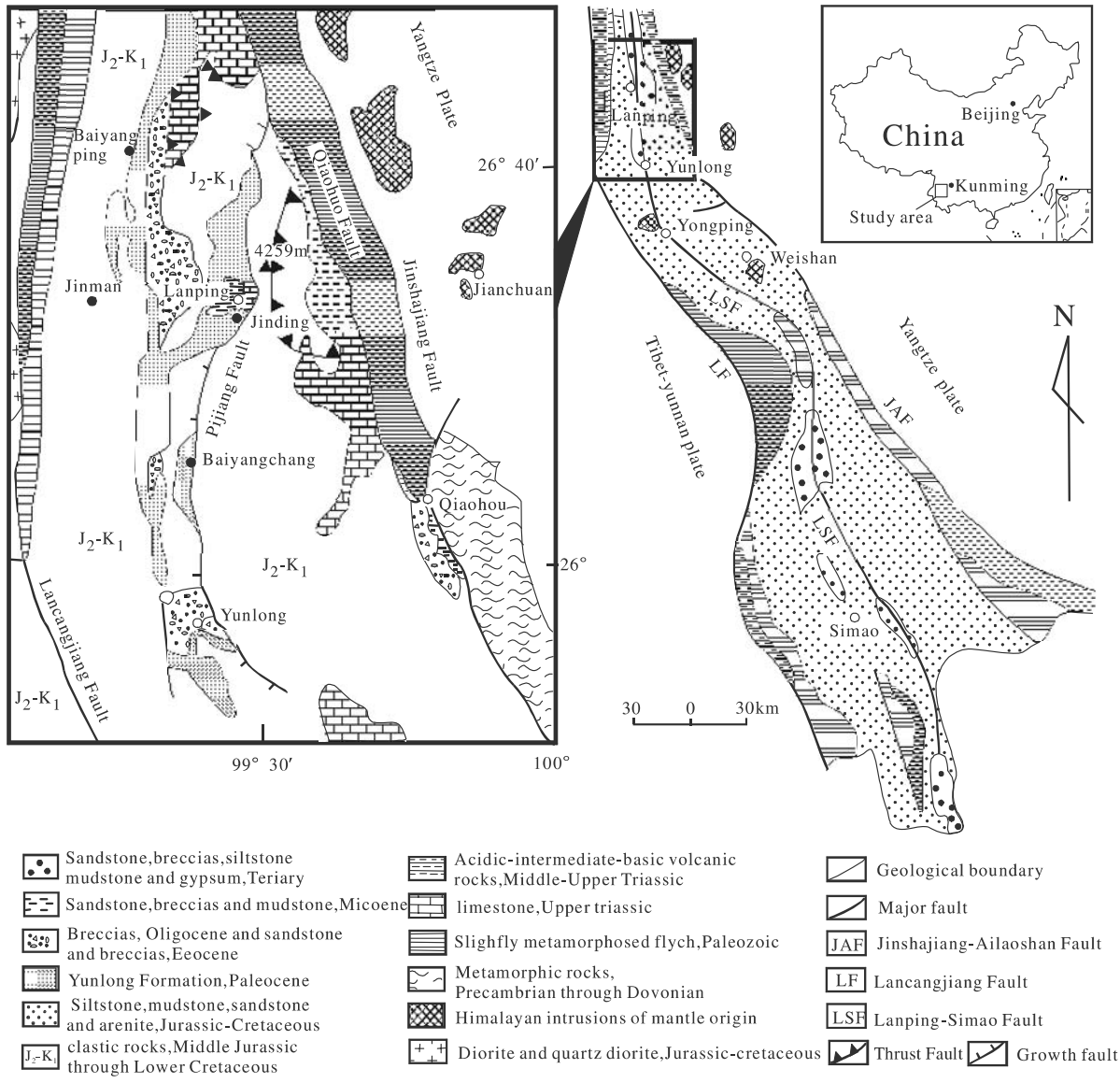

Figure 1: Location of the Jinding Deposit and a simple geology of the Lanping Basin.

eral intergrowth in the ore. They are the stage of quartz-sphalerite-galena, the stage of sphalerite-galena-celestite and the stage of galena-calcite-celestite-gypsum. The galena of the third stage is coarse grained and associated with calcite in veins and vugs, whereas the galena of the earlier stages is fine-grained and disseminated. The celestite of the third stage occurs in veins and associated with the remobilized bitumen, which is different from the sedimentary celestite in strata and the disseminated hydrothermal celestite in the ore. Pyrite occurs in every stage, but most commonly in the second and the third stages. Disseminated bitumen formed before Zn-Pb mineralization and was hydrothermally matured during the mineralization.

4 Jinding mineralization fluid process

Fluid inclusions have been found in sphalerite and associated quartz, celestite, calcite and gypsum in the Jinding ores. Fluid inclusions show a variation in size 3~20 microns (Fig. 3). Fluid inclusions distributed in healed fractures were not studied. The results of 73 melting- temperature and 94 homogenization- temperature have been obtained.

The homogenization temperatures range 54°~309°C with the average 182°C in quartz, 154°C in sphalerite, 140°C in celestite, 126°C in calcite and 98°C in gypsum. 3 homogenization temperature peaks are revealed in the

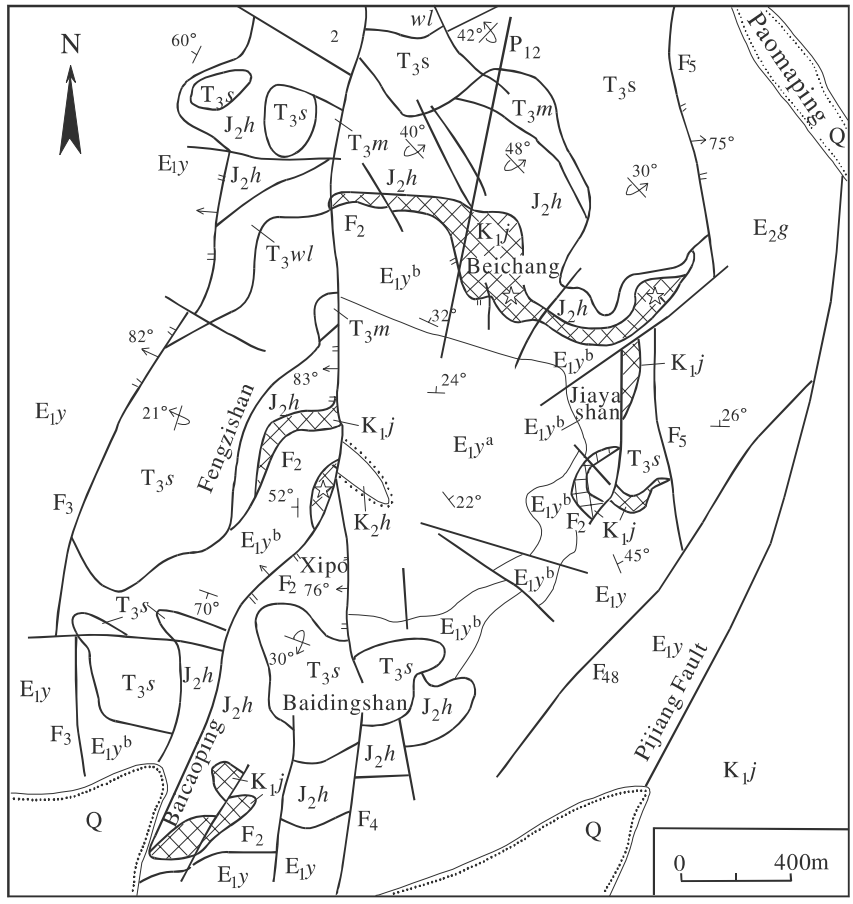

Figure 2: A geological map of the Jinding Deposit (after Third Geological Team 1984).

stacked histogram, i.e., a 170°C~190°C peak mainly consisting of quartz, sphalerite and celestite, a 110°C~140°C peak of sphalerite, celestite and calcite, and a 80°C~100°C peak of calcite and gypsum. These peaks broadly correspond to the three hydrothermal stages recognized by ore petrography and mineralparagenesis. There is a general trend of westward decrease in homogenization temperatures in the Jinding ore district.

Salinities of fluid inclusions range from 1.6 to 18.0 wt% NaCl equivalent, with an average of 6.1 wt% and a mode around 4~5 wt% NaCl equivalent. The average salinity is 8.7 wt% NaCl equivalent for fluid inclusions in quartz, 10.5 wt% in sphalerite, 10.0 wt% in celestite, 5.2 wt% in calcite, and 3.6 wt% in gypsum. Salinity values show a systematic increase from east to west in the ore district.

The westward decrease in homogenization temperatures and increase in salinity indicate a negative correlation between temperature and salinity, which is also reflected in the temperature-salinity diagram, especially for data from sphalerite, celestite and quartz (Fig. 4).

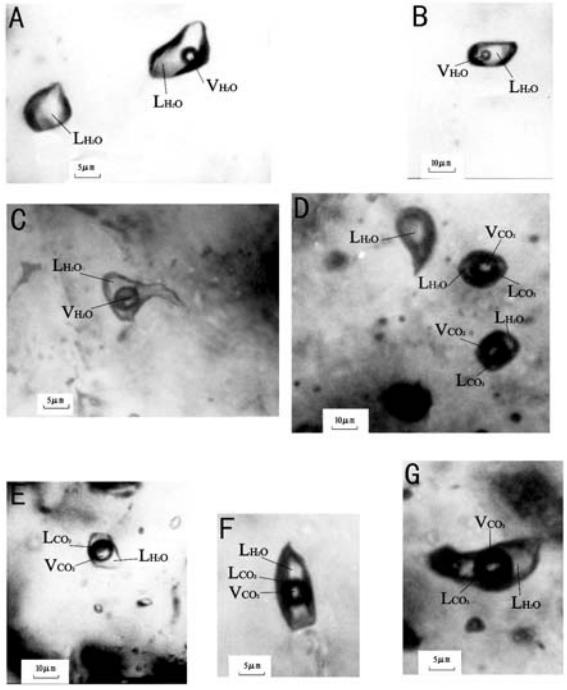

Figure 3: Photomicrographs of the fluid inclusion types from sphalerite and associated quartz, celestite, and calcite in the Jinding ores (room temperature). (A) a single-phase liquid H_2O inclusion (left) and a two-phase vapor-liquid H_2O inclusion (right) in celestite; (B) a two-phase vapor-liquid H_2O inclusion in calcite; (C) a two-phase vapor-liquid H_2O inclusion in quartz; (D) a single-phase liquid H_2O inclusion (upper) in quartz and two three-phase liquid H_2O-liquid CO_2-vapor CO_2 inclusions (the other two on right) in sphalerite; (E) a three-phase liquid H_2O-liquid CO_2-vapor CO_2 inclusion in quartz; (F) a three-phase liquid H_2O-liquid CO_2-vapor CO_2 inclusion in celestite; (G) a three-phase liquid H_2O-liquid CO_2-vapor CO_2 inclusion in celestite.

5 Conclusions

The temperature increases and the salinity decreases during the early stage, the temperature is stable and the salinity decreases during the main stage, and both of temperature and salinity decreases during the later stage.

The negative temperature-salinity trend probably results from mixing of a high-temperature and low-salinity fluid with a low-temperature and high-salinity fluid during the main stage of mineralization.

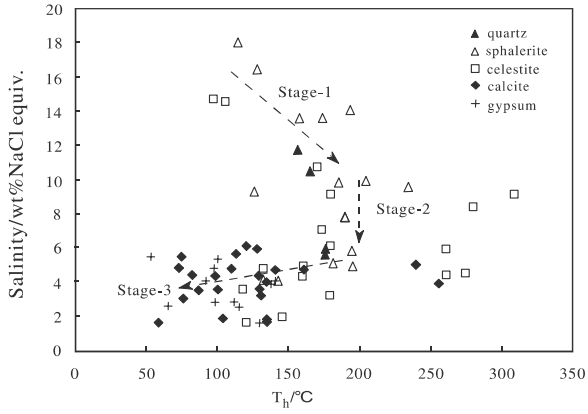

Figure 4: Homogenization temperature vs. salinity, the Jinding mineralizing fluid.

Acknowledgements

This work was supported by the NSFC (40272050, 40427054), the State Key Basic Research Development Plan of China (2002CB4126007, G1999043201) and NSERC.

References

Bian QT (2000) A discussion about the relationship between the super large-scale ore deposits and the tectonics of the mantle-crust structure: taking Yunnan as example. In: Tu G C (Ed.) Super Large-scale Ore Deposit in China (I). Beijing: Science Press, 545-569 (in Chinese with English abstract)

Luo JL, Yang JZ (1994) The Tethyan Evolution and the Mineralization of the Main Metal Deposits in Western Yunnan. Publishing House, Geological Beijing: 149-239 (in Chinese with English abstract)

Geochemistry of PGE and Au in ferromanganese crusts from seamounts in the west Pacific Ocean

Xue Ting[1], Sun Xiaoming[1,2], He Gaowen[3], Wang Shengwei[1], Lu Hongfeng[1], Zhang Mei[1]
[1]*Departmartment of Earth Sciences, Sun Yat-sen University, Guangzhou 510275, China*

[2]*Key Laboratory of Marginal Sea Geology, Guangzhou Institute of Geochemistry & South China Sea Institute of Oceanology, Chinese Academy of Sciences, Guangzhou 510640, China*

[3]*Guangzhou Marine Geological Survey, The Ministry of Land and Resoures, Guangzhou 510760, China*

Abstract. Ferromanganese crusts and their basaltic substrates from the Magellan Seamount are greatly enriched in PGE (ΣPGE = 70.09 to 629.26 ppb) and Au (0.60 to >1500 ppb). Chondrite-normalized patterns and noble gases isotopic analyses suggest that the PGE and Au were sourced from water/rock reaction between the basaltic substrates and seawater, and enrichments from iron meteorite dusts.

Keywords. Platinum group element (PGE), ferromanganese crust, west Pacific Ocean

1 Introduction

Platinum group elements (PGE) are an important mineral resource for China and the world (Wang et al. 2001; Xu et al. 2003). Previous studies have shown that ferromanganese crusts from Pacific seamounts can be enriched in many metal elements, including PGE (Shi et al. 2000; He et al. 2001; Bu et al. 2003). This study reports the PGE and Au contents of ferromanganese crusts and their basaltic substrates from the Magellan seamounts in west Pacific Ocean. Comparisons with chondrite-and primitive mantle-normalized patterns and previously reported noble gas analyses are used to suggest sources and mechanisms of PGE enrichment in the crusts.

2 Samples and analytical methods

Samples were collected by dragnet in the Haiyang 4/DY105-11 and the 13th cruises in Magellan seamounts from water depths of greater than 2km. The collected crusts have a single-, double- or three-layered structure. Our emphasis was on the three-layered crusts because of their greater thickness (>10cm).

Samples were dried and crushed to a less than 75μm-sized powder. A 10g sample split for Pt, Pd, and Au analyses was dissolved in hydrochloric acid/hydrogen peroxide, pre-concentrated with active charcoal and subsequently ashed. A 0.25 mg split of the residue was mixed with a spectral buffer, and determined with a DC arc spectrometer and a computerization photo plate determination system. The detection limits were 0.2 ppb for Pt and 0.1 ppb for Pd and Au. A 10g subsample was dissolved and pre-concentrated with nickel sulphide mini fire assay. The button was rinsed in distilled water and pulverized, dissolved in heated hydrochloric acid, and subsequently filleted in order to remove Fe and Ni. The residue was fused with sodium pyrophosphate and extracted with distilled water. One aliquot of the solution was used for the determination of Rh with catalysis polarography in vitriol-hexamethyleneteramine system. The other was used for the determination of Ir with catalysis photometric method in As(III)-Ce(IV)-Ag(I) system. The detection limits were 0.02 ppb for both elements. A 5g sample for Ru and Os was decomposed with sodium peroxide fusion, extracted with distilled water and acified with sulfuric acid. Distillation was used for separation of Ru and Os from matrix and from each other with potassium bromate-potassium dichromate- sodium chloride as oxidant and ethanol- vitriol as a splitting agent. The Ru and Os is determined by catalysis photometric method with As(III)-Ce(IV) system. The detection limits were 0.02 ppb. Standards for this work are GPT series standards provided by Institute of Geohysical-Geochemical Exploration, CAGS.

3 Analytical results and discussion

PGE and Au contents in the ferromanganese crusts and their respective chondrite- and primitive mantle-normalized patterns are presented in Table 1, Figure 1, and Figure 2. The results show that (1) the contents of PGE and Au in the ferromanganese crusts are variably enriched with ΣPGE (70.09 to 629.26 ppb), Os (1.19 to 3.09 ppb), Ir (1.05 to 7.04 ppb), Ru (11.63 to 23.92 ppb), Rh (4.17 to 30.11 ppb), Pt (42.82 to 567.90 ppb), Pd (0.51 to 1.99 ppb) and Au (0.60 to >1500 ppb). (2) In the three-layered ferromanganese crusts the ΣPGE contents of porous (339.37 to 545.82 ppb) and compact (280.09 to 629.26 ppb) are significantly higher than the outer (70.09 to 133.27 ppb) layers. Although the Au contents of the outer

Table 1: Contents of platinum group elements (PGE) and Au of ferromanganese in West Pacific Ocean (ppb)

Sample	Sample No.	Os	Ir	Ru	Rh	Pt	Pd	ΣPGE	Au
Outer layer	0303-1	2.35	1.24	18.11	5.06	42.82	0.51	70.09	0.60
Porous layer	0303-2	1.91	1.35	23.92	24.92	286.61	0.66	339.37	2.21
Compact layer	0303-3	1.01	1.05	13.94	17.65	245.72	0.72	280.09	1.44
Platy crust	0311	2.53	1.14	18.35	11.38	208.81	1.99	244.20	1.35
	0312	2.94	1.19	22.10	10.94	176.89	1.38	215.44	1.43
	0314-1	2.38	1.09	20.03	9.15	213.67	1.03	247.35	138.42
	0320	3.04	4.18	23.76	9.15	215.07	1.12	256.32	2.36
Outer layer	0321-1	2.11	7.04	21.24	5.58	89.91	0.94	126.82	10.35
Porous layer	0321-1	1.57	6.83	19.71	15.64	500.62	1.48	545.85	29.88
Compact layer	0321-3	1.47	5.66	23.06	30.11	567.90	1.06	629.26	8.28
Outer layer	0346-1	3.09	1.76	20.43	5.26	105.96	0.77	137.27	237.95
Porous layer	0346-2	2.35	2.13	29.47	24.79	372.57	1.22	432.53	5.09
Compact layer	0346-3	1.25	2.03	12.17	16.14	411.58	0.90	444.07	86.90
Platy crust	0349	2.38	1.65	17.82	6.88	227.23	1.39	257.35	56.08
	0361	1.57	1.84	18.35	12.46	444.49	1.04	479.75	>1500.00
	0366	1.19	1.54	15.16	6.48	149.29	0.66	174.32	>1500.00
	0370	2.65	1.61	22.99	9.15	324.00	1.15	361.55	160.50
Knotty crust	0374	1.55	1.21	17.03	4.17	58.78	1.20	83.94	132.49
Platy crust	0392	2.32	1.15	13.28	4.82	119.84	1.42	142.83	172.33
	0395	1.46	2.40	11.63	17.00	286.98	1.77	321.24	>1500.00
Altered basalt	0340	0.80	1.17	2.63	1.40	56.41	1.92	64.33	227.63
Primitive mantle*		3.40	3.20	5.00	0.90	7.10	3.90	23.50	1.00
C1 chrondrite*		490.00	455.00	710.00	130.00	1010.00	550.00	3345.00	140.00

*After McDonough et al. 1995.

layer were the highest measured, there is no obvious correlation between layers and Au content. (3) The variation of ΣPGE (83.94 to 479.75 ppb) in the single-layered crusts is relatively small, and Au (as high as 1.5 ppm) is higher than in the three-layered crusts. (4) Chondrite- and mantle-normalized normalized patterns of PGE and Au in the three-layered ferromanganese show Au-Pt enrichments and Ir-Pd depletions. The ΣPGE and Au of the crusts are lower than chondrite, while Ir-Ru-Rh-Pt are higher than primitive mantle (Fig. 1).

Several studies have explored the source and enrichment mechanism of PGE in the ferromanganese crusts. Halbach et al. (1989) proposed that PGE in ferromanganese crusts were sourced from seawater and meteorite dusts that co-deposited with MnO_2 from seawater. Baturin et al. (1991) interpreted gradually decreasing enrichments of Pt>Ru>Pd>Rh as indicating a crustal-seawater source. The Re-Os isotopic analyses of Shi et al. (2000) and Yao et al. (2002) suggested that that some of the PGEs in ferromanganese crusts were derived from cosmic particles. While Stuben et al. (1999) and Le et al. (1989) suggested that negative Pd anomalies in the chondrite-normalized patterns in ferromanganese crusts eliminate chondrites as a major source of PGE. Similarly, Koide et al. (1991) suggested that Pd should co-vary with other PGE if the source was cosmic particles.

Figure 2 shows that the chondrite-normalized PGE and Au patterns of the three-layered ferromanganese crusts are similar to average crustal compositions and the altered basaltic substrates. Values are, however, different than those of seawater and primitive mantle. These plots suggest that PGE and Au was leached from the basalt through water/rock reaction with seawater and deposited in the crusts. In addition, previously reported noble gas isotopic analyses indicate that cosmic particles such as meteorite dusts might also have contributed PGE and Au, especially in the porous layers of three-layered crusts (Sun et al. 2005). The similarity between our chondrite-normalized patterns and those of iron meteorites, including negative Pd anomalies, imply that the PGE and Au were partly sourced from iron meteorites rather than chondrite. This is consistent with microscope observation and electronic probe analyses of Halbach et al. (1989) that indicate iron meteorites dusts in ferromanganese crusts from middle Pacific Ocean seamounts.

This page intentionally blank

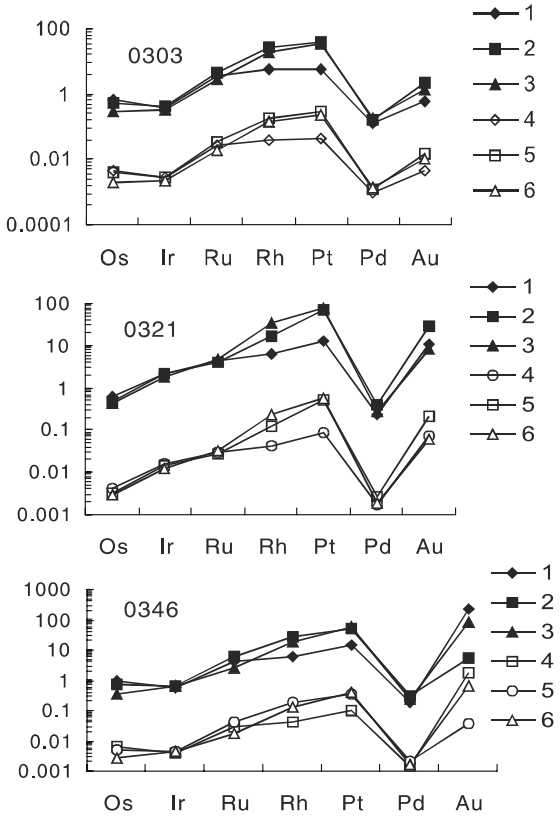

Figure 1: Normalized patterns of PGE and Au for ferromanganese crusts. 1,4: outer layer; 2,5: porous layer; 3,6: compact layer; 1,2,3: primitive mantle- normalized patterns; 4,5,6: chondrite-normalized patterns.

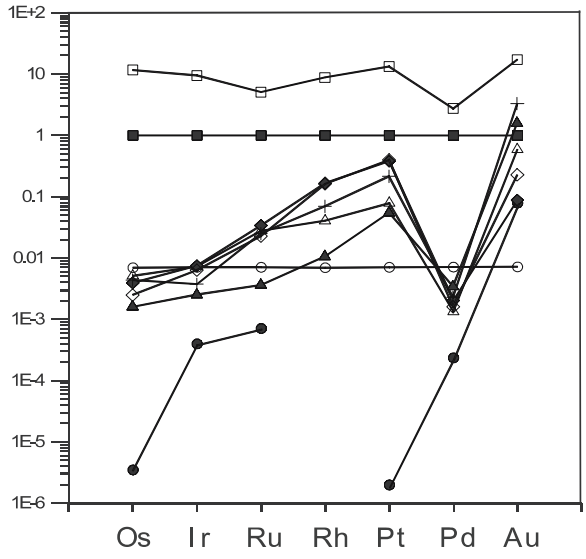

Figure 2: Comparative PGE and Au chondrite normalized patterns of ferromanganese crusts. ● seawater; ○ primitive mantle; ■ C1 chondrite; □ iron meteorite; ▲ basaltic substrate; △ outer layer; ◆ porous layer; ◇ compact layer; + average composition of crust.

Acknowledgements

This work is jointly supported by the NSFC (No. 40473024, 40343019), Project of 10th Five Year Research and Development of International Seabed (No. PY105-2-01-04-13, DY105-01-02-1), Project of Key Laboratory of Marginal Sea Geology, Guangzhou Institute of Geochemistry & South China sea Institutes of Oceanology, CAS (No. MSGLCAS03-4), Specialized Research Fund for the Doctoral Program of Higher Education (No. 20040558049) and the Trans-century Training Program Foundation for Talents by the Ministry of Education.

References

Bu WR, Shi XF, Peng JT, Qi L (2003) Geochemical characteristics of seamount ferromanganese nodules from mid-Pacific Ocean. Chinese Sciences Bulletin, 48: 98-105

Evans NJ, Chai CF (1997) The distribution and geochemistry of platinum-group elements as event markers in the Phanerozoic. Palaeogeography, Palaeoclimatology, Palaeoecology 127: 373-390

Halbach P, Kriete C, Prouse B, Puteanus D (1989) Mechanisms to explain the platinum congcentration in ferromanganese seamout crusts. Marine Geology, 76: 95-106

He GW, Zhao ZB, Zhu KC (2001) Cobalt-rich Crust Resources in the West Pacific. Geological Publishing House: 1-92, Beijing

Koide M, Goldberg ED, Niemesyer S, Gerlach D, Bertine KK, Padova A (1991) Osmium in marine sediments. Geochim. Cosmochim. Acta 55: 641-648

Le Suave R, Pichocki C, Pautot G (1989) Geological and mineralogical study of Co-rich ferromanganese crusts from asubmerged atoll in the Tuamotu Archipelago (French Polynrsia). Marine Geology 87: 227-247

Shi XF, Peng JT, Bu WR (2000) Pilot study on platinum-group elements of ferromanganese crust from Pacific Ocean. Bulletin of Mineralogy, Petrology and Geochemistry 19, 4: 339-340 (in Chinese)

Stuben D, Glasby GP, Eckhardt JD, Berner Z, Mountain BW (1999) Enrichments of Platinum-group element in hydrogenous, diagenetic and hydrothermal marine manganese and iron deposits. Exploration and Mining Geology 8: 233-250

Sun XM, Xue T, He GW (2005) Noble gas isotopic composition of ferromanganese crust from west Pacific Ocean and its geological significances. Acta Geologica Sinica (in press)

Wang SL (2001) Actuals of platinum group element reserve in China. Chinese Geology, 28,8:23-27 (in Chinese)

Xu C, Huang ZL, Liu CQ (2003) Review on geochemistry of platinum group element. Earth Science Frontiers 10(4): 520-528 (in Chinese with English abstract)

Yao D, Zhang LJ, Wiltshire JCW (2002) PGE and Re-Os isotope compositions and their significance of Co-rich ferromanganese crusts. Marine Geology & Quaternary Geology 22, 3: 53-58

Mirror-image coupling between sedimentary depression and the upper mantle uplifting in the Shengli oil/gas region, China: Implications for tectonics and exploratory practice

Liqiang Yang
State Key Laboratory of Geological Processes and Mineral Resources, China University of Geosciences, Beijing, 100083, China

Zhongjie Zhang
Institute of Geology and Geophysics, Chinese Academy of Sciences, Beijing, 100029, China

José Badal
Physics of the Earth, University of Zaragoza, Sciences B, Pedro cerbuna 12, 50009 Zaragoza, Spain

Abstract. For the purpose of exploring the connection between some structural features of the crust and the abundance of oil/gas content, we have defined and computed some characteristic structure parameters which have allowed us to study the mirror-image coupling between sedimentary depression and the upper mantle uplifting in oil/gas-bearing basins. We have obtained quantitative results concerning different tectonic elements on a multi-scale tectonic partition in the oil/gas region of Shengli, China. Factors measuring the activity degree of the crust-mantle interaction and the deviation of the crust from the isostatic equilibrium, together with other parameters related to the sedimentary structure and the deep-seated crust, have allowed us to discuss the implications of the mirror-image symmetry for tectonics and exploratory practice.

Keywords. Mirror-image symmetry, crust-mantle interaction, isostasy, oil/gas exploration

1 Introduction

The conditions of the sedimentary cover are mainly taken into account in the oil/gas exploration, but the data of the deep-seated structure are seldom used. In recent years, after exploring the characteristics of the deep structure of the crust under the regions with oil/gas content, it has been suggested that the abundance of oil/gas content in a sedimentary basin depends on the general pattern of crustal structure, and on the existent correlation between the bottom of the basin and the top of the uplifting mantle materials, described as mirror-image symmetry (Zhang et al. 2004). From such a relationship, we can investigate the state of internal activity – isostasy – of different tectonic systems and their classification (Egorkin et al. 1987), without giving quantitative results.

Bohai Bay Basin is located in the eastern part of China (see Fig. 1, top right). In this paper, we present below four unpublished geological-geophysical profiles located at the Shengli oil/gas region to the southeast of the basin (Fig. 1), and look for the mirror-image symmetry on a multi-scale

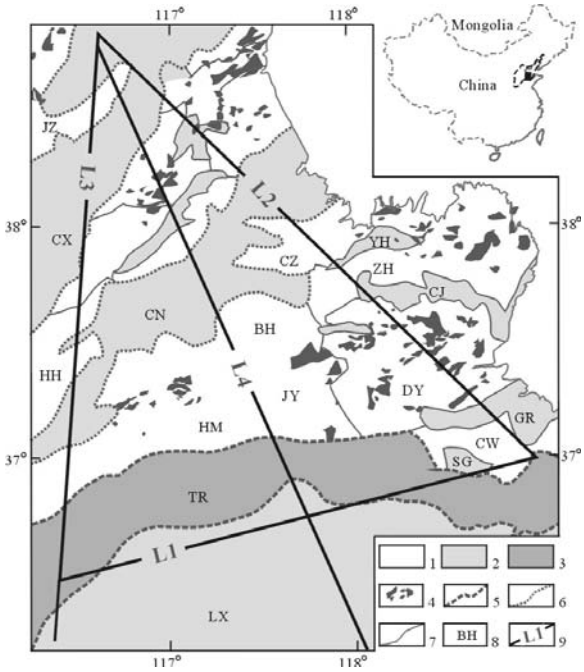

Figure 1: Location of the Bohai Bay Basin (dashed line) and the study area (small full rectangle) to east of China (upper right corner). A zoom view of the probed region showing the deep seismic profiles (from L1 to L4) on a multi-scale tectonic partition (lower right corner). 1, depression or lag; 2, uplift; 3, trisition zones; 4, oil/gas; 5, the boundary of larger tectonic elements; 6, the boundary of intermediate tectonic elements; 7, the boundary of smaller tectonic elements; 8, symble of tectonic elements; 9, deep seismic profiles and their number. Key to symbols: BH, Bohai Bay Basin; LX, Luxi uplift; TR, transition zone; JY, Jiyang Depression; HH, Huanghua Depression; JZ, Jizhong Depression; CX, Cangxian Uplift; CN, Chenning Uplift; DY, Dongying Lag; HM, Huiming Lag; ZH, Zhanhua Lag; CW, Changwei Lag; CZ, Chezheng Lag; CJ, Chenjiazhuang Uplift; GR, Guangrao Uplif; YH, Yihezhuang Uplift; SG, Shouguang Uplift.

tectonic partition: basin/uplift on a large-scale, depression/uplift on an intermediate-scale and lag/uplift on a small-scale. We also discuss the implications for tectonics and geophysical exploration.

2 Multi-scale tectonic partition and related geophysical data

The collected field information supplies a good database for estimating the thickness of Mesozoic-Cenozoic sedimentary cover and the Moho depth in the region. We have considered three deep seismic soundings that are labeled from L1 to L3 and make up a triangular area of observation, together with a fourth seismic profile labeled L4 crossing this area.

All these profiles are plotted in Figure 1 by straight lines and are 240 km (L1), 300 km (L2, L3) and 320 km (L4) long.

Two kinds of data have been used in this study: the thickness data of the Mesozoic-Cenozoic sedimentary covering (t) that are available from the 2D and 3D seismic exploration works, geological surveying and exploration wells, and the Moho depth data (H) provided by the four wide-angle seismic profiles mentioned above. Based on these data, the thickness of both the sedimentary cover and the crust of the different tectonic elements of the study area were grouped according to its tectonic order (large-, intermediate- or small-scale).

3 Method and results

If t represents the thickness of the sedimentary cover and h is the thickness of the consolidated crust, then we can write the linear equation

$$h = T + at \tag{1}$$

where T is the average thickness of consolidated crust, so characterizing the degree of closing between the bottom of the sedimentary cover and the top of the upper mantle lid. The coefficient a in equation (1) is defined as the mirror-image symmetry factor, and it express the symmetrical behavior of the bottom of a sedimentary basin with respect to the Moho depth and therefore to the thickness of the consolidated crust. Here we follow the procedure applied in previous work by Zhang et al. (2004). From a quantitative viewpoint, the results for T and a concerning different tectonic elements are plotted all together in Figure 2, where a comparison for the three classes of tectonic orders can be seen.

4 Tectonic implications

The mirror-image symmetry of the crust seems to be related with the isostatic compensation of the tectonic elements (Zhang et al. 2004), according to the results obtained after studying the lithosphere in Siberia (Egorkin et al. 1987), a mirror-image symmetry factor of about -1.6 is interpreted to correspond to an isostatically compensated tectonic element.

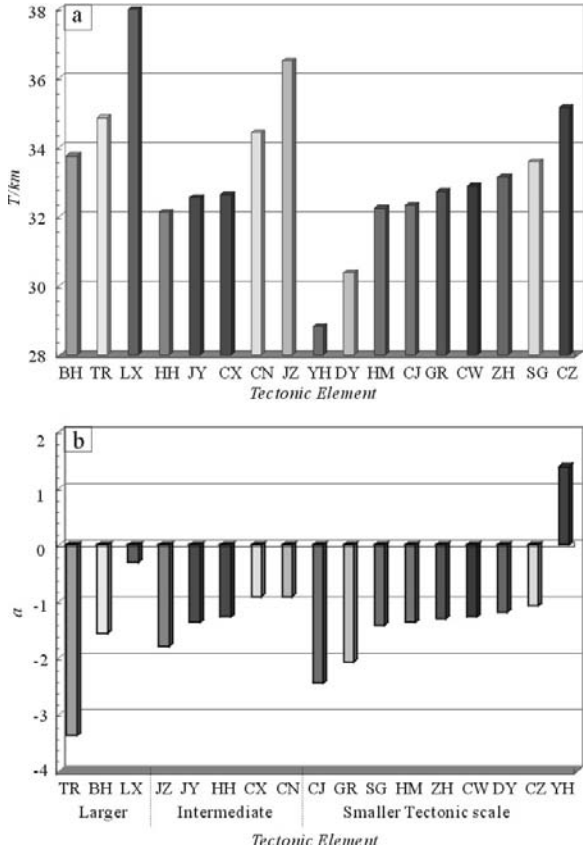

Figure 2: Histogram in the upper part (a): Average thickness of the consolidated crust (T) for the different tectonic units taken into account in this study. Histogram in the lower part (b): Mirror-image symmetry factor (a) for the geological formations of reference. Key to symbols as in Figure 1.

Regarding the three types of tectonic elements to take into account, sedimentary regions, uplifts and transition or slope zones, we are able to do the following considerations. In the Mesozoic-Cenozoic sedimentary regions the sediments are comparatively thicker, the average thickness of the consolidated crust is thinner, and the mirror-image symmetry factor nears to -1.6. In these regions the crust-mantle interaction is remarkable and the crust seems to be isostatically compensated.

5 Implications for exploratory practice

In previous work we defined the ratio R as the ratio between the thickness of the consolidated crust and the absolute value of the symmetry factor, and we found that there exists a connection between R and some tectonic units of China with oil/gas content (Zhang et al. 2004).

This page intentionally blank

The ratio *R* for these tectonic units range in a narrow band 19.4~37.4, being about 31.5 in the western part and 25.5 in the eastern part separated by the earthquake belt. Therefore, we have calculated the ratio *R* from the previous results. As can be seen, in Bohai Bay Basin, Luxi Uplift and transition zone *R* takes the values 21.68, 113.41 and 11.28, respectively, which are not similar. On an intermediate scale, the *R*-value is practically the same for Jiyang, Huanghua and Jizhong Depression, 23.72, 25.23 and 20.34, respectively, although different but of the same order for Chenning, 35.88, and Cangxian Uplift, 37.62. On the smaller scale *R* falls in three intervals: 23.47~32.45 for the five lags, Dongying, Huiming, Zhanhua, Changwei and Chezheng; 13-19~15.84 for the two uplifts, Chenjiazhuang and Guangrao; 21.00 for Yihezhuang Uplift and 23.65 for Shouguang Uplift. After seeing the sites where oil/gas reservoirs have been found up to date and according to our results, the connection of *R* with oil/gas content is obvious.

Clear differences between the sites with oil/gas reservoirs and the regions without them can be observed from the figures defining their respective structure parameters. The collected data may be correlated as follows: In the case of regions that are rich in oil/gas: (1) the upper mantle uplifts sharply up to 8~10 km; (2) the sedimentary cover is a sharply depressed zone up to 10~20 km; (3) the average thickness of the consolidated crust, *T*, and the mirror-image symmetry factor, *a*, are parameters constrained in a narrow band near to the global average: 36 km and -1.6, respectively, so that the ratio *R* is in his turn closed within a narrow interval; for example it takes a value near to 26.5 in Eastern China. The ratio *R* is a very important parameter as it is indeed a prognostic tool for oil/gas-bearing regions. In relation to all tectonic elements that are rich in oil and gas in Eastern China, the thickness of the most of the sedimentary covers is more than 7.0 km; the least thickness of the consolidated crust is less than 32 km; the average thickness of the consolidated crust is more than 33.65 km and less than 38.79 km; the mirror-image symmetry factor is near to -1.6, actually between -1.13 and -1.88; and the ratio between average thickness of consolidated crust and the mirror-image symmetry factor is close to 26.5, actually between 19.39 and 30.76 (Zhang et al. 2004).

In the case of regions with a poor or nonexistent content in oil/gas: (1) the upper mantle uplifts a little, even depress, usually less than 5 km; (2) the sedimentary cover may be a sharply depressed zone, although it is usually less than 10 km; (3) the *T*-, *a*- and *R*-values deviate enough from the global average (Shao et al. 1999; Zhang et al. 2004). There is however a kind of tectonic element having a crust far from the isostatic equilibrium and a very active crust-mantle interaction, without oil/gas or with a poor content of these natural resources, although with presence of them in the surroundings: Yihezhuang Uplift belonging to the investigated area and the Southeast China fold system are two clear examples.

The structure parameters have not why to be totally coincident in some and other cases. For example, in North China platform the *T*-, *a*- and *R*-values are 38.78 km, -1.47 and 26.45, respectively (Zhang et al. 2004), and in Bohai Bay Basin those values become 33.76 km, -1.56 and 21.70. A small deviation exists between both groups of data, and the same thing happens with respect to the results on intermediate- and small-scale. The cause may be the different thickness of the sediments, the heterogeneity of the deep-seated structures and the variable abundance of oil/gas among all the tectonic elements on multiscale.

Acknowledgements

We are indebted to all those who supplied us original information and contributed to data acquisition for this study. Helpful comments and suggestions from anonymous reviewers are gratefully acknowledged. The present work takes advantage of the Collaboration Agreement between the Institute of Geology and Geophysics, Chinese Academy of Sciences, and the University of Zaragoza, Spain. The Chinese National Nature Sciences Foundation and China Postdoctoral Science Foundation supported this research through the projects 40304007, 40234044 and 2003033238.

References

Egorkin AV, Zuganov SK, Pavlenkova NA, Chernyshev NM (1987) Results of lithosphere studies from long-range profiles in Siberia. Tectonophysics 140: 29-47

Zhang Z, Yang L, Teng J, Badal J (2005) Mirror image symmetry between the thickness of sedimentary basin and the crust in China. Earth. Plan. Sci. Lett. (in press)

An ore-forming model for Pb-Zn deposits in the Qinling orogenic belt, China

Yao Shuzhen, Ding Zhenju, Zhou Zonggui, Lü Xinbiao
China University of Geosciences, Wuhan, Hubei, 430074, China

Abstract. The Qinling polymetallic belt is one of the important producers of Pb-Zn in China, as it contains numerous large to super-large Pb-Zn ore deposits. Especially VHMS, SEDEX, and MVT Pb-Zn type deposits possess important economic value and potential for exploration. The VHMS Pb-Zn deposits are mainly hosted in volcano-sedimentary formations along a Late Proterozoic arc and arc-back basin. The SEDEX Pb-Zn deposits are associated with hydrothermal sediments that primarily formed in Paleozoic an intraplate rift basin. And the MVT lead-zinc ore deposits are controlled by fault-induced brecciated zones mainly distributed along the foreland basin margin of the Qinling orogen and hosted within Sinian system carbonate formations. These deposits are products of different stages during orogenic evolution and respectively show characteristics of zonal distribution and sublevel concentrations. Generation of the deposits is related to multi-episode tectonic-fluid events during orogenic processes.

Keywords. Qinling orogen belt, lead-zinc metallogenic series, VHMS, SEDEX, MVT

1 Metallogenic geological background

The Qinling orogen is bounded in the north by the Baijiluonan fault and in the south by the Yangpingguan-Dabashan arc fault. It is further subdivided into three parts form north to south by the Shangdan and Mianlue ophiolite zones: the southernmost margin of North China Craton, Qinling microplate, and northernmost margin of Yangtze Craton. The Shangdan ophiolite and Mianlue ophiolite zones represent the remnants of two limited oceanic basins that developed during Proterozoic to Early Paleozoic and Devonian- Carboniferous, respectively. The Qinling microplate between the two main sutures formed as a result of breakup of the Yangtze Plate and the Mianlue ocean, ever as a part of the passive continental margin of the Yangtze plate prior to the Late Paleozoic.

Qinling and its adjoining area have experienced multiple periods of structural-fluid-thermal and ore-forming events (Yao et al. 2002). The main Pb-Zin mineralization types in the Qinling include VHMS, SEDEX, MVT, and porphyry type,. Among these, VHMS, SEDEX type, and MVT ore deposits have important economic value and exploration potential.

2 VHMS type metallogenic series

The VHMS type deposits mainly formed in a middle to late Proterozoic island arc or backarc basin; for example, the Donggouba Pb-Zn-Au-Ag and Liushanyan Pb-Zn deposits. Taking Donggouba deposit as a example to explain the VHMS type mineralization characteristics, the Donggouba deposit host rocks are mainly tuff in which orebodies display layer or lens-like shape, are parallel and in accordance with bedding of the volcanic clastic rocks as a whole. The profitable component of ore mainly consist of Pb, Zn, Au, Ag, while major metallic minerals are sphalerite, galena, pyrite, with minor or rare chalcopyrite, electrum, aphonite, argentite, nature silver, zincite, and magnetite; major gangue minerals are quartz, barite, sericite, chlorite, and carbonate. The ore is characterized by massive, laminated striation, rhythmic banding, and dissemination structures, and with partial residue of sedimentary structures. In addition, later-generation vein shapes and rootless folding and intense structure replacement phenomena are observed. Wall rock alteration includes silication, pyrite-sericite-quartzite, and baritization. The deposit underwent two mineralization periods and four stages (Wang et al. 1991): Early synsedimentary hydrothermal exhalative mineralization which is marked by the formation of bed and bed-like orebodies and the appearance of colloidal pyrite and fine-grained barite; subsequent metamorphic fluids superimposed mineralization with 3 stages, (1) barite–galena –pyrite-sphalerite-gold-silver mineralization stage, marked by enlargement of mineral grains, (2) barite-sphalerite-containing gold and silver pyrite mineralization stage, formation of vein orebodies, (3) barite-carbonate-sericite mineralization stage, marked by stringer orebody appearance. REE geochemistry shows that the ore and its host rocks, on the whole, have similar distribution patterns except for Eu and Ce. Ores have apparent positive Eu anomalies and weak negative Ce anomalies; at the same time they display evidence for convective mixing of some seawater and hydrothermal fluids to be involved in ore deposition. Moreover, based on LREE enrichment, positive Eu and negative Ce anomalies appear in barites and other ore. From this we conclude that the ore-forming hydrothermal fluid contained a component of magmatic fluid (Ding et al. 2003). This notion is consistent with the observation of mixed Pb and S isotopic compositions (Wang and Li 1992; Lu et al. 1998). The ore Pb isotopic compositions show a mixing trend of two end member components of mantle and crust that were involved in the ore-forming processe, whereas S isotopic compositions show the S originated from volcanics and seawater (Wang and Li 1992;

Lu et al 1998). These observations indicate that ore formation was mainly related with ancient seafloor hydrothermal fluid activity, and late-stage superposition of mineralization.

3 SEDEX type metallogenic series

The Devonian in the Qinling is exposed as a concentric area of exhalative sedimentary type of lead zinc ore deposits of China. The Qinling microplate interior developed as a series of graben and horst style basins in the Devonian, where the fault activity induced a large scale of hydrothermal fluid exhalation and deposition of Pb-Zn on the seafloor. As a result, a series of large and superlarge polymetallic ore deposits with Pb-Zn predominant components are distributed along the contemporaneous faults, and are especially concentrated in the Xicheng, Fengtai, and Shanzha subdivisions. The Changba-Lijiagou, Bijiashan deposit in Chengxian, and Qiantongshan, Bafangshan in Fengxian represent this type of ore deposit. Combined with some recent discoveries and exploration in the Daijiazhuang, Shuiguanzi ore deposits show that Qinling SEDEX type deposits still have relatively significant prospecting potential.

There are two main Pb-Zn ore-producing units in the Devonian system: (1) Middle Devonian Anjiacha formation, and (2) Middle Devonian Xihanshui formation. Similarly, the Devonian Pb -Zn deposits can be divided into two classes of hydrothermal sedimentary (Changba style) and reworked hydrothermal sedimentary deposit (Bijianshan-Qiantongshan style). The hydrothermal sedimentary type of ore deposit is one of high-grade, large-tonnage superlarge deposits such as the Changba-Lijiagou Pb-Zn deposit. The host rocks for this kind of ore deposit mainly are carbonates to fine clastic formations. The orebodies can be farther grouped into two classes according the lithological characteristics of their host rock: (1) orebodies occurring in biotite quartz schist; (2) orebodies occurring in biomicrite. The stratiform or stratiform-like orebodies are in conformable contact with the surround rocks and with stockwork mineralization or alteration envelope in footwall of orebody (Ma et al. 1996). The major ore minerals are pyrite, galena and sphalerite, with minor pyrrhotite. Major gangue minerals are quartz and calcite, with minor barite, muscovite, tremolite, plagioclase, biotite, chlorite, epidote, and fluorite. The major ore components are lead and zinc, associated with Ga, Ge, In, Cd, Tl, Ag, As, Sb, and S. Ores have major rhythmic-banded structures and minor massive structures, as well as later deformation-induced concentric corrugation and quasi-gneissic structure. The hydrothermal sedimentary -reworked deposit type is another important but slightly less important than Changba style of ore deposit in Qinling. Its host rock series are reef quartzite suites. The major orebodies showing saddle shape are located in the cores of anticlines and associated with siliceous rocks; some minor orebodies show quasi-bed or lens form and occur in reef limestone or phyllite formations. The ore components are more complex than of the hydrothermal sedimentary type, with major metal minerals being sphalerite, galena, pyrite, and minor chalcopyrite, tetrahedrite, bornite, leukargyrite, arsenopyrite, marcasite, stibnite, and siderite, and with major gangue minerals of quartz, calcite, and barite, and minor ankerite, sericite, chlorite, and fluorite. The major ore structures are banding and brecciated, with minor massive, dissemination, spot, and stockworks. The major alteration types are silication and ankeritization, with minor baritization, sideritization. The ores components are major Pb and Zn, with minor Ag and Cu. The ore-forming temperatures of hydrothermal sedimentary ore deposit (Changba style) and hydrothermal sedimentary reworked ore deposit (Bijiashan or Qiantongshan style) types range from 300 to 200 degree Celsius and 300 to 150 degree Celsius, respectively. The ores show relatively rich isotopically heavy S and have similar isotopic ratios of average seawater sulphate in the middle Devonian (18%). Ore lead, with a small amount of radioactive origin Pb, mostly belongs normal Pb, its values are limited to between 9.51 to 9.65 per mil. Model ages vary from 401 Ma to 476 Ma, are concentrated at about 440 Ma, thus obviously older than the age of ore host strata. These facts suggest that the ore matter derived from basement rocks and was leached out from the rocks and transported to the seabed by heated water. In addition, recent discoveries have been made in the Middle Silurian Shuanghezhen formation and the early Silurian Meiziya formation where more than 20 ore deposits or occurrences, such as Guanzigou, Sirengou, and Nanshagou ore deposit, have been located. Our results suggest that the hydrothermal ore-forming process started during the Silurian and reached its peak in middle Devonian.

4 MVT metallogenic series

The MVT metallogenic deposits are located mainly along the margins of paleo-uplifts in the foreland basin in the southernmost part of the Qinling, such as the Hannan-Beiba and Shennongjia uplifts, with stable host rock horizons and a large extent of mineralization. This type of deposit also occurs along the northwest margin of the Yangtze platform in Sichuan Province. The mineralization mostly occurs in Sinian Deingying formation, which composes of upper banding dolomite and lower algal dololaminite. Mineralization along fissures or edges of rubble was controlled by interlayer structures and structural breccias. The mineralization intensity is irregular, generally stronger in the centre to weaker along the rim and correspondingly the change from massive to fissure

This page intentionally blank

veinlet on ore structure. The orebodies show quasi-layers, lenses, and banding along interlayer breccia zones, or cut strata at slight angles, with obvious branching and combinations of enlargement and narrowing phenomena along strike and dip. Ore elements include major Pb and Zn, and subordinate Ge, Cd, and Ag. Major ore minerals include sphalerite, galena, smithsonite, and hemimorphite, with minor pyrite and pyrrhotite. Major gangue consitutents are dolomite, barite, calcite, quartz, fluorite, and organic matter. In ore bodies and the overlying rocks asphaltic bitumen and vugs are common and indicate the mineralization characteristics of filling by low temperature and organic matter-rich hydrothermal fluid.s The source of organic matter in ore fluid is tentatively inferred to have derived from the middle and lower algal dolomite of the Dengying formation. Ore S isotopic ratios are $10.8\sim12.8x10^{-3}$ and relatively rich in heavy S. These features are similar to MVT Pb-Zn ore deposits in USA.

The ore formation in this type of ore deposit displays not only stratabound and lithologically-controlled features but also obvious epigenetic mineralization characteristics. The ore fluid was low temperature and rich in hydrocarbon from algal dolomite. In recent years, sedimentary sphalerite mineralization has been discovered in algal dolomite of the Sinian Dengying Formation at Baijihe and Yichang. Ores are likely to be the product of infilling and replacement of breccia by infiltration and circulation of fluid driven by tectonic force during orogen evolution. The basement uplift and decollement structures provide a favorable space for fluid movement and the location of orebodies.

5 Regional metallogenic model

The Qinling lead and zinc ores were formed during several cycles. Ore formation began in the middle to late Proterozoic and early Paleozoic, continued during the Hercynian and Indosinian, and ended in Yanshanian. The peak of ore formation occurred during the Hercynian and Indosinian-Yanshanian. The middle Proterozoic is the late evolution stage of Bikou rift-ocean basin-island arc metallogenic system, when VHMS deposits of lead and zinc related with island arc volcanic rocks were formed. Subsequently a series of lead zinc (or copper) deposits formed. For example, sedimentary ore seams or ore source beds formed during the Sinian along the north margin of Yangtze plate; early Paleozoic Pb-Zn-Cu metallogenic series formation formed during Erlangping volcanism in a backarc basin; in the Silurian and Devonian SEDEX type deposits formation occurred in a series of rift basins. The large scale of hydrothermal fluid exhalative processes began with Silurian in intraplate rift basins and reached a peak in the middle Devonian and formed widespread regional large or super-large Pb-Zn ore deposits. Even

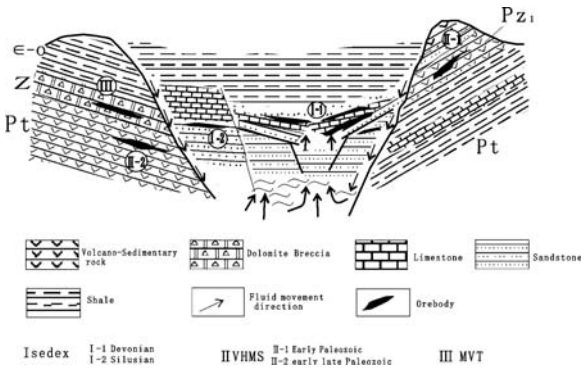

Figure1: Regional metallogenic model of Pb-Zn in Qinling.

for single ore deposits, the cyclicity of hydrothermal activity is apparent and shows characteristics of episodic-style sedimentation (intermittent), and formed multilayers of ore bodies with rhythmic or banded structure. Following the formation of the Qinling orogenic belt during the final stages of the Indosinian, Qinling changed into a intracontinental orogenic cycle, where ore source material produced during the Sinian was reworked to generate MVT ore deposits by tectonically driven fluid processes.

Regionally, ore deposit distribution displays apparent zonal and sublevel concentrated features. The VHMS type of Pb-Zn deposit was mainly hosted in volcano-sedimentary formation along late Proterozoic arc and arc-back basins. The SEDEX type of Pb-Zn deposit is closely associated with hydrothermal sediments that primarily formed in a Paleozoic intraplate rift basin. And the MVT lead-zinc ore deposits were controlled by fault-induced brecciated zones mainly distributed along the foreland basin margin of Qinling orogen, and arfe hosted in Sinian system carbonate formations. According to the above findings, we have summarized the regional metallogenic model, in Figure 1.

References

Ding Z, Yao S, Liu C, Zhou (2003) The characteristics of exhalation-sedimentary deposit of Donggouba polymetal deposit: evidence from ore's REE composition. Acta Petrologica Sinica, 19: 792-798

Lu W, Zhang P, Yang S (1998) Isotopic geological features of the Donggouba multimetal deposit. Journal of Chengdu University of Technology, 25: 447-456

Ma G, Qi S, Li Y (1996) A study of the exhalative origin of the Chengba lead-zinc deposit, Gansu Province. Review of Geology and Exploration, 11: 36-44

Wang D, Li S (1991) Origin of the pyrite-barite type Au-Ag polymetallic deposit of "Donggouba type": a study on physical and chemical condition of ore-forming and stable isotope geochemistry. Northwestern Geology ¨ 12: 25-32

Yao S, Ding Z, Zhou Z, Chen S (2002) The metallogenic systems of Qinglin orogen. Earth Science-Journal of China University of Geosciences, 27(5): 599-604

Platinum-group elements in Cambrian black shale in southern China: Differential enrichment of platinum and palladium

Guangdi Zhang, Jiuling Li, Qunyao Xiong
Institute of Mineral Resources, Chinese Academy of Geological Sciences, Baiwanzhuang 26,Beijing 100037, China

Fangyuan Chen
Institute of Geology, Chinese Academy of Geological Sciences, Baiwanzhuang 26,Beijing 100037, China

Abstract. We have conducted electro-microprobe analysis, X-ray scanning image, SEM+EDS, X-ray powder diffraction and X-ray photoelectron spectroscopy (XPS) of PGE-bearing sulfide-rich ores collected in the Cambrian black shale in Guizhou and Hunan provinces, southern China. Our results show that platinum-group minerals (PGM) have not been found in Mo-Ni-PGE-rich sulfide ores. Pt and Pd are enriched in different minerals or mineral assemblages. Pt is highly enriched in micrometer-scale As-bearing Fe-vaesite mixed assemblages. Pd is mainly enriched in a phase similar to MoSC, which has previously been referred to as "jordisite". The XPS clearly shows double peaks of Pd3d. Palladium in the samples may therefore form a compound like PdSC or $Pd(SPh)_2$, (where Ph stands for benzene). The double peaks of Pt4f are located in the range of nanometer clusters of native platinum, which might occur in a nanometer-cluster form in black shale.

Keywords. Pt topo-accumulation, Pd, carbon-bearing S-Mo phase

Extensive research has been done on platinum-group elements (PGE) from the Cambrian Mo-Ni beds in southern China by means of numerous approaches (Fan et al. 1973; Zhang et al. 1987; Li. 1994 and Li et al. 1995). The PGE from the Cambrian black shales in south China are concentrated in Ni-Mo sulfide beds, but the nature of their occurence is an open question. No platinum-group minerals (PGM) have been reported in this area thus far and Pt and Pd have not been concentrated during the ore dressing process.

This study focuses on metal-rich horizons with high concentrations of nickel and molybdenum from the Cambrian black shales in southern China. The PGE-rich samples were collected from Huangjiawan, Guizhou Province and Dayong, Hunan Province. The maximum contents of Pt and Pd from the ore are 569 ppb (0.569g/t) and 554 ppb (0.554g/t), respectively.

Four concentrates with Pt contents of more than 1000 ppb were obtained from the samples. They all belong to electromagnetic or weakly electromagnetic Ni-rich concentrates (contain up to 25.2wt% of Ni) and were used for our further analyses. Their Pt contents are 2780, 1520, 1290 and 1180 ppb respectively. The highest Pd content is 960 ppb and the contents of all other Pd concentrates are lower than 610 ppb. Samples were characterized by more than 100 WDS point analyses, a large number of X-ray scanning images and SEM+EDS analyses. Some inhomogeneous distribution and topo-accumulation of Pt were observed in the As-bearing Fe-vaesite mixed assemblage M. The X-ray scanning images of Pt show the position of the increase of Pt concentration (Fig. 1). It is worth noting that such Pt enrichment is just a relative phenomenon. The absolute Pt content is too low to be compared with that of regular Pt minerals and the Pt-rich portions of the sample do not show high reflectance, which is a common feature of regular PGM. The Pt X-ray scanning image and profile illustrate inhomogeneous distribution and enrichment of Pt of concentrate sample Y2a in the microlitic mixed assemblage, which has the highest content of Pt (Fig. 1).

The only sulfide mineral in which Pt and Pd could be detected is tennantite. There is no positive relation between Pt and Pd. Comparatively speaking, Pt was more detected in in the As-bearing Fe- vaesite mixed assemblage, Pd was clearly detected more in the carbon-bearing Mo-S phase than in other assemblages. As with WDS, SEM+EDS analysis indicated that the content of Pt is commonly higher than that of Pd in Ni- minerals especially in the assemblage M (e.g. in Fig. 1). The Pd content is always higher than the Pt content in the carbon-bearing Mo-S phase (e.g. in Fig. 2). Three Ni-rich samples with the highest Pt content, selected from more than 27 concentrates, were analyzed by X-ray photoelectron spectroscopy (XPS) at Tsinghua University. The Pt4f line is the characteristic XPS spectral line of Pt, which displays double peaks. The space between the two peaks is about 3.33eV and the binding energy is $Pt4f_{7/2}$ = 71.2eV for metallic platinum (Fig. 3-b)(Moulder et al. 1992). The full-scanning images, As3d, Fe2p, Ni2p, Ni3p+Al2p (+Pt4f), Mo3d+S2s+ As3s, S2p and Pd3d were obtained. The peaks of Pt in two of the three samples could not be observed due to being sheltered (maybe by the minor Al3p in the sample) and interfered with by Ni3p. Pt4f was shown more or less only in one sample (see Fig 3-a), though still interfered by Ni3p. $Pt4f_{7/2}$ might be 71.85eV and $Pt4f_{5/2}$ is 75.25eV. The space between the two peaks is about 3.4 eV.

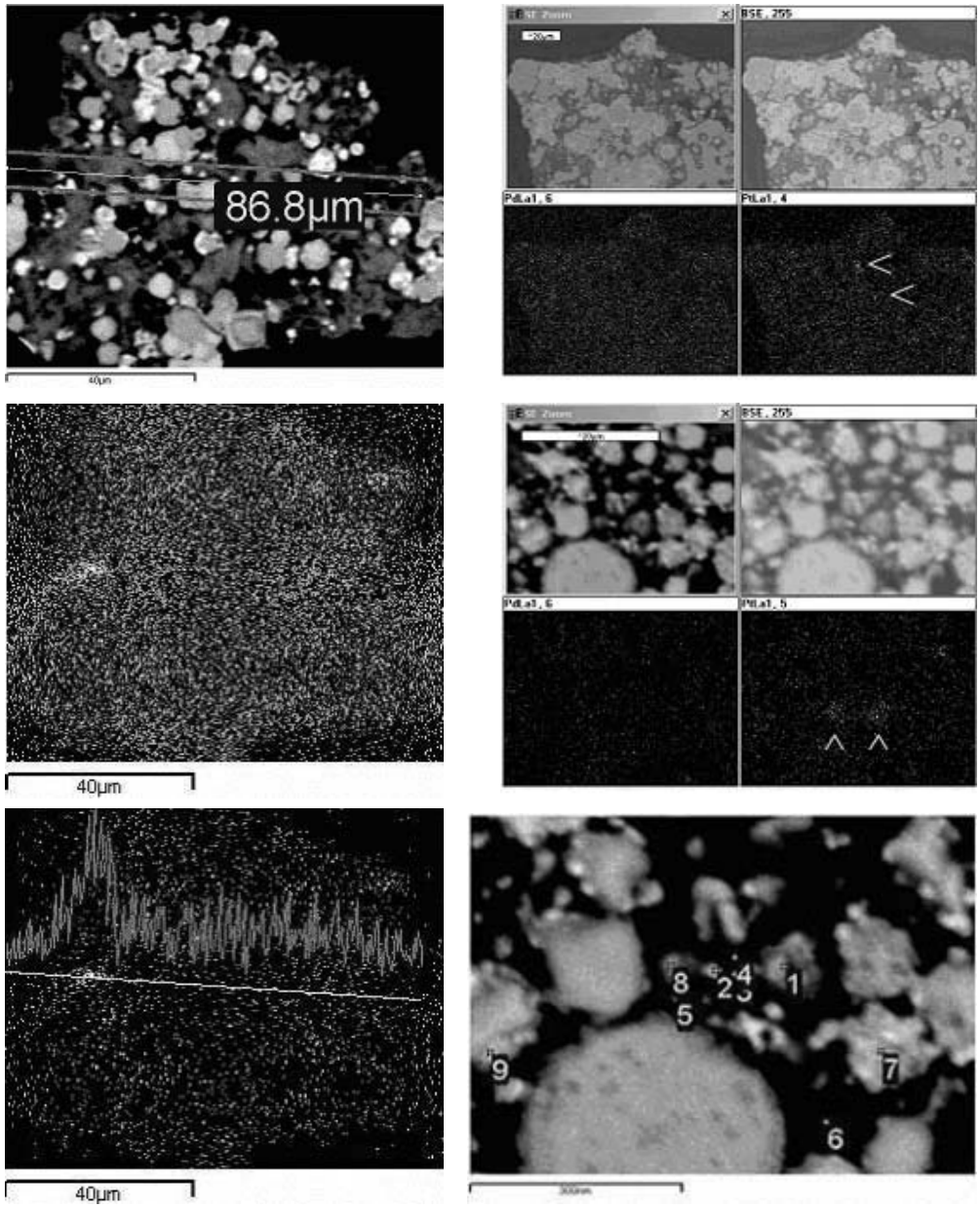

SEM+EDS：5266

atom%	O	Na	Si	S	Ca	V	Cr	Fe	Ni	Cu	Zn	As	Pd	Cd	Pt	Total
1	15.84	4.85	1.02	37.07	0.52		1.15	2.57	0.72	0.79	33.71	0.88	0.10	0.35	0.42	100.00
2	21.91			46.97				9.81	3.04		14.05	3.53	0.17		0.51	100.00
3	24.17			45.06				7.50	7.54		6.23	8.73	0.11		0.66	100.00
4	21.11			47.42				11.06	6.66		5.70	7.42	-0.06		0.68	100.00
5	20.00			50.35		0.34		10.64	5.83		5.94	6.24	0.04		0.60	100.00
6	27.20			44.52				9.09	9.53			9.54	-0.21		0.32	100.00
7	13.81			51.49				20.51	8.17			5.24	0.18		0.60	100.00
8	18.79			49.01				11.91	6.62		5.37	7.80	-0.01		0.51	100.00
9	11.75		0.63	49.06				25.48	8.59		0.44	3.47	0.18		0.42	100.00

Figure 1: SEM + EDS analysis of Ni-Fe-As-S mixed assemblage(sample y-2a and sh-1); upper left: SEM image No. 1003; middle left: X-ray scanning image of Pt; low right: X-ray scanning profile of Pt; upper and middle right:BSE, X-ray scanning image of Pt and Pd,the topo -accumulation of Pt signed by white arrows<; low right: SEM+EDS image 5266&analyzed points.

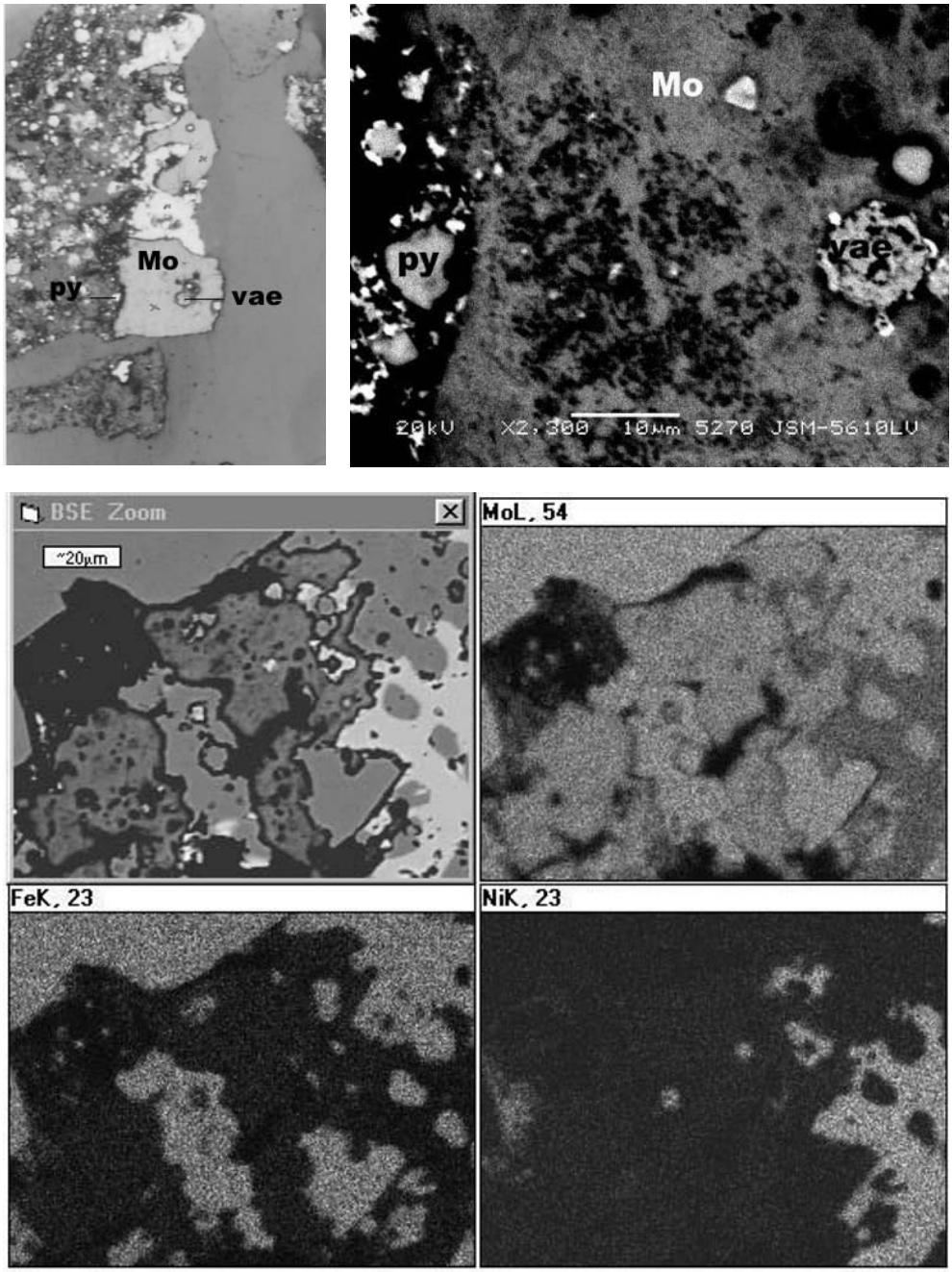

Wt%	As	S	Ni	Mo	Cu	Pd	Fe	Pt	Zn	Sb	
4-b-1	0.96	24.56	2.64	25.31	0.02	0.11	3.83	0.02	0.00	0.00	57.43
4-b-2	0.92	23.20	2.53	23.67	0.05	0.10	3.64	0.00	0.01	0.00	54.11
7-d-5	0.67	34.22	2.68	37.26	0.05	0.12	7.11	0.04	0.00	0.00	82.16
7-d-6	0.42	26.95	2.21	28.42	0.04	0.12	5.53	0.03	0.00	0.00	63.71
7-d-6	0.50	26.74	2.09	28.32	0.01	0.10	5.39	0.00	0.00	0.00	63.14

Figure 2: Microprobe WDS and SEM analyses for "jordisite" (carbon-bearing S-Mo phase). Sample Sh-1-mo, upper left: "jordisite"(Mo) under microscopy; upper right: SEM image in the same region; WDS analysis numbers for WDS: 4-b-1 and 4-b-2. Sample Z-6, lower: BSE, X-ray scanning image of Mo+S, Fe and Ni; analysis numbers for WDS: 7-d-5 and 7-d-6(2)

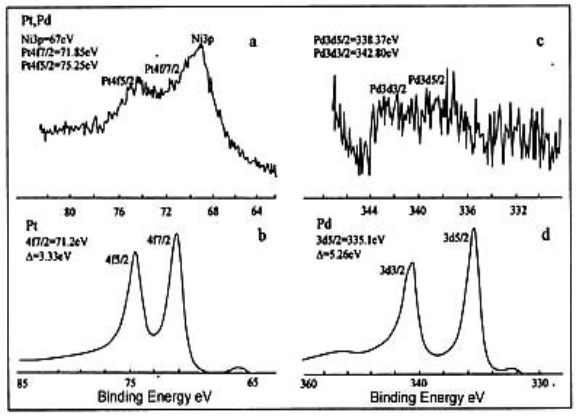

Figure 3: XPS spectra of Pt4f and Pd3d; a. Sample Sh-1-Ni4, the spectra Ni3p and the appraised Pt4f; b. standard double peaks of Pt4f; c. sample Y2-a, spectra Pd3d; d. standard double peaks for metal Pd3d.Calibrated by C1s (284.6eV) of the assuming carbon. Analyzed by Ms. Ye Xiayan, Tsinghua University.

XPS data collected from nanometer-scale clusters of Pt on carbon surfaces and activated carbon containing 1wt% and 10% Pt indicate that when the Pt particle sizes (i.e. expression in coverage θ) decrease the binding energy shifts will increase (Mason 1983; Cheung 1984; Lin et al. 1999). The $Pt4f_{7/2} \approx 71.8$eV in the activated carbon containing 1% Pt is located in the nanometer region with positive shifts relative to metallic Pt. The platinum in the activated carbon containing 10% Pt is inferred to be present as native Pt. Platinum in the samples was hardly recognized with the XPS because of relatively low content and interference of Ni3p. However, A small positive shift (Pt4f 71.85eV relative to metal platinum Pt4f 71.2eV) might be recognized. In consideration of the above data, the characteristic binding energy appears to be characteristic of nanometer-scale clusters of Pt. The XPS spectral line of Pd is the Pd3d double peaks. For metallic palladium the binding energy is $Pd3d_{5/2} = 335.1$ eV and the space between the two peaks is about 5.26eV (see Fig 3-d) (Moulder et al. 1992). Pd3d of sample Y2a is clearly displayed in the narrow-scanning image (Fig 3-c). Pd3d has double peaks and $Pd3d_{5/2}$=338.37eV. The space between the two peaks is close to that for metallic Pd and the binding energy of Pd in the sample has a clear positive shift compared with $Pd3d_{5/2}$=335.1eV for metallic Pd. Pd is mainly enriched in carbon-bearing S-Mo facies in black shale. The Pd3d spectra of sample Y2-a are assigned to $Pd3d_{5/2}$ =338.37eV with the associated peak $Pd3d_{3/2}$ (Fig 3-c). Referring to the XPS database related to binding energy of $Pd3d_{5/2}$, occurrence of the palladium in the samples is similar to that of several kinds of Pd-salts or PdO_2, including $Pd(SPh)_2$ (benzyl was showed as Ph). Considering that Pd is mainly enriched in the carbon-bearing S-Mo facies, the palladium should exist as a form to approach carbon and sulfur-bearing matter, i.e. $Pd(SPh)_2$, or as a PdSC component in the MoSC phase (c.f., Kao et al., 2001).

References

Cheung TTP (1984) X-ray photoemission of small platinum and palladium clusters. Surface Science 140: 151-164

Fan D, Yang X, Wang L (1973) Petrological and geochemical characteristic of a nickel - molybdenum- multe- element- baring lower-cambrian black shale from a certain district in south China. Geochimica 3: 143-164

Kao LS, Peacor DR, Coveney RM, Zhao GM, Dungey KE, Curtis MD, Penner-Hahn JE (2001) A C/MoS2 mixed-layer phase (MoSC) occurring in matalliferous black shales from southern China, and new data on jordisite. American Mineralogist 86: 852-861

Li S, Gao Z (1995) A review on geological and geochemical studies of PGE in black shale and its significance. Sichuan dizh ikeji qingbao (in Chinese)4(247)19-22, 31

Li S (1994) Study on geochemistry of gold, silver and PGEs in the lower Cambrian black rocks of Hunan-Guizhou Region. Post-doctor thesis. Geochemical Institute, Chinese Academy of Sciences, Guiyang

Lin P, Zhu Y, Su S (1999) Support effect of ultrafine platinum catalysts prepared by X-ray radiation method. Chinese Journal of Catalysis 20(1): 17-20

Mason MG (1983) Electronic structure of supported small metal clusters. Physical review B 27(2): 748-762

This page intentionally blank

Session 3

Uranium deposits: metallogeny and exploration

Geochemistry, geothermometry, and K-Ar dating of episyenitic rocks associated with the Guarda uraniferous granites, Portugal

I. Bobos, L. Jaques, F. Noronha
GIMEF – Centro de Geologia, Faculdade de Ciências, Praça Gomes Teixeira, 4099-002 Porto, Portugal

N. Clauer, N. Liewig
Centre de Géochimie de la Surface (ULP-CNRS), 1 Rue Blessig, 67084 Strasbourg, France

Abstract. The Guarda granite underwent a continuous hydrothermal alteration process from K/Na- to H- and to Ca-metasomatism. No changes of REEs distribution were observed during late- to post-magmatic processes. U remobilization and enrichment occur in the argillic zone. K-Ar ages of episyenitic rocks are around 245 Ma, whereas the argillization zone gives ages around 209 to 225 Ma.

Keywords. Episyenite, hydrothermal alteration, major, trace and rare earth elements, fluid inclusions, K-Ar ages, Guarda, Portugal

1 Introduction

The late Hercynian granites of Central and Western Europe in the Variscan belt are commonly present a magmatic to post-magmatic evolution accompanied by U, Sn and W mineralizations. Fluid flows along the fracture systems in granitic environments may produce dequartzification of the granite, which is well known as "episyenitization". A permeable porous-rock reservoir controlled by fractures is formed, which could be later mineralized, as a result of hydrothermal fluid circulations between a deep heated zone and a colder superficial zone. Such episyenitic rocks were previously described in the French Massif Central (Leroy 1971; Cuney 1978; Cathelineau 1986), Bohemian Massif (Hecht et al. 1999) and Central Iberian Massif (Recio et al. 1997) and other parts of the world.

The present contribution focuses on episyenite rocks unrelated to economic U mineralizations. The aim of this study is to characterise the mineralogical and geochemical episyenitic rocks, hydrothermal fluids from a microthermometric study of fluid inclusions in quartz and to date the minerals from the episyenite and argillic rocks by the K-Ar technique.

2 Geology

The Hercynian orogenic belt mainly consists of metamorphosed sediments and granitic rocks originated during the convergence and collision of two major continents at the end of Palaeozoic times (Matte 1991). The Guarda monzogranite is located in the western part of Iberian Peninsula (Fig. 1) and belongs to the intermediate series of Carboniferous synorogenic granitoids.

Episyenitic rocks occur as bodies elongated N40ºE and ranging from a few decimetres up to 10 meters in thickness. Their location is structurally controlled by NE-SW faults and fractures or local shear zones. The contact between episyenite body and protolith is gradual, marked by a reddish transition zone of a few centimetres.

3 Materials and methods

Mineralogy was carried out using optical microscopy, X-ray diffraction (XRD) and scanning electron microscopy (SEM). Electron microprobe analysis (EMPA) was carried out with a Cameca Camebax. Whole-rock compositions were analysed by ICP-AES, for the major and trace elements and by ICP-MS for the REE. Chondrite-normalization was carried out according to Taylor and McLennan (1985). Estimating the gains or losses of elements during a mass transfer processes were determined by the methods of Grant (1986). Fluid inclusions studies were performed using a Chaixmeca and Linkam TH600 heating-freezing stages. Volatile analyses were performed using a LABRAM micro-Raman spectrometer.

The K-Ar determinations were made using a method close to that of Bonhomme et al. (1975). The K was measured by flame spectrophotometry with accuracy better than 1.5%. The analytical precision was periodically controlled by measuring the international standard mineral GLO, which averaged 24.40 ± 0.15 (2σ) x 10^{-6} cm^3/g STP of radiogenic ^{40}Ar for 5 independent measurements during the course of the study, and the atmospheric $^{40}Ar/^{36}Ar$ ratio, which averaged 299.8 ± 3.3 (2σ).

4 Results

4.1 Alteration stages

Previous mineralogical and petrographycal studies on epysienitic rocks from Guarda (Jaques et al. 2003) have identified a complete evolution from K/Na- to H- and to Ca-metasomatism characterized by microclinization, albitization, sercitization, argillization and propyliti-

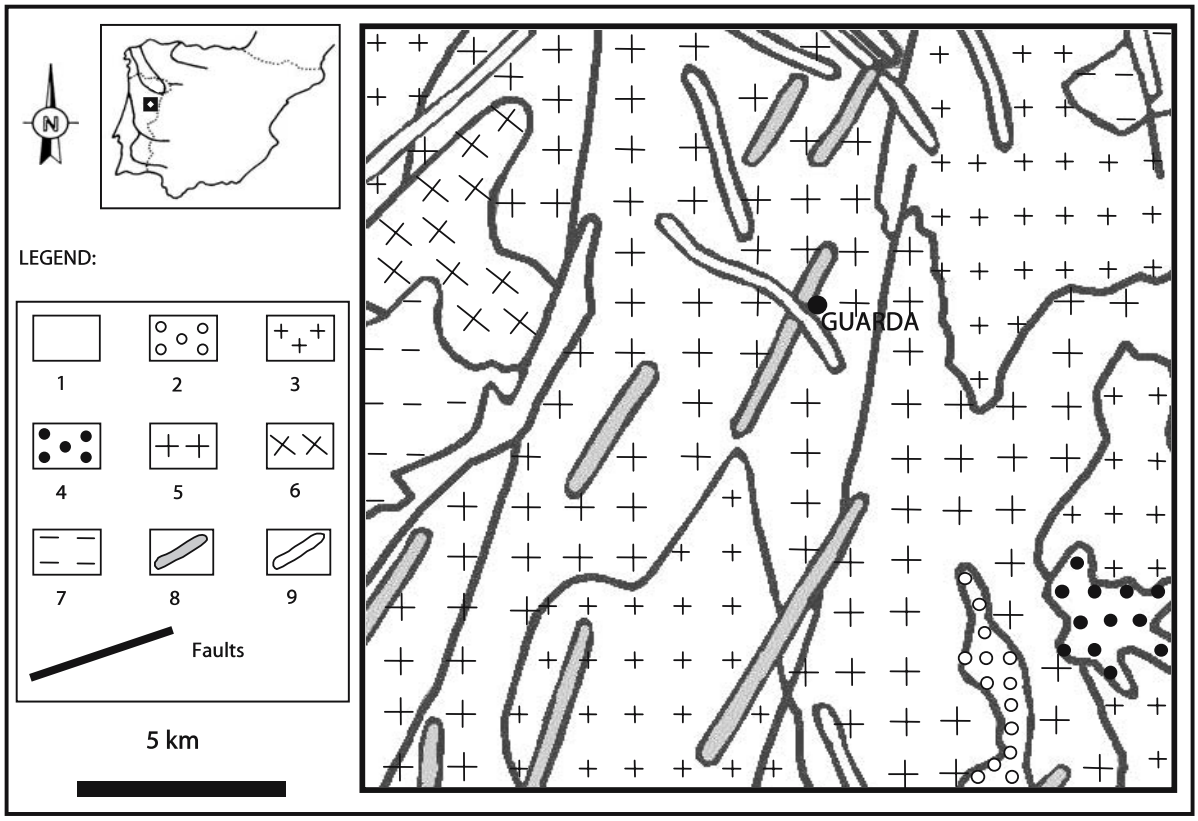

Figure 1: Geological map of the Guarda region. LEGEND: 1 - Schists and graywackes; 2 - Muscovite-biotite granites; 3 - Porphyritic monzonitic granites; 4 - Biotite quartzdiorites and granodiorites; 5 - Porphyritic granites and granodiorites of Guarda; 6 - Biotite granodiorites; 7 - Two-mica granites; 8 - Quartz and quartz-carbonate veins; 9 - Microdiorites, microandesites, lamprophyres and dolerites.

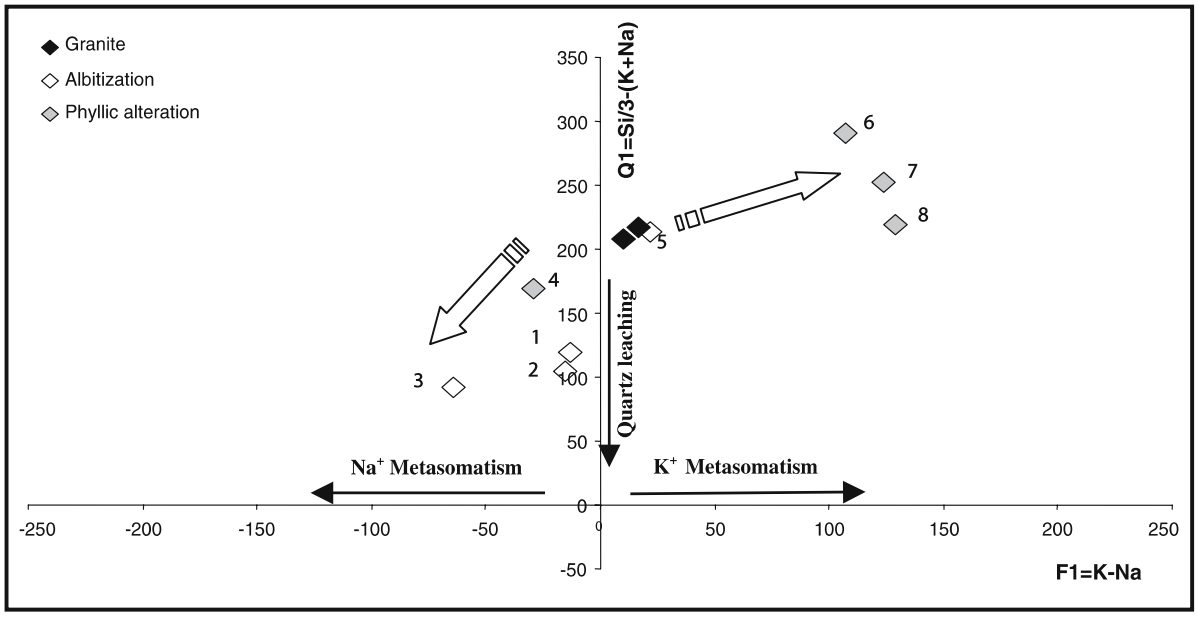

Figure 2: Three main alteration trends appear in the Q_1-F_1 diagram: 1) dequartzification, 2) albitization with silica depletion; 3) strong sericitization and argillization

zation. Episyenitization is limited to quartz leaching accompanied by a strong alkali metasomatism especially characterized by albitization of plagioclase and K-feldspar transformation into chessboard-like albite. Later alteration processes led to pervasive sericitization of plagioclase (muscovite-phengite) and chloritization of biotite. The episyenitic column exhibits a strong argillization characterised by illite-smectite ordered mixed layers (I-S). A vermicular chlorite-calcite-epidote assemblage occurs similar to the propylitic alteration observed in other granites.

4.2 Geochemistry

The mobility of major and trace elements during hydrothermal alteration processes was estimated by comparison with the composition of fresh Guarda granite. In the Q_1–F_1 diagram (Fig. 2) are observed three distinct reaction processes: dequartzification (samples 1 and 2 closest to the Q1 axis), slight dequatzification-albitization (sample 4) towards albitization (sample 3), followed by phyllic to argillic alteration (samples 5, 6, 7, 8), which corresponds to strong leaching of Na and H-metasomatism increases. A small increase of CaO, K_2O and Al_2O_3 were observed in propylitic zone, being associated with the presence of epidote- calcite-adularia assemblage. Zr, Th, Hf and Ti show a coherent behaviour. Trace elements are almost immobile excepted Rb, Ga and U. The ratio of U/Th increases with increasing the argillization process. Thus, significant amount of U (50 ppm) is associated to argillic zone. No mass transfer of REEs was observed during late to post-magmatic hydrothermal alteration (Fig. 3). No evident alteration of REE-bearing accessory mineral phases (i.e., zircon, allanite and monazite) was found along the hydrothermal alteration stages. Therefore, theseare nearly immobile during the episyenitization process.

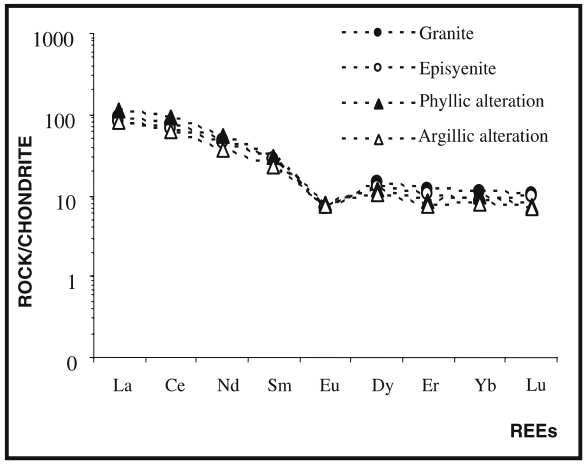

Figure 3: Chondrite-normalized REEs patterns

4.3 Fluid inclusions

Microthermometric analyses were performed in secondary fluid inclusions (FI) in healed microcracks from magmatic quartz and in primary or pseudo-secondary FI from later authigenic quartz crystallized in open spaces. Fluid inclusions planes (FIP) in magmatic quartz are two-phase with crystal negative shape. The homogenization temperature (Th) ranges in the 200-300 °C, whereas ice melting temperature (Tm_{ice}) between -0,5 and -6,6 °C (0,9 to 9,9 wt.% eq. NaCl). The Th-Tm_{ice} relation decreases in salinity as Th diminishing (Fig. 4). FI from authigenic quartz are two-phase and one-phase, containing few solid phases, namely quartz and chlorite. The Th ranges from 145 to 270°C, with a mode around 220°C.

The melting temperatures of hydrohalite (Tmh) is close to 0.0-0.3°C, indicating a salinity less than 26.3 wt.% eq. NaCl. The Th variation at constant salinity may be due to "necking-down" and/or metastability of several FI, occurring at temperatures below the real Th values of the fluid. The results obtained show that both fluids belong to the H_2O–NaCl system. No volatile species were detected by micro-Raman analysis.

4.4 K-Ar ages

K-Ar age dating of K-feldspar and mica has been used to date geological events such as overthrustings, hydrothermal alterations, among others (Clauer and Chaudhuri 1995). Absolute ages were obtained using K-Ar geochronology on K-feldspar and I-S collected from fresh granite, episyenitic and argillic rocks. K-feldspar from episyenite gives 245 ± 4.8 Ma whereas K-feldspar from granite gives 260 ± 3 Ma. Illite ages give values ranging 209.1 to 225.5 ± 3.4 Ma.

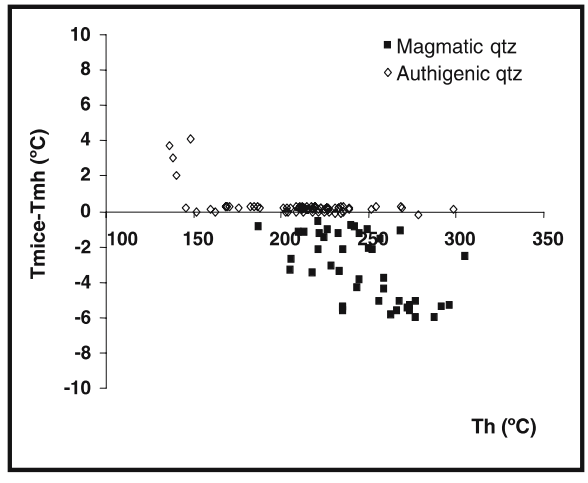

Figure 4: Th/Tm_{ice}–Tmh plot of FIP from magmatic quartz and FI hosted in authigenic quartz

5 Discussion

The new data obtained confirm a series of alteration from K/Na- exchange to H- and Ca-metasomatism, resulting from several stages of hydrothermal alteration. The results obtained confirm the paleofluid migration, where at least two successive alteration stages did occurred. The first is related to an alkaline metasomatism, where the moderate saline fluids have migrated along the microcrack networks in granitic rock, initially at elevated temperatures, higher than 300ºC. A progressive cooling of fluid was probably promoted by a dilution process with a poorly aqueous saline fluid. The later alteration stages are associated to the highly saline fluids of lower temperatures (< 200ºC).

Such alteration events were related to post-Variscan metallogenesis. The Early Permian was a period of major uranium mobility and concentration (Pagel 1990). Nevertheless, across the Hercynian belt some of the U ores result from strong remobilization of the Permian ores during later (mainly Liassic) hydrothermal events (Cathelineau et al. 1990). In the Guarda granite, U remobilization and enrichment occur in the argillic zone with an upper Triassic age. The Triassic hydrothermal event supported by K-Ar ages allowed the mixing of connate reducing fluids and of meteoric oxidising fluids, able to leach uranium at low temperatures.

Acknowledgements

The investigation was made possible through the financial support of the GRICES – CNRS project. L.Jaques thanks to Portuguese Foundation for Sciences (POCTI Project SFRH/BD/4646/2001). We thank M. Pagel for his carefully review and B. Manson for English improvements.

References

Bonhomme M, Thuizat R, Pinault Y, Clauer N, Wendling R, Winkler R (1975) Méthode de datation Potassium-Argon. Appareillage et technique. Inst. Géol. Univ. Louis Pasteur, Strasbourg, note technique 3 :53

Cathelineau M (1986) The Hydrothermal Alkali Metasomatism Effects on Granitic Rocks: Quartz Dissolution and Related Subsolidus Changes. Journal of Petrology 27; 945-965

Cathelineau M, Boiron MC, Holliger P, Poty B (1990) Metallogenesis of the French part of the Variscan orogen. Part II: time-space relationships between U, Au, Sn-W ore deposition and geodynamic events: mineralogical and U- Pb data. Tectonophysics 177: 59–79

Clauer N, Chaudhuri S (1995) Clays in Crustal Envionments - Isotope Dating and Tracing. Springer Verlag, Heidelberg, 359.

Cuney M (1978) Geologic Environment, Mineralogy, and Fluid Inclusions of the Bois Noirs-Limouzat Uranium Vein, Forez, France. Economic Geology 73:1567-1610

Grant JA (1986) The Isocon Diagram – A Simple Solution to Gresen's Equation for Metasomatic Alteration. Economic Geology 81:1976-1982

Hecht L, Thuro K, Plinninger R, Cuney M. (1999) Mineralogical and geochimical characteristics of hydrothermal alteration and episyenitization in the Königshain granites, northern Bohemian Massif, Germany. Journal of Earth Sciences 88:236-252

Jaques L, Bobos I, Noronha F (2003) Episyenitization and Hydrothermal alteration in the Guarda granites from the Uraniferous Province of Portugal. Preliminary data. In: Eliopoulos et al. (eds), Mineral Exploration and Sustainable Development, Millpress, Rotterdam 287-289

Leroy J (1971) Les épisyénites non minéralisées dans le massif de granite à deux micas Saint-Sylvestre (Limousin-France). Equilibres entre minéaux et solutions. Unp. Thesis, Nancy I, Univ., 87

Matte P (1991) Accretionary history and crustal evolution of the Variscan belt in Western Europe. Tectonophysics 196 :309-337

Pagel M (1990) Le Permien et la métallogénie de l'uranium. Chron. Rech. Min. 499:57–68

Recio C, Fallick AE, Ugidos JM, Stephens WE (1997) Characterization of multiple fluid-granite interaction processes in the episyenites of Avila-Béjar, Central Iberian Massif, Spain. Chem. Geol. 143:127-144

Taylor SR, McLennan SM (1985) The Continental Crust: its Composition and Evolution. Blackwell Scientific Publ., 266

Petroleum-related origin for sandstone-hosted uranium deposits in the Dongsheng area, Ordos Basin (China)

Chunfang Cai, Hongtao Li, Xiaorong Luo
Key Lab of Mineral Resource, Institute of Geology and Geophysics, CAS, P.O. Box 9825, Qijiahuozi, Beijing 100029, China

Abstract. Sandstone-hosted roll-type uranium deposits were found to occur in the Middle Jurassic Zhiluo Formation sandstone in Dongsheng area, north of the Ordos basin. The uranium occurs mainly as coffinite. Some of the coffinite is intergrown intimately with secondary pyrite, indicating simultaneous precipitation. The pyrite has $\delta^{34}S$ values from -34‰ to +18‰, suggesting an origin of bacterial sulfate redu ction. Calcite cement of the host sandstones has $\delta^{13}C$ values from +0.3‰ to -27.6‰. The most negative $\delta^{13}C$ value is more negative than those of terrestrial higher plants-derived organic matter in the Jurassic in the basin, thus the carbon of the calcite cement is likely derived from oil and natural gas, most likely from mixing of preexisting inorganically derived CO_2 and methane-derived CO_2. The hypothesis is supported by the great number of oil/gas inclusions found in the calcite cement and healed fractures through quartz grains. Interestingly, in the sandstone with high content of uranium, secondary pyrite has $\delta^{34}S$ as light as -34‰, calcite cement has $\delta^{13}C$ lower than -10‰. Thus, it can be concluded that sulfate reducing bacteria likely oxidized hydrocarbons, and directly or indirectly reduced uranium (VI) to uranium (IV).

Keywords. Bacterial sulfate reduction (BSR), petroleum, $\delta^{34}S$, $\delta^{13}C$, uranium, sandstone

1 Introduction

Sandstone-hosted uranium deposit are commonly observed to coexist with organic matter including petroleum in sedimentary basins. The roles of organic mater is considered to include adsorption, concentration and reduction of U(VI) (e.g. Jensen 1958; Rackley 1972; Curiate et al. 1983; Reynolds and Goldhaber 1982; Nakashima et al. 1984; Spirakis 1996). Uranium reduction by organic matter may be thermochemical or biological. The experimental studies (Nakashima et al. 1984) have shown that direct reduction of uranyl species by lignite occurs at the temperatures higher than 120°C. Thus, under conditions of significantly lower than this temperature, the microbial process may be a main mechanism for direct or indirect uranium reduction. Sulfate reducing bacteria (SRB) were considered to deplete organic acids generated during organic matter maturation or from hydrocarbon metabolization by oxic bacteria (e.g. Reynolds and Goldhaber 1982; Cai et al. 1997), resulting in the generation of H_2S and pyrite. The sulfur species subsequently reduced uranyl species to precipitate U(IV) (e.g. Rackley 1972; Reynolds and Goldhaber 1982). However, recent studies have shown that SRB deplete methane and other hydrocarbons directly or coupled with organic acids (e.g. Aharon and Fu 2000; Boetius et al. 2000; Cai et al. 2002; Zhang et al. 2002), and that both SRB and iron-reducing bacteria can reduce U(VI) to U(VI) directly (Lovely et al. 1991; Spear et al. 2002; Sani et al. 2004).

In his paper, we present sandstone micro-texture, fluid inclusion, calcite cement $\delta^{13}C$, and secondary pyrite $\delta^{34}S$ data. We seek to confirm that SRB are responsible for uranium precipitation in the deposits, and to address what kind of organic matter (kerogen, coal, petroleum) was involved in BSR.

2 Geological setting

The Ordos basin in the middle-west of China is rich in coal, oil and natural gas, and uranium deposits (Fig. 1). Its basement is composed of Archeaean and Lower Proterozoic metamorphosed rock, and intermediate-acidic rocks such as granite with relatively high uranium abundance. Middle and Upper Proterozoic terrestrial and marine clastics lie over this basement.

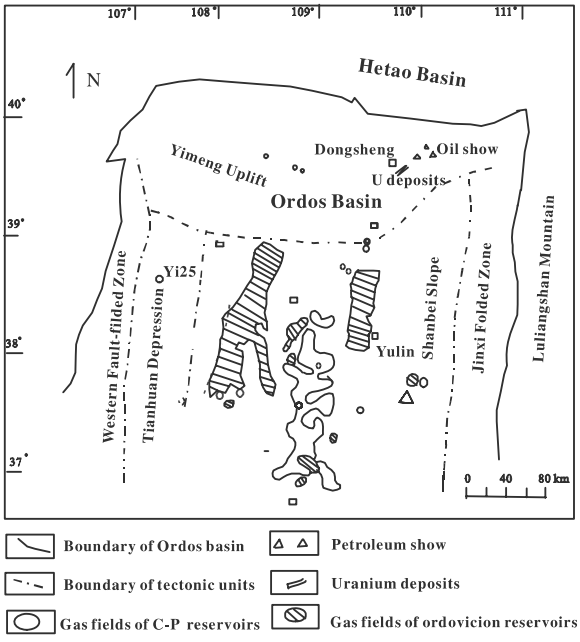

Figure 1: Map showing location of uranium deposits and gas fields, petroleum show in outcrops

During the early Paleozoic, most of the basin belonged to a passive continental margin. The Cambrian and Ordovician are dominated by platform facies carbonates. From the end of the Ordovician to Middle Carboniferous, the whole basin was uplifted and exposed to the surface. Transgression occurred during the Middle Carboniferous. The Carboniferous - Permian sequence is composed of alternating marine and terrestrial coal-bearing detrital rock and bioclastics. The Triassic - Lower Cretaceous sequence is composed of lacustrine and fluvial clastic rocks that produce oil and coal. Uranium ore was found in the Middle Jurassic Zhiluo Fm. in the Dongsheng area. During the Early Cretaceous, regional structure changed dramatically, the eastern part was uplifted and formed a westward gently sloping monocline. Subsequently, oxidized ground water that originated by recharge from the surface near the Hetao area, northeast of the basin flowed down towards the Dongsheng area supplying a main source of uranyl species for the deposits. The Hetao area was then rifted, subsided and formed a fault bounded depression which was covered by 1000m to 2600m thick Eocene and about 10,000m thick Neogene sediments.

The Middle Jurassic Zhiluo Fm. was deposited under braided to sinuous river environments. The Zhiluo Fm. can be divided into an Upper and a Lower member. The Upper member was deposited under a dry to semi-dry climate and is composed of purplish red, brownish red, or dark purple massive mudstone and sandstone with abundant limonite. The Lower member is grey to light grey middle-grained and middle- to coarse-grained sandstone, which were deposited under semi-humid to humid climate.

U-Pb dating of uranium minerals has indicated that the uraniferous mineralization was deposited or remobilized during several episodes: 120±11Ma, 77±6Ma, 20±2Ma and 8±1Ma, respectively (Xia 2003). During the earlier stages of mineralization during the Early and Late Cretaceous, the uranium was supplied from the Hetao area, northeast of the basin. In contrast, the source of uranium for the later mineralization during the Middle and Late Pleistocene was from oxidation of preexisting uranium ore (Xia 2003).

3 Sampling and analytical methods

Sandstone samples were obtained from the Zhiluo Formation grey-green sandstones, grey sandstones and mineralized sandstone in between grey-green sandstones and grey sandstones. The samples were observed for polished thin sections, electron microprobe. Fluid inclusions were observed under UV fluoroscope. Calcite cement was analyzed for carbon and oxygen isotopes, and pyrite analyzed for sulfur isotopes. Uranium content was measured using ICP-MS with a precision of better than 8%. The methods have been published in Cai et al. (2001).

4 Results and discussion

4.1 Petrography and fluid inclusions

Observation of outcrops, polished thin sections and electron microprobe show that abundant Fe(III)-rich minerals such as limonite, hematite, and iron chloride are found to occur in the oxidation zones in the Lower member of Zhiluo Fm. in Redstone Gorge outcrop, to the south of the Dongsheng area. Pyrite, coal and plant debris are rich in the reduced zone. Sandstones in mineralization zones in the Dongsheng area are rich in ore-stage secondary pyrite, and some contain calcite cement and plant debris. The main uranium mineral is coffinite. Some of the coffinite is intimately intergrown with secondary pyrite, suggesting simultaneous precipitation. The pyrite occurs as aggregation, and replaced quartz grains and clay matrix and grew along quartz fractures. The features indicate fast crystalline growth for the pyrite under low-temperature epigenetic conditions. The low-temperature diagenetic environment is supported by low vitrinite reflectivity R_o values from 0.35 to 0.55% for Jurassic mudstone and coal in the basin.

Gas and oil inclusions occur in the calcite cement and healed quartz fractures. Gas inclusions are rich in methane and carbon dioxide. Oil inclusions show a shallow blue to bright white UV fluorescence. GOI values (e.g. George et al. 1994), measuring the abundance of quartz and feldspar grains containing oil-bearing fluid inclusions (FIs) in sandstones, are used to determine the extent of oil saturation in the geological past. In the Dongsheng deposits, most of the Zhiluo Fm sandstones have GOI values from 0.2 to 1%. Only a small proportion of the sandstones have GOI higher than 5%. The GOI values from 0.2% to 6% indicate that the sandstones may have been utilized as oil migration pathways, and that oil most likely escaped during calcite cementation and quartz fracturing.

4.2 Isotopic composition of cements

The mineralized and uranium-poor reduced zones have pyrite $\delta^{34}S$ ranging from -34‰ to +18‰ (n=12). The most negative value of -34‰ is more negative than the known lightest value of organically derived sulfur (-17‰, Cai et al. 2002), indicating that the reduced sulfur unlikely derived from organic matter. In addition, no sulfur-rich organic matter was found to occur in petroleum source rocks in the area, indicating the no significant sulfur content was derived from organic matter. Such negative $\delta^{34}S$ values originated from bacterial sulfate reduction because a maximum fractionation of -46‰ has been obtained during one step bacterial sulfate reduction on pure culture experiments (Kaplan and Rittenberg 1964) and down to -72‰ by Ulrich et al. (2001). Thus, the sulfur of pyrite

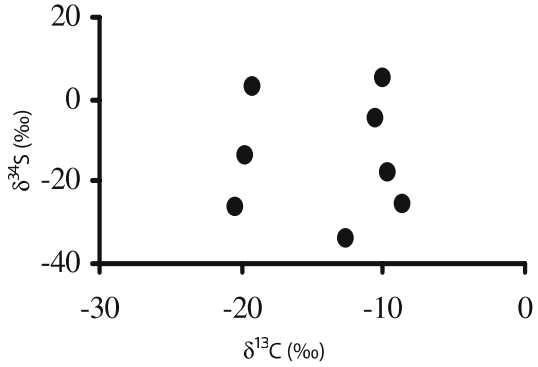

Figure 2: Cross plot of calcite $\delta^{13}C$ and pyrite $\delta^{34}S$ value of host sandstones

with the most negative value in the area may result from multi-step reaction, including sulfate reduction, pyrite oxidation and re-reduction (e.g. Rackley 1972; Reynolds and Goldhaber 1982), or from one-step reaction (Ulrich et al. 2001).

The positive $\delta^{34}S$ values of the pyrite may result from BSR under a relatively closed system conditions. In such a system, the rate of sulfate supply has to be lower than the rate of sulfate reduction. With the progression of the reduction, newly generated sulfides and residual sulfate are expected to have heavier $\delta^{34}S$ values.

Calcite cement of sandstones in the Dongsheng deposits has $\delta^{13}C$ of +0.3‰ to -27.6‰ (n=20), most of the samples having $\delta^{13}C$ more negative than -10‰, suggesting a significant contribution from organic matter (OM). Potential OM sources include mudstone, coal in the Jurassic in situ and petroleum from deeper strata (most likely Carboniferous – Permian). Wood and Boles (1991) has shown that associated dissolved HCO_3^- would be about 10‰ heavier at 50°C and about 5‰ heavier at 100°C than parent OM. Thus, parent OM for the isotopically lightest calcite is expected to have $\delta^{13}C$ value of about -33‰ if the whole calcite is generated from oxidization of the OM at about 100°C. OM from mudstone and coal in the Jurassic in the basin is dominated by higher plants and has $\delta^{13}C$ values higher than -24.0‰ and about -22.4‰, respectively (Chen and Huang 1994). The Jurassic OM $\delta^{13}C$ values are significantly higher than -27.6‰, thus it is unlikely for the carbon at least for the calcite presenting the most negative $\delta^{13}C$ values to be derived from the Jurassic OM. Instead, the carbon is likely derived from hydrocarbon oxidation, most likely from mixing of CO_2 produced from methane anoxic oxidation ($CH_4+SO_4^{2-}=CO_2+H_2S+2OH^-$) (Cai et al. 2002) with pre-existing inorganically derived CO_2 (Cai et al. 2001). The most negative $\delta^{13}C$ values of calcite cement together with occurrence of petroleum inclusions in the host sandstones consistently indicate that the petroleum is derived from deeper strata.

In the uranium-rich sandstone, secondary pyrite has $\delta^{34}S$ as negative as -34‰, and calcite cement has $\delta^{13}C$ lower than -10‰ (Fig. 2) associated with intimate intergrowth of coffinite with secondary pyrite indicate that SRB may have utilized petroleum (most likely methane) as nutrients, resulting in the generation of organic CO_2 and the reduction of sulfates to H_2S. Subsequently, H_2S reduced U(VI) to U(IV) (Rackey 1972). Alternatively, SRB may have reduced sulfates simultaneously with U(VI) reduction to U(IV) thus leading to U(IV) precipitation. However, it is hard to distinguish the two mechanisms in nature.

5 Conclusions

1. Uranium ore hosted in the Middle Jurassic Zhiluo Formation sandstone from the Dongsheng area occurred mainly as coffinite.
2. Coffinite was precipitated simultaneously with pyrite aggregates under low-temperature epigenetic conditions.
3. Bacterial sulfate reduction was responsible for both the generation of pyrite aggregates with $\delta^{34}S$ down to -34‰ and probably for direct or indirect uranium (VI) reduction and uranium (IV) precipitation as coffinite.
4. Sulfate reducing bacteria have oxidized petroleum (likely methane) migrated from depth rather than terrestrial organic matter *in situ*, to produce CO_2, resulting in the precipitation of calcite with $\delta^{13}C$ value down to -27.6‰.

Acknowledgements

The research is financially supported by China National Major Basic Development Program "973" (2003CB214605) and FANEDD.

References

Aharon P, Fu B (2000) Microbial sulfate reduction rates and sulfur and oxygen isotope fractionations at oil and gas seeps in deepwater Gulf of Mexico. Geochim Comochim Acta 64: 233-246

Boetius A, Ravenschlag K, Schubert CJ, Rickert D, Widdel F, Gleseke A, Amann R, Jorgensen BB, Witte U, Pfannkuche O (2000) A marine microbial consortium apparently mediating anaerobic oxidation of methane. Nature 407: 623-626

Cai CF, Hu WS, Worden RH (2001) Thermochemical sulfate reduction in Cambro-Ordovician carbonates in Central Tarim. Marine and Petroleum Geology 18: 729-741

Cai CF, Mei BW, Ma T, Chen CP, Li W, Liu CQ (1997) Approach to Fluid-Rock Interaction in Tarim Basin. Beijing, Geological Publishing House (in Chinese)

Cai CF, Worden RH, Wang QH, Xiang TS, Zhu JQ, Chu XL (2002) Chemical and isotopic evidence for secondary alteration of natural gases in the Hetianhe Field, Bachu Uplift of the Tarim Basin. Organic Geochemistry 43: 1415-1427

Chen JP, Huang DF (1997) The source of oils in Jurassic coal mine in the southeast of Ordos basin. Acta Sedimentologica Sinica 15(2): 100-104 (in Chinese)

Curiale JA, Bloch S, Rafalska-Bloch J, Harrison WE (1983) Petroleum-related origin for uraniferous organic-rich nodules of southwestern Oklahoma. AAPG Bull 67: 588-608

George SC, Ahmed M, Liu K, Volk H (2004) The analysis of oil trapped during secondary migration. Orgc Geochem 35: 1489-1511

Jensen ML (1958) Sulfur isotopes and the origin of sandstone-type uranium ore deposits: Economic Geology 53: 598-616

Kaplan IR, Rittenberg SC (1964) Microbiological fractionation of sulfur isotopes. J Gen Micro 34: 195-212

Lovley DR, Philips EJP, Gorby YA, Landa ER (1991) Microbial reduction of uranium. Nature 350: 413-416

Nakashimima S, Disnar JR, Perruchot A, Trichet J (1984) Experimental study of mechanisms of fixation and reduction of uranium by sedimentary organic matter under diagenetic or hydrothermal conditions. Geochim Comochim Acta 48: 2321-2329

Rackley RI (1972) Environment of Wyoming Tertiary uranium deposits AAPG Bull 56: 755-774

Reynolds RL, Goldhaber MB (1982) Biogenic and nonbiogenic ore-forming processes in the South Texas Uranium District: Evidence from the Panna Maria deposit. Economic Geology 77: 541-556

Sani RK, Peyton BM, Amonette JE, Geesey GG (2004) Reduction of uranium (VI) under sulfate-reducing conditions in the presence of Fe (III)-(hydr) oxides. Geochim Cosmochim Acta 68: 2639–2648

Spear JR, Figueroa LA, Honeyman BD (2002) Modeling the removal of uranium U (VI) from aqueous solutions in the presence of sulfate reducing bacteria. Applied Microbiology and Biotechnology 60: 192-199

Spirakis CS (1996) The roles of organic matter in the formation of uranium deposits in sedimentary rocks. Ore Geology 11: 53-69

Ulrich GW, Stefano MB, Michael EB (2001) Hypersulfidic deep biosphere indicates extreme sulfur isotope fractionation during single-step microbial sulfate reduction. Geology 29: 647–650

Xia YL, Lin JR, Liu HB, Fan G, Hou Y (2003) Research on geochronology and sandstone-hosted uranium ore formation in major uranium productive basins, northern China. Uranium Geology 19(3): 129-136 (in Chinese)

Zhang CL, Li YL, Wall JD, Larsen L, Sassen R, Huang YS, Wang Y, Peacock A, White DC, Horita J, Cole DR (2002) Lipid and carbon isotopic evidence of methane-oxidizing and sulfate-reducing bacteria in association with gas hydrates from the Gulf of Mexico. Geology 30: 239-242

Mesozoic - Neozoic structural evolution and its relationship to the formation of sandstone-type uranium deposits in the Yili Basin

Yuqi Cai, Shengxiang Li, Xiaozhong Han
Beijing Research Institute of Uranium Geology, 100029, China

Enjiu Zheng, Xigen Li
Geologic Party No.216, CNNC, Urumqi 830011, China

Abstract. The Yili Basin is a uranium-producing basin and large quantities of uranium deposits and occurrences have been discovered there. Since the Mesozoic – Neozoic, geologic events in the basin have played an important role in forming the uranium-productive formation and uranium deposits. This paper discusses the relationship between the structural evolution of the basin and uranium mineralization, and it is concluded that the structural evolution of the basin not only controlled the formation and distribution of the uranium- producting formation, but also the occurrence and spatial orientation of sandstone-type uranium mineralization.

Keywords. Yili Basin, structural evolution, uranium-productive formation, uranium mineralization

1 Geologic setting

The Yili Basin is a Mesozoic – Neozoic intermontane basin that developed on a Precambrian ancient block. Its tectonic location is at the junction of the Kazakhstan plate, west Siberia plate and Tarim plate. Its basement consists of Middle-Upper Proterozoic and Palaeozoic folded rock series and Hercynian granite. Its cover is composed of Mesozoic – Neozoic continental coal-bearing clastic rock formation and red clastic rock formation. The ore-bearing rock series are coal bearing clastic rocks of Shuixigou Group ($J_{1\text{-}2}$sh) of Middle - Lower Jurassic. Shuixigou Group can be further divided into Badaowan Formation (J_1b), Sangonghe Formation (J_1s) and Xishanyao Formation (J_2x) and it can be divided into seven cycles according to the sedimentary rhythm (Li et al. 2002), where I-V cycles are equivalent to Badaowan Formation, VI cycles are equivalent to Sangonghe Formation and VII cycle is equivalent to Xishanyao Formation. 13 layers of coal seams in total have been developed in the seven sedimentary cycles and relatively stable coal seams in the region include No.5, No.8 and No.10 coal seams (Fig. 1).

2 Mesozoic – Neozoic geologic events and structural evolution characteristics of the basin

Whether a basin is a uranium-forming basin depends on various geologic events undergone in the course of its formation and evolution. The formation of uranium-productive the formation, and the accumulation of uranium in the ore-hosting rocks commonly happen during special stages of the structural evolution or structural transformation (Chen et al 2002). Since the Mesozoic – Neozoic, the Yili Basin has undergone five stages in its structural evolution, namely, weak squeezing, weak stretching, strong squeezing, weak squeezing, and differential subsidence.

In the early Triassic, the Yili Basin was in the structural stage of weak squeezing and continental lucastrine clastic rocks with small thickness are developed due to the influence of geologic events such as squeezing and orogenesis, subduction and closure of southwest Paleotethys.

From the middle Triassic to the middle Jurassic, accompanying the opening, spreading and northward subduction of the Bangonghu – Nujiang Sea, the northern branch of southwest Neotethys, the eastern section of Kazakhstan and Traim block rotated deasil and the Yili Basin is in the weak stretching structural environment.

The development history of this stage is relatively long (Ca. 53Ma) and the uranium-productive formation – Shuixigou Group is formed with the thickness of 600-1100m.

From the late Jurassic to the early Cretaceous, the basin was in the weak stretching structural environment due to the northward subduction of Bangonghu – Nujiang Sea and J_3 - K_1 sedimentation is basically absent in the basin.

From the late Cretaceous to the Paleocene, the basin was in the structural stages of weak squeezing and slack stretching and in this stage, the deposition thickness is thin, usually from tens of meters to over 200m in the basin, and often absent near the margin of the basin.

From the Eocene to Quaternary, the basin was in the structural stage of differential subsidence; with the uplifting of Qinghai-Tibet Plateau, two important tectonic processes, namely, slow uplifting in the late Eocene – Miocene and strong uplifting in the Pliocene – Quaternary, happened in the Basin.

This page intentionally blank

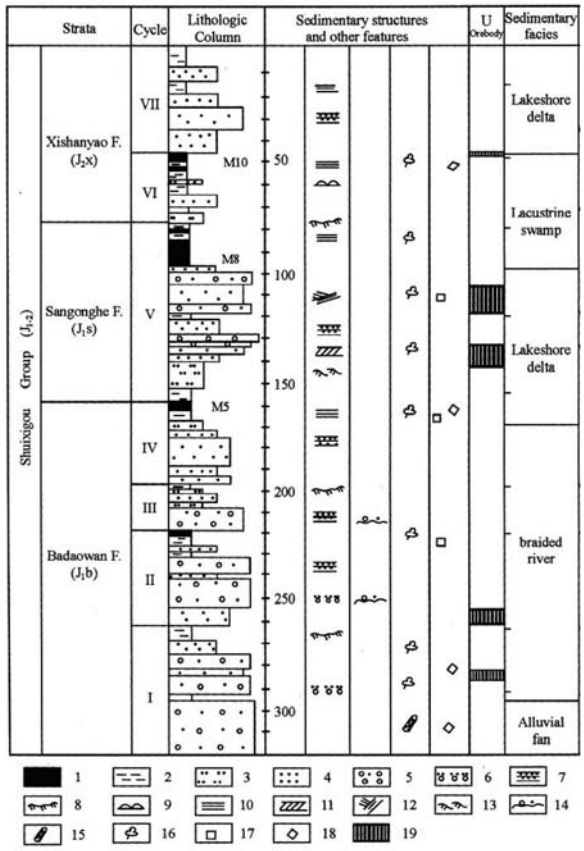

Figure 1: Sedimentary facies and features of sequence stratigraphy of Shuixigou Group in the southern part of Yili basin (after Li et al. 2002) 1-coal seam, 2-mudstone, 3-siltstone, 4-sandstone, 5-pebbly sandstone, and conglomerate, 6-graded bedding, 7-parallel bedding, 8-wavy bedding, 9-lenticular bedding, 10-horizontal bedding, 11-planar cross bedding, 12-wedge shaped cross bedding, 13-ripple cross bedding, 14-swash mark, 15-plant trunk, 16-plant leaf fragment,17-pyrite, 18-siderite, 19-uranium orebody

3 Relationship of structural evolution of the basin with uranium mineralization

Regional geologic setting and structural evolution characteristics show that the Yili Basin, located in Tianshan tectonic belt, is a composite intramontane basin of faulting and depression. It is of favorable geologic conditions for the formation of interlayer oxidation zone type sandstone-hosted uranium deposits and the formation of uranium deposits is closely related to the geologic events undergone in various structural stages of the basin (Han et al. 2004).

1. Weak extension during middle Jurassic led to the formation of favorable uranium-productive formation in the basin under the warm and humid palaeoclimate conditions, namely, Shuixigou Group, which provides favorable ore-hosting sand bodies and reductive agents for the accumulation of uranium.
2. Compression from the late Jurassic to the early Cretaceous gave rise to the uplifting, denudation and outcropping at the surface of the uranium-productive formation, and made the ore-hosting sandstone bodies be continuously worked by uranium- and oxygen-bearing water for a long time; so the initial pre-enrichment of uranium was formed (Li 2002).
3. Two tectonic movements since the Eocene led to the tilting of early uranium-productive formation, and made the uranium- and oxygen- bearing water continuously infiltrating and migrating in the ore- bearing sand bodies; and in consequence, the major uranium mineralization of the basin was formed. Uranium mineralization ages of 11.4Ma, 7.1Ma, 3.5Ma and 2Ma (Xia 2002) also reveal a close relationship of the structural evolution of the basin to the uranium mineralizations.

Acknowledgements

The research is subsided by the National Fundamental Research and Development Project (2001CB409808). Thanks are due to professor Lin Shuangxing and professor Wang Baoqun for their help in the study of this paper.

References

Chen ZY, Li ZY (2004) Formation-evolution Model of Uranium-productive Basin and Its Recognition Criteria. China Nuclear Science and Technology Report 1: 156

Han XZ, Li SH (2004) Neotectonic Activity Characteristics of Yili Basin and Its Relation to the Formation of Sandstone-type Uranium Deposits. Xinjiang Geology 22 (4): 381

Li SX, Chen DS (2002) Geologic Evolution and Uranium Metallogenic Regularity of Yili Basin. Sandstone-type Uranium Deposits in China; In: Geology and Exploration Techniques. Beijing: Atomic Energy Press, 2002: 53-64

Li X (2002) Characteristics of Sandstone-type Uranium Mineralization and Ore-controlling Factors in Wukuerqi Ore District at Southern Margin of Yili Basin, Xinjiang. Uranium Geology 18(1): 34-35

Xia YL, Lin JR (2002) Characteristics of Isotope Geology of Sandstone-type Uranium Deposit in Yiii basin, Xinjiang. Uranium Geology 18(3): 153

Geodynamic setting of Mesozoic magmatism and its relationship to uranium metallogenesis in southeastern China

Chen Pei-rong, Zhang Min, Chen Wei-feng
State Key Laboratory for Mineral Deposits Research and Department of Earth Sciences, Nanjing University, Nanjing 210093, China

Keywords. Mesozoic magmatism, geodynamic setting, Indosinian granite, southeastern China

Abstract

In southeastern China, Mesozoic magmatism is widespread and formed abundant rare metal and nonferrous metal deposits.

An analysis on the macroscopic geological conditions of large-scale granite-type and volcanic-type uranium deposits shows that Indosinian granites are likely to have played an important role in the uranium deposit-forming process.

Based on the above, in large-scale uranium deposits of South-China lithologies of Yanshanian volcanic rocks or intrusive rocks are altered, with some acidic granites or volcanic rocks, and basic volcanic rocks. However, the basement and wall rocks are commonly Indosinian two-mica and biotite granites. In south China, Yanshanian magmatism has no obvious uranium metallogenic specific attributes, but the temporal and spatial relationships between Indosinian granites and uranium metallogenesis are very close.

So the following conclusions can be reached: Indosinian granites hold obvious uranium metallogenic specific attributes, and were likely the source for the uranium. Yanshanian tectonic-magmatism thermal events mainly provided the thermal energy, mineralizing fluids and dynamic conditions. Indosinian granites, as basement or wall rocks of Yanshanian igneous rocks, are favorable for the formation of large-scale hydrothermal uranium deposits. The geodynamic setting for uranium metallogenesis is the complex Indosinian syntectonic intraplate orogenesis and Yanshanian rifting movement. Late Yanshanian taphrogenesis provided mineralizing fluids which were mostly CO_2, promoted the convection and circulation of fluid, and confined the uranium metallogenic era. So in south-Chinese uranium exploration, research on the distributing framework and metallogenic factors of Indosinian granites should be strengthened.

This research has been funded by the National Science Fund, and the projects numbers are 40372036 and 40132010.

References

Carter A, Roques D, Bristow C (2001) Understanding Mesozoic accretion in Southeast Asia: Significance of Triassic thermotectonism (Indosinian orogeny) in Vietnam. Geology, 29: 211-214

Chen PR, Kong XG, Ni QS (1999) Ascertainment and implication of the early Yanshanian biomodal volcanic associations from south Jiangxi province. Geol Rev, 45(suppl): 734-741

Chen PR, Kong XG, Wang YX (1999) Rb-Sr isotopic dating and significance of early Yanshanian bimodal volcanic-intrusive complex from South Jianxi Province. Geol J China University, 5(4): 378-383

Chen PR, Zhang BT, Kong XG (1998) Geochemical characteristics and tectonic implication of Zhaibei A-type granitic intrusives in South Jiangxi Province. Acta Petrol Sinica, 1998, 14(3): 289-298

Fan CF, Chen PR (2000) Geochemical characteristics and tectonic implication of Beitou A-type granitic intrusive in South Jiangxi Province. Geochimica, 29(4): 358-366

Hua RM, Mao JW (1999) A preliminary discussion on the Mesozoic metallogenic explosion in East China. Mineral Deposits, 18(4): 300-307

Kong XG, Chen PR, Zhang BT (2000) Confirmation of A-type volcanics in Baimianshi and Dongkeng Basin, South Jiangxi Province and their geological implication. Geochimica, 29(6): 521-524

Lauri LS, Manttari I (2002) The kynsijarvi quartz alkali feldspar syenite, Koillismaa, eastern Finland-silicic magmatism associated with 2.44 Ga continental rifting. Rrecambrian Reach, 119: 121-140

Neumann ER (1980) Petrogenesis of Oslo Region larvikites and associated rocks. J Petrol, 21:449-513.

Rejesh HM, Santosh M, Yoshida M (1996) Journal of Southeast Asian Earth, 14(3/4): 275-291

Cenozoic tectonic movement and its control on sandstone-type uranium deposits in the northern Junggar Basin

Z.-L. Chen, J. Liu, H.-L. Gong
Institute of Geomechanics, Chinese Academy of Geological Sciences, 100081, Beijing, P.R. China

E.-J. Zheng, X.-H. Wang
Geology Party No.216, CNNC, Urumuqi 830001, Xinjiang, P.R. China

Abstract. The Dingshan area, located in the northern Junggar Basin, is a significant prospecting area for sandstone-type uranium deposits. Field investigation and interpretation of remote-sensing images show that Cenozoic tectonic movement in this area is characterized by reactivation of deep thrust-faults, resulting in extensional fractures and formation of large billabongs at the surface. Measurement of slickensides and joints indicates that there are at least two stages of new tectonic movement during the Late Cenozoic. The tectonic evolution process during the Cenozoic is, therefore, reconstructed based on sedimentary filling features and neotectonic movement, and the Sangequan block is suggested as a favorable metallogenic area for sandstone-type uranium deposit.

Keywords. Junggar Basin, Cenozoic tectonics, sandstone-type uranium deposit

1 Introduction

The Dingshan area is located in the northern part of the Junggar Basin (JB), where some mineralized locations were discovered in 2003 (Lin et al. 2003), suggesting that it may potentially be a significant prospecting area for sandstone-type uranium deposit in China. This paper discusses the character of the neotectonic movement and its control on the formation of sandstone-type uranium deposits during the Cenozoic by both field investigation and interpretation of remote-sensing images.

2 Sedimentary features

Cenozoic sediments are divided into four lithostratigraphic units by Xinjiang BGMR (1993), including Paleocene-Eocene Honglishan Formation (HF), Eocene-Oligocene Wulunguhu Formation (WF), Miocene Suosuoquan Formation (SF), and Quaternary (Fig. 1). The HF is up- and southward-fining fluvial material, and is composed of conglomerates, cobble sandstones, and fine-layered mudstones at the bottom, thick-layered sandstones with mudstones further up and conglomerates at the top. It overlies Paleozoic and Mesozoic rocks with an angular unconformity. The WF can be divided into three sedimentary cycles (Wang 2003). The lower one, which has an unconformable contact with the HF, is composed of conglomerates, sandstones, with plant-bearing thick mudstones on the top, suggesting pebble alluvial fan facies settings. The middle one is of braided fluvial and gravity fluid origin, and consists of conglomerates, sandstones, and thin-layered mudstones. The upper one is composed of sandstones and mudstones with widespread calcite surficial nodules, indicating a meandering fluvial and shallow-water fluvio-lacustrine environment. The SF is composed of red fine-grained sediments, mainly mudstones, muddy sandstones, and siltstones, full of calcite cement. This stratum is of shallow-water fluvio-lacustrine, or swamp origin, and only locally exposed in some depressions. The Quaternary in our study area is predominantly composed of the Upper Pleistocene Xinjiang conglomerates, which has an unconformable contact with lower sections.

3 Neotectonic movement

The northern Junggar basin is virtually barren, where few plants grow. One of the typical features of this landscape is the development of many billabongs of variable size and depth. They are usually lower in topography, and generally behave as a concentration area for temporary runoff water from surface drainages. Most of them have no outlet, and are internally drained. Peng (1987) has suggested that their formation is associated with water and wind erosion at the surface.

Our field investigation shows that these billabongs are usually situated at the surface above the intersection of faults of different orientations at depth or commonly above NWW- to EW-trending faults, which are proven to be thrust faults by petroleum data (1998). Hereby, we suggest that the billabongs could be controlled by thrusting of faults at depth. Although the youngest strata that are cut by the thrusts at depth are Jurassic units, the thrusting leads to upwarping and folding of overlying Cretaceous and Cenozoic units, and to the extensional setting at the surface. Therefore, extensional fissures are widespread in the poorly consolidated, near horizontal Cretaceous and Cenozoic rocks. Then, the runoff water at the surface continually incises the rocks along fissure-planes, and transports alluvium at the same time. After the wa-

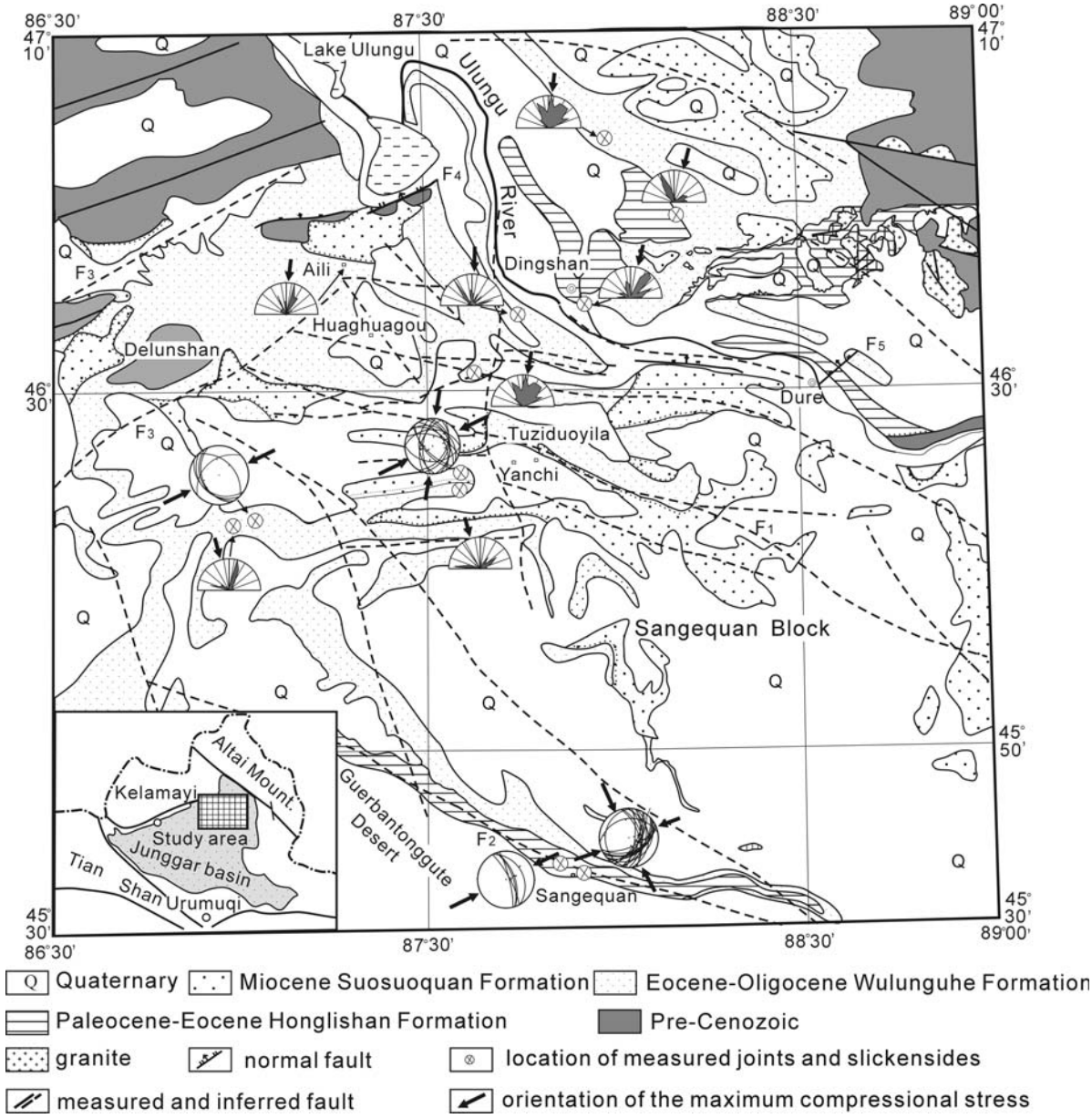

Figure 1: Simplified geological map of the northern Junggar Basin and its location in northern Xinjiang, mainly modified from Lin et al (2003) and Xinjiang BGMR (1993). Measure results and the orientation of maximum compressional stress inferred from slickensides (Wulff-projection) and joints (Rose diagram) are also shown in this map.

ters recede, the alluvium is reworked and moved by the wind before it can be cemented. As the time goes on, more and more rocks are eroded and weathered material is transported by the runoff water and wind. The influenced area grows in area and depth, and eventually forms a billabong.

On the ETM Landsat images, there are series of NWW- to EW-trending, NE-trending, and NW- trending faults developed in the northern part of the basin. The NE-trending faults are usually developed in the western part of the area, while EW-trending faults are distributed in the middle part of the basin. The study area are cut by these various oriented faults, forming many blocks isolated at the surface and connected at depth (Fig. 1). Large-scale NWW-EW- trending faults include the Tuziduoyila fault (F_1 in Fig. 1) and Sangequan fault (F_2 in Fig. 1), which are only developed at depth. However, as described above, slip on these faults at depth results in extensional fracturing and tilting of blocks and then formation of billabongs at the surface.

This page intentionally blank

A NEE-trending fault is newly recognized in the northeast side of the town Dure (F_5 in Fig. 1). The fault is striking to NEE 60° with near vertical dip and behaves as a strike-slip and normal fault. A 20-30 centimeter thick fault gouge is developed along the fault and is composed of red-purple mudstones and conglomerates.

Field measurement of joints and slickensides developed in the WF and SF sandstones and mudstones was completed in order to better constrain the direction of maximum stress. The Rose diagram of the strike of joints infers that the regional maximum compressional stress is orientated nearly NS in both units. The Wulff projection of slickensides shows that the main stress is directed to the NNW or NEE in the HF, while in the SF it is the NNE or NE, suggesting that NWW- and NEE-directed compressional stresses are earlier than the NEE-direction stress. Therefore, two regional stress stages can be recognized.

4 Cenozoic Tectonic evolution and its control on the formation of sandstone-type uranium deposit in the northern Junggar Basin

Sedimentary filling processes and neotectonic features reveal that the northern Junggar basin has experienced various stages of tectonic movements in the Cenozoic. During the Paleocene to Eocene, thrusting of northern boundary faults resulted in thick-layers of coarse-grained sediments along the front edge of the fault, and fluvial plain sediments in areas far away from the fault (the HF) (Shi 2002). The tectonic movement from the Eocene to Oligocene is characterized by the uplift of mountains in northern Xinjiang and new thrusting on the northern boundary faults, resulting in the alluvial fan sedimentation close to mountains and thrust fault, and fluvial sedimentation in areas far away from active belts (the WF). A slight uplift might have happened during the later Oligocene. The study area subsided locally, and was filled by red material during a relatively torrid climate in the Miocene (the SF). During the Late Miocene to Middle Pleistocene, the sedimentation was scarce in northern Junggar basin. Joints and slickensides of various orientations formed during this time period. Most parts of northern Junggar basin may have subsided again during the Late Pleistocene, getting filled by the Xinjiang conglomerates. Slip on thrusts at depth since the Late Pleistocene led to tilting and rotation of blocks and created local extensional settings at the surface.

Although the neo-tectonic movement in northern Junggar basin is relatively mild, it is highly correlated with the formation of uranium deposits. First, the basin subsided due to gentle tectonic activity during the Cenozoic, causing the sedimentation of fluvial plant-bearing sandstones in a reducing environment. Moderate tectonic movement in the Late Cenozoic led to uplift and tilting of Tertiary packages, and formed an integrated supply-flow-discharge cycle for groundwater on a monoclinal slope. The exposure and denudation of the ore-bearing strata is also favored by the infiltration of uranium- and oxygen-bearing groundwater into the sandstone bodies and flow along the layer. Secondly, the development of faults at depth allow oil and gas to move along the fault and interact with the sandstone bodies, increasing the reducing agent which is essential for mineralization of sandstone-type uranium deposits. Thirdly, fault slip at depth leads to the formation of billabongs, which then work as the local discharge areas of groundwater. However, the slip on the thrust faults between various blocks can block groundwater flow, preventing the oxygen- and uranium-bearing groundwater from traveling and transporting the uranium from strata into the groundwater on a large scale.

Our analyses suggest that blocks, which are relatively stable during the neo-tectonic movement, should be favorable mineralization regions, such as the Sangequan slope block (Fig. 1). There the ore-bearing strata is relatively shallow and is stably plunging to the south with the dip less than 10°, forming a south-directed monoclinal slope and an integrated and independent supply-flow-discharge cycle for the groundwater. Fissures provide conduits for flow of oil and gas fields that are developed at depth (EGOX 1993) and provide a reducing environment for the sandstone bodies, which is favorable for the formation of sandstone-type uranium deposits.

Acknowledgements

This work was supported by the Major State Basic Research Program (No. 2001CB409808, and 2001CB7110013), and the National Natural Science Foundation (No. 40102022) of People's Republic of China.

References

EGOX (Editors group of gas and oil in Xinjiang) (1993) Petroleum in China (15): Junggar Basin (in Chinese with English abstract). Beijing: Petroleum Industry Publishing House, 37-385

Lin SX, Wang G (2003) Discovery of interlayer oxidation zone sandstone-type uranium mineralization in Lower Tertiary and its significance, Dingshan area, Junggar basin, Xinjiang. Uranium Geology19: 264-270(in Chinese with English abstract)

Peng XL (1986) Formation process of the billabong in n orthern Junggar basin. Xinjiang Petroleum Geology 7: 83-87(in Chinese)

Shi ZL (2002) Compressional and thrust structures of the Early Paleogene and their coupling sedimentary processes in the northern Junggar basin of Xinjiang. Xinjiang Geology 20:115-117(in Chinese with English abstract)

Wang G (2003) Characteristic of rock geochemistry for W-1 cycle of Wunlunguhe Formation at Dingshan area in north Jungar basin. Xinjiang Geology 21:415-418(in Chinese with English abstract)

Xinjiang BGMR (Xinjiang Bureau of Geology and Mineral Resources) (1993) Regional Geology of Xinjiang Uygur Autonomous Region. Beijing: Geological Publishing House, 1-481(in Chinese with English abstract).

The evolution of prototype basin and its relation to sandstone-hosted uranium ore-formation in northwestern China

Chen Zu-yi, Guo Qing-yin, Liu Hong-xu
Beijing Research institute of Uranium Geology, Beijing 100029, China

Abstract. Meso-Cenozoic sedimentary basins in northwestern China are superimposed composite basins starting with the extensional down-faulting prototype basin and then turning to compressional down-warping prototype basin. Based on the general law of Meso-Cenozoic tectonic evolution of northwestern China - two-time extensional down- faulting and two-time compressional uplifting - four stages of prototype basin evolution are classified. By analyzing characteristics of depositional systems and sedimentary facies developed in each stage of prototype basin evolution, authors emphasize that most favourable sand bodies for hosting uranium ores are those developed in the stage of extensional down-faulting prototype basin. In addition, six possible kinds of tectonic reworking pattern are discussed. It is proposed that the regional tilting occurring in the stage of compressional foreland prototype basin is the most advantageous for uranium ore-formation in sand bodies.

Keywords. Prototype basin, tectonic evolution, uranium ore-formation, sandstone-hosted uranium deposit

1 Introduction

Sandstone-hosted uranium deposits mostly occur in Meso-Cenozoic sedimentary basins and are attributed to exogenic epigenetic ones. So do sandstone-hosted uranium deposits in northern China. Generally speaking, ore-hosting sand bodies are of specific sedimentary facies occupying a fixed location in the stratigraphic column of the region, and appear in a specific prototype basin stage of the basin evolution, occupying a determinated space location of the basin. Meanwhile, the time for uranium infiltration into ore-hosting sand bodies occurs in certain prototype basin stage after the deposition of ore-hosting sand bodies experiencing a period of special pattern of tectonic reworking. If such period was absent or the basin experienced another pattern of tectonic reworking, uranium mineralization would not happen, and the basin could not be an important uranium –productive one.

2 Favourable ore-hosting sand bodies

2.1 Depositional system and sedimentary facies characteristics of ore-hosting sand bodies

Sandstone-type uranium deposits are hosted in sand bodies, but not all sand bodies can be the host of uranium mineralization. Sand bodies at known important uranium deposits basically are characterized by following features: I) They must be thick enough and be stable in extension. Usually, the thickness of sandstone bed ranging from 10 to 40m is regarded as suitable and the extension of hundreds of meters or more is favourable. II) The lithification of sandstone should be low and the permeability must be high for the easy infiltration of groundwater into sand bodies. III) Sand bodies should contain certain amount of reductant, such as coalcified plant debris and sulfide.

Sand bodies with above-mentioned features are mostly of delta (including braided delta and normal delta), fluvial (mainly braided stream, minor meandering stream) sedimentary facies in braided stream – braided delta – lacustrine and dew-delta – fan delta – lacustrine depositional systems, while sand bodies of lacustrine, flood plain and anastomosing facies usually do not host important uranium mineralization.

2.2 Evolutional stage advantageous for the occurrence of uranium-hosting sand bodies

The general trending of basin evolution in Meso-Cenozoic time can be summarized as two-time extension down-faulting and two time compression uplifting. Correspondingly, Meso- Cenozoic basins in the northwest of China experienced four stages of prototype basin evolution, i.e.

I The rift-like down-faulting prototype (J_{1-2})
II The intramontane (piedmont) down-warping prototype
III The taphrogenic extension prototype
IV The down-warping foreland compression prototype

Based on the associated relation of depositional system, sedimentary facies of sand bodies and prototype basin, the graben-like down-faulted basins are unfavourable for the occurrence of uranium-hosting sand bodies, because at the marginal sites of such basin only fan-delta, turbidite fan, subaqueous stream channel are developed, and sand bodies of these facies could not become good hosts for their low content of reductant or limited size. At the steep bank of half graben-like down-faulted basin the depositional system is similar to that of graben-like basin. How-

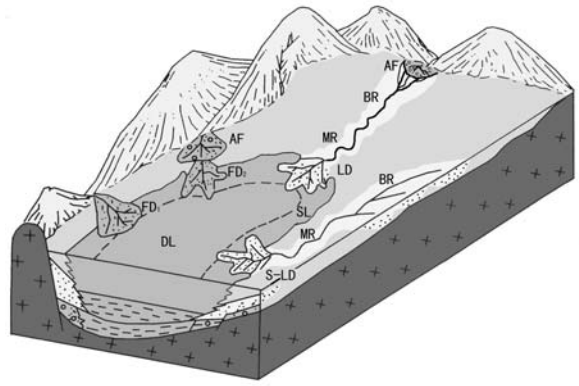

Figure 1: The sketch 3D-diagram showing the distribution of sand bodies of a down-faulted basin in contraction phase after WU Chong-jun,1993; AF – Alluvial fan; BR – Braided steam; MR – Meandering stream; FD1– Fan delta (closed to mountain); FD2 – Fan delta (closed to fan); SL – Shallow lake; DL – Deep lake; S-LD – Short-long fluvial delta)

ever, the flattish bank of half graben-like down-faulted basin is characterized by the development of braided delta, normal delta and quite wide range of fluvial (both braided and meandering) sand bodies (Fig.1), especially in the uplifting-contracting step of the late extensional down-faulting stage of down-faulted basins (Yu 2002).

In marginal areas of down-warping basins, including piedmont and intramontane down- warping basins, only narrow zone of fluvial and delta sand bodies can occur for the rapid subsidence of basin bottom. However, minor near-bank sand bodies may be developed during the uplifting –contracting stage of such basins (Yu 2002). No important target horizons could be formed in this stage of prototype basin evolution.

3 Special tectonic reworking for sandstone-hosted uranium ore-formation

Uranium ore-formation for sandstone-hosted uranium deposits occurs when ore-hosting sand bodies have been accumulated and the groundwater infiltrates into host sand bodies and makes it geochemically altered, and uranium in sand bodies becomes concentrated. However, the fundamental factor leading to the change of hydrogeologic regime and geochemical alteration is the tectonic reworking the sand bodies experience. Not all kinds of tectonic interference can guarantee the infiltration of uranium and oxygen bearing groundwater into potential ore-hosting sand bodies. For this reason, six kinds of tectonic reworking patterns are classified depending on the rigidity and contraction of the basin basement. These are:

I Graben-like differential uplifting-subsidence
II Half graben-like down-faulting
III Regional uplifting as a whole
IV One-side thrusting or two-side opposite thrusting of the basin
V Intense folding and deformation
VI Regional tilting

The successive subsidence of the potential target horizon (case I and case II) would make the target horizon more deeply buried and unavailable for prospecting and exploration. Regional uplifting (case III) would totally erode away sand bodies (such as delta sand bodies, fluvial sand bodies etc.) previously developed in the marginal areas of the basin and make the basin of no prospecting significance. Thrusting (case IV) would result in the accumulation of thick younger strata overlying the target horizon. The intense folding and deformation (case IV and V) would make rocks of target horizon more compact and reject the groundwater infiltration. Only in case of regional tilting (case VI) which may happen under the moderate tectonic stress and certain plastic state of the basement, can the target horizon be slightly uplifted and flat-lying and can groundwater successfully infiltrate into sand bodies and make it oxidized. It is well known that uranium exists basically in uranyl carbonate complex ions in surface and ground waters and migrate together with groundwater to the deep subsurface. When oxygen in the groundwater is completely consumed, uranyl complex ions would be disintergrated and U^{6+} would be reduced into U^{4+} and would become precipitated at the redox front forming so-called "roll-type" sandstone-hosted uranium deposit.

4 Conclusions

On the basis of the above description and analysis, following conclusions may be summarized.

1. The Meso-Cenozoic tectonic evolution of the northwestern China can be generally summarized as two-time extension ($J_{1\text{-}2}K_1$) and two-time compression (J_3, K_2~Q). Meso-Cenozoic sedimentary basins in the region are superimposed composite basins, and basically start with the stage of extensional down-faulting prototype basin and then turn to the stage of compressional down-warping foreland prototype basin.
2. The evolution stage of extensional down-faulting prototype basin is the best time for the formation of ore-hosting sand bodies. Thus, Lower-Middle Jurassic and Lower Cretaceous are the most important prospecting target horizons.
3. Uranium ore-formation in sand bodies occurs in the period of regional titling after the deposition of ore-hosting sand bodies. Other patterns of tectonic reworking such as continuous subsidence, one-side thrusting or two-side opposite thrusting of the basin, or the intense folding and deformation are unfavourable for the

This page intentionally blank

concentration of uranium in potential ore-hosting sand bodies.

4. The basic regularity of ore-formation in sandstone-hosted uranium deposited can be expressed as: "The target horizon for sandstone-hosted uranium deposit is formed in the evolution stage of extensional down-faulting prototype basin, and uranium ore-formation occurs in the evolution stages of compressional down-warping foreland prototype basin." It may be applied to preliminary determination of prospecting target horizon in a working region, and to the assessment of uranium potential in a basin. The knowledge could be of reference significance in uranium prospecting in other regions as well.

References

Franz J, Dahlkamp (1991) Uranium Ore Deposits, Springer-Verlag

Guo QY (2003) An evaluation system for uranium potential in continental basins dominated by recognizing favourable sand body, World Nuclear Geosciences 21(2): 69-76 (in Chinese)

Yu XH (1998) Petroliferous Reservoir Sedimentology of Clastic Rock Series, Beijing: Petroleum Industry Press (in Chinese)

World-class unconformity-related uranium deposits: Key factors for their genesis

M.L. Cuney
Unité Mixte: Géologie et Gestion des Ressources Minérales et Energétiques, and UMR G2R 7566 - CREGU - UHP, BP 239, F-54 501 Vandoeuvre les NANCY Cedex, France

Abstract. Unconformity related uranium deposits from the Athabasca basin (Saskatchewan, Canada) represent the world largest high-grade U ore-bodies. They are located in the vicinity of an unconformity between an Archean to Paleoproterozoic basement and a Paleo- to Meso-proterozoic intracontinental clastic basin. Their exceptional grade and size results from the combined efficiency of a series of U-fractionation mechanisms, which will be reviewed here. U-enrichment of the basement is exceptional. U-extraction efficiency from source rocks is shown by the alteration of highly refractory minerals such as monazite and zircon in the sandstone, the regolith, and the basement by slightly acidic, hot (160 to 220°C, about 1kbar), oxidized and Na-Ca-Mg rich (up to 6 molar Cl) basinal diagenetic brines generated within continental, oxidized, organic free, clastic formations. Exceptional trapping conditions resulted from (i) the strong redox gradient developed between the oxidized Paleo- to Meso-Proterozoic sediments and the epicontinental Paleoproterozoic organic-rich metasediments of the basement and (ii) the creation of large openings by the combined effects of reverse faulting and intensive quartz dissolution in the sandstone. U-Pb geochronology and REE patterns of the U-oxides provide evidence for a succession of mineralization events rather than one unique ore-forming event.

Keywords. Uranium, unconformity related, Proterozoic, metallogenesis

1 Introduction

Unconformity related uranium deposits from the Athabasca basin (Saskatchewan, Canada) represent more than half a million tons U @ more than 10 % in average. With the development of the Sue, Midwest and the high grade - large tonnage McArthur (225,000t @15.34 %U) and Cigar Lake (142,000t @ 15 % U) deposits, the production of Canadian unconformity-type deposits is expected to reach about 18,000 metric tons U by 2007. Most of the results presented here derive from recent studies of the Athabasca Uranium Province (AUP) with offers more than 30,000 continuously cored drill holes through the basin, generally down to the basement, and to a lesser extend from the East Alligator Rivers Uranium Province (EARUP) with large but lower grade deposits. The understanding of the mechanisms leading to the formation of such metal accumulations at that time represents a major scientific challenge. The efficiency of the successive fractionation processes occurring during metal extraction from the source, its transport and its deposition will be evaluated here.

2 Relative importance of the uranium sources

A first parameter to consider is the level of the metal concentration in the potential source rocks and the stability of each metal hosting phase. Possible uranium sources of unconformity related deposits were the basement and the sandstone cover.

2.1 Potential U sources in the basement

Archean in the AUP is mainly composed of U-poor magnetite bearing tonalities and cannot have represented an uranium source, but in the EARUP high K-Th-U Archean granites does exist. **Paleoproterozoic sediments** in both provinces consist of epicontinental clastic to chemical deposits. During Paleoproterozoic, the strong oxygen increase in the earth atmosphere, led to a worldwide storage of considerable amounts of uranium and carbon matter in these sediments. Graphitic schist, meta-arkose and calc-silicate show syngenetic U-enrichments in both provinces. Graphitic schist, cannot have been a major U-source because the reducing conditions created by graphite and associated sulfides, prevent uranium leaching. But, uraninite bearing calcsilicates and meta-arkoses may have been easily leached by oxidizing fluids. **Leucogranites and pegmatoids** derived by partial melting of the Paleoproterozoic metasediments (Sibbald et al. 1976; Annesley et al. 2003) are frequently enriched in uraninite and monazite. **Paleoproterozoic high-K calc-alkaline granitoids**, rnriched in Th and U represent up to 50% of the basement rocks in the Western AUP (Brouand et al. 2003) and also exist in the Eastern AUP (Annesley & Madore, 1991) and in the EARUP (Ferguson et al 1980). They are 1800±30 Ma old, in EAUP and EARUP, but of Taltson age (1930±30 Ma) in the WAUP (Brouand et al., 2003). **Late Hudsonian vein type U-deposits** (e.g. Beaverlodge, Gunnar) also demonstrate the ability of the Paleoproterozoic basement to represent a favorable U-source and these deposits may also themselves have contributed as U-sources for the unconformity related deposits.

2.2 Potential U sources in the cover

The clastic sediments are considered as the major U-source by many authors because they hosted oxidized fluids able to transport uranium. However, average U-con-

tent of the sandstones, away from the mineralized areas, is below 1 ppm, and 50 to 80% of U is presently bound to zircon. But, original U-contents may have been higher and leached during the diagenetic events (Kotzer and Kyser 1995). In clastic sediments, U can be distributed among 4 major sites: (i) in detrital accessories, (ii) adsorbed on clay minerals and Ti-Fe oxides, (iii) precipitated in organic matter bearing layers, (iv) bound to acidic volcanic ash. However, the amount of U, originally present as U-oxide, must have been very low, owing to the oxidizing conditions during deposition of these Proterozoic continental sandstone, free of organic matter. Only monazite may have represented a significant U-source.

3 Efficiency of uranium extraction

Incongruent dissolution of monazite with new formation of a Th-U silicate with lower Th/U ratio and Ca-REE-Sr Al-phosphates-sulfates (APS), both in the clastic sediments and in the altered sections of the basement allowed the extraction of about 75% of its uranium (Hecht and Cuney 2000a, b). Zircon was also altered with enrichment in U, Ca, LREE, Al, P, elements typical of the monazite alteration products (Hecht and Cuney 2000a). Such alterations, first observed in the Franceville basin, Gabon (Cuney and Mathieu 2001) also occur basin wide in the Athabasca and Kombolgie clastic sediments. Average Th content of the sandstone being below 10 ppm (except in the lower Manitou Falls Formations of the Eastern Athabasca), the amount of U deriving from monazite alteration was limited. Moreover, a significant part of the liberated U was trapped in altered zircon (U increase from a few hundreds to several thousand ppm), in Fe-Ti oxides deriving from detrital Fe-Ti oxide alteration.

4 Efficiency of uranium transport

4.1 Fluid characteristics

Most authors agree that U was transported by the basinal brines. U solubility was favored by their high fO_2 (well within the hematite field) and chlorinity (up to 6 molal). High fO_2 resulted from the lack of organic matter in the sandstone. The pH, controlled by the kaolinite-illite paragenesis, was slightly acidic (ca. 4.5 at 200°C) because of the lack of feldspar in highly mature quartzose sandstones or from its alteration during diagenesis. Early diagenetic brines from detrital quartz overgrowths are Na-rich and derive from evaporitic layers in the upper part of the basin, whereas the brines trapped later in pervasively silicified zones and drusy quartz, close to the mineralized zones, were enriched in Ca through their interaction with Ca-rich basement lithologies (Derome et al. 2003, 2005). One of the key factors for the genesis of high grade U-ore is the high-Ca content in the mineralizing fluid which led to: (i) dissolution of U, even from monazite, (ii) new formation of U-poor APS, (iii) Ca, REE, U, Al, P enrichment of zircon altered zones (Hecht and Cuney 2000a, b; Cuney et al. 2000), (iv) strong change in quartz solubility, which may have contributed to its dissolution in the mineralized zones. No experimental data exist to quantify the effect of such fluid compositions on U-solubility, but laser ablation ICP-MS analyses (ongoing studies, coll. C. Heinrich, ETH, Zürich) reveal that the Ca-rich brines are the richest in uranium. U solubilities of 30 ppm were calculated by Raffensperger & Garven (1995) for 5 molal Na-Ca chloride solutions at 200°C for a fO_2 of –20. The concentrations of U-ligands other than chlorine (F, P, CO_2, S) was severely limited by the low solubility product of fluorite, apatite, calcite and gypsum imposed by high Ca-activity in the brines.

4.2 Temperature regime

The temperature at the base of the basins during the mineralization event was assumed to be slightly higher than during early diagenesis and to be constant everywhere at about 200-250°C (Kotzer and Kyser 1995). Such high temperatures would mean anomalously high thermal gradients: 40-50°C/km for a 5 km thick basin. New fluid inclusion studies (Derome 2003, 2005) show that T and P at the unconformity decrease from the early diagenetic (160-220°C, 1-1.25 kbar) to the mineralization stage (140-160°C, 0.6 kbar). A late, low saline, CH_4 bearing fluid, deriving from the basement which mixed with the basinal brines is common in the EARUF but rare in the AUF.

4.3 Duration and age of ore deposition

The duration of the alteration and mineralization processes cannot be quantified by geochronology. U-Pb ages on U-oxides have an error of several tens of Ma. The scatter of the data can be explained by Pb diffusion out of U-oxides because of its larger ionic radius. Duration of the processes obtained by numerical modeling require numerous parameters which are not all well constrained. The formation of an ore body, such as Cigar Lake, requires a few million years and several tens of km^3 of fluid, using 5 to 10 ppm U in the solution and a 0.lm/year fluid percolation rate. Mass balance calculations using the amount of dissolved silica in a volume derived from GOCAD 3D modeling of chlorite breccias associated with U-ore deposition, gives a minimum fluid volume of about 1 km^3 in the EAUP, and a fluid/rock ratio of ~10,000 (Lorilleux et al., 2003). Recent U-Pb dating by ion probe have given ages up to 1570 Ma (Alexandre and Kyser 2003) much older than previous estimations. Combined U-Pb isotopic dating and REE analyses by ion probe (Bonhoure et al. 2005) show that different U-oxide generations in the same deposit may have different ages and distinct REE

abundance, but all generations having the same REE pattern. Bell shaped REE patterns centered on the middle HREE seems to be typical of the uranium oxides from unconformity related uranium deposits. However, it is still uncertain to certify if accretion of multiple stages of U deposition is required to explain the high grade-large tonnage of these deposits.

5 Efficiency of trapping conditions

Accumulation of such high-grade ore requires the creation of open space and an efficient reaction to destabilize the U-complexes and to reduce U^{VI+}.

5.1 Tectonic reactivation

Space can be first created by tectonic reactivation of basement faults. Most unconformity-type deposits are related to tectonic contraction leading to reverse faulting of the basement and creation of preferential opening near the strong mechanical anisotropy represented by the unconformity. Such faults were already active during the retrograde orogenic events affecting the basement with graphite-sulfide deposition and during sedimentation. If faulting is important to create or rejuvenate the permeability of the structures, the magnitude of the displacement along the fault does not seem to control the size of the ore-body. For the two largest deposits, the offset of the reverse fault reach 85 m at McArthur River, but just a small bump exists at Cigar Lake.

5.2 Quartz dissolution

Another major way of creating space is the huge quartz dissolution associated with U-mineralization and associated breccia bodies (Lorilleux et al. 2003). A volume loss up to 90% was estimated from mass balance calculations in altered sandstone. The upward decrease of alteration intensity from the unconformity and the input of basement-derived elements (Mg for sudoïte and dravite, K for illite) indicate that the fluids derived from the basement (Kister et al. 2005). As no temperature increase, no boiling or unmixing is observed during this event, quartz dissolution may be related to the sharp decrease of silica solubility in the basement derived Ca-rich aqueous fluid with respect to basinal Na-rich or to less saline aqueous fluid as shown by experimental data (Marshall and Chen 1982).

5.3 Basement derived reduced fluid

A basement derived reduced fluid was proposed to explain U deposition, the source of Mg (dravite and sudoite alteration), B (dravite) in the sandstones, and Ni, Co, Cu, Zn, Au in the polymetallic deposits. However, direct evidences for such a reduced fluid are still very weak. Current studies in the AUP and EARUP have identified CH_4 in the gas phase of some highly saline inclusions and in gas-rich inclusion in the basement. Hydrocarbons reported in the Rabbit Lake (Pagel et Jaffrezic 1977) and Nabarlek and Jabiluka (Wilde et al. 1989) deposits have only been detected by global analyses of crushed quartz. Leaching of iron in the sandstone in the alteration envelope of the U-deposits represents a further indication of the percolation of a reducing fluid (Kister et al. 2005).

5.4 Role and origin of organic compounds

A genetic link between basement graphite and bitumens associated with the U-deposits has been rejected by several authors. But, the similar isotopic composition of barren bitumens and basement graphite suggests a derivation of the bitumens by hydrogenation of carbon (Landais 1996), as well as the intimate relations between graphite and hydrocarbons determined by synchrotron (Annesley et al. 2001). Sangely et al. (2005) from in situ analyses of C-isotopic composition by ion probe and aliphacitic by Fourier Transform Infrared Microspectroscopy propose an abiogenic origin for bitumens. Thus, the genetic link between organic matter and U-deposition is still controversial.

6 Conclusions

Advanced analytical techniques, and geochemical and 3D modeling have permitted to reassess the various hypotheses proposed for the genesis of the exceptionally large tonnage high-grade unconfor-mity-related U deposits. The degree of U and graphite enrichment of the Paleoproterozoic basement was a key factor, but, the extreme reactivity of the oxidized, highly saline, Ca-Na brines generated at the base of thick, organic matter and K-feldspar free, Proterozoic sandstone basins, able to scavenge U even from very refractory minerals such as monazite, seems to be the most important key factor. The intensive quartz dissolution produced by large volumes of basement derived reduced and silica undersaturated fluids was also a key factor for creating the space necessary for high-grade ore deposition. The role of a reducing fluid remains not well understood. At the world scale, several Proterozoic basins (e.g. Thélon, Canada; Riphean of Siberia, Jotnian of the Baltic shield with the Karku deposit) share similarities with the Athabasca and Kombolgie basins, but need to be better characterized to evaluate their potentialities for hosting unconformity-related deposits. More recent continental clastic basins contain interstratified formations rich in organic matter, preventing the genesis of large volumes of highly oxidized fluids.

References

Alexandre P, Kyser K (2003) In Prog. Abstracts, Uranium Geochemistry 2003 Conference, Cuney M (ed), Nancy, France, 37-40

Annesley IR, Madore C (1991) Sask Resear Counc, Publ. R-1230-4-C-91, 140

Annesley IR, Madore C, Cutler J (2001) Summary of Investigations 2001, Sask. Geol. Surv, Sask. En. Mines, Misc Rep 2001-4.2. 132-140

Annesley IR, Madore C, Hajnal Z (2003) Uranium Geochemistry 2003, Conference Proceedings, Nancy, Cuney M (ed.), 55-58

Bonhoure J, Kister P, Cuney M, Deloule E (2005) IAEA Tech. Doc., Vienna, in press.

Brouand M, Cuney M Deloule E (2003) Uranium Geochemistry 2003, Conference Proceedings, Nancy, Cuney M (ed.), 91-94

Cuney M, Brouand M, Hecht L, Bruneton P (2000) GeoCanada 2000, Calgary, Conf. CD, 179

Cuney M, Mathieu R (2001) Geology 28(8): 743-746

Derome D, Cuney M, Cathelineau M, Dubessy J, Bruneton P (2003) J. of Explor. Geochim. 80: 259-275.

Derome D, Cuney M, Cathelineau M, Fabre C, Lhomme T (2005) Evidences of brine mixings in the McArthur River unconformity-type uranium deposit (Saskatchewan, Canada). Implications on genetic models. Econ Geol., in press

Ferguson J, Chappel BW, Goleby AB (1980) in Ferguson J, Goleby AB (eds) IAEA Tech. Doc., Vienne, 73-90

Hecht L, Cuney M (2000a) GeoCanada 2000. Calgary, Conference CD, ext. abstract, 191

Hecht LM, Cuney (2000b) Mineralium Deposita 35: 791-795

Kister P, Laverret E, Quirt D, Cuney M, Patrier P, Beaufort D, Bruneton P (2005) Clays Clay Miner, in press.

Kotzer T, Kyser TK (1995) Chem. Geol. 120: 45-89

Landais P (1996) Ore Geology Review 11: 33-51

Lorilleux G, Cuney M, Jebrak M, Rippert JC (2003) J. Geochem. Explor. 80:241-258

Marshall WL, Chen CTA (1982) Geochim. Cosmochim. Acta 46: 289-291

Pagel M, Jaffrezic M (1977) Aspect méthodologique et importance génétique. C. R. Acad. Sci. 284:113-116

Raffensberger JP, Garven G (1995) The formation of unconformity-type uranium ore deposits: Coupled hydrochemical modeling. Am. J. Sci. 295: 639-696

Sangely, Michels R, Chaussidon M, Brouand M, Cuney M (2005) Geochim Cosmochim Acta, submitted

Sibbald TII, Munday RJC Lewry JF (1976) (DUNN, C.E., Ed.); Saskatchewan Geo.l Soc., Spec. Publ. 3: 51-98

Wilde AR, Mernach TP, Bloom MS, Hoffman CF (1989) Economic Geology 84: 1627-1642

Alteration characteristics of the sandstone-type uranium deposit in Qianjiadian, Inner Mongolia

Wenming Dong, Jinrong Lin, Yuliang Xia, Daneng Qi
Beijing Research Institute of Uranium Geology, P.O. Box 9818, 100029 Bejing, China

Abstract. The Qianjiadian deposit is a typical epigenetic sandstone-type uranium deposit. The host Yaojia Formation of the Upper Cretaceous age was reduced and altered due to migration of organic fluids from a deeper part of the basin. The main types of alteration comprises reducing of iron, argilitization, carbonatization, and pyritization of host rocks. The uranium mineralization is closely related to those alterations, and the uranium ore-bodies occur mostly in the gray altered sandstone and associate closely with matrix pyrite, albanite and clay minerals that were formed during alteration. The post-ore oxidations locally lead to further enrichment of uranium in ore bodies.

Keywords. Qianjiadian deposit, sandstone-type uranium, Yaojia Formation, alteration, uranium mineralization

1 Introduction

The Qianjiadian uranium deposit in Inner Mongolia is located in the Qianjiadian depression in the southwest part of the Songliao basin and represents a typical epigenic sandstone-hosted type of uranium mineralization (Xia et al. (2002). The major ore-bearing strata in the deposit is the Yaojia Formation of the Upper Cretaceous age, and in general, the ore forms sheet-like or lenticular bodies, which are distributed parallel to the host rocks bedding. In ore bodies, uranium occurs as uraninite, or absorbed on a surface of clastic grains or within cement.

2 Characteristics of host rocks

The ore-bearing horizon of the Yaojia Formation consists mostly of thick sandstone and thin mudstone bodies that were deposited in the distributary streams of a braided delta system. The host rocks are mainly medium to fine grained felspathic sandstone (or lithic sandstone) with high amount of cement (Yin et al. 2000). The clastic components are mainly quartz, feldspar and lithic fragments, the cement being formed by clay minerals and calcite.

Because of an arid and semi-arid palaeo-climate in the time of deposition, most sediments of the Yaojia Formation are red in color. They contain an extremely small amount of organic matter and sulfide and a high amount of carbonate. Therefore, rocks are geochemically alkaline and oxidized.

3 Types of alteration

During the Nengjiang and Mingshui compressive phase of (Hou et al. 2004), host rocks were deformed and underwent alteration due to a migration of organic fluids (oil- and gas-bearing brines) from deep parts of the basin. The alterations of thee sandstone can be classified into several types: (1) the reduction of Fe^{3+}minerals, (2) argilitization, (3) carbonatization and, (3) pyritization. These types of alterations are contemporaneous with the uranium deposition. After uranium deposition, a part of reduced lithologies was oxidized due to the infiltration of phreatic oxygen-bearing water from the surface host rocks from shallow aquifers. This post-ore alteration is characteristic by the oxidation of ferrous iron.

3.1 Reduction

Due to the migration of acid and strongly reduced organic fluids seeped from deep parts of the basin, the host rocks were to various degrees reduced. The rock color changed from original red to mottle (weakly altered) and gray (strong altered) with an increasing degree of alteration. The Fe_2O_3/FeO ratio and pH value decreases substantially while the ΔEh value increases (Table 1) The decrease of Fe_2O_3/FeO and pH values and the increase of delta Eh values indicate that the rock geochemical properties changed from alkaline and oxidized to acid and reduced, and its reducing capacity increased substantially.

3.2 Argilitization

As the acidification and reduction of sandstone increases, a great part of unstable components in the rocks (feldspars, lithic fragments) were altered to form clay minerals. In argilitic alterations, kaolinite is a dominant mineral and accounts for more than 60 % of the total amount

Table 1: Geochemical indexes of unaltered red sandstone and altered sandstones

Lithology	Red sandstone	Mottle sandstone	Gray sandstone	Yellow sandstone
n*	3	10	219	8
Fe_2O_3/FeO	5.26	2.66	0.84	4.58
S (wt.%)	0.02	0.16	0.17	0.13
pH	9.64	9.51	9.12	9.57
ΔEh (mV)	17.33	27.00	29.11	21.50

Note: * number of analyzed samples.

of clay minerals. Illite, chlorite and I/S mixed layered clay minerals are less abundant (< 30 %).

3.3 Carbonatization

The process of carbonatization associated with the seepage of acid and reduced fluid is manifested either by the partial corrosion of early diagenetic carbonate cement, either by the replacement of quartz grains, lithic fragments and clay minerals formed during fluids migration.

The corrosion improves greatly the permeability of host rocks, forming favorable conditions for the migration of underground water. The secondary replacement of clastic grains and clay minerals furthermore substantially changes the geochemical characteristics of rocks. These two processes are quite favorable for the origin of uranium mineralization.

Two different types of carbonate can be recognized in rocks. The first type was formed during diagenesis, the second one during the alteration of rocks. Both types differ in their carbon izotopic composition. The average $\delta^{13}C$ value of the diagenic carbonate is -0.87‰, which equals approximately to the $\delta^{13}C$ values of sedimentary carbonates. In contrast, carbonates deposited during migration of oil and gas-bearing water are depleted in ^{13}C (up to -6.8‰). The depletion in ^{13}C isotope indicates that the organic carbon or carbon from a deep crustal reservoir ("magmatic carbon") can be considered as a source of CO_2 in migrating fluids (Lou et al. 2002).

3.4 Pyritization

Two types of pyrites can be identified in host rocks: (1) the diagenetic pyrite that forms idiomorphic grains or accumulations in sandstone matrix and, (2) pyrite that forms tiny veins or bands in host rock.

The diagenetic pyrite, which presumably originated due to a bacterial reduction of the marine sulfate in intergranular spaces of sediments, occurs only locally in some gray, thin mudstone and in adjacent sandstone.

The grains of pyrite that originated during alteration yrite are similar to marcasite in shape. The marcasite-like morphology of pyrite grains is attributed to the acid character of the environment of their formation.

The pyrite of this type associates closely to the albanite and appears to be widely distributed in the gray, reduced sandstone, forming tiny veins parallel to sedimentary bedding or crevices, which show many features typical of late filling.

Sulfur isotope composition of the two types of pyrites displays significant difference. The diagenetic pyrite is enriched in ^{34}S isotope ($\delta^{34}S_{V\text{-}CDT}$ up to +15.3‰). In contrast, pyrite related with alterations is depleted in ^{34}S izotope. Its average $\delta^{34}S_{V\text{-}CDT}$ value is close to -34.0‰), thus indicating biogenic source of sulfur in deep-seated source rocks.

Table 2: Geochemical indexes of mineralized rocks in different grades and non-mineralized rocks. Post-ore alteration increases from gray to yellow sandstone

Lithology	Gray sandstone				Yellow sandstone
n*	12	67	143	8	7
U ($x10^{-6}$)	1544.2	299.9	37.2	5.5	4.8
Fe_2O_3/FeO	0.67	0.55	0.61	1.15	5.03
S (%)	0.91	0.20	0.11	0.02	0.02
pH	7.84	9.11	9.17	9.76	9.67
ΔEh (mV)	43.58	30.63	27.11	18.25	19.29

Note: * number of analyzed samples.

3.5 Oxidation of ferrous iron

After the formation of uranium mineralization, a part of pyrite and Fe-carbonate, formed during the reduction of host rocks by oil and gas-rich fluids, was oxidized due to infiltration of the phreatic oxygen-bearing water. Oxidation of iron and sulfur is envidenced by a local formation of jarosite. The Fe_2O_3/FeO ratios of the oxidized rocks and their pH gradually increase while Eh values decrease (Table 2), The data suggest that geochemical properties of rocks changed from acid and reduced to alkaline and oxidizing during the post-ore stage.

4 Relation of alteration to U- mineralization

The uranium mineralization in the studied area is closely related to alterations, especially to the reduction of ferric iron in host rocks. The uranium ore bodies occur mostly in gray "reduced" sandstone, and they associate closely with pyrite, albanite and clay minerals that were formed in course of alteration. The uranium contents in ores are distinctly correlated to Fe_2O_3/FeO ratios, contents of sulfide, and to changes in the pH and delta Eh values of the host rocks (Tab.2). The more the host rocks are altered, the more it is favorable for the enrichment in uranium.

During the post-ore oxidization, a new phase of the re-concentration of uranium took place in the studied area. The uranium ore bodies were locally impoverished, locally enriched in uranium. As a consequence of the secondary enrichment, the grade of ore in some ore bodies was improved.

5 Conclusions

1. The Qianjiadian uranium deposit is a typical epigenetic sandstone-hosted type of uranium deposit. The

This page intentionally blank

ore-bearing strata of the deposit are the Yaojia Formation of the Upper Cretaceous age. This formation consists of thick sandstone and thin mudstone of a braided delta system origin.

2. Host rocks are mainly medium- to fine-grained felspathic sandstone or lithic fragments sandstone. The rocks are red in color because of an arid paleo-climate in the depositional period. During the seepage of gas- and oil-rich fluids from the deeper parts of the basin, the rocks were reduced and acidified.
3. Alteration of sandstones comprises reduction of trivalent iron, argilitization, carbonatization and pyritization. The post-ore alteration is typical of the oxidation of ferrous iron as a result of the infiltration of phreatic oxygen-bearing water.
4. The uranium mineralization in the studied area is closely related to the alterations, especially to the reducing of trivalent iron, argilitization and pyritization. The late oxidization further lead to an enrichment of uranium in some ore bodies.

Acknowledgement

Thanks are to Dr. Li Sheng-xiang for geological data and fruitful discussion, and to Prof. Huang Zhi-zhang, Li Xiuzheng Xie Yu-xin, Fang Xi-heng, Li Yue-xiang for their study of thin sections and data analysis.

References

Hou GT, Feng DC, Wang WM, Yang MH (2004) Reverse structures and their impacts on hydrocarbon accumulation in Songliao Basin. Oil & Gas Geology 25:50-53 (in Chinesse)

Lou ZH, Yao YM, Jin AM, Cai XY (2002) Geochemical properties of underground fluids in Songliao Basin, China. Acta MineralogicaA Sinica 22:344-349

Xia YL, Lin JR, Li ZY, Li SX, Liu HB, Wang ZM, Fan G, Zheng JW, Li ZJ, Zhang MY (2003) Perspective and resource evaluation and metallogenic studies on sandstone-type uranium deposit in Qianjiadian Depression of Songliao Basin. China Nuclear Science & Technology Report, 105-117

Yin JH, Zhang H, Zan GJ, Li XC (2000) Sedimentation factors analysis of uranium mineralization of Qianjiadian Depression, Kailu Basin, East Inner Mongolia Autonomous Region. Journal of Palaeogeography 2: 76-83

Simple deposition versus replacement and re-equilibration at the Crescencia Ni-(Co-U) deposit (Central Pyrenees, Spain)

I. Fanlo, I. Subías, J. Manuel, A. Paniagua
Cristalografíay Mineralogía. Universidad de Zaragoza. 50009-Zaragoza, Spain

S. Morales
Dpto. de Mineralogía y Petrología. Facultad de Ciencias. Universidad de Granada. 18002-Granada. Spain

Abstract. The mineral assemblage of the Crescencia mine contains Ni sulfarsenides, arsenides and diarsenides, uraninite and pyrite. Three stages of mineral deposition can be distinguished: Stage I: nickeline, gersdorffite I, and rammelsbergite; Stage II: gersdorffite II; Stage III: uraninite. Gersdorffite II has been subdivided into six groups on the basis of textural and compositional criteria. Some of these gersdorffite types are clearly pertained to disequilibrium processes. Gersdorffite B, C, E and F represent intermediate steps during the nickeline replacement and progressive re-equilibration with residual fluids, representing by gersdorffite D. Thus, compositional variations found in gersdorffite are the result of nickeline replacement and reequilibration processes rather than a direct precipitation under different conditions of the ore-forming fluids.

Keywords. Nickeline, gersdorffite, uraninite, mineral replacement, dissolution-precipitation, recrystallization front, reaction rims, Pyrenees

1 Introduction

In the Pyrenees there are two groups of small-scale Ni-Co deposits hosted by Palaeozoic metasomatized limestones, according to whether Co or Ni is dominant: Co dominant, such as San Juan de Plan deposits and Ni dominant, as Crescencia mine (this study).

The extent of the solid-solution fields of the cobaltite-gersdorffite series along with the presence of alloclasite suggest that San Juan de Plan deposits were formed at temperatures as high as 600ºC (Fanlo et al. 2004), what strongly disagree with field geology. Textural and compositional characteristics of Crescencia ore minerals may allow us to test whether the extent of the mentioned solid solution is due to high temperatures or re-equilibrium processes at lower temperatures.

2 Geology of the deposit

The Crescencia mine is located in the central part of the Pyrenees, a doubly vergent collisional mountain belt, which resulted from Mesozoic to Cenozoic interaction between the Afro-Iberian and European plates.

The ore is enclosed by limestones, which alternate with black shales in the early Devonian sequence. This ore-bearing unit is extensively dolomitized. The deposit consists of an E-W vein, 50 m long and 10 cm wide, located in the contact between the limestones and black shales. An irregular, discordant zone of disseminated or vein mineralization occurs all over the vein. The Hercynian structure of both host rocks and ore is disrupted by Alpine E-W thrust verging to the south. The deposit is not obviously related to igneous intrusions.

3 Mineralogy

The mineral assemblage is characterized by Ni sulfarsenides, arsenides and diarsenides, uraninite and rare pyrite along with ankerite and dolomite as gangue minerals. Three stages of mineral deposition can be distinguished:

Stage I comprises masses of coarse anhedral aggregates of nickeline that contain small (<20μm) scattered euhedral gersdorffite (Gd I) grains, being, in some cases, aligned among the grain boundaries of nickeline. Frequently, nickeline shows a distinct cleavage that is accented by weathering along exceptionally well-developed lamellar twinning (Fig. 1A). Rammelsbergite occurs as inclusions in nickeline. Sometimes both minerals occurred as inclusions in Gd II, showing replacement evidences.

Stage II is dominated by gersdorffite (Gd II), which overgrows nickeline grains and replaces and fills small cracks in these crystals. Locally replacement follows nickeline crystallographic directions. Gd II has been subdivided into six groups on the basis of its texture and compositional variability. The groups are named gersdorffite A, B, C, D, E and F throughout the text and figures. (A) euhedral gersdorffite overgrowing the pyrite grains disseminated in the black shales close to the vein. Although has been included in gersdorffite II, there is not any textural relation among this type and the rest of gersdorffite types; (B) small idiomorphic crystals, twinned and with variable compositions in the As-S contents (Fig. 1B). (C) Rhythmic reaction rims with high arsenic content produced by the replacement of nickeline by gersdorffite (Figure 1C); (D) masses of coarse subhedral aggregates with small remnants of nickeline and rammelsbergite; (E) irregular patches of arsenic-rich gersdorffite included in gersdorffite with “normal” As

contents (As: S-1) (Fig. 1D); (F) euhedral crystals with irregular growth-bands (Fig. 1E) characterized by variations in the As and S contents but with no variation in the metal content.

Stage III is characterized by the deposition of uraninite following a recrystallization front affecting both, nickeline and gersdorffite (Fig. 1F). Texturally, uraninite forms concentric structures, coalescing and producing tabular aggregates. Sometimes, these aggregates grow along crystallographic directions of gersdorffite crystals.

4 Mineral composition

Electron-microprobe analyses show a Sb-bearing nickeline: $Ni_{0.98\text{-}1.01}Fe_{0.00\text{-}0.01}As_{0.97\text{-}1.03}Sb_{0.00\text{-}0.03}\ S_{0.00\text{-}\ 0.08}$ while rammelsbergite composition is within the range of $(Ni_{0.96\text{-}1.01}Fe_{0.00\text{-}0.02})As_{1.94\text{-}2.00}\ S_{0.00\text{-}0.04}$-$Sb_{0.00\text{-}\ 0.02}$. Gersdorffite I (cubic crystals) exhibits the following compositional variability $(Ni_{0.80\text{-}1.01}\ Co_{0.02\text{-}0.18})As_{1.01\text{-}1.55}Sb_{0.00\text{-}0.05}S_{0.40\text{-}0.98}$, ranging As/S ratio from 1.03 to 3.88. Gersdorffite A (overgrowing pyrite crystals) shows the highest Co, Fe and lowest As contents and is the only Sb-free gersdorffite: $(Ni_{0.57\text{-}0.78}Co_{0.18\text{-}0.39}Fe_{0.02\text{-}0.12})As_{0.97\text{-}1.10}\ S_{0.90\text{-}1.01}$. Gersdorffite B (twinned crystals) is characterized by a Co contents up to 7 wt.% and very variable As and S ones (As:S ratio from 1.13 to 4.23): $(Ni_{0.76\text{-}0.88}Co_{0.10\text{-}0.22})As_{1.07\text{-}1.65}Sb_{0.00\text{-}0.02}S_{0.39\ \text{-}0.95}$. The higher S content there is, the higher Co content there is (R=0.88), and, comparably, the correlation between As and Ni is positive too (R = 0.87). This is in agreement with the idea that high As contents favour the incorporation of Ni in the crystal lattice (Hem et al. 2001). Gersdorffite C (reactions rims) displays As/S ratio ranging from 1.03 to 4.46, with a composition of: $Ni_{0.96\text{-}1.01}\ As_{1.02\text{-}1.65}Sb_{0.00\text{-}0.02}S_{0.37\text{-}0.99}$. Gersdorffite D (massive) is the most abundant phase, showing the As and S values closest to the theoretic composition: $(Ni_{0.61\text{-}1.03}Co_{0.00\text{-}0.29}Fe_{0.00\text{-}0.08})\ As_{0.97\text{-}1.17}\ Sb_{0.00\text{-}0.07}\ S_{0.83\text{-}1.01}$. The As:S ratio varies between 0.98-1.40. Gersdorffite E, with the irregular patches of arsenic-rich gersdorffite shows compositions very similar to those from gersdorffite F: $(Ni_{0.94\text{-}1.01}Co_{0.00\text{-}0.15}\ Fe_{0.00\text{-}0.05})As_{1.04\text{-}1.43}Sb_{0.02}S_{0.54\text{-}0.94}$. Finally, gersdorffite F (euhedral crystals with growing bands), displays As values ranging between those of gersdorffite C and stoichiometric ones (gersdorffite D). The general composition is: $(Ni_{0.84\text{-}1.02}\ Co_{0.00\text{-}0.15}\ Fe_{0.00\text{-}0.05})\ As_{1.01\text{-}1.37}\ Sb_{0.00\text{-}0.03}\ S_{0.64\text{-}0.99}$.

5 Discussion and conclusions

The nickeline-rammelsbergite-gersdorffite mineral assemblage is a common association in ore deposits and frequently, these minerals are intimately intergrown each other or, nickeline core are enclosed by rammelsbergite and/or gersdorffite. The As/S ratio and cation contents have been used to distinguish among different gersdorffite varieties in high temperature deposits since both As and Ni contents in gersdorffite-cobaltite$_{ss}$ are controlled by the As fugacity of the mineralizing fluid (Hem et al. 2001

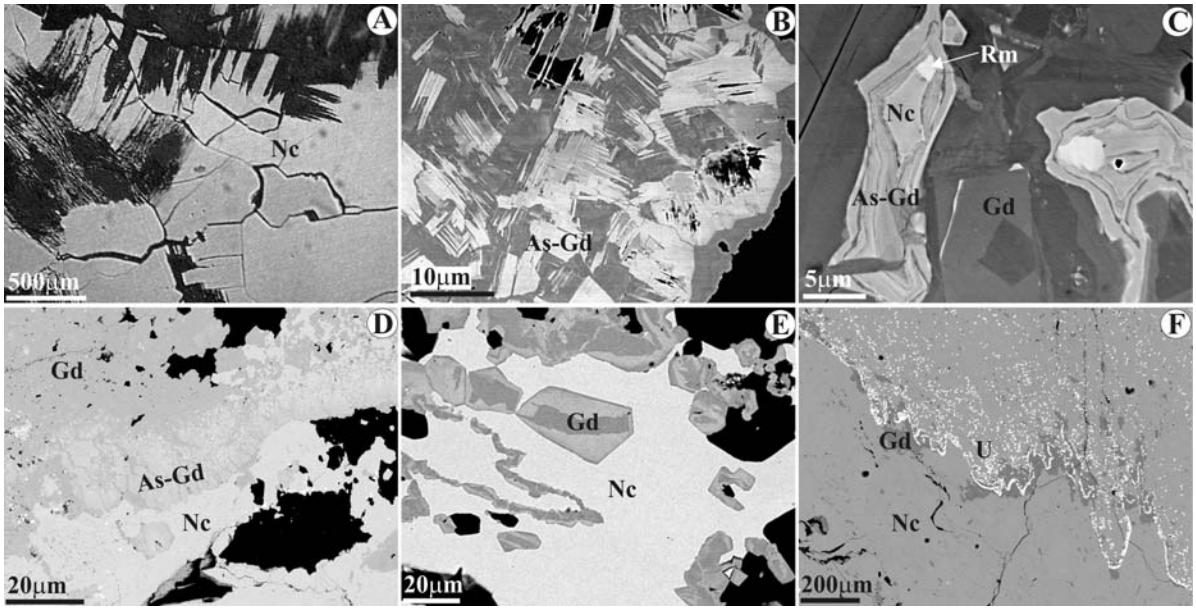

Figure 1: Textures of ore minerals from Crescencia mine. All photomicrographs are BSE images, except Figure 2A (reflected light image). A) Anhedral aggregates of nickeline showing a cleavage parallel to (0001). B) Twinned gersdorffite crystals (type B). C) Nickeline crystal hosting a tiny rammelsbergite inclusion, partially replaced by gersdorffite C, both minerals are included in gersdorffite D. D) Irregular patches of arsenic-rich gersdorffite (type E). E) Euhedral crystals of gersdorffite F. F) A recrystallization front of uraninite. Symbols: Gd I: gersdorffite from stage I; Nc: nickeline; As-Gd: As-rich gersdorffite; Rm: rammelsbergite; U: uraninite.

This page intentionally blank

Hem and Makovicky 2004). However, a question arises when low temperature deposits, such as Crescencia mine, are studied. Are the complex textures and the As variation in gersdorffite the result of a direct precipitation, or the result of reequilibration processes?

The textural and compositional features of gersdorffite B and C cannot be explained as a simple precipitation processes. With respect to the complex twinning of gersdorffite B, Bayliss (1982) from heating experiments on gersdorffite specimens, suggested that those samples with twins might be explained as $Pca2_1$ structure, an intermediate and metaestable form between the Pa3 (the high form) and the low temperature form, $P2_13$. On the other hand, compositional variations in gersdorffite C may be explained by variation in the solution composition and degree of supersaturation at solid-solution interfaces due to diffusion-controlled concentration gradients (Oen et al. 1984). Far from the reaction rims, gersdorffite attains re-equilibrium, showing nearly stoichiometric As and S contents.

Gersdorffite E and F represent and intermediate situation between gersdorffite C and gersdorffite D (As/S ratio ~ 1). Above all, the gersdorffite E must be considered as the classic mineral replacement reaction, which proceeds via a moving interface (Figure 1D). The separation of transformed (As-enriched gersdorffite) and untransformed phase (nickeline) by the interface suggests a coupled dissolution-reprecipitation process, rather than one controlled by diffusion or simple anion exchange (Putnis 2002). The rates of this process must be equal to preserve the integrity of the interface between nickeline and As-enriched gersdorffite. It seems a common phenomenon that the replacement results in porosity in the product phase, and the gersdorffite shows porosity as we move father away the interface and it attains a re-equilibrium with an As/S~1.To sum up, the compositional variations found in gersdorffite types can be considered the result of nickeline replacement and subsequent re-equilibrium steps with the residual solutions rather than a deposition under different conditions of the ore-forming fluids. The As-rich gersdorffite (type C) would represent the first product of nickeline replacement while gersdorffite D would represent end equilibrium (As/S~1). During this process, a shrinkage in As content is produced (types E and F). A better understanding of the factors controlling replacement reactions between nickeline and gedorffite require the study of the interface between them by TEM, what is now in progress.

Acknowledgements

The Ministerio de Educación y Ciencia financially supports this research project (grant CGL2004-05055/BTE).

References

Bayliss P (1982) A further crystal structure refinement of gersdorffite. Am. Mineral. 67:1058-1064

Fanlo I, Subías I, Gervilla F, Paniagua A, García B (2004) The composition of Co-Ni-Fe sulfarsenides, diarsenides and triarsenides from the San Juan de Plan deposit, Central Pyrenees, Spain. Can. Mineral 42:1221-1240

Hem SR, Makovicky E (2004) The system Fe-Co-Ni-As-S. II. Phase relations in the (Fe, Co, Ni) As1.5S0.5 section at 650 and 500°C. Can. Mineral 42: 63-86

Hem SR, Makovicky E, Gervilla F (2001) Compositional trends in Fe, Co and Ni sulpharsenides and their crystal-chemical implications: results from the Arroyo de la Cueva deposits, Ronda peridotite, Southern Spain. Can. Mineral. 39: 831-853

Oen IS, Dunn PJ, Kieft C (1984) The nickel-arsenide assemblage from Francklin, New Jersey: description and interpretation. Neues Jahrb. Mineral, Abh. 150:259-272

Putniss A (2002) Mineral replacement reactions from macroscopic observations to microscopic mechanism. Min. Mag. 66: 689-708

Evolution of Mezozoic to Cenozoic basins in the Beishan-Gansu Corridor region with respect to uranium ore formation

Qingyin Guo, Zuyi Chen, Hongxu Liu
Beijing Research institute of Uranium Geology, Beijing 100029, China

Abstract. Mezozoic to Cenozoic basins in the Beishan-Gansu Corridor region experienced six evolutional stages. During sedimentation, uranium mineralization of synsedimentary origin was formed. Subsequently, during regional uplift, the interlayer oxidation- and coal type uranium mineralization originated in sand bodies developed at the flat banks of the down-faulted basins. Taking in account differences in paleoclimatic conditions, and sandstone bodies' morphology and properties, the Lower to Middle Jurassic and Lower Cretaceous periods were recognized as the most promising target for uranium prospecting.

Keywords. Beishan-Gansu corridor region, basin evolution, uranium ore

1 Geologic setting

Beishan-Gansu Corridor region is located amidst the Tarim-Karakum, North China, Kazakhstan and Siberia plates (Fig. 1). During the end of Late Paleozoic period, the Hercynian orogeny welded all plates together into a large continental block that successively experienced Indosinian, Yanshanian and Himalayan orogenies More than 20 medium- to small-sized superimposed continental basins were formed during Mezozoic.

2 Evolution of Mezozoic to Cenozoic basins

The structural evolution of Mezozoic to Cenozonic basins in the studied region began in Early Jurassic (Zhang et al. 1981; Yang 1987; Li et al. 1991; Zhai et al. 2002). Based on the angular unconformity positions in stratigraphic column, filling sequence lithology and burial history of the basins cover, the evolution of Mezozoic to Cenozoic basins in the region can be divided into six stages. The tectonic and sedimentary characteristics of each stage are described below:

2.1 The extension-down-faulting stage, Early to Middle Jurassic

The horizontal compression during Indo-sinian period was accompanied with extension in some areas where extensional basins of down-faulttype were opened (Chen and Wang 2000). The extensional environment resulted in the emplacement of basic lava flows that intercalate

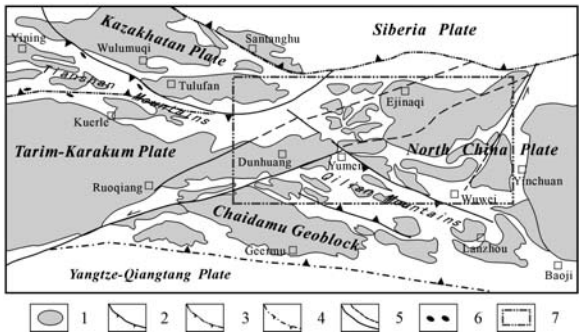

Figure 1: Map showing the geotectonic location of the studyiedregion. 1.Sedimentary basin; 2. Suture zone of the Caledonian period; 3. Suture zone of the Hercynian period; 4. Suture zone of the Indo-sinian period; 5. Fault structure; 6. Ophiolite; 7. Location of the studied region.

withLower to Middle Jurassic sediments. The taphrogenic center was located in the Dunhuang- Jiuquan area.

The early basin-controlling faults cut the basement and produced a series of half graben-like down-faulted blocks. During the subsequent filling, the regional extension of basins gradually expanded during the sedimentation of Middle Jurassic Qingtujing Group. Basins developed in that stage are mostly of half graben down-faulted type with one side normal growth fault on its boundary. As a rule, at the steep bank of down-faulted basins, the alluvial fan- fan-delta- and subaqueous fan depositional system was developed with less stable sand bodies. However, at the flat banks of basins, braided stream- and brained delta depositional systems dominated and sand bodies were well developed with better interconnection between each other. As the humid climate was predominant at that time, coal-bearing formation with high content of organic matter was deposited in all basins of the region.

2.2 The intracontinental down-warping stage, Late Jurassic

During the Late Jurassic period, reflecting the of Bangonghu-Nujiang oceanic basin closure, the tectonic setting of the studied region turned into compressional and intracontinental down-warping basins were formed. The sedimentary area was greatly contracted (restricted?) and Upper Jurassic sediments are missing in some ba-

sins. The compressional regime resulted not only in an unconformity formation between Middle Jurassic and Upper Jurassic, but also in intense folding and deformation of Lower to Middle Jurassic sediments in the Beishan area. However, some basins, for example, Chaoshui basin, were subjected only to slight compression resulting only in tilting of pre-existing strata offlap.

2.3 The extension-subsidence stage, Early Cretaceous

The studied area was affected by an extension once more during the Early Cretaceous period. The argument in favor of the extensional tectonic regime is the formation of multi-bed basalts in the Bayingobi and Jiuxi basins. Down-faulted basins of this stage basically inherited the paleogeomorphologic pattern of the Early toMiddle Jurassic half graben-type basins. During this stage, the faulting activity was weak and basin areas were entirely subsided and sedimentary range (rate or areal extent of sedimentation?) reached the maximum in Mesozoic time. The paleoclimatic condition was characterized by a repetition of arid andhumid intervals, thus leading to the deposition of variegated red terrigenous clastic formations. The deposition of predominantly fine-grained clastics with high content of carbonate, characteristics of sedimentary structures and filling sequence of this stage point to the lacustrine origin of sediments. At that time, shallow water lake occupied an extensive area. Therefore, sediments were basically of the coastal lacustrine— and shallow lacustrine subfacies. Alluvial fan- and fluvial facies occurred only at the periphery of basins. During the late evolution of down-faulted basins, because of the reduction of clastic material imput and intense evaporation, an evaporite sequence including limestone, marl, gypsum and salt was formed.

2.4 The compression uplifting stage, Late Cretaceous

During the Late Cretaceous, the studied region was again subjected to the compressional tectonic regime, which reflected subduction and closing of the Indian-Yarlung Zanbo Ocean to the north. Most areas of the studied region were uplifted and exposed to the surface. The western Qilian, Dunhuang and Beishan areas were connected into a united uplift (zone?) (Zhai et al. 2002) and sedimentation in many basins (Bayingobi, Chaoshui, Yabulai) was restricted. Representative sediments of their evolution stage are represented by red coarse-grained clastics that accumulated in down-warping basins.

2.5 The piedmont down-warping stage, Oligocene to Miocene

During the early period of Tertiary, the compressional tectonic regime of the Late Cretaceous uplift stage persisted and, therefore, the Paleocene and Eocene sediments are usually absent. Starting with Oligocene, the Tethys Ocean was closed and Indian and Eurasian plates were welded together. The compression resulted in a rapid uplift of the pre-existing orogenic belts and in the formation of a great number of separated compressional down-warping basins filled with red coarse-grained clastic sediments. (Zhai et al. 2002; Liu 2004). Because of the prevailing arid climate at that time, sediments were usually intercalated with evaporates, such as gypsum.

2.6 The foreland stage, Pliocene to Pleistocene

Along with a quick rise of the Qinghai-Tibet Plateau, the studied region experienced strong tectonic compression. Under such conditions, the Arjin region fault system shows sinistral strike-slip kinematics and simultaneously, thick fluvial- and lacustrine facies sediments accumulated in the Dunhuang, Beishan and Gansu Corridor compressional foreland basins. Ones, Area to the north of Gansu Corridor experienced less compression, and small-sized subsided depression appeared in the Chaoshui and Yabulai basins with local deposition of alluvial- and fluvial tolacustrine clastic sediments. During this stage, the paleoclimate was relatively humid, and sediments are mostly earth-yellow and less grey in color.

3 Evolution of Mezozoic to Cenozoic basins with respect to uranium ore formation

The Mezozoic to Cenozoic basins in the Beishan-Gansu Corridor region experienced a long-term evolution that comprised two periods of down faulting and four periods of uplifting. Repetition of the compressive and extensive tectonic regimes resulted in the formation of numerous superimposed basins with complicated structure. During the different stages of basin evolution, geological process, such as the sediment filling, the tectonic uplifting, deformation and tilting might resulted in the remobilization, migration and concentration of uranium and in the uranium ore-formation.

3.1 Uranium ore-formation during sediment filling of basins

This type of uranium mineralization occurred mainly in the of late Early Cretaceous period. Under arid climatic conditions, the uranium in basement (?) and in uranium-rich source rocks was easy to be mobilized and transported into basins. High evaporation under arid climatic condition made the uranium concentrated in surface water (why? is there any agrument for it? probably better to delete this sentence). At the end of basins evolution, the terrigenous material input as well as sedimentary rate decreased. When the evaporite sequences were formed, the concentration of CO_3^{2-}became lower and lower. (Why? HCO3 and CO3 concentrations were buffered by precipi-

tated carbonate) As a result, uranyl complex ions $[UO_2(CO_3)_2]^{2-}$ and $[UO_2(CO_3)_3]^{4-}$ became unstable and U^{6+} might be reduced to U^{4+} and precipitated or was absorbed by clay minerals and organic matter to form so called mudstone (marl)-hosted uranium deposits. (Note: mostly U^{6+} is absorbed).

Such type of uranium mineralization is relatively widespread in the studied region and is distributed in the interior of lake basin or in small water collecting depressions. Uranium bodies at such uranium deposits are generally lenticular, stratiform, and occur within thin-bedded mudstone and siltstone with minor marl intercalations. The ore is of low grade. The U-Pb isotopic age of this mineralization type shows the identical age as ore-hosting sediments and indicate the synsedimentary origin of uranium mineralization.

3.2 Uranium ore-formation in regional uplifting processes

Mezozoic to Cenozoic basins in the region experienced multistage tectonic uplifting. The tectonic pattern favorable for the formation of uranium mineralization includes tilting,uplifting and erosion of the potential ore-hosting horizons. Large-scale folding and deformation was not favorable for the formation of uranium ore-formation.

However, the tilting of crustal blocks during Lower to Middle Jurassic as well as intracontinental down-warping in Late Jurassic made most areas of the studied region uplifted, exposed to the ground surface and eroded, which led to the infiltration of ground water into Lower toMiddle Jurassic rocks. This event lasted some 11 Ma and resulted in early uranium ore-formation in some basins. Based on the above analysis, the late Yanshan and early Himalaya tectonic uplifting were the most favorable stages (periods?) for the uranium ore-formation. This is because the tectonic interference during these two stages was moderate (Note: it is difficult to understand) and, moreover , the paleoclimate was arid and oxygen and uranium-bearing groundwater might continuously infiltrate to sediments to form uranium ore deposits. This period lasted from the late Cretaceous to Miocene, i.e. about 90 Ma, and might be the most important ore-forming period in the studied region. The post-Miocene tectonic activity was obviously disadvantageous to uranium ore-formation because of rapid uplift of basin areas and the strong deformation of potential ore hosting horizons.

During the two uplifting stages, two types of uranium mineralization might occur, namely, the interlayer oxidation type and uranium-bearing coal type. The interlayer oxidation type is developed in the Lower to Middle Jurassic gray coal-bearing series and Lower Cretaceous gray sandstones. Braided stream- and braided delta sand bodies that were developed at the flat banks of the Early-Middle Jurassic down-faulted basins are the best host rock for the interlayer oxidation type uranium mineralization. Interlayer oxidation has been observed in Lower Cretaceous variegated clastics in some basins. However, important interlayer oxidation type uranium deposit still has not been found. Authors suggest that there is some potential for a discovery of small-sized uranium deposits of such type.

Uranium mineralization of the uranium-bearing coal type is hosted in stable coal beds overlain by permeable sandstones in the upper part of the Qingtujing Group. Uranium ore-formation occurred under arid climatic condition as the uranium concentration in surface water or groundwater in the region of arid climate is much more higher (an order of magnitude). As uranium-bearing water infiltrated into permeable layer, a well-defined zone of physical-chemical changes appeared at the contact between coal and permeable sandstones resulting in the uranium precipitation and concentration. In general, such type of uranium mineralization occurs in phreatic oxidation zone above the table of groundwater, and is absent below the table. Obviously, the regional successive uplifting and a long-term infiltration of the uranium oxygen-bearing water are the main ore-controlling factor of such a type of uranium mineralization.

4 Conclusions

Based on the above analysis, the following conclusions can be summarized.

1. Mezozoic to Cenozoic basins in the studied region experienced six evolutional stages, i.e. extensional down-faulting, intracontinental down-warping, extensional subsidence, compressional uplifting, piedmont down-warping and foreland compression, and two prospecting target horizons- Lower to Middle Jurassic and Lower Cretaceous- were recognized.
2. Two types of uranium mineralizations in Mezozoic to Cenozoic basins of the studied area were recognized: (1) Synsedimentary mudstone (marl) –hosted uranium mineralization formed during sedimentation and (2) interlayer oxidation zone- and uranium-bearing coal types of mineralization were formed when ore-hosting horizons were tilted and uranium bearing groundwater infiltrated into potential ore hosting horizons.

References

Chen FJ WANG XW (2003) Prototype analysis of early-middle Jurassic in northwestern China, Earth science Frontiers 7(4): 459-469 (in Chinese)

Li DS (1991) The geological characteristics of petroliferous basins in western China. Petroleum Exploration and Development 2:1-10 (in Chinese)

Liu X (2004) Palaeogeography of the Meso-Cenozoic and crustal tectonic evolution of basin-mountain area in northwestern China. Journal of palaeogeography 6:448-458 (in Chinese)

Tang LJ (2003) The main tectonic characteristics of superimposed basins, northwestern China. Earth Science Frontiers10:118-124 (in Chinese)

Yang KS (1987) The types and the evolution of structures in Hexi Corridor petroliferous basins. Petroleum Exploration and Development 5:1-6 (in Chinese)

Zhai GM (2002) Plate tectonic evolution and its relationship to petroliferous basins. Beijing: Petroleum Industry Press, (in Chinese)

Zhang K (1981) The discussion on evolution of continental plate and characteristics of petroliferous basins in China. Petroleum Exploration and Development 1:13-25 (in Chinese)

Study of methods and techniques of aeroradiometric weak information extraction for sandstone-hosted uranium deposits based on GIS

Han Shao-yang
Beijing Research Institute of Uranium Geology, Beijing, No, 10,Xiao Guan Dong Li, Anwai, Beijing, China

Hou Hui-qun
China Research Institute of Nuclear Science and Technique Information and Economy, No, 43, Fucheng street, Beijing, China

Ke Dan
Beijing Research Institute of Uranium Geology, Beijing, No,10,Xiao Guan Dong Li , Anwai, Beijing, China

Abstract. The weak information extraction method is an important research aspect in the current sandstone-type uranium prospecting in China. This paper introduces the connotation of aeroradiometric weak information extraction discusses the formation theories of aeroradiometric weak information and establishes some effective mathematic models for weak information extraction. Models for weak information extraction are realized based on a GIS software platform. Application tests of weak information extraction are completed in known uranium mineralized areas. Research results show that prospective areas of sandstone-type uranium deposits can be rapidly delineated by extracting aeroradiometric weak information.

Keywords. Sandstone-type uranium deposits, aeroradiometric survey, weak information extraction, methods and techniques

1 Introduction

Quite a number of successful examples have been reported in China and abroad through the application of gamma-spectrometric surveys to locate uranium deposits. According to the theory of radioactivity measurement, the measured radioactivity values just represent the radioactive intensity from the layer of tens of centimeters below the surface. Best results may be obtained if radiometric survey are used to directly locate the uranium deposits near the ground surface. However, sandstone-hosted uranium deposits mainly occur in the medium-large sized Mesozoic or Cenozoic sedimentary basins at relatively deep depth with no obvious radioactive anomaly on ground surface. Thus, measured abnormal information in aeroradiometric field related to uranium deposits must be very weak. If no special data-processing techniques are adopted, the weak information might be lost.

In order to directly recognize the weak abnormal information originated from aeroradiometic data above sandstone-hosted uranium deposits, which is called aeroradiometric weak information in short, formation mechanism of weak information above the deep-seated uranium deposits is studied and a series of weak information extraction methods have been developed, and ideal application effects have been obtained in practice.

2 Connotation of aeroradiometic weak information extraction

Weak information is a relative and fuzzy concept, and its application depends on the difference of buried depth, scale and grade of the sandstone-hosted uranium deposits. Abundant geological information may be obtained by aeroradiometric survey; of them some information is very obvious and some can be recognized only by special data-processing. Weak information extraction is only one kind of mathematic processing of measurement data, and can enhance some information by changing the Signal-to-Noise ratio of anomaly, but cannot produce new information which does not exist. Therefore, one prerequisite for applying weak information extraction is that the weak information must be detected by aerometric instruments.

There are two approaches in obtaining the effective weak information in aeroradiometric survey as it is seen from the development trends at home and abroad; one is improving the detector precision and the measuring and data-acquisition techniques in order to reduce the noise of aerometric survey; and the other is restraining the disturbance noises originated from geologic background, and improving the signal-to-noise ratio by adopting effective mathematic and physical models.

3 Formation theory of aeroradiometric weak information

Extraction of radioactive weak information is based on Rn migration and the geogas theories. The content of equivalent uranium in γ spectrometric survey is actually the content of ^{214}Bi ,which is a daughter element of Rn gas in Ra series. Migration of Rn may bring information of deep-seated uranium mineralization. In the mean time, some influential factors must be considered as well, such as: fault structures which act as moving channels of Rn, the action of groundwater and the change of temperature etc., and Rn originated from deep uranium ore bod-

ies may probably be transferred to the earth's surface through all kinds of pathes above. Thus, ^{214}Bi – the daughter element of Rn – may make the deep information more obvious on the surface.

The geogas theory suggests there is a geogas flow in the deep earth crust. When ascending geogases pass through sandstone-hosted uranium ore-bodies and surrounding primary and secondary haloes, they carry the super-tiny particles of uranium metal and move together upwards to the earth's surface. Thus, information of deep-seated uranium is transferred, and the superimposed mobile uranium brings information of deep-seated uranium mineralization. Some deep information associated with uranium mineralization is included in the gamma spectrometric data; and it is possible to obtain the useful weak information and to predict prospective areas of uranium deposits if high-sensitivity measurement equipment and effective data-processing technique are adopted.

4 Methods for extracting aeroradiometric weak information

4.1 Noise adjusted singular value decomposition (NASVD)

NASVD analyses multi-channel survey data to identify all statistically significant spectral shapes. These "spectral components" are used to reconstruct new potassium, uranium and thorium window values, which then have significantly less noise than that of the original raw windows. For the uranium window, in particular, it is possible to achieve a reduction of statistical noise equivalent to an increase of detector volume by a factor of three or more. The spectral component method results in more accurate measurement of the ground concentration, which improves considerably the discrimination among different geologic units with similar concentrations of radioactive elements.

4.2 Enrichment coefficient of uranium migration

Enrichment coefficient of uranium can be performed as below:

$$U_c = U \cdot (U / Th) \cdot (U / K) = U^3 / (Th \cdot K)$$

Where U_c is the enrichment coefficient of uranium, and U, Th and K are content of uranium, thorium and potassium at the measuring points respectively.

According to the characteristics of hydrogenic uranium deposits, the U_c is designed. Namely, U above uranium-mineralized areas is characterized by high value while U/Th and U/K also show high value. Thus, U_c obtained from the overlapping of several factors can indicate the relatively uranium enriched areas in the basin. In order to extract weak information during the data processing, every parameter in the mathematic model may be transformed to its standard deviation format; such change not only maintains the radioactivity features of every sampling point unchanged, but also reflects the dispersion of radioactive elements relative to the geologic units.

4.3 Analysis of spatial correlation for radioactive elements

A great deal of cases show that uranium mineralized areas are redistributed areas of natural radioactive nuclides, making correlation coefficient between U and Th elements lower above the uranium mineralized areas. In order to identify the weak information associated with uranium minera-lization, the following model of spatial correlation has been designed based on practice experiences. According to the design, the whole study area is divided into mangy rectangular windows, and correlation coefficient between U and Th elements in each window is calculated; Thus, correlation coefficient with central coordinates of different windows, can be used to generate the correlative anomaly map of the study area by "Kring" gridding method.

4.4 Integrated favorable index U_5 for predicting uranium deposits

Integrated favorable index U_5can be performed as below:

$$U_5 = \frac{[U_i + (U_i - MeU) + U_h] \times \sigma_u}{MeTh / MeU}$$

where $U_h = U_i - [Th_i / (MeTh / MeU)]$, content in square brackets shows the contents of uranium when rocks are formed; U_h is the content difference between original and recently measured uranium after rocks experienced geological or geochemical process (positive value indicates the introduction and negative value indicates the removal of uranium); U_i and Th_i are content of uranium and thorium at the measuring point; $MeTh$ and MeU are mean value of uranium and thorium in the window; σ_u is the standard deviation of uranium in the window. The bigger U_5 values, the more favorable corresponding prospective targets in the study area are.

5 Realization of weak information extraction models based on GIS

In the field of mineral resources evaluation, GIS provides the capability of the integrated management, the effective integration and analysis for multi-source information including geological, geophysical, geochemical and remote sensing data with the assistance of a computer. GIS has become a kind of powerful tool for the extraction and integration of metallogenic information.

The authors have applied GIS techniques to study radiometric weak information extraction in the prospect-

This page intentionally blank

ing and exploration of sandstone-hosted uranium deposits. The compact integration between GIS software – ArcView3.2 and weak information extraction models is completed by mixed programming: at first, the kernel computation programs of mathematic models realized by Visual C++ programming language, are rewritten to be Dynamic Link Library (DLL), in which function interfaces are designed; secondly, data input, calling DLL and data out programming are performed by the Avenue language, which is a kind of second development language in Arcview3.2; Thus, visual data processing for extracting weak information enters GIS spatial analysis.

6 Analysis of test effects

In a certain basin, authors have completed data-processing of whole energy spectrum by using NASVD, and NASVD greatly decreased the statistic noise of spectrometric data equivalent to an increase of detector volume by a factor of nine to sixteen. Authors have performed application tests of weak information extraction methods, such as enrichment coefficient of uranium, analysis of spatial correlation between U and Th and integrated favorable index U_5 based on GIS, and quite good effects have been obtained in known uranium mineralized areas. Results from analysis of spatial correlation between U and Th indicate, that all the boreholes where uranium mineralization or anomalies were met, are almost corresponding to the areas with lower correlation coefficient, and the redox zone located by borehole drilling also falls into the same areas. So this kind of method may play an important role in the medium-scale prediction of sandstone-hosted uranium deposits. Areas with higher value on the anomaly map of enrichment coefficient of uranium and U_5 disclose the spatial location of uranium mineralization and anomaly, and the two kinds of methods may be used to guide large-scale prospecting of sandstone-hosted uranium deposits.

7 Conclusions

During the prospecting for sandstone-hosted uranium deposits, more significant uranium mineralizaiton information may be rapidly obtained by the effective methods and techniques of weak information extraction. No doubt, uncertainty still exists if only the single aeroradiometic weak information is applied to prospecting for uranium deposits. However, it is possible to rapidly delineate the prospective areas just by integrating all kinds of aeroradiometric weak informaiton based on GIS in a region geologically favorable metallogenentic perquisites; at the same time, the predictive precision may be greatly improved. Recently, extraction of aeroradiometric weak information has become one of the effective methods in predicting prospective areas of sandstone-hosted uranium deposits in China.

References

Bai YS (1995) Discussion of Rn's migration mechanism for uranium prospecting. Uranium Geology 11(4):224-230 (in Chinese)

Hou HQ (2002) Geophysical methods and its application in the prospecting for exogenetic uranium deposits. Beijing: Ocean Press, 60-63 (in Chinese)

Hovgaard J, Grasty RL (1997) Reducing statistical noise in airborne gamma-ray data through spectral component analysis. Proceeding of Exploration 97:753-764

A new sandstone type uranium metallogenetic type - "Structure – Oil, Gas Type"

Huang Xian-fang, Liu De-chang, Du Le-tian, Zhao Ying-jun
Beijing Research Institute of Uranium Geology, Key Laboratory of Remote Sensing, National Defence Science and Technology, P.O.Box 9818, Beijing, 100029, China

Abstract. A new sandstone type uranium metallo- genetic type – "structure – oil, gas type" is recommended and its regional setting, structure features, metallogenetic environment, uranium mineralization characteristics, and genesis are elaborated in this paper. The new sandstone type uranium metallogenetic type – "structure – oil, gas type" is different from traditional interlayer oxida- tion zone type uranium deposits, emphasizing on regional penetrating fault and oil and gas which play an important role in uranium mineralization. It is useful for uranium reconnaissance and exploration.

Keywords. Structure – oil, gas type, regional penetrating fault, uranium mineralization characteristics, reconnaissance and exploration

1 Introduction

Based on practice and research on sandstone type uranium deposits which are located in north-east, south-east, and south-west part of Ordos basin respectively, a new sandstone type uranium metallo- genetic type – "structure – oil, gas type" is put forward. Using remote sensing technique, geologic methods in combination with field investigation and indoor analysis, the regional setting, structure features, metallogenetic environment, mineralization characteristics, and genesis of "structure – oil, gas type" uranium deposits are systematically studied. The result has showed that the new "structure – oil, gas type" is different from traditional interlayer oxidation zone type deposit, indicating that fault and oil and gas play an important role in uranium metallization.

2 New discovery

In the light of the practice and research on test ore-field in north - east part of Ordos basin, the difference between traditional interlayer oxidation zone type uranium deposits and new type uranium deposit has been discovered. The differences are as follows.

1. The test ore-field in the north part of Ordos basin is separated from Yin - shan mountain by He-tao downfaulted basin. So, since early Eocene Epoch, there is no sub-orogenic belt tectonic environment for uranium minera- lization in this area, but expressing as fault block environment.
2. The dip angle of ore-bearing horizon is very gentle, only 1-2° It is not favorable for driving uranium-bearing, oxygen-bearing solution move downward along the horizon to form oxidation-reduction zone.
3. The uraniferous mineral is coffinite. It differs from Yi-Li basin and Song-liao basin in China, where uraniferous mineral is pitchblende (the mixture of U^{+4} and U^{+6}), showing the origin is quite different.
4. Uranium mineralization is obviously controlled by fault. All of these have indicated that tectonic setting; provenance supply, mineralization Characteristics, and origin of "structure – oil, gas type" uranium deposit are distinct from those of traditional interlayer oxidation zone type uranium deposits.

3 Proposal of a new uranium metallogenetic type

According to the research on regional setting, metallogenetic environment, structure features and mineralization characteristics, two amazing identical Characteristics of these deposits have been found, i.e. uranium mineralization is controlled by fault and related with oil and gas. As a result, a new sandstone type uranium metallogenetic type – "structure – oil, gas type" is put forward.

4 Main characteristics

The main characteristics of "structure – oil, gas type" sandstone uranium deposits are as follows:

4.1 Regional setting

"Structure – oil, gas type" sandstone uranium deposits are situated in petroleum and natural gas basin. The tectonic background is fault-block environment.

4.2 Structure features

One of important structure features is that regional penetrating faults are developed in this kind of sandstone uranium deposit. The uranium deposits and occurrences are remarkably controlled by fault, expressing as linear distribution along the fault.

1. Image feature: The penetrating faults usually pass through the uranium ore-field, exhibiting linear signature and color zone in the image (Fig. 1). The texture

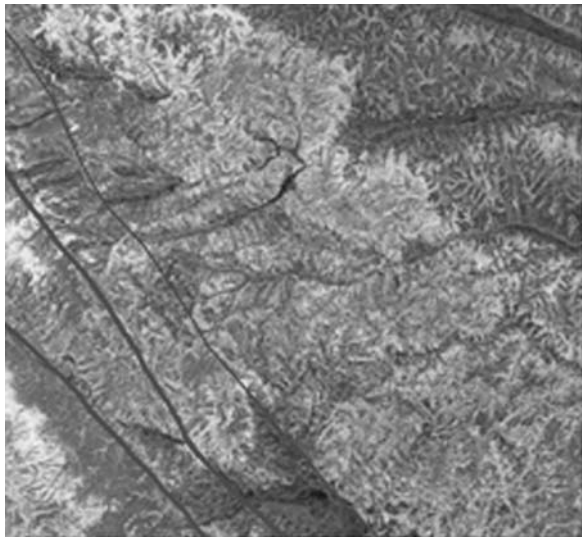

Figure 1: Penetrating fault (dark line) pass through the uranium ore-field, exhibiting linear signature

and color on both sides of the fault are quite different, expressing as boundary of two different image textures.

2. Geophysical feature: The penetrating faults can be interpreted from airborne spectral contour map. A fault in the north - east part of the basin has been delineated according to the radiometric contour map.
3. Geological feature: The penetrating fault has remarkable fault plane, usually displaying as fracture zone (Fig. 2). The distinctive fault triangle plane can be seen in the field.
4. Fault movement: multi-stage movement is one of important features. At early stage, the fault is usually expressed as compress or compress-shear fault, while at late stage, it is exhibited as tension fault.
5. The depth of the fault: The penetrating fault often cuts through the basin basement from the surface. The older strata are usually trusted over the younger strata.
6. Tectonite: Carbonatization and multi -stage carbonate veins can be seen in the fault zone. Microscopic identification has showed that the bitumen is replaced by calcite. It implies that the calcitization is alteration product of the bitumen.

4.3 Metallogenetic environment

Oil and gases seepage phenomena and reducing gases anomaly can be seen on the ore-field surface.

1. The oil and gases seepage phenomena are expressed as oil-soaked sandstone that can be found on the surface. Employing remote sensing technique, the oil and gases seepage area is conspicuously displayed in the image. The dark blue spots (White circles) that show oil and gas seepage districts are clearly displayed in the light blue background image (Fig. 3).

Figure 2: Penetrating fault is expressed as fracture zone

Figure 3: Oil and gas seepage areas (dark grey spots in white circle) are clearly displayed in the light blue background image

2. According to the gas - geochemical survey and analysis result, the reducing gas anomalies do exist in the ore-fields in the south - west part and north - east part of the basin.

4.4 Alteration

There are blue-green alterations in the sandstone uranium deposit districts, the north - east part of the basin. The blue-green alteration can be subdivided into blue alteration and green alteration. The former is concordant with uranium mineralization spatial distribution.

The light color alteration or fade alteration is developed in the south - west part of the basin. There is an abundance of liquid and gas hydrocarbon in the alteration sandstone. The light color alteration or fade alteration is caused by hydrocarbon participation and reduction, accompanying with distinct calcitization.

4.5 Spatial distribution of uranium mineralization

There are three characteristics for spatial distribution of uranium mineralization.

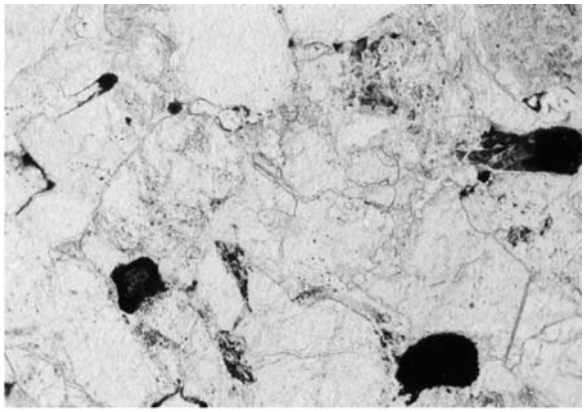

Figure 4: Residual asphalt (dark spots) is showed as pear-ball shape in sandstone

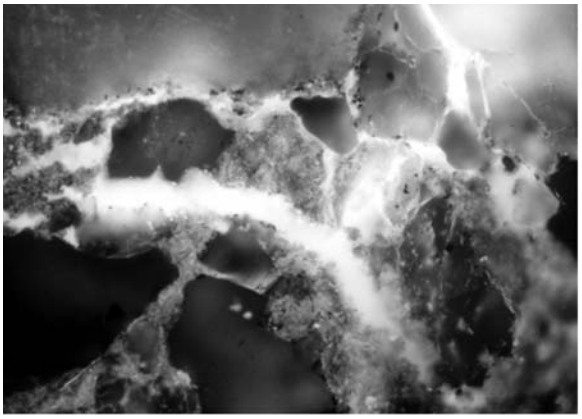

Figure 5: Oil and gas are filled in the intergranular space of sandstone

1. Uranium mineralization is controlled by fault, expressing as linear distribution.
2. Uranium mineralization is controlled by oil-soaked sandstone. In the light of borehole information in test deposit, the ore-bodies are located in the lower part of oil-soaked sandstone and faded alteration zone.
3. Uranium mineralization is connected with blue alteration and light color alteration.

4.6 Features of ore-bearing rock

1. Ore-bearing sandstone is usually undergone oil permeation. So, oil and bituminous matter are often found in the ore-bearing rock. Microscopic identification has recognized that a lot of oil and pitch do exist in the rock (Fig. 4). Pitch veins that cut through sandstone stratification can be seen in the field. Samples analysis has revealed that the bituminous matte and hydrocarbon are caused by oil and gas.
2. There are an abundance of gas-fluid inclusions in the ore-bearing rock. The oil, gas and bituminous matter are usually filled in the intergranular space (Fig. 5).
3. A distinctive texture – "oil-pressure-fracture texture" is found by microscopic identification (Fig. 6). The "oil-pressure-fracture texture" is a distinct texture, reflecting that the quartz grains are crashed under high oil pressure and filled with oil (now it has become residual asphalt). It is favorable for uranium-bearing solution permeation and uranium concentration.

4.7 Uranium mineralization characteristics

1. Uraniferous mineral is mainly coffinite, and associated mineral is clausthalite etc., showing that metallogenetic process was taken place in a strong reducing environment.
2. The age of high-grade ore is quite young.
3. The oil plays an important role in uranium mineralization, when the seepage oil has become the asphalt. The asphalt is considered to be a main enrichment medium since it can absorb part of uranium in the ground water for uranium concentration.
4. Uranium concentration is expressed as a tower-type increment process (pre-concentration series).

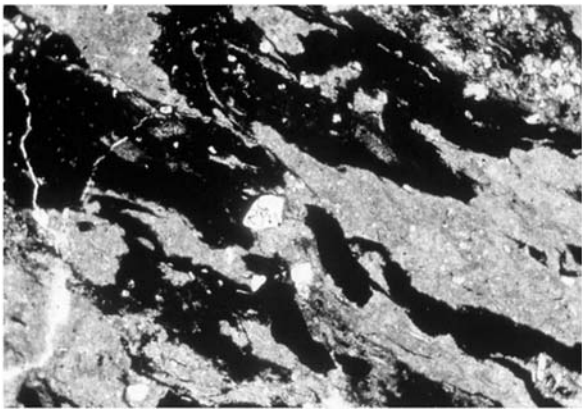

Figure 6: Oil-pressure-fracture texture

1. Uranium content of original red sandstone in the study area is only 0.9×10^{-6}
2. When purple-red sandstone become fade alteration sandstone, the reducing environment is created. The fade sandstone uranium content increase 4 times more than background content.
3. Then, the gray-white sandstone is super- imposed by oil and gas, uranium content increase up to 5.1×10^{-6} (10 samples).
4. After the oil-soaked sand-body has become bituminous matter, uranium is once again concentrated due to bituminous matter absorption.
5. Finally when the bituminous matter undergoes calcitization the clay minerals (kaolinite) are precipitated from bituminous matter, it is favorable for uranium further enrichment, forming industrial uranium ore.

4.8 Analysis of deposit genesis

1. Petroleum is an important carrier of uranium. Trace element analysis has indicated that the trace elements in the uranium ore are Ti, Ni, As, Zr, Hf, Nb, Ta, Sb, Cs, W, Pb, Li, etc. Except for Li, Cs, they all are unsolvable in ground water. It is inferred that uranium is not carried by ground water but by oil.
2. Gamma intensity in oil-soaked sandstone is higher than in normal sandstone. According to gamma measurement in the field, the gamma intensity of the normal sandstone is 10-20γ, while the oil-soaked sandstone is 20-40γ, the highest can be up to 500γ, indicating that the oil seepage may result in uranium preliminary concentration.
3. Uranium concentration can be seen in asphalt-bearing sandstone. Chemical analysis has indicated that uranium content in the asphalt -bearing sandstone is 0.12%, showing that asphalt - bearing sandstone has preliminary concentration.
4. Uranium concentration is mainly related with oil and gas that come from the depth. Industrial uranium mineralization is controlled by multi-active faults that cause oil and gas multi-migration upward and result in tower type increment concentration.

Based on above mentioned, uranium mineralization (especially high grade ore) is mainly controlled by two factors, - fault and oil, gas. The fault is a conduit for oil and gas migrate upward from the depth. The oil and gas can create reducing environment. Industrial uranium mineralization is the result of tower type increment enrichment.

5 Conclusions

By means of comprehensive research and analysis, the results are summarized as follows.

1. The "structure – oil, gas type" is a new sandstone type uranium metallogenetic type. It differs from the traditional interlayer oxidation zone type uranium deposit.
2. There are two main ore-controlling factors. The one is that mineralization is controlled by fault which provides conduit for water, oil gas migration upward from the depth. The other is oil and gas that can create reducing environment and take as absorption medium.
3. The new "structure – oil, gas type" theory is useful for uranium reconnaissance and exploration. Great attention should be paid to fault and oil and gas for the future reconnaissance and exploration.
4. Remote sensing technique in combination with geologic methods has proven to be an effective method in geology research.

References

Huang XF (1999) Remote Sensing Technology Prospecting Methods of Interlayer Oxidation Zone Type Sandstone Uranium Deposit in Yili Basin. Beijing: Atomic Energy Press

Huang XF (2001) Remote Sensing Technique and Prognosis of Sandstone Type Uranium Deposit. International Conferences on Info-tech and Info-net Proceedings, 64-69

Huang XF (2003) Research on Generalization Integration Technology of Uranium Resource Prospecting in the Covered Area Using Remote Sensing and Airborne Spectrometric Survey Data (unpublished report)

Huang XF (2004) Research on Generalization Integration Technology of Uranium Resource Prospecting in the Covered Area Using Remote Sensing and Geo-science Data (unpublished report)

Liu DC (2004) New Discovery and Study of Remote Sensing Image Characteristics at Sandstone – Type Uranium Deposit in China and its Important Significance, Uranium Geology 20:352-357

Mantle-derived fluid and uranium mineralization: Evidence from the world-class Xiangshan uranium deposit, SE China

Yaohui Jiang, Hongfei Ling, Shaoyong Jiang
State Key Laboratory for Mineral Deposits Research, Department of Earth Sciences, Nanjing University, Nanjing 210093, China

Abstract. Locally enriched mantle-derived fluids played an important role in the genesis of the world-class Xiangshan uranium deposit. Its ore-forming fluid and U, Th, alkali metals, LILE, REE and HFSE were mainly derived from locally enriched mantle sources. The Early Cretaceous back-arc extensional tectonic setting and deep boundary faults of the Gan-Hang basin enabled upward migration of the local enriched mantle-derived fluid. The mineralisation precipitated in multiple fracture zones in the Xiangshan volcanic rocks. The shallowly circulated meteoric water in fractures of volcanic rocks resulted in temperature decrease and solution dilution of the deep-seated ore-forming fluid and subsequent precipitation of uranium ores.

Keywords. Mantle-derived fluid, uranium mineralization, Xiangshan, China

1 Introduction

It has been demonstrated that mantle-derived fluids played an important role in gold mineralization such as in the gold deposits of the Yilgarn Block, Western Australia (Barley et al. 1989; Kerrich and Wyman 1990; Groves 1993), copper-gold-uranium mineralization such as the Olympic Dam deposit, South Australia (Johnson and McCulloch 1995), and REE mineralization such as the Bayan Obo deposit, Northern China (Cao and Zhu 1996). However, U and Th have generally been considered to be of crustal origin. Thus, it is important to discuss the possibile involvement of enriched mantle-derived fluid in the formation of uranium mineralization.

In this study, we report isotopic and geochemical data from the Xiangshan uranium deposit, which we suggest has a locally enriched mantle origin for the ore-forming fluid.

2 Geological setting

The Xiangshan uranium ore field is located in Jiangxi Province, southeast China, close to the south side of the suture zone between the Yangtze and Cathaysia blocks. During the late Mesozoic, extensive magmatism took place in SE China, forming a volcanic-intrusive complex belt of about 600 km wide parallel to the coastline of SE China. During this period, magmatic-related mineralization occurred widely, forming several metallogenetic belts with different ore deposits such as W, Sn, Cu, Au and U in this region, one of which is the Mesozoic Gan-Hang uranium metallogenetic belt. The Cretaceous Gan-Hang extension basin (the "Gan-Hang Rift" of Gilder et al. 1996) overlaps the Gan-Hang Mesozoic volcanic-related uranium metallogenetic belt, and the Xiangshan ore field is located in the southwestern part of this belt. The extensional setting and concurrent magmatism of the Gan-Hang basin are important factors in the uranium mineralization.

3 Characteristics of the Xiangshan ore field

The world-class Xiangshan uranium deposit is located in a resurgent caldera (collapse caldera and resurgent dome association), distributed in the northwestern volcanic-intrusive complex belt of SE China (Jiang et al. 2005). The caldera was formed in the late Jurassic (158-135 Ma) and overlay the basement composed of Paleo- to Mesoproterozoic and Sinian metamorphic rocks (Fig. 1).

A lamprophyre dike was intruded into the Xiangshan volcanic rocks at 109 Ma, concurrent with the eruption of shoshonite lavas (104-99 Ma) in the Cretaceous Gan-Hang extension basin close to the Xiangshan ore field.

The lamprophyre has an Epsilon Nd (T) value of –7.2 and initial $^{87}Sr/^{86}Sr$ ratios of 0.7090, concordant with the shoshonite lavas that have Epsilon Nd (T) values of –6.6- –8.5 and initial $^{87}Sr/^{86}Sr$ ratios of 0.7089-0.7090. The lamprophyre also has high contents of transition elements, LREE and LILE, and a negative Ce anomaly, implying a metasomatic enrichment event associated with subducted oceanic sediments in the local lithospheric mantle source.

Uranium mineralization, as hydrothermal veins in fractures within the volcanic rocks, occurred at 115 Ma (early stage) and 98 Ma (main stage) and therefore post-dated the caldera volcanic activity but was concurrent with formation of the lamprophyre dike and shoshonite lavas. The ore-forming fluid was enriched in CO_2 ($CO_2 >> H_2O$) with moderate salinity (15.0 wt% NaCl equiv.) and homogenization temperature (174 °C) at the main mineralization stage. The evolving ore-forming fluids displayed large ranges of stable isotope compositions ($\delta^{13}C$ = –5.5- –20.0‰, δD = –45- –174‰ and $\delta^{18}O$ = +1.8- –9.8‰). The uranium ores are enriched in alkali metals, LILE, REE (especially HREE), HFSE and transition elements besides

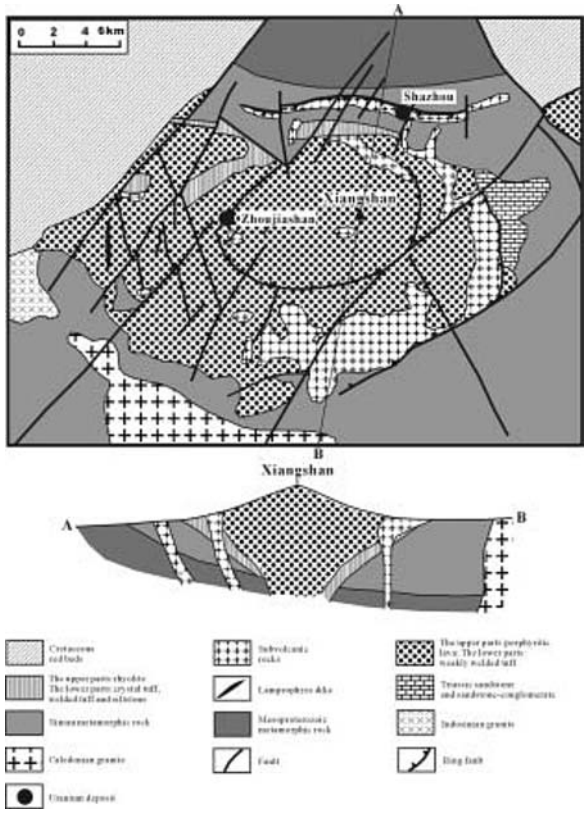

Figure 1: Simplified geological map of the Xiangshan resurgent caldera, showing a cross section and two major uranium ore deposits of Zhoujiashan and Shazhou

U and Th. From the uranium ore veins toward the host volcanic rocks, there are trends of gradual decrease in U, Th, alkali metals and HFSE, and of gradual increase in Rb/Cs and Th/U ratios. Compared with the host volcanic rocks (Rb/Cs=17.1-22.5, Th/U=2.1-5.4), uranium ores have much lower Rb/Cs (1.7-3.4) and Th/U (0.02-0.5) ratios, which are closer to those of the lamprophyre (3.1 and 1.4, respectively).

Hydrothermal fluorites, which are closely associated with the Xiangshan uranium mineralization, have variable Sr contents of 295-1136 ppm and initial $^{87}Sr/^{86}Sr$ ratios of 0.7145-0.7207. There is a positive linear correlation (r^2 = 0.998) between $^{87}Sr/^{86}Sr$ and 1/Sr of the fluorites, which is interpreted to reflect a mixing relationship as a result of reaction between local enriched mantle-derived fluid that has low $^{87}Sr/^{86}Sr$ ratios of 0.7089-0.7106 (at 98 Ma) and high Sr contents, and the basement that has high $^{87}Sr/^{86}Sr$ ratios of 0.7234-0.7720 (at 98 Ma) and low Sr contents of 38-300 ppm. In contrast, the initial $^{143}Nd/^{144}Nd$ ratios of these fluorites are relatively uniform (0.51209-0.51217, avg. 0.51212), rather similar to those of the lamprophyre (0.51214, at 98 Ma) and shoshonite lavas (0.51207-0.51217, at 98 Ma), suggesting that the Nd in the ore-forming fluid was dominantly of local enriched mantle origin.

The Xiangshan uranium mineralization is interpreted to have formed as a result of contributions from a local enriched mantle-derived fluid. During the late stage of the Early Cretaceous, when the lamprophyre dike and shoshonite lavas were emplaced, the local enriched mantle-derived fluid, containing a significant amount of U, Th, alkali metals, LILE, REE and HFSE, migrated upward along the deep faults to fracture zones in the Xiangshan volcanic rocks. This deep-seated fluid may have leached some Sr (and probably other metals) from the basement during its ascent, and was finally precipitated in fractures as aresult of temperature decreases accompanying dilution resulting from mixing with the shallowly circulated meteoric water.

4 Discussion and conclusions

A number of studies have revealed that the igneous rocks derived from partial melting of the enriched mantle source have high U content. The Tsaolingshan (Taiwan) high-Mg potassic rocks, derived from partial melting of the phlogopite-bearing harzburgite metasomatised by slab-released hydrous fluid, show very high U concentrations ranging from 17.2 to 22.1 ppm with a mean of 19.1 ppm (Chung et al. 2001). The potassic volcanic rocks in SW Tibet, which are considered being derived from metasomatised lithospheric mantle, have high U contents of 20-27 ppm with a mean of 23 ppm (Miller et al. 1999). The Xiangshan lamprophyre which, as we suggested, was derived from the enriched mantle source related with the paleo-Pacific plate subduction also contains high U content (6.4 ppm), seven times as much as U abundance in general basic rocks (0.9 ppm). Previous studies also indicate that the enriched mantle-derived fluids may contain a significant amount of U. By developing a new method, Rosenbaum et al. (1996) was able to determine U concentration (13 ppm) of metasomatic fluids trapped as inclusions within minerals in the Nunivak lherzolite xenoliths from the mantle where phlogopite metasomatism had occurred. Schrauder et al. (1996) analyzed the trace element contents of micro-inclusions in the fibrous diamonds from Botswana, which represent syngenetic mantle fluids under high pressure and revealed that the mantle fluids contained high U contents of 6-51 ppm with a mean of 21 ppm. Our recent studies (Jiang and Yang 2000; Jiang et al. 2002a,b) suggest that the late-orogenic granitoids with high U contents were formed by partial melting of the lower crust caused by an influx of enriched mantle-derived fluid which was responsible for the high U contents. Therefore, we believe that such an enriched mantle-derived fluid containing a significant amount of uranium can directly contribute to formation of uranium ores. Our elemental and isotopic data of the Xiangshan uranium deposits suggest that the ore-forming fluid and components such as alkali metals, REE, LILE and HFSE are most

This page intentionally blank

likely of enriched mantle origin. We also suggest that the U in the ore-forming fluid was mainly derived from the local enriched mantle source. The Th/U ratios (0.02-0.5) of the Xiangshan uranium ores, which are much lower than those of the host volcanic rocks (2.1-5.4), are also significantly lower than those estimated for the continental crust (e.g. Rudnick and Fountain 1995) and for the mantle (Hofmann 1988; McDonough et al. 1992; McDonough and Sun 1995). As the mobility of incompatible elements during dehydration of the subducting slab increases with the ionic radius (Tatsumi et al. 1986), the enrichment factors of LILE such as U in the slab-released hydrous fluid would be the greatest. Mineral-aqueous fluid partitioning experiments (Brenan et al. 1995; Keppler 1996; Ayers 1998) also show that U is preferentially transported, relative to Th, from the subducting slab to the mantle wedge. Therefore, the enriched mantle-derived fluids related with dehydration of subducting slab would be enriched in U and have low Th/U ratios. The rocks, derived from the enriched mantle related with slab-released hydrous fluid, also have high U contents and low Th/U ratios, such as the Tsaolingshan (Taiwan) high-Mg potassic rocks (19.1 ppm, 1.1) (Chung et al. 2001) and Xiangshan lamprophyre (6.4 ppm, 1.4).

Acknowledgements

We would like to Acknowledge X. Huang from the Institute of Geology, Academica Sinica for his assistant with measurements of Nd and Sr isotope compositions. This study was supported by a National Key Basic Research Project (No. G1999043211) and an Excellent Research Group grant from the National Natural Science Foundation (No. 40221301).

References

Ayers J (1998) Trace element modeling of aqueous fluid– peridotite interaction in the mantle wedge of subduction zones. Contributions to Mineralogy and Petrology 132: 390– 404

Barley ME, Eisenlohr B, Groves DI, Perring CS, Vearncombe JR (1989) Late Archean convergent margin tectonics and gold mineralization: a new look at the Norseman-Wiluna Belt, Western Australia. Geology 17: 826-829

Brenan JM, Shaw HF, Ryerson FJ , Phinney DL (1995) Mineral – aqueous fluid partitioning of trace elements at 900°C and 2.0 GPa: Constraints on the trace element chemistry of mantle and deep crustal fluids. Geochimica et Cosmochimica Acta 59: 3331– 3350

Cao RL, Zhu SH (1996) Mantle fluids and metallogeny. In: Du LT (ed), Geochmistry of Mantle Fluids and Asthenosphere (Asthenoliths): Beijing, Geological Publishing House, pp 436-459

Chung SL, Wang KL, Crawford AJ, Kamenetsky VS, Chen CH, Lan CY, Chen CH (2001) High-Mg potassic rocks from Taiwan: implications for the genesis of orogenic potassic lavas. Lithos 59: 153-170

Gilder SA, Gill J, Coe RS, Zhao X, Liu Z, Wang G, Yuan K, Liu W, Kuang G, Wu H (1996) Isotopic and paleomagnetic constraints on the Mesozoic tectonic evolution of south China. Journal of Geophysical Research 101: 16137-16154

Groves DI (1993) The crustal continuum model for late-Archean lode-gold deposits of the Yilgarn Block, Western Australia. Mineralium Deposita 28: 366-374

Hofmann AW (1988) Chemical differentiation of the Earth: the relation between mantle, continental crust, and oceanic crust. Earth and Planetary Science Letters 90; 297-314

Jiang YH, Jiang SY, Ling HF, Zhou XR, Rui XJ ,Yang WZ (2002a) Petrology and geochemistry of shoshonitic plutons from the western Kunlun orogenic belt, China: implications for granitoid geneses. Lithos 63: 165-187

Jiang YH, Ling HF, Jiang SY, Fan HH, Shen WZ, Ni P (2005) Petrogenesis of Late Jurassic peraluminous volcanic complex and its high-Mg, potassic, quenched enclaves at Xiangshan, Southeast China. Journal of Petrology 46: in press

Jiang YH, Ling HF, Jiang SY, Zhou XR, Rui XJ, Yang WZ (2002b) Enrichment of mantle-derived fluids in the formation process of granitoids: evidence from the Himalayan granitoids around Kunjirap in the Western Qinghai-Tibet plateau. Acta Geologica Sinica (English Edition) 76: 343-350

Jiang YH, Yang WZ (2000) High contents of Th, U in late-orogenic granitoids to track lithospheric delamination: evidence from granitoids in the Western Kunlun orogenic belt, China. Chinese Journal of Geochemistry 19: 267-272

Johnson JP, McCulloch, MT, 1995, Sources of mineralizing fluid for the Olympic Dam deposit (South Australia): Sm-Nd isotopic constrains: Chemical Geology 121: 177-199

Keppler H (1996) Constraints from partitioning experiments on the compositions of subduction-zone fluids. Nature 380: 237– 240

Kerrich R, Wyman D (1990) The geodynamic setting of mesothermal gold deposits: an association with accretionary tectonic regimes. Geology 18: 882-885

McDonough WF, Sun S-S (1995) Composition of the Earth. Chemical Geology 120: 223– 253

McDonough WF, Sun S-S, Ringwood AE, Jagoutz E, Hofmann AW (1992) Potassium, rubidium, and cesium in the Earth and Moon and the evolution of the mantle of the Earth. Geochimica et Cosmochimica Acta 56: 1001– 1012

Miller C, Schuster R, Klotzli U, Frank W, Purtscheller F (1999) Post-Collisional Potassic and Ultrapotassic Magmatism in SW Tibet: Geochemical and Sr–Nd–Pb–O Isotopic Constraints for Mantle Source Characteristics and Petrogenesis. Journal of Petrology 40: 1399-1424

Rosenbaum JM, Zindler A, Rubenstone JL (1996) Mantle fluids: evidence from fluid inclusions. Geochimica et Cosmochimica Acta 60: 3229-3252

Rudnick RL and Fountain DM (1995) Nature and composition of the continental crust: a lower crustal perspective. Rev. Geophys 33: 267–309

Schrauder MS, Koeberl C, Navon O (1996) Trace element analyses of fluid-bearing diamonds from Jwaneng, Botswana. Geochimica et Cosmochimica Acta 60: 4711-4724

Tatsumi Y, Hamilton DL, Nesbitt RW (1986) Chemical characteristics of fluid phase released from a subducted lithosphere and origin of arc magmas: evidence from high-pressure experiments and natural rocks. Journal of Volcanology and Geothermal Research 29: 293– 309

Forecasting the occurrence of sandstone-type uranium deposits by spatial analysis: An example from the northeastern Ordos Basin, China

Yangquan Jiao, Liqun Wu, Minfang Wang, Zhicheng Xu
Faculty of Earth Resources, China University of Geosciences, Wuhan, 430074, China

Abstract. Spatial orientation analysis of sandstone-type uranium mineralization is closely linked to sedimentology in the northeastern Ordos Basin. The Zhiluo Formation in this area is an integrated third-order sequence, which can be divided into three depositional system tracts. The sandstone-type uranium deposits mainly lie in the lowstand systems tract (LST) which can be divided into two parasequence set- an upper parasequence set and a lower parasequence set by outcrop study, drill core analysis, and sand distribution system mapping. The lower parasequence set comprises a braided stream system and a braided delta system. The braided delta system mainly consists of a delta plain, which has extensive sandstones and good connectivity and favours uranium mineralization and is thus the main uranium mineral host unit. The upper parasequence set, which comprises a meandering river system, and a meandering river delta system has less sandstone, and is the secondary uranium mineral host unit. The high-grade mineralization zone is mainly in a braided distributary channel, which sandstone heterogeneity research shows to be a transfer sedimentary facies from the braided stream sedimentary system to the braided delta sedimentary system. The highest-grade zones always exist in the branching area of the braided distributary channel at the margin of channel sandstones where isolated barrier bedcause abrupt facies changes. The frequency and quality of uranium mineralization decrease when the number and thickness of isolated barrier beds increase. Statistical results show that medium grained and fine-grained sandstones are best for uranium mineralization. Uranium deposits always occur in the middle-lower part of braided distributary channel sandstone in each vertical sequence unit. These sedimentological features are the basis of analysis of the spatial orientation and forecasting of uranium mineralization.

Keywords. Lowstand systems tract, braided distributary channel, sandstone heterogeneity, sandstone-type uranium deposit, Zhiluo Formation, Ordos basin

1 Introduction

Sandstones can provide both fluid migration channels and void spaces for deposition of uranium minerals. Sandstones with extensive high connectivity are particularly favourable for uranium mineralization and so research on large-scale skeleton sandstones in sedimentary basins can provide valuable data about the spatial orientation of uranium mineralization.

The concept of sandstone heterogeneity was first applied by petroleum geologists to describe the complexity of oil-gas accumulation and oil-gas exploitation caused by sandstone heterogeneity, see Miall (1985), Van et al. (1989), Qiu (1992) , Jiao et al. (1998) and Jiao et al. (2005). The first author has already applied this concept successfully to spatial analysis of a sandstone-type uranium deposit in a sedimentary basin, the Ordos Basin; see Jiao et al. (2005). In the northeastern part of the Ordos Basin, this research showed that the sandstone-type uranium deposit had mainly accumulated in a lowstand systems tract ($J_2z^{1\text{-}1}$) of a third-order sequence (the Zhiluo Formation) (Fig. 1). Before 2001, no useful mineral resources had been found in the Zhiluo Formation, so they had received little attention and there was no published information about the mineralization. However, its sedimentary characteristics were well understood, particularly of the large-scale sandstone at the base of the sequence, the Zhiluo Formation that formed in a braided stream system, see Zhang (1989), Li (1996), and Cheng et al. (1997). Between 2003 and 2004 as part of an extensive program of uranium prospecting, the first author made a detailed study of the rules controlling the spatial distribution of sandstone, their modes of formation and the causes of their heterogeneity in the Zhiluo Formation of the Dongsheng and Shenmu areas, and analyzed the relationship between these features and the spatial distribution of uranium mineralization.

2 Sequence stratigraphy

The Zhiluo Formation in the northeastern Ordos basin is an integrated third-order sequence. Its important characteristics and the marker horizons used to identify the sequence are as follows (Fig. 1):

1. The coarse clastic sandstone at the bottom of the Zhiluo Formation is the most prominent marker horizon of the Zhiluo Formation;
2. The base of the Zhiluo Formation may have a basal conglomerate;
3. There are regional scour surfaces and an unconformity at the base of the Zhiluo Formation, see Li et al. (1992). This surface is the sequence stratigraphic base (SB1) of the third-order sequence;
4. The top of the Yan'an Formation has a weathered crust, with local sandstone-type kaolin Deposits (Li et al. 1992);
5. The coal measures of the Yan'an Formation show obvious differences from the alluvial deposits of the Zhiluo Formation see Li et al. (1992);

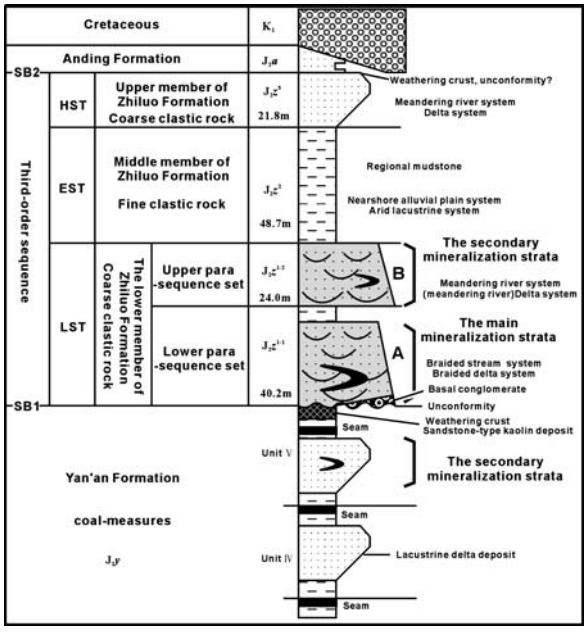

Figure 1: Simplified strata sequence of the Northeastern Ordos basin and the main symbols used in this paper.

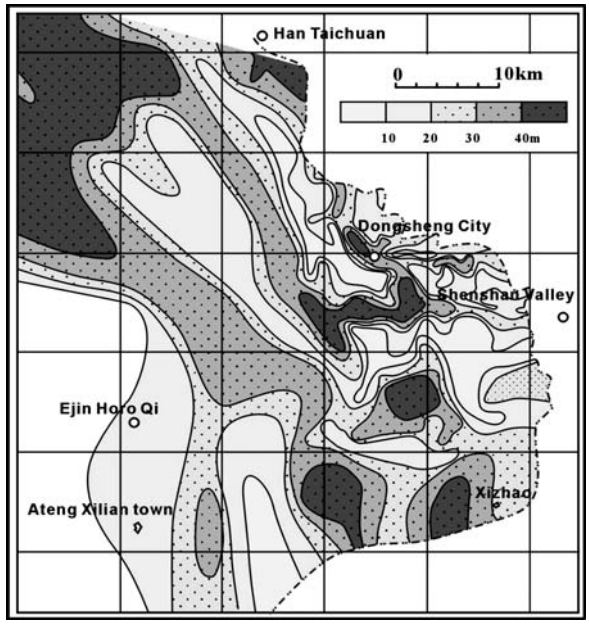

Figure 2: Isopach map of the lower parasequence set ($J_2z^{1\text{-II}}$) sandstone in the study area

6. There is a regional unconformity at the top of the Zhiluo Formation where it is in contact with Cretaceous strata in the Dongsheng area and with the Jurassic Anding Formation in this Shenmu area. This surface is the sequence stratigraphic top (SB2) of the third-order sequence.

The Zhiluo Formation shows a good correspondence between sequence stratigraphic units and lithostratigraphic units. The Zhiluo Formation sequence can be divided into three depositional system tracts: a lowstand systems tract (LST), a lacustrine-expanding systems tract (EST) and a highstand systems tract (HST). The LST is composed of coarse clastic rocks and is the same as the lower member of the Zhiluo Formation (J_2z^1); the EST is composed of fine clastic rocks, and is the same as the middle member of Zhiluo Formation (J_2z^2); the HST once again develops coarse clastic rocks and is the same as the upper member of the Zhiluo Formation (J_2z^3). As shown in Figure 1, the LST can be divided into two parasequence sets- a lower parasequence set and an upper parasequence set, which are each the same as the lower sub-member of Zhiluo Formation ($J_2z^{1\text{-}1}$) and the upper sub-member of Zhiluo Formation ($J_2z^{1\text{-}2}$) respectively. The lower parasequence set is the most important uranium mineral host rock.

3 Sedimentary systems of the LST and uranium mineralization

Outcrop study, drill core analysis, and sand distribution system mapping show that the lower parasequence set ($J_2z^{1\text{-}1}$) of the LST comprises a braided stream system and a braided delta system. In the braided delta system a braided stream delta plain constitutes the main body, most of the braided stream delta front and prodelta having been eroded away. The sandstones of the delta plain, which are extensive and have good connectivity are not only good for mineralizing fluid migration but also offer void space for uranium mineralization, and therefore the lower parasequence set ($J_2z^{1\text{-}1}$) is the main uranium mineral host rock (Fig2). The upper parasequence set ($J_2z^{1\text{-}2}$) comprises meandering river systems and meandering river delta systems, and sandstone are less extensive, so it is the secondary uranium mineral host rock.

4 Sandstone heterogeneity and uranium mineralization

The sandstones show horizontal and vertical heterogeneity. Horizontal sandstone heterogeneity is shown on sand distribution maps, while vertically, it is shown by the isolated barrier bed and sediment granularity; see Jiao et al. (2005).

The main mineralization zone is distributed horizontally along a braided distributary channel, which is the transfer zone from the braided stream sedimentary system to the braided delta sedimentary system. The highest-grade mineralization always occurs in the branching area of the braided distributary channel (Fig 3). Statistical research shows that the frequency of uranium mineralization is highest in the area where the sandstone thickness is between 25-40m and the sand ratio is between 75%-90%.

Vertically, uranium mineralization occurs close to isolated barrier beds in sandstone and areas of sediment

This page intentionally blank

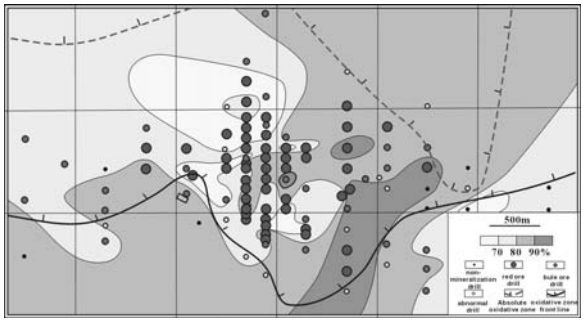

Figure 3: Sand ratio, interlayer oxidized zone and uranium mineralization in the study area

Heterogeneity mineralization model	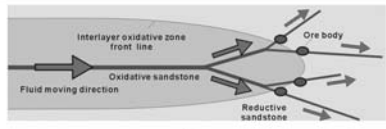	
Skeleton sandstone	Braided channel sandstone	Braided distributary channel sandstone
Sedimentary process (facies change)	Large scale channel sandstone coarse-grained deposit	Frequent channel forking the number of isolate barrier bed increasing fine-grained deposit
	Reductive matter increasing	
The connectivity and heterogeneity of sandstone	good	bad
Mineralization fluid state	(equal to highway) the channel of mineralization moving and conveying quickly	(equal to the exit of highway) distributary and decelerating
Ore-forming process	Advantaged development space of interlayer oxidative zone	Advantaged development space of uranium mineralization

Figure 4: Uranium mineralization process controlled by sandstone heterogeneity

granularity. The high-grade mineralization zone is always in the branching area of braided distributary channels and the margins of channel sandstone where individual isolated barrier beds change abruptly. Therefore, the frequency and quality of uranium mineralization decrease where the number and thickness of isolated barrier beds increase. The middle sandstone has the highest probability of uranium mineralization, fine sandstone the second highest. So, uranium deposits always occur in the middle-lower part of braided distributary channel sandstones in each vertical sequence units.

5 The uranium mineralization process

Sandstone heterogeneity obviously controls uranium mineralization. It does so first by controlling uranium mineralization by affecting the rate of migration of mineralized fluid and secondly by changes of sedimentary facies leading to increase of organic reducing agents that promote uranium mineralization.

The braided channel sandstone and braided distributary channel sandstone usually have better connectivity and homogeneity and act like a highway where mineralizing fluids move and convey uranium quickly, and interlayer oxidative zones are widely developed. The areas where the sandstone begins to fork, the number of isolate barrier beds begins to increase and sediment granularity reduces are like the exits of the highway. The mineralizing fluids diverge and decelerate because of the increased resistance. In addition, the change of sedimentary facies may lead to an increase of reductive matter. All these factors restrain the development of interlayer oxidative zones, and control uranium mineralization (Fig 4), see Jiao et al. (2005).

References

Chen S, Huang Y, Fu X (1997) Paleogeography reconstruction of the Early-Middle Jurassic large Ordos basin and development and evolution of continental downwarping, Acta Sedimentologica Sinica 15(4): 43-49

Jiao Y, Chen A, Yang Q, Peng Y, Wu L, Miao A, Wang M,. Xu Z (2005) Sand body heterogeneity: one of the key factors of uranium metallogenesis in Ordos basin, Uranium Geology 21(1):8-15

Jiao Y, Li S (1998) Heterogeneity of porosity and permeability in clastic rock reservoirs, Gas & Gas Geology 19(2): 89-92

Jiao Y, Yan J, Li S, Yang R, Lang F, Yang S (2005) Architectural Units and Heterogeneity of Channel Reservoirs in Karamay Formation, Outcrop Area of Karamay Oilfield, Junggar Basin, Northwest of China, AAPG Bulletin 89(4): 529–545

Li S (1996) Depositional systems in energy- resources bearing basins- case studies of the continental and paralic depositional systems in China. Wuhan: China University of Geosciences Press, 32-45

Li S, Chen S, Yang S, Huang Q, Xie X, Jiao Y, Lu Z, Zhao G (1992) Sequence stratigraphy and depositional system analysis of the northeastern Ordos basin. Beijing:Geological Publishing House, 22-174

Miall AD (1985) Architectural-Elements Analysis: A new Method of Facies Analysis Applied to Fluvial Deposits. Earth Science Reviews 22(4): 261-308

Qiu Y (1992) Developments in reservoir sedimentology of continental clastic rocks in China. Acta Sdeimentologica Sinica 10(3): 16-24

Van WJE, Graff D, Ealey PJ (1989) Geological Modeling for Simulation Studies. AAPG Bulletin 73(11). 1436-1444

Zhang K (1989) Tectonics and resourses of Ordos facult block. Xi'an: The Science and Technology Press of Shannxi

Hydrothermal alteration of the graphitized organic matter at the Kansanshi Cu (Au-, U-) deposit, Zambia

B. Kríbek, I. Knésl, J. Pasava, K. Malý
Czech Geological Survey, Geologická 6, 152 00 Prague 5, Czech Republic

H. Caruthers
First Quantum Minerals Zambia Ltd, P. O. Box 22 000 Kitwe, Zambia

I. Sykorová
Institute of Structure and Mechanics of Rocks, Academy of Sciences of the Czech Republic, V Holesovickách 41, 182 09 Prague 8, Czech Republic

J. Jehlicka
Institute of Geochemistry, Mineralogy and Raw Materials, Faculty of Sciences, Charles University, Albertov 6, 128 43 Prague 2, Czech Republic

Abstract. Hydrothermal alteration of greenschist facies metamorposed organic matter in host rocks of the Kansanshi vein-type copper (Au-, U-) deposit produced ^{13}C depleted amorphous carbon phase (pyrobitumen) and CO_2 >> CH_4 volatile phase. Compared with graphitized organic matter in non-altered rocks, FTIR spectra of amorphous carbon phase in altered rock display significant increase of C=O and C=C vibrations, C-H deformation vibrations and C-O vibrations of ethers. Depletion of hydrothermal carbonates with ^{13}C indicates that the interaction between graphitized organic matter and hydrothermal fluids was a major source of carbon in the fluids. A large volume of bleached carbonaceous schists at the Kansanshi deposit suggests that the hydrothermal decomposition of graphitized organic matter to a great extend controlled the redox state of the ore fluids.

Keywords. Copper and uranium deposits, organic matter, hydrothermal alteration, Zambia

1 Introduction

Although many authors speculated about the role of graphitized organic carbon (semigraphite, disordered graphite) in the origin of epigenetic uranium, copper and gold vein- and disseminated mineralization in metamorphic rocks (for review, see for example Gize 2000) examples of semigraphite hydrothermal decomposition are few. Several authors (Kyser et al. 1989, Kotzer and Kyser 1990, Ettner et al. 1994) noticed a "bleaching halo" i.e. decoloration of organic matter-rich metamorphic rocks around the epigenetic uranium, copper and gold deposit. The process of the hydrothermal alteration of highly graphitized organic matter, however, was never studied in detail. The Kansanshi Cu (Au-, U-) vein-type epigenetic deposit in Zambia is hosted by epizonally metamorphosed rocks (phyllites) rich in graphitized organic matter. The gradual transition from unaltered black schist to albitized and carbonatized rocks adjacent to the quartz veins with Cu mineralization enabled us to study the mechanism of the hydrothermal decomposition of highly graphitized organic matter and to evaluate its role in the ore genesis.

2 Geology

The Kansanshi Cu (Au-, U-) deposit is located in Northwest province, Zambia (Fig. 1) and display many similarities with the Lubumbashi (Cu) and Shinkolobwe (U) deposits in DRC Congo. Recent exploration has indicated an open-pit resource of 267 million tonnes averaging 1.28 percent Cu and 0.16 g/t Au, making Kansanshi one of the largest known Zambian copper resources outside the Copperbelt (Broughton et al. 2002). The deposit occurs in the center of the Lufilian arc, a Pan-African fold-and-thrust belt active from Late Proterozoic until Late Cambrian. The Neoprotero-zoic Kansanshi Mine Formation contains virtually all mineralization at the deposit. The unit consists of a sequence of calcareous biotitic schists, graphitic phyllites, knotted schists, and marbles. The biotite-garnet mineral assemblage of the unaltered rocks within the Mine Formation is indicative of the upper greenschist facies regional metamorphism. Metamorphic

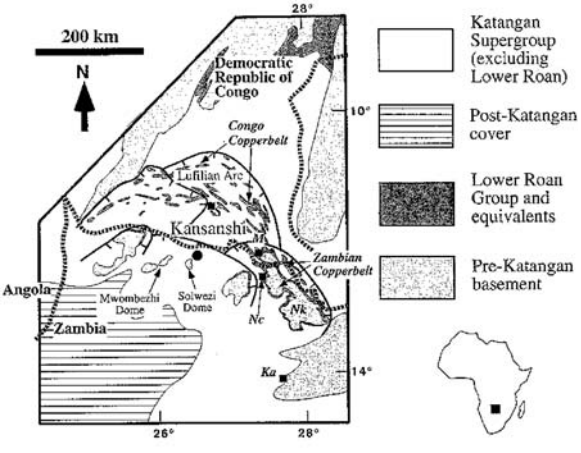

Figure 1: Location of the Kansanshi Cu (-Au, -U) deposit within the Lufillian Arc. After Broughton et al. (2002)

biotite has yielded Ar-Ar ages 499.3 ± 2.9 Ma and 492.9 ± 2.9 Ma at Kansanshi (Torrealday et al. 2000).

3 Mineralization and alterations

The Kansanshi mineralization occurs predominantly within undeformed, high-angle veins and their associated alteration halos. Mineralized veins formed in three overlapping stages: stage I quartz-carbonate (ferroan dolomite and calcite)-sulphide (chalcopyrite, pyrrhotite, pyrite, bornite) veins, stage II uranium (brannerite, monazite, uraninite) carbonate-sulphide (chalcopyrite, pyrite, pyrhotite) veins, and stage III late sulphide (chalcopyrite, pyrite) veins. The age of mineralization at the Kansanshi deposit determined by a number of geochronological techniques ranges between 511 and 500 Ma (Torrealday et al. 2000). Fluid inclusion studies indicate that the mineralizing fluids responsible for the stage I and II veins were saline (+30 wt.% NaCl eq.) and CO_2 rich. Only traces of CH_4 were recorded in fluid inclusions. The Th data range between 280 and 340°C (Torrealday 2000). The alteration halo widths vary from centimeters to 40 meters and are only crudely related to the vein width. A narrow, intensely bleached inner alteration zone is comprised mainly of albite with minor ferroan dolomite and low chalcopyrite-pyrrhotite content. The distal part of the halo contains less albite and more abundant ferroan dolomite, chalcopyrite, pyrrhotite and remnants of organic carbon.

4 Results

4.1 Organic petrology

The average organic carbon content of 25 samples of unaltered and unmineralized pyrrhotite-bearing graphite phyllites is 0.52 percent. In contrast, the organic carbon content of altered phyllites ranges from 0.40 percent to less than 0.001 percent (average grade 0.08 %). Thus, the alteration halo around mineralization lost approximately 84.6 percent of its carbon content.

In unaltered rocks, graphitized organic matter occurs as (1) fine-grained (< 2μm) particles, oriented mostly parallel to the metamorphic foliation and (2) larger (2-15.2 μm), lath-shaped or isometric particles. The reflectance values of fine-grained particles (average Romin = 0.95%, Romax =7.60%) and lath-shaped particles (average Romin =2.30%, Romax=11.50%) plot outside the semigraphite and graphite field in the classification of Teichmuller et al. (1979).

In hydrothermally altered rocks, reflectance of fine-grained- and lath-shaped particles decreases (Romax = 5.70%, Romin = 1.1%). With an increasing intensity of the hydrothermal alteration, only small carbon accumulations (carbon-rich specks) are preserved in strongly albitized and carbonatized rocks. In spite of the almost complete lack of organic carbon, the original metamorphic foliation is still preserved in altered rocks (Fig. 2).

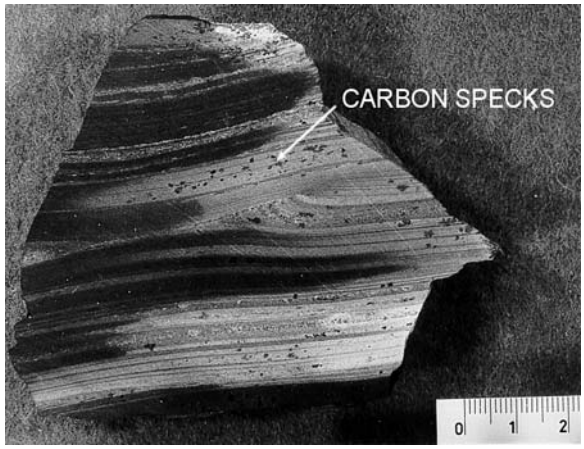

Figure 2: Handsample of black schist from the Kansanshi deposit showing gradual decrease of carbon content during hydrothermal alteration. Only small specks of carbon are preserved in strongly albitized and carbonatized schist

4.2 H/C ratio, XRD and FTIR patterns of bulk carbonaceous matter

Compared with atomic H/C ratios of organic matter in unaltered schists (0.21-0.40), hydrothermally altered organic matter displays higher amount of hydrogen (H/C = 0.42-0.51).

The XRD pattern of the bulk organic matter in unaltered schists is characterized by an asymmetric shape of the (002) graphite reflection attributed to the occurrence of particles in variable stages of structural ordering. The d(002) peak position (3.3547 nm) and peak width measured as full width at half maximum (FWHM) value (0.30) is indicative of low-ordered graphite (Landis 1971). In hydrothermally altered rock, hovewer, the d(002) and FWHM values gradually increase (d = 3.3586-3.3606, FWHM = 0.31-0.32), thus indicating a decrease of the organic matter crystallinity.

FTIR spectra of the bulk organic carbon in non-altered schist confirm that the graphitization process in host rocks is almost complete. Only a weak band in the in the 1630 cm^{-1} region (C=C vibrations of aromatic and polyaromatic rings) was recorded in the FTIR spectrum. In contrast, FTIR spectra of bulk organic matter in hydrothermally altered rocks revealed, in addition to absorption band in the 1630 cm-1, other bands located in the 1400-1000 region (C=O and C=C vibrations, C-H deformation vibrations and C-O bands of ethers).

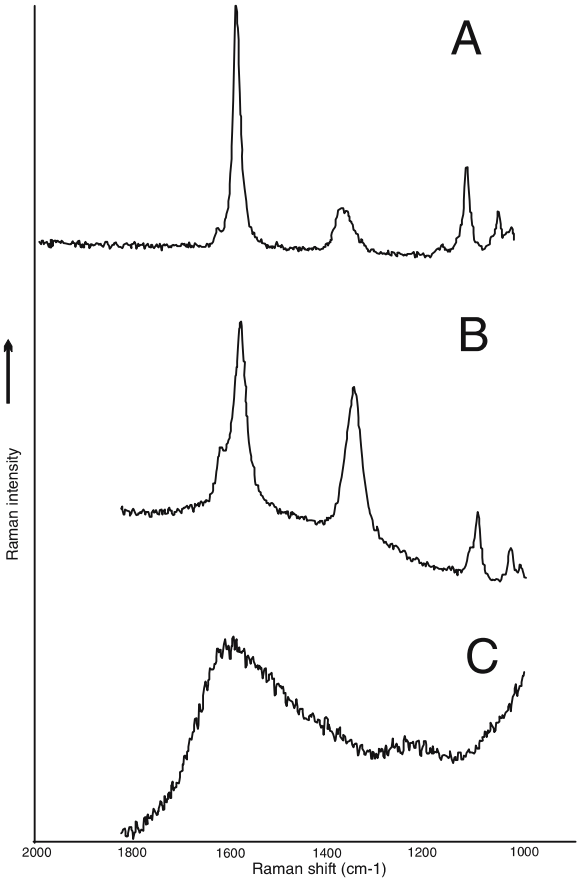

Figure 3: Raman spectra of the graphitized organic matter from greenschist-facies metamorphosed host rocks of the Kansanshi deposit (A), from hydrothermally altered rocks (B) and spectrum of disordered carbon (pyrobitumen) from carbon speck in strongly altered rocks (C)

4.3 Raman spectroscopy of organic particles

Raman spectra of organic matter in unaltered rocks yield consistent results: a small, broad symmetrical peak around 1367 cm^{-1} and a narrower, high peak at around 1580 cm^{-1} (Fig. 3). The 1580 cm^{-1} peak width measured as full width at half maximum is around 20 cm^{-1}. These consistent Raman spectra correspond to a high degree of graphitization, indicating upper greenschist facies metamorphic conditions (Wopenka and Pasteris 1993). In slightly hydrothermally altered rocks, a decrease of graphitized organic matter crystallinity is documented by an increasing intensity of the 1350 cm^{-1} region and additional small hump formation at about 1620 cm^{-1}. In highly altered rocks, a broad band centered at about 1600 cm^{-1} indicates dramatic decrease in graphitized organic matter crystallinity.

Spectra of this type are characteristic of solid bitumens that occur in many types of uranium deposits (Kríbek et al. 1999).

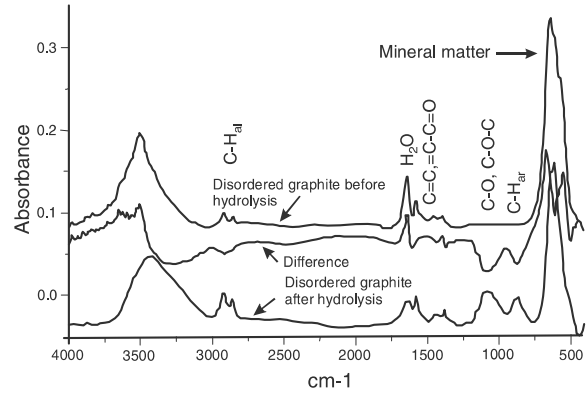

Figure 4: The FTIR spectrum of graphitized organic matter from slightly altered rocks of the Kansanshi deposit and FTIR spectrum of the same sample after reaction in water- vapor saturated stream of air.

4.4 Isotope composition of organic and carbonate carbon

Graphitized organic matter in unaltered schists have $\delta^{13}C$ values, which group around -21.6 ‰ (PDB). In altered shales, $\delta^{13}C$ values gradually increase with increasing intensity of alteration ($\delta^{13}C$ = -25.6 - -26.5). The highest $\delta^{13}C$ values were recorded in carbon accumulations displaying very low crystallinity (carbon specks).

The depletion of carbon specks in ^{13}C can be explained as due to in-situ condensation/oxidation of methane and complex hydrocarbons derived from the hydrothermal decomposition of the graphitized organic matter (Kríbek et al 1999).

The $\delta^{13}C$ values in hydrothermal ferroan dolomite range from -1.6 to -5.6 ‰. Carbon-isotope values around 6.1 ‰ (PDB) are typical for host rock marbles. Hydrothermal carbonates and marble display $\delta^{18}O$ values 12.7-23.5‰ and 21.1‰, respectively.

4.5 Experimental decomposition of graphitized organic matter in FTIR temperature programmed cell

Graphitized organic matter from the host rocks of the Kansanshi deposit was experimentally oxidized in water-vapor saturated stream of air in a high temperature cell of FTIR spectrometer (Nicolet Magna-550) at temperature 400°C for a period of 12 hours.

It was found that after hydrolysis/oxidation (12 hour) the FTIR spectra of hydrolysed material displayed increasing absorption in the range 2800-2960 cm^{-1} (aliphatic C-H structures), 1600-1630 cm^{-1} (skeletal vibrations of aromatic cycles), 1000-1300 cm^{-1} (vibrations of various types of C-O bonds) and in 800-900 cm^{-1} (aromatic C-H structures). The resulting FTIR spectra resemble spectra of organic matter from hydrothermally altered rocks from the Kansanshi deposit.

5 Discussion

The results presented in previous chapter indicate that highly graphitized organic matter can react with hydrothermal solutions at temperatures between 280 and 340°C During the reaction, structure of graphitized organic matter is gradually disordered and resulting material reacts with water oxygen and hydrogen to produce carbon phase enriched in -CH, $-CH_2$ and -C-O groups. Ohmoto and Kerrick (1977) showed that at high PT the main constituents of a fluid in equilibrium with graphite (graphitized organic matter) are CO_2, and CH_4. Hydrolysis of graphitized organic matter could account for the CO_2 and/or CH_4-rich fluids, although the ratio in which CO_2 and CH_4 occur in the fluid would be governed by the equilibrium constants of the different reactions. At high oxygen fugacities and/or high concentrations of SO_4^{2-} in fluids, CH_4 can be oxidized to CO_2. Predominantly CO_2-rich fluid inclusion in Kansanshi gangue minerals is consistent with the methane oxidation scenario. During the CH_4 partial oxidation a number of intermediate species (complex hydrocarbons) can condensate to form liquid or solid phase (pyrobitumen), displaying depletion in ^{13}C (Kríbek et al. 1999). The occurrence of ^{13}C depleted pyrobitumen was observed in many uconformity-type uranium deposits (Mossman et al. 1993).

6 Conclusions

All information gained from the study of altered rocks at the Kansanshi deposit indicate that organic matter graphitized under conditions of upper greenschist facies metamorphism can react with fluids to produce substantial amount of CH_2 and CO_2. High activation energy of semigraphite hydrolysis is probably reduced during its gradual disordering and the formation of disordered products with higher content of hydrogen and oxygen. Gradual decomposition of graphitized organic matter in host rocks can substantially reduce the fO_2 of the fluids, thus resulting in lower solubility of dissolved copper, gold and uranium species. Methane (and probably other hydrocarbons) that originates during the hydrothermal decomposition of organic matter can condensate to form authigenic solid phase resembling bitumens.

Acknowledgments

This study was funded through the Czech Technical Assistance Programme to the Republic of Zambia in the year 2004. The experimental hydrolysis of organic matter was carried out by Z. Sobalík, from the J. Heyrovsky Institute of Physical Chemistry, Academy of Sciences of the Czech Republic.

Australia's uranium endowment: Metallogeny, exploration and potential

Ian Lambert, Subhash Jaireth, Aden McKay, Yanis Miezitis
Minerals Division, Geoscience Australia, GPO Box 378, Canberra, ACT 2601 Australia

Abstract. Australia has a rich uranium endowment. This is considered to reflect the widespread emplacement of uranium-enriched felsic igneous rocks in three main periods of igneous activity. While some uranium deposits appear to have formed during these igneous events, including the giant Olympic Dam deposit, most formed by subsequent low temperature processes from uranium-enriched source rocks. There has been limited exploration since 1980 and considerable potential exists for discoveries of various types of uranium deposits.

Keywords. Uranium deposits, Australia, uranium-rich felsic igneous rocks, ore genesis

1 Introduction

Ore genesis researchers have long debated whether metalliferous mineral deposits require sources that are enriched in the relevant metals. Magmatic, pegmatitic, greisen, and skarn deposits are clearly linked to igneous processes, which produce metal rich phases. Placer deposits are generally related to regions in which there are elevated abundances of the minerals of interest. On the other hand there is a growing recognition that for many hydrothermal deposits the sources are often present within or in close proximity to the fluid flow systems and it is debatable whether the sources need to be enriched in metals.

This paper considers the metal sources for Australia's numerous uranium deposits by investigating the spatial and temporal relationships between these deposits and uranium-enriched igneous rocks. It draws on information from Geoscience Australia's OZCHEM database (http://www.ga.gov.au/gda/index.jsp).

2 Australia's uranium endowment

Australia has the world's largest resources of low cost uranium (675,000t U), with roughly 40% of world resources in this category. Some 75 uranium deposits, varying in size from small to very large, are scattered across the Australian continent. Approximately 86% of total uranium resources (1,054,000t U) occur in two main types of deposits: hematite-rich breccia complexes and unconformity-related deposits (McKay and Miezitis 2001).

- *Hematite-rich breccia complex deposits:* some 70% of resources occur in Proterozoic hematite-rich granitic breccias at Olympic Dam in South Australia, which is the world's largest uranium deposit. Broadly similar hematite-rich breccia mineralisation is being evaluated elsewhere in the same geological province, at Prominent Hill.
- *Unconformity-related deposits:* about 18% of resources are associated with Proterozoic unconformities, mainly in the Alligator Rivers field, Northern Territory (Ranger, Jabiluka, Koongarra).
- Other significant resources occur in:
- *Sandstone uranium deposits:* constitute about 6% of resources, mainly in the Frome Embayment field, South Australia (Beverley, Honeymoon) and the Westmoreland area, Queensland.
- *Surficial (Calcrete) deposits*: constitute about 4% of Australia's uranium resources, mostly in the Yeelirrie deposit (Western Australia).

3 Uranium-rich felsic igneous rocks

As shown in Figure 1, the uranium deposits show a marked spatial relationship at the regional scale with widespread uranium-rich felsic igneous rocks, comprising mainly granitoid intrusives and associated rhyolitic volcanics. Some associated sedimentary strata also have elevated uranium contents. Roughly 22,000 felsic igneous rocks and gneisses in OZCHEM have been analysed for uranium, and over 2,700 of these have 10ppm U or more (that is at least 4 times crustal average).

Figure 2 shows the ages of uranium mineralisation in relation to the ages of the uraniferous igneous rocks. The uraniferous felsic igneous rocks, which are highly fractionated and/or have alkaline affinities, were emplaced during major magmatic events in the late Archaean (2.69 – 2.65 Ga (Champion and Sheraton 1996), the Palaeo-Mesoproterozoic. (~1.8 – 1.5 Ga) and, in eastern Australia, Silurian to Permian (0.43 – 0.25 Ga). Of these, intervals, the Proterozoic produced the greatest volumes of uraniferous igneous rocks.

In the case of Olympic Dam, mineralisation is of similar age to felsic igneous activity. Together with the close spatial association, this supports the concept that the uranium was concentrated during associated hydrothermal activity (Reynolds 2000). Some small intrusive and volcanic style uranium deposits also have temporal association with felsic host rocks, including the intrusive style Crocker Well deposit in Mesoproterozoic granitoids in

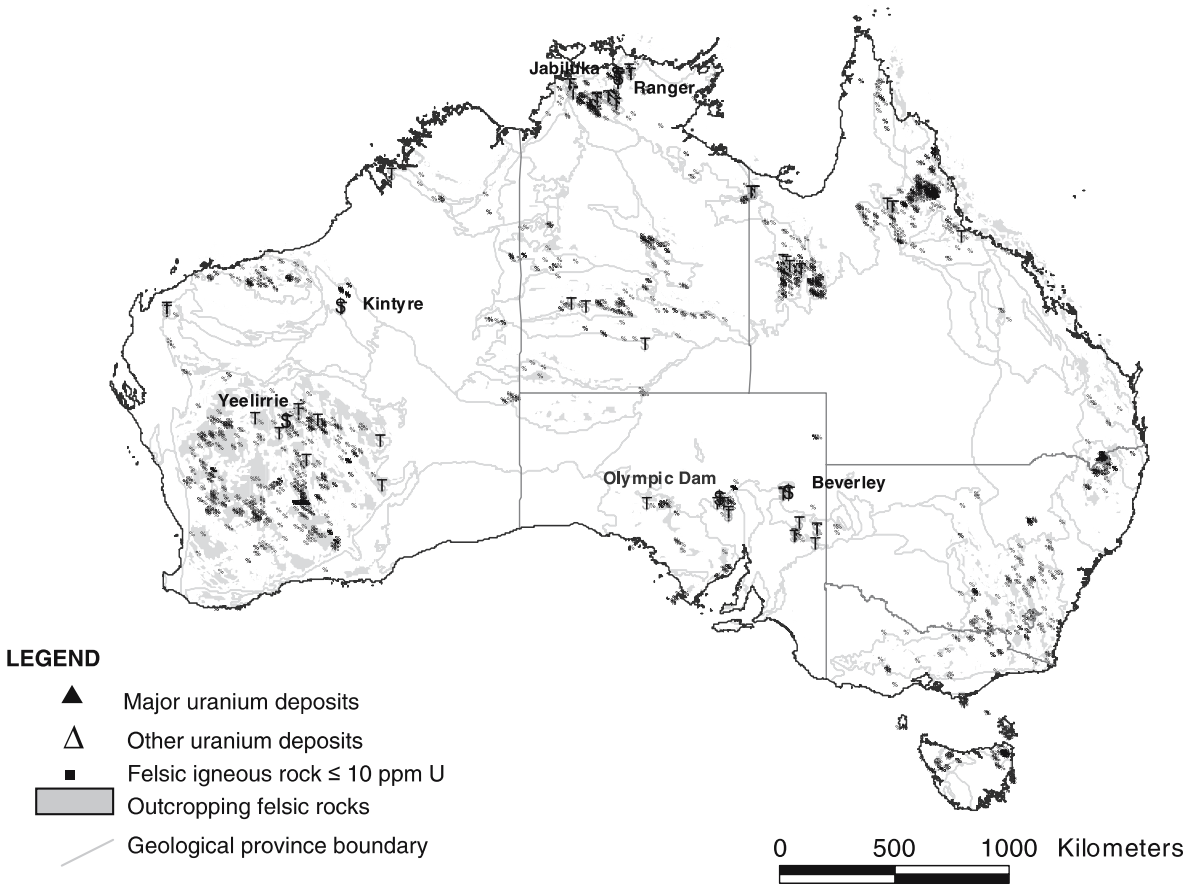

Figure 1: Significant Australian uranium deposits in relation to occurrences of felsic igneous rocks known to have at least 10 ppm uranium

South Australia and the Ben Lomond volcanic style deposit in Carboniferous rhyolitic tuffs in northeastern Queensland (McKay and Miezitis, 2001).

More generally, the uranium mineralisation is considerably younger than the spatially-related igneous rocks. This is the case for calcrete, sandstone-hosted deposits and unconformity-related deposits. In general, these deposits appear to have formed where uranium was mobilised from the older uranium-enriched source rocks under low temperature oxidising conditions and precipitated by redox reactions. In particular:

- In the western part of the continent there is a clear spatial relationship of the Cainozoic calcrete type uranium deposits, including the large Yeelirrie deposit, with the uranium-rich Archaean felsic rocks in northeast Yilgarn. The ages of the probable source rocks are approximately 2.6 billion years older than the uranium deposits.
- Sandstone uranium deposits are the most widely distributed type of uranium deposit in Australia and range in age from Neoproterozoic for the Westmoreland group of deposits (Ahmad and Wygralak 1990) in Queensland to Cainozoic for those of Honeymoon and Beverley in the Frome Embayment, South Australia. The Mulga Rock sandstone deposit in Western Australia, was sourced from uranium in the Archaean basement (Fulwood and Barwick 1990) to the west. Those in the Frome Embayment are derived from the adjacent exceptionally uranium-rich Proterozoic felsic rocks (Curtis et al 1990).
- Unconformity-related uranium deposits, which formed in the late Palaeoproterozoic to early Mesoproterozoic, are variably younger than the spatially associated Palaeoproterozoic to late Archaean felsic igneous rocks.

It is of interest that, although Archaean rocks are widespread in the western part of the continent, there are no known uraniferous deposits in Late Archaean quartz pebble conglomerate in Australia. Further, it is possible that the absence of known uranium deposits in the southeastern part of Australia reflects the paucity of exploration in this region, as a result of state government policies.

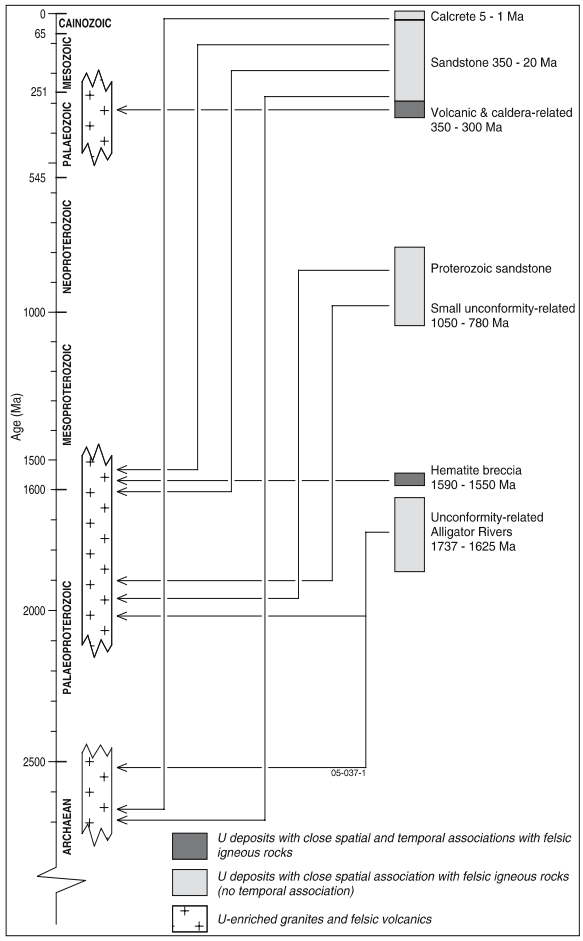

Figure 2: Ages of uranium deposits and uranium-enriched felsic igneous rocks. Lines link each deposit type to the age of its probable source rocks.

4 Exploration

The bulk of discoveries were made during the period 1969 to 1980 which also clearly coincided with peak expenditure in uranium exploration (Fig. 3).

Early uranium discoveries relied extensively on airborne radiometric surveys. The 1960s and early 1970s saw extensive testing of surficial radiometric anomalies. This progressed to more sophisticated approaches, often based on conceptual geological modelling and led to major discoveries at Jabiluka and Olympic Dam.

In more recent exploration, airborne electromagnetic surveys have been used to locate palaeo-channels in the vicinity of the Honeymoon sandstone uranium deposit in South Australia.

There have only been two notable discoveries since 1980 with the unconformity-related Kintyre deposit in 1985 and the breccia hosted copper-gold-uranium deposit at Prominent Hill in 2001. Nevertheless, uranium resources have continued to increase substantially due to ongoing delineation of mineralisation, particularly at Olympic Dam.

Given the limited modern exploration, there is significant potential for additional uranium deposits in Australia, including:

- Sandstone deposits in sedimentary strata in various regions adjacent to uranium-enriched basement.
- Unconformity-related deposits, including relatively high grade deposits at and immediately above the unconformity, particularly in Arnhem Land in the Northern Territory but also in the Granites-Tanami region (Northern Territory-Western Australia), the Paterson Province (Western Australia) and the Gawler Craton (South Australia).
- Hematite-rich breccia deposits, particularly in the Gawler and Curnamona cratons of South Australia.

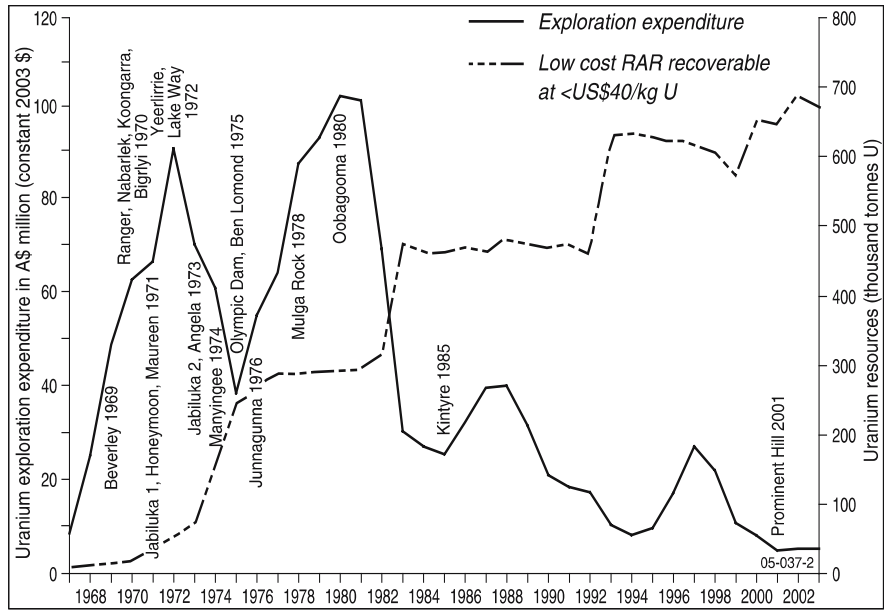

Figure 3: Trends in uranium exploration expenditure and discovery in Australia, in relation to resource levels. Resources have increased markedly as a result of ongoing evaluation of known deposits

References

Ahmad M, Wygralak AS (1990) Murphy Inlier and environs - regional geology and mineralisation. In: Geology of the Mineral Deposits of Australia and Papua New Guinea (editor Hughes FE). The Australasian Institute of Mining & Metallurgy, Melbourne, 819–826

Champion DC, Sheraton JW (1996) Geochemistry and Nd isotope systematics of Archaean granites

Curtis JL, Brunt DA, Binks PJ (1990) Tertiary palaeochannel uranium deposits of South Australia. In: Geology of the Mineral Deposits of South Australia and Papua New Guinea (editor Hughes FE). The Australasian Institute of Mining & Metallurgy, Melbourne, 1631–1636

Fulwood KE, Barwick RE (1990) Mulga Rock uranium deposits, Officer Basin. In: Geology of the Mineral Deposits of Australia and Papua New Guinea (editor Hughes FE). The Australasian Institute of Mining & Metallurgy, Melbourne, 1621–1623

McKay AD, Miezitis Y (2001) Australia's uranium resources, geology and development of deposits. AGSO – Geoscience Australia, Mineral Resource Report 1

Reynolds LJ (2000) Geology of the Olympic Dam Cu-U-Au-Ag-REE deposit. In: Porter TM (eds), Hydrothermal iron oxide copper-gold & related deposits - A global perspective. Australian Mineral Foundation Inc, 9-26

Features of mylonite and its relationship to uranium ore-formation in the Xiazhuang uranium ore field

Jianhong Li
Beijing Research Institute of Uranium Geology, Beijing, 100029, China

Liang Liang
East China Geological Institute, Fuzhou, 344000, China

Abstract. Based on geological features, the mylonite at the Xiazhuang uranium ore field may be divided into two types, namely mylonite in ductile shear zone and mylonite in silicic cataclastic rocks. The first of these basically results from single shear strain, while the second formed mainly as a result of pure shearing strain. The two types of mylonite are different in characteristics such as their petrofabric diagram, strain parameters and dynamic vorticity number. The main ductile-shearing zones at the uranium ore district have been recognized as reverse faults. The formation ages of mylonite have been obtained as 140 Ma and 141 Ma (2 samples), close to those of the peak stage of later granitic magmatic activity, and identical to those of the early uranium mineralization. It is suggested that ductile-shearing zones in the area originated from the deformation of an earlier granitic body in a pseudoplastic state. The ductile deformation is closely associated with uranium ore-formation both in space and time, and ore-controlling factors are intimately related to ore-formation mechanism and mechanism of ductile shearing. Such information is useful in the prospecting and exploration for uranium mineralization in this region.

Keywords. Mylonite, geologic age, Xiazhuang uranium ore field

1 Introduction

The Xiazhuang uranium ore-field is located in the east of Guidong granitic massif in Nanling sublatitudinal tectonic belt. Two main groups of fault structures are developed; these are sublatitudinal and NE-NNE-trending ones (Fig. 1). Rock forming and uranium ore-forming processes in the ore field are characterized by multiple stages and phases. The earlier uranium mineralization (with a mineralization age more than 100 Ma) mainly occurs in mylonitized rocks of ductile-shearing zone, or in mylonitized rock bands of cataclastic rocks. Later uranium mineralization (with the mineralization age less than 100 Ma) is localized in altered silicified veins in the silicic cataclastic zone or in quartz veins. Previous exploration work has proven some large-scale younger uranium deposits associated with the silicified zone. Recently, with the discovery of older uranium mineralization, genetically related to mylonitization, as well as the new theory of ductile shearing and new prospecting achievements in this field, it is suggested that there must be great potential in prospecting for older uranium deposits controlled by sublatitudinal fault structures. Mylonite is one of the early-formed ore-hosting rocks in Xiazhuang uranium ore-field, so the study of mylonite is of practical significance for prospecting in the region.

2 Features of mylonite

Mylonitic zones in the range of Xiazhuang uranium ore-field are divided into two groups. The first group is of sublatitudinal striking. Mylonitic zones F_1 and No. 120, and the Shitoulin and Zhangguangying foliation zones are included in this group. The second group has submeridional trending including mylonitic zones No.6009, No.202 and No.6004. In addition, smaller mylonitic zones occur sporadically. Mylonitic zones F_1 and

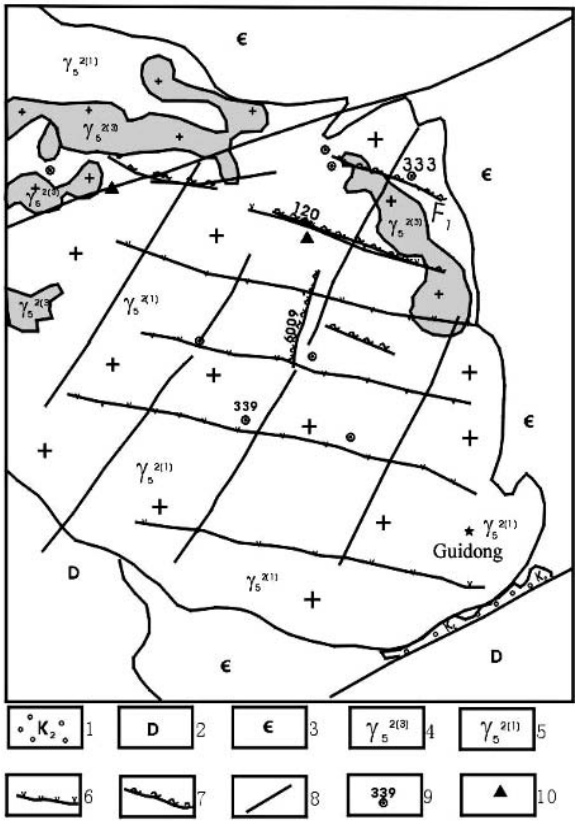

Figure 1: Sketch geologic map of Xiazhuang uranium ore-field. 1-Upper Cretaceous; 2-Devonian; 3-Cambrian; 4-Granite of the third episode Early Yanshnian phase; 5-Granite of the first episode Early Yanshnian phase; 6-Swarm of intermediate-basic dykes; 7-Ductile-shearing zone and its number; 8-Siliceous fault zone; 9-Deposit and its number; 10-Age-dating sample

No.120 are those in ductile shearing zones. In addition, mylonitic bands and mylonitic breccia are developed in silicic cataclastic rocks.

There are two types of mylonite, namely mylonite in ductile shear zones and mylonite in silicic cataclastic rocks. The former basically results from single shearing strain, while the latter originated mostly from pure shearing strain. The two types of mylonite are different in characteristics such as petrofabric diagram, strain parameters and dynamic vorticity number. The main ductile-shearing zones at the uranium ore district are recognized as reverse faults. The average paleo-stress is determined as 50 Mpa, and strain rate value is determined as 4.8×10^{-2}/s. Fabric features include big-ring band, small-ring band, incomplete band and extremely dense points reflecting different genesis and formation environment of mylonites. Strain measurements show that the mylonite in ductile-shearing zone is the product of shearing strain, and mineralized mylonite—product of flat- compression.

3 The relationship between mylonite and uranium ore-formation

The relationship between mylonite and uranium ore-formation is expressed in following aspects:

1. The formation age of mylonite (104.41~ 104.48 Ma) is close to that of late small granitic massifs and early intermediate-basic dykes, which show certain genetic relationships. It is established that the country rocks of the mylonitic zones are mainly granite of main phase, and minor the late small granitic massifs. The intrusion of early sublatitudinal intermediate-basic dykes is another feature of the peak period of magmatic activity, following the emplacement of main phase granite. At that time, the consolidated main phase granite was transformed into a pseudo-plastic state again as a result of the emplacement of intermediate-basic dykes. When the eastern part of the main phase granite was subject to the regional stress and its distribution direction turned to the south as a whole, the granitic mylonitic zones were generated as the main phase granite adjacent to small granitic massif was in a pseudo-plastic state. The NE-NNE-striking silicic cataclstic zones that contain mylonitic breccia were also in a ductile deformation state, but were subject to structural reworking later. The ductile deformation occurred everywhere suggesting its spatial-temporal and genetic relationship to late-small granitic massif in the ore district.
2. According to ore-formation characteristics and mineralization ages, two major uranium ore-formation periods can be recognized, namely, the first one with mineralization ages more than 100 Ma, and the second one with mineralization ages less than 100 Ma. The formation ages of mylonite obtained by the authors are 140~141 Ma showing close relationship to early uranium mineralization with the formation age more than 100 Ma. Some uranium orebodies at uranium deposits No.333, No337 and No.339 are hosted just in mylonite or foliated rocks. The ages of early uranium mineralization are close to those of mylonite (140~141 Ma) indicating that the ductile deformation and uranium ore-formation are closely, genetically associated in space and time. Experiments on rock-forming and uranium ore- formation processes prove (Yue et al., 1990, Chen et al., 1999, Li et al., 2001) that structural dynamic differentiation might occur in rocks under structural shearing stress leading to changes in mineralogical and chemical compositions. Thus, fluids of dynamic metamorphic origin are generated. In the mean time, the metamorphic water originated from the deep source, the magmatic water and atmospheric water may join the fluids. These fluids flow through rocks leaching and extracting ore-forming materials. When the fluids flow, circulate in close vicinity of mylonitic zone; the ore-forming materials may be unloaded in fractured space and micro-fissure to form orebodies. Such orebodies that are spatially and temporarily associated with mylonitic zones and whose ore-controlling factors and ore-formation mechanism are closely related to ductile shearing deformation can be termed mylonite-type uranium deposits.
3. The NE-NNE-trending silicic fractured zones, as the main fault zones in the ore district, are mostly silicified zones or silicified cataclastic zones. These fault zones and their relation to uranium mineralization have been systematically studied for a long time (Du et al. 1982, Du 2001) for its close relation to later uranium mineralization. In fact, these fault zones are characterized by multistage activities, the alternation of ductile, brittle, and brittle-ductile deformation, the complexity of deformation environments. Analytic data of age-dating samples taken from mylonitic breccia in silicic cataclastic zone and from mylonite in ductile shearing zone indicate, that in the late stage of Yanshanian orogeny (140 Ma) an extensive ductile deformation event occurred in the region of the ore district generating a series of mylonitic zones. Besides those mylonitic zones F_1 and No.120 that can be seen at present, mylonitic zones exist in NE-NNE trending silicic cataclastic zones regarded as the main fault zones in the ore district. However, these mylonitic zones have been reworked by silicic cataclastic rocks of later brittle deformation, and the remainder mylonitic zones are limited and difficult to find. The Huangpi cataclastic zone where an age-dating sample has been taken is a remnant mylonite. It is expected

This page intentionally blank

that many more remnant mylonites (mylonitic breccias) will be discovered and studied. It has been proven that the ductile shearing zone and early (120~140 Ma) uranium mineralization are inseparably associated, and the study of the ductile shearing zone is the key to successful prospecting for early uranium mineralization, and much attention should be paid to this in the future.

4. Present exploration work in the ore district indicates, uranium mineralization has been found in all these kinds of country rocks, even in mylonitized rocks, no matter what the genesis (single-shearing or pure-shearing) of the mylonite, and no matter what composition (silicic, granitic or diabasic) the mylonitic breccias have. Usually, mylonitic breccias in silicic fractured zone are lack of uranium mineralization, but mylonitic bands in silicic fractures may host rich uranium mineralization. The intersection or the superimposition of ductile shearing zone (mylonitic zone) and silicic fractures may result in rich uranium mineralization, such as the fault zone F_1 at uranium deposit No.333. As a rule, mineralized mylonite has experienced intense hydrothermal alterations such as silicification and hematitization. Mylonites with no alteration are lack of uranium mineralization. Therefore, mylonite may be regarded as a prospecting criterion. Mineralized districts and districts with rich uranium mineralization can be found by studying the genetic relationships between mylonitic zones and various geologic bodies.

References

Bonnemaison M, Marcoux E (1990) Auriferous mineralization in some shear zone: A three-stage.model of metallogenesis. Mineral Deposit 25: 96-104

Boyle, RW (1979) The geochemistry of gold and its deposits. Geol. Survey Canada 278-280

Chen BL (1999) Ore-forming model of ductile shear zone type gold deposits. Geological Review 45: 186-192

Christie JM, Ord A (1980) Flow Stress from Microstructure of Mylonites Example and Curreud Assessement. J Geophys Res 85: 6253-6262

De Paor DG (1983) Orthograptric analysis of geologicstructures- I. Deformation Theory. J. Struct Geol. 5: 323-333

Kerrich R (1988) The formation of gold deposit with particular reference to Archean greenstone belts and Yellow Knife, Contrib. Geol NW Tevritories (Canada) 3:37-62

Li XF (2001) Deformation-metamorphism and gold mineralization in ductile shear zone. Journal of Gulin Institute of Technology 3: 207-212

Liu ZM (2001) Basic features of the Hehe-Yindian Shear zone Along the Xincheng-Huangpi fault. Geology and Mineral Resources of South China 62-69

Ramsay JG (1980) Shear Zone geometry, A review. Struct. Geol. 2: 83-99

Sibson RH (1977) Fault rocks and fault mechanism. London: Geol. Soc. 133: 191-213

Zhang GL (2002) The measurement of kinematic Vorticity number and its structure significance in general Shear Zone. Journal of Gulin Institute of Technology 97-104

Zheng YD (1993) Kinematic Vorticity Number and Shear type related to the Yagan metamorphic core Complex on China-Mongolian border, Scientia Geologica Sinica 34: 273-280

Zhong ZQ (1990) Petrological study on the ductile shear zones in the core of the eastern Qinling orogenic belt, weastern Henan, Acta Geologica Sinica 121-130

Zhong ZQ (1997) Shear zone arrays in Yunkai uplifted area and its relationship with gold mineralization. Earth Science-Journal of China University of GeoSciences 22: 20-26

Mineralization characteristics and origin of the Qianjiadian uranium deposit

Shengxiang Li, Yuqi Cai, Yuliang Xia, Guangxi Ou, Jinrong Lin, Wenming Dong
Beijing Research Institute of Uranium Geology, P.O. Box 9818, Beijing, 100029, China

Abstract. The Qianjiadian uranium deposit occurs in variegated clastic rocks of the Upper Cretaceous Yaojia Formation. The primary color of the ore-bearing sandstone is purple to red; the ore-bearing host rocks show gray or grayish white colors due to secondary alteration of oil-gas and oil-field water. The uranium ore bodies are of tabular shape. The uranium ores have low ratios of Fe_2O_3/FeO and U^{6+}/U^{4+}, but high contents of CH_4 and total hydrocarbon. In the uranium ores, U content is positively correlated to S content and delta Eh value, and negatively correlated to pH; however, it has no evident correlation with the content of organic matter. The mixing of the infiltrating oxygen-bearing supergene water with ascending oxygen-free hypogene oil-gas and oil-field water plays a key role in forming Qianjiadian uranium deposit.

Keywords. Sandstone-type uranium deposit, oil-gas and oil field water, secondary reduction, and double mixing metallogenesis, Qianjiadian

1 Geologic setting

The Qianjiadian uranium deposit is located in the north of Qianjiadian sag, Kailu depression, in the southwestern Songliao basin. The Qianjiadian sag is a NNE-striking narrow sag, with a length of about 100km, a width of 9-20km and covering an area of about 1280km^2. The E-W-trending Xilamulun deep-seated fault traverses the sag, and a series of NNE-striking and nearly S-N-striking faults are also developed at the margin and in the inside of the sag. These faults provide pathways for the upward migration of the deep oil and gas.

Uranium mineralization in the Qianjiadian deposit occurs in the Upper Cretaceous Yaojia Formation, which is characterized in the ore district by sandy braided stream facies. It comprises a lithologic combination of mudstone-sand- stone-mudstone, and the thickness of the sandstone ranges from 0 to 40m. These features suggest that the Yaojia Formation in the study area is a favorable horizon for the formation of in-situ leachable sandstone type uranium deposits.

2 Mineralization characteristics of the Qianjiadian uranium deposit

Mineralization characteristics of the Qianjiadian uranium deposit are as follows:

1. The ore-bearing sand bodies in the ore district have undergone intense epigenetic alteration, mainly in three periods.

   The first period is the secondary reduction of oil-gas and oil-field water during pre-ore stage. Due to secondary reduction of oil-gas and oil-field water, the rocks of the ore-bearing layers have changed from primary purple or red to gray or grayish white in color, and kaolinization, dolomitization, and pyritization are extensively developed. As a result of the decolorising alteration, Fe_2O_3/FeO ratio of gray or grayish white sandstone rocks in the ore-bearing layers is obviously lower than that of the unaltered purple or red sandstone rocks, but the uranium content of the former is obviously higher than that of the later (see Table 1). These features indicate that the decolorized alteration can largely increase the uranium content of the sandstone, and lead to the pre-enrichment of uranium in the ore-bearing layers.

   The second period is the mixing of the infiltrating oxygen-bearing supergene water with ascending oxygen-free hypogene oil-gas and oil-field water in the metallogenic epoch. Their mixing ore-formation is the most important ore-controlling factor and directly results in the formation of Qianjiadian uranium deposit.

   The third period is the secondary reduction of the oil-gas during post-ore stage, which leads to the fact that the interlayer oxidation zones has been partially reduced and as a consequence, it is difficult to find direct contact of the uranium orebodies with the interlayer oxidation zone in the deposit.
2. U^{6+}/U^{4+} ratios in various rocks of the ore-bearing sand bodies are quite low. They are 1.33, 1.2 and 0.9 in the oxidized yellow or brown sandstone, uranium ores and altered gray or grayish white sandstone respectively. They are clearly lower than those of various rocks in the ore-bearing sand bodies in Kujieertai uranium deposit (which is a typical sandstone-hosted uranium deposit of interlayer oxidation type with the U^{6+}/U^{4+}

Table 1: Analytical result of uranium and iron oxides in altered and unaltered sandstone rocks

Rocks	U(10^{-6})	FeO(%)	Fe_2O_3(%)	Tfe(%)	Fe_2O_3/FeO
Altered S.*	42.89	1.30	0.91	2.21	0.70
Unaltered S.**	3.76	0.42	1.9	2.36	4.58

Note: * Altered sandstone with gray or grayish white color;
** Unaltered sandstone with purple or red color.

ratios of 1.34-2.41), Yili Basin. These indicate that uranium source of the ore-formation may be partially from hypogene tetravalent uranium.

3. Uranium orebodies show tabular shape rather than the roll shape peculiar to the typical interlayer oxidation type sandstone-hosted uranium deposits.
4. In the uranium ores, the uranium content is positively correlated with sulfur content and ΔEh and negatively correlated with pH; however, there is no evident correlation with the content of organic matter. While in the uranium-mineralized sandstone, the uranium content is positively correlated to the content of CH_4. This suggests that uranium ore-formation may be closely related to the secondary reduction of CH_4- and H_2S-rich oil-gas rather than the fragments of syngenetic organic matter in the sandstone.
5. In the uranium ores, many oil-gas inclusions are found in the cleavages or fractures of the minerals such as dolomite, feldspar and so on.
6. Contents of CH_4 and total hydrocarbon in the ores are 479.83 μl/kg and 691.97 μl/kg respectively, obviously greater than those in the country rocks around the ore-bearing sand bodies. This indicates that hydrocarbon of the oil-gas played an important role on the precipitation and enrichment of uranium in the ores.
7. U-Pb isotopic age dating of the ores yields 53Ma, which demonstrates that the Qianjiadian uranium deposit is supports, the epigenetic reworking origin, closely related to the epigenetic uplifting and denudation of the basin.

3 Origin of the Qianjiadian uranium deposit

The Qianjiadian uranium deposit is of multi-stage and superimposition origin, and the uranium source is from the provenance area, infiltrating supergene waters in the ore-bearing layers and the hypogene oil-field water.

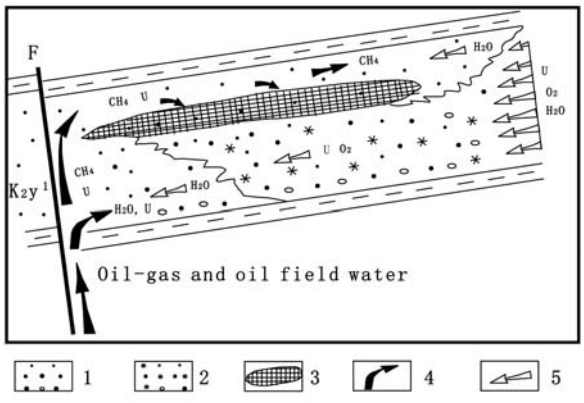

Figure 1: The metallogenic model map of Qianjiadian uranium deposit; 1-gray or grayish white sandstone; 2-yellow sandstone; 3-industrial U orebody; 4-migration direction of oil, gas and oil field water; 5-migration direction and relative speed of infiltration oxygen- and U-bearing water

During the compressional and shrinking stage of the basin (late Cretaceous), hypogene oil-gas and oil-field water moved upwards along fault fractures. After entering the ore-bearing layers, alteration of the primary variegated sandstone of Yaojia Formation occurred into gray or grayish white sandstone, and resulted in the pre-enrichment of uranium in the ore-bearing layers. During the uplifting and denudation stage (Eogene), the Yaojia Formation in the southeast of Qianjiadian uranium deposit was extensively exposed to the surface, and was reworked by oxygen-bearing supergene water for a protracted period. With the development of interlayer oxidation zone toward the deeper of the ore-bearing layers, the infiltrating fluid (oxygen-bearing groundwater) with high Eh value and pH value encountered with the ascending fluid (oxygen-free oil-gas and oil-field water) with low Eh, pH values and abundant reductive. The mixing of the two fluids of different geochemical properties led to abrupt changes in the Eh value and pH value of the fluids and led to the reduction and precipitation of uranium from the infiltrating oxygen-bearing groundwater, Figure 1 shows schematically how fluid mixing led to the formation of this sandstone- hosted uranium mineralization.

4 Conclusions

1. Oil-gas and oil-field water from depth in the sedimentary basin moved upwards along the fault fractures and altered the primary variegated sandstone of Yaojia Formation to gray or grayish white sandstone, and led to the pre-enrichment of uranium in the ore-bearing layers.
2. The mixing of the infiltrating oxygen-bearing supergene water with ascending oxygen-free hypogene oil-gas and oil-field water is the main ore-controlling factor.
3. The reduction alteration of the oil-gas after the metallogenic epoch partially reduced the interlayer oxidation zones so that the uranium ore bodies display little direct contact with the interlayer oxidation zones.

Acknowledgements

The research is subsided by the National Fundamental Research and Development Project (2001CB409808). Thanks are due to professor Chen Zhaobo, professor Chen Zuyi, and professor Li Ziying for their advice in the study of this paper.

References

Chen DS, Wang RY, Li SX (1997) The metallogenic model of the sandstone-type uranium deposits in interlayer oxidation zone in Yili basin. Atomic Energy Press, 1-12(in Chinese)

Chen ZB, Li SX, Cai YQ (2002) Geologic evolution and uranium metallogenic regularity in Yili basin. In: Mineral Deposits, 21(sup.): 849-852 (in Chinese)

Li SX, Chen DS, Wang RY (1998) Ore controls of the sandstone-type uranium deposits in interlayer oxidation zone in Yili basin. In: Mineral Deposits, 17(sup.): 461-464(in Chinese)

Metallogenetic conditions and exploration criteria of the Dongsheng sandstone type uranium deposit in Inner Mongolia, China

Ziying Li, Xiheng Fang, Yuliang Xia, Xinjian Xiao, Ye Sun
Beijing Research Institute of Uranium Geology, P.O. Box 9818, Beijing 100029, China

Anping Chen
Geological Exploration Team 208, Inner Mongolia, China

Yangquan Jiao
China Geological University, Wuhan, China

Ke Zhang
Zhongshan University, Guangzhou, China

Abstract. The Dongsheng uranium deposit differs from other sandstone type deposits. It has unique signatures and is generally controlled by a transitional zone between greenish and grayish sandstones; both of them indicate reduced geochemical environments. It is genetically different from ordinary sandstone uranium deposits and of more complex origin. Understanding metallogenetic conditions and concluded exploration criteria of this type uranium deposit are of both theoretical and practical significances in exploration for similar kind of uranium deposits.

Keywords. Metallogenetic conditions, exploration criteria, sandstone type uranium deposit, Dongsheng Geological Setting

1 Introduction

The study area is located in the north of the Ordos basin (Fig. 1), The Ordos basin is a large Meso-Cenozoic depression basin developed in North China Platform, with its size of approximately 250000 km^2 and is well known as an important "energy resources basin" because of abundance of coal, oil and gas deposits.

The pre-Jurassic basement of the basin can be divided into two parts: one is the crystalline basement consisting of Archean and Proterozoic highly metamorphic rocks and migmatic granites, and another is Paleozoic lightly metamorphic rocks (Fig. 1).

The Mesozoic sedimentary covers of the Dongsheng area are of Upper-Triassic, Jurassic and Lower-Cretaceous ages. The Upper-Triassic Yanchang Formation is mainly composed of gravel-bearing sandstone with siltstone and mudstone interbeds that are oil- and coal-productive. The Jurassic system can be divided into three series: (1) Fuxian Formation, the Lower Jurassic, mainly composed of siltstone and arkosic sandstone, with a parallel unconformity to the underlying Yanchang Formation. (2) Yanan Formation, coal-productive beds with arkosic sandstones, siltstone and mudstone interbeds, in which uranium anomalies have been found, being one of uranium target horizons; Zhiluo Formation, the Middle Jurassic, composed of gray, greenish sandstone, siltstone and mudstone, the main uranium-productive horizon in Dongsheng area, which is separated by a parallel, and locally angular, unconformity from the underlying Yanan Formation; Anding Formation, the Middle Jurassic, mainly composed of fine-grained red or brownish red siltstone and mudstone, with a parallel unconformity to the underlying Zhiluo Formation. (3) Fenfanghe Formation, Upper Jurassic, poorly developed in the study area, mainly composed of brown-red conglomerate, with an angular unconformity to the underlying Anding Formation. The Lower Cretaceous series is mainly composed of red and gray sandstone and mudstone of alluvial, fluvial and eolian origins, which has angular unconformities with overlying and underlying horizons. In general, Upper Cretaceous and Lower Tertiary series are poorly developed in the study area. Quaternary sands and soils are scattered through the region and can reach tens of meters thick.

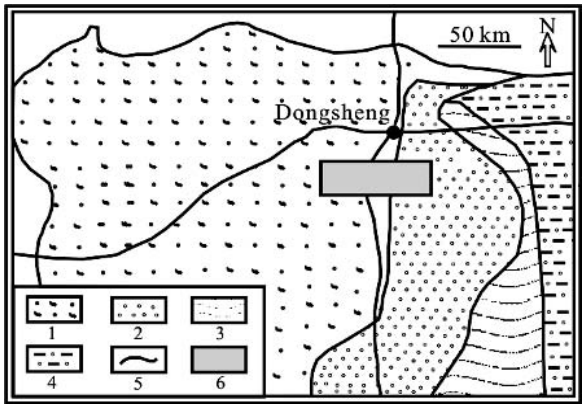

Figure 1: simplifies geological map of Dongsheng area in Ordos Basin. 1-Lower Cretaceous series, 2-Jurassic system, 3- Triassic system, 4- Paleozoic erathem, 5- road, 6-study area

The Dongsheng area underwent multiple tectonic events, leading to changes of contact relations between sedimentary strata, sedimentary facies, hydrological conditions and erosion etc., having close relationship to uranium mineralization.

2 Metallogenetic conditions

Metallogenetic conditions of Dongsheng sandstone type of uranium deposit can be summarized in three aspects of tectonics, formation and reworking processes.

2.1 Tectonic conditions

1. The Dongsheng uplift block: The block is one of important tectonic features, which is located in the north of Dongsheng area (Fig. 1). The block began to be uplifted in Middle Proterozoic, and did not stop uplifting until Early Carboniferous, when sedimentation occurred in the block area. The block tectonics resulted in a gentle slope dipping southwards or southwestwards with the dip angle of 2°-5°. This gentle slope controlled not only sedimentary formation, but also ancient or even present hydrodynamic regime. Fluvial sedimentation was dominant in Middle Jurassic (Fig.2), and a major hydrological recharge-runoff-discharge system was formed. So, the Dongsheng block provided the basic conditions for uranium mineralization.
2. Tectonic evolution: The Dongsheng area underwent multiple tectonic events after the Yanan and uranium-bearing Zhiluo Formation. A): The Dongsheng area was regionally uplifted and was subjected to erosion after Yanan Formation, at approximately 175 Ma. This led to uranium enrichment in its upper part because of downwards leaching processes. This regional uranium anomaly is detected by borehole logging, and could provide uranium sources for the uranium concentration in Zhiluo Formation, which is indicated by the isotopic U-Pb age of 177 Ma. B): During the period from 154 Ma (Late Jurassic) to 125 Ma (Early Cretaceous), tectonic movements were dominated by uplifting and erosion, and sedimentation took place only in some local sections, which provided suitable conditions for the paleo-phreatic oxidation and led to corresponding uranium enrichment. This was an important time of uranium enrichment, and laid the foundation for further uranium enrichment, which is indicated by the isotopic U-Pb age of 124 Ma and geochemical signatures to be discussed. c): During the period from 96 Ma (Late Cretaceous) to 32 Ma (Oligocene), tectonic movements were also dominated by uplifting and erosion, and sedimentation did not take place, resulting in suitable conditions for the interlayer oxidation and leading to corresponding uranium enrichment. This appears to have been the main phase of uranium mineralization, leading to the formation of Dongsheng deposit, indicated by the isotopic U-Pb age of 85 Ma and metallogenetic features. d): The multiple Cenozoic tectonic movements obviously impacted on the pre-existing uranium mineralization mentioned above, resulting in redistribution and recrystallization to form coffinite, and down-dip movement of the roll-fronts, which are indicated by the isotopic U-Pb age of 20 Ma determined from coffinite and 8 Ma from roll-front ore samples. Radium and uranium are not in equilibrium, and the equilibrium coefficients vary from zone to zone, implying that the reworking process is still active.
3. The Zhungeerzhao-Wangjiata Fault: This fault, which is located to the south of deposit area and is considered to intersect both the basement and Meso-Cenozoic rocks, is clearly seen in the satellite images. It appears to be a long-lived and multiply-activated faul, which has made two contributions to uranium mineralization: the first was to provide a suitable discharge condition for hydrodynamic regime, and the second was to generate a reducing environment as reducing materials (organic gases etc.) move upward it, where oxidized uranium was precipitated.

2.2 Sedimentary formation conditions

1. Braided stream facies sedimentation: The lower section of Zhiluo Formation is the main target horizon of Dongsheng deposit. It belongs to braided stream depositional system (Fig. 2). Its lithology is dominated by coarse-grained arkosic sandstones with a thickness from 20 to 40 meters, which contain uranium from 3 to 5 ppm and are loosely cemented. The braided stream sandstone plays a basic role in the formation of the uranium deposit.

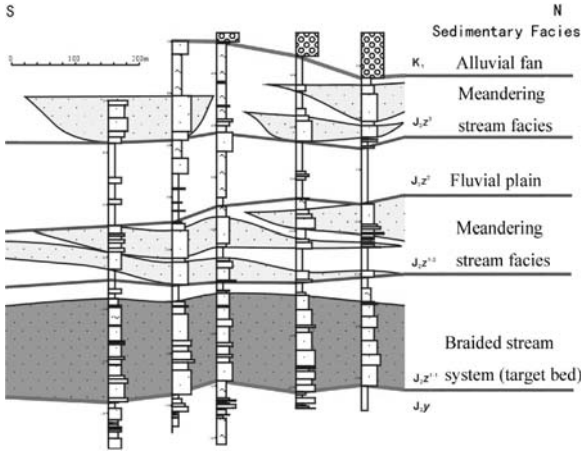

Figure 2: Construction of middle Jurassic series and their sedimentary facies

2. Favourable mud- and sandstone distributions: The formation of sandstone type uranium deposits, especially those amenable to in-situ leaching, requires favourable sandstone to mudstone ratios, from 3:1 to 1:1. The 2:1 ratio of sandstone to mudstone in Dongsheng area is suitable. In addition, these sandstone or mudstone beds should be stable in extension, i.e. single sandstone or mudstone bodies should be connected to each other (Fig. 2). These features make it possible for ore-forming fluids to flow only in the sandstone horizons. Furthermore, interlayer oxidation can be developed, resulting in mineralization.
3. Occurrence of ore-hosting horizons: The target horizon of Zhiluo Formation is buried at the depth generally ranging from 150 to 500 meters, being acceptable depth for exploration at present time. Dip angle are favourable for water movement, being in the range from 2 to 4 degrees.
4. Reductants: The target horizon of Zhiluo formation has suitable content of reducing materials ranging from 0.5 to 1.5%. In addition, some reductants are thought to have been originated from the depth through faults mentioned before, which can be confirmed by a lot of oil and gas inclusions found in the ore samples. The reductants are necessary for uranium to be reduced from mobile 6^+ to stable 4^+ valence, leading to uranium precipitation.

2.3 Subsequent reworking conditions

1. Redox condition: Dongsheng deposit occurs in the redox zone, i.e. transitional zone between oxidation and original zones. The redox transitional zone was formed by both paleo-phreatic and interlayer oxidation processes. So, it has both vertical and horizontal zonations, which are also confirmed by geochemical and mineralogical zonations. Analytical data for U, Se, Mo, V, Re and S show systematic increases from oxidation to original zones in both vertical and horizontal directions. Goethite, kaolinite, hemitite are typical in the oxidation zone, in contrast with pyrite in the original zone. The ore bodies show roll-front shape with long tails. These features show that uranium mineralization are controlled by oxidation and reduction processes.
2. Secondary reduction processes: Mineralogical studies show that secondary reduction processes took place after the formation of uranium deposit in the Zhiluo Formation. These processes make the sandstones in the paleo-oxidation zone green or gray-green, indicating geochemical reduction environments. The greenish color mainly results from chloritization and epidotization. The ore bodies are clearly located in the transitional zone between gray and green colored sandstones. This is a special feature of Dongsheng deposit, different from other ordinary sandstone type uranium deposits. The greenish alteration is related to oil and gas secondary reduction processes. A lot of oil and gas inclusions have been found not only in the paleo-oxidation zone, but also in the ore body zone, which show multiple oil and gas penetrating and reworking processes.
3. Tectono-hydrothermal events: Dongsheng uranium deposit records tectono-hydrothermal reworking events, which resulted in uranium redistribution and coffinitization in the ore bodies (Fig. 3). The appearance of coffinite indicates that uranium mineralization was formed at relatively higher temperature and more reducing environment than those of the ordinary deposits. In addition, homogenization temperatures measured from inclusions in vein carbonate range from 70°C to 170°C, and the salinity from 8% to 20%, which also indicate that Dongsheng area underwent hydrothermal events.
4. Climatic evolution: The paleo-climate evolved from humid in the Yanan and early Zhiluo epochs to arid in the time later than Zhiluo epoch. The humid climate in the Yanan and early Zhiluo epochs was favorable to generation and preservation of organic materials in sediments, and later arid climate was favorable for oxidation process to make uranium mobile. This climatic evolution is favorable for uranium mineralization.

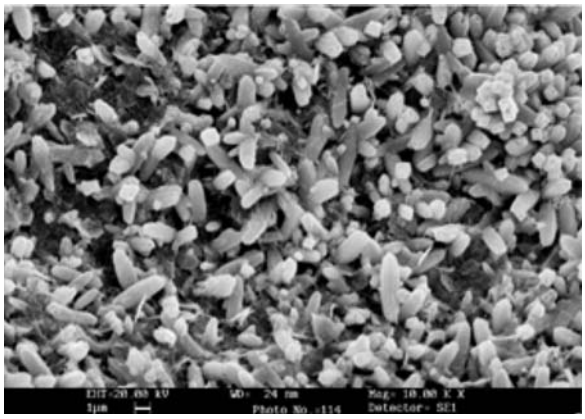

Figure 3: Coffinite crystal found in uranium ore sample

3 Exploration criteria

As discussed above, the Dongsheng deposit is characterized by its unique features, which are related to its complicated origin. The deposit was formed not only under redox processes, but also underwent oil-gas and hydrothermal reworkings conditions. Therefore, the correctly understood origin and concluded exploration criteria are of both theoretical and practical significances in exploration for similar type uranium deposit. Criteria for exploration are concluded as follows:

1. Tectonic slope: The slope must have a favorable dipping angle not larger than 10 degrees and undergo suitable subsidence and uplifting movements to keep acceptable depth of target horizons and erosion period for uranium mineralization.
2. Connected sandstone bodies and lithologically transitional zone: Braided stream sandstone bodies should be well connected as stable sandstone horzons, with suitable occurrence state. Uranium mineralization often occurs in the transitional zone in lithologic, grain-size, facies or color changes.
3. Paleo-oxidation zone identified from presently displayed reduction area: Greenish or green sandstones are special features, which reflect secondary reduction processes. They are actually secondary-reduced paleo-oxidation zones. Uranium mineralization is controlled by transitional zone between gray (original rock) and green (paleo-oxidized) sandstones. To identify this kind of transitional zone is very important in exploration.

References

Li ST (1992) Sequence stratigraphy and depositional system in Northeast Ordos Basin. Beijing: Geological Publication House (in Chinese)

Li ZY, Dong WM, Guo QY (2002) Metallogenetic features and perspective evaluation of sandstone-type uranium mineralization in Hailaer Basin, NE China. In "Sandstone-type Uranium Deposits in China: Geology and Exploration Techniques" edited by Bureau of Geology CNNC. Beijing: Atomic Energy Press

Wang SM (1996) Coal accumulative pattern and resource evaluation of Ordos Basin. Beijing: Coal Industry Press

New discovery in the study of remote sensing image characteristics in sandstone-type uranium districts in China and its significance

Dechang Liu, Xianfang Huang, Fawang Ye
Beijing Research institute of Uranium Geology, Key Laboratory of Remote Sensing, National Defence Science and Technology, Beijing 100029, China

Abstract. Sandstone-type uranium deposits are now one of the main targets for uranium prospecting in China. Prospecting commonly emphasizes lithology, stratigraphy, lithofacies, and ore-controlling factors, while the influence of faulting is usually neglected. Systematic research of features from remote sensing images of sandstone-type uranium deposits shows fault-controlled commercial mineralization occurs in most major sandstone-type uranium ore districts. This paper discusses characteristics of faults and their roles in controlling mineralisation, particularly faults penetrating the basin and basement rocks. Based on the above research, a new ore-controlling model- "structure-geochemical barrier model" is put forward. It is pointed out that the "structure-geochemical barrier model" is a metallogenic model that differs from the traditional interlayer oxidation zone model. The new metallogenetic model proposes that gases, water and oil migrate upward along faults as a result of fault mobilization and form a geochemical variation zone where uranium is precipitated. These are distinct from uranium-bearing and oxygen-bearing water migrating along ore-hosting horizons from oxidizing to reducing environments, with uranium precipitated in redox transition zone. This is an important model for non-typical geosyncline platform environments. It is of significance for uranium reconnaissance and prospecting in China. Attention should be paid not only to lithology and lithofacies research but also to the roles of ore-controlling faults.

Keywords. Remote sensing image, ore-controlling fault, structure-geochemical barrier model

1 Remote sensing research

According to systematic research on remote sensing image features of major sandstone type uranium ore-fields in China, an important discovery has been obtained, showing that ore-controlling faults are present in most major sandstone-type uranium ore districts. Since the faults are covered with Quaternary strata, they are difficult to find in the field and it is difficult to detect an enhanced image signature of fault using general image processing methods. Therefore, the existence of faults and their ore-controlling roles have been neglected for a long time. The evidences for faulting and the relationship with uranium mineralization are discussed here.

1.1 Indications of ore-controlling faults

There are two cases that are described as follows.

I) Linear signature of ore-controlling fault is very clear in the light color image background, expressing as dark and dim color zone and longer extension along strike. In the cross profile, the width of the color zone is quite large, sometime, there is no remarkable textural feature in the margin, and the boundary line is indistinct.
II) The ore-controlling fault is expressed as a boundary of two different image districts. Although the linear signature is not clear, the color, lamination, geographic landscape on both sides are obviously different. In the thermal image of Dong Sheng district, the image feature is displayed as the boundary line between the high geothermal field and low geothermal field.

1.2 Geophysical indications of ore-controlling faults

The ore-controlling faults interpreted from image is usually coincident with those interpreted from geophysical data (including gravity data, magnetic data, seismic data). In addition, airborne radioactivity surveys often show distributions of uranium along faults in some ore-fields.

1.3 Topography, geomorphology, and drainage indications of ore-controlling faults

These kinds of faults are difficult to recognize by geologists in the field due to Quaternary cover and are often neglected in research. By means of remote sensing image analysis, very weak trace signatures can be discerned. They are expressed as geomorphic cliff and valley, river and drainage direction changed, springs and wetland and vegetation linear distribution (Zhu et al. 2002).

1.4 Field checking of interpreted faults

Field checking has indicated that some ore-controlling faults occur beneath Quaternary cover. Although difficult to identify, the macro-image features are very clear. Multi-information comprehensive indications are conspicuous. Borehole information shows that mineral alteration is developed along the fault. Water leakage can be seen in some boreholes. All of these reflect that the fault is objectively existed in the ore-field. The spatial relationships

show that uranium mineralization is clearly controlled by fault. In plan, the uranium deposits and occurrences are distributed along the fault, expressing as pearl-string and belt distribution. The direction of fault controls mineralization belt orientation. In profile, the ore-body is located close to local oxidation-reduction transition zone or in strong reducing zone related to the fault. Double faults control double oxidation-reduction transition zone and control the formation of double roll bodies (Huang et al. 1999).

2 Characteristics and role of ore-controlling fault

2.1 Fault characteristics

In the light of comprehensive study and analysis of ore-controlling faults in major ore-fields in China, the characteristics are summarized as follows:

The interpreted fault from remote sensing interpretations coincides with the faults interpreted from gravity, magnetic and seismic information. Most of them are penetrating faults that cut through the basin basement from above covering strata. Multi-stage mobilization. The ore-controlling fault is usually expressed as compressive or compressive-shear fault at early stage, while displayed as tension or tension-shear fault at late stage. All the ore-controlling faults cut through the ore-bearing strata. The intersection and fault mobilization are favorable for uranium-bearing and oxygen-bearing ground water migrating toward the fault along the ore-bearing horizon. Ore-controlling faults are displayed as water-rich or oil and gas seepage zones.

2.2 Role of faulting in ore formation

Analysis of many uranium deposits shows that faulting plays important roles in uranium mineralization. One is to drive circulation of uranium-bearing and oxygen-bearing groundwater. The other is to create a favorable environment for uranium precipitation. Both control the distribution of uranium occurrences.

How does the fault control uranium mineralization? The explanations are as follows:

The fault is a decompression zone: Fault movements form decompressive physical environments and result in uranium-bearing and oxygen-bearing groundwater moving toward the fault. The fault is discharge zone: In the most cases, the fault is a discharge zone. Both decompressive and discharge zones can result in groundwater circulation and ensure that uranium-bearing and oxygen-bearing groundwater continuously migrates towards the ore-controlling fault. This is favorable for uranium mineralization formation. The fault is connection zone: The fault is a conduit which links with gas, water, oil at depth. It is also a conduit for uranium element moving upward and precipitating in the favorable environment. Based on above research, a conclusion can be drawn that when the uranium resource condition is determined, the fault plays an important role in uranium mineralization of sandstone type uranium deposits in China. Accordingly, a new ore-controlling model- "structure -geochemical barrier model" is put forward, after analyzing distribution feature of main sandstone type uranium deposits in China (Liu et al. 2004).

3 Structure-geochemical barrier model

The structure-geochemical barrier model of main sandstone type uranium deposits in China differs from foreign traditional interlayer oxidation front zone model. It is a new ore-controlling model.

3.1 The difference of two ore-controlling models

In terms of uranium source, hydrodynamic condition, uranium precipitation and concentration mechanism or thinking for prospecting, both models are quite different.

1. Uranium source: The traditional viewpoint is that the uranium source of interlayer oxidation front model is derived from provenance area, ore-hosting horizon, or above uranium - containing horizon; while the structure-geochemical barrier model considers that besides above-mentioned uranium sources, the uranium source can also derived from uraniferous layer below the ore-hosting horizon.

2. Mechanism of forming hydrodynamic condition: Traditional viewpoint is that the forming hydrodynamic mechanism of traditional interlayer oxidation front zone is due to strata tilt, and gravity process; while structure -geochemical barrier model considers that besides gravity process, fault decompress is an important factor. When the ore-bearing layer is near horizon, hydrodynamic condition mechanism is mainly caused by fault decompress which drive the water migration from higher pressure place to lower pressure place (fault). So, when the ore-bearing layer is near horizon, structure -geochemical barrier model can also form uranium deposit.
3. The origination of uranium concentration precipitation: Traditional viewpoint thinks that the uranium precipitation and concentration of interlayer oxidation front zone takes place in the oxidation-reduction zone, when the uraniumbearing and oxygen-bearing groundwater moves from oxidation zone to reducing zone. While structure -geochemical barrier model considers that fault can connect with the gas, water, and oil in depth, forming local reducing or strong reduc-

This page intentionally blank

ing environment, making uranium precipitation. The origination is fault motion. The traditional viewpoint emphasizes on provenance area, lithology, stratigraphy, lithofacies, and eglects fault role in uranium mineralization. The structure-geochemical barrier emphasizes lithology, stratigraphy, lithofacies plus fault condition. According to the structure -geochemical barrier, prospecting should pay attention to both the ore-hosting layer, but also to ore-controlling fault (water-rich zone or oil seepage zone), and to the intersection of these.

3.2 Significance of structure-geochemical barrier controlling model

Structure -geochemical barrier controlling model shakes off viewpoint that considers uranium source is only derived from provenance area, ore-bearing horizon, and above strata, considering that uranium source can also derived from below the strata. Structure -geochemical barrier controlling model do not follow the classical viewpoint that the prerequisite for forming interlayer oxidation zone mineralization is tilting of strata, and considering that decompression of fault can result in favorable hydrodynamic mechanism for forming uranium deposit, even though the strata is near horizon. Structure-geochemical barrier model deepens interlayer oxidation zone theory that considers forming uranium mineralization concentration not only is due to uranium-bearing and oxygen-bearing groundwater moves downward along the ore-hosting layer and forms oxidation-reduction but also due to gas, water, and oil in the depth migrates upward along the fault and forms favorable uranium concentration environment and widens uranium metallogeny theory. The structure-geochemical barrier model emphasizes composite controls of lithology, stratigraphy, lithofacies, and fault (water-rich zone or oil, gas seepage zone). So, prospecting should especially pay attention to areas where the lithology, stratigraphy, lithofacies, and ore-controlling fault is favorable. The structure-geochemical barrier model is the main ore-controlling model for sandstone type uranium deposits in China. The structure-geochemical barrier model is restricted by exceptional tectonic background. So, further prospecting should pay attention to Chinese tectonic characteristics favourable for fault controlled uranium mineralization in sandstones.

References

Huang XF, Liu DC (1999) Remote Sensing Technology Prospecting Methods of Interlayer Oxidation Zone Type Sandstone Uranium Deposit in Yili Basin.Beijing: Atomic Energy Press

Zhu MQ, Yu DG (2002) Remote Sensing Geologic Research on Structure and Uranium Mineralization in Bayantala Basin, the Inner Mongolia Autonomous Region, Remote Sensing for land & resource 51(1)

Controls on Precambrian uranium ore formation: The role of ancient oil (and evaporates?)

I.G. Mineeva
Institute of Mineral Resources (VIMS), Moscow, Russia

Abstract. The relationship between Precambrian rifting, greenstone belts, iron-rich- and carbonaceous rocks formation, alkaline metasomatism, ancient oil generation and the origin of Proterozoic U deposits on Precambrian shields is revealed. Interrelated processes of the Proterozoic economical U ore deposition and oil generation occurred in ancient rift basins, in zones of structural and stratigraphical discordance between greenstone crystalline basement and overlying volcanogenic-sedimentary sequences. High-grade complex U deposits were formed at the final stage of the oil and gas reservoirs degradation.

Keywords. Precambrian shields, greenstone belts, rifts, U deposits, oil

1 Introduction

A comparative study of the Proterozoic U-Th-REE-, U, U-Au-, U-Au (REE, Fe)-, and U, Au-U, U-Ni, U-Au-Co-Ni-complex deposits on Precambrian shields of Russia, Ukraine, Canada, Brazil, South Africa, and Australia revealed general similarities in their formation. Particular attention was paid to their worldwide confinement to ancient rift basins, which contain abundant carbonate and siliclastic sequences with high organic carbon content. Such sequences could act as oil-source rocks, as confirmed by the presence of economic-grade ancient oil reservoirs (1850-1450 Ma) in the Australian rift basins that occur close to large North and South-Australian U-bearing provinces (Summons et al. 1988).

2 Geological setting of Precambrian U deposits: A role of greenstone belts and ancient rifts

The oldest long-lived Precambrian U-bearing ore systems of Precambrian shields formed within a rift environment at the Archean to Early Proterozoic boundary.

Protorifts were open at the early stage of the Earth's crust evolution and are traced by greenstone belts (Condie 1983). Precambrian U deposits developed in riftogenic troughs, which were initiated within greenstone belts in Early or Late Proterozoic.

The Precambrian U deposits are confined to structural-stratigraphic unconformities between Archean granite-greenstone crystalline basement and overlaying Early Proterozoic protoplatform volcanogenic-sedimentary sequences consisting of quartz conglomerates, phosphorites, ferriferous carbonaceous-carbonate deposits, and submarine volcanic rocks. Carbonaceous marine sediments are typical of the most subsided rift parts. They usually rest on iron formations.

Greenstone belts can be used as a key for deciphering Precambrian riftogenic structures.

3 Main genetic types of Precambrian U deposits

3.1 Primary Precambrian U deposits

Primary U deposits may be divided into four main genetic types based on their chemical elements association and geological, petrological, and mineralogical characteristics (Table 1). The uranium deposits of the Type I are associated with granites, granite pegmatites and feldspathic-silicate skarns in the Precambrian granite-greenstone basement. The uranium deposits of the Types II – IV developed within the upper parts of the stratigraphic sections of greenstone belts, containing conglomerates and sandstones (Type II), iron quartzites (Type III), carbonates and carbonaceous shales (Type IV - unconformity-type).

Two geochemical associations of elements are typical for Precambrian U deposits: the first one includes lithophile elements: Th, REE and Zr; the second one sid-

Table 1: Major genetic types of Proterozoic complex U deposits on Precambrian shields

No	Type	Geological setting	Examples
I	U-Th-REE deposits in granites, pegmatites and skarns	Structures of greenstone and granulite belts, zones of regional granitization, pegmatitization and skarn-formation	Sharlebua, Canadian shield; Mary Kathleen, Australian shield
II	U, U-Au deposits in pyritic quartz pebble conglomerates	Periphery of Archean greenstone belts	Witwatersrand, S.African shield; Serra de Jacobina, E.Brazilian Shield
III	U-Au (REE, Fe) deposits in iron formations	Structures of greenstone belts, zones of brecciation in iron quartzites	Radium Hill, Olympic Damp, Australian shield
IV	U, Au-U, U-Ni, U-Au-Co-Ni deposits in carbonaceous shales-"unconformity" type	Structures of destroyed greenstone belts, zones of ancient regional unconformities	Jabiluka, Australian shild; Kee Lake, Canadian shield

Table 2: Transformed (?) genetic types of Proterozoic complex U deposits by Na metasomatism (related to albitization?)

No	Types	Examples
Ia	U deposits in polyzonal albitites (apogranitic, apopegmatitic, aposkarn)	Kirovogradsky region, Ukrainian shield; Beaverlodge, Canadian shield
IIa	U deposits in local zones of albitization in conglomerates	Krivorozhsky region, Ukrainian shield; Pronto, Canadian shield
IIIa	U - Fe deposits in ferriferous Na-metasomatites	Zheltorechenskoye, Ukrainian shield; Iron Quaadrangle, E. Brazilian shield
IVa	U, PGE-Au-U-V deposits in albitites after carbonaceous shales ("unconformity" type)	Padma, Kuusamo, Baltic shield

erophile and chalcophile elements: PGE, Au, Ag, Bi, Cu, Co, Ni, Mo, V, Fe, Sc, Cr, Mn, S, Se and Te. The major aspect of U, Au, PGE, V, and Ni geochemistry is their affinity with organic matter.

3.2 Transformed (?) Precambrian U deposits (related to albitization and carbonatization?)

The oxidized (are there any arguments for oxidation?) Na-carbonaceous (sodium and carbonate?) metasomatism (albitization and carbonatization?) occurred essentially on all Precambrian shields at about 1.8 Ma. It was probably (?) connected with an uplift of large tectonic blocks of the Earth´s crust along long-lived riftogenic structures. The most intense uraniferous Na-carbonaceous metasomatic processes (albitization and carbonatization?) are developed on Ukrainian, Baltic, Canadian, and East Brazilian shields. The Na- metasomatic solutions destroyed rock-forming- and ore minerals, oxidized elements of alternative valence (U, Au, Fe, S, C), and created favorable conditions for the redeposition and separation of U and accompanying elements. Principally new genetic types of U deposits, uraniferous albitites, were formed instead of earlier complex U deposits that are not accompanied by large-scale alterations (Table 2). U mineralization developed within the most brecciated and permeable parts of metasomatite bodies.

4 Ancient rifting and participation of ancient oil in the formation of complex U deposits on Precambrian shields

Highgrade Precambrian complex unconformity-type deposits occur in ancient rift structures, where they are confined to sedimentary rocks enriched in organic carbonaceous material. Strong sagging under lithosperic extensional conditions associated with repeated volcanic activity regularly led to the intense heating of sedimentary

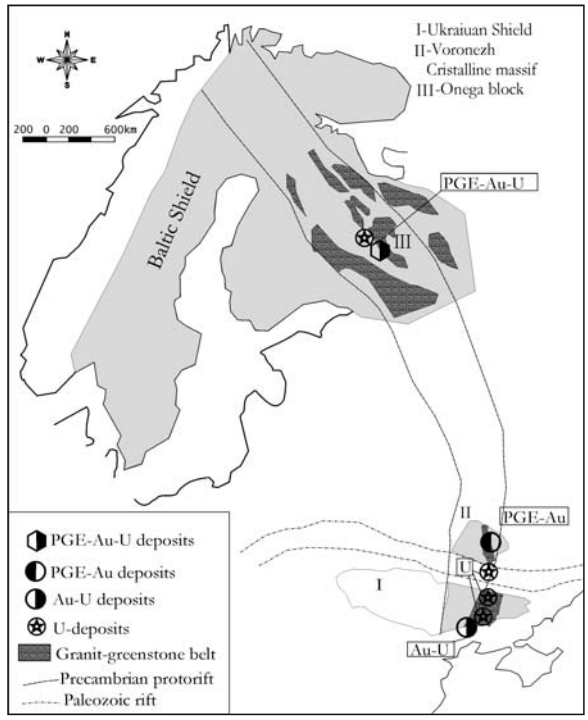

Figure 1: Location of complex U deposits in the Precambrian Eastern-European rift

rocks and ancient oil accumulation. Our investigations (Mineeva and Guseva 2001) showed that complex U (Au-U and PGE-Au-U) deposits developed in the oldest rifting structures retain traces of Precambrian oil, which probably participated in the ore formation (Fig. 1).

4.1 Relicts of ancient oil in ores of the Proterozoic Padma PGE-Au-V-U deposit (Baltic shield)

The Padma PGE-Au-V-U deposit was formed at 1900 Ma in a brecciation zone at the contact between the Proterozoic shungite schists and dolomites in the Onega rift of the Baltic shield (Mineeva and Guseva, 2001). Rocks similar to shungite schists are not known in the other parts of the world. Based on the carbon content, five shungite varieties were distinguished. The latest shungite-I (70-95 wt. %C) forms cross cutting veins, irregular inclusions, conformable interlays and lenses in surrounding rocks. Shungite has a globular permolecular structure and light carbon isotopiccomposition ($\delta^{13}C$ -23.3‰ to -42‰) that is typical for Precambrian oil. The solubile bituminoids extracted from the sample of ore metasomatites show significant content of aromatic hydrocarbons. The distribution of n-alkanes in shungites and ore-bearing metasomatites after shungites is similar and shows maximum at n-C_{21}. The pristane/phytane ratios are similar (0.68-0.60) in host rocks, wall rock metasomatites and ore zone. Gas chromatography revealed traces of steranes and hopanes. The aromatic hydrocarbons,

n-alkanes, isoprenoids, styrenes (steranes?) and hopanes, as well as relict biomarkers, i.e. phytane and pristane preserved in transformed (?) ores indicate participation of the Early Proterozoic marine biogenic oil in the PGE-Au-V-U ore formation. Therefore, disruption (extinction?) of the oil-bearing rift basins and oil migration can facilitat formation of the economic-grade U mineralization. The dissolving of ancient evaporite caps of oil reservoirs can be regarded as the most probable source of Na in metasomatic processes that transform all (?) genetic types of the Precambrian U deposits, completely obliterating all traces of ancient oil participation in the ore formation.

4.2 Relicts of ancient oil in res of the Witwatersrand Au-U deposit

The preservation of relicts of the previously existed oil in the oldest economic-grade Witwatersrand Au-U deposit was reported by Spangenberg et al. (1999). The deposit is confined to the Early Proterozoic riftogenic trough located among (along?) the Archean Barberton greenstone belt. The Au-U ores in the Witwatersrand pyritized quartz conglomerates are restricted to reefs, where native gold, uraninite, and pyrite are closely associated with bitumens. Organic matter in the reefs occurs in two forms (Spangenberg et al. 1999): (1) stratiform carbon seams and (2) spherical glassy disrupted nodules of solid bitumen. These forms are similar to shungite generations. Both these forms have light carbon isotopic composition ($\delta^{13}C$ = -23.6 ‰ to -39.2 ‰).

Soluble bitumen extracts show significant contents of aromatic hydrocarbons. The pristane/phytane ratio varies from 0.21 to 0.82. The isotopic composition of normal alkanes (n-C_{15} to n-C_{27}) and isoprenoids (Pr and Ph) in extracts from vein carbon varies from -28.5‰ to -34.8‰ and from -29.1‰ to -33.9‰, respectively.

Therefore, the occurence of relict biomarkers (Pr and Ph) in the ancient Witwatersrand bitumens and light carbon isotopic composition of normal alkanes and isoprenoides also indicate that marine biogenic oil participated in the Au-U ore genesis in the riftogenic basin of the South African shield at the Archean-Early Proterozoic boundary.

4.3 Proterozoic oil of Australia and U-bearing provinces of North and South Australia

The Earth's oldest preserved oil (1400 Ma) was found in the Upper Proterozoic McArthur rift basin. Intracontinental East Australian rift, like East European rift (Fig. 1 and 2), extends longitudinally through the entire Australia over many thousands kilometers and includes three oil & gas bearing basins (McArthur, Georgina, and Adelaide). The rift controls the location of large U-bearing provinces. The McArthur basin rims the eastern part of the Pine Creek U-bearing province, which hosts the unique Precambrian U, Au-U, and PGE-Au-U unconformity-type deposits (Rum Jungle, Jabiluka, Coronation Hill, and others), while the Adelaide basin hosts Olympic Dam complex U-Fe-Au-Ag-Cu-REE deposit. The central part of the McArthur basin is filled with Upper Proterozoic terrigenous and carbonate sediments up to 12 km thick, which contain up to tenstrongly disrupted (segmented?) ferruginous beds of the Roper group. The Kyalla ore-bearing member consists of dark gray and black tuffaceous mudstones located at a depth of 968-1714 m. The C_{org} content in the Kyalla formation ranges from 2 to 9 wt %. The Pr/Ph ratio is close to 1. The average carbon isotopic composition of ancient oil $\delta^{13}C$ is -31.69 ‰, which is consistent with isotopic composition of the ancient relict oil found in the Precambrian complex U deposits in the Baltic and South African shields.

5 Possible role of oil in the formation of U deposits of the Atabaska basin

It is known that the U-bearing province of the Athabasca basin hosts the richest known economic-grade unconformity-type U deposits (Cluff Lake, Rabbit Lake, Kee Lake, McArthur, and others). Riftogenic nature of was by On the basis of geophysical field study; Darnley (1981) interpreted the Athabasca basin as a riftogenic structure. The ancient paleorift was deeply subsided, extending NE over 1500 km beneath the Middle Proterozoic Athabasca trough (1450 Ma). The ancient rift structure controls the location of the richest Upper Proterozoic economic-grade uncon-formity-type U deposits.

The giant, in terms of hydrocarbon reserves, unique Athabasca asphalt deposit is located 180-200 km southward of the uranium province, on the slope of the Canadian shield (Fig. 3). High-sulfur oil occurs there at a depth more than 1000 m. Bituminous sandstones (age??) unconformably overlay eroded Devonian carbonate deposits and are covered by Lower Cretaceous clayey sequence. The oil content in sandstones widely varies, occasionally reaching up to 20 wt.%. Total geological reserves of oil hydrocarbons in sandstone are estimated on the level of 50 billion tons. The age of the Athabasca asphalts bitumens is controversial. Acccording to Perrodon (1985), oil was supplied from the underlying Devonian deposits, which in the west of the Athabasca River host the richest reservoirs of the heavy resinous oil. It is highly probable that ancient Athabasca rift, strongly affected by brittle deformation similarly as the McArthur Basin, accumulated oil since Upper Proterozoic. (!!this is very speculative. Athabaska tars are very young in relation to the uranium deposition. However, there is evidence that some oil formed a part of hydrothermal fluids. (See for example Mossman et al. 1993, Kotzer and Kyser 1990, Pagel and Landais and many others).

6 Conclusions

1. Ancient oil took part in the formation of the Precambrian high-productive complex unconformity-type U deposits developed in the volcano-sedimentary sequences of ancient riftogenic structures.
2. The large economic-grade U deposits of the Precambrian shields formed simultaneously with decomposition of the Early Precambrian oil & gas bearing riftogenic basins (Archean and Early Proterozoic). The oil migration and decomposition is inevitable if rifting is accompanied by volcanism. Volcanic processes cause oil pyrolysis, which facilitates formation of natural fullerenes that form complex compounds with many ore components.
3. Subsequent transformation of the complex U mineralization was caused by alkaline metasomatism. The destruction of salt domes can be considered a source of sodium for metasomatic processes and for the formation of albitites that accompany U-mineralization.
4. Petroleum potential of Precambrian rocks was presumably higher than that of Phanerozoic rocks, which was reflected in the formation of economic-grade giant unconformity-type U deposits on the Precambrian shields. However, only traces of hydrocarbons were preserved in uranium deposits due to oxidative character of ore-bearing solutions.

References

Condie KC (1981) Archean Greenstone belts. Amsterdam-Oxford-New York: Elsevier Scientific Publishing Company

Darnley AG (1981) The relationship between distribution and some major crustal features in Canada.Miner. Mag. 44: 425

Mineeva IG, Guseva NN (2001) Primary and transformed carbonaceous PGE-Au-U ores on Precambrian shields: role of petroleum. In A. Piestrzynsky et al. (eds), Mineral Deposits at the Beginning of the 21st Century 63-66. Lisse: Swets & Zeitlinger

Spangenberg J, Frimmel H (1999) Tracking the origin of organic matter in the Witwatersrand Basin using $^{13}C/^{12}C$ analysis of individual hydrocarboms. In Stanly CJ et al. (eds), Mineral Deposits: Processes to Processing, A.A.Balkema Publishers 1: 271-275

Summons RE, Taylor D, Boreham CJ (1994) Geochemical tools for evaluating petroleum generation in Middle Proterozoic sediments of the McArtur basin, Northern Territory, Australia. APEA Journal 674-691

Uranium deposits in the Arlit area (Niger)

Maurice Pagel, Sabine Cavellec, Pierre Forbes, Olivier Gerbaud, Pierre Vergely, Ibrahim Wagani
Laboratoire CNRS-UPS IDES et Equipe Tectonique, Bât 504, Université de Paris-Sud, 91405 Orsay Cedex, France

Régis Mathieu
COGEMA, 2, rue Paul Dautier, 78141 Velizy-Villacoublay, France

Abstract. In the Arlit area (Niger), the uranium deposits are located in the Visean Guezouman Formation and in the Namurian Tarat Formation, near the Arlit In Azawa fault. Sedimentological and structural controls of the mineralized zones are evidenced. The age of the mineralizing event is not precisely determined but is younger than the age of sedimentation. According to fluid inclusions studies, brines were recorded during the main mineralizing event at temperatures ranging from 85 to 175°C. The presence of Zr, Mo, V and Zn in the deposits is related to volcanic sources for uranium and these metals.

Keywords. Visean, Namurian, sediments, volcanism, brine

1 Introduction

The Tim Mersoï sub-Basin (Niger) is part of the Iullemmeden Basin, located about 200 km north of Agadez and west of the Air Mountains. Several uranium deposits have been discovered since 1958 in this area. They have been the subject of very few scientific studies, different to and compared with other areas in the world particularly the unconformity-type deposits. However, the tonnage is important (160 000 tons U) with a grade ranging from 0,2% to 0,5% and mineralization reaching to a depth of 220m. This paper summarizes the data already obtained and points out the many questions still to be answered.

The main U deposits are mined by Cominak and Somair using underground and open pit methods respectively. They are located in the Visean Guezouman Formation for Cominak (44 000 tons U) and in the Namurian Tarat Formation for Somair (50 000 tons U), 50 km westward of the Air basement. The Imouraren deposit of lower grade (0,12% U, 66 000 tons U) is located 80 km south in the Tchirezrine 2 sandstones (Jurassic). These deposits are located near the Arlit In Azawa (AIA) normal fault but other U mineralizations are known close to the Aïr basement, in the Madawela area. Therefore, several types of deposits exist in the Tim Mersoï basin but their characteristics still need to be examined in further detail.

To present and discuss the different possible uranium models and following a brief description of these U deposits, five questions remain to be answered: (1) what is (are) the sources of uranium and associated metals (Mo, Zn, V and Zr)? (2) What are the sedimentological controls? (3) What are the structural (and tectonic) controls? (4) What is (are) the age(s) of U deposition? (5) What are the nature and origin of the mineralizing fluids?

The laboratory data used in the present discussion are mainly based on a PhD thesis realized by Pierre Forbes under the supervision of Maurice Pagel. Most of the geological field observations have been acquired by many geologists from CEA, GOGEMA, COMINAK and SOMAIR over the past years.

2 Mineralogy of the deposits

Five mineralizing phases have been distinguished by Forbes (1989) in the Akouta deposit: (1) an early replacement of wood fragments by pyrite and formation of quartz overgrowths on detrital quartz grains, (2) a sulphate phase with formation of barite, (3) the U-Mo-V-Zn-Zr deposition phase, (4) the alteration of feldspars and formation of kaolinite on the west side and (5) the formation of iron oxides and manganese-rich cements. The ore in the Guezouman and Tarat deposits consists of pitchblende, V-chlorite, corrensite, jordisite, montroseite, pyrite, marcasite, sphalerite and dolomite. Pitchblende contains about 3% ZrO2 in the Akouta deposit. A comparable paragenesis has been cited by Elhamet for the deposits in the Tarat formation. A different paragenesis is present in the stratabound Imouraren deposit that mainly consists of hexavalent uranium minerals (uranotile) with abondant Cu (chalcocite, chalcopyrite, native copper). This type is absent in the Arlit zone.

3 Source of uranium and associated metals

The presence of significant amount of Zr replacing U in the uraninite structure implies that Zr was in solution during the deposition of uranium. Only Zr located in volcanic glasses may be liberated easily into solution. The association of Mo, V and Zn also suggests an alkaline volcanic source for these elements. Several explanations are possible: (1) volcanic complexes exist in the Aïr Mountains, such as the Goundaï and the Bilete complexes, which are rich in uranium, especially the vitroclastic tuffs (about 20 ppm in ther Goundaï massif and 15 ppm in the Bilete massif) with large amount of zirconium (between 2000 and 2500 ppm in the Goundaï massif and about 1000 ppm in the Bilete massif). Numerous data obtained on granitic complexes show that their U content is significantly lower. (2) In the Guezouman Formation, occurrences of volcanic shard ghosts are present and suggest that volcanic components were introduced into the sediment by

aerial transportation. However, no volcanism of Carboniferous age is known in the Aïr massif, it is therefore necessary to consider an other scale and look for volcanic activities in entire Western Africa. (3) Furthermore, volcanic components are also present in other formations in this area, including the Jurassic.

Therefore, several choices for the source(s) of U may exist: (1) erosion of the Aïr massif and its volcanic and granitic complexes and supply of detrital grains in the sedimentary formations. These detrital components were rapidly altered and subsequently were suitable for the main mineralizing event. (2) U and the other metals could have been leached and concentrated at redox fronts from the dispersed tuffs from different formations. In our opinion, the U potential of the Aïr massif is relatively well known. This is not the case for volcano-sedimentary rocks that can be also an important source of uranium.

4 Sedimentological controls

The Guezouman Formation and the Tarat Formation were deposited in a fluvio-deltaic environment. This environment is well known as particularly suitable for the enrichment of uranium because organic matter is accumulated rapidly and favourable permeable formations exist where aqueous fluids may circulate. The sedimentological control of the mineralization is undisputed. The Akouta mineralization is characterized by U-Zr-Mo-V-Zn concentration along the N 80 paleochannels located in a floodplain environment. Sanguinetti et al. (1982) have also shown that the mineralization is located in bottom-sets layers and along basal fore-set layers. In these sandstone bodies, there is a preferential accumulation of organic matter, mainly replaced by pyrite. All these features were interpreted by Cazoulat (1985) as a proof of a syn-sedimentary concentrations of U and associated metals. This interpretation is often supported by a Pb-Pb age of 338 ± 5 M.a. on one sample quoted in the literature. This age is based on an unpublished report by Devillers and Menes (1977) where four other samples have been dated by Pb-Pb and gave ages between 150 and 370 Ma. Nineteen other Pb-Pb data sets (Turpin et al., 1991) revealed ages between 69 and 409 Ma. The explanation for such a discrepancy may be explained with the Ra mobility in these deposits discrediting the values of the Pb-Pb ages. One should clearly distinguish the emplacement of the reductant which is without doubt related to the sedimentation process (organic matter distribution) and the U deposition. At the present time, only the Akouta deposit has been studied in sufficient detail. The remnants of syn-sedimentary mineralization, if they exist, should be investigated for all types of mineralization and especially near the Aïr massif. It will be also very important to investigate the Guezouman and the Tarat formations on the West side of the Arlit-In Azzawa fault.

The sedimentary control of the mineralization may result from the differences in porosity and permeability combined with the distribution of the reductants and the circulation paths of the mineralizing fluids.

5 Structural and tectonic controls

The first control is the location of the main uranium deposits in close proximity to the eastern edge of the normal Arlit-In Azawa (AIA) fault in contact with oxidized rocks on the western side of the fault. Additional local control exists as demonstrated in the Akouta deposit. The higher U grades are located at the N40 post depositional syncline and the intersection with the N80 Akouta channel. Recent observations in the Tarat formation show also a strong influence of faulting during sedimentation, with coarse sandstones along faults (NS, N140, N70) controlling a significant part of the mineralisation.

The discovery of all the deposits near the AIA fault may have biased the model for the distribution of the U deposits. A survey of all structures, their timing and their relation to different types of mineralisation is necessary. The role of the AIA could be: (1) generating a redox front between the West (oxidized) and the East (reduced) and (2) providing a conduit for the circulation of hot deep fluids, which may or not have been circulating during the mineralizing process.

6 Age of uranium deposition

Turpin et al. (1991) have dated several minerals (uraninite, chlorite, corrensite) and rocks (organic matter-rich rocks, sandstones) by the U-Pb, K-Ar and Sm-Nd isotopic methods. The K-Ar data suggest that there are two stages, one close to 190 Ma and the other close to 150 Ma, whereas the U-Pb discordia method gives an age of 197±63 Ma. The Sm-Nd method does not provide any age information. This study rules out the hypothesis of a syn-sedimentary genesis of stratabound U ore-deposits in Niger. Because, as it will be shown after, temperatures were largely higher than 120°C during the main mineralizing event. Fission tracks data on apatite could be an other way to determine the age of mineralization. Sampling along a section from the AIA fault to the Aïr basement has been done in order to solve this important question.

7 Nature and origin of the mineralizing fluid(s)

Two-phase aqueous inclusion microthermometry has been studied in sphalerite and dolomite. In sphalerite, homogenization temperatures range from 85 to 175°C and in dolomites they are closer to 120 ± 15°C. These temperatures cannot be explained by burial, because at the age of mineralization, the thickness of the sediments along the reconstructed section was only less than 1200 m. Ac-

This page intentionally blank

cording to the temperatures of melting of ice, the salinities of the brines were high. These brines should be studied in more details similar to the studies done by Derome (2002) for the unconformity-type deposits from the Athabasca Basin (Canada) and the Pine Creek geosyncline in Northern Australia. In the basin the pH is basic (abundance of carbonate) and oxidizing conditions where U and Zn could be transported in the same fluid. An interesting chemical orbservation remains unexplained for the Akouta deposit: phosphorus and thorium are depleted in the deposit. This may be the result of brine-monazite interactions as suggested by Hecht and Cuney (2000).

8 Concluding remarks

The models and type for the uranium deposits in Niger, which could be the tabular-type or the roll-type, remains to be further explored.

From a geometric point of view they are not like a roll, probably because the host rocks have had a different distribution of reductants, permeabilities and structuration but roll structures do exist in the deposits. In the Akouta deposit, it looks like a stable redox front deposit (oxidizing in the West, reducing in the East). This is our preferred hypothesis at the moment but the presence of a white rock in the western altered tongue rather than the characteristic red rock associated to the altered tongue in the roll-type deposits poses some problems. One possible explanation could be that this white zone is related to circulation of deep-seated reduced acid fluid along the AIA fault after the emplacement of the U mineralization and the transformation of hematite to pyrite and of feldspar to kaolinite.

The structural and tectonic events related to fluid-rock interactions are very important to establish. Different types of U deposits are present in the Tim Mersoi Basin. Fission track thermochronology may provide an answer as large-scale tectono-thermal events are known in Western Africa at about 200 Ma (numerous intrusions of mafic dykes) and at about 140 Ma with an important Late Jurassic rifting episode (Bénoué Trough).

Acknowledgments

We especially thank COMINAK and SOMAIR for access to the mines, and CREGU for the scientific and financial support of the PhD thesis of Pierre Forbes. In 2003, Cogema has initiated a new R and D program on the Niger deposits in cooperation with Paris-Sud University, the Niamey University and School of Mines and Geology of Niamey. Several pHD thesis have started, with Sabine Cavellec on the diagenetic history (supervisor M. Pagel and H. Moussa), Olivier Gerbaud on the structural and tectonic history (supervisor P. Vergely) and Ibrahim Wagani on the volcanic and plutonic complexes of the Aïr massif and related volcano-sediments (supervisor M. Pagel and A. Liboré in cooperation with M. Cuney, CREGU).

References

Cazoulat M (1995) Geological environment of the uranium deposits in the Carboniferous and Jurassic sandstones of the Western margin of the Aïr Mountains in the Republic of Niger. In: Geological Environment of Sandstone Type Uranium Deposits. I.A.E.A., Vienna, TECDOC, 328 :247-263

Derome D (2002) Evolution et origine des saumures dans les bassins protérozoïques au voisinage de la discordance socle/couverture. L'exemple de l'environnement des gisements d'uranium associés aux bassins Kombolgie (Australie) et Athabasca (Canada). Thèse Université Henri Poincaré, Nancy I

Devillers C, Menes J (1977) Datation de la minéralisation d'Akouta, République du Niger: compléments. Rapport DRA/SAECNI/77, DR62/123/CD/DT, 7-15

Elhamet MO (1993) Analyse géologique et pétrographique de la formation du Tarat dans les carrières de la Somaïr (Paléozoïque inférieur). Région d'Arlit, Niger septentrional. Thèse de doctorat de 3ème cycle, Université de Dijon et Niamey 279

Forbes P (1989) Rôle des structures sédimentaires et tectoniques, du volcanisme alcalin régional et des fluides diagénétiques-hydrothermaux pour la formation des minéralisations à U-Zr-Zn-V-Mo d'Akouta (Niger). Géol. Géochim. Mém 17:387

Forbes P, Pacquet A., Chantret F, Oumarou J, Pagel M(1984) Marqueurs du volcanisme dans le gisement d'uranium d'Akouta (République du Niger) C. R. Acad. Sci. Paris, 298, Sér II, 15:647-650

Hecht L, Cuney M (2000) Hydrothermal alteration of monazite in the Precambrian basement of the Athabasca basin: implications for the genesis of unconformity related deposits. Mineral. Depos 35:791-795

Sanguinetti H, Oumarou J, Chantret F (1982) Localisation de l'uranium dans les figures de sédimentation des grès hôtes du gisement d'Akouta,, République du Niger. C.R. Acad. Sci. Paris, Sér II, 591-594

Turpin L, Clauer N, Forbes P, Pagel M (1991) U-Pb, Sm-Nd and K-Ar systematics of the Akouta uranium deposit, Niger. Chem. Géol. (Isot. Géosci. Sect.) 87: 217-230

Metallogeny of the uranium-bearing sedimentary basins

I.G. Pechenkin, I.F. Volfson, A.N. Sysoev
All-Russian Research Institute for Mineral Resources (VIMS). 31, Staromonetny per., Moscow, 119017, Russia

V.G. Pechenkin
FSUE "Urangeo". Build. 3, h. 49, Bol. Ordynka, Moscow, 115184, Russia

G.V. Grushevoy
All-Russian Research Geological Institute (VSEGEI). 74, Sredniy pr., St. Petersburg, Russia

Abstract. The leading role of geochemical conditions in the formation of hydrogenous mineralization within the covers of young platforms has been shown. Tectonic regionalization of Central Asia for the recent time on the mobilistic basis has been accomplished, which has made it possible to characterize the interrelations of individual large geological structures. The ore-bearing regions, which served as standard sites for modeling ore forming processes, have been distinguished. The whole spectrum of interrelations between ore-forming systems has been reduced to five typical models representing various geological and structural settings. The important achievement is a new method of prediction for the locations of uranium deposits of the sandstone group based on the compilation of series of paleohydrogeological maps on the paleotectonic base. It gives the possibility to predict deposit locations in different temporal shears under the complicated structural conditions in Neogene-Quarternary time.

Keywords. Central Asia, sedimentary basin (SB), ore-forming system (OFS), dynamic model, uranium deposit

1 Introduction

The last decade has been marked by the application of a complex approach to the study of the sedimentary basins. These geological structures are characterized by a complicated structure due to their localization in large blocks of the Earth's crust and, as a consequence, by the multivariance of ore formation processes.

The study of metallogeny of the Turan Plate and its mountainous framing, where the formation of ore objects can be observed *in situ,* displayed the leading role of epigenetic processes. The ore formation is governed by the collision tectonics related to the collision of Eurasia (the Turan Plate) with the Indian subcontinent. The region may serve as a satisfactory test site for elaborating the models of formation of various mineral deposits on the modem mobilistic geodynamic basis.

The temporal regularity that has been established in the manifestation of ore-forming systems (stadial ? exfiltration ? infiltration) and performed analysis of their spatial location point to the complexity and irreversibility of this process in the sedimentary cover of platforms. The interrelations of ore-forming systems (OFS) are determined by the geostructural position of the ore district. The geodynamic conditions connected with the manifestation of plate tectonics play a major role in the determination of particular regularities in the development of individual blocks both in space and time.

2 Ore-forming systems in sedimentary basins

In order to establish the interrelations of OFS with various geostructural positions of the regions, we have elaborated typical dynamic models of ore formation. These models offer a graphic representation of the processes of geodynamics, hydrodynamics, epigenesis, and ore formation. All the schemes are tied to individual ore-bearing sectors. They encompass the whole life-periods of OFS, to which the epigenetic processes are related.

Three (stadial, exfiltration, and infiltration) OFS have been distinguished. Each of them creates prerequisites for the formation of a specific type of epigenetic deposit and favorable conditions for the transition to the next system.

The stadial OFS represents a hydrodynamically closed system and is characterized by the formation of liquid and gaseous mineral resources. Their formation is intimately connected with the catagenetic transformation of rocks during their subsidence to the depths corresponding to the development of the principal phase of oil or gas formation. This process can be accelerated due to the stress increase during the orogenesis. The stadial OFS is also a preparatory one for the subsequent (exfiltration) system. This is manifested in the generation of various useful components in the gaseous liquid fluid.

The onset of exfiltration OFS functioning is triggered by the accumulated potential energy within the geodynamically open structures as a result of the exposure of sedimentary complexes. The fluid degassing leads to the equilibrium shift in the solution and to its differentiation, which is connected, with an abrupt drop of intra-stratal pressures and temperatures. The resultant deposits can be combined into several groups depending on the degree of fluid transformations (Fig. 1).

The action of infiltration OFS begins in reservoirs, both in the strata and ground regimes of subsurface waters. Folded rocks of the mountainous framing serve as recharge zones, while the rocks filling large basins and intermontane depressions serve as host rocks for mineralization. The directed movement of strata waters is governed by the localization of regional and local discharge zones. These waters, as a rule, are oxygenated or gleyey, and carry a number of elements (U, Se, Me, Re, Cu, V, etc.). They form the oxidative-series epigenetic zonality and the stratal oxidation zone, in particular. The stratal, roll, or analogous (in shape) ore lodes are formed at the reductive (both syngenetic and epigenetic) geochemical barriers.

The infiltrational system of OFS predominates when forming polymineral uranium ores of the sandstone type.

3 Typical models of ore formation

The *first model* is elaborated for the region, and represents the inherited (residual) oceanic basin and its mountainous framing (zone of up-thrusts and over-thrusts of the foreland), e.g., the West Turkmen depression and its northern flank.

The *second model* was elaborated for the Kopet Dagh thrust region and represents the conjugation of the up-thrust and over-thrust zone with the foreland basin.

The *third model* has been elaborated for the region where the joint troughs are conjugated with the up-thrust and over-thrust zone. It is divided into several subtypes, based on the geological structure.The *first subtype of the third model* is represented by the region of conjugation of the joint trough and the up-thrust and over-thrust zone in the eastern part of the Afghan-Tadzhik depression.The *second subtype of the third model* is represented by the region of conjugation of the joint troughs and the up-thrust and over-thrust zone in the areas where saliferous sequences are usually absent but the subsidence depth of rocks is favorable for the principal phases of oil and gas formation. The *third subtype of the third model,* which is represented by the region of conjugation between the up-thrust and over-thrust zone and the activized part of the platform, is characterized by more complicated interrelations of the OFS (e.g., Gaurdak-Kugitang region). The Northern Fergana represents the *fourth subtype of the third model.*

The *fourth model* unites a large number of various settings with the predominant action of infiltration OFS and the similar conditions of ore genesis.

The *first subtype of the fourth model* is established in the joint troughs with a thick sedimentary cover, where catagenetic transformations of rocks are at the initial stage. It is inherent to depressions of the Northern and Central Tien Shan. The different conditions of epigenesis are established within large depressions in the activized part of the Turan Plate, in particular, within the Chu-Sary Su depression *(second subtype)*. With the onset of Neogene-Quaternary tectonic activization, the regional SOZ starts to develop here. It advances as a united front, forming the uranium and associated mineralization at the wedging.

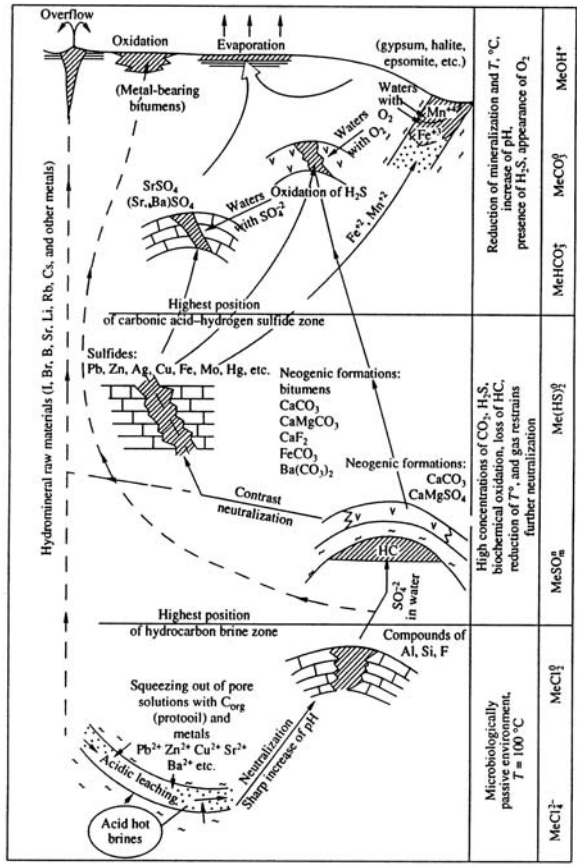

Figure 1: Scheme of gaseous liquid fluid transformations in the exfiltrational ore-forming system

If larger sedimentary basins (e.g. Syr Darya), characterized by substantial thicknesses of the sedimentary cover are present within the activized part of the plate *(third subtype)*, the regional SOZ advances predominantly in the upper parts of the section.

Minor artesian basin groups, separated by small horst-anticlines, which are composed of older crystalline rocks and serve, as recharge zones, can also exist within the activized part of the plate.

Within the Turan Plate, such a structural position is inherent to the Central Kyzyl-Kum uplift. It represents the *fourth subtype of the fourth model.*

The *fifth model* has been elaborated for the areas of conjugation of the platform-type uplifts with the passive part of the platform (e.g., the Mangyshlak and Tuarkyr regions).

4 Uranium-bearing sedimentary basins

Uranium deposits occur within the covers of the young and ancient platforms and intermountain areas of orogenic regions. The most studied territories are the western part, from the Atlantic Ocean to the Pamirs. They are disposed intermittently and the ore-bearing territories alternate with ore-free ones for a distance of 10 000 km.

The research is based on two postulates: 1) the large uranium deposits of the sandstone type are located in sedimentary basins (SB) of different types, the number of which is limited, 2) each SB passes several consecutive stages of development that correspond to ore-forming systems (OFS). The sedimentary basin is considered to be an independent geological structure, but in its development it is connected with the tectonic evolution of the continental block that adjoins it.

The analysis that was carried out revealed the exceptional role of ore-concentrated process, stipulated by the effect of oxygenated uranium-bearing, underground waters in the artesian basins. This process is well known; it is based on the example of the uranium deposits of the sandstone type of the Neartienshan province. At the same time, the limitations of the earlier known methods were revealed on the regional stage of prediction. Therefore, the original methods of working out schemes from a paleotectonic basis were devised. The schemes open new approaches to search for hydrogenous deposits under complicated structural conditions. The comparison of sedimentary basins of the Pamirs and the Himalayas sectors, which were forming in Neogene – Quaternary period, showed that against a background of the general principles of infiltrational ore formation individual preconditions were manifested determining the intensity of uranium-ore process in each of them. The Pamirs "wedge" shows the result of the prolonged collision of the Indian plate treading on the Eurasian one. It predetermined the unique ore concentration of the area. As a rule, large deposits of the roll type are situated on the acute point within the most distant from the orogen suborogenic (activated) part of the adjoining Turan platform and its southwestern margin, the edge of the Kazakh shield.

In the western and central part of the Eurasian continent the uranium deposits of the sandstone type of Mz-Kz age are widely spread in the SB, and are related to intermountain areas and covers of the young and ancient platforms. Metallogenic analysis of ore-bearing SB shows that large uranium deposits are concentrated within two belts (Collisional and Suborogenic). The sedimentary basins of the North belt (covers of the platforms) are not the source of uranium. The location of the industrial uranium deposits is determined by geodynamic factors. They are connected with the area of joining the young Mediterranean-Himalayan collisional belt with the ancient and young platforms. The zoning in distribution of uranium-bearing SB in the direction from the Volitional to the North platform belt is marked. Within the intermountain areas of the Collisional belt there are the small, medium and large uranium deposits of the sandstone type in the terrigenous, carboniferous and carbonated deposits of the SB. In the Suborogenic belt, there is the nodal distribution of uranium-bearing SB within separate blocks (median massives, activated parts of the platforms). The medium, large and unique uranium deposits of the roll type are located in these SB. Structural features of the Collisional and Suborogene belts predetermine the variety of interrelation of ore systems (catagenetic, exfiltrational and infiltrational) in SB and manifestation of the thermal process within ore fields of separate uranium deposits (Gamr, Kenigshtain, etc.).

SB located in the North uranium-bearing belt, control the distribution of the small and medium sheet deposits of paleovalley. The uniformity of morphology of sheet deposits and ore composition both in cover of the young and ancient platforms is typical. At present, the uranium deposits of the basal type of the Mesozoic age, related to the southern board of the young Western Siberian platform, are gaining industrial value. The possibility of exposure of uranium paleovalleys in the cover of the Russian platform, developing not only from the boundaries but also from the large massifs of the Central type (Voronezh massif) is grounded. Lately the considerable perspectives of the Baikal-Gobi belt (Zabaikalye, Mongolia, s-w China) where under different tectonic conditions the uranium-bearing SB are exposed. The regional prospecting criteria of uranium mineralization in SB are worked out insufficiently. The positional connection of the young mineralization with covers of Cenozoic basalts is marked.

Within the Suborogenic belt the Pamirs and Himalayas sectors are chosen. Three types of metallogenic zones are related to them. Within metallogenic zones giant roll deposits are moved off at the largest distance from the border of suborogene (up to 200 km). The comparison of infiltrational ore formation (according to uranium), catagenetic and exfiltrational process in the mentioned sectors showed that this process had manifested in different ways. In N-Q time in the Pamirs sector the staged unidirectional development of tectonic processes led to the continuous of growth accumulation of the zone of oxidation-reduction and accordingly, to the increase of uranium deposits. In the Himalayas sector, the collisional process conditioned more complicated mosaic structural drawing, with frequent displacement of the direction of the infiltrational ore forming process in the SB and shifting of the hearth of relief of the stratum waters in time. It predetermined more simple development of the ore forming process in the SB of the given sector. For all this, it should be emphasized that this process study is far lesser in comparison with the Pamir sector. The leading role of exogenetic factors in distribution

of all uranium deposits (except unique giant deposits) in all four belts (Collisional, Suborogenic, North and Baikal-Gobi) is self-evident and is stipulated by the active "work" of oxygenated uranium waters to exact uranium from the enclosed ore sediments and rocks of the local areas of recharge in the upper coating of the earth's crust.

5 Conclusions

Consideration of the impact of epigenesis on the transformation of rocks of the sedimentary cover and gaseous liquid fluids generated in them, as well as the regularities in this process, which are dominated by tectonic factors due to movement of lithosphere plates, allow us to substantiate the distinction of three interrelated ore-forming systems. The study of interrelations between these systems at the recent stage of geological evolution in the territory of Central Asia within the boundaries of large crustal blocks with a certain ore potential in the spatiotemporal coordinates has enabled us to distinguish a number of geostructural settings with the hydrogenous ore formation.

Reduction of fluids in the Bashbulak sandstone type uranium deposit in the Tarim Basin, China

Mingkuan Qin, Wenming Dong, Guangxi Ou
Beijing Research Institute of Uranium Geology, 100029, China

Abstract. This paper concentrates on the main evidence for reducing fluid in the Bashbulak uranium deposit, its fluid properties, stages and source. Based on these considerations, the origin of the deposit is discussed and an "extraction of reducing thermal fluid–metallogenesis" model is put forward. The formation of the deposit resulted from the internal action between infiltration water and the multi-stage reducing thermal fluids from multiple sources. The reducing thermal fluid plays an important role in three aspects: 1) resulting in the formation of host rock with relatively high reduction capacity; 2) leading to pre-concentration of uranium; 3) leading to local superposed concentration of uranium and increasing the grade of uranium ore.

Keywords. Bashbulak uranium deposit, mineralogical-geochemical indicator, reduction of fluid, extraction of reducing thermal fluid – metallogenesis

1 Introduction

The Tarim Basin is the largest sedimentary basin in China and its prospectivity for sandstone type uranium deposits is considered excellent. Bashbulak is the largest uranium deposit discovered in the basin is very close to the reduction of oil and gas from deep-lying strata (Qin et al. 2000). However, the properties, stages and source of reducing fluids of the deposit and the action of different fluids upon uranium mineralization are not clear. This paper addresses thee issues in order to improve the understanding of the genesis of the deposit, and also to be beneficial in future exploration for uranium in the Tarim Basin.

2 Geological setting

The deposit occurs in continental red clastic rocks of Lower Cretaceous age. From base to top, the clastic rocks can be divided into four lithologic members: conglomerate at the base, red mudstone in the lower, ore-bearing sandstone in the middle and red mudstone in the upper. The ore host rock can be divided into 3 zones zone along the dip i.e. oxidation zone, uranium ore zone and reduction zone. The typical alteration rock in above 3 zones is yellow sandstone (including oil-soaked sandstone), gray mineralized sandstone and blue-gray sandstone respectively.

There are 12 layers in total hosting lenticular ore bodies, which are concordant with the host rock. The principal uranium mineral is pitchblende, but most of the uranium is adsorbed in asphalt stone. In the uranium ore zone, other metal minerals include pyrite (which is most widespread), sphalerite, galena and chalcopyrite. Asphalt and oil seeps occur in the deposit and uranium concentrations around the ore (Qin 2000; Dong et al. 1998).

3 Mineralogical-geochemical indicators of reduction

3.1 Mineralogical indicators

Results of bulk-rock X-ray diffraction analysis reveal that whether in yellow sandstone or in oil soaked sandstone, gray mineralized sandstone and blue-gray sandstone, carbonate minerals occur to different degrees, and halite halite is also present; dolomite is dominant in the carbonate minerals, and its minimum content is 7.5% and maximum content is up to 43.0%. However, pyrite occurs mainly in the ore band and reduction zone with the content of 0.7% - 1.4% (see Table 1); microscope observations show that the degree of crystallinity of pyrite is poor and most is a secondary reduction product in gel form.

Major clay minerals are illite, illite/smectite and chlorite; chlorite is relatively abundant in the range 5%-40%; no smectite occurs and kaolinite is only found in some samples with the content not more than 11%. Clay minerals of sandstone-type uranium deposits in a typical infiltration interlayer oxidation zone consist mainly of kaolinite and illite (Qin Mingkuan et al. 1998). This suggests that strong chloritization of ore-bearing host rock is another important indicator of reducing fluids. In short, the mineral assemblages of dolomite + calcite + pyrite + halite and strong chloritization are the most typical mineralogical indicator for reduction from deep reducing fluids in the deposit.

3.2 Geochemical indicators

1. No charred plant fragment is found in the ore-bearing host rock, but albanite veins and nodules are found and the abundance of organic carbon is relatively low. The average content of organic carbon in oxidized sandstone is 0.04%, and that in oil soaked sandstone is 0.15%, that in mineralized sandstone is 0.06% and in reduction sandstone is 0.03%.

Table 1: Mineral composition table of ore-bearing host rock in Bashibulake deposit (wt%)

Sample No.	Lithology	Quartz	Feldspar	Albite	Calcite	Dolomite	Pyrite	Halite	Gypsum	Clay	Total
BS-17	Light yellow sandstone	42.4	0.5	7.1	0.7	19.6		1.2		28.5	100.0
BS-18	Yellow sandstone	55.5	10.2	15.5						18.8	100.0
BS-19	Light yellow sandstone	44.0	0.6	7.0		27.7		0.6	0.4	19.7	100.0
BS-20	Brown-yellow oil soaked sandstone	42.2	0.1	5.3		35.0		0.6		16.8	100.0
BS-35	Gray mineralized sandstone	35.5	6.0	7.3		43.0				8.2	100.0
BS-36	Gray mineralized sandstone	42.6	0.1	5.1		31.3	1.0			19.2	99.3
BS-47	Blue-gray fine sandstone	42.7	3.4	9.3		24.2	1.2	0.7		18.6	100.1
BS-48	Gray fine sandstone	35.2	9.6	12.5		37.3	0.7	0.6		4.7	100.6
BS-49	Blue-gray fine sandstone	40.4	3.0	8.6		26.2	0.8			20.4	99.4
BS-50	Gray fine sandstone	49.0	18.0	14.9		7.5	1.4	0.6		9.2	100.6

2. The average content of soluble organic matter (chloroform bitumen A) in the ore-bearing host rock and albanite is 0.02%. The soluble organic matter mainly consists of non-hydrocarbon, asphaltene, saturated hydrocarbons and aromatic hydrocarbons; their average contents are 46.8%, 24.7%, 23.2% and 5.3%, respectively. The average content of hydrocarbon (saturated and aromatic hydrocarbon) is up to 28.5%, which is evidently higher than that in the ore-bearing host rock in the coal seams (for example, the hydrocarbon content in the ore-bearing host rock in Shihongtan uranium deposit in the southern margin of the Turpan-Hami Basin is universally less than 20% (Xiang 1999).
3. The range of carbon number of saturated hydrocarbon in the ore-bearing host rock and albanite is relatively small and the main peak carbon is distributed mainly at the range of C14 - C17; $\delta^{13}C$ of saturated hydrocarbon is in the range of –27.0 - -33.3‰ and that of asphaltene is in the range of –25.1 to -29.5‰, which shows that the maturity of organic matter is relatively high and the type of organic matter is mainly sapropelic and some is humic-sapropelic.

4 Characteristics of fluid inclusions

Relatively abundant fluid inclusions can be found in all kinds of altered sandstone. In general, two stages of inclusions can be found and three stages of inclusions are developed in some samples. As the ore-bearing host rock is concerned, the three stages of inclusions are secondary. The size of inclusions is generally 4-7 microns and types of inclusions include fluid inclusion, gas-liquid inclusion and gaseous hydrocarbon inclusion. Inclusions mainly occur in: 1) early closed microfissures before quartz and feldspar were enlarged secondarily; 2) inside calcite grains or their secondary enlargement margins; 3) in secondary enlargement margins of quartz grains.

Fluid inclusions: are mainly liquid hydrocarbon inclusions. Most are brown-yellow, yellow-brown, gray-brown or yellow and they often have yellow and brown fluorescence.

Gas-liquid inclusions: are mainly hydrocarbon-bearing salt-water inclusions, secondarily hydrocarbon-bearing oil inclusions; most are black-brown or gray-brown, and the ratio of gas/liquid is less than or equal to 5%. The homogenization temperature of hydrocarbon-bearing salt-water inclusions is 85°C - 137°C and thus they are low-temperature thermal fluid.

Gaseous hydrocarbon inclusion: are gray or dark gray and often have blue or light blue fluorescence.

Early and intermediate inclusions are mostly liquid hydrocarbon and gas-liquid inclusions and late inclusions are mostly gaseous hydrocarbon inclusions.

5 Discussion of metallogenesis

According to the characteristic parameters such as type of organic matter, content and distribution of organic carbon etc., the organic matter in the ore-bearing formation is evidently from allochthonous sources, and its source rocks are marine strata. In another word, the organic matter in the deposit is mainly from the marine oil source rocks of Carboniferous and Permian Systems in the southwestern depression in Tarim Basin.

Research on the fluid inclusions in the deposit and the degree of development oil sand and albanite reveal that the host rocks were subjected to multi-stage reducing fluids and the main pathways for migration of fluids were faults. In general, three stages of fluids can be identified: early, intermediate and late stage fluids.

Early stage fluid: this occurred before the interlayer oxidation zone was formed. The fluid is believed to represent a deep oil & gas and hot brine, rich in reducing gas such as H_2S and CH_4 and metal ions such as Ca^{2+}, Mg^{2+}, Na^{+}, $Pb^{2+}$and Zn^{2+} and at the same time, it is also abundant in Cl^{-}, HCO_3^{-}, CO_3^{2-}. On the one hand, the early stage fluid leads to the formation of metal minerals such as a great amount of pyrite gel, crystalline galena and sphaler-

This page intentionally blank

ite and on the other hand, it also gives rise to the strong carbonatization and chloritization and to the formation of nonmetallic minerals such as halite.

Intermediate stage fluid: this occurred after the interlayer oxidation zone was formed and the fluid in properties is mainly liquid petroleum. The fluid caused heterogeneous reducing action on the ore-bearing rock and there may be 2-3 times intermittent invasion and as a sequence, albanite veins cut each other and lumpy yellow oil soaked sandstone formed in the deposit, among which, the albanite veins are very significant to the local accumulation of uranium in the deposit.

Late stage fluid: a large amount of gaseous hydrocarbon in the ore-bearing host rock indicates the existence of the late stage fluid, which also shows that the reducing action of late fluid in the deposit is mainly "gas reduction" and its component is mainly light hydrocarbon such as CH_4 and so on. As a whole, the reduction intensity of the fluid of this stage is not strong and thus the direct mineralogical indictor left at the surface is not very evident.

The uranium content of primary red sandstone around the deposit is 2.6 ppm, the average uranium content in the blue-gray reduced sandstone is 8.5 ppm, that in the oxidized sandstone is 19.3 ppm and that in the oil soaked sandstone in the oxidization zone is 6.9 ppm. These data show:

1. The uranium source of the deposit was from the external allochthonous source, namely, mainly from the peripheral source areas.
2. The deep reducing fluid brought some of the uranium, which led to the fact that the uranium content of ore-bearing host rock increased by over three times.
3. The transport of uranium may have been mainly related to the deep reducing hot brine, but was not related to the migration of petroleum. The obvious evidence for this is that the uranium content of oil soaked sandstone in the oxidation zone is less than that of non-oil soaked sandstone. Not only was the temperature of deep brine is relatively high, but also it it had high volatile components, and thus it continuously exchanged materials and energy with its country rocks in the course of upward migration and the quadrivalent uranium in the country rocks may have entered into the fluid in the mode of physical action due to "extraction" and finally it was precipitated in the ore-bearing formation due to supersaturation, which led to considerable increases in the uranium background values. It is considered that this increase played a very important role in later accumulation and metallogenesis of uranium. The above phenomenon is called "extraction of reducing thermal fluid – metallogenesis" for short. In essence, the reducing thermal fluid did not directly lead to the formation of sandstone-type uranium deposits, but provided a good basis for uranium mineralization; the thermal fluid was involved in the uranium mineralization and the important evidence for this is the mineral assemblages of pitchblende + pyrite + galena + sphalerite in the uranium ore.

6 Conclusions

In conclusion, the formation of Bashibulake uranium deposit was a very complex process. It involved the alternately internal action of infiltrated oxidizing water and multi-stage reducing thermal fluids of multiple sources. The reducing thermal fluid played an important role in three ways: 1) the formation of ore-bearing formation with relatively large reduction capacity; 2) increasing the background value of uranium, which led to pre-concentration of uranium; 3) leading to local superposed concentration of uranium and increasing the grade of uranium ore.

Acknowledgements

The research is subsidized by the National Natural Science Foundation of China (Project No. 49903004).

References

Dong DZ, Xiao AC (1998) The petroleum geological characters and oil & gas resources in southwestern depression, Tarim basin. Beijing: Petroleum industry publishing house, 176-178

Qin MK, Wang ZB, Zhao RQ (1998) Characteristics of clay minerals and their relationship with uranium mineralization in uranium deposit No.512, yili basin. Earth Science 23(5): 508-512

Qin MK, Zhao RQ (2000) New understanding in genesis of uranium deposits Bashblak in Tarim basin. Uranium geology 16: (1): 26-30

Xiang WD (1999) Studies on metallogenic conditions and regularities of interlayered oxidation zone type sandstone uranium deposit in southwestern Turpan-Hami basin, Northwestern China. Ph.D. Thesis, Beijing Research Institute of Uranium Geology, 139

Study on the relationship between coal-derived hydrocarbon and formation of sandstone-type uranium deposits in the basins of North China

Sun Ye, Li Zi-ying
Beijing Research institute of Uranium Geology, Beijing 100029, China

Abstract. This study investigates the relationship between uranium mineralization and organic geochemistry. It is pointed out that an inherent genetic relationship exists between the coal-derived hydrocarbon and ore formation in sandstone-type uranium deposit in the Ordos basin. The coal-derived hydrocarbon provides double reducing agents (internal and external) for uranium mineralization.

Keywords. Coal-derived hydrocarbon, sandstone-type uranium deposit

1 Introduction

Many studies show that a relationship exists between sandstone-type uranium deposits and organic matter. Sandstone-type uranium deposits occur in the same basins as oil, gas and coal deposits in many basins of the world (Chen et al. 2001). The authors have noted an interesting phenomenon that the ore-hosting formations are within to coal-bearing or -productive sequences, where coal seam and debris are usually developed. They are usually of Jurassic or Mesozoic age, with the Jurassic an important coal-forming period in China. The phenomenon of coexistence between coal formation and uranium deposits suggests that there is a fundamental genetic relation between coal and uranium deposits. The focus of this paper is the role that coal-derived hydrocarbons play in uranium mineralization processes. Previous discussions of the relationship between coal strata and sandstone-type uranium deposits have mainly involved humic acid, and few studies have dealt with coal-derived hydrocarbons in relation to sandstone-type uranium deposits.

2 Evidence of the coal-forming hydrocarbons

Abundant evidence for coal-derived hydrocarbon has been found in sandstone-type uranium deposits distributed in the basins of northern China.

2.1 Hydrocarbon material

We have found the source materials for coal to form hydrocarbons in the uranium deposit. The major hydrocarbon-forming source materials in the study area are resinite and fluorinite. The content of resinite in some samples can reach over 20 %, constituting an important source of the coal-derived hydrocarbons (Figs. 1, 2).

2.2 Residual material after derivation of hydrocarbons

The authors have found that micrinite is the residual material after hydrocarbon formation from materials such as resinite and fluorinite. The abundant micri-nite remains are the indicator of the existence of coal-derived hydrocarbon in the study area (Fig. 1). The coexistence of micrinite and resinite indicates their close affinity.

2.3 Evidence of the primary migration of coal-derived hydrocarbon

Evidence has been discovered that coal-derived hydrocarbons have migrated in the uranium deposit, and the important indicator is that the liquid hydrocarbon oc-

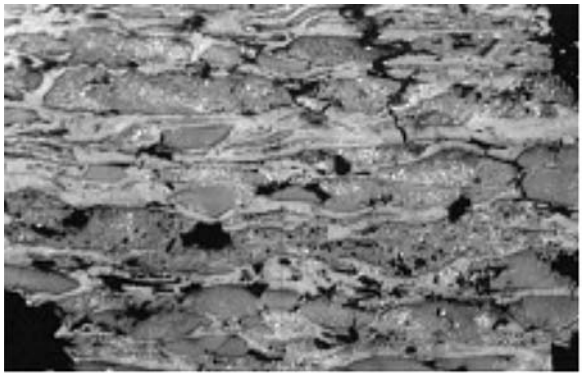

Figure 1: Resinite in coal strata of uranium deposit

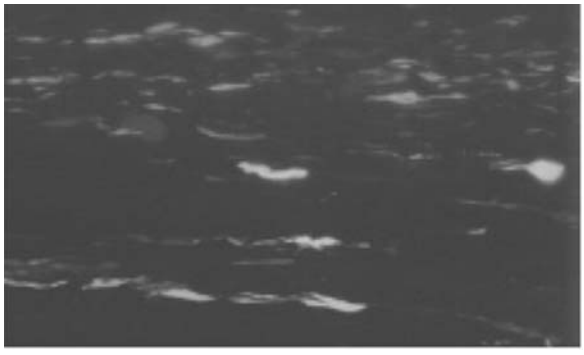

Figure 2: Fluorinite in coal strata of uranium deposit

This page intentionally blank

curs in the exsudatinite and micro-fractures in coal bearing rocks. Their occurrence and hydrocarbon-forming material are products and indicators of hydrocarbon generation and migration.

2.4 Evidence of late migration of coal-derived hydrocarbons

It has been also found that the coal-derived hydrocarbons migrated into the ore-hosting sandstone at later stages. The important biomarker of coal-derived hydrocarbon in the uranium ore is sesquiterpenoids i.e., which is a typical indicator derivation from coal strata (Fig. 3, Cheng et al. 1995). The coal-derived hydrocarbon migrated into the sandstone beds and contributed to formation of the uranium deposit.

3 Episodic expulsion of hydrocarbons

Our research has shown that the coal-formed hydrocarbons in the study area were expelled at various times. It has been shown that the major hydrocarbon-forming material, resinite, had at least two major phases of expulsion, while fluorinite had at least three phases of expulsion. The migration model of coal-derived hydrocarbons such as formation, migration, conglomeration and dispersion provide a basis for understanding uranium ore genesis.

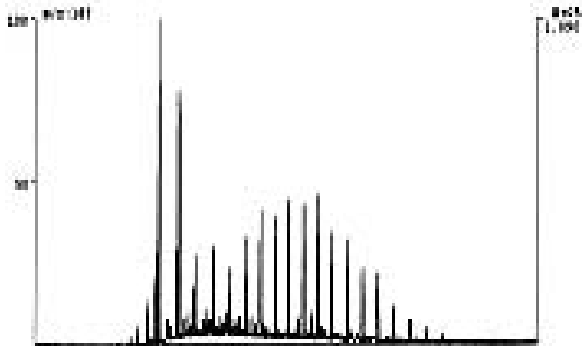

Figure 3: The biomarker sesquiterpenoids distribution of the the uranium ore sample

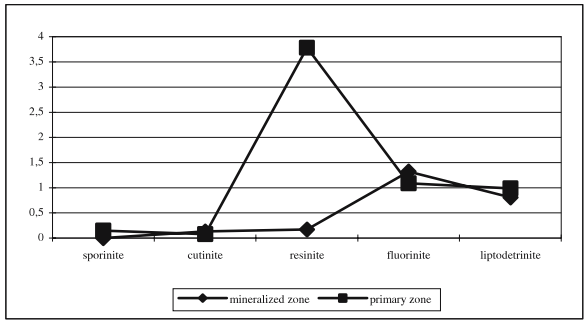

Figure 4: The content of coal-derived hydrocarbon in different zones of the Dongsheng uranium deposit

4 Distribution of coal-derived hydrocarbon and its relationship with oil-gas inclusion

Zoning is apparent in the concentration of coal-derived hydrocarbons in the uranium deposits, i.e. very low in the primary zone, and high concentrations in the mineralized zone (Fig. 4). As shown in Figure 4, the hydrocarbon-forming material resinite is clearly enriched in the transitional ore zone, which can be considered to be an important indicator to prospecting using organic matter. It has been that the coal-derived hydrocarbons generate oil-gas inclusions, that the phases of coal's expulsion can have excellent correspondent relationship with the development phases of the oil-gas inclusion, which plays a very important role in ore forming period of the Dongsheng uranium deposit.

5 Timing of hydrocarbon formation and reducing capacity

It is considered that the time of hydrocarbon formation from coal is earlier than the major uranium mineralization, which indicates that the hydrocarbons provided the reducing capacity prior to uranium mineralization for the ore-hosting horizon and created the reducing condition for uranium reduction and precipitation. It is shown in this analysis that the coal-derived hydrocarbons constitute the reducing geochemical barrier, together with the natural gas migrating upwards from the depth. Therefore, the coal-derived hydrocarbons can also play important roles in the preservation of mineralization. The reducing capacity of the coal-derived hydrocarbon is relatively large and depends on size of coal formation.

The coal-derived hydrocarbons have no comercial value, beyond playing a significant role in uranium ore formation.

Conclusions

The relationship between the coal-derived hydrocar-bons and uranium ore-formation has been discussed.

The coal can produce hydrocarbons, which migrate and are enriched in the ore beds and have a genetic relation with ore-formation in sandstone-type uranium deposits. The coal-derived hydrocarbons provide double reducing agents (internal and external).

The relationships described between coal and uranium deposits contribute to the understanding of uranium metallogenesis.

References

Chen ZY (2001) A new round of strategic target area selection for ISL-amenable sandstone-hosted uranium deposits in China. A final scientific research report, Beijing Research Institute of Uranium Geology, 40-65

Cheng KM, Wang TG, Zhong NN (1995) Geochemistry of hydrocarbon-source rocks. Beijing: Publishing Company of Science, 22-35

Analysis of pegmatitic granite-uranium deposit formation conditions and exploitation prospects in the Shaanxi Shang-Dan triangular region, China

Jianguo Wang, Changwei Mu, Zhongduo Wang
Unit 224, Nuclear Geologic Bureau of Shaanxi Province, China

Keywords. Shang-Dan triangular region, pegmatitic granite uranium deposit, uranium resource base, process test

Abstract

By adopting a new deposit formation theory, that is, that landscape, field, mineragraphy and deposit evolve in turn to form a mineral deposit, together with combining macro and microanalysis, we have analyzed the geological environment, deposit formation mechanisms and prospects of uranium deposit formation in the Shang-Dan triangular region. We conclude that a uranium mine with resource/reserves of ten thousand tons might be verified in the Shang-Dan triangular region following geologic exploration. Heap leaching technology and research at different scales have been conducted on ore from the Guangshigou uranium deposit. This deposit is located in this region. In this research, systematic and economically rational processing flow and technical parameters were acquired, which were up to the domestic advanced level of the same field and there had been no preceding pegmatitic granite uranium ore heap leaching technique in China. Scientific foundation has been laid for the exploration and exploitation of this uranium mineral deposit and other deposits of the same kind. There are good prospects for the exploration and exploitation of pegmatitic granite uranium deposits.

References

Liu GQ. The Granite Feature and the Relationship of its Uranium Mineralization in the Red Phoenix Triangle Region. Unit 224, Nuclear Geologic Bureau of Shaanxi Province

Mu CW. The Feature of Exploring with Physical and Chemical Method and the Prospect of Seeking Mineral in the Red Phoenix Triangle Region. Unit 224, Nuclear Geologic Bureau of Shaanxi Province

Pei RF (2001) The appraisemant to potential geology of difficultily identified and hidden, big and rich Mine. Geography press

Shen BF, Lu SN (2000) Theory and Method of Prediction to Swarming Mineral Deposit. Geography press

The Forecast of Uranium Resource Amount in Red Phoenix Triangle Region. Research Institute 203 in Nucleus Industry Geology Office

The Investigation and the Evaluate Report of Uranium Deposit in Guangshigou Uranium Mine of Shangnan County in Shaanxi Province. Unit 224, Nuclear Geologic Bureau of Shaanxi Province

The Research Report of 500 Tons of Half Industrial Test in Guangshigou Uranium Mine. Uranium mine project group in team 224

Xiang D, He RS, Liu DC. The Geological Background in which Uranium is Analyzed and the Mine Distant View in the Red Phoenix Triangle Region. Unit 224, Nuclear Geologic Bureau of Shaanxi Province

Table 1: Comparison of the Technique and Economic Parameters of Guangshigou Uranium Ore heap leaching Technology

Item	Days (d)	Solid-to-liquid ratio (T : m3)	Raw ore grade (%)	Acid consumption (Kg/T_{ore})	Consumption of B (Kg/T_{ore})	Consumption of A (Kg/T_{ore})	Extraction ratio (%)	Cost of Extraction Material	
								Yuan/T_{ore}	Yuan/TMe
Test	50	3.40	0.072	32.2	2.06	1.65	81.45	26.8	32774.8
20T test	42	1.11	0.076	15.6	2.06	0.50	66.06	13.3	26670.6
50T test	95	1.98	0.088	20.0	1.892	0.3986	89.05	14.6	19045.9

Note: Leaching return difference is calculated as 7.5%.

Late Mesozoic-Cenozoic tectono-sedimentary evolution and sandstone-hosted uranium mineralization of the Erlian basin

Sanyuan Wei, Mingkuan Qin, Yuexiang Li, Zhongbo He
Beijing Research Institute of Uranium Geology, Box 9818, Beijing, 100029, China

Anping Chen, Kefeng Shen
Geologic party No. 208, CNNC, Baotou, 014010, Inner Mongolia, China

Abstract. The tectono-sedimentary evolution of the Erlian basin can be divided into 3 stages: continental extension and down-faulting, transformation of down-faulting to down-warping, weak compression and differential uplifting-subsidence. Clastic rocks developed in the transformation stage of down-faulting to down-warping are the main ore-hosting beds. The stages of weak compression and differential uplifting-subsidence provide conditions for uranium mineralization. Uranium metallogenic conditions have been analyzed, and a metallogenic model of uranium deposits discovered recently in the Baiyiwula area are summarized.

Keywords. Erlian basin, tectono-sedimentary evolution Sandstone-type uranium deposits

1 Introduction

Generally speaking, various mineral resources in a basin are products of certain stage of tectono-sedimentary evolution of the basin. These mineral resources may form during different stages because of their different metallogenic mechanisms. Sandstone-hosted uranium deposits are generally developed in the late stage of the basin evolution (Mesozoic – Cenozoic).

2 Geologic setting of the Erlian Basin

The total area of Erlian basin is about $10x10^4km^2$. Its tectonic setting is characterized by being located in the suture zone of North China plate and Siberia plate. It is a Mesozoic and Cenozoic basin developed on the Xing'an-Mongolian Hercynian folded basement. The structural characteristics are demonstrated in Figure 1.

3 Tectono-sedimentary evolution of the Erlian Basin

Since Late Mesozoic-Cenozoic the basin has experienced three evolution stages: continental extension and down-faulting, transformation of down- down-warping, and weak compression and differential uplifting-subsidence.

3.1 Continental extension and down-faulting

During Early Cretaceous the basin was in the back-arc tensional area, under the stress of the NW-SE extension, and the basin entered a stage of continental extension and down-faulting, which also can be divided into two

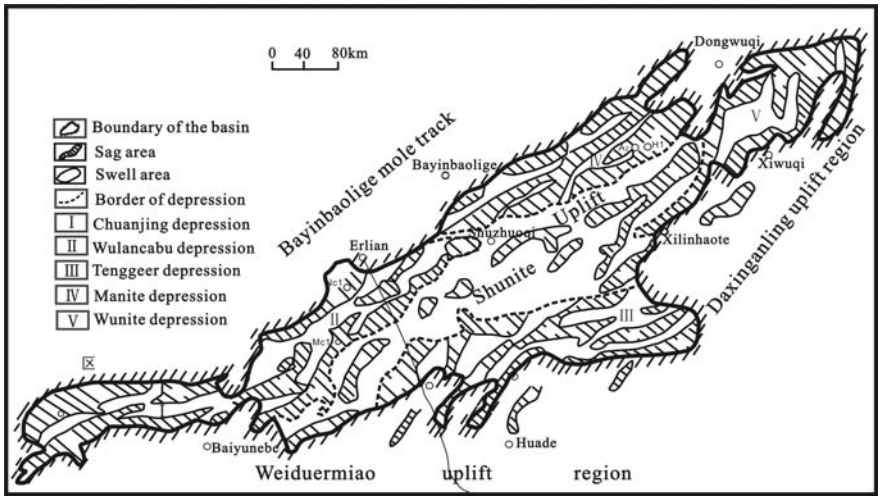

Figure 1: Sketch map showing the tectonic division of basement of the Erlian basin

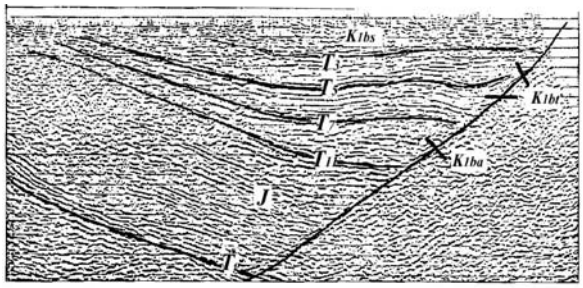

Figure 2: Seismic interpretation section of a sag in the basin

substages. Correspondently Arasan Formation (K_1ba) and Tengeer Formation (K_1bt), Bayanhua Group, were accumulated during these substages, and it is quit clear the seismic reflection profile (Fig. 2).

In the early stage of basin down-faulting, NE and NEE thrust faults were developed from the contraction-compression in pre-Cretaceous time, happened reversion, and down-faulting occurred in the basin. As the horizontal tensile force was weak, the differential block-faulting movement was not obvious. The sedimentation rate exceeded the subsidence velocity; and the sedimentation is characterized by rapid accumulation. Arshan Formation (K_1ba) became a set of grey-green, brown-red continental variegated coarse clastic formation.faulting to the later substage, continental extension and down-faulting of the basin were the peak time.

Its tectonic activity is characterized by horizontal extension and vertical deep-subsidence, the subsidence rate was faster than that of deposition, and set of grey, dark-grey, grey-green lacustrine mudstone was deposited, with a maximum thickness of 2400m.

3.2 Transformation of down-faulting to down-warping

After an intense down-faulting phase of the basin the seduction of the west Pacific plate toward Eurasian plate was strengthened. NNE-SSW compression made the basin area raised, and short-time denudation-eneplanation occurred. Subsequently the basin began to be downwarped again.

Saihan Formation (K_1bs) is marked by following characteristics: 1. Its sedimentation area became contracted; 2. Its lithology and sedimentary facies is homoplasy in every sag, but the thickness became smaller, generally it is 400~500m thick; 3. Although the activity of the depression-controlling border faults was weakened, the sedimentation pattern was controlled by the same previous structure; 4. The formation can be divided into three members: the lower coarse-grained, the middle mudstone, and the top coarse-grained, suggesting that the basin experienced three evolution stages: regression under weak-compression, transgression under weak-extension, again regression under weak-compression. The above-mentioned phenomena indicated that the nature of the basin became down-faulting to downwarping transformed. Saihan Formation (K_1bs) is a set of grey coal-bearing clastic rocks, and is ore-hosted series for sandstone type uranium deposits.

3.3 Weak compression and differential uplifting-subsidence

During Late Cretaceous the basin was in relatively uplifting state resulting from the NW-SE compression caused by the subduction of the Pacific plate towards the Eurasian continent. The NE trending basement faults became sinistral strike slipping ones. The compression stress was stronger in the east than that in the west, and differential uplifting-subsidence occurred. As a result, the Wunite and Tenggeer depressions to the east of Shunite uplift were an uplifted and eroded region without sedimentation, and the Chuanjing, Wulanchabu, Manite depressions to the west of Sunite uplift experienced weak compression becoming a subsided region, and a set of variegated clastic rocks under semiarid climatic conditions, with a thickness from tens of meters to 300 m, was setted (Erlian Formation, K_2e).

The neotectonic framework of china and its adjacent areas can be divided into three domains: the western compressional domain, the middle transitional domain, and the eastern extensional domain. Erlian basin is located on the middle transitional domain.

The geodynamic mechanism of the basin in Paleogene was fundamentally changed. The subduction of Pacific plate changed its direction from NNW to NWW, while the continent-continent collision of Indian and Eurasian plates engendered strong impact to the interior of Eurasia. As a result of two above processes the geodynamic nature of the basin was changed into dextral extension-shearing, and Chuanjing and Wulanchabu depressions with less rigid basement began to sink. The sedimentation in Wulanchabu depression showed the shallow water in the west and the deeper water in the east, and the depocenter was on its southeastern side. In Chuanjing depression the north was uplifted and the south was subsided. The Paleogene represents a set of red gypsiferous clastic rocks with its main lithology of mudstone. Its thickness is stable range form tens of meters to over 100m. Generally the Paleogene is absent in the north and the east of the basin, and it was thick in the east and was thin in the west of the basin (Fig. 3).

In Neogene, the Himalayan movement became much more intense. The crust of western China was compressed, resulting in the crust shortening and uplifting; the crust of eastern china was extended, leading to the crust thinning and down-faulting. The structural movement of Erlian basin showed weak compression and differential uplifting-sbsidence because it was located on the middle transition domain. On the west and north of the basin the Neogene was absent owing to the uplifting. The sedimen-

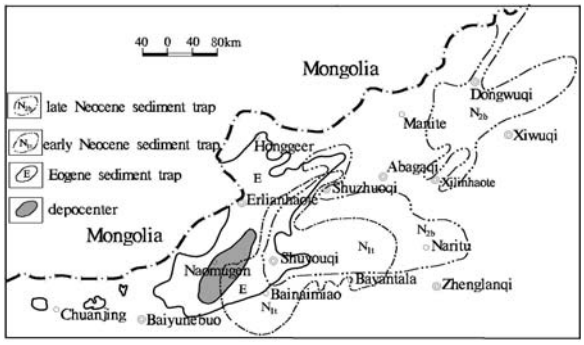

Figure 3: Map showing the Distributing of Tertiary system in Erlian basin

tation moved eastwards, the Tengguer(N_1t) and Baogedawula (N_2b) Formations were deposited. The Neogene is characterized by a set of brick-red mudstone and variegated clastic rocks, with a thickness from tens of meters to over 100 m.

4 Effect of tectono-sedimentary evolution on metallogenesis of sandstone-hosted uranium deposits

4.1 Genetic mechanism of sandstone-hosted uranium deposit formation

Sandstone-hosted uranium deposits usually include two kinds: the diagenetic uranium deposits, and the epigenetic uranium deposits. Authors mean the latter ones in the paper. The epigenetic uranium deposits can be divided into interlayer oxidation zone subtype and phreatic oxidation zone subtype. Their genetic mechanism is as follows: under conditions of the normal temperature and pressure, the surface water, which contains oxygen and uranium, vertically infiltrates or laterally along permeable aquifers, extracting uranium from the layer at the same time. Along with the consumption of oxygen and the increase of salinity, pH and Eh will changed to a certain extent. When these changes reach the critical value of geochemical environments the uranium and other associated elements are precipitated, forming uranium deposit.

According to the above mentioned, there should be four necessary prerequisites for the formation of sandstone-hosted uranium deposits: 1. Uranium source must exist; 2. There must be large-sized stable permeable aquifers and stable aquifuges; 3. There must be a stable hydrodynamic system of ground water for driving the infiltration of groundwater to form an oxidation zone; 4. There must be geochemical barriers (mostly reducing barriers) where the uranium may be precipitated and concentrated. These prerequisites are all related to the tectono-sedimentary evolution of the basin. Especially, the structural movement of the basin must not be too intense during the period when the sandstone was formed and afterwards. The intense structural movement is unfavorable for the development of large-sized stable water-bearing permeable sandstone bodies, and for the development of stable groundwater hydrodynamic system.

4.2 Discussion on uranium mineralization

According to previous analysis, Erlian basin was located on the middle transitional domain, and the structural nature of the basin was of weak compression and differential uplifting-subsidence during Neotectonic movement. So tectonic conditions are very favorable for formation of the uranium mineralization.

Grey sandstone beds with abundant coalified remains and pyrites developed at the stage of down-faulting to downwarping transformation are target horizons of uranium deposits.

The Erlian Formation (K_2e) is absent in the east of the basin and locally absent in Manite depression, and the Neogene is also absent in the west of the basin, providing possibilities for the development of interlayer oxidation zone and phreatic oxidation zone in sandstone bodies of Saihan Formation (K_1bs) and of Poleogene.

Since Tertiary Erlian basin has been in slow tilting state of: the uplifting in the west and the subsidence in the east, leading to the development of a series of NE-and NNE-trending half graben in Manite, Wulanchabu depressions and the west of Tenggeer depression. These half-graben like sags are characterized by the development of a normal fault at its eastern border, and the overlapping in the west of the sag. The above mentioned indicates that a stable hydrodynamic system of groundwater occur with the flow direction from NW to SE. These are favorable for the development of interlayer oxidation zone.

Furthermore, based on characteristics of tectonic evolution and the sedimentation of the basin since Late Mesozoic, different types uranium deposits might have been developed at different places. Wulanchabu and Manite depressions are advantageous for developing interlayer oxidation-type uranium deposits, while Wunite and Tenggeer depressions are advantageous for developing phreatic oxidation-type uranium deposits. The reasons for this are: after the settlement of Saihan Formation (K_1bs) the sedimentation in two depressions was absent until Neogene period.

4.3 Uranium metallogenic model

Recently, several important uranium deposits have been found in the transitional area of Wulanchabu and Manite depressions. Especially in Baiyinwula area the uranium deposits developed in grey fluvial clastic rocks of Saihan Formation (K_1bs), may be of good prospecting signifi-

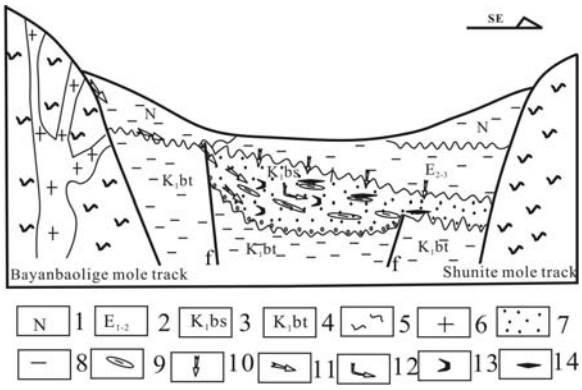

Figure 4: Diagram showing uranium metallogenic model of Sandstone-hosted Uranium deposits in Baiyinwula area 1. Neogene 2. Eocene and Oligocene 3. Saihan Formation 4. Tenggeer Formation 5.Basement metamorphic rocks 6.Granite 7. sandstone 8. Mudstone 9. Mudstone interlayer 10. Flow direction of paleo-phreatic water 11. Flow direction of interlayer water 12.Interlayer water transformed from phreatic groundwater 13. Interlayer oxidation type ore-body

cance and commercial value because uranium at this deposit can be extracted by in-situ leach technology. Based on borehole data and the evolution of the basin, a model for sandstone-hosted uranium deposits is summarized as follows: There are numerous Hercynian granitic massifs in the range of bayinbaolige uplift that may offer plenty of uranium; After the deposition of Saihan Formation (K_1bs) Baiyinwula area showed a complete lack of Late Cretaceous and Paleocene sediments; meanwhile weathering and leaching process were predominant during that period and the vertical infiltration of groundwater in grey fluvial sandstone bodies of Saihan Formation might result in the formation of phreatic oxidation type uranium mineralixation. During the deposition of Eocene and Oligocene the western area was uplifted and eroded, but the sedimentation occurred in the eastern subsided area. At that time the uranium-containing ground water coming from the western uplift flowed to the east, and might lead to the formation of interlayer oxidation zone type uranium deposits in Saihan formation (Fig. 4).

Geologic features and mineralization of the uranium-bearing Vonsenite deposit in the LiaoDong rift

Xuehui Xia, Fei Yan, Yuhai Zhao, Wenzong Chang
Geological Institute of Bureau of Geology & Mining of China Chemical Industry, China

Abstract. The uranium-bearing vonsenite deposit in LiaoDong is a unique and super-large deposit. In this paper, we study the ore composition, mineralization epoch, REE characters, and stable isotope, based on the detail introduction of the geological feature of this type of deposit. The research indicates that submarine hot-water deposition is the main mineralization of uranium-bearing vonsenite deposit, and that the industrial deposit was formed after further enrichment of boron and ferrum by the superposition and transformation by regional metamorphism and migmatization.

Keywords. Uranium-bearing vonsenite deposit, geological features, mineralization

1 Metallotectonic setting

The uranium-bearing vonsentile deposit is located in a Proterozoic fold belt in Liaodong of North China platform, and was controlled originally by the structural setting of Liaodong rift. During the later proterozoic period, the Liaodong-south JiIin region folded and rose to craton by the An Shan movement. Then, after a long period of disintegration and shearing off, the rift valley was formed by Wu Tai movement, which occurred 2300 Ma years ago. This rift valley started from Yingko in the west, through Kuandian to the east, turned to north east to Jilin, doubled over Korea peninsula to the east, and formed an arc basin projecting at east north direction. Within the boundaries of China, at the south of Anshan-Nanfen-Huairen-Tonghua, north of Gaixian-Xiuyan-Dandong, were formed leucogranulitite granulitite of B-rich of Liaohe group in rift basin. The initial rocks of B-bearing rock formation is a set of submarine volcano eruptive rock, clay rock and with interbeds of megnesian carbonate formation.

The rift valley is 400km long and more than hundreds kilometers wide, and in the west-east direction at the area of YingKou-KuanDian, where the main fault inclined to the north, take the shape of dustpan. The subsidence center distributed at the north side of main fault where the Hupiyu-Hongshilazi is located, the slope area of basin is at the north side where there is an outcropping of the Archaeozoic basement at the Anshan area, which gradually increases in thickness to the south. Submarine volcanic activity occurred frequently at the subsidence center, with the result that the content of B at B-bearing metamorphic volcanic rocks from decades to hundreds times higher than it is in the same type volcanic rocks elsewhere, this is also resulted in the formation of boron deposit, prepared the material resource, located in a certain layer and certain lithology of Mg-rich carbonate rocks. Wongquangou is a huge deposit hosted in the second basin of rift valley.

2 Geological feature of uranium-bearing vonsenite deposits

The Wongquangou uranium-bearing vonsenite deposit occurs in a set of marine facies volcano sedimentary formation, which was controlled by an ore-bearing formation of the Liaodong rift during the ancient Proterozoic period. The mineralazation happened at the second volcano-sedimentary fault basin of the rift valley. Acidic volcano-hydrothermal rock in the lower part of Liaohe group Lieryu formation created boron-bearing formations (Feng 1995; Xia 1995 1997), of which the initiate rock successively as Na-rich rhyolite ash tuff intercalated with Fe-rich and Mg-rich silicalite; Mg-rich felsic pyroclastic rock, K-rich kahuste, ash tuff intercalated with striatus magnetic silicalite. By regional metamorphism and hydrothermal reconversion, a set of amphibolite facies metamorphic consociation was formed, which is, from the bottom to the top ,biotite magnetite amphibole magmatite, biotite granulitite, tourmaline, biotite pyroxenolite, dolomite-marble, serpentinite, phlogopite tremolite rock, amphibole pyroxene granulitite, leucogranulitite, apatite-granu-litite and rutile-lecogranulitite etc. are intercalated in leucogranulitite bed.

The Uranium-bearing vonsenitite ore body mainly hosted in a (Ca, Mg)-silicate rock layer, located in a syncline of a horseshoe-shaped zone in a stable bed (Fig. 1), the facies of ore-bearing formation changes distinctly in the horizontal direction with the difference in rock formation, while there were serpentine rocks changes to calamite from east to west of the ore-bearing bed at the north top of the syncline.

The ludwigite has vanished with the gradual thinning out of serpentine, and instead of this id found apatite, which formed the unique B.Fe-P metallogenetic series in this area. (Ca, Mg)-silicate, carbonate rock and leucoganulitite alternated repeatedly, showing a sedimentary rhythm in vertical direction, with the ore-bearing formation varying with changes in the facies.

The deposit was controlled strictly by synclinal structure, the ore body takes the shape of a planar horseshoe, and occurrence of leucogranlitite take the form of layer

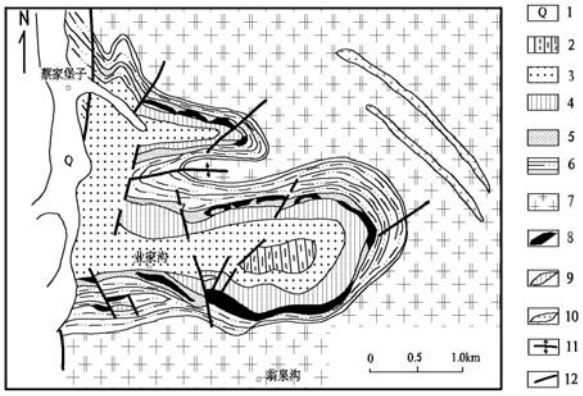

Figure 1: Diagrammatic geological map of the wengquangou. 1-quaternary system; 2-biotite pyroxene granulitite; 3-leucoguanlitite; 4-amphibole pyroxene granulite; 5-boron-bearing iron ore bed marble, metasomatic rock; 6-biotite granulitite; 7-biotite amphibole magmatite; 8-vonsentite ore bed; 9-apatite ore bed; 10-amphibolite; 11-anticiline; 12-fault

and pod, the top angle of the ore body changes greatly: it is higher in the shallow part and lower in the deep part, this is due to later reconversion, in which the ore body was superimposed or pulled out.

The deposit shows a clearly wall-rock alternation, there is a metasomatic belt close to the ore body roof, which varies dramatically in thickness, from 0.2m to several dozens meters.

It is known from analysis of chemical composition of deposit that, wongquangou deposit is a synthetic deposit paragenesised with B and Fe, associated with P, containing uranium, sulfur, and REE in general.

The ore, according to the contents of borate mineral and magnetite, can be divided into four types,ludwigite-magnetite type, szaibelyite-magnetite type, szaibelyite-suanite-ludwigite-magnetite type, and magnetite type. The former two types are dominant and account for more than 85% of total ore in this area.

2.1 Ore types and its characters

Ludwigite-magnetite ore type: this is one of the major ore types of the Wongquangou mining area, and is evenly distributed over five deposits, Wongquangou, Yejiagou, Caijiagou, Dongtaizi and Zhoujiadayuan. The ore is composed of lewisite, magnetite, szaibelyite and serpentine, phlogopite. The amount of the essential mineral of the ore, ludwigite varies at 40%-50%, magnetite varies at 3%-12%, szaibelyite varies from 1%-5%. For the gangue mineral, serpentine varies from 5%-25%, phlogopite from 2%-15%, tourmaline from1%-3%, olivine from 1%-2%, and crystalline uranium and rutile in negligible amounts.

The primary ludwigite occurs in a columnar form, with ore composed of ludwigite mosaic with each other, having a particle diameter varying from 1.25×0.35mm to 0.8×0.3mm ,the smaller part of it discomposed followed the crack to produce fibrous szaibelyite and fine-grained magnetite. Incompletely discomposed ludwigite from a hydrothermal process forms an irregular residual. In most cases, magnetite in the form of idiomorphic-half idiomorphic, of which the particle diameter varies from 0.2mm to1.2mm, connects to serpentine with brokenline, paragensised with olivine in granular form. In lesser amounts,szaibelyite mostly in form of fibrous mosaicing closely with fine-granular magnetite, take a tabular shape distributed in the ore.

The tectonic fabric of this ore type is a block structure, bent structure, granular and mosaic texture, replacement remnant texture.

The chemical composition is shown in Table 1. Which indicates that the content of SiO_2 varies from13.17% to15.38%, B_2O_3varies from 5.58% to 7.66%, and FeO varies from 12.10% to14.64%, this is less than szaibelyite – magnetite type ore.

Szaibelyite-magnetite ore type: This ore type was formed by decomposition of ludwigite after regional metamorphism and hydrothermal synthesis, which are generally distributed and tend to concentrate highly in certain areas. It is composed of szaibelyite, magnetite, serpentine and clinohumite. The contents of the essential mineral, szaibelyite varies from17% to 20%, and magnetite from 40% to 45%. The contents of gangue mineral, serpentine varies from 18% to 20%, clinohumite from 8% to 10%, pyrrhotite from 3% to 5%, chlorite from 2% to 3%, and contents of other minerals vary from 1% to 2%.

This ore type is discomposed mainly by szaibelyite, therefore the grain size of mineral is very small and mosaic is complicated. It occurs mainly in fibrous patterns and in groups, its grain size varying from 0.005 to 0.02mm,a closed mosaic with micrograined and fine-grained magnetite. A part of the fibrous szaibelyite interlocks with fibrous serpentine. The grain size of a small part of the columnar szaibelyite, varying from 0.2mm to 1.3mm,is distributed in an uneven crumber structure in the ore. This type of szaibelyite takes the shape of columns in its external form, but takes a fibrous form internally; this might be a result of alternation of early suanite. The magnetite exists mainly in fine grains with different forms, with grain sizes varying from 0.005mm to 0.02mm, and mosaic closely with fibrous szaibelyite, which forms a fibrous granoblastic texture.

This ore type has a complicated texture, including densified massiveness, banding, taxitic texture, fibrous texture, granular texture, fibrous szaibelyite and granular magnetite which takes the shape of a jigsaw-like, graphic texture: the magnetite and sziabelyite are decomposed by ludwigite existing in a graphic texture, in the form of a cloud, with stock work and radial texture. The szaibelyite formed in later periods takes the shape of stock work and radial, pseudomorph structure: It remains the co-

lumnar pseudomorph of ludwigite after decomposed into szaibelyite and magnetite by the hydrothermal process.

The chemical composition of szaibelyite-magnetite ore type shows that the content of boron is higher in this ore type than in the ludwigite-magnetite ore type, with the content of B_2O_3 varying from 10.66% to 12.35%. The content of SiO_2 is lower than in the ore type mentioned above, which varies from 4.28% to 8.05%, and the content of FeO varies from 20.09% to 20.52%, twice as high as the ludwigite-magnetite, the variation content of B_2O_3 and FeO, reflects the result of abruption of Fe and B during the decomposing process of ludwigite.

2.2 The character and forming generation of essential ore mineral

The essential mineral of Wongquangou uranium-bearing vonsenite deposit are: magnetite, szaibelyite, luwdigite, serpentine, and clinohumite. The auxiliary minerals: are suanite, tourmaline, pyrrhotine, phlogopite, chlorite, calcite, brucite, graphite, and apatite, microcomponents are: uraninite, quartz, olivine, tremolite, albite, rutile, and pyrite. Every mineral is distributed unevenly in different types of ore body and with a big diversity in contents.

It can be divided into three generations, depending on the mineral-producing sequence of magnetite: magnetite of the first generation occurs mostly in the form of euhedral crystal, the particle diameter varying from 0.2mm to1.3mm and with lower content, about 1% to 2% of total content of magnetite, which was synchronously produced with olivine.

The magnetite in the second generation is the product of ludwigite decomposed by hydrothermal process, with different shapes and in fine granular, pilotaxtic paragenetic with fibrous szaibelyite. The magnetite of the third generation is in the form of thread vein, with small contents and could be intercalated in the fissure of different types of ore.

According to its order of formation, the szaibelyite can be divided into two generations: Szaibelyite in the first generation is mostly in the form of lath-shaped, with large grain size, and distributed in the ore body in an uneven crumb structure. it may be the product of alteration of suanite in the early stage. Szaibelyite in the second generation is the result of decomposition of ludwigite, by the hydrothermal process in the late stage, fibrous magnetite, and fine-grained magnetite mosaiced closely, 90% of the total content is szaibelyite.

The chemical composition of szaibelyite indicates that there are small variation in the contents between the early stage and the late stage. Ludwigite is mostly the product of the early stage of the first generation, and most of it was decomposed during the hydrothermal process and regional metamorphism during the late stage. The degree of decomposition of ludwigite is the direct cause influencing the comprehensive utilization of boron mineral. The areas with higher degrees of ludwigite decomposition have a higher utilization ratio of boron ore body.

3 REE features of the uranium-bearing vonsenite deposit

The REE contents of ore in the boron-bearing rock series in Liaodong rift are shown in Table 3. It indicates that the contents of REE of different types of ores are very small, ΣREE varying from 4.60 to 34.78×10^{-6}, with an average content of 18.30×10^{-6}. It is 6 to10 times lower than in marble, granulitite of which are normally marine sedimentary. The Eu value in different ore types less than 1, varying from 0.24 to 0.77. Eu/Sm value average below 3.5. The distribution pattern of REE take a valley shape at Eu point, and belongs to the Eu depletion model. The curve of the REE distribution pattern roughly takes the shape of a "W", forming two-wave trough at Eu and Er. This REE feature of ores has a certain similarity with hydrothermal sedimentary rock, which reflects the inner relation of their genesis, the ore body and hydrothermal sedimentary rock experienced similar geological process, and the Uranium-bearing vonsenite is a product of boron-rich, Si-rich hot- water deposit.

4 Stable isotope characters of uranium-bearing vonsenite deposit

4.1 Carbon isotope features

The analysis of carbon isotope of ore and surrounding rocks (magnesian marble) indicate that there is a clear difference between ore and surrounding rocks, $\delta^{13}C$ of ore varies from –2.69‰ to -1.04‰. it is very close to the $\delta^{13}C$ of volcanic rock and volcanic gas, showing the close relation of carbonaceous origin and volcanic activity. The $\delta^{13}C$ of magnesiam marble varies from –2.6‰~+2.69‰, with a mean value of 0.29‰, close to the $\delta^{13}C$ value of marine dolomite in the Proterozoic era.

4.2 S isotope features

There are sulfide, especially pyrite and pyrrhotite, distributed unevenly in the ore and surrounding rocks in the boron deposit of the Lliaodong rift, and submarine exhalation sulfide deposit was formed at the top of boron-bearing rock series in some areas.

There is little variation of $\delta^{34}S$ of different rocks in boron-bearing rock series in Liaidong rift, varying from –3.2‰ to 10.99‰, the $\delta^{34}S$ value of sulfide varying from1.58‰ to 9.8‰.

In different types of boron ores. In comparison with $\delta^{34}S$ value, it shows that the S isotope composition of sulfide for host rocks and different types of ores ,varying in

a limited scope, is similar to the S from deep resource. Compared with the S isotope composition of sulfide in different geological setting, the S isotope composition in this area is similar to that in volcanic S. Combined with the analysis of structural setting of boron deposit, we can conclude that volcanic exhalation-hot water sedimentary was the main effect during the early stage of the boron deposit formation, S was provided by submarine volcanic exhalation. S isotope composition homogenized during the late stage.

5 Mineralization in the uranium-bearing vonsenite deposit

The Liaodong rift developed under a foundation of granite greenstone terrene in the Archeozoic era, it went through stretching extension, fault depression, depositing, compression, and folding, consuming a great quantity volcanic products, and hot-water sediment products spouted out during the process, Meanwhile, a set of volcanic rocks——hot-water sedimentary rocks was formed, which is rich in Na, Fe, B. This is called the boron-bearing rock series. The mineralization of uranium-bearing vonsenite deposit can be divided into two stages based on the analysis of the ore fabric.

In the second volcanic-sedimentary fault basin at the ancient rift environment of the Proterozoic era, a boron-rich mantle current from deep earth entered into sedimentary basin at the intermittence of volcanic activity, Due to a change in the physical-chemical condition, BO_3^{-2} complex anion combined with Mg^{2+} of water mass formed borate of Fe and Mg, resulting in the original ore bed after depositing.

During the period of the Lvliang movement, this area experienced alteration of regional metamorphism of amphibolites facies and deformation in two stages, highly hydrothermal alteration occurred at the mining district due to hydrous mineral and sulfide. Favorable evidence of hydrothermal process in phlogopite tremolite metasomatic rock zone exists at the roof of the uranium-bearing vonsenite seam. By regional metamorphism and hybridization, after highly superposition and transformation for source bed or hot-water sedimentary boron deposit, B and Fe was further enriched during the process, This caused a relocation, resulting in the formation of the industrial deposit.

Geology and origin of the Dongsheng uranium deposit in the Ordos basin, North China

Weidong Xiang, Xiheng Fang, Tiangang Li, Xiaolin Chen, Yaqing Pang, Huahan Cheng
Beijing Research institute of Uranium Geology, Beijing 100029, China

Abstract. The Dongsheng uranium deposit in the Ordos basin, Northern China occurs in fluvial sandstones in the Zhiluo Formation, Middle Jurassic. Geologic characteristics of the deposit such as depositional environments of host sandstones, the distribution of ore bodies, uranium minerals, the mineralization age etc. are described in this paper. A "Multi-stage Uranium Mineralization" model is proposed for uranium ore-formation of the deposit. The mineralization process can be divided into four main stages, namely the preconcentration during diagenesis, the interlayer infiltration mineralization during Late Jurassic to Paleocene time, the reconcentration in Miocene, and the last stage of ore preservation exerted by reducing fluids after Eocene time.

Keywords. Dongsheng uranium deposit, host sandstone, metallogenic model, multi-stage uranium mineralization

1 Introduction

Since 1990, China has shifted its prospecting emphasis from hardrock-hosted uranium deposits mostly located in southeastern China to sandstone- hosted ones in northern China. The sandstone targets expect to be amenable by low cost ISL mining. From then on, several ISL-amenable sandstone-type uranium deposits have been explored in China. The Dongsheng uranium deposit, a newly discovered large-scale sandstone uranium deposit, is located in the Ordos basin in the middle of Northern China with an area of 250,000km^2. The crystalline basement of the Ordos basin was formed in Archean and Early Proterozoic time. The basin was attributed to a part of the North China Platform from Middle Proterozoic to Triassic time. The platform regime was kept stable and a secession of marine-dominated sediments was deposited during the period. Since Late Triassic, the basin was successively transferred from a platform into an independent intracratonic basin. In response to the transformation, deposition in the basin changed from marine-dominated sediments in Paleozoic to continental ones in Mesozoic.

2 Geology of the Dongsheng uranium deposit

The Zhiluo Formation, the ore-hosting horizon, can be divided into two lithologic members, namely, the upper member and lower member in the ore district. The lower member of the Zhiluo Formation is recognized as a set of sediments of braided-stream system deposited in humid paleoclimatic conditions, whereas the upper one is attributed to a meandering-stream system in semi-arid or arid climate conditions. Ore bodies of the Dongsheng uranium deposit mostly occur in the lower member of the Zhiluo Formation, especially at or near the contact between gray sandstones and gray-greenish sandstones (Figure 1). The gray sandstones of the lower member contain abundant

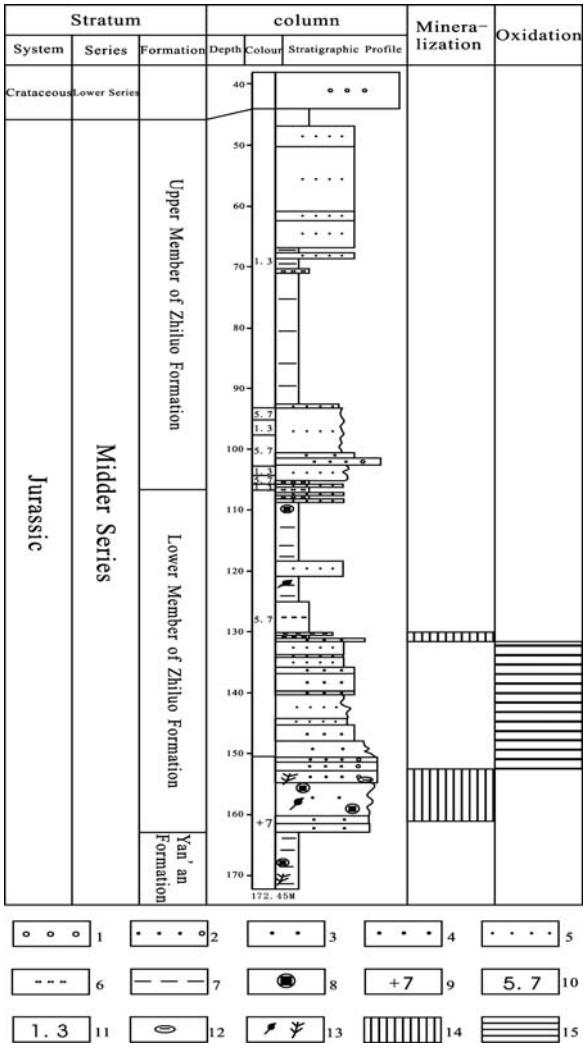

Figure 1: Column showing the lithology of host sandstones and uramium mineralization in Dongsheng uraium deposit 1-Conglomerate, 2-Pebbly gritstone, 3-Coarse-grained sandstone, 4-Medium-grained sandstone, 5-Fine-grained sandstones, 6-Siltstone, 7-Mudstone, 8-Pyrite, 9-Gray color, 10-Gray-greenish color, 11-Pink or red color, 12- Muddy gravel, 13-Plant debris, 14-Ore body, 15-Alterated sandstone

carbonous plant remains, coal debris and sulfides, and usually are loosely cemented. In contrast, some plant debris and pyrite occur in green, gray-greenish sandstones, but argillic alteration was intensely developed in green sandstones.

2.1 Host sandstones

The host sandstones of the Zhiluo Formation are dominantly presented as lithiclastic arkose, being loosely consolidated and moderately sorted. Monomineral debris of the host are mainly composed of feldspar, rock debris, quartz and biotite. Heavy minerals of host sandstones consist of essonite, monazite, sphene, zircon, epidote, black tourmaline, etc. Opaque minerals are mostly pyrite. The composition of the host shows that the sediments were originated and transported in a short distance and the provenance rocks mainly consist of granitoids and metamorphic rocks. The thickness of host sandstones varies from 17m to 55m.

2.2 Gray-greenish host sandstones

Geochemical and mineralogical data show that the ferrous iron content in silicate minerals of gray-green host sandstones is significantly higher than that of gray host sandstones and uranium ores, respectively being 2.04%, 1.52% and 1.50% in average. Mineralogically, the total content of clay minerals is 30.82% on average in gray-green sandstones, 20.84% and 20.96% in gray host sandstones and ores by X-ray diffraction analysis. In the aspect of relative contents of clay minerals, chlorite is 11.6% in average in gray-green sandstones, 3.2% and 5.4% in gray host sandstones and uranium ores. In conclusion, it is proposed that the high contents of Fe^{2+} in gray-green host sandstones are considered as the most important reason why those sandstones are in gray-greenish or green color. Mineralogically, there are more clay minerals, especially more chlorite, existing in gray-green sandstones. As it is well known, clay minerals are attributed to sheet silicates, and usually certain cations can be adsorbed in interlayers of crystal lattices. In gray-green or green sandstones, Fe^{2+} can occur in the crystal lattice of clay minerals.

2.3 Orebodies

The sedimentary environments of ore-hosting sandstones are mainly attributed to fluvial systems, especially braided-stream systems. Uranium ore bodies mostly are tabular, roll-shaped and partly lenticular in cross section, and elongated and sinuous in plan along the contact between the gray host sandstones and gray-greenish or green sandstones. Some tabular ore bodies seem to float within a sandstone layer with no obvious relation to mudstone interbeds or overlying and underlying mudstones. Uranium ores mostly occur in medium- and coarse-grained sandstones with loose cementation and high permeability. The gray host sandstones usually contain a great amount of reductants such as carbonaceous plant debris, pyrite, coal debris, etc.

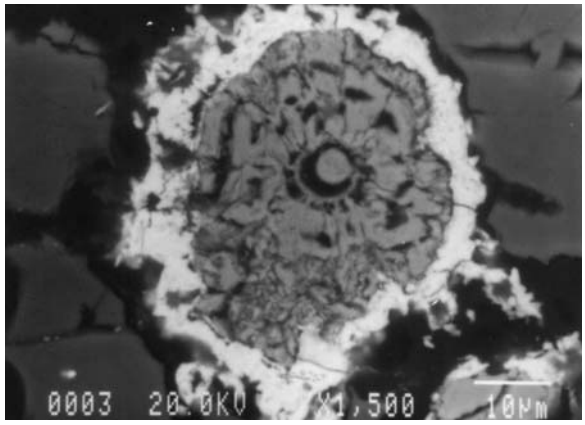

Figure 2: Photo of electronic microprobe showing coffinite in light-gray color surrounds the pyrite core in dark-gray color

2.4 Uranium minerals

Uranium mainly occurs in uranium minerals and adsorption form. Data of the electron microprobe and X-ray powdered crystal analysis show that uranium minerals are mainly coffinite, minor brannerite and uraniferous Ti-Fe oxides.

According to electron microprobe data, the composition of coffinite is: UO_2 (63.50%-74.98%), SiO_2 (15.26%-18.78%), ThO_2 (0.08%-0.36%) and other elements with very low content. Coffinite, existing in the colloform texture or the form of fine columnar crystal (usually less than 3 micron), is usually associated with pyrite and occasionally independent in the matrix of host sandstones. A photo of coffinite is shown in Figure 2. Uraniferous Ti-Fe oxides seem to be alteration products of leucoxene or ilmenite. Adsorbed uranium is closely associated with clay minerals, carboniferous materials, zeolite and powdery pyrite.

3 Origin and metallogenic model for the Dongsheng uranium deposit

There exist some distinctive differences between the Dongsheng uranium deposit and previously discovered sandstone-type uranium deposits in the Yili basin and Turpan-Hami basin, NW China (Lin et al. 2002; Xiang et al. 2001).

Important aspects related to the formation of the Dongsheng uranium deposit have been studied in detail, such as tectonic setting and evolution, lithofacies and epigenic alteration of host sandstones, paleohydrology,

paleoclimatic conditions, uranium mineralization age, etc. (Xiang et al. 2002). The authors discuss the mineralization process and genesis of the uranium deposit. The newly obtained research results suggest that a long and multistage process lasted in the formation of the Dongsheng uranium deposit. The metallogenic model of the Dongsheng uranium deposit is interpreted and proposed as a "Multistage Uranium Mineralization" model. The mineralization process could be divided into four main stages, namely the pre-concentration during diagenesis, the interlayer infiltration mineralization, the reconcentration in Miocene, and the stage of ore preservation exerted by reducing fluids.

3.1 Stage I: Pre-concentration

The uranium concentration of some tabular protores seems to have begun shortly after the sedimentation and burial of overlying sediments. Indeed, some uranium could have been preconcentrated during the deposition of overbank boggy mudstone. The mineralization appeared to be accompanied by the diagenetic process of host rocks. These tabular protores seem to be precipitated at chemical interfaces between the connate pore solution and infiltration solution.

3.2 Stage II: Interlayer infiltration mineralization

The tectonic evolution of the Ordos basin shows that the eastern margin of the basin was uplifted from Late Jurassic time, and the paleo-topographic conditions with the highland in the east and lowland in the west were maintained from Late Jurassic to Miocene time. The Sanxi massif at the eastern margin of the basin was uplifted from Late Jurassic time and became the recharge area of meteorically-derived uranium-bearing solutions which infiltrated host aquifers, and the Yinshan uplifting area in the north of the basin also became recharge regions from Late Jurassic to Paleocene time (Except for Early Cretaceous). From Late Jurassic, paleoclimate conditions of the basin became arid being favourable for the enrichment uranium in recharge solutions from provenance rocks.

The oxidizing, uraniferous groundwater was driven by a regional hydrologic gradient and interlayer pressure, and moved into reductant-enriched host sediments of the Zhiluo formation, Middle Jurassic along exposed basin margins. The oxidizing solution replaced the reducing materials, to form an oxidation-reduction (redox) boundary, and resulted in uranium concentration at the redox front. Most roll-type orebodies, namely the interlayer oxidation type ones, were formed during the stage that lasted from Late Jurassic to Paleocene time (155-56Ma), being particularly favorable for uranium mineralization in Late Jurassic (about 135Ma), the third episode of Yanshanian tectonism (about 85-88Ma), and Late Paleocene (about 56Ma).

3.3 Stage II: Uranium reconcentration

Although most uranium mineralization of the Dongsheng uranium deposit seems to be formed prior to Tertiary, some high-grade ores were formed in Miocene time. Three uranium-lead isotopic ages of the uranium mineral-coffinite in typical high-grade ores of the uranium deposit show 20.2Ma, 16.5Ma and 9.8Ma. The process and origin of uranium reconcentration in the stage might be mulriple, either in the redox process or in hydrothermal process. Some low-grade ore bodies could be destroyed and redistributed in subsequent tectonic movements, especially in the second episode of the Himalayas tectonism in Micocene time. On the other hand, recent research results suggest that some high-grade ores were formed in a thermal process according to evidences obtained by investigations of fluid inclusion (Xiao et al. 2003) mineral associations and mineral replacement.

3.4 Stage IV: Ore preservation exerted by reducing fluids

Prospecting drilling indicates that most of uranium orebodies are located at or near the contact between gray-greenish or green sandstones and gray or light-black sandstones. It is proposed that the gray-greenish host sandstones were previously oxidized sandstones and subsequently were reduced by introduced fluids after Eocene time. Because of the oxidation process (from Late Jurassic to Paleocene time), reductants such as carbonificated plant remains, sulfides were destroyed and disappeared off the gray-greenish or green host sandstones. The reduction process covered up the previously oxidized sandstones and could protect uranium accumulations from the destruction originated from infiltrating oxidizing water. In some cases, the oxidized sandstone remains with pink or red color can be observed in gray-greenish or green host sandstones. The remaining sandstones usually are cemented by carbonates.

It is stated that the reduction process in the Dongsheng area was simultaneously and genetically related with the formation and development of the Hetao down-faulted basin located to the north of the Ordos basin. The formation process of the Hetao basin began from Eocene time and continues at the present. Before the subsidence of the Hetao basin, the region was uplifted and denudated and served as a recharge area of groundwater at the north margin of the Ordos basin. The appearance of the Hetao basin changed the hydraulic system in the following way: the interlayer infiltration of groundwater stopped; then seepage and reduced solutions began to move out from the deep to shallow subsurface of the Ordos basin; at last, the host sandstones were reduced by ascending reducing fluids such as oil field water and gas. A lot of oil-soaked sandstones and evidences of oil and gas in Lower Cretaceous in the north of the Dongsheng upwelling area can

verify the relation between the subsidence of the Hetao down-faulted basin and filtration solutions from oil and gas fields.

4 Summary and conclusions

1. The ore bodies of the Dongsheng uranium deposit mostly occur at the interface between gray sandstones and gray-greenish sandstones.
2. The high content of Fe^{2+} in gray-greenish host sandstones is considered to be the most important reason why those sandstones are in gray-greenish or green color. In mineralogical aspect, there are more clay minerals, especially more chlorite, existing in gray-greenish sandstones. The gray-greenish host sandstones were previously oxidized sandstones and subsequently were reduced by introduced fluids after Eocene time.
3. The reduction process in the Dongsheng region was simultaneously and genetically related with the formation and development of the Hetao down-faulted basin.
4. The mineralization process can be divided into four main stages, namely the pre-concentration during the diagenesis, the interlayer infiltration mineralization during Late Jurassic to Paleocene time, the reconcentration and accretion of ore bodies in Miocene, and the last stage of ore preservation exerted by reducing fluids after Eocene time.

References

Lin SX, Wang BQ, Li SX (2002) Chararacteristics of Uranium Mineralization and Ore-Controls of Kujieertai Deposit, Yili Basin, Xingjiang Autonomous Region. Sandstone-type Uranium Deposits in China: Geology and Exploration Techniques. Beijing: Atomic Energy Press, 65-76

Xiang WD, Chen ZB, Chen ZY, Yin JS (2001) Metallogenic Condition and Regularity of Interlayered Oxidation Zone-type Sandstone Uranium Deposit in Southwestern Part of Turpan-Hami Basin, Northwestern China. China Nuclear Science & Technology Report, Beijing: Atomic Energy Press, 1-12

Xiang WD, Fang, XH, Li TG, Cheng HH (2002) Metallogenic Process and Perspective Technology of Sandstone-type Uranium Deposits in the Middle and East Part of North China. An Annual Inner Report of the Research Project, 67-86

Xiao XJ, Li ZY (2003) The Evidences and Significances of Epithermal Mineralization Fluid in Dongsheng Sandstone-type Uranium Deposit, Inner Mongolia. Annual Report of Beijing Research Institute of Uranium Geology, 20: 64-69

On the "complex three member fluids genesis" sandstone type uranium deposit in Dongsheng district, Inner Mongolia, NW China

Xinjian Xiao, Ziying Li, Xiheng Fang, Guangxi Ou, Ye Sun
Beijing Research Institute of Uranium Geology, Beijing, 100029, China

Anping Chen
Geologic Party No.208, Bureau of Geology, CNNC, Batou, Inner Mongolia, 014010, China

Abstract. The Ordos basin is one of the main oil-, gas- and coal-producing basins in China. The Dongsheng sandstone type uranium deposit is located in the northeast of the basin.The Dongsheng sandstone type uranium deposit has unique metallogenic features. Based upon detailed studies of geological setting, geological characteristics of ore deposit, epigenetic wall-rock alteration and ore-forming fluid of the deposit, this paper emphasizes the evolution of the low-temperature fluids during the mineralization processes and geochemistry characteristics of fluid metallogeny. Based on analysis of fluid evolution and uranium mineralization, we propose a "complex three member fluids genesis" model for the Dongsheng sandstone type uranium deposit, which relates to tectonic and alteration history.

Keywords. Ordos basin, Dongsheng sandstone type uranium deposit, low temperature hydrothermal fluid, "complex three member fluids genesis" model

1 Geological setting

The Ordos basin is one of the main oil-, gas- and coal-producing basins in China The Dongsheng sandstone type uranium deposit is located in the northeast of the basin. Research on the characteristics of Ordos basin and metallogenic setting of Dongsheng sandstone type uranium deposit indicates that faulting, tilting, uplift and depression of the whole rigid block of the basin occurred during the Indo-sinian-Yanshanian and Himalayan movement. During the mid-Jurassic and early-Cretaceous orogenic movement especially, uplift of the basin, sedimentation interruption, infiltration of the surface-water and groundwater and lateral migration of oil supplied the material source and fluid dynamics for the Dongsheng sandstone type uranium deposit (Wu 1997; Yeet et al 1997; Gao et al. 2000). The neotectonic movement (uplift and denudation) of the basin aided in U element remobilization and multiple interlayer oxidations. Furthermore, around the Dongsheng district is the NE striking Langshan rock mass on the northwest, the EW striking Yinshan rock mass on the north, with their granitic rocks and volcanic rocks possibly supplying the uranium source for the deposit.

2 Geology of the sandstone type uranium deposit

Our studies show that the ore-bearing strata of Zhiluo group have two parts (Fig. 1), the top layer is middle-fine motley sandstone and claystone; the lower layer can further be divided into two sub-layers, with the top sub-layer mostly gray-green sandstone and claystone, and the lower sub-layer gray uranium-bearing sandstone. Mineralogical analysis, of the sandstone of ore-bearing stratum confirms it to be lithic arkose (Xiao et al. 2004a, b). Chemical analysis indicatesd that there are the same chemical compositions between the Zhiluo group sandstone and the granitic rocks of the Yinshan and Langshan area.

The ore bodies are blurry roll type shaped, more plank type, layer type and lensoid type. Most of the uranium element is absorbed, and the coffinite is the primary uranium mineral, there are also some brannerite and uraninite.

The contents variety of organic matter, S, Mn and Fe element in the different parts of the Zhiluo group under layer show that the gray-green sandstone rock has been subject to interlayer oxidation. The varieties of U, Se, V, Mo and Re elements in drill and section plane support the interlayer oxidation mineralization of the Dongsheng sandstone type uranium deposit. According to the analysis results, it is obviously the Zhiluo group contains uranium-rich sandstone rocks, with the U contents of 4 to 4.6 ppm.

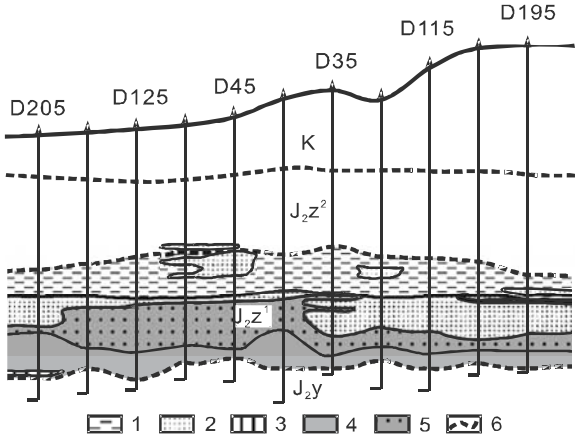

Figure 1: Section map of exploration line (NO.X) in the Dongsheng sandstone type uranium deposit 1.gray-green claystone, 2.gray-green sandstone, 3.gray claystone, 4.gray sandstone, 5.gray sandstone with bearing uranium, 6.the borderline of stratum

3 Alteration zones

There are obvious epigenetic alteration zones associated with the deposit. The plane alteration zones indicate the interlayer oxidation in the sandstone strata. There is three-layer alteration in lengthways: the top alterations are limonitize, clay and carbonation which are in the upper layer of Jurassic system Zhiluo group, and middle alterations are chloritization of biotite and plagioclase, epidotization of plagioclase, clay alterations and carbonation in top sub-layer, under-layer alterations are epidotization of plagioclase and carbonation in under sub-layer of Zhiluo group which is the host rock of uranium deposit (Xiao et al. 2004a).

4 Uranium mineralization of the low temperature fluids

In this deposit, there are three type alterations created by three mineralizing fluids, i.e., the first type is the acid oxygenic alteration with kaolinization, hematitization, limonitzation and the oxidation of organic matters; the second type is the weak acid and alkalescent reductive oil-gas alteration with epidotization, carbonation, chloritization, sericitization, montmorillonitzation and pyritization; the third type is alkalescent and strongly reductive hydrothermal fluid alteration with epidotization, carbonation, montmorillonitzation, pyritization and the mineral assemblage of brannerite, anatase and coffinite.

We distinguished three periods of carbonation: the first period carbonation occurred before the green alteration as the cryptocrystalline, microcrystalline and finely-crystalline calcite cement; the second occurred as the finely-crystalline calcite cement and the third as sparry-calcite cement or calcite vein. There are plenty of the oil-gas fluid inclusions in the calcite cement. The second and third period carbonations are the results of oil-gas and hydrothermal alteration after the primary uranium mineralization, and gloss over the early alterations.

The study on the uranium mineralization fluids shows the three type important fluids on the sandstone type deposit. The first type fluid, the acid oxygenic fluid, is the primary mineralization fluid for the Dongsheng sandstone type uranium deposit; the second type fluid is oil-gas fluid, which supplied a part of reducers and made the carbonation and green alteration for the deposit; the third type fluid is the low temperature hydrothermal fluid with alkali enrichment, this type fluid transformed the ancient interlayer oxidation type ore bodies and occurred the assemblage of coffinite-bannerite-anatase.

5 Fluids conduit system

Drawing on the studies of many geologists (Ren et al. 1994; Zhao et al. 1996; Sun et al. 1997), we also analyzed the tectonic thermal events during later Jurassic and early Cretaceous period. Those events activated the basement, resulting in large-, mid-, small- scales system of cracks, along which fluids moved.

6 Conclusions

Based on analysis of the fluid evolution and uranium mineralization, we propose a "complex three member fluids genesis" model for the Dongsheng sandstone type uranium deposit. The three member fluids are the normal temperature acid oxygenic fluid, the oil-gas fluid and low temperature hydrothermal fluid. This model is considered to involve tectonic activity and alteration under the different dominant geologic agents in different periods.

Acknowledgements

The authors gratefully thank Dr. Chunfang Cai (IGG of CAS, China) for the useful discussions. This study is financially supported by China Nuclear Bureau of Geology's Program (HDKY20020501) and China National Major Basic Development Program "973" (2003CB214608). Finally, the authors wish to thank the anonymous reviewer for the insightful review comments.

References

Ding YY (2000) Structural characteristics of northern ordos basin reflected by aeromagnetic data. Geophysical & Geochemical exploration, 24(3): 197-202 (in Chinese with English abstract)

Gao SL, Han QJ, Yang H (2000) Yanshanian movement in ordos basin and its relationship with distribution of oil and gas. Journal of Changchun university of science and technology 30(4): 353-358 (in Chinese with English abstract)

Ren ZL, Zhao ZY, Zhang J (1994) Research on Paleotemperature in the Ordos Basin. Acta sedimentologica sinica, 12(1): 56-65 (in Chinese with English abstract)

Sun SH, Li XM, Gong GL (1997) Study on the tectonical thermal events of Ordos basin. Chinese science bulletin 42(3): 306-309

wu CL, Zhou JY, Wang GF (1997) Relationship between paleotechtonic stress fields and major gas fields in ordos basin. Oil & gas geology 18(4): 267-275 (in Chinese with English abstract)

Xiao XJ, Li ZY, Chen AP (2004a) Preliminary study on features of mineralogical zoning of epigenetic alteration at sandstone-type uranium deposit, Dongsheng area, Ordos basin. Uranium Geology 20 (3): 136-140 (in Chinese with English abstract)

Xiao XJ, Li ZY, Fang XH (2004b) The evidences and significances of epithermal mineralization fluid in Dongsheng sandstone type uranium deposit, Inner Mongolia. Bulletin of Mineralogy, Petrology and Geochemistry 23(4): 301-305 (in Chinese with English abstract)

Ye J.R, Lu MD (1997) Geohistory modeling of cratonic basins: a case study of the Ordos Basin, NW China. Journal of Petroleum Geology. 20: 347-362

Zhao MW, Hans A, Klaus W (1996) The application of the K-Ar dating to the determination of diagenetic ages of sedimentary rocks – a case study from the ordos basin. Acta sedimentologica sinica 14(3): 11-21 (in Chinese with English abstract)

Establishment of a virtual geological environment: A case study from the Dongsheng U-mineralized area, China

Fawang Ye, Yingjun Zhao, Dechang Liu
Beijing Research Institute of Uranium Geology, P.O.Box 9818, Beijing, 100029, China

Abstract. Beginning with an introduction of basic concepts, this paper deals with the key techniques and operating approach to the implement of virtual geological environment for uranium exploration. A tentative study has been conducted in Dongsheng sandstone-type uranium mineralized area, based on the virtual reality platform of Multigen software. As a result, a primary computer system of virtual geological environment was firstly established in China including both function of virtually roaming run-time and function of inquiring information. This is an important step for the application of virtual reality technique in uranium exploration.

Keywords. Virtual geological environment, Dongsheng U mineralized area, multigen virtual reality software platform

1 Introduction

The geological environment is considered as the target space where uranium exploration is processed. The higher the digitalized degree of geological environment is, the more increased exploration efficiency will be. So, raising the digitalization of geological environment is an important issue to change the traditional exploration approach and to improve uranium exploration information. The virtual geological environment is established by means of importing related data into computer, forming and displaying a multi-scale environment to simulate the real field geological environment. Differentiating from virtual terrain or virtual physiognomy sight studied by others currently (Song et al. 2002; Li and Gong 2002), virtual geological environment manifests all of geological exploration information, including strata occurrence, geological structure besides the spatial geographical situation and hypsography. Moreover, virtual geological environment should provide researchers with function of real-time roaming, information inquiry, information synthesis and analysis, and making decision, etc. Recently, the establishment of virtual geological environment is realized, based upon the association of various techniques of Virtual Reality (VR), Remote Sensing (RS), Geographical Information System (GIS), Global Position System (GPS), and Database. It seems reasonable to perform the study of geological phenomena in virtual geological environment, such as topography and hypsography, strata occurrences, faulting and folding, and wall rock rather than doing that in real field. It will reduce a great deal of manpower, material and financial input, representing a great step to make the dream of "indoor search for mineral resources" true (Ye et al. 2004). The paper deals with the Dongsheng uranium mineralized area as an attempt in uranium exploration.

2 Key techniques to establishing a virtual geological environment

To establish the virtual geological environment, a series of key techniques are applied as follows:

2.1 Modeling techniques for vivid field geological phenomena

It is necessary for describing the natural geological setting in multi-temporal and spatial scale to establish virtual geological environment with help of physiognomy cliff, river and gulch, vegetation, and water body; and more proper geological phenomena including strata occurrences, color of rock, geological structure (faulting and folding) as well. Consequently, how to form morphologic expression of high precision and how to simulate such vivid geological phenomena are of remarkable significance, and will greatly prescribe the visual effect of virtual geological environment.

2.2 Techniques for real-time transmission, processing and displaying mass data

Virtual geological environment is established upon mass data including high accurate Digital Elevation Model (DEM) data, high-resolution remote sensing image, filed real photos, and those related to search for mineral resources. Roaming, inquiring, and analyzing the information data will be processed in virtual environment by Model operation, dynamic forming and real-time visualization according to users. Therefore, it plays a role of the key techniques how to transmit, process, and display the information data at real-time for establishing and applying virtual geological environment. Recently, most of domestic and foreign VR software platform are not so available in dealing with geo-scientific data, which increase difficulties for the establishment of virtual geological environment.

2.3 Technique to combine VR with GIS

As an advanced scientific research and decision platform to support mineral resources exploration, the functions of information display, inquiry, analysis and data mining, etc. are indispensable for virtual geological environment. VR and GIS have their advantages on realizing such functions respectively. It seems reasonable that the establishment of virtual environment mainly depends upon how to combine GIS and VR in practice.

3 The means of realizing a virtual geological environment

The research and realization of virtual geological environment are carried out using the support of various modern techniques.

3.1 Association of software with hardware

Virtual reality system is recently established on the basis of software and hardware. According to the current level of techniques, the software study as a dominant factor is popular for all kinds of virtual reality system in various application domains. Moreover, it is easier to be achieved.

3.2 Association of VR with GIS

The association of VR with GIS is implemented at different levels. At the early stage of research, the association demonstrates mainly is mostly in mutual operation on the data The second level of association is characterized by the establishment and application of common database on the basis of the same data model and data structure. The third level indicates sufficient integration of VR and GIS in technical realization and function, that is, the basic function of VR and GIS merges into an organic whole via software realization. Recently, the research and application of virtual geological environment remains at the first stage.

4 The tentative establishment of a virtual geological environment: The Dongsheng uranium mineralized area

A most basic virtual geological environment at least deals with three groups data: the elevation data to present morphology; the geo-scientific feature information associated with mineral resources, and the texture data describing vivid physiognomy of the earth's surface. The virtual geological environment of Dongsheng uranium mineralized area in this paper, the DEM data (Fig. 1) is obtained automatically through processing high-resolution Spot5 stereoscopic images by digital photogrammetry technology based on software module of OrthBASE in RS software platform of ERDAS 8.6.

Figure 1: The three-dimension presentation of DEM data, Dongsheng uranium mineralized area (vertical exaggerated factor is 4)

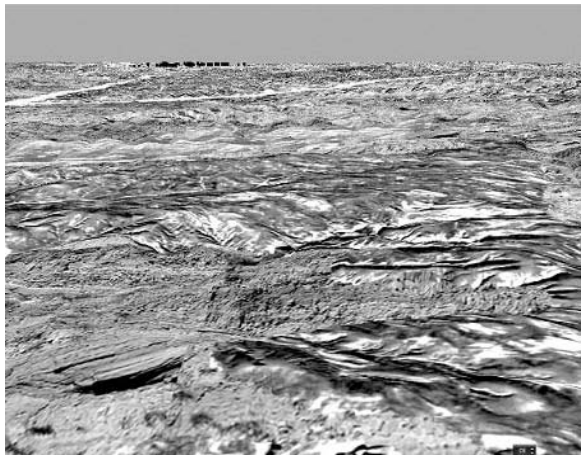

Figure 2: A sight of virtual geological environment, Dongsheng uranium mineralized area (northward sight angle)

Some geoscience professional information is provided by ARCGIS database in Shape file or Coverage format, including geological map and those related to search for mineral resources. In addition, the data conversion between GIS and VR software platform by means of FME (Feature Manipulation Engine) or programming. Association of satellite image of high precision with field photos in order to make the virtual object more vivid collects texture data.

The modeling of virtual geological environment is processed and supported by Multigen Creator VR platform after preparation of above-mentioned three groups data, producing a database of virtual geological environment in Openflight data format. During the study mentioned in this paper, the strata information is taken into account as the only geo-scientific feature information needed by virtual geological environment. Besides, to make better visual effect, local projection of strata information is

This page intentionally blank

adapted. The virtual geological environment acquired is presented in Figure 2.

How to roam and display the virtual geological environment achieved through Multigen Creator platform, and develop the inquiry function according to user's requirement present key techniques for establishing geological environment as well. Those are studied and realized through VR tools software "Mulitgen Vega" (Gong 2002; Wang 2003). An Application Defined File (ADF) is firstly defined in Lynx interface of Multigen Vega software, followed by the program compilation to develop the function of information inquiry and sight driving by association of Microsoft Function Class (MFC) with Vega function library (Li et al. 2002). In the study, the following objects need to set parameter when an ADF is set up: Window, Object, Scene, Motion Models, Observer, etc. Of them, such original values are set for Motion Models:

- Input device: default;
- Initial position: x=86000, y=95000, z=4000;
- Motion Model type: walk;
- Max step depth: 10;
- Walking speed: 100

In general, walking is the main way for geological researchers to make field investigation, resulting in the observation of all geological phenomena in details. Thus, the roaming way is set as walk in study.

There exist two executing programs of virtual geological environment, either compiling an executive file in the VC (Visual Studio C), or opening the ADF file in Lynx interface, followed by executing the menu command: Preview\Active preview.

5 Conclusions

A real-time roaming system of virtual geological environment has been tentatively established for the Dongsheng uranium mineralized area, as shown in the paper. The system displays and simulates the phenomena of the Dongsheng U mineralized area vividly, including morphology, physiognomy, and the occurrence of upper and lower members of Zhiluo Group (J_2) and Cretaceous system (K_1). It plays an important role in improvement and development of uranium exploration techniques.

Acknowledgements

We are very grateful to Professor Zhou for his great efforts to revise this paper carefully.

References

Gong ZR (2002) Design of VEGA program (in Chinese). National Defence Industry Press

Li H, Gong JH (2002) On virtual geographic environments (in Chinese). Acta Geodaetica et Cartographica Sinica 31(1): 1-6

Li R, Liu PY, Zhang XE (2002) Application of Vega software design in MFC (in Chinese). Computer Engineering and Design 23(8): 55-57

Song Y (2002) The design of large terrain 3D visualization system (in Chinese). Journal of Sichuan University (Natural Science Edition) 39(3): 439-442

Wang YJ (2003) An initial exploration of desktop virtual reality based on Multigen Creator and Vega (in Chinese). Journal of Geomatics 28 (4): 14-16

Ye FW, Liu DC, Zhang BJ (2004) Study on application of virtual reality to uranium geology (in Chinese). Uranium Geology 20(1): 56-62

Correlation between shoshonitic rocks and uranium mineralization in the Xiangshan uranium ore field

Shuming Zhang
China University of Geoscience, Wuhan, 430074, China, and East China Institute of Techology, Fuzhou, Jiangxi, 344000, China

Dagan Yu
East China Institute of Techology, Fuzhou, Jiangxi, 344000, China

T.S. Brewer
Department of Geology, University of Leicester, Leicester, LE1 7RH, UK

Abstract

The Xiangshan basin contains signifycant volcanic units and is located in the area between Lean country and Chongren Country of Jiangxi Province, China. The basin appears has an oval form with an area of 309 km^2; it is approximately 26.5 km in length from east to west, and about 15km width from north to south. The basement rocks onto which the Xiangshan basin were deposited are predominantly Proterozoic lower greenschist facies to lower amphibolite facies metamorphic rocks. The basin deposits are composed of upper Jurassic intermediate to acidic volcanic rocks. The upper Jurassic volcanism in the Xiangshan basin can be divided into two cycles. The first volcanic cycle is composed mainly of fissure eruptions of dellenite and dacite porphyry, whereas, the second volcanic cycle is composed of discrete eruptive centres that produced pyroclastic lavas (Xia et al 1992; Shen et al 1995).

The dellenite and dacite porphyry of the first volcanic cycle was formed during a ca.30 Ma period (Liu et al 1985; Li et al 1989; Xia et al 1992; Shen et al 1995; Wang et al 2000). But the eruptive sequence is composed of two different rock types. The early stage rock assemblage was dominated by dellenite with zircon U-Pb age and whole rock Rb-Sr ages in the interval 158 -169Ma. The later stage volcanism produced mainly porphyritic dacite, with zircon U-Pb age and whole rock Rb-Sr ages in the interval 125-134Ma.

We argue that the later porphyritic dacites belong to inter-plate shoshonitic style volcanism, with the key lines of evidence being:

1 The major element, trace element and rare earth element character of porphyritic dacites have shoshonitic affinities (Morrison 1980). These dacites have SiO_2=66.73% -69.88%, high alkali (K_2O+Na_2O = 6.06%-8.41%), high K_2O/Na_2O ratio (1.53-3.49), high Al_2O_3 (13.24% -15.96%), lower TiO_2 (<0.5%); enriched LILE and LREE; P, Sr and Ti negative anomalies and weak Nb and Ta negative anomalies.
2 In the discrimination diagrams of Morrison (1980) and Turner et al. (1996) all the dacites plot the shoshonitic fields.
3 Our model for the Xiangshan shoshonitic dacites involves meting of subduction enriched lithospheric mantle triggered by under plating of basalt magma (Li et al. 2000; Zhou et al. 2000).

In the Xiangshan basin,uranium mineralization can be correlated with the distribution of the dacitic volcanics. Supporting evidence for which comes from:

1 The timing of uranium mineralization (100-120Ma; Chen et al. 1997) in Xiangshan basin is somewhat similar to that of the dacitic volcanism (125-134Ma). And the timing of uranium mineralization (100-120Ma) was corresponded approximately with the mid-late of cosmically mineralization timing limit (110-160Ma) in the east China (Mao and Wang 2000).
2 The host rocks for the uranium deposits in the Xiangshan basin are mainly the dacites (Shen et al. 1995; Wu et al. 2003).
3 The chemistry of the U-ore bearing fluids has characteristics consistent with derivation from a mantle source. The C isotopic values of ore-forming fluids vary from -4‰ to -8‰, which indicates that the CO_2 in ore-forming fluids was probably mantle-derived. The $^3He/^4He$ of the Xiangshan uranium deposit is 0.1-2.02Ra, which shows there existed a lot of mantle-derived He in the fluids (Hu et al. 2004).
4 There existed the uranium and thorium enrichment strip under lithosphere, which offered uranium source for uranium mineralization (Bao and Zhang 1998), and enriched and formed the Xiangshan uranium deposit (Jiang et al. 2004). The characteristic of shoshonitic magma was just made the uranium fluid differentiation entirely (Rock 1991; Muller et al. 1995).

References

Bao XZ, Zhang AL (1998) Geochermistry of U and Th and its influence on the origin and evolution of the Earth's crust and the biological evolution. Acta Petrological & Mineralogica 17: 160-172(in Chinese with English abstract)

Chen YH, Chen ZY, Cai YQ, Chen ZB (1997) Space-time evolution of Meso-Cenozoic extensional tectonics and distributions of uranium mineralization in southeastern China. Uranium Geology 13(3): 129-146 (in Chinese with English abstract)

Hu RZ, Bi XW, Su WC, Peng JT, Li CY (2004) The relationship between uranium metallogensis and crustal extension during the cretaceous-tertiary in south China. Earth Science Froniters 11(1): 153-160(in Chinese with English abstract)

Li KY, Shen JL, Wang XP (1989) The isotopic geochronology of Mesozoic volcanics in Zhejiang, Fujian and Jiangxi provinces. Bull.Nanjing Inst.Geol. M.R., Chinese and Geol.Sei.,supplementary Issue, 5 (in Chinese with English abstract)

Li XH, Zhou HW, Liu Y, Le CY, Sun M, Chen ZH (2000) Shoshonitic intrusive suite in SE Guangxi: Petrology and geochemistry. Chinese Science Bulletin 45(7): 653-659

Liu JY (1985) Xiangshan igneous pluton - a granitic hypabyssal intrusive volcanic complex. Geochimica 2: 142-149(in Chinese with English abstract)

Mao JW, Wang ZL (2000) A preliminary study on time limits and geodynamic setting of large-scale metallogeny in East China. Mineral Deposits 19(4): 289-297(in Chinese with English abstract)

Morrison GW (1980) Characteristics and tectonic setting of the shoshonite rock association. Lithos 13: 97-108

Muller D, Groves DI (1995) Potassic Igneous Rocks and Associated Gold-copper Mineralization. Berlin: Springer-Verlag

Pearce JA (1982) Trace element characteristics of lavas from destructive plate boundaries. In: Thorpe RS (ed.), Andesite: Orogenic Andesites and Related Rocks. New York: John Wiley 525-548

Rock NMS (1991) Lamprophyres . Glasgow: Blackie

Rogers NW, James D, Kelley SP (1998) The generation of potassic lavas from the eastern Virunga Province. J Petrol 39: 1223-1247

Shen F, Chen RZ, Li F (1995) Metallogenetic conditions and prospects of the Xiangshan uranium orefield in south China. Uranium Geology 11(5): 259-265 (in Chinese with English abstract)

Turner S, Arnaud N, Liu J, Rogers N, Hawkesworth C, Harris N, Kelley S, Calsteren PV, Deng WM (1996) Post-collisional,shoshonitic volcanism on the Tibetan plateau: Implications for convective thinning of the lithosphere and the source of ocean island basalts. J Petrol 37: 45-71

Wang DZ, Zhou XM (2000) The origin about later Mesozoic of the volcanic-intrusive complexes in east-south China and the crust evolution. Beijing: Science Press (in Chinese)

Wu RG, Yu DG, Zhang SM (2003) Identification of rhyolite-dacie porphyry and its relation to uranium mineralization at Xiangshan uranium ore-field. Uranium Geology 19(2): 81-87 (in Chinese with English abstract)

Xia LQ, Xia ZC, Zhang C (1992) Petrogeochemistry of Mesozoic uraniiferous volcanic complex from Xiangshan, China. Beijing: Geology Press (in Chinese with English abstract)

Zhou XM, Li WX (2000) The origin of later Mesozoic igneous rock in east-south China: the model of combine lithosphere subducting and basalt underplating. Progress in Natural Science 10(3): 240-247(in Chinese)

Metallogenic time-space evolution of the Xiangshan Uranium ore field in China

Wanliang Zhang
270 Research Institute, China National Nuclear Corporation, Nanchang County, Jiangxi province, China

Ziying Li
Beijing Research Insititute of Uranium Geology, China National Nuclear Corporation, Beijing, China

Abstract. The Xiangshan field is situated in a volcanic rock belt along the margin of East-Asia continent it is a hydrothermal vein type uranium ore field with the biggest size and the highest grade occurring in the Xiangshan volcanic intrusive complex. From the early to the late period, and from deep to shallow levels, and from the east to the west side in the field, the metals content generally increases, with temperatures decreasing, the alteration type varies in albilization–apatitization- carbonatization-chloritization-fluoritization-hydrosericite-silication, the hydrothermal features change from alkalinity to acidity, and $w(HCO_3^-)$ in the solution tend to decrease, and $w(F^-)$ to increase.

Keywords. Metallogenic evolution, uranium ore field, China Xiangshan

The Xiangshan field is situated in a volcanic rock belt along the margin of East-Asia continent, and represents a hydrothermal vein type uranium ore field with the biggest and the highest grade occurring in the Xiangshan volcanic intrusive complex (Xia et al. 1992). After more than 40 years of uranium ore geological explorations and investigations, more than 20 deposits have been discovered within about 300km^2 in the Xiangshan field (Fig. 1). These deposits have different metallogenic features and types, but they are interrelated. The Xiangshan field is of an overall metallogenic fluid evolution system.

The field is governed by the Mesozoic Xiangshan volcanic intrusive complex, and the main host rocks of the U- mineralization are porphyroclastic lava, granite-porphyry, rhyodacite-porphyry, basement metamorphic rocks, pyroclastic rocks, sandstone, cryptoexplosion breccia and so on. There may be several ore-bearing wall rocks in a deposit and no typical rocks for U-mineralization. Ore bodies present the shape of vein or cluster veins, controlled by fault or fissures with steeply dipping, chimney-like ore bodies in the shape of the cryptoexposion breccia body (Chen 1981).

The ore minerals contain Th-bearing pitchblende, pitchblende, brannerite, uranothorite, coffinite, thorite, auerlite, U-bearing collophane, U-bearing anatase, hematite, pyrite, galena, chalcopyrite, etc., as well as gangue minerals albite, apatite, chlorite, calcite, dolomite, fluorite, hydrosericite, and microcrystal quartz. According to the alteration mineral assemblage, the ores may be classified into five types: U-apatite, U-chlorite, U-carbonate, U-fluorite and U-hydrosericite. The assemblage features of each type are shown in table 1.

Hydrothermal alteration can be divided into three epochs: pre-ore, mineralization and post-ore. The pre-ore alteration presents albilization. The alteration of the mineralization phase presents apatitization, carbonatization, fluoritization and hydrosericitetization. And the post-alteration presents silicification.

U-apatite, U-chlorite and U-carbonate type are all products of alkaline hydrothermal processing, belonging to alkaline metasomatism type. However, U-fluorite and U-hydrosericite types are all products of acidic hydrothermal processing, entitling fluorite-hydrosericite type. In general, the former is a single U-mineralization with more simpler mineral assemblage, lesser accompanying element, lower Th content and lesser mineral species, but the latter is a multiple U-mineralization with complicated mineral assemblage, more U-Th minerals.

The albilization, which formed prior to alkaline metasomatism type U-mineralization, was formed at 330-300°C. The lilac and aqua fluorite was formed at the later stage of fluorite-hydrosericite type U-mineralization (at around

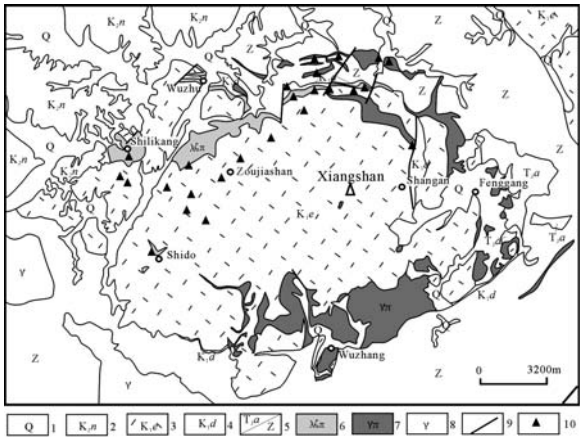

Figure 1: Distribution of uranium deposits in Xiangshan field. 1-Clay and gravel of Quaternary system; 2-Red sandstone and sand conglomerate rock of Upper Cretaceous Nanxong formation; 3-Porphyroclastic lava of Lower Cretaceous Ehuling formation; 4-Purplish red sandstone and welded tuff of Lower Cretaceous Daguding formation; 5-Quartz sandstone and shale of Upper Trissic Anyuan formation and Schist and phyllite of Sinian system; 6- Rhyodacete-porphyry; 7- Granite-porphyry; 8- Granite; 9- Fault; 10-Uranium deposit

Table 1: Ore types of Xiangshan uranium field

Ore type	Major Gangue minerals	Second gangue minerals	Uranium minerals	Metallic minerals
U-apatite	albite, apatite	Calcite	pitchblende, a few of coffinite	
U-chlorite	albite, chlorite	Calcite, dolomite	Pitchblende	Pyrite
U-carbonate	Albite, carbonate	Chlorite, calcite	Pitchblende	Pyrite, galena, sphalerite
U-fluorite	Fluorite	Hydrosericite	Th-bearing pitchblende	Molybdenite, galena, sphalerite, pyrite
U-hydrosericite	hydrosericite	Fluorite	Th-bearing pitchblende, a few of brannerite, uranothorite, auerlite	Molybdenite, galena, sphalerite, Pyrite

Table 2: Metallogenic time-space evolution serials of Xiangshan uranium field

	Depth (East) → shallow (west)						
Alteration type	**Albilization**	**Apatitization**	**Carbonatization**	**Chloritization**	**Fluoritization (hydrosericite)**	**Hydrosericite (fluoritization)**	**Silication**
Forming age	135Ma → 88Ma						
Forming temperature	330? → normal temperature						
Hydrothermal features	alkalescence → acidity						
HCO_3^- concentration in hydrothermal solution	high → low						
F^- concentration in hydrothermal solution	low → high → low						
Metallogenic components			U → U, Th				
Accompanying elements			fewness → many				
Ore minerals	simpleness → compexity						
Deposit case			Yunji	Hongwei	Shimashan, Huangjian, Zoujiashan		

122-86°C). And the temperature of silication of the post-mineralization could be lower.

The study of gas-liquid inclusion in minerals for different ore-forming stages, which is the reflection of ore-forming fluid components, shows that the solution of the albilization is alkaline (pH=9.36-9.55), and the alkalinity of the solution at calcitization and fluoritization stage has decreased. It is estimated that the alkalinity of the solution of post-ore silication could be less, and the acidity higher.

In the ore-forming hydrotheramal solution, the cation is mainly Ca^{2+}, Na^+, K^+, Mg^{2+}, and the anion mainly HCO_3^-, SO_4^{2-}, F^-, Cl^-. From pre-ore albilization stage to the calcitization and flurilization stage, w (Na^+) fell gradually, w (Ca^{2+}) fell to the lowest at fluorilization stage, w (K^+) and w (Mg^{2+}) varied randomly, w (F^-) tended to increase, w (Cl^-) and w (HCO_3^-) tended to decrease, w (SO_4^{2-}) reached the highest level at fluoritization stage.

There are many age data in the ores in Xiangshan field, and the age range of U-mineralization is in the range of 143 -88Ma. The age range has been divided into early and late period, and has been combined with the features of the two types U-mineralization by the precursors. The former is about 120Ma, and the later is about 100Ma (Du 2001). But a detailed study of these age data shows that the age is related to ore type, and the ore-forming age coul't be simply classified into two or more periods. In fact, the two U-mineralization types are transitional to each other, and they coexist in most deposits. They are all products of the long hydrothermal processin. Thus it is argued that there is single U-mineralization period in Xiangshan field. Because the granite-porphyry formed at 135Ma (Chen et al. 1999), and Yuanji deposit was formed after the granite-porphyry, the lower limit age of U-mineralization in Xiangshan area is 135Ma, and the upper limit age should be less than 88Ma.

The spatial distribution of the deposits across the plane is the following. Firstly, the deposits are concentrated in the northern and the western part of the field,

This page intentionally blank

and only one deposit is located in the eastern part. Only small ore-spot are located in the central section and southern part. Secondly, alkaline metasomatism type U-deposit occurred mainly in the eastern and north-eastern part. The Yunji deposit is a typical alkaline metasomatism type U-deposit. It contains U-apatite, U-carbonate as well as U-chlorite type ores. Thirdly, the single U-deposit occurred only in the eastern or north-eastern part of the field carries Th/U about 0.01-0.08 in ores, while U-Th composite deposits are centered largely in the western or north-western part of the field, with Th/U higher than 0.2.

In the vertical direction, the distribution of the deposits is the following. Firstly, the alkaline metasomatism type U-mineralization is located underneath fluorite-hydrosericite type, and Zoujiashan deposit has the distinct "upper acid lower alkali" regularity of mineralization-alteration zoning. It is shown that from upper to lower, the contents of Fe_2O_3, MgO, P_2O_5 in the ores increased obviously, and that apatitiation, chloritization and calcitization becomes stronger and stronger. Secondly, the vertical scope ranges from 200m to 300m in general, sometimes, to 1000m. And in volcanic rocks, the scope is larger than in hypabyssal-ultrahypabyssal intrusive (Fan 2001). The metallogenic time-space evolution of Xiang-shan uranium ore field is summarized in Table 2.

References

Chen XM, Lu JJ, Liu CS, Zhao LZ, Wang DZ, Li HM(1999) U-Pb age of the Single Zircon from the Volcanic-Intrusive Complexes in Lujiang-Zongyang and Xiangshan. Acta Petrologica Sinica 15(2): 272-277(in Chinese with English abstract)

Chen ZB (1981) "Double Mixing"genetic model of uranium doposits in volcanic rocks and relationship between China's Mesozoic vein-type uranium deposits and Pacific plate tectonics. Metallogensis of Uranium.Proceedings of the 26th IGC, Geoinstitute, Beogard, 65-97

Du LT (2001) Basic Metallogenic Regularities of Hydrothermal Uranium Deposit and General Hydrothermal Metallogeny in China. Beijing: Atonic Energy Press, 39-56(in Chinese)

Fan FH (2001) Xiangshan crust-source type volcano-intrusive complex and its deep mineralization in Jiangxi Province. Nanjing University Doctoral Dissertation, (in Chinese with English abstract)

Xia LQ, Xia ZH, Zhang C, Clocchiatti R, Dardel J, Joron JL (1992) Petrogeochemistry of Mesozoic Uraniferous Volcanic Complex From Xiangshan, China. Beijing: Geological Press, 12-43(in Chinese with English abstract)

Alkali-metasomatism and uranium mineralization

Fengmin Zhao
Beijing Research Institute of Uranium Geology, Beijing 100029, China

Keywords. Alkali-metasomatism, uranium deposits, brannerite, uranium-bearing titanium minerals

Alkali-metasomatism is a geological process developing widely in nature in accompany with the multimetallic mineralization that is studied extensively by many geologists. In the aspect of uranium geology, the geologists in the former USSR and China also carry out special research on alkali-metasomatism and uranium metallogenesis, with important results being achieved, which plays an important role in guiding exploration, but there exists different views on some important problems, some aspects are not studied profoundly. Some aspects on alkali-metasomatism and uranium metallogenesis have been discussed in this paper on the basis of the information on the alkali-metasomatic type uranium deposits in our country.

Alkali-metasomatism refers to the geological behavior by which alkali (K or Na)-rich hydrothermal fluids interact with the country rocks and form the altered rocks mainly composed of albite or potassium feldspar and accompanied by some other altered minerals. It is impossible for potassium and sodium in the nature to occur simultaneously in the hydrothermal fluids, the main alteration could be observed in alkali-metasomatism is single albitization or single feldsparization, when the albitization dominates, it could be called as alkali-metasomatism; when the feldsparization dominates, it could be called as potassium-metasomatism. Alkali-metasomatism is divided into two types of high temperature alkali-metasomatism and middle-low temperature one. High temperature alkali-metasomatism has genetic relationship with metalliferous mineralization of niobium, tantalum, lithium, beryllium; middle-low temperature alkali-metasomatism has genetic relationship with uranium mineralization.

Alkali-metasomatic type uranium deposit is one of the main industrial uranium deposits, has been discovered around the world. Some large, super-large alkali-metasomatic type uranium deposits have been also indicated in Ukraine Shield, Kokchetav intermedium massif in Kazakhstan and Aldan Shield in Russia, where the uranium resources of Elicon potassium-metasomatic uranium deposit exceed 30,000 t. A lot of medium and small size alkali-metasomatic type uranium deposits have been discovered in northwestern and southeastern China.

Alkali-metasomatic uranium deposits all occur in the cataclastic zone in relation to the regional deep several metres to dozens of metres wide and vary in and large scale fractures. The cataclastic zones vary in length from several hundred metres to several hundred thousands of metres. The relationship between the (vein-like) zone; albite-calcite (spotted) –sericite zone; albite-sericite zone; chlorite (as the pseudomorph of melanic minerals)-secondary quartz zone, its macroscopic features are that it is red-coloured and maintains the original rock structure. The redness is caused by the hematitization, stronger the metasomatism becomes, stronger the hematitization is. The color of the most altered central zone remains purpish red; the altered rock maintains the original rock structure, because the pseudomorphic metasomatism is dominant. Some researchers in Jiling District classified the incataclastic and weak metasomatic altered granites into a single phase of flesh-colored granite just because of this feature. The chemical composition of rocks clearly represents the mineral zoning of alkali-metasomatite. Na and Ca decrease from the center to the outer parts, whereas SiO2 increases towards the outer parts of the altered zone which shows that the minerals forming by the alteration in the center of the metasomatic body are the products of the interaction between calc-alkaline elements and the country rocks; the minerals forming in the transitional zone and the surrounding zone is the results of the replaced elements in the minerals in the central zone transporting outwards along with the well-developed alkali-metasomatite from the center to outside can be successively divided into the alteration cataclastic zone and the nomal country rock is gradual transition, there are mylonite in the center and strong cataclastic rock, cataclastic rock, weak cataclastic quartz and so on, which have clear spatial zonation. A subzone: albite-calcite (vein-like, massive) –chlorite rock and normal country rock successively from the center to the outside. The extent of alkali-metasomatism often extends beyond the cataclastic zones and into normal country rocks. Middle-low temperature alkali-metasomatites in relation with uranium metallogenesis in the granitoids are composed of the altered minerals, such as albite (or potassium feldspar), calcite, chlorite, hydromica, hematite, secondary hydrotherm and interacting with the country rock. This should be pointed out that the alkali-metasomatism could take place in all kinds of rocks, besides widely developed in granite and granodiorite, it could be also identified in all kinds of metamorphic rocks, pegmatites, subvolcanic rocks and volcanic rocks, and there all exists industrial uranium mineralization. The characterristics of the alteration zoning are quite similar, although the original

country rock of the alkali-metasomatite remains different. For example, the alteration zoning of the sodium-metasomatic body at the Biandoukou uranium deposit occurring in sandstone is nearly identical with that occurring in granite, the altered mineral assemblage in the internal zone is albite-dolomite-hematite-ferrichlorite; in the transitional zone is albite-dolomite-hematite; in the external zone is albite-dolomite.

The increase in uranium content could be found out in the whole middle-low temperature alkali-metasomatic zone, uranium mineralization could only be identified in the alkali-metasomatized cataclastic rocks and strong cataclastic rocks in the center. The mineralization intensity weakens grandually from the center to the outer part, but mylonite in the central part has the weakest mineralization intensity due to its compaction and poor permeability. Uranium orebody is usually lenticular, several metres to dozens of metres wide, dozens of metres to several hundred metres long, extending hundreds of metres downwards. At the superlarge Elicon deposit, the longest orebody reaches 6.1km, drilling has shown that mineralization is 1800 m in depth, and also extends deeper in places. Sodium-metasomatic type uranium ore usually belongs to the low grade which all reaches 0.01%, it can reach 0.3% in the rich area. The mineralized rock is usually strongly altered, the feldspar is completely altered into albite or potassium feldspar, quartz disappears completely with strong hematization, and its color remains dark red or purpish red. Alkali-metasomatic type uranium mineralization has specific uranium mineral assemblage; the most obvious is brannerite and uranium-bearing titanium minerals. The identified assemblages include: single brannerite assemblage, brannerite-pitchblende assemblage and single pitchblende assemblage. Brannerite-coffinite assemblage also developed at the alkali-metasomatic deposit at abroad. It must be pointed out that uranium-bearing titanium minerals are not simple chemical composition rather; they are a kind of mineral aggregates with a range in compositions. It is usually the pseudomorph of titanium mineral (sphene, ilmenite)-bearing source rock, composed of the latticed anatase and uranium-bearing substances. A clear spectral line of anatase can be achieved by the X-ray analysis. Uranium usually occurs among the substance in the lattice of anatase. Brannerite is massive, sometimes has well-developed columnar crystal. Brannerite is usually metamict, its texture was completely destroyed. After heating the brannerite at the Yangmeiwan occurrence up to 900°C, the mixed X-ray diffraction spectral lines of U_3O_8 and brannerite can be observed.

Alkali-metasomatic type uranium mineralization developed in many uranium metallogenic epochs, mainly 1 800-1 600 Ma, 440 - 250 Ma and 145 - 47 Ma.

With regards to the source of alkali-metasomatic fluid, all of the researchers consider as anatectic origin, and ascended to the crustal surface along the deep and large fracture. The isotopic analysis at the Jinling uranium deposit shows that the whole rock $\delta^{18}O$ of sodium-metasomatite ranges from +9.86‰ to +10.25‰, and +10.05‰ on average; δD of the calcite's liquid inclusion in the sodium-metasomatite ranges from 74.2‰ to 74.4‰. After calculation, $\delta^{18}O$ value of the media liquid in the sodium-metasomatite ranges from +5.54‰ to +6.09‰, showing that the alkali-metasomatic hydrotherm has an crustal origin. In the research at the alkali-metasomatic type uranium deposit, one of the largest different points of view is on the relationship between alkali-metasomatism and uranium mineralization. Most of the researchers consider alkali-metasomatism as a kind of metasomatized alteration prior to the uranium mineralization, creating conditions for the later-stage uranium mineralization. It is considered that the albitization can make the source rock more porous, and make the mechanical intensity of the rock decrease owing to the ionic radius of sodium is smaller than that of potassium. Hence the alkali-metasomatic is quite easy to fracture and could create a very favourable country rock condition for the supersition of the deuterogenic structure and hydrothermal activity. There exist two points of view on the aspects of the uranium behavior in alkali-metasomatism: one is that sodium-metasomatism can cause uranium pre-enrichment in the rock, but cannot form the high grade mineralization; the other considers that sodium-metasomatism lead to the loss and depletion of uranium in the source rock. The increase in uranium content in alkali-metasomatite could be identified is only a falsappearance, i.e. as the result of the infiltration of the deuterogenic uranium-bearing hydrothermal fluids. However, some geologists (including the author) engaged in the research of alkali-metasomatism and uranium mineralization consider that the structural activity, alkali-metasomatism and uranium mineralization are an integrated process. The main evidences are:

1. *The geological phenomenon that the alkali-metasomatites refractured doesn't exist.* The geologists who maintain that alkali-metasomatism and uranium mineralization are two separate stages consider that alkali-metasomatism took place at first, then alkali-metasomatite fractured, the uranium-bearing hydrotherm came into and formed uranium mineralization. But the middle-low temperature alkali-metasomatism is a kind of pseudomorphic replacement, the present breccia structure are actually the one formed before the hydrothermal activity stage or the structural activity of the same stage, this is exactly this kind of breccia providing the site location for the hydrothermal activity. Any breccia must be cemented after the reformation of hydrothermal activity. If the new structural activity appears, the formed cataclastic zones would be different in the as-

pects of occurrence, morphology and scale because of the orientation of the structural stress and the differences of the intensity. It produces the phenomenon of containing old breccia among the new one. Two phases of sodium-metasomatites developed in Yangmeiwan occurrence include 2 phases: the early one is high temperature white sodium-metasomatite; the latter is middle-low temperature red sodium-metasomatite. These two phases both have obvious differences in the aspect of scale, occurrence, the alteration feature and mineralized elements. The researchers advocating uranium mineralization and sodium metasomatism are two phases of hydrothermal activities don't provide the geological evidence for two structural activities, do not point out the structural trace controlling alkali-metasomatic hydrothermal activity of the early phase. As to the mentioned sodium-metasomatism can caust the pority of the rocks to increase and form the spongy one. It is similarly reasonable to explain by the smaller sodium ionic radium than potassium ionic radium, but on the contrary, it is very difficult to explain potassium-metasomatism; it is more difficult to explain through the comparison that the porosity of alkali-metasomatite is higher than the normal country rocks, the porosity of the cataclastic rock is originally high. It must be emphasized here that a phase of structural activity the author refers is process of structural activity, including a relatively weak structural activity before and after a major structural activity phase, hence the hydrothermal lode system-filling microfracture can be identified through out the cataclastic rocks.

2. *Middle-low temperature alkali-metasomatic hydrotherm is the favorable medium for the uranium activation and transportation.* By the comparison of the chemical composition of sodium-metasomatites and the normal country rocks, it is certain that sodium, calcium and HCO_3 are rich in the alkali-metasomatic hydrotherm; their temperature is below 300°C according to the temperature measurement results of the inclusion; widely developed hematization shows that the oxygen fugacity in this hydrotherm is quite high. This geochemical condition makes it easy to let uranium active in the rock come into the fluids and form the carbonated uranyl complex of sodium or calcium which is stable and can be transported. After the uranium-bearing hydrotherm comes into the fractured zone, the carbonated uranyl complex decomposes to form albite and carbonate, uranium precitates and enriches correspondently because the pressure decreases and interacts with the country rocks. The high temperature sodium-metasomatites which don't associate with hematization are infavorable for the activation and transportation of uranium due to the high temperature and low oxygen fugacity. Compared with the normal country rock, the uranium content in the niobium-bearing and tantalum-bearing high temperature sodium-metasomatite in Yichun of Jiangxi, beryllium-bearing high temperature sodium-metasomatite don't change basically, the uranium content in the strongly albitized zone decrease a little, it increases a little in the transitional zone. These changes may be caused by the uranium activation and transportation of near range when the alkali-metasomatism took place. This indicates that uranium is in the stable state in the environment of high temperature, it is quite difficult for the high temperature alkali-metasomatism to become the uranium source of uranium mineralization of the later phase, hence middle-low temperature alkali-metasomatism has genetic relationship with uranium mineralization, which is decided by the chemical behavior of the relative elements.
3. *Unique uranium mineral assemblages.* Alkali-metasomatic type uranium deposit is characterized by the brannerite or uranium-bearing minerals, sometimes brannerite can be identified in some hydrothermal veinlike uranium deposits, but all the brannerite occurs in the albitized area without any exception, this is the typomorphic uranium mineral produced by the interaction of alkali-metasomatic hydrotherm with the country rocks. The titanium bearing minerals in the source rocks are easy to decompose in the carbonate-rich hydrothermal activity and form the hydroxided titanium, which is a strong absordant absording a large amount of uranium from the fluid. After the hydrothermal activity stops, the substable hydroxided titanium changes into the stable titanium bearing oxidized minerals – anatase. Brannerite only occurs in the alkali-metasomatic orebody of high hydrothermal temperature and strong alteration, and has well-developed columnar crystal, showing that the titanium bearing minerals in the source rock decompose completely, titanium come into the mineralizing fluid to combine with the uranium and form the brannerite. According to the temperature measurement data of the relative minerals, the formation temperature of brannerite in Yangmeiwan occurrence of Zhejiang province ranges from 230 to 290°C, the formation temperature of brannerite in Elicon uranium deposit is from 200 to 230°C, the formation temperature of uranium bearing titanium minerals in Jiling uranium deposit of Gansu province is from 175°C to 185°C, the temperature of mineralizing fluid and the intensity of metasomatism are the key factors deciding whether the titanium bearing minerals in the source rock decompose and the titanium comes into the fluid to form brannerite. As stated above, titanium mainly comes from the source rock with a limited amount; as a result, the relict uranium forms pitchblende or coffinite after the uranium

combines with the titanium to form brannerite. Brannerite or uranium-bearing titanium minerals could not be formed in some alkali-metasomatic type uranium deposit, the main reason is that CO_3 content in the mineralizing fluids is quite low and the metasomatism is weak, which could not cause the titanium minerals decompose and make the titanium activize. For example, C_A and loss on ignition are only 0.*n* % in the strong sodium-metasomatite with the pitchblende association in Huangfengling uranium deposit; Na_2O content in the strong sodium-metasomatite in Biandoukou deposit ranges from 4.86% to 5.99%. In consequence, alkali-metasomatism exists in brannerite or uranium bearing titanium minerals, alkali-metasomatism cannot be simply denied when it is not developed, concrete analysis should be made yet.

In summary, the author considers that alkali-metasomatic type uranium mineralization is the product that sodium-rich, calcium-rich, uranium-rich, deep-seated, high oxygen fugacity middle-low temperature hydrotherm comes into the cataclastic zone to interact with the country rocks; the results of the synchronous structure-hydrothermal activity; having the unique uranium mineral assemblages. All of the alkali-metasomatisms occurring surrounding the deep and large-scale fractures could develop in any lithologies. The macroscopic characteristics of uranium-bearing alkali-metasomatite are red and deep red and having calcite and iron-rich chlorite. Middle-low temperature alkali-metasomatism is a kind of hydrothermal activity quite favorable for the uranium mineralization and can form large and superlarge uranium deposit; consequently, it must be emphasized in the uranium geology prospecting work.

Evidence of early oxidation related to sandstone-type uranium mineralization within the Zhiluo Formation (J_2z), Ordos Basin, China

Minqiang Zhu, Rengui Wu, Dagan Yu
East China Institute of Technology, Fuzhou, Jiangxi 344000, China

Abstract. Based upon research on alteration in the Dongsheng and Huangling uranium mineralised areas, Ordos Basin, three stages have been distinguished in the lower member of the Zhiluo Formation: an early-stage red oxidation of hematization and goethitization; a middle-stage yellowish green and greyish blue hydrocarbon related reduction of smectitization, chloritization, pyritization; and a late-stage yellow oxidation of goethitization and limonitization. The fact that the mean TOC value of red sandstone and yellowish green and greyish blue sandstone are evidently lower than that of the original grey sandstone may indicates that the yellowish green and greyish blue sandstone have suffered oxidation before hydrocarbon reduction. In addition, residual red alteration sand bodies are observed as inclusions in the yellowish green and greyish blue sandstone in Dongsheng area, while in Huangling area the oil-immersed sands occur along fractures and unconformity interfaces in red widespread altered sandstone. The brown-black oil-immersed sands are surrounded by yellowish green sandstone, which have locally been bleached due to later reduction. Evidence favouring the existence of early-stage oxidation also include that the yellowish green and greyish blue sandstone with abundant oil stains on the outcrop, and rock slices contain much more acidolysis hydrocarbon content than that of red and yellow sandstone; and that the early formed limonite is replaced by secondary pyrite in yellowish green and greyish blue sandstone. The major U metallogenic epoch has been dated at 120 ±11 Ma and 80 ±5 Ma. During this time, the surface oxidation water supply remained abundant and flowed from the north southwards as the Ordos was not uplifted and the Hetao basin was not down-faulted until Eocene. Exploration has verified that the uranium ore bodies are situated at the front of yellowish green and greyish blue alteration zone in Dongsheng area. The yellowish green and greyish blue sandstone were sourced from the early-stage red sandstone by hydrocarbon reduction, so the front of yellowish green and greyish blue alteration zone is considered to be an indicator of the early-stage red alteration front zone. This might be helpful to outline promising areas for exploration in the Ordos Basin.

Keywords. Ordos Basin, early-stage red oxidation, uranium mineralization

1 Introduction

The Ordos Basin is located in the centre of northern China and covers an area of about 250,000 km^2. It is well known in China as a "basin of energy resources" for its large reserves of coal, petroleum and natural gas. The Changqin oil field, Sulige gas field and Shenfu-Dongsheng coalfield are the most important oil, gas and coal producers in China (Fig. 1). Systematic exploration for sandstone type uranium resources started in 2000. Since then, some uranium-mineralised areas have been found in the strata with ages ranging from late Jurassic to early Cretaceous. Of them, the largest one is the Dongsheng area where ore bodies are hosted in Middle Jurassic Zhiluo Formation. Studies have shown that the alteration and mineralization in the area are somewhat unique, evidently different from those in famous ore fields in Middle Asia or those in S. Yili Basin. Thus, the ore-forming mechanism remains unsolved so far. Some researchers attributed the uranium mineralization in the area to palaeo-oxidation roll-front type (Chen et al. 2004). Others proposed a multistage oxidation model (Xa 2004), or a genesis of lower temperature hydrothermal activity (Ou 2004). Doubtlessly, the alteration investigation plays an important role in clarifying the uranium mineralising process.

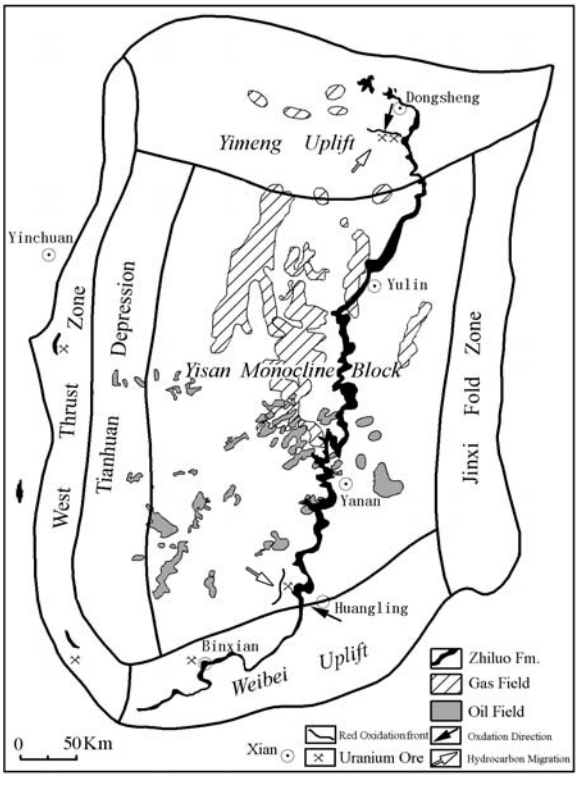

Figure 1: The diagram illustrating the tectonic pattern, the outcrop of Zhiluo Fm. and the oil/gas fields of Ordos Basin

2 Geological setting

In the Ordos Basin, the late Triassic - Jurassic continental strata are well developed, including Yanchang Fm. (T_3), Fuxian Fm. (J_1f), Yanan Fm. (J_2y), Zhiluo Fm. (J_2z) and Anding Fm. (J_2a) from the bottom to the top. Of them, the Zhiluo Fm. (J_2z), as host sediments, outcrops along the Dongsheng - Yulin - Yanan - Huangling - Binxian in eastern basin (Fig. 1), presenting a set of varied colour fluvial deposits. The Zhiluo Fm. un-conformably overlies the Yanan Fm. (J_2y) delta to lacustrine facies dark coal-bearing sediments, and is conformably covered by the Anding Fm. (J_2a) fluvial to lacustrine facies red sediments, or by the lower Cretaceous sediments — Zhidan Group (K_1z) red alluvial, fluvial and eolian deposits with slight angle unconformity (Fig. 2). The basin fill inclines smoothly and gently westwards with a dip angle of 1°-3° without intense tectonic deformation. The groundwater flowed in the period of early Jurassic to early Cretaceous from the basin margin to the basin center (Chen 2004). Structures are mainly of block movement constrained by regional deep faults and basement faults. The remote sensing interpretation shows that a nearly EW-trending fault zone might play a role of pathway for hydrocarbon micro-seepage in the south of Dongsheng mineralised area (Zhu 2002).

3 Alteration and mineralization in the Zhiluo Formation

The uranium mineralization is mainly hosted in lower Zhiluo Fm. sand bodies that were distributed along several braided channels and connected each other in general. The sand bodies are mostly spread in the areas between Yisan Monocline, Yimeng Uplift, and Weibei Uplift, and comparatively well developed in the Dongsheng - Yulin and Huangling - Binxian areas (Fig. 1).

The mineralization related alteration zones were originally developed in the lower member of the Zhiluo Fm. deposited in alluvial plain facies of braided fluvial system (Fig. 2). The alteration zone distributed in the south of Dongsheng area is about 40km long in EW trend. The colour change in the alteration zone implies a developing tendency from the north southwards because of the yellowish green and greyish blue in the north, and gradually to grey and greyish black in the south. The width of the yellowish green and greyish blue sub-zone ranges from several km to more than 20 km (Chen et al, 2004). Similar alteration zones distributed in the SN trending Huangling area obtain widths of several km to 10 km with developing from east westwards.

Based on research of alteration characteristics in Dongsheng Area (Zhu 2002) and Huangling Area, three stages have been distinguished in the lower member of Zhiluo Formation: the early-stage red oxidation of hematization and goethitization; the middle-stage yellowish green and greyish blue hydrocarbon related reduction of smectitization, chloritization, pyritization; and the late-stage yellow oxidation of goethitization and limonitization.

4 Evidence of early oxidation

4.1 Organic contents

The mean values of TOC of early-stage red altered sandstone and yellowish green and middle-stage greyish blue altered sandstone are of 0.03 % - 0.05 % and 0.03 % - 0.06 % respectively, lower than that of original grey sandstone (0.12 - 0.13 %) (Table 1). The organic carbon detritus are quite rarely found on the outcrop and in the core of yellowish green and greyish blue sandstone. This evidence indicates that the yellowish green and greyish blue sandstone have been suffered a de-carbonation oxidation before hydrocarbon reduction.

4.2 Residual red alteration sandstone

The residual red altered sand bodies, with higher carbonate content and more compact, are included in the yellowish green and greyish blue sandstone in Dongsheng area. Besides, outcrops of red sandstone

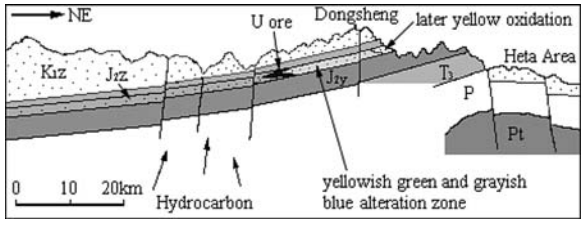

Figure 2: The schematic profile of alteration zone in Dongsheng Uranium Area

Table 1: The mean values of TOC, ΣS and F^{3+}/F^{2+} in Zhiluo Fm. Sandstone

Sandstone Type	TOC (10^{-2})	ΣS (10^{-2})	F^{3+}/F^{2+} (10^{-2})	Amount of Samples	Refrences
Grey original sandstone	0.13		1.03	7	Zhu Minqiang
	0.12	0.42	0.99	86	Geo. Team No. 208
Yellowish green and greyish	0.03		2.52	13	Zhu Minqiang
blue altered sandstone	0.06	0.13	1.29	20	Geo. Team No. 208
Red and Yellow altered	0.03		3.30	3	Zhu Minqiang
sandstone	0.05	0.08	1.84	25	Geo. Team No. 208

This page intentionally blank

occur widely in Huangling area where the oil-immersed sands are spread along the fractures and unconformity interface. It is observed that the yellowish green sandstone surrounds the brown-black oil-immersed sandstone, and bleached sandstone due to afterward reduction (Fig. 3). It seems reasonable that the bleached, yellowish green and greyish blue alterations were resulted from hydrocarbon reduction as many oil stains are discovered on the outcrops and in rock slices and their content of acidolysis hydrocarbon is higher than that of red and yellow sandstone.

4.3 Alteration mineralogy

In Zhiluo Fm, the main alteration minerals include hematite, goethite, limonite, smectite, chloritite, pyrite and calcite. The early-stage red altered sandstones mainly contain hematite and goethite. The hematite is originated from dehydration of early limonite and hydrous-goethite. The smectite and chloritite, having high concentration of Fe^{2+} (Xiao et al. 2003), are originated from feldspar and biotite by hydrocarbon-related reduction and hydrolytic dissociation. In addition, the early-formed limonite was replaced by secondary pyrite in yellowish green and greyish blue sandstone (Fang et al. 2004). The latest yellow-coloured oxidising goethitization and limonitization were produced by modern groundwater activity.

4.4 Metallogenic epoch and paleo-climate

The major U metallogenic epoch has been dated at 120 ±11Ma and 80 ±5Ma by U-Pb age determination in the Dongsheng uranium mineralised area (Xia et al. 2004). During this time the surface oxidation water supply remained abundant and flowed from the north southwards as the Ordos was not uplifted as a plateau and the Hetao basin was not down-faulted until Eocene. Of coarse, the arid climate in early Cretaceous was also favourable to the development of the early-stage oxidation.

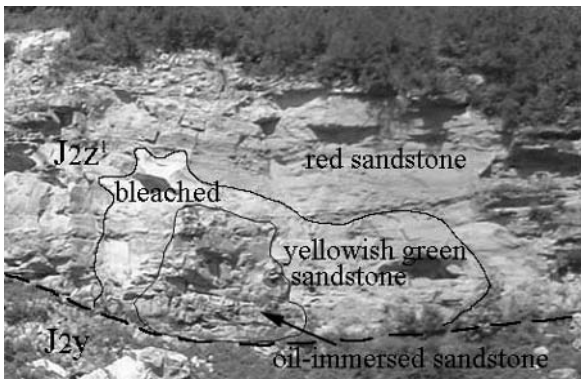

Figure 3: The early-stage red altered sandstone partly reduced by oil seepage in lower member of Zhiluo Fm. (J_2z^1) in Diantou, Huangling

4.5 Geological exploration

Since 2000, the Geology Team No.208 has verified that the uranium ore bodies are situated at the front of yellowish green and greyish blue alteration zone in Dongsheng area. The yellowish green and greyish blue sandstone were sourced from the early-stage red sandstone by hydrocarbon reduction, so the front of yellowish green and greyish blue alteration zone is considered to be the indicator of the early-stage red alteration front zone.

5 Conclusion

In the Zhiluo Formation (J_2z), there is a series of evidence to support the presence of early-stage red oxidising alteration that is closely related to the sandstone-type uranium mineralization and mainly formed in early Cretaceous time. However, it was followed by hydrocarbon-related reduction, becoming the yellowish green and greyish blue sandstone now. So the front of yellowish green and greyish blue alteration zone is considered to be an indicator of the early-stage red alteration front zone. This might be helpful to outline promising areas for exploration in Ordos Basin.

References

Chen AP, Miao AS (2004) Mineralization Characteristics of Dongsheng Uranium Mineralized Area. Proceeding of Technical Meeting of Recent Developments in Uranium Resources and Production with Emphasis on In Situ Leach Mining, Beijing, China, Sep.18 – 22, 2002. IAEA-TECDOC-1396: 69-78

Chen FZ (2002) Analysis on Paleohydrogeologic Conditions and Prospects of Uranium Metallogenesis Northern Part of Ordos basin. Uranium Geology 18: 287 – 294 (in Chinese)

Fang XH (2004) Characteristics of Uranium Mineralization and Ore Component in Dongsheng District. Ordos Basin Sandstone-type Uranium Metallogenesis Annual Workshop, Fuzhou, China (in Chinese)

Li ST, Lu FX (1997) Evolution of Mesozoic and Cenozoic Basin in Eastern China and Their Geodynamic Background. Wuhan: China University of Geosciences Press (in Chinese)

Ou GX (2004) Lower Temperature Hydrothermal and Uranium Mineralization in Northern Ordos Basin. Ordos Basin Sandstone-type Uranium Metallogenesis Annual Workshop, Fuzhou, China (in Chinese)

Xa YL (2004) Isotope Geochemistry of Sandstone-type Uranium Mineralization in Dongsheng District. Ordos Basin Sandstone-type Uranium Metallogenesis Annual Workshop, Fuzhou, China (in Chinese)

Xiao XJ, Li ZY (2003) Preliminary Study on Features of Mineralogical Zoning of Epigenetic Alteration at Sandstone-type Uranium Deposit, Dongsheng Area, Ordos Basin. Uranium Geology 20: 136–140 (in Chinese)

Zhu MQ (2002) Multi-source Information Integration Techniques of Sandstone-type Uranium Deposits Exploration Based on GIS in Ordos Basin. Ph.D Dissertation. Beijing Research Institute of Uranium Geology, Beijing, China (in Chinese)

Zhu MQ, Wu RU (2004) Sedimentary Characteristics of Zhiluo Fm. (J2z) and Uranium Mineralization in Southern Ordos Basin. Ordos Basin Sandstone-type Uranium Metallogenesis Annual Workshop, Fuzhou, China (in Chinese)

Zhu XY, Wang YL (2003) Trace Element Geochemistry of Sandstone-type Uranium Deposit in Dongsheng Area. Geology-Geochemistry31: 39–45 (inChinese)

This page intentionally blank

Session 4

Magmas and base-metal ore deposits

Factors controlling palladium and gold contents in the Aksug porphyry Cu-Mo deposit (Russia)

A.N. Berzina, V.I. Sotnikov
Institute of Geology, Koptyug Avenue, 3, Novosibirsk 630090, Russia

M. Economou-Eliopoulos
Department of Geology, University of Athens, Panepistimiopolis, Ano Ilissia, GR-15784 Athens, Greece

D.G. Eliopoulos
Institute of Geology and Mineral Exploration, 70 Messoghion Street, GR-11527 Athens, Greece

Abstract. Two stages of economic copper mineralization can be distinguished in the Aksug porphyry Cu-Mo deposit. The first stage, consisting mainly of pyrite and chalcopyrite is accompanied by abundant rutile and monazite. The second stage, consisting mainly of chalcopyrite, is associated with the telluride PdTe2 (merenskyite), electrum (18 wt% Ag) and monazite. Mineralogical, geochemical and textural data indicate that precious metals are closely associated with zones of propylitic alteration, vein-type chalcopyrite and a strongly evolved mineralized system.

Keywords. Palladium, gold, REE, Cu-Mo porphyry, Aksug

1 Introduction

Porphyry Cu-Mo deposits are among the world's most important sources of Au and PGE. However, the published data on PGE contents and their distribution in ores of these deposits are limited (Economou-Eliopoulos and Eliopoulos, 1996, 2000, 2001; Stribrny et al. 2000, Tarkian and Stribrny, 2000), in particular, for deposits from Russia (Kovalenker et al. 1996; Sotnikov et al. 2001). Our study of the composition of flotation and sulfide concentrates as well as mineralized rock samples from the Aksug porphyry Mo-Cu deposit provides new information concerning the precious metal contents of porphyry ores.

The Aksug porphyry Cu-Mo deposit occurs in the northeastern part of Tuva republic (Fig. 1). The deposit was discovered in 1952 and explored from 1982 to 1985, and is not active now. Estimated reserves and grades are 2.26 Mt Cu @ 0.67 wt. %, 52 kt Mo @ 0.015 wt.%, 39 t Au @ 0.12 g/t, and 370 t Ag @ 1.09 g/t (Lebedev and Kuzhuget 1998).

2 Geological setting

The Aksug deposit is hosted by the Aksug granitoid pluton, composed mainly of sodic, calc-alkaline quartz diorites and tonalites, with subordinate diorites and gabbro (Fig. 1). The pluton has been cut by stocks and dikes of quartz diorite, tonalite and granodiorite porphyries (the Aksug series). Low-grade (0.1 to 0.2 %Cu, ~0.003% Mo) molybdenite-pyrite-chalcopyrite mineralization is related to stage I granodiorite porphyries. Emplacement of a second generation of granodiorite porphyries (stage II) superimposed high grade chalcopyrite – bornite - molybdenite ore (0.3 to 1.0 % Cu; 0.01–0.02% Mo) onto the low-grade proto-ore.

A general sequence of mineral assemblages at the Aksug deposit has been distinguished in: (1) quartz-pyrite with hematite, (2) quartz-molybdenite with pyrite and chalcopyrite, (3) quartz-chalcopyrite with bornite, pyrite, and molybdenite, (4) fahlore, enargite, galena, and sphalerite, (5) quartz-calcite (Sotnikov et al. 2001).

Quartz-sericite and propylitic alteration are predominant at the deposit, while the early potassic alteration is subordinate. All magmatic rocks of the Aksug ore region have strontium isotopic compositions consistent with a predominantly mantle source regime $(^{87}Sr/^{86}Sr)_0$ = 0.70454–0.70496. $^{40}Ar/^{39}Ar$ dating of plagioclase from tonalite porphyries returned an age of 404–401 Ma (Sotnikov et al. 2003).

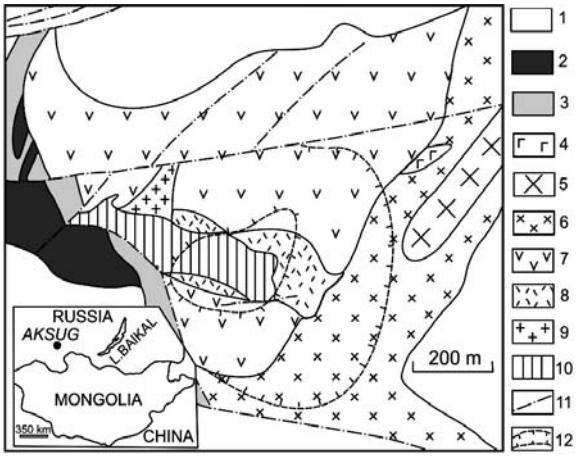

Figure 1: Geological map of the Aksug deposit. Inset: location map. 1 – recent sediments, 2 – rhyodacite porphyry, 3 – sandstone, conglomerate; the Tannu-Ola series (4-7): 4 – gabbro, 5 – diorite, 6 – quartz diorite, 7 – tonalite; the Aksug series (8-10): 8 – porphyry tonalite, 9 – granodiorite porphyry I, 10 – granodiorite porphyry II; 11 – faults; 12 – ore body outline.

Table 1: Pd, Pt and Au contents of wall-rock samples and flotation concentrates from the Aksug porphyry Cu-Mo deposit.

Sample number	Sample description	Au ppb	Pd ppb	Pt ppb	Cu ppm	Mo ppm	Pd/Pt	Cu/Mo
wall-rock samples, (alteration type/silicates)								
s-0463b	sericitic/quartz, sericite	30	11	17	1550	8	0.65	194
s-0464	potassic/K-feldspar, quartz	51	9	17	2090	10	0.53	209
s-0468	silicification-sericitic/sericite, quartz	47	12	21	950	55	0.57	17
s-0474	silicification-sericitic/sericite, quartz, albite	200	12	21	2400	55	0.57	44
s-0486	silicification-potassic/K-feldspar, sericite, quartz, albite	72	20	34	1010	72	0.59	14
s-0487	potassic/K-feldspar, quartz, albite, biotite	26	23	20	350	43	1.15	8
s-0488	silicification-sericitic/sericite, quartz, albite	24	31	21	154	128	1.48	1
s-0497a	potassic/K-feldspar, quartz, albite	36	12	24	3800	<1	0.5	>3800
representative ore sample, flotation and sulphide concentrates								
4T/1	sulphide ore (chalcopyrite, pyrite, molybdenite, silicates)	178	17	29	10 840	224	0.59	48
4T/2	copper flotation concentrate	5450	62	96	196 500	980	0.64	201
4T/3	copper-molybdenum flotation concentrate	2740	83	76	102 000	14 080	1.1	7
s-2392b	copper (chalcopyrite) sulphide concentrate	1210	920	25	53 600	85	37	630

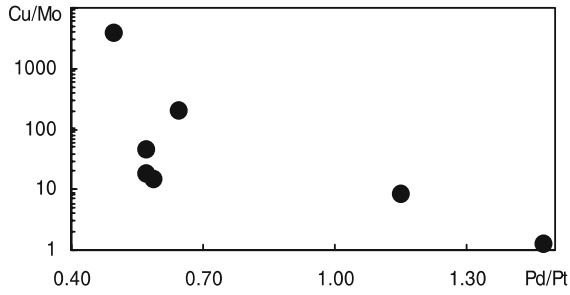

Figure 2: Pd/Pt versus Cu/Mo values in mineralized wall-rock samples of the Aksug deposit.

3 Analytical methods

Pt, Pd and Au contents of concentrates and rock chip samples were determined at both X-ray Assay Laboratories (XRAL), Ontario, Canada, and the National University of Athens, using ICP/MS and AAS (heated graphite atomizer), respectively, after preconcentration by the Lead Fire Assay technique from samples of mineralized rocks and sulfide concentrates. The amount analysed was 30g. Detection limits are 1 ppb for Pd and Au, and 10 ppb for Pt. The Cu and Mo contents were determined by the AAS method in the National University of Athens with a detection limit of 1 ppm.

Analyses of PGM were carried out by a (SEM) JEOL JSM-5600 combined with an Oxford Link ISIS Series 300 EDX at the National University of Athens. Accelerating voltage and beam current were kept at 20.0 kV and 0.5 nA, respectively.

4 Platinum, palladium and gold distribution

4.1 Pt, Pd and Au contents of the mineralized porphyry

Pd and Pt contents in wall rock samples with minor mineralization (Cu: 0.01–0.4 wt.%; Mo: 0–0.01 wt.%), from the different alteration types, range between 9 and 31 ppb, and from 17 to 34 ppb, respectively (Table 1). Average PGE contents in mineralized rocks of the Aksug deposit are 17 ppb Pd and 22 ppb Pt. Gold contents in mineralized rocks are generally low, ranging from 24 to 200 ppb, with an average of 60 ppb.

The variation of Pd/Pt ratios in wall-rock samples is small (0.5–1.5). Even though the data base is relatively small, it seems likely that higher Pd/Pt ratios in wall rock samples (1.15–1.5) are linked to the samples with lower Cu/Mo value (1–8; Fig. 2). In wall rock samples Pd correlates positively with Mo ($r = 0.83$) and negatively with Cu ($r = -0.70$), Pt shows weak positive correlation with Mo ($r = 0.31$) and no correlation with Cu ($r = -0.03$). Evidently, there is no consistent relationship between alteration type and Pt, Pd and Au content.

4.2 Pt, Pd and Au in flotation and sulphide concentrates

We have analysed four samples for their noble metal contents (Table 1). Sample 4T/1 is a bulk sulphide ore sample, which was crushed and milled for geochemical analysis. It is considered to be representative of the bulk composition of the orebody. Two flotation concentrates (Cu – 4T/2; Cu-Mo – 4T/3) were prepared from the bulk sample. A chalcopyrite-rich rock chip sample of propylitic alteration

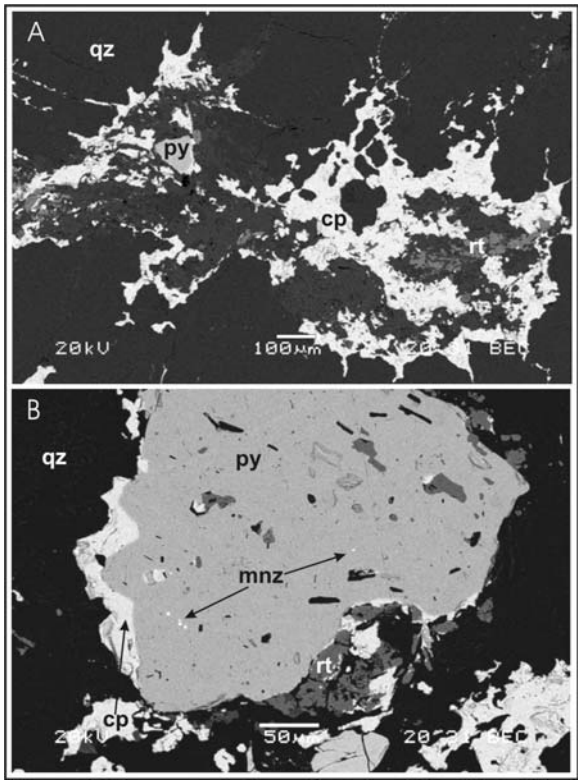

Figure 3: a, b. Back scattered images, showing textural relationships between base and precious metal minerals. Py – pyrite, cp – chalcopyrite, rt – rutile, mnz – monazite, qz – quartz

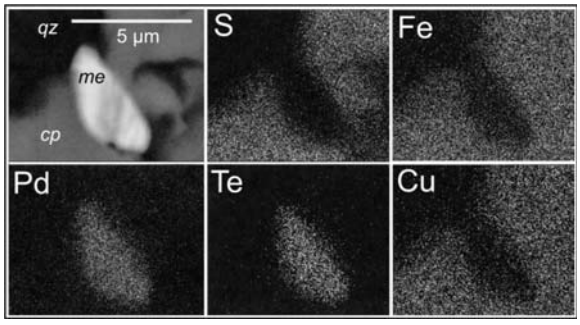

Figure 4: SEM image and X-ray scanning photographs for S, Pd, Te, Fe and Cu of merenskyite (me) inclusion in chalcopyrite (cp). Qz - quartz.

was also analysed (sample S-2392b; Table 1). The bulk sulphide ore sample contains 178 ppb Au, 17 ppb Pd and 29 ppb Pt (Table 1). The copper flotation concentrate and copper-molybdenum flotation concentrate have Au, Pd and Pt contents of 5450, 62, 96 and 2470, 83, 76 ppb respectively (Table 1). The chalcopyrite-rich propylitic altered rock chip sample (S-2392b) has relatively high Pd and Au contents (920 and 1210 ppb respectively; Table 1).

We undertook a detailed investigation of the most Pd- and Au-enriched sample (s-2392b) using SEM and the electron microprobe. Our results show that copper mineralization occurred in two stages. Stage 1 consists of pyrite and chalcopyrite and is associated with abundant Ti-minerals (mostly rutile), REE-minerals, such as monazite (Fig 3 a, b), F-apatite and zircon. Palladium occurs as Pd-telluride (merenskyite), containing 23–25 wt.% Pd and small amounts of Pt. Merenskyite is hosted as small (2-5 µm) rounded to oval inclusions within stage II chalcopyrite, along with electrum (Fig. 4; Table 2). Several Pd-bearing grains occur as intergrowths and as composite grains with other minerals such as cobaltite, chalcopyrite (Table 2, analysis 3), and as-yet and unidentified Au, Ag, As-bearing minerals. Monazite inclusions have also been recognized in stage 2 chalcopyrite, and small grains of Sr-bearing barite (4.6 to 18 wt% Sr) occur along fractures through the metallic minerals, and as disseminations in quartz and silicate minerals.

Table 2: SEM EDX analyses of merenskyite (*1*), electrum (*2*) and composite Pd-bearing grain (*3*) from the Aksug deposit

Element	1	2	3
Pd	25.20	n.d.	12.38
Pt	1.21	n.d.	0.65
Ag	n.d.	18.96	n.d.
Au	n.d.	79.92	n.d.
Cu	0.46	n.d	10.10
Fe	0.38	n.d	9.54
S	n.d.	n.d	21.78
Te	72.31	n.d	12.00
Co	n.a.	n.a.	11.74
As	n.a.	n.a.	21.81

5 Discussion

The Aksug deposit is associated with a suite of sodic calc-alkaline porphyries, inferred to be derived from volatile-rich, strongly fractionated parent magmas (Kuz'min 1985, Sotnikov et al. 2003). Mineralizing fluids at Aksug were Cl-rich and of magmatic derivation (Sotnikov et al. 2003). Mineralization formed under relatively oxidized conditions, as indicated by the presence of abundant anhydrite and low $(CO/CH_4)/CO_2$ ratios, as determined by gas chromatography (Berzina et al. 2005). Such conditions should favor the transport of Au, Pd and Pt as chloride complexes (Economou-Eliopoulos and Eliopoulos 2000, Wood et al. 1992, Xiong and Wood 2000).

Although the Pd and Pt contents at Aksug are much lower than those reported at Skouries, Santo Tomas, Biga, Elatsite, Majdanpek and Mamut (Economou-Eliopoulos and Eliopoulos, 2000, 2001; Stribrny et al. 2000, Tarkian and Stribrny 2000), there are similarities in terms of (a) the occurrence of merenskyite as the main Pd-bearing

mineral (Table 2), (b) the association of merenskyite with chalcopyrite, (c) the association of merenskyite with Au, Ag, As-bearing minerals and (d) the oxidized nature of mineralizing fluids. The low Pd and Pt contents at Aksug (Table 1) may relate to low precious metal contents of the parent magma, or to inefficient processes of PGE deposition at the trap site.

The positive correlation between Pd/Pt and Cu/Mo in the mineralized samples (Fig. 2) implies that Pd at Aksug may occur as an impurity in molybdenite. The high Pd contents of the molybdenum sulphide concentrate (684 ppb Pd; Table 1) supports this, as does the report of elevated Pd (up to 270 ppb Pd) in molybdenite samples from the Zhireken Mo-Cu porphyry deposit, Russia (Sotnikov et al. 2001).

The PGE and Au distribution in porphyry Cu-Mo deposits is controlled by a complex interplay of several factors. The association of merenskyite with stage II chalcopyrite in relatively Pd-enriched samples, coupled with the lower temperature of formation and higher $^{87}Sr/^{86}Sr$ values for Aksug compared to other porphyry Cu-Mo deposits of Russia (Sotnikov et al. 2001) suggest that additionally to the physico-chemical conditions of crystallization (fO_2, Cl activity), major controlling factors were the compositions of the parent magma and the ore-forming solutions.

Acknowledgements

The authorities of the University of Athens, Russian Foundation for Basic Research (grant 04-05-64238) and President Grant for Leading Scientific Schools in Russia (1573.2003.5) are thanked for the financial support of this work.

References

Berzina AN, Sotnikov VI, Economou-Eliopoulos M, Eliopoulos DG (2005) Distribution of rhenium in molybdenite from porphyry Cu-Mo and Mo-Cu deposits of Russia (Siberia) and Mongolia. Ore Geol. Rev. vol 26, No 1-2

Economou-Eliopoulos M, Eliopoulos DG (1996) Distribution of rhenium (Re) in molybdenites and Mo-bearing minerals of Greece and its economic significance. Final Report, University of Athens: 30 (in Greek with English abstract)

Economou-Eliopoulos M, Eliopoulos DG (2000) Palladium, platinum and gold concentration in porphyry copper systems of Greece and their genetic significance. Ore Geol. Rev. vol. 16: 59-70

Economou-Eliopoulos M, Eliopoulos DG (2001) Factors controlling the Pd and Pt potential of the Skouries porphyry-Cu deposit, Chalkidiki Peninsula, N. Greece. In K. Mayer (ed) Mineral deposits at the beginning of the 21st century. Proc. 6th Biennial SGA-SEG Meeting. Balkema, Rotterdam: 579-582

Kovalenker VA, Myznikov IK, Kochetkov AYa, Naumov VB (1996) PGE-bearing gold-sulphide mineralization in the Ryabinovyi alkaline massif, Central Aldan, Russia. Geology of Ore Deposits, vol. 38, No 4: 307-317

Kuz'min MI (1985) Geochemistry of igneous rocks of phanerozoic mobile belts. Nauka, Novosibirsk: 199 (In Russian)

Lebedev VI, Kuzhuget KS (1998) Mineral potential of Tuva Republic: possibility of utilization in 1999-2001 and in future. TuvIKOPR, Kyzyl: 26 (in Russian)

Sotnikov VI, Berzina AN, Economou-Eliopoulos M, Eliopoulos DG (2001) Palladium, platinum and gold distribution in porphyry Cu±Mo deposits of Russia and Mongolia. Ore Geol. Rev., vol. 18, No. 1-2: 95-111

Sotnikov VI, Ponomarchuk VA, Shevchenko DO, Berzina AN (2003) The Aksug porphyry Cu-Mo deposit in northeastern Tuva: $^{40}Ar/^{39}Ar$ geochronology and sources of matter. Russian Geology and Geophysics, vol. 44, No. 11: 1119-1132

Stribrny B, Wellmer FW, Burgath KP, Oberthur T, Tarkian M, Pfeiffer T (2000) Unconventional PGE occurrences and PGE mineralization in the Great Dyke: metallogenic and economic aspects. Miner. Deposita, vol. 35: 260-281

Tarkian M Stribrny B (1999) Platinum-group elements in porphyry copper deposits: a reconnaissance study. Mineral. Petrol. vol. 65: 161-183

Wood SA, Mountain BW, Pan P (1992) The aqueous geochemistry of platinum, palladium and gold: recent experimental constraints and re-evaluation of theoretical predictions. Can. Mineral. vol. 30: 955-981

Xiong Y, Wood SA (2000) Experimental quantification of hydrothermal solubility of platinum-group elements with special reference to porphyry copper environments. Mineral. and Petrol. vol. 68: 1-28

The Boyongan porphyry Cu-Au deposit: Repeated hydrothermal cycles tied to discrete intrusive events

D.P. Braxton, D.R. Cooke

Centre for Ore Deposit Research, University of Tasmania, Private Bag 79, Hobart, 7001, Tas., Australia

Abstract. The recently-discovered Boyongan porphyry copper-gold deposit is part of an emerging belt of intrusion-centered gold-rich deposits in the Surigao district of NE Mindanao, Philippines. Core logging of this blind porphyry system has revealed that Cu-Au mineralization is controlled by stockworked quartz-sulfide veins centered around two multi-phase diorite porphyry stocks. Detailed paragenetic reconstructions reveal a characteristic progression of vein and potassic alteration styles that is repeated with the emplacement of each discrete intrusive event. Quartz-poor wispy magnetite-biotite-K-feldspar veinlets characterize *Stage 1*. *Stage 2* veins consist of quartz with selvage and/or disseminated magnetite and/or biotite and K-feldspar halos. *Stage 3* quartz veins have K-feldspar halos but generally lack magnetite and biotite. *Stage 4* veins consist of massive bornite-chalcopyrite and chalcopyrite-pyrite with K-feldspar halos.

Bornite and chalcopyrite are the dominant hypogene copper sulfides, with hypogene gold occurring as fine inclusions in copper sulfides and as rare free grains in quartz. Stage 3 quartz veins and Stage 4 sulfide veins host Cu-Au mineralization of the greatest volumetric significance, reflecting the general paucity of sulfide in the earlier vein stages.

Keywords. Vein paragenesis, hydrothermal cycles, potassic alteration

1 Introduction

While the spatial and temporal relationship between hypogene mineralization and intrusive events in calc-alkalic porphyry systems is well recognized (e.g. Gustafson and Hunt 1975), relationships between vein and alteration progressions and discrete intrusions is not well appreciated. Understanding the complex interplay of magmatism, hydrothermal activity, and mineralization is of fundamental importance in the understanding of porphyry systems.

Features encountered during exploration of Boyongan suggested that the vein stockworks and associated Cu-Au mineralization were products of multiple hydrothermal cycles punctuated by the emplacement of discrete intrusions. Such features included stockworked intrusions truncated by successive intrusive phases which are themselves cut by veins, and the presence of vein quartz xenoliths in these same intrusive stages.

2 Location

The Boyongan porphyry Cu-Au deposit is located in the Surigao Gold District of NE Mindanao (Fig. 1), known previously for its epithermal and sediment-hosted gold mineralization (Waters 2004).

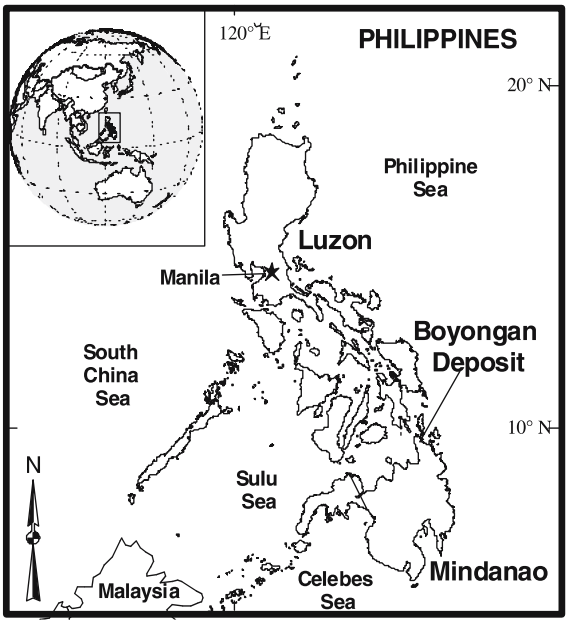

Figure 1: Location of Boyongan Porphyry Cu-Au deposit in NE Mindanao, Philippines.

The deposit, currently undeveloped, is covered by Quaternary material. Anglo American geologists discovered Boyongan by diamond drilling in August 2000 (Waters 2004).

3 Geological framework

At least nine discrete intrusive events are evident in the Boyongan Intrusive Complex. Magmatism began with the emplacement of a suite of three pre-mineral porphyritic diorite stocks into an Oligocene to Early Pliocene-aged sequence of basalts, marine clastics, and carbonates. The development of an extensive pre-mineral diatreme-like breccia body followed this early magmatism, resulting in the fragmentation of a large proportion of the earlier intrusions and the adjacent host rock.

Cu-Au mineralization followed the formation of the rock-flour-matrix breccia body, in association with the emplacement of narrow, multi-phase, pipe-like diorite porphyry stocks within two discrete areas in the breccia complex. Known respectively as the Eastern and Western High-Grade Zones (EHGZ, and WHGZ), Cu-Au mineralization developed in quartz vein stockworks focused in

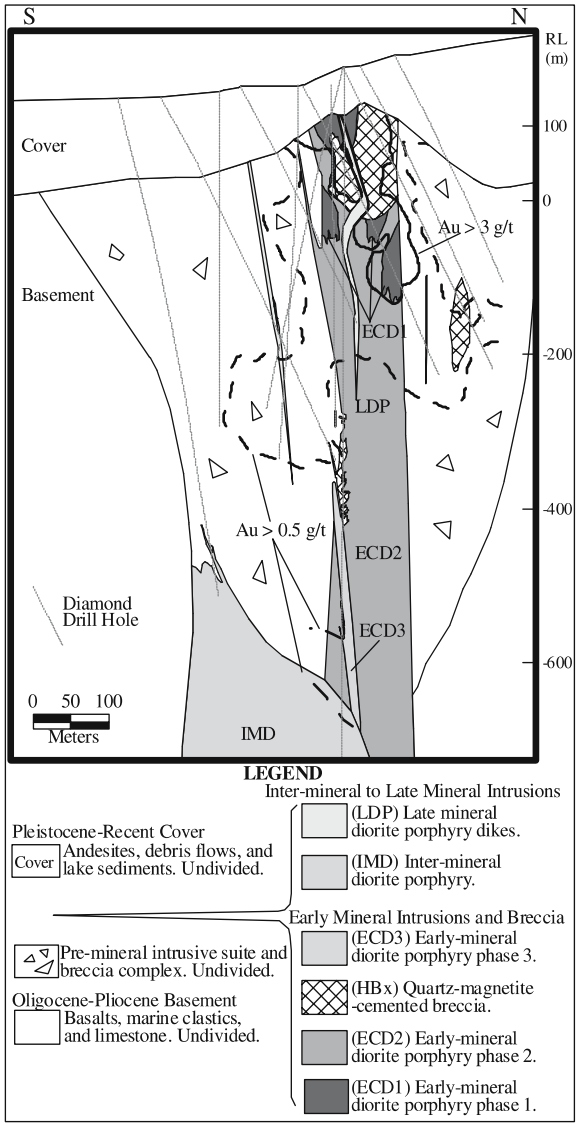

Figure 2: N-S cross-section along easting 779900 through the Eastern High-Grade Zone. Three phases of the Early Mineral Diorite Porphyry (ECD) are present, with highest gold (and copper) grades coinciding with stockworking events associated with the cupola of ECD1 and ECD2.

and around the cupolas of these two intrusive centers. These early intrusions are collectively termed the Early Mineral Coarse-grained Diorite Porphyry (ECD). At least two phases of the ECD intruded the WHGZ (ECD0 and ECD1), while at least three early mineral intrusive phases (ECD1, ECD2, and ECD3) occur in the EHGZ (Fig. 2).

A large inter-mineral diorite porphyry stock (IMD) truncated intrusions of the Western and Eastern High-Grade Zones at depth (Fig. 2), developing weak Cu-Au mineralization. Narrow, late-mineral diorite porphyry (LDP) dikes represent the last pulse of magmatism in the Boyongan Intrusive Complex.

Uplift, exhumation, and weathering followed the emplacement of the diorite porphyry suite at Boyongan, and a deep supergene oxidation profile, locally exceeding 500 meters, developed during this time. Oxidation depth and intensity is greatest in the WHGZ, with only partial oxidation of primary sulfides in the upper portion of the EHGZ.

A localized extensional tectonic regime brought an end to supergene oxidation at Boyongan. Debris flows, andesitic flows and volcaniclastic products associated with the nearby Maniayo volcanic complex shed into an actively extending fluvio-lacustrine basin. These processes led to extremely rapid burial of the Boyongan deposit, preserving the unusually thick supergene profile (Waters 2004).

4 Vein paragenesis

Paragenetic reconstructions at Boyongan are based on systematic core logging through the Eastern and Western High-grade Zones. Vein features described included dimensions, external form, internal texture, vein mineralogy, vein selvages, alteration halos, cross-cutting relationships, and influence on Cu-Au grades.

Documentation of vein truncations at intrusive contacts, abrupt changes in quartz vein density, and quartz vein xenoliths constrained the timing and spatial relationships between specific veining and intrusive events.

Petrographic observations made on 79 polished thin sections helped to refine the mineralogical identifications and cross-cutting relationships documented during core logging. All petrographic offcuts, and an additional 210 slabs, were stained with sodium cobaltinitrate to identify K-feldspar.

We present below the hypogene vein paragenesis for the Eastern High-Grade Zone, where hypogene features are best preserved. For most of the intrusions in the EHGZ, veining and attendant potassic alteration follow a progression that is characteristic of most gold-rich porphyry deposits (Sillitoe 2000). The vein stage progression described hereunder clas-

Table 1: Generalized vein progression for intrusive-related vein stages at Boyongan.

Vein Stage	Description
Stage 1	Wispy magnetite or biotite veinlets with K-feldspar alteration halos. Small miarolitic cavities with biotite, K-feldspar and quartz.
Stage 2	Irregular quartz veins with disseminated and/or selvage biotite or magnetite and K-feldspar alteration halos.
Stage 3	Irregular quartz veins with little or no biotite or magnetite and with moderate to weak K-feldspar alteration halos.
Stage 4	Chalcopyrite or bornite veins with K-feldspar alteration halos.

sifies veins on the basis of the equilibrium mineral assemblage, vein form and vein texture (Table 1).

Stage 1 veinlets are generally thin (0.5-1 mm) and discontinuous with narrow K-feldspar alteration halos. Three Stage 1 veins can be defined by the dominant mineral: magnetite, biotite, or K-feldspar.

Although similar to the 'M' veinlets described by Clark and Arancibia (1995) the magnetite-dominated Stage 1 veinlets at Boyongan lack actinolite, and have K-feldspar alteration halos. These veinlets are best developed within and immediately adjacent to ECD diorite intrusions.

Stage 1 biotite occurs either as thin discontinuous wispy veinlets, or as relatively coarse-grained euhedral crystal aggregates growing with subsidiary quartz and K-feldspar in miarolitic cavities. Both features have intense K-feldspar alteration halos. Stage 1 biotite-quartz-K-feldspar miarolitic cavities are restricted to the upper portions of the IMD stock. Wispy biotite veinlets are common to the ECD, IMD, and LDP intrusions, and are equivalent to the 'streaky' biotite veinlets of Sillitoe (2000).

Stage 2 is characterized by quartz-dominated veins occurring with subsidiary magnetite or biotite. There are two styles of Stage 2 infill: irregular quartz veins, and quartz-magnetite breccia cement.

Stage 2 quartz veins are generally massive with disseminated and/or selvage biotite or magnetite. Veins are irregular in form, variable in width (1-90 mm), and consist of granular sugary quartz grains ranging in size between 0.2 and 1 mm. K-feldspar alteration halos are common and are locally intense.

Stage 2 minerals also occur as cement to polymict angular to sub-rounded, clast-supported breccias particularly in the Eastern High-grade Zone ("HBx" in Figure 2). K-feldspar alteration halos flood the breccia clast margins.

Table 2: Vein stages in the Eastern High-Grade Zone that are temporally and spatially associated with discrete intrusive events.

Vein	Intrusive Stage				
	Early				Late
Stage	ECD1	ECD2	ECD3	IMD	LDP
1	■	■	■	■	■
2	■	■	■	■	■
3	■	■	■	■	■
4	■	■	■	■	■

■ Vein stage observed

■ Vein stage with significant Cu-Au mineralization

Intrusive Stages: *ECD* Early-mineral Coarse-grained Diorite Porphyry; *IMD* Inter-mineral Diorite Porphyry; *LDP* Late-mineral Diorite Porphyry.

Stage 3 quartz veins are the most abundant at Boyongan, locally forming stockworks containing 10-30% quartz by volume. These veins host most of the hypogene Cu-Au mineralization in the EHGZ.

A lack of biotite and magnetite distinguishes Stage 3 quartz veins from earlier vein sets. Stage 3 consists of irregular quartz veins otherwise similar in form and internal sugary texture to Stage 2 veins. Stage 3 veins commonly display distinctive textures such as banding parallel to vein walls defined by variations in quartz grain size (e.g. "ribbon" veins). K-feldspar halos, although present, are generally weaker and more diffuse than in earlier vein stages. In the shallow portion of the EHGZ sulfide mineralization occurs in Stage 3 veins as disseminated bornite-chalcopyrite grains which are locally concentrated along quartz banding.

Stage 4 sulfide veins with moderate-intense K-feldspar alteration halos make up the final stage in the potassic cycle at Boyongan. In the shallow portion of the EHGZ, Stage 4 consists of irregular bornite- chalcopyrite veinlets and locally as breccia cement, and locally contribute

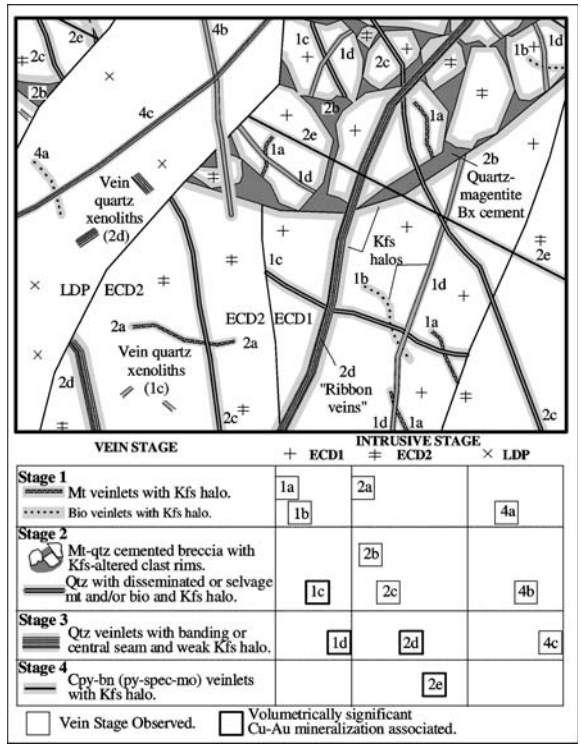

Figure 3: Schematic summary of the vein paragenesis in the Eastern High Grade Zone. A similar progression of vein stages affects all three intrusive phases present. Cross-cutting relationships clearly demonstrate that each successive intrusion truncates earlier vein progressions, and that a discrete hydrothermal system follows each intrusion. Qtz quartz; Mt magnetite; Kfs K-feldspar; Bio biotite; Cpy chalcopyrite; Bn bornite; Py pyrite; Spec specularite; Mo molybdenite.

significantly to Cu-Au grades. In the deeper, lower-grade portions of the EHGZ, thin chalcopyrite-pyrite veinlets with minor bornite represent Stage 4.

5 Repeated hydrothermal cycles

Table 2 summarizes the progression of potassic alteration and veining compiled for the intrusive phases in the Eastern High-Grade Zone.

From this compilation it is clear that a similar progression has affected each the intrusions of the EHGZ. Figure 3 represents schematically the complex paragenetic relationships associated with intrusions in the shallow portions of the EHGZ.

6 Discussion

The paragenesis for the EHGZ at Boyongan demonstrates that following initial stock emplacement (ECD1), hydrothermal systems evolved from producing early magnetite and biotite-rich veins (Stages 1 and 2), to forming magnetite-poor, biotite-poor, sulfide-rich, and well-mineralized veins (Stages 3 and 4). This vein progression is similar to that described by Redmond et al.(2004) for the Bingham porphyry Cu-Au deposit. At Boyongan, subsequent intrusive events truncated earlier vein stages, initiating renewed cycles of potassic alteration and mineralization tied to each successive intrusive event. These observations highlight the role that multiple magmatic-hydrothermal cycles play in modifying grade and contained metal of gold-rich porphyry copper deposits either by superposition of multiple mineralizing cycles, or through dilution by the emplacement of weakly-mineralized intrusions.

Acknowledgements

The authors wish to thank Anglo American Exploration Philippines Inc. for the generous financial and logistical support that made this study possible.

References

Clark AH, Arancibia ON (1995) Occurrence, paragenesis, and implications of magnetite-rich alteration-mineralization in calc-alkaline porphyry copper deposits. In: Clark AH (ed) Giant Ore deposits II Workshop. Kingston, Ontario: 511-581

Gustafson LB, Hunt JP (1975) The porphyry copper deposit at El Salvador, Chile. Economic Geology and the Bulletin of the Society of Economic Geologists 70: 857-912

Redmond PB, Einaudi MT, Inan EE, Landtwing MR, Heinrich CA (2004) Copper deposition by fluid cooling in intrusion-centered systems; new insights from the Bingham porphyry ore deposit, Utah. Geology 32: 217-220

Sillitoe RH (2000) Gold-rich porphyry deposits; descriptive and genetic models and their role in exploration and discovery. Reviews in Economic Geology 13: 315-345

Waters PJ (2004) Exploration models for giant copper-gold deposits at the district scale: examples from the SW pacific. SEG Conference 2004 Proceedings: Predictive Mineral Discovery Under Cover. Perth, AUSTRALIA: 51-56

Endoskarn and Cu-Zn mineralization at the Empire mine, Idaho, USA

Zhaoshan Chang
Centre for Ore Deposit Research, University of Tasmania, Private Bag 79, Hobart, TAS 7001, Australia

Lawrence D. Meinert
Department of Geology, Clark Science Center, Smith College, Northampton, MA 01063, USA

Abstract. The Empire mine is a Cu-Zn skarn associated with the granite porphyry phase of the Mackay Stock, which consists of quartz monzodiorite, granophyre, granite porphyry, Mackay Granite, and numerous dikes. Both granite porphyry and Mackay Granite have high F and also have unusual, extremely vermicular quartz phenocrysts. Both endoskarn and exoskarn are developed at the Empire mine, with more endoskarn than exoskarn. The alteration of the intrusive rocks began with weak disseminated diopsidic pyroxene, actinolite, and titanite. Further endoskarn formed by veins or as massive replacements of intrusive rocks. The earliest formed endoskarn veinlets contain scapolite, with or without wollastonite halo. This was followed by wollastonite-dominant (± Ca-rich plagioclase and hedenbergitic pyroxene) veins as fronts or envelopes on garnet-dominant veins. Early pyroxene is diopsidic whereas pyroxene in distal/late veinlets is hedenbergitic. Similarly, garnet becomes more Fe-rich with time. In exoskarn, all the pyroxene is diopsidic and garnet andraditic. Magnetite precipitated after garnet-pyroxene in both endoskarn and exoskarn. Zn sulfide precipitated together with Cu in proximal locations, associated with retrograde quartz+calcite+chlorite. Massive endoskarn and exoskarn replacement formed at 500-550 °C, whereas slightly higher temperatures were recorded by late minerals at the metasomatic front, >600 °C. The highest temperatures, >700 °C, occur in garnet-dominant veins that probably represent conduits insulated by earlier skarn. During retrograde alteration, quartz, calcite, chlorite, fluorite, and chalcopyrite precipitated in both endoskarn and exoskarn at 250-300 °C. The extremely vermicular texture of quartz phenocrysts, abundant endoskarn, and proximal deposition of Zn, are all caused by the high F contents of the magma and magmatic fluid.

Keywords. Endoskarn, proximal Zn mineralization, high F activity, fluid inclusion, Empire

1 Introduction

Discovery of the world class Antamina Cu-Zn skarn deposit in Peru has sparked renewed interest in exploration for large skarn deposits worldwide. Besides the large amount of ores, this deposit also has several unusual features, such as abnormally abundant endoskarn, and a high Zn/Cu ratio. Typically skarn deposits have much more exoskarn than endoskarn because carbonate wall rocks are more easily dissolved and replaced by dilute to moderately acidic hydrothermal fluids whereas silicate rocks are relatively hard and insoluble (e.g. Einaudi et al. 1981). The high Zn/Cu ratio is also unusual because most Zn skarns are located distal to intrusions whereas Cu occurs in proximal locations due to the precipitation of Zn sulfides at lower temperatures than Cu sulfides (e.g. Einaudi et al. 1981; Meinert 1992, 1997). Skarns with large amounts of endoskarn and relatively high Zn/Cu ratios in proximal locations are not well understood, and need further study. The Empire mine in Idaho is a small but representative example of these phenomena (Chang 2003; Chang and Meinert 2004). Recent drilling provides excellent 3-D exposures of fresh rocks.

2 Empire mine

The Empire mine is located in Custer County, south-central Idaho, USA (Fig. 1). It was mined intermittently from 1884-1982 and produced 899,517 tons of high grade ore yielding 30,730 tons Cu, 456 tons Zn, 41,159 ounces Au, and 1,293,208 ounces Ag (Wilson et al. 1995). Recent drilling indicates an oxide resource of 18 Mt at 0.49% Cu, 0.19% Zn, 13.5 g Ag/t and 0.48 g Au/t.

The Empire district lies east of the Idaho batholith and north of the Snake River Plain. It is within the Cordilleran thrust belt, and at the edge of the Basin and Range structural province. The deposit occurs in the White Knob horst that is bounded by 2 Cretaceous faults and 2 Eocene faults (Skipp and Harding 1985). Sedimentary rocks include Lower Mississippian Copper Basin Formation argillites and Upper Mississippian White Knob Limestones that have been intruded by the multiphase Eocene Mackay Stock.

The intrusive rocks in the Mackay Stock are described in detail in Chang and Meinert (2004). In general, the Mackay Stock is composed of, from oldest to youngest, quartz monzodiorite, granophyre, granite porphyry, Mackay granite, and numerous dikes. The skarn and mineralization is closely associated with the granite porphyry. Both the granite porphyry and the Mackay granite have extremely vermicular quartz phenocrysts. The F contents of biotite and amphibole in granite porphyry and Mackay granite are high. In addition, granophyre, granite porphyry, and Mackay granite contain fluorite as an accessory mineral, which indicates high F activity in the magma.

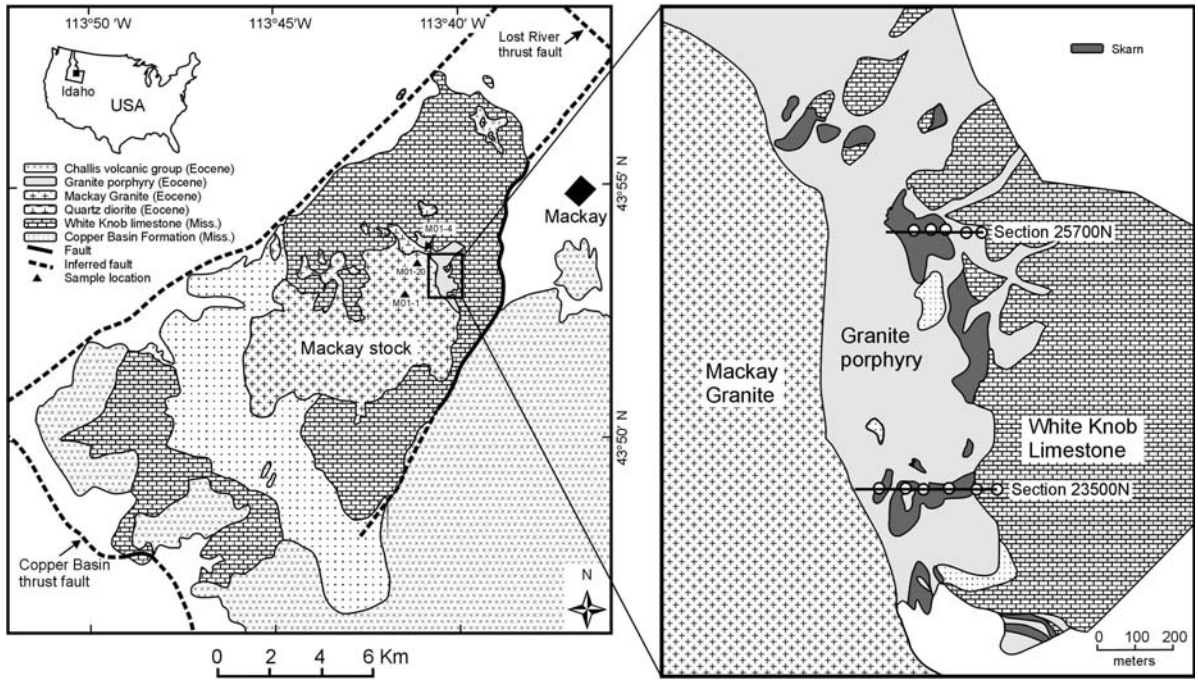

Figure 1: Geologic Setting of the Empire mine (modified from Wilson et al.1995) and simplified geologic map of the Empire mine (after the geologic map Cambior Inc. 1997)

3 Alteration of the intrusive rocks and skarn

The earliest alteration is represented by weak but pervasive, disseminated diopsidic pyroxene ($Di_{64}Hd_{36}$ to $Di_{88}Hd_{12}$) replacing the granite porphyry, especially the groundmass and mafic minerals. The pyroxene occurs as clusters of very fine grains. With slightly stronger alteration, actinolite and titanite also are present and the pyroxene becomes more Mg-rich. At this stage, the carbonate wall rock is thermal-metamorphosed to marble.

Following this, endoskarn and exoskarn form replacing the intrusive rocks and the White Knob limestone wall rocks, respectively. There is more endoskarn than exoskarn (Fig. 2). Exoskarns are massive. Endoskarn appears mostly as veins, but where multiple veins intersect, it locally appears as massive replacement. Skarn minerals in the veins are typically fine-grained on the margin, and become coarser toward the vein center. The formation of endoskarns starts with Na and Cl-rich scapolite (Me_{18} to Me_{35}, mostly $Me_{18\text{-}26}$) veinlets, with or without wollastonite halos. This was followed by a wollastonite-dominant assemblage as vein fronts or envelopes on garnet-dominant veins. This assemblage may or may not contain Ca-rich plagioclase (An_{56} to An_{89}) and mostly hedenbergitic pyroxene ($Di_{19}Hd_{78}$ to $Di_{55}Hd_{43}$). Many of the endoskarn veins have a halo of very fine-grained, disseminated wollastonite ± Ca-rich plagioclase whose intensity decreases over a short distance into background disseminated alteration. Early pyroxene is diopsidic whereas pyroxene in distal/late veinlets is hedenbergitic. Similarly, garnet becomes more Fe-rich with time and towards vein centers. Development of alteration and endoskarn within the intrusion is illustrated in Figure 3. In exoskarn, all the pyroxene is diopsidic ($Di_{79}Hd_{20}$ to $Di_{99}Hd_1$) and garnet andraditic (Gr_0Ad_{100} to $Gr_{30}Ad_{69}$).

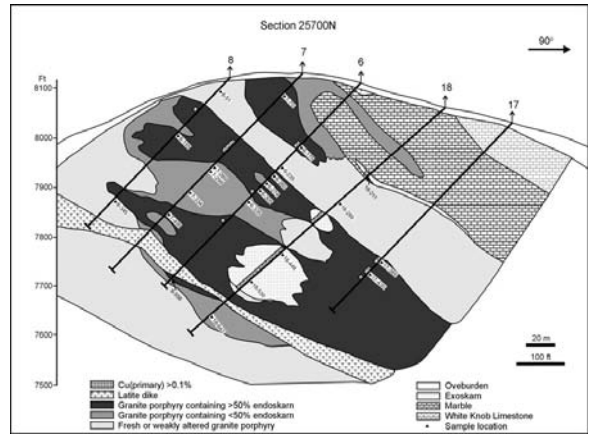

Figure 2: Cross Section 25700N.

All the endoskarn garnet is pink-brown to dark brown in color, whereas for exoskarn, the garnet color is brown to dark brown closer to the intrusion, and becomes yel-

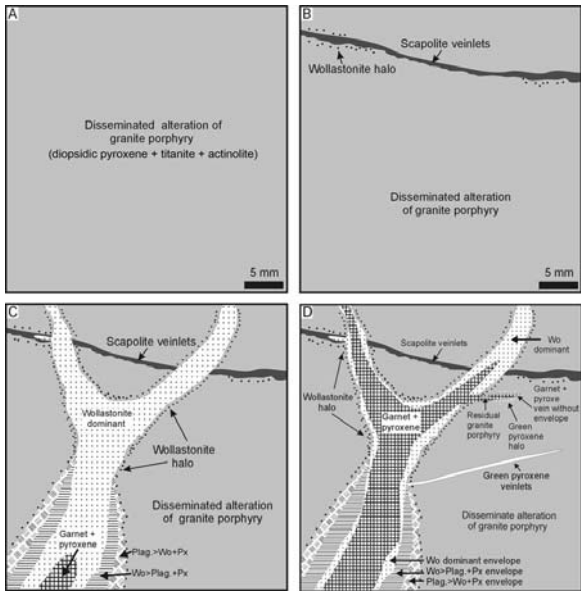

Figure 3: Development of endoskarn veins. A. Weak disseminated alteration of granite porphyry. B. Early scapolite veinlets with or without wollastonite halo. C. Wollastonite + Ca-rich plagioclase + pyroxene assemblage as front of garnet-dominant + minor pyroxene vein. This assemblage cuts across the earlier scapolite veins or utilizes its channel. Sometimes this assemblage has zoning, with the centre dominated by wollastonite, and toward vein margin, the amount of Ca-rich plagioclase increases. Usually a wollastonite halo is around the vein. D. Increasing garnet + pyroxene take over the vein and extend beyond the vein. Now the wollastonite + Ca-rich plagioclase + pyroxene assemblage is the envelope to the garnet-dominant vein. Some garnet + pyroxene veins without envelope have hedenbergite haloes.

low farther away. Endoskarn pyroxene is dark-green to light-green, whereas all the exoskarn pyroxene is light-green in color.

Retrograde alteration is limited in both endoskarn and exoskarn. It mainly consists of quartz and calcite replacing, filling the interstices of, or as veins cutting across prograde skarns, as well as minor chlorite, talc, and fluorite.

4 Mineralization

Both Cu and Zn are important in the Empire mine, and Zn sulfide precipitated together with Cu in proximal locations. In time sequence, magnetite precipitated after garnet-pyroxene in both endoskarn and exoskarn. Chalcopyrite and sphalerite also are present in both of them but later than magnetite. They are mostly associated with retrograde quartz+calcite±chlorite. Other ore minerals include minor molybdenite, native gold, pyrite, hematite, galena, arsenopyrite, as well as supergene minerals such as chrysocolla, malachite, azurite, native Cu, and limonite.

5 Fluid inclusion study

Fluid inclusions are found in pyroxene, garnet, quartz, and calcite. Eutectic, last-ice-disappearing, daughter mineral dissolving, and vapor homogenization temperatures were measured on a Linkam THMSG600 stage and a USGS gas flow stage.

Massive endoskarn and exoskarn replacement formed at 500-550 °C, whereas slightly higher temperatures were recorded by late minerals at the metasomatic front, >600 °C. The highest temperatures, >700 °C, occur in garnet-dominant veins that probably represent conduits insulated by earlier skarn. During retrograde alteration, quartz, calcite, chlorite, fluorite, and chalcopyrite precipitated in both endoskarn and exoskarn at 250-300 °C. Eutectic temperatures of fluid inclusions in quartz and calcite indicate that the fluid contains multiple components including at least KCl, $MgCl_2$, NaCl, $CaCl_2$, and $FeCl_2$ or $FeCl_3$, similar to what is revealed by SEM-EDS analyses of daughter minerals in fluid inclusions in quartz phenocrysts of the intrusive rocks (Chang and Meinert 2004). The salinity of fluid inclusions in garnet and pyroxene is 26 - 60 wt%NaCleq, mostly >40 wt%NaCleq, whereas for retrograde quartz and calcite, the salinity is 1.4 to 19 wt% NaCleq, mostly <10 wt% NaCleq. This trend is consistent with what has been measured for other skarn systems (e.g. Meinert et al. 1997).

6 Discussion

The extensive presence of endoskarn, the zonation of endoskarn veins with respect to mineralogy, mineral composition, mineral color, and the temperature of fluids, and the decrease of fluid temperature from skarns hosted inside the intrusion to skarns hosted in the wall rocks indicate that the fluid originates from the magma. The garnet-dominant veins may represent the fluid conduits as indicated by the very high temperature (>700°C) of the fluid inclusions in garnet and pyroxene.

The high temperature of garnet and pyroxene indicates that hydrothermal fluid exsolution started at high temperature and relatively early in the magma cooling history. Other evidence includes the large amount of Fe, Mg, and Ca in fluid inclusions, the presence of chalcopyrite (high Cu) in fluid inclusions of quartz phenocrysts, and the large amount of magnetite in the mine (Chang 2003; Chang and Meinert 2004). If water had saturated late, these elements would have been mostly incorporated into magmatic minerals (e.g. Candela and Piccoli 1995). However, the termination of the exsolution may be at lower than normal temperature when the magma totally solidified, due to the high F in the magma as discussed below.

Chang and Meinert (2004) demonstrated that both the magma and the hydrothermal fluid are high in F as evidenced by high F content in igneous biotite and amphibole and hydrothermal vesuvianite, fluorite as accessory minerals in igneous, endoskarn, and exoskarn rocks, and fluorite as daughter minerals in fluid inclusions. It was argued that the high F activity was one of the major causes of the extremely vermicular texture of the quartz phenocrysts in the intrusive rocks at the Empire mine, according to 3-D imaging, cathodoluminescence, microprobe/BSE, and fluid inclusion studies (Chang and Meinert 2004).

The high F activity may also have caused the abundant endoskarn and proximal Zn mineralization at the Empire mine. High F in hydrothermal fluids makes it easier to dissolve/decompose silicate minerals, creating space for endoskarn formation and/or promoting the reactions to form endoskarn. Fluorine also lowers the solidus temperature of the magma and prolongs the exsolution of magmatic hydrothermal fluid from the magma. In the end stages of magma solidification , the hydrothermal fluid is lower temperature compared to low-F systems. Therefore, it is cool enough to precipitate Zn sulfides in proximal locations, in contrast to distal Zn mineralization in typical Pb-Zn skarns.

References

Candela PA, Piccoli PM (1995) Model ore-metal partitioning from melts into vapor and vapor/brine mixtures. In: Thompson JFH (ed) Magmas Fluids and Ore Deposits. Mineralogical Association of Canada Short Course 23:101-128

Chang ZhSh (2003) Magmatic-hydrothermal transition, skarn formation, and mineralization at the Empire Mine, Idaho. PhD dissertation, Washington State University, 337

Chang ZhSh, Meinert LD (2004) The magmatic-hydrothermal transition - evidence from quartz phenocryst textures and endoskarn abundance in Cu-Zn skarns at the Empire mine, Idaho, USA. Chem Geol 210:149-171

Einaudi MT, Meinert LD, Newberry RJ (1981) Skarn deposits, Economic Geology, 75th Anniversary Volume 317-391

Meinert LD (1992) Skarns and skarn deposits. Geoscience Canada 19:145-162

Meinert LD (1997) Application of skarn deposit zonation models to mineral exploration. Explor. Mining Geol 6:185-208

Meinert LD, Hefton KK, Mayes D, Tasiran I (1997) Geology, zonation, and fluid evolution of the Big Gossan Cu-Au skarn deposit, Ertsberg District, Irian Jaya. Econ. Geol. 92: 509-534

Skipp BA, Harding ST (1985) Preliminary report on geology of Borah Peak area, Idaho, including interpretation of seismic and gravity data, in Stein RS, Bucknam RC (eds) Proceedings of Workshop 28 on the Borah Peak, Idaho, earthquake: U.S. Geological survey Open-File Report 85-290-A, 657-671

Wilson AB, Soulliere SJ, Skipp BA (1995) Mineral deposits of the Mackay and Copper Basin mineralized areas, White Knob Mountains, south-central Idaho. U. S. Geological Survey Bulletin, 2064:I1-I16

The Rosario porphyry Cu-Mo deposit, northern Chile: Hypogene upgrading during gravitational collapse of the Domeyko Cordillera

David R. Cooke, Glenton J. Masterman[1], Ron F. Berry
Centre for Ore Deposit Research, University of Tasmania, Private Bag 79, Hobart, TAS 7001, Australia
[1]current Address: Bolnisi Gold NL, Chihuahua, Mexico

John L. Walshe
CSIRO Exploration and Mining, ARRC, 26 Dick Perry Av, Kensington, WA 6151, Australia

Abstract. Porphyry style mineralisation at the Rosario deposit in northern Chile formed during the waning stages of the Incaic Orogeny (~34 – 32 Ma). Early-formed copper-molybdenum mineralisation formed in association with potassic and intermediate argillic alteration during the emplacement of the Rosario Porphyry. Late-stage high sulfidation state epithermal veins (including the Rosario Vein) formed when NW-trending, SW-dipping normal faults cut the Rosario Porphyry. The massive sulfide veins overprinted earlier-formed potassic alteration and related mineralization, producing a high grade core of copper-silver mineralization associated with advanced argillic and phyllic alteration. Pressure-depth estimates from fluid inclusion analyses imply that more than a kilometer of overburden was removed in 1.8 m.y., from the time of porphyry ore formation to the deposition of high sulfidation veins. Gravitational collapse of the Domeyko Cordillera at the end of the Incaic Orogeny promoted rapid exhumation of the porphyry system. This allowed for the formation of an extensional vein array infilled by high sulfidation state mineralization in a terrane undergoing compressional tectonism.

Keywords. Porphyry, epithermal, hypogene, structure, faulting, uplift

1 Introduction

This paper discusses the origins of high grade mineralisation at the Rosario porphyry Cu-Mo deposit in the Collahuasi district of northern Chile (Fig. 1). We begin with a brief review of the geodynamic setting of Northern Chile, and of the mineral deposits of the Collahuasi district, before focusing on the physical processes that promoted hypogene upgrading of porphyry copper proto-ore at Rosario.

2 Geodynamic setting

Several of the world's largest known porphyry copper deposits (defined in terms of contained copper metal) occur in northern and central Chile. The ore deposits are related to intrusive complexes that have rare earth element and radiogenic isotopic compositions consistent with emplacement within compressional tectonic settings, where uplift and crustal thickening are occurring synchronous with ore formation (Kay et al. 1999; Hollings et al. 2005). Changes to 'steady-state' plate tectonic conditions appear to have been caused by 'small' collisional events that occurred in the Eocene-Oligocene and again in the Miocene to Recent. These 'small' collisions have occurred between the South American continental plate

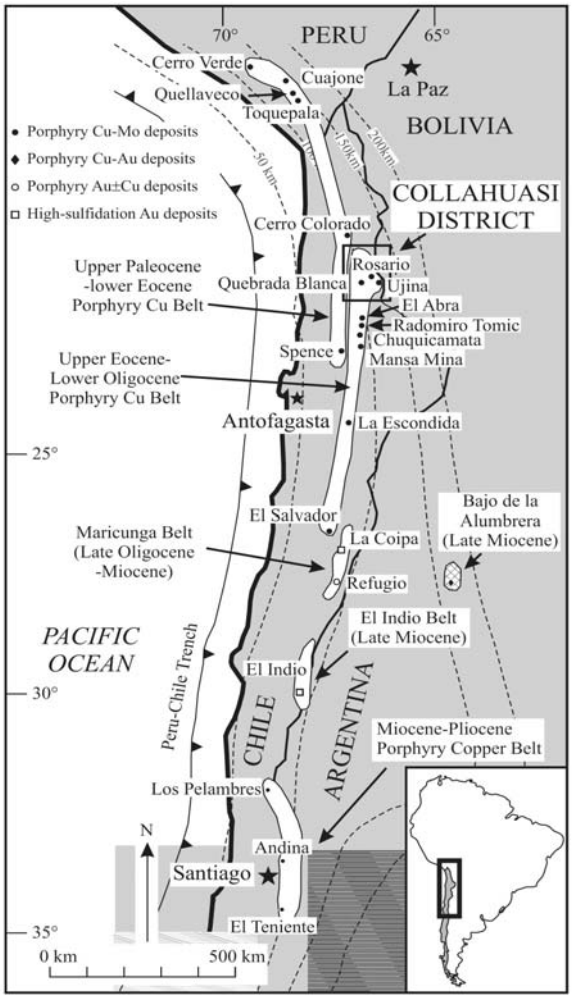

Figure 1: Location of the major porphyry and epithermal deposits of northern Chile. The Rosario porphyry deposit occurs in the Collahuasi district, at the northern end of the Eocene-Oligocene porphyry belt (modified from Masterman et al. 2005).

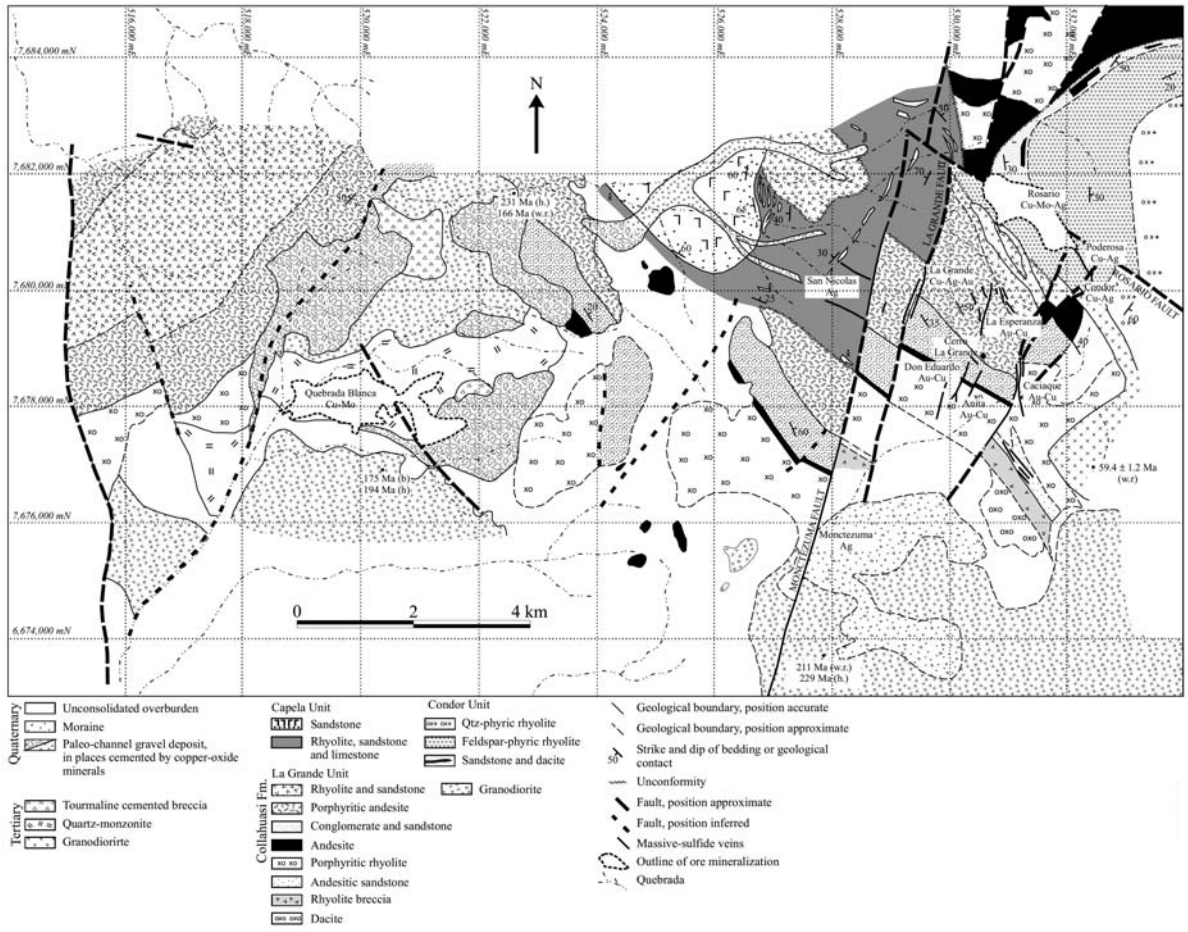

Figure 2: Geology of the Collahuasi district, showing the location of the major porphyry and epithermal mineral deposits (modified from Munchmeyer et al. 1984; Masterman et al. 2005).

and ridge segments on the subducting Nazca oceanic plate. They did not cause a cessation or reversal of subduction or an obduction event (as can be the case for 'large' collisions, where two continents or a continent and a large oceanic plateau such as the Ontong-Java plateau collide). Instead, Cooke et al. (2005) and others have argued that these 'small' collisions have caused the subduction zone to flatten, leading to thrust stacking and crustal thickening, 'giant' earthquakes (magnitude > 8) and a cessation of volcanism (except for minor alkaline or adakitic volcanism).

James and Sacks (1999) summarized the effects of transitions from normal to flat to normal subduction in southern Peru and northern Chile during the Eocene-Oligocene period. These included: i) a broad zone of low-volume alkalic magmatism; ii) horizontal shortening via thrusting; iii) hydration of the lithosphere above the flat slab (most intense above the zone of normal subduction, and above the initial zone of flat subduction); iv) abnormally low heat flow (due to advective cooling of the lithosphere as a result of dehydration of the oceanic plate?); v) return to normal subduction - interaction of hot asthenosphere and hydrated mantle, causing wet melting; vi) substantial crustal melting due to passage of mantle melts through the continental lithosphere; and vii) lithospheric thinning and weakening via heating and fluid advection, leading to formation of a ductile block where Neogene crustal shortening and uplift has been focused.

3 Collahuasi District

The Domeyko Cordillera in northern Chile hosts several giant Eocene-Oligocene porphyry copper-molybdenum deposits, including the super giant Chuquicamata and La Escondida systems, together with other major systems such as La Fortuna (Paleczek et al., this volume), El Salvador, Radomiro Tomic, El Abra and Mansa Mina. The northernmost cluster of porphyries occurs in the Collahuasi district (Fig. 2), and includes the supergiant Rosario (3.11 Gt @ 0.82 % Cu, 0.024 % Mo and 0.01 g/t Au), and the giant Ujina (636 Mt @ 1.06 % Cu), and Quebrada Blanca porphyry deposits (400 Mt @ 0.83 %

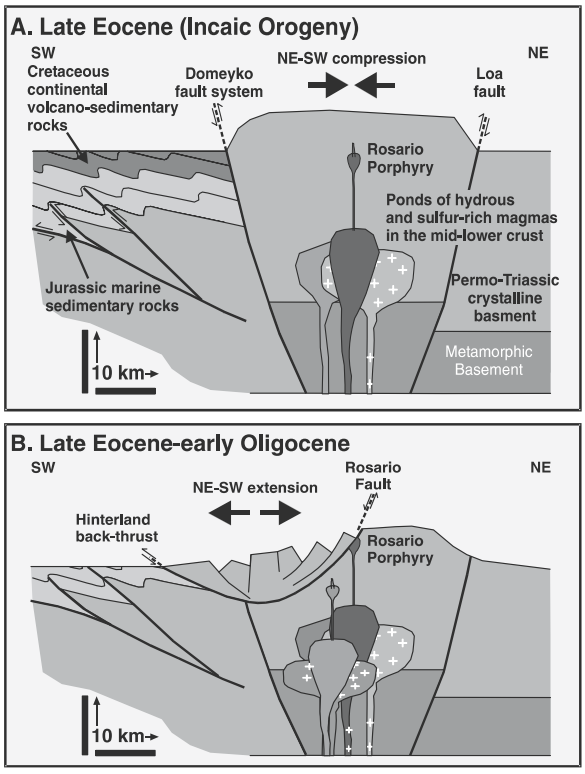

Figure 3: Model for the formation of porphyry and epithermal mineralization in the Collahuasi district. A: emplacement of the Rosario Porphyry under compressive stress during the Incaic Orogeny. B: gravitational collapse of the Domeyko Cordillera and superposition of the Rosario vein into the Rosario porphyry along a SW-dipping normal fault (modified from Masterman et al. 2005).

Cu, 0.015 % Mo and 0.1 g/t Au; Camus 2002). The district also contains high sulfidation epithermal copper-silver veins (including La Grande and Rosario), the intermediate sulfidation state Montcezuma epithermal silver vein system and the Huinquintipa exotic copper deposit.

Epithermal veins in the Collahuasi district have been mined since at least 1400 AD, with a peak of activity occurring between 1907 and 1920 (Moore and Masterman 2002). The porphyry potential of the district was not realised until the advent of modern exploration in the latter half of the twentieth century, and significant difficulties were encountered in bringing the mines into production. Claims staked in the late 1950s resulted in the discovery of the supergene-enriched Quebrada Blanca deposit in 1977 (production commenced in 1994). Subsequent exploration resulted in the discovery of Rosario in 1979 (first mined in 2002) and Ujina in 1991 (initial production in 1998).

4 Rosario porphyry Cu-Mo deposit

Alunite at the La Grande epithermal vein system, 2 – 4 km south of Rosario (Fig. 2), formed simultaneous with alunite at Rosario, based on a weighted mean plateau $^{40}Ar/^{39}Ar$ age of 32.7 ± 1.6 Ma (Masterman et al. 2004).

The K-feldspar-altered core at Rosario formed from hypersaline brines (40 to 45 wt. % NaCl) that coexisted with vapour between 400° and >600°C (Masterman et al. 2005). Weakly mineralised illite-chlorite (intermediate argillic) alteration was caused by moderate temperature (250° to 350°C), moderate salinity brines (10 to 15 wt. percent NaCl). These early-formed alteration assemblages were by structurally-controlled quartz-alunite-pyrite, pyrophyllite-dickite and muscovite-quartz (phyllic) alteration assemblages. The quartz-alunite-pyrite and pyrophyllite-dickite alteration assemblages formed from 250° to 400°C and 5 to 10 wt. percent NaCl fluids. Thick veins (0.5 to 2 m wide) of fault-hosted fluids. Thick veins (0.5 to 2 m wide) of fault-hosted fluids. Thick veins (0.5 to 2 m wide) of fault-hosted massive pyrite, chalcopyrite and bornite precipitated from 30 wt. percent NaCl brines at 250° to 300°C.

5 Discussion

At the Rosario porphyry deposit, high sulfidation state massive sulfide epithermal veins have been superimposed into the core of the porphyry system, resulting in significant hypogene upgrading of the porphyry proto-ore. This phenomenon is a feature common to the largest northern Chilean porphyry deposits (Chuquicamata, La Escondida). It produces 'reverse alteration zonation' with central domains of advanced argillic and phyllic alteration that have overprinted more laterally extensive potassic and propylitic alteration zones.

The Rosario porphyry was emplaced at 34.4 ± 0.4 Ma (Masterman et al. 2004). Potassic alteration and the mineralised quartz vein stockwork formed at depths of around 2km below the paleosurface, based on fluid inclusion results (Masterman et al., 2005). Exhumation of the porphyry system allowed for superposition of massive sulfide epithermal veins and advanced argillic alteration into the core of the porphyry system at 32.6 ± 0.3 Ma. The epithermal veins at Rosario formed at depths of approximately 600 m below the paleosurface, implying that at least 1 km of rock was eroded at Rosario over a period of approximately 1 m.y.

The Rosario Porphyry intruded immediately after the Incaic tectonic phase, implying that it was emplaced as the Domeyko Cordillera underwent gravitational collapse. Gravitational sliding along normal faults, such as the Rosario Fault, potentially accelerated exhumation and helped to promote telescoping of the high-sulfidation environment onto the Rosario Porphyry (Fig. 3).

This mechanism has proven highly effective at generating giant, high-grade hypogene resources throughout northern Chile, and should be a focus for exploration in other porphyry provinces.

Acknowledgements

The authors thank Compañia Minera Doña Inés de Collahuasi, Falconbridge and AngloAmerican for their generous financial and logistical support, and Renmin Hua for his scientific review. Thanks also to the sponsors and other research team members of AMIRA project P511.

References

Camus F (2002) The Andean porphyry systems: CODES Special Publication No. 4, University of Tasmania: 5-22

Cooke DR, Hollings P, Walshe JL (2005) Giant porphyry deposits – characteristics, distribution and tectonic controls: Economic Geology, v. 100 (in press)

Dick LA, Chavez WX, Gonzales A, Bisso C (1994) Geologic setting and mineralogy of the Cu-Ag-(As) Rosario vein system, Collahuasi District, Chile: Society of Economic Geologists Newsletter: 6-11

Hollings P, Cooke DR, Clark A (2005) Regional geochemistry of Tertiary igneous rocks in central Chile: implications for the geodynamic environment of giant porphyry copper and epithermal gold mineralization: Economic Geology, v. 100 (in press)

James D, Sacks IS (1999) Cenozoic formation of the Central Andes: A geophysical perspective: Society of Economic Geologists, Special Publication No 7: 1-25

Kay SM, Mpodozis C, Coira B (1999) Neogene magmatism, tectonism and mineral deposits of the Central Andes: Society of Economic Geologists, Special Publication No 7: 27-59.Lee AW (1994) Evolution of the Rosario copper-molybdenum porphyry deposit and associated copper-silver vein system, Collahuasi District, I Region, Northern Chile: Unpub. Masters thesis, Queens University, Kingston, Ontario, Canada: 75

Masterman G, Berry R, Cooke DR, Walshe JL, Lee AW, Clark AH (2005) Fluid chemistry, structural setting and emplacement history of the Rosario Cu-Mo porphyry and Cu-Ag-Au epithermal veins, Collahuasi district, Northern Chile: Economic Geology (in press)

Masterman GJ (2003) Structural and geochemical evolution of the Rosario Cu-Mo porphyry deposit and related Cu-Ag veins, Collahuasi district, Northern Chile: Unpublished PhD thesis, University of Tasmania, Tasmania, Australia: 253

Masterman GJ, Cooke DR, Berry RF, Clark AH, Archibald DA, Mathur R, Walshe JL, Duran M (2004) $^{40}Ar/^{39}Ar$ and Re-Os geochronology of porphyry copper-molybdenum deposits and related copper-silver veins in the Collahuasi district, northern Chile: Economic Geology, v. 99: 673-690

Moore RL, Masterman GJ, (2002) The geology and corporate discovery history of the Collahuasi district porphyry copper deposits, Chile: CODES Special Publication 4, University of Tasmania, Hobart, Australia: 23-50

Munchmeyer C, Hunt JP, Ware H (1984) Geología del Distrito de Collahuasi y del pórfido cuprífero Rosario: Internal Company Report: Compañia Doña Inés de Collahuasi, Santiago: 84

Copper mineralization in the western Longbohe area, SE Yunnan, China – a comparison with the Shengquan copper deposit, Vietnam

Yinliang Cui[1], **Dexian Qin**
Department of Land and Resource, Kunming University of Science and Technology, Kunming, 650093, China
[1]current address: Yunnan Nonferrous Geology Bureau, Kunming, 650051, China

Yaoguang Chen
Yunnan Nonferrous Geology Bureau Kunming, 650051, China

Abstract. This paper discusses the geological background, characteristics of copper mineralization, geophysical and geochemical characters of copper deposits in the Longbohe area, Jinping County, Yunnan province, China, and compares them with the Shengquan copper deposit in Vietnam. There are many similarities between Longbohe and Shengquan, This implies great potential for discovery of a large-size Shengquan-type copper deposit in the Longbohe area.

Keywords. Copper, Longbohe, Yunnan, China, Shengquan, Vietnam

1 Introduction

The Longbohe copper deposit is located in southeastern Yunnan Province, China, at the southern end of the Ailaoshan mountain range. Longbohe consists of two mineralization zones that are bounded by the Honghe fault. The host rocks in the eastern zone are a suite of intermediate-basic metavolcanics. The proven resource of copper metal in the eastern zone is 1 Mt at the Class of $333+334_1$ (Chinese Resource/Reserve Classification System). The western zone occurs at the southern end of the Ailaoshan metamorphic terrain and extends for 20 km within Ailaoshan metamorphic host rocks (Fig. 1). Little exploration has been done in the western zone, but it is thought to have good potential for a large-size copper deposit, because of similarities to the nearby Shengquan copper deposit in Vietnam (Fig. 1). Shengquan is a large copper deposit characterized by an association of Cu-Co-Ni-REE that occurs in the same mineral belt as Longbohe. Based on the data published by the Mine Bureau of Vietnam (ESCAP 1990; GIIMV 1990), the proven reserves of copper metal at Shengquan is 5.5 Mt with a grade of 0.5 to 11.58% Cu and an average grade of 1.03%. The deposit also contains 3.3 Mt REE, 34.42 tonnes gold, 25.3 tonnes silver and 8.4 Mt sulfur. This paper compares the characteristics of copper occurrences in the western Longbohe area with the Shengquan copper deposit.

2 Geological setting

The western Longbohe zone is hosted by Proterozoic rocks of the Wudoukeng Formation, which is part of the Ailaoshan Group. The formation contains sericite schist, marble, leucogranulite, biotite-plagioclase granulite, migmatite, felsic mylonite and gneiss. Structurally, this entire zone is a deformed syncline, cut by NW-trending faults. Granitoid intrusions have been emplaced along the Honghe fault. Biotite granite is predominant, and is typified by gneissic, mylonitic and granophyric textures.

The Shengquan copper deposit is located in Vietnam at Laojie, near the border with China. It is the largest copper deposit in Vietnam and occurs within the Fantuban Fe-Cu-REE mineral belt (Fig. 1). Proterozoic gneissic granite, schist and granulite host Shengquan. Most of the copper orebodies occur as banded sulfides parallel to the cleavage in the schists. Some copper also occurs in the form of veins and disseminated ores.

3 Copper mineralization

In the Longbohe area, several copper showings have been found on the Maocaoping, Daliangzi, Gongjishan and Longbohe riverbanks. Results of a stream sediment program at a scale of 1:100,000 indicate that the geochemical anomalies are zoned along a NW trend, and distributed extensively with an apparent anomalous center. The highest copper value detected is 1826 ppm, with an average of 374 ppm, the anomalous association is Cu-Co-Ni-REE. Together with the results of a surface magnetic survey and IP survey, a copper anomaly 7 km in length, 50 m in width and 400 m depth has been outlined.

3.1 West Longbohe copper zone

Results of exploration work has indicated that the western Longbohe mineralized zone is 2100 m long and 1.6 to 24.5 m thick, with copper grades of 0.54 to 9.91 %. The zone generally strikes NW and dips NE at an angle of 60-70°. The copper orebodies occur in a series of lens. The main metallic minerals are chalcopyrite, magnetite, pyrrhotite, pyrite, azurite and malachite. The host rocks are biotite amphibole granulite, migmatite, mica schist and lateritic rocks. The main rock type in outcrop is magnetite-bearing biotite amphibole granulite. Copper mineralization has been

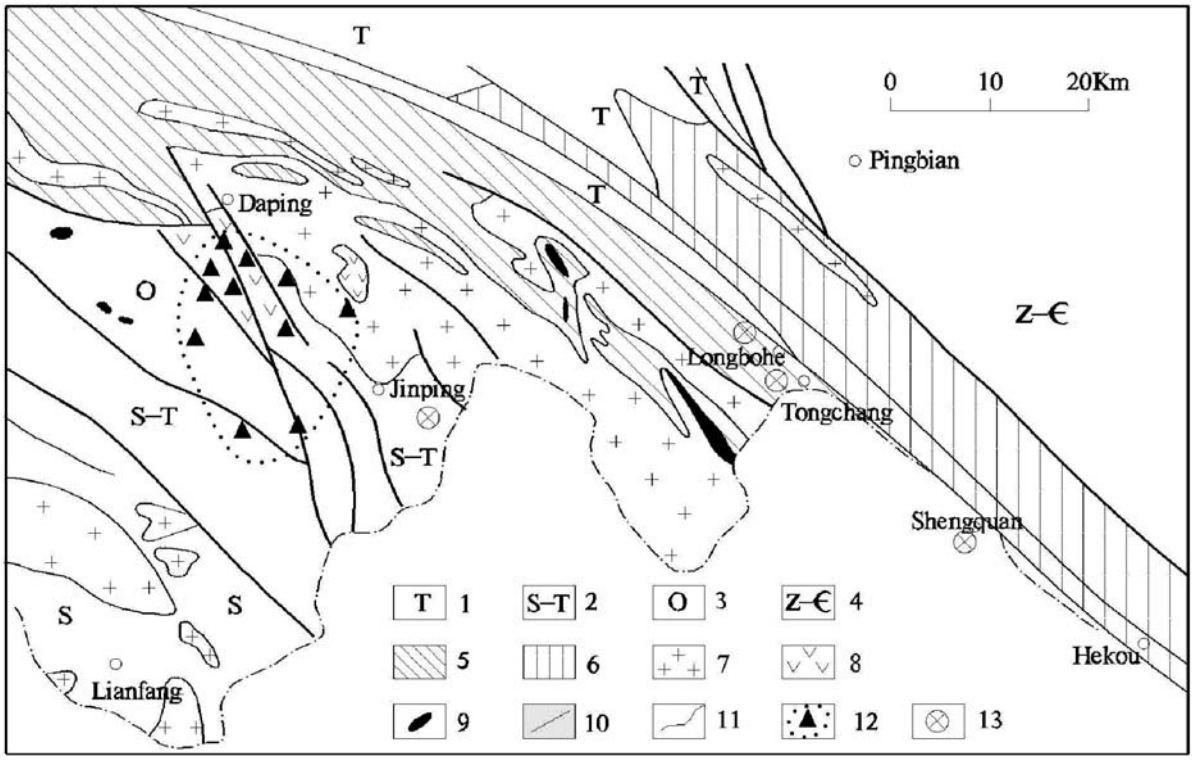

Figure 1: Geological map of the Fantuban Fe-Cu-REE mineral belt, Vietnam and China, showing the Longbohe area in Jinping, Yunnan. 1 – Triassic rocks. 2 – Silurian-Triassic rocks. 3 – Ordovician rocks. 4 – Sinian-Cambrian rocks. 5 – Proterozoic Ailaoshan Group. 6 – Proterozoic Yaoshan Group. 7 – granite. 8 – diorite. 9 – ultramafic rocks. 10 – fault 11 – stratigraphic boundary. 12 – gold deposit 13 – copper deposit.

classified into two types: banded copper ore, where chalcopyrite occurs parallel to the cleavage within the country rocks; and vein mineralisation, where chalcopyrite has infilled vertical fractures. Chang and Zhu (1996) inferred the presence of a large copper orebody at depth, based on lead isotope results.

3.2 Shengquan copper deposit

A total of three copper-mineralized zones, i.e., the East, Central and West zone, have been outlined over a strike length of 40 km at Shengquan and in the surrounding area. The known copper reserve is contained within the central zone, which strikes NW293-298° and dips NW at a angle of 70-80°. A total of 17 vein-type copper orebodies have been outlined in the central zone. The country rock is biotite plagioclase granulite. The main metallic minerals are magnetite, chalcopyrite and pyrite. The copper orebodies consist of a series of chalcopyrite-bearing lenses that are similar to those in the western Longbohe zone.

4 Geophysical characteristics

A high-precision surface magnetic survey and a dual-pole and dual-frequencies IP survey have been completed over the western Longbohe zone. These surveys covered an area of 10 km^2 at a scale of 1:20,000, with a grid of 200 m by 20 m. There is an apparent moderate-high magnetic anomaly coincident with the copper anomaly detected by stream sediment sampling. The frequency amplitude is 17% and the time-domain intensification at low-resistivity of 5Ω.m is 28.5%. The western Longbohe copper zone is inferred to be associated with a gentle positive magnetic anomaly at the surface, because it is thought to be more strongly mineralized at depth.

Table 1 compares the magnetic (deltaT) parameters of the measured rock specimens collected from the western Longbohe zone with samples from the Shengquan copper deposit. The main magnetite-bearing rocks are the biotite-plagioclase granulite in the western Longbohe zone and the copper ore samples in the Shengquan copper deposit. The highest magnetic value measured in the biotite-plagioclase granulite is 180 nT, whereas the maximum value obtained from the Shengquan copper ore is 21845 nT. In contrast, the granulite, gneissic granite and the weathered soil have weak magnetic responses.

Table 2 compares the electrical parameters measured from western Longbohe and Shengquan. From electrical parameters listed in Table 2, the frequency amplitude and the time-domain intensification of the biotite plagioclase

This page intentionally blank

Table 1: Magnetic (deltaT) parameters for the western Longbohe and Shengquan areas.

Area	Lithology	Samples	K ($4\pi.10^{-6}$ ST)		J (10^{-3} A/m)	
			Range	Mean	Range	Mean
West Longbohe	Copper-bearing biotite plagioclase granulite	15	57.5–57907.8	293.4	22.9–23676.5	220.5
	Plagioclase amphibole granulite	7	35.1–1073.8	326.5	17.4–339.5	100.4
Shengquan	Banded granulitic copper ore	3	104289.7–109510	106123.9	7052.2–12077.3	8296.6

Table 2: Electrical parameters for rocks from the western Longbohe zone and Shengquan copper deposit.

Area	Lithology	Samples	F_s%		ρΩsM	
			Range	Mean	Range	Mean
West Longbohe	Copper-bearing biotite plagioclase granulite	13	3.5 - 20.2	11.6	17 - 471	162
	Plagioclase amphibole granulite	7	0.1 - 1.4	0.7	191 - 1393	652
Shengquan	Banded granulitic copper ore	5	0.5 - 26.3	11.7	2377	48

granulite in the western Longbohe zone are 11.6% (Fs) and 162Ω.m (Ps), respectively. These compare favourably to those at Shengquan, i.e., 11.7% (Fs) and 48Ω.m (Ps). In the western Longbohe zone, there are apparent low resistivity and high frequency values in the biotite plagioclase granulite, carbonate-bearing migmatite and carbonate-bearing slate, which contrasts markedly with other rock types.

In summary, there are many similarities in the magnetic and electrical properties of rocks in the western Longbohe zone and at Shengquan.

5 Geochemical characteristics

5.1 Rare-earth elements

The REE contents of four samples collected from the western Longbohe zone and one sample collected from the Shengquan copper zone have been analyzed. Results indicate that the samples are all enriched in REE (SREE = 0.0075 to 1.36%), and are particularly enriched in LREE. LREE/HREE varies from 42 to 146. Plots of REE data show similar trends for both deposits. These results show that samples from the western Longbohe zone has same REE characteristics as the copper ores, granite, felsic vein and amphibolite in the Shengquan copper zone. Calculated Sm/Nd and dEu values are also similar for samples from both areas, which is consistent with a similar genesis for copper mineralization in both areas.

5.2 Lead isotopes

Based on the results of Sun et. al. (1996), copper ores from Shengquan have similar lead isotopic compositions to mineralized rocks from the western Longbohe zone. The lead isotope results are characterized by radiogenic lead, consistent with a similar source of lead in both systems.

6 Conclusions

The Proterozoic country rocks, structural setting and intrusions in the southern Ailaoshan belt are similar to those in northern Vietnam. The characteristics of minor mineral occurrences in western Longbohe are also similar to the major Cu-Co-Ni-REE-Au-Ag deposit at Shengquan. It is therefore concluded that there is good potential for the discovery of a large, Shengquan-style copper deposit in western Longbohe. As yet, no significant copper deposit has been found in western Longbohe. However, discovery of Fe-Cu showings on the Maocaoping and Gongjishan riverbanks is encouraging for continued exploration in the area.

References

ESCAP (1990) Atlas of Mineral Resources of the ESCAP. In: United Nations Economic and Social Commission for Asia and the Pacific in Cooperation with the General Department of Mines and Geology of Vietnam. Volume 6. Region: Vietnam Explanatory Brochure. Bangkok

Geological Institute under Industry Ministry of Vietnam. (1990) Geology of Laos, Vietnam and Cambodia, Hanoi: GSV, 1990. Vol. 2, No. 12

Sun DZ (1996) Assessment of the Potential for Prospecting the Copper Deposit in the Longbohe area, Eastern Yunnan, China. Guangzhou Geochemical Research Institute under China Academic Institute, 31-44

Yunnan Bureau of Geology and Mineral Resources (1990) Yunnan Regional Geology Bulletin. Geological Publishing House, 1-728

Sulfur isotope zonation at the Mt Polley alkalic porphyry Cu-Au deposit, British Columbia, Canada

C.L. Deyell
Centre for Ore Deposit Research, University of Tasmania, Private Bag 79, Hobart, Tas., 7001, Australia

Abstract. The Mt Polley alkalic porphyry deposit is located in the Quesnel terrane, British Columbia, Canada. A newly discovered mineralized zone (the NE Zone) is dominated by plagioclase and potassium feldspar–phyric intrusions and large zones of intrusion breccias. Sulfide mineralization is strongly zoned from a core of bornite outwards to a chalcopyrite halo and peripheral pyrite.

The goal of this study was to examine the sulfide sulfur isotope composition in the NE Zone to determine if any zonation is present. Previous studies at other alkalic porphyry deposits (e.g. Afton, Britise for Mt Polley. Results from this study indicate that $\delta^{34}S_{sulfide}$ values in the NE Zone are strongly negative, ranging from -1.1 to -7.0‰. There is a strong spatial zonation in the data, with minimum $\delta^{34}S_{cpy}$ values slih Columbia; Cadia District, NSW, Australia; Didipio, Philippines), have shown a systematic lateral and vertical zonation in $\delta^{34}S_{sulfide}$ data around a mineralized core. No similar data were previously availablghtly offset from the core of bornite mineralization, zoning outwards to less negative values. This zonation cannot be attributed to the effects of cooling alone and the data suggest that redox controls were significant during sulfide deposition.

Keywords. Mt Polley, alkalic, porphyry, sulfur isotopes, sulfides

1 Introduction

Mt Polley is a porphyry Cu-Au deposit located in the Quesnel terrane in south-central British Columbia, Canada (Fig. 1). The Mt Polley deposit was mined between 1997 and 2001, with a production of 27.7 Mt of ore from the Cariboo and Bell pits (Fig. 2). The property has been inactive since 2001, but it still contains an estimated 31.9 Mt of ore in the Bell and unexploited Springer deposits (Fig. 2; Imperial Metals; writ. comm. 2004). In August 2003, the discovery of the high-grade NE Zone (Fig. 2) by Imperial Metals initiated a major exploration and drilling program in the region. This led to the identification of several mineralized zones and on-going exploration continues to intersect significant copper and gold grades.

Mt Polley is characterized as an alkalic Cu-Au porphyry system due to its affiliation with alkalic igneous rocks (Fraser et al. 1995). Many of the world's best-known examples of alkalic Cu-Au porphyry deposits are located in B.C. (e.g. Mt Polley, Galore Creek, Afton/Ajax, and Copper Mountain). The Lachlan Fold Belt of New South Wales (Australia) is the other major alkalic porphyry province (e.g. Cadia, Goonumbla). Other isolated alkalic systems are known from the Philippines (Dinkidi), Greece (Skouries), and Colorado (Allard Stock).

Initial research in alkalic porphyry deposits of Australia and the Philippines suggests that a systematic sulfur isotopic zonation surrounds several mineralized complexes (e.g. Goonumbla and Cadia in NSW; Lickfold, 2002; Wilson 2003: Didipio in the Philippines; Wolfe 2001). These findings have significant implications for both the explora-

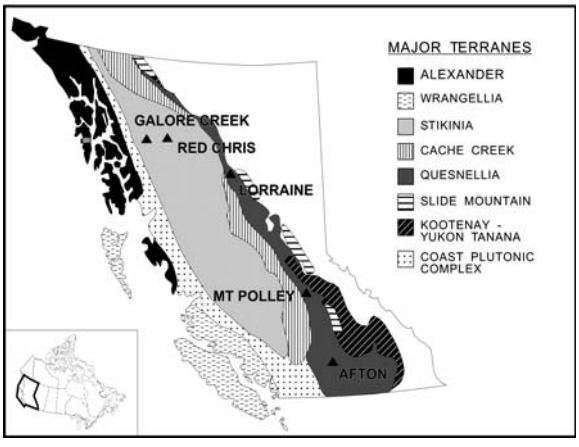

Figure 1: Map of British Columbia, Canada (see inset map for location) showing major terranes and selected alkalic porphyry Cu-Au deposits.

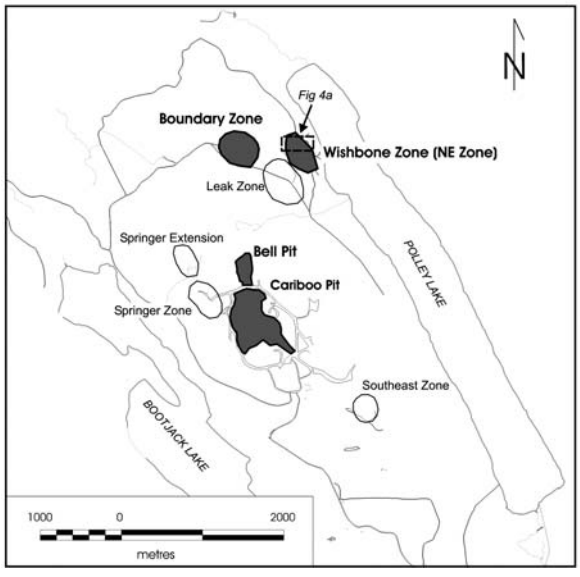

Figure 2: Map of the Mt Polley deposit showing locations of major mineralized zones. Approximate location of Figure 4a is indicated.

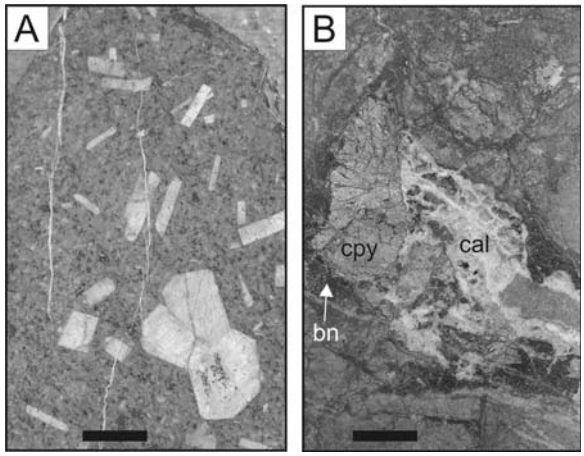

Figure 3: Photos of NE Zone Mt Polley drill core. A. K-feldspar megacrystic porphyry (DDH 04-26, 109.0m). B. Breccia-hosted bornite (bn) and chalcopyrite (cpy) mineralization overprinted by late calcite (cal) (DDH 04-29, 100.5m). Scale bars = 1 cm.

Table 1: Summary of Mt Polley $\delta^{34}S$ data (as per mil values).

	NE Zone*	Cariboo Zone**
Mean	**-4.1**	**0.2**
Max	-1.1	2.4
Min	-7.0	-2.3
1σ	1.0	1.0

* n=70 (60 chalcopyrite, 6 bornite, 4 pyrite)
** n=60 (53 chalcopyrite, 2 bornite, 5 pyrite)

tion and understanding the genesis of these deposits (Wilson et al. in press). Similar data are not available for many deposits in B.C. The goal of this study is therefore to determine the sulfur isotopic signature of sulfide minerals within the NE Zone of the Mt Polley deposit and establish whether a systematic zonation pattern can be identified.

2 Mt Polley deposit geology

The Mt Polley area is underlain by Jurassic and Triassic intrusive rocks of the Mt Polley intrusive complex (Fraser et al. 1995). This complex consists of multiple intrusions of diorite to plagioclase porphyry to monzonite compositions that intruded sedimentary and volcanic rocks of the late Triassic to early Jurassic Nicola Group (Fraser et al. 1995). The intrusions are associated with several igneous-cemented breccia bodies, as well as numerous hydrothermal breccias.

The geology of the NE zone is dominated by plagioclase and potassium feldspar–phyric intrusions that are locally megacrystic (Fig. 3a) In addition, there are lesser monzonite with late augite porphyry and mafic dykes. The Cu-Au mineralization in the Bell, Springer, and Cariboo zones

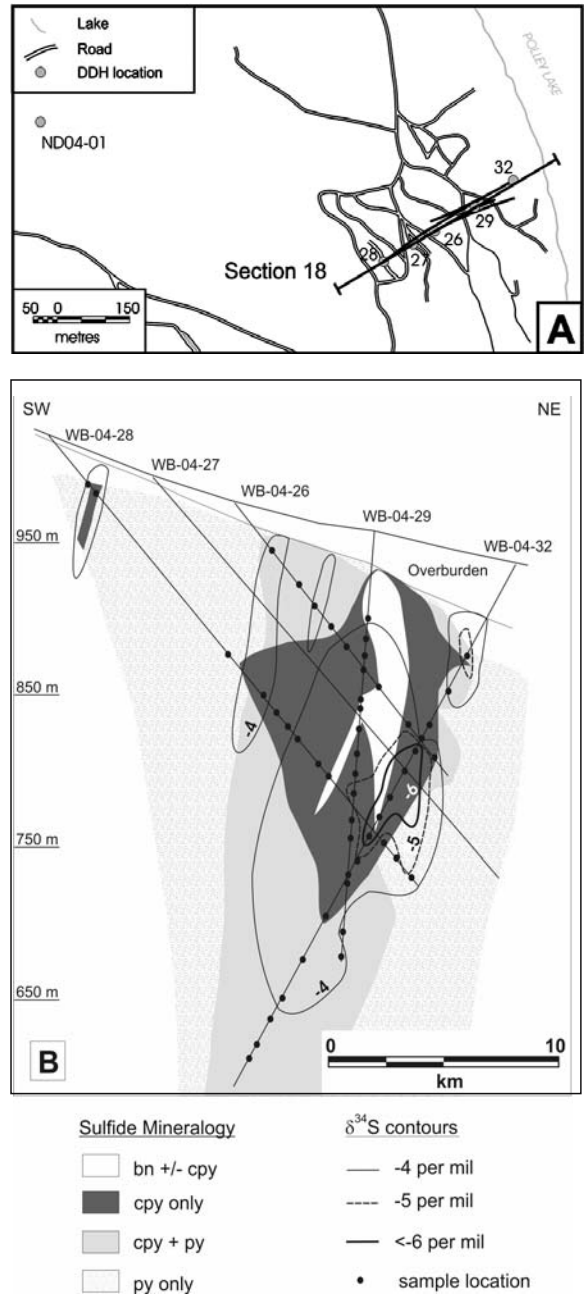

Figure 4: Schematic cross-section through the NE Zone, Mt Polley. A. General location of Section 18 (mine grid) across the NE Zone that was sample for this study. B. Sulfide mineral zonation and contours of $\delta^{34}S_{cpy}$ data from this study.

(Fig. 2) is spatially associated with igneous-cemented breccia that is heterolithic, matrix- to clast-supported, with an equigranular monzonite cement. Sulfide minerals are dominated by bornite, chalcopyrite, and lesser pyrite. The sulfides form coarse-grained clots, irregular veins, or fine disseminations overprinting the igneous cement and locally

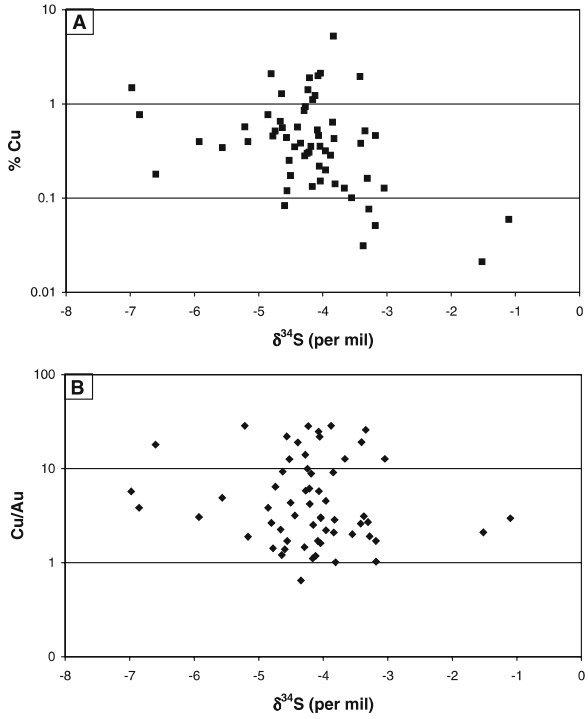

Figure 5: $\delta^{34}S_{cpy}$ data from NE Zone, Mt Polley. A. $\delta^{34}S_{cpy}$ vs. Cu grade (as %). B. $\delta^{34}S_{cpy}$ vs. Cu/Au ratios (Cu as %, Au as g/t).

breccia clasts as well (Fig. 3b). Sulfide minerals also occur in veins and as disseminations in coherent intrusive phases. A sulfide zonation was recognized in cross-section with a core of bornite±chalcopyrite, rimmed by chalcopyrite-dominant sulfide assemblages, with pyrite ± chalcopyrite at the margins (Fig. 4).

Alteration in the NE Zone (K Ross; writ. commun. 2004) consists of an early, pervasive, potassium metasomatism associated with little to no biotite. A distinct magnetite-garnet-apatite assemblage is pre- to syn-mineral. This assemblage may overlap with a slightly later syn- to post-mineral assemblage dominated by a Ca-Al silicate (clinozoisite or prehnite?) and is associated with albite-calcite, lesser garnet, and minor diopside (K Ross; writ. commun. 2004). Late alteration consisting of calcite-sericite-albite-chlorite is widespread. Chlorite-carbonate-pyrite alteration is rare but is locally peripheral to the brecciated zones and occurs within the country rocks to the east of the main mineralized centre.

3 Sulfur isotope study

Sampling for this study was focused along one cross-section through the core of the NE zone (Section 18; Fig. 4). Sulfides were selected from diamond drillhole (DDH) samples collected on-site at Mt Polley and were extracted manually using a hand-held drill (Dremel tool). Sulfur isotopic analyses were completed at the U.S. Geological Survey (USGS) Isotope Laboratory in Denver (Colorado, U.S.A.). Samples were analyzed using an on-line method with an elemental analyzer coupled to a Micromass Optima mass spectrometer following the method of Giesemann et al. (1994). Analytical uncertainties are estimated at ±0.1 per mil (‰.).

Analytical results are summarized in Table 1. Samples from the NE Zone consisted mostly of chalcopyrite with lesser pyrite and bornite, and have $\delta^{34}S_{sulfide}$ values ranging from -1.1 to -7.0‰. Table 1 also gives a summary of $\delta^{34}S_{sulfide}$ data for the Cariboo and Bell deposits (details see Deyell and Tosdal, 2005).

The $\delta^{34}S_{sulfide}$ data from the NE Zone are on average significantly more negative than data from the Cariboo and Bell deposits. In cross-section (Fig. 4b), $\delta^{34}S_{cpy}$ values are strongly zoned with minimum values concentrated at depth to the E-NE, slightly offset from the core of bornite mineralization. The more negative $\delta^{34}S$ values are spatially associated with igneous-cemented breccia, although a range of values is recognized through this unit.

A comparison of $\delta^{34}S_{cpy}$ with metal values shows a general trend of increasing Cu grade with more negative $\delta^{34}S$ values (Fig. 5a). In contrast, there is a relatively constant relationship between $\delta^{34}S_{cpy}$ values and Cu/Au ratios (based on 2m assay intervals; Fig. 5b) although significant scatter is present in the dataset.

4 Discussion and conclusions

The NE Zone at Mt Polley is characterized by a strong sulfide mineral zonation with a core of bornite rimmed by chalcopyrite and peripheral pyrite. This mineralogical zoning coincides broadly with a sulfur isotope zonation, with low $\delta^{34}S_{sulfide}$ values (-5 to -7‰) in the core of the deposit (although slightly offset from the bornite mineralization). The $\delta^{34}S_{sulfide}$ zonation recognized at Mt Polley is comparable to several other alkalic porphyry deposits (e.g., Afton, Deyell and Tosdal, 2005; Goonumbla, Lickfold, 2002; Cadia District, Wilson et al. in review). This zonation pattern, with more negative values in the core of the deposit zoning outwards to more positive values, cannot simply be explained by sulfide deposition via cooling (cooling would produce an opposite trend; Rye, 1993). Instead, this pattern suggests that redox controls were significant during sulfide deposition and the observed zonation could be produced by the progressive reduction of sulfate-rich, metal-bearing fluids outwards from the deposit core. The recognition of a systematic sulfur isotope zonation at Mt Polley, in addition to the other porphyry deposits mentioned above, has implications for the exploration of Cu-Au alkalic systems and may help explorers to better predict the proximity to a high-grade core.

Acknowledgements

This project was funded through the Rocks to Riches program (managed by B.C. and Yukon Chamber of Mines) and special thanks are extended to Imperial Metals (Patrick McAndless, Leif Bjornson and the Mt Polley exploration crew). Additional assistance by R. Tosdal, S. Ebert, D. Cooke, and K. Ross is gratefully acknowledged. Special thanks to R. Rye and C. Bern (USGS) for the sulfur isotope analyses. Reviews and editorial handling by SGA session conveners (D. Cooke, F. Pirajno, J. Walshe) are thankfully acknowledged.

References

Deyell CL, R Tosdal (2005) Sulfur Isotopic Zonation in Alkalic Porphyry Cu-Au Systems: Applications to Mineral Exploration in British Columbia. B.C Ministry of Energy and Mines, Geological Fieldwork Vol 2004: 191-208

Fraser TM, CR Stanley, ZT Nikic, R Pesalj, D Gorc (1995) The Mount Polley alkalic porphyry copper-gold deposit, south-central British Columbia. In: Porphyry Deposits of the Northwestern Cordillera of North America, T.G. Schroeter (Ed.), Canadian Institute of Mining and Metallurgy (CIMM) Special Vol 46: 609-622

Giesemann A, HJ Jager, AL Norman, HR Krouse, WA Brand (1994) Online sulfur-isotope determination using and elemental analyzer coupled to a mass spectrometer. Analytical Chemistry 65: 2816-2819

Lickfold V (2002) Volatile evolution and intrusive history at Goonumbla, central western NSW. Unpub. PhD, University of Tasmania, Australia: 243

Ross KV (2004) Alteration study of the Northeast Zone, Mount Polley Mine, British Columbia. Report prepared for Imperial Metals Corporation: 23

Rye RO (1993) The evolution of magmatic fluids in the epithermal environment; the stable isotope perspective. Economic Geology 88: 733-752

Wilson A (2003) The genesis and exploration context of porphyry Cu-Au deposits in the Cadia district, NSW. Unpub PhD, University of Tasmania, Australia: 335

Wilson A, DR Cooke, BJ Harper, CL Deyell (in review) Sulfur isotope zonation in the Cadia district, NSW: Exploration significance and implications for the genesis of alkalic porphyry copper-gold deposits. Mineralium Deposita.

Wolfe RC (2001) Geology of the Didipio region and paragenesis of the Dinkidi Cu-Au porphyry deposit. Unpub PhD, University of Tasmania, Australia: 200 p.

Genesis of regionally metamorphosed skarns from the Bohemian Massif: Contact metasomatic versus sedimentary-exhalative

P. Drahota, Z. Pertold, M. Pudilová
Institute of Geochemistry, Mineralogy and Mineral Resources, Charles University, Albertov 6, Prague 2, 128 43, Czech Republic

Abstract. Several skarns were studied in the northern part of the high-grade Moldanubian zone, Bohemian Massif (Czech Republic). Three different kinds of skarn were distinguished on the basis of their host environment, and their mineralogical and isotopic compositions. Regionally metamorphosed skarns reflect post-peak metamorphic decompression after high pressure-high temperature regional metamorphism (approximately 800°C and 12 kbars) and younger regional metamorphism (670°C, 6-8 kbars) accompanied by intrusion of an orthogneiss body. Analysed d18O values from the skarn minerals are not compatible with a post-peak metamorphic contact metasomatic origin associated with emplacement of the orthogneiss. The skarn precursors are interpreted to have been an integral part of the primary (volcano-) sedimentary successions in these Moldanubian localities, and a submarine exhalative origin is inferred.

Keywords. Skarn, geothermobarometry, oxygen isotopes, metamorphism

1 Introduction

Skarn is a relatively simple rock type defined by its mineralogy, which reflects the physical and chemical stability of the constituent minerals rather than implying any particular geological setting or protolith composition (Einaudi et al. 1981). Although most are found adjacent to plutons, they also occur along faults and major shear zones, in shallow geothermal systems and at lower crustal depths in deeply buried metamorphic terranes.

Skarn bodies of the Variscan Bohemian Massif occur in the highest-grade metamorphic units. They have been regionally metamorphosed, together with their host rocks (gneisses), to amphibolite, granulite and eclogite facies. Because of a very complex metamorphic history of these geological units, it is difficult to decide, if skarn precursors were a part of sedimentary series (e.g. Pertold et al. 1997, Drahota et al. 2005) and therefore metamorphosed during all events, such as "classic" skarns of the Bergslagen District, or if they originated during later events, as contact skarns (e.g. Nemec 1991) in association with metagranitoids or migmatites.

The aim of this paper is to discuss the origin of the Holsice, Zliv and Vápenka skarns in the Moldanubicum (Bohemian Massif) on the basis of their geologic situation, mineral composition, metamorphic history and isotopic composition, and to contribute to the interpretation of skarns in high-grade terranes in general.

2 Geologic setting

Moldanubicum is the most complicated unit of the Bohemian Massif, with protolith ages from 2.05 Ga to Lower Paleozoic. The Holsice, Zliv and Vápenka skarns are believed to be located in the uppermost tectonic unit (Gföhl terrane), which comprises predominantly lower crustal rocks with mantle-derived units in its basal portions and also acidic gneisses of Paleozoic protolith ages (e.g. Neubauer and Handler 2000). While most of the gneisses and amphibolites have been retrogressed to different degrees, some granulite, eclogite and ultramafic rocks contain evidence for high pressure-high temperature (HP/HT) metamorphic equilibration.

The study area has been described in detail by Drahota et al. (2005). It consists of biotite-sillimanite paragneiss and a leucocratic two-mica Kácov orthogneiss body, probably of Variscan age, accompanied by migmatites. The complex is intercalated with layers and bands of quartzite gneisses, and abundant calc-silicate rocks, which contain sporadic marbles and skarns. In an area encompassing approximately 3 km^2, there are three types of skarn occurrences that have been distinguished according to their geological settings and their mineralogical and isotopic compositions.

The first skarn type includes layers and lenses enclosed in calc-silicate gneisses. Together, they form the Holsice skarn body, which is located in the footwall of the Kácov orthogneiss body. Banded garnet-clinopyroxene skarn contains quartz, feldspar, epidote and titanite as accessory minerals. The dominant rock type within the Holšice body is banded calc-silicate gneiss, consisting of feldspar, quartz, garnet, pyroxene and amphibole, with titanite, hisingerite and epidote as minor and accessory minerals.

The second skarn type is typified by the Zliv skarn body. It occurs in migmatized paragneisses, close to one of the apophyses of the orthogneiss body. Similarly to other skarn localities of the Bohemian Massif (Nemec 1991), the oldest metamorphic association in the Zliv skarn consists of andradite and hedenbergite with minor magnetite in massive garnet-clinopyroxene skarn, which occurs mostly within the central part of the skarn body. This rock gradually passes into granoblastic garnet-amphibole skarn or amphibole skarn towards the margins

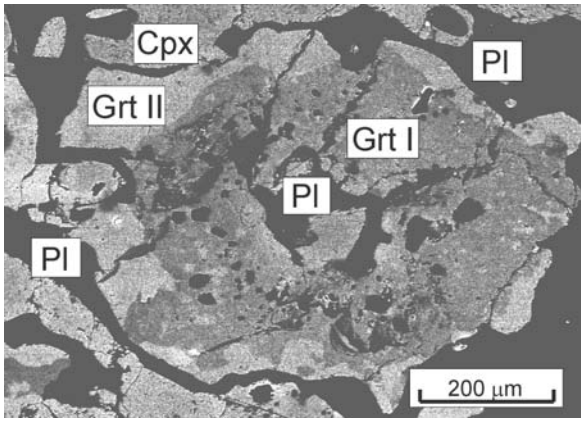

Figure 1: BSE image of calc-silicate gneiss with garnet (Grt) and clinopyroxene (Cpx) from the Holšice skarn. A younger Ca-depleted Grt II (light-colored) occurs along contact with plagioclase (Pl).

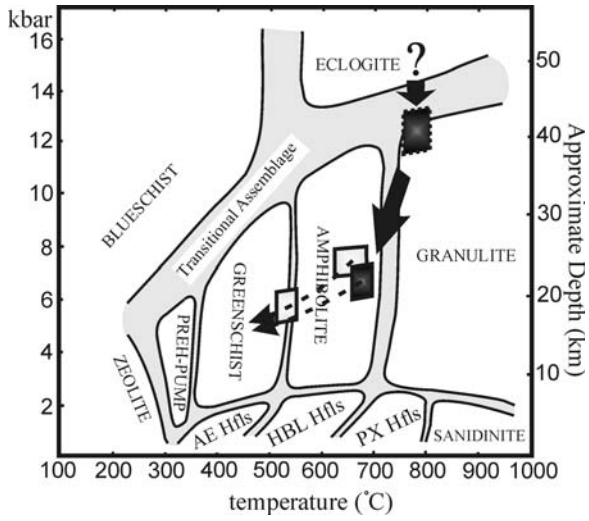

Figure 2: P-T diagram illustrating the retrograde PT path of skarns (dark grey) and surrounding gneisses (light grey) from the Holsice and Zliv localities.

of the skarn body. Magnetite mineralization is bound mainly to the massive clinopyroxene skarn and partly to local cummingtonite skarn. In very rare cases, garnet-amphibole gneiss was found as a several-cm-thick reaction rim between the garnet-amphibole skarn and the surrounding migmatites.

The third skarn type is characterized by a small skarn band at Vápenka. This calc-silicate band (4-8 cm wide) locally contains a mineral assemblage corresponding to garnet-amphibole skarn, which has formed at the contact between marble and the Kácov orthogneiss. The main minerals are quartz, feldspar, amphibole and spessartine-almandine garnet. Scheelite and sulfides are minor minerals.

3 Mineral chemistry and metamorphic history

Clinopyroxene in the Holšice and Zliv skarns belongs to the diopside-hedenbergite series. Al and Na contents are low, and exhibit slight depletion towards the rims in the calc-silicate gneiss of the Holsice skarn (especially in association with plagioclase and garnet).

No compositional zoning has been found in almandine-grossular garnets from the Holsice garnet-clinopyroxene skarn, in contrast to garnet from the calc-silicate gneiss. Although Ca contents are high in the red interiors of garnets from the Holsice calc-silicate gneiss, X-ray imaging (Fig. 1) indicates a distinct drop in Ca content adjacent to large plagioclase inclusions and intergranular plagioclase (between garnet and clinopyroxene).

Plagioclase in the Holsice calc-silicate gneiss has a broad range of compositions (An_{20-41}). Inclusions in garnet and in the intergranular aggregate between garnet and clinopyroxene show a slightly more calcic composition (An_{32-44}).

Of all the garnet-clinopyroxene skarn and calc-silicate gneiss samples studied, only a few of the gneiss samples correspond to the chemical conditions recommended for geothermobarometers by Ravna (2000) and Kohn and Spear (1990). Calculated temperatures and pressures range 760-810 °C and 11.5-13.4 kbars, corresponding to high-grade metamorphic conditions of the Holšice skarn. The equilibration temperature of Ca-rich ferro-actinolite with abundant cummingtonite exsolution-lamellae in amphibole skarn of the Zliv skarn (based on Cameron 1975) is in reasonable agreement with the restricted temperature range of 670-690 °C calculated for the garnet-amphibole skarn (Zliv locality) using the Graham and Powell (1984) thermometer. Also the estimated pressures of 6.0-6.5 kbars by the garnet-plagioclase-amphibole-quartz geobarometer (Kohn and Spear 1990) well describe the metamorphic mineral association of the Zliv marginal skarn rocks.

Formation temperatures and pressures of approximately 640°C and 6.8-8.0 kbars have been determined for the paragneisses and the Kácov orthogneiss. These correspond to the PT conditions of the marginal parts of the Zliv skarn body (Fig. 2).

Retrograde metamorphism is apparent from biotite II growth, formation of chlorite at the expense of biotite, and garnet zoning similar to the youngest zoning in garnets of Holsice calc-silicate gneiss. Retrograde metamorphic conditions are estimated to have been approximately 540°C and 5.3-6.3 kbars.

4 Oxygen and carbon isotopes

The $\delta^{18}O$ values for the skarn minerals are systematically lower than those for minerals of the surrounding rocks. (Fig. 3). Minerals from the Vápenka skarn band are enriched in ^{18}O, which is consistent with the isotopic composition of the orthogneiss (Fig. 3).

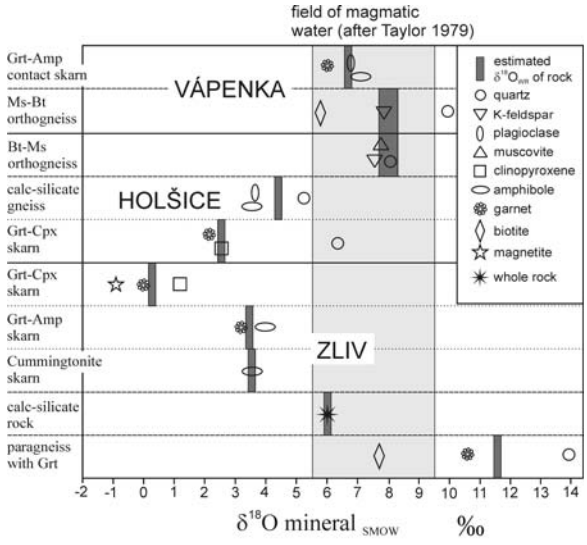

Figure 3: $\delta^{18}O$ values for minerals and rocks from skarns, orthogneisses, and surrounding paragneiss of the study area.

At the Vápenka site, $\delta^{18}O$ and $\delta^{13}C$ isotopic compositions were analyzed over a short profile of the marble from the contact with the garnet-amphibole skarn band. The values ($\delta^{18}O_{SMOW}$ = +14.8‰ and $\delta^{13}C_{PDB}$ = –2.9 ‰) inside the marble correspond to regionally metamorphosed limestone of Upper Proterozoic to Palaeozoic age (Taylor 1979).

5 Discussion and conclusions

Based on their geological environments, the Holsice and the Zliv skarn bodies seem to be an integral part of the more regionally extensive calc-silicate layers in the paragneiss unit. Isoclinal folds of decimetre dimensions in banded skarn of the Holsice body preserve older structures than the ductile fabrics in the surrounding paragneisses. At Vápenka, only a narrow band (cm) of calc-silicate rock, which locally passes into thicker skarn, was found at the direct contact of orthogneiss with a lens of marble.

The Holsice and Zliv skarn bodies underwent HT/HP metamorphism. This is indicated by zonation and chemical composition of garnet, clinopyroxene and plagioclase in the calc-silicate gneisses of the Holšice skarn body, which are characterized by post-peak decompression conditions of 760-810°C and 11.5-13.4 kbars (Fig. 2). There is an apparent similarity of the metamorphic evolution with high-pressure granulites of the Bohemian Massif (e.g. Cook et al. 2000). Numerous fractures in the analyzed garnets occur close to plagioclase inclusions. These connected the inclusions with the matrix, allowing participation of matrix phases (clinopyroxene + quartz) in decompression-driven reactions. The prograde growth zonation in garnet grains is not preserved, because increased diffusion rates during the assumed HT/HP metamorphism led either to the growth of chemically homogeneous garnet or to elimination of previously developed zoning. The subsequent metamorphism in the amphibolite facies at 640-690°C and 6-8 kbar fully affected the metasediments of the paragneiss unit, but affected the skarn bodies only in their border zone. This metamorphic event was accompanied by intrusion of the Kácov orthogneiss body, the related migmatization of the surrounding gneisses and the invasion of younger fluids into the border zone of the skarn bodies. A further metamorphic retrogression (to ~ 540°C and 5-6 kbar) is reflected in the spessartine component enrichment in rim zones of garnets in skarns and gneisses, the formation of biotite II in gneisses, and epidote with albite in the skarn.

Genetic relationships are well-established between certain types of skarn mineralization and various types of granitoid rocks (Meinert 1993). This does not mean, however, that the magnetite skarn at Zliv and the Fe-rich skarn at Holsice must be related genetically to the neighboring Kácov orthogneiss body. Instead, the orthogneiss chemistry is compatible with the scheelite-bearing Vápenka skarn band (Drahota et al. 2005).

The $\delta^{18}O_{WR}$ values of garnet-pyroxene skarn rocks at Holsice and Zliv range from +0.3 to +2.7‰. These low values cannot have resulted from high-temperature metasomatism of the marble by solutions derived from the nearby orthogneiss. Elevated $\delta^{18}O_{WR}$ values in the marginal skarn rocks at Zliv and in the calc-silicate gneiss at Holsice are interpreted to reflect elevated ^{18}O contents in the protolith. Retrograde metamorphic solutions, which influenced the peripheral parts of the skarn body, may have also caused some ^{18}O enrichment. The skarn band at Vápenka has an overall $\delta^{18}O$ composition of 6.8 ‰, consistent with the whole-rock composition of the neighboring orthogneisses, (7.5 to 8.3‰; Fig. 3). This band of skarn and calc-silicate rock appears to have formed at high temperature in isotopic equilibrium with the orthogneiss.

The temperature and pressure conditions of regional metamorphism were not relevant to primary mineral formation in the Holsice and Zliv skarns. Furthermore, their ^{18}O compositions are not consistent with skarn formation from fluids derived from the adjacent orthogneiss body or migmatites. Consequently, we interpret the precursors of the Holsice and Zliv skarn bodies to have been an integral part of the paragneiss unit prior to HP/HT metamorphism. Because of their abnormal chemical and mineral compositions, geological settings and oxygen isotope compositions, the skarn protolith may have had a submarine exhalative origin. Consequently, the Holsice and Zliv skarns probably represent rare examples of high-grade skarn of regionally metamorphic origin. This study indicates that garnet-clinopyroxene skarns in high-grade terranes are likely to preserve old structures and mineral assemblages. Their oxygen isotopic signature, due to low diffusion rate in garnet and clinopyroxene, survived metamorphic events and is an important guide for discrimination between a metasomatic and sedimentary-exhalative origin.

References

Cameron KL (1975) An experimental study of actinolite-cummingtonite phase relations with notes on the synthesis of Fe-rich anthophyllite. Am Mineral 60: 375-391

Cooke RA, O'Brien PJ, Carswell DA (2000) Garnet zoning and the identification of equilibrium mineral compositions in high-pressure-temperature granulites from the Moldanubian Zone, Austria. J Metamorphic Geol 18: 551-569

Drahota P, Pertold Z, Pudilová M (2005) Three types of skarns from Holšice (northern part of the Moldanubian Zone, Bohemian Massif)-implications for their origin. J Czech Geol Soc (in print)

Einaudi MT, Meinert LD, Newberry RJ (1981) Skarn deposits. Econ Geol 75th Anniversary Volume: 317-391

Graham CM, Powell R (1984) A garnet-hornblend geothermometer: calibration, testing, and application to the Pelona schist, Southern California. J Metamorphic Geol 2(1): 13-31

Kohn MJ, Spear FS (1990) Two new geobarometers for garnet amphibolites, with applications to southern Vermont. Am Mineral 75: 86-96

Nemec D (1991) Regional typization of the iron skarns of the Bohemian–Moravian Heights (Ceskomoravská vrchovina). Acta Musei Moraviae 76: 51-82

Neubauer F, Handler R (2000) Variscan orogeny in the Eastern Alps and Bohemian Massif: How do these units correlate? Mitt Österr Geol Ges 92:35-59

Pertold Z, Pertoldová J, Pudilová M (1997) Metamorphic history of skarns in the Gföhl unit, Moldanubicum, Bohemian Massif, and implications for their origin. Acta Univ Carolinae–Geologica 41(3-4): 157-166

Ravna EJK (2000) The garnet – clinopyroxene Fe^{2+} – Mg geothermometer: an updated calibration. J Metamorphic Geol 18: 211-219

Taylor HP (1979) Oxygen and hydrogen isotope relationships in hydrotermal mineral deposits. In: Barnes HL (ed) Geochemistry of hydrotermal ore deposits. Wiley, New York, pp 236-277

Sm-Nd isotope dating of fluorites from the Xiangquan thallium deposit, Anhui Province, East China

Y. Fan, T.F. Zhou, F. Yuan
School of Resources and Environment Engineering, Hefei University of Technology, Hefei 230009, China

M.A. Wu, M.J. Hou
Academy of Geological Survey of Anhui Province, Hefei 230001, China

G. Voicu
Department of Earth and Atmospheric Sciences, University of Quebec at Montreal (UQAM), Canada

Q.H. Hu, Q.M. Zhang
327 Geological Team, Geological Bureau of Anhui Province, Hefei 23000, China

Abstract. The Xiangquan thallium (Tl) deposit is the first example of a thallium-only deposit in the world. It is located in Anhui province, in the northeast margin of the Yangtze block, east China. Sm–Nd isotopic compositions of early- and late-stage fluorites in the deposit fall on two well-defined lines on an isochron plot, with isochrons corresponding to 131.9 ±2.6 and 79 ±9.7 Ma. The isochron ages suggest that thallium mineralization took place in the Early Cretaceous period. The thallium deposit was subsequently altered by hot spring activity in the Late Cretaceous period.

Keywords. Sm-Nd isotope dating, fluorite, thallium, China

1 Geological setting

The Xiangquan thallium (Tl) deposit is located in the transition zone between the Yangtze and North China Blocks. Magmatic activity is minor in this region and sedimentary rocks predominate. The foreland fold-thrust belt trends northeast and consists of several thrust-detachment systems. The fold-thrust belt is divided into the eastern (Hanchao) and the western (Chouzhou) sub-belt by the Chu River fracture (Chang and Dong 1996). The deposit occurs in the middle part of the Xiaolongwang Mountain anticline. Only the southwest limb of the anticline crops out at the surface. The major stratigraphic units in the Xiangquan district are Lower Ordovician Honghuayuan Group, Lunshan Group and Lower Silurian Gaojiabian Group (Wu, 2000). The host rocks of the orebodies are calcilutite of Lunshan Group. Orebodies are conformable with the country rocks. The ores are dominated by Tl-rich pyrite, and by thallium-bearing minerals such as lorandite ($TlAsS_2$), hutchinsonite ($TlFeS_2$) and avicennite (Tl_2O_3). The gangue minerals include fluorite, quartz, calcite and barite. Hydrothermal alteration includes pyritization, silicification, fluoritization, carbonation, and baritization.

The fluorite in the deposit can be classified into two stages. The early stage (main mineralization stage) fluorites are purple, white and yellow, fine grained fluorites that coexist with pyrite and thallium minerals, while the late stage fluorites are white, canary yellow or transparent, large crystal fluorites that commonly occur in cavities and fractures. Veins containing late stage fluorites have cut early stage fluorites and pyrite.

2 Results and discussion

Based on field observations, and textural and microscopic observations, ten fluorite samples were selected for Sm-Nd isotopic analyses. Fluorites chips were cut from hand specimens and lightly crushed to 0.3 to 0.5 mm in size, and then the separated pure fluorites were handpicked under a binocular microscope. Finally they were crushed to 200 mesh in an agate mortar. All the specimens analyzed in this study were collected from drill cores. Isotope ratio measurements were taken on a MAT-261 mass spectrometer at Tianjin Institute of Geology and Mineral Resources, CAGS.

Two stages of fluorites display remarkable differences in Nd concentrations, $^{147}Sm/^{144}Nd$ and $^{143}Nd/^{144}Nd$ ratios. For the early stage fluorites, the Nd abundances are obviously higher than those for the late stage fluorites, and the $^{147}Sm/^{144}Nd$ and $^{143}Nd/^{144}Nd$ ratios of the late stage of fluorites are remarkably higher than those of the early fluorites. In the $^{147}Sm/^{144}Nd$–$^{143}Nd/^{144}Nd$ diagrams, the fluorites from the early and late-stage, respectively, display a good linear relationship (Figs. 1 and 2), which probably represents an isochron or a mixed line with two end-members with different $^{147}Sm/^{144}Nd$ and $^{143}Nd/^{144}Nd$ ratios. Because no linear relationships exist in the 1/Nd–$^{143}Nd/^{144}Nd$ diagrams for the early stage fluorites or the late stage fluorites, we can rule out the possibility of mixing. Early fluorites have an isochron slope corresponding to an age of 131.9 ±2.6 Ma and an intercept of 0.5112808 ±0.0000069 (initial = -23.2), the mean square of weighted deviates (M.S.W.D) is 0.43 (Fig.1). The late stage fluorites define a slope corresponding to an age of 79 ±9.7Ma and an intercept of 0.5120651 ±0.0000071 (initial ε_{Nd} = -9.2); the M.S.W.D is 0.035 (Fig. 2).

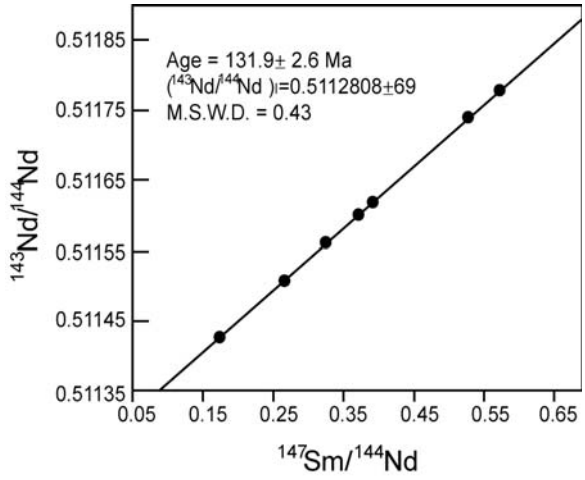

Figure 1: Sm–Nd isochron for the early stage fluorites from the Xikuangshan deposit.

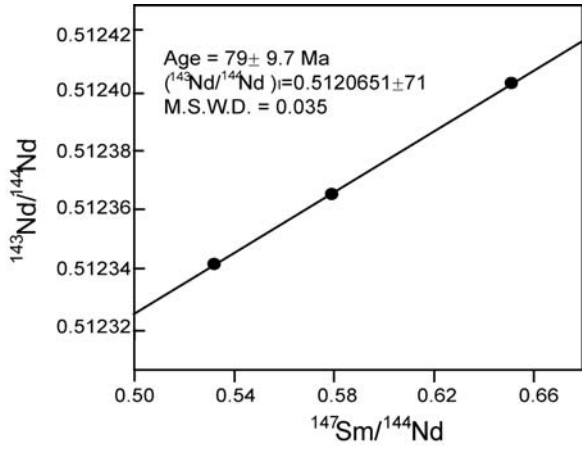

Figure 2: Sm–Nd isochron for the late stage fluorites from the Xikuangshan deposit.

It is noticeable that the initial ε_{Nd} values for the two regression lines are different (-23.2 and -9.2, respectively). The initial $^{143}Nd/^{144}Nd$ value of early stage fluorites is close to those of the host rocks of Lunshan Group. This may indicate that the Nd in the ore-forming solution originated from the host sedimentary rocks. The initial $^{143}Nd/^{144}Nd$ value of the late stage fluorites is close to those of the underlying intrusive bodies (Wu 1997), suggesting some genetic association; e.g. the Nd was possibly leached from underlying intrusions by deeply circulating hot spring-waters.

C, O and Sr isotopic and REE data studies (Fan et al. in press) also indicate that early and late stage fluorites from the Xiangquan deposit were probably precipitated from different hydrothermal solutions, Their data show that there were two hydrothermal systems and that the main thallium mineralization took place in Early Cretaceous period followed by hot spring alteration in Late Cretaceous period.

It is well known that copper (iron)-gold deposits in the Middle and Lower reaches of the Yangtze River metallogenic belt in the northeast margin of the Yangtze block mostly formed during the Mesozoic Yanshanian period (137 ±5 Ma; Zhai et al. 1992; Pan et al. 1999; Zhou et al. 2000; Mao et al. 2004). A copper skarn deposit located 50km east of Xiangquan has been dated at 137 Ma (Zhai et al. 1992). The main age of thallium mineralization at Xiangquan (131.9 ±2.6 Ma) indicates that this episode of thallium mineralization occurred soon after copper (iron)-gold skarn mineralization in the Middle and Lower reaches of the Yangtze River.

Thallium is a diagnostic trace element for gold exploration. Thallium and gold have similar physicochemical characteristics in low temperature solutions and they can be transported together (Sobott 1987). The occurrence of thallium is used as a favourable pathfinder for epithermal mineralization, and may help to detect epi-thermal metallogenic provinces (Jankovic 1989). The discovery of the Xiangquan thallium deposit may indicate the existence of an epithermal metallogenic event of late Yanshanian age in the district, and elsewhere in the Yangtze Block.

3 Conclusions

Our main conclusions are as follows:

1. Main stage fluorites at Xiangquan define a Sm–Nd isochron age of 131.9 ±2.6 Ma (ε_{Nd} = -23.2, M.S.W.D. = 0.43), while late stage fluorites define a Sm–Nd isochron age of 79 ±9.7 Ma (ε_{Nd} = -9.2, M.S.W.D. = 0.035). These two Sm–Nd isochron ages indicate that thallium mineralization at Xiangquan took place initially during the Early Cretaceous period, with modification via hot spring alteration in the Late Cretaceous.
2. The Xiangquan thallium deposit is the first example of a Tl-only deposit reported from anywhere in the world. This deposit formed soon after copper (iron)-gold skarn mineralization in the Middle and Lower reaches of the Yangtze River. An epithermal metallogenic province may exist in the northeast margin of the Yangtze Block.

Acknowledgements

This research has been supported by the National Natural Science Foundation of China (Grant No. 40272048), the Anhui Provincial Excellent Youth Science and Technology Foundation (Grant No. 04045063) and the Anhui provincial Natural Science Foundation (Grant No. 01045202). We thank Prof. Chang Yinfo for his input.

This page intentionally blank

References

Chang YF, Dong SW (1996) On tectonics of "Poly-Basement with one cover" in Middle-Lower reaches of Yangtze Craton China. Volcanology and Mineral Resources 17: 17-25

Jankovic S (1989) Sb-As-Tl mineral association in the Mediterranean region. International Geology Review 31:262-273

Mao JW, Holly S, Du AD, Zhou TF, Mei YX, Li YF, Zang WS, Li JW (2004) Molybdenite Re-Os precise dating for Molybdenite from Cu-Au-Mo Deposits in the Middle-Lower Reaches of Yangtze River Belt and its implications for mineralization. Acta Geologica Sincina 78: 121-131

Pan YM, Dong P (1999) The lower Changjiang (Yangtze River) metallogenic belt, east central China: intrusion and wall rock-related Cu-Fe-Au, Mo, Zn, Pb, Ag deposits. Ore Geology Review 15: 177-242

Sobott RJ, Klaes R and Moh G H (1987) Thallium containing Mineral Systems. Chem. Erde 47:195-218

Wu MA, Tu YJ, Wang XY (2000) Exploration study on gold and silver mineral resources in north Changjiang region. Unpublished report, Hefei, 1-198

Zhai YS, Yao SZ, Lin XD (1992) Iron and copper deposits in the middle and lower reaches of Yangtze River. Geological Publishing House, Beijing, 1-254

Zhou TF, Yuan F, Yue SC, Zhao Y (2000) Two series of copper-gold deposits in the middle and lower reaches of the Yangtze River area and the O, S, Pb isotopes of their ore-forming hydrothermal systems. Science in China (Series D) 43 (supp): 208–218

Geochemical characteristics and genesis of Na-rich rocks in the Bayan Obo REE-Nb-Fe deposit, Inner Mongolia, China

Hongcai Fei[1], Rongge Xiao, Lan Cheng, Cuizhi Wang
Key Laboratory of Lithosphere Tectonics and Lithoprobing Techology of Ministry of Education, China University of Geosciences, Beijing 100083, China
[1]current address: Institute of Mineral Resources, Chinese Academy of Geological Sciences, Beijing, 100037, China

Abstract. The giant Bayan Obo REE deposit is hosted mainly by middle and late Proterozoic Na-rich rocks, dolomitic rock and K-rich slate. Ore-bearing dolomitite and K-rich slate occur together with Na-rich rocks. The Na-rich rocks include albitite, albitite dyke, arfvedsonite dyke and arfvedsonitized dolomitite. Albitite is the most common variety of sodic rock at Bayan Obo. REE in the original dolomitic rock has been enriched by hydrothermal processes, which has caused redistribution of REE, but did not introduce additional REE to the system.

Keywords. Sodic, albitite, arfvedsonite, dolomitite, Bayan Obo

1 Introduction

Bayan Obo is the world's largest REE deposit (Fig. 1). It has received considerable attention globally since its discovery by Prof. Ding Daoheng in 1927. Previous studies were focused on ore-bearing rocks, dolomitic rock and K-rich slate, and their sedimentary or magmatic genesis (Yang et al. 1998; La Bas 1992). Chao (1992, 1993, 1997) conducted research on sodic alteration at the deposit but did not make any detailed study of the Na-rich rocks. We describe the lithological and geochemical characteristics and occurrence of ore-bearing Na-rich rocks at Bayan Obo and provide the first discussion of their genesis.

2 Regional geology

There are three ore zones at Bayan Obo: Main, East and West Ore zones. Na-rich rocks are distributed widely (Fig. 2), especially in the south area of the Main orebody and East orebody. They also occur in the ore-bearing country rocks and the altered footwall (Fig. 2). Na-rich rocks include albitite, arfvedsonite-bearing albitite dyke, arfvedsonite dyke, and arfvedsonite-bearing carbonatite dyke and arfvedsonitized dolomitite. Each has a distinct origin. We have focused our research on the Na-rich rocks in the Main orebody, East orebody and in the hanging wall and footwall.

3 Na-rich rocks

3.1 Albitite

We use the term 'albitite' to describe albitic volcanic rocks, albite-riebeckite rock and biotite-albite- riebeckite schist. These all occur together in one geologic unit but differ slightly in their compositions (Fig. 2). Previous workers (Institute of Geochemistry 1998; Bai 1996; etc.) only described the ore-bearing dolomitic marble, and K-rich slate and their mineral combination. No previous worker has studied the albitite in detail.

Laminated or stripped albitite is well exposed in the open pit at the southern end of the main orebody. Pure albitite is milky white in colour, while most albitites are white and black stripped structure- interlayer of arfvesonitite and albitite. The albitite has a gradational contact with K-rich slate and biotite schist.

Whole rock analyse of the albitites has revealed Na-rich compositions. Na_2O contents of most of the analysed samples are much higher than 6 wt % (Table 1). The $NaO+K_2O$ content is more than 8 wt %, with Na_2O in excess of K_2O. The Rittmann index (?) of the albitite is between 2.96 and 8.56. Al/(K+Na) is more than 1 and Al/(K+Na+Ca) less than 1, indicating that these are alkali metaluminous rocks. The albitite is characterized by enrichment of crustally-derived incompatible trace element, and depletion of mantle-derived elements (Fig. 3). Rare earth elements, especially light REE in the albitites are extremely abundant. There is no distinct Eu anomaly. The total amount of REE in the albitite is lower than that of mineralized dolomitic rocks (Fig. 4). These characteristics are similar to those of the dolomitic volcanic rocks (Xiao 2003; Zhai et al. 2002). Based on their occurrence, structure and. chemical compositions, the albitite protolith is inferred to have been Na-rich volcanic rocks.

3.2 Albitite dyke

Albitite dykes mainly occur in the ore-bearing dolomitite, albitic volcanic rock and K-rich slate. The major, trace and REE, chemical composition of the albitite dykes are consistent with those of the albitic volcanic rocks, implying a common origin (Figs. 3 and 4).

3.3 Albite-arfvedsonite dyke

Albite-arfvedsonite dykes occur mainly within the albitite, quartzite, ore-bearing dolomitite, and carbonatite dykes. We have studied arfvedsonite-dominated dykes and arfvedsonite-bearing carbonatite dykes in the quartzite.

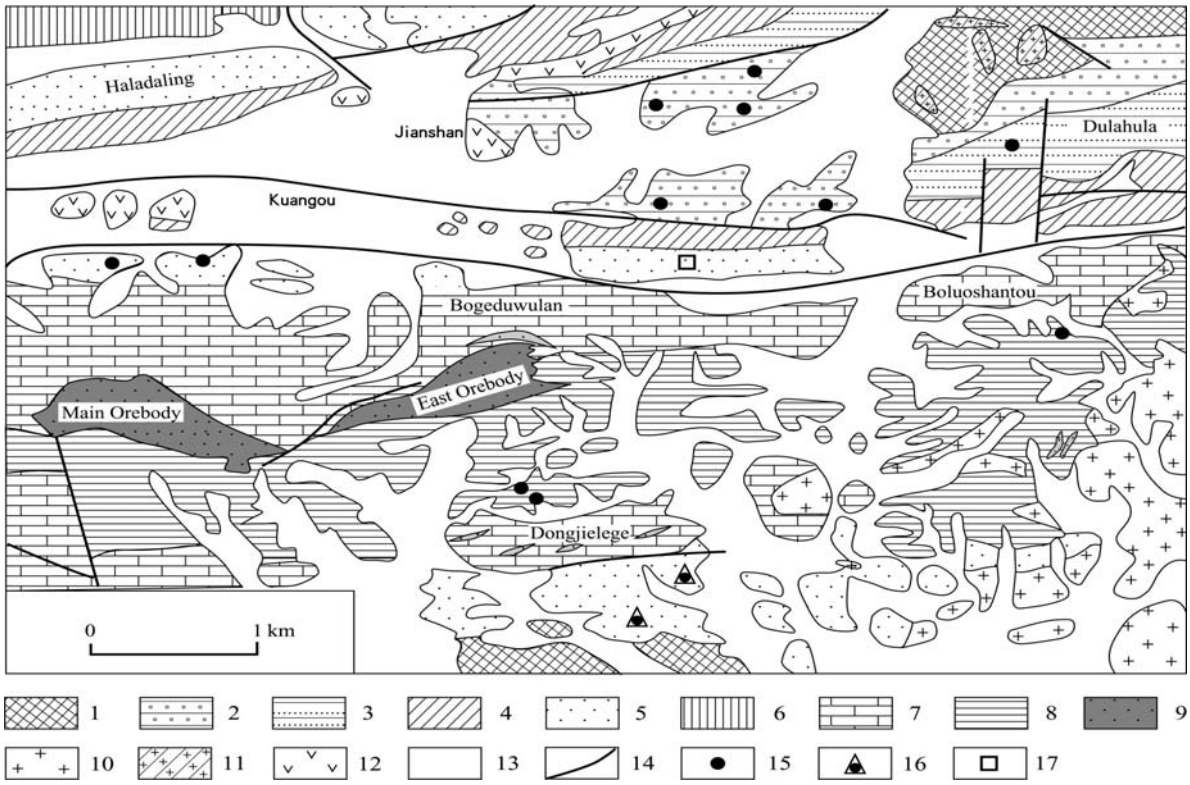

Figure 1: Geological map of the Bayan Obo area . 1. Tertiary sediments; 2. H9 K-rich slate; 3. Dolomite; 4. H5 dark slate; 5. H4 dark quartzite; 6. H3 dark slate; 7. H2 white quartzite; 8. H1 quartz conglomerate; 9. Basal complex; 10. Hercynian granite; 11. Alkali dyke; 12. Basic dyke; 13. Orebodies; 14. Fault; 15. Outcrop positions of carbonatite dykes; 16. Sample localities; 17. Arfvedsonite dyke

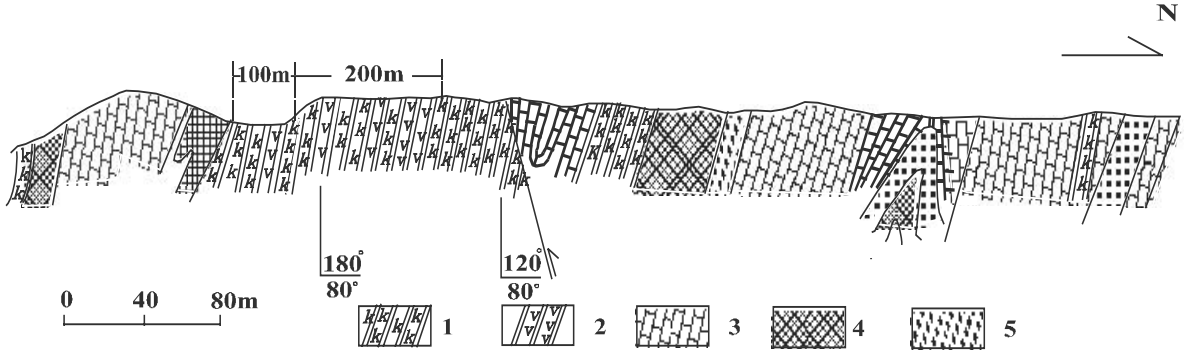

Figure 2: South-north cross section through the Eest Orebody, Bayan Obo. 1. K-rich slate; 2. Biotite schist, albite-arfvesontite volcanic rock and albitite; 3. Fluorite- and REE-bearing mineralized dolomitic rock; 4.Fluorite-bearing Fe layers; 5. REE layers.

Both the arfvedsonite-bearing carbonatite dykes and the arfvedsonite-rich dykes have the same geochemical features, with crustal and incompatible element enrichment, mantle element depletion, total amounts of REE that are higher than for the albitite and a weak negative Eu anomaly with Eu less than 1 (Figs. 3 and 4). The dykes are inferred to be co-genetic. The arfvedsonite-bearing carbonatite is a magmatic-hydrothermal feature, whereas the arfvedsonite-rich dykes formed by magmatic differentiation. According to Samson et al. (2000), Potassium and sodium in magmatic fluids can react with the surrounding country rocks during eruption of alkali carbonate magma forming arfvedsonite and leaving a residuum of pure carbonate magma (Olson 1954). This could explain the formation of dolomitic volcanic rock via carbonate magma eruption.

3.4 Arfvedsonitized dolomitite

Sodic alteration at Bayan Obo mainly occurs in the form of fenitization, arfvedsonization and albitization. In ad-

Table 1: Mean chemical compositions of Na-rich rocks from Bayan Obo.

No	SiO_2	TiO_2	$A1_2O_3$	Fe_2O_3	FeO	MnO	CaO	MgO	K_2O	Na_2O	P_2O_5	Loss	Total
1(8)	61.03	0.32	14.24	3.22	2.43	0.20	2.69	2.75	1.41	8.22	0.23	2.42	99.13
2(4)	35.08	0.86	0.91	37.77	4.85	0.37	5.199	5.30	0.74	2.92	0.73	4.39	99.14
3(4)	44.59	0.37	9.37	3.59	1.36	0.33	10.50	3.93	3.48	5.67	0.46	16.65	100.30
4(8)	2.46	0.05	0.80	3.29	3.10	0.77	33.85	12.87	0.12	0.40	6.82	35.30	99.80
5(2)	24.83	0.30	1.03	7.75	0.98	0.23	18.30	15.40	2.18	2.10	0.09	26.33	99.50

1. albitite, 2. arfvedsonite dyke, 3. amphbole-bearing carbonatite dyke, 4. dolomitite, 5. altered dolomitite. (Note: number of samples in brackets).

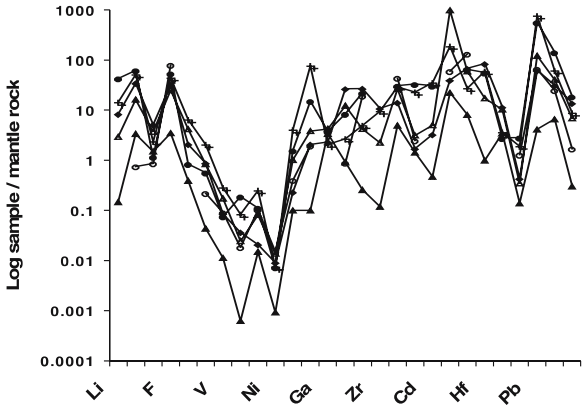

Figure 3: Average trace element spider diagrams normalized to primordial mantle. Note: the numbers in bracket are the quantity of the samples.

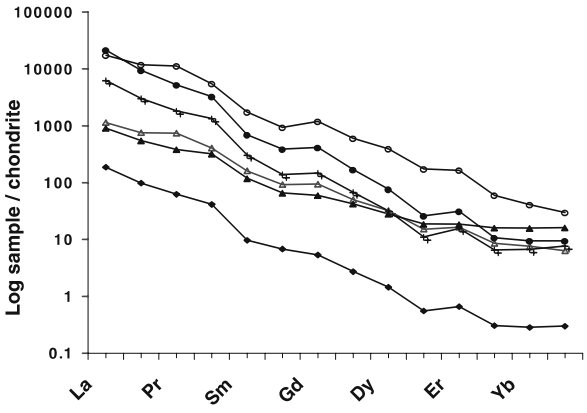

Figure 4: Average chondrite-normalised REE patterns of mineralized dolomitite (8), altered dolomitite (3), arfvedsonite dyke (4), albitic rock (6), carbonatite (from top to bottom).

dition, the reaction of Na-rich fluid with dolomitite has produced an arfvedsonitized dolomitite. This alteration assemblage occurs mainly within the dolomitite in the hanging wall and footwall of the Main and East ore zones, and West ore zone. Alteration products are dependent on the composition of the protolith and of the fluid. Na-metasomatism is invariably associated with K-metasomatism, which has resulted in phlogopite and biotite alteration. The most intensive alteration at Bayan Obo occurs in the Main and East orebodies, where REE have also been enriched. The REE enrichment appears to be related to sodic replacement.

The dolomitite has a grey-black colour along the contact-metasomatic zone due to the presence of arsfedsonite. Inclusions of dolomitite occur in the amphibole grains. When compared the compositions of unaltered and altered dolomitites in terms of bulk rock, trace elements and REE (Figs. 3 and 4), alteration has caused REE differentiation and a weak negative Eu anomaly. The arfvedsonitized dolomitite is high in SiO_2, TiO_2, K_2O and Na_2O, and depleted in P_2O_5 compared to the protolith.

Based on whole rock geochemistry of these rocks, it is indicated that REE had already been enriched in the original dolomitite prior to sodic alteration (fenitization). Hydrothermal process caused modification and redistribution of REE but we believe that this did not add any significant new REE to the deposit.

4 Conclusions

Based on the spatial distribution, lithological and geochemical features of the Na-rich rocks at Bayan Obo, along with the age data (Yang et al. 2000; Fan et al. 2002; Hao et al. 2002), three main origins of the sodic rocks are proposed: (1) volcanogenesis, which was mainly responsible for the formation of the albitite; (2) intrusion of arfvedsonite-bearing dolomitic magma; and (3) postmagmatic hydrothermal metasomatism of various arfvedsonite dykes with local replacement of country rocks.

Acknowledgements

We appreciate the advice of Dr. David Cooke, Dr. Richard Goldfarb and Dr.Kurt Friehauf. This study was supported financially by the McKinsky Students Research Grants of SEG and the National Natural Science Foundation of China (No.40073013). Also thanks to the geologists Ms. Guo Aifang and Xiao Guowang for their kind help at Bayan Obo.

References

Ba G, Yuan ZX, Wu CY, Zhang ZQ (1996) Demonstration on the Geological Featrues and Genesis of the Bayan Obo Deposit, Geological Publishing House, pp.1-104

Chao ECT, Back JM, Minkin JA (1992) Host-rock controlled epigenetic, hydrothermal and metasomatic origin of the Bayan Obo REE-Fe-Nb ore deposit, Inner Mongolia, P.R.C. Applied Geochem.7 (3), pp.443-458

Chao ECT, Tasumoto M, Minkin JA (1993) Multiple line of evidence for establishing the mineral paragenetic sequence of the Bayan Obo rare earth ore deposit of Inner Mongolia, China, In: Procedings of International Association on the Genesis of Ore Deposits, 8thSymposium volume (Maurice Y. T.). Stuttgart: E Schweizerbart, pp. 53-73

Chao ETC, Back JM, Minkin JA (1997) The sedimentary carbonate-hosted giant Bayan Obo REE-Fe-Nb ore deposit of Inner Mongolia, China: A cornerstone example for giant polymetallic ore deposits of hydrothermal origin. US Geol. Surv Bull. 2143: 1-65

Fan HR, Chen FK, Wang KY, Xie YH (2002) Zircon U-Pb Age of a Carbonatite dyke of the Bayan Obo Deposit and Its Significance, Acta Petrologica Sina, 18(03), pp. 363-368

Hao ZG, Wang XB, Li Z, Xiao GW, Zhang TR (2002) Petrological Study of alkaline basic dyke and carbonatite dyke in Bayan Obo, Acta Petrologica et Minralogica, 21 (4), pp. 429-444

Hao ZG, Wang XB, Li Z, Xiao GW, Zhang TR(2002) Bayan Obo Carbonatite REE-Nb-Fe Deposit: A Rare Example of Neoproterozoic Lithogeny and Metallogeny of a Damaged Volcanic Edifice, Acta Geol Sinica, 76(4), pp. 525-540

Institute of Geoschemistry, Chinese Academy of Sciences (1998) Geochemistry of the Bayan Obo Depsit: Beijing, Science Press, in Chinese.pp.519-528

Olson JC (1954) Rare-Earth Mineral Deposits of the Mountain Pass District San Bernardino Country California. United States Government Printing Office, Washington

Samson, IM, Al-Aasm, IS, and Zhu L (2000) Dolomitization and Mineralization in the Rock Canyon Creek fluorite-REE deposit, B C.Program and Abstracts, Geo CA 2000, Calgary.

Xiao RG, Fei HC, Zhang HC (2003) Lithology and Genesis of Dolomite in Bayan Obo, Inner Mongolia, Geoscience, 17(3), pp.287-293

Yang XY, Zhang YF, Yang XY, Zhang PS, Le Bas MJ (2000) A Geochemical Study of an REE-rich Carbonatite Dyke at Bayan Obo, Inner Mongolia, N China, Acta Geol Sin, 74(3): 605-611

Zhai YS, Deng J, Tang ZL, Xiao RG (2002) Metallogenic System of Paleocontinental Margin, Geological Publishing House, pp. 210-230

Tsav: A shoshonite-hosted intermediate sulfidation epithermal Ag-Pb-Zn deposit, eastern Mongolia

H. Gantumur
Mineral Resource Authority of Mongolia

D. Batulzii
Mongolian University of Science and Technology

Wang Lijuan, Zhu Heping
Institute of Geology and Geophysics Chinese Academy of Science

Abstract. Epithermal Ag-Pb-Zn mineralization at the Tsav deposit, Eastern Mongolia is characterized by intermediate sulfidation state mineral assemblages, and is hosted by shoshonitic volcanic rocks. Hydrothermal alteration varies from propylitic to argillic. Galena, sphalerite and silver form the ore mineral association. Ores have banded to crustiform, colloform and open space fill textures. Mn – carbonates are the dominant gangue minerals. Fluid inclusion studies have shown that the hydrothermal fluids were dominated by H_2O, CO_2 and NaCl, and had low salinities.

Keywords. Intermediate sulfidation, propylitic, argillic alteration, shoshonite

1 Introduction

The late Mesozoic volcanic-plutonic belt of Eastern Mongolia contains approximately seventy percent of Mongolia's lead and zinc deposits and 90% of the country's total lead and zinc endowment. Uranium, molybdenum, silver, gold and fluorite occurrences in Eastern Mongolia are also associated with this magmatic belt. Rift-related volcanic activity during the Late Mesozoic produced bimodal and shoshonitic volcanic rock series. Based on exploration results to date, the shoshonitic series have greater ore potential. This manuscript describes the characteristics of the Tsav Ag-Pb-Zn epithermal vein, which is associated with shoshonitic volcanic rocks in Eastern Mongolia.

2 Host rocks

Shoshonitic rocks at Tsav were deposited in a volcano-hypabyssal dome complex. The volcanic complex defines an elongated structure 12 by 15 km in diameter, and was the end product of many eruptions of effusive hypabyssal and subvolcanic rocks. The volcanic rocks include shoshonite, andesite, trachyandesite, latite, dacite, and quartz latite to high-K rhyolite including ignimbrite and tuffaceous rocks. Hypabyssal and sub-volcanic monzodiorite, syenite and granite have intruded the volcanic rocks. A porphyritic texture is common to all rocks. Chemical analyses reveal a range of compositions from high-K calc-alkaline to shoshonitic when plotted on a K_2O-SiO_2 diagram (Fig. 1). The rocks are enriched in Ba, and Th, and also have high Rb, Sr, Nb, La, Zr, and Nd contents. They are depleted in Co, Ni, and Cr.

3 Mineralisation and alteration

Silver-lead-zinc-bearing veins at Tsav have characteristics typical of intermediate sulfidation state mineralization (Hedenquist et al. 2000; Sillitoe and Hedenquist 2003). A total of 21 ore zones have been distinguished. The ore zones are controlled by near-vertical northwest-trending faults along which veins and related alteration zones have developed. The orebodies comprise thin veins, veinlets, sulfide-rich pockets, lenses, and breccias. Sharp boundaries separate the orebodies from their host rocks. The largest mineralized veins are 3.5 to 4 km long.

The orebodies comprise quartz - sulfide and carbonate - sulfide veins. Individual banded quartz - sulfide veins (e.g., Fig. 2) can be traced along strike for 70 to 150 m, and for 100 to 300 m down-dip. The quartz - sulfide orebodies are spaced from a few meters to 100 m apart, with vein thicknesses varying from 0.3 to 3 m. Average grades are 7.21 wt % Pb, 3.42 wt % Zn, 0.23 wt % Cu and

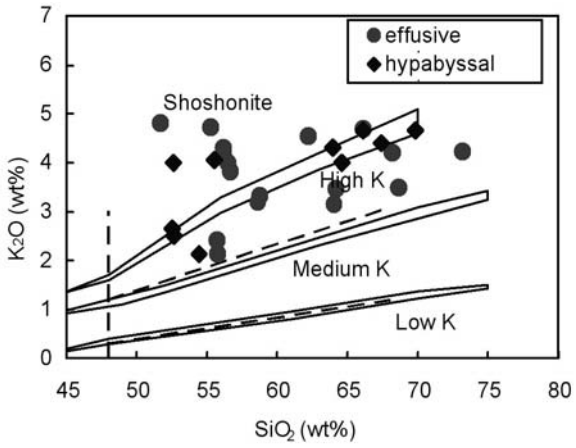

Figure 1: Chemical composition of intrusive and extrusive rocks from Tsav, plotted on a K_2O-SiO_2 discrimination diagram (fields from La Meitre et al. 1989; Peccerillo and Taylor 1976).

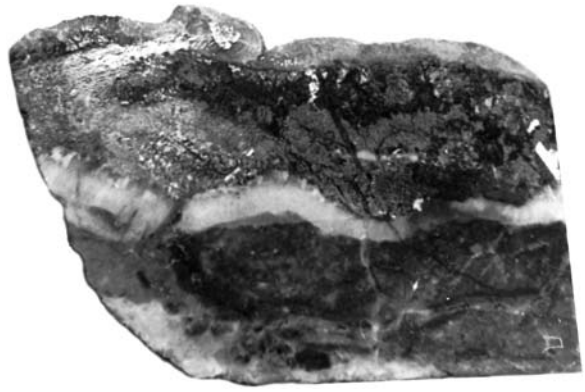

Figure 2: Banded quartz-sphalerite-galena vein.

Figure 3: Crustiform and breccia textures defined by cryptocrystalline quartz - lybasite in a carbonate-sulfide vein (1 and 2 are grains of native silver).

141 g/t Ag. The quartz-sulfide veins contain quartz – pyrite - arsenopyrite, quartz – chalcopyrite – galena - sphalerite, and quartz – chalcopyrite – galena - tetrahedrite mineral associations.

In the zone where carbonate - sulfide orebodies are dominant, the carbonate - sulfide veins have moderate dips (45° to 65°), spacing between each vein varies from 0.2 to 4.9 m and the zone does not exceed 50 to 100m in any dimension. Average metal grades in the carbonate - sulfide orebodies are 3.61 wt % Pb, 2.66 wt % Zn, 0.08 wt % Cu and 372 g/t Ag. The carbonate-sulfide veins consists of carbonate – sphalerite - galena and cryptocrystalline quartz – carbonate - sulfoantimonite mineral associations. They are characterised by disseminated, veinlet, colloform, crustiform, cockade and breccia textures (e.g., Figs. 3 and 4).

Gangue minerals include quartz, rhodochrosite and Mn-siderite. Narrow cryptocrystalline quartz veinlets with polybasite and pyrargyrite from the carbonate - sulfide veins have overprinted the quartz- sulfide veins.

The composition of ore and gangue minerals changed during each stage of hydrothermal activity at Tsav. From

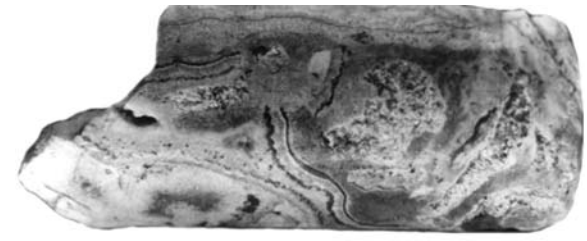

Figure 4: Colloform banded sphalerite and galena in a carbonate – sulfide vein.

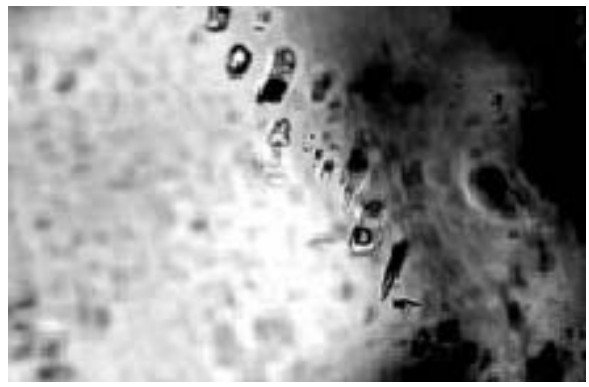

Figure 5: Primary two-phase liquid rich fluid inclusions along a growth zone in quartz.

earlest to latest, the paragenesis is interpreted to be as follow: (i) quartz; (ii) quartz + oligonite; (iii) quartz + rhodochrosite; (iv) rhodochrosite; (v) cryptocrystalline quartz + calcite.

The main sulfide mineral associations are as follows: galena, galena + bismuthinite, bismuth, martite + sphalerite + cleophan + greenocite. The precious metal-bearing minerals are gold, electrum, tetrahedrite, freibergite, polybasite, argentite and native silver.

Propylitic and argillic alteration assemblages have formed adjacent to the Tsav quartz-sulfide and carbonate-sulfide epithermal veins, respectively. The propylitic assemblage is composed of epidote, chlorite, calcite, smectite and illite. The argillic alteration consists of manganoan chlorite, illite-smectite and kaolinite.

4 Fluid inclusions

Petrographic analyses of fluid inclusions from Tsav have shown that the ore-related fluid inclusions are simple two-phase liquid + gas inclusions (Fig. 5, 6). The gas phase occupies 16-24% of the total inclusion volume when observed at room temperature. We have observed elongated primary fluid inclusions in growth zones at the edges of quartz grains (Fig. 5), whereas fluid inclusions in the central parts of the quartz grains have a circular or isometric distribution. Fluid inclusions in cleophane also occur

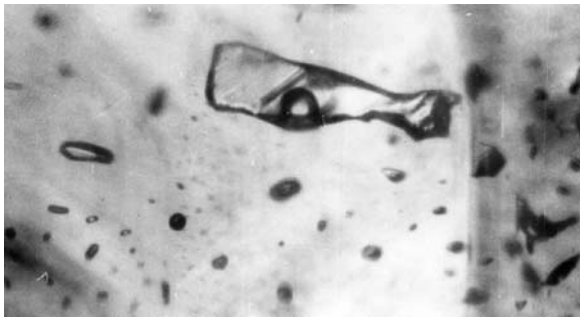

Figure 6: Primary two phase fluid inclusions on a growth zone in cleophane. These inclusions homogenized between 112° and 210°C.

Table 1: Summary of the microthermometric data on fluid inclusions of different ore mineral association.

Ore mineral association	Inclusion host mineral	Th (°C)	Tm (°C)	Salinity (eq.wt% NaCl)
Carbonate sphalerite-galena	Cleophane (green sphalerite)	112 to 210		
Quartz-tetrahedrite chalcopyrite galena	Quartz	210 to 230	-2.2 -1.2	1.9 to 3.6
Quartz-galena-sphalerite chalcopyrite	Quartz Sphalerite	217 to 254 230 to 265	-1.2 -4.6	2.6 to 7.2
Quartz, arsenian pyrite, pyrite	Quartz	196 to 330		

along growth zones and have isometric or elongated shapes (Fig. 6).

Measured homogenization temperature of fluid inclusions from quartz and tourmaline in pre-ore mineral assemblages vary between 330° and 260°C. Table 1 summarises the homogenization temperature from the ore stages at Tsav. Fluid inclusions from quartz-sulfide stage minerals have homogenization temperatures from 254° to 210°C. Ice melting temperature (Tm °C) range from -1.2° to -4.9°C Homogenization temperature from cleophane (carbonate-sulfide stage) vary from 210° to 112°C.

Analyses of gases contained within quartz-hosted fluid inclusions associated with galena - sphalerite chalcopyrite mineralization revealed the following concentrations: H_2O - 80.047%, CH_4 - 0.79%, C_2H_6 - 2.29%, H_2S - 0.21%, Ar - 0.594%, CO_2 - 16,1%. Analyses of gases in quartz-hosted fluid inclusions associated with tetrahedrite –chalcopyrite - galena mineralisation detected: H_2O - 76.792 %, CH_4 - 1.363%, C_2H_2 - 3.9%, H_2S - 0.13%, Ar - 0.83%, CO_2 – 16.9%. When plotted on a homogenization temperature versus NaCl content diagram, the fluid inclusions from ore stage minerals at Tsav plot within the field most characteristic of epithermal deposits (Fig. 7).

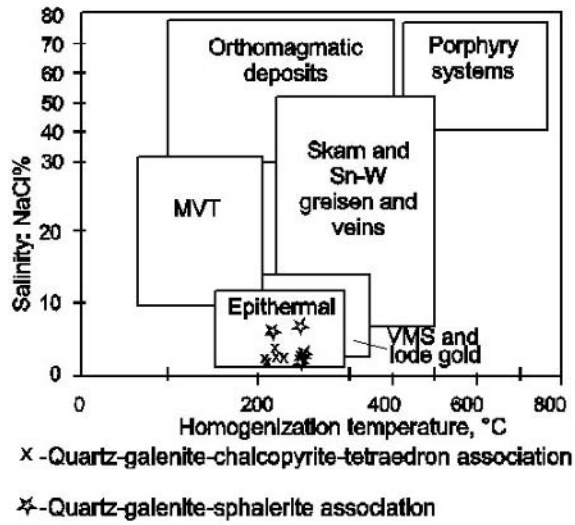

Figure 7: Th°C and NaCl data from Tsav, plotted on a Th°C-NaCl diagram (Lattanzi 1997).

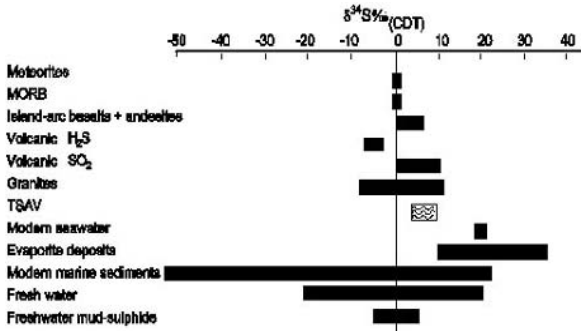

Figure 8: sulphur isotope data from Tsav compared to the common range of sulfide sulfur isotopic compositions from a variety of geological environments.

5 Sulfur isotopes

Sulfur isotopic measurements of galena, sphalerite and pyrite from ore zones at Tsav have indicated $\delta^{34}S$ values from +2.8 to +5 per mil, which correspond to values of magmatic sulfur (Fig. 8).

6 Conclusions

Based on our fluid inclusion and sulfur isotopic data, the ore stage sulfides at Tsav precipitated from magmatic-hydrothermal solutions. Table 2 compares the characteristics of Tsav with those of intermediate sulfidation epithermal deposits, as described by Hedenquist et al. (2000) and Sillitoe

Table 2: Characteristics of intermediate sulfidation deposits (Hedenquist et al. 2000, Sillitoe and Hedenquist 2003) compared to the Tsav deposit, Mongolia.

Criterion	Intermediate sulfidation characteristic	Tsav
Setting	Extensional	Extensional
Depth of formation	300 - 800m, rarely >1000 m	650 m
Typical host rocks	Domes, diatremes pyroclastic and sedimentary volcanic rocks	Volcanic- hypabysal dome, shoshonite series rocks
Deposit form	Vein, breccia	Vein
Texture	Coarse banded veins	Banded, veinlet cockade, crustiform
Gangue	Quartz, carbonate rhodochrosite	Quartz, oligonite rhodochorosite
Sulfides	Pyrite, Au, Ag-sulfides, sulfosalts galena, variable sphalerite, tetrahedrite/tennantite	Pyrite, Au, sphalerite, galena, Ag-chalcopyrite, tetrahedrite, polybasite
Metals	Ag, Au, Pb, Zn, Ba, Mn, Se,	Ag, Pb, Zn, Cu, Au
Fluids	3-20 wt % NaCl, 220-280^{o}C	2.1-6.7 wt % NaCl, 254-110^{o}C

and Hedenquist (2003). Based on this comparison, we classify Tsav as an intermediate sulfidation style of epithermal deposit. As has been noted elsewhere, there is potential for this style of epithermal deposit to be related to porphyry style mineralisation (Sillitoe and Hedenquist 2003)

References

Hedenquist JW, Arribas AJr, Gonzalez-Urien E (2000) Exploration for epithermal gold deposits. In: Reviews in Economic Geology 13:245-277

Lattanzi P (1991) Applications of fluid inclusions in the study and exploration of mineral deposits. Eur J Mineral 3:689-70.

Le Maitre RW (ed) (1989) A classification of igneous rocks and glossary of terms. Blackwell, Oxford: 193 p.

Peccerillo R, Taylor SR (1976) Geochemistry of Eocene calc-alkaline volcanic rocks from the Kastamonu area, Northern Turkey. Contrib Mineral Petrol 58: 63-81.

Sillitoe R, Hedenquist JW (2003) Linkages between volcanotectonic settings, ore fluid compositions, and epithermal precious-metal deposits. Society of Economic geologists and Geochemical Society, Special Publication 10:285-313

White NC, Hedenquist JW (1990) Epithermal environments and styles of mineralization: variation and their causes, and guidelines for their exploration. Journal of Geochemical Exploration 36: 445-474.

White NC, Hedenquist JW (1995) Epithermal gold deposits: Styles, characteristics and exploration. Society of Economic Geologists Newsletter, October, pp. 9-13.

Timing of volatile and magma ascent in the formation of the Bajo de la Alumbrera porphyry Cu-Au deposit

A.C. Harris, D.R. Cooke, N.C. White
Centre for Ore Deposit Research, University of Tasmania, Private Bag 79, Hobart, 7001, Australia

W.J. Dunlap, C.M. Allen, I. Campbell
Research School of Earth Sciences, Australian National University, Canberra, 2006, Australia

P.W. Reiners
Geology & Geophysics Department, Yale University, 06520-8109, New Haven, CT

Abstract. Dacitic rocks at the Bajo de la Alumbrera porphyry Cu-Au deposit (NW Argentina) preserve textures that suggest volatiles streamed upwards through intrusions temporally related to ore formation and hydrothermal alteration. There is evidence that volatile phases accumulated in the carapace of some intrusions. Phase transformations measured from fluid inclusions in comb-quartz layered textures suggest pressure fluctuations, and imply that Cu-bearing volatiles were catastrophically released from the ascending magma into the adjacent wallrock. Other findings (including the results of low temperature thermochronology) also argue that magmatic volatiles were introduced independent of any new batches of magma. These volatiles must have been episodically sourced from deeper-seated magma bodies or blind intrusions beneath Bajo de la Alumbrera over millions of years.

Keywords. Porphyry, copper, ore-forming fluids, thermochronology, longevity

1 Introduction

In porphyry-related ore deposits, alteration assemblages and associated mineralization develop in hydrothermal systems largely dominated by magmatic-hydrothermal fluids. These systems form in and adjacent to subvolcanic (typically silicic) porphyritic intrusions that are apophyses to deeper-seated magma bodies. High-temperature K-silicate alteration develops within and around the intrusions and is interpreted to have a short duration, whereas longer-lived low-temperature alteration migrates inwards during thermal collapse of the system.

We discuss here petrographic features (including aqueous phase transformations measured from fluid inclusions) that preserve evidence of volatile ascent and subsequent release from porphyritic intrusions associated with formation of the Au-rich Bajo de la Alumbrera porphyry Cu deposit. Using several different chronometers (including U-Pb, $^{40}Ar/^{39}Ar$ and (U-Th)/He techniques), it appears that these intrusions were emplaced episodically over a few millions of years. It also appears that hydrothermal alteration can occur tens of thousands to millions of years after the emplacement of the final intrusion associated with the porphyry deposit. These findings have implications in understanding volatile exsolution from upper crustal magma bodies beneath porphyry Cu deposits.

2 Deposit geology

At Bajo de la Alumbrera, Cu-Fe sulfide-bearing pervasive and fracture-controlled alteration assemblages have overprinted several dacitic porphyries (Fig. 1). These intrusions define a complex ~800 m in diameter and up to 1 km in known vertical extent (Proffett 2003). At least four broad groups occur, including, the plagioclase-phyric dacite P2 porphyries (including the Northeast Porphyry and Los Amarillos Porphyry); biotite-plagioclase-phyric dacite Early P3 porphyries (including the Quartz Eye Porphyry); hornblende-plagioclase-phyric dacite Late P3 porphyries and the post mineralization intrusions (Proffett 2003). Paragenetic studies have revealed that the Cu-Au vein stages cut both the P2 and Early P3 porphyries, with lesser ore found in the Late P3 porphyries (e.g. Fig. 14 of Proffett 2003). The youngest know intrusion

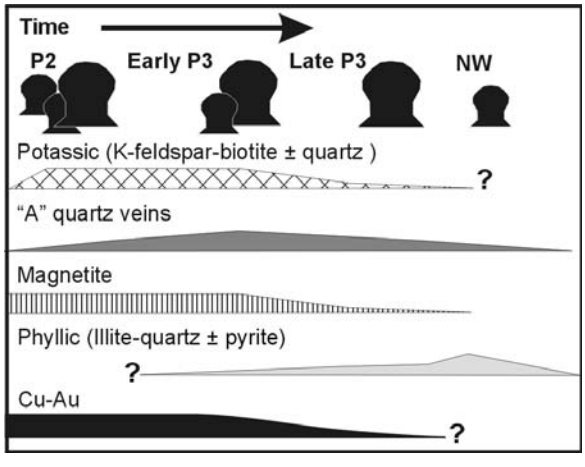

Figure 1: Timing of intrusion phases, alteration and Cu-Au ore at Bajo de la Alumbrera (modified after Proffett, 2003).

that was emplaced after mineralization, is the NW Porphyry (Proffett 2003).

Hydrothermal alteration assemblages are zoned from a chalcopyrite-rich potassic core (biotite- K-feldspar ± quartz) outwards to propylitic (chlorite-illite-epidote-calcite) assemblages. Quartz-magnetite (±chalcopyrite) veins crosscut the deepest parts of the potassic alteration. Intermediate argillic alteration assemblage (chlorite-illite ± chalcopyrite ± pyrite) has overprinted the potassic alteration zone, and is itself zoned outwards into phyllic (illite-quartz ± pyrite) alteration (Harris et al. in press).

Fluid inclusion and stable isotope geochemistry show that high temperature (up to 845°C) and saline (over 30 wt.% NaCl eq.) fluids of magmatic origin were responsible for the potassic alteration assemblages (Ulrich et al. 2002; Harris et al., in press). These studies also show that the less saline (less than 15 wt.% NaCl eq.) magmatic fluid and/or admixtures with meteoric water form the late-stage overprinting assemblages (Ulrich et al. 2002). Modelling of isotopic data shows that meteoric water becomes important below 200°C (Harris et al. in press).

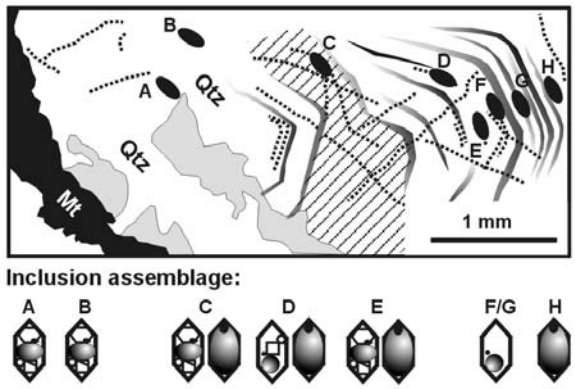

Figure 2: Sketch of comb-quartz layer texture from a phase of Late P3 Porphyry. Magnetite (Mt) defines the contact. Apical terminations of the quartz (Qtz) crystals are oriented perpendicular to the intrusion contact. Four inclusion groups occur: 1) inclusion that homogenize by halite dissolution (A-B), 2) boiling trails (C-E), 3) inclusions that exhibit 'near-critical' behaviour (F-G), and 4) vapor-rich inclusions (H).

3 Magmatic-hydrothermal textures

Based on vein distribution and cross cutting relationships, Proffett (2003) envisaged that magmatic volatiles ascended with an effervescing magma or immediately after porphyry emplaced, or both. Petrographic studies have identified textures that confirm the intrusions were a dynamic mixture of crystals and magmatic volatile phases (Harris et al. 2004a). For example, miarolitic pods and interconnected miarolitic cavities (e.g., Candela and Blevin, 1995) are present in porphyritic intrusions associated with mineralization.

Miarolitic pods occur as elliptical sugary aggregates of quartz (± alkali feldspar ± magnetite). These have been found in the P2 and P3 group of porphyries (Harris et al. 2004a). The Late P3 porphyries contain interconnected miarolitic cavities that comprise irregular zones of aplite and graphic quartz-alkali feldspar (± biotite ± magnetite) intergrowths. Crystals are typically coarser grained (0.2-0.5 mm) than the surrounding groundmass. Feldspar phenocrysts adjacent to these cavities are overgrown by alkali feldspar and intergrown with myrmekitic quartz and biotite.

Comb-quartz layered textures also occur along the contact of a single Late P3 phase. These textures define alternating bands (5-20 mm thick) of prismatic quartz, plumose biotite and aplite. Typically, apical terminations of the quartz crystals are perpendicular to the intrusion contact. Cathodoluminescene (CL) imaging of this quartz reveals internal complexity: luminescence bands of varying widths commonly define concentric growth zones in prismatic quartz. Moreover, this CL imaging shows that quartz in the aplite bands is typically bipyramidal; i.e., consistent with it being high-temperature β-quartz (Harris et al. 2004a).

3.1 Fluid inclusion petrography

Fluid inclusions in the comb-quartz layered textures include chalcopyrite-bearing brine inclusions that homogenize by halite dissolution (Harris et al. 2004a). Heating experiments have found that vapour disappearance occurs between 198 and 365°C, whereas halite typically disappears by 405°C (n = 28). Salinity is estimated between 45 and 47 wt.% NaCl eq. The true trapping temperature must have been much higher (>573°C), given that these inclusions were trapped during the growth of bipyramidal β-quartz.

Successively younger primary inclusion trails include, coexisting brine and vapor-rich (boiling) inclusions, low-salinity liquid-rich inclusions and vapor-rich inclusions (see Fig. 2). Brine inclusions in the boiling trails homogenize (typically by vapor disappearance) between 410 and 550°C (n = 10). Salinity is up to 45 wt.% NaCl eq. No phase transformation data has been measured from coexisting vapor-rich inclusions. Younger liquid-rich inclusions have final ice-melting temperatures ranging from -2.1° to -1.7°C (n = 7), which assuming a pure H_2O-NaCl system equals ~3.0 wt.% NaCl eq. These inclusions homogenize by vapor bubble disappearance between 300° and 332°C (n = 10). On cooling, the bubble reforms within 5° to 12°C of the temperature of homogenization. Typically the bubble reforms in the same position from where it disappeared. Younger vapor-rich inclusions (up to 80 volume percent vapor) have salinities up to 10 wt.% NaCl eq. (n = 7).

4 Timing of events

U-Pb zircon geochronology show that porphyry emplacement occurred during two periods. The earliest (P2) mineralized porphyries have U-Pb ages of 8.02±0.14 Ma and 7.98±0.14 Ma, whereas late stage (Early and Late P3) porphyries have much younger ages (7.10±0.07 Ma; Harris et al. 2004b). A post-mineralization intrusion has been dated via $^{40}Ar/^{39}Ar$. Sasso (1997) reported ages 6.78±0.15Ma (hornblende) and 6.48±0.85Ma (biotite), with the later biotite age considered disturbed (Sasso 1997).

Sasso and Clark (1998) published several key ages that constrain the timing of hydrothermal alteration for the Bajo de la Alumbrera deposit. Two biotite $^{40}Ar/^{39}Ar$ ages (7.10 ± 0.13 Ma and 6.83 ± 0.07 Ma), originally interpreted as the age of igneous crystallization (Sasso 1997), were determined from intrusions in and temporally associated with potassic alteration (including secondary biotite). Discrepancies between the $^{40}Ar/^{39}Ar$ ages and the U-Pb zircon ages of from the same porphyry, suggest that Sasso's $^{40}Ar/^{39}Ar$ ages have been reset and represent the timing of potassic alteration that overprints the porphyritic intrusions (Harris et al. 2004b). Sasso and Clark (1998) also reported a $^{40}Ar/^{39}Ar$ age of 6.75±0.09 Ma (whole rock) for pervasive phyllic alteration, slightly younger than the biotite ages (and the U-Pb ages).

Additional chronologic studies have been undertaken on one of the least altered Late P3 phases. It is coarser grained (up to 12 mm) than most P3 porphyries; twinned clusters of alkali feldspar and plagioclase occur with lesser biotite and hornblende. Bipyramidal crystals of quartz are dispersed throughout. The groundmass comprises quartz and feldspar. Interconnected miarolitic cavities have also been observed.

The newly acquired $^{206}Pb/^{238}U$ zircon age ($n = 24$; mean = 6.9 Ma) for this Late P3 porphyry is indistinguishable from the age of Sasso's (1997) $^{40}Ar/^{39}Ar$ age for a post-mineralization intrusion. We have also acquired incremental ($n = 42$) heating $^{40}Ar/^{39}Ar$ age spectra for phenocrystic alkali feldspar; the feldspar is unaltered and is not recrystallized. The spectra is characterized by high and geologically meaningless initial ages (during the first 10% of gas release), which decrease to ages between 6.3 and 6.1 Ma, before rising again to a plateau-like segment (at approximately 45% of gas release). This 'plateau' coincides with the total fusion age ~7.3 Ma for the alkali feldspar and is slightly older than the U-Pb age for the zircon separates (~6.9 Ma). This spectrum pattern is explained in terms of an apparent diffusion loss of essentially homogeneous alkali feldspar.

We have used multi-diffusion domain modelling (Lovera et al. 1989) of the alkali feldspar age spectrum to better define the timing and magnitude of this thermal event. The thermal history was characterized by rapid initial cooling from magmatic temperatures to 260°C by 6.6 Ma; cooling to 180°C by 5.8 Ma; isothermal conditions till 5.0 Ma and waning of the system (through 100°C) prior to 4.5 Ma.

Low-temperature chronometers confirm the thermal history predicted by multi-diffusion domain modelling (from 6.6 Ma to 4.5 Ma). Single-grain (U-Th)/He ages ($n = 2$) for zircon from P2 and P3 intrusive phases imply that the system last cooled through 180°C by 5.3 Ma. The thermal collapse (to below 70°C) of the system most likely occurred around 4.0 Ma, based on a single apatite (U-Th)/He age determination.

5 Discussion and conclusions

At Bajo de la Alumbrera, the magmatic-hydrothermal system developed in and around multiple silicic intrusions that are thought to emanate from a larger upper crustal magma body (Proffett 2003). Although this deep magma body evolved by open-system fractionation, magma mingling and incomplete mixing has been shown to be important in the evolution of the mineralized dacitic intrusions (Sasso 1997). Repeated influx of hydrous mafic magma would have resulted in the sudden release of metal-rich magmatic volatiles (and melt). In part, these volatiles were transported to the ore deposit with compositionally evolved silicic magmas. Evidence for this comes from the occurrence of miarolitic cavities and comb-quartz layered textures in the porphyries. Fluid inclusions in the comb-quartz layered texture appear to preserve evidence of volatile accumulation (including over-pressure) and release from these silicic intrusions. Fluids escaping from the intrusions would cause hydrothermal alteration of the adjacent wallrock explaining the close spatial and temporal relationship between successive intrusions and hydrothermal minerals (Proffett 2003).

By using a variety of chronometers, it can be shown that the Bajo de la Alumbrera porphyries were subjected to one or more low-temperature thermal events long after their emplacement. Our (U-Th)/He data (combined with limited inverse modelling of $^{40}Ar/^{39}Ar$ data) reveals that the magmatic-hydrothermal system last cooled through 200°C, approximately 1.5 m.y. after the last porphyry intrusion. This finding suggests that the magmatic-hydrothermal system was active for much longer than is expected from heat flow modelling of cooling of the small, high-level intrusions typically found associated with porphyry ore deposits (c.f. Norton 1982). For this to occur, heat and/or volatiles must have been sourced from deeper-seated magma bodies or blind intrusions.

Stable isotope studies confirm that the bulk of the hydrothermal alteration at Bajo de la Alumbrera was caused by repeated influx of magmatic volatiles (Ulrich et al. 2002; Harris et al. *in press*). Textures found in the silicic porphyries, imply that a portion of the volatiles once streamed upwards through these vertical intrusions into the de-

posit area. Moreover, low temperature thermochronologic data confirms that new batches of magmatic volatiles were introduced into the deposit area independent of any new batches of magma. This finding implies that the magma bodies underlying the Bajo de la Alumbrera deposit must have been continually replenished and/or new magma batches intruded the upper crust to ensure the longevity of the entire system. Without replenishment, crystallization of the magma body will occur and volatile exsolution will stop, leading to rapid cooling.

References

Candela PA, Blevin PL (1995) Do some miarolitic granites preserve evidence of magmatic volatile phase permeability? Econ Geol 90: 2310-2316

Harris AC, Allen CA, Bryan SE, Campbell IH, Holcombe RJ, Palin MJ (2004b) Measuring the longevity of regional volcanism hosting the Bajo de la Alumbrera Cu-Au deposit: Implications for the genesis of porphyry ore deposits: Mineralium Deposita 39: 46-67

Harris AC, Golding SD, White NC (in press) The genesis of Bajo de la Alumbrera deposit: Stable isotope evidence for a porphyry-related hydrothermal system dominated by magmatic aqueous fluids. Econ Geol.

Harris AC, Kamenetsky VS, White NC, Steele DA (2004a) Volatile phase separation in silicic magmas at Bajo de la Alumbrera porphyry Cu-Au deposit, NW Argentina. Resource Geology 54: 341-356

Lovera OM, Richter FM, Harrison TM (1989) The $^{40}Ar/^{39}Ar$ thermochronometry for slowly cooled samples having a distribution of diffusion domain sizes J Geophysical Research, B, Solid Earth and Planets 94: 17917-17935

Norton DL (1982) Fluid and heat transport phenomena typical of copper-bearing pluton environments; southeastern Arizona. In: Titley SR (ed) Advances in geology of porphyry copper deposits; southwestern North America. University of Arizona Press, Tucson: 59-73

Proffett JM (2003) Geology of the Bajo de la Alumbrera porphyry copper-gold deposit, Argentina. Econ Geol 98: 1535-1574.

Sasso AM, Clark AH (1998) The Farallón Negro group, northwest Argentina: magmatic, hydrothermal and tectonic evolution and implications for Cu-Au metallogeny in the Andean back-arc. Soc Econ Geol Newsletter 34: 1,8-18

Sasso, AM (1997) Geological evolution and metallogenetic relationships of the Farallón Negro volcanic complex, NW Argentina: Unpublished Ph.D. Thesis, Queens University: 842

Ulrich T, Günthur D, Heinrich CA (2002) The evolution of a porphyry Cu-Au deposit, based on LA-ICP-MS analysis of fluid inclusions: Bajo de la Alumbrera, Argentina. Econ Geol 96: 1743-1774

Trace element content of quartz from the Ehrenfriedersdorf Sn-W deposit, Germany: Results of an acid-wash procedure

S. Haßler, U. Kempe, T. Monecke, J. Götze
Institut für Mineralogie, TU Bergakademie Freiberg, Germany

Abstract. The trace element content of quartz from the Ehrenfriedersdorf Sn-W deposit has been determined by ICP-MS. It has been tested whether acid-washing of the finely crushed samples modifies the composition of the bulk quartz samples. In the case of the pure quartz analyzed, untreated and treated sample splits show very similar trace element contents suggesting that this method of sample preparation can be used to remove traces of associated minerals such as calcite without influencing the contents of elements required for genetic interpretation. The quartz samples from the Ehrenfriedersdorf deposit show high concentrations of Li, Rb, and K suggesting that these elements were enriched in the ore-forming hydrothermal-magmatic system. High Al concentrations in quartz are interpreted to result from the elevated temperatures of quartz formation. The REE patterns of the quartz samples are similar to those previously observed in fluorite.

Keywords. Trace element geochemistry, quartz, granite-related tin deposits

1 Introduction

Trace elements in minerals are considered to represent important indicators of the physicochemical conditions of mineral formation and alteration. Due to the common occurrence of quartz, several attempts have been made to study the geochemistry of this mineral (Novgorodova et al. 1984; Heynke et al. 1992; Peucker-Ehrenbrink and Behr 1993; Monecke et al. 2002a; Götze et al. 2004). Although pronounced differences in the trace element signatures were observed for bulk quartz samples collected from different geological environments, detailed interpretation has to take into account that there are several mechanisms of trace element uptake into quartz. Foreign elements may enter the crystalline structure of quartz by substitution into the Si tetrahedron or by incorporation into interstitial places. In addition, fluid inclusions and, in particular, mineral impurities are likely to represent important hosts of trace elements in bulk quartz samples (Gerler 1990; Götze et al. 2004).

In the present contribution, the results of systematic experiments are reported that where carried out to determine the trace element content of pure bulk quartz samples prior and after acid-washing. These experiments were mainly conducted to test whether such a cleaning procedure modifies the trace element composition of bulk quartz samples, e.g., by removing the trace elements contained in fluid inclusions opened during the crushing of samples. Previous investigations have shown that the application of an acid-wash procedure is essential during sample preparation of bulk quartz samples containing traces of finely dispersed calcite that cannot be removed by hand-picking (Monecke et al. 2002a).

2 Sample selection

The present study is based on three quartz samples collected from the Ehrenfriedersdorf Sn-W deposit, Germany. The geology of the deposit has been studied intensively and is summarized by Hösel (1994). Briefly, the mineralization is related to a Li-F granite that intruded a sequence of metamorphic rocks mainly comprising gneiss, mica schist, and phyllite. Cassiterite mineralization is mainly confined to greisen bodies within the endocontact of the granite and to vein zones within the exocontact.

The samples investigated originate from geologically distinct positions within the deposit. The quartz ED-507 was collected from a pegmatite body located in the endocontact of the Li-F granite. Sample ED-504 was sampled from a quartz vein hosted by an endocontact greisen zone whereas quartz ED-1050 was taken from a cassiterite-bearing hydrothermal quartz vein occurring in the exocontact of the granite within the altered metamorphic country rocks by an endocontact greisen zone whereas quartz ED-1050 was taken from a cassiterite-bearing hydrothermal quartz vein occurring in the exocontact of the granite within the altered metamorphic country rocks.

3 Materials and methods

The quartz samples were initially studied in thin section to identify mineral impurities by optical microscopy, cathodoluminescence microscopy, and scanning electron microscopy. The microscopic investigations revealed that the quartz samples contained relatively large zones of quartz lacking mineral inclusions. These zones of pure quartz were carefully crushed and samples (ca. 300 mg) of pure quartz without visible mineral inclusions were then hand-picked using a binocular microscope.

The preparation of the samples was followed by tests to confirm the purity of the quartz. A representative frac-

Table 1: Trace element content of quartz samples from the Ehrenfriedersdorf Sn-W deposit, Germany.

	Untreated bulk quartz samples			Acid-washed bulk quartz samples		
	ED-507	ED-504	ED-1050	ED-507	ED-504	ED-1050
Concentrations in ppm						
Li	61.2	21.6	15.0	65.3	21.7	14.4
Na	65.5	32.6	19.9	52.8	34.7	19.6
Al	642	215	153	618	210	160
K	39.7	30.8	30.2	37.1	28.3	15.3
Ca	10.7	7.9	9.5	7.3	12.2	8.1
Mn	1.82	1.39	1.03	1.12	0.60	0.47
Rb	0.91	1.20	0.85	0.84	0.95	0.70
Sr	0.06	0.08	0.09	0.07	0.11	0.08
Σ	822	311	230	783	309	219
Concentrations in ppb						
La	9.3	4.2	14.7	4.3	6.8	4.1
Ce	10.9	6.1	20.8	6.8	9.5	10.9
Pr	0.8	0.4	1.9	0.4	0.3	0.5
Nd	3.1	1.3	6.0	1.1	0.8	1.8
Sm	0.7	0.3	0.6	0.4	<0.2	0.3
Eu	<0.2	<0.2	0.4	<0.2	<0.2	0.4
Gd	0.4	0.2	0.5	<0.2	0.3	0.4
Dy	0.6	0.6	0.5	<0.2	1.0	0.5
Er	0.4	0.3	0.3	<0.2	0.6	0.7
Yb	0.6	0.5	0.4	<0.2	0.9	1.3

tion of each sample was investigated by infrared stimulated optical luminescence as described by Monecke et al. (2002a). All three samples yielded counting rates below a pure synthetic quartz sample indicating that the hand-picked samples lacked mineral impurities such as feldspar. After these investigations, the samples were repeatedly washed with 2 mol l^{-1} HNO_3 and ultra-pure water to clean the surfaces of the quartz grains. The samples were then crushed to a grain size of approximately 30 µm using a carefully precleaned agate mortar and pestle. A representative fraction of each powdered sample was utilized for Fourier-transform infrared spectroscopy. This spectroscopic test confirmed that the hand-picked samples were of high purity.

The finely ground quartz samples were split into two sub-samples of approximately equal weight. One sample split was treated with 14.4 mol l^{-1} HNO_3 for 5 min and then repeatedly washed with ultra-pure water. It was assumed that acid-washing removes the content of the fluid inclusions opened during the crushing of the samples. In contrast to this sample, the other sample split was not acid-washed to preserve the trace element signature of the bulk sample. The obtained quartz samples were then digested by HF/HNO_3 in glassy carbon vessels and analyzed by ICP-MS. Details on the analytical procedure including blank levels and detection limits are given by Monecke et al. (2000).

4 Results

The results of the trace element analyses of the untreated and acid-washed samples are listed in Table 1. Inspection of the data reveals that the acid-washing only resulted in minor changes in the overall trace element concentrations, the total amount of trace elements was only decreased by 1 to 5 %. Taking analytical errors and possible sample inhomogeneities into account, Rb represents the only monovalent element that was significantly affected by the procedure of acid-washing. No consistent trend was observed for Ca. However, the concentration of Mn in the quartz samples decreased significantly due to the treatment. The Al concentrations were not modified. Acid-washing generally resulted in a decrease of the light REEs whereas the heavy REEs were apparently not influenced significantly.

The chondrite-normalized REE patterns of the samples investigated are shown in Figure 1. The samples from the endocontact exhibit kinked REE patterns with REE concentrations that decrease from La to Sm and increase from Gd to Yb. In contrast, the REE pattern of the untreated sample ED-1050 from the exocontact quartz vein decreases from La onwards. The two samples from the endocontact are typified by pronounced negative Eu anomalies whereas quartz from the exocontact is typified by a positive Eu anomaly.

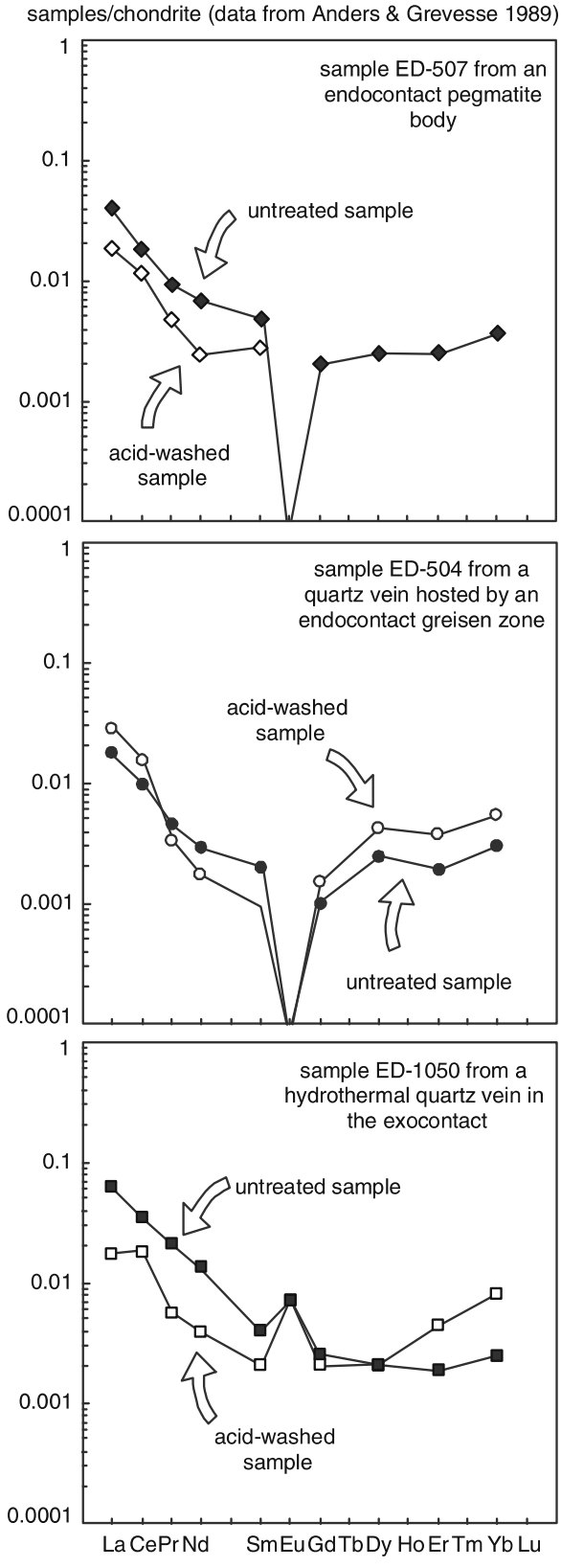

Figure 1: REE patterns of the quartz samples investigated.

5 Discussion

The results of the present study demonstrate that the applied procedure of acid-washing results only in minor changes in the trace element content of bulk quartz samples if the finely crushed samples do not contain mineral inclusions that can be dissolved in 14.4 mol l^{-1} HNO_3 such as calcite. This finding is surprising given the fact that earlier studies showed that a number of elements are concentrated in fluid inclusions. For instance, Götze et al. (2004) showed that the Na, K, Ca, and Mg contents of fluid inclusions of pegmatite quartz amount to trace element concentrations in the ppm level for bulk quartz samples. In addition, these authors suggested that the REEs and Rb are mainly hosted by fluid inclusions although the concentrations of these elements were too low to be directly measured in fluid inclusion leachates from quartz.

A possible explanation for the observation of the present study is the fact that quantitative removal of the trace element content of fluid inclusions from the quartz matrix by acid-washing is hampered by the absorption of elements to the quartz surfaces freshly produced during the crushing of the samples (Bottrell et al. 1988). It appears possible that a simple treatment with 14.4 mol l^{-1} HNO_3 is insufficient to prevent the absorption of elements released from the fluid inclusions. However, because no detailed fluid inclusion study was carried out, it cannot be ruled out with certainty that the fluid inclusions contained in the analyzed quartz samples possessed only small sizes and/or low element concentrations and, therefore, did not significantly contribute to the overall trace element contents of the samples.

Comparison of the obtained analytical results with data given by previous workers (Monecke et al. 2002a) reveals that the samples from the Ehrenfriedersdorf Sn-W deposit are enriched in a characteristic suite of trace elements. The samples are, in particular, characterized by a high Al content (≥150 ppm) when compared to metamorphic quartz collected from the wall rocks of the deposit (Al ≤ 30 ppm). The high Al contents of the quartz samples investigated are probably related to the temperature of quartz formation because increasing amounts of Al are incorporated at the Si site of the quartz crystal structure at elevated temperatures (Dennen et al. 1970). The samples from the Ehrenfriedersdorf Sn-W deposit were also found to be enriched in Li (≥15 ppm), Rb (≥0.7 ppm), and K (≥30 ppm) when compared to metamorphic quartz (Li ≤ 0.4 ppm, Rb ≤ 50 ppb, and K ≤ 35 ppm). The relative enrichment of these elements in the pegmatite quartz and the hydrothermal quartz vein samples is in good agreement with the results of previous geochemical and mineralogical studies that suggest that Li, Rb, and K were extremely enriched in the deposit-forming hydrothermal-magmatic system (Hösel 1994). Another important observation is the relative en-

richment of the HREEs in the normalized patterns of the quartz samples collected from the endocontact. A similar enrichment of the HREEs has been observed for fluorite collected from various granite-related rare metal deposits (Monecke et al. 2002b) implying that the relative enrichment of the HREEs is a universal feature of endocontact samples in this deposit type. The relative depletion of Eu in quartz from the endocontact and the corresponding enrichment of this element in the exocontact sample is also in agreement with fluorite REE data (Monecke et al. 2002b).

6 Conclusions

The results of the present study show that a simple procedure of acid-washing of finely crushed quartz samples does not result in significant changes in the trace element content of bulk quartz samples (except possibly for Rb and Mn). The acid-washed samples contain trace element concentrations that are similar to untreated samples. Thus, the applied procedure can be used for the preparation of monomineralic quartz samples to remove traces of associated minerals such as carbonates. The contents of trace elements and their ratios required for genetic interpretation are apparently not influenced by simple acid-washing.

Acknowledgements

We thank G. Bombach, M. Krebetschek, and S. Tesch for their help during the analytical investigations. The study benefited from critical comments by D. Wolf and W. Klemm.

References

Anders E, Grevesse, N (1989) Abundances of the elements: Meteoritic and solar. Geochim Cosmochim Acta 53: 197-214

Bottrell SH, Yardley B, Buckley F (1988) A modified crush-leach method for the analysis of fluid inclusion electrolytes. Bull Minéral 111: 279-290

Dennen WH, Blackburn WH, Quesada A (1970) Aluminum in quartz as a geothermometer. Contrib Mineral Petrol 27: 332-342

Gerler J (1990) Geochemische Untersuchungen an hydrothermalen, metamorphen, granitischen und pegmatitischen Quarzen und deren Flüssigkeitseinschlüssen. Ph.D. thesis, Georg August Universität Göttingen

Götze J, Plötze M, Graupner T, Hallbauer DK, Bray CJ (2004) Trace element incorporation into quartz: A combined study by ICP-MS, electron spin resonance, cathodoluminescence, capillary ion analysis, and gas chromatography. Geochim Cosmochim Acta 68: 3741-3759

Heynke U, Leeder O, Schulz H (1992) On distinguishing quartz of hydrothermal or metamorphogenic origin in different monomineralic veins in the eastern part of Germany. Mineral Petrol 46: 315-329

Hösel, G. (1994) Das Zinnerzlagerstättengebiet Ehrenfriedersdorf/Erzgebirge. Landesamt für Umwelt und Geologie und Oberbergamt Freiberg

Monecke T, Bombach G, Klemm W, Kempe U, Götze J, Wolf D (2000) Determination of trace elements in the quartz reference material UNS-SpS and in natural quartz samples by ICP-MS. Geostandards Newslett 24: 73-81

Monecke T, Kempe U, Götze J (2002a) Genetic significance of the trace element content in metamorphic and hydrothermal quartz: A reconnaissance study. Earth Planet Sci Lett 202: 709-724

Monecke T, Kempe U, Monecke J, Sala M, Wolf D (2002b) Tetrad effect in rare earth element distribution patterns: Geochim Cosmochim Acta 66: 1185-1196

Novgorodova MI, Veretennikov VM, Boyarskaya RV, Drynkin VI (1984) Geochemistry of trace elements in gold-bearing quartz. Geochemistry Int 21: 101-113

Peucker-Ehrenbrink B, Behr HJ (1993) Chemistry of hydrothermal quartz in the post-Variscan "Bavarian Pfahl" system, F.R. Germany. Chem Geol 103: 85-102

Three large-scale metallogenic events related to the Yanshanian Period in Southern China

Renmin Hua, Peirong Chen, Wenlan Zhang, Jianjun Lu
State Key Laboratory of Mineral Deposit Research, Department of Earth Sciences, Nanjing University, Nanjing 210093, China

Abstract. Post-orogenic magmatism during the Yanshanian Period in southern China caused three major metallogenic events in South China. The first took place from ~180 to 170 Ma (Early Yanshanian), and produced Cu, Pb-Zn and polymetallic mineralization in northeastern Jiangxi and southeastern Hunan. The second event, which occurred from ~150 to 139 Ma (Mid-Yanshanian), produced rare metal mineralization (e.g. Nb-Ta) and W and Sn deposits, closely related with S-type granitoids. The third, and most important, large-scale metallogenic event occurred mainly from ~125 to 98 Ma in the Late Yanshanian period. It produced Sn and U mineralization in the Nanling Range region and Au-Cu-Pb-Zn-Ag mineralization in the southeast coast zone. These three large-scale metallogenic events were the products of lithospheric evolution of southern China. They occurred mainly within extensional geodynamic settings, involving crust-mantle interaction, and participation of heat and fluids from deep sources.

Keywords. Metallogeny, Yanshanian, lithospheric evolution, South China

1 Introduction

The Mesozoic Era was a time of intensive metallogenesis in eastern and southern China. It has been termed a "metallogenic explosion" by some authors (Hua and Mao 1999; Mao et al. 1999). The Yanshanian Period was the most important within the Mesozoic for metallogenesis. In most Chinese geological literature, the Yanshanian Period is commonly accepted to be the time interval from 180 Ma to about 65 Ma. In this paper, we identify three major metallogenic events within this >100 m.y. time interval, and clarify the tectonic settings for these large-scale events in southern China (Fig. 1).

2 Indonsinian orogeny

The Mesozoic Era in South China started with the Indochina Orogeny, which was caused by collision and accretion between the Sibumasu plate and Indochina plate between 258 ±6 and 243 ±5 Ma (Carter et al. 2001). This orogenic movement caused compression, collision and uplift within the South China plate. The Central Orogenic Belt formed at this time, linking the North China plate and South China plate into a united continent. Ages of ultra-high pressure metamorphic rocks in the Dabieshan belt (Sun et al. 2002) show that the main collision during the Indosinian orogeny occurred at 250~230 Ma in South China.

Indosinian granitoids, especially peraluminous granites, were emplaced mainly from 238 Ma to 205 Ma. They resulted principally from collision and subsequent crustal thickening (Wang et al. 2002b). Some I-type granites also were emplaced at this time, possibly relating to post-collisional extension and initial lithospheric delamination.

No large-scale metallogenesis occurred during the Indosinian Period. However, there is a spatial relationship between some Indosinian granites and later uranium mineralization.

3 Early Yanshanian Cu-Pb-Zn metallogenesis

After a period of subdued igneous activity from about 200 to 185 Ma, Southern China entered a geodynamic stage of post-orogenic lithospheric extension and break-up, marking the beginning of the Early Yanshanian Period. Magmatic activity began at 185 Ma, but was mostly between ~180 and 170 Ma. Four types of magmatism occurred during this period. Basaltic magmatism occurred in southeastern Hunan between ~178 and 175 Ma (Zhao et al. 1998). Bimodal magmatism occurred in southern Jiangxi and also in southwestern Fujian. The mafic units were emplaced between 179 Ma and 158 Ma (Chen et al. 1999). A-type granitic magmatism produced the Zhaibei and Pitou granites in southern Jiangxi at 176 Ma and 178 Ma, respectively (Chen et al. 1998; Fan et al. 2000). High-K calc-alkaline magmatism occurred in two areas: north-

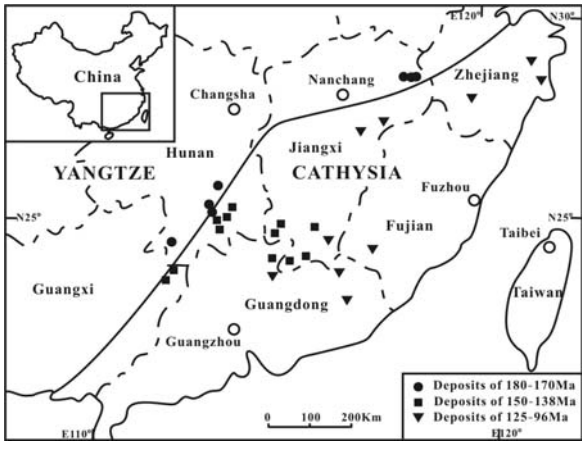

Figure 1: Sketch map of South China showing localities of major mineral deposits of the Yanshanian Period

eastern Jiangxi and southeastern Hunan. These granodioritic rocks were intruded between ~184 and 170 Ma (Zhu et al. 1983; Hua and Dong 1984) and ~181 to 172 Ma (Wang et al. 2002a), respectively.

Most of the Early Yanshanain magmatism of southern China formed in a post-orogenic geodynamic setting due to lithospheric extension, thinning and break-up in limited areas (Chen et al, 2002). The high-K igneous suite may have been related to a tectono-magmatic event that occurred along the boundary between the older Yangtze and Cathaysia blocks.

Copper, lead-zinc and polymetallic (Au-Ag-Cu-Pb-Zn) deposits associated with high-K calc-alkaline granodioritic rocks in northeastern Jiangxi and southeastern Hunan define the Early Yanshanian metallogenic province. The largest ore deposits include the Tongchang porphyry copper deposit (which is the largest copper mine in China), the Yinshan polymetallic deposit in northeastern Jiangxi, and the Shuikoushan lead-zinc deposit in southern Hunan. There are also several large ore deposits, including Fujiawu, Baoshan, and Tongshanling.

4 Middle Yanshanian W-Sn-Nb-Ta metallogenesis

From about 170 Ma, the Mid-Yanshanian Period was characterized by large-scale post-orogenic lithospheric extension, which caused significant crustal thinning in southern China. This resulted in abundant S-type granitoid magmatism, in association with underplating of mantle-derived basaltic magma. The granitoids were derived primarily from partial melting of metasedimentary continental crust. The compositions of these S-type granites are distinct from the igneous rocks of the Early Yanshanian.

The S-type granitoids were mostly emplaced in the Nanling Range region, in the central part of southern China. Magmatism was confined mostly to the earliest stage of the Mid-Yanshanian Period, i.e. from 170 Ma to 150 Ma. The granitic plutons include Qianlishan and Qitianling in southern Hunan, Xihuashan and Dajishan in southern Jiangxi, Fogang, Guidong, and Hongling in northern Guangdong, and Huashan and Guposhan in northeastern Guangxi.

The Mid-Yanshanian granitoids are closely related to rare metal mineralization, especially W, Sn, Nb, Ta, Li, Be, etc, making the Nanling Range region one of the largest rare metal provinces in the world. Mineralization apparently post-dated the host granitoids. Most tungsten mineralization, for example, started from about 150 Ma, and tin mineralization occurred even later in the evolution of the province. The limited number of age determinations prevents accurate timing of ore formation during the Mid-Yanshanian. The available data imply that most rare metal mineralization took place from ~150 to 139 Ma. The Xihuashan tungsten deposit was dated at 139 Ma by Li et al (1993), which is about 10 m.y. later than the Xihuashan granite (McKee et al. 1987; Maruejol et al. 1990). We have used the $^{40}Ar/^{39}Ar$ method to date mica in wolframite-bearing quartz veins at the Dajishan W-Nb-Ta deposit. Our results show that ore formation occurred between ~147 and 144 Ma, about 15 m.y. after the emplacement of the host granite (Sun et al. 1989).

The period from ~150 to 139 Ma was characterized by further evolution of crustally-derived granitic magmas, with development of highly-evolved smaller intrusions, including shallow (porphyritic) granitic bodies, and also by the intrusion of lamprophyre and mafic dykes in the Nanling Range region (Liu et al. 1997, 2002; Zhao et al. 2003). Volcanic activity became more prevalent at this time. These phenomena indicate further extension and break-up of the lithosphere, and upwelling of deep-sourced heat and fluid, which favored ore deposit formation.

5 Late Yanshanian Sn, U, Au-Cu-Pb-Zn-Ag metallogenesis

The late Yanshanian period was another high tide of tectono-magmatic activity in southern China. Volcanism was more intensive at this time, compared to the Early and Mid Yanshanian periods. At this time, the Pacific tectonic system began to play an important role in the metallogenesis and tectonics of eastern China.

The most abundant Late Yanshanian igneous rocks in the Nanling Range region are shallow-crustal sub-volcanic granitic rocks, classified as S-type by Wang et al. (1991). Some of these intrusive complexes are associated with tin mineralization, as typified by the Yanbei deposit in southeastern Jiangxi. The granite porphyry at Yanbei was dated at ~136 to 126 Ma (Xiong et al. 1994), whereas Sn ore formation occurred between ~122 and 100 Ma (Wang et al. 1993).

Sub-volcanic granitoids related to uranium mineralization include those at the Xiangshan deposit in Jiangxi. Age determinations for volcanic rocks and related granite porphyry at Xiangshan are mainly from ~141 to 126 Ma, whereas the ages of uranium ores are ~120 to 100 Ma (Li et al. 1989; Chen et al. 1993; Chen et al. 1999).

Late Yanshanian calc-alkaline volcanic rocks were intensively developed in the southeastern coastal area of China, related to subduction of the Pacific plate beneath the Eurasian plate. Shoshonitic rocks were emplaced along deep-rooted fault zones, such as those in the lower and middle reaches of the Yangtze River (Wang et al. 1996). Both calc-alkaline and shoshonitic rocks are associated with Au, Ag, Cu, Pb and Zn mineralisation. Typical ore deposit examples include Lengshuikeng (Ag-Pb-Zn) in Jiangxi, Zhilingtou (Au-Ag) and Wubu (Pb-Zn) in Zhejiang, and the Zijinshan porphyry-epithermal Au-Cu deposits in Fujian (Zhang et al. 2001).

The Late Yanshanian period was an important time for the remobilization and concentration of uranium from Indosinian granitoids. The uranium deposits of the Xiazhang ore field in northern Guangdong typify this process (Deng et al. 2000).

The Late Yanshanian Period (~125 to 98 Ma) was the third, and perhaps the most intensive large-scale metallogenic event in southern China. This period coincides with ore formation in many other areas within eastern China, including the gold deposits of the eastern Shandong Peninsula (Mao et al. 2003).

6 Conclusions

While there was no significant mineralization associated with the Early Mesozoic Indosinian Orogeny, Southern China subsequently underwent three major metallogenic events during the Yanshanian period, primarily in relation to post-collisional geodynamic processes. The first metallogenic event occurred from ~180 to 170 Ma, and is represented by copper and lead-zinc deposits in northeastern Jiangxi and southeastern Hunan. Mineralization was related to tectono-magmatic activity along the boundary between the old Yangtze and Cathaysia plates. The second metallogenetic event took place from ~150 to 139 Ma, and was connected to post-orogenic extension, resulting in tungsten, tin and rare metal mineralisation. The third and most intensive metallogenic event occurred at about ~125 to 98 Ma. This event caused tin and uranium mineralization in the Nanling Range region within an extensional geodynamic setting, and subduction-related base and precious metal mineralization in the southern coastal area.

The three Yanshanian metallogenic events were the products of lithospheric evolution. Although granitoids can form within compressional tectonic settings, Yanshanian metallogenesis mainly took place in extensional geodynamic environments, with heat, fluid, and other components derived from mantle sources.

Acknowledgements

This study was supported by a State Key Fundamental Research Project of China (Grant No. G1999043209) and a key project of National Natural Science Foundation of China (Grant No. 40132010). The authors would thank Dr David Cooke and Dr John Walshe for their help in preparing this manuscript.

References

Carter A, Roques D, Bristow C (2001) Understanding Mesozoic accretion in Southeast Asia: Significance of Triassic thermotectonism (Indosinian Orogeny) in Vietnam. Geology 29: 211-214

Chen DY, Zhou WB, Zhou LM (1993) Isotope geology of the Xiangshan uranium orefield. Mineral Deposits, 12 (4): 370-377 (in Chinese with English abstract)

Chen PR, Hua RM, Zhang BT (2002) Early Yanshanian post-orogenic granitoids in the Nanling region. Science in China (Series D) 45(8): 757-768

Chen PR, Kong XG, Wang YX, (1999) Rb-Sr isotopic dating and significance of early Yanshanian bimodal volcanic-intrusive complex from South Jiangxi Province. Geological Journal of China Universities 5(4): 378-383 (in Chinese with English abstract)

Chen PR, Zhang BT, Kong XG (1998) Geochemical characteristics and tectonic implication of Zhaibei A-type granitic intrusives in South Jiangxi Province. Acta Petrologica Sinica 14: 289-298 (in Chinese with English abstract)

Chen XM, Lu JJ, Liu CS (1999) Single-grain zircon U-Pb isotopic ages of the volcanic-intrusive complexes in Tonglu and Xiangshan areas. Acta Geoscientia Sinica 15 (2): 272-278 (in Chinese with English abstract)

Deng P, Tan ZZ, Wu LQ (2000) Tectono-magmatism of granite and uranium metallogenic sequences in North Guangdong. Uranium Geology in South China 17 (1-2): 32-43 (in Chinese)

Fan CF, Chen PR (2000) Geochemical features and tectonic implication of Beitou A-type granitic intrusive in South Jiangxi Province. Geochimica 29(4): 358-366 (in Chinese with English abstract)

Hua RM, Dong ZQ (1984) The characteristics and origins of granitic rocks of two genetic series in Dexing, Jiangxi. In: Xu KQ, Tu GC, Geology of Granites and Their Metallogenetic Relations. Beijing: Science Press: 347-366

Hua RM, Mao JW (1999) A preliminary discussion on the Mesozoic metallogenic explosion in East China. Mineral Deposits 18(4): 300-308 (in Chinese with English abstract)

Li HQ, Liu JQ, Wei L (1993) Study on geo-chronology of fluid inclusion in hydrothermal ore deposits and its geological applications. Beijing: Geological Publishing House (in Chinese)

Li KY, Shen JL, Wang XP (1989) Isotopic geochronology of Mesozoic terrestrial volcanic rocks in the Zhejiang-Fujian-Jiangxi area. Journal of Stratigraphy 13(1): 1-13 (in Chinese with English abstract)

Liu YM, Dai TM, Lu HZ, (1997) Ar/Ar and Sm/Nd isotopic ages of the lithogenesis and mineralization of the Qianlishan granite. Science in China (Series D) 27(5): 425-430 (in Chinese)

Liu YM, Xu JF, Dai TM (2002) Ar/Ar isotopic ages of the Qitianling granite and their geological significance. Science in China (Series D) 32, Supp: 40-48 (in Chinese)

Mao JW, Hua RM, Li XB (1999) A preliminary study of large-scale metallogenesis and large clusters of mineral deposits. Mineral Deposits 18(4): 291-299 (in Chinese with English abstract)

Mao JW, Zhang ZH, Yu JJ, (2003) Geodynamic settings of Mesozoic large scale mineralization in North China and vicinity: revealed from the accurate age determination of ore deposits. Science in China (Series D) 33(4): 289-299

Maruejol P (1990) Magmatic and hydrothermal REE fractionation in the Xihuashan granites (SE China). Contribution to Mineralogy and Petrology 104: 668-680

McKee EH, (1987) Geochronology of the Xihuashan composite granitic body and tungsten mineralization, Jiangxi Province, south China. Economic Geology 82: 218-223

Sun GA, Shi MK, Zhang HL (1989) Study on petrology, geochemistry, and metallogeny of Dajishan granite. In: Yichang Institute of Geology (ed). Scientific Reports of Geology and Mineral Resources in Nanling (2). Wuhan: University of China Geoscience Press: 326-363 (in Chinese)

Sun WD, Li SG, Chen YD (2002) Timing of synorogenic granitoids in the South Qinling, central China: Constraints on the evolution of the Qinling-Dabie orogenic belt. Journal of Geology 110(4): 457-468

Wang DZ, Liu CS, Shen WZ (1991) Discovery of Mesozoic S-type volcanic belt in Dongxiang-Xiangshan, Jiangxi, and its geological significance. Chinese Science Bulletin 36(19): 1491-1493 (in Chinese with English abstract)

Wang DZ, Liu CS, Shen WZ (1993) Volcanic-intrusive complex in Yanbei porphyry tin mine, Jiangxi. Journal of Nanjing University 29(4): 625-650 (in Chinese with English abstract)

Wang DZ, Ren QJ (1996) The Mesozoic Volcanic-Intrusive Complexes and Their Metallogenic Relations in East China. Beijing: Science Press

Wang YJ, Fan WM, Guo F (2002a) U-Pb dating of Mesozoic granodioritic intrusions in southeastern Hunan Province and its petrogenetic implication. Science in China (series D) 44(3): 270-280

Wang YJ, Zhang YH, Fan WM, (2002b) Numerical modeling for generation of Indo-Sinian peraluminous granitoids, Hunan Province: basaltic underplating vs. tectonic thickening. Science in China (series D) 45(11): 1042- 1056

Xiong XL, Zhu JC, Liu CS (1994) Alteration zoning of the Yanbei porphyry tin deposit in Jiangxi and geochemical characteristics of its main altered rocks. Mineral Deposits 13 (1): 1-10 (in Chinese with English abstract)

Zhang DQ, Li DX, Feng CY (2001) The temporal and spatial framework of the Mesozoic magmatic system in Zijinshan area and its geological significance. Acta Geoscientia Sinica 22 (5): 403-408 (in Chinese with English abstract)

Zhao ZH, Bao ZW, Zhang BY (1998) Geochemical features of Mesozoic basalts in South Hunan. Science in China (series D) 28, Supp: 102-112 (in Chinese)

Zhao ZH, Tu GC (2003) Super-large Ore Deposits in China Vol. 2. Beijing: Science Press: 54-56 (in Chinese)

Zhu X, Huang CK, Rui ZY (1983) The Geology of Dexing Porphyry Copper Ore Field. Beijing: Geological Publishing House (in Chinese with English abstract)

Intercummulus massive Ni-Cu-Co and PGE-bearing sulphides in pyroxenite: a new mineralization type in the layered gabbroic sequence of the Beja Igneous Complex (Portugal)

Ana P. Jesus, António Mateus, José Munhá, Álvaro Pinto
CREMINER/Centro Geologia/Dep. Geologia, U. Lisboa, Ed. C6, Campo Grande, 1749-016,Lisboa, Portugal

Abstract. Coarse-grained pyroxenite cumulates occurring within an olivine leucogabbro/pyroxenite gabbro rhythmic suite host a new sulphide mineralization type in the Beja Layered Gabbroic Sequence, Portugal. The sulphides formed in an intercummulus phase as a result of the coalescence of disseminated blebs of pyrrhotite with abundant pentlandite and chalcopyrite exsolutions, gradually disrupting the silicate matrix. Intra- and inter-granular veinlets are sealed by Ni-rich minerals of the linnaeite group, with decreasing Co content from earlier to later generations. The deposition of Ni (± Co)-rich pyrite represents the late mineral infill in the linnaeite veins. Pyrite veinlets and subhedral grains in the pyrrhotite groundmass display gradually lower Ni contents with time. Chalcopyrite is the latest sulphide phase, sealing micro-fractures and replacing pre-existing sulphides. EPMA data revealed concentrations up to 1500 ppm of Pt, Pd, Au, Ag Cd and Bi in pentlandite, chalcopyrite and in minerals of the linnaeite group.

Keywords. Layered gabbros, pyroxenite, intercummulus, massive sulphides

1 Introduction

The Beja Igneous Complex is an intrusive belt that can be followed for *ca.* 100 km along the southwestern border of the Ossa Morena Zone in Portugal (Fig. 1). The Beja Igneous Complex records syn-orogenic Variscan magmatic activity, extending from Upper Devonian to Late Visean (Dallmeyer et al. 1993). Three units are classically defined within the Beja Igneous Complex: 1) the Beja Layered Gabbroic Sequence (LGS), mainly consisting of olivine-bearing gabbroic rocks, rimmed by heterogeneous diorites resulting from variable extents of magma mixing and crustal assimilation; 2) the Cuba-Alvito Complex comprising granodioritic and gabbroic rocks; and 3) the Baleizão Porphyry Complex, a late, shallow intrusion consisting of porphyritic granitoids (Andrade 1983; Santos et al. 1990; Silva et al. 1970).

In order to assess the metallogenic potential of the Beja Layered Gabbroic Sequence, significant efforts were made to determine its internal architecture and related ore-forming systems. Two main styles of mineralization have been recognized previously (Jesus 2002; Jesus et al., 2003b): 1) massive Fe-Ti-V oxide accumulations within ultramafic cumulate lenses; and 2) anastomosing (locally stockwork) Cu(-Ni) sulphide vein arrays within strongly developed metasomatic halos. This paper is the first documentation of a new type of mineralization: intercummulus massive Ni-Cu-Co sulphides hosted by a pyroxenitic cumulate facies.

2 Geological framework

Detailed mapping of the Beja Layered Gabbroic Sequence (inset, Fig. 1) has revealed NW-trending magmatic layering that dips approximately 30ºSW, typically associated with a magmatic lamination. Field and geochemical cri-

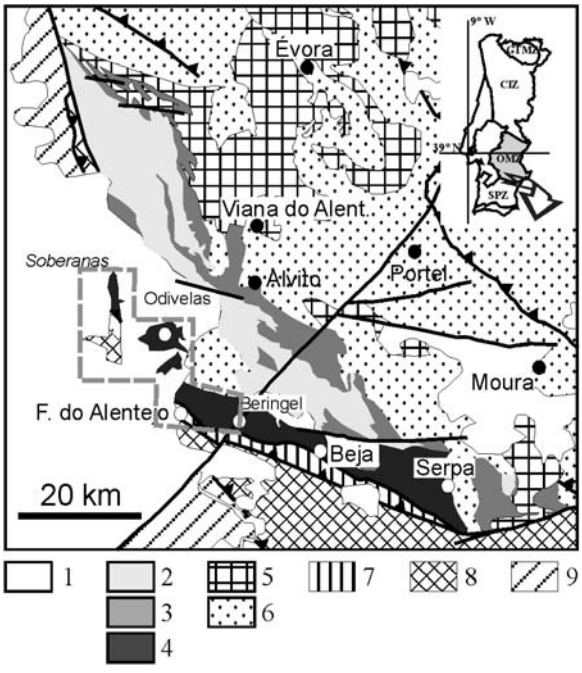

Figure 1: Location of the Beja Igneous Complex (BIC) with indication of the major geotectonic units of SW Iberia: CIZ, Central-Iberian Zone; GTMZ, Galicia – Trás-os-Montes Zone; OMZ, Ossa-Morena Zone; SPZ, South Portuguese Zone. Schematic geological map: 1) Cenozoic sedimentary cover; 2) Baleizão Porphyry Complex (BIC); 3) Cuba-Alvito Complex (BIC); 4) Beja Layered Gabbroic Sequence LGS (BIC). 5) Undifferentiated Variscan Granitoids. 6) Undifferentiated meta-sedimentary and meta-volcanic sequences and ultramafic rocks. 7) Beja-Acebuches Ophiolite Complex; 8) Meta-sediments and meta-volcanics of Pulo do Lobo Group. 9) Meta-sedimentary and meta-volcanic sequences of SPZ.

teria suggest that the intrusion had a multiphase history. This resulted from the input of several batches of magma, which each correspond to a distinctive series of gabbroic rocks.

Five main magmatic series were defined, from NW to SE: Soberanas I, Soberanas II, Odivelas I, II and III. The contact between Soberanas I and Soberanas II is tectonic. Soberanas I is composed of coarse-grained coronitic (leuco-) troctolite and fine grained wehrlite, whereas Soberanas II comprises fine-grained leuconorite to leucogabbro. The transition to Odivelas I is covered by Cenozoic sediments. Odivelas I consists mostly of olivine leucogabbro and includes in its lower section an intercummulus enrichment zone of vanadiferous Ti-magnetite + ilmenite, where massive type I Ti-V ores have developed (Jesus et al. 2003b). Odivelas II is a rhythmic succession of olivine gabbro with discontinuous anorthosite layers at its uppermost section. Odivelas III comprises a rhythmic sequence of well-layered olivine (leuco-)gabbro. Intercalations of fine-grained pyroxenite layers contain disseminated sulphide and sulpho-arsenide blebs, as well as anastamosing veins of pyrrhotite + chalcopyrite ± pyrite ± mackinawite, which have late-stage metasomatic haloes. These veins comprise type II mineralization (Jesus 2002; Jesus et al. 2003a). The contact between Odivelas II and III series is obscured by sedimentary cover.

Several suites of gabbroic rocks occur between Ferreira do Alentejo and Beringel. These gabbroic suites host Ni-Cu-Co- and PGE-bearing sulphide mineralization and can be correlated with Soberanas I and Odivelas II/III series. This new mineralization type occurs near Ferreira do Alentejo (Fig. 1) within a thick and rhythmic sequence of (coarse-grained) olivine leucogabbros (enclosing minor anorthosite) and pyroxenitic gabbros. Locally, these pyroxenitic gabbros grade to cumulate lenses of pyroxenite, which constitutes the preferential host of Ni-Cu-Co PGE-bearing sulphide mineralization.

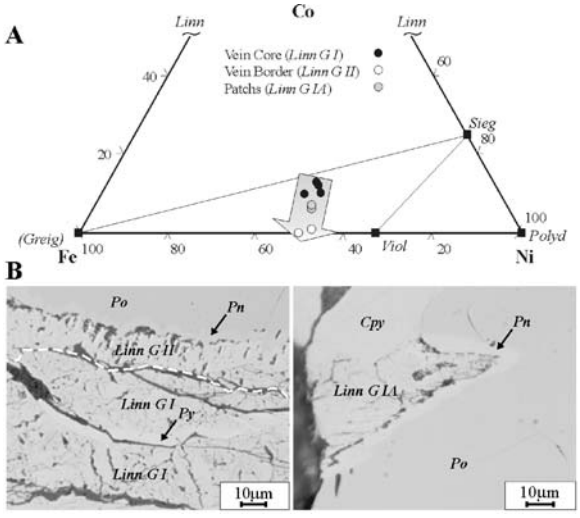

Figure 2: Chemical (A) and textural (B) features of the linnaeite group minerals. A- Compositional space of the analysed minerals. End-member composition (according with the AB_2S_4 formula): Linn, linnaeite s.s. $(Co^{2+})(Co^{3+})_2S_4$; Viol, violarite $(Fe^{2+})(Ni)_2S_4$; Sieg, siegenite $(Ni,Co)(Ni,Co)_2S_4$ (plotted empirical formula: $Ni_{2.25}Co_{0.75}S_4$); Polyd, polydymite $(Ni)(Ni)_2\ S_4$; Greig, greigite $(Fe^{2+})(Fe^{3+})_2S_4$. B- Left: typical zonation of linnaeite s.l. veins, white line indicates transition of Co-rich core (linnaeite GI) to Co-poor vein borders (linnaeite GII). Right: linnaeite s.l. GIA patches in pyrrhotite (Po) matrix bordered by pentlandite (Pn).

3 Ni-Cu-Co mineralization

Pyroxenites hosting the massive Ni-Cu-Co- and PGE-bearing sulphide are mainly composed of randomly oriented, subhedral grains of clinopyroxene ($En_{43}Wo_{45}Fs_{12}$). Millimetre-sized blebs of pyrrhotite with pentlandite-chalcopyrite exsolutions occur as inclusions within the coarser clinopyroxene grains, forming graphic intergrowths. As the sulphide modal proportion increases, clinopyroxene grains are disrupted, displaying abundant corrosion gulfs but only mild retrograding effects. Rare plagioclase (An_{60}) occurs interstitially or included within the clinopyroxene-sulphide framework. Silicate phases do not show any significant compositional zoning or retrograde textures, suggesting equilibrium with the sulphide phases. Minor magnetite ($Fe^{3+}{}_{1.59}Ti_{0.1}Cr_{0.1}V_{0.03}Al_{0.07}\ Fe^{2+}{}_{1.08}\ Mg_{0.04}Mn_{0.01}O_4$) and ilmenite ($Fe^{2+}{}_{0.84}Mg_{0.06}\ Mn_{0.06}Fe^{3+}{}_{0.05}V_{0.05}\ Ti_{0.95}O_3$) coexist with pentlandite-pyrrhotite-chalcopyrite blebs suggesting fO_2 conditions of late stage (~620 ºC) crystallization close to QFM.

Groundmass and disseminated pyrrhotite blebs display similar Fe:S (0.87) and Ni contents (0.01 (atoms per unit formula) suggesting that the massive ores developed by coalescence of monosulphide droplets as sulphide saturation was achieved. pentlandite exsolutions have an almost invariant (Co+Ni):Fe ratio of 1.2-1.4 and an average formula $Fe_4Ni_{4.3}Co_{0.6}S_8$. Linnaeite group minerals (*linnaeite s.l.*) have sealed a network of intra- and intergranular millimetric veinlets that crisscross the pyrrhotite matrix. Electron microprobe data confirms that these veins have complex compositional zoning that results from multiphase infilling, as indicated by petrographic observations (Fig. 2).

Early *linnaeite s.l.* Co-rich vein cores are rimmed by a dissymmetric (sometimes absent) Co-poor border, whereas irregular patches with intermediate Co contents are observed in the pyrrhotite matrix; pentlandite occurs on the edges of these patches (Fig. 2B). Ideal metal site distribution according with the (thio-) spinel-like structure of linnaeite group minerals shows that the analysed minerals are non-stoichiometric: *linnaeite s.l.* Co-rich vein cores $(Fe)_1(Fe_{0.3}Ni_{1.5}Co_{0.4})_{\Sigma 2.2}\ S_{3.9}$; *linnaeite s.l.* Co-poor vein borders $(Fe)_1(Fe0_{.5}Ni_{1.5})_{\Sigma 2}S_4$ and *linnaeite s.l.* patches in pyrrhotite matrix $(Fe)_1(Fe_{0.3}Ni_{1.5}Co_{0.2})_{\Sigma 2}\ S_4$. The resulting deviation is due to exceeding Fe in the B position, displacing the trend towards a greigite composition

This page intentionally blank

Table 1: EPMA trace element average contents (ppm) of the sulphide phases (maximum and minimum in parenthesis) normalized for 100 wt%. N = number of analyses; nd= below detection limit. Py VL = pyrite late veinlets occurring in the core of linnaeite s.l. zoned veins; Py G = early pyrite grains in the pyrrhotite matrix; Py VG = pyrite veins in pyrrhotite matrix; Ccp = chalcopyrite exsolutions in pentlandite blebs; Po = pyrrhotite blebs and groundmass; Pn = pentlandite exsolutions in pyrrhotite blebs; Linn GI = linnaeite s.l. Co-rich vein cores; Linn GII = linnaeite s.l. Co-poor vein borders; Linn GIA = linnaeite s.l. patches in pyrrhotite matrix.

	Pd	Ag	Cd	Pt	Au	Bi	N
Py VL	26 (51-1)	268 (535-1)	479 (956-1)	*nd*	275 (550-1)	262 (522-1)	*2*
Py G	*nd*	137 (273-1)	56 (110-1)	48 (94-1)	*nd*	*nd*	*2*
Py VG	183 (537-1)	65 (160-1)	386 (1308-1)	271 (874-1)	19 (89-1)	196 (790-1)	*5*
Ccp	879 (1034-723)	334 (667-1)	646 (1291-1)	*nd*	346 (692-1)	427 (698-156)	*2*
Po	298 (708-1)	172 (925-1)	570 (1075-1)	133 (593-1)	126 (751-1)	284 (1244-1)	*6*
Pn	*nd*	694 (1116-459)	382 (1447-1)	497 (1235-2)	360 (1768-1)	289 (958-1)	*6*
Linn GI	197 (784-1)	40 (158-1)	253 (732-1)	535 (1614-2)	206 (822-1)	112 (327-1)	*4*
Linn GII	295 (588-1)	213 (425-1)	27 (53-1)	*nd*	*nd*	136 (234-39)	*2*
Linn GIA	405 (810-1)	699 (1078-320)	196 (391-1)	155 (308-2)	*nd*	*nd*	*2*

(Fig. 2A). The *linnaeite s.l.* Co-rich vein cores present the maximum deviation accompanied by sulphur deficiency, a common feature in non-stoichiometric minerals of the linnaeite group. Late veinlets of Ni-rich pyrite in the *linnaeite s.l.* zoned veins ($Fe_{0.9}Ni_{0.1}S_2$) include trace amounts of Co (726-1147ppm). Millimetric veinlets of pyrite in the groundmass and occurring as early-formed subhedral grains display gradually lower Ni contents from 11666 to 7300 ppm. Late-stage chalcopyrite occurs in microfractures and has locally replaced earlier-formed sulphides.

Semi-quantitative EPMA data for trace elements in sulphide phases are shown in Table 1. Higher Pt, Ag and Au contents were measured consistently from the rims of pentlandite, suggesting that cryptic mineral exsolutions incorporating those metals may be present. Chalcopyrite has the highest analysed Pd concentration (1034 ppm). Pd/(Pt+Au) is strongly partitioned between chalcopyrite and pentlandite with (Pt+Au) displaying higher affinity with the Co-Ni-rich phase. All *linnaeite s.l* phases display negative correlation between Co contents and Pd/(Pt+Au) ratio. Thus, *linnaeite s.l* compositional (Co) variations may represent a suitable pathfinder for high (Pt+Au) grades.

4 Conclusions and future research

The results of this study demonstrate the occurrence of primary magmatic Ni-Cu-Co and PGE-bearing sulphide mineralizations in the Beja Layered Gabbroic Sequence, providing new insights into the metallogenic potential of this igneous complex. Further research is underway to fully explore the economic significance of these new findings.

Acknowledgements

The authors acknowledge the financial support of CREMINER and Centro de Geologia-FCUL. Part of this work was supported by the research project 12/2.1/CTA/82/94– PROGEREMIN. Ana Jesus acknowledges a PhD Grant SFRH/BD/6355/2001. D. Cooke is gratefully acknowledged for is reviews of this paper.

References

Andrade AS (1983) Contribuition à l'analyse de la suture Hercynièn ne de Beja (Portugal), perspectives metallogéniques. Ph.D. thesis, INLP, Univ. of Nancy, France (English abstract)

Dallmeyer RD, Fonseca PE, Quesada C, Ribeiro A (1993) $^{40}Ar/^{39}Ar$ mineral age constraints to the tectonothermal evolution of the Variscan Suture in SW Iberian. Tectonophysics 222: 177-194

Jesus AP (2002) Fe-Ti-V mineralizations and sulphide occurrences in gabbroic rocks of the Beja Igneous Complex (Odivelas–Ferreira do Alentejo). M.Sc. thesis, University of Lisbon (English abstract)

Jesus AP, Mateus A, Oliveira, V Munhá J (2003a) Ore forming systems in the Layered Gabbroic Sequence of the Beja Igneous Complex (Ossa Morena Zone, Portugal); state of the art and future perspectives. In: Eliopoulos, DG et al. (eds), Mineral Exploration and Sustainable Development. Proceedings Volume of the 7th Biennial SGA Meeting, Athens, Greece, August 24 - 28, 2003. Milpress, Rotterdam Netherlands: 591-594

Jesus AP, Mateus A, Waerenborgh JC, Figueiras J, Cerqueira L, Oliveira V (2003b) Hypogene titanian, vanadian maghemite in reworked oxide cumulates in the Beja Layered Gabbro Complex, Odivelas, Southeastern Portugal. Canadian Mineralogist 41: 1105-1124

Santos JF, Andrade SA, Munhá J (1990) Orogenic magmatism in the meridional border of the Ossa Morena Zone. Comunicações Serviços Geológicos de Portugal 76: 91-124 (English abstract)

Silva LC, Quadrado R, Ribeiro L (1970) Preliminary notes about the existence of a zoned structure and of anorthosites in the gabbro-dioritic massif of Beja. Boletim Museu Laboratório Mineiro Geológico da Universidade de Lisboa 11: 223-232 (English abstract)

Geochemical characteristics of ores from the Tangziwa deposit, Gejiu district, Yunnan province, China

Run-Xing Jia, Wei-Xuan Fang, Zhen-Min Gao, Hong-Yang Li
Open Laboratory of Ore Deposit Geochemistry, Institute of Geochemistry, Chinese Academy of Sciences, Guiyang, 550002, Guizhou, China

Ying He
Key Laboratory of Continental Dynamics of the Ministry of Education, Department of Geology, Northwest University, Xi'an, 710069, Shaanxi, China

Abstract. Trace element and REE concentrations of ores and wallrocks have been determined for the Tangziwa tin - polymetallic deposi, Gejiu, Yunnan province, China. Analyses of trace element contents of the metamorphosed mafic volcanic host rocks has revealed an elevated average tin content of 117ppm. This implies that the volcanic wallrocks could have been an important source of tin mineralization, in addition to copper, nickel and zinc, which are also present in high concentrations.

Keywords. Geochemistry, tin, polymetallic mafic, genesis, Gejiu

1 Introduction

The Gejiu tin-polymetallic district in Yunnan province, China, is one of the most important tin-producing regions in the world. The district contains skarn, vein-type and stratabound carbonate-hosted ores. The area has been studied extensively by previous workers (Huang 1984; Peng 1985; Yu et al. 1988; Li et al. 1993; Zhuang et al. 1996; Zhou et al. 1997; Fang et al. 2001; Jia et al. 2004). Despite this, there is still controversy regarding the origin of the ores. Some workers (e.g., Huang 1984; Peng 1985; Yu et al. 1988; Zhuang et al. 1996) have argued that mineralization was magmatic - hydrothermal in origin. Zhou et al. (1997) argued that the ores are purely hydrothermal, with no magmatic contribution. Others have argued for a sedimentary proto-ore that has been upgraded and modified by magmatic activity (Li et al. 1993).

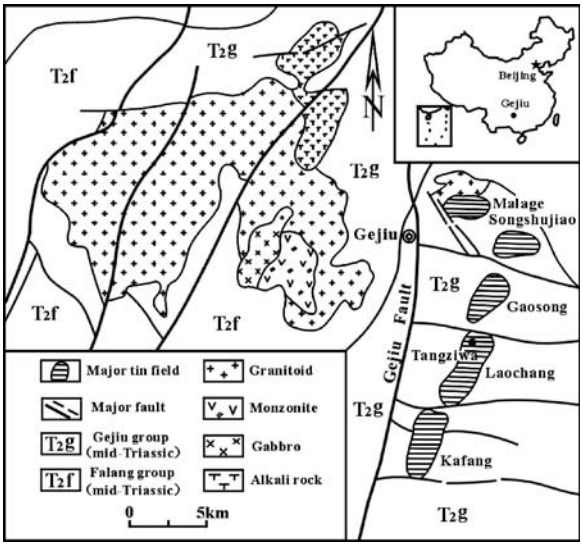

Figure 1: Geological map of the Gejui district, China, showing the location of the major tin fields and granitoids.

2 Location

The tin-polymetallic deposits of Gejiu are located in the southeastern part of Yunnan province in China (Fig. 1). Sedimentary rocks cover more than 60% of the district (Fig. 1). Strata from the Triassic to the Quaternary are exposed in the region. Major fault have N-, NW- and NE-trends. Multiple episodes of volcanism and plutonism have occurred from the Proterozoic to the Cenozoic (Fang et al. 2002). The tin granites have a Rb/Sr whole-rock isochron age of 84 to 81 Ma (Zhuang et al. 1996).

3 Mineralization

Tin and sulfide mineralization in the Tangziwa deposit are associated with Cretaceous leucogranites, whcih were emplaced into volcano-sedimentary rocks of the Gejiu Group. The wallrocks at Tangziwa consist mainly of Mid-Triassic carbornate rocks intercalated with mafic volcanics.

4 Sampling and analysis

The trace element and REE compositions of samples of the host rocks and ores from Tangziwa have been determined by ICP-MS (Qi et al. 2000) at the Open Laboratory of Ore Deposit Geochemistry, Institute of Geochemistry, Chinese Academy of Sciences. Samples analyzed include altered granite (n = 4), skarn-type ores (n = 3), metavolcanic rocks (n = 2) and marbles (n = 3; all data listed in Table 1).

Table 1: Trace element (ppm) of rocks and ores from Tangziwa deposit, Gejiu

	leucogranite				skarn-type ore			metavolcanic rock		marble		
sample	GR-15	GR-16	GR-18	GR-19	TSK-21	TSK-23	TSK-24	MRG-1	MRG-2	MA37	MA39	MA40
V	0.516	0.263	1.42	1.99	25.6	15.6	42.6	256	292	8.27	11.0	11.5
Co	0.977	0.756	1.175	1.31	78.3	3.86	2.84	44.1	46.4	4.16	4.49	3.51
Ni	--	0.148	0.417	1.24	5.33	6.71	4.03	217	268	22.2	13.1	12.5
Cu	285	7.03	12.5	18.2	11260	113	388	198	144	7.84	32.9	13.1
Zn	31.3	6.99	9.27	16.6	176	136	75.7	199	217	4.27	9.38	26.1
Ge	4.49	3.54	3.84	2.90	7.34	21.9	4.05	3.14	2.68	0.547	0.485	0.544
As	101	13.9	12.3	9.85	6.49	12.3	103	15.0	9.55	40.8	7.57	16.5
Rb	841	923	924	816	48.4	11.7	2203	704	1331	1.40	3.46	4.57
Sr	89.8	60.5	47.1	78.5	17.0	818	29.3	768	864	645	802	787
Y	131	102	97.2	59.5	23.2	2.95	52.3	22.4	22.4	0.661	0.961	2.27
Zr	70.3	66.5	63.6	60.4	15.0	6.86	9.64	128	162	1.54	2.94	14.4
Nb	48.5	49.2	46.0	52.2	3.46	13.5	27.0	27.0	33.2	0.246	0.342	1.76
Mo	0.502	1.34	0.727	4.49	0.308	78.7	1.97	10.5	9.36	0.945	1.27	0.159
Cd	0.536	0.573	0.616	0.453	4.05	131	0.613	3.36	2.44	0.126	0.165	0.004
In	0.416	0.042	0.084	0.069	2.98	19.7	0.366	0.658	0.416	0.011	0.033	0.019
Sn	10.6	13.9	24.2	18.9	111	4089	30.1	135	99.6	1.65	3.56	0.63
Sb	4.64	1.43	1.33	1.26	0.792	1.21	1.25	1.88	1.71	0.528	0.663	1.18
Cs	18.8	32.2	40.8	24.7	8.32	4.02	289	147	328	0.151	0.47	1.09
Ba	27.2	37.6	21.8	47.3	3.39	74.3	18.3	121	224	2.84	6.00	9.20
Hf	7.29	6.55	5.52	5.46	0.396	0.119	0.277	3.74	4.90	0.01	0.124	0.479
Ta	17.0	15.3	14.3	12.7	0.157	0.929	4.27	1.63	2.23	0.024	0.015	0.071
W	97.7	38.2	38.2	325	1.84	822	1814	8.85	96.2	2.59	0.642	3.52
Tl	3.62	4.14	4.94	4.42	0.208	0.085	7.65	4.9	8.3	0.039	0.135	0.091
Pb	103	65.9	69.5	72.4	3.81	3.05	2.06	6.52	8.24	1.84	6.04	1.82
Bi	29.7	1.53	6.61	2.08	116	1.15	63.4	0.682	0.367	0.048	0.131	0.193
Th	19.8	20.5	26.0	27.5	0.768	0.645	0.332	2.99	3.70	0.064	0.087	0.446
U	36.7	17.3	32.6	24.7	3.89	1.13	30.2	1.24	1.18	0.574	0.943	1.29
La	10.5	9.42	13.9	22.1	0.448	1.42	0.524	22.7	25.5	0.829	1.26	2.09
Ce	29.4	26.3	32.9	50.8	1.49	4.15	1.45	48.4	55.0	1.33	2.41	4.99
Pr	4.46	3.90	4.43	6.23	0.25	0.658	0.238	5.93	6.82	0.212	0.26	0.623
Nd	21.2	18.2	20.2	25.5	1.13	3.18	1.59	26.5	28.6	0.485	0.913	2.42
Sm	11.0	9.59	9.80	8.03	0.779	0.934	1.08	5.82	6.51	0.131	0.277	0.365
Eu	0.075	0.102	0.069	0.088	0.051	0.074	0.046	1.82	1.77	0.049	0.074	0.138
Gd	13.8	11.2	11.1	8.04	1.29	0.569	1.89	5.79	5.68	0.174	0.15	0.479
Tb	3.05	2.32	2.22	1.73	0.344	0.111	0.388	0.742	0.986	0.022	0.014	0.084
Dy	19.9	14.5	15.5	10.5	2.37	0.676	3.24	4.58	5.03	0.093	0.181	0.376
Ho	3.97	2.87	3.14	2.17	0.494	0.073	0.785	0.858	0.791	0.019	0.033	0.068
Er	11.8	8.39	8.78	6.05	1.48	0.246	2.34	1.86	2.19	0.052	0.092	0.264
Tm	1.77	1.32	1.35	0.912	0.26	0.044	0.325	0.248	0.288	0.016	0.01	0.038
Yb	13.5	10.2	10.4	6.78	1.75	0.295	2.30	1.60	1.90	0.033	0.126	0.208
Lu	1.84	1.47	1.42	0.944	0.245	0.048	0.364	0.231	0.238	0.007	0.016	0.032

The trace elements for the samples were analyzed ICP-MS method in the Open Lab of Ore Deposit Geochemistry, Institute of Geochemistry, Chinese Academy of Sciences, Guiyang; -- no data. GR-granite. TSK-skarn type ore. MRG- metamorphosed mafic volcanic rock. MA-mable.

5 Results

The metamorphosed mafic volcanic rocks contain elevated Cu, Co, Ni, V, Zn, Sn, Mo, Cd, In and LILEs (such as Rb, Cs and Ba) compared to the altered granites (Table 1). The granite samples are enriched in U, Bi, Pb, Ta and Th compared to the metavolcanics.

The normalized REE pattern determined for the skarn-type ores is similar to that in the granite, with no obvious Ce anomaly and a sharp negative Eu anomaly (Fig. 2); The normalized REE patterns for the metavolcanic rocks and marbles are characterized by slight enrichment of LREE with no obvious Ce and Eu anomalies (Fig. 2).

6 Discussion and conclusions

Mineralization at Gejiu is primarily related to granitoid emplacement in the Cretaceous. Volcanism during the Indo-Chinese orogeny may, however, have been an important precursor. Metavolcanic country rocks occur at several major tin deposits in addition to the Gejiu district, including Chahe and Baotan in China, (Li 1984; Liu et al. 1984), and Nam Salu in Indonesia (Schwartz and Surjono 1990). The high average concentrations of Sn (117 ppm), Cu (171 ppm), Zn (208 ppm) and Ni (243 ppm) for the metavolcanic rocks at Gejiu (Table 1) indicate that the wallrocks could have been an important source of tin and base metals.

This page intentionally blank

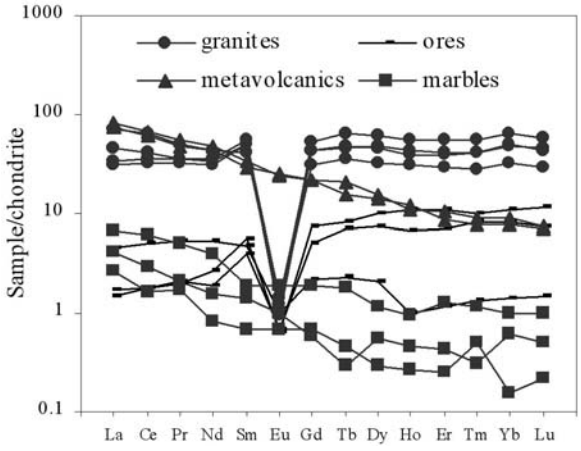

Figure 2: Normalised REE patterns for ores, granites, metavolcanic and marble samples from the Tangziwa deposit.

Acknowledgements

This study was supported jointly by the Chinese State Key Project on Fundamental Research Planning (Grant No 2001CB409805), and by the Ministry of Science and Technology of China (2004BA615A-03).

References

Fang WX, Hu RZ, Xie GQ, Su WC (2001) On characteristics of the metallogenic systems of continental dynamics and metallogenic series as well as prospecting orientations at the southern margin of the Yangtze massif and its vicinities. Acta Mineralogical Sinica 21(4): 561-570 (in Chinese with English abstract)

Huang TR (1984) Generality for the typical deposits of Gejiu primary tin deposits. Yunnan geology 3 (1): 36-46 (in Chinese)

Jia RX, Fang WX, HE Y, Gao ZM, Li HY(2004) Geochemical Characteristics of Rare Earth Elements in Gejiu Tin Polymetallic Deposits, Yunnan Province, China. Journal of Rare Earths 22(5):714–720.

Li L Z (1984) The geological characteristics and mineralized indicators of Chahe tin deposit, Sichuan. Yunnan geology 3 (1): 59-71 (in Chinese with English abstract)

Li XJ, Yang Z, Shi L, Deng BL (1993) Chinese tin deposits, in "chinese deposits" editor committee, Chinese deposit], mid-volume. Beijing: Geological publishing house 105-188 (in Chinese)

Liu YZ, Zhong K, Ma LQ (1984) The genetics and distributed law of tin deposits in Guangxi. Geology of Guangxi, First Issue: 11-19. (in Chinese with English abstract)

Oi L, Hu J, Gregoire DC (2000) Determination of trace elements in granites by inductively coupled plasma mass spectrometry. Talanta, 51: 507-513

Peng CD (1985) Discussion on the mineralizing condition and the type model of the tin deposits in Gejiu district. Yunnan geology 4 (1): 18-32 (in Chinese with English abstract)

Schwartz MO, Surjono (1990) The strata-bound tin deposit Nam Salu, Kelapa Kampit, Indonesia. Economic. Geology 85 (1):76-98

Yu CW, Tang YJ, Shi PF, Deng BL (1988) The dynamic system of endogenic ore formation in Gejiu tin-polymetallic ore region, Yunnan province. Wuhan: China University of Geosciences Press 1-304 (in Chinese with English abstract)

Zhou JP, Xu KQ, Hua RM, Zhao YY (1997) A discussion on genesis of the tin Polymetallic sulfide deposits of southeastern Yunnan. Yunnan geology 16(4): 309-349 (in Chinese with English abstract)

Zhuang YQ, Wang RZ, Yang SP, Yi JM (1996) Geology of Gejiu Tin-Copper Polymetallic Deposit. Beijing: Seismological press 1-145 (in Chinese with English abstract)

Ni-Cu-PGE mineralization in the Upper Proterozoic Ioko-Dovyren mafic-ultramafic massif, Russia

E.V. Kislov
Geological Institute SD RAS, Ulan-Ude, Russia

Abstract. Sulphide PGE-Ni-Cu and low sulphide PGE mineralization has been discovered in a Rifean (Upper Proterozoic) Ioko-Dovyren mafic-ultramafic intrusion at Nort Baikal region, Russia. The age, geodynamic setting, contact processes and mineralization of the Ioko-Dovyren massif are comparable with other known layered intrusive complexes such as Duluth (USA), Muskox, Voisey's Bay and several other examples in Canada, China and Brazil. Mineralization is associated with volcano-plutonic complexes related to continental paleorift structures. The Rifean metallogenical epoch belongs together with the Archean and Lower Proterozoic epochs as major periods of Ni-Cu-PGE metallogenesis.

Keywords. Mafic-ultramafic intrusions, continental rift, plume

1 Introduction

The world's main sources of Ni and platinum group elements (PGE) are the Archean komatiite bodies of Kambalda, the Lower Proterozoic norite massif at Sudbury, picrodolerite bodies of Pechenga, and the Permo-Triassic picrodolerite massifs of the Norilsk-Talnakh area, in addition to various laterites. Archean and Lower Proterozoic dunite-garzburgite-bronzitite-gabbronorite massifs at Bushveld, Stillwater, and the Great Dike are the principal sources of low-sulphide PGE ores.

Sulphide PGE-Ni-Cu and low sulphide PGE mineralization has been discovered in Rifean (Upper Proterozoic) Ioko-Dovyren mafic-ultramafic intrusion at Nort Baikal region, Russia. Mineralization is associated with conduits within a volcano-plutonic complex that formed within a continental paleorift structure. This discovery places the Rifean metallogenical epoch alongside the Archean and Lower Proterozoic epochs as major periods of Ni-Cu-PGE metallogenesis.

2 Geology of the Ioko-Dovyren intrusion

The Ioko-Dovyren layered dunite-troctolite-gabbro intrusion is located in the North Baikal region (56°30'N and 110°E; Fig. 1). It is a 26 km long and up to 3.5 km wide sill-like body, which was intruded almost concordantly into Neoproterozoic carbonate-terrigenous rocks within the axis of the Synnyr rift zone.

The sediments of the Synnyr rift zone are overlain by the Inyaptuk picrite-basaltic and Synnyr subalkali basalt-basalt-trachydacitic volcanics suites of Rifean age. The Inyaptuk suite was deposited in a submarine environment (pillow lavas), whereas the Synnyr suite formed under subaeral conditions (based on the presence of hematite).

Small bodies of peridotites, pyroxenites, diabases and the Ioko-Dovyren layered massif intruded the carbonate-terrigeneous sediments. The Ioko-Dovyren intrusion was emplaced in the Late Proterozoic with estimated ages of 780 to 730 ± 30 Ma (K-Ar on phlogopite; Gerling et al. 1962; Gurulev 1965), 739 ± 55 Ma (Rb-Sr isochron; Kislov et al. 1989) and 673 ± 22 Ma (Sm-Nd isochron; Amelin et al. 1996). The Ioko-Dovyren intrusion appears to be an eroded sub-volcanic chamber for the Synnyr volcanic suite, based on their similar geochemistry (Manuylova and Zarubin 1981; Konnikov et al. 1988, 1994; Kislov and Konnikov 1992). The age of the Synnyr volcanic suite (700 ± 35 Ma, U-Pb zircon method; Neymark et al. 1991) overlaps the age of Ioko-Dovyren.

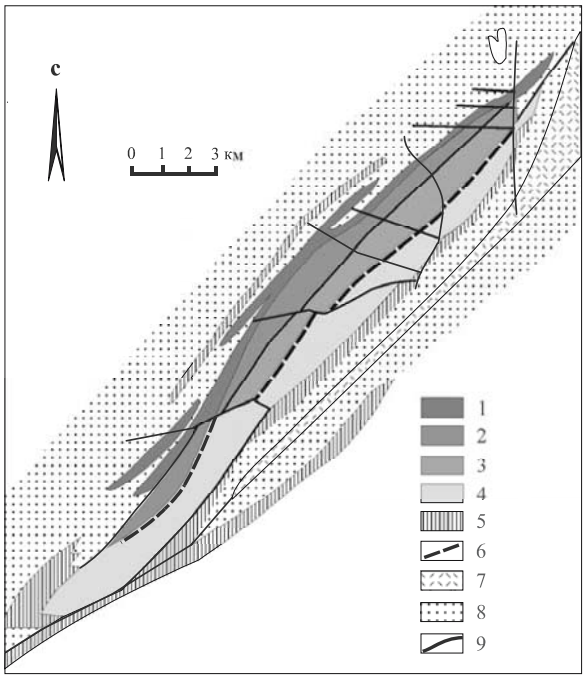

Figure 1: Geology of the Ioko-Dovyren dunite-troctolite-gabbro massif. 1 – plagioclase peridotites; 2 – dunites; 3 – rhytmic layering of plagioclase dunites, troctolites, olivine gabbro; 4 – olivine gabbro, olivine gabbronorites; 5 – gabbronorites; 6 – PGE-bearing horizon; 7 – volcanics (trachiliparites, trachidacitec, andesites); 8 - quartsites, limestones, schists, sandstones; 9 – faults.

The wall rocks at the northwestern end of the massif are fine-grained schists interlayered with dolomites and sulphide-bearing metapelites. These have been folded and metamorphosed to greenschist to lower amphibolite facies. Pyroxene hornfels and partial melting veinlets occur at the contact zone with the intrusion. The intrusion and country rocks (Fig. 1) are covered by a sequence of Vendian conglomerates and sandstones which overlie the north-east flank of the massif unconformably.

The massif consists, from the bottom upward, of: lower marginal zone (up to 200 m thick), ultramafic zone (up to 1000 m), layered zone (up to 1000 m), and a gabbroic zone (up to 1100 m).

The rocks of the massif are characterised by the assemblage olivine + plagioclase + clinopyroxene, with a change of cumulus minerals as follows: olivine + chromespinel – olivine + plagioclase + chromespinel – olivine + plagioclase + clinopyroxene – olivine + plagioclase + clinopyroxene + orthopyroxene.

Ophitic granophyric gabbronorites occur as a sill in the uppermost portion of the massif. These rocks were produced by injection of a younger basalt melt into the chamber from an intermediate, deeper-seated reservoir (Konnikov et al. 1988; Kislov and Konnikov 1992). Similar noritic rocks form a belt of sills and dikes, which cut basal plagioperidotites at the massif and the adjacent country rocks.

The Ioko-Dovyren intrusion contains widely distributed metasedimentary xenoliths derived from the wallrocks. Magnesian skarns are common in upper part of the ultramafic zone, and also occur in the base of the layered zone. A layer of xenoliths from 2-3 cm up 100-150 m in width occurs about 1000 m above the basal contact in the central part of the massif. This zone contains brucite marbles and forsterite – monticellite - spinel, brucite - forsterite, mervinite and vesuvianite - fassaite skarns. Xenoliths of terrigenous rocks are less common, occuring mainly in the plagioperidotites and mafic rocks near the roof of the massif.

3 Mineralization

Ni-Cu mineralization in the Ioko-Dovyren massif has been known since 1949, with the area subjected to geological prospecting from 1959 to 1963 (Gurulev 1965; Kislov 1998). Mineralization is confined to the plagioperidotites of the Ioko-Dovyren massif and to sills of the same composition that have penetrated the intrusion footwall. Both disseminated (locally net-textured) and massive sulphide Ni-Cu mineralization occurs. Mineralization is irregularly distributed, and is best developed where plagioperidotites have cut by the dikes and sills of granophyric gabbronorites and gabbro-pegmatites.

Disseminated mineralization is considerably more abundant than net-textured and massive ores. Bodies of disseminated mineralization have been traced along strike for 1400 to 1700 m in surface exposures. Their width typically varies from 8 to 25 m, locally reaching 80 m. The lenses of disseminated mineralization are oriented parallel to the sills and the bottom zone plagioperidotites. Veins of massive sulphide mineralization most commonly occur inside the disseminated ore zones. The largest sulphide vein occurs in the northeastern part of the massif. It extends along the base of the massif for 650 m and is 0.7 - 1.0 m wide. Sulphide veins of smaller size (15 - 50 m long and 0.2 - 1.5 m thick) are confined to tectonic zones of sublatitudinal and submeridional directions. Drilling data indicate that the veins dip almost vertically and extend to depths of more than 500 m.

The disseminated ore is characterized by low grades (average 0.5% Ni, 0.28% Cu and 0.03% Co). The massive sulphide veins have much higher grades (average 2.1% Ni, 0.64% Cu and 0.1% Co). The Ni/Cu ratio of both types of sulphide mineralization (1.9 and 3.3, respectively) is similar to other sulphide Ni-Cu deposits, but the Ni/Co is notably lower (16.7 and 21.0, respectively). Elevated Co contents are a distinctive characteristic of the Ioko-Dovyren massif.

Sulphide mineralized zones at Ioko-Dovyren are enriched in PGE (up to 0.5 ppm Pt, 2.2 ppm Pd, 0.24 ppm Rh), Au (up to 0.32 ppm), Ag (up to 16 ppm), Se (up to 23 ppm) and Te (up to 14 ppm).

The presence of low-sulphide PGE mineralization in the Ioko-Dovyren intrusion was documented by Konnikov et al. (1994). This mineralization is confined to horizons of heterogeneous rocks within the gabbroic part of the massif, and has been traced along strike for 20 km.

The lowest and richest horizon (I) is confined to the transition zone between rhythmic layered troctolite - olivine gabbro and the olivine gabbro zones (500 to 600 m above the first zone of cumulus plagioclase). The PGE ore zone is composed of concordant veins and lenses of coarse-grained and taxitic troctolites, olivine gabbros, pegmatites and anorthosites. The most common are schlieren and lens-like bodies of anorthosites surrounded by gabbro-pegmatites. The anorthosite bodies are mostly a few cm to 1 m thick and extend for 2 to 5 m along strike (rarely >40 m), forming discontinuous ore zones with an en echelon-like distribution. Horizon I consists of three separate layers over a 200 m vertical interval.

The PGE-bearing rocks contain olivine, plagioclase and chromespinels in a cumulate paragenesis. The intercumulus domains contain clinopyroxene, plagioclase and rare orthopyroxene.

Pd is more abundant then Pt in the Ni-Cu mineralized plagioperidotites. The low sulphide PGE horizons are marked by elevated Pt concentrations compared to Pd, and high Au concentrations. This suggests that different mechanisms of Pt and Pd fractionation occured in the ultramafic and mafic parts of the intrusion. Pt accumu-

lation in the mafic melt seems to have been associated with alteration of cumulate layers and evolution of the intercumulate melt, the residual derivative of which was enriched in fluid components and sulphide liquid.

4 Comparisons with other systems

The age, geodynamic setting, contact processes and mineralization of the Ioko-Dovyren massif are comparable with other layered intrusive complexes, such as Duluth (Minnesota, USA), Muskox (Northwest Territories, Canada), Voisey's Bay (Labrador, Canada) Crystal Lake, Geordie Lake and Two Duck Lake (Ontario, Canada), Jinchuan (Gansu, China) and Niquelandia (Goias, Brazil). Summaries for each system are provided below, and list the following information: name of the intrusive complex; age, Ma; geodynamic setting; rock types; contact interaction; mineralization; references. **Ioko-Dovyren**: 740 Ma; continental rift, plume, volcano-plutonic complex; dunite, troctolite, gabbro; skarn xenoliths, contamination; sulphide Ni-Cu, low-sulphide PGE. **Duluth**: 1120 Ma; continental rift, plume, volcano-plutonic complex; troctolite, anorthosite; hornfel xenoliths, contamination; sulphide Ni-Cu, low-sulphide PGE (Naldrett 1997, 1999; Weiblen et al. 1989). **Muskox**: 1270 Ma; continental rift, plume, volcano-plutonic complex; dunite, peridotite, pyroxenite, gabbro; contamination; sulphide Ni-Cu, low-sulphide PGE (Barnes and Francis 1995; Barnes et al. 1997). **Voisey's Bay**: 1333 Ma; troctolite, anorthosite; gneiss xenoliths, contamination; sulphide Ni-Cu; (Naldrett 1997, 1999; Amelin et al. 1999). **Crystal Lake**: continental rift; peridotite, norite, anorthosite; low-sulphide PGE; (Naldrett 1997). **Geordie Lake**: 1108 Ma; continental rift; troctolite, gabbro; low-sulphide PGE; (Good and Crocket 1994b; Mulja and Mitchell 1990, 1991). **Two Duck Lake**: continental rift; gabbro; volcanic and gabbro xenoliths, contamination; low-sulphide PGE; (Good and Crocket 1994a; Watkinson and Ohnenstetter, 1996). **Jinchuan**: 1501 Ma; continental rift; peridotite; skarns, contamination; sulphide Ni-Cu; (Chai and Naldrett 1992; Naldrett 1997). **Niquelandia**: 1560-1600 Ma; continental rift; dunite, troctolite, anorthosite; chromite, magnetite-ilmenite, Ni laterite; (Ferreira-Filho et al. 1994).

5 Discussion

The Rifean metallogenic epoch is distinct from the Archean and Lower Proterozoic in that a change of initial melt composition of Ni-Cu-PGE-bearing intrusions from komatiitic to tholeitic (typical for Rifean Ni-ferrous intrusions) occurred at the boundary between the Lower and Upper Proterozoic. The main part of the Rifean intrusions belong to the dunite-troctolite-gabbro series.

The Rifean intrusions are related to mantle plumes and continental rifts. Significant volumes of magma, which were saturated in sulphides, must have been emplaced in order to generate the large ore body. The development of mantle plumes promoted a high degree of partial melting, so that the ore components could not remain within the mantle. Foundering of the crust took place probably during early stages of rifting on the periphery of the plume. This created space for the emplacement of the intrusive complex. Initial melt interacted with basement rocks, friable carbonate and terrigeneous xenoliths. Melt contamination occurred, causing enrichment in water, alkali, S and probably also Cl, SiO_2 and reduced carbon. This contamination of the melt had a significant influence on ore genesis.

Low-sulphide PGE mineralization and Ni-Cu-PGE ores characterize the Ioko-Dovyren intrusion. This is compatable to other layered mafic-ultramafic complex such as Duluth and Muskox. In contrast, only Ni-Cu-PGE ores characterise the Voisey's Bay and Jinchuan intrusions and low-sulphide PGE mineralization characterises intrusions of the Superioir Lake region.

Acknowledgements

This work was supported by the Russian Foundation for Basic Research grant 05-05-97246, RAS Siberian department integration grant 210 and Russia President grant for leading science school 2284.2003.5. I am grateful to Eduard Konnikov, Dmitry Orsoev and Zhargal Tsydypov for long time collaboration and David Cooke for his review, which have significanly improved the manuscript.

References

Amelin Y, Li C, Naldrett AJ (1999) Geochronology of the Voisey's Bay intrusion, Labrador, Canada, by precise U-Pb dating of coexisting baddeleyite, zircon, and apatite. Lithos 47: 33-51

Amelin Y, Neymark LA, Ritsk EY, Nemchin AA (1996) Enriched Nd-Sr-Pb isotopic signatures in the Dovyren layered intrusion (eastern Siberia, Russia):evidence for source contamination by ancient upper-crustal material. Chemical Geology 129: 39-69

Barnes SJ, D Francis (1995) The distribution of platinum-group elements, nickel, copper, and gold in the Muskox layered intrusion, Northwest Territories, Canada. Economic Geology 90: 135-154

Barnes SJ, ML Zientek MJ, Severs en (1997) Ni, Cu, Au, and platinum-group element contents of sulphides associated with intraplate magmatism: a synthesis. Canadian Journal of Earth Sciences 34: 337-351

Chai G, AJ Naldrett (1992) Characteristics of Ni-Cu-PGE mineralization and genesis of the Jinchuan deposit, Northwest China. Economic Geology 87: 1475-1495

Ferreira-Filho C.F, SL.Kamo, RA. Fuck, TE Krogh, AJ. Naldrett (1994) Zircon and rutile U-Pb geochronology of the Niquelandia layered mafic and ultramafic intrusion, Brazil: constraints for the limiting of magmatism and high grade metamorphism. Precambrian Research 68: 241-255

Gerling EK, Koltsova TV, Matveeva II, Shukolyukov YA, Yakovleva SZ (1962) Dating of mafic rocks by the K-Ar method. Geokhimiya 11: 1055-1062(In Russian)

Good DJ, JH Crocket (1994 a) Genesis of the Marathon Cu-Platinum-group element deposit, Port Coldwell alkaline complex, Ontario: a Midcontinent rift-related magmatic sulphide deposit. Economic Geology 89: 131-149

Good DJ, JH Crocket (1994 b) Origin of albite pods in the Geordie Lake gabbro, Port Coldwell alkaline complex, Northwestern Ontario: evidence for late-stage hydrothermal Cu-Pd mineralization. Canadian Mineralogist 32: 681-701

Gurulyev SA (1965) The geology and formation conditions of the Ioko-Dovyren gabbro-peridotitic massif. Nauka, Moskaw: 1-122(In Russian)

Kislov EV, EG Konnikov (1992) Specific character of interaction between gabbro-norite melt and plagioperidotites from the Ioko-Dovyren massif. Rus. Geol. Geofyz 33: 58-66

Kislov EV, Konnikov EG, Posokhov VF, Shalagin VL (1989) Isotopic evidence of crust contamination in the Ioko-Dovyren Pluton. Sov. Geol. Geofys 30: 126-129

Kislov EV. (1998) Ioko-Dovyren layered massif. Publishing House of Buryatian Scientific Centre, Ulan-Ude: 1-265 (In Russian)

Konnikov EG, EV Kislov, DA Orsoev (1994) Ioko-Dovyren layered pluton and associated ore mineralization. Geol. Ore Deposits 36: 490-498

Konnikov EG, EV Kislov, LN Kacharovskaya (1988) New data about petrology and ore content of the Ioko-Dovyren nickel-bearing pluton. Sov. Geol. Geofys 29: 33-41

Manuylova MM, VV Zarubin (1981) Volcanogenic rocks of the Precambrian of the North Baikal region. Nauka, Leningrad: 1-88 (In Russian)

Mulja T, RH Mitchell (1990) Platinum-group minerals and tellurides from the Geordie Lake intrusion, Coldwell complex, Northwestern Ontario. Canadian Mineralogist 28: 489-501

Mulja T, RH Mitchell (1991) The Geordie Lake intrusion, Coldwell complex, Ontario: a palladium- and tellurium-rich disseminated sulfide occurrence derived from an evolved tholeiitic magma. Economic Geology 86: 1050-1069

Naldrett AJ (1997) Key factors in the genesis of Noril'sk, Sudbury, Jinchuan, Voisey's Bay and other world-class Ni-Cu-PGE deposits: implications for exploration. Australian Journal of Earth Sciences 44: 283-315

Naldrett AJ (1999) World-class Ni-Cu-PGE deposits: key factors in their genesis. Mineralium Deposita 34: 227-240

Neimark LA, E Yu, Rytsk BM, Gorokhovskiy GV, Ovchinnikova EI, Kiseleva VD, Konkin (1991) Lead isotope composition and genesis of Pb-Zn ores in the Olokit zone, North Baikal region. Geol. Ore Deposits 33(6): 34-49(In Russian)

Watkinson DH, D Ohnenstetter (1992) Hydrothermal origin of platinum-group mineralization in the Two Duck Lake intrusion, Coldwell complex, Northwestern Ontario. Canadian Mineralogist 30: 121-136

Weiblen PW, B Saini-Eidukat, JD Miller (1989) Duluth complex and associated rocks of the Midcontinental rift system. 28th International Geological Congress. Field Trip Guidebook T345: 1-42

Pb-Zn-Cu mineralization in the Filfila Massif, northeastern Algeria

O. Kolli
Laboratoire de Métallogénie et Magmatisme de l'Algérie, Faculté des Sciences de la Terre, FSTGAT-USTHB, BP n° 32-El Alia, Alger-16111, Algeria

Abstract. The Filfila Massif, Algeria, comprises four stacked units. They are, from bottom to top, a para-autochthonous unit of limestone and dolomite, a metamorphic unit and its Tertiary cover, a pelitic-sandstone unit and an upper Numidian sandstone unit. The lower units have been intruded by the Filfila Granite.

Fe, Cu and Cu-Pb-Zn sulphide mineralization is hosted by the Meçadjet vein set. The Meçadjet Vein is several hundred meters long and has a width of 0.5 to 3 m. It trends NE and dips 60° SE. This vein has cross-cuts the basal stacked units of the Filfila Massif. Ore minerals include pyrrhotite, hematite, sphalerite, chalcopyrite, pyrite, arsenopyrite, galena, sulfosalts, melnicovite, fluorite and barite. This mineralization is related to the post-orogenic Filfila granite, and is late Miocene in age.

Keywords. Meçadjet Vein, Miocene, granite, Fe-Cu-Pb-Zn mineralization

1 Introduction

This paper documents the characteristics and paragenesis of mineralization in the Mecadjet Vein, northeastern Algeria. The vein is hosted by rocks of the Filfila Massif, and has a protracted history of exploitation. Mining activities appear to extend as far back as Roman times, followed later by the French (1885-1942) and more recently by Geological Survey of Algeria (OGRM). Fracture-filling mineralization found in the Mecadjet Vein and elsewhere in the Filfila Massif is linked to metasomatism and hydrothermal solutions generated by the Miocene Filfila granite.

2 Geological setting

The Filfila Massif is located in the easternmost part of the Petite Kabylie region, and adjoins the Cap de Fer-Edough Massif. In this region, the Alpine Orogeny caused Miocene southward-directed overthrusting of Kabylie basement rocks onto the Tellian zones in northeastern Algeria (Perrin 1969; Lemoy 1969; ORGM 1969; Semroud 1970; Mahdjoub 1991; Ouabadi 1994; ORGM 1998). The region consists of three superimposed thrusted nappes. The basal package is the Tellian Nappe, which comprises Mesozoic and Tertiary sediments of African affinity. These have been overthrust by the flysch Nappe, which is composed of Cretaceous and Eocene flysch, and Jurassic, Permo-Triassic and Paleozoic sub-autochthonous sediments (Durand Delga 1969; Raoult 1974; Bouillin 1978; Vila 1980; Wildi 1983). The overlying nappe comprises a metamorphic complex, which is in turn overlain locally by unmetamorphosed Paleozoic and Upper Jurassic to Lutetian sediments, which constitute the "Dorsal Kabyle" (Durand Delga 1969). Granitoids, including the Filfila granite, have crosscut the entire pile of tectonic nappes.

The structural evolution of the Petite Kabylie in this area can be summarized as a pile of four tectonic units (Fig. 1). These are described below.

The Para-autochthonous unit, Djebel Filfila (Fig. 1), forms the lowest and most complex unit and appears to be a window through the metamorphic complex. Perrin (1969) recommended a four-fold subdivision of lithostratigraphic formations: the lower and upper carbonate formations, and the lower and upper detrital formations. The lower carbonate formation is composed of

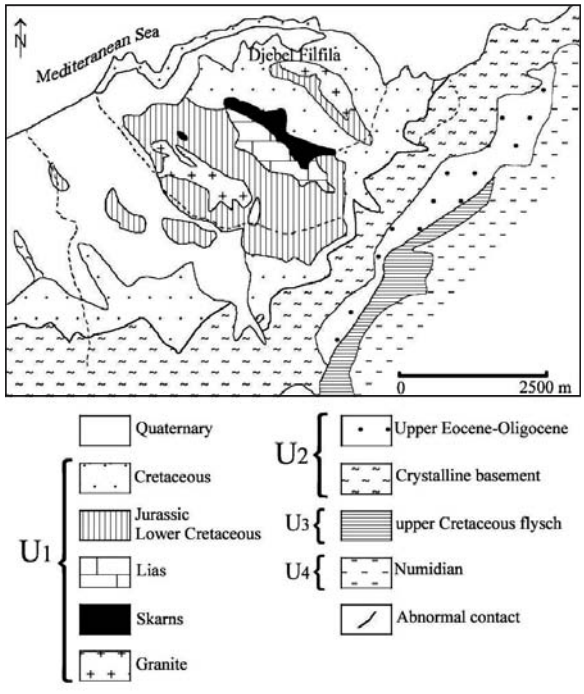

Figure 1: Geological map of the Filfila Massif (Perrin, 1969). Tectonic units labelled U1 – U4 are defined as follows: U1 - Para-autochthonous tectonic unit (Djebel Filfila); U2 - Kabylian basement and overlying Oligo-Miocène Kabyle; U3 – Upper Cretaceous Flysch unit; U4 - Lower Miocene Numidian flysch unit.

bioclastic limestones of Liassic age; the upper carbonate formation of Dogger-Malm age consists of limestone, dolomite and thin pelitic beds. The lower detrital formation of Neocomian age consists of interbedded grey shale and sandstones, dominated by thin- to moderately-bedded sandstone, olive-grey shale and black slate. This sequence is a flysch-type sequence. The Aptian-Albian Upper detrital formation consists of white bedded sandstones with argillite intercalations.

The Kabylian basement (metamorphic complex; Fig. 1) is composed of blue-grey sericite schists and grey-green chlorite schists. It is overlain unconformably by the Oligocene-Miocène Kabyle (OMK), a sequence of coarse conglomerates, pebbly sandstones and argillites.

The Flysch unit (Fig. 1) is Upper Cretaceous in age. It occurs as large outcrops and has been subdivided into three members. The lower member is mainly composed of sandstones and pelites with thin layers of fine siliceous schists and radiolarites. The middle member consists essentially of grey shale with green-greyish sandstone intercalations. The upper member is composed mainly of yellowish shale with some limestone micro-breccia interbeds. The uppermost part of this member consists of grey-yellow pelites with scarce micaceous sandstones interbeds.

The Numidian flysch unit of Lower Miocene age has a wide distribution throughout the study area (Fig. 1). It comprises thick massive beds of nearly pure quartzitic sandstones, with thin pelitic intercalations.

The Filfila granite complex has intruded Unit 1 (Fig. 1). The granite has a contact aureole that contains andalusite, cordierite, and muscovite, and locally reaches hornblende hornfels facies (Bourefis 1994). Granite emplacement coincided with an extensional tectonic episode (Bouillin 1983) and has been dated at ca 15 Ma (Langhian; Borsi et al. 1967). The Filfila pluton is clearly discordant, has been emplaced at shallow crustal levels and has a post-tectonic timing (Ouabadi 1994).

3 Mineralization

We have grouped Fe-Cu-Pb-Zn-bearing veins in the Filfila Massif according to their spatial locations. These are from east to west: Méçadjet; Mechhada; n° 1 vein and Oued Saboun. The veins are a few hundred metres in length and up to a metre thick. They are hosted by the Tellian and metamorphic units, and are characterized by a complex paragenesis. The Meçadjet vein is the most significant economically, and is the focus of the following discussion.

3.1 Méçadjet

Méçadjet is located in the extreme northeastern part of the Filfila Massif, east of the Filfila granite intrusion. The deposit was discovered in 1885. Pb-Zn-Ag mining commenced in 1924 and ceased by the end of 1942. A total of 14,780 tons were mined during this period. In 1969, th remaining ores reserves were estimated to be 87,000 tons with grades of 3.4 % Pb, 12.30 % Zn, 0.37 % Cu and 8.1 g/t Ag. A new exploration programme was started in 1998 by ORGM with the purpose of re-evaluating known mineralization, and to investigate the potential for additional sulphide ores at depth.

The Méçadjet vein system has a strike of N80°E and dips 60-80° south. The lengths of individual veins are between 60 m and 1000 m. The thickness of the veins changes along strike from 10s of centimetres up to 3 m or more.

The veins have cross-cut the Albo-Aptian upper detrital formation, and also the metamorphic unit. Rheological properties of the wallrocks have controlled the morphology and enrichment of the vein. Vein thickness increase and the grade is enriched in the metamorphic unit.

The main Méçadjet vein is characterized by horizontal and vertical mineral zonation. Pb is enriched in the eastern part, whereas Zn is enriched to the west, and Cu is dominant at depth.

The Méçadjet veins consist mainly of quartz and calcite. Quartz is dominant throughout the vein, but calcite is more abundant at deeper levels in the western part of the main vein. Quartz is typically coarse-grained (locally fine grained), whereas calcite tends to be relatively coarse-grained.

The veins commonly display open space-filling textures, although multistage crack- and fill-textures are also observed. Vugs are common. Minor chlorite and hematite, and rare late-stage barite and fluorite are also present. Chlorite occurs typically as fine selvages along vein walls, and is particularly abundant in areas of vein breccia. Hematite and calcite occur in pre-ore quartz veins at lower levels.

Open space fill textures are characteristic, with evidence of sequential filling, beginning with medium-grained zoned quartz on the vein walls, followed by sulphides and coarse-grained quartz then by fine-grained quartz with yellow brown sphalerite, purple fluorite and central white barite.

Breccia occurs locally within the veins. It is composed of silicified and chloritized wall-rock and ore fragments cemented by quartz ± calcite. Replacement of black slate clasts by chlorite and metamorphic rock fragments by quartz is ubiquitous. Late-stage carbonate alteration has overprinted vein sulphides at deeper levels.

Banded vein textures are best developed in the northeastern strike extension of the vein system. There is a preponderance of banded ore over breccia-hosted and disseminated ore throughout the deposit. The disseminated ore is mostly composed of scattered granular galena and sphalerite with minor chalcopyrite.

The main sulphide minerals, in descending order of abundance, are sphalerite, galena, pyrite and chalcopyrite. Accessory minerals are tetrahedrite, arsenopyrite,

chalcocite, hematite, cerusite, smithsonite, pyromorphite and malachite. Boulangerite, melnicovite and pyrrhotite have also been reported (ORGM, 1969). The gangue consists of black slate and metamorphic rock clasts, quartz, fluorite, barite, calcite and minor chlorite.

3.2 Ore mineralogy and paragenesis

Minerals observed microscopically in this study include hematite, sphalerite, chalcopyrite, pyrite and galena, as well as non-sulphides such as quartz, calcite, chlorite, fluorite and barite.

Sphalerite is the dominant ore mineral, and occurs as massive aggregates in the disseminated ore and as fine to coarse grains in the banded ores. In general, sphalerite is intergrown with chalcopyrite, arsenopyrite and quartz in the massive aggregates, whereas fine-grained sphalerite is more commonly associated with galena in the banded ore. Sphalerite in the massive aggregates typically contains exolutions of chalcopyrite.

There are three distinctive types of pyrite. The first is coarse-grained and zoned (from 0.8 to 5 mm), the second is medium-grained (0.2 – 0.5 mm) and the third is fine-grained (< 0.2 mm). In general, the former is intimately associated with hematite and chalcopyrite and also displays some evidence of brittle deformation. It has been replaced locally by sphalerite and also occurs in early-stage quartz. The second type is associated with dark- and honey-colored sphalérite. The third type of pyrite commonly occurs in microfractures that have cross-cut all earlier-formed minerals. In most cases, medium crystalline pyrite grew idiomorphically, typically as cubes.

Galena occurs interstitially to the earlier-formed sulphides. Hematite occurs as needles cemented by quartz. Arsenopyrite appears as idiomorphic crystals included in sphalerite and chalcopyrite.

Paragenetic relationships previously described, represent a sequence consisting of pre-ore, ore, and post-ore stages (Fig. 2). In the pre-ore stage, the vein mineralization started with the deposition of quartz and hematite, together with minor pyrite, sphalerite and chalcopyrite. The veins were then deformed, resulting in pre-ore cataclasis. During the ore stage, most of the sphalerite and galena, and subsequently fluorite and barite, were precipitated. Quartz was the main gangue mineral together with chlorite and calcite during the ore stage. In the post-ore stage, minor amounts of pyrite were deposited.

4 Conclusions

The Filfila veins cross-cut the terrains of stacked units, clearly post-dating thrust tectonics of the late Lutetian (Raoult, 1974). The veins are similar to those of the Ain Barabr district, which are related to Miocene magmatic activity (Marignac 1985). Similarly, we interpret the Filfila polymetallic vein deposits to be related to Miocene magmatic activity. The veins have a strong structural control, occurring in NE-trending subvertical fractures that have cross-cut stacked thrust terrains. The Méçadjet veins exhibit lateral and vertical mineral zonation and a complex paragenetic assemblage.

Acknowledgements

Thanks to two unknown referees from the JAES Team and also to Assoc. Prof. David Cooke and Dr Tafao Zhao for their reviews.

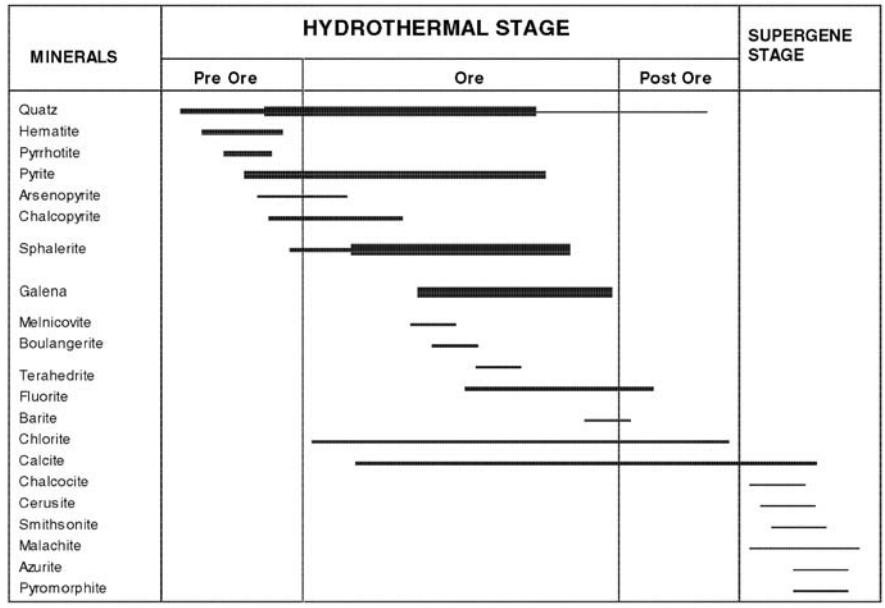

Figure 2: Schematic paragenetic sequence of Pb-Zn-Cu-Fe vein mineralization at Méçadjet, Filfila district, Algeria.

References

Borsi S, Ferrara G, Tangiorgi E (1967) Determinazione con metodo K-Ar dell'eta delle rocce magmatiche della Toscana. Bull. Soc. Geol. Italia, 86, 403-410

Boullin JP (1978) Géologie alpine de la Petite Kabylie dans les régions de Collo et d'El Milia (Algérie). Thèse d'Etat, Univ., Paris

Boullin JP (1982) Mise en évidence d'importantes structures tangentielles au sein du socle de Petite Kabylie (Algérie). C. R. Acad. Sci. Paris, 294 (11), 1271-1274

Bourefis A (1994) Etude pétrographique, minéralogique et métallogénique des skarns du dj. Filfila (Skikda, Algérie). Thèse Magister, Univ., Constantine

Durand Delga M (1969) Mise au point sur la structure du Nord-Est de la Berbérie. Bull. Serv. Carte géol., Algérie, 39, 89-131

Lemoy C (1969) Stratigraphie des Unités Allochtones : Structures et Métamorphisme du Massif. Thèse 3ème Cycle, Univ., Nancy

Mahdjoub Y (1991) Cinématique des déformations et évolution P-T anté-alpines et alpines en Petite Kabylie (Algérie nord-orientale) : un modèle d'évolution du domaine tellien interne. Thèse d'Etat, Univ., USTHB, Alger

Marignac C (1985) Les minéralisations filoniennes d'Aïn Barabar (Algérie): un exemple d'hydrothermalisme lié à l'activité géothermique alpine en Afrique du nord. Thèse Doct. Etat, INPL, Nancy (Fr), 2 vol., 1163 p

ORGM (1969) Recherches géologiques dans l'oued Méçadjet (région de Skikda), rapp. Interne

ORGM (1998) Recheerches minières dans la région de Filfila (Skikda), rapp. Interne

Ouabadi A (1994) Pétrologie, géochimie et origine des granitoïdes peralumineux à cordiérite (Cap Bougaroun, Beni Toufout et Filfila), Algérie Nord-Orientale. Thèse d'Etat, Univ. USTHB, Alger

Perrin C (1969) Contribution à l'étude géologique du Massif du Filfila (Algérie Nord-Orientale). Stratigraphie et sédimentologie de la série mézosoïque de l'unité inférieure. Thèse 3ème Cycle, Univ., Nancy

Raoult JF (1974) Géologie du centre de la chaîne numidique (Nord du Constantinois, Algérie). Mem. Soc. Géol., France, 53/121

Semroud B (1970) Eude pétrographique du granite du Filfila (Skikida). Thèse 3ème Cycle, Univ, Alger

Vila M (1980) La chaîne alpine d'Algérie Orientale et des Confins Algéro-Tunisiens. Thèse d'Etat, Univ., Paris

Wildi W (1983) La chaîne tello-rifaine (Algérie, Maroc, Tunisie) : structure, stratigraphie et evolution du Trias au Miocène. Rev. Géol. Dyn. Géogr. phy., 24, 201-297

Mass-balance analysis of mineralized skarn systems: Implications for replacement processes, carbonate mobility, and permeability evolution

D.R. Lentz
Department of Geology, University of New Brunswick, PO Box 4400, Fredericton, New Brunswick, E3B 5A3 Canada

Abstract. In infiltrative skarn systems, especially those associated with sulphide and oxide mineralization, there are pronounced depletions in CO_2 and Ca coincident with increasing abundance of Si, Al, Fe, etc. This is regardless of the mass-balance technique used to examine skarns. The assumption of constant volume (Lindgren's law) is not entirely justified. Net mass changes, however, are generally small except in the most proximal endoskarn and exoskarn, although this depends a lot on the nature of the infiltrative magmatic system. The outer distal reaction margin exhibits the greatest change. This reflects the infiltrative decarbonation front enhanced by the dissolution of excess carbonates by carbonic acid generated by the skarn reactions, as well as the acidity (HCl) of the magmatically-dominated hydrothermal fluid. Using infiltrative solubility constraints, it is possible to estimate the minimum fluid-rock ratio (F/R) associated with each part of the skarn. The distal skarn has the lowest F/R and the proximal exoskarn having the highest F/R. Net mass increases are related to hydrofracturing processes coupled with F/R reaction. Enrichment of sulphides occurs just within the outer (distal) reaction margin, indicating that acid neutralization is key to sulphide saturation. Because the reaction front continually changes, resolution-precipitation reactions must typify sulfide-bearing exoskarns.

Keywords. Skarn, mass-balance, constant-volume, contact-metasomatism, mineralization

1 Introduction

During infiltrative skarn formation, numerous chemical changes are evident that are associated with mineralization. Determination of mass-balance relationships can allow the gains and losses of elements from the system to be described. This can help to constrain the mineralization processes. With this comes the assumption(s) that part of the system did not change during alteration. The challenge is to determine, or convincingly justify, the immobility of certain elements or of the amount of volume change (Leitch and Lentz 1994). The problem is that in high-temperature, contact metasomatic settings that form endoskarns and complimentary exoskarns, many elements can be mobilized.

2 Mass balance analysis

In skarn systems, few elements are known to be immobile. High-field strength trace-elements, such as Zr, may have potential as an immobile element (see Leitch and Lentz 1994; Ague 1996), although their distribution in carbonate rocks is very low and generally erratic, so proper sampling would be fundamental. Lindgren's Law (constant volume hypothesis) is based on the observation that there is no volume change evident during exoskarn formation. This was based principally on his studies at the Morenci and Bingham Cu deposits (Lindgren 1924, 1925). Since then, others have made similar observations, in particular Kwak's (1978) detailed mass-balance study of the King Island scheelite skarn (Tasmania). Rose and Burt (1979) noted that few others have documented the constant volume observations. In fact, they have found that

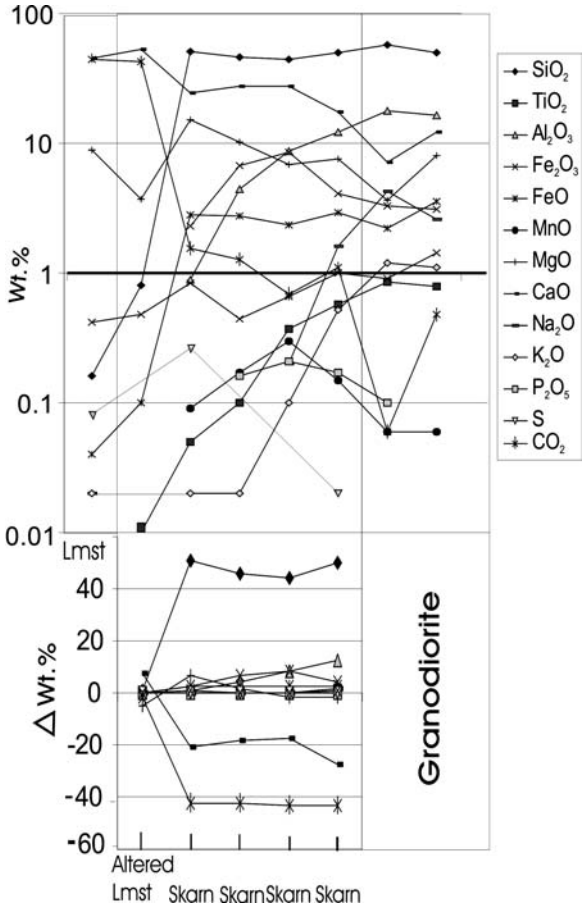

Figure 1: Geochemical variations and constant volume mass balance calculations in dolomitic limestone at the Arctic Chief deposit (Yukon, Canada; Boyle 1979).

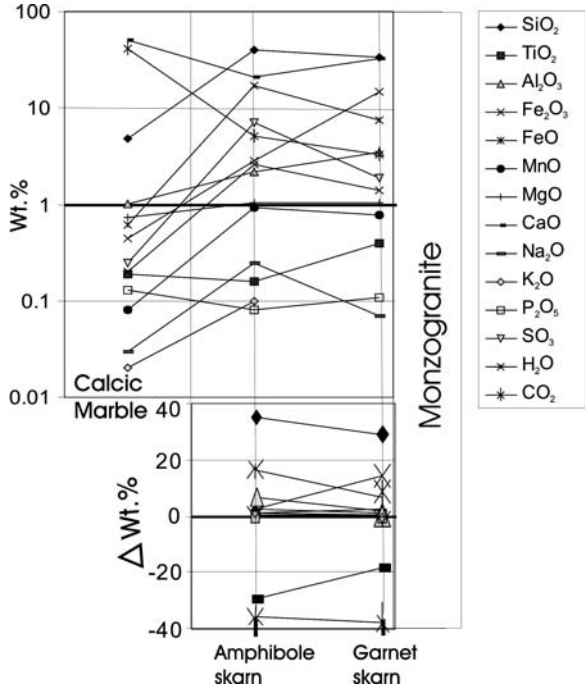

Figure 2: Geochemical variations and constant volume mass-balance variations in a calcic marble, King Island W skarn (Tasmania, Australia; Kwak 1978).

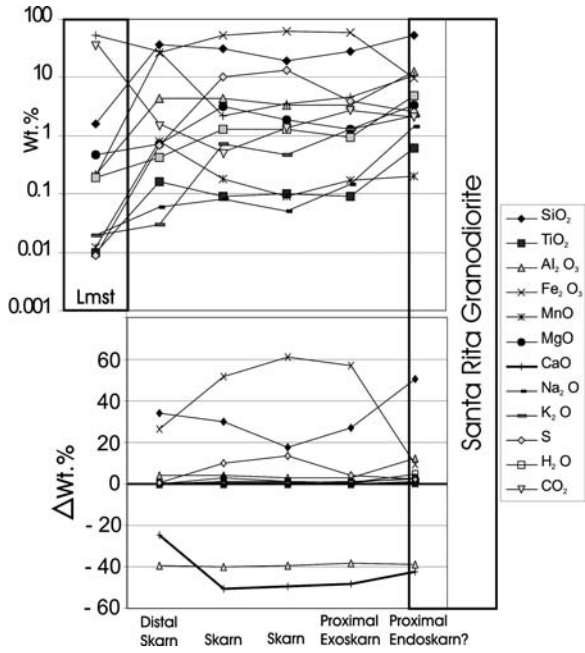

Figure 3: Geochemical variations and constant volume mass-balance variations in the Oswaldo Formation limestone (New Mexico, USA; Nielson 1970).

some authors have documented overall mass loss (small), and so they advocated caution with this approach.

Several other mass-balance studies have been conducted, including the Santa Rita Cu skarn (Nielson 1970), Ely Cu skarn (Nevada; James 1971), Arctic Chief Cu skarn (Yukon, Boyle 1979), Moina F-Sn-W skarns (Tasmania; Kwak and Askins 1981), Cu-W Traversella skarn (Italy; Vander Auwera and Verkaeren 1993), Millstream Cu-Fe skarn (Lentz et al. 1995), and Celebi Fe-Cu skarn (Kuscu 2001), among others. Many of these mass balance studies have tried to justify the constant volume assumption. In contrast, Lentz et al. (1995) justified using Al_2O_3 as the immobile monitor at Millstream.

Compositional profiles are reproduced here that show the overall geochemical variations in the skarn at the Arctic Chief Cu-Au deposit (Fig. 1; Boyle 1979), King Island W deposit (Fig. 2; Kwak 1978), Santa Rita Cu deposit (Fig. 3; Nielson 1970), and Crestmore skarn (Fig. 4; Burnham 1959) as examples. SiO_2, Al_2O_3, FeO, Fe_2O_3, TiO_2, MnO, alkali elements, S and many other elements have been added to each of these skarns. There is a pronounced decrease in CO_2 and variable changes in CaO and MgO with CaO generally decreasing (see Barton et al. 1991). CO_2 depletion is well known from skarn systems, in particular at the calc-silicate reaction front where metasomatically-induced decarbonation reactions begin. If specific gravities are included, the changes in CaO and MgO would be less pronounced, although in places they are still quite significant. Lindgren (1924) calculated that a cubic metre of limestone lost 460 kg of CaO and 1190 kg CO_2 coupled with the addition of significant amounts of Si and Fe, etc. associated with andradite exoskarn formation. Similarly, Nielsen (1970) noted substantial loss of CaO and CO_2 with the addition of Si, Fe, Al, alkalis etc. in the Santa Rita Cu skarn. If the solubility of silica in the intrusive-derived fluid can be estimated, then a lower estimate of the infiltrative fluid-rock ratio (F/R) can calculated, because the solubility of silica at the skarn reaction front is extremely small (Lentz 1998; Lentz and Suzuki 2000). For example, if the solubility of SiO_2 equaled 1 wt.% (0.25 moles SiO_2 aq), then to add 25 wt.% SiO_2 to the exoskarn requires a minimum F/R (wt.) of at least 25 (Lentz and Suzuki, 2000). Net mass increases in proximal environments mainly reflect hydrofracture- induced permeability coupled with concurrent calc-silicate and silicate saturation reactions.

Variations in Mg concentrations are significant. They generally show an enrichment in the outer (distal) skarn located near the skarn front, but decrease systematically into the skarn toward the intrusion contact. In other skarns, no real Mg changes are usually observed, although there are exceptions (e.g. Vander Auwera and Verkaeren 1993). Overall, this is consistent with very low mobility of Mg in quartz-saturated, calc-silicate systems, but slightly higher mobility at low $\boldsymbol{a}(SiO_2)$ in distal skarns (Luce et al. 1985). Notice Mg enrichment is common in the distal skarns, consistent with higher mobility og Mg at low $\boldsymbol{a}(SiO_2)$ such that Mg is in part mobilized to near the outermost reaction front.

3 Carbonate mobility

The net decrease in CaO, which is in some cases substantial, is worthy of note considering that the permeability of skarns is the key to infiltrative skarnification and mineralization as well as hydrofracturing. If a 0.25 m SiO_2 solution forms 0.25 m wollastonite, then 0.25 m CO_2 is released into 55.5 m H_2O (0.45 % or 0.005 $X(CO_2)$ in the fluid). The close relationship between CO_2 loss and CaO loss indicates that a high proportion of CaO is dissolved in this fluid and is not forming calc-silicates. Permeability is initiated by contact metamorphic decarbonation reactions, then assisted by variable degrees of hydrofracturing associated with H_2O infiltration. If this hypothesis is correct, then substantial CaO can be mobilized. $Ca(OH)_2$ and $CaCl_2$ are high in skarn fluids (Kwak and Tan 1981; Kwak 1986). High Ca solubilities are possibly related to reactions such as:

$$CaCO_3 + 2\,H_2O \longrightarrow H_2CO_3 + Ca(OH)_2 \quad [1]$$

$$CaCO_3 + 2\,HCl \longrightarrow H_2CO_3 + CaCl_2 \quad [2]$$

$$CaCO_3 + 2\,NaCl \longrightarrow Na_2CO_{3aq} + CaCl_2 \quad [3]$$

The solubility of carbonates is very low (retrograde) at high temperature, but increase with higher salt contents, acidity, and higher pressure (Fein and Walther 1989). Calcite solubility increases with increasing CO_2 to a maximum of 0.02 to 0.05 $X(CO_2)$, which is consistent with the amount of CO_2 generated from infiltrative skarn (see above). However, the solubility of carbonate is still quite low. HCl and salts must therefore be involved to increase Ca solubility and explain the removal of substantial carbonate in some skarns. Otherwise, the fluid/rock ratios would need to be extremely high. One possible alternative is that carbonate melt (Ca-Mg) of very low viscosity is generated during infiltrative reaction (Lentz 1998, 1999), if fluid/rock ratios are too low to support a hydrothermal dissolution mechanism.

The acid neutralizing aspect of carbonates near the outer reaction front explains the localization of sulphides near that reaction zone. These pH-sensitive, sulphide preciptation reactions particularly enhance destabilization of metal-chlorine ligands (Rose and Burt 1979). Therefore, there is typically evidence of remobilization of sulphides as the reaction front progresses outward during progressive infiltration (Fig. 1).

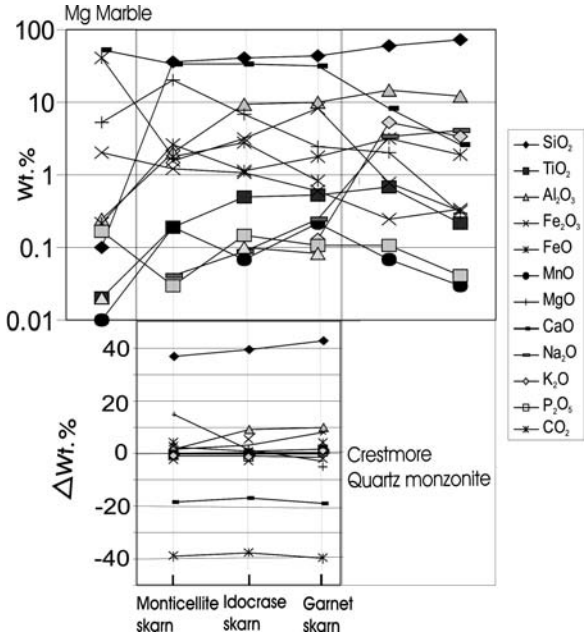

Figure 4: Geochemical variations and constant volume mass-balance variations in the Sky Blue Mg marble (Crestmore, California; Burnham 1959).

4 Conclusions

Decarbonation coupled with decalcification of the exoskarn is associated with infiltrative magmatic hydrothermal skarn reactions. Mass addition of Si, Al, Fe, etc. helps drive these reactions, and is propogated by hydrofracturing, which aids reaction progress. Dissolution of excess carbonates is evident in the distal skarn. The acid neutralization process at the reaction front control the precipitation of ore-forming constituents sensitive to these pH increases. However, redissolution-precipitation reactions are evident in many proximal skarns. These are related to remobilization at the outer reaction front.

Acknowledgements

I appreciated discussions with D.M. Burt about mass balance constraints in skarns. I thank David Cooke for valuable comments on this manuscript. This research is supported by a NSERC Discovery grant.

References

Ague JJ, van Haren JLM (1996) Assessing metasomatic mass and volume changes using the Bootstrap with application to deep crustal hydrothermal alteration of marble. Economic Geology 91: 1169-1182

Barton MD, Ilchik RP, Marikos MA (1991) Metasomatism. In: Kerrick, DM (ed) Contact Metamorphism. MSA Reviews in Mineralogy 26: 321-350

Boyle RW (1979) The Geochemistry of Gold and its Deposits. Geol. Surv. Canada Bull 280: 584

Burnham CW (1959) Contact metamorphism of magnesian limestones at Crestmore, California. Geological Society of America Bulletin 70: 879-920

Fein JB, Walther JV (1989) Calcite solubility and speciation in supercritical NaCl-HCl aqueous fluids. Contributions to Mineralogy and Petrology 103: 317-324

James LP (1971) Zoned alteration in limestone at porphyry copper deposits, Ely, Nevada. Economic Geology 71: 488-512

Kuscu I, (2001) Geochemistry and mineralogy of the skarns in the Celebi District, Kirikkale, Turkey. Turkish Journal of Earth Sciences 10: 121-132

Kwak TAP (1978) Mass balance relationships and skarn-forming processes at the King Island scheelite deposit, King Island, Tasmania, Australia. American Journal of Science 278: 943-968

Kwak TAP (1986) Fluid inclusions in skarns (carbonate replacement deposits). Journal of Metamorphic Geology 4: 363-384

Kwak TAP, Askins PW (1981) Geology and genesis of the F-Sn-W(-Be-Zn) skarn (wrigglite) at Moina, Tasmania. Economic Geology 76: 439-467

Kwak TAP, Tan TH (1981) The importance of $CaCl_2$ in fluid composition trends – evidence from the King Island (Dolphin) skarn deposit. Economic Geology 76: 955-960

Leitch CHB, Lentz DR (1994) The Gresen's approach to mass balance constraints of alteration systems: Methods, Pitfalls, Examples. In: Lentz, DR (ed) Alteration and Alteration Processes Associated with Ore-forming Systems. Geological Association of Canada, Short Course Notes 11: 161-192

Lentz DR (1998) Late-tectonic U-Th-Mo-REE skarn and carbonatitic vein-dyke systems in the southwestern Grenville Province: a pegmatite-related pneumatolytic model linked to marble melting (limestone syntexis). In: Lentz DR (ed) Intrusion-related Skarns Systems. Mineralogical Association of Canada Short Course Handbook 26: 519-657

Lentz DR (1999) Carbonatite genesis: a re-examination of the role of intrusion-related pneumatolytic skarn processes in limestone melting. Geology 27: 335-338

Lentz DR, Susuki K (2000) A low-F pegmatite-related MO skarn from the southwestern Grenville Province, Ontario, Canada: phase equilibria and petrogenetic constraints. Economic Geology 95: 1319-1337

Lentz DR, Walker JA, Stirling JAR (1995) Millstream Cu-Fe skarn deposit: an example of a Cu-bearing magnetite-rich skarn system in northern New Brunswick. Exploration and Mining Geology 4: 15-31

Lindgren W (1924) Contact metamorphism at Bingham, Utah. Geological Society of America Bulletin 35: 507-534

Lindgren W (1925) Metasomatism. Geological Society of America Bulletin 36: 247-261

Luce RW, Cygan GLJ, Hemley J, D'Angelo WM (1985) Some mineral stabilities relations in the system CaO-MgO-SiO_2-H_2O-HCl. Geochimica et Cosmochimica Acta 49:525-538

Nielsen RL (1970) Mineralization and alteration in calcareous rocks near the Santa Rita stock, New Mexico. In: Geological Society of New Mexico Guidebook, 21st field conference: 133-139

Rose AW, Burt DM (1979) Hydrothermal alteration. In: Barnes, HL (ed) Geochemistry of Hydrothemal Ore Deposits. Wiley: 173-235

Vander, Auwera J, Verkaeren J (1993) Occurrence of contrasting skarn formations in dolomites of the Traversella deposit (Ivrea, Italy). Geologische Rundschau 82: 726-740

Numerical simulations of heat and mass transfer for the Tongchang porphyry copper deposit, Dexing, Jiangxi Province, China

Jiankang Li, Dehui Zhang
China University of Geosciences, 29 Xueyuan Rd.,100083 Beijing, China

Denghong Wang
Institute of Mineral Resources, Beijing,26 Baiwanzhuang Rd.,100037, China

Abstract. Numerical simulations of heat and mass transfer have been used to investigate the genesis of the Tongchang porphyry copper deposit, China. Early stages of hydrothermal activity are predicted to have been dominated by magmatic-derived fluids, with fluid flow centred on granodiorite contact zones. During the middle period of hydrothermal activity, there was potential for mixing of magmatic water and groundwater. Late stage hydrothermal activity is predicted to have been dominated by groundwater convection.

Keywords. Numerical simulation, heat-mass transfer, porphyry, Dexing

1 Introduction

Cathles (1977), Norton and Knight (1977) and Norton (1982) reported pioneering results of numerical simulations of heat and mass transfer in porphyry systems. Their findings provided many useful insights into fluid flow around shallow crustal intrusions, but suffered from some defects, including problems associated with selecting false force, and neglecting changes of density and porosity. Subsequent workers have provided more sophisticated models of heat and mass transfer in magmatic-hydrothermal settings. Guozhang and Qijiang (1994) reported simulations of heat and mass transfer for porphyry-style mineralization from Dexing, China. But they did not have a precise geological model for their simulations.

In this paper, we revisit the topic of fluid flow at the Tongchang porphyry copper deposit, Dexing, China. Our numerical simulations include a revised dynamic model, highly efficient numerical arithmetic methods to solve simultaneous equations, and are based on a precise geological model. We use our results to interpret the likely spatial and temporal evolution of the temperature field and stream functions, in order to help explain the genesis of the Tongchang porphyry copper deposit.

2 Geology

Host rocks to the Tongchang porphyry deposit are part of the Jiuling Group (Fig. 1a) of Presinian (Late Proterozoic) age. The main rock type is sericite phyllite. The rocks are folded around the Xiyuanling anticline, and the core of the fold has been intruded by a mineralised

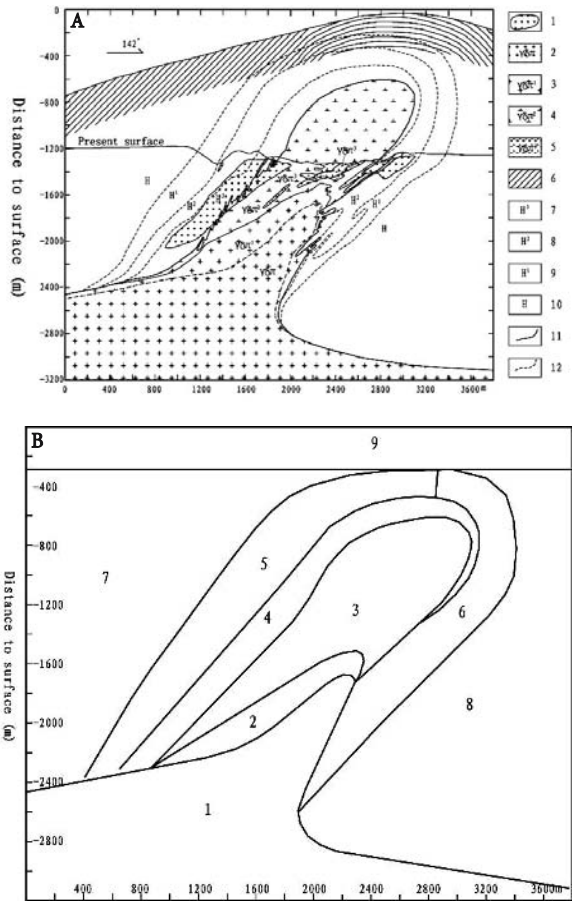

Figure 1: (A) Geological model of the Tongchang porphyry deposit. 1 – orebody; 2 – granodiorite porphyry; 3 – weakly altered granodiorite porphyry; 4 – medium-altered granodiorite porphyry; 5 – strongly altered granodiorite porphyry; 6 – strata and schistosity; 7 – strongly altered metamorphic rocks; 8 – medium-altered metamorphic rocks; 9 – weakly altered metamorphic rocks; 10 – metamorphic rocks; 11 – geological contact; 12 – alteration zone. (B) Geological domains defined for the purposes of our numerical simulations (modeling parameters listed in Table 1).

Parameter	Code of area								
	1	2	3	4	5	6	7	8	9
Porosity (φ)/%	1	1	1	12	9	9	3	3	1
permeability (κ)/md	1	1	1	100	20	10	6	1.5	1
Heat conduction coefficient (K) /W. m^2 K^{-1}	2.1	2.1	2.1	3.2	3.2	2.32	3	2.32	2.31
Density of rock (ρ)/kg. m^{-3}	2600	2600	2600	2600	2600	2600	2600	2600	2600
Specific heat (C)/J.kg^{-1} K^{-1}	1000	1000	1000	1000	1000	1000	1000	1000	1000

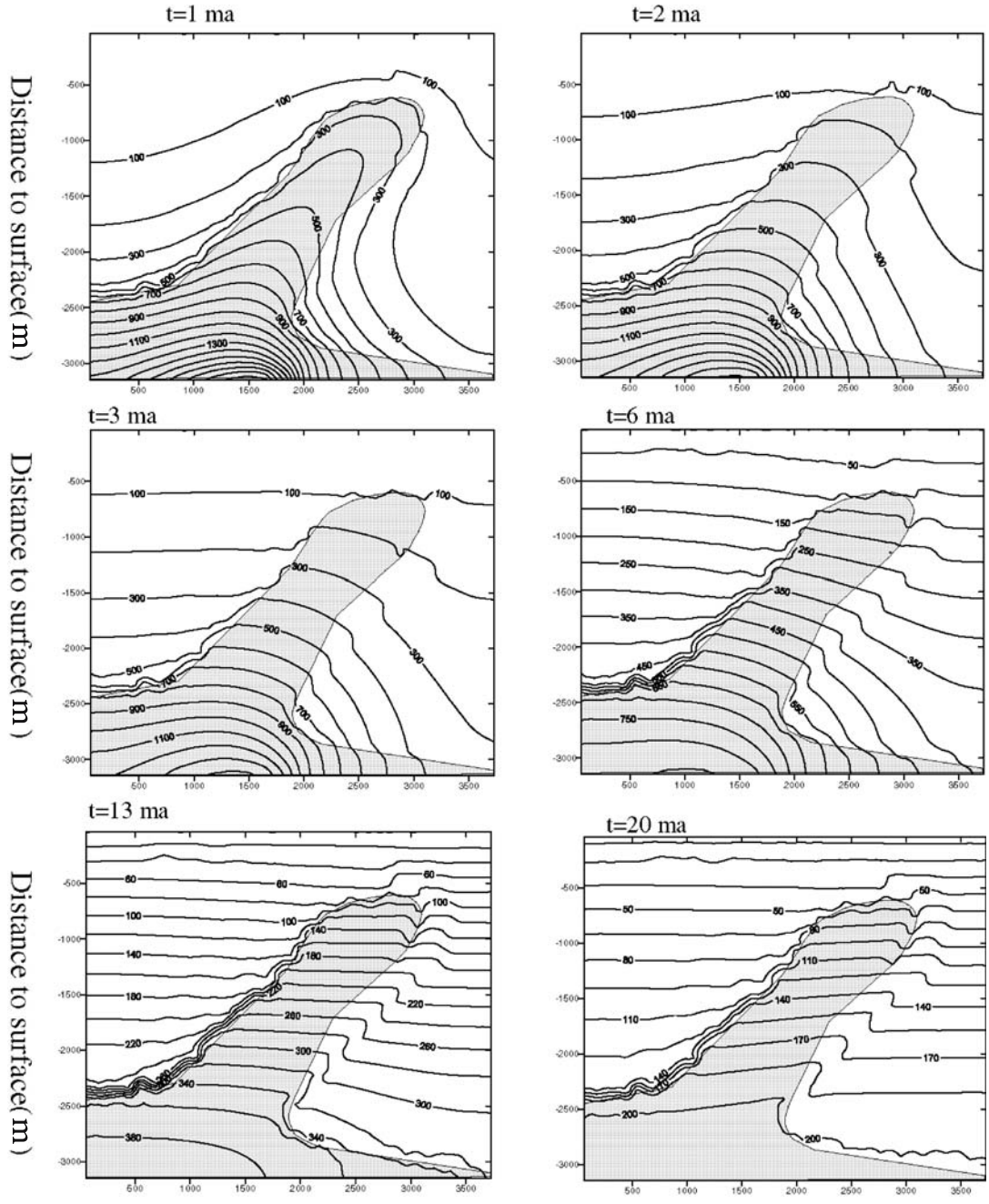

Figure 2: Spatial and temporal evolution of the temperature field (unit: °C; grey pattern - granodiorite porphyry)

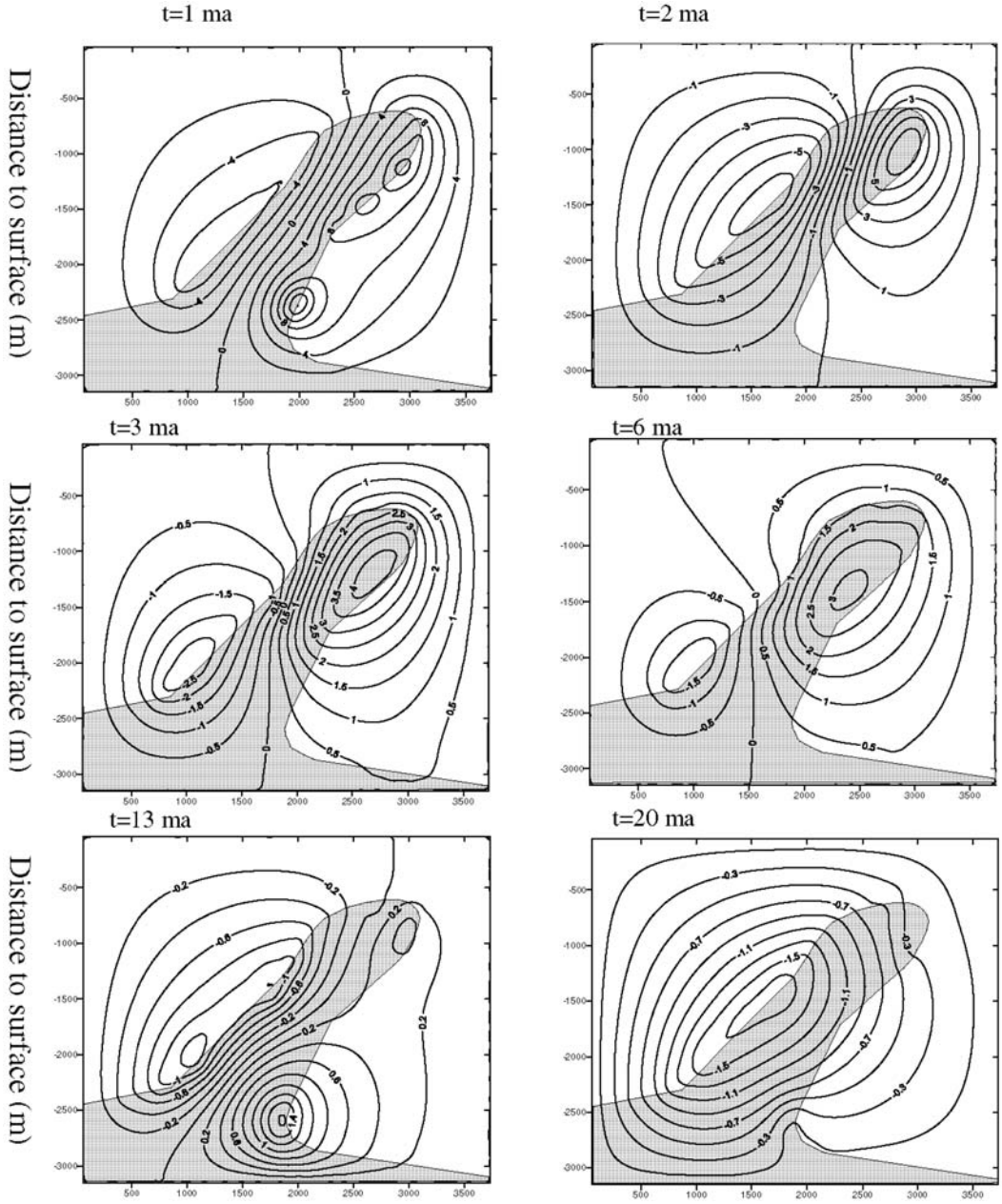

Figure 3: Spatial and temporal evolution of the stream function (unit: $10^{-6}m^2s^{-1}$; negative values refer to anti-clockwise convection, positive values refer to clockwise convection; grey pattern - granodiorite porphyry)

granodiorite porphyry (Fig. 1a). Bedding-parallel schistosity on the limbs of the Xiyuanling anticline appears to have facilitated fluid flow. In contrast, the Xiyuanling anticlinal axis appears to have acted as a fluid flow barrier, preventing ore-forming fluids from dissipating and resulted in mineralization being focused within the interior of the granodiorite and its immediate contact zone. The host rocks adjacent to the granodiorite porphyry have been contact metamorphosed to varying degrees, with metamorphism intensifying with depth.

3 Model parameters

Based on the available geological data (Fig. 1a), we have defined a series of geological domains (Fig. 1b). For each domain, we selected initial values for each of the main variables required to undertake our numerical simulations (Table 1).

With decreasing temperature, the permeability of a rock body will change. Based on the research results of Hanson (1995) among others, when temperatures were less than

500°C, we have assumed that the permeability was 200md. Similarly, when the temperature was less than 400°C, permeability was set to 300md, and when temperature dropped below 200°C, a permeability of 500md was assumed.

4 Numerical modeling results

The results of our numerical simulations, specifically the predicted spatial and temporal changes in temperature and stream function are shown on Figures 2 and 3 respectively. Our modeling predicts that the temperature field evolved as follows: (1) During the early period of intrusive activity, the highest temperatures were localized within and around the granodiorite (Fig. 2a). The granodiorite was considerably hotter than the surrounding wallrocks. Temperatures are predicted to have then homogenized gradually over a 2 – 3 m.y. period (Fig. 2b and c).

During the early phase of intrusive activity, temperatures in the granodiorite are predicted to have been higher than in the underlying metamorphic rocks (Fig. 2a). This relationship reversed with time (Fig. 2b), because permeability was higher in the intrusion, allowing heat to dissipate from the intrusion more rapidly.

Based on the results of our stream function calculations (Fig. 3), we infer that during the early period of magma intrusion, centers of convection were localised on the margins of the granodiorite. Convection was symmetrical (Fig. 3a), despite the pronounced inclination of the intrusion (Fig. 1a). After 2 m.y., the center of convection is predicted to have moved from the contact zone gradually. The interface of double convection is predicted to have moved to the left (Fig. 3b). During late stage fluid flow, clockwise convection is predicted to weaken. After 20 m.y.; (Fig. 3f), clockwise convection had disappeared entirely and anti-clockwise convection dominated the simulation.

5 Discussion

Evolution of the temperature field and stream function at Tongchang is predicted to have been controlled by dynamic evolution of the granodiorite and its wallrocks. During prograde heating, fluid production from metamorphic reactions and thermal expansion of pore fluids would have acted to raise fluid pressures in individual pores. Similarly, prograde metamorphic reactions tend to result in a decrease in solid phases volumes. This process, which may open pores, also acts on the scale of individual grains. Together these would lead to continual creation of micro-cracks. In addition, bulk thermal expansion, ductile strain accompanying metamorphism, and pore collapse, crack-sealing, and pressure solution driven by any sudden decrease in fluid pressure would inhibit the formation of large-scale permeability. Under these conditions, fluid would have flowed from the granodiorite into the host rocks, and granodiorite temperatures would have remained high. Thermal buoyancy drove fluid flow, so that convection was localized at the igneous contact zone. During this period, magmatic fluid was dominant.

As peak temperatures were achieved, fluid generation by chemical reactions and pore fluid expansion ceased. Cooling would have progressed outward from the contact zone and downward from the surface. Fluid being generated at depth, in the outer aureole, and even residual magmatic fluid would still escape, but it must have become more difficult to generate a grain-scale porosity network through the overlying rocks. Hydrofracturing would have formed macroscopic fractures at this time. Any retrograde reactions will have increased solid volumes, closing fine pores. Overall, the permeability of the rock body is predicted to have increased, causing convection to move from the contact zone. A double convection system would have allowed groundwater and magmatic fluid to mix. As the rocks cooled, they would have also contracted. Eventually, discrete fractures will have formed, having orientations reflecting the orientation of the thermal stress regime and the failure mechanism. As the entire system cooled, thermal contraction may have become the dominant mechanism of producing permeability. This could have allowed a groundwater convection system to dominate late-stage fluid flow at Tongchang.

References

Cathles LM (1977) An analysis of the cooling of intrusives by groundwater convection which includes boiling. Econ. Geol.,72: 804-826.

Guozhang G, Qijiang R (1994) Computer simulation for hydrothermal fluid migration during mineralization of Dexing porphyry copper deposit, Jiangxi province. Geochim Cosmochim Acta, 23: 402-410.

Hanson RB (1995) The hydrodynamics of contact metamorphism. Science, 107: 595-611.

Norton D (1982) Fluid and heat transport phenomena typing of copper –bearing pluton environments: Southeast America, in Titley SR (ed.) Advances in Geology of the porphyry copper deposits. University of Arizona Press, 1982, 59-72.

Norton D, Knight J (1997) Transport phenomena in hydrothermal system: Cooling plutons. America Journal of Science, 277: 937-81.

Magmatic Ni-Cu-PGE deposits in the Qilian-Longshou mountains, Northwest China – part of a Proterozoic large igneous province

Li Wenyuan, Wang Wei
Xi'an Institute of Geology and Mineral Resources, CGS, Xian 710054, China

Guo Zhouping
School of Earth Science and Resources Management, Chang'an University, Xi'an 710054, China

Abstract. The Jinchuan intrusion occurs in the Qilian-Longshou mountains, China and contains a world-class Proterozoic Ni-Cu-PGE deposit. It has a Sm-Nd isochron age of 1508 ± 31Ma. Zangbutai is a non-mineralized complex of metamorphic and ultramafic rocks with komatiite features located on the western side of the Jinchuan intrusion, and has been dated at 1511 ± 67 Ma. Proterozoic continental flood basalts form part of the Zhulongguan group of the Jingtieshan micro-continental block in the western part of North Qilian, and in the Hualong micro-continental block of South Qilian Lashuixia. Small intrusive-hosted Ni-Cu-sulfide (PGM) deposits are associated with other mafic-ultramafic intrusions of Proterozoic age. The Proterozoic continental flood basalts, komatiites, mafic-ultramafic rock bodies and magmatic Ni-Cu sulfide (PGM) deposits are interpreted to define a Proterozoic large igneous province in the Qilian-Longshou mountains. This province was created by large scale magmatism in response to rifting of the Columbia super-continent and extension of the Qilian paleocontinent at about 1.5Ga. At Jinchuan, up to 60% of the rock body is sulfide mineralized, whereas at Lashuixia sulfides comprise up to 90%. Such high concentrations of metallic sulfides imply formation via injection of metallic sulfide-bearing magma and/or metallic sulfide liquid.

Keywords. Magmatic sulfide, large igneous province (LIP)

1 Introduction

The giant Proterozic Jinchhuan magmatic Ni-Cu-PGE sulfide deposit, China, has large ore reserves and high grades of copper, nickel and PGE. Consequently its geological environment of formation is of great interest, in order for us to understand how explore for similar systems elsewhere. An important question to resolve is how such a large magmatic ore deposit formed in such a small rock body (Tang & Barnes 1998). In this paper we propose a new metallogenic model for the Jinchuan deposit, specifically that it is a product of a previously unrecognized Proterozoic large igneous province in the Qilian paleocontinent.

2 Geological Setting

The Qilian and Longshou mountains are located in northwestern China (Fig. 1). The Qilian mountains are considered to be a component of the western segment of the Central Orogen. The Longshou mountains are part of the uplift of the southern margin of Alax block in the western part of the North China Plate (Huang et al. 1985; Xu et al. 2003). The Qilian and Longshou mountains are separated by the Hexi Corridor (Fig. 1). There are two models for relationships between the Qilian Orogen and the Longshou Uplift zone: (i) both the basement of the Qilian Orogen and Qaidam Block are part of the South China Landmass Group, whereas the Longshou mountains are located at the southwestern margin of the North China Landmass Group, so that the Qilian mountains formed in the Caledonian orogeny due to collision of these landmasses in the latter stages of the Early Palaeozoic (Feng and He, 1996); (ii) both the remnant blocks of basement of the Qilian Orogen and the basement of Longshou mountains belong to same landmass (Wan et al. 2000; Lu et al. 2002), and the Qilian oceanic basins formed in response to breakup of Rodinia at the end of the late Proterozoic (Fig. 1; Xia et al. 2003; Xu et al. 2003).

3 Evidence for a large igneous province

We infer the existence of large scale magmatism in Qilian-Longshou region during the early Middle Proterozoic from the similar isotopic ages of Precambrian continental flood basalts, komatiite and the magmatic Ni-Cu-PGE sulfides ores associated with layered intrusions and mafic dyke swarms. Specifically, we infer that the continental flood basalts may represent an intracontinental large igneous province (LIP) event related to a mantle plume, and that the Jinchuan deposit is an important component of this province.

3.1 Jingtieshan continental flood basalts

Xia et al. (1999) identified Precambrian continental flood basalts in the Qilian-Longshou micro-landmass, specifically in the Middle Proterozoic Zhulongguan Group of the Changcheng System. These rocks occur in the western segment of North Qilian as a very thick volcanic rock package comprising lower tholeiite and upper alkali basalts. They are similar to continental flood basalts of the Indian Deccan Traps. The Qilian discrimination basalts

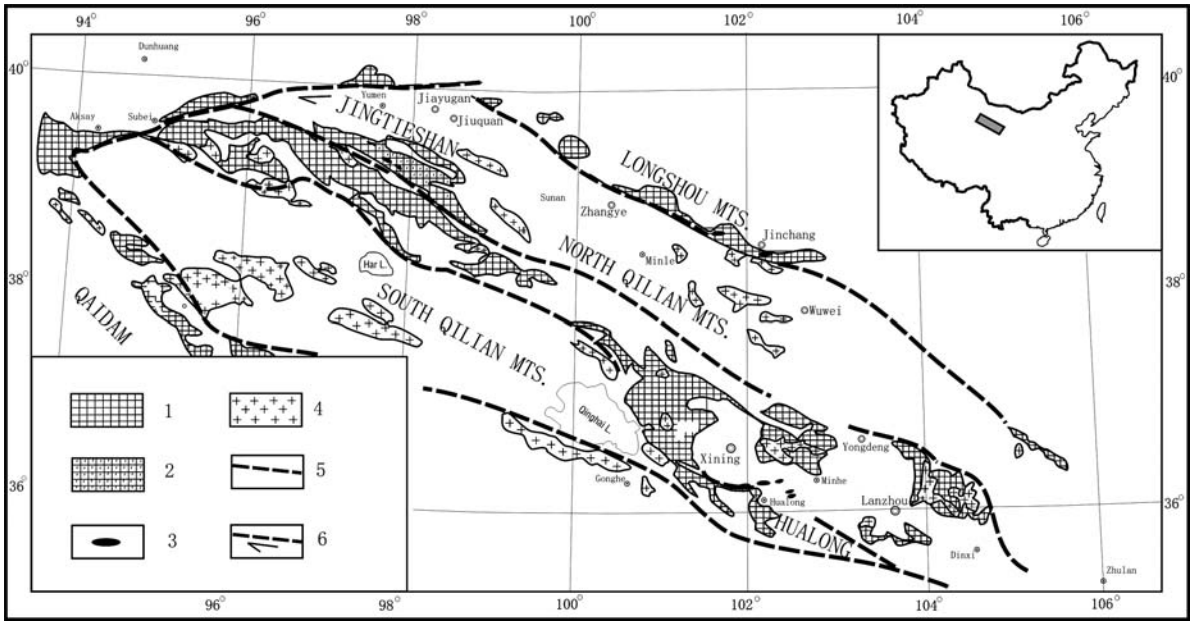

Figure 1: Geological distribution of Qilian-Longshou tectonic elements. 1 - Precambrian basement; 2 - Middle Proterozoic continental flood basalts; 3 - mafic-ultramafic rocks; 4 - granite; 5 – structural boundary of major tectonic unit; 6- strike-slip fault. Inset: locality map.

plot in the intraplate field on a Zr-Zr/Y diagram. They have La/Nb=0.8~1.5, similar to characteristics of other flood basalt provinces (La/Nb=0.5~7), and chondrite-normalized trace element patterns show a Rb, K, Sr, P and Ti trough, also similar to known lower P_2O_5-TiO_2 type flood basalts from other provinces.

Isotopic dating of the Jingtieshan continental flood basalts confirm that they formed in the Changcheng Period of the Middle Proterozoic. In the Baidahe area, the lower basalts have been dated using a Sm-Nd isochron at 1770.9 ± 333 Ma (Mao et al. 1997). The overlying Jingtieshan Group jasperoids of the Iron Range were deposited in the Jixian Period, with a Sm-Nd isochron age of 1309 ± 80 (Xia et al. 2003). Continetnal flood basalt volcanism therefore occurred in the early stages of the Middle Proterozoic, about 1.7~1.5Ga.

3.2 Zangbutai komatiite

The Zangbutai komatiite occurs in the western segment of the Longshou mountains, and was first recognised by Dong et al. (1990). The komatiite contains high-Mg extrusive rocks, about 50~250m thick, which contain distinctive layering and have conformable contacts with the surrounding strata. The komariites have a siliceous glassy matrix that preserves spinifex texture (Fig. 2), and belong to the komatiite-meta-basalt association. On a (TiO_2+Fe_2O_3+FeO)-Al_2O_3-MgO diagram, samples plot in the fields of komatiitic peridotite, komatiitic basalt and Fe-tholeiite. A mineral-rock Sm-Nd isochron age of 1511 ± 168 Ma has been obtained from this unit (Li et al. 2004).

3.3 Mafic dyke swarms

Mafic dyke swarms in the Qilian and Longshou mountains have not been studied systematically. Available data from regional geological surveys show that they have wide distributions. In the Longshou mountains, there are a large number of mafic dyke swarms. In the Jingtieshan micro-continental block in the western segment of North Qilian (Fig. 1), some mafic dyke swarms have also been recognised. Mao et al. (1997) obtained U-Pb zircon dates of 1840 to 1784 Ma from the lower diabases of the Zhulongguan Group in the Aoyougou area. These diabase dykes could represent part of the early stages of a large scale mantle plume.

4 Magmatic Ni-Cu-PGE sulfide deposits

We have used the existence of continental flood basalts, komatiite and mafic dyke swarms in the Qilian-Longshou landmass to infer the existence of an intracontinental Large Igneous Province (LIP) in the Middle Proterozoic, about 1.5Ga. In this province, a large scale mantle plume caused rifting of the Columbia super-continent. This lead to the Longshou mountains becoming China's most important metallogenic belt for Proterozoic magmatic Ni-Cu-PGE deposits.

4.1 Mafic-ultramafic complexes

We believe that a rising mantle plume originated in the 'D' layer of the core-mantle boundary and base of the

This page intentionally blank

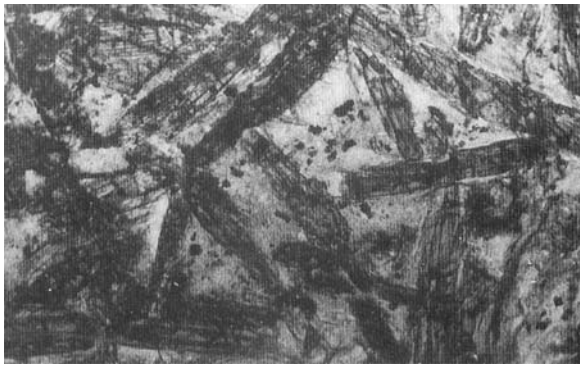

Figure 2: Spinifex textures in Zangbutai komatiite

lithospheric mantle. It caused parting melting and yielded a large scale magma source that generated the ancient Qilian large igneous province, including continental flood basalts, komatiite, picrite and mafic dyke swarms. It formed large volumes of closely spaced gabbro sills in the Longshou mountains, along with layered intrusive complexes and magmatic Ni-Cu sulfide (PGE) ore bodies that comprise zoned mafic-ultramafic complexes with local domains of highly-mineralized rock.

4.2 Jinchuan magmatic Ni-Cu-PGE deposit

The Jinchuan intrusion is dominated by lherzolite, and contains sixty percent sulfide mineralization. At Lashuixia, the intrusion contains ninety percent sulfides. Such concentrations of metallic sulfides could only results from injection of metallic sulfide-bearing magma and/or metallic sulfide liquid derived from an immiscible phase in a larger magma chamber at depth. The Jinchuan lherzolite has εNd(t) = -1.9 to -4.3, $(La/Yb)_N$ = 5.39 to 79.15 (average = 15.04), $(^{87}Sr/^{86}Sr)_I$ = 0.702547 to 0.711761, $Nd_{Sr}(t) > 0$ (and as high as +128.8). These values indicate that the mineralizing magma was crustally contaminated. The unmineralised Zangbutai ultramafic rocks occur adjacent to Jinchuan. They have eNd(t) = +2.6 to +2.9, and are inferred to have remained sulfur-unsaturated due to no crustal contamination.

There is a remarkable difference between the composition of the western segment of the Jinchuan intrusion (SREE = 3.39 to 23.57 ppm, average 14.12 ppm, $(La/Yb)_N$ = 5.39 to 14.01, average 7.50, PGE enrichment) and the eastern segment (SREE = 15.25 to 55.87 ppm, average 30.64 ppm, $(La/Yb)_N$ = 7.02 to 79.15, average 23.52, lower quantities of PGE). This implies that there were several injections of magmas. Depletion of nickel and cobalt in early olivine and chromite accumulations indicates that sulfide immiscibility occurred in the early stages, within a deep-seated chamber.

5 Conclusions

Most of the world's well-known large igneous provinces occur on stable cratons. The Qilian province is different, because after its formation, discrete Qilian palaeocontinental blocks were separated during the Palaeozoic era, and became incorporated into an orogenic belt that extended though the western part of China. This makes it difficult to restore Qilian's palaeo-large igneous province. However, this should be a high priority for research, given that the province contains the exceptional Jinchuan magmatic Ni-Cu-PGE deposit.

References

Dong X, Zeng H,Wang L (1990) The komatiite is found in western Lonshoushan, China[J]. Bulletin of the Xian Institute of Geology and Mineral Resources, CAGS, 30: 136-139.

Feng Y, He S (1996) Geotectonics and orogeny of the Qilian Mountains. Bejing: Geological Publishing House, 1-135(in Chinese).

Huang J, Zhang Z, Zhang Z (1985) The eugeosyncline and Miogeosycline in China and its polycyclic development. Bejing: Chinese Inndustrial Press, 5–41(in Chinese).

Li W, Tang Z, Guo Z, Wang W (2004) Diagenetic epoch and geochemical characteristics of mafic-ultramafic rocks on the southern margin of Alashan Massive in North China. Acta Petrologica et Mineralogica, 23(23):117-126.

Lu SN, Yang CL, Li HK (2002) A group of rifting events in the terminal Paleoproterozoic in the North China Craton. Gondwana Research, 5(1): ,23-131.

Mao J, Zhang Z, Yang J (1997) Zircon in Precambrian Strate geochronometry and its geological significance western of Northern Qilian Mountains. Chinese Sci. Bull., 42(3): 1414–1417(in Chinese with English abstract).

Tang Z, Barnes SJ (1998) Mineralization mechanism of magmatic sulfide deposits[M]. Bejing: Geological Publishing House, 1-70.

Wan Y, Yang J, Xu Z, Wu C (2000) Geochemical characteristics of the Maxianshan Complex and Xinglongshan Group in the eastern segement of the Qilian Orogenic Belt. Geol. Rev., 43(1): 52-68.

Xia L, Xia Z, Xu X (1999). Proterozoic continental flood basalts from Qilian Mountains. Geologica Review, 45(Sup.): 1028–1037 (in Chinese with English abstract).

Xia LQ, Xia ZC and Xu XY (2003) Magma genesis in the Ordovician backarc basins of the Northern Qilian Mountains, China. Geological Society of America, 115(12):1510-1522.

Xu Z, Zhao Z, Yang J (2003) Tectonics beneath plates and mantle dynamics. Geological Bulletin of China, 22(3): 149–159(in Chinese with English abstract).

A study of clay mineralogy and illite Kübler index with respect to hydrothermal alteration in the Yinshan polymetallic deposit, South China

Li Xiaofeng, Mao Jingwen
Institute of Mineral Resources, Chinese Academy of Geological Sciences, Beijing 100037, China

Hua Renmin
Earth Science Department, State Key Laboratory of Mineral Deposit Research, Nanjing University, Nanjing 210093, Jiangsu, China

Abstract. The Yinshan polymetallic deposit is a hydrothermal deposit spatially associated with Late Jurassic felsic to intermediate volcanic-subvolcanic rocks. Illite is the dominant clay mineral formed via hydrothermal alteration of feldspar during fluid-rock interaction. The Kübler index of illite has been used to map paleo-fluid flow associated with hydrothermal mineralization. In the Pb-Zn-Ag mineralizing episode (136-130 Ma), fluid/rock ratios were relatively low, fluid flow was mainly by pore osmosis, and the solute transported slowly. Illite formed at this time and contains some swelling layers. In the second Cu-Au mineralizing episode (125-122 Ma) fluid/rock ratios were relatively higher, and fluid flow was mainly through fractures or channels. Illite associated with stage 2 hydrothermal activity has no swelling layers and a lower Kübler index. The third hydrothermal episode (104 Ma) has no economic mineralization, and produced only minor illite. The clay mineral assemblages, their distributions, and the micro-structural features and variations in the Kübler index of illite are indicators of temperature changes, and the type and intensity of hydrothermal alteration. Consequently, the Kübler index can be used to aid exploration for Cu, Au, Pb, Zn and Ag mineralization in the district.

Keywords. Illite, Kübler index, Yinshan, China, polymetallic

1 Introduction

Illite is a ubiquitous clay mineral that forms at moderate to low-temperatures (100-300°C) in hydrothermal, burial diagenetic and low-grade metamorphic environments. There have been relatively intensive studies of illite formed during sedimentary diagenesis, modern geothermal activity and low-grade metamorphism (Eberl 1993; Inoue 1995; Ji and Browne 2000). However, the formation of illite and its relation to fluid processes during hydrothermal alteration-mineralization are still poorly understood (Bechtel et al. 2000; Celik et al. 1999; Li et al. 2003). This paper presents studies of the Kübler index and X-ray diffraction (XRD) peak intensity of illite and the clay mineral assemblages in altered volcanic-subvolcanic rocks and altered phyllite in the Yinshan polymetallic ore district, and discusses the origin of illite and chlorite in relation to the ore-forming fluids.

2 Geological setting

The Yinshan lead-zinc-silver-copper-gold deposit is located on the southeastern margin of the Yangtze plate, between the northeastern Jiangxi fault and Le'anjang fault on the northeastern margin of the Leping-Dexing volcanic basin (Hua 1987; Fig. 1). The strata exposed in the ore district and the surrounding area consists predominantly of low-grade metamorphic rocks of the Lower Subgroup of the Mesoproterozoic Shuangqiaoshan Group. Late Jurassic calc-alkaline intermediate-felsic rocks have intruded the metamorphic basement. The Yinshan polymetallic deposit is interpreted to be related to this volcanic-subvolcanic activity (Hua 1987; Liu 1994).

Within the Yinshan ore district volcanism falls into three phases, or three eruptive cycles, between which there were pronounced breaks of eruption. The three phases are the felsic, intermediate-felsic and intermediate phase, with the first and second phases being predominant. Each phase began with pyroclastic eruption, followed by lava eruption and then intrusion of subvolcanic rocks. The first phase caused rhyodacitic-rhyolitic volcanism on the northeastern and eastern sides of the ore district. The eruption was notably of fissure type, occurring mainly along the intersection position between E-trending and NE-trending structures. Subvolcanic quartz porphyry was intruded later as E-trending irregular dikes into the Shuangqiaoshan Group on the basin margin. This activity was located in the vicinity of Jiulongshangtian and Beishan in the northern part of the ore district, as exemplified by intrusions units 4, 5 and 13. The second phase of magmatism was dacitic. Subvolcanic dacitic porphyry is distributed mainly around Xishan Mountain and its surroundings, as exemplified by units units. 1 and 3 (Fig. 1). The third phase of volcanic activity resulted in the eruption of minor andesitic lava, which is restricted to the Xishan volcanic edifice (rock body No. 11; Fig. 1; Hua 1987).

Mineralization of the Yinshan deposit produced large, steeply dipping, fissure filling veins which are generally more than 5 cm wide, and associated veinlets and disseminations. The orebodies mainly occur in phyllite of the Shuangqiaoshan Group. The dominant ore minerals are pyrite, chalcopyrite, galena, sphalerite, enargite and tennantite. Gold mainly occurs within copper minerals and pyrite, whereas silver is concentrated mainly in lead- and zinc-bearing minerals. There are significant amounts

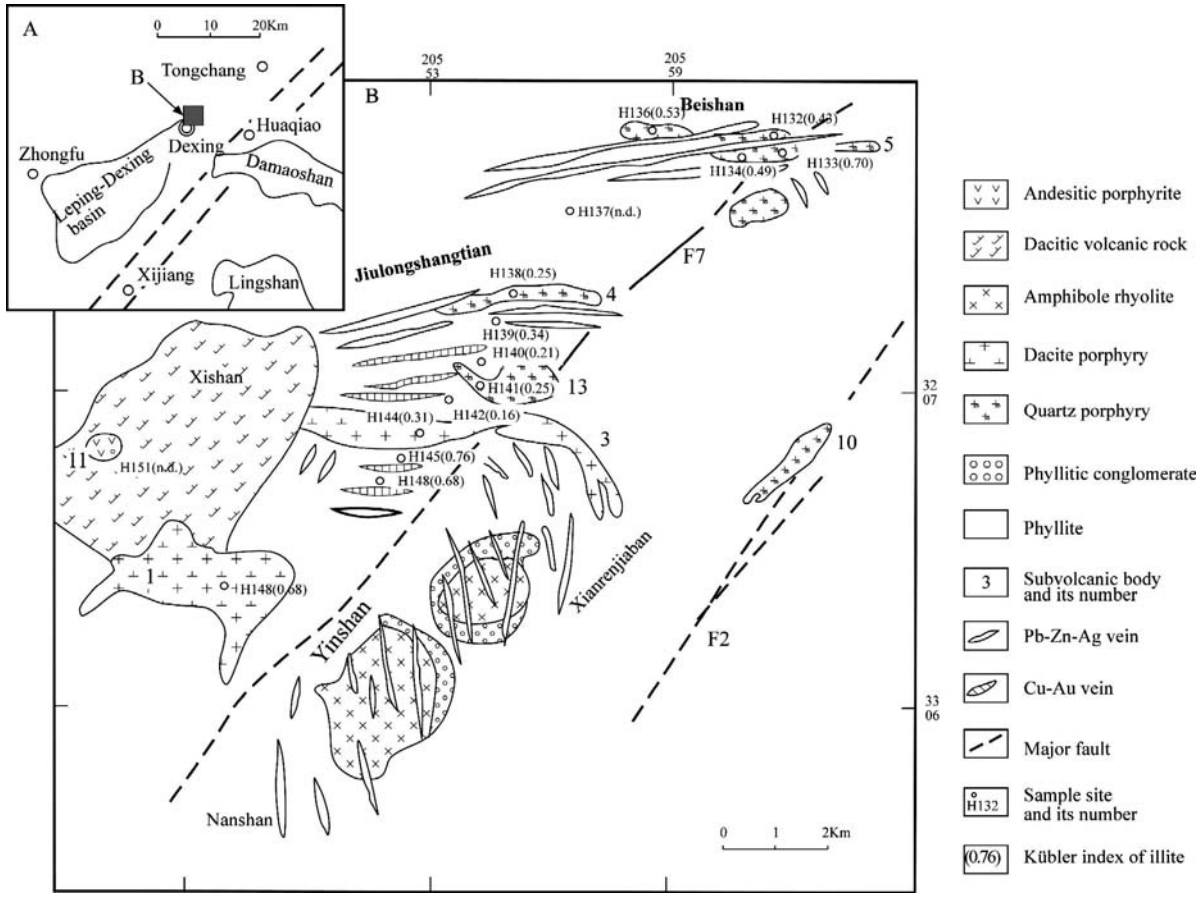

Figure 1: Geological sketch map of the Yinshan ore district, Dexing (B) and its adjacent areas (A); modified from Hua (1987).

of arsenopyrite, enargite and tennantite in the Beishan and Shangtianjiulong areas (Fig. 1), whereas these phases are not in the southern part of the study area. Sphalerite in the north is Fe-rich. Lower-temperature wurtzite occurs in the south.

3 Clay mineral assemblages

Clay minerals in the altered subvolcanic rocks and phyllite at Yinshan can be divided into two assemblages. One is composed dominantly of illite (e.g. samples H132, H133, H134, H136, H137, H140, H141, H145, H148 and H151; Fig. 1). The others consist dominantly of illite and chlorite, or illite and kaolinite (e.g. samples H138, H139, H142, H144, H146; Fig. 1). In terms of spatial distribution, the illite dominates assemblages associated mainly with a lead-zinc-silver ore zone. Areas dominated by chlorite, or by illite plus chlorite are associated mainly with a copper-gold ore zone. Clay assemblages in unaltered phyllite consist of illite (70%) and chlorite (30%).

Clay minerals in porphyry units 5 and 13 (Fig. 1) consist mainly of illite, whereas unit 4, is altered to illite + kaolinite. Unit 3 (dacite porphyry) is mostly altered to chlorite + illite. Weakly unaltered andesite porphyry (Unit 1; Fig. 1) contains a very small amount of illite. Clay minerals in altered phyllite include illite and minor chlorite and kaolinite, whereas those in the altered slate mainly include mixed-layer illite/montmorillonite.

4 Illite Kübler index and XRD peak-intensity ratios

The illite Kübler index is an integrated reflection of the size of the crystal domain, percentage of expandable layers, crystal defects and heterogeneity of the chemical composition (Eberl and Velde 1989). The percentage of expandable layers reflects the degree of expansion of the crystal structure. Whether illite contains expandable layers may be judged by the Ir value. If Ir=1, illite contains no expandable layer; if Ir>1, illite contains expandable layers (Srodon and Eberl 1989).

Analyses of the altered rocks from have revealed the lead-zinc-silver ore zone and copper ore zone vary from 0.43 to 0.76 with a mean of 0.54 and from 0.16 to 0.34 with a mean of 0.25 respectively. Before and after the treatment of hexandiol, the illite Kübler index does not change much, and in some cases the values are essentially equal.

This page intentionally blank

This suggests that these illite crystals contain few or almost no expandable layers. In the copper ore zone, the Kübler index of illite is lower than that in the lead-zinc-silver zone and the Ir value is generally equal to 1, suggesting that its degree of crystallinity is relatively high.

The Kübler index of illite in altered country rocks varies from 0.16 to 0.76, with a mean of 0.39, and the XRD peak-intensity ratio varies from 0.98 to 1.19. The Kübler index of illite in altered subvolcanic rocks varies from 0.25 to 0.76, with a mean of 0.48 and the XRD peak-intensity ratio varies from 0.97 to 1.43. The Kübler index of illite in unaltered phyllite in the surrounding areas is 0.11, which is consistent with greenschist facies metamorphism. The difference in clay mineral assemblages in the altered phyllite and altered slate suggests a lithological constraint on clay mineral compositions. Based on this difference, and on the clay mineral assemblage and the Kübler index of illite in unaltered, low-grade phyllite in the surrounding areas of the ore district, we propose that illite in the altered phyllite and altered subvolcanic rocks is the product of hydrothermal activity.

5 Disscusion and conclusions

Yinshan is a typical polymetallic hydrothermal ore deposit and resulted from superimposition of two stages of mineralization (Hua 1987). There were also two major phases of hydrothermal alteration at Yinshan. The first phase was associated with subvolcanic hydrothermal activity and was centered on rock body units 5, when ore fluids migrated from north to south. The second phase of hydrothermal activity centered on units 3 or 13 (Fig. 1), when ore fluids migrated both toward the south and north but still mainly toward the north based on the Kübler index. The differences in characteristics of clay mineral assemblages of the altered subvolcanic rocks and country rocks and distribution and texture of illite are consistent with multi-stage mineralization.

In the first stage of mineralization (136-130 Ma) the fluids centered on rock body unit 5 and the fluids mainly migrated in the manner of diffusion. As the water/rock ratio was lower, plentiful K^+ was released into the fluids by feldspar hydrolysis and caused the fluids to change from acidic to neutral. As the formation of illite immobilizes K, the K content in the system may directly affect the rate of illitization of feldspar. Therefore in this stage, illite is inferred to have been precipitated directly from the fluids. As the ore-forming fluids floated along fault F7 (Fig. 1), the fluids inside unit 5 flowed from east to west, and the temperatures of the fluids decreased gradually, thus resulting in a westward increase of the Kübler index of illite unit 5 (Fig. 1). During southward migration of fluids within and around unit 5, the temperatures of ore fluids fell and the water/rock ratio diminished gradually, and accordingly the Kübler index of illite increased progressively (Fig. 1). Due to the relatively poor permeability of slate, the clay minerals in altered slate were mainly mixed-layer illite-smectite minerals.

In the second stage of mineralization (125-122 Ma), the fluid flow was centered on units 3 or 13 (Fig. 1). This stage was characterized by large flow volumes, high water/rock ratios, as well as relatively high temperatures, resulting in a low Kübler index of illite. Because the dacite porphyry has higher Fe and Mg contents than the quartz porphyry, more Fe and Mg could be leached allowing chlorite to form during hydrothermal alteration. The high water/rock ratio meant that feldspar hydrolysis was unable to neutralize H^+ completely, so fluids remained acid throughout hydrothermal activity. Kaolinite was precipitated during the latest stages. Migration of the stage 2 fluids toward the north and south caused superimposition of chlorite and illite on the first phase of hydrothermal alteration. This resulted in lower Kübler index values for illite in the mineralization zone.

Acknowledgements

This study was supported by the general project (40403006) of the National Natural Science Foundation of China.

References

Bechtel A, Shieh YN, Elliott WC, Wampler JM, Oszcepalski, Hoernes S. (2000) Mineralogy, crystallinity and stable isotopic composition of illitic clays within the Polish Zechstein basin: implication for the genesis of Kupferschiefer mineralization. Chemical Geology 163: 189-205

Celik M, Karakaya N, Temel A (1999) Clay minerals in hydrothermally altered volcanic rocks, Eastern Pontides,Turkey. Clays and Clay Minerals, 47: 708-717

Eberl DD (1993) Three zones for illite formatioesis and metamorphism. Clays and Clay Minerals 41:26-37

Eberl DD, Velde B (1989) Beyond the Kubler Index. Clay Minerals 24: 571-577

Harvey CC, Browne PRL (1991) Mixed-layer clay geothermometry in the Wairakei geothermal field, New Zealand. Clays and Clay Minerals 39: 614-621

Hua R-M (1987) A discussion on the mechanism of lead, zinc and copper metallogeneses in Yinshan, Jiangxi Province. Mineral Deposits 6(2): 90-96 (in Chinese with English abstr.)

Inoue A (1995) Formation of clay minerals in hydrothermal environments. In Origin and Mineralogy of Clays, Veide B. ed.. Springer. Berlin, 268-330

Ji J-F, Browne PRL (2000) Relationship between illite crystallinity and temperature in active geothermal systems of New Zealand. Clays and Clay Minerals, 48: 139-144

Li, X-F, Hua, R-M, Mao, J-W, Ji, J-F, Wang, C-Z (2003) A study of liite Kübler indexes and chlorite "crystallinities" with respect to shear deformation and alteration, Jinshan gold deposit, east China. Resource Geology, 53(4): 283-292

Liu J-J (1994) Subvolcanic magmatism and Au, Cu polymetallization in Yinshan, Jiangxi Province, Journal of Guilin College of Geology 14(3): 244-253 (in Chinese with English abstract)

Srodon J, Eberl DD (1984) Illite [A]. In: Bailey SW, ed. Micas, Reviews in Mineralogy 13: 495-544

Structural controls on copper skarn mineralization in the Fenghuangshan copper deposit, Tongling, China

Liangming Liu, Shenglin Peng
Computational Geosciences Research Centre, Central South University, Changsha 410083, China

Yanhua Zhang, Chongbin Zhao
CSIRO Division of Exploration and Mining, PO Box 1130, Bentley, WA 6102, Australia

Abstract. This paper presents field data and numerical modeling results for structural controls on copper skarn mineralization in the Fenghuangshan copper deposit. Tensional fractures overlapping the igneous contact zone are well-mineralised and developed as a result of far-field tectonic stress and/or contraction of cooling igneous intrusions. Results of numerical modeling suggest that these dilatant zones were important for fluid focusing and ore formation.

Keywords. Structure, skarn, copper, dilation, numerical modeling

1 Introduction

Tongling is one of the most important copper mining districts in China. The district is characterized by copper skarns. Because of their economic value and scientific significance, these deposits have been studied intensively (Chang et al. 1991; Zhang and Ling 1993; Zhai et al. 1996; Yu et al.1996; Pan and Dong 1999). These metal-bearing skarns were formed by magmatic-related metasomatic processes. The igneous rocks and their contact zones, and also the skarn itself, have been studied intensively by previous workers. The structural controls on copper skarn mineralization in the district are also important, but have not been as intensively studied and are poorly understood. This paper presents our research into structural controls at the Fenghuangshan copper deposit in the Tongling district.

2 Geological setting

The Tongling copper district is located in the central segment of the Lower-middle Yangtze metallogenic belt, which is one of the most important polymetallic belts in China (Chang et al. 1991; Zhai et al. 1996; Pan and Dong 1999). The copper deposits in the Tongling district are mostly of skarn type, and are clustered in three ore fields, Tongguangshan, Shizishan and Fenghuangshan. Each field corresponds to an area of extensive felsic magmatism.

The Fenghuangshan ore field is located in the west part of the Tongling district, and includes six copper deposits along the contact zone of the Xingwuli intrusion. The largest deposit, also called Fenghuangshan, occurs on the western contact zone of the Xingwuli intrusion. It has a reserve of 30.58 million tons of Cu with an average grade of 1.26%. The Xingwuli intrusion mainly consists of calc-alkaline granodiorite and quartz monzodiorite. Their K-Ar isotopic ages are 149 to 124 Ma (APGB 1987). The host rocks are mainly Triassic and Permian limestones and dolomitic limestones.

The ore bodies in the Fenghuangshan copper deposit have NE-, NW- and NWW-trends, and form an arc-shaped array along the western contact zone of the intrusion (Fig.1). The main ore bodies (Nos. I and II) have a NW trend. They have irregular to tabular shapes and are located in the contact zone. Massive Cu-bearing magnetite/hematite and siderite ore is dominant, which contains more than 30% Fe. Minor ore types include disseminated copper sulfides in quartz monzodiorite, granitoid and skarn, and Cu-bearing breccias (including brecciated felsic magmatite, brecciated limestone and brecciated skarn). The copper-bearing minerals are chalcopyrite and bornite. Pyrite and chalcopyrite typically occur along grain-boundaries and fractures through earlier-formed magnetite and hematite.

3 Structural analysis

Although Fenghuangshan is classified as a copper skarn deposit (Chang et al. 1991; Pan and Dong 1999), the localization of copper ore cannot only be ascribed to chemical processes. Skarns mainly occur along the northern segment of the Xingwuli intrusion contact zone, but the main copper ore bodies are located in the southern segment, where fewer skarns and more breccias have formed (Fig. 1). Mechanical processes, including brecciation, must have also played important roles in copper mineralization.

Evidence for structural controls on copper mineralization at Fenghuangshan is provided by:

1. Copper-bearing sulfides that occur as disseminated veinlets in the oxides or skarns.
2. The spatial location of the largest ore body, which occurs on the southern segment of the western contact zone, where a major NW-trending tensional fault has cut the NW-trending contact zone (Fig. 1).
3. The main ore bodies occurring in fault contact with marble. The jagged nature of the contact and the ir-

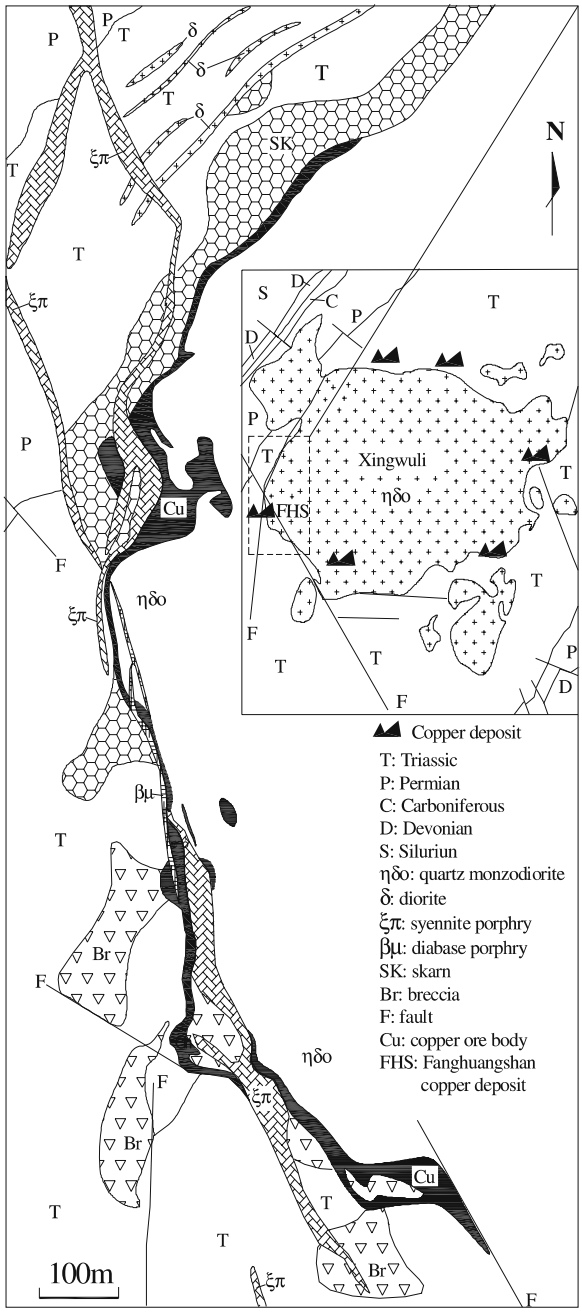

Figure 1: Surface geological map of the Fenghuangshan copper deposit. Inset: The location of Fenghuangshan and other skarn deposits in the Fenghuangshan ore field, relative to the Xingwuli intrusion.

regularly-shaped clasts of marble that occur within the ores indicate that the sulfides formed in space created by tensional fracturing.

4. Z- and S-shaped ore bodies, in both plan and cross sections, which occupy two sets of conjugate shear fractures. The attitudes of the conjugate shear fractures are not uniform along the contact zone. Their strikes vary from NE and NNW in the northern segment of the contact zone, to SEE and NNW in the southern segment. This most likely resulted from variations in the local stress field, possibly influenced by cooling and contraction of the Xingwuli intrusion, and/or changes in the far-field stress regime.
5. A close association between mineralized breccias, fractures and faults. There is a gradual transition from fractured host rocks through brecciated rocks to copper-bearing hydrothermal breccias. The morphological and compositional features of the breccias include jigsaw-fit textures, where angular wall rock fragments occur in a hydrothermal sulfide and carbonate cement. These textures are consistent with hydrothermal brecciation, probably caused by explosion of over-pressured hydrothermal fluids. Brittle failure and hydrothermal brecciation would have caused a significant drop in fluid pressure, possibly triggering copper sulfide deposition.

In summary, structural processes on copper skarn mineralization at Fenghuangshan produced the dilatant zones that were favourable sites for high grade ore formation. They may have also triggered copper sulfide deposition by causing phase separation during brecciation.

4 Numerical modeling results

Numerical modeling of fluid flow and heat transfer was undertaken using FLAC (Fast Lagrangian Analysis of Continua; Coetzee et al. 1995). The aim was to evaluate possible effects of syn-deformation cooling and fluid flow evolution after emplacement and crystallization of the Xingwuli intrusion. For the purposes of our simulations, it was assumed that $\sigma 1$ was 4×10^7Pa in the NW-SE direction, $\sigma 3$ was 2×10^7 Pa in the NE-SE direction, the initial temperature of the intrusion was 650°C, and the country rocks were 300 °C. These assumptions are consistent with the findings of Liu and Peng (2004).

Our simulations predict dilatant zones to be distributed along the contact zone (Fig. 2), and the predicted sites coincide well with all the known ore bodies. More importantly, more dilatant zones correlate with the locations of the larger ore bodies, suggesting that dilation has controlled both the location and size of the ore bodies in the Fenghuangshan ore field. The close spatial association of the existing ore deposits with the dilatant zones can be ascribed to dilatant deformation controls on fluid flow. Fluid focusing was essential for high grade ore formation. The western dilatant zone, where the Fenghuangshan ore deposit is located (Fig. 1), is predicted by our modeling to be the most dilatant zone, and also the site for most intense fluid-focussing. Magmatic-hydrothermal fluids sourced from the Xingwuli intrusion, and pore fluids derived from the host rocks, are all predicted to flow to-

This page intentionally blank

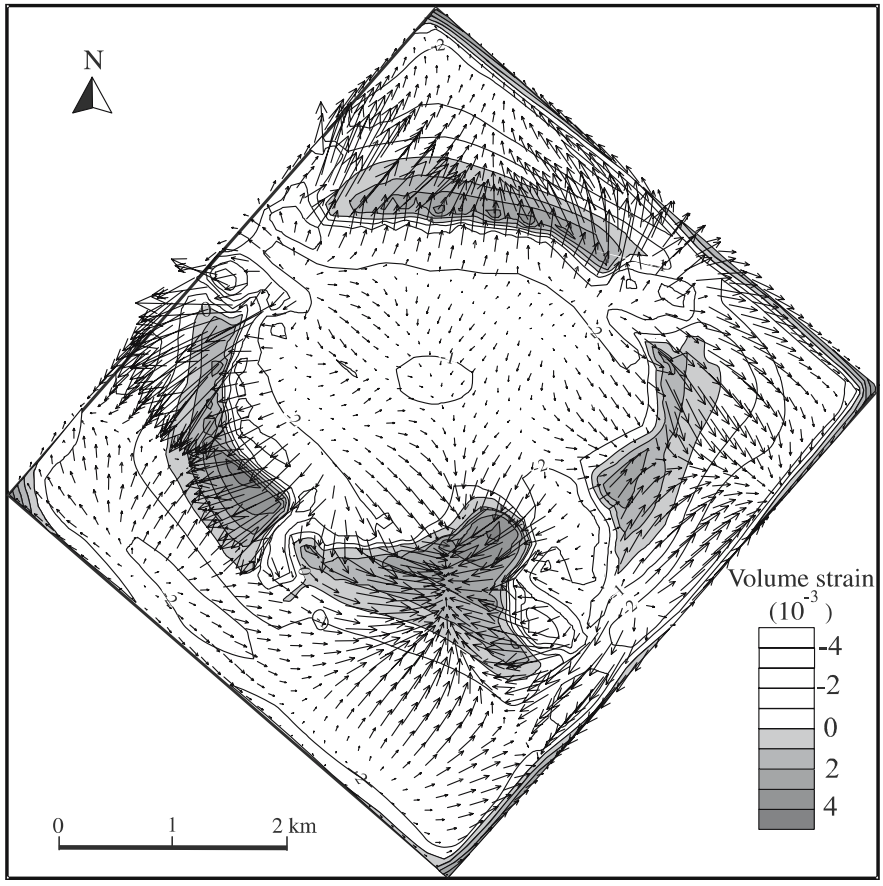

Figure 2: Numerical modelling results, showing Darcy fluid flow velocities (arrows) and total volume strain contour at 7000 year, the maximum fluid flow velocity is 2.61×10^{-11} m/s.

wards the Fenghuangshan dilatant zone (Fig. 2), where they could have undergone fluid mixing, in addition to phase separation. This is predicted to be a very favourable site hydrologically for mineralization.

5 Conclusions

Both field evidence and numerical modeling results demonstrate that structural controls were important for copper mineralization at Fenghuangshan. The most favorable structures for mineralization were tensional fractures that overlapped the contact zone and were closely associated with hydrothermal brecciation. The mineralised fractures were formed in a local stress regime influenced by local cooling and contraction of the Zingwuli intrusion, and also possibly by far-field tectonic stress. The mechanical processes at Fenghuangshan not only created space for copper mineralization, but also may have influenced ore deposition by triggering phase separation, and/or facilitating fluid mixing (further work is required to evaluate the most likely ore-forming process). The highly dilatant zones at Fenghuangshan provided favorable sites for fluid flow, an essential requirement for any style of hydrothermal mineralization.

References

Anhui Provincial Geological Bureau (1987) The Regional Geology of Anhui Province. Geological Publish House, Beijing: 1-721 (in Chinese)

Chang Y, Liu X, Wu Y (1991) The Copper-Iron Belt of the Low and Middle Reaches of the Changjiang River. Geological Publish House, Beijing: 1-359 (in Chinese)

Coetzee MJ, Hart RD, Varona PM, Cundall PA (1995) FLAC Basics. Itasca Consult Group, Minneapolis: 1-125

Liu LM, Peng SL (2004) Prediction of hidden ore bodies by synthesis of geological, geophysical and geochemical information based on dynamic model in Fenghuangshan ore field, Tongling district, China. Journal of Geochemical Exploration 81: 81-99

Pan Y, Dong P (1999) The lower Changjiang (Yangzi / Yangtze River) metallogenic belt, easter central China: intrusion- and wall rock-hosted Cu-Fe-Cu,Mo,Zn,Pb, Ag deposits. Ore Geol Rev 15: 177-242

Yu CW, Jiang Y, Xiao Z (1996) Dynamics of ore-forming processes of the stratabound skarn copper deposits of Tongling, Anhui Province. Acta Geologica Sinica (English Edition) 9: 59-73

Zhai YS, Xiong YL, Yao SZ. Lin XD (1996) Metallogeny of copper and iron deposits in the Eastern Yangtze Craton, east-central China. Ore Geol Rev 11: 229-248

Zhang S, Ling Q (1993) Characteristics of skarn copper deposit; an example from Dongshizishan copper deposit in Tongling County, Anhui Province. Journal of China University of Geosciences 18: 801-810 (in Chinese)

Rutile - the tin-tungsten host in the intrusive tourmaline breccia at Wheal Remfry, SW England

A. Müller
Norges Geologiske Undersøkelse, N-7491 Trondheim, Norway

C. Halls
Natural History Museum, Department Mineralogy, Cromwell Road, London SW7 5BD, United Kingdom

Abstract. Trace element compositions (Al, Si, Ca, Zr, Nb, V, Cr, Fe, Sn, W) have been analysed from accessory rutile from the tourmaline breccia of Wheal Remfry, SW England. The analyses show that rutile is the main carrier of Sn in the tourmaline breccia of Wheal Remfry. High Fe (Sn, W) in the final outer growth zones of rutile and tourmaline suggest open-system behaviour during breccia formation, with an increasing contribution from relatively oxidizing formation waters. The tin, present as Sn^{4+} in the mineralising fluid, enters the structure of the rutile which coexists in intergrowths with tourmaline in the breccia matrix. The amount of Sn^{4+} in the fluid was probably too low for cassiterite to form as a separate phase.

Keywords. Rutile, tin, tourmaline, breccia, Wheal Remfry

1 Introduction

Tourmaline breccia dykes and pipes are found worldwide in tin-bearing granite intrusions at both plutonic and subvolcanic levels in provinces of different ages (e.g. Slack 1996 and references therein). The concentration of boron and water in the late-Variscan granite magmas of SW England led to the explosive release of volatiles during the transitional stage of magmato- hydrothermal evolution. This resulted in tourmaline breccia dykes and pipes and the intimate paragenetic association between cassiterite and tourmaline in hydrothermal mineral lodes of the Cornubian metalliferous province (e.g. Allman-Ward et al. 1982; Halls 1994). Halls et al. (1977) gave the first description of an intrusive hydrothermal tourmaline breccia at the Wheal Remfry china clay pit in the western part of the St. Austell pluton, Cornwall. The explosive brecciation took place at temperatures of 300-400°C, in the presence of a highly saline fluid (36-46 wt.% eq. NaCl) at minimum depths of 1-1.5 km (Halls et al. 1977). Brecciation probably began at a depth of ~4 km (Halls 1994).

The main accessory phase in the breccia matrix is rutile. Cassiterite has not been found despite the fact that the rock contains elevated tin-concentrations. Rutile can accommodate a wide range of highly charged trace elements up to percent level, e.g., V, Cr, Fe, Al, Nb, Sn, Sb, Ta and W (e.g. Graham and Morris 1973; Deer et al. 1992; Zack et al. 2002). According to Harris (1986), Rice et al. (1998) and Michailidis (1997), rutile formed in hydrothermal mineral deposits can be expected to contain V, Nb, Sn, Sb and/or W as major (>1 wt. %) components. Tourmaline can be also a significant carrier of Sn (Nemec 1973, Williamson et al. 2000). For this reason, tourmaline from the breccia matrix of Wheal Remfry has been analysed for tin and other diadochic metals.

Here we report trace element analyses of rutile and tourmaline from the tourmaline breccia of Wheal Remfry. We show that rutile is the principle host for Ti, Sn, W and Nb in this breccia.

2 Field setting

The tourmaline breccia pipe is exposed in the Wheal Remfry china clay pit at the western end of the St. Austell pluton. The host rock is a strongly kaolinised K-feldspar megacrystic biotite granite (e.g. Dangerfield et al. 1980). The exposed breccia body extends about 400 m in N-S-direction with a width of 40 to 100 m. Its geometry is controlled by sub-vertical, N-S-striking fracture systems (Allman-Ward et al. 1982). The breccia pipe post-dates the consolidation of the outer carapace of megacrystic granite, but incorporates rheomorphic enclaves of porphyritic granite drawn up from the underlying magma body during adiabatic decompression when brecciation took place. The breccia is matrix-supported and composed of variably tourmalinised killas and granite fragments that show a wide variation in size, degree of sorting and roundness set in a dark matrix of microcrystalline tourmaline and quartz with silicified mineral and lithic fragments (Allman-Ward et al. 1982). The volume proportion of fragments varies between 40% and 70% (Allman-Ward et al. 1982). In some parts, large blocks of granite reaching 2 m in diameter occur, but most of the fragments are smaller than 0.5 m. The presence of killas mixed in with the granite fragments is evidence of the turbulent mixing of fragments within a fluidised system at the time of formation (Allman-Ward et al. 1982).

3 Petrography of the breccia matrix

The matrix-forming minerals are tourmaline and quartz. The crystal size of the anhedral quartz ranges form 5 to 500 μm. There are three tourmaline generations: (1) the oldest is inherited from the host granite, and has brown maximum absorption colours. It occurs as anhedral frag-

ments of up to 1 mm in size. The brown tourmaline is partially replaced by blue tourmaline of generation (2). The youngest generation forms thin, pale green needles 5 to 800 µm in length. The needles are commonly intergrown with quartz. The backscattered electron image (BSE) in Fig. 1a reveals a complex zoning of the pale green needles.

The main accessory phase in the breccia matrix is rutile. It forms dendritic and corroded but overall lath-shaped crystals which are up to 1 mm long. In the BSE images four different domains within the crystals can be distinguished. In order of age from older to younger these are: (1) homogeneous grey dendritic, (2) grey corroded spongy, (3) bright grey and (4) white domains (Fig. 2a, b). From 70 to 80 vol.% of the rutile crystals consist of domains 1 and 2. Occasionally, small (<50 µm) bright crystals with planar crystal faces (domains 3 and 4) occur as overgrowths on the dendritic crystals (Fig. 2a).

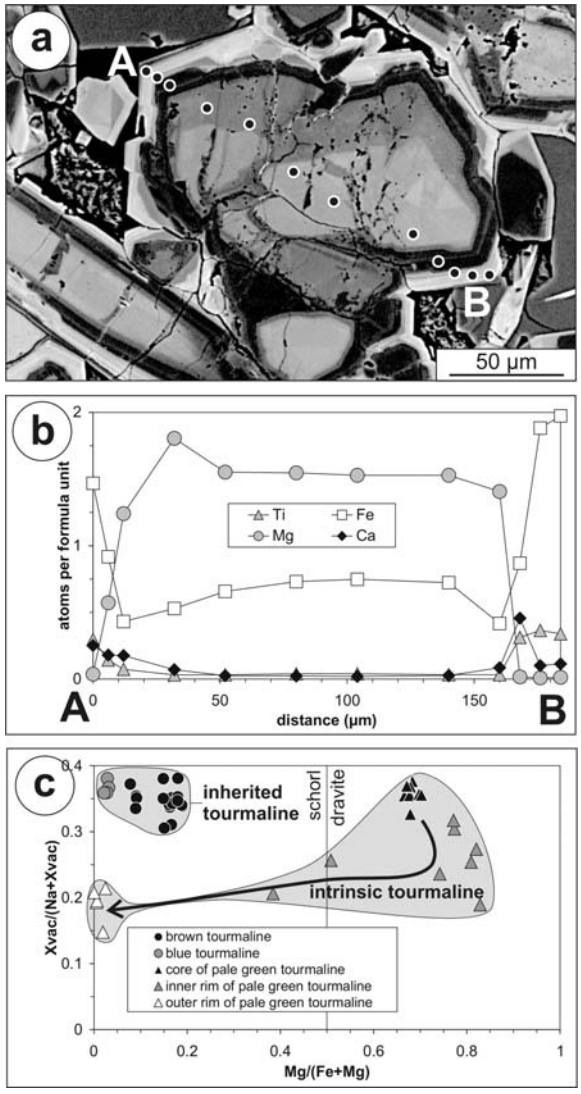

Figure 1: a - Backscattered electron image (BSE) showing the zoning of pale green tourmaline perpendicular to the c-axis. The dots mark the location of the micro probe traverse A-B shown in (b). b – Electron micro probe traverse A-B across the pale green tourmaline shown in (a). The outer rim of the tourmaline is enriched in Fe, Ti and Ca and depleted in Mg in comparison to the crystal core and inner rim. c – variation diagram for tourmaline of Mg/(Fe + Mg) vs Xvac/(Na + Xvac). The inherited and intrinsic tourmalines plot in two separated fields. The arrow indicates the crystallisation trend of the pale green tourmaline.

4 Rutile and tourmaline chemistry

Quantitative analysis of tourmaline and rutile was carried out using the Cameca SX50 microprobe in the laboratories of the Department of Mineralogy at the Natural History Museum, London. For tourmaline analysis an accelerating voltage of 20 kV and a beam current of 25 nA were used. For rutile an accelerating voltage of 20kV and a beam current of 20 nA were used. In both cases the electron beam was focussed to a spot size of ~5 µm. Calculated limits of detection of the trace elements in rutile are listed in Table 1.

The analytical profile across the pale green tourmaline in Fig. 1b shows that the crystal has a relatively homogenous core with high Mg and moderate Fe. Fe decreases slightly towards the margin but then reaches a maximum in the outermost zone (the brightest zone in Fig. 1a). Also, Ti and Ca are slightly enriched in the outer zone. In the tourmaline discrimination diagram (Fig. 1c), the core of the pale green tourmaline plots in the dravite field whereas the outermost zone has a schorl composition. Fragments of inherited brown and blue tourmaline plot in a narrow field which is clearly separated from the field of pale green tourmaline (Fig. 1c). The composition of the brown tourmaline plots with tourmaline from granites and pegmatites of SW England (London and Manning 1995), whereas the blue tourmaline is hydrothermal in origin (Charoy 1982). Sn is below the 480 ppm detection limit in all tourmaline generations.

Rutile contains highly variable amounts of Fe, Nb, V, W and Sn as shown by the high contrast of the BSE signal within the zones of rutile crystals (Fig. 2a). Fe (300-5,200 ppm), W (<3,300 ppm) and Sn (<6,900) are less enriched in domain 1 and 2, more enriched in domain 3 (Fe: 6,400-10,000 ppm; W: 8,500-11,300 ppm; Sn: 3,500-5,600) and strongly enriched in domain 4 (Fe: 14,300-14,700 ppm; W: 16,700-19,500 ppm; Sn: 18,000-18,800). Thus, these elements reach a maximum in the latest overgrowth. The brightness of rutile shown by BSE imaging is predominantly due to the Fe, W and Sn contents so that the most enriched zones form the brightest domains in the image. Nb and V behave in a different way. Domain 1 has the highest V (4,100-5,800 ppm) and high Nb (10,700-18,500 ppm). The corroded spongy domain 2 contains relatively low Nb (6,700-8,400 ppm) and lower V (1,100-3,300 ppm). Domains 3 and 4 have the lowest V (800-1,800 ppm) but elevated Nb (8,400-20,500 ppm).

Table 1: Trace element composition (ppm) of rutile from the tourmaline breccia of the Wheal Remfry, Cornwall. Detection limits (LOD) were calculated from 3σ of 12 background measurements. Note the strong enrichment of Sn, W and Fe in domain 4.

domain		1	1	1	1	2	2	2	2	3	3	4	4
analysis#	LOD	6	5	8	9	4	11	16	19	3	14	2	10
Ca	227	<227	1730	<227	<227	572	<227	629	658	1051	<227	250	300
Al	100	1651	1080	1403	1392	1313	1133	1043	1191	1471	900	619	1148
Cr	400	801	623	718	883	<400	<400	<400	<400	<400	<400	<400	<400
Fe	335	5068	3583	4656	2954	4539	3762	5239	4703	10089	6421	14707	14310
Si	1340	<1340	<1340	<1340	<1340	<1340	<1340	1800	2608	<1340	1449	<1340	<1340
Nb	657	18511	10688	15889	13177	8319	8437	6732	7242	15617	20489	8430	11828
V	350	5781	4128	5299	5702	1692	2403	2818	2000	1132	829	1798	1619
W	509	<509	<509	<509	<509	1142	1078	1316	3266	11345	8546	19479	16673
Sn	541	1000	1906	<541	<541	6467	6033	5600	6931	3513	5600	18801	17982

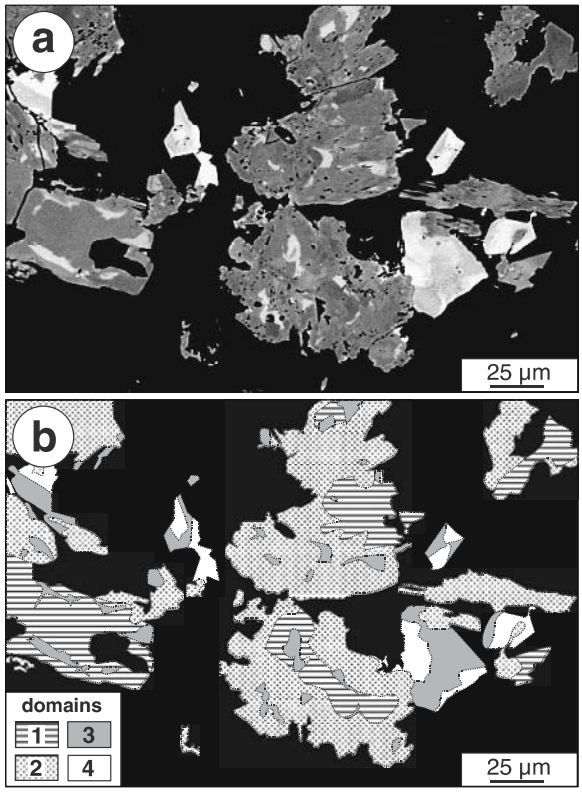

Figure 2: a – Backscattered electron (BSE) image of rutiles in the matrix of the tourmaline breccia of Wheal Remfry. Rutiles have different grain textures and domains contrasted by BSE within the crystals. b – Distribution map of four different domains within the rutiles shown in (a).

5 Discussion

The substitution of Sn, W and Fe in rutile increases progressively during the history of crystallisation at Wheal Remfry. During the last growth stage, up to 1.9 wt.% Sn, 1.9 wt.% W and 1.5 wt.% Fe were incorporated in the rutile. These elements fit very well into the rutile structure but the charge variations of $Fe^{3+}(Fe^{2+})$ and W^{6+} require coupled substitutions to maintain electrical neutrality. Similar atomic quantities of Fe and W in the same rutile domain suggest that double substitutions of the kind $2Ti^{4+} \rightarrow Fe^{3+} + W^{6+}$ or $2Ti^{4+} \rightarrow Fe^{2+} + W^{6+}$ have occurred (Rice et al. 1998). The excess positive charge produced by the first kind of substitution could be balanced by Ti or O vacancies. In common with rutile, the paragenetically associated tourmaline contains the greatest amount of iron as Fe^{2+} and Fe^{3+} in the final overgrowth. This indicates that conditions were relatively oxidizing during the formation of this zone. This demonstrates that the level of substitution of Fe in rutile and tourmaline is directly related to the concentration of Fe in the mineralising fluid. The strong increase in Fe in the last overgrowth in rutile and tourmaline suggest open-system behaviour during breccia formation, with increasing contributions from relatively oxidizing formation waters (Williamson et al. 2000). Rutile incorporated highest Sn and W concentrations at this stage.

The presence of Sn^{4+} in hydrothermal fluids is likely to be a transient phenomenon, as it would normally be precipitated and fixed in the crystal structure of cassiterite. However, the absence of cassiterite in the tourmaline breccia at Wheal Remfry is attributed to the fact that Sn^{4+} simply enters the sites available in rutile which forms a common accessory constituent of the breccia matrix. The amount of Sn^{4+} in the fluid was probably too low to give rise to precipitation of cassiterite as a separate phase.

Complex zoning in rutile and tourmaline indicates changing fluid conditions during breccia formation. Different crystal growth textures of rutile (corroded spongy versus homogeneous) and the highly variable trace element contents in rutile and paragenetically associated tourmaline can be attributed to variations in the composition of the rock-forming fluid and variations in pressure and/or temperature. The apparently uniform brec-

cia matrix records stages of hydrothermal evolution in the system from a transitional magmatic state to one in which more oxidised formation waters entered and reacted with the magmatic residue.

Acknowledgements

This study was supported by the Natural History Museum of London, Geological Survey of Norway and the Deutsche Forschungsgemeinschaft (MU 1717/2-1). Thanks to J. Spratt of the Department of Mineralogy at the Natural History Museum, London, who supervised the acquisition of the microprobe analyses of rutile and tourmaline.

References

Allman-Ward P, Halls C, Rankin A, Bristow CM (1982) An intrusive hydrothermal breccia body at Wheal Remfry in the western part of the St Austell granite pluton, Cornwall, England. In: Evans AM (ed) Metallization associated with acid magmatism. John Wiley & Sons Ltd, London: 1-28

Charoy B (1982) Tourmalinisation in Cornwall, England. In: Evans AM (ed) Metallization associated with acid magmatism. John Wiley & Sons Ltd, London: 63-70

Dangerfield J, Hawkes JR, Hunt, EC (1980) The distribution of lithium in the St. Austell granite. Proc Ussher Society 5: 76-80

Deer WA, Howie RA, Zussmann J (1992) An introduction to rock-forming minerals. Longmans Scientific and Technical

Graham J, Morris RC (1973) Tungsten- and antimony-substituted rutile. Min Mag 39: 470-473

Halls C (1994) Energy and mechanism in the magmato-hydrothermal evolution of the Cornubian Batholith: A review. In: Seltmann R, Möller P, Kämpf H (eds) Metallogeny of collisional orogens. Czech Geological Survey Prague: 275-294

Halls C, Rankin A, Ferriday IL, Blain CF, Bristow CM, Gronow, C (1977) A tourmalinized hydrothermal intrusion breccia at Wheal Remfry in the western part of the St. Austell pluton, Cornwall. Trans Inst Mining Metallurgy Section B 86: B163

Harris DC (1986) Mineralogy and chemistry of the main Hemlo Gold deposit, Hemlo, Ontario, Canada. Proceedings of the Gold 1986 Symposium, Toronto: 297-310

London D, Manning DAC (1995) Chemical variation and significance of tourmaline from Southwest England. Econ Geol 90: 495-519

Michailidis KM (1997) An EPMA and SEM study of niobian-tungstenian rutile from the Fanos aplitic granite, Central Macedonia, Northern Greece. N Jahrb Mineral Monatsh: 549-563

Nemec D (1979) Tin in tourmalines. N Jahrb Mineral Monatsh 2: 58-63

Rice CM, Darke KE, JW Still (1998). Tungsten-bearing rutile from the Kori Kollo gold mine, Bolivia. Min Mag 62: 421-429

Slack JF (1996). Tourmaline associated with hydrothermal ore deposits. In: Grew ES, Anovitz LM (eds) Boron: Mineralogy, petrology and geochemistry. Review in Mineralogy, vol. 33: 559-643

Williamson BJ, Spratt J, Adams JT, Tindle AG, Stanley CJ (2000) Geochemical constraints from zoned hydrothermal tourmalines on fluid evolution and Sn mineralisation: an example from Fault breccias at Roche, SW England. J Petrol 41: 1439-1453

Zack T, Kronz A, Foley SF, Rivers T (2002) Trace element abundances in rutiles from eclogites and associated garnet mica schists. Chem Geol 184: 97-122

Intrusion-related gold occurrences in the Astaneh-Sarband area, west central Iran

N. Nezafati
Department of Economic Geology and Leibniz Laboratory for Applied Marine Research, Freiberg University of Mining and Technology, Brennhausgasse 14, D-09596 Freiberg, Germany

P.M. Herzig
Leibniz-Institut für Meerewissenschaften, IFM-GEOMAR, Dienstgebaeude Ostufer, Wischhofstr. 1-3, Geb 4, D-24148 Kiel, Germany

E. Pernicka
Institute of Prehistoric Archaeology, University of Tuebingen, Schloss Hohentuebingen, D-72070 Tuebingen, Germany

M. Momenzadeh
Zarneh Research Institute, 34 Forth 12m Street, Jenah Highway, Tehran, Iran

Abstract. The Astaneh-Sarband area is located in the Sanandaj-Sirjan metamorphic belt in west central Iran. The area hosts five intrusion-related tungsten and/or gold systems, including the Deh Hosein and Astaneh gold occurrences and Nezam Abad tungsten-gold occurrence. The Astaneh-Sarband area contains Mesozoic schist, Late Cretaceous-Early Tertiary intrusive rocks and related contact metamorphic aureoles, and pegmatites. The Astaneh and Nezam Abad systems are hosted in granitic to granodioritic intrusive rocks of Early to Late Eocene age. At Deh Hosein, mineralization occurs mainly in Jurassic-Triassic meta-sedimentary rocks which have undergone greenschist facies metamorphism and intrusion by the Astaneh granite-granodiorite complex. Gold occurs in quartz and quartz-sulfide veins and veinlets, and as disseminations. Major ore minerals are arsenopyrite, chalcopyrite, pyrite, pyrrhotite, sphalerite, marcasite, bismite, native bismuth, bismuthinite, cassiterite, scheelite, ferberite, galena, native gold, and rare stannite. Adjacent to and within zones of intense quartz veining the predominant alteration assemblage is quartz + sericite + tourmaline + chlorite. The sulfide mineral content in the veins is generally less than 3 vol. %. The gold contents of samples from Deh Hosein, Astaneh and Nezam Abad range up to 9.5, 13.3, and 36.2 ppm respectively. Gold contents correlate moderately well with As, Bi, and Se. Arsenopyrite geothermometry yields deposition temperatures of 580° to 380° C for these occurrences. Stable-isotope data include $\delta^{18}O$ values of 11.5 to 19.2 (quartz), and $\delta^{34}S$ values of -5.6 to 4 (galena, pyrite, arsenopyrite, chalcopyrite). The sulfur data are compatible with a magmatic fluid source. Lead isotope results are consistent with a lower crustal source for the ores at Deh Hosein.

Keywords. Intrusion-related gold, Deh Hosein, Iran

1 Introduction

Recently a specific class of intrusion-related gold deposits has been defined, based largely on deposits in the Fairbanks district, Alaska, and similar deposits in the Yukon Territory (McCoy et al. 1997; Lang et al. 2001). These deposits are mainly of Phanerozoic age and are located mainly in magmatic provinces, formerly best known for tungsten and/or tin deposits. The provinces contain granitic to granodioritic intrusions that have been emplaced into metasedimentary rocks in continental settings well inboard of convergent plate margins. These intrusions are moderately reduced and of dominantly crustal origin. The deposits are characterized by a reduced (pyrrhotite-stable with no magnetite or hematite), low-sulfide (<5 vol %) ore assemblage and geochemical enrichment in gold, bismuth, arsenic, tungsten, molybdenum, tellurium, and/or antimony with usually strong correlation of gold and bismuth. Gold commonly occurs in sheeted quartz veins (McCoy et al. 1997; Thompson et al. 1999; Lang et al. 2001; Baker 2002).

For decades, the Astaneh-Sarband area in Iran was known for tungsten and gold. The discovery of a new polymetallic occurrence (Deh Hosein) has encouraged more investigation in the area (Momenzadeh et al. 2002). This paper introduces the metal occurrences of the Astaneh-Sarband area and provides a description of the geology, ore paragenesis and distribution of gold as well as some relevant elements in these occurrences in order to compare them with the newly defined class of intrusion-related gold deposits (Lang et al. 1997, 2000; McCoy et al. 1997; Thompson et al. 1999).

2 Geologic setting

The Astaneh-Sarband area is located west-southwest of the town of Astaneh in west-central Iran (33°40´-33°50´ N, 49°08´-49°20´ W). There are five known tungsten and gold occurrences in the area. We have studied the Astaneh gold, the Deh Hosein polymetallic, and the Nezam Abad tungsten occurrences in detail. All of these mineral occurrences were recognized from the relics of ancient copper, tin and/or gold mining in the area. The study area is located in the northern part of the Sanandaj-Sirjan tectonic unit and consists mainly of Mesozoic schist, Late Cretaceous-Early Tertiary intrusive rocks and related contact metamorphic aureoles, and pegmatites. The Sanandaj-Sirjan zone (Stocklin 1968) is a metamorphic belt aligned NW-SE. This belt is

parallel to the Zagros Mountains and extends from Sanandaj in the northwest to Sirjan in the southeast of Iran.

Regional metamorphism in the area has reached a peak of greenschist facies, but further metamorphism has occurred locally, associated with granitoid emplacement. Magmatism has produced large intrusive bodies along a general northwest trend. The granitoids have been emplaced in Jurassic and Triassic rocks, and having well-developed contact metamorphic aureoles. The three major intrusive bodies of Astaneh, Boroujerd and Tavandasht-Gousheh consist of granite, granodiorite and quartz diorite (Radfar 1987; Masoudi 1997). The main trend of the faults, fractures and other structural features of the area is NW-SE, which corresponds with the main trend of the Sanandaj-Sirjan zone and the Zagros chain.

3 Geology of the mineral deposits

The Deh Hosein system is hosted by greenschist facies Jurassic-Triassic metasedimentary rocks, which have been intruded by the Astaneh complex. Mineralization continues into the southern part of the Astaneh intrusion. The meta-sedimentary rocks consist of alternating meta-sandstone, phyllite, schist, spotted slate and hornfels. The main faults and other structural features trend NW and NE. Both orientations have controlled mineralization, which occurs in the form of quartz, quartz-sulfide and quartz-gossan veins and veinlets, partly sheeted in structure. These veins show mainly NW-, NE- and sporadically E-trends, and are up to 1.5 m wide and several to tens of meters long. Mineralization also occurs as disseminations and impregnations, especially in the vein selvages. Adjacent to and within zones of intense quartz veining, the predominant alteration assemblage is quartz + sericite + tourmaline + monazite + hematite.

At Astaneh, gold mineralization is confined to the NW-SE trending Astaneh intrusion that is composed mainly of biotite granite (98.9 ± 1.0 Ma; Masoudi 1997), which is locally accompanied by granodiorite and quartz diorite. These rock units are locally altered and/or intersected by quartz or aplitic veins. The northeastern part of the Astaneh intrusion has been cut by the Shirmazd granodiorite. This stock is about 400 m in diameter and we have dated it at 35.05 ± 0.92 Ma (Rb/Sr age, unpublished data). The Shirmazd granodiorite has been cut by NE-trending microgranodioritic dykes. Gold mineralization occurs mainly in the Shirmazd stock and the intersecting microgranodioritic dykes, and in some nearby, smaller, altered microgranodioritic stocks. The dykes contain mostly disseminated chalcopyrite and pyrite, and are in some cases accompanied by arsenopyrite veins. Gold mineralization occurs in NE-trending quartz- and quartz-sulfide veins and veinlets, as well as in disseminations. Alteration minerals include sericite, chlorite, quartz, calcite and local kaolinite (Hashemi 2002).

Nezam Abad is hosted by a quartz diorite stock with an age of approximately 52 to 40 Ma (Lower-Mid Eocene; Farhadian 1991). The quartz diorite stock has been cut by several aplitic and quartz or quartz-tourmaline veins; the latter hosts mineralization. The faults of the area are NW-, NE- and N-trending, with the former the most abundant. The quartz and quartz-tourmaline veins have a general NW-trend, and contain sulfide minerals and malachite stains. There is also a NE-trend apparent in the mineralized veins. Alteration minerals include biotite, quartz, chlorite, sericite, and tourmaline.

4 Ore mineralogy

A total of 36 metalliferous minerals have been detected at Deh Hosein: anglesite, arsenopyrite, azurite, beaverite, bismite, native bismuth, bismuthinite, bornite, cassiterite, cerussite, chalcopyrite, native copper, covellite, cuprite, delafossite, ferberite, galena, goethite, native gold, kobellite, krupkaite, ilmenite, limonite, lollingite, malachite, marcasite, plumbojarosite, pyrite, pyrolusite, pyrrhotite, scorodite, sphalerite, stannite, sulphotsumoite, sztrokayite, and tenorite. The sulfide content in the ore is generally less than two volume percent. Arsenopyrite is dominant, with lesser amounts of chalcopyrite > pyrite > pyrrhotite. Early-formed arsenopyrite typically contains 1-150μm inclusions of native bismuth, bismite and bismuthinite. The latter also occur as individual grains in quartz veins.

At Astaneh the following ore and gangue minerals were observed: arsenopyrite, azurite, bornite, calcite, chalcocite, chalcopyrite, covellite, digenite, galena, goethite, native gold, illmenite, lepidochrosite, limonite, malachite, marcasite, molybdenite, pyrite, pyrrhotite, rooseveltite, scheelite, scorodite, and sphalerite. Chalcopyrite and arsenopyrite are the major sulfide minerals, of which the latter contains 1-50 μm sized inclusions of native bismuth and bismite. Chalcopyrite sporadically contains exsolved sphalerite "stars", which suggests formation temperatures greater than approximately 400°C (Hutchison and Scott 1981).

At Nezam Abad, metalliferous minerals include arsenopyrite, chalcopyrite, azurite, baksanite, bismuth, bismuthinite, cassiterite, covellite, joseite, makovickyite, malachite, marcasite, pyrite, pyrrhotite, rooseveltite, scheelite, schneiderhoehnite, scorodite, sphalerite, stannite, and wurtzite. Scheelite, chalcopyrite and arsenopyrite are the most abundant ore minerals. It seems that scheelite has formed in earlier stages, as it does not show a good correlation with gold.

5 Metal associations and distributions

At Deh Hosein and Nezam Abad, we failed to find any native gold associated with the ore, despite the investigation of more than 65 polished sections. This led to the conclusion that the gold must occur as "invisible gold",

either as submicroscopic metallic particles or as "chemically bound" gold (Maddox et al. 1998). At Astaneh visible gold has been reported in the form of very fine grained particles (<15 μm) either in goethite produced from the oxidation of chalcopyrite or in sericitized plagioclase (Hashemi 2002). At Deh Hosein and Nezam Abad, the highest gold concentrations were found in samples containing visible arsenopyrite, chalcopyrite, pyrite, sulfosalts and highly oxidized iron (gossan) whereas at Astaneh they were found in quartz-hematite veinlets, disseminated chalcopyrite grains in granodiorite of the Shirmazd stock and microgranodioritic dykes, and in arsenopyrite veins. In all three occurrences, gold shows positive correlation with arsenic, bismuth, selenium and weak positive correlation with tellurium and antimony. Bulk gold contents determined by NAA ranged from 0.05 to 13.3 ppm for Deh Hosein, from 0.05 to 9.5 ppm for Astaneh (Samim resources 2001) and 0.05 to 36.2 ppm for Nezam Abad. The Cu, Sn, and W concentrations of veins range up to 6%, 6.7%, and 2420 ppm for Deh Hosein, 1%, 0.05%, and 100 ppm for Astaneh and %10, %0.14 (Farhadian 1991), and 3300 ppm for Nezam Abad.

6 Arsenopyrite geothermometry

The refractory nature of the arsenopyrite, which is the most abundant sulfide mineral in the Astaneh-Sarband area, allows estimation of the conditions of its formation by relating its composition to the sulfur fugacity and the temperature (Kretschmar and Scott 1976; Scott 1083; Sharp et al. 1985). Arsenopyrites from Deh Hosein, Astaneh and Nezam Abad contain 32.3 to 34.3, 30.7 to 31.4, and 33.6 to 35.8 atomic percent of arsenic. Average compositions lead to the conclusion that mineralization occurred at temperatures of 470° to 450°C, 410° to 380°C and 580° to 510 °C, respectively.

7 Isotope studies and geochronology

Analysis of a sample from the Shirmazd stock by the Rb/Sr method yielded an age of 35.05 $\pm$ 0.92 Ma (Priabonian, Late Eocene). Oxygen isotope ratios for gold-bearing quartz veins in the area range from 13.6 to 19.2‰ for Deh Hosein, from 11.5 to 13.7‰ for Astaneh and from 11.6 to 15‰ for Nezam Abad. Measured sulfur isotope values for pyrite, chalcopyrite, galena and arsenopyrite in quartz veins of the Deh Hosein, Astaneh and Nezam Abad range from -5.6 to 0‰, -0.5 to 1.8‰ and 1.2 to 4‰, respectively. The sulfur-isotope values of all these occurrences are compatible with a magmatic sulfur source. Pb isotope ratios from twenty Deh Hosein sulfide samples range from 18.415 to 18.547 for $^{206}Pb/^{204}Pb$, 15.643 to 15.661 for $^{207}Pb/^{204}Pb$ and 38.578 to 38.833 for $^{208}Pb/^{204}Pb$. According to the plumbotectonic model of Zartman and Doe (1981) the lead in the ores has a significant lower crustal Pb component.

8 Discussion and conclusions

The Deh Hosein, Astaneh and Nezam Abad deposits occur in a magmatic province of the northern part of the Sanandaj-Sirjan zone in Iran. Mineral deposits in the region are characterized by a gold-tungsten association, low sulfide mineral contents (generally less than 3 vol %), abundant arsenopyrite, a paucity of pervasive hydrothermal alteration, and a close correlation of gold with As, Bi, and Se. All of these features are similar to intrusion-related gold deposits that have been described from Alaska, the Yukon and other parts of the world (e.g., Lang et al. 1997, 2000; McCoy et al. 1997; Thompson et al. 1999). The Iranian intrusion-related gold occurrences display similar characteristics in mineralogy, their form of the mineralization, their $\delta^{18}O$ and $\delta^{34}S$ signatures, their formation temperatures, alteration, metal association and distribution as well as the ages of their host rocks (in case of Astaneh and Nezam Abad). According to the present data it appears that a fertile magmatic source (probably of lower crustal origin) has caused intensive gold mineralization in the area during the Pyrenean Orogeny. The ore-bearing hydrothermal fluids were primarily of magmatic derivation.

Acknowledgements

The authors acknowledge the financial support of the DAAD (German academic exchange service), the PHD-Program and the Leibniz laboratory for applied marine research at the TU Bergakademie Freiberg, and Zaryaban Exploration who supported this research program. The research was carried out in the course of Nima Nezafati's PhD thesis project. We thank Marion Tichomirowa and her coworkers for performing stable-isotope and Rb/Sr analyses, K.P. Becker for assisting with the electron microprobe at the Institute of Mineralogy and Bernd Höppner for lead isotope analyses at the Institute of Archaeometry, TU Bergakademie Freiberg.

References

Baker T (2002) Emplacement depth and carbon dioxide-rich fluid inclusion in intrusion-related gold deposits. Economic Geology 97: 1111-1117

Farhadian MB (1991) Geochemical and mineralogical investigation into Nezam Abad tungsten deposit, Arak, Iran. Unpublished MSc thesis (in Persian), Tehran University, Iran

Hashemi M (2002) Probable gold mineralization associated with igneous body of Astaneh, Arak, Iran. Unpublished MSc thesis (in Persian), Teacher Training University of Tehran, Iran

Hutchison MN, Scott SD (1981) Sphalerite geobarometry in the Cu-Fe-Zn-S system. Economic Geology, 76: 143-153

Kretschmar U, Scott SD (1976) Phase relations involving arsenopyrite in the system Fe-As-S and their application. Can Mineral. 14:364-386

Lang JR, Baker T (2001) Intrusion related gold systems: the present level of understanding, Mineralium Deposita. 36: 477-489

Maddox LM, Bancroft GM, Scaini MJ, Lorimer JW (1998) Invisible gold: Comparison of Au deposition on pyrite and arsenopyrite. American Geologist. 83: 1240-1245

Masoudi F (1997) Contact metamorphism and pegmatite development in the region SW of Arak, Iran. PhD thesis. The University of Leeds, UK

McCoy D, Newberry RJ, Layer P, DiMarchi JJ, Bakke A, Masterman DL (1997) Plutonic-related gold deposits of Interior Alaska. In: Goldfarb RJ, Miller LD (eds) Mineral Deposits of Alaska. Economic Geology Monograph 9: 191-241

Momenzadeh M, Nezafati N, Pernicka E (2002) First indication of tin at the ancient mining site near Deh Hosein, West central Iran: a possible source for Luristan bronze, Abstract, 33rd International symposium on Archaeometry, Amsterdam, The Netherlands

Radfar J (1987) Petrology of granitic rocks from Astaneh area, Iran. Unpublished MSc thesis (in Persian), Tehran University, Iran

Sharp ZD, Essene EJ, Kelly WC (1985) A re-examination of the arsenopyrite geothermometer: pressure considerations and applications to natural assemblages. Can Mineral. 23: 517-534

Thompson JFH, Sillitoe RH, Baker T, Lang JR, Mortensen JK, (1999) Intrusion-related gold deposits associated with tungsten-tin provinces, Mineralium Deposita 34: 323-334

Zartman RE, Doe BR (1981) Plumbotectonics-The model. Tectonophysics 75: 135-162

The La Fortuna Cu-Au porphyry deposit, Chile

Piotr Paleczek, Waldo Cuadra
Av. Andres Bello 2777, Piso 8, Las Condes, Santiago, Chile

Michael Donnelly, Robert Page
Noranda Inc. / Falconbridge Ltd., 207 Queen's Quay, Queen's Quay Terminal, Toronto, Ontario, Canada

Abstract. La Fortuna is a newly-discovered porphyry deposit that occurs at the southern end of the Eocene-Oligocene metallogenic province in northern Chile. This paper describes the geological features of the deposit, and comments on the implications for mineral exploration.

Keywords. Porphyry, copper, gold, Chile, Eocene-Oligocene

1 Introduction

The La Fortuna deposit is a 35 m.y. old Cu-Au porphyry located 650 km north of Santiago in the Andean Cordillera of Region III, Chile. The deposit occurs within the La Fortuna porphyry cluster of the El Morro District. It is situated 300 km south of El Salvador at the south end of the prolific Eocene-Oligocene porphyry belt (Fig. 1). The deposit was discovered in 2001 as part of the El Morro Joint Venture between Metallica Resources and Noranda Chile Ltda. An Inferred Resource estimate of 466 Mt grading 0.61% Cu and 0.50 g/t Au has been defined based on forty-one diamond drill holes totalling 19,009 m.

Cu-Au mineralization centers on a near vertical, multiphase, quartz monzonite to diorite porphyry stock intruding Mesozoic and Cenozoic sedimentary and andesitic to dacitic volcanic rocks. Porphyry-style hypogene mineralization exhibits uniform Cu/Au ratios, and has been recognized to a depth of 970 m. Leached capping is partially exposed beneath Atacama gravels, and important secondary enrichment is preserved in a discontinuous supergene blanket. Strong potassic and clay-sericite-chlorite alteration accompanied the main stage of mineralization, and is locally overprinted by white quartz-sericite-pyrite and advanced argillic assemblages. This paper describes briefly the geologic setting, and the principal mineralization and alteration features at La Fortuna.

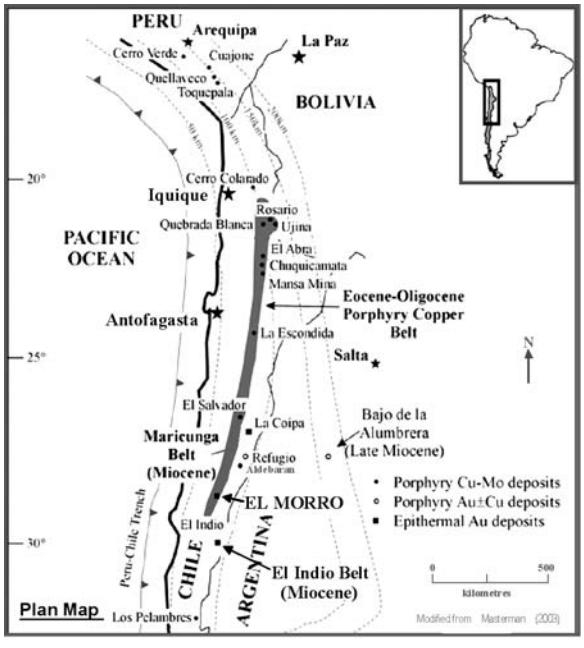

Figure 1: Location of the major porphyry and epithermal deposits of northern Chile. La Fortuna occurs in the El Morro district, at the southern end of the Eocene-Oligocene porphyry belt. Modified from Masterman (2003).

2 Geologic setting

The El Morro District lies in a N-S, 15 by 30 km graben. The western boundary fault is correlated with the southern extension of the Domeyko fault system, which has controlled the location of the great porphyry deposits of the northern Chile Eocene-Oligocene belt. The basement rocks consist of Carboniferous to Permo-Triassic granitoids and Permo-Triassic rhyolite tuffs, capped by Mesozoic sedimentary and volcanic rocks. All are intensely folded along north-trending thrusts.

A series of Eocene-Oligocene aged granodioritic to dioritic porphyry stocks and dikes, i.e. the La Fortuna porphyry cluster, intruded older units in a 7 km by 7 km central portion of the graben. Alteration-mineralization accompanied this magmatic activity and was covered by Miocene volcanics and by Tertiary Atacama gravels. Quaternary erosion has mostly exhumed the La Fortuna porphyry cluster and associated alteration systems.

There are two major structural systems in the El Morro District of which the strongest is a NNE to NS system of reverse faults marking the southern extension of the Domeyko fault system. The second is defined by lesser faults and fractures with a NW trend that has provided a conspicuous control on emplacement of porphyries and mineralization, something that is typical along the length of the Domeyko fault system.

3 La Fortuna geology

The mineralized porphyries at La Fortuna are emplaced in a gently east-dipping sequence of Upper Jurassic - Cretaceous siliceous tuffs, sediments and andesitic conglomerates (Fig. 2). The mineralized area is spatially related to a NW trending fault system with the porphyry stocks found mostly between the sub-parallel La Fortuna and Cantarito faults, which are separated by 600 to 800 m. The La Fortuna deposit is developed in a multiphase porphyry system where the distinction between the different phases is difficult owing to compositional similarity and extensive alteration. The porphyries are separated into three main units and several lesser small dikes.

The main productive unit, the Quartz-Feldspar Porphyry (Qfp), is a quartz monzonite with a medium to fine-grained quartz–feldspar groundmass and plagioclase phenocrysts. Scarce mafic minerals have been altered to biotite, sericite, chlorite or clays. Emplacement of the main body of the Qfp (700 by 400 m elongate NNE) was controlled by the intersection of the La Fortuna-Cantarito fault with a NNE fault zone. The average Qfp primary grade is 0.62% Cu and 0.58 g/t Au.

The second productive porphyry is the Biotite-Amphibole Porphyry (Bap). It has a granodioritic to quartz monzonite composition with plagioclase, biotite, and hornblende phenocrysts. Alteration and veining are less intense than in the Qfp, and the mafic minerals are still visible. Mineralization is lower in copper but higher in gold than in the Qfp. Average grades in the primary zone are 0.48% Cu and 0.64g/t Au. The Bap does not outcrop but drilling has identified at least 4 bodies cutting Qfp. The largest body is 250 by 500 m elongate NW.

The last major porphyry, the Amphibole Porphyry (Ap), is a late intrusive and is found in two NW trending bodies. One is 300 by 100 m and is located in the middle of the deposit. It is weakly altered and veined. The other body is at the west end of the deposit and is effectively unaltered and unveined. The average grade of the Ap is low, with 0.11% Cu and 0.14 g/t Au.

Breccias are common along the contacts of the porphyries and the siliceous country rocks but are not volumetrically extensive. Some breccias appear to be of fault origin with rock flour matrix and others appear hydrothermal with quartz- or tourmaline-bearing matrix. Breccia fragments are mostly of the wall rock but do include some porphyry clasts.

4 Alteration and mineralisation

Alteration assemblages typical of copper-gold porphyries are present at La Fortuna. The outcropping portion of

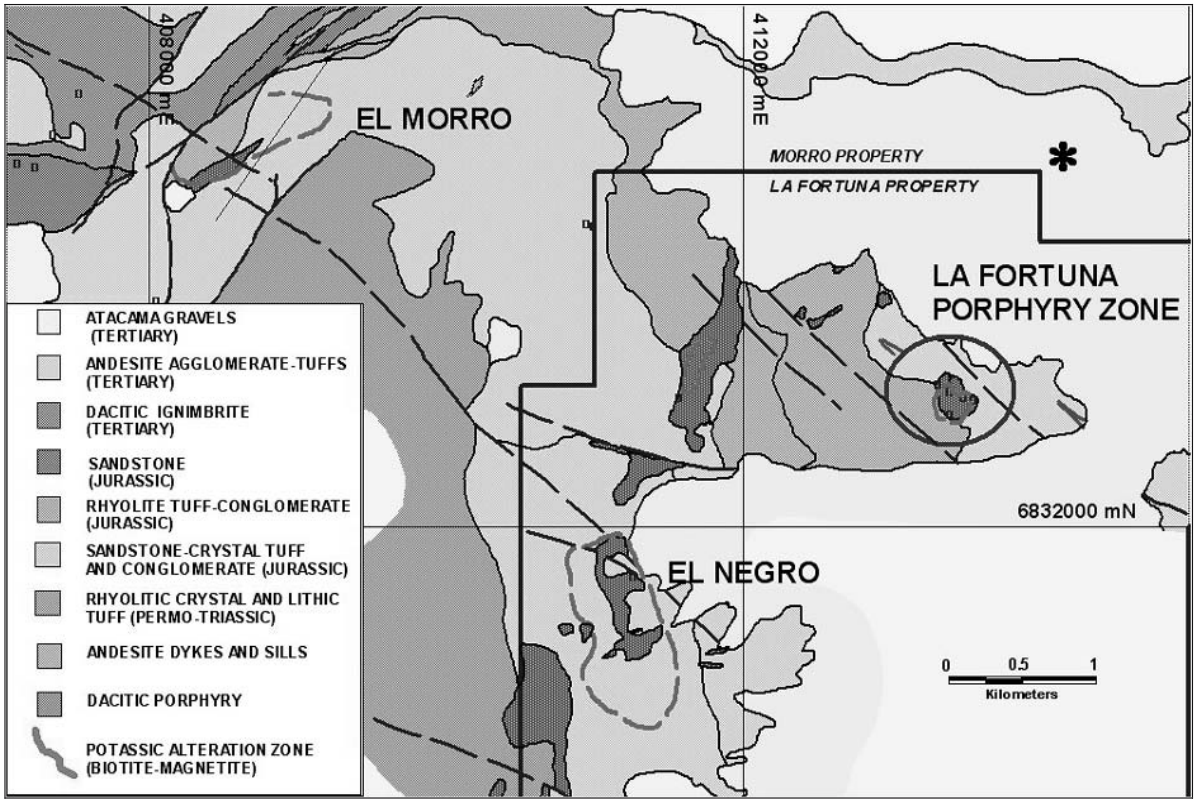

Figure 2: Geology of the La Fortuna porphyry deposit.

the deposit shows a telescoped suite of assemblages from early high temperature potassic (biotitic) and clay-chlorite-sericite assemblages to later phyllic and advanced argillic assemblages in the upper reaches of the system over an exposed vertical distance of 200m (Fig. 3).

Potassic alteration has affected both Qfp and Bap and is characterized by development of biotite in the groundmass and by shreddy biotite as replacement of hornblende phenocrysts. The potassic zone, where not overprinted, is cut by a stockwork of thin bio-mt +/- cpy seams, and q-cpy-py veins and hosts disseminated magnetite, chalcopyrite and in the deepest levels bornite. In that case, the pyrite:chalcopyrite ratio is less than 1.

Below 3500 m elevation, secondary biotite in the potassic zone has been partially overprinted by sericite, chlorite, magnetite, and chalcopyrite, giving the altered rocks a gray-green coloration. At the deepest levels drilled, overprinting and pyrite content increases and the cpy/py ratio and copper grades decrease. Above 3500 meter elevation, the intermediate argillic (IA) is the dominant alteration assemblage. It consists of iron-rich green sericite, smectite, chlorite and orthoclase (after plagioclase phenocrysts). Biotite is generally altered to chlorite. The alteration assemblage gives the rock a distinct green color. This zone is developed on a stockwork of qz-ksp-cpy-mt veins, qz-cpy ("B") veins, and thin cpy-mt veins with green sericite halos. There is a higher pyrite content in this zone than the potassic zone but most of the iron is in magnetite keeping py/cpy ratio around 1. Both early alteration types, potassic and IA, extend upwards to 4200 m where they overlap and host the highest protore grades in the La Fortuna deposit.

Overprinting by late white quartz-sericite-pyrite+/- tourmaline (QSP) alteration extends along significant structures at least as deep as the deepest hole (3100 m elevation). The deeper, structurally controlled QSP zones are generally less than 5 m thick but expand greatly at higher levels as the late QSP zone blossoms out. In the QSP zones early chalcopyrite and magnetite can be completely replaced by pyrite and when combined with the pyritic "D" veins controlling this alteration gives QSP altered rock the highest py/cpy ratio at greater than 5 to 1. The "D" veins controlling QSP have preferred orientations, following major structures and pre-existing fractures. The abundance of pyrite-rich veins and associated QSP alteration increases upwards and outwards, merging with advanced argillic alteration (AA) characterized by a quartz-alunite-kaolinite-pyrite assemblage. The AA zone is extensive at the highest levels of exposure but dies out even along major structures below 4100 m.

La Fortuna was subjected to moderate supergene leaching and enrichment in the 10 m.y. following formation of the deposit. At this time La Fortuna was buried under a thick cover of Atacama gravels. Only recently has the district been exhumed. As a general rule, where mineralized porphyry is close to surface, leaching is not well developed. At shallow depths atacamite, chrysocolla and minor cuprite are found above a 30 to 60 m thick weakly enriched supergene chalcocite zone. The oxide zone over porphyry is usually less than 10m thick and grades just 0.4% Cu. Outside the porphyries, owing to a combination of higher permeability and higher pyrite contents, leaching has been complete and extensive, reaching depths of 250 m. While hypogene grades are much lower in the wall rocks, the highly efficient leaching of a thick column of rock has resulted in development of a sheet of ore grade copper extending outside the limits of the porphyry intrusions. Within the stocks there is locally strong enrichment adjacent to structures but most of the 30 to 60m thick chalcocite zone grades only 0.6 to 0.8% Cu – indicating inefficiency in the enrichment process over the stock.

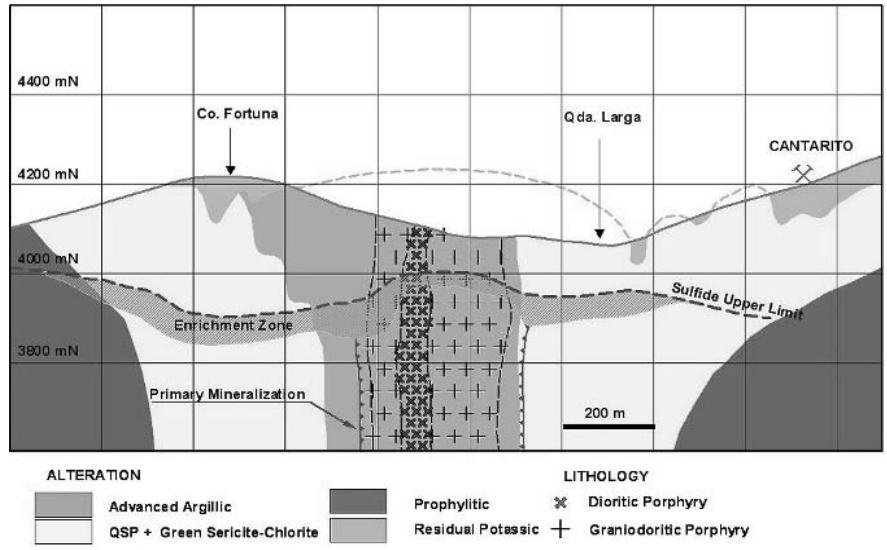

Figure 3: La Fortuna idealized cross section showing alteration patterns.

5 Gold and copper

Copper and gold are the main hypogene metals of economic interest in the system, with only minor molybdenum (<100 ppm). In the primary zone, grade distribution in the porphyries is laterally and vertically uniform for copper as well as gold, in an almost 1:1 ratio. A few higher-grade gold intervals have been intersected in the main mineralized zone in the Qfp and Bap. Assay data through the mineralized zone shows that the better gold grades, above 0.8g/t Au, are distributed around the barren Ap dyke in the middle of the deposit. This zone of higher gold grades and higher gold/copper ratios covers an area of 200 x 300m oriented roughly NE. Possible explanations are anomalously intense stockwork quartz veining, strong QSP alteration with tourmaline, outright silicification, and presence of a fine-grained aplitic phase of porphyry. In some special cases, this ratio may pass to 2:1, with gold reaching 3 g/t. Despite gold grades in this range it is only rarely seen in polished section owing to its fine grain size. It has been observed as inclusions in pyrite and bornite (0.5 to 6.4μ), and more rarely as free grains to 36μ. Metallurgical tests indicate that most gold is bound in some way to chalcopyrite.

6 Summary

The La Fortuna copper-gold porphyry, along with La Esperanza at 443 Mt @ 0.63% Cu and 0.26 g/t Au and Potrerillos at 210 Mt @ 1.1% Cu and 0.25 g/t Au, are rare examples of this type of deposit in Chile. Cerro Casale with 1.3 billion tones could be considered similar at 0.69 g/t Au and 0.27% Cu, but it lies in the Miocene gold belt and is more of a gold porphyry. La Fortuna is now the southernmost known Eocene-Oligocene porphyry copper deposit, extending this highly prospective belt 300km further south than previously recognized.

The La Fortuna system is the largest and longest-lived of three copper-gold porphyry hydrothermal systems found to date in the district. The fully zoned alteration system of La Fortuna is typical of porphyry copper deposits with late phyllic overprinting. Alteration began with a high temperature potassic stage, defined by the presence of secondary biotite, and extended from the highest surface exposures at 4200m to at least the 3100 meter elevation. The potassic zone has been overprinted by coeval green sericite-chlorite alteration (IA) and subsequently by white QSP and AA alteration. The latter alteration types mushroom upwards from structurally confined zones to broad areas of pervasive alteration at surface that have mostly wiped out the early potassic assemblage in the upper reaches of the deposit.

Most of the copper and gold at La Fortuna were introduced during the main potassic and IA stages of alteration and are confined to a vertically dipping cylindrical body defined by the two main porphyry phases. Outside this pipe-like body siliceous volcanics and sediments are much less altered and copper-gold grades drop precipitously over a few meters, to less than 0.1% and 0.1 g/t respectively.

Reference

Masterman GJ, (2003) Structural and geochemical evolution of the Rosario Cu-Mo porphyry deposit and related Cu-Ag veins, Collahuasi district, Northern Chile: Unpublished PhD thesis, University of Tasmania, Tasmania, Australia:253

Fe-Ti-V oxide mineralization in the Permian Panzhihua Gabbro, Emeishan large igneous province, SW China

Kwan-Nang Pang, Mei-Fu Zhou
Department of Earth Sciences, The University of Hong Kong, Hong Kong, China

Yuxiao Ma
Department of Science and Technology, Chengdu University of Technology, Chengdu, China

Abstract. Massive concentrations of Fe-Ti oxide minerals occur as lenticular, sill or dyke-like bodies in the Permian Panzhihua intrusion, SW China. Although the intrusion is characterized by well-developed igneous layering, major oxide orebodies are intimately associated with massive oxide gabbro devoid of layered structure. Magnetite crystals in one of the main orebodies do not show any cryptic variations at different stratigraphic heights, thereby precluding settling of magnetite crystals as an oxide concentration mechanism. Instead, the oxides crystallized from an immiscible oxide melt that separated from a crystallizing gabbroic magma. Oxide immiscibility may have been caused by an abrupt change in oxygen fugacity and/or introduction of volatiles induced by assimilation of carbonate wallrock into the gabbroic magma.

Keywords. Layered intrusion, magnetite, Emeishan, oxide immiscibility

1 Introduction

Rocks that are composed essentially of Fe-Ti oxides are associated with a wide range of igneous rocks including anorthosite massifs, felsic to intermediate volcanic rocks and layered intrusions (Kolker 1982; Eales and Cawthorn 1996). These rocks are considered enigmatic because an effective mechanism is required to concentrate oxides from a magma (Johnson et al. 2002).

The Panzhihua intrusion, SW China, hosts massive oxide bodies that have been mined for more than 30 years. The oxide deposit is one of the largest in the country and has 1333 Mt of ore reserves, with an average ore grade of 45 wt% FeO, 12 wt% TiO_2, and 0.3 wt% V_2O_5. The oxide orebodies are suggested to have crystallized from immiscible oxide liquid (Zhou et al. 2005). However, more information is required to better constrain the mechanism by which the oxides concentrate.

Fe-Ti oxide minerals exhibit wide compositional variations and can be a useful petrogenetic indicator (Leeman et al. 1978). For instance, magnetite formed early in the crystallization sequence should be enriched in compatible elements such as Cr and V compared with later-formed equivalents. In the Panzhihua intrusion, oxide minerals are present in many rock types, allowing for a detailed study of their compositional variations in space and time. This paper reports a microprobe investigation on magnetites in the Panzhihua intrusion. Analyses were performed in the Electron Microscopy Center, University of South Carolina.

2 Geological setting

The Panzhihua intrusion is one of several layered intrusions in the Permian Emeishan Large Igneous Province, SW China. The gabbroic intrusion is a sill-like body ~19-km-long and 2-km-wide (Fig. 1). It is divided, from the bottom to the top, into four stratigraphic units: the Marginal zone composed of hornblende microgabbro, the Lower zone composed of massive oxide gabbro, the Middle zone composed of layered gabbro, and the Upper zone composed of layered leucogabbro. Oxide orebodies occur as lenticular, sill or dyke-like bodies concentrated mainly in the lower parts of the intrusion. The contacts between the orebodies and their host rocks are either sharp or gradational.

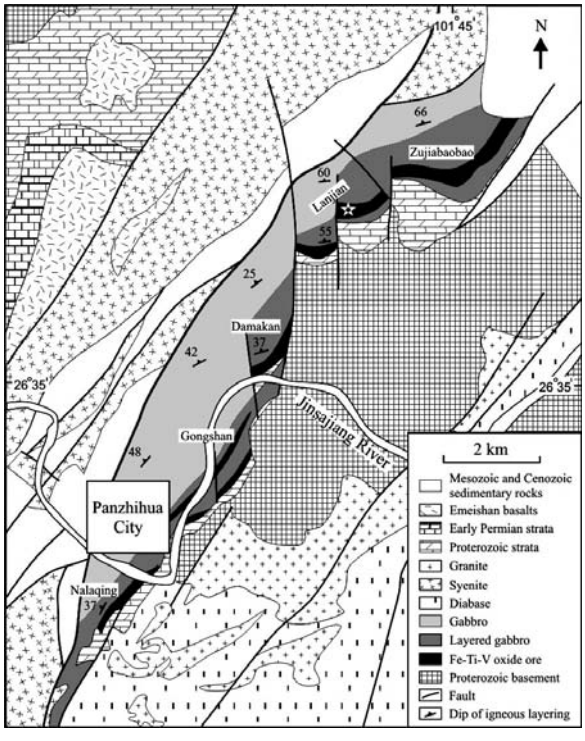

Figure 1: Geological map of the Panzhihua intrusion. Major oxide orebodies are shown in black.

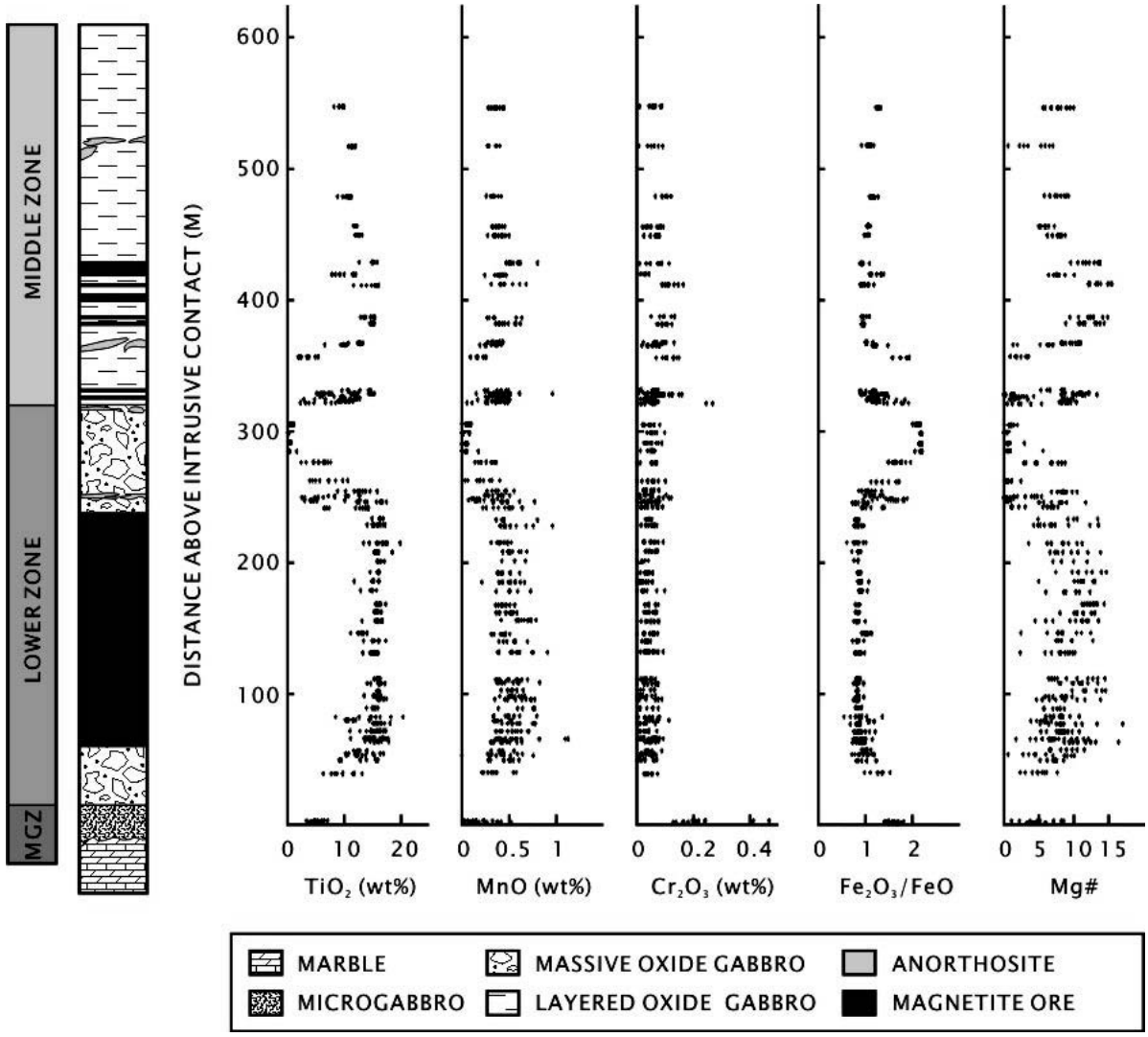

Figure 2: Compositional variation of magnetite as a function of stratigraphic height, illustrated with the sampled column section. MGZ: Marginal zone.

3 Oxide chemistry

Figure 2 shows the variation of magnetite compositions at different stratigraphic heights. Magnetite in the major orebody of the Lower zone has similar composition with increasing stratigraphic heights, e.g. 15 wt% TiO_2, 0.5 wt% MnO and 0.05 wt% Cr_2O_3. In the massive oxide gabbro above the oxide orebody, certain minor elements in magnetite decrease rapidly with stratigraphic height, e.g. TiO_2 and MnO, with the corresponding increase in the Fe_2O_3/FeO ratio and decrease in Mg#. The Lower zone-Middle zone boundary is marked by an abrupt reversal for most elements. Magnetite composition is less variable in the Middle zone relative to the Lower zone and is marked by several minor reversals.

In terms of texture, magnetite can be classified into three types: (i) massive magnetite, with common shared grain boundaries in oxide ore, (ii) disseminations in gabbro, and (iii) magnetite inclusions in cumulus clinopyroxene and plagioclase. Figure 3 shows binary plots of selected elements in different types of magnetite. There is considerable overlap in compositions between massive and disseminated magnetite. Except for a few analyses, almost all magnetite inclusions plot in the massive magnetite region.

4 Genetic implications

In the oxide orebody of the Lower zone, magnetite at different stratigraphic heights has similar compositions. This is not consistent with fractionation of magnetite as a concentration mechanism. In contrast, our data suggest that most of the oxides crystallized in-situ at about the same time, presumably from an oxide liquid. Although it is ar-

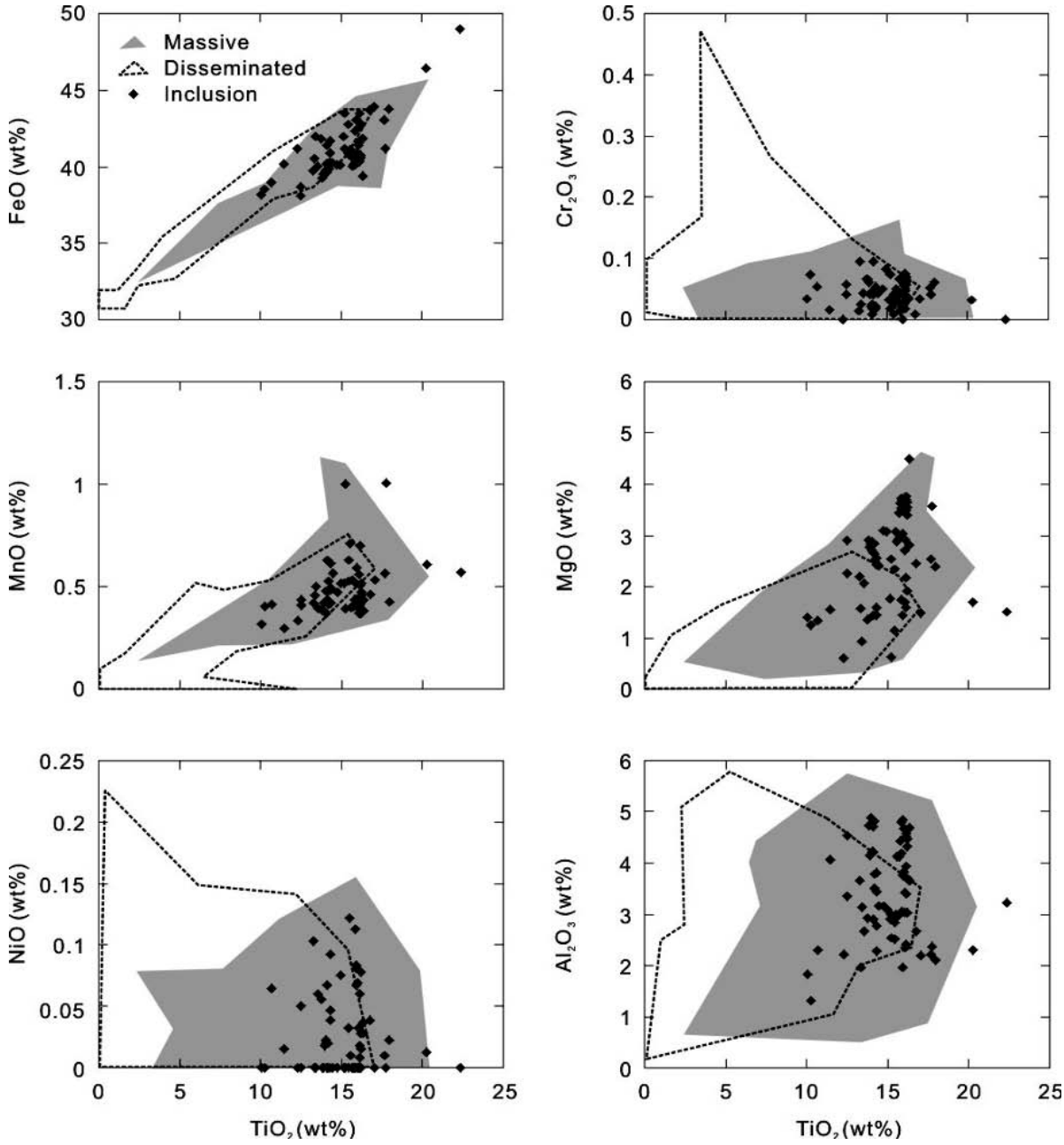

Figure 3: Binary plots for selected elements in different types of magnetite of the Panzhihua intrusion.

guable that the primary compositions of magnetite might have been modified by subsolidus processes, it is unlikely that any subsolidus process is capable of homogenising magnetite compositions in a 100-m-thick orebody. The oxide melt model is also consistent with field and petrographic observations. The lensoidal, sill and dyke-like geometry of the oxide bodies seems to indicate magmatic injection of an oxide liquid. Silicate minerals in the orebody are usually outlined by embayed grain boundaries saturated with oxides. Reaction rims of brown hornblende at the silicate– magnetite interface imply that the latter was a liquid phase. All available evidence apparently points to the existence of an oxide melt which subsequently gave rise to the Fe-Ti-V orebodies.

The formation of oxide melt is thought to be related to immiscible separation because crystal fractionation alone might only result in an Fe-rich silicate melt, not an oxide melt (Duchesne 1999). In the Panzhihua intrusion, magnetite inclusions in cumulus clinopyroxene and plagioclase have irregular boundaries but similar chemis-

try as massive and disseminated magnetites. In textural terms, magnetite included in clinopyroxene should crystallize much earlier compared to disseminated magnetite which is interstitial to these cumulus silicate minerals. However, their similar chemistry could only be explained if the inclusions represent oxide melt trapped when the silicate host crystallized. This implies the coexistence of the silicate magma and the oxide melt, consistent with immiscible separation.

The cause of oxide immiscibility cannot be evaluated with available information but it might be related to Neoproterozoic marble (i.e. the Dengying Formation) which is common in the region and could be extensively buried in Permian times. There is a clear intrusive boundary between the Panzhihua intrusion and the marble, suggesting potential interaction between the parental magma and the carbonate rocks. Assimilation of carbonate rocks could have caused dramatic changes to the oxygen fugacity of the magma, and may also have introduced volatiles such as CO_2 into the magma. This may have triggered the separation of immiscible oxide liquid from the crystallizing gabbroic magma (e.g. Lester 2002). However, it remains uncertain as to how the mantle source that gave rise to the Panzhihua intrusion contributed to generation of the oxide melt, and further studies are required.

5 Conclusions

The massive oxide orebodies in the Panzhihua gabbroic layered intrusion crystallized from an oxide melt, which might have separated immiscibly from a crystallizing gabbroic magma. The formation of oxide melt may be triggered by the assimilation of carbonate wallrock.

Acknowledgements

Lily Chiu, Gregory Shellnutt and Christina Yan Wang are thanked for their assistance in sample preparation and data processing. This study is supported by grants from the Research Grant Council of Hong Kong, China (HKU7056/03P).

References

Duchesne JC (1999) Fe-Ti deposits in Rogaland anorthosites (South Norway): geochemical characteristics and problems of interpretation. Mineralium Deposita 34: 182-198

Eales HV, Cawthorn RG (1996) The Bushveld Complex. In Cawthorn RG (ed) Layered Intrusions, Development in Petrology 15, Elsevier, Amsterdam

Johnson K, Barnes CG, Browning JM, Karlsson HR (2002) Petrology of iron-rich magmatic segregations associated with strongly peraluminous trondhjemite in the Cornucopia stock, northeastern Oregon. Contributions to Mineralogy and Petrology 142: 564-581

Kolker A (1982) Mineralogy and geochemistry of Fe-Ti oxide and apatite (nelsonite) deposits and evaluation of the liquid immiscibility hypothesis. Economic Geology 77: 1146-1158

Leeman WP, Ma M-S, Murali AV, Schmitt RA (1978) Empirical estimation of magnetite/liquid distribution coefficients for some transition elements. Contributions to Mineralogy and Petrology 65: 269-272

Lester GW (2002) The effects of excess H_2O, and H_2O in combination with F, Cl, S, or P on liquid immiscibility in the system Si-Fe-Al-K-O, at 2 Kbar: implications for the genesis of Fe-oxide magmas: Unpublished M.A. thesis, Binghamton, New York, State University of New York, 66p

Zhou M-F, Robinson PT, Lesher CM, Keays R.R, Zhang C-J, Malpas J (2005) Geochemistry, petrogenesis, and metallogenesis of the Panzhihua gabbroic layered intrusion and associated Fe-Ti-V oxide deposits, Sichuan Province, SW China. Journal of Petrology (accepted)

Nodular chromite deposits in some Tethyan ophiolites

M. Rahgoshay, H. Shafaii Moghadam, V. Forouzesh
Earth Sciences Faculty, Shahid Beheshti University, Tehran, Iran

Abstract. Nodular chromites form part of the specular chromite ores that occur within the mantle peridotite layers of ophiolites. This paper documents the geochemical and structural characteristics of these peculiar chromite concentrations in some Tethyan ophiolites.

Keywords. Ophiolites, podiform chromites, geochemistry, genesis

1 Introduction

Tethyan ophiolites on the eastern side of the Mediterranean Sea contain podiform chromite deposits. These deposits have been described previously by Rahgoshay et al. (1981), Rahgoshay and Juteau (1982), Rahgoshay (1986), Usumezsoy (1990), Paktunc (1990) and Rahgoshay et al. (2005). Nodular chromites, which are dense concentrations of lensoid masses of chromite, are common in some of these massifs. Hypotheses regarding the genesis of the nodular chromites include: (1) aggregation of chromite crystals in magma before final crystallisation (Denis 1932, Johnston 1936, Thayer 1969); (2) mechanical aggregation by the rotation of grains on the floor of a magma chamber floor that has more than a 50° dip (Borchert 1964); (3) erosion of chromites during plastic flow prior to consolidation (Kaaden 1970); (4) dissemination of chromiferous globules in an immiscible silicate liquid (Pavlov et al. 1977, Shams 1964); (5) spontaneous crystallization and agglomeration of chromites in a turbulent magmatic zone (Greenbaum 1977, Leblanc 1980, Leblanc and Nicolas 1992); (6) agglomeration of chromites in cavities within ascending magmatic conduits in the upper parts of convective flows (Cassard et al. 1981, Lago et al. 1982); and (7) segregation and downward-spouting of nodules in a basaltic system that was oversaturated with water (Matveev and Ballhous 2002). This manuscript documents the characteristics of several Tethyan nodular chromite deposits, and discusses their likely genesis.

2 Nodular chromite deposits

Textural observations of nodular chromites from some of the Tethyan ophiolites show distinctive relationships between the nodules and chromite layers. These are described below.

2.1 Fethiye district, Turkey

Ophiolite in the Fethiye district, southeastern Turkey, contains a 3-4 mm thick chromite-rich layer that separates two dunitic layers. The upper dunitic layer contains 10-15% disseminated chromites with a grainsize of 0.1 to 0.6 mm. The lower dunitic layer contains nodular chromites with diameters of about 5 to 13 mm (Fig. 1). The smallest chromite nodules are detached from and elongated perpendicular to the main chromite layer. Chemical analyses of olivine and chromite crystals do not show any significant compositional variations (Fig. 1). The chromites

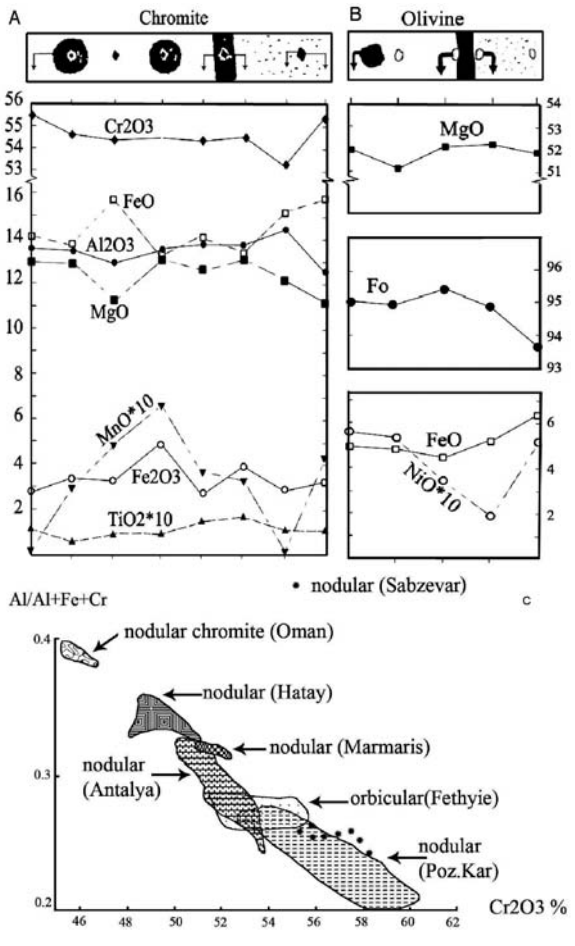

Figure 1: Geochemical analyses of (A) chromite and (B) olivine from a nodular chromite-bearing sample collected from the Fethiye district, Turkey. As indicated by the sketches, from left to right, the chromite and olivine crystals were analysed from (i) nodules in the lower dunite layer, (ii) disseminations between nodules, (iii) the main chromite layer and (iv) disseminations in the upper dunite layer. (C) Comparison of nodular chromite compositions from Fethyie with those from other Tethyan massifs.

are rich in Cr_2O_3 (54.5 to 55.5% wt), irrespective of whether they are disseminated or massive, or whether they occur in the main chromite layer or as separate nodules. Analyses of olivine associated with the different varieties of chromite have revealed a positive correlation between Fo contents (93.5 to 95.5) and MgO contents of the associated chromites. The limited textural and chemical variations of these Fethiye chromites most likely require a homogenous magmatic environment for their formation. Gravitational settling of the nodules from the main chromite layer due to contrasting densities of the chromite and the dunite silicate liquid is considered to be the most likely formation mechanism.

One sample collected from a chromite pod at Fethiye contains a centimeter-wide chromite layer that is separated by a range of nodules, which forms a chromitic layer with a dip of about 40^0. A rounded nodule at the base of the layer has textures reminiscent of a rolling snowball. A series of nodules are aligned parallel to the primary chromite layer, forming a schlieren nodular structure. The upper part of the rock contains a schlieren of disseminated chromites that occurs oblique to the primary chromite layer. This sample shows textural evidence for the separation of nodules from the main chromitic layer, and also the formation of snowball nodules. As for other samples from Fethyie, the chemical compositions of chromites and olivines in this sample are very homogenized.

2.2 Pozanti-Karsanti district, Turkey

In the Pozanti-Karsanti massif (southern Turkey), dunitic bands of about 3 cm thicknesses are separated by millimeter-thick chromite layers that contain chromite

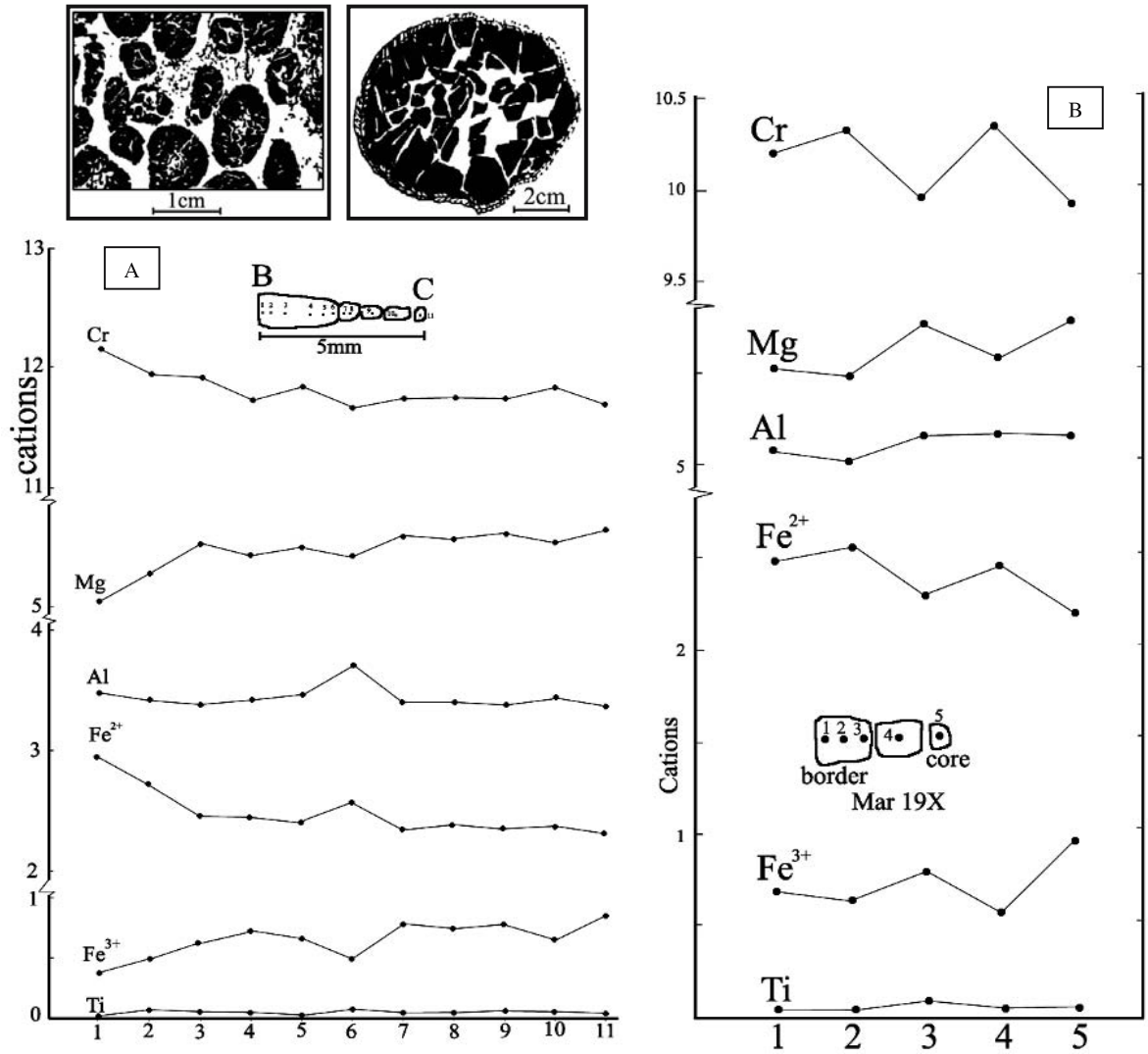

Figure 2: Chemical variations within two chromite nodule samples, from their centers (left) to their margins (right). Data from a sample from the Pozanti-Karsanti massif (left side) and from Mar19X sample (right side), from Marmaris (Turkey)

nodules and disseminations. The nodules are arranged parallel or oblique to the igneous layering. As for Fethiye separation of the nodular chromite nuclei from the main chromite layers in dynamic conditions appears likely.

2.3 Sabzevar district, Iran

Nodular chromites in Sabzevar (northern Iran) occur as circular to ellipsoidal masses, which have locally been stretched due to plastic deformation. They are always associated with massive podiform chromites. The formation of these chromite nodules seems to have involved water, based on the presence of OH-bearing minerals as inclusions in chromite grains (Matveev and Ballhous 2002). This type of chromite nodule is common in subduction zone-related ophiolites, and such a setting has been proposed previously for Sabzevar (Noghreyan 1982).

2.4 Semail ophiolite, Oman

In the Semail massif, Oman, nodular chromites with shapes similar to a rugby ball contain sodic and chromiferous amphibole (pargasite/edenite). The crhomite nodules can have net or fragmental textures.

3 Compositional and chemical variations

Chromite nodules that are either in dunitic and/or pyroxenitic gangue are generally very chromiferous (Cr_2O_3 = 50 to 58 wt %, Al_2O_3 = 9 to 17 wt %, MgO = 12 to 15 wt %). At the district scale, type 2 nodules are richer in Cr than type 1 nodules. In the scale of nodule, the chemical composition is almost constant. From rim to core, the nodules are characterized by: (i) decreasing of Cr and Fe^{+2}; (ii) increasing Mg and Fe^{+3}; and (iii) constant Al (Fig. 2). There is one exception where a chromite grain that occurs at the contact with chromiferous chlorite has a very large zonation of Al. There is an increase of chromite grainsize toward the center of nodules. Enrichment of Mg in small chromite crystals toward the center of the nodules is opposite to that observed in the massive chromitites, where the smaller crystals are less magnesian than the larger ones. This probably relates to intensive re-equilibrium between the periphery of the nodules and their dunitic hosts. Mg migrated towards the chromite when the crystals in the center of the nodules had only a limited exchange of components with the trapped silicate liquid.

4 Conclusions

The chromite nodules and their associated chromititic layers essentially have the same chemical compositions, which imply that crystallization conditions were the same. It is possible that some nodules formed via direct crystallization and/or under turbulent magmatic conditions. But in cases where the nodules have a secondary origin, the textural evidence implies that they have been formed by mechanical separation from chromititic layers. This involved separation in a viscous and dynamic media via gravity-induced instabilities. Formation of the nodules from an immiscible liquid is physically impossible, because it is not possible for an oxide liquid to separate from a basic silicate liquid under the conditions of formation relevant to the formation of podiform chromite deposits (i.e. low oxygen fugacity and high temperature). On the other hand the composition of nodules and disseminated chromites are rich in Cr and these two types of chromites have the same chemical composition; in these cases the formation of nodules by the immiscible liquid is not reasonable. In Sabzevar massif, the formation of nodules is different from other above-mentioned massifs. Genesis in back arc setting is proposed for the formation of Sabzevar ophiolites. So we suggest the role of liberating water from a subducting slab to enhance the aggregation of chromite grains in order to form nodules around hydrous agents.

References

Borchert H (1964) Principles on the genesis and enrichment of chromite ore deposits. In: Ostle D, Woodtliand D (eds) Methods of prosecution for chromite. Economic Coop Devel Paris 175-202

Cassard D, Nicolas A, Rabinowith M, Moutte J, Leblanc M, Prinzhofer A (1981) Structural classification of chromite pods in southern New Caledonia. Econ. Geol. 76: 805-831

Denis BT (1932) The chromite deposits of the eastern townships of the province of Quebec. Bull Miner Ann Report

Greenbaum D (1977) The chromiferous rocks of the Troodos plutonic complex and associated chromite deposits, Cyprus. Unpub Ph.D Thesis, University of Leeds

Johnston WDJ (1936) Nodular, orbicular and banded chromite in northern California. Econ Geol 31: 417-427

Kaaden VG (1970) Chromite bearing ultramafic and related gabbroic rocks and their relationship ophiolitic extrusive basic rocks and diabases in Turkey. Geol Soc South Afr, Symposium on the Bushveld igneous complex and their layered intrusions 511-531

Lago BL, Rabinowicz M, Nicolas A (1982) Podiform chromite ore bodies: a genetic model. J Pet 23: 103-125.

Leblanc M (1980) Chromite growth, dissolution and deformation from a morphological viewpoint: SEM investigation. Min Deposita 15: 201-210

Leblanc M, Nicolas A (1992) Les chromitites ophiolitiques. Chron. Rech. Min. 507: 3-25

Matveev S, Ballhaus C (2002) Role of water in the origin of podiform chromitite deposits. Earth Planet Sci. Lett. 203:235-243

Paktunc D (1990) Origin of podiform chromite deposits by multistage melting, melt segregation and magma mixing in the upper mantle. Ore Geol. Reviews 5: 211-222

Pavlov N V, Grigoryeva I, Tsepin A I (1977) Chromite nodules as an indicator of liquation of a magmatic melt. Int. Geol. Rev. 19: 43-56

Rahgoshay M (1986) Les Chromites et Leurs Gisements dans les Complexes Ophiolitiques de la Chaine du Taurus (Turquie), Comparaison avec les Gisements Omanais. These Doc d'Etat l'Universite Louis Pasteur Strasbourg France

Rahgoshay M, Juteau T (1982) Nouvelles observations sur des chromites nodulaires et orbiculaires dans les gisement podiformes ophiolitiques. C.R. Acad. Sc. Paris 295: 225-230

Rahgoshay M, Juteau T, Whitechurch H (1981) Kizilyuksek Tepe: un gisement exceptionnel de chromite stratiforme dans un complexe ophiolitique (massif de Pozanti-Karsanti, Taurus, Turquie). C.R. Acad. Sc. Paris 293: 765-770

Rahgoshay M, Shafaii Moghadam H, Forouzesh V (2005) Petrology of podiform chromitites in Kuh-Siah, north of Sabzevar. Proceeding of Crystallographic and Mineralogical conference Ahwaz Iran in press.

Shams FA (1964) Structures in chromite bearing serpentinites, Hindubagh, Zhob Valley, West Pakistan. Econ. Geol. 59: 1343-1347

Thayer TP (1969) Gravity differentiation and magmatic re-emplacement of podiform chromite deposits. In: Wilson HDB (ed) Mafic ore deposits. Eco Geol Mon 4: 132-146

Usumezsoy S (1990) On the Formation Mode of the Guleman Chromite Deposits (Turkey). Mineralium Deposita 25: 89-95

Sulfosalt mineral compositions from the No 10 vein, Zletovo lead-zinc deposit, Macedonia

T. Serafimovski, P. Lazarov, G. Tasev
Department of Mineral Deposits, Faculty of Mining and Geology, Goce Delcev 89, 2000 Stip, Macedonia

Abstract. This paper presents results obtained from electronic microprobe of analyses of sulfosalt minerals and other phases from ore vein ¹ 10 at the Zletovo lead zinc deposit, Macedonia. The vein contains galena, sphalerite, pyrite, chalcopyrite, siderite, tetrahedrite-tennantite, luzonite, stibioluzonite and pearceite. The tetrahedrite-tennantite series ranges from pure tetrahedrite to pure tennantite. Pearceite and luzonite have near-ideal stochiometric compositions.

Keywords. Zletovo, sulfosalts, tetrahedrite, tennantite, luzonite, pearceite

1 Introduction

The Zletovo lead-zinc deposit is located in Macedonia. It formed during hydrothermal activity that was intimately associated with Tertiary volcanism along an active continental margin. The major rock types in the area are andesite, dacite, dacitic ignimbrite and volcanic tuff (Serafimovski 1990; Serafimovski and Alexandrov 1995; Tasev 2003). Dacitic ignimbrite is the most common volcanic unit.

Pb-Zn mineralization at Zletovo is spatially and genetically related to fracture zones that trend NW, NNW and ENE. These fractures appear to have served as the main conduits and depositional sites for hydrothermal fluids. Mineralization has infilled joints and brecciated zones, and has replaced wallrocks. The orebodies comprise numerous veins and associated stockwork mineralization in areas of altered wallrocks. Most of the veins have a strike length of more than 1 km. Ore vein No 10 is exceptional because it can be followed for up to 10 km along strike. Vein thickness ranges from a few cm up to 2m. The veins generally dip from 40° to near-vertical, averaging about 60°. The veins have been intersected at depths of up to 500 m.

The morphologies and compositions of the ore veins from Zletovo are generally similar. We use ore vein No 10 as the type example (Fig. 1). The central vein consists primarily of massive sulphide ore, and contains clay-altered clasts of volcanic rocks. Sulfides have impregnated the intensely clay-altered wallrocks adjacent to the veins. Siderite bands occur near the vein walls (Fig. 1).

The ore mineral association comprises galena as the principal ore mineral together with sphalerite and subordinate pyrite, siderite and chalcopyrite, and rare pyrrhotite, marcasite, and magnetite. Minor occurrences of U-mineralization (pitchblende) have also been discovered. Detailed information about the mineral parageneses and geochemical features of the major minerals in ore veins is provided in Mudrinic and Serafimovski (1991) and Serafimovski and Tasev (2003).

The veins typically contain large clasts or screens of altered dacitic and andesitic wallrocks. The altered clasts are weakly mineralized or barren.

2 Methodology

We have examined sulfides and sulfosalts petrographically from five samples of ore vein No. 10 (Fig. 2). Selected minerals were then analyzed for S, Fe, Co, Cu, Zn, Ge, As, Ag, Cd, In, Sn, Hg, Pb and Bi using wavelength dispersive spectrometry electron microprobe analysis using a CAMECA / CAMEBAX microprobe. The estimated precision is low for Sb, Zn, As, and Ag (1–3%, 3–10%, 10–15%, respectively) and somewhat worse for Pb, Cd, In and Sn (2–5%, 5–15%, 15–30%, respectively).

Detectable contents of Sn and In were only found in some tetrahedrites, whereas Co, Ge, Hg and Bi were always below detection limits. Detection limits for Hg and Bi, were fairly high (>0.4–0.6%), partly because of interference between different elemental X-ray spectra. Detection limits for As and Pb were also high (0.25%) compared to other elements (Fe 0.05; Co, Cu 0.07; Zn, Ag, In, Sn 0.1; Cd, Ge 0.13).

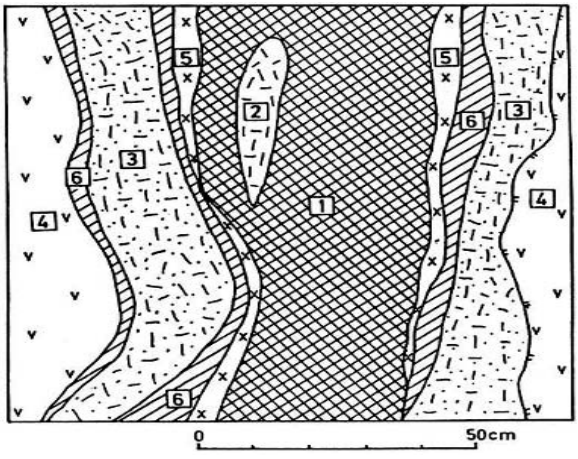

Figure 1: Schematic section through ore vein No 10, Zletovo mine. 1. Massive Pb-Zn sulfide ore; 2. Clast of Dacitic-andesitic ignimbrite (slightly kaolinized); 3. Dacitic-andesitic ignimbrite (intensely kaolinized); 4. Dacitic-andesitic ignimbrite; 5. Siderite; 6. Dacitic-andesitic ignimbrite, with galena impregnations

3 Results and discussion

Composition of pearceite, luzonite and tennantite-tetrahedrite are listed in Tables 1 and 2.

3.1 Luzonite (Cu_3AsS_4)

Luzonite was observed in samples #3 and #5. Luzonite in sample #3 is slightly more Fe-rich (0.15–0.66 %) and Sb-poor (0.17–2.5 %) relative to sample #5 (Fe?0.14 %; Sb 1.7–3.8 %). Luzonite contains minor Zn (?0.26 %), Ag (?0.17 %) and Cd (?0.15 %) in sample #3, but these elements are lower or absent in sample #5. Analysis 5-3Lu2 is close to the ideal stochiometric compositions of luzonite (Table 1).

3.2 Pearceite ($Ag_{13-11}Cu_{3-5}As_2S_{11}$)

A pearceite grain with 59 % Ag and $Sb/(Sb + As)_{mol}$ = 0.14 was analyzed from sample #5 (Table 1). Pearceite occurs as rare, small grains associated with luzonite + tennantite + galena + pyrite + chalcopyrite.

3.3 Tetrahedrite ($Cu_{12}Sb_4S_{13}$) – Tennantite ($Cu_{12}As_4S_{13}$)

Our microprobe analyses (Table 2) have revealed that Zletovo tetrahedrites are members of the tetrahedrite–tennantite solid solution [Sb/(Sb + 1%). Within individual samples, Ag is systematically higher in more Sb-rich grains or portions of composite grains and Ag decreases in areas that have more tennantitic compositions. The highest Ag contents occur in fine (a few microns diameter) droplets of tetrahedrite inside galena crystals in sample #4, which comes from a galena + sphalerite + pyrite + tetrahedrite-tennantite veinlet. These may actually represent the main Ag-bearing sites within what have previously been reported as Ag-bearing galena from Zletovo (up to 1250 ppm; $As)_{mol}$ = 0.04–0.94]. They contain significant Zn (usually 7–8 %) and Ag (from none to 5.5 %). Fe contents are always relatively low (?3%, usually Mudrinic and Petkovic 1982). Cd contents in tetrahedrite can be significant. They are typically <0.3 %, but locally can be as high as 1.1 % in some of the abovementioned droplets. A tetrahedrite droplet contains detectable In (0.15 %). Sn contents just above the detection limit (0.10–0.12 %) have been measured in more Sb-rich parts of the grains. Sample #2 has a particularly coarse grainsize, and has tetrahedrite – tennantite compositions characterized by an intermediate $Sb/(Sb + As)_{mol}$ ratio of 0.44.

Analyses of fine grained tetrahedrites may have been affected by contamination from neighboring phases. This may be the source of the locally significant Pb contents (up to 0.48%). Overall, the tetrahedrite analysis with the closest composition to ideal stochiometry is 3-5 Tet2 (Table 2).

Tennantites from Zlotovo contain significant Zn (1.72–8.33 %) and Sb (1.32-7.38%; Table 2). Fe is relatively low (0.1-3.06%). Within individual samples, the content Ag

Table 1: Results of WDS microprobe analyses of pearceite (Pea) and luzonite (Lu) from ore vein No 10, Zletovo ore deposit. All data listed as atomic %.

	5-2 Pea3	5-2 Lu3	5-2 Lu4	5-3 Lu2	3-5 Lu?	3-5 Lu?	3-1 Lu6	3-1 Lu7
S	17.41	32.04	31.84	32.62	32.29	32.55	32.87	32.68
Fe	0.03	0.05	0.14	0.01	0.53	0.66	0.15	0.19
Co	0.00	0.00	0.00	0.00	0.00	0.03	0.00	0.02
Cu	15.18	47.24	46.74	48.00	46.97	47.23	47.86	47.59
Zn	0.03	0.03	0.14	0.00	0.04	0.12	0.23	0.26
Ge	0.09	0.00	0.03	0.01	0.00	0.00	0.01	0.06
As	6.31	16.67	16.21	17.79	17.50	18.92	18.27	18.03
Ag	58.63	0.03	0.08	0.03	0.17	0.15	0.03	0.09
Cd	0.34	0.00	0.03	0.00	0.01	0.15	0.01	0.02
In	0.00	0.03	0.00	0.00	0.00	0.03	0.00	0.03
Sn	0.00	0.00	0.00	0.00	0.02	0.00	0.03	0.01
Sb	1.64	3.12	3.77	1.67	2.48	0.17	0.75	0.67
Hg	0.05	0.00	0.17	0.00	0.12	0.00	0.00	0.15
Pb	0.18	0.00	0.10	0.00	0.15	0.14	0.00	0.07
Bi	0.29	0.00	0.00	0.20	0.00	0.00	0.00	0.00
Sum	100.17	99.20	99.25	100.33	100.27	100.14	100.21	99.87

Table 2: Results of WDS microprobe analyses of tetrahedrite (Tet) and tennantite (Ten), from ore vein No 10, Zletovo ore deposit. All data listed as atomic %.

	3-4 Ten	3-1 Ten4As	5-2 Ten (2)	5-2 Ten3	3-5 Tet1	3-5 Tet2	3-4 Tet
S	27.27	28.00	28.04	28.03	25.16	26.48	26.48
Fe	0.10	0.36	0.22	3.06	0.37	0.17	0.05
Co	0.01	0.00	0.02	0.03	0.00	0.01	0.00
Cu	40.74	41.73	42.26	45.37	35.42	37.97	38.92
Zn	8.31	8.33	8.13	1.72	7.37	7.81	8.20
Ge	0.00	0.00	0.05	0.04	0.04	0.06	0.08
As	14.94	18.86	18.06	17.85	3.59	9.35	9.53
Ag	0.49	0.44	0.03	0.15	1.89	1.15	1.13
Cd	0.24	0.17	0.18	0.61	0.30	0.24	0.12
In	0.00	0.07	0.01	0.00	0.02	0.01	0.04
Sn	0.00	0.01	0.00	0.05	0.11	0.10	0.10
Sb	7.38	1.32	2.56	2.55	24.52	15.98	15.55
Hg	0.14	0.14	0.07	0.10	0.14	0.02	0.00
Pb	0.08	0.38	0.17	0.21	0.48	0.09	0.00
Bi	0.00	0.00	0.00	0.00	0.16	0.33	0.00
Sum	99.68	99.81	99.77	99.77	99.56	99.75	100.20

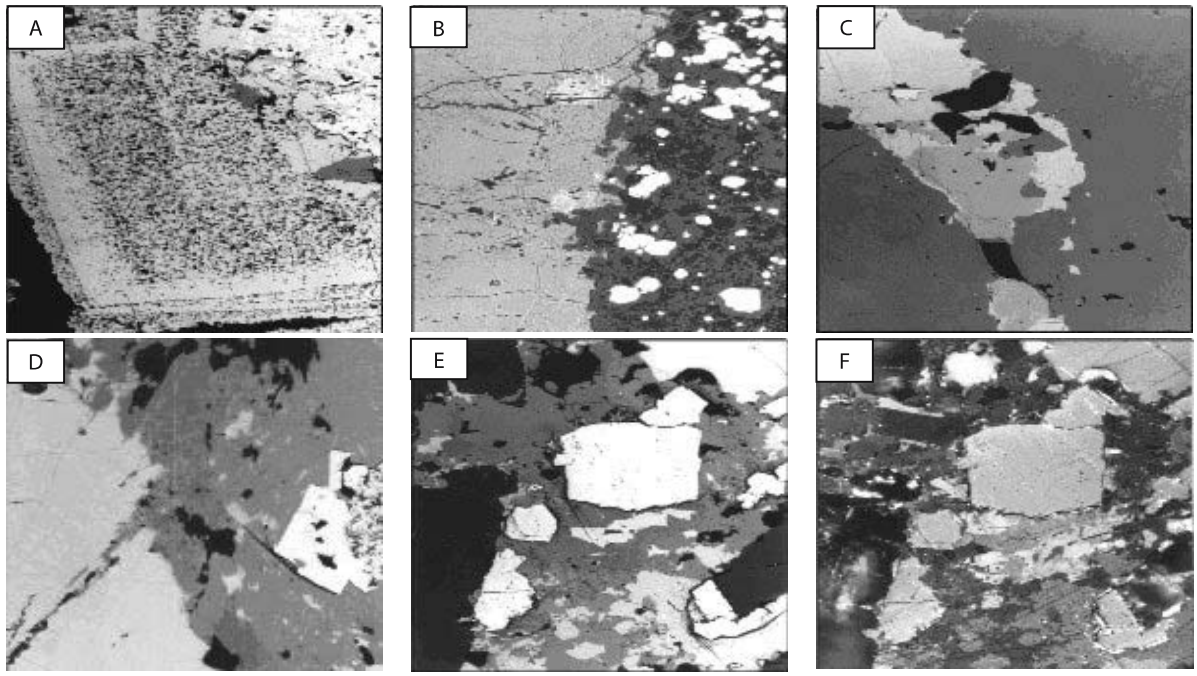

Figure 2: Photomicrographs of sulfides and sulfosalts from Zletovo (ore vein No10). A) Late generation of zoned galena with abundant quartz inclusions. An earlier generation of galena-sphalerite-pyrite-tetrahedrite ore comprises the background. B) Contact between intensively pyritized volcanic fragments and massive zoned sphalerite (gray). C) Sphalerite cut by vein composed of galena (light gray), tetrahedrite (gray), chalcopyrite (medium gray, upper part), quartz and traces of pyrite. D) Pyrite (white), chalcopyrite (light gray, left part), tenantite (gray in lower and central part) with inclusions of galena (light gray) and luzonite-stibioluzonite (dark gray, lower central part). Oil immersion. E) Complex intergrowth of pyrite crystals (white), sphalerite (dark gray), galena (white, irregular shapes), chalcopyrite (light gray, center) tennantite (middle to dark gray, central area) and luzonite-stibioluzonite (dark gray, strongly pleochroic, central part). Oil immersion. F) Partially crossed nicols. Lamellar twinning in one direction in luzonite-stibioluzonite (light to middle gray, central and lower part), and "flashy" internal reflections of tennantite (dark gray, left part).

decreases as end-member tennantite compositions are approached. Cd contents are significant in some samples, usually between 0.17 and 0.61%. Two samples contained detectable In (0.01 and 0.07%). Sn contents are just above the detection limit (0.01-0.05%).

3.4 Galena

Galena from the No. 10 vein is almost pure PbS. It locally contains significant Cu (0.7 %), Zn (<0.4 %), Fe (0.16 %) and Cd (0.16%). It is not clear whether these elements occur as fine inclusions or within the galena crystal lattice.

3.5 Sphalerite

The Zlotovo sphalerite is characterized by low Fe contents (usually ?1 %). Higher Fe contents have been detected locally in sample #3 (?6 %) and #5 (?2 %). Grain-to-grain and within-grain variations in Fe tenors show no systematic patterns. The highest Fe contents are typically associated with the lowest Cd contents, which reach 0.5–0.8 % in the least ferrous compositions. Minor amounts of Cu, Sb and Pb have been detected in some grains. Late-stage schalenblende has been detected in sample #3. It is distinctly cathodoluminescent under the electron beam and has a composition of almost pure sphalerite, with detectable As (0.3 %) and low Cd (0.15 %).

3.6 Chalcopyrite

Our analyses have shown that chalcopyrite is virtually pure $CuFeS_2$. All other elements were below detection limits.

3.7 Pyrite

Significant As contents are found in all generations of pyrite from Zlotovo. They can probably be ascribed to fine, unresolved intergrowths with arsenopyrite, as suggested by the crystal chemical formulae (S+As=Fe). Minor Cu (0.7%) has been detected in late euhedral or partially resorbed pyrite grains that occur with galena, sphalerite, tetrahedrite-tennantite and luzonite. Early pyrite grains are virtually Cu-free, except for sample #5, where an early pyrite grain contains significant Cu (0.36 %) and high As (4.4 %) contents. Detectable Pb (0.26 %) has been found in early and late-stage pyrite grains.

4 Conclusions

Results from the latest field and laboratory studies of ore vein No. 10 in Zletovo lead-zinc mine have shown an unusual group of sulfosalt minerals associated with the massive lead-zinc sulfide vein. Galena and sphalerite are associated with tetrahedrite, tennantite, pyrite, chalcopyrite, quartz, calcite, siderite luzonite and pearceite. Results of electron microprobe analyses have shown a huge range in tetrahedrite and tennantite compositions from essentially pure tetrahedrite through to pure tennantite.

Acknowledgements

For all the efforts during the field sampling in the Zletovo Mine and help about the laboratory analysis of samples we express our sincere gratitude to our colleague Dr Paolo Nimitz from the Department of Mineralogy and Petrology, University in Padova, Italy.

References

Mudrinic C, Petkovic M (1982) Geohemijska ispitivanja. "Regionalna i detaljna metalogenetska istrazivanja rudnog polja Zletovo". RGF-Beograd, 125-165

Mudrinic, C, Serafimovski T (1991) Geochemical and geochronological examinations by isotopes in Zletovo ore field. Geologica Macedonica, T 5, Nr.1, 105-120.

Serafimovski T (1990) Metallogeny of the Lece-Halkidiki zone. Doctoral thesis, Faculty of Mining and Geology, Stip, 390 p (in Macedonian)

Serafimovski T, Aleksandrov M (1995) Lead-zinc deposits and occurrences in the Republic of Macedonia. Faculty of Mining and Geology, Stip, Special Issue no 4, 387 p (in Macedonian)

Serafimovski T, Tasev G (2003) The Zletovo Subvolcanic Hydrothermal Pb-Zn Mineral Deposit in the Republic of Macedonia. Geodynamics and Ore Deposit Evolution of the Alpine-Balkan-Carpathian-Dinaride Province. Final GEODE-ABCD Workshop. Programme and Abstracts. Seggauberg, Austria, 22-24 March, 2003, 50-51.

Tasev G (2003) Polymetallic mineralizations related to the Tertiary magmatism in the Republic of Macedonia. Faculty of Mining and Geology, Stip. Masters thesis, 176 p. (in Macedonian)

Magmatic sulfide deposits in the Permian Emeishan large igneous province, SW China

Xie-Yan Song, Hong Zhong, Yan Tao
Key Lab. Of Ore Deposit Geochemistry, Chinese Academy of Sciences, Guiyang 550002, China

Mei-Fu Zhou
Department of Earth Sciences, The University of Hong Kong, Hong Kong, China

Abstract. Four genetic types of magmatic sulfide mineralization have been identified in the Emeishan large igneous province. These are: 1). Ni-Cu-(PGE) sulfide deposits produced by *in-situ* sulfide segregation, 2). PGE-enriched layers within layered intrusions, 3). Ni-Cu sulfide mineralization related to sulfide-bearing mush, and 4). PGE sulfide mineralization distributed throughout ultramafic rock. The distribution of the sulfide mineralization is associated with dynamics of the mantle plume.

Keywords. Sulfide mineralization, Emeishan, large igneous province

1 Introduction

Magmatic Ni-Cu-(PGE) sulfide deposits in large igneous provinces typically form in magmatic environments (Naldrett 1999). There are numerous small Ni-Cu-(PGE) sulfide deposits and occurrences in the Emeishan large igneous province, SW China. However, the spatial and temporal associations of these deposits and the Emeishan plume structure are not well-understood. We have divided the deposits into four major types and discuss their possible origins.

2 Geological setting

The Emeishan province covers more than 5 x 10^5 km^2 in SW China, and extends southwards into the northern Vietnam. It comprises the Emeishan Continental Flood Basalts (ECFB) and associated mafic-ultramafic intrusions, which were produced by a Late Permian mantle plume (Zhou et al., 2002a; Song et al., 2001). The central Emeishan province is characterized by thick flood basalt sequences, layered intrusions hosting giant V-Ti-magnetite deposits and syenite bodies (e.g. Zhang et al. 1988). The ECFB is mostly high-Ti basalts. Low-Ti basalts are only presented in the lower parts of the lava sequences in the central Emeishan province. The lava sequence is thinner around the margin of the Emeishan province (Xu et al. 2004). Most of the ECFB in the central region had been eroded because of Cenozoic uplift. The concentric distribution of the intrusive bodies, thickness of the lavas, and stratigraphic position of the low-Ti and high-Ti basalts display the temporal and spatial structure and dynamic progress of the Emeishan mantle plume. The magmatic activity was more extensive in the central part of the Emeishan province than on its periphery. It also produced small volumes of low-Ti basalts, followed by larger volumes of high-Ti basaltic magmas.

3 Magmatic Ni-Cu-(PGE) sulfide deposits

Most of the magmatic sulfide deposits and occurrences are in the central Emeishan province. Others occur on the northern and southern margins (Song et al. 2003, 2004). On the basis of their possible origin and lithological association, four types of sulfide deposits in the Emeishan province are identified.

3.1 Ni-Cu-(PGE) sulfide deposit produced by in-situ sulfide segregation

This type of deposit is hosted in mafic-ultramafic sills. Well-studied examples are those in the Yangliuping area, in the northern segment of the Emeishan province (Song et al. 2003, 2004). At Yangliuping, four sulfide-mineralized sills are present in Devonian quartz schist and marble, subparallel to the sedimentary bedding, within the Yangliuping tectonic dome. The Yangliuping and Zhengziyanwuo sills host economic Ni-Cu-(PGE) sulfide deposits. These two deposits contain 0.27 Mt tons Ni (average grade = 0.45 wt %), 0.10 Mt tons Cu (0.16 wt %), 10,177 tons Co (0.016 wt %), and 35 tons PGEs (0.55 ppm).

The two sills are more than 2 km long and up to 300 m thick, and extend 300 to 500 m down dip. Screens of Devonian rocks occur in the lower parts of the sills. In stratigraphic order, both the Yangliuping and Zhengziyanwuo sills consist of serpentinite, talc schist, tremolite schist, and minor altered gabbro.

The main disseminated sulfide orebody in the Yangliuping sill occurs in the lower part, within the serpentinite zone. The orebody extends intermittently along the sill for more than 1,500 m. The disseminated orebody is generally 10-50 m thick (locally up to 90 m). Concentration of sulfide decreases regularly from > 30 modal % in the lower part to < 20 % in the upper part of the orebody. Weakly mineralized zones, with <10 % sulfide, up to 100 m thick, occur above the disseminated orebody.

Massive sulfides occur at the bottom of the sills, and in the footwall along fractures. The massive orebodies show sharp boundaries with the footwall rocks. The massive ores contain 85-95 modal % sulfides, locally < 20 % in net-textured ores at the margins of the orebodies. The average metal contents in the massive ores are 4.66 wt % Ni, 0.67 wt % Cu, 0.069 wt % Co, and 2-3 ppm Pt + Pd.

Major sulfides in the sulfide ores are pyrrhotite, pentlandite, and chalcopyrite. In addition, Pd-bearing cobaltite-gersdorffite solid solution and platinum-group minerals, including Pd-Sb-Bi-telluride, Pt- and Os-arsenide, and Pd-antimonide had been identified in the massive ores.

The ECFB in the Yangliuping area is 1000 to 1500 m thick, and is divided into three units. Most of the lavas are high-Ti basalts, with exception of a low-Ti basalt subunit of the Upper unit. The Middle unit shows large oxide content variations, Nb-Ta depletion in primitive-mantle normalized spider diagram, and PGE-depletion, suggesting a close genetic linkage with the sulfide concentration in the mafic-ultramafic sills. The Lower and Upper units have 10 to 20 ppb Pt or Pd, comparable with typical continental flood basalts. Song (2004) proposed that crustal contamination was an important prerequisite for S-saturation in the magmas. However, S-saturation was finally triggered by crystallization of mafic minerals in the sills. Sulfide segregation then formed the deposits, while the residual magmas erupted, forming the PGE-depleted Middle unit.

3.2 PGE-enriched layer in layered intrusions

In the central Emeishan province, several layered intrusions contain PGE-enriched layers and also host V-Ti-magnetite deposits. The best-known PGE enrichment occurs in the Xinjie intrusion, a 7.5 km long, 1 to 1.5 km wide, and 1200 m thick ultramafic-mafic sill, which intruded the lower sequence of the ECFB at 259 ± 3 Ma (Zhou et al., 2002). Another good example of a PGE-enriched layer occurs in the lower part of the Anyi layered intrusion. As for Xinjie, Anyi also hosts a V-Ti-magnetite deposit.

The Xinjie intrusion exhibits well-developed igneous layering and has been divided into three cycles. Both Cycles I and II are composed of, from the base upwards, peridotite, clinopyroxenite, and gabbro, while Cycle III is dominated by clinopyroxenite, gabbro and quartz diorite.

Both the magnetite ore and PGE enrichment are associated with the magmatic cycling. V-Ti-magnetite ores occur mainly at the top of Cycles I and II, composed of Ti-bearing chrome, V-Ti-magnetite and ilmenite. The PGE mineralization is associated with disseminated sulfides with interbedded thin oxide layers (Zhong et al. 2004). There are at least three major 3-5m thick, PGE-enriched layers at the bottom of Cycle I that contain 1 to 3 g/t PGE. The sulfide content within the PGE-enriched layers ranges from 0.1% to 1%, and locally, up to 2%. The sulfides are dominated by pyrrhotite, pentlandite, chalcopyrite and cubanite.

Zhong et al., (2004) proposed that PGE mineralization in the Xinjie intrusion formed via magma mixing. Distribution of the PGE-enriched layers is controlled by the segregations of Fe-Ti oxides and sulfides.

3.3 Ni-Cu sulfide mineralization related to sulfide-bearing mush

This is perhaps the most important type of sulfide deposit in the Emeishan province. The deposits occur in mafic-ultramafic bodies in the central and the southern margin of the Emeishan province.

The Limahe deposit is a typical example. It is hosted in a lopolithic-shaped complex, which is located 30 km southwest of the town of Huili. Indicated reserves are estimated at 2.49 million tonnes grading 1.11 wt% Ni. The mine produced from 1958 to 1985, with about 22,700 tonnes of Ni produced (Zhang 1996).

The Limahe complex, dated as 262±2 Ma, is 900 m long, 20-180 m wide and hosted in the Proterozoic metamorphic rocks (Zhou et al. 2002; Zhou 2004). Rock types (from base to top) include olivine pyroxenite, peridotite, gabbro, and diorite.

Both disseminated and massive Ni-Cu sulfide ores are present. The main disseminated ore body occurs within the peridotite on the west side of the complex. The main orebody is 500 m long and ranges in thickness from 2 to 29 m. The main massive orebody is irregularly-shaped and generally surrounded by the disseminated ores. It also cuts through the disseminated ore body and has a direct contact with the wallrocks locally.

Proterozoic limestone blocks, contained in the base of the complex, have been sulfide mineralized. Small sulfide veins occur within the country rock on the west side of the complex.

The major sulfide minerals in the ores include pyrrhotite, pentlandite, and chalcopyrite, with smaller amount of pyrite, magnetite, and galena.

Some small dike-like ultramafic bodies in the Huili area, such as Qingshuihe and Shuiping (<1000 m long and <100 m wide), are highly sulfide mineralized (up to 50%). Sulfide orebodies may occur in the upper part of the intrusions.

The Baimazai Ni-Cu sulfide deposit occurs in Jinping, at the southern margin of the Emeishan province. It is hosted in a concentrically zoned ultramafic body (< 200 m in diameter) rimed by gabbro. Massive sulfide body is hosted by disseminated sulfide bearing peridotite, which is in turn surrounded by pyroxenite (Wang et al. 2004).

The characteristics of this type of sulfide deposit suggest that sulfide separation occurred in staging chambers at depth. Sulfide-free magma, sulfide-bearing mush, and sulfide melt were then intruded sequentially along faults and formed the sulfide deposits and intrusions.

This page intentionally blank

3.4 PGE sulfide ores in ultramafic body

This type of deposit was found in the central Emeishan province east of Dali, in the Jinbaoshan ultramafic sill, which is one of a series of mafic-iultramafic intrusions in the area. It is 5000 m long, 600-1000 m wide, and < 170 m thick. It has intruded the Devonian limestone and dolomite and has a thermally metamorphosed contact zone.

The Jinbaoshan intrusion is dominated by wehrlite. Nonetheless, Brozdowski et al. (2004) identified six distinctive horizons from the bottom to the top of the intrusion. The horizons are marked by variations in olivine grainsize, chromite contents, and/or appearance of sulfides. In addition, cumulate-orthocumulate textures are preserved well in the rocks. Geochemical studies suggested that the primitive magmas were high-MgO low-Ti tholeiitic (Tao et al. 2000).

Economic Pt-Pd sulfide ore layers are mainly hosted in two sub-horizontel layers with thickness of 4-16 m. One of the major Pt-Pd sulfide ore layer (K_1) is hosted within the first horizon at the base of the sill. Another major one (K_2) occurs at the base of the fifth horizon. The Pt-Pd rich layers are characterized by 3-5 model % sulfides and 9-20% chromite. The sulfides are interstitial phases between olivine and chromite grains and present an assemblage of pyrrhotite + chalcopyrotite + pentlandite. Minor platinum group minerals occur in the sulfides (Yang and Li 1993).

Previous exploration indicated that the Jinbaoshan sill contains 9.44 Mt ore with PGE contents averaging 0.9-1.66 ppm. The ores are poor in Ni and Cu (< 0.2% and < 0.3% respectively), but Pt and Pd are positively correlated with Cu (Tao et al. 2004).

The stratigraphic horizons and thermal metamorphism in the contact zone indicate that the Jinbaoshan sill was a conduit of multiple pulses of high-Mg low-Ti tholeiitic magmas. In this magma tunnel, the magmas reached S-saturation, thereby precipitating Pt-Pd sulfide ore layers.

This type of PGE sulfide mineralization also occurs at the base of the Hetaoshu intrusion, Huili area, which mainly consists of clinopyroxene peridotite.

4 Temporal and spatial associations

The previous descriptions indicate that both high-Ti and low-Ti basaltic magmas are related to Ni-Cu-(PGE) sulfide mineralization in the Emeishan province. Most of the magmatic sulfide deposits are located in the central part of the province. However, in this region, the intrusions hosting different type of sulfide deposits have distinctive characteristics. Composite intrusions produced from crystal- and sulfide-bearing mush, e.g. the Limahe body, and those that represent a magma conduit, such as the Jinbaoshan sill, do not contain V-Ti-magnetite ores and always have high proportions of ultramafic rocks. In contrast, the layered intrusions that contain PGE-enriched layers also host V-Ti-magnetite deposits, e.g. the Xijie intrusion.

Distribution of the low-Ti basalts in the central Emeishan province suggests that the intensively upwelling of the mantle plume during its early stages caused significant partial melting of the upper mantle. Lithological and geochemical features indicated that the Jinbaoshan sill was associated with high-MgO low-Ti tholeiitic magmas. We conclude that these two types of magmatic sulfide mineralization were closely related to high degree partial melting of the upper mantle in the early stages of the plume activity.

Layered intrusions containing V-Ti-magnetite are genetically linked to the high-Ti basalts, which formed mostly after the eruption of low-Ti basalts (Xu et al. 2003). Thus, the PGE-enriched layers in layered intrusions are temporally later than the sulfide deposits not association with magnetite ores in the central Emeishan province.

In the Yangliuping area, in the northern part of the Emeishan province, Ni-Cu-(PGE) sulfide deposits were genetically related to the high-Ti basalts. This implies that the S-undersaturated primary magmas were derived from a mantle source depleted in sulfur (Song 2004).

5 Conclusions

Four types of magmatic sulfide mineralization have been identified in the Emeishan province. Most of them are located in the central region. Ni-Cu-(PGE) sulfide mineralization within mafic-ultramafic bodies without V-Ti-magnetite ore are associated with the low-Ti tholeiitic magmas. They formed in early stages of mantle plume activity in the central province. PGE-enriched layers in the layered intrusions are related to high-Ti basaltic magma. Ni-Cu-(PGE) sulfide deposits in the margins of the Emeishan province are associated with high-Ti basalts.

References

Song XY, Zhou MF, Cao ZM, (2004) Genetic Relationships Between Base-Metal Sulfides and Platinum-Group Minerals in the Yangliuping Ni-Cu-(PGE) Sulfide Deposit, SW China, The Canadian Mineralogist, 42, 469-484.

Song XY, Zhou MF, Cao ZM, Sun M, Wang YL (2003) The Ni-Cu-(PGE) Magmatic Sulfide Deposits in the Yangliuping Area Within the Permian Emeishan Large Igneous Province, SW China, Mineral Deposita, 38, 831-843.

Zhong H, Yao Y, Prevec SA, Wilson AH, Viljoen MJ, Viljoen RP, Liu BG, Luo YN (2004) Trace-element and Sr-Nd isotopic geochemistry of the PGE-bearing Xinjie layered intrusion in SW China, Chem Geol, 203, 237-252.

Zhou MF (2004) Geochemical constrains on the diversity of igneous assemblages within the Permian Emeisan large igneous province, SW China, Recent Advances in magmatic ore systems in mafic-ultrmafic rocks, abstract vol. of IGCP 479 Hong Kong workshop, J.G. Shellnutt, M.F. Zhou and K.N. Pang eds., 61-63.

Zhou MF, Yang ZX, Song XY, Keays RR, Lesher CM (2002) Magmatic Ni-Cu- (PGE) sulfide deposits in China. In: Cabri LJ (ed) The geology, geochemistry, mineralogy, mineral benification of the PGE. Canadian Institute of Mining, Metallurgy and Petroleum, Spec Vol 54, 619-636.

Composition and mineralisation potential of A-type granites of the Kolyma tectonic block (northeast Yakutia)

Vera A. Trunilina, Sergey P. Roev
Diamond and Precious Metal Geology Institute, Siberian Division, Russian Academy of Sciences, Yakutsk, 677980, Russia

Abstract. Late Proterozoic – Early Paleozoic granitoids in the northern part of the Kolyma tectonic block are A-type granites. They formed in an intraplate setting. They have chemical affinities with ultrametamorphic granites and rapakivi, and have potential for rare elements and gold mineralization. The granitoids crystallized under conditions of high oxygen and volatile fugacities, which is favourable for mineralization.

Keywords. A-type granites, rare metals, Kolyma, tectonics

1 Introduction

The tectonic history and metallogeny of the Kolyma tectonic block (Fig.1) are widely debated. Some researchers consider the block to be a part of the Kolyma-Omolon median massif (Gusev et al. 1985). Others interpret it as an exotic complex microcontinent (superterrane) foreign to the Siberian continent (Parfenov, 2001). Still others treat it as an eugeosynclinal structure that originally developed on oceanic or transition-type crust (Lychagin et al. 1977). The different interpretations relate to limited data on magmatic activity at the early evolutionary stages of the province. The composition and geochemistry of the oldest granitoids of the Kolyma tectonic block are discussed in this paper, helping to some extent fill this knowledge gap.

2 Geology

From geophysical data, areas of crystalline crust underlie a vast region to the southwest of the South Anyui suture zone (Fig. 1). Despite this, outcrops of pre-Riphean crystalline rocks can only be observed within the Omolon terrane, where gneisses and crystalline schists of varying composition, quartzites, quartzitic sandstones, and para- and orthoamphibolites crop out with a total thickness of up to 6 km. Their age (3.4 Ga +/- 150 Ma) (Bibikova et al. 1981) and architecture is comparable to the Archean stratotype sections in the Aldan shield (Gusev et al. 1985). The Omolon terrane hosts 300-500 m thick lenses and sheets of Proterozoic granite-gneisses and granites (Rb-Sr ages of 1.8-2.2 Ga; Gusev et al. 1985). Outside of the Omolon terrane, the pre-Riphean basement is exposed in separate tectonic blocks. Rb-Sr dating of these schists yielded ages of 723 +/- 15 and 602 +/- 5 Ma (Gorbov and Zagruzina, 1971). Alkali feldspathic granites intruded between 590 and 550 Ma (Grebennikov, 1974). $^{40}Ar/^{39}Ar$ dating of amphibole schists gave ages ranging from 900 to 310 Ma (Layer et al. 1993), due to repeated reworking of the rocks. The basement rocks include meta-basalts, meta-diabases, meta-gabbroids and meta-hyperbasites. Normative compositions of the meta-basites correspond to gabbro-norites and olivine gabbros, and are similar to those of gabbroids from layered continental intrusions (Trunilina et al. 1999).

3 Granitoids

Granitoids were emplaced in the northern part of the Omulevka mountains, and in the Uyandina river basin.

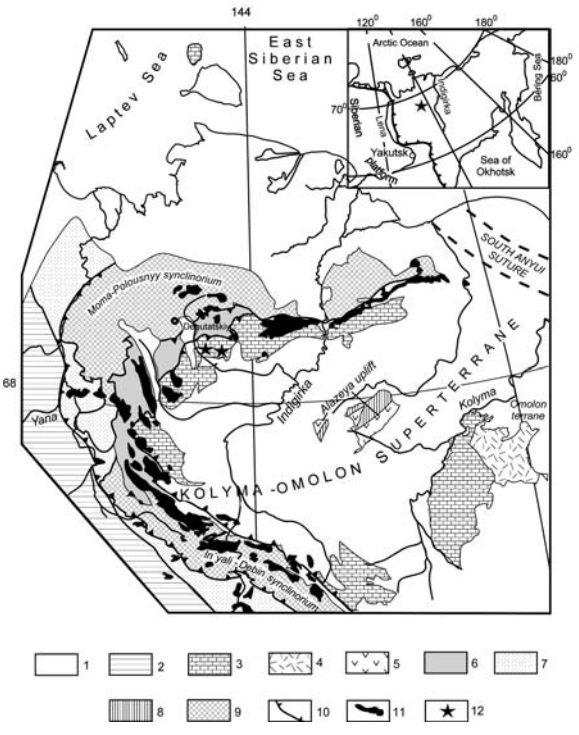

Figure 1: Tectonic structure of northern part of the Verkhoyansk-Kolyma orogenic region (Parfenov, 2001). 1 - Cenozoic cover, 2 - Verkhoyansk fold-and-thrust belt, 3 - miogeoclinal terranes, 4 - Omolon craton terrane, 5 - island-arc terranes, 6 - turbidite terranes, 7 - Kular-Nera continental margin turbidite terrane (slate belt), 8 - accretionary wedge terranes, 9 - Polousnyy-Debin terrane, 10 - strike stile fault, 11 - Mesozoic granitoids, 12 - Late Proterozoic granites of Uyandina basin.

In the Uyandina river basin, granitic gneisses grade into granites. These large intrusions are hosted by muscovite-chlorite-calcite-quartz, sericite-chlorite-quartz, and garnet-feldspar-quartz crystalline schists. Marbles are also cut by granite apophyses. The granites are mesocratic to leucocratic, alkali-feldspathic, with banded structures and cataclastic granoblastic textures. The rocks are composed of latticed microcline-perthite, albite, oligoclase-albite, quartz, biotite and muscovite, with some tourmaline and rare pyroxene crystals (Trunilina et al. 1999).

4 Mineralogy

We have determined the crystallization history of the granites. First to crystallize from the melt were magnesian enstatite-diopside and diopside with Fe/(Fe+Mg) = 10-12 %, calculated crystallization temperature of 1100 to 1210°C (Pertchuk, 1977). As the crystallization temperature decreased to 1030°C, the Fe/(Fe+Mg) of the pyroxenes increased to 20 %, accompanied by an increased content of chermackite (1 to 10.9 %). At 1150°C (Brown and Parsons, 1985), soda-potash feldspar (An17 Ab35 Ort48) began crystallizing synchronous with pyroxenes. At 1100°C (Negrei, 1983), halogen-rich (F = 2.99-3.49%, Cl = 0.15-0.20 %) magnesian biotite (Fe/(Fe+Mg) = 25-29 %) began to crystallize. The biotite is similar compositionally, to that which occurs in A-type granites of mixed mantle-crystal origin (Brimhall and Crerar, 1987). Crystallization of biotite occurred at high oxygen (log f_{O2} = -8.4 to -9) and F (log f_{HF} = 0.8 to 2.28) and anomalously high H_2O and Cl (log f_{H2O} = 3.8 to 4.5; log f_{HCl} = 4.5 to 6.5) fugacities. The initial water content of the parent melt did not exceed 0.7 % (Brown, 1970).

Principal accessory minerals in the granites are orthite (allanite) and monazite, the latter being anomalously enriched in thorium. Also present are chromian titanomagnetite (11.6-13.9 % TiO_2; 0.5-1.7 % Cr_2O_3) and ilmenite (0.1-0.4 % Cr_2O_3; 0.6-1.6 % MgO); Cl-apatite and F-apatite with elevated Cl; zircon with high ("gabbroic", after Lyakhovich, 1979) ZrO_2/HfO_2 ratios (up to 73) and increased UO_3 and ThO_2 contents (1.15 and 2.6 %, respectively); thorite; and Sn-rich (up to 0.1 %) pyrite. The accessory mineral compositions are consistent with high temperature and low-water contents of the parent melts. Compositions of accessory garnets (almandine = 70-71 %, pyrope = 13-15 %, grossular = 9-12 %, spessartine = 1-5 %) and a positive correlation between F in apatites and Na_2O in the host rocks (Figs. 2, 3) indicate the initial melt was derived from the granulite facies metamorphic substrata. As determined from garnet compositions, the pressure in the magmatic chambers attained 10 kbar (Smirnov et al. 1988).

5 Geochemistry

Chemically, the granites are characterized by high alkalinity, elevated alumina contents, prevalence of normative albite over orthoclase, and an almost complete absence of anorthite. The rocks have trachytic compositions and an anorogenic intraplate geodynamic setting is inferred. The mineralogical, petro- and geochemical characteristics [mean values: Al/(2Ca+Na+K) = 1.21; K/(Na+K) = 0.44; K/Rb = 205; Ce/Yb = 7; Rb/(Y+Nb) = 3.22), differentiated REE trends with enrichment in both LREE

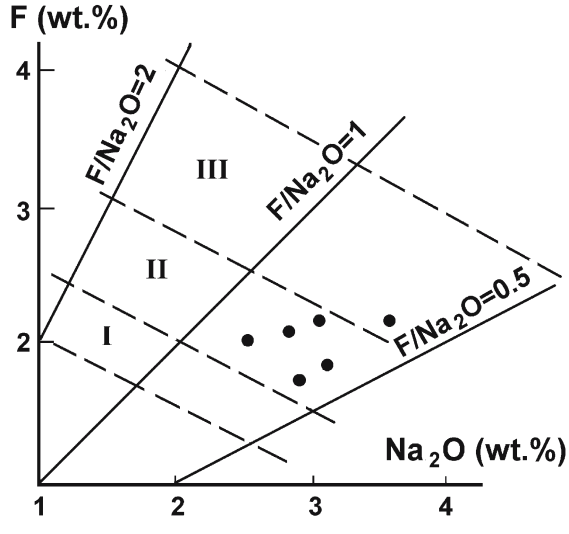

Figure 2: Correlation of F contents in accessory apatites with the Na_2O contents of their host granites in the Kolyma tectonic block. Fields from Bushlyakov and Kholodnov (1986) - derivatives melts, generated in: I - limits of eclogite facies, II - granulite facies metamorphic substrata, III - amphibolite facies metamorphic substrata.

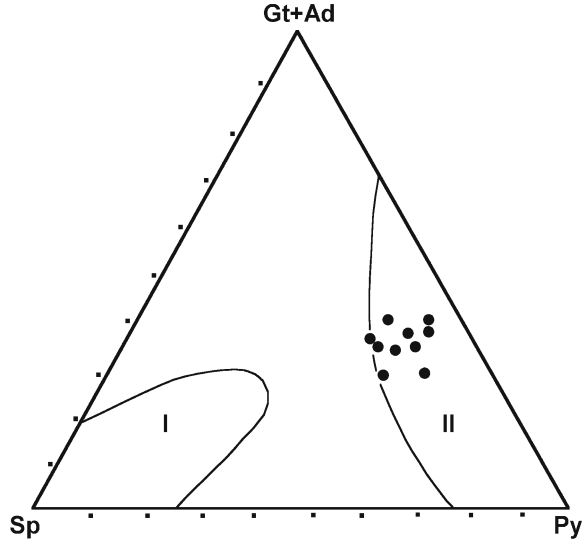

Figure 3: Normative compositions of garnets from the Kolyma granites. Fields from Rub et al. (1977): garnets from granites derived for I - gneiss-amphibolite horizons, II - gneiss-granulite horizons.

This page intentionally blank

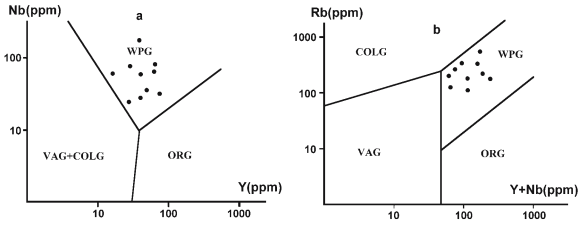

Figure 4: Nb - Y and Rb – (Y+Nb) diagrams for Kolyma granites. Fields from Pearce et al. (1984): VAG - volcanic arc granites, COLG - collisional granites, WPG - within plate granites, ORG - oceanic granites.

and HREE [$(La/Yb)_N$ = 1.9-3.5; $(La/Sm)_N$ = 4-7.7; $(Gd/Yb)_N$ = 0.2-1.9] and a distinct Eu-minimum (Eu* = 0.1-0.4), as well as Rb/(Nb+Y) and Nb/Y ratios (Fig. 4) are consistent with intraplate continental A-type granites (Nenakhov et al. 1992; Whalen et al. 1987). Trace elements contents are similar to ultrametamorphic granites and rapakivi (Tauson 1984), which are associated with rare metal, REE, and Au ores in the Aldan and Baltic continental shields (Nedaschkovskiy and Lennikov, 1991; Nenakhov et al. 1992).

6 Regional context and metallogenesis

No outcrops of Proterozoic basement have been identified in the structures that bound the Kolyma block. However, crystalline schists, granite-gneisses and intrusive alkali-feldspathic granites similar to those described above have been recognized in large xenoblocks that hosted by andesite-dacite volcanics in the northern part of the Moma-Polousny synclinorium in the Verkhoyansk margin of the Siberian continent surrounding the Kolyma block, and in numerous xenoliths and microxenoliths in dikes of the Deputatskiy ore field (fig. 1). Rb-Sr ages of the granites from xenoliths range from 350 up to 500 Ma (our data). Their petro- and geochemical coefficients are also close to A-type granites (Trunilina et al. 1999). All these data suggest the presence of a common Late Proterozoic continental basement at the base of the Kolyma tectonic block and the Verkhoyansk continental margin.

The Kolyma granites are rich in Bi, Mo, Sn, W, Ag, Au, Cu, Hf and Th. Based on their F – (Li+Rb) – (Ba+Sr) ratios, they have compositions typical of ore-bearing granites (Fig. 5). The total ore content index of the rocks has been calculated following the technique of Kozlov and Svadkovskiy (1977). It varies from 60 to 100, which corresponds to productive magmatic systems (Sn, W, Li, Be). Sn, W and Au occurrences are known from the vicinity of the Kolyma granites. Anomalously high water and halogen fugacities, especially with early crystallization of biotite, should have been favourable for aqueous fluid separation. These parameters indicate that the Kolyma block has significant potential for ore deposit discoveries.

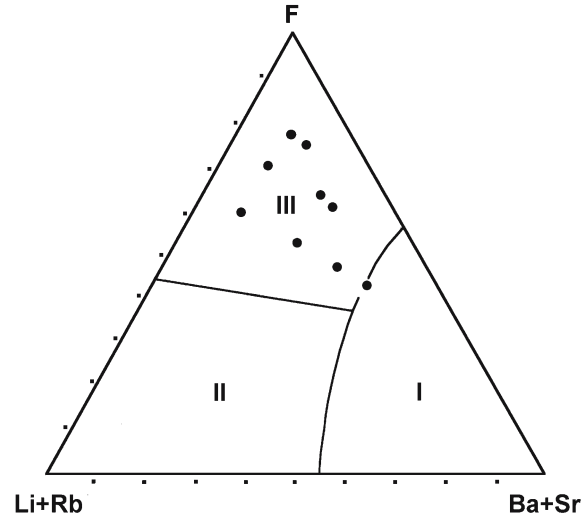

Figure 5: (Li+Rb) vs (Ba+Sr) vs F for Kolyma granites. Fields from Kozlov and Svadkovskiy (1977): I - barren granitoids, II - limited ore-bearing granitoids, III - granitoids with anomalous rare metal contents.

7 Conclusions

Proterozoic granites of the Kolyma tectonic block are comparable with continental intraplate A-type granites. Compositionally similar granites are found in xenoliths of magmatic rocks in the nearby Verkhoyansk continental margin of Siberia. The Kolyma block appears to define the eastern extremity of the Proterozoic continental margin. Prior to this study, the Late Proterozoic - Early Paleozoic rocks in this region were only considered to have potential for stratiform Pb, Zn and Cu deposits (Parfenov 2001). We have shown that the Proterozoic granitoids of the Kolyma region had the potential to exsolve hydrothermal fluids, opening new opportunities for exploration for granite-related rare metals, REE and Au ore deposits.

References

Bibikova EV, Makarov VA, Gracheva TV, Kalinkina OM (1981) The ancientest rocks of the Omolon massif. In*:* The ancientest granitoids of USSR. Leningrad: Nauka:137-146

Brimhall GH, Crerar DA (1987) Ore fluids: Magmatic to supergene. In termodynamic modeling of geological materials In: Minerals, Fluids and Melts. Reviews in mineralogy. Michigan Vol. 17:235-321

Brown GG (1970) A comment on the role of water in the partial fusion of crystal rocks. Earth and Planet. Sci. Lett. Vol. 9:355-358

Brown W, Parsons J (1985) Calometric and phase-diagram approaches to two-feldspar geothermometry a critique. Amer. Mineral. Vol. 70, No. 3-4:356-361

Bushlyakov IN, Kholodnov VV (1986) Halogens in petrogenesis of granitoids. Moscow: Nedra:192

Gorbov GS, Zagruzina IA (1971) The first definitions of the absolute age metamorphic rocks of the Kolyma massif. Doklady AN SSSR. Vol. 197, No. 5:1131-1132

Grebennikov GA (1974) Geologic map of the USSR. Scale 1: 200 000. Explanatory note. Sheet R-54 – XXXIII, R-54 – XXXIV. Leningrad: VSEGEI:95

Gusev GS, Petrov AF, Fradkin GS (1985) Structure and evolution of the Earth's crust in Yakutia. Moscow: Nauka:248

Kozlov VD, Svadkovskiy LN, Petrochemistry, geochemistry and ore-bearing potential of granitoids of the Central Transbaykalia. Novosibirsk: Nauka:150

Layer PW, Parfenov LM, Surnin AA, Timofeev,VF (1993) First $^{40}Ar/^{39}Ar$ age determinations of magmatic and metamorphic rocks of the Verkhoyansk-Kolyma Mesozoides. Doklady AN SSSR. Vol. 329, No. 5:621-624

Lyakchovitch VV (1979) Accessory minerals of the rocks. Moskow: Nedra:296

Lychagin PP, Merzlyakov VM, and Terekhov MI (1977) Geology of the Alazeya plateau. In: Problems of geology of median massifs in the northeast USSR. Magadan: SVKNII DVO AN SSSR:18-55

Nedaschkovskiy PG, Lennikov AM (1991) Petrology and geochemistry of Aldan rapakivi. Moscow: Nauka:134

Negrei EV (1983) Petrology Late Paleozoic granites of Central Kazakhstan. - Moscow: Nauka: 168

Nenakhov VM, Ivannikov VV, Kuznetsov LV, Strik YN (1992) Specificity of studying and geologic mapping of collisional granitoids. Moscow: Roskomnedra:101

Parfenov LV (editor) (2001) Tectonics, geodynamics and metallogeny of Republic Sakha (Yakutia) territiry. Moscow: MAIK, Nauka/Interperiodika:571

Pearce JA, Harris NBW, Tindle AG (1984) Trace element discrimination diagrams for the tectonic interpretation of the granitic rocks. J. Petrol. Vol. 25, pt. 44:956-963

Rub MG, Ashimina NA, Gladkov NI (1977) Typomorphic features of accessory minerals and their meaning by ascertain of genesis and ore-bearing of the granitoids. In: Granitoids of the folded and activity regions. Moskow: Nauka:197-235

Smirnov VN, Chashchukhina VA, Pushkarev EV, Vedernikov VV (1988) On the nature of accessory garnets in the rocks of the gabbro-granite series of the Ural region. Doklady AN SSSR. Vol. 298, No. 4:955-960

Tauson LV (1984) Typification of magmatites and their ore potential. In: The 27th International Geologic Congress. Vol. 9: Petrology. Moscow: Nauka:221-228

Trunilina VA, Roev SP, Orlov YuS, Oxman VS (1999) Magmatism of various deodynamic environments (zone of junction of the Verkhoyansk margin of the Siberian continent and the Kolyma-Omolon microcontinent). Yakutsk: YaNTs SO RAN:168

Whalen GB, Kenneth L, Currie KL, Chappel BW (1987) A-type granites: geochemical characteristics, discrimination and petrogenesis. Cotrib. Miner. Petrol. Vol. 95, No 2:407-419

New porphyry - Cu ± Mo occurrences in the north-eastern Aegean, Greece: Ore mineralogy and epithermal relationships

Panagiotis Voudouris
Department of Mineralogy–Petrology, Faculty of Geology, University of Athens, Panepistimioupolis 15784 Athens, Greece

Dimitrios Alfieris
S&B Industrial Minerals S.A., Athens, Greece

Abstract. New discoveries of porphyry Cu±Mo mineralization have been made on Limnos and Lesvos islands, in areas covered by hydrothermally altered Miocene shoshonitic volcanic and subvolcanic rocks. The Fakos prospect has many typical features of porphyry Cu±Mo deposits: K-silicate alteration, barren advanced argillic lithocap, tourmaline-sericite veins and breccias and late quartz veins rich in base and precious metals. Gold and silver are present as electrum, hessite, petzite and an unknown Ag-sulfotelluride, and are mainly enriched in the late veins. The Stipsi prospect is a molybdenum-enriched porphyry system, consisting of a quartz stockwork that contains molybdenite, bismuthinite, galena and sphalerite. Both porphyry systems evolved through several stages of magmatic-hydrothermal action with the late polymetallic quartz veins representing either epithermal style overprints.

Keywords. Porphyry, copper, molybdenite, electrum, tellurides, epithermal

1 Introduction

Post-collisional orogenic magmatism occured in northern Greece during the Oligocene to Miocene. This resulted in the formation of several magmatic-hydrothermal ore deposits and prospects that contain Au, Cu, Mo and other base metals. Examples include Olympias and Skouries in Chalkidiki (Kroll et al. 2002) and Maronia, Sappes, Perama and Pefka in western Thrace (Arikas and Voudouris 1998). In the northeastern Aegean, exploration work by the authors focused mainly in two areas on Limnos island (Fakos and Sardes prospects) and on Lesvos island (Stipsi; Figs. 1 and 2). This study documents the geological, geochemical and mineralogical features of these areas, which are reinterpreted here to be porphyry rather than epithermal styles of mineralization. The Limnos and Lesvos areas represent a southward extention of the Oligocene-Miocene northeastern Greek porphyry belt into the Miocene volcanic islands of the central Aegean Sea, previously known only to be prospective for epithermal style mineralization.

2 Geology

Limnos island comprises molasse deposits of Middle Eocene – Lower Miocene age, which are overlain by high-K calc-alkaline to shoshonitic volcanic rocks of Lower Miocene age (21-18 Ma, Innocenti et al. 1994). Two bodies of quartz monzonite porphyry have intruded the volcanic and sedimentary rocks in the central part of Fakos peninsula, as well as near Sardes in the northwestern part

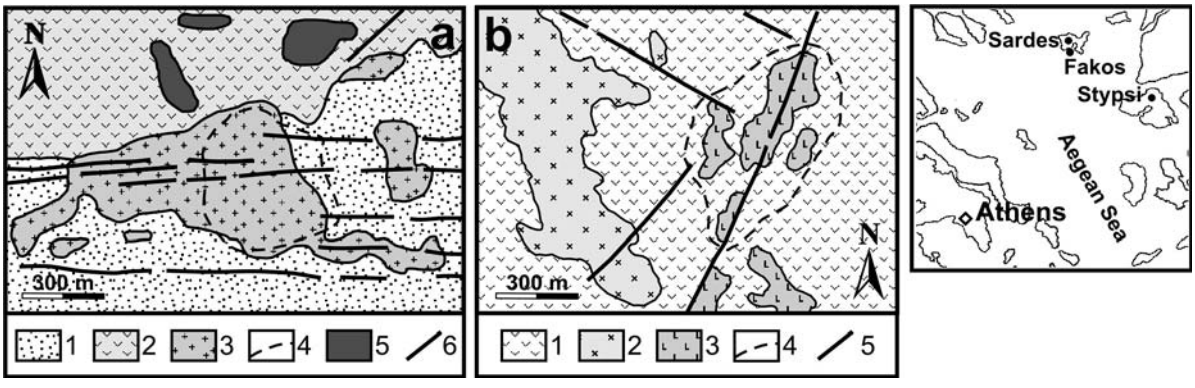

Figure 1: (a) Simplified geologic map of Fakos prospect, Limnos 1. Middle Eocene-Lower Miocene sediments; 2. Lower Miocene volcanic and pyroclastic rocks - intensively altered localy; 3. Lower Miocene monzonite porphyry; 4. Faults and mineralized veins; 5. Surface outcrop of porphyry-type stockworks. (b) Simplified geologic map of the Stipsi prospect, Lesvos. 1. Andesitic lavas (Middle Miocene); 2. Dacitic andesite porphyry (Middle Miocene); 3. Dacite porphyry (Middle Miocene); 4. Faults and mineralized veins; 5. Surface outcrop of porphyry-type stockworks. (c) Locality map.

of the island (Fig. 1). Limnos is dominated by two fault systems striking NNW and NE to ENE.

The island of Lesvos comprises Middle to Upper Miocene volcanic rocks of shoshonitic to calc-alkaline affinity (Pe–Piper 1980) that overlie a metamorphic Paleozoic basement. Three major fault systems have been recognized: NW-, NNE- and E-trending. The Stypsi prospect in the north-central part of the island is hosted by shoshonitic subvolcanic and volcanic rocks (Fig. 2). The prospect is bounded on the north and west by a caldera structure, and to the east by a northeast-trending fault zone (Rokos et al. 2000).

3 Mineralization and alteration

3.1 Limnos island

Fakos prospect: Mineralization occurs in two structurally controlled stages. The Early porphyry stage comprises a stockwork of clear or grey quartz veinlets (A- and B-type) hosted in the monzonite and surrounding sediments. The quartz veinlets have K-silicate alteration haloes composed of K-feldspar, biotite, apatite and magnetite. Hypogene mineralization consists of iron oxides (magnetite and hematite) and minor sulfides (bornite, chalcopyrite, pyrite, galena and sphalerite), which occur as disseminations, fracture fillings and in quartz veinlets. Petrographic observations indicate initial deposition of magnetite and chalcopyrite + bornite, followed by pyrite, hematite, galena and sphalerite. The second stage of mineralization is hosted by a series of E-W trending parallel and sub-parallel siliceous brecciated fault zones that have overprinted earlier-formed A- and B-type veins and the K- silicate alteration. The vein system extends over an area of about 2km within argillized subvolcanic, volcanic and sedimentary rocks. It comprises early monomineralic black tourmaline veins and breccias (with minor amounts of pyrite and arsenopyrite), which are cut by late polymetallic quartz±barite veins (Voudouris and Skarpelis 1998). Both vein types are related to quartz + sericite + tourmaline + pyrite alteration of the wallrocks. The polymetallic quartz veins include sulfides, sulfosalts, tellurides and electrum (Fig. 3a and b). Paragenetic relationships suggest initial deposition of pyrite, Fe-poor sphalerite and minor bornite followed by the deposition of fahlore group minerals, chalcopyrite, bournonite and galena together with minor hessite, petzite, Ag-sulfotelluride and electrum. Calcite is a late gangue phase.

Volcanic-hosted silicic and advanced argillic alteration zones (lithocap) in the northern part of the prospect comprising alunite and kaolinite are juxtaposed on the K-silicate and sericitic alteration and are barren of mineralization.

Bulk-rock analyses of 50 rock chip samples from the Fakos prospect, analyzed using ICP-MS, established the widespread occurrence of gold (max. 11 ppm), Ag (up to 11.3 ppm), Cu (up to 780 ppm), Pb (3500 ppm), Zn (256 ppm), Sb (300 ppm), Bi (26 ppm), As (4630 ppm), Mo (83 ppm) and Se (18 ppm).

Sardes prospect: The Sardes area has many similarities to Fakos, except for the absence of K-silicate alteration. The prospect comprises a stockwork of milky quartz + pyrite + molybdenite veinlets hosted within quartz + sericite + tourmaline altered sedimentary rocks and also within the monzonite. Gold grades reach 1.1 ppm. Anomalous Cu (up to 200 ppm), Pb (up to 200 ppm), Zn (up to 130 ppm) and As (up to 1400 ppm) have been detected, similar to the Fakos prospect.

3.2 Lesvos island

Stipsi prospect: The Stipsi prospect is characterized by an area of intense hydrothermal alteration, ranging from propylitic to argillic and locally to silicic (Kelepertsis and Esson 1987). A dacitic andesite porphyry body in the western part of the has been altered to kaolinite, illite and smectite. Mapping has delineated a target area that consists of a stockwork of grey to black silica veinlets crosscutting a dacite porphyry body (Fig. 2). Early veinlets that contain grey quartz + actinolite + minor magnetite, chalcopyrite and pyrite are related to K-Na-silicate alteration of the porphyry. These are cut by black quartz ± calcite veins associated with sericite-carbonate alteration. The black quartz veinlets contain early magnetite, which is overgrown by pyrite, chalcopyrite, bismuthinite, molybdenite and then by galena and sphalerite (Fig. 3c and d). Late-stage milky to amethystine quartz and platy calcite veins with pyrite and galena were formed along the ma-

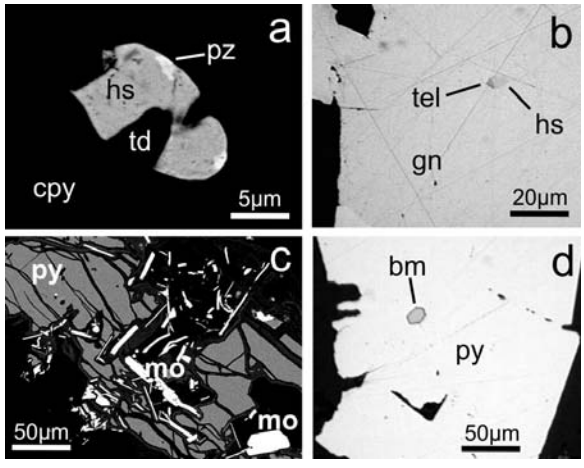

Figure 2: (a) Inclusions of hessite (hs), petzite and tetrahedrite (td) in chalcopyrite (cpy), BSE image, (Fakos prospect); (b): hessite (hs) and Ag-sulfotelluride (tel) in galena (gn) Reflected light, (Fakos prospect). (c) Molybdenite (mo) postdating pyrite (py), BSE-image, (Stipsi prospect). (d) Bismuthinite (bm) included in pyrite (py) Reflected light, (Stipsi prospect).

Table 1: Electron microprobe data from Sardes (1) and Stipsi (2-5) molybdenites.

wt %	1	2	3	4	5
Mo	60.26	60.63	59.46	59.59	59.23
Re	0.38	0.08	0.14	0.64	1.06
Fe	0.34	0.00	0.00	0.01	0.00
S	39.87	40.12	40.43	40.54	40.35
Total	100.85	100.82	100.03	100.78	100.64

Table 2: Electron microprobe data on hessite (1-3) petzite (4) and unknown sulfotelluride (5).

wt %	1	2	3	4	5
Ag	62.59	63.57	63.60	45.08	67.61
Au	0.11	0.05	0.24	19.88	0.12
Te	37.86	37.86	38.03	34.86	28.37
S	0.06	0.18	0.05	0.00	4.73
Total	100.75	101.69	101.9	99.82	101.3

1. $Ag_{1.98}Te_{1.01}S_{0.01}$, hessite; 2. $Ag_{1.98}Te_{1.00}S_{0.02}$, hessite
3. $Ag_{1.99}Te_{1.09}S_{0.01}$, hessite; 4. $Ag_{3.16}Au_{0.76}Te_{2.07}$, petzite
5. $(Ag_{3.12}Cu_{0.03})(Te_{1.11}S_{0.73})$ unknown sulfotelluride

jor NNE-SSW trending fault zone, and have overprinted earlier-formed alteration and mineralization. Barren jasperoidal silicic alteration, which overlies kaolinitized ± minor alunite volcanics is well exposed at higher elevations to the north of the prospect area. Maximum assay values returned from surface samples of the Stipsi prospect were 0.48 ppm Au, 1330 ppm Cu, 170 ppm Mo, 1020 ppm Pb, 1.7 ppm Ag, 21 ppm Sn and 16 ppm Se. Kelepertsis and Esson (1987) reported up to 330 ppm Mo from Stipsi and first postulated that this prospect may be of porphyry-Mo style.

4 Ore mineralogy

Ore minerals were investigated using a Cameca-SX 100 wavelength-dispersive electron microprobe at the Department of Mineralogy and Petrology, University of Hamburg. Selected results are presented in Tables 1 and 2.

Molybdenite is absent at Fakos. In both Sardes and Stipsi, it occurs as elongated laths postdating pyrite. EMPA data indicate generally low Re-contents (0.03-1.1 wt %, Table 1) that contrast to high Re-contents (up to 4.2 wt % Re) reported from western Thracian molybdenites (Melfos et al. 2001). Bismuthinite is observed only in Stispi as small inclusions within pyrite. It contains Bi (77.6 wt %) and small amounts of Cu (0.19 wt %), Fe (1.77 wt %) Sb (1.1 wt %) and Se (0.09 wt %).

Arsenopyrite (Au <0.07 wt %) is very abundant in Fakos and Sardes and absent in Stipsi. Small amounts of galena and sphalerite occur in the K-silicate alteration of Fakos and within the black quartz stockworks at Stipsi, but they are interpreted to be late hydrothermal overprints. They are more abundant in the late-stage milky quartz veins in all three prospects. EPMA data on sphalerite indicates Fe contents in the order between 0.23 and 1.57 wt % Fe for Fakos and between 1.24 and 1.43 wt % Fe for Stipsi.

Tetrahedrite group minerals from the polymetallic veins of Fakos are characterized by both As (2.4-20.3 wt %), and Sb (0.2-27.3 wt %)-rich varieties coexisting in one sample. Silver contents of up to 9.22 wt % have been detected, along with elevated Sn (<0.17 wt %), Te (<0.20 wt %) and Hg (<0.23 wt %).

Hessite, petzite and an unknown Ag-sulfotelluride occur rarely as small grains (up to 30μm) included in galena, tetrahedrite, and chalcopyrite in the polymetallic veins of Fakos. Hessite (Ag_2Te) contains small amounts of Au (<0.11 wt %) and S (<0.18 wt %). Petzite has a composition intermediate between end-member petzite and the x-phase, and occurs as very small (1μm) grains surrounding hessite (Fig. 3a). Microprobe analysis of petzite has revealed a Au content of 19.9 wt % Au. An unknown sulfotelluride containing about 5 wt % S, 68 wt % Ag and 28 wt % Te with a composition approaching $Ag_3(TeS)_2$ occurs in contact with hessite. Electrum with 21.4 to 22.7 wt % Ag is closely associated with hessite and petzite.

5 Discussion and conclusions

Newly-recognized porphyry-style mineralizations at Fakos, Sardes and Stipsi extend the northeastern Greece porphyry belt south into the Aegean Sea. The deposits are associated with shoshonitic monzonite and dacite plugs, and occur within Miocene shoshonitic to calc-alkaline lavas and sediments. Fakos and Sardes evolved through several stages of magmatic-hydrothermal pulses, as indicated by the early formation of K-silicate alteration, high-level advanced argillic alteration, later tourmaline-sericite veins and superimposition of epithermal-style polymetallic quartz veins enriched in base metals and precious metal tellurides. Fakos and Sardes are in many aspects similar to many other tourmaline-bearing porphyry systems worldwide as Aldebaran, Chile (Vila and Sillitoe 1991) and Bulagidun, Indonesia (Lubis et al. 1994). The Fakos system is enriched in tellurides which is consistent with the shoshonitic nature of the intrusion (Jensen and Barton 2000), a feature typical of many northern Greek porphyry and epithermal systems (Tarkian and Stribny 1999; Voudouris et al. 2004).

The Stipsi porphyry system is distinct in that it displays widespread sericite-carbonate alteration combined with an enrichment in molybdenite, bismuthinite and galena, features uncommon for other porphyry systems in Greece. This prospect is overprinted by low-sulfidation style quartz-carbonate veins, which extend northwards to Megala Therma, where they host economic precious metal mineralization (Kontis et al. 1994).

References

Arikas K, Voudouris P (1998) Hydrothermal alterations and mineralizations of magmatic rocks in the southern Rhodope Massiv. Acta Vulcanologica, 10(2): 353-365

Innocenti F, Manetti O, Mazzuoli R, Pertusati P, Fytikas M. Kolios N (1994) The geology and geodynamic significance of the island of Limnos, North Aegean Sea, Greece. N Jb Geol Palaont Mh, 11: 661-691

Jensen EP, Barton MD (2000) Gold deposits related to alkaline magmatism. Rev Econ Geol 13: 279-314

Kelepertsis AE, Esson J (1987) Major- and trace element mobility in altered voncanic rocks near Stypsi, Lesvos, Greece and genesis of a kaolin deposit. Appl Clay Sci 2: 11-28

Kontis E, Kelepertsis AE, Skounakis S (1994) Geochemistry and alteration facies associated with epithermal precious metal mineralization in an active geothermal system, northern Lesvos, Greece. Min Deposita, 29:430-433

Kroll T, Muller D, Seifert T, Herzig PM, Schneider A (2002) Petrology and geochemistry of the shoshonite-hosted Skouries porphyry Cu-Au deposit, Chalkidiki, Greece. Min Deposita 37: 137-144

Lubis H, Prihatmoko S, James LP (1994) Bulagidun prospect: a copper, gold and tourmaline bearing porphyry and breccia system in northern Sulawesi, Indonesia. Jour Geoch Expl 50: 257-278

Melfos V, Voudouris P, Arikas K, Vavelidis M (2001) Rhenium-rich molybdenites in Thracian porphyry Cu±Mo occurrences, NE Greece, Bull Geol Soc Greece 34: 1015-1022 (in Greek with English abstract)

Pe–Piper G (1980) The Cenozoic volcanic sequence of Lesvos, Greece. Zt Dtsch Geol Ges 131: 889-901

Rokos D, Argialas D, Mavrantza R, Seymour KSt,Vamvoukakis C, Kouli M, Lamera S, Paraskevas H, Karfakis I, Denes G (2000) Structural analysis for gold mineralization using remote sensing and geochemical techniques in a GIS environment: island of Lesvos, Hellas, Nat Res Research 9(4): 277-293

Tarkian M, Stribny B (1999) Platinum group elements in porphyry copper deposits: a reconnaissance study. Miner Petrol 65: 161-183

Vila T, Sillitoe RH (1991) Gold rich porphyry systems in the Maricunga belt, northern Chile. Econ Geol 86: 1238-1260

Voudouris P, Alfieris D, Fiori M, Grillo SM (2004) Te-rich magmatic-hydrothermal systems in northeastern Greece and Sardinia: a comparative study of ore mineralogy and sulfidation state. In: Khanchuk et al. (eds). Tectonics, magmatism and metallogeny. Dalnauka publ. Vladivostock:572-575

Voudouris P, Skarpelis N (1998) Epithermal gold-silver mineralizations at Perama (Thrace) and Lemnos island. Bull Geol Soc Greece XXXII/3: 125-135

Five questions for fun and profit: A mineral systems perspective on metallogenic epochs, provinces and magmatic hydrothermal Cu and Au deposits

John L. Walshe
CSIRO Exploration and Mining, ARRC, 26 Dick Perry Av, Kensington, Western Australia 6151

David R. Cooke
Centre for Ore Deposit Research, University of Tasmania, Private Bag 79, Hobart, TAS, 7001, Australia

Peter Neumayr
School of Earth and Geographical Sciences, The University of Western Australia, 35 Stirling Highway, Crawley, Western Australia 6009

Abstract. We argue that the empirical basis of deposit classification schemes is an inhibitor of the adventurous conceptual thinking required to aid efficient mineral exploration. It ought to be possible to construct a limited number of process - based, scale-integrated, system models to describe mineral and hydrocarbon deposits, provinces and epochs. We suggest that the geodynamic controls on reservoir construction and focused fluid release may be a unifying theme across many classes of deposits, effecting the formation of mineral provinces and epochs. The common architectural, geodynamic and fluid reservoir characteristic of porphyry Cu-Au and orogenic Au classes of deposits serve to illustrate the concept. The "Five Question" description of mineral systems is utilized.

Keywords. Mineral systems, architecture, geodynamics, reservoirs, gradients

1 Introduction: process to prediction

The question underlying the drive for enhanced methods of mineral discovery is how to "see" the deposit at scales significantly larger than the deposit scale, including the "whole-of-Earth" scale. Are there ways of determining productive from non-productive terrains? Are there fluid reservoirs and pathways and distal "haloes" as yet not recognised (Kesler, pers. comm. 2004)? Woodall (2004) called for "an adventure in new ways of thinking … a renascence of thought" to stimulate progress on these issues.

Arguably, a significant inhibitor of adventurous conceptual thinking is the present method of cataloguing knowledge of mineral deposits: i.e. the empirical nature of mineral deposit classification schemes. Ore deposit classes and models remain largely defined by selected deposit-scale characteristics and some micro-scale information e.g. porphyry Cu-Mo-Au, VHMS, shale hosted Pb-Zn, MVTs, IOCGs, BHTs etc. Any process understanding is an overlay on this class/type classification scheme. There is a need to develop genuine mineral system models that are independent of types/classes and are constrained by data at all scales, spatial as well as temporal.

Conceivably, no more than say six end-member process - based models, are required to account for the plethora of existing mineral and hydrocarbon deposit models. Building models of this ilk will involve making assumptions of commonality of processes across different classes of deposits and an assumption that data from apparently quite different systems can be interpreted in ways that reduce cross-scale and cross-class ambiguity to permit the building of a limited number of mineral system models. Models that account for the distribution of deposits and/or provinces through Earth history as well as province-, deposit- and micro-scale characteristics may well look quite different to models that do not need to satisfy such diverse data. The models need to be holistic in that they must take account of the physical and chemical processes/constraints in source rocks, reservoirs, flow paths and trap sites, and must balance heat and mass transfer across the whole system.

2 The "Five Questions" paradigm

The emphasis on understanding where deposits are located led to a restatement of the "source" "transport" and "trap" paradigm by the AGCRC (Australian Geodynamics Cooperative Research Centre) and its successor, the pmd*CRC (predictive mineral deposits Cooperative Research Centre). The "Five Question" description (Price and Stoker 2002) explicitly highlights the problem of understanding the system in space and the temporal evolution of the system at all scales. Question 1 asks: "What is the architecture and size of the system?" and question 2 asks: "What is P-T and the geodynamic history of the system. Hence the issues of "source" "transport" and "trap" are addressed within the context of an understanding of the architectural and geodynamic history of the whole system, taking account of information from the deposit to the terrain scale. Thus Question 3: "What is the nature of the fluids and fluid reservoirs in the system?" is not only

a question about the chemical characters of fluids and potential source regions. It is also a question about the location of the fluid reservoirs within the system. Question 4 enquires as to the nature of fluid pathways and processes driving fluid flow, and explicitly links the "transport" question to the architecture and dynamic history of the system. This is also achieved by question 5, which deals with the chemistry of metal transport and deposition in space as well as time (Walshe 2004).

3 Beginning with metallogenic epochs and provinces

Why did the major porphyry Cu deposits of northern Chile form in a relative short interval of approximately 10 Ma from the Late Eocene to Early Oligocene, given the existence of a convergent margin since the Carboniferous with subduction related magmatism occurring over some 200 Ma. Is it a co-incidence that the Carlin-style Au province of Northern Nevada, also formed in this time interval as did the Eocene Bingham Canyon Cu-Au porphyry in Utah. On the western Pacific rim, why is the Cu-Au province associated with an Ordovician volcanic arc in central west NSW and not with the much more extensive and voluminous Siluro-Devonian I-type volcanic and intrusive rocks of the Eastern Lachlan Orogen? What information is required at the terrain scale that combined with deposit & micro scale data will lead to development of scale-integrated mineral system models that predict terrain-scale phenomena such as mineral provinces and epochs? The need to elucidate architectural constraints, lithological as well as structural, on the spatial distribution of deposits is obvious enough. But what data have potential to explain/constrain metallogenic epochs? The Eocene metallogenic epoch on the eastern Pacific rim suggests that some factor(s) operated at least at the scale of the Pacific plate. Linking metallogenic epochs to geodynamic factors: changes in convergence rates and direction, changes in slab dip, high exhumation rates, etc., reinforces the sense of plate-scale processes at work but doesn't actually shed light on the mechanism(s) that constrain the metallogenic epoch. The current explanation for Cu deposits of central Chile invokes additional water release due to depth of melt generation. Such a mechanism, while satisfying the petrochemical constraints from central Chile, doesn't provide a mechanism that will work across all classes of deposits, magmatic and non-magmatic and wont aid the construction of a limited number of mineral system models.

4 Geodynamic controls on reservoir construction: a key to metallogenic epochs

A number of workers have talked about magma chambers becoming reservoirs at the time of porphyry copper production but this is a process that could apply across the system to many different types of reservoirs. Potentially metallogenic epochs can be linked to capacity of the Earth's crust to store fluids and release fluids in a focused way. Certainly the geodynamic observations are consistent with models of transient or episodic fluid flow. Hence mineral system models need to accommodate long periods of fluid dispersion or fluid storage and periodic/episodic fluid release.

The concept of creating reservoirs in the system is attractive because of the parallels with oil and gas generation. However, prediction within mineral systems is more challenging than in oil/gas systems precisely because the process has two critical stages rather than one, i.e.

- Creation of fluid reservoirs
- Focused release of fluids from the reservoirs to trap sites.

Fluid pressure may be considered the effective messenger that makes it possible for a whole terrain with a common and potentially "productive" architecture to act in unison – hence the clustering effect ("elephant country" concept) observed in many metallogenic provinces. Undoubtedly the rock record contains quite specific signals related to building and maintaining fluid pressure in the system. Many such signals are likely to reflect evolution of the partial pressures of the acid volatile species (CO_2, H_2S, SO_2, HCl). It is the values of these parameters that will determine the acidity, redox state and sulfur concentration of fluids, maintain the balance of metal and the sulfur components and sustain the geochemical gradients that ultimately control where metals are mobilized, stored in fluid reservoirs and / or concentrated / dispersed along fluid pathways. A productive epoch will require relatively limited pressure release. Sustained loss of fluid pressure is likely to lead to a degradation of reservoirs and pathways, both in terms of volume of available fluid and the chemical potential of key fluid parameters. Catastrophic pressure loss will mark the death of a productive system (e.g., El Teniente, Chile). It follows that one of the key elements we need to identify in the architecture of a system (Q1) are the seals – be they lithological or structural.

5 Towards a mineral system view of the porphyry Cu-Au and orogenic Au classes of deposits

Identifying potential seals in porphyry Cu-Au, and orogenic Au classes of deposits would seem to be a useful beginning point for developing genuine mineral system models that are independent of current classification schemes. Examples from the circum Pacific of competent lithological elements of the architecture that appear to have acted a seals in the system include the Darai/Mendi Limestone or equivalents in New Guinea, and the lavas of

the Farellones Formation in central Chile. These plates appear to have acted to impede magma ascent, as well as forming a cap on a magma and/or fluid system being pressurized by collision and orogenesis. Deposits commonly occur below the seal but may also occur above it e.g. the Porgera, Ok Tedi deposits c.f. the Grasberg deposit in New Guinea. The reduction (perhaps even cessation) of volcanism but not plutonism associated with porphyry Cu production in northern and central Chile (Camus 2002) is consistent with the idea of sealing the system by tectonic loading and storing the fluids. Hence, the absence of volcanic activity or transition from volcanic activity to plutonic activity, or vice versa, at the time of mineralization may be one of the "terrain-scale" signals of a productive mineral system. In the Au and Cu provinces of Northern Nevada and Utah these is a switch from plutonism to volcanism around 40 Ma; the time of mineralization. In the Tasmanides it was the Middle to Late Ordovician hiatus in volcanism in central west NSW that heralded the onset of Cu-Au metallogenesis (Glen et al. 2004). By contrast the Siluro-Devonian in the Eastern Lachlan is marked by coeval S and I type volcanism and plutonism and an absence of world class deposits. In South Australia, the Gawler Range Volcanics appear to have acted as the major seal on a system that includes the IOCG deposits of the eastern Gawler, including Olympic Dam, and the gold deposits of the central Gawler. Both the Au and Cu-Au systems formed at 1580-1590 Ma (Skirrow et al. 2002, Budd and Fraser 2004). In the Archean gold systems of the eastern Yilgarn, Western Australia, it is the late siliciclastic basins and the Black Flag Beds that appear to have acted as regional seals.

6 Multiple fluid reservoirs and chemical gradients along pathways and at trap sites

Large-tonnage, high-grade deposits require both sustained fluid flow and sustained contrasts in thermo-chemical conditions at trap sites. One of the most efficient ways to sustain thermo-chemical gradients is to mix two fluids of contrasting chemistry. An implication is that multiple and chemically different fluid reservoirs will most likely be a feature of mineral systems that produced the giant deposits. Another is that it should be possible to characterise the elements of the architecture (Q1) that were pathways of chemically contrasting fluids and build scale-integrated models from deposit to at least district scale of the pathways and styles of alteration to aid mineral exploration. In the eastern Yilgarn district-scale alteration and geochemical dispersion patterns combined with paragenetic, fluid inclusion and stable isotope studies at deposit- scale point to three main fluid types/reservoirs in the systems (Neumayr et al. this volume): (1) ambient aqueous carbonic fluids with the CO_2 largely derived from the greenstone host sequences; (2) oxidized magmatic sourced from 2665-2650 Ma mafic and syenitic granite-magmas; and (3) highly reduced fluids inferred to be have been sourced from the deep crust or mantle. Fluid inclusion studies (e.g. Petersen et al. 2005) indicate a wide range of fluid compositions (aqueous, salt- rich, CO2-rich and CH4-rich) consistent with diverse origins. Mixing of fluids of contrasting chemistry controlled Au deposition. A similar diverse range of fluid types and iron sulfides and oxides, occur in the Gawler and Isa IOCG provinces (although relative abundances are different) implying multiple fluid reservoirs in these systems. Oliver et al. (2004) invoke the mixing of evolved magmatic brines with sulfur-bearing fluids as one of the mechanisms for depositing Cu-Fe-sulfides. Reservoirs of reductant (H_2) and H_2S beyond the magma chamber are also required to sustain physicochemical gradients in redox and reduced sulfur activity at sites of Cu-Fe-sulfide precipitation in porphyry Cu-Au systems (Walshe et al. 1993) and there are certainly radiogenic isotope data sets (e.g. Mathur et al. 2000; Frikken et al. 2005) to support a role for deep - sourced non-magmatic fluids in porphyry Cu-Au systems.

7 Conclusions

The "Five Questions" provide a framework to describe the key elements of productive mineral systems and are arguably promoting "the right questions" across different classes of deposits. The emphasis on cross-scale integration is leading to an appreciation of the size of systems and the diversity of fluid types. A better understanding of the interplay between architecture, geodynamics and fluid reservoirs, at various scales, is probably the process key to enhanced prediction.

Acknowledgements

We acknowledge pmd*CRC, MERIWA and CODES for support and permission to publish.

References

Budd AR, Fraser GL (2004) Geological relationships and $^{40}Ar/^{39}Ar$ age constraints on gold mineralisation at Tarcoola, central Gawler gold province, South Australia. Australian Journal of Earth Science, v. 51: 685–699

Camus F (2002) The Andean porphyry systems, Cooke, DR, Pongratz J, Giant ore deposits – characteristics, genesis and exploration: CODES Special Publication No. 4, University of Tasmania: 5-22

Frikken PH, Cooke DR, Walshe JL, Archibald D, Skarmeta J, Serrano L,Vargas R (2005) Mineralogical and isotopic zonation in the Sur-Sur Tourmaline Breccia, Río Blanco-Los Bronces Cu-Mo deposit, Chile - Implications for ore genesis: Economic Geology, in press

Glen, RA Crawford, AJ Cooke, DR Percival, IG Meffre, S Scott, RJ Squire, R Barron, L M (2004) The Macquarie Arc: a key component of the Ordovican and earliest Silurian tectonics of the Lachlan Orogen. Abstracts of the Geological Society of Australia 73: 162

Neumayr P, Petersen KJ, Gauthier L, Hodge J, Hagemann SG, Walshe JL, Prendergast K, Conners K, Horn L, Frikken P, Roache A, Blewett R. (2005) Mapping of hydrothermal alteration and geochemical gradients as a tool for conceptual targeting: examples from Western Australia, this volume

Oliver NHS, JS Cleverley, G Mark, PJ Pollard, Bin Fu, LJ Marshall, MJ Rubenach, PJ Williams, T Baker (2004). Modeling the Role of Sodic Alteration in the Genesis of Iron Oxide-Copper-Gold Deposits, Eastern Mount Isa Block, Australia. Economic Geology 99: 1145-1176

Petersen KJ, Neumayr P, Hagemann SG, Walshe JL (2005) Palehydrologic evolution of the St. Ives gold camp. this volume

Price GP, Stoker P (2002) Australian Geodynamics Cooperative Research Centre's integrated research program delivers a newminerals exploration strategy for industry. Australian Journal of Earth Science, v 49: 595–600

Skirrow RG, Bastrakov E, Davidson GJ, Raymond OL, Heithersay PS (2002) The geological framework, distribution and controls of Fe-oxide Cu–Au mineralisation in the Gawler Craton, South Australia. In: Porter T. M. ed. Hydrothermal Iron Oxide Copper-Gold and Related Deposits: a Global Perspective, Vol 2: 33–47. Porter Geological Consultancy Publishing, Adelaide

Walshe JL (2004) Mineral systems to mineral discovery: The metallogeny of the Lachlan Orogen 10 years on. In. Bierlein, F.P., Hough, M.A. (editors), Tectonics to Mineral Discovery – Deconstructing the Lachlan Orogen. Proceedings Volume and Field Guide, MORE-SGEG Conference, Orange, NSW, July 6 – 8, 2004. Geological Society of Australia Abstracts No. 74: 45-48

Walshe JL, Cooke DR, Cannell J, Frikken P, Hollings P, Masterman G, Skarmeta J, Camus F, Gow PA, Midgley G (2003) Physicochemical gradients and architectural constraints on fluid-mixing models of porphyry Cu formation In Eliopoulos D.G. et al., eds, Mineral Exploration and Sustainable Development, Proceedings of the 7th Biennial SGA meeting, Athens, Greece: 419-422

Woodall R (2004) The challenge of discovering mineral deposits undercover: What can we learn from the past? Opening Address to the Society of Economic Geologist's Conference, Predictive Mineral Discovery Under Cover, Perth September 2004

Mineral chemistry of Fe-Ti oxides from the Xinjie PGE-bearing layered mafic-ultramafic intrusion in Sichuan, SW China

Christina Yan Wang, Mei-Fu Zhou
Department of Earth Sciences, University of Hong Kong, Hong Kong, China

Abstract. The Xinjie intrusion is a typical example of a mafic-ultramafic body that hosts both Fe-Ti oxide and Cu-Ni-(PGE) sulphide mineralization. Both the oxide-rich and sulphide-rich layers occur as part of an igneous layered sequence. The layered sequence can be divided into three cycles. Chromite mineralization occurs at the lower part of each cycle, whereas magnetite and ilmenite mineralization occur in the upper part. The intergrowth of chromite and ilmenite, and titanomagnetite and ilmenite are common in the ores. High temperatures and oxygen fugacities together with isotopic evidence of crustal contamination indicate that ilmenite- titanomagnetite grains were crystallized at greater depths, prior to assimilation of crustal materials. Two possible mechanisms can explain the oxide mineralization: (1) immiscible oxide melts formed within the magma started crystallization of olivine and chromite, and (2) formation of these ore zones by magma mixing.

Keywords. Fe-Ti oxides, Xinjie, mineral chemistry, petrogenesis

1 Introduction

Large layered intrusions, such as the Bushveld and Stillwater complexes, contain chromite deposits in their lower part and Fe-Ti oxides in the upper part. However, some giant magnetite deposits are hosted in gabbroic intrusions, such as the Stella layered intrusion in South Africa (Maier et al. 2003). How such large amount of Fe-Ti oxides can be formed from these magmas remains an unanswered question.

The Xinjie layered intrusion, which occurs in Sichuan, SW China, is a typical example of a mafic-ultramafic body that hosts both Fe-Ti oxide and Cu-Ni-(PGE) sulphide mineralization. Both oxide-rich and sulphide-rich layers occur as part of the layered sequence. The whole sequence is 1200 m thick, including 70-m-thick ilmenite-rich layers, 62-m-thick V-Ti magnetite-rich layers and 11-m-thick chromite-rich layers. The ores contain 5 to 50 modal % Fe-Ti oxides. Such high concentrations of oxides are hard to explain by either in-situ crystal fractionation or by liquid immiscibility from the parental magma. In this paper, we document the characteristics of Fe-Ti oxide mineralisation in the Xinjie intrusion and discuss possible genetic models.

2 Geological background

The Pan-Xi area is located on the western margin of the Yangtze Block, east of the Tibetan Plateau. There are a number of mafic-ultramafic layered intrusions associated with the 260 Ma Emeishan Large Igneous Province in this area, which host giant Fe-Ti-V deposits (Yao et al. 1993) and Cu-Ni-(PGE) sulphide mineralization (Liang et al. 1998). From north to south, they include the Taihe, Baima, Xinjie, Hongge and Panzhihua intrusions. The Panzhihua, Baima and Taihe intrusions are mafic, whereas the Hongge and Xinjie intrusions are mafic-ultramafic complexes (Zhong et al. 2002; 2004). The intrusions have been related genetically to the high-Ti Emeishan basalts because of their similar compositions and close spatial relationships (Xu et al. 2001).

The Xinjie intrusion is a sill-like body about 2 km long and 1-1.5 km wide. It has intruded the Emeishan flood basalts and syenitic rocks. The sill strikes NW-SE and dips 70° SW, and has been differentiated, with well-developed igneous layering. Three cycles are recognized (Fig. 1).

Cycle I consists of peridotite, olivine clinopyroxenite, plagioclase clinopyroxenite, gabbro and quartz-bearing gabbro. Cycle II contains olivine clinopyroxenite, gab-

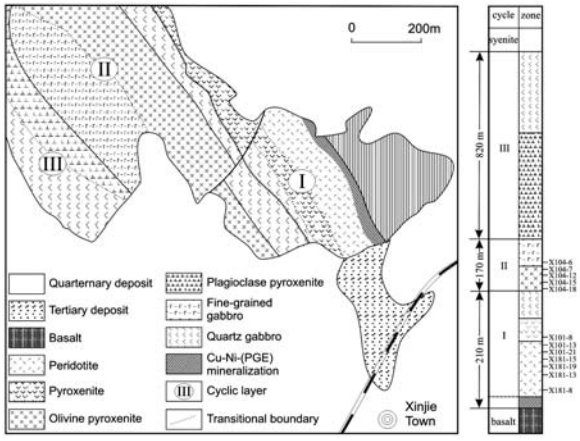

Figure 1: Geological map of the Xinjie intrusion

bro and quartz-bearing gabbro. Cycle III consists of plagioclase clinopyroxenite, gabbro and quartz diorite. Contacts between different rock types are transitional within individual cycles. The base of the intrusion is marked by a marginal zone composed of gabbro with abundant blocks of felsic material.

Chromite mineralization occur in Cycles I and II, whereas magnetite and ilmenite mineralization occurs in all three cycles. Chromite-rich layers with chromite veinlets occur mostly within the lower part of each cycle, whereas magnetite- and ilmenite-rich layers are typically concentrated in the upper part of each cycle. The PGE mineralization is located near the base of Cycle I and II and the marginal zone.

3 Petrography

Cycle I: Olivine clinopyroxenite consists of cumulus olivine up to 61 modal %, titanaugite (15 to 75%), intercumulus titanaugite (5 to 50%) and plagioclase (6 to 45%). Gabbro consists of cumulus titanaugite (25 to 55%), olivine (<30%), plagioclase (10 to 60%), intercumulus plagioclase (20 to 40%), titanaugite (12 to 60%) and quartz (<5%). Cycle II: Olivine clinopyroxenite comprises cumulus olivine (<35%) and titanaugite (30 to 85%), intercumulus plagioclase (7 to 55%) and titanaugite (20 to 50%). Gabbro contains cumulus plagioclase (40 to 65%), and interstitial titanaugite (25 to 30%). Cycle III: cumulus plagioclase (45 to 80%) and interstitial quartz contents (<6%) increase upwards as the rocks change from clinopyroxenite to quartz diorite. Major Fe-Ti oxides including magnetite, ilmenite and chromite are disseminated in the ores.

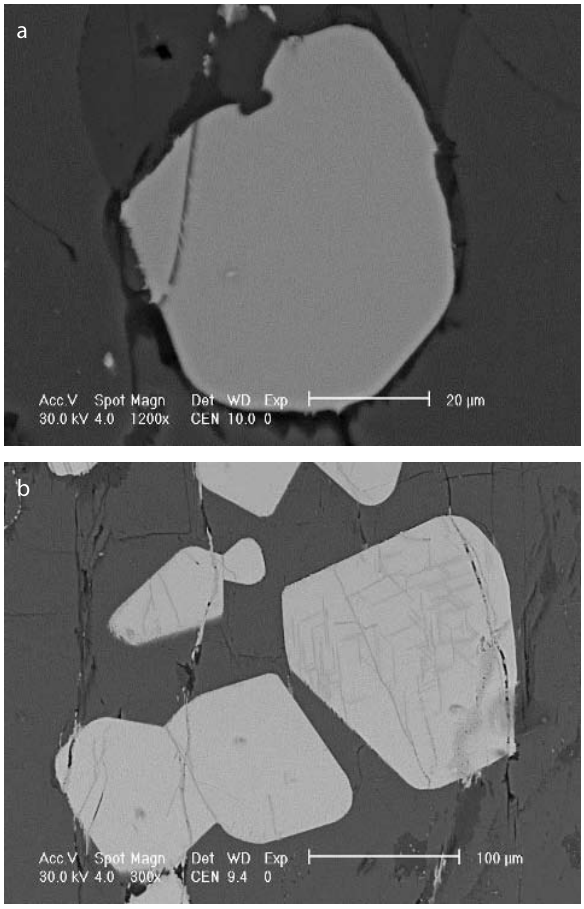

Figure 2: Photomicrographs of chromites. (a) Optically homogeneous chromites; (b) ilmenite lamellae in chromites

Euhedral-subhedral chromites are enclosed within olivine or clinopyroxene, and typically vary from 0.04 to 0.2 mm in diameter. Although the chromites are in most cases optically homogeneous (Fig. 2a), a small number of exsolved ilmenite lamellae have developed in the chromite host (Fig. 2b). The chromite host usually contains = 15% ilmenite lamellae, typically <0.01 mm in width. Some of the chromites have thin magnetite rims.

There are two types of magnetites. One type is characterized by euhedral to subhedral grains ranging from 0.1 to 0.8 mm in size, and occurs as inclusions in clinopyroxene and plagioclase (Fig. 3a). The other type occurs as interstitial phase between clinopyroxene, olivine and plagioclase (Fig. 3b). Intergrowths of magnetite and ilmenite lamellae are common in the ores. Ilmenite occurs along cracks, boundaries and cores of magnetite grains, and as densely spaced domains throughout the magnetite host. The magnetite host contains 8-25 % oriented ilmenite lamellae ranging in width from 0.005 to 0.03 mm, forming trellis and sandwich textures (Fig. 3c). Ilmenite lamellae are evenly space densely through the magnetite host (Fig. 3d). Ilmenite lamellae occur in two generations. The first exhibits large sandwich-type lamellae, followed by a finer-grained, second generation of trellis-type.

There are two types of ilmenites. One type occurs as fine subhedral inclusions in silicate grains within the gabbro (Fig. 4a). The subhedral grains are typically 0.1 to 0.4 mm in diameter, with some up to 1.9 mm. The second type occurs as an interstitial phase between silicate grains and typically has irregular magnetite rims and magnetite lamellae in the cores (Fig. 4b). As for magnetite, intergrowths of magnetite and ilmenite have also been observed in ilmenite. The magnetite lamellae are oriented are spaced mainly through the core of the host ilmenite (Fig. 4c).

Two generations of subparallel oriented magnetite lamellae can be recognized. The first magnetite generation is represented by elongated crystals (length >50 µm), whereas the second is extremely fine-grained (a few µm) and does not occur in contact with the first generation (Fig. 4d).

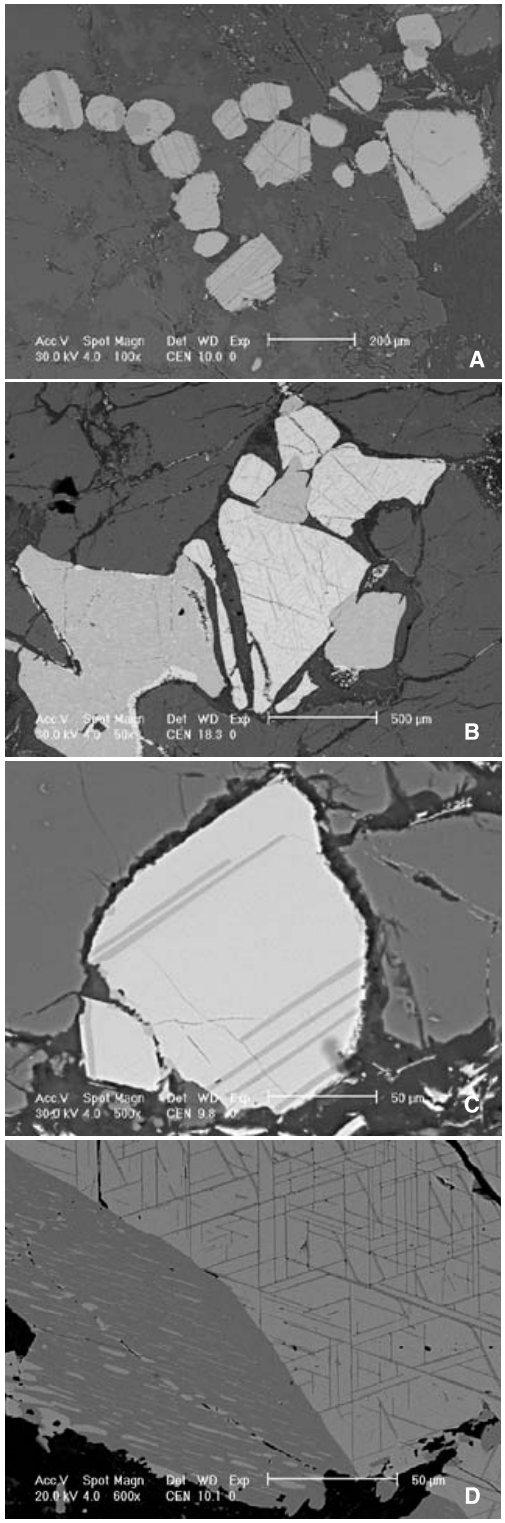

Figure 3: Photomicrographs of magnetites. (a) Euhedral to subhedral magnetites ranging from 0.25 to 0.8 mm in size occurs as inclusion in pyroxene; (b) Interstitial magnetites and ilmenites; (c) oriented ilmenite lamellae in magnetite forming sandwich textures; (d) Ilmenite lamellae space densely in magnetite host.

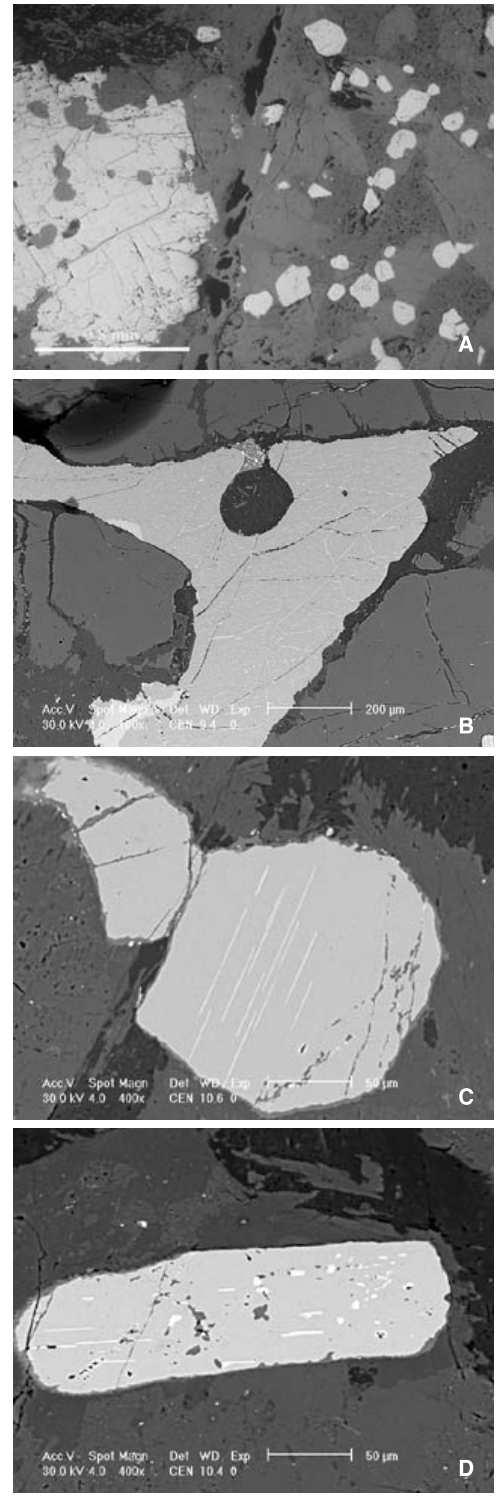

Figure 4: Photomicrographs of ilmenites. (a) Ilmenite grains isolated in silicates; (b) Interstitial ilmenite; (c) Magnetite lamellae are oriented parallel to {0001} planes of the host ilmenite; (d) Two generations of subparallel oriented magnetite lamellae. 1: elongated crystals (length >50 µm), 2: extremely fine-grained (few µm) and does not occur in contact with the first generation.

This page intentionally blank

4 Results

4.1 Chromite

The chromites are defined as high-Fe chromites because of their high Fe contents (45 to 83 wt % FeO_T). The chromites have 6.55 to 29.9 wt % Cr_2O_3, 0.49 to 8.82 wt % Al_2O_3, 29.8 to 35.6 wt % FeO, 11.0 to 57.1 wt % Fe_2O_3, and 0.09 to 2.86 wt % MgO. Cr_2O_3 co-varies positively with Al_2O_3 and MgO, and negatively with Fe_2O_3. Al_2O_3 correlates negatively with Fe_2O_3, and positively with MgO. There is a negative correlation between MgO and FeO_T. Chromites in Cycle I contain higher Cr_2O_3, Al_2O_3 and MgO but lower Fe_2O_3 content than those in Cycle II. The FeO contents of the chromites in both cycles vary in a relatively small range although there is a larger variation in Cycle I than those in Cycle II. In Cycle II, FeO contents of the chromites are relatively constant (31.3 to 33.3 wt %) whereas Fe_2O_3 vary largely from 37.9 to 57.1 wt %. Mg#'s and Cr#'s of all chromites vary from 0.5 to 14 and from 75 to 90, respectively.

4.2 Magnetite and ilmenite

Homogeneous magnetite and ilmenite have not been observed. The magnetites are titanomagnetite because of their high TiO_2 content in a range from 0.4 to 31 wt %. The ilmenite have high TiO_2 content, ranging from 38 to 53 wt %, higher than that of pure ulvite (Fe_2TiO_4, 36 wt %).

The compositions vary slightly between host and guest magnetite, and between host and guest ilmenite. In Cycle I, magnetite host grains have 30 to 55 wt % FeO, 3.6 to 60 wt % Fe_2O_3, 0.4 to 29 wt % TiO_2 and 0.52 to 1.7 wt % V_2O_3 whereas magnetite inclusions have 35 to 57 wt % FeO, 5.4 to 58 wt % Fe_2O_3, 3.2 to 31 wt % and 1.2 to 1.7 wt % V_2O_3. Ilmenite host grains have 37 to 41 wt % FeO, 3.0 to 14 wt % Fe_2O_3, 46 to 51 wt % TiO_2 and 2.1 to 2.3 wt % V_2O_3 while ilmenite inclusions have 26 to 44 wt % FeO, 1.8 to 27 wt % Fe_2O_3, 38 to 52 wt % TiO_2 and 1.8 to 2.9 wt % V_2O_3. The magnetites and ilmenites in Cycle II are similar compositionally to Cycle I. Magnetite host grains have 33 to 41 wt % FeO, 47-66 wt % Fe_2O_3, 10-11 wt % TiO_2 and 1.0 to 1.1 wt % V_2O_3 whereas magnetite inclusions have 35-57 wt % FeO, 19 to 60 wt % Fe_2O_3, 3.1 to 27 wt % TiO_2 and 0.61 to 1.6 wt % V_2O_3. Ilmenite host grains have 41 to 45 wt % FeO, 4.9 to 11 wt % Fe_2O_3, 47 to 51 wt % TiO_2 and 2.5 to 2.7 wt % V_2O_3 whereas inclusions have 44-46 wt % FeO, 3.2 to 4.7 wt % Fe_2O_3, 50 to 53 wt % TiO_2 and 2.4 to 2.6 wt % V_2O_3.

5 Discussion

Equilibration temperatures and oxygen fugacities of crystallization were calculated based on the co-existing ilmenite-magnetite mineral phases using an ilmenite-magnetite geothermometry and barometry program (ILMAT120, Lepage 2003), based on the geothermometer of Anderson and Lindley (1985). Oxygen fugacity values (as $-\log fO_2$) vary from 8.1 to 25.0 in Cycle I and from 13.3 to 21.5 in Cycle II. The maximum and minimum temperatures obtained for magnetite (host) / ilmenite (inclusions) are 1146° and 541°C in Cycle I, and 610° and 572°C in Cycle II. The crystallized temperatures of ilmenite (host) / magnetite (inclusions) in Cycle II vary from 931° to 637°C. The temperature variations are possibly due to (a) changes in the type and quantity of contaminants, (b) early or late appearance of ilmenite-magnetite during crystallization of the magma and (c) different sources of the magma and their differentiation at various levels of the Earth's crust. Comparatively higher temperatures are inferred as an approximate temperature of emplacement of the magmas. Phase relationships in Fe-Ti system shows that the melting point of ilmenite is 1470°C and that of magnetite is 1591°C (Vincent and Phillips 1954). The low Fe-Ti oxide equilibration temperature indicates that the plagioclase and pyroxene have already been crystallized before the Fe-Ti oxide re-equilibrated, and the Xinjie intrusion was derived from multiple differentiated magmas (Ahmad and Shrivastava 2004). Thus, the liquidus temperature of the host rocks was much higher than that of the observed temperature of equilibration for ilmenite-magnetite phases. This is supported by an association of plagioclase and pyroxene with ilmenite and magnetite. High temperature and oxygen-fugacity values together with isotopic evidence of crustal contamination indicate that some Fe-Ti oxides were crystallized at greater depths before assimilation of crustal materials.

The common intergrowths of magnetite and ilmenite in the Xinjie intrusion cannot be explained by the model of Buddington and Lindsley (1964). According to their model, the two intergrowths would originate from oxy-exsolution (magnetite host + ilmenite lamellae) and from reduction-exsolution (ilmenite host + magnetite lamellae) and, thus cannot properly occur in the same paragenesis. The ilmenite/magnetite lamellae in the core of the magnetite/ilmenite host form true exsolution textures which are generally able to change the host-inclusion relationships depending on the composition of the precursor. However, it is possible that the ilmenite lamellae along crack and grain boundaries of the magnetite host form because of oxy-exsolution. There may be two other possible mechanisms to explain the formation of oxide deposits within the Xinjie intrusion: (1) immiscible oxide melts formed within the magma when crystallization of olivine and chromite commenced, and (2) the formation of these ore zones may have resulted from magma mixing.

Acknowledgements

This study was substantially supported by a RGC grant, Hong Kong (7056/03P).

References

Ahmad M, Shrivastava JP (2004) Iron-titanium oxide geothermometry and petrogenesis of lava flows and dykes from Mandla lobe of the eastern Deccan volcanic province, India. Gondwana Res 7: 563-577

Anderson AT, Lindsley DH (1985) Model for the Ti magnetite or ilmenite geothermometers and oxygen barometers. Trans. Geophysical Union 66: 416

Buddington AF, Lindsley DH (1964) Iron-titanium oxide minerals and synthetic equivalents. J Petrol 5: 310-357

Lepage, Luc D (2003) ILMAT: an Excel worksheet for ilmenite-magnetite geothemometry and geobarometry. Comp and Geosci 29: 673-678

Liang YB, Liu TY, Song GR, Jin ZM (1998) Platinum Group Element Deposits in China Metallurgical Industry Press, Beijing: 185 (in Chinese)

Maier WD, Barnes SJ, Gartz V, Andrews G (2003) Pt-Pd reefs in magnetitites of the Stella layered intrusion, South Africa: a world of new exploration opportunities for platinum group elements. Geology 31: 885-888

Vincent EA, Phillips R (1954) Iron titanium oxide minerals in layered gabbros of Skaergaard intrusion, East Greenland. Geochim Cosmochim Acta 6: 1-26

Xu YG, Chung SL, Jahn BM, Wu GY (2001) Petrologic and geochemical constraints on the petrogenesis of Permain-Triassic Emeishan flood basalts in southwestern China. Litho 58: 145-168

Yao PH, Wang KN, Du CL, Lin ZT, Song X, (1993) Records of China's Iron Ore Deposits. Metallurgic Industry Press, Beijing: 638-641 (in Chinese)

Zhong H, Yao Y, Prevec SA, Wilson AH, Viljoen MJ, Viljoen RP, Liu BG, Luo YN (2004) Trace-element and Sr-Nd isotopic geochemistry of the PGE-bearing Xinjie layered intrusion in SW China. Chem Geol 203: 237-252

Zhong H, Zhou XH, Zhou MF, Sun M, Liu BG (2002) Platinum-group element geochemistry of the Hongge layered intrusion in the Pan-Xi area, southwestern China. Mineral Deposit 37: 226-239

Volcanism and mineralization in the North Qilian Orogenic Belt, Northwestern China

Xue-Yi Xu, Lin-Qi Xia, Zu-Chun Xia
Xi'an Institute of Geology and Mineral Resources, Xi'an, 710054, China

Abstract. The bedrocks of the North Qilian Mountains have been subjected to episodes of continental rifting, ocean basin opening, subduction, basin closing and plate collisions. This has, resulted in a diversity of volcanic rocks that were deposited from the Proterozoic to the Silurian in the North Qilian orogenic belt. Proterozoic continental rift volcanism produced flood basalts in the western parts of the North Qilian Mountains, with Fe and Cu as the major mineral resources. Cambrian volcanic rocks are rift-related, and can be divided into two groups based on their textural characteristics (flow dome complexes versus fissure complexes) and their associations with Cu deposits. Early Paleozoic submarine mid-ocean ridge volcanic rocks are preserved as obducted slices of the North Qilian ocean basin. The subduction complex which marks the site of the Paleozoic paleo-trench is located on the northeastern side of the Paleozoic submarine volcanic belt. A Late Cambro-Ordovician belt of arc-related volcanic rocks is located to the northeast of the subduction complex, along the southern Zhulang Mountains. Middle-Late Ordovician volcanism occurred in a back-arc basin setting, as exposed on the northern slope of Zhulangnanshan. Within this back-arc environment, ophiolite suites developed with Cu and Zn deposits hosted in basic lava in the upper parts of the ophiolites. Late Ordovician volcanism occurred in a passive continental rift setting with minor Cu- and Pb-Zn sulfide mineralization.

Keywords. North Qilian mountains, volcanism, paleosubmarine, mineralization

1 Introduction

The North Qilian orogenic belt is a large, composite orogenic belt located in northwestern China (Fig. 1). It extends across Gansu and Qinghai Provinces and has a history of formation that extends from the late Proterozoic to the Paleozoic. With regards the Paleozoic geological evolution, some authors have considered that the North Qilian ocean was a part of paleo-Tethys ocean and its evolution can be attributed to Tethyan tectonics (Xu et al. 1994; Ge et al. 2000). Others have proposed that North Qilian was a restricted oceanic basin in the Paleozoic that formed at the margin of the north China Plate, and it developed three kinds of tectonic systems since the Proterozoic: continental rift, subduction-related arc and intracontinental orogeny respectively, similar to the evolution of the western Pacific today (Xia et al. 1998a,b; 1999a,b; 2000). In this paper, we discuss the most likely tectonic settings for the various volcanic belts of the North Qilian Mountains, from the Proterozoic through the Paleozoic.

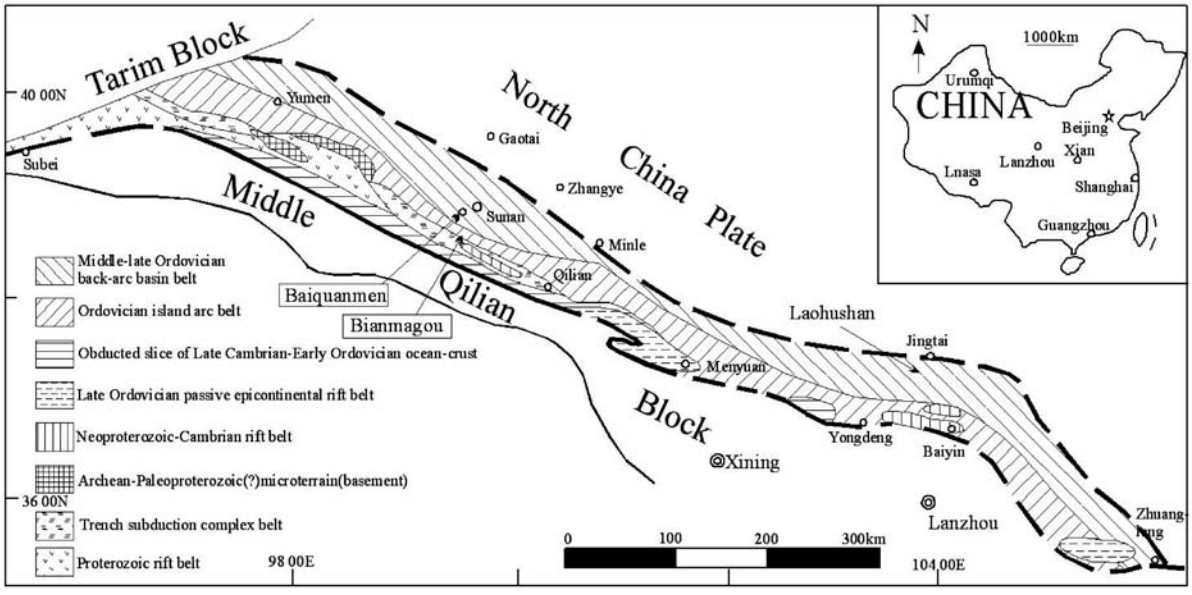

Figure 1: Geology of the North Qilian Mountains, China, highlighting major Proterozoic and Paleozoic geological and tectonic elements. Fault-bound blocks of Archean-Paleoproterozoic basement are also present in the region. Inset: locality map.

This page intentionally blank

2 Proterozoic rift volcanism

During the middle Paleoproterozoic, an asthenospheric mantle plume triggered continental rift volcanism in the North Qilian region. Continental flood basalts developed on Archean-Proterozoic basement during rifting and extension of continental crust. Rifting eventually progressed to the point where oceanic crust formed. The Proterozoic continental flood basalts crop out in the western section of the North Qilian Mountains (Xia et al. 1999a,b; Fig. 1). There are several units. The lowermost is composed of tholeiitic lavas intercalated with dolomite, and ranges in age from 2349 to 1780 Ma (Xia et al. 1999a,b; Mao and Zhang 2000). The 1309 Ma middle package consists of microclastic rocks that contain an Fe-bearing layer. These rocks have undergone low grade metamorphism. The upper package consists of dolomites and alkali basalts, which were erupted between 1032 and 604 Ma. The Proterozoic volcanic rock sequences are preserved in fault blocks in the North Qilian Mountains, and cover an area of over 1000 km^2. They are similar in character to the Deccan continental flood basalts.

3 Neoproterozoic-Cambrian rift volcanism

Volcanic rocks that formed in the Neoproterozoic - Cambrian period (Fig. 1) can be divided into two groups based on their modes of occurrence: (1) Large, bimodal volcanic domes formed by a combination of explosive and effusive volcanism, and shallow-level intrusive activity, and were important for mineralization; (2) Flow-banded lavas formed by fissure-type eruptions. The Heishishan volcanic dome complex is associated with the Baiyinchang orefield, Gansu Province. Other significant volcanic domes include Qingshuigou - Bailiugou and Shitougou - Xiangzigou in Qinghai Province. In each of these domes, the mafic volcanic rocks are dominated by alkali basalts. Acid volcanic rocks developed in the central and lower parts of the domes. The Baiyinchang and Gadaban copper deposits and Xiangzigou pyrite deposit all occur in acidic volcanic rocks within these dome complexes.

4 Late Cambrian - Early Ordovician mid-ocean ridge volcanism

By the Late Cambrian, continued continental break-up had led to the transformation from a continental rift setting to an oceanic basin. Mid-ocean ridge volcanism produced a belt of Late Cambrian - Early Ordovician (522 to 495 Ma) rocks that are preserved as obducted slices in the north Qilian Mountains (Fig. 1). These rocks define the North Qilian Early Paleozoic oceanic basin, and extend from the Yushigou (522 Ma) and Chuancigou (495 Ma) areas on the northern slope of Telaishan, northwest to Diaodaban, southeast to Yongan old city in northwest Menyuan County, and disjointedly to Dakecha in Tianzhu County. The source magmas had low-K tholeiitic series and ocean island alkali and tholeiitic series compositions with E-MORB and T-MORB features (Xia et al. 1998a,b; Ge et al. 1999; 2001, Zhang et al. 2000).

5 Ordovician arc volcanism and mineralization

With continued ocean basin opening, the oceanic lithospheric plate became cold and dense, and began to subduct beneath the North China continental plate. Northwest-directed subduction generated a subduction complex from 486 to 445 Ma along the southern slope of Zoulangnanshan. The subduction complex crops out to the northeast of the belt of Paleozoic submarine volcanic rocks (Fig. 1) on the north slope of South Tuolai mountains, and extends for over 400 km from Yingzuishan in the west to Changma, Bianmagou, Qinshuigou, Baijingshi and Jingyangling. The complex contains a forearc accretionary wedge, two belts of blueschist rocks, fault blocks of mafic-ultramafic volcanic rocks, volcanic rock microlithons, mélange accumulations, remnants of radiolarian siliceous rocks. The accretionary wedge sediments include abundant soft sediment deformation, turbiditites and flysch (Xu et al. 1994). Paleozoic gold deposits occur within the subduction complex.

The Late Cambrian - Ordovician (523Ma - 455 Ma) belt of arc volcanic rocks developed on the northeastern side of the subduction complex (Fig. 1). The arc volcanics crop out along the south Zoulang Mountains, with the type locality at Shihuigou, Yongdeng County, Gansu Province. The arc volcanics evolved with different stages of island-arc evolution from early to late, and with distance from the subduction belt. The oldest sequences are dominated by tholeiitic basalts. These were followed by the eruption of dominantly marine calc-alkaline volcanic rocks, and by intermediate volcanic rocks. During the Late Ordovician (457Ma - 445Ma), a series of alkali volcanic rocks of shoshonitic character were erupted. These marked the final stage of the island arc system in the North Qilian Mountains.

Xia et al. (1998b; 2000) noted that the Ordovician island arc volcanic rocks extend for more than 1000 km from northwest to southeast. The belt contains orogenic gold deposits in the western section of the North Qilian Mountains. These deposits occurs in island-arc fine pyroclastic rocks. Gold mineralisation is inferred to have been related to the tectonic-thermal events during or after collision in the North Qilian Mountains.

6 Ordovician back-arc volcanism and mineralization

Rocks that were deposited in a Middle to Late Ordovician (469 to 444 Ma) back-arc basin crop out on the north slope of Zhulangnanshan (Fig. 1). The back-arc volcanic

belt extends from east of Laohushan, Jingtai County, Gansu Province, to Baiquanmen – Huoshixia, Sunan County. The width of the belt increases to the west. Ophiolite sequences and submarine volcanic rocks that were erupted from back-arc spreading ridge are well exposed in the Laohushan region to the east, and at Dacha-Daban, in the Huoshixia - Baiquanmen region in the west. The composition of the ophiolites and volcanic rocks, and the presence of locally overturned layers, indicates that they are obducted seafloor slices of a back-arc basin. Different volcanic rocks in the belt have either MORB-like or island-arc-like chemical affinities. The mafic volcanic packages in the upper parts of the ophiolite suites contain copper and zinc deposits. The origin of these deposits is inferred to have been similar to that of Cu-Zn deposits currently forming in modern mid-ocean ridge volcanic settings.

7 Late Ordovician - Silurian passive margin volcanism and mineralization

Closing of the ocean basin in the North Qilian Mountains region was caused by collision of the Ordovician island arc with the Middle Qilian Massif in the Late Ordovician. Following on from this, continental rift volcanism occurred in a Late Ordovician (445 Ma; Xia et al. 1998b) passive margin setting in some parts of Binggou in Qilian County, at Honggou in Menyuan County and also at Huluhe in Jingning, Zhuanlang Counties. Volcanism in these areas is inferred to have been the product of small-scale passive continental rifting caused by lithosphere spreading induced by local relaxation after the arc-continental plate collision. The Honggou Cu deposit in Qinghai Province and Jiaolongzhang Pb-Zn sulfide deposit in Gansu Province appear to be related to this phase of post-collisional volcanism.

After the cessation of volcanism in the Silurian, the Middle Qilian Massif in the south collided with Alashan Massif (north part of China Plate) beneath the North Qilian orogenic belt in the Devonian. This caused huge masses to be overthrust in fan shapes towards the north and south respectively, forming a collisional-type "kepa tectonic" zone (Xu and Cui, 1996, 1997, 1999). The North Qilian region entered a phase of post-orogenic extension after the Late Devonian, resulting in crustal thinning and the development of ductile shear zones.

References

Cross TA, Pilger JRH (1982) Controls of subduction geometry, location of magmatic arcs, and tectonics of arc and back-arc regions. Bull. Geol. Soc. Am. 93: 545-562.

Ge XH, and Liu J (1999) Formation and tectonic background of the Northern Qilian Orogenic belt. Earth Science Frontiers 6: 223-230 (in Chinese with English abstract)

Karig DE (1971) Origin and development of marginal basins in the western pacific. J. Geophys. Res. 76: 2542-2561

Mao JW, Zhang ZH (2000) U-Pb zircon dating of the Yeniutan granitic Intrusion in the western part of the North Qilian Mountains. Geological Review 46: 616-620 (in Chinese with English abstract)

Xia LQ, Xia ZC, Ren YX, (1998a) The Volcanism and Mineralization from Qilian Mountains and Adjacent Regions. China Geological Press Beijing, 5, pp. 215 (in Chinese).

Xia LQ, Xia ZC, Ren YX, Xu XY (2001) The Tectono-Volcanic Magma-Metallogenic Dynamics of North Qilian Mountains. China Land Press, Beijing, pp. 296 (in Chinese).

Xia LQ, Xia ZC, Ren YX, Xu XY (1999a) Paleosubmarine volcanism and mineralization from North Qilian Mountains. Journal of China University of Geosciences 10: 34-37.

Xia LQ, Xia ZC, Xu XY (1998b) Early Palaeozoic Mid-Ocean Ridge, Ocean island and Back-Arc Basin volcanism in the North Qilian Mountains. Acta Geological Sinica 72: 301-312.

Xia LQ, Xia ZC, Xu XY, Yang HQ (1999b) Proterozoic Continental Flood Basalts from Qilian Mountains. Geological Review 45: 1028-1037 (in Chinese with English abstract)

Xia LQ, Xia ZC, Zhao JT, Xu XY, Yang HQ, Zhao DH (1990) Determination of Proterozoic continental flood basalt of western part from North Qilian Mountains. Science in China (series D). 42, pp. 506-514

Xu ZQ, Cui JW (1996) Defromation Tectonic Dynamics of Continental Mountain Chains. China Metallurgical Industry Pess, Beijing, pp. 246 (in Chinese with English abstract).

Xu ZQ, Xu HF, Zhang JX (1994) Caledonian subducted complex accretionary massif and its dynamics in South Zulang Mountains form North Qilian Mountains. Acta Geological Sinica 68: 1-15.

Xu ZQ, Yang JS, Zhang JX (1999) The Comparison of tectonic units along the sides of Altin faults and the shearing mechanism of lithosphere, Acta Geologicai Sinica 73: 193-205 (in Chinese with English abstract).

Xu ZQ, Zhang JX, Xu HF, Wang ZX, Li HB, Yang TN, Qiu XP, Zeng LS, Shen K, Chen W (1997) Ductile Shear Zone and Its Dynamics of Major Continental Mountain Chains in China. China Geological Press, Beijing, pp. 294 (in Chinese with English abstract).

Zhang Q, Wang Y, Qian Q (2000) The North Qilian Oceanic basin of the early Paleozoic age. a discussion with Ge, X., H. Geoscience 35: 121-128 (in Chinese with English abstract)

Zhang ZC, Zhou MF, Robinson PT (2001). SHRIMP dating of the Aaoyougou ophiolite in the west sector of the North Qilian Mountains and its geological significance. Acta Petrologica Sinica 17: 222-226 (in Chinese with English abstract)

The Shaxi porphyry Cu-Au deposit, Anhui Province, eastern China

Xiao-Yong Yang, Yong-Fei Zheng
School of Earth and Space Sciences, University of Science & Technology of China, Hefei 230026, China

Abstract. The middle and lower Yangtze valley is one of the most important metallogenic regions in Eastern China, where more than 200 polymetallic Cu–Fe–Au, Mo, Zn, Pb, Ag deposit occur. The Shaxi porphyry Cu-Au deposit is located in the central Anhui Province, and is related to Jurassic-Cretaceous intrusions. Measured sulfur isotope compositions of sulfides are consistent with a mantle sulfur source, and there is little evidence for sedimentary sulfur input. Hydrogen and oxygen isotopic compositions shows that the ore-forming fluids were of magmatic derivation, whereas post-mineralization fluids had a component of meteoric water.

Keywords. Porphyry, copper, gold, stable isotopes, Yangtze

1 Introduction

The Eastern Yangtze Craton of central to eastern China is an important Fe-Cu metallogenic province (Chang et al. 1991; Zhai et al. 1996), The metallogenic belt is controlled by faults and aulacogens formed during the Early Yanshan epoch (Jurassic). West-northwest- and east-trending faults controlled the distribution of copper mineralization. The belt occurs on the northern margin of the Yangtze platform and in the southeastern part of the Sino-Korean platform (Ren et al. 1980; Chang et al., 1991). The Yangtze River deep fracture zone extends approximately 450 km from southeastern Hubei Province eastwards to Jiangsu Province. It controlled the emplacement of numerous Mesozoic igneous intrusions which are associated with copper, iron, gold and sulfur ores. The region is one of the most important Cu-Fe mining bases in China, including more than 200 polymetallic Cu–Fe–Au, Mo, Zn, Pb and Ag deposits (Chang et al. 1991; Zhai et al 1996; Pan and Dong 1999).

Igneous rocks in the Anhui province can be grouped into two associations according to their relationships to mineralisation: Fe-related and Cu-related groups. In this paper, we focus on the latter. Specifically, we discuss the geochemistry and mineralization of the Shaxi porphyry Cu-Au deposit.

2 Geological setting

Igneous rocks in the middle and low Yangtze valley have been studied throughout the past century. Back in the 1920's, Chinese geologists recognized that granitoids in the lower Yangtze region were markedly different from those in southeastern China. Figure 1 shows the regional geology and tectonic belts of the lower Yangtze region, and the distribution of granitoids related to Cu-Au mineralization. The granitoids include the Shaxi porphyry and Huangtun diorite, both of which are related to porphyry Cu-Au mineralisation. The Anqing diorite, Tongling granite and Chuxian diorite are closely related to skarn Cu-Au deposits.

The Luzong Basin crops out near the Shaxi porphyry deposit. It contains Paleozoic and Mesozoic sedimentary strata, including red sandstone and conglomerate.

3 Mineralogy and metallogenesis

3.1 Ore types

Five types of Cu-Au ores have been recognized at Shaxi. They are characterized by chalcopyrite, Cu-bearing pyrite, magnetite-chalcopyrite, pyrite-bornite-chalcopyrite and chalcopyrite-molybdenite mineral assemblages. All five types are distributed heterogeneously. Metal-bearing minerals include chalcopyrite, pyrite, specular hematite, bornite, magnetite, chalcocite, covellite and arsenopyrite with average grade of 0.2 to 0.4% Cu. Gangue minerals include quartz, K-feldspar, calcite, gypsum, and anhydrite. Average grades of up 3.16 ppm occurr in some parts of the ore blocks (Yang 1996; Yang et al. 2002).

3.2 Alteration zonation and paragenesis

Shaxi has a core of K-feldspar alteration, succeeded by a sericitic alteration domain and an outer propylitic zone. These zones overlap locally, but occur as discrete domains in the quartz-phyric and biotite-quartz-phyric diorite porphyries. The diorites have intruded middle and lower Silurian sandstones and mudstones. Three mineralized stages have been distinguished (Anonymous 1982): (1) Early biotite - K-feldspar - magnetite stage, with associated quartz, oligoclase and sericite, and formation temperature above 400°C based on fluid inclusion analyses of quartz; (2) Sericite – quartz – sulfide stage, with temperatures ranging from 250-300°C. This is the main stage of Cu mineralization at Shaxi. (3) Late stage quartz – carbonate – sulphide, where copper mineralisation is associated with carbonates, chlorite, sericite, kaolinite and albite. Fluid inclusion homogenisation temperatures range from 200 to 150°C.

This page intentionally blank

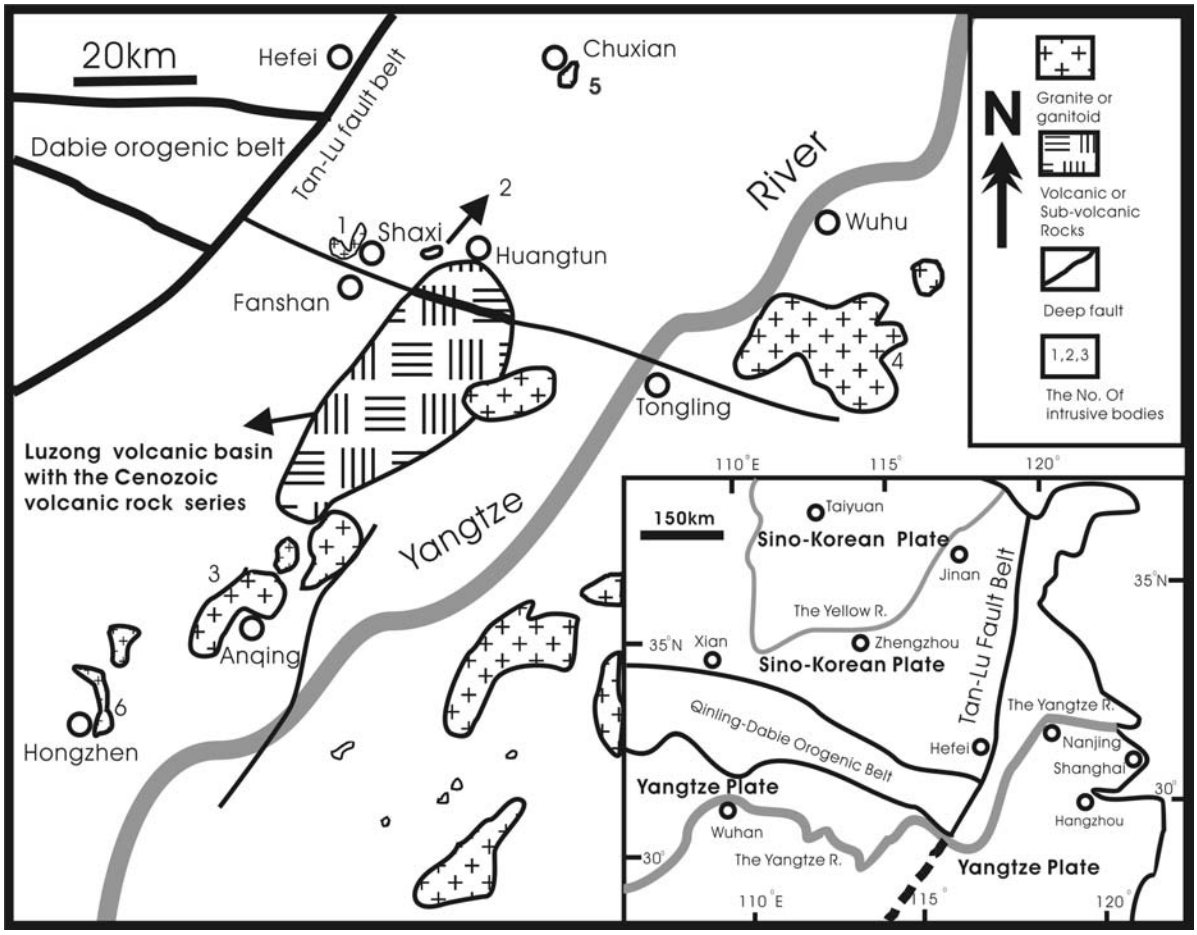

Figure 1: Regional geological and tectonic map, showing the distributions of granitoids related to Cu-Au mineralization along the lower part of Yangtze metallogenic valley in eastern China (after Chang et al. 1991). 1 Shaxi porphyry; 2 Huangtun diorite; 3 Anqing diorite; 4 Tongling granite; 5 Chuxian granite; 6 Huangzhen granite.

4 Igneous petrochemistry

Two periods of magmatic activity occurred in the lower Yangtze region (Chang et al. 1991): (1) quartz diorite intrusions related to copper-gold mineralization; (2) Late stage eruptions and intrusions of basic, intermediate and acid magmas without any associated copper-gold mineralization.

Stage 1 igneous rocks crop out widely in the Lower Yangtze region. They intruded Neoproterozoic low-grade metamorphic rocks and Paleozoic to Triassic sedimentary strata. They vary from basaltic trachyandesite and trachyandesite to syenite in composition. The Shaxi porphyry intrusion has a shoshonitic (ultrapotassic) composition, with Na_2O+K_2O of 8.1 to 12.0 wt %, K_2O contents of 4.1 to 8.5 wt %, and a K_2O/Na_2O ratio from 0.8 to 1.4 (Anhui 1987; Yang 1996; Xing and Xu 1999). These alkalic rocks are closely associated with copper, iron, sulfur and gold ore deposits in the region (Chang et al. 1991).

5 Stable isotope geochemistry

5.1 Sulfur isotopes

Measured sulfur isotopic compositions of sulfides from the Shaxi deposit range from –0.1 ‰ to +3.0‰. The sulfur isotope compositions of chalcopyrite grains are more restricted than those of pyrite. The calculated bulk $\delta^{34}S$ value is about +1.09‰ based on sulfide paragenesis. The very narrow variation of $\delta^{34}S$ values is similar to many other porphyry copper deposits, including Dexing, Yulong and Duobaoshan (Rui et al. 1984). This is consistent with a magmatic sulfur source and reducing (H_2S-predominant) conditions at Shaxi. In contrast, the sulfur isotope compositions of sulfides from the Luzong basin, and from Yueshang and Tongling, where different types of copper deposits occur, shows significant differences in their sulfide sulfur isotopic compositions, which is best explained by different geological processes and fluid interaction.

5.2 Oxygen and hydrogen isotopes

Calculated δD and $\delta^{18}O$ values of ore-forming fluids at Shaxi range from -71.7‰ to –84.0‰ and from +0.4‰ to +4.6‰ during the mineralization stage, respectively. The whole rock $\delta^{18}O$ values range from +8.3‰ to +11.8‰, with a general trend tendency of decreasing ^{18}O with increasing depth. These results show that the fluids during the ore-forming process were of magmatic derivation, with an increasing input of meteoric water with time.

6 Exploration potential

A large geochemical and geophysical anomaly has been detected in Changpushan, adjacent to the Shaxi deposit. Given the character of the Shaxi system, it seems that there is good potential for further discoveries of porphyry Cu-Au mineralization in the lower Yangtze River region (Yang 1996; Yang et al. 2001).

Acknowledgements

Dr. Yang XY has been supported by funding from the Chinese Ministry of Science and Technology (G1999043204) and Korean Foundation for Advanced Studies. Assoc. Prof. Cooke reviewed the manuscript and improved it greatly.

References

Anhui Bureau of Geology and Mineral Resources of Anhui Province (1987) Regional geology of Anhui Province (Geological Memoirs, SW. 1, No. 5). Geological Publishing House, Beijing, pp1-72l (in Chinese with English abstract).

Anonymous (No.327 Geol. Party) (1982) A report of geological survey on Shaxi porphyry copper deposit. Report, Publishing by Anhui Bureau of Geology and Mineral Resources, pp1-163 (in Chinese).

Chang YF, Liu X, Wu YC (1991) The Copper-Iron Belt of the Middle and Lower Reaches of the Changjiang River. Geological Publishing House, Beijing, pp1-379 (in Chinese with English abstract).

Pan YM, Dong P (1999) The Lower Changjiang (Yangzi/Yangtze River) metallogenic belt, east central China: intrusion- and wallrock-hosted Cu–Fe–Au, Mo, Zn, Pb, Ag deposits. Ore Geology Reviews 15:177–242.

Ren QJ, Liu XS, Xu ZW (1991) Luzong volcanic basin of Mesozoic era and the mineralization, Anhui, East China. Geological Publishing House, Beijing, pp1-206 (in Chinese).

Rui ZY, Huang ZK, Qi GM, Xu Y, Zhang HT (1984) Porphyry copper (molybdenum) deposit of China. Geological Publishing House, Beijing, pp201-241 (in Chinese).

Shelton KL, Lofstro M (1988) Stable isotope and fluid inclusion studies of W-Sn-Ag deposits, Silver Mine district, southeastern Missouri, Tectonic control of water-rock interaction in a magma tic hydrothermal system. In Kisvarsanyi G & Grant SK (eds), Proceedings Volume. North America Conf. on Tectonic Control of Ore Deposit and the Vertical and Horizontal Extent of Ore System. Rolla, Missouri University Missouri-Rolla 567, pp 368-377.

Xing FM, Xu X (1999) Yangtze Magmatic Belt and Metallogenesis. Anhui People's Publishing House, Hefei, pp1-170 (in Chinese).

Yang X-Y (1996) The Cu-Au metallogenic prospecting areas from middle-lower reaches of Changjiang River:A study on metallogenic geochemistry of some typical copper and gold ore deposits. Unpubl. Ph.D. Thesis of University Science Technology Of China, Hefei, pp1-214 (in Chinese with English abstract).

Yang Xiao-Yong, Wang Kuiren, Sun Liguang, Yang Xueming, Li Yingxian, Shi Kunfa (2001) A prospecting porphyry Cu-Au deposit in Changpushan area by geochemical and geophysical exploration, central Anhui, east China. Chime der Erder-Geochemistry 61:254-276.

Yang Xiao-Yong, Wang Kuiren, Yang Xue-Ming, Sun Liguang (2002) Characteristics of mineralization and gold occurrence in Shaxi porphyry copper-gold deposit, central Anhui, China. Neues Jahrbuch für Mineralogie 177: 293-320.

Zhai Y, Xiong Y, Yao S, Lin X (1996) Metallogeny of copper and iron deposits in the Eastern Yangtze Craton, east-central China. Ore Geol Rev 11: 229-248.

Evidence for evolution of fluorine-chlorine activity in intrusion-related gold systems, southwestern New Brunswick, Canada

X.M. Yang, D.R. Lentz
Department of Geology, University of New Brunswick, PO Box 4400, Fredericton, New Brunswick, E3B 5A3, Canada

Abstract. Chemical composition of biotite in two groups of Appalachian granitoid intrusions, i.e., Late Silurian to Early Devonian granodioritic to monzogranitic series (GMS), and Late Devonian granitic series (GS), southwestern New Brunswick, was used to constrain volatile exsolution and fluorine-chlorine activity of fluids associated with these gold-related intrusions. Oxidized to reduced I-type GMS rocks appear to have higher magmatic temperatures, variable levels of emplacement, a range of $f(O_2)$, and relatively low f_{HF}/f_{HCl} ratios in exsolved fluids, compared to fractionated I-type GS rocks. Reduced GMS intrusions bear higher gold potential, thus may be prospective targets for intrusion-related gold systems in the region.

Keywords. Biotite, granitoid, intrusion-related gold systems, halogen

1 Introduction

Biotite chemistry has been widely used to deduce the origin of granitoids, magmatic to hydrothermal processes and related $f(O_2)$ and f_{HF}/f_{HCl} ratios, relationships to metal mineralization, and even tectonic setting (cf. Ague and Brimhall 1988; Lentz 1994). The principle is to use internally consistent thermodynamic data of biotite that contains hydroxyl and halogens, to predict the fluoride and chloride activity of fluids from the measured F and Cl contents in the mineral.

Recent studies have shown a high potential for formation of intrusion-related gold systems in southwestern New Brunswick, a segment of the Canadian Appalachians (Yang et al. 2003, 2004a,b), which is well known for W-Sn-Mo-Sb mineral resources associated with granitoids. Many gold deposits and occurrences (e.g. Clarence Stream, Lake George, Poplar Mountain, McDougall Brook, Jimmy Hill, Kedron, Tower Hill) (Fig. 1) in the region share similarities with intrusion-related gold systems elsewhere (Thompson et al. 1999; Lang and Baker 2001). An essential question about intrusion-related gold systems is: did these intrusions supply mineralizing components and how were they transported? This contribution uses chemical composition of biotite together with petrology to constrain the relative fluorine-chlorine activity in fluids associated with these gold-related granitoid intrusions and to provide clues as to the genesis of intrusion-related gold systems.

2 General geology

In southwestern New Brunswick, two major granitoid batholiths and associated satellite plutons are intruded into the Gander and Avalon zones of the Canadian Appalachian Orogen (Fig. 1), namely, the Pokiok Batholith (415 to 402 Ma) and the Saint George Batholith (423 to 360 Ma; Whalen 1993; Yang et al. 2004b). On the basis of field relations, ages, petrologic and petrochemical features, two groups of granitoid intrusions associated with gold mineralization are recognized: 1) Late Devonian granitic series (GS), and 2) Late Silurian to Early Devonian granodioritic to monzogranitic series (GMS) rocks (Yang et al. 2004b). The GS intrusions collectively show high-level, highly evolved characteristics typical of fractionated I-type, whereas GMS intrusions are less evolved in composition and show more variable emplacement levels and are oxidized to reduced I-type. Hornblende is present, and plagioclase (An > 10) is more abundant relative to K-feldspar in GMS rocks, which are associated with quartz, biotite, apatite, titanite, zircon, monazite, ± pyroxene, ± magnetite, ± ilmenite, and ± sulfide. GS rocks are composed of quartz, K-feldspar, plagioclase (An < 10), micas, zircon, monazite, apatite, sulfide ± ilmenite, magnetite, topaz, columbite, and xenotime.

3 Biotite chemistry

The color of biotite is variable in GMS intrusions from fox-red to brown (e.g., the reduced I-type Lake George Granodiorite) through dark brown to greenish (e.g. the oxidized I-type Magaguadavic Granite Suite, Bocabec Granitoid Suite), reflecting differences in their redox conditions. Biotite is light brown to fox-red in GS rocks, indicative of their relatively reduced nature. Biotite in the granitoids is trioctahedral and within the series annite, siderophyllite, phlogopite, and eastonite.

Biotite in GS rocks is Fe-rich biotite (e.g., the Mount Douglas, True Hill, Beech Hill, Sorrel Ridge, and Mount Pleasant granites). Although intra-intrusion variations are present, the Mg/(Mg + Fe) ratio (atomic) of biotite, decreases from the Mount Douglas (0.44 ± 0.02 - 0.09 ± 0.01) through Beech Hill (0.43 ± 0.06), to Sorrel Ridge (0.26 ± 0.01 - 0.18 ± 0.01) → Mount Pleasant (0.01 ± 0.02). In addition, biotite is char-

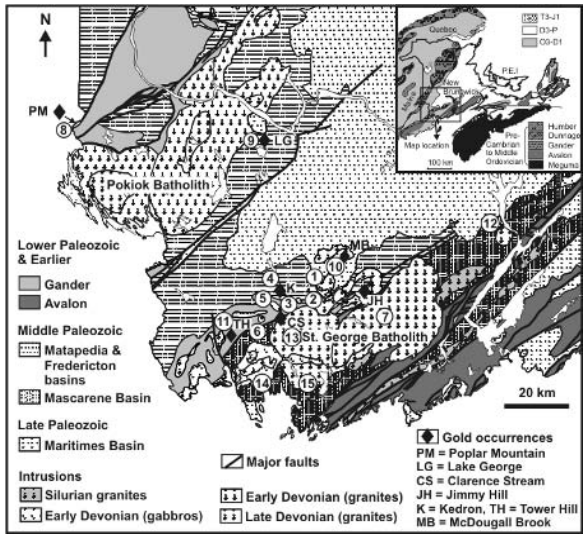

Figure 1: Geological map of southwestern New Brunswick (modified from Yang et al. 2004b), showing the location of two groups of granitoid intrusions, i.e., Late Devonian Granitic series (GS): 1 - Mount Pleasant Granite Suite, 2 - True Hill Granite, 3 - Beech Hill Granite, 4 - Kedron Granite, 5 - Pleasant Ridge Granite, 6 - Sorrel Ridge Granite on the northwest margin of Sainte George Batholith (SGB), and 7 – Mount Douglas Granites, the eastern part of the SGB. Late Silurian to Early Devonian Granodioritic to Monzogranitic series (GMS): 8 - Poplar Mountain Volcanic Suite, 9 - Lake George Granodiorite, 10 - McDougall Brook Granitoid Suite, 11 - Tower Hill Granite, 12 - Evandale Granodiorite, 13 - Magaguadavic Granitoid Suite, 14 - Bocabec Granitoid Suite, 15 - Utopia Granite; 13-15 constitute the western part of the SGB. Also shown are the location of gold deposits and/or occurrences: PM - Poplar Mountain, LG - Lake George, CS - Clarence Stream, MB - McDougall Brook, K - Kedron, JH - Jimmy Hill, TH - Tower Hill.

acterized with appreciable F contents, up to 2.18 ± 0.13 wt% (e.g., Mount Douglas). Total ΣAl of biotite is < 3.0 apfu (atoms per formula unit), except for the biotite in the Mount Pleasant Granite Suite, which is close to end member siderophyllite. Fluorine contents also decrease from the Mount Douglas to Sorrel Ridge Granite (0.39 ± 0.15 wt%), but F is high in biotite (4.39 ± 0.75 wt%) in the Mount Pleasant Granite owing to extreme fractionation (Yang et al. 2003).

Biotite in GMS rocks has generally high Mg/(Mg + Fe) ratios, with inter- and intra-intrusion variations evident. Total ΣAl of the biotite is < 3.0 apfu, except for those in the Tower Hill Granite that show relatively low Mg/(Mg + Fe) ratios. The F contents of biotite are variable in different intrusions. Biotite in the Utopia Granite contains the highest F contents of 2.90 ± 0.49 wt%. It is noted that Mg/(Fe + Mg) ratios increase with increasing ΣAl (e.g. the Magaguadavic Granite Suite, Bocabec Granitoid Suite).

4 T - P - f(O_2) conditions

Magmatic equilibrium among rock-forming minerals in granitoids is disturbed by subsolidus hydrothermal fluids, based upon estimates from hornblende-plagioclase geothermometry and ternary feldspar thermometry, although GMS intrusions formed at higher temperatures than GS rocks in terms of zircon-, apatite-, and (or) monazite-saturation models (Yang et al. 2004b).

Al-in-amphibole geobarometry is used to estimate the pressures of igneous hornblende crystallization with the assemblage of quartz, plagioclase, orthoclase, biotite, amphibole, titanite, and ilmenite and/or magnetite in GMS intrusions. Varying pressures are evident for different intrusions, i.e., the Evandale Granodiorite (~ 0.6 kb), the Magaguadavic Granite Suite (~ 1.1 - 1.5 kb), and the Bocabec Granitoid Suite (~ 2.8 kb), suggesting that hornblende began to crystallize in these intrusions at lower pressures than the Lake George Granodiorite stock (~ 3.4 - 4.6 kb). In terms of textural characteristics, thickness of reconstructed strata, and the system Q-Ab-Or-H_2O phase diagram, the final emplacement pressures for these intrusions are approximately ~ 1.5 kb for the Evandale Granodiorite, ~ 2.0 - 3.0 kb for Magaguadavic Granite Suite, and ~ 1 kb for Bocabec Granitoid Suite, and < 2 kb for Lake George Granodiorite stock.

Amphibole minerals are absent in GS rocks. The emplacement pressures have been estimated qualitatively in terms of rock textures, strata reconstruction, and the system Q-Ab-Or-H_2O phase diagram, which yielded pressures around 1 kb.

The $f(O_2)$ conditions for the granitoids were assessed from the Mg/(Fe + Mg) ratios of biotite associated with K-feldspar and magnetite in terms of the calibration of Wones and Eugster (cf. Lentz 1994). For reduced I-type granitoids that do not contain primary magnetite, such as the Lake George Granodiorite, the calibration of Ague and Brimhall (1988) was used to estimate $f(O_2)$. The results indicate that GS rocks and reduced GMS have lower values of $f(O_2)$ than those of normal I-type (oxidized) GMS rocks. For example, the values of $f(O_2)$ for the Lake George Granodiorite are between $10^{-16.5}$ and $10^{-13.7}$ bars, and for the Tower Hill Granite between $10^{-16.7}$ and $10^{-13.4}$ bars, comparable with strongly contaminated reduced I-type granites (Ague and Brimhall 1988). The $f(O_2)$ values of GS rocks (i.e. Sorrel Ridge, Beech Hill, Mount Pleasant, and Mount Douglas) are between $10^{-17.7}$ to $10^{-15.8}$ bars. However, oxidized I-type GMS rocks (i.e., the Magaguadavic Granite Suite, Bocabec Granitoid Suite) display high $f(O_2)$ values ranging from $10^{-14.0}$ to $10^{-10.5}$ bars, similar to weakly to moderately contaminated I-type granitoids elsewhere (Ague and Brimhall 1988).

The GMS rocks from southwestern New Brunswick have comparable geochemical characteristics and thus have similar sources (Yang et al. 2004b), the difference in $f(O_2)$ for reduced and normal (oxidized) I-type granitoids observed in this study requires further discussion. The reduced I-type Lake George Granodiorite stock intruded Kingsclear Group metasedimentary sequence containing

reduced organic-carbon, which may result in assimilation-hybridization plus interaction with circulating of hydrothermal systems (bearing CO_2-CH_4) driven by the intrusion (Yang et al. 2004a). In the Bocabec Granitoid Suite, a granitoid that intruded a gabbro body with appreciable magnetite, retains its high redox condition. This oxidized state is reflected in the assemblage of magnetite + titanite + quartz in the granitoid. Therefore, local redox buffers in the country rocks may play an important role in affecting the granitoid intrusion oxidation state and indirectly control the genesis of intrusion-related gold systems.

GS rocks exhibiting lower redox than GMS rocks, may reflect their different petrogenesis as is also shown in their distinction in geochemistry (Yang et al. 2004b). Yang et al. (2004b) suggested that GS granites might have been derived from partial melting of quartzofeldspathic rocks (igneous) at relatively shallow crustal level, and then the magmas may have experienced extensive low-T fractionation. Thus, source control on redox may be important for GS rocks.

5 Estimated f_{HF}/f_{HCl} conditions

Although the hydroxyl site of biotite is susceptible to Cl-OH exchange during its interaction with hydrothermal fluids, the systematics of F, Cl, and OH are useful for qualitatively inferring the relative HF, HCl, and H_2O fugacity in the volatiles associated with felsic melts (Munoz 1992; Lentz 1994). On the diagram of the mole fraction X_{Mg} in the octahedral site versus $\log(X_F/X_{Cl})$ of biotite (Fig. 2) where X_F and X_{Cl} are respectively the mole fraction of F and Cl in the hydroxyl site, biotite has a significant range of $\log(X_F/X_{Cl})$ ratios for particular intrusions, suggesting that biotite may have interacted with subsolidus hydrothermal fluids. For example, the large range of calculated halogen fugacity ratios [$\log(f_{HF}/f_{HCl})$ = -3 to -1, at 400°C] for magmatic fluids in equilibrium with biotite in the Lake George Granodiorite, suggests that the halogens in biotite might have been reequilibrated with various Cl-rich magmatic fluids. These fluids probably emanated from the crystallizing granodiorite magma at depth and differentially partitioned the volatiles and solutes from that magma during progressive crystallization. The data illustrated in Figure 2 also indicate that either the biotite compositions represent a crystallization sequence, an unreasonable conclusion for the Lake George Granodiorite, or that the biotite has been reequilibrated with orthomagmatic to exogenetic fluids of variable composition (i.e. those with different f_{HF}/f_{HCl} ratios). If magmatic, these fluids could have changed with time as the magma cooled and solidified at depth, such that the f_{HF}/f_{HCl} ratios of the fluids would progressively increase (Fig. 2).

Biotite in the Tower Hill Granite have lower values of X_{Mg} (0.15 - 0.20) than those in the Lake George Granodiorite (Fig. 2), but seemed to have equilibrated with a fluid with relatively higher $\log(f_{HF}/f_{HCl})$ ratios (-1.5 ~ -0.1, at 400°C). The Magaguadavic Granite Suite contains two groups of biotite, i.e., high X_{Mg} and low X_{Mg} ones, although the calculated $\log(f_{HF}/f_{HCl})$ ratios in fluids associated with these biotite are mostly confined between -1 and –2 (Fig. 2). Notably, in the Bocabec Granitoid Suite biotite with high X_{Mg} values require a fluid with low $\log(f_{HF}/f_{HCl})$ ratios (-3 to -2), whereas those with low X_{Mg} values require a fluids having higher $\log(f_{HF}/f_{HCl})$ ratios (-1.5 ~ -1.0).

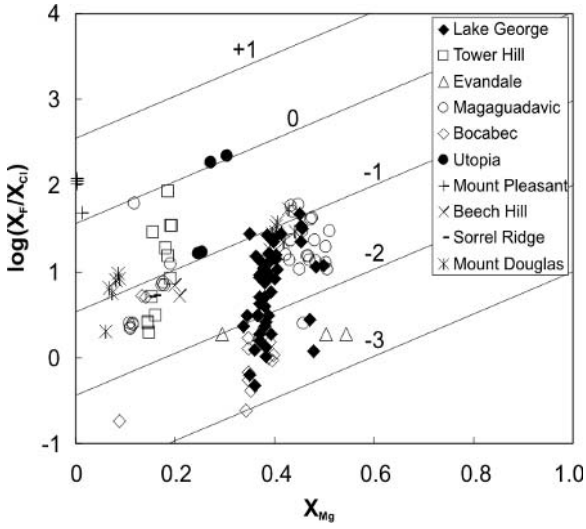

Figure 2: X_{Mg} versus $\log(X_F/X_{Cl})$ of biotite from the granitoids of southwestern New Brunswick. X_F and X_{Cl} are the mole fractions of F and Cl in the hydroxyl site, respectively. Contours are the logarithm of the fluorine-chlorine fugacity ratios (f_{HF}/f_{Cl}) for a fluid in equilibrium with biotite (Munoz 1992), calculated at 400°C.

Biotite in GS rocks commonly has low X_{Mg} values, and the fluids associated with these biotite normally display relatively high $\log(f_{HF}/f_{HCl})$ ratios (-1.5 ~ +0.5) (Fig. 2). It is noted that the Mount Douglas Granite has biotite with high X_{Mg} values (0.40 ~ 0.42), but the calculated $\log(f_{HF}/f_{HCl})$ ratios (~ -1.5 ~ -0.7) in related fluid are similar to those with low X_{Mg} values (~ 0.06 – 0.10) (Fig. 2). This indicates the fluids associated with the Mount Douglas Granite intrusion remain relatively constant f_{HF}/f_{HCl} ratios through fractionation.

6 Conclusions

Magmatic equilibrium among the rock-forming minerals in both GS and GMS rocks may have been disturbed by subsolidus hydrothermal fluids. These fluids display variable f_{HF}/f_{HCl} ratios and may result from sequential emanations from progressively cooling magmas at depth. The fluids associated with GS intrusions commonly have higher f_{HF}/f_{HCl} ratios than GMS granitoid intrusions. Within a granitoid suite, f_{HF}/f_{HCl} ratios usually increase with fractionation. Magmatic fluids associated with GMS

intrusions have relatively lower f_{HF}/f_{HCl}, which imply that gold may be transformed as chloride complex in Cl-rich fluids at high T.

Evolved I-type GS granites are characterized by reduced features, thus exhibiting lower $f(O_2)$ than GMS granitoids. GMS granitoid intrusions display two groups regarding $f(O_2)$ (i.e. reduced and oxidized), which is interpreted that these intrusions are intruded into distinctive country rocks that occur as redox buffers. Local redox conditions play a key part in the genesis of intrusion-related gold systems. Fox-red biotite is a petrographic indicator for reduced I-type GMS granitoids, which is significant to exploration for intrusion-related gold systems.

References

Ague JJ, GH Brimhall (1988) Regional variations in bulk chemistry, mineralogy and the compositions of mafic and accessory minerals in the batholiths of California. Geological Society of America Bulletin 100: 891-911

Lang JR, Baker T (2001) Intrusion-related gold systems: the present level of understanding. Mineralium Deposita 36: 477-489

Lentz DR (1994) Exchange reactions in hydrothermally altered rocks: examples from biotite-bearing assemblages. In:Lentz DR (ed.) Alteration and alteration processes associated with ore-forming systems. Geological Association of Canada Short Course Notes 11: 69-99

Munoz JL (1992) Calculation of HF and HCl fugacities from biotite compositions: revised equations. Geological Society of American, Abstracts with Programs 24:221

Thompson JFH, RH Sillitoe, T Baker, GJR Lang, JK Mortensen (1999). Intrusion-related gold deposits associated with tungsten tin provinces. Mineralium Deposita 34: 323-334

Whalen JB (1993). Geology, petrography, and geochemistry of Appalachian granites in New Brunswick and Gaspésie, Quebec. Geological Survey of Canada Bulletin 436:124

Yang XM, DR Lentz, G Chi, KG Thorne (2004b) Petrochemical characteristics of gold-related granitoids in southwestern New Brunswick, Canada. Exploration and Mining Geology(in press)

Yang XM, DR Lentz, G. Chi, TK Kyser (2004a) Fluid-mineral reaction in the Lake George granodiorite, New Brunswick: implications for Au-W-Mo-Sb mineralization. Canadian Mineralogist 42: 1443-1464

Yang XM, DR Lentz, SR McCutcheon (2003) Petrochemical evolution of subvolcanic granitoid intrusions within the Late Devonian Mount Pleasant Caldera, southwestern New Brunswick, Canada: comparison of Au versus Sn-W-Mo-polymetallic mineralization systems. Atlantic Geology 39: 97-121

Geochemistry of the Kalatongke layered intrusion, Xinjiang NW China: Implications for the genesis of a magmatic Cu-Ni sulfide deposit

Zhaochong Zhang, Jingwen Mao, Zhou Gang, Fengmei Chai
State Key Laboratory of Geo-Processes and Mineral Resources, China University of Geosciences, Beijing, 100083, China

Shenghao Yan, Bailin Chen
Chinese Academy of Geological Sciences, Beijing, 100037, China

Abstract. The Kalatongke mafic-ultramafic intrusions that hosts large Cu-Ni sulfide deposit is located in the Junggar Variscan orogenic belt. Four intrusive types are recognized, which from top to bottom of the intrusive complex, include biotite diorite, biotite-hornblende norite, biotite-hornblende-olivine norite and biotite hornblende-gabbro-dolerite. The low $(^{87}Sr/^{86}Sr)_t$ ratios of the intrusions (0.70375 to 0.70504), and high $(\varepsilon_{Nd})t$ from (+6.3 to +8.2), the strong enrichment of lithophile elements, and the low Nb and Ta abundance and the high $\delta^{18}O$ values of separated clinopyroxene (mostly>6‰) suggest that the primary magmas were derivedfrom MORB-type mantle source involved in previously subducted oceanic crust, which released aqueous liquid that promoted partial melting. The intrusions were generated by fractional crystallization in situ accompanying assimilation of upper crust at the upper part of the intrusions within high-level magma chamber. The distinct boundaries between massive ores and disseminated ores suggest that the massive ores were formed by immiscible sulfide liquid formed within deep-seated crust chamber following physicochemical change, which was transported upwards to their present locations. In contrast, the gradual change relationship between disseminated ores and barren wallrocks were formed by crystal fractionation of the settling of sulfides in situ within high-level magma chamber.

Keywords. Magmatic Cu-Ni sulfide deposit, layered intrusion, MORB-like mantle, genesis of ores

1 Introduction

Although it is generally accepted that the Cu, Ni, platinum-group elements (PGE) of Cu-Ni sulfide deposit were derived from the magmas, the processes of sulfide segregation and concentration have been received quite debate. In China, the Cu-Ni sulfide deposits are characterized by the small mineralized mafic-ultramafic intrusions hosting large proportions of sulfides relative to the volume of silicates. For example, over 40% in volume of the Jinchuan intrusion in Gansu province (the second-largest Cu-Ni sulfide deposits in the world) and over 50% in volume of the Honqiling intrusion in Jilin province are sulfides (Tang and Ren, 1988). They have been explained as forming by multiple injections of compositionally different magmas, whereas the massive sulfide bodies are considered to be the last injection of sulfide melts (Tang 1993; Barnes 1998).

The Kalatongke copper-nickel sulfide deposit, located in Xinjiang, SW China, is one of the largest one in China. The Cu-Ni ore-bearing Kalatongke intrusion is a typical example of a small layered intrusion. However, unlike other deposits occurring in cratonic setting, it is located in the Variscan orogenic belt. Thus, the interests on the processes that led to the accumulation of the ore sulfides have been received much attention.

In this paper, we first present new analytical data on trace elements and Sr-Nd and O isotopic data, and use these data to discuss the source and evolution of magmas that yielded the ore sulfides and the processes that led to formation of the ore deposits.

2 Geology of intrusions

Nine layered intrusive bodies are recognized in the Kalatongke area, and three in the southern part of the area (named Y1, Y2 and Y3 respectively) contain economic sulfide mineralization whereas six in the northern part (named Y4-Y9 respectively) are weakly differentiated and lack economic mineralization. All intrusions intrude the middle and upper portions of the Lower Carboniferous strata, which consists predominantly of clastic metasedimentary rocks and metatuff. The contact metamorphic zone surrounding the intrusion is generally less than 20 meters in width. Radiometric Rb-Sr and Sm-Nd isochron ages and SHRIM U-Pb zircon age of the Y1, Y2 and Y3 yield a wide spread of 285 to 297 Ma (Wang & Zhao, 1991; Li et al., 1998).

Y1, Y2 and Y3 have the similar features. Y1 at the surface displays irregular lens that is 695-m-long and 39- to 289-m-wide with an area of about 0.1km^2. In the cross-section, it appears inclined funnel-shaped and becomes more vein-like at depth. Four lithologic zones can be recognized in Y1. From top to bottom, they range from biotite-rich diorite (5vol.%), biotite-hornblende norite (38 vol.%), biotite-hornblende-olivine norite (29.6 vol.%) and biotite-hornblende gabbro-dolerite (27.4 vol.%). Biotite-hornblende gabbro-dolerite is a marginal intrusive phase. The boundaries between the igneous phases are obscure,

and change gradually. The mafic components in the intrusion are getting high downward, and usually containing olivine, whereas its upper part is more felsic and usually contains quartz. In general, the most mafic rocks contain economic Cu-Ni ores whereas relatively felsic rocks are weakly mineralized. Y2 and Y3 are buried intrusive bodies. Compared with Y1, they contain less volume of biotite- hornblende-olivine norite and massive ores.

Biotite-hornblende diorite is fine- to medium-grained, with 2-5 mm in diameter. It consists chiefly of andesine-oligoclase (60-70 vol%), hornblende (10-15 vol%) with secondary biotite(2-10 vol%), quartz as well as accessory apatite, magnetite, zircon and sphene. Biotite-hornblende gabbro-dolerite, is fine- to medium-grained (0.2-1 mm in diameter). It usually has poikilotopic fabric and diabase-like textures, with minor sideronitic texture. Labradorite (30-50 vol%) and bronzite (10-30%) are dominant, with minor augite, olivine (5-25%), biotite (3-7 vol%) and hornblende (5-10% vol), and with accessory minerals of apatite, magnetite and ilmenite. Biotite-hornblende norite is medium-fine to medium-coarse grained. Poikilotopic texture is dominant, with gabbroic and reaction rim textures. It consists of labradorite (30-50 vol%), bronzite (20-30 vol%), with brown hornblende (3-15 vol%), biotite (2-10 vol%), quartz (less than 5 vol%) and augite (less than 5 vol%), and accessory apatite, magnetite and sphene. Biotite-hornblende-olivine norite is dominantly medium-coarse grained. It consists of labradorite (15-40 vol%), bronzite (10-30 vol%) and olivine (10-40 vol%), with minor brown hornblende (5-20 vol%), biotite (5-15 vol%) and augite (less than 3 vol%), and accessory apatite, magnetite and ilmenite.

3 Ore geology and geochemistry

The detail exploration shows that about 60 percent of Y1 in volume is mineralized. Economic ores are hosted in biotite-hornblende norite and biotite-hornblende-olivine norite at depths of 550-1 000 m below the surface. The orientation of the orebodies is almost consistent with that of the intrusion. The orebodies are both irregularly- and lens-shaped in the vertical section and nest- or pocket-like in shape in the horizontal section. The mineralization has a clear circular zoning pattern, from high-grade massive ore in the center, outward to disseminated ores that gradually grade into subeconomic grades where sulfides are more widely disseminated. Accordingly, the copper and nickel contents decrease outward from the massive ores. The boundary between disseminated ores and massive ores is distinct, whereas the disseminated ores and barren country rocks change gradually, and often only defined by grade analysis. In the disseminated ores, the Cu and Ni grades increase downward.

The $\delta^{34}S$ values of 96 sulfide samples from Y1 vary from -3.5 – +3.0‰ averaging 0.17‰, and a normal distribution surrounding a value of approximately 0‰, which suggests that the sulfur was dominantly derived from the mantle. The δD values of inclusions in calcite and pyrrhotite range from –57.5 to –42 per mil, which falls the range of magmatic water. This suggests that the mineralization fluids were derived from magma rather than a mixture of the two sources.

4 Geochemistry of the intrusions

Samples collected from drill cores of Y1 and Y2 were utilized for analyses of major elements, trace elements and Sr, Nd isotopes. Separated clinopyroxene minerals were analyzed for oxygen isotopes. The analyzed results show that the contents of Y1 and Y2 range from 41 to 55% for SiO_2, 8 to 17.5% for Al_2O_3. Their TiO_2 contents are quite low, generally less than 1%. Their Mg# values (Mg#=Mg/(Mg+Fe)) vary from 0.51 to 0.74. When plotted on a diagram of A-F-M, most of them lie in the tholeiitic field, and only a few are plotted in the calc-alkaline field.

Both Y1 and Y2 display similar chondrite-normalized rare earth element (REE) patterns. They are in the range of 23 to 58 times chondrite for La, and display that the light REE are strongly fractionated from the heavy REE, which have contents 4 to 8 times chondrite in the case of Yb and Lu, with $(La/Yb)_N$ ratios of 4.6 to 13. The strong incompatible element enrichment, especially large ion lithophile element (LILE) is also visible in the MORB-normalized plots. All rocks display a closely similar pattern. They show remarkably negative anomalies for Nb, Ta, Zr and Ti. In addition, Ti, Y and Yb are depleted compared with MORB.

The initial $^{87}Sr/^{86}Sr$ ratios range from 0.70375 to 0.70504, and $(^{143}Nd/^{144})t$ varies from 0.51259 to 0.51268 with $(\varepsilon Nd)_t$ of +6.3 to +8.2, implying that they originated from depleted MORB-type mantle. $\delta^{18}O$ values determined by laser fluorination (LF) on separated clinopyroxene minerals range from 5.4 to 10.6 per mil. Excluding sample Z2-2, the overall range in $\delta^{18}O$ values of 5.4-6.8 is quite restricted. These values are significantly higher than those observed in typical MORB (5.7 per mil ±0.3 for fresh glasses; Ito et al., 1987), oceanic island basalts (<5.8 per mil for fresh whole-rock; Kyser et al. 1982) and in mantle clinopyroxene analysed by LF (5.57 ±0.32 per mil, Mattey et al. 1994).

5 Source of parental magmas and magma evolution

Both Y1 and Y2 are characterized by low initial $^{87}Sr/^{86}Sr$ ratios and high $(\varepsilon Nd)_t$ values (6.3-8.2), suggesting that they were derived from the depleted MORB-type mantle source. This is also supported by some incompatible ele-

ment ratios, such as Zr/Nb (~15) and Sm/Nd (0.22). MORB-normalized patterns exhibit the enrichments of LILE relative to LREE and Th, in particular to HFSE. Thus, it can be easily explained by a mantle comprising MORB-source +LILE-rich fluid since the LILE are fluid-soluble relative to HFSE and HREE (Keppler 1996). This is consistent with the fact that the intrusions contain a lot of hydrous minerals, such as hornblende and biotite. On the other hand, the MORB-normalized patterns display remarkably negative Nb and Ta anomalies, which suggest that the sources contain crustal materials or that the magmas were generated in the mantle sources with residual rutile and ilmenite because these two minerals/fluid partition coefficients are high for Nb and Ta (Ayers et al. 1997). Thus, the magmas would be depleted in Nb and Zr if these two minerals are residual phases. However, the negative Zr anomalies on the MORB-normalized patterns are not obvious. Therefore, it is unlikely that rutile and ilmenite are residual phases during melting. Zr/Sm ratios are essentially constant, ranging from 20.5 to 39.0, close to those of MORB (27-32). Crustal contamination can't lead to reduce Zr/Sm ratios as the crust has the Zr/Sm ratios of ~32. Thus, Negative Nb anomalies can be attributed to source mixing, i.e., MORB-type mantle mixing with crust. This is supported by relatively homogeneous elevated $\delta^{18}O$ values. Considered the subduction event during Devonian era, the contaminants might be subducted oceanic crust. Ti/V ratios range from 22 to 61. Since Ti is less compatible than V for mantle, it was inferred that the Kalatongke intrusions with higher than Ti/V ratios than those MORB (~25.4 in average, Pearce & Parkinson, 1993) were generated by lower partial melting of MORB-like mantle.

One sample (Z2-4) have the highest $\delta^{18}O$ value of 10.6‰, which suggests that it was contaminated by upper crust, probably sediments. In summary, the primary magmas for the Kalatongke intrusions are generated by partial melting of MORB-type mantle source containing previously subducted oceanic crust, which released fluid. The primary mantle-derived melts have ascended into the crust where crystal fractionation was accompanied by upper crustal contamination (AFC).

6 Implications for ore genesis

As previously mentioned, the disseminated ores and barren wallrocks change gradually, and the different rock types also change gradually. Furthermore, the sulfide minerals increase downward. This strongly supports the conclusion that the Y1, Y2 and Y3 were produced by crystal fractionation in situ, and the disseminated ores were formed by in situ settling of sulfide from the magmas. In contrast, a distinct boundary between massive ores and disseminated ores indicates that the massive ores were formed slightly later than the consolidation of the intrusion with its contained disseminated ores. Thus it can be inferred that the massive ores were formed by injection of a pulse of sulfide liquid, which was formed by immiscibility within the deep magma chamber. The immiscible sulfide liquid ascended through the same channel and superimposed on the disseminated ores.

The main criterion for the formation of an immiscible sulfide liquid is that the host magma should be over-saturated in sulfur and in addition contain a reasonably high proportion of immiscible sulfide droplets which can then settle rapidly to form a continuous, thick sulfide blanket (Naldrett et al., 1995). The production of a high proportion of immiscible sulfides at a given stage in the history of a magma body can be brought about in a number of ways: 1) physicochemical change (e.g., temperature, pressure, oxygen fugacity and sulfur fugacity) within magma column or magma chamber (e.g. Brugmann et al. 1993; Rad'ko 1991); 2) the addition of crustal S (e.g., Naldrett et al. 1995; Lightfoot and Hawakesworth 1997); 3) mixing of mafic magma that was nearly saturated in sulfide with felsic magma (Irvine 1975). As stated previously, the trace element and oxygen isotopic characteristics of the Kalatongke intrusions indicate that the primary magma was generated by partial melting of depleted MORB-type mantle involved oceanic crust, and not contaminated by crust within the deep magma chamber. Moreover, S isotopic data ($\delta^{34}S$) are within a narrow range close to 0 per mil, suggesting that they are predominantly derived from the mantle, rather than addition of crustal S. It can therefore be concluded that the immiscible sulfide magma was not triggered by crustal contamination or addition of crustal S, but by physicochemical change, such as decreasing temperature and increasing oxygen fugacity because there has been an evidence that temperature of immiscibility (850°C) is much lower than the temperature of primary magma generation (1300°C; Wang and Zhao 1991).

Acknowledgement

We thank the management of the Kalatongke Cu-Ni Mine for logistical support for field work at the Kalatongke deposit. Financial support was provided by 305 Project from Ministry of Sciences and Technology (No. 2001BA609A - 07-02) and 973 Project (No. G1999043205).

References

Ayser JC, Dittmer SK, Layne GD (1997) Partitioning of elements between peridotite and H_2O at 2.0-3.0 GPa and 900-1100°, and application to models of subduction zone processes. Earth Planet. Sci. Lett., 150: 381-398

Brugmann GE, Naldrett AJ, Asif M (1993) Siderophile and chalcophile metals as tracers of the evolution of the Siberian Traps in the Noril'sk Region, Russion. Geochim. Cosmochim. Acta, 57: 2001-2018

Irvine TN (1975 Crystallisation sequence of the Muskox Intrusion and other layered intrusions: II Origin of the chromitite layers and similar deposits of other magmatic ores. Geochim. Cosmochim. Acta, 39: 991-1020

Keppler H (1996) Constraint from partition experiments on the composition of subduction-zone fluid. Nature, 380, 237-240

Kyser TK, O'Neil JR, Carmichael ISE (1982) Genetic relations among basic lavas and ultramafic nodules: evidence from oxygen isotope compositions. Contrib. Mineral. Petrol., 81: 88-102

Li H, Xie C, Chang H (1998) Study on Metallogenetic Chronology on Nonferrous and Precious Metallic Ore Deposits in North Xinjiang, China. Geological Publishing House, Beijing, 264pp (in Chinese)

Lightfood PC, Hawkesworth J (1997) Flood basalts and magmatic Ni, Cu, and PGE sulphide mineralization: comparative geochemistry of the Noril'sk (Siberian Traps) and West Greenland sequences. In J. J. Mahoney (ed.): Large Igneous Provinces: Continental, Oceanic, and Planetary Flood Volcanism. Geophysical Monography 100, American Geophysical Union, 357-380

Mattey, D., Lowry, D., Macpherson, C., 1994. Oxygen isotope composition of mantle periotite. Earth Planet. Sci. Lett., 128, 231-241

Naldrett AJ, Fedorenko VA, Lightfoot PC, Kunilov VI, Gorbachev NS, Doherty W, Johan Z (1995) Ni-Cu-PGE deposits of Noril'sk region, Siberian; their formation in conduits for flood basalt volcanism. Institution of Mining and Metallurgy, Transaction, Section B: Aplied Earth Science, 104, 18-36

Rad'ko, V. V., 1991. Model of dynamic differentiation of intrusive traps in the northwestern Siberian platform, Soviet Geol. and Geophys., 32(7): 70-77

Tang Z, Ren, D (1988) Types and metallogenic model of nickel sulfide deposits of China. Acta Geologica Sinica, 1: 193-206

Tang, Z. & Barnes, S. J., 1998. Mineralization mechanism of magmatic sulfide deposits. Geological Publishing House, Beijing

A preliminary investigation of autometasomatic phenomena in the host rocks to the Bayan Obo Fe-Nb-REE deposit, Inner Mongolia, China

Yuan Zhongxin, Bai Ge
Institute of Mineral Resources, CAGS, 26 Baiwanzhuan Rd., Beijing 100037, China

Zhang Zongqing
Institute of Geology, CAGS, 26 Baiwanzhuan Rd., Beijing 100037, China

Abstract. Host rocks to the Fe-Nb-REE orebodies at Bayan Obo, Inner Mongolia, China, include dolomitic marble and K-rich slate. Microphotographic evidence demonstrates that these rocks formed by autometasomatic phenomena. The protolith of the dolomitic marble is magmatic carbonatite, whereas the protolith of the K-rich slate is trachytic volcaniclastic rock or volcanic tuff.

Keywords. Bayan Obo, host rocks, autometasomatism, petrogenesis

1 Introduction

The Bayan Obo Ore deposit, Inner Mongolia, China is renowned as the largest REE ore deposit in the world, and is also a large Fe-Nb ore deposit. The host rocks to the Fe-Nb-REE orebodies in the district are mainly Proterozoic dolomitic marble and K-rich slate. Although these two host rocks have been studied by numerous researchers, their petrogenesis has remained in dispute. Sedimentary or sedimentary-metamorphic origins (Zonglin 1989; Qingrun 1982) or magmatogenic origins (Zhenling 1980; Zhongxin 1992) have been considered for the dolomitic marble. For a long time, the K-rich slate in the ore district had been called light slate, dark slate, siliceous slate, K-rich slate or potassic feldspar rock, implying a K-rich clay-rich rock of sedimentary origin. A possible volcanogenic origin, in that the rock is a trachyte instead of K-rich slate, was first suggested by Yuan Zhongxin (1995). In this paper, we document thin section evidence of autometasomatic phenomena in these rocks, and comment on their genetic significance.

2 Host rocks

2.1 Dolomitic marble

Based on mineralogical compositions of the rock, dolomitic marble in the Bayan Obo district can be divided into three varieties: dolomitic or ankerite – dolomite marble, calcite – dolomite marble and calcitic marble. The dolomitic marble can be further subdivided into coarse-grained and fine-grained dolomitic marble. The former has a grain size of 0.5 to 3 mm, and consists mostly of anhedral crystals with obvious cleavage (Fig. 1a). Crystals in the fine grained dolomitic marble (0.02 to 0.5 mm) have a polygonal texture. Triple junctions are common, where three mineral grain boundaries radiate out at 120° (Fig. 1b).

The dolomitic marbles consist of 70 to 90% dolomite and ankerite. Minor minerals include calcite, magnetite, fluorite, riebeckite, aegirine, arfvedsonite, phlogopite, barite, apatite and pyrite. There is a vast amount of rare earth minerals in the rock, which occur mainly as monazite and bastnaesite. The fine grained dolomitic marble rock contains a large number of rare earth elements and volatile components, with a close relationship to the orebodies in space, composition and genesis.

2.2 K-rich slate

The K-rich slate has a microcrystal-cryptocrystal texture. It can be divided into dark and light varieties, with the two types occurring as discrete bands in some outcrops (Fig. 1c).

The grain size of the K-rich slate was measured using an SEM-IPS image analyzer. The minerals in the light rock have a minimum grain size of 0.6μm and a maximum of 30.0μm, with an average of 4.3μm (Fig. 1d).

The rocks consist of up to 80% microcline. Minor minerals are biotite, aegirine, riebeckite, albite, quartz, calcite, dolomite, apatite, fluorite, magnetite, pyrite and barite. Rare element and REE minerals include monazite, bastnaesite, aeschynite, Nb-rutile and columbite.

3 Autometasomatic phenomena

3.1 Dolomitic marble

The fine grained dolomitic marble shows the effects of many autometasomatic phenomena. Figure 1e shows the end-products of riebeckitization. Aegirine of autometasomatic genesis is shown in Figure 1f. Figure 1g shows a veinlet of fluorite in the fine grained dolomitic marble and Figure 1h shows veinlet-disseminated magnetite. Figure 1b shows aggregates of the monazite as veinlet-disseminated ore, which have cut and corroded the early dolomite.

This page intentionally blank

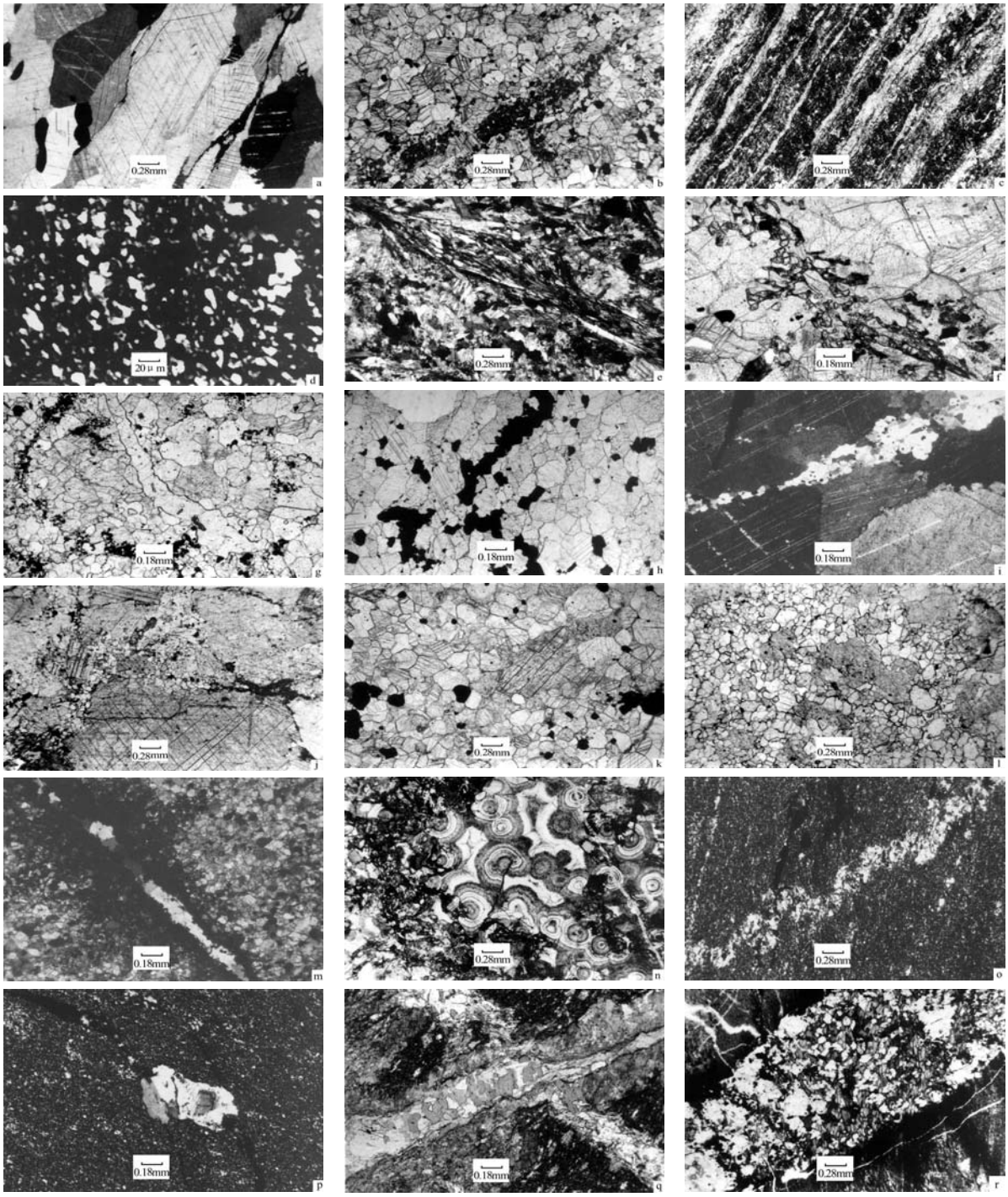

Figure 1: Photomicrographs of ore-bearing rocks from Bayan Obo. A: dolomite crystalline strips in coarse-grained dolomite, cross polarized light (xpl). B: dolomite and monazite distributed as fine veins in fine-grained dolomite, plane polarized light (ppl). C: dark-colored and light-colored strips in trachyte (ppl). D: image of light-colored trachyte grain. E: late riebeckite in fine-grained dolomite, (xpl). F: alkali-pyroxene aggregates distributed as networks in fine-grained dolomite (ppl). G: late fluorite veins in fine-grained dolomite (ppl). H: magnetite veins in fine-grained dolomite (ppl). I: late fine-grained dolomite veins in coarse-grained dolomite, (xpl). J: fine-grained dolomite distributed around coarse-grained dolomite (ppl). K: coarse-grained dolomite relicts in fine-grained dolomite (ppl). L: coarse-grained dolomite relicts in fine-grained dolomite (ppl). M: late dolomite veins in fine-grained dolomite, (xpl). N: Spherulite dolomite (ppl). O: late anastamosing microcline veins in trachyte (xpl). P: early microcline crystal fragments corroded by late feldspar in trachyte (xpl). Q: late feldspar veins cut by later microcline and biotite veins in trachyte (ppl). R: late veins of fluorite, magnetite, biotite, REE minerals and microcline in trachyte (ppl).

Figure 1i shows a veinlet of late stage fine grained dolomite in the coarse-grained rock. Figure 1j shows an aggregate of fine grained dolomite occuring as a stockwork around a coarse grain of dolomite. Figures 1k and 1l show remnants of coarse grained dolomite in the fine grained rock. Fine grained dolomite is characterized by clear crystals whereas coarse-grained dolomite is turbid and has a fragmental texture. Figure 1m shows a calcite veinlet in the fine grained rock. Figure 1n shows a calcite nodule with oolitic texture in the fine grained rock.

3.2 K-rich slate

The most clear autometasomatic phenomenon of the K-rich slate is microclinization. Figure 1o shows an anastamosing veinlet of microcline. Figure 1p shows a fragment of microcline with a reaction rim. The outer rim obviously is a result of corrosion and alteration. Locally, remnant crystals of early-formed microcline occur in later microcline. Figure 1q shows a early microcline veinlet that has been cut by a microcline-biotite veinlet. Many late veinlets contain biotite, fluorite, magnetite, microcline and rare earth minerals (Figure 1r).

4 Genetic significance

Paragentically early minerals, dolomite and K-feldspar in particular, have been deformed, cut, corroded, and replaced by later minerals. These textures reflect autometasomatic phemomena, because the late metasomatic minerals have no immediate relation to the earlier formed minerals in the rock. The veinlets, with widths of less than 1 mm and short lengths, are not relict features preserved from sedimentary and metamorphic protoliths.

The autometasomatic textures in the Bayan Obo host rocks are interpreted to indicate that the dolomite and K-rich slate are mostly products of magmatic evolution, and should be considered as magmatic rocks. The coarse grained dolomite rock is interpreted to be the early-crystallized product of a carbonatitic magma, whereas the fine grained dolomite rock is a product of the late stage evolution of the melt, which may have exsolved a hydrothermal fluid. Such processes have been documented by Le Bas (1997), Smith (2000) and Kaiyi, (2002). Formation of the fine-grained dolomite rock probably occurred via condensation and solidification of the magma that initially formed the coarse-grained dolomite rock. The coarse grained dolomite has been replaced by fine grained dolomite, riebeckite, aegirine and fluorite. This is reflected in the chemical composition of the fine grained dolomite rock, which is rich in F, H_2O, CO_2 and other volatiles. It is likely that the melt which formed this rock was a carbonatitic magma, rather than a silicate melt. The magma may have had a transitional state between igneous melt and hydrothermal solution, or it may have been a hybrid fluid caused by mixing of melt and hydrothermal fluid.

At Bayan Obo, the structure, texture, chemical compositions and metasomatic phenomena of the K-rich slate are consistent with formation via condensation and solidification of a trachytic magma. The late alteration products were formed by a K-rich hydrothermal solution, or a hybrid K-rich melt-solution.

References

Chao ETC, Back JM, Minkin JA, Ren Y (1992) Host-rock controlled epigenetic hydrothermal metasomatic origin of the Bayan Obo REE-Fe-Nb ore deposit, Inner Mongolia, PRC. Appl. Geochem, 7: 443-456

Hou (1989) The Bayan Obo Fe-Nb-REE deposit: its basic geological featutes, metallogenesis and genetical model. Geology and Prospecting 25(7): 1-5

Le Bas MJ, Spiro B, Yang X (1997) Oxygen, Carbon and Strontium isotopes study of the carbonatitic dolomite host of the Bayan Obo Fe-Nb-REE deposit, Inner Mongolia, N. China. Mineralogical Magazine 61(4): 531-541

Meng Q (1982) The genesis of the host rock-dolomite of the Bayan Obo iron are deposit and the analysis of its Sedimentary environment. Geological Review 28(15): 481-489

Smith MP, Henderson P, Camball LS (2000) Fractionation of the REE during hydrothermal processes: Constraints from the Bayan Obo Fe-REE-Nb deposit, Inner Mongolia, China. Geochimica et Cosmochimica Acta 64(18): 3141-3160

Wang K, Fan H, Xie Y (2002) Geochemistry of REE and Other trace elements of the carbonatite dykes at Bayan Obo: implication for its formation. Acta Petrdogica Sinica 18(3): 340-348.

Yuan Z, Bai G, Wu C, Ding X (1995) Petrological features of volcanic rocks in H9 formation of the Bayan Obo ore district, Inner Mongolia and their significance. Mineral Deposits, 14(3): 197-205

Yuan Z, Bai G, Wu C, Zhang Z, Ye X (1992) Geological features and genesis of the Bayan Obo REE ore deposit, Inner Mongolia, China. Applied Geochemistry 7: 429-442.

Zhou Z, Li G, Song T, Liu Y (1980) On the geological characters and genesis of the dolomitic carbonatites at Bayan Obo, Inner Mongolia. Geological Review, 26(1): 35-41

REE-Nb (Fe, U,Th)-bearing alkaline skarns of China

Zhao Yiming, Bai Ge, Li Daxin
Institute of Mineral Resources, Chinese Academy of Geological Sciences, Beijing, 100037, China

Abstract. Alkaline skarns consist of special Na (K, Ca, Mg, Fe, Al) silicate metasomatic minerals, such as aegirine, aegirine-augite, sodic diopside, richterite, arfvedsonite, eckermannite, magnesio-arfvedsonite, sodic tremolite and phlogopite, and are typically associated with REE, Nb (Fe, U, Th) mineralization. They occur chiefly in the contact zones between syenite or alkaline granitoid and dolomitic marble, and also in carbonatite in the form of metasomatic lenses. They have a rift-related tectonic setting, occurring at the northern border of the China platform. Three alkaline skarn subtypes can be defined on the basis of geological setting and deposit characteristics (1): hydrothermal metasomatic alkaline skarn in carbonatites; (2) alkaline skarn related to alkalic granitoids, and (3) alkaline skarn related to syenites.

Keywords. Alkaline skarn, REE-Nd (Fe, U, Th) mineralization, China

1 Introduction

Skarns are generally divided into two types according to their mineral compositions: calcic skarn and magnesian skarn (Korshinskii, 1955; Zharikov, 1968; Einaudi el al., 1981). The calcic skarn consists mainly of grossular-andradite series, diopside-hedenbergite series, wollastonite, vesuvianite and scapolite in limestone or marble host rocks. The magnesian skarn consists mainly of forsterite (or its alteration product, serpentine), diopside, phlogopite, spinel, tremolite and the humite group, in dolomite or dolomitic marble host rocks. Based on studies of numerous skarn deposits of China and in comparison with skarn deposits in other parts of the world, Zhao et al. (1986; 1990; 1997; 2003) proposed two other types of skarn: manganoan skarn and alkaline skarn. Manganoan skarn consists of special Mn (Ca, Mg, Fe, Al) silicate minerals, such as manganoan diopside, manganoan hedenbergite, johannsenite, bustamite, pyroxmangite, rhodonite, spessartine, tephroite, and are typically associated with Pb-Zn (Ag) mineralization (Zhao et al. 1990; 2004).

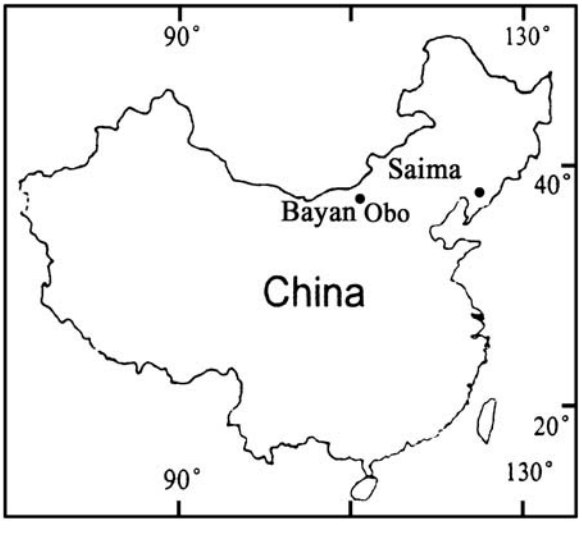

Figure 1: Location map of the alkaline skarns.

In this paper, we provide a preliminary discussion of the alkaline skarn types: (1) hydrothermal metasomatic alkaline skarn in carbonatites; (2) alkaline skarn related to alkaline granitoids, and (3) alkaline skarn related to syenites. The former two subtypes are located separately in the main Bayan Obo deposit and its eastern part in Inner Mongolia, while the latter occurs in the Saima deposit, Liaoning Province (Fig. 1). Their occurrence at the northern border of the China platform suggests a rift-related tectonic setting.

2 Fe-Nb-REE-bearing alkaline skarns related to dolomitic carbonatite

The Bayan Obo ore deposit in Inner Mongolia, China is the largest rare earth metal deposit in the world and contains ~75% of the world's known reserves. The deposit is also a significant iron resource, with reserves of around 1468 Mt. Nb, Sc, apatite, fluorite and barite are byproducts of mining.

The origin of the Bayan Obo deposit has been debated for a long time. Two main hypotheses have been proposed. The first is that the deposit formed in the Caledonian (around 532 to 418 Ma) by hydrothermal replacement of Mesoproterozoic carbonate rocks (Chao et al. 1992). The other hypothesis is that the host rocks are carbonatites and that the deposit belongs to the alkali-carbonatite genetic type. Alternatively, the REE (Fe) ores may have formed as a result of volcanic-exhalative processes (Bai et al. 1985; Yuan et al. 1992).

Detailed study of the age and geochemistry of the Bayan Obo ore deposit suggests that the Main orebody and East orebody were probably formed in the last stage of the Mesoproterozoic (1305 to 1250 Ma), whereas the West orebody probably formed in Late Proterozoic period at about 809 Ma. Strong deformation of the ore deposits occurred during the Caledonian (475 to 441.8 Ma; Zhang et al. 2003).

The alkaline skarns are mainly distributed in the Main, East and West orebodies, and occur as lenses within the dolomitic carbonatites. The main skarn minerals are aegirine, arfvedsonite, magnesio- arfvedsonite, phlogopite, richterite, and ferrorichterite associated with abun-

This page intentionally blank

Table 1: Represetative etectron microprobe analyses of sodic pyroxenes in the alkaline skarns.

Sample no	By-31	By-36	By-52	By-4	By-8	By-9	Sap-6	Sap-9	Sap-17
Location	Bayan Obo			East of Bayan Obo			Saima deposit		
SiO_2	52.44	50.55	52.41	53.75	54.52	53.46	52.45	53.04	52.83
TiO_2	1.67	0.08	0.57	0.05	0.12	0.06	3.44	1.83	2.81
Al_2O_3	0.44	1.28	0.60	0.49	0.26	0.47	0.75	0.87	0.55
Fe_2O_3	29.47	32.86	32.37	4.47	3.02	9.78	27.09	27.96	25.85
FeO	0.00	0.00	0.00	5.81	6.14	6.43	0.88	1.94	2.97
MnO	0.22	0.03	0.02	1.23	0.71	0.38	0.37	0.17	0.33
MgO	1.23	0.17	0.12	11.76	12.86	9.53	1.06	0.32	0.71
CaO	0.50	0.39	0.12	21.32	20.50	16.98	1.34	0.27	1.29
Na_2O	13.65	14.01	13.96	1.70	1.83	4.14	12.92	13.38	12.82
K_2O	0.00	0.00	0.00	0.00	0.01	0.00	0.00	0.00	0.00
Total	99.62	99.37	100.17	100.58	99.97	101.23	100.30	99.78	100.16
$NaFe^{3+}Si_2O_6$	95.4	98.7	99.4	12.9	11.2	28.9	93.4	95.1	89.9
$CaMgSi_2O_6$	4.6	1.3	0.6	67.5	73.6	53.5	4.4	1.2	3.5
$CaFe^{2+}Si_2O_6$	0	0	0	19.5	15.2	17.6	2.2	3.7	6.6

dant fluorite, magnetite, and bastnaesite, monazite, niobite, aeschynite, pyrochlore, fergusonite and ilmenorutile.

The alkaline skarns have an obvious infiltrational hydrothermal metasomatic character, but no obvious zonation has been determined.

3 REE-Nb-bearing alkaline skarn related to alkalic granitoids and carbonatite

This type of alkaline skarn occurs in the eastern part of the Bayan Obo Fe-Nb-REE ore deposit. The skarn occurs in the form of lenses and veins at the contact zones between Variscan (280-249 Ma, Zhang et al. 1986; Zhang et al. 2003) alkaline granitoid and Proterozoic dolomite carbonatite. The alkaline skarn is mainly composed of sodic diopside, aegirine-augite, phlogopite, richterite, sodic tremolite, and perthite. The associated REE and Nb-bearing minerals are pyrochlore, monazite, allanite, fersmite, fergusonite. Zonation is well-developed in the alkaline skarn: alkalic granodiorite ⟶ perthite metasomatite (± sodic diopside) ⟶ REE (Nb)-bearing alkaline skarn ⟶ REE (Nb)-bearing dolomite carbonatite.

Systematic chemical analyses of the alkaline skarns suggest that the average RE_2O_3 contents are 0.78%, which is similar to average RE_2O_3 contents of the carbonatite wall rocks in this area. But close to the endocontact zone, the skarn is enriched in RE_2O_3, up to 4.31%.

4 U-Nb (REE, Th)-bearing alkaline skarns related to syenite

The Saima alkaline massif is one of the unique alkaline complexes in the world, and is dominated by aegirine-nepheline syenite. It is located in Fengcheng County, Liaoning Province and was formed in the Indosinian period (240 to 213 Ma; Chen et al. 1996). Geotectonically, the massif is situated at the contact between the old craton (China platform) and the Proterozoic mobile zone. Intense contact-metasomatic phenomena developed on the steep-dipping fault zone located at the western margin of the Saima massif. U-Nb-bearing alkaline skarns occurr at the contact between aegirine-nepheline syenite and Proterozoic dolomitic marble. The skarns are mainly composed of aegirine, arfvedsonite, eckermannite, magnesioriebeckite, richterite, orthoclase, albite, and phlogopite. U-Nb mineralization occurs in the alkaline skarns (including aegirine – orthoclase metasomatite in the endocontact zone).

The most important U (REE) mineralization occurs in a grass green aegirine nepheline syenite near the alkaline skarns. Rinkolite [(Ce, La, Th, U) Na Ca_4 Ti $(Si_2O_7)_2OF_3$] is the major ore mineral (Chen et al. 1996). The representative electron microprobe (chemical)0 analyses of major sodic pyroxenes and sodic amphiboles of the alkaline skarns are shown in Table 1 and Table 2 respectively.

Birkett et al. (1998) described the Kipawa Y-Zr-REE alkaline skarn in Quebec, Canada. It is a metamorphosed skarn formed at the contact between peralkaline granite (presently gneiss) and marble. Within and near the deposit, rocks containing sodic- calcic pyroxene, sodic amphibole, and phlogopite are intimately associated with eudialyte and Y mineralization. Y, Zr and REE mineralization is located at the contact zone between former carbonate rocks, which are now preserved as remnants of marble in the syenite gneisses. The skarns formed in association with feldspathization reactions (mainly albitization), and with widespread, general enrichment of Y, REE, Zr, Th, and U.

Table 2: Representative electron microprobe (chemical) analyses of sodic amphiboles in the alkaline skarns.

Sample no	By-34	By-36	By-24	By-32	By-9-1	By-6	Sa-21	Sa-26*	Sa-27*
Location	Bayan Obo			East of Bayan Obo			Saima deposit		
SiO_2	54.10	53.49	56.08	51.24	55.10	55.80	55.46	54.53	48.00
TiO_2	0.04	0.06	0.02	0.79	0.17	0.01	0.53	0.58	1.34
Al_2O_3	0.72	0.59	0.21	3.20	1.27	0.45	0.38	2.43	2.00
Fe_2O_3	–	–	–	–	–	–	–	5.66	11.24
FeO	20.66	30.93	14.00	13.40	8.44	11.15	6.26	4.37	8.06
MnO	1.63	0.21	0.34	0.59	0.40	0.79	1.60	1.50	2.34
MgO	9.99	4.15	15.67	14.75	18.64	16.66	19.04	13.12	7.41
CaO	2.10	0.14	0.54	6.75	5.95	10.78	5.59	3.61	4.27
Na_2O	7.03	7.58	8.88	4.67	4.96	1.29	6.88	6.41	6.44
K_2O	1.31	0.31	1.36	1.45	3.17	0.41	2.64	3.98	2.18
H_2O	–	–	–	–	–	–	–	1.22	2.27
F	–	–	–	–	–	–	–	1.82	1.58
-O=F								99.23 -0.76	97.13 -0.66
Total	97.56	97.45	97.11	96.84	98.10	97.34	98.38	98.47	96.47

* Chemical analyses (analyst: Liu Lanfen and Xie Xiuying).

5 Conclusions

In the classification of skarns, besides calcic, magnesian, and manganoan skarns, there is also an alkaline skarn type, which is composed of metasomatic Na (K, Ca, Mg, Fe, Al) silicate mineral assemblages. The main skarn minerals are sodic pyroxene, sodic amphibole, and phlogopite, and there is an association with REE-Nb (U, Fe, Zr, Th) mineralization. The alkaline skarns have formed in rift-related settings of different ages.

According to their formation geological conditions, geological characteristics, and associated mineralization, three alkaline skarn subtypes can be defined in China: (1): hydrothermal metasomatic alkaline skarn in carbonatites; (2) alkaline skarn related to alkalic granitoid, and (3) alkaline skarn related to syenite.

Alkaline skarns are one of the important vectors that can help in the discovery of REE-Nb (U, Fe, Zr, Th) skarn deposits.

References

Bai, G, Yuan, ZX (1985) Carbonatites and related mineral resources. Bulletin of the Institute of Mineral Deposits, Chinese Academy of Geological Sciences, No 13, pp. 107-140 (in Chinese with English abstract).

Birkett, TC, Sinclair, WD (1998) Rare-metal replacement deposits (skarns and fenites) associated with alkalic and carbonatite complexes. In: Mineralized intrusion-related skarn systems. Short Course Volume 26, Series Editor: Jambo, J. L., Quebec, pp. 445-474.

Chao, ECT, Back JM, Minkin JA (1992) Host rock controlled epigenetic, hydrothermal and metasomatic origin of the Bayan Obo REE-Fe-Nb ore deposit, Inner Mongolia, PRC. Applied Geochem. 7: 443-458.

Chen ZB, Fan J, Guo ZT, He ZJ, Wan S, Ren KC (1996) Saima alkaline rocks and relevant metallogenesis. Beijing: Atomic Energy Press, pp: 1-305 (in Chinese with English abstract)

Einaudi MT, Meinert LD, Newberry RT (1981) Skarn deposits. Econ. Geol., 75th Anniv., pp. 317-391.

In: Fundamental Problems in Theory of Magmatogenic

Korzhinskii, DS (1995). An outline of metasomatic process.

Ore Deposits. 2nd Ed., Izd. AN SSSR, M., pp. 335-456 (in Russian).

Yuan ZX, Bai G, Wu CY, Zhang ZQ, Ye XJ (1992) Geological features and genesis of the Bayan Obo REE ore deposit, Inner Mongolia, China. Applied Geochemistry 7: 429-442.

Zhang PS, Tao KJ (1986) Bayan Obo mineralogy. Beijing: Science Press, pp. 1-208 (in Chinese).

Zhang ZQ, Yuan ZX, Tang SH, Bai G, Wang JH (2003) Age and geochemistry of the Bayan Obo ore deposit. Beijing: Geological Publishing House, pp. 1-222 (in Chinese with English abstract).

Zhao YM (1986) A discussion on genetic classification of metasomatites and their associated mineralizations. Mineral Deposits 5 (4): 1-13 (in Chinese with English abstract).

Zhao YM, Li DX (2003) Amphiboles in skarn deposits of China, Mineral Deposits, 22(4): 345-359 (in Chinese with English abstract).

Zhao YM, Lin WW, Bi CS, Li DX, Jiang CJ (1990) Skarn deposits of China. Beijing: Geological Publishing House, pp. 1-354 (in Chinese with English abstract).

Zhao YM, Zhang YN, Lin WW (1997) Characteristics of Pyroxenes and pyroxenoids in skarn deposits of China and their relationship with mineralization. Mineral Deposits, 16 (4): 318-329 (in Chinese with English abstract).

Zhao, Y. M. and Li D. X. (2004). Pb-Zn-Ag-bearing manganoan skarns of China. Acta Geologica Sinica, 78 (2): pp. 524-528.

Zharikov VA (1968) Skarns. In: Genesis of Endogenic Ore Deposits. Moscow: Izd. Nauka, 220-300 (in Russian).

Origin of giant Fe-Ti-V oxide deposits in layered gabbroic intrusions, Pan-Xi district, Sichuan Province, SW China

Mei-Fu Zhou, Christina Yan Wang, Kwan-Nang Pang, Gregory J. Shellnutt
Department of Earth Sciences, University of Hong Kong, Hong Kong, China

Yuxiao Ma
Department of Science and Technology, Chengdu University of Technology, Chengdu 610059, China

Abstract. The Pan-Xi region, SW China, is part of the Emeishan large igneous province, which comprises voluminous flood basalts and spatially associated mafic-ultramafic intrusions. The ~260 Ma gabbroic intrusions at Pan-Xi host giant Fe-Ti-V oxide deposits. Unlike the oxide deposits in classic layered intrusions, such as the Bushveld Complex, those in the Pan-Xi region occur as layers and/or lenses within the gabbros and are generally concentrated in the lower parts of the intrusions. Available geochemical evidence suggests that the intrusions were formed from highly evolved Fe-Ti-V-rich ferrogabbroic or ferropicritic magmas. Ore textures and associated mineral assemblages indicate that the orebodies were formed by late-stage crystallization of V-rich titanomagnetite from oxide liquids. The abundant accessory hydrous phases suggest that addition of fluids from upper crustal rocks might have induced the separation of the immiscible oxide melts and subsequently gave rise to the oxide orebodies.

Keywords. Pan-Xi, gabbro, oxide melt, Fe-Ti-V mineralization

1 Introduction

In the Pan-Xi (Panzhihua-Xichang) area, SW China, several mafic-ultramafic intrusions host giant Fe-Ti-V oxide deposits. This region is the most important Fe-Ti-V metallogenic district in China (Zhong et al. 2002; 2003; Ma et al. 2003). Some of the oxide deposits are being mined currently, whereas others are under re-evaluation or have not been mined as yet. The Panzhihua Fe-Ti-V oxide deposit has been mined for more than 30 years and has produced large quantities of Fe, Ti and V. Estimated ore reserves in the Pan-Xi area are over 7544 million tonnes, with average grades of 36 wt % Fe, 0.28 wt % V_2O_5 and 12.6 wt % TiO_2.

Mafic-ultramafic intrusions in the Pan-Xi region exhibit various scales of igneous layering, which are generally similar to those documented in classic layered intrusions such as the Skaergaard intrusion and the Bushveld Complex (Cawthorn 1996). Oxide ore occurs as layers and lenticular bodies in the lower parts of the Pan-Xi intrusions, in contrast to magnetite layers in the upper part of the Bushveld Complex. This difference in morphology of the orebodies and relative stratigraphic positions seems to reflect the complexity of the formation of these oxide bodies in layered intrusions. Genetic and exploration models of the Pan-Xi oxide deposits are poorly constrained, despite their tremendous economic significance. Likewise, the relationship between the Fe-Ti-V oxide orebodies and their host rocks is not known. This paper documents the geology of the Pan-Xi oxide orebodies and discusses their likely mechanism of formation.

2 Local geology

The Pan-Xi layered intrusions occur in the western portion of the Permian (~260 Ma) Emeishan large igneous province, which covers 500,000 km^2 in SW China and northern Vietnam. The province is dominated by voluminous flood basalts with minor intrusive rocks. Exposure of the intrusive rocks was generally controlled by large-scale N-trending faults. The felsic plutons and layered intrusions occur along a zone about 300 km long and 10-30 km wide. The oxide ore-bearing mafic-ultramafic intrusions extend from Taihe in the north to Baima, Panzhihua and Hongge in the south (Fig. 1). These intrusions are divided into mafic and mafic-ultramafic bodies on the basis of the predominant rock types (Zhong et al., 2002, 2004). Three large Fe-Ti-V oxide ore deposits have been explored in the Pan-Xi District: Panzhihua (1,333 Mt ore reserves), Baima (1,497 Mt), and Hongge (4,572 Mt; Ma et al. 2003), but only Panzhihua is currently being mined for its Fe-Ti-V ores.

The oxide orebodies have a variety of geometries, including lenses, layers and dyke-like bodies. Some orebodies are intimately associated with layered igneous rocks. Most of the oxide orebodies occur in the lower parts of the intrusions, although there are some smaller occurrences at higher levels within the igneous stratigraphy. Due to limited exposure, it is not clear as to whether the oxide ore is part of the layered sequence. Nonetheless, several field observations suggest that the deposits are magmatic in origin: (1) the orebodies are integral parts of the intrusions, regardless of whether layering is conspicuous; (2) both the oxide ores and host rocks are characterized by fresh igneous mineral assemblages; (3) the geometries of the orebodies (e.g. lenses, dykes) are consistent with a magmatic origin; and (4) the sharp contacts observed in certain well-exposed orebodies are characteristic of igneous contacts.

This page intentionally blank

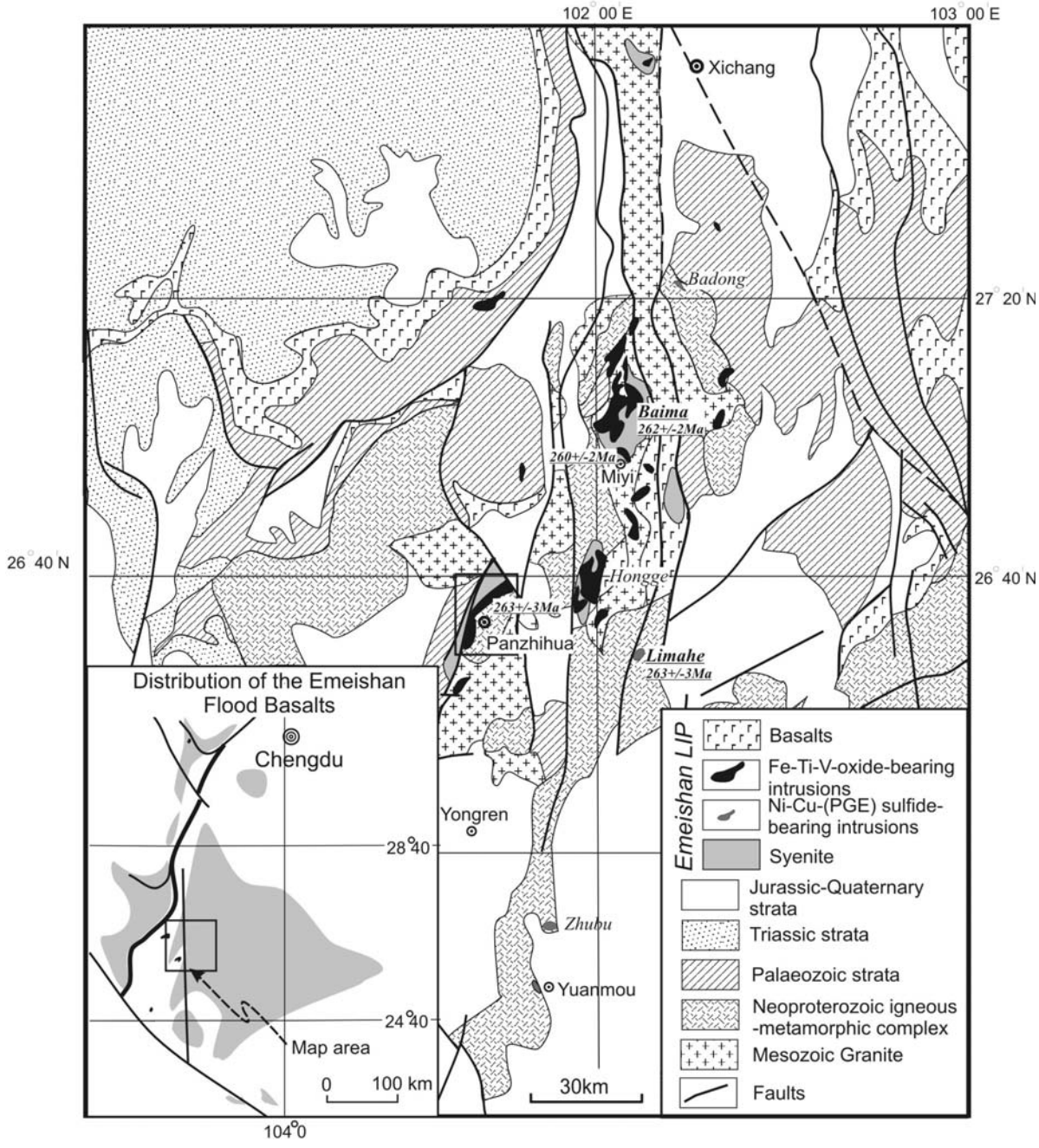

Figure 1: Fe-Ti-V oxide-bearing intrusions in the Pan-Xi district of the Emeishan large igneous province, SW China.

3 Ore textures

The textures of the oxide ores range from massive, through net-textured to disseminated. Massive ore is dominated by titanomagnetite with minor ilmenite. Accessory minerals typically comprise less than 10% of the rock. The oxide grains are medium to coarse and have polygonal shapes outlined by straight to slightly curved boundaries. Similar subsolidus textures have been documented from magnetite layers in the Bushveld Complex (Reynolds, 1985; von Gruenewaldt et al., 1985

Compared to the massive ores, net-textured ores have a larger modal amount of silicate minerals such as olivine, plagioclase and/or clinopyroxene. The ratios between oxide and silicate minerals, and those between different silicates are highly variable. For example, certain net-textured ores contain magnetite and olivine without any other silicate phases. The silicate minerals in the net-textured

ores typically have sub-rounded grain shapes and are surrounded by oxides. They commonly have embayed grain boundaries.

Disseminated ores consist of oxide gabbro or oxide peridotite, both of which generally contain less than 20% oxides. The oxides invariably occur interstitial to the silicate minerals.

Hydrous minerals are important accessory phases in almost all of the oxide ore types. The hydrous phases include brown hornblende and lesser biotite, and are typically associated with oxides. Brown hornblende occurs as small grains with irregular boundaries, or as reaction rims at certain oxide-silicate interfaces, particularly those involving plagioclase.

4 Genesis

The Panzhihua layered intrusion at Pan-Xi is interpreted to have crystallized from highly evolved, Fe- and Ti-rich parental magmas (Zhou et al. 2005). Supporting arguments for this model include (1) enrichment in LREE relative to HREE; (2) enrichment in Ti relative to elements with similar compatibilities; (3) depletion in U, Th, Zr, and Hf relative to elements with similar compatibilities. It is possible that Fe-enrichment may be a primary feature of the parental magma attributable either to the mantle source composition or conditions of partial melting. However, it is difficult to envision how such dense, high-Fe magmas could migrate from the mantle into the lower crust. A more likely mechanism is that high-Fe liquids formed through fractionation and thus were highly evolved magmas.

Ore textures suggest that the oxide orebodies crystallised from oxide melts. The interstitial character of the oxides and the hornblende reaction rims indicate that such a melt may have invaded a silicate crystal mush and reacted with the silicate minerals. The dense, viscous oxide melt was presumably developed within the magma chamber rather than being transported from elsewhere. The oxide melt most likely required immiscible separation, because fractional crystallization alone could only produce a Fe-rich silicate liquid, and not an oxide liquid (Duchesne 1999).

The formation of an immiscible oxide melt from a silicate magma may be related to mineral fractionation, magma mixing, abrupt changes in oxygen fugacity, or introduction of fluids. The presence of minor disseminated sulfides and apatite suggest that S, P, F and/or Cl may have acted as fluxing agents that facilitated development of the immiscible liquids. The association of brown hornblende and oxides suggests that water and other fluids might also play a part in this process. Volatile-bearing fluids may have been introduced through magma/wall rock interaction during or after the emplacement of the Fe-rich gabbroic magmas. The abundance of hydrous minerals in the Panzhihua intrusion suggests that fluids were introduced into the system during crystallization.

Acknowledgements

This study was substantially supported by a RGC grant, Hong Kong (7056/03P).

References

Cawthorn RG (1996) Re-evaluation of magma compositions and processes in the uppermost Critical Zone of the Bushveld Complex. Mineralogical Magazine 60: 131-148

Duchesne JC (1999) Fe-Ti deposits in Rogaland anorthosites (South Norway): geochemical characteristics and problems of interpretation. Mineralium Deposita 34: 181-198

Ma YX, Ji XT, Li JC, Huang M, Min ZZ (2003) Mineral resources of Panzhihua, Sichuan Prvince, SW China. Chengdu University of Technology, p 275

Reynolds IM (1985) The nature and origin of titaniferous magnetite-rich layers in the upper zone of the Bushveld Complex: a review and synthesis. Economic Geology 80: 1089-1108

von Gruenewaldt G, Klemm DD, Henckel J, Dehm RM (1985) Exsolution features in titanomagnetites from massive magnetite layers and their host rocks of the upper zone, eastern Bushveld Complex. Economic Geology, 80: 1049-1061

Zhong H, Yao Y, Hu SF, Zhou XH, Liu BG, Sun M, Zhou MF, Viljoen MJ (2003) Trace-Element and Sr-Nd isotopic geochemistry of the PGE-bearing Hongge layered intrusion, Southwestern China. International Geological Review 45: 371-382.

Zhong H, Zhou XH, Zhou M-F, Sun M, Liu BG (2002) Platinum-group element geochemistry of the Hongge layered intrusion in the Pan-Xi area, Southwestern China. Mineralium Deposita 37: 226-239.

Zhou M-F, RobinsonPT, Lesher CM, Keays RR, Zhang CJ, Malpas J (2005) Geochemistry, petrogenesis, and metallogenesis of the Panzhihua gabbroic layered intrusion and associated Fe-Ti-V-oxide deposits, Sichuan Province, SW China. Journal of Petrology (in press).

Xiangquan: The World's first reported sediment-hosted thallium-only deposit, northeastern margin of the Yangtze Block, eastern China

T.F. Zhou, Y. Fan, F. Yuan
School of Resources and Environment Engineering, Hefei University of Technology, Hefei 230009, China

M.A. Wu, M.J. Hou
Academy of Geological Survey of Anhui Province, Hefei 230001, China

G. Voicu
Department of Earth and Atmospheric Sciences, University of Quebec at Montreal (UQAM), Canada

Q.H. Hu, Q.M. Zhang
327 Geological Team, Geological Bureau of Anhui Province , Hefei 23000, China

Abstract. Thallium is a dispersed element that seldom occurs as independent minerals. Consequently it is difficult to form a discrete thallium mineral deposit. This paper reports the first example of a thallium-only ore deposit discovered in the northeast margin of the Yangtze block, eastern China. Hydrothermal enrichment on the ancient sea floor and hydrothermal reworking during the Yanshanian orogeny are the two important metallogenic events that led to the formation of the thallium deposit.

Keywords. Xiangquan, thallium, epithermal metallogenic, Yangtze, China

1 Geological characteristics of the thallium deposit

The Xiangquan thallium deposit is located in the transition zone between the Yangtze Block, North China Block and Dabie orogenic belt. There are only minor intrusions in the district, with sedimentary rocks in abundance. The foreland fold-thrust belt trends northeast and consists of several thrust-detachment systems (Fig 1). The fold-thrust belt is divided into the eastern (Hanchao) and the western (Chouzhou) sub-belt by the Chu River fracture (Chang and Dong 1996).

1.1 Stratigraphy and structure

There are three major stratigraphic units in the Xiangquan district; these include: (1) Lower Ordovician Honghuayuan Group (Fig. 1) which consists mainly of gray micrite and dolomite. These rocks crop out in the Xiao, Xiaolongwang, Mei and Dalongwang Mountains. The carbonaceous rocks crop out as yellow-white silicified breccias due to weathering. (2) Lower Ordovician Lunshan Group, which consists of gray micrite, calcilutite and marl containing siliceous concretions or banding. These rocks crop out in the core of the anticline (Fig. 1). They are characterized by the presence of bedded syngenetic pyrite. (3) Lower Silurian Gaojiabian Group, which crops out sporadically on both limbs of the anticline (Fig. 1). These rocks consist of yellow-white silty shale and sandstone (Wu 2000).

The main factors that controlled the distribution of thallium ore are stratigraphic contacts, folds and faults. Orebodies occur in the middle part of the Xiaolongwang Mountain anticline. Beds of the Honghuayuan Group and the Lunshan Group crop out in the core of the anticline, whereas both limbs of the fold consist of the Gaojiabian Group.

Faults in this district can be classified into two groups: Northeast-striking faults (F_1 and F_2) and northwest striking faults (F_3, F_4, F_5 and F_6). Faults F_3, F_4, F_5 and F_6 cut across and offset faults F_1 and F_2 (Fig. 1).

1.2 Mineralisation and alteration

The thallium orebodies are hosted in calcilutite of the Lunshan Group. Three main thallium orebodies (I, II and III) have been defined using a cut-off grade value of 0.05% Tl. Individual orebodies are generally 120~400 m long, 10~15m wide and 0.9 to 1.2 m thick. The orebodies are conformable with the country rocks. The thallium metal reserve at Xiangquan is about 250t. The orebodies are dominated by pyrite, and contain independent thallium minerals including lorandite ($TlAsS_2$), hutchinsonite ($TlFeS_2$) and avicennite (Tl_2O_3).

Pyrite at Xiangquan occurs in two modes. Colloform pyrite is inferred to be diagenetic, whereas euhedral pyrite is hydrothermal. Very fine grained (<10 μm) colloform pyrite is associated with quartz and clay minerals, and occur in beds with typical sedimentary characteristics. Cubic crystals (>1mm) of hydrothermal pyrite are distributed widely and generally coexist with fluorite or quartz. They occur in pelitic siltstones as veinlets, nodules and disseminations. Thallium minerals are generally submicroscopic (<10 μm) and occur as individual minerals on the margins of colloform pyrite. Some thallium minerals have grain sizes greater than 2mm and coexist with hydrothermal pyrite. A significant

This page intentionally blank

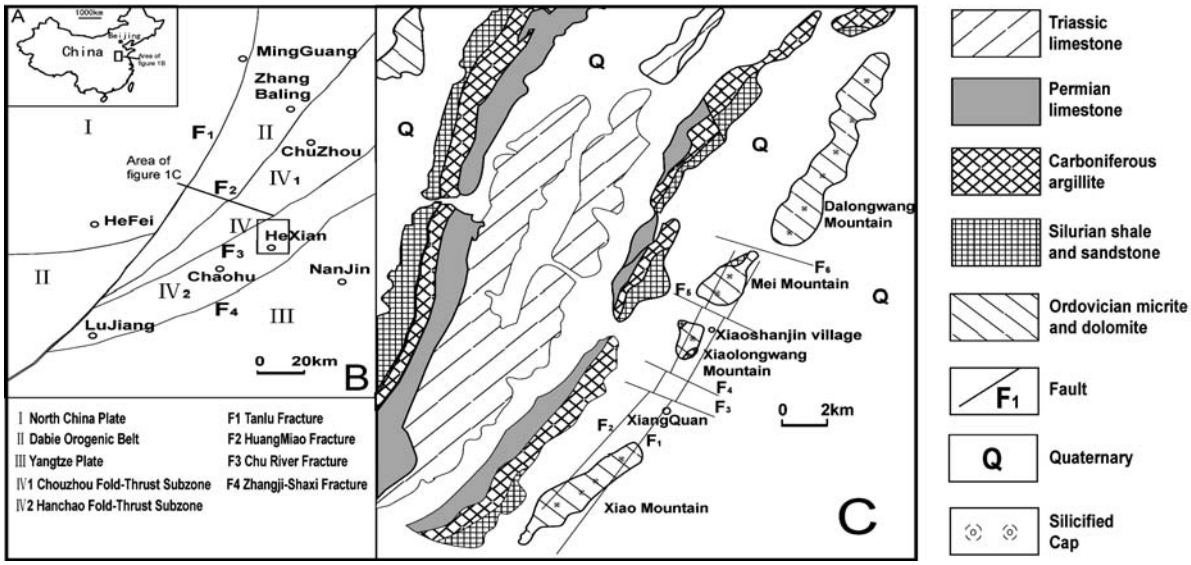

Figure 1: Location and geological map of the Xiangquan district

amount of thallium occurs within pyrite, either as inclusions or in solid solution.

Hydrothermal alteration has produced secondary fluorite, carbonate, barite and hydrothermal breccias. Fluorite mostly formed in the micrite and dolomite. The intensity of fluorite alteration decreases with depth. Fluorite formed during two stages: early stage fine grained purple fluorite coexists with pyrite, while the late stage fluorite is white, canary yellow or transparent colored and usually occurs in open caverns or fractures. Carbonate also formed in two stages but does not coexist with fluorite and pyrite. Some bladed calcite can be found in open veins. Barite generally coexists with later stage fluorite. Abundant hydrothermal breccias are found in the transition position of faults. Most of the breccias have been silicified and there is a silica cap at the surface. Near-surface pyrite has been weathered to limonite (Fig. 1).

2 Geochemistry and metallogenesis

2.1 Trace element geochemistry

Only thallium has been enriched economically at Xiangquan. The thallium content is positively correlated with pyrite (Table 1), and is very low in the late stage hydrothermal gangue (fluorite, barite and quartz). Several samples of weathered rocks have high thallium (up to 1250 ppm). Enrichment appears to have occurred during weathering of thallium-bearing pyrite to limonite (Table 1).

2.2 Fluid inclusion geochemistry

We have analyzed fluid inclusion in early stage fluorites. Those primary fluid inclusions in fluorites homogenize to liquid between 140 and 340°C, with a cluster between 200 and 260°C. The calculated salinities range from 0.5 to 6.0 wt% NaCl eq., with a cluster between 3.8 and 5.0 wt% NaCl eq. The temperature and salinity of the ore-forming fluids at Xiangquan are similar to those which form low sulfidation epithermal ore deposits.

2.3 Metallogenic epoch

Seven fluorite samples which are closely associated with the thallium-bearing hydrothermal pyrite have been analyzed for their Sm-Nd isotopic compositions, which were determined using a MAT-261 mass spectrometer at Tianjin Institute of Geology and Mineral Resources, CAGS. The calculated isochron age is 131.9 ±2.6 Ma, and the M.S.W.D is 0.43. This indicates that thallium hydrothermal minerali-sation occurred during the late Yanshanian period.

Most of the mineral deposits in the Middle and Lower reaches of the Yangtze River metallogenic belt formed during 130~138Ma, the Mesozoic Yanshanian period (Zhai et al. 1992; Zhou et al. 2000, 2003; Mao et al. 2004). The discovery of the Xiangquan thallium deposit indicates the existence of another metallogenic event of late Yanshanian age in this region, possibly of epithermal character. It is possible that such mineralisation could have a broad distribution along the northeastern margin of the Yangtze Block.

2.4 Metallogenic model

Thallium mineralisation at Xiangquan appears to have formed during two stages: syngenetic pyrite deposition and subsequent hydrothermal enrichment. During the late

This page intentionally blank

Table 1: Content of Tl, As, Hg, Au and Ag in minerals and rocks in Xiangquan Tl deposit ($\times 10^{-6}$).

No.	Samples	Tl	As	Hg	Au	Ag
1	Colloid pyrite(6)	1,100~25,000	3,500~26,000	80~400	0.01~0.05	0.12~1.08
2	Pyrite(5)	2,300~35,000	2,000~12,000	50~230	0.01~0.05	0.33~0.82
3	Tl-ore(25)	532~16,000	459~55,00	12~60	0.01~0.23	0.21~1.32
4	Barite(2)	0.5~0.8	-	-	-	-
5	Quartz(8)	0.7~0.9	-	-	-	-
6	Fluorite(10)	0.5~0.7	-	-	-	-
7	Weathering sample(20)	3.5~1250	8.6~546	1.6~9.8	0.01.~0.12	0.12~1.24

Analytical unit: National Research Center for GeoAnalysis of Chinese Academy of Geological Sciences. Numbers in bracket represent sample analyzed.

Ordovician, thallium-bearing ore-forming solutions deposited colloform pyrite and fine grain thallium minerals on the sea floor. Hydrothermal reworking took place in the late Yanshanian period (about 132 Ma). At this stage, a series of extensional fractures and faults provided favorable pathways for hydrothermal fluid flow. Fluid-rock interaction between the epithermal solution and syngenetic pyrite led to the deposition of thallium minerals, pyrite, fluorite, quartz, barite, and calcite. The epithermal stage of thallium mineralisation occurred immediately after formation of copper (iron)-gold mineralization (130~138Ma) in the Middle and Lower reaches of the Yangtze River (Zhai et al. 1992; Zhou et al. 2000; Mao et al. 2004).

3 Conclusions

Our major conclusions are as follows.

1. The Xiangquan thallium deposit formed by a two-stage process. Syngenetic thallium-enriched pyrite was deposited in the late Ordovician. The thallium was then reworked by epithermal fluids in the Yanshanian.
2. The Xiangquan thallium deposit is the first example of a thallium-only deposit reported anywhere in the world. It is possible that other epithermal thallium deposits formed in the NE Yangtze block in the late Yanshanian period. The epithermal event has occurred soon after the Yanshanian (130~138Ma) copper (iron)-gold mineralization that occurred in the middle and lower reaches of the Yangtze River.

Acknowledgements

This research is supported by the National Natural Science Foundation of China (Grant No. 40272048), the Anhui Provincial Excellent Youth Science and Technology Foundation (Grant No. 04045063) and the Anhui provincial Natural Science Foundation (Grant No. 01045202). We thank Prof. Chang Yinfo for his input during the study. Special thanks are due to Dr. David Cooke and Dr. Khin Zaw, Center for Ore Deposit Research, University of Tasmania, Hobart, Australia for their constructive advice and helpful comments.

References

Chang YF, Dong SW (1996) On tectonics of "Poly-Basement with one cover" in Middle-Lower reaches of Yangtze Craton China. Volcanology and Mineral Resources 17: 17–25

Mao JW, Holly S, Du AD, Zhou TF, Mei YX, Li YF, Zang WS, Li JW (2004) Molybdenite Re-Os precise dating for Molybdenite from Cu-Au-Mo Deposits in the Middle-Lower Reaches of Yangtze River Belt and its implications for mineralisation. Acta Geologica Sincina 78: 121-131

Wu MA, Tu YJ, Wang XY (2000) Exploration study on gold and silver mineral resources in north Changjiang region. Unpublished report, Hefei: 198

Zhai YS, Yao SZ, Lin XD (1992) Iron and copper deposits in the middle and lower reaches of Yangtze River. Geological Publishing House, Beijing: 254

Zhou TF, Yuan F, Yue SC, Zhao Y (2000) Two series of copper-gold deposits in the middle and lower reaches of the Yangtze River area and the O, S, Pb isotopes of their ore-forming hydrothermal systems. Science in China (Series D) 43 (supp): 208–218

Zhou TF, Yuan F, Yue SC (2003) $^{40}Ar/^{39}Ar$ fast neutron activation dating of quartz from the Tongniujing Cu, Mo, Au vein-type hydrothermal deposit, Anhui. Geological Review (in Chinese with English abstract) 49 (2): 212-216

Session 5
Epigenetic gold systems

Geochemical and isotopic constraints on Palaeozoic orogenic gold endowment and crustal evolution of the south central Andes, NW Argentina

Frank P. Bierlein
School of Geoscience, Monash University, Melbourne, VIC 3800, Australia, and Tectonics Special Research Centre, The University of Western Australia, Crawley, WA 6009, Australia

Beatriz Coira
CONICET and Instituto de Geología y Minería, Universidad Nacional de Jujuy, 4600 San Salvador de Jujuy, Argentina

Holly Stein
AIRIE Program, Department of Earth Resources, Colorado State University, Fort Collins, CO 80523-1482 USA

Abstract. Major and trace element concentrations, and Nd isotope compositions of Ordovician volcano-intrusive rocks in the Puna of northwestern Argentina point to their formation in a pericratonic setting above thickened and evolved continental crust. Input from juvenile sources was limited and there is no evidence for oceanic crust or the presence of a terrane-bounding suture in the region. In contrast to analogous terrains elsewhere in the Central Andes (e.g., in Peru and Bolivia), relatively minor orogenic gold mineralisation is known to occur in the Palaeozoic succession in northwestern Argentina. Possible explanations for the lack of more substantial orogenic gold endowment include the absence of hydrated oceanic substrate in the Puna, lack of 1st-order conduits and the limited extent of crustal shortening and thickening during Ordovician orogenic events.

Keywords. Orogenic gold, Puna Argentina, Re-Os, endowment, petrogenesis

1 Introduction

Orogenic gold mineralisation is developed within virtually all Palaeozoic metamorphic belts of the Pacific Rim (e.g., Lachlan Orogen, SE Australia; Hodgkinson-Broken River Province, NE Australia; Mongol-Zabaikal belt, Russian Far East; Buller Terrane, New Zealand; Eastern Andean Cordillera in Peru, Bolivia and Argentina; Goldfarb et al. 2001). In each of these terrains, orogenic gold mineralisation formed in response to crustal shortening and thickening, and from hydrothermal fluid systems that operated (intermittently) throughout uplift and exhumation of the orogenic belts. However, within this geological framework significant variations exist to the overall endowment in orogenic gold deposits and provinces. These variations are likely to be influenced and controlled by geological, structural and physico-chemical factors that operate on the province scale. The spatial association of major orogenic gold deposits with terrane-bounding sutures, and meta-sedimentary rocks that are typically interbedded with 'primitive' oceanic crust, implies that these rock sequences, as well the subduction of spreading ridges and/or mantle plumes, play important roles in the ore-forming process (Bierlein and Crowe 2000). Thus, it can be hypothesised that variations in the volume and composition of mafic rocks underlying a metasedimentary succession represent key elements in the economic evaluation of a given fold belt.

In this study, we report results of petrogenetic and isotopic investigations aimed at characterising and fingerprinting mafic intrusives, related volcanic rocks, and metasedimentary rocks in the Puna Argentina. In addition to providing insight into the tectonic evolution of Palaeozoic northwestern Argentina, these findings may allow for a more accurate assessment of gold endowment, fertility and future potential of this region, and contribute to an improved understanding of the processes that control the genesis of orogenic gold deposits.

2 Geological framework of orogenic gold deposits in the Puna Argentina

Gold deposits in the Sierra de Rinconada in the Puna of northwestern Argentina are hosted by low-grade metamorphosed and upright folded turbidites of mid-Ordovician age in the Ocloyic fold belt (Rodriguez and Bierlein 2002). Wallrock alteration associated with the predominantly laminated- to massive vein-hosted deposits is characterised by chloritisation, sericitisation, (de)silicification, and sulphidation. Notably, carbonatisation is only very weakly developed. A number of hard-rock deposits are known in the Palaeozoic of northern Argentina, with gold production typically dating back to Incaic times, but production figures are not recorded. Since 1890 only minor production has come from several deposits characterised by rich accumulations of very coarse, vein-hosted gold, with the vast majority of gold produced from about 20 deposits in the Sierra de Rinconada having come from placer workings. The total production of about 2 tonnes from this part of Eastern Andean Cordillera is in stark contrast to

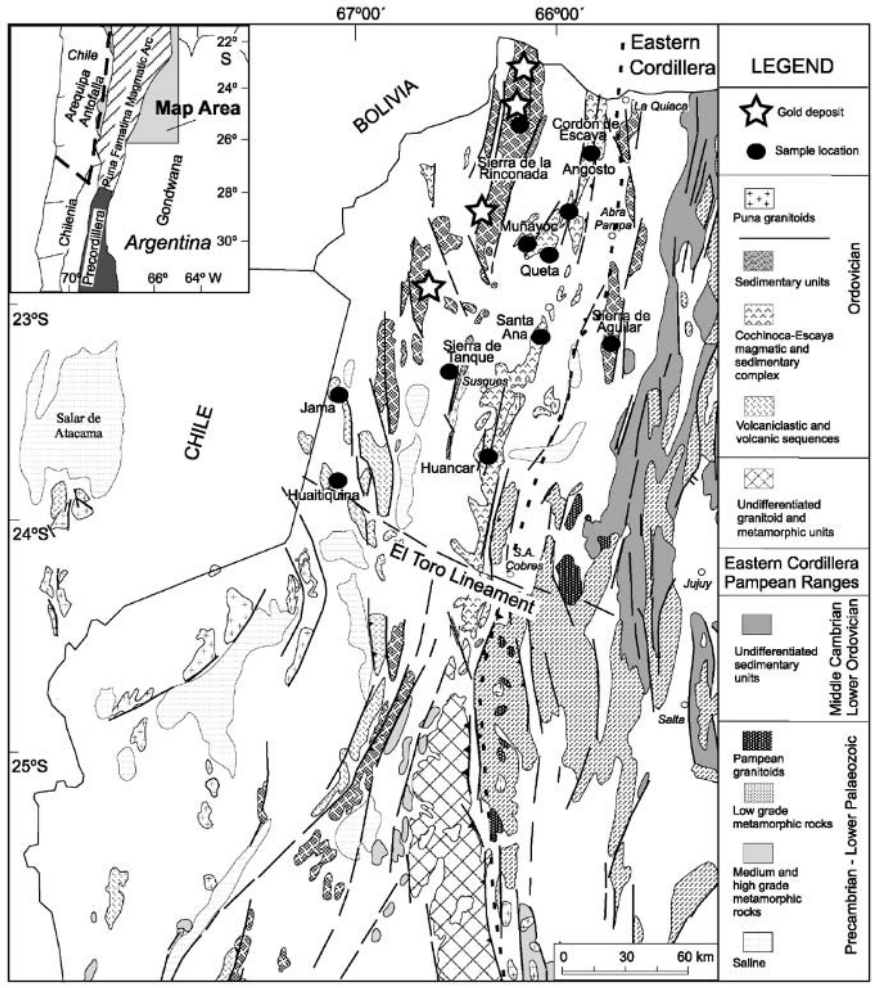

Figure 1: Map of part of the Puna in northwestern Argentina showing the distribution of principal Precambrian – Lower Palaeozoic volcano-intrusive and sedimentary units, location of orogenic gold deposits and position of samples analysed in this study (modified from Coira et al., 1999).

the > 160 tonnes of turbidite- and granite-hosted gold that have come from the Pataz Province in northern Peru, and the ~15 tonnes of placer gold from southeastern Peru and central-southern Bolivia (Haeberlin et al. 2002). In sharp contrast to these belts in the Eastern Andean Cordillera, as well as many other metamorphic terrains hosting orogenic gold mineralisation, there is no direct evidence of syn- or post-tectonic magmatism in the Sierra de Rinconada (e.g. Coira et al. 1999).

3 Crustal evolution of the Puna Argentina - insights from whole-rock and Sm-Nd data

The geodynamic setting and tectonic evolution of the Palaeozoic of northwestern Argentina is poorly constrained, but formation of the Puna turbidite complex is inferred to have occurred in response to the change from an extensional to a foreland basin setting in the Middle Ordovician times (Bahlburg 1990). Very little is known about the nature of the basement underlying the Puna turbidite complex. Therefore, we determined the petrogenetic characteristics of 15 volcano-intrusive rock units from the Puna Argentina in an attempt to i) constrain the nature of the substrate beneath the Ordovician-Devonian sedimentary succession, ii) assess evidence for crustal growth along the Pacific margin of Gondwana, and iii) consider the presence of an obscured terrane boundary/suture in the south central Andes of northwestern Argentina. Crustal growth would be indicated by a pronounced contrast in petrogenetic character of sampled material across the Puna and mark the appearance of juvenile or exotic sources across a lithospheric break. Conversely, homogenous data from volcano-intrusive rocks could indicate their derivation from a common magmatic source, with those of sedimentary rocks implying recycling of pre-existing material. If Ordovician volcano-intrusive and sedimentary rocks in the Puna originated in a setting involving active subduction and arc magmatism, the juvenile nature of the material should be reflected by trace elements and radiogenic Nd isotope signatures.

Ordovician metasedimentary rocks from the Puna Argentina are characterised by acidic arc signatures, with

La/Th ratios close to the field of upper continental crust. They have Th/Sc ratios of about 1 and trace element characteristics that are consistent with upper crustal derivation. Rare earth element patterns of all samples are also similar to the pattern of upper crust with light rare earth enrichment, pronounced negative Eu anomalies and relatively flat heavy rare earth patterns. On the basis of Hf-Th-Ta and Zr-Nb-Y relations, the volcano-intrusive rocks have implied sources that range from alkaline within-plate-type to back-arc-like chemistry. The majority of the samples are characterised by moderate to steep REE slopes, low La/Ta ratios and weakly elevated Th and U concentrations. These patterns are consistent with the formation of Ordovician volcano-intrusive rocks in the Puna involving a transition from a waning arc regime to a setting dominated by oblique convergence or strike-slip tectonics, as proposed by Coira et al. (1999). In such a setting, limited crustal melting could occur along sub-parallel fault zones cutting attenuated continental crust, with mantle decompression giving rise to alkaline magmatism along short-lived pull-apart basins in the former back-arc.

$Epsilon_{Nd}$ (450 Ma) isotope compositions for Ordovician volcano-intrusive rocks from the northern Puna range from 7.4 to -6.4, with samples of silicic units in the eastern belt yielding between -6 and -5, and the less abundant mafic units between -2 and 7 (indicative of some juvenile mantle input). Magmatic rocks of the western belt show a more pronouncned arc signature and yield $Epsilon_{Nd}$ values from -5 to –2, indicative of juvenile, differentiated material mixed with an old crust, or derived in part from a crust with an inherit arc signature. The Nd isotope compositions of all these rocks correspond to a substantial range in depleted-mantle model ages (TDM) from 0.56 to 1.84 Ga. Trace element patterns of Ordovician turbidites that are slightly younger than the magmatic sequences in the Puna point to a decreasing to absent juvenile contribution. This trend is indicated by smaller negative Eu anomalies, less marked high field strength depletion, lower Ba/La, less variation in Th/Sc ratios with values >1 and, as reported by Bock et al. (2000), homogeneous, evolved crustal ε_{Nd} (450 Ma) values of –7.0 ± 1 and TDM of 1.6 to 1.8 Ga. All these data suggest that input of juvenile (arc-related) material in the northern Puna during the Ordovician was rather limited and short-lived.

4 Timing of gold mineralisation

In a preliminary study, we analysed two samples of auriferous quartz vein-hosted pyrite from the Minas Azules and El Torno gold deposits in the Sierra de Rinconada. Both samples are low-level, highly radiogenic with variable 187Re/188Os ratios. The choice of the initial ratio affects the calculated ages but since the samples occur in rocks of predominantly continental-character crustal provenance (as discussed above), a crustal initial ratio of ~0.9 can be assumed. Sample Py-03 from the Minas Azules has Re (2.5 ppb) and Os (22.3 ppt) that can be well measured. Its $^{187}Re/^{188}Os$ ratio is 1054 and a model age with an initial of 0.9 yields approximately 360 Ma. However, the error on this model age is rather large at ± 50 Ma. Sample Py-06 from the El Torno deposit has notably higher Re (5 ppb) with low Os (34 ppt). It yields a $^{187}Re/^{188}Os$ ratio of 2630 and a reasonably well-constrained calculated model age of 440 ± 18 Ma, corresponding to the timing of the Ocloyic orogeny. Field evidence supports the notion of multiple ore genesis across the Sierra Rinconada in the Palaeozoic (Rodriguez and Bierlein 2002), but further geochronological data are required to ascertain the age(s) of orogenic gold formation.

5 Make-up of the orogen - a possible explanation for low gold endowment?

Whole-rock data and Nd isotopic compositions of Ordovician volcano-intrusive and sedimentary rocks do not support a tectonic setting that involved significant crustal growth during the Palaeozoic in the south central Andes of northwestern Argentina. In agreement with the findings of Bock et al. (2000), our data do not indicate the appearance of allochthonous terranes, neither does it support the presence of oceanic crust or a terrane-bounding suture in the study area. The dominance of evolved crustal material suggests that the Ordovician magmatic arc that gave rise to the volcano-intrusive succession, as well as the Puna turbidite complex developed on attenuated continental crust. In the absence of more pronounced subduction and reduced mantle input (at least in the eastern belt), contributions from juvenile sources were likely to be of limited importance. If the Ordovician orogenic event in the Puna of northwestern Argentina was restricted both in its extent and intensity, it could also explain the absence of more substantial crustal melting and syn- to post-tectonic granite generation north of the El Toro Lineament (Fig. 1).

The consistent correlation between the (confirmed) presence and volume of oceanic-character substrate and elevated gold endowment in orogenic belts throughout space and time almost necessitates that compositional variations of the sub-crust underneath the meta-sedimentary successions in each of these terrains can, at least to some extent, account for the significant disparity in their apparent gold endowment. Furthermore, chemical modelling by Mernagh and Bierlein (2004) has highlighted the importance of CO_2 in generating 'fertile', orogenic gold-bearing fluids. The requirement to generate sufficient amounts of CO_2 from, for example, carbonate-rich mafic rocks, serpentinised ultramafics or mantle melts thus lends further support to the notion that primitive, hydrated and oceanic-character terranes are more likely

to be gold-rich than pericratonic and dehydrated blocks that are characterised by a felsic and more fractionated composition.

The nature and composition of the pre-Ordovician substrate, together with the limited extent of Ordovician orogenic events in the Puna of northwestern Argentina, thus may explain the low gold endowment of this region and also suggests that potential for major orogenic gold discoveries in the Palaeozoic volcanogenic-sedimentary succession of this part of the southern Central Andes is limited.

Acknowledgements

G. Rodriguez and Iamgold Pty. are thanked for assistance with field work and provision of sample material; we are grateful to R. Markey for carrying out Re-Os analyses. FPB acknowledges support via ARC Discovery Grant DP0342488.

References

Bahlburg H. (1990) The Ordovician basin in the Puna of NW Argentina and N Chile: geodynamic evolution from back arc to foreland basin: Geotektonische Forschungen 75: 1-107

Bierlein FP, Crowe DE (2000) Phanerozoic orogenic lode gold deposits. In: Hagemann, SG, Brown PE (eds), Gold in 2000, Society of Economic Geologists Reviews in Economic Geology 13, pp. 103-139

Bock B, Bahlburg H, Worner G, Zimmermann U (2000) Tracing crustal evolution in the southern Central Andes from Late Precambrian to Permian with geochemcial and Nd and Pb isotope data. The Journal of Geology 108: 515-535

Coira B, Peréz B, Flores P, Kay SM, Woll B, Hanning M, (1999) Magmatic sources and tectonic setting of Gondwana margin Ordovician magmas, northern Puna Argentina and Chile. Geological Society of America Special Paper 336, pp. 145-170

Goldfarb RJ, Groves DI, Gardoll S (2001) Orogenic gold and geologic time: a global synthesis. Ore Geology Reviews 18: 1-75

Haeberlin Y, Moritz R, Fontboté L (2002) Paleozoic orogenic gold deposits in the eastern Central Andes and its foreland, South America. Ore Geology Reviews 22: 41-59

Mernagh TP, Bierlein FP (2004) Chemical controls on the Endowment of turbidite-hosted gold deposits in the Lachlan Fold Belt. In: Bierlein FP, Hough MA (eds), Tectonics to Mineral Discovery - Deconstructing the Lachlan Orogen. Proceedings Volume and Field Guide, MORE-SGEG Conference, Orange, NSW, July 6 - 8, 2004. Geological Society of Australia Abstracts No 74, pp 139-140

Rodriguez GA, Bierlein FP (2002) The Minas Azules deposit – an example of orogenic lode gold mineralisation in the Sierra de Rinconada, northern Argentina. International Geology Reviews 44: 1053-1067

Models for epigenetic gold exploration in the northern Cordilleran Orogen, Yukon, Canada

Mike Burke, Craig J.R. Hart, Lara L. Lewis
Yukon Geological Survey, Box 2703 (K-10), Whitehorse, Yukon, Y1A 2C6, Canada

Abstract. A variety of gold deposit styles formed in response to Mesozoic and Cenozoic metamorphic, plutonic and volcanic events associated with the formation of the northern Canadian Cordilleran orogen. Orogenic lodes are two ages. The oldest are as old as Jurassic and formed after peak metamorphism of the Yukon-Tanana terrane. These lodes likely contributed to the Klondike placer deposits. The youngest orogenic veins formed during the Eocene during metamorphism and uplift of more outboard terranes. Intrusion-related gold ores are mainly related to far-inboard post-orogenic, reduced mid-Cretaceous intrusions. These occurrences comprise the Tombstone Gold Belt as well as other gold districts in Yukon. Epithermal gold ores formed in association with Late Cretaceous to Eocene subaerial volcanism. Differentiation of the gold deposit models are important first steps for exploration targeting in regions of complex geology.

Keywords. Yukon, Cordillera, gold, epigenetic, epithermal, intrusion-related, orogenic

1 Introduction

Yukon Territory in the northern Canadian Cordillera is underlain by a mosaic of late Paleozoic and Mesozoic suspect (arc and oceanic) and pericratonic terranes that have been accreting to the Noeproterozoic and early Paleozoic miogeocline-dominated continental margin since the Early Jurassic. Upon this complex geological framework are an array of gold deposits and occurrences that are categorized as orogenic, intrusion-related, skarns and epithermal. Gold mineralization formed in response to, Mesozoic to Cenozoic metamorphic, plutonic, and volcanic events during the evolution of the North American Cordilleran orogen.

2 Orogenic gold

Orogenic gold mineralization in the Yukon is mostly associated with the polydeformed, greenschist-grade pericratonic metasedimentary and metaigneous rocks of the Yukon-Tanana Terrane. The orogenic lodes occur as low-sulfide quartz veins in fissures and shears, that postdate metamorphism. The oldest veins are ca. 170-145 Ma having formed after Early Jurassic (~185 Ma) terrane accretion and metamorphism. The youngest veins occur in more outboard (coastal) locations and are likely ca. 55 Ma having formed in response to metamorphism and uplift associated with emplacement of coastal batholiths (Coast Plutonic Complex).

Orogenic gold has not traditionally been a focus of exploration in Yukon, despite approximately 20 million ounces of placer gold having been recovered from the historic Klondike placer district, and associated goldfields. An orogenic source is suspected but significant motherlodes have not been discovered. Recent exploration activity however, has focused on orogenic gold lodes targets in the Klondike, and on other areas underlain by Yukon-Tanana terrane that also yield significant placer gold (such as Stewart River). Much of this region escaped Quaternary glaciation and bedrock exposure is poor with thick colluvial cover and inhibits effective exploration. The Lone Star deposit, at the headwaters of Bonanza Creek in the heart of the Klondike, is one of the few, small historical lode producers in the district with a reported production of 7650 tonnes grading 5.1 g/t Au from the early 1900's. Ore was produced from discordant quartz and quartz-pyrite veins. Gold grades are erratically distributed in the nuggety veins and new exploration efforts at Lone Star include bulk sampling. Controls on vein location and gold enrichments in the Klondike are not well understood but are pivotal for successful exploration of orogenic vein gold mineralization in this region.

Approximately 80 km south of the Klondike district, active placer mining in the White River-Thistle Creek area, an area also underlain by Yukon-Tanana terrane, has been targeted for orogenic gold. Gold-rich quartz vein specimens were reported by Dominion of Canada Land Surveyor William Ogilvie in 1887. Efforts directed towards finding the source of the specimens is unclear but recently discovered quartz vein float, in an area with historical hand trenching, assayed >50 g/t Au. Subsequent exploration has exposed parallel quartz veins with visible gold and minor chalcopyrite and galena. The veins are hosted in sericite-altered quartz-muscovite schist proximal to a small gabbroic intrusion. A coincident Au-As-Sb (Au to 1580 ppb, As to 1080 ppm, Sb to 97 ppm) soil geochemical signature overlaps the apparently faulted margins of the intrusion. Geological mapping indicates areas with similar potential in proximity to placer gold bearing creeks in the area, but geological controls on mineralization remain poorly understood.

Orogenic gold veins have also recently been discovered in the Coast Belt metamorphic rocks (Kluane Schist metasedimentary rocks), between upper greenschist and amphibolite isograds in the footwall of the Coast Plutonic

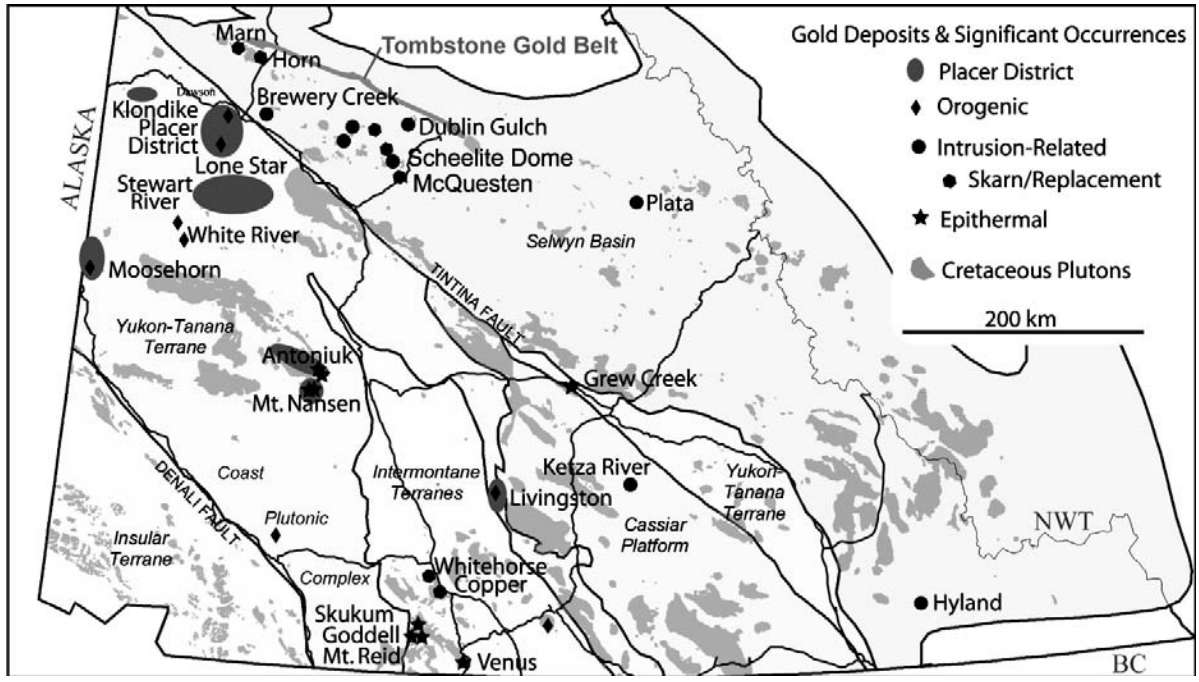

Figure 1: Distribution of differing types of gold deposits and occurrences in southern Yukon with respect to Cretaceous plutons.

Complex, also in an area with current and historic placer gold production. These rocks were metamorphosed and uplifted in response to mid-crustal magmatic emplacement during the Eocene and the veins are likely similarly aged. The recognition of orogenic gold veins in association with some of the richer placer gold districts in Yukon suggests that other placer districts with similar geologic settings and metamorphic histories, such as the Stewart River and Livingston areas, should be targets for orogenic vein gold deposits.

3 Intrusion-related gold

Intrusion-related gold deposits with elevated primary oxidation states (magnetite-series) have a close association with copper porphyry-like systems and intrude accreted terranes, but reduced (ilmenite-series) intrusion-related systems have a gold-bismuth-tungsten association, lack associated base metals and intrude miogeoclinal basinal strata (Selwyn Basin) of the ancient continental margin. These reduced gold systems are associated with mid-Cretaceous (94 Ma), slightly metaluminous, and slightly alkalic plutons and form the Tombstone Gold Belt (Hart et al. 2000, 2002). Related metal associations are zoned but variable depending on the nature of host rocks and distance from the pluton, but gold is associated with Bi, Te, W (proximal), As (medial), and Ag-Pb (distal). As well, epizonal variants of reduced intrusion-related systems such as Brewery Creek, have lower temperature metal associations (Au-As-Hg-Sb) and gold is associated with refractory arsenian-rich rims on pyrite, similar to Carlin-type deposits. These intrusion-related gold systems show a wide variability in occurrence style from sheeted arrays of low-sulphide gold bearing quartz veins hosted within the intrusion, to gold-rich and tungsten-rich skarns, solitary Au-As veins near the intrusion margins, to auriferous replacements, stockworks, and disseminations in the thermal aureoles. Reduced intrusion-related gold systems are a relatively new model and exploration for these styles of deposits began in the late-1980's after the discovery of the Fort Knox deposit in Alaska. Exploration efforts directed towards intrusion-hosted occurrences such as Dublin Gulch, Clear Creek and Scheelite Dome which are the closest analogies to the Fort Knox deposit, continue. A resource of ~ 2 Moz was defined at Dublin Gulch prior to the late 1990s declining gold market, but is the current focus of exploration efforts. Researchers and explorationists recognized the variable styles of mineralization around these intrusions in the 1990s but exploration of these newly recognized targets was limited by the lack of available exploration funds during these times. The epizonal ores of the Brewery Creek mine (17 Mt of 1.44 g/t Au) emphasized the metal variability in ore types associated with this model. Mining of the unglaciated and oxidized ores allowed low cost mining and heap-leach solvent extraction (280,000 ounces production, 1996 to 2002). This deposit is undergoing a new phase of exploration due to recognized similarities with the large Donlin Creek deposit in Alaska. Renewed exploration interest has focused attention on some of these systems due to an

improved understanding of their geological settings, such as at Ketza River where approximately 100,000 ounces were produced from oxidized sulfide replacement bodies in lower Cambrian limestone. The Ketza ore bodies are related to an unexposed mid-Cretaceous pluton presumed to exist at depth as evidenced by regional uplift, local extensional deformation, and hornfelsing and silicification of argillaceous country rocks. As well, the Hyland property, in southeastern Yukon, is characterized by intense silicification and sulfide replacement of phyllite and quartzite along the axis of an overturned antiformal structure. The property is underlain by a prominent magnetic low feature and a few narrow intrusive dykes are exposed suggesting that the mineralization may also be underlain by a large intrusive body.

4 Gold skarns

Gold-rich skarns are associated with both oxidized and reduced intrusions. Only a few of the skarns are gold-only, as most have either associated copper or tungsten mineralization depending on the pluton's metallogenic character as imparted by their redox state. The most significant gold skarn deposits in Yukon are located in the Whitehorse Copper Belt where Upper Triassic carbonate of the Stikine island arc terrane are in contact with the Cretaceous Whitehorse Batholith. Two types of skarns are present, iron-rich skarns are characterized by retrograde magnetite and serpentine whereas calc-silicate skarns are characterized by prograde garnet and diopside. The belt contains 28 deposits along 32 km of the western margin of the Whitehorse Batholith, a body of metaluminous, magnetite-series quartz diorite and granodiorite. Production from 1900 to 1982 came from 10 Mt with an average grade of 1.5% Cu, 0.7 g/t Au, 13.0 g/t Ag. Recent exploration has uncovered several new areas of skarn mineralization and drilling has intersected sheeted quartz-chalcopyrite-bornite veins within granodiorite intrusion. Many skarns are developed in Selwyn Basin strata in association with the moderately reduced, mid-Cretaceous (94 Ma) Tombstone and Mayo plutonic suite intrusions. The Marn and Horn skarn deposits are examples of gold-rich skarns with a copper-bismuth association. The Marn deposit consists of pyroxene-garnet with retrograde sulphide mineralization consisting mainly of pyrrhotite and chalcopyrite hosted in Permian limestone in contact with the Cretaceous Mt. Brenner stock. The deposit contains a resource of approximately 250,000 tonnes grading 8.56 /t Au, 1.0% Cu and 0.1% W. In a similar geological setting is the Horn deposit, a small but high grade gold-copper-bismuth skarn, in a limestone pendant within the Cretaceous Tombstone pluton syenite stock. Other skarn occurrences associated with the mid-Cretaceous Tombstone Plutonic Suite include the Tom zone on the Scheelite Dome property where gold mineralization in pyroxene skarn is developed within calcareous rocks of the Neoproterozoic to Lower Cambrian Hyland Group. Drill intersections to 6.4 m of 7.09 g/t Au have been obtained. The McQuesten occurrence hosts weakly skarned mineralization with disseminated to semi-massive pyrrhotite developed in calcareous metasedimentary rocks but a quartz monzonite dyke is the only exposed magmatic rock. Widespread mineralization is indicated as gold mineralization is exposed over 1.4 kilometres of strike length with values up to 5.81 g/t Au over 7.7 metres. The Mahtin occurrence forms at the contact between the Cretaceous Sprague Creek stock of the and Upper Cambrian-Ordivician Rabbitkettle Formation silty limestone. Numerous anomalous and mineralized areas occur within the limestone adjacent to the intrusion. Calc-silicate skarn in boulders have disseminated pyrrhotite-pyrite-arsenopyrite mineralization and values to 6.5 g/t Au.

5 Epithermal gold

Epithermal gold mineralization in Yukon is associated with either porphyry to epithermal transitions (e.g. Mount Nansen, Mount Freegold), or with arc-like calderas (Mt. Skukum) or rift-related subaerial volcanics (Grew Creek). Most systems area characterized by low sulfidation epithermal characteristics, but those in the epithermal-porphyry transition are of "intermediate" sulfidation character having high silver contents but lacking copper enrichments or acid-related alteration. The former producing Mt. Nansen and Venus mines are two examples of deposits formed in association with post-orogenic Late Cretaceous calc-alkaline arcs and having intermediate sulfidation character. The Mt. Nansen mine has minor production (1089 kg Au, 4,276 kg Ag) from veins containing dark grey silica and pyrite, arsenopyrite, sphalerite, galena, sulphosalts, bornite, stibnite and chalcopyrite along the margins of a feldspar porphyry dyke. The deposit occurs in basement rocks below the volcanic strata. The Venus deposit has limited historical production and is also silver-rich. Mineralization consists of coarsely crystalline quartz and carbonate within vein-marginal bands and pods of quartz, pyrite and arsenopyrite. Gold is associated with second stage vein fillings with galena and sphalerite with minor tetrahedrite and chalcopyrite. The Venus vein, which averages 0.9 m in width, has been traced for 1.2 km and is hosted in Cretaceous andesitic rocks. Fourteen similar vein occurrences are located in the district. The Mt. Skukum deposit is a former producer and an example of a low-sulfidation deposit (McDonald and Godwin 1986; Love et al. 1998). Quartz-carbonate gold-silver veins, andesitic and felsic dykes occupy fault structures cutting porphyritic andesitic flows and tuffs of the Eocene Mt. Skukum caldera complex. Vein marginal phyllic alteration is mineralized with minor wallrock pyrite being the only significant sulfide mineral. Boiling tex-

tures are common. Au:Ag ratios are approximately 1:1. Mining produced approximately 95,000 ounces of gold with grades of 25 g/t Au and 20 g/t Ag. The Grew Creek deposit is a quartz-adularia dominated low-sulfidation epithermal vein system hosted in Eocene volcanic and sedimentary rocks in a rift environment within a pull-apart zone in the Tintina fault zone (Christie et al. 1992). A resource of 773 000 tonnes grading 8.92 g/t Au and 33.6 g/t Ag is reported but will increase due to recent successful exploration that is targeting north-trending extensional zones. The deposit consists of a high-grade quartz-adularia vein that is faulted into four segments and surrounded by a low-grade stockwork.

6 Conclusions

A variety of styles of epigenetic gold mineralization occurs in Yukon in a wide range of geological settings in response to a several deformation and magmatic events. Much recent exploration in Yukon has focused on mid-Cretaceous intrusion-related systems, mainly intrusion-hosted occurrences after the discovery of the Fort Knox Mine in Alaska in the late-1980's. Exploration has more recently broadened to the variable styles of intrusion-related systems which were recognized but only received minimal exploration during the prolonged period of low exploration activity. Several styles of epithermal gold deposits have been explored and exploited historically in Yukon. All are associated with Late Cretaceous-Eocene magmatic activity. Current exploration success may rekindle interest of Yukon's epithermal gold potential. Orogenic lodes, which have been accepted as a contributor to the Klondike's placer gold, are becoming increasingly recognized as a significant target both in the Klondike and in many of the Yukon's other placer gold camps. These potentially high-grade veins are attractive, but challenging exploration targets due to the lack of understanding of the metamorphic and structural history of Yukon-Tanana terrane.

Characteristics and evolution of hydrothermal fluids from the Archean orogenic New Celebration gold deposits, Western Australia

J.L. Hodge, S.G. Hagemann, P. Neumayr
School of Earth and Geographical Sciences, The University of Western Australia, 35 Stirling Highway, Crawley, Western Australia 6009, Australia

Abstract. The western segment of the Boulder Lefroy fault zone in the Eastern Goldfields province of Western Australia hosts the New Celebration gold deposits (~20,000,000t @ 2.40g/t Au for ~ 1,500,000 oz Au). Detailed petrography and microthermometry on fluid inclusions hosted in Early (Porphyry- and Mylonite-styles) and Late (Fracture-style) gold-related quartz and quartz-carbonate veins at New Celebration revealed a progression from early methane-rich fluids, which may represent deep-crustal fault-zone fluids, to low salinity, aqueous-carbonic gold -related fluids, to late, dense, highly saline brines.

Porphyry- and Mylonite- style gold mineralization formed at temperatures between 330° and 450°C and pressures between 3 and 4kbars, whereas Fracture-style mineralization, which post-dates both Porphyry- and Mylonite-style mineralization formed at similar pressures but lower temperatures, between 290° and 350°C. Isochors calculated from representative fluid inclusions trapped in quartz and quartz-carbonate veins associated with both mineralizing events, in conjunction with independent pressure estimates suggest an isobaric cooling path.

Preliminary fluid inclusion data revealed no evidence for phase immiscibility or fluid mixing.

Keywords. Boulder Lefroy fault zone, New Celebration, gold, fluid inclusions, Archean

1 Introduction

Worldwide, Archean orogenic lode gold deposits typically show a close spatial relationship to first-order, trans-crustal fault systems (Eisenlohr et al. 1989; Neumayr et al. 2000). At a camp- to deposit-scale, however, second- and third-order splays typically host the majority of world-class (>100t Au) deposits (Eisenlohr et al. 1989; Groves et al. 1990; Cox and Ruming 2004). While much research has been undertaken into the fluid chemistry and P-T-X-t evolution of hydrothermal fluids in the ore-bearing lower order structures, fluid analyses in first order faults have been largely ignored.

The New Celebration gold deposits are located within the Boulder segment of the first-order, trans-crustal Boulder Lefroy fault zone (Swager 1989) in the Eastern Goldfields Province of the Yilgarn Craton, Western Australia. The fault zone forms the eastern margin of the Kalgoorlie Terrane, a NNW-trending, elongated volcano-sedimentary terrane (Swager 1997), and is spatially associated with the world-class Golden Mile and St Ives gold camps, which are hosted in adjacent lower-order splays. Orogenic lode gold deposits hosted in first-order structures are rare, so the New Celebration gold deposits provide a unique opportunity to study the P-T-X-t evolution of hydrothermal fluids in a first-order fault zone segment, and evaluate the role regional scale structures play in focusing mineralizing and non-mineralizing fluids.

This abstract presents the results of preliminary investigations into the hydrothermal fluid system at New Celebration and constrains the P-T-X-t conditions of deformation, hydrothermal alteration and gold mineralization. A preliminary hydrothermal fluid evolution model is presented and the constraints on gold precipitation evaluated.

2 Geological setting

The New Celebration gold deposits are hosted within a sequence of ultramafic and differentiated mafic rocks, which is metamorphosed to upper greenschist facies and intruded by a number of felsic and lamprophyric dykes (Langsford 1989).

2.1 Structural and magmatic evolution, hydrothermal alteration and gold mineralization

Nichols (2003) identified three major deformation events at New Celebration: 1) $D2_{NC}$, represented by upright folding, which predates gold mineralization; 2) $D3_{NC}$, represented by oblique slip fault movement, which is spatially and temporally associated with an Early gold mineralizing event; and 3) $D4_{NC}$, associated with strike-slip fault movement, which is synchronous with a Late gold mineralizing event.

Nichols (2003) also recognized two major magmatic events at New Celebration: 1) early plagioclase porphyries (denoted M1), which are intensely altered and have a penetrative $S3_{NC}$ foliation; and 2) later, weakly altered, unfoliated to weakly foliated quartz-K-feldspar porphyries, which cross-cut M1 porphyries.

The Early gold event comprises Mylonite- (hosted in mylonitized M1 porphyry), Porphyry- (hosted in foliated M1 porphyry) and Contact- (hosted at the contact between M2 porphyry and high-Mg basalt) styles of mineralization, whereas the Late gold event comprises Fracture-style (hosted in M2 porphyry) mineralization.

Pyrite in textural equilibrium with biotite $S3_{NC}$ foliation planes hosts gold in the Early mineralization styles and is associated with quartz and zoned quartz-calcite shear and extension veins and proximal biotite-ankerite-sericite-pyrite alteration. Porphyry and Mylonite mineralization styles display a strong telluride association

Thin (1-2mm) fractures developed on the margins of M2 porphyries host Fracture-style mineralization. Pyrite hosts gold as intragranular inclusions or along grain boundaries and is spatially associated with quartz breccia veins. Proximal alteration comprises pyrite-sericite±chlorite and is restricted to the fracture fill. Tellurides are absent. Quartz breccia veins associated with Fracture-style mineralization clearly crosscut $S3_{NC}$ fabrics and are interpreted as post-$D3_{NC}$.

3 Fluid inclusions

3.1 Types and timing relationships

Early gold at New Celebration is predominantly wall rock hosted, and occurs primarily as inclusions in pyrite within iron-rich rocks, whereas sericite-chlorite-filled fractures host Late gold. It is therefore not directly possible to measure the fluids responsible for Early and Late mineralization, so veins directly spatially and temporally related to gold mineralization were selected for fluid analysis as the best proxy for gold mineralizing fluids. Detailed petrography and microthermometry of primary, pseudo-secondary and secondary inclusions from Early gold-related quartz and quartz-calcite veins in Porphyry- and Mylonite-style samples, and Late gold related quartz breccia veins in Fracture-style mineralization revealed four inclusion types and a number of different fluid inclusion assemblages. A fluid inclusion assemblage comprises one or more inclusion types contemporaneously trapped in clusters or trails (Diamond 1990). The following section outlines, in chronological order from oldest to youngest, the fluid inclusion types and assemblages observed in Porphyry, Mylonite and Fracture mineralization styles.

Porphyry-style mineralization:
1. CH_4
2. H_2O-CO_2-NaCl-CH_4 - H_2O-NaCl - CO_2-CH_4
3. H_2O-NaCl
4. CH_4±N_2

Mylonite-style mineralization:
1. H_2O-NaCl - CO_2-CH_4 - H_2O-CO_2-NaCl-CH_4
2. H_2O-NaCl

Fracture-style mineralization:
1. H_2O-CO_2-NaCl-CH_4 - H_2O-NaCl - CO_2-CH_4
2. H_2O-NaCl (low salinity)
3. H_2O-NaCl (high salinity)

3.2 Microthermometric results

3.2.1 Low-temperature measurements

Where observed, the eutectic temperature of aqueous inclusions in all mineralization styles occurred at approximately -24° to -22 °C, indicating that these inclusions are likely within the H_2O-NaCl±KCl system (Shepherd et al. 1985). Final ice-melting temperatures (Tm_{ICE}) for aqueous inclusions typically ranged between -10° and 0°C in all mineralization styles, however, in Fracture-style mineralization, low temperature measurements delineated two populations: 1) Tm_{ICE} between -5° and 0°C, and 2) Tm_{ICE} between -15° and -21°C.

In Porphyry and Fracture mineralization styles the majority of mixed aqueous-carbonic inclusions displayed CO_2 melting temperatures around the CO_2 triple-point (-56.6°C), indicating that the CO_2 phase of these inclusions was almost pure. Clathrate melting temperatures ranged between 6° and 9°C, while CO_2 homogenized to liquid between 6° and 31°C.

Low temperature measurements on methane inclusions delineated two populations: 1) homogenized to liquid at around -75°C and 2) homogenized to liquid at around -90°C. In the absence of laser Raman analyses these inclusions are interpreted to be methane rich, however other gas phases may be present.

3.2.2 High-temperature measurements

Aqueous inclusions in the Porphyry-style sample homogenized to liquid at temperatures between 180° and 360°C, whereas aqueous inclusions in the Mylonite-style sample homogenized to liquid at slightly lower temperatures, between 220° and 290°C. The highly saline aqueous inclusions in Fracture-style mineralization homogenized to liquid at very low temperatures, between 87° and 102°C.

Aqueous-carbonic inclusions in calcite from the Porphyry-style sample either homogenized to liquid or decrepitated via expansion of the vapor bubble at temperatures between 267° and 271°C. Aqueous-carbonic inclusions in quartz from both Porphyry and Fracture mineralization styles homogenized to liquid or decrepitated via vapor bubble expansion between 220° and 290°C; rare inclusions homogenized to liquid at temperatures up to 360°C.

3.3 Fluid composition and density

The salinity of aqueous inclusions in Porphyry and Mylonite mineralization styles ranged from 6-11equiv. wt% NaCl and 11-14 equiv. wt% NaCl, respectively, whereas in Fracture-style mineralization two aqueous

inclusion populations were observed: a low salinity (5-9 equiv. wt% NaCl) group and a high salinity (19-23 equiv. wt% NaCl) population. Aqueous-carbonic inclusions in Porphyry and Fracture mineralization styles contained between 0 and 10 equiv. wt% NaCl, with rare outliers of up to 18 equiv. wt% NaCl.

Aqueous-carbonic inclusions in Porphyry-style mineralization contained between 10 and 30 mole % CO_2 while similar inclusions in Fracture-style mineralization showed a wider range, between 10 and 70 mole % CO_2. Methane in aqueous-carbonic and carbonic inclusions from all mineralization styles was less than 3 mole % CH_4. The bulk density of all inclusion types in all mineralization styles typically ranged between 0.75 and 1.00g/cm^3, with outliers as low as 0.60 and as high as 1.20g/cm^3

4 Fluid inclusion processes and implications for gold mineralization

Early gold mineralization at New Celebration is hosted in the wall rocks (mylonites and M1 porphyries) and therefore is interpreted to be the result of desulfidation reactions between gold-bearing fluids and iron rich wall rocks (Williams 1994). This is consistent with the present lack of evidence for fluid immiscibility and fluid mixing in veins associated with Porphyry and Mylonite styles of mineralization. The likely depositional mechanism for Fracture-style mineralization is equivocal.

5 P-T-t history and hydrothermal model

Pressures determined from pressure-corrected aqueous inclusions, maximum homogenization temperatures of aqueous-carbonic inclusions and an independent pressure estimate from phengite geobarometry (Williams 1994) indicate that Porphyry- and Mylonite-style mineralization formed between 3 and 4kbars and at temperatures between 330° and 450°C, whereas Fracture style mineralization formed at similar pressures and at temperatures between 290° and 350°C. Calculations of isochors from fluid inclusions within representative quartz and quartz-calcite veins from the different mineralization styles suggest isobaric cooling during both Early and Late mineralizing events.

The following section presents a preliminary hydrothermal model for hydrothermal fluid flow and associated gold mineralization during $D3_{NC}$ and $D4_{NC}$ deformation events:

- The earliest observed $CH_4 \pm CO_2$ fluid inclusions possibly represent a regional-scale fault-zone fluid of unknown source (mantle or deep-crustal metamorphic fluid).
- The fault experienced a localized pulse of hot fluid of unknown origin. As this fluid cooled isobarically, it interacted with iron-rich wall rocks, precipitating Porphyry, Mylonite and Contact style gold in the host rock due to desulfidation reactions.
- A second, localized fluid pulse, slightly cooler than the first, ascended along the fault. This fluid was responsible for the Late gold mineralizing event. It is presently unclear whether this event was also the result of wall rock reaction, or whether it occurred by some other mechanism such as fluid immiscibility or fluid mixing.
- Low-salinity aqueous fluids overprinted all gold mineralization styles.
- Methane rich fluids were the latest observed in Porphyry-style mineralization whereas cool, highly saline fluids were the latest observed in Fracture-style mineralization.

6 Conclusions

Interpretation of the vein system and detailed petrography of the fluid inclusion assemblages associated with gold mineralization at the New Celebration gold deposit leads to the following preliminary conclusions:

1. Porphyry-style mineralization took place at temperatures between 360 and 450°C and between 3- 4kbars from low salinity fluids containing approximately 30 mole % CO_2 and little or no CH_4. Mylonite style mineralization occurred between 330 and 360°C and at 3-4kbars from similar low salinity, moderately CO_2-rich fluids.
2. Fracture-style mineralization occurred at around 300 and 350°C and between 3 and 4kbars from a second pulse of low salinity, moderately CO_2-rich, low CH_4 hydrothermal fluid.
3. Isochors from representative fluid inclusions from all mineralization styles, in conjunction with independent pressure estimates suggest an isobaric cooling history during Early and Late gold mineralization stages.
4. Low salinity aqueous fluids overprinted both Early and Late mineralizing events.
5. Methane dominated fluids post-dated all other fluids in Early mineralization.
6. Cool, dense, highly saline brines overprinted all other fluids in Late mineralization.

Acknowledgements

The first author acknowledges receipt of an Australian Post-graduate Award and a pmd*CRC supplementary scholarship. This research is supported by Harmony Gold Australia.

References

Cox SF, Ruming K (2004) The St Ives mesothermal gold system, Western Australia - a case of golden aftershocks? Journal of Structural Geology 26: 1109-1125.

Diamond LW (1990) Fluid inclusion evidence for P-V-T-X evolution of hydrothermal solutions in late alpine gold quartz veins at Brusson, Val d'ayas, Northwest Italian Alps. American Journal of Science 290: 912-958.

Eisenlohr BN, Groves DI, Partington GA (1989) Crustal scale shear zones and their significance to Archaean gold mineralisation in Western Australia. Mineralium Deposita 24: 1-8.

Groves DI, Barley ME, Ho SE (1990) Nature, genesis and tectonic setting of mesothermal gold mineralisation in the Yilgarn Block, Western Australia. Economic Geology Monograph 6: 71-85.

Langsford N (1989) Stratigraphy of Locations 48 and 50 Kalgoorlie Gold Workshop. pp 6.

Neumayr P, Hagemann SE, Couture JF (2000) Structural setting, textures and timing of hydrothermal veins systems in the Val d'or camp, Abitibi, Canada: Implications for the evolution of transcrustal, second- and higher-order fault zones and gold mineralisation. Canadian Journal of Earth Sciences 37: 95-115.

Nichols S (2003) Structural control, hydrothermal alteration and relative timing of gold mineralisation at the New Celebration gold deposits, Kalgoorlie, Western Australia School of Earth and Geographical Sciences. University of Western Australia, Pert, pp 62.

Shepherd TJ, Rankin AH, Alderton DHM (1985) A practical guide to fluid inclusion studies. Blackie, Glasgow.

Swager C (1989) Structure of Kalgoorlie greenstones - Regional deformation history and implications for the structural setting of the Golden Mile gold deposits Geological Society of Western Australia Report 25, pp 59-84.

Swager C (1997) Tectono-stratigraphy of late Archaean greenstone terranes in the southern Eastern Goldfields, Western Australia. Precambrian Research 83: 11-42.

Williams H (1994) The lithological setting and controls on gold mineralization in the Southern Ore Zone of the Hampton-Boulder gold deposit, New Celebration Gold Mine, Western Australia School of Earth and Geographical Sciences. University of Western Australia, Perth.

Source of ore fluids in Carlin-type gold deposits, China: Implications for genetic models

A.H. Hofstra, P. Emsbo, W.D. Christiansen, P. Theodorakos
U.S. Geological Survey, MS-973, Box 25046, Denver, CO 80225, USA

X.-C. Zhang, R.-Z. Hu, W.-C. Su, S.-H. Fu
Key Lab of Ore Deposit Geochemistry, Inst. of Geochem., Chin. Acad. Sci., Guiyang, 550002, China

Abstract. Fluid inclusion and isotopic data on quartz, carbonate, and clay minerals from Carlin-type deposits in two gold provinces of southwest China suggest the deposits formed at epizonal levels where metamorphic fluids discharged into foreland fold and thrust belts, reacted with sedimentary rocks, and mixed with local meteoric ground waters.

Keywords. China, Carlin, gold, δD, $\delta^{18}O$, Na-Cl

1 Introduction

Carlin-type gold deposits in the Dian-Qian-Gui area (Golden Triangle) and West Qinling belt of SW China contain significant Au (ca. 400 t each) and are scientifically important because of their similarity to giant deposits in Nevada. Recent descriptions of the geology of these gold provinces and deposits within them are provided in Liu et al. (2000), Wang and Zhang (2001), Gu et al. (2002), Hu et al. (2002), Mao et al. (2002), Peters et al. (2002), Vielreicher et al. (2003), and Zhang et al. (2003a). To improve understanding of published results and identify fluid sources, the $\delta^{18}O$ of quartz and carbonate minerals and δD and $\delta^{18}O$ values of clay minerals of known paragenesis were determined and displayed relative to published data for minerals of unspecified paragenesis. Na-Cl-Br ratios of fluid inclusions were also analyzed to constrain the source of salt in ore fluids. The deposits sampled are in southwestern Guizhou province (Lannigou, Zimudang, Shuiyindong, Getang, and Nibao), northwestern Sichuan province (Dongbeizhai, Zheboshan, Manaoke, La'erma) and western Shaaanxi province (Jianchaling). In combination with the tectonic settings of each gold province, this information is used to refine genetic models for Carlin-type gold deposits in China.

2 Tectonic setting

The Dian-Qian-Gui area is in a foreland fold and thrust setting on the east side of the Triassic-Cretaceous Indochina orogen and northwest side of the Late Jurassic-Cretaceous Yanshanian orogen. Subduction-related magmatism does *not* extend into the area. The diversity of fold orientations in the area is due to polyphase contraction and transpression along basement faults (Peters et al., 2002; Zhang et al., 2003a). Carlin-type gold deposits are in Cambrian to Triassic platform carbonate, transitional, and basinal siliciclastic rocks and locally in mafic intrusives and volcaniclastic rocks. Unconventional isotopic dates permit mineralization ages between 140 and 75 Ma (Hu et al., 2002).

The West Qinling belt is in the western part of the Triassic-Jurassic Dabie-Qinling collisional orogen (Mao et al., 2002). It is intruded by post-collisional granitoids and contains mesozonal orogenic gold deposits in metamorphosed Devonian-Carboniferous siliciclastic rocks of the accretionary prism, Carlin-type gold deposits in the adjacent foreland fold and thrust belt to the south, and a few gold skarns (Mao et al., 2002). Carlin-type gold deposits are in deformed Triassic Songpan-Ganzi basin flysch, Neoproterozoic-Permian miogeoclinal rocks, and locally felsic to mafic dikes, sills, or volcaniclastic rocks. Both gold deposit types are inferred to have formed during the final stages of contraction, transpression, or post collisonal uplift of the orogen (Mao et al., 2002; Vielreicher et al., 2003). Mao et al. (2002) proposed that the Carlin-type gold deposits may be epizonal analogues of the mesozonal orogenic gold deposits.

3 Paragenesis of quartz, carbonate, and clay minerals

Carlin-type gold deposits in the Dian-Qian-Gui area and West Qinling belt frequently contain early milky quartz veins, jasperoid (pervasively silicified wallrock), and late clear drusy quartz. They also contain several stages of calcite or dolomite veins (Fig. 1). Kaolinite, illite, or smectite are usually present in altered rocks and dickite occurs locally in fractures and vugs on drusy quartz. Some of the milky quartz veins in these deposits are colored orange or gray by inclusions of realgar or stibnite and locally cement ore controlling structures suggesting that at least some are ore related. The presence of disseminated Au- and As-rich pyrite in jasperoid and altered rocks and orpiment, realgar, stibnite, cinnabar, lorandite, pyrite, or marcasite with late drusy quartz and calcite or dolomite in fractures indicates they are ore related. This paragenesis is like that of gold deposits in Nevada, except that milky quartz veins there lack inclusions of stibnite or realgar and predate Carlin-type gold mineralization (Hofstra and Cline, 2000).

4 Fluid inclusion studies

Aqueous carbonic (CO_2, CH_4, N_2) fluid inclusions in milky quartz veins from Dian-Qian-Gui area deposits have Th of 215-307°C, salinities of 3.0-8.5 wt.%, and minimum pressures of 1.5 to 2.3 kbar corresponding to depths of 6.0 to 9.2 km, assuming fluid pressure equaled lithostatic load (Hu et al., 2002; Zhang et al., 2003a; Su W-C unpublished data, 2004). Lithostatic fluid pressures also are suggested by the nearly horizontal dips of milky quartz veins in some deposits (e.g Shuiyindong, Niboa). In contrast, late stage drusy quartz, fluorite and calcite contain aqueous liquid-vapor inclusions that are frequently necked and have lower Th (98-360°C), gas contents, and salinities (0-5.8%) suggestive of lower pressures and influx of dilute ground water (Zhang et al., 2003a).

Fluid inclusions in West Qinling belt Carlin-type gold deposits (Wang and Zhang, 2001) have Th (135-280°C), salinities (2-14%), and pressures (<400 bars) that overlap those of mesozonal orogenic gold deposits (215-475°C, 1-22%, 210-1750 bars) in adjacent areas (Wang and Zhang, 2001; Zhang et al., 2003b). Carbonic (CO_2>CH_4±N_2) inclusions are more abundant in orogenic gold deposits and less common in Carlin-type gold deposits. Fluid inclusions with lower Th and salinities are typically in late drusy quartz and calcite or dolomite veins.

To evaluate the source of salt in hydrothermal fluids, Na/Cl/Br ratios of fluid inclusions were determined a la Hofstra and Emsbo (2005). Based on ion chromatographic analyses of fluid inclusions from a varied selection of ore deposit types, they demonstrate that the source of salt in hydrothermal fluids can be discriminated on Na/Cl vs. Cl/Br plots. These data are subject to the same mass balance limitations as all other bulk extraction techniques (e.g. δD analyses of fluid inclusions, below) where more than one generation of inclusions are trapped and analyzed together. In this case, the Na/Cl/Br ratios measured are most representative of the most saline population of inclusions present in the sample. On Figure 1, their results from Nevada Carlin-type gold deposits (gray field) are shown relative to the fields for diverse magmatic hydrothermal deposits and Phanerozoic mesozonal orogenic gold deposits. Superimposed on these fields are new data (white diamonds) from several Dian-Qian-Gui area deposits. Fluid inclusions in milky, jasperoidal, and drusy quartz, orpiment, realgar, and pyrite generally plot within the field for orogenic gold deposits. Although milky quartz from Lannigou plots near the bottom of the magmatic hydrothermal field, independent evidence for an intrusion, such as igneous dikes or a high amplitude aeromagnetic anomaly, are lacking. As in Nevada, the Na/Cl/Br results from Dian-Qian-Gui area deposits suggest magmatic fluids were not important in their formation. Analyses of samples from West Qinling belt deposits are in progress.

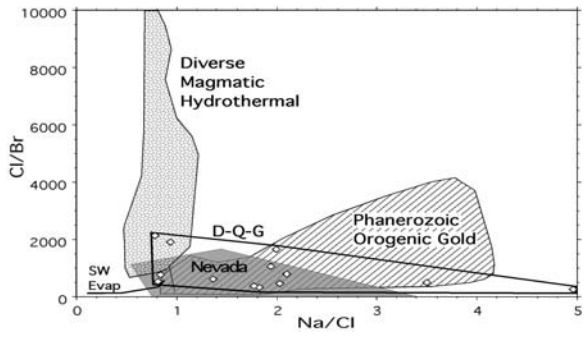

Figure 1: Na/Cl vs. Cl/Br plot of fluid inclusions from Dian-Qian-Gui area gold deposits (white diamonds) relative to fields for magmatic, orogenic, and Nevada Carlin-type gold deposits and the seawater evaporation curve.

5 $\delta^{18}O$ of quartz and carbonate

Figure 2 compares $\delta^{18}O$ ranges for quartz and carbonate of known paragenesis with those of unspecified paragenesis from the literature. In the Dian-Qian-Gui area (Fig. 2a), milky quartz veins have a narrow range of high $\delta^{18}O$ values, including a representative example containing inclusions of realgar. Jasperoid and drusy quartz and calcite veins have a wider range of lower values. Drusy quartz usually has lower values than jasperoid. Late calcite veins containing realgar or cinnabar plot near the center of the range of published data.

Carlin-type gold deposits in the West Qinling belt exhibit a similar pattern (Fig. 2b). Milky quartz with and without inclusions of realgar or stibnite have the highest values. Jasperoid and drusy quartz have values that are similar to, or lower than, milky quartz veins. Late calcite

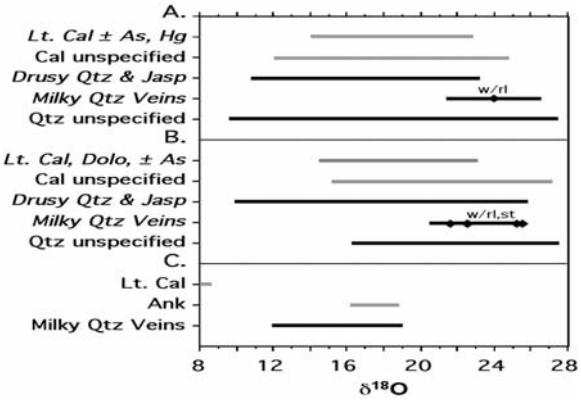

Figure 2: $\delta^{18}O$ of quartz (black bars) and carbonate minerals (gray bars) from A. Dian-Qian-Gui area Carlin-type gold deposits, B. West Qinling belt Carlin-type gold deposits, and C. West Qinling belt orogenic gold deposits. "unspecified" refers to the paragenesis of minerals analyzed in the literature. Based on data in Wang, 1996, Wang and Zhang, 2001, Hu et al., 2002, Zhang et al., 2003a,b, Feng et al., 2004, and this study (headings in italics).

or dolomite veins with and without realgar are on the lower end of the range of published values. Milky quartz veins in mesozonal orogenic gold deposits (Fig. 2c) have lower values than those in Carlin-type gold deposits. If milky quartz veins in both deposit types formed from similar fluids, this difference can be explained by a decrease in temperature as fluids moved from mesozonal to epizonal depths and exchanged with marine sedimentary rocks.

6 δD and $\delta^{18}O$ of ore fluids

Most published isotopic data for ore fluids are based on $\delta^{18}O$ analyses of quartz, calcite, or dolomite and δD analyses of fluid inclusion water extracted from these minerals by crushing or thermal decrepitation (Fig. 3a,b). For these data to be representative of ore fluids, the host mineral must be ore-related and the fluid inclusions must be dominantly primary or pseudosecondary in origin, which is commonly uncertain or not well documented. In many cases, the largest veins present in the deposits were analyzed because 2-10 grams of material is required to yield sufficient fluid inclusion water (e.g. >1 µl) for conventional δD analysis. The larger veins are typically comprised of milky quartz which may or may not be ore related. Furthermore, secondary inclusions often trap meteoric ground water which will shift bulk fluid inclusion analyses to lower δD values. Consequently, the upper part of the field for each deposit on Fig. 3a is likely to be most representative of ore fluids. These fluid compositions are well away from the meteoric water line within, or below, the metamorphic water box. Likewise, in the West Qinling belt (Fig. 3b), the upper parts of the fields for most Carlin-type gold deposits overlap those of orogenic gold deposits in adjacent areas.

To evaluate this rationale, we determined the mineralogy and isotopic composition of < 2 µ clay minerals in altered and mineralized rocks and late dickite from Dian-Qian-Gui area deposits. With one exception, the calculated fluid compositions at 200°C for the dickite, kaolinite, illite, and smectite analyzed (white squares) plot within or just below the metamorphic water box (Fig. 3a). Given the paucity of intrusive centers in this area, the resulting distribution of values are best explained by a metamorphic ore fluid (e.g. δD=-50‰, $\delta^{18}O$=9‰) that evolved by reactions with sedimentary rocks and mixing with variably exchanged meteoric ground water. The highest δD values for dickite from a West Qinling belt deposit (Fig. 3b) are suggestive of a similar fluid source.

7 Conclusions

The paragenetic controls on quartz and carbonate minerals and new $\delta^{18}O$ data suggest that published data is from several different stages. Carlin-type deposits in both

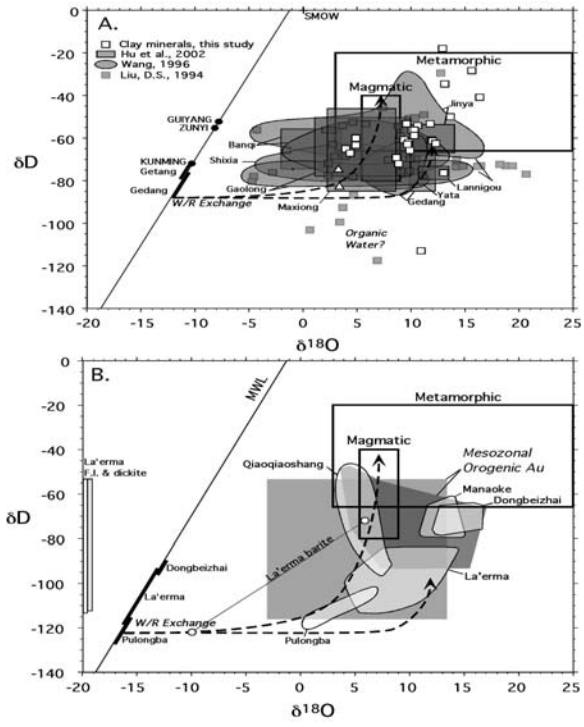

Figure 3: δD and $\delta^{18}O$ of hydrothermal fluids in A. Dian-Qian-Gui area Carlin-type gold deposits and B. West Qinling belt mesozonal orogenic (dark fields) and Carlin-type (light fields w/ black border) gold deposits. In A., the black dots on the MWL are the mean δD and $\delta^{18}O$ of precipitation for the cities listed. The δD of fluid inclusions and dickite from Laerma are plotted along the y-axis of B. Black bars along the MWL are for present day waters or supergene minerals from the deposits listed. Dashed arrows are meteoric water/rock exchange curves. Produced from data in Liu, 1994; Wang, 1996; Wang and Zhang, 2001; Hu et al., 2002; Zhang et al., 2003a,b; Feng et al., 2004, and this study.

gold provinces frequently contain milky quartz veins of uncertain relation to ore with high $\delta^{18}O$ values and hot, aqueous, carbonic, moderate salinity, inclusions with δD values that extend into or near the metamorphic water box. Some of these veins appear to be ore related because they (1) cement fault zones that localize ore, (2) contain inclusions of realgar or stibnite, (3) have $\delta^{18}O$ values only slightly greater than the highest values from jasperoid and drusy quartz that are ore related, and (4) have fluid inclusions with δD values similar to calculated values for late dickite and other clay minerals from altered rocks. The general decrease in $\delta^{18}O$ values through the paragenetic sequence from early milky quartz veins, through jasperoid, to late drusy quartz and carbonate veins are suggestive of variable dilution of these fluids by meteoric ground water during later stages.

The Na-Cl-Br ratios of fluid inclusions in Dian-Qian-Gui area and Nevada deposits are similar to one another and to those of orogenic gold deposits. Unlike Nevada, the setting in this area precludes significant inputs of

magmatic water from subduction-related magmas. Together these data suggest a model for Carlin-type gold deposits involving inputs of metamorphic fluids from below.

Data from Carlin-type gold deposits in the West Qinling belt are also consistent with a metamorphic ore fluid, although the abundance of intrusives and aeromagnetic anomalies permit fluid contributions from magmas. The presence of mesozonal orogenic gold deposits and Carlin-type gold deposits in adjacent areas at different levels in the crust and the isotopic similarity of their ore fluids support the proposal of Mao et al. (2002), in which case, orogenic fluids discharged from mesozonal levels may have migrated upward and laterally along thrust faults into the adjacent fold belt to form Carlin-type gold deposits at epizonal levels. If this interpretation is correct, Carlin-type gold deposits in China are variants of epizonal orogenic gold deposits developed in continental foreland settings.

References

Feng J, Wang D, Wang X, Zeng Y, Li T (2004) Magmatic gold mineralization in the Western Qinling orogenic belt: Geology and metallogenesis of the Baguamiao, Liba and Xiaogouli gold deposits. Acta Geologica Sinica, 78: 529-533.

Gu X-X, Liu J-M, Schulz O, Vavtar F, Zheng M-H (2002) Syngenetic origin for the sediment-hosted disseminated gold deposits in NE-Sichuan, China: Ore fabric evidence. Ore Geol Rev, 22: 91-116.

Hofstra AH, Cline JS (2000) Characteristics and models for Carlin-type gold deposits. Rev in Econ Geol, 13: 163-220.

Hofstra AH, Emsbo P (2005) Source of salt in hydrothermal fluids based on Na-Cl-Br of fluid inclusions: Geochimica et Cosmochimica Acta, Supplement, Abstracts of the 15th V.M. Goldschmidt Conference, Moscow, Idaho, May 20-25.

Hu R-Z, Su W-C, Bi X-W, Tu G-Z, Hofstra AH (2002) Geology and geochemistry of Carlin-type gold deposits in China. Min Dep, 37: 378-392.

Liu D-S, Tan Y-J, Wang J-Y, Wei L-M 1994, Carlin-type gold deposits in China: in Liu D-S, Tan Y-J, Wang J-Y and Jiang S-F, eds., Chinese Carlin-type Gold Deposits: University of Nanjing Press, Nanjing, p. 1–36.

Liu J, Zheng M, Liu J, Su W (2000) Geochemistry of the La'erma and Qiongmo Au-Se deposits in the western Qinling Mountains, China. Ore Geol Rev, 17: 91-111.

Mao J, Qiu Y, Goldfarb R, Zhang Z, Garwin S, Ren F (2002) Geology, distribution, and classification of gold deposits in the western Qinling belt, China. Min Dep, 37: 352-377.

Peters SG (2002) Geology, geochemistry, and geophysics of sedimentary-hosted Au deposits in P.R. China. U.S. Geological Survey Open-File Report: 02–131.

Vielreicher RM, Vielreicher NM, Hagemann SG, Jones G (2003) Fault zone evolution and its controls on ore-grade distribution at the Jian Cha Ling gold deposit, western Qinling region, central China. Min Dep, 38: 538-554.

Wang X-C, Zhang Z-R (2001) Geology of sedimentary rock-hosted disseminated gold deposits in northwestern Sichuan, China. Inter Geol Rev, 43: 69-90.

Wang, X-C (1996) On isotope geology of micro-disseminated type of gold deposits in China: in Geology and Mineral Resources Proceedings of Ministry of Metallurgical Industry, The Chinese Society of Metals, International Academic Publishers Beijing, p. 109-113.

Zhang X-C, Spiro B, Halls C, Stanley CJ, Yang K-Y (2003a) Sediment-hosted disseminated gold deposits in southwest Guizhou, PRC: Their geological setting and origin in relation to mineralogical, fluid inclusion, and stable isotope characteristics. Inter Geol Rev, 45: 407-470.

Geology and ore genesis of the Nanjinshan gold deposit in Beishan Mountain area, northwestern China

Si-hong Jiang, Feng-jun Nie
Institute of Mineral Resources, Chinese Academy of Geological Sciences, Baiwanzhuang Road 26, Beijing, 100037, China

Abstract. Located in the western part of the Beishan Mountain area, the Nanjinshan gold deposit occurs within Carboniferous pyroclastic rocks. The ore geology of this deposit is described and its origin is discussed in this paper. It can be concluded that the Nanjinshan gold deposit was formed during Indosinian (250~205Ma) magmatism, and belongs to the intrusion-related, meso- to epi- thermal type of gold deposit.

Keywords. Deposit geology, ore genesis, gold deposit, Nanjinshan, Beishan Mountain area, China

1 Introduction

Located in the western part of Tianshan-Yinshan-Great Hinggan metallogenic belt, and the conjunction area of Inner Mongolia Autonomous Region, Gansu Province and Xinjiang Uygur Autonomous Region, Northwest China, the Beishan Mountain area is one of the most important gold metallogenic provinces in northwestern China. To date, about 100 gold deposits and prospects have been discovered, explored and mined, among which Nanjinshan, Mazhuangshan, Liushashan, Jinwozi, Zhaobishan and Xiaoxigong are the most important ones.

The Nanjinshan gold deposit is situated in the northwestern part of Beishan Mountain (Mt.) area , and is the first discovered through geochemical exploration in Gansu province. It is important to study the ore deposit geology and its genesis, in order to guide the mineral exploration for gold in this area.

2 Geological setting

The Beishan Mt. area can be divided into three tectonic units by the Liuyuan-Daqishan and Hongshishan-Heiyingshan deep-seated faults (Zuo and He, 1990; Liu and Wang, 1995; Nie et al., 2002) (Fig.1). These tectonic units are (1) Tarim plate to the south, which is composed of Dunhuang and Anbei-Jiusidun terranes from south to north, respectively; (2) Kazakhstan plate, consisting of Liuyuan-Daqishan, Huaniushan, Mazongshan, Gongpoquan-Yueyashan and Hongshishan- Heiyingshan terranes from south to north; and (3) Siberian plate, comprising Queershan and Wuzhuergashun terranes. It is noted that the area has been influenced by repeated distinct tectono-magmatic activities.

2.1 Stratigraphic sequences

The oldest stratigraphic unit exposed in the Beishan Mt. area is the Archean Dunhuang Group, which occurs in the southernmost part of the area. It consists of quartzite, gneiss, amphibolite, marble and schist, and constitutes the basement of the Tarim plate.

The Proterozoic strata crop out in the Anbei-Jiusidun, Huaniushan, Mazongshan and Hongshishan-Heiyingshan terranes. They are mainly composed of granulite, schist, marble, crystalline limestone and dolomite.

The early Paleozoic marine sedimentary and volcanic rocks are located mainly in Mazongshan, Gongpoquan-Yueyashan and Queershan terranes, which are composed of rhyolite, dacite, andesite, basalt, tuff, sandstone, limestone, slate and siltstone. In contrast, the late Paleozoic marine sedimentary and volcanic rocks are widely distributed in the Beishan Mt. area, and notably consist of rhyolitic dacite, rhyolite, conglomerate, sandstone, limestone, tuff and slate. They are one of the most important host rocks for gold deposits in the area.

The Mesozoic and Cenozoic continental sedimentary rocks are distributed primarily in basins developed unconformably on the Precambrian and Paleozoic rocks. The rocks comprise mainly sandstone, conglomerate and shale.

2.2 Intrusions

Ultramafic to granitoid batholiths, stocks and dykes are common throughout the Beishan Mt. area. The most common intrusive bodies are Hercynian (405~250Ma), which are distributed widely in the area as batholiths, stocks and dyke swarms. These are composed of ultramafic rocks, gabbro, quartz diorite, diorite, tonalite, granodiorite, monzonitic granite and K-feldspar granite, which are closely related to the formation of most gold deposits in the area.

Indosinian (250~205Ma) and Yanshanian (205~66Ma) granite and K-feldspar granite batholith and stocks mainly crop out in the eastern and southeastern parts of the study area. Some of the Indosinian intrusions have genetic relationships with the formation of gold deposits in the region. The Nanjinshan gold deposit is a typical example.

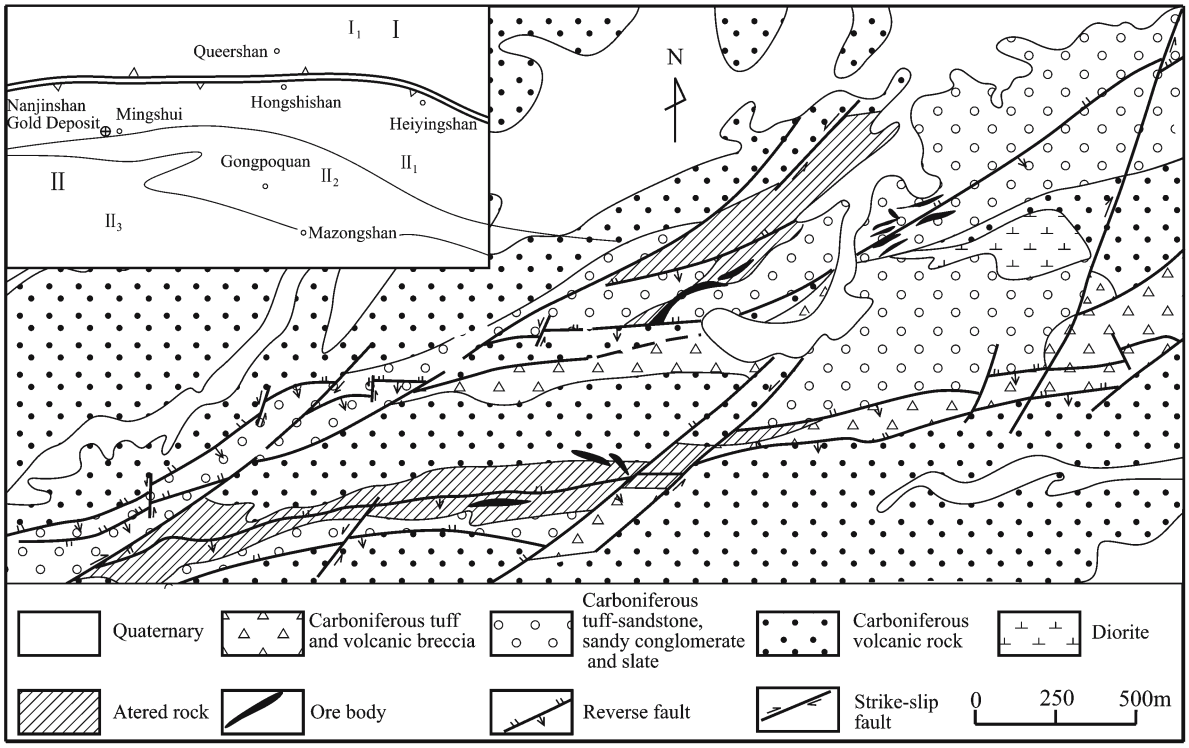

Figure 1: Schematic geological map of the Nanjinshan gold deposit (modified from Cui et al., 1996). Tectonic units in the inlet of this figure: I - Siberian plate, I_1 – Queershan terrane; II – Kazakhstan plate, II_1 – Hongshishan-Heiyingshan terrane, II_2 – Gongpoquan-Yueyashan terrane, II_3 – Mazongshan terrane

2.3 Tectonics

EW-, NE-, NS- and NW-trending faults are widely distributed in the study area. The most predominant structural style is EW trending deep-seated faults, which are composed of Hongshishan-Heiyingshan, Mingshui-Shibanjing-Xiaohuangshan and Liyuan-Daqishan faults, and control the spatial distribution of the intrusive bodies and stratigraphic units, extending more than 500 km. The locality of the Hongshishan-Heiyingshan fault is also the suture zone of Kazakhstan and Siberian plates, while the locality of the Liuyuan-Daqishan fault represents the suture zone of the Tarim and Kazakhstan plates.

3 Ore deposit geology

The Nanjinshan deposit was also discovered in the 1980s by Geophysical Party of Gansu Bureau of Geology during geochemical exploration. Ten tonnes of gold metal have been verified, with an average Au of 7 g/t.

The host rocks of the Nanjinshan deposit are composed of Carboniferous tuff, breccia sandstone, sericite slate, tuff breccia, dacitic tuff and carbonaceous shale (Fig. 1). The structural style at the deposit is dominated by NNE trending reverse faults, which dip 60°~70°to SSE, with a length of more than 3000 m. The displacement of these reverse faults ranges from 40 to 190 m. The mylonite with various width can be seen along these faults, where hematitization, silicification, sericitization and pyrophyllitization are well developed.

The only intrusive body, i.e. diorite stock, crops out in the center of the ore district , with an area of 0.3 km^2. ^{40}Ar-^{39}Ar isotopic dating on the biotite separates from the diorite near the ore district yields an age of 244±0.3Ma (analyzed by Isotopic Lab of Institute of Geology, Chinese Academy of Geological Sciences).

The gold ore bodies occur within silicified volcanic rocks as gold-bearing quartz veinlets and disseminated bodies. To date, two gold and silver mineralization zones have been outlined: northern and southern zones, of which the northern zone includes 58 gold ore bodies and 5 silver ore bodies, and the southern zone 5 gold ore bodies and 1 silver ore bodies. The gold ore bodies vary from 25 to 555 m long, and 1 to 41m wide, with a downdip extent of 5 to 200 m. In contrast, the silver ore bodies range from 25 to 200 m in length, 1 to 17 m in width, with a downdip extent of 16 to 100 m.

Mineralogical constituents of the gold ores at Nanjinshan are pyrite, galena, sphalerite, arsenopyrite, chalcopyrite, pyrrhotite, magnetite, native Au, native Ag and electrum. Isotopic dating on the sericite from the gold ore yields a ^{40}Ar-^{39}Ar age of 242.8±0.8 Ma (analyzed by

Isotopic Lab of Institute of Geology, Chinese Academy of Geological Sciences). It has been suggested that the gold mineralization is essentially contemporaneous with the emplacement of the diorite stock, or that the sericite K-Ar has been reset by the magmatic event.

4 Isotope studies

4.1 Sulfur isotopes

Four pyrite, three arsenopyrite and one pyrrhotite separates from the gold ores of the Nanjinshan deposit show $\delta^{34}S$ values ranging from 2‰ to 7.8‰, 8.1‰ to 8.4‰ and 7.4‰, respectively, and clustering between 7‰ and 9‰.

These $\delta^{34}S$ values are typical for that in mesothermal gold deposits from many parts of the world (Lambert et al., 1984; Peters and Golding, 1987; Groves and Foster, 1991; Trumbull et al., 1992). According to Ohmoto and Rye (1979) and Ohmoto (1986), such $\delta^{34}S$ values are consistent with a deep-seated source of sulphur either from leaching of metamorphic rocks or from igneous intrusions. Since no metamorphic rocks are exposed in Nanjinshan district, it is suggested that the sulphur was dominantly derived from the magmatic rocks.

4.2 Lead isotopes

Eight sulfides from the gold ore in Nanjinshan deposit give $^{206}Pb/^{204}Pb$ ratios from 18.365 to 18.540, $^{207}Pb/^{204}Pb$ from 15.538 to 15.636 and $^{208}Pb/^{204}Pb$ from 38.087 to 38.434, while whole rocks from Carboniferous volcanic rocks, diorite and granodiorite show $^{206}Pb/^{204}Pb$ ratios from 18.756 to 20.477, $^{207}Pb/^{204}Pb$ from 15.540 to 15.673 and $^{208}Pb/^{204}Pb$ from 38.380 to 39.415. These data indicate that the gold ore contains much lower radiogenic lead than their wall rocks. Even so, the μvalues from the gold ores and their wall rocks are very close to each other. It is suggested that the lead of the gold ore may be dominantly derived from their wall rocks.

5 Fluid inclusion study

Fluid inclusion microthermometry was conducted on 5 samples of gold-bearing quartz veins from different places of the Nanjinshan gold deposit. The primary fluid inclusions are typically composed of two-phase H_2O-rich inclusions, and two-phase and three-phase CO_2-rich inclusions.

The two-phase H_2O-rich inclusions show a degree of fill of about 75 to 95 percent. The inclusions are about 10 to 20 μm in diameter and exhibit irregular, ellipsoid-like or incomplete negative crystal shapes. By comparison, the CO_2 inclusions have the same size as the two-phase H_2O-rich inclusions, but display a degree of fill of about 20 to 95 percent for CO_2.

Fluid inclusion microthermometry was conducted on a calibrated France-made CHAIXMECA heating and freezing stage. The homogenization temperatures of 67 two-phase H_2O-rich inclusions range from 74 to 330°C, with a bimodal distribution from160 to 180°C and 220 to 240°C. In general, these data indicate a moderate to low ore-forming temperature, which is consistent with the appearance of pyrophyllite occurring under low temperature. The salinities of 48 two-phase H_2O-rich inclusions vary from 0.88 to 11.81 wt% NaCl equiv, with a mode between 6 and 7wt% NaCl equiv. Comparatively, the homogenization temperatures of 14 two-phase and 12 three-phase CO_2-rich inclusions vary from 242 to 274°C and 222 to 352°C, respectively, with the salinities from 3.76 to 11.84 wt% NaCl equiv (18 inclusions) and 4.51 to 11.29 wt%NaCl equiv(14 inclusions). The estimated ore-forming pressure is about 100~160 MPa, according to the microthermometric data of the two-phase and three-phase CO_2-rich inclusions.

The salinities in these samples do not display a linear correlation with temperature, but show three distinct clusters. The first cluster is composed of salinities less than 3 wt%NaCl equiv , the second one between 3~7.5 wt%NaCl equiv , and the third one larger than 7.5 wt%NaCl equiv. It can be inferred that the fluids with high- and low-salinity were mixed at the same temperature during the ore-forming process.

6 Discussion and conclusions

According to the data presented above, the ore-forming age of the Nanjinshan gold deposit is very close to the emplacement age of the diorite occurring near the ore district. The sulfur and lead isotope data also suggest that a certain amount of ore-forming material derived from intrusive bodies or volcanic rocks was involved in the formation of gold deposits. In addition, based on the study on fluid inclusions, the formation of the Nanjinshan deposit is mainly controlled by fluid mixing with low- and high- salinities at meso- to epi- thermal temperatures. The fluid with relatively high salinity may be sourced from the magmatic water, while the fluid with relatively low salinity from meteoric water. Therefore, the Nanjinshan gold deposit is inferred to belong to the intrusion-related meso- to epi- thermal gold deposit.

So far, although most gold deposits in Beishan Mountain area were formed during Hercynian (Nie et al., 2002; Jiang et al., 2004), it is certain that some gold deposits are controlled by Indosinian tectono-magmatism, which is neglected by most economic geologists. Since the Indosinian magmatism was so intimately related to the formation of Nanjinshan gold deposit in the Beishan Mt. area, it is believed that there is great potential of gold remaining to be discovered around the Indosinian intrusions.

Acknowledgements

This research is financed by the State Basic Research Programme of China (No. 2002CB412606), Geological Survey of China (200310200001-1), and Ministry of Science and Technology (2001BA609A-03). Many thanks are sent to the staff members working with the Nanjinshan gold mine for their support to our field geological investigation.

References

Cui HW Chen, ZY (1996) Gold deposit geology of Beishan area, Gansu Province. Geological Publishing House, Beijing, 104p. (in Chinese with English abstract)

Groves DI, Foster RP (1991) Archean lode gold deposits. In: Foster, R.P.(Ed.), Gold Metallogeny and Exploration. Blackie, Glasgow, 63-103

Jiang SH, Nie FJ, Liu Y (2004) Gold Deposits in Beishan Mountain, Northwestern China. Resource Geology: 325–340

Lambert IB, Phillips GN, Groves DI (1984) Sulfur isotope composition and genesis of Archean gold mineralization, Australia and Zimbabwe. In: Foster, R.P. (Ed.), Gold'82. Balkema, Rotterdam, 373-387

Liu X-Y., Wang Q (1995) Tectonics of orogenic belts in Beishan Mts., western China and their evolution. Dixue Yanjiu (Geoscientific Research), No.28, 37-48 (in Chinese with English abstract)

Nie F-J, Jiang S-H, Bai D-M, Wang X-L, Su X-X, Li J-C, Liu Y, Zhao X-M (2002) Metallogenic studies and ore prospecting in the conjunction area of Inner Mongolia Autonomous Region, Gansu Province and Xinjiang Uygur Autonomous Region (Beishan Mt.), northwest China. Geological Publishing House, Beijing, 408p (in Chinese with English abstract)

Ohmoto H (1986) Stable isotope geochemistry of ore deposits. Rev. Mineral. 16: 491-560

Ohmoto H, Rye RO (1979) Isotopes of sulfur and carbon. In: Barnes, H.D. (Ed.), Geochemistry of Hydrothermal Ore Deposits. Wiley, New York, 509-567

Peters SG, Golding SD (1987) Relationship of gold-quartz mineralization to granodioritic phase and mylonites at Charters Tower goldfield, northeastern Queensland. The Geology, Structure, Mineralization and Economics of the Pacific Rim. Proceedings of Pacific Rim Congress. Australasian Institute of Mining and Metallurgy, Carlton Victoria, Australia, 363-367

Trumbull RG, Morteani G, Li Z, Bai H (1992) Gold metallogeny in the Sino-Korean Platform. Springer-Verlag, Berlin, 202p.

Zuo G-C, He G-Q (1990) Plate tectonics and metallogenic regularities in Beishan region. Beijing University Publishing House, Beijing, 209p. (in Chinese with English abstract)

Age and origin of advanced argillic alteration at the Bor Cu-Au deposit, Serbia

C. Lerouge, L. Bailly, E. Béchu, C. Fléhoc, A. Genna, J.L. Lescuyer, G. Stein
BRGM, BP 6009, 45060 Orléans cédex 2, France

P.Y. Gillot
Laboratoire de Géochronologie, bat. 504, 91405 Orsay, France

D. Kozelj
Bor Copper Institute, Bor, Serbia

Abstract. Stable (O, S, H) isotopic data on alunite from the Bor high-sulfidation Cu-Au deposit in Serbia indicate a magmatic-hydrothermal origin. Hydrogen and oxygen isotopes indicate fluids are dominantly magmatic. Oxygen and sulfur isotopes suggest a H_2S/SO_4 ratio around 7-8 that is similar to those of other high-sulfidation ore deposits around the world. A K/Ar date on alunite of 84.6 ± 1.2 Ma is within the range of early V1 Volcanism in the district. Stable isotopic data on alunite from the Kupjatra prospect are quite similar to the Bor ore deposit ; fluids are dominantly magmatic with a greater meteoric component.

Keywords. K/Ar dating, stable isotopes, advanced argillic alteration, Bor district, Serbia

1 Introduction

Alunite is a typical mineral of advanced argillic alteration by acidic, sulfate-bearing fluids generated by several ways in epithermal and supergene environments. Its different origins can be distinguished by associated minerals and S, H, O isotope compositions (Rye et al., 1992). Advanced argillic alteration occurs as a main alteration type in the Bor district, Serbia. It is associated with the large copper-gold deposit of Bor, the small base metals/gold deposit at Coka Marin, and large quartz-alunite carapaces associated with gold anomalies identified during an extensive exploration program in the Bor district, such as Coka Kupjatra (Kozelj 2002). These alteration zones and ore deposits are hosted by Upper Cretaceous Volcano-plutonic rocks of the Timok complex in Serbia. Exhumation of the Carpatho-Balkanic belt suggests that a part of alunite might be supergene.

This paper presents a K-Ar date and (S, O, H) isotopic data on alunite from the Bor ore deposit and from the prospect of Coka Kupjatra in order to constrain the origin of the advanced argillic alteration zones in the district.

2 Geology

The Bor district in Serbia is part of the Carpatho-Balkans metallogenic province which lies within the larger Tethyan Eurasian metallogenic belt (TEMB). The Bor metallogenic zone is developed in the so-called Timok Complex (TC) (80km long, 20 km wide) comprised of three main calc-alkaline Volcanic episodes (V1 to V3).

The major types of mineralization in the district are located along the eastern margin of the TC mainly within the V1 hornblende±biotite andesitic lavas and pyroclastics, dated at around 90-80 Ma (Jankovic et al., 1981). There are porphyry copper deposits (Majdanpek, Veliki Krivelj), a cupriferous massive pyrite deposit (Bor) and a gold-bearing polymetallic massive sulfide deposit (Coka Marin). Other gold prospects associated with advanced-argillic alteration are hosted within V2 hornblende±pyroxene andesites dated around 80-72 Ma (Jankovic et al., 1981). They are characterized by low volume and low grade Cu-Au mineralization, such as Coka Kupjatra, where the Au content is around 1 g/t in surficial samples and below 0.1 g/t at deeper levels and laterally (Kozelj, 2002). The Bor mineralization consists of series of massive cigar-shaped and pipe-like bodies related to fracture zones and Volcanic breccias. The largest body is Tilva Ros. The massive ore is comprised of up to 70 Volume % fine-grained pyrite with chalcosite, covellite and enargite. Barite is common in upper parts of the system, whereas anhydrite/gypsum occur as vein networks in lower parts of the system. Associated advanced argillic alteration contains pyrophyllite, diaspore, alunite, andalusite, zunyite and corundum (Karamata et al. 1983).

3 Sampling

In the BOR mine, samples were collected along a vertical cross-section in the advanced argillic alteration of the Tilva Ros orebody, at the 0, -16, and -31m levels, and at the deepest -155m level of the Borska Reka orebody. At Tilva Ros, mineralization is represented by disseminated pyrite and veins of pyrite-covellite, pyrite-sulvanite, or enargite associated with an advanced argillic alteration (AAA), overprinted by a late sericitic alteration. The AAA affects massively volcanics, with scarce relics of biotite and plagioclase phenocrysts. It is characterized by different mineral assemblages depending of the depth and lateral zon-

ing relative to fluid conduits. Vertically in the system, alunite, alumino-phosphato-sulfate phases (APS) and pyrophyllite are present at all the levels, whereas dickite/kaolinite occurs at level 0m and zunyite and diaspore occur at levels -16m and -31m. Lateral to fluid conduits, alunite is proximal to sulfide veins whereas kaolinite/dickite and scarce APS occur far from veins. At Borska Reka, level -155m, mineralization is characterized by fine-grained pyrite impregnation, chalcopyrite, grey copper, sphalerite and galena with minor enargite, associated with intense sericitic alteration and F-apatite. A vein network of anhydrite crosscuts this alteration and reworks a part of the sulfides. Samples of advanced argillic alteration from Coka Kupjatra hosted in V2 Volcanics have been collected for comparison with those from the Bor mine.

4 Analytical methods

Sulfides and quartz were separated by handpicking. Alunite was separated by heavy liquids. On the sample from Coka Kupjatra, a complementary clean up with hydrofluoric acid was used to eliminate silicate impurities.

Alunite was dated by the K–Ar method at the UPS-IPGP geochronology laboratory at Orsay, France. K was measured by flame emission and compared with reference materials MDO-G and ISH-G (Gillot et al., 1992). Ar was measured with a mass spectrometer described by Gillot and Cornette (1986), using the Cassignol-Gillot technique (Cassignol and Gillot, 1982) which is based on an atmospheric argon comparison. The interlaboratory standard GL-O, with the recommended value of 6.679 x 10^{14} at/g of $^{40}Ar^*$ (Odin et al., 1982), was used for ^{40}Ar signal calibration. Typical uncertainties of 1% are achieved for the ^{40}Ar signal calibration and for the K determination. Decay constants of Steiger and Jäger (1977) were used and uncertainties are quoted at the 1 j level throughout.

Oxygen , hydrogen and sulfur isotopic analyses were performed at the Laboratory of Stable isotopes and Low radioactivity of the BRGM, Orléans, France. Sulfides were analyzed for sulfur isotopes using the method of Thode et al., (1961). Quartz was analyzed for oxygen isotopes by laser-CO_2 fluorination (Fouillac and Girard, 1996). Oxygen and sulfur isotopes of alunite and anhydrite were analyzed after their conversion into a $BaSO_4$ precipitate, after Wasserman et al. (1990), and Sakai and Krouse (1971). Sulfur isotopes of sulfides were analyzed according to the method of Thode et al. (1961). Hydrogen isotopes of alunite were analyzed by extraction of water at 800°C and water reduction on hot uranium, according to Bigeleisen et al. (1952). Results are reported in δ units relative to international standards (V-SMOW for oxygen and hydrogen and CDT for sulfur). Analytical reproductibility on standards is better than ± 3 per mil for hydrogen and better than ± 0.3 per mil for oxygen and sulfur.

Table 1: K and Ar contents, deduced age

% K	% radiogenic ^{40}Ar	radiogenic ^{40}Ar (10^{14} at.g^{-1})	age
4,536	85,55	4,130	85,1±1,2
	85,68	4,080	84,1±1,2

5 Geochronology

Alunite from advanced-argillic alteration in the Bor mine (Table 1) yields a mean $^{40}K/^{40}Ar$ date of 84.6 ± 1.2 Ma (2s). This age is close to the age of V1 magmatic activity at Bor (Jankovic, 1981; Lips et al., 2003).

6 Stable isotopes

In the Bor mine, sulfides and alunite from Tilva Ros and sulfides and anhydrite from the deeper level of Borska Reka were analysed. For comparison, alunite from the prospect of Coka Kupjatra was analyzed. Isotopic results are given in Table 2.

The $\delta^{34}S$ of sulfides from the Bor mine vary between -3.0 and -0.6 ‰. They are slightly lower than sulfides from porphyry copper deposits of the district. Alunite from Tilva Ros (+19.8 ‰) has a $\delta^{34}S$ value close to previous data on anhydrite and barite from Tilva Ros, whereas the $\delta^{34}S$ of anhydrite from Borska Reka (+17.5 ‰) is lower than that of anhydrite from Tilva Ros (Drovenik et al., 1974). Within the Bor mine, the $\delta^{34}S$ of sulfides and sulfates are slightly lower in Borska Reka, at level -155m, than in Tilva Ros, at level -16m. The $\delta^{34}S$ and $\delta^{18}O$ of alunite from Coka Kupjatra are similar to those of alunite from the Bor mine.

7 Formation temperatures

At Tilva Ros, level –16 m, the alunite-pyrite sulfur isotope thermometer gives a temperature of 307 °C (after Stoffregen et al, 1994). This temperature is consistent with the diaspore + dickite + APS + zunyite assemblage and the position at bottom of the high-sulfidation orebody. At Borka Reka, level –155m, the anhydrite-pyrite thermometer gives a similar temperature of 326°C (after Ohmoto and Rye, 1979) in good agreement with the temperature range predicted from the mineral assemblages. Together these data confirm the hydrothermal origin of advanced argillic alteration in the Bor deposit.

8 Constraints on the source of fluids advanced argillic alteration

Stable (S, H, O) isotopes are useful tools to determine the origins of the fluids. Based upon the regional geology,

Table 2: Sulfur, oxygen and hydrogen isotope data

		$\delta^{34}S$	$\delta^{18}O$	δD
Tilva Ros	Cov	-1.8		
Level -16m	Py	-0.6		
	Alu	19.8	10.4	-43
	Qtz		11.5	
BOR112	Cpy	-3		
Borska Reka	Py	-2		
Level -155m	Anh	17.5	10.9	
Coka Kupjatra	Alu	19.4	11.1	-60

advanced argillic alteration may have formed from magmatic fluids and Volcanic vapors, meteoric waters and possibly Cretaceous seawater, each of which has its own isotopic signature. In the Bor district, the $\delta^{34}S$ and $\delta^{18}O$ values of alunite from advanced argillic alteration at Tilva Ros and Coka Kupjatra are indicative of a magmatic-hydrothermal origin. These values were reported in a $\delta^{18}O$ vs. $\delta^{34}S$ diagram (Fig. 2), in which the assumed $\delta^{34}S_{\Sigma}$ and the $\delta^{18}O$ of the hydrothermal fluid (magmatic dominant) and the predicted composition of alunite deposited from this fluid over a range of H_2S/SO_4 values (1 to 8) at estimated formation temperature of alunite are indicated by a line for each occurrence (adapted from Rye et al., 1992).

At Tilva Ros, the H_2S/SO_4 ratio was estimated around 7 – 8, considering a formation temperature of alunite around 300°C. In the pyrite-free sample from Coka Kupjatra, the isotopic composition of alunite is consistent with H_2S/SO_4 ratios around 2 – 4 assuming a formation temperature around 250°C.

H_2S/SO_4 ratios >1 are common in other high-sulfidation epithermal Cu-Au deposits (e.g. Summitville: Rye et al., 1990; Pueblo Viejo: Vennemann et al., 1993; Nansatsu: Hedenquist et al., 1994; Rodalquilar: Arribas et al., 1995; Lepanto: Hedenquist et al., 1998).

The $\delta^{18}O$ and δD values of waters in equilibrium with alunite from the Bor mine and Coka Kupjatra were calculated using the alunite-water fractionation data of Stoffregen et al. (1994) and formation temperatures estimated above. They were compared with potential fluid reservoirs in the district: Volcanic vapors, primary magmatic waters, the meteoric water line and seawater (Taylor, 1987; Giggenbach, 1992). Calculated $\delta^{18}O$ and δD values for water at Tilva Ros (Bor mine) of +4.2‰ and -35 ‰, respectively, are consistent with precipitation from magmatic fluids or vapors. However its tendency toward lower $\delta^{18}O$ values suggests a slight dilution with surficial waters. The lower $\delta^{18}O$ (+0.2 to +2.7‰ estimated for a temperature range of 200-250°C) and δD (–53 ‰) values at Coka Kupjatra are indicative of a more important dilution by meteoric water.

9 Conclusions

K-Ar date of alunite from the Bor high-sulfidation ore deposit is 84.6 ± 1.2 Ma. This Upper Cretaceous date is sub-synchronous of the first stage of volcanism, as the other main ore deposits of the district. O, H, and S isotopic compositions of alunite in the Bor district require a magmatic-hydrothermal origin for advance argillic alteration (Rye et al., 1992). Hydrothermal fluids were hot (>300°C), had H_2S/SO_4 ratios of 2 to 8, and comprised dominantly of magmatic fluid or condensed vapor with a minor meteoric component. The isotopic compositions of alunite from ore deposits and uneconomic prospects are similar. Our results are quite similar to those obtained on advanced argillic alteration in the Srednogorie zone in Bulgaria (Lerouge et al., 2003). A common feature of high-sulfidation ore deposits in Serbia and Bulgaria is the presence of zunyite at depth and alunite with high PO_4 (and Sr, Ba) contents (Bailly et al., in prep.).

References

Arribas A, C.G. Cunningham, J.J. Rytuba, R.O. Rye, W.C. Kelly, M.H. Podwysocki, E.H. Mc Kee, and R.M. Tosdal (1995). Geology, geochronology, fluid inclusions and isotope geochemistry of the Rodalquilar gold alunite deposit, Spain. Econ. Geol., Vol. 90, pp. 782-823.

Bigeleisen, J., M.L. Perlman, and R.H. Prosse (1952). Conversion of hydrogenic materials to hydrogen for isotopic analysis. Analytical Chemistry, Vol. 24, p. 1356.

Cassignol, C., P-Y. Gillot (1982). Range and effectiveness of unspiked potassium-argon dating: experimental groundwork and applications. In « numerical dating in stratigraphy », G. S. Odin Edit., Willey pub., chap. 9, pp. 159-179.

Claypool, G.E., W.T. Holser, I.R. Kaplan, H. Sakai, I. Zak (1980). The age curves of sulfur and oxygen isotopes in marine sulfate and their mutual interpretation. Chem. Geol., Vol. 28, pp. 199-260.

Drosenik, M., H. Leskovsek, J. Pezdic (1974-75). Isotpic composition of sulfur in the ore deposits of the Timok Volcanic district. Rud. Metal. Zb, Vol. 4, pp. 319-362 (in Serbian).

Fouillac, A.M., J.P. Girard (1996). Laser oxygen isotope analysis of silicate/oxide grain separates: Evidence for a grain size effect?. Chem. Geology, Vol. 130, pp. 31-54.

Giggenbach, W.F. (1992). Isotopic shifts in waters from geothermal and Volcanic systems along convergent plate boundaries, and their origin. Earth and Planetary Science Letters, Vol. 113, pp. 495–510.

Gillot, P-Y., Y. Cornette (1986). The « Cassignol technique » for potassium-argon dating, precision and accuracy: examples from the Late Pleistocene to recent Volcanics from Southern Italy. Chem. Geol. (Isot. Geos. Sect.), Vol. 59, pp. 205-222.

Hedenquist, J.W., A. Arribas, T.J. Reynolds (1998). EVolution of an intrusion-centered hydrothermal system: Far Southeast-Lepanto porphyry and epithermal Cu-Au deposit, Philippines. Econ. Geol., Vol. 93, pp. 373-404.

Hedenquist, J.W., Y. Matsuhisa, E. Izawa, N.C. White, W.F. Giggenbach, M. Aoki (1994). Geology, geochemistry, and origin of high sulfidation Cu-Au mineralization in the Nansatsu district, Japan. Econ. Geol., Vol. 89, pp. 1-29.

Jankovic, S., M. Jovanovic, S. Karamata, A. Lovridj, (1981). Isotopic age of some rocks from Timok eruptive zone: Srpska Akademija Nauka i Umetnosti, Glas. Odeljenje Prir, pp. 87-94.

Karamata, S., V. Knezevic, P. Djordjevic, and D. Milovanovic (1983). Alterations in the Bor copper deposit and their significance for explanation of the ore genesis. Geologica Carpathica, Vol. 34, pp. 45-52.

Kozelj, D. (2002). Morphogenetical types of epithermal gold mineralization in the Bor metallogenic zone. In: Geology and metallogeny of copper and gold deposits in the Bor metallogenic zone. D. Kozelj and R. Jelenkovic (Eds), Serbia and Montenegro, pp. 57-70.

Lerouge C., Bailly L., Fléhoc C., Petrunov.R., Kunov.A., Georgieva.S., Velinov.I. (2003). Preliminary results of a mineralogical and stable isotope systematic on alunite in Bulgaria - Constrain on its origin.. In Mineral Exploration and Sustainable Development, SGA - Athènes - Grèce - 24-28/08/2003, pp. 495-498.

Lips, A., R.J. Herrington, G. Stein, D. Kozelj, K. Popov, J.R. Wijbrans (2004). Refined timing of porphyry copper formation in the Serbian and Bulgarian portions of the Cretaceous Carpatho-Balkan Belt. Economic Geology and the Bulletin of the Society of Economic Geologists, Vol. 99, pp. 601-609.

Odin, G.S., et al. (1982). Interlaboratory standards for dating purposes. In: Numerical Dating in Stratigraphy, Odin, G.S. (Ed.), Wiley, Chichester, pp. 123– 150.

Ohmoto, H., R.O. Rye (1979) Isotopes of Sulfur and Carbon. In : Geochemistry of Hydrothermal Ore Deposits, Barnes H. , Wiley J. and Sons (Eds.), New York.

Rye, R. C., R.E. Stoffregen, P.M. Bethke (1990). Stable isotope systematics and magmatic and hydrothermal processes in the Summitville, CO gold deposit. Open-File Report - U. S. Geological Survey, open file report 90-0626, 31 pp.

Rye, R.O., P.M. Bethke, M.D. Wasserman (1992). The stable isotope geochemistry of acid sulfate alteration. Economic Geology, Vol. 87, 225–262.

Sakai, H., H.R. Krouse (1971). "Elimination of memory effects in 18-O/16-O determinations in sulfates". Earth Planet. Sci. Letters, Vol. 11, pp. 369-373.

Steiger, R.H., E. Jäger (1977). Subcomission on geochronology: Convention on the use of decay constants in geo- and cosmochronology. Earth Planet Sci. Let., 36, pp. 359-362.

Stoffregen, R.E., R.O. Rye, M.D. Wasserman (1994). Experimental studies of alunite: Part I, ^{18}O - ^{16}O and D-H fractionation factors between alunite and water at 250-450 degrees C. Geochimica et Cosmochimica Acta, Vol. 58, pp. 903-916.

Taylor, H.P. (1987). Stable isotope geochemistry of ore-forming fluids. Shortcourse Handbook, Canada 13.

Thode, H.G., J. Monster, H.B. Dunford (1961). Sulfur isotope geochemistry. Geochim. Cosmochim. Acta., Vol. 26, pp. 159–174.

Wassermann, M.D., R.O. Rye, P.M. Bethke, A. Arribas (1992). Methods for separation and total stable isotope analysis of alunite. USGS open file Report 92-9, 20p.

Turbidite-hosted gold deposits of SE Guizhou, China: Their regional setting, mineralizing styles, and some genetic constrains

Huan-Zhang Lu[1,2], Zhonggang Wang[2], Wenyi Chen[2], Xueyi Wu[2], Ruizhong Hu[2], Moussa Keita[1]
[1]Sciences de la terre, CERM, University of Québec at Chicoutimi, Chicoutimi, Québec, G7H 2B1, Canada
[2]Institute of Geochemistry, Chinese Academy of Sciences, Guiyang, Guizhou Province, China

Abstract. Turbidite-hosted gold deposits have been found in SE Guizhou province, China. They are characterized by bedding-parallel, gold-bearing quartz veins that are structurally controlled by NE folds and faults. Research shows that the gold deposits formed during the Caledonian orogeny. The source of gold may be from hydrothermal fluids that reacted with pyrite in the host beds.

Keywords. Turbidite, gold deposits, quartz vein, SE Guizhou

1 Introduction

Auriferous deposits hosted by turbidites have a wide distribution throughout the world, occurring in rocks ranging in age from Archean to Tertiary. Turbidite-dominated terranes have been an important sources of gold, particularly in Victoria of Australia, and the Meguma Terrane of Nova Scotia, Canada (Boyle 1986; Cox et al., 1995; Ramsay et al., 1998; Ryan and Smith 1998; Large 2004,). But in China, this type of gold deposits has only recently been discovered in SE Guizhou Precambrian turbidite terrane (Lu et al. 2005). This paper summarizes the relationship between gold deposits and structures, turbidite and hydrothermal fluids.

2 Regional geology of SE Guizhou Province, China

SE Guizhou province is a gold region with primary gold mineralization richly-developed in the Precambrian rocks of the SE Guizhou and SW Hunan Caledonian fold belt (Fig.1). More than 20 gold deposits have been found in the area and gold was produced both from primary quartz veins and from alluvial placer deposits. In the West Hunan province, several large gold deposits including Xiangxi, Muoping and Youxi (more than 50 tons in reserve), are

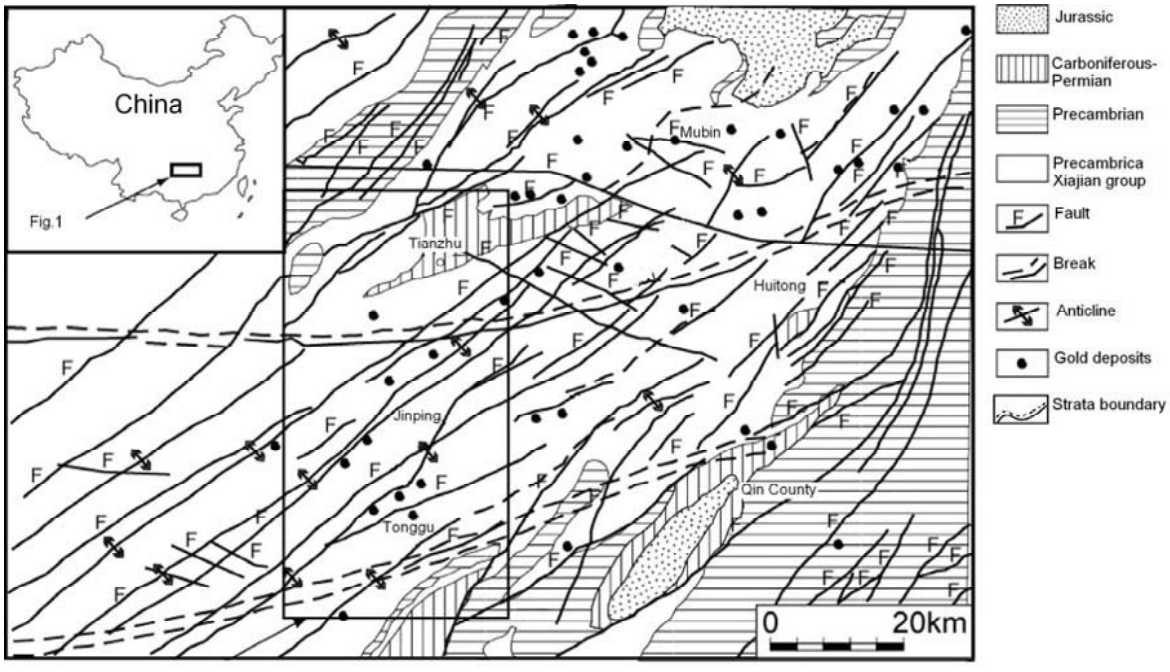

Figure 1: Regional geological map of turbidite-hosted gold deposits, SE Guizhou, China. This map show the SE Guizhou- SW Hunan Caledonian fold belt. Most gold deposits occur in the Precambrian turbidite Xiajiang group (Lu et al. 2005). The square frame is the location of Figure 2.

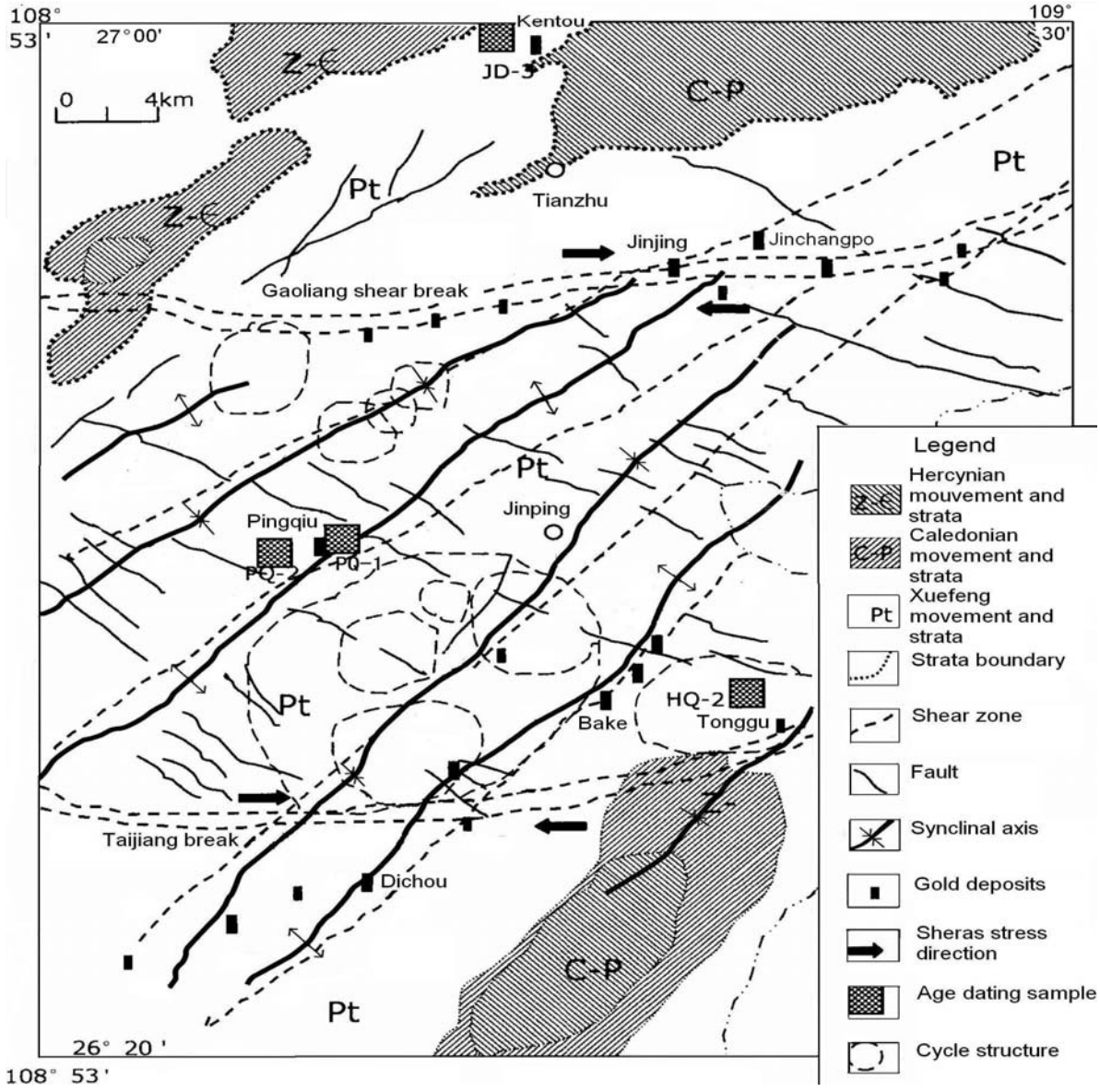

Figure 2: Geological and structural map of Tianzhu –Jinping area, SE Guizhou (this study) showing two E-W break structures, six NE direction anticlines and synclines, several NE direction shear zones and faults. The gold deposits are controlled by fold and faults in the Precambrian fold belt.

hosted by Proterozoic, weakly-metamorphosed turbidite rocks. In the SE Guizhou, five shear zones including the Jingjing, Kentou, Pingqiu, Wenjiang, and Tonggu shear zones, and 6 anticlines in orientation of NEE or NE, have been recognized (Lu et al. 2005). At least four major gold deposits including Huaqiao, Kentou, Pingqiu, and Jingjing (more than 10 tons in reserve) and about 10 gold showings have been found. Geologically, the region lies on the southwestern edge of the Yangtze paleo- platform, which is composed of crystalline rocks of Proterozoic age, and overlain by shallow-marine Cambrian to Jurassic age rocks.

The majority of the deposits are hosted by Proterozoic slate-tuff, and sandstone. These Proterozoic rocks suffered a greenschist phase metamorphism prior to gold mineralization. But this is not the case of the Cambrian to Jurassic age rocks.

There are several orogenesis in the region: Xuefeng; Caledonia; Yanshanian and Himalayan. Among of them the Caledonia movement is the major one. The Caledonian deformation resulted in NE folding and shearing. Structurally, the deposits are located in a composite anticline, with Proterozoic rock in the center and Cambrian to Jurassic rocks in the limbs. The five shear zones are located on the south and North limbs of the anticline: the Kentou and

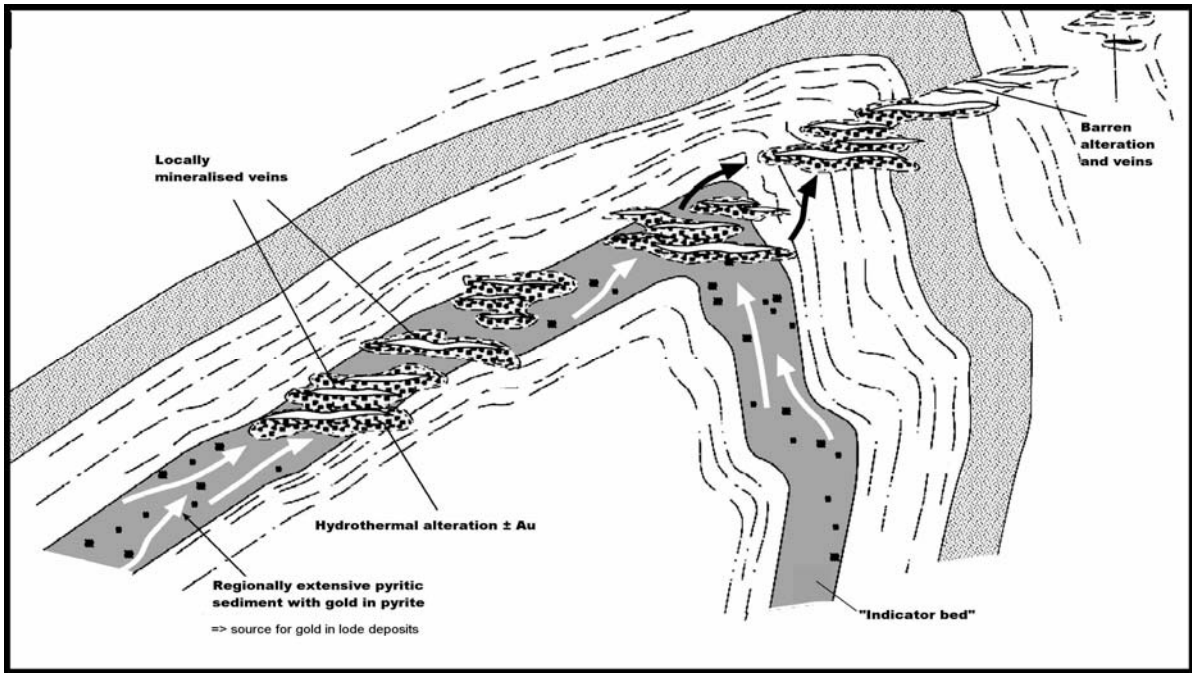

Figure 3: Possible genetic model for forming gold deposits be turbidite (after Large 2004).

Jingjing shear zones are located in the North limb and the Wenjiang and Tonggu shear zones occur in the south limb and the Pingqiu shear zone is located near the axis of anticline (Fig. 2). These shear zones produced subsidiary structures including ductile, ductile-brittle and brittle structures. The quartz veins are filled mostly into the interbeds structures. No intrusion has been found in the region, but far away (about 400 km away) from south and North region there are mafic and felsic magmatic intrusions (the age of these intrusions, according to the geological Map of Guizhou (1:400,000, 1978), are Caledonian.

The native gold-bearing quartz veins strike NE and about 200-1000m in length, 0.1 to 1.0 m in width and about 200 to 300m in depth. The en echelon distribution pattern of gold-bearing quartz veins is found in Pingqiu, Huaqiao, Kentou and Jingjing gold mines. The gold grade is from 2 g/t to 30 g/t. Native gold is associated with quartz and a minor pyrite. The alteration is dominated by chloritization, sericitization and silicification.

3 Mineralization style and age

Three mineralization types have been identified in the region: auriferous quartz veins mostly parallel to the bedding (BPV); disseminated type and placer deposits. The vein type deposits can be subdivided into three sub-types: (1) high grade (approximately 16 g/t Au) narrow gold bearing veins ; (2) low grade (0.5- 4 g/t Au) thicker (0.8 to 1.2 m) gold bearing quartz veins; and (3) bedding discordant quartz veins (3-6 g/t Au) with intensive alteration than type 1 and 2.

Using Rb-Sr dating, samples (quartz from the quartz veins in 7 different locations of same mine from 5 gold mines, yield ages from 370 to 514 Ma, which corresponds to Caledonian movement.

4 Discussion

The gold deposits- the bed parallel quartz veins in SE Guizhou province are formed during syn or post Caledonia orogeny. Fluid inclusion study indicates homogenization temperatures ranging from 250 to 320 oC and rich of CO_2 in composition (about 6 to 12 mole%)

Our recent study (electron microprobe analysis) shows the Au contents in turbidite and in pyrite of turbidite (from 6 to 100 ppb) are higher than the Au Clarke value (4 ppb), this indicates the turbidite and pyrite as a possible source of gold with the probable hydrothermal fluids reacted with them to form this type of deposits (Fig. 3). The ore-forming fluids along the structures generated by folding and faulting, form the bedding paralleled gold bearing quartz veins deposits in the turbidite.

Acknowledgements

We thank the geologists in gold mines of SE Guizhou for their assistansce and the finance support for this project by the Chinese Academy of Sciences, Institute of geochemistry, Science and technology foundation of Guizhou government, FUQAC, and Hong Kong W.H. Wong foundation.

References

Boyle RW (1986) Gold deposits in turbidite sequences: Their geology, geochemistry and history of the theories of their origin in Keppie, Boyle and Haynes eds, Turbidite-Hosted gold deposits: Geological Association of Canada special paper 32, p.1-13.

Cox SF, Sun S-S, Etheridge MA, Wall VJ, Potter TF (1995) Structural and geochemical controls on the development of turbidite hosted gold quartz vein deposits, Wattle Gully mine, Central Victoria, Australia: Econ. Geol. 90: 1722-1746.

Large RR (2004) A new approach to the terrane selection, deposit vectoring and ore-deposit characterization for sediment-hosted gold systems. CODES research project C330, 42p.

Lu H-Z, Wang Z, Chen W, Wu X, Hu R (2005) Turbidite-hosted bedding parallel gold quartz veins in SE Guizhou, China: Acta Geologica 1: 22-26.

Ramsay WRH, Bierlein FP, Arne DC, VandenBerg AHM (1998) Turbidite hosted gold deposits of Central Victoria, Australia; their regional setting, mineralizing styles, and some genetic constrains: Ore Geol Rev 13: 131-151.

Ryan RJ, Smith PK (1998) A review of the mesothermal gold deposits of the Meguma group, Nova Scotia, Canada. Ore Geol Rev 13: 153-183.

Carlin-like gold mineralization in the Gaspé Peninsula, Canadian Appalachians

M. Malo
Institut national de la recherche scientifique – Eau, Terre et Environnement, Université du Québec, 490 de la Couronne, Québec, Québec, G1K 9A9, Canada

B. Dubé
Geological Survey of Canada – Québec, 490 de la Couronne, Québec, Québec, G1K 9A9, Canada

V. Garnier, A. Chagnon
Institut national de la recherche scientifique – Eau, Terre et Environnement, Université du Québec, 490 de la Couronne, Québec, Québec, G1K 9A9, Canada

Abstract. In the Gaspé Peninsula of the Canadian Appalachians, the Saint-André-de-Restigouche gold prospect is spatially associated with the Acadian dextral strike-slip Grand Pabos-Restigouche fault system. Mineralized veins hosted by Lower Silurian argillaceous and silty limestones are enclosed in a large halo of propylitic alteration. The veins are composed of quartz, stibnite, arsenopyrite and altered angular fragments of the host-rocks with arsenopyrite and framboidal pyrite. Grades average 6 g/t Au with the best values reaching 39 g/t. The host-limestone is silicified with local massive silica replacement. At a greater distance from the vein, the host-rock is carbonatized. Idiomorphic grains of pyrite are rimmed by arsenian pyrite. The metallic signature of the mineralization is characterized by Au-As-Sb-Hg without Ag and base metals. The geological setting, style of alteration, metallic signature and presence of auriferous arsenic-rich pyrite rims indicate that the Saint-André-de-Restigouche prospect has many attributes of Carlin-type gold deposits in Nevada. It also shares analogies with distal disseminated gold deposits.

Keywords. Carlin, gold, distal disseminated, sedimentary rocks, Appalachians, Canada

1 Introduction

Different styles of gold mineralization have been discovered along major faults in the Canadian Appalachians (Dubé et al. 2001). The Saint-André-de-Ristigouche (SAR) gold prospect in southern Gaspé Peninsula shows affinities with Carlin-type gold deposits (Malo et al. 1998). Herein, we describe regional-scale, district-scale and prospect-scale characteristics which allow comparisons with those of Carlin-type and distal disseminated gold deposits in Nevada (Hofstra and Cline 2000).

2 Geological setting of the Gaspé Peninsula in the Canadian Appalachians

The Gaspé Appalachians consist of Paleozoic rocks, mainly sedimentary with minor volcanics, which are divided into three rock assemblages (Fig. 1): 1) Cambrian to Upper Ordovician rocks, 2) Upper Ordovician to Middle Devonian rocks, the Gaspé Belt, and 3) Carboniferous rocks. The first rock assemblage was affected by the Late Ordovician Taconian and Middle Devonian Acadian orogenies, whereas the second rock assemblage was mainly deformed by the Acadian Orogeny and also records Salinic structural features during Late Silurian.

The SAR gold prospect is hosted by Silurian rocks of the Gaspé Belt along the Grand Pabos-Ristigouche fault system (Fig. 1).

3 Regional-scale characteristics

The Gaspé Belt consists of four broad temporal and lithological assemblages (Bourque et al. 2000). From the base to the top (Fig. 2), these are : (I) the Upper Ordovician-lowermost Silurian fine-grained carbonate-siliciclastic facies, (II) the Silurian-lowermost Devonian shallow to deep shelf and basin facies, (III) the Lower Devonian mixed siliciclastic and carbonate fine-grained deep shelf and basin facies, and (IV) the Lower to Middle Devonian nearshore to terrestrial coarse-grained facies. Upper Silurian and lower Devonian continental tholeiitic basalts and andesites are present in rock assemblages II, III and IV. Rocks of the Gaspé Belt are bounded by two major unconformities between Cambrian to Upper Ordovician assemblages, at the base, and the overlying Carboniferous rocks (Fig. 1). A Late Silurian unconformity associated with extensional tectonics is recognized in the Gaspé Belt sequence (Fig. 2). The Gaspé Belt rocks were affected by regional anchimetamorphism to low-grade metamorphism usually attributed to burial metamorphism. Local zones of high-grade metamorphic rocks are spatially associated with Devonian intrusions and dike swarms along major Acadian faults. Intrusions are restricted to the northern part of the peninsula. Several stocks and dike swarms intrude the Gaspé Belt rocks further south. The Gaspé Peninsula host several Cu deposits including the world-class Mines Gaspé and Mines Madeleine in

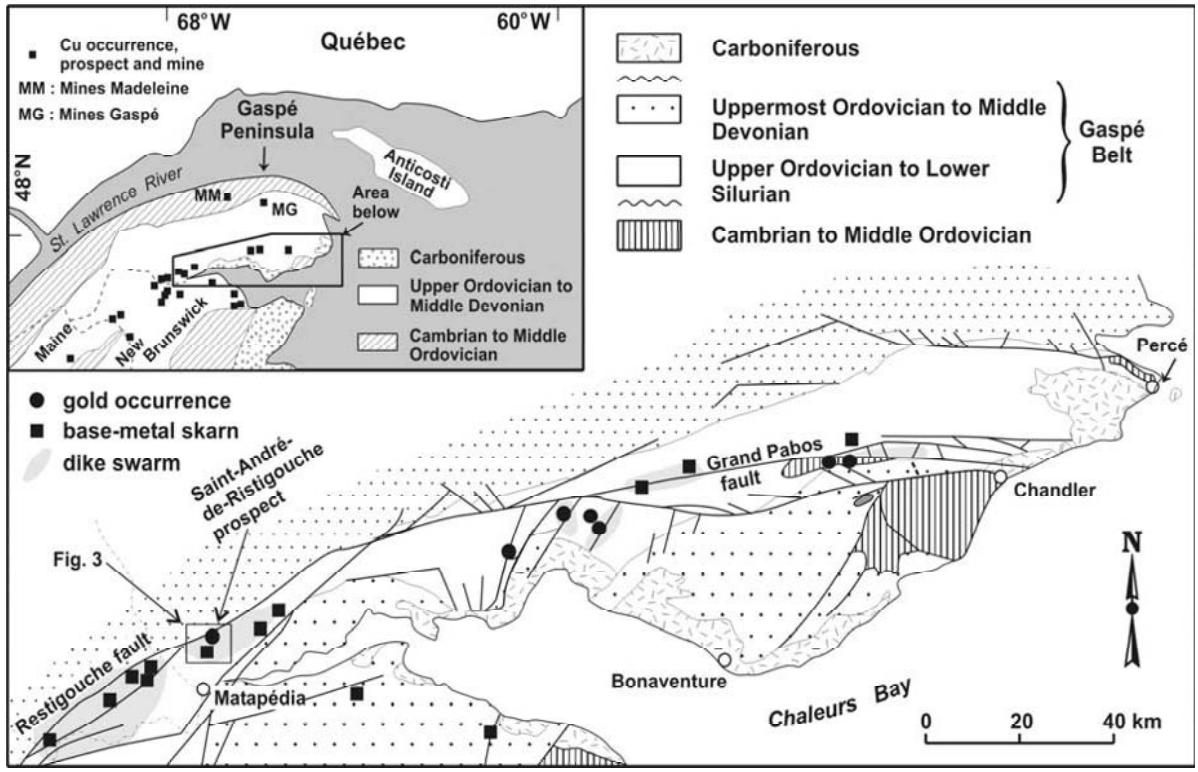

Figure 1: Simplified geology of the southern Gaspé Peninsula and location of the study area.

the north, and numerous polymetallic Cu-Pb-Zn-Ag-Au prospects (Fig. 1). They are part of the northern Appalachian porphyry-skarn province that stretches from northern Maine to northwestern New Brunswick and Gaspé Peninsula (Fig. 1) (Hollister et al. 1974).

4 District-scale characteristics

The Grand Pabos fault with its western extension, the Restigouche fault, and their subsidiary faults is a major Acadian strike-slip fault system of the Canadian Appalachians (Figs. 1). The SAR gold prospect, as well as base-metal skarns (Fig. 1), is hosted by rocks of the lower assemblage of the Gaspé Belt which consists of a conformable sequence of terrigenous rocks (Garin) passing gradually upward to silty and shaly limestones (White Head) through an intermediate facies of calcareous and terrigenous rocks (Pabos) (Fig. 2). Igneous intrusive activity is restricted to isolated or swarms of felsic dikes along major Acadian faults (Fig. 1). The regional structural trend of Gaspé Belt rocks in southern Gaspé Peninsula is northeast. Major E- to ENE-trending dextral strike-slip faults cut this trend (Fig. 1). NE-trending faults, such as the Sellarsville fault in southwestern Gaspé Peninsula, are SE-directed, high-angle reverse faults. Several gold occurrences consisting of Au-bearing veins are located close to secondary faults (Fig. 1).

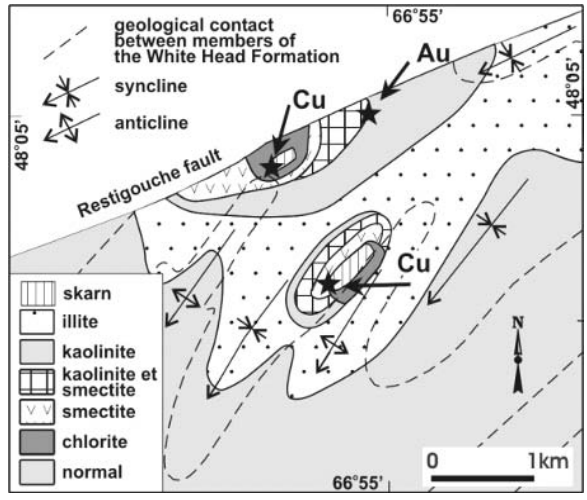

Figure 2: General lithostratigraphy of the Gaspé Belt.

5 Prospect-scale characteristics - SAR

The SAR gold prospect consists of quartz-stibnite veins hosted by the Silurian calcilutite and laminated silty and argillaceous limestone of the White Head Formation (Fig. 2) along the Restigouche fault (Fig. 1). Several NE- and NW-trending, fine-grained and porphyritic, granodioritic dikes intrude the sedimentary rocks on both sides of the fault.

South of the Restigouche fault, NE-trending regional folds are upright, tight and plunge moderately to the NE (Fig. 3).

The SAR gold prospect is enclosed in a large halo of propylitic hydrothermal alteration which includes two Cu-skarn mineral occurrences (Fig. 3). From the unaltered limestone to the centre of the halo, clay mineral assemblages are: illite, kaolinite, kaolinite/smectite, smectite, and chlorite (Fig. 3). The Cu-skarn occurrences are associated with the chlorite zone whereas the SAR gold prospect is in the kaolinite zone (Fig. 3).

The mineralization consists of two NW-trending subvertical mineralized veins cutting across a meter-wide As-Sb-rich quartz stockwork. Grades average 6 g/t Au with the best values reaching 39 g/t. Quartz represents 40 to 50% of the vein. Carbonates, which account for 10 to 15% of the vein, occur as crystals of sparite with mm to cm fragments of the host limestone. The latter fragments are angular and contain arsenopyrite and framboïdal pyrite. Stibnite, the dominant sulfide, represents 30 to 35% of the vein. Arsenopyrite, comprising 5% of the vein, is enclosed in the quartz, the stibnite, and the host rocks. Host limestones are commonly silicified at the vein contact. This silicification is expressed by massive silica replacement of the limestone, with locally up to 90% quartz with disseminated arsenopyrite and sericite, and 1 to 2 m thick stockwork of quartz veinlets, with variable proportion of As and/or Sb, and up to 11 g/t Au. This silicification is followed, away from the vein, by a zone of abundant calcite-quartz veinlets, subparallel to the main vein. In addition to calcite-quartz veinlets, quartz replaces lime muds of calcilutite and argillaceous limestone beds in the silicification zone. Other constituents of the silicification alteration zone are arsenopyrite, representing 5% of the host limestones, 1% of framboïdal and hydrothermal pyrite and traces of kaolinite either disseminated or in veinlets. This silicification shares analogies with the jasperoids of Carlin-type deposits. At a greater distance from the vein, the host-rock is carbonatized with up to 95% of carbonates, 2% of quartz and 1 % of pyrite and arsenopyrite. About 5 to 10% of the carbonates occur in late veinlets. In both the silicified and carbonatized zones, pyrite is present as framboids and as hydrothermal idiomorphic grains.

Most of the later are rimmed by arsenian pyrite (Fig. 4). Gold, which was not observed in thin sections, is included in arsenopyrite and rims of arsenian pyrite.

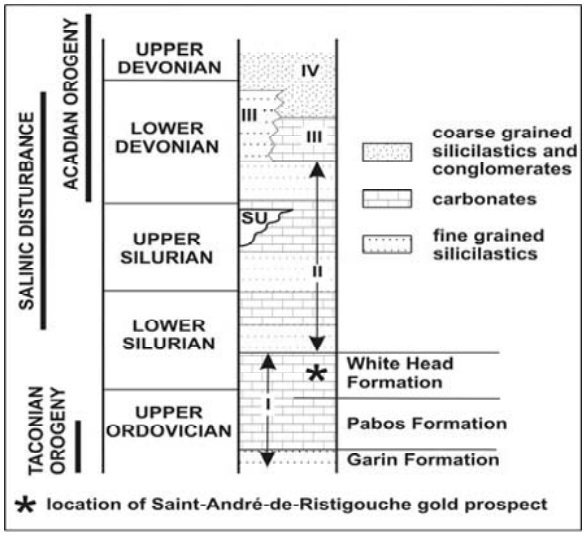

Figure 3: Geology and alteration zoning at the Saint-André-de-Ristigouche gold prospect.

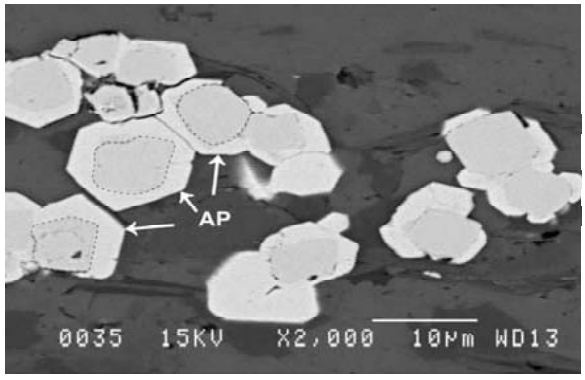

Figure 4: Rims of arsenian pyrite around pyrite grains.

Table 1: Metallic signature of channel samples across the main vein at SAR gold prospect. hr: host rock, sb: stibnite, sil: silicification, stock: stockwork. From Malo et al. (1998).

#	Description	Au ppb	As ppm	Sb ppm	Hg ppb	Cu ppm	Zn ppm	Mo ppm	Ag ppm
6051	hr + calcite vein	96	529	86	160	13	42	6	<0,1
6052	hr + calcite vein	177	926	83	150	7	39	4	<0,1
6053	hr ± sil + traces sb	4923	11900	2120	455	16	37	3	<0,1
6054	hr ± sil + stockwork quartz-sb	6693	14200	415	350	17	46	2	<0,1
6055	hr ± sil + stockwork quartz-sb	15260	20100	99000	630	21	21	2	<0,1
6056	Sb-rich quartz vein	8093	7430	112000	305	12	9	2	<0,1
6057	sil hr + stock quartz-calcite-sb	4783	2880	502	125	9	28	3	<0,1
6058	sil hr + stock quartz-calcite-sb	1719	1520	457	110	9	29	4	<0,1
6059	hr + calcite vein	2127	1710	114	160	12	39	6	<0,1
6060	hr + calcite vein	32	131	61	85	9	25	9	<0,1

The metallic signature of the mineralization (Table 1) is characterized by a significant enrichment in Au-As-Sb-Hg without Ag and base metals (Pb, Zn, Cu). Electron microprobe analyses show that the arsenian rims are characterized by 3 to 15wt% As, up to 2280ppm Au and 2500ppm Sb. Au and Sb are also contained in less-abundant arsenopyrite (up to 2500 and 2400ppm respectively).

6 Conclusions

The geological setting (regional and district-scale characteristics) and prospect-scale characteristics (composition of host rocks, proximity to a crustal scale fault and Cu-skarn, style of alteration, metallic signature and presence of auriferous arsenian pyrite rims) clearly indicate that the SAR gold prospect has many attributes of Carlin-type gold deposits in Nevada [see Poulsen (1999), and Hofstra and Cline (2000) for summaries of characteristics]. Its distal position in an intrusion related zonation pattern centered on a Cu skarn suggests also analogies with distal disseminated gold deposits (Hofstra and Cline 2000). The SAR gold prospect in the Gaspé Peninsula highlights the potential for sedimentary rock-hosted disseminated gold deposits within the carbonate rock-units of the Canadian Appalachians.

References

Bourque PA, Malo M, Kirkwood D (2000) Paleogeo-graphy and tectono-sedimentary history at margin of Laurentia during Silurian-Earliest Devonian time: the Gaspé Belt, Québec. Geol Soc Am: 112, 4-20.

Dubé B, O'Brien S, Dunning GR (2001) Gold deposits in deformed terranes: examples of epithermal and quartz-carbonate shear-zone-related gold systems in the Newfoundland Appalachians and their implications for exploration. North Atlantic Mineral Symposium, St. John's, NF, Canada. Ext abs, 2001, pp. 31-35.

Hofstra AH, Cline JS (2000) Characteristics and models for Carlin-type gold deposits. SEG Rev: 13, 163-220.

Hollister VF, Barker AL, Potter RR (1974) Porphyry-type deposits of the Appalachian orogen. Econ Geol: 69, 618-630.

Malo M, Moritz R, Dubé B, Chagnon A, Roy F, Pelchat C (2000) Base-metal skarns and Au occurrences in the southern Gaspé Appalachians: Distal products of a faulted and displaced magmatic-hydrothermal system along the Grand Pabos-restigouche fault system. Econ Geol: 95, 1297-1318.

Malo M, Pelchat C, Dubé B, Chagnon A (1998) Contrasting styles of gold mineralization along the Grand Pabos-Ristigouche fault system: implication for Carlin-like Au-mineralization in the southwestern Gaspé Appalachians. Expl Min Geol: 7, 217-236.

Poulsen KH (1999) Geological environnements for Carlin-type gold deposits in Canada. In: New developments in the geological understanding of some major ore types and environments, with implications for exploration. PDAC, Toronto, pp. 155-178.

Fluid inclusion study of quartz veins from the orogenic Klecza gold deposit in the Kaczawa Mountains (SW Poland)

S.Z. Mikulski, S. Speczik
Polish Geological Institute, 4 Rakowiecka St., 00-975 Warsaw, Poland

A. Kozlowski
Institute of Geochemistry, Mineralogy and Petrology of the Warsaw University, Al. Zwirki i Wigury 93, 02-089 Warszawa, Poland

Abstract. Primary fluid inclusions in different generations of auriferous quartz from the Klecza orogenic gold deposit crystallized from 340 to 244°C with decreasing salinity of fluids of 12.3 to 6.4 wt % NaCl equivalent and at pressure drop of 0.9 to 0.7 kb. Fluids revealed the presence of moderate to low saline two-phase aqueous fluids with CO_2, N_2 and CH_4. In ore fluids beside sodium cations there occurred especially high concentration of K and low to moderate contents of Al and Fe cations that caused Au precipitation. Post-ore fluids are characterized by domination of Na. The correlation between gold and sulphur as well as common occurrence of gold inclusions in pyrite and arsenopyrite of the first ore stage mineralization suggest that gold was transported as reduced bisulphide complexes. The values of the sulphur isotope compositions of the considered above sulphides reflect a strong sulphur contribution from the graphitic schists beside the magmatic source of sulphur.

Keywords. Orogenic gold, fluid inclusion, Klecza, Kaczawa Mountains, Western Sudetes, SW Poland, Bohemian massif, European Variscides

1 Introduction

The Klecza deposit is located within the abandoned gold mining area of the Klecza-Radomice ore district (KROD) in the SW part of the Kaczawa Mountains. The Kaczawa Mountains constitute the west-central part of the Western Sudetes, where the Palaeozoic crystalline basement continues from the Saxothuringian zone of the European Variscan belt in the NW part of the Bohemian massif. In the KROD, gold-sulphide mineralization in quartz veins and fractures is of unknown economic significance. It was classified as the orogenic type (Mikulski 2003). Genetic classification of those gold deposits was based on the geological setting between metamorphic terranes, strong structural control of ores, low Au/Ag ratio in gold ores, insignificant base-metal sulphides content, and low salinity of mineralizing fluids (<7 wt% NaCl equivalent). In this contribution we present new results of fluid inclusion studies in auriferous quartz veins from the Klecza area.

2 Geological setting of Klecza Au orogenic deposit

At the Klecza deposit gold mineralization is hosted by Ordovician – Silurian epimetamorphosed slates of the Pilchowice unit that belongs to the Kaczawa complex. Gold-bearing quartz-sulphides mineraliza-tion occurs in fractures, veins and vein arrays in folds (saddle reefs), and diagonal veins. Bigger lodes are preferentially located in fractured zones discordant to the bedding. In Klecza two main ore fields exist with several recognised veins. Fractures and veins have major NE-SW and minor NW-SE strike directions, and steeply dip (65-85^0) to the west. They were examined along their lengths of about 90-120 m and down to 100 m below surface. These veins change in thickness from 0.1 to 1.2 m (an average thickness is about 0.25 m). All these mineralised structures have small post-mineraliza-tion displacement (less than 1 m) at different angles. In shallower parts of the veins auriferous arsenopyrite dominates (with the gold content up to 20 ppm). Auriferous pyrite increases as the vein depths increase (30-34 ppm Au, as noted earlier by Grimming, 1933).

3 Ore mineralization in quartz veins and host rocks

Gold-bearing sulphide and gold mineralization occurs in quartz breccia veins and cataclassed sericite-quartz schist and quartz-graphite schist. Pyrite and arsenopyrite are most common sulphides, however, often either of them prevails. Base metals sulphides are subordinate and carbonates are associated with the ores. Arsenopyrite and pyrite occur in two characteristic forms. The first one as euhedral crystals up to 3-5 mm in size exhibits cataclastic deformation textures accompanied by the second form as very fine euhedral crystals from 10 to 200 μm in size. These fine-grained sulphides may form pyrite- or arsenopyrite-rich bands cementing cataclased quartz and coarse-grained ores. Chalcopyrite and less frequently galena occur as fillings of fractures in the coarse-grained sulphides, as inclusions, and as overgrowths. Sphalerite is rare and may contain inclusions of chalcopyrite, aligning along planes.

Gold mineralization was found both in sulphide-rich and sulphide-poor samples. Gold occurs as inclusions in pyrite and arsenopyrite as well as microveinlets associ-

ated with chalcopyrite and galena and as grains. Free grains of gold occur in the cataclastic quartz veins cemented by chalcedony and younger ankerite. Host rocks represented by graphite-quartz-chlorite schists contain very fine pyrite, which is abundant in places. Pyrite of an early generation consists of framboidal clusters from 1 up to 20 μm in size associated with graphite. Late pyrite occurs as anhedral crystals recrystallized from framboidal pyrite. In the quartz-sericite schists very fine crystalline hematite and titanium oxides commonly occur. Most of the hematite and titanium-oxide crystals are disseminated and evenly distributed but some occur in bands within sericite laminae and fill fractures as well. Alteration processes are manifested by first strong silicification and sulphidization followed by extensive sericitization and carbonatization of quartz-muscovite schists hosting quartz veins and gold-bearing fractures. Amorphous silica, fine-fibrous quartz, and chalcedony formed as a result of hydrothermal low temperature precipitation. Chalcedony was fractured again and cemented by the younger generation of carbonate and Fe-hydroxides.

4 Fluid inclusion studies

4.1 Methods

The investigations were performed with double-side polished preparations, ca. 0,3 mm thick, on the *Fluid Co.* microscope heating stage, calibrated on the commercial and self-prepared standards. The uncertainty of the measurements in the temperature range 80–500°C was ±1°C, and from –70 to +50°C,±0.05°C. The heating stage was assembled with the Leitz Laborlux S microscope. Standard physico-chemical plots and the programme *Fluids* supplied by Dr. R. Bakker were used to calculate contents of the salts in the inclusion solutions. Pressures were determined by the crossed isochors method on the basis of the data obtained from aqueous and pure carbon dioxide inclusions. The percentage of the individual salts in inclusion solutions were calculated as the part of the total salt dissolved. Similarly, the percent values of the gas refer to the total gas equal 100 percent.

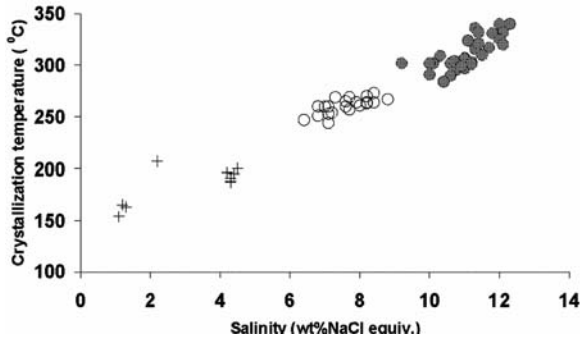

Figure 1: Calculated crystallization temperatures vs. salinity diagram of fluid inclusions hosted by quartz veinlets of various generations at the Klecza gold deposit. Symbol explanation: grey dot – 1st generation of grey quartz; circle – 2nd generation of white quartz; cross – late generations of quartz.

4.2 Fluid inclusions in quartz veins from Klecza

All samples used for the fluid inclusion studies contain gold from several to a few tens g/t. The inclusion studies were carried out in quartz veins cutting sericite-quartz-chlorite schists. Veins, in general, contain at least three or four generations of quartz. The first generation includes massive, deformed and recrystallized grey quartz. The second one is whitish quartz that formed veinlets (up to 1 cm in diameter) and/or cement of earlier brecciated quartz and rock fragments. The third one comprises clear quartz forming eu-, to subhedral crystals inside the veinlets. Sulphides, mostly arsenopyrite with minor pyrite, are cataclased and associate with grey quartz. Base-metal sulphides are less common and associate white quartz matrix and/or carbonates of various compositions. These sulphides are disseminated or form aggregates, filling fractures in the older sulphides. Separate grains of native gold were also observed in chalcedonic quartz matrix or micro-veinlets. Fluid inclusions were investigated in quartz from veinlets, matrix and in quartz fragments. The results indicate that crystallization of grey massive quartz fragments, rich in brecciated sulphides, were at temperature from 340 to 284°C with the salinity of fluids of 12.3 to 9.2 wt% NaCl equivalent (Fig. 1) and under pressure of 0.9 kb. These fluid inclusions homogenized into the liquid phase.

They have sizes from 4 to 14 μm in diameter. The composition of salts indicates the presence of *NaCl* (60-76 % of total salts), *KCl* (11-23 %), $CaCl_2$ (4-15%) and $AlCl_3$ (up to 5%), (Fig. 2). Two-phase aqueous inclusions in ad-

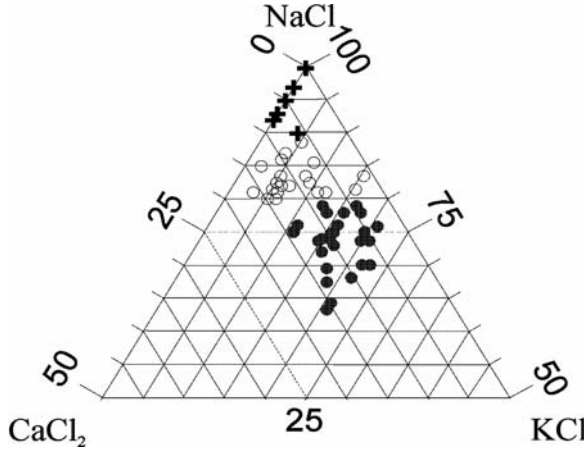

Figure 2: Composition of salts in fluid inclusions in quartz of various generations at the Klecza deposit, symbols explained in Figure 1.

dition to CO_2 may contain up to 10 % N_2. The early event of grey quartz crystallization corresponds to auriferous arsenopyrite and pyrite precipitation.

The second generation of quartz of white colour that forms veinlets and rock matrix seems to be related to pyrite and base-metals sulphides precipitation also associated with crystallization of carbonates of various compositions (mainly ankerite). This quartz crystallized within the temperature ranges from 273 to 244°C with the salinity of fluids of 8.5 to 6.4 wt % NaCl equivalent and at pressure of 0.7 kb. The contents of salts in comparison to the inclusion solution composition in grey quartz are characterized here by higher *NaCl* contents up to 85% and lower content of *KCl*, $CaCl_2$ and $AlCl_3$ (Fig. 2). In the sample richest in gold (>60 ppm Au) $FeCl_3$ appears in the amount up to 5% of total salts. Furthermore, in two-phase aqueous fluid inclusions beside CO_2 methane appears commonly (up to 10% CH_4). The third generation of quartz crystallized from 200 to 180^{0}C with salinity of fluids about 4.5 of wt % NaCl equivalent and pressure at 0.7 kb. The salts in inclusion fluids are dominated by *NaCl* (92-97 % of total salts) and low contents of $CaCl_2$ (3-7 % of total salts). The lowest crystallization temperatures from 165 to 154°C are measured in quartz veinlets of the next generation. Fluid inclusions in that quartz homogenized into the liquid phase and are characterized by presence of NaCl dissolved in water, exclusively. The data in Fig. 1 shows a clear linear trend, due to hypothetical dilution by formation waters?

5 Sulphur isotope in sulphides from Klecza

The sulphur isotope compositions (δ^{34}S CDT) have been determined in several pure sulphide samples from the Klecza area. Contents of sulphur δ^{34}S CDT in medium- and fine-grained arsenopyrite from Klecza range from +2.25 to +7.88 ‰ δ^{34}S and in coarse-grained pyrite they are from –1.62 to –1.49 ‰ δ^{34}S. The values of the sulphur isotope compositions of the considered sulphides reflect a sulphur contribution from the host rocks beside the magmatic input of sulphur into mineralizing fluids during precipitation of the sulphides. However, there is no direct evidence of magmatism in the surrounding area. Especially, samples of massive arsenopyrite aggregates hosted by a quartz vein in chlorite-sericite schists have heavier sulphur isotope compositions (up to 7.88 ‰) that indicate for sulphur contribution from the host rocks.

6 Discussion and conclusions

Primary fluid inclusions in different generations of auriferous quartz from rock samples from the Klecza gold deposit revealed the presence of moderate to low saline two-phase aqueous fluids with CO_2, N_2 and CH_4. Reported crystallization temperatures for the refractory sulphide-bearing grey quartz ranges from 340 to 284°C with the salinity of fluids of 12.3 to 9.2 wt% NaCl equivalent and pressure of 0.9 kb. The white quartz associated with non-refractory gold, base metal sulphides, and carbonates crystallized at temperatures range from 273-244°C with the salinity of fluids of 8.5 to 6.4 wt % NaCl equivalent and at pressure of 0.7 kb. The features of fluid inclusions in gold-bearing quartz were considered by Kozlowski and Metz (1989). They are: temperatures 250-350°C, pressure 0.4-1 kbar, abundance of CO_2, especially hetero-genisation (splitting of the one phase medium into two- or more-phase medium) of aqueous and carbon dioxide fluids (Popivnyak 1975), methane in the ore-forming fluids (Kalyuzhnyi et al. 1975) and presence of other than sodium cations in fluids, especially high contents of K and occurrence of Al, Ca, and Fe in gold-precipitating solutions, and strong domination of Na in pre- and post-ore fluids.

These features were recognized in fluid inclusions in quartz of the studied deposit. The changes of the ore-forming solution like separation of carbon dioxide and aqueous fluids, replacement of sodium by potassium and other ions and presence of methane influencing the oxygen fugacity may cause the instability of the gold-transporting chloride, carbonate or bisulphide complexes, leading to precipitation of native gold. Gold mineralization zones are hosted in quartz ± sericite ± graphitic schists. Common presence of organic matter and graphite has been recognized in the studied samples from Klecza. Contents of TOC (Total Organic Carbon) range from traces up to 18.7 %. Graphitic schists horizons are common in the Pilchowice unit and formed during recrystallization and redistribution of carbon in metamorphosed black argillites. Carbon present in the country rocks reacted with water from fluids to produce carbon dioxide and methane according to reaction: $2C + 2H_2O = CO_2 + CH_4$. In this study methane was always measured in fluid inclusions (up to 10 %) in the most auriferous samples. Presence of methane causes reduction of the oxygen fugacity and destabilizes gold complex inducing gold precipitation (Cox et al. 1991). Graphitic schists with their reducing character, acted as preferential site for gold precipitation. The correlation between gold and sulphur as well as common occurrence of gold inclusions in pyrite and arsenopyrite of the first ore stage mineralization suggest that gold was transported as reduced bisulphide complexes [Au $(HS)^-_2$] during this stage of ore precipitation. However, the composition of fluid inclusions indicates also for chloride complexes as gold transporting during next stages of Au precipitation.

The role of nitrogen in the fluids is not obvious. It may come either from the decomposing organic matter or from dissolved potassium feldspars or micas, where it may be present in form of ammonia ions. In any of the above-listed cases it may migrate into the system together with

potassium, and in the first one – with methane or carbon dioxide. The latter may change the equilibria in the solution bearing gold complexes causing the precipitation of gold, thus nitrogen beside methane could be an indicator of the approaching formation of gold ore. The fluid inclusions in the latest quartz generation contain only NaCl, being the evidence of solutions, which either were again capable to transport, not to precipitate gold, or did not contain gold in amounts, which could cause origin of recognisable mineralization.

Acknowledgements

The analytical work was supported by the NCSR Grant 5T12B00122 and by the Faculty of Geology Grant BW1642/17.

References

Cox SF, Wall VJ, Etheridge MA, Potter TF (1991) Ore geology Reviews, 6: 391-423

Grimming H (1933) Centralne Archiwum PIG, Warszawa, pp. 1-96

Kalyuzhnyi VA, Davidenko NM, Zinchuk IN, Svoren JM, Pisotskiy BJ (1975), Lvov, pp. 80-81

Kozlowski A, Metz P (1989) Fluid inclusion studies in quartz from the reportedly gold-bearing veins from Lower Silesia, SW Poland. Proc. International Symp. on Gold Geology and Exploration, Shenyang, pp. 731-735

Mikulski SZ (2003) In: Eliopoulos DG et al. (eds), Mineral Exploration and Sustainable Development. Proceedings of the Seventh Biennial SGA meeting Athens / Greece / 24-28 August 2003, Millpress, Rotterdam, pp. 787-790

Popivnyak IV (1975) Role of CO_2 in formation of the lodes of the Muy gold ore deposit (North Buryatia). Carbon and its compounds in endogene processes of mineral formation, Lvov, pp. 84-86

Deformation history and multiple gold mineralisation events within the Bardoc Tectonic Zone, Eastern Goldfields, Western Australia

Anthony A. Morey, Roberto F. Weinberg
*pmd*CRC, Australian Crustal Research Centre, School of Geosciences, Monash University VIC 3800 Australia*

Frank P. Bierlein
*pmd*CRC, School of Geosciences, Monash University, VIC 3800, Australia, and Tectonics Special Research Centre, The University of Western Australia, Crawley WA 6009 Australia*

Abstract. This study focuses on three gold deposits within the late-Archaean Bardoc Tectonic Zone (BTZ) Western Australia, namely Paddington, New Boddington and Yunndaga. The styles, characteristics and relative timing of deformation and gold mineralisation have been constrained at each of these deposits. These local events have then been correlated to provide an understanding of regional controls of gold mineralisation within the BTZ.

Results imply that gold mineralisation chiefly occurred relatively early (D_2) within the deformation history of the region. However at Paddington, there are two phases of gold mineralisation. One is associated with D_2 and the other is associated with a local NNW–SSE-directed shortening event (D_{NS}) that has been interpreted to occur between D_2 and D_3.

These findings are in contrast with other regional studies of gold endowment within the Eastern Goldfields, which have reported that gold mineralisation occurred late (D_3-D_4) within this terrane. Furthermore, no large-scale strike-slip faulting (D_3) has been observed and late oblique faults (D_4) are unmineralised. Associating gold mineralisation with relatively early D_2 and D_{NS} deformation provides important relative timing constraints on gold mineralisation within the BTZ.

Keywords. Gold mineralisation, shear zones, Late Archaean, Yilgarn Craton

1 Introduction

The Late Archaean Eastern Goldfields Province (EGP) within the Yilgarn Craton, Western Australia hosts one giant and over ten world-class orogenic lode-gold deposits (Hagemann and Cassidy 2001). These types of gold deposits are genetically associated with major regional shear zones and are commonly sited on second- or third-order faults that splay off first-order structures (e.g. Groves et al. 2000).

The BTZ has been a significant gold-producing shear system, but it has received little scientific attention in comparison to the along-strike Boulder-Lefroy Shear Zone (BLSZ) (Fig. 1), which hosts the giant Kalgoorlie gold camp and other world-class gold deposits (e.g. Weinberg et al. 2004).

This study has focussed on three well-spaced gold deposits within a portion of the BTZ that stretches between the Paddington and Menzies areas. These are Paddington, New Boddington and Yunndaga (Fig. 1). The outcomes of field-based structural and gold mineralisation studies are reported herein, and provide a new framework for understanding structural deformation and gold mineralisation within the BTZ. Evidence is presented to introduce a previously undocumented gold mineralisation event as well as further constraining the relative timing of gold mineralisation within the shear zone.

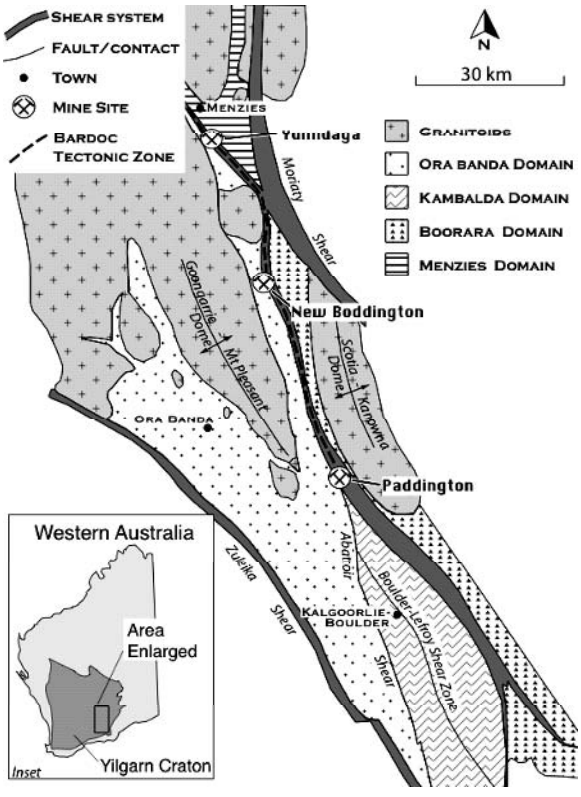

Figure 1: Map of a section of the southern Eastern Goldfields Province showing the location of the deposits studied and a selection of its tectono-stratigraphic domains and shear zones (modified from Swager and Griffin 1990).

2 Regional geology

The composite Yilgarn Craton (inset, Fig 1) is dominated by metamorphosed granitoid rocks, as well as less abundant portions of greenstones. The Late Archaean EGP constitutes the eastern portion of the Yilgarn Craton, and is characterised by a number of elongate NNW-trending granite-greenstone sequences that have been partitioned into various tectono-stratigraphic terranes and domains (e.g. Swager and Griffin 1990; Swager 1997). A number of major shear systems exist either at the boundary of, or within these domains and they control the location of many of the EGP's gold deposits.

The BTZ is an example of one of these mineralised shear systems. It is regarded as a major, deep-penetrating shear system that is also the boundary structure between the Ora Banda and Boorara domains (Fig 1) (Swager and Griffin 1990).

3 Local deformation and gold mineralisation events

3.1 Deformation at the Paddington gold deposit

The Paddington gold deposit (~37 t Au, Fig. 1) is made up of two elongate NNW-trending open pits. Out cropping lithologies comprise ultramafic schists, mafic extrusive and intrusive rocks, interbedded shales and volcano-sedimentary rocks.

At Paddington, the first recognised deformation event (D_{1P}) is characterised by a pervasive NNW-trending foliation that is axial-planar to a number of upright, tight to isoclinal folds (F_{1P}). This foliation also defines the regional fabric of the BTZ. These folds and associated foliations are overprinted by moderate, easterly-dipping reverse faults. Both of these structures can be attributed to a maximum shortening axis oriented in an ENE–SWS direction (D_{1P}).

Post-D_{1P} shortening is characterised by open F_{2P} structures that fold $S_0//S_{1P}$. These fold axes are steeply plunging, trend N70° and indicate that shortening was directed towards NNW–SSE, orthogonally to the D_{1P} maximum shortening axis.

The final deformation event (D_{3P}) at Paddington is characterised by NE-trending, brittle-ductile faults that divide the deposit in two. Movement along these steeply-dipping faults is indicated by drag folds, which give a composite dextral/reverse movement sense. These faults indicate a change to strike-slip motion through ENE–WSW shortening.

3.2 Gold mineralisation at the Paddington gold deposit

There are two major styles of gold-bearing lode structures at Paddington; *laminated* and *ladder* lodes. Both types of lode are hosted within the competent mafic units. The quartz-carbonate laminated lode trends NNW, dips steeply east and runs along the length of the open pit. It characteristically has alternating selvages of vein and wall rock material at its margins. Arsenopyrite (asp)-dominated + gold assemblages occur within the highly sericitised wall rock to this lode. The alteration assemblages at the margin of the lode are sheared in a reverse fashion by the pervasive D_{1P} fabric. This implies that the laminated lode and its gold-bearing alteration assemblage are either syn- or pre-D_{1P}.

The ladder lodes are an array of thin (1-10cm thick) quartz-carbonate veins not affected by D_{1P} folding or reverse faulting – and hence must have post-dated D_{1P}. From analysis of diamond drill core, Sheehan and Halley (2002) also reported the ladder lodes overprinted the laminated lode. A stereo plot (Fig. 2) shows that the poles to ladder veins define a great circle, and indicates that a maximum shortening axis oriented NNW–SSE can explain the formation of these veins. This is the same shortening direction inferred for D_{2P}, and suggests the ladder lodes formed after the laminated lode and that these veins represent two different generations of gold mineralisation.

3.3 Deformation at the New Boddington gold deposit

The New Boddington gold deposit (~2 t Au) is situated approximately half way between Paddington and Menzies (Fig. 1). Lithological contacts trend towards NNW and have a steep westerly dip. The exposed rock units comprise an ultramafic schist unit on its western flank and two mafic units within its central and eastern portions. There is a thin (<1 m) shale unit at the contact between these mafic units.

A steep, westerly-dipping, NNW-trending foliation (S_{1NB}) pervades all units and is the first, most prominent deformation structure. Stretching lineations (L_{1NB}) are steep towards N335° with limited variation, indicating the maximum stretching axis is down-dip. Kinematic indicators orthogonal to S_{1NB} and parallel to L_{1NB} consistently show reverse movement along foliation planes. This movement sense on S_{1NB} therefore suggests a maximum shortening axis oriented ENE–WSW (D_{1NB}).

Faults with sub-metre dextral displacement striking N310 overprint S_{1NB} planes. This faulting event has also been noted by Colville et al. (1990), and requires N–S-directed shortening (D_{2NB}) to explain its movement.

3.4 Gold mineralisation at the New Boddington gold deposit

Gold mineralisation within this open pit is hosted within the mafic rocks, associated with a number of stockwork and planar lode structures. Based on the observation that lodes are undeformed, Colville (1990) inferred that gold mineralisation was relatively late. Witt (1992) further reported that gold mineralisation was associated with sinistral strike-slip shearing.

Our field work failed to find evidence for strike-slip deformation at New Boddington. Instead, microstructural and structural analysis of mineralised stockwork and planar lodes demonstrate that the veins and wall rock sulphide assemblages are deformed by S_{1NB}. These results challenge the previous conclusions of Colville (1990) and Witt (1992) and imply that gold mineralisation occurred prior to or during D_{1NB}.

3.5 Deformation at the Yunndaga gold deposit

The Yunndaga deposit (~9 t Au) is located approximately 5km south of the township of Menzies (Fig. 1). This open pit exposes NNW-trending quartz-rich sedimentary rocks, minor ultramafic schist, a carbonaceous shale and a mafic doleri-te rock unit. The western contact between the mafic unit and the sedimentary rocks hosts the gold-bearing lode structure.

As with the previous two deposits, D_{1Y} is characterised by a NNW-trending, steep westerly-dipping pervasive foliation (S_{1Y}) that is most pronounced within the sedimentary and ultramafic rock units. S_{1Y} is axial planar to a number of tight to isoclinal folds (F_{1Y}) that plunge moderately to the south. In contrast to the other deposits, lineations along S_{1Y} have a shallow to moderate plunge, which indicate that a component of strike-slip movement occurred during D_{1Y}. Kinematic analysis suggests reverse-sinistral movement along these planes. This folding and shearing (D_{1Y}) can be related to a maximum shortening axis oriented in a ENE–WSW direction.

Within the northern section of the deposit, prominent sets of NW-trending, steeply-dipping, dominantly brittle faults cut across all lithologies and structures. The reverse-sinistral movement sense along these faults can be explained by the same shortening direction associated with D_{1Y}, however the offset of earlier S_0//S_{1Y} structures, as well as their brittle nature suggest that they are later (i.e. D_{Y2}) than D_{1Y}.

3.6 Gold mineralisation at the Yunndaga gold deposit

Gold mineralisation at Yunndaga is localised at the contact between the dolerite and sedimentary rock unit. Mineralised structures are characterised by boudinaged laminated quartz-carbonate veins with asp-dominated + gold assemblages within wall rock. The boudinaged lodes, as well as the deformed and rotated asp + gold grains, are deformed by D_{1Y} deformation. Gold mineralisation is thus syn- or pre-D_{1Y}.

4 Regional synthesis of deformation and gold mineralisation within the BTZ

Figure 3 summarises the local deformation and gold mineralisation events at each deposit. These local events are also correlated with other regional deformation events, e.g. D_1–D_4 of Swager (1997).

This study has found that there is no evidence in the strongly deformed BTZ for early D_1 N–S-directed, recumbent folding and associated thrusting. Instead, the first known deformation at all localities is characterised by NNW-trending tight to isoclinal, upright folding and faulting, indicating pronounced ENE–WSW shortening. This style of deformation can be correlated with regional D_2. The majority of gold mineralisation within the BTZ is also associated with this relatively early event, and this provides the earliest timing constraint on gold mineralisation for this shear system. Results also indicate that there is a later gold mineralisation event at Paddington that occurred after D_2, and is associated with NNW–SSE shortening (herein termed D_{NS}, Fig.3). Evidence for ~N-S-directed shortening has been reported for the EPG (e.g. Ellis 1939), but it has not been placed within a contemporary regional deformation regime. Duuring et al. (2001) have reported that mineralisation within the Tarmoola gold deposit was linked to a similar shortening direction as D_{NS} (subhorizontal NW-SE shortening). These results highlight the potential for gold-bearing events within the EGP to be associated with shortening events that are at an angle to regional D_2. No large-scale sinistral strike-slip deformation (D_3) has been recognised within the BTZ. Small-scale, NNW-trending strike-strike slip deformation has been observed at the Yunndaga deposit but this was a result of transpressional

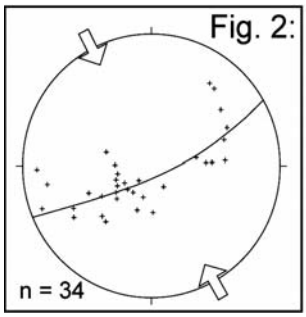

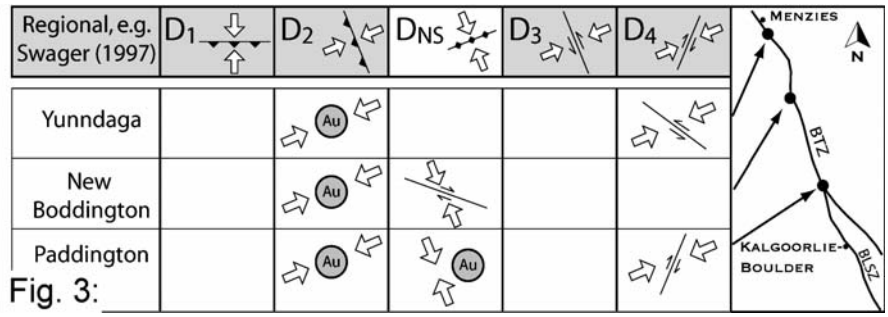

Figure 2: Lower hemisphere stereonet projection of poles to planes of ladder lodes from Paddington, indicating a NNW-SSE shortening axis.
Figure 3: Correlation between deformation and gold mineralisation events from each deposit studied and regional deformation phases.

movement related to D_2. The relatively late NE-trending dextral faults at Paddington and the NW-trending sinistral faults at Yunndaga are associated with D_4 of Swager (1997). These faults consistently overprint gold-bearing structures and indicate that D_4 deformation is not associated with gold mineralisation within the BTZ. Regional studies such as Groves et al. (2000) reported that mineralisation was relatively late within the deformation sequence (i.e. D_3-D_4). In contrast, this study has found that gold within the BTZ is mainly associated with earlier D_2 and D_{NS} deformation, implying that gold within the BTZ was protracted and occurred earlier than elsewhere within the EGP.

Acknowledgements

This abstract has been released with the permission of the CEO, *pmd**CRC. The continuing support of Placer Dome Asia Pacific, WMC, AngloGold Australia Ltd and Harmony are gratefully acknowledged for field assistance and discussions. Reviews by Feng-Jun Nie and Richard Blewett are greatly appreciated for improving the quality of this abstract.

References

Colville RG, Kelly D., Fish BL (1990) Goongarrie gold deposits, In: Hughes FE (ed) Geology of the mineral deposits of Australia and Papua New Guinea. Australian Institute of Mining and Metallurgy Monograph No 14, pp. 363–366

Duuring P, Hagemann SG, Love RJ (2001) A thrust model for gold mineralization at the Archean Trondhjemite-hosted Tarmoola Deposit: The importance of heterogeneous stress distributions around granitoid contacts. Economic Geology 96: 1379–1396.

Ellis HA (1939) The geology of the Yilgarn gold field, south of the Great Eastern Railway. Geological Survey of Western Australia Bulletin 97

Groves DI, Goldfarb RJ, Knox-Robinson CM, Ojala J, Gardoll S, Yun GY, Holyland P (2000) Late-kinematic timing of orogenic gold deposits and significance for computer-based exploration techniques with emphasis on the Yilgarn Block, Western Australia. Ore Geol Rev 17: 1–38

Hagemann SG, Cassidy KF (2001) World-class gold camps and deposits in the Eastern Goldfields Province, Yilgarn Craton: diversity in host rocks, structural controls, and mineralization styles, In Hagemann SG, Neumayr P, Witt WK (eds) World-class gold camps and deposits in the eastern Yilgarn Craton, Western Australia, with special emphasis on the Eastern Goldfields Province. Geological Survey of Western Australia Record 2001/17: pp. 7–44

Sheehan P, Halley S, (2002) Paddington Review 2001, Paddington Gold Pty. Ltd. Internal report, Unpublished.

Swager CP, Griffin TJ (1990) An early thrust duplex in the Kalgoorlie-Kambalda greenstone belt. Precambrian Research 48: 63–73

Structural control of mineralization in metamorphic core complexes

F. Neubauer
Department Geography, Geology and Mineralogy, University of Salzburg, Hellbrunnerstr. 34, A-5020 Salzburg, Austria

Abstract. The structural styles of epigenetic mineralization of two metamorphic core complexes in contrasting geodynamic settings have been investigated. The Tauern metamorphic core complex (Alps) formed due to continental plate collision. Corresponding mineralization, mainly Au-Ag, is structurally related to indentation and lateral extrusion, and occurs at accommodation zones at the termination of a shear zone and confining strike-slip and normal faults of the core complex. In contrast, the Sifnos metamorphic core complex exhumed during two distinct stages of back-arc extension triggered by retreat of the Hellenic subduction zone. Gold-quartz veins formed during terminal stages of NNE-directed ductile extension, subsequent Fe-Mn-Pb-Zn-Ag mineralization above a rolling hinge at a wide antiform associated with brittle trench-directed (SW) shear.

Keywords. Exhumation, rolling hinge, lateral extrusion, slab retreat, back arc extension

1 Introduction

Mineralization within terminal orogenic stages involves such associated with exhumation of metamorphic core complexes with mesothermal gold deposits as common features (Groves et al., 2003). Here, structural styles of mineralization associated with two Tertiary-aged metamorphic core complexes of different geodynamic settings are shown.

2 Tauern window

The Tauern window exposes an initially subducted, cool piece of stacked oceanic and continental crust (Penninic units) metamorphosed during Early Tertiary. Neogene exhumation of the Tauern metamorphic core complex is closely linked with oblique shortening of the Eastern Alps due to indentation during plate collision (Rosenberg et al. 2004). Several types of mineralizations are known that closely link to structures formed during exhumation (Fig. 1; Neubauer, 2002; Weber et al. 1997): (1) sub-vertical NNW-trending Au-Ag-Cu-Pb-quartz-carbonate veins (type Hirzbach-Schiedalpe-Kloben; Weber et al. 1997) close to the northern margin of the Tauern window where internal structures of the Tauern window form a bend with a ca. 30° opening angle; (2) sub-vertical earlier NE-, later NNE-trending Au-quartz veins at the termination of the sinistral Möll fault (Paar in Weber et al. 1997); (3)

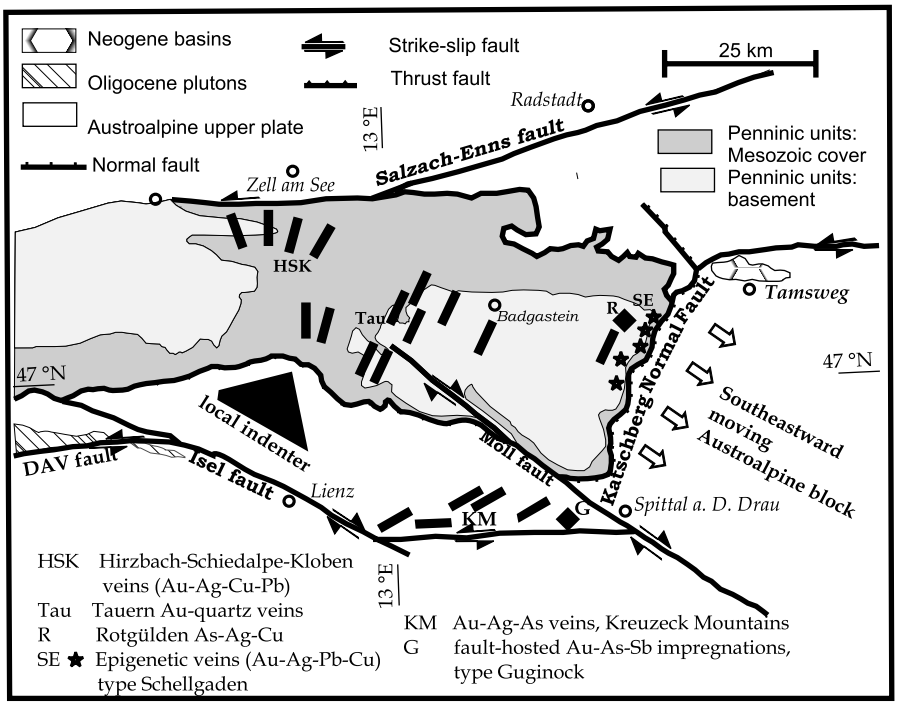

Figure 1: Mineralization in the central Eastern Alps related to the exhumation of the Tauern metamorphic core complex in an oblique convergent system (modified from Neubauer, 2002).

saddle reefs and replacement ores in marbles (type Rotgülden; Horner et al. 1997); (4) Au-Ag-Pb-Cu-W veins and quartz lenses (type Schellgaden) within ductile low-angle normal shear zone at the upper margin of the Tauern window (Amann et al. 1997); (5) ENE-trending Au-Ag-As veins in the Kreuzeck Mountains, which are interlinked with intermediate sub-volcanic rocks (Feitzinger et al. 1995); and (6) Au-As-Sb impregnations along E-trending sinistral fault zones (type Guginock; Amann et al. 2002). All these ores were formed after peak temperature conditions at ca. 30 Ma of metamorphism and crosscut regional structures like foliation, except most of the Schellgaden-type. The Au-quartz lodes are widely distributed over eastern–central sectors of the Möll fault, which formed at ca. 20–16 Ma (Ar-Ar sericite and adularia ages) as tension gashes, which show an apparent rotation from NE to NNE-trends during progressive development. The Au-Ag lodes of the southern Kreuzeck Mountains postdate calc-alkaline dykes (40–26 Ma; Deutsch 1984) and follow a ca. 50 km long E-trending, semi-brittle shear zone.

The metals of all these ore bodies include Au, Ag, Pb, Zn, and Cu. Fluid inclusion studies display maximum homogenisation temperatures of ca. 400–200°C (Pohl and Belocky 1998; Horner et al. 1997). Lead isotopic data constrain variable, distinct, mostly continental sources, and no inter-linkage between various hydrothermal systems (Horner et al. 1997; Köppel in Weber et al. 1997).

The data presented above from the Neogene mineralization in and around the Tauern Window show that all the ore deposits were formed during indentation and exhumation of the Tauern metamorphic core complex in a sinstral E-trending wrench corridor (Neubauer 2002). Mineralized strike-slip faults and sub-vertical tension gashes argue for ca. NNE–SSW shortening in a dominant strike-slip regime during formation. Furthermore, seismic pumping of metamorphogenic fluids may have contributed to development of brittle fault systems (according to models proposed by, e. g., Sibson and Scott 1998). As a model for the formation of these ore bodies, I propose that they formed by initial brittle failure during exhumation of the Tauern metamorphic core complex after motion through the ductile-brittle transition zone within the crust.

2 Sifnos (Aegean Sea)

The Attic-Cycladic metamorphic belt has been exhumed in response of back arc extension of a previously thickened, metamorphic Alpine orogenic edifice over the southwestward retreating Hellenic subduction zone (Fig. 2). The metamorphic belt comprises a number of mineralizations in part related to arc-related subvolcanic and plutonic rocks, in part entirely controlled by exhumation structures of high-pressure units in a back-arc setting (Skarpelis 2002).

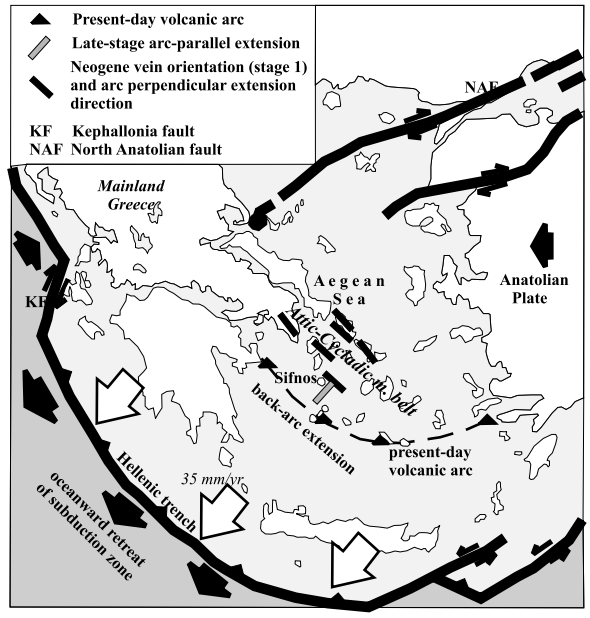

Figure 2: NE-SW extension in the Attic-Cycladic metamorphic complexes of the Aegean Sea is induced by oceanward retreat of the Hellenic trench/subduction zone. Rare NW–SE extension like on Sifnos is created by lateral spreading of back-arc area.

Sifnos exposes four lithotectonic units including a eclogite-blueschist unit. Eclogites were formed at ca. 20 kbar (Trotet et al., 2001) later decompressed and brought to shallower crustal levels and were affected by a pervasive greenschist-facies overprint at a depth of 15–20 km at 20–25 Ma (Wijbrans et al. 1993; Avigad 1993).

Three basically distinct types of mineralization in Sifnos have been distinguished by Vavelidis (1997; Vavelidis et al. 1985; Fig. 3):

1. Subconcordant, 10–40 cm thick ore bodies occur in the region between Faros and NW Platys Gialos within the Greenschist-Gneiss unit (GGU) (Fig. 2). The ores often show cataclastic fabrics and pervasive chlorite alteration along shear zones at lithological boundaries. They comprise Fe-rich carbonates, pyrite, chalcopyrite and quartz.
2. Subvertical, 10–20 cm wide quartz-Au veins are a common feature of the GGU in the footwall of low-angle normal faults, which separate it from the overlying Lower Marble unit (LMU; south-eastern Sifnos; Fig. 2). Two sets of quartz veins, dominating WNW-trending and subordinate NNW-trending ones formed during subhorizontal extension. Gold contents range from 1.5 to 12.2 ppm (av.: 6 ppm). The ore comprises pyrite, chalcopyrite, pyrrhotite and an unidentified silver mineral (Vavelidis 1997). Fluid inclusions in quartz are of a low-salinity type (1.5 to 12.4 wt % NaCl equ.) and homogenization temperatures range from 240 to 475°C.

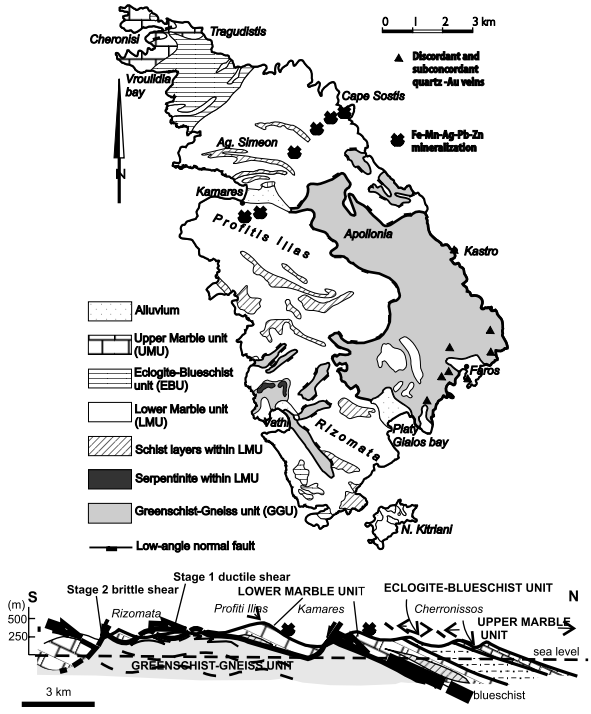

Figure 3: Simplified geological map and section of Sifnos Island with locations of abandoned mines and simplified cross-section across southern Sifnos showing the location of oxidized Fe-Mn-Pb-Zn-Ag mineralization above a brittle, S-directed normal fault parallel to the contact between GGU and LMU (map modified after Avigad 1993).

3. Ag-bearing Fe-Mn-Pb-Zn-Ag ores are always located within the LMU in the crest of a wide E-trending antiform (east) or synform to the south of a major S-directed normal fault (west; Fig. 2). At Cape Sostis, two different types of ore bodies are exposed: (i) Subhorizontal, discordant layers and lenses comprise idiomorphic, coarse-grained siderite. (ii) Oxidized Fe-Mn-Pb-Zn-Ag ores form irregular, max. ca. 10 m thick bodies with sharp boundaries to marble. The NNW-trending ca. 40–150 cm thick veins are associated with marble breccia veins and affected by two stages of subsequent faulting which formed by N–S strike-slip contraction and subsequent NW–SE extension. Structural relationships suggest that ore formation occurred above a rolling hinge of a major SSW-directed stage 2 normal fault (Fig. 3).

4 Discussion and conclusions

The conditions of Au-quartz vein formations are mesothermal in both cases, a type which was identified as characteristic for Au-quartz veins in metamorphic core complexes. Mineralization likely has been assisted by crack propagation, by uprising metamorphic fluids which may have their origin in devolatization deeper in the crust, likely within the operating subduction zone (according to the "deep-latter" model proposed by Stüwe 1998). At Sifnos, ore formation occurred within extensional kinematic conditions, when the Sifnos metamorphic core complex reached a near-surface level. Both Au-quartz vein and Fe-Mn-Pb-Zn-Ag mineralization occurred within brittle conditions. Two distinct events are responsible for that: subordinate ca. E–W extension during operation of a NNE-directed semiductile normal fault in the hangingwall of the GGU for formation of Au-quartz veins, and subordinate ca. NNE–SSW extension for formation of Mn-Fe-Pb-Zn-Ag mineralization during subsequent top-SSW brittle normal faulting. Both events are related to SW-ward retreat of the Hellenic subduction zone (e. g. Jolivet et al. 1994; Fig. 2). Fluid uprise was assisted by extensional kinematic conditions, which are in correspondence to large-scale kinematics of the Aegean Sea.

Geodynamic settings of Au-quartz systems in Alps and Aegean Sea differ in many details: active subduction and extension in the Aegean Sea and collisional/post-collisional setting of Alps. However, the governing structures are similar in the scale of the individual metamorphic core complexes. These include: (1) rapid extension, which thinned the upper part of the crust, mainly by decoupling of the brittle upper crust from the ductile middle/lower crust; (2) pervasive flushing by hydrous, low- to medium-salinity fluids, which come from a deeper source; (3) fluid channelling along crests of domes and specific locations in the hanging wall of low-angle normal faults, at transitional locations between high-angle to low-angle dips respectively rolling hinges; (4) rheological control of ore locations as ore deposits formed mainly in brittle behaving rocks which are underlain by weak, semiductilely behaving rocks, and finally (5) chemical control as ore deposits, like the Fe-Mn-Pb-Zn-Ag ores of Sifnos, formed by reaction of acidic hydrous fluids with carbonates.

Acknowledgements

The author gratefully acknowledges discussion with Nikos Skarpelis, review by Yasushi Watanabe and support by grants P14.028-TEC (FWF), 7153 and 6172 (ÖNB).

References

Amann G, Daxner G, Neubauer F, Paar WH, Steyrer HP (1997) Structural evolution of the Schellgaden Gold-District, eastern Tauern window, Austria - a preliminary report. Zentralblatt für Geologie und Paläontäontologie Teil I, 1996: 215-228

Amann G, Paar WH, Neubauer F, Daxner G (2002) Auriferous arsenopyrite-pyrite and stibnite mineralization from the Sifnitz-Guginock area (Austria): indications for hydrothermal activity duringe Tertiary oblique terrane accretaion in the Eastern Alps. Geological Society Special Publication 204: 103-117

Avigad D (1993) Tectonic juxtaposition of blueschists and greenschists in Sifnos island (Greece) – implications for the structure of the Cycladic blueschist belt. Journal of Structural Geology 15: 1459–1469.

Davis EN (1966) Der geologische Bau der Insel Sifnos. Institute of Geology and Subsurface Research 10/3: 161-220

Deutsch A (1984) Young Alpine dykes south of the Tauern Window (Austria): A K-Ar and Sr isotopic study. Contribution to Mineralogy and Petrology 85: 45-57

Feitzinger G, Paar WH, Tarkian M, Reche R, Weinzierl O, Prochaska W, Holzer H (1995) Vein type Ag-(Au)-Pb,Zn, Cu-(W-Sn) mineralization in the Southern Kreuzeck Mountains, Carinthia Province, Austria. Mineralogy and Petrology 53: 307–332

Groves DI, Goldfarb RJ, Robert F, Hart CJR (2003) Gold Deposits in Metamorphic Belts: Overview of Current Understanding, Outstanding problems, future Research, and Exploration Significance. Economic Geology 98: 1–29

Horner J, Neubauer F, Paar WH, Hansmann W, Koeppel V, Robl K (1997) Structure, mineralogy, and Pb isotopic composition of the As-Au-Ag deposit Rotgülden, Eastern Alps (Austria): significance for formation of epigenetic ore deposits within metamorphic domes. Mineralium Deposita 32: 555–568

Jolivet L, Brun JP, Gautier P, Lallemant S, Patriat M (1994) 3D-kinematics of extension in the Aegean region from the early Miocene to the Present, insights from the ductile crust. Bulletin de Societé géologique de France 165: 195–209

Kurz W, Neubauer F (1996) Strain partitioning during formation of the Sonnblick Dome (southeastern Tauern Window, Austria). Journal of Structural Geology 18: 1327–1343

Neubauer F (2002) Contrasting Late Cretaceous to Neogene ore provinces in the Alpine-Balkan-Carpathian-Dinaride collision belt. Geological Society Special Publication 204: 81–102

Pohl W, Belocky R (1998) Metamorphism and metallogeny in the Eastern Alps. Mineralium Deposita, 34: 614–629

Rosenberg C, Brun JP, Gapais D (2004) Indentation model of the Eastern Alps and the origin of the Tauern Window. Geology 32: 997–1000

Sibson RH, Scott J (1998) Stress/ fault controls on the containment and release of overpressed fluids: Examples from gold-quartz vein systems in Juneau, Alaska; Viktoria. Australia and Otago, New Zealand. Ore Geology Reviews 13: 293-306

Skarpelis N (2002) Geodynamics and evolution of the Miocene mineralisation in the Cycladic-Pelagonian belt, Hellenides. Bulletin of the Geological Society of Greece 34: 2191–2206

Stüwe K (1998) Tectonic constraints on the timing relationships of metamorphism, fluid production and gold-bearing quartz vein emplacement. Ore Geology Reviews 13: 219-228Trotet F, Jolivet L, Vidal O (2001) Tectono-metamorphic evolution of Syros and Sifnos islands (Cyclades, Greece). Tectonophysics 338: 179–206

Vavelidis M (1997) Au-bearing quartz veins and placer gold on Sifnos island, Aegean Sea, Greece.. In: Papunen, H. (ed.), Mineral Deposits, pp. 335–338, Balkema, Lisse.

Vavelidis M, Bassiakos I, Begemann F, Patriarcheas K, Pernicka E, Wagner GA (1985) Geologie und Erzvorkommen von Sifnos. Anschnitt Beihefte 3: 59–80

Weber L and 27 others (1997) Handbuch der Lagerstätten der Erze, Industrieminerale und Energierohstoffe Österreichs. Archiv für Lagerstättenforschung an der Geologische Bundesanstalt 9: 1–607

Wijbrans JR, van Wees JD, Stephenson RA, Cloetingh SAPL (1993) Pressure-temperature-time evolution of the high-pressure metamorphic complex of Sifnos, Greece. Geology 21: 443-446

Using remote sensing technology for the determination of mineralization in the Kal-e-Kafi porphyritic deposit, Anarak, Iran

M.H. Nezampour, I. Rassa
Department of Geology, Faculty of Earth Science, Shahid Beheshti University, Tehran, Iran

Abstract. The Kal-e-Kafi is located in the northeast of Anarak, Central Iran. The Central Iran contains several Tertiary porphyritic deposits, which are important sources for Cu, Mo and locally Au. In this research, the aim is search for exploration targets by remote sensing technology in Anarak. Landsat TM data were used to study petrology, hydrothermal alterations and tectonic structures. Different approaches were used in this project such as band ratioing, principle component and digital filtering. The structures were identified using low pass filter, edge sharping detector filter, Laplacian detector and Sobel edge detector. As a result, two limiting ring structures as well as a number of faults have been located in Kal-e-Kafi porphyry deposit. RGB TM175, RGB TM735 and RGB TM531 methods were used to determine rock unites. By this method, several rock units have been determined; such as porphyritic diorite, granodiorite, granite and monzogranite as well as dacite, andesite, trachyandesite, carbonates, marble and schist. The developed selective method on bands of TM1, TM4, TM5 and TM7 as well as TM1, TM2, TM3, TM4, TM5 and TM7, in addition TM5/TM7, TM5/TM4, TM3/TM1 ratios of Landsat-TM were used for determination of alteration haloes around this porphyritic deposits. Based on the studies mentioned above, it is suggested that five areas are favorable for further exploration.

Keywords. Remote sensing, porphyritic deposits, Kal-e-Kafi body, Khuni Mt

1 Introduction

Porphyritic deposits are the most important sources of copper in the world. These deposits may be exposed at surface or placed in near surface environments. Remote sensing has emerged as a powerful tool in recent years for assessing/predicting resources or isolating the favorable areas from unfavorable ones. Remote sensing data are mainly used to: (1) update the geological (lithology and structures) maps of the area; and (2) map the hydrothermally altered minerals.

Rock types and structures are important, because certain rock types are more favorable for hosting these deposits and tectonic structures provide means by which hydrothermal fluids can ascend. Alteration zones are often broader than the ore body itself even if covered by other rocks; they are useful for determining the location of deposits.

Remote sensing technology has been an useful tool for targeting the porphyritic deposits in the Central Iranian volcanic belt (CIVB) (Ranjbar et al. 1996, 2000, 2002; Tangestani and Moore 2000, 2002;). This study has focused on the determination of the location of the Kal-e-Kafi deposit by remote sensing technology.

2 Study area

The study area (54° 07' 38" – 54° 21' 35" E, 33° 20' 26" - 33° 29' 49" N) is situated in the northern part of CIVB, northeast of Anarak town, Isfahan province. The main part of the study area consists of the Kal-e-Kafi body (Fig. 3) metamorphic, sedimentary, volcanic and intrusive rocks. The oldest and youngest exposures are upper Proterozoic including metamorphic rocks and the Quaternary alluvial, respectively. The regional data indicate that the upper Proterozoic comprise graphite schist, serpentine schist and marble which form the fold basement and crops out as two isolated blocks (Perfiliew et al. 1979). Sedimentary rocks consist of Cretaceous sandy limestone to limy sand stone. The Eocene volcanic-sedimentary consists of andesite, trachyandesitic tuff, lava flow, porphyryes, tuffs, trachyandesitic, andesitic and dacitic rocks. The intrusive rocks are diorite to monzodiorite, monzonite, granite and granitoide belong to Eocene-Oligocene. Copper, Copper-molybdenum and polymetallic deposits and prospects are widely distributed in this area (Yankovenko et al. 1981). Two main types of mineralization were identified: porphyritic and type mineralization. Porphyritic type mineralization occurs in the post Eocene intrusive bodies (Kal-e-Kafi body), and vein type mineralization, can be found in upper Proterozoic dolomite and marble (Khuni Mt.). Chloritization, sericitization, kaolinitization, talcization, carbonization, and silicification are developed in intrusive, volcanic and metamorphic rocks.

3 Used data and data processing

Satellite data (Seven Landsat Thematic Mapper), Mearaji toposheet 1:50000 (Geographic Survey of Iran), Kabudan geological map 1:100000 (Geological Survey of Iran), ground geological and geochemical data were used in this project.

This page intentionally blank

3.1 Pre-processing

Prior to using the data from Landsat TM data, we had to pre-process the data to increase image quality. These pre-processing activities consist of data correction, geometric correction and atmospheric correction.

3.2 Processing

Our processing procedures consist of contrast increasing, creating color images, and operations between images, Principal Component Analysis (PCA) and different filters. After this processing, we have several images for interpretation and conclusion. Meanwhile, the geological phenomena are explained.

3.2.1 Tectonic structures

To recognize tectonic structures we used low pass filter, Laplacian detector, Sharping detector filter and Sobel edge detector. Project structures consist of several faults (Fig.1). These faults orientations are northeast-southwest and north west-southeast; however a few faults exist with north-south orientations that have an important role in the regional tectonics. Two ring structures were recognized in the Kal-e-Kafi_Khuni and the southeast area. The Kal-e-Kafi_Khuni ring structure was recognized by geophysical activity, in the past (Yankovenko et al 1981). These rings structures and faults are of interest as to which mineralization can be found at joint area of the two type structures.

3.2.2 Rock types

The study area is located in arid terrain with low density vegetation; because of TM175, RGB TM735 and RGB TM531 were used to determine rock units. Results of this activity are shown in table1. Granites and marbles are host rocks for ore body mainly occur in these rock types.

Table 1: Rock types recognized by different methods in the study area.

Rock type	Lithological association
Volcanic rocks	Andesite (and tuffite) Trachyandesite Dacite Gabbro
Intrusive rocks	Diorite Monzonite Monzonite to Diorite Granite Granitoid Granodiorite
Metamorphic rocks	Marble Serpentinite schist Amphibulite schist Other type of schist
Sedimentary rocks	Detritial carbonate

3.2.3 Hydrothermal alteration

To determine alteration zones, we used the classic TM5/TM7 ratio for identifying clay mineral zone, 7M5/TM4 and TM3/TM1 ratio for iron minerals and ferric oxides zone.

The Feature Principal Component Selection (FPCS) methods proposed by Crosta and Moore (1980) achieved good results. TM1, TM4, TM5 and TM7 were used to characterize hydroxyl minerals and the subset TM1, TM3, TM4 and TM5 for iron oxide mapping. Figure 2 shows an integrated image resulting from processing for alteration zones.

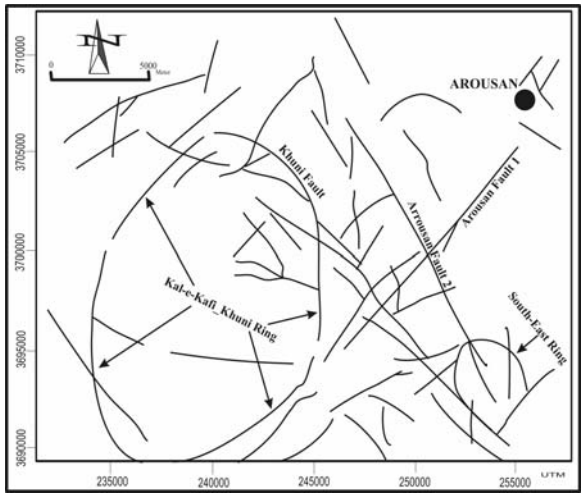

Figure 1: Sketch map showing the major structures of the studied area.

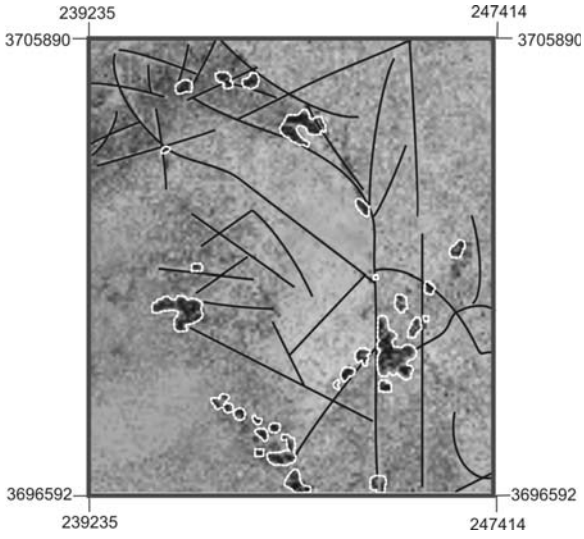

Figure 2: Alterations map, this picture clearly shows altered points controlled by tectonic structures.

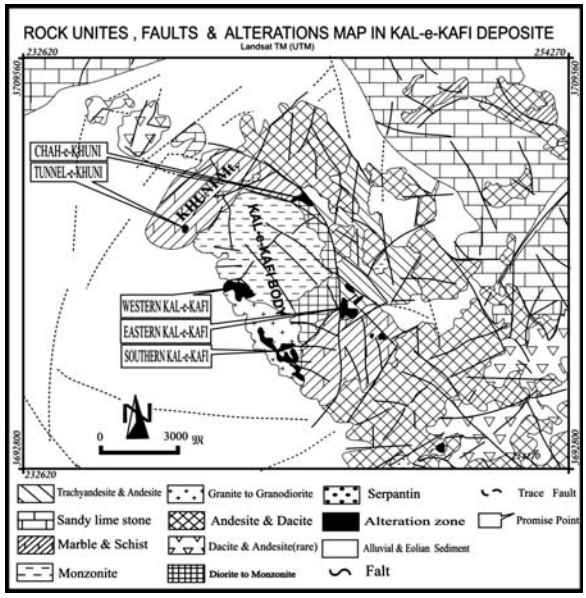

Figure 3: Simplified geological map showing the rock units, faults and alteration in Kal-e-Kafi deposit.

4 Integration and conclusion

According to three principals: 1) hydrothermal alteration is the most important factor; 2) there are relations between fractional phases in the intrusive rocks of this area with mineralization and 3) there are clear relations between faults and ring structures with mineralization; the integration of remote sensing results shows five suggested areas as promising points for subsequent exploration. These areas are shown in Figure 3. Fieldwork indicates that three of these regions correlate to ancient mines in the Kal-e-Kafi body and Khuni Mt.

References

Arnold,RH (1997) Interpretation of Airphotoes and Remotely Sensed Imagery. Upper Saddle Rever, N.J.:Prentice-Hall, p 249

Chicha-Olmo M, Abaraca, F (2002) Development of a Decision Support System Based on Remote Sensing and GIS Technique for Gold-rich Area Identification in SE Spain. International Journal of Remote Sensing 23(22): 4801-4814

Crosta AP, Rabelo A (1993), Assessing Landsat TM for Hydrothermal Alteration Mapping in Centeral-Weastern Brazil. Proceedings of the Ninth Thematic Conference on Geologic Remote Sensing, Pasadena, California, USA, 8-11 February 1993(Ann Arbor, MI: Environment Research Institute of Michigan), pp.1053-1061

Floyd FS (1997) Remote Sensing: Principles and Interpretation (3 ed). Freeman and co., p 495

Srivastav SK, Bhattacharya A, Kamaraju MVV, Sreenivasareddy G, Shrimal AK, Mehta, DS, List FK, Burger FK (2000) remote sensing and GIS for locating favorable zones of lead-zinc-copper mineralization in Rajpura-Dariba aera, International Journal of Remote Sensing 21(17):3253-3267

Tangestani MH, Moore F (2001) Comparison of Three Principal Component Analysis Technique to Porphyry Copper Alteration Mapping: A Case Study Meiduk Area; Kerman, Iran. Canadian Journal of Remote Sensing, 27:176-182

Tangestani MH, Moore F (2002) Porphyry copper alteration mapping at the Meiduk area. International Journal of Remote Sensing 23(22): 4815-4825.

Tosdal RM, Richards JP (2001) Magmatic and Structural Controls on the Development of Porphyry Cu ±Mo ±Au Deposits. Society of Economic Geologists 14:157-181.

Yankovenko V, Chinakov I, Kokorin Y, Krivyakin B (1981) Report on Detailed Geological Prospecting in Anarak area (Kal-e-Kafi, khuni locality), Technoexport Company, Moscow

New observations on W-Sb-Au mineralization at Woxi, western Hunan, China

B. Peng
Faculty of Resource and Environment Science, Hunan Normal University, Changsha, 410081, China

A. Piestrzynski, J. Pieczonka
Ore Geology Department, University of Mining and Metallurgy, 30-059 Cracow, Poland

Abstract. W-Sb-Au mineralization at Woxi was carefully studied, and native gold and Au-Sb mineral phases were observed under ore microscope and using EMPA with EDS techniques. The results show that the Au-Sb mineral phases include aurostibite ($AuSb_{2.13}$) and antimony gold ($Au_{1.02}Sb$) which interlaced with native gold as inclusions in microfractures of pyrite. The development of native gold and Sb-Au minerals as inclusions in microfractures of pyrite indicates that the mineralization processes might have evolved from a Au-Sb coexisting ore-forming fluid in temperature higher than 350°C. The temperature decreasing from higher to less than 350°C likely caused the precipitation of minerals including native gold, aurostibite, and antimony gold.

Keywords. W-Sb-Au mineralization, aurostibite, antimony gold, scheelite-quartz vein, Woxi

1 Introduction

The Woxi Deposit is located in the center of the so-called Xuefeng uplift belt in western Hunan, China (Peng et al. 1999; Peng and Frei 2004). Host rocks for the mineralization are the purple-red slates of the Madiyi Formation, Banxi Group (Luo et al. 1996; Peng et al. 1999, 2003). The W-Sb-Au mineralization recognized in the mining district are in three different modes: (1) quartz veins planar to bedding; (2) sheeted quartz veins; and (3) network veins and veinlets. Among them, the planar quartz veins controlled by bedded shear faults are the major host to ores and account for about 70 percent of total ore reserves (Peng et al. 2003; Peng and Frei 2004). The V4 vein we sampled for this study is one of the planar quartz veins exploited at present. The ores contain major minerals including scheelite, wolframite, stibnite, native gold, pyrite, and minor arsenopyrite, sphalerite, galena, chalcopyrite, cinnabar, and others (Peng et al. 1999, 2003).

The deposit was found in early 1875, but the presence of aurostibite in the ores was recognized only very recently (Zhang et al. 1996), and relative data are very rare. The W-Sb-Au mineralization is genetically very interesting, which has attracted a number of researchers since early 1950s, and has been the subject to a long-standing debate (Peng et al. 2003; Peng and Frei 2004). Because there are no magmatic rocks and dykes found throughout the mining district, the relations of the mineralization to magmatism were doubted by many researcher such as Luo et al. (1996), Ma (1997), and Gu et al. (2000). However, isotopic studies show that the ore-forming fluids might be related to granitoids distributed far away from the deposit (Peng and Frei 2004). Besides its diagnostic problems (Jedwab and Chuva 1992), aurostibite has some interesting mineralogical properties that may shine light on the understanding of the genetic relation of the mineralization to magmatism, and this composes the primary purpose of the present study.

2 Materials and methods

Samples for this study were selected from an extensive suite of quartz vein material collected from underground workings at Shangwoxi (Woxi District). These from the massive scheelite-quartz vein of V4 were cut both for double polishing sections and mineral separation for binocular microscope checking. The sections were then inspected under reflected light microscope, under the scanning electron microscope (SEM) and the electron microprobe fitted with an energy dispersive spectrometer (EDS) using a Filter Fit method on

TRACOR TN-2000, at the Institute of Geological Sciences, Jagiellonian University (Poland). Electron microprobe analyses (WDS) were carried out under the following environments: the accelerating voltage of 20 kV, and sample current of 15 nA. The following standards and spectral lines were used: CaKa($CaCO_3$), WLa(100%), MoLa(100%), FeKa(iron), SKa(100%), AuLa(100%), SbLa(100%).

3 Results

The massive scheelite-quartz vein (V4) consists of mainly scheelite (about 45%) and quartz (35%), with minor wolframite, pyrite, stibnite, native gold, and others. No direct relation between scheelite and pyrite could be observed under ore microscope, but pyrite grains in pentagonal dodecahedron form frequently observed under binocular microscope were probably formed after scheelite (Peng et al. 1999; 2003). Usually, native gold occurs as short microveinlets (up to 300μm) in scheelite and stibnite, and

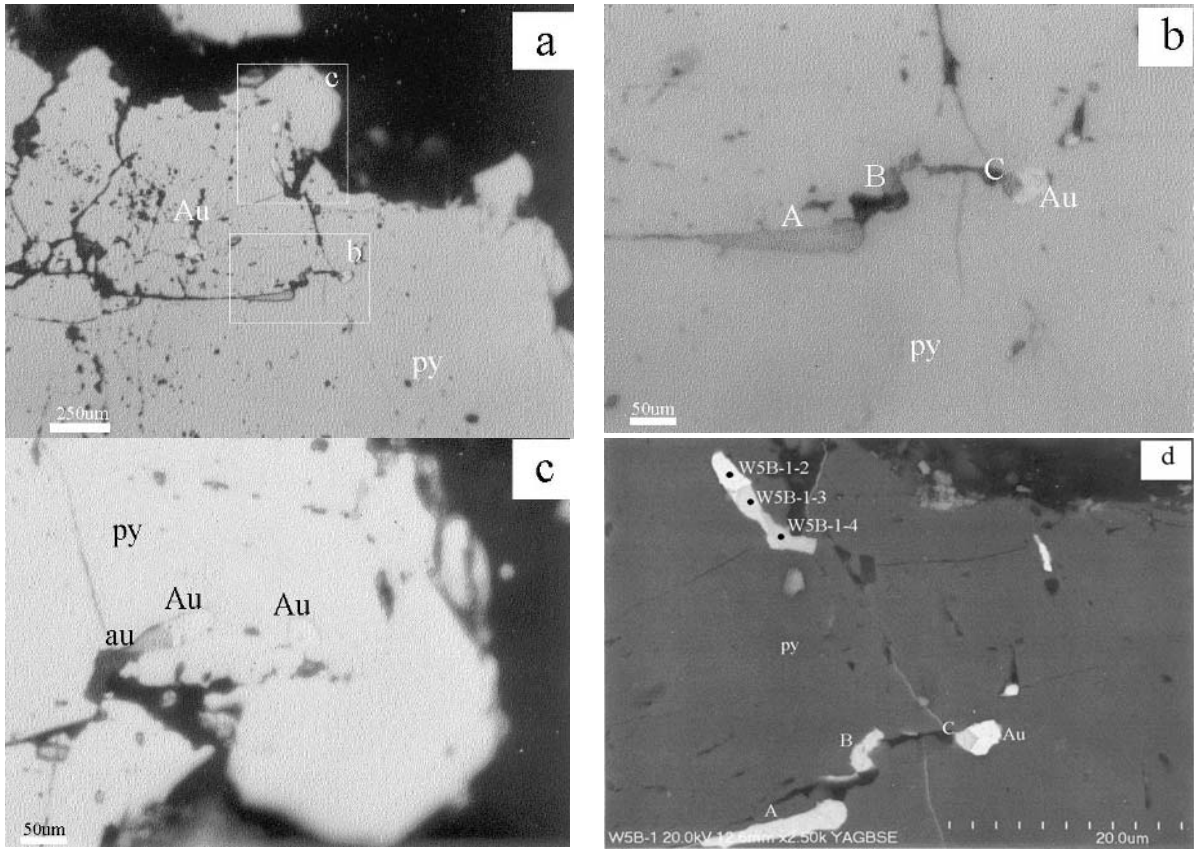

Figure 1: Microphotographs of gold and Au-Sb occurrences in pyrite. (a) Native gold as inclusions and in microfractures of pyrite; (b) Enlarged area of b in Figure 1a, showing native gold and intergrown dark gery mineral along microfractures of the pyrite; (c) Clockwisely rotated and enlarged area of c in Figure 1a, showing native gold and intergrown dark gery mineral in microfractures of the pyrite; (d) SEM imagine of all native gold and dark gery mineral in microfractures of the pyrite, the numbered points are corresponding to the analyzing results listed in Table 1. py = pyrite; Au = gold; aur = aurostibite; q = quartz; for details see text.

also commonly as inclusions in pyrite and sphalerite (Peng et al. 1999). However, the native gold we observed this time is not simply isolated, it occurs in paragenesis with other mineral grains that are in dark grey colour and in very small size within the microfractures of a pyrite grain (Fig.1a, b, c). It is difficult to identify these minerals even under ore microscope of very high amplification mainly because of their too small grain size and very rare occurrence. The SEM imagining (Fig. 1d) shows that one of these small mineral grains is actually composed of two paragenetic grains: one in white or light grey (W5B-1-3); and another in dark gery (W5B-1-4), of which the optical features are similar to that of the rest dark grey grains marked A, B, and C in Fig. 1b and d. The EMPA with an EDS analyzing results (Table 1) indicate that the grain in white/bright grey colour (W5B-1-3, in Fig. 1d) is aurostibite with chemical form of $AuSb_{2.13}$, of which the Au content is a bit lower than that of Zhang et al. (1996) reported. However, the grain in dark grey (W5B-1-4, in Fig. 1d) seems to be a mineral phase with chemical form as $Au_{1.02}Sb$, which may be antimony gold similar to that identified from the Primorye polymetallic deposit (Kazachenko et al. 1979), but with much higher antimony content. The native gold (W5B-1-2 in Fig. 1d) is also interlaced with aurostibite. Pyrite is one of the major sulfides in massive scheelite-quartz veins (Peng et al. 1999; 2003), the filling of the Au-Sb minerals including native gold, aurostibite ($AuSb_{2.13}$), and antimony gold ($Au_{1.02}Sb$) in microfractures indicates the percolation of Au-Sb bearing ore-forming fluid after pyrite formation and during deformation.

Aurostibites commonly occurs also as microveinlets ranging from 8 to 750 μm, and in white grey colour with hardness of 3 to 4 and VHN_{25} of 356 kg/mm (Zhang et al. 1996). The present results (Table 1) show that trace elements including Al, Si, S, and Fe, are also presented in both aurostibite and antimony gold ($Au_{1.02}Sb$) which is recognized for the first time from the W-Sb-Au ores of the deposit. However, the mineralogical data regarding antimony gold ($Au_{1.02}Sb$) at the moment are very limited and further study is required.

Table 1: Microprobe Analyses of Sb-Au in pyrite contained within a massive scheelite vein sample from V4 at Woxi, China

Sample	Item	Atom (%)	Element (wt%)	Err (±1δ)
W5A-1	Ca	50.25	18.11	0.35
	W	49.28	81.48	0.28
	Mo	0.48	0.41	0.35
	Total	100.00	100.00	Sch
W5B-1-1	S	66.84	53.65	0.38
	Fe	33.16	46.35	0.70
	Total	100.00	100.00	Py
W5B-1-2	Al	5.06	0.78	0.14
	Fe	10.14	3.25	0.48
	Au	84.80	95.96	2.88
	Total	100.00	100.00	Au
W5B-1-3	Al	3.00	0.63	0.09
	Si	2.78	0.61	0.09
	S	3.68	0.92	0.23
	Sb	57.12	53.99	0.60
	Fe	6.63	2.87	0.24
	Au	26.8	40.99	3.17
	Total	100.00	100.00	Aur
W5B-1-4	Al	6.34	1.41	0.11
	Si	5.30	1.23	0.11
	S	9.89	2.62	0.33
	Sb	33.87	34.06	0.57
	Fe	10.16	4.69	0.52
	Au	34.42	55.99	2.56
	Total	100.00	100.00	Aus

ZAF corrections; Sch = scheelite; Py = pyrite; Au = native gold; Aur = aurostbite; Aus = antimony gold

4 Discussion and conclusions

Aurostibite as a trace mineral has been discovered in many gold deposits in the world, such as Yakutia (Gamyanin et al. 1952), Primorye (Kazachenko et al. 1979), Yangshanzhuang (Yuan et al. 1989), Mobale gold mine (Jedwab and Chuva 1992), and Woxi (Zhang 1989; Zhang and Luo 1992). Most reported aurostibites (Graham and Kaiman 1952; Jedwab and Chuva 1992) occurs as a secondary reaction rim between gold and antimony, however, the aurostibite and antimony gold identified from the Primorye polymetallic deposit appears to be primary (Kazachenko et al. 1979). The finding of aurostibite and antimony gold in the Primorye polymetallic deposit (Russia) indicates unusual conditions for the formation of the deposit, during which the temperature might change abruptly (Kazachenko et al. 1979). Aurostibite ($AuSb_{2.13}$) identified by Zhang et al. (1989) and recognized by us this time from the Woxi Deposit is very similar to the aurostibite ($Au_{0.9}Sb_{2.10}$) identified at the Primorye deposit (Kazachenko et al. 1979) in composition. However, the antimony gold ($Au_{1.02}Sb$) we identified this time from the Woxi Deposit is quite different from that ($Au_{0.95}Sb_{0.05}$) identified at the Primorye polymetallic deposit (Kazachenko et al. 1979), in that the antimony gold from Woxi has an Au : Sb ratio of approximately 1.

The coexistence of native gold, aurostibite ($AuSb_{2.13}$), and antimony gold ($Au_{1.02}Sb$) in microfractures of a pyrite at least indicates that an Au-Sb coexisting ore-forming fluid was developed locally during mineralization.

Theoretically, the binary phase diagram of Au-Sb system shows that the Au-Sb coexisting as liquid phase (ore-forming fluid) should be under a temperature of higher than at least 350°C, and the precipitations of native gold, aurostibite, and native antimony from the Au-Sb system require necessarily a temperature decreasing (Cherolier 1989; Kim et al. 2002). Also the study of intermixing at Au/Sb interfaces using photoelectron-spectoscopy methods indicate that polycrystalline Au and Sb can be formed under very low temperature (Boyen et al. 1995). For the Woxi Deposit, when we complement the present observation results, the deposition of native gold, aurostibite, and antimony gold, with native antimony identified by Peng et al. (1999) in other samples from V4, it can been seen that the aurostibite ($AuSb_{2.13}$) and antimony gold ($Au_{1.02}Sb$) represent the intermediate mineral compositions between the two end member minerals: the native gold and native antimony, which are corresponding to the mineral compositions at less than 200°C in the binary phase diagram of Au-Sb system (Cherolier 1989; Kim et al. 2002). From this theoretical analogy, here we deduce that the temperature decreasing of an Au-Sb coexisted ore-forming fluid from higher to less than 350°C likely caused the precipitation of native gold, aurostibite ($AuSb_{2.13}$), and antimony gold ($Au_{1.02}Sb$) within microfractures of the pyrite during mineralization. If this deduction is tenable, that is to say, if the original ore-forming fluid was under temperature of higher than 350°C, then the ore-forming fluid might be evolved from magmatic intrusions. Therefore, the genesis of the W-Sb-Au ore deposit at Woxi could be closely related to magmatic intrusions developed in depth and outside the mining district, as implied by isotopic results (Peng and Frei 2004).

Acknowledgements

This study was made possible by funding from the Natural Science Foundation Committee of China (grant No. 40002021). WDS analyses were partly supported by the AGH University of Science and Technology, project no 11.11.140.258. We are grateful to M S Tkiewica at the Institute of Geological Science, Jagiellonian University (Poland) for help the EDS study. We are grateful to Drs. Chen Yanshao and Frank Bierlein for formal reviews.

References

Boyen H, Cossy-Favre A, Oelhafen D, Siber A, Ziemann P, Lauinger C, Moser T, Haussler P, Bauman F (1995) Low-temperature interface reaction in the layered Au/Sb of an amorphous phase. Physical Review, 151(3): 1791~1802

Cherolier PY (1989). Binary phase of the Au-Sb system. Therochinica Acta, 66: 211~225

Graham AR, Kaiman S (1952) Aurostibite, $AuSb_2$: a new mineral in the pyrote group. American Miner, 37(5,6): 461~469

Gu XX, Liu JM, Zhen MH (2000) Evidence from texture and geochemistry of W-Sb-Au ore deposit at Woxi: implication for ore formation by ancient sea floor spring deposition. J Mineralogy, Petrology, and Geochemistry, 19(4): 235~240 (in Chinese with English abstract)

Jedwab J, Chuva JM (1992) Reflected-light microscope and SEM/EMP observations on the behaviour of aurostibite ($AuSb_2$) during amalgamation. Mineralogical Magazine, 56: 561-565

Kazachenko VT, Chubarov VM, Basova GV (1979) Ore minerals in a polymetallic deposit of Primorye, U.S.S.R. American Miner, 64: 432-435

Kim JH, Jeong SW, Lee HM (2002) A thermodynamic study of phase equilibria in the Au-Sb-Sn solder system. J Electronic Matterials, 31(6): 557~563

Luo Xl, Zhong DS, Li GS (1996) Geology of Woxi-Type stratabound gold deposits in Hunan province (in Chinese with English abstract). Seismal Press, Beijing, 81-90 (in Chinese with English abstract)

Ma DS (1997) Geochemical tracing of the crustal fluid flow and mineralization: examples from low-temperature hydrothermal ore deposits in Jiangnan region, China. J Nanjing University, Geofluids Spec Publ, 33:1~10 (in Chinese with English abstract)

Peng B, Chen GH, Piestrzynski A (2003) Ore mineralogy of stibnite ore veins and its genetic implications for the W-Sb-Au ore deposit at Woxi, western Hunan, China (in Chinese with English abstract). Acta Mineralogica Sinica, 23(1): 82-90 (in Chinese with English abstract0

Peng B, Frei R (2004) Nd-Sr-Pb isotopic constrains on metal and fluid sources in W-Sb-Au mineralization at Woxi and Liaojiaping, western Hunan, China. Mineralium Deposita, 39(3): 313-327

Peng B, Piestrzynski A, Huang RH (1999) W-Sb-Au mineralization at Woxi deposit in western Hunan, China. Mineralogia Polonica. 30(1): 33-47

Yuan BQ, Tian SZ, Chen QY (1989) The discovery of aurostibite in China. Acta Miner Sinica, 9(4): 330 (in Chinese with English abstract)

Zhang SZ, Luo SH (1992) Metallic minerals in Hunan. Centeral-South University of Science and Technology Press, Changsha, 30 (in Chinese)

Zhang ZR (1989) Mineralogy of gold ores. Centeral-South University of Science and Technology. Press, Changsha, 1-300 (in Chinese)

Zhang ZR, Yang SX, Chen MX (1996) Mineralogy of the Woxi W-Sb-Au ore deposit in Hunan province. In Luo XL, Zhong DQ, Li GS (eds) Geology of Woxi-type stratabound gold deposits in Hunan province. Seismic Press, Beijing, 216-232 (in Chinese)

Paleohydrologic evolution of the St. Ives gold camp

Klaus J. Petersen, Peter Neumayr, Steffen G. Hagemann
School of Earth and Geographical Sciences, The University of Western Australia, 35 Stirling Highway, Crawley, Western Australia 6009, Australia

John L. Walshe
CSIRO Exploration and Mining, ARRC, 26 Dick Perry Av, Kensington, Western Australia 6151, Australia

Abstract. In the St. Ives gold camp in the Yilgarn Craton of Western Australia, several stages of hydrothermal alteration are pre-dating (epidote - calcite - magnetite 1- pyrite 1 - chalcopyrite – quartz), synchronous with (plagioclase - carbonate - pyrite 1 ± Au ± magnetite 2 ± hematite) and post-dating (quartz vein system - pyrite 2 - chlorite) gold mineralization. Hydrothermal fluids are characterized throughout the alteration history to gain an in depth understanding of chemical processes which controlled gold precipitation and the site of gold ore bodies.

Hydrothermal fluids in the camp evolve over time from low salinity aqueous, to low salinity aqueous-carbonic to carbonic followed by late stage saline aqueous-carbonic. The fluids show broadly and increase in CO_2, salinity and decrease in temperature with time. Importantly, during gold mineralization, hydrothermal fluids show rapid salinity decrease and CO_2 increase as monitored in syn-gold, growth-zoned carbonate grains.

Keywords. Yilgarn, St. Ives, fluid inclusion, fluid evolution, gold, hydrothermal alteration

1 Introduction

The Yilgarn Craton hosts several of the most studied ore deposits in the world and still presents challenges for the understanding of the complex geometry of fluid flow and the chemical evolution of hydrothermal fluids that lead to the formation of world class gold deposits. Most of the previous studies focussed strongly on the composition of hydrothermal fluids immediately in the gold environment and exactly at the time of gold mineralization. However, a much better understanding of the chemical processes involved in gold precipitation and the formation of world-class resources can be achieved, if the chemical compositions of hydrothermal fluids are understood spatially within the camp as well as temporally throughout the systems evolution.

This paper presents preliminary data on hydrothermal fluids in the St. Ives gold camp with the aim to: 1) establish a relationship between the hydrothermal alteration assemblages and the fluid inclusion associations, 2) characterize the P-T-x conditions of the hydrothermal fluids resulting in the deposition of the major alteration assemblages, and 3) develop a fluid evolution model.

2 Geological setting

The St. Ives gold camp is located in the southern part of the Norseman-Wiluna greenstone belt within the Eastern Goldfields Province of the Yilgarn Craton of Western Australia. The camp is hosted in predominantly mafic-ultramafic lavas and intrusions that have been metamorphosed to upper greenschist and lower amphibolite facies. The greenstone sequence has been intruded by felsic to intermediate porphyry stocks that predate, are synchronous with and post-date gold mineralization (Nguyen 1997).

The St. Ives gold camp is bounded by two major NNW-trending regional structures: the Boulder- Lefroy fault to the east and the Merougil fault to the west, and has undergone four major Archaean deformation events. The first (D1) produced regional south-over-north thrusts. The second (D2) produced upright, NNW-trending, gently plunging folds, such as the Kambalda anticline. The third event (D3) generated brittle-ductile, NNW-trending, oblique-sinistral wrench fault systems that show locally major N-trending, reverse, gold-bearing shear zones. During the fourth event (D4), NE-trending, dextral faults offset stratigraphy and earlier fault systems, and caused dextral±reverse reactivation of these earlier faults. Gold mineralization is mainly controlled by the D3 and D4 deformation events (Nguyen 1997).

3 Alteration petrography

In the St. Ives gold camp, a range of hydrothermal alteration assemblages can be documented (Neumayr et al. 2003, 2005). Numbers after the mineral name (e.g., pyrite 1, pyrite 2) indicate a different relative timing based on textural observations. Observed assemblages are:

- Carbonate alteration associated with deformation along the transcrustal Lefroy fault structure;
- epidote-calcite-magnetite1-pyrite1-chalcopyrite - quartz alteration in mafic rocks spatially associated with porphyry stocks (contact aureole);
- magnetite 1 halo around gold-bearing structures, i.e., interpreted to represent oxidized hydrothermal fluid (Neumayr et al. 2003, 2005);
- pyrrhotite±pyrite alteration (i.e., interpreted to represent reduced hydrothermal fluid);
- distal (to Au) chlorite-carbonate and intermediate biotite-carbonate alteration;
- proximal (to Au) plagioclase (mainly albite)-carbonate (Fe-rich dolomite to ankerite)-pyrite 1 (with mineral inclusions)±Au±magnetite 1 ±hematite, i.e., in-

terpreted to represent very oxidized hydrothermal fluid (Neumayr et al. 2003, 2005), related to fault zones; and
– quartz vein system (+Au?) with pyrite 2 (without mineral inclusions)+chlorite (hostrock alteration), which overprinted at least alterations assemblages (b) and (f).

The following discussion concentrates on the alteration assemblages (b), (f), and (g).

The alteration assemblage (b) occurs in mafic rocks up to 1 meter from the intermediate porphyry intrusions. Importantly, this style of alteration is unmineralized with respect to gold. Based on macro- and micro-textures the relative timing of the alteration assemblages (b) in mafic rocks is:

– amphibole (key metamorphic mineral);
– alteration assemblage (b);
– carbonate-pyrite (?)±quartz veins; and
– assemblage (g)±chalcopyrite±magnetite (?)± carbonate (?).

The alteration assemblage (f) comprises the gold-associated hydrothermal system. Mafic host-rocks are completely replaced by this alteration assemblage, which hosts the majority of pyrite 1 and contains abundant visible gold as well as magnetite and hematite inclusions. Later quartz veins related to alteration assemblage (g) partially replaced plagioclase alteration (f) based on dissolution textures and quartz pseudomorphs of plagioclase and carbonate. Where quartz veins are in contact with pre-existing pyrite 1, an overgrowth of clean pyrite 2 formed. However, the majority of quartz veins do not contain pyrite. Based on macro- and micro-textural observations the relative timing of this alteration in mafic rocks is:

– actinolitic hornblende/actinolite (key metamorphic mineral);
– total replacement of wallrock alteration assemblage (f); and
– assemblage (g).

Both alteration assemblages (b) and (f) are spatially associated, but appear to have forming during separate events based on overprinting textures (consequently fluid inclusions within the two assemblages are discussed separately). The hydrothermal quartz vein system (g) overprints both alteration assemblages, and is interpreted to be the result of the same hydrothermal event due to similar fluid inclusion properties, so the associated fluid inclusions are discussed together.

4 Fluid inclusions

Samples were taken from representative diamond core profiles through the ore zones of the Revenge and Conqueror mines at St. Ives gold camp.

Approximately 30 doubled-polished sections, which represent the various alteration systems with and without gold mineralization, were examined petrographically, and of these 5 were selected for microthermometric analysis.

Within each alteration assemblage, primary and pseudosecondary fluid inclusions were examined in different host minerals (e.g., carbonate, plagioclase, epidote) which allows the reconstruction of the fluid(s) evolution through time.

The fluid inclusion associations are subdivided according to the hydrothermal alteration assemblages discussed above into three stages: Stage 1 for (b), Stage 2 for (f) and Stage 3 for (g).

Hydrothermal alteration (b) contains primary inclusions in epidote, carbonate and quartz and shows no evidence of post-entrapment modifications. These irregular to negative crystal shaped fluid inclusions (<15 µm in length) occur as individual, isolated inclusions or as clusters that show random three-dimensional distribution throughout a single grain.

Hydrothermal alteration (f) showed primary fluid inclusions in albite with sizes between 2 and 10 µm and irregular to regular forms in carbonate with 5 to 10 µm in size showing negative crystals to irregular forms, and in isolated quartz inclusions in pyrite 1, 10 to 20 µm in size and irregular to regular forms. Detailed analysis on euhedral carbonate grains (Fig. 1) that grew in the host plagioclase of alteration assemblage (f) showed a strong zonation that preserved part of the fluid evolution history. The carbonate crystals displayed at least three distinctive zonations and/or events characterized by:

– Core with small (<5 µm) predominantly aqueous inclusions with a gas bubble of unknown composition;
– Intermediate zone with up to 20 µm aqueous-carbonic inclusions that is interpreted as a change of crystal growth velocity and sudden influx of CO_2 associated with mineral inclusions (e.g. scheelite);
– Rim with up to 10 µm aqueous-carbonic fluid inclusions.

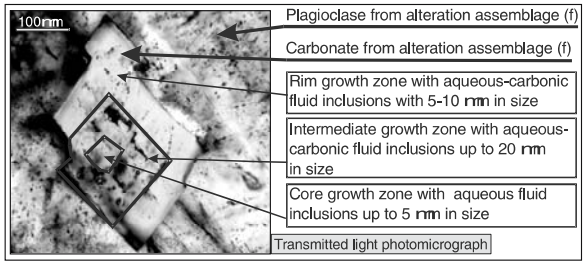

Figure 1: Hydrothermal alteration assemblage (f) showing the carbonate growth zones with preserved flincs that reveals the micro fluid evolution trough time.

The intermediate growth zone in the carbonate crystal is interpreted to be synchronous with the pyrite 1 core that contains abundant mineral (Au inclusive) and fluid (?) inclusions. The rim growth zone of the carbonate grain is interpreted to be synchronous with the "clean" pyrite 2 rim.

Hydrothermal alteration (g) contains primary fluid inclusions in carbonate with sizes between 3 and 10 µm showing negative crystals, regular to irregular shapes, and primary to pseudosecondary fluid inclusions in quartz, 5 - 25 µm in size, and irregular to regular shapes. Daughter crystals of halite and carbonate (dolomite) are observed.

4.1 Stage 1 fluid inclusions

Fluid inclusions of the Stage 1 are predominantly aqueous and show a small gas bubble at room temperature. The eutectic temperatures for epidote-hosted fluid inclusions varies from -38 to -49°C suggesting the presence of Ca and/or Mg cations, The total homogenization temperature into liquid are between 219 and 276°C, the salinity varies from 0.8 to 7.3 wt% equiv. NaCl, and density is in the range of 0.8 to 0.9 g/cm^3.

4.2 Stage 2 fluid inclusions

Plagioclase contains fluid inclusions (<5 µm in length) that are predominately carbonic, and locally aqueous-carbonic. Syngenetic carbonate contains mostly carbonic-aqueous inclusions possibly indicating that apparently purely carbonic inclusion in plagioclase contain also minute amounts of H_2O. The carbonic fluid inclusions in plagioclase do not contain any other gases than CO_2 (e.g., methane) and show a eutectic temperature range of -37 to -44°C. Salinity varies from 1.0 to 4.1 wt% equiv. NaCl, and density is about 0.3 to 0.6 g/cm^3.

A growth-zoned carbonate grain (Fig. 1) reveals a complex fluid evolution from lower-temperature saline aqueous to low salinity, higher temperature aqueous-carbonic: a) fluid inclusions in the carbonate core homogenize to liquid between 138 and 154°C and contain between 22 and 23 wt% equiv. NaCl at a density of 1.0 g/cm^3, b) fluid inclusions in the intermediate/rim zone homogenize to liquid between 268 to 277°C, and contain between 0.4 and 1.6 wt% equiv. NaCl at a density of 0.8 g/cm3.

Overall, fluid inclusion in carbonate show eutectic temperatures between -38 and -45°C and homogenization temperatures to liquid from 268 to 310°C. The salinity is highly variable showing values between 0.0 to 15.2 wt% equiv. NaCl and a density of 0.3 g/cm^3.

4.3 Stage 3 fluid inclusions

The Stage 3 fluid inclusions are related to the late alteration assemblage (g) and are hosted in the quartz and carbonate close to alteration assemblages (b) and/or (f). Microthermometry was conducted in primary/pseudosecondary fluid inclusions in quartz and carbonate in areas close to epidote in the alteration assemblage (b) and close to plagioclase-carbonate-pyrite in the alteration assemblage (f).

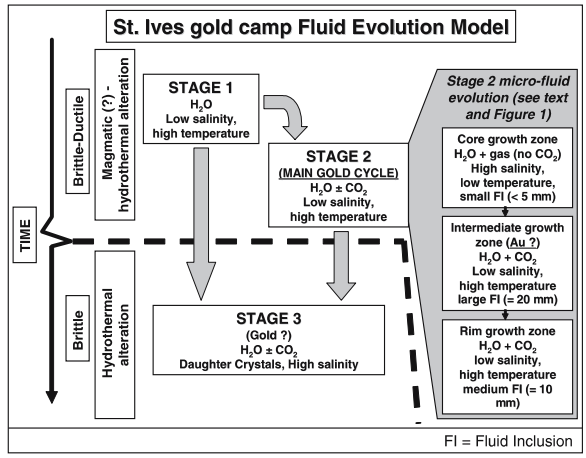

Figure 2: Fluid evolution model for the St. Ives Gold Camp.

Stage 3 fluid inclusions in quartz are aqueous, carbonic and aqueous-carbonic in nature with variable H_2O/CO_2 ratios. The eutectic and homogenization temperatures vary from -32 to -58°C and from 53 to 337°C (to liquid), respectively. Salinity ranges from 0 to 37 wt% equiv. NaCl and density from 0.4 to 1.2 g/cm^3.

Stage 3 fluid inclusions in carbonate are aqueous, carbonic and aqueous-carbonic (variable CO_2/H_2O ratios). Eutectic and homogenization temperatures range from -30 to -59°C and from 80 to 300°C (to liquid), respectively. Salinity varies between 0 and 22.8 wt% equiv. NaCl and density 0.7 to 1.1 g/cm^3.

The large range of values can be explained by post-entrapment modifications of fluid inclusions (e.g., temperature of total homogenization and density) and variable release of chemical components into the fluid during dissolution of plagioclase and carbonates (e.g., salinity).

5 Fluid evolution at St. Ives gold camp

Camp to micro-scale hydrothermal alteration and fluid inclusion studies indicate that three main fluid systems occurred in the same space but at different relative timing (Fig. 2). The igneous (porphyry) related epidote-calcite-magnetite 1-pyrite 1-chalcopyrite-quartz alteration (b) contains a predominantly aqueous fluid with low salinity. This fluid phase is marked by several pulses (magnetite with several crystal growth zonations) and vesicles now occupied by epidote-magnetite (alteration assemblage (b)).

The main gold mineralization event is related to the plagioclase-carbonate-pyrite 1±Au±magnetite 2 ±hematite alteration (f) which represents a relatively oxidized hydrothermal fluid. Cross-cutting macro textures revealed a later timing for this alteration in relation to the epidote dominant alteration assemblage (b). Fluid showed a suddenly enrichment in the CO_2 content which maybe the result of a new fluid entering the system (deep fluid source driven by aftershocks? Cox and Rumming 2004), associated with relatively faster crystal growth as indicated by the larger fluid inclusions.

The late quartz system (hydrothermal alteration (g)) is characterized by fluids that are out of chemical equilibria which regards to the plagioclase alteration (f) as indicated by dissolution textures of the plagioclase and carbonate. The predominantly brecciated pathways for this alteration indicate brittle conditions. Large variations in the H_2O/CO_2 ratios, salinities (0 to up to 37 wt% equiv. NaCl) and presence or absence of daughter crystals (halite and/or carbonate) may be partially caused by dissolution of pre-existing carbonate and plagioclase from the alteration wallrocks.

Conclusions

The preliminary data on the hydrothermal fluid evolution at St. Ives indicate: 1) an overall increase in CO_2, salinity and decrease of temperature with time; and 2) a rapid chemical change of the hydrothermal fluid during gold precipitation with dramatic increases of CO_2 in the system.

Acknowledgements

The study is financially supported by the Predictive Mineral Discovery Cooperative Research Centre (pmd*CRC) Y3 project, MERIWA and St. Ives Gold Mining Company (Pty) Ltd. (SIGMC) The authors acknowledge the permission to publish. Geologists at SIGMC are thanked for their support.

References

Cox SF, Ruming K, Nguyen PT, Stone WE (2001) The behaviour of faults, fluids and gold in a crustal scale shear system, St. Ives Goldfield, WA; a case of golden aftershocks? Specialist Group in Tectonics and Structural Geology conference, Ulverstone, Tasmania, Australia, Feb. 20:12-16.

Neumayr P, Hagemann SG, Walshe J, Horn L (2004) Sulphide-oxide mineral relationships on camp to deposit scale: vectors to orogenic gold deposits? SEG 2004: Predictive Mineral Discovery Under Cover; Poster Abstracts. Centre for Global Metallogeny, The University of Western Australia, Publication 33:451.

Neumayr P, Hagemann SG, Walshe J, Morrison RS (2003) Camp- to deposit-scale zonation of hydrothermal alteration in the St. Ives gold camp, Yilgarn Craton, Western Australia: evidence for two fluid systems? In Min. Exploration and Sustainable Development, Seventh Biennial SGA Meeting, Athens, pp. 799-802.

Neumayr P., Petersen KJ, Gauthier L, Hodge J, Hagemann SG, Walshe J, Prendergast K, Conners K, Horn L, Frikken P, Roache A, Blewett R (2005) Mapping of hydrothermal alteration and geochemical gradients as a tool for conceptual targeting: examples from Western Australia, this volume.

Nguyen TP (1997) Structural controls on gold mineralization at the Revenge Mine and its tectonic setting in the Lake Lefroy area, Kambalda, Western Australia. Unpub. Ph.D. thesis, The University of Western Australia, 195 pp.

Tectonic setting of epithermal deposits in mainland China

Jinping Qi
Laboratory of Orogen and Crust Evolution, Department of geology, Peking University, Beijing, China

Yanjing Chen
Institute of Geochemistry, Chinese Academy of Sciences, Guiyang, China

Franco Pirajno
Geological Survey of Western Australia, Perth, Australia, 100 Plain Street, East Perth 6004, Australia

Abstract. This paper documents selected epithermal deposits in Mainland China. The deposits cluster in four regions, namely northeast China, northern margin of the North China craton, southeast China and northwest China. Geological and geochemical characteristics of the epithermal deposits are summarized and metallogenic trends are revealed. The ore-forming fluid-systems were dominated by meteoric water, occasionally with inputs of magmatic fluid. Ore metals were mainly sourced from host-rocks and parent intrusions, with many deposits formed in epithermal-to-mesothermal conditions, suggesting a link with porphyry systems. Large-scale metallogenesis and magmatism postdated local oceanic closure by ca. 50 Ma, and was coeval with the transition from collisional compression to extension tectonic regime. Hence a model of collision-metallogeny- fluid flow (CMF) is applicable to interpret the origin of epithermal ore provinces in Mainland China.

Keywords. Epithermal deposits, tectonic setting, collisional orogen, CMF model, Mainland China

1 Introduction

Epithermal Au/Ag ore systems are globally very important. Recent discoveries in China include several large epithermal deposits, such as the Tuanjiegou Au deposit in Heilongjiang province, the E'rentaolegai Ag deposit in Inner Mongolia, the Zijinshan Au-Cu deposit in Fujian province and the Axi Au deposit in Xinjiang province. Unlike the epithermal ore systems in the Circum-Pacific rim, most epithermal deposits of China are associated with continental collision orogens and consequently cannot be related to arc magmatism caused by B-type subduction. Therefore, the tectonic setting and origins of most epithermal ore systems in Mainland China remain unresolved. To provide some insight into this issue, we summarize the geological, geochemical and geochronological data from 86 epithermal deposits in Mainland China, and suggest that these relate to A-type subduction during collisional orogeny. We argue that the CMF model (Chen and Pirajno, 2005; Pirajno and Chen, 2005; this volume) is applicable to interpret the origins of epithermal ore systems in Mainland China.

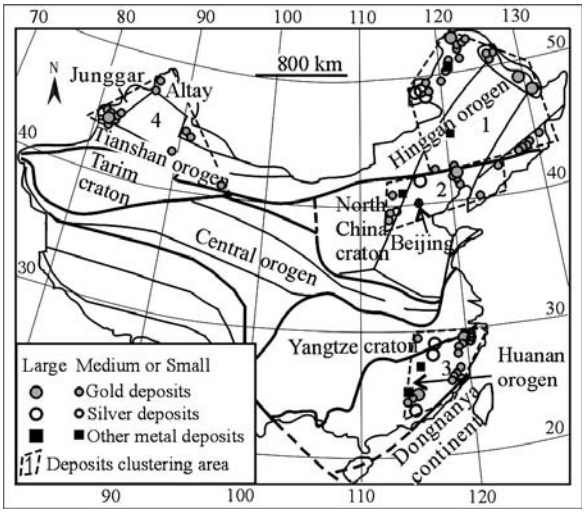

Figure 1: Sketch distribution map of epithermal deposits in Mainland China

2 Epithermal metallogeny in space and time

Epithermal deposits in Mainland China cluster in four areas: NW China, NE China, the northern margin of the North China craton and SE China (Fig. 1). In NW China, epithermal deposits mainly occur in the Tianshan (including Beishan), Junggar and Altay orogens. Ore-hosting rocks include Devonian-Carboniferous volcanic sequences that formed in arc settings, e.g. the Axi deposit (Chen et al., 2003), and Permian volcanic sequences that developed during continental collision. Isotopic dating yields two groups of ages, i.e. >320 Ma and 300-210 Ma. In NE China, deposits are distributed in four regions, namely Derbugan, Lesser Hinggan, southern Great Hinggan and Eastern Jilin- Heilongjiang. Along the northern margin of North China craton, epithermal deposits cluster from west to east at the northern end of the Taihang Mountains, the Yanshan orogen, and the Liao-Ji block. In SE China, epithermal deposits cluster in the Huanan Orogen and its collisional orogenic belt with the Yangtze craton. Most epithermal ore systems appear to have formed during the Yanshanian orogenic event (180-90 Ma) and are hosted in Mesozoic volcanic sequences overlain on the Hercynian (405-270 Ma) or Indosinian (270-208 Ma) orogens, or on the Precambrian rocks of the Yangtze and North China cratons. The majority of isotopic ages (Rb-Sr, K-Ar, Ar-Ar, U-Pb) for epithermal ores and their related intrusions in eastern China fall in a range of 90-170 Ma.

3 Ore deposits geology

Paucity of comprehensive descriptions of individual deposit makes it difficult to distinguish between high- and low-sulfidation types. Favorable host rocks include high-potassium calc-alkaline andesite, rhyolite, dacite, volcanic tuff, and breccia. A few deposits are hosted by granite, sedimentary rocks and metamorphic rocks. Ore systems tend to be sited in or close to calderas, volcanic domes, and fault systems. Ore body styles include stratiform, vein-like, lenticular, cylindric and irregular, depending on the types of controlling structures. Massive, disseminated, stockwork and breccia ores are common. Major ore minerals are pyrite, pyrrhotite, arsenopyrite, sphalerite, galena, chalcopyrite, bornite, native gold, native silver, and tellurides. Gangue minerals are dominantly quartz, sericite, illite, adularia, laumontite, chlorite, calcite, and epidote.

4 Isotope geochemistry

The $\delta^{18}O$ and δD data of 35 epithermal deposits throughout China suggest that ore fluids were mainly sourced from meteoric water. Some deposits, especially in SE China and along the northern margin of the North China craton, such as the Zijinshan gold deposit and Yinshan silver deposit, formed in an epithermal system with input of magmatic water. Tao et al. (1998) considered these deposits to be a continuum between porphyry and epithermal types.

The sulfur isotopic data of ore sulfides for 42 epithermal deposits in mainland China show that the $\delta^{34}S$ values of the epithermal ores along the northern margin of the North China craton and NW China, primarily range between 0 and 8 ‰, and those in NE and SE China between –5 ‰ and 5 ‰. In SE China, where the host rocks have high sedimentary/volcanic ratios or the fluid-systems are dominant of meteoric water, exhibit a wide range of $\delta^{34}S$ values.

Pb-isotope ratios ($^{206}Pb/^{204}Pb$, $^{207}Pb/^{204}Pb$, and $^{208}Pb/^{204}Pb$) show that epithermal ores in SE China and NE China have more radiogenic components than those of the northern margin of the North China craton where Pb-isotope ratios range widely and are consistent with regional variations addressed by Zhang (1995). In NW China epithermal ores have high $^{206}Pb/^{204}Pb$, $^{207}Pb/^{204}Pb$, and $^{208}Pb/^{204}Pb$ ratios similar to those in the SE China and NE China. In $^{207}Pb/^{204}Pb$ vs. $^{206}Pb/^{204}Pb$ or $^{208}Pb/^{204}Pb$ vs. $^{206}Pb/^{204}Pb$ plots, samples of individual deposits or from individual metallogenic provinces usually define a linear trend. This can be interpreted to represent a mixing line of two end-members, i.e. a deep magmatic source and a shallow source. For example, the ore-metals of the Zhilingtou Au deposit, with a linear Pb-isotope trend, were interpreted to have sourced from both the basement metamorphic host rocks and magma (Lu et al., 1997).

5 Tectonic setting and origins

Epithermal deposits and epithermal ore provinces are generally interpreted to have originated from oceanic crust subduction, such as the epithermal systems of the Southwest Pacific (White et al., 1995). However, the fact that isotopic ages (Rb-Sr, K-Ar, Ar-Ar, U-Pb) for epithermal metallogenesis in NW China fall into two time spans (>320 Ma and 300-210 Ma) suggests two possibilities. The >320 Ma event can be related to the subduction of the Paleo-Asian Ocean, and this is supported by the presence of Devonian-Early Carboniferous andesites and ophiolite suites in NW China. The 300-210 Ma time span must be related to continental collision, because the Paleo-Asian Ocean was closed by the middle Carboniferous and thereafter the tectonism in NW China entered into a continental collision regime.

Mesozoic epithermal deposits and associated igneous rocks in eastern China (NE China, northern margin of the North China craton and SE China) are generally accepted to be linked with the subduction of the Paleo-Pacific Ocean. However, this view is not supported by the following observations: (1) in eastern China, no suture has been recognized to represent Yanshanian subduction of the Paleo-Pacific plate; if present it must lie in the Japanese Sea and is far (500~2000 km) from the epithermal ore provinces of eastern China; (2) unlike those of the Circum-Pacific metallogenic belts, the Yanshanian metallogenic belts or provinces are perpendicular to and not parallel to the Mesozoic and present-day trenches; (3) Yanshanian magmatism and metallogenesis did not occur in Southern Hebei, Northern Henan, Western Shandong, Northern Anhui, and Northern Jiangsu; (4) the petrological and geochemical characteristics of the Yanshanian granitoids and volcanic rocks have S-type affinity, significantly different from those of the Andean magmatic arcs, which is characterized by calc-alkaline trends dominated by andesitic volcanics; (5) the Pb-isotope ratios of Yanshanian magmatic rocks and ores along the northern margin of North China craton show that they were mainly sourced from Precambrian basement and not from the Paleo-Pacific lithosphere. These observations suggest the magmatic rocks and associated epithermal ore systems are different from those of the Circum-Pacific metallogenic belts and therefore can not be related to the subduction of the Paleo-Pacific Ocean.

In summary, the epithermal ore systems of eastern China and the 300-210 Ma epithermal ore-forming epoch in NW China both occurred during continental collision with an A-type subduction regime. The origin of these epithermal systems can be interpreted with the CMF model as proposed by Chen et al. (2005), Chen and Pirajno (2005, this volume), and Pirajno and Chen (2005, this volume).

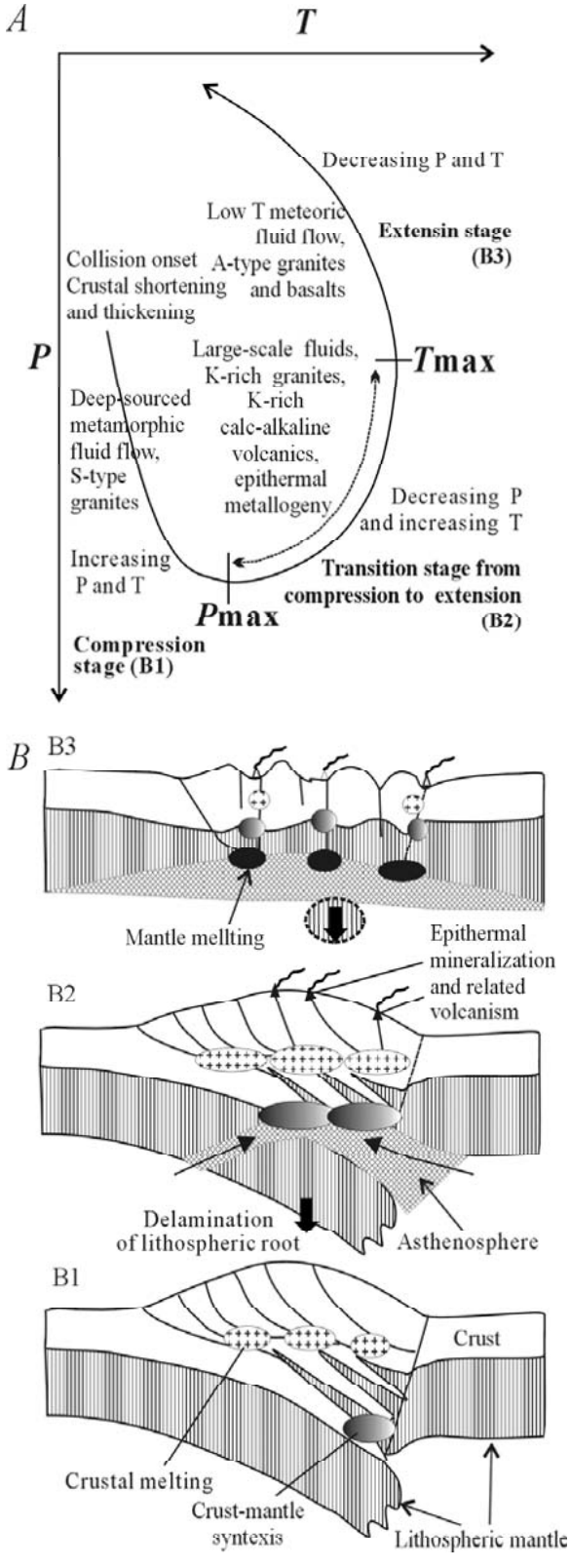

Figure 2: CMF model for epithermal deposits occurring in intracontinental collisional orogeny

Epithermal mineralization in eastern China, for example, is linked with the Permo-Triassic continental collisions in East China along the Solonker suture, followed by Triassic multi-continental collisions to the south, and the Early Jurassic Dongnanya-Eurasia collision (Chen et al., 2005). Eastern China was affected by an A-type subduction regime, experiencing a compression stage (increasing P and T), through a transition stage from compression to extension (decreasing P and increasing T) to an extension stage (decreasing P and T), roughly corresponding to Triassic-mid Jurassic, late Jurassic-Cretaceous, and mid Cretaceous respectively in time (Chen et al., 2005; Chen and Pirajno, 2005, this volume).

During the compression stage, slab stacking, shortening, and thickening develop, leading to the emplacement of crustal-sourced S-type granite (Fig. 2A, Fig. 2B1). Ages of epithermal ores reveal that some epithermal mineralization, especially in SE China, occurs during this stage. Following the maximum of compression, shortening, and thickening (P_{max}), the stage of transition from compression to extension begins (Fig. 2A). The lithospheric root and the continental subducting slab tend to sink, and upwelling of asthenospheric mantle will replace the space created by the sinking lithosphere, resulting in partial melting of the subcontinental mantle lithosphere and the base of the crust (Pirajno and Chen, 2005, this volume) (Fig. 2B2). Decompression (decreasing P) of downgoing slab and increasing geothermal gradient (increasing T) (Fig. 2A) result in large-scale decompression melting and fluid generation at depth, leading to emplacement of granitoids represented by K-rich and K-feldspar porphyritic calc-alkaline granitoids (Pirajno and Chen, 2005, this volume), and K-rich calc-alkaline volcanics as for example those in SE China (Tao et al., 1998). Meanwhile structures dilation caused by decompression provide the necessary channels for shallow-sourced fluid circulation, which is driven by increased geothermal gradient. Ages of epithermal ores and related igneous rocks in eastern China show a peak around 130Ma, which demonstrates that primary epithermal mineralization occurs during this stage; epithermal ore fluids characterized by meteoric water indicate that ore systems are mainly controlled by shallow-sourced fluid, driven by high geothermal gradients. Where magmatic water participates, resulting in mixing of deep- and shallow-sourced fluids, the mineralization shows a combination of epithermal and porphyry types, and usually results in formation of large-scale deposits, such as Zijinshan Au-Cu and Yinshan Ag deposit. In the extension stage (Fig. 2A, Fig. 2B3), the geothermal gradient decreases and depletion in mobile components reduces the generation of deep-sourced fluids and melts. Granitoids of this stage are characterized by A-type granites and basalts, like those in SE China (Lu et al., 1997). During this stage only low temperature meteoric fluids will circulate, thermal anomalies are weakened and only few important deposits will form.

Acknowledgements

Dr. Wu Guang is thanked for offering geologic data of deposits in NE China; we acknowledge Dr. Zhao Caisheng for helping to format this abstract. Franco Pirajno publishes with the permission of the Director of the Geological Survey of Western Australia.

References

Chen YJ, Bao JX, Zhang ZJ, Chen HY, Liu YL (2003) Laumontitization as exploration indicator of epithermal gold deposits: A case study of the Axi and other epithermal systems in West Tianshan, China. Chinese Journal of Geochemistry, 22, pp.289-303.

Chen YJ, Chen HY, Zaw K, Pirajno F, Zhang ZJ (2005) Tectonic setting of skarn-type gold deposits in China, an overview. Ore Geology Review, in print.

Chen YJ, Pirajno F (2005) Linking the CMF model to metallogenic zoning in the east Qinling Orogen, central China. Extended Abstract of SGA2005 Conference, Springer, Beijing, this volume.

Lu ZG, Tao KY, Xie JY, Xie DK, Wang WB, Chen HN (1997) Volcanic geology and mineral resources of southeast China continent. Geological Publishing House, Beijing, 431pp (in Chinese).

Pirajno F, Chen YJ (2005) Hydrothermal ore systems associated with the extensional collapse of collision orogens. Extended Abstract of SGA2005 Conference, Springer, Beijing, this volume.

Tao KY, Gao TJ, Lu ZG (1998) Basement tectonics of volcanic rock and volcanic-intrusion related to mineralization of coastal area of southeast China. Geological Publishing House, Beijing, 371pp.

White NC, Leake MJ, McCaughey SN, Parris BW (1995) Epithermal gold deposits of the southwest Pacific. Journal of Geochemical Exploration, 54: 87-136.

Zhang LG (1995) Block geology of eastern Asia lithosphere. Science Press, Beijing, 252pp (in Chinese).

Gold deposits rich in bismuth minerals: An important type of gold deposits

Ren Yunsheng, Liu Liandeng
College of Earth Sciences, Jilin University, 2199 Jianshe Street, Changchun 130061, China

Zhang Huihuang
Guangzhou Institute of Geochemistry, Chinese Academy of Sciences, Guangzhou 510640, China

Abstract. Several gold deposits, both in China and abroad, are drawing attention because of their abundant bismuth minerals. Comparative studies on some of them indicate that certain characteristics can aid in identifying standards and exploration criteria of the type of gold deposits. Firstly, the lode gold ore bodies are structurally controlled. Secondly, the gold ore is rich in bismuth minerals, most of which are major gold-bearing minerals. Thirdly, there is a prominent positive correlation of Au with Bi in the gold ore. Moreover, the phase separation of ore-forming fluid during the major gold metallogenic stage can frequently be shown. Although the Bi-rich gold deposit may belong to a variety of genetic types, high content of elements of Au and Bi in associated igneous rocks, the phase separation of ore-forming fluid play important roles in the mineralizing process.

Keywords. Bismuth minerals, correlation of Au with Bi, phase separation of ore-forming fluid, exploration criteria

1 Introduction

There have been an increasing number of reports that bismuth minerals are found in some gold deposits in China and closely associated with gold mineralization, for example, the Tongguan deposit in Shaanxi province (see Ye and Li 1989), the Wulong deposit in Liaoning province (see Zhao et al. 1994), the Lanjia deposit in Jilin province (see Zhong and Han 1998), Baocun and Chaoshan deposits in Anhui province (see Ren et al. 2004), as well as some deposits in Jiaodong region of the Shandong province (see Pan 1994). These gold deposits are similar in that bismuth minerals in the gold ore are usually closely associated with gold minerals in both space-time and genesis.

Since 2002, the authors have mainly studied the Baocun and Chaoshan gold deposits in Tongling area in China (see Fig. 1). The purpose of the present paper is to describe essential features of the type of gold deposits, discuss their ore-controlling factors and genesis, and to contribute to the exploration and further studies of the type of gold deposits.

2 Characteristics of the gold deposit rich in bismuth minerals

2.1 Gold ore body

Baocun and Chaoshan deposits represent two of the known gold only skarn deposits in Tongling area. Main gold ore bodies in the two deposits, ranging in shape from lentiform to lode, are located in the contact zones between the Mesozoic alkaline or calc-alkaline igneous rocks and their carbonate wall rocks of the Triassic system. Some lie in compressional fracture zones in the Triassic strata. In strike and dip direction, gold ore bodies appear as expanding and thinning, pinching and recurrent, branching and converging. It can be shown that ore bodies are obviously controlled by structures.

The gold skarn in the Lanjia deposit in Jilin province is located in the contact zone between the metallogenic quartz diorite body and its wall rocks. Auriferous quartz in the Wulong deposit in Liaoning province is distributed in the associated granite body, and those in Tongguan in Shaanxi province are in the metamorphic rock. Ore bodies in these mines are similar in morphology and spatially changing with those in Baocun and Chaoshan deposits (see also Zhong and Han 1998; Zhao et al. 1994; Ye and Li 1989). On the basis of these observations, we can assume that the gold ore bodies in these Bi-rich gold deposits show similar morphology and controlled by structure.

2.2 Bismuth minerals and their relationship with gold minerals

Native bismuth and bismuthinite are major bismuth minerals in all gold deposits mentioned above. Montanite, pavonite, hedleyite, wehrlite, joseite, emplectite, galenobismutite, gustavite, ikunolite and maldonite may also be identified by microscope or electron probing analysis sometimes. Spatially, bismuth minerals are usually disseminated in the auriferous quartz. Thin bismuth gold ore veins, composed of bismuth minerals, quartz and a few other metallic sulphides, can sometimes be seen in some fractures in gold ore bodies. Bismuth minerals, together with native gold and a few of metallic sulphides, deposit in the middle and late metallogenic stage, namely the independent bismuth-gold stage.

In the Baocun deposit, thin bismuth-gold ore veins located in copper skarn are wide from 1 to 25mm and obviously controlled by fractures. The vein is mainly composed of native bismuth, bismu- thinite, native gold and copper pyrite. In the hand specimen, needle-like or radial bismuth minerals are mainly paragenetic with the lumpy and sugary- grained quartz.

This page intentionally blank

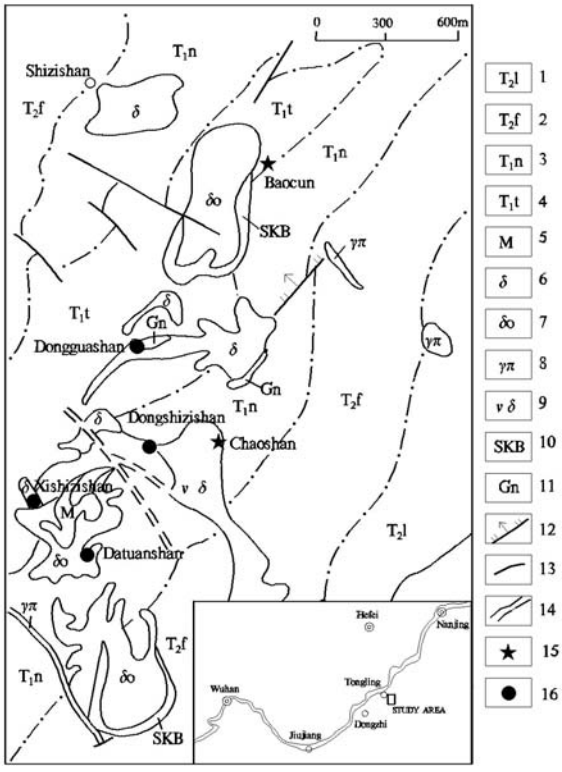

Figure 1: Geological sketch map of the Shizishan orefield in Tongling area, Anhui province,China; 1-Longtoushan formation; 2-Fenshuiling formation; 3-Nanlinghu formation; 4-Tashan formation; 5-marble; 6-diorite; 7-quartz-diorite; 8-granite-porphyry; 9-augite diorite; 10-skarn; 11-gossan; 12-normal fault; 13-fault; 14-geological boundary; 15-study gold deposits; 16-other gold deposit

Ren et al. (2004) reported that twenty-three among ninety-six gold minerals in eight polished sections in Baocun and Chaoshan deposits are paragenetic with bismuth minerals (see Fig. 2). Other sixteen are in the same fields of microscope with native bismuth or bismuthinite. Eighty-one among ninety-six gold minerals are distributed in polished sections rich in bismuth minerals. All of this suggests that bismuth minerals be closely associated with gold minerals.

Bismuth minerals in the Wulong deposit are formed in the stage of metallic sulphide crystallization and paragenetic with native gold. Bismuth minerals with various shapes can coexist with native gold. Moreover, more complicated bismuth minerals are in shape, more paragenetic gold minerals can be found.

Seventy-five percent of native gold in the Lanjia deposit are packaged in or paragenetic with native bismuth, bismuthinite and some bismuth sulfates. Data show that gold mineralization took place in the hydrothermal metallogenic stage, which superimposed in the earlier skarn. Gold minerals accompanying bismuth minerals are commonly distributed in thin structures and intergranular fractures.

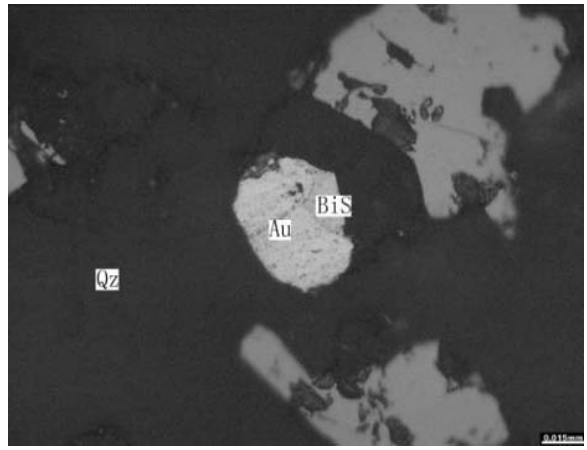

Figure 2: Intergrowth of bismuth minerals with gold minerals in the Baocun deposit in Tongling area. Au Native gold; BiS Bismuthinite; Qz Quartz.

2.3 Correlation of Au with Bi

Correlation coefficient matrix of eight trace elements in forty-one pieces of gold ore in the Baocun deposit indicates that the correlation coefficient of Au with Bi is 0.6916, that of Cu with Bi is 0.5030 and Ag with Bi is 0.5836. There is a prominent positive correlation of Au, Ag and Cu with Bi. All show that gold minerals and bismuth minerals are synchronously deposited in the gold-bismuth metallogenic stage in which copper and silver mineralization also formed, to some degree.

In the Buckhorn Mountain deposit, bismuth and telluride minerals are common and often intimately associated with the gold. The best field determination of whether or not gold is present is visible bismuthinite, which is almost always associated with gold. Geochemical data from chip holes were plotted on log-log plots of gold vs. Bi, Ag, As, Cu, Pb, and Zn. These plots show a logarithmic correlation coefficient of gold with bismuth is 0.514 and not with any of the other metals(see Hickey 1992).

In the Wulong mine, Xiang et al. (1980) carried out a factor analysis of trace elements in both surface and deep-seated samples from two major auriferous quartz veins. It is clearly indicated that there is close correlation coefficient of Au with Bi ranges from 0.72 to 0.90. In different levels, elements of Au and Bi are in the principal factor, which suggests that Au and Bi be major metallogenic elements in the major metallogenic stage.

3 Discussion

3.1 High content of Au and Bi in metallogenic igneous rocks

Studies on regional geochemical background data in the Tongling area show that concentration coefficients of metallogenic elements of Au, Ag, S, Cu and Bi in the Me-

sozoic middle-acid metallogenic igneous rocks are obviously higher than those in strata. Associated intrusive rocks are assumed to be the main source of metallogenic elements (see Zhang 1989). Contents of Bi in Baocun and Chaoshan intrusive rocks are 3.75×10^{-6} and 10.01×10^{-6}, respectively, which together high contents of Au indicate that the associated igneous rock is the major source of Au and Bi.

In the Wulong deposit, contents of Au, Ag, As and Bi in the metallogenic intrusive rock and dikes are tens of times of their Clarke values, and the ratio of Au/Ag in the gold lode is nearly same as that in metallogenic igneous rock and dikes. All show that there is inheritance of metallogenic elements in gold lode, intrusive rock and dikes (see Peng 1994).

3.2 Phase separation of ore-forming fluid and its metallogenic significance

Ren et al. (2004) analyzed fluid inclusions from quartz deposited in gold-bismuth metallgenic stages. Specimens were collected from main ore bodies underground in the Baocun and Chaoshan mines.

Four types of inclusions can be identified in the quartz grains. They are the pure CO_2 inclusion, three-phase inclusion rich in CO_2, gas-liquid inclusions and three-phase inclusions containing daughter minerals of halite. Not only are different types of inclusion distributed in different quartz grains formed in the same stage, but they can also be found in the same quartz grain. Determination and comparison of homogenization temperature and salinity of different types of inclusion can define the boiling of ore-forming fluid.

The phase separation of ore-forming fluid can lead to the escape of CO_2 and H_2S from the ore-forming fluid, which causes declination of fs_2 of hydrothermal system (see Drummond and Ohmoto 1985). Moreover, the maldonite in such deposits as Baocun and Chaoshan mines may decompose into native gold and native bismuth with the descending of fs_2, which causes the intimate intergrowth of native gold and bismuth minerals.

4 Summary and conclusion

In spite of their different genesis, Bi-rich gold deposits often have some common geological characters. The first is that the ore is rich in bismuth minerals which are major minerals containing gold. Secondly, there is a prominent positive correlation of Au with Bi in the gold ore.

Mineralised igneous rocks are the main source of metallogenic elements such as Au, Ag, Cu and Bi. The main cause of gold minerals closely associated with bismuth minerals is decomposing of S-Au-Bi complex, induced by declination of fs_2 of ore- forming hydrothermal system. On the other hand, the phase separation of ore-forming fluid may result in the declination of fs_2 of the ore-forming fluid. It is of value to better study the causes and processes involved in the escape of ore-forming fluids rich in Au and Bi from a magma system.

Bismuth minerals can provide an important targeting clue, especially for the bonanza type. Furthermore, examination of bismuth minerals and investigation of intergrowth of gold minerals with bismuth minerals are beneficial to raise the gold recovery ratio during the ore dressing.

References

Drummond SE, Ohmoto H (1985) Chemical evolution and mineral deposition in boiling hydrothermal system. Econ. Geo. 87:126-147

Hickey RJ (1992) The Buckhorn Mountain (Crown Jewel) gold skarn deposit, Okanogan, Washington. Econ. Geo.1:125-141

Liu GZ (1994) Typomorphic characteristics of quartz in auriferous quartz vein and exploration significance in Wulong gold deposit. Journal of Shenyang Institute of Gold Technology 1:10-16

Pan YC (1994) Discovery and geological meanings of opaque minerals containing bismuth in gold deposits in Jiaodong area, China. Gold Geology 1:80-83

Peng YD (1994) Study on genesis of Wulong dold deposit in Liaoning province. Journal of Precious Metallic Geology 1: 21-31

Ren YS et al (2004) A study on the relationship between bismuth minerals and gold mineralization in skarn gold deposits in Shizishan orefield. J Mineral Petrol 2:41-45

Ren YS et al (2004) Discussion on the metallogenic depth of skarn type gold deposits in Tongling area, Anhui province. Geotectonica et Metallogenia.4:397-403.

Ye F, Li YQ (1989) Gold-bismuth solid solution and its bismuth compound in Xiaoqinling gold deposit in Tongguan area, Shaanxi province, China. In: International Symposium on Geology and Exploration of Gold Deposits. Northeast Industry Institute Publishing House, Shenyang, pp571-574.

Zhao YS et al (1994) A study on the relationship between bismuth minerals and gold mineralization in the Wulong gold deposit, Liaoning province. ACTA Mineralogica Sinca 1:88-91

Zhong CL, Han YJ (1998) A brief introduction on the geological features of deposit in the Lanjia area, Jilin provinc. Jilin Geology 2:59-64.

Analysis of Au content in sedimentary rocks around the Hishikari gold deposit, Japan

Kenzo Sanematsu, Akira Imai, Koichiro Watanabe
Department of Earth Resources Engineering, Kyushu University, 6-10-1 Hakozaki, Higashi-ku, Fukuoka 812-8581, Japan

Tetsuya Nakanishi
Kyushu University Museum, Kyushu University, 6-10-1 Hakozaki, Higashi-ku, Fukuoka 812-8581, Japan

Abstract. The basement rock of the Hishikari low sulfidation type epithermal gold deposit, Japan is the Cretaceous Shimanto Supergroup consisting of sandstone and shale. Rock samples of the Shimanto Supergroup were collected from the surface and drill cores and the Au contents were analyzed by ICP-MS. Since Au is commonly present in organic matter of sedimentary rocks, organic matter was decomposed by heating using a microwave oven. The Au content of the unaltered rock samples of the Shimanto Supergroup collected from the surface ranges from 1.9 ppb to 7.1 ppb in sandstone and 15.7 ppb in shale. The Au contents were relatively high, however, it may be necessary to analyze the same samples from leaching more than two times to determine more precisely their Au content because of the heterogeneous distribution of Au in the samples. In the Hishikari deposit, $\delta^{13}C$ value in calcite veins was lower than average crustal $\delta^{13}C$ value and this result suggests that carbon of low $\delta^{13}C$ value in veins resulted from organic matter in the basement rock (Morishita 1993). Although Au in organic matter might be transported to the deposit by hydrothermal fluid in the Shimanto Supergroup, the result of rock samples containing organic matter collected below the deposit could not corroborate this notion.

Keywords. Gold, sedimentary rocks, ICP-MS, microwave oven, organic matter, Hishikari gold deposit

1 Introduction

The association of Au with organic matter in sedimentary rocks or sediments has been reported by many researchers (e.g., Gatellier and Disnar 1989, Kettler et al. 1990, Terashima 1995). Although Au is commonly present in organic matter, it is difficult to determine Au concentrations in the order of ppb or sub-ppb levels. In this study, the Au content in sedimentary rocks was determined by Inductively Coupled Plasma Mass Spectrometer (ICP-MS) after decomposition of organic matter using microwave oven and solvent extraction of Au.

The basement rock of the Hishikari gold deposit is the Cretaceous Shimanto Supergroup consisting of sandstone and shale. This study is aimed to investigate the potentiality of the Shimanto Supergroup as the source of Au to the Hishikari deposit.

2 Geological setting

The Hishikari low sulfidation type epithermal gold deposit is located in southern Kyushu, Japan. In the Hishikari deposit, Au - Ag bearing adularia – quartz veins are hosted by the Pliocene to Pleistocene andesite and the Cretaceous Shimanto Supergroup overlain by the andesite unconformably (Izawa et al. 1990). Although the Shimanto Supergroup consisting of sandstone and shale does not outcrop around the Hishikari deposit, it can be observed commonly in southwestern Japan. The accretionary prism of the Shimanto Supergroup distributed in the Shimanto Terrane, Southwest Japan was formed from Early Cretaceous to Miocene. Thus, the age of the stratigraphy becomes older northward in the Shimanto Supergroup (Fig. 1). The Shimanto Supergroup can be classified into the Lower Shimanto group from Cretaceous to Early Palaeogene and the Upper Shimanto group from Palaeogene to Early Miocene (Teraoka and Okumura 1992) and the basement rock of the Hishikari deposit is the former. The terrigenous sediments of the Shimanto Supergroup consist mainly of clastics of felsic to intermediate volcanic and granitic rocks, and the most of them were supplied from southwestern Japan and the eastern part of the Asian continent (Teraoka et al. 1999).

3 Sample description

Two sandstone samples and one shale sample were collected in Southern Kyushu, and three sandstone samples were collected in Shikoku. The samples that were not weathered in appearance were obtained from the outcrop of the Lower Shimanto Group.

Drill core samples were taken at depths of 797 m, 861 m, 922 m, 950 m and 988 m in the drilling of 8MAHAK-5 (MITI (Ministry of International Trade and Industry) 1997), at depths of 778 m, 806 m, 846 m and 899 m in drilling hole 12MAHA-1 and at the depth of 848 m, 879 m and 999 m in drill hole12MAHA-2 (MITI 2001). Two samples (797 m and 861 m) in 8MAHAK-5 were shale and the others were all sandstone. All samples were collected from parts including no veinlets. The location of drilling of 8MAHAK-5 was located in 1 km east of the Hishikari deposit at 300 m sea level. Quartz veinlets were commonly observed in the drill core samples indicating that this area was influenced by the mineralization. The location of drilling of 12MAHA-1 and 12MAHA-2 was located in 6 km north-northeast of the Hishikari deposit at 560 m sea level.

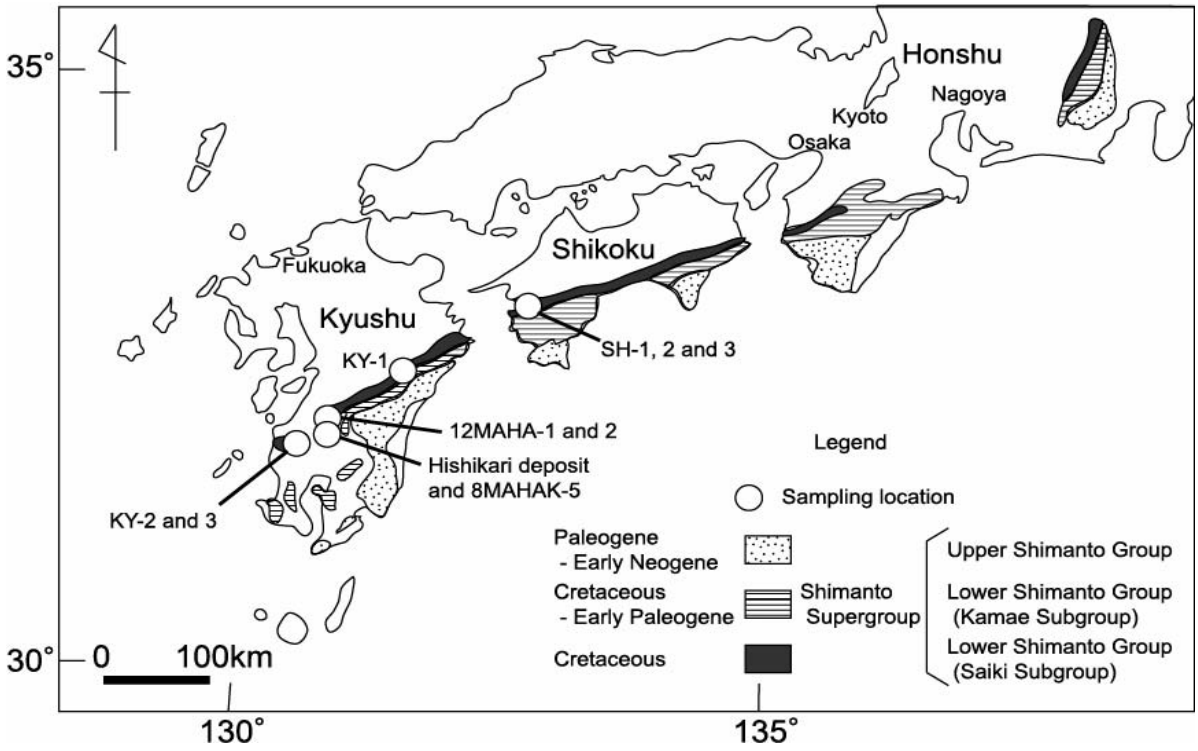

Figure 1: The geologic map showing the distribution of the Shimanto Supergroup in southwestern Japan (modified from Teraoka et al. 1999).

Two sediments samples of GSJ (Geological Survey of Japan) geochemical reference samples were analyzed for comparison with the results of these rocks from the Shimanto Supergroup. The sample of JLk-1 is lake sediment and the other sample of JSl-1 is slate.

The sandstone of the Shimanto Supergroup analyzed in this study consists mainly of clastics of quartz, plagioclase, K-feldspar and rock fragment, and illite, chlorite and calcite. The sandstone commonly contains a small amount of heavy minerals such as biotite, muscovite, pyrite and zircon. Pyrite is commonly observed in organic matter existing as cement in sandstone and shale.

4 Experimental

The samples of sandstone and shale were crushed and roughly ground by a jaw crusher with alumina jaws. A sample of about 0.5 g in weight was leached by HF 10 ml. After vaporizing HF, the sample was dissolved with HNO_3 1m and perchloric acid ($HClO_4$) and was heated by microwave until the organic matter in the sample was decomposed. After vaporizing HNO_3 and perchloric acid, Au was dissolved by aqua regia. After vaporizing much of aqua regia, Au was collected by 1.5 M HBr. The solution was mixed with diethylether 20 ml and phosphoric acid (H_3PO_4) 0.5 ml in a separatory funnel. The diethylether layer dissolving Au was collected and diethylether was vaporized at room temperature. Eventually Au was prepared by dissolving in 0.1 M HCl. All analytical instruments were washed by aqua regia before using to prevent them from Au contamination.

The analysis of Au concentration was conducted using ICP-MS (Agilent 7500c) at the Center of Advanced Instrumental Analysis, Kyushu University. In ICP-MS analysis, a portion of Ta in solution can be oxidized to TaO. Since the mass of TaO is equivalent to the mass number of Au, signal of TaO can be counted as that of Au in high Ta solution. The concentration of Au and Ta was determined by averaging the data measured 5 times.

5 Results and discussion

Although 0.28 % of Ta in solution could be oxidized to TaO and Au concentration became apparently higher than real Au concentration in ICP-MS analysis (Nakanishi 1997), in this study Ta concentration in solution was less than the background. Therefore, Ta concentration could not affect Au concentration using ICP-MS. The result of Au contents is shown in Table 1. All the values of relative standard deviation were below 5 %.

The Au contents of JLk-1 and JSl-1 were 4.89 ± 0.08 ppb and 1.04 ± 0.05 ppb, respectively. These results were roughly concordant with 4.59 ppb and 0.93 ppb reported by Terashima et al. (1992). Two samples of JLk-1 were

Table 1: Au contents in sedimentary rocks.

Sample name	Rock type	Au content (ppb)	
JLk-1	lake sediment	4.89	± 0.08
JLk-1(no microwave)	lake sediment	4.20	± 0.10
JSl-1	slate	1.04	± 0.05
SH-1	sandstone	2.97	± 0.10
SH-2	sandstone	1.93	± 0.02
SH-3	sandstone	2.00	± 0.02
KY-1	shale	15.71	± 0.26
KY-2	sandstone	7.06	± 0.30
KY-3	sandstone	3.27	± 0.07
8MAHAK-5 797m	shale	7.91	± 0.16
8MAHAK-5 861m	shale	24.69	± 1.11
8MAHAK-5 922m	sandstone	15.03	± 0.13
8MAHAK-5 950m	sandstone	9.72	± 0.23
8MAHAK-5 988m	sandstone	8.91	± 0.42
12MAHA-1 778m	sandstone	0.67	± 0.02
12MAHA-1 806m	sandstone	3.00	± 0.07
12MAHA-1 846m	sandstone	4.54	± 0.07
12MAHA-1 899m	sandstone	4.69	± 0.06
12MAHA-2 848m	sandstone	2.73	± 0.03
12MAHA-2 879m	sandstone	2.15	± 0.07
12MAHA-2 999m	sandstone	3.05	± 0.07

prepared to compare with the influence of decomposition of organic matter by microwave oven. One sample was heated by microwave oven and the other one was not heated. The Au concentration of the former was 4.89 ± 0.08 ppb and that of the latter was 4.20 ± 0.10 ppb. This result indicates the importance of decomposing organic matter to determine Au content because Au can be contained in organic matter. Terashima et al. (1995) suggests that Au in terrigenous sediments is present mostly in elemental form and that some of Au in pelagic sediments is present in organometallic complexes.

The Au contents of the Lower Shimanto Group in Kyushu were 7.06 ± 0.30 ppb and 3.27 ± 0.07 ppb in sandstone, and 15.71 ± 0.26 ppb in shale. The Au contents of the Lower Shimanto Group in Shikoku were 2.97 ± 0.10 ppb and 1.93 ± 0.02 ppb in sandstone. According to Terashima et al. (1992), the Au contents in sedimentary rocks and sediments of GSJ geochemical reference samples that are not related to mineralization range from 0.07 to 4.59 ppb. These results imply that the potentiality of the relatively high Au content in sedimentary rocks of the Shimanto Supergroup. And the result shows that the shale sample contains apparently a large quantity of Au in comparison with the sandstone samples.

Since the number of analyses in this study might not be enough to determine the Au content in sedimentary rocks of the Shimanto Supergroup, more samples should be analyzed. It is considered that the heterogeneous distribution of Au particles may influence Au content because Au is present in the order of ppb or sup-ppb. Therefore, the analysis of Au content including the process of leaching should be conducted at least two times for the same sample.

The drilling of 8MAHAK-5 was close to the Hishikari deposit and the Au content of the drill core samples at 797 m, 861 m, 922 m, 950 m and 988 m deep were 7.91 ± 0.16 ppb, 24.7 ± 1.1 ppb, 15.03 ± 0.13 ppb, 9.72 ± 0.23 ppb and 8.91 ± 0.42 ppb, respectively. The Au content in these samples was apparently higher than that in the samples taken at the surface. Homogenization temperatures of fluid inclusions in quartz vein indicate 184 to 245 °C at 845 m deep and 169 to 247 °C at 969 m deep (MITI 1997). It is considered that the elevated Au contents are due to mineralization in the Hishikari deposit.

The drilling of 12MAHA-1 and 12MAHA-2 were relatively far from the Hishikari deposit and the Au contents of the drill core samples of 12MAHA-1 at 778 m, 806 m, 846 m and 899 m were 0.67 ± 0.02 ppb, 3.00 ± 0.07 ppb, 4.54 ± 0.07 ppb and 4.69 ± 0.06 ppb, respectively. The Au contents of the drill core samples of 12MAHA-2 at 848 m, 879 m, 999 m deep were 2.73 ± 0.03 ppb, 2.15 ± 0.07 ppb and 3.05 ± 0.07 ppb, respectively. These samples showed slightly higher Au contents than the samples taken from the surface. Homogenization temperatures of fluid inclusions in quartz veins indicate 221 to 281 °C in 12MAHA-1 and 202 to 269 °C in 12MAHA-2 (MITI 2001). The sampling location was located in north of the Hishikari deposit and west of the Masaki hydrothermal alteration zone. The slightly high Au contents are considered to result from the mineralization from both or either of the Hishikari deposit and Masaki alteration zone.

The drill core samples of 8MAHAK-5 were collected at –250 to –400 m sea level approximately. And the drill core samples of 12MAHA-1 and 12MAHA-2 were collected at 0 to –300 m sea level approximately. The level of the drill core samples was much deeper than the level of the working face at present (about –20 m sea level). The hydrothermal fluid associated with the mineralization of the Hishikari deposit was present at least –400 m sea level. Calcite veins from the Hishikari deposit showed that $\delta^{13}C$ value ranged from –10.8 to –4.7 ‰ (Morishita 1993, Imai and Uto 2002). Morishita (1993) suggests that relatively low $\delta^{13}C$ value in calcite compared with average crustal $\delta^{13}C$ value resulted from organic carbon in the basement rock of the Shimanto Supergroup. Because of the relatively high Au content ranging from 1.9 to 15.7 ppb in the Lower Shimanto Group, Au might be transported from the basement rock by hydrothermal fluid. However, organic matter expected to contain Au was commonly observed in sandstone and shale samples using microscope in the drill core samples taken below the deposit. It was not confirmed the evidence of Au transportation from the sedimentary rocks.

Acknowledgements

We acknowledge Sumitomo Metal Mining Co. Ltd. for permission to collect drill core samples in the Hishikari mine.

References

Gatellier JP, Disnar JR (1989) Organic matter and gold-ore association in a hydrothermal deposit, France. Applied Geochemistry 4: 143-149

Imai A, Uto T (2002) Association of electrum and calcite and its significance to the genesis of the Hishikari gold deposits, southern Kyushu, Japan. Resource Geology 52: 381-394

Izawa E, Urashima Y, Ibaraki K, Suzuki R., Yokoyama T, Kawasaki K, Koga A, Taguchi S (1990) The Hishikari gold deposit: high-grade epithermal veins in Quaternary volcanics of southern Kyushu, Japan. Journal of Geochemical Exploration 36: 1-56

Kettler RM, Waldo GS, Penner-Hahn JE, Meyers PA, Kesler SE (1990) Sulfidation of organic matter associated with gold mineralization, Pueblo Viejo, Dominican Republic. Applied Geochemistry 5: 237-248

MITI (Ministry of International Trade and Industry) (1997) Research report on precision geological structure, 1996 fiscal year. (in Japanese).

MITI (Ministry of International Trade and Industry) (2001) Research report on precision geological structure, 2000 fiscal year. (in Japanese).

Morishita Y (1993) Carbon and oxygen isotopic characteristics of epithermal veins in the Hokusatsu gold district, southern Kyushu, Japan. Resource Geology Special Issue 14: 103-114

Nakanishi T, Yokoyama T, Izawa E (1997) Determination of trace gold in rock samples by ICP-MS. Report of the Center of Advanced Instrumental Analysis, Kyushu University 15: 36-41, (in Japanese with English abstract)

Teraoka Y, Okumura K (1992) Tectonic division and Cretaceous sandstone compositions of the Northern Belt of the Shimanto Terrane, Southwest Japan. Memoirs of the Geological Society of Japan 38: 261-270 (in Japanese)

Teraoka Y, Okumura K, Suzuki M, Kawakami K (1999) Clastic sediments of the Shimanto Supergroup in Southwest Japan. Bulletin of Geological Survey of Japan 50: 559-590 (in Japanese with English abstract)

Terashima S, Itoh S, Ando A (1992) 1991 compilation of analytical data for silver, gold, palladium and platinum in twenty-six GSJ geochemical reference samples. Bulletin of the Geological Survey of Japan 43: 141-15

Terashima S, Nakao S, Mita N, Inouchi Y, Nishimura A (1995) Geochemical behavior of Au in terrigenous and pelagic marine sediments. Applied Geochemistry 51: 35-44

A case study of structure-controlled mineralization – the Huangtuliang gold deposit, northwestern Hebei, China

A.Q. Sun, J.Z. Zhang, S.Y. Niu, H.B. Hu, F.J. Fu
College of Resources, Shijiazhuang University of Economics, Hebei 050031, China

Y.C. Han
Third Geological Survey Team of Hebei, Zhangjiakou, Hebei 075000, China

F. Li
Huangtuliang Gold Mine, Chicheng, Hebei 075500, China

Abstract. The Huangtuliang gold deposit, with 10.7 tons of gold reserves at shallow levels (<150 m in depth), is situated in the Zhaojiagou-Erbaozi secondary brittle-ductile shear zone along the northern margin of the North China craton. The dominant structure in the Huangtuliang gold deposit is a steeply north-dipping, brittle-ductile shear zone south of the ore zone. Helium and argon, sulfur and oxygen isotope studies suggest that mantle fluids were involved in the mineralization. Detailed studies of ore field structures and engineering data suggest that the Huangtuliang gold deposit has potential for a major to world-class gold resource.

Keywords. Huangtuliang gold deposit, structure-controlling, isotope, prospecting, North China craton

1 Introduction

The Huangtuliang gold deposit was discovered in the 1990s. It, together with the Dongping and Xiaoyingpan gold deposits, forms a well-known metallogenic belt in the North China craton. Previous studies focused on the Dongping and Xiaoyingpan gold deposits (Song 1991; Cheng 1995; Fan 2001), with the Huangtuliang gold deposit less studied. The Huangtuliang gold deposit is characterized by its broad veins, dense distribution of ore bodies, and continuous extension along strike. Geological surveys at shallow levels (< 150 m in depth) alone suggest that the resource is of an average size (10.7 tons of contained Au). In this study we report results of investigations of its geological characteristics, ore-controlling structure, and geochemistry, and a breakthrough made in gold prospecting at its deep levels and peripheries according to the available data.

2 Geological setting

The Huangtuliang gold deposit is located in Chongli County, northwestern Hebei Province, and situated tectonically at the south side of the Shangyi-Chongli-Chicheng deep fault. The strata exposed in the area are mainly the Huajiaying and Jiangouhe formations of the Archean Sanggan Group, Proterozoic Changcheng and Jixian groups, and Jurassic volcanic-sedimentary rocks. The Archean Sanggan Group has a whole-rock Rb-Sr isochron age of 2790±155 Ma and a zircon U-Pb age of 2715±21 Ma (Nie 1998) and consists of a suite of amphibolite facies to granulite facies metamorphic rocks, including garnet-biotitic-plagioclase gneiss, eclogitic plagioclase gneiss, two-pyroxene-plagioclase granulite, migmatite, and itabirite. The Proterozoic Changcheng Group is a sequence of clastic rocks, with a zircon U-Pb age of 1776 Ma (Cheng 2000).

The Shangyi-Chongli-Chicheng deep fault, as a regional EW – trending structure, separates the Inner Mongolian axis from the Yanliao depression. The Huangtuliang gold deposit occurs in the Zhaojiagou-Erbaozi secondary brittle-ductile shear zone on the south side of the Chongli-Chicheng brittle-ductile shear zone (Fig. 1).

In the area magmatic rocks are well developed, including Proterozoic ultrabasic rocks and the Mesozoic Indosinian Huangtuliang alkaline complex and Yanshanian granite stock, of which the Huangtuliang complex is closely related to the gold deposit. Rectangular in shape, the Huangtuliang complex has an outcrop area of ~2 km^2 and consists predominantly of syenite. The rock has a medium- to coarse-grained texture and a massive structure. The principal minerals are microcline and perthite (70–80%), albite (10–15%), and quartz (1–5%), and the accessory minerals are magnetite and apatite (1%).

3 Geology of gold deposits

Ore bodies generally strike nearly E-W (85°) and dip steeply toward the north, being ~1000 m long from east to west and 60–150 m wide from north to south. The ore veins extend nearly parallel and the spacing between the veins is close at the east and west ends, generally 3–10 m, and wide in the middle part, generally 5–16 m. Most ore bodies occur as veins, large veins, and lenses. In plan and section, they are irregular in outline and show the features of branching and merging, pinching-out and reappearance, and even flame-shaped pinching and swelling. Drilling and 40 m-spaced trenching have revealed that the gold reserves at shallow levels of this deposit are 10.7

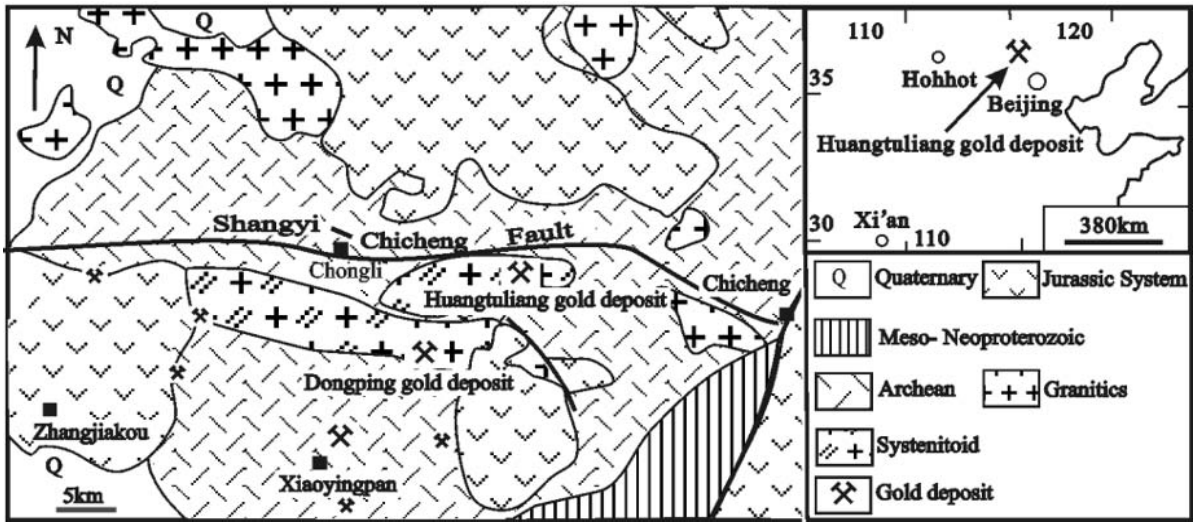

Figure 1: Geological sketch map of the Huangtuliang gold deposits

tons, with a gold grade ranging from 3 to 6 g/t and averaging 4.83 g/t. Wall-rock alteration types include potassic alteration, silicification, pyritization, chloritization, carbonization, and kaolinitization. The first three alteration types are widespread in the deposit and intimately associated with gold mineralization.

Native gold, the only ore mineral of gold, is golden-yellow, granular or flaky in shape, ranging in size from 0.001 to 0.06 mm, with a mean of 0.017 mm and a maximum of 0.078 mm. Scanning electron microscopy (SEM) analysis shows that it contains 89.18% Au, 8.5% Ag, and 2.32% Fe.

The metallic minerals contribute ~3% of the ore components. They are dominated by pyrite with minor galena, chalcopyrite, and sphalerite. Gangue minerals include K-feldspar, plagioclase, quartz, and sericite. Pyrite, an important gold carrier, mostly occurs as subhedral granular or granular aggregates disseminated in gangue minerals and are of nonuniform distribution. Its grain size is commonly <0.5 mm and may reach a maximum of 2.0 mm.

Chalcopyrite occurs as grains or veinlets set at margins or in fissures of pyrite, and sometimes occurs as disseminations in ores. The mineral is 0.005 to 0.3 mm in size. SEM analysis shows that it contains 34.44% Cu, 30.05% Fe, and 35.51% S.

4 Discussion of metallogenetic structures

The Huangtuliang gold deposit is characterized by its broad veins and dense distribution and continuous extension of the veins along strike. However, deep drilling of three holes(ZK8-1, ZK8-2, and ZK8-4)have revealed that gold mineralization at deep levels is not ideal. Hole ZK8-1 shows no sign of mineralization, while holes ZK8-2 and ZK8-4 have not encountered mineralization either though they have penetrated the known ore veins. Therefore, whether ore veins exist at deep levels of the Huangtuliang gold deposit is uncertain.

During detailed field surveys, we found a 3–6 m wide mylonite belt on the southern side of the ore zone, which generally strikes nearly E-W and dips steeply north at 70°–80°. In the belt quartz grains are markedly stretched with the ratio of the XZ axis = 6–20 and even stretched to form a ribbon structure. It is a brittle-ductile shear zone with very distinct structural features, generally dipping 80°–90° at 70°–80°. According to the distribution of the mylonite belt and ore bodies at shallow levels, we think that the dominant ore-controlling factor for the Huangtuliang gold deposit is the steeply north-dipping brittle-ductile shear zone, and that the ore-forming fluids migrated and gathered to form ore bodies in a number of secondary faults in the hanging wall of the shear zone. Because hole ZK8-4 was drilled in the footwall of the shear zone, we made a futile effort. As to holes ZK8-1 and ZK8-2, after penetrating the mylonite belt at 1038–1100 m depth, they also intersected the footwall of the brittle-ductile shear zone, so they did not find mineralization either (Fig. 2).

The features of branching and merging and pinching and swelling along the dip of the ore bodies were produced by normal faulting. Ore veins become wide in the steep-dipping segment of the fault and become narrow in its gentle-dipping segment, thus giving rise to the podiform features in space (Fig.2).

Based on an analysis of ore-controlling structures, it is inferred that similar secondary faults should also exist at deep levels along the dip of the shear zone, i.e. ore bodies similar to those at shallow levels should also exist at deep levels along the dip of the shear zone. The mineralization found in the upper part of hole ZK-2 ought to be the top haloes of the ore bodies at depths.

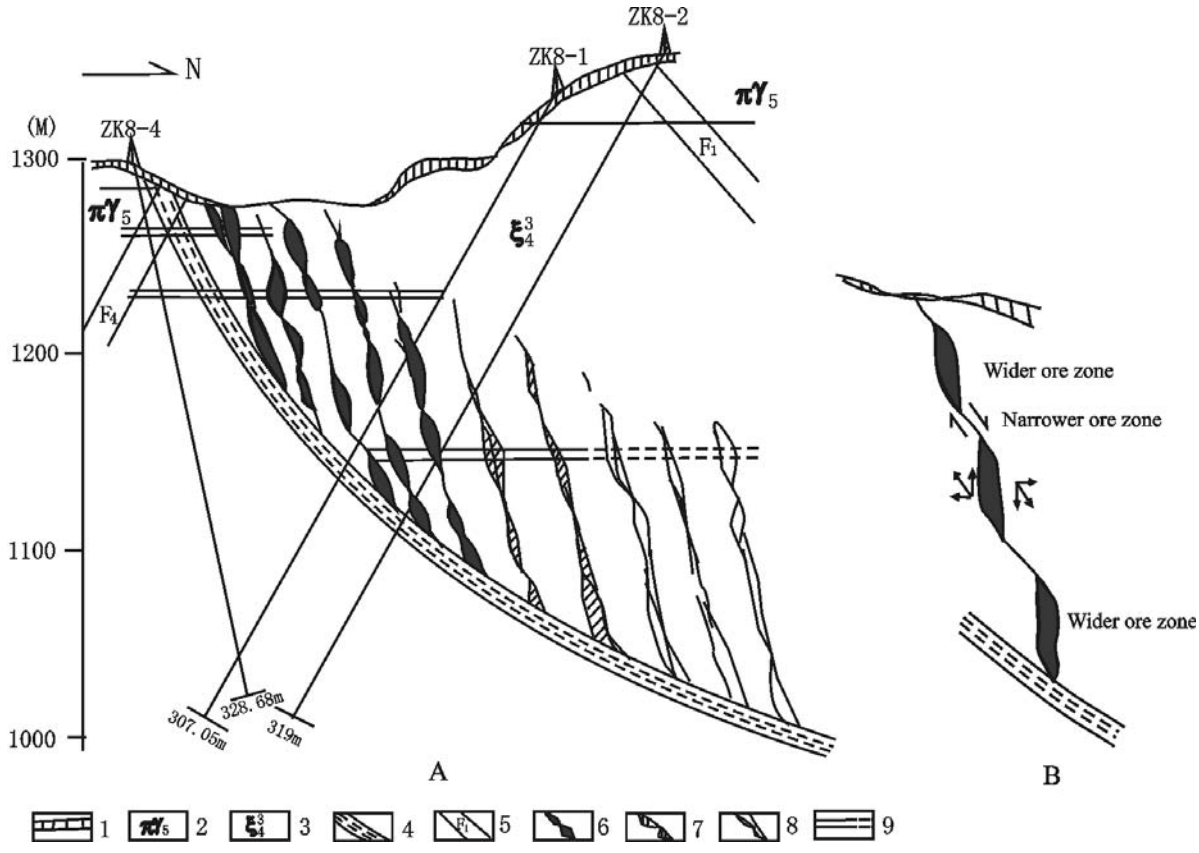

Figure 2: Metallogenetic Prediction of Huangtuliang Gold Deposit A: Characteristics of Prospected and Predicted Ore Bodies; B: Dynamic Analysis of Metallogenesis1-Quaternary; 2-Yanshanian monzonitic granite; 3- Hercynian sienite; 4- brittle-ductile shearing zone; 5-fault; 6-prospected ore bodies; 7-verified ore prediction; 8-predicted ore bodies; 9-finishen and scheduled tunnel

5 Engineering check and verification of ore bodies

Exploration engineering was carried out in order to check and verify whether there exist hidden ore veins at depths along the north dip of the brittle-ductile shear zone in the Huangtuliang gold deposit. According to the characteristics of the ore-controlling structure, a transverse drift was directly driven from the mined level at depths northward to prospect for ores. Just as we expected, several predicted ore bodies were discovered. The first blind ore vein is 18 m wide. In 2003, based on the aforesaid breakthrough and according to the characteristics of deep ore bodies, five drill holes arranged at three exploratory profiles all encountered ores with good mineralization. This further verifies that several ore bodies do exist at deep levels of the hanging wall of the shear zone. They occur en echelon and extend northward.

In 2004, additional three wide-spaced exploratory profiles made by the Third Geological Survey Party of Hebei Province confirmed that the ore bodies of the Huangtuliang gold deposit extend generally persistently eastward along strike, and that good gold mineralization is present farther along line 88. Therefore, the Huangtuliang gold deposit has potential for a major to world-class resource.

6 Source of ore-forming fluids - a discussion

6.1 The contents of gold in host rocks

The content of gold in the host strata – Archean Jiangouhe Formation and Huajiaying Formation – of the Huangtuliang gold deposit is high, ranging from 7.0 to 9.3 ppb, and the content of gold in the host magmatic rock - syenite and porphyritic granite - is also high, ranging from 7.6 to 12.48 ppb, suggesting a relation between gold mineralization and host rocks.

6.2 Helium and argon isotopes

Helium and argon isotope analyses were performed on pyrite from the Huangtuliang, Dongping, Xiayingpan and Hougou gold deposits, Niuquan silver-gold deposit, and Zhaojiagou silver-lead deposit in the whole northwestern Hebei metallogenic province. The 3He/4He values of fluid inclusions in pyrite range from 0.93×10-6 to 4.05×10-6,40Ar/36Ar values range from 397 to 2073, and the R/Ra values range from 0.66 to 2.91, which are very close to the data (R/Ra =0.3–5.2) of quartz from the Dongping gold deposit (Mao and Li 2001; Mao et al. 2003). The helium and argon isotopic composi-

tions reflect to some extent that mantle fluids were involved in gold mineralization.

6.3 Sulphur isotopic composition

The $\delta^{34}S$ values of 12 pyrite samples are all negative, ranging from –1.6 to –7.4‰ with a mean of –4.99 ‰. The total $\delta^{34}S$ value of the hydrothermal fluids in the Dongping gold deposit is 1.85‰ (Wang et al. 2003), indicating the feature of deep-source sulfur.

6.4 Oxygen isotopic composition

$^{\delta 18}O_{SMOW}$ values of quartz range from 11.1 to 10.3‰ with a mean of 10.7‰. According to the quartz-water fractionation equation (Clayton, 1972) and the average homogenization temperature of fluids inclusions in quartz, the $\delta^{18}O$ values of the mineralizing fluids were calculated to be 1.48 – 1.81‰, reflecting that the ore-forming fluids were mixed with meteoric water during mineralization.

Acknowledgements

This study was supported by the State Development and Planning Programs for Basic Researches in Key Areas of China (No. 1999043211) and the National Natural Science Foundation of China (No. 40272088).

References

Chen J (1995) Geological characters and genesis of Dongping gold deposit in Hebei Province, in Typical Gold Deposits in China, Beijing: Geological Publishing House, 84-92 (in Chinese).

Cheng Y (1994) Regional geology of China: Beijing, Geological Publishing House, pp. 575 (in Chinese).

Clayton RN (1972) Oxygen isotope exchange between quartz and water, J. Geophys. Res. 77: 3057-3607.

Fan H, Xie Y, Zhai M (2001) Ore-forming fluids in the Dongping gold deposit, northwestern Hebei Province, Science in China (Series D) 44: 748-757.

Mao J., Li Y. (2001). Fluid Inclusions of the Dongping gold Telluride Deposit in Hebei Province, China: Involvement of Mantle Fluid in Metallogenesis. Mineral Deposit, Vol. 20, No.1, pp.23-36 (in Chinese with English abstract).

Mao JW, Li YQ, Goldfarb R, He Y, Zaw K (2003) Fluid inclusion and nobale gas studies of the Dongping Gold deposit, Hebei province,China: a mantle connection for mineralization? Econ. Geol. 98: 517-534.

Nie F (1998) Geology and origin of the Dongping alkalic- type gold deposit, northern Hebei province, People's Republic of China, Resource Geology 48: 139-158.

Song G (1991) A gold deposit associated with alkali-complex: Dongping deposit in north Hebei, Geology & Prospecting, Vol.27, No.8, pp.1-8 (in Chinese with English abstract).

Wang B, Niu S., Sun A (2003) Source of ore-forming material of Mesozoic Au-Ag polometallic deposits in North Hebei province and restriction of deep process, Acta Geologica Sinica 77: 379-386 (in Chinese).

Gold systems in northeastern Queensland: A key to tectonic evolution of the northern Tasman Fold Belt System, Australia

I.M.A. Vos
*ACRC / pmd*CRC, School of Geosciences, Monash University, PO Box 28e,VIC 3800, Australia*

F.P. Bierlein
*TSRC / pmd*CRC, School of Earth and Geographical Sciences, University of Western Australia, 35 Stirling Hwy, Crawley, WA 6009, Australia*

Abstract. The nature and style of ore deposits can provide important constraints on the overall tectonic framework of orogenic systems. Characteristics of epigenetic gold-antimony systems in the northern part of the Tasman Fold Belt System in Australia are investigated. We report on sulphide paragenesis, structural relationships and fluid inclusion studies of gold-antimony deposits in the Hodgkinson and Broken River provinces. Strong similarities between the deposits in both provinces allows for inter-regional correlation, which provides important insights into the tectonic evolution of the northern portion of the Tasman Fold Belt System. The 'orogenic' style of gold mineralisation and relative timing of gold deposition in both provinces imply that gold mineralisation occurred during several episodes of deformation in a subduction-accretion system along the Pacific margin of Palaeozoic Australia.

Keywords. Epigenetic gold, tectonic evolution, Hodgkinson, Broken River, Tasman Fold Belt

1 Introduction

The characteristics, spatial distribution and timing of emplacement of base and precious metal deposits can be directly related to the tectonic setting in which they originated (e.g. Kerrich et al. 2000; Bierlein et al. 2002). In this study, we address these criteria by investigating epigenetic gold deposits in the northern part of the Tasman Fold Belt System, Australia that encompasses the Hodgkinson and Broken River provinces (Fig. 1).

The Tasman Fold Belt System in eastern Australia forms a composite of fold belts that have developed from accretion of oceanic sequences, volcanic arcs and micro-continental blocks. The development of these fold belts was controlled by subduction-related processes outboard of the Australian craton throughout the Palaeozoic (e.g. Veevers 2000). The tectonic framework in which the various fold belts of the Tasman Fold Belt System formed remains a contentious issue.Here, we compare the results of paragenetic, structural and fluid inclusion studies of gold deposits in the Hodgkinson and Broken River provinces and utilise our findings to place these deposits in a tectonic framework. This study is the first attempt to employ the characteristics of epigenetic gold systems in northeastern Australia as a tool for inter-regional correlation. Our study provides important constraints on the tectonic evolution of the northern portion of the Tasman Fold Belt System.

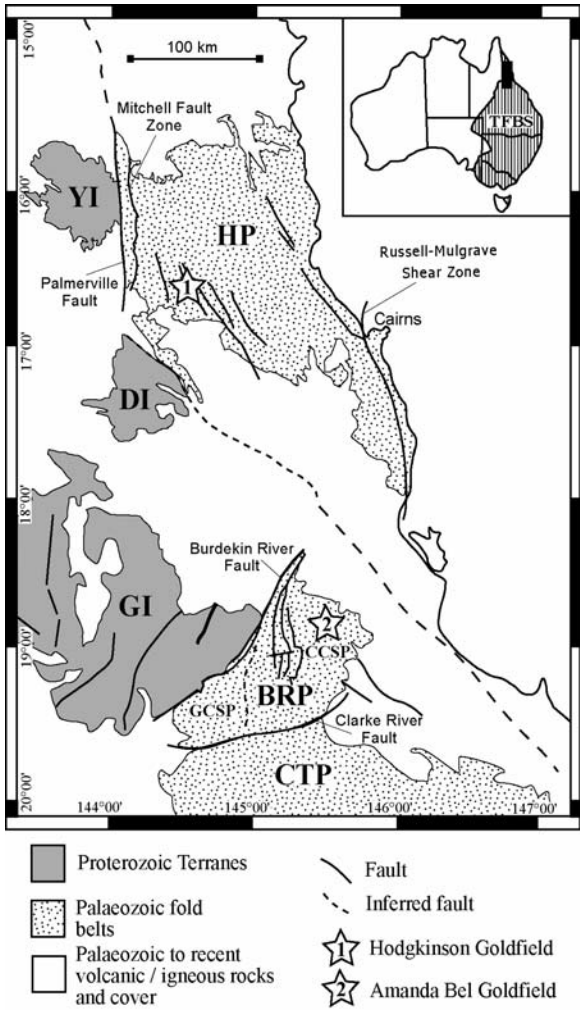

Figure 1: Location of Palaeozoic fold belts forming the northern section of the Tasman Fold Belt System (black region in inset). Location of studied goldfields indicated by stars. YI = Yambo Inlier; DI = Dargalong Inlier; GI = Georgetown Inlier; HP = Hodgkinson Province; BRP = Broken River Province; CTP = Charters Towers Province. GCSP / CCSP = Graveyard / Camel Creek Subprovince

2 Gold systems in the Hodgkinson Province

2.1 Geological setting

The Hodgkinson Province consists mainly of shallow to deep marine siliciclastic sequences that were deposited on the margin of the Precambrian craton during the Ordovician to Devonian (Bultitude et al. 1997). Metallogeny of the Hodgkinson Province is diverse and includes gold, antimony, copper, lead, silver, zinc, tungsten and tin deposits. Most of these deposits are associated with Carboniferous and Permian granites and related sedimentary rocks.

2.2 Hodgkinson Goldfield

The Hodgkinson Goldfield is located in the central southern portion of the Hodgkinson Province and hosts a number of mining districts. We have investigated selected gold-antimony deposits in the Northcote and Tregoora Districts of the Hodgkinson Goldfield. These occur along distinctive northwestern trends and are associated with major fault structures (Figure 2). At least two phases of gold mineralisation can be distinguished in the gold-antimony deposits of the Northcote and Tregoora Districts. Antimony is introduced after, or during the later stage of the second gold mineralisation episode.

Microthermometric data support results from previous studies in the adjacent districts in the Hodgkinson Goldfield (e.g. Peters et al. 1990). These report homogenisation temperatures between 170 and 305°C and fluid salinities ranging between 3 and 11 weight percent NaCl equivalent. The occurrence of gold-bearing quartz veins in shear zones and faults indicates a close relationship between mineralisation and deformation. Based on sulphide paragenesis, structural relationships and fluid inclusions studies, the mineralisation style for gold deposits of the Northcote and Tregoora Districts can be classified as 'orogenic' (cf. Groves et al. 1998). Furthermore, our results indicate that the gold-antimony deposits have developed during two deformation phases in the Late Devonian to Carboniferous.

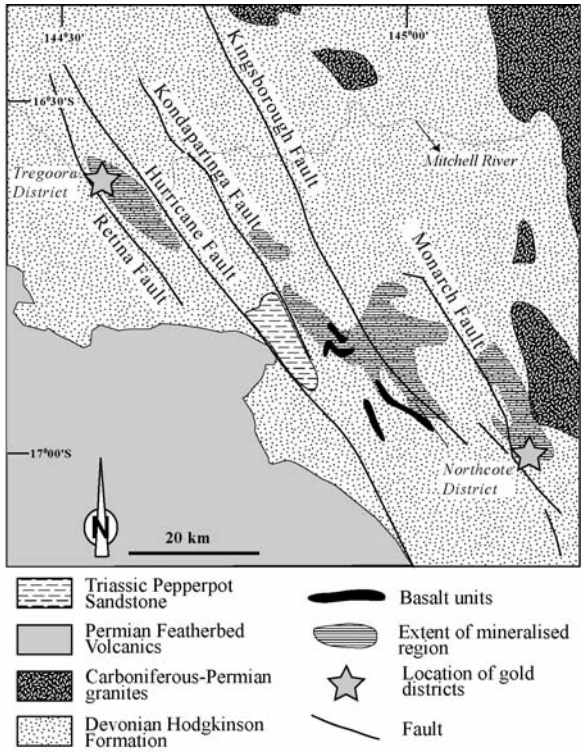

Figure 2: Detailed geology of the Hodgkinson Goldfield indicating the extent of mineralised regions and the location of the studied gold-antimony districts within the goldfield. Note the close relationship with major fault.

3 Gold systems in the Broken River Province

3.1 Geological setting

The Broken River Province is dominated by an open to tightly folded sequence of sedimentary and volcanic rocks of Late Ordovician to Early Carboniferous age that are structurally juxtaposed in the northwest against the Precambrian Georgetown Inlier. The Broken River Province hosts a variety of deposits, including gold, antimony, uranium, nickel, tin and minor copper and tungsten deposits. Most of these deposits are associated with Carboniferous and Permian granites, apart from the gold-antimony deposits that are structurally controlled and generally predate felsic igneous activity.

3.2 Amanda Bel Goldfield

The Amanda Bel Goldfield is located in the northeastern part of the Camel Creek Subprovince (Fig. 1). We have investigated a number of gold-antimony-arsenic and gold-arsenic deposits in the Amanda Bel Goldfield, which occur along distinctive northeastern trends (Fig. 3). Three phases of mineralisation can be distinguished in the gold-antimony deposits of the Amanda Bel Goldfield. The first two phases are associated with gold deposition, where the third phase represents mainly antimony mineralisation. Microthermometric data from fluid inclusion studies indicate homogenisation temperatures between 140 and 300°C and fluid salinities up to 6.5 weight percent NaCl equivalent. Field observations indicate a close relationship between mineralisation and deformation.

Based on sulphide paragenesis, structural relationships and fluid inclusions studies, the style of gold mineralisation in the Amanda Bel Goldfield can also be classified as 'orogenic' (cf. Groves et al. 1998). As with the Hodgkinson Province, the formation of major gold-antimony deposits can be constrained to two deformation phases in the Late Devonian to Carboniferous.

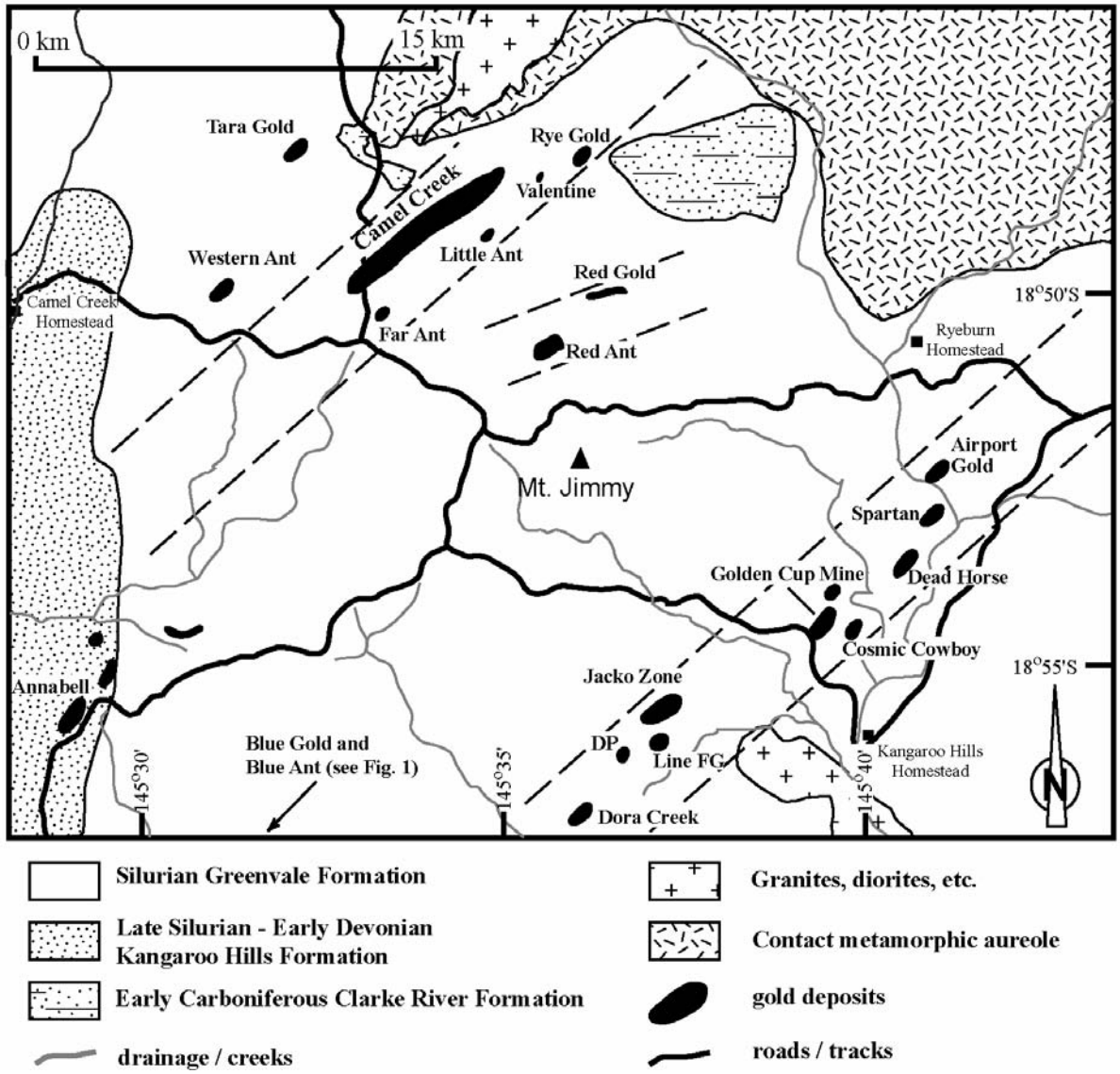

Figure 3: Detailed geology of the Amanda Bel Goldfield and the location of gold-antimony deposits. Dashed lines indicate the distinct northeastern trend along which gold-antimony deposits occur, probably related to structures in the subsurface.

4 Tectonic evolution of the northern Tasman Fold Belt System

Overall strong similarities exist between the Hodgkinson and Amanda Bel goldfields that include nature and style of mineralisation and relative timing of mineralisation episodes. Based on our findings, we suggest that both goldfields may have formed during periods of overall contraction as part of a continuous fold belt inboard of a subduction system in the Late Devonian and Carboniferous. Radiometric ages for a number of gold deposits from both goldfields further constrain the approximate timing of deformation and mineralisation events in the northern part of the Tasman Fold Belt System.

The tectonic environment and setting for rocks in the northern portion of the Tasman Fold Belt System are uncertain. Previous interpretations include fore-arc / accretionary prism and back-arc settings (e.g. Bultitude et al. 1997). The close relationship between deformation and mineralisation and the occurrence of gold deposits along a distinct trends in the Hodgkinson and Amanda Bel goldfields, suggests a strong structural control for their formation. The described style of gold mineralisation in these goldfields is characteristic of 'orogenic' gold deposits, which are almost invariably associated with collisional tectonics and continental growth in the vicinity of major structures (cf. Groves et al. 1998). Changes in the stress field that affect movement along these major faults are often considered

This page intentionally blank

important key factors that control gold mineralisation (cf. Bierlein and Crowe 2000). As such, the timing of formation of the gold deposits in the Hodgkinson and Broken River provinces can provide important constraints on the tectonic evolution of the orogenic system.

Acknowledgements

The study reported herein was conducted as part of a PhD project funded by the predictive mineral discovery Cooperative Research Centre (pmd*CRC). The presenting author wishes to acknowledge the financial support of the pmd*CRC. We thank G. Teale (Teale & Associates Pty Ltd) and C. Roberts (Republic Gold Pty Ltd) for their support during the various facets of this study.

References

Bierlein FP, Crowe DE (2000) Phanerozoic orogenic lode gold deposits. Rev. Econ Geol, 13: 103-139

Bierlein FP, Gray, DR, Foster DA (2002) Metallogenic relationships to tectonic evolution; the Lachlan Orogen, Australia. Earth Planet Sci Lett 202: 1-13

Bultitude RJ, Garrad PD, Donchak PJT, Domagala J, Champion DC, Rees ID, Mackenzie DE, Wellman P, Knutson J, Fanning CM, Fordham BG, Grimes KG, Oversby BS, Rienks IP, Stephenson PJ, Chappell BW, Pain CF, Wilford JR, Rigby JF, Woodbury MJ (1997) Cairns region. In: Bain JHC, Draper JJ (eds) North Queensland geology, AGSO Bulletin 240: 225-325

Groves DI, Goldfarb RJ, Gebre-Mariam M, Hagemann SG, Robert F (1998) Orogenic gold deposits; a proposed classification in the context of their crustal distribution and relationship to other gold deposit types: Ore Geol Rev 13: 7-27

Kerrich R, Goldfarb R, Groves D, Garwin S (2000) The geodynamics of world-class gold deposits; characteristics, space-time distribution, and origins. Rev Econ Geol 13: 501-551.

Peters SG, Golding SD, Dowling K (1990) Melange- and sediment-hosted gold-bearing quartz veins, Hodgkinson Gold Field, Queensland, Australia. Econ Geol 85: 312-327

Veevers JJ (ed) (2000) Billion-year earth history of Australia and neighbours in Gondwanaland. Gemoc Press, North Ryde, NSW, 388 p

Session 6

Submarine ore systems and ancient analogues: Global comparisons of VMS (IGCP 502)

Polymetallic VMS deposits of the Andes Fueguinos (southernmost Argentina): Preliminary report

R.D. Acevedo
CADIC -CONICET. Av Malvinas Argentinas, Ushuaia, Tierra del Fuego 9410, Argentina

I. Fanlo, I. Subías, A. Paniagua
Cristalografía y Mineralogía. Universidad de Zaragoza. Pedro Cerbuna, 12. 50009 Zaragoza, Spain

D.E. Buffone
Empresa Minera Marifil, S.A. Caronti 348, 2D, Bahía Blanca 8000, Argentina

Abstract. The polymetallic volcanic-hosted massive sulphide deposits of the Andes Fueguios occur in a highly deformed but coherent stratigraphic succession of Late Jurassic metavolcanic and metasedimentary rocks. Local stratigraphy consists of porphyries along with rhyolitic lava, acidic tuff, breccias, conglomerates, radiolarian lutites and basaltic rocks. Mineralization occurs as massive stratiform, massive replacement and sulphide stringer veins. Sulphides are typically massive, fine-grained, layered and locally brecciated andconsists of pyrite and sphalerite, with lesser pyrrhotite, chalcopyrite, galena, tetrahedrite-freibergite, bournonite, cobaltite and arsenopyrite. Styles of hydrothermal alteration identified in the host rocks include proximal silicification and more distal chloritization, sericitization and, in places, carbonatization. Future research will be focused on identifying the salient physico-chemical controls on the mineralization process and their implications for volcanic-hosted massive sulphide exploration in the district.

Keywords. Tierra del Fuego, VHMS, mineralogy, bimodal volcanism, back-arc, Jurassic

1 Exploration history

The ore deposit potential of the Andes Fueguinos was virtually unknown until the 1970s and early 1980s, when exploration was initiated by several companies (Aguilar-St. Joe 1970-72, 1980-82; Noranda 1994-96; Yamana-Polimet 1995-96; Westmin 1996-97). These efforts have been mostly directed to pursue discovery of volcanic-hosted polymetallic massive sulphide deposits, with two regional targets regions of Sierra Sorondo and Sierra Alvear (Fig. 1). This effort has led to the recognition of several targets which have recently been advanced to the drill stage in three specific prospects: Arroyo Rojo (best intercept: 18.5 metres @ 1%Cu, 1.4% Pb, 3% Zn), Sargent (surface grades of *4.4%* Cu were tested in depth but failed to reach zones due to bad drilling conditions) and Lago Guanaco (surface grades of 3%Cu, 11.3% Pb, 22.6% Zn, 147 g/t Ag – with two holes drilled which failed to find any deep continuity). Further potential exists, and most of targets appear are open in some direction.

In this contribution, we briefly update and expand upon the geological setting, field and mineralogical characteristics. In particular, we focus on the major host lithologies, the types and styles of mineralization present, and the related hydrothermal alteration.

2 Regional geology

The Andes Fueguinos is a portion of the Andes Cordillera lying south of 50ºS lat, forms an arcuate orogenic belt, which extends for some 1000 km parallel to the continental margin. Rocks exposed in this area represent deep-marine volcano-tectonic rift basin environments formed during Gondwana supracontinent fragmentation. In the Isla Grande de Tierra del Fuego, where the study area is located, four different suites can be recognized from south to north (Olivero et al 2001 and references therein): (1) A Cretaceous-Cainozoic plutonic suite interpreted as the roots of the Pacific magmatic arc which is located in the Chilean Archipielago; (2) A complex and heterogeneous terrane Palaeozoic to Late Cretaceous in age, consisting of schists, granitic rocks, volcanics, deep-marine volcanoclastic turbidites and slope mudstones. Late Jurassic ophiolitic rocks and Early Cretaceous volcanic rocks represent the oceanic floor and the volcanic arc of the Marginal Basin, respectively. These materials belong to the so-called *Complejo Deformado* (Quartino et al. 1989; Acevedo 1988). Most of the aforementioned rocks are lower greenschist facies regional metamorphic grade (Olivero and Martinion 2001); (3) A suite of Late Cretaceous to Palaeogene slope and platform black shales, marls, and minor sandstones and limestones belonging to the fold and thrust belt of Austral and Malvinas foreland basins; (4) A suite of deep to shallow foreland molasses (conglomerates, sandstones, shales, limestones) of Late Palaeogene-Neogene age. A dextral strike-slip faulting resulted in the final separation of South America from Antarctica.

The massive sulphides are hosted by the late Jurassic volcano-sedimentary sequence belonging to the Complejo Deformado of suite 2). This complex sequence has a variety of local formational names: Tobifera Formation (Thomas 1949) in Chile and Lemaire Formation (Borrelo 1969) in Argentina. Despite greenschist-grade metamorphism

and a high degree of deformation, it is possible to recognize volcanic, volcaniclastic and sedimentary protoliths.

The Jurassic volcanism in the Andes of the southernmost Argentina and Chile are represented by a vast rhyolitic volcanic field forming a linear belt (Figure 1) of outcrops inboard of the Cretaceous marginal basin terrane. Kranck (1932) first recognized a submarine volcanic complex consisting of porphyries along with rhyolitic lava, acidic tuff, breccias, conglomerates and radiolarian lutites. Basaltic rocks of tholeiitic-calc-alkaline and spilitic affinities (Quartino et al. 1989) are commonly interstratified or intruded within the acidic volcanic and volcanoclastic rocks forming a bimodal assemblage.

3 Styles of mineralization

On the basis on geological and mineralogical criteria, four different styles of mineralization with variation in host rock and deposit style:

I. Volcanic-hosted massive sulphides (Arroyo Rojo, Sargent and Lago Guanaco prospects; see Fig. 1). Mineralization consists of massive sulphide bodies that varies from 0.3 to more than 25 metres thick, which in the case of the Arroyo Rojo prospect, has been traced for over 500 m along strike. In general the massive sulphides occur immediately below a feldspar phyric, locally amygdaloidal, rhyolite unit. Most of the mineralization occurs in tabular, homogeneous massive sulphide lenses composed of pyrite and sphalerite with lesser amounts of galena and chalcopyrite. Tetrahedrite-freibergite is the predominant sulphosalt mineral which is distributed locally together with lesser bournonite. Locally, the massive sulphides are dominated by fine-grained pyrite with bands of reddish brownsphalerite and minor galena. In most places, layers are parallel to the regional foliation and are likely a result of deformation, although some of the layering may be primary sedimentary features. In a few localities, such as in two drill holes of the Arroyo Rojo prospect, there are two sulphide lenses separated by rhyolite. These multiple lenses may represent distinct exhalative horizons (i.e., stacked sulphide lenses), or may be the result of structural repetition due to folding or structural dismemberment.
II. Stratiform sulphide lenses hosted by the sedimentary portion of Lemaire(=Tobifera) Fm. (Mina Beatriz, Rancho Hambre prospect; see Fig. 1). Sulphide minerals are generally fine grained and, millimeter- to centimeter-scale layering, parallel to stratification and/or regional foliation, is common. Layering along with other sedimentary structures like load cast and, locally, slumping (Zubia et al. 1989) as well as the presence of pyrite framboids, strongly support sedimentary deposition. The mineral assemblage is composed of pyrite, sphalerite, galena, arsenopyrite, minor chalcopyrite, pyrrhotite, marcasite, cobaltite and rare tetrahedrite and gold.
III. Pyrite layers and/or lenses interbedded with chert and black shales. They all are fine-grained and have abundant sedimentary structures, that indicate direct precipitation on the sea floor.
IV. Quartz–pyrite-chalcopyrite stockwork hosted by both rhyolites and shales. . All these veins are concordant or crosscut the regional foliation, locally cause brecciation of massive sulphides, yet lack significant alteration envelopes.

4 Sulphide textures

Pyrite is the principal sulphide mineral in all deposits and it typically occurs as coarsely grained porphyroblasts, which are set in a matrix of finer grained pyrite and/or sphalerite. Pyrite shapes vary from euhedral to more foam-like textures. Although such cubic pyrite grains have been noted as a primary feature in active massive sulphide fields such as the TAG field (Brown and McClay 1998), thermal annealing of the massive sulphide ore is inferred from triple point junctions of some of the grains, and is most likely due to regional metamorphism. Pyrite also forms fine-grained, anhedral masses and framboids. Abundant, medium-grained, sphalerite forms delicate, wispy, submillimetre- to centimetre-scale layers. These layers are largely responsible for the bedded appearance of the massive sulphide mineralization. Some sphalerite also occurs as very small grains interstitial to massive pyrite. Chalcopyrite occurs as medium-grained masses on the edges of large patches of pyrite as well as disseminations and irregular blebs hosted by pyrite and sphalerite. Galena, tetrahedrite, and bournonite are all common sulphide minerals in the massive sulphide lenses, although they are difficult to distinguish from one another in hand specimen. They typically occur together as medium- to fine-grained, anhedral aggregates within sphalerite-rich layers. Tetrahedrite also occurs as fine grains interstitial to pyrite, although this is difficult to identify due to the fine-grained nature of the mineralization. Arsenopyrite and cobaltite have been recognized at Mina Beatriz only occurring as subhedral to euhedral grains.

5 Hydrothermal alteration

Hydrothermally altered rocks are found predominantly in the immediate footwall to the massive sulphide mineralization, where permeable felsic volcaniclastic rocks have been preferentially altered. Four main styles of hydrothermal alteration are intimately associated with mineralization at the deposits. The alteration types, in order of decreasing abundance, are (1) sericite, (2) chlorite, and (3) silica (quartz). The main features of each are discussed below.

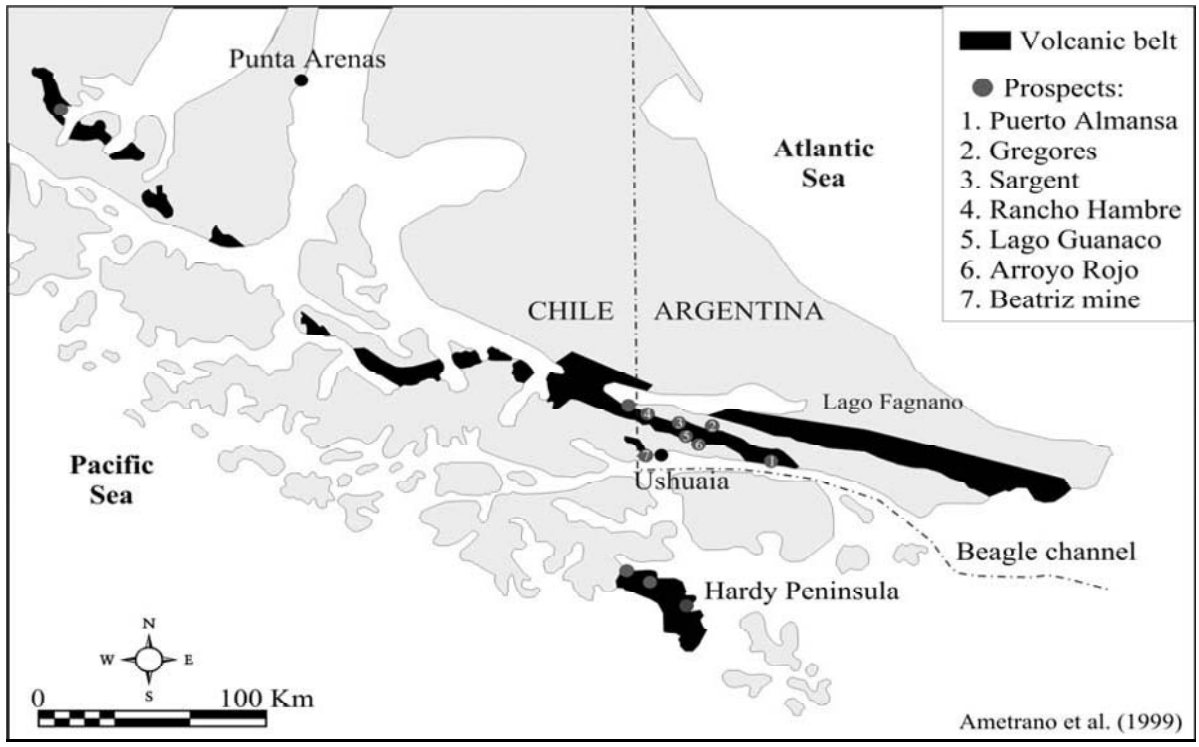

Figure. 1: Location of VHMS deposits and prospects in the rhyolitic belt of the Andes Fueguinos.

1. Sericite alteration is the most extensive and widespread alteration type. Sericite alteration is characterized by moderate to pervasive development of sericite in fine- to coarse-grained felsic volcaniclastic rocks and occurs throughout the deposit, both within, below, and lateral to (or outside of) the zone of chlorite alteration, but occurs most commonly in the footwall to massive sulphide mineralization. Sericite-altered volcaniclastic rocks are intensely foliated. It should be noted that it is difficult, in places, to distinguish hydrothermal sericite alteration from that which formed in the felsic rocks in response to both seafloor alteration (keratophyres and regional metamorphism and deformation, particularly where the former is only weakly developed. Sericite alteration has not been recognized in the massive sulphides hosted by shales, possibly because it is obliterated by regional metamorphism.
2. Chlorite alteration is characterized by the intense development of chlorite in fine- to coarse-grained, felsic volcaniclastic rocks. The result is a dark green chloritized rock with moderately to coarsely flattened felsic volcanic rock fragments with, or without quartz and feldspar crystals. Chlorite alteration is most strongly developed in the immediate footwall to the massive sulphide mineralization. In most drill holes, where chlorite alteration is present, there is a gradual transition from chlorite to sericite zones with increasing distance from the massive sulphide lens.
3. Silica alteration is characterized by the pervasive development of quartz in rocks at the top of massive sulphide mineralization. This alteration-type is minor and may be confined to narrow zones where rhyolite is intensely silicified and contains quartz-pyrite-sphalerite veins ranging up to 3 cm in width. Silica alteration is particularly strong in the hanging wall of the drill hole S-97-8 (Sargent prospect; see location on Fig. 1).

6 Future work

Research on the Andes Fueguinos is only in its preliminary stages. Future research includes continued petrographic studies of the sulphide mineralization, host rocks, and hydrothermal alteration in combination with geochemical characterization of the mineralization and the hydrothermally altered and unaltered host rocks. Since there may be a compositional difference between sericite and chlorite forming the different genetic types of alteration coexisting in the volcanics, these studies will define further the temporal and spatial nature of alteration. Acquisition of such data will permit the quantification of the physico-chemical conditions of ore formation and place constraints on material transfer processes accompanying hydrothermal alteration. The ultimate aim of the project is to produce a genetic model and develop exploration criteria that may be applied to the search for further VHMS deposits in the district.

Acknowledgements

We gratefully acknowledge the Dirección General de Recursos Mineros de la provincia de Tierra del Fuego, which provided access to drill holes. The stay of IF and IS was supported by Research Group of Gobierno de Aragón. This study was supported by the Spanish Ministry of Education and Ciencia (grant CGL2004-05055/BTE).

References

Acevedo RD (1988) Estudios geológicos areales y petroestructurales en el Complejo Deformado de los Andes Fueguinos. Unpubl Ph. D., Universidad de Buenos Aires, 247.

Ametrano S, Etcheverry R, Echeveste H, Godeas M, Zubia M (1999) Depósitos polimetálicos (tipo VMS) en la cordillera fueguina, Tierra del Fuego. In: Zapettini EO Recursos Minerales de la República Argentina, SEGEMAR, Buenos Aires: 1029-1038.

Borrelo AV (1969) Los geosinclinales de la Argentina Dirección Nacional de Geología y Minería Anales 14: 1-118

Brown D, McClay KR (1998) Data report: sulfide textures in the active TAG massive sulfide deposit, 26 N, Mid-Atlantic Ridge. In: Herzig, P.M., Humphris, S.E., Miller, D.J., Zierenberg, R.A. (eds.), Proceedings of the Ocean Drilling Program, Scientific Results:. 193– 200

Kranck EH (1932) Geological investigations in the Cordillera of Tierra del Fuego. Acta Geographica 4: 1-231

Olivero EB, Martinioni DR (2001) A review of the geology of the Argentinian Fuegian Andes. Journal of South American Earth Sciences 14: 175-188

Quartino BJ, Acevedo RD, Scalabrini Ortiz J (1989) Rocas eruptivas volcanogenas entre Monte Olivia y Paso Garibaldi, Isla Grande de Tierra del Fuego. Revista de la Asociación Geológica Argentina 44: 328-335

Thomas CR (1949) Geology and petroleum exploration in Magallanes province, Chile. Bull. Am. Ass. Petrleum Geologists 33: 1553-1578

Zubia M, Godeas, M., Ametrano, S (1989) Area mina Beatriz, Territorio Nacional del Tierra del Fuego, República Argentina: una manifestación de metales de base estratoligada y singenética. In: Brodtkorb M and Schalamuk, I (eds.) Simposios sobre el Cretácico de América Latina IGCP 242 C15-C44

Mineralogical and geochemical hydrothermal evidences on sediments from the serpentinite-hosted Saldanha hydrothermal field

Ágata S.C.M.A. Dias[1], Fernando J.A.S. Barriga[1,2]
[1]*CREMINER, Faculdade de Ciências, Universidade de Lisboa, Portugal*

[2]*Dep. Geologia, Faculdade de Ciências, Universidade de Lisboa, Portugal*

Abstract. Mineralogical and geochemical data of hydrothermal sediments collected from the Saldanha site are presented. The Saldanha hydrothermal field is located at the top of a serpentinized massif Mount Saldanha (MS), at a non-transform offset (NTO5) along the Mid-Atlantic Ridge (MAR), south of the Azores. It is one of the rare known sites where direct evidence of low-temperature hydrothermal activity has been provided by direct observation of hydrothermal fluid venting through small orifices in the ocean floor sedimentary cover. This study reveals that these hydrothermal sediments are highly "diluted" within dominant foraminiferal nanofossiliferous ooze and that the mineral assemblage of the hydrothermal component is characterized by sulphides, poorly crystallized Mn oxihydroxides, Mn brucite and hydrothermal clays. Sediments with a stronger hydrothermal component are located at the top of the mount, where hydrothermal activity was observed. Here the sediments are enriched in Cu, Zn and Fe sulphides, Mn-Mg oxy-hydroxides and putative manganobrucite. Total geochemical analyses show that all sediments are enriched in elements such as Mn, Fe, Cu and Zn, derived from hydrothermal fluids, Mg, P and V, scavenged from seawater, and Ni, Cr and Co derived from ultramafic rocks. Sediments collected next to the vents are particularly enriched in Mn. The geochemical data together with the observed mineral assemblage and the geological setting suggest that the hydrothermal fluids have much higher temperature than those measured at the escape orifices (max. 9ºC), and a strong enrichment in Mg, mainly at the top of the mount, agrees with extensive mixing of the hydrothermal fluid with unmodified seawater.

Keywords. Hydrothermal sediments, low temperature vents, ultramafic-hosted hydrothermal field, Mount Saldanha

1 Introduction

Mount Saldanha (MS) is a modern seafloor hydrothermal field located at the Mid Atlantic Ridge (MAR), south of Portugal's Azores Archipelago (N36º34'; W33º26'), between the Pico Fracture Zone (PFZ), 38ºN, and the Oceanographer Fracture Zone (OFZ), 35º40'N (Fig. 1A). This region of the MAR is composed of six left-lateral non-transform offsets (NTOs) characterised by peridotite massifs detached from their segment flanks and are commonly associated with hydrothermal vents (e.g. German et al. 1996). The exposure of ultramafic rocks is consistent with low magma budgets, relatively thin crust and irregular faulting patterns (Gràcia et al. 2000).

Mount Saldanha (MS) is located on NTO5, between the FAMOUS and AMAR second-order segments (Fig. 1B), and consists of a faulted massif detached from its segment flanks, almost parallel to the ridge segment. It is composed mainly of ultramafic and gabbroic rocks and a strong methane anomaly within the overlying water column (Charlou et al. 1997). At the summit of MS, hydrothermal fluid was directly observed to be venting through centimetric orifices in the ocean floor sedimentary cover over an area of approximately 400 m^2 and at depths between 2200 and 2220 m.

Peridotites, serpentinites and steatites were identified. *In situ* temperature measurements of the discharge fluid at the hydrothermal orifices revealed maximum fluid temperatures of 9ºC, whereas the adjacent seawater at the seafloor was at around 2ºC (Barriga et al. 2003). The source of the heat at the MS hydrothermal field has been suggested to be derived from the exothermic serpentinization process (Barriga et al. 1998).

Heat balance models by Lowell and Rona (2002) suggest that heat released upon serpentinization of peridotites can explain hydrothermal venting only at temperatures ranging from a few degrees to a few tens of degrees Celsius, as happens at MS. Bach et al. (2002) reached the same conclusion after calculating that the serpentinization process can heat circulating water to 25-150 ºC.

Unlike many other systems sampled so far along the MAR, at MS the hydrothermal discharge takes place through the sediments. Here the hydrothermal fluids react not only with the underlying crystalline rocks but also with the sedimentary cover.

2 Sampling and analytical methods

Hydrothermal sediments were collected at MS, during the Saldanha (Barriga et al. 1998), Seahma (Barriga et al., 2008) and CD167 (Sinha et al., 2005) missions by push- and gravitic-cores. Cores were on average 15cm long and were collected between 2200 and 3000m depth. The samples were examined by several different analytical techniques: mineralogy by optical microscopy, X-ray diffraction (XRD) and electron microprobe; bulk analysis by ICP, ICP-MS and INAA. Mn oxy-hydroxides were also examined by scanning electron microscopy (SEM).

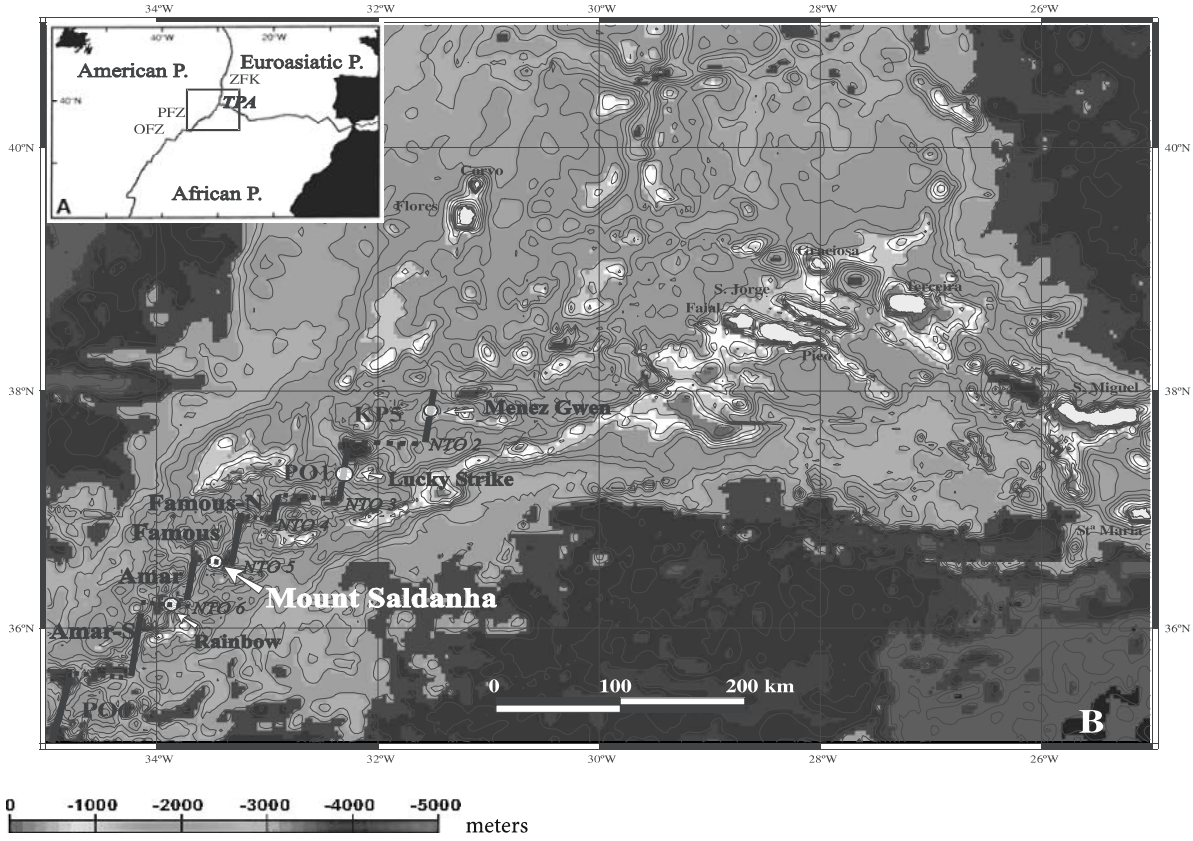

Figure 1: (A) Area between Pico Fracture Zone (PFZ) and Oceanographer Fracture Zone (OFZ) along the Mid-Atlantic Ridge, south of Azores Triple Junction (TPA); (B) relief map showing the location of Mount Saldanha at a non-transform offset (NTO5) between FAMOUS-S and AMAR segments

3 Results

3.1 Mineralogy

At the top of MS the sediments are covered by a Mn-oxides crust (Fig. 2A) that forms a millimetric cap poked by millimetric holes interpreted as micro-chimneys. XRD and SEM analyses of these crusts revealed that the interior layers consist of todorokite (tk) and/or birnesite (br) and that columnar vernardite (vr) grows in the outer massive layers, exhibiting elongated structures (Fig. 2B) formed by spheroids with honeycomb textures.

Microprobe analyses of Mn oxy-hydroxides display a low content in minor elements, a typical feature of hydrothermal origin, a large variation of MnO_2, MgO and FeO wt% and a strong substitution of Mn by Mg in the oxides structure. More reflective minerals of these oxy-hydroxides show compositions similar to tk and/or br while less reflective minerals show a vr composition. In close association with these oxides, at the top of the mount, an uncommon and transparent mineral was identified (Fig. 2B and 3A). Chemical analyses of these crystals show an average of MnO and MgO of 22.6 and 41.6 wt%, respectively, and low totals (range: 58.8-71.7%). The small size and scarcity of the crystals precluded an XRD investigation. The mineral is most probably manganobrucite, an extremely rare, poorly known variety of brucite with (Mg, Mn) $(OH)_2$ as its ideal formula.

MS sediments are mainly foraminiferal nanofossili-ferous ooze (>80%) with hydrothermal precipitates and small fragments of lithoclasts and minerals from the underlying rocks (serpentinites, steatites and basic rocks). Ore microscopy and microprobe studies confirm the presence of fine-grained pyrite and isocubanite disseminated within sediments collected near the vent area. Sphalerite was only found in sediments collected at the top of the mount. Here tubular millimetric structures formed by isocubanite surrounded by sphalerite interpreted to be micro-chimneys were found (Fig. 3B) X-ray diffraction also suggests the presence of smectite-chlorite and nontronite. Putative nontronite (Al-poor Fe-smectite) is particularly abundant in samples collected near the hydrothermal orifices. Experimental data on nontronite synthesis (Harder, 1976) suggests that the solution from which this mineral forms has a low temperature (3 to 29ºC), nearly neutral pH (7 to 9) and is slightly reduced (Eh= -0.2 to -0.8). At MS the presence of sulphide minerals and nontronite suggest that the hydrothermal fluids

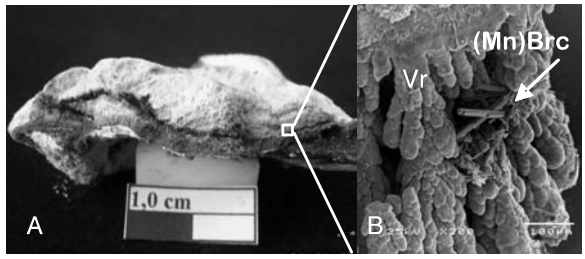

Figure 2: (A) Black-layered Mn-rich crust; (B) SEM image of Mn oxy-hydroxides elongated structures and Mn-brucite (Mn-brc).

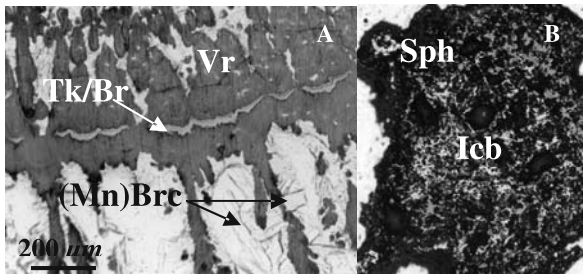

Figure 3: Photomicrographs of polished sections of: (A) poorly crystalline Mn-oxides minerals. High reflectance bands are formed by Todorokite/Birnessite (Tk/Br) and elongated structures, comprise the poorly crystalline phase identified as vernadite (Vr). Transparent fine crystals of Mn-brucite (Mn-brc) grow into open spaces at poorly crystalline Mn-oxides; (B) isocubanite surrounded by sphalerite.

have much higher temperatures than those measured at the vents (max. = 9ºC). The low measured temperatures of the hydrothermal fluids are probably a consequence of cooling effects during conductive circulation and of extensive mixing with seawater in the discharge areas.

3.2 Bulk analyses

Bulk geochemical analyses show that MS sediments have high Ca and C concentrations that are in agreement with the carbonate content (average Ca = 37.6% and C=11.6%). The lowest concentration of Ca was found in a hydrothermal sediment collected at a venting orifice (Ca = 28.7% and C = 9.1%). The concentration of Mn and Mg was also higher in sediments collected near the hydrothermal vents (Mn = 3.2%; Mg=4.2%) in comparison with the remaining MS samples (average Mn = 0.3% and Mg = 0.7%). The higher Mg enrichment at the top of the mount suggests a more intense mixing of seawater with hydrothermal fluids in this area. In contrast, the Mn enrichment is derived from the hydrothermal fluids and was most visible in the hydrothermal orifice samples.

When MS sediments were normalized to pelagic sediments, enrichments in P, V, Mn, Fe, Cu and Zn were observed, revealing a clear hydrothermal signature, especially in samples from the top of the mount where Mn is particularly high. A correlation between Fe+Cu+Zn and

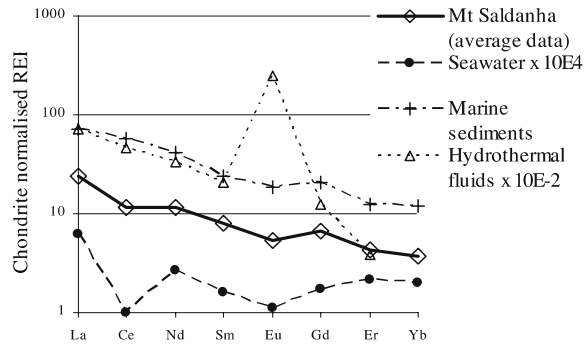

Figure 4: Chondrite-normalized REE patterns

S concentration (r = 0.66; N = 14; p < 0.01) confirms that these metals are present as sulphides.

High abundances of Co, Cr and Ni are likely to be due to the presence of ultramafic rocks in the sediments. Indeed, the Cr/Al and Ni/Al ratios are higher at sediments where larger amounts of ultramafic rocks were found, reflecting the presence of an ultramafic component.

Chondrite normalized REE show similar patterns (Fig. 4). They exhibit a depletion of HREE and negative Eu and Ce-anomaly (averages Ce/Ce* = 0.61 and Eu/Eu* = 0.73). Comparing our REE data with seawater, pelagic sediments and hydrothermal fluids from Rainbow, it is clear that MS sediments have a negative Ce anomaly, less pronounced than seawater, and lack the positive Eu anomaly of the hydrothermal fluids, presenting instead a slightly negative Eu anomaly as in seawater and pelagic sediments. Michard (1989) shows that hydrothermal fluids below 250ºC are characterized by negative Eu anomalies, in agreement with MS fluids. However, the possibility remains that at greater depths the fluids are warmer and are cooled when mixed with unmodified seawater nearer the surface. The REE patterns of MS sediments clearly show that seawater and the dominant pelagic fraction overprint the REE hydrothermal signature.

4 Summary and conclusions

The hydrothermal component is strongly "diluted" in a pelagic carbonate ooze and is dominated by sulphides, Mn oxides, Mn-brucite and clay minerals. The strongest hydrothermal evidence was registered at the top of the mount where hydrothermal activity was observed.

The Mg enrichment, together with the occurrence of Cu, Zn and Fe sulphide minerals, may be explained by the interaction between seawater percolating down into the sediments with the upwelling modified seawater. Metal enrichment in sediments is either directly hydrothermally sourced (e.g., Fe, Mn, Cu and Zn) or scavenged from the seawater (e.g., V and P). Some samples also show a Co, Ni and Cr enrichment derived from ultramafic fragments. The REE pattern shows that seawater is the dominant fluid in the

sediments which is consistent with the dominant pelagic ooze fraction.

The mineralogical and geochemical data from MS sediments suggest an environment of deposition with percolation of low temperature hydrothermal fluids through pelagic sediments. However, these fluids seem to have a much higher temperature than those measured at the escape orifices, and a strong enrichment in Mg, mainly at the top of the mount, agrees with extensive mixing of the hydrothermal fluid with unmodified seawater.

Precipitation of hydrothermal minerals is likely to occur mainly inside sediments where a Mn-Mg oxidized cap prevents direct contact of the evolved hydrothermal fluid with the oxidizing unmodified seawater. Similar caps were postulated for the formation of sub-seafloor massive sulphide mineralization, both modern and fossil.

These data, together with the lack of a magmatic heat source, the presence of peridotite altered to serpentinites and steatites, and the occurrence of a strong methane anomaly within the overlying water column, agree with the system being driven mainly by heat released during the serpentinization process. Additional geophysical and geochemical data are needed to understand the heat sources of these systems.

Acknowledgements

We thank all Saldanha, Seahma and CD167, CREMINER researchers and technicians and the financial support from FCT (Portugal). Reviews by Steve Scott and Elitsa Hrischeva greatly improved the final version.

References

Barriga F, Almeida A, Biscoito M, Colaço A, Company R, Costa R, Costa V, Cruz V, Dias Á, Ferreira P, Gadanho M, Iyer S, Kadar E, Lopes C, Lourenço N, Marques A, Martins V, Pinto Á, Relvas J, Rohais S, Segonzac M, and Serafim M (2003) Seahma-1 Cruise Report. In Creminer (ed. FCT). Faculty of Sciences University of Lisbon

Barriga F, Fouquet Y, Almeida A, Biscoito M, Charlou J-L, Costa R, Dias A, Marques A, Miranda M, Olu K, Porteiro F, and Queiroz P. (1998) Discovery of the Saldanha Hydrothermal Field on the FAMOUS Segment of the MAR (36º 30'N). AGU - Fall Meeting, Eos Transaction 79(45):F67

Charlou J-L, Donval J-P, Douville E, Knoery J, Fouquet Y, Bougault H, Baptiste P, Stievenard M, and German C (1997) High methane flux between 15ºN and the Azores Triple Junction, Mid-Atlantic ridge, hydrothermal and serpentinization processes. Eos trans. AGU 78(F831)

German C, Parson L, and Team H (1996) Hydrothermal exploration near the Azores Triple Junction: Tectonic control of venting at slow-spreading ridges? Earth and Planetary Science Letters 138:93-104

Gràcia E, Charlou J-L, Radford-Knoery J, and Parson L (2000) Non-transform offset along the Mid-Atlantic ridge south of the Azores (38ºN-34ºN): ultramafic exposures and hosting of hydrothermal vents. Earth and Planetary Science Letters 177:89-103

Lowell R, Rona P (2002) Seafloor hydrothermal systems driven by the serpentinization of peridotite. Geophysical Research Letters 29(11):1-4

Michard A (1989) Geochimica et Cosmochimica Acta 53:745-750

Sinha M, Dzhatieva Z, Santos F, Silva N, Dias A, Marques A, Dean S, Morris E, Maxey A, Ellis M, Team C (2005) Active electromagnetic survey of hydrothermal venting area at Saldanha Massif, Mid-Atlantic Ridge. Geophysical Research Abstracts 7:07706, 2005

Geological features and sulphur isotope study of the Meixian-style Pb-Zn-(Ag) deposits in Fujian Province, South China

Feng Chengyou, Zhang Dequan, She Hongquan, Li Daxin
Institute of Mineral Resources, Chinese Academy of Geological Sciences, 100037 Beijing, China

Wu Jianshe
Fujian Geological Survey, 350001 Fuzhou, China

Abstract. The central Fujian rift is a new and important metallogenic province of volcanogenic massive sulfide deposits in China, where several large- and middle-size Pb-Zn deposits were recently discovered. All of the VMS deposits, here called Meixian-style, occur within Meso-NeoProterozoic greenschists that outcrop as metamorphic basement inliers and are characterized by higher LILE contents, enrichment in LREE and a small Eu anomaly, and formed in the continental rift. The orebodies are in stratiform, stratiform-like or lenticular form and ores display banded, disseminated, taxitic and massive textures with higher content of Pb+Zn. Sulphur isotope data for ores in four major deposits are within a narrow range of -3.5‰ to +5.6‰. It is concluded that the sulphur in these deposits was derived largely from magmatic sources, although either volcanic exhalation or leaching from hosted volcanic rocks are possible.

Keywords. Meixian-style deposit, VMS, Pb-Zn deposit, sulphur isotope

1 Introduction

Volcanogenic massive sulfide deposits are an important base-metal deposit type in China. Hou et al. (1999) reported the systematics of their geologic setting, classification, features and style. On a whole, Paleozoic, Proterozoic and Triassic are the most important metallogenic epochs, and this type of deposits is concentrated in the Northern Qilian (Wang et al. 2001), Sanjiang (Hou et al. 1995) and Altai (Ye et al. 1997; Wang, 1999) metallogenic provinces. The central Fujian rift is another new VMS metallogenic province in China, where several large- and middle-size Pb-Zn deposits have been discovered in Meso-NeoProterozoic felsic volcano-sedimentary sequence in recent years. The objective of this contribution is to provide a description of the geologic setting, mineralization and sulfur isotope geochemistry of the major Pb-Zn-Ag deposits of Dingjiashan, Fengyan, Bawaiyang and Shuiji.

2 Geologic setting

2.1 Regional geology

The Meixian-style Pb-Zn-Ag deposits occur tectonically in the central Fujian rift which is an important paleotectonic setting for volcanogenic massive sulfide deposits in China. The central Fujian rift, controlled by NE-striking Zhenhe-Dapu and Pucheng-Wuping deep faults, lie in the superimposed position of three first-order tectonic elements including Northwestern Fujian mole trac, Southwestern Fujian geotectogene and Eastern Fujian volcanic fault belt. It is a part of the South China fold system. Moreover, it is also an important metallogenic province of tungsten, tin, lead, zinc and gold (Ye et al. 1999), which belongs to the West Pacific metallogenic belt.

The outcropping stratigraphy is from Lower Archean to Cenozoic in the central Fujian rift, where the Proterozoic is distributed most widespread and hosts most significant mineralizations of lead, zinc and gold. The Lower Archean Tianjingping formation just outcrops sporadically and is composed of metamorphosed sandy to argillaceous sediment and volcanic rocks. Fu et al. (1994) reported a Sm-Nd isochron age of 2678 Ma for plagioamphibolite in Qiuyuan, Pucheng county. The PaleoProterozoic Mayuan group is a suite of amphibolite facies metamorphic rocks consisting of terrigenous detrital sediments with intercalated carbonate rocks and medium- to basic volcanic rocks. It can be divided mostly into two formations, in which only the Nanyuan formation hosts small-size Cu-Pb-Zn deposit. The Meso-NeoProterozoic Mamianshan group is composed of volcano-sedimentary rocks metamorphosed to greenschist and low amphibolite facies. Bimodal volcanic rocks of the spilite-keratophyre series are distributed in basement inliers along a NEE-striking belt. It was divided into two formations comprising the lower Dongyan and the upper Longbeixi formations as named by Sun (1991), while Zhang (2002) proposed a four-fold division for the basement rocks including the Xiafeng, Huangtan, Dongyan and Longbeixi formations from upper to lower based on rock association, deformation, metamorphism and contact relationship. Of these, the Dongyan and Longbeixi formations are the hosts of a great deal of zinc, lead, copper and silver mineralization, which are important sources for the Meixian-style deposits. The Daling formation contains significant gold mineralizations in ductile shear zones such as the Xiaoban and Shuangqishan gold deposits. The upper Paleozoic stratigraphy is dis-

tributed sporadically in the southern part of the central Fujian rift, while the Cenozoic is restricted to some fault basins.

The host rocks of the Meixian-style Pb-Zn districts are cut by late Yanshanian intermediate to acidic dikes striking NE. For instance, the Gengzhuyuan-Guandou granite-porphyry, 6 km in length and 0.1-0.5 km in width, and the Oingzhai-Nanyang quartz porphyry, nearly 6 km in length and 0.05-0.3 km in width cut across the the Meixian orefield from NE to SW. The granite-porphyry yielded a Rb-Sr isochron age of (127 ±6) Ma (Feng, unpublished). Numerous diorite veins, which strike S-N and are more than 1.2 km in length and 4-20 m in width, occur in the Shuiji district along the F_{11} fault belt.

2.2 The massive sulphide deposits

The Meixian-style volcanogenic massive sulfide deposits are widespread in central Fujian rift, especially in Meixian ore field. Dingjiashan, Fengyan, Bawaiyang and Shuiji are the main deposits. In addition, there are also some small-size deposits such as Xiashan, Wangdihou and. Of these, the Shuiji deposit was discovered earliest in 1959. To date, Dingjiashan, Fengyan, Bawaiyang and Shuiji have Pb+Zn reserves of >1Mt, 1.64 Mt, 1Mt and 0.6 Mt, respectively.

All massive sulfide deposits occur within a unit of the Meso-NeoProterozoic Mamianshan group (mainly the Dongyan and Longbeixi formations) metamorphic rocks, which are overlain discordantly by Mesozoic continental volcano-sedimentary rocks. The Longbeixi formation in Dingjiashan district comprises three lithological units. The uppermost one is dominated by chlorite schist and epidote schist and is characterized by significant lead and zinc mineralizations. The Dongyan formation is widespread in the Fengyan mine and can be divided into five lithological units. Units 1, 3 and 5 are also composed of epidote schist, chlorite schist and actinolite schist, and are the hosts to economic zinc, lead and silver mineralizations. The leptynites in Units 2 and 4 are free of mineralizations. Wang (1998) and Zhou (2001) have done some research on petrochemistry, REE and trace element geochemistry of the greenschists and leptynites. They concluded that the former originated from basic volcanics (basalt) and the latter from acidic volcanics (rhyolite). Therefore, they represent a bimodal volcanic suite formed in a continental rift setting. Both of them are characterized by higher LILE contents, LREE enrichment and small Eu anomalies.

All of the orebodies occur in the Meso-NeoProterozoic greenschists and extend parallel to the host strata with generally stratiform or lenticular shapes. The characteristics of the orebodies change considerably in different deposits and even in the same deposit. For instance, at Yugongshan ore block of the Fengyan deposit, six orebodies strike NE-NNW and dip 10°-35°. At the Dingjiashan deposit, the known lengths of the main orebodies range from 450 m to 1800 m with average thickness from 1.29 m to 6.92 m and a maximum of 25.77 m. The mean grade is 0.96% Pb, 4.21% Zn and 40.88 g/t Ag, with a maximum of 20% Pb+Zn. There are more than thirty orebodies in the Fengshanlin ore-block of the Shuiji Pb-Zn-Ag deposit. Their lengths range from 300 m to 930 m with average thickness from 1.71 m to 5.35 m and an average grade of 2.08% Pb, 1.49% Zn and 49.4 g/t Ag. At the newly-discovered Bawaiyang deposit, individual orebodies are 100 to 650 m long and 1 to 19.95 m thick with average grades of 0.5%-7.01% Pb and 0.60%-25.76% Zn and maximums of 8.72% Pb and 25.76% Zn. The ores

Table 1: Features of the major Meixian-style ore deposits in Fujian Province, South China

Deposit	Commodities Major (minor)	Mineralogy Major (minor)	Host unit	$\delta^{34}S$ (per mil)
Dingjiashan	Pb, Zn, (Ag)	Sph, Pyr, Py, Di, Ep, Act, Chl (Gn, Cp, Gr, Cal, Q)	Dongyan Formation	Py = 0 – 2.6[1,2] Sph = 2.2 – 3.8[1,2] Gn = 1.1 – 2.4[1] Pyr = 2.5 – 2.7[2]
Fengyan	Zn, Pb, Ag	Sph, Gn, Py, Ep, Di, Act (Cp, Pyr, Gr, Cal, Q)	Dongyan Formation	Sph = 2.0 –2.5[1] Gn = 0.5 – 0.8[1]
Bawaiyang	Pb, Zn	Gn, Sph, Di, Ep, Q, Act (Cp, Py, Pyr, Cal, Chl)	Longbeixi Formation	Py = -0.7 – 1.9[1] Sph = -3.3 – -2.0[1] Gn = -3.5 – -2.9[1] Pyr = -2.0[1]
Shuiji	Pb, Zn, (Ag)	Gn, Sph, Py, Pyr, Di, Act (Cp,Chl, Cal)	Meso-NeoProterozoic volcanics	Py = 5.3 – 5.4[1,3] Sph = 4.3 – 5.6[1,3] Gn = 1.9 – 4.5[1,3] Pyr = 4.1[1]

Sph=sphalerite, Gn=galena, Py=pyrite, Cp=chalcopyrite, Pyr=pyrrhotite, Ep=epidote, Di=diopside, Act=actinolite, Chl=chlorite, Gr=garnet, Cal=calcite, Q=quartz, [1] = this study, [2] = Zhou Bin et al.(1999), [3] = Shu Youqin (1992).

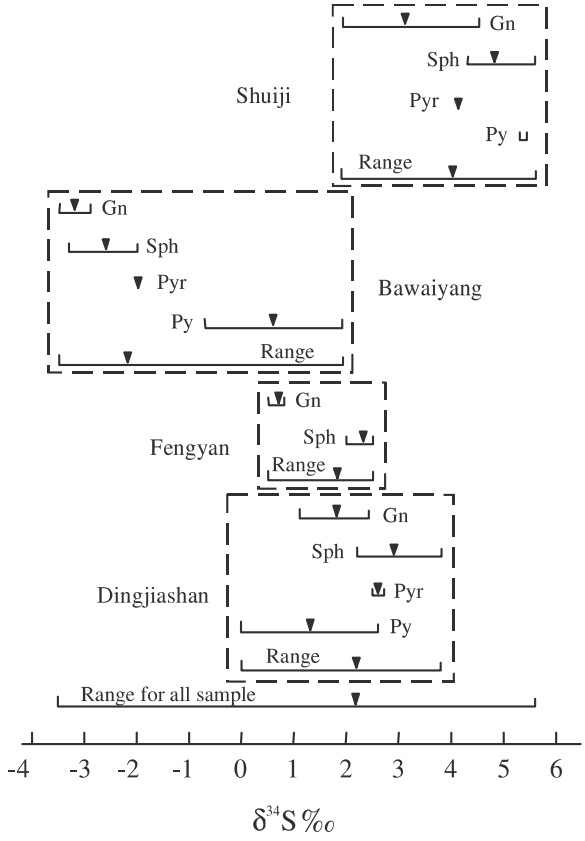

Figure 1: Range of $\delta^{34}S$ values for pyrite, sphalerite, galena and pyrrhotite from the Meixian-style Pb-Zn-Ag deposits

display banded, disseminated, taxitic and massive textures. Ore minerals in the Meixian-style deposits are dominated by sphalerite, galena, pyrite and pyrrhotite with minor chalcopyrite, magnetite, tetrahedrite and silver minerals. Some silver minerals such as stephanite, polybasite, freibergite and argyrodite have been recognized in the Shuiji deposit. Gangue minerals comprise dominantly diopside, epidote, chlorite and actinolite, and minor quartz, feldspar, calcite, apatite and garnet.

Despite wallrock alteration being widespread in the Meixian-style deposits, it is very weak and exhibits no systematic zonation. Alteration minerals are dominated by chlorite, epidote, diopside, sericite, quartz and carbonates. Epidotization, silicification and carbonation are thought to be genetically related to lead and zinc mineralizations.

3 Minerals and methods

A total of 36 ore and adjacent mineralized wall-rock samples were selected for sulfur isotope study. The sulfide minerals, including pyrite, sphalerite, galena and pyrrhotite, were drilled and separated manually. Sixty sulfide mineral samples were analyzed. The sulfur isotope analyses were carried out at the Isotopes Laboratory of the Institute of Mineral Resources, Chinese Academy of Geological Sciences on a MAT 252 isotope ratio mass spectrometer. The reproducibility of the sulfur analyses are better than 0.2‰, and the values are reported relative to the Canyon Diablo Troilite (CDT).

4 Results and discussion

Variations of the $\delta^{34}S$ values of sphalerite (-3.3 to +5.6‰, median = +2.8‰), galena (-3.5 to +4.5‰, median = +1.6‰), pyrite (-0.7 to +5.4‰, median = +2.1‰), and pyrrhotite (-2.0 to +4.1‰, median = +1.8‰) are within a small range of 9.1‰ (Fig. 1). The $\delta^{34}S$ vary little between individual base-metal deposits (Table 1). The $\delta^{34}S$ signature for Dingjiashan varies from 0 to 3.8‰ (mean 2.2‰) with pyrite from 0 to 2.6‰, sphalerite from 2.2 to 3.8‰, galena from 1.1 to 2.4‰, and pyrrhotite from 2.5 to 2.7‰. The $\delta^{34}S$ values for Fengyan are very similar to those of Dingjiashan, ranging from 0.5 to 2.5‰ (mean 1.8‰) with sphalerite from 2.0 to 2.5‰ and galena from 0.5 to 0.8‰. Sulphides from the Bawaiyang mine have the majority of negative $\delta^{34}S$ values ranging from -3.5 to 1.9‰ (mean -2.2‰) with pyrite from -0.7 to 1.9‰, sphalerite from -3.3 to -2.0‰, galena from -3.5 to -2.9‰, and pyrrhotite -2.0‰. The Fengshanlin ore block of the Shiji mine has $\delta^{34}S$ values of 5.3 to 5.4‰ for pyrite, 4.3 to 5.6‰ for sphalerite, 1.9 to 4.5‰ for galena, and 4.1‰ for pyrrhotite. The relations of $\delta^{34}S$ values between different sulphide minerals indicate that all the deposits except Dingjiashan have the following trend: $\delta^{34}S_{pyrite} > \delta^{34}S_{sphalerite} > \delta^{34}S_{galena}$. This trend suggests suggest that coexisting sulfides in most ore deposits have attained isotopic equilibrium. Recent studies (Solomon et al. 1988; Jia 1996) show that there are two main sources for sulfur in the volcanogenic massive sulfide deposits, i.e., sulfur reduced from seawater sulfate and magmatic sulfur. Although sulfur isotope compositions for four main zinc-lead deposits of the Meixian-style are in different ranges, the averages are very close to zero, which suggests that sulphur in these deposits was derived largely from magmatic sources. Both volcanic exhalation and leaching from the volcanic host rocks are also possible mechanisms for the derivation of the sulphur.

Acknowledgements

This work is financially supported by the project of National Geological Survey (20031020000 - 2). The authors are grateful to Mr. Luo Jinchang for access to these mines and their valuable materials. Mr. Zhuang Jianmin and Jie Yujin from Fujian Regional Geological Surveying Team are thanked for accompanying with us during fieldwork.

References

Hou ZQ, Deng J, Sun HT, Song SH (1999) Volcanogenic massive sulfide deposits in China: setting, feature, and style. Exploration and Mining Geology 8:149-175

Hou ZQ, Hou LW, Ye QT, Liu FL, Tang GG (1995) The tectono-magmatic evolution and volcanogenic massive deposits in the Yidun island arc, Sangjiang region, southwestern China. Earthquake Publishing House, Beijing, 220 (in Chinese)

Jia QZ (1996) Mineralization characteristics and formation environment of the Ashele massive sulfide depoait, Xingjiang. Mineral deposits 15:267-277

Shu YQ (1992) S-isotope characteristics of ore in Shuji Pb-Zn mine and the Genesis. Contributions to Geology and Mineral Resources Research 7: 85-97 (in Chinese with English abstract)

Solomon M, Eastoe CJ, Walshe JL (1988) Mineral deposits and sulfur isotope abundances in the Mount Read Volcanics between Que River and Mount Darwin, Tasmania. Econ. Geol. 83:1307-1328

Wang DH (1999) Geological setting and features of the Ashele Cu-Zn deposit, Xingjiang, China. Exploration and Mining Geology 8:197-210

Wang HN, Sun CY (1999) Trace element geochemistry and tectonic setting of greenschists in the central part of Fujian Province. Geological J of China Universities 4: 383-392 (in Chinese with English abstract)

Wang Y, Zhang Q, Xu RH, Qian Q (2001) A discussion on the metal source of Baiyin volcanic hosted massive sulfide deposit from the North Qilian mountains. Geological Science and Technology Information 20:46-50 (in Chinese with English abstract)

Wu JS, Huang RS (2001) Potentials of lead, zinc and silver resources and their prospecting direction at Fengyan, Youxi, Fujian. Chinese Geology 28:13-18(in Chinese with English abstract)

Ye QT, Fu XJ, Zhang XH (1997) Geological characteristics and genesis of the Ashele copper-zinc massive sulfide deposit, Xinjiang. Mineral Deposits 16:97-106 (in Chinese with English abstract)

Ye SQ, Tang RL, Zhang YM (1999) The metallogenic system of central Fujian rift. Geological Exploration for Non-ferrous Metals 6:400-403(in Chinese with English abstract)

Zhang KB, Li XX, Li JH (2002) Classification and comparison of Meso-Neoproterozoic Mamianshan terrain in northwestern Fujian. Geology of Fujian 21:176-186 (in Chinese with English abstract)

Zhou B, Gu LX (1999) Geological characteristics and formation environment of the Meixian massive sulfide deposit. Mineral Deposits 18:99-109(in Chinese with English abstract)

Formation mechanism of oreshoots in massive sulphide orebodies at Hongtoushan, NE China

Gu Lianxing, Tang Xiaoqian, Zheng Yuanchuan, Wu Changzhi, Lu Jianjun, Ni Pei, Xiao Xinjian
State Key Laboratory for Endogenic Metal Deposits Research (Nanjing University), Department of Earth Sciences, Nanjing University, Nanjing 210093, China

Tian Zeman
Hongtoushan Copper Ltd., Fushun 113321, China

Abstract. The Hongtoushan volcanic-exhalative massive sulphide Cu-Zn-Au-Ag deposit of Liaoning Province occurs in an Archaean greenstone belt of the North China craton. Ores and the confining strata were metamorphosed to upper amphibolite facies and underwent three phases of deformation in the period between 2.8 and 2.5 Ga. There are more than 30 oreshoots that occur inside the main massive sulphide orebodies. These oreshoots range from 2 m to 30 m in length, 0.1 m to 1.5 m in width and 2 to 30 m in depth extension. Studies on composition and fabrics indicate that these oreshoots were actually local ore mylonite zones, which were overprinted by hydrothermal fluids during retrograde metamorphism from amphibolite to greenshcist facies.

Keywords. Massive sulphide, mylonite, metamorphism, remobilization, Hongtoushan

1 Introduction

Ductile shear zones have been recognized as important ore-hosting structures, particularly in relation to structurally controlled gold deposits (Kerrich 1989; Pirajno et al. 2003). Furthermore, ore mylonites are common features of metamorphosed and deformed submarine exhalative massive sulphides (Marshall and Gilligan 1989; Duckworth and Rickard 1993), yet ore mylonites enriched in metals with respect to surrounding massive ores have not been well documented. This paper aims to describe the mechanism of metal enrichment in ore mylonites based on the research of more than 30 oreshoots highly enriched in copper, gold and silver inside the massive sulphide orebodies of the Hongtoushan deposit.

2 Deposit geology

The Hongtoushan Cu-Zn-Au-Ag massive sulphide deposit of Liaoning Province occurs in an Archaean greenstone belt of the North China craton. Ores and the confining strata were metamorphosed to upper amphibolite facies under T-P conditions of 600 to 650°C and 0.8 to 1.6 GPa (Zhao and Cui 1987) and underwent three phases of deformation in the period between 2.8 and 2.5 Ga (Zhang et al. 1984; Liu et al. 1994).

The Hongtoushan deposit has proven ore reserves of 30 Mt at average grades of 1.80 wt% Cu, 2.5 wt% Zn, 20 wt% S, 0.68 g/t Au, 40 g/t Ag, 56 g/t Cd and 25 g/t Se. Sulphides in the massive ores are dominated by pyrite, pyrrhotite, chalcopyrite and sphalerite with minor galena, cubanite, electrum, chalcocite and magnetite. Gangue minerals are dominated by quartz with lesser plagioclase, garnet, amphibole, biotite and muscovite. The ores are characterized by well-developed pyrite porphyroblasts in matrices composed of varying amounts of pyrrhotite, pyrite, chalcopyrite, sphalerite and gangue minerals (Gu et al. 2004).

Investigation of ore composition and texture indicates that pre-metamorphic massive sulphide ores are dominated by pyrite, pyrrhotite, chalcopyrite and sphalerite with minor galena (Gu et al. 2004). However, sedimentary textures have been obliterated almost completely, and the present textures were largely formed during peak metamorphism and retrograde processes. Pyrite porphyroblasts with cubic crystal form and grain size from 5 to 30 mm are thought to have been produced both by prograde recrystallization of sedimentary pyrite and by retrograde growth with sulphur derived by exsolution from pyrrhotite. Deformation textures of porphyroblastic pyrite are weak and dominated by cataclastic fractures.

3 Characteristics of oreshoots

There are at least 30 oreshoots inside the main massive sulphide orebodies. These oreshoots range from 2 m to 30 m in length, 0.1 m to 1.5 m in width and 2 to 30 m in depth extension. They are gradational towards the nearby massive ores, but have sharp boundaries when they are in contact with the metamorphic rocks (Fig. 1). Deformation and remobilization textures are characteristic of the oreshoots (Fig. 2).

3.1 Deformation textures

Constituents of the originally massive ores in the oreshoots have undergone intense ductile shearing. Foliations can be clearly seen in handspecimen (Fig. 2-A). Quartz grains have been elongated and recrystallized. Plagioclase is affected by cataclastic flow, resulting in fragments aligned along shear directions. Curved flakes, undulose extinc-

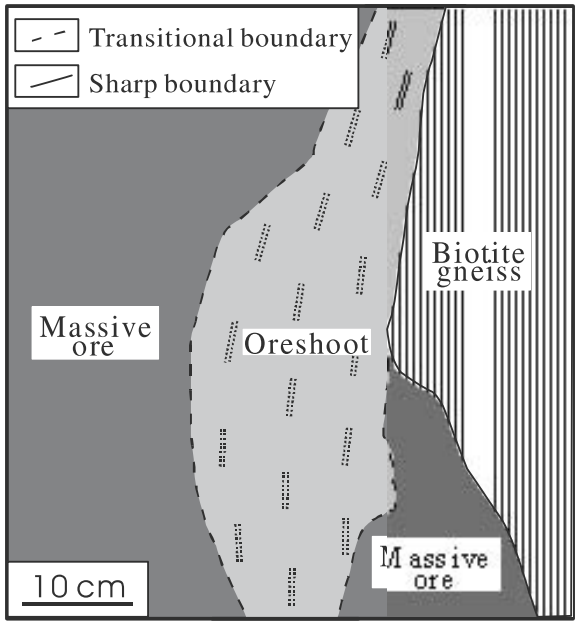

Figure 1: Sketch showing contact relationships of an oreshoot with biotite gneiss and massive sulphide ore at a mining surface on Level –347 of the Hongtoushan mine.

tion and kink bands of micas are commonly seen, and some flakes have been sheared into typical mica fishes.

Sulphide minerals vary in rheology in the oreshoots. Pyrite is characterized by cataclastic deformation and porphyroclastic textures. The fragments are mostly smaller than 200 microns in size, which is in sharp contrast to the mm- or cm-sized pyrite crystals in the massive sulphide ores. Initial shearing of a pyrite metablast in the massive sulphide ore resulted in rhombohedral or nearly rectangular pull-apart fragments cut by a set of microfractures. Further shearing has made fragments of a single grain separated by plastic minerals (e.g. chalcopyrite and pyrrhotite) and aligned along shear direction (Fig 1- B). Some pyrite catablasts show concentric fractures and are surrounded by a zone of peeled-off tiny grain fragments, indicating that rotation of the pyrite grains occurred locally. Etching with chromate acid revealed abundant slip lines and dislocation walls on the polished surfaces of pyrite porphyroclasts, indicating initial plastic deformation has occurred to this mineral. Lens-shaped outlines of some grains suggest that pressure solution of pyrite has also occurred.

As principal matrix-forming minerals, pyrrhotite, chalcopyrite and sphalerite behaved more plastically. Intense stretching of the grains resulted in alternating stripes of these minerals (Fig 2- A, C). Post-shear annealing is typically indicated by strain-free pyrrhotite grains with straight to gently curved boundaries (Fig 2- C). Foam textures of this mineral are also commonly seen. Recrystallized and strain-free pyrrhotite grains (Fig 2- C), microns to tens of microns in size, are significantly smaller than those in the undeformed massive sulphide ores. The pyrrhotite is almost purely hexagonal and lacks lamellar intergrowths of the monoclinic variety, as is also the case of the recrystallized pyrrhotite in the Norwegian sulphide deposits (Gu and Vokes, 1996). By contrast, no evidence has been found for recrystallization of pyrite.

3.2 Remobilization textures

A variety of textures indicate that significant amounts of chalcopyrite, pyrite, arsenopyrite, electrum and other minerals have been introduced by late-stage remobilization fluids.

Chalcopyrite, and in fewer cases sphalerite and pyrrhotite, commonly fill cracks of pyrite porphyroclasts in the oreshoots (Fig. 2-D). Embayed and non-matching walls of some veins (Fig. 2-D) indicate that replacement corrosion has affected the host pyrite. Sulphides, particularly chalcopyrite, are also ubiquitously seen filling cracks, fissures and cleavages of quartz, plagioclase, mafic silicates and lithoclasts.

Besides the cataclastically-deformed pyrite, there is a remobilized generation of pyrite in the oreshoots. This generation is deformation-free and occurs as irregular grains, mostly 5 to 20 μm in size, in the matrices or as microscopic veins cutting chalcopyrite and pyrrhotite. Some fractures of the deformed pyrite have been healed by this generation of pyrite.

Arsenopyrite is commonly seen in the oreshoots although not found in the massive sulphide ores. It typically occurs in a matrix of chalcopyrite as columnar euhedra with rhombus cross-sections. Deficiency of deformation textures indicates that arsenopyrite was precipitated later than ductile shearing of the massive ores.

Electrum occurs as rectangular or irregular grains in a matrix of chalcopyrite or as fissure filling material in cracks of arsenopyrite, indicating that this mineral is a post-shear precipitate and was introduced by fluids subsequent to the crystallization of arsenopyrite.

Various hydrothermal alteration products, such as hornblende, actinolite, epidote, clinozoisite, biotite, muscovite, albite, carbonate and quartz are extensively developed in the oreshoots. These alteration minerals can occur either as replacive patches or in veinlets cutting deformed minerals. Such alteration assemblage and the greenish blue pleochroism of the replacive hornblende are likely to indicate an environment transitional from the amphibolite to greenschist facies.

3.3 Metal enrichment

Based on the mine records, metal grades in the oreshoots average 15.20 wt% Cu, 1.54 g/t Au and 231.40 g/t Ag, and

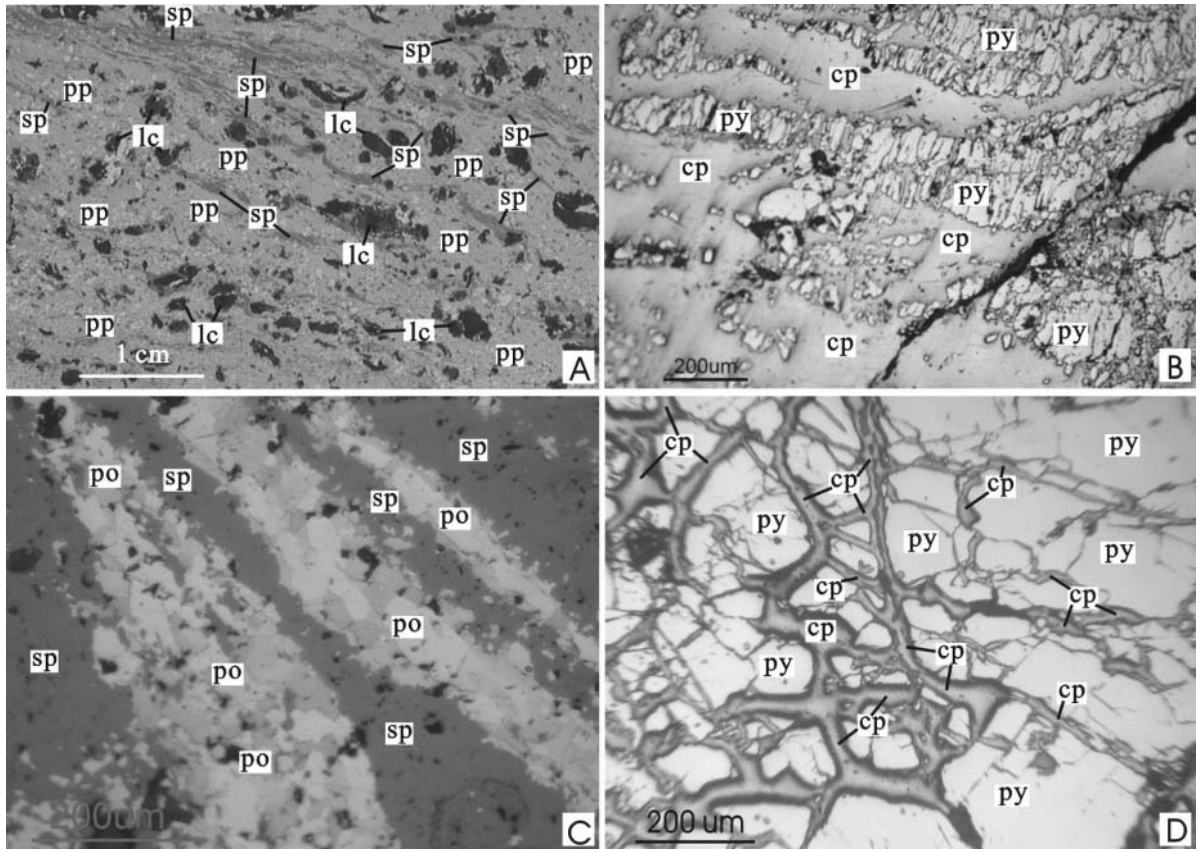

Figure 2: Ore fabrics of the oreshoots. Abbreviation for minerals: *cp,* chalcopyrite; *lc,* lithiclast; *po*, pyrrhotite; *pp*, pyrrhotite + pyrite + chalcopyrite; *py*, pyrite; *sp*, sphalerite; A – Handspecien of the ore from an oreshoot, indicating foliations; B- Intensely sheared pyrite in a matrix of pyrite; C – Foliation indicated by alternating sphalerite and pyrrhotite bands with recrystallized and strain-free pyrrhotite grains; D – Chalcopyrite filling cracks of a pyrite porphyroclast. Some of the vein walls are non-matching and embayed, indicating metasomatism has occurred during precipitation of the chalcopyrite.

are much higher than the massive sulphide ores which average 3.69 wt% Cu, 0.46 g/t Au and 59.96 g/t Ag. Analyses of the present authors are in good consistency with these records.

4 Concluding remarks: Genesis of the oreshoots

Ductile deformation and remobilization textures suggest that the oreshoots are actually ore mylonites overprinted by late-stage hydrothermal fluids. Ductile shearing of the massive sulphide ores and overprinting of the ore mylonite occurred during retrograde metamorphism transitional from the amphibolite to greenschist facies. This is evidenced by restricted distribution of the oreshoots in the originally massive sulphide orebodies, less strong recrystallization of the minerals than in surrounding massive ores, and the greenschist assemblage of alteration minerals. It has been demonstrated that prominent annealing of pyrrhotite and pyrite can only occur at temperatures higher than 450oC and 550oC, respectively (Cox et al. 1981; Marshall and Gilligan 1987). Thus, the presence of annealing textures of pyrrhotite, the absence of annealed pyrite, and the dislocation textures revealed by etching appear to suggest that formation and succeeding annealing of the ore mylonite took place over the temperature range from 550oC to 450oC. At such temperatures, pyrrhotite, chalcopyrite and sphalerite are sufficiently ductile, but pyrite remains in the field of brittle deformation (McClay and Ellis 1983). Pressure solution of quartz and other pressure-sensitive gangues during ductile shearing might have caused initial enrichment of the metals, but the extreme enrichment is linked to overprinting fluids. Enhanced porosity and permeability of the ore mylonite facilitated fluid focusing and percolation. Reduced grain size of the shear zones raised their reaction and overgrowth rates and thus accelerated precipitation of metals from fluids. Distribution of the oreshoots basically restricted to the main massive sulphide orebodies is likely to indicate that remobilizing metals including Cu, Au, Ag and As were derived essentially from the surrounding massive sulphide ores.

References

Cox SF, Etheridge MA, Hobbs BE (1981) The experimental ductile deformation of polycrystalline and single crystal pyrite. Econ Geol 76:2105-2117

Duckworth RC, Rickard D (1993) Sulphide mylonites from the Renström VMS deposit, Northern Sweden. Mineral Mag 57:83-92

Gu LX, Tang XQ, Zheng YC, Wu CZ, Tian ZM, Lu JJ, Xiao XJ, Ni P (2004) Deformation, metamorphism and ore-component remobilization in the Archean massive sulphide deposit at Hongtoushan, Liaoning Province (in Chinese with English abstract). Acta Petrol Sinica 29(4): 923-934

Gu LX, Vokes FM (1996) Intergrowth of hexagonal and monoclinic pyrrhotites in some sulphide ores from Norway. Mineral Mag 60(2):304-316

Kerrich R (1989) Geodynamic setting and hydraulic regimes: shear zone hosted mesothermal gold deposits. In: Bursnall JT (Ed), Mineralization and Shear Zones. Montréal: Geological Association of Canada, short course notes, 89-128

Liu LD, Zhu YZ, Dai SB (1994) Relationships between gold deposits and ductile shear zones and overprint structures. In: Zhang YX, Liu LD (eds) Precambrian Ore Deposits and Tectonics in China (in Chinese). Seismol Publ House, Beijing, 39-77

Marshall B, Gilligan LB (1987) An introduction to remobilization: information from ore-body geometry and experimental considerations. Ore Geol Rev 2(1-3):87-131

Marshall B, Gilligan LB (1989) Durchbewegung structures, piercement cusps, and piercement veins in massive sulphide deposits: formation and interpretation. Econ Geo 84:2311-2319

McClay KR, Ellis PG (1983) Deformation and recrystallization of pyrite. Mineral Mag 47:527-538

Pirajno F, Thomassen B, Dawes PR (2003) Copper–gold occurrences in the Palaeoproterozoic Inglefield mobile belt, northwest Greenland: a new mineralisation style? Ore Geol Rev 22:225–249

Zhang QS, Li SY, Liu LD (1984) Geology and Metallogeny of the Early Precambrian in China (in Chinese). Jilin People's publ House, Changchun, 1-536

Zhao YX, Cui WY (1987) Mineralogy and P-T conditions of crystallization of Archaean metamorphic complex from Qingyuan district, Liaoning Province (in Chinese). J Changchun Univ of Earth Science, Special Issue of Metamorphic Geology, 191-204

The Khandiza Zn-Pb-Cu-Ag VMS deposit: Part of a new 'Bathurst District' in southern Uzbekistan?

R.J. Herrington
Centre for Russian and Central Asian Mineral Studies, Department of Mineralogy, Natural History Museum, London, SW7 5BD, U.K.

N.A. Achmedov
State Committee on Geology and Mineral Resources of the Republic of Uzbekistan, 11a Shevchenko Str. Tashkent 700060 Republic of Uzbekistan

W.J. Charter
Marakand Minerals Limited, 63, Vosit Vokhidov St., Tashkent, Republic of Uzbekistan

Abstract. The Lower Carboniferous Khandiza VMS deposit is located in southeast Uzbekistan close to the border with Tajikistan. Currently awaiting development by Marakand Minerals Limited ("Marakand"), the deposit comprises more than 14 Mt of resource grading 7.2% Zn, 3.5% Pb, 0.9% Cu, 130g/t Ag and 0.4 g/t Au. The deposit is hosted in Lower Carboniferous (Visean) rhyolite and dacite extrusives and pyroclastics, closely associated with a rhyolitic subvolcanic system.. Geochemistry suggests the volcanics show both tholeiitic and calc-alkaline affinity, consistent with being forming in a rifted continental margin above the south-facing active destructive plate margin to the north of the Paleotethys Ocean. The sulphides form multiple lenses of massive banded ore with sulphide-cemented clastic volcanic breccias and footwall disseminations. Mineralogy of the sulphides is fairly simple comprising sphalerite, galena, chalcopyrite and pyrite with minor sulphosalts. Silver reports to sulphosalts and galena as well as other minor silver-rich sulphide phases. Minor gold appears to be paragenetically late. The Khandiza region has many features comparable to the Bathurst district of Canada where rifting at a supra-subduction continental margin is responsible for generating the host volcanics to deposits such as the Brunswick 12 deposit. In southern Uzbekistan, Khandiza is the only VMS deposit that has so far been well explored. A further 34 mineral occurrences and base metal anomalies have been identified, all associated with volcanics, and warranting further exploration. 12 of these targets are within 10km of Khandiza itself, and associated with the Chornova volcanic complex.

Keywords. VMS Deposit, Khandiza, lead-zinc-copper-silver, Uzbekistan

1 Introduction

The Carboniferous-age Khandiza zinc-lead- copper-silver VMS deposit lies within the Baisun-Kugitang Tectonic Zone of the South Tien Shan in southern Uzbekistan. This zone is south of the east-west trending South Gissar and Zaravshan-Alai structural formations. The Zaravshan-Alai is one of the terranes in the 'Tien Shan Gold Belt' which contains the major Muruntau gold deposits to the northwest. The Khandiza deposit was discovered by Soviet geologists in 1957, yet it was only in 1970 that diamond drilling located significant massive sulphide mineralisation. Further drilling and underground development delineated nine separate orezones before exploration work ceased in 1974. Oxus Resources Corporation ("Oxus") commenced evaluation of the property in July 1996 identifying the style and setting of the VMS mineralisation and recognizing additional resource potential. Oxus carried out further drilling and underground investigations, then in December 2003 transferred the deposit into the AIM listed Marakand Minerals Limited who have since completed a feasibility study. The quoted resource for Khandiza following this work is 14.412 Mt @ 7.24% Zn, 3.50% Pb, 0.86% Cu, 134 g/t Ag and 0.38 g/t Au. (Marakand's 2004 Feasibility Study and Annual Report).

2 Geological setting of the deposit

In the Early Carboniferous, the region in which Khandiza formed lay at the northern edge of the Baisun-Kugitang microcontinental block, the most southerly of the Tien Shan continental terranes (Figure 1). The deposit region faced the South Gissar rift which at the time formed a probable back arc basin to the northward dipping subduction of the oceanic plate of the Paleothethys, which lay to the south of Baisun-Kugitang (Filippova 2001). Correlation of this zone to the west is tentative at best, but clearly structures can be traced around the margin of the Kazakh craton into the Uralide orogen. The main period of VMS development in the South Urals was Mid Devonian (Herrington et al. 2005) but the Uralian Ocean was still open to the east. Western Kazakhstan formed an Andean-type margin which can be traced through to the Kurama-Chatka zone in Uzbekistan. It is possible that the Baisun-Kugitang block has an analogue in one of the continental slivers located between the Kazakh Plate and the western Uralides (Yakubchuk et al. 2001, Herrington et al. *in review*).

Khandiza is associated with the Chornova volcanic complex, peripheral to which are a series of satellite rhyolite centres or 'domes' both occurring along a linear trend parallel to, the southern limb of the Hodjaharkan Syn-

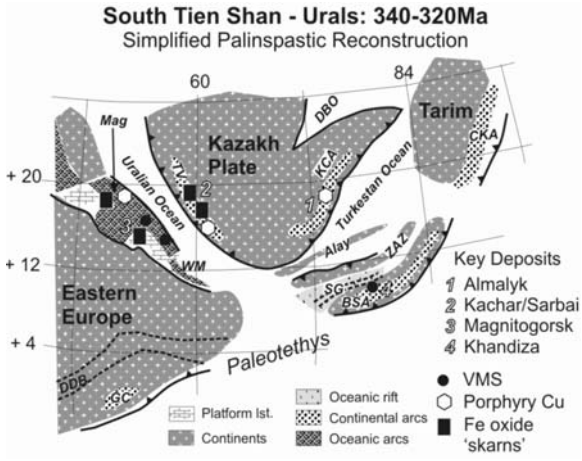

Figure 1: Simplified palinspastic reconstruction of the Southern Tien Shan to Urals in the Early Carboniferous showing position of Khandiza Mag= Magnitogorsk, TV= Turgai-Valerianovka, M= West Mugodzhar, KCA= Chatka-Kurama, SG= South Gissar, BSA= Baisun arc, DDB= Dnepr-Donetsky, GC= Greater Caucasus, DBO= Djunggar/Balkash Ocean, KCA= Central Kazakh arc (modified from Filippova et al. 2001)

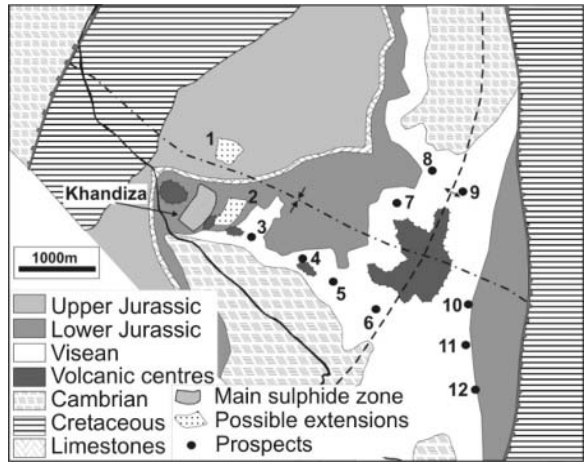

Figure 2: Simplified geology map of the Khandiza deposit showing related prospects (modified from Charter 2004) Legend to prospects : 1 Khandiza North; 2 Khandiza East; 3 Vodnisay; 4 Chinarsay; 5 Maidansay; 6 Novasay; 7 Chornova; 8 Dalney; 9 Gurud; 10, 11 & 12 Yangaklik North, Central and South.

cline (Figure 2), and also around the Chornova volcanic complex itself. The Chornova volcanic complex comprises units of the regionally identified Vakshivar Formation, a sequence of Lower Carboniferous (Upper Visean) sediments, rhyolitic volcanics and pyroclastics which is overlain by a unit of largely dacites. Mineralisation consists of massive sulphides in at least three main horizons intercalated within the rhyolitic and dacitic volcanic sequence.

Within the Khandiza area, basal Cambrian schists and gneisses are overlain by an unconformable Lower Carboniferous basal conglomerate, which marks the start of the Vakhshivar Suite, which is sub-divided into a Lower, Middle and Upper suite (Charter 2004). The Lower Vakhshivar Suite includes the basal conglomerate, above which is a limestone overlain by a sandstone and siltstone sequence with volcanic tuffs representing the onset of volcanism. The Middle Vakhshivar Suite has been divided into two stratigraphic packages, the lower comprising limestones, dolomites, and a thick (up to 500m) volcanic stratigraphy composed of porphyritic rhyolites, rhyolitic tuffs (liparites) and dacites.

3 Nature of host volcanics

The rhyolitic volcanic rocks of the Middle Vakhshivar host the Khandiza massive sulphide mineralisation. The upper package comprises limestones and shales of Upper Visean age. The limestone is characteristically siliceous and is a stratigraphically persistent unit overlying volcanic rocks that mark the effective division between the Middle and Upper Vakhshivar. The Upper Vakhshivar Suite is a distinct dominantly sedimentary sequence of sandstone/siltstones, shales, minor limestones of Namurian age with interstitial porphyritic dacites and late stage rhyolites that represent the waning stage of volcanism. The Vakhshivar Suite, which can be traced to the east through Vodnisay, Chinarsai and Maidansai, and then north to Chornova, dips below unconformable cover sediments of Triassic, Mesozoic and Quaternary age.

Volcanic rocks of the Middle Vakhshivar host the Khandiza massive sulphide deposit and preliminary analyses of these rocks indicates that they may show both tholeiitic and calc-alkalic affinity with some of the volcanics and the related subvolcanic intrusives showing rift-related settings rather than typical volcanic arc (Figure 3). The uppermost massive sulphide unit is overlain by a massively bedded dacite unit with rare earth patterns typical of calc-alkaline lavas, distinct from the apparently more primitive suites hosting mineralisation (Fig. 4b, c). This change in the nature of the volcanics is often marked by distinct red jasper horizons, up to 10cm thick which clearly mark some kind of volcanic hiatus. The Khandiza sulphide mineralisation appears to be closely related to rhyolite / quartz porphyry sub-volcanics, which have been mapped underground at the eastern margin of the deposit, with a similar chemistry to presumably co-magmatic rhyolite extrusives (Fig. 4a).

Mineralisation close to the subvolcanic unit is largely massive sulphides with peripheral brecciated ores. Immediately to the west of Khandiza, a further sub-volcanic 'rhyolite dome' has been identified by drilling (see Fig. 2). A significant fault is interpreted as separating the Khandiza massive sulphides and this 'Khandiza West' dome and massive sulphide mineralization is interpreted

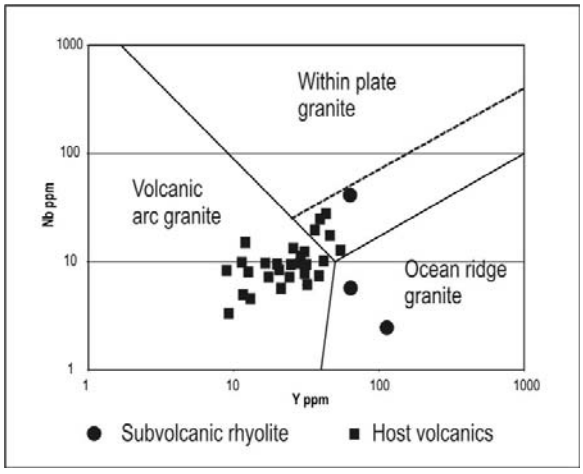

Figure 3: Nb/Y plot of Khandiza rhyolites, dacites and subvolcanic dacite intrusives (after Winchester and Floyd 1977)

as being located in a 'sea-floor trough', in-between the two 'domes'. Three stages of pre- to syn- and post-mineralisation deformation are noted. The first is best shown by northeast trending faults which appear to have controlled the distribution of volcanism and so may be considered synvolcanic. The second phase of deformation involves folding before deposition of the Triassic sediments and resulted in major east-southeast trending folds and flexures, principally the Hodjaharkan Syncline to the north of Khandiza, and parallel flexures which affected the Khandiza mineralisation. The third phase relates to Alpine deformation resulting in the gentle regional dip of the Mesozoic strata to the west and the exposure of north-northeast trending fault-bounded Palaeozoic–Mesozoic inliers. The average dip of the Carboniferous strata in the Khandiza region is moderately to the north-northeast.

4 Mineralisation

The sulphide ores consist of massive, brecciated and disseminated ore types.

Massive ores are common at the eastern edge of the deposit and towards the top of each ore zone, especially with regard to the largest Ore zone No 3, where massive sulphides generally overlie brecciated ores, which in turn overlie disseminated ores. Massive sulphide grades tend to be very high, ranging from 8 – 30% zinc. Massive ores are dominated by sphalerite (25-50%), galena (10-20%) and pyrite (6-15%). Chalcopyrite is less common (1.5 to 6%) together with sulphosalts (1-3.5%).

Brecciated ores for the most part consist of clasts of barren rhyolitic clasts in a fine-grained sulphide matrix. The volcanic clasts vary from to sub-angular. Obviously grades here are variable but range from 2 – 12% zinc.

Disseminated ores are the lowest grade ore, and tend to form the base of each ore zone. Mineralization may

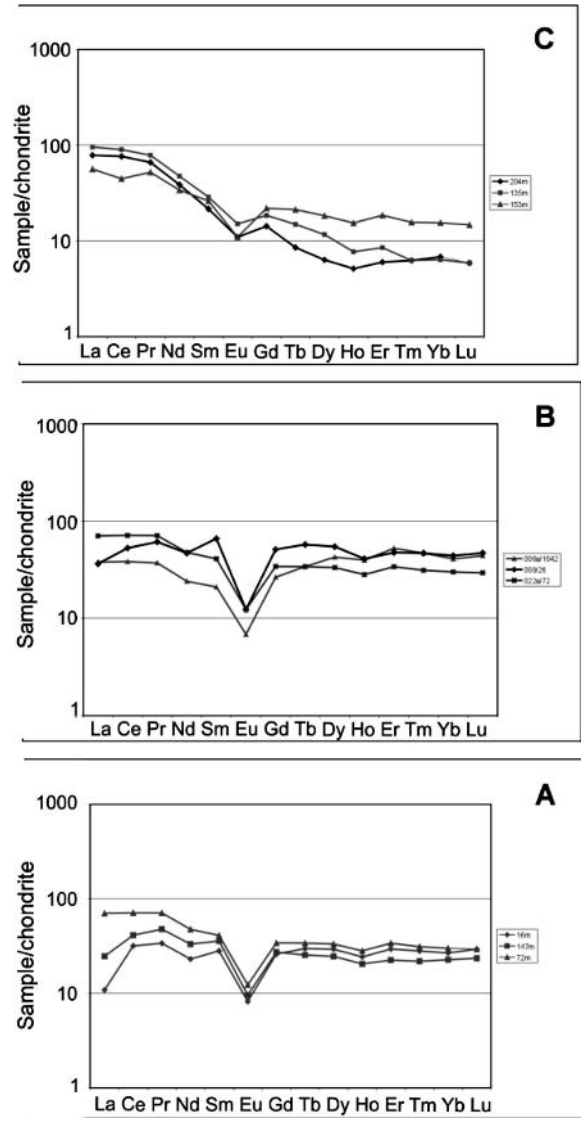

Figure 4: Chondrite normalised REE plots for Khandiza volcanic and subvolcanic rocks. A: Quartz porphyry subvolcanic rocks (note charateristic La, Ce depletion from alteration); B: Sulphide host rhyolite units; C: Hanging wall dacite units.

consist of disseminations or segregations of fine grained sulphides, particularly pyrite, within altered footwall rocks. Veinlet mineralization is also common, containing coarser secondary sulphide crystals. Alteration varies from silicification to chloritization and whole rock geochemistry confirms major changes to alkali chemistry with losses of sodium with concomitant potassium enrichment. Grades range from 2 – 7% zinc

Detailed mineralogy performed by TsNIGRI between 1972 and 1974 (Charter 2004) identified sphalerite, galena, chalcopyrite and pyrite as major sulphides. Minor phases include sulphosalts, arsenopyrite, pyrrhotite and magnetite. The main non-ore minerals include quartz,

sericite, chlorite, and carbonate (dolomite and calcite). Silver is shown to have a close relationship with galena and chalcopyrite and is present in the sulphosalts, freibergite, argentite, polybasite and pyrargyrite. Rare native silver is recorded. Gold is present within sulphides but also in late stage quartz veining along the hanging wall contacts.

5 Conclusions

The metal suite and volcano-sedimentary association indicate that Khandiza fits the siliciclastic-felsic VMS class of Barrie and Hannington (1999) with features broadly comparable to the settings of the Bathurst, New Brunswick, and the Iberian Pyrite Belt deposits. The sedimentary assemblages at Khandiza, comprise conglomerates, sandstones, siltstones and bioclastic limestones, typical for oceanic basins developed close to continental margins where the clastic material is sourced from denuded land masses. Palinspastic reconstructions indicate that the Baisun region lay south of the South Gissar rift which formed a back-arc basin with formation of true oceanic crust behind the proposed 'Andean' style continental margin to the south. Volcanic rock geochemistry confirms the similarity between the composition of the subvolcanic host rhyolites and rhyolites from the Bathurst District (Lentz 1998, Rogers et al. 2003). The affinity of the Carboniferous sediments confirm an affinity with European and North American faunas and extrapolation of the Baisun zone westwards indicates probable linkage with zones to the west of the Kazakh plate. The Magnitogorsk arc in the Urals which itself hosts giant Cu-Zn VMS deposits had already docked with the East European plate suggesting that Khandiza may actually correlate with regions east of this. The broad conclusion is that Khandiza appears to be developed in a continental rift setting outboard of the Kazakh Plate but associated to it geographically, in an environment somewhat similar to that being interpreted for the Bathurst VMS district of eastern Canada (van Staal 1987).

Acknowledgements

The State Committee of Geology and Mineral Resources of the Republic of Uzbekistan, Marakand Minerals Limited and the Natural History Museum are thanked for permission to publish this abstract. This is a contribution to the IGCP Projects #502 and #473 "

Massive sulfide deposits in continental volcanic basins at the lower Yangtze Valley, Southeast China

Wenxuan Hu, Wenlan Zhang, Lianxing Gu, Yucai Song
State Key Laboratory of Mineral Deposits Research, Department of Earth Sciences, Nanjing University, 210093, Nanjing, China

Abstract. Two Mesozoic continental basins in the Lower Yangtze Valley of Southeast China host a number of iron oxide and sulfide ore deposits that have been previously interpreted as magmatic-hydrothermal mineralization associated with porphyry intrusions. Our work indicates, however, that a significant part of the metallogenic history in this area predated the sub-volcanic emplacement of the porphyry intrusive rocks. The ore-forming process is thought to have included an early event of massive sulfide formation in continental fault-bounded basins, which products were subsequently reworked and metal-enriched by the porphyry-related hydrothermal system. Detailed reconstruction of the geological relationships between the ores and their host-rocks, coupled with interpretation of the textural, mineralogical and paragenetic characteristics of the various types of ores in several different deposits in the area, collectively suggest a syngenetic, volcanic -exhalative origin for the lens-shaped, massive pyrite-anhydrite ores related to Mesozoic volcanic activity. Evidence for this includes synsedimentary structures and soft-sediment deformation features, widespread, siliceous and anhydrite-rich chemical sediments (exhalites) associated with the massive sulfides, and iron sulfide-oxide replacement relationships.

Keywords. Massive sulfide deposits, continental volcanic basin, exhalative sedimentation, hydrothermal overprinting, Southeast China

1 Introduction

The massive sulfide deposits (MSDs) found in the Mesozoic continental volcanic basins of Southeast China possess high economic potential. They may also be of significant scientific interest as the formation of massive sulfide deposits, both modern and fossil, has been widely described in marine (seafloor) environments but not extensively in continental settings (e.g., Hutchinson, 1984; Solomon et al., 1979; Spooner et al., 1973).

The Ningwu (Nanjing-Wuhu) and the Luzong (Lujiang-Zongyang) basins are two important continental volcanic basins in the Lower Yangtze Valley. They enclose abundant mineral resources, including iron, sulfur, copper, gold and alunite. Some of the deposits located therein contain ore reserves in excess of a hundred million tons. The formation of these deposits has been interpreted in the light of a general magmatic-hydrothermal model in relation to a porphyry intrusion (NIDP research group, 1978; Zhao, 1990). According to this model, the pyrite-rich (± anhydrite) ores and the iron oxide ores are interpreted to result from a single metallogenic event. A temperature- controlled reverse evolutionary path is envisaged to explain the hydrothermal activity responsible for the precipitation of magnetite, hematite, pyrite and anhydrite at successive stages of the ore-forming process. The final consequence is hypothesized to be the generation of several different types of mineralization, and different alteration patterns around an intrusive body.

The porphyry model was put forward mainly on the basis of data from the iron oxide deposits as, by that time, little attention has been paid to the massive pyrite deposits. Later studies by Hu (1990) and Hu et al. (1991), which have focused on the pyrite-anhydrite ores, have provided evidence for a number of characteristics that do not conform to a simple porphyry-type model for the entire ore-forming system. These authors have shown that the pyrite-anhydrite ores formed prior to the iron oxide ores, with the former being largely replaced by magnetite, hematite and related gangue minerals in some deposits.

In this paper, we report the main results of a recent investigation of several massive sulfide deposits in the area. It is shown that these deposits exhibit many characteristics that are similar to those of massive sulfide deposits found in marine sequences. We propose a volcano-exhalative history for their origin, followed by hydrothermal overprinting due to subsequent interaction with magmatic-hydrothermal solutions.

2 Geological setting

The Ningwu and Luzong basins are two large, Late Jurassic to Early Cretaceous, volcanic basins in Southeast China, each covering an area of about 1000 km^2. They are located in the Lower Yangtze down warping-faulted subsidence belt, between the Dabie Terrane-Huaiyin block and the Jiangnan old land (circum-Pacific volcanic and metallogenic belt; Wang 1982; Ren et al. 1991; Zhai et al. 1996; Lianxing et al. 2000). These basins owe their origin to tectonic activity. They are both bound by important faults and cut by numerous tectonic features of smaller order. The Luzong Basin lies between the well-known Tancheng-Lujiang fault zone and the Yangtze River fault zone, whereas the Ningwu basin is bordered by the Yangtze River fault zone and by several second-order faults.

The basement strata underlying the volcanic sequence consist mainly of the Triassic System and Lower-Middle

Jurassic Series. These units are composed of various clastic rocks, which are exposed at the periphery of the basins, with a total thickness of more than 3 km. Within the basins, the volcanic sequence is up to 1-2 km thick. It comprises four formations, representing four volcanic cycles. The volcanic products are lithologically varied, including a series of intermediate to basic rocks, such as andesite, pyroxene-andesite, trachyandesite, trachyte, phonolite, sedimentary-pyroclastic rocks and pyroclastic-sedimentary rocks, together with some fine-grained, clastic intercalations (Wu 1982; Ren et al. 1991, 1993).

Each volcanic extrusive cycle was generally followed by high level, magmatic intrusive events that account for the widespread occurrence of sub-volcanic porphyry bodies in the area. The extrusive and the intrusive igneous rocks are geochemically affiliated. Geochemical data, including trace elements, rare earth elements, Rb-Sr and Pb isotopes, suggest that the magmatism resulted from partial melting of the upper mantle, ascribed to the subduction of the paleo-Pacific plate under the Eurasian margin (Zhang 1981; Ren et al. 1991 1993; Zhai et al. 1996). The spatial distribution of the deposits inside the basins is zoned. The deposits characterized by predominant pyrite-anhydrite ore associations are preferentially located in the central part of the basins (e.g,. the Xiangshannan and the Mashan MSDs in the Ningwu Basin, and the Dabaozhuang, Luohe, Hejiaxiaoling and Huangcun MSDs in the Luzong Basin). The (pyrite)-sphalerite-galena and layered iron-oxide mineralizations occur mostly in the marginal depressions, showing a strong genetic relationship with the paleotopography of the basins. The occurrence of the iron oxide deposits seems not to have been controlled by this primary zoning as they occur either in the central or in the peripheral areas of the basins. The spatial coexistence and intimate relationship among several different types of mineralization in these basins is one of their most interesting features.

3 Exhalative-sedimentary features

The pyrite-anhydrite ores occur either as stratiform or lens-shaped orebodies, meters to tens of meters thick, and extend horizontally for several hundreds to one thousand meters. The orebodies are conformably hosted by the tuffaceous and/or sedimentary-pyroclastic rocks and occupy a well-defined position in the stratigraphic sequence, between the first and second volcanic cycles. The pyrite-anhydrite ores distribution in the basins indicates that these ores are preferentially hosted by pyroclastic strata, suggesting a permeability- controlled genetic relationship with these rocks (*cf.* Solomon et al. 1979). The deposits are commonly overlain by siliceous rock layers. No vertical or lateral spatial dependence seems to exist between the location of these ores and the timing and location of the neighboring intrusive rocks. It is believed that the generation of these deposits has depended exclusively of syngenetic, hydrothermal activity. Moreover, their stratabound morphology does not conform to the characteristics usually portrayed by porphyry-related mineralizations (Ren et al. 1991, 1993).

Banded Structures. The pyrite-anhydrite ores often exhibit internal structures that can be banded, striped or laminated. Bands can be parallel or oblique to bedding, with thicknesses ranging between about a millimeter and several centimeters. Some bands are very compacted, with a micro-scale massive structure, whereas others are loose, with uneven banding. In some ores, the size of the pyrite grains and/or of its aggregates varies laterally into ribbon structures, or vertically generating rhythmic banding. Pyrite and anhydrite bands are commonly interbedded.

"T"-type Structures. "T"-type structures were found in the Dabaozhuang, Hejiaxiaoling and Xiangshannan deposits. In these deposits, minor growth faults clearly control the deposition of the pyrite ores (and of coeval tuffs), whose thicknesses are variable in each side of the faults. This is interpreted to reflect a syn-depositional origin for these ores (Hu 1990; Hu et al. 1991).

Syn-depositional Breccia Structures. The pyrite-anhydrite ores frequently exhibit breccia structures. Abundant pyrite fragments, cemented by fine-grain pyrite, tuff and/or chalcedony can be found. Pyrite fragments vary considerably in size, but generally are one millimeter to several centimeters across. They show sharp angles, irregular shapes and are typically more massive than the cementing pyrite. Other kinds of fragments observed in these ores include siliceous and tuffaceous rocks. Pyrite clasts are probably derived from ore beds that formed earlier in the sequence.

Soft-sediment Deformation. In some pyrite- anhydrite ores, plastic deformation of the anhydrite beds was responsible for internal disturbance of the pyrite bands, which are curved and thinned. In places, dropping of pyrite fragments produced bends the underlying ore laminae. These deformation features are interpreted to have been generated at the syn-sedimentary stage when the sediments were still poorly consolidated.

Jasper. Siliceous exhalites are typical products of the MSD-forming processes (Gu et al. 1989, 2000; Humphris et al. 1995). Jaspers occur widespread in the studied deposits of both basins. These siliceous rocks do not correspond to "silicification caps" covering intrusive porphyry bodies. Instead, they occur as large conformable beds, typically with tabular or lens-shaped morphology, and extend for hundreds to about a thousand meters in length and tens to a hundred meters in thickness. They show no

spatial dependence relative to the porphyry intrusions. Most siliceous sediments overlie pyroclastic sequences and occur in close association with the pyrite-anhydrite-rich horizons, capping the ores or interbedded with them. The pyrite and some anhydrite ore beds commonly grade laterally into siliceous hydrothermal sediments.

Banded structures are relatively common in the jaspers. These can alternate with pyrite and/or anhydrite bands or beds at the millimeter to larger scales. Syn-depositional siliceous clasts can also be found in the ore-horizons.

Anhydrite. Precipitation of anhydrite and gypsum were common processes in the massive sulfide deposits of the two basins. In four of the studied deposits (Xiangshan, Xiangshannan, Dabaozhuang and Luohe; all located in central, basinal depressions), these processes were prominent enough to account for the formation of well-developed anhydrite beds. These anhydrite layers generally overlie the sulfide ore bodies and/or the siliceous beds, forming sulfide-jasper-anhydrite associations similar to those of the Kuroko deposits in Japan.

Sedimentary structures, such as laminations and bandings, are common in the anhydrite ores. Syn-depositional clasts of pyrite, of siliceous exhalites and of volcanic rocks are also common in this type of ore. The anhydrite beds consist mainly of anhydrite but may contain variable amounts of pyrite, silt, tuff and, occasionally, barite.

Unlike in most porphyry (iron-rich) deposits, where the paragenetic sequence of iron minerals usually evolved from high-temperature to low-temperature minerals, in the studied pyrite-anhydrite deposits, the lower-temperature minerals (e.g., pyrite, anhydrite, silicate, sericite) were extensively replaced by high-temperature ones (magnetite, hematite, garnet, diopside, actinolite). Several kinds of replacement relationships have been recognized, either involving ore minerals, or (and) gangue minerals, as follows:

1. Pyrite was extensively replaced by magnetite and/or hematite. The massive pyrite ores are commonly cut by magnetite veinlets. Relics of incompletely replaced pyrite enclosed in magnetite crystals can easily be observed. In places, the replacement process yielded a chalcopyrite "by-product".
2. Anhydrite and microcrystalline quartz were commonly replaced by albite, diopside, actinolite and apatite. The former minerals were typically preserved as relics within the latter.
3. The pyritic (plus hematite) ores were commonly affected by late albitization, accompanied by the formation of diopside and apatite; the siliceous hydrothermal sediments underwent extensive magnetitization.
4. A late generation of pyrite may complicate the interpretation of the paragenetic relationships described above. In one sample, euhedral to subhedral crystals of magnetite and hematite, resulting from the replacement of early massive pyrite, are partially replaced by a subsequent generation of pyrite of different optical and textural characteristics.

4 Discussion and conclusions

Unlike in previously proposed metallogenic models, two main mineralizing events, which cannot be attributed to a single ore-forming process, are clearly distinguished in the studied deposits. The lower temperature mineral association (e.g. pyrite, anhydrite, and siliceous exhalites) is thought to have formed prior to the higher temperature, silicate/iron oxide paragenesis (e.g., magnetite, hematite, albite, diopside, actinolite). Whereas the former appears to have resulted from an early event of volcano-hydrothermal exhalative activity, the later event is believed to have resulted from subsequent magmatic-hydrothermal activity associated with the sub-volcanic porphyry intrusions. The alteration/mineralization consequences of the later event are superimposed upon and heavily obscure the former event.

The sedimentary-exhalative process is thought to have occurred during the waning stage of the first volcanic cycle. By that time, the two basins had suffered deep subsidence. Some restricted depressions might have developed in the central part of the basins, which could have supplied the volcanic-hydrothermal system with water. Active faults were common in this volcanic setting. These would have favored the focusing of the rising hydrothermal fluids, leading to the precipitation of siliceous exhalites, massive sulfide ores and anhydrite beds in a number of relatively large (and deep) depressions (e.g. Dabaozhuang in Luzong, and Xiangshan in Ningwu basins).

The overprinting and strong modification of the hydrothermal products by higher-temperature ore and gangue mineral assemblages took place at the final stage of the second volcanic cycle, coeval with the intrusion of most sub-volcanic porphyry rocks in the area. Combined with intensive momentum, this extensive magmatic activity brought tremendous heat energy and a large volume of metal-bearing solutions up to shallow levels in the crust. High-temperature, hydrothermal reworking and mineral precipitation, superimposed on the earlier exhalative associations, led to a series of replacement reactions and new iron mineralization associations. As a consequence, the pyrite-anhydrite deposits in the two basins studied display some characteristics that denote the superimposition of an iron-rich porphyry hydrothermal system over a sedex-type massive sulfide deposit. It is emphasized that the deposits have developed in continental basins rather than in marine basins. This observation widens the spectrum of geological settings considered of interest to economic geologists in the search for massive sulfide deposits.

References

Gu L, Zheng S (1989) A Review on the Study of Massive Sulphide Deposits. Geological Science and Technology Information 8(2):67~73

Gu LG, Hu W, He J (2000) Regional Variations in Ore Composition and Fluid Features of Massive Sulphide Deposits in South China: Implications for Genetic Modelling. Episodes 23(2):110-118

Hu W (1990) Exhalative Sedimentation and Hydrothermal Superimposition-transformation Characteristics of the Xiangshannan Pyrite Deposit, Anhui Province. Mineral Deposits 9 (4):375-384

Hu W, Xu K, Hu S, Ren Q (1991) Exhalative sedimentation and hydrothermal transformation- superimposition iron and pyrite deposits in the Ningwu-Luzong continental volcanic basins. Beijing: Geological publishing house

Humphris SE, Herzig PM, Miller DJ (1995) The Internal Structure of an Active Sea-floor Massive Sulphide Deposit. Nature 377(.26):713-716

Hutchinson RW (1984) Massive Sulphide Deposits and Their Significance to Other Ores. Paper for fifth regional congress on geology, mineral and energy resources of Southeast Asia

Ningwu Iron Deposit Project (NIDP) Research Group (1978) Ningwu-type porphyrite-iron deposits, Beijing: Geological Publishing House

Ren Q, Liu X, Xu Z (1991) The Mesozoic Volcanic Depression and Ore-forming Processes in the Lujiang-Zongyang Area, Anhui Province. Beijing: Geological Publishing House

Ren Q, Wang D (1993) Formation and Development of the Mesozoic Lujiang-Zongyang Volcanic-structural Depression in Anhui Province and Their Relation to Mineralization. Acta Geologica Sinica 67(2):131-145

Solomon M, Walshe JL (1979) The Formation of Massive Sulfide Deposits on the Sea Floor. Economic Geology, l74:797-813

Spooner ETKC, Fyfe WS (1973) Sub-sea Floor Metamorphism, Heat and Mass Transfer. Contr. Mineralogy Petrology 42:287-304

Wang Z (1982) Lujiang-Zongyang Cauldron Subsidence, Bulletin of the Nanjing Institute of Geology and Mineral resources. Chinese Academy of Geological Sciences 3 (1): 16-36

Wu L (1982) Mesozoic Volcanic Rocks in the Eastern Part of China, Acta Geologica Sinica, l56(3):223-234

Siting of gold and characteristics of gold-bearing massive sulfides from the interior of the felsic-hosted PACMANUS massive sulfide deposit, eastern Manus basin (PNG)

T. Ihle
Department of Economic Geology and Petrology, Freiberg University of Mining and Technology, Germany

S. Petersen, P.M. Herzig
Leibniz-Laboratory for Marine Sciences, IFM-GEOMAR, Kiel, Germany

M.D. Hannington
Department of Earth Sciences, University of Ottawa, Canada

Abstract. Precious- and base metal-rich massive sulfides from the interior of the active Roman Ruins site (PACMANUS) locally contain abundant native gold in two distinct mineralogical associations: (I) with chalcopyrite-sphalerite dominated mineral assemblages and (II) with sphalerite-barite-amorphous silica-rich mineral assemblages. The silver content is variable and is lower for Cu-Zn-hosted gold (avg. 3.6 wt. % Ag; range from 1.2 to 8.7 wt.% Ag) and higher for Zn-Ba-hosted gold (avg. 11.3 % Ag; range from 8.0 to 16.4 wt.% Ag). The latter is in marked contrast to previously published results for surface samples from PACMANUS that showed only high gold fineness values. The FeS-content of sphalerite associated with native gold is low in the Cu-Zn-rich core section (0.1 to 6.0 mole % FeS; avg. 0.6 mole % FeS), but higher in Zn-Ba-rich mineral assemblages (0.1 to 18.7 mole % FeS; avg. 6.5 mole % FeS) indicating a larger variability in the sulfur activity than previously documented. The combination of the siting of gold at Roman Ruins and the variability of the gold fineness and the Fe-content of associated sphalerite is distinct from most other seafloor hydrothermal systems and indicates that refining of primary gold is not responsible for the enrichment of gold in Zn-rich sulfide assemblages at Roman Ruins.

Keywords. Drilling, PACMANUS, gold-rich VMS, gold-fineness

1 Introduction

Primary gold enrichment in seafloor massive sulfides is common both in deposits in back-arc basins or volcanic arcs, where they are associated with bimodal or felsic volcanic rocks, and in ultramafic-hosted deposits along the Mid-Atlantic Ridge (Herzig et al. 1993; Moss and Scott 2001; Watanabe and Kajimura 1994; Murphy and Meyer 1998). In modern seafloor hydrothermal systems gold enrichment is commonly associated with Zn-rich mineral assemblages (Hannington et al. 1999). Native gold generally shows low Ag-contents and, in addition, the associated sphalerite is largely Fe-poor indicating a high activity of sulfur and oxygen during formation (Hannington et al. 1995). Investigations of surface samples from Satanic Mills at PACMANUS and Susu Knolls, both in the Eastern Manus Basin, documented a Cu-As-rich mineral assemblage hosting native gold (Moss and Scott 2001). Here, native gold grains are almost Ag-free and are largely hosted by tennantite and chalcopyrite in Zn-Cu-rich assemblages. In 2002, we successfully deployed the British Geological Survey (BGS) Rockdrill from the German R/V SONNE and drilled 10 holes (up to 5 m in length) at the Roman Ruins site at PACMANUS (Petersen et al. 2003). Here we report on the siting and mineral chemistry of gold from the precious-metal enriched drill core samples in order to document the similarities and differences to previously published results from the Eastern Manus Basin.

2 Geological setting

The Manus Basin is a rapidly opening (~ 10 cm/yr) back-arc basin located north of the active New Britain subduction zone (Fig. 1). The regional tectonic complexity is a consequence of the northward subduction of the oceanic Solomon Microplate beneath the South Bismarck Microplate. True seafloor spreading occurs in the Central and Western Manus Basin whereas the Eastern Manus Basin is characterized by extensional rifting.

The Eastern Manus basin, host to several hydrothermal sites including PACMANUS, DESMOS, and SuSu knolls, represents a pull-apart structure in former island arc crust, and is situated between two sinistral fault zones (Binns et al. 2002). The PACMANUS hydrothermal field is situated near the bathymetric minimum of the elongated Y-shaped NE-SW trending Pual Ridge. The Ridge itself is terraced and consists of stacked 5-30 m thick lava flows representing a suite of eruptives formed by magmatic differentiation starting with basalt and ending with rhyodacite (Binns et al. 2002).

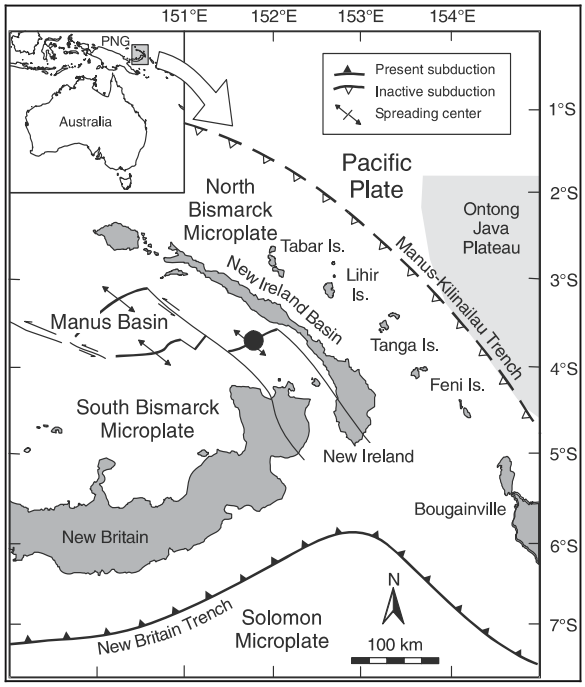

Figure 1: Location and plate tectonic setting of the PACMANUS hydrothermal field (solid circle).

Table 1: Mode of occurrence of gold grains in drill core samples from Roman Ruins in comparison to published data from the Eastern Manus Basin (EMB = Satanic Mills and SuSu Knolls; Moss and Scott, 2001). [1] – fractures in minerals.

	65RD	69RD	EMB
Inclusions in chalcopyrite	172	65	49
sphalerite	6	394	5
pyrite	27	1	-
amorphous silica	2	69	-
galena	-	1	-
tennantite	-	-	232
bornite	-	-	1
Grain boundaries	11	82	7
Cavity fill	12	35	4
Other	-	46	5[1]
Total	230	693	303

3 Results

Two days of drilling at the active Roman Ruins vent site recovered 9 m of precious- and base-metal enriched massive sulfides with up to 57 g/t Au and up to 585 ppm Ag. Average precious and base metal contents of individual drill core samples (¼ core sections, between 20 and 50 cm in length) are 10.8 ppm Au, 156 ppm Ag, 17.4 wt.% Zn, 4.2 wt. % Cu and 0.5 wt. % Pb (N=35). The gold is heterogeneously distributed in the cores and the highest grades are in sections that are mineralogically distinct. Section 65RD(010-030cm), which contains 57.2 g/t Au, 135 g/t Ag, 12.7 wt. % Cu, 12.2 wt. % Zn and 0.1 wt. % Pb consists of abundant chalcopyrite in close association with dark-brown sphalerite, whereas section 69RD(085-120cm) is dominated by porous, brown sphalerite plus barite and contains 30.4 g/t Au, 403 g/t Ag, 0.4 wt. % Cu, 44.7 wt. % Zn and 1 wt. % Pb.

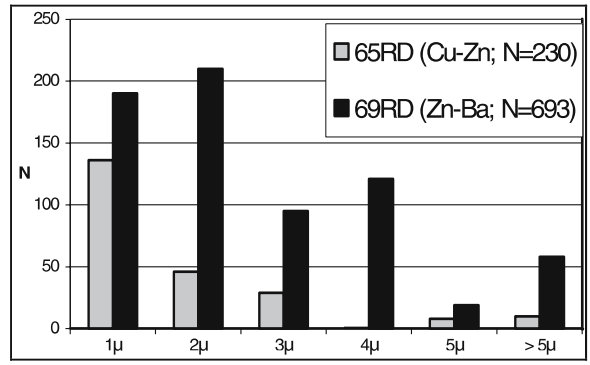

Figure 2: Grain size distribution of native gold in massive Cu-Zn- and Zn-Ba-rich assemblages from the interior of the Roman Ruins site at PACMANUS.

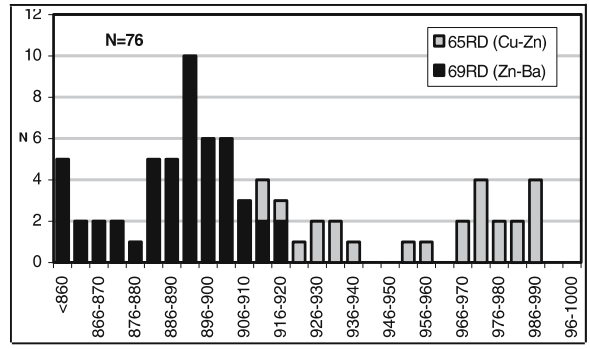

Figure 3: Gold-fineness (1000*Au/(Au+Ag)) of native gold in massive Cu-Zn- and Zn-Ba-rich assemblages from the interior of the Roman Ruins site at PACMANUS (N=76).

Native gold in the Zn-Ba-rich section 69RD(085-120cm) occurs predominantly as micron-sized inclusions in chalcopyrite, sphalerite and to a lesser extent in amorphous silica (Table 1). Other, minor sulfides co-precipitated with sphalerite in this core, such as galena and pyrite, do not contain native gold. Gold grains in the Cu-Zn-rich section 65RD(010-030cm) are found as inclusions in chalcopyrite and pyrite, with few grains hosted by sphalerite and amorphous silica. Some grains are situated on grain boundaries between early co-precipitated chalcopyrite and sphalerite. Larger, isolated grains commonly occur at grain boundaries and in cavities of early chalcopyrite. Several

gold grains in both mineral assemblages occur as late-stage cavity-fillings.

The gold grains observed in both drill-core sections are mostly rounded and small (75% less than 4 μm; only few are between 6 and 10 μm), with smaller grains often occurring in clusters. The gold grains of the Zn-Ba mineral assemblage are distinctly larger than those in the Cu-Zn-rich core section 65RD(010-030cm), however, none of the grains is larger than 10 μm in diameter (Fig. 2).

Gold grains contained in the Cu-Zn assemblage are generally Ag-poor (avg. 3.6 wt. % Ag, gold fineness (1000*Au/(Au+Ag)) varies from 912 to 988, N=25) in contrast to the gold grains in Zn-Ba assemblages (avg. 11.3 % Ag, gold fineness varies from 836 to 920, N=51, Fig. 3).

Microprobe analyses of sphalerite from the Cu-Zn-rich core section 65RD(010-030cm) reveal a low Fe-content (avg. 0.6 mole % FeS, N=288; Fig. 4) indicating a high activity of sulfur during precipitation of this Cu-Zn-rich mineral assemblage. In contrast sphalerite from the Zn-Ba-rich section 69RD(085-120cm) is characterized by a more variable and higher Fe-content (avg. 6.6 mole % FeS, N=474) indicating a distinctly lower activity of sulfur for this mineral assemblage.

4 Discussion

The behavior of gold in seafloor hydrothermal systems has been discussed in detail in terms of solubility models based on aqueous chloride ($AuCl_2^-$) and reduced sulfur complexing ($AuHS_2^-$ or $AuHS^0$; Hannington et al. 1986; Huston and Large 1989; Moss and Scott 2001). Gold may be transported as $Au(HS)_2^-$ in fluids of weakly acid to near-neutral pH, low salinity, temperatures less than 350°C and moderately reducing conditions and high αH_2S (Seward and Barnes 1997). Benning and Seward (1996) and Gibert et al. (1998) have shown that the AuHS°-complex is the dominant complex for fluids with a lower pH and lower αH_2S, while chloride complexing is only important for high-temperature fluids with a low pH, low sulfur concentrations and high salinities. The $Au(OH)^0$-complex may also play an important role in gold transport at temperatures between 300° and 500°C (Gammons and William-Jones 1997).

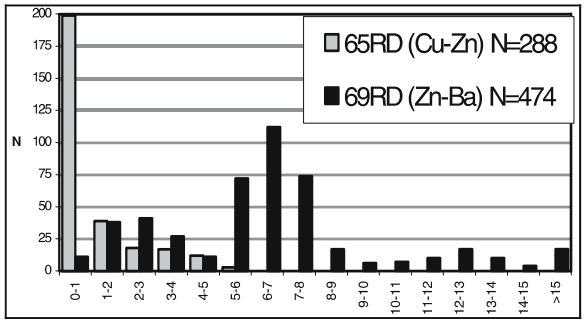

Figure 4: Mole % FeS in sphalerite from two Au-rich massive sulfide core sections from Roman Ruins, PACMANUS.

Our study revealed distinct differences between Satanic Mills and Roman Ruins with regard to the mineralogy of gold-bearing massive sulfide assemblage, and the host and fineness of native gold grains. Tennantite, the major host in samples studied by Moss and Scott (2001) is only a rare component in drill core samples from Roman Ruins and, when present, does not contain inclusions of native gold. Bornite another mineral commonly found at Satanic Mills is also rare or absent in samples from the interior of Roman Ruins. Also, the sulfur activity for the Zn-Ba-assemblage at Roman Ruins seems to be distinctly lower than documented for Satanic Mills by Moss and Scott (2001).

At Roman Ruins the association of native gold with two distinct mineral assemblages (Cu-Zn, Zn-Ba), the variability in gold fineness and inferred sulfur activity suggest differences in transport and/or depositional controls between the two Au-rich mineral associations. Native gold in the Zn-Ba-rich mineral assemblage may be the result of remobilization, transport and re-precipitation of gold as suggested for other sites by Hannington et al. (1995), however, gold is commonly refined during this process separating Au from Ag and resulting in native gold containing distinctly less silver. This is not the case in our samples and indicates that refining of primary gold is not responsible for the enrichment of gold in Zn-rich sulfide assemblages at Roman Ruins. Gold may be precipitated by a large decrease in temperature in order to overcome the solubility maximum between 150° and 250°C or by oxidation of H_2S during mixing with seawater (Hannington et al. 1989). The presence of barite in the Zn-rich section 69RD(085-120cm) may be an indication for this mixing.

Precipitation of gold in the interior of Roman Ruins may therefore have proceeded from a chalcopyrite-rich stage with high-temperature fluids and relatively high αH_2S, as indicated by the low Fe-content of sphalerite and the high fineness of the native gold grains. Gold precipitation may then have continued to lower temperatures as a consequence of lowering αH_2S during continued precipitation of sulfides, probably with associated mixing with seawater. However, it is possible that the two different paragenetic relationships may be related to two different mineralizing events under different physico-chemical conditions.

Moss and Scott (2001) have shown that the $AuHS^0$-complex is likely responsible for the transport of gold in fluids from PACMANUS. This is likely also true for the Zn-Ba mineral assemblage at Roman Ruins, since $AuHS^0$ is stable at lower sulfur activities and the $AuHS_2^-$-complex is only important at higher sulfur activities, not present at Roman Ruins.

Acknowledgements

This project is funded by the German Federal Ministry for Education and Research through a grant to PMH (grant: 03G0166A). Additional funding was provided by the Leibniz Program of the German Research Association. TI thanks the Society of Economic Geologists for a student research grant (2003).

References

Benning LG, Seward TM (1996) Hydrosulphide complexing of Au(I) in hydrothermal solutions from 150 to 400°C and 500 to 1500 bars. Geochim Cosmochim Acta 60:1849-1871

Binns RA, Barriga, F Miller DJ (2002) Leg 193 summary. In: Binns RA, Barriga FJAS, Miller DJ (eds) Proc ODP, Init Rep. 193. College Station, TX: 1-84

Gammons CH, Williams-Jones AE (1997) Chemical mobility of gold in the porphyry-epithermal environment. Econ Geol 92: 45-59

Gibert F, Pascal ML, Pichavant M (1998) Gold solubility and speciation in hydrothermal solutions: experimental study of the stability of hydrosulphide complex of gold (AuHS°) at 350 to 450°C and 500 bars. Geochim Cosmochim Acta 62: 2931-2947

Hannington MD, Poulsen KH, Thompson JFH, Sillitoe RH (1999) Volcanogenic gold in the massive sulfide environment, in Barrie, C. T., and Hannington, M. D., eds., Volcanic-associated Massive Sulfide Deposits: Processes and Examples in Modern and Ancient Settings. Rev Econ Geol 8:325-356

Hannington MD, Tivey MK, Larocque AC, Petersen S, Rona PA (1995) The occurence of gold in sulfide deposits of the TAG hydrothermal field, Mid-Atlantic Ridge. Can Mineral 33: 1285-1310.

Herzig PM, Hannington MD, Fouquet Y, von Stackelberg U, Petersen S (1993) Gold-rich polymetallic sulfides from the Lau back-arc and implications for the geochemistry of gold in sea-floor hydrothermal systems in the Southwest Pacific. Econ Geol 88: 2182-2209

Huston DL, Large RR (1989) A chemical model for the concentration of gold in volcanogenic massive sulfide deposits. Ore Geol Rev 4:171-200

Moss R, Scott SD (2001) Geochemistry and mineralogy of gold-rich hydrothermal precipitates from the Eastern Manus Basin, Papua New Guinea. Can Mineral 39:957-978

Murphy PJ, Meyer G (1998) A gold-copper association in ultramafic-hosted hydrothermal sulfides from the Mid-Atlantic Ridge. Econ Geol 93:1076-1083

Petersen S, Herzig PM, Hannington MD, Gemmell JB (2003) Gold-rich massive sulfides from the interior of the felsic-hosted PACMANUS massive sulfide deposit, Eastern Manus Basin (PNG). In: Eliopoulos DG (ed) Mineral Exploration and Sustainable Development, Proceedings of the 7th biennial SGA meeting Athens, Greece. Millpress, Rotterdam:171-174

Seward TM, Barnes HL (1997) Metal transport by hydrothermal fluids, in Barnes, H. L. (ed) Geochemistry of Hydrothermal Ore Deposits. John Wiley, Sons Inc. New York:435-486

Watanabe K, Kajimura T (1994) The hydrothermal mineralization at Suiyo Seamount, in the central part of the Izu-Ogasawara Arc. Res Geol 44:133-140

Volcanic stratigraphy, chemical stratigraphy and alteration system of the Storliden massive sulphide deposit, Skellefte district, northern Sweden

Marcello Imaña
Division of Ore Geology and Applied Geophysics, Luleå University of Technology, SE-987 71 Lulea, Sweden

Rodney Allen
Volcanic Resources Limited, Strömforsvägen 87, Boliden 936 91, Sweden

Tim Barrett
Ore Systems Consulting, 29 Toronto St. S., Markdale, Ontario, ON N0C 1H0, Canada

Abstract. The Storliden massive sulphide deposit is hosted by a thick tholeiitic volcanic succession that mainly comprises andesitic and rhyolitic volcaniclastic rocks and felsic synvolcanic sills. Metamorphic recrystallization of hydrothermally altered rocks associated with the massive sulphides has produced a distinct coarse grained "spotty" mineralogy, composed of muscovite-biotite, cordierite-phlogopite, and spinel-orthoamphibole-humite assemblages, which obscures the original stratigraphy. Using a combination of physical facies mapping and immobile-element-based litho-geochemical methods, the stratigraphy in the alteration zone has been identified and correlated with the more distal least altered areas. The application of this lithogeochemical approach to several cross sections has enabled interpretation of synvolcanic structures and cross cutting relationships between alteration and stratigraphy. Quantification of the alteration effects is based on the calculation of mass changes, which indicates that significant amounts of Mg, Si and Fe have been added near the orebody.

Keywords. Chemostratigraphy, massive sulphide, tholeiitic, Storliden, Skellefte district

1 Introduction

Palaeoproterozoic tholeiitic volcanic rocks host the Storliden deposit in the NW part of the Skellefte district. The lower part of the stratigraphy consists of weakly deformed and weakly metamorphosed basaltic to andesitic tuffaceous sandstones and subordinate Al-rich porphyritic pillow lavas and fire fountain deposits. The upper part consists of a bimodal sequence that includes andesitic tuffaceous sandstones, felsic syn-volcanic sills and juvenile resedimented pyroclastic rocks. The whole succession has moderate to gentle dips towards the northeast (Fig. 1).

2 The Storliden deposit

Storliden is a high-grade Zn-Cu ore deposit, containing 1.8 Mt at 10.3% Zn, 3.5% Cu, 0.25 g/t Au and 24 g/t Ag. In contrast to other massive sulphide ores in the Skellefte district, the Storliden ore is very coarse-grained, composed of sphalerite, chalcopyrite, pyrrhotite and calcite, and contains almost no pyrite. The orebody forms a single, flat-lying, stratabound lens within the uppermost part of a felsic pumiceous crystal-rich unit (Fig. 2).

Storliden has a distinct, asymmetric alteration system, which consists of six metamorphosed alteration facies. The innermost zone comprises intensely silicified rocks and is surrounded by a distinct and persistent layer of spinel-orthoamphibole-humite. This is succeeded outward by spotted cordierite-anthophyllite, cordierite-phlogopite and biotite-muscovite as-

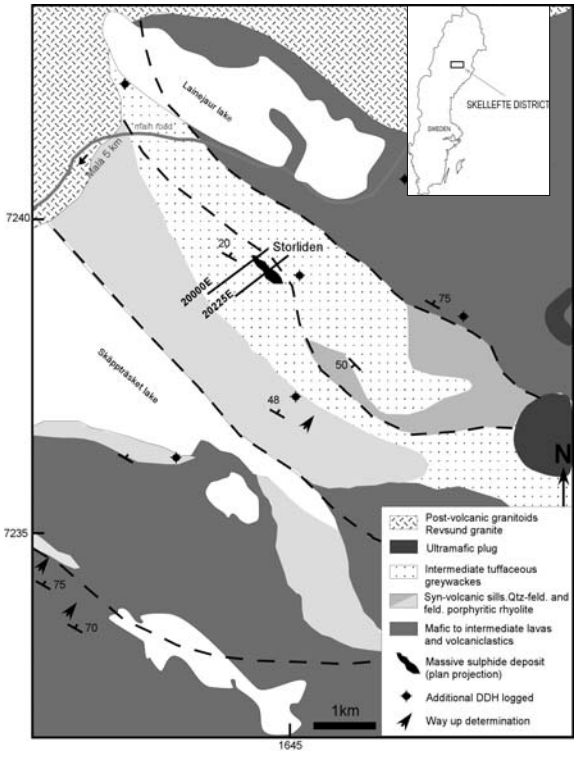

Figure 1: General geology of the Storliden area, location of the orebody and cross sections.

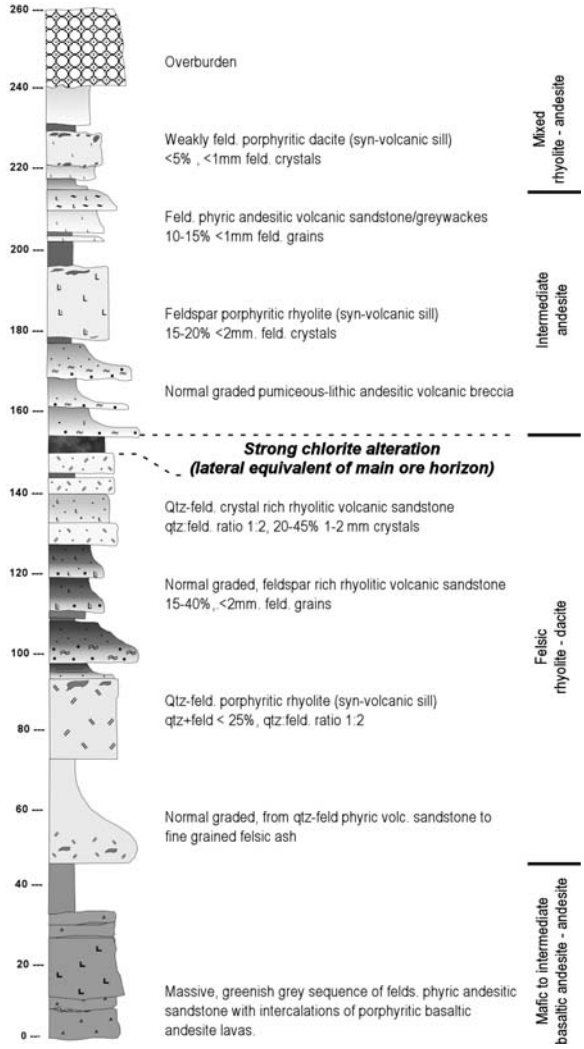

Figure 2: Local stratigraphic column located 300 metres from the Storliden deposit.

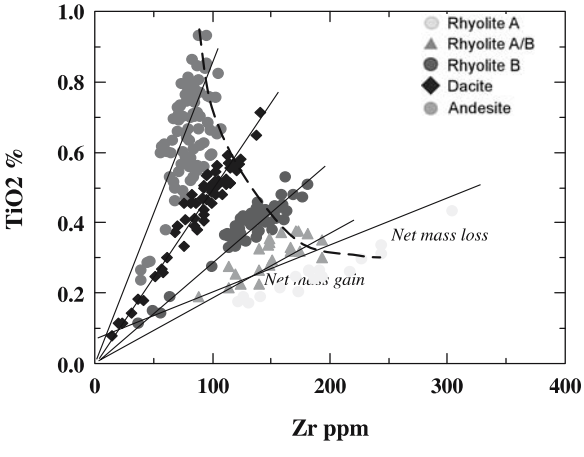

Figure 3: Alteration lines for chemical units. Dashed lines indicate a primary fractionation curve based on the least altered samples

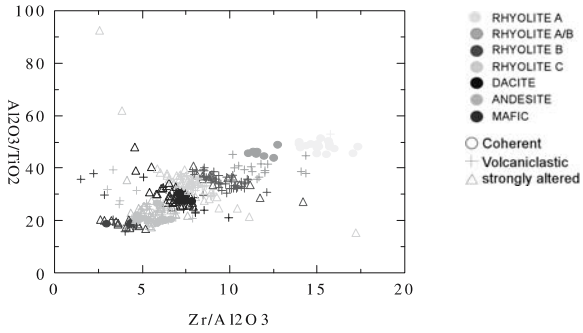

Figure 4: Immobile element ratios are plotted against each other. Chemical groups show a continuous trend from basalt to rhyolite. Scatter in some samples is produced by sedimentary enrichment of feldspars in some clastic beds.

semblages. Skarn alteration is common and forms mainly where the inner alteration zones overprint earlier diagenetic pods of calcitic alteration. Relicts of silicified volcaniclastic rocks within the ore lens suggest that the ore formed by replacement of the volcaniclastic sedimentary rocks.

3 Lithogeochemical classification

Thirty six drillholes, comprising four cross sections from proximal to distal areas of the orebody, were selected for systematic litho-geochemical sampling. Samples were taken every 15-20 m along the drill cores and were analysed by ACME Laboratories (Vancouver) by ICP-MS techniques.

Ratios of "immobile" elements such as Al, Ti, Zr, Y and REE proved to be very useful in reconstructing the original composition of altered and metamorphosed rocks. Using the approach of MacLean and Kranidiotis (1987), seven chemically distinct units have been identified and correlated throughout the mine area. In Fig. 3, plots of TiO2 versus Zr define alteration trends associated with addition or subtraction of mobile components within each of these chemically distinctive units.

The rock units show an almost continuous range in composition from basaltic to rhyolitic; this effect is clearly seen in a ratio-ratio plot involving immobile elements (Fig. 4). Barrett et al. (2004) stated that a ratio-ratio plot of immobile elements assists to discriminate chemical rock types by removing effects of alteration. Despite this, a few samples plot outside the general trend in Fig. 4. This effect is attributed to mechanical enrichment of phenocrysts during sedimentation of crystal-rich graded beds as documented by Imaña et al. (2004) in least altered areas at Storliden.

In contrast to other areas in the Skellefte district, Storliden represents an entirely tholeiitic volcanic domain; both mafic and felsic rocks have Zr/Y ratios < 4, and flat REE patterns, with $La_n/Yb_n < 2.5$ (Fig. 5a, b).

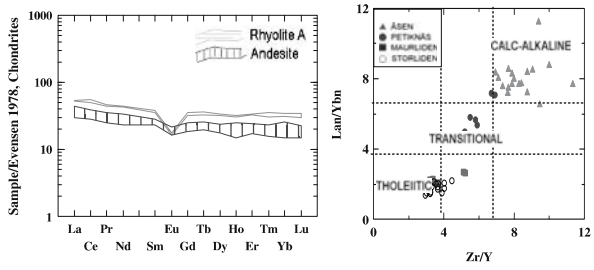

Figure 5: a. Typical REE patterns of volcanic rocks from the Storliden area. b. Plot indicating the magmatic affinity of representative least altered felsic rocks from different volcanic

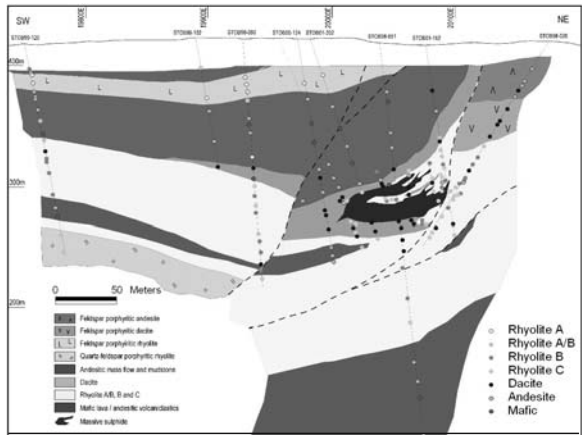

Figure 6: Chemostratigraphic relations on section 20225 east.

4 Chemostratigraphy

The distribution of chemically defined units on geological sections enables correlation of four different packages across the alteration zone in the mine area (Fig. 6). The ore-bearing unit is a 60 to 130 m thick rhyolitic interval, mainly composed of rhyolite B, rhyolite C and rhyolite A/B. The orebody occurs towards the top of this rhyolitic unit, and coincides with a series of small dacitic intercalations. Andesitic and basaltic rocks occur in two units, the uppermost one is a 70-100 m thick unit that lies immediately above the felsic ore horizon. A second mafic unit occurs lower in the stratigraphy and its total thickness is at least 140 m in the mine area, while in other areas more than 350 m have been reported from drillholes.

A series of coherent andesitic, dacitic and rhyolitic synvolcanic sills pass from unaltered areas into the alteration zone, and due to their homogeneous nature, they provide an unequivocal test to the immobility of Ti, Zr, Y and the REE in the Storliden alteration system.

5 Alteration

In order to quantify the chemical effects of alteration on each sample, a multiple precursor method (MacLean 1990) has been carried out to calculate mass changes in each element. The mass change calculations indicate that the main effects of alteration were strong Na depletions and significant additions of Si, Mg and Fe towards the orebody, Alteration effects extend asymmetrically at least 100 metres along strike and above the orebody, and 10-15 metres below it. The amount of Mg added varies from 40 wt. % near the thickest part of the ore to <5 wt. % in the distal areas. The added Mg is clearly distinguished in the central part of the system where metamorphic assemblages form distinct zones of orthoamphibole, spinel and cordierite. These metamorphic assemblages envelope the southwestern part of the ore lens as illustrated on Fig. 7. Similarly, intense Si additions are prominent in rocks within and adjacent to massive sulphides, with typical Si gains of >40 wt. %. (not shown). Silicification has been identified in most synvolcanic sills and some pumiceous crystal rich deposits, but in contrast to the ore-related Si additions, this alteration type has discrete Si and Na gains and very low metal values. This later type of silicification is attributed to pre-mineralization processes involving local remobilisation of alkalis and concentrations of silica due to quenching and cooling of the synvolcanic intrusions. A similar process has been documented to occur in welded pyroclastic rocks in Snowdonia (Howells et al. 1991).

6 Conclusion and implications

Integration of physical volcanology and lithogeochemical techniques has enabled reconstruction and correlation of the stratigraphic succession in strongly metamorphosed and hydrothermally altered areas at Storliden.

Fracture controlled alteration zones are well developed near the central part of the orebody and cut the stratigraphy. Despite this, the bulk of the mineralization at Storliden occurs near the contact between a thick crystal- and pumice-rich volcaniclastic unit and an overlying andesitic tuffaceous unit. Local lateral facies changes seem to be controlled by syn-volcanic faults. Consequently, study of volcanic facies and correct identification of prospective horizons can improve exploration strategies. Once a prospective horizon is identified, quantification of alteration effects by the aforementioned methods provides geochemical vectors towards mineralization.

The coherent sills and volcaniclastic rocks at Storliden have similar REE patterns and similar primary mineralogy and porphyritic textures, which suggest that they are genetically related. The marine paleoenvironment, the predominantly tholeiitic andesitic to basaltic compositions together with geochemical evidence for subduction and primitive Sm-Nd isotopic characteristics, suggest that the Storliden volcanic rocks formed in a relatively primitive and marine volcanic arc environment that was none-

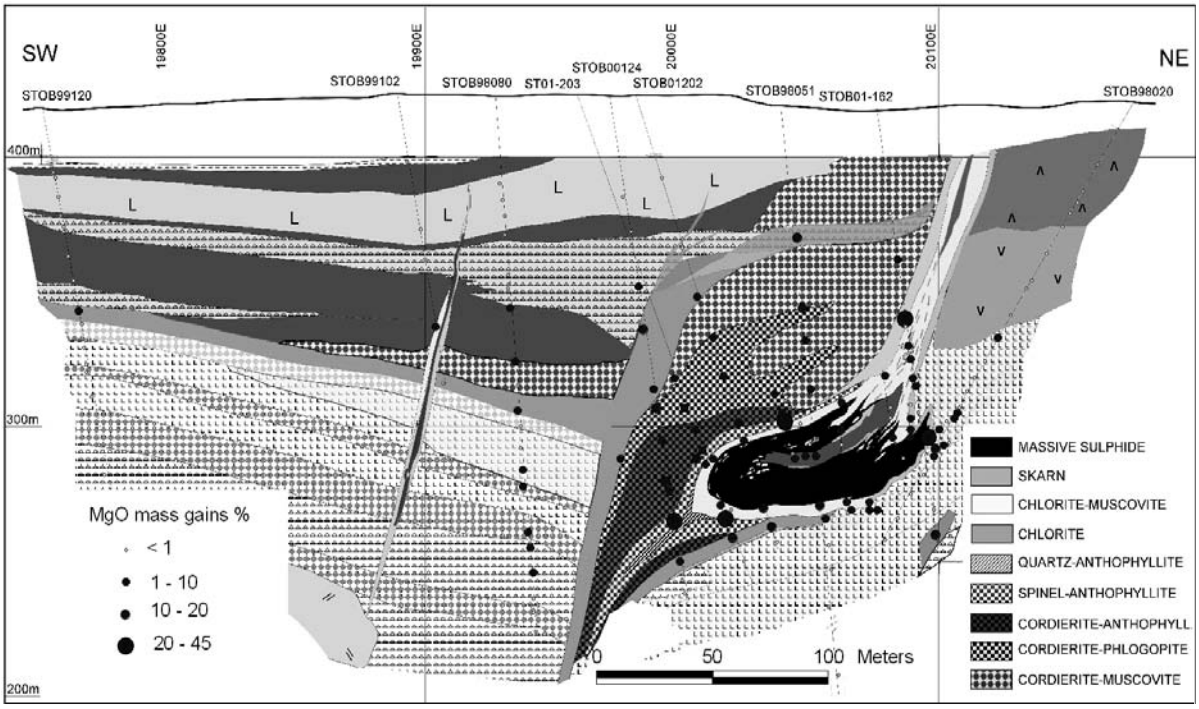

Figure 7: Alteration pattern and Mg mass changes in section 20225 east.

theless spatially associated with the rhyolite-dacite-andesite dominated Skellefte arc. This environment may have been a less mature part of the arc (thin arc crust?) or an extensional (back-arc or intra-arc) basin, possibly floored by oceanic crust, within the arc terrane. The Fe-Cu-Zn-rich and Pb-poor composition of the Storliden massive sulphides is also consistent with this interpretation. An alternative interpretation is that the Malå-Storliden domain could represent an intra-oceanic arc basin that has subsequently docked and amalgamated with the Skellefte arc terrane. Massive sulphide mineralization has also been reported in modern intra-oceanic arc basins settings in the Philippines, British Columbia and the Flin Flon region in Canada, (Barrett and MacLean 1999; Sherlock and Barrett 2004). These scenarios open new exploration potential in similar more primitive volcanic areas in the Skellefte district.

Acknowledgements

This paper forms part of the doctoral research of MI founded by the Georange. Stig Liedberg and Magnus Leijd are thanked for fruitful discussions.

References

Barrett TJ, MacLean WH (1999) Volcanic-associated massive sulphide deposits: processes and examples in modern and ancient settings. In: Barrie C, Hannington MD (eds) Reviews in economic geology 8: 101-131

Barrett TJ, MacLean WH, Arebäck H (2003) Chemostratigraphy, alteration and metamorphism of Paleoproterozoic volcanic rocks at the Kristineberg VHMS deposit, northern Sweden. In: Eliopoulos DG et al. (eds), Proceedings of the seventh biennial SGA meeting, Athens, Greece, August 24-28, 2003, 1: 107-110

Howells MF, Reedman AJ, Campbell SDG (1991) Ordovician (Caradoc) marginal basin volcanism in Snowdonia (north-west Wales) London: HMSO for the British Geological Survey 30-165

Imaña M, Allen RL, Barrett TJ (2004) The origin of crystal-rich tuffaceous sandstones in the Storliden area, Skellefte district, Sweden: evidence for deposition by syneruptive subaqueous gravity flows. Proceedings of the IAVCEI meeting Pucon, Chile, November 14-19, 2004

MacLean WH (1990) Mass changes calculations in altered rock series. Mineralium Deposita 25:44-49

MacLean WH, Kranidiotis P (1987) Immobile elements as monitor of mass transfer in hydrothermal alteration: Phelps Dodge massive sulphide deposit, Matagami, Quebec. Economic Geology 82: 951-962

Sherlock RL, Barrett TJ (2004) Geology and volcanic stratigraphy of the Canatuan and Malusok volcanogenic massive sulphide deposits, southwestern Mindanao, Philippines. Mineralium Deposita 39:1-20

Silica gel microtextures in siliceous exhalites at the Soloviejo manganese deposit, Spain

R.C.G.S. Jorge, J.M.R.S. Relvas, F.J.A.S. Barriga
CREMINER /Dep. Geologia, Fac. Ciências, U. Lisboa, Ed. C6, Campo Grande, 1749-016 Lisboa, Portugal

Abstract. Well-preserved primary textural features were recognized in cherts and jaspers that form one of the manganese ore-hosting units of the Soloviejo Mn deposit, in the Iberian Pyrite Belt. These include (i) spherulitic, (ii) banded and (iii) brecciated. The spherulites (0.04-0.3 mm) consist of a central core of minute grains of hematite or quartz, rimmed by chalcedony or microcrystalline quartz. Banded jaspers show no spherulitic textures. Banded textures are made up by alternations of micro- to meso-bands of silica and hematite. They often show soft-sediment deformation features, such as microslumps, pinch-and-swell, and load cast. Diagenetic brecciation overprints these pristine textures. Breccias consist of jasper fragments (mm to cm), affected by total or partial recrystalization, cemented by different proportions of microcrystalline quartz. Primary textures in siliceous hydrothermal precipitates reflect different stages of formation and diagenetic maturation of its silica gel precursor. Their interpretation helps in constraining the initial conditions assisting the hydrothermal activity at the Soloviejo deposit, and its early evolving stages.

Keywords. Siliceous exhalites, gel, diagenesis, manganese mineralization, Iberian Pyrite Belt

1 Introduction

Fe-Mn-Si rich exhalites have been recognized in numerous active seafloor hydrothermal systems and volcanic-hosted massive sulphide (VHMS) districts worldwide. Well-established genetic models consider the formation of these hydrothermal products as consequence of VHMS generative processes. In the Iberian Pyrite Belt (IPB), the exceptional expression of these hydrothermal sedimentary facies, now mainly represented by jaspers and cherts, is one of its more salient characteristics (Leistel et al. 1998, and references therein). The meta-exhalites occur regionally, frequently are tens of meters thick, and lie in various stratigraphic positions within the massive sulphide-hosting Volcanic-Siliceous Complex (VS; Late Devonian-Early Carboniferous). Meaningfully, the maximum development of these chemical sedimentary rocks occurs generally either above or along strike from the massive sulphide orebodies. In addition, more than three hundred large and small manganese occurrences are known in the IPB. These are hosted by several different lithologies, namely jaspers, cherts, tuffites, and siliceous shales.

Soloviejo was the largest manganese deposit in the IPB. During 87 years of continuous mining, which was interrupted only in 1973, production was *ca.* 0.2 Mt of manganese ores at 35% Mn (del Villar and Aranda 1995). Jorge (2000) and Jorge et al. (2002) have shown that, like in many other locations of the IPB, at Soloviejo large-scale, low-temperature hydrothermal activity formed extensive deposits of siliceous precipitates on the paleo-seafloor, its local thickness and degree of preservation being severely conditioned by paleo-topographic constraints. The study of primary textures in these siliceous exhalites, which enables us to go through their initial stages of formation, is only possible because, in places, their pristine features are exceptionally preserved from recrystalization. Our approach is based on detailed optical and SEM inspection of a very large number of samples taken from a previously investigated sample set collected at the Soloviejo deposit in 1997-1999 (see Jorge 2000 for sample location, complimentary geochemical and XRD data, and detailed description of the methods used).

2 Mine geology

The Soloviejo deposit is located in the Huelva Province of Spain, in the eastern sector of the IPB. The deposit lies in the northern, inverted limb of the Rio Tinto syncline, and is composed by a series of small orebodies, which align roughly E-W. Most ore-grade mineralization was hosted by cherts and jaspers belonging to the so-called Jasper Unit (JU). The latter is part of the Manganiferous Formation (MF), which in turn represents the uppermost part of the local volcano-sedimentary column. The VS footwall sequence also includes felsic volcanic rocks, which consist mostly of fine- to medium-grained autoclastic tuffs, with minor intervening massive coherent lava pods and flows of rhyolitic composition. The stratigraphic sequence of the Manganiferous Formation at Soloviejo is characterized by considerable lateral and vertical lithological variations, and comprises gray, purple, and reddish shales, argillaceous/siliceous metapelites, fine-grained felsic tuffs, tuffites, and the siliceous sediments of the Jasper Unit. The latter consist mainly of jaspers, both radiolarian-rich and banded, with only minor cherts (Jorge 2000). In the Soloviejo area, the Jasper Unit is exposed almost continuously over 3.5 km along strike (N 94º-105º E, dipping 80º-86º N), ranging in thickness from tens of centimeters to more than 30 m. The contact between jaspers and the footwall sequence is commonly sharp. However, in places where the JU is underlain by thin horizons of purplish-red shale, the transition can be gradational as the shales

are often strongly silicified, fading into jaspers almost in an imperceptive way. Where preserved from tectonic disruption, the jasper bodies are often lens-shaped, with their basal outline seeming to have mimicked variably large topographic depressions or morphologic irregularities on the paleoseafloor.

Jorge et al. (2002) distinguished several types of mineralization facies in the Soloviejo deposit. These include three types of primary facies: (1) oxide (pyrolusite + romanechite ± manjiroite and plagioclase + quartz + pyrolusite + hollandite + hematite), (2) siliceous (rhodonite + quartz ± friedelite ± persetensite ± caryopilite ± rhodochrosite ± chlorite), and (3) carbonate (rhodochrosite + caryopilite ± rhodonite ± manganopyrosmalite *s.l.*); and two types of secondary facies: (4) tectonically remobilized Mn (pyrolusite + manganomelane *s.l.* + braunite ± cryptomelane ± romanechite ± todorokite), and (5) supergenically altered/enriched (quartz + pyrolusite + lithiophorite ± cryptomelane ± romanechite ± manganomelane *s.l.* ± nsutite and vernardite ± pyrolusite ± rhodonite ± quartz).

3 Mineralogy and primary textures of siliceous exhalites

In the Jasper Unit, cherts are clearly subordinate relative to jaspers. The former represent local facies variations of the later. Cherts consist always of equigranular microcrystalline quartz, seldom covered by a fine dust of hematite and sericite. The biogenic fraction of these rocks is strongly variable, ranging from <1% to 60% in volume, and consists mostly of radiolarian carapaces usually heavily obscured by recrystalized quartz (40-220 μm in diameter).

The jaspers are made up of microcrystalline quartz with varying proportions of fine hematitic dust. These

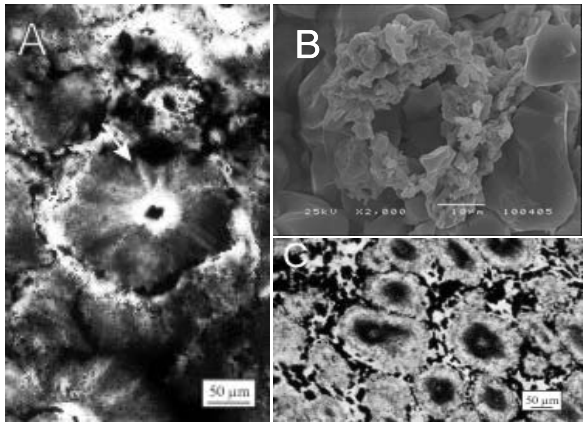

Figure 1: Photomicrographs of: (A) spherulite exhibiting radial microfractures filled with microcrystalline quartz; (B) SEM image of a spherulite with preserved fibroradial chalcedony; (C) coalescing spherulites surrounded by hematite.

rocks are also recrystalized to variable extents. However, in less recrystalized domains of the silica matrix, many pristine features are nicely preserved. Several syn- and post-depositional phenomena were recognized. For clarity, below these characteristics are grouped into three major categories: (a) spherulitic structures; (b) banded structures; and (c) brecciation features.

Well-preserved spherulites (0.04 - 0.3 mm) consist of a central core surrounded by a "halo" of length-slow chalcedony or, in other cases, of microcrystalline quartz. The core is composed of anhedral grains of hematite, which occur either alone, or intergrown with microcrystalline quartz (Fig.1). The core is frequently rimmed by minute grains of hematite. The outer portion of the spherulites comprises one or more concentric layers colored with different grades of red due to the variable dissemination of fine-grained iron oxides.

Spherulites are either in direct contact with each other, or are joined together by microcrystalline quartz and/or finely crystalline hematite. Isolated pairs or larger groups of spherulites are often coalesced, sometimes assuming a chain-like, wavy form, interpreted as being reminiscent of plastic movements of soft, unconsolidated sediments. In places where spherulites are surrounded by hematite, fine polygonal microfractures filled with microcrystalline quartz are frequent in the hematitic domains. Moreover, many spherulites exhibit radial microfractures filled by microcrystalline quartz. Both textural features are interpreted as syneresis cracks resulting from dehydration of a silica-iron oxide colloidal sediment.

Banded structures result from the alternation of micro- to meso-bands made of silica and hematite. The hematitic bands either consist of (i) massive hematite, or (ii) finely crystalline hematite intergrown with microcrystalline quartz. The silica-rich bands consist of microcrystalline quartz spotted by fine hematitic dust. Thin disseminations of sericite occur associated with both types of bands. Radiolarian vestiges are abundant in both types of bands. Usually, they have been replaced by microcrystalline quartz or, less commonly, by hematite and sericite. The bands are laterally uniform, with planar or wavy surfaces and sharp contacts. In places, bands are cut by sets of polygonal cracks filled by microcrystalline quartz. Many bands show evidence for soft-sediment deformation such as microslumps, pinch-and-swells, and load casts.

Syn-sedimentary brecciation is well recorded in the Soloviejo jaspers and affects all types of primary textures. Commonly, millimetric to centimetric fragments of jaspers (pseudoclasts) occur cemented by different proportions of microcrystalline quartz. The pseudoclasts either display very sharp edges or angular to subrounded shapes. They frequently exhibit mutually-fitting broken walls. In places, scattered pseudoclasts show subrounded to rounded shapes and smooth edges, and their disposi-

tion strongly suggests internal rotation. These features appear to record local fluid flow movements during the early diagenetic stages of these rocks. Also, hematitic bands in banded jaspers are often disrupted into fragments of variable shape and size. This internal disturbance laterally fades away along the band passing to domains completely devoid of any kind of deformation. Morevoer, these bands are often sandwiched between undisrupted bands.

4 Effects of tectono-metamorphism

The recrystallization of the siliceous sediments imposed by Hercynian tectonics and low-grade regional metamorphism (lower greenshist facies) is strongly heterogeneous. Recrystallization of chalcedony and microcrystalline quartz results in the formation of a non-uniform quartz mosaic, which frequently encloses domains with almost unmodified primary textures. The boundaries between coarse-grained quartz and microcrystalline quartz are usually gradational, but in some cases are sharp, suggesting the existence of a variety of processes leading to recrystallization/generation of coarsely-crystalline quartz (e.g., coalescence, neoformation). Iron oxide remobilization and coalescence of dispersed iron oxide dust always accompanies the recrystallization of hematite. As a result, hematite becomes patchy and forms massive aggregates on the boundaries of megaquartz grains. Intensely recrystallized samples show total overprinting of the primary textures; quartz forms an almost uniform mosaic with triple-point junctions. In these cases, hematite occurs under the form of large euhedral sections (>0.20 mm) that may or may not exhibit exsolution of magnetite lamellae. Multiple tectonic microfractures filled by quartz or, less commonly, by hematite and/or sericite cut a recrystallized siliceous matrix where the identification of early formational features is not possible.

5 Discussion and conclusions

The primary textural features of the Soloviejo siliceous sediments reflect the diagenetic evolution of a silica-iron oxide colloid/gel precursor. Spherulitic textures are relict features that testify to the formation of the first silica polymorph (opal-A) formed during crystallization of the silica gel. Indeed, in low-temperature hydrothermal systems the kinetics of the different silica polymorph-producing reactions favor the precipitation of opal-A at temperatures of <300ºC, even though the fluid would be supersaturated with respect to other silica polymorphs (Williams and Crerar 1985).

Similar to spherulites found in siliceous exahalies elsewhere (e.g., Duhig et al. 1992, Grenne and Slake 2003a), the Soloviejo spherulites exhibit siliceous or, in most cases, hematitic "nuclei" representing inorganic impurities that act as crystallite nucleating centers. This fact reflects the relevance of the Fe-O-OH groups in diagenetic evolution of iron-silica gel, due to their ability to trigger the bridging together of mutually repellent silica colloids in a pH range of 4 to 7 (Williams and Crerar 1985; Grenne and Slack 2003b).

Soloviejo spherulites are comparable to those from deposits of amorphous silica found in modern diffuse, low-temperature (<100º) hydrothermal vent fields (e.g. Hopkinson et al. 1999 and references therein). However, unlike these modern analogues, at Soloviejo chains or filamentous aggregates of spheroids have not been observed. The data obtained so far do not permit us to infer a role for biogenic activity in the iron-silica gel precipitation mechanisms. The spherulites from Soloviejo consist mineralogically of length-slow chalcedony and/or microcrystalline quartz. Local preservation of pristine fabrics is most probably related to grain-by-grain replacement which results from slow dissolution of early siliceous polymorphs and rapid local precipitation of quartz or chalcedony. The spherulitic textures are not ubiquitous throughout the Jasper Unit. In the banded jaspers (hematitic or manganiferous) these textures have not been observed, suggesting a different mechanism of silica crystallization. It is widely accepted today that the formation of spherulites is limited to colloidal solutions of high viscosity, with diffusion rate of impurities being much slower than the rate of crystal growth. In Fe- or Mn-rich solutions, an excess of metal cations leads to rapid precipitation of silica and subsequent lowering of solution viscosity. Consequently, the diffusion rates in these types of solutions do not favor the formation of spherulites. Breccia structures are widespread in the Soloviejo Jasper Unit. The extensive shrinkage cracks observed and frequent radial fracturing of spherulites suggest that diagenetic dehydration/contraction of silica-iron oxide colloidal sediment played an important role in the origin of these structures. However, these processes alone cannot account for all types of brecciation observed in Soloviejo. All amorphous silica phases are thermodynamically unstable with respect to α-quartz at low temperature and pressure. The diagenetic sequence occurs via transition to other metastable phases of increasing stabilility, following dissolution-precipitation pathways. The rate of silica phase transformations can be influenced by several factors, such as time and temperature, pressure, porewater chemistry, and host rock lithology. On the other hand, most silica phase transformations are dehydration reactions, which are paralleled by a decrease in porosity, thus leading to an increase in fracture susceptibility of siliceous sediments. The large volume of siliceous sediments and the multistage hydrothermal activity at Soloviejo (Jorge et al. 2002) should have contributed to a strongly heterogeneous lithification of these sediments.

In synthesis, Soloviejo jaspers exhibit breccia textures of distinct origins, observed on micro- to macroscopic scale and often superimposed on each other: (a) Large fraction of the textures observed formed during diagenesis as a result of dehydration/contraction of siliceous sediments. Variations in the rate of dehydration led to differential movement between beds, producing slumpage, plastic-flow structures, and penecontemporaneous breccias. (b) Hydraulic fracturing resulted from growing fluid pore pressure, built up as a consequence of compaction/fluid expulsion and accompanying decrease in porosity of the siliceous sediments. This type of brecciation is texturally superimposed on the former one. (c) The evolution of hydrothermal activity at Soloviejo resulted in the injection of mineralized fluids through the semiconsolidated siliceous exhalites and consequent Mn-enrichment of jaspers, accompanied by the formation of hydrothermal pseudobreccias that were superimposed on the previous textural types.

Acknowledgements

This study is a contribution to research project ARCHYMEDES (FCT-SAPIENS 2001/41393). T. Grenne, J. Slack and F. Tornos are gratefully acknowledged for their detailed reviews.

References

del Villar RC, Aranda SM (1995) Boletin Geologico y Minero 106-2:21-31

Duhig NC, Stolz J, Davison GJ, Large RR (1992) Cambrian microbial and silica gel textures in silica iron exhalites from the Mount Windsor volcanic belt, Australia: their petrography, chemistry, and origin. Economic Geology 87: 764-784

Grenne T, Slack JF (2003a) Bedded jaspers of the Ordovcian Lokken ophiolite, Norway: seafloor deposition and diagenetic maturation of hydrothermal plume-derived silica-iron gels. Mineralium Deposita 36:625-639

Grenne T, Slack JF (2003b) Paleozoic and Mesozoic silica-rich seawater: Evidence from hematitic chert (jasper) deposits. Geology 31:319-322

Hopkinson L, Roberts S, Herrington R, Wilkinson J (1999) The nature of crystalline silica from the TAG submarine hydrothermal mound, 26° N Mid Atlantic Ridge. Contributions to Mineralogy and Petrology 137:342-350

Jorge RCGS (2000) Estudo mineralógico e metalo-genético do depósito manganesífero de Soloviejo, Huelva, Spain. MSc Thesis, University of Lisbon, 155 pp.

Jorge RCGS, Relvas JMRS, Barriga FJAS (2002) Siliceous Exhalites and Manganese- Rich Horizons as Guides to VHMS Exploration in the Iberian Pyrite Belt: the Example of the Soloviejo Manganese Deposit (Spain). In: Global Exploration-Integrated Methods for Discovery, SEG. Marsh E, Goldfarb RJ, Day WC (eds) 107-108

Leistel JM, Marcoux E, Deschamps Y (1998) Chert in the Iberian Pyrite Belt. Mineralium Deposita 33:59-81

Williams LA, Crerar DA (1985) Silica diagenesis, II. General mechanisms. J Sed Pet 55:312-321

'T'-type mineralisation – a pseudo-epithermal style of VHMS associated gold mineralisation, Cyprus

S.M. Jowitt
University of Leicester, Department of Geology, University Road, Leicester, LE1 7RH, UK

R.G.M. Osborn
Camborne School of Mines, University of Exeter in Cornwall, Tremough Campus, Treliever Road, Penryn, Cornwall, TR10 9EZ, Cornwall, UK

R.D.H. Thomas
Imperial College, Department of Earth Science and Engineering, London, SW7 2AZ, UK

J. Naden, A.G. Gunn
British Geological Survey, Kingsley Dunham Centre, Keyworth, Nottingham, NG12 5GG, UK

R.J. Herrington
Natural History Museum, Department of Mineralogy, Cromwell Road, London, SW7 5BD, UK

S. Nicolaides
Geological Survey Department, Ministry of Agriculture and Natural Resources, 1415, Nicosia, Cyprus

Abstract. A recent investigation of five VHMS prospects located in the Troodos ophiolite, Cyprus (Tourounjia, Alestos, Papoutsi, Kokkinovounaros and Agrokipia B), has indicated the possible presence of a pseudo-epithermal style of mineralisation. This is based on the presence of anomalous Au concentrations and hydrothermal brecciation. Short wavelength infrared (SWIR) analysis using a portable infrared mineral analyser (PIMA) was carried out to investigate the alteration mineralogy of these deposits and compare them with Cyprus-type mineralisation. Three distinct styles of alteration are present; two represent typical Cyprus-type VHMS alteration, with acidic alteration, not previously documented in Cyprus-type VHMS deposits, being the third. A process of sub-seafloor boiling, as inferred to be occurring presently in the Lau basin, most easily explains the formation and spatial link between acidic alteration and the zones of explosive hydrothermal brecciation present in the Tourounjia and Alestos deposits. It also provides a model to account for the high Au content found in the boreholes from Tourounjia.

Keywords. VHMS, epithermal, Troodos ophiolite, gold

1 Introduction

Cypriot copper deposits are considered to be a type example of a massive sulphide deposit produced at an oceanic spreading ridge (e.g. Hannington et al. 1998). These deposits, formed at the seawater-lava interface and underlain by a mineralised stockwork zone are derived from metal-bearing exhalative fluids. Modern analogues are black smokers, as seen in mid-ocean and supra subduction zone ridge settings today (e.g. the TAG mound on the Mid-Atlantic Ridge, and the Lau Basin).

Recent investigation of the Kokkinovounaros, Papoutsi, Alestos and Tourounjia prospects (Figure 1) located in the Troodos ophiolite, Cyprus, has led to the proposal of a possible pseudo-epithermal style of mineralisation on account of high Au grades and explosive hydrothermal brecciation (Maliotis and Herzig 2000). Short wavelength infrared (SWIR) analysis of core and chippings from each of these deposits was undertaken using a portable infrared mineral analyser (PIMA-SP) with a total of over 500 analyses. The project aimed to evaluate the alteration mineralogy of these deposits and to compare them with a typical Cyprus-type VHMS deposit, Agrokipia B (Cyprus Crustal Project, Borehole CY-2A—Herzig and Friedrich, 1987).

2 Discussion

The data obtained show three distinct styles of alteration. Two of these, named P and M-type alteration (Richards 1989), are typical of Troodos VHMS deposits. They have similar external alteration zones, but different internal zones. P-type (named after the Pitharokhoma deposit) alteration is generally characterised by a chlorite-illite facies with a leached core. Conversely, M-type (from the Mathiati deposit) alteration shows no illite or rectorite in the core of the alteration halo and possesses a central zone with a chlorite, quartz, pyrite and anatase assemblage, referred to as chlorite-quartz-pyrite facies alteration. Chlorite in the chlorite-illite-pyrite facies is more Fe-rich. The third type (discussed below) shows the presence of possible hypogene acidic alteration minerals—dickite and nacrite.

The boreholes from the Agrokipia B, Kokkinovounaros and Papoutsi deposits are associated with alteration minerals typical of Cyprus-type VHMS deposits. The Agrokipia B and Kokkinovounaros deposits contain P-type alteration with abundant chlorite and illite in addition to epidote and minerals of a supergene origin. Illite

This page intentionally blank

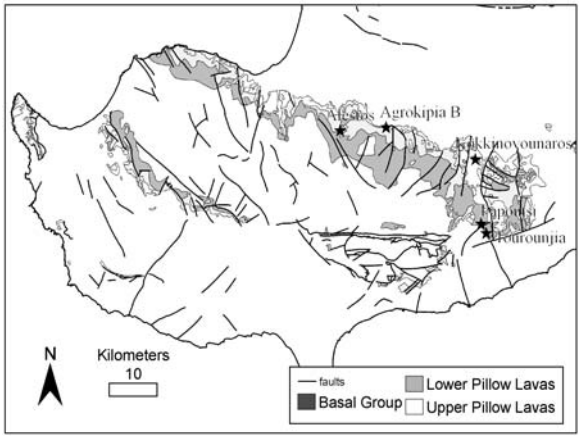

Figure 1: A map of the Troodos ophiolite showing the locations of the five deposits studied in relation to host rock lithologies.

was not recorded in the Papoutsi prospect alteration assemblage implying an M-type alteration style, although the chlorites exhibited Mg-rich spectral characteristics more consistent with P-type alteration. No sign of hydrothermal brecciation was found in these deposits and it is likely that the brecciation present is tectonic in origin.

Analysis of drill core from Alestos revealed a predominately P-type alteration with chlorite and illite being identified. Dickite was identified in three samples taken from minor zones of hydrothermal brecciation, identified by the presence of sub-angular to rounded clasts supported by a silicic matrix. Field observations at Tourounjia also suggest the brecciation present is also of hydrothermal origin. PIMA analysis of two boreholes from Tourounjia showed that the kaolin group minerals are dominant with the frequent identification of kaolinite, nacrite and dickite as well as supergene minerals. Kaolinite was the most commonly identified mineral in the Tourounjia boreholes, although nacrite was also common, present in around 40% of analyses of borehole material, and dickite subsidiary. The spatial link between the occurrences of the kaolin group minerals to zones of hydraulic brecciation implies that their genesis is related and, as nacrite is a relatively high temperature mineral, is most likely to have occurred at a similar time. Though supergene processes cannot be discounted, the presence of relatively abundant high-temperature kaolinite polymorphs (nacrite and dickite) suggests that at least some of the elevated gold, silver and arsenic values are the result of hypogene mineralisation. In one of the Tourounjia boreholes chlorite, illite and epidote were also identified. Advanced argillic-style alteration, which formed the kaolin group minerals, has not hitherto been identified in Cyprus-type VHMS deposits and is named here T-type alteration (after Tourounjia).

Au grades are at least an order of magnitude greater than in other VHMS deposits on Cyprus, with As grades ~20 times higher and Ag grades five times higher. It is considered unlikely that supergene enrichment alone could have increased the content of Au, Ag or As within the Tourounjia deposit as the increase in grades, compared to levels seen in other deposits both affected and unaffected by supergene enrichment, is too high to reflect merely supergene enrichment. This implies that the grades of these deposits reflect the primary mineralisation processes within the deposit rather than later supergene enrichment of a typical VHMS deposit. Mineralisation at Tourounjia is hosted by silicified breccia units, and consists of dominant pyrite, with subsidiary covellite, chalcopyrite and sphalerite. Minor amounts of arsenopyrite and cinnabar, minerals rarely associated with VHMS deposits but common in epithermal deposits, are present as overgrowths on pyrite, sphalerite and copper sulphides. Chalcopyrite and sphalerite are seen as early phases with covellite replacing and coating pyrite, chalcopyrite and sphalerite. Small amounts of galena were also identified through the use of scanning electron microscopy, although no gold was identified.

3 Formation of 'T' type mineralization

The kaolin minerals present in the Tourounjia deposit may have been formed by three hypogene processes: (i) the genesis of acidic fluids through oxidation of H_2S; (ii) magmatic input or (iii) by boiling. The last two methods are analogous to the genesis of terrestrial high or low sulphidation epithermal deposits. Oxidation of H_2S requires a sulphur content higher than the S_2:Fe ratio and more oxidising conditions than those in which the other Cyprus VHMS deposits formed. The input of magmatic fluids to create acidic fluids is another possible method, as proposed by Sillitoe et al (1996) to explain acidic alteration within shallow Kuroko-type VHMS deposits and the presently active Hine Hina hydrothermal field of the Lau Basin, a supra-subduction zone spreading centre analogous to the possible setting of the Troodos ophiolite. However, it is questionable whether the magmas that formed the Troodos ophiolite are sufficiently rich in magmatic volatiles to provide the necessary input to form the Au-rich zones seen in the Tourounjia deposit.

Our preferred process for acidic fluid generation at Tourounjia is one of sub-seafloor boiling, as inferred to be occurring presently in the Lau basin. This most easily explains the formation and spatial link between acidic style alteration and zones of explosive hydrothermal brecciation in the Tourounjia and Alestos deposits. It also provides a model to account for the high Au content found in the boreholes from Tourounjia. Boiling has been well documented in Kuroko-type systems, but has not been encountered in VHMS deposits in the Troodos ophiolite as the depths inferred from overlying sediments and modern analogues implied that at these depths (2000-2500m) mineralising fluids of up to 350°C would not boil.

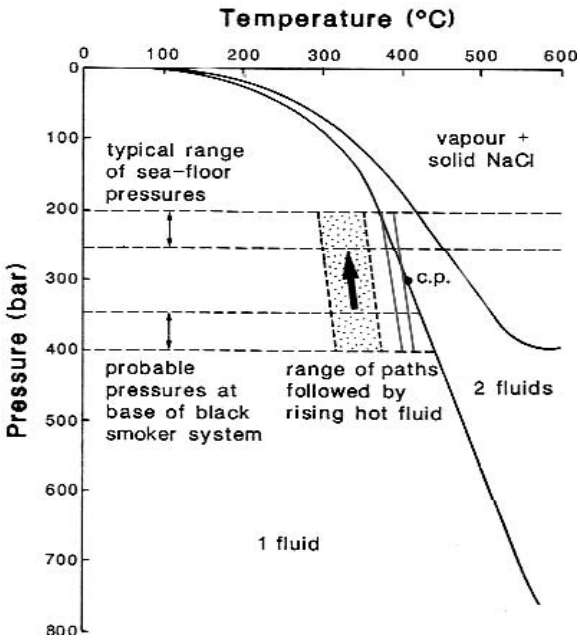

Figure 2: A P-T diagram for a NaCl-H_2O solution of seawater salinity (3.2wt%). c.p is the critical point for seawater. The typical range of seafloor pressures corresponds to normal mid-ocean ridge depths of 2000 to 2500 m. The probable pressures at the base of the hydrothermal system correspond to hydrostatic pressure 1500 to 2000 m below the seafloor. The path of normal Cyprus type mineralising fluids rising from the base of the system to the seafloor is plotted in the stippled region. The path of the raised temperature fluids needed to produce boiling is outlined. (Adapted from Cowan and Cann 1988)

As the phase diagram in Figure 2 indicates, decreasing pressure (e.g. uplift of the hydrothermal field by ~500m) or increasing the temperature of the hydrothermal fluids could cause subcritical phase separation and boiling. These conditions are encountered in modern-day hydrothermal black smokers – such as the Vai Lili hydrothermal field in the Lau Basin (Herzig et al. 1993) and the Northern Fiji basin (Luders et al. 2002). This boiling also allows the deposition of Au, not commonly encountered in the Troodos VHMS deposits, as the typical temperatures encountered inhibit the precipitation of Au (from Au(HS)) until after the fluids have been vented from the black smoker. However, boiling of the hydrothermal fluids beneath the seafloor would allow the precipitation of Au, Ag and As seen in the Tourounjia prospect.

Further work currently being undertaken using XRD analyses will clarify the alteration assemblages and mineralisation processes within these atypical Au-rich Cyprus-style VHMS deposits. Stable isotope studies of samples taken from Tourounjia may allow the source of the hydrothermal fluids to be determined.

Acknowledgements

This work is part of a collaborative research programme between the Geological Survey Department, Cyprus and the British Geological Survey and is funded by the Government of the Republic of Cyprus. The Hellenic Mining Company Ltd, Eastern Mediterranean Minerals (Cyprus) Ltd. and Oxiana Resources NL are also thanked for access to a variety of proprietary information. Permission to publish for JN, & AGG is by the Director, BGS, NERC, UK and for SN by the Director, GSD, Cyprus.

References

Cowan J, Cann JR (1988) Supercritical two-phase separation of hydrothermal fluids in the Troodos ophiolite. Nature 333: 259-261

Hannington MD, Galley AG, Herzig PM, Petersen S (1998) Comparison of the TAG mound and stockwork complex with cyprus-type massive sulfide deposits. Proceedings of the Ocean Drilling Program, Scientific Results, Leg 158:389-415

Herzig PM, Friedrich GH (1987) Sulphide mineralisation, hydrothermal alteration and Chemistry in the drill hole CY2-a. in: Cyprus Crustal Study Project: Initial Report: Holes CY-2 and CY2a, Robinson, R.T., Gibson I.L and Panayiotou, A., (eds.). Geological Survey of Canada, Paper 85-29, Ottawa, Canada, 103-152

Herzig PM, Hannington MD, Fouquet Y, Stackelberg UV, Petersen S (1993) Gold-rich polymetallic sulphides from the Lau back arc and implications for the geochemistry of gold in sea-floor hydrothermal systems of the southwest Pacific. Economic Geology 88:2182-2209

Luders V, Banks D, Halbach P (2002) Extreme Cl/Br and δ^{37}Cl isotope fractionation in fluids of modern submarine hydrothermal systems. Mineralium Deposita 37:765-771

Maliotis G, Herzig PM (2000) Potential for epithermal-style gold mineralization in the Troodos ophiolite, Cyprus, Confidential company report, Eastern Mediterranean Minerals (Cyprus) Ltd

Richards HG, Cann JR, Jensenius J (1989) Mineralogical zonation and metasomatism of the alteration pipes of Cyprus sulphide deposits. Economic Geology, 84:91-115

Sillitoe RH, Hannington MD, Thompson JFH (1996) High sulfidation deposits in the volcanogenic massive sulfide environment. Economic Geology 91(1):204-212

Some new constraints on hydrothermal alteration and deformation of the Paleoproterozoic serpentinite-hosted Outokumpu Cu-Co-Ni-Zn-Au deposits, Finland

A. Kontinen, P. Sorjonen-Ward, P. Peltonen
Geological Survey of Finland, PO Box 1237, 70210 Kuopio, Finland

U. Kuronen
Polar Mining Oy, PO Box 15, Kummunkatu 34,83501 Outokumpu, Finland

Abstract. Although the Outokumpu ore deposit has been long regarded as having affinities with ocean floor exhalative deposits, recent studies have shown that the host serpentinites are depleted mantle harzburgites and that the putative silicous exhalites are in fact leached serpentinite.The intense structural reworking and metamorphic overprint precludes further assessment of the original nature of the Cu enrichment, although limited Pb isotope data militate against an interaction with continental crust.

Keywords. Outokumpu, Paleoproterozoic, serpentinite, silica alteration, deformation

1 Introduction

The Paleoproterozoic Outokumpu Cu-Co-Ni-Zn-Au deposits occupy an important place in the history of mining and metals processing in Finland. Between its discovery in 1910 and closure in 1988, the main Outokumpu deposit produced 28.54 Mt or ore grading 3.8% Cu, 0.24% Co, 0.12% Ni, 1.1 % Zn, 8.9 ppm Ag and 0.8 ppm Au. The Vuonos deposit contained 5.82 Mt at lower grades and was mined from 1972-1984. Current mining operations are restricted to extraction of significant talc deposits in the eastern part of the district, where metamorphic grade is lower. The blind Kylylahti deposit, which was discovered in 1984 at depth along strike from the mined deposits, has yet to be exploited, but contains around 2 Mt of semimassive sulfide ore with proven reserves at 2.63% Cu, 0.39% Co, 0.13% Ni, 0.76% Zn, 0.9 ppm Au and 20.6% S. The somewhat unusual metal association of the Outokumpu deposits occurs within an equally distinctive host rock assemblage, comprising (metamorphosed) serpentinites, metalliferous black shales and banded quartz rocks and Cr-diopside skarns, all enclosed within an isoclinally folded and monotonous sequence of turbidites. While the highly strained and allochthonous nature of the Outokumpu assemblage, and tectonic remobilization of the ore have long been recognized (Koistinen 1981), the prevailing interpretation has been that the Outokumpu deposits originally formed as massive sulfide accumulations associated with seafloor exhalative processes. However, a recent collaborative joint venture (GEOMEX) between Outokumpu Mining and the Geological Survey of Finland, aimed at an enhanced understanding of the mineral system and refinement of exploration strategies has led to a reappraisal of the origin of mineralization and relationships between hydrothermal alteration, deformation and metamorphism. Here we summarize the principal findings of the GEOMEX research, with particular emphasis on the constraints and remaining uncertainties regarding the relationships between alteration and mineralization, metamorphism and deformation.

2 Ophiolites, mantle plumes and the origin of the Outokumpu serpentinites

The Outokumpu assemblage lies within an allochthonous nappe sequence that was emplaced onto the Karelian craton margin during the early stages of the Svecofennian Orogeny. The timing of this event is constrained between 1.94-1.92 Ga for detrital zircons in enclosing turbidites, and 1.885 Ga, for granitoids truncating deformed and metamorphosed fabrics. The tectonically disrupted, but otherwise complete 1.95 Ga Jormua ophiolite (Kontinen 1987; Peltonen et al. 1998), several hundred kilometers north of Outokumpu, is clearly part of the same tectonostratigraphic terrain and has provided a basis for analyzing the origin of the more highly strained and metamorphosed Outokumpu rocks. While the ultimate cause of oceanic crust formation at this time is unknown, evidence exists for plume impingement in Fennoscandia between 2.0-1.95 Ga, as recorded by picritic flood basalt provinces erupted on the Archean craton (Puchtel et al. 1998). Gabbros intruding the serpentinites within the Outokumpu ore district are of similar age to those at Jormua (Koistinen 1981). However, in contrast to the Jormua ophiolite, the Outokumpu assemblage contains only very limited evidence of volcanic rocks. Chloritic schists are locally abundant at Outokumpu, transecting the serpentinites, but not the country rocks and presumably represent mafic dykes; these too show the effects of hydrothermal alteration. In addition, a volumetrically minor, highly strained sequence of tholeiitic rocks has been identified (Park 1988). Although these have a distinct low-

Ti character, typical of Phanerozoic suprasubduction zone wedge melting, the overall trace element and Sm-Nd characteristics at both Jormua and Outokumpu are more consistent with a 1.95-2.0 Ga plume scenario than derivation from a MORB reservoir affected by continental lithospheric contamination. Felsic schists encountered in exploration drilling at the Kylylahti deposit have also been found to be chemically equivalent to rhyolites from the Kidd Creek district, strengthening the argument for plume-related magmatism (cf. Prior et al. 1999).

3 Tectonic and metamorphic evolution of the Outokumpu assemblage

The process by which the turbidites, black shales and serpentinites became juxtaposed is not understood, although it is clear from regional mapping and microstructural studies (Koistinen 1981; Park 1988) that this occurred before formation of the first recorded tectonic and metamorphic fabrics. So far, no convincing record of mud or serpentinite diapirs or tectonic mélange has been found, as might be expected in an accretionary tectonic wedge, and relict depositional features may still be preserved in close proximity to highly strained serpentinite and talc schist lenses. On the other hand, the preservation of relict mantle tectonite fabrics and mineralogy can be used to argue against such extensive mobilization during serpentinization. Limited observations of chaotic slumping and debris flow deposits, and a tendency for massive pelitic units with isolated psammitic clasts to occur in proximity to Outokumpu assemblage lithologies, nevertheless provide some evidence of tectonic instability and rapid sedimentation. We also interpret the chemical homogeneity and textural immaturity of the enclosing sediments as an indication of abundant supply and rapid sedimentation, prograding across a continental foreland onto the oceanic substrate.

A ubiquitous feature of the Outokumpu assemblage is the presence of zones of banded quartz rocks and talc-carbonate or olivine-enstatite-carbonate rocks in the outer parts of serpentinite bodies. The quartz rocks had long been interpreted as hydrothermal silica precipitates, within the context of a seafloor exhalative model (Koistinen 1981; Park 1988). However, geochemical and textural studies demonstrate, together with the presence of relict chromite grains, that the quartz rocks represent extreme hydrothermal leaching of serpentinite. Based on limited oxygen isotope data and analogies with less metamorphosed Paleozoic deposits in Quebec (Auclair et al. 1993) and numerical reaction modelling (Peabody and Enaudi 1992), this appears to be a relatively low-temperature (70-150°C) process. Textural evidence indicates that this silicification and carbonate formation predated metamorphism and significant deformation. On the other hand, the primitive Pb isotopic composition of the Outokumpu ores precludes this silica-carbonate alteration from being related to Cu mineralization via fluid and metal exchange between serpentinite, black shale and turbidites, since the latter have more evolved crustal radiogenic Pb signatures. On the other hand, adequate amounts of nickel could have been supplied by breakdown of silicate minerals such as olivine and pyroxene during serpentinization, provided that sulfur was also available. Indeed, this may explain why the distribution patterns of Cu and Ni differ, as well as account for the distinctive Ni enrichment at Outokumpu, compared to typical oceanic seafloor hydrothermal systems.

Further upgrading of nickel might also have been facilitated by differential deformation of silica-sulfide lithologies and silica mobilization during subsequent deformation and metamorphism. This also applies to the chalcopyrite-pyrite-pyrrhotite ores, where an obvious structural remobilization, dynamic recrystallization and coarsening of grain size is apparent. Complex fluid rock reaction occurred during prograde and retrograde metamorphism (cf. Gole et al. 1987, O'Hanley 1996), with the formation of significant talc reserves.

The present large scale geometry of the ore bodies can be understood in terms of mobilization associated with progressive deformation under prograde metamorphism. This peaked at upper amphibolite facies conditions around 1.86-1.85 Ga, resulting in the formation of spectacular chrome-tremolite and chrome-diopside skarns overprinting the lower grade silica-carbonate alteration assemblages and olivine-enstatite-anthophyllite assemblages in serpentinites. Peak metamorphism was accompanied by emplacement of granitoids derived from melting of the underthrust Archean craton margin, during late orogenic crustal scale contractional deformation. The structural pattern of the Outokumpu province is thus defined by refolded domes and basin, with a prominent NE-SW axial trend.

The subsurface geometry of the main synform in the Outokumpu district can be further constrained to a depth of about 5 km by combining recently acquired seismic reflection data with down-plunge projections of surface intersections. Within this framework, the Outokumpu ore bodies can be interpreted both geometrically and kinematically as being mechanically remobilised within a NW-vergent structurally duplexed lense of serpentinite.

4 Potential sources and mechanisms for copper mineralization

Inferences from chemistry and analogies with the Jormua ophiolite mantle section indicate that the Outokumpu serpentinites represent refractory depleted mantle harzburgites. Although the timing of this depletion event is

not well constrained, the mantle section is cut by mafic dykes, which are only weakly deformed and metasomatized, and which contain late Archean xenocrystic zircons (Peltonen et al. 1998, 2003). This implies that the serpentinites most likely represent late Archean subcontinental lithospheric mantle, exhumed from beneath the Karelian craton during continental breakup. Mass balance considerations of Cu endowment at Outokumpu preclude the current exposed volume of serpentinites from being a sufficient metal source, even with extremely efficient extraction. Therefore, alternative sources and mechanisms for Cu supply and enrichment are required. These could include addition of Cu to the lithospheric mantle during a metasomatizing event. However, Late Archean carbonatite magmatism in the Karelian craton does not appear to have left a tangible record in the Jormua or Outokumpu serpentinites, nor are the Jormua ophiolite mafic units, or picrites with the 2.0-1.95 Ga plume signatures enriched in chalcophile elements. Moreover, lower crustal and mantle xenoliths suites from kimberlites intruding the Outokumpu district only record a much younger latest Proterozoic mantle metasomatizing event (cf. Peltonen et al. 1999).

Alternatively, the Cu mineralization in the serpentinites may represent the deep levels of a subseafloor convective system, with a former hydrothermally altered basaltic crustal carapace having been excised during extensional exhumation. Such a process could be reconciled with pelagic sedimentation of black shales, followed by progradation of a clastic turbidites across a serpentinized lithospheric mantle substrate

The ubiquitous spatial association between the Outokumpu ores and metal-enriched graphitic and sulfidic black shale makes derivation of copper and sulfur from the shales a logical and attractive proposition, and a common hydrothermal source has indeed been invoked to explain metal enrichment in both rock types (Loukola-Ruskeeniemi 1999). However, Pb and Sm-Nd isotopic data indicate that the black shales are an integral part of the regional turbidite sequence. The systematic alternation between turbidites and black shales, and the lack of volcanogenic detritus and hydrothermal alteration in the turbidites militates against syndepositional hydrothermal processes. It must be emphasized however, that the rejection of the black shale as a potential metal source is at present largely contingent upon acceptance of the lead isotope data, though the issue could in principle be resolved if it were conclusively proven that the serpentinites were mineralized prior to deposition of the black shale

The same isotopic arguments can be used to refute the concept of introduction of copper during structural focussing and trapping of metalliferous fluids within a regional scale synmetamorphic hydrothermal regime. While the regional structural architecture might be appropriate, there is an apparent lack of obvious hydrothermal alteration in regional scale thrust systems and shear zones.

5 Concluding remarks

In conclusion, by elimination of mechanisms inconsistent with available constraints, we are still left with the proposition that a cryptic early subseafloor hydrothermal process enriched the Outokumpu serpentinites in copper. There is only indirect and limited evidence to support this, namely the Pb isotope data and the presence of remnant mafic dykes, gabbroic intrusions within the serpentinites, sporadic low-Ti mafic volcanics and some recently discovered rhyolitic volcanics or plagiogranites. Nevertheless, all Outokumpu deposits show a strong structural control, with synmetamorphic textural recrystallization and mobilization. Indeed, the structural geometry of the main lode at Outokumpu is readily interpreted as mobilization, if not introduction of ore by duplexing of ore during late stage folding under peak metamorphic conditions.

References

Auclair M, Gauthier M, Trottier J, Jébrak M, Chatrrand F (1993) Mineralogy, geochemistry, and paragenesis of the Eastern Metal serpentinite-associated Ni-Cu-Zn deposit, Quebec Appalachians, Economic Geology 88:123-138

Gole MJ, Barnes SJ, Hill RE (1987) The role of fluids in the metamorphism of komatiites, Agnew nickel deposit, Western Australia, Contributions to Mineralogy and Petrology 96: 151-162

Koistinen TJ (1981) Structural evolution of an early Proterozoic stratabound Cu-Co-Zn deposit, Outokumpu, Finland, Transactions of the Royal Society of Edinburgh: Earth Sciences 72: 115-158

Kontinen A (1987) An early Proterozoic ophiolite – the Jormua mafic-ultramafic complex, northern Finland, Precambrian Research 35: 313-341

Loukola-Ruskeeniemi K., 1999, Origin of black shales and serpentinite-associated Cu-Zn-Co ores at Outokumpu, Finland, Economic Geology, 94, 1007-1028

O'Hanley DS (1996) Serpentinites: records of tectonic and petrological history, Oxford University Press

Park AF (1988) Nature of the Early Proterozoic Outokumpu assemblage, eastern Finland, Precambrian Research 38:131-146

Peabody CE, Einaudi MT (1992) Origin of petroleum and mercury in the Culver-Bear cinnabar deposit, Mayacmas District, California, Economic Geology 87:1078-1103

Peltonen P, Huhma H, Tyni M, Shimuzu N (1999) Garnet-peridotite xenoliths from kimberlites of Finland: nature of the continental mantle at an Archaean craton – Proterozoic mobile belt transition. Proceedings of the 7th International Kimberlite Conference, Cape Town, South Africa: 664-676

Peltonen P, Kontinen A, Huhma H (1998) Petrogenesis of the mantle sequence of the Jormua Ophiolite (Finland): Melt migration in the upper mantle during Palaeoproterozoic continental breakup, Journal of Petrology 39: 297-329

Peltonen P, Mänttäri I., Huhma H, Kontinen A (2003) Archean zircons from the mantle: the Jormua ophiolite revisited, Geology 31: 645-648

Prior GJ, Gibson HL, Watkinson DH, Cook RE, Hannington, MD (1999) Rare earth and high field strength element geochemistry of Kidd Creek Rhyolites, Abitibi Greenstone belt, Canada: Evidence for Archean felsic volcanism and massive sulphide ore formation in an Iceland-style rift environment, Economic Geology, Monograph 10:457-484.

Puchtel IS, Arndt NT, Hofmann AW, Haase KM, Kröner A, Kulikov VS, Kulikova VV, Garbe-Schönberg CD, Nemchin AA (1998) Petrology of mafic lavas within the Onega plateau, central Karelia: evidence for 2.0 Ga plume-related continental growth in the Baltic Shield, Contributions to Mineralogy and Petrology 130:134-153.

Transport and deposition of selenium in felsic volcanic-hosted massive sulfide deposits of the Finlayson Lake District, Yukon Territory, Canada

D. Layton-Matthews, S.D. Scott
Department of Geology, University of Toronto, 22 Russell Street, Toronto, Ontario, M5S 3B1

J.M. Peter
Geological Survey of Canada, Central Canada Division, 601 Booth Street, Ottawa, Ontario, K1A 0E8

M.I. Leybourne
Department of Geosciences, University of Texas at Dallas, 2601 N. Floyd Rd., Richardson, Texas, 75080

Abstract. The mobility and hydrothermal transport of selenium are a function of the fluid pH, fO_2 and temperature. At high temperatures (>200 °C) and relatively acidic (pH <6) conditions, H_2Se is the dominant aqueous species. At ambient seafloor temperatures, reduced forms of selenium are relatively immobile, but the element becomes increasingly mobile under oxidized conditions. Deposition of selenium from a hydrothermal fluid results when relatively hot, acidic, reduced hydrothermal fluid mixes with cold (1-10°C), oxidized ambient seawater. The selenium content of the precipitating sulfide is controlled by the reaction: $MtSe_2 + H_2S_{(aq)} = MtS_2 + H_2Se_{(aq)}$, where Mt is a transition metal, and therefore H_2Se/H_2S approximates the Se/S of the fluid at the time of sulfide precipitation. However, in modern and ancient volcanic-hosted massive sulfide (VHMS) systems the final residence site of transition metals (and Se), or their redistribution, is ultimately a function of the solubility product (log Q/K) and temperature of precipitation of the sulfide minerals, which produce metal zoning in sulfide mounds as a result of hydrothermal fluid interaction/ dissolution with previously precipitated sulfide minerals (a.k.a., zone refining). Observations and data from ancient VMS deposits in the Finlayson Lake District (FLD), Yukon, Canada show a strong positive correlation between high-temperature (>300°C), copper-rich sulfide assemblages at the base of VHMS and the selenium content of all sulfide minerals. Thermodynamic calculations for selenide and sulfide minerals indicate significantly higher temperatures and lower solubility indices for the formation of selenide versus sulfide pairs, which is consistent with petrographic observations and can explain the distribution of selenium in zone-refined VMS deposits.

Keywords. Selenium, volcanic-hosted massive sulfide, Yukon, seafloor mineralization, ore deposit

1 Introduction

In the mid 1990's three polymetalic volcanic-hosted massive sulfide deposits of potential economic significance (Kudz Ze Kayah – KZK, Wolverine and GP4F) were discovered in the Finlayson Lake District (FLD) of the Yukon, Canada, these have a combined resource of 21.5 million tonnes grading 8.2% zinc, 0.97% copper, 1.7% lead, 203 g/t silver and 1.6 g/t gold (see Figure 1). The Wolverine and KZK deposits have elevated selenium contents, whereas the GP4F deposit does not. Elevated selenium contents at Wolverine and KZK massive sulfide ores were recognized during metallurgical testing and in the prefeasibility stages of exploration. Low base metal prices during and following these discoveries hindered further development of these resources, until recently.

In this study we present field, petrographic, bulk geochemical and mineral chemical data on the mineralogical residence sites and bulk distributions of selenium within the KZK, Wolverine and GP4F VHMS deposits in the FLD. Whole-rock compositional data for host felsic volcanic and carbonaceous argillite host-rocks, sulfide mineralization, and altered host-rocks are presented together with thermodynamic models using the Geochemists Workbench® 4.0 computer program in order to quantitatively elucidate transport and depositional processes that resulted in elevated selenium contents of the Wol-

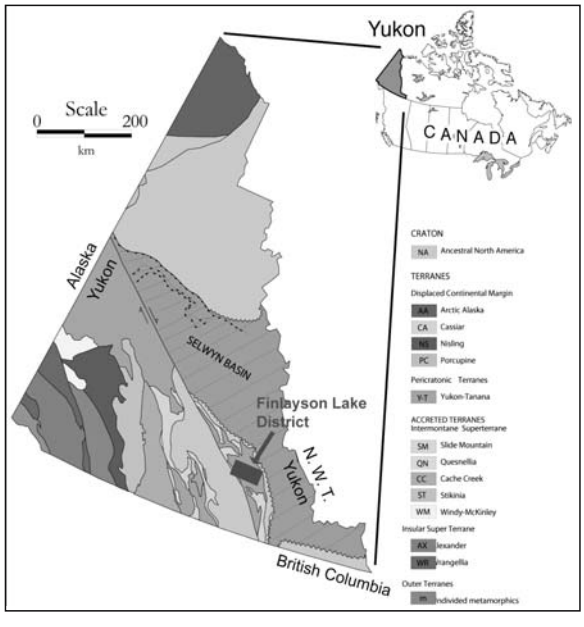

Figure 1: General tectonic map of the Yukon and location of the FLD.

verine and KZK deposits. Thermodynamic modeling results are then compared to actual selenium distributions in both the Wolverine and KZK deposits, and modern seafloor analogs.

2 Selenium distribution

The study of the distribution of selenium in VHMS deposits provides important insights into the physiochemical nature of the fluids responsible for selenium-rich and selenium-poor mineralization. Recognition of selenium mineralogical associations within particular mineralization types may also be of relevance to metallurgical considerations and may contribute to the economic potential of a Se-rich deposit (i.e., selective mining or concentrate blending).

Sulfide deposits in the FLD are variable, exhibit a wide range of mineralization styles and sulfide intersections have been broadly divided into six mineralization types based on mineralogy, mineral textures and spatial location relative to regards to proximal stratigraphic footwall alteration. Progressing upward in order from stratigraphic footwall to hanging wall, these are: 1) footwall, 2) chalcopyrite – pyrite – pyrrhotite predominant, 3) pyrite – sphalerite predominant, 4) sulfide breccia, 5) barite-rich, and 6) remobilized sulfides.

In areas of thick sulfide intersections, well-defined systematic base-metal zoning is observed from stratigraphic footwall to hanging wall contacts is present at both the Wolverine and KZK deposits. At Wolverine, in both the Lynx and Wolverine zones, there is a strong positive correlation of selenium with Cu/Cu+Pb+Zn at the stratigraphic base of both sulfide lenses ($r = 0.66$). In diamond drill hole WV96-39 from the western edge of the Wolverine zone, a ~7 m massive sulfide interval was intersected. At the base a 1.6 m interval of Type 1 (footwall mineralization) was intersected with concentrations of up to 14.1 wt % Cu (0.54 Cu/Cu+Pb+Zn) and 2120 ppm Se. Conversely, Pb abundances and tenors are low at 0.48 wt % and 0.18 Pb/Cu+Pb+Zn, respectively. Immediately above this intersection occurs a narrow 0.6 m intersection of Type 2 chalcopyrite mineralization with up to 10.8 wt % Cu (0.41 Cu/Cu+Pb+Zn) and 3420 ppm Se. Selenium and Cu tenor drastically decrease in Type 3 mineralization stratigraphically up section, whereas Pb and Zn contents generally increase up section, reaching 2.97 wt % Pb (0.12 Pb/Cu+Pb+Zn) and 20.3 wt % Zn (0.83 Zn/Cu+Pb+Zn).

At the KZK deposit, the thickest sulfide intersections are in the eastern down-dip portions of the deposit within the fold nose where meter-scale m-folds have structurally thickened the sulfide intersection. Within this area, diamond drill holes commonly intersect two stratigraphic hanging wall and footwall contacts with repeated Type 1, 2, 3 and 4 mineralization sequences and sulfide intersections of ~20 m. At the stratigraphic footwall contacts there is commonly a ~2 m interval of Type 1 mineralization with up to 4.2 wt % Cu (0.79 Cu/Cu+Pb+Zn) and 210 ppm Se. Conversely, Pb abundances and Pb tenor are low, 0.28 wt % and 0.05 Pb/Pb+Cu+Zn, respectively. Stratigraphically above this, a ~1.75m interval of Type 2 mineralization with concentrations of up to 10.2 wt % Cu (0.86 Cu/Cu + Pb + Zn) and 551 ppm Se occurs. Selenium and Cu tenor decrease stratigraphically upward, whereas Pb and Zn contents increase through Type 3 mineralization, reaching 5.3 wt % Pb (0.33 Pb/Pb + Cu + Zn) and 13.9 wt % Zn (0.87 Zn/Zn+Pb+Cu).

At the GP4F deposit, sulfide intersections are comparatively thinner than those at the Wolverine and KZK deposits and have poorly developed base-metal zoning in areas of thick sulfide intersection. Within these intersections there is commonly a thin (<0.5m) interval of stratigraphic footwall mineralization (Type 1) that has elevated Cu contents (up to 0.4 wt %) compared to Type 3 mineralization within the same drill hole. These areas of weakly developed Type 1 mineralization comprise sphalerite, pyrite, chalcopyrite, and arsenopyrite and have selenium contents up to 78 ppm. Selenium contents sharply decrease to below detection in whole-rock analyses at the Type 1 – Type 3 contact (d.l. = 50 ppm). Type 2 mineralization is notably absent from the GP4F deposit.

In areas of thin sulfide intersections at the Wolverine and KZK deposits, base-metal zoning is poorly developed. In such areas, selenium abundance, although much lower than in thick sulfide intersections, demonstrate weak trends of increase near the base of sulfide intersections. Similarly, Cu contents in thin sulfide intersections are relatively low and show no systematic distribution within the intersections. Base-metal tenor within thin intersections is generally low, reflecting their pyrite-rich nature.

3 Selenium thermodynamic modeling

Deviations from homogeneous selenium contents within sulfide minerals can arise from three possible mechanisms (Huston et al., 1995), namely: 1) changes in fluid Se/S ratio by sulfide precipitation/dissolution reactions, 2) fractionation of Se with temperature, and 3) fractionation of Se with redox or pH changes. Changes in temperature, redox or pH conditions can be brought about by either sulfide saturation caused by conductive heat loss, or convective heat loss involving seawater mixing, or most likely a combination of both mechanisms.

The KZK and Wolverine deposits demonstrate base-metal and sulfide mineral distributions that are consistent with temperature dependant mineral solubilities. An exception to this temperature control is the textural evidence of temporally co-existing chalcopyrite and galena, which is inconsistent with other VHMS models that infer

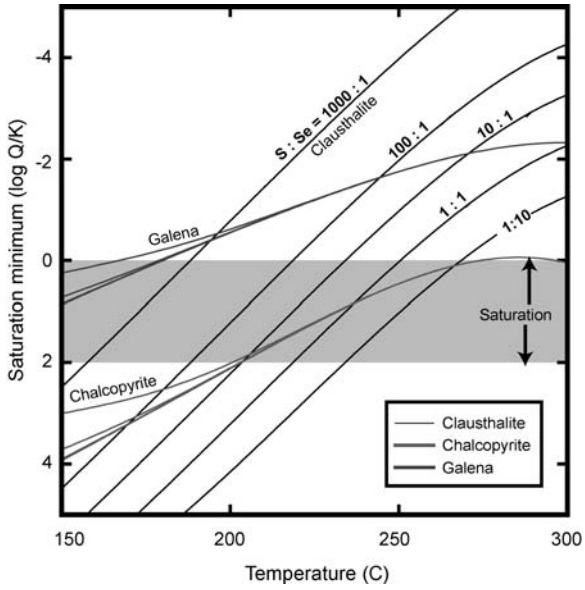

Figure 2: GWB® cooling model of sulfide and selenide saturation.

a lower temperature of galena saturation (i.e., (Eldridge et al., 1983; Ohmoto, 1996). The Se-rich nature of galena (clausthalite) and the corresponding decrease in selenium content with increasing stratigraphic height and decreased temperatures suggests a correlation of high selenium contents with higher temperatures of clausthalite precipitation. Below, we identify the thermodynamic parameters (i.e., fO_2, fS_2, ΣSe/ΣS, etc…) of the mineralizing fluid for the KZK and Wolverine deposits and model the solubility of selenium in a cooling hydrothermal fluid from >300 to 200 °C.

The coexistence of pyrite, pyrrhotite, chalcopyrite and the presence of relict high Fe-sphalerite near the stratigraphic bases of the FLD deposits indicates a predominantly low and narrow range of fO_2 (-35 to –43) and fS_2 (-8 to –13) conditions within the sulfide mounds (Barton, 1978; Helgeson, 1969). The absence of pyrrhotite, chalcopyrite and the presence of Fe-poor sphalerite near the stratigraphic tops of the FLD deposits indicate a somewhat higher fO_2 (-35 to –30) and decreased temperature (< 250 °C) of the hydrothermal fluid.

In hydrothermal fluids above 200 °C the dominant aqueous Se and S species are H_2Se and H_2S, respectively (D'yachkova and Khodakovkiy, 1968; Yamamoto, 1976). Furthermore, at temperatures above 220 °C, melting of native selenium occurs. It has been also shown in metal-rich fluids that native selenium is not stable even at very low temperatures (150 °C) regardless of thermodynamic predictions (Elrashidi et al., 1987). Therefore, at temperatures > 150 °C, m_{H2Se}/m_{H2S} approximates $m_{\Sigma Se}/m_{\Sigma S}$ of the hydrothermal fluid, and native selenium is not stable within hydrothermal fluids. As such, the partitioning of selenium and sulfur between a hydrothermal fluid and sulfide minerals should be recorded in the sulfide minerals and the $\Sigma H_2Se/\Sigma H_2S$ of the volcanogenic fluid can be calculated given the appropriate $K_{reaction}$ data and mineral compositions (Huston et al., 1995).

The high selenium contents at the stratigraphic base of KZK are similar to those for modern Cu-rich chimneys at seafloor hydrothermal black smoker sites (e.g., up to 1000 ppm at East Pacific Rise 13°N; (Auclair et al., 1987). However, pyrite compositions within Type I and 2 from the Wolverine deposit are more variable and consistently higher (3200 to 1000 ppm) than those of KZK. Calculations indicate that a significantly higher selenium concentration in the hydrothermal fluid would be required (perhaps >1000 ppb).

The textural coexistence of chalcopyrite and clausthalite within Type 1 and 2 mineralization provides further evidence for the high activity of H_2–Se in the ore-forming fluid at the Wolverine deposit. The solubility products of clausthalite from D'yachkova and Khodakokiy (1968) and Xiong (2003) indicate significantly higher temperatures of precipitation of selenides than the sulfide solid solution end members. A first-order estimate of the hydrothermal fluid was modelled for a conductively cooling system from 300 to 150°C using the Geochemists Workbench® 4.0 computer program (Bethke, 2001). Variation of the activity of H_2Se from values equivalent to end-member fluids venting on the modern seafloor ($7x10^{-8}$ to $8x10^{-8}$ *m*) (Von Damm et al., 1985) to estimates based on pyrite compositions from Type 1 and 2 mineralization at the Wolverine deposit demonstrate that at very high aH_2Se (1 mg kg^{-1}) the solubility minimum (log Q/K) for clausthalite and chalcopyrite will overlap and thus these minerals will co-precipitate (see Figure 2). This is consistent with our petrographic observations and mineral compositional data for Type 1 and 2 mineralization.

Unlike in other deposits (i.e., Mount Lyell, Rosebery, Tazmania) in which bulk selenium contents sharply decreases to zero at the stratigraphic top of the sulfide lenses (Huston et al., 1995), at the edges of the Wolverine and KZK deposits the selenium contents of bulk sulfide and individual sulfide phases increase non-uniformly, as observed in Type 4 mineralization. This observed relationship is supported by the different stabilities of H_2S and H_2Se at higher fO_2 (~-30), the absence of native Se in the presence of high metal concentrations (Elrashidi et al., 1987), and the likely ingression of seawater. The ingress and mixing of seawater with the mineralizing fluids near the stratigraphic tops and edges of these deposits created an environment where SO_4^{2-} was the dominant sulfur species but H_2Se was the stable selenium species; this created a unique assemblage of selenide and sulfate minerals, consistent with our petrographic and field observations.

References

Auclair G, Fouquet Y, Bohn M (1987) Distribution of selenium in high-temperature hydrothermal sulfide deposits at 13 degrees North, East Pacific Rise: The Canadian Mineralogist 25: 577-587

Barton PB Jr, (1978) ore textures involving sphalerite from the Furutobe mine, Akita Prefecture, Japan: Mining Geology 28:293-300

Bethke CM (2001) The Geochemist's Workbench® Release 4.0, A Users Guide to Rxn, Act2, Tact, React, and Gtplot: Urbana, University of Illinois 184

D'yachkova IB, Khodakovkiy I L (1968) Thermodynamic equilibria in the systems S-H2O.Se-H2O and Te-H2O in the 25-300°C temperature range and their geochemical interpretations: Geochemistry International 5:1108-1125

Eldridge CS, Barton PB, Jr, Ohmoto H (1983) Mineral textures and their bearing on formation of the Kuroko orebodies: Econ. Geol. Mon. 5:241-281

Elrashidi MA, Adriano DC, Workman SM, Lindsay W L (1987) Chemical-Equilibria of Selenium in Soils - a Theoretical Development: Soil Science 144:141-152

Helgeson HC (1969) Thermodynamics of hydrothermal systems at elevated temperatures and pressures: American Journal of Science 267:729-804

Huston DL, Sie SH, Suter GF, Cooke DR, Both RA (1995) Trace elements in sulfide minerals from eastern Australian volcanic-hosted massive sulfide deposits.1. Proton microprobe analyses of pyrite, chalcopyrite, and sphalerite, and.2. Selenium levels in pyrite: Comparison with delta S-34 values and implications for the source of sulfur in volcanogenic hydrothermal systems: Economic Geology 90:1167-1196

Ohmoto H (1996) Formation of volcanogenic massive sulfide deposits: the Kuroko perspective: Ore Geology Reviews 10:135-177

Von Damm KL, Edmond JM, Measures CI, Grant B (1985) Chemistry of submarine hydrothermal solutions at Guaymas Basin, Gulf of California: Geochimica et Cosmochimica Acta 49:2221-2237

Yamamoto M (1976) Relationship between Se/ S and sulfur isotope ratios, hydrothermal sulfide minerals: Mineralium Deposita 11:197-209

Rare mineral assemblages in black and white smoker vent chimneys from Uralian VHMS deposits, Russia

V.V. Maslennikov, S.P. Maslennikova
Institute of Mineralogy of RAS, 456317 Miass, Russia

Abstract. A variety of fossil vent chimneys ranging from pyrite-chalcopyrite "black smoker" to sphalerite-quartz-barite "white smoker" assemblages has been studied from the Silurian Ymana-Kasy and the Devonian Alexandrinskoye VHMS deposits in the southern Urals. Within this range of chimney types changes in the mineralogy from tellurides and sulphoarsenides to assemblages of native gold-rich galena-sulphosalts have been established. These changes are related to a decrease in formation temperature, Te_2 activity and relative increase of S_2 and O_2 activities as a consequence of mixing of hydrothermal fluids with cold oxygenated seawater.

Keywords. Silurian and Devonian VHMS deposits, Urals, vent chimney, mineralogy, tellurides, native gold, sulphoarsenides, sulphosalts, black and white smokers

1 Introduction

The occurrence of fossil vent smoker chimneys in ancient volcanic-hosted massive sulphide deposits is very rare. The VHMS deposits in the south Urals are characterized by the abundance of well-preserved sulphide vent chimneys especially in the Devonian Oktyabr'skoye, Alexandrinskoye, Saphyanovskoye and the Silurian Yaman-Kasy deposits (Herrington et al., 1998, Maslennikov, 1999).

The mineralogical diversity of the vent chimneys can be understood when changes in the physico-chemical conditions of the fluids, that are documented by the various paragenetic mineral assemblages, are resolved.

2 Geological setting

The Yaman-Kasy VHMS deposit is situated in the Mednogorsk region of the western part of Urals, which is considered to be a fragment of the Ordovician-Silurian Sakmara marginal sea (Zaykov et al. 1995). The Alexandrinskoye VHMS deposit is related to the rifted East-Magnitogorsk island arc. Both deposits are hosted by dacite-rhyolite-basalt sequences that are nearly unmetamorphosed. The steep mound-style of the orebody, the presence of clastic ore, chimney fragments and abundant vent fauna relics indicate that the Yaman-Kasy deposit is an ancient analogue of a modern "black smoker" sulphide mound complex (Zaykov et al. 1995; Herrington et al., 1998). The Alexandrinskoye deposit is considered to be the clastic sulphide stratum formed after dismembering of sulphide mounds and is characterized by abundant sulphide breccias and sulphide sandstones (Maslennikov 1999).

3 Fossil vent chimney types

Six different vent chimney types have been documented and range from pyrite-chalcopyrite to sphalerite-quartz-barite. For each type several mineralogical zones and subzones can be distinguished and are described from the outside (zone A) to the inner wall (zone B) and to the central conduit (zone C). All six types were observed in samples from Yaman Kasy while the Alexandrinskoye deposit contains only chimney types 5 and 6.

- (Type 1) Pyrite-chalcopyrite vent chimneys. The outer wall (zone A) of the chimney consists of colloform and boytroidal pyrite (subzone A1) followed by massive pyrite pseudomorphing tabular anhydrite or pyrrhotite crystals (subzone A2). This pyrite is replaced by euhedral pyrite and chalcopyrite towards the innermost part of this zone (subzone A3). The inner wall (zone B) and conduit (zone C) of these chimneys are filled by drusy chalcopyrite. The majority of the samples of this chimney type 1 lacks any rare minerals (Table 1).
- (Type 2) Pyrite-marcasite-chalcopyrite vent chimneys. This is a variety of the previous type, and the main difference is the presence of marcasite and quartz in the outer wall (zone A) and of minor pyrite and sphalerite in the central conduit. Rare minerals observed in this type include frohbergite-sylvanite, altaite-tellurobismu-thite, petzite-hessite-stuetzite and galena-native tellurium mineral assemblages in the inner wall (zone B; Table 1). Coloradoite and mattagamite were observed in some quartz-rich chimneys.
- (Type 3) Sphalerite-pyrite-marcasite-chalcopyrite vent chimneys. This type is characterized by the increased replacement of colloform pyrite by chalcopyrite and sparry marcasite towards the inner part of the outer wall (zone A). The rare mineral assemblages observed in this type are similar to those observed in type 2, with the exception of frohbergite, which is absent (Table 1). Tellurides are located in fine-grained pyrite-chalcopyrite aggregates of zone B, while coarse-grained chalcopyrite in the same zone lacks rare minerals. The conduit (zone C) consists of intergrowths of euhedral chalcopyrite, sphalerite and quartz with small grains of löllingite.

- (Type 4) Pyrite or marcasite-sphalerite-chalcopyrite vent chimneys. Colloform pyrite and marcasite are mostly replaced by sphalerite in zone A. Tellurides are common and are interstitial to areas of isocubanite and chalcopyrite. Rare minerals include volynskite instead of tellurobismuthite (Table 1). Tellurides are partly replaced by native tellurium in association with galena and Ag-sulphosalts. Relics of cobaltite were also observed. The axial conduit (zone C) is infilled by spheroidal marcasite. Colloform to drusy sphalerite, quartz and minor barite with disseminated tennantite + goldfieldite, native gold and sylvanite may also be found in this chimney type.
- (Type 5) +/-Pyrite+/-marcasite+/-quartz- chalcopyrite-sphalerite vent chimneys. The quartz-sphalerite dominated outer wall (zone A) is characterized by only minor or the complete lack of pyrite and marcasite. The inner wall (zone B) consists of a discontinuous layer of chalcopyrite with inclusions and intergrowths of sphalerite and marcasite. Dendritic chalcopyrite-sphalerite intergrowths are common. The axial conduit (zone C) is subsequently infilled by marcasite, sphalerite, quartz or barite.

  Tennantite, galena and bornite occur as rare minerals in all zones of this chimney type (Table 1). Native gold occurs in association with galena and euhedral pyrite in chalcopyrite (Yaman-Kasy) or sphalerite (Alexandrinskoye).
- (Type 6) +/-Pyrite-chalcopyrite-sphalerite-quartz-barite vent chimneys.The peculiarity of this chimney type is the presence of abundant barite and quartz in the axial conduit and the scarcity of chalcopyrite. Rare minerals include abundant tennantite and galena, minor bornite and traces of native gold (Table 1).

Table 1: Rare mineral distribution in the vent chimney type: black – wide spread; gray – occasional.

Rare mineral	Types of vent chimneys					
	1	2	3	4	5	6
Native tellurium						
Frohbergite						
Sylvanite						
Tellurobismuthite						
Altaite						
Petzite						
Coloradoite						
Volynscite						
Empressite						
Stuetzite						
Hessite						
Löllingite						
Cobaltite						
Tellurite						
Ag-sulphosalts+Te						
Goldfieldite						
Tennantite						
Galena						
Bornite						
Native gold						

4 Temperature zonality of the vent chimney types

The following attempt to assess the temperature of formation is based on mineral thermometers and fluid inclusions data.

Zone A: The colloform pyrite was likely formed at temperatures less than 80°C (Maslennikov, et al., 1999), while the presence of marcasite indicates a temperature below 240°C (Murowchick and Barnes, 1986). Higher temperatures in the inner part of this zone allow the inversion of marcasite to euhedral pyrite.

Zone B: The equilibrium of marcasite and pyrite in this zone in chimney types 4, 5 and 6 suggests a temperature of about 240°C. The local presence of isocubanite indicates temperatures around 300°C (Halbach et al. 2003). The sylvanite melting point (354°C), the upper stability of frohbergite (272°C) and stuetzite (265-295°C) restrict the maximum for-mation temperatures for chimney type 1 (Afifi et al. 1988). The association of sylvanite, native tellurium and stuetzite + hessite (y-phase) may be useful as a geothermometer since Cabri (1965) has shown that gold-rich sylvanite ($Au_{1.14}Ag_{0.86}Te_4$), present in chimney type 2, forms at a high temperature of about 300°C. The stoichiometric sylvanite (23.5-24.2 wt.% Au) in chimney type 4 formed at temperatures between 120°C and 230°C (Cabri 1965). This is in agreement with the presence of empressite, which also indicates formation temperatures around 210°C (Honea, 1964).

The temperature of formation of native gold precipitated in chimneys of type 5 may be around 150-200°C (Hannington and Scott 1989). Abundant low-temperature mineral assemblages including galena and sulphosalts indicate that the fluid temperature may have been even less (<150°C) during the formation of chimneys of type 6 (Halbach et. 2003).

Thus the temperature differences between zone B and zone A in the various chimney types is in the range of 100-200°C.

Zone C: The presence of marcasite in zone C of some of the chimney types (type 2 and type 3) indicates a decrease in temperatures to values lower than 200°C in the waning stages of hydrothermal activity. Homogeni-

zation temperatures recorded in fluid inclusions indicate medium to low temperature formation in the range from 110-230°C for sphalerite, 160-210°C for quartz, and 103-180°C for barite (Herrington et al. 1998; Bailly et al. 1999).

5 Activity of Te_2, S_2, and O_2

The highest values of $logTe_2$ and the lowest values of aS_2 are indicated by the presence of frohbergite ($FeTe_2$) in chimney type 1 and 2 (Afifi et al. 1988). The transition from frohbergite to pyrite suggests an increase in aS_2 for all other chimney types. The occurrence of volynscite ($AgBiTe_2$) instead of tellurobismuthite (Bi_2Te_3) in chimneys of type 4 and the presence of native gold rather than sylvanite in chimneys of type 5 shows the further decrease of aTe_2. This tendency is coincident with the depletion of altaite and the prevalence of galena in chimneys of type 5 and 6. The change from tellurides to Ag-Bi-rich galena, sulphosalts and bornite documents the relative increase in aS_2. The later formation of tellurium oxides, sulphosalts, and abundant barite demonstrates higher oxidation conditions during this stage. This is also indicated by the changes in the stability fields of the following minerals with respect to the oxidation state of the fluids in the order $FeTe_2$-Bi_2Te_3-PbTe (Afifi et al. 1988).

6 Discussion and conclusion

The models for chimney formation and growth of Paleozoic and modern black smokers seems to be very similar (Haymon 1983). However, telluride-rich VHMS such as those in the Urals have not yet been found on the modern seafloor. The various chimney types in the Uralian deposits show different temperatures of formation. The prevalence of chalcopyrite or sphalerite in certain samples is an indication of these temperatures differences. The concentration of copper in reduced, hot and acid hydrothermal fluids displays a sharp decrease in fluid concentration at temperatures below 320° (Metz and Trefry 2000), while temperature effects of Zn solubility are more important at temperatures below 250°C (Janecky and Seyfried 1984). The chimneys that formed from these lower temperature fluids mainly consist of sphalerite, silica and barite and their formation is related to conductive cooling and mixing of the hydrothermal fluid with seawater (Halbach et al. 2003). The six chimney types present at Yaman-Kasy and Alexandrinskoye are comparable with a range of chimneys from black to white smokers that follow a temperature gradient, with some representing intermediate gray smoker chimneys.

Within the range of chimney types (from type 1 to type 6), Te-rich minerals pass to low-Te species and into native gold-galena-sulphosalt associations. These mineralogical changes may be interpreted as related to a decline in temperature and aTe_2 with a relative increase in aS_2 and aO_2.

The absence of telluride mineral assemblages in type 1 chimneys may indicate that these formed at temperatures above 350°C. This may also be true for some parts of zone B of chimney types 2,3, and 4, that lack tellurides. Favourable conditions for the precipitation of tellurides (200-250°C) occurred mainly in the outer and inner part of subzone B in chimney types 3 and 4. However, it is also possible, that tellurides are being dissolved at lower temperatures, high sulphidation and oxidation conditions as well as with increasing pH (Jareth 1991). These conditions probably hold true for the chimney types 5 and 6 that are similar to modern white smoker chimneys with their low-temperature assemblages (e.g. galena, sulphosalts; Halbach et al., 2003).

Given the right geotectonic conditions, the discovery of telluride-rich mineralization might be anticipated in modern seafloor sulphides. Generally, the detailed study of ancient massive sulphide deposits on land can help to identify processes that are not currently known on the modern seafloor and is therefore a valid contribution to the project "Global comparison of massive sulphide deposits (IGCP502)".

Acknowledgements

The author is grateful to Dr. V. Kotlyarov, C. Stanley, Dr. R. Herrington, K. Becker, John Spratt, Tony Wighton, Terry Greenwood and Dr.D. Steele for help in electron microprobr analyses and thank Dr. F.Tornos, Dr. S. Petersen and Dr. D. Heydon for useful remarks and the careful edition of the text. This research is supported by of Presidium of the Russian Academy of Sciences in the Priority Program "World Ocean" and Russian Base Research Foundation project (N 05-05-645332).

References

Afifi A.M, Kelly WC, Essene EJ (1988) Phase relations among tellurides, sulfides, and oxides: I. Thermodynamical data and calculated equilibria. Econ. Geol. 83: 377-394

Bailly, L, Orgeval JJ, Tessalina SG, Zaykov VV, Maslennikov VV (1999) Fluid inclusion data of the Alexandrinka massive sulfide deposit, Urals. In: Mineral Deposits: Processes to Processing, Stanley C (ed) 13-16

Cabri LJ (1965) Phase relation in the Au-Ag-Te system and their mineralogical significance. Econ. Geol. and Bull. of the Society of Econ. Geol. 60(8):1569-1606

Halbach PE, Fouquet Y, Herzig P (2003) Mineralization and compositional patterns in deep-sea hydrothermal systems. In: Enegry and Mass Transfer in Marine Hydrothermal. Halbach P, Tannicliffe V, Hein JR (eds). Berlin: Dahlem university press, 85-122

Hannington MD, Scott SD (1989) Sulfidation equilibria as guides to gold mineralization in volcanogenic massive sulphides: evidence from sulphide mineralogy and composition of Sphalerite. Econ. Geol. 84: 1978-1995

Haymon RM (1983) Growth history of hydrothermal black smoker chimneys. Nature 305: 695-698

Herrington RJ, Maslennikov VV, Spiro B, Zaykov VV, ST Little S (1998) Ancient vent chimney structures in the Silurian massive sulphides of the Urals. In: Modern Ocean Floor Processes and the Geological Record. Mills R and Harrison K (eds) 148: 241-257

Honea RM (1964) Empressite and stuetzite redefined. Amer. Minerat 49: 325-338.

Janecky DR, Seyfried WE (1984) Formation of massive sulfide deposits on oceanic ridge crests: Incremental reaction models for mixing between hydrothermal solutions and seawater. Geochim. Cosmochim. Act 48: 2723-2738

Jareth S (1991) Hydrothermal geochemistry of Te, Ag_2Te and $AuTe_2$ in epithermal precious metal deposits. EGRU Contribution, 37: 1-21

Maslennikov VV (1999) Sedimentogenesis, halmyrolysis and ecology of the massive sulphide-bearing fields (in Russian). Miass: Geotur, 342

Metz, S., J.H. Trefry (2000). Chemical and mineralogical influences on concentrations of trace metals in hydrothermal fluids. Geochim. Cosmochim. Acta 64:. 2267-2279

Murowchick JB, Barnes HL (1986) Marcasite precipitation from hydrothermal solution. Geochim. Cosmochim. Acta 50: 2615-2629

Oudin E, Constantinou G (1984) Black smoker chimney fragments in Cyprus sulfide deposits. Nature 308: 349-353

Shimazaki H, Horikoshy Ei (1990) Black ore chimney from the Hanaoka Kuroko deposit, Japan. Mining Geolog 40(5): 313-321

Zaykov VV, Shadlun TN, Maslennikov VV, Bortnikov NS (1995) Jaman-Kasy sulphide deposit – ancient "black smoker" of Urals paleoocean (in Russian). Geol. Rudn. Mesto. 37: 511-529

Back-arc basin constraints on the genesis of Ordovician volcanogenic massive sulfides in the Flat Landing Brook Formation, Bathurst Mining Camp, Canada

S.H. McClenaghan
Department of Geology, University of New Brunswick, PO Box 4400, Fredericton, New Brunswick, E3B 5A3 Canada

D.R. Lentz
Department of Geology, University of New Brunswick, PO Box 4400, Fredericton, New Brunswick, E3B 5A3 Canada

J.A. Walker
Geological Surveys Branch, New Brunswick Department of Natural Resources, PO Box 50, Bathurst, New Brunswick, E2A 3Z1 Canada

Abstract. Volcanic sediment hosted massive sulfide (VSHMS) deposits and coeval iron formation in the Middle Ordovician Bathurst Mining Camp (BMC) are generally hosted by tuffaceous sedimentary rocks of Nepisiguit Falls Formation. However, several volcanogenic massive sulfide (VMS) deposits occur within effusive volcaniclastic rocks and felsic domes associated with felsic dominated bimodal volcanism of the Flat Landing Brook Formation. Their setting higher in the stratigraphic pile is accompanied by base-metal contents that are atypical of the deposits hosted by the Nepisiguit Falls Formation within the BMC. The Louvicourt deposit, which occurs within felsic hyaloclastite (Flat Landing Brook Formation) at the contact with an overlying sequence mafic volcanic rocks (Little River Formation) has a Pb/Zn ratio of 2.6, the highest recorded for any massive sulfide deposit in the BMC (Pb/Zn avg. 0.39). The persistence of exhalative hydrothermal activity at the terminal stages of felsic volcanism, with an evolution towards extensional mafic magmatism, highlights the exploration potential for VMS systems along the contact between the Flat Landing Brook and Little River formations within the Middle Ordovician Tetagouche Group.

Keywords. Volcanogenic, massive sulfide , Flat Landing Brook, Louvicourt, Bathurst Mining Camp, New Brunswick

1 Introduction

Historically, Zn, Pb, Cu, and Ag production in the BMC has come principally from VSHMS deposits associated with felsic volcaniclastic rocks of the Tetagouche Group. The Brunswick and Heath Steele belts (Figure 1), hosted by tuffaceous sedimentary rocks of the Nepisiguit Falls Formation have accounted for over 125 Mt of massive sulfide production (McCutcheon et al. 2003). The large size and preservation of these deposits can be attributed to their deposition in a restricted back-arc basin (Tetagouche-Exploits) that was conducive to the formation of massive sulfide deposits. Although not a major focus of exploration efforts, the overlying Flat Landing Brook Formation, characterized by felsic domes, flows and volcaniclastic rocks, does host massive sulfide deposits and smaller occurrences.

2 Geological setting

The BMC is a Cambro-Ordovician bimodal volcanic and sedimentary sequence that formed on a stable continental margin in response to subduction- related rifting (Skinner 1974). The base of the BMC consists of a continentally derived turbidite sequence of quartz wacke, quartzite, siltstone, and shale (Miramichi Group) that forms a flysch apron on the Avalonian margin. The Miramichi Group is conformably to disconformably overlain by felsic volcaniclastic, sedimentary and mafic volcanic rocks of the Tetagouche Group (van Staal et al. 2003). These volcanic rocks are interpreted to have formed in a back-arc basin (similar to the Japan Sea back-arc basin; Rogers and van Staal 2003; Rogers et al. 2003) and represent ensialic to ensimatic portions of the Tetagouche-Exploits basin formed as a result of rifting of the Popelogan arc between 475 and 455 Ma (van Staal et al. 2003). The entire sequence has undergone complex polyphase deformation and has been intruded by Ordovician and Devonian felsic to mafic plutons (Skinner 1974; van Staal et al. 2003).

Felsic volcanic rocks of the Tetagouche Group formed as successive high temperature partial melts (mantle-derived basaltic magma) of the same crustal block (Lentz 1999; Rogers et al. 2003) and have been divided into subalkalic volcanic rocks of the Nepisiguit Falls Formation and felsic dominated bimodal volcanic rocks of the Flat Landing Brook Formation (Rogers et al. 2003). Coarse-grained, quartz-feldspar-crystal-rich tuffs and tuffaceous sandstones of the Nepisiguit Falls Formation (~474-469 Ma; Rogers et al. 2003) are conformably overlain sparsely feldspar-phyric to aphyric lavas, domes, and pyroclastic flow/fall rocks of the Flat Landing Brook Formation (466 ± 2 Ma; Rogers et al. 1997). The Flat Landing Brook Formation is overlain by the mafic-dominated bimodal Little River Formation (459 ± 3 Ma; Sullivan and van Staal 1996), which is composed of alkalic pillow basalts, hyaloclastite, mudstone, ferromanganiferous shale, chert and black shale with lesser rhyolite and comendite (Rogers et al. 2003; van Staal et al. 2003).

3 VMS setting of the Flat Landing Brook Formation

Massive sulfides and coeval exhalite from the Stratmat, Taylor Brook, and Louvicourt deposits (Llanvirnian, 467-465 Ma; van Staal et al. 2003) represent the last significant hydrothermal activity in the BMC (Fig. 1) prior to mafic volcanic rift volcanism (Little River Formation). Their association with felsic domes, flows and hyaloclastite of the Flat Landing Brook Formation has led to a range of deposit settings and hydrothermal signatures that differ from the more well known deposits along the Brunswick Horizon (Figure 1), which occur predominantly along a single horizon within the Nepisiguit Falls Formation (469-468 Ma; van Staal et al. 2003). Massive sulfide occurrences in the Flat Landing Brook Formation are unique to the BMC, possessing a number of similarities with the Kuroko deposits of Japan (Ohmoto 1996), namely the abundance of barite, and the close spatial association with felsic domes.

These proximal autochthonous deposits formed through syngenetic hydrothermal exhalative activity that was likely related to emergent felsic domes. Sulfides are pyrite, sphalerite, and galena with lesser chalcopyrite, tetrahedrite and arsenopyrite; pyrrhotite is subordinate to pyrite and is generally scarce. Metal zonation is developed in massive sulfide lenses with a Pb+Zn-rich top that grades into a Cu-rich base and is commonly autochthonous upon an epigenetic stockwork sulfide system composed of pyrite, pyrrhotite, and chalcopyrite. Overall, base-metal contents of deposits hosted by the Flat Landing Brook Formation are systematically higher with an average Pb+Zn of 10.8 wt%, significantly higher than the BMC average of 6.52 wt% (Goodfellow and McCutcheon 2003). These deposits are also notably enriched in Pb with 3.11 wt% Pb (BMC average, 1.78 wt%) and a Pb/Zn ratio of 0.53 (BMC average, 0.39).

Trace-element contents also vary between deposits hosted by the Flat Landing Brook Formation. Despite their elevated base-metal contents, trace-element contents of the Stratmat deposits resemble typical Bathurst-style deposits. The Taylor Brook and Louvicourt deposits differ from the Stratmat deposits with massive sulfides containing elevated contents of Tl (63 to 300 ppm) and abundant barite.

The 0.14 Mt Louvicourt Au-Ag-Cu-Zn-Pb sulfide deposit is hosted by felsic volcaniclastic rocks at the top of the Flat Landing Brook Formation. The base- and precious-metal content of the Louvicourt deposit is atypical of BMC massive sulfide deposits. Assessment file assay data from the sulfide intersections (n=27) yield a Pb/Zn ratio of 2.6, the highest of any massive sulfide deposit in the BMC (Pb/Zn avg. 0.39). Lead exhibits a strong Spearman Rank correlation (r'=0.92) with other base metals throughout the sequence indicating a preponderance of galena in the stockwork and massive sulfides (n = 80). The deposit also has elevated Ag and Au contents, among the highest in the BMC. Barite-rich exhalative pyrite (n=10) exhibits a moderate Au correlation with Ag (r'=0.77) and Cu (r'=0.76). This Au-Ag-Cu association displays a strong correlation with Pb/Zn suggesting precipitation of Au in Pb-enriched portions of the exhalative sulfides.

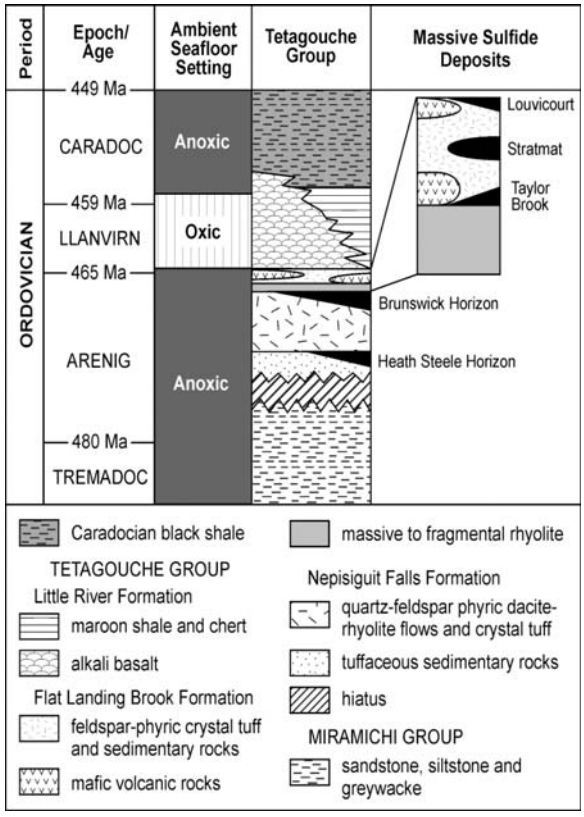

Figure 1: Stratigraphic distribution of massive sulfide deposits in the Bathurst Mining camp (modified from Goodfellow and McCutcheon 2003).

4 Constraints on deposit genesis

The Louvicourt deposit, situated atop the Flat Landing Brook Formation, was deposited at a time when the Tetagouche-Exploits basin had reverted to more oxygenated conditions. These conditions would have been unfavourable for sulfide accumulation and subsequent preservation, and may have been compounded by their proximity to an emerging felsic dome that resulted in an unstable seafloor topography. The small size and low base-metal contents of the Louvicourt deposit may also indicate that the hydrothermal system which formed the deposit was not as long lived as that for the larger base-metal-rich Stratmat deposits. Barite is typically rare for Bathurst-type deposits due to the limited content of SO_4^{2-} in the dominantly anoxic Tetagouche-Exploits back-arc

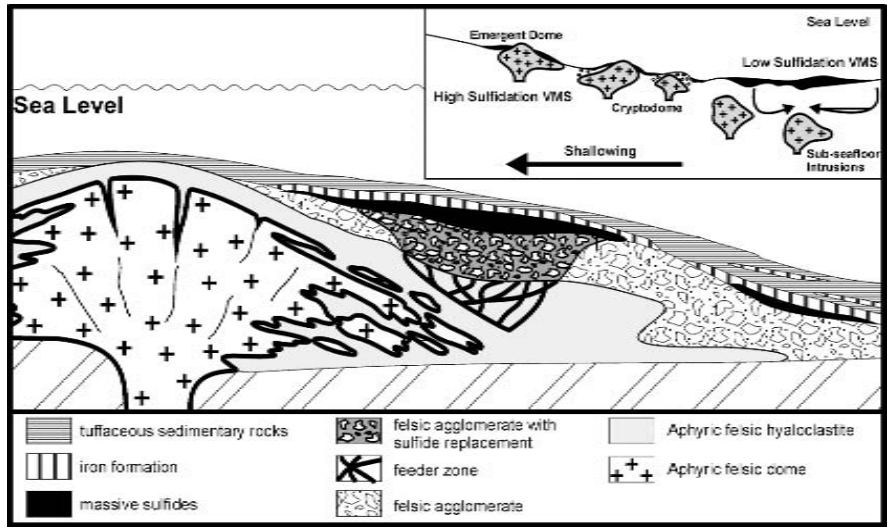

Figure 2: An idealized cross-section through a felsic cryptodome with a volcanogenic massive sulfide deposit analogous to the Louvicourt deposit generated along its flanks. The hydrothermal signature and setting is similar to high sulfidation VMS deposits described by Hannington et al. (1999), whereas typical low sulfidation, Bathurst deposits occur in thick tuffaceous sequences.

basin during the deposition of the Nepisiguit Falls Formation and in part the Flat Landing Brook Formation (Goodfellow et al. 2003). The metal signature of massive sulfides from the Louvicourt deposit is atypical for the BMC with a Pb/Zn of 2.6 and with elevated contents of Ag, Au, Sb, Hg, and Tl. The unique hydrothermal signature of the deposit may suggest an increased role of magmatic volatiles in low pH hydrothermal fluids, analogous to high sulfidation VMS systems (Figure 2).

5 Implications for exploration

The Flat Landing Brook Formation has the potential to host large Zn+Pb-rich VMS deposits, as exemplified by the Stratmat deposits. However, these deposits are associated with thicker sequences of tuffaceous sedimentary rocks that are indicative of quiescent basin conditions. The size and preservation of these deposits are further enhanced by their occurrence in deeper, more isolated sub-basins where anoxia prevailed later in the evolution of the Tetagouche-Exploits back-arc basin. However, this does not preclude the occurrence of VMS deposits at the top of the Flat Landing Brook Formation prior to the eruption of the Little River Formation. Rift volcanism was preceded by an extended period of quiescence (466 to 459 Ma), which would have been conducive to sulfide accumulation at the top of the Flat landing Brook Formation.

Similarly, VMS deposits of the Pelly Mountains in Canada and the Avoca Cu-Pb-Zn deposit in Ireland are associated with the initiation of highly alkaline rift volcanism, highlighting the role of extensional dynamics in the generation of VMS systems (Lentz 1998). An extensional setting was important in the formation of the Kuroko deposits that occur within an aborted intra-island-arc rift. In the BMC, the occurrence of the Louvicourt deposit demonstrates that hydrothermal activity persisted during the later stages of extension in the Tetagouche Group, and offers a unique exploration target at the top of the Flat Landing Brook Formation.

Acknowledgements

This project was funded by a NSERC Discovery grant to David Lentz and the New Brunswick Department of Natural Resources. Research benefited from discussions with Warna Downey, Peter Gummer, Don Hattie, Jonathan Lafontaine, Roger Moss, Adrian Park, and Xueming Yang.

References

Goodfellow WD, Peter JM, Winchester JA, van Staal CR (2003) Ambient marine environment and sediment provenance during formation of massive sulfide deposits in the Bathurst Mining Camp: importance of reduced bottom waters to sulfide precipitation and sulfide preservation. In: Goodfellow WD, McCutcheon SR, Peter JM (eds) Massive Sulfide Deposits of the Bathurst Mining Camp, New Brunswick and northern Maine, Economic Geology Monograph 11: 129-156

Hamilton A (1992) Geology of the Stratmat Boundary and Heath Steele N-5 zones, Bathurst Camp, Northern New Brunswick. Exploration and Mining Geology, 1: 131-135

Lentz DR (1999) Petrology, geochemistry, and oxygen isotope interpretation of felsic volcanic and related rocks hosting the Brunswick 6 and 12 massive sulfide deposits (Brunswick Belt), Bathurst Mining Camp, New Brunswick, Canada. Economic Geology, 94: 57-86

Lentz, DR (1998) Petrogenetic evolution of felsic volcanic sequences associated with Phanerozoic volcanic-hosted massive sulphide systems: the role of extensional geodynamics. Ore Geology Reviews, 12: 289-327

McClenaghan SH, Goodfellow WD, Lentz DR (2003) Gold in massive sulfide deposits, Bathurst Mining Camp: distribution and genesis. In: Goodfellow WD, McCutcheon SR, Peter JM (eds) Massive Sulfide Deposits of the Bathurst Mining Camp, New Brunswick and northern Maine, Economic Geology Monograph 11: 303-326

McClenaghan SH, Lentz DR, Beaumont-Smith CJ (in press) The gold-rich Louvicourt volcanogenic massive sulfide deposit, New Brunswick: A Kuroko analogue in the Bathurst Mining Camp. Exploration and Mining Geology

McConnell BJ, Stillman CJ, Hertogen J (1991) An Ordovician basalt to peralkaline rhyolite fractionation series from Avoca Ireland. Journal of the Geological Society of London, 148: 711-718

McCutcheon SR, Luff WM, Boyle RW (2003) The Bathurst Mining Camp, New Brunswick, Canada: history of discovery and evolution of geologic models. In: Goodfellow WD, McCutcheon SR, Peter JM (eds) Massive Sulfide Deposits of the Bathurst Mining Camp, New Brunswick and northern Maine, Economic Geology Monograph 11: 17-36

Mortensen JK, Godwin CI (1982) Volcanogenic massive sulfide deposits associated with highly alkaline rift volcanics in southeastern Yukon Territory. Economic Geology, 77: 1225-1230

Rogers N, van Staal CR (2003) Volcanology and tectonic setting of the northern Bathurst Mining Camp: Part II. mafic volcanic constraints on back-arc opening. In: Goodfellow WD, McCutcheon SR, Peter JM (eds) Massive Sulfide Deposits of the Bathurst Mining Camp, New Brunswick and northern Maine, Economic Geology Monograph 11: 181-202

Rogers N, Wodicka N, McNicoll V, van Staal CR (1997) U-Pb zircon ages of the Tetagouche Group felsic volcanic rocks, northern New Brunswick. Current Research, Geological Survey of Canada 1997-F: 113-119

Skinner R (1974) Geology of Tetagouche Lakes, Bathurst and Nepisiguit Falls map areas, New Brunswick. Geological Survey of Canada, Memoir 371, 133

Sullivan RW, van Staal CR (1996) Preliminary chronostratigraphy of the Tetagouche and Fournier groups in northern New Brunswick., Radiogenic Age and Isotopic Studies. Current Research, Geological Survey of Canada, 1995-F: 43-56

van Staal CR, Wilson RA, Rogers N, Fyffe LR, Langton JP, McCutcheon SR, McNicoll V, Ravenhurst CE (2003) Geology and tectonic history of the Bathurst Supergroup, Bathurst Mining Camp, and its relationships to coeval rocks in southwestern New Brunswick and adjacent Maine - a synthesis. In: Goodfellow WD, McCutcheon SR, Peter JM (eds) Massive Sulfide Deposits of the Bathurst Mining Camp, New Brunswick and northern Maine, Economic Geology Monograph 11: 37-60

Walker JA (1999) Geology of the Taylor Brook massive sulphide deposit (NTS 21 O/08E), Bathurst Mining Camp, New Brunswick. In: Carroll, BMW (ed) Current Research 1998. New Brunswick Department of Natural Resources and Energy, Minerals and Energy Division, Mineral Resource Report 93-1: 57-87

The submarine volcanic succession hosting the massive sulfide and sulfosalt Eskay Creek deposit, Canada

T. Monecke
Department of Earth Sciences, University of Ottawa, Canada

D. Gale, T. Roth
Barrick Gold Corporation, Vancouver, Canada

M.D. Hannington
Department of Earth Sciences, University of Ottawa, Canada

Abstract. Volcanic facies analysis shows that the unusual polymetallic, precious-metal rich volcanic-rock hosted massive sulfide and sulfosalt Eskay Creek deposit in northern British Columbia, Canada, formed on top of a submarine felsic volcanic center. The footwall rhyolite formed by multiple rhyolite generations involving extrusive and intrusive emplacements. Extrusive volcanism involved phreatic-hydrothermal explosive eruptions and the deposition of associated volcanic rocks. Despite the fact that the mineralization is largely hosted by carbonaceous mudstone overlying the sedimented phreatic-hydrothermal explosion deposits, it can be demonstrated that the ore-forming event took place contemporaneously with the youngest intrusive emplacement of rhyolite. The mineralizing event overlapped with the onset of a period of intense basaltic volcanism.

Keywords. Volcanic facies architecture, massive sulfides, shallow marine gold deposits

1 Introduction

Eskay Creek is an unusual polymetallic, precious-metal rich volcanic-rock hosted massive sulfide and sulfosalt deposit that is located in the Iskut River area of northern British Columbia, Canada. In 2003, total production of the mine reached 1.53 Mt at average grades of 52.5 g/t Au and 2,398 g/t Ag. The mineralization comprises stratiform beds of clastic ore as well as discordant zones of sulfide veins and disseminations. The deposit represents an important example of massive sulfide formation in a relatively shallow water environment where boiling of the hydrothermal fluids was an important ore-forming process. It shares many physical and chemical attributes with epithermal Au-Ag deposits occurring on land (Roth et al. 1999; Sherlock et al. 1999).

Hitherto, different models for the volcanic facies evolution of the Eskay Creek deposit have been proposed that differ in the interpretation of the volcanic facies occurring in the immediate footwall and hanging wall of the mineralization (Rye 1992; Allen 1993; Bartsch 1993; Roth et al. 1999). Because facies relationships in this stratigraphic position are particularly important for the understanding of the depositional environment of the mineralization, additional logging of volcanic facies in exploration drill core was carried out.

2 Deposit geology

The Eskay Creek deposit is hosted by a Middle Jurassic bimodal volcanic sequence that is folded into a shallowly north-plunging, northeast-trending anticline. The stratigraphic footwall of the mineralization is dominated by rhyolite. These volcanic rocks are overlain by a relatively thick interval of carbonaceous mudstone and basalt (MacDonald et al. 1996; Roth et al. 1999).

The bulk of the ore is contained in the stratiform ores of the 21 zones (Fig. 1) that are located within the carbonaceous mudstone at or near the contact with the underlying rhyolite. The 21A zone is a stibnite-realgar-cinnabar-rich sulfide lens whereas the high-grade 21B zone is composed of bedded clastic sulfides and sulfosalts . Stratiform mineralization also occurs in the barite-rich 21C zone and the fault-complicated mineralization of the NEX zone. The massive, fine-grained sulfides of the HW zone are located in a stratigraphically higher position within the carbonaceous mudstone. Discordant zones of sulfide veins and disseminations are hosted by the footwall rhyolite below and adjacent to the 21B zone in the Pumphouse and 109 zones (Roth et al. 1999).

3 Facies architecture

The facies architecture of the Eskay Creek deposit was studied by examining ~1200 m of exploration diamond drill core that intersected a stratigraphic interval of approximately 100 m over a strike extent of 850 m (Fig. 1). The principal volcanic facies recognized are summarized in Table 1.

Logging revealed that the immediate footwall of the stratiform mineralization is dominated by coherent facies and blocky to slabby rhyolite breccias (Fig. 1). This breccia facies formed by different processes including autobrecciation, quench fragmentation, and hydraulic brecciation caused by the expansion and volatilization of seawater entrained into the rhyolite or the migration of over-pressured hydrothermal fluids (Allen 1993). A stratified sandstone and rhyolite breccia facies has been ob-

Table 1: Principal volcanic lithofacies recognized in representative exploration drill core from the Eskay Creek deposit. Note that additional facies have been identified in the lower part of the footwall and the upper portion of the hanging wall.

Lithofacies (interpretation)	Characteristics
Rhyolite facies	
Massive or flow-banded rhyolite (coherent rhyolite)	Aphyric, massive or flow banded rhyolite; flow banding ranges from centimeter-scale layers to laminations that are only few millimeters wide; rhyolite is white to cream in color, siliceous and very hard; formerly glassy; contains abundant perlitic cracks and locally spherulitic textures
Blocky to slabby rhyolite breccia (autobreccia and hyaloclastite, or hydraulic breccia)	Non-stratified and poorly sorted; clast- to matrix-supported; blocky to slabby clasts that are aphyric, sometimes perlitic; curviplanar, planar, ragged or serrated clast margins with local evidence for abrasion; clasts are typically several centimeters in size and commonly flow banded; jigsaw-fit or random orientation of clasts; monomictic, but breccia with flow-banded and massive clasts occur; frequently intense hydrothermal alteration of the matrix, pseudoclastic textures are common
Sediment-matrix rhyolite breccia (peperite)	Non-stratified and disorganized; typically matrix-supported, locally clast-supported or sediment veined; rhyolite clasts are texturally diverse, polyhedral and blocky or serrated and sinuous; monomictic; clasts are typically several centimeters in size; matrix consists of mudstone or stratified sandstone and rhyolite breccia; mudstone beds are commonly distorted; preferential hydrothermal alteration of matrix is common; facies has sharp to gradational contacts
Stratified sandstone and rhyolite breccia (phreatic-hydrothermal explosion deposit)	Diffuse stratification, moderately to well sorted; normal grading is common; coarse sandstone has a granular to gravelly texture, larger rhyolite fragments are blocky, slabby or subrounded; clasts are polymictic, not pumiceous and variably altered; clasts range up to approximately 5 cm in size; mudstone intraclasts are common
Mudstone facies	
Mudstone (hemipelagic sediment and syn- to posteruptive volcaniclastic mass flow deposits)	Laminated, thinly bedded, or massive; black and distinctly carbonaceous, variably calcareous and siliceous; intercalated beds of coarser volcaniclastic material; abundant sulfide laminations, frequently flame structures at the base of beds of coarser volcaniclastic material or clastic sulfide laminations; intervals ranging in thickness from several centimeters to tens of meters; rare belemnite fragments; abundant prehnite porphyroblasts in intervals hosting massive basalt
Basalt facies	
Massive basalt (coherent basalt)	Aphyric to moderately porphyritic; pale to medium green; occasional jointing; non to moderately amygdaloidal; amygdales are round to ellipsoidal in shape; trails of elongated amygdales sometimes define a flow foliation; abundance of amygdales commonly increases towards the margins of individual basalt units; basalt is frequently chilled at the contacts to adjacent sedimentary facies
Non-stratified basalt breccia (autobreccia and hyaloclastite)	Monomictic; chaotic and very poorly sorted breccia; clast- to matrix-supported; frequently jigsaw-fit textures; polyhedral, blocky, or splintery clasts with distinctly planar to curviplanar margins; clast sizes vary from a few millimeters to several centimeters; facies is gradational to massive basalt
Mudstone-matrix basalt breccia (peperite)	Monomictic; disorganized, matrix-supported breccia or sediment veined breccia; clasts are angular and blocky with planar to curviplanar margins or bulbous to lobate; clast margins typically show evidence for quenching; clast sizes range from a few millimeters to several centimeters; mudstone matrix is indurated or partially replaced by secondary minerals; bedding of mudstone is absent, destroyed, or intensely contorted; facies is gradational to massive basalt
Polymictic basalt breccia (talus breccia)	Polymictic, aphyric and porphyritic basalt clasts; massive, clast-supported and poorly sorted breccia; clasts are polyhedral and blocky with distinctly subrounded to rounded corners, locally well rounded, gravelly clasts; clast sizes range up to several tens of centimeters; locally clasts of chilled and quenched basalt or pillow fragments, orientation of internal foliation of clasts is random, mudstone intraclasts are present

served in several drill holes. This facies probably formed by phreatic-hydrothermal explosions. The observed stratification and sorting indicates that this facies deposited on the ancient sea floor. According to Rye (1992) and Roth et al. (1999), the sedimented phreatic-hydrothermal explosion deposits are particularly abundant in the footwall of the 21A and 21B zones. In contrast to this facies, the occurrence of sediment-matrix rhyolite breccia, interpreted to be peperite, is indicative for the intrusive emplacement of rhyolite. Peperite has been observed at the margins of coherent facies that is in contact with the stratified sandstone and rhyolite breccia as well as carbonaceous mudstone. The latter represents the host to the stratiform sulfide and sulfosalt mineralization (Fig. 1). The upper portion of the investigated stratigraphic interval is dominated by carbonaceous mudstone and basalt (Fig. 1). The frequent occurrence of peperite along the top and bottom margins of coherent basalt bodies indicates that the basaltic lava commonly intruded into the wet and unconsolidated mudstone. Intrusions are particularly common in the lower portion of the hanging wall. Non-stratified basalt breccias are more common

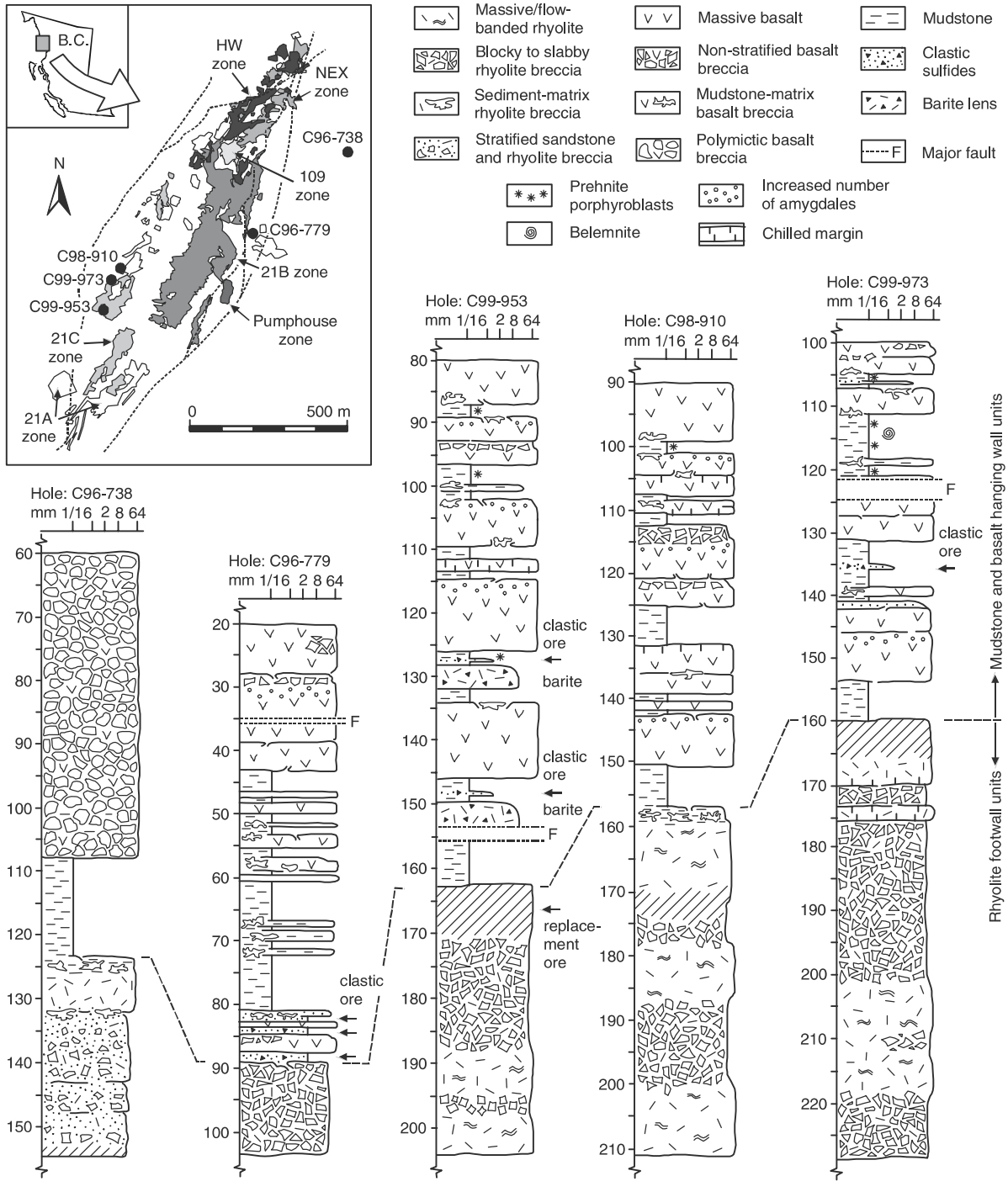

Figure 1: Simplified stratigraphic logs showing the distribution of volcanic facies at the Eskay Creek deposit.

along the top margins of coherent basalt units occurring in the upper portion of the hanging wall where basalt forms intervals exceeding tens of meters in thickness. The occurrence of hyaloclastite and basaltic talus breccia indicates that these thick basalt intervals include a significant extrusive component.

4 Reconstruction of the volcanological setting

The precious-metal rich sulfide and sulfosalt mineralization of the Eskay Creek deposit formed in proximity to a submarine felsic volcanic center that has previously been considered to represent a row of rhyolite flow domes

(Bartsch 1993). Logging carried out as part of the present research supports the finding of Allen (1993) that the footwall rhyolite formed by multiple rhyolite generations involving extrusive and intrusive emplacements. The geometry and facies relationships observed are inconsistent with the model of Bartsch (1993). Correlation of different rhyolite generations between adjacent drill holes is, however, difficult due to the absence of phenocryst populations that can be used to identify separate units of rhyolite.

The footwall rhyolite emerged at the ancient seafloor causing phreatic-hydrothermal explosive eruptions. Because the related deposits are immediately overlain by the stratiform mineralization, and locally contain sulfide clasts (Rye 1992), the ore must have formed in close temporal and spatial association with the extrusive part of the felsic volcanic center. However, the footwall rhyolite contains a currently unconstrained, but possibly significant, intrusive component. At least locally, rhyolite sills intruded along the contact of the still wet and unconsolidated deposits of the phreatic-hydrothermal explosions and the mudstone that was deposited on top of the extrusive parts of the footwall rhyolite (Fig. 1). These rhyolite sills have been subject to hydrothermal alteration. Therefore, there was clearly no time hiatus between the rhyolitic volcanism and the formation of the deposit. The hydrothermal alteration of the basalt indicates that the onset of basaltic volcanism occurred prior to the waning of the hydrothermal activity. These observations suggest that the sulfide and sulfosalt mineralization of the Eskay Creek deposit formed essentially coeval with the youngest emplacement of rhyolite units in the footwall and the onset of basaltic volcanism in the hanging wall. From an exploration point of view, it is important to note that the bulk of the mineralization is spatially associated with the sedimented phreatic-hydrothermal explosion deposits. Due to the common intrusive nature of basalt in the lower part of the hanging wall, exploration strategies should not be based on a stratigraphic distinction of mudstone occurring below and above the basalt as initially proposed by Britton et al. (1989).

Acknowledgements

TM gratefully acknowledges financial support by the Emmy Noether Program of the German Research Foundation. Field work was supported by Barrick Gold Corporation and a grant provided by the Michael-Jürgen-Leisler-Kiep Foundation.

References

Allen RL (1993) Volcanic facies analysis of massive sulphide deposits in British Columbia: Preliminary results from field work August-September 1993. MDRU report. University of British Columbia, Vancouver

Bartsch RD (1993) A rhyolite flow dome in the Upper Hazelton Group, Eskay Creek area (104B/9,10). British Columbia Ministry of Energy, Mines and Petroleum Resources, Geological Fieldwork 1992: 331-334

Britton JM, Blackwell JD, Schroeter TG (1989) #21 zone deposits, Eskay Creek, northwestern British Columbia. British Columbia Ministry of Energy, Mines and Petroleum Resources, Exploration in British Columbia 1989: 197-223

Macdonald AJ, Lewis PD, Thompson JFH, Nadaraju G, Bartsch RD, Bridge DJ, Rhys DA, Roth T, Kaip A, Godwin CI, Sinclair AJ (1996) Metallogeny of an Early to Middle Jurassic Arc, Iskut River Area, northwestern British Columbia. Econ. Geol. 91: 1098-1114

Roth T, Thompson JFH, Barrett TJ (1999) The precious metal-rich Eskay Creek deposit, northwestern British Columbia. Rev Econ. Geol. 8: 357-373

Rye K (1992) Geological and geochemical report on the 1991 Eskay Creek diamond relog program. Internal report for International Corona Corporation

Sherlock RL, Roth T, Spooner ETC, Bray CJ (1999) Origin of the Eskay Creek precious metal-rich volcanogenic massive sulfide deposit: Fluid inclusion and stable isotope evidence. Econ. Geol. 94: 803-824

Unraveling mineral isotope signatures from whole-rock oxygen and hydrogen isotope data: A case study

T. Monecke
Department of Earth Sciences, University of Ottawa, Canada

H. Paulick
Mineralogisch-Petrologisches Institut, Universität Bonn, Germany

R. Kleeberg
Institut für Mineralogie, TU Bergakademie Freiberg, Germany

Abstract. The present contribution proposes a method that allows the calculation of the stable isotope signatures of minerals contained in fine-grained altered volcanic rocks by combining isotope measurements and quantitative XRD analysis on whole-rock samples and grain size separates. Application of this method to samples from the Waterloo VHMS deposit, Australia, revealed that hydrothermal alteration associated with the formation of pyrite-rich massive sulfides proceeded at higher temperatures than that related to the precipitation of sphalerite-rich sulfides. The calculated $\delta^{18}O$ and δD values of the hydrothermal fluids are 0.5 to 5.5 ‰ and -0 to -25 ‰, respectively.

Keywords. Oxygen and hydrogen isotopic fractionation, hydrothermal alteration, massive sulfides

1 Introduction

Over the past decades, numerous oxygen and hydrogen isotope studies have been conducted on hydrothermally altered volcanic rocks hosting massive sulfide deposits. It has been well established that these deposits are usually enveloped by alteration halos that are characterized by distinct isotopic signatures (cf. review by Huston 1999). Although the recognition of isotopic gradients around massive sulfides has important exploration implications, whole-rock oxygen and hydrogen isotope data are only of limited use in genetic studies. The temperature of hydrothermal alteration and the isotopic composition of the mineralizing hydrothermal fluids can only be derived from isotope data of alteration minerals with known isotope fractionation coefficients. The determination of the stable isotopic signatures of individual alteration minerals is, however, problematic because the fine-grained nature of the hydrothermally altered rocks typically precludes the preparation of monomineralic samples.

In the present contribution, a method is proposed that allows the calculation of mineral oxygen and hydrogen signatures from isotope and mineral abundance data determined on whole-rock samples and grain size separates. Particular care has been paid to the propagation of analytical errors. The proposed method has been applied to samples from the Waterloo deposit, Australia.

2 Geological background

The Waterloo VHMS deposit is situated in the Charters Towers region in northern Queensland. It is located in the central part of the Seventy Mile Range Group, a major relict of Cambro-Ordovician back-arc volcanism at the northern end of the Tasman Fold Belt System. The mineralization consists of several dismembered massive sulfide lenses representing a base metal resource of 372,000 t at 3.8 % Cu, 19.7 % Zn, 2.8 % Pb, 94 g/t Ag, and 2 g/t Au.

The blanket-like massive sulfide mineralization of the Waterloo deposit is located on top of an andesite-dominated facies association and is overlain by coarse volcaniclastic rocks that have been intruded by a dacite cryptodome. The sulfides are enveloped by an extensive and mineralogically zoned hydrothermal alteration halo (Monecke et al. 2001).

3 Materials and methods

The present study is based on five intensely altered whole-rock samples that have been collected from the immediate footwall of the massive sulfides. Sample 22-277 was taken from a drill hole that lacked significant base metal mineralization whereas the samples 9A-218 and 9A-228 originated from the immediate footwall of sphalerite-rich massive sulfides. The samples 16-276 and 16-292 were collected from drill holes penetrating pyrite-rich massive sulfides. The mineralogical composition of the samples was determined by XRD analysis. Initially, the whole-rock samples were finely crushed and powdered. A split of each powdered sample was further prepared for XRD analysis following the procedure of Monecke et al. (2001). In addition, a set of samples with changed relative phase abundances was prepared by grain size separation of the powdered whole-rock samples. Grain size separation of the <2 μm fractions was conducted by gravity sedimentation. Step-scan XRD data of the whole-rock samples and the <2 μm fractions were collected on an URD-6 (Seifert-FPM) diffractometer. Qualitative and quantitative phase analysis was conducted by the Rietveld

Table 1: Mineralogical and isotopic composition of selected silicic-altered samples from the Waterloo VHMS deposit, Australia

	Whole-rock samples					Muscovite-enriched samples				
	22-277	9A-218	9A-228	16-276	16-292	22-277T	9A-218T	9A-228T	16-276T	16-292T
Phase abundances (wt.%)										
Ms	33.2±0.7	16.6±0.5	23.2±0.5	35.1±0.7	26.4±0.6	77.7±0.7	48.3±0.7	64.6±0.7	76.5±0.7	73.6±0.8
Py	8.0±0.2	6.9±0.2	3.1±0.1	5.9±0.2	9.3±0.2	1.1±0.2	2.8±0.2	0.5±0.1	0.6±0.2	1.3±0.2
Qtz	58.8±0.6	76.5±0.5	73.7±0.5	59.0±0.7	64.3±0.6	21.2±0.6	48.9±0.7	34.9±0.7	22.9±0.7	25.1±0.7
Oxygen isotopic compositions (‰, SMOW)										
$\delta^{18}O$	8.4±0.2	9.8±0.2	9.4±0.2	8.1±0.2	8.1±0.2	5.6±0.2	8.4±0.2	7.9±0.2	7.0±0.2	6.8±0.2
Hydrogen isotopic compositions (‰, SMOW)										
δD	-60±3	-57±3	-54±3	-52±3	-60±3	-63±3	-37±3	-46±3	-47±3	-61±3

method using the procedure described by Monecke et al. (2001).

The $\delta^{18}O$ and δD ratios of the whole-rock sample and <2 µm fractions were determined at the University of Bonn. In order to remove atmospheric moisture and non-structural water, the powders were pre-heated overnight under vacuum at 120 °C. The silicate oxygen was extracted and converted to CO_2 in a fluorination line using F_2 gas as a reagent following procedures described by Clayton and Mayeda (1963). The hydrogen was extracted by heating the sample powders in vacuum up to 1,300 °C and the vapor was reduced by passing it over hot uranium oxide (Bigeleisen et al. 1952). A VG Isogas SIRA-9 instrument was used for the measurements. The overall precision of the analytical procedure is 0.2 ‰ for $\delta^{18}O$ and 3 ‰ for δD. Quartz standards, calibrated against NBS-28 quartz, as well as NBS-30 biotite were used to evaluate the accuracy of the analytical method.

4 Results

The intensely altered rocks investigated are composed of quartz, muscovite, and pyrite (Tab. 1). Rutile was detected by XRD, but was neglected during Rietveld refinement due its low content (<1.5 wt.%). Table 1 illustrates that the procedure of gravity sedimentation changed the relative phase abundances, the <2 µm fractions possess significantly higher muscovite and lower quartz and pyrite contents than the original whole-rock samples.

The stable isotopic composition of the whole-rock samples and their muscovite-enriched equivalents are also given in Table 1. The whole-rock samples are typified by $\delta^{18}O$ values that are distinctly higher than those of the muscovite-enriched samples indicating that the major constituent phases quartz and muscovite have different oxygen isotopic signatures ($\delta^{18}O_{Ms} < \delta^{18}O_{Qtz}$). The recorded δD values show no systematic changes in response to the procedure of gravity sedimentation because muscovite represents the only major hydrogen-bearing phase in the samples.

5 Discussion

Notes: Equilibrium fractionation coefficients from * = Matthews & Schliestedt (1984) and ‡ = Chako et al. (1996). The errors of $\delta^{18}O_{Qtz}$, $\delta^{18}O_{Ms}$, $\Delta_{Qtz\text{-}Ms}$ and δD_{Ms} were determined by lowest order Taylor expansion. However, due to the large errors in $\Delta_{Qtz\text{-}Ms}$, the errors of T could not be determined in this way. The reported ranges of T correspond to the ranges in $\Delta_{Qtz\text{-}Ms}$.

Based on the data given in Table 1, the oxygen isotopic signatures of quartz and muscovite were derived. The $\delta^{18}O$ values of these two minerals were calculated from a set of equations that was built from the data given in Table 1. Because muscovite is the only hydrous phase, the δD signature of this mineral was simply assumed to be the arithmetic mean of the independent isotopic measurements on the whole-rock samples and the muscovite-enriched equivalents. The analytical errors were propagated by Taylor expansion to estimate the er-

Table 2: Calculated mineral isotopic compositions and alteration temperatures. See text for explanation

	22-277	9A-218	9A-228	16-276	16-292
Oxygen isotopic compositions (‰, SMOW)					
$\delta^{18}O_{Qtz}$	10.8±0.6	10.6±0.5	10.3±0.5	9.1±0.6	8.9±0.5
$\delta^{18}O_{Ms}$	4.2±0.5	6.2±0.9	6.6±0.6	6.4±0.5	6.1±0.5
$\Delta_{Qtz\text{-}Ms}$	6.6±1.1	4.4±1.4	3.7±1.1	2.8±1.1	2.9±1.0
Hydrogen isotopic composition (‰, SMOW)					
δD_{Ms}	-62±3	-47±3	-50±3	-50±3	-61±3
Alteration temperatures (°C)					
T[a]	175-256	243-449	298-502	360-687	364-629
T[b]	136-229	213-413	269-463	329-636	333-582

Notes: Equilibrium fractionation coefficients from [a] = Matthews & Schliestedt (1984) and [b] = Chako et al. (1996). The errors of $\delta^{18}O_{Qtz}$, $\delta^{18}O_{Ms}$, $\Delta_{Qtz\text{-}Ms}$ and δD_{Ms} were determined by lowest order Taylor expansion. However, due to the large errors in $\Delta_{Qtz\text{-}Ms}$, the errors of T could not be determined in this way. The reported ranges of T correspond to the ranges in $\Delta_{Qtz\text{-}Ms}$.

rors of the mineral $\delta^{18}O$ and δD values (Tab. 2). Assuming that alteration in the footwall of the Waterloo deposit proceeded under conditions comparable to equilibrium conditions attained in experimental studies conducted in closed systems, the temperature of hydrothermal alteration can be reconstructed from the calculated mineral $\delta^{18}O$ values using experimentally defined oxygen isotope equilibrium fractionation coefficients of the mineral pair quartz and muscovite. The alteration temperatures calculated according to different sets of equilibrium fractionation coefficients given in the literature are listed in Table 2. In general, the oxygen isotope geothermometers given by Matthews and Schliestedt (1984) and Chako et al. (1996) appear to slightly overestimate the alteration temperatures because temperatures exceeding approximately 400 °C are unlikely to occur in the massive sulfide forming environment (Large 1992). Table 2 also illustrates that significant uncertainties in the estimated temperatures of alteration are introduced by the large errors of the calculated $\Delta_{Qtz\text{-}Ms}$ values (Tab. 2).

Although the alteration temperature cannot be precisely estimated, some important information can be drawn from the relative differences between the samples investigated. Sample 22-277 from the drill hole lacking significant base metal mineralization yielded the lowest alteration temperature. The alteration temperatures calculated for the samples 9A-218 and 9A-228 are consistently lower than those obtained for the samples 16-276 and 16-292. The temperature difference between both groups of samples amounts to approximately 100-200°C. This finding is in agreement with current models of massive sulfide formation predicting that hydrothermal alteration associated with the formation of sphalerite-rich mineralizations takes place at a lower temperature than that associated with the precipitation of pyrite-rich massive sulfides (Large 1992).

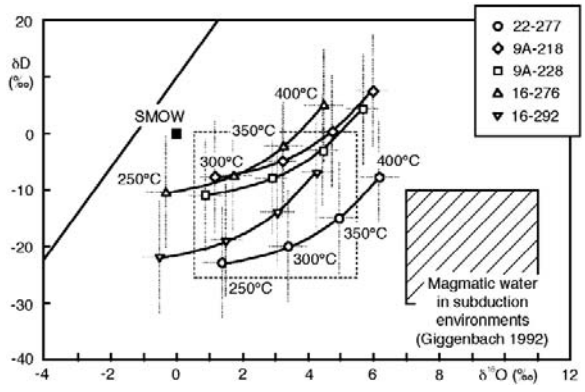

Figure 1: Hydrogen and oxygen isotope ratios calculated for the hydrothermal fluids in equilibrium with quartz and muscovite in altered rocks from the Waterloo deposit. The isotope signatures are given for different alteration temperatures.

The oxygen isotopic composition of the hydrothermal fluids involved in the alteration process was determined from the $\delta^{18}O$ values calculated for the quartz contained in the samples using the fractionation coefficients of Zhang et al. (1989). The muscovite δD values were used to constrain the hydrogen signature of the hydrothermal fluids using the fractionation coefficients given by Vennemann and O'Neil (1996) in combination with those of Suess (1949). The calculation was based on the assumption that the hydrothermal fluids were dominated by liquid H_2O. Since the temperature of alteration could not be precisely determined from the mineral pair quartz-muscovite, the isotopic signature of the hydrothermal fluids was calculated at temperatures ranging from 250 to 400 °C (Fig. 1). Based on these temperature estimates, the hydrothermal fluids must have had $\delta^{18}O$ and δD values of 0.5 to 5.5 ‰ and -0 to -25 ‰, respectively.

The derived stable isotopic signature of the mineralizing fluids at Waterloo broadly overlaps with the composition of massive sulfide forming fluids as constrained by previous authors (cf. review by Huston 1999). The agreement between the different data sets highlights the fact that the method applied in the present study provides geologically meaningful results. Figure 1 shows that the oxygen isotopic composition of the mineralizing fluids at Waterloo is shifted towards higher values when compared to seawater. This deviation has previously been interpreted to result from the interaction of seawater-derived fluids with the volcanic wall rocks (Pisutha-Arnond and Ohmoto 1983). The negative δD values cannot, however, be easily explained by the interaction of the fluids with the volcanic rocks because such a process would produce a positive shift in the δD composition (Huston 1999). The observed stable isotopic signatures and, in particular, the low δD values are probably best explained by a mixing process of seawater-derived fluids with a magmatic component because magmatic water in subduction environments possesses a strongly negative δD signature.

6 Conclusions

In the present study, a method is proposed that allows the calculation of mineral stable isotope signatures from the analysis of whole-rock samples without making any assumptions on the alteration temperature or the composition of the fluid involved in the alteration. The proposed method was used to identify gradients in the isotopic composition of quartz and muscovite within the alteration halo of the Waterloo VHMS deposit. Application of the technique revealed that pyrite-rich massive sulfides formed at higher temperatures than sphalerite-rich sulfides. The calculated stable isotope compositions of the hydrothermal fluids involved in the alteration process were found to be consistent with the mixing of seawater-derived fluids and a magmatic component.

References

Chako T, Hu X, Mayeda TK, Clayton RN, Goldsmith JR (1996) Oxygen isotope fractionations in muscovite, phlogopite, and rutile. Geochim Cosmochim Acta 60: 2595-2608

Clayton RN, Mayeda TK (1963) The use of bromine pentafluoride in the extraction of oxygen from oxides and silicates for isotopic analysis. Geochim Cosmochim Acta 27: 43-52

Huston DL (1999) Stable isotopes and their significance for understanding the genesis of volcanic-hosted massive sulfide deposits: A review. Rev Econ Geol 8: 157-179

Large RR (1992) Australian volcanic-hosted massive sulfide deposits: Features, styles, and genetic models. Econ Geol 87: 471-510

Matthews A, Schliestedt M (1984) Evolution of the blueschist and greenschist facies rocks of Sifnos, Cyclades, Greece. Contrib Mineral Petrol 88: 150-163

Monecke T, Köhler S, Kleeberg R, Herzig PM, Gemmell JB (2001) Quantitative phase-analysis by the Rietveld method using X-ray powder-diffraction data: Application to the study of alteration halos associated with volcanic-rock-hosted massive sulfide deposits. Can Mineral 39: 1617-1633

Pisutha-Arnond V, Ohmoto H (1983) Thermal history, and chemical and isotopic compositions of the ore-forming fluids responsible for the Kuroko massive sulfide deposits in the Hokuroku district of Japan. Econ Geol Mon 5: 523-558

Suess HE (1949) Das Gleichgewicht H_2+HDO=HD+H_2O und die weiteren Austauschgleichgewichte im System H_2, D_2, und H_2O. Z Natur 4A: 328-332

Vennemann TW, O'Neil JR (1996) Hydrogen isotope exchange reactions between hydrous minerals and molecular hydrogen: I. A new approach for the determination of hydrogen isotope fractionation at moderate temperatures. Geochim Cosmochim Acta 60: 2437-2451

Zhang LG, Liu JX, Zhou HB, Chen ZS (1989) Oxygen isotope fractionation in the quartz-water-salt system. Econ Geol 84: 1643-1650

Osmium isotope systematics in the Iberian Pyrite Belt

J. Munhá, J.M.R.S. Relvas, F.J.A.S. Barriga, P. Conceição, R.C.G.S. Jorge
Centro Geologia/CREMINER/Dep.Geologia, U. Lisboa, Ed. C6, Campo Grande, 1749-016 Lisboa, Portugal

R. Mathur
Department of Geology, Juniata College, Huntingdon, Pa 16652, USA

J. Ruiz
Department of Geological Sciences, U. Arizona, Tucson, Arizona 85721, USA

C.C.G. Tassinari
Centro Geocronologia (CPGeo), Universidade São Paulo, P.O. Box 11.340, São Paulo, Brasil

Abstract. New Re and Os analyses of pyrites from Aljustrel, Lagoa Salgada and Neves-Corvo deposits yield concentrations that are similar to those previously reported for the Rio Tinto and Tharsis deposits, all at the Iberian Pyrite Belt. Osmium contents in IPB pyrites increase from the deeper stockwork zones towards the upper massive sulphides. Pyrite samples from IPB sulphide orebodies plot on a major $^{187}Re/^{188}Os$ – $^{187}Os/^{188}O$ linear array, yielding an age of 359 ±26 Ma and an initial $^{187}Os/^{188}O$ ratio of *ca.* 0.57. Five samples from Neves-Corvo sulphide-rich stockwork ores yield an age of 358 ±29 Ma and an initial $^{187}Os/^{188}O$ ratio of 0.49 ±0.07, in accord with palynological and isotopic age constraints for ore formation at the IPB. Pyrites from Neves-Corvo copper-tin ores have Re/Os ratios and osmium concentrations that are similar to those in pyrites from sulphide-rich stockwork ores; however, their highly radiogenic initial $^{187}Os/^{188}O$ ratios (4.89 – 7.85, if preserving original isotope systematics) preclude derivation from the same sources as the remaining IPB sulphides. The overall Re-Os geochemical data conform to previous Sr, Nd and Pb isotopic studies supporting multiple sources for IPB metallogenesis.

Keywords. Iberian Pyrite Belt, VHMS deposits, metal sources, osmium isotope systematics

1 Introduction and geological setting

A total accumulation of 1700 Mt of massive sulphide ores, distributed over 88 known deposits and containing more than 21 Mt of copper, 34 Mt of zinc, 12 Mt of lead and 0.8 Mt of gold, is the impressive balance of about 6 Ma of highly productive hydrothermal activity in the Iberian Pyrite Belt (IPB; Barrie et al., 2002; Oliveira et al. 2004). Massive sulphide deposition occurred within a relatively thin volcanic-siliceous complex during the wanning stages of felsic volcanism (VS Complex; seldom thicker than 600-m; upper Devonian-lower Carboniferous). The ore-hosting unit lies on a thick sequence of shallow platform sediments (>2000-m-thick, base unknown; Phyllite-Quartzite Group – PQ -, upper Devonian and older), and is overlain by a synorogenic flysch succession (>1600-m-thick; Baixo Alentejo Flysch Group; early to middle Carboniferous) (Leistel et al. 1998; and references therein).

The predominance of modified seawater in the fluid budget of typical IPB deposits is widely acknowledged, but its exclusivity has been questioned by a number of authors, who invoke, at least concerning to some particular deposits, the participation of possibly significant proportions of connate waters equilibrated with the PQ metasediments, fluids resulting from low-grade metamorphic dewatering, direct contributions of magmatic waters, and/or different combinations of either of these fluids in the IPB ore-forming systems (e.g, Relvas et al. 2001; Tornos et al., in press; and references therein).

2 Sampling and methods

The 12 samples used in this study were selected from, previously investigated, large sample sets collected in drill core intersections carried out at the Aljustrel (Gavião orebody) and the Lagoa Salgada deposits, and in the underground workings of the Neves Corvo deposit (Corvo/Graça orebodies). The analysed material consists exclusively of pyrite that was separated from ore samples, representing (1) sulphide (chalcopyrite - pyrite) -rich stockwork ores at Corvo, Graça (Neves-Corvo) and Lagoa Salgada, (2) Sn/Cu (cassiterite–calchopyrite-pyrite) stockwork ores at Corvo, and (3) massive pyrite ores from Gavião and Corvo orebodies; pyrite separated from a mineralised late tectonic fault breccia at Corvo orebody was also analysed for comparative purposes. Re and Os concentrations and Os isotopic compositions were determined by negative thermal ionisation spectrometry (NTIMS); detailed analytical procedures, blank values and analytical errors were described by Mathur et al. (1999). Taken together with results previously reported by Mathur et al. (1999) for Tharsis and Rio Tinto deposits, the data obtained during this study should provide a fairly representative picture of Re-Os isotope systematics in the Iberian Pyrite Belt major sulphide deposits.

3 Results

The Iberian Pyrite Belt (IPB) pyrites analysed during this study have highly variable rhenium and osmium contents, ranging from 0.25 up to 55 ppb and from 9 up to 598 ppt, respectively; these values are comparable to those reported

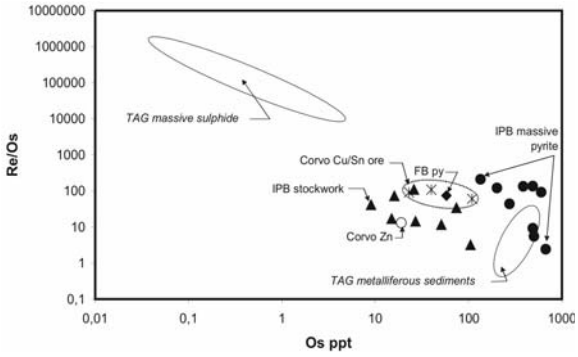

Figure 1: Re-Os distribution in Iberian Pyrite Belt ores compared to data from the TAG hydrothermal system (Ravizza et al., 1996; Brugmann et al., 1998).

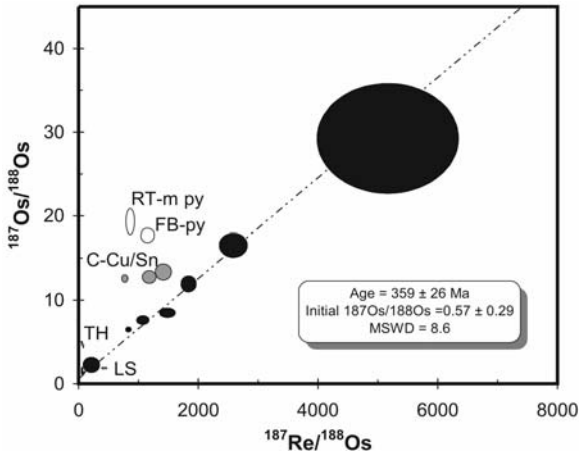

Figure 2: $^{187}Re/^{188}Os$ – $^{187}Os/^{188}Os$ isochron plot for Iberian Pyrite Belt ores. C-Cu/Sn: Corvo cooper-tin ores; FB-py: pyrite from fault breccia at Corvo deposit; LS: Lagoa Salgada; TH and RT-m py: massive pyrite from Tharsis and Rio Tinto (Mathur et al. 1999).

by Mathur et al. (1999) for Rio Tinto and Tharsis deposits (Re = 0.34 – 66 ppb; Os = 51 – 669 ppt). Modern TAG (Mid-Atlantic Ridge) sulphides exhibit similar rhenium concentrations (0.1 up to 72 ppb), but have a much wider range of osmium contents (0.04 up to 3990 ppt; Ravizza et al., 1996; Brugmann et al., 1998) than IPB ores (Fig. 1). Osmium concentrations, as well as Re/Os ratios in IPB pyrites clearly discriminate the different ore facies (Fig. 1). The osmium contents are lowest within the deeper stockwork ore zones (sulphide-rich = 9 - 105 ppt; cassiterite-rich = 23 – 109 ppt) and increase towards the upper massive (pyrite) sulphide ores (19 – 669 ppt). Similar patterns are reported in both modern TAG hydrothermal system (Brugmann et al., 1998) and Paleozoic southern Urals VHMS deposits (Tesalina et al., 2003), being ascribed to mobilization and re-deposition of osmium by the hydrothermal fluids (Brugmann et al., 1998). Contrasting with the osmium behaviour, there are no clear relationships for rhenium distribution patterns in IPB ores. Some IPB massive sulphides tend to be enriched in Re relative to stockwork pyrites, contrasting with low Re concentrations that were found in TAG distal metalliferous sediments (Ravizza et al., 1996). However, pyrite from the sphalerite-rich Corvo marginal massive sulphide facies (Corvo-Zn; Fig. 1) has the lowest rhenium concentration (0.25 ppb) of all the analysed IPB samples; this low Re concentration could be explained by higher rhenium solubility (and consequent removal) under increased pH-fO_2 (Xiong & Wood, 2001) that should have prevailed under seawater dominated conditions at the distal facies of the massive sulphide deposit.

Os isotope compositions of VHMS deposits have been used to find the age of mineralization, as well as evidence for the source of ore-forming metals. In recent hydrothermal ore-forming systems (e.g., Brugmann et al., 1998) Re-Os isotopes can be used to directly constrain the source of metals; however, for ancient orebodies it is necessary to take into account the long-term increase in ^{187}Os as a result of ^{187}Re decay. For modern TAG deposits, the limited range of $^{187}Os/^{188}Os$ values (0.439 – 1.070; Ravizza et al. 1996; Brugmann et al. 1998) is controlled by the extent to which the hydrothermal fluid has mixed with seawater. In the Late Devonian IPB sulphides, $^{187}Os/^{188}Os$ ratios display a much wider range, from 0.416 up to 29.11 (Mathur et al. 1999; this study), indicating significant ^{187}Os enrichment. The highest and the lowest $^{187}Os/^{188}Os$ isotope ratios were determined for massive pyrite ores. However, most sulphide-rich stockwork ores have lower $^{187}Os/^{188}Os$ isotope ratios (typically, within the range 0.98 - 2.03) than massive pyrite. Conversely, pyrites from Corvo cassiterite-rich stringer ores are highly radiogenic, with $^{187}Os/^{188}Os$ = 12.3 – 13.1.

Five pyrite samples from Neves-Corvo sulphide-rich stockwork ores yield an age of 358 ±29 Ma, which agrees with both palynological (Oliveira et al., 2004; Rosa et al., 2005) and U/Pb age constraints of ore formation in the IPB (Aznalcóllar = 345 ±5 Ma, Nesbitt et al., 1999; Rio Tinto = 349.8 ±0.9 Ma, Aljustrel = 352.9 ±1.9 Ma, Lagoa Salgada = 356.4 ±0.8 Ma, Barrie et al. 2002). A combination of fourteen samples from the different IPB sulphide ore deposits (Mathur et al. 1999; this study) yield an age of 359 ±26 Ma, which is indistinguishable from the age obtained using only the samples from Neves-Corvo. Considering that these (14) samples represent orebodies that lie >100 km apart, the major linear array in the isochron diagram (Fig. 2) suggests a dominant isotopically homogeneous source for sulphide-ore forming metals in the whole IPB. The remaining samples (including the Corvo tin ores) lie well above the reported isochron; the observed deviations may be associated with late disturbance of the isotope system during Variscan regional tectonics and metamorphism (e.g., late pyrite in fault breccia cutting through Corvo massive sulphides; Fig. 2), or they may have been caused by isotopic heterogeneity of the IPB hydrothermal ore-forming system.

4 Discussion and conclusions

Calculated initial $^{187}Os/^{188}Os$ isotope compositions of IPB ores are shown in Figure 3. Three samples yield negative initial $^{187}Os/^{188}Os$ ratios; these reflect either analytical imprecision (extrapolation from high $^{187}Re/^{188}Os$ values), or isotope resetting during late-stage hydrothermal/metamorphic activity. Nevertheless, the overall results are consistent with the previous uncorrected osmium isotope distribution in ore facies. Initial $^{187}Os/^{188}Os$ isotope compositions in sulphide-rich stockwork ores (0.451 – 1.08) are much lower than those in pyrites from Corvo cassiterite-rich stockwork ores (4.89 – 7.85), whereas massive pyrite displays wide variations of initial Os isotope compositions, ranging from 0.376 up to (abnormally high; see Mathur et al. 1999) 14.1. The estimated initial $^{187}Os/^{188}Os$ values are all too radiogenic for mantle sources ($^{187}Os/^{188}Os$ = 0.105 – 0.152; Shirey and Walker 1998) and indicate a large crustal component for ore-forming metals in the IPB.

Sulphide-ores that plot on the linear array in Figure 2 have initial osmium contents and $^{187}Os/^{188}Os$ ratios overlapping those of TAG hydrothermal sulphides and metalliferous sediments (Fig. 3). An important source of osmium in those modern TAG deposits consists of seawater (Ravizza et al. 1996). According to best-fit calculations on the isochron in Figure 2, a (poorly constrained) initial $^{187}Os/^{188}Os$ of 0.57 ±0.29 can be defined; precision of the initial Os is improved by using only the five Neves-Corvo (sulphide-rich stockwork) samples, yielding $^{187}Os/^{188}Os$ = 0.49 ±0.07. This value is similar to that inferred for Late Devonian (358 Ma) seawater ($^{187}Os/^{188}Os$ = 0.59 ±0.05; Creaser et al. 2002), implying that metals in IPB sulphide-ores should include significant contributions from a seawater-derived component. Despite considerable scatter, data in Figure 3 indicate that the more radiogenic sulphide ore metal sources were enriched in osmium. Black shales have both high osmium concentrations and isotope ratios (e.g., Horan et al., 1994), and could provide a plausible Os source for the massive sulphide ores in deposits which footwall sequence include a significant proportion of shales (radiogenic/Os-rich), like Aljustrel, and especially in shale-hosted deposits, of which Tharsis is a remarkable example. Thus, Re-Os data (Fig. 3) suggest that the main fluid precipitating the IPB sulphides had a component of contemporary seawater and fluids that possibly leached metals from the black shales in the volcanic-sedimentary sequence.

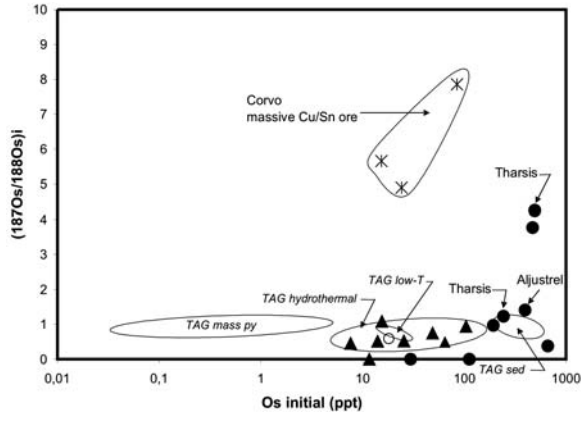

Figure 3: Initial $^{187}Os/^{188}Os$ ratios vs. Os content distribution in the Iberian Pyrite Belt ores, compared to modern TAG deposits (Ravizza et al., 1996; Brugmann et al. 1998).

Comparatively high initial osmium isotope ratios of pyrites in Corvo cassiterite-stringer and massive copper-tin ores could either reflect late hydrothermal and Variscan metamorphic isotope disturbances or pristine isotope values. If preserving original isotope systematics, the data indicate that metals in Corvo tin ores cannot be (exclusively) derived from the same crustal sources as the remaining IPB sulphides (Fig. 3). Recent studies (Chesley and Ruiz 1998) have shown that some portions of the lower continental crust comprise highly radiogenic, large-scale, Os reservoirs. From this perspective, osmium isotope data is consistent with the highly radiogenic lead and low-εNd values reported for Corvo tin ores (Relvas et al. 2001). Whereas sulphide-ore compositional variations are consistent with significant incorporation of "typical" IPB seawater-derived hydrothermal components, the much more radiogenic osmium and lead signatures, as well as low-εNd values preserved in high-grade tin and copper-tin ores require a predominant derivation from external sources. This could be either a highly evolved magmatic source (different from the typical IPB felsic magmas), or metamorphic fluids deeply circulated through older basement rocks.

Acknowledgements

This study is a contribution to research projects MODELIB (POCTI/35630/CTA2000-FEDER) and POCA-PETROLOG (Centro Geologia U. Lisboa, UI: 263; POCTI/FEDER) and ARCHYMEDES (FCT-SAPIENS 2001/41393). Reviews by S. Tessalina and F. Tornos contributed to improve the presentation and are gratefully acknowledged.

References

Barrie TC, Amelin,Y, Pascual,E (2002) U-Pb geochronology of VMS mineralization in the Iberian Pyrite Belt. Mineral. Deposita 37: 684-703

Brugmann GE, Birck JL, Herzig PM, Hofman AW (1998) Os isotopic composition and Os and Re distribution in the active mound of the TAG hydrothermal system, Mid-Atlantic Ridge. Proceeding of the Ocean Drilling Program, Scientific Results 158: 91-100

Chesley JT, Ruiz J (1998) Crust-mantle interaction in large igneous provinces: implications from Re-Os systematics of the Colombia River flood basalts. Earth Planet. Sci. Letters 154: 1-11

Creaser RA, Sannigrahi P, Chacko T, Selby D (2002) Further evaluation of the Re-Os geochronometer in organic-rich sedimentary rocks: A test of hydrocharbon maturation effects in the Exshan Formation, Western Canada sedimentary basin. Geomchim. Cosmochim. Acta 66: 3441-3452

Horan M, Morgan JW, Coveney R, Murowchick J, Hubert L (1994) Rhenium and osmium isotopes in black shales and Ni-Mo-PGE rich sulphide layers, Yukon territory, Canada and Hunan and Guiznoun province, China. Geochim. Cosmochim. Acta 58: 257-265

Leistel JM, Marcoux E, Thieblemont D, Quesada C, Sanchez A, Almodovar GR, Pascual E, Saez R (1998) The volcanic-hosted massive sulphide deposits of the Iberian Pyrite Belt. Review and preface to the special issue. Mineralium Deposita 33: 2-30

Mathur R, Ruiz J, Tornos F (1999) Age and sources of the ore at Tharsis and Rio Tinto, Iberian Pyrite Belt, from Re-Os isotopes. Mineral Deposita 34: 790-793

Nesbitt RW, Pascual E, Fanning CM, Toscano M, Saez R, Almodóvar GR (1999) First zircon U-Pb age from the Iberian Pyrite Belt, Spain. J. Geo. Soc. London, 156: 7-10

Oliveira JT, Pereira Z, Carvalho P, Pacheco N, Korn D, (2004) Stratigraphy of the tectonically imbricated lithological succession of the Neves Corvo mine area, Iberian Pyrite Belt, Portugal. Mineralium Deposita 39: 422-436

Ravizza G, Martin CE, German CR, Thompson G (1996) Os isotopes as tracers in seafloor hydrothermal systems: metalliferous deposits from the TAG hydrothermal area, 26ºN Mid-Atlantic Ridge. Earth Planet. Sci. Letters 138: 195-219

Relvas JMRS, Tassinari CCG, Munhá J, Barriga JAS (2001) Multiple sources for ore-forming fluids in the Neves Corvo VHMS Deposit of the Iberian Pyrite Belt (Portugal): strontium, neodymium and lead isotope evidence. Mineral. Deposita 36: 416-427

Rosa C.PJ, McPhie J, Relvas JMRS, Pacheco N, Pereira Z, (2005) Felsic pyroclastic and effusive volcanic facies hosting the Neves Corvo massive sulphide deposit, Iberian Pyrite Belt, Portugal. 8th Biennial Meeting of the Society for Geology Applied to Mineral Deposits (SGA), Beijing, China

Shirey SB, Walker RJ (1998) The Re-Os isotope system in cosmochemistry and high temperature geochemistry. Annual Review of Earth Planetary Sciences 26: 423-500

Tesalina SG, Gannoun A, Bourdon B, Birck JL, Alègre JC (2003) Os isotopes distribution within Paleozoic seafloor hydrothermal system in Southern Urals. In: Elliopoulos et al. (eds) Mineral Exploration and Sustainable Development (Millpress, Roterdam) 187-190

Tornos F, Casquet C, Relvas JMRS, in press. Transpressional tectonics, lower crust decoupling and intrusion of deep mafic sills: a model for the unusual metallogenesis of SW Iberia: Ore Geology Reviews

Xiong Y, Wood SA (2001) Hydrothermal transport and deposition of rhenium under subcritical conditions (up to 200 ºC) in light of experimental studies. Econ. Geology 96: 1429-1444

Lead isotopic systematics of Urals massive sulphide deposits

Jean-Jacques Orgeval, Catherine Guerrot
Bureau de Recherches Géologiques et Minières (BRGM), 3 Avenue Claude-Guillemin, BP 6009, 45060 Orléans Cedex 2, France

Svetlana G. Tessalina, Bernard Bourdon
Laboratoire de Géochimie et Cosmochimie, Institut de Physique du Globe de Paris (IPGP), 4, place Jussieu, 75252 Paris Cedex 05, France

Victor Zaykov
Institute of Mineralogy of RAS,456301 Miass, Russia

Claudia Buley, Berndt Bushmann
Technische Universität Bergakademie, Freiberg, Germany

Richard Herrington
Natural History Museum, Cromwell Road, London SW7 5BD, UK

Rex Taylor
Southampton Oceanography Centre, UK

Abstract. The isotopic composition of lead from a total of 53 samples of galena from 18 VHMS deposits shows a range between 17.437 and 18.111 for $^{206}Pb/^{204}Pb$; 15.484 and 15.630 for $^{207}Pb/^{204}Pb$ and 37.201 – 38.027 for $^{208}/^{204}Pb$. The results show a systematic trend with the leads of the Sibay, Barsuchiy Log and Djusa deposits being most radiogenic by comparison with those of Bakr-Tau and Oktiabrskoe which are the least radiogenic deposits. The Bakr-Tau and Oktiabrskoe deposits occur within most primitive fore- arc rocks at the lower part of the Baymak-Buribay formation, which contain lavas of boninitic affinity. The Sibay, Barsuchiy Log and Djusa deposits are found in intra- and back-arc setting and are hosted by a sequence of bimodal tholeiites. The deposits in "arc" settings such as the Balta-Tau, Gai and Alexandrinka deposits occupy an intermediate position. This trend is explained in term of mixing between mantle wedge and continental blocks.

Keywords. Lead isotopes, Urals, massive sulphide deposits

1 Introduction

Subduction zones are widely regarded as major sites of crust-mantle differentiation, with key roles in the generation of new continental crust. The isotopic composition of lead from deposits and host rocks of the Mid-Oceanic ridges is remarkably homogeneous and corresponds to the host MORB. In contrast, the isotopic composition of lead in massive sulphides and rocks from the island arcs varies more widely as it is a case within Mesozoic Japanese Island arc (Tatsumoto 1969). This has been explained in terms of the variable contribution from the subducted oceanic crust and sediments to the ore-forming system.

Urals offer a possibility to study a complete cross-section across the well-preserved Paleozoic island-arc system from boninitic-like and calc-alkaline fore-arc sequence to island-arc mainly tholeiitic formation. A number of massive sulphide deposits occur within fore-arc, arc and back-arc geotectonic settings. In this paper, the use of Pb isotope compositions as a means of testing the role of underthrusted oceanic lithosphere as a source of lead in the VHMS deposits of the Urals arc is investigated.

2 Geological setting of Urals massive sulphide deposits

The structural formation of the Urals has been explained by Zonenshain (1984) in terms of the thrusting of ocean-floor beneath a Palaeozoic island arc, a concept further developed by, for example, Puchkov (1997), Koroteev (1997) and Zaykov (1996).

The Urals is a meridional orogenic belt of some 2000 km in length. It forms the natural topographic boundary between Europe and Asia. The Urals belt formed during Late Devonian – Early Carboniferous time as a result of the collision between the proto-Uralian island arc and the East European and Kazakhstan continents. The structure of the South Urals is well-preserved. The following subdivisions can be made:

1. Main Urals Fault suture zone with relics of ophiolite in a tectonic melange containing blocks ranging in age from Ordovician up to Late Devonian.
2. Magnitogorsk island arc zone, consisting of volcanics and sediments of Devonian age. An intermediate "intra-arc" basin, filled by Late Devonian-Lower Carboniferous volcanics and sediments, divides the Magnitogorsk structure into the West and East-Magnitogorsk zones;

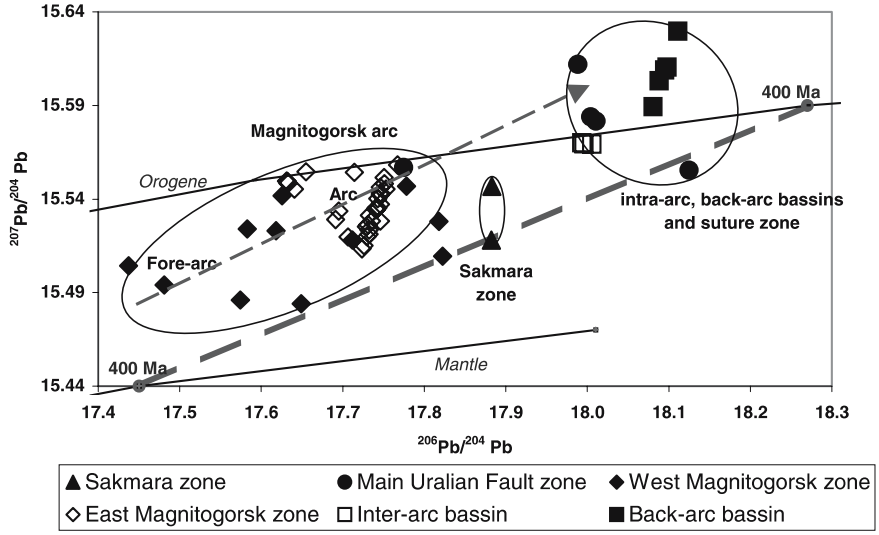

Figure 1: Lead isotopic composition of the studied Urals massive sulphide deposits according to their tectonic settings.

3. Sakmara allochthon, the origin of which is not clear. There are two main hypotheses regarding its tectonic origins: (1) It may be a displaced fragment of the main Urals island arc; (2) it may be a remnant of an independent island arc (Herrington et al. 2002).

The overview of Urals VHMS deposits and their geotectonic settings have been done by Prokin et al. (1999) Herrington et al. (2002). Formation of the massive sulphide deposits in the Urals began in Silurian time with the formation of the Yaman-Kasy deposit. The deposits found in the Baimak-Buribai formation were formed in Emsian time, whereas the majority of the deposits hosted by the Karamalitash formation were formed in Eifelian (Middle Devonian) time.

3 Results

The isotopic composition of lead from a total of 53 samples of galena and 5 whole ore samples from 18 VHMS deposits shows a range between 17.437 and 18.111 for $^{206}Pb/^{204}Pb$; 15.484 and 15.630 for $^{207}Pb/^{204}Pb$ and 37.201 – 38.027 for $^{208}/^{204}Pb$ (Fig. 1). Most of the galenas were obtained from massive ores and the footwall stockwork zones of the deposits. The variations in isotopic composition on the scale of the Urals province is 0.67 ‰ for $^{206}Pb/^{204}Pb$, though the range is quite similar to that measured for modern VHMS deposits from Mid Ocean Ridge and back-arc basins of Pacific ocean, up to 0.8 ‰ for $^{206}Pb/^{204}Pb$ (Fouquet and Marcoux, 1995). This range is higher than that seen in the closely clustered data from massive sulphide deposits in the IPB of Spain (Marcoux, 1998). The lead isotope composition from some ancient VHMS deposits in the arc setting exhibits larger variations, e.g. highly variable Miocene Kuroko deposits of Japan (1.62 for $^{206}Pb/^{204}Pb$) (Sato, 1975).

The results show a systematic trend with the leads of the Sibay, Barsuchiy Log and Djusa deposits being most radiogenic by comparison with those of Bakr-Tau and Oktiabrskoe which are the least radiogenic deposits. The Sibay deposit is found in a inter-arc setting and hosted by a sequence of tholeiites. The Bakr-Tau and Oktiabrskoe deposits occur in a fore-arc setting and are hosted by the calc-alkaline Baymak-Buribay formation. The deposits in arc settings such as the Balta-Tau and probably the Gai deposit occupy an intermediate position.

In order to reconstruct the source of lead in volcanogenic massive sulphide deposits, the 32 rocks and sediments samples from the Main Uralian Fault zone, Karamalytash formation, Mednogorsk ore region and two plagiogranite massifs were analysed for lead isotopic composition. The range of age corrected lead isotopic ratios is also quite large: 17.25-17.96 for $^{206}Pb/^{204}Pb$; 15.48-15.56 for $^{207}Pb/^{204}Pb$, and match these of ores. The anomalous ratios were obtained for serpentinites and altered volcanics from Main Uralian Fault zone, ranging from 6.36 up to 23.73 ‰ for the $^{206}Pb/^{204}Pb$ ratio. The lead isotopic composition of volcanics is mostly similar to that of hosted sulphides. For example, lead isotopic composition of basalt from Sibay ore field matches these of Sibay ores. The most complete set of ore hosted volcanics and sediments are presented for the Alexandrinka VHMS deposit. Most of them are identical in lead isotopic composition to the sulphide ores. Only three dacites from Alexandrinka ore field, as well as plagiogranite clast are less radiogenic (~0.36 lower on $^{206}Pb/^{204}Pb$). They are characterised by relatively low Pb contents (2.5-4 ppm) and high U/Pb ratio of about 0.3.

4 Sources of lead

The island arc systems are considered as the major sites of crust-mantle interaction where the lithospheric mate-

rial of various types is returned to the deep mantle and the continental lithosphere beings to be created. The significant differences among lead isotopic ratios within volcanic rocks in subduction zones are usually interpreted as a mixture of material derived from subducted slab and mantle wedge. The subducted slab consists of oceanic crust (usually MORB with low μ) and oceanic sediments carapace (high radiogenic component).

Internal growth of radiogenic lead due to decay of U and Th during the time of Urals island arc formation (about 22 Ma) would not be greater than 0.15. However the difference between the least radiogenic lead of the Oktiabrskoe and the most radiogenic lead of the Sibay deposit is 4.5 times higher. Indeed, the model ages calculated according to the two-stage model vary from Proterozoic to Devonian. The only reasonable age (about 400 Ma), corresponding to that of the host rocks, has been obtained for the Dergamish, Ivanovka, Sibay, Djusa, Barsuchiy Log and Yaman-Kasy deposits. Thus, the different sources have contributed to the formation of the lead in many of the Urals VHMS deposits.

The linear arrow on uranogenic lead diagram (Fig. 1) could be explained in term of plumbotectonic model by a mixture of two or more components with different μ-values.

The average isotopic composition of lead of modern low-μ oceanic crust which is largely MORB is less radiogenic than the lead in higher-μ island arc volcanics. Model points for Average Mantle Lead and Average Orogenic Lead at 400 My are plotted on Fig. 1. It can be seen that, the lead isotope data for the Urals VHMS deposits forms a trend which is parallel to the mixing line between these two points. The Baimak-Buribai group deposits in a "fore-arc" setting are closer to the "Average oceanic crust" point, and the lead isotopes from inter-arc and back-arc Sibay, Djusa and Barsuchiy Log deposits are close to the "Average Orogene" point. The μ-value ($^{238}U/^{204}Pb$) increases in the same range from the Baimak-Buribai series hosted VHMS deposits (8.87-8.97) to the Sibay, Barsuchiy Log and Djusa deposits (9.0-9.15).

The isotopic composition of sulphide ores reflects these of host rocks with toleiitic basalt from Sibay ore field being more radiogenic than calc-alkaline volcanics from the Alexandrinka ore region.

Various petrochemical, geochemical and isotopic characteristics reflect the increase of continental character of igneous rocks eastward the Magnitogorsk island arc system. The increase of U, Th and Pb is consistent with increase of initial Sr isotopic composition, La/Lu ratio, as well as K, Rb and other large-ion lithophile elements, typical for continental crust and island arcs (Bobokhov 1994; Puchkov, 1997). This asymmetrical geochemical and petrochemical zonality reflect the eastward dipping of subducted plate (seismo-focal zone) underneath the Magnitogorsk island arc.

The Baimak-Buribai tholeiitic to calk-alcaline formation is characterised by higher Pb contents and lower U/Pb ratios. The indirect confirmation of high Pb contents in a calc-alkaline volcanics is a high Pb grade in Baymak type deposits. The low $^{206}Pb/^{204}Pb$, $^{207}Pb/^{204}Pb$, $^{208}Pb/^{204}Pb$ ratios and μ-values, as well as high ε_{Nd}, low γ_{Os}, and low $^{87}Sr/^{86}Sr$ ratios are typical for MORB-type depleted material, which could consist the subducted slab.

The lead isotopic composition of basement could be estimated to be close to that of Precambrian sediments of the Bashkirian anticlinorium in the Southern Urals and Ordovician carbonate sequence in Polar Urals (Sundblad et al. 1996). The lead isotopic composition of Pb-Zn mineralization points within Bashkirian anticlinorium is similar to that of arc-related VHMS deposits, and lead from Polar Urals match this of the VHMS deposits in intra-arc and back-arc setting. Moreover, the deposits in intra-arc and back-arc setting have been formed without addition of subduction fluid. Thus, at the time of these deposits formation the continental crust has been completely entered into subduction zone. The reasonable model ages about 400 Ma for the VHMS deposits in intra-arc and back-arc setting show the uniform crustal lead source.

Acknowledgements

This work was carried out in the framework of the EU-funded MinUrals project INCO COPERNICUS ICA2 CT-2000-10011.

References

Bobokhov AS (1994) Evolution of Palaeozoic magmatism and problem of continental crust formation in the Southern Urals according to geochemical and isotopic data (in Russian), Institute of Geology, Ufa, 44

Fouquet Y, Marcoux E (1995) Lead isotope systematics in Pacific hydrothermal sulfide deposits, Journal of Geophysical Research, 100, No B4: 6025-6040

Herrington RJ, Armstrong RN, Zaykov VV, Maslennikov VV, Tessalina S, Orgeval JJ, Taylor RNA (2002) Massive sulphide deposits in the south Urals: Geological setting within the framework of the Urals orogen, In: "Mountain Building in the Uralides: Pangea to the Present", Eds. Brown D., Juhlin C., and Puchkov V., Geophysical Monograph Series 132: 155-182

Koroteev VA, de Boorder H, Netcheukhin VM, Sazonov VN (1997) Geodynamic setting of the mineral deposits of the Urals, Tectonophysics 276: 291-300

Marcoux E (1998) Lead isotope systematics of the giant massive sulphide deposits of the Iberian Pyrite Belt, Mineralium Deposita 33: 31-44

Prokin VA, Buslaev FP (1999) Massive copper-zinc sulphide deposits in the Urals, Ore Geology Reviews 14: 1-69

Puchkov VN (1997) Structure and godynamics of the Uralian orogen, From Burg, J.-P. and Ford, M. (eds), Orogeny through time, Geologial Society Special Publication 121: 201-236

Sato K (1975) Unilateral isotopic variation of Miocene ore leads from Japan, Economic Geology 70: 800-805

Sunblad K, Bibikova E, Kontar E, Neymark L, Beckholmen M, Prokin VA (1996) Source of lead in sulphide ores in the Urals, Uralides and SW-Iberia workshop, Granada, Spain, Programme with Abstracts 12

Tatsumoto M (1969) Lead isotopes in volcanic rocks and possible ocean-floor thrusting beneath island arcs, Earth and Planetary Sciences Letters 6: 369-376

Zaykov VV, Maslennikov VV, Zaykova EV, Herrington RJ (1996) Hydothermal activity and segmentation in the Magnitogorsk – West Mugodjarian zone on the margins of the Urals paleo-ocean. Tectonic, Magmatic, Hydrothermal and biological segmentation of the Mid Ocean Ridges, London, 199-210

Zonenshain LP, Korinevsky VG, Kuzmin DM, Pechersky DM, Khain VV, Matveenkov VV (1984) Plate tectonic model of the South Urals, Tectonophysics 109: 95-135

Local and regional geochemical variations in VHMS-related felsic volcanic series in the Iberian Pyrite Belt

Emilio Pascual, Teodosio Donaire, Alfonso Valenzuela
Departamento de Geología. Facultad de Ciencias Experimentales. Universidad de Huelva Campus Universitario del Carmen. 21071 Huelva, Spain

Abstract. The study of volcanic architecture in several selected areas in the Spanish Iberian Pyrite Belt (IPB) has been correlated with the chemical variation of the volcanic rocks. Results have been compared with those recently reported in the literature, both at a regional and at a local scale, in order to assess the spatio-temporal relationships of the bimodal IPB volcanism, generally agreed to consist of a basic series and a roughly continuous dacite-rhyolite series. In the studied areas, however, dacitic and rhyolitic rocks occur as clearly separate volcanic pulses, which can be distinguished by their petrographic and geochemical features. In areas such as that of the Odiel river, it is also shown that chemical composition, either dacitic or rhyolitic, is characteristic of entire volcanic packages, irrespective of the volcanic mechanisms. Variations within each of the two felsic groups also occur, partly overlapping the differences between them. We propose that the IPB felsic volcanic series may consist of two separate pulses, respectively dacitic and rhyolitic. Accordingly, we suggest that in VHMS areas where separate volcanic episodes occur, each of these may have a characteristic age and relation with the interbedded VHMS deposits.

Keywords. Iberian Pyrite Belt, felsic volcanism, geochemistry, Spain

1 Introduction

The Iberian Pyrite Belt (IPB) is one of the largest massive sulphide provinces on Earth. It occupies the SW corner of the Iberian Peninsula, from Seville in Spain to the Atlantic Ocean, south of Lisbon, in Portugal, making a belt in which many massive sulphide deposits occur, including several giant and supergiant deposits such as Riotinto, Tharsis, La Zarza, Sotiel, and Aznalcóllar in Spain, or Neves Corvo and Aljustrel in Portugal. Even after continuous metal extraction for more than 5000 y, it retains exceptionally large metal reserves. In addition, the very numerous deposits it hosts, their diversity and mineralogical, chemical and isotopic features make this province peculiar. Accordingly, an "Iberian type" of VHMS has been proposed (Sáez et al. 1999).

2 Geological setting

The IPB forms a part of the South Portuguese Zone of the Hercynian Iberian Massif, now interpreted as a tectonostratigraphic terrane sutured to the Iberian Massif during Variscan times (Quesada 1991). The most conspicuous features are the abundant volcanic rocks and the huge massive sulphide deposits, both intercalated between Devonian and Lower Carboniferous sediments. The succession in the IPB has been classically subdivided into three main units, distinguishing the Devonian pre-volcanic sediments (PQ group), the volcano-sedimentary complex (VSC) and the post-volcanic group (Culm group)

The VSC group mainly consists of an alternation of felsic and mafic, volcaniclastic and coherent rocks, together with other sedimentary rocks. On a regional scale, several felsic and mafic volcanic episodes have been distinguished. Mafic rocks are either sills or submarine flows, exhibiting pillow structure, whereas felsic volcanics have been claimed to be pyroclastic in many localities in the IPB, either subaerial or deposited in a shallow marine environment. Subvolcanic felsic rocks also occur as domes, dykes or sills. These interact in places with sediments to produce hydroclastic rocks, that have also been locally formed by interaction with mafic sills (Boulter 1993). In general, intense regional deformation makes detailed petrographic studies difficult. A well-defined volcanological interpretation is only possible in selected areas.

In order to account for the complexities of the felsic volcanism, we present here new geochemical data (major- and trace-element analyses, including REE) from several areas in the Spanish IPB that show contrasting volcanic features, which can be considered representative of the volcanic facies listed above (Fig. 1). The areas include the Odiel River, close to the Riotinto area, Villanueva de los Castillejos, at the southern limb of the Puebla de Guzmán antiform and Paymogo, close to the northern border of the Spanish IPB. These data are compared with regional, geochemical data in the IPB (Thiéblemont et al. 1998).

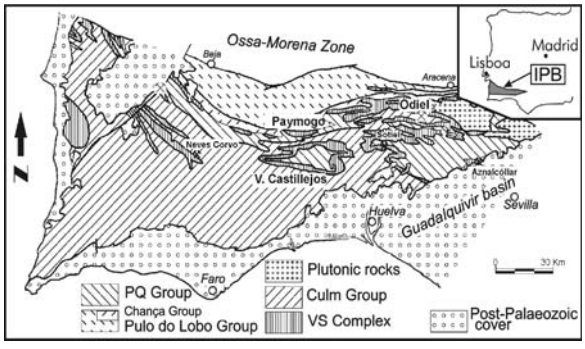

Figure 1: sketch map of the Iberian Pyrite Belt with the location of the selected areas. See text for explanation

This page intentionally blank

3 Volcanic architecture of felsic volcanism in the selected areas

The Odiel River area, located at the northern flank of the Riotinto antiform, has an approximate extension of 10 km^2. We have distinguished felsic and basic coherent rocks, as well as felsic volcaniclastics and siliciclastic rocks. Regarding felsic rocks, two separate sub-units occur in the area. One consists of a large, coherent igneous dacitic body emplaced between the PQ Group and the VSC basic subvolcanics. Field relationships with the PQ and VSC are uncertain. The rest of the felsic sequence consists of a thick pile formed by rhyolitic volcaniclastic rocks of direct, submarine volcanic origin intruded by rhyolitic sills. These latter show peperitic contacts, indicating an age coeval with the volcaniclastic pile (Valenzuela et al. 2001).

The Villanueva de los Castillejos area is located at the southernflank of the La Puebla de Guzmán anticline, in a zone where VHMS do not occur. Although volcanic architecture is here more obscured by tectonics, it is apparent that the volcanic style is very different. Here rhyolitic, felsic rocks largely consist of domes and some probably pyroclastic rocks, showing collapsed pumice clasts within a possibly welded matrix. Although the contact with the PQ group is tectonic, these rocks have been considered to represent the early stages of the IPB volcanism.

The Paymogo area is located at the northwestern Spanish IPB, where several small- to medium-sized VHMS occur. Here felsic volcanism starts with dacitic, coherent and volcaniclastic facies, followed by rhyolitic volcaniclastics and sediments. The whole sequence is intruded by later dacitic rocks.

4 Geochemical data

In all of the localities studied, a clear distinction between rhyolite and dacite is shown both by petrographic and chemical rock features. Rhyolite are mostly aphyric or only with quartz phenocrysts, rarely accompanied by *scarce* feldspar crystals. They have low TiO_2 and P_2O_5 contents and steep LREE spectra ($La_N/Sm_N > 4$), with pronounced, negative Eu anomaly (Eu/Eu* from 0.56 to 0.20) and flat HREE patterns ($Gd_N/Yb_N<1$). In contrast, dacites contain abundant feldspar (plagioclase) and quartz phenocrysts, as well as pyroxene or amphibole crystals, abundant in some localities. These features correlate well with higher TiO_2 and P_2O_5 contents, as well as with relatively flat REE patterns, with low Eu anomaly (Eu/Eu* from 0.76 to 0.50). LREE slopes tend to be similar, whereas HREE always show a negative slope ($Gd_N/Yb_N>1$).

In the studied areas, the persistence of a single geochemical pattern is irrespective of the physics of the eruptive process within a *single volcanic episode*. This is clearly shown by the volcaniclastic-peperitic series in the Odiel river, where all of the studied rocks are rhyolitic and the rhyolitic clasts

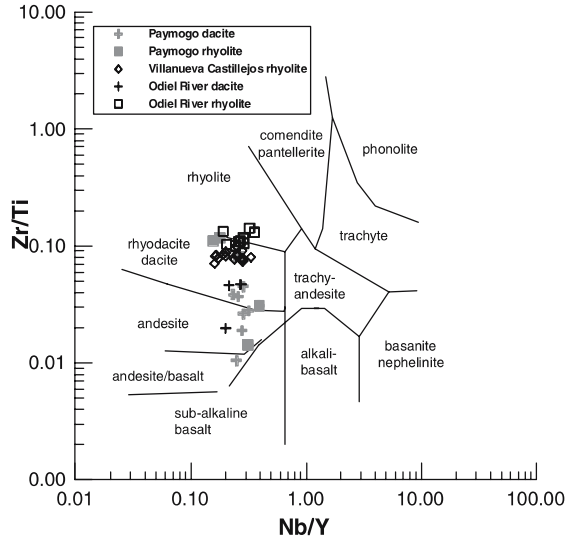

Figure 2: Selected chemical analyses of felsic rocks from the Iberian Pyrite Belt on the diagram by Winchester and Floyd (1977). See text for explanation.

in the volcaniclastic sequence are equivalent in composition to their corresponding peperitic sills.

In each of these areas, however, an internal chemical variation occurs. For instance, volcani-clastic rocks and the related peperitic sills in the Odiel River show chemical variations that must be assigned to fractional crystallization, including REE evolving patterns. Similarly, dacitic rocks in Paymogo evolve from less to more pronounced negative Eu anomalies, and so on.

Comparing *different episodes*, however, it is apparent that each of the major groups distinguished in the volcanologic study has contrasting chemical features, either dacitic or rhyolitic (Fig. 2). For instance, all of the volcaniclastic and coeval coherent rocks in the Odiel River are more or less differentiated rhyolites, whereas in this area dacites occur as a separate, non-coeval coherent unit. In Villanueva de Los Castillejos, only rhyolites occur, and in the Paymogo area dacites and rhyolites also correspond to separate volcanic events. In all, the data suggest that in none of the studied areas a *single* volcanic episode has produced dacites *and* rhyolites, but only one of the two rock types. First detailed studies in the Portuguese IPB also seem to support this idea, as in the Mértola section only dacitic rocks occur (Rosa et al. 2004).

Both the bimodal character of the IPB volcanism and the importance of fractional crystallization in the chemical variation of volcanic rocks have been repeatedly stressed (Munhá 1971; Thieblémont el al. 1998). However, these works do not distinguish between dacitic and rhyolitic episodes, mainly for two reasons: a) these two rock types have chemical properties that partly overlap, and b) the scarcity of volcanological studies has impeded a precise separation of volcanic episodes and therefore a correlation between volcanology and geochemistry.

5 Conclusions

On the basis of a volcanologic study in selected IPB areas, we show that volcanic each felsic volcanic episode in the IPB is characterized by distinct chemical features, either dacitic or rhyolitic, with minor internal chemical variations. This suggests that, in VHMS areas where separate volcanic episodes occur, each of these may have different age and a characteristic relationship with the interbedded VHMS deposits.

Geochemical distinction of volcanic episodes needs to be completed with isotopic studies and age determinations to assess the role of volcanism in the genesis of the VHMS in the IPB. Ultimately, this work will lead to know a more precise relationship between volcanism and the VHMS deposits in the region.

In spite of some interpretations tending to minimize the role of the magmatic activity in the VHMS genesis, we contend that volcanism is still to be considered relevant to VHMS genesis, at least as their main heat source but also, at least in part, in the geochemistry of the deposits Only a careful study, combining volcanology, geochemistry and dating, may be a key in deciphering such a link.

References

Boulter CA (1993) Comparison of Rio Tinto, Spain, and Guaymas Basin, Gulf of California: an explanation of a supergiant massive sulfide deposits in an ancient sill-sediment complex. Geology 21: 801-804

Munhà J (1983) Hercynian magmatism in the Iberian Pyrite Belt. Mem Serv Geol Portugal 29: 39-81

Quesada C (1991) Geological constraints on the Paleozoic tectonic evolution of tectonostratigraphic terranes in the Iberian Massif. Tectonophysics 185: 225-245

Rosa DRN, Inverno CMC, Oliveira VMJ, Rosa CJP (2004) Geochemistry of Volcanic Rocks, Albernoa area, Iberian Pyrite Belt, Portugal. International Geology Review 46: 366-383

Sáez R, Pascual E, Toscano M, Almodóvar GR (1999) The Iberian type of volcano-sedimentary massive sulphide deposits. Mineralium Deposita 34: 549-570

Thiéblemont D, Pascual E, Stein G (1998) Magmatism in the Iberian Pyrite Belt: petrological constraints on a metallogenic model. Mineralium Deposita 33: 98-110

Valenzuela A, Donaire T, Pascual E (2001) The Odiel River section: an example on complexities in volcanic evolution of the Volcano-Sedimentary Complex in the Iberian Pyrite Belt, Spain. In: Tornos F, Pascual E, Sáez R, Hidalgo R (eds) Massive sulphide deposits in the Iberian Pyrite Belt: New advances and comparison with equivalent systems GEODE Workshop 61-62

Winchester JA, Floyd PA (1977) Geochemical discrimination of different magma series and their differentiation products using immobile elements. Chemical Geology 20: 325-343

Volcanic sequences, lithostratigraphy and geochemistry of altered rocks at the Jbel Malek deposit: Clues for the origins of a Neoproterozoic gold deposit, High-Atlas, Morocco

Ewan Pelleter, Alain Cheilletz
CRPG-CNRS UPR A2300, BP 20, F54501 Vandoeuvre-lès-Nancy, France

Abdellah Mouttaqi, Abdelkhalek El Hakour
ONHYM,BP 99, Rabat, Morocco

Gasquet Dominique
CISM-EDYTEM, CNRS UMR5204, F73376 Le Bourget du Lac cedex, France

Abstract. The Jbel Malek gold deposits are situated in the Tamlalt-Menhouhou Palaeozoic-Neoproterozoic inlier, at the eastern edge of the High Atlas belt of Morocco. The inlier is composed of a bimodal volcano-sedimentary sequence intruded by a microgranodiorite stock. The entire rock sequence was severely deformed by the Variscan tectono-thermal events. Native gold is associated with goethite and barite, and seems to have been remobilised. The mineralised area shows intensive alteration halos comprising predominantly albitisation and silicification, then chloritisation, hematisation, carbonatation, sericitisation and tourmalinisation. Banded iron formations (BIF) indicate the presence of an exhalative mineralization, and hydrothermal activity.

Keywords. VMS-type, Gold deposit, albitisation, silicification, Neoproterozoic, Variscan orogen

1 Introduction

The Moroccan Proterozoic inliers are thighly mineralised. Among the mineralisation are the Pb-Zn-Cu-Ag Bou Madine deposit, the Co-Ni-As-Au-Ag Bou Azzer deposit, the Au-Ag-Cu Tiouit deposit and the Zgounder and Imiter Ag deposits. The latter is one of the largest silver deposits in the world (Cheilletz et al. 2002; Levresse et al. 2004). All these base and precious metal deposits belong to the Neoproterozoic inliers located in the Anti-Atlas Mountains.

The Jbel Malek gold deposit is located in the High-Atlas Mountains, Morocco (Fig.1). It belongs to the Tamlat-Menhouhou Palaeozoic-Neopro-terozoic inlier. Drilling reveals gold grades varying from 1 to 20 ppm (with intersections at 500 ppm; El Hakour 2002). Houari and Hoepffner (2003) show an important overprint of the Variscan orogen in the Tamlalt-Menhouhou inlier characterized by development of foliation, followed by uplift and thrusting during the Alpine orogen of the High Atlas belt. This multiphase history has led to the present structural situation of the Jbel Malek area, bordered by a set of E-W faults. The aim of this paper is to characterize the lithostratigraphy and geochemistry of volcanic and volcano-sedimentary rocks of the Jbel Malek gold deposit and to reveal clues to the understanding of this new type of mineralization in the High Atlas of Morocco.

2 Lithostratigraphy

The studied area contains four main sequences (Fig. 2); These are from bottom to top (i) a felsic volcano-sedimentary sequence (f.v.s.1), (ii) a mafic to intermediate volcano-sedimentary sequence (m.v.s.) (iii) a second felsic volcano-sedimentary sequence (f.v.s.2). The first felsic volcano-sedimentary series is composed by metatuffite and rhyolitic ash. The mafic to intermediate volcano-sedimentary unit is formed by metatuffites, andesitic ash, andesites and dolerites. The second felsic volcano-sedimentary series is composed of metatuffites, dacites breccia and ignimbrites. These units are cut by an intrusive microgranodiorite. Two main generations of quartz veins host the gold mineralization. The first one is constituted by quartz, calcite, siderite, goethite, chlorite ± muscovite ± hématite ± tourmaline ± gold ± malachite. These quartz veins form a stockwork-type dense network. The second quartz veins generation is composed of quartz, goethite ± pyrite ± muscovite ± gold. These veins display an horizontal saddle reef shape. In both quartz generations, gold is essentially associated with goethite minerals (Fig. 3) and sometimes with barite. Gold seems thus to have been remobilized from secondary alteration of sulphur (e.g. pyrite).

The whole area is subjected to the development of pervasive hydrothermal alteration: albitisation, silicification, chloritisation, hematisation, carbonatation, sericitisation and tourmalinisation . Albitisation appears to be the main alteration, and lead to the formation of albitites (Fig. 4). Furthermore, most of the plagioclase of the volcanic rocks (felsic and mafic) present a typical composition of albite.

One of the noteworthy feature of the Jbel Malek gold deposit is the presence of banded iron formations (BIF).

They display fine-grained alternation of quartz and hematite layers (Fig. 5). Most of them have been remobilised as indicate the late calcite and barite veins.

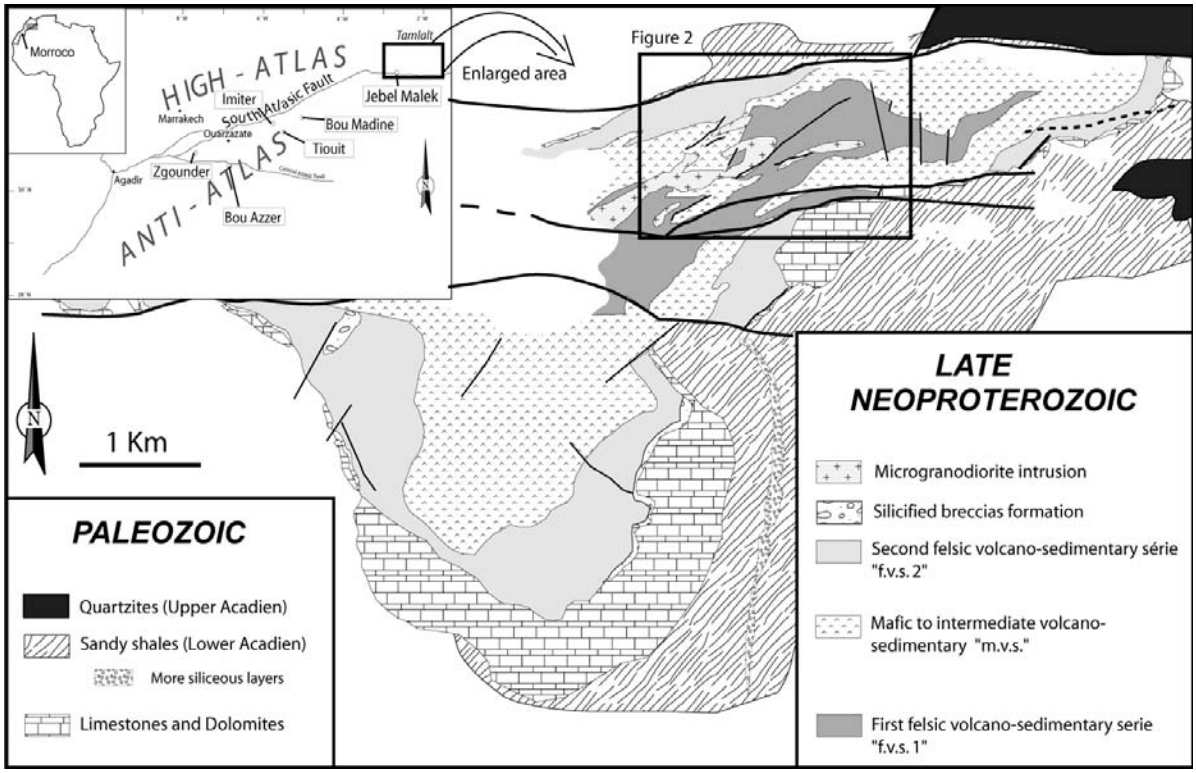

Figure 1: Geological map of the Menhouhou inlier, and localisation of the Jbel Malek sector.

Figure 2: Geological map of the Jbel Malek sector.

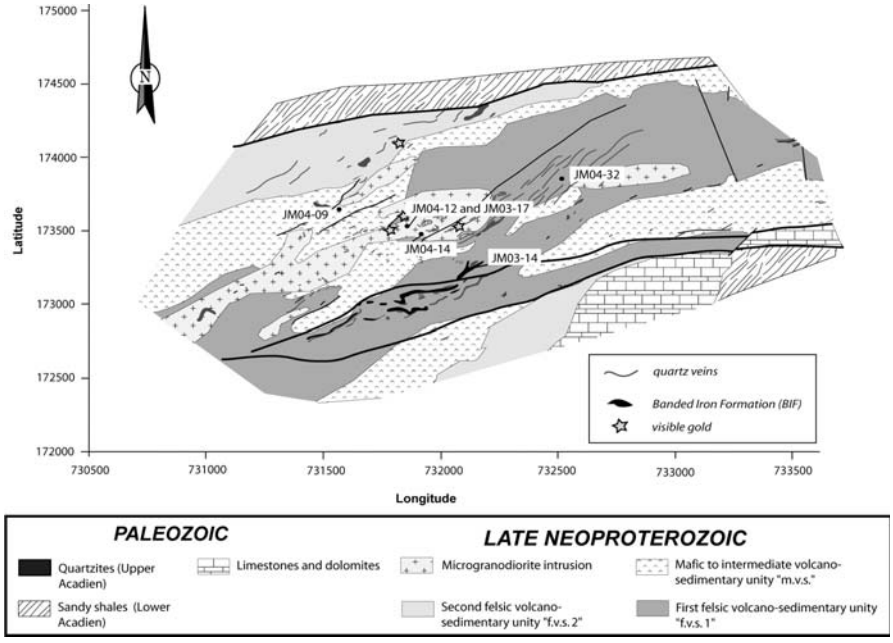

3 Geochemistry

Chemical-mineralogical change in hydrothermally altered rocks have been identified using a parametric procedure (La Roche and Marchal 1978, Charoy 1971).Two specific diagrams (Fig.6 and Fig.7) clearly indicate the progressive albitisation suffered by the wall-rock including the microgranodiorite stock. We can also distinguish weak silicification (Fig. 6).

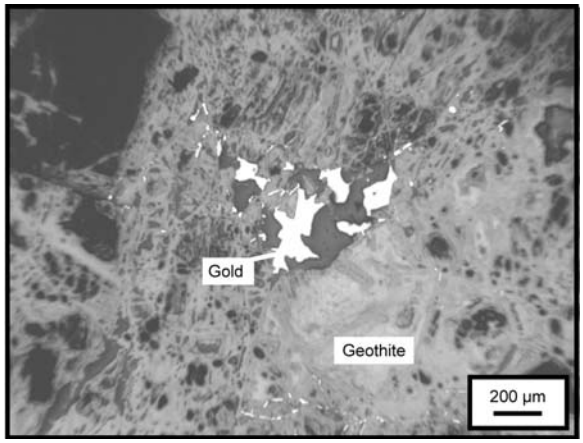

Figure 3: Quartz vein of first generation (JM03-17). Gold inclusions in goethite (replacement of pyrite), reflected light.

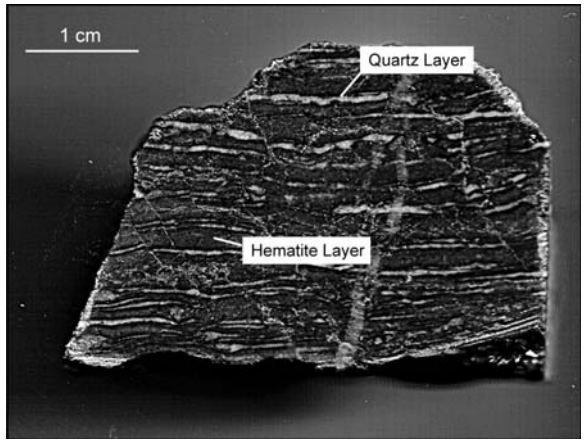

Figure 5: Hand specimen of fine-grained Banded Iron Formation (BIF) (JM03-14). Dark=hematite, light=silica.

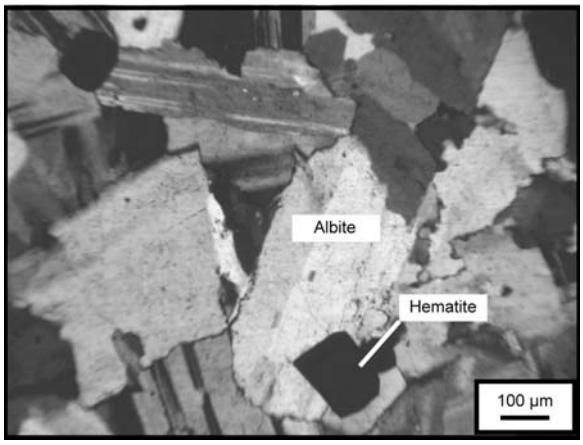

Figure 4: Microphotograph of albitite (JM04-12) in cross polarized light.

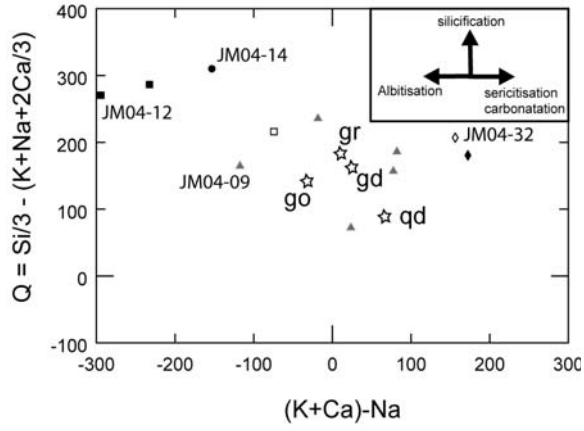

Figure 6: Chemical and mineralogical characterization of the Jbel Malek volcanic successions (modified after Charoy 1971). Triangle: mafic volcanic formation; diamond: felsic volcano-sedimentary unity (empty: f.v.s.1; fill: f.v.s.2); square: altered rocks (fill: albitite and strongly albitised rocks; empty: albtitised and chloritised rock); circle: microgranodiorite. Empty stars represent the mean values for fresh gabbro (go), granodiorite (gd) and granite (gr).

The chemical-mineralogical diagrams have been used to select samples with different degree of alteration in order to test their behaviour with respect to hydrothermal alteration and their magmatic affinities. The microgranodiorite (JM04-14) and f.v.s.1 sample (JM04-32), in spite of different degree and type of alteration (Figs.6, 7) display rather similar distribution of MREE, HREE and HFSE (Fig.8). On the opposite, LREE and especially alkalies are highly variable due to the high solubility of these elements during alteration. The albitite shows depleted spectrum in trace elements related to its highly altered nature and its complete mineralogical change. Zr appears conserved even in the albitite. Using the most immobile elements (MREE, HREE, HFSE) for the microgranodiorite and the f.v.s1 sample, these rocks seems to have a common magmatic origin.

The mafic rock sample (JM04-09) has been albitised but has not suffered propyllitic alteration. It is the less altered mafic rocks and it shows similar trace elements values than E-MORB, with a negative anomaly in Nb interpreted as representative of a metasomatised mantle source.

4 Conclusion

The Jbel Malek gold deposit may show some evidence for having formed from an earlier VMS-type system. The evidence is: (i) volcano-sedimentary rocks, (ii) bimodal volcanism, (iii) strong alteration of country rocks, including albitisation and silicification, and (iii) an exhalative mineralization characterized by the presence of banded iron formations. Nevertheless, the typical mineralogical association (gold remobilization associated with goethite and barite) indicate that overprinting tectonic events post date the Late Neoproterozoic and appear to overprint the system.

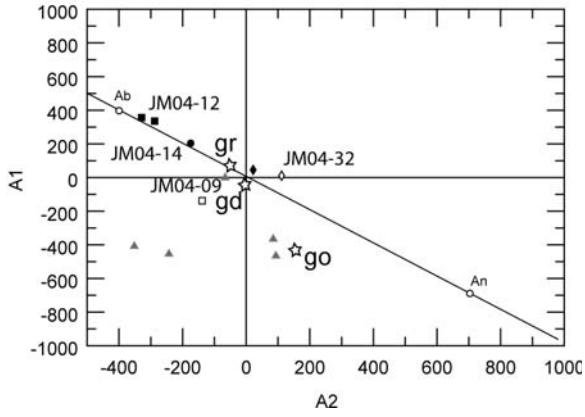

Figure 7: A1/A2 diagram for rocks evolution (modified after La Roche and Marchal 1978). A1 = (Al-K)-(Fe-Mg)-2Na and A2 = (Al-K)+(Fe-Mg)-4Ca. Symbols as Figure 6.

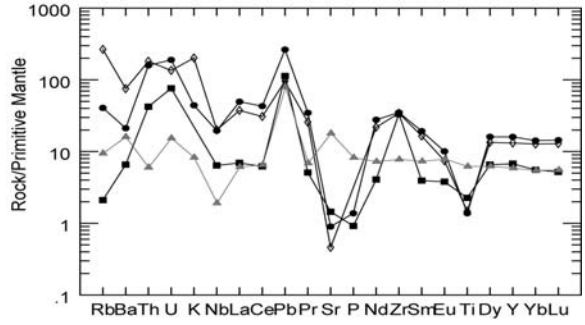

Figure 8: Multi-elements spidergram (Sun and McDonough, 1979) for microgranodiorite (circles), f.v.s.1 (empty diamonds), albitite (squares) and dolerite (triangles).

Acknowledgements

This work was supported by the Bureau de Recherches et de Participations Minières (BRPM-ONHYM, Morroco) and the Ministry of Industry (France). The Service d'Analyses des Roches et Minéraux (SARM, Nancy) which carried out the analyses is thanked. The Service Commun de Microanalyses (UHP, Nancy) is gratefully acknowledged for the SEM and electron probe analyses.

References

Charoy B (1971) Différenciations pétrographiques et géochimiques dans les granites à deux micas du massif de Questembert (Morbihan). Sci. Terre (Nancy), 16, 5-44.

Cheilletz A, Levresse G, Gasquet D, Azizi-Samir MR, Zyadi R, Archibald DA, Farrar E (2002) The giant Imiter silver deposit: Neoproterozoic epithermal mineralization in the Anti-Atlas, Morocco. Mineralium Deposita, 37, 772-781.

El Hakour A (2002) Minéralisation aurifère de la bordure Sud de la Boutonnière de Tamlalt: avancement des travaux et résultats obtenus. BRPM 431-78 GAL 54, 16 p.

Houari M.C, Hoepffner C (2003) Late Carboniferous dextral wrench-dominated transpression along the North African craton margin (Eastern High-Atlas, Morocco). J. Afr. Earth Sci., 37, 11-24.

La Roche (de) H, Marchal M (1978) Leucogranites et granites du massif de Valencia de Alcantara (Espagne): Relations entre compositions chimiques et faciès minéral. Sci. Terre (Nancy), 22, 179-200.

Levresse G, Cheilletz A, Gasquet D, Reisberg L, Deloule L, Marty B, Kyser K (2004). Osmium, sulphur, and helium isotopic results from the giant Neoproterozoic epithermal Imiter silver deposit, Morocco: evidence for a mantle source. Chemical Geology, 207, 59-79

Sun S-S, McDonough WF (1979). Geol. Soc., Sp. Pub., 313-345.

Factors controlling precious and base-metal enrichments at the ultramafic-hosted Logatchev hydrothermal field, 14°45'N on the MAR: New insights from cruise M60/3

S. Petersen, T. Kuhn, P.M. Herzig
Leibniz-Laboratory for Marine Sciences, IFM-GEOMAR, Kiel, Germany

M.D. Hannington
Department of Earth Sciences, University of Ottawa, Canada

Abstract. Massive sulfides from the Logatchev hydrothermal field are characterized by strong enrichments in Cu and Au (up to 56 wt. % Cu and 135 ppm Au) in secondary Cu-sulfides. Gold enrichment also occurs in porous, chalcopyrite-dominated chimney conduits that contain minor sphalerite as well as in oxidized sulfides from the mound surface. The presence of a strongly silicified caprock overlying Cu-Au-rich massive sulfides suggests that conductive cooling and/or mixing of hydrothermal fluids and seawater are responsible for at least some of the Au and Cu enrichment. Sulfur isotope ratios provide further evidence for the interaction of hydrothermal fluids and oxidized seawater in the formation of the secondary sulfides.

Keywords. Ultramafic-hosted, Logatchev, gold-rich VMS

1 Introduction

The Logatchev hydrothermal field on the Mid-Atlantic Ridge is one of the few submarine massive sulfide occurrences currently known where black smoker activity is related to ultramafic host rocks (Batuev et al. 1994). A distinct Au-Cu association was reported for the massive sulfides at Logatchev with Au concentrations up to 56 ppm and an average of 8.4 ppm Au (Krasnov et al. 1995, Murphy and Meyer 1998; Mozgova et al. 1999). However, high Cu-contents between 40 and 50 wt. % in several Au-rich samples indicated that Au enrichment was at least partially related to secondary processes. Even higher average Au concentrations (23.8 ppm Au) were reported by Lein et al (2003) for the nearby inactive Logatchev-2 site.

The Hydromar I cruise M60/3, carried out with the German R/V Meteor, took place from January 14th to February 13th, 2004. The principal scientific aim of the cruise was to investigate the interrelationship of geological and biological processes in an active, ultramafic-hosted hydrothermal field. Seafloor investigations and sampling were performed using the deep-sea ROV Quest provided by the University of Bremen.

Here we report field observations and preliminary geochemical and S-isotopic data on samples obtained during cruise M60/3 and try to establish important factors contributing to the enrichment of Au and Cu at Logatchev.

2 Geological setting

The Logatchev hydrothermal field is located at 14°45'N on the Mid-Atlantic Ridge, about 35 miles south of the 15°20'N fracture zone. This area is characterized by a blocky and irregular morphology, oblique faults and extensive outcrops of serpentinized ultramafic rocks on both sides of the rift valley indicating a high ratio of tectonic to magmatic extension (Fujiwara et al. 2003).

Hydrothermal activity was first documented in 1994 along the eastern wall (Batuev et al. 1994). At least three hydrothermal fields occur off-axis along a WNW-ESE trending structure where it intersects with N-S trending faults: the Logatchev-1 and –2 fields (Cherkashev et al. 2000, Lein et al. 2003) as well as a hydrothermal site at 14°42.38'N / 44°54.50'W, discovered during M60/3 (Kuhn et al. 2004). Several scarps along the wall are covered with large "land slides" forming poorly sorted talus made up of large blocks consisting of mafic and ultramafic material. The presence of large irregular bulged features in the bathymetry is believed to represent slumped structures derived from the eastern valley wall (Kuhn et al. 2004).

3 Results

The Logatchev-1 hydrothermal field is situated on a plateau immediately below a 350 m-high cliff between 3060 m and 2900 m water depth on the eastern wall of the rift valley. It consists of two main areas of high-temperature hydrothermal activity: (I) an area of "smoking craters" (termed Anna-Louise, Irina and site "B" by the Russians) and a black smoker chimney (site "A") to the SE and (II) the Irina II mound area with a chimney complex at its top. An additional smoking crater "Quest" was discovered in the NW of Irina II during M60/3 (Kuhn et al. 2004).

The smoking craters are characterized by 1-2 m high rims with a central depression. Anna-Louise is the largest of the smoking craters with a diameter of about 15 m, whereas Irina, site "B" and Quest have distinctly smaller diameters.

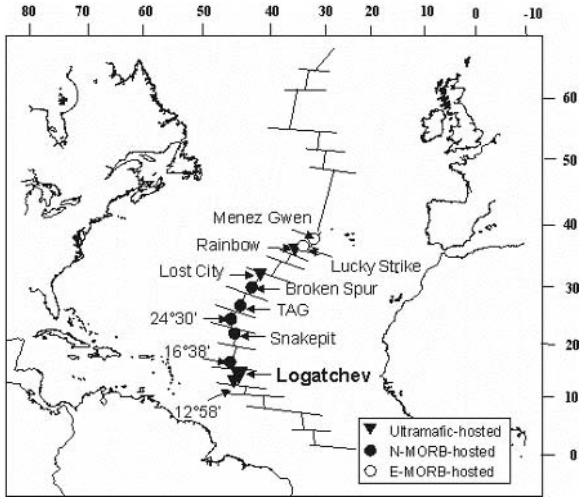

Figure 1: Location and plate tectonic setting of the Logatchev hydrothermal field.

The Irina II site consists of a hydrothermal mound with steep slopes rising about 15 m above the surrounding seafloor. The round to elongate structure has a basal diameter of about 60 m. Four vertical chimneys, up to 2 meters high, with emanating black to gray high-temperature fluids mark the top of the mound. Some of the smokers resemble beehives and the fluids are venting diffusely. The chimneys are densely covered by mussels and shrimp and are surrounded by densely populated mussel beds and by a few inactive chimneys. A single, very active black smoker occurs about 15 m to the south of the Irina II chimney complex. There, the fluids escape almost directly from the seafloor and distinct chimney structures are not present. This is very similar to a number of black smokers at smoking craters elsewhere in the Logatchev field, that also have comparatively small chimneys sitting atop (dm- to m-high) sulfide talus material or emitting fluids from the floor of the depressions. Strong bottom currents are dispersing the plume rapidly.

A large variety of hydrothermal samples were recovered during cruise M60/3 including active and inactive sulfide chimneys, massive sulfides, silicified breccias and crusts, secondary Cu-sulfides, abundant goethite, Fe-Mn-oxyhydroxides, atacamite, Mn-oxides as well as carbonate-cemented Cu-sulfide clasts with rare native copper and cuprite.

Active chimneys from smoking craters are composed of chalcopyrite with variable amounts of isocubanite and minor to rare sphalerite, pyrite and pyrrhotite. Locally, hematite and magnetite are present as inclusions in chalcopyrite. Other chimneys contain substantial amounts of sphalerite/wurtzite and pyrrhotite mixtures. Anhydrite is present in active Zn-rich chimneys from the Irina II mound. Some black smokers from the "smoking craters" are thin-walled (< 1 cm) and banded, and consist entirely of chalcopyrite with only a thin coating of Fe-oxyhydroxides on the outside. The reason for the layering is not clear, but might represent multiple growth zones indicating episodic hydrothermal activity.

Three TV-guided grabs recovered strongly silicified black crusts often containing fragments of altered wallrock as well as orthopyroxene crystals. Small (mm-sized) chalcopyrite and pyrite clasts are common and are disseminated throughout the crusts. During one attempt to sample a dense mussel bed, we collected some of the silicified crusts that were broken on impact by the TV-guided grab. The underlying soft material had an *in-situ* temperature of 106°C after recovery on deck, and the mussels sitting atop the crusts were baked. Conductive cooling is currently taking place underneath some of these crusts, cementing the immediate subseafloor by precipitating amorphous silica and, at the same time, providing the ideal temperature gradient for the dense mussel beds above.

Unconsolidated sulfides occur immediately underneath this caprock and usually contain a more pyrite-rich section at the top followed by more Cu-rich sulfides underneath. In this Cu-rich part, irregular fragments of chalcopyrite are common, and are variably replaced by secondary Cu-Fe- and Cu-sulfides such as bornite, digenite and chalcocite reflecting decreasing Fe and H_2S and increasing Cu activities. These secondary Cu minerals likely formed from conductively cooling hydrothermal fluids. A fluid channel, 5 cm wide, consisting mainly of Cu-rich sulfide crosscuts the silicified caprock (inactive). Similar features may be present elsewhere and may form some of the black smokers in the smoking craters and emanating fluids directly from the seafloor without obvious chimney structures. Gray to green-gray indurated mud underlying the sulfides in these TV-grab samples is common, and likely related to the alteration of host rock material. Thus, the massive sulfides along the flanks of the deposit might only be a thin veneer directly below the seafloor.

The amount of sulfide talus, the state of oxidation and the widespread occurrence of abundant atacamite suggest that this is an old hydrothermal system. Abundant Cu-sulfides formed under supergene conditions at ambient temperatures during interaction of sulfides with oxidized seawater.

Preliminary geochemical analyses (instrumental neutron activation for trace elements and ICP-ES for major elements) show strong enrichments of Cu and Au in samples from Logatchev. The highest Cu-grades (up to 56 wt. %) are in secondary Cu-sulfides, Au concentrations reach up to 135 ppm, also in secondary Cu-sulfides. This is the highest Au concentration yet reported from a submarine massive sulfide deposit in the modern ocean. In addition to the high values found in secondary Cu-sulfides, Au-enrichment also occurs in porous, chalcopyrite-dominated chimneys that contain minor sphalerite and in oxidized sulfides from the mound surface (up to 51

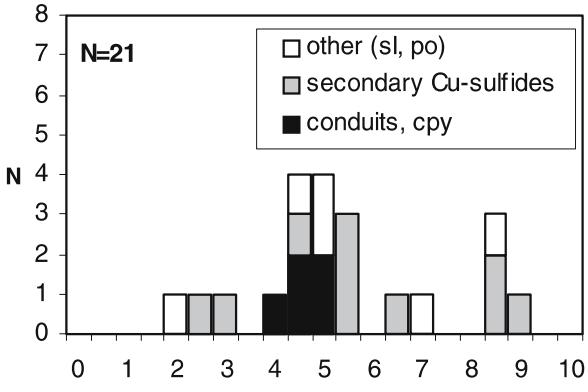

Figure 2: Histogram of sulfur isotope ratios from the ultramafic-hosted Logatchev hydrothermal field.

ppm Au). In contrast, primary thin-walled chalcopyrite conduits, mostly from smoking craters, contain less than 1 ppm Au. This indicates that the fluids are initially undersaturated with respect to Au and precipitate Au only after conductive cooling and/or mixing with seawater in the porous walls of the chimneys. Similar processes might occur underneath the silica cap or where ascending hydrothermal fluids percolate through porous massive sulfides. Other elements enriched at Logatchev include Co and Se. The concentration of Mo, which is commonly enriched in high-temperature hydrothermal precipitates is relatively low (on aver. 36 ppm Mo). Sulfur isotope ratios vary from 2.2 to 8.9 ‰ (N=21) and are within the range of previously reported values, from 0.7 to 13.8 ‰ $\delta^{34}S$ (Bogdanov et al. 1997). Chalcopyrite-rich chimney conduits are characterized by a narrow range of $\delta^{34}S$ (4.1 to 4.8 ‰, N=5), whereas secondary Cu-sulfides show a much larger spread with heavier values indicating a higher contribution of sulfur from seawater (Fig. 2).

4 Discussion

High Cu- and Au concentrations are a characteristic feature of the ultramafic-hosted Logatchev hydrothermal field. The reason for this enrichment is not entirely known. Primary enrichments in the source rocks, favorable conditions for Au transport in the fluids, phase separation or certain depositional controls are possible reasons for the enrichments. In the absence of geochemical results from other ultramafic-hosted sites, especially from the high Arctic we currently do not know if this is a particular feature of the Logatchev hydrothermal field or if it is common to all ultramafic-hosted deposits.

A primary Au enrichment in the source rock is not yet established. Although it has been suggested that some of the venting at ultramafic-hosted sites is driven by the heat of serpentinization, the high-temperature black smokers are considered to require a magmatic heat source (Kelley et al. 2002). The vent fluid geochemistry at the Rainbow hydrothermal field shows higher Fe and lower SiO_2 concentrations when compared to the Logatchev site, suggesting a more pronounced ultramafic input at Rainbow (Douville et al., 2002). The formation of massive sulfide deposits at Logatchev is believed to result from the circulation of hot fluids through fissured and faulted terrain associated with slumped material, but fluids in the reaction zone may have equilibrated with mafic rocks in addition to ultramafic rocks at depth. The heat is probably supplied from basaltic melts or intrusions localized underneath the adjacent rift valley and/or off-axis intrusions.

Boiling might be another process in enriching massive sulfides. Reversed plumes, reported earlier and thought to indicate venting of high-salinity fluids, were not encountered during our cruise, rather strong bottom currents dispersed the plume rapidly away from the source. Also, Douville et al. (2002) did not find evidence for high-salinity fluids when analyzing the vent fluids. However, high-salinities were documented by Bortnikov et al. (1997) in fluid inclusions in gypsum, confirming the presence of high-salinity fluids.

The observation of a strongly silicified caprock overlying massive sulfides that are enriched in Cu and Au suggest that conductive cooling and/or mixing and constant up-grading of the sulfides takes place at Logatchev and is responsible for at least some of the Au and Cu enrichment observed. Mixing of the hydrothermal fluids with sea-water would also have increased oxygen fugacity, which would have promoted deposition of Au assuming that this metal was transported as a bisulphide complex. Sulfur isotope ratios provide further evidence for the interaction of hydrothermal fluids and oxidized seawater in the formation of these secondary sulfides.

Acknowledgements

This project is carried out within the framework of the German DFG Priority Program 1144: " From Mantle to Ocean: Energy-. Material- and Life-cycles at Spreading Axes". We are grateful for the excellent work done by both, the ROV crew and the crew of R/V Meteor under captain M. Kull.

References

Batuev BN, Krotov AG, Markov VF, Cherkashev GA, Krasnov SG and Lisitsyn YD (1994) Massive sulfide deposits discovered and sampled at 14°45'N, Mid-Atlantic Ridge: Bridge Newsletter 6: 6-10

Bogdanov YA, Bortnikov NS, Vikentyev IV, Gurvich EG and Sagalevich AM (1997) A new type of modern mineral-forming systems: black smokers of the hydrothermal field at 14°45'N latitude, Mid-Atlantic Ridge. Geology of Ore Deposits 39: 68-90

Bortnikov NS, Krylova TL, Bogdanov YA, Vikentyev IV and Nosik LP (1997) The 14°45'N hydrothermal field, Mid-Atlantic Ridge: Fluid inclusion and sulfur isotope evidence for submarine phase separation. In Papunen H (ed) Mineral Deposits: Research and Exploration. Where do they meet. Proceedings of the 4th Biennial SGA Meeting, Turku, Finnland. Balkema, Rotterdam 353-356

Cherkashev GA, Ashadze AM, Gebruk AV and Krylova EM (2000) New fields with manifestations of hydrothermal activity in the Logatchev area (14°N, Mid-Atlantic Ridge). InterRidge News 9: 26-27

Douville E, Charlou JL, Oelkers EH, Bienvenu P, Jove Colon CF, Donval JP, Fouquet Y, Prieur D and Appriou P (2002) The Rainbow vent fluids (36°14'N, MAR): the influence of ultramafic rocks and phase separation on trace metal content in Mid-Atlantic Ridge hydrothermal fluids. Chem. Geol. 184: 37-48

Fujiwara T, Lin J, Matsumoto T, Kelemen PB, Tucholke BE and Casey JF (2003) Crustal Evolution of the Mid-Atlantic Ridge near the Fifteen-Twenty Fracture Zone in the last 5 Ma, Geochem. Geophys. Geosys. 4: doi:10.1029/ 2002 GC 000364

Kelley DS, Baross JA and Delaney JR (2002) Volcanoes, fluids, and life at mid-ocean ridge spreading centers. Annual Reviews of Earth and Planetary Science 30: 385-491

Krasnov SG, Cherkashev GA, Stepanova TV, Batuyev BN, Krotov AG, Malin BV, Maslov MN, Markov VF, Poroshina IM, Samovarov MS, Ashadze AM, Lazareva LI and Ermolayev IK (1995) Detailed geological studies of hydrothermal fields in the North Atlantic. In Parson LM, Walker CL and Dixon DR (eds) Hydrothermal Vents and Processes. Geol. Soc. Spec. Publ. 87: 43-64

Kuhn T, Ratmeyer V, Petersen S, Hekinian R, Koschisky-Fritsche A, Seifert R, Borowski C, Imhoff J, Türkay M, Herzig P, Alexander B, Augustin N, Birgel D, de Carvalho LM, Engemann G, Ertl S, Franz L, Grech C, Jellinek T, Klar S, Küver J, Kulescha F, Lackschewitz K, Renken J, Ruhland G, Scholten J, Schreiber K, Süling J, Westernstöer U and Zielinski F (2004) The Logtachev hydrothermal field - revisited: new findings of the R/V Meteor cruise Hydromar (M60/3): InterRidge News 13: 1-4

Lein AY, Cherkashev GA, Ulyanov AA, Ulyanova NV, Stepanova TV, Sagalevich AM, Bogdanov YA, Gurvich EG and Torokhov MP (2003) Mineralogy and geochemistry of sulfide ores from the Logatchev-2 and Rainbow fields: similar and distinctive features. Geochem Int 41: 271-294

Mozgova NN, Efimov AV, Borodaev YS, Krasnov SG, Cherkashov GA, Stepanova TV and Ashadze AM (1999) Mineralogy and chemistry of massive sulfides from the Logatchev hydrothermal field (14°45'N Mid Atlantic Ridge). Expl. Mining Geol. 8: 379-395

Murphy PJ and Meyer G (1998) A gold-copper association in ultramafic-hosted hydrothermal sulfides from the Mid-Atlantic Ridge. Econ. Geol. 93: 1076-1083

Gold mineralization in recent and ancient volcanic-hosted massive sulfides: The PACMANUS field and the Neves Corvo deposit

A.M.M. Pinto, J.M.R.S. Relvas, F.J.A.S. Barriga, J. Munhá
CREMINER/Centro Geologia/Dep.Geologia, U. Lisboa, Ed. C6,Campo Grande, 1749-016 Lisboa, Portugal

N. Pacheco
SOMINCOR, Sociedade Mineira de Neves-Corvo, SA, Mina de Neves-Corvo, 7780 Castro Verde, Portugal

S.D. Scott
Department of Geology, University of Toronto, 22 Russell Street, Toronto ON M5S 3B1, Canada

Abstract. Gold mineralization in the Neves Corvo copper stockworks occurs in two geochemical associations: (1) Au+Co+Bi(±Te) and (2) Au+Cu+Ag(±Hg).Type 1 gold occurs in the deeper parts of the feeder zones. Its associated mineralogical assemblage is consistent with low sulfur activity of the fluid and high temperature (360º- 400ºC) conditions. The second type of gold geochemical association reflects pH increase and/ or temperature decrease as the fluid moves upwards in the stockwork and reaches the base of the massive sulfide lenses. Conversely, gold in the bornite-rich massive sulfide ores of Neves Corvo is accompanied by high sulfidation parageneses. These might have resulted either from the long-lived maturation of the ore-forming system, which would have led to extreme zone refining effects, and/or from the late input of an external fluid component (possibly magmatic?) in the Neves Corvo hydrothermal system. In the PACMANUS hydrothermal field, native gold also occurs in both high and low sulfidation mineral associations. Gold occurs at the seafloor level either associated with: (1) chalcopyrite + sphalerite + tennnatite, or (2) chalcopyrite + bornite ± covellite. At depth, instead, gold occurs in sphalerite as small native gold inclusions (silver-poor). Following the process of copper enrichment by zone-refining, gold frequently concentrates in the borders of the sphalerite grains.

Keywords. Gold, seafloor hydrothermal activity, PACMANUS, Iberian Pyrite Belt, Neves Corvo

1 Introduction

Full understanding of gold mineralization patterns in volcanic-hosted massive sulfide (VHMS) deposits is often difficult to achieve due to the complex behaviour of gold during the syn- and post-metallogenic histories of most ancient deposits. This difficulty can possibly be overcome by seeking in modern seafloor and sub-seafloor analogues the pieces of knowledge that frequently are missing in the fossil systems.

Regardless of significant differences, like geotectonic setting and host-rock succession, sulfide mineralization in the PACMANUS field and in the Neves Corvo deposit, in the Iberian Pyrite Belt, display some interesting resemblances, mainly concerning the possible involvement of magmatic fluid and metal contributions in the budget of their hydrothermal ore-forming systems (Relvas et al. 2001; Yang and Scott 2002). The base metal concentrations at Neves Corvo and PACMANUS are locally similar. As in PACMANUS, there are some ore types in Neves Corvo where gold concentrations exceed 20 ppm. The hybrid character of the Neves Corvo mineralization has been recently emphasized (Relvas et al. 2001), and this may well be the case at PACMANUS as well. Binns et al. (2002) advocated a significant magmatic fluid and metal input for the PACMANUS hydrothermal field. Subsequent shallow drilling of the sub-seafloor massive sulfides revealed strong textural and mineralogical similarities with the seafloor sulfides (Herzig et al. 2003). However, the deeper facies of the system, drilled during ODP Leg 193, appear to be surprisingly insensitive to external fluid signatures. Hydrothermal alteration/mineralization patterns there do not show significant imprints of magmatic fluid/metal contributions (Roberts et al. 2003).

Here we report the results of an on-going study devoted to characterizing and comparing the gold mineralization in the Neves Corvo deposit with that of the PACMANUS hydrothermal field.

2 Gold in the Neves Corvo deposit

The Neves Corvo deposit is located in the Portuguese segment of the Iberian Pyrite Belt (IPB). The deposit is hosted by an upper Devonian to lower Carboniferous Volcanic-Siliceous Complex and embraces five orebodies: Graça, Corvo, Neves, Zambujal and Lombador (Relvas et al. 2001; and references therein).

Gold in VHMS deposits occurs in two different types of metal associations: Au-Cu and Au-Zn-Pb-Ag (Huston 2000). In the IPB deposits, previous mineralogical and geochemical studies of gold mineral assemblages allowed the definition of two geochemical, mineralogical and spatial associations for gold, in accordance with the classic metal zonation in this type of deposits: (1) Au+Co ±Bi in the stockwork and interaction zones at the base of the

massive sulfide orebodies; and (2) Au+Zn+Ag ±Tl ± Hg in the uppermost part of the orebodies or in their lateral and distal extensions (Leistel et al. 1998).

In the Neves Corvo deposit, gold occurs in close proximity to the copper-rich ores. Significant gold contents and high maximum gold grades (up to 95 ppm) have been found in the stockwork and at the base of the copper-rich ores at the Lombador and Neves North orebodies. No significant gold grades have been found to date in the zinc-rich polymetallic ores of the deposit. Random fire assays performed in drill cores intersections in zinc-rich ores repeatedly yield gold grades below 1 g/t.

In the Neves Corvo stockworks, gold is distributed in two different types of stringer mineralization: the copper-rich stockwork ores and the barren stockworks. In copper-rich stockwork ores, gold clearly belongs to the Au-Cu association type. Based on detailed mineralogical, textural and geochemical studies, two sub-type associations were defined for this gold: 1) Au+Co+Bi(±Te), and 2) Au+Cu+Ag(±Hg).

Gold of the Co+Bi(±Te) geochemical association occurs as native gold with low silver contents. Its mineralogical association consists of arsenopyrite (FeAsS), cobaltite (CoAsS), alloclasite ([Fe,Co] AsS) and rare glaucodot ([Co,Fe]AsS). Bi minerals are bismuthinite (Bi_2S_3), galenobismutite ($PbBi_2S_4$), native bismuth (Bi), lindstromite ($Cu_3Pb_3Bi_{10}S_{19.5}$), tetradymite (Bi_2Te_2 S), and joseite–B ($Bi_{4-x}Te_{2-x}S$). Other associated ore minerals include chalcopyrite, pyrite, fahlore, sphalerite, pyrrhotite, galena, stannite, kosterite, and minor cassiterite. Gold grains of almost pure Au (Au>85%, Ag<10%, and 0.3-1.3% Hg) occur as inclusions (5-25 μm) within cobaltite and alloclasite, commonly associated with bismuth minerals (Fig. 1A). In the Au+Cu+Ag(±Hg) geochemical association, gold occurs as electrum (10-250 μm), associated with chalcopyrite, Ag-tetrahedrite, and minor sphalerite. The electrum composition is typically characterized by Au<75%, Ag>20%, and Hg ranging 3-5% (Fig. 1B). Gold (+Co+Bi±Te) occurring as inclusions in arsenic and cobalt minerals is texturally interpreted as an early phase. The gold (+Cu+Ag±Hg) that occurs as larger electrum grains in chalcopyrite is thought to have resulted from subsequent hydrothermal reworking of the previous gold generation.

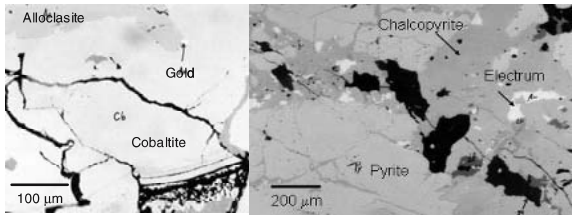

Figure 1: A – Photomicrograph of gold in Co+Bi(±Te) geochemical association occurring as native gold (>85% Au) in the contact between alloclasite and cobaltite (plain polarized reflected light (pprl)). B – Photomicrograph of the gold in Au+Cu+Ag(±Hg) geochemical association occurring as electrum (<75% Au) associated with later copper sulfides (pprl).

Gold is also present in the barren stockworks as submicroscopic grains within the structure of the sulfides. Detailed optical microscopy has shown a simple mineralogy consisting of arsenopyrite and pyrite, with minor chalcopyrite, stannite, and galena. No "visible gold" has been noticed. EMPA has shown that arsenopyrite is the gold-bearing mineral whereas pyrite and chalcopyrite do not carry any gold. The gold content in arsenopyrite varies from 15 to 1020 ppm with rims enriched (avg. 400 ppm) relative to core (avg. 60 ppm). Arsenopyrite occurs as a late phase, cementing and overprinting the pre-existing sulfides.

Gold has also been found in the bornite-rich massive sulfide ores where it occurs as extremely fine grains, in averaging less than 5μm across. Gold is associated with naumannite ($Ag_{1.95}Se_{0.94}$), galena-clausthalite ($Pb_{0.95}(S,Se)_{1.00}$), and wittichenite ($(Cu,Fe,Ag)_{3.01}Bi_{1.01}S_{2.98}$). Bornite ($(Cu,Ag)_{4.93}Fe_{0.97}$ $S_{4.10}$) is part of this mineral assembla -ge together with nekrasovite / colusite ($(Cu,Ag)_{26.83}$ $V_{1.56}$ $(As,Sn,Sb,Fe)_{6.57}$ $S_{31.00}$), and an unidentified Ag phase. Bi- and Hg-rich tennantite is the main In-bearing mineral in this association $((Cu,Ag,Fe,Zn,Hg,In)_{11.76}(As,Sb,Bi)_{4.01}S_{13.24})$.

3 Gold in the PACMANUS field

The PACMANUS vent field is located in the Manus Basin (active New Britain volcanic arc), offshore eastern Papua New Guinea. This hydrothermal field consists of five active vent sites, named Roger Ruins, Roman Ruins, Satanic Mills, Tsukushi and Snowcap (Binns et al. 2002). The Roman Ruins high temperature vent field is one of the three where gold has been found (Moss and Scott 2001). Roman Ruins is located in the northern edge of the ridge crest at a water depth of 1693-1710 meters below sea level (mbsl). It was first drilled during ODP Leg 193, Nov.2000-Jan.2001 (Binns et al. 2002). In another oceanographic mission, in September 2002, the shallow sub-seafloor portion of the Roman Ruins mound was repeatedly intersected by drilling with recovery (small length drill holes: 2.1 to 5.0 m of penetration), enabling the continuous sampling of gold-rich massive sulfide mineralifation in the immediate sub-seafloor (Herzig et al. 2003). Thus, Roman Ruins is one of the rare vent sites that have been studied at several different depths – seafloor, shallow sub-seafloor and deep sub-seafloor.

Roman Ruins contains numerous large columnar broken chimneys (Binns et al. 2002). Mineral composition is dominated by sphalerite and barite, chalcopyrite, tennantite, bornite, covellite and gold. The Roman Ruins precipitates average 17.2 ppm Au. Gold enrichment occurs both in the interior (Cu-rich), and in the outer rims of the chimneys (Zn-rich). However, the zinc-rich portions generally possess the higher gold contents. Gold was found within two different mineral associations: (1) chal-

copyrite + sphalerite + tennnatite and (2) chalcopyrite + bornite ± covellite. Native gold tends to occur as inclusions in tennantite (Moss and Scott 2001).

The shallow sub-seafloor interface contains massive sulfides dominated by light brown to dark brown sphalerite, together with varying proportions of barite, pyrite, chalcopyrite, and minor galena and sulfosalts. Textures are similar to those of seafloor sulfides. Gold averages 12 g/t, with a maximum value of 57 g/t (Herzig et al. 2003).

The Roman Ruins sub-seafloor sulfide mineralization represents less than 10% of the recovered material in the deep drill holes carried out during ODP Leg 193. Sulfide mineralogy consists of pyrite occurring in association with chalcopyrite-diseased and light brown sphalerite, chalcopyrite, galena, marcassite and gold. This gold occurs at 118 mbsf, as micrometric grains of silver-poor (0.1 to 3.5 wt.% Ag) native gold, mostly as inclusions in sphalerite. Sphalerite grains are generally zoned with nicely developed chalcopyrite-diseased borders and chalcopyrite rims, which speak for significant zone-rifining processes. The early sphalerite generation carries significant gold contents, averaging more than 0.1wt.% Au. Textural zonation in sphalerite is underlined by variation of the iron contents from the core (Fe-poor) to the chalcopyrite-diseased border of the grains (Fe-richer). Gold inclusions are concentrated near the boundary between the core and the chalcopyrite-diseased borders, or in the outer part of the sphalerite grains. Gold appears to migrate with copper during the advance of a zone refining front.

4 Discussion and conclusions

Occurrences of Au-Cu associations in ancient VHMS deposits have been interpreted to have resulted from chloride complexing of gold in high temperature fluids (>300°C) (Huston and Large 1989). Gold deposition is mainly controlled by pH increase and, to a lesser degree, by temperature fall as the gold-carrying fluids move through the stringer zone and lower part of the massive sulfide lens (Huston 2000). Most gold mineralization at Neves Corvo ores is consistent with this mechanism. Native gold in the Neves Corvo stockwork ores occurs as inclusions in cobaltite and alloclasite. The cobaltite-alloclasite association denote conditions of low sulfur activity for a temperature range of 360°-400° C (Scott 1983). The presence of native bismuth and bismuth tellurides in the deeper parts of the stockworks also conforms to prevalent conditions of low sulfur activity. The upward transition to a different regime of Bi fixation, which is accommodated in bismuthinite towards the upper part of the feeder zones, should reflect an increase of sulfur activity following the up-flow pathway of the mineralizing fluid and likely enhancement of fluid mixing with seawater. Continuous increase of sulfur activity and progressive availability of different metals as a function of their relative solubility, promote new changes in the equilibrium mineralogy. Bi is partly replaced by Pb+Cu to first form lindstromite, followed by galenobismutite. The presence of galenobismutite indicates that this part of the hydrothermal system has reached temperatures close to 375 – 390°C (Marcoux et al. 1996). Gold occurrence in the uppermost part of the feeder zone is represented by a mineral assemblage that includes electrum, chalcopyrite, fahlore and minor sphalerite. This mineral assemblage is consistent with depositional temperatures of about 300 – 350°C.

Gold, associated with a complex metal suite that includes extremely high concentrations of copper, and also Sn, Sb, Se and In, was found in the Neves Norte bornite ores in clear association with high sulfidation mineral assemblages. Huston and Large (1989) emphasized the importance of bornite as an ore mineral in Au-rich deposits of the Au-Cu association, and established a genetic parallel among high-sulfidation VHMS deposits and high-sulfidation epithermal deposits, namely possible copper-gold direct magmatic inputs to these systems (Huston 2000). Gold occurring as "invisible gold" in the arsenopyrite structure is interpreted as a late stage phase in Neves Corvo. The latter probably relates with tectono-metamorphic redistribution of metals in response to the Hercynian orogeny.

In the PACMANUS hydrothermal field, gold enrichments are associated both with Zn-rich and Cu-rich mineral assemblages. At the seafloor, native gold is precipitating mainly as inclusions in tennantite in zinc-rich assemblages (Moss and Scott, 2001). According to these authors, in the PACMANUS hydrothermal system, gold should have been preferentially transported in solution as $Au(HS)^o$ complexes. The high activity of sulfur testified by the mineralogical assemblages produced, suggests that part of the gold might have been sourced by a direct magmatic contribution (Yang and Scott 2002).

In contrast, subsurface sulfide mineralogy is of low-sulfidation nature. The sulfide paragenesis shows a classic temperature-controlled evolutionary pattern. Early pyrite, followed by pyrite-sphalerite-minor galena and, finally, by sphalerite-chalcopyrite associations represents the prograde path of the isotherms and associated zone-refining processes. Gold preferentially precipitates as inclusions in sphalerite, especially in the borders of light brown sphalerite grains. Frequently, however, dark brown to black sphalerite replaces the earlier grains, developing gold-containing, chalcopyrite-diseased borders in the new formed sphalerite grains. The gold distribution in the early sphalerite is thus severely constrained by zone-refining processes.

Irrespective of other possible sources, an early generation of gold should have been supplied by leaching of the footwall rocks as it clearly correlates with the low-temperature precipitation of the zinc-rich assemblage. Subsequent partial gold depletion in sphalerite, gold migration with chalcopyrite and silver enrichment of the mobilized generation of gold collectively indicate significant zone-refining of gold in parts of the hydrothermal system.

Acknowledgements

This study is a contribution to research project ARCHYMEDES (FCT-SAPIENS 2001/41393). AP acknowledges the FCT for financial support for his research activities (SFRH/BD/6240/2001). M. Solomon and F. Tornos are gratefully acknowledged for their reviews of this paper.

References

Binns RA, Barriga FJAS, Miller DJ (2002) Proceedings ODP, Initial Reports, 193. In: Ocean Drilling Program, Texas A&M University, College Station TX 77845-9547, USA

Herzig P, Petersen S, Kuhn T, Hannington M, Gemmell J, Skinner A, SO-166 Shipboard Scientific and Technical Party (2003) Shallow drilling of seafloor hydrothermal systems using R/V Sonne and the BGS Rockdrill: Conical Seamount (New Ireland Fore-Arc) and PACMANUS (Eastern Manus Basin, Papua New Guinea). In: International Research: Back Arc Basins 12(1): 22-26

Huston David L (2000) Gold in volcanic-hosted massive sulfide deposits: Distribution, Genesis, and Exploration. In: SEG Reviews: Gold in 2000. Hagemann & Brown (eds) Vol. 13, Lake Tahoe, USA, 401-426

Huston L, Large R (1989) A chemical model for the concentration of gold in volcanogenic massive sulfide deposits. In: Ore Geology Reviews 4: 171-200

Leistel JM, Marcoux E, Deschamps Y, Joubert M (1998) Antithetic behaviour of gold in the volcanogenic massive sulfide deposits of the Iberian Pyrite Belt. In: Mineralium Deposita 33: 82-97

Marcoux E, Moëlo Y, Leistel J (1996) Bismuth and cobalt minerals as indicators of stringer zones to massive sulfide deposits, Iberian Pyrite Belt. In: Mineralium Deposita 31: 1-26

TAG hydrothermal field: A key to modern and ancient seafloor hydrothermal VMS ore-forming systems

Peter A. Rona
Institute of Marine and Coastal Sciences and Department of Geological Sciences, Rutgers University, 71 Dudley Road, New Brunswick, New Jersey 08901-8521, USA

Abstract. The TAG hydrothermal field, situated in the axial valley of the slow-spreading Mid-Atlantic Ridge near 26°N, 45°W, is one of the largest and best-studied seafloor hydrothermal fields in the world. This paper applies what we are learning about the TAG field that may guide exploration for modern and ancient Volcanogenic Massive Sulfide (VMS) deposits. Consideration includes water column and seafloor signals distal to the field and tectonic, magmatic, hydrothermal, alteration, and serpentinization processes with diagnostic features in the axial valley proximal to the field; the role of replacement, sulfate deposition and dissolution, and zone refinement in individual sulfide mounds; the concentration of large deposits by superposition of multiple short episodes of high-temperature hydrothermal activity (episodes to hundreds of years; episodicity thousands of years); and the clustered mode of occurrence of an assemblage of large sulfide mounds by synchronous and asynchronous episodic hydrothermal activity over more than 100,000 years.

Keywords. Hydrothermal, Volcanogenic Massive Sulfides (VMS), mid-ocean ridge, Mid-Atlantic Ridge, seafloor

1 Introduction

The TAG hydrothermal field comprises a cluster of active and inactive sulfide mounds and at least two active low-temperature zones in an area of about 5 km by 5 km on the eastern floor and wall of the axial valley of the slow-spreading Mid-Atlantic Ridge near 26°N, 45°W (Figure 1, Rona et al. 1993). The TAG field has been the subject of ongoing international collaborative interdisciplinary studies since its discovery in 1985, as the first high-temperature hydrothermal field, massive sulfide deposits, and vent ecosystem, found in the Atlantic Ocean (Rona et al. 1986), and the first such field found on a slow-spreading ocean ridge. The groundwork of multidisciplinary studies at TAG provides a framework to address fundamental questions of magmatic, tectonic, hydrothermal, and biologic processes at a slow-spreading ocean ridge, and to resolve linkages between these processes (Rona and Von Herzen 1996). The knowledge being gained from studies at the TAG field provides insights to guide exploration for other such large modern and ancient VMS deposits, which is the subject of this paper.

2 Asymmetric tectonic, magmatic, hydrothermal, and serpentinization processes

Exploring for a modern or ancient VMS deposit follows a procedure of progressively closing range from far to near by sensing chemical and physical properties of the source in a setting where such deposits occur (Rona 1999-2000, Table 2). Approaching the TAG field the first hydrother-

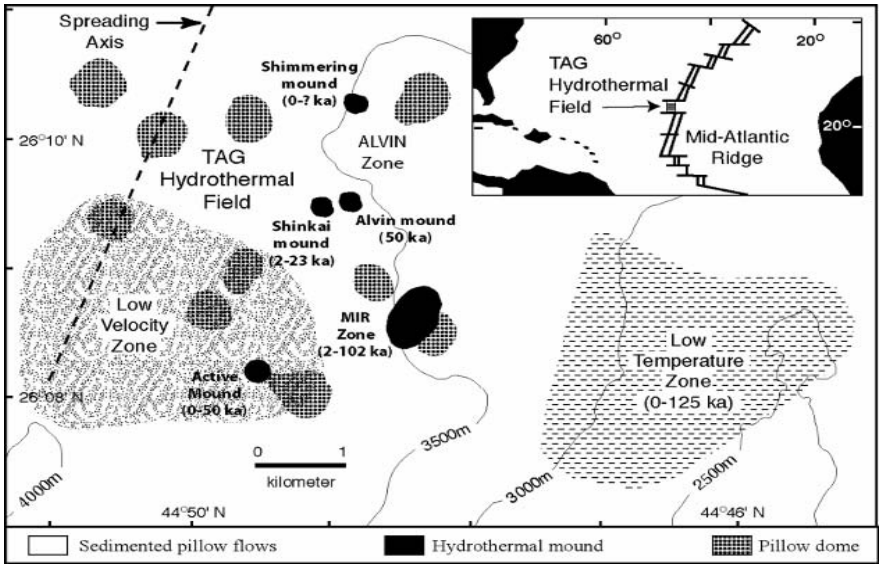

Figure 1: Map of the TAG hydrothermal field in the axial valley of the Mid-Atlantic Ridge near 26°N, 45°W (index map in upper right corner) showing spatial and temporal distribution of large VHS mounds and low-temperature deposits (Rona et al. 1993).

mal signal detected is weak acid soluble iron and manganese oxide particles suspended in the water column at the depth of the Mid-Atlantic Ridge crest (2,000 m) at a distance of 750 km west of the ridge crest, which may be an integrated signal from a region of the Mid-Atlantic Ridge (Rona, 1980). Continuing eastward, the concentration of Fe and Mn in particulate and dissolved phases and of the conservative primordial gas ^{3}He (expressed as δ^3He) would be expected to gradually increase, leading to a neutrally buoyant hydrothermal plume. The neutrally buoyant plume is connected to the source vents by a narrow (c. 15 m diameter) buoyant plume discharging from a group of black smokers vigorously venting high temperature (365°C) solutions (Edmonds et al. 1996) from multiple chimneys on top of a sulfide mound 250 m in diameter and 35 m high at a water depth of 3670 m. The plume extends from the source vents tens of kilometers east-northeast at an altitude of several hundred meters above the seafloor (Rudnicki 1995). The corresponding signal on the seafloor is a trail of metalliferous sediments produced by fallout from the water column increasing from a trace component diluted by normal deep-sea sediments to distinct layers within kilometers of the source vents within the axial valley (Shearme et al. 1983; Metz et al. 1988). The signal of suspended hydrothermal particulates detected to the west of the Mid-Atlantic Ridge is absent to the east, indicating transport by unidirectional deep ocean currents (Rona 1980).

The active high-temperature sulfide mound lies near the center of a 40 km-long NE-SW-trending spreading segment, 2.4 km east of the spreading axis,adjacent to a marginal fault at the base of the east wall of the axial valley. The active sulfide mound onlaps a pillow mound of similar size to the east. These two mounds are situated at the intersection of axis-parallel with axis-oblique fault systems within a faulted and fissured zone that occupies the eastern half of the 7 km-wide valley floor (Karson and Rona 1990; Kleinrock and Humphris 1996; Bohnenstiehl and Kleinrock 1999). The fault intersections are inferred to act as past conduits for magma and present conduits for hydrothermal solutions, and are kept open by ongoing microearthquake seismicity (Kong et al. 1992; Smith et al. 2004; R. Reves-Sohn personal communication). A neovolcanic zone occupies the western half of the axial valley characterized by constructional volcanic morphology of linear volcanic ridges and hummocks (Kleinrock and Humphris 1996) and patchy sheet flows.

Both walls of the axial valley are constructed of outward-tilted listric normal fault blocks. The east wall that hosts the TAG field is higher (2,400—3,600 m), steeper, and smoother than the west wall (2,800—3,600 m), where hydrothermal activity is absent (Karson and Rona 1990; Kleinrock and Humphris 1996). Zonenshain et al. (1989) observed sheeted dikes and recovered gabbro from mid-depth (~3,000 m) on the east wall indicating uplift of the plutonic layer of ocean crust, which they ascribed to expansion by serpentinization of the underlying peridotites of the upper mantle by circulating hydrothermal fluids accompanied by thinning of the basaltic layer of ocean crust. An axis-parallel linear magnetization low extends several kilometers northeast of the active sulfide mound over the east wall (Tivey et al. 1996). This magnetization low is modeled as a product of crustal thinning (Tivey et al. 2003), attributed either to uplift by serpentinization (Zonenshain et al.,1989), or by 4 km of horizontal extension along a normal (detachment) fault (Tivey et al. 2003). In either case, the mantle uplift and crustal thinning on a scale of kilometers are seismically and magnetically detectable exploration targets. The exothermic serpentinization reaction beneath the east wall provides a heat source to drive hydrothermal circulation (Lowell and Rona 2002), in addition to magmatic heat sources beneath the axial valley.

3 Distribution and characteristics of active and relict sulfide mounds of the TAG field

An assemblage of at least four large massive sulfide mounds in the TAG field ranges from young-hot to old-cold. The sulfide mounds are fresh where forming on the floor of the axial valley and recrystallized, silicified, and deformed where undergoing uplift in the east wall. The sulfides span a radiometrically dated age range of about 140,000 years (Lalou et al. 1995 1998). Short-wavelength (<100 m) lows in magnetic intensity measured near the seafloor within the broader magnetic low of the east wall are associated with individual active and relict sulfide mounds and are attributed to hydrothermal alteration of the magnetic mineral component in pipe-like upflow zones through the host basalts (Rona, 1978; Tivey et al. 1996). The mounds and related hydrothermal features of the TAG field are clustered in 4 zones, as follows (Figure 1; Rona et al. 1993):

High-temperature zone: The central black smoker complex of the active high-temperature sulfide mound is surrounded by lower temperature diffuse flow from large areas of the mound surface and white smokers produced by internal mixing of the high-temperature solutions with seawater (Tivey et al. 1995). The internal stratigraphy of this mound reconstructed from cores drilled on Ocean Drilling Program (ODP) Leg 158 in 1994 (Humphris et al. 1995) exhibits a classic VMS form of a feeder or stockwork zone connecting upwards to a sulfide lens (Figure 2). The lens contains a zone of sulfides with a clastic texture and sulfate (anhydrite) matrix. The clastic texture of the sulfides, similar to that in certain ancient VMS deposits like those of the Troodos ophiolite, is attributed to precipitation of the sulfate matrix from conductively heated seawater circulating through the mound, dissolution of the

sulfate when cut off from the hot water, and collapse of the sulfides (Tivey et al. 1995; Hannington et al. 1998). Radiometric dating of sulfides within the mound as a whole range in age to about 50,000 years old and record short episodes of high-temperature activity (duration to hundreds of years) alternating with longer intervening episodes of quiescence (duration thousands of years; Lalou et al. 1998; You and Bickle 1998). The multiple episodes of high-temperature hydrothermal circulation build the mound, and concentrate copper, zinc, silver and gold in the upper 10 m beneath the seafloor by the process of zone refinement. Pyrite remains as the primary mineral in the underlying volume of the 3.9 million tonne mound (Hannington et al. 1998).

Mir zone: The Mir zone lies on listric normal fault blocks of the lower east wall 1.5 km east of the active high-temperature sulfide mound and 4 km from the spreading axis. This zone is about 1 km in diameter and contains a central area of relict massive sulfides ranging in age from about 2,000 to 102,000 years old, bounded by marginal areas of low-temperature hydrothermal deposits (manganese and iron oxides, hydroxides, silicates), ranging in age up to about 140,000 years old with minor ongoing patchy diffuse flow;

Alvin zone: The Alvin zone extends about 2 km along strike on the lower east wall about 1.5 km northeast of the active high-temperature sulfide mound and 2.2 km east of the spreading axis. This zone contains inactive sulfide mounds up to 50,000 years old (Shinkai mound 2,000 to 23,000 years old; Alvin mound 50,000 years old) of comparable size to the active sulfide mound (Lalou et al., 1995). An actively venting low-temperature mound topped with low-temperature hydrothermal deposits (Shimmering mound) is also present in the Alvin zone.

Low-temperature zone: This zone is situated higher on the east wall between water depths of 2,300 m and 3,100 m 5 to 8 km east of the spreading axis and contains primarily highly fractionated manganese oxyhydroxides (~50 weight percent manganese primarily as birnessite (Thompson et al. 1985) with radiometrically dated ages up to 125,000 years; patchy low-temperature venting is present. This hydrothermal activity may be driven by heat from the inferred underlying serpentinization reactions.

A hydrothermal event at about 50,000 years B.P. correlates between the different hydrothermal zones indicating that the TAG field as a whole developed as an episodically interactive hydrothermal system over a period of at least 140,000 years. The clustered mode of occurrence of sulfide mounds in the TAG field corresponds to the clustered mode in certain ancient VMS deposits, such as the Archean Noranda deposits of eastern Canada (Knuckey et al. 1982).

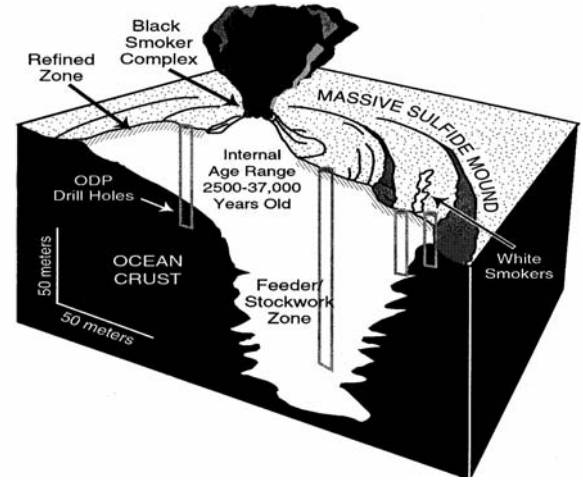

Figure 2: Cross-section of active high-temperature sulfide mound in the TAG hydrothermal field (Figure 1) showing massive sulfide lens, stockwork zone, refined zone, and ages of internal deposits based on Ocean Drilling Program Leg 158 (modified from Humphris et al., 1995).

Summary

Guidelines from multidisciplinary investigation of the TAG hydrothermal field that can be applied to exploration for modern and ancient VMS deposits include metalliferous particulates unidirectionally distributed for hundreds of kilometers from source vents, distinctive asymmetric along- and across-axis tectonic and magmatic features of the axial valley, uplift produced by serpentinization of the mantle associated with crustal thinning, diagnostic magnetic lows as signatures of crustal thinning and hydrothermal alteration, patterns of high- and low-temperature hydrothermal deposition, and spatial and temporal relations of clustering of large sulfide mounds. The crustal thinning, mantle uplift, and magnetic signatures remain with the sulfide mounds to guide exploration, as the mounds are rafted eastward by seafloor spreading.

References

Bohnenstiehl DR, Kleinrock MC (1999) Faulting and fault scaling on the median valley floor of the trans-Atlantic geotraverse (TAG) segment, ~26°N on the Mid-Atlantic Ridge, J. Geophys. Res. 104: B12: 29,351-29,364.

Edmonds HN, German CR, Green DRH, Huh Y, Gamo T, Edmond JM (1996) Continuation of the hydrothermal fluid chemistry time series at TAG and the effects of ODP drilling, J. Geophys Research 23:23:3487-3489.

Hannington MD, Galley AG, Herzig PM, Petersen S (1988) Comparison of the TAG mound and stockwork complex with Cyprus-type massive sulfide deposits, in, Herzig., P.M., Humphris, S.E., Miller, D.J., and Zierenberg, (Eds.), Proc. ODP, Scientific Results, 158, College Station, TX (Ocean Drilling Project) 389-415

Humphris S, Herzig PM, ODP Leg 158 Scientific Party (1995) The internal structure of an active sea-floor massive sulfide deposit, Nature 377: 713-716

Karson JA, and Rona PA (1990) Block-tilting, transfer fault, and structural control of magmatic and hydrothermal processes in the TAG area, Mid-Atlantic Ridge 26°N, Geol. Soc. Am. Bull. 102: 1635-1645

Kleinrock MC, Humphris SE (1996) Structural control on sea-floor hydrothermal activity at the TAG active mound, Nature 382: 149-153

Knuckey MJ, Comb CDA, Fiverin G (1982) Structure, metal zoning, and alteration at the Millenbch deposit, Noranda, Quebec, in Precambrian Sulphide Deposite, edited by Hutchinson, R.W., Spence, C.d., and Franklin, J.M., Geol. Assoc., Canada Spec. Paper 25: 255-296

Kong L, Solomon SC, Purdy GM (1992) Microearthquake characteristics of a mid-ocean ridge along axis high, J. Geophys. Res. 97: 1659-1685

Lalou C, Reyss JL, Brichet E (1998) Age of sub-bottom sulfide samples at the TAG active mound, Herzig, P.M, Humphris, SE., Miller, D.J., an Zierenberg, R.A., (Eds.), Proc. ODP Sci., Results, 158, College Station, TX, (Ocean Drilling Program) 111-117

Lalou CE, Reyss JL, and Brichet E (1995) Hydrothermal activity on a 10^5-year scale at a slow-spreading ridge, TAG hydrothermal field, Mid-Atlantic Ridge 26°N, J. Geophys. Res. 100(B9):17,855-17,862

Lowell RP, Rona PA (1988) History and geochemistry of a metalliferous sediment core from the Mid-Atlantic Ridge at 26°N, Geopys Res. Letters 29:11:10.1029/2001 GL014411, 26-1-26-4

Metz S, Trefry JH, Nelsen TA (1988) History and geochemistry of a metalliferous sediment core from the Mid-Atlantiuc Ridge at 26° N, Geochim. Cosmochim. Acta 52(10): 2369-2378

Rona PA (1978) Magnetic signatures of hydrothermal alteration and volcanogenic mineral deposits in oceanic crust, J. Volcanol., Geotherm. Res. 3: 219-225

Rona PA (1980) The TAG hydrothermal field, Mid-Atlantic Ridge crest at latitude 26°N, J. Geol. Soc. London, 137:385-402

Rona PA (1999-2000) Deep-diving manned research submersibles, Marine Tech. Soc. J. 33:4:13-25

Rona PA, Hannington MD, Raman CV Thompson G, Tivey MK, Humphris SE, Lalou C, Petersen S (1993) Active and relict seafloor hydrothermal mineralization at the TAG hydrothermal field, Mid-Atlantic Ridge, Econ. Geol. 88: 1989-2017

Rona PA, Klinkhammer G, Nelsen TA, Trefry JH, Elderfield H (1986) Black smokers, massive sulfides, and vent biota on the Mid-Atlantic Ridge, Nature 321: 33-37

Rona PA, Von Herzen RP (1996) Introduction to special section on measurements and monitoring at the TAG hydrothermal field, Mid-Atantic Ridge 26°N, 45°W, Geophys. Res. Letters 23(23): 3427-3430

Rudnicki MD (1995) Particle formation, fallout and cycling within the buoyant and non-buoyant plume above the TAG vent field, in Parson, L.M., Walker, C.L., and Dixon, D.R. (eds.), Hydrothermal Vents and Processes, Geological Society special Publication No. 87: 387-396

Shearme S, Cronan DS, Rona PA (1983) Geochemistry of sediments from the TAG hydrothermal field, MAR at latitude 26°N, Marine Geol. 51: 269-291

Smith DK, Dziak RP, Matsumoto H, Fox CG, Tolstoy M (2004) Autonomous hydrophone array monitors seismic activity at Northern Mid-Atlantic Ridge, Eos, Trans. Am. Geophys. Un. 85(1): 1, 5

Thompson G, Mottl MJ, Rona PA (1985) Morphology, mineralogy and chemistry of hydrothermal deposits from TAG area, 26°N, Mid-Atlantic Ridge, Chemical Geology 49: 243-257

Tivey MA, Rona PA, Kleinrock MC (1996) Reduced crustal magnetization beneath relict hydrothermal mound: TAG hydrothermal field, Mid-Atlantic Ridge, 26°N, Geophys. Res. Letters 23(23): 3511-3514

Tivey MA, Schouten H, Kleinrock MC (2003) A near-bottom magnetic survey of the Mid-Atlantic Ridge axis at 26°N: Implications for the tectonic evolution of the TAG segment, J. Geophys Res. 108, B5, 2277, doi:10.1029/2002JB001967

Tivey MK, Humphris SE Thompson G, Hannington MD Rona PA (1995) Deducing patterns of fluid flow and mixing within the active TAG mound using mineralogical and geochemical data, J. Geophys. Res. 100: 12,527-12, 555

You CF, Bickle MJ (1998) Evolution of an active sea-floor massive sulfide deposit, Nature 394: 668-671

Felsic pyroclastic and effusive volcanic facies hosting the Neves Corvo massive sulfide deposit, Iberian Pyrite Belt, Portugal

C.J.P. Rosa, J. McPhie
CODES, University of Tasmania, Private Bag 79, Hobart, Tasmania, 7001 Australia

J.M.R.S. Relvas
CREMINER/Dpt.Geologia, U. de Lisboa, Edifício C6, Piso 4, Campo Grande, 1749-016 Lisboa, Portugal

Z. Pereira
INETI, Apartado 89, 4466-956, S. Mamede de Infesta, Portugal

N. Pacheco
SOMINCOR, Sociedade Mineira de Neves-Corvo, AS, Mina de Neves-Corvo, 7780 Castro Verde, Portugal

Abstract. The combination of biostra- tigraphic data with the facies architecture of the Neves Corvo massive sulfide deposit allows dating of the two major volcanic events identified in the mine stratigraphy. Both volcanic episodes are represented by submarine and proximal to source vent deposits, with intrabasinal origin and rhyolitic composition. Thick pyroclastic pumice-rich facies of the late Famennian and younger lavas of the late Strunian (latest Famennian) constitute the host sequence of the massive sulfides. The hydrothermal mineralizing event occurred after the emplacement of the rhyolitic lavas.

Keywords. Felsic volcanism, palynostratigraphy, Iberian Pyrite Belt

1 Introduction

The Iberian Pyrite Belt (IPB) in the south of Portugal and Spain hosts more than 85 giant massive sulfide deposits amounting to more than 1700 million metric tonnes of sulfide ore. The deposits are hosted by a submarine felsic volcanic succession and mudstones that constitute the Upper Devonian to Lower Carboniferous Volcanic-Sedimentary Complex (VSC). Regionally this unit overlies the Phyllite-Quartzite Group (PQ) (Upper Devonian, base unknown) and is overlain by the Baixo Alentejo Flysch Group (BAFG) (Lower to Upper Carboniferous). The Neves Corvo massive sulfide deposit (Fig 1) contains more than 300 Mt of sulfides, of which100 Mt contain 3.46% Cu and 3.54% Zn and 50 Mt contain ~6% Zn. These high grades combined with 300 000 t of tin, mainly in the form of cassiterite and stannite make Neves Corvo a unique case in the belt.

Disruption of the IPB stratigraphy by low-angle thrust faults, and subsequent folding of these structures to form NW-SE or W-E trending anticlines occurred during the Variscan orogeny in the Upper Devonian-Carboniferous (Silva et al. 1990).

The depositional environment in the IPB is considered to be submarine due to the widespread presence of diverse marine fossils and abundant massive sulfide deposits. Thick intervals of black mudstone and abundant sandstone and mudstone turbidites also suggest that much of the submarine environment was below wave base.

2 Facies analysis

Reconstruction of the volcanic and sedimentary facies architecture was done using data from drill-core distributed throughout the mine area. Original primary volcanic textures are well preserved in areas where the hydrothermal alteration is negligible and away from the strongly cleaved intervals near thrust faults.

The principal volcanic facies identified at Neves Corvo are grouped into two facies associations: pumice-rich facies and coherent and monomictic rhyolite breccia facies.

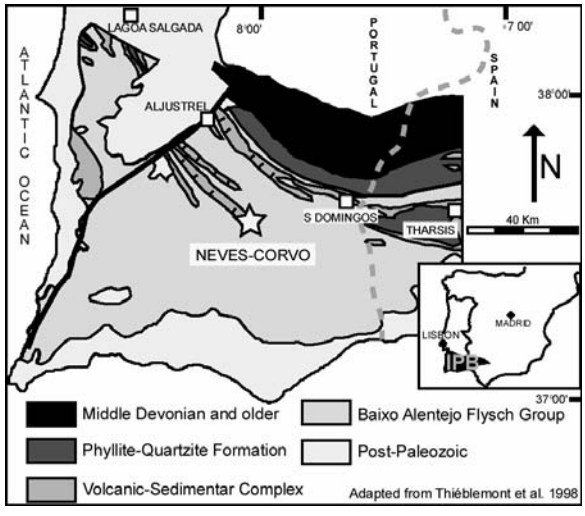

Figure 1: Location of Neves Corvo in the IPB. Inset map shows location of the IPB in the Iberian Peninsula.

Pumice-rich facies have considerable thickness (up to 60 m) and extend over the Neves Corvo mine area, overlying black mudstone. Two main facies are present: pumice breccia and pumice-crystal sandstone. There are two pumice breccia intervals: pumice breccia A is overlain by pumice breccia B.

The pumice breccia A is on average 60 m thick, has an irregular, discordant and erosive basal contact with black mudstone and is overall graded. The lower zone (average 40 m) is thick, massive, poorly sorted and polymictic, and composed of irregular and angular clasts of black mudstone, dense spherulitic rhyolite clasts, pumice, and quartz crystal fragments. The intermediate zone is on average 10 m thick, massive, finer grained than the lower zone and composed of pumice, and quartz crystal fragments. The top zone is on average 7 m thick and composed of laminated siliceous mudstone containing pumice clasts 6-10 cm across. Contacts between adjacent zones are gradational, as are contacts with the overlying sedimentary facies.

Pumice breccia B overlies pumice breccia A at an irregular and erosive or faulted contact and it is very similar in terms of internal structure and composition. The major differences are that it is thinner, on average 20 m, and it is more hydrothermally altered. Pumice breccia B also lacks black mudstone clasts in the lower zone, containing instead abundant grey siliceous mudstone clasts, similar to the mudstone forming the top zone of pumice breccia A.

Both pumice breccia A and B grade laterally into pumice-crystal sandstone. Beds of this facies are generally massive or normally graded, 0.3-1.5 m thick and intercalated with mudstones. The main components are pumice clasts, angular quartz crystal fragments, and rare mudstone and dense rhyolite clasts. Beds generally have gradational contacts but sharp contacts also occur, as well as some load casts.

Clasts in the pumice-rich facies association thought to have originally been pumice are porphyritic. They contain euhedral to sub-euhedral quartz phenocrysts up to 2 mm across, indicating a rhyolitic composition, and have a groundmass composed of fine grained phyllosilicates, quartz and feldspar. No vesicular texture is preserved in the groundmass and the clasts are lenticular and aligned parallel to bedding.

The criteria used to consider these clast as pumice are the presence of euhedral quartz phenocrysts that imply an igneous origin; the flattening parallel to bedding which indicates that they were easily compacted (presumably vesicular) in a sequence where other clasts are not flattened, and finally, because the presence of these clasts in the laminated mudstones of the top zone of the pumice breccias A and B, suggesting that the quartz-phyric clasts and mud were deposited from suspension simultaneously, and therefore had similar low densities.

Flattening of the pumice clasts probably occurred when vesicles were empty, the glassy vesicle walls were altered, so the clasts do not preserve any vesicular texture as has been described for other old successions (McPhie and Allen 2003; Gifkins et al. 2000).

The pumice clasts in the pumice breccia are probably pyroclasts, given their angular or ragged shape, high abundance and relatively fine grain size. The bedforms of the pumice breccia units are typical of deposits from high-concentration, voluminous gravity flows and water settled fall-out. In addition, the great thicknesses and lack of other facies imply rapid aggradation. Hence, we conclude that the pumice breccias are syn-eruptive pyroclastic deposits. The source vent(s) has not been located but the dominance of lapilli-size pumice and the relatively good hydraulic sorting could indicate that the vent(s) was submarine (McPhie and Allen 2003; Kano et al. 1996).

The pumice-crystal sandstone facies is considered to be the distal equivalent of the pumice breccias. The sandstone was deposited by relatively low concentration gravity flows down-current from the pumice breccias. The pumice-rich facies, although largely composed of juvenile pyroclasts, show no evidence for hot emplacement.

The coherent and monomictic rhyolite breccia facies association extends throughout the Neves Corvo area, except for the western part. This facies association overlies the pumice-rich facies association or black mudstone and is composed of three facies: coherent rhyolite, *in-situ* and clast-rotated monomictic breccia, and stratified monomictic breccia and sandstone.

Coherent rhyolite is compositionally uniform throughout the Neves Corvo area. The intervals of coherent rhyolite are up to 10 m thick and are enclosed by monomictic rhyolite breccia. Texturally, the coherent rhyolite is evenly quartz- and feldspar-phyric. Phenocrysts are 1-5 mm across, euhedral to sub-euhedral, and the quartz is frequently embayed. Groundmass textures include well preserved spherulites, perlitic cracks, rare vesicles and flow banding.

This facies has gradational contacts with the coherent rhyolite intervals. The groundmass textures and phenocryst assemblages of the clasts are identical to those of the coherent intervals. These clastic intervals are up to 250 m thick, massive, non-stratified, monomictic and poorly sorted. Most are clast-supported although matrix-supported intervals also occur. Clasts vary in size from <1 cm up to 30 cm and occur in a matrix of compositionally similar, finer rhyolite clasts and crystal fragments. Clast margins are planar or curviplanar and clast shapes are blocky, irregular or tabular. Margins of tabular clasts are generally parallel to flow banding in flow-banded clasts. In intervals of the *in-situ* monomictic breccia facies, jigsaw-fit organisation of the clasts is typical and especially

conspicuous in flow-banded domains. Intervals of the clast-rotated monomictic breccia facies can be up to 40 m thick. These intervals are relatively matrix-rich and jigsaw-fit texture is uncommon.

This facies gradationally overlies *in-situ* and clast-rotated monomictic breccias, is up to 10 m thick and crudely bedded. Beds are poorly sorted and weakly defined. Breccia and sandstone are monomictic, being composed of clasts similar in composition and texture to those in the *in situ* and clast-rotated monomictic breccias. This facies grades to overlying grey, black or green siliceous mudstone.

The coherent and monomictic rhyolite breccia facies association is typical of the products of submarine effusive silicic eruptions (McPhie et al. 1993) and corresponds to a near vent setting. Gradational contacts between all facies and their uniform composition indicate that they are genetically related. The gradation to overlying sedimentary facies suggests that the rhyolites were extrusive. The fragmentation mechanism that generated the clasts was mainly autobrecciation and quenching, with no evidence of explosivity.

The coherent facies is interpreted as the coherent interior of lavas or domes surrounded by *in-situ* to clast-rotated autoclastic breccia envelopes. The stratified facies accumulated as aprons of remobilised and resedimented autoclastic debris.

3 Age constraints

The biostratigraphy of the Neves Corvo mine was defined by Oliveira et al. (2004) based in palynomorphs and ammonoid associations from 700 samples collected in 39 drill-holes. The samples were collected from black mudstones occurring below, within or above the volcanic facies and the massive sulfides ore bodies, close to their contacts. The volcanic-sedimentary sequence extends from the late Famennian (Upper Devonian) to the late Visean (Lower Carboniferous) and the age of the sulfides is within the time span of 354.8 to 354.0 Ma, an interval that falls in the late Strunian (Upper Devonian). Integrating the age data with the facies architecture allows the following conclusions to be drawn:

1. The pumice-rich facies association is from the late Famennian and therefore older than the late Strunian (latest Famennian) coherent and monomictic rhyolite breccia facies association.
2. There is a gap of at least 1 Ma between the two volcanic episodes that corresponds to a stratigraphic hiatus.
3. The late Strunian age of the massive sulfides means they are probably contemporaneous with the emplacement of the coherent and monomictic rhyolite breccia facies association.

4 Geochemistry and mineralization

The geochemical data distinguish the two volcanic facies associations although on classification diagrams both associations are rhyolitic. Plots of immobile elements show two suites that correspond to the two main volcanic facies associations. A spider diagram of the REE also distinguishes the two facies associations. Both show a negative Eu anomaly, but the HREE trend of the pumice-rich facies association is flatter than that of the coherent and monomictic rhyolite breccia facies association. The hydrothermal activity that generated the massive sulfides and altered the volcanic-sedimentary host sequence affects all the facies with more or less intensity, regardless of the facies type. However, the morphology of the stockworks and disseminated mineralisation appears to be related with initial differences in porosity and permeability of the facies type. The pumice-rich facies association hosts disseminated, widespread and stratabound stockworks whereas the coherent and monomictic rhyolite breccia facies association hosts vein-dominated and cone-shaped stockworks in which veins have sharp contacts.

5 Conclusions

The first volcanic event occurred in the late Famennian (Upper Devonian) and generated water-supported, pumiceous pyroclastic gravity flows of rhyolitic composition. The gravity flows were probably sourced from one or more, submarine vents. Both the proximal (pumice breccias) and distal (pumice-crystal sandstones) facies lack evidence of hot emplacement.

During the late Strunian the second volcanic event took place with rhyolitic lavas originated from submarine vents emplacing on the basin. The lavas underwent intense quench fragmentation and autobrecciation. The two volcanic episodes temporarily interrupted deposition of black mud in a deep submarine setting.

In the final stages of volcanism, hydrothermal activity affected the volcanic facies and generated mineralised stockworks and massive sulfides in proximity to intrabasinal effusive volcanic centres.

Acknowledgements

This study is part of the project ARCHYMEDES (FCT-SAPIENS 2001/ 41393). E. Clavijo and F. Tornos are acknowledged for their reviews.

References

Gifkins CC, McPhie J, Allen RL (2002) Pumiceous rhyolitic peperite in ancient submarine volcanic successions. Jour. Volc. Geo. Res. 114: 181-203

Kano K, Yamamoto T, Ono K (1996) Subaqueous eruption and emplacement of the Shinjima Pumice, Shinjima (Moeshima) Island, Kagoshima Bay, SW Japan. Jour. Volc. Geo. Res. 71: 187-206

McPhie J, Allen RL (2004) Submarine, silicic, syn-eruptive pyroclastic units in the Mount Read Volcanics, western Tasmania: Influences of vent setting and proximity on lithofacies characteristics, In: Explosive Subaqueous Volcanism (White JL, Smellie JL, Clague DA, eds): AGU 245-258

McPhie J, Doyle MG, Allen RL (1993) Volcanic Textures: A guide to the interpretation of textures in volcanic rocks. Hobart: CODES, University of Tasmania 198

Oliveira JT, Pereira Z, Carvalho P, Pacheco N, Korn P (2004) Stratigraphy of the tectonically imbricated lithological succession of the Neves Corvo mine area, IPB, Portugal. Mineralium Deposita 39: 422-436

Silva JB, Oliveira JT, Ribeiro A (1990) Structural Outline of the South Portuguese Zone. In: Pre-Mesozoic Geology of Iberia (Dallmeyer RD, E. MG, eds). Berlin: Springer-Verlag, 348-362

Dufrenoysite and marumoite from the Okoppe Mine, Japan

M. Shimizu, Y. Ishizaki, T. Honma
Department of Earth Science, University of Toyama, 3190 Gofuku, Toyama 930-8555, Japan

S. Matsubara, R. Miyawaki
Department of Geology, National Science Museum, 3-23-1 Hyakunin-cho, Shinjuku, Tokyo 169-0073, Japan

Abstract. Dufrenoysite and marumoite (IMA 1998-004) from high sulfidation-type epithermal Cu-Pb-Zn disseminated-massive sulfide deposits of the Okoppe mine, Japan are reported based on their chemical compositions and powder XRD patterns. Marumoite from Okoppe is the second occurrence.

Keywords. Dufrenoysite, marumoite, jordanite, Okoppe mine, high sulfidation type, epithermal

1 Introduction

High sulfidation-type epithermal Cu-Pb-Zn disseminated-massive sulfide deposits of the Okoppe mine are located in Ohma Town, Shimokita-gun, Aomori Prefecture, northern Japan. There are two localities of jordanite in Japan; the Yunosawa mine also in Aomori Prefecture in addition to the Okoppe mine. Tsugaruite and gratonite are observed from the Yunosawa mine, and some of Pb-As-S sulfosalt minerals from the Okoppe mine are here reported. Arsenic is one of characteristic elements enriched in hydrothermal solution in back-arc basin (e.g., Fouquet et al., 1991), which is different from that in oceanic ridges.

2 Occurrence

The deposits of the Okoppe mine are embedded in the altered dacitic to andesitic rocks of the "Green Tuff" of middle to late Miocene age. Argillic alteration of pyrophyllite, kaolinite, sericite and less chlorite is dominated in the deposits whereas propylitic and smectite alteration occurs far from them.

The ores are composed of pyrite, enargite, chalcopyrite, barite and small amounts of jordanite, wurtzite, and covellite. Some of Pb-As-S sulfosalt minerals also occur as acicular crystals of lead-gray color associated with jordanite-barite (J type) or pyrite (P type). Hydrothermal activity here in a back-arc basin (Japan Sea) is characterized by low pH and Ba-, As-, Pb-rich solutions.

Table 1: Chemical compositions for dufrenoysite, marumoite and baumhauerite

	1	1'	2		2'	3	3'	4	4'	5	6
Wt.%											
Pb	55.08	53.75 ~ 57.09	51.82		51.64 ~ 52.09	57.42	57.20	47.5	51.38	47.1	50.92
Ag	0.12	0.03 ~ 0.27	0.13		0 ~ 0.26					1.4	0.44
Tl	0.17	0 ~ 0.36	0.14		0 ~ 0.26			0.8		0.5	0.83
As	20.99	20.15 ~ 21.98	22.75		22.46 ~ 23.12	20.89	20.68	27.9	24.77	26.8	23.42
Sb	0.14	0.04 ~ 0.29	1.37		1.10 ~ 1.64						0.28
S	23.12	22.65 ~ 23.56	23.25		23.06 ~ 23.35	22.55	22.12	24.6	23.85	23.9	23.46
total	99.62		99.46			100.86	100	100.8	100	99.7	99.35
Atomic Proportions											
Pb	14.74		12.42	31.74		15.76	16	10.7	12	10.9	30.91
Ag	0.06		0.06	0.15						0.6	0.51
Tl	0.04		0.04	0.09				0.2		0.1	0.51
As	15.54		15.08	38.54		15.86	16	17.4	16	17.3	39.30
Sb	0.06		0.56	1.42							0.46
S	40		36	92		40	40	36	36	36	92

1; Dufrenoysite from the Okkope mine, Aomori Prefecture.
2; Marumoite from the Okkope mine, Aomori Prefecture.
3; Dufrenoysite from Binntal, Switzerland (Palache et al., 1946).
4; Baumhauerite from Binntal, Switzerland (Pring et al., 1990).
5; Baumhauerite-2a from Binntal, Switzerland (Pring et al., 1990).
6; Marumoite from Binntal, Switzerland (Ozawa, personal communication).
1'; range
2'; range
3'; $Pb_{16}As_{16}S_{40}$
4'; $Pb_{12}As_{16}S_{36}$

This page intentionally blank

Table 2: X-ray powder diffraction data for dufrenoysite

1				2			1				2		
d_{obs}	d_{calc}	I	$h\,k\,l$	d	I	$h\,k\,l$	d_{obs}	d_{calc}	I	$h\,k\,l$	d	I	$h\,k\,l$
7.69		9	B				2.405	2.402	10	3 3 1			
7.53	7.54	9	1 1 0	7.50	10	1 1 0	2.346	2.346	30	1 $\underline{10}$ 1	2.36	60	1 $\underline{10}$ 1
7.02	7.01	7	0 2 1				2.310	2.314	10	2 9 0			
6.71	6.72	7	1 2 0	6.81	20	1 2 0	2.262	2.263	15	1 9 $\bar{2}$			
5.81	5.80	7	1 3 0	5.99	10	1 3 0	2.239	2.241	16	3 6 0			
4.98	4.98	12	1 4 0	4.98	20	1 4 0	2.216	2.218	24	3 0 $\underline{2}$	2.23	60	3 1 2
4.32	4.31	11	1 5 0				2.164	2.168	18	3 6 $\bar{1}$	2.16	20	2 $\underline{10}$ 0
4.26	4.27	42	1 4 1	4.27	20	1 4 1		2.161		3 6 1			
4.12	4.13	17	0 1 2	4.11	20	0 1 2	2.137	2.138	14	3 7 0			
3.945	3.942	23	2 0 0	3.93	10	2 0 0	2.090	2.091	20	0 0 4	2.09	30	2 $\underline{10}$ 1
3.894	3.897	31	2 1 0				2.066	2.068	44	3 7 1			
3.854		24	B					2.064		0 2 4			
3.805		48	B				2.033	2.035	34	3 8 0	2.03	30	1 1 $\bar{4}$
3.767	3.766	100	1 6 0	3.74	100	1 0 $\bar{2}$	2.027	2.028	27	2 9 $\bar{2}$			
3.681	3.684	23	1 0 $\underline{2}$				1.972	1.971	20	4 0 0			
3.576	3.576	30	2 0 $\bar{1}$	3.56	50	2 0 1	1.955		13	B			
3.477		17	B				1.948	1.948	13	4 2 0			
3.437	3.438	21	1 6 $\bar{1}$				1.926	1.925	30	1 4 4			
3.401	3.401	25	1 3 $\bar{2}$	3.40	50	1 3 2	1.921	1.921	33	4 3 $\underline{0}$			
3.334	3.330	36	1 7 0				1.907	1.908	16	3 7 $\bar{2}$	1.910	40	4 1 1
3.220	3.215	63	0 8 0	3.21	60	1 4 2		1.906		3 0 $\underline{3}$			
3.125	3.125	36	2 4 $\bar{1}$				1.873	1.873	10	3 3 $\bar{3}$			
3.100	3.097	18	1 7 $\bar{1}$				1.855	1.854	15	2 8 3			
3.004	3.007	56	1 5 $\bar{2}$	3.00	90	1 5 2	1.850	1.848	15	2 1 $\bar{4}$			
2.899	2.902	34	2 6 $\underline{0}$	2.90	50	2 6 0	1.832	1.831	13	1 6 $\bar{4}$			
2.868	2.861	21	2 1 $\bar{2}$				1.825	1.826	14	1 6 4	1.831	40	3 4 3
2.833	2.841	16	2 1 2					1.824		2 2 $\underline{4}$			
2.790	2.791	23	2 2 2	2.80	40	0 0 3	1.808	1.811	13	2 3 $\bar{4}$			
2.763	2.760	30	0 7 $\underline{2}$				1.793	1.794	18	3 $\underline{10}$ 1			
2.730	2.729	30	2 3 $\bar{2}$				1.787	1.787	17	3 5 $\underline{3}$			
2.698	2.704	58	0 9 1	2.70	80	1 9 0	1.772	1.773	15	1 7 $\bar{4}$			
2.615	2.615	16	3 1 0				1.753	1.753	10	0 8 4			
2.572	2.572	20	0 $\underline{10}$ 0	2.58	10	1 2 3	1.741	1.742	20	3 6 3	1.746	10	3 6 3
2.486	2.491	10	3 1 1					1.741		4 3 $\underline{2}$			
2.443	2.445	8	1 $\underline{10}$ 0	2.44	10	1 8 $\bar{2}$	1.703	1.703	14	4 7 $\bar{1}$			

1: Dufrenoysite + "baumhauerite (B)" from Okkope mine. ***a*** 7.885 (1), ***b*** 25.72 (1), ***c*** 8.365 (1) Å, ***β*** 90.4 (1)°
2: Dufrenoysite from Binntal, Switzerland (ICDD 10-453). ***a*** 7.88, ***b*** 25.85, ***c*** 8.41 Å, ***β*** 90.5°.

In polished sections, in plane-polarized light, the two minerals (dufrenoysite and marumoite) are weakly bireflectant, weakly pleochroic, and strongly anisotropic similar to jordanite.

Homogenization temperature of fluid inclusions in barite from the mine ranges from 300 to 170°C.

3 Chemical data

Chemical analyses were carried out by means of an electron microprobe using the following standards: synthetic PbS (Pb-Mα), Cu_3AsS_4 (As-Lα), ZnS (S-Kα), $AgBiS_2$ (Ag-Lα), $Cu_{10}Fe_2Sb_{1.4}As_{2.6}S_{13}$ (Sb-Lα) and lorandite (Tl-Lα). The analyses of jordanite give a composition $Pb_{14}(As,Sb)_6S_{23}$. The average of 15 analyses of Pb-As-S sulfosalt minerals associated with jordanite-barite (J type) is: Pb 55.08, Ag 0.12, Tl 0.17, As 20.99, Sb 0.14, S 23.12, total 99.62 wt.%, and those (6 analyses) associated with pyrite (P type) are: Pb 51.82, Ag 0.13, Tl 0.14, As 22.75, Sb 1.37, S 23.25, total 99.46 wt.%, shown in Table 1. The empirical formulae based on S = 5 and S = 92 are: $(Pb_{1.84}Ag_{0.01}Tl_{0.01})_{1.86}(As_{1.94}Sb_{0.01})_{1.95}S_{5.00}$ and $(Pb_{31.74}Ag_{0.15}Tl_{0.09})_{31.98}(As_{38.54}Sb_{1.42})_{39.96}S_{92.00}$, respectively. They can be simplified to $Pb_2As_2S_5$ and $Pb_{32}As_{40}S_{92}$, respectively.

4 X-ray crystallography

Powder XRD patterns for J- and P-type samples (Tables 2 and 3) were obtained but both samples are thought to be a mixture of dufrenoysite and a small amount of "baumhauerite", and that of "baumhauerite" or marumoite (IMA 1998-004) and a small amount of dufrenoysite, respectively. The cell parameters for defrenoysite refined from the data are: a = 7.885(1), b = 25.72(1), c = 8.365(1) Å, and β = 90.4(1)°.

5 Discussion and conclusion

It is difficult to distinguish the powder XRD patterns of baumhauerite, baumhauerite-2a and marumoite, probably because they can easily form mixtures in the lattice order and a large single crystal is generally very rare. They seem to be complicated mixtures with lattice defects. It is concluded that two Pb-As-S sulfosalt minerals, dufrenoysite and marumoite occur to the exclusion of jordanite in the Okoppe mine, Japan as products of typical hydrothermal activity in a back-arc basin (Japan Sea).

Acknowledgements

Mr. Shizuo Tamura and Mr. Tohru Shino are thanked for their help during the field survey.

Reference

Fouquet YU, Stackelberg V, Charlou JL, Donval JP, Foucher J P, Erzinger J, Herzig P, Muche R, Wiedicke M (1991) Hydrothermal activity in the Lau back-arc basin: Sulfides and water chemistry. Geology 19: 303-306

Trace and rare earth element chemistry of garnet and apatite as discriminant for Broken Hill-Type mineralization, Namaqua Province, South Africa

Marcel Stalder, Abraham Rozendaal
Department of Geology, University of Stellenbosch, Private Bag X1, Matieland 7602, South Africa

Abstract. This paper reports trace and rare earth element data of garnet and apatite from the Broken Hill-type Gamsberg Zn-Pb deposit and several occurrences of Fe-rich but base metal sulphide-poor metahydrothermal rocks in the Namaqua Province of South Africa. Garnet and apatite within ore-bearing assemblages at Gamsberg are characterised by a prominent positive Eu anomaly, which is not developed in metahydrothermal host rocks at Gamsberg and the investigated ferruginous rocks in the Namaqua Province. The positive Eu anomaly is interpreted as a premetamorphic signature related to the initial ore-forming fluids. It indicates that relatively hot (200-250°C) and reduced metal-rich brines were responsible for the emplacement of the ores. This distinct ore-related signature may serve as geochemical discriminant in the exploration for Broken Hill-type deposits.

Keywords. Broken Hill-type deposits, Namaqua Province, rare earth elements, indicator minerals, garnet, apatite

1 Introduction

The rapid development of micro-analytical techniques such as laser ablation ICP-MS and PIXE in recent years has opened up new possibilities for the exploration of Broken Hill-type (BHt) deposits (Walters 2002). In particular, geochemical signatures of certain indicator minerals (e.g. garnet, gahnite) have previously been used as guides to mineralisation (Schwandt et al. 1993, Spry et al. 2000, 2004). Of vital importance to this approach, however, is the identification and characterisation of geochemical discriminants that allow to differentiate between minerals in BHt ore systems and those in less prospective rock types, such as Algoma-type iron formations and pegmatites, which commonly occur in the same Proterozoic terranes.

In this paper, we present preliminary trace and REE data of garnet and apatite from the Gamsberg deposit and from Fe-rich but base metal sulphide-poor metahydrothermal rocks that occur throughout the Namaqua Province. The objective of the study is to compare and contrast the trace and REE patterns from the different localities, with the aim of identifying geochemical signatures that are characteristic for BHt deposits. Garnet and apatite were particularly suited for this approach, since they readily incorporate REE and form a common constituent of ores and metahydrothermal host rocks at the Gamsberg deposit and the regionally developed ferruginous metahydrothermal rocks.

2 Geological background

The study area is situated in the central Namaqua Province of South Africa (Fig. 1). The dominant rock types in the area belong to a late PalaeoProterozoic (2000 – 1600 Ma) supracrustal succession of multiply deformed and metamorphosed sedimentary and interbedded volcanic rocks (Bushmanland Group), which overlie a suite of granitic gneiss. In the Aggeneys-Gamsberg area, four major BHt deposits are present that are intimately associated with complex assemblages of Fe-Mn-Ca-rich metahydrothermal rocks. Similar although more Fe-rich metahydrothermal rocks (hereafter referred to as iron formations) are present at various localities in the Namaqua Province, but are not associated with economic concentrations of base metals (Rozendaal 1982). The present study focused on two specific occurrences of iron formations in the Namaqua Province, namely Koeris and Lemoenpoort (Fig. 1).

2.1 Gamsberg ore body and metahydrothermal host rocks

The Gamsberg ore deposit (150 Mt at 7% Zn, 0.5% Pb) is the most easterly of four giant BHt deposits in the area, and is interpreted as the metamorphosed product of synsedimentary to early syndiagenetic submarine mineralisation (Stalder and Rozendaal 2004). The ore body occurs in the northern hinge zone of a large sheath-fold structure and consists of a lower unit of metapelite-hosted ore, a central horizon of phosphorite-hosted ore, and an upper unit of chemogenic garnet-apatite ore. These Fe- and base metal sulphide-rich rocks are enveloped by subeconomic but mineralised metahydrothermal rocks that are interpreted as metamorphosed chemical sediments, including Fe-Mn-Ca-rich silicate and silicate-carbonate rocks, magnetite-quartz-apatite rocks and quartz-hematite-gahnite rocks (Stalder and Rozendaal 2004, 2005).

Garnet forms a common component of all rock types in the mineralised horizon except metapelite-hosted ore. It occurs as small- to medium-grained porphyroblasts or as massive monomineralic masses. Some Mn-rich rocks may be composed almost entirely of garnet ('garnetites'). Apatite forms a characteristic minor component of the Gamsberg ores and metahydrothermal host rocks. In phos-

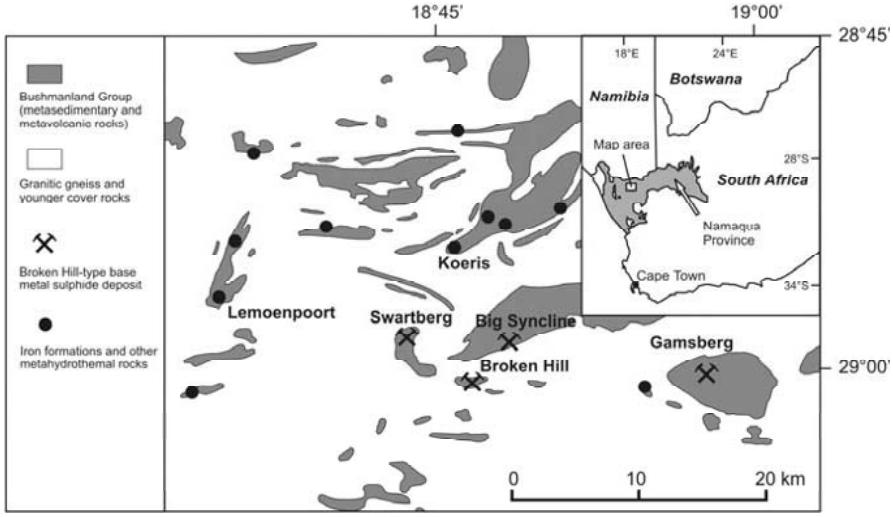

Figure 1: Locality map showing the distribution of BHt deposits and Fe-rich metahydrothermal rocks in the central Namaqua Province (modified from Rozendaal 1982).

phorite-hosted ore, it occurs as recrystallised and zoned nodules (10 – 30 mm in diameter) that are interpreted as products of early diagenesis (Stalder and Rozendaal 2004). In garnet-apatite ore and metahydrothermal host rocks, apatite occurs as small rounded grains (< 300 μm) or coarse euhedral crystals (< 2 mm), which may in places be concentrated in monomineralic layers.

2.2 Iron formations at Koeris

At Koeris, a complex sequence of ferruginous metapelite and interbedded iron formation is confined to a unit of aluminous biotite schist. Stratigraphically, the iron formation is not equivalent to the Gamsberg ore horizon, but appears to be interbedded with the aluminous schist that underlies the Gamsberg ore body (Rozendaal 1982). The iron formation occurrence is present as large lensoid bodies varying from 1 to 80 m in thickness and 1 to 500 m in continuous strike length. Mineralogically, it is dominated by medium- to coarse-grained poikiloblastic garnet in association with coarse acicular amphibole and variable concentrations of quartz, clinopyroxene, olivine and apatite. Magnetite is generally only a minor component, but some banded rocks may contain up to 20% magnetite in association with anomalous apatite. The latter occurs as rounded to euhedral grains ranging in size up to 500 μm.

2.3 Iron formations at Lemoenpoort

Iron formations at the Lemoenpoort synform are present as impersistent lenses, up to 15 m thick, within a biotite-sillimanite schist that overlies a unit of white quartzite. The iron formations are mineralogically diverse and display abrupt lateral and vertical variation in silicate, oxide and sulphide mineralogy. In the northern limb of the Lemoenpoort structure, the iron formations consist of fine-grained and well laminated magnetite-garnet rocks, which grade laterally into poorly banded amphibole-garnet-quartz rocks with variable amounts of olivine, biotite, apatite, magnetite and Fe sulphides. Iron formations in the southern part of the synform consist of well-banded garnet-quartz-magnetite rocks, magnetite-quartz-garnet-amphibole and garnet-amphibole-quartz rocks, which locally contain lenses of pyrite-rich quartzite.

3 Geochemistry

3.1 Composition of garnet and apatite

The composition of garnet from Gamsberg, Koeris and Lemoenpoort in general closely reflects the bulk chemical composition. At Gamsberg, most assemblages contain spessartine-almandine garnet, but in more Ca-rich rocks the garnet may be enriched in andradite or grossular. Garnet in oxidised assemblages is predominantly andradite-calderite, with variable concentrations of spessartine (Stalder and Rozendaal 2005). In comparison to garnet from Gamsberg, garnet from Koeris and Lemoenpoort is more Fe-rich and dominated by the almandine component. Apatite from Koeris and Lemoenpoort is close to stoichiometric fluorapatite. At Gamsberg, apatite may be enriched in MnO (up to 5.50 wt.%), FeO (up to 2.09 wt.%) and PbO (up to 7.76 wt.%).

3.2 Trace and rare earth element composition

The REE patterns of garnet and apatite from selected assemblages is shown in Figure 2. Garnet in ore-bearing assemblages at Gamsberg is characterised by enrichment of heavy REE (HREE) relative to light REE (LREE), and the presence of a positive Eu anomaly (Fig. 2a).

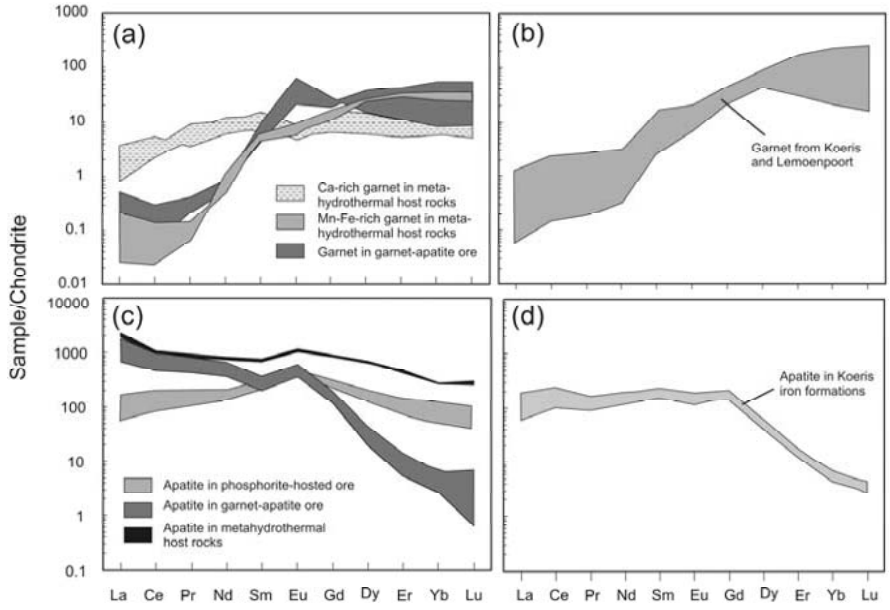

Figure 2: Chondrite-normalised REE patterns of garnet and apatite **a** Garnet from Gamsberg **b** Garnet from Koeris and Lemoenpoort **c** Apatite from Gamsberg **d** Apatite from Koeris.

Spessartine-almandine garnet in base metal sulphide-free host rock assemblages displays a similar pattern but lacks the positive Eu anomaly. Calcium-rich garnet is characterised by enrichment in LREE, therefore displaying a relatively flat pattern with no or a slight negative Eu anomaly. In comparison, garnet from Koeris and Lemoenpoort is characterised by LREE-depleted, HREE-enriched patterns with no Eu anomaly, similar to garnet in other regionally metamorphosed terranes (Fig. 2b, Grauch 1989). Garnet from ore-bearing assemblages at Gamsberg is enriched in Zn and V, but depleted in the relatively immobile elements Ti and Zr compared to garnet in Gamsberg host rock assemblages and iron formations at Koeris and Lemoenpoort.

Apatite from Gamsberg shows significant variation in the degree of fractionation between LREE and HREE. The REE patterns range from strongly LREE-enriched, HREE-depleted to middle REE enriched, concave-down patterns (Fig. 2c). Similar to garnet, apatite in ore-bearing assemblages and proximal host rocks is characterised by a positive Eu anomaly. Preliminary data from Koeris indicates that apatite displays a relatively flat pattern from La to Gd, strong depletion in the HREE and a small negative Eu anomaly (Fig. 2d).

4 Discussion and conclusions

The trace and REE data illustrate that there is a positive Eu anomaly in garnet and apatite from ore-bearing assemblages at Gamsberg. However, this pattern is not developed in metahydrothermal host rocks that envelop the deposit, nor in base metal sulphide-poor iron formations that occur at various stratigraphic levels in the Bushmanland Group. The positive Eu anomaly indicates that relatively hot (200-250°C) and reduced hydrothermal fluids were responsible for formation of the Gamsberg ores, since reduction of Eu^{3+} to Eu^{2+} only takes place at temperatures above ca. 200°C (Sverjensky 1984). Such fluids are capable of transporting significant concentrations of Zn and Pb in solution (e.g. Cooke et al. 2000). The metahydrothermal host rocks that envelop the Gamsberg deposit are interpreted to have formed from lower temperature Fe-Mn-rich fluids that pre- and postdated base metal sulphide deposition. The iron formations at Koeris and Lemoenpoort probably formed from fluids with similar characteristics, suggesting the presence of a regionally active low-temperature hydrothermal system and periodic pulses of Fe- and Mn-rich metalliferous brines. Only at a specific point in the development of the Bushmanland Group were the basinal and brine characteristics conducive for the precipitation of major amounts of base metals and resulted in deposition of the four BHt deposits at a comparable stratigraphic level. This ore-forming event has been preserved as a geochemical indicator in the form of a positive Eu anomaly in ore-related minerals such as Mn-Fe-rich garnet and apatite. The positive Eu anomaly, however, is only developed in the immediate ore environment, which limits the use of REE patterns as a regional scale vector to ore. Potential applications for exploration arise from the interpretation of trace and REE signatures in resistate heavy minerals in stream sediment samples. The presence of positive Eu anomalies in such minerals should be regarded as high-priority indicator and can help to identify prospective terranes hosting BHt or related ore systems.

References

Cooke DR, Bull SW, Large RR, McGoldrick PJ (2000) The importance of oxidized brines for the formation of Australian Proterozoic stratiform sediment-hosted Pb-Zn (Sedex) deposits. Economic Geology 95: 1-18.

Grauch RI (1989) Rare earth elements in metamorphic rocks. In: Lipin, B, McKay, GA (eds), Geochemistry and Mineralogy of Rare Earth Elements. Reviews in Mineralogy 21: 147-167.

Rozendaal A (1982) The petrology of the Gamsberg zinc deposit and the Bushmanland iron formations with special reference to their relationships and genesis. PhD thesis (unpublished), University of Stellenbosch

Schwandt CS, Papike JJ, Shearer K, Brearley AJ (1993) A SIMS investigation of REE chemistry of garnet in garnetite associated with the Broken Hill Pb-Zn-Ag orebodies, Australia. Canadian Mineralogist 31: 371-379.

Spry PJ, Heimann A, Messerly JD, Houk RS, Teale GS (2004) Discrimination of metamorphic and metasomatic processes at the Broken Hill lead-zinc-silver deposit, Australia: rare earth element signatures of garnet in garnet-rich rocks. Proceedings of the Annual Geological Society of America meeting 2004, Denver

Spry PJ, Peter JM, Slack JF (2000) Meta-exhalites as exploration guides to ore. In: Spry PG, Marshall B, Vokes FM (eds), Metamorphosed and Metamorphogenic Ore Deposits. Reviews in Economic Geology 11: 163-201.

Stalder M, Rozendaal A (2004) Apatite nodules as indicators of depositional environment and ore genesis for the mid-Proterozoic Broken Hill-type Gamsberg Zn-Pb deposit, Namaqua Province, South Africa. Mineralium Deposita 39: 189-203

Stalder M, Rozendaal A (2005) Calderitic garnet and franklinitic spinel in amphibolite-facies hydrothermal sediments, Gamsberg Zn-Pb deposit, Namaqua Province, South Africa. Canadian Mineralogist (in press)

Sverjensky DA (1984) Europium equilibria in aqueous solution. Earth and Planetary Science Letters 67: 70-78.

Walters SG (2002) Advances in micro-analytical techniques – new exploration applications using indicator minerals. In: Robb, LJ, Montjoie, R (eds), Proceedings of the 11th Quadrennial IAGOD Symposium and Geocongress 2002, Geological Society of Namibia, Windhoek, CD-Rom

The effect of weathering on reflectance spectra of hydrothermal white micas and chlorites: Implications for alteration mapping

S. Ehara Suryantini
Department of Earth Resource Engineering, Kyushu University, 6-10-1 Hakozaki, Higashi-ku, Fukuoka 812-8581, Japan

F.J.A. van Ruitenbeek, F.D. van der Meer
Department of Earth System Analysis, International Institute for GeoInformation Science and Earth Observation (ITC) P.O. Box 6, Hengelosestraat 99, 7500 AA Enschede, The Netherlands

Abstract. Reflectance spectra of fresh and weathered rock were compared in order to determine the effect of weathering on hydrothermal white mica and chlorite. A total of 46 rock samples from the Panorama Volcanic Massive Sulphide (VMS) District in Australia were analyzed. The study area lies in an arid area and the degree of weathering is low. The reflectance spectra from fresh and weathered rocks were analysed for mineralogical composition and spectral characteristics.

The results show that the spectral characteristics of the hydrothermally altered rocks were modified during weathering. Chlorite disappears during weathering while white micas persist. Newly formed minerals are halloysite and Fe-(hydr)oxides. The exact wavelength position of the main absorption feature of white micas near 2200 nm, which is a measure of their chemical composition, shifts due to weathering. This wavelength shift depends on the wavelength position in the unweathered rock. Three different wavelength ranges, reflecting different white mica species in unweathered rock, have been identified. In each range, weathering processes have a different effect on the absorption wavelength. During weathering, the absorption wavelength of Al-rich white mica (having an absorption wavelength < 2198 nm) shifts toward a longer wavelength of 2200-2202 nm. That of Al-poor white mica (having an absorption wavelength > 2208 nm) shifts toward a shorter wavelength of 2203-2205nm. This can be explained as a change in composition of the micas or a changing mineralogy, i.e. an increase in halloysite. The absorption wavelength of white mica of intermediate Al-content (having an absorption wavelength between 2198 and 2208 nm) does not change during weathering, indicating that this white mica is unaffected by weathering.

We conclude that white micas are potentially useful indicators for alteration mapping using remote sensing methods since it survives low degrees of weathering. However care has to be taken when interpreting the wavelength position of its main absorption feature since weathering modifies it. Chlorite is potentially less useful for mapping alteration since it disappears during weathering.

Keywords. Reflectance spectra, alteration mapping, chlorite, white mica, weathering

1 Introduction

The application of Short Wave Infrared Reflectance (SWIR) spectroscopy for alteration mapping has been widely used in mineral exploration (Herrman et al. 2001; Sun et al. 2001). Reflectance spectra can be obtained using a field portable spectrometer or by airborne remote sensing.

Alteration mapping with airborne remote sensing is most successful in areas with low degrees of weathering. However, in these areas, the detection of spectra of alteration minerals is hampered by weathering products. In this research the effect of weathering on reflectance spectra of white micas (such as illite, muscovite, and phengite) and chlorite is investigated. These minerals are key minerals for detection of hydrothermal alteration facies that are related to, for example, Volcanogenic Massive Sulphide (VMS) deposit forming processes. The study area is the Panorama VMS District in Australia, which includes the Kangaroo Caves and Sulphur Springs deposits. These VMS deposits are hosted by Archean greenstone sequences and alteration assemblages include chlorite-quartz, sericite-quartz, feldspar-sericite-quartz, and least altered rocks (Brauhart et al. 1998). The degree of weathering of the rocks is low and the climate is arid. Weathering processes have formed a thin layer of clay and iron oxides several millimeters thick that have accumulated on the surface of the rocks.

The results of this research help to: (1) improve the identification of minerals and mineral composition from remote sensing spectral imagery, and (2) identify zones of alteration related to VMS mineralization. The objective of the research is two fold: (1) to examine spectral difference between weathered and fresh rock in the 400-2500 nm wavelength region (commonly used in spectral remote sensing), and (2) to identify what minerals, that contribute to the spectral signal, were formed due to weathering.

2 Methodology

From a total of 46 rock samples that represent various lithologies and alteration styles in the study area, reflectance spectra were obtained using an ASD Filedspec-Pro spectrometer. A weathered and a fresh surface were measured for each rock sample. The reflectance spectra were interpreted in terms of mineral composition and mineral chemistry using the software program The Spectral Geologist (TSG), version 3. The reflectance spectra of unweathered and weathered rock faces were compared and the effect of weathering was assessed.

The mineral identification was conducted automatically by the TSG software and is based on spectral matching with library spectra. The software identifies a maximum of two minerals, assigns relative weights to the minerals, and an error of matching. The weight reflects the relative proportion of one mineral to another and is influenced by the distribution of the minerals and the grain size in the samples. Thus it does not refer to the abundance of the mineral in the samples. The error shows the level of confidence of the mineral identification. The results were crosschecked by comparison with a spectral library (USGS and ASTER spectral library). Thin sections of selected rock samples were studied to validate the mineralogical results.

The following spectral characteristics were studied: (1) the shifting of wavelength positions of diagnostic absorption features; and (2) the shape of diagnostic absorption and/or reflection features, such as the relative depth of absorption or relative peak of reflectance, the width of features and deflection in main absorption features.

Shifting of wavelength positions of diagnostic absorption features represents the change of compositional variation of minerals (Duke, 1994) or the formation of new minerals or the disappearances of the existing minerals. Wavelength shifting together with the appearance of an inflection in the main Al-OH absorption feature in, for instance, white mica indicates the formation of new clay minerals. The variation in depth and width of absorption or reflectance feature may reflect the variation in crystallinity or the grain size or the relative abundances of the mineral (Pontual, et al. 1997).

We studied absorption features in the SWIR that are related to white micas, chlorites, and clay minerals. Figure 1 provides a brief overview of the diagnostic wavelength of white mica (illite and muscovite), chlorite and halloysite. The diagnostic absorption feature of white mica is centered near 2200 nm. Muscovite has a shallow or weak water (H_2O) absorption depth near 1900 nm. In illites, this H_2O absorption feature is commonly deeper (Figure 1a and 1b) (Pontual et al. 1997).

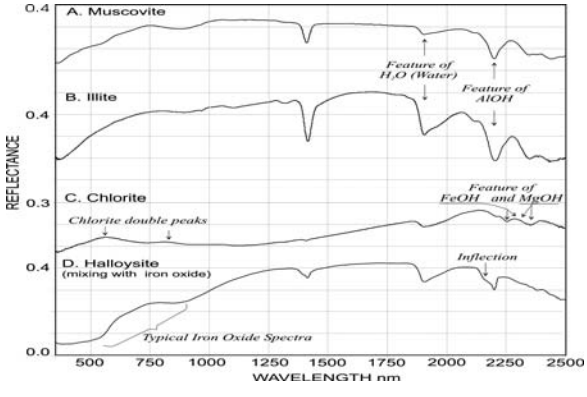

Figure 1: Reflectance spectra of muscovite (a), illite (b), chlorite (c) and halloysite mixed with Fe-(hydr)oxides (d).

Chlorite spectra show absorption features between 2300 and 2360 nm related to Mg-OH bonds and between 2230 and 2300 nm related to Fe-OH bonds (Pontual et al., 1987). The wavelengths of these absorption features increase as the iron content of chlorite increases. Other absorption features occur in VNIR centered near 400-450 nm, 700 nm, 900 nm, 1100 nm and 1400 nm. The absorption near 400-550 nm often occurs as a slope near 550 nm toward ultra violet (Clark and King, 1989). Consequently, chlorite spectra form double peaks or high reflectance centered near 550 nm and 800 nm (Fig. 1c).

Halloysite spectra show a double Al-OH absorption feature centered near 2166 nm and 2206 nm (Figure 1d). The feature at 2166 nm is sometimes only present as an inflection point.

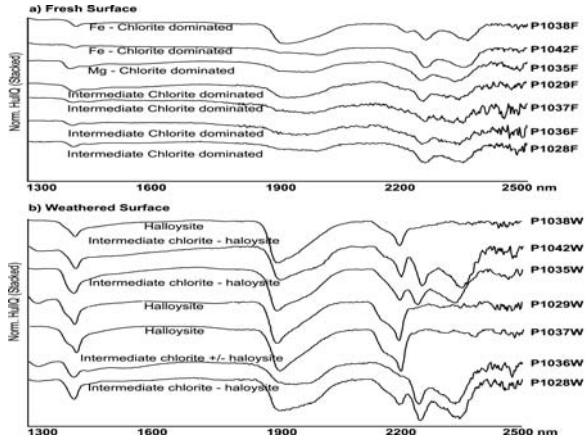

Figure 2: Reflectance spectra of chlorite containing rock.

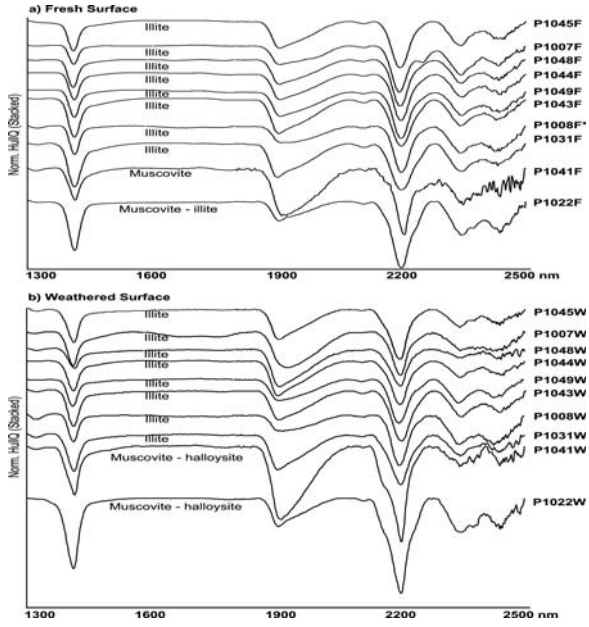

Figure 3: Reflectance spectra of white mica containing rock.

3 Results and discussion

The results show that weathering modifies the spectral characteristic of the hydrothermally altered rocks. The change in spectral modification reflects both mineralogical changes and compositional changes of minerals. The following mineralogical changes take place due to weathering. Chlorite that dominates in unweathered chlorite-quartz or least altered rock disappears.

This is apparent by the extinction of Fe-OH and Mg-OH related absorption features in weathered rock. In these rocks, illite and halloysite are formed as a result of weathering which is indicated by the appearance of an inflection point near the 2156-2190 nm and an absorption feature near 2200 nm, respectively (Fig. 2). However, in some cases, chlorite persists in the weathered surfaces. Microscopic study in thin sections shows that the weathering products occur in a patchy arrangement and they do not cover the entire weathered surface leaving some of the chlorite exposed. The double reflectance peaks of chlorite in the VNIR range of the spectra disappear and are replaced by typical iron oxide reflectance spectra.

In unweathered rock where white micas dominate, the reflectance spectra, such as in sericite-quartz, feldspar-sericite-quartz, and some least altered rock, the main absorption feature near 2200 nm related to Al-OH bond persists after weathering (Fig. 3). Where only muscovite is present in the unweathered rock, halloysite is formed as a weathering product.

Where only illite is present, illite persists after weathering. Weathering reduces the average reflectance values (or brightness) and enhances the water absorption feature due to the formation of Fe-(hydr)oxides and clay minerals, respectively. Fe-(hydr)oxides are formed mainly at the expense of mafic minerals, such as chlorite.

In fresh rock where both chlorite and white micas are present, such as in some least altered rocks (Fig. 4), weathering destroys chlorite whereas illite and muscovite persist. Newly formed minerals are halloysite and Fe-(hydr)oxides.

Interestingly, the exact wavelength position of the main absorption feature of white micas near 2200 nm, which is a measure of their chemical composition (Duke, 1994), shifts due to weathering. This wavelength shift depends on the wavelength position in the unweathered rock (Fig. 5).

Three different wavelength ranges, reflecting different white mica species in unweathered rock, have been identified. In each range weathering processes have a different effect on the absorption wavelength: 1. (B in Figure 5) In this range (< 2198 nm), Al-rich white micas are

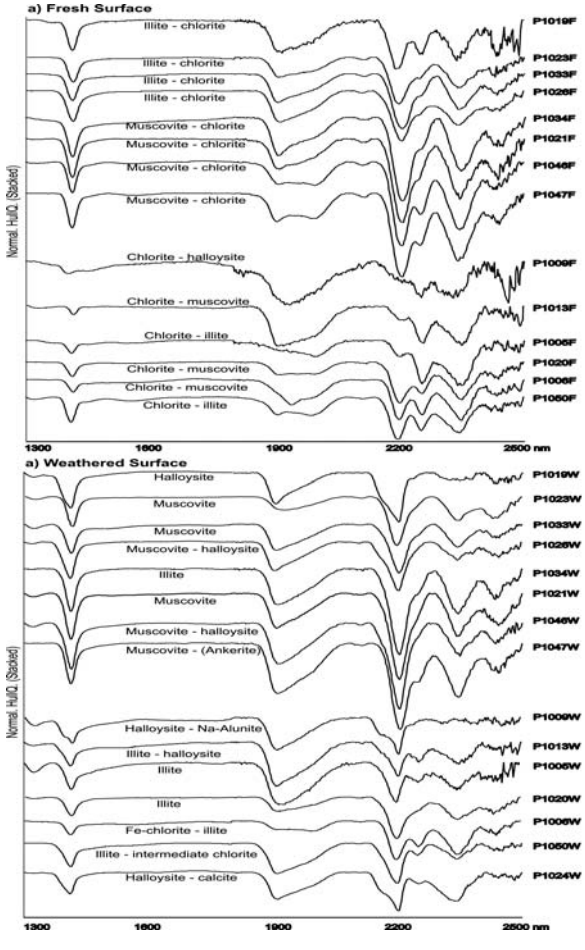

Figure 4: Reflectance spectra of rocks containing a mixture of chlorite and white mica.

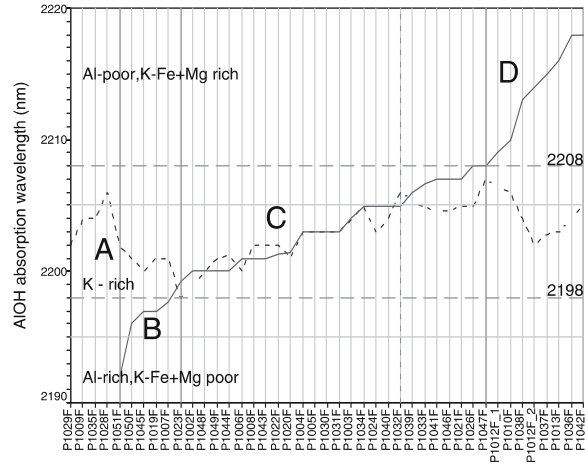

Figure 5: Plot of samples, of which (the) absorption wavelength of the Al-OH absorption feature in unweathered rock are arranged in increasing order, versus the absorption wavelength of the Al-OH absorption feature in unweathered rock (continuous line) and in weathered rock (dashed line). A: No white micas in unweathered rock, B: Unweathered rock contains Al-rich white micas, C: Unweathered rock contains white micas of intermediate Al-content, D: Unweathered rock contains Al-poor white micas.

present. Weathering shifts the absorption wavelengths toward longer wavelengths (2200-2202 nm). This suggests that Al-rich white micas are not stable during weathering; 2. (C in Figure 5) In this range (2198-2208 nm) white micas of moderately high Al-content are present. Weathering does not affect the wavelength position, except in the range between 2205 and 2208 nm, where the position shifts slightly to shorter wavelengths. This indicates that these white micas are stable during weathering. 3. (D in Figure 5) In this range (> 2208 nm) Al-poor white micas are present. Weathering strongly affects the wavelength position and shifts it to shorter wavelengths at around 2203-2205 nm. This suggests that Al-poor white micas are not stable during weathering. In unweathered rocks containing no white mica (A in Figure 5), an absorption feature having a wavelength position of 2203-2205 nm, appears after weathering. This is most likely due to the formation of halloysite at the expense of feldspars

The results of this study show (1) that chlorite disappears during weathering, and that the mineral is difficult to detect in even slightly weathered areas. Only if the weathering surface is thin and patchy, are there possibilities for detection. (2) White mica generally persists during weathering and can therefore be used for spectrally based alteration mapping. However the wavelength position of its main absorption feature around 2200 nm is modified during weathering. This modification depends on the type of the white mica species present in the unweathered rock.

References

Brauhart CW, Groves DI, Morant P (1998) Regional alteration systems associated with volcanogenic massive sulfide mineralization at Panorama, Pilbara, Western Australia. Economic Geology 93: 292-302

Clark NR, King TVV, Klejwa M, Swayze GA (1990) High spectral resolution reflectance spectroscopy of minerals. J of Geophysical Research 95, no 88: 12653-12680

Duke EF (1994) Near infrared spectra of muscovite, Tschermak substitution, and metamorphic reaction progress: implications for remote sensing. Geology 22: 621-624

Herrman W, Blake M, Doyle M, Huston D, Kamprad J, Merry N, Pontual S (2001) Short Wavelength Infrared (SWIR) spectral analysis of hydrothermal alteration zones associated with base metal sulfide deposits at Rosebery and Western Tharsis, Tasmania, and Highway-Reward, Queensland. Economic Geology 96: 939-955

Pontual S, Merry N and Gamson P (1997). Volcanic Hosted Massive Sulphide. AusSpec International, Australia

Sun Y, Secombe PK, Yang K (2001) Application of shortwave infrared spectroscopy to define alteration zones associated with the Elura zinc-lead-silver deposit, NSW, Australia. J of Geochemical Exploration 73: 11-26

Gold and silver in Cu-Zn massive sulphide deposits of the Urals

I.V. Vikentyev
Institute of Geology of Ore Deposits, Russian Academy of Sciences, Staromonetny per. 35, Moscow 119017, Russia

Abstract. The increasing production of processed ores of VMS deposits of the Urals (15 million ton per year) has aggravated a problem of gold recovery: 50-80% of gold and 33-50% of silver are lost in the pyritic concentrates and tailings. Gold and silver are relatively uniformly distributed in massive sulphide ores (Au: 0.5-1.5 ppm, Ag: 10-50 ppm), but local enrichments occur (up to 90 ppm Au and 600 ppm Ag). Au contents in Cu and Zn concentrates are commonly 20-50% more than those in ores and vary from 1.5 to 5 ppm. Most (50-90%) of the gold in common VMS ores containing 0.5-2 ppm Au are incorporated in the sulphides, mainly in pyrite and chalcopyrite, which have an Au range of 0.7-20 ppm. Au enrichment in reniform pyrite (5.5-20 ppm) and sphalerite with emulsion-like chalcopyrite (1.8-10.6 ppm) has been recognized. Tennantite-tetrahedrite is the main host of Ag, low-iron tennantite (0.05-0.6 wt% Ag, 1.2-2200 ppm Au) being the dominant variety. While Au contents in the ores are greater than 3-5 ppm, Au generally occurs as electrum and native gold (fineness 520-974), which form individual minute grains and/or aggregates with size of about 2-50 μm (up to 150 μm). These mineral parageneses were usually formed in the latest stage of mineralisation.

Keywords. Gold, silver, massive sulphides, Urals

1 Introduction

Reserves of by-product Au in the world-wide massive sulphide ores exceed 4000 t, accounting for 5% of its annual production. The Uralian orogen is the largest ore belt with about 2 billion tones of ore reserves and 70 Mt of nonferrous metals in massive sulphide deposits associated with volcanic rocks (VMS deposits). It is comparable to the Iberian Pyrite Belt in total reserves, but contains more Au and Ag. The majority of the deposits are located within the main greenstone belt of the Urals - Tagil-Magnitogorsk trough extending longitudinally along 60°E over 2000 km (Prokin and Buslaev 1999). VMS deposits related to a sodium rhyolite-basalt bimodal suite, were developed during the primitive arc stages of the Lower Silurian (Tagil megazone) and Middle Devonian (Magnitogorsk megazone). World-class deposits with 3-10 Mt of (Cu+Zn) reserves are located within the Magnitogorsk megazone (Fig. 1). These VMS deposits belong to the Uralian or Cu-Zn-pyritic type with either Cu≥Zn (Gaisk, Sibai, Degtyarsk, Jubilein, Podolsk, Safyanovsk) or Zn>Cu (Uchaly and Uzelginsk).

Among them, seven deposits contain Au of > 100 tonnes in massive sulphide ores. A few small deposits in the Magnitogorsk megazone are classified as the Bajmak or Au-pyritic type (Bakrtau, Baltatau, Tashtau, Maysk). The ores in these deposits are rich in Cu, Zn, Pb, Ba, Au and Ag, suggesting an analogue to the Kuroko type deposits (Prokin and Buslaev 1999). Cyprus type deposits associated with pillow lavas in ophiolitic suites are usually small and rare (Dombarovsk region: Letnee, Vesenee, Osennee).

In terms of the total reserves of associated Au in VMS deposits, the Uralian province is very significant relative to other massive sulphide regions in the world. So far, more than a half of Uralian gold has been produced as by-product of sulphide ores from 20 large and giant VMS deposits. Each individual deposit has gold reserves of 50-500 tonnes. The increasing amount of processed ores from the massive sulphide deposits in the Urals (15 million ton per year) has aggravated a problem of gold recovery. Loss of 50-80% of gold in the pyritic concentrates and tailings can amount to 10-12 tonnes annually. About 33-50% of silver is also lost in the tailings.

2 Samples and analytical methods

The study was based on open pit and underground mapping and sampling of drill core and mill products of major Uralian mines. We studied the distribution of noble metals and composition of electrum and native gold in ores and sulphide concentrates from the Gaisk, Uchaly, Uzelginsk, Aleksandrinsk, Safyanovsk, Degtyarsk, and other deposits in the Urals. Physicochemical conditions for the formation of Au-bearing mineral assemblages were estimated on the basis of electrum-sphalerite and arsenopyrite geothermometers and fluid inclusion thermometric determinations.

Ore samples mainly collected from Au-rich zones of the deposits were studied. The contents of Au, Ag, and base and rare metals were determined by INAA for bulk samples, ultra-heavy concentrates and hand-made mineral concentrates. In order to detect the noble metal minerals in massive sulphide ores, we separated ultra-heavy fractions from large samples (0.5-1 kg) with elevated Au contents. Ore concentrates in thin sections and mounts were studied with microanalyzers. The composition of electrum, native gold and other sulphide minerals was determined on a Camebax SX-50 microprobe (EPMA with 100 sec counting time for PGE and Au) and a JSM-5300 electron microscope equipped with energy-dispersive device LINK ISIS.

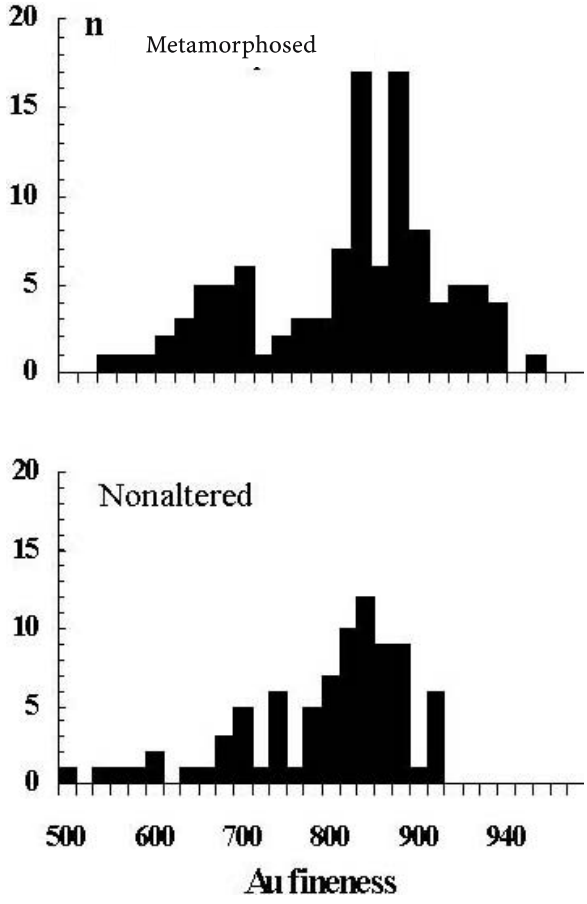

Figure 1: Gold fineness of electrum in ores of VMS deposits of the Urals, microprobe data.

3 Ore geochemistry

Massive sulphide ores predominate with subordinate disseminated ores (commonly 5-15 vol%) for most of the VMS deposits. Gold and silver are relatively uniform in distribution throughout the massive sulphide ores (Fig. 2). Most Cu-Zn massive ores are enriched in gold (>1.5-2 ppm), but Zn-Cu massive ores have lower gold concentrations. Gold contents in ores usually range between 1-2 ppm (Uralian type) and 2-5 ppm (Bajmak type), but can amount to 15-90 ppm in Au-rich zones in the deposits of both ore types. Cu-Zn ores with Au contents of 1.5-2 ppm or more are characterized by high concentrations of Pb, Ba and Ag. Silver contents range from 5 to 50 ppm (up to 600 ppm). Other metal contents have ranges of 1-100 ppm (up to 1200 ppm) for Pt, 1-50 ppm (up to 340 ppm) for Pd, 10-200 ppm (up to 2100 ppm) for Te and 20-100 ppm (up to 450 ppm) for Se.

4 Ore mineralogy

Pyrite is the dominant mineral of the ores (40-90 vol%). Chalcopyrite and sphalerite are the major commercial minerals (1-10 vol %, up to 30 vol %). Tennantite-tetrahedrite (usually tennantite) and galena are common minerals (0.2-1, up to 5 vol% and 0.1-0.5 vol%, respectively). Bornite, digenite, pyrrhotite, marcasite, magnetite are noteable in some deposits. The paragenetic Au-Ag mineral assemblages are mainly composed of argentiferous tennantite, Ag-bearing galena, bornite, various tellurides (altaite, hessite, petzite, stützite, krennerite, sylvanite, montbrayite, mutmanite), sulphides (acanthite, argentite, petrovskaite, argentopentlandit, Ag-Sn sulfides: stromeyerite, jalpaite and mackinstryite), sulphotellurides (tetradymite) and sulphobismuthides (aikinite, wittichenite), amalgams, and native elements (Au-Ag, Ag, Te). Irregular distribution of these parageneses in the orebodies could be genetically related to latest hydrothermal processes (e.g. Vikentyev and Yudovskaya 2004). Native gold and electrum form individual small grains and aggregates with size of about 2-50 μm up to 150 μm, larger grains being rare. Fineness of electrum and native gold ranges from 538 up to 974 for highly metamorphosed deposits and from 520 up to 918 for slightly transformed deposits (Fig. 1). Ag content in electrum varies from 2.56 to 39.45 wt %. Moreover, admixtures (wt%) of Pt up to 2.23, Pd up to 0.85, Te up to 1.17, Hg up to 0.89, Fe up to 0.5 and Se up to 0.49 also occur in the sulphide ores. Compositions of electrum are approximately Au_3Ag and Au_2Ag. An inverse correlation of electrum composition with Fe concentration in the associated sphalerite has been found. Direct correlation of the Au content with metamorphic grade and hydrothermal alterations is less remarkable. This trend of sphalerite composition may be related to an increase of fS_2 in the fluid or a decrease of sphalerite crystallization temperature. However, the role of sulphur fugacity is probably more important. Its increase raised the stability of Ag_2S relative to electrum and lead to the crystallization of high-Au electrum (Gammons and Williams-Jones 1995, Shikazono and Shimizu 1987).

Large gold flakes (100-1000 μm or more) are found in strongly metamorphosed VMS deposits (Gai, Degtyarsk, Karabash, and San Donato). In weakly metamorphosed ore deposits (Uzelginsk, Uchaly, Molodezhn, Aleksandrinsk, Safyanovsk), native gold is observed as rare tiny grains (5-25 μm). Larger grains (up to 150-200 μm) are detected in areas characterized by overprinting of late hydrothermal processes (recrystallized ores) and a mineral assemblage of quartz + sulphide - barite - tennantite veinlets. Evidently, the appearance of gold minerals was mainly related to the release of isomorphous Fe from sulphides during epigenetic hydrothermal alterations.

Native gold and other gold minerals occur in ores with Au content of >5 ppm (rarely <3 ppm). Based on mineral geothermometers, such high-grade ores were mainly formed at high sulphur fugacity and low temperature conditions. The $\log fS_2$ deviation from the chalcopyrite-bornite equilibrium line is relatively insignificant and ranges from

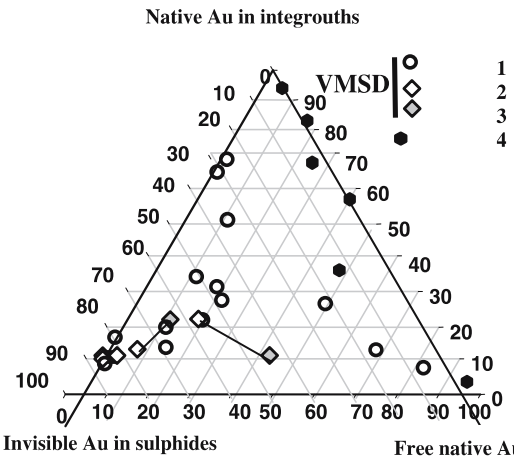

Figure 2: Gold in ores of VMS deposits of the Urals and Berezovsk gold deposite. Gold occurrence forms by the results of step-by-step autoclave leaching of technological probes. 1-3 ores of VMS deposits Metamorphosed (1), Nonaltered (2) and tailings (3), cannodes are connected figurative points of ore and related tailings; (4) - sulphide ores of Berezovsk deposit.

-12 to -5 for the majority of the studied associations. The temperature varies from 150 to 380°C. Under such conditions, the bornite + tennantite-tetrahedrite and chalcopyrite + tennantite-tetrahedrite paragenetic associations are most typical. At each examined temperature, the fugacity needed for the formation of Au-rich ores is one to two orders of magnitude higher relative to ores with normal Au content of approximately 1 ppm. Data on the stability of tellurium minerals suggest that the studied mineral associations fall into the hessite-native gold field in the logfTe_2 - t(°C) diagram (Afifi et al. 1988; Cabri 1965; Moloshag et al. 2002): from log f_{Te2} = -16~-6 (300°C) to log f_{Te2} = -21 ~ -13 (150°C).

5 Au and Ag in massive sulphides

Most gold grains are invisible, and occur in association with pyrite and chalcopyrite, which contain 0.7 to 20 ppm Au. INNA reveals that pyrite has 0.1-2.5 ppm Au and 5-60 ppm Ag. Au enrichment in reniform pyrite (5.5-20 ppm) that commonly has chalcopyrite inclusions is recognized. In contrast, euhedral pyrite associated with the reniform pyrite is characterized by an order of magnitude lower concentrations of Au, Ag, and As. Gold enrichment in the reniform As-pyrite may be related to the isomorphous replacement of Fe in the As-pyrite lattice by Au. Gold may have become visible as a result of recrystallization of the ores and migration of As from pyrite to tennantite, which is typical of late parageneses. Tellurides, native tellurium and tennantite-tetrahedrite, together with main sulphides, are detected as microinclusions in pyrite. Gold contents in chalcopyrite average 1.5-3 ppm with Au and Ag ranges being 1-18.6 ppm and 10-100 ppm, respectively. Sphalerite with very fine emulsion-like chalcopyrite inclusions contains 1.8 to 10.6 ppm Au, while gold content in pure sphalerite grains detected by INNA is 0.3 to 3 ppm. Therefore tiny gold-bearing chalcopyrite inclusions in sphalerite can be considered to be responsible for the most of the gold in the latter mineral. Composition of galena is characterized by admixtures of 0.05-0.41 wt% Au, 0.01-0.34 wt% Ag, up to 0.14 wt% Pd, up to 0.24 wt% Pt, 0.1-0.2 wt% Se, 0.1-0.14 wt% Te and 0.1-0.25 wt% Hg (EPMA). Some precious metals occur in bornite (0.02-0.27 wt % Au, EPMA). Additionally, Au is present as a trace element in some tellurides, such as altaite (0.02-5.2 wt%) and hessite (0.02-0.63 wt%). Tennantite-tetrahedrite is the main host of Ag with low-iron tennantite (0.05-0.6 wt% Ag, 1.2-2200 ppm Au) being the dominant variety and Ag-bearing tennantite (up to 6-8.4 wt% Ag) scarce.

A positive correlation between gold and silver in sulphides and a high dispersion of their contents is likely to indicate the occurrence of some of the gold as microinclusions of electrum and native gold. Elevated contents of other components (Sb, As, Hg, Te and Se) in some gold-bearing sulphide grains point to the occurrence of other Au and Ag compounds. Most (47-87%, Fig. 2) of the gold in common VMS ores (Au 0.2-3 ppm) are incorporated into sulphides as "invisible" gold, resulting in the loss of Au in tailings with pyrite and other sulphides. The fraction of electrum and native gold as Au-hosts ranges from 13 to 90%, but only 13-53% if technological probes enriched in Au (7.9-21.2 ppm) are excluded.

Metamorphism of sulphide ores resulted in the redistribution of non-ferrous and precious metals and the formation of submicron isolations of Au-Ag alloys and Au compounds with Te, Se, S, As, Sb and Hg. Sulphide precipitation is likely to have occurred under conditions favorable for the incorporation of isomorphous gold into the lattice of common sulphides during high temperature (250-380°C) stages. The paragenesis of native metals (gold, silver, tellurium and rhenium), tellurides and sulphosalts was formed at the latest stage of the hydrothermal process at 130-200°C.

Evidently, dispersed invisible gold in the major ore-forming sulphides is an essential form of its concentration in the studied deposits. Visible segregations of gold (~1 μm or more) and tellurides appeared in massive sulphides during the recrystallization of ores as a result of late (low-temperature) hydrothermal processes and low-pressure metamorphism (prehnite-pumpellyite-greenschist facies). These processes led to coarsening of gold grains and increased amount of free gold. This conclusion is supported by an inverse correlation of Au and Ag contents in the major ore-forming sulphides (sphalerite, chalcopyrite, and pyrite) with metamorphic grade of the ores (Vikentyev et al. 2000).

Gold in hydrothermal sulphide edifices on the modern seafloor is primarily confined to iron and copper

sulphides as isomorphous fine-grained disseminations of Au-bearing chalcopyrite and sphalerite (Bortnikov et al. 2003). Free gold is atypical for massive ores. According to our data, native gold can be formed with temperature decrease to 150-200°C (Bortnikov et al. 2003). This condition corresponds to the late (low-temperature) stage of ore recrystallization.

Acknowledgements

The author wishes to thank N. Bortnikov, V. Moloshag, V. V. Murzin and M. Judovskaya for help and fruitful discussion. Analyses were performed by A.Mokhov (JSM-5300+LINK ISIS), A. Tsepin (EPMA) and A. Kerzin (INNA). The study was supported by Russian Science Support Foundation (proj. 04-05-65040), the Ministry of Science, Industry and Technology of the Russian Federation (proj. Nanomineralogy), and the Russian Science Support Foundation.

References

Bortnikov NS, Kabri L, Vikentyev IV (2003) Invisible gold in sulphides of modern sulphide edifices. Geol. Ore Dep. 45 (3): 232-245

Gammons, CH and Williams-Jones AE (1995) The solubility of Au-Ag alloy + AgCl in HCl/NaCl solutions at 300°C: New data on the stability of Au (I) chloride complexes in hydrothermal fluids. Geochim. Cosmochim. Acta 59 (17): 3453-3468

Moloshag, VP, Vikentyev IV, Grabezhev AI, Gulyaeva TYa (2002) Tellurides of massive sulphide deposits of the Urals. Proc. Zavaritsky Inst. Geol.Geochem. Uralian branch RAS 189-195 (in Russian)

Prokin, VA, Buslaev FP (1999) Massive copper-zinc sulphide deposits in the Urals. Ore Geol. Rev 14: 1-69

Shikazono, N, Shimizu M (1987) The Ag/Au ratio of native gold and electrum and the geochemical environment of gold vein deposits in Japan. Miner. Deposita 22:309-314

Vikentyev IV, Yudovskaya MA, Mokhov AV, Kerzin AL, Tsepin AI (2004) Gold and PGE in massive sulphide ore of the Uzelginsk deposit, Southern Urals, Russia. Canadian Mineralogist 42:651-665

Vikentyev, IV, Belenkaya YuA, Ageev BI (2000) Alexandrinsk pyrite-polymetallic deposit on the Urals. Geol. Ore Dep 42 (3):248-274

Spherulitic pyrite in seafloor hydrothermal deposits: Products of rapid crystallization from mixing fluids

Qidong Xu
Faculty of Earth Resources, China University of Geosciences, 388 Lumo Road, Wuhan, Hubei 430074, China

Steven D. Scott
Department of Geology, University of Toronto, 22 Russell Street, Toronto, Ontario M5S 3B1 Canada

Abstract. Some framboid and colloform textures of pyrite in seafloor hydrothermal deposits actually are fibroradial spherulites of pyrite when viewed in partially polarized reflected light. "Colloform bands" in these pyrites are ring-cracks. This disequilibrium texture reflects rapid crystallization with undercooling caused by mixing between hot vent fluid and cold ambient seawater. In principle, different morphologies of spherulitic pyrite may indicate different degrees of mixing between vent fluid and seawater.

Keywords. Spherulite, pyrite, seafloor hydrothermal deposit, disequilibrium texture, mixing process

1 Introduction

Pyrite is the most widespread sulfide mineral in many types of ore deposits. Its morphology, texture and composition have been used in determining environments of ore formation, identifying different types of ore deposits and as a signature in ore exploration (Bralia et al. 1979; Roberts 1982; Campbell et al. 1984; Brown et al. 1993; Huston et al. 1995; Raymond 1996; Craig et al. 1998; Clark et al. 2004). For ancient volcanogenic massive sulfide (VMS) deposits, many sulfides are modified and recrystallized owing to late metamorphism and deformation. Only a few minerals, such as pyrite, are sufficiently refractory to preserve some pre- and/or syn-metamorphic development (Scott 1983; Craig 1998). It is not clearly understood what the textures in remnant pyrite mean, so there are issues for applying textural evidence to the origins and exploration for ore deposits. Seafloor hydrothermal deposits are considered to be modern analogues of ancient VMS deposits and the knowledge gained from them can be used to explain phenomena in ancient VMS deposits as an aid to understanding their formation processes (Humphris et al. 1995; Scott 1997; Gibson et al. 1999).

This study arose from an observation of presently forming hydrothermal samples from SuSu Knolls, eastern Manus basin, Papua New Guinea, and southern Explorer Ridge, northeast Pacific Ocean. Microtextural examination of pyrite (including a few examples of marcasite) commonly shows two generations: the first occurs as spherulites (formerly called framboid and colloform textures) and the second as cubic euhedral-subhedral aggregates. The first-formed pyrite, having so-called framboid and colloform textures, is actually found to be spherulitic, a polycrystalline aggregate of radiating fibres as seen in partially polarized reflected light. Some band boundaries in this "colloform" texture are shrinkage cracks. This spherulite is a disequilibrium texture that probably reflects rapid crystallization under highly undercooled conditions, a crystallization behaviour of pyrite that might be expected during mixing between hot vent fluid and cold ambient seawater.

2 Observations

The hydrothermal fields of SuSu Knolls and southern Explorer Ridge occur in, respectively, a back-arc extensional basin and a mid-ocean ridge. At SuSu Knolls, the typical mineral assemblage in the studied chimney samples is barite-pyrite- chalcopyrite-sphalerite-tennantite in the outer zone of the chimneys. At southern Explore Ridge, the main mineral assemblage in the studied samples is similar to that at SuSu Knolls. The pyrite in both is divided into two generations: the first generation has so called framboidal and colloform textures and the second generation is cubic euhedral-subhedral aggregates. More detail microtextures of the pyrite cannot be seen in plain reflected light, or even by SEM, but they are revealed in partially polarized reflected light. Such observations show that the first generation of pyrite is composed of fine-grained wisps of pyrite, as in Figure 1, and that the texture is spherulitic, a polycrystalline pyrite aggregate of radiating fibres.

Typical single spherulitic pyrite is shown in Figures 1A and B. The sizes of the spherulites are about 150 to 300 μm in diameter. Tiny wisps of pyrite grew radially from the centre to the outside. Every tiny wisp in the spherulite of Figure 1A has the same interference colour and optical orientation, and their width increases from the centre to the outside. Tiny needle-like crystals in the spherulite of Figure 1B appear to be merged into several larger fan-like shapes. Similar features are seen in more complex spherulites in Figures 1C and E, where perfect and imperfect spherulites are intergrown, implying rapid crystallization with multiple centres of nucleation.

Spherulitic pyrite in Figure 1D appears to be colloform in plain reflected light and grew where debris in the centre acted as a core onto which a late succession of pyrite

This page intentionally blank

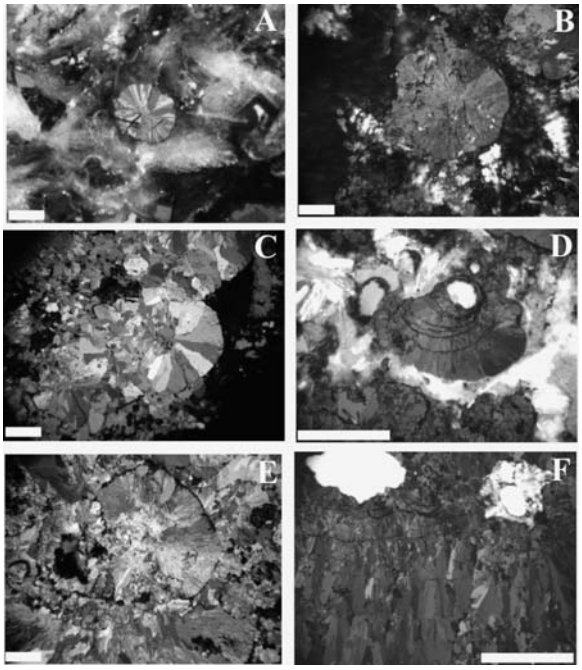

Figure 1: Photomicrographs of spherulitic textures in ores from seafloor hydrothermal deposits. A, D, F from southern Explorer Ridge (Sample D10-10); B, C, E from SuSu Knolls (Sample MD94). The scale bar is 100 microns, partially polarized reflected light.

was coated, resulting in a banded colloform texture. In fact, though, this is a fibroradial spherulite and the "band boundary" of the so-call colloform pyrite is a group of ring-cracks where fibroradial pyrite was cut off. It is clear from Figure 1F that some ring-cracks disappear or are connected to another crack. The development of the ring-cracks in pyrite may be similar to ring-cracks in igneous intrusions that are caused by shrinkage upon cooling. About 20 spherulitic pyrites having an appearance of colloform texture were chemically analysed with a Cameca SX-50 electron microprobe at the University of Toronto. Neither major nor trace elements (Fe, S, Co, Ni, As) show any change across the "colloform" texture. This is different from some researchers' results (e.g. Raymond 1996; Craig et al. 1998) that bands in pre-metamorphic pyrite from ancient VMS deposits showed regular change in some elements such as Co and Ni. These remnant bands in pyrite of ancient VMS deposits obviously are not analogous to the spherulitic pyrite in modern seafloor hydrothermal deposits.

3 Discussion

There are some problems in nomenclature in describing and explaining ore textures because many different genetic textures are applied to the same textural term. Framboidal and colloform textures are such examples. Framboidal pyrite initially consists of tiny spherical aggregates of cubic pyrite euhedra, as a result of microbial processes in sediments, but now nearly all fine spherical aggregates of pyrite are called framboid. Colloform texture was initially thought to have been formed by colloidal deposition but later it was found that it was possible to be crystallized from a fluid. It is accepted that the colloform banding represents some change in the ore fluid or the conditions of precipitation (Craig and Vaughan 1994). However, difficulties are inevitable in recognizing and explaining special textures.

The character of spherulitic pyrite in Figure 1 is different from the original intention of framboidal pyrite but is similar to fibroradial spherulite in basalt (Fowler et al, 1987). These are radially symmetrical arrays of crystalline fibres having the same fibre axis and they need not be spherical, as they do form conical arrays, sections through which yield fan-like shapes. The fibroradial spherulite is a disequilibrium mineral texture having a fractal feature (Fowler et al. 1989, 1995). These disequilibrium textures, such as spherulites, are produced by rapid crystallization in undercooled conditions or rapid crystallization with multiple centres of nucleation from supersaturated liquid or rapid crystallization at a hot fluid-seawater- sediment interface (Roedder 1968; Fowler et al. 1987; Pichler et al. 1999). During the early period of chimney formation, hot vent fluid first mixes with cold ambient seawater creating intense fluctuation of temperature and produces undercooling in the mixed fluid, causing precipitation of finely radial anhydrite and barite. Our samples are from the outer part of the chimney where fibroradial spherulites of pyrite have intergrowth with barite. We interpret that pyrite, anhydrite and barite are quickly crystallized from the mixing fluid, contemporaneously to form fine- and tiny-fibrous aggregates, only each has different crystallization behaviours.

Fowler et al. (1987) showed that crystal morphology changes with decreasing degree of undercooling: tiny to small fibroradial spherulites coarse-fibre spherulites ->branching forms dendritic forms, consistent with the result of plagioclase-undercooling experiments (Loggren 1974). Likewise, morphology changes of pyrite in Figure 1 B and E -> A and C ->D and F could be equivalent to fibroradial spherulites ->coarse-fiber spherulites ->branching forms, and Hannington and Scott (1988) observed dendritic forms of pyrite in sulfides from the Juan de Fuca Ridge. These can also be a series of morphological changes in pyrite with degree of undercooling of fluid. Because undercooling of the fluid depends on the amount of mixing between vent fluid and seawater, the morphological changes of pyrite should reflect the degree of mixing between these two fluids.

As the mixing between vent fluid and ambient seawater decreases, the undercooling effect gradually disappears while the chimney is growing. Crystallization of pyrite from the inner part of a chimney is a near-equilibrium

situation, forming cubic euhedral-subhedral aggregates. The polycrystalline pyrite (and marcasite) aggregate will recrystallize to a new euhedral-subhedral aggregate and growth zoning may develop in these pyrites after the large chimneys collapse to form a mound. Because these cubic euhedral-subhedral aggregates of pyrite, sometimes with growth zoning, cannot be entirely precipitated from vent fluid, and spherulitic pyrite is not easily preserved in ancient ores, it is necessary to use chemical composition of pyrite and remnant growth zoning in pyrite to determine the origin of this mineral in ancient VMS deposits.

References

Bralia A, Sabatini G, Troja F (1979) A revaluation of the Co/Ni ratio in pyrite as geochemical tool in ore genesis problems: evidences from southern Tuscany pyritic deposits. Mineralium Deposita 14: 353–374

Brown D, McClay KR (1993) Deformation textures in pyrite from the Vangorda Pb-Zn-Ag deposits, Yukon, Canada. Mineralogical Magazine 57: 55-66

Campbell FA, Ethier VG (1984) Nickel and cobalt in pyrrhotite and pyrite from the Faro and Sullivan orebodies. The Canadian Mineralogist 22: 503-506

Clark C, Grguric B, Mumm AS (2004) Genetic implications of pyrite chemistry from the Palaeoproterozoic Olary Domain and overlying Neoproterozoic Adelaidean sequences, northeastern South Australia. Ore Geology Reviews 25: 237-257

Craig JR, Vaughan DJ (1994) Ore Microscopy and Ore Petrography. Second edn, John Wiley and Sons, Inc, New York, pp167-168, pp 273-274

Craig JR, Vokes FM, Solberg TN (1998) Pyrite: physical and chemical textures. Mineralium Deposita 34: 82-101

Fowler AD (1995) Mineral crystallinity in igneous rocks – fractal method. In: Barton CC and LaPointe PR (eds), Fractals in the earth sciences, Plenum Press, New York, 237-249

Fowler AD, Jensen LS, Peloquin SA (1987) Varioles in archean basalts: products of spherulitic crystallization. The Canadian Mineralogist 25: 275-289

Fowler AD, Stanley HE, Daccord G (1989) Disequilibrium silicate mineral textures: fractal and non-fractal features. Nature 341: 134-138

Gibson HL, Morton RL, Hudak GJ (1999) Submarine volcanic processes, deposits, and environments favorable for the location of volcanic-associated massive sulfide deposits. In: Barrie CT, Hannington MD (eds), Volcanic-associated massive sulfide deposits: processes and examples in modern and ancient settings, Society of Economic Geologists Review in Economic Geology 8: 13-51

Hannington M, Scott SD (1988) Mineralogy and geochemistry of a hydrothermal silica-sulfide-sulfate spire in the caldera of Axial seamount, Juan de Fuca ridge. The Canadian Mineralogist 26: 603-625

Humphris SE, Herzig PM, Miller DJ (1995) The internal structure of an active sea-floor massive sulphide deposit. Nature 377: 713-716

Huston DL, Sie SH, Suter GF (1995) Trace elements in sulfide minerals from Eastern Australian volcanic-hosted massive sulfide deposits: part 1. Proton microprobe analyses of pyrite, chalcopyrite, and sphalerite, and part 2. Selenium levels in pyrite: comparison with $\delta^{34}S$ values and implications for the source of sulfur in volcanogenic hydrothermal systems. Economic Geology 90: 1167-1196

Lofgren GE (1974) An experimental study of plagioclase crystal morphology: isothermal crystallization. American Journal of Science 274: 243-273

Pichler T, Giggenbach WF, McInnnes BIT (1999) Fe sulfide formation due to seawater-gas-sediment interaction in a shallow-water hydrothermal system at Lihir Island, Papua New Guinea. Economic Geology 94: 281-288

Raymond OL (1996) Pyrite composition and ore genesis in the Prince Lyell copper deposit, Mt Lyell mineral field, western Tasmania, Australia. Ore Geology Reviews 10: 231-250

Roberts FI (1982) Trace element geochemistry of pyrite: a useful guide to the occurrence of sulfide base metal mineralization. Journal of Geochemical Exploration 17: 49–62

Roedder E (1968) The noncolloidal origin of "colloform" textures in sphalerite ores. Economic Geology 63: 451-471

Scott SD (1983) Chemical behaviour of sphalerite and arsenopyrite in hydrothermal and metamorphic environments. Mineralogical Magazine 47: 427-435

Scott SD (1997) Submarine hydrothermal systems and deposits. In: Barnes HL (ed) Geochemistry of Hydrothermal Ore Deposits, Third edn, John Wiley & Sons, Inc, New York, 797-975

Magmatic sources of volatiles and metals for volcanogenic massive sulfide deposits on modern and ancient seafloors: Evidence from melt inclusions

Kaihui Yang, Steven D. Scott
Department of Geology, University of Toronto, Toronto M5S 3B1, Canada

Abstract. Ore metal-rich magmatic fluids are found in the vapor bubbles of melt inclusions in phenocrysts of felsic volcanic rocks that host the hydrothermal fields in the presently active eastern Manus Basin of the western Pacific and the large Ordovician massive Zn-Pb-Cu sulfide deposits in the Bathurst Mining Camp of New Brunswick, Canada. The fluids contain Fe, Ni, Cu, Zn, Mn, Pb, Ag and Au chlorides, sulfides and oxides. Degassing of such fluids from magma into seafloor hydrothermal systems can contribute large quantities of ore metals for the formation of massive sulfides on modern and ancient seafloors.

Keywords. Magmatic fluid, hydrothermal system, melt inclusions, massive sulfide

1 Introduction

Magmas may degas their volatiles and metals into active subaerial volcanoes, fumaroles and geothermal systems as well as submarine volcanic systems (e.g., Hedenquist 1995; Hekinian et al. 2000). Such a high-temperature magmatic fluid is considered to be essential for the formation of epithermal and porphyry-type ore deposits (Hedenquist and Lowenstern 1994) and probably to have played an important role, but less well understood, in the genesis of some volcanogenic massive sulfide (VMS) deposits (Stanton 1994; Yang and Scott 2002; 2003). In this paper, we demonstrate the degassing processes of pre-erupted magma, and the contribution of magmatic volatiles and their contained ore metals to a seafloor hydrothermal system through the study of melt inclusions in phenocrysts in volcanic rocks that host a presently-active seafloor hydrothermal site and an ancient analogous VMS deposit. The active site is PACMANUS in the eastern Manus pull-apart backarc basin offshore Papua New Guinea in the western Pacific where we examined dredged and ODP Leg 193 volcanic samples from the Pual ridge that hosts the actively forming sulfide chimneys at PACMANUS (1700-2000 m water depth, 10.9% Cu, 26.9% Zn, and 1.7% Pb, n = 26; Scott and Binns, 1995). The ancient site is the large Ordovician massive sulfide deposits in the Bathurst Mining Camp of New Brunswick, Canada, thought to have formed in a continental backarc setting (>1000 m estimated water depth at time of formation, >280 million tonnes of ore with average grades of 2.28% Pb, 6.60% Zn and 0.46% Cu; McCutcheon 1992; Van Staal et al. 2003).

2 Methodology

Melt inclusions provide an effective approach to the study of pre-eruptive degassing or boiling processes in the magma chamber. When a crystallizing magma is depressurized and becomes saturated with volatiles, bubbles of volatiles will nucleate. The vesiculation event may generate a distinct population of volatile bubbles in the melt (Cashman and Mangan 1994), most preferably on the surfaces of the suspended crystals (Herwitz and Navon 1994). These surficial bubbles will likely be entrapped to become part of the melt inclusions in the growing crystals. Thus, the trapped melt inclusions in the phenocrysts record the processes of volatile exsolution from the melt. Detailed examination and measurement of these melt inclusions yield insights into the abundance and composition of the magmatic volatile phase.

For this study, we have measured the sizes of melt inclusions and their coeval vapor bubbles and have analyzed the major element and volatile contents of the glass in phenocryst olivine, pyroxene (Fig. 1) and plagioclase of representative volcanic rocks collected from PACMANUS, and in quartz phenocrysts of felsic rocks from Bathurst. The studied samples range in composition from basaltic andesite to rhyolite.

3 Composition of melt inclusions and their fluid phases

High concentrations of H_2O (0.9 to 2.5 wt%) are detected in the glass of melt inclusions in olivine and pyroxene of the andesite from PACMANUS. A fluid phase occurs in the melt inclusions in olivine, pyroxene, plagioclase or quartz of the felsic rocks from both of the studied areas (Figs. 1 and 2A), indicating that the magmas were saturated with volatiles. At PACMANUS, CO_2-rich bubbles are found in the mafic melt inclusions (Yang and Scott, 1996) and H_2O-rich bubbles in the evolved felsic glasses (also see Kamenetsky et al. 2001).

Ore-forming metals including Fe, Cu, Zn, Ni, Mn, Pb, Ag and Au are found as precipitates in the gaseous bubbles of melt inclusions in phenocrysts as well as in vesicles in the matrix glass of the felsic rocks from Manus and

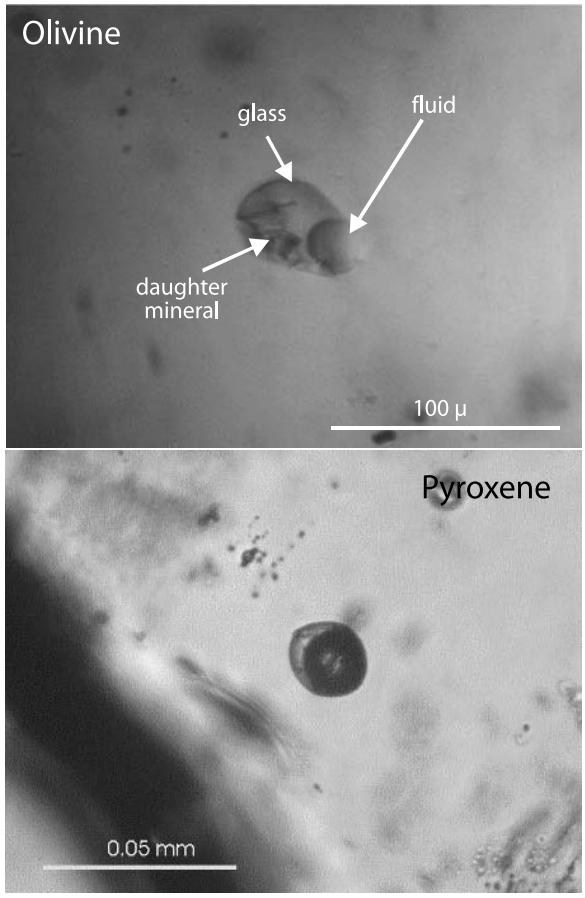

Figure 1: Melt inclusions in olivine (upper) and pyroxene (lower, with a large bubble) phenocrysts of andesite from the PACMANUS hydrothermal field.

Bathurst (Fig. 2). At PACMANUS, the magmatic fluid is estimated to contain 1.1% Ni, 2.3% Zn, 7.2% Cu, and 2.7% Fe (Yang and Scott 1996). This is compatible with the data from other melt inclusion studies (e.g., Lowenstern 1995) and analyses of precipitates in lavas, tuffs and sublimates collected from active subaerial volcanoes as well as associated fumaroles (e.g., Hedenquist 1995). These observations confirm experimental results that the high-temperature, supercritical fluids degassed from magma are capable of transporting high concentrations of metal species (e.g. Ballhaus et al. 1994).

Saline inclusions accompany the melt inclusions in quartz phenocrysts of rhyolite from Bathurst (Fig. 2B). The quartz crystal also trapped high-F apatite and zircon mineral inclusions that contain aqueous fluid inclusions (Yang and Scott 2003). These observations indicate that a saline magmatic fluid was associated with the felsic magma, and are consistent with the data from porphyry-epithermal systems in active subaerial volcanoes (Hedenquist and Lowenstern 1994).

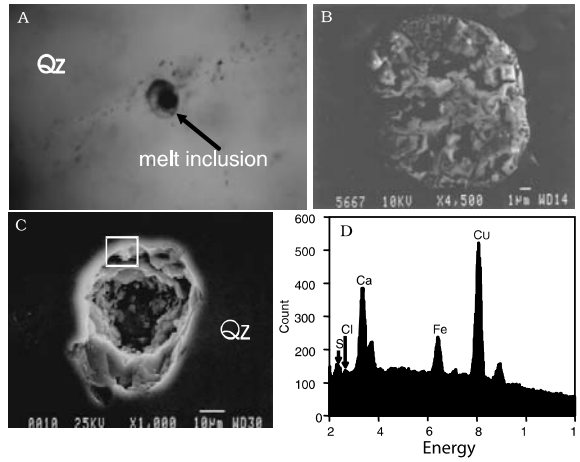

Figure 2: A, melt inclusion with a gaseous bubble in quartz (Qz) phenocryst in rhyolite from Bathurst, Canada; B, opened brine inclusion in quartz; C, opened bubble with precipitates (boxed) in a melt inclusion in quartz; D, EDS spectrum of the precipitates in C, with S, Cl, Fe and Cu peaks.

4 Vapor bubbles of melt inclusion as evidence for magma boiling

A bubble in a melt inclusion may be primary or secondary. The secondary bubbles are formed, for example, by leakage (Lowenstern 1995) after the melt inclusion was trapped in a crystal. The primary bubbles in melt inclusions, which are of interest here, may be formed by (1) the shrinkage of trapped melt on cooling, (2) the exsolution of volatiles from the homogeneous melt after entrapment and (3) the entrapment of a volatile phase together with the melt by the growing phenocrysts in the magma (Roedder 1979). The maximal volume of a bubble formed by the shrinkage of the entrapped melt is estimated to make up about 3.6 vol% of the melt inclusion (bubble/melt inclusion volume ratios, V_b/V_m). The shrinkage bubble may be vacuum or filled with volatiles that exsolved from the trapped melt. Inclusion of a melt that is particularly rich in volatiles may nucleate a bubble as a result of exsolution of the volatiles on cooling. If a shrinkage bubble does not occur, the exsolved volatile phase that nucleates at 1000°C and 170 bars (1700 m below sea level at PACMANUS) and has a density of 0.07 g/cm^3 may create a bubble with the maximal V_b/V_m ratio of 3.7 vol%, about the same as that of a shrinkage bubble.

The observed melt inclusions, ranging in size from <2 µm to >150 µm, contain one or more bubbles. Most of the bubbles have V_b/V_m of >5.5 vol%, higher than those for the melt inclusions with their bubbles generated from shrinkage (V_b/V_m, 3.6 vol%) or post-entrapment exsolution of volatiles (V_b/V_m, 3.7 vol%). This, together with the presence of vapor bubbles with little melt (V_b/V_m, 80 to >95 vol%) in pyroxene and olivine phenocrysts (Fig. 1, lower), suggests that a vapor phase was formed

from vigorous exsolution of volatiles or the boiling of a magma in the crystallizing magma chamber. The V_b/V_m ratios show distinct distribution patterns in the phenocryst minerals, indicating that there was more than one vesiculation event in the magma chamber as the phenocrysts would have formed on the liquidus at different times.

5 Pre-eruptive degassing and its contribution to a hydrothermal system

Melt inclusions with no visible bubbles have the highest contents of H_2O (2.1 - 2.5 wt%, Yang and Scott 2005). The H_2O contents of the glass in the melt inclusions are negatively related to the size of the coeval bubbles. Significant variation of H_2O contents (1.0 to 2.5 wt%) in the melt inclusions suggests that the H_2O was degassed from the crystallizing magma. Positive correlations of S, Cl and possible F with H_2O indicate that all these volatiles were exsolved from the melt into the vapor phase. The negative correlation of H_2O with alkali content in the glass of melt inclusions suggests that the magma was crystallizing in the presence of a fluid phase. It is estimated that the magma might have lost up to 65% of its volatiles while crystallizing (Yang and Scott 2005).

Significant amounts of magmatic fluid can be degassed from magma during its fractionation in a shallow magma chamber. At PACMANUS, the depletion of H_2O, Cl and S in the matrix glass relative to the melt inclusions gives a minimum estimate of 1.1-1.7 wt% of degassed fluid from a mafic magma (Yang and Scott 1996; 2002). More fluids are expected to have been degassed from the magma as it fractionated from mafic to felsic compositions.

Such a pre-eruptive degassing process may last at least 5 to 48 years, as estimated from the size and growth rate of the phenocrysts. This estimate is a minimum because not all the phenocrysts crystallize at the same time. The exsolved fluid may be discharged along a favorable structural zone that extends to the sea floor, and contribute large quantities of volatiles and ore metals directly to a seafloor hydrothermal system that is forming sulfide chimneys at PACMANUS. The estimated life of a black smoker chimney at PACMANUS is 5 to 40 years, which is of the same order as the duration of the pre-eruptive degassing process. This implies that the magmatic fluid may be a major source of ore metals for the sulfide chimneys.

6 A magmatic genetic model

Magmatic fluids may have played an important role in the formation of large ancient volcanogenic massive sulfide deposits by providing a major source of ore metals beyond that which can be derived by leaching of rocks in a high temperature reaction zone adjacent to a magma (e.g. Cathles 1993). Only 1% of such metal-rich magmatic fluid (27000 ppm Fe, 23000 ppm Zn, 72000 ppm Cu; Yang and Scott 1996) mixed with heated sea water that has leached its metals from rocks (80 ppm Fe, 6 ppm Zn and 2 ppm Cu; Von Damm 1990), would contribute over 85% of the total metals to form an orebody. Such magmatic fluids are most likely to be formed from volatile-rich felsic magmas that are prevalent in island arcs and, if added to the normal circulation system, the fluids could be responsible for the formation of "giant" ore deposits (Fig. 3). If a magma plays an active role providing metals to a circulating hydrothermal system rather than simply being a passive "heat engine" during hydrothermal circulation, this may be recorded in the geochemistry or mineralogy of the crystallized magma. Reliable detection of this elusive signal in subvolcanic intrusions would constitute a significant exploration guide for volcanogenic massive sulfide ores and related hydrothermal deposits.

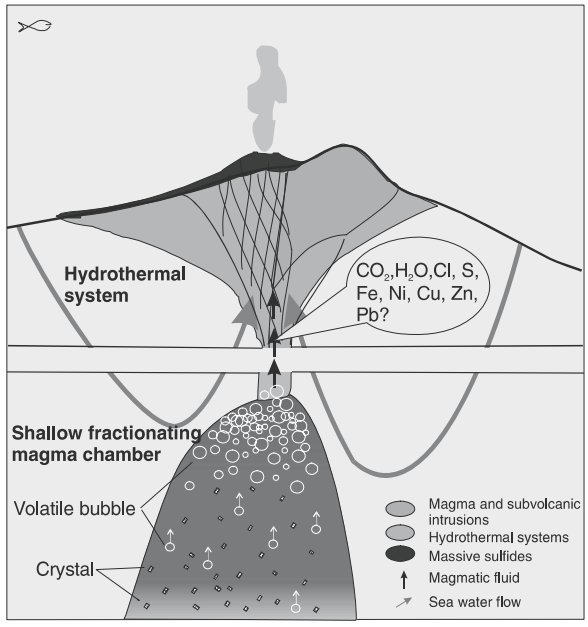

Figure 3: Magmatic genetic model for large volcanogenic massive sulfide deposits.

Acknowledgements

This research was funded by grants from the Natural Sciences and Engineering Research Council of Canada.

References

Ballhaus C, Ryan CG, Mernagh, TP, Green, DH (1994) The partitioning of Fe, Ni, Cu, Pt, and Au between sulfide, metal, and fluid phases: a pilot study. Geochim Cosmochim Acta 58: 811-826

Cashman KV, Mangan MT (1994) Physical aspects of magmatic degassing II. Constraints on vesiculation processes from textural studies of eruptive products. In: Carroll MR, Holloway JR (eds) Volatiles in Magmas. Mineral Soc America 30: 447-478

Cathles LM (1993) A capless 350°C flow zone model to explain megaplumes, salinity variations, and high-temperature veins in ridge axis hydrothermal environments. Econ. Geol. 88: 1977-1989

Hedenquist JW (1995) The ascent of magmatic fluid: discharge versus mineralization. In: Thompson JFH (ed) Magmas, Fluids and Ore Deposits. Mineral Assoc Canada, short course series 23: 263-290

Hedenquist JW and Lowenstern JB (1994) The role of magmas in the formation of hydrothermal ore deposits. Nature 370: 519-527

Hekinian R, Pineau F, Shilobreeva S, Bideau D, Gracia I, Javoy M (2000) Deep sea explosive activity on the Mid-Altantic Ridge near 34°15'N: magma composition, vesicularity and volatile content. J Volcano Geoth Res 98: 49-77

Hurwitz S Navon O (1994) Bubble nucleation in rhyolitic melts: Experiments at high pressure, temperature, and water content. Earth Planet Sci Lett 122: 267-285

Kamenetsky VS, Binns RA, Gemmell JB, Crawford AJ, Mernagh TP, Maas R, Steele D (2001) Parental basaltic melts and fluids in eastern Manus backarc basin: implications for hydrothermal mineralization: Earth Planet Sci Lett 184: 685-702

Lowenstern JB (1995) Applications of silicate-melt inclusions to the study of magmatic volatiles. In: Thompson JFH (ed) Magmas, Fluids and Ore Deposits. Mineral Assoc Canada, short course series 23: 71-100

McCutcheon SR (1992) Base-metal deposits of the Bathurst-Newcastle district: characteristics and depositional models. Explr. Mining Geol. 1: 105-119

Roedder E (1979) Origin and significance of magmatic inclusions: Bull Mineral 102: 487-510

Scott SD Binns RA (1995) Hydrothermal processes and contrasting styles of mineralization in the western Woodlark and eastern Manus basins of the western Pacific. In: Parson LM, Walker CL, Dixon DR (eds) Hydrothermal vents and processes. Geol Soc London Sp Pub 87: 191-205

Stanton R.L (1994) Ore Elements in Arc Lavas 391 Oxford Sci Pub

Van Staal CR, Wilson RA, Rogers N, Fuffe LR, Langton JP, McCutcheon SR, McNicoll V, Ravenhurst CE (2003) Geology and tectonic history of the Bathurst supergroup, Bathurst Mining Camp, and its relationships to coeval rocks in southwestern New Brunswick and adjacent Maine— A synthesis. Econ. Geol. Monog 11: 37-60

Von Damm KL (1990) Seafloor hydrothermal activity: black smoker chemistry and chimneys. Ann. Rev. Earth Planet Sci. 18: 173-204

Yang K, Scott SD (1996) Possible contribution of a metal-rich magmatic fluid to a sea-floor hydrothermal system. Nature 383: 420-423

Yang K, Scott SD (2002) Magmatic degassing of volatiles and ore metals into a hydrothermal system on the modern sea floor of the eastern Manus back-arc basin, western Pacific. Econ. Geol. 97: 1079-1100

Yang K, Scott SD (2003) Geochemical relations of felsic magmas to ore metals in massive sulfide deposits of the Bathurst Mining Camp, Iberian Pyrite Belt, Hokuroku District and the Abitibi belt. Econ. Geol. Monog 11:457-478

Yang K, Scott SD (2005) Magma boiling beneath a hydrothermal system on the modern sea floor of the eastern Manus back-arc basin, western Pacific: Evidence from melt inclusions. Econ. Geol. accepted

Anhydrite-pyrite-magnetite-pyroxene-type deposits in volcanic basins of a Mesozoic continent, Yangtze River Valley, China

Ronghua Zhang, Shumin Hu, Xuetong Zhang
Open Research Lab. of Geochemical Kinetics, Institute of Mineral Resources, Chinese Academy of Geological Sciences, Baiwanzhuang Road 26, Beijing 100037, China

Abstract. Anhydrite–pyrite–magnetite–pyroxene type deposits occur in volcanic basins of the Mesozoic continental crust, Yangtze River valley, China. These types of mineral deposits consist of large magnetite ore bodies, pyrite ores, and an anhydrite layer. The deposits have mainly two types of alteration zoning, melanocratic alteration and leucocratic alteration. Magnetite ores occur in association with melanocratic alteration. Pyrite ores and the anhydrite layer occur in leucocratic altered rocks. Investigations indicate that isopleths of the major- and trace-element compositions in minerals are all parallel to the boundaries of alteration zones. The spatial distribution of various mineral solid solutions and polymorphs has been documented in the alteration profile, from the lower level upward stratigraphically and from the inner part outward (proximal to distal). These compositional variations indicate the presence of a temperature and a concentration gradient in the ore-forming hydrothermal system during ore formation. The temperature for separating two sets of ores and alteration zones was at 300-350°C, near the critical point of water. Intersecting and crossing the H_2O critical curve changes the property of hydrothermal fluids resulting of precipitation of magnetite ores, which is coincident with the transition from melanocratic to leucocratic alteration types.

Keywords. Anhydrite–magnetite-pyroxene equilibrium, Mesozoic volcanic area, alteration zone

1 Introduction

Massive sulfide deposits formed in ancient oceanic volcanic areas are generally considered to be similar to and comparable with the products of hydrothermal activity at modern mid-ocean ridges (MOR); and Cyprus-type deposits are commonly regarded as deposits of old mid-ocean ridge type (Humphris et al.1995). Seafloor drilling has revealed that the accumulation of hydrothermal ores at MOR include substantial sulfide and sulfate minerals that are commonly closely associated with silicified rocks (Seyfried et al. 1991; Alt 1995; Seyfried and Ding 1995). The pyrite-anhydrite-quartz assemblage may form an important alteration product that may have a brecciated structure. Deposits of this type are characterized by the presence of abundant accumulated anhydrite (Anh). However, many Cyprus-type deposits do not contain much anhydrite. In the Mesozoic continental volcanic basins formed within fault depressions in the Middle-Lower Yangtze river valley in China are deposits dominated by pyrite-anhydrite-magnetite (Py-Anh-Mt) ores.

The Luohe deposit in the Anhui Province in China is typical of these Py-Anh-Mt type deposits (Zhang 1979; Zhang 1986). Such a deposit can be divided into two parts: the deeper and the shallower. The shallower part, called the leucocratic alteration zone, consists of substantial pyrite and anhydrite ores and silicified rocks, constituting extensive pyrite-anhydrite-quartz rocks (sometimes breccias) that are associated with argillized, sericitized, and propylitized ores. Those alteration features and internal breccia structures are very similar to MOR hydrothermal systems. The deeper parts of the Luohe deposit, called the melanocratic alteration zone, consists of anhydrite and magnetite ores that are associated with alteration minerals such as pyroxene, uralite, apatite, garnet, scapolite, plagioclase (dominated by albite and oligoclase), titanite, potassium feldspar, and phlogopite. The Luohe deposit belongs to a special deposit type formed in fault-controlled, intracontinental volcanic basins. Describing the compositional evolution of the minerals through the vertical alteration zoning profile in this Mesozoic volcanic system will provide further understanding of this ancient hydrothermal system.

2 Geological setting

In the Middle-Lower Yangtze River valley, there are marine basins of Early Paleozoic to Triassic age. These basins contain a thick marine sedimentary sequence, which is dominated by limestone, with less sandy shale. The thick Triassic carbonate sedimentary strata are intercalated with anhydrite. In the Mesozoic, a series of continental faulted basins were formed. In the Early Jurassic, continental sedimentary sandy shale occurred. In the Late Jurassic, volcanic activity began, producing a sequence comprising mainly alkaline basalts and multiple eruptions involving basalt rich in potassium, alkaline basalt, trachyandesite, trachyte and volcanic clastics took place and continued into the Early Cretaceous. Associated with the volcanism was the intrusion of gabbros, monzonite and dioritic porphyry. The Luohe deposit, located in the Lu-Zong Basin, is a large deposit dominated by an anhydrite-magnetite-pyrite-pyroxene assemblage (Zhang 1979; Zhang 1986; Zhang et al. 1997; Zhang et al. 2002). There is a thick an-

This page intentionally blank

hydrite bed, which is underlain by massive pyrite ore (occasionally containing copper) or pyrite-anhydrite ore. The alteration zone is thick and typically composed of pyrite, quartz, and anhydrite. At its periphery, silicified, kaolinized (argillized) and carbonate- sericite altered rocks, some with widespread propylitic alteration, occur successively outwards. The anhydrite layer extends up to 1500 m, whereas the anhydrite-quartz-pyrite zone extends for 2000 m. Between the two alteration zones is a superimposed alteration zone that contains quartz, sericite and clay with carbonate minerals (leucocratic alteration commonly contains hematite and pyrite ore) overprinting early melanocratic altered rocks.

3 Hydrothermal alteration zones

The compositions of the mineral solid solutions, their trace elements and the coexisting aqueous solutions vary systematically from bottom to top of the profile in the anhydrite-magnetite-pyroxene type Luohe deposit (Table 1).

From the data obtained from homogenization temperature and salinity of primary fluid inclusions in anhydrite, it can be inferred that, during the formation of the deposit, there existed a temperature gradient and a NaCl salinity gradient for aqueous species in the fluid coexisting with the ore minerals. Two type of alteration zones can be defined in the profile with the boundary between the two at about 350°C. In the upper type, leucocratic alteration is composed mainly of the products of hydrolysis reactions. The lower melanocratic alteration is composed of anhydrite, pyrite, magnetite, pyroxene, plagioclase, K-spar and phlogopite. The main features in the early hydrothermal stage are characterized by high salinity, 21.2 wt% NaCl, and high temperatures, up to 548°C (fluid inclusion data on anhydrite). Some fluid data suggests that the homogenisation temperature of fluid inclusion in apatite is 600°C.

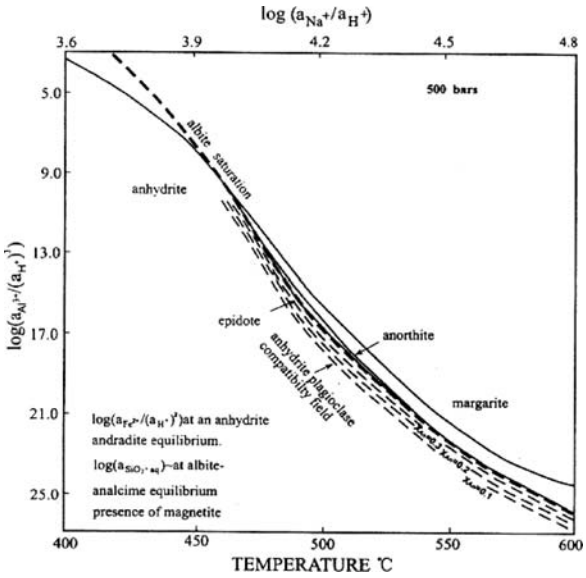

Figure 1: Mineral stability fields within the coordinated activity ratio versus temperature diagram for the system CaO-FeO/Fe_2O_3-Al_2O_3-SiO_2-H_2SO_4-HCl-H_2O, in the presence of magnetite and pyrite and with aH_2O = 1, P = 500 bars, log ($a_{Fe}^{+2}/a^2_{H}^{+}$) values buffered by anhydrite-andradite equilibrium, and log(a_{SiO2}) corresponds to albite-analcime equilibrium. There is a small field for epidote stability.

In the early stage of the mineralization, anhydrite coexisted with pyroxene, plagioclase and potassium feldspar. When the temperature dropped below the critical temperature and pressure for saline water, the pyrite–anhydrite assemblage (pyrite ore and alteration) was formed. During late stage hydrolysis reactions, anhydrite was rarely preserved. Many ore deposits in the Middle-Lower Yangtze River valley do not contain much anhydrite, but have anhydrite relicts in the silicified zones, which are buried at the depths of less than 400m.

4 Thermodynamic analysis of the anhydrite-magnetite-pyroxene-albite quilibria, coexisting solutions, and discussion

A theoretical phase equilibrium analysis of major mineral assemblages and coexisting hydrothermal fluids in the system K_2O -Na_2O – CaO – MgO – FeO/Fe_2O_3 – Al_2O_3 – SiO_2 – H_2SO_4 – H_2S – H_2O – HCl in the temperature range 350-600°C and 50 MPa was done. Activity diagrams were used to depict chemical constraints on these equilibria with the coexisting hydrothermal fluids.

In the inner part of the high-temperature and high-pressure alteration zone at depths of 500-1000m, the composition, temperature, salinity (m_{NaCl}) and pH of the hydrothermal fluid in melanocratic alteration are defined by the equilibria of the major minerals, anhydrite–pyroxene– plagioclase, and the coexisting aqueous solutions in this system, expressed in activity diagrams, e.g., Figure 1.

In the temperature range 400-550°C at 50MPa, the anhydrite-pyrite-magnetite-diopside mineral assemblage is stable in the systems within the chemical constraints of log ($a_{Ca}^{2+}/ a^2_{H}^{+}$) from 6 to –2, log ($a_{Fe}^{2+}/ a^2_{H}^{+}$) from 1.8 to –8 and a_{SiO2} less than the activity of SiO_2 at quartz saturation.

In the upper part of the alteration zone, at a depth of 300 to 600m, gradual evolution to temperatures less than the critical for water, at low pH and low m_{NaCl}, yielded coexisting pyrite and anhydrite in the alteration zone and exhalative layer and overlying anhydrite layer.

Hot brines at depth reacted with basalt resulting in alteration, with resultant alteration assemblages acting as buffers to redox, pH and various aqueous species in the hydrothermal fluid. This in turn affected the mineral–aqueous solution equilibria and evolution of these fluids

This page intentionally blank

Table 1: Principle compositional characteristics of minerals and the coexisting fluids from the various alteration zones in the Anhydrite-Pyrite-Magnetite-Pyroxene type, Luohe deposit.

Alteration zone	Aalinity[a]	T_h °C	T_m °C	$T_{anh\text{-}py}$ °C	$\delta^{34}S_{Anh}$	$\delta^{18}O_{Mt}$	TiO_2 in mt wt%	Co+Ni in py wt%	An of Pl	Al_2O_3 in Pyx	F in Ap
Pyx-Ab-Anhn	21.1-18.25	500-400	520-435	548-527	16-17.86	4.5-4.7	2.7-1.5	0.05	23-5	2-9.12	2.8-3.2
Pyx-Anh-Mtn	19.5-12.5	400-300		560-344	17-18.2	4.3-4.5	1.5-0.5	0.03-0.05	5-0	1-2	2.6-1
Superposed Alt.	15.3-10.1	370-300	(440-380)	360-350	17-19			0.03-0.02			
Leuco. Alt.	13.7-8.1	300-180	(300)	310-230	18-19.3			0.02-0			

Note: salinity (a) is measured from fluid inclusions in anhydrite; T_h means homogenizition temperature of fluid inclusion in anhydrite. T_m°C is from the feldspar geothermometer; $T_{anh\text{-}py}$°C is the temperature according to the sulfur isotopic fractionation factor between anhydrite and pyrite (Zhang 1986); $\delta^{34}S_{Anh}$ refers to $\delta^{34}S$ of anhydrite; $\delta^{18}O_{Mt}$ express $\delta^{18}O$ in magnetite. TiO_2 in mt is weight percentage of TiO_2 in magnetite. Co+Ni in py wt% is weight percentage of Co + Ni in pyrite. An is anorthite number in plagioclase. Al_2O_3 in Pyx is weight percentage of Al_2O_3 in pyroxene. F in ap is weight percentage of F in apatite. (440-380) is from Taishan deposit.

in late stage mineralization. Those fluid-rock buffers can be depicted on activity ratio diagrams.

The anhydrite-andradite-bearing equilibrium assemblage can be used as the redox buffer (to determine the activity of Fe^{2+}), whereas the albite - analcime assemblage acts as a buffer of activity of $SiO_{2(aq)}$. Plagioclase-epidote, prehnite-epidote, K-spar-annite and albite-epidote-anhydrite equilibria can also act as redox buffer or Fe^{2+} concentration buffer for the hydrothermal fluids (see Fig. 1).

The plagioclase-pyroxene–anhydrite zone occurs over an extensive thickness (at depths of 500-1000m). The plagioclase, pyroxene, and garnet solid solutions in the profile gradually co-vary in composition. Once local equilibrium was achieved between the minerals and coexisting solution, the mineral composition gradually changed with the fluid composition in an evolving temperature gradient evident now within the observed alteration profile.

When these buoyant hydrothermal solutions were reacting with basalts, they became subcritical due to decreasing temperature and pressure. The saline fluids reacted with basalt resulting in two types of alteration zones, consistent with phase separation at depth "near-the critical region".

Acknowledgements

This study is supported by 2001 DEA30041,2001DEA20023B 2002DEA30084 and 2003DEA2c021, G1999CB403212, Chinese NSF 20373064.

References

Alt JC (1995) Subseafloor processes in mid-ocean ridge hydrothermal systems. In: Humphris SE, Zierenberg RA, Mullineaux LS and Thomson RE (eds) Seafloor hydrothermal systems: physical, chemical, biological and geological interactions. American Geophysical Union, Geophysical Monograph 91: 85-114.

Berndt ME, Seyfied Jr WE, Janicky DR (1989) Plagioclase and epidote buffered of cation ratios in mid-ocean ridge hydrothermal fluids: Experimental results in the near supercritical region, Geochimica et Cosmochimica Acta 53: 2283-2300.

Humphris SE, Herzig PM, Miller DJ (1995) The internal structure of an active sea-floor massive sulphide deposit. Nature 377(26): 713-716.

Seyfried Jr WE, Ding K, Berndt, ME (1991) Phase equilibria constrains on the chemistry of hot spring fluids at mid-ocean ridges. Geochimica et Cosmochimica Acta 55: 3559-3580.

Seyfried Jr, WE, Mottl MJ (1995) Geologic setting and chemistry of deep-sea hydrothermal vents. In: Karl (ed) The microbiology of deep-sea hydrothermal vents. CRC press 1-34.

Zhang R (1986) Sulfur isotopes and pyrite-anhydrite equilibria in a volcanic basin hydrothermal system of the Middle-Lower Yangtze valley. Economic Geology 81: 32-45.

Zhang R, Hu S, Su Y (2002) Alteration zoning and kinetic process of mineral - water interactions. Acta Geologica Sinica 76(3): 351-366z

Zhang R, Hu S, Yu W, Wang J (1997) Chemical Kinetics in hydrothermal systems: alteration minerals, Proceedings of 9th Quadrennial IAGOD Symposium Beijing, 1996, (E.Schweizerbart'sche Verlagsbuchhandlung) 223-238.

Zhang RH (1979) Geochemical zoning of altered country rocks of perphyrite iron deposits, Yangtz river valley. Geologica Acta Sinica 53(2): 137-153.

Session 7

Understanding ore systems though precise geochronology, isotope tracing and microgeochemistry

Origin of titanomagnetite-ilmenite mineralization, Arsentyev gabbro-syenite massif, Transbaikalia, Russia

Roza Badmatsyrenova, Dmitriy Orsoev
Geological Institute SD RAS, Ulan-Ude, Russia

Abstract. The study of endogenic titanomagnetite-ilmenite ores are of interest as they present a number of petrologic problems. One such problem is determining their genetic connection with alkali-mafic and mafic complexes and associated phosphorus enrichment. The Arsentyev gabbro-syenite massif is representative of these systems and provides an ideal situation in which a detailed study allows further understanding of interrelated magmatic and ore-formation processes. It is shown that an oxide-ore liquid separated from a parental silicate melt during early stages of subalkaline mafic magma crystallization.

Keywords. Liquid immiscibility, geochemistry, ore mineralization

1 Introduction

Titanomagnetite-ilmenite ores sourced from various deposits are considered as a premier source of commercial iron and vanadium. Select deposits additionally contain significant titanium enrichment providing a mineral source for titanium production. Currently ores from large tonnage, high grade deposits are now mined from Bushveld (the South Africa Republic), Lac-Tio (Canada), Panzhihuan (China), Kachkanar (Russia). Ore occurrences are known in the Urals, Kareliya, East Sayan, Transbaikalia, and Far East. The Arsentyev gabbro-syenite massif with titanomagnetite-ilmenite mineralization is representative of this association. Understanding iron ore deposit genesis is problematic, with particular difficulties in rectifying magmatic titanomagnetite-ilmenite deposits formation, yet a comprehensive understanding is essential for exploration. Therefore, studies identifying genetic processes occupies a special place in the analysis of ore genesis in magmatic systems. In addition to fundamental understanding, the study of already known of ore complexes is necessary for development of prospecting criteria and interpretations of results, which may form the basis for rating production feasability of titanomagnetite-ilmenate ores.

2 Geological setting and structure

The Arsentyev massif is located at the central part of the Monostoy ridge west of the Arsentyevka village (Fig. 1a). The massif outcrops over a 20 km^2 area.

The Arsentyev massif is defined by intrusions of syenite-pyroxenite-gabbro with a high titanium ultramafic-mafic association (Badmatsyrenova et al. 2004). These intrusions are related to rift-like structures of various ages and have the geochemical signature of alkaline basalts. Two intrusive phases, each of them being followed by formation of dike complexes, form the Arsentyev massif (Fig. 1b). The first phase consists of a stratified series pyroxenites, olivine and kersutite gabbros, gabbros, anorthosites and syenite. The second phase includes the rocks of the syenite series.

The titanomagnetite-ilmenite mineralization is confined to the stratified gabbro-anorthosite series. This mineralization is subdivided into syngenetic and epigenetic by morphological features and degree of localization. The widespread syngenetic mineralization is represented by disseminated and net-textured ores while the restricted epigenetic mineralization is represented by massive ores. As a rule, disseminated ores are confined to apatite-free and apatite ore gabbros and pyroxenites with 10 to 25 vol.% ore minerals. Ore gabbros are advanced among most differentiated intrusive region, where they alternate with leucogabbro (up to anorthosite) and gabbro.

The thickness of orebodies are highly variable but prevail as ventricular and vein ore. The massive ores are usually contained within area associated with disseminated and net-textured ores and are related to protomagmatic fracturing. The contact between ore bodies with host gabbroids are tectonic as a rule.

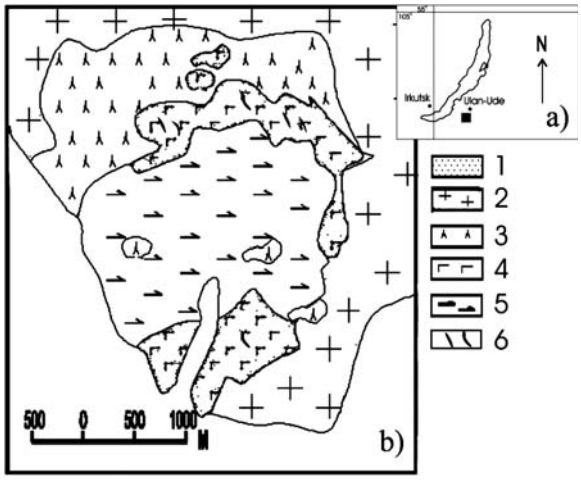

Figure 1: Location (a) and geological map (b) of the Arsentyev massif (after Bogatikov 1966, modified from Badmatsyrenova et al. 2004). 1-Quaternary sediments, 2-Granite, 3-Syenite, 4-Layered series, 5-Leucogabbro and anorthosite, 6-ore bodies

This page intentionally blank

3 Mineral composition and geochemistry

The disseminated ores are divided into titanomagnetite-ilmenie ore and apatite-titanomagnetite-ilmenite ore with apatite contents of 10-15 wt.%. Apatite-titanomagnetite-ilmenite ores have a subordinate value. Magnetite and ilmenite are the main ore minerals. They are intimately associated, forming xenomorphic aggregates interstial to silicate minerals and always crystallizing after the silicates. The grains size varies from 0.04 to 3 mm. They also occur as small inclusions in pyroxene, kersutite and plagioclase but in insignificant amounts. The separate grains of magnetite and ilmenite display variable degrees of isomorphism depending on their quantitative ratio. Both "homogeneous" magnetite having roughly a pure iron composition and titaniferous magnetite with dissolution structures are observed. Ilmenite also has variable composition based on the concentration of Fe^{3+}.

In addition to ore minerals and apatite, the ores contain varying amounts of olivine, pyroxene and plagioclase. Amphibole and biotite are also present. Sulphides and spinel are present but economically insignificant compared to the apatite-titanomagnetite-ilmenite ores. The apatite-bearing ores have significantly more sulphides and spinel compared to the massive and disseminated iron-titanium ores.

The mineral composition of massive ores is rather restricted. The ore is dominated (70-90 vol.%) by aggregates of magnetite, titanomagnetite and ilmenite. Magnetite is the dominant ore mineral with a half to a third as much ilmenite. The grains of ore minerals are larger, up to 5 mm, in massive ores compared with disseminated ore minerals. Separate, fine-grained pyrite, pyrrhotite, chalcopyrite, marcasite and pentlandite are present in the ores at insignificant amounts. The constant presence of apatite at insignificant amounts and increased contents of spinel (up 10-30%) are characteristic of the massive ores. Kersutite is also present.

Titanomagnetite from the massive ore contains 6.48 wt.% TiO_2 and is seen as thin intergrowths of magnetite, ilmenite, spinel and ulvöspinel(?). Trellised or reticulated titanomagnetite from ore gabbros contain appreciablly less TiO_2 (0.18-0.91 wt.%). Finally, titanomagnetite from host gabbros contains only TiO_2 (0.06-0.08 wt.%).

The concentration of TiO_2 in ilmenite forming lamellar inclusion in titanomagnetite found in disseminated ore is 48.68 wt.% while concentration of TiO_2 in massive ore is 53.31 wt.%. Spinel in disseminated ores contain 0.1 to 0.3 wt.% TiO_2, whereas spinel from massive ores forming tear-shaped structures of immiscibility in magnetite contains TiO_2 up 4.94 wt.% and in ilmenite in massive ore contains 0.96 wt.% TiO_2. Manganese concentration in ilmenite is 0.52 to 1.57 wt.%. Mn in magnetite is 0.07 to 0.19 wt.%. The magnesium contents in magnetite-bearing ore much more exceeds (up to 1.57 wt.%) contents in ore gabbro and gabbro (0.08 wt.%). Mg concentrates in lamella of ilmenite in massive ores are 7.94 wt.%. The aluminium in magnetite in massive ores contains up to 1.73 wt.%. The maximum contents Al in rocks are 0.11 wt.%. Ilmenite is aluminum-poor (0.06 wt.% Al_2O_3). Dissolution structures in massive ores are present with Al_2O_3 up to 5.55 wt.%. Aluminium in titanomagnetite is associated with spinel intergrowths.

Amphibole (TiO_2 up to 6 wt.%) is identified as an accessory mineral in ores. Large kersutite crystals are distinctly brown colour and pleochroic suggesting greater Fe and Ti content. Analyzed amphibole have the high contents Al_2O_3, Ti and alkalis in comparison with gabbro from other units.

Biotite in massive ore is FeO deficient with proportionaly more MgO, TiO_2, Na_2O than in dissiminated ores.

Clinopyroxene composition directly correlates to plagioclase composition. The most magnesian pyroxene (MgO 14.56 wt.%) is associated with the most basic plagioclase (An_{40}). The pyroxene Mg# changes from 80 to 74 %.

Fayalite olivine is enriched with increasing ore abundances. Nickel contents correlate with the olivine.

Apatite is often the only mineral in mafic rocks that yield information about volatile composition. Fluorapatite is found in gabbros and ores of the Arsentyev massif. The fluorine contents in ores (1 to 2 wt.%) is noticeably less than in gabbro (2 to 3.5 wt.%). High fluorine and phosphorus concentrations in connection with increased alkalinity of the primary basalt magma facilitates volatile immiscibility and support ore cluster formation. REE concentrations in apatite from gabbro have typical for basalt distribution: the relative concentration of lanthanides increases from HREE to LREE, the degree of division is marginal (La/Yb = 21-36), and a negative Europium anomoly is evident. Conversely, apatite from ores does not have a negative Europium anomoly. The new data does not contradict immiscibility of titanomagnetite-ilmenite ores and apatite formation.

The geochemical data suggest an iron-bearing silicate melt of large anion trivalent iron complexes ($Fe_2O_4^{2-}$) formed after oxidation by interaction with alkaline oxide components and water. The predominance of oxidic iron in magnetite points to an oxidizing environment. It is probable that the formation of anion complexes $Fe_2O_4^{2-}$ instead of cation of bivalent iron facilitates initiation of immiscibility in the melt system resulting in an ore-forming and a silicate liquid.

4 Conclusions

Microprobe analysis shows that magnetite, ilmenite, amphibole and biotite of the massive ores are significantly richer in TiO_2, Al_2O_3, MgO and Na_2O than the minerals

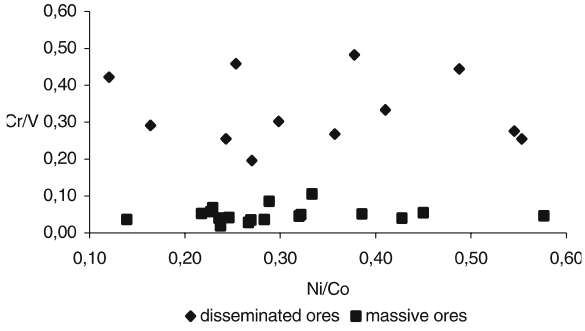

Figure 2: Diagram illustrating the dependence Cr/V and Ni/Co in disseminated and massive ores.

of the disseminated ores. The massive ores are characterized by high V (1400 to 1600 ppm), Zn (200 to 500 ppm), and Cr (21 to 36 ppm) concentrations and low concentrations of Sr (60 to 210 ppm), Co (73 to 112 ppm) and P_2O_5 (0.06 to 0.21 ppm) compared to the disseminated ores that have very high concentrations of the main components (TiO_2, Fe_2O_3 and FeO). Variations in ore compositions are illustrated on the ratio plots of petrogenic and trace elements. A later independent formation of the massive ores is indicated by significantly lower values of Cr/V and Ni/Co ratios than in the disseminated ores if using these ratios as indicators of ore formation stages. Using classification based on chemical composition, the ores of the Arsentyev massif belong to the iron-titanium-vanadium type.

The study of distribution of noble metals has shown that the ores have platinum enrichment: Pt contents of massive ores are up to 6.3 ppb and Ag contents up to 2.8 ppm while Pt contents of disseminated one are < 2 ppb and Ag 1 ppm.

Conditions favorable for phosphorus induced liquid immiscibility can be expected in silicate-salt melts (Krigman, Krot 1991), or immiscibility may be induced by another component, possibly ferrous iron complexes. For example, it is possible to form gabbroid complexes associated with apatite-ilmenite and titanomagnetite mineralization, which, in opinion of some researchers (McBirney, Nakamura 1974, Marakushev 1987), is connected to immiscibility decomposition of the parental melt into a salic and a femic melt, where the latter representing an ore magma with the contents P_2O_5 7 to 8%.

Two genetic ore types in the Arsentyev massif are allocated: the first type, massive titanomagnetite-ilmenite ores, are of immiscibility genesis while the second type, ore gabbro, formed in result of crystallization differentiation of a basalt magma.

Acknowledgements

This work was supported by the Russian Foundation for Basic Research (grant No 05-05-97246), Russia President grant for leading science school No Sh-2284.2003.5, Russian Science Support Foundation.

References

Badmatsyrenova RA, Orsoev DA (2004) Computer simulation of titanomagnetite-ilmenite mineralization formation, Arsentyev massif, Transbaikalia, Russia. In: Proc. of the Interim IAGOD Conference, Vladivostok, Russia, 1-20 September, 2004, pp. 407-410

Krigman LD, Krot TV (1991) Stable phosphate-aluminosilicate liquation in magmetic melts Geokhimia. 11: 1548-1561 (in Russian)

Marakushev AA (1987) Geology and mineralogy of the anorthosite associations. Vladivostok, p.17 (in Russian)

McBirney A.K., Nakamura Y (1974) Ann. Report Director geophys. Lab. Washington, 348 pp

Direct dating of ore minerals: A feasibility study of the Pb-Pb isotope step-leaching technique

K. Bassano, J. Hergt, R. Maas, J. Woodhead
*pmd*CRC, School of Earth Sciences, The University of Melbourne, Australia*

Abstract. Pb-Pb step-leaching (PbSL) is a digestion technique based on sequential acid treatment of a mineral resulting in the selective recovery of radiogenic and common Pb components from the crystal lattice, making single-phase Pb-Pb dating possible. Developed originally by R. Frei and colleagues at Bern, the technique was recently applied to Proterozoic garnets to test the reliability of PbSL as a dating tool in multiply deformed terranes (Tonelli 2002).

This study builds on previous observations and tests the reliability of PbSL in directly dating ore minerals such as sulfides (chalcopyrite, pyrite, pyrrhotite/pentlandite) and oxides (magnetite), thereby obtaining the timing of mineralisation from a phase that is unambiguously linked to the ore-forming process. This is based on the often surprisingly high U contents (relative to what might be anticipated), yielding rather higher than expected initial U/Pb ratios in several types of low-Pb sulfides. The technique is applied to well-constrained samples from a number of predominately Australian mineral deposits covering a range of mineralization types.

Keywords. Pb-Pb, step-leaching, ore minerals, direct dating

1 Introduction

The mechanism of Pb isotope unmixing in step-leaching was examined by Frei et al. (1997) who proposed two main processes; the surface/crystallographic site dependent hydrolysis of metal cations, and the progressive remobilisation of radiogenic Pb from the leached gel-like structure. Different rates of these processes during progressive leaching results in an effective separation of common and radiogenic Pb, producing generally linear unmixing arrays with age significance in the $^{206}Pb/^{204}Pb$ vs $^{207}Pb/^{204}Pb$ diagram.

Benefits of PbSL over bulk U-Pb and Pb-Pb techniques include the ability to:

- detect sub-microscopic U-rich inclusions using the distinct variations in $^{208}Pb/^{206}Pb$ (i.e. time-integrated Th/U) between host mineral and inclusions such as zircon or monazite
- date a wide range of minerals with low-U; minerals generally thought to be unfavourable for conventional U/Pb dating
- obtain 'single'-mineral isochron ages without the need for analysing associated minerals to produce isotopic dispersion on isochrons

Although previous authors (eg Collerson et al. 2002) have obtained age estimates on (mixed) ore minerals using PbSL prior to this study, further investigation is required into the circumstances in which this technique may/may not be reliably applied.

2 Discussion

In this study the technique has been applied to well-constrained samples from a number of Australian ore deposits, including the analysis of chalcopyrite and magnetite from Broken Hill (BHT), Mt Isa, Ernest Henry (IOCG) and Osborne (IOCG). Magnetite and pentlandite/pyrrhotite from the Merensky Reef in the Bushveld Complex have also been studied.

Studies of chalcopyrite from Copper Blow (Broken Hill) yielded promising results. Lead isotope ratios obtained, particularly in the second leach step, indicate the presence of radiogenic Pb with $^{206}Pb/^{204}Pb$ ratios ranging up to ~57. As chalcopyrite at Copper Blow occurs with torbernite (U-rich), typical grains were interrogated using the SEM to confirm that the Pb compositions reflect those of the chalcopyrite and not inclusions. Results for magnetite from the same deposit display greater spread in the $^{206}Pb/^{204}Pb$ (~23 to 183). The age estimates obtained from these co-genetic minerals are the same (magnetite: 1094±89Ma; MSWD=250; chalcopyrite: 1071±210; MSWD=213), to within error, although the uncertainties are quite large. Unlike the $^{206}Pb/^{204}Pb$ and $^{207}Pb/^{204}Pb$ ratios of these samples, $^{208}Pb/^{204}Pb$ displays very little variation, retaining values typical of common lead (~37 to 38). This indicates that the mineralising fluid from which these phases grew carried U but not Th into the system.

Both chalcopyrite and magnetite were also analysed from the Osborne deposit. The chalcopyrite displays radiogenic values ($^{206}Pb/^{204}Pb$ ~20 to 48) that generate an age estimate of 1252±190Ma.

Preliminary studies at Ernest Henry indicate the samples are also highly radiogenic. Chalcopyrite shows a large spread in $^{206}Pb/^{204}Pb$ (~18 to 257) generating an age estimate of 1590±17Ma (MSWD=1). The variation in $^{206}Pb/^{204}Pb$ ratios displayed by the associated magnetite is even greater (~214 to 965) although the scatter is considerable. These data yield a poorly constrained age of 1044±450Ma because, although the range in ratios is considerable, 'gaps' in the array contribute to the large errors obtained as the isochrons become dominated by one or two points. Further analyses of these samples with varied leaching protocols produced consistently scattered data sets.

In order to determine if the technique is producing the 'correct' age estimates, three samples from the Merensky Reef in the Bushveld Complex, South Africa (two magnetites and one mixed pyrrhotite /pentlandite sulfide) where analysed. Samples from this orthomagmatic deposit were selected due to the generally widely excepted age of the Bushveld Complex ore system. The resulting leach steps from each of these samples displayed little or practically no spread in $^{206}Pb/^{204}Pb$ and $^{207}Pb/^{204}Pb$. The majority of the age estimates generated from this data fall within error of the "known" age of the Merensky Reef, however the uncertainties are large, most likely due to the minor data spread.

3 Evaluation of the leaching process

ICPMS trace element analyses of the study samples have been undertaken in order to examine possible causes for the apparently variable success of this technique. First, the U and Pb contents of bulk-separates will clearly influence how much radiogenic ingrowth can occur relative to the common Pb component, and hence how great the spread in the Pb isotope ratios may be during step-leaching. How this varies between particular ore deposit types is a central question of this study. Another important question is to determine the factors that control the retention or mobility of different elements (particularly Pb, but also how this behaves relative to other trace elements). The acid leaching mechanism cannot be the same as that determined in the step-leaching experiments of silicates (where Si-O bonds are broken during hydrolysis reactions). The assessment of trace element mobility is conducted via analysis of the leachates from different leach steps, and comparisons between these and data for bulk-separates. Finally, the extent to which variations in the initial Pb isotope composition within samples has influenced the scatter in isochrons will be explored. This involves the analysis of numerous separate aliquots of material to check for levels of heterogeneity in their Pb isotope compositions.

Acknowledgements

The authors would like to thank the many members of the *pmd**CRC who have provided us with the well-constrained materials required for this study.

References

Collerson KD, Kamber BS, Schoenberg R (2002) Applications of accurate, high-precision Pb isotope ratio measurements by multi-collector ICP-MS. Chem Geol 188: 65-83

Frei R, Villa IM, Nagler ThF, Kramers JD, Przybylowicz WJ, Prozesky VM, Hofmann BA, Kamber BS (1997) Single mineral dating by the Pb-Pb step leaching method: Assessing the mechanisms. Geochim Cosmochim Acta 61: 393-414

Tonelli M (2002) An evaluation of Pb step leaching geochronology as applied to high-grade metamorphic terranes. PhD Thesis, University of Melbourne (unpubl)

Rutiles in eclogite from the Sulu UHPM Terrane: A preliminary study

Chen Zhenyu, Chen Yuchuan, Wang Denghong, Xu Jue, Zhou Jianxiong
Institute of Mineral Resources, Chinese Academy of Geological Science, Beijing, 100037, China

Abstract. In recent years more than 40 rutile-bearing eclogite ore bodies have been discovered among the thousands of eclogite bodies in the Sulu Utra-High Pressure Metamorphic (UHPM) terrene. Rock- and ore-cores obtained by the Chinese Continental Scientific Drilling (CCSD) Project revealed the presence of several hundred meters of rutile-bearing eclogites. This paper presents a preliminary petrographic, trace element, and Pb isotope study of rutile ores in eclogite. Rutiles occur as inclusions, intergranular infillings, remnant replacements, and hydrothermal infillings in the host rocks. The ore minerals define four stages of rutile mineralization and metamorphic evolution in the eclogites. Electron microprobe (EMP) trace element analysis of three rutile specimens show that different occurrences of eclogite also have different trace element compositions in rutile. These compositional differences may reflect different source rocks for the eclogites. Peak metamorphic temperatures were calculated using the Zr geothermometer in rutile. The Pb isotopic compositions of rutile obtained by step-fuse analysis of single grains of rutile did not fall on one growth line, but show similar variation between different samples. This implies that the Pb isotopic compositions of rutile may have been disturbed during its growth. This variation could be used to trace the growth history of the rutile, and further to trace the process of continental subduction- exhumation.

Keywords. Rutile, eclogite, petrography, trace elements, Pb isotope, Sulu UHPM terrene

1 Introduction

The Sulu ultra-high pressure metamorphic (UHPM) terrene is the product of the Triassic collision involving the north China and Yangtze cratons. There are thousands of eclogite bodies of different size and occurrence in the UHPM belt in the Sulu terrene, and more than 40 rutile-bearing eclogite ore bodies have been recently discovered. The total reserves of rutile ore amount to several million tons (Huang J P., et al. 2003). The main hole of the Chinese Continental Scientific Drilling (CCSD) project is located at Maobei, Donghai, in the southern part of the Sulu UHPM terrene (a simplified geological map is showed in Fig. 1). Drilling to 5100m at this locality has recently completed. Rock- and ore-cores obtained by the CCSD revealed rutile-bearing eclogites amounting to several hundred meters (Xu et al. 2004).

The rutile deposit in the Sulu UHPM terrene is a typical eclogite-type rutile deposit. To assess the relationship between UHPM and the mineralization of rutile in eclogite, we have conducted a preliminary study on the rutile from the main hole of the CCSD. In this study we focus on the different rutile occurrences, petrography, trace element composition and Pb isotopic composition.

2 Petrography of rutile and titanium minerals in eclogite

The rutile ore bodies mainly occur in massive eclogites, as strips and lenses. Rutile-bearing eclogites have at least three different occurrences: (1) xenoliths in ultra-mafic serpentines, e.g. in Xugou and Jiangzhuang; (2) lenses in marbles e.g. in Yanmachang and Banzhuang; (3) metamorphosed intrusive complex rocks in Donghai. The eclogites show variable mineral assemblages and chemical compositions, and indicate diverse origins for their protoliths (Zhang et al. 2004). The observation and documentation of both the rock- and ore-cores obtained by CCSD reveal that the major titanium mineral phases of economic interest are rutile and titano-magnetite. The most important ore-bearing rock types are normal rutile eclogite, quartz eclogite associated with phengite-rutile eclogite and kyanite-rutile eclogite. The modal content of rutile in eclogite is 2%~5% (vol.) and is as high as 8%~10% (vol.) (Xu et al. 2004).

Detailed petrographic investigation reveals that rutile in eclogite mostly occurs in four types: (1) as inclusions in garnets, omphacites or zircons, which may have crystallized during prograde metamorphism (coesite or its pseudomorph can be found coexisting with rutile in the same garnet, omphacite or zircon host); (2) as intergranular infilling grains between garnets and omphacites. In

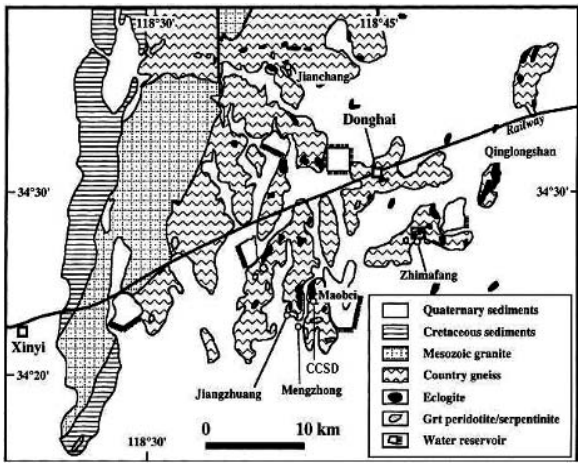

Figure 1: Simplified geological map of Donghai, the southern part of the Sulu UHPM terrene (after Yang and Jahn 2000).

This page intentionally blank

this stage, metamorphism reached its peak conditions, and rutile crystallized simultaneously with eclogite-face minerals such as garnets and omphacites. This is the main crystallization stage of rutile; (3) as replacement remnant, at the amphibolite-face retrograde metamorphism stage. Garnets and omphacites are altered to hornblende and plagioclase. Rutlie is also partly altered to ilmenite or titanite; (4) as hydrothermal infilling forms. Rutile fills in the cleavages and cracks as veins, strings or megacrysts. This rutile occurrence may have crystallized at the greenschist-facies metamorphic stage. At this time, hydrothermal fluids extracted components of mineralization from wall rocks and deposited them in cleavages and cracks in the rocks. On the other hand, the early rutile phase is partly or totally altered to ilmenite or titanite. As for the above-mentioned four occurrences, the second one is the most abundant, and accounts for about 90% of the gross rutile ore reserves. Rutile and titano-magnetite that were altered to ilmenite and titanite during retrogressive metamorphism led to a drop in grade of the titanium mineralization.

3 Trace elements in rutile

Rutile has long been considered to be an important carrier of high field strength elements (HFSE; Zr, Nb, Mo, Sn, Sb, Hf, Ta, W). It also plays a key role in subduction zones by retaining HFSE in the restite/residuum during dehydration and melting reactions. Recent studies by Zack et al. (2002, 2004a, 2004b) show that the trace elements in rutile can give us more information than just the dominant control of HFSE in eclogite. For example, the Nb, Cr content in rutile can be used to distinguish different protoliths of rutile-bearing eclogites. Additionally, the Zr content in rutile is temperature dependent and can be used as a geothermometer in rutile. In this study, we used a JXA-8800R electron microprobe to determine the trace element composition of rutiles in eclogites from Machang, Qinglongshan and Banzhuang. The Machang and Qinglongshan samples occur in metamorphosed intrusive complex rocks, and the Banzhuang samples occur as lenses in marbles. Particular operating conditions were used to obtain low detection limit (20kV, 100nA and 100~300s counting time, which resulted in a detection limit of elements of interest in the 20~30ppm range). Analytical results (Table 1) show that rutiles in eclogite from Machang have the lowest content of Cr and Nb, averaging ~89ppm and mostly below the detection limit. However, these rutiles also have the highest Fe and V content, averaging 5390ppm and 3853ppm respectively. Rutiles in eclogite from Banzhuang show the highest Cr and Nb content, averaging ~1574ppm and ~385ppm respectively; but they also show the lowest Fe and V content, averaging 2602ppm and 2114ppm respectively. Rutiles in eclogite from Qinglongshan have moderate content of these elements, averaging 615ppm, 324ppm, 3457ppm and 3333ppm for Cr, Nb, Fe and V respectively. In the Nb-Cr diagram defined by Zack, et al. (2004b), protoliths of these three eclogites all plot in the "mafic rocks" field. Temperature calculated from Zr content in rutile showed that the peak temperature of metamorphism for these eclogites was 550~575° for Qinglongshan, 565~615° for Banzhuang and ~716° for Machang. These temperature values are comparable with those calculated by the cation-exchange geothermometer of host minerals.

Table 1: Trace elements in rutile analyzed by electron microprobe, (in average, in ppm).

Sample	Cr	Nb	Fe	V	Zr
Machang	89	-	5390	3853	246
Qinglongshan	615	324	3457	3333	71
Bazhuang	1574	385	2602	2114	81

4 Pb isotopic composition of rutile

To obtain the U-Pb age of rutile in eclogite from the Sulu UHPM terrene, we selected three rutile specimens for U-Pb isotope analysis by the step-fuse method. Unfortunately, we could not obtain a correct age because of the very low content of radiogenic Pb isotopes in rutile. But, to our surprise, the Pb isotopic compositions ($^{206}Pb/^{204}Pb$, $^{207}Pb/^{204}Pb$, $^{208}Pb/^{204}Pb$) obtained from a series of step-fuse analyses of a single grain from its shell to its core can not be plotted on one growth line. This means that Pb isotopic ratios can not be attributed to in-situ Pb growth. Franz et al. (2001) found a similar phenomenon when they tried to determine the U-Pb age of a rutile specimen in an eclogite-facies quartz vein within a metabasalt in South Dabieshan. In their case, one 4-cm-long single crystal was divided into 3 small fragments, and each fragment was analyzed. The isotopic variability among these fragments was too large to be attributable to in situ Pb growth, and patterns on the $^{206}Pb/^{204}Pb$-$^{207}Pb/^{204}Pb$ and $^{206}Pb/^{204}Pb$-$^{208}Pb/^{204}Pb$ are incompatible with secondary addition or removal of Pb (Franz et al. 2001) . The rutile in the quartz vein may have been crystallized in the retrograde fluid, so they considered the initial Pb composition of this specimen to be isotopically heterogeneous, which implies that the Pb in the fluid is isotoptically variable during rutile crystallization. In our case, the Pb isotopic compositions of these three specimens have shown abrupt variations at a certain middle step and at the final step of fuse analysis in a similar way. This implies that these three rutile specimens have similar Pb growth history. The two abrupt variations indicate that Pb isotopic compositions of rutile were disturbed twice during its crystallization. These disturbances may reflect the variation of geologic settings

during rutile growth, which can be used to infer continental subduction-exhumation processes. This suggests to us that the variation of Pb isotopic composition in rutile by step-fuse analysis may be used to trace the growth history of the rutile, and further to trace the process of continental subduction- exhumation. Although this is a preliminary discussion and needs further study and more evidence to support it, this approach has shown great potential in the study of the geodynamics of subduction zones.

5 Conclusions

The rutile deposit in the Sulu terrene is genetically related to the UHPM. Rutile is mainly mineralized during eclogite-facies metamorphism. The alteration by retrogressive metamorphism leads to a drop in grade of the titanium mineralization.

EMP was used to obtain trace element composition of different occurrences of rutile in eclogites. These analyses show variations in Nb, Cr, Fe and V content between each occurrence, which may be used to infer the protolith of these eclogites. Temperatures calculated from the Zr geothermometer in rutile are comparable with the results from other methods. This implies that the Zr geothermometer in rutile is a feasible and effective method for calculating peak metamorphic temperatures.

Pb isotopic compositions obtained from step-fuse analysis of single grains of rutile may be potential tracers of rutile growth history. If so, this analytical technique could play an important role in furthering the understanding of continental subduction- exhumation processes.

Acknowledgements

This study is supported by the Major State Basic Research Development Program (2003CB716501). We thank Parham Gardner for her critical reviews, which improved this paper significantly.

References

Franz L, Romer RL, Klemd R, Schmid R, Oberhansli R, Wagner T, Dong S (2001) Eclogite-facies quartz veins within metabasites of the Dabie Shan (eastern China): Pressuretemperature-time- deformation path, composition of the fluid phase and fluid flow during exhumation of high-pressure rocks. Contrib Mineral Petrol 141: 322-346

Huang JP, Ma DS, Liu C, Wang CL (2003) Character and origin of rutile deposit in eclogite in Xiaojiao, Xinyi, Jiangsu province. Geoscience 17: 435-443

Xu J, Chen YC, Wang DH, Yu JJ, Li CJ, Fu XJ, Chen ZY (2004) Titanium mineralization in the ultrahigh-pressure metamorphic rocks from Chinese Continental Scientific Drilling 100~2000m main hole. Acta Petrologica Sinica 20: 119-126

Yang JJ, Jahn BM. (2000) Deep subduction of mantle-derived garnet peridotites from the Su-Lu UHP metamorphic terrane in China. J. metamorphic Geol., 18: 167-180

Zack T, von Eynatten H, Kronz A (2004b) Rutile geochemistry and its potential use in quantitative provenance studies. Sediment Geol. 171: 37-58

Zack, T, Kronz, A, Foley S., River T (2002) Trace element abundances in rutiles from eclogites and associated garnet mica schists. Chem. Geol. 184: 97-122

Zack, T, Moraes, R, Kronz A (2004a) Temperature dependence of Zr in rutile: empirical calibration of a rutile thermometer. Contr. Min. Petrol. 148: 471- 488

Zhang ZM, Xu ZQ, Liu FL, Shen K, Yang JS, Li TF, Chen SZ (2004) Geochemistry of eclogites from the main hole (100~2050m) of the Chinese Continental Scientific Drilling Project. Acta Petrologica Sinica 20: 27-42

A non-magmatic component in fluids of South American Fe oxide-Cu-Au deposits inferred from $\delta^{37}Cl$, $^{87}Sr/^{86}Sr_i$ and Cl/Br

M. Chiaradia[1], **D. Banks, R. Cliff**
School of Earth Sciences, University of Leeds, Leeds LS2 9JT, U.K.
[1] *Present address: Department of Mineralogy, University of Geneva, 1205-Geneva, Switzerland*

R. Marschik
Department of Earth and Environmental Sciences, Ludwig-Maximilians University, 80333-München, Germany

A. de Haller
Department of Mineralogy, University of Geneva, 1205-Geneva, Switzerland

Abstract. The magmatic versus basinal brine origin of the hypersaline fluids associated with iron oxide-copper-gold (IOCG) deposits is controversial. In this study we present and discuss the first stable chlorine and strontium isotope data, combined with Cl/Br ratios, of inclusion fluids of South American IOCG deposits. The isotopic and elemental signatures of South American IOCG deposits suggest either mixing of juvenile magmatic fluids with up to several tens wt.% of crustal brines or magmatic fluids leaching up to few wt.% of evaporite.

Keywords. Iron oxide Cu-Au deposit, chlorine isotope, strontium isotope, fluid inclusion, Andes

1 Introduction

Iron oxide-copper-gold (IOCG) deposits represent a hydrothermal mineralization style characterized by abundant magnetite and/or hematite, variable amounts of Cu-sulfides, pyrite, gold and REE, and intense and voluminous sodic ± calcic and potassic alteration (Hitzman et al. 1992). These deposits form at shallow to mid-crustal levels within cratonic or continental margin settings (Hitzman et al. 1992), and although they usually occur within magmatic rocks, they are not always clearly related to igneous activity. The most controversial aspect of IOCG deposits is the origin of their hypersaline fluids as either (i) fluids exsolved from magmas (e.g., Pollard 2002), or (ii) basinal brines heated by nearby intrusions (e.g., Barton and Johnson 1996).

We report the first stable chlorine and strontium isotope data, as well as Cl/Br ratios, for inclusion fluids of four IOCG deposits and one magnetite-apatite deposit from South America. Chlorine is the dominant metal ligand in IOCG hypersaline fluids and behaves conservatively during fluid-rock interaction. Therefore, chlorine isotopic compositions, combined with strontium isotopes and Cl/Br ratios, may provide tighter constraints, compared to O and S stable isotope data, on the origin of IOGC fluids. The mean mantle $\delta^{37}Cl$ value is 4.7‰ with a range between 3 and 7‰ (Magenheim et al. 1995) whereas crustal chlorine has $\delta^{37}Cl$ values around 0‰ (Eggenkamp et al. 1995). In principle, therefore, chlorine isotopes are able to discriminate between heavy mantle- and light crust-derived chlorine. Additionally, since IOCG deposits constitute an end-member of a continuum with magnetite-apatite (Kiruna-type) deposits (Hitzman 2000), combined investigations of these two mineralization types increase our understanding of the origin of their hypersaline fluids resulting in improved exploration strategies.

2 Ore deposits investigated, samples and techniques

The investigated deposits belong to the Carajás Mineral Province (CMP), Brazil, and to the Peruvian and Chilean Andes (Fig. 1). The CMP consists of a Late Archean volcano-sedimentary sequence deposited upon high-grade tonalitic and trondhjemitic gneisses of the southern part of the Central Brazilian Shield. The region is subsequently intruded by 2.56-2.76 Ga alkaline and calc-alkaline granites and by 1.8-1.9 Ga anorogenic granites (Machado et al. 1991). Either a continental rift (Olszewski et al. 1986) or a subduction-related arc (Dardenne et al. 1988) geodynamic setting is suggested. Investigated CMP mineralization includes the Archean to Early Proterozoic Sossego and Gameleira deposits.

The Cretaceous IOCG deposits of Candelaria (Chile), and Raul-Condestable (Peru) and the magnetite-apatite deposit of El Romeral (Chile) occur in the Andean Cordillera of Peru and Chile in extensional to transpressional arc settings (e.g. Sillitoe 2003).

Geological, mineralogical, and stable isotope data (mostly O, S) indicate dominantly magmatic fluids formed Gameleira (Lindenmayer et al. 2001) and El Romeral, whereas mixed magmatic and non-magmatic fluids characterize Sossego (Marschik et al. 2003) Candelaria (Marschik and Fontboté 2001) and Raul-Condestable (de Haller et al. 2002).

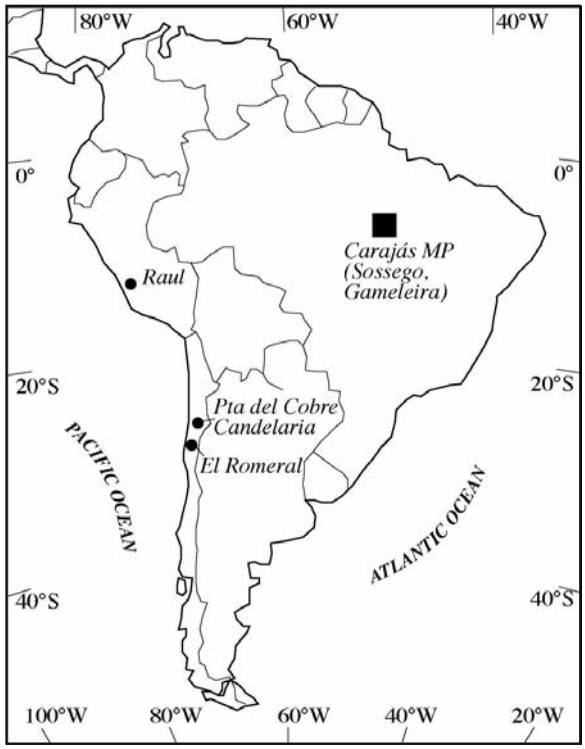

Figure 1: Map of South America with location of the investigated deposits.

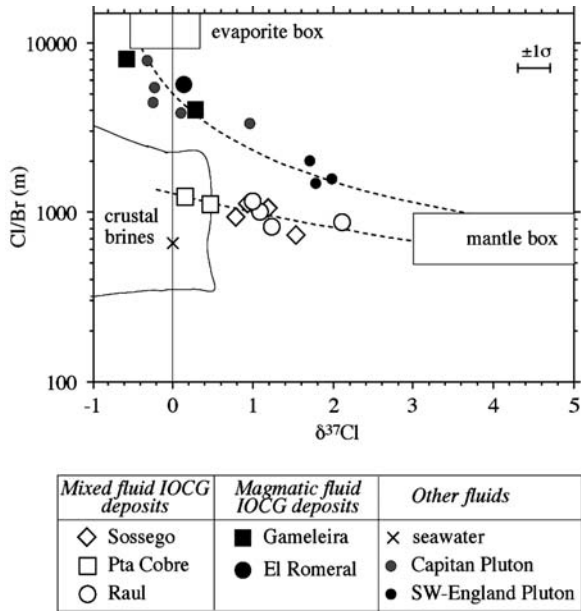

Figure 2: Cl/Br (molar) vs. $\delta^{37}Cl$ diagram of fluids of the investigated deposits. The brine, mantle and halite fields are from data of Eastoe et al. (2001), Magenheim et al. (1995), Johnson et al. (2000), and Eggenkamp et al. (1995). Calculated mixing lines between mantle and crustal sources are also drawn.

Selected fragments of quartz representing the primary ore stages at Raul-Condestable, Candelaria, Gameleira, and Sossego, apatite from El Romeral, as well as two calcites from the late ore stage at Sossego were sampled and crushed. The inclusion fluids were analyzed for stable chlorine and strontium isotope compositions by thermal ionization mass spectrometry (TIMS) and for Cl^- and Br^- concentrations by ion chromatography at the School of Earth Sciences (University of Leeds, U.K.).

3 Sources of chlorine and strontium in inclusion fluids

Chlorine isotope compositions and Cl/Br ratios of hydrothermal fluids of South American IOCG and magnetite-apatite deposits plot along two distinct arrays (Figure 2), allowing discrimination between magmatic fluid-dominated deposits (Gameleira and El Romeral) and deposits with mixed magmatic and non-magmatic fluids (Sossego, Candelaria, Raul) consistent with previous geochemical studies. We interpret the two trends defined by fluids of the magmatic fluid-dominated (Gameleira, El Romeral) and mixed fluid (Candelaria, Raul-Condestable, Sossego) deposits as the result of mixing between a common mantle-derived magmatic fluid and two distinct crustal sources of chlorine both with near 0‰ $\delta^{37}Cl$ values but with different Cl/Br values (Fig. 2).

The trend defined by the magmatic fluids of Gameleira and El Romeral integrated with data from the magmatic fluids of the Capitan and SW-England plutons (Banks et al. 2000: Figure 2) is shifted to high Cl/Br values suggesting that chlorine is a mixture between mantle and halite-derived chlorine, probably resulting from variable magmatic interaction with evaporites. A non-magmatic component at El Romeral is supported by the significantly more radiogenic strontium isotopic composition ($^{87}Sr/^{86}Sr_i = 0.7065$) of the fluid compared to that of the associated magmatic rocks ($^{87}Sr/^{86}Sr_i \sim 0.703$-$0.704$). The Sr isotope data addtionally suggest evaporite assimilation by high-temperature exsolved magmatic fluids rather than evaporite assimilation by the magma itself is responsible for the observed Cl and Sr isotope systematics of the inclusion fluid at El Romeral.

We have calculated that assimilation of 2 to 9 wt.% halite by a mantle-derived magmatic fluid could cause the shift to the near 0‰ $\delta^{37}Cl$ values and high Cl/Br ratios observed in the Gameleira, El Romeral and Capitan pluton fluids. The existence of evaporites in the host sequences of El Romeral (Chile) and Capitan pluton (Mexico) yields geological support to the above scenario. However, there is no evidence for evaporites in the CMP. As a result a fluid souce with ~0‰ $\delta^{37}Cl$ and high Cl/Br ratios such as a hypersaline crustal brine may explain the data of Gameleira.

The other IOCG deposits investigated (Sossego, Candelaria, Raul-Condestable) define a linear array in the

Cl/Br-$\delta^{37}Cl$ space that may result from mixing of the mantle-derived magmatic-hydrothermal fluid with a crustal brine characterized by Cl/Br ratios significantly lower than evaporites but higher than seawater (Figure 2). The fact that all these IOCG deposits plot along a common mixing line (despite the large compositional field of crustal brines) is intriguing and appears to indicate that the mantle-derived magmatic fluid has interacted with a crustal brine characterized by virtually identical Cl/Br ratios despite the different ages and geographic locations of the deposits. The presence of a non-magmatic fluid component in these IOCG deposits is again supported by strontium isotope compositions of the inclusion fluids, which are significantly more radiogenic ($^{87}Sr/^{86}Sr_i$ = 0.7053-0.7056 at Candelaria and 0.7051-0.7062 at Raul-Condestable) than those of the associated magmatic rocks ($^{87}Sr/^{86}Sr_i$ = 0.7031 at Candelaria and 0.7042 at Raul-Condestable). In addition, at Candelaria-Punta del Cobre chalcopyrite, secondary biotite, ore-related calcite and anhydrite also have $^{87}Sr/^{86}Sr_i$ (0.7043-0.7063) higher than the magmatic rocks (R. Marschik, unpublished data). Calculated chlorine contributions from the crustal brine range between 50 and 95% assuming $\delta^{37}Cl_{mantle}$ = 4.7‰ (Magenheim et al., 1995) and a $\delta^{37}Cl_{brine}$ = -0.4‰. However, due to the ten- to hundred-fold higher chlorine content of crustal brines compared to (non-boiled) magmatic fluids, these figures correspond to 4 and 30 wt.% crustal brine contribution.

The above calculations are highly sensitive to assumptions about Cl and Br concentrations in brines and magmatic fluids, to the poorly constrained $\delta^{37}Cl$ composition of the mantle-derived magmatic fluid and crustal brines, and to the relatively large analytical uncertainty of $\delta^{37}Cl$ values (±0.2‰), yet they clearly indicate the presence of a measurable non-magmatic, crustal Cl (and Sr) component in fluids of IOCG deposits.

4 Conclusions

Chlorine and strontium isotope data combined with Cl/Br ratios indicate that ore fluids in the investigated IOCG and magnetite-apatite deposits result from variable mixing of mantle-derived magmatic-hydrothermal fluids with crustal brines or evaporites. The Gameleira IOCG deposit and the El Romeral magnetite-apatite deposit formed by magmatic-hydrothermal fluids leaching evaporites from the host sequence or by mixing with crustal brines characterized by high Cl/BR ratios. Fluids of these deposits preserve a pristine magmatic O and S isotope signatures, yet minimal interactions with evaporites (e.g., 2-9 wt.%) are sufficient to produce the observed evaporite-type Cl and Sr isotope signatures as well as Cl/Br ratios.

In contrast, the IOCG deposits of Candelaria, Raul-Condestable and Sossego formed by the mixing of magmatic-hydrothermal fluids with up to a few tens percent of crustal brine (4-30 wt.%). The significant contribution of crustal brines in these deposits is suggested by Cl and Sr isotope data as well as by Cl/Br ratios. The results are consistent with mixed magmatic and non-magmatic hydrothermal fluid signatures inferred from other isotope systems (oxygen, sulfur). Chlorine isotope data combined with Cl/Br ratios and strontium isotope compositions suggest a measurable contribution of crustal brines and/or evaporites to the ore fluids in IOCG and magnetite-apatite deposits of South America. This conclusion may help to refine strategies for IOCG deposit exploration in South America.

Acknowledgements

We thank Rolf Romer (GFZ, Potsdam) and Holly Stein, Aaron Zimmerman, and Parham Gardner (AIRIE Program, Colorado State University, U.S.A.) for their comments that helped to improve an earlier version of the manuscript.

References

Banks DA, Green R, Cliff RA, Yardley BWD (2000) Chlorine isotopes in fluid inclusions: determination of the origins of salinity in magmatic fluids. Geochim Cosmochim Acta 64: 1785-1789

Barton MD, Johnson DA (1996) Evaporitic-source model for igneous-related Fe oxide-(REE-Cu-Au-U) mineralization. Geology 24:259-262

Dardenne MA, Ferreira Filho CF, Meirelles MR (1988) The role of shoshonitic and calc-alkaline suites in the tectonic evolution of the Carajás district, Brazil. J South Amer Earth Sci 1: 363-372

de Haller A, Zúñiga Alvarado J, Corfu F, Fontboté L (2002) The iron oxide-Cu-Au deposit of Raul-Condestable, Mala, Lima, Peru. In: Sociedad Geologica del Peru (ed) Conf Abst Vol XI Congr Peruano Geol, Lima: p. 80

Eastoe CJ, Long A, Land LS, Kyle JR (2001) Stable chlorine isotopes in halite and brine from the Gulf Coast Basin: brine genesis and evolution. Chem Geol 176: 343-360

Eggenkamp HGM, Kreulen R, van Groos FK (1995) Chlorine stable isotope fractionation in evaporites Geochim Cosmochim Acta 59: 5169-5175

Hitzman MW (2000) Iron oxide-Cu-Au deposits: what, where, when, and why? In: Porter TM (ed) Hydrothermal iron oxide-copper-gold and related deposits: a global perspective, vol 1. PGC Publishing, Adelaide, Australia, p 9-25

Hitzman MW, Oreskes N, Einaudi MT (1992) Geological characteristics and tectonic setting of Proterozoic iron oxide (Cu-U-Au-REE) deposits. Precamb Res 58: 241-287

Johnson LH, Burgess R, Turner G, Milledge HJ, Harris JW (2000) Noble gas and halogen geochemistry of mantle fluids: comparison of African and Canadian diamonds. Geochim Cosmochim Acta 64: 717-732

Lindenmayer ZG, Pimentel MM, Ronchi LH, Althoff FJ, Laux JH, Araújo JC, Fleck A, Bortowski DC, Nowatzki AC (2001) Geologia do depósito de Cu-Au do Gameleira, Serra dos Carajás, Pará. In: Jost H, Brod JA, Queiroz ET (eds) Caracterização de depósitos auriferous brasileiros. ADIMB-DNPM, Brasília, p. 79-139

Machado N, Lindenmayer Z, Krogh TE, Lindenmayer D (1991) U-Pb geochronology of Archean magmatism and basement reactivation in the Carajás area, Amazon shield, Brazil. Precambrian Res 49: 239-354

Magenheim AJ, Spivack AJ, Michael PJ, Gieskes JM (1995) Chlorine stable isotope composition of the oceanic crust: implications for Earth's distribution of chlorine. Earth Planet Sci Lett 131: 427-432

Marschik R, Fontboté L (2001) The Candelaria-Punta del Cobre iron oxide Cu-Au(-Zn-Ag) deposits, Chile. Econ Geol 96: 1799-1826

Marschik R, Spangenberg JE, Leveille RA, de Almeida AJ (2003) The Sossego iron oxide-Cu-Au deposit, Carajás, Brazil. In: Eliopoulos D et al (eds) Mineral Exploration and Sustainable Development v 1. Millpress, Rotterdam, p. 331-334

Olszewski WJ, Wirth KR, Gibbs AK, Gaudette HE (1989) The age, origin and tectonics of the Grão-Pará Group and associated rocks, Serra dos Carajás, Brazil. Precambrian Res 42: 229-254

Pollard PJ (2002) Evidence of a magmatic fluid and metal source for Fe-oxide Cu-Au mineralisation. In: Porter TM (ed) Hydrothermal iron oxide copper-gold and related deposits – A global perspective v 1. PGC Publishing, Linden Park, Australia: 27-41

Sillitoe RH (2003) Iron oxide-copper-gold deposits: An Andean View. Mineral Deposita 38: 787-812

Origin of hydrothermal ore-forming processes in the Dapingzhang polymetallic copper deposit in the Lanping- Simao Basin, Yunnan Province

Dai Baozhang, Jiang Shaoyong
State Key Laboratory for Mineral Deposits Research, Department of Earth Sciences, Nanjing University, Nanjing, 210093, China

Liao Qilin
Jiangsu Geological Survey Institute, Nanjing, 210018, China

Abstract. The newly discovered Dapingzhang polymetallic copper deposit in the Lanping-Simao Basin is hosted in volcanic rocks. The orebodies include an upper stratiform and lentiform massive sulfide orebody, and a lower vein type and disseminated sulfide orebody. The Rb-Sr isotopes of quartz fluid-inclusions in the vein type orebody yield an isochron age of 118 ±12 Ma. Fluid-inclusion analysis shows that the ore-forming fluid is of low to middle salinity (2.0-8.0 wt%NaCl), and of low to middle temperature (90~200°C). The $\delta^{34}S$ values of pyrite and chalcopyrite minerals in this deposit concentrate at about 0‰. Our modeling and water/rock ratio calculations using available hydrogen-oxygen isotope data suggests an evolved meteoric water origin for the ore-forming fluids, instead of mixture of seawater and magmatic fluids. The Pb isotope composition indicates radiogenic Pb sources, and suggests Pb from sedimentary rocks and mantle-derived volcanic rocks in the basin both contribute to this deposit. In conclusion, the Dapingzhang deposit shares many similar geochemical characteristics with vein type copper deposits in the Lanping-Simao Basin. These data support the conclusion that the Dapingzhang polymetallic copper deposit is a hydrothermal deposit formed during Yanshanian period, not a massive sulfide deposit of submarine-exhalative-sedimentary origin as proposed by previous researchers.

Keywords. Isotope geochemistry, quartz fluid inclusion, Rb-Sr isochron age, Yanshanian period, hydrothermal deposit

1 Introduction

The Dapingzhang polymetallic copper deposit is an important recent discovery in Lanping-Simao Basin. It is composed of an upper stratiform and lentiform massive sulfide orebody, and a lower vein type and dissiminated sulfide orebody. Previous researchers have identified it as a massive sulfide deposit with submarine- exhalative-sedimentary origin (Li 2000; Li et al. 2000; Li and Zhuang 2000; Li and Zhang 2001; Zhong et al. 2000). In this paper, new results of fluid inclusion, sulfur isotope and mineralization age are taken into account. The data lead to a different perspective on ore-forming process, which is also consistent with previous data. The Dapingzahng deposit was formed by extensive interaction between meteoric water (or brine) and host rocks. This is similar to the oreforming process identified in the vein type deposits in Lanping-Simao Basin.

2 Rb-Sr isochron age

Determining the age of mineralization is essential for understanding any deposit. In this study, mineralization was dated using Rb-Sr analysis of fluid inclusions. The Rb-Sr isotopic compositions of fluid inclusions in 8 selected quartz samples were analyzed. The data were then plotted using the ISOPLOT program with λ (^{87}Rb) $1.42x10^{11}$/a. The input error was $^{87}Rb/^{86}Sr$ = 0.5%. The 6 samples from the vein type and disseminated sulfide orebody yield an isochron age of 118 ±12Ma, MSWD = 0.46. Previous isotope dating (Zhong et al. 2000) shows that the age of the host rock is 500~530 Ma. The ages of a variety of intrusions in this area are between 300 Ma and 150 Ma, which indicate that the Dapingzhang deposit formed after these local intrusions.

Two samples from the massive orebody evidently depart from the isochron and show higher $^{87}Sr/^{86}Sr$ values (Fig. 1). This could be caused by increased contribution from materials with higher $^{87}Sr/^{86}Sr$ values (e.g., sediments in the basin). This could be because the massive orebody is relatively shallower than the vein type deposits. The limited sample number in this case (2) prevents the possibility of obtaining an age for the massive orebody. Some

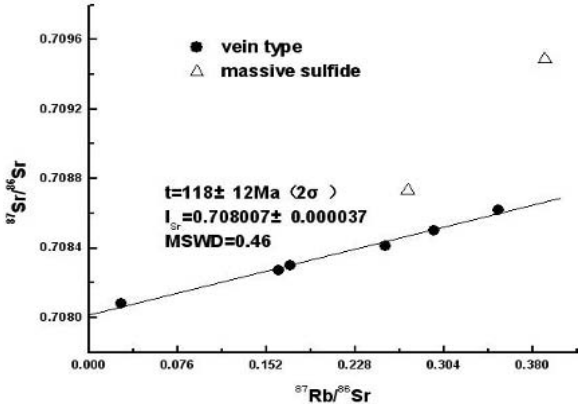

Figure 1: Fluid inclusion Rb-Sr isochron of quartz in ore-bodies from the Dapingzhang deposit.

This page intentionally blank

direct dating methods such as Re-Os isotope analysis of metal sulfides (Jiang et al., 2000) should be adopted in further research. The reliable age of 120 Ma for the vein type and disseminated sulfide orebody indicates that this deposit mainly formed in Yanshanian period.

3 Fluid inclusions

In this study, quartz and calcite minerals from variety of samples were carefully selected for fluid inclusion analysis in order to acquire information about the composition of ore-forming fluids. The results show that the range of homogeneous temperatures is 90~200°C (mainly from130°C to 160°C), and the salinity of the ore-forming fluid varies from 2.0 to 8.0 wt%NaCl. These results are relatively lower in temperature and salinity than previous data; however this could be due to the fact that these samples originate from shallower depths than those from previous studies.

As shown in Figure 2, the ore-forming fluid of Dapingzhang deposit is similar to that of the vein type deposit series in Lanping-Simao Basin composed by Jinman, Shuixie and Bailongchang.

On the other hand, temperature of ore-forming fluids in massive sulfide deposits mainly ranges from 200°C to 350°C, which is much higher than that of the Dapingzhang deposit.

4 Isotope research

4.1 Sulfur isotopes

Chalcopyrites and pyrites from variety of samples were selected in this study for sulfur isotope analysis. Both the results in this study and previous studies (Li et al. 2000; Zhong et al. 2000) indicate that $\delta^{34}S$ values of all sulfides concentrate at about 0‰, implying that sulfur in this deposit is mainly mantle-derived. Sulfur with such characteristics can either come directly from volcano exhalative, or can be leached from volcanic rocks. For the Dapingzhang deposit, the latter is more reasonable.

4.2 Hydrogen-oxygen isotopes

To determine the origin and evolution of the ore-forming fluid, available hydrogen and oxygen isotope data (Li and Zhuang 2000; Zhong et al. 2000) are compiled ($\delta^{18}O_{H2O}$ values of -2.5 to +2.9‰, and δD values of –84 to –59‰ for the ore-forming fluids) and further analyzed. The calculation of water/rock interaction is taken in this study with the δD and $\delta^{18}O_{H2O}$ values of meteoric water are -120‰ and -16‰ (Liu et al., 2000) and the δD and $\delta^{18}O_{H2O}$ values of volcanic rocks are -65‰ and 8‰ (Shen 1997).

Figure 4 shows that the available hydrogen and oxygen data are consistent with the two evolution curves at 150°C

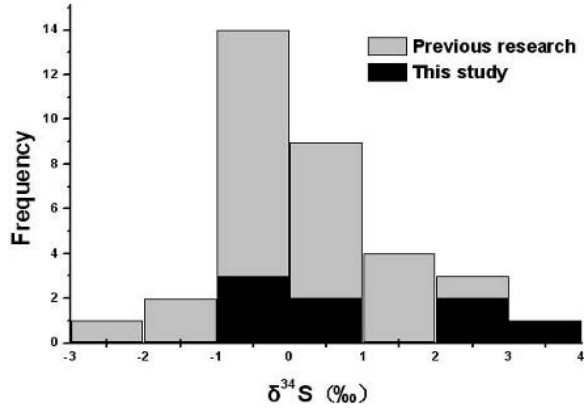

Figure 3: Sulfur isotope composition of sulfides in the Dapingzhang deposit.

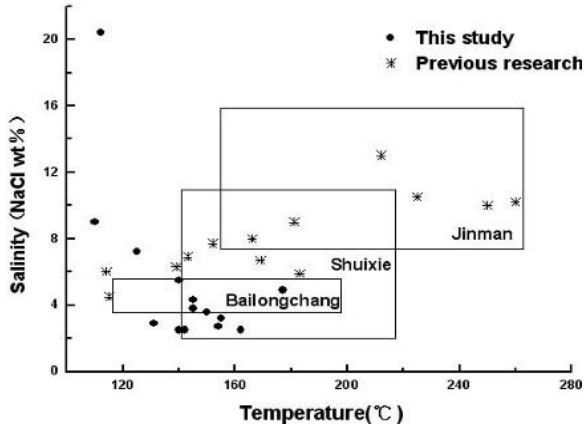

Figure 2: Temperature and salinity distribution of ore-forming fluid in the Dapingzhang deposit (Data cited mainly from Li et al. 2000; Wu 2003).

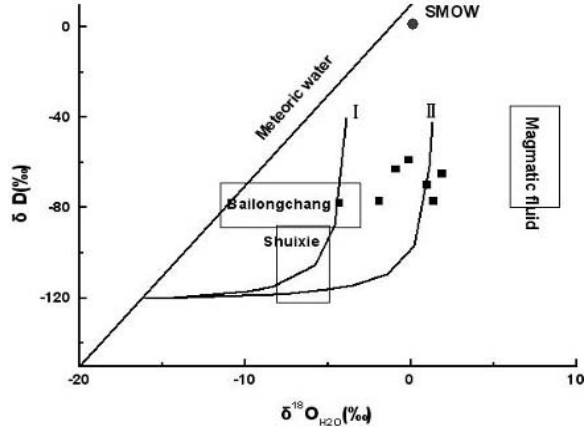

Figure 4: H-O isotope composition of ore-forming fluids in the Dapingzhang deposit (I and II represent calculated water- rock interaction curve at 150 °C and 250 °C, respectively).

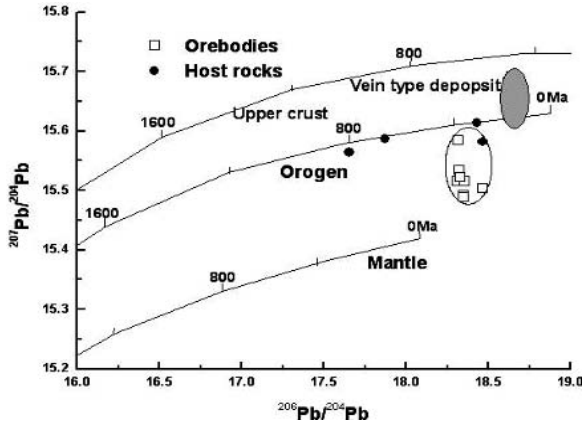

Figure 5: Pb isotopic composition of the Dapingzhang deposit (after Zartman and Doe 1981).

and 250°C, respectively. Thus, it is most likely that the ore-forming fluid is extensively evolved meteoric water.

4.3 Lead isotopes

Available lead isotope data are plotted onto the Zartman Pb isotope diagram. Lead in this deposit is relatively rich in radiogenic Pb. Fig. 5 shows that host-rock samples lay on the orogen curve, while orebody samples lie between the orogen curve and the mantle curve, implying some contribution from a magmatic source. It is likely that host rocks supply most of the ore-forming metal to both the vein type deposit series and the Dapingzhang copper polymetallic deposit.

5 Conclusions

Combining the new results in this study and the available data of previous researchers, we acquire some essential perspectives on the Dapingzhang copper polymetallic deposit:

1. The fluid-inclusion Rb-Sr isotopes of quartz in the vein-type orebody yield an isochron age of 118 ±12 Ma. This indicates that the orebody was formed in late Yanshanian period.
2. The ore-forming fluid is similar to that of the vein type deposit series, with low to middle salinity and low to middle temperature. Hydrogen-oxygen isotope data indicate an evolved meteoric water origin for the fluid.
3. Sulfur and lead isotope data imply that the host volcanic rocks are the main source for sulfur and ore-forming metals.
4. It is most likely that mineralization of the Dapingzhang deposit is similar to that of the vein type deposit series in Lanping-Simao Basin. The Dapingzhang polymetallic copper deposit is a hydrothermal deposit.

References

Jiang S, Yang J, Zhao K (2000) Re-Os isotope tracer and dating methods in ore deposits research. Journal of Nanjing University (Natural Sciences) 36(6): 669~677

Li F (2000) Volcanic-exhalative-sedimentary ore- forming model of Dapingzhang Cu-polymetal deposit, western Yunnan. Bulletin of Mineralogy, Petrology and Geochemistry 19(4): 296~297

Li F, Zhang F (2001) Volcanic-exhalative- sedimentary genesis of Dapingzhang Cu-polymetal deposit, western Yunnan. Geology and Prospecting 37(4): 5~8

Li F, Zhuang F (2000) Fluid inclusion characteristics and its metallogenic significance of the Dapingzhang Cu-polymetal deposit in Simao, western Yunnan. Geotectonica et Metallogenia 24(3): 237~243

Li F, Zhuang F, Yang H (2000) Fluid inclusions analysis of Dapingzhang Cu-polymetal deposit, western Yunnan. Acta Petrologica Sinica 16(4): 581~586

Liu J-J, Li C-Y, Pan J-Y (2000) Isotopic Geochemistry of copper deposits in sandstone and shale of Lanping-Simao basin, western Yunnan. Mineral Deposits 19(3): 223~234

Ohmoto H, Skinner BJ (1983) The Kuroko and related volcaogenic massive sulfide deposit. Economic Geology (Monograph) (5): 604

Shen W (1997) Textbook on isotopic geology. Atomic energy publishing house, Beijing.

Wu N (2003) Geochemistry of the vein-type copper deposits in Lanping-Simao Basin, Yunnan Province, China. Paper for master's degree of Department of Earth Sciences, Nanjing University

Wu N (2003) Lead and sulfur isotope geochemistry and the ore sources of the vein-type copper deposits in Lanping-Simao Basin, Yunnan Province. Acta Petrologica Sinica 19(4): 799~807

Zhong H, Hu R-Z, Ye Z-J (1999) Isotopic chronology of the spilite-ceratophyre formation in Dapingzhang, Yunnan Province and its geologic significance. Science in China (D) 29(5): 407~412

Zhong H, Hu R-Z, Ye Z-J (2000) Sulfur, lead, hydrogen and oxygen isotopic geochemistry of the Dapingzhang copper- polymetallic deposit, Yunnan Province. Geochemica 29(2): 136~142

Stable isotope geochemistry of the gold-sulfide mineralized zone of the Kottapalle block of the Ramagiri greenstone belt, Dharwar Craton, South India

M. Deb, K. Bheemalingeswara
Department of Geology, University of Delhi, Delhi 110007, India

Abstract. The Neo-Archean Ramagiri-Penakacherla belt is located in the eastern Dharwar craton of South India. It hosts auriferous quartz bodies in altered mafic and felsic volcanic rocks, intimately interlayered and co-folded with carbon phyllites. The sequence is metamorphosed to low greenschist facies. Pervasive quartz-carbonate alteration is a conspicuous feature in the gold-sulfide mineralized zone of the Kottapalle block of this greenstone belt.

The carbonate compositions spread along the dolomite-ankerite or calcite-ankerite join. The host volcanics are of tholeiitic basalt, andesitic and dacitic compositions representing a probable island-arc setting. The majority of carbonaceous samples fall in the range of – 20 and – 28 per mil $\delta^{13}C_{org}$ (PDB), suggesting a biogenic derivation of the reduced carbon and a sedimentary origin of the strata. Carbonate $\delta^{13}C$ (PDB) have median values of -2.4 per mil and mean of – 4.0 per mil. $\delta^{34}S$ (CDT) values of pyrite and pyrrhotite cluster around +2 per mil. Primary fluid inclusions, rich in CO_2 with subordinate CH_4, as observed in preliminary microthermometric studies, demonstrate the pervasive presence of a CO_2-rich hydrothermal fluid responsible for the extensive carbonation of the auriferous host rocks.

Absence of any sedimentary carbonate strata in the sequence, and the stable-isotope data support the role of mantle-derived fluids in producing the quartz-carbonate alteration. The $\delta^{13}C$ values of carbonates indicate that the hydrothermal fluid did not have any significant interaction with the reduced carbon in the ore zone. The sulphur isotope data points to the mantle-source of sulphur in the ore-bearing hydrotherms.

Keywords. Shear gold, quartz-carbonate alteration, Dharwar craton, stable-isotope geochemistry

1 Introduction

The Ramagiri-Penakacherla belt is one of a series of auriferous greenstone belts in the eastern Dharwar craton of South India. This belt, considered to be of Neo-Archean age (2746± 64 Ma; Zachariah et al. 1995) is located in the Anantapur district of Andhra Pradesh. The belt forms a Y-shaped outcrop of prominently mafic volcanic rocks, which are surrounded on all sides by the Peninsular Gneiss. The litho-units present in the area (Ghosh et al. 1970) are:

- Dolerite dyke
- Ultrabasic rocks
- Pyroclastics
- Light and dark phyllites
- Greenstones with chert layers
- Quartz-chlorite schists
- Quartzite
- Banded Iron Formation
- Hornblende schist
- Metagabbro
- Granitic rocks, massive and banded

The light grey phyllite consists essentially of carbonate and chlorite, with minor amounts of sericite and quartz. The dark grey phyllite on the other hand has chlorite as the dominant phase over carbonates. Auriferous quartz bodies of different types and generations occur in this part of the sequence (shown in italics above) in the form of reefs, pods and veinlets along the pervasive foliation.

In the Kottapalle block of the Ramagiri ore zone (Fig. 1) the altered volcanics are intimately interlayered and co-folded with carbon phyllite. In the auriferous zone these rocks contain sulfide minerals such as, pyrite, chalcopyrite, pyrrhotite, sphalerite and minor arsenopyrite..The metamorphic mineral assemblage indicates that the grade of metamorphism has attained low green schist facies.

Pervasive quartz-carbonate alteration is a conspicuous geological feature noted in the gold-sulfide mineralized zone in the Kottapalle block. It has affected both the felsic and mafic volcanic units of the greenstone belt. The carbonates co-exist as grains, bands and patches with the carbonaceous matter in the carbon phyllites. Thus, carbon, either as graphitic carbon or as carbonate is invariably associated with the Au-sulfide mineralization.

This first stable isotope study in this belt was conducted to ascertain the source of carbon and sulfur in the ore-host rock association. This work would also provide useful insight into the oregenetic process and environment of ore emplacement. Towards this end, three bore holes drilled by the Geological Survey of India in the Kottapalle block (cf. Fig. 1) were logged and sampled systematically and subjected to XRD, XRF, CHNS (elemental), EPMA analyses and stable isotope mass spectrometry.

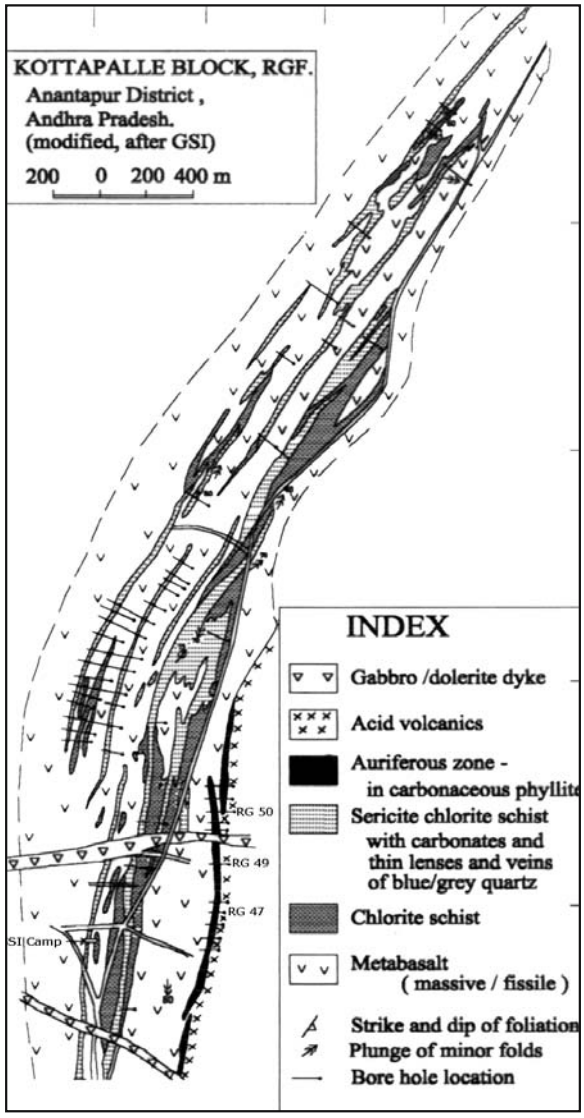

Figure 1: Geological map of Kottapalle Block of Ramagiri Greenstone belt (modified after GSI).

2 Results

2.1 Petrology and geochemistry

Based on discriminant diagrams, using their major and trace element abundances, the mafic and felsic volcanics in the host sequences were found to be of tholeiitic basalt, andesite and dacite compositions. In tectonic discriminant diagrams, the Kottapalle metabasalts plot in the IAB field, suggesting the possibility of subduction-related volcanism in an island arc setting in the Archean Dharwar craton (cf. Zachariah et al. 1997). The volcanic rocks have been so severely altered and metamorphosed that the two main protoliths, tholeiitic basalt and dacite, can hardly be distinguished petrographically. Both the

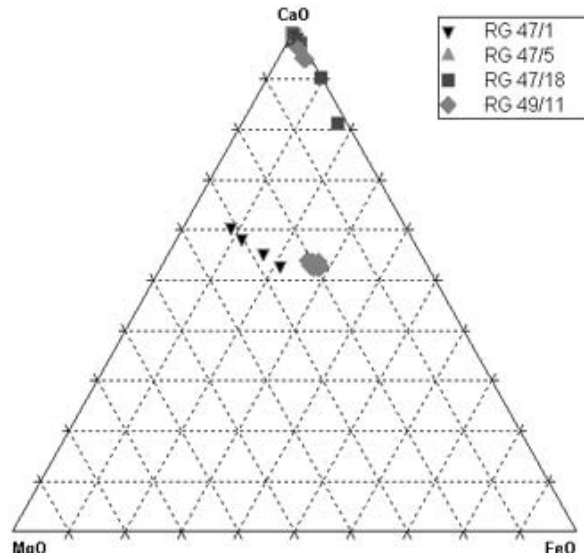

Figure 2: Triangular plot of carbonate compositions.

volcanics have turned into fine grained chlorite-sericite schists, the only distinction being the fine grained quartzofeldspathic matrix in the felsic compositions. These schists have been described as light and dark phyllites in field parlance.

Carbonate grains in three samples of metabasalt and felsic volcanics were investigated through XRD, CL and EPMA (JEOL JXA 8600 superprobe) analyses. All carbonate grains analysed contain manganese as a minor component, with MnO content ranging from nil to 0.9 wt.%. Their compositional characteristics, in terms of the three major components, CaO, MgO and FeO, are presented in Figure 2. Coarse quartz-carbonate veins and lenses occur in contact with finely schistose carbonaceous and carbonate interlayerings in sericite-quartz schists (RG49/11). Compositions of carbonates in them showed the predominance of ankerite over dolomite molecule along the dolomite-ankerite join. Coarse brownish carbonates in lenses and bands in another section (RG47/1) within sericite-chlorite-quartz schist showed a trend of increasing dolomitic and calcitic molecules. This section showed excellent microstructural relationships, with the schistosity transected by tightly folded late quartz veinlets. In yet another section (RG47/18) brownish pre- to syntectonic carbonate-quartz-sulfide lenses show compositions along the calcite-ankerite join. In this section, two types of carbonates are observed. The late carbonates, identified under CL, are clearly more calcitic. They are located along the grain boundaries of earlier carbonate grains. Fe-rich carbonates, as noted in this study, are typically related to gold mineralization in greenstone belts the world over.

Total carbon content of 48 analyzed samples from the ore zone rocks ranged from 7.3 to 0.27 wt.%, with a mean of 3.11 wt.% (std. dev. 1sigma = 1.67%). C_{org} content mea-

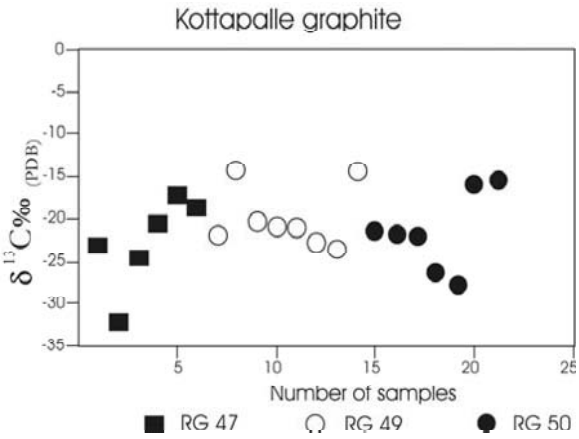

Figure 3: Plot of reduced carbon isotope data from carbon phyllites.

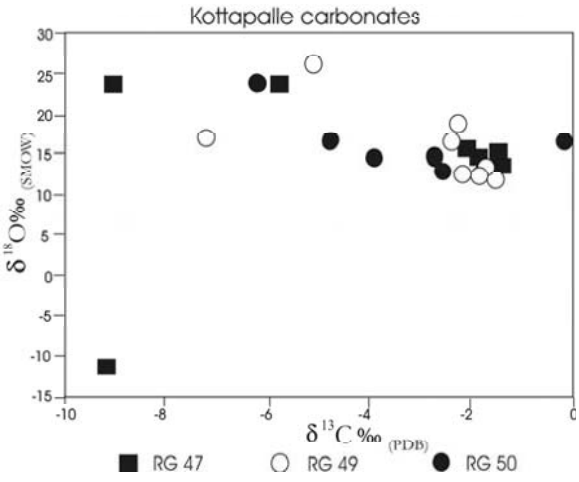

Figure 4: Plot of $\delta^{13}C$ vs $\delta^{18}O$ per mil of carbonates from Kottapalle ore zone.

sured in 15 samples ranged from 5.8 wt.% to nil, while $C_{carb,}$ estimated as the difference between C_{total} and C_{org} in 15 samples, ranged between 5.9 wt.% to nil.

2.2 Stable isotope composition

Twenty one analyses of $\delta^{13}C_{org}$ in three carbonaceous samples (Fig. 3) ranged between – 14.2 and – 32.4 per mil (PDB), with the majority of samples falling in the range of – 20 and – 28 per mil. These values suggest a biogenic source for the carbon, and thus, a sedimentary origin for the carbonaceous strata. Values heavier than – 20 per mil probably reflect partial equilibration with co-existing carbonates or thermal maturation to heavier values by liberation of CH_4. $\delta^{13}C_{Carb\text{-}graphite}$ of 11.6 and 13.8 per mil in co-existing carbonate and reduced carbon suggest an equilibration temperature of about 300 to 225°C (cf. Oberthür et al. 1996). A plot of $\delta^{13}C$ (PDB) per mil against

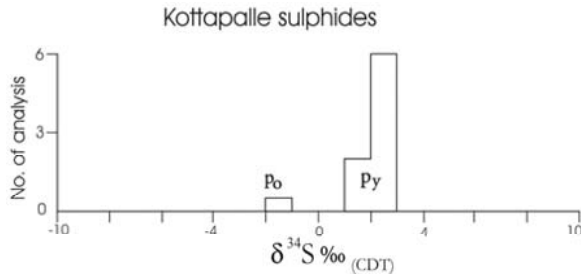

Figure 5: Histogram showing $\delta^{34}S$ values of sulphide separates from Kottapalle ore zone.

$\delta^{18}O$ (SMOW) per mil of 21 carbonates from Kottapalle ore zone (Fig. 4) show spread of $\delta^{13}C$ values from 0 to -9.2 per mil with a mean of – 4.0 and a median of – 2.4 per mil. $\delta^{18}O$ values range from 26.0 to 12.5 per mil. One pure calcite from a late veinlet had an unusual composition of -9.2 per mil $\delta^{13}C$ and -11.2 $\delta^{18}O$. While only one sample showed sea water-derived carbonate $\delta^{13}C$ value near zero, the majority clustered between – 1.5 and – 2.7 per mil. A few values were spread between – 3.9 and - 6.2 per mil while 2 samples gave values around – 9 per mil. Limited sulfur isotope analyses of 8 monomineralic pyrite and 1 pyrrhotite separates gave a range of $\delta^{34}S$ (CDT) between +2.8 and -1.7 per mil, with the majority clustering around +2 per mil (Fig. 5).

3 Discussion and conclusion

For shear- or fault-controlled Archean epigenetic gold-quartz deposits, controversy prevails regarding the source of the ore components and fluids. There are two end-member genetic hypotheses - one metamorphic and the other magmatic - which continue to compete. Since most deposits of this type show pervasive carbonate alteration and sulfide association, determination of the source of carbon and sulfur in the ore zone can lend significant support to either of the two hypotheses. Extensive quartz-carbonate alteration of the host volcanics, absence of any sedimentary carbonate strata in the sequence and presence of primary fluid inclusions rich in CO_2 with subordinate CH_4, as observed in preliminary microthermometric studies, demonstrate the pervasive presence of a CO_2-rich hydrothermal fluid. This type of fluid is necessary for carbonation of the auriferous host rocks in the Kottapalle block of the Ramagiri greenstone belt. The variation in the composition of the carbonates, noted above, may be attributed to episodic fluctuations in the temperature and composition of the fluids in the structural conduits (cf. Mumin et al. 1996). The median $\delta^{13}C$ of -2.4 per mil composition of the carbonates is too negative to have been derived from metamorphically remobilized CO_2 from sea water-derived carbonate. This median value of ore zone carbonates and their spread upto -6.2 per mil conforms closely to the range

of -2.0 to -6.0 recorded by Groves et al. (1988) for fault-controlled regional carbonation involving CO_2 of magmatic or mantle origin. The median value is also close to the -3.1 ± 1.3 per mil $\delta^{13}C$ value of undoubted magmatically-derived carbonates found in association with molybdenite mineralization in a granodiorite intrusion in Canada (Burrows et al. 1986). Direct involvement of mantle fluids in the ore-bearing hydrotherm is envisaged instead of reworking of mantle-derived carbonates into metamorphic fluids, as an alternative process of ore formation. This is supported by the limited variation in the $\delta^{13}C$ values of carbonates and the near-zero (+2 per mil) mantle signature in the associated sulfides. Absence of strongly negative (> -10 per mil) $\delta^{13}C$ values in the carbonates also imply that the hydrothermal fluid did not have any significant interaction with reduced carbon.

Acknowledgements

This study was made possible by the kind permission granted by the Deputy Director General (Southern Region), Geological Survey of India for the logging and collection of bore hole samples. The help received in the field from senior geologist, K.N.Reddy is gratefully acknowledged. The EPMA, CL, XRD and Mass spectrometry were carried out during a revisit of the first author (MD) to the Geochemisches Institut, Göttingen, Germany with an Alexander von Humboldt Foundation fellowship. He is grateful to Prof. J.Hoefs for extending all laboratory facilities at Göttingen. Thanks are also due to Dr. Andreas Hoppe, Director, Landesamt fur Bodenforschung, Wiesbaden, for help in generating the XRF data. This study was supported by a research grant (ESS/CA/A5-11/95) from the Department of Science & Technology, Govt. of India, to the first author.

References

Burrows DR, Wood PC, Spooner ETC (1986) Carbon isotope evidence for a magmatic origin for Archean gold-quartz vein ore deposits. Nature 321 851-854

Ghosh DB, Sastry BBK, Rao AJ, Rahim AA (1970) Ore environment and ore genesis in Ramagiri Gold Field, Andhra Pradesh, India. Econ. Geol. 65 801-814

Groves DI, Golding SD, Rock NMS, Barley ME, McNaughton NJ (1988) Archean carbon reservoirs and their relevance to the fluid source for gold deposits. Nature 331: 254-257

Mumin AH, Fleet ME, Longstaffe FJ (1996) Evolution of hydrothermal fluids in the Ashanti gold belt, Ghana: stable isotope geochemistry of carbonates, graphite and quartz. Econ. Geol. 91: 135-148

Oberthür T, Schmidt Mumm A, Vetter U, Simon K, Amanor, JA (1996) Gold mineralization in the Ashanti belt of Ghana: genetic constraints of the stable isotope geochemistry. Econ. Geol. 91: 289-301

Zachariah JK, Hanson GN, Rajamani V (1995) Postcrystallisation disturbance in the neodymium and lead isotope systems of metabasalts from the Ramagiri schist belt, southern India. Geochimica et Cosmochimica Acta 59: 3189-3203

Zachariah JK, Rajamani V, Hanson, GN (1997) Petrogenesis and source characteristics of metatholeiites from the Archean Ramagiri schist belt, eastern part of Dharwar craton, India. Contrib. Mineral. Petrol. 129: pp. 87-104

Isotope systematics of ore-bearing granites and host rocks of the Orlovka-Spokoinoe mining district, eastern Transbaikalia, Russia

A. Dolgopolova, R. Seltmann, C. Stanley
Natural History Museum, Dept. Mineralogy, CERCAMS, Cromwell Road, London SW7 5BD, UK

D. Weiss
Imperial College, London, Prince Consort Road, London SW7 2BP, UK

B. Kober
Institute of Environmental Geochemistry, Im Neuenheimer Feld 234, D-69120 Heidelberg, Germany

W. Siebel
Dept. of Earth Sciences, Eberhard-Karls-University, Wilhelmstr. 56, D-72074 Tübingen, Germany

Abstract. Pb, Rb and Sr isotope data are reported for the Khangilay, Orlovka and Spokoinoe granite massifs and their host rocks in the Orlovka-Spokoinoe mining district, Eastern Transbaikalia, Russia. Pb isotope analyses indicate a common Pb source for all three granite massifs reflecting a homogenous source melt from which all magmatic members evolved. Pb isotope systematics identify two possible scenarios for the source of Li-F granites: 1) a crust-mantle source where a mixture of MORB and continental-derived material were brought together in an orogenic environment; and 2) a type II enriched mantle source where subducted continental material could have been strongly implicated in volcanic suites. New Rb-Sr isotope age data yield a 143.8±4.2 Ma age for barren granites of the Orlovka and Khangilay massifs.

Keywords. Pb Rb Sr isotope systematics, ore-bearing granite, Eastern Transbaikalia

1 Introduction

The rare-metal granite-related Orlovka tantalum deposit and the Spokoinoe tungsten vein quartz-greisen deposit are located in Eastern Transbaikalia 140 km and 148 km SE of Chita, respectively. Both deposits are hosted by the Khangilay granite pluton and are believed to be its satellites (Fig. 1) (Badanina et al. 2004; Beskin et al. 1994; Kovalenko et al. 1999; Syritso et al. 2001). In recent years, the evolution of rare-metal granites, their formational stages, and their relation to intraplate magmatism have been studied. Specifically, Rb-Sr and Sm-Nd isotopic systems were used to reveal the source(s) of rare-metal granite melts from the study area, and the results indicate that sources were likely to be either crustal, mantle or combined crustal-mantle (Kostitsyn 2001; Kovalenko et al. 1999, 2002, 2003; Yarmolyuk et al. 2001, 2003). Our study uses Pb isotopes for the granites of the Orlovka, Spokoinoe, and Khangilay massifs and their host rocks with the goal to study the evolutionary trends and features of the Khangilay pluton and the Orlovka and Spokoinoe deposits (barren versus mineralized granites, ores, host rocks). By examining fluid-rock and crust-mantle interaction in the development of granitoid magmatism, the genetic relationship between the three massifs and similarities and differences among them may be identified. Rb-Sr isotopes provide additional insights into the age of granites from the Orlovka-Spokoinoe mining site.

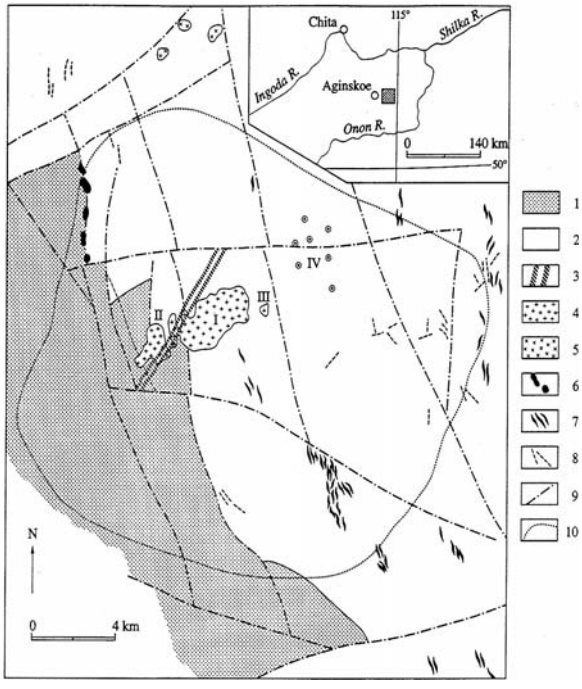

Figure 1: Schematic geological map of the Khangilay pluton (after Beskin et al., 1994). 1-Triassic terrigenous rocks and volcanoclastic sediments; 2-Paleozoic metasedimentary rocks; 3-Cenozoic diabase dikes; 4-6-Mesozoic intrusives: 4- granites, 5-granodiorites, 6-gabbro-diorites; 7-granite-porphyry; 8-pre-granite lamprophyres; 9-faults; 10-contour of a hidden granite pluton (based on gravity data). I-IV-Granite massifs and hosted deposits: I-Khangilay Massif; II -Orlovka Massif; III-Spokoinoe Massif; IV-minor W and Sn deposits and showings.

2 Geological setting

The Orlovka-Spokoinoe mining district belongs to the Central Asian Orogenic Belt (CAOB) (Jahn et al. 2000) or Transbaikal-Mongolian orogenic collage where multiple oroclinally bent magmatic arcs separated by accretionary complexes and ophiolitic sutures are located between the major cratons. Rare-metal Li-F enriched granites and pegmatites are widespread as products of continental crustal growth and associated intraplate magmatism. The Khangilay pluton is located in the central portion of the Paleozoic Aginskaya microplate, which is made up of predominantly sandstone and shales (Beskin et al. 1994; Syritso et al. 2001). The granitoids of the pluton cut Proterozoic to Carboniferous shales and volcanics, a Triassic terrigenous and volcano-sedimentary sequence, and gabbro-diorite, granodiorite, and lamprophyre bodies (Kovalenko et al. 1999). The microplate was intruded by granite plutons, the largest of which is 24 km by 22 km in dimension at a depth of 500-2500 m based on gravimetric data.

It is exposed at the surface as three separate granitic (Khangilay, Spokoinoe and Orlovka) massifs. The Khangilay granite massif is composed of biotite granite and biotite-muscovite granites. The Orlovka satellite is a highly differentiated Ta-(Nb-Sn-) bearing intrusion of lithionite-amazonite-albite granite. The Spokoinoe body is a muscovite-albite granite with W (Sn, Be) mineralization.

To assess magma–host-rock interactions of the Khangilay-Orlovka intrusions within the regional geochemical framework, greisenized Spokoinoe granites and a representative suite of host rocks (volcanics, hornfelses, metasediments, gabbro-diorite) were included in the study.

3 Results and discussion

The mixing diagram (Fig. 2) shows a strong relationship between the barren parental granites of the Khangilay pluton and the ore-bearing granites of the Orlovka and Spokoinoe massifs. They all plot within a single linear array. Despite a wide range of Pb isotope compositions within each granite body, they do not differ significantly among all three granite massifs (Dolgopolova et al. 2004). It hints at fractionation from a homogenous (or homogenized) source melt with uniform initial $^{206}Pb/^{204}Pb$ and $^{207}Pb/^{204}Pb$ ratios. The overall data trend demonstrates a simple mixing of the uniform Pb composition with different radiogenic components in the rocks and a strong relation of the barren parental rocks to the ore-bearing rocks. Lead isotope signatures of the host rocks are more scattered than those of the granite rocks and are off the granite's mixing line.

The Orlovka ore-bearing amazonite granites, with the highest Pb concentration, were used to identify the initial Pb isotopic signature subsequently transferred to the

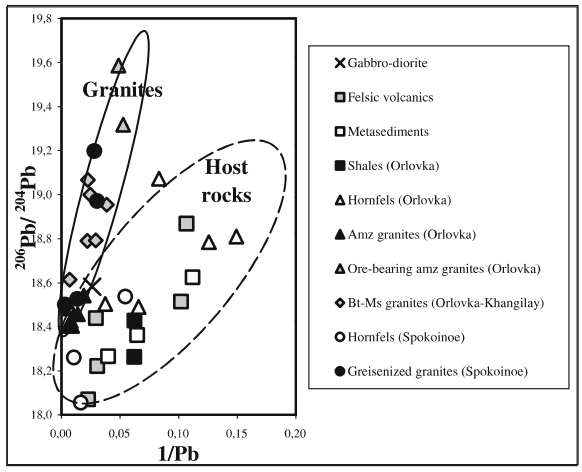

Figure 2: $^{206}Pb/^{204}Pb$ vs. 1/Pb mixing plot for Khangilay-Spokoinoe-Orlovka granites and their host rocks.

Table 1: Pb isotope composition of Orlovka K-feldspars.

$^{206}Pb/^{204}Pb$	*±2SE (%)*	$^{207}Pb/^{204}Pb$	*±2SE (%)*	$^{208}Pb/^{204}Pb$	*±2SE (%)*
18.387	*0.003*	15.564	*0.002*	38.331	*0.016*
18.384	*0.001*	15.562	*0.001*	38.329	*0.013*
18.384	*0.003*	15.563	*0.002*	38.326	*0.016*
18.374	*0.002*	15.547	*0.002*	38.272	*0.014*

ore-bearing rocks. The high Pb concentrations, up to 190 ppm, found in ore-bearing amazonite granites minimize the effects of fluid-wall rock interaction and associated perturbation to Pb systematics. The amazonite granites are characterized by the lowest rate of radiogenic Pb accumulation because of their very low $^{238}U/^{204}Pb$ ($\mu_{average}$ = 1.3). The calculated initial values for these "least sensitive" ore-bearing granites are very similar and their averages are: $^{206}Pb/^{204}Pb = 18.41 \pm 0.02$; $^{207}Pb/^{204}Pb = 15.56 \pm 0.006$; and $^{208}Pb/^{204}Pb = 38.3 \pm 0.03$ (Dolgopolova et al. 2004). Pb isotope compositions were also determined in two separate grains of K-feldspar from the ore-bearing amazonite granite of the Orlovka Ta-Nb deposit. Pb isotope analyses and U-Pb isotope dilution measurements were carried out for blue-green cores and white feldspar rims. Differences between core and rim Pb isotopic compositions are negligible within the limits of statistical significance. The averages of measured initial Pb isotope compositions of feldspars are shown in Table 1.

The average values of initial Pb isotope composition of ore-bearing granites were calculated previously to assess sources of the granitic magmas and were in the range of: $^{206}Pb/^{204}Pb = 18.49 \pm 0.05$; $^{207}Pb/^{204}Pb = 15.57 \pm 0.01$ and $^{208}Pb/^{204}Pb = 38.23 \pm 0.06$ (Dolgopolova et al. 2004). Our new data on Pb isotope compositions of K-feldspar (Table 1) show very good agreement with the calculated

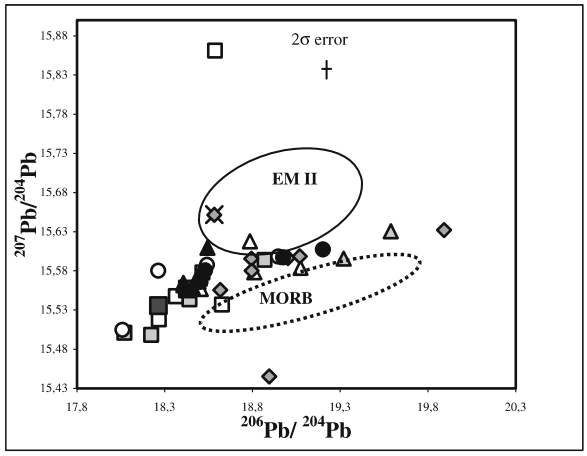

Figure 3: Pb^{206}/Pb^{204} vs. Pb^{207}/Pb^{204} diagram for Khangilay-Spokoinoe-Orlovka granites and their host rocks. All symbols are identical to those in Figure 2. EM II (type II enriched mantle) and MORB (mid-ocean ridge basalt) represent two types of mantle end members (Zindler and Hart 1986).

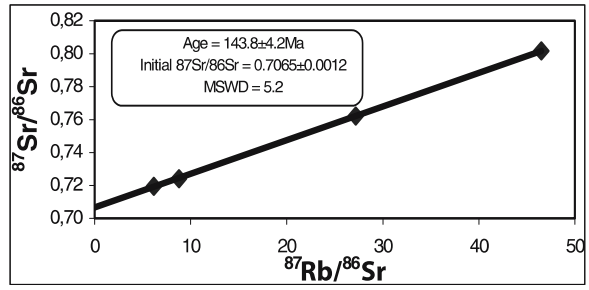

Figure 4: Rb-Sr isochron for barren biotite–biotite-muscovite granites of the Orlovka-Spokoinoe mining site.

initial Pb isotopic composition of the Orlovka granite pluton.

Pb isotope systematics show the presence of a mantle signature transferred during the formation of the studied granites (Figure 3). A mantle-derived component is in a transitional field between mid-ocean ridge basalt (MORB) and type II enriched mantle (EM II) (Zartman and Doe 1981) but closer to the latter. There is a mixture of different epochs presented on Figure 3. The mantle arrays indicate present-day mantle Pb isotopes while granite data reflects "frozen" Jurassic Pb isotope compositions. If the mantle arrays are traced back to a Jurassic age with less radiogenic EM II and MORB sources than the plotted arrays, they would slightly shift to the lower left part of the plot and indicate EM II input.

Therefore, Pb isotopic data suggest two possible sources contributed to the formation of the studied granites: 1) a crust-mantle source where a mixture of MORB and upper crustal-derived material were brought together in an orogenic environment; and 2) type II enriched mantle source where subducted continental material could have been strongly implicated in several island-arc volcanic suites and the corresponding isotopic signatures, thus reflecting a strong similarity of EM II with upper continental crust or continentally derived sediment.

4 New Rb-Sr age data

Seven samples of barren and ore-bearing granites of Khangilay and Orlovka massifs were analyzed for Rb and Sr isotope compositions. Analyses of four samples from the barren granites yield a whole rock isochron age of 143.8 ± 4.2 Ma with an initial $^{87}Sr/^{86}Sr$ ratio of 0.7065 ± 0.0012 (Fig. 4). The data for barren biotite-muscovite granites are in excellent agreement with published data of the Orlovka-Spokoinoe granites, where the determined age of granites was 142.9 ± 1.8 Ma at initial $^{87}Sr/^{86}Sr$ of 0.706 ± 5 (Kovalenko et al. 1999).

5 Regional evidence for the proposed model

Evidence from Sr, Nd and O isotope investigations (Kovalenko et al. 1999, 2002, 2003; Yarmolyuk et al. 2003) is consistent with our lead isotope data reaffirming the two possible common sources for granitic magmas of the Orlovka-Spokoinoe mining district. However, there is no unequivocal data implicating either a mixed upper crust-mantle source or a type II enriched mantle source.

Regional studies of Transbaikalian granitoids incorporating geochemical, geophysical and geodynamic data indicate both crustal and mantle inputs triggering granitic melt generation of all petrochemical series (Jahn et al. 2000; Kovalenko et al. 1996; Litvinovsky et al. 2002). The isotopic heterogeneity of these granites was predetermined by the isotopic heterogeneity of their sources (Kovalenko et al. 1996). Blocks of consolidated pre-Riphean crust were overthrust during the accretionary collision of the foldbelts onto the younger crustal complexes of within-block oceanic basins contributing to an anomalous crustal thickness. The Riphean-aged crust in Caledonian structures most likely reflects the same average composition of a mixed source (basites + pelites) of the granitoid magmas; the source formed at 450-500 Ma. The isotopic evolution of this source resulted in $\varepsilon Nd_{(T)} \sim 0$ of the mixed source by 100-200 Ma. Some of the young (~120 Ma) granites show evidence of assimilation of pre-Riphean crust (Kovalenko et al. 1996). Some metaluminous and peralkaline syenite-granite suites and closely associated comendites of Transbaikalia constrain A-type granitoid magma generation emplaced at ca. 280 Ma as a result of fractional crystallization of syenite magmas. Alkali-rich silicic magma formed at an estimated depth of 50-60 km far exceeding the normal crust thickness. The Sr-Nd isotope data advocate the main role of mantle-de-

rived material in the source region from which the alkali-rich syenitic and granitic magmas were produced (Litvinovsky et al. 2002). Also, widespread Transbaikalian alkali monzodiorite-syenite series are explained by fractional crystallization from tephritic magma intrusions at ca. 130 Ma. In contrast to calc-alkaline granite batholiths generated during continental crustal growths, subalkaline granites of Transbaikalia are often accompanied by basalt-trachyte-pantellerite-alkaline granite associations marking rift structures of intraplate "hotspots" (Kovalenko et al. 1996). The related Li-F and alkaline granites represent A-type granites with high heat production. Sr, Nd and O isotope investigations of late Oligocene–Holocene volcanics from the adjacent area of the Southern Baikal region (Yarmolyuk et al., 2003) show that the isotopic signature of the magma source is a mixture of moderately depleted mantle and enriched mantle reservoirs of types I and II enriched mantle (EM I and EM II). EM II source has been reported to be one of the mantle sources contributing to the formation of Early Mesozoic rocks of the Mongolia-Transbaikalia magmatic area and has been listed among mantle sources for the CAOB as a whole (Kovalenko et al. 2002). The published data on Sr and Nd isotopes for the Orlovka massif with the values of initial $^{87}Sr/^{86}Sr$ of 0.706 ± 0.005 and $\varepsilon Nd = 0.1$ (Kovalenko et al. 1999) also favor EM II mantle input. Data hints at the possibility that an EM II source controlled intraplate activity in Eastern Transbaikalia during late Mesozoic times including formation of the Orlovka and Spokoinoe deposits.

6 Conclusions

Pb isotope data of crustal rocks and ore deposits of the Orlovka-Spokoinoe mining district complement the existing Nd and Rb-Sr data for this region. Our results indicate that the three granite massifs have uniform Pb isotope compositions and show a strong genetic relationship between the barren biotite-muscovite granites of Khangilay and the Spokoinoe and Orlovka ore-bearing granites suggesting a common source for the three massifs. Pb isotope data also confirm that the Khangilay pluton can be considered as the parental intrusion for its hosted mineralized apical intrusions. Pb isotope systematics outline two possible scenarios for the source of granitic melts: a mixed upper crust-mantle source, and a type II enriched mantle source.

New Rb-Sr isotope data confirms the age of 143.8±4.2 Ma for biotite and biotite-muscovite granites of the Khangilay and Orlovka massifs.

Acknowledgements

The authors would like to thank Russian colleagues who participated in the INTAS 97-0721 project for inspiring discussions, assistance in field sampling and analytical support. Continuous assistance of the EMMA laboratory at the Natural History Museum London and of Barry Coles (Imperial College London) with the analytical part of the project is acknowledged. This is a contribution to the IGCP Project #473 "GIS Metallogeny of Central Asia".

Syn-metamorphic dates for tourmaline formation around Mount Isa, north-west Queensland, Australia

Robert J. Duncan, Andy R. Wilde
*pmd*CRC, School of Geoscience, Monash University, Melbourne, VIC 3800, Australia*

Roland Mass, Katherine Bassano
*pmd*CRC, School of Earth Sciences, Melbourne University, Melbourne, VIC 3010, Australia*

Abstract. Pb stepwise leaching of tourmaline from the Palaeoproterozoic Western Fold Belt of the Mount Isa Inlier yield dates of 1559±17 Ma, 1577±52 Ma and 1480±90 Ma. Structural, petrological and textural data suggest that 1559±17 Ma is the best estimate for peak metamorphism in the area. Estimates of Pb closure temperature and comparison with peak metamorphic temperatures indicate that this age represents tourmaline crystallisation. These dates represent syn-metamorphic fluid flow and indicate metal mobility during the Isan Orogeny. A result of this event is regional-scale silicification that has the same relative timing as extensive silica deposition in the rocks that now host the Cu orebodies at Mount Isa.

Keywords. Mount Isa, metamorphism, tourmaline, hydrothermal fluid flow, Pb stepwise leaching

1 Introduction

To further constrain the timing of the Isan Orogeny in the Western Fold Belt of the Mount Isa Inlier we applied the Pb step-leaching (PbSL) technique to tourmaline. PbSL involves sequential acid leaching of low-U minerals to generate Pb-Pb isochrons for old (>400 Ma) rocks (Frei and Kamber 1995). The tourmaline samples dated here can be demonstrated to have formed under, or close to, peak metamorphic conditions using structural, petrographical and geochemical evidence.

As tourmaline is generally considered metasomatic in origin, this work not only allows an improved understanding of the timing of peak metamorphism, but also new insights into the nature of fluid flow associated with compressional deformation. The timing and nature of this hydrothermal event has potential implications for the Cu mineralisation at Mount Isa.

2 Previous work

The polydeformed mid- to late Proterozoic Mount Isa Inlier in north-west Queensland was tectonically active between 1900 and 1500 Ma (Blake and Stewart 1992). The most intense period of deformation is considered to be largely synchronous with peak high temperature-low pressure metamorphism that resulted from crustal shortening during the Isan Orogeny from 1590 to 1500 Ma (Connors and Page 1995; O'Dea et al. 1997).

Previous attempts to date peak metamorphism have focused on U-Pb analysis of zircon and monazite (Connors and Page 1995; Hand and Rubatto 2002), but their relationship to metamorphic reactions and structural features is ambiguous (e.g. Roberts and Finger 1997). Published Ar-Ar biotite dates (Perkins et al. 1999) are likely to represent cooling ages past the closure temperature. Table 1 summarises the current age estimates of peak metamorphism on single mineral phases.

Table 1: Summary of published age data for peak metamorphism from around Mount Isa

System	Mineral	Age ± Error	Source
U-Pb	Monazite	1575 ± ?	(1)*
U-Pb	Zircon	1532 ± 7	(2)*
U-Pb	Zircon	1565 ± 5	(2)†
U-Pb	Zircon	1480 ±14	(2)†
Ar-Ar	Biotite	1534 ± 4	(3)*

?=not reported; *=interpreted as peak metamorphic
†= other data from same sample; [1]Hand and Rubatto (2002); [2]Connors and Page (1995); [3]Perkins et al. (1999)

3 Tourmaline occurrence, petrography and geochemistry

Tourmaline-rich lithologies are abundant in areas around Mount Isa. Tourmaline is especially prevalent in the Eastern Creek Volcanics (ECV) west of the Mount Isa fault. In this area it occurs in quartz-K feldspar-mica-apatite pegmatites around the contact of the Sybella Batholith and apparently stratabound, but not stratiform, tourmalinites (representative of extensive silicification). Minor tourmaline occurrences have been identified in the ECV to the east of Mount Isa. The three samples selected for dating are from within a 25 km radius of Mount Isa and are in close proximity to small mineral occurrences (Fig. 1).

Tourmaline has been identified as an accessory phase in the silica dolomite alteration halo to the Cu orebodies at Mount Isa (Mathias and Clark 1975). The silicification at the mine is considered to have occurred prior to Cu mineralisation, synchronous with D_2 or D_3 deformation (Swager 1985; Wilde et al. this volume) during the peak of deformation. The orebody tourmaline is dravitic in

composition and is concentrated in the Paroo Fault in the footwall of the Cu orebodies (W. Perkins and J. Knights pers. comm. 2004).

Tourmaline from close to the King Cu deposit is stratabound, but not stratiform within quartzite and psammopelitic units of the Myally subgroup. Tourmaline growth overprints the S_2 fabric, defined by biotite and sillimanite, and is deformed by D_3 NNW-trending shear zones and NNW gently plunging meso-scale folds (Fig. 2a). The sample consists of zoned glomerocrysts and coarse-grained strained quartz, along with minor amounts of titanite, sphalerite and Fe-Ti oxides.

Adjacent to the Eldorado U deposit (hosted by the ECV) is a quartz-tourmaline-K feldspar-mica pegmatite. The pegmatite is parallel to the S_2 fabric and is boudinaged by D_3 structures. Tourmaline in the pegmatite selvages defines a steeply plunging mineral lineation (L_2) and pseudomorphs cordierite poikiloblasts in the wall rock (Fig. 2b). Primary fluid inclusions within tourmaline from this sample contain up to 436 ppm U (Duncan and Wilde 2004).

At Anderson's Lode (a small U deposit hosted by the ECV) a quartz-fibrous tourmaline vein is deformed by D_3 shearing. Host rock tourmaline is overprinted by a biotite-chlorite metamorphic matrix (Fig. 2c). These relationships suggest that tourmaline crystallisation was early to syn-metamorphic and pre-D_3 in timing. Paragenetically associated with the quartz-tourmaline vein are minor amounts of pyrite and chalcopyrite.

Electron-microprobe analyses demonstrate the transitional Fe-Mg composition of all the tourmaline samples. Tourmaline from Anderson's Lode is schorlitic, whilst samples from Eldorado and King are dravitic. Trace element analysis by laser ablation ICP-MS reveals that the tourmalines are relatively enriched in light rare earth elements with variable Eu and Ce anomalies, indicative of crystallisation from a metamorphic fluid (cf. Jiang et al. 2004).

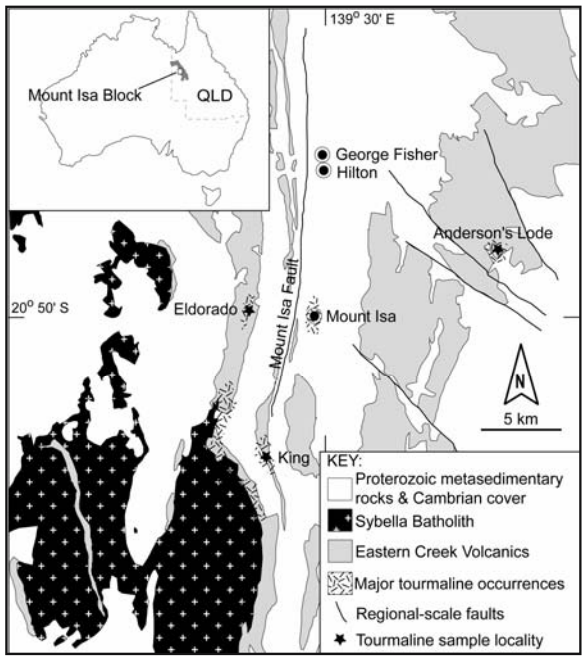

Figure 1: Regional distribution of tourmaline around Mount Isa and key sample locations.

4 Pb stepwise leaching

PbSL was carried out at the University of Melbourne. The main advantage of PbSL over bulk U-Pb dating is the ability to chemically separate Pb from U-rich and U-poor domains within the samples, thus generating Pb isotopic dispersion from a single mineral separate. $^{208}Pb/^{206}Pb$ systematics can be used to recognise, and discard if necessary, results from leach steps dominated by unequilibrated impurities with distinct Th/U ratios, such as zircon and monazite.

Tourmaline concentrates (200 to 400 μm) were produced by conventional dense medium separation and purified by hand-picking. After removal of surficial Pb contamination with distilled water, samples weighing 80 to 100 mg were sequentially leached with 1.5 N HCl-2N HBr mix, 1N and 8N

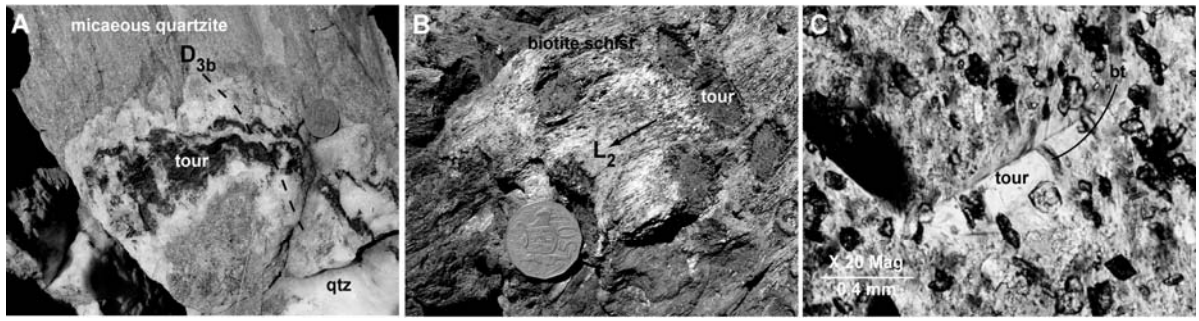

Figure 2: Typical tourmaline occurrences at key locations (A) tourmalinite (tourmaline + quartz) deformed by eastwards verging D_3 fold at King (B) tourmaline delineating L_2 and pseudomorphing cordierite at Eldorado (C) tourmaline at Anderson's Lode overprinted by biotite

HBr, 7N and 15N HNO_3 and 48% HF on a hot plate at ~100°C for periods of five minutes to 120 hours. Pb from each leach step was extracted using a single pass over 0.1 ml columns of EICHROM^{TM} Sr resin following the method of Thériault and Davies (1999). Pb isotopic ratios were determined by multi-collector ICP-MS (Woodhead 2002).

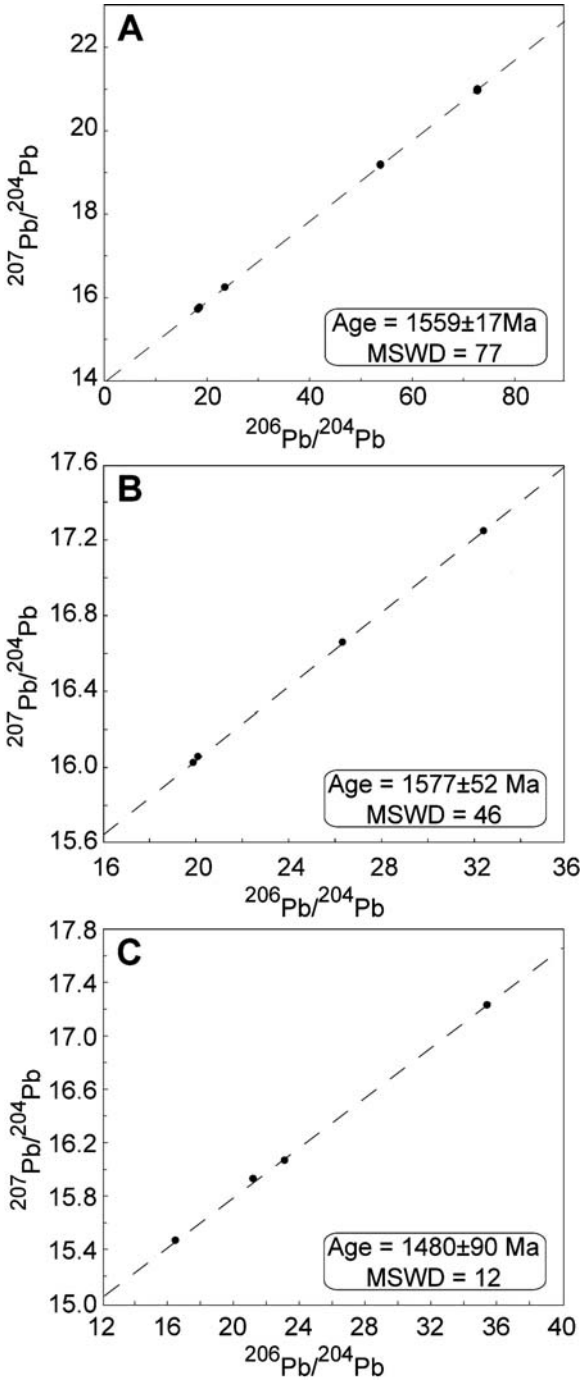

Figure 3: Pb-Pb stepwise leaching isochrons for tourmaline from (A) Anderson's Lode (B) Eldorado (C) King.

Pb-Pb isochrons parameters and ages were calculated using ISOPLOT (Ludwig 2003). External $2sigma_m$ (±0.03%) or internal ($2sigma_m$) errors (whichever is greater) and error correlations derived from these uncertainties were used as input errors for the isochron calculations. No blank corrections were applied.

Tourmaline from Anderson's Lode yielded five leach steps, with a range in $^{206}Pb/^{204}Pb$ of 17.2 to 72.9. A regression of all five leach steps identifies some scatter (MSWD 77), but a relatively precise Pb-Pb isochron age of 1559±17 Ma (Fig. 3a).

Seven leach steps derived from the tourmaline at Eldorado gave a range in $^{206}Pb/^{204}Pb$ from 19.9 to 67.2, regression of all the data indicates a excessive amount of scatter (MSWD >6000). Inspection of the $^{208}Pb/^{206}Pb$ data shows that three leach steps are affected by Pb from Th-rich micro-inclusions. Omission of these points results in a four-point age of 1577±52 Ma (MSWD 46; Fig. 3b).

The five leach spectra of the tourmaline from King yield the narrowest range in $^{206}Pb/^{204}Pb$ (16.4 to 35.3). After the removal of one step with anomalously high $^{208}Pb/^{206}Pb$ (i.e., Pb derived from Th-rich inclusions), this short data array produce an imprecise age of 1488±90 Ma (MSWD 16; Fig. 3c).

5 Interpretation of ages

Estimates of Pb closure temperatures in tourmaline for compositions similar to these samples were calculated according to the method outlined by Dahl (1997) and range from 580°C to 630°C. The Anderson's Lode area is characterised by low to mid-greenschist facies rocks, so the 1557 Ma date reflects tourmaline formation. Around Eldorado peak metamorphic temperatures are estimated at 540°C to 640°C (Rubenach 1992) and at King temperatures of ~600°C are likely to have been encountered during peak metamorphism (Connors 1992). At these two locations the ages and associated large errors may represent a period of elevated heat flow, when the ambient geothermal gradient was above the Pb closure temperature and Pb could diffuse easily. The may explain the range of U-Pb zircon dates (Table 1; 1565 to 1480 Ma from one sample in Connors and Page (1995)).

Comparing age data derived from Pb-Pb dating of tourmalines with other metamorphic dates it is clear that between ~1575 and ~1530 Ma the Western Fold Belt around Mount Isa was undergoing high-temperature/low-pressure peak metamorphism. This metamorphic window reflects the prolonged duration of tectonic shortening during the Isan Orogeny. It appears that regional tourmalinisation resulted from prolonged hydrothermal activity related to this compressional deformation. The best estimate of peak metamorphism is now ca. 1557±17 Ma.

The occurrence of tourmaline with small Cu and U deposits and paragenetic relationships with minor

sulphides suggests that during hydrothermal fluid movement driven by metamorphism, metals of economic interest were mobile. The regional spatial and temporal association of tourmalinisation with silicification indicates that the silica-rich halo around the Cu orebodies may have formed at a similar time.

Acknowledgements

The PbSL routines are based largely on unpublished experiments by M Tonelli, J Hergt and J Woodhead (Univ. of Melbourne). The work reported is part the *pmd**CRC with support from Xstrata Copper. Thanks to R. Romer for reviewing this abstract.

References

Blake DH, Stewart AJ (1992) Stratigraphic and tectonic framework, Mount Isa Inlier. In: Stewart AJ, Blake DH (eds) Detailed studies of the Mount Isa Inlier. Aust Geol Surv Organ Bull 243: pp 1-11

Connors KA (1992) Tectonothermal evolution of the Mount Novit Ranges, Mount Isa Inlier, Australia. PhD Thesis, Monash University

Connors KA, Page RW (1995) Relationships between magmatism, metamorphism and deformation in the western Mount Isa Inlier, Australia. Precambr Res 71: 131-153

Dahl PS (1997) A crystal-chemical basis for Pb retention and fission-track annealing systematics in U-bearing minerals, with implication for geochronology. Earth Planet Sci Lett 150: 277-290

Duncan RJ, Wilde AR (2004) Tourmaline at Mount Isa, Australia: a tracer of metal-rich hydrothermal fluid flow. In: Muhling J et al. (eds) SEG 2004: Predictive Mineral Discovery Under Cover, Perth, Western Australia; Extended Abstracts, Centre for Global Metallogeny, The University of Western Australia Publication 33: 413

Frei R, Kamber BS (1995) Single mineral Pb-Pb dating. Earth Planet Sci Lett 129: 261-268

Hand M, Rubatto D (2002) The scale of the thermal problem in the Mt. Isa Inlier. In: Preiss VP (ed) Geoscience 2002: Expanding Horizons. Abstracts of the 16th Australian Geological Convention, Adelaide, SA, Australia 67: 173

Jiang SY, Yu JM, Lu JJ (2004) Trace and rare-earth element geochemistry in tourmaline and cassiterite from the Yunlong tin deposit, Yunnan, China: implications for migmatic-hydrothermal fluid evolution and ore genesis. Chem Geol 209: 193-213

Ludwig KR (2003) User's Manual for Isoplot 3.00: A geochronological toolkit for Microsoft Excel. Berkeley Geochronology Center Spec Publ 4, California, p 70

Mathias BV, Clark GJ (1975) Mount Isa copper and silver-lead-zinc ore bodies; Isa and Hilton mines. In: Knight CL (ed) Economic Geology of Australia and Papua New Guinea. Aust Inst Mining Metall, pp 351-371

O'Dea MG, Lister GS, MacCready T, Betts PG, Oliver NHS, Pound KS, Huang W, Valenta RK (1997) Geodynamic evolution of the Proterozoic Mount Isa terrain. In: Burg JP, Ford M (eds) Orogeny through time. Geol Soc Spec Publ 121: 99-122

Perkins C, Heinrich CA, Wyborn LAI (1999) $^{40}Ar/^{39}Ar$ geochronology of copper mineralization and regional alteration, Mount Isa, Australia Econ Geol 94: 23-36

Roberts MP, Finger F (1997) Do U-Pb zircon ages from granulites reflect peak metamorphic conditions? Geology 25: 319-322

Rubenach MJ (1992) Proterozoic low-pressure/high-temperature metamorphism and an anticlockwise P-T-t path for the Hazeldene area, Mount Isa Inlier, Queensland, Australia. J Meta Geol 10: 333-346

Swager CP (1985) Syndeformational carbonate-replacement model for the copper mineralization at Mount Isa, Northwest Queensland; a microstructural study. Econ Geol 80: 107-125

Thériault RJ, Davies WJ (1999) Rapid extraction of Sr and Pb by ion-specific chromatography for thermal ionisation mass spectrometry analysis. In Radiogenic age and isotopic studies, report 12, Geol Surv Can Current Research 1999-F: 9-12

Wilde AR, Gregory MJ, Duncan RJ, Gessner K, Kühn M, Jones P (2005) Geochemical process model for the Mt Isa Cu-Co-Ag deposits, this volume

Woodhead JD (2002) A simple method for obtaining highly accurate Pb isotope data by MC-ICP-MS. J Anal Atom Spec 17: 1-6

Potassic alteration and veining and the age of copper emplacement at Mount Isa, Australia

Melissa J. Gregory, Andy R. Wilde, Bruce F. Schaefer, Reid R. Keays
*pmd*CRC, School of Geoscience, Monash University, Melbourne, VIC 3800, Australia*

Abstract. Preliminary $^{187}Re/^{188}Os$ dating of whole rocks and sulphide separates from the Mount Isa copper orebody has generated an isochron age of 1367 ± 80 Ma (MSWD = 49; n = 6). This age is approximately 150 myr younger than published biotite $^{40}Ar/^{39}Ar$ ages previously assumed to date the copper-forming event at ca. 1523 Ma. These older ages are from rocks in which biotite is likely to be metamorphic rather than hydrothermal in origin. Unambiguous potassic alteration related to copper formation is characterised by biotite replacement of metabasalt (brownstones) and potassium feldspar replacement of meta-tuffs. Previous $^{40}Ar/^{39}Ar$ dating of biotite from brownstone yields 1352 Ma to 1385 Ma ages, while $^{87}Rb/^{86}Sr$ dating of potassium feldspar altered tuffs gives 1323 Ma. Muscovite from the Buck Quartz Fault, considered a conduit for copper mineralising fluids, yields an $^{40}Ar/^{39}Ar$ age of 1324 Ma. We suggest that these ages more accurately reflect the age of copper emplacement, whereas the older $^{40}Ar/^{39}Ar$ ages more likely relate to cooling from peak metamorphism.

Keywords. Mount Isa, Re-Os, potassic alteration

1 Introduction

The Mount Isa copper deposit contains over 13 million tonnes of copper at 3.3 wt.%, and is hosted within the Proterozoic Urquhart Shale (Perkins 1990). Textural evidence suggests that chalcopyrite-pyrrhotite mineralisation occurred late in the tectonic history of the Mount Isa Inlier (Perkins 1984; Swager 1985; Valenta 1994; Waring 1990). The absolute age of copper mineralisation, however, is poorly defined. In this paper we discuss the available radiometric data and their significance. Most published data are from potassic phases, such as biotite, muscovite and potassium feldspar so it is necessary to review evidence for the relationship of such phases to copper deposition.

2 Metamorphic biotite

2.1 Eastern Creek Volcanics

The Eastern Creek Volcanics below and to the east of the Mount Isa copper deposit have undergone lower greenschist facies metamorphism. Stable assemblages in the metabasalts include chlorite, albite, actinolite, epidote, calcite, titanomagnetite, magnetite, sphene and biotite. Biotite and chlorite define a metamorphic foliation in some areas.

2.2 Urquhart Shale

Biotite is a common phase in metasedimentary rocks of the Mount Isa Group, including the Urquhart Shale. It defines the peak metamorphic foliation, and ranges in composition from Fe-rich to more magnesian phlogopite, depending on the host rock composition.

Biotite is rare in the intense silica-dolomite alteration associated with economic copper mineralisation, but distinctive biotite-magnetite-stilpnomelane bearing rocks occur in close proximity to Pb-Zn ore (Fig. 1). Swager et al. (1987) interpret these zones to be the result of the interaction of the copper mineralising fluid with pre-existing iron-rich metasomatic rocks in the Urquhart Shale. Conversely, Waring (1990) suggests that these zones were the result of greenschist facies metamorphism. He notes that the biotite-magnetite-stilpnomelane assemblage is cut by dolomite veins considered to be contemporaneous with copper emplacement.

3 Absolute age of metamorphism

The absolute age of the peak (maximum temperature and pressure) of regional metamorphism is poorly constrained. Biotite from the Eastern Creek Volcanics 14.5 km east of the mine, gave $^{40}Ar/^{39}Ar$ ages of 1534 ± 4 Ma and 1524 ±3 to 1554 ± 2 Ma (Perkins et al. 1999). These ages were interpreted to reflect hydrothermal activity at the end of regional metamorphism at 1534 Ma. This date is consistent with the SHRIMP U-Pb zircon ages of 1532 ± 7 Ma by Connors and Page (1995) and the whole rock $^{87}Rb/^{86}Sr$ ages of 1544 ± 12 Ma from Page and Bell (1986).

U/Pb monazite dating by Hand and Rubatto (2002) suggests that peak metamorphism is older at ca. 1575 Ma. This older age is supported by new metamorphic tourmaline dates of 1559 ± 17 Ma and 1577 ± 52 Ma using Pb-Pb step leaching (Duncan et al. this volume).

4 Potassic alteration

4.1 Urquhart Shale

There are over 60 potassium-rich layers within the Urquhart Shale throughout the Mount Isa mine sequence (Croxford 1964). These layers are typically less than 5 cm

thick, and characterised by an unusual pale gray colour. Croxford (1964) interpreted these layers as tuffs, based on the rare presence of glass shards. The tuffs consist of microcline (after adularia), quartz, rutile, hematite, sericite and carbonate. Perkins (1997), however, found that only the tuffs in the mine area were potassium-rich, suggesting a hydrothermal origin for potassium.

4.2 Eastern Creek Volcanics

Detailed logging of drillcore at the northern end of the Mount Isa copper deposit (mine section 38,000 mN) has defined a zone of potassium-rich alteration within the Eastern Creek Volcanics, below copper mineralisation in the Urquhart Shale (Fig. 1). This zone, which is dominated by biotite, has previously been called brownstone and has been reported in many deep drillholes that have intersected the Eastern Creek Volcanics below the Mount Isa copper deposit (e.g. Hannan et al. 1993).

This biotite-rich alteration parallels the Paroo Fault (Fig. 1) and is thicker (up to 70m) where copper mineralisation overlies the fault. In thin section, the biotite-dominated rocks have a groundmass of chlorite, albite and ilmenite that is overprinted by a fine network of biotite veinlets. Undeformed biotite also pseudomorphs weakly foliated chlorite.

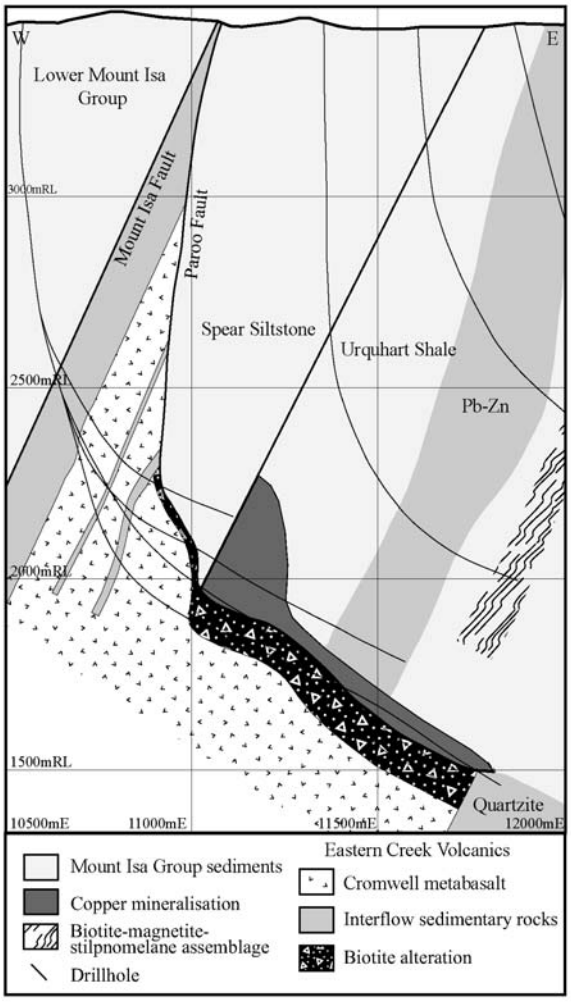

Figure 1: Mine cross section 38,000 mN showing general geology and distribution of mineralisation and alteration. Geological interpretation adapted from work done by Xstrata Copper geologists.

4.3 Potassium feldspar veining

Away from biotite-rich zones, potassium-rich veins are observed in the metabasalts of the Eastern Creek Volcanics. These veins are dominated by potassium feldspar, calcite, quartz and chalcopyrite and are commonly 2 to 5 mm thick. Typically the veins are zoned with potassium feldspar lining the metabasalt contact and calcite with lesser quartz in the core. Chalcopyrite is intergrown with the potassium feldspar. The vein boundaries are sharp and cross cut the peak metamorphic foliation found within the metabasalts.

5 Absolute age of ore formation

Preliminary $^{187}Re/^{188}Os$ isotopic analyses of whole rocks and sulphide separates from the Mount Isa copper orebody define an imprecise isochron age of 1367 ± 80 Ma (Fig. 2).

$^{87}Rb/^{86}Sr$ dating of potassic altered tuff horizons from the mine area define isochron ages from 1341 ± 21 Ma to 1474 ± 202 Ma (Farquharson and Richards 1975; Page

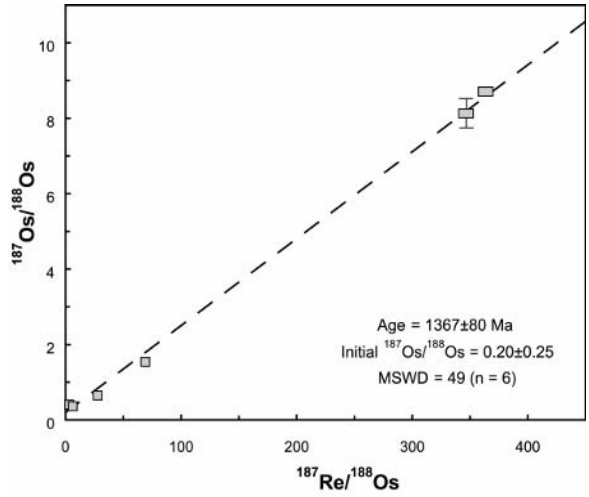

Figure 2: Re-Os isochron for Mount Isa copper orebody. Errors are smaller than sample points except where indicated. Re and Os abundances range from 0.0394 to 3.7847 ppb and 0.0078 to 0.4027 ppb respectively. Samples are blank corrected with corrections <5% and 1% for Os and Re respectively, with the exception of one sample which had corrections of 8.7% for Os and 7% for Re due to low abundances.

Table 1: Published age data associated with the Mount Isa copper deposit.

System	Mineral/rock type	Age (Ma)
Ar/Ar	Biotite - magnetite-stilpnomelane zone	1523 ± 3[1]
	Biotite - magnetite-stilpnomelane zone	1516 ± 3[1]
	Biotite - pyrrhotite vein	1505 ± 3[1]
	Muscovite - Buck Quartz Fault	1324 ± 2[1]
	Biotite - Brownstone	1385 ± 3[1]
	Biotite - Brownstone	1352 ± 3[1]
	Biotite - ECV-Anderson's Lode	1534 ± 4[1]
	Biotite - ECV-Anderson's Lode	1554 ± 2[1]
	Biotite - ECV-Anderson's Lode	1524 ± 3[1]
Rb/Sr	Pooled whole rock tuffs	1323 ± 12[2]
Re/Os	Whole rock ore and sulphide separates	1367 ± 80

[1]Perkins et al. 1999; [2]Gregory et al. 2004; ECV = Eastern Creek Volcanics.

1981). A significantly more precise age is achieved by combining the two data sets (as all samples are from the same lithology and area) to give an age of 1323 ± 12 Ma (Gregory et al. 2004). A radiogenic initial ratio of 0.7418 ± 0.0061 suggests isotopic resetting may have occurred at this time (Farquharson and Richards 1975; Gregory et al. 2004; Page 1981).

Perkins et al. (1999) reported numerous $^{40}Ar/^{39}Ar$ dates for biotite and muscovite from the Urquhart Shale and the Eastern Creek Volcanics (Table 1). Biotite and phlogopite from stilpnomelane-magnetite zones gave $^{40}Ar/^{39}Ar$ ages of 1523 ± 3 Ma and 1516 ± 3 Ma, from which 1523 Ma was interpreted as the most likely date of copper ore deposition (Perkins et al. 1999).

Perkins et al. (1999) also dated biotite separates from brownstones within the Eastern Creek Volcanics adjacent to the copper deposit. $^{40}Ar/^{39}Ar$ dating of these separates gave distinct plateau ages at 1352 ± 3 Ma and 1385 ± 3 Ma, which was interpreted as the age of late stage fluid flow.

Muscovite from the Buck Quartz Fault, interpreted to be the inflow zone for the copper bearing fluids (Waring 1990), gave an $^{40}Ar/^{39}Ar$ age of 1324 ± 2 Ma, also interpreted as due to minor late stage fluid flow (Perkins et al. 1999).

6 Discussion and conclusions

Biotite and phlogopite are virtually absent from intensely altered and mineralised rocks which form the Mount Isa copper deposit but there is a close spatial relationship between biotite-rich alteration below the Paroo Fault and copper mineralisation above the fault. The biotite overprints the metamorphic foliation and the spatial relationships and timing supports the idea of hydrothermal fluid flow along the fault, as suggested by Hannan et al. (1993) and Heinrich et al. (1995).

Chalcopyrite-bearing potassium feldspar veins overprint the metamorphic foliation and therefore have the same relative timing as the biotite-rich alteration and the copper ore. The presence of both biotite-rich alteration below the Paroo Fault and potassium feldspar-rich veins demonstrates the presence of a potassium and copper-rich fluid. This fluid post-dates regional metamorphism and is spatially associated with the Mount Isa copper deposit.

A number of isotopic dating techniques suggest that the peak of metamorphism at Mount Isa occurred prior to 1532 Ma and possibly prior to 1575 Ma. Emplacement of the Mount Isa copper deposit, based on numerous studies, clearly postdates the metamorphic peak. The absolute age of copper emplacement however, and particularly the gap between the conclusion of metamorphism and ore formation has been poorly defined.

Our re-evaluation of published $^{40}Ar/^{39}Ar$ and $^{87}Rb/^{86}Sr$ data on potassic hydrothermal alteration, together with our preliminary $^{187}Re/^{188}Os$ dating of sulphide ore suggest that copper mineralisation was emplaced between 1300 Ma and 1400 Ma, at least 130 million years after the metamorphic peak.

An alternative interpretation may be that the terrain remained above the closure temperature for these systems for several hundred million years after the peak of metamorphism.

We suggest that the ca. 1523 Ma age of Perkins et al. (1999), previously assumed to be the date of copper ore formation, instead dates cooling from the metamorphic peak. The maximum temperature of ore formation is suggested to be between 300 and 350°C (Heinrich et al. 1989; Heinrich et al. 1995), and may not have exceeded the Ar closure temperature range of the metamorphic biotite.

Therefore, there is significantly more evidence to support a ca. 1350 Ma age for copper mineralisation compared with the previously accepted ca. 1523 Ma age. This has implications for the genetic models proposed for the formation of the Mount Isa copper deposit.

Acknowledgements

Work reported here was conducted as part of the *pmd**CRC with support from Xstrata Copper.

References

Connors KA, Page RW (1995) Relationships between magmatism, metamorphism and deformation in the western Mount Isa Inlier, Australia. Precambr Res 71:131-153

Croxford NJW (1964) Origin and significance of volcanic potash-rich rocks from Mount Isa. Inst. Min. & Met. Tr. 74:33-43

Duncan RJ, Wilde AR, Maas R, Bassano K (2005) Syn-metamorphic dates for tourmaline formation around Mount Isa, North-west Queensland, Australia, this volume

Farquharson RB, Richards JR (1975) Isotopic remobilization in the Mount Isa tuff beds. Chem Geol 16:73-88

Gregory MJ, Wilde AR, Keays RR, Schaefer BF (2004) Preliminary Re-Os dating of the Mount Isa copper ores, Northwest Queensland. Barnicoat AC, Korsch RJ (eds) Predictive Mineral Discovery Cooperative Research Centre – Extended Abstracts, Geoscience Australia Record 2004/09, pp 79

Hand M, Rubatto D (2002) The scale of the thermal problem in the Mt Isa Inlier. In: Preiss VP (ed) Geoscience 2002: Expanding Horizons, 16th Australian Geological Convention, Adelaide, South Australia, pp 173

Hannan KW, Golding SD, Herbert HK, Krouse HR (1993) Contrasting alteration assemblages in metabasites from Mount Isa, Queensland; implications for copper ore genesis. Econ Geol 88:1135-1175

Heinrich CA, Andrew AS, Wilkins RWT, Patterson DJ (1989) A fluid inclusion and stable isotope study of synmetamorphic copper ore formation at Mount Isa, Australia. Econ Geol 84:529-550

Heinrich CA, Bain JHC, Mernagh TP, Wyborn LAI, Andrew AS, Waring CL (1995) Fluid and mass transfer during metabasalt alteration and copper mineralization at Mount Isa, Australia. Econ Geol 90:705-730

Page RW (1981) Depositional ages of the stratiform base metal deposits at Mount Isa and McArthur River, Australia, based on U-Pb zircon dating of concordant tuff horizons. Econ Geol 76:648-658

Page RW, Bell TH (1986) Isotopic and structural responses of granite to successive deformation and metamorphism. Journal of Geology 94:365-379

Perkins C, Heinrich CA, Wyborn LAI (1999) $^{40}Ar/^{39}Ar$ geochronology of copper mineralization and regional alteration, Mount Isa, Australia. Econ Geol 94:23-36

Perkins WG (1984) Mount Isa silica dolomite and copper orebodies; the result of a syntectonic hydrothermal alteration system. Econ Geol 79:601-637

Perkins WG (1990) Mount Isa copper orebodies. In: Hughes FE (ed) Geology of the mineral deposits of Australia and Papua New Guinea. Aust Inst Mining Metall, pp 935-941

Perkins WG (1997) Mount Isa lead-zinc orebodies; replacement lodes in a zoned syndeformational copper-lead-zinc system? Ore Geol Rev 12:61-111

Swager CP (1985) Syndeformational carbonate-replacement model for the copper mineralization at Mount Isa, Northwest Queensland; a microstructural study. Econ Geol 80:107-125

Swager CP, Perkins WG, Knights JG (1987) Stratabound phyllosilicate zones associated with syntectonic copper orebodies at Mt. Isa, Queensland. Aust J Earth Sci 34:463-476

Valenta R (1994) Syntectonic discordant copper mineralization in the Hilton Mine, Mount Isa. Econ Geol 89:1031-1052

Waring CL (1990) The Genesis of the Mount Isa Copper Orebodies. PhD, Monash University

Contact metamorphism at the manganese deposits of the Noda-Tamagawa Mine, northeast Japan: Insight from oxygen isotope data of manganese minerals

Ken-ichiro Hayashi
Doctoral Program in Earth Evolution Sciences, Graduate School of Life and Environmental Sciences, University of Tsukuba, Tsukuba 305-8572, Japan

Abstract. Manganese ores of the Noda-Tamagawa mine are metamorphosed equivalents of bedded-type sedimentary manganese deposits. The ore lenses are typically zoned with a central pyrochroite-hausmannite zone, outer tephroite zone, and outermost rhodonite zone closest to the wall rock chert. The $\delta^{18}O$ (VSMOW) values of 65 tephroite, 32 rhodonite and eight quartz samples from the manganese ores and chert are in the ranges of 9.9–20.0‰, 11.7–20.3‰ and 23.0–23.9‰, respectively. The overall order of ^{18}O-enrichment corresponds to the order of equilibrium fractionation among these minerals. However, the temperatures calculated from quartz-rhodonite and rhodonite-tephroite pairs from neighboring ore zones do not give temperatures consistent with those estimated from the mineral assemblages in the wall rocks. These data suggest that equilibrium was not established among neighboring mineral pairs, H_2O, and CO_2 during metamorphism. The fluid/rock ratios during metamorphism were very low (<< 1).

Keywords. Manganese deposit, oxygen isotope, contact metamorphism, metamorphic fluid

1 Introduction

Manganese ores of the Noda-Tamagawa mine are highly metamorphosed and folded. This metamorphism makes it difficult to obtain information on the primary features of the deposits, such as the original mineralogy, chemical composition, and environment of deposition. Despite these difficulties, the deposit is interpreted to be the metamorphosed equivalent of bedded-type sedimentary manganese deposits. The main objective of this study is to elucidate the origin and metamorphic history of the manganese ores at Noda-Tamagawa using the $\delta^{18}O$ relationships among various metamorphic Mn-bearing silicate minerals. These data constrain the temperatures of metamorphism, fluid/rock ratios, and composition of the metamorphic fluids.

2 Geology of the Noda-Tamagawa mine

The manganese deposits of the Noda-Tamagawa mine are situated in the northeastern part of a roof pendant of the granodiorite body. The roof pendant is ca. 8 km (N-S) x 12 km (E-W) in area, and is comprised of the Jurassic Formation. In the vicinity of the Noda-Tamagawa mine, these rocks have been hornfelsed due to the thermal metamorphism by the granodiorite. Sillimanite, andalusite, and cordierite are present in some pelitic hornfels near the manganese ore bodies.

As a result of the thermal metamorphism, a distinct zoning of manganese minerals developed in each ore lens, on a scale of 2 to 5 m. Pyrochroite ($Mn(OH)_2$) and hausmannite (Mn_3O_4) typically occupy the central part of the ore lens (0 to 1 m in thickness), surrounded by a tephroite (Mn_2SiO_4) ore, and an outer rhodonite ($MnSiO_3$) ore.

The major Mn-bearing minerals in the Noda-Tamagawa mine can be represented in the MnO-SiO_2-Al_2O_3 system. The principal zoning sequence in the ore lenses of the Noda-Tamagawa mine corresponds to a trend of decreasing MnO content (and increasing SiO_2 content) toward the wall rocks. Bulk chemical compositions of the manganese ores change along the MnO-SiO_2 join from near the MnO apex for pyrochroite-hausmannite ore in the central part of the bed to rhodonite near the wall rock.

3 Oxygen isotope study

Mineral grains were hand picked from thick sections of ~0.5 mm under a binocular microscope. Since most ore samples of this study are monomineralic in nature, the purities of mineral separates were better than 95 %.

Extraction of oxygen from quartz, rhodonite and tephroite was carried out using a CO_2-laser and BrF_5 by a fluorination method similar to that described by Hayashi et al. (2001). The reproducibility of the $\delta^{18}O$ values was better than ±0.2 ‰.

4 Results and discussion

The $\delta^{18}O$ values of quartz samples from 3 localities of the mine have a narrow range from 23.0 to 23.9 ‰. Quartz from thin quartz layers in rhodonite ore has essentially the same $\delta^{18}O$ value as quartz in the wall rock chert. Thirty-two samples of rhodonite from rhodonite ore have $\delta^{18}O$ values that range from 11.7 to 20.3 ‰; 65 samples of tephroite from tephroite ore and have values from 9.9 to 20.1 ‰. The order of ^{18}O enrichment is generally quartz > rhodonite > tephroite, which corresponds to the ex-

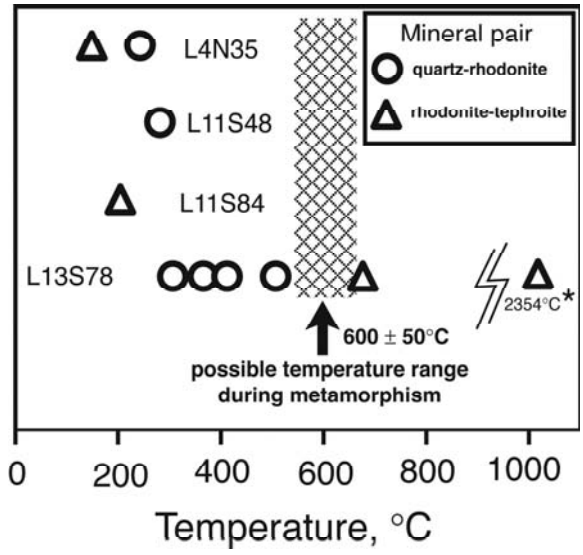

Figure 1: Isotopic temperatures calculated from the non-coexisting but neighboring quartz-rhodonite and rhodonite-tephroite pairs. Note the discrepancy between the isotopic temperatures and the temperatures inferred from the metamorphic mineral assemblage. The temperature with asterisk (*) indicates an improbable value.

pected order of enrichment for isotopic equilibrium between minerals. Reversals in the order of ^{18}O enrichment (i.e., nonequilibrium relationships) was observed for some rhodonite and tephroite pairs that were collected from zones separated by a distance of less than 1 m.

The $\delta^{18}O$ values for the series of samples from ore stope L13S78 do not show a symmetrical pattern from the wall rocks toward the center of the ore lens. In general, the $\delta^{18}O$ values of both rhodonite and tephroite are higher in the footwall of the ore zone than those in the hanging wall.

Because the manganese ores in the Noda-Tamagawa mine are generally monomineralic on a hand specimen scale, truly coexisting mineral pairs are difficult to obtain. However, if the Mn-silicates and oxides were both formed from $MnCO_3$ and SiO_2 (i.e., the most probable primary mineral assemblage of the Mn ores before metamorphism) in conditions accompanying a large amount of metamorphic fluid, isotopic equilibrium may be expected among minerals in samples up to a few meters apart.

Isotopic equilibrium temperatures were calculated for mineral pairs in the neighboring zones within individual ore lenses (Fig. 1). Except for one very high temperature, three quartz-rhodonite and four rhodonite-tephroite pairs give temperatures between 545°C and 145°C. These temperatures are much lower than the estimated metamorphic temperatures and suggest that the minerals did not equilibrate at peak temperature. The presence of sillimanite, although it is rare in the pelitic hornfelses near the manganese ore bodies suggests that the peak metamorphic temperature was near the stability limits for andalusite and sillimanite (ca. 600°C at P= 2kb).

The $\delta^{18}O$ values for H_2O and CO_2 in equilibrium with quartz, rhodonite and tephroite at the calculated temperatures are variable, 7.6 to 18.4 ‰ for H_2O and 16.7 to 33.6 ‰ for CO_2. These data suggest that the equilibrium was not established among neighboring mineral pairs, H_2O, and CO_2 during the metamorphism. At high fluid/rock ratios, isotopic equilibrium between the neighboring (but non-coexisting) minerals would be expected. Therefore, our data suggest that the fluid/rock ratios during metamorphism were very low ($<< 1$) or that fluids with different isotopic compositions were present. A comparison of $\delta^{18}O$ values between the manganese silicate minerals of this study and calc-silicate minerals from skarn deposits provides constraints on the nature of metamorphism and the origin of the isotopic composition of the Mn-minerals. As the skarn minerals were probably equilibrated with magmatic or meteoric water (e.g. El Rhazi and Hayashi 2002), the relatively narrow range of $\delta^{18}O$ values of the skarn minerals was probably controlled by the $\delta^{18}O$ values of skarn-forming water. In contrast, the wide range of $\delta^{18}O$ values for the manganese minerals in this study suggests that their isotopic compositions mainly reflect the precursor minerals. The contribution of ^{18}O-depleted fluids during metamorphism was not important.

References

El Rhazi M, Hayashi K (2002) Mineralogy, geochemistry, and age constraints on the Beni Bou Ifrour skarn type magnetite deposit, northeastern Morocco. Resource Geology 52: 25-39

Hayashi K, Maruyama T, Satoh H (2001) Precipitation of gold in a low-sulfidation epithermal gold deposit: insights from a submillimeter-scale oxygen isotope analysis of vein quarts. Economic Geology, 96: 211-216

Isotopic geochemistry of Mesozoic igneous rocks and mineralization of Shanmen silver deposit in Yi-Su Basin, Jilin Province

Huang Wenbin
Institute of Mineral Resources, Chinese Academy of Geological Sciences, Beijing 100037, and Chinese Geological Library, Beijing 100083, China

Shen Haoche
Jllin University, Changchun Jilin, 130021, China

Fen Lin
Research Institute, China Water Northeastern Investigation Design and Research Co. Ltd., Changchun, 130021, China

Abstract. The present study focuses on isotopic geochemistry of the Mesozoic igneous rocks and the Shanmen silver deposit in Yi-Su basin. Petrochemistry, isotopic geochemistry and isotopic geochronology are used to explore the relationship between regional magmatic activity and the formation of the ore deposit. In this study, we explore the isotopic geochemistry in the deposit and the surrounding igneous rocks by studying Rb, Sr, Pb, S, H and D isotopes. This helps us to discern the source of the economic minerals and the metallogenetic mechanism responsible for the formation of the Shanmen silver deposit.

Keywords. Igneous rock, isotopic geochemistry, silver deposit, source of ore material

1 Introduction

The Yi-Su basin is located in the fold zone of the TianShan-Xinan orogenic belt, where two deep parallel faults known as the Yi-Su fracture zones, are oriented 45~50°E and extend to the base of the lithosphere. The strata from the Paleozoic group to the Cenozoic group lie along the side of the basin. Metamorphosed igneous rocks that have experienced alteration and compressional deformation, outcrop around the outer edge of the basin. Many economic deposits have been discovered in this region, including iron, copper, gold, silver, and coal, fluorite deposits. These deposits are controlled by fractures and show an intimate relationship with Mesozoic igneous rocks.

The Shanmen silver deposit is located in the Yi-Su basin. In this paper, we present a detailed study of isotopic geochemistry of the Mesozoic igneous rocks and the sliver ore in order to determine the relationship between magmatic activity and mineralization.

2 Isotopic geochemistry and formation of igneous rocks

2.1 Petrochemistry

A variety of igneous rocks from the Herynian to Himalayan can be found in the Yi-Su basin.Neutral and acidic magmatic rocks comprise about 70% of the igneous rocks. The petrochemical composition of neutral and acidic igneous rocks shows that the younger rocks are relatively richer in Si and alkali elements. As rocks get older, Na_2O content, and especially K_2O content gradually rise. With the evolution of magma from neutral to the acidic-alkali, the petrochemical composition of the rocks shows a range in SiO_2 content from 51.0% to 78.9%. Alkalinity ranges from $Na_2O>K_2O$ to $K_2O<Na_2O$. Initial $^{87}Sr/^{86}Sr$ ratios vary from 0.74 to 0.70. These geochemical characteristics indicate that the netural and acidic magma was derived from the deep earth.

2.2 Genesis of igneous rocks

2.2.1 Mantle–derived (M-Type) igneous rocks

Mantle-derived igneous rocks occur sparsely in this region, with the exception of large scaleHimalayan alkali basalts which are found along the Yi-Su deep fault. The $^{87}Sr/^{86}Sr$ ratio determined for olivine inclusions in basalt is 0.738. Because the geologic age of these basalts is relatively young, the ^{87}Rb content is fairly low. The half-life of ^{87}Rb is 48.8 b.y.. We suggest that the 0.738 may represent the initial $^{87}Sr/^{86}Sr$ ratio in the basalt. This indicates that the basaltic magma was derived from the upper mantle.

2.2.2 Mantle-crust mixed (MC-type) igneous rocks

The rocks derived from both mantle and crustal materials are controlled by a basement rift, which lies in the topographically lower region of the basin. Most of the neutral-acidic and acidic igneous rocks occur in this locality. The initial $^{87}Sr/^{86}Sr$ ratio in these rocks ranges from 0.705 to 0.710. The $\delta^{18}O$ value in the quartz varies from 7.8‰ to 8.5‰. The Rb/Sr ratio ranges from 0.6 to 0.4. SiO_2 content varies form 57% to 72%, whereas $Na_2O>K_2O$, $Al_2O_3/Na_2O+CaO+K_2O = 1$, and f' (ω%) varies from 0.1

to 0.4. These characteristics can be used to identify igneous rocks derived from both crustal and mantle material in the relative deeper earth.

2.2.3 Crustal-derived (C-Type) igneous rocks

Crustal-derived igneous rocks are mainly located in the folded region of the basin, and are controlled by regional fracture zones and folds. In this locality, the crust is thick. The initial $^{87}Sr/^{86}Sr$ ratio of these igneous rocks ranges from 0.716 to 0.720. The $\delta^{18}O$ value in the quartz is l0‰, and the Rb/Sr ratio is high. The rocks are rich in Si and K, and poor in Ca. SiO_2 content varies from 74% to 98% $K_2O>Na_2O$, f' (ω%) varies from 0.4~0.7. These characteristics can be used to identify rocks derived from crustal materials.

3 Isotopic and geochemical features of the silver deposit

3.1 Regional geology

The Shanmen silver deposit is located along the western margin in the Jihei fold system of the TianShan-Xinan orogenic belts. The main strata are the Cambrian-Ordovician Baoan group and the Middle Ordovician Huangyingtun group. The latter has undergone silicification, sericitization and carbonatization. Igneous rocks outcrop in the uplifted area, which intrudes along deep fractures, mainly consisting of monzogranite, biotite granite, and quartz diorite (Fig. 1). The Indosin Kaodaozi diorite, Wuolong hornblende pyroxenite and Yanshanian granites display a close relationship with the silver deposit. The Kandaozi pluton, which controls the distribution of the main ore body, is located near the upper section of the silver deposit, and overlaps the Huangyintun group. The Wuolong pluton, which forms the base of the ore body, lies on the eastern edge of the Kaodaozi pluton. It has a skewed contact with the main fracture, and forms the wall rock for the deposit. The silver deposit is 10 km long, 1~2 km wide, and is distinctly controlled by NE-NNE factures. These fractures divide the deposit into 5 ore blocks from south to north: the Zhangjiatun block, the Longwang block, the Wuolon block, the Gudong block and the Yingpan block. The Wuolong block contains the majority of the ore reserves, which occur in marbles and meta-siltstones from the middle-upper Huangyingtun group. The ore minerals are mainly silver (50%), galena, sphalerite, secondly pyrite and chalcopyrite.

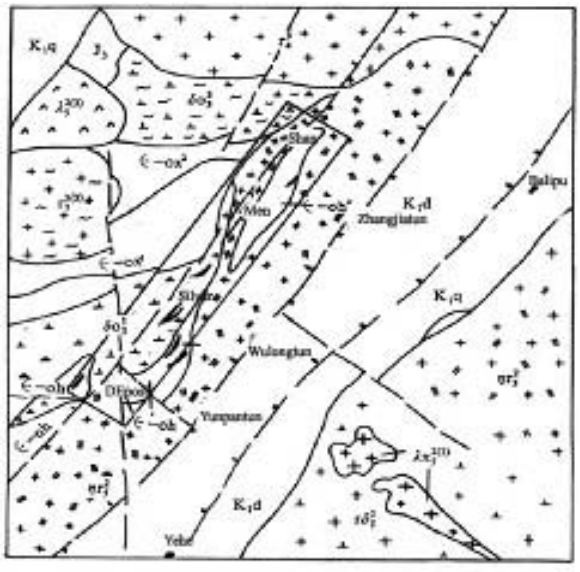

Fig 1 Geology map of Shanmen silver deposit

3.2 Petrography and petrochemistry of the mine region

The Kaodaozi pluton is the host rock for the main ore body. It consists mainly of diorite, with lesser quartz diorite and quartz monzonite. The petrochemical composition is as follows: $K_2O/Na_2O<1$, $Al/K+Na+2Ca<1$, $[Fe_2O_3+FeO+1/2(MgO+Ca)]$ is 11.65, $(Si+Na+K)/Fe^{2+}+Fe^{3+}+Mg)$ is 6.03, $(Cao+Na_2O+K_2O/(Al_2O_3+CaO+Na_2O)$ is 1.70, and the coefficient of consolidation is 24.37. The main accessory minerals are titanite, apatite and barringerite.

The geochemistry of the rock is as follows: the $^{207}Pb/^{204}Pb$ ratios vary from 15.56 to 15.64, the $^{206}Pb/^{204}Pb$ ratios from 18.32 to 18.35, the $^{208}Pb/^{204}Pb$ ratios from 38.24 to 38.47, respectively. The initial $^{87}Sr/^{86}Sr$ ratio is 0.70544. The δEu values range from 0.92 to 1.02. The L_{Ree}/H_{Ree} is 5.93. Therefore, we suggest the Kaodaozi diorite is likely derived from the mantle-crust melting. Whole rock U-Th-Pb dating, measured by MS, produces an age of 193.3 Ma. Pb-Pb dating of zircon in the quartz diorite produces an age of 187.8 Ma.

The Wuolong pluton forms the base of the ore body, and is the wall rock for the deposit. It consists mainly of adamellite, with lesser granite and moyite. The petrochemical composition is as follows: $K_2O/Na_2O>1$, $Al/K+Na+2Ca>1$, SiO_2 content is 73.4%. The main accessory minerals are zircon, apatite and magnetite.

The geochemistry of the rock is as follows: the $^{207}Pb/^{204}Pb$ ratios vary from 15.58 to 15.61, the $^{206}Pb/^{204}Pb$ ratios from 18.56 to 18.61, the $^{208}Pb/^{204}Pb$ ratios from 38.71 to 38.85, respectively. The initial $^{87}Sr/^{86}Sr$ ratio is 0.7158. The δEu value is 0.45. Therefore, we suggest the Wuolong pluton is likely derived from mantle-crust melting. U-Th-Pb dating for zircon, measured by MS, produces an age of 150Ma. Whole rock K-Ar dating produces an age of 158 Ma.

3.3 Isotopic and geochemical evidence of genesis of the Shanmen silver deposit

A histogram is plotted for the 22 ore samples. The results show that the $^{208}Pb/^{204}Pb$ ratio shows normal distribution with a single population except one. This indicates that Pb isotopes come from a distinct parental material, and that the source of mineralization is separate.

The model age, computed by a Doe single-stage model using Pb isotopes, is a negative age. This reveals that Pb isotopic values within the ore zone are similar to isotopic values expected from Pb derived from the upper mantle The model age computed by the Stacey two-stage formula is 180 Ma. This model age, which represents the age of the formation of the silver deposit, is close to the age of formation of Kaodaozi and Wuolong plutons. Moreover, the Pb isotopic composition in the ore is the same as the Pb isotopic composition of the two plutons, but differs from the stratum of Hangyintong group. Therefore, the source of Pb isotopes in the ore has an intimate relationship with magmatic activity.

The Pb isotopic composition in galena ore may be compared with Pb isotopic composition in the rocks which come from the modern mantle or the crust, in order to discern the source of minerals for the younger deposits (Y. W. Cheng, 1983). Fig. 2, Fig. 3 illustrate that Pb isotopic composition of the galena is between the Pb composition of the tholeiite found at mid-oceanic ridges (representing the upper mantle), and the Pb composition of island-arc magmas found along the western coast of the Pacific Ocean. The results reveal that the mineral material is derived from the deep earth, and formed from a magma composed of mixed upper mantle and crust. We compare the Pb isotopic composition in the galena in the Shanmen deposit with the Phanerozoic metal deposits in China. The Pb isotopic composition in the metal deposits, which are related to the Mesozoic lava or granodiorite in China is as follows (Cheng 1984): the Pb composition is steady, The $^{207}Pb/^{204}Pb$ ratios vary from 15.3 to 15.6, and the $^{206}Pb/^{204}Pb$ ratios >17.5. In the Shanmen silver deposit, the $^{206}Pb/^{204}Pb$ ratios vary from 18.017 to 18.149, whereas the $^{207}Pb/^{204}Pb$ ratios vary from 15.418 to 15.525. Therefore, we suggest the minaeralization may be related to the intrusion of the granodiorite.

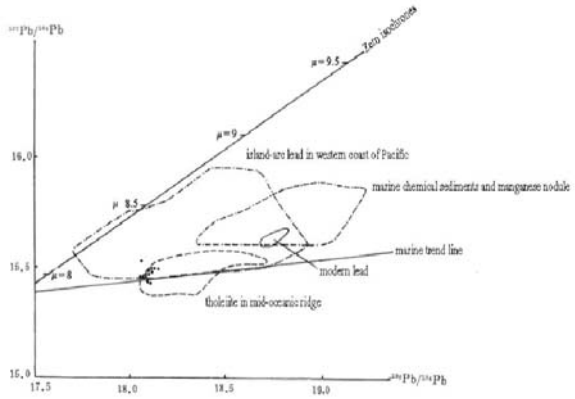

Fig 2 206Pb/204Pb vs. 207Pb/204Pb diagram for galena in ore in Shanmen silver deposit,compared with modern lead

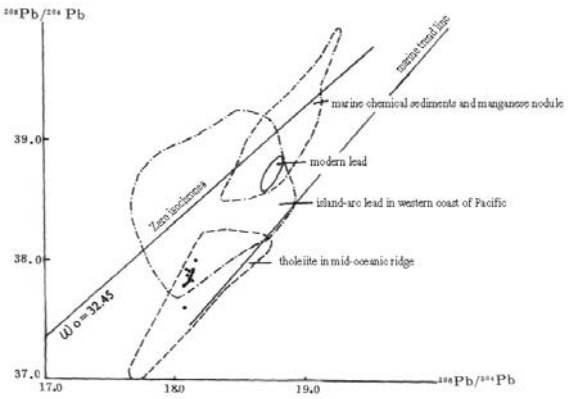

Fig 2 206Pb/204Pb vs. 208Pb/204Pb diagram for galena in ore in Shanmen silver deposit, compared with modern lead from 3 different geological environment

We measured the $\delta^{34}S$ values in galena, sphalerite and pyrite in the ore bodies, wall rocks, and local strata. (Table 1). The $\delta^{34}S$ data is as follows: the variation of the $\delta^{34}S$ values is narrow, the $\delta^{34}S$ values are low in the ore bodies and the wall rocks, This is similar to the $\delta^{34}S$ values in meteorites. The $\delta^{34}S$ values are negative in the stratum. The average $\delta^{34}S$ values in pyrite are -1.37‰. This is within the range of $\delta^{34}S$ values in meteorites. These results indicate that the mineral material is derived from the deep earth.

The $\delta^{34}S$ values from different ore bodies show a normal distribution. Most of them cluster around -2.0‰. The $\delta^{34}S$ values in the ore minerals are as follows: $\delta^{34}S$ (FeS) > $\delta^{34}S$(ZnS) > $\delta^{34}S$(PbS). This agrees with the equilibrium conditions for sulfur isotopes in hydrothermal systems. Therefore, these minerals are paragenetic. Thermometry of sphalerite galena shows that the metallogenic temperature was between 160 to 300°C.

Table 1: $\delta^{34}S$ values in main geological bodies.

Geological body	Name	Num	$\delta^{34}S$‰		2σ
			range	mean	
Plagiogranite quartz diorite	FeS_2	3	+0.5~-1.9	-0.76	2.4
Meta-silty marble	FeS_2	8	-1.86~-30.3	-12.09	28.4
Beresite	FeS_2	12	-1.2~-9.6	-4.2	8.4
Ore body mineralized belt	FeS_2	23	+1.79~-4.6	-1.47	6.39
	ZnS	12	1.18~-8.7	-3.89	7.52
	PbS	13	-2.7~-1 1.4	-8.24	8.7
Quartz vein bearing chalcopyrite and galena	FeS_2	1	-3.9	-6.76	1.3
	PbS	1	-12.6		
	$FeCuS_2$	3	-6.3~-7.6		

The $\delta^{18}O_{H2O}$ values in quartz show that mineralized fluids consisted of magmatic water in the early stages, and meteoric waters mixed with magmatic waters during the later stages. The δD values range from -92% to -106%. Thereby, we suggest the silver deposit was formed in the same hydrothermal system.

4 Conclusions

The genesis of the igneous rocks in the study region falls into two groups: crustal-derived igneous rocks, and mantle-crustal mixed igneous rocks. These two groups of igneous rocks have distinct differences in petrochemistry, mineral assemblage, and geologic environment of formation.

On the basis of detailed study of geology and isotopic geochemistry of Rb, Sr, Pb, S, H, and O in both ore and wall rock, we suggest the silver deposit is a mesothermal ore deposit, and the mineral material is derived form the mixed upper mantle and crust. The metallogenesis of Shanmen silver deposit has an intimate relationship with magamatic activity. The origin of mineral material and mineralizing fluids is complex. Magmatic activity is the metallogenetic mechanism of formation for this silver deposit.

References

Amstrong BL, Hales WH (1977) Rb-Sr and K-Ar geochemistry of Mesozoic grantic rock and their isotopic composition. Ball, Geol. Soc. Am 88

Cheng YW, Zhu BQ (1984) The feature of isotopic composition of ore lead and genesis. Geochemica 3: 35-45

Hu X, Xu C, Niu S (1990) Evolution of the early Paleozoic continental margin in northern margin of the North China Platform. Beijing: Peking University Publishing House, 6-34

Li L, Zheng YF, Zhou JB (2001) Dynamic model for isotope Pb evolution in the Continental Crust of China. Acta Petrologica Sinica 1:63-67

Liang YH, Zheng, XS, Zhang S (1996) The discussion on the relation between the magmatite and the silver deposit and exploration of the mechanism of the formation of the silver deposit in Sipin. Songliao Journal (Nature Science Edition) 1: 41-45

Liu, JQ (1987) Geochronology Study of Cenozoicin Lava in North East China. Acta Petrologica Sinica 4: 21-31

Taylor SR, Mclennan SM (1985) The continental crust: Its composition and evolution. Oxford: Blackwell, 67-96.

Wang FK (1994) Analysis on metallogenetic conditions of the Shanmen Silver Deposit in Sipin, Jilin Povice. Jilin Geology 3: 9-16

Wang FK (1997) A new understanding of the Mesozoic intrusive rock genesis and relationship with metallogeny in the Shanmen Silver Deposit, Sipin Area. Jilin Geology 3: 9-26

Platinum group elements as useful genetic tracers for the origin of polymetallic Ni-Mo-PGE-Au sulfide ores in Lower Cambrian black shales, Yangtze Platform, South China

S.-Y. Jiang, Y.-Q. Chen, H.-F. Ling, J.-H. Yang, H.-Z. Feng
State Key Laboratory for Mineral Deposits Research, Department of Earth Sciences, Nanjing University, Nanjing, China

Abstract. The polymetallic Ni-Mo-PGE-Au sulfide ores occur in the Lowermost Cambrian Niutitang Formation of a thick black shale sequence in Yangtze Platform of South China. The origin for this special type of sulfide ore has been hotly debated. Three genetic models have been proposed: (1) extraterrestrial impact origin (Fan et al. 1984); (2) submarine hydrothermal exhalative origin (Coveney et al., 1992; Lott et al. 1999; Steiner et al. 2001); (3) seawater scavenging origin (Mao et al. 2002). In this paper, we discuss the origin for this special type of sulfide ore based on platinum group element geochemistry. We suggest that the chondrite-normalized PGE patterns of the sulfide ores show some distinctive difference from the seawater pattern and may indicate a submarine hydrothermal input for the metal enrichments in the sulfide ore. We defined a new parameter, namely Pt anomaly (Pt/Pt*), and found that the Pt anomaly in the polymetallic Ni-Mo-PGE-Au sulfide ores is similar to those ancient and modern sea-floor massive sulfide deposits. Other platinum group element pairs, such as Pt/Pd, Ir/Pd, and Au/Pd ratios of the Ni-Mo sulfide ores also share some similarity with those of ancient and modern submarine massive sulfide deposits. In conclusion, we support the submarine hydrothermal exhalative origin for the sulfide ores, and suggest that this is a new type of sediment-hosted submarine hydrothermal exhalative sulfide deposits.

Keywords. PGE, sulfide ore, black shale, Lower Cambrian, South China

1 Introduction

The polymetallic Ni-Mo-PGE-Au sulfide ores occur in the Lowermost Cambrian Niutitang Formation of a thick black shale sequence on the Yangtze Platform of South China, which extend over 1600 kilometers length along a NE trending belt. Although this type of polymetallic Ni-Mo-PGE-Au mineralization has been known for more than 30 years, its origin has long been debated (Fan et al. 1984; Coveney et al. 1992; Horan et al. 1994; Lott et al. 1999; Steiner et al. 2001; Mao et al. 2002; Coveney 2003; Lehmann et al. 2003). Our study in recent years suggest that the occurrence of PGE and other metal anomalies and mineralizations in black shales may belong to a special class of sedimentary-exhalative sulfide deposits that can potentially provide economically significant PGE and other metal resources in the future.

2 Geological setting

In South China, the polymetallic enrichment bed in the Lowermost Cambrian Niutitang Formation accounts for extreme enrichments of a large spectrum of metals, such as Mo, Ni, Se, Re, Os, As, Hg, Sb, Ag, Au, Pt, and Pd, with up to 10^6 to 10^9 fold enrichment relative to seawater values. Although this belt extends over 1600 km, economically minable ores occur mostly within the provinces of Guizhou and Hunan, with the most famous deposits being Huangjiawan near Zuuyi (Guizhou province) and Dayong near Zhangjiajie (Hunan province).

Steiner et al. (2001) suggested that the linear trend of the Ni-Mo sulfide ore occurrence in South China may relate to structural controls by a major deep fault zone in the transitional area between the Neoproterozoic back arc basin and the platform. Lott et al. (1999) found footwall hydrothermal quartz-sulfide stockworks for the sulfide deposit, which may represent submarine hydrothermal venting systems. Mao et al. (2002) reported a Re-Os age for the Ni-Mo sulfide ores of 541 ± 16 Ma. Chen et al. (2003) also obtained a similar age using the Pb-Pb dating technique for the host black shales (531 ± 24 Ma).

The major ore minerals are vaesite, bravoite, jordisite, and MOCs; and minor ore minerals include arsenopyrite, chalcopyrite, covellite, sphalerite, millerite, polydymite, gersdorffite, sulvanite, pentlandite, tennantite, tiemannite, violarite, and native gold. Gangue components consist of organic debris, siliceous rock, carbonate, clay, and phosphorite.

3 Platinum group element geochemistry

The Platinum group element and their chondrite-normalized patterns are very useful indicators for the origin of ore deposits including those within black shales and submarine hydrothermal exhalative massive sulfide deposits (e.g., Coveney et al. 1992; Pasava 1993; Pan and Xie 2001; Pasava et al. 2004).

3.1 The Ir anomaly

The polymetallic Ni-Mo-PGE-Au sulfide ores in South China were first reported by Fan et al. (1973) and were regarded as an entirely new type of sulfide ore, which contains up to several percent of Ni, Mo, As, together with substantial amounts of PGE and Au. In 1984, Fan et al. (1984) found high Ir values for these polymetallic Ni-Mo-

This page intentionally blank

PGE-Au sulfide ores, and consequently they suggested a meteorite impact model for the origin of these ores. However, this model was doubted and discarded by Conveney et al. (1992) who found that the Ir contents are actually relatively low (<0.02-2 ppb, average 1.7 ppb) compared with other PGEs (up to 700 ppb Pt and 1255 ppb Pd). Hence, Conveney et al. (1992) concluded that an extraterrestrial source seems unlikely for the Chinese polymetallic Ni-Mo-PGE-Au sulfide ores.

3.2 The Pt anomaly (Pt/Pt*)

Jiang et al. (2003) proposed a new PGE parameter of Pt anomaly (Pt/Pt*), which can be used as a sensitive genetic tracer. By analogy with the Eu anomaly in chondrite-normalized REE patterns, a Pt anomaly can be defined using the following equation:

$$Pt/Pt^{*} = \frac{Pt_N}{\sqrt{Rh_N * Pd_N}}$$

where the Pt_N, Rh_N, and Pd_N are the chondrite-normalized values of the samples. The Pt/Pt* values are generally larger than 1 (positive Pt anamaly) for most crustal sources. In contrast, the mantle-derived sources display negative Pt anomaly with Pt/Pt* close to or less than 1. We found that the Pt/Pt* values for the host rocks of phosphorites, siliceous shales, and black shales in South China are significantly larger than 1, but the Pt/Pt* values for the Ni-Mo sulfide ores are close to 1, overlapping the values for Kuroko VMS-type sulfide ores. This similarity may imply a similar submarine hydrothermal origin for the Chinese Ni-Mo sulfide ores. This hypothesis supports other studies that favor a hydrothermal origin for the Chinese polymetallic Ni-Mo-PGE-Au sulfide ores (Murowchick et al. 1994; Li and Gao 1996; Lott et al. 1999; Steiner et al. 2001).

3.3 Platinum group element ratios

The Platinum group element ratios are diagonastic tools to trace ore genesis. Lehmann et al. (2003) suggested that the Chinese Ni-Mo sulfide ores have Pt/Pd and Au/Pd ratios around 1, quite close to seawater ratios (Pt/Pd= 0.8, Au/Pd=0.3), but are different from the Serra Pelada Au-Pd-Pt deposit of northern Brazil and the Rammelsberg deposit of Germany (Au>Pd>Pt).

However, we found that the Pt/Pd ratios of magmatic Ni-Cu sulfide deposits are also commonly close to 1 (Barnes et al. 1985; Brugmann et al. 1989). In fact, the Pt/Pd ratio for the Chinese Ni-Mo ores and their host rocks, as well as for many modern and ancient sea-floor massive-sulfide deposits and Fe-Mn crusts show a relative large variation. We found that the Pt/Pd ratios of the Chinese Ni-Mo sulfide ores (0.3-20) are similar to their host rocks (0.5-14), and are also comparable to the modern sea-floor metalliferous sediments (0.1-3.3) and the ancient massive sulfide ores (0.4-1.0), although the range in these deposits seems to be smaller. The Fe-Mn crusts, which scavenged PGEs from seawater, also show large Pt/Pd ratios ranging from 6 to 272, whereas Au/Pd ratios show even larger variations.

Hence, we suggest that a simple comparison of these noble metal ratios to those of seawater is by no means an adequate way to prove or disprove their derivation. Instead, we suggest that the correlations between the noble metal ratio pairs are more useful to differentiate hydrothermal origin from seawater origin. The comparison of Chinese Ni-Mo sulfide ores with submarine hydrothermal exhalative sulfide ores and Fe-Mn nodules and crusts in Pt/Pd vs Pt/Pt*, Pt/Pd vs. Ir/Pd, Au/Ir vs. Au/Pd diagrams demonstrate the similarity between the Chinese Ni-Mo sulfide ores with Kuroko VMS-type sulfide ores and modern sea-floor metalliferous sediments and sulfides, but a distinct contrast to Fe-Mn nodules and crusts.

Taken together, we suggest that the Chinese Ni-Mo ores are likely to have a similar hydrothermal origin to modern and ancient sea-floor massive sulfide deposits.

4 Conclusions

The ore genesis for the Chinese polymetallic Ni-Mo-PGE-Au ores within the Lowermost Cambrian Niutitang Formation has been hotly debated. The increasing amount of data from field geology, fluid inclusions, geochemistry (trace, rare earth elements, and platinum group elements), and isotopes support a formation of these deposits via submarine hydrothermal venting systems, in an anoxic environment where abundant organic matter promotes extreme enrichment of redox-sensitive metals. According to our systematic PGE investigation, we propose a genetic model for the submarine hydrothermal ore-forming process, and suggest this is a new type of sediment-host Sedex deposits.

Acknowledgements

This research was supported by China National Science Foundation grants (40221301, 40372059, 40172041). Profs. Zhu Maoyan, Zhang Junming, and Wu Xianhe are thanked for their very helpful assistance in field work and for critical discussion. This is a contribution to the Sino-German joint project of Biological and Geological Processes of the Cambrian Explosion.

References

Barnes SJ, Naldrett AJ, Gorton MP (1985) The origin of fractionation of platinium-group elements in terrestrial magmas. Chem Geol 53: 303-323

Brugmann GB, Naldrett AJ, MacDonald AJ (1989) Magma mixing and constitutional zone refining in the Lac des Iles Complex, Ontario: Genesis of platinum-group element mineralization. Econ Geol 84: 1557-1573

Chen Y-Q, Jiang S-Y, Ling H-F, Feng H-Z, Yang J-H, Chen J-H (2003) Pb-Pb isotope dating of black shales from the Lower Cambrian Niutitang Formation, Guizhou Province, South China. Progr Nat Sci 13: 771-776

Coveney RM Jr (2003) Re-Os dating of polymetallic Ni-Mo-PGE-Au mineralization in Lower Cambrian black shales of South China and its geological significance-A discussion. Econ Geol 98(3): 661-662

Coveney RM Jr, Murowchick JB, Grauch RI, Michael D, Glascock D, Denison JD (1992) Gold and platinum in shales with evidence against extraterrestrial sources of metals. Chem Geol 99: 101-114

Fan D, Yang R, Huang Z (1984) The Lower Cambrian black shales series and the iridium anomaly in south China. Development in Geoscience, Inter Geol Congr, 27th, Moscow, 1984, Beijing, Science Press, 215-224

Fan D, Yang X, Wang Y, Chen N (1973) Petrological and geochemical characteristics of a nickel-molybdenum-multe-element-bearing Lower Cambrian black shale from a certain district in south China. Geochim 3:143-163

Horan MF, Morgan JW, Grauch RI, Coveney RM Jr, Murowchick JB, Hul-bert LJ (1994) Rhenium and osmium isotopes in black shales and Ni-Mo-PGE-rich sulfide layers, Yukon Territory, Canada, and Hunan and Guizhou Provinces, China. Geochim Cosmochim Acta 58: 257-265

Jiang S-Y, Yang J-H, Ling H-F, Feng H-Z, Chen Y-Q, Chen J-H (2003) Re-Os isotopes and PGE geochemistry of black shales and intercalated Ni-Mo polymetallic sulfide bed from the Lower Cambrian Niutitang Formation, South China. Progr Nat Sci 13: 788-794

Lehmann B, Mao J, Li S, Zhang G, Zeng M (2003) Re-Os dating of polymetallic Ni-Mo-PGE -Au mineralization in Lower Cambrian black shales of South China and its geological significance-A reply. Econ Geol 98(3): 663-665

Li S, Gao Z (1996) Siliceous rocks of hydrothermal origin in the Lower Cambrian black rock series of South China. Acta Mineral Sinica 16: 416-422

Lott DA, Coveney RM Jr, Murowchick JB (1999) Sedimentary exhalative nickel-molybdenum ores in South China. Econ Geol 94: 1051-1066

Mao J, Lehmann B, Du A, Zhang G, Ma D, Wang Y, Zeng M, and Kerrich R (2002) Re-Os dating of polymetallic Ni-Mo-PGE-Au mineralization in Lower Cambrian black shales of South China and its geologic significance. Econ Geol 97: 1051-1061

Murowchick JB, Coveney RM Jr, Grauch RI, Eldridge CS, and Shelton KL (1994) Cyclic variations of sulfur isotopes in Cambrian stratabound Ni-Mo-(PGE-Au) ores of southern China. Geochim Cosmochim Acta 58: 1813-1823

Pasava J (1993) Anoxic sediments- an important environment for PGE: An overview. Ore Geol Rev 8: 425-445

Steiner M, Willis E, Erdtmann BD, Zhao YL, and Yang RD (2001) Submarine-hydrothermal exhalative ore layers in black shales from South China and associated fossils- insights into a Lower Cambrian facies and bio-evolution. Palaeogeo Palaeoclim Palaeoeco 169: 165-191

Chemical and mineralogical characteristics of tourmaline in pegmatites from Vavdos, Chalkidiki peninsula, N Greece

M.D. Laskou
Department of Geology and Geoenvironment, Section of Mineralogy and Petrology, Athens University, Greece

Abstract. Pegmatite veins crosscutting dunites and serpentinites of the ophiolitic complex of the Vavdos (Gioldaki and Loukoviti), northern Greece contain tourmalines with a wide variation in size and composition. Pegmatite veins mainly consist of quartz crystals, microcline, albite, perthitised-feldspars. The accessory minerals include mostly coarse to medium grained zoned tourmaline, and lesser amounts of sericite (only occasionally biotite). There are also trace amounts of some rare earth element minerals, such as morazite, xenotime and minerals of the bastnaesite group (epigenetic products of monazite). The pegmatite veins host also fine-grained tourmalile, which shows an orientation parallel to the schistosity of the rock. They are composed of quartz, low-T albite and K-feldspars. Hydroxy apatite, chlorite, Nb-bearing REE minerals (koragoite), garnet, zircon and talc are also present in lesser amounts.

Keywords. Tourmaline, quartz, pegmatites, Chalkidiki Greece

1 Introduction

Pegmatites occur in veins crosscutting dunites and serpentinites of the ophiolitic complex of Vavdos in the western part of the Chalkidiki peninsula, N. Greece (Fig. 1).

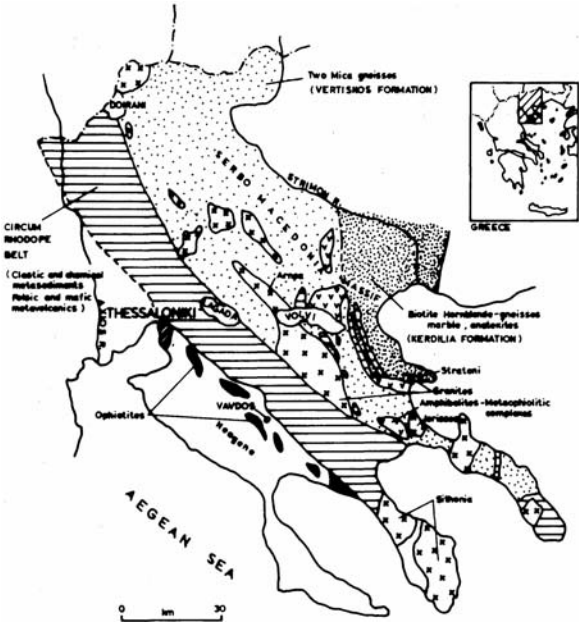

Figure 1: Geological map of the Chalkidiki peninsula (modified after Kockel et al. 1977).

The Vavdos ophiolitic complex forms an elongate fault-bounded body within the Circum-Rhodope Belt. It is one of several similar complexes of Middle to Upper Jurassic age, extending in NW-SE direction, from north-east of Thessaloniki to Sithonia (Kockel et al. 1977; Musallam and Jung, 1986). It consists of dunite, websterite, olivine clinopyroxenite, gabbroic rocks and serpentinite. It also hosts a major deposit of cryptocrystalline magnesite (Dabitzias 1980).

Pegmatites crosscutting the ultramafic sequence of the Vavdos ophiolite complex contain tourmaline dispersed throughout the whole tourmaline mass (Kassoli-Fournaraki 1990).

The present study focuses on two particular occurrences of tourmaline within the unit. These occurrences have coarse, medium and also fine-grained tourmaline hosted in pegmatite. The description of the mineral assemblages and their composition are given.

2 Analytical methods

The phase mineral analyses were carried out using SEM JEOL JSM-5600 combined with an Oxford Link ISIS Series 300 EDX (University of Athens). ZAF corrections were applied using SEMQuant™ software. Accelerating voltage and beam current were kept at 20.0 kV and 0.5 nA, respectively.

3 Mineralogical characteristics

Pegmatites from the area of Vavdos (Gioldaki and Loukoviti) have a thickness ranging from 0.5 to 3m, and are characterized by a medium- to coarse-grained texture (Fig. 2). The coarse and medium grained pegmatite veins mainly consist of quartz crystals, microcline, albite, and perthitised-feldspars. The accessory minerals include coarse-grained, medium to fine-grained and the mostly zoned tourmaline, plus small quantities of sericite and rarely biotite. Lesser amounts of rare earth element minerals are also present (morazite, xenotime and minerals of the bastnaesite group, which are epigenetic products of monazite). Tourmaline occurs in sub to euhedral crystals. Optical zoning in coarse-grained tourmaline is well pronounced, with core color ranging from greenish-blue to brown, while rims range from green brown to olive-

Figure 2: Coarse grained tourmaline in pegmatite sample from Vavdos. Irregular development of tourmaline (black) and associated quartz (grey) in a matrix of feldspar (white) and quartz. Bar scale = 2 cm.

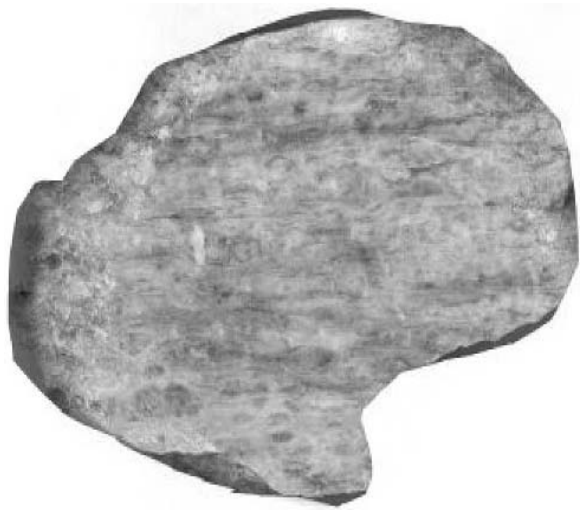

Figure 3: Fine-grained tourmaline (black) hosted in pegmatite shows an orientation parallel to the schistosity.

green. Tourmaline of medium size exhibits green-pale cores and olive-green rims. The textural association of tourmaline and quartz (Fig. 2) indicate that these two minerals are genetically related.

Fine grained tourmalines in pegmatite veins occur in crystals with a wide range in grain size, from 250-500 μm to 1000-1500 μm. (Fig. 3). These pegmatites are composed of quartz, low-T albite, K-feldspars and tourmaline.

Table 1: Zoned coarse grained tourmalines from the type 1 (Fig. 2)

	1M1		2M1	
	core	**rim**	**core**	**rim**
SiO_2	36.85	36.86	36.28	37.08
TiO_2	0.62	0.73	1.52	1.09
Al_2O_3	37.92	37.40	36.69	36.60
FeO	10.07	10.65	10.35	10.27
MnO	-	-	-	-
MgO	2.35	1.90	2.35	2.47
CaO	-	-	-	-
Na_2O	1.63	1.44	2.03	2.18
K_2O	0.23	-	-	-
Cl	-	-	-	-
NiO	-	-	-	-
	89.67	88.98	89.22	89.69

Hydroxyapatite, chlorite, Nb-bearing REE minerals (koragoite), garnet, zircon and talc are present in lesser amounts.

Tourmaline is visible in hand specimens and in thin section, and is identified as green grains with fine brown rims. The fine-grained tourmaline associated with quartz and microcline occurs along shear zones within the host pegmatite, which seem to have formed by re-crystallization during a subsequent event

4 Mineral chemistry

Tourmalines from the area of Vavdos show wide compositional variation, in particular in the SiO_2 (33.94-38.93wt%), Al_2O_3 (34.55-39.92wt%), FeO (3.78-12.29wt%), TiO_2 (0.00-3.33wt%), NaO (0.00-1.51wt%), MgO (0.00-6.14wt%) and MnO (0.00-1.8wt%).

The range of the FeO/(FeO+MgO+MnO) and Fe/(Fe+Mg) ratios are generally comparable to those given in granitic systems (Deer et al. 1986). The majority of tourmaline cores fall in the schorl field. Tourmaline rims are depleted in FeO and enriched in Al_20_3 in Table 2 only.

All tourmaline cores data are plotted in two areas: the field 2 [Li-poor granitoids and their associated pegmatites and aplites] and the field 3 [Fe^{3+}-rich quartz-tourmaline rocks (hydrothermally altered granites)] (Fig. 5).

5 Concluding remarks

Although much more research is required to establish the origin of the Vavdos tourmalines, their textural, mineralogical and chemical characteristics suggest a multistage genesis. Changes in the chemical composition of tourmalines and associated minerals are probably the result of epigenetic processes.

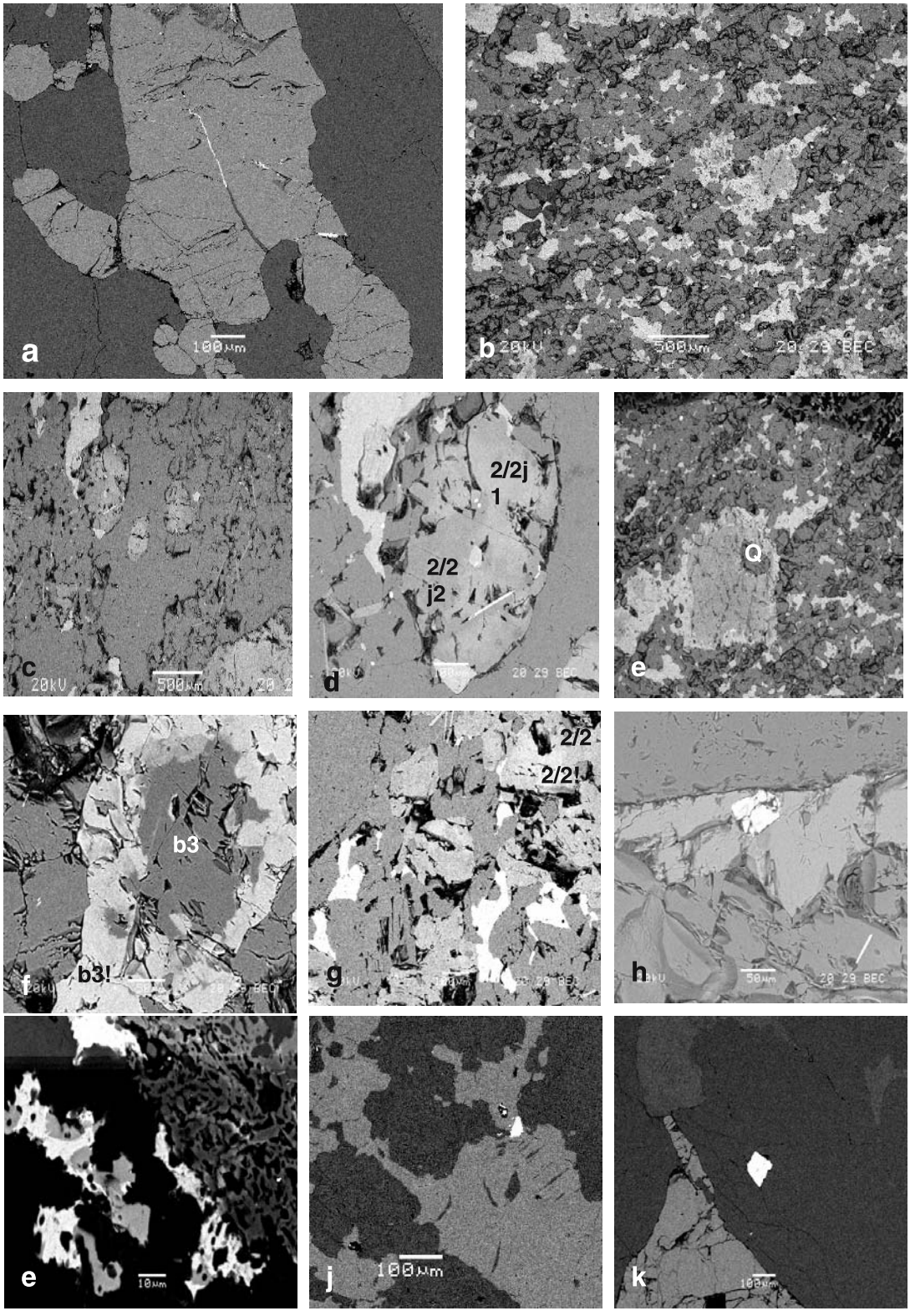

Figure 4: Backscattered electron images of representative tourmaline crystals in pegmatites from Vavdos. Examples of zoned tourmalines (d, e, f and g). The electron microprobe compositional data are shown in the Tables1,2 and 3. REE minerals in the coarse and fine grained types: koragoite (h), bastnaesite with apatite (e), monazite (j) and xenotime (k).

Table 2: Zoned tourmalines from the type 2 (Fig. 3)

	2/2j1		2/2	
	core	**rim**	**core**	**rim**
SiO_2	35.83	36.89	36.43	37.27
TiO_2	0.39	0.99	0.90	0.72
Al_2O_3	36.18	36.92	35.33	37.66
FeO	11.86	8.35	10.90	8.06
MnO	0.41	1.04	0.49	1.26
MgO	0.75	0.65	0.97	0.36
CaO	0.00	0.00	0.00	0.00
Na_2O	0.83	1.67	1.18	1.58
K_2O	0.00	0.00	0.00	0.00
Cl	0.00	0.00	0.00	0.00
NiO	0.00	0.00	0.00	0.00
	86.25	86.51	86.20	86.91

Table 3: Zoned tourmalines from the type 2 strongly schistosed (Fig. 3)

	1/b2		1/b3		1/b5	
	core	**rim**	**core**	**rim**	**core**	**rim**
SiO_2	38.56	36.79	36.75	36.67	36.70	36.80
TiO_2	0.36	1.04	0.39	1.04	0.40	0.97
Al_2O_3	38.24	31.19	35.90	30.39	36.32	2.37
FeO	8.30	12.50	10.43	13.42	12.07	13.74
MnO	0.00	0.73	0.00	0.63	0.00	0.35
MgO	3.45	3.29	2.28	3.26	2.01	4.03
CaO	0.29	0.35	0.00	0.28	0.00	0.79
Na_2O	0.77	1.92	0.61	1.80	1.06	1.32
K_2O	0.00	0.15	0.00	0.00	0.00	0.00
Cl	0.00	0.00	0.00	0.00	0.00	0.00
NiO	0.00	0.00	0.00	0.00	0.00	0.00
	89.97	87.96	86.36	87.49	88.56	87.37

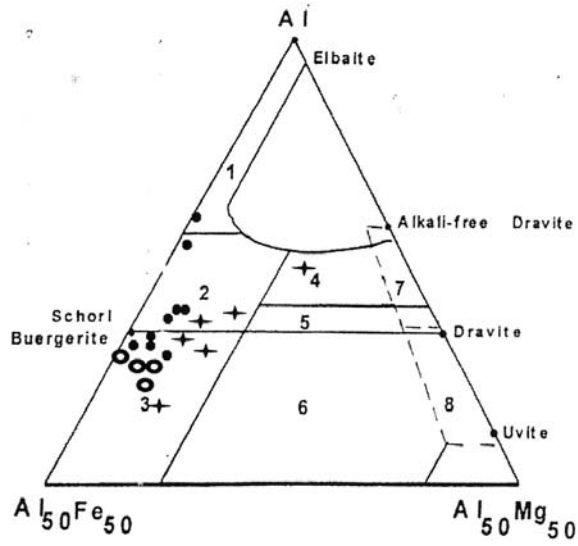

Figure 5: Microprobe data are projected on an Al-Fe-Mg ternary diagram (after Henry and Guidotti 1985).

References

Dabitzias S (1980) Petrology and genesis of the Vavdos cryptocrystalline magnesite deposits, Chalkidiki Peninsula, Northern Greece. Econ Geol 75:1138-1151

Deer WA, Howie RA, Zussman J (1986) Rock-forming minerals: volum 1B, Disilicates and ring silicates: London, Longman Scientific and Technical, 629p

Henry DJ, Guidotti CV (1985) Tourmaline as a petrogenetic indicator mineral: an example from the staurolite-grade metapelites of NW Maine. Am. Mineral. 70, 1-15.

Kassoli-Fournaraki A (1990) Chemical varuations in tourmalines from pegmatite occurrences in Chalkidiki Peninsula, Northern Greece. Scheiz Mineral Petrogr Mitt 70: 55-65

Kockel F, Mollat H, Walther HW (1977) Erlauterung zur geologischen Karte der Chalkidiki und angrenzender Gibiete 1:100000, Nordgriechenland. 119 S, Hanover

Mussalam K, Jung D (1986) Petrology and geotectonic significance of salic rocks preceding ophiolites in the eastern Vardar Zone, Greece. Tscher Min Petr Mitt 35:217-242

Geochemical characteristics of He-Ar and Pb isotopes in the Dajiangping pyrite deposit, western Guangdong, South China

Kuang Li, Kai Hu, Shaoyong Jiang, Shiming Song
State Key Laboratory for Mineral Deposits Research, Department of Earth Sciences, Nanjing University, Nanjing, 210093, China

Abstract. He-Ar isotopes were measured from fluid inclusions in six samples of the Dajiangping pyrite orebody III and orebody IV., The $^{3}He/^{4}He$ values range from 0.13 to 2.55Ra, and the $^{40}Ar/^{36}Ar$ values range from 348 to 443. These data indicate that mantle-derived fluids contributed to the ore-forming fluids. This study suggests that the hot fluids from the deep mantle intruded into the ore body along a thrust fault, and hydrothermed the orebody. This caused differentiation of the orebody resulting in the formation of the banded orebody III and the massive orebody IV. Pb isotopes from the ore and wall rocks were also measured in this study. $^{206}Pb/^{204}Pb$ values range from 18.075 to 18.292, $^{207}Pb/^{204}Pb$ values range from 15.654 to 15.737, and $^{208}Pb/^{204}Pb$ values range from 38.401 to 38.781. These ratios indicate that orebody III is very similar to the wall rock, whereas orebody IV has lower Pb/Pb ratios than wall rock. The data support the interpretation that mantle fluid intruded into the entrapping Pre-Sinian basement migmatite, causing lower Pb isotope ratios in orebody IV.

Keywords. He-Ar isotope, Pb isotope, Crust fluid, Mantle fluid, Thrust fault

1 Introduction

The Dajiangping pyrite deposit lies in the northeastern part of the of Yunkai ridge, south China. It is a unique ultra-large pyrite deposit in the south of Sinian (period) layer (Chen and Chen 1998). The ore genesis model for the Dajiangping deposit has long been in dispute, and the major debate focuses on whether the orebodies formed during hydrothermal sedimentation reform, by a vapour-liquid superimposition event (Zhang et al. 1992, 1993, 1994), or whether formation was the product of hydrothemal sedimentation (Chang and Chang 1998). Noble gases, especially helium and argon have distinct isotopic compositions in the crust and mantle. Due to this characteristic, He and Ar isotopes have been widely applied in tracing the origins and water-rock interactions of contemporary crustal fluids. Recently, these isotope systematics have also been successfully applied to the study of the origin of ancient ore-forming fluids and mineralization (Turner and Stuart 1992; Turner et al 1993; Burnard et al. 1994; Hu 1997; Zhao et al. 2002; Sun and Wang 2003; Zheng et al. 2003). In this note, we report He and Ar isotopic data for the Dajiangping ore deposit first time, and discuss the origin and evolution of the hydrothermal fluid.

2 Sampling and analytical methods

He and Ar isotope were measured in fluid inclusions from six pyrites in the Dajiangping Deposit. These samples were collected from orebody III, orebody IV, CK36 core and wall rock. The samples were dispersed to 0.1~0.2mm grain size, through dressing by both magnetic separation and heavy-liquid separation, then the pyrites were selected by stereomicroscope.

The He and Ar isotope compositions were analyzed in the Open Laboratory for Isotope Geology at the Institute of Mineral Deposits at the Chinese Academy of Geological Sciences. All samples were cleaned for 20 min in ultra-sonic bath using acetone and then dried. The samples were heated under vacuum at 120°C for 24 h to remove absorbed atmospheric gases. They were crushed to extract inclusion-trapped noble gases. The released gases were purified four times through two titanium sponge pumps, a Zr-Al pump and an active-carbon cooling trap filled with liquid nitrogen.

Active gases were frozen and completely absorbed. Then comparatively pure He and Ne were introduced into the analyzing system. He and Ne were purified further to remove traces of impure gases such as H_2 and Ar using a titanium sublimation pump filled with liquid nitrogen. He isotopes were analyzed by mass spectrometer. Finally Ar was released at -78°C and Ar isotopes were then analyzed. The instrument used in this study is an MI 120l IG noble gas mass spectrometer. The ^{3}He values were measured by an electronic multiplier detector. ^{4}He was measured by a Faraday cup. The resolutions are 1200 for the electronic multiplier detector, and 760 for the Faraday cup. The standard gas air is atmospheric air with a $^{3}He/^{4}He$ ratio of $1.4x10^{-6}$.

3 He-Ar isotope analysis and discussion

The results of helium and argon isotope data are given in table 1. As shown in table 1, the fluid inclusions from pyrite have $^{3}He/^{4}He$ ratios of $0.18\sim3.55x10^{-6}$(0.13~2.55Ra). The values of $^{40}Ar/^{36}Ar$ ratios show slight variation between 348~443, which is higher than Air-saturated water's $^{40}Ar/^{36}Ar$ ratios of 295.5.

Table 1: He–Ar isotope compositions of fluid inclusions in pyrites from Dajiangping (^{4}He & ^{40}Ar in cm^3 STP/g, Ra=1.4x10^{-6}).

Sample No.	Sampling location	^{3}He/^{4}He×10^{-6}	^{4}He×10^{-7}	^{40}Ar/^{36}Ar	^{40}Ar/^{38}Ar	^{40}Ar×10^{-7}	R/Ra*
DJP3-3	III orebody	1.38±0.27	1.37	348±1	1870±12	5.93	0.99±0.19
DJP3-14	III orebody	2.11±0.30	7.75	402±2	2185±7	8.92	1.52±0.22
DJP4-12	IV orebody	3.17±0.50	17.32	443±2	2389±10	4.15	2.28±0.36
DJP4-13	IV orebody	3.55±0.18	3.21	365±1	1993±21	5.71	2.55±0.13
CK36-14	CK36 core	0.95±0.22	2.99	383±1	2080±5	5.84	0.68±0.16
DP-11	wall rock	0.18±0.09	1.17	385±2	2090±17	2.24	0.13±0.06

Three possible noble gas sources exist in hydrothermal fluids (Burnard et al. 1999): (1)Air-saturated water (ASW), including meteoric water and seawater. This is characterized by atmospheric He and Ar isotopic compositions, i.e. ^{3}He/^{4}He=1.4×10^{-6} = 1Ra, ^{40}Ar/^{36}Ar=295.5. (2) Radiogenic He and Ar accumulated in the crust. In this source, the ^{3}He/^{4}He ratio varies from 0.01 to 0.05 Ra, and the ^{40}Ar/^{36}Ar ratio usually higher than 295.5. (3) Mantle-derived volatiles. These are characterized by high ^{3}He with a well-defined ^{3}He/^{4}He ratio of 6–9 Ra. The ^{40}Ar/^{36}Ar ratio varies widely, and are usually higher than 400. By comparing the isotopic composition of the sample to the isotopic compositions of the three possible sources of noble gases, we can determine the origin of the noble gases in hydrothermal fluids.

As shown in the plot of ^{3}He/^{4}He vs. ^{40}Ar/^{36}Ar ratios (Fig. 1), the data fall among three sources district, which indicates that the hydrothermal fluid did not originate from the single source, and instead may be a product of crust-mantle mixture. There are two orebody IV samples, two orebody IV samples, one CK36 drill core sample (depth 133 m), and one wall sample of all the six samples. We find that the ore-forming fluids of orebody IV fall in between mantle-derived fluids and ASW. In contrast, the others lie lower on the graph; the CK-36 and DP-11 even lie between ASW and crust fluids.

We can make use of the ^{3}He/^{4}He ratios to Figure out the mantle fluids (Rm) ratio and the crustal fluids (Rc) ratio of the ore-forming fluids. By following formula[13], we can Figure out the helium from mantle fluids:

$$\text{Helium from mantle fluids} = [(R-Rc)/(Rm-Rc)] \quad (1)$$

The Rm, Rc and R represent the ^{3}He/^{4}He ratios of mantle fluids, crust fluids and the samples. Rm=6~9 Ra, Rc=0.01~0.05 Ra. According to formula (1), the six samples' helium content from mantle fluids declines from orebody IV, orebody to wall rock, indicating that the degree of mantle fluids participating in the ore-forming processes was decreasing. The reason for this may be that the ore deposit's formation passed through a few different stages. Zhu and Meng (1999) found that the

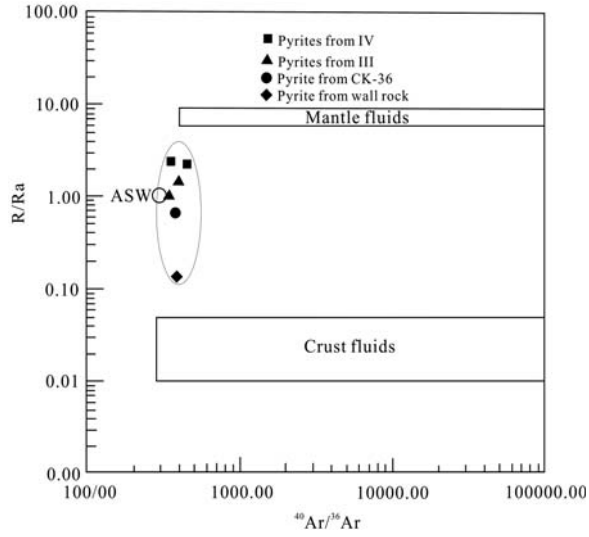

Figure 1: ^{40}Ar/^{36}Ar–R/Ra diagram of fluid inclusions in pyrites from Dajiangping.

Dajiangping pyrite deposit was located on the thrust slip fault of a nappe structure in the western Guangdong. The deposit was controlled by both a large overturned fold; which has an axial plane to the southeast; and a secondary rotational fault. We can find out the tectonic characteristics from Figure 2. It is conjectured that after the orebodies underwent the hydrothemal sedimentaion event, thrust faults formed by intensive crustal tectonic movement, which pushed the Sinian layer onto limestone of Devonian and Carboniferous.

Then mantle fluids rose with the intensive tectonic movement. Finally the hydrotherm from deep mantle fluids entered into, and transformed the orebodies along the fault. Therefore, the characteristics of noble gas isotope signature changed systematically during formation, as shown in Figure 1. At the same time the hydrotherm transformed the shape of orebodies, and caused differentiation resulting in the formation of the banded pyrite ore (orebody III) and the massive pyrite ore (orebody IV).

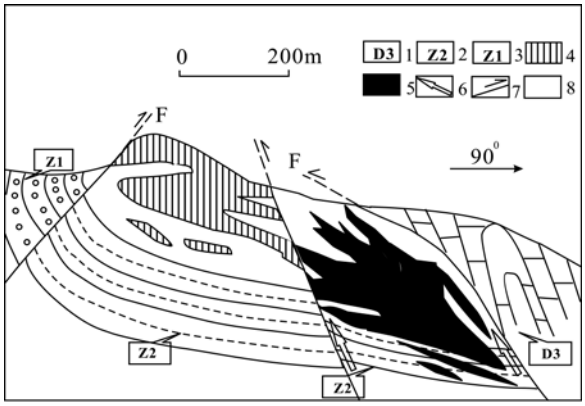

Figure 2: Schematic section of the Dajiangping pyrite deposit (after information by the Dajiangping mine). 1Upper Devonian series 2 Upper Sinian series 3Lower Sinian series 4 Orebody III 5 Orebody IV 6 Mantle fluids' invasion 7 Thrust fault 8 Wall rock

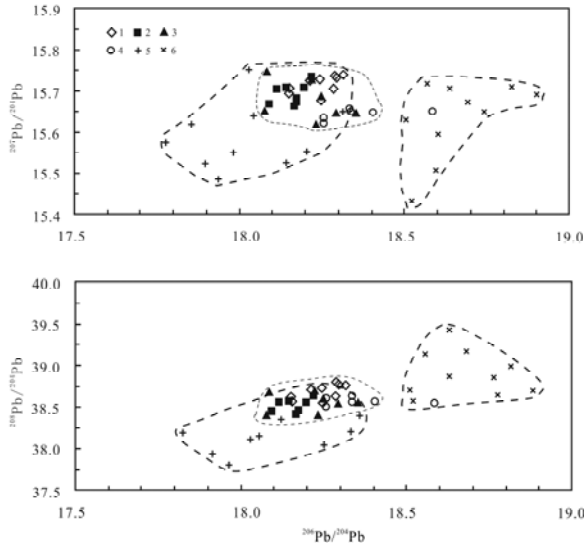

Figure 3: the Pb isotope composition of Dajiangping pyrite deposit (Some data were analyzed in State Key Laboratory for Mineral Deposits Research, Nanjing University. Others were quoted from [15]). 1 Banded orebody 2 Massive orebody 3 Fragmentary rock 4 Limestone 5 Basement migmatite 6 Yunkai ridgy granite

4 Pb isotope geochemical characteristics

Lead isotopes are a powerful tool to trace the origin of metal deposits. We also measured lead isotope of 11 samples including orebody III, orebody IV, and wall rock. The data in Figure 3 also incorporate Pb isotope data of Yunkai ridge area magmatic rock and basement migmatite in Pre-Sinian period, as well as other Pb isotope data from pyrites. The lead isotope data from the pyrites differs from the lead isotope data from the magmatic rocks. This indicates that the ore deposit must not be the product of igneous magmatism. It also shows that the lead isotope compositions of minerals and wall rocks are mainly consistent.

Although the lead isotope compositions of the two ore types partially overlap, the massive orebody has lower Pb isotopic values than the banded orebody. It is possible that the lead from mantle fluid had been added to the orebody. Therefore, the Pb isotope characteristics of the Dajiangping pyrite deposit strengthen our conclusion that the orebody IV was formed by late mantle fluid, which migrated along a thrust fault and altered the original shape of the orebody.

5 Conclusions

The ore-forming fluid of pyrites in Dajiangping orebodies mainly consists of air-saturated water (seawater), which leached lithospheric ore-forming material. The original R/Ra ratio of Helium Isotope was less than 1, but after the deposit was altered by the late mantle fluid, the R/Ra ratio rose by about 50 points.

We conclude that in the Sinian layer, the air-saturated water (seawater) was cyclically heated in the growth faults, absorbed by the ore-forming matter of the crustal basement rocks, and eventually formed the mixing hydrotherm. Then, the fluid burst out of sea floor from growth faults and formed stratiform deposits in the reducing environment. The formation of the thrust fault was initiated by teconic movement at the spot of ore deposits. Later, the deep mantle hydrotherm entered into, and reformed the orebodies. Though no new element was added in, the hydrotherm changed the orebody shape and differentiated the deposit into two distinct members: the banded orebody III and the massive orebody IV.

Acknowledgements

This work was supported by the Youth Excellent-Group Program No.40221301 and No.40172035 in the National Science Foundation of China.

References

Burnard PG, Hu RZ, Turner G (1999) Mantle, crustal and atmosphere noble gases in Ailaoshan, yun-nan Province, China. Geochimica et Cosmochimica Acta, 63,pp. 1595-1604

Burnard PG, Stuart F, Turner G (1994) C-He-Ar variations with in a dunite nodule as a function of fluid inclusion morphology. Earth Planet Sci.Lett,128: 243-258

Chen D, Chen Q (1998) Characteristics of the hydrothermal sedimentation of the Dajiangping super-large pyrite deposit in Yunfu, Guangdong. Geochimica 27: 12-19

Chen DF (1998) Pb and Nd Isotopes of the dajiangping Pyrite deposit, Guangdong Province, and its metallic ore source. Mineral deposits: 215-222

Hu R (1997) Geochemistry of He, Ar isotopes in ore forming fluids. Bulletin of Mineralogy, Petrology and Geochemistry 16: 120-124

Li X, Mao J (2004) Helium and Argon Isotope Systematics in Fluid Inclusion of the Gold Deposits along the Daduhe River, Sichuan Province, Southwestern China. Acta Geologica Sinica 78: 203-210

Sun X, Wang M (2003) He-Ar isotopic systematics of fluid inclusions in pyrites from PGE-polymetallic deposits in lower Cambrian black rock series, southern China. Geological Journal of China Universities 9: 661-666

Turner G, Burnard PB, Ford JL (1993) Tracing fluid sources and interaction. Phil Trans R Soc Lond A 344: 127-140

Turner G, Stuart F (1992) Helium/heatratios and deposition temperatures of sulfides from the ocean floor. Nature 357: 581~583

Zeng Z, Qin YS (2003) He, Ne and Ar isotope compositions of fluid inclusions in massive sulfides from the Jade hydrothermal field, Okinawa Trough. Acta Oceanolog 25: 36-42

Zhang B, Zhang Q, Pan J (1994) Trace element characteristics and their geological significance of Dajiangping pyrite deposit, western Guangdong. Geology and Prospecting 30: 66-71

Zhang Q, Zhang B, Cao Y (1993) Preliminary discussion on sulfur and lead isotope compositions of the Dajiangping pyrite deposit in western Guangdong province. Acta Geologica Sinica, 67(3), pp. 232-242

Zhang Q, Zhang B, Pan J (1992) Silicalite characteristics and rare-earth element model of Dajiangping pyrite deposit in western Guangdong province. Chinese Science Bulletin 37: 1588-1592

Zhao K, Jiang S, Xiao H (2002) Origin of ore-forming fluids of the Dachang Sn-polymetallic ore deposit: Evidence from helium isotopes. Chinese Science Bulletin 47: 1041-1045

Zu D, Meng X (1999) Primary study on the western Guangdong nappe structure in the hercynian and indo-Chinese epoch. Journal of geomechanics 5: 51-58

Precise Re-Os dating of molybdenite from the east Qinling molybdenum belt in central China and its geodynamic implications

Yong-Feng Li, Jing-Wen Mao, Feng-Jun Bai, Bao-Jian Guo
Faculty of Geosciences and Resources, China University of Geosciences, Beijing 100083, China

Zhi-Guang Wang
Bureau of Geology and Mineral Resources for Nonferrous Metals, Henan Province, 107 Zhongyuandong Road, Zhengzhou 450052, Henan, China

Abstract. Located in central China on the southern margin of the North China craton, the East Qinling molybdenum belt is one of the important large molybdenum belts in China. This study provides reliable Re-Os isotopic dating results for the metallogenetic epoch of four deposits by inductively coupled plasma mass spectrometry (ICP-MS), with analytical errors of Re and Os between 0.11-0.4% (2sigma). The results show that the Re-Os model ages are 141.8±2.1Ma for the Nannihu deposit, 145.4 ±2.0 to 144.5 ±2.2 Ma (averaging 145.0 ±2.2 Ma) for the Sandaozhuang deposit, 145.8±2.1 to 143.8±2.1 Ma (averaging 144.8 ±2.1 Ma) for the Shangfanggou deposit, and 133.1±1.9 to 131.6±2.0 Ma (averaging 132.4±2.0 Ma) for the Leimengou deposit. According to these ages, combined with the results of previous work in the molybdenum belt, it is suggested that the age of the molybdenite deposits in the East Qinling molybdenum belt is mainly ~140 Ma. These deposits are the product of transformation from the N-S to the nearly E-W tectonic regime in eastern China. Except for the Huanglongpu Mo deposit, which originated at ~220 Ma, the deposits appear to have geodynamically formed in the extensional stage of the post-collisional orogeny between the North China craton and the Yangtze craton.

Keywords. Mo deposit, Re-Os dating, geodynamics, East Qinling, China

1 Introduction

The East Qinling molybdenum belt contains the most important large molybdenum deposits in China. This belt is the second largest molybdenum belt in the world subsequent to the Climax-Henderson porphyry molybdenum belt. The molybdenum deposits occur along a tectonic lineament of trending nearly east-west. They are mostly concentrated in a region extending from the Jinduicheng-Huanglongpu area, south to the Shaanxi, eastward to the Nannihu area in Luanchuan County and the Leimengou area in Songxian County, western Henan. There are a total of more than 30 superlarge, large and intermediate molybdenum polymetallic ore deposits in the belt, which contribute 52 percent of the total identified Mo reserves in China (Zhang et al. 2001). Stein et al. (1997) have reported the Re-Os ages for the Jinduicheng-Huanglongpu area. This study provides the reliable Re-Os isotopic dating results for the other two clusters, including four large deposits: the Nannihu porphyry Mo (W) deposit, Sandaozhuang skarn Mo (W) deposit, Shangfanggou porphyry Mo (Fe) deposit and Leimengou porphyry Mo deposit. These results, combined with the results of previous work in the Mo belt, provide further insight into the geodynamic setting for the formation of these ore deposits.

2 Geological setting

Located on the southern margin of the North China craton, The East Qinling belt is used to be a part of the North China craton (Fig. 1). Recently, it has also been described as a component part of the northern margin of the Qinling orogen because of its involvement in the Qinling intracontinental orogenic movement during the Meso-Cenozoic, accompanied by intense magmatic activities dominated by acid magma (Jurassic to Cretaceous), as the Wuzhangshan batholith, the Haoping, Heyu and Huashan batholiths. Concomitantly with the intrusion of the above-mentioned large granite bodies, a number of small, hypabyssal to near-surface granite porphyries (such

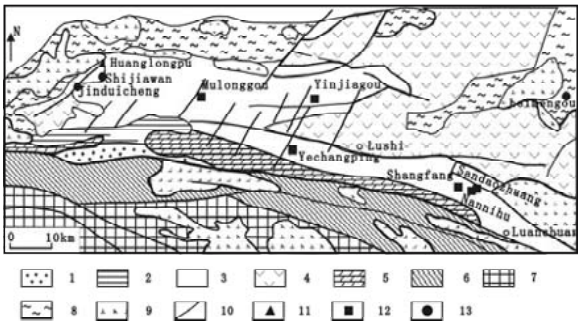

Figure 1: The geological sketch map of East Qinling Mo belt. 1-Cretaceous, sandstone, shale; 2-Cambrian, limestaone; 3-Late Proterozoic Guandaokou and Luanchuan Group, carbonate; 4-Middle Proterozoic Xiong'er Group, metavolcanics; 5-Middle Proterozoic Taowan Group, marble; 6-Middle Proterozoic Kuanping Group, greenschist; 7-Lower Proterozoic Qinling Group, metamorphic rock; 8-Archean Taihua Group, amphibolite gneiss; 9-Yanshanian monzogranite; 10-Fault; 11-Carbonatite Mo-Pb deposit; 12-Porphyry-skarn Mo-W deposit; 13-Porphyry Mo deposit

as the Leimengou granite porphyry) and their genetically related cryptoexplosive breccias, were emplaced. They form a NW-trending tectonomagmtic belt in the region and provide the source of ore materials for molybdenum polymetallic mineralization. The Qinling molybdenum belt may be approximately divided into three molybdenum clusters. The first cluster is found in the Jinduicheng-Huanglongpu area (Huang et al. 1984), and can be described as a mineralization cluster. The second cluster, is located in the Nannihu-Sandaozhuang area about 75 km ESE of the Jinduicheng-Huanglongpu area, and consists of porphyry skarn-type Mo-W mineralization,. The third cluster is located in the Leimengou area, and includes the Leimengou porphyry type Mo deposit and the Huangshuian Mo-Pb deposit, which occurs in carbonatite veins.

According to the geological characteristics, ore element assemblage, ore genesis, mode of occurrence and metallogenic mechanisms of the ore deposits, the molybdenum deposits in the Qinling belt may be classified into three distinctly different groups; porphyry type, skarn-porphyry type and hydrothermal carbonate vein type.

3 Previous dating

In the East Qinling molybdenum belt, there have been numerous attempts to date molybdenum mineralization. For many years the mineralization ages in this area were indirectly estimated by using the ages of mineralization-related granites, alteration minerals or by dating accessory minerals and nearby plutonic rocks. The development of new dating techniques, such as Re-Os dating of molybdenite, has allowed for direct dating of mineralization., In the past several years, Re-Os analyses of molybdenite from the East Qinling belt have been performed by Huang et al. (1994, 1996) and Stein et al. (1997). These data are summarized in Table 1.

4 Samples and analytical methods

A total of eight ore samples were collected from the East Qinling Mo deposits for Re-Os dating in this study. One of them came from the Nannihu deposit, three from the Sandaozhuang deposit, two from the Shangfanggou deposit, and two from the Leimengou deposit. The samples were carefully identified under the binocular microscope and then molybdenite separates were picked out by hand. The separates were fresh, non-oxidized and pollution-free. Samples were sealed in tubes and dissolved, following the Carius tube digestion technique (Mao et al. 2003b). The Re and Os isotopic compositions were determined by using the ICP-MS (VG PQ-EXCELL). In this study, the average blanks for the Carius tube procedure as described above are ca.10 pg for Re and ca.1 pg for Os.

Table 1: Comparison of molybdenite Re-Os ages with mineralization ages obtained by other methods in the East Qinling area.

Deposits	Ages±absolute error (Ma)	Method	Mineral analyzed	Number of runs	Reference
Huanglongpu	221.5±0.3	Re-Os	Molybdenite	7	Stein et al. 1997
Huanglongpu	216±2	Re-Os	Molybdenite	3	Du et al. 1995
Huanglongpu	222±4	Re-Os	Molybdenite	5	Huang et al. 1994
Jinduicheng	138.4±0.5	Re-Os	Molybdenite	2	Stein et al. 1997
Jinduicheng	141±4	Re-Os	Molybdenite	5	Du et al. 1995
Jinduicheng	127±7	Re-Os	Molybdenite	1	Huang et al. 1994
Jinduicheng	129±4	Re-Os	Molybdenite	1	Huang et al. 1994
Jinduicheng	137±2	Re-Os	Molybdenite	7	Du et al. 1995
Jinduicheng	135±6	Ar-Ar	Molybdenite	No data	Du et al. 1995
Jinduicheng	124±6	K-Ar	Biotite	1	Nie et al. 1994
Shijiawan	136±8	Re-Os	Molybdenite	1	Huang et al. 1994
Shijiawan	124	K-Ar	Unknown	No data	Huang et al. 1985
Nannihu	142±15	Rb-Sr	Whole rock	7	Hu et al. 1988
Nannihu	141.8±2.1	Re-Os	Molybdenite	1	Li Y F et al. 2004
Nannihu	148±10	Re-Os	Molybdenite	1	Huang et al. 1994
Shangfanggou	144.8±2.1	Re-Os	Molybdenite	2	Li Y F et al. 2004
Sandaozhuang	145.0±2.2	Re-Os	Molybdenite	3	Li Y F et al. 2004
Leimengou	132.4±2.0	Re-Os	Molybdenite	2	Li Y F et al. 2005
Leimengou	136.2±1.5	SHRIMP	Zircon	11	Li Y F et al. 2005

Table 2: Re-Os isotopic data of Mo ores from the Nannihu deposits, eastern Qinling.

Sample No.	Sample weight (g)	Re (μg/g)	^{187}Re (μg/g)	^{187}Os (ng/g)	Model age (Ma)
SDZ-1	0.01475	27.5 (0.4)	17.3 (0.2)	41.7 (0.4)	144.5 (2.2)
SDZ-2	0.03005	15.2 (0.2)	9.58 (0.11)	23.2 (0.2)	145.4 (2.0)
SDZ-3	0.01543	25.2 (0.4)	15.9 (0.2)	38.4 (0.3)	145.0 (2.2)
SF-1	0.02077	20.2 (0.2)	12.7 (0.2)	30.5 (0.3)	143.8 (2.1)
SF-2	0.02219	19.0 (0.2)	12.0 (0.2)	29.1 (0.2)	145.8 (2.1)
NNF-1	0.01753	24.9 (0.4)	15.7 (0.2)	37.1 (0.3)	141.8 (2.1)
LMG-1	0.02286	18.4 (0.3)	11.5 (0.2)	25.3 (0.2)	131.6 (2.0)
LMG-2	0.0182	25.9 (0.3)	16.2 (0.2)	36.1 (0.3)	133.1 (1.9)

5 Results

Common Os was not detected in the eight samples of molybdenite Table2.shows the isotopic components of the samples. The decay constant used for ^{187}Re of $1.666\times10^{-11}yr^{-1}$, which has an uncertainty of about ±1.02%. The results show that the Re-Os model ages are 141.8±2.1 Ma for the Nannihu deposit, 145.4 ±2.0 to 144.5 ±2.2 Ma (averaging 145.0 ±2.2 Ma) for the Sandaozhuang deposit, 145.8±2.1 to 143.8±2.1 Ma (averaging 144.8 ±2.1 Ma) for the Shangfanggou deposit, and 133.1±1.9 to 131.6±2.0 Ma (averaging 132.4±2.0 Ma) for the Leimengou deposit.

6 Metallogenic environment and geodynamical setting

The North China craton had been in a stage of steady development from the Cambrian until the Early Triassic. The isotopic age data suggest the following: the Yangtze craton collided and converged with the North China craton at about 218 to 238 Ma (Li et al. 1989), This was followed by an intracontinental orogeny, which ended in the Jurassic (Chen and Fu 1992). During the late Jurassic and early Cretaceous, the regional tectonic regime in the whole of eastern China began to change. The main stress field began to shift from N-S to nearly E-W, signaling the beginning of the Pacific tectonic evolution stage (Ren 1991). During this stage the southern margin of the North China craton, including the East Qinling area, transformed into the extensional tectonic environment. The Indosinian-Yanshanian magmatic activity corroborates the features of the tectonic evolution in this period.

First, in the Middle-Late Jurassic mafic magma rose and intruded along tenso-shear steep-dipping fractures, forming diabase dikes or dike swarms in the area. Later, widespread acid magmatic activity formed large granite batholiths and numerous granite porphyry stocks and dikes. During the Early Cretaceous, large amounts of intermediate-acid magma were erupted along the Sanmenxia-Lushan deep fault, forming volcanic basins at Tianhu of Songxian County, Jiudian of Ruyang County and other areas (Wang et al. 1997). Magmatism intensified, and the magma evolved successively from the alkaline through subalkaline to calc-alkaline compositions. This suggests a change in the character of the magamitic activity during that period. The fact that more than 80% of Mesozoic intrusive rocks occurred in the Early Cretaceous indicates that the transition of the tectonic regime began at the turn of the Jurassic-Cretaceous. The Re-Os isotope model ages obtained in this study are between 145.8±2.1 and 131.6±2.0Ma. It can be concluded that the East Qinling metallogenic molybdenum belts originated during this great transition of the tectonic regime in eastern China. This time period belongs to the second phase of large-scale metallogenesis in East China during the Mesozoic (Mao et al. 2000; 2003b).

Acknowledgements

This study was supported by the National Natural Science Foundation of China (grant 40434011) and the State Development and Planning Program for Basic Researches in Key Areas of China (grant 1999043211).

References

Chen Y, Fu S (1992) Mineralization of gold deposits in Henan, China. Beijing: Seismological Press: 1-146 (in Chinese)

Huang D, Du A, Wu C, Liu L, Sun Y, Zhou X, (1996) Metallochronology of Mo(-Cu) deposits in the North China plateform: Re-Os age of molybdenite and its geological significance. Mineral Deposits 15: 365-373

Huang D, Wu C, Du A, He H (1994) Re-Os isotope ages of molybdenum deposits and in East Qinling their geological significance. Mineral Deposits 13; 221-230 (in Chinese with English abstract)

Li S, Hart SR, Zheng S (1989) The collision time of North China plate and South China plate: evidence from Sm-Nd ages. Scientia Sinica(B):19: 312-319 (in Chinese)

Li Y, Mao J, Guo B (2004) Re-Os dating of molybdenite from the Nannihu Mo(W) orefield in the east Qinling and Its Geodynamic significance. Acta Geologica Sinica 78: 463-470

Mao J, Wang Z (2000) A preliminary study on time limits and geodynamic setting of large-scale metallogeny in East China. Mineral Deposits 19:289-296 (in Chinese with English abstract)

Mao J, Yang J, Qu W, Du A, Wang Z, Han C (2003b) Re-Os age of Cu-Ni ores from the Huangshandong Cu-Ni sulfide deposit in the east Tianshan Mountains and its implication for geodynamic process. Acta Geol Sinica 77: 220-226.

Mao J, Zhang Z, Yu J, Wang Y, Niu B (2003a) The geodynamics setting of Mesozoic large-scale mineralization in North China: the revelation from accurate timing of metal deposits. Science in China (series D) 33:289-299

Ren J (1991) A discussion on the basic features of the lithosphere tectonics in Chinese continents. Regional Geology of China 2: 289-293 (in Chinese with English abstract)

Stein HJ, Markey RJ, Morgan JW, Du A, Sun Y (1997) Highly precise and accurate Re-Os ages for molybdenite from the east Qinling molybdenum belt, Shaannxi Province, China. Economic Geology 92:827-835

Wang Z, Cui B, Xu M (1997) The tectonic evolution and mineralization in the south margin of North China block. Beijing: Metallurgical Industry Press. pp1-296 (in Chinese)

Zhang Z, Zhu B, Chang X, Qiang L, Wen M (2001) Petrogenetic metallogenetic background and time space relationship of the East Qinling molybdenum ore belt, China. Geological journal of China University 7(3):307-315(in Chinese with English abstract)

Studies on the genesis of adjacent Changkeng gold- and Fuwang silver-deposits, Guangdong Province, China

Hua-Ying Liang, Ping Xia, Xiu-Zhang Wang
Laboratory of Marginal Sea Geology, Guangzhou Institute of Geochemistry and South China Sea Institute of Oceanology, Chinese Academy of Sciences, 510640 Guangzhou, China

Heng-Xiang Yu
Guilin Institute of Technology, Guilin 541004, China

Abstract. The Changkeng Au- and Fuwang Ag-deposits represent an economically significant and distinct member of the Au–Ag deposit association in China. The two deposits are immediately adjacent, but the Au- and Ag-orebodies separated from each other. Changkeng is hosted in brecciated cherts and jasperoidal quartz and is characterized by disseminated ore minerals. Fuwang, hosted in the Lower Carboniferous Zimenqiao group bioclastic limestone, has vein and veinlet mineralization associated with alteration comprised of quartz, carbonate, sericite, and sulfides. The Changkeng gold and Fuwang silver deposits overlap in homogenous temperature and salinity of fluid inclusions. The δD_{H2O}, $\delta^{18}O_{H2O}$, $\delta^{13}C_{CO2}$ and $^{3}He/^{4}He$ values of the fluid inclusions suggest the ore fluids of the Changkeng Au-ore come from the meteoric water and the ore fluids of the Fuwang Ag-ore are derived from mixing of magmatic water and meteoric water. The Changkeng gold- and the Fuwang silver deposits show different Pb isotope signatures, suggesting different sources of ore-forming material. Rb-Sr isochron age (68 ± 6 Ma) and ^{40}Ar-^{39}Ar age (64.3 ± 0.1 Ma) of the ore-related quartz veins from the Ag-deposit indicate that the Fuwang deposit formed during the Cenozoic Himalayan tectono-magmatic event. The adjacent Changkeng and Fuwang deposits could, however, represent a single evolved hydrothermal system. The deposits are alternatively the product of the superposition of two different geological events. Our work indicates that the Pacific Coastal Volcanic Belt in the South China Fold Belt has greater potential for Himalayan precious metal mineralization than previous realized.

Keywords. Himalayan, gold, silver, Guangdong, ore genesis

1 Geological setting

The adjacent Changkeng gold- and Fuwang silver-deposits are located along the southwestern rim of the Shanshui basin (Fig. 1). Sedimentary rocks in the region range from Proterozoic to Cenozoic.(Bureau of Geology and Mineral Resource of Guangdong Province 1985; Du et al. 1993). Eocene volcanic and sedimentary rocks are widespread (Tang 1987) and a small Tertiary volcanic rocks hosted-silver deposit was discovered (Fig. 1).

The adjacent Changkeng gold- and Fuwang silver- deposits differ in their geologic characteristics, stratigraphic position, and metal contents, but are both located at the same locality (Fig. 1), The Changkeng gold orebodies are present in the upper part of the stratigraphic section (Du et al. 1993). The Fuwang silver orebodies are located in the lower parts of the stratigraphic section. The gold and silver ore bodies are separated from each other. The Changkeng gold deposit is hosted in brecciated siliceous rocks on the top of rocks of the Zimenqiao Group bioclastic limestone and is characterized by disseminated mineralization. Ore minerals in the gold deposit include disseminated anhedral pyrite, native gold, stibnite, realgar, and orpiment. Gangue minerals include quartz, illite, dickite, calcite, less fluorite, and barite (Du et al. 1993). The silver content in the gold orebodies is low (generally <11 ppm).

The Fuwang silver deposit is hosted in Early Carboniferous Zimenqiao bioclastic limestone along the contact fault zones between the limestone and the overlying Changkeng gold-hosting siliceous rocks. The Fuwang silver is characterized by vein and veinlet mineralization with zones of silicification. The main sulphide minerals are sphalerite and galena, with lesser pyrite and rare arsenopyrite, chalcopyrite, and bornite. The deposit is poor in gold (< 0.2 ppm). The crosscutting relationship indicates that the gold deposit is older than the silver deposit.

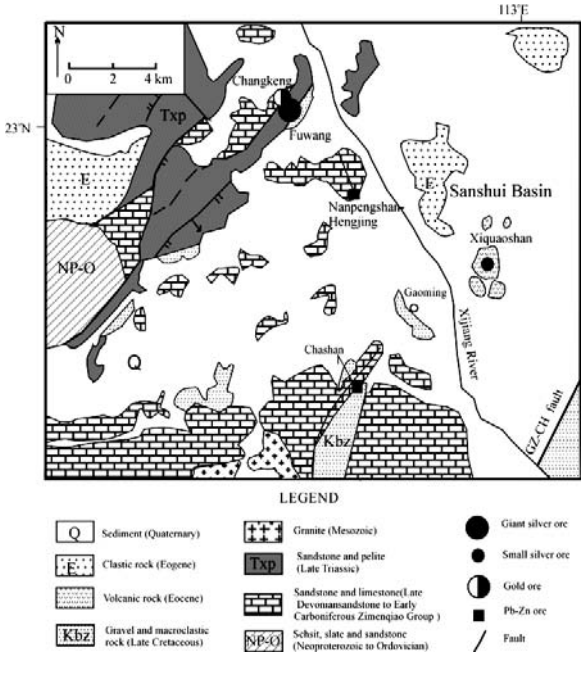

Figure 1: Simplified regional geologic map of the Changkeng gold- and Fuwang silver-deposits (after Du et al. 1993).

This page intentionally blank

2 Genesis of the gold-hosting siliceous rocks

Genesis of the gold-hosting siliceous rocks has been debated extensively. Du et al. (1993) argues that the gold-hosting siliceous rocks are jasperoid quartz formed from limestone. However, Xia et al. (1996) suggest that these rocks are syngenetic chert. Gold-hosting silicious rocks consist of thin-bedded and laminated, massive, and brecciated black material. Some radiolaria, which suggest an age of between Carboniferous and Permian, are present in some of the laminated and massive siliceous material. This suggests that some parts of the gold-hosting siliceous laminated and massive material is radiolarian chert. The limestone-siltstone contacts are common sites of deep burial diagenetic silicification. Some of the massive zones contain framboidal pyrite, and therefore may have formed by diagenetic processes as diagenetic chert. The Changkeng gold ore is hosted mainly in the breccia. Thus, the gold-bearing breccias imply that the gold was introduced after the diagenetic silicification. The gold-hosting rocks, therefore, formed by multistage silicification that at least includes syngenetic-, diagenetic-, and hydrothermal- silicification. The hydrothermal silicification is related to gold deposition. The syngenetic silicification and the diagenetic silicification have high background abundances of gold and may indicate that a pre-existing enriched of gold in the stratigraphic section contributed to the Changkeng gold deposit, similar to processes suggested for the Meikle and neighboring Carlin-type deposits of Nevada (Emsbo et al. 2003).

3 Geochemical studies of the adjacent Changkeng gold and Fuwang silver deposits

3.1 Geochemistry of the ore-forming fluid

The gold and silver deposits overlap in homogenization temperature, in the ranging 210 ± 80 °C and 230 ± 50 °C, respectively. Salinities of the fluid inclusion from the gold and silver deposits are also overlap, ranging from 1.6 - 7.3 wt % and 1.6 - 2.6 wt % equiv. NaCl, respectively.

The adjacent Changkeng gold- and Fuwang silver- deposits are different in δD_{H2O}, $\delta^{18}O_{H2O}$, $\delta^{13}C_{CO2}$ and $^{3}He/^{4}He$ isotope composition (Guo et al. 1996; Sun et al. 1999). The δD_{H2O}, $\delta^{18}O_{H2O}$, $\delta^{13}C_{CO2}$ and $^{3}He/^{4}He$ values of the fluid inclusions from the Changkeng gold deposit range from –80 to -30 ‰, -7.8 to –3.0 ‰, -16.6 to -17.0 ‰ and 0.0100 to 0.0054 Ra, respectively. The δD_{H2O}, $\delta^{18}O_{H2O}$, $\delta^{13}C_{CO2}$ and $^{3}He/^{4}He$ values of fluid inclusions from the Fuwang silver deposit range from –59 to -45 ‰, -0.9 to 4.1 ‰, -6.7 to –0.6 ‰ and 0.5930 to 0.8357 Ra, respectively. The δD_{H2O}, $\delta^{18}O_{H2O}$, $\delta^{13}C_{CO2}$ and $^{3}He/^{4}He$ values of the fluid inclusions suggest the ore fluids of the Changkeng gold ore come from the meteoric water and the ore fluids of the Fuwang silver ore come from mixing of magmatic water and meteoric water.

3.2 Pb Isotopes of the adjacent Changkeng gold- and Fuwang silver- deposits

The adjacent Changkeng gold- and Fuwang silver- deposits show different lead isotopic signatures. The Changkeng gold deposit has Pb isotope ratios ($^{206}Pb/^{204}Pb$: 18.580-19.251, $^{207}Pb/^{204}Pb$: 15.672-15.801, $^{208}Pb/^{204}Pb$: 38.700-39.104) similar to those ($^{206}Pb/^{204}Pb$: 18.578-19.433, $^{207}Pb/^{204}Pb$: 15.640-15.775, $^{208}Pb/^{204}Pb$: 38.925-39.920) of its host rocks and different from those ($^{206}Pb/^{204}Pb$: 18.820-18.891, $^{207}Pb/^{204}Pb$: 15.848-15.914, $^{208}Pb/^{204}Pb$: 39.579-39.786) of the Fuwang silver deposit. The Pb in the gold deposit is derived from the local sources. The Pb isotope composition of the Fuwang silver deposit is similar to those of the Neoproterozoic metamorphic basement of the western Guangdong region (Zhang et al. 1993), suggesting that the Pb of the Fuwang silver deposit is derived from the Neoproterozoic metamorphic basement.

3.3 $^{40}Ar/^{39}Ar$ age and Rb-Sr isochron age of mineralized quartz veins

The mineralized quartz sample from the Fuwang silver deposit yields $^{40}Ar/^{39}Ar$ a plateau age of 64.3 ± 0.1 Ma and isochron age of 64.0 ± 0.1 Ma with an initial $^{40}Ar/^{36}$ ratio of 294.5 ± 0.4. The Rb and Sr isotopic data obtained from six samples define an Rb-Sr isochron, with an age of 68 ± 6 Ma, MSWD = 4.14. Quartz $^{40}Ar/^{39}Ar$ *age s and* Rb-Sr isochron age are concordant within error, and correspond to the Himalayan tectono-magmatic event (Himalayan is a period <90 Ma; Wang and Mo 1995).

4 Origin of Changkeng gold and Fuwang silver deposits

The Changkeng gold deposit is hosted in siliceous rocks and limestone and shows similar mineralization and mineral associations to many Carlin-type deposits (Hofstra and Cline 2000; Hu et al. 2002; Peters et al. 2002).

Age evidence suggests that the Fuwang silver deposit bear a genetic relation to the Himalayan magmatic event in the Shanshui Basin. Given the close temporal and broad spatial association of the silver deposit with Early Tertiary magmatism, the D, O, C, and He isotope data are consistent with ore fluids that consisted of a mixture of deeply sourced magmatic and local meteoric water.

The most plausible explanation is to ascribe these combined mineralized ages and isotopic results for the Fuwang silver deposit to the Himalayan tectono-magmatic event. The presence of disseminated gold in brecciated siliceous rocks along with epigenetic quartz, orpiment, realgar, and stibnite, together with meteoric D, O, C, and He isotopic values and fluid inclusion salinity and temperature data that overlap those from Fuwang silver deposit, suggests that the gold was deposited by an epigenetic meteoric hydrothermal system.

The adjacent Changkeng gold- and Fuwang silver-deposits could represent a single evolved hydrothermal system where the ore fluids deposited gold at first in the brecciated silicification, and then mixed with the magmatic water and deposited silver in the fracture zone in the limestone. Alternatively, the second ore genetic model is that the adjacent Changkeng gold- and Fuwang silver-deposits may have resulted from the superposition of different geological events. Given the close proximity of the two deposits and the overlap of fluid inclusions salinities and temperatures, the adjacent Changkeng gold and Fuwang silver deposits were most likely formed by the first model.

Early Tertiary isotopic ages from the Fuwang silver deposit and the nearby Xiqiaoshan Tertiary volcanic rock-hosted silver deposit suggest that the South China Fold Belt underwent a Himalayan event of precious metal mineralization.

Acknowledgements

The work was supported by the the NSFC (No.49872035, 40472049), and the important project of CAS (No. KZCXZ-SW-117 and No. GIGCX-03-04).

References

Bureau of Geology and Mineral Resource of Guangdong province (1985) Regional geology of Guangdong province. Geol Pub House, Beijing, China, 1-350 (in Chinese)

Du JE, Ma CH, Zhang GH (1993) Mineralization characteristics of the Changkeng gold-silver deposit, Guangdong province. Guangdong Geology 8: 1-8. (in Chinese with English abstract)

Emsbo P, Hofstra AH, Lauha EA, Griffin GL, Hutchinson RW (2003) Origin of high-grade gold ore, source of ore fluid components, and genesis of the Meikle and Neighboring Carlin-type deposits, Northern Carlin trend, Nevada, Econ Geol 98: 1069-1105

Guo XS, Du JE (1996) Study on the fluid inclusions and geochemistry of the Changkeng Gold-Silver deposit. Min Res Geol 10: 187-193. (in Chinese with English abstract)

Hofstra A H, Cline JS (2000) Characteristics and models for Carlin-type gold deposits, Rev Econ Geol 13: 163-220.

Hu RZ, Su WC, Bi XW, Tu GZ, Hofstra AH (2002) Geology and geochemistry of Carlin-type gold deposits in China. Miner Depos 37: 378-392

Peters SG, Huang JZ, Jing CG (2002) Introduction to and classification of sedimentary rock-hosted Gold deposits in P.R. China. In: Peters S.G. (ed), Geology, geochemistry, and geophysics of sedimentary rock-hosted gold deposits in P. R. China. Open-File Rep 02-131, versi 1.0: 1-60

Sun XM, Norman DI, Sun K, Chen BH (1999) Characteristics and source of ore-forming fluids of Changkeng Gold-Silver deposits in middle Guangdong province, evidences from N_2-Ar-He. Scie China (Series D) 29: 240-246 (in Chinese)

Tu GZ (2000) The super-large deposits in China. Vol. 1. Scie China Press, Beijing, pp. 3-9 (in Chinese)

Wang HZ, Mo XX (1995) An outline of the tectonic evolution of China. Episodes 8: 6-16

Xia P, Zhang H, Wang XZ, Chen JP (1996) Geology-geochemistry and genesis of chert from Changkeng Au-Ag deposit, west Guangdong province, China. Geochemica 25: 129-139 (In Chinese with English abstract)

Zhang Q, Zhang BG, Pang JY, Cao YB, Hong DH (1993) The isotope signature and source rocks of Chadong Silver-Gold deposit. Mineral Deposits 12: 349-355 (in Chinese with English abstract)

Zhang WH, Lu WJ, Jiao YQ, Li ST (2000) Composition and source study of ore-forming fluid in the Changkeng gold-silver deposits, Guangdong province, China. Acta Petrol Sinica 16: 521-527 (in Chinese with English abstract)

Fluid inclusion and stable isotope geochemistry of the Ernest Henry Fe oxide-Cu-Au deposit, Queensland, Australia

Geordie Mark[1], Patrick J. Williams, Nick H.S. Oliver
School of Earth Sciences, James Cook University, Townsville 4811, Australia
[1] Current address: School of Geosciences, Monash University, Melbourne 3168, Australia

Chris Ryan
CSIRO Exploration and Mining, School of Geosciences, Monash University, Melbourne 3168, Australia

Terry Mernagh
Geoscience Australia, GPO Box 378, Canberra 2601, Australia

Abstract. Ernest Henry is an iron oxide-copper-gold deposit characterized by magnetite>>hematite, chalcopyrite as the only significant hypogene copper mineral. It occurs within a large, zoned, medium to high temperature alteration system. Pre- to synmineralization quartz contains three broad populations of fluid inclusions. Type 1 (L-V-H±nS) inclusions decrepitate or homogenise at 200-500° C, have salinities of 32-55 wt% $NaCl_{equiv}$, display chemical variations that parallel the paragenetic sequence of alteration, and have variable Br/Cl mostly less than magmatic brines. Type 2 (L-V) inclusions homogenise at temperatures of 120-350°C have salinities up to 20 wt% NaClequiv and inferred to contain $CaCl_2$. Type 3 L-rich CO_2 inclusions were entrapped at 130-370MPa. dD and dO of pre- to synmineralisation fluids are estimated to have been -23 to -66 and 8 to 11 per mil respectively. dS in main ore pyrite and chalcopyrite is -1.6 to +5.4 per mil. The data are compatible with a substantial magmatic contribution to Ernest Henry fluids but also suggest the system was complex and involved fluids and other components with different sources. Ernest Henry is distinguished from the giant Olympic Dam deposit by evidence for high temperature/salinity fluids and for no major involvement of surficial waters during mineralization.

Keywords. Ernest Henry, copper, gold, fluid inclusions, stable isotopes

1 Introduction

The sources of ore fluids and mechanisms of mineralization in iron oxide-copper-gold (IOCG) deposits are poorly-understood and could differ amongst the geologically diverse members of the group (e.g. Barton and Johnson 2004). Ernest Henry is the largest known magnetite-dominated IOCG deposit in Australia (Mark et al., in press; cf. Williams and Pollard 2003). In contrast to the giant hematite-rich Olympic Dam deposit in South Australia, it is characterized by complex high temperature alteration zoning and has chalcopyrite as the only significant copper mineral (Mark et al. in press; cf. Reeve et al. 1990). This paper reports on fluid inclusion and stable isotope studies that were undertaken to characterize Ernest Henry ore fluids. It is the first fluid inclusion study to have been attempted at the deposit where such work is challenging because of the low abundance of quartz compared to most other hydrothermal deposits and a general tendency for fluid inclusions to be small and difficult to work with. New stable isotope data augment earlier work by Twyerould (1997) and include the first reported δD data for the deposit.

2 Geological context

Ernest Henry is the largest of several magnetite bearing IOCG deposits in the Cloncurry mining district, which encompasses the eastern part of the Proterozoic Mount Isa inlier in northwest Queensland, along with its extensions beneath shallow cover in the surrounding area (Williams and Pollard 2003). Late Palaeoproterozoic supracrustal rocks and early ca 1.74 and 1.66 Ga intrusions were deformed and metamorphosed at greenschist to amphibolite facies between 1.58 and 1.50 Ga and extensively intruded by granitoids from 1.55 to around 1.50 Ga (Page and Sun, 1998; Williams and Pollard, 2003). The Ernest Henry deposit is hosted in a sequence of metamorphosed, predominantly intermediate volcanic rocks and is spatially-associated with bodies of ca 1.66 Ga diorite. U-Pb dating of titanite from pre-ore alteration assemblages suggests that the Ernest Henry hydrothermal system was broadly contemporaneous with the later (1.55-1.50) granitoids, examples of which are present within 15 km of the ore deposit (Mark et al. in press). Proterozoic basement near Ernest Henry is obscured by Mesozoic to recent cover. However, extensive drilling around the deposit has demonstrated there is a very large volume of altered rocks that extends for at least several kilometres in all directions near the current erosion level (Mark et al. in press).

3 Paragenesis of alteration and mineralization

Twyerould (1997) and Mark et al. (in press) documented the time-space evolution of the Ernest Henry hydrothermal system. Distal stage 1 alteration produced secondary albitic plagioclase and calc-silicates and was similar to regional-scale sodic-calcic metasomatism elsewhere in the

district (De Jong and Williams 1994). It is preserved with variable overprints by younger alteration at distances of 1-3 km from the orebody. Stage 2 formed a potassic-iron-(manganese) association represented predominantly by biotite, magnetite, K feldspar, almandine-spessartine garnet and quartz rich veins. Stage 2 alteration is preserved around the periphery of the mine and along NE-trending structures extending away from it. Stage 3 potassic alteration was pervasive in the immediate vicinity of the orebody where the rocks were replaced by hematite-stained and variably barian K-feldspar. Stage 3 altered rocks were selectively affected by Stage 4 which formed a SE-plunging breccia lens up to 300m thick in which magnetite, sulphides and a very complex association of other minerals form the matrix to K-feldspar-dominated clasts. Stage 5 calcite-dominated veins are predominantly localized near the footwall contact of the ore lens.

4 Sampling and methods

Samples were obtained from drill cores where the geological context and paragenetic setting was well known from detailed logging undertaken as part of general geological description of the deposit and the surrounding altered rocks (Mark et al. in press). The fluid inclusion study focussed on interpreted primary inclusions hosted by quartz from paragenetic stages 2, 3 and 4 (i.e. pre- to synmineralization). The inclusions were investigated by conventional and electron microscopy, subjected to microthermometric experiments, and selected examples were analyzed by Laser Raman spectrometry and proton induced X-ray excitation (PIXE) analysis (cf. Ryan et al. 2001). Hand-picked separates were prepared of minerals from stages 1-5 and analyzed using conventional methods as appropriate for δD in biotite and amphibole (n=10, SUERRC, East Kilbride, Scotland), $\delta^{13}C$ and $\delta^{18}O$ in carbonates (n=36, Monash University), $\delta^{18}O$ in silicates and magnetite (n=42, Monash University) and $\delta^{34}S$ in sulphides (n= 32, University of Tasmania).

5 Fluid inclusion types and geochemistry

Quartz-hosted fluid inclusions from stages 2 to 4 can be classified into three broad groups (Fig. 1). Type 1 (L-V-H±nS) inclusions contain liquid, a small H_2O vapour bubble (<10% of total volume) and a halite solid at room temperature. Most have additional solids in a variety of assemblages containing one or more of ferropyrosmalite, sylvite, Fe-chloride, magnetite, hematite, calcite and kutnahorite ($CaMn(CO_3)_2$). Brown ice forms on freezing and low first melting temperatures indicate the presence of Ca and other divalent metals. A small proportion of Type 1 inclusions decrepitate without homogenising on heating while the remainder homogenise by halite or ferropyrosmalite dissolution at temperatures between 200 and 520°C (65% > 300°C). Salinities estimated from halite dissolution temperatures are 32-55 wt% $NaCl_{equiv}$. Type 2 (L-V) inclusions occur in both primary and secondary

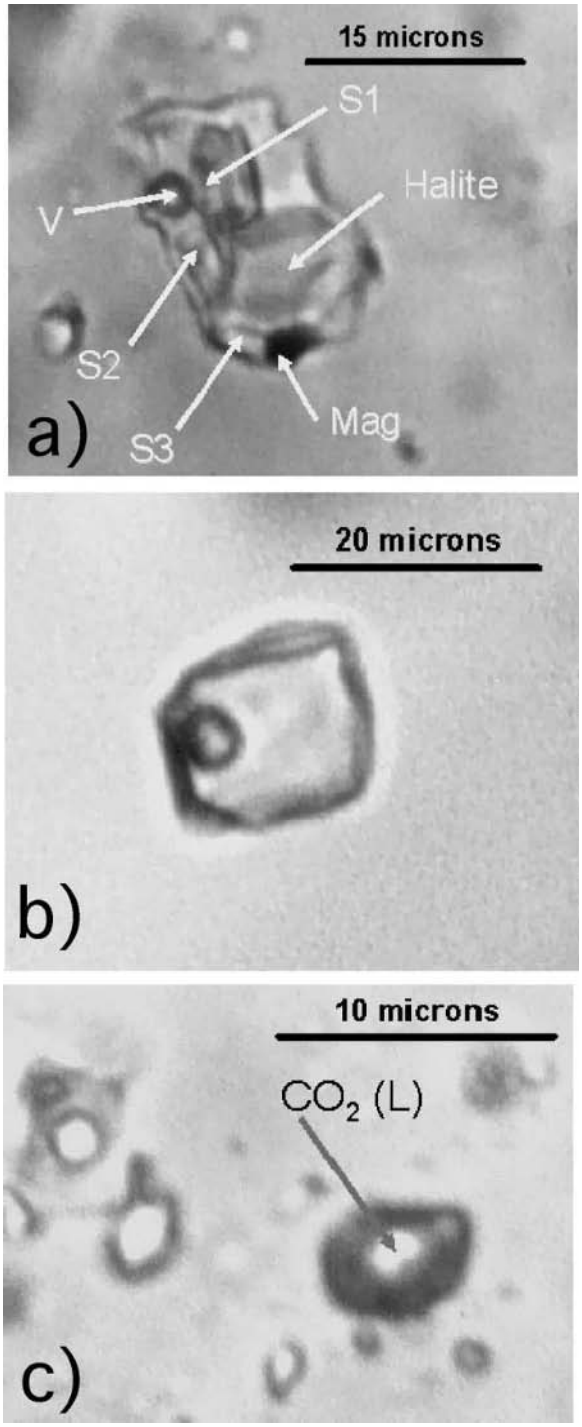

Figure 1: Examples of the main types of fluid inclusions found at Ernest Henry. a) Type 1 inclusion with halite, magnetite (Mag), a small vapour bubble (V) and three unidentified solids (S1-S3); b) Type 2 liquid + vapour inclusion; c) Type 3 liquid CO_2 inclusion.

settings (i.e. some of them represent the youngest fluid type). At room temperature they contain liquid and an H_2O vapour bubble which occupies up to 25% of the volume of the inclusion. They homogenise at temperatures of 120-350°C. Type 2 inclusions form brown ice on freezing and are deduced to be $CaCl_2$-bearing. Salinities range up to 20 wt% $NaCl_{equiv.}$ Type 3 inclusions are dominated by CO_2 and are liquid-rich (>90%) at room temperature. Some contain a small proportion of liquid H_2O and/or a nahcolite ($NaHCO_3$) solid. Their densities suggest entrapment at pressures of 130-370 MPa during stages 2 to 4.

PIXE studies were undertaken on populations of single fluid inclusions from stages 2, 3 and 4 (total analyses = 40). The results are quantitative at an accuracy of around ±50% for Cl, K, Ca, Mn, Fe, Cu, Zn, As, Br, Rb, Sr, Ba and Pb. Accuracy for many interelement ratios is far better than this as the main sources of error have similar effects on all elements. Analytical detection limits were mostly in the range 30-300 ppm. Type 1 inclusions display systematic stage to stage variation. All are distinguished by high Mn:Fe ratios (mostly > 1) compared to complex brine inclusions from other Cloncurry Fe oxide Cu-Au deposits such as Osborne, Starra and Eloise (Williams et al. 1999; 2001). Stage 3 (K feldspar-related) Type 1 inclusions have lower (Mn+Fe)/K than those from stages 2 and 4 (magnetite/biotite/garnet-related). With the exception of one outlying result, Br/Cl ratios in Type 1 inclusions are less than 0.0013 and in some cases in which Br was undetected must be less than 0.0005. Cu was only detected in Type 1 inclusions at concentrations of 30-200ppm. Analyses of the eight analyzed ore stage Type 1 inclusions have previously been reported by Mark et al. (2005). These are distinguished by the highest K/Ca ratios and absolute concentrations of Ba (mean 2.8 wt%), Zn (mean 4800 ppm), As (mean 590 ppm), and Pb (mean 2300 ppm) but all had estimated Cu below 120 ppm.

6 Stable isotope results

δD values are -80 to -88 per mil in three stage 1 amphiboles, -85 and -91 per mil in two stage 2 biotites, - 69 to -95 in four stage 4 biotites, and -72 in a stage 5 amphibole. Allowing for the likely fractionations this suggests that the fluids in the Ernest Henry system had δD of -23 to -66 per mil Mean $\delta^{18}O$ values (per mil) are: Stage 1, amphibole = 5.8, calcite = 15.7; Stage 2, biotite = 6.4, calcite = 12.5, K feldspar = 11.3, magnetite = 4.6, quartz = 10.7; Stage 3, biotite = 5.7, calcite = 12.5, K feldspar = 9.0, magnetite = quartz = 11.8; Stage 4, biotite = 6.2, calcite = 12.6, K feldspar = 10.1, magnetite = 3.1, quartz = 11.7; Stage 5, amphibole = 10.5, calcite = 14.9. In conjunction with data from Twyerould (1997) these results suggest that fluid $\delta^{18}O$ remained in the range 8-11 per mil in the time period represented by stages 1-4. The data for carbonate-rich stage 5 are consistent with an influence from metamorphosed carbonates either involving an external fluid with higher $\delta^{18}O$ of 13-16 per mil that had equilibrated with such rocks or from their presence in the protoliths of the highly deformed rocks in the footwall of the deposit where the carbonate veining is localized.

Mean $\delta^{13}C$ values (per mil) in calcite are; Stage 1, -2.4; Stage 2, -4.2; Stage 3, -3.5; Stage 4 -3.0; Stage 5, -2.1. ^{34}S ranged from - 0.5 to +5.4 per mil (mean 2.2) in ore stage chalcopyrite and from -1.6 to +4.8 (mean 1.6) in ore stage pyrite. The two common sulphide minerals are not preserved in isotopic equilibrium.

7 Discussion

The pre- to synmineralization (Stages 2-4) mineral parageneses at Ernest Henry that distinguish the system from from regionally sodic-calcic altered rocks are deduced to have formed in a hydrothermal system dominated by compositionally complex fluids. Type 3 (high density CO_2) inclusions may have formed by unmixing from aqueous brine phase. The Type 1 and 2 inclusions imply that at least two fundamentally different types of aqueous brine were present echoing the situation that has been found in other Cloncurry district Cu-Au deposits (e.g. Williams et al. 2001). High salinity brines are most likely to have cotransported Cu and Au in the system though ore-stage Type 1 inclusions studied by PIXE have much lower Cu concentrations than were found at the much smaller Starra Au-Cu deposit (Williams et al. 2001). They do however high concentrations of Zn, Pb and Ba compared both to premineralization Type 1 inclusions and the relatively Cu-rich brines from Starra. This suggests ore deposition was associated with the influx of a distinct mineralizing brine and although the studied Type 1 inclusions could indicate that the ore was deposited by efficient Cu precipitation from a very large mass of fluid a more plausible explanation maybe that the analyzed inclusions represent a "spent" fluid after chalcopyrite precipitation (cf. Mark et al. 2005). Assuming that fluid Br/Cl ratios would have been essentially insensitive to fluid-rock interactions, then the variable measured values in Type 1 inclusions imply they derived their salinity from more than one source and including a component with Br/Cl similar to evaporitic halite. The rocks near Ernest Henry have evidently undergone extensive fluid-rock interactions at elevated temperatures. The O-H stable isotopic data are consistent with substantial magmatic contributions of these elements during the main presyn mineralization stages but given that immediate host rocks are igneous, cannot be taken to demonstrate an exclusively magmatic fluid source. Compared to Olympic Dam, Ernest Henry seems to have formed from relatively high temperature and salinity fluids without a significant contribution from surfice waters (cf. Oreskes and Einaudi 1992).

Acknowledgements

This research was supported by the Australian Research Council, Ernest Henry Mining and MIM Exploration. The project was planned and executed in collaboration with Richard Crookes and Rick Valenta.

References

Barton MD, Johnson DA (2004) Footprints of Fe-oxide(-Cu-Au) systems. SEG 2004: Predictive Mineral Discovery Under Cover. Centre for Global Metallogeny, The University of Western Australia, Special Publication 33: 112-116

De Jong G, Williams PJ (1995) Giant metasomatic system formed during exhumation of mid crustal Proterozoic rocks in the vicinity of the Cloncurry Fault, NW Queensland: Australian Journal of Earth Sciences 42: 281-290

Mark G, Oliver NHS, Williams PJ (in press) Mineralogical and chemical evolution of the Ernest Henry Fe oxide-Cu-Au ore system, Cloncurry district, northwest Queensland, Australia: Mineralium Deposita

Mark G, Wilde AR, Oliver NHS, Williams PJ (2005) Predicting alteration patterns in the outflow zones of hydrothermal ore systems: a case study using the "spent" fluids from the Ernest Henry Fe-oxide-Cu-Au deposit: Journal of Geochemical Exploration 85: 31–46

Oreskes N, Einaudi MT (1992) Origin of hydrothermal fluids at Olympic Dam: preliminary results from fluid inclusions and stable isotopes: Economic Geology 87: 64-90

Page RW, Sun S-S (1998) Aspects of geochronology and crustal evolution in the Eastern Fold Belt, Mt Isa Inlier: Australian Journal of Earth Sciences 45: 343-361

Reeve JS, Cross KC, Smith RN, Oreskes N (1990) Olympic Dam copper-uranium-gold-silver deposit: Australasian Institute of Mining and Metallurgy Monograph 14:1009-1035

Ryan CG, McInnes BM, Williams PJ, Guoyi Dong, Tin Tin Win, Yeats CJ (2001) Imaging fluid inclusion content using the new CSIRO-GEMOC nuclear microprobe: Instruments and Methods in Physics Research B 181: 570-577

Twyerould SC (1997) The geology and genesis of the Ernest Henry Fe-Cu-Au deposit, NW Queensland, Australia: Unpublished PhD thesis, University of Oregon. 494pp

Williams PJ, Dong Guoyi, Pollard PJ, Perring C, Ryan CG Mernagh TP (1999) Fluid inclusion geochemistry of Cloncurry (Fe)-Cu-Au deposits: In: Stanley CJ et al. (eds) Mineral Deposits: Processes to Processing. Balkema, Rotterdam, pp 111-114

Williams PJ, Guoyi Dong, Ryan CG, Pollard PJ, Rotherham, JF, Mernagh TP, Chapman LH (2001) Geochemistry of high salinity fluid inclusions from the Starra (Fe)-Cu-Au deposit, Cloncurry district, Queensland: Economic Geology 96: 875-883

Williams PJ, Pollard PJ (2003) Australian Proterozoic iron oxide-Cu-Au deposits: An overview with new metallogenic and exploration data from the Cloncurry district, northwest Queensland. Exploration and Mining Geology 10: 191-213

The Re-Os age for molybdenite from the Variscan Strzegom-Sobótka massif, SW Poland

Stanislaw Z. Mikulski
Department of Economic Geology, Polish Geological Institute, 4 Rakowiecka St., 00-975 Warsaw, Poland

Holly J. Stein
AIRIE Program, Department of Geosciences, Colorado State University, Fort Collins, CO 80523-1482 USA
Norges Geologiske Undersøkelse, Leiv Eirikssons vei 39, 7491 Trondheim, Norway

Abstract. Molybdenites from quartz veins in a late Variscan granite from the Fore-Sudetic block in southwest Poland yield ages of 309 to 304 Ma with the Re-Os method. The ages of the molybdenites reflect post-magmatic hydrothermal activity associated with leucogranite porphyry (aplogranite) related to regional uplift and shear deformation during Westphalian time within this part of the Saxothuringian zone of the European Variscan belt.

Keywords. Molybdenite, Re-Os, Strzegom-Sobótka granites, Fore-Sudetic block, SW Poland, Bohemian Massif

1 Introduction

Re-Os dating of molybdenite has been successfully employed to date magmatic and metamorphic pulses within orogenic cycles (Bingen and Stein 2003; Requia et al. 2003). Magmatism associated with deformation and hydrothermal activity in regional scale shear zones has also been dated using molybdenite geochronology (Stein et al., in press). In northern Sweden, over 100 m.y. of Svecofennian orogenic history is recorded in molybdenite, both within magmatic and metamorphic assemblages, and low Re concentrations are attributed to molybdenite derived by local biotite breakdown (Stein, in press).

In the northeastern part of the Bohemian massif that constitutes the Saxothuringian zone of the European Variscan belt, exposed crystalline rocks in the Western Sudetes continue under the Cenozoic cover across the Sudetic Marginal fault into the Fore-Sudetic block to the Odra Fault Zone, which defines the northeastern boundary of the massif. During the Carboniferous and early Permian, a major post-orogenic episode of granitic magmatism and coeval volcanism occurred. Most of the granites in this region are generally late to post-tectonic I-type and S-type intrusions with a span of Rb-Sr ages from ~330 to 280 Ma (Pin et al. 1989; Duthou et al 1991; Oberc-Dziedzic et al. 1996; Kennan et al. 1999).

2 The Strzegom-Sobótka granitoid Massif

The Strzegom-Sobótka granites (SSG) are classified as I-type granites, based on their generally low A/CNK (commonly less than 1.1). The $^{87}Sr/^{86}Sr$ initial ratios determined for the SSG range from 0.703 to 0.707 (Kennan et al. 1999). However, for some of petrographic variants this ratio is as high as 0.708-0.709 probably due to crustal contamination (Pin et al. 1989). The Strzegom-Sobótka granites are calcic to calc-alkaline in character (Oberc-Dziedzic et al. 1999). Using the Pearce et al. (1984) classification scheme, the SSG are within the late orogenic to syn-collisional granite groups.

Numerous faults divide the SSGM into an elevated western part and downthrown middle and eastern parts. The SSGM contains three petrographic varieties (Majerowicz 1972; Maciejewski and Morawski 1975; Puziewicz 1985, 1990):

1. equigranular to porphyritic monzonite granite (Kostrza type, western SSGM),
2. equigranular biotite granodiorite (Chwalków type, central and eastern SSGM),
3. equigranular two-mica monzonite granite (eastern SSGM).

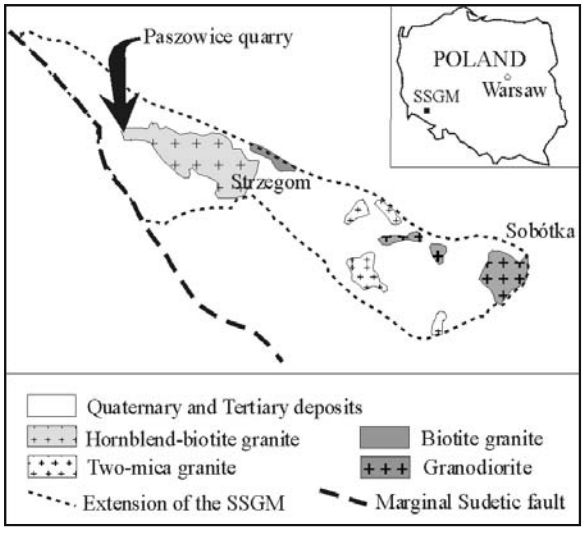

Figure 1: Location of the Mo mineralization at the Paszowice quarry in the eastern part of the Strzegom-Sobótka granitoid massif (SSGM) after Kural and Morawski (1968).

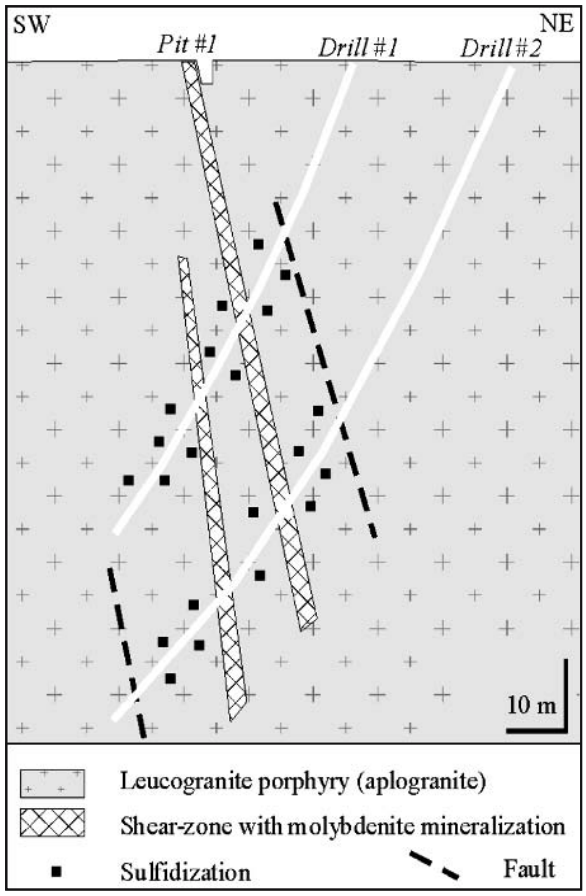

Figure 2: Geologic cross-section through zone of molybdenite mineralization in vicinities of the Paszowice quarry (Kanasiewicz and Mikulski 1989).

The granite intrusion has two phases. A younger phase is represented by Kostrza-type granite and leucogranite from the Paszowice quarry. Rb-Sr ages for two-mica granite from the SSGM provide an age of ca. 330-325 Ma (± 22 Ma), whereas some of monzogranites have a reported age of ca. 290 Ma (Pin et al. 1989). Based on Rb-Sr whole-rock isochron ages, Kennan et al. (1999) suggest that post-tectonic Carboniferous granites in the Western Sudetes, including some of the Strzegom-Sobótka massif, were emplaced over a short time interval at ~328 Ma and derived from a source with similar $^{87}Sr/^{86}Sr$ initial ratios. The present U/Pb dating of monazite and xenotime from two-mica granites of SSGM yielded ages of 309.1 ± 0.8 Ma and 306.4 ± 0.8 Ma, respectively and indicate for the younger emplacement of the two-mica granites during the late Westphalian (Turniak and Bröcker 2002). The relation of the leucogranite porphyry (aplogranite) from the Paszowice quarry to the entire SSGM is not well understood (Pendias and Walenczak 1956; Majerowicz 1972).

3 Molybdenite mineralization from the Paszowice quarry

In the NW part of the Strzegom-Sobótka granitoid massif (SSGM), numerous occurrences of molybdenite mineralization have been documented (Pendias and Walenczak 1956; Salacinski 1978). Among other localities, Mo mineralization is found in the abandoned aplogranite quarry near the Paszowice village (Fig. 1). Here, mineralization occurs in a system of gray quartz veinlets up to 2 cm thick that cut fine-grained leucogranite porphyry (aplogranite). The veins are oriented at 290-300° and dip steeply to the NE. The ore veinlets are cut by massive but barren milky quartz veinlets striking 240°. Molybdenite is a major sulfide present in veinlets forming either monomineral concentrations or may occur in paragenetic association with other sulfides (chalcopyrite, pyrite) native bismuth, or rarely with oxides such as wolframite and cassiterite (Pendias and Walenczak 1956; Salacinski 1973). The ore mineralization is accompanied by feldspathization, albitization, silicification, sericitization and chloritization. The deposit has a moderate to high temperature hydrothermal origin based on ore paragenesis (Salacinski 1978). According to fluid inclusion studies of sulfide-bearing quartz veinlets the deposit has been classified as mesothermal based on temperatures and pressures of 361-236°C and ~0.9 MPa, respectively (Ilnicki 1998). Ore-bearing quartz veinlets have also been found in three oriented prospecting holes drilled in 1957 in the surrounding area (Chilinska, *unpublished*). The average content of Mo is 0.34 wt% and of Cu 0.13 wt%. Existing data from these boreholes and from the surface geochemical prospecting led to the classification of the mineralization as Mo-Cu stockwork type (Kanasiewicz and Mikulski 1989). Two zones of quartz vein Mo-Cu mineralization are now identified, extending to 100 m below the surface (Fig. 2). They occupy shear zones oriented NW-SW and dipping 70-80° NE. The shear zones range from about 2 to 5 m in thickness.

4 Sample description for Re-Os data

Two molybdenite samples for Re-Os dating were collected from the lowest level in the central part of the quarry within the Strzegom-Sobótka granitoid massif. Molybdenite in quartz veins represents the main stage of mineralization. Euhedral molybdenite was selected from fine-crystalline gray quartz veins (up to 2 cm thick) cutting fine-grained leucogranite porphyry (aplogranite). Some crystals form rosette aggregates 3-5 mm in diameter. The length of single molybdenite flakes is usually <1 mm with a width of ~0.1 mm. Larger molybdenite crystals are curved and overgrown by chalcopyrite or pyrite, or they may contain fine-grained chalcopyrite and pyrite grains

Table 1: Re-Os data for molybdenite from quartz veins, Paszowice quarry.

Sample	Re, ppm	^{187}Os, ppb	Age, Ma
MDID-311	0.6847 (6)	2.219 (2)	309 ± 1
MDID-304	0.932 (1)	2.975 (4)	304 ± 1
MDID-315	0.5428 (1)	1.744 (3)	306 ± 1

Comments to table 1:
(1) Assumed initial ^{187}Os/^{188}Os for age calculation = 0.2 ± 0.1.
(2) Absolute uncertainties at 2σ for last digit indicated.
(3) Decay constant used for ^{187}Re is 1.666 x 10^{-11}yr^{-1} (Smoliar et al. 1996) and age calculated using ^{187}Os = ^{187}Re ($e^{\lambda t}$ – 1).
(4) Ages corrected for Re blank = 8.41 ± 0.57 pg, total Os = 1.9 ± 0.1 pg, ^{187}Os/^{188}Os = 0.3 ± 0.05 for MDID-311, 304.
(5) For MDID-315, blanks are Re = 1.33 ± 0.06 pg, total Os = 1.9 ± 0.1 pg, ^{187}Os/^{188}Os = 0.25 ± 0.001.
(6) 2σ ages include analytical and ^{187}Re decay constant error.

intergrown within molybdenite crystal cleavage, indicating an intimate temporal relationship. Albite crystals may be found within quartz veinlets, but more commonly albite together with chlorite (after biotite) is found marginal to the quartz veins.

5 Methods and results

Re-Os dating of molybdenite is described in Stein et al. (2001). We present the results of high precision Re-Os age determinations for two molybdenite samples using procedures and techniques outlined in Markey et al. (2003). A mixed double Os spike was used (^{185}Re, ^{188}Os-^{190}Os). The samples have low Re contents, all < 1 ppm, and the resulting ages range from 309 to 304 Ma. A replicate of sample #3, is provided in MDID-315. Sample weights ranged from 41 to 73 mg.

6 Discussion

Re-Os dating of molybdenites from the Paszowice quarry from the western part of the Strzegom-Sobótka granitoids massif yields ages from 309 to 304 Ma. Their markedly low Re concentrations (<1 ppm) are consistent with a derivation related to metamorphic processes (Stein, in press). The Mo mineralization clearly postdates emplacement of leucogranite porphyry (aplogranite), but is considered as either (1) related to post-magmatic processes associated with the emplacement of evolved and Mo-specialized leucogranite magma (Kanasiewicz and Mikulski 1989), or (2) related to metamorphic processes and the development of shear zones. Field relationships permit an interpretation whereby the Paszowice leucogranite and mineralized quartz veins were emplaced during shear deformation in late Variscan time. Re-Os dating of molybdenite provides an age for this deformation of about 310-305 Ma. Thus, the Mo mineralization formed during uplift of the Variscan orogen. The unidirectional NW-SE strike of the ore veinlets at the Paszowice quarry and the vein-hosted Mo zones recognized by boreholes are similar to the direction of the Marginal Sudetic fault, which was also active during the Upper Carboniferous (Zelazniewicz et al. 1997).

Mo mineralization of similar type and age (307 ± 3 Ma) has been reported from the southern margin of the Variscan orogen (Langthaler et al. 2004) and similarly, but slightly younger Re-Os ages from Sardinia are also latest Variscan (289 ± 1 Ma; Boni et al. 2003). In Sardinia, at least two ages of leucogranites are recognized, with only the younger one displaying Mo mineralization and the older (~310-300 Ma) being barren (Boni et al. 2003). The molybdenite Re-Os ages from the SSGM also coincide with a sharp increase in the rate of uplift in the Massif Central (310-305 Ma; Bouchot et al. 2000) that consitute the western part of European Variscides.

Acknowledgements

The analytical work was supported by the National Committee Scientific Research, Grant 5 T12B 001 22. Special thanks goes to Dr. S. Ilnicki for providing one of molybdenite samples.

References

Bingen B, Stein HJ (2003) Molybdenite Re-Os dating of biotite dehydration melting in the Rogaland high-temperature granulites, S Norway. Earth and Planet Scientific Letter 208: 181-195

Boni M, Stein HJ, Zimmerman A, Villa IM (2003) Re-Os age for molybdenite from SW Sardinia (Italy): A comparison with Ar/Ar dating of Variscan granitoids. In: Eliopoulos et al (eds), Mineral Exploration and Sustainable Development: pp 247-250. Millpress, Rotterdam

Bouchot V, Milesi JP Ledru P (2000) Crustal scale hydrothermal Paleofield and related Au, Sb, W orogenic deposits at 310-305 Ma (Massif Central). SGA News 10: 6-10

Duthou JL, Couturie JP Mierzejewski MP, Pin C (1991) Next dating of granite sample from the Karkonosze Mountains using Rb-Sr total rock isochrones method. Przeglad Geologiczny 39:75-79

Ilnicki S (1998) Conditions of hydrothermal alterations in aplite from Paszowice (Strzegom-Sobótka massif). Mineralogia Polonica 29: 29-42

Kanasiewicz J, Mikulski SZ (1989) On the occurrence possibility of the molybdenium deposit of Cu-Mo formation on the Strzegom granites massif. Przeglad Geologiczny 37: 129-133

Kennan PS, Dziedzic H, Lorenc MW Mierzejewski MP (1999) A review of Rb-Sr isotope patterns in the Carbo-niferous granitoids of the Sudetes in Poland. Geologia Sudetica 32: 49-53

Kural S, Morawski T (1968) Strzegom-Sobótka granitic massif. Biuletyn Instytutu Geologicznego 227: 33-85

Langthaler KJ, Raith JG, Cornell DH, Stein HJ, Melcher F (2004) Molybdenum mineralization at Alpeiner Scharte, Tyrol (Austria): results of in-situ U-Pb zircon and Re-Os molybdenite dating. Mineralogy and Petrology 82: 33-64

Maciejewski S, Morawski T (1975) Petrographic diversity of granites of the Strzegom massif. Kwartalnik Geologiczny 19: 47-65

Majerowicz A (1972) The Strzegom-Sobótka granite massif. Geologia Sudetica 6: 7-96

Markey R, Hannah JL, Morgan JW, Stein HJ (2003) A double spike for osmium analysis of highly radiogenic samples. Chemical Geology 200: 395-406

Oberc-Dziedzic T, Zelazniewicz A, Cwojdzinski S (1999) Granitoids of the Odra Fault Zone: late- to post-orogenic Variscan intrusions, SW Poland. Geologia Sudetica 32: 55-71

Pearce JA, Harris NB, Tindle AG (1984) Trace Element Discrimination Diagrams for the Tectonic Interpretation of Granitic rocks. Journal Petrology 25: 956–983

Pendias H, Walenczak Z (1956) Signs of mineralization in the NW part of Strzegom Massif. Biuletyn Instytutu Geologicznego 227: 209-228

Pin C, Puziewicz J, Duthou JL (1989) Ages and origins of a composite granitic massif in the Variscan belt: a Rb-Sr study of the Strzegom-Sobótka Massif. Neues Jahrbuch Mineralogische Abhandlungen 160: 71-82

Puziewicz J (1985) Origin of chemical, structural and textural variations in aplites from Strzegom granite (Poland). Neues Jahrbuch Mineralogische Abhandlungen 153: 19-31

Puziewicz, J., 1990. Strzegom-Sobotka granitic massif (SW Poland). Summary of recent studies. Archiwum Mineralogiczne 45: 135-154

Requia K, Stein HJ, Fontboté L, Chiaradia M (2003) Re-Os and Pb-Pb geochronology of the Archean Salobo iron oxide copper-gold deposit, Northern Brazil. Mineralium Deposita 38: 727-738

Salacinski R (1973) Ore mineralization in granite at Paszowice. Acta Geologica Polonica 23: 587-596

Salacinski R (1978) Ore mineralization and its origin in the granitoids of the Strzegom massif. Biuletyn Instytutu Geologicznego 308: 41-90

Smoliar MI, Walker RJ, Morgan JW (1996) Re-Os ages of group II1, IIIA, IVA and IVB iron meteorites. Science 271: 117-133

Stein HJ, Hannah JL, Zimmerman A, Markey R, Sarkar SC, Pal AB, in press, A 2.5 Ga porphyry Cu-Mo-Au deposit at Malanjkhand, central India: implications for Late Archean continental assembly. Precambrian Research.

Stein HJ, in press, Low-rhenium molybdenite by metamorphism: recognition, sampling, genesis, economics, and regional implications based on examples from northern Sweden. Lithos.

Stein HJ, Markey RJ, Morgan JW, Hannah JL, Scherstén A (2001) The remarkable Re-Os chronometer in molybdenite: how and why it works. Terra Nova 13: 479-486

Turniak K, Bröcker M (2002) Age of the two-mica granite from the Strzegom Massif: new data from U/Pb monazite and xenotime study. Mineralogical Society of Poland Special Papers 20: 211-213

Zelazniewicz A, Cwojdzinski S, England P, Zientara P (1997) Variscides in the Sudetes and the reworked Cadomian orogen: evidence from the GB-2A seismic reflection profiling in southwestern Poland. Geological Quarterly 41 (3): 289-308

Re-Os ages for auriferous sulfides from the gold deposits in the Kaczawa Mountains (SW Poland)

Stanislaw Z. Mikulski
Department of Economic Geology, Polish Geological Institute, 4 Rakowiecka St., 00-975 Warsaw, Poland

Richard J. Markey[1], Holly J. Stein[1, 2]
[1] *AIRIE Program, Department of Geosciences, Colorado State University, Fort Collins, CO 80523-1482 USA*
[2] *Norges Geologiske Undersøkelse, Leiv Eirikssons vei 39, 7491 Trondheim, Norway*

Abstract. A Re-Os six-point isochron age of 317 ± 17 Ma has been obtained for auriferous sulfides from sheeted quartz-veins representing the first stage of ore precipitation at the Radzimowice Au-As-Cu deposit. The age uncertainty is dominated by the fact that sulfides contain very little common Os. Extremely low Re concentrations for gold-bearing sulfides from another gold district, Klecza-Radomice, permitted dating of only one Co-arsenopyrite sample G-4 from Klecza – analyzed as a Low Level Highly Radiogenic (LLHR) sample. A precise age of 316.6 ± 0.4 Ma was obtained. Re-Os ages indicate gold mineralization in Late Namurian time associated with post-collisional extension and regional uplift in a continental arc setting. Opening of deep-seated structures, marked also by the presence of lamprophyre dykes, may have allowed for the migration of post-magmatic mineralizing fluids from various magmatic sources at about 317 Ma.

Keywords. Gold, Re-Os, low level and highly radiogenic sulfides (LLHR), Kaczawa Mountains, SW Poland, Bohemian Massif

1 Introduction

The Re-Os method has been successfully applied to molybdenite and can be similarly applied to other sulfides with much lower concentrations of Re and Os, provided the Re/Os ratio is very high. These sulfides have been named LLHR (low level highly radiogenic), as their Os isotopic composition mimics molybdenite (Stein et al. 2000). LLHR sulfides are samples whose ^{187}Os dominates the total Os. They are common in some hydrothermal environments, and may be particularly common in small crustally-derived deposits (Stein et al. 2000). The first Re-Os isotopic ages for LLHR sulfides closely associated with Au mineralization were reported from Bendigo, Australia (Arne et al. 2001). Recently, the giant Muruntau Au deposit was successfully dated using LLHR samples of arsenopyrite (Morelli et al. 2004). Analysis of samples with extremely low-level Os contents is dominated by Os contributions from procedural blanks (Markey et al. 2003). Subtraction of blank contributions in such cases may result in significant adjustments to the $^{187}Os/^{188}Os$ ratio, with a commensurate increase in the uncertainties of both the isotopic composition and the concentration of Os in the samples.

2 Geological setting

In the northwestern part of the Bohemian Massif, i.e., the Western Sudetes that constitute the eastern fragment of the Saxothuringian Zone of the European Variscides, several abandoned small and medium size gold-bearing arsenic-polymetallic deposits are found (Manecki 1965; Paulo and Salamon 1974; Mikulski 2001). Among them, there is still a high potential for exploration in vein deposits in Radzimowice and the Klecza-Radomice gold ore district (KROD) in the Kaczawa Mountains. In these deposits the major gold, silver, and arsenic production came from the sheeted quartz-sulfide veins, and vein arrays in folded flysch-like sediments deformed and metamorphosed to lower greenschist facies during Upper Devonian-Lower Carboniferous. At the Radzimowice and Klecza deposits the most important ore minerals are refractory gold-bearing Co-arsenopyrite and pyrite. This stage of mineralization underwent strong cataclasis and was later overprinted by base metal sulfides and non-refractory gold associated with quartz and carbonates. The Radzimowice auriferous ore mineralization is considered transitional between a porphyry and epithermal type around the Upper Carboniferous composite Zelezniak porphyry intrusion of subalkaline to alkaline igneous rocks formed in a post-collisional arc setting (Mikulski 2005). The genesis of gold mineralization at the Klecza-Radomice ore district was commonly assumed to be a hydrothermal type connected with Variscan Karkonosze-Jizera granites. Recently auriferous mineralization is classified as orogenic type (Mikulski 2003).

3 Sample description for Re-Os data

The auriferous sulfide samples for Re-Os dating were collected from the old mining wastes and underground workings of the *Luis* shaft in the northern part of the Radzimowice Au-As-Cu deposit and from the old mining wastes of the Klecza Northern Ore Field of the KROD. Auriferous sulfide mineralization occurs as massive or semi-massive ores in quartz veins that have been brecci-

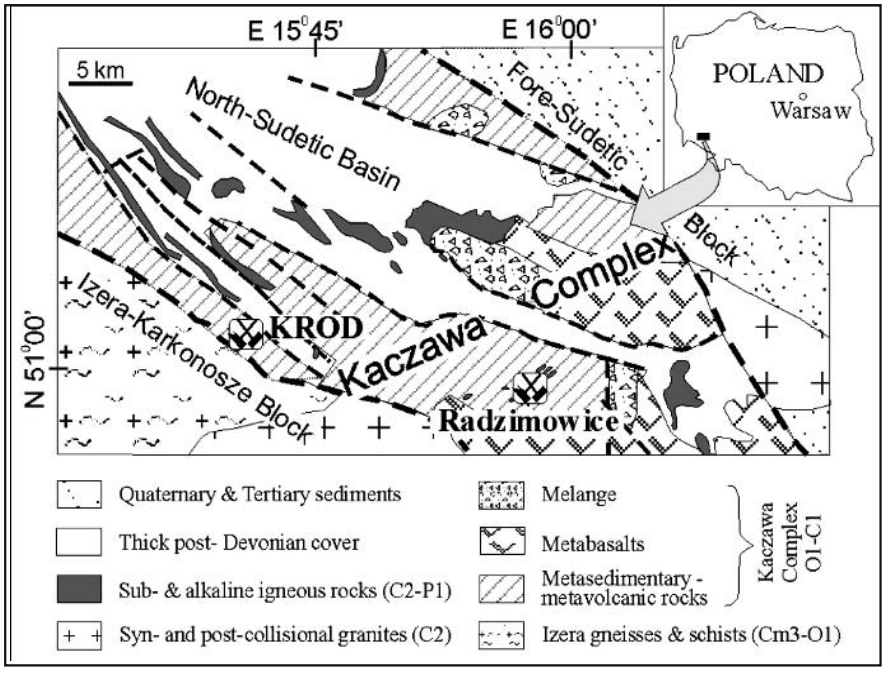

Figure 1: Simplified geologic map of the Kaczawa Mountains (part of the Western Sudetes) with location of the abandoned Radzimowice Au-As-Cu deposit and the Klecza-Radomice gold ore district (KROD).

ated and cemented by a younger generation of quartz-carbonate and base metal sulfides with non-refractory gold. For Re-Os measurements we selected medium-, and fine-grained (0.5 to 3 mm) euhedral Co-arsenopyrite, pyrite and chalcopyrite non-fractured crystals. Arsenopyrite crystals from Radzimowice display compositional variability in their As contents (34.8 to 37.4 at.%) and high admixtures of cobalt (up to 6.4 at.%) and refractory gold. Refractory gold (ca. 70 ppm) appears as sub-microscopic inclusions within Co-bearing arsenopyrite and is less abundant in pyrite. Arsenopyrite from Klecza has arsenic contents between 31.5 and 33.4 at.% and a cobalt admixture from 0.1 to 0.9 at.%.

4 Methods and results

Re and ^{187}Os concentrations in selected sulfides were determined at AIRIE, Colorado State University, using procedures and techniques outlined in Stein et al. (2000) and Markey et al. (2003). Analyses of auriferous Co-arsenopyrites from the Radzimowice Au-As-Cu deposit yield Re concentrations of 0.13-3.5 ppb with total Os in the very low ppt range (Table 1). Nearly all analyzed auriferous sulfide samples from the KROD were characterized by extremely low Re concentrations (near blank level), so age information based on those samples, with the exception of one, is not possible. Co-arsenopyrite sample G-4 from Klecza – analyzed as a LLHR sample – gave an age 316.6 ± 0.4 Ma assuming an initial $^{187}Os/^{188}Os$ ratio of 0.2 (Table 1). The LLHR arsenopyrite from Radzimowice with the highest Re content (run LL-99) yields a Re-Os model age of 317 Ma that is fairly insensitive to the assumed $^{187}Os/^{188}Os$ initial ratio ($^{187}Re/^{188}Os > 10^5$). A four-point isochron based on auriferous Co-arsenopyrites yields a Re-Os age of 314 ± 31 Ma (initial ratio = 0.8 ± 2.2, MSWD = 2.1). However, the large uncertainties for two Co-arsenopyrite analyses (LL-28, 29) resulting from extremely low Os contents, precludes a precise age. We note that there

Table 1: Re-Os concentration data for low level and LLHR auriferous sulfides from the Radzimowice and Klecza deposits. Refer to Figure 2 for isotopic composition data.

AIRIE Run No; Sample	Re, ppb (± 2σ)	Os, ppb (± 2σ)	Model Age, Ma[1]
Samples from Radzimowice deposit			
LL-28; Co-asp[2]	0.129 (2)	0.0013 (1)	ca. 323
LL-29; Co-asp[2]	0.3448 (4)	0.0019 (1)	ca. 327
LL-30; Co-asp[2]	0.357 (6)	0.0028 (2)	ca. 384
LL-97; cp[3]	0.0072 (4)	0.00022 (2)	ca. 411
LL-98; py[3]	0.0253 (7)	0.0048 (2)	ca. 294
LL-99; Co-asp[3]	3.51 (9)	0.01327 (6)	317
Sample from Klecza deposit			
MDID-350; G-4 Co-asp[(1,3,4)]	310.0 (2)	1.030 (1)	316.6± 0.4

Abbreviations: asp = arsenopyrite; cp = chalcopyrite; py = pyrite
Notes:
(1) Assuming an initial $^{187}Os/^{188}Os$ ratio of 0.2.
(2) Analytical blanks: Re = 1.97 (2) pg, Os = 4.68 (5) pg with $^{187}Os/^{188}Os = 0.182$ (4).
(3) Analytical blanks: Re = 2.5 (1) pg, Os = 0.635 (6) pg with $^{187}Os/^{188}Os = 0.190$ (8).
(4) LLHR (i.e. Os is almost entirely radiogenic ^{187}Os).

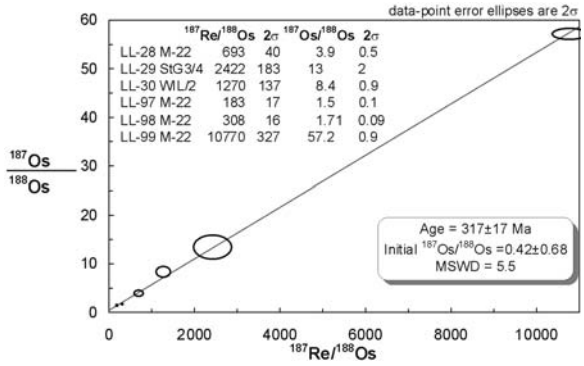

Figure 2: Six-point isochron for auriferous sulfides from the Radzimowice Au-As-Cu deposit.

is general agreement between model ages for these samples when an Os initial ratio of 0.2 is used. We support our arsenopyrite analyses by additional analyses of a pyrite and chalcopyrite sample from the Radzimowice deposit. These sulfides also contained low to very low ppt level Re and Os (Table 1). Collectively, all sulfide analyses from Radzimowice provide a six-point isochron with a Re-Os age of 317 ± 17 Ma (Fig. 2). The six-point isochron has a reduced uncertainty compared to the four-point isochron based only on Co-arsenopyrite samples. The still relatively large uncertainty is due to the very low Os concentrations of most of the samples (<5 ppt total Os in all cases but one). Within uncertainty, the Re-Os isochron age overlaps with a much more precise model age of 316.6 ± 0.4 Ma for Co-arsenopyrite sample G-4 (run MDID-350) from the Klecza deposit.

5 Discussion

According to $^{40}Ar/^{39}Ar$ data presented by Marheine et al. (2002), in the Western Sudetes, host rock schists of Ordovician-Lower Carboniferous represent shaly flysch-type sediments that were recrystallized during regional uplift-related greenschist metamorphism in the Viséan at 344-333 Ma and the upper limit of the Variscan tectonometamorphic and magmatic activity was dated at 314-312 Ma (Namurian / Westphalian boundary). Re-Os data suggest that refractory gold- sulfide mineralization in the Kaczawa Mountains postdates regional metamorphism of host rocks and orogenic deformation. Refractory gold mineralization is related to Late-Namurian tectonometamorphic and magmatic processes. At the Radzimowice Au-As-Cu deposit, the schist unit was intruded by the Zelezniak Intrusion (ZI) (Mikulski 2005). Gold-bearing sulfide veins cut dacite porphyries and postdate lamprophyre dykes, but are spatially associated with the dykes. SHRIMP ages for zircons from the fine-grained rhyolite are similar to zircon ages from the medium-grained microgranites of ZI, and indicate that the main magmatic event was restricted to the Late Namurian (weighted mean $^{206}Pb/^{238}U$ at 316.7 ± 1.2 Ma; Muszynski et al. 2002). The Re-Os age of ca. 317 Ma for arsenopyrite sample LL-99 in the context of SHRIMP ages from ZI support an association between post-orogenic felsic magmatism and auriferous Co-arsenopyrite mineralization. This is further supported by the six point 317 ± 17 Ma Re-Os isochron age. The spatial association of quartz-sulfide veins with lamprophyre dykes implicates them in the ore-forming process, and suggests they are also of similar age. Genesis of the gold mineralization in Klecza, like other Au deposits and occurrences in the KROD, is suggested to be of orogenic type (Mikulski 2003). The KROD deposit is located in the Intra Sudetic Fault zone that separates two different terranes (Aleksandrowski et al. 1997). At KROD there is no evidence for a direct magmatic origin for hydrothermal fluids responsible for the gold mineralization, despite the widely held belief that mineralization is related to the Karkonosze-Jizera granites located ca. 10 km to the south. Re-Os data for auriferous Co-arsenopyrite from Klecza (316.6 ± 0.4 Ma), the first stage of refractory gold mineralization, may be slightly younger than the porphyritic granites of the Karkonosze-Jzera pluton dated at 325-330 Ma by the Rb-Sr method (Duthou et al. 1991) or date at 320 ± 2 Ma by $^{40}Ar/^{39}Ar$ on biotite (Marheine et al. 2002). Au mineralization is most likely associated with lamprophyre dykes dated at 314 ± 6 Ma $^{40}Ar/^{39}Ar$ (Marheine et al. 2002) or with aplitic granites date at 310 ± 5 Ma by Rb-Sr (Duthou et al. 1991).

Summarizing, our Re-Os results indicate that one of the major Late Namurian post-orogenic extension episodes and regional uplift in the Kaczawa Mountains took place ca. 317 Ma. Deep-seated structures allowed mineralizing fluids, mostly likely associated with magmatic sources, to migrate upwards, forming auriferous sulfide mineralization. The age of auriferous mineralization (ca. 317 Ma) recognized in the Kaczawa Mountains is not coeval with gold events described from the Central Bohemian province (ca. 338 Ma; Bouchot et al. 2001; or at 344 ± 2.8 Ma by Re-Os method on molybdenite by Zachariáš et al. 2001) and Massif Central (310-305 Ma; Bouchot et al. 2000).

Acknowledgements

The analytical work was supported by NCSR, Grant no. 5 T12B 001 22.

References

Aleksandrowski P, Kryza R, Mazur S, Zaba J (1997) Kinematics data on major Variscan strike-slip faults and shear zones in Sudetes. Geol Magazine 134: 727-739

Arne DC, Bierlein FP, Morgan JW, Stein HJ (2001) Re-Os dating of sulfides associated with gold mineralization in Victoria, Australia. Economic Geology 96: 1455-1459

Bouchot V, Faure M, Feybesse JL, Correira P, Zachariáš J (2001) Variscan orogenic Au district related to a regional Visean detachment in the Central Bohemian province. In: Eliopoulos et al (eds) Mineral Exploration and Sustainable Development. Millpress, pp 747-750

Bouchot V, Milesi JP Ledru P (2000) Crustal scale hydro-thermal Palaeofield and related Au, Sb, W orogenic deposits at 310-305 Ma (Massif Central). SGA News 10: 6-10

Duthou JL, Couturie JP, Mierzejewski MP, Pin C (1991) Rb/Sr whole rock samples isochrones method of the age determination of the Karkonosze granite (in Polish). Przeglad Geologiczny 32: 75-79

Manecki A (1965) Petrographic-mineralogical studies of the polymetallic veins from Wojcieszow vicinities (Lower Silesia). Prace Mineralogiczne PAN, 47 (2): pp 65

Marheine D, Kachlik V, Maluski H, Patocka F, Zelazniewicz A (2002) The $^{40}Ar/^{39}Ar$ ages from the West Sudetes (NE Bohemian Massif): constraints on the Variscan polyphase tectonothermal development. In: Winchester JA, Pharaoh TC, Verniers J (eds) Palaeozoic Amalgamation of Central Europe. Geological Society of London Special Publication 201: 133-155

Markey R, Hannah JL, Morgan JW, Stein HJ (2003) A double spike for osmium analysis of highly radiogenic samples. Chemical Geology 200: 395-406

Mikulski SZ (2001) Late-Hercynian gold-bearing arsenic-polymetallic mineralization in Saxothuringian zone in the Polish Sudetes, NE Bohemian Massif. In: Piestrzynski et al (eds), Mineral Deposits at the Beginning of the 21st century. Balkema, pp 787-790

Mikulski SZ (2003) Orogenic quartz-sulfide-gold veins from the Klecza-Radomice ore district in the Kaczawa Mountains (Western Sudetes) – NE part of Bohemian Massif. In: Eliopoulos et al (eds), Mineral Exploration and Sustainable Development, Millpress, pp 787-790

Mikulski SZ (2005) Geological, mineralogical and geochemical characteristics of the Radzimowice Au-As-Cu deposit from the Kaczawa Mts. (Western Sudetes, Poland) - an example of the transition of porphyry and epithermal style. Mineralium Deposita 39: 904-920

Morelli, R, Creaser, RA, Seltmann, R (2004) The age of gold mineralization at the Muruntau Au deposit, Uzbekistan, from Re-Os arsenopyrite geochronology. Geological Society America Abstracts with Programs 36 (5): 444

Muszynski A, Machowiak K, Kryza R, Armstrong R (2002) SHRIMP U-Pb zircon geochronology of the Zelezniak rhyolite intrusion, Sudetes – preliminary results. Mineral Society of Poland – Special Papers 19: 156-158

Paulo A, Salamon W (1974) Contribution to the knowledge of the Stara Gora deposit. Kwartalnik Geol 18: 266-276

Stein HJ, Morgan JW, Scheresten A (2000) Re-Os of low level highly radiogenic (LLHR) sulfides: The Harnas gold deposit, southwest Sweden, records continental-scale tectonic events. Economic Geology 95: 1657-1671

Zachariáš J, Pertold Z, Pudilová M, Zák K, Pertoldová J, Stein H, Markey R (2001) Geology and genesis of Variscan porphyry-style gold mineralization, Petráčkova hora deposit, Bohemian Massif, Czech Republic. Mineralium Deposita 36: 517-541

Dating of gold occurrences in the Sayan-Baikal Fold Belt, Southern Siberia, Russia

A.G. Mironov
Geological Institute of SB RAS, Sakhyanova 6a, Ulan-Ude, 670047, Russia

H. Stein, A. Zimmerman
AIRIE Program, Department of Geosciences, Colorado State University, Fort Collins, CO 80512-1482 USA

S.M. Zhmodik
Institute of Geology UIGGM SB RAS, Koptyuga 3, Novosibirsk, 630090, Russia

Abstract. The complex geologic history of the Tain gold-porphyry deposit in the Sayan-Baikal Fold Belt (South Siberia) makes direct age determinations problematic. Timing of porphyry gold mineralization, magmatism, and hydrothermal alteration are constrained to an interval of 670-280 Ma based on dating of the host granodiorites, altered rocks, and ores by the Rb-Sr, Ar-Ar, and Re-Os techniques, respectively.

Keywords. Sayan-Baikal Fold Belt, gold-porphyry deposit, dating, Ar-Ar, Rb-Sr, Re-Os techniques

1 Introduction

The gold-bearing Sayan-Baikal Fold Belt is known for its important ore reserves. Both quartz lode deposits (Pioneer, Granite, Dynamite, Irokinda, etc.) and gold-sulfide polymetallic deposits, along with sub-economic ore occurrences (Zun-Kholba, Zun-Ospin, etc.), are located in the Belt (Mironov and Zhmodik 1999). Only recently, new types of gold mineralization such as those at Tain, Konevinskoye, and Kharalginskoye have been discovered. The Tain deposit is of particular significance as it appears genetically different from previously studied deposits in the region and has unique geolocial features.

The Tain gold deposit lies in the central Ospin-Kitoi massif of ultrabasic rocks comprising the ophiolitic Ilchir plate. Regionally, the Gargan Craton consists of Archean-Proterozoic volcanogenic-sedimentary strata, ophiolite sequences of the Neo-Proterozoic age, and granitoids of the Sumsunur (PZ_{1-2}) and Samsal (PZ_{2-3}) sequences. The Ospin-Kitoi ultrabasic massif is defined by the convergence of ophiolite outcrops from north to south in the eastern Gargan Craton. The massif is suggested to be a single unit later dissected by erosion associated with uplift of the Gargan Craton and preserved along its periphery (Belichenko et al. 1988).

2 Gold deposit description

The Tain deposit is localized in 300 m by 700 m granodiorites and plagiogranites stocks that crosscut local serpentinites and serpentinized harzburgites (Fig. 1). The massif hosting gold mineralization is shaped like two attached lenses. The inner massif is composed of the grey mid- to fine-grained diorites and quartz diorites (granodiorites) that are variably altered and deformed. The marginal areas of the massif are variably enriched in yet to identified carbonaceous matter. The carbonaceous matter is commonly encountered as fine dust in quartz, along zone planes, or as dust-like spotted disseminations in plagioclase. The carbonaceous matter is also observed in the cross-cutting microfractures, occasionally associated with epidote-clinozoisite. The granulated aggregates of albite replacing calcic plagioclase are also pigmented by dust-like carbonaceous matter (Mironov et al. 2001).

The beresitized rocks and beresites (mineral association of quartz, sericite, pyrite, and calcite) are the dominant rock type in the massif. They are greenish-grey fine- and medium-grained rocks composed of sericitized plagioclase, quartz, sericite, calcite, chlorite, sulfides (pyrrhotite predominates), leucoxene, apatite, and zircon. Quartz is characterized by two varieties, i.e., pressed, fractured grains (quartz 1) and almost undeformed aggregates (quartz 2). Sulfides are represented by impregnations (0.1-1.5mm) of pyrrhotite. Pyrite is associated with quartz 2, iron hydroxides, and calcite or chlorite. The low SiO_2 concentrations, higher concentrations of MgO and CaO and dominantly more Na_2O than K_2O are characteristic of beresitized rocks.

In the southern part of the massif, accompanying and hosting gold mineralization are medium to dark grey, variably grain-sized, porphyritic plagiogranites. They have an irregularly grained texture of quartz and plagioclase aggregates 0.2-5mm in size and porphyry-like quartz impregnations with traces of deformational cataclasite. Muscovite is developed along fractures in plagioclase and locally intense alteration results in completely replaced plagioclase. Calcite (up to 1-2 wt.%), sulfides (to 3-5 wt.%), sericite, biotite, sphene, rutile, apatite, and carbonaceous matter (0.1-0.5 wt.%). The carbonaceous matter gives the dark grey colour to the rock and is best developed on altered plagioclase, infilling of microfractures in quartz grains, and along fractures intersecting mineral aggregates.

This page intentionally blank

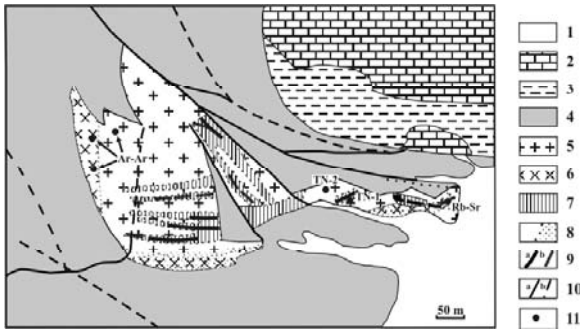

Figure 1: Map of the Tain gold-porphyry deposit geological structure and points of sampling for dating. (1) Quaternary deposits; (2) limestones of the Ilchir suite; (3) blackschists of the Ilchir suite; (4) serpentinites and harzburgites; (5) granodiorites and plagiogranites of the Tain massif; (6) diorites; (7) zones of beresitization and veinlet-impregnated mineralization; (8) carbonatization; (9) quartz veins (a) and quartz sulfide veins (b); (10) tectonic faults: established (a) and suggested (b) ones; (11) points of sampling for dating.

Geochemically all the varieties of the stock granitoids have low Th and U concentrations, moderate Ba and Sr concentrations with Sr prevailing in the unaltered or weakly altered rocks, and sharp increase of Ba concentrations in muscovitized and dyke formations. The precious metal contents significantly vary, reaching maximum in the muscovitized and carbonatized rocks.

Three types of orebodies: (1) quartz-veined low sulfide bodies, (2) quartz-muscovite-pyrrhotite ores and (3) veinlet-impregnated ores are identified at the Tain deposit.

Quartz veined low sulfide bodies occur as 0.3 to 1.5 m thick bodies observable for 230 m along strike. The quartz veins are characterized by the carbonaceous matter-induced dark gray color and intensive boudinage structures with a clear tectonic orientation. Quartz grains within the boudins elongate by unidirectional fracturing and dislocation with equigranular grains showing pressure-induced dissolution-reprecipitation. In some locations brittle deformation is seen as cataclasis and brecciation of host granitoids.. Muscovite, chlorite, biotite, amphibole and iron hydroxides (1-3 wt.%) are locally developed in microfractures.

The major ore minerals (0.1-10 wt.%) occur as nest-like features (1-8cm across) of pyrite, pyrrhotite, galena, sphalerite and chalcopyrite. These minerals also occur as fine impregnations. Rare ore minerals hessite, wehrlite, argentite, native gold and silver are associated with net-like features as well.

Quartz-muscovite-pyrrhotite ores are differientiated by high sulfide contents, mainly pyrrhotite, comprising up to 70% of the total rock, hosted in light grey and white quartz muscovite granitoids. The vein-like bodies are up to 0.6 m thick in the quarry walls, hardly accessible, and dominantly studied from rockfall in talus piles.

In contrast to the quartz veins, this type of ore is characterized by lighter colored quartz without carbonaceous matter, high precious metal contents between 150 to 200 ppm Au and 300 to 450 ppm Ag, and a peculiar paragenesis of gold and sulfide minerals. Hexagonal pyrrhotite is the dominant sulfide mineral comprising 95-98 vol.% of ore minerals. Chalcopyrite (0.1-3 vol.%) occurs as thread veinlets and impregnations at the contact between massive pyrrhotite ores and quartz-muscovite aggregates. Pyrite, cobaltite, sphalerite, galena, kustelite, and native gold occur in subordinate amounts. Cobaltite (CoAsS) is always seen as impregnations of small (0.01-0.09mm) crystals in pyrrhotite. The important peculiarity of this ore type is the partitioning of Au and Ag into kustelite rather than other Au and Ag minerals. Kustelite forms isometric grains 0.01-0.06mm in size that localize at the contact of pyrrhotite with chalcopyrite and quartz.

Ores of veined-impregnated type are found within the dark grey carbonatized, muscovitized and cataclased porphyry-like plagiogranites. The ore consists of quartz veinlets 0.5-3 cm thick and a few meters long with impregnations (0.1-5 mm) of pyrrhotite and chalcopyrite (0.5-5 vol.%) and noticably subordinate pyrite, sphalerite and galena. The plagiogranite host rocks are five to thirty meters thick and 100's of meters long zones made of quartz-sericite-muscotite rocks with variable amounts of calcite, sulfides, and carbonaceous matter. Mineralogical analysis of this ore type identify native gold, silver, argentite, and Ag-bearing bornite. Gold is present as two distinctly different morphologies. The first is represented by middle and large native gold particles (0.1-0.3 mm and 0.7-1.0 mm, respectively) of bright yellow color and cloddy-laminar shape with high purity (915-965). The second variety is composed by small and middle (0.01-0.3 mm) gold particles of low purity (429-323) and kustelite.

Molybdenite is found as flakes and little nests in both dark grey quartz and beresite ores. In the veinlets of dark grey quartz, molybdenite is found together with gold and, in beresite ore, it is found as "dry" veinlets along fractures.

The Tain gold deposit has a number of features that are atypical of East Sayan hydrothermal deposits. The veinlet-impregnated type of ore mineralization in porphyry-like granitoids are dominant here unlike the Pioneer, Barun-Kholba, Granite, and other lode deposits. The presence of carbonaceous material, predominance of pyrrhotite among sulfides, that of kustelite among gold minerals, and of methane in the gas phase are peculular as well. In our view, it is interpreted that the Tain deposit formed in different conditions and due to the magmatism of another type.

The granitoids of the Tain stock belong to the granitoids of the island arc type based on geochemical data. Although variable in absolute composition, the stocks generally corresponds to the island arc granites according to the main indices (for example, Nb-Y, Rb-(Nb+Y) ratios) in discrimination plots. Predominance of Sr and Ba and low contents of U and Th are typical of unaltered varieties. Ba, Cu, and Zn concentrations increase in the beresitized and carbonatized granodiorites and granites. The maximum contents of Ba (1100-1600 ppm) have been found in the carbonatized dykes of granite-porphyries. Co and Ni predominance as well as low concentrations of U (1.3-3.2 ppm) and Th (0.4-3.9 ppm) are also characteristic of the granite porphyries. Analyzed rare earth elements form a trend similar to the REE trend of granitiods from the Amur-Alyaska island arc system. Some decrease of their contents is observed in ores at their enrichment in quartz and pyrrhotite.

The massif rocks are intensly tectonized by subhorizonal faulting. Small, spotted occurences of plagiogranites, diorites and dacite-porphyries are known in other areas of the ophiolite cover (Ekhe-Shigns, Borto-Gol rivers, etc.). All this testifies to the fact that the Tain stock granitoids and analogous rocks formed in the island arc stage suffered deformation during the subsequent collision and obduction. In contrast, the granitoids of the Sumsunur and other younger sequences (PZ_{2-3}) are clearly syn- and postcollisional.

3 Dating results

The study of absolute age in rocks and ores of the Tain deposit shows significant variations in obtained data. A Rb-Sr isochron indicates 670±19 Ma and 87Sr/86Sr =0.7120±0.0010 on the altered porphyry-like granites and muscovite. Two Ar-Ar ages of 435±9 Ma (samples Тн–330 and Тн–331) and 280±4.1 Ma (Тн–329) were obtained from amphiboles taken from the Tain massif diorite. Those ages are likely to indicate the later metamorphism and hydrothermal alteration of rocks.

The question arises which process is associated with and/or reponsible for gold mineralization. The answer may be obtained from Re-Os data on molybdenite associated with gold mineralization. A sample of molybdenite as a rosette-like inclusion in a veinlet (6mm thick) of dark grey quartz (TN-1) and a sample of molybdenite from a “dry” veinlet (molybdenite powdery coating on the fracture surface 0.5-1.5mm thick) (sample TN-2) were selected.

TN-1 was taken from a single molybdenite bleb in an 0.8 cm vein of dark gray quartz, of the variety associated with Au mineralization. Although the rock is quite weathered and Fe stained, the vein and molybdenite are moderately fresh. The rock appears to be a fine-grained granitoid that is highly altered, including silicification and a vuggy nature due to leaching of mm scale feldspar. This molybdenite-bearing vein yielded a Re-Os age of about 550 Ma, but additional molybdenite separates will be taken and dated to confirm this result.

TN-2 is also a fine-grained granitoid with mm scale euhedral crystals of feldspar with diffuse margins due to silicification. The rock is also sericitized. Fe-oxide staining is locally prevalent. Molybdenite occurs in abundance along a surface that appears to be the margin of an irregular, not planar, vein. The Re-Os age is about 860 Ma, but additional mineral separates are necessary to affirm geologic accuracy of this somewhat weathered occurrence.

Thus, the gold mineralization in the massif has the age that is close to the island arc and island arc type granitoid formation (800-600 Ma). The Tain gold deposit contains the mineralization formed by reducing fluids and has obvious features typical of gold porphyry deposits. Its specific features are caused by granitoid emplacement in an area of ultrabasites and black shales that are enriched in carbonaceous matter of both biogenic and mantle nature. It is likely the earliest gold mineralization in the region in the massif of island arc granitoids that were subsequently subjected to obduction within the ophiolite cover and accompaning turbidite and craton terranes (Bogatikov and Tsvetkov 1988).

Acknowledgements

The work has been carried out with the grant support of the leading research schools No -2208.2003.5 and RFBR grant 03-05-65162.

References

Belichenko VG, Butov YuP, Dobretsov NL (1988) Geology and metamorphism of the East Sayan. Novosibirsk, Nauka.

Bogatikov OA, Tsvetkov AA (1988) Magmatic evolution of island arcs. Moscow, Nauka.

Mironov AG, Zhmodik SM (1999) Gold deposits of the Urik-Kitoi metallogenic zone (East Sayan, Russia). Geology of ore deposits. V. 41, N1, 54-69

Mironov AG, Zhmodik SM, Ochirov YuCh, Borovikov AA, Popov VD (2001) The Tain gold deposit (East Sayan, Russia) is rare type of gold-porphyry formation. Geology of ore deposits. N5, 395–413

Jurassic magmatism and Au-Ag mineralization in the Deseado Massif (Patagonia Argentina): Lead and sulfur isotopic studies

P. Moreira, R.R. Fernández, I.A. Schalamuk, R.O. Etcheverry
Instituto de Recursos Minerales (INREMI), Universidad Nacional de La Plata, CICBA, Argentina

A.P. Rolando
Pará-Iso Laboratory, Instituto de Geociencias, Universidade Federal do Pará, Belém, Brazil

Abstract. Lead isotope analyses of volcanic rocks and hydrothermal minerals and sulfide isotope analyses of sulfurs from Au-Ag La Josefina prospect (Deseado Massif geological province, Argentina) are reported. Lead isotope ratios for sphalerite and pyrite have mean values of 18.48, 15.69 and 38.61 for $^{206}Pb/^{204}Pb$, $^{207}Pb/^{204}Pb$ and $^{208}Pb/^{204}Pb$, respectively, and are similar to Pb isotope ratios for the Jurassic volcanic rocks of Bajo Pobre and Chon Aike Formations. $\delta^{34}S$ ‰ values of sphalerite, pyrite and galena cluster between 1.3 and 3.8 ‰, suggesting that the sulfur at La Josefina was primarily of magmatic origin. These results are interpreted to indicate that the Jurassic volcanic rocks are closely related with low sulfidation Au-Ag occurrences.

Keywords. Pb isotopes, S isotopes, epithermal deposits, Jurassic volcanism, Patagonia Argentina

1 Introduction

The Deseado Massif (DM) is located in the southern Argentinean Patagonia (Fig. 1). In this region, the most important unit is a volcanic complex of upper to middle Jurassic age with bimodal features marked by andesitic and rhyolitic magmas that conform the Bajo Pobre and Chon Aike Formations, respectively. These units crop out over more than half the area of a wide plateau. The geochemical analyses of the Jurassic volcanism show a calc-alkaline magmatism with a volcanic arc affinity.

These volcanic rocks are related to the early history of the Gondwana break-up and were deposited in the back-arc Patagonian Andes during a long period (187 to 144 My) of extension (Riley et al. 2000). The geotectonic environment of Patagonia in the Jurassic times was characterized by very slow subduction in the Pacific margin of Gondwana (Ramos 1988). Pankhurst et al. (2000) support the idea that the volcanic rocks were probably generated by a variety of mechanism, among which the melting of pre-existing continental crust was a dominant process.

These volcanic rocks host the Au-Ag veins of Cerro Vanguardia, the principal ore deposit currently in production, and also host the Ag-ore shoot worked in the Marta Mine, as well as some other important prospects like Manantial Espejo, Huevos Verdes-Cerro Saavedra-El Pluma, El Dorado-Monserrat, Cerro Negro and La Josefina. Most of these prospects (Schalamuk et al. 1997) correspond to the low sulfidation epithermal type of deposits. The last prospect, currently under exploration, is located in the central part of the DM and the mineralization is represented by Au-Ag bearing vein systems (up to 300 g Au/t).

The objective of this paper is to present the lead and sulfur isotopic data from samples of hydrothermal sulfides and volcanic rocks obtained at the La Josefina prospect.

There are few isotopic studies of the DM, only two lead isotope data for the Jurassic volcanic rocks are indicated by Kay and Gorring (1999) and five lead isotope measurements on galena from several ore deposits of the DM were showed by Schalamuk et al. (1997). Theses analyses show isotopic values between 18.48-18.72, 15.73-15.95 and 38.70-39.53 for $^{206}Pb/^{204}Pb$, $^{207}Pb/^{204}Pb$ and $^{208}Pb/^{204}Pb$, respectively.

Isotope sulfur ratios carried out in samples from Au-Ag epitermal prospects (Cerro Vanguardia, Manantial Espejo, El Dorado-Monserrat and Cerro León) in the DM, were reported by Echavarría (1997), Schalamuk et al. (1998) and Jovic et al. (2004). The $\delta^{34}S$ values range between –2.8 and 4.2 ‰, indicating a magmatic source for the sulfur.

2 La Josefina geology

The La Josefina prospect (Fig. 1) includes lower Paleozoic low grade metamorphic muscovitic schists, metavolcanic and calk-silicate rocks with minor magnetitic levels and tourmalinites of La Modesta Formation (Moreira et al. 2005).

The Bajo Pobre and Chon Aike Formations represent the Jurassic volcanic rocks. The Bajo Pobre Formation, mainly andesitic-dacitic rocks, include porphyritic and aphanitic flows partially self-brecciated, porphyries, sills that intrude the low angle dip schist of the La Modesta Formation, and ring-dikes surrounding rhyolitic domes. The Chon Aike Formation cover approximately a 60 % of the area. The lower member outcrop on the west part, and consists of crystal-rich quartz-feldspar-biotite welded ignimbrite with some flatten pumice-rich levels that was dated at 153.2 ±3.6 My (K/Ar on biotite; Arribas et al.

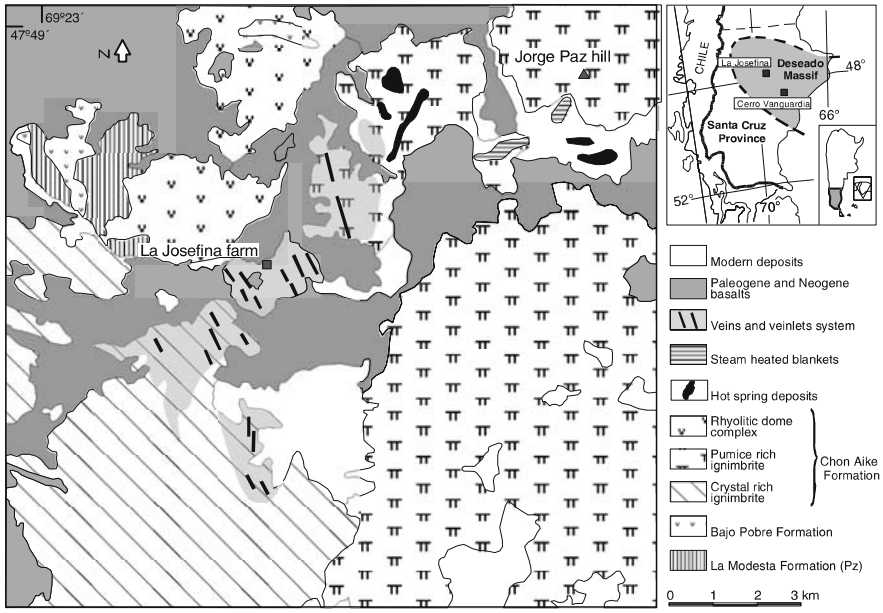

Figure 1: Geology and location of La Josefina prospect.

1996). On the eastern part dominate a welded pumice-rich, crystal-poor welded ignimbrite whose lower levels carrying 5-20 cm crystal-rich-ignimbrite lithic fragments, whereas in the upper levels these lithics are smaller and sporadic. A rhyolitic dome-complex outcrops on 10 km^2 in the north-northwest of the area and some smaller rhyolitic domes extend to the northwest, both with slowly propylitic, pyritic and argillic patch of hydrothermal alteration. These domes intruded the Paleozoic metamorphic rocks (La Modesta Formation).

Paleogene and neogene basaltic flows cover the Jurassic volcanic rocks.

3 La Josefina Au-Ag epithermal ocurrences

The mineralization at the La Josefina prospect consists of system of low sulphidation epithermal veins and veinlets filled mainly by quartz and chalcedony with minor adularia, barite and platy calcite. The primary assemblages are composed by native gold, electrum, specularite and pyrite, arsenopyrite, galena with freibergite inclusions, sphalerite, chalcopyrite and bornite and a supergenic association consist in limonites, chalcocite-covelite, cerusite-anglesite and malachite.

These occurrences are distributed in a curved belt about N-S 12 km long and between 500 and 1200 m wide. The age of the mineralization is not well constrained; a Rb-Sr errorchron gave an age of 156 ± 2 My (Fernández et al. 1999). The veins are spatially associated with superficial epithermal occurrences, like hydrothermal eruption breccias, silica sinter terraces, geyserites, carbonate stromatolitic deposits, and steam heated blankets, mainly to the north of the prospect.

4 Samples and results

4.1 Samples

The samples collected for the lead isotopic study of the La Josefina prospect consisted in intermediate-acid Jurassic volcanic rock from Bajo Pobre and Chon Aike Formation (feldspar separates) and hydrothermal minerals from veins (pyrite and sphalerite). The isotopic Pb composition were determinate on 13 samples in the Pará-Iso Laboratory, Instituto de Geociencias, Universidade Federal do Pará, Belém, Brazil.

Seven sulfide paragenetic samples, including separates of pyrite (3), sphalerite (3), and galena (1), were analyzed for their sulfur isotope composition. Analyses were carried out at the Stable Isotopic Service from Salamanca University (Spain). The results are given as $\delta^{34}S$ ‰ values relative to the CDT standard.

4.2 Results

The analyses of Pb in samples from La Josefina prospect are summarized in the Table 1 and plotted in the Zartman and Doe (1981) diagrams (Fig. 2).

The volcanic Jurassic samples have an average ratios of $^{206}Pb/^{204}Pb$= 18.44, $^{207}Pb/^{204}Pb$= 15.65 and $^{208}Pb/^{204}Pb$= 38.50 and the elongate trends in the general cluster indicate mainly an orogenic model fit, suggesting variable mixing of lead from different sources, mainly model upper crust and to a lesser extent model mantle and lower crust reservoirs.

The Pb isotopic compositions of pyrite and sphalerite from La Josefina are near $^{206}Pb/^{204}Pb$= 18.48, $^{207}Pb/^{204}Pb$=

Table 1: Lead isotope composition of volcanic rocks and sulfides from La Josefina.

	Sample	$^{206}Pb/^{204}Pb$	$^{207}Pb/^{204}Pb$	$^{208}Pb/^{204}Pb$
Chon Aike Fm	2728	18.543	15.712	38.722
	2719	18.475	15.659	38.563
	2762	18.307	15.59	38.29
	2862	18.494	15.67	38.558
	2800	18.48	15.656	38.566
	2705	18.515	15.653	38.573
Bajo Pobre Fm	10bp	18.424	15.64	38.475
	2733	18.391	15.626	38.405
	2760	18.424	15.64	38.475
	2795	18.397	15.621	38.414
py	1678	18.496	15.68	38.611
	1693	18.416	15.633	38.46
sph	1681	18.541	15.762	38.769

Table 2: $\delta^{34}S$ ‰ values of La Josefina Au-Ag occurrence

Sample	Mineral	$d^{34}S_{CDT}‰$	Yield %
1678	py	3.1	64.9
1677	py	3.8	81
1725	py	2.7	69.8
1681	sph	13.1	92.7
1687	sph	2.1	82.8
1687 bis	sph	2	84.7
1699	ga	1.3	90.2

15.69 and $^{208}Pb/^{204}Pb$= 38.61. The lead isotope composition of these sulfides are in general slightly more radiogenic than the volcanic host rocks.

The analyses of $\delta^{34}S$ ‰ are summarized in the Table 2. Sulfur samples in La Josefina show $\delta^{34}S_{mineral}$ values between 1.3 and 3.8 ‰. The $\delta^{34}S$ high value for sphalerite (13.1 ‰) demonstrate an overall increase. This could be explained by changes of the hydrothermal fluid pH produced by the interaction with the volcanic rocks.

5 Conclusions

The $\delta^{34}S$ values of pyrite, sphalerite and galena indicate that their sulfur was derived from a magmatic sulfur source with scarce supergene activity. Pb isotope ratios of pyrite and sphalerite, are most similar to those of the volcanic rocks and suggest that they are the likely source.

The correspondence of both sets of values with the orogenic growth curve of Zartman and Doe (1981) suggests further that varied sources contributed to the lead of the magma.

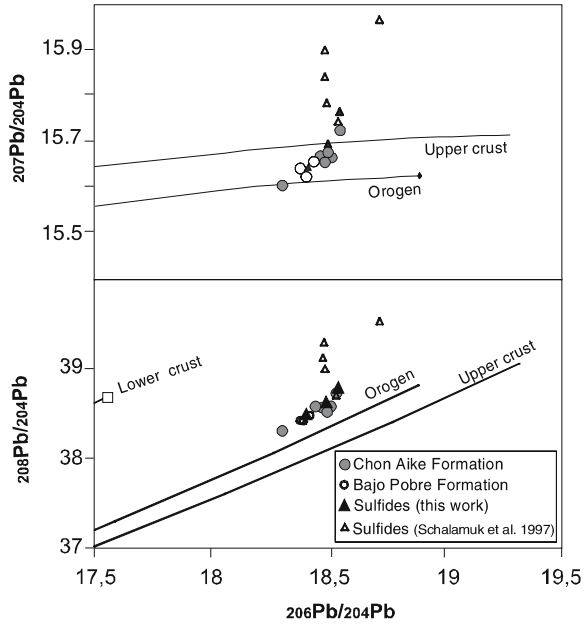

Figure 2: Detailed $^{206}Pb/^{204}Pb$ versus $^{207}Pb/^{204}Pb$ and $^{208}Pb/^{204}Pb$ versus $^{206}Pb/^{204}Pb$ plots of lead isotopes from La Josefina samples.

Lead isotopes obtained from galena samples by Schalamuk et al. (1997) although have slightly higher values, do not show significant differences from the samples studied here. The $\delta^{34}S$ results in La Josefina are similar to those in several ore deposits in the DM.

Based on these features, there is a genetic link between the DM low sulfidation epithermal deposits and the bimodal magmatism of the Bajo Pobre and Chon Aike Formation.

Acknowledgements

The authors are grateful to the Agencia Nacional de Promoción Científica y Tecnológica (FONCyT) and the Santa Cruz state mining company (FOMICRUZ S.E.) for the support and close cooperation during this research.

References

Arribas Jr A, Schalamuk I, de Barrio R, Fernández R, Itaya T (1996) Edades Radimétricas de Mineralizaciones Epitermales Auríferas del Macizo del Deseado, Provincia de Santa Cruz, Argentina. In: XXXIX Congresso Brasileiro de Geología, pp 254-257

Echavarría LE (1997) Estudio geológico-minero del área El Dorado-Monserrat, Departamento Magallanes, provincia de Santa Cruz. Tesis Doctoral Facultad de Ciencias Naturales y Museo, Universidad Nacional de La Plata. Unpublished

Fernández R, Echeveste H, Tassinari C, Schalamuk I (1999) Rb-Sr age of the La Josefina ephitermal mineralization and its relation with host volcanic rocks. Macizo del Deseado, Santa Cruz Province, Argentina. In: 2º Simposio Sudamericano de Geología Isotópica, pp 462-465

Jovic SM, Guido D, Tiberi P, Schalamuk I (2004) Cerro Leon, una variación del modelo epitermal de baja sulfuración del Macizo del Deseado. In: VII Congreso de Mineralogía y Metalogenia, pp 225-230

Kay SM, Gorring ML (1999) Evolution of the Patagonian Mantle: evidence from isotopic studies of Tertiary to recent plateau lavas. II South American Symposium on Isotope Geology, pp 556-565

Moreira P, González P, Fernández R, Echeveste H, Schalamuk I, Etcheverry R (2005) El basamento de bajo grado de las Estancias La Modesta y La Josefina, Macizo del Deseado, Provincia de Santa Cruz. Revista de la Asociación Geológica Argentina 60-1

Pankhurst RJ, Riley TR, Fanning CM, Kelley SR (2000) Episodic silicic volcanism in Patagonia and the Antarctic Peninsula: chronology of magmatism associated with the break-up of Gondwana. J Petrol 41: 605-625

Ramos V. (1988) Late Proterizoic-Early Paleozoic of South America. A collisional history. Episodes, 11:168-175

Riley T, Leat P, Pankhurst R, Harris C (2000) Origin of large volume rhyolitic volcanism in Antartic Peninsula and Patagonia by crustal melting. J Petrol 42: 1043-1065

Schalamuk I, Echeveste H, Etcheverry RO, Ametrano S (1998) Metalogénesis del yacimiento "Manantial Espejo", Macizo del Deseado, provincia de Santa Cruz. In: Academia Nacional de Ciencias Exactas, Físicas y Naturales, Anales 50: 217-236

Schalamuk I, Zubia M, Genini A, Fernández R (1997) Jurassic epithermal Au-Ag deposits of Patagonia, Argentina. Ore Geol Rev 12: 173-186

Zartman RE, Doe BR (1981) Plumbotectonic-the model. Tectonophys 75: 135-162

Re-Os ages for molybdenite from the Tepeoba breccia-centered Cu-Mo-Au deposit, western Turkey: Brecciation-triggered mineralization

Hiroyasu Murakami
Institute for Geo-resources and Environment, Geological Survey of Japan, AIST, 1-1-1 Higashi, Tsukuba 305-8567, Japan

Yasushi Watanabe
Institute for Geo-resources and Environment, Geological Survey of Japan, AIST, 1-1-1 Higashi, Tsukuba 305-8567, Japan

Holly Stein
AIRIE Program, Department of Geosciences, Colorado State University, Fort Collins, CO 80523-1482 USA, and Norges Geologiske Undersøkelse, Leiv Erikssons vei 39, 7491 Trondheim, Norway

Abstract. The Tepeoba breccia-centered Cu-Mo-Au deposit is associated with the Miocene Eybek granodiorite complex in western Turkey. The ages for molybdenite samples in the hydrothermal breccia and two molybdenite samples in veins surrounding breccia, one in metasedimentary rocks and one in the granodiorite, were dated by the Re-Os method using a double Os spike. Re-Os ages of molybdenite are 25.03 ± 0.14 and 25.11 ± 0.14 Ma for the veins and 25.62 ± 0.09 Ma for the breccia-hosted sample. These results indicate that the hydrothermal breccia in the Tepeoba deposit formed prior to the vein formation. We conclude, based on the Re-Os ages, that hydrothermal activity at Tepeoba lasted at least half a million years.

Keywords. Re-Os, ^{188}Os-^{190}Os double spike, hydrothermal breccia, Cu-Mo-Au deposit, Turkey

1 Introduction

Re-Os dating of molybdenite (MoS_2) is an effective tool for directly dating mineralization. Notably, molybdenite posses the unique property of accommodating Re at the ppm level, while incorporating essentially no initial (common) Os, thus providing a suitable single mineral chronometer utilizing the ^{187}Re-^{187}Os method (Stein et al. 2001). The ^{188}Os-^{190}Os double spike may be essential for young or low Re molybdenites (Markey et al. 2003). This method can precisely determine and correct for common Os and mass fractionation. The method thus provides a precise mineralization age associated with formation of molybdenite even in young samples with low Re contents.

In this study, we report three Re-Os ages of molybdenite, dated by the double Os spike method, in the Tepeoba Cu-Mo-Au deposit in western Turkey. We discuss duration of mineralization and the spatial and temporal evolution of the Tepeoba hydrothermal system.

2 Geologic background

Western Turkey is comprised of Permo-Triassic metamorphic and sedimentary rocks (Fig. 1A). A series of intrusions was emplaced into these basement rocks during the Oligocene and Early Miocene period. A ~24 Ma rapidly exhumed high-grade metamorphic core complex in the Kazdað mountain range was uplifted from ~14 km to ~7 km along a thick shear zone (Okay and Satir 2000). The Eybek granodiorite is situated on eastern margin of the Edremit graben bounded by ENE-WSW trending high-angle normal faults. The granodiorite is a typical calc-alkaline, I-type, magnetite-series. Granite body with S-type and ilmenite-series signatures occurs locally along the margin of the granodiorite body (Fig. 1B). A two-component mixing pattern of strontium isotope values suggests the "granite" formed by mixing between the granodiorite and the host meta-sedimentary rocks. Early to Middle Miocene volcanic and sedimentary rocks overlie the basement rocks.

3 Tepeoba breccia-centered Cu-Mo-Au deposit

The Tepeoba deposit was discovered in 2002, by diamond drilling conducted by the General Directorate of Mineral Research and Exploration of Turkey. A drill hole shows the upper 100 m with an average grade of 0.5 % Cu and ~1 g/t Au, with the upper 53 m at 1 % Cu, and 0.05 % Mo. The deposit occurs along and above the south granite body, located at the southern margin of the Miocene Eybek granodiorite complex. This deposit is hosted by metamorphic and sedimentary rocks of Permo-Triassic age, metamorphosed to andalusite-biotite schist due to the contact metamorphism by the granodiorite. The deposit consists of semicylindrical hydrothermal breccia 200 m wide, and extends for 800 m southwards with a maximum thickness of 100 m (Fig. 1B). This hydrothermal breccia includes fragments of surrounding rocks (e.g., andalusite-biotite schist and granite) except granodiorite in a matrix mainly of phlogopite. The ratio of granite fragments to andalusite-biotite schist fragments is greater nearer to the granite. The breccia ore is composed of chalcopyrite

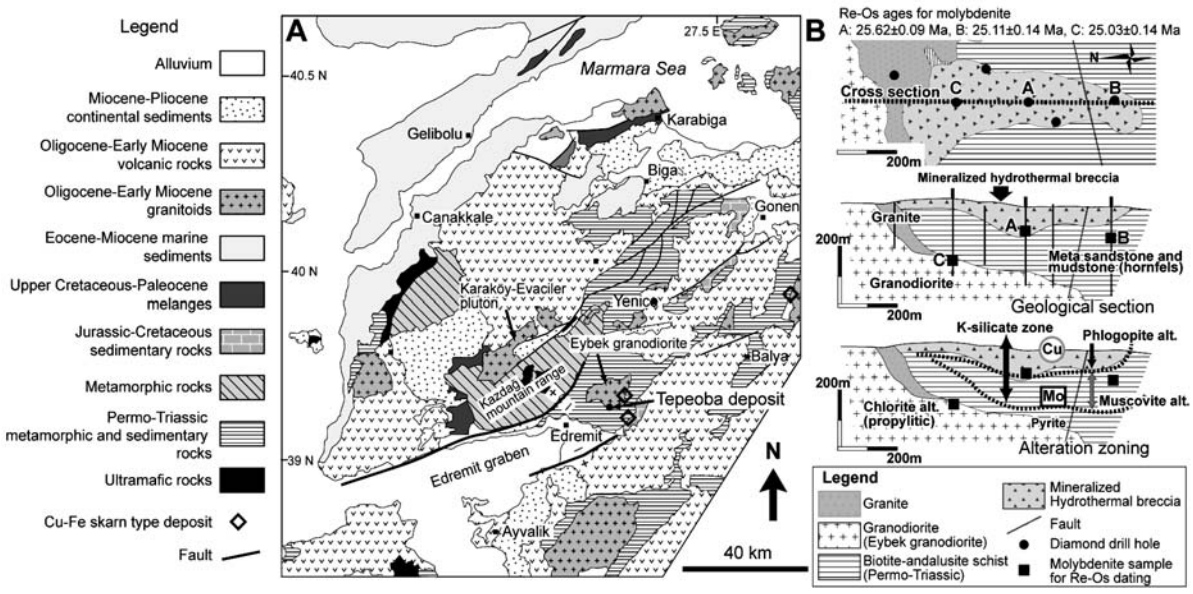

Figure 1: A Simplified geologic map of northwest Turkey showing location of the Tepeoba deposit and Eybek granodiorite (modified from Okay and Satir 2000); B Geologic map and cross section of the Tepeoba deposit showing location of molybdenite samples used for Re-Os dating. Alteration zoning and associated ore types are also illustrated.

and phlogopite with accessory molybdenite, pyrite, calcite, quartz, tourmaline, sphalerite, and electrum. In the hydrothermal breccia, post-brecciation hydrothermal activity is limited to thin quartz veining.

It has been proposed that the Tepeoba deposit has been tilted almost 90° with its top to the south due to Miocene normal faulting, resulting in full exposure of hydrothermal alteration zones associated with the granodiorite-granite complex on the present surface (Murakami et al, 2004). We suggest that alteration and mineralization at Tepeoba resemble types seen at porphyry-style Cu-Mo deposits. The alteration sequence in order of increasing proximity to mineralized breccia is a propylitic zone, muscovite zone, and K-silicate zone. The propylitic and muscovite zones are characterized by the presence of small amounts of chlorite and pyrite, and the presence of muscovite partly replacing biotite and quartz-calcite-molybdenite veins, respectively. These alteration zones surround the breccia dominated by K-silicate alteration, depicted by phlogopite with disseminated chalcopyrite and molybdenite. K-Ar ages for phlogopite in the matrix of the mineralized breccia are 23.8 ±1.2 and 23.8 ±1.4 Ma (hereafter, all ages are shown with two sigma uncertainty), and K-Ar ages for muscovite surrounding the breccia are 22.8 ±1.4, and 24.6 ±1.4 Ma. Ages of the intrusions have also been dated by K-Ar. Biotite in the granodiorite is dated at 20.3 ±1.0 and 21.4 ±1.2 Ma. K-feldspar in the granite is older at 34.7±2.0 Ma. Integration of stable isotope data, together with geologic relations and fluid inclusion data indicate that boiling, high-salinity fluids were responsible for the K-silicate and muscovite alteration and Cu-Mo-Au mineralization is related to the granodiorite intrusion and subsequent brecciation (Murakami et al. 2004).

4 Samples and analytical procedures of Re-Os dating

The three molybdenite samples used for Re-Os dating are (A) molybdenite cementing a matrix of a granite-fragment rich hydrothermal breccia, with phlogopite, quartz and chalcopyrite, (B) molybdenite in a hydrothermal calcite-quartz vein in andalusite-biotite schist, and (C) molybdenite in a vein containing chlorite (after igneous biotite) found along cracks in the granodiorite (Fig. 1B).

Molybdenite was extracted from these samples in a targeted, occurrence-specific manner using a diamond-tipped, slow-speed drill (Stein et al. 2003). Chemical procedures follow Markey et al. (2003). Isotopic compositions were determined using NTIMS on two NBS spectrometers at AIRIE. Age is calculated by applying the equation $^{187}Os = ^{187}Re\,(e^{\lambda t}-1)$, where λ is the decay constant for ^{187}Re and t is the age. The ^{187}Re decay constant used is $1.666 \cdot 10^{-11}$ yr^{-1} with an uncertainty of 0.31%. During this study, blanks were Re = 4.77 ± 0.04 pg, total Os = 4.09 ± 0.02 pg, and $^{187}Os/^{188}Os = 0.229 \pm 0.002$ pg.

5 Relationship between granodiorite and hydrothermal alteration

Re-Os and K-Ar ages for hydrothermal minerals, granodiorite and granite from the Tepeoba Cu-Mo-Au deposit are summarized in Figure 2.

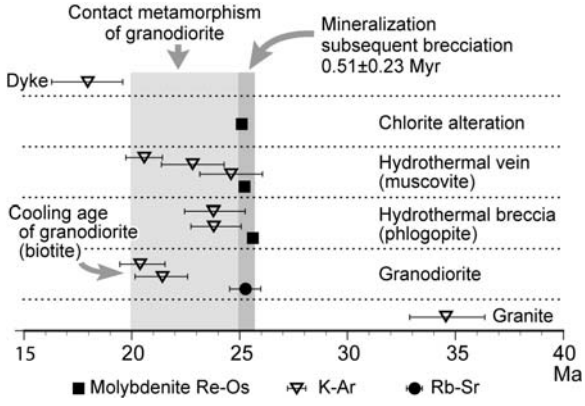

Figure 2: Re-Os and K-Ar ages for hydrothermal minerals and intrusions from the Tepeoba Cu-Mo-Au deposit (Rb-Sr age from Yılmaz and Karacık (2001)). Bars associated with data points denote two sigma analytical uncertainty.

Re-Os dates are consistently older than all K-Ar dates. The Re-Os system has been shown to remain closed at the scale of the molybdenite phase even through high-grade ductile deformation and metamorphism of a porphyry system (Stein et al. 2004b). On the contrary, the temperatures where minerals begin to lose radiogenic argon are of 300 ± 50 °C, 350 ± 50 °C, and the interval ranging from 400 to 470°C, for biotite, muscovite, and phlogopite, respectively (Dodson and McClelland-Brown 1985). Additionally, K-Ar dates in a contact metamorphic aureole generally reflect cooling ages for the associated intrusion. A pluton showing a close temporal and spatial association with the Eybek granodiorite has a Rb-Sr age of 25 ± 0.4 Ma (Yilmaz and Karacik 2001 and references therein), which is close to the Re-Os molybdenite ages. Therefore, K-Ar ages for biotite in the granodiorite should correspond to final cooling of the granodiorite, and that of hydrothermal minerals rejuvenated due to contact metamorphism.

During cooling of the granodiorite, contact metamorphism may cause continuous loss of radiogenic argon from hydrothermal minerals, because the youngest age of granodiorite is accord with that of hydrothermal muscovite. The K-Ar age of the hydrothermal phlogopites is somewhat older than that of muscovite, which is consistent with the observation that phlogopite commonly retains its radiogenic argon better than muscovite at higher temperature (Dodson and McClelland-Brown 1985).

6 Style of Tepeoba mineralization relative to porphyry copper

For porphyry-style Cu deposits, hydrothermal breccia generally forms at the close of major hydrothermal activity, although there are exceptions (e.g. Sillitoe 1985). Based on Re-Os dating results, mineralized hydrothermal breccia at the Tepeoba deposit formed prior to the vein formation.

Re-Os ages for molybdenites yield a time-span from 25.62 ± 0.09 to 25.03 ± 0.14 Ma, a period > 0.5 m.y., slightly longer than 0.3 m.y. estimates for the Far Southeast porphyry deposit (Arriibas et al. 1995) and 0.16 m.y. for the Batu Hijau porphyry deposit (Garwin 2002). Recent Re-Os dating indicates that some porphyry Cu-Mo deposits have longer mineralization periods (e.g. Los Pelambres, El Teniente, Stein et al. 2004a). Dilles et al. (2004) interpreted extended mineralization at Butte to overprint of multiple mineralization events.

There is no syn- or post-hydrothermal activity except a single stage of mineralized breccia at the Tepeoba deposit with a lack of significant veining in the hydrothermal breccia body. Molybdenite of ca. 25.03 Ma also coexists with low-temperature assemblages compare to those in the breccia. These occurrences suggest that the 0.5 m.y.mineralization period of Tepeoba is more likely to represent an extended mineralization event such as pro and retro-grade alteration in skarn type deposit, rather than possible multiple mineralization events.

We have determined formation pressure for the granodiorite using plagioclase-hornblende geobarometry. The crystallization pressure is estimated at ~2 kbar. According to geobarometry, if rock density is 2.7 g/cm^3, depth of crystallization of the Eybek granodiorite is considered to be ~7.5 km, which is consistent with depth estimates for surrounding metasedimentary rocks (Okay and Satir 2000). Such a deeper depth relative to many other porphyry copper deposits (ca. 1-4 km) may utilize a more static regime for skarn formation (e.g. controlled by diffusion rate rather than infiltration), and to limit hydrothermal activity accompanying mineralization in the vicinity of hydrothermal source without disturbance such as meteoric water circulation. This may be supported by the presence of small-scale skarn type Cu-Fe deposits which are sporadically distributed in and around the Eybek granodiorite at almost the same depth as the Tepeoba deposit.

Although a period of hydrothermal activity at the Tepeoba deposit related to the granodiorite and subsequent brecciation is consistent with the time interval for common porphyry-style deposits, there is a huge difference in the scale between these types. This is interpreted that volume and scale of mineralization of intrusion-related style should be controlled by number of cycles of hydrothermal alteration linked to magmatic fluid derived from intramineral intrusion (e.g., giant Cu-Mo porphyry deposits in Chilean Andes).

Acknowledgements

We are grateful to Dr R Sari and Mr S Küçükefe of the General Directorate of Mineral Research and Exploration of Turkey for helping a field survey and providing geologic data of the Tepeoba deposit.

References

Arribas AJr, Hedenquist JW, Itaya T, Okada T, Concepción RA, Garcia, JSJr (1995) Contemporaneous formation of adjacent porphyry and epithermal Cu-Au deposits over 300 ka in northern Luzon, Philippines. Geology 23: 337-340.

Dilles JH, Stein H.J, Martin MW (2004) Re-Os and U-Pb ages for the duration of the giant Butte, Montana, porphyry Cu-Mo and Cordilleran base metal lode ore deposit. IAVCEI general assembly Pucón, Chile

Dodson MH, McClelland-Brown E (1985) Isotopic and paleomagnetic evidence for rates of cooling, uplift and erosion. Geol Soc Mem 10: 315-325

Garwin S (2002) The Geologic Setting of Intrusion-Related Hydrothermal Systems near the Batu Hijau Porphyry Copper-Gold Deposit, Sumbawa, Indonesia, Global Exploration 2002: Integrated Methods for Discovery, Colorado, USA. Soc Econ Geol 9: 333-366

Markey R, Hannah JL, Morgan1 JW, Stein HJ (2003) A double spike for osmium analysis of highly radiogenic samples. Chemi Geol 200: 395-406

Murakami H, Watanabe Y, Sari R, Küçükefe S (2004) Newly discovered Tepeoba breccia-centered Cu-Mo-Au deposit in western Turkey: (electronic, session 1c) IAVCEI general assembly Pucón, Chile

Okay A, Satir M (2000) Coeval plutonism and metamorphism in a latest Oligocene metamorphic core complex in northwest Turkey. Geol Mag 137: 495-516

Sillitoe RH (1985) Ore-Related Breccias in Volcanoplutonic Arcs. Econ Geol 80: 1467-1514

Stein HJ, Cannell J, Cooke D, Sillitoe R, Perelló J (2004a) Metalliferous moments inside the lifespan of porphyry-style Cu-Au-Mo deposits: (electronic, session 12a) IAVCEI General Assembly, Pucón, Chile

Stein HJ, Hannah JL, Zimmerman A, Markey R, Sarkar SC, Pal AB (2004b) A 2.5 Ga porphyry Cu-Mo-Au deposit at Malanjkhand, central India: implications for Late Archean continental assembly. Precambr Res 134: 189-226

Stein HJ, Markey, RJ, Morgan JW, Hannah JL, Scherstén, A (2001) The remarkable Re-Os chronometer in molybdenite: how and why it works. Terra Nova 13: 479-486

Stein HJ, Scherstén, A, Hannah, JL, Markey R (2003) Sub-grain scale decoupling of Re and ^{187}Os and assessment of laser ablation ICP-MS spot dating in molybdenite. Geochim Cosmochim Acta 67: 3673-3686

Yilmaz Y, Karacik Z (2001) Geology of the northern side of the Gulf of Edrem it and its tectonic significance for the development of the Aegean grabens. Geodin Acta 14: 31-43

U-Pb SHRIMP dating of zircon from quartz veins at the Yangshan gold deposit: Evidence for multiple magmatic-hydrothermal events

Qi Jinzhong, Li Li, Yuan Shisong, Liu Zhijie
Gold Geological Institute of China Armed Police Force, Langfang 065000, China

Abstract. The Yangshan gold deposit is a fine-grained disseminated gold deposit located in south Gansu province. The metallogenic age was determined by cathodoluminescence imaging and U-Pb SHRIMP techniques. Zircons associated with quartz veins containing fine-grained disseminated gold ore have typical magmatic features including pillar idiomorphism, rhythmic zoning, and Th/U ratio of 0.5 to 1.5. Average $^{206}Pb/^{238}U$ ages of 197.6 ±1.7 Ma, 126.9±3.2 Ma, and 51.2±1.3 Ma define three primary zircon populations. The former age correlates to K-Ar ages (189.4±7.2 Ma mean) for plagiogranite dikes, while the later two ages suggest buried Cretaceous and Tertiary intrusives in or near the ore field. The Yangshan gold deposit is genetically related to the three magmatic-hydrothermal events.

Keywords. Disseminated gold, zircon, quartz vein, SHRIMP dating, Gansu

1 Introduction

The recently discovered found Yangshan gold deposit, located in south Gansu province, China, is a large deposit containing fine-grained disseminated gold. Four discovered ore blocks occur in metamorphosed Devonian sandstone, phyllite and limestone. The ore belt is primarily controlled by the Anchanghe- Guanyinba fault as well as small secondary faults. Locally, plagiogranite dikes lie along the fault, and gold mineralization is concentrated in the contact zone between the dikes and the Devonian phyllite. The orebodies, roughly sigmoidal in plane and tabular in profile, are hosted in pyritized, arsenopyritized, sericitized and argillized phyllite and plagiogranite. Late-stage pyrite-quartz veinlets crosscut the orebodies. Native gold, mainly electrum, is found as microscopic to sub-microscopic (<3μm) inclusions in pyrite and arsenopyrite.

Previous K-Ar and ^{39}Ar-^{40}Ar dating of the deposit give early Jurassic ages for the plagiogranite dikes, which were spatially associated with the mineralization (Qi 2003). In order to refine the metallogenic age of the Yangshan gold deposit, zircons from quartz veinlets are analyzed using cathodoluminescence images (CL) combined with SHRIMP U-Pb dating.

2 Sample description and experimental method

Sample YM is from 305# gold vein in the Caopingliang adit while sample AB from 314# gold vein in the Anba adit. Both samples are from pyrite-quartz veinlets hosting fine-grained disseminated gold ore. The quartz veinlets (often 1 to 2 cm wide) occur in the contact zone between the plagiogranite dikes and the Devonian phyllite. The samples consist mainly of quartz (95 wt.%) with subordinate sericite and clay minerals (4 wt.%), minor arsenopyrite and pyrite (1 wt.%), and rare electrum.

Representative zircon grains from the samples were selected under microscope. The grains together with a slice of standard zircon SL13 and grains of standard zircon TEM from Australia State University were mounted in epoxy, ground, and polished to expose the interior. Cathodoluminescence (CL) images were made on the zircons prior to analyses at the electronic probe laboratory of Institute of Mineral Deposits, CAGS. U, Th, Pb isotopic compositions of zircons were analyzed on a SHRIMP II at the ion probe center of Geological Institute, CAGS. Analyses followed the established methods of Composton et al (1992) and Williams et al (1998). Programs SQUID 1.02 and ISOPLOT were utilized for data processing. Reported uncertainties for U/Pb ratios are at the 1σ level. Common Pb is corrected from measured ^{204}Pb. Weighted mean ages are quoted at the 95% confidence level.

3 Result of SHRIMP dating

Fourteen analyses were made on zircon grains from sample YM representing fine-grained disseminated ore. Three age groups are defined and shown in the U-Pb concordia diagram (Fig. 1). The first group consists of three analyses giving $^{206}Pb/^{238}U$ ages of 195.4 to 200.9 Ma. These zircons are prismatic with concentric zoning (Fig. 3) suggesting a magmatic genesis (Yang 2002; Wu 2002). The second group consists of six analyses yielding $^{206}Pb/^{238}U$ ages between 121.8 and 137.0 Ma with a 128.2±5.5 Ma mean. These oscillatory zoned zircons are also prismatic (Fig. 3) and regarded as magmatic. The third group consists of four analyses giving $^{206}Pb/^{238}U$ ages between 48.1 and 51.7 Ma (50.0±3.0 Ma mean). These zircons are also prismatic with clear oscillatory zoning and are interpreted as magmatic (Fig. 3). The remaining analyses are scattered in the diagram.

Zircon samples YM-13 and YM-15 are short prisms with concentric zoning yielding $^{206}Pb/^{238}U$ ages of 1069±22 Ma and 809±17 Ma, respectively. They likely represent

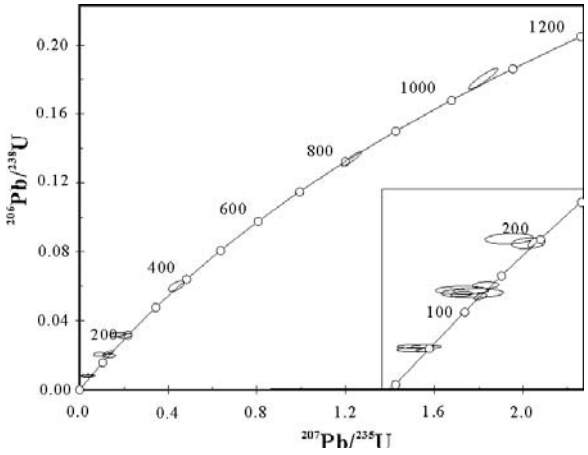

Figure 1: U-Pb concordia diagram showing SHRIMP data for YM sample.

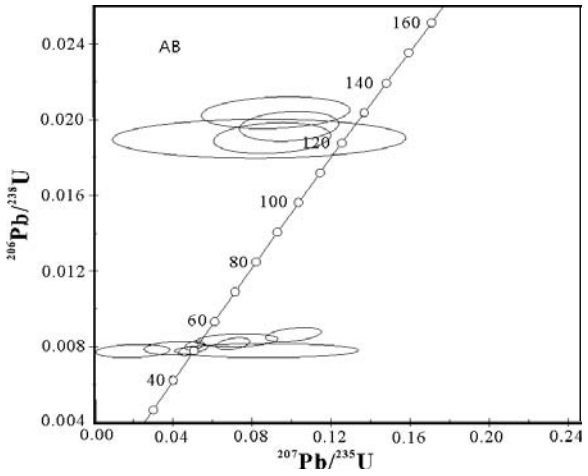

Figure 2: U-Pb concordia diagrams showing SHRIMP data for sample AB.

captured zircons from late Proterozoic intrusives. Analysis on zircon YM-12 gives an $^{206}Pb/^{238}U$ age of 375±11 Ma and might be captured from the Devonian strata.

16 zircons from sample AB representing the quartz veinlet of fine-grained disseminated ore were analyzed. These zircons are small and their common lead concentrations are slightly high. One analysis with significantly high common lead content was rejected. Two age groups were obtained as shown in the U-Pb concordia diagram (Fig. 2). The first group consists of five analyses giving $^{206}Pb/^{238}U$ ages between 121.4 and 130.2 Ma (125.3±4.9 Ma mean). These zircons are interpreted to be magmatic from their prismatic morphology and oscillatory zoning (Fig. 4). The second group consists of eight analyses which yield $^{206}Pb/^{238}U$ ages of 49.8 to 55.3 Ma (51.7±1.6 Ma in average). These concentrically zoned zircons are also primsatic (Fig. 4) and regarded as magmatic zircons.

4 Geological significance of the SHRIMP age and discussion

With high U-Pb isotope closure temperature of 700 to 750°C (Harrison et al. 1987; Tilton et al. 1991) and a strong resistence to thermal disturbance (Meger et al. 1997), zircon is widely used to constrain the timing of geological events. Although it has been proposed that "hydrothermal zircon" may form at lower temperatures (Corfu et al. 1984; Claoue-long et al. 1990), published ages of "hydrothermal zircons" from quartz veins in some gold deposits are very close to the ages of their host rocks, so whether "hydrothermal zircon" do exist in quartz veins is suspicious (Luo et al. 2000). The relatively low temperature of the hydrothermal fluid (150 to 250°C, Qi et al. 2003) at Yangshan could hardly result in the formation of "hydrothermal zircon". Furthermore, among the 30 analyses, only 3 zircons have Th/U ratios close to or less than 0.1, indicating that typical metamorphic zircons are not well-developed in the district (Gebauer et al, 1985; Yang J S et al. 2002). Therefore, zircons from the quartz veins in the district should be the ones captured during hydrothermal activity. The zircons may be captured from intrusives (including intrusives in the source area and those near the path of the hydrothermal fluid flow) and those captured from strata (mainly from older rocks that supplied source material to the Devonian strata).

Three analyses on zircons from sample YM constitute the first group age, giving the $^{206}Pb/^{238}U$ ages between 195.4 and 200.9 Ma. Having short prism form with concentric zoning and Th/U ratios of 0.44 to 0.87, these are regarded as Jurassic igneous zircons. As the age is consistent with the whole rock K-Ar ages of five plagiogranite samples in the gold field (171 to 209 Ma, Qi et al. 2003), these zircons may be captured from the plagiogranite dikes. Furthermore, the age coincides with the ^{39}Ar-^{40}Ar plateau age of 195.40±1.05 Ma of the quartz veinlet (Qi et al. 2003), suggesting that the intrusion of the plagiogranite dikes is responsible for hydrothermal activity in the district.

Cretaceous and Tertiary zircon groups were detected in samples YM and AB. Analyses revealed eleven Cretaceous zircons yielding an average $^{206}Pb/^{238}U$ age of 126.9±3.2 Ma and twelve Tertiary zircons give an average $^{206}Pb/^{238}U$ age of 51.2±1.3 Ma. These zircons are prismatic with concentric oscillatory zoning and dominant Th/U ratios between 0.5 and 1.5 indicating their magmatic genesis. These zircons could not be captured from the nearby strata as no Cretaceous or younger strata is found in the district. Furthermore, no intrusives other than the Jurassic plagiogranite are found related to the ore belt suggesting these zircons are captured from buried Cretaceous and Tertiary intrusives. Consequently, after the intrusion of plagiogranite dikes, two major magmatic events occurred in early Cretaceous and in early Tertiary, with a later ore fluid capturing the zircons from the intrusives.

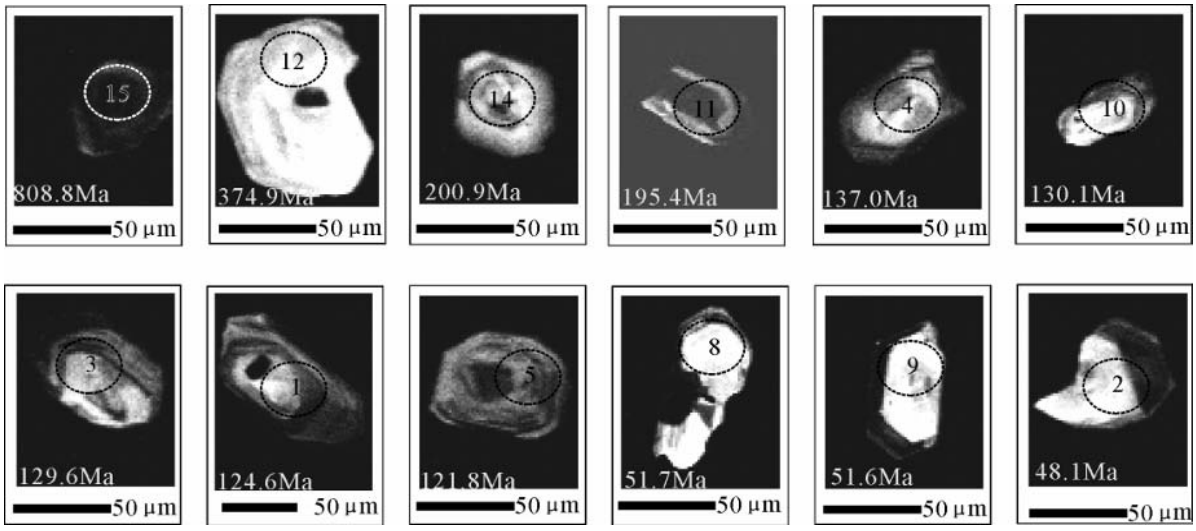

Figure 3: CL images of zircons from quartz veinlet (sample YM).

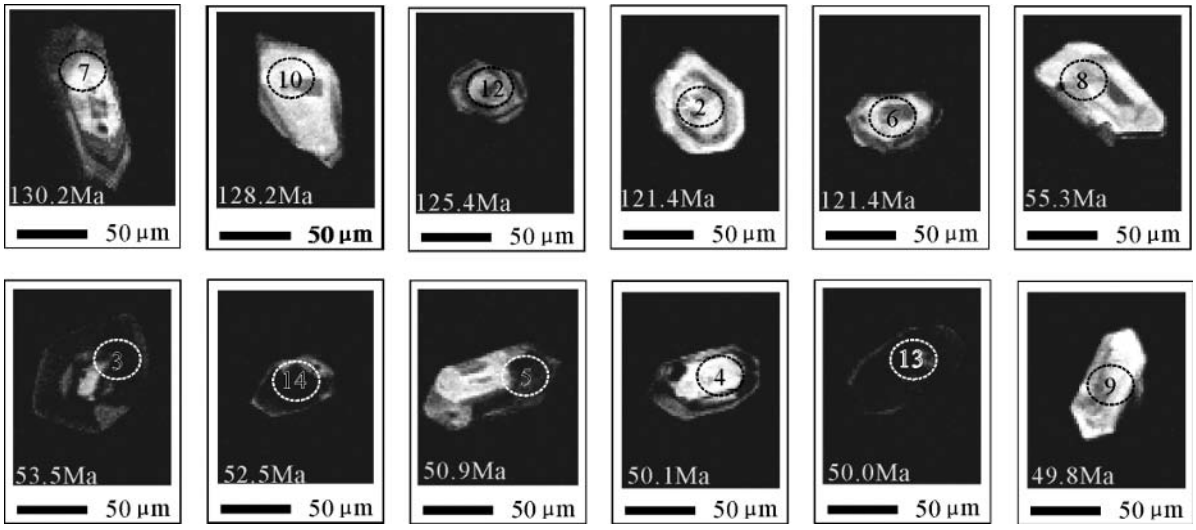

Figure 4: CL images of zircons from quartz veinlet (sample AB).

Therefore, the gold field was influenced by three magmatic and associated hydrothermal events.

Comparing Yangshan magmatic-hydrothermal events with the magmatic events in western Qinling, we can see that the early Jurassic hydrothermal epoch coincides with one fastigium of felsic intrusions in western Qinling (190Ma to 220Ma, Zhang et al. 1994), while the early Cretaceous hydrothermal epoch corresponds to another fastigium of granite activities in western Qinling (120Ma to 150Ma, Du et al. 1998). These two epochs were also considered to be the fastigiums of gold mineralization in China (Zhai et al. 2002; Mao et al. 2002). The early Tertiary magmatic-hydrothermal epoch is consistent with the major metallogenic age of gold deposits in southwestern China (Chen et al. 2001), and the magmatic-hydrothermal activity may be linked to the continental-continental collision of the penetrating Indian plate and Eurasian plate. The gold mineralization at Yangshan may be directly linked to multiple, localized magmatic-hydrothermal events in the district and major magmatic-tectonic events in the region.

5 Conclusion

1. Zircons from quartz veinlets associated with ore are dominantly prismatic with concentric oscillatory zoning and Th/U ratios of 0.5 to 1.5 indicating a magmatic genesis.
2. The magmatic zircons with $^{206}Pb/^{238}U$ ages of 195.4 to 200.9 Ma in quartz veinlet sample YM are captured from the early Jurassic plagiogranite intrusives.

3. The two zircon groups with average $^{206}Pb/^{238}U$ ages of 126.9±3.2 Ma and 51.2±1.3 Ma in quartz veinlets are captured from buried Cretaceous and Tertiary intrusives, respectively. The early Jurassic, early Cretaceous, and early Tertiary magmatic-hydrothermal events affected Yangshan gold field and the deposit was genetically related to the three magmatic-hydrothermal events.

References

Chen YC, Wang DH (2001) Study of Himalayan endogenic mineralization. Bejing: Seismic Publishing House. 1-138 (in Chinese with English abstract)

Claoue-long J, King RW, Kerrich R (1990) Archean hydrothermal zircon in the Abitibi greenstone belt: constrains on the timing of gold mineralization. Earth Planet Sci. Letters 98:109-128.

Composton W, Williams IS, Kirschvink JL, Zhang Z, Ma G (1992) Zircon U-Pb ages for the Early Cambrian time scale. Journal of the Geological Society London 149:171-184.

Corfu F, Ayres LD (1984) U-Pb age and genetic significance of heterogeneous zircon populations in rocks from the Favourable Lake area, Northwestern Ontario. Contrib Mineral Petrol 88: 86-101

Du ZT, Wu GG (1998) Study on tectonic systems and gold metallogenic tectono-dynamics in the region of west Qinling. Bejing: Geological Publishing House. 1-145 (in Chinese with English abstract)

Gebauer D, Lappin MA, Grunenfelder M (1985) The age and origin of same Norwegian eclogite: A U-Pb zircon and REE study. Chemical Geology 52: 227-248

Harrison TM, Aleinkoff JN, Compston W (1987) Observation and controls on the occurrence of inherited zircon in concord-type granitoids, New Hampshire. Geochem Cosmochim Acta5 1: 2549-2568

Luo ZK, Miao LC, Guan K (2000) Discussion on the metallogenetic epoch of gold deposit on north fringe of North China platform, Gold Geology 6: 70-75 (in Chinese with English abstract)

Mao JW, Qiu YM, Goldfarb RJ, Zhang Z, Garwin S, Fengshou R (2002) Geology, distribution, and classification of gold deposits in the western Qinling belt, central China, Mineralium Deposita 37:352-377

Mezger K, Krogstad E J (1997) Interpretation of discordant U-Pb zircon ages: An evaluation. J. Metamorphic Geol. 15:127-140

Qi JZ, Yuan SS, Li L, Sun B, Guo JH (2003) Geological and geochemical study of yangshan gold deposit, gansu province. Mineral Deposits. 22:24-31 (in Chinese with English abstract)

Tilton GR, Schreyer W, Schertl HP (1991) Pb-Sr-Nd isotopic behavior of deeply subducted crustal rocks from the Dora Maira massif, Western Alps, Italy-II: what is the age of the ultra-high pressure metamorphism? Contrib. Mineral. Petrol, 108:22-33

Williams I S. (1998) U-Th-Pb Geochronology by Ion Microprobe, in McKibben MA, Shanks III WC and Ridley WI (eds), Applications of microanalytical techniques to understanding mineraling processes. Reviews in Economic Geology 7:1-35.

Wu CL, Jone W, Yang JS, Li HB (2002) margin of Qilian mountains: evidence from zircon SHRIMP age of the Aolaoshan granite, Acta Geologica Sinica, 76(1): 118-125

Yang JS, Xu ZQ, Wu CL, Liu FL, Shi RD, Wooden J, Maruyama S (2002) SHRIMP U-Pb dating on coesite bearing zircon: Evidence for Indosinian ultrahigh-pressure metamorphism in Su-Lu, East China, Acta Geologica Sinica, 76(3): 354-372 (in Chinese with English abstract)

Zhai YS, Miao LC, Xiang YC, Deng J, Wang JP (2002) Preliminary discussion on ore-forming system in greenstone belt-type of north China Craton. Earth Science-Journal of China University of Geosciences. 27: 522-529 (in Chinese with English abstract).

Zhang BR, Gao S, Luo TC (1994) Lithosphere structure of Qinba area and metallogenic geochemistry. Wuhan: Publishing House of China University of Geosciences. 1-446 (in Chinese with English abstract)

$^{87}Sr/^{86}Sr$, $^{3}He/^{4}He$, REE and stable isotope ($\delta^{34}S$, $\delta^{18}O$) constraints on the hydrothermal fluid evolution of the PACMANUS system, Manus Basin

Stephen Roberts
School of Ocean and Earth Science, Southampton Oceanography Centre, University of Southampton, Southampton, SO14 3ZH, UK

Wolfgang Bach
Department of Marine Chemistry and Geochemistry, Woods Hole Oceanographic Institution, Woods Hole, MA 02543, USA

Adrian Boyce
Scottish Universities Environmental Research Centre, Scottish Enterprise Technology Park, Rankine Avenue, East Kilbride, G70 0QF, UK

Ray Burgess
Department of Earth Sciences, University of Manchester, Manchester, M13 9PL, UK

Abstract. $\delta^{34}S$, $^{87}Sr/^{86}Sr$, $\delta^{18}O$, REE and $^{3}He/^{4}He$ analyses of anhydrite from the PACMANUS hydrothermal system suggest a complex interplay between hydrothermal fluid, magmatic fluid, and seawater during alteration and mineralization. These new data significantly expand the subsurface data on seafloor hydrothermal systems and may begin to explain the earliest processes of multistage mineralization and alteration history that typify ancient massive sulfide systems.

Keywords. Hydrothermal vents, sulfides, anhydrite, isotopes

1 Introduction

Ocean Drilling Program Leg 193 investigated two sites of hydrothermal activity along the crest of the Pual Ridge in the eastern Manus Basin. A site of low-temperature diffuse venting, Snowcap (Site 1188), and a high-temperature black smoker site, Roman Ruins (Site 1189), were drilled to depths of 386 and 206 meters below sea floor, respectively (Binns et al. 2002; Roberts et al. 2003; Bach et al. 2003; Vanko et al. 2004). Although the two sites are <1000 m apart, the geochemical signatures of anhydrite recovered at both sites are very different. Measured anhydrite $^{87}Sr/^{86}Sr$ ratios vary between 0.7050 and 0.7086; the most radiogenic values occur just beneath the variably altered dacitic cap at both sites (Fig. 1).

At Snowcap (Site 1188) there is a clear trend downhole to less radiogenic $^{87}Sr/^{86}Sr$ values, from 0.7086 beneath the dacite cap to values of 0.7060 at ~100 mbsf, and these low values are broadly maintained to the base of the hole.

The measured anhydrite $\delta^{34}S$ values vary between 18.1‰ and 22.5‰. For Snowcap, most of the values are less than 21.0‰ and trend significantly toward lower values downhole. In contrast, anhydrite $\delta^{34}S$ values at Roman Ruins are mostly equal to or greater than the seawater value and show no obvious downhole trends.

The $^{87}Sr/^{86}Sr$ and $\delta^{34}S$ data for anhydrite from Snowcap (Site 1188) and Roman Ruins (Site 1189) suggest contrasting fluid evolution and flow regimes.

The rare-earth element (REE) contents of anhydrite from PACMANUS show extreme variability, in terms of both absolute concentrations (e.g., 0.08–28.3 ppm Nd) and pattern shape (La_N/Sm_N=0.08–3.78, Sm_N/Yb_N=0.48–23.1,

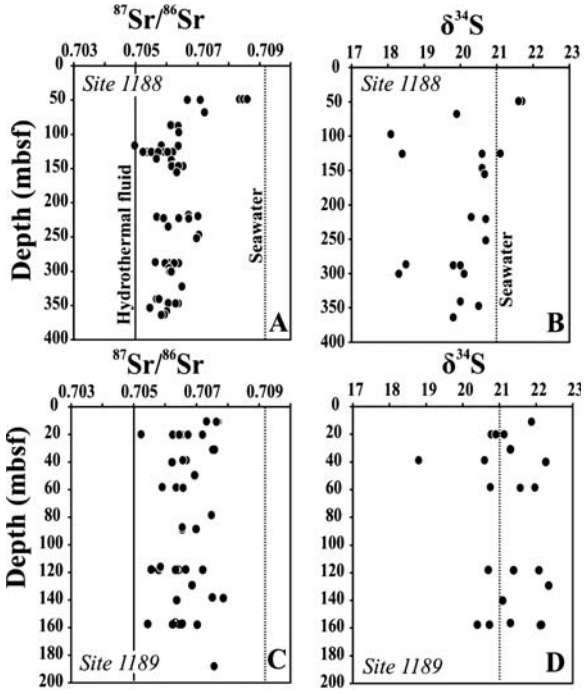

Figure 1: Strontium and sulfur isotope downhole variations in anhydrite.

This page intentionally blank

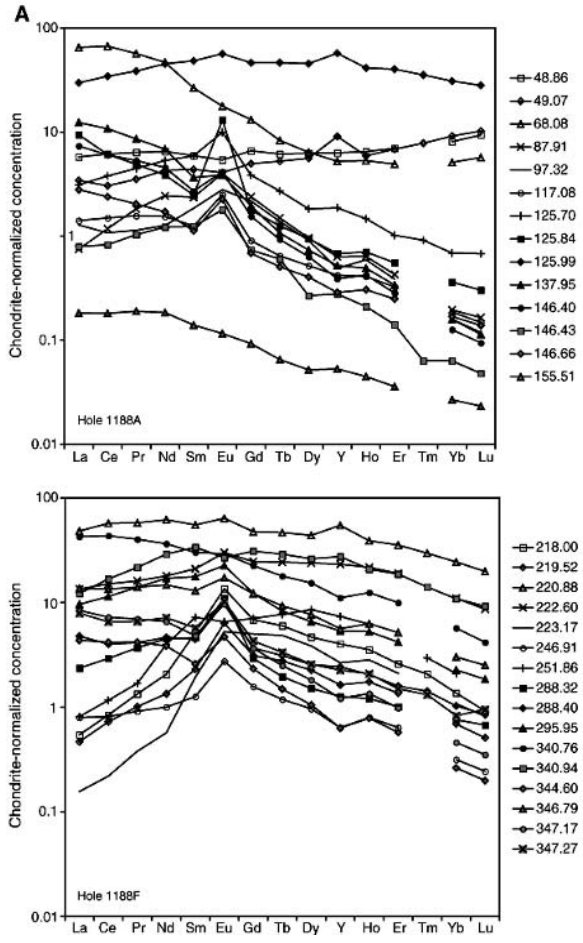

Figure 2a: Anhydrite REE data 1188.

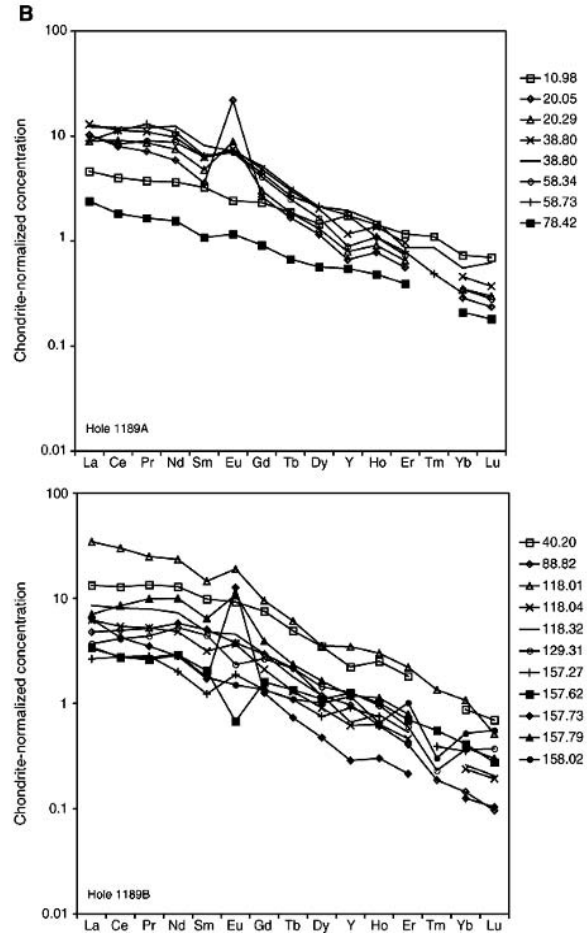

Figure 2b: Anhydrite Data 1189.

Eu/Eu*=0.59–6.1). The range of REE patterns in anhydrite includes enrichments in the middle and heavy REEs and variable Eu anomalies (Fig. 2a,b). The REE patterns of anhydrite from hole 1188 differ markedly from those of anhydrite recovered during ODP Leg 158 from the TAG hydrothermal system at the Mid-Atlantic Ridge, which display uniform LREE-enriched patterns, in contrast the 1189 data are more comparable.

The anhydrite and sulfides from both sites show variable $^{3}He/^{4}He$ ratios with R/Ra in the range 0.29-6.91 (R/Ra Seawater = 1.05) (Fig. 3). The data show correlations with depth, $\delta^{34}S$ and $^{87}Sr/^{86}Sr$ data. Oxygen isotope data for the anhydrite are relatively uniform, $\delta^{18}O$ varies between 8 and 10‰, and show no downhole correlation.

2 Discussion

The Snowcap data are consistent with higher sulfate concentrations of the hydrothermal end-member fluid. If the sulfate concentration is increased because of magmatic SO_2 disproportionation and dissociation, it would predict a lower fluid pH. This is consistent with the dominance of pyrophyllite at Snowcap and secondary feldspar at Roman Ruins.

Furthermore, Bach et al. (2003) have suggested that the range of REE patterns in the anhydrites from Snowcap reflects the waxing and waning input of magmatic volatiles (HF, SO_2) and variable complexation of REEs in the fluids. Taken together, these observations strongly suggest a magmatic contribution to the hydrothermal system drilled at Snowcap. In contrast, Roman Ruins data are characterized by $^{87}Sr/^{86}Sr$ ratios of ~0.7065, with significant intrasample variation, and $\delta^{34}S$ ratios that are at seawater or slightly elevated values. The $^{87}Sr/^{86}Sr$ and S isotope data show no systematic downhole trends and are very similar to data reported for anhydrites recovered during the TAG drilling, ODP Leg 158 and are consistent with the mixing of a low-sulfate hydrothermal fluid and seawater.

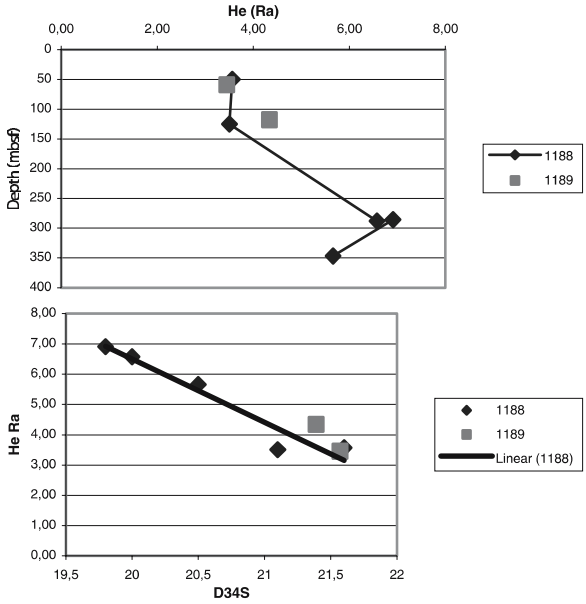

Figure 3: Anhydrite helium isotope data, plotted against depth and coexisiting sulfur isotope signature.

Overall, the data suggest a complex interplay among hydrothermal fluid, magmatic fluid, and seawater during alteration and mineralization of the PACMANUS system.

References

Bach W, Roberts S, Vanko DA, Binns RA, Yeats CJ, Craddock PR, Humphris SE (2003) Controls of fluid chemistry and complexation on rare earth element contents of anhydrite from the PACMANUS subseafloor hydrothermal system, Manus Basin, Papua New Guinea. Mineralium Depos, 38: 916-935

Binns RA, Barriga FJAS, Miller DJ (2002) Proc. ODP, Init. Repts., 193 [CD-ROM]. Available from: Ocean Drilling Program, Texas A&M University, College Station TX 77845-9547, USA

Roberts S, Bach W, Binns RA, Vanko DA, Yeats CJ, Teagle DAH, Blacklock K, Blusztajn J.S, Boyce AJ, Cooper MJ, Holland N, McDonald B (2003) Contrasting evolution of hydrothermal fluids in the PACMANUS system, Manus Basin: The Sr and S isotope evidence. Geology 31: 805-808

Vanko DA, Bach W, Roberts S, Yeats CJ, Scott SD (2004) Fluid inclusion evidence for subsurface phase separation and variable fluid mixing regimes beneath the deep-sea PACMANUS hydrothermal filed, Manus Basin back arc rift, Papua New Guinea. J Geophys Res 109: B03201-03214

U-Pb dating of micro-inclusions: The age of the Ehrenfriedersdorf tin deposit (Erzgebirge, Germany)

R.L. Romer, R. Thomas
GeoForschungsZentrum Potsdam, Telegrafenberg, D-14473 Potsdam, Germany

Abstract. Multiple reworking of ore deposits may disturb geochronologic systems and eventually render incorrect ages for ore deposition or different stages of ore formation. Micro-inclusions may beprotected from later disturbances by their host mineral and, thus, yield reliable age information. Major problems in dating micro-inclusions include their genetic connection with various stages of ore formation and technical aspects, such as loss of daughter isotopes by α-recoil and the initial isotopic composition of the daughter element. The problem of daughter-loss from a high-μ microinclusion (μ = $^{238}U/^{204}Pb$)by α-recoil can be avoided by analyzing the inclusion together with its low-μ host. The philosophy behind the presented analytical approach is to "trade" radiogenic composition of the daughter element (i.e., high $^{206}Pb/^{204}Pb$, $^{207}Pb/^{204}Pb$, and $^{208}Pb/^{204}Pb$) against closed-system behavior. This approach is demonstrated for <10 microns small uraninite inclusions in darkmica from Ehrenfriederdorf, Erzgebirge, Saxony. Our data demonstrate that micro-inclusions may yield precise and accurate age data for early ore forming processes.

Keywords. Micro-inclusions, U-Pb dating, Ehrenfriederdorf, tin deposits

1 Introduction

Precise and accurate dating of many kinds of ore deposits is problematic because later hydrothermal and tectonic overprint (resulting in the repeated redistribution of elements or the introduction of various metals at different time) may disturb geochronometers that are genetically and texturally related to early stages of deposit formation. For instance, U deposits in the Aue-Niederschlema district (Erzgebirge, Saxony) yield ages of c. 280-270 Ma, 190 Ma, 120 Ma, 80 Ma, and 30 Ma (Förster 1996), the oldest age related with the introduction of U into the deposit, the younger ages reflecting redistribution of U in conjunction with multiple tectonic reactivation of the Gera-Jachymov zone, along which numerous U deposits occur.

Many of the ambiguities and complexities arising from the redistribution of the ore metals during multiple overprint and alteration can be avoided by (i) dating the economically interesting minerals, which is possible for minerals of the columbite-tantalitetapiolite series (e.g. Romer and Wright 1992; Romer and Smeds 1996), molybdenite (e.g. Stein et al. 1998, 2001; Stein and Bingen 2002), and U-minerals (e.g. Ludwig and Simmons 1991; Förster 1996), (ii) by dating minerals that have formed cogenetically with the economically interesting minerals, which for skarn ores may involve titanite, vesuvianite, and garnet (e.g., Romer 1992; Romer and Soler 1995) and for hydrothermal vein deposits may involve gangue minerals such as white mica or quartz (e.g. Franzke et al. 1996; Romer and Linnemann 2004), and (iii) by dating fluid inclusions in economically interesting minerals or associated gangue minerals (e.g. Glodny 1997; Pettke and Diamond 2000). In this paper, we demonstrate that U-Pb dating of micro-inclusions is technically possible and yields accurate results as long as precautions are taken (i) to avoid micro-minerals along grain-boundaries and fractures and (ii) to sample in a way that compensates for recoil-related open-system behavior in the U-Pb system.

2 Advantages and disadvantages of the use of micro-inclusions in mineral dating

Dating micro-inclusions entirely enclosed in other minerals has the advantage that the host prevents interaction of the micro-inclusion with later fluids. The host-mineral represents a container that makes the geochronologic system of the inclusion behave as a closed system even for inclusions (e.g., uraninite) that are known to react readily with fluids. The host mineral, however, should neither react with the inclusion nor incorporate those elements that define the geochronologic system of the inclusion. Otherwise there may be exchange of the geochronologically relevant element between host and inclusion. The major problem in the use of micro-inclusions for dating originates from ambiguities in the genetic connection between inclusion and host and the representativity of the inclusion.

3 Requirements on micro-inclusions to be suitable for dating

There are basically three requirements that must be fulfilled for micro-inclusions to become potentially attractive for dating attempts: (i) closed system, (ii) strong daughter-to-parent (D/P) fractionation, and (iii) high P contents.

i. Closed system behavior requires that neither the P nor the D element is lost from the inclusion. Major processes for possible daughter loss include diffusion and recoil, both of which are more likely to become more important for smaller grain size. Loss by diffusion de-

pends not only on temperature, the diffusion constant of the considered element, the cooling history of the sample, and the distance to the grain surface, but also on the transport of the lost ions away from the grain surface. If a host that does not accept ions lost from the inclusion, these ions will concentrate at the contact between the two minerals and prevent additional loss from the inclusion. An example for an inclusion that remained a closed system to high temperature has been presented by Kühn et al. (2000). They showed that biotite in Sveconorwegian granulite-facies garnet recorded this older event rather than the Caledonian eclogite facies overprint. α-recoil refers to the displacement of the daughter isotope due to the emission of an α-particle (Fig. 1). The daughter nucleus

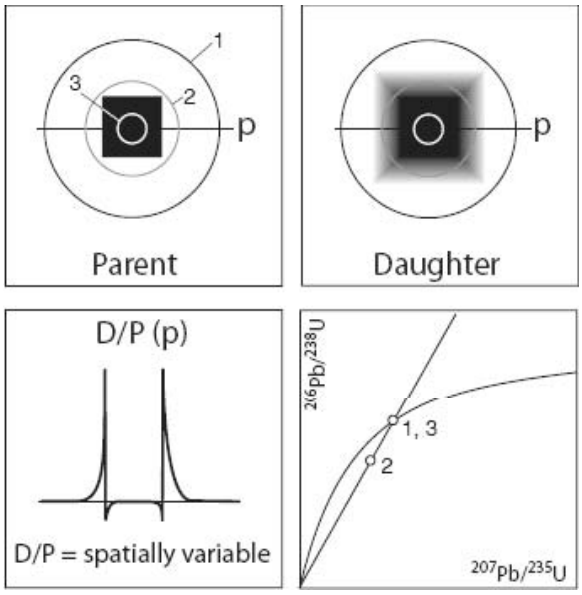

Figure 1: Parent (P) and daughter (D) isotope distribution in a heterogeneous mineral. (p) represents a hypothetical profile line along which the D/P ratio is determined. There occur important variations in D/P in the border zone between two areas of contrasting P content. There is a deficit of D in the area of high P and there is an excess of D in the area of low P. Note that the excess of D may represent a much larger portion of a sub-sample than the D deficit (modified from Romer 2003). Circles represent three hypothetical samples yielding the following $^{206}Pb/^{238}U$ results: (1) The sample is large enough to include the high-μ phase and the volume of the low-μ phase that contains the recoiled daughters. This sample is concordant at the true age; (2) The sample encompasses the entire high-μ phase, but only part of the low-μ phase doped with recoiled daughter isotopes. Thus, there is a daughter deficit, the sample has a too low $^{206}Pb/^{238}U$ and falls below the concordia; (3) The sample includes only the innermost part of the high-μ phase. Daughter isotopes lost by recoil from the sample volume are compensated by daughter isotopes originating from the surrounding sample. The sample is concordant at the true age. Note that the perfect separation of the phase with high P content from the surrounding phase results in a too low $^{206}Pb/^{238}U$.

typically is displaced by some 20 to 30 nm (e.g., Matzke 1982). At the contact between a high-μ phase and a low-μ phase, the loss of daughter isotopes from the high-μ phase is more important than the addition of daughter isotopes. Thus, the high-μ phase eventually shows a deficit in daughter isotopes and the low-μ phase shows an excess (cf. Ludwig 1978; Mattinson et al. 1996; Romer 2001, 2003). This effect becomes more important, the smaller the high-μ phase (cf. Romer 2003). Because of α-recoil, isolated small high-μ inclusions are beyond doubt open systems showing a daughter deficit. The same inclusion and its immediate host in combination, however, may represent a closed system as the daughter isotopes lost from the inclusion are collected in the host. This behavior is shown in Figure 1. Note that the isolated inclusion would fall below the concordia and the separated host would fall above the concordia.

ii. High P/D values result with time in highly radiogenic D-element compositions, which makes uncertainties about the initial composition of D irrelevant for the age calculation and allows to constrain the slope of an isochron more closely, i.e., to deduce more precise ages. High P/D are restricted to element-pairs of contrasting geochemical behavior, such as Rb-Sr, U-Pb, and Th-Pb and to mineral phases that strongly prefer P over D.

iii. Analytical uncertainties originating from counting statistics depend on signal intensity. To obtain small uncertainties, the signal has to be strong, i.e., many ions have to be available for counting. For small inclusions to yield high signal intensities, the content of D has to be high, which is a function of time and P. Thus, for an optimal analytical result, P has to be high.

Only few phases fulfill above three requirements. For the U-Th-Pb systems, minerals that have high P/D and high P contents include xenotime, monazite, and uraninite; for the Rb-Sr system, the requirements may be fulfilled by micas and Rb-rich phases. To obtain a closed system, the inclusions should be analyzed together with their host. Thus, the host should yield very low or no contributions of P and D to the bulk sample.

4 High-μ inclusions (monazite, xenotime, and uraninite)

Because of alpha-recoil, micro-inclusions are notoriously open systems. Separating inclusions results in too young apparent 206Pb/238U ages as there is a deficit in radiogenic Pb. Drilling the inclusions together with a rim of their host directly from thin sections solves the problem. (i) Recoiled daughter isotopes are collected by the host. (ii) U-rich and Th-rich minerals are readily recognized by their pleochroitic haloes (Fig. 2) and can be iden-

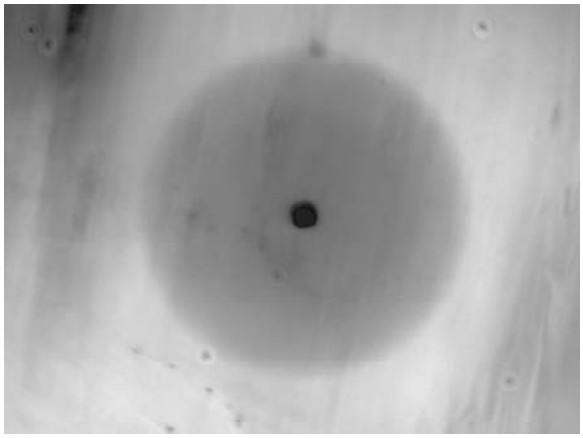

Figure 2: Typical uraninite micro-inclusion in Li-bearing dark mica (Li-siderophyllite to protolithionite) with pleochroitic halo. The pleochroitic halo is caused by the emission of α-particles and their interaction with ions in the crystal lattice. Since α-particles are much lighter than the recoiled nuclei, they travel for a larger distance into the crystal and interact to a lesser extent than recoiled ions with the ions in the crystal lattice. For instance, α-particles of the ^{238}U, ^{235}U, and ^{232}Th decay series travel 9.9 to 29.5 µm in zircon, depending on the energy of the decay (cf. compilation of Nasdala et al. 2001). The volume of recoil implantation is about 3·107 times smaller than the halo of radiation damage.

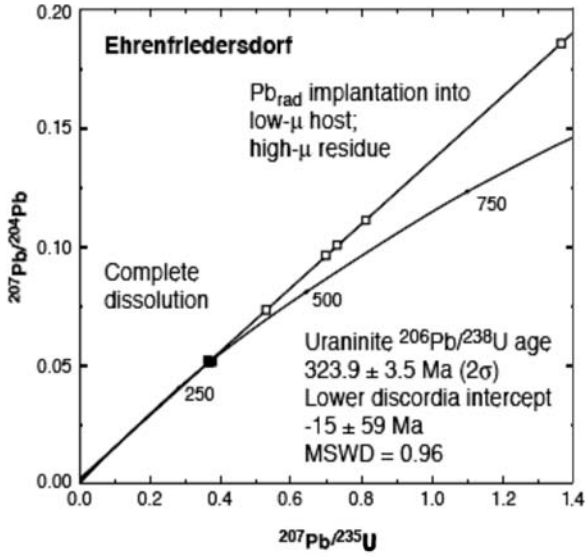

Figure 3: Concordia diagram for micro-inclusions from the Greifenstein granite (Ehrenfriedersdorf). Discordia is forced through 324 ± 2 Ma (concordant uraninite inclusions). Reverse discordant samples represent selectively dissolved host minerals (residual xenotime and monazite inclusions) that illustrate the effect of recoil-implantation of U-daughters.

tified by micro-Raman. For sampling, special care should be taken to collect only inclusions that are entirely enclosed in the host. Outcropping inclusions always show a deficit in radiogenic Pb. (iii) The radius of pleochroitic haloes is more than 100 times larger than the distance of recoil displacement of U-daughters. Thus, drilling samples that include the entire pleochroitic halo must yield closed systems. In thoroughly altered or multiply overprinted rocks, inclusions that are protected by their host mineral from interaction with late fluids may represent the only datable minerals from the early evolution of the altered rock.

5 Uraninite inclusions in mica from the Ehrenfriederdorf tin deposit

Extensive high-temperature Sn-mineralizations that form skarns, pegmatites, greisen, and pneumatolyitc- hydrothermal vein deposits are closely associated with Late Variscan granites in the Ehrenfriedersdorf-Geyer area (cf. Oelsner 1952). The granite is dominated by quartz, alkali-feldspar, plagioclase (<An12), and up to 5 vol-% mica. Accessory minerals include topaz, cassiterite, zircon, monazite, xenotime, uraninite, apatite, tourmaline, and Sn-rich pyrrhotite. Melt inclusions in topaz prove that this mineral is magmatic and did not form during pneumatolytic or hydrothermal overprinting. High Sn contents (up to 800 ppm) in melt inclusions in quartz demonstrate that the granite is closely related with the formation of the Sn deposits in the marginal greisen and skarns (Thomas et al. 2003). The radioactive elements U and Th are predominantly hosted in tiny crystals of zircon, uraninite, monazite, and less common xenotime that are readily recognized as they show distinctive pleochroitic haloes in mica (Fig. 2). The small crystal size of the radioactive minerals and the distinctive pleochroitic haloes are typical for most late Variscan granites of the Ehrenfriedersdorf-Geyer district.

We analyzed three uraninite inclusions that gave concordant data (filled symbols, Fig. 3). The best age estimate, obtained from the weighted mean of the $^{206}Pb/^{238}U$ ages, is 323.9±3.5 Ma (2sigma). It falls within the expectation range for these post-kinematic granites, which is defined by 40Ar/39Ar ages of intruded metamorphic rocks and the age of tectonically comparable granites from Fichtelgebirge, Oberpfalz, and the Bavarian Forrest (e.g., Werner and Lippolt 2000; Siebel et al. 2003). The age also agrees well with chemical ages obtained on uraninite, monazite, and xenotime from numerous geochemically corresponding granites of the Erzgebirge (Förster et al. 1999). Thus, our data demonstrate that complete dissolution of inclusion and host yields concordant data that give accurate age constraints. Data from samples with incompletely dissolved monazite and xenotime (open symbols, Fig. 3) show an excess of radiogenic Pb that represents Pb implanted by α-recoil into the host.

References

Förster B (1996) U/Pb Datierung an Pechblenden der U-Lagerstätte Aue-Niederschlema (Erzgebirge). Dissertation, Universität Giessen Förster H-J, Tischendorf G, Trumbull RB, Gottesmann B (1999) Late-collisional granites in the Variscan Erzgebirge, Germany. J Petrol 40: 1613-1645

Franzke HJ, Ahrend H, Kurz S, Wemmer K (1996) K-Ar Datierungen von Illiten aus Kataklasiten der Flossbergstörung im südöstlichen Thüringer Wald und ihre geologische Interpretation. Z geol Wiss 24:441-456

Glodny J (1997) Der Einfluß von Deformation und fl uidinduzierter Diaphthorese auf radioaktive Zerfallssysteme in Kristallingesteinen. Dissertation, Universität Münster Kühn A, Glodny J, Iden K, Austrheim H (2000) retention of Precambrian Rb/Sr phlogopite ages through Caledonian eclogite facies metamorphism, Bergen Arc Complex, WNorway. Lithos 51: 305-330

Ludwig KR (1978) Uranium-Daughter Migration and U/Pb Isotope Apparent Ages of Uranium Ores, Shirley, Basin, Wyoming. Econ Geol 73: 29-49

Ludwig KR, Simmons KR (1991) U-Pb dating of uranium ores in collapse-breccia pipes, Grand Canyon region. In: Pagel M, Leroy JL (eds) Source, transport and deposition of metals. A.A. Balkema, Rotterdam, pp 405-408

Mattinson JM, Gaubard CM, Parkinson DL, McLelland WC (1996) U-Pb reverse discordance in zircons: the role of fi ne-scale oscillatory zoning and sub-microscopic transport of Pb. Am Geophys Union Geophys Monogr 95: 355-370

Matzke H (1982) Radiation damage in crystalline insulators, oxides and ceramic nuclear fuels. Rad Effects 64: 3-33

Nasdala L, Wenzel M, Vavra G, Irmer G, Wenzel T, Kober B (2001) Metamictisation of natural zircon: Accumulation versus thermal annealing of radioactivity-induced damage. Contrib Mineral Petrol 141: 125-144

Oelsner O (1952) Die pegmatitisch-pneumatolytischen Lagerstätten des Erzgebirges mit Ausnahme der Kontaktlagerstätten. Freib Forschh 9: 80 pp

Pettke T, Diamond LW (2000) Rb-Sr Dating of Sphalerite based on fl uid inclusion-host mineral isochrons: A clarifi -cation of why it works. Econ Geol 91: 951-956

Romer RL (1992) Vesuvianite — a new tool for the U-Pb dating of skarn ore deposits. Mineral Petrol 46: 331-341

Romer RL (2001) Isotopically heterogeneous initial Pb and continuous 222Rn loss in fossils: The U-Pb systematics of Brachiosaurus brancai. Geochim Cosmochim Acta 65: 4201-4213

Romer RL (2003) Alpha-recoil in U-Pb geochronology: effective sample size matters. Contrib Mineral Petrol 145: 481-491

Romer RL, Linnemann U (2004) U-Pb dating the Schlottwitz agate-amethyst vein (Erzgebirge, Saxony). Eur J Mineral 16 (Beiheft 1): 116

Romer RL, Smeds S-A (1996) U-Pb columbite ages of pegmatites from Sveconorwegian terranes in southwestern Sweden. Precambr Res 76: 15-30

Romer RL, Soler A (1995) U-Pb age and lead isotopic characterization of Au-bearing skarn related to the Andorra granite (central Pyrenees, Spain). Mineral Deposita 30: 374-383

Romer RL, Wright JE (1992) U-Pb dating of columbites: a geochronologic tool to date magmatism, metamorphism, nand ore deposits. Geochim Cosmochim Acta 56: 2137-2142

Siebel W, Chen F, Satir M (2003) Late-Variscan magmatism revisited: new implications form Pb-evaporation zircon ages on the emplacement of redwitzites and granites in NE Bavaria. Int J Earth Sci 92: 36-53

Stein HJ, Bingen B (2002) 1.05-1.01 Ga Svenconorwegian metamorphism and deformation of the supracrustal sequence at Saesvatn, South Norway: Re-Os dating of Cu-Mo Mineral occurances. In: Blundell DJ, Neubauer F, von Quadt A (eds) The timing and location of major ore deposits in an evolving orogen. Geol Soc London Spec Publ 204: 319-335

Stein HJ, Markey RJ, Morgan JW, Hannah JL, Schersten A (2001) The remakable Re-Os chronometer in molybdenite: how and why it works. Terra Nova 13: 479-486

U-Pb data of Au-Pd-Pt-bearing quartz-hematite veins, Quadrilátero Ferrífero, Minas Gerais, Brazil

R.L. Romer, V. Lüders
GeoForschungsZentrum Potsdam, Telegrafenberg, 14473 Potsdam, Germany

D.A. Banks
School of Earth Sciences, University of Leeds, Leeds, LS2 9JT, UK

J. Schneider
Inst. Geowissenschaften und Lithosphärenforschung, Universität Gießen, 35390 Gießen, Germany

Abstract. Fluid inclusions hosted in specular hematite from auriferous (jacutinga) and barren veins in the Quadrilátero Ferrífero either contain fluid inclusions assemblages of high-temperature aqueouscarbonic and multiphase high-salinity, high-temperature aqueous inclusions or multiphase aqueous fluid inclusions showing narrow ranges of salinity and homogenization temperatures. Fluid inclusions in quartz and hematite are characterized by uniform Na/K ratios and considerable SO_4 contents indicating similar formation conditions and perhaps fluid origin from a common source. The formation of specular hematite veins may be related to retrograde metamorphic fluids being released during the Brazilian orogenic cycle (600-700 Ma). The Pb isotopic characteristics of all jacutinga-type samples is readily reconciliated in a simple model that (i) involves different Palaeoproterozoic or Archaean source lithologies for lead and gold and that (ii) possibly reflects contrasting depths of fluid percolation during the Braziliano orogeny and (iii) heterogeneous Au distribution in the greenstone source.

Keywords. Fluid inclusions, U-Pb, jacutinga, Au-Pd-Pt, Minas Gerais

1 Introduction

Palladian gold mineralization is unusual worldwide and only Brazilian occurrences are of economic importance. In the Quadrilátero Ferrífero of Minas Gerais, which includes Paleoproterozoic clastic and chemical sedimentary sequences (Minas Supergroup) underlain by an Archean greenstone belt (Riodas Velhas Supergroup) and granite-gneiss terrains (Fig. 1), the auriferous portions of itabirites have traditionally been denoted as jacutinga. This peculiar mineralization occurs as Au-Pd-Pt-bearing quartzspecular hematite veins crosscutting the metamorphosed host itabirites. The gold is coarse-grained and commonly black (ouro preto) due to coatings of Pd-O species and Fe-oxyhydroxide. A number of jacutinga-style gold deposits were worked in the 18th and 19th centuries in the Quadrilátero Ferrífero. Openpit iron ore mining-operations have exposed sections of jacutinga mineralization. Gold is currently an intermittent by-product of iron ore mining at Gongo Soco (several tens of kg Au per year) and Itabira, where gold production amounted to about 600 kg Au per year in 2000.

2 Results

Fluid inclusions have been studied in specular hematite from two auriferous jacutinga-style mineralization and two barren hematite veins using infrared microscopy. Hematite from barren veins of the Fábrica and Córrego do Feijão iron ore mines contain only one compositional type of fluid inclusions. These are aqueous inclusions with a vapour bubble and with more than 90% having one or more solid phases. Hematite-hosted fluid inclusions from the jacutinga style mineralization of Gongo Soco are similar to those of barren veins. Hematite from jacutinga-style mineralization at Itabira contain two compositional types of fluid inclusions, (i) aqueous carbonic inclusions, and (ii) multiphase aqueous inclusions with at least one solid phase. Both types of inclusions occur together in isolated clusters or as isolated fluid inclusion pairs within individual samples.

Two-phase and multiphase aqueous inclusions with solid phases in specular hematite from jacutinga veins of

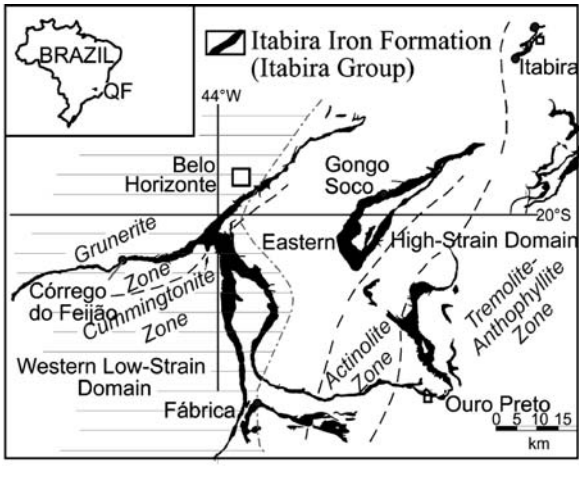

Figure 1: Simplified geological map of the Quadrilátero Ferrífero; metamorphic zones (dashed lines) and strain domains in the Itabira iron formation (modifed after Rosière et al. 2001).

the Gongo Soco mine as well as from barren veins show narrow ranges of salinity between 7.2–11.7 wt.% NaCl equiv. and homogenization temperatures between 148 and 229°C (Fig. 2). Fluid inclusions in specular hematite from the Itabira area are comparatively more complicated. The ice melting temperatures of multiphase aqueous inclusions cover a wide range between -26.1 and -10.7°C (Fig. 2). The majority of the homogenization temperatures of multiphase aqueous inclusions range between 317 and 365°C (Fig. 2). In contrast, aqueous carbonic inclusions have considerably higher total homogenization temperatures when compared with multiphase aqueous inclusions and higher ice melting temperatures (Fig. 2). Crush-leach analyses on samples of quartz and hematite show that Cl and SO_4 are the major anions in the fluid inclusions. The fluids are dominated by Na and show significant but variable amounts of K and Ca, and lesser amounts of Mg and Li. The low Cl/Br and Na/Br ratios of the analyzed inclusions are indicative of halite dissolution and reprecipitation by a halite saturated fluid. During dissolution and reprecipitation, Br is excluded from halite and enriched in the fluid, just as during halite precipitation from seawater. The salinity of the fluid inclusions, however, is below halite saturation and indicates dilution after they have gained Br by interaction with halite. The Na/K ratios of the analysed fluids fall into the narrow range (mean 4.5±2.2). The Na/K ratios in brines are likely to be controlled by equilibrium reactions with alkali feldspars and muscovite. Therefore, the elevated K and Li concentration in the fluids are likely to derive from water-rock interaction between the ore-forming fluids and granites and/or gneisses of the crystalline basement.

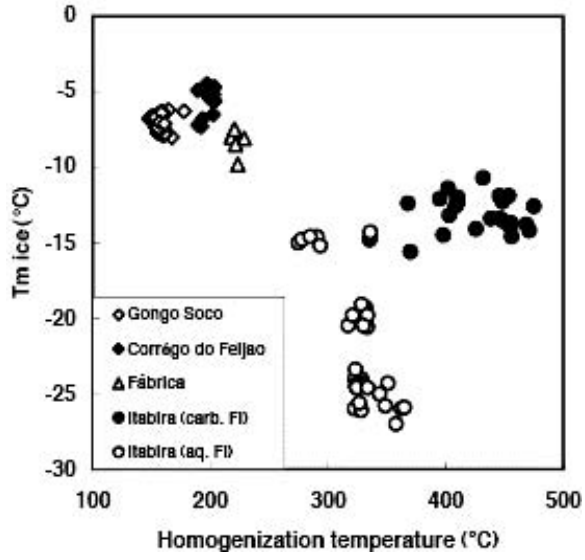

Figure 2: Th vs. Tmice diagram of fluid inclusions in specular hematite from auriferous (jacutinga) and barren veins in the Quadrilátero Ferrífero.

3 U-Pb systematics of hematite and gold

3.1 Hematite

The Pb isotope data of the hematite samples scatter widely in the $^{206}Pb/^{204}Pb$ – $^{207}Pb/^{204}Pb$, $^{206}Pb/^{204}Pb$–$^{208}Pb/^{204}Pb$, and $^{206}Pb/^{204}Pb$–$^{238}U/^{204}Pb$ diagrams (Fig. 3a-c). The data do not define isochrons. Although the scatter among samples from individual deposits is smaller than for the entire data set, there is significant excess scatter, which may originate from (i) initial isotopic heterogeneity within single deposits and contrasting Pb composition in different deposits, (ii) addition of isotopically distinct Pb at some time after formation of the deposits, and (iii) fractionation between U and Pb (modification of the $^{238}U/^{204}Pb$ ratio) during a later event. Furthermore, there may have been some redistribution of radiogenic Pb between hematite host and fluid inclusions by recoil. These potential non-idealities make the derivation of a precise age impossible. Nonetheless, the Pb isotope systematics of the fluid-free hematite samples imposes several constraints on the evolution of the hematite deposits. (1) The data fall in a triangular area in the $^{206}Pb/^{204}Pb$–$^{207}Pb/^{204}Pb$ diagram (shaded area, Fig. 3a), which may reflect a heterogeneous source or a poly-stage evolution of the hematite veins. The steepest $^{207}Pb/^{206}Pb$ trend corresponds to a mixing line of Pb that evolved from ca. 2.7 Ga to 1.9-2.0 Ga. Since the sampled jacutinga–style veins are hosted by Palaeoproterozoic itabirite-type iron deposits, variations along the 2.7-1.9 Ga trend possibly reflects derivation of Pb from an isotopically heterogeneous source during the Palaeoproterozoic formation of the iron deposits. (2) In the $^{206}Pb/^{204}Pb$–$^{238}U/^{204}Pb$ isochron diagram (Fig. 3c), most data scatter about a linear trend, whose slope corresponds to an age of c. 635 Ma. This age has no strict geochronological meaning as the requirements for an isochron (common initial, single stage evolution) are not met. There are numerous samples that fall above this Palaeozoic reference line, which either implies that these samples had a more radiogenic initial Pb isotopic composition (dashed line, Fig. 3c) or that they record an older age. (3) Hematite from each deposit shows a relatively narrow range in $^{208}Pb/^{204}Pb$, but shows distinct differences between deposits (Fig. 3b). (4) The initial Pb isotopic composition of all deposits is characterized by $^{207}Pb/^{204}Pb$ values, which implies that the initial Pb of the hematite deposits was dominantly derived from an old crust.

3.2 Gold

The Pb isotopic composition of gold flitters from jacutinga veins at Gongo Socco align along the steep trend in the $^{206}Pb/^{204}Pb$–$^{207}Pb/^{204}Pb$ diagram (Fig. 3a) with some samples being displaced to the right of this trend. In situ Pb growth (shift to the right) was insignificant for most

samples. The Pb from the gold samples is distinctive by its higher $^{207}Pb/^{204}Pb$ and lower $^{208}Pb/^{204}Pb$ values (at comparable $^{206}Pb/^{204}Pb$) than the hematite samples (Figs. 3a and 3b), the itabirites, or the wall-rocks. This implies that trace Pb in gold may have been derived from a different source than the iron. Hematite from the barren deposit Córrego do Feijão is in its $^{208}Pb/^{204}Pb$ signature closest to the host-rocks and the itabirite deposits, whereas hematite from the Au-bearing jacutinga-style veins have $^{208}Pb/^{204}Pb$ values that are closer to the signature of Au.

4 Discussion

Specular hematite ores from barren veins and Au-Pd-Pt-bearing jacutinga–style mineralization at Gongo Soco were deposited from fluids that show narrow ranges of salinity and homogenization temperatures. This may be due to similar formation conditions or fluid origin from a common source, although the barren veins do not contain Au, Pd, and Pd. Crush-leach analyses demonstrate Cl and SO_4 to be the major anions in the ore-forming fluids. The high sulfate concentrations of the analyzed fluids may also be derived by leaching of evaporites (gypsum). The formation of schistose high-grade specular hematite veins at Itabira can be related to acid Cl-SO_4-CO_2 retrograde metamorphism fluids that interacted intensively with crystalline rocks. The absence of CO_2 in hematite-hosted inclusions from veins in the low-strain domain may be attributed to carbonate precipitation or conversion of CO_2 to bicarbonate due to cooling during fluid migration from the highto low-strain domain. A Brasiliano age can be derived from the $^{238}U/^{204}Pb$–$^{206}Pb/^{204}Pb$ diagram (Fig. 3c) where specular hematite samples from the Itabira district and fluid inclusions therein fairly plot on or close to the reference line for 635 Ma. The least radiogenic Pb isotopic composition from the investigated region was measured on galena from stratiform gold deposits in the Archaean Rio das Velhas Supergroup. Starting from such a composition and lasting until the Transamazonian orogeny in situ Pb growth would yield values that fall on the red array in Fig. 3. Samples with low μ values would have evolved less from their starting composition, whereas samples with high μ values would have evolved to more radiogenic composition. There may be a lithologic control on the μ values, which higher values in more evolved felsic units than in mafic units. Depending on source regions for the itabirite-type iron deposits in the Palaeoproterozoic clastic-chemical sediments of the Minas Supergroup, different deposits may have a constrasting Pb isotopic composition. Undisturbed in situ Pb growth in itabitirite-type iron deposits until the present would result in Pb isotopic compositions that fall between the 1.83 Ga reference line of Olivo et al. (1996) and the Archaean-to-Transamazonian Pb trend (Fig. 3). As the Pb isotopic composition of most samples falls to the right of

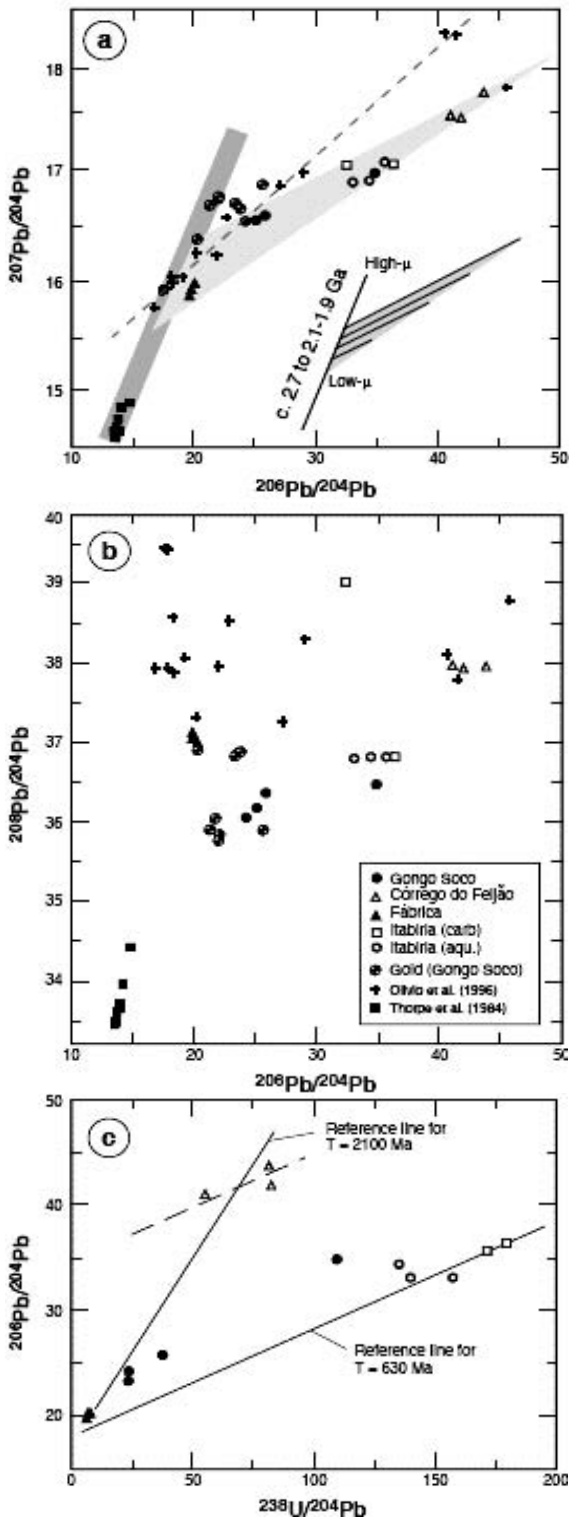

Figure 3: Pb-Pb and U-Pb isotope systematics of hematite, gold, and whole-rock samples. The dashed reference line corresponds to the 1.83 Ga age preferred by Olivo et al. (1996) for the Cauê mine. This data set includes another three samples (206Pb/204Pb > 60) that fall below the reference line.

the 1.83 Ga reference line, lead evolution to highly radiogenic compositions occurred mainly after the Braziliano orogeny (see also Fig. 3c). The scatter of the data in the $^{206}Pb/^{204}Pb$ vs. $^{238}U/^{204}Pb$ diagram either may reflect several events, most prominantly a Braziliano and a Transamazonian event (Fig. 3c) or it may reflect that the initial Pb isotopic compositions of some deposits was highly radiogenic at the time of the Braziliano orogeny (dashed line in Fig. 3c).

The Pb isotopic composition of trace Pb in gold generally has lower $^{208}Pb/^{204}Pb$ values than the hematite samples. Furthermore, this trace Pb plots above the 1.83 Ga reference line and above the hematite field (Fig. 3). The contrasting Pb isotopic composition between hematite and gold in the jacutinga-style veins possibly suggests that hematite incorporated significant amount of locally derived material and that the veins in part even may contain hematite grains originating from the older wallrock. The relation of the trace Pb from gold is compatible with a derivation from an Archaean source rock that is characterized by high $^{238}U/^{204}Pb$ values and relatively low $^{232}Th/^{204}Pb$ values. In this context, Archaean source does not only refer to the Archaean basement, but also to its cover of Palaeoproterozoic clastic sediments that were derived from the Archaean basement. The relation of the trace Pb from gold is incompatible with a derivation from the same source as the Pb in the itabirites or from the itabirites itself. If the Archaean felsic basement is the source of the trace Pb in gold, the same source could also be the source of U, which eventually gave rise to radiogenic Pb isotopic compositions in hematite. This source may also have had controlling influence on the homogeneous Na/K ratios in hematite-hosted fluid inclusions. A felsic Archean basement, however, could not provide Au and Pd. Instead, these two elements may be derived from the Archaean supracrustal rocks that include voluminous units of mafic volcanic rocks. Since the Pb contents in felsic rocks are much higher than in mafic and ultramafic rocks, the Pb isotopic composition reflects the signature of the felsic basement rather than the mafic units. Thus, the fluid that transported Au and Pb into the jacutinga–style veins may carry the Pb isotopic signature of a source rock that does not correspond to the source of Au and Pd. This explanation allows the fluid to acquire its Pb isotopic signature either in the felsic basement below the greenstone unit or in the Palaeoproterozoic clastic sediments between the Archaean basement and the units hosting the itabirite-type iron deposits. The occurrence of Au (and Pd), however, is controlled by the distribution of Au-bearing mafic to ultramafic supracrustal rocks in the Archaean basement. Thus, there may be a spatial correspondance between stratiform Archaean and jacutinga-type Braziliano gold deposits. Au in both deposits would have been mobilized from the same source rocks.

The formation of the jacutinga–style veins during the Brazilian orogenic cycle explains both the homogeneous nature of the fluids with respect to dissolved major components, e.g., Na/K, Cl/Br ratios, high-SO_4 content, and the heterogeneous character of the fluids with respect to CO_2 content and trace (Au, Pd, Pb, and U) constituents, as differences in proportions of major components reflect contrasting evolution histories of the fluid in terms of unmixing and cooling.

Constraints on the source and evolution of mineralising fluids in the Norrbotten Fe oxide-Cu-Au province, Sweden

Martin Smith
School of the Environment, University of Brighton, Brighton, BN2 4GJ, U.K.

Sarah A. Gleeson
University of Alberta, Edmonton T6G 2E, Canada

Abstract. Norrbotten County, Sweden, is well known for the iron oxide-apatite deposits of the Kiruna and Malmberget areas. These are spatially associated with iron oxide Cu (± Au) deposits and a genetic link between the two has been suggested as a part of the IOCG spectrum of deposits. Here, we report the results of a fluid inclusion microthermometry and bulk crush leach halogen and chlorine stable isotope study, carried out to test that hypothesis. Quartz veins from late stage veins from Fe oxide-apatite deposits and Cu-(Au) deposits contain hypersaline brine inclusions, with a salinity range of 32 to 38wt. % NaCl eq. in Fe-oxide bodies, and of 38 to 47wt % NaCl eq. in Cu-Au deposits. In Cu-(Au) deposits these are sometimes accompanied by CO_2-rich inclusions.

The Cl/Br ratio of the fluid inclusion leachates is consistent with magmatic fluid compositions, and ranges between 859 and 9597, with no distinction between the Fe-oxide samples and the Cu-mineralizing brines. $\delta^{37}Cl_{(SMOW)}$ values range from –0.99 to –5.63‰. The data are far removed from both mantle ($\delta^{37}Cl$ = +4.7‰) and crustal ($\delta^{37}Cl$ = 0‰) values and must represent fractionation of the isotopes during the mineralizing process. We suggest this fractionation occurred during the formation of Cl-rich mineral phases commonly found associated with the deposits e.g. scapolite, biotite and amphibole.

Keywords. Fluid inclusions, halogens, IOCG, chlorine isotopes

1 Introduction

The original classification of iron oxide-copper-gold type deposits by Hitzman et al. (1992) postulated a link between Fe oxide-apatite deposits ('Kiruna-type') and the IOCG deposits themselves. Northern Norrbotten County, Sweden, is well known for the Kirunavaara deposit, and also hosts several Cu-(Au) deposits (Bergman et al., 2001). However, magnetite-apatite bodies and epigenetic Cu-Au bodies formed in the range 1900-1860Ma (Romer et al., 1994; Billstrom and Martinsson, 2000), but with the Cu-Au systems potentially post-dating the Fe oxide-apatite bodies. Younger deposits still (~1800-1750Ma) are associated with regional scale shear zones. All these deposits show similar alteration types and association with regional sodic alteration (Frietsch, 1997), and have been suggested to belong to the IOCG group. A knowledge of fluid source in all three deposit types is therefore of value for metallogenetic models, and will help to define any common mineralising processes related to episodic metamorphism or magmatism. As a part of the EU-RDF Georange program we have investigated the fluid sources for quartz veins from the late stage of Fe oxide-apatite ore formation and from a range of Cu-(Au) deposits and prospects using a bulk crush leach technique to analyse for cation, anion, and chlorine isotope composition within the inclusion fluids.

2 Sample sites

The geology of the Norrbotten area consists of a Palaeoproterozoic supracrustal sequence overlying Archaean basement, which was deformed and intruded by grantoids during the Svecofennian orogeny (1.96-1.85Ga). The Palaeoproterozoic sequence within the area studied is broadly separated into the Greenstone Group metabasic rocks, and the overlying Porphyry Group, which consists of intermediate to acid volcanics and intercalated sediments. Within Fe oxide-apatite bodies, quartz veins cross-cut both the ore itself, and altered footwall rocks. Samples of this kind were collected from the magnetite-hematite-apatite bodies of the Kiruna area and from the Valkommen deposit, which forms a part of Malmberget Fe oxide-apatite body.

Samples from Cu-(Au) deposits where collected from sites hosted in the Greenstone and Porphyry Group volcanics at Pahtohavare (Lindblom et al. 1996), Kallosalmi and Gruvberget, and from younger deposits associated with the Nautanen Deformation Zone (Fig. 1).

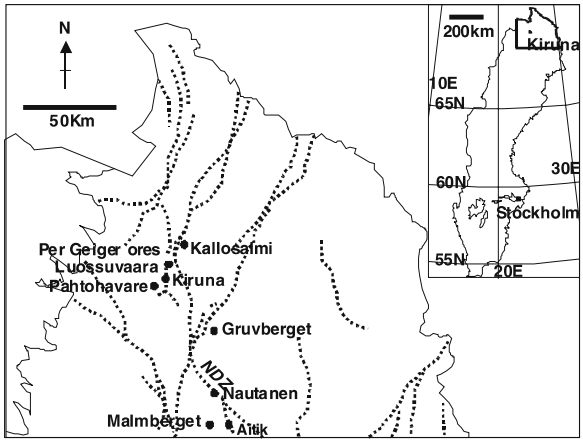

Figure 1: Sketch map of northern Norrbotten, showing locations mentioned in the text, and major structural lineaments (after Bergman et al. 2001).

3 Techniques

Samples were initially characterised petrographically and microthermometrically using a Linkam TMS600 heating-freezing stage at the University of Brighton. Samples were then crushed and hand picked to provide approximately 5g of pure quartz for crush leach analysis. Samples were electrolytically cleaned prior to crushing, and the leachates analysed for Na, Li and K using atomic absorption spectroscopy, for other cations using ICP-MS, and for halogens, sulphate and phosphate using ion chromatography at the University of Alberta. Chlorine isotope analyses were carried out on the leachates using gas source mass spectrometry at Environment Canada, Saskatoon.

4 Results

4.1 Microthermometry

Late stage quartz veins cutting Fe-oxide apatite bodies or their wall rocks contain a consistent fluid population across the area (salinity 30-40 wt. % NaCl eq.; T_h=100-150°C). Fluids associated with quartz veins from Cu-(Au) deposits and prospects, range from much higher salinities (around 50-60 wt % NaCl eq.) to those comparable with the late stage veins associated with the Fe-oxide bodies. Two veins from the Gruvberget body contain lower salinity, Ca-rich inclusions, which probably represent a post-ore fluid.

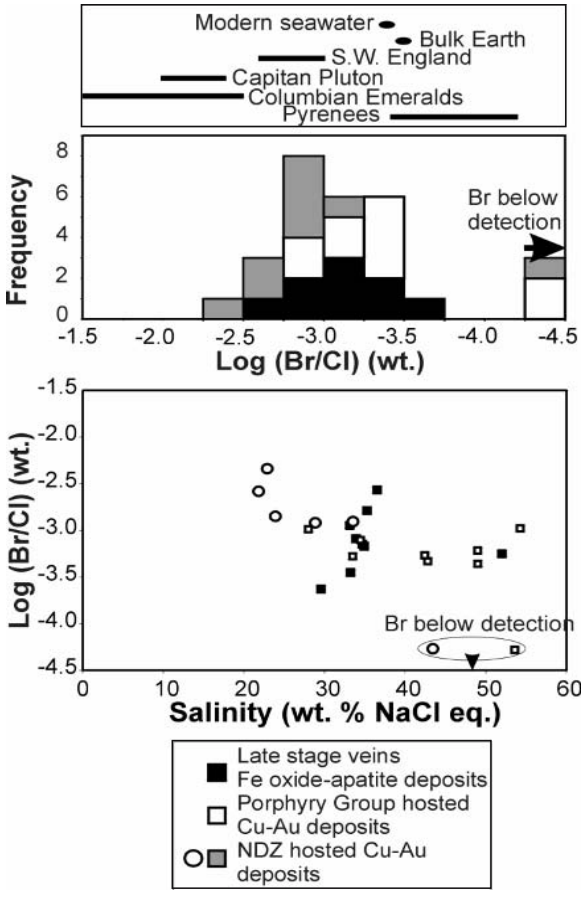

Figure 2: Halogen chemistry of inclusion fluids from Norrbotten.

The inclusion assemblage from deposits associated with the NDZ is more complex, with coexisting Lw+Sh+V, Lw+Lc+V and Lc+V inclusions. In some instances these are preserved along the same secondary fluid inclusion trails. Lw+Sh+V inclusions from the Valkommen body, and from some veins at Nautanen show similar salinities and homogenisation temperatures to those from the Fe-oxide and Cu-Au deposits already discussed. At Nautanen complex inclusion assemblages are hosted on secondary trails. These are indicative of phase separation. Salinities vary from ~12-18 wt. % NaCl eq. for Lw+Lc+V inclusions to ~29wt % NaCl eq. for halite bearing inclusions. Total homogenisation temperatures for Lw+Lc+V inclusions are typically around 250-300°C, whilst partial L-V homogenisation for halite bearing inclusions is around 100-120°C. At both Nautanen and Ferrum a further assemblage of Ca-rich brines is observed similar to those observed in some veins at Gruvberget. Many of the observations made here are in agreement with previous work by Broman and Martinsson (2000).

4.2 Halogen chemistry

Log Br/Cl ratios within leachates from these fluids (Fig. 2) range from approximately –2.5 to -3.7, with two exceptional analyses at –2.3 and –4.4. The majority of analyses fall in the range –2.8 to –3.5 with no distinction between Fe-oxide related and Cu-related brines. These data are compared with a selection of previous data from Yardley et al. (2000) in Figure 2. They are most comparable to S.W. England granite related fluids, and are clearly distinct from fluids associated with the Capitan Pluton, New Mexico and Columbian Emerald deposits. This is significant as these are both interpreted as deriving their salinity either from magmatic interaction with evaporites, or from metamorphism of evaporites. Our data are therefore consistent with magmatic sources for mineralising fluids in Norrbotten, and not with a meta-evaporitic source. The more Br enriched samples are lower salinity fluids from the NDZ, and possibly indicate interaction of a magmatic fluid with the surrounding metasediments.

4.3 Chlorine isotopes

The chorine isotopic composition of leachates from vein quartz samples from Fe oxide-apatite bodies, and from epigenetic Cu-Au deposits ranges in δ^{37}Cl relative to standard mean ocean chlorine (SMOC) from -5.63 to -0.99‰. These data are compared with previous data from inclu-

sion fluids, natural porewaters and rocks and minerals in Figure 3. Norrbotten inclusion fluids are consistently enriched in ^{35}Cl relative to all previously analysed fluid inclusions, most rocks and minerals and most natural porewater samples. The only comparable data are from subduction zone porewaters sampled in the Barbados and Nankai accretionary prisms (Ransom et al. 1995). Luders et al. (2002) showed that submarine hydrothermal fluids could be enriched in ^{37}Cl by extraction of ^{35}Cl into a vapour phase during boiling, and consequently a condensate from a low density fluid or vapour could show low $\delta^{37}Cl$ values.

However, the high salinity of these fluids would seem to preclude their origin as a condensate. Equally ^{35}Cl enriched fluids can be formed by the evapo-concentration of seawater and precipitation of halite (Eastoe et al. 1998), but such fluid have not yet been reported with the low $\delta^{37}Cl$ values seen here. The most likely explanation for the Cl isotope data is the preferential extraction of ^{37}Cl into silicate mineral phases (in this case scapolite, biotite and amphibole) results in a passive enrichment of hydrothermal fluids in ^{35}Cl. Chlorine isotope analyses of silicate minerals are relatively limited at the present time, but those available from biotites in the Stillwater complex (Boudreau et al. 1997), Porphyry Cu related biotites (Arcuri and Brimhall 2003) show uniformly positive $\delta^{37}Cl$ values. Experimental data from. Pan and Dong (2003) show that Br/Cl ratios of marialitic scapolite closely reflect the halogen composition of co-existing fluids, and hence this process would not be expected to affect the Br/Cl signature of hydrothermal fluids.

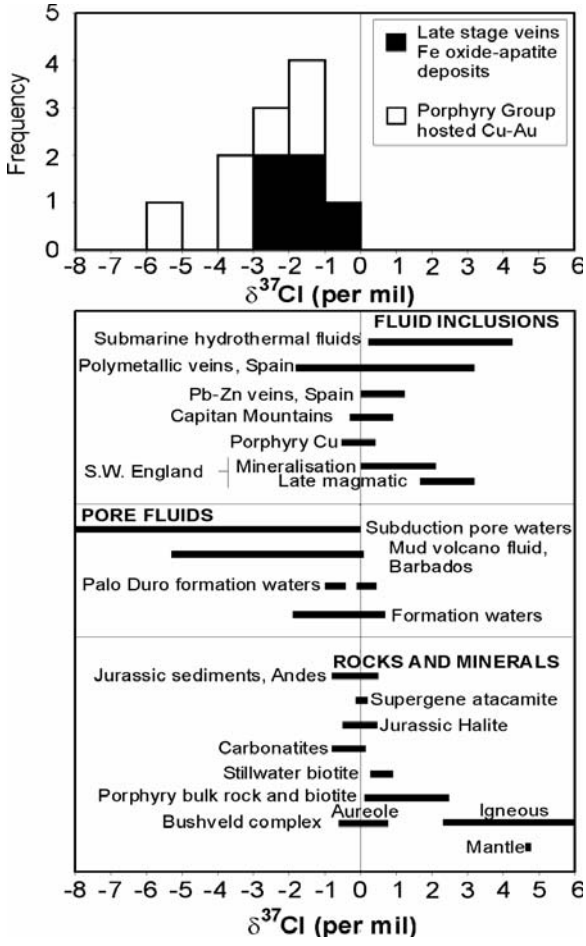

Figure 3: Chlorine isotope composition of inclusion fluids compared with previous data. Individual citations given in reference section.

5 Discussion and conclusions

The data presented here are consistent with a magmatic fluid source for Porphyry and Greenstone Group hosted Cu-(Au) mineralization in Norrbotten, and for late stage fluids associated with Fe oxide-apatite bodies. The microthermometric data do not, however, indicate that directly comparable fluids were involved in the formation of the Fe oxide- apatite bodies and the Cu-(Au) mineralization. The displacement of $\delta^{37}Cl$ values to lower values in the epigenetic Cu-(Au) mineralising fluids may reflect extensive water rock interaction and Na-Cl metasomatism during this stage of the regions evolution.

Fluids associated with younger, shear zone hosted deposits are also potentially magmatic, although the inclusion of several fluid inclusion populations reflects the modification over an extended period and possibly the input of metamorphic fluids. Temporal constraints indicate that the highly saline ore fluids present in all deposits must have been generated during several magmatic events, with the additional input of non-magmatic fluids into the younger, shear zone hosted deposits at Nautanen.

Previous workers have suggested that meta-evaporites may have played a role in generating the highly saline brines and regional sodic alteration in Norrbotten (Frietsch et al. 1997). We find no evidence to support this idea. Halite typically shows heavy $\delta^{37}Cl$ values relative to the fluid from which it precipitates, so halite dissolution is unlikely to form strongly ^{37}Cl depleted fluids. We have not yet, however, analysed samples containing a significant proportion of the Ca-rich brine, and this may preserve such a signature (Wanhainen et al. 2003).

References

Arcuri T, Brimhall G (2003) The chloride source for atacamite mineralization at the Radomiro Tomic porphyry copper deposit, Northern Chile. Econ Geol 98:1667-1681

Banks DA, Gleeson SA, Green R (2000) Determination of the origin of salinity in granite-related fluids: evidence from chlorine isotopes in fluid inclusions. J Geochem Expl 69-70: 309-312

Banks DA, Green R, Cliff R, Yardley BWD (2000) Chlorine isotopes in fluid inclusions: Determination of the origins of salinity in magmatic fluids. Geochim Cosmochim Acta 64:1785-1789

Bergman S, Kübler L, Martinsson O (2001) Description of regional geological and geophysical maps of northern Norrbotten county (east of the Caledonian orogen). Sver Geol Unders Ba 56.

Billstrom K, Martinsson O (2000) Links between epigenetic Cu-Au mineralisations and magmatism/deformation in the Norrbotten county, Sweden. In: LuT research report 2000:06. 2nd GEODE Fennoscandian Shield field workshop on Palaeoproterozoic and Archaen greenstone belts and VMS districts in the Fennoscandian Shield.

Boudreau AE, Stewart MA, Spivack AJ (1997) Stable Cl isotopes and origin of high-Cl magmas of the Stillwater Complex, Montana. Geology 25 791-794

Broman C, Martinsson O (2000) Fluid inclusions in epigenetic Fe-Cu-Au ores in northern Norrbotten. In: L..T research report 2000:06. 2nd GEODE Fennoscandian Shield field workshop on Palaeoproterozoic and Archaen greenstone belts and VMS districts in the Fennoscandian Shield.

Eastoe CJ, Long A, Kinaith LP (1998) Stable chlorine isotopes in the Palo Duro Basin, Texas: Evidence for preservation of Permian evporite brines. Geochim Cosmochim Acta 63: 1375-1382

Frietsch R, Tuisku P, Martinsson O, Perdahl JA (1997) Early proterozoic Cu-(Au) and Fe ore deposits associated with regional Na-Cl metasomatism in northern Fennoscandia. Ore Geol Rev 12: 1-34

Hitzman MW, Oreskes N, Einaudi MT (1992) Geological characteristics and tectonic setting of proterozoic iron-oxide (Cu-U-Au-REE) deposits. Precambr Res 58: 241-287

Lindblom S, Broman C, Martinsson O (1996) Magmatic-hydrothermal fluids in the Pahtohavare Cu-Au deposit in greenstone at Kiruna, Sweden. Mineralium Depos 31: 307-318

Luders V, Banks DA, Halbach P (2002) Extreme Cl/Br and δ^{37}Cl isotope fractionation in fluids of modern submarine hydrothermal systems. Mineralium Depos 37: 765-771

Pan Y, Dong P (2003) Bromine in scapolite-group minerals and sodalite: XRF microprobe analysis, exchange experiments, and application to skarn deposits. Can Mineral 41: 529-540

Ransom B, Spivack AJ, Kastner M (1995) Stable Cl isotopes in subduction-zone pore waters - implications for fluid-rock reactions and the cycling of chlorine. Geology 23:715-718

Romer RL, Martinsson O, Perdahl JA (1994) Geochronology of the Kiruna iron ores and hydrothermal alterations. Econ Geol, 89:1249-1261

Yardley BWD, Banks DA, Barnicoat AC (2000) The chemistry of crustal brines: tracking their origins. In: TM Porter (ed) Hydrothermal iron oxide copper-gold and related deposits: A global perspective. Austral Min Found, Adelaide, pp. 61-70.

LA-ICPMS U-Pb dating of titanite: New constraints on multistage geological evolution of the Norrbotten mining district, Sweden

Martin Smith, Craig Storey
School of the Environment, University of Brighton, Brighton, BN2 4GJ, U.K.

Teresa Jeffries
Department of Mineralogy, The Natural History Museum, London, SW7 5BD, U.K

Abstract. Established techniques for the laser ablation ICP-MS U-Pb analysis of zircon have been developed for application to common Pb bearing phases, including titanite and allanite. A novel common Pb correction procedure has been developed for deriving mineral ages, and has been tested using well characterised samples. This technique has been applied to samples from the mining district of Norrbotten, Sweden, with the aim of constraining the timing of iron oxide-copper-gold (IOCG) mineralization in relation to the formation of Fe-oxide-apatite deposits and the regional geological evolution. Titanites from three of the Fe oxide apatite deposits studied show complex multistage growth textures implying a prolonged metasomatic history. Cores from these samples show ages in the range 2070 to 2000 Ma before present, indicating that the age of the host supracrustal sequence in Norrbotten may be significantly older than previously thought. The rims of these crystals, which show distinct trace element signatures to the cores, as well as unequivocally metasomatic titanites and allanites from other areas give ages in the range ~1875-1820Ma. These ages probably indicate the time of primary mineralization of both the late stages of Fe oxide and Cu-Au types. Younger ages in the range ~1790-1700Ma are interpreted to relate to subsequent metamorphism of the deposits, and remobilisation of sulphide mineralization along long lived, regional scale structures.

Keywords. U-Pb, geochronology, titanite, Norrbotten, Kiruna, IOCG

1 Introduction

Northern Norrbotten County, Sweden, is well known as a region of Fe oxide-apatite mineralization, and also hosts a range of copper-gold deposits (Bergman et al. 2001). These deposits have been proposed to be related as a part of the iron oxide-copper-gold (IOCG) spectrum of deposits. A more detailed understanding of this relationship will be of great use to defining ore genetic and exploration models in terms of both the relationship of Cu-Au mineralization to Fe oxide mineralization, and the relationship of both mineralization types to the regional geological evolution. As a part of the EU-RDF Georange program we have investigated this relationship via the development of a novel U-Pb geochronological technique, which allows the use of in situ laser ablation ICP-MS for analysis of titanite and other common lead-bearing phases within polished thick sections.

2 Technique

In this study we have extended established U-Pb techniques by LA-ICPMS (quadrupole) to titanite and allanite. Titanite and other common U hosting minerals readily incorporate up to ppm levels of (common)Pb into their lattice alongside U and Th during crystallisation, making the necessity for common Pb correction paramount. In this study we have used both a mathematical based ^{207}Pb-correction, and the far more robust TIMS-style correction. The TIMS-style correction is based upon measurement of the stable ^{204}Pb isotope to assess the amount of common Pb in the analysis. This requires an independent measurement or estimate of the common Pb composition to be corrected for. We have made measurements of common Pb composition by utilising in line gold traps to reduce interferances on the ^{204}Pb peak from mercury stable isotopes. In samples with low analytical signal intensity we combine this approach with a novel appraoch based on 3 dimensional U-Pb concrodia.

3 Sites investigated

The geology of the Norrbotten area consists of a Palaeoproterozoic supracrustal sequence overlying Archaean basement, which has subsequently been deformed and intruded by grantoids during the Svecofennian orogeny (1.96-1.85Ga). The Palaeoproterozoic sequence within the area studied is broadly separated into the Greenstone Group metabasic rocks, and the overlying Porphyry Group, which consists of intermediate to acid volcanics and intercalated sediments.

For the purpose of this study we have examined material from both Fe oxide-apatite and copper deposits (Bergman et al. 2001) including titanite intergrown with magnetite from deformed vesicle fills within the sodically altered footwall trachyandesites at Luossavaara, and titanite hosted in quartz-carbonate veins cutting magnetite cemented brecciated metavolcanics in the footwall of the Kirunavaara magnetite-apatite body. Within the Kiruna area samples were also analysed from Cu-(Au) deposits and prospects at Rakkurijarvi (Porphyry Group hosted) and Kallosalmi (Greenstone Group hosted). We

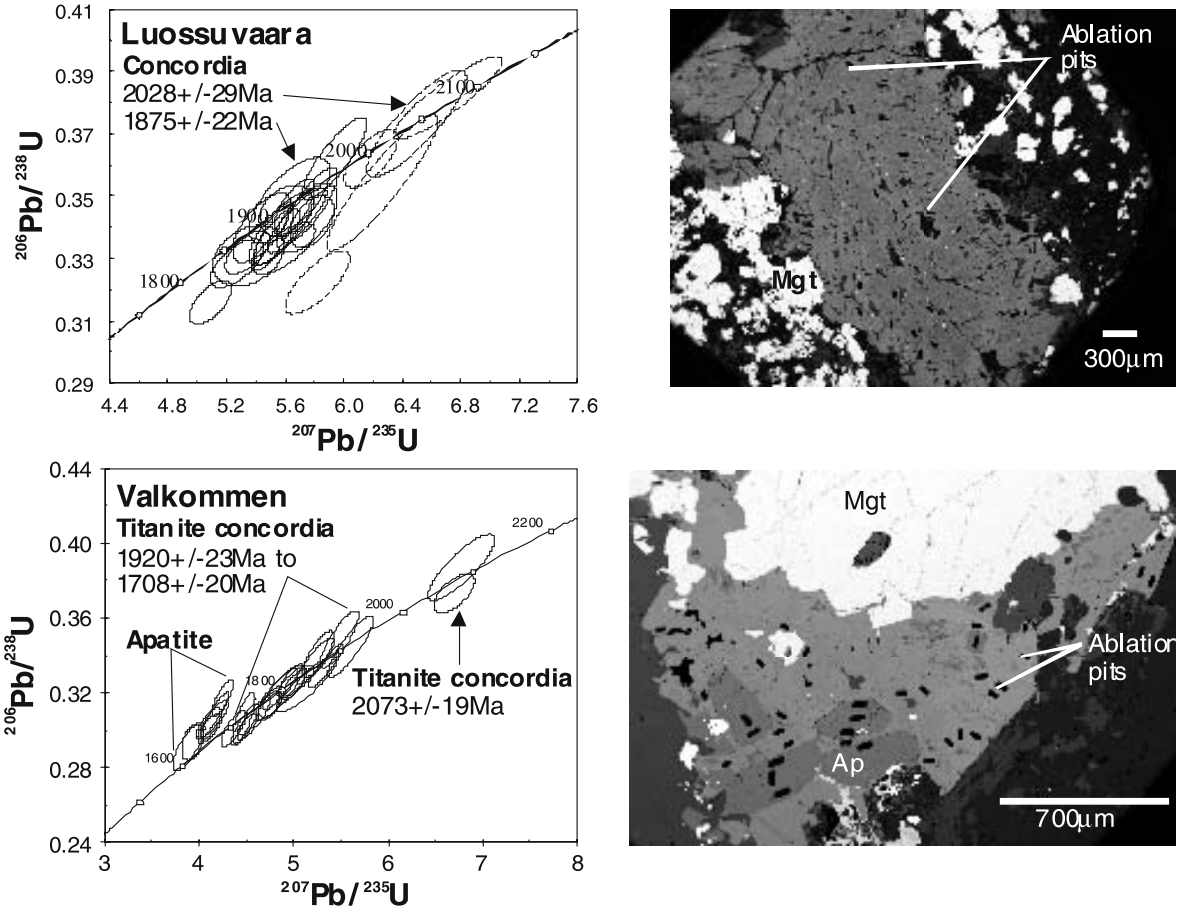

Figure 1: Examples of U-Pb data from titanite grains from Fe oxide-apatite deposits, showing evidence of multistage growth in back scattered electron images

have also analysed samples from the Gruvberget Cu deposit, developed in the footwall to a magnetite-hematite-apatite body, again hosted by intermediate metavolcanics.

The third area studied was around Malmberget to the south of Kiruna. The Malmberget body itself is an Fe oxide-apatite body exposed in a large fold structure. It is interpreted to be a metamorphosed Kiruna type deposit. Samples where taken from the hanging wall of the Valkommen ore body. To the east of the Malmberget body both the supracrustal sequences and the Svecofennian granitoids are cut by a regional scale shear system (the Nautanen Deformation Zone). This hosts the working Cu-(Au) mine at Aitik, and a historically worked prospect at Nautanen.

4 Results of geochronological studies

A number of samples show complex multistage growth (Fig. 1). Samples from Luossavaara, Gruvberget, and Malmberget show core ages in the range 2073-2028 Ma. All these bodies are Fe-oxide (and sometimes copper) deposits hosted in Porphyry group metavolcanics, supposedly of Svecofennian age. The BSE light rims of most of these

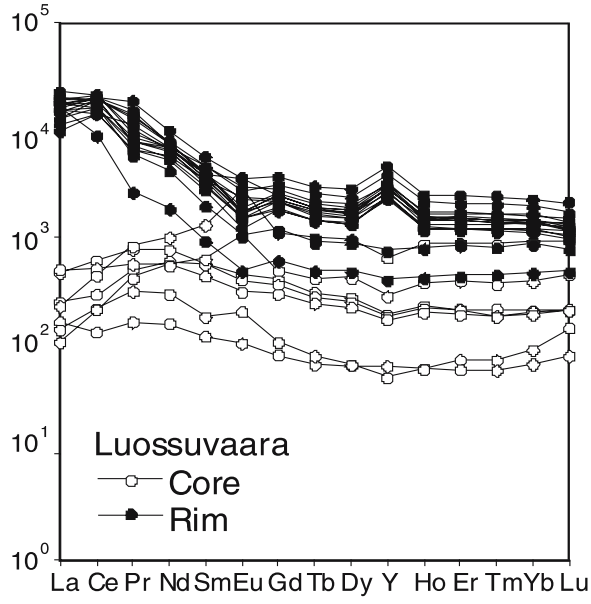

Figure 2: Chondrite normalised REE content of Luossavaara titanite.

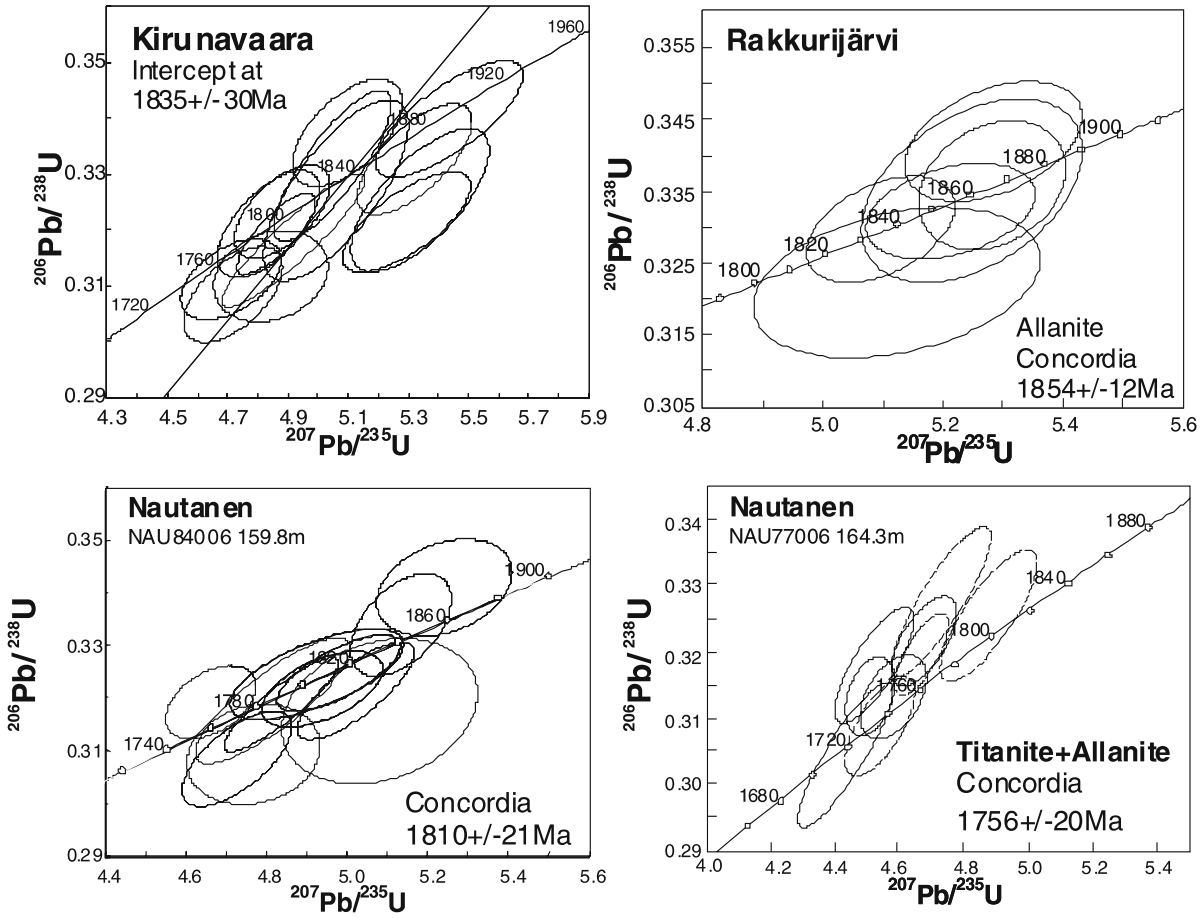

Figure 3: Examples of U-Pb data from alteration surrounding Fe-oxide-apatite and Cu-(Au) deposits.

titanites give ages in the range 1920 to 1826 Ma. LA-ICPMS trace element analyses from corresponding sites in the same grains show a clear distinction between core and rim analyses (Fig. 2). The younger, rim zones are strongly LREE enriched relative to the core zones. These patterns are comparable to the composition of unequivocally metasomatic titanites from other deposits. The rim zones are volumetrically the most significant parts of the crystals. The ages obtained from these zones are reflected in previous TIMS data from Norbotten titanite which analysed bulk crystals. The range of ages from the alteration surrounding Fe-oxide and Cu-deposits is previously unreported from the Porphyry Group and the deposits which it hosts. These data suggest a minimum age of the Porphyry group of between ~2070-2028 Ma, significantly older than currently thought. Analyses of titanites from regional alteration (Nunasvaara) and the alteration surrounding Fe-oxide and Cu-Au deposits hosted by the Porphyry Group range from 1902+/-8 Ma (Nunasvaara) to 1758+/-18 Ma (Tjarrajäkka). The data in the range of 1920-1826 Ma correspond to the time range of the Svecofennian metamorphism, and the main intrusive activity in the area. Our data are consistent with either metamorphic growth of titanite during this period or metasomatic growth of titanite during hydrothermal activity. The youngest ages so far encountered are from the Valkommen body, with titanite at 1708±20 Ma, and apatite at 1584±12 Ma. The very young age recorded in apatite from Valkommen is related to the lower closure temperature of apatite relative to either titanite or zircon. We suggest that these ages record subsequent metamorphism of the deposits in question.

Data from deposits hosted by, or associated with, the NDZ range from 1826+/-15 Ma to 1756+/-20 Ma. Two samples from the Nautanen deposit gave ages of 1810+/-21 Ma and 1756+/-20 Ma respectively. These data indicate a prolonged history of deformation and fluid flow along the NDZ, probably involving multiple episodes of ore deposition and remobilisation. The REE patterns of these titanites are LREE depleted; indicating different chemical conditions of titanite formation in the NDZ compared to other Cu-(Au) deposits. This may be related to contrasting fluid chemistry, or may reflect ore-forming processes, particularly the co-precipitation of allanite and LREE enriched epidote.

5 Discussion and conclusions

The data presented here are generally in agreement with previous data on mineral deposits within the Norrbotten region. The Kirunavaara and Luossavaara mineralization has previously been dated at 1888+/-6 Ma between 1876+/-9 Ma by Billstrom and Martinsson (2000), who reported U-Pb titanite ages for Cu-Au mineralization in the ranges 1880-1860Ma and 1800-1750Ma. These ages are also in broad agreement with our data; however, a number of deposits in the younger group in their study gave ages in the older group in this study. This is likely to represent a difference in the scale of sampling, and suggests that the age heterogeneity seen in these deposits is the result of metamorphic remobilisation of ore in the period 1800-1750Ma. In complex zoned grains we interpret the data from the cores as indicating the timing of initial metamorphism (and a minimum age for magmatism), and data from the rims as indicating the timing of metasomatic fluid flow associated with mineralization.

Previous constraints on the age of the Porphyry group come from U-Pb dating of zircon (Welin 1987; Skiöld and Cliff 1984). Our new data now suggest these ages may represent recrystallisation of zircon during a later metamorphic/metasomatic event. In summary, the data from titanite cores suggest that Porphyry and Porphyrite group volcanism occurred significantly earlier than previously thought. This has significant implications for the timing of rifting and subduction during the early tectonic evolution of the Fennoscandian shield. It may also have implications for correlation of Norrbotten stratigraphy with that of the Skellefte district (Bergman et al. 2001). The timing of Fe oxide and Cu-Au deposit formation corresponds to that of the Svecofennian metamorphism, and the intrusion of the Haparanda and Perthite-monzonite suite granitoids. A second stage of mineralisation, or metamorphism of previously formed deposits occurred in association with the younger stage of metamorphism. This possibly accompanied movements on the Nautanen Deformation Zone.

References

Bergman S, Kübler L, Martinsson O (2001) Description of regional geological and geophysical maps of northern Norrbotten county (east of the Caledonian orogen). Sveriges geologiska undersökning Ba 56

Billstrom K, Martinsson O (2000) Links between epigenetic Cu-Au mineralisations and magmatism/deformation in the Norrbotten county, Sweden. In L.U.T. research report 2000:06. 2nd GEODE Fennoscandian Shield field workshop on Palaeoproterozoic and Archaen greenstone belts and VMS districts in the Fennoscandian Shield

Romer RL (1996) What is the significance of lead isotope data from stilbite, a low temperature natural ion exchanger? The 22nd Nordic Geological Winter Meeting, Turku, Åbo, Abstracts, 172

Romer RL, Martinsson O, Perdahl JA (1994) Geochronology of the Kiruna iron ores and hydrothermal alterations. Economic Geology 89: 1249-1261

Skiöld T, Cliff RA (1984) Sm-Nd and U-Pb dating of Early Protoerozoic mafic-felsic volcanism in northernmost Sweden. Precambrian Research 26: 1-1

Welin E (1987) The depositional evolution of the Svecofennian supracrustal sequence in Finland and Sweden. Precambrian Research 35: 95-113

Metamorphic to magmatic transition captured at the Myszków Mo-W deposit, southern Poland

H.J. Stein
AIRIE Program, Department of Geosciences, Colorado State University, USA, and Norges Geologiske Undersøkelse, Trondheim, Norway

M. Markowiak, S.Z. Mikulski
Polish Geological Institute, Sosnowiec and Warszawa, Poland

Abstract. Millimetre scale drilling of paragenetic ally-specific sulphide occurrences represented by ten Myszków molybdenite samples provides a temporal framework for this Mo-W deposit, associated with the transcontinental Hamburg-Kraków tectonic zone. With replicates (second mineral separates) for two samples, a total of twelve Re-Os model ages pin high temperature molybdenite-scheelite-(chalcopyrite) mineralization to a narrow time window, from 300 ± 1 to 296 ± 1 Ma (2-sigma). Published $^{40}Ar/^{39}Ar$ ages (305-290 Ma) for potassium feldspar, white mica, and biotite do not precisely pin the timing of mineralization, but provide information on the regional cooling history. Alteration is characterized by local metasomatism of hosting Vendian to Cambrian metamorphic rocks, and spatial patterns for Mo-W-(Cu) mineralization support a relationship between metasomatism and mineralization. Dehydration melting of middle crust was followed by local intrusion of magmas along structurally vulnerable zones. Melting of hosting metaclastic sequences influenced local metallic assemblages and provided the magmatic apophyses and crustal enclaves associated with much of the Myszków mineralization. Even though local stockwork may be found, the overall architecture of the Myszków deposit does not support a calc-alkaline porphyry-style deposit, and this interpretation should be reconsidered. We attribute Myszków mineralization to unroofing of the Variscan orogen, rapid late Variscan uplift, and exhumation melting.

Keywords. Re-Os, molybdenite, Mo-W deposit, metasomatism, Myszków, Poland

1 Introduction

Late Variscan (~300 Ma) Mo-W mineralization at Myszków has been classified as a calc-alkaline porphyry-type deposit situated in a poorly defined belt of magmatic rocks in south-central Poland (Podemski et al. 2004; Markowiak et al. 2001). Features defining of calc-alkaline porphyry-style mineralization, however, are conspicuously absent, not the least an intrusion centered brittle-planar stockwork and attendant alteration types.

Re-Os data for molybdenites have provided key information on the timing and genesis of a broad spectrum of deposits, in particular, metamorphically-derived deposits versus classic Cu-Mo-Au porphyry-style mineralization (e.g. Stein, in press). The former tend to be small in size, of erratic but locally high-grade, and display widely dispersed rather than focussed ore zones. They are associated with moderate-low ppm to sub-ppm levels of Re. In contrast, true porphyry systems have high to very high Re contents (hundreds to thousands of ppm) associated with main stage molybdenites, and are the product of a vertically and laterally communicative magmatic-hydrothermal system that moved from deep to shallow crustal levels, over a period of several million years, importantly, without venting. With these characteristics in mind, we apply Re-Os dating of molybdenite through the paragenetic history of Myszków to document the timing and duration for its formation and to improve our understanding of this unusual deposit.

2 Geologic setting

The Myszków deposit is situated along the NE margin of the NW-trending Kraków-Lubliniec tectonic zone, a segment of the transcontinental Hamburg-Kraków tectonic zone. In southern Poland, the tectonic history of this zone is poorly known but strike-slip movement appears to be an important component. Mafic to felsic magmatism with granodiorite prevailing is common along the 15 km segment of the Kraków-Lubliniec tectonic zone that includes the Myszków Mo-W region. Magmatic rocks are hosted by intensely folded, predominantly fine-grained Vendian to Cambrian clastic units at regional greenschist facies. Upper amphibolite-granulite facies (metasomatic) is locally present in the vicinity of magmatic rocks. A NW-trending granodiorite body with subvolcanic dacite and rhyolite porphyry dikes intruded the metasedimentary rocks, and contact relations vary from sharp to ill-defined. The overall character of the Myszków granodiorite is one of a moderately flat-top intrusion extending over tens of kilometres, and dissected by normal faults (Fig. 1). Interfingering and foliation parallel magmatic units intersected in drill holes in the vicinity of the granodiorite are interpreted as apophyses to the granodiorite body (Podemski et al. 2001). Associated alteration is described both as metasomatic and hydrothermal vein type, with significant K-feldspar, silica, sericite, and carbonate. While potassic alteration is prevalent, secondary biotite, magnetite, and significant pyrite are conspicuously sparse. Some alteration assemblages have been described as greisen-like at Myszków.

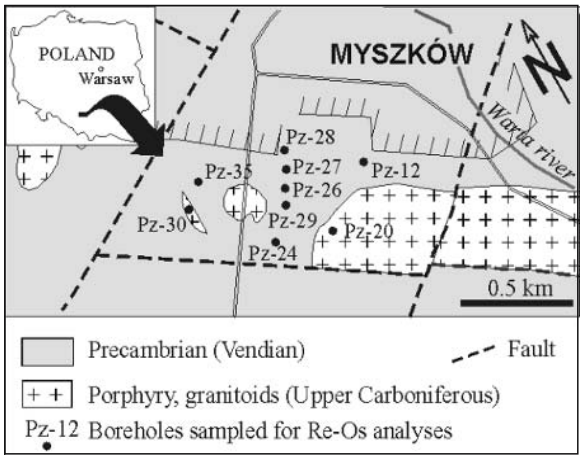

Figure 1: Myszków geology with borehole localities providing molybdenite samples (after Podemski et al. 2001).

The Myszków deposit, outlined by 35 boreholes from 1985 to 1993, is estimated to contain 800 million tons of ore at 0.15% Cu, 0.05% Mo, and 0.04% W and continues to at least 1250m depth (Podemski et al. 2001). Several similar deposits were also discovered in this region. Significantly, Cu mineralization (chalcopyrite) bears little spatial relation to W and Mo mineralization (scheelite and molybdenite). And, W and Mo also exhibit differences. In general, W (and Mo) are associated with magmatic rocks, whereas Cu and to some extent Mo, are associated with contact regions between granodiorite and metaclastic host units. Molybdenite is generally associated with quartz veins and patches in pink (potassic) granodiorite, but these ill-defined and scattered veins do not constitute stockwork in the classical sense. Also, the richest ore body is contained in an enclave of metaclastic host rock within the upper portion of the granodiorite (Chaffee et al. 1997), rather than exhibiting an intrusion-wide association to the granodiorite. Myszków mineralization and paragenesis have been described in detail by Piekarski (1982, 1995) and Ślósarz (1985, 1993), including vein, pegmatitic, metasomatic, disseminated, and skarn varieties (see Podemski et al. 2001).

3 Molybdenite samples dated

This Re-Os study utilizes different ore occurrences to determine the relative timing of ore-forming environments at Myszków. Even at the hand-specimen scale, molybdenite was drilled from occurrence-specific sites, a critical step for successful age determinations in complex metamorphic settings (Stein in press). Replicate ages for two samples were acquired from new mineral separates exploiting the same occurrence. This is an indisputable test for age accuracy.

Three periods of mineralization are defined at Myszków: Early Skarn (Period I), Main Hydrothermal (Period II), and Late Post-Ore (Period III). The first two are molybdenite-bearing. Within Period I, early skarn consists of magnetite-sulfide mineralization. Within Period II, different stages of ore deposition are proposed (Stage 1, feldspar-molybdenite veins with biotite; Stage 2, quartz-feldspar pegmatite veins; Stage 3, quartz-molybdenite stockwork with scheelite; Stage 4, black quartz veins with microsulfide; Stage 5, quartz polymetallic veins without molybdenite and late brecciated quartz veins with sulfide. The Period-Stage classification (Ślósarz 1985, 1993) was used for our molybdenite samples (Table 1), and is summarized in Podemski et al. (2001).

4 Re-Os analytical results

Twelve Re-Os ages representing paragenetically defined Myszków molybdenites provide a remarkably narrow age range, 300 ± 1 to 296 ± 1 Ma (2-sigma). Re concentrations are moderate, ranging from an about 40 to 74 ppm. The lower value (40 ppm) is an estimate of the true Re concentration as up to 95% dilution of the molybdenite separate by quartz was unavoidable during drilling of some samples. Such samples consist of very fine-grained grey streaks of molybdenite in quartz (see footnote, Table 1). This does not affect the age calculation, as diluting quartz contains essentially no Re and Os. Four samples with abundant and coarser crystalline molybdenite suggest that ~70 ppm Re was common to the fluids forming quartz-molybdenite veins.

Notably, the Re values reported in Podemski et al. (2001), 0.07 to 0.17% (700 to 1700 ppm), bear no resemblance to our Re values determined by isotope dilution. It is highly unlikely that both data sets can be correct for a single deposit.

5 Discussion and conclusions

The moderate and fairly consistent Re levels (about 40 to 75 ppm) for Myszków molybdenites do not support a subduction-related porphyry-style origin (Stein et al. 2001). A better fit would be a moderately local derivation utilizing a crustal reservoir with fairly consistent Re, rather than one dependent on batch additions of material from different reservoirs, mixing, and system wide fluid separation (porphyry model). At Myszków, development of local veins, stockwork, and pegmatite likely depended on local separation and volatile enhancement of hydrothermal fluids that were not far-travelled.

Re-Os ages have a very tight range (300-296 Ma) and $^{40}Ar/^{39}Ar$ ages (305-290 Ma) overlap the molybdenite age range but should be interpreted as recording the cooling history at the sampled localities for the minerals dated

Table 1. Re-Os data for molybdenites from the Myszków Mo-W deposit, south-central Poland

AIRIE Run #	Drill Hole, Depth	Paragenesis	Brief Description of Molybdenite Dated	Re, ppm	^{187}Os, ppb	Age, Ma
MDID-232	PZ-12, 193.0 m	Period I, Early Skarn	massive dark grey magnetite-kspar-quartz skarn rock with fg mo + cp + py disseminations to patchy networks hosted in altered metaclastic rock	0.8394 (1)	2.607 (3)	**296 ± 1**
MDID-406	PZ-12, 193.0 m	REPLICATE	REPLICATE (SECOND MINERAL SEPARATE)	0.7177 (2)	2.244 (1)	**298 ± 1**
MDID-186	PZ-24, 984.0 m	Period II, Stage 1, Main Hydrothermal	1 mm disseminations to 15 mm clots and patches of mo + lesser cp in potassic red biotite-bearing granitoid	69.8 (4)	217.07 (9)	**296 ± 2**
MDID-233	PZ-24, 984.0 m	REPLICATE	REPLICATE (SECOND MINERAL SEPARATE)	67.82 (2)	211.8 (1)	**298 ± 1**
MDID-235	PZ-28, 564.5 m	Period II, Stage 2, Main Hydrothermal	interval to ill-defined vein-pegmatite of fg quartz + kspar + disseminated mo + cp + py hosted in silicified clastic metasedimentary rock	3.637 (5)	11.353 (9)	**297 ± 1**
MDID-236	PZ-29, 602.0 m	Period II, Stage 2, Main Hydrothermal	interval of massive fg quartz pegmatite with disseminated fg mo + lesser cp + py and clasts of slightly argillized pink granitoid	33.731 (8)	105.41 (3)	**298 ± 1**
MDID-237	PZ-26, 1091.5 m	Period II, Stage 3, Main Hydrothermal	2 cm qtz + mo + cp veins with locally diffuse margins in pink biotite-bearing porphyritic granitoid with sparse mm cp + mo disseminations	60.90 (4)	190.53 (5)	**298 ± 1**
MDID-410	PZ-26, 1009.3 m	Period II, Stage 3, Main Hydrothermal	5-8 mm qtz-mo veins in pink fg granitoid with sparse diss cp + py and fracture with cp + py	67.95 (6)	212.25 (8)	**298 ± 1**
MDID-238	PZ-35, 976.0 m	Period II, Stage 3, Main Hydrothermal	1 cm qtz + mo vein with mo forming well-defined selvages and ~40% of the vein volume cutting pink granitoid	74.049 (4)	232.3 (1)	**299 ± 1**
MDID-239	PZ-30, 332.5 m	Period II, Stage 3, Main Hydrothermal	1-2 cm banded qtz + fg mo veins with lesser kspar and minor cp + py, hosted in silicified fg metaclastic rock	28.262 (9)	88.92 (1)	**300 ± 1**
MDID-407	PZ-27, 1296.5 m	Period II, Stage 4, Main Hydrothermal	massive very fg mo + qtz with lesser kspar constituting a grey lacey silica rock with local mo slickensides	0.5116 (1)	1.589 (1)	**296 ± 1**
MDID-255	PZ-20, 921.2 m	Period II, Stage 5?, Main Hydrothermal	slightly argillized kspar rock with 1-2 cm breccia veinlets containing host material + mo + cp + py + sl + qtz + kspar + carb, locally vuggy	33.17 (5)	103.74 (6)	**298 ± 1**

Assumed initial $^{187}Os/^{188}Os$ for age calculation = 0.2 ± 0.1
Absolute uncertainties shown, all at 2-sigma level, for last digit indicated
Decay constant used for ^{187}Re is 1.666 x 10^{-11} yr^{-1} (Smoliar et al. 1996)
Carius tube dissolution using double Os spike (Markey et al. 2003), sample weights from 10 to 80 mg
Ages calculated using $^{187}Os = {}^{187}Re(e^{\lambda t} - 1)$ include all analytical and ^{187}Re decay constant uncertainties
Blank corrections during study were Re = 1.33 ± 0.06, 8.41 ± 0.57, 1.95 ± 0.02 pg, total Os = 1.9 ± 0.1, 0.635 ± 0.006 pg, $^{187}Os/^{188}Os$ = 0.245 ± 0.010, 0.388 ± 0.010, 0.1905 ± 0.
MDID-232, 235, 406, 407 mo separates >90% diluted by quartz, true Re concentrations much higher; MDID-236, 239, 255 silica dilution estimated at 40%, 40%, 10%, respectively

(potassium feldspar, biotite, white mica). Argon geochronology should not be used to define ages of high temperature Mo-W-Cu mineralization (Stein et al. 2001). General agreement between Re-Os and $^{40}Ar/^{39}Ar$ ages suggests that the region cooled very quickly, and has not seen any further thermal activity.

Mineralogy (e.g. lack of abundant chalcopyritee, fluorite, and Au), lack of an intrusion-centered relationship for mineralization, lack of correlation between Cu and Mo, the abundance of W, lack of planar-brittle vein styles, and lack of classic porphyry-style alteration collectively do not support a Mo-W calc alkaline intrusion-related, porphyry model (Podemski et al. 2001).

Re-Os ages and the preserved regional greenschist facies character of host rocks with local high temperature contact metamorphism suggest rapid uplift with structurally favourable but localized discontinuities serving as focussing sites for intrusion. This was accompanied by local and brief *in situ* melting and metasomatism. As a result, erratic mineralization of variable grade covers a large region. This includes the Myszków deposit and other prospects in the Kraków-Lubliniec tectonic zone. Small perturbations in pressure permitted local formation of thick (cm scale) "stockwork" veins but true and abundant stockwork never formed system wide as defines classic Cu-Mo-Au-W porphyry-style mineralization. Furthermore, there is no evidence for a regional tectonic environment conducive to classic porphyry-style mineralization, as at ~300 Ma the Variscan orogeny is not characterized by subduction. We suggest that the Myszków Mo-W deposit is the product of exhumation melting associated with rapid unroofing of the Variscan orogen.

Acknowledgements

Re-Os analytical work was carried out by AIRIE graduate students A Zimmerman and N Loeppke, and supported by NSF EAR-0087483. Salary support for HJS was provided by Edward Warner.

References

Chaffee MA, Eppinger RG, Lasón K, Mlósarz J, Podemski M (1999) A geological, alteration, and geochemical model of the Myszków porphyry Cu-Mo deposit, southern Poland, in Papunen (ed). Mineral Deposits, Balkema, Rotterdam, 851-854

Markey RJ, Hannah JL, Morgan JW, Stein HJ (2003) A double spike for osmium analysis of highly radiogenic samples. Chemical Geology 200: 395-406

Markowiak M, Ślósarz J, Lasón K, Podemski M, Karwowski L, Chaffee MA (2001) Palaeozoic porphyry molybdenum-tungsten mineralization in the Myszków area, southern Poland, in Piestrzynski et al. (eds). Mineral Deposits at the Beginning of the 21st Century, Swets & Zeitlinger Publishers Lisse, 445-448

Piekarski K (1982) Molybdenum schists in the vicinities of Myszków (Eng Sum). Prz Geol 30(7): 335-340

Piekarski K (1995) Geologic setting and ore mineralisation characteristics of the Myszków area (Poland). Geol Quart 39(1): 31-42

Podemski M (editor), Buła Z, Chaffee MA, Cieśla E, Eppinger R, Habryn R, Karwowski L, Lason K, Markiewicz J, Markowiak M, Snee LW, Ślósarz J, Truszel M, Wybraniec S, Zaba J (2001) Palaeozoic porphyry molybdenum-tungsten deposit in the Myszków area, southern Poland. Polish Geological Institute Special Papers 6: 1-87

Ślósarz J (1985) Stages and zonality of ore mineralization in Palaeozoic rocks of the environs of Myszków. Ann Soc Geol Pol 53(1-4): 267-288

Ślósarz J (1993) The main paragenetic stages for molybdenum mineralisation in the Palaeozoic rocks of the Myszków area and their importance to the formation of the ore deposits of that area (Eng Sum). Pol Tow Mineral Pr Spec 3: 123-128

Stein HJ (in press) Low-rhenium molybdenite by metamorphism in northern Sweden: recognition, genesis, and global implications. Lithos.

Stein HJ, Markey RJ, Morgan JW, Hannah JL, Scherstén A (2001) The remarkable Re-Os chronometer in molybdenite: how and why it works. Terra Nova 13(6): 479-486

New K-Ar, $^{87}Sr/^{86}Sr$, REE, and XRF data for Tertiary volcanic rocks in the Sasa-Toranica ore district, Macedonia

G. Tasev, T. Serafimovski, P. Lazarov
Department of Mineral Deposits, Faculty of Mining and Geology, Goce Delcev 89, 2000 Stip, Macedonina

Abstract. The latest K-Ar, $^{87}Sr/^{86}Sr$, and REE data for samples from Sasa-Toranica ore district are presented. Whole rock XRF analyses confirm host rock composition as dacites, quartz-latites, trachyandesites and rhyolites. K-Ar absolute ages range from 31 to 14 Ma confirming Oligocene-Miocene age as previously determined by relative methods. $^{87}Sr/^{86}Sr$ ratios (0.70954 to 0.71126) suggest material is sourced from the contact zone between the lower crust and upper mantle where contamination of primary melt occured. New REE data including negative Eu anomalies along with previously determined La/Yb ratios ranging from 13.3 to 43.0 (Serafimovski 1990) confirm inferred material source. These new data reconfirm previous results, provide insight into the Tertiary magmatic history of the district, and suggest the exact origin of the material that produced the Tertiary magmatic rocks.

Keywords. Sasa, Toranica, volcanic rocks, age, origin, contamination, Tertiary

1 Introduction

Tertiary volcanic rocks in the Osogovo-Besna Kobila (Sasa-Toranica ore district) area regionally strike NW-SE for 100 km on both sides of Macedonia-Bulgaria border. Volcanic rocks in the area occur as ~50 m thick elongate dykes oriented roughly east-west (260°). From the Osogovo Mountain to the Besna Kobila Mountain (Osogovo-Luke-Karamanica), volcanic rocks are present as pyroclastics (Deve Bair), volcanic domes, dykes, necks and veins. Volcanic rocks at the Osogovo-Besna Kobila mountains cut the Paleozoic and Riphean-Cambrian metamorphic and igneous rocks and overlie Upper Eocene sedimentary sequences. The volcanics are mainly dacitic tuffs (Deve Bair), dacites, quartzlatites, rhyolites, trachyandezites, andesite-latites and occasionally lamprophyre veins (Sasa and Toranica localities).

2 Methodology

After detailed sampling and preparation at the Faculty of Mining and Geology in Stip, samples were sent to the Geological Department, University of Padova, Italy for whole rock XRF analysis, Actlabs in Canada for ICP-MS and INAA REE analysis, the Geology Department, Royal Holloway University of London, U.K. for TIMS $^{87}Sr/^{86}Sr$ ratios, and the Geological Institute in Budapest, Hungary for K-Ar dating.

3 Results and discussion

The new K-Ar, Sr isotope, REE, and whole rock XRF data from Sasa-Toranica host rocks provide insight into the composition, timing, and sources of volcanic activity in the region.

Dacites in the Luke-Kiselica area occur from the Karamanica mountain to the southeast at the Osogovo mountain (Serafimovski and Alexandrov 1995). The dacites contain plagioclase (37% An), small amount of orthoclase, quartz, biotite and amphibole phenocrysts. Their matrix is holocrystaline to hypocrystaline with glassy domains. Apatite, sphene and zircon were identified as accessory minerals; while sericite, chlorite, kaolinite, carbonate and metallic minerals are present as secondary minerals.

Quartzlatites are found near the springs of Lucka River and Kuprina Padina as dykes and at Samar and Karamanica as dykes and volcanic flows (Samar and Crcorija) over the volcano-sedimentary rocks. They are characterized by a porphyritic coarse grained texture with sanidine and plagioclase (35-40% An) phenocrysts, with secondary amphibole and augite phenocrysts. Sphene and zircon are accessory minerals. These rocks also contain metallic secondary minerals.

Hialoandesites appear as necks and lava flows over the Upper Pliocene sediments at Gradeska Mountain. These rocks are porphyry-vitrophyric with phenocrysts of plagioclase (37% An), biotite, amphibole and augite; apatite and zircon occur as accessory minerals.

Hypoabyssal and subvolcanic dacites and quartzlatites dominate the Sasa-Toranica zone (Osogovo). All the dacites and quartzlatites in the Sasa-Toranica zone experienced hydrothermal alteration. Dacites are holocrystalline with ~ 30% phenocrystals of andesine (5-16%), quartz (2-3%) and smal amount of orthoclase and coloured minerals (13-20%), mainly replaced by epidote, chlorite and carbonates. Hydrothermal alteration of andesites result in various new mineral assemblages. Illitization, seritization and propylitization dominante andesite alteration. Apatite, zircon, sphene and magnetite are present as accesory minerals, while pyrite, chalcopyrite, sphalerite and galena represent economic mineralization.

Table 1: Chemical composition of rocks in the Toranica-Sasa ore region (%).

No.	SiO_2	TiO_2	Al_2O_3	Fe_t	MnO	MgO	CaO	Na_2O	K_2O	P_2O_5	LOI
MK1	63.93	0.65	14.35	4.34	0.11	3.15	3.91	2.56	6.32	0.6	3.96
MK2	69.1	0.43	14.92	3.04	0.08	1.38	2.78	3.38	4.58	0.24	3.43
MK3	60.48	0.54	16.43	3.18	0.1	2.86	6.85	3.67	5.57	0.28	3.05
MK4	68.46	0.44	15.47	3.15	0.08	1.24	2.69	2.66	5.47	0.23	4.03
MK5	69.09	0.44	15.0	3.02	0.1	1.4	2.89	3.4	4.37	0.24	4.06
MK6	67.62	0.46	15.53	3.11	0.07	1.42	3.27	3.24	4.98	0.24	3.87
MK7	65.73	0.63	14.94	3.98	0.09	2.86	3.14	2.88	5.19	0.49	3.69
MK8	69.19	0.4	14.72	3.16	0.31	1.87	2.51	1.58	5.93	0.27	2.77
MK9	68.35	0.41	15.15	3.35	0.34	1.46	3.7	1.46	5.37	0.25	5.31
MK10	68.59	0.42	15.29	3.22	0.3	1.38	2.85	1.95	5.66	0.24	4.33
MK11	68.65	0.4	15.29	3.02	0.24	1.32	2.55	2.85	5.35	0.24	3.56
MK12	63.0	0.52	16.24	5.12	0.1	2.0	4.04	3.28	5.36	0.28	4.96
MK13	66.83	0.56	15.52	4.14	0.4	2.58	2.47	2.43	4.66	0.21	4.93

Note: 1. MK-1 Trachydacite; 2. MK-2 Trachyte-rhyolite-dacite; 3. MK-3 Trachyandesite-trachydacite; 4. MK-4 Trachydacite; 5. MK-5 Dacite; 6. MK-6 Trachydacite; 7. MK-7 Trachydacite; 8. MK-8 Dacite; 9. MK-9 Dacite; 10. MK-10 Dacite; 11. MK-11 Trachydacite; 12. MK-12 Trachydacite; 13. MK-13 Dacite.

Quartzlaties are the most common rocks in the zone mentioned above. They occur as elongated dykes a few kilometers in length. These rocks are characterized by large phenocrysts of sanidine, andezine and femic minerals biotite, amphibole and rarely augite. Sanidine crystals are fresh and quite large (up to 5-6 cm). Quartzlatites were intensively hydrothermaly altered.

Transition rocks from quartzlatites to rhyolites are found at a few locations at Osogovo Mountain. Rocks with increased SiO_2 content occur near the Sekirica Tower close to the Macedonian-Bulgarian state border. These rocks were intensly propylitized and hydrothermaly altered.

The volcanic rocks from the Kozja River and Svinja River (Sasa Mine area) are dominantly dacites and quartzlatites. The volcanic rocks from this area are intensly propylitized and hydrothermaly altered. In addtion to previously mentioned secondary minerals, these rocks also contain ore minerals including pyrite, galena, sphalerite, sometimes chalcopyrite and occasionally traces of ceruzite, anglezite and malachite.Trachyandesites occur as small bodies at subvolcanic-volcanic levels in the Sasa-Toranica zone and its western borders. They are characterized by porphyry structure (fine grained porphyry) and crystalized microlitic or microtrachytic matrix. Phenocrystals of large, around 2 to 3 mm, andezine, sanidine, biotite, augite and hornblende are present. Apatite, sphene, and zircon occurs as accessory minerals. In comparison to the quartzlatites, the trachyandesites are characterized by lower SiO_2 concentrations. Similar rocks were identified in Pecovska Maala on the Osogovo Mountain on the Bulgarian side of the Bulgaria-Macedonian border.

Lamprophyres occur as small dykes near Sredno Brdo and Toranica. They are dark grey to brown rocks with a fine-grained porphyrtic texture and glassy matrix. Pyroxene, amphibole and biotite pheocrysts are identified. Accessory minerals are apatite, sphene and zircon.

Data obtained after geochemical analyses were entered into the computer software IGPET 2000 and Microsoft Excel; results are displayed in Table 1.

Use of IGPET 2000 software facilitated determination of rock types by the Total Alkali Silica (TAS) classification scheme, their classification under the calk-alkaline or tholeiitic series of rocks (Fig. 1, 2), and subsequent interpretations based on the classifications.

Graphical view of those determinations is presented in Figure 1.

TAS classification indicate that the rocks of interest mostly plot in the areas that define dacites, trachydacites, trachyandesites and rhyolites. All analyzed rocks plot in the area of calk-alkali series. Selected samples were analyzed for rare earth element (REE) concentrations. The analyses were performed at the *Active Labs, Canada*. REE concentration data for four samples are presented in Table 2 and plotted in a chondrite-normalized spider diagram in Figure 2.

From the spider diagram (Fig. 2) it can be seen that the rare earth elements in the Sasa-Toranica ore region have a decreasing trend. Comparing the left and right side of the diagram suggests there is a decrease in heavy rare earth elements, HREE with an atomic number higher than 63 (Eu), in comparison with light rare earth elements, LREE with an atomic number lower than 63 (Eu). The trend is typical as the product of fractionation of light

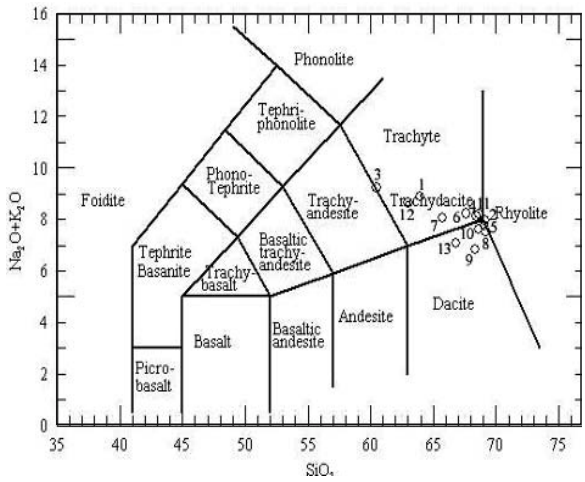

Figure I: Chemical classification and nomenclature of volcanic rocks in the Sasa-Toranica ore region, using diagram total alkalias vs. silica (Le Maitre et al. 1989).

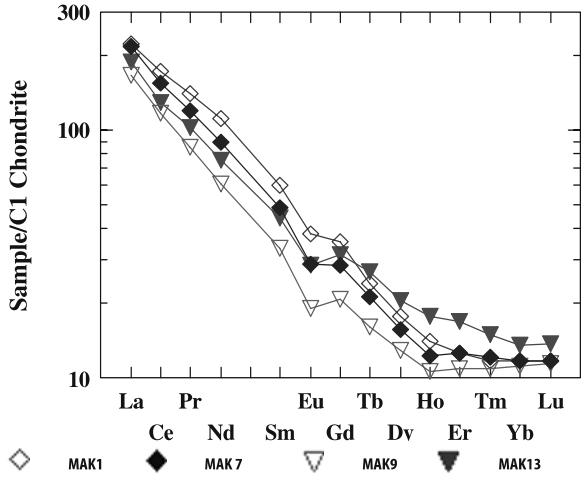

Figure 2: Diagram of normalized values of rare earth elements in comparison to those in chondrites, for rock samples from the Sasa-Toranica ore region.

Table 2: Rare earth elements content in rocks from the Sasa-Toranica ore region (ppm).

Element	MAK-1 I	MAK-7 I	MAK-9 II	MAK-13 II
La	53.10	52.00	39.60	44.90
Ce	106.00	95.40	72.10	79.30
Pr	13.30	11.40	8.08	9.72
Nd	52.50	42.10	28.30	35.20
Sm	9.20	7.50	5.10	6.80
Eu	2.22	1.68	1.11	1.65
Gd	7.30	5.90	4.30	6.50
Tb	0.90	0.80	0.60	1.00
Dy	4.50	4.00	3.30	5.20
Ho	0.80	0.70	0.60	1.00
Er	2.10	2.10	1.80	2.80
Tm	0.30	0.31	0.28	0.38
Yb	2.00	2.00	1.90	2.30
Lu	0.30	0.30	0.29	0.35

Table 3: Values of Eu anomaly in samples from the Sasa-Toranica deposit.

Samples	Value of Eu anomaly
MAK-1 I	0.8289057
MAK-7 I	0.7740283
MAK-9 II	0.7276697
MAK-13 II	0.759748

rare earth elements and their increase in comparison to the chondritic values. Fractionation occurred as a direct consequence of partial melting, which according to the angle of the line in the diagram was not of high intensity.

Looking at the middle part of the diagram the value of Eu is slightly and negatively displaced from the "ideal" linear line between Sm and Gd defining a distinct negative Eu anomaly. A chondrite normalized, geometric mean calculation of the Eu anomaly is shown in Table 3.

From the table it can be seen that Eu anomaly values are in range from 0.727669702 up to 0.828905716, and all are less than 1, which implies a negative Eu anomaly (Rollinson 1992). Eu anomalies are controled by presence of feldspars. Eu^{2+} is compatible in plagioclase and K-feldspar, in contrast to the Eu^{3+} which is incompatible. Thus the removal of feldspar from a felsic melt by crystal fractionation or the partial melting of a rock in which feldspar is retained in the source will result in a negative Eu anomaly in the melt.

Accordingly, the data for Eu in analyzed samples and its negative anomaly it can be concluded that Eu has been removed from the melt as a compatible Eu^{2+}, by the processes of crystal fractionation or partial melting.

With the analyses of strontium isotopes (Table 4) was performed to construct a general model of formation for rock complexes at the Osogovo Mountain (Sasa-Toranica ore field). Strontium isotope analyses of rock samples from the volcanic rocks from the Sasa-Toranica ore field results in strontium ratios that range from 0.70954 up to 0.71125. The results suggest the magma forming Neogene magmatic complexes at the Osogovo Mountain is a product of primary magmatic melt originating from the border zone between upper mantle and continental crust where mixing and contamination of primary magma occurred.

The new data complies with previous $^{87}Sr/^{86}Sr$ data for Upper Tertiary calk-alkaline complexes formed in the Serb-Macedonian metallogenic province. $^{87}Sr/^{86}Sr$ ratios

Table 4: $^{87}Sr/^{86}Sr$ ratios in volcanic rocks from the Osogovo Mountain.

No.	Locality	Rock type	$^{87}Sr/^{86}Sr$
1	Golema R.950, Sasa	Quartzlatite	0.71051
2	Kozja R. IV_o, Sasa	Quartzlatite	0.70994
3	Svinja R. IV_o, Sasa	Quartzlatite	0.71126
4	Toranica – 2	Quartzlatite	0.71016
5	Toranica, TO-1	/	0.70979
6	Sasa	Andesite-latite	0.71064
7	Sasa	Quartzlatite	0.71024
8	Sasa, SA-2	/	0.70954
9	Toranica, MK-1	Trahydacite	0.71055
10	Sasa, MK-9	Dacite	0.71096

Table 5: Absolute age determination of volcanic rocks in the Sasa-Toranica ore region by the K/Ar method (Tasev 2003).

No.	Locality	Rock type	K-Ar age (m.y.)
1	Mal Ruen	Quartzlatite	28.38±1.09
2	Toranica-I	Quartzlatite	28.36±1.09
3	Sasa (Kozja R.)	Quartzlatite	30.72±1.19
4	Sasa (Kozja R.)	Andesite	29.25±1.13
5	Sasa (Crvena R.)	Granodiorite	31.16±1.40
6	Sasa	Andesite-latite	14.0±3.0
7	Sasa	Quartzlatite	24.0±3.0

of samples from Kozuf Mountain range from 0.7088 to 0.7090 and those for volcanic rocks from the Rogozna range between 0.7074 and 0.7085 (Serafimovski 1990).

Osogovo Tertiary igneous rocks are characterized by interesting distributions of Pb, Ba, Sr, Rb, Li, Cs and Be. Compared to Clark standard values Pb, Ba, Sr and Be are enriched while Li, Rb and Cs are similar to Clark standard values. Also, in magmatic processes it was noticed trend of increasing Li, Pb, Cs, Be, Rb and Ba concentrations going from fine-grained porphyry quartzlatites to coarse-grained porphyry quartzlatites (Serafimovski 1993a; Serafimovski et al. 2003). Tendencies in concentration distribution of elements show that the magmatic rocks originated from one magmatic chamber but during different time intervals producing different rock types. K-Ar isotopic age data give Tertiary magmatic ages in the study area. Results of this study are shown in Table 5.

The range of ages (Oligocene-Miocene) confirms the age determined by the relative methods.

4 Conclusion

This study of the volcanic rocks in the Sasa-Toranica ore region identified the distinct and uniform chemical composition of these rocks. The rocks are characterized as dacites, trachydacites, trachyandesites and rhyolites based on the TAS scheme. New K-Ar ages range from 31.16 ± 1.40 to 14.0±3.0 Ma confirming Oligocene-Miocene ages. Strontium isotope ratios and REE analyses identify magmatic material originated from the contact zone between the upper mantle and lower continental crust where certain contamination of primary melts occurred.

References

Rollinson H (1992) Using Geochemistry Data: evaluation, presentation, interpretation. pp. 352. Prentice Hall, an imprint of Pearson Education, Harlow, England.

Serafimovski T (1990) Metallogeny of the Lece-Halkidiki zone. Doctoral thesis, Faculty of Mining and Geology, Stip, p. 390 (in Macedonian)

Serafimovski T (1993a) Structural - Metalogenic features of the Lece-Halkidiki zone: Types of Mineral Deposit and Distribution. Faculty of Mining and Geology. Stip, Special Issue N. 2, 325 p, Stip.

Serafimovski T, Aleksandrov M (1995) Lead-zinc deposits and occurrences in the Republic of Macedonia. Faculty of Mining and Geology, Stip, Special Issue 4, p. 387 (in Macedonian)

Serafimovski T, Jelenkovic R, Tasev G (2003) Geodynamic Evolution and Metallogeny in the Southern Parts of the Balkan Peninsula. Geodynamics and Ore Deposit Evolution of the Alpine-Balkan-Carpathian-Dinaride Province. Final GEODE-ABCD Workshop. Programme and Abstracts. pp. 50. Seggauberg, Austria.

Serafimovski T, Jelenkovic R, Tasev G, Lazarov P (2003) Mineral Deposits Related to Tertiary Magmatism in the Southern Part of the Balkan Peninsula. Geologica Macedonica, Volume 17, pp. 19-23, Stip.

Tasev G (2003) Polymetalic mineralizations related to the Tertiary magmatism in the Republic of Macedonia. Faculty of Mining and Geology, Stip. Master thesis, p. 176. (in Macedonian)

Sources of rhenium and osmium enrichment in fumaroles, sulphide sublimates and volcanic rocks from the Kudriavy volcano

Svetlana G. Tessalina, Françoise Capmas, Jean-Louis Birck, Claude-Jean Allègre
Laboratoire de Geochimie et Cosmochimie, Institute de Physique du Globe, 4 pl. Jussieu, 75252 Paris, France

Marina A. Yudovskaya, Vadim V. Distler, Ilya V. Chaplygin
Institute of Geology of Ore Deposits, Petrography, Mineralogy, and Geochemistry (IGEM), RAS, Moscow, Russia

Abstract. Rhenium loss through magma degassing could be partly balanced by rhenium enrichment in fumarolic magmatic gases and Re-bearing precipitates, as may be the case for the Kudriavy volcano associated with an active subduction zone. The relatively unradiogenic $^{187}Os/^{188}Os$ isotope ratios (0.122 up to 0.152) and high Os contents (averaging 0.6 ppb) of fumarolic gas condensates imply that significant Re and Os are remobilised from depleted MORB mantle. Involvement of a Re-rich component is evident from high Re concentrations in high-temperature gas condensates, ranging from 7 to 200 ppb. Indeed, Re-rich Os-poor components such as organic-rich subducted sediments and volcanic rocks do not significantly shift the isotopic composition of fumarolic products. The relatively radiogenic composition of the dacite-andesite-basaltic arc volcanics ($^{187}Os/^{188}Os$ ratio up to 0.58), however, could result from significant Os (and Re) input from subducted sediments.

Keywords. Re-Os, subduction zone, rheniite, Kurile Islands, Kudriavy

1 Introduction

Subduction zones are major sites of continental crust formation and elemental recycling between the mantle and crust. The great difference between Re contents in degassed subaerially deposited arc volcanics (~0.19 ppt, Lassiter 2003) and in melt inclusions from undegassed primary arc volcanics (~2 ppb, Sun et al. 2003) requires Re loss during magma degassing. Substantial Re loss from arcs can be partly balanced by high Re contents in magmatic gases and the presence of pure Re sublimates in arc systems (Korzhinsky et al. 1994), as reported for the Kudriavy volcano, above an active subduction zone in the Kurile Islands. The Re-Os systematics should provide important information on the source of Re-rich magmatic volatiles and sulphide precipitates with regard to contributions from the mantle, crust, subducting slab, and seawater, because of compatible Os and slightly incompatible Re behaviour.

2 Tectonic setting of the Kudriavy volcano

The Kurile Islands are the result of Pacific plate subduction beneath the Eurasian plate. Subducted Pacific plate comprises oceanic crust (MORB), oceanic lithospheric mantle and associated sediments. The 400 m-thick seafloor sediments are almost completely subducted beneath Kurile Island arc (Von Huene and Scholl 1991). The lower part of the sedimentary section consists of the Cretaceous chert (120 to 92 Ma) of carbonate composition with abundant siliceous organisms. The radiolarian and diatom ooze accumulated during the middle to late Miocene (14 to 5 Ma) represents the upper part of the sedimentary section (Bailey 1993).

The Kudriavy volcano has been passively degassing at 500-940° C, as recorded in fumarole activity for the last 100 years. The unique occurrence of rhenium disulphide (rheniite ReS_2) has been discovered around high-temperature fumaroles on the Kudriavy volcano, together with elevated PGE contents.

3 Sample description and analytical methods

In order to understand mechanisms for rhenium and osmium enrichment, we undertook integrated studies of fumarolic gases, sulphide sublimates and volcanic rocks at Kudriavy. The sulphide sublimates are represented by molybdenite (MoS_2), rheniite (ReS_2) and Pb-Bi sulphosalt. The suite of volcanic rocks ranges from basaltic to dacitic in composition. Two fractions of fumarolic gas condensates were analysed: = 0.2 mm (Fraction 1) and bulk fumaroles condensates (Fraction 2). Re and Os concentrations and Os isotopic compositions was determined by negative thermal ionisation mass spectrometry (NTIMS) on a Finnigan MAT 262 at the IPGP. Analytical procedure has been described previously (Birck et al. 1997).

4 Re-Os isotope systematics

The Re contents in Kudriavy volcano rocks range from 3.5 to 17 ppb (Fig. 1) averaging 7 ppb, which is about 20 times higher than the estimated average Re abundance for arc lavas (0.3 ppb) and 3 times higher than for melt inclusions from primitive arc lavas, southern Pacific (Sun et al. 2003). The Os contents (ave. 11 ppt.) are similar to those of MORB (Roy-Barman and Allègre 1994). The $^{187}Os/^{188}Os$ ratios vary from 0.205 in basalt to 0.588 in dacite with an average of 0.385. This range of Os isotopic com-

This page intentionally blank

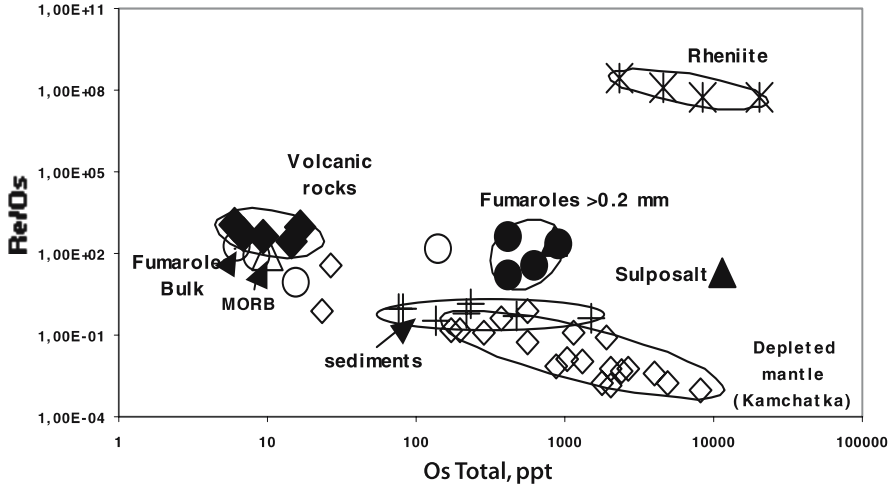

Figure 1: Re and Os concentrations of fumarolic gases, sulphosalt, rheniite, and volcanic rocks from Kudriavy volcano in comparison with depleted mantle peridotite xenoliths from Kamchatka (Widom et al. 2003) and organic-rich Pacific sediments (Peucker-Ehrenbrink et al. 1995).

position in volcanic rocks could be explained by mixing of an unradiogenic MORB-type reservoir with more radiogenic components. Our mass balance calculations are based on the following parameters (Table 1).

The unradiogenic MORB-type component could represent Os-poor oceanic crust. The Os contribution from high-Os depleted mantle is limited to 10% in basalts and almost negligible in felsic volcanic rocks formation. Fluid–saturated sedimentary slab from the subduction zone can be considered as the more radiogenic end-member. Thus, the relatively radiogenic Os signatures for Kudriavy volcanic rocks could be explained by significant Os and Re input (up to 50 %) from slab-derived fluids and melts contaminated by more radiogenic (0.29 to 0.64 for $^{187}Os/^{188}Os$) organic-rich sediments from the subducting Pacific plate (Peucker-Ehrenbrink et al. 1995) (Fig. 2) .

Previous studies of fumarolic gases using H, He and C isotopic systematics (Taran et al. 1995; Fischer et al. 1998) showed that the subducted slab and mantle wedge were the main sources for fluids in the Kudriavy volcanic system. The Re-Os contents and isotope composition of gas condensates vary significantly depending on the method of analytical sampling. Fractions = 0.2 mm (Fraction 1) are characterised by high Re and Os contents (average values are 85 ppb and 0.6 ppb, respectively) and unradiogenic $^{187}Os/^{188}Os$ compositions (0.122 to 0.152). In contrast, bulk condensates (Fraction 2) are characterised by lower Re and Os concentrations (~0.4 ppb Re and 2-37 ppt Os) and slightly more radiogenic Os isotope compositions (0.12 to 0.45), similar to those of the hosting volcanic rocks. This difference can be explained by chemical procedure (incomplete digestion of Fraction 2 due to the absorption of Re and Os complexes by coarse sulphur particles coagulated during acid decomposition), or by the presence of rocks particles in a Fraction 2. Thus, the data obtained for Fraction 1 can be considered as representative of bulk gas condensate composition. The relatively unradiogenic $^{187}Os/^{188}Os$ ratios (0.122 to 0.152) and high Os contents

Table 1: Parameters for mass balance calculations

Reservoir	Os ppt	$^{187}Os/^{188}Os$	Reference
Mantle (Kamchatka)	1880	0.133	Widom et al. 2003
MORB	11	0.13	Roy-Barman and Allègre 1994
Sediments (Carboniferous)	200	0.5	Ravizza et al. 2001; Peucker-Ehrenbrink et al. 1995

(averaging 0.6 ppb) for fumarolic gas condensates imply that a significant part of Re and Os was remobilised from depleted MORB mantle (Table 1). Involvement of a Re-rich component is evident from high Re concentrations in gas condensates, ranging from 7 to 200 ppb. But this radiogenic, Re-rich and Os-poor component, possibly organic-rich subducted sediments (up to 20%) and volcanic rocks (up to 20%), does not significantly shift the Os isotopic composition of fumarolic products.

Rheniite is highly radiogenic due to its high Re content (74.5 wt.% Re). Repeated analyses of two rheniite samples provide model ages of 79±11 yr, which agree with the known 100 year period of fumarolic activity. The initial $^{187}Os/^{188}Os$ ratio is not well defined (0.32±0.15), but appears to be higher than ratios associated with gas condensates. The Pb-Bi sulphosalts have much lower Re contents (~250 ppb) and relatively unradiogenic osmium isotopic compositions (0.125 to 0.176), similar to that of gas condensates.

5 Conditions of Re enrichment

Experimental work has shown that rhenium can be mobilized by high-temperature, saline, and sulphide-poor hydrothermal solutions (Xiong and Wood 1999). According to these experimental data, Re concentrations at 510°C in 0.5 m KCl solution are about 8 x 10^{-6}moles/kg H_2O (~1 ppm). Thus, Re could be easily remobilised from the host rocks and sediments by high temperature (700-940°C)

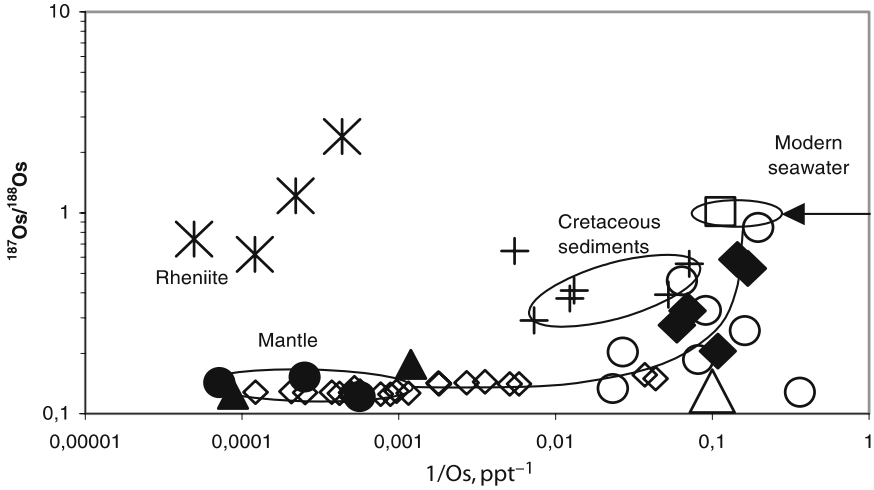

Figure 2: $^{187}Os/^{188}Os$ vs. 1/Os diagram showing reconstruction of fumarolic gases, sulphide sublimates and volcanic rocks osmium isotopic composition and Os concentrations in comparison with depleted mantle (Kamchatka peridotite xenoliths), Pacific sediments and modern seawater. Filled symbols labelled in Figure 1.

fumarolic gases with 0.5 mol% of Cl (Taran et al. 1995). On the other hand, Re and Os enrichment in fumarolic gases could depend on melt-vapor fractionation processes. Deposition of Re-bearing sulphide could be induced by subaerial conditions, which exclude the possibility for dissolution of Re-complexes in water.

6 Importance for Re resources

Until now, molybdenite-bearing Cu-porphyry deposits have been the primary source of Re. High Re concentrations in molybdenite from Cu-porphyry environments have been attributed to mantle involvement in a subduction setting (Stein et al. 2003; Zimmerman et al. 2003) The occurrence of high levels of rhenium in gases and sulphides from the Kudriavy volcano may represent a new and unexplored resource for Re. The Re resources of Kudriavy volcano are still under considerations.

References

Bailey JC (1993) Geochemical history of sediments in the northwestern Pacific Ocean. Geochem. J 27: 71-92

Birk JL, Roy-Barman M, Capmas F (1997) Re-Os isotopic measurements at the femtomole level in natural samples. Geostandards newsletter 20: 19-27

Fischer TP, Giggenbach WF, Sano Y, Williams SN (1998) Fluxes and sources of volatiles discharged from Kudriavy, a subduction zone volcano, Kurile Islands. Earth Planet Sci Lett 160: 81-96

Korzhinsky MA, Tkachenko SI, Shmulovich KI, Taran YA, Steinberg GS (1994) Discovery of a pure rhenium mineral at Kudriavy Volcano. Nature 369: 51-52

Lassiter JC (2003) Rhenium volatility in subaeral lavas: constraints from subaeral and submarine portions of the HSDP-2 Mauna Kea drillcore. Earth Planet. Sci. Lett. 214: 311-325

Peucker-Ehrenbrink B, Ravizza G, Hofmann AW (1995) The marine $^{187}Os/^{188}Os$ record of the past 80 million years. Earth Planet Sci Lett 130: 155-167

Roy-Barman M, Allègre CJ (1994) $^{187}Os/^{186}Os$ ratios of mid-ocean ridge basalts and abyssal peridotites. Geochim Cosmochim Acta 58: 5043-5054

Stein H, Scherstén A, Hannah J, Markey R (2003) Sub-grain scale decoupling of Re and ^{187}Os and assessment of laser ablation ICP-MS spot dating in molybdenite Geochim Cosmochim Acta 67: 3673-3686

Sun W, Benett VC, Eggins S, Kamenetsky VS, Arculus R (2003) Enhanced mantle-to-crust rhenium transfer in undegassed arc magmas. Nature 422: 294-297

Taran YuA, Hedenquist JW, Korzhinsky MA, Tkachenko SI, Shmulovich KI (1995) Geochemistry of magmatic gases from Kudriavy volcano, Iturup, Kuril Islands. Geochim Cosmochim Acta 59: 1749-1761

Von Huene R, Scholl DW (1991) Observations at convergent margins concerning sediment subduction, subduction erosion, and the growth of continental crust. Reviews in Geophysics 29: 279-316

Widom E, Kepezhinskas P, Defant M (2003) The nature of metasomatism in the sub-arc mantle wedge: evidence from Re-Os isotopes in Kamchatka peridotite xenoliths. Chemical Geology 196: 283-306

Xiong Y, Wood SA (1999) Experimental determination of the solubility of ReO_2 and the dominant oxidation state of rhenium in hydrothermal solutions. Chem Geol 158: 245-256

Zimmerman A, Stein H, Markey R, Fanger L, Heinrich C, von Quadt A, Peytcheva I (2003) Re-Os ages for the Elatsite Cu-Au deposit, Srednogorie zone, Bulgaria: *in* Eliopoulos, D.G. et al. (eds), Mineral Exploration and Sustainable Development, Millpress, Rotterdam: 1253-1256

Muluozhai REE deposit in Sichuan Province, China: Stable isotope data and their implications on the dynamics of mineralization

Shihong Tian, Zengqian Hou, Tiping Ding
Institute of Mineral Resources, Chinese Academy of Geological Sciences, Beijing 100037, China, and Key Laboratory on Isotope Geology, Ministry of Land and Resources, Beijing 100037, China

Yuling Xie
Civil & Environmental Engineering School, Beijing University of Science and Technology, Beijing 100083, China

Zhongxin Yuan, Ge Bai, Tianren Zou
Institute of Mineral Resources, Chinese Academy of Geological Sciences, Beijing 100037, China

Abstract. The Muluozhai REE deposit, located about 60 km to the southwest of the Mianning County, Sichuan Province, is the third largest light REE deposit in Sichuan. The Muluozhai REE deposit is tectonically located on the northern Jinpingshan Mountains, a Cenozoic intracontinental orogenic belt in southwestern China. The authors analyzed the essential ores from two tunnels for their carbon, hydrogen, oxygen, and sulfur isotopic compositions of the mineralizing fluid. The $\delta^{13}C_{V\text{-}PDB}$ values of fluid from fluid inclusions of the quartz and fluorite vary from - 2.5 to - 9.0 per mil, which show characteristics of mantle-derived carbon. The $\delta D_{V\text{-}SMOW}$ values of fluid from fluid inclusions of the calcite, quartz, fluorite, and bastnaesite range from - 63 to - 87 per mil, which are characteristics of mantle-derived hydrogen. The $\delta^{34}S_{V\text{-}CDT}$ values of barite and galena vary in a narrow range of + 0.1 to + 2.2 per mil and - 8.6 to - 9.3 per mil, respectively, showing the isotopic characteristics of mantle-derived sulfur. The $\delta^{13}C_{V\text{-}PDB}$ values and the $\delta^{18}O_{V\text{-}SMOW}$ values of calcite range from - 6.6 to - 6.8 per mil and from + 8.4 to + 9.1 per mil, respectively, which are fallen into the range of the "primary carbonatites", showing the carbon and oxygen in the ores of the Muluozhai ore veins were mainly derived from depths. The stable isotopic data suggest a mantle source for the rare earth elements mineralization and a dynamic process involving mantle materials and tectonics.

Keywords. Rare earth element deposit, stable isotopes, mantle source, mineralization dynamics, Muluozhai in Sichuan Province

1 Introduction

The Muluozhai REE deposit (28°22' N Lat. and 101°50' E Long.), located about 60 km to the southwest of the Mianning County, Sichuan Province, is the third largest light REE deposit in Sichuan. Along with other REE deposits in the Panzhihua-Xichang area, it forms one of the three major REE deposit producing regions in China. Although known since the 1960s, it has not attracted nearly as much interest as the Maoniuping and the Daluchao REE-deposits in the Panxi REE ore belt, and, therefore, only little research has been performed concerning its geological characteristics, geochemistry, isotopic geochemistry, mineralogy, and fluid inclusions. Because it is an important part of the Panxi REE ore-forming belt and is situated at the eastern margin of the Tibetan Plateau, it is necessary to understand regional metallogenic rules and the collision between the Indian plate and the Eurasia plate. In this paper, we present systematic studies on the characteristics of S, C, O, and H isotopes of the ores to ascertain the sources of the mineralizing fluids and the dynamic process related to the mineralization.

2 Geologic setting and REE mineralization

The Muluozhai REE deposit is tectonically located on the northwest margin of the Panxi (Panzhihua-Xichang) rift zone at the western side of the Yangtze Platform (Fig. 1). According to Luo et al. (1985), the Panxi rift zone formed on the Yangtze platform starting in the early Paleozoic. Deposition continued during the late Paleozoic into the Mesozoic and ended in the early Cenozoic with the beginning of the Himalayan Orogeny. The Panxi rift was bordered by the Ganluo-Xiaojiang Fault to the east and Qinghe-Chenghai Fault to the west. It extends north-south for over 300 km and reaches a width of about 100 km. Large amounts of alkali-rich ultramafic, basic, and intermediate-acid rocks with a great deal of REE were intruded or erupted in the Panxi rift zone and its neighboring areas. In the region, the Devonian, Permian, Triassic and Jurassic strata are distributed scatteredly because of the destruction of the developed igneous rocks. The latter are distributed extensively in the region and the main rocks are Indosinian quartz diorite, granite, and Yanshanian alkali-feldspar granite.

On the basis of orebody distribution, three kinds of ores have been identified: (i) massive fluorite-bastnaesite, (ii) impregnated, and (iii) banded. The ore minerals are mainly bastnaesite, whereas the gangue minerals include fluorite, barite, calcite, feldspar, quartz, mica and aegirine-augite. The textures and structures are allotriomorphic inequigranular, tabular, subhedral, and massive, banded, respectively. The wall-rock alteration is characterized by

This page intentionally blank

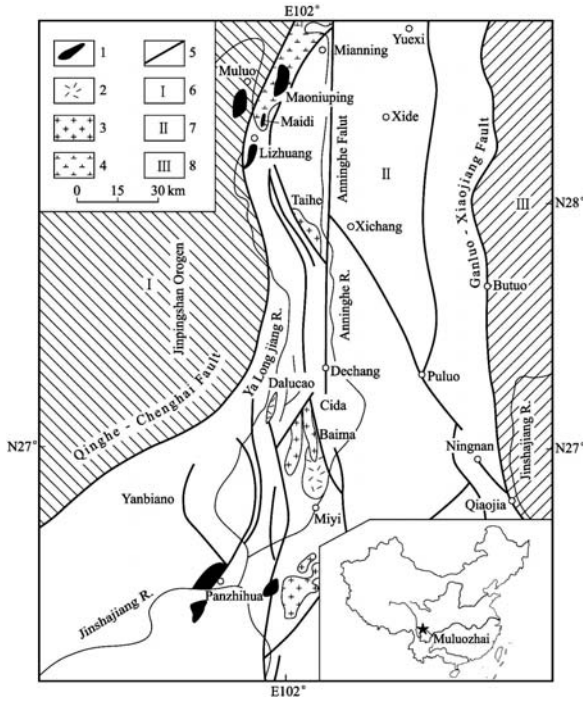

Figure 1: Regional geological map showing the location of the Maoniuping district (modified after Wang et al. 2001). 1 Late Cenozoic REE–bearing nordmarkite; 2 Late Mesozoic syenite; 3 Late Mesozoic alkali granite; 4 Late Mesozoic alkali-feldspar granite; 5 regional fault; 6 Early Mesozoic sedimentary rocks; 7 Precambrian metamorphic rocks; 8 Paleozoic sedimentary rocks.

contact metamorphism and hydrothermal alteration, which includes sericitization, pyritization, baritization, and carbonatization.

3 Stable isotope analysis

3.1 Experiments

Sulfur, carbon, oxygen, and hydrogen isotopes of mineral separates from the Muluozhai deposit have been analyzed. SO_2 was prepared from the samples for sulfur isotope analysis with the method of Robinson and Kusakabe (1975). For oxygen and carbon isotope analysis, calcite was reacted with phosphoric acid at 25° (McCrea 1950) to release CO_2. The $\delta^{18}O_{V\text{-}PDB}$ values of calcite samples were directly obtained from the $\delta^{18}O$ values of their CO_2 against the CO_2 of PDB. For converting the $\delta^{18}O_{V\text{-}PDB}$ to $\delta^{18}O_{V\text{-}SMOW}$, the equation by Friedman and O'Neil (1977) was used, $\delta^{18}O_{V\text{-}SMOW} = 1.03086 \cdot \delta^{18}O_{V\text{-}PDB} + 30.86$. For analysis of hydrogen isotopes, the water in fluid inclusion was released by the decrepitation method. Then, the water was reacted with Zn at 400° to produce H_2 (Coleman et al. 1982), which was collected in a sample tube with activated charcoal at liquid N_2 temperature. For the analysis of carbon isotopes from the fluid, the CO_2 in fluid inclusions in quartz and fluorite was released by the decrepitation method and collected in sample tube at liquid N_2 temperature. All SO_2, CO_2, and H_2 were analyzed using a Finnigan MAT 251 mass spectrometer at the Key Laboratory on Isotope Geology, Ministry of Land and Resources. Analytical reproducibility in this study is ± 0.2 per mil for C, O, and S isotopes, and ± 2 per mil for H isotope.

3.2 Results

Sulfur isotope analyses have been done on 3 barite and 3 galena samples. The $\delta^{34}S_{V\text{-}CDT}$ values vary in a narrow range of + 0.1 to + 2.2 per mil with an average of + 0.8 per mil for the barite, and - 8.6 to - 9.3 per mil with an average of - 9.0 per mil for the galena, respectively. According to the theory by Ohmoto (1972), the $\delta^{34}S_{V\text{-}CDT}$ values of ore-forming fluid in the Muluozhai deposit vary from - 9.0 to + 0.8. On account of barite more than galena, the $\delta^{34}S_{V\text{-}CDT}$ values of ore-forming fluid is more than 0 per mil, but less than + 2.2 per mil, which shows the isotopic characteristics of mantle-derived sulfur (Lu 1986).

Five calcite samples were analyzed for their carbon and oxygen isotopes. The $\delta^{13}C_{V\text{-}PDB}$ values and the $\delta^{18}O_{V\text{-}SMOW}$ values range from - 6.6 to - 6.8 per mil with an average of - 6.7 per mil and from + 8.4 to + 9.1 per mil with an average of + 8.7 per mil, respectively. These values fall into the range of "primary carbonatites", showing that carbon and oxygen in the ores of the Muluozhai deposit were mainly derived from the mantle (Keller and Hoefs 1995).

Carbon isotope analyses of fluid from fluid inclusions were made on 2 quartz and 5 fluorite samples. The $\delta^{13}C_{V\text{-}PDB}$ values range from - 2.5 to - 3.6 per mil for quartz with an average of - 3.1 per mil and - 5.5 to - 9.0 per mil for fluorite with an average of - 7.1 per mil. Quartz and fluorite samples show narrow ranges in $\delta^{13}C_{V\text{-}PDB}$ values, which are close to the estimated value of mantle carbon (Pineau and Methez 1990).

Hydrogen isotope analyses of fluid from fluid inclusions have been done on 2 quartz, 5 fluorite, 5 calcite, and 5 bastnaesite samples. The $\delta D_{V\text{-}SMOW}$ values range from - 69 to - 76 per mil for the quartz with an average of - 73 per mil, - 73 to - 87 per mil for the fluorite with an average of - 81 per mil, - 70 to - 82 per mil for the calcite with an average of - 76, and - 63 to - 86 per mil for the bastnaesite with an average of - 71 per mil. All minerals show a narrow range in $\delta D_{V\text{-}SMOW}$ values that fall close to the estimated value (-60 to -80 per mil) of mantle hydrogen (Mao and Li 2004).

4 Discussion and conclusions

REE mineralizations in rift belts are characterized by multiphase and multistage processes. Mineralizing types

vary through time. Correspondingly, geological, mineralogical, petrological, and geochemical features differ also. For example, in the Liaodong rift belt, REE mineralizations in pegmatites and migmatites formed during an early stage of rift formation, REE-Fe-rich formation of metamorphism volcano-sedimentary rocks during the mid-stage of rift formation, and REE-U-rich aegirine and aegirine-nepheline syenites are related to the postrift evolution (Chen 1984). In the Bayan Obo rift belt, Inner Mongolia, the famous Bayan Obo Fe-Nb-REE ore deposit formed during the Proterozoic, in the evolved rift (Bai 1996) and REE-rich hydrothermal vein and skarn deposits formed during the Caledonian and Hercynian. These late mineralizations reworked the Proterozoic mineralizations (Yuan et al. 1992). The REE mineralizations of the Panxi rift belt are also characterized by multiphase and multistage processes.

REE-rich nordmarkites, alkali granites, syenite porphyries, and albitites. formed during the Hercynian-Indosinian epoch in the developed stage of the Panxi rift, which were mostly associated with alkaline and basic bedded rocks in the region. Affected by the collision between the Indian plate and the Eurasia plate, the rift closed during the Himalayan epoch and changed into an intracontinental orogenic belt, i.e. the Jinpingshan Orogen (Fig. 1), which was formed during Cenozoic and became the eastern margin of the Tibetan Plateau (Burchfiel et al. 1995).

The Muluozhai REE deposit is located in the transitional zone between the Panxi rift and the Longmenshan-Jinpingshan orogenic zone, where the Yangtze plate penetrated as a wedge into the crust at Longmenshan, resulting in a Moho dislocation, thereby inducing partial melting of the mantle materials (Xu et al. 1999). This tectonic environment may have caused intensive faulting and magmatism, possible metamorphic dehydration and upwelling of mantle fluids along the deep faults in the western margin of the Yangtze. The fluids that were responsible for the formation of the Muluozhai REE deposit have S, C, O, and H isotopes similar to mantle or mantle-derived rocks.

Acknowledgements

This work was supported by grants from the State Science and Technology Commission (contract No. 2002CG412610 and G1999043211) and China Natural Sciences Foundation (Grant No. 40425014). We thank Luo Yaonan of Sichuan Bureau of Geology and Mineral Resources and Pu Guangping, Yu Bo and other engineers of the No. 109 Geological Team during our field investigation. We are grateful to Professor Wang Denghong and Professor Chen Wenming at the Institute of Mineral Resources, CAGS, for their constructive suggestion. We also thank Professor Wan Defang, Senior Engineer Li Jincheng, Senior Engineer Bai Ruimei, and Engineer Luo Xurong at the Key Laboratory on Isotope Geology, Ministry of Land and Resources, for their performance of analyses.

References

Bai G, Yuan ZX, Wu CY (1996) Geotectonic setting of the Bayan Obo deposit, Inner Mongolia. Acta Geosci Sinica 17 (supl): 1-8 (in Chinese with English abstract)

Burchfiel BC, Chen, ZL, Liu, YP, Royden LN (1995) Tectonics of the Longmen Shan and adjacent regions, central China. Intern Geol Rev 37: 661-735

Chen RD (1984) A Proterozoic rift basin-Liaodong rift. Liaoding Dizhi 2: 125-133 (in Chinese with English abstract)

Coleman ML, Sheppard TJ, Durham JJ, Rouse JE, Moore GR (1982) Reduction of water with zinc for hydrogen isotope analysis. Anal Chem 54: 993-995

Friedman I, O'Neil JR (1977) Compilation of stable isotope fractionation fraction factors of geochemical interest. In: Fleischer M (ed) Data of geochemistry. Sixth Edition. Geol Surv Profl Pap US P. 117

Keller J, Hoefs J (1995) Stable isotope characteristics of recent natrocarbonatites from Oldoinyo Lengai. In: Bell K (ed) Carbonatites volcanism: Oldoinyo Lengai and Petrogenesis of Natrocarbonatites. LAVCEI Proceeding in Volcanology. LAVCEI, 113-123

Lu CW (1986) Stable Isotopic geochemistry. Chengdu Univ Technol, Publ House, Chengdu, pp. 40-43 (in Chinese)

Luo YN (1985) Panzhihua-Xichang paleo-rift zone, Southwest of Sichuan. In: Zhang YX (ed) Contribution to Panzhihua-Xichang rift, China. Geol Publ House, Beijing, pp. 1-25 (in Chinese with English abstract)

Mao JW, Li XF (2004) Mantle-derived fluids in relation to ore-forming and oil-forming process. Mineral Deposits 23: 520-532 (in Chinese with English abstract)

McCrea JM (1950) On the isotope chemistry of carbonates and a paleotemperature scale. J Chem Phys 18: 849-857

Ohmoto H (1972) Systematics of sulfur and carbon isotopes in hydrothermal ore deposits. Econ Geol 67: 551-578

Pineau F, Methez EA (1990) Carbon isotopes in xenoliths from the Hualalai volcano, Hawaii, and the generation of isotopic variability. Geochim Cosmochim Acta 54: 2117-2127

Robinson BW, Kusakabe M (1975) Quantitative preparation of sulphur dioxide for $^{34}S/^{32}S$ analyses from sulphides by combustion with cuprous oxide. Anal Chem 47: 1179

Wang DH, Yang JM, Yan SH, Xu J, Chen YC, Pu GP, Luo YN (2001) A special orogenic-type rare earth element deposit in Maoniuping, Sichuan, China: Geology and Geochemistry. Resource Geol 15: 177-188

Xu ZQ, Yang JS, Jiang M, et al., (1999) Continental subduction and uplifting of the orogenic belts at the margin of the Qinghai-Tibet Plateau. Earth Sci Front 6: 139-150 (in Chinese with English abstract)

Yuan ZX, Bai G, Wu CY, Zhang ZQ, Ye XJ (1992) Geological features and genesis of the Bayan Obo REE ore deposit, Inner Mongolia, China. Appl Geochem 7: 429-442

Stable isotope composition of the Dalucao rare earth deposit in western Sichuan

Wan Defang, Tian Sihong
Institute of Mineral Resources, Chinese Academy of Geological Sciences, Beijing 100037, China

Luo Mei
Chengdu University of Technology, Chengdu 610059, Sichun China

Jiang Shaoyong
Department of Earth Sciences, Nanjing University, Nanjing 210093, Jiangsu, China

Abstract. Ore-forming solutions and the origin of mineralizing material in the Dalucao rare earth deposit were studied by means of H, O, C, and Si isotope analyses. The δ13C of the bastnasite range narrowly from -8.1‰ to-8.0‰, while the δD values range from -89‰ to -79‰. The quartz δ30Si of the orebody is -0.3‰, and the δD and δ18O of the quartz-fluid inclusion range from -87‰ to +6.0‰, respectively. The δD and δ18O values of the fluorite-fluid inclusion in the ore body are -99‰ to -11.6‰, respectively. The study shows that the compositions of hydrogen and oxygen isotopes in ore-forming fluid of Dalucao rare earth deposit lie in the region between magmatic water and meteoric water. Therefore the ore-forming fluid was mixed from magmatic and meteoric water. The carbon isotopic features suggest that carbon of the bastnasite was from the mantle, carbon of fluorite-fluid inclusions in the ore body was from a mixture carbon source, and carbon of quartz-fluid inclusions was from the mantle.

Keywords. Stable isotope composition, quartz-fluid inclusion, fluorite-fluid inclusion, rare earth deposit, Dalucao

1 Introduction

The Dalucao rare earth ore deposit, one of the largest rare earth ore deposits of China, is located 20 km southwest from Dechang county town, Sichuan Province. It covers an area of about 3 km^2. Tectonically, the deposit is situated in the middle part of the Panxi rift belt, a famous epicontinental rift in the western border of the Yangtze platform.

Rare earth ore bodies of Dalucao rare earth ore deposit are mainly hosted in the aegirine-augite syenite, bordering to quartz diorite, and are related to hydrothermal activations associated with the quart diorite. Geological and geochemical features demonstrate that the deposit is a hydrothermal deposit that formed at medium to low temperature. Based on the C, H, O, and Si isotopes and in the context of the regional geology and tectonics of the Panxi rift, it is further suggested that the source rocks of the ore-bearing aegirine-augite syenite are probably early-formed alkali-rich rocks of the Hercynian epoch that are present at depth. The ore-bearing aegirine-augite syenite was mostly formed by remelting, ascending, and emplacement of the source rocks under the activation of mantle plume and tectonic mobilization in the Himalaya period.

2 Geological survey of Dalucao rare earth deposit

Dalucao rare earth ore deposit is located in the middle part of the Panxi rift belt, which is a famous epicontinental rift in the western border of the Yangtze platform. The distributive strata of the deposit are mainly Previndean system, Vindean-Cambrian system and Jurassic system (Fig. 1). Previndean strata are mainly composed of Yanbian formation strata of Huili group, Vindean-Cambrian strata are consisted of Guanyinyan formation and Dengying formation, and Jurassic system is made up of Baiguowan group and Yimen formation.

The deposit is situated in part between Shuenhe syncline and Xincun syncline, located at intersections with the Dalucao (F_1), Nanmuhe (F_7)and Xincun syncline, located at intersections with the Dalucao (F_1), Nanmuhe (F_7) and Zhangmenzha (F_6) faults. The regional structural framework was mainly made up of SN-striking, NW-striking and NE-striking faults. The ore body is cut through by Dalucao fault (F_1), and affected by the fault.

Outcropping magmatic rocks in the mineral district include quartz diorites of the Jinning epoch, alkali granites of the Indo-Chinese epoch, aegirine-augite syenites, and syenites of the Himalaya epoch. The Daluxiang quartz diorite (853Ma) is emplaced into the Presinian Huili group and is covered by the Jurassic Baiguowan formation. Rare earth ore bodies are hosted in the 64.9 Ma old aegirine-augite –syenite, which is emplaced in Daluxiang quartz diorite. The major ore body is lens-shaped and shows net-veining and mineralization of structural fissures in the aegirine-augite syenite. The major mineral assemblage in the ore is made up of bastnasite, celestobarite, barytocelestite, aegirine-augite, fluorite, calcite, quartz, mica, minor sulphide, and rare earth titanite.

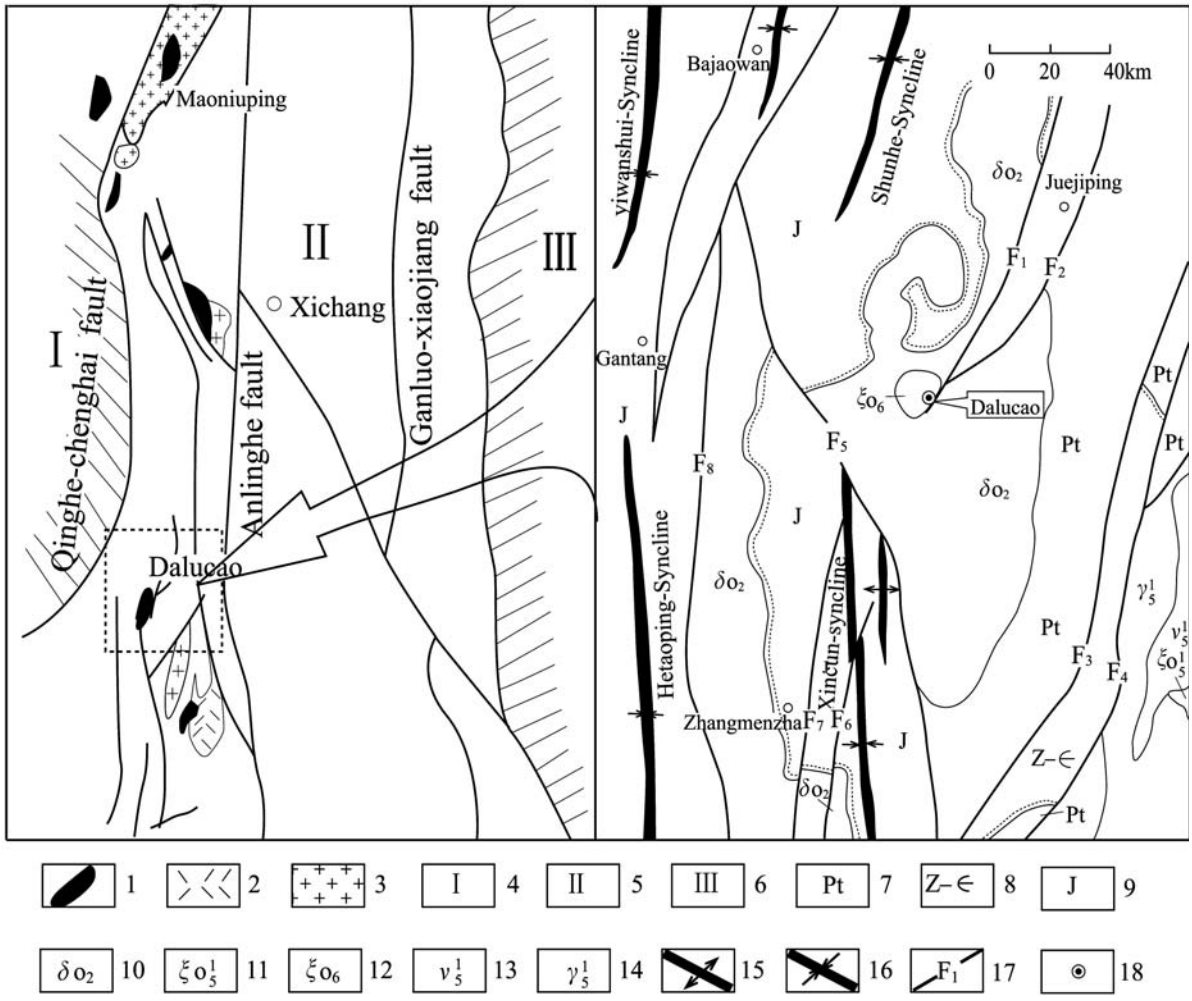

Figure 1: Geological structural map of Dalucao area (modified after the Regional Geology of Yanbian Range). 1- rare earth rich alkali-complex of Cenozoic period; 2- syenite of Triassic period; 3- alkali granite of Triassic period; 4- distributive province of marine Mesozoic group; 5- distributive province of Previndean land; 6- distributive province of Paleozoic group and continental Mesozoic group; 7- Previndean system; 8- Vindean-Cambrian system; 9- Jurassic system; 10- quartz diorite of Proterozic; 11- aegirine-augite syenite of Triassic period; 12- aegirine-augite syenite of Cenozoic period; 13- gabbro of Triassic period; 14- granite of Triassic period; 15- anticline axis; 16- syncline axis; 17- fault and its number; 18- REE deposit

3 Geochemistry of stable isotopes

3.1 Signature of silicon and oxygen isotopic compositions

We measured the silicon and oxygen isotope compositions of many wall rock and quartz samples from the rare earth ore body in order to elucidate the origin and the evolution of ore-forming fluid in the deposit. Table 1 shows the Si and O isotope compositions of the deposit. Quartz $\delta^{18}O$ in quartz diorite has values around 9.1‰ to 9.3‰, and the quartz diorite $\delta^{18}O$ is +7.1‰.

It is suggested that the quartz diorite belongs the granitoid (Talor 1968). The quartz $\delta^{30}Si$ in quartz diorite is 0.0‰, hornblende -0.2‰ and the quartz diorite $\delta^{30}Si$ 0.1‰, which is close to the granitoid average.

The $\delta^{18}O$ and $\delta^{30}Si$ of quartz in the ore body are respectively +10.1‰ and -0.3‰, the $\delta^{18}O_{H2O}$ of fluid inclusions in quartz is 6.0‰, and bastnasite $\delta^{18}O$ is from +19.2‰ to +19.3‰.

3.2 Signature of H, O and C isotopic compositions

Table 2 displays H, O, and C isotope compositions of mineral-hosted fluid inclusions in the REE deposit.

The quartz δD in quartz diorite is -96‰ and the $\delta^{13}C_{PDB}$ of its CO_2 is -11.9‰.

δD and $\delta^{18}O_{H2O}$ of quartz in the ore body are respectively -87‰ and +6.0‰, the fluite inclusion $\delta^{13}C_{PDB}$ of quartz in the ore body is -8.4‰, which show the H, C and O isotope compositions of the magmatic water.

Table 1: Silicon and oxygen isotopic compositions of minerals and rock samples (‰).

number	mode of occurrence	determined mineral	homogenization temperature °C	$\delta^{18}O_{V\text{-}SMOW}$	$\delta^{18}O_{H2O}$	$\delta^{30}Si_{NBS\text{-}28}$
Dlx-4-1	quartz diorite	whole rock		+7.1		–0.1
Dlx-4-2	quartz diorite	hornblende		+6.8		–0.2
Dlx-4-3	quartz diorite	quartz		+9.1		0.0
Dlx-4-4	quartz diorite	quartz		+9.3		0.0
Dlx-7	Ore body	quartz	400 ±10	+10.1	+6.0	–0.3
Dlx-8	Ore body	bastnasite		+19.2		
Dlx-23	Ore body	bastnasite		+19.3		

Note: $\delta^{18}O_{H2O}$ is the result calculated with $\delta^{18}O_{quartz} - \delta^{18}O_{H2O} = 3.34 \times 10^6 T^2 - 3.31$ (Matsuhisa 1979).

Table 2: Hydrogen, carbon and oxygen isotopic compositions of minerals-hosted fluid inclusions (‰)

number	mode of occurrence	determined mineral	$\delta D_{V\text{-}SMOW}$	$\delta^{18}O_{H2O}$	$\delta^{13}C_{PDB}$
Dlx-4	quartz diorite(wall rock)	quartz	-96		-11.9
Dlx-7	Ore body	quartz	-87	+6.0	-8.4
Dlx-2-1	Ore body	fluorite	-83	-13.6	-17.1
DLx-2-2	Ore body	fluorite	-104		-19.0
DLx-2-3	Ore body	fluorite	-91		−17.0
Dlx-14	Ore body	fluorite	-119	-9.6	-16.0
Dlx-8	Ore body	bastnasite	-89		-8.0
Dlx-23	Ore body	bastnasite	-79		-8.1
	surface water	water	-83	-14.7	

Note: quartz $\delta^{18}O_{H2O}$ is the result calculated with $\delta^{18}O_{quartz} - \delta^{18}O_{H2O} = 3.34 \times 10^6 T^2 - 3.31$ (Matsuhisa 1979), fluorite $\delta^{18}O_{H2O}$ is the determination value of the fluid inclusions, and bastnasite $\delta^{13}C_{PDB}$ is the determination value of the mineral.

Fluorite δD of in the ore body range from -119‰ to -83‰, averaging around -99‰. Its $\delta^{18}O_{H2O}$ range from -13.6‰ to -9.6‰, with an average of -11.6‰, indicating that the ore-forming fluid is a mixed fluid of the magmatic water and the meteoric water.

The fluid inclusion δD of the bastnasite range from -89‰ to -79‰, showing that the ore-forming fluid is a magmatic water. The bastnasite $\delta^{13}C_{PDB}$ is about -8.0‰, indicating the characteristic of mantle carbon.

3.3 Derivation of the metallogenetic material

In the graph of $\delta^{18}O$ vs δD for ore-forming fluids (Fig. 2), it is evident that the fluid-inclusion water in quartz belong to magmatic water, and the fluid-inclusion water in fluorite belong to meteoric water, indicating that the ore-forming fluid was a mixed fluid of the magmatic water and the meteoric water.

According to the Si isotope compositions of the ore body quartz and whole rock, it can help us infer that the Si may be from a deep magmatic source area.

The carbon isotopic features suggest that carbon of the bastnasite was from mantle, the fluid inclusion carbon of fluorites in the ore body was from a mixed carbon source, and the fluid inclusion carbon of quartz was from mantle.

The rare earth partitioning of the bastnasite, the ore and the alkali complex is all Ce>La>Nd, and Ce-rich, showing the mantle features of the metallogenetic material in the rare earth deposit. The $^{134}Nd/^{144}Nd$ of the rare earth deposit range from 0.512297 to 0.512313, indicating that the rare earth elements were mainly derived from the upper mantle.

4 Conclusions

The rare earth elements of Dalucao deposit are mainly from the mantle. Si may also be from a deep magmatic source. The ore-forming fluid was a mixture fluid of the magmatic water and the meteoric water. The carbon of bastnasite was deduced from the mantle and the carbon of the ore-forming fluid in bastnasites was from a mixture carbon source area. It is further suggested that the source rocks of the ore-bearing aegirine-augite syenite are probably early-formed alkali rich rocks in Triassic period or Carboniferous-Permian period. The ore-bearing aegirine-augite syenite was mostly formed by remelting, ascending and emplacement of the source rocks under the activation of mantle plume

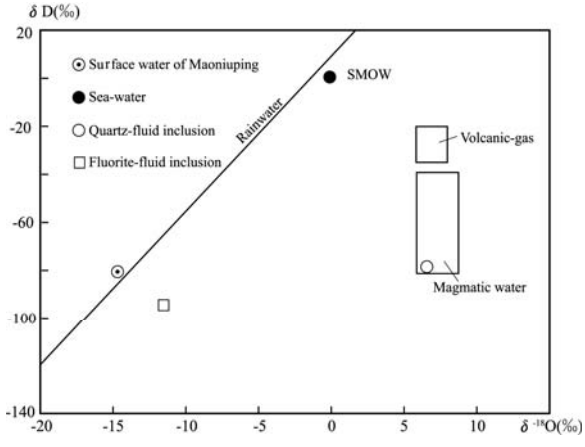

Figure 2: Graph of $\delta^{18}O$ vs δD for ore-forming fluids.

and tectonic mobilization in the Tertiary-Quaternary period. C, H, O, and Si isotope compositions of the deposit indicate that Dalucao rare earth deposit was a hydrothermal vein type deposit of the rich light rare earth element, which was formed in the Tertiary-Quaternary period.

References

Clayton RN, O'Neil JR, Mayeda TK (1972) Oxygen isotope exchange between quartz and water. J Geophys Res 77: 3057-3059

Ding T (1994) Silicon isotope geochemistry. Geol Pub House, Beijing, 23-30

Matsuhisa Y, Goldsmith JR, Clayton RN (1979) Oxygen isotopic fractionation in the systemquartz-albite-water. Geochim. Cosmochim Acta 43: 1131-1140.

O'Neil JR, Taylor HP (1967) The oxygen isotope and cation exchange chemistry of feldspars. Am Mineral 52: 1414-1418

Pu G (2001) REE mineralization evolution in Panxi rift and basic metallogenic feature in Himalaya age. Study on the endogenetic minerallization in Hymalaya age, China. China Seismol Press, Beijing, 104-113 (in Chinese)

Shen W (1987) Geology of stable isotope. Atom Ener Pub House, Beijing: 123-125 (in Chinese)

Tang L, Yang D, Liu S, Wang Z, Ye X, Chen Z (1985) The double structural feature of Panxi rift. The collected works of Panxi rift, China. Geol Pub House Beijing: 72-84 (in Chinese)

Taylor HP (1968) $^{18}O/^{16}O$ ratios coexisting minerals in glancophane-bearing metamorphic rock: Bull Geol Soc Am 79: 1727-1756

Yuan Z, Shi Z, Bai G, Wu C, Li X (1995) Mouniuping REE deposit, Mianning County, Sichuan Province. China Seismol Press, Beijing: 103-105 (in Chinese)

Preliminary study on the Chinese continental mineralization system

Wang Denghong
Institute of Mineral Resources, CAGS, Beijing, 100037, China

Chen Yuchuan
Chinese Academy of Geological Sciences (CAGS), Beijing, 100037, China

Abstract. China is enriched in mineral resources. How to systematically deduce the regularity of mineralization in order to serve for prospecting is the main purpose of this paper. The Chinese continental mineralization system (CCMS) can be referred to as the whole group of mineral deposits located in the present continent of China and their genetically related geological factors. The CCMS consists of 214 minerogenic series of 11 geological periods from Early Archean to Cenozoic, including at least 978 patterns of representative mineral deposits. The CCMS is the final result of mineralization formed through the whole evolution history of Chinese continental crust.

Keywords. Chinese continental mineralization system, minerogenic series, metallogenic prognosis, evolution regularity

1 Introduction

After a long history of mining (at least 3000 years), especially large-scale geological exploration conducted since the founding of the People's Republic of China (1949), 171 kinds of mineral resources have been discovered up to present. Among these, 156 commodities have explored reserves, including 9 types of energy resource, 54 metallic minerals, 90 industrial minerals, plus groundwater, mineral water, and carbon dioxide gas. The total value of potential reserves places China third in the world. Various deposits are among the richest in the world, including rare earths, W, Sn, Sb, Mo, Bi, Be, coal, magnesite, barite, fluorite, talc, graphite, bentonite, fireclay, asbestos, gypsum, wollastonite, diatomaceous earth, and building stone. On the other hand, the country is lacking oil, high-grade iron, Cr, Mn, Cu, PGE, potash salt, and diamond. By now, about 200,000 localities of ore deposits or mineral occurrences have been discovered. Among these, 20,000 ore deposits have been investigated in detail, including 90 super giant deposits (Fig. 1; Chen 1999). However, little geological work has been done in the vast western territory of China and for depths greater than 500 m, suggesting a great potential for further discoveries. Owing to the diversity of geological settings for mineralization in China, there is great potential for ore prospecting (Guo, 1987; Chen 1999).

2 Concept of Chinese continental mineralization system and related terms

In this paper, we refer the Chinese continental mineralization system (CCMS) as the whole group of mineral deposits located in the present continental crust of China and their genetically related geological factors. All mineral deposits located in the present continental crust of China formed during the history of continent evolution. The concept of CCMS contrasts with the term Chinese oceanic mineralization system (COMS), both the CCMS and the COMS compose the Chinese Mineralization System (CMS), while the CMS is part of the global mineralization system (GMS). The global mineralization system can be divided into a series of sub-systems geographically. The GMS can be divided into sub-systems according to different classification systems, such as spatial sub-systems, temporal sub-systems (Mesozoic mineralization system, Cenozoic mineralization system and so on), and genetically sub-systems (magmatic mineralization system, sedimentary mineralization system and metamorphic mineralization system). Thus, the CCMS is in fact a complex big system composed of different levels of sub-systems, which related to each other structurally, regularly, inevitably and recognizably. By the study of CCMS, the wholly, knowledge about mineralization can be concluded systematically and sequentially, instead of individually, fragmentally or randomly. In this paper, we will pay more attention to the CCMS, because it's forming history shows an important aspect of the continental evolution history of China and provides valuable clues and indispensable examples for the understanding of global mineralization system. The relationships among different deposits and the relationships between mineralization and its geological history and tectonic setting are very important for the study of CCMS.

The present Chinese continental crust includes relative stable regions (paleo-plates or massif) and active belts (suture zones and/or collision belts). There are three large landmass or plates and four active belts in China (Fig. 2). The three main landmass include: (1) the North China landmass, which were formed after the Lvliang Movement (1800 Ma) and includes a basement of Archean and/or Lower Proterozoic metamorphic rocks; (2) the Tarlimu landmass, formed after the Jinning Movement (1000 Ma) and has a basement of pre-Sinian metamorphic rocks; (3) the Yangtze landmass, also formed after the Jinning Movement and its basement consists mainly of Proterozoic metamorphic rocks.

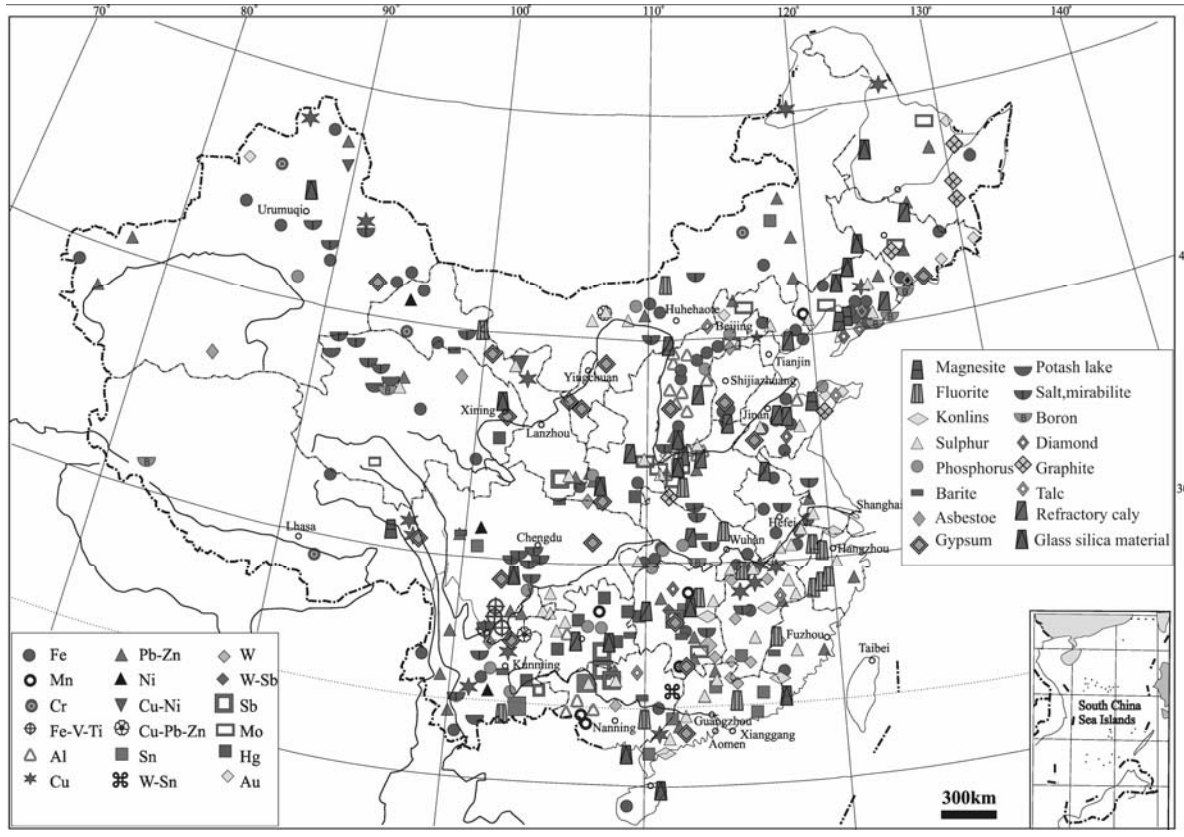

Figure 1: Sketch map showing the distribution of the chief metal and nonmetal deposits of China

The main active belts include: (1) the Tianshan- Xing'an active belt, which consist with a series of fold belts and micro-plates and formed after the Caledonian- Hercynian movement; (2) the Kunlun-Qilianshan- Qinling active belt, located between North China and South China and activated at different epochs of Jinning, Caledonian, Hercynian, Indo-Chinese, Yanshanian and Himalayan; (3) the Sichuan-Yunnan-Qinghai-Tibet active belt, which is the most important active belt of Tethys- Himalayan in the southwestern China; and (4) the western circum-Pacific active belt, mainly overprinted on the Paleozoic and pre-Paleozoic tectonic belts in the eastern China and featured by strong activation of Mesozoic-Cenozoic volcanism-magmatism in East China, large-scale granitoid intrusion in the Nanling Region (Chen et al. 1989), NE-NNE-trending movement of blocks and rifting-magmatism in the margin area of paleo-landmass.

3 Manifestation of the CCMS

Generally speaking, the CCMS is a natural system consisting of more than 200 thousand localities of ore deposits or mineral occurrences. Obviously, it is difficult to reveal the nature and complexity of CCMS by single deposits, deposit types, mineralized belts, host rocks, or other factors related to mineralization. In this paper, we apply the terminology of minerogenic series to describe the CCMS in brief. The concept of CCMS is different from that of minerogenic series presented by Cheng et al. (1979, 1983), which groups a series of mineral deposits related to each other genetically within a certain setting of geological environment and within a certain stage of geological history (Wang et al. 2002). However, because each minerogenic series bases on the four most important factors (ore-forming age, tectonic setting, geologic event and mineral assemblage and/or metal association), it is suitable to apply the nomenclature of minerogenic series to construct the framework of CCMS. Generally speaking, we have divided the CCMS into different sub-systems according to geological time, and each sub-system consist of secondly sub-system of mineralization based on geological setting of the same geological time. Given a certain geological setting of a certain geological time, each minerogenic series refers to a certain group of metals and/or mineral resources and/or energy resources related to a certain geologic process. Thus, minerogenic series is the preferred and integrant unit to make up of the CCMS. As a whole, the CCMS consists of 214 minerogenic series of 11 geological periods from Early Archean to Cenozoic, including at least 978 patterns of representative mineral deposits.

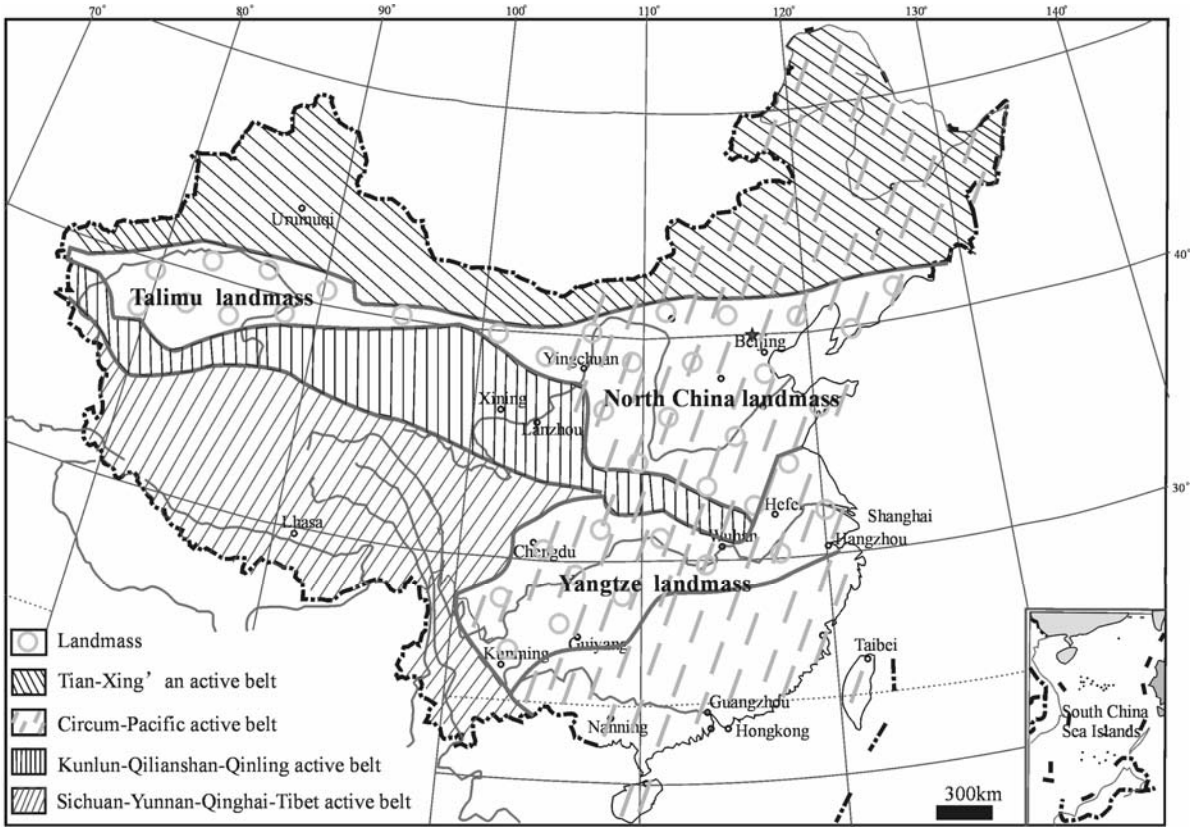

Figure 2: General tectonic setting of China continent

4 Application significance of the CCMS

Because the CCMS can be build up by basic unit of minerogenic series, minerogenic series and their relationship with the evolution history of China continental crust then become the most important aspect of our present research. As to each minerogenic series, all the mineral deposits are grouped together genetically rather than randomly. For example, the Triassic sedimento-minerogenic series of salt and coal deposits associated with marine carbonaceous rocks and paralic clastic rocks within the Sichuan basin, which is one of the above 214 minerogenic series of the CCMS, consists of a series mineral deposits including the gypsum deposits (named as Nongle-type) and the celestite deposits (named as Chongqing-type) hosted within the Jialingjiang Formation (T_1^2j), including the polyhalite deposits (named as Quxian-type) within the Jialingjiang Formation and the Leikoupo Formation (T_2^1l), including the halite deposits (named as Weixi-type) within the Leikoupo Formation, and including the coal deposits (named as Yongrong-type) within the Xujiahe Formation ($T_3^{2\text{-}3}x$). The evolution trend of mineral deposits from salt to coal gradually is in accordance with the evolution history of the Sichuan basin changing from oceanic to terrestrial facies at its waning stage. Such trend of mineralization evolution can thus be deduced as a piece of regularity for prospecting in the Sichuan basin and in other similar basins further.

In a broad sense, in a geosyncline's environment such as the Northern marginal belt of the North China Platform of Proterozoic, the Kunlun- Qilianshan-Qinling belt of Proterozoic-Paleozoic, the Altay tectonic belt of Paleozoic ,and the Tethys belt of Mesozoic, mineral deposits usually change from base metal deposits of VHMS-type formed at its early stage to rare metal deposits associated with magmatism at its folding or mountain building stage, and to gold deposits controlled by regional structures at its late stage of structural adjustment within an actually continental setting. Such trend is partly similar to that of an Wilson cycle, but each minerogenic series is different from each other because of its unique geological time of ore-forming, tectonic environment, special association of mineral resources and genetic relationship with other geologic process. Thus, the study of CCMS also can provide a new approach for deduction the evolution history of the Chinese continent crust.

In addition, the study of CCMS can contribute to metallogenic prognosis. For instance, the number of minerogenic series become more and more from Archean to Proterozoic to Paleozoic to Mesozoic and to Cenozoic.

However, the number of Yanshanian minerogenic series shows a negative anomaly calculated on the same scale of geological time, suggesting that there is still a good potential for prospecting Yanshanian minerogenic series in China. Recently, numerous new deposits of Mesozoic age have been discovered both in northwestern China (such as the Baishan Mo deposit in Xinjiang, dated at 229±3Ma by a Re-Os isochron on molybdenite) and in south-eastern China (such as the Taoxikeng wolframite deposit in south Jiangxi, the Baolun gold deposit in Hainan). Some important deposits discovered earlier have also been proved to be of Mesozoic age by systematic dating. For example, the famous rare metal deposit hosted within the No.3 pegmatite-vein in Keketuohai mine, North Xinjiang, yields $^{40}Ar/^{39}Ar$ isochron ages ranging from 177.9 Ma to 148 Ma (Wang et al. 2002). This deposit has been recognized as a Hercynian deposit for nearly a century.

5 Evolution of the CCMS

In general, the concept of CCMS can also be summarized as the systematic combination of all the minerogenic series that formed during the whole evolution history of the present continental crust in China. So, the CCMS can be divided into Archean, Proterozoic, Paleozoic, Mesozoic, and Cenozoic sub-systems of mineralization as follows:

1. Archean sub-systems occurred in nucleus of the Chinese continental crust, dominated by BIF-type deposits, VHMS-type Fe, Cu, Pb, and Zn deposits, gold, graphite, and sillimanite deposits associated with metamorphic rocks;
2. Proterozoic sub-systems occurred in the marginal rift setting peripheral to the Archean Chinese continental shield, also dominated by Fe, Cu, Ni, REE, Pb, Zn deposits related to magmatism and sedimentary process and Au, B, P, magnesite, graphite, andalusite, and sillimanite deposits related to metamorphic process, and featured by massive Cu-Ni deposits related to mafic-ultramafic rocks;
3. Paleozoic sub-systems occurred in the main orogenic belts around the Proterozoic Chinese continent, featured by more complex association of elements and/or mineral resources than that of Proterozoic and by typical plate tectonic environment;
4. Mesozoic-Cenozoic sub-systems occurred both around and within the Paleozoic Chinese continent (Chen and Wang 2001), featured by porphyry-type copper deposits, skarn-type Fe-Cu deposits, granite-related W, Sn, Bi, Mo, REE, Rare metal, Pb, Zn, Sb, Ag, Au, Hg deposits, placer deposits, industrial mineral deposits formed within weathering crust, energy resources formed within continental basins and so on, with banded iron formation and mafic-ultramafic massive Cu-Ni deposits disappearing (Wang et al. 2000).

Origin and evolution of Sn- and Cu-rich fluids in the Dajing tin-polymetal deposit - evidence from LA-ICP-MS analysis of individual fluid inclusions

Wang Lijuan, Wang Yuwang, Wang Jingbin
Beijing Institute of Geology for Mineral Resources, Beijing 100012, and Key Laboratory of Mineral Resources Institute of Geology and Geophysics, Chinese Academy of Sciences, Beijing, 100029, China

Zhu Heping
Key Laboratory of Mineral Resources Institute of Geology and Geophysics, Chinese Academy of Sciences, Beijing, 100029, China

Günther Detlef
ETH, Swiss Federal Institute of Technology, 8092 Zürich, Switzerland

Abstract. LA-ICP-MS analysis of the composition of individual fluid inclusions indicate that shallow-originated Sn-rich fluids and deep-originated Cu-rich fluids mix at moderate to low temperature and low salinity, eventually resulting in the formation of Cu and Sn mineralization in the Dajing deposit.

Keywords. Dajing, single inclusion, LA-ICP-MS anslysis, Cu-rich fluids, Sn-rich fluids

The Dajing tin-polymetal deposit is located at the northern margin of North China Craton (Zhao and Zang 1997; Wang et al. 2001). Quartz and fluorite are intergrown with cassiterite and chalcopyrite. Chalcopyrite can be found included in fluorite. Abundant fluid inclusions were found in fluorite. They are large with a gas/liquid ratio of 10%. Chalcopyrite crystals can be found in some fluid inclusions. It is deduced that these fluid inclusions with chalcopyrite crystals are trapped from Cu-rich fluids. Cassiterite can be found included in quartz. Fluid inclusions in quartz are small in size and some are gas inclusions with high gas/liquid ratios. Microthermometric data show that the chalcopyrite-bearing fluid inclusions in chlorite have low to moderate temperature and low to moderate salinity whereas gas inclusions in quartz have moderate to high temperature and low salinity. Therefore, it is inferred that Cu-rich fluids are low to moderate temperature and low to moderate salinity whereas the Sn-rich fluids are moderate to high temperature and low salinity. The intergrowth of Sn and Cu probably resulted from mixing of Cu-rich fluids and Sn-rich fluids (Wang et al. 2000).

To further ascertain the origin and evolution of the Sn-rich and Cu-rich fluids in the Dajing deposit, LA-ICP-MS analyses on individual fluid inclusions with different temperature, salinity, and occurrence in quartz and fluorite from the Sn-Cu orebodies were carried out at Swiss Federal Institue of Technology, Switzerland in February, 2004. LA-ICP-MS is the most advanced analysis method for the composition of single fluid inclusions. Most of the reseach focused on fluids of high temperature and high salinity (Audeat et al. 1998; Günther et al. 1998; Günther and Heinrich 1999). Because some fluid inclusions in fluorite contain chalcopyrite crystals, we made LA-ICP-MS analysis of individual fluid inclusions on them and take their compositions as representative of the Cu-rich fluids. Near the Dajing deposit, there is a tin deposit named Huangganglіang, which belongs to the same tin-mineralization belt as the Dajing deposit. Both deposits have quite similar geological background (Li et al. 2001; Wang et al. 2001). We analyzed the fluid inclusions in quartz associated with cassiterite from the Dajing deposit and primary fluid inclusions in fluorite from the Huangganglіang deposit with LA-ICP-MS analysis. The

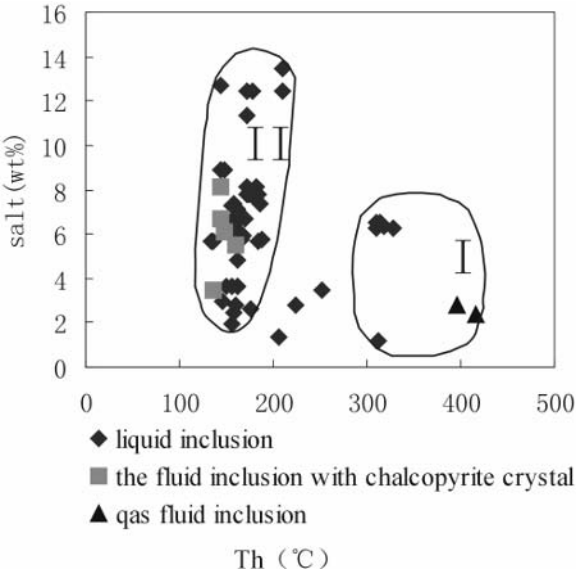

Figure 1: Relation between homogeneous-temperature and salinity of fluid inclusion from Dajing mine I-Sn-rich fluid; II-Cu-rich fluid.

This page intentionally blank

results are quite similar. Therefore, the LA-ICP-MS analytic results of individual fluid inclusions in quartz associated with cassiterite from the Dajing deposit were taken as representative of the Sn-rich fluids.

Tables 1 and 2 are the LA-ICP-MS analytic results of individual Cu-rich and Sn-rich fluid inclusions, respectively.

Table 1 shows that the Cu-rich fluids have higher Cu contents than Sn, have Sr contents one to several order of magnitude higher than Rb, and are relatively richer in Na than K. Table 2 shows that the Sn-rich fluids have higher Sn contents than Cu, have Rb contents one to several oder of mragnitude higher than Sr, and are relatively richer in K than Na. Based on the compositions of representative Cu-rich and Sn-rich fluids, we infer whether other fluid inclusions with different occurrence, temperature and salinity in quartz and fluorite belong to Cu-rich or Sn-rich fluids, and thereby trace the origin and evolution of these fluids.

Cu-rich and Sn-rich fluid inclusions are listed in Tables 3 and 4, respectively.

Figure 2 shows that both the Cu-rich and the Sn-rich fluids have a similar evolutionary trend from high to low temperature and the two kinds of fluids probably mix at moderate temperature, resulting in mineralization.

The Sr and Rb concentrations in the fluids are important indicators for the fluid source. According to Zhao et

Table 1: The composition of fluid inclusion including chalcopyrite in fluorite from Daing mine.

Test No.	Sample	Tm-Ice	Th	Na/K	Sn/Cu	Na/Sn	Na/Cu	Na/Rb	Na/Sr	Rb/Sr	Sn/Fe	Cu/Fe
fb04a06	n22-4	-3.9	150	0.25	0.53	0.01	0.003	19	0.37	0.02	0.62	1.17
fb04b05	n7-3	-3.5	148	5.1	0.06	0.12	0.01	120	7.6	0.06	0.06	0.97
fb06a25	n19-2	-4.9	180	2.1	0.03	0.61	0.02	916	5.5	0.01	0.01	0.44
fb06b03	n19-3	-4.4	216	20	0.70	34	23	1565	254	0.16	0.01	0.01

Table 2: The composition of original fluid inclusion in fluorite from tin ore-body in Huangganglang mine.

Test No.	Sample	salt (wt%)	Na/K	Sn/Cu	Na/Sn	Na/Cu	Na/Rb	Na/Sr	Rb/Sr	Sn/Fe	Cu/Fe
fb10a07	n42-1	30	0.23	1.5	10	15	2.6	40	16	0.010	0.007
fb10a08	n42-2	30	3.61	3.7	87	324	112	600	5. 4	0.016	0.004
fb10a09	n42-3	30	2.67	4.9	69	343	79	1540	19	0.022	0.004

Table 3: The composition of Cu-rich fluid inclusion from flurite and quartz in Dajing mine.

Test No.	Sample	(Tm-Ice, Th)	Na/K	Sn/Cu	Na/Sn	Na/Cu	Na/Rb	Na/Sr	Rb/Sr	Sn/Fe	Cu/Fe
fb04a25	n6-2	Cu(-4.8, 129)	2.8	0.1	3140	350	402	27	0.066	0.023	0.21
fb04b03	n7-1	Cu(-3.6, 148)	55	0.2	140	25	4800	113	0.024	0.14	0.74
fb04b06	n7-4	Cu(-3.5, 148)	62	0	–	52	–	660	0	–	–
fb04b07	n7-5	Cu(-3.5, 148)	15	0.07	520	37	–	61	0	0.063	0.88
fb04b08	n7-6	Cu(-2.8, 164)	3.3	0.05	9.1	0.4	316	4.1	0.013	0.033	0.73
fb04b12	n9-2	(-7.8, 136)	1.1	0.15	241	37	58	21	0.36	0.008	0.05
fb04a04	n22-2	Cu(-10.5, 264)	2.4	0.39	12000000	4600000	146	55	0.38	0.008	0.02
fb06b11	n13-1	Cu(-5.2, 298)	11900	0.33	55	21	3400000	58400	0.017	0.029	0.09
fb06b12	n13-2	Cu(-5.4, 312)	1451	0.03	25800	740	1200000	7900	0.007	0.028	0.99
fb09a06	n16-4	(-3.7, 146)	–	0.44	7.7	3.4	–	0.2	0	–	–
fb06b09	n4-3	Cu(-3.0, 162)	0.2	0.47	99	47	–	38	0	0.057	0.12
fb09a12	n16-8	(-3.8, 146)	–	0.28	3.8	1.1	2.7	0.04	0.015	–	–
fa11b09	n53-2	* (-4.0, 175)	2.4	0	–	19	88	62	0.70	0	0.12
fb06a24	n19-1	(-3.0 , 180)	10	–	–	–	660	35	0.054	–	–
fb04a29	n17-3	Cu(-4.9, 300)	29	–	–	–	7900	312	0.040	–	–

"–" denotes divider below detection limits, "0" denotes dividend below detection limits. The host minerals are fluorite except for those marked with *, which are quartz. Cu denotes chalcopyrite was found included in fluorite.

Table 4: The composition of Sn-rich fluid inclusion from flurite and quartz in Dajing mine.

Test No.	Sample	(Tm-Ice, Th)	Na/K	Sn/Cu	Na/Sn	Na/Cu	Na/Rb	Na/Sr	Rb/Sr	Sn/Fe	Cu/Fe
fa11a04	n31-2	* (-4.5, 188)	1.8	–	31.4	–	406	900	2.2	0.33	0
fa11a05	n31-3	* (-4.5, 188)	49	–	94.0	–	403	–	–	–	–
fa11a08	n32-2	* (-3.9, 154)	36	–	–	–	2460	–	–	0.05	0
fa11b08	n53-1	* (-4.0, 175)	7.1	1.52	70.8	107	–	–	–	–	–
fa11a06	n31-4	* (-4.5, 188)	5.86	–	–	–	162	310	1.9	0	0
fa11a07	n32-1	* (-4.4, 330)	1.36	–	–	–	350	1300	3.7	–	–
fb04a12	n5-2	Cu(-4.2, 162)	1.60	–	–	–	91	–	–	–	–
fb06b04	n19-4	Cu(-3.0, 156)	0.11	2.29	3.0	6.9	11	99	9.2	0.16	0.07
fb09a07	n16-5	(-4.6, 146)	–	5.65	41	233	–	–	–	–	–
fb04a11	n5-1	Cu(-4.2, 154)	1.73	–	4700	–	200	7550	38	0.01	0

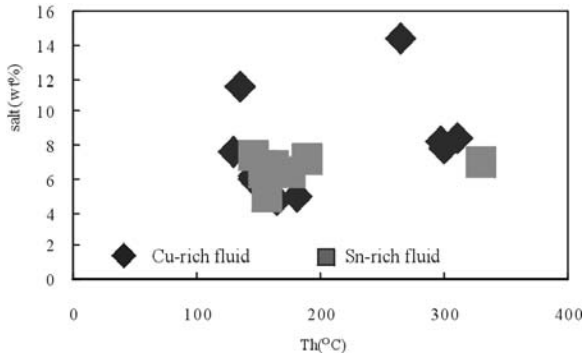

Figure 2: Relation between homogeneous-temperature and salinity of the fluid inclusions that are rich in Cu and Sn, respectively, from the Dajing mine.

al (1997), Sr is enriched in the early stage of magma differentiation, whereas Rb is enriched in the late stage of magma differentiation. Therefore, the ratio of Rb/Sr increases with magma differentiation, from an average of about 0.5 at the early stage to above 10 at the late stage. The Cu-rich fluid in the Dajing deposit are highly enriched in Sr, indicating that the fluids are derived from the deep, whereas the Sn-rich fluids are enriched in Rb, reflecting their derivation from the shallow.

Based on the analyses, several conclusions can be reached:

1. The Cu-rich fluids have higher Cu contents than Sn, higher Sr contents than Rb, and are relatively rich in Na. The fluids are derived from a deep source and are mainly trapped in fluorite.
2. The Sn-rich fluids have higher Sn contents than Cu, higher Rb contents than Sr, and are relatively rich in K. The fluids are shallowly derived and mainly trapped in quartz.
3. Both the Cu-rich and Sn-rich fluids have an evolutionary trend from high temperature to low temperature. The shallow-originated Sn-rich fluids and the deep-originated Cu-rich fluids mix at the stage of moderate to low temperature and low salinity and result in the formation of Cu and Sn mineralization in the Dajing deposit.
4. To our knowledge, there have been no reports about LA-ICP-MS analysis on individual fluid inclusions with such low temperature, low salinity and small size as in the Dajing deposit. The results demonstrated that the LA-ICP-MS analysis of individual fluid inclusions has practical applications in studying ore-forming processes in polymetal ore deposits.

References

Audetat A, Günther D, Heinrich CA (1998) Formation of a magmatic-hydrothermal ore deposit: Insights with LA-ICP-MS analysis of fluid inclusions. Science 279: 2091-2094

Günther D, Heinrich CA (1999) Enhanced sensitivity in laser ablation-ICP mass spectrometry using helium-argon mixtures as aerosol carrier. J Anal Atom Spectrom 14: 1363-1368

Günther, D Audetat A, Frischknecht R, Heinrich CA (1998) Quantitative analysis of major, minor and trace elements in fluid inclusions using laser ablation-inductively couple plasma mass spectrometry. J Anal Atom Spectrom 13: 263-270

Li JW, Shimazaki H, Yoshihide S (2001) Skarns and genesis of the Huanggang Fe-Sn deposit, Inner Mongolia, China Resource Geol 51: 359-376

Wang L, Wang J, Wang Y, Shimazaki H (2001) Ore-forming fluid and metallization of the Huangganglang skarn Fe-Sn deposit, Inner Mongolia. Sci China (Series D) 44: 735-747

Wang L, Wang Y, Wang J, Jin X, Zhu H (2000) Metallogenetic fluid study of tin and copper stage from Dajing deposit and its genetic significance. Acta Petrol Sinica 16: 609-615 (in Chinese with English abstract)

Wang YW, Wang JB, Uemoto T, Wang LJ (2001) Geology and mineralization at Dajing tin-polymetallic ore deposit, Inner Mongolia, China. Resource Geol 51: 307-320

Zhao Y, Zhang D (1997) Metallogeny and prospective evaluation of copper-polymetallic deposits in the Da Hinggan Mountains and its adjecent regions Seismo Press, Beijing: 125-144

Zhao Z (1997) The principle of trace elements geochemistry. Science Press 1-153 (in Chinese)

Lead and zinc-rich fluid inclusions in Broken Hill-type deposits: Fractionates from sulphide-rich melts or consequences of exotic fluid infiltration?

Patrick J. Williams, Dong Guoyi
School of Earth Sciences and [1]Predictive Mineral Discovery CRC, James Cook University, Townsville 4811, Australia

Bruce Yardley
School of Earth Sciences, University of Leeds, Leeds LS2 9JT, UK

Thomas Ullrich
Geology Department, The Australian National University, 0200 Canberra, Australia

Chris Ryan
CSIRO Exploration and Mining, School of Geosciences, Monash University, Melbourne 3168, Australia

Terry Mernagh
Geoscience Australia, GPO Box 378, Canberra 2601, Australia

Abstract. High salinity fluid inclusions (Th = 200-550° C) from the Broken Hill and Cannington "Broken Hill-type" ore deposits in Australia have been analysed by PIXE and LA-ICP-MS. They have high Pb (>1%) and Zn (>1000 ppm) and Pb/Zn ratios much higher than those of the majority of crustal brines. Laser Raman studies reveal the presence of methane and PIXE images show that Pb and Zn are respectively concentrated in a Pb-K-Cl solid, and the liquid phase. This indicates that the inclusions have very low total sulphur contents. The Pb/Zn ratios are similar to those of eutectic melts in the Gn-Sp-Po system whereas Pb/Fe ratios are variable and lower than those of such melts. If these brines originated by fractionation from synmetamorphic sulphide-rich melts, then they must been greatly modified prior to entrapment. An alternative origin involving late- to post-metamorphic interaction of externally-derived brines with pre-existing sulphide accumulations should also be considered. In either case, the unique brine chemistry would appear to relate to the large amounts of sulphides in these systems.

Keywords. Lead, zinc, fluid inclusions, Broken Hill-type deposits, PIXE, LA-ICP-MS

1 Introduction

Yardley et al. (2003) used compiled natural brine and fluid inclusion analyses to show that concentrations of many metals vary systematically with temperature and salinity. This was taken to indicate that rock buffering is a powerful control on other major chemical influences of solubility, such as pH, fO_2 and sulphur abundance. Concentrations of elements such as Mn, Fe, Cu, Zn and Pb in natural fluids can be predicted within about an order of magnitude for known temperature and salinity and this can be viewed as a limiting chemical framework for hydrothermal ore-forming processes

Large and very distinctive Pb-Zn-Ag ore deposits occur in partially melted metamorphic rocks at Broken Hill, New South Wales (2 pyroxene granulite) and Cannington in NW Queensland (upper amphibolite). Along with just a few other ore deposits worldwide these are referred to as "Broken Hill-type" (BHt) deposits which are defined more by their high grade metamorphic settings than any consensus on their origin (e.g. Walters, 1998). It has recently emerged that very Pb- and Zn-rich aqueous fluid inclusions occur in both large Australian BHt deposits (Williams et al. 1999). In this paper we show that the chemistry of these brines is unlike any others previously known and discuss the possible processes by which they may have formed.

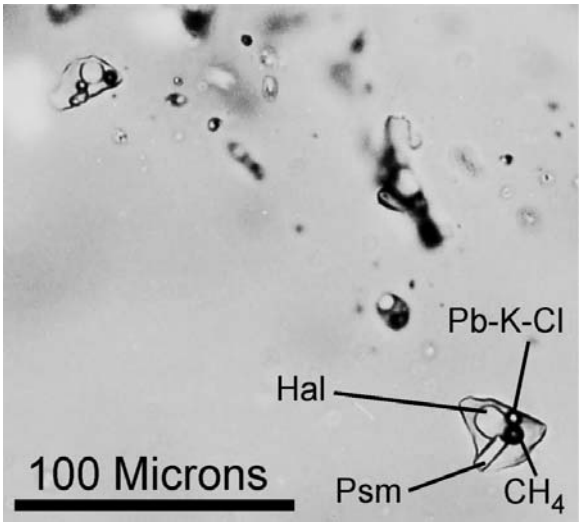

Figure 1: Part of a fluid inclusion trail from Cannington sample 42170 including a large inclusion with labelled phases (Hal = halite; Psm = pyrosmalite).

2 Petrography and microthermometry

A large variety of fluid inclusions have previously been observed in the Broken Hill ore deposit but this have received little attention in the literature (Wilkins 1977; Spry 1978). The current study used rocks displaying evidence of hydrothermal modification during the retrograde metamorphic history of the deposits. Sample 147001 from Broken Hill is a partly recrystallized quartz-rich rock from Western A lode in which older "blue quartz" is overprinted by late stage "white quartz" as described by Wilkins (1977). Fluid inclusions, predominantly less than 15 microns in diameter are very abundant as secondary trails in the older quartz and belong to the same fracture association that formed the white quartz. Sample 42170 from Cannington is an example of a quartz vein associated with a form of Fe- and Cl-rich hornblende alteration which is very common in the deposit (Chapman and Williams 1998). Fluid inclusions are again abundant in secondary trails (Fig. 1) and in this case can be very large (up to circa 100 microns).

In both samples, the vast majority of inclusions at room temperature are composed of liquid, a small vapour bubble, and number of solids. The latter have been investigated by microprobe in opened inclusions, in PIXE images and (42170 only) by laser Raman probe and were consistently found to include halite, pyrosmalite, and a Pb-K chloride.Some inclusions additionally contain sylvite and/or a Mn-rich carbonate mineral. Vapour bubbles were investigated by laser Raman probe in 42170 only and were found to consist of methane. The inclusions in 147001 homogenise by vapour bubble disappearance at temperatures between 270 and 410° C and have NaCl equivalent salinities between 30 and 40 wt %. Those in 42170homogenise by pyrosmalite dissolution at 400-450° C and have NaCl equivalent salinities between 30 and 40 wt %. In both samples the Pb-K-Cl phase dissolves at temperatures 100-200° below those of total homogenisation.

3 Fluid inclusion geochemistry

In situ microanalysis of fluid inclusions is a new and rapidly developing field and to date there has been a general lack of studies comparing results obtained using different techniques and in different laboratories. High salinity brine inclusions from Cannington and Broken Hill were investigated using both proton induced X-ray excitation (PIXE) analysis (method of Ryan et al. 2001), and laser ablation inductively coupled plasma mass spectrometry (LA-ICP-MS) using Excimer laser ablation systems (cf. Heinrich et al. 2003) at the Australian National University and Leeds University. The PIXE method is (a) relatively insensitive to contamination from the host quartz and any solid inclusions it contains, (b) able to provide quantitative data for halogens (Cl, Br) that were not analyzed by LA-ICP-MS owing to a lack of suitable external standards, and (c) able to image the distribution of elements between the phases present in the inclusions at room temperature. Coupled with microthermometric and laser Raman gas phase data, the images throw light on the likely abundance and speciation of the critical element sulphur which can not be determined at normal geological abundance by either microanalytical technique. PIXE analyses give a quantitative estimate of element abundances to an accuracy of ± circa 50 % though interelement ratios are determined to a much better level of accuracy as the main sources of error have similar effects on all elements. LA-ICP-MS data are determined as ratios and estimation of absolute concentrations depends on an independent internal standard such as the estimated abundance of a component by PIXE or microthermometric salinity estimates (Heinrich et al. 2003). PIXE analysis can only be undertaken of shallow inclusions (typically < 20 microns). Attempts to achieve controlled laserablation of shallow inclusions were generally unsuccessful and the analyses obtained by the two techniques were undertaken on different groups of inclusions.

Pb and Zn data from the three different laboratories are very consistent (Fig. 2). The average concentrations estimated by PIXE are 3150 ppm Zn, 36500 ppm Pb in 147001 and 4950 ppm Zn, 30300 ppm Pb in 42170 (ex-

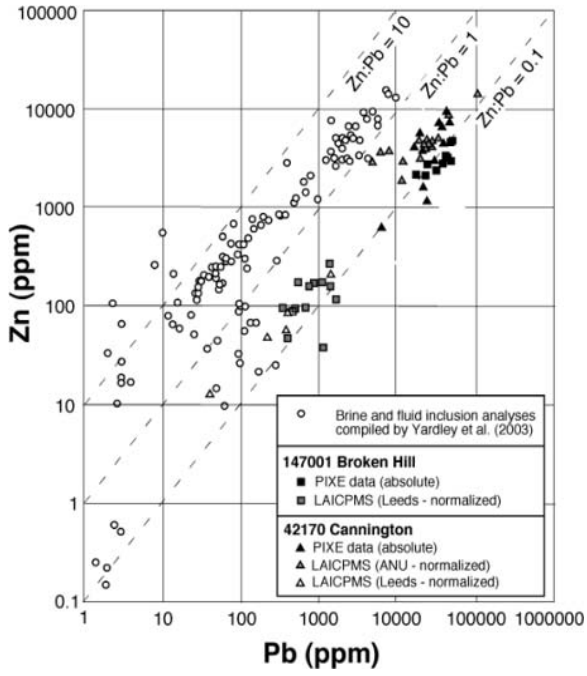

Figure 2: Zn versus Pb plot for the Broken Hill and Cannington fluid inclusions compared the natural brine and fluid inclusion analyses compiled by Yardley et al. (2003). ANU LAICPMS data were normalized to Mn as estimated by PIXE. Leeds LAICPMS data are arbitarily normalized to Na = 1000 ppm to facilitate their discrimination on the diagram.

cluding one outlying analysis with lower concentrations - cf. Fig. 2). The PIXE images reveal that Zn is codistributed with Ca and Br in the liquid phase of the inclusions at room temperatures. Zn/Pb ratios determined by both techniques are all less than 1 and on average around an order of magnitude below those of high temperature and high salinity brines in the data set compiled by Yardley et al. (2003). This reflects much higher concentrations of Pb in the Broken Hill and Cannington inclusions than have been measured in other natural high salinity fluids excepting a single case where extreme Pb enrichment was deduced to occurred in a fluid involved in retrograde hydration of granulites (Svenson et al. 1999). Pb/Ag ratios measured by LA-ICP-MS are between 640 and 1470 in sample 147001 and between 200 and 800 in sample 42170.

Br/Cl ratios determined by PIXE in sample 42170 are in the range 0.0003 to 0.0016 which is distinctly lower than seawater and magmatic brines as measured from porphyry copper deposits (cf. Kendrick et al. 2003). The PIXE investigation of sample 147001 was undertaken under conditions of comparatively poor instrumental performance and meaningful data were not obtained for Br in this case.

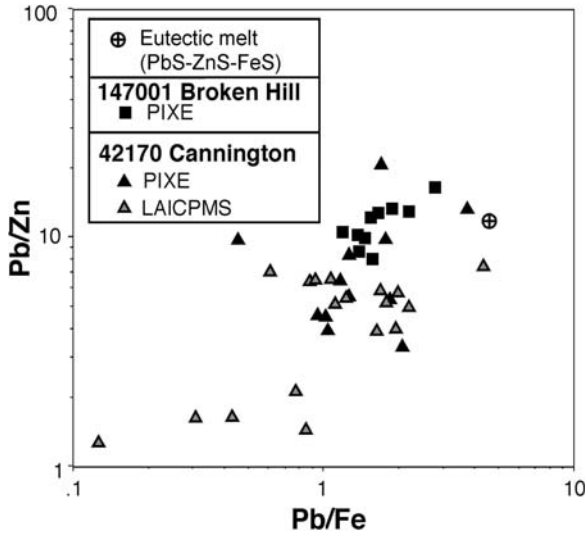

Figure 3: Plot of Pb/Zn ratio against Pb/Fe ratio in analyzed fluid inclusions compared with eutectic melt composition in the system FeS-ZnS-PbS from Mavrogenes et al. (2001).

4 Discussion

The studied fluid inclusions from Broken Hill and Cannington have much higher Pb concentrations and Pb/Zn ratios than fluid inclusions with similar salinities from other geological settings suggesting that they result from some process which is specific to this sort of ore deposit. Mavrogenes et al. (2001) have shown that compositions in the FeS-ZnS-PbS-Ag_2S system would have been partially-molten under peak metamorphic conditions at Broken Hill (though it is not clear that this would also have been the case at Cannington). One possible explanation for the unusual fluid inclusions is that they represent aqueous phases that equilibrated with sulphide melts. If this is the case then element abundances in the inclusions should reflect their activity ratios in the melt. The FeS-ZnS-PbS eutectic as determined by Mavrogenes et al. (2001) has Pb:Fe:Zn (by weight) approximating to 12:2.5:1 (Fig. 3) and all melts below 900° C have low ZnS compared to the other two components. High Pb/Zn ratios are therefore to be expected in fluids equilbrated with FeS-ZnS-PbS melts and the average ratios measured in the fluid inclusions from samples 147001 and 42170 are very similar to the ratio of the eutectic composition Furthermore, Mungall and Brenan (2003) established that Cl has an affinity for Fe-Cu-Ni-S melts (due to similarities with sulphur) and predicted that aqueous fluids evolved from such melts should have low Br/Cl ratios (cf. the fluid inclusions in 42170). This would be also expected to be a feature of other sulphide melt systems. However, it is not a diagnostic feature as low ratios could also reflect salinity derived from evaporitic halite or its preserved signature in metamorphic rocks.

Other features of the fluid inclusions are less easily reconciled with a relationship to sulphide melts. Thermometric results and paragenetic associations with retrograde hydrous and Cl-bearing silicates suggest the inclusions were trapped at temperatures several 100°s below those of the metamorphic peaks in the two systems. At Cannington, metamorphic hornblendes did not pass through their ^{40}Ar-^{39}Ar blocking temperatures until some 40 million years after the partial melting event recorded in the gneissic host rocks (Pollard et al. 1997; Giles and Nutman 2002). Aqueous fluids present at peak conditions would have somehow had to have avoided extraction by silicate melts and remained trapped in the system throughout this period to have been preserved in fluid inclusions. Fluids from both locations were evidently strongly undersaturated in Pb and Zn when trapped and must have very low reduced sulphur contents given the phase distribution of metals at room temperature. Large chemical variations are present including those of Pb/Fe (all lower than eutectic melt; Fig. 3) and Pb/Ag (different in the two samples) suggesting that the fluids were involved in chemical reactions at the time the inclusions were trapped. An alternative origin involving late- to postmetamorphic interaction of externally-derived brines with pre-existing sulphide accumulations should also be considered. In this case the high Pb/Zn ratio might reflect the higher solubility of galena compared to sphalerite in high temperature brines (Hemley et al. 1992). In either case the unique chemistry would appear to relate to the large concentrations of sulphides in these systems.

Acknowledgements

This work was supported by AMIRA, the ARC and the Predictive Mineral Discovery CRC.

References

Chapman LH, Williams PJ (1998) Evolution of pyroxene-pyroxenoid-garnet alteration at the Cannington Ag-Pb-Zn deposit, Cloncurry district, Queensland, Australia: Econ Geol 93: 1390-1405

Giles D, Nutman AP (2002) SHRIMP U-Pb monazite dating of 1600-1580 Ma amphibolite facies metamorphism in the southeastern Mt Isa Block, Australia. Austr J Earth Sci 49: 455-465

Heinrich CA, Pettke T, Halter WE, Aigner-Torres M, Audétat A, Günther D, Hattendorf B, Bleiner D, Guillong M, Horn I (2003) Quantitative multi-element analysis of minerals, fluid and melt inclusions by laser-ablation inductively-coupled plasma mass-spectrometry: Geochim Cosmochim Acta 67: 3473-3496

Hemley JJ, Cygan GL, Fein JB, Robinson GR, D'Angelo WM (1992) Hydrothermal ore-forming processes in the light of studies in rock-buffered systems: I, iron-copper-zinc-lead sulfide solubility relations: Econ Geol 87: 1-22

Kendrick MA, Burgess R, Pattrick RAD, Turner G (2001) Fluid inclusion noble gas and halogen evidence on the origin of Cu-porphyry mineralising fluids: Geochim Cosmochim Acta 65: 2651-2668

Mavrogenes JA, Macintosh JW, Ellis DJ (2001) Partial melting of the Broken Hill galena-sphalerite ore. Experimental studies in the system PbS-FeS-ZnS-(Ag_2S). Econ Geol 96: 205-210

Mungall JE, Brenan JM, (2003) Experimental evidence for the chalcophile behavior of halogens. Can Mineral 41: 207-220

Pollard PJ, Perkins C (1997) $^{40}Ar/^{39}Ar$ geochronology of alteration and Cu-Au-Co mineralization in the Cloncurry district, Mount Isa Inlier. AMIRA P438 Cloncurry Base Metals and Gold Final Report, Section 3, 40pp

Ryan CG, McInnes, BM, Williams PJ, Guoyi Dong, Tin Tin Win, Yeats CJ (2001) Imaging fluid inclusion content using the new CSIRO-GEMOC nuclear microprobe. Instr Meth Physics Res B 181: 570-577

Spry PG (1978) The geochemistry of garnet-rich lithologies associated with the Broken Hill orebody, N.S.W., Australia. Unpubl MSc thesis, University of Adelaide, 129pp

Svenson H, Jamtveit B, Yardley B, Engvik AK, Austrheim H, Broman C (1999) Lead and bromine enrichment in eclogite-facies fluids: extreme fractionation during lower-crustal hydration. Geology 27: 467-470

Walters SG (1998) Broken Hill-type deposits. AGSO J Austr Geol Geophys 17: 229-237

Wilkins RWT (1977) Fluid inclusion assemblages of the stratiform Broken Hill ore deposit, New South Wales, Australia. Science 198: 185-187

Williams PJ, Dong Guoyi, Prendergast K, Pollard PJ, Ryan CG (1999) Metasomatism and metal mobility in Broken Hill-type deposits. In: Stanley CJ et al. (eds) Mineral Deposits: Processes to Processing. Balkema, Rotterdam, pp 999-1002

Yardley B, Bennett A, Banks D (2003) Controls on the chemical composition of crustal brines. J Geochem Expl 78/79: 133-135

Isotopic composition and source of lead in the Jinding Zn-Pb Deposit, Yunnan, China

Zeng Rong, Zhao Shihua, Gao Yongbao, Li Yongqiang
Faculty of Earth Sciences and Territory Resources, Chang'an University, Xi'an, Shaanxi 710054, China

Abstract. The Jinding Zn-Pb deposit is the largest Zn-Pb deposit so far discovered in China. To study the source of the mineralizing materials, we analyzed its lead isotopes. We found that the isotopic composition of lead in coarse-grained and fine-grained galenite crystals are very different. The ratio of lead isotopes in fine-grained galenite is higher, and lead isotopes are distributed over the lead development curve of the orogenic belt which is located in the range of upper crustal lead. All these indicate that the lead of fine-grained galenite comes mainly from stratigraphy. In contrast, the ratio of lead isotopes in coarse-grained galenite is lower and lead isotopes are distributed beneath the lead development curve of the orogenic belt, as well as in the upper mantle and lower crust.

Keywords. Lead isotope, composition, source, Jinding Pb-Zn deposit, Yunnan, China

1 Previous research

The Jinding Zn-Pb deposit is one of the seventeen giant Zn-Pb deposits in the world, with more than 10 million tons of Zn+Pb reserves. It is also the largest Zn-Pb deposit so far discovered in China. The Jinding Zn-Pb deposit is sediment-hosted, however its genetic origin differs from other sediment-hosted Zn-Pb deposits such as Mississippi Valley-type (MVT) deposits, Sedimentary exhalative (Sedex) deposits and Sandstone-type (SST) deposits. The Jinding Zn-Pb deposit may represent a new type of sediment-hosted deposit. Geologists have been studying the Jinding Zn-Pb deposit intensively since the 1980s, and during the twenty years of study there have been many different opinions about the genesis of the lead ores. Some think the lead in the ores comes mainly from the deep mantle, with minor input from the crust (Zhao 1989). Some argue that the lead in the ores is derived from the mantle, but has been hybridized by lead from the crust (Zhou and Zhou 1992). And others consider that the lead in the ores is derived from the lower crust and is related to the interaction between lead in the lower crust and in the sedimentary rocks (Zhang and Shao 2002).

2 Geologic characteristics of the ore zone

The Jinding Zn-Pb deposit occurs in a Cenozoic dome structure whose center is eroded. There are six ore blocks (Beichang, Paomaping, Jiayashan, Xiponanchang, Baicaoping and Fengzishan) surrounding the dome. The slaty, veined, phacoidal and stratoid orebodies are distributed around the center of dome and tilt in towards the deep dome. At the top of the dome the orebody is thicker. Two stratigraphic systems are present in the Jinding area, referred to as the autochthonous system and the allochthonous system. The former refers to strata of the Cretaceous Hutousi Formation (K_2h) and the Paleocene Yunlong Formation (E_1y^a-E_1y^b). The allochthonous system includes the Lower Cretaceous Jingxing Formation (K_1j), Mid-Jurassic Huakaizuo Formation (J_2h), the Upper Triassic Maichuqing Formation (T_3m) and the Sanhedong Formation (T_3s). The Zn-Pb ores are hosted in the sandstones of the Lower Cretaceous Jingxing Formation (K_1j) and the Upper Yunlong Formation (E_1y^b), which are separated by a thrust-nappe structure (F_2). There are two distinct types of ores at the Jinding deposit, breccia-type ores and sandstone-type ores. The textures associated with the breccia-type ores include metasomatic and solutional texture, concentric zonal texture, massive structure, brecciated structure and reticular vein structure. These ores are hosted in the Upper Yunlong Formation (E_1y^b), east of ore district. The sandstone-type ores consist mainly of cementation texture and disseminated structure and are hosted in the middle and west of the ore district.

3 Isotopic composition and source of lead

To study the source of the mineralizing materials of the Jinding Zn-Pb deposit, we choose the homogeneous galenite samples to do comparative study on lead isotopes (Table 1). We find that the composition of lead isotopes from coarse-grained and fine-grained galenite is different (Fig. 1): Fine-grained galenite $^{206}Pb/^{204}Pb$ 18.15~18.60, $^{207}Pb/^{204}Pb$ 15.612~15.64, $^{208}Pb/^{204}Pb$ 38.287~38.66; Coarse- grained galenite $^{206}Pb/^{204}Pb$ 18.03~19.21, $^{207}Pb/^{204}Pb$ 15.252~15.55, $^{208}Pb/^{204}Pb$ 37.800~38.930. The ratio of lead isotopes in fine-grained galenite is higher, and lead isotopes are distributed over the lead development curve of the orogenic belt which is located in the range of upper crustal lead. All these indicate that the lead of fine-grained galenite comes mainly from stratigraphy.

In contrast, the ratio of lead isotopes in coarse-grained galenite is lower and lead isotopes are distributed beneath the lead development curve of the orogenic belt, as well as in the upper mantle and lower crust. The composition of lead isotopes in three plagioclases crystals and garnets

This page intentionally blank

Table 1: Lead isotopes in the Jinding lead-zinc deposit.

Serial number	Sample number	Sample name	$^{206}Pb/^{204}Pb$	$^{207}Pb/^{204}Pb$	$^{208}Pb/^{204}Pb$	Data origin
1	Ty-37	G-B (C)	18.283	15.463	38.297	G
2	Ty-38	G-B (C)	18.222	15.423	38.093	G
3	Ty-39	G-B (C)	18.208	15.377	38.007	G
4	Ty-40	G-B (C)	18.214	15.400	38.046	G
5	Ty-41	G-B (C)	18.138	15.252	38.921	G
6	Ty-42	G-B (C)	18.169	15.362	38.042	G
7	Ty-43	G-B (C)	18.265	15.410	38.226	G
8	Ty-44	G-B (C)	18.289	15.421	38.301	G
9	Ty-45	G-B (C)	18.286	15.453	38.433	G
10	Ty-46	G-B (C)	18.22	15.407	38.155	G
11	Yn-10	G-B (C)	18.29	15.340	38.12	G
12	Yn13-1	G-B (C)	18.31	15.470	38.13	G
13	Yn16-1	G-B (C)	18.29	15.500	38.22	G
14	Yn16-2	G-B (C)	19.21	15.370	38.93	G
15	Yn-16	G-B (C)	18.27	15.470	38.12	G
16	Yn-23	G-B (C)	18.27	15.440	38.03	G
17	Yn-25	G-B (C)	18.24	15.400	38.9	G
18	Yn-31	G-B (C)	18.32	15.500	38.18	G
19	Yn31-1	G-B (C)	18.35	15.520	38.28	G
20	Yn38-2	G-B (C)	18.28	15.450	38.04	G
21	Yn-41	G-B (C)	18.37	15.540	38.32	G
22	Yn41-1	G-B (C)	18.37	15.450	37.99	G
23	Yn41-2	G-B (C)	18.29	15.550	38.36	G
24	Yn42-2	G-B (C)	18.4	15.530	38.29	G
25	Yn-45	G-B (C)	18.35	15.520	38.29	G
26	Yn46-2	G-B (C)	18.35	15.490	38.16	G
27	Yn10-55	G-B (C)	18.31	15.510	38.2	G
28	Yn-59	G-B (C)	18.31	15.390	38.89	G
29	Yn-61	G-B (C)	18.19	15.500	38.17	G
30	Yn10-87	G-B (C)	18.32	15.490	38.15	G
31	Ding-1	G-B (C)	18.32	15.396	38.113	G
32	Ding -2	G-B (F)	18.15	15.634	38.481	G
33	Ding -3	G-B (F)	18.52	15.634	38.287	G
34	Ding -4	G-B (F)	18.416	15.637	38.639	Yin hanhui
35	82j-31	G-B (F)	18.588	15.617	38.321	Zhang qian
36	82j-33	G-B (F)	18.6	15.622	38.359	Zhang qian
37	82j-2	G-S (F)	18.4	15.612	38.463	Zhang qian
38	28j-11	G-S (F)	18.42	15.628	38.536	Zhang qian
39	Yn-91	G-B (C)	18.33	15.450	38.23	Zhang qian
40	Yn-31	G-B (C)	18.03	15.270	38.17	Zhang qian
41	Yn-55	G-B (C)	18.19	15.510	38.2	G
42	Yn-87	G-B (C)	18.33	15.490	38.15	G
43	82j-5	G-S (F)	18.441	15.632	38.660	Zhang qian
44	82j-27	G-S (F)	18.506	15.640	38.557	Zhang qian
45	82j-35	G-S (F)	18.493	15.619	38.488	Zhang qian
46	82j-26	G-B (C)	18.321	15.450	38.235	Zhang qian
47	82j-18	G-B (C)	18.232	15.476	38.174	Zhang qian
48	82j-19	G-B (C)	18.283	15.493	38.295	Zhang qian
49	82j-7	V-G-S (C)	18.285	15.491	38.300	Zhang qian
50	82j-9	V-G-S (C)	18.303	15.501	38.290	Zhang qian

G-B: Galenite in Breccia-type ores, G-S: Galenite in Sandstone-type ores, V-G-S: Veined galenite in sandstone fracture, C: coarsed grain, F: fine grained, G: Geology and minerals bureau, Yunnan province.

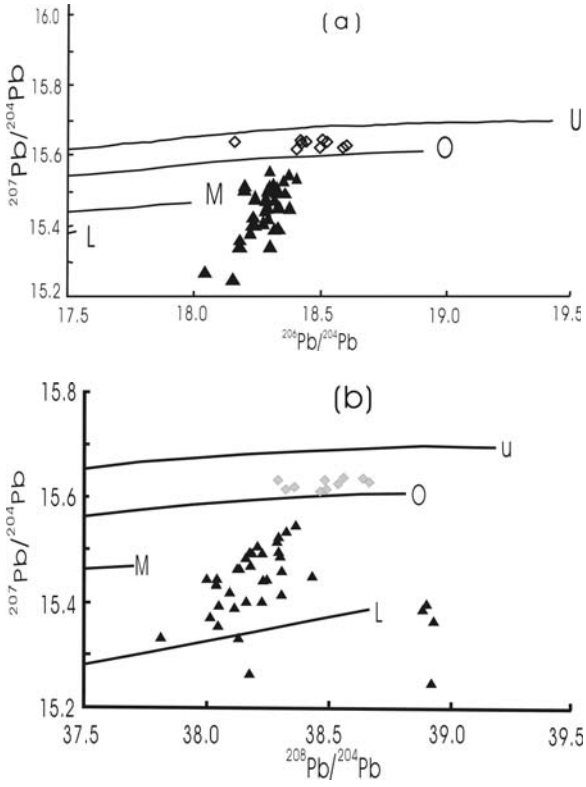

Figure 1: Lead isotope composition of Jinding lead-zinc deposit Triangles:coarse-grained galenite, square: fine-grained galenite, U: upper crust, O: orogenic belt, M: upper mantal, L: lower crust.

derived from the enclosures of the lower crust in alkalic rocks of western Yunnan is: $^{206}Pb/^{204}Pb$ 18.135~18.187, $^{207}Pb/^{204}Pb$ 15.335~15.388, $^{208}Pb/^{204}Pb$ 37.836~38.899. These values are identical to the coarse-grained galenite samples whose values are the lowest, so we can conclude that coarse-grained galenite come from the lower crust. The REE geochemical data indicate that the mineralizing materials of the Jinding Zn-Pb deposit are mainly mantle-derived fluids rich in CO_2 (jingdin and Chaoyang 1991). The isotopes of He, Ne, Xe also indicate that there are mantle components in the Jinding Zn-Pb deposit (Xue and Chen 2003). These data are consistent with the lead isotope data from coarse-grained galenite distributed in the upper mantle. According to the data, we may conclude that there are at least two metallogenic epochs in the Jinding Zn-Pb deposit: (1) The epoch of fine-grained galenite; (2) The epoch of coarse-grained galenite. The source of the mineralizing materials is different between the two epochs. The mineralizing materials of fine-grained galenite come mainly from stratigraphy, while mineralizing materials of coarse-grained galenite come mainly from the upper mantle and lower crust. The study on the controlling factors of evolution of the Lanping-Simao basin also indicates that the mineralization of the Jinding Zn-Pb deposit involves the interaction between crust and mantle (Yin and Fan 1990). All the data and analyses validate the theory of a multiperiod and multisource origin for the Jinding Zn-Pb deposit.

References

Wang J, Li C (1991) REE geochemistry of the Jinding superlarge Pb-Zn deposit Geochemica 19: 359~365

Xue C, Chen Y (2003) Geology and isotopic of Helium, Neon, Xeon and Metallogenic age of the Jinding and Baiyangping Ore Deposits Northwest Yunnan, china. Science in China, Ser. D, 46:789~800

Yin H, Fan W (1990) Deep processes and mantle-crust compound mineralization in the evolution of the Lanping-Simao Mesozoic-Cenozoic Diwa Basin in Western Yunnan, China 4: 113~124

Zhang Q, Shao A (2002) Lead isotopic composition and lead soure of polymetallic deposits in the Large Ore Assembly District in the Langping Basin. Acta Mineralogica Sinica 22: 147~153

Zhao X (1989) stable isotope geochemistry of the Jinding lead-zinc ore deposit, Yunnan, Science in the Earth–The Journal of Geology University of China 14: 495~501

Zhou W, Zhou Q (1992) A study on the isotopic composition of Pb and Sinc in the Lanping Pb-Zn Deposit, Yunnan, Geochemica 2: 141~148

Geology and geochemistry of the Furong Tin Deposit, Hunan Province, P. R. China

Zhao Kuidong, Jiang Shaoyong, Jiang Yaohui
State Key Laboratory for Mineral Deposits Research, Department of Earth Sciences, Nanjing University, Nanjing, China

Abstract. Recently, a giant tin deposit, the Furong deposit, has been discovered in the Qitianling granitoid, Hunan, South China. The tin mineralization occurs as disseminated crystals or veins of cassiterite. The cassiderite is found in narrow envelopes of chlorite alteration within the granite. The Qitianling granite has distinctly different petrology and mineralogy from common S-type tin granites. The oxygen and hydrogen isotope data indicate a dominant influence of surface-derived meteoric water associated with chlorite alteration. Variations in $\delta^{18}O$ of fresh and altered granites are due to continuous isotopic exchange reaction between hydrothermal fluids and granites at variable water/rock ratios. The sulfur isotope compositions of sulfides from the tin ores indicate that both the granite and the strata supported the sulfur for mineralization. The Pb isotopic compositions of sulfides are same as those of feldspars from the granite. Thus, Pb in the ores might come from the granite. Fractional crystallization of the magma and tin deposition directly from exsolved magmatic-hydrothermal fluids may not be the major mechanism for the tin mineralization in this deposit. Instead, we suggest that interactions between fluids of meteoric origin and the granite may contribute to the release and deposition of tin.

Keywords. Geochemistry, Furong tin deposit, Qitianling granite, South China

1 Introduction

The Furong deposit is a newly discovered giant tin deposit in Hunan Province, P. R. China (Fig. 1). The tin reserve in this deposit has been estimated to be about 600,000 tons (Wei et al. 2002). Tin orebodies mainly occur as veins in the Qitianling granite, which lies in the middle of the Nanling Granite Belt in South China. Previous workers mainly focused on the geology of this deposit (e.g. Wei et al. 2002; Huang et al. 2003; Wang et al. 2003; Mao et al. 2004). The main objectives of the present study are to investigate the source of the ore-forming materials, and to determine the origin and evolution of the hydrothermal fluids and its relationship with the Qitianling granite. We review the geology of the deposit and present the geochemical and isotopic data of the granites and the ores. These data provide important insights into the genetic model of this deposit.

2 Regional geology

The Qitianling granite and the Furong tin deposit lie in the middle of the Nanling granitic magma intrusive belt, South China. The belt is an important granitic intrusion and metallic mineralization zone. The Nanling zone has been suggested as one of the domains of the transition from the Paleo-Asian to the Paleo-Pacific tectonic system (Shu and Zhou 2002). The Qitianling granite is ellipse shaped and is one of the largest stocks in the Nanling Granite Belt with a total outcrop area of 520km^2. Coutry rocks intruded by the Qitianling granite are Permo-Carboniferous carbonates and Permo- Triassic sandy shales.

3 Geology of the Furong deposit

Most of the cassiterite ores occur as veins hosted by altered granites. There are about 40 cassiterite-bearing veins, in which the No. 19 and the No. 10 veins contain 90% of the tin reserve in the deposit. The main granite alterations are chloritization, phyllic and potassic feldspar alteration, in which chloritization is mostly associated with tin mineralization. Cassiterite occurs as disseminated mineralization in the altered granites. There are minor skarn-type tin orebodies, which forms at the contact between the granites and the country rocks. Other metallic minerals include scheelite, pyrite, chalcopyrite, sphalerite, arsenopyrite, and rutile. An interesting fact is that cassiterite is generally precipitated together with rutile as disseminations in chlorite. Chlorite has been used as a useful exploration guide for tin mineralization in the granites.

4 Petrology and mineralogy of the Qitianling Granite

The Qitianling Granite is complex, with different intrusive phases (Zheng and Jia 2001). Tin mineralization mainly occurs in the Furong phase. Geochemical characteristics of the granite are distinctly different from common S-type tin granites. The Furong phase is composed of potassic feldspar (40%), plagioclase (24%), quartz (27%), biotite (7%) and minor amphibole (2%). Accessory minerals are mainly magnetite, ilmenite, zircon, fluorite, apatite, monazite, sphene. The granite is metaluminous with a ACNK ratio (molar ratio of $Al_2O_3/(CaO+K_2O+Na_2O)$) of 0.88~1.05, which is different from common strongly peraluminous tin granites. The granite is alkaline-enriched and shows low initial $^{87}Sr/^{86}Sr$ value (0.708), high εNd value (-5.1~-5.8) and young Nd model ages, which suggests contribution of mantle materials in granite genesis. Zircon SHRIMP U-Pb dating gave a crystallization age of 157.1±1.2Ma.

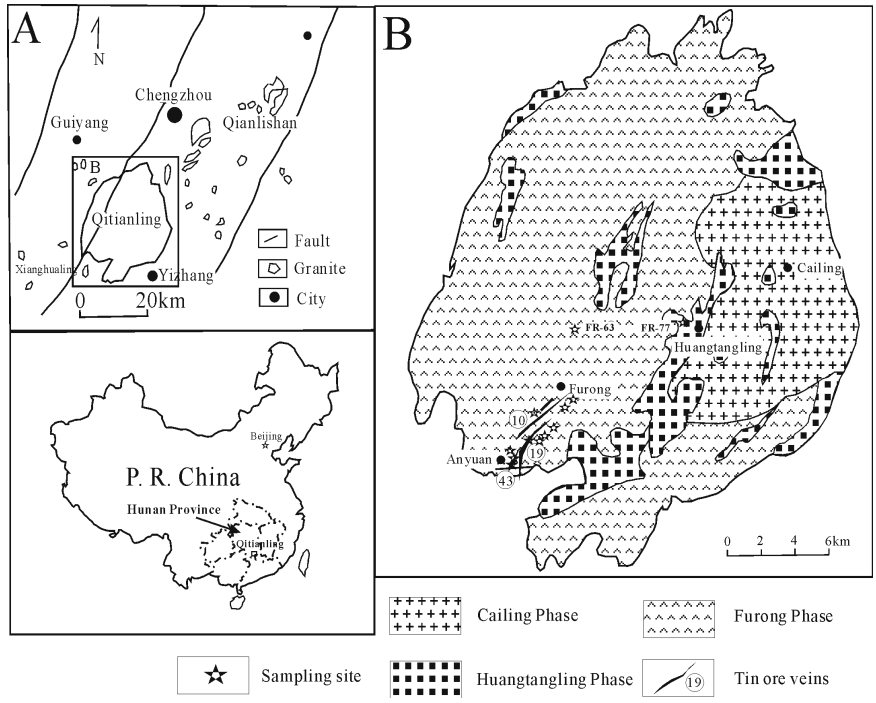

Figure 1: Simplified geological map of the Qitianling granitoid and the Furong tin deposit, Hunan Province, P. R. China

5 Geochemical studies of the granite and the deposit

5.1 Mineral chemistry

The main rock-forming minerals (amphibole, biotite, plagioclase and ore minerals such as cassiterite and rutile) were analysed for chemical composition by electron microprobe (Zhao et al., 2004). The biotite is Fe-rich annite, and has high Ti, Cl and Sn concentrations. The biotite has high $Fe^{3+}/(Fe^{2+}+Fe^{3+})$ ratios and the oxygen fugacity calculated by biotite compositions is above Ni-NiO (NNO), and near the Fe_2O_3-Fe_3O_4 (MH). The amphiboles are ferropargasite and ferro-edenite hornblende. The pressure of the granite, estimated by Al-in-hornblende barometer, is 3.6 ±0.9kbar. Amphibole- plagioclase thermometry and a semiquantitative hornblende thermometer yield a forming temperature of 750~820°C. The chlorite from the orebody has negligible K_2O, Ti_2O, F, and Cl, but shows similar Fe/(Fe+Mg) ratios with amphibole and biotite. Disseminated cassiterite is closely associated with rutile in chlorite alteration veins and envelopes. The ore-forming temperature is estimated to be 290~405°C from chlorite geothermometry. The studied cassiterites are nearly pure SnO_2 (>98%). The concentrations of Nb_2O_5 and Ta_2O_5 in cassiterite are very low and almost negligible ($Nb_2O_5+Ta_2O_5$<0.1%).These values are distinctly different from cassiterites found in granites or pegmatites, but similar to cassiterite from epithermal or hydrothermal ore deposits.

5.2 REE geochemistry

REE contents of both fresh and altered granites are analyzed. Fresh granites show a LREE-enriched and large negative Eu anomaly REE pattern. Altered granites have a similar REE pattern to fresh granites. It suggested that REEs were immobile during hydrothermal alteration of granites in this case.

Most sulfides have very low REE contents and show similar REE patterns with granites. Because REEs have distinctly different ionic radii from those of base metal elements, it is difficult for REEs to substitute into crystal lattices of sulfides. Thus, it may be assumed that a major part of REE content of sulfides comes from fluid inclusions in these minerals. REE patterns of sulfides may represent those of ore-forming fluids.

Fluorites coexisting with sulfides have relatively high REE contents and show a different REE pattern. Fluorites show a HREE-enriched pattern. Marchand et al. (1976) studied the REE partition between fluorite and a solution of calcium chloride. The REE distribution coefficients strongly favor fluorite, and those for the HREE are greater than those for the LREE.

5.3 H-O isotopes

Cassiterites have $\delta^{18}O$ values from -4.8‰ to 1‰. Chlorites from the ores have $\delta^{18}O$ values from 0.5‰ to 2.5‰, and δD values from -62‰ to -68‰. The estimated oxygen isotope compositions of the hydrothermal fluid from

cassiterites and chlorites vary from -2.0‰ to +3.8‰. The values are lower than those of magmatic-hydrothermal fluids, and are higher than those of Mesozoic meteoric water (-8‰~-9‰) in the studied area. Involvement of surface water of meteoric origin during mineralization of the Qitianliang granite can be ascertained by the oxygen and hydrogen isotope data.

Oxygen isotopic compositions of fresh and altered granites have also been measured. The fresh granite far away from tin mineralization has the highest oxygen isotopic composition (+10.5‰). The fresh and slightly altered granites near the tin veins have lower $\delta^{18}O$ values from +6.0‰ to +10.0‰. The completely chloritized granites collected from the tin orebodies have the lowest oxygen isotopic composition (5.4‰~6.6‰). The oxygen isotopic variations of the whole rocks are the result of fluid-rock interactions. The W/R ratios of completely chloritized granites are estimated to be 0.3~0.5.

5.4 Sulfur isotopic data

Sulfur isotopic compositions of twelve sulfides were analyzed. The $\delta^{34}S$ values of sulfides vary from -20.4‰ to 3.2‰. The sulfur isotopic compositions were divided into two groups in the histogram plot. In one group, the sulfur isotopic compositions vary from -0.5‰ to +3.2‰. Sulfur in this group might come from the granite. In the other group, the sulfur isotopic compositions vary from -20.4‰ to -10‰. Sulfur in this group might come from sulfides in strata.

5.5 Lead isotopic data

Thirteen sulfides from the ores and ten feldspars from the Qitianling granite were analyzed for Pb isotopic composition. The Pb isotopic composition of both sulfides and feldspars is relatively homogeneous. $^{206}Pb/^{204}Pb$, $^{207}Pb/^{204}Pb$ and $^{208}Pb/^{204}Pb$ ratios of sulfides are 18.615~18.898, 15.726~15.766 and 38.893~39.077, respectively. The Pb isotopic ratios of feldspars are 18.682~18.970, 15.747~15.774 and 39.030~39.183, respectively. The similarity in Pb isotopic composition in sulfides and feldspars indicates that lead in sulfides might come from the Qitianling granite. The lead isotope data of both sulfides and feldspars were plotted on the upper crust Pb growth curve in a Zartman Pb diagram (Zartman et al. 1981). This suggests that Pb is of crustal origin.

6 Conclusions

Tin mineralization in the Furong tin deposit is related to hydrothermal alteration of the Qitianling granite. The ore-forming fluids might be derived from meteoric water. Both the granite and the strata supported the sulfur for mineralization. Water-rock interaction might have released tin and other metals (e.g. Pb and Ti) from the granite.

Acknowledgements

This work was supported by funding from China National Science Foundation (40221301).

References

Huang GF, Gong SQ, Jiang XW, Tan SX, Li CB, Liu DH (2003) Exploration on the ore-forming regularities of tin deposits in Qitianling area, southern Hunan. Geological Bulletin of China 22: 445-451

Mao JW, Li XF, Lehmann B, Chen W, Lan XM, Wei SL (2004) ^{40}Ar-^{39}Ar dating of tin ores and related granite and its geodynamic significance for rock and ore formation. Mineral Deposits 22: 164-175

Marchand L, Joseph D, Touray JC, Treuil M (1976) Critères d'analyse géochimique des gisements de fluorine basés sur l'étude de la distribution des lanthanides- application au gîte de Maine (71-Cordesse, France). Mineralium Deposita 11: 357-379

Shu LS, Zhou XM (2002) Late Mesozoic tectonism of Southeast China. Geological Review 48:249-260

Wang DH, Chen YC, Li HQ, Chen ZH, Yu JJ, Lu YF, Li JY (2003) Geochemical and geochemical features of the Furong tin deposit in Hunan and their significance for mineral prospecting. Geological Bulletin of China 22: 50-56

Wei SL, Zeng QW, Xu YM (2002) Characteristics and ore prospects of deposits in the Qitianling area, Hunan. Geology in China 29: 67-75

Zartman RE, Doe BR (1981) Plumbotectonics - the model. Tectonophysics 75: 135-162

Zhao KD, Jiang SY, Jiang YH, Wang RC (2004) Mineral chemistry of the Qitianling granitoid and the Furong tin ore deposit in Hunan Province, South China: Implication for the genesis of granite and related tin mineralization. Accepted by European Journal of Mineralogy

Zheng JJ, Jia BH (2001) Geological characteristics and related tin-polymetallic mineralization of the Qitianling granite complex in southern Hunan Province. Geology and Mineral Resources of South China 4: 50-57